SOVIET PHYSICS
CRYSTALLOGRAPHY

Volume 18 **July 1973—June 1974** Index

a translation of the journal **КРИСТАЛЛОГРАФИЯ**, Kristallografiya
(Crystallography), Vol. 18, July 1973—June 1974
published by the American Institute of Physics

SOVIET PHYSICS CRYSTALLOGRAPHY

GOVERNING BOARD

H. Richard Crane, *Chairman*
H. William Koch, *ex officio*
Robert T. Beyer
J. V. Bouyoucos
Joseph A. Burton
James L. Flanagan
Kenneth W. Ford
William A. Fowler
Laurence W. Fredrick
James B. Gerhart
J. E. Goldman
Martin Greenspan
Janet B. Guernsey
W. W. Havens, Jr.
Sherwood K. Haynes
Gerald Holton
G. A. Jeffrey
E. Leonard Jossem
Robert P. Kraft
J. A. Krumhansl
John S. Laughlin
A. I. Mahan
Sidney Millman
Philip M. Morse
E. R. Piore
Jarus W. Quinn
R. S. Rivlin
Arthur H. Rosenfeld
Arthur L. Schawlow
Frederick Seitz
F. Dow Smith
A. A. Strassenburg

GENERAL ADMINISTRATION

H. William Koch, *Director*

Sidney Millman, *Secretary*

Gerald F. Gilbert, *Treasurer*

Lewis Slack
Associate Director, General Activities

Robert H. Marks
Associate Director, Publishing

DIRECTORS OF PROFESSIONAL DIVISIONS

A. W. K. Metzner, *Publications*

Theodore Metaxas
Brookhaven Publishing Operation

Harold L. Davis, *Physics Today*

Joan N. Warnow, *Acting Physics History*

Audrey Likely, *Public Relations*

Dion W. J. Shea, *Education*

Raymond W. Sears, *Manpower*

PUBLISHING SERVICES

Edward P. Greeley, *Advertising*

Mitchell Koch
Managing Editor

Mimie Yin, *Translations*

Leon Benedict, *Composition*

Gerald Goodman, *Indexing*

Jo-Ann Wasserman
Sr. Editorial Supervisor

Robert Will
Sr. Journal Supervisor

John Di Caro, *Fulfillment*

10/74

American Institute of Physics Translations Advisory Board:

Robert T. Beyer, *Chairman*
J. George Adashko
Freeman Dyson
Dwight Gray
Morton Hamermesh
David Harker
Howard A. Robinson

Advisory Editor of *Soviet Physics–Crystallography:*
Marc H. Richman, Department of Engineering, Brown University, Providence,
Rhode Island 02912

Soviet Physics–Crystallography, a translation of the journal КРИСТАЛЛОГРАФИЯ, *Kristallografiya*, is published bimonthly by the American Institute of Physics, with the cooperation of the American Crystallographic Association, for the purpose of making available in English reports of current Soviet research in crystallography as contained in the journal *Crystallography* of the Academy of Sciences of the USSR (editorial address: Leninskii prospekt 59, Moscow V-333, USSR). The translations began with the 1957 issues.

The American Institute of Physics and its translators propose to translate faithfully all the material appearing in the original articles. The views expressed in the translations are therefore those of the original authors, and not of the translators nor of the American Institute of Physics.

The transliteration of the names of Russian authors follows essentially the standard agreed upon by the British Standards Institute and the American National Standards Institute (Committee Z39).

Soviet Physics–Crystallography is translated and produced for the American Institute of Physics by Consultants Bureau, a division of Plenum Publishing Corporation. One volume is published annually beginning with the July-August issue.

Subscriptions, renewals, address changes, and single-copy orders should be addressed to: Subscription Fulfillment Division, American Institute of Physics, 335 East 45th Street, New York, N.Y. 10017. Allow at least six weeks advance notice. For address changes please send both old and new addresses, and, if possible, include an address-stencil imprint from the mailing wrapper of a recent issue. For your convenience **a change of address form is included in every issue of *Physics Today;*** please use it.

Subscription prices (for Vol. 19, July 1974–June 1975):

U.S.A., Canada, Mexico	Europe, Middle East, North Africa (mandatory) air freight	Foreign (surface mail)	Optional air freight (Asia)	Single copies	Cumulative index (Vols. 1-10)
$90.00	$94.00	$93.00	$98.00	$16.00	$20.00

Complete volumes of *Soviet Physics-Crystallography* are available on microfilm (16 mm or 35 mm on reels or cartridges): Vols. 1-17 (January 1956–June 1973) $535; Vol. 18 (July 1973–June 1974) $50.

Soviet Physics–Crystallography also appears on a monthly basis in *Current Physics Microform* (CPM) Section II ($2000 per year) along with 15 other translation journals published by the American Institute of Physics and its member societies. A subject index to CPM, *Current Physics Titles*, is published monthly in 3 sections (Atoms & Waves, Solid State, Nuclei & Particles) at $15 per section for members and $35 for nonmembers. Abstracts of articles to be published in *Soviet Physics–Crystallography* appear two or more months ahead in *Current Physics Advance Abstracts*, available in 3 sections at $20 per section for members and $50 for nonmembers.

Copyright: All the material published in this journal is Copyright © 1974 by the American Institute of Physics, and all rights are reserved. Address inquiries to Director, Publications Division, American Institute of Physics, 335 East 45 Street, New York, N.Y. 10017.

Second-class postage paid at Lancaster, Pa.

Soviet Physics—Crystallography Vol. 18, Index, July 1973-June 1974

(Russian original: Kristallografiya, Vol. 18, July 1973-June 1974)

Analytic subject index to volume 18:

829 1 Communication, education, history, and philosophy
829 3 Classical and quantum mechanics
829 29 Experimental methods and instrumentation for elementary particle and nuclear physics
829 31 Atoms
829 32 Molecules
829 34 Collision processes and interactions of molecules, atoms, or ions
829 35 Macromolecules and polymers
830 51 Structure of liquids and solids; crystallography
834 52 Mechanical and acoustic properties of condensed matter
834 53 Lattice dynamics
834 54 Equations of state, phase equilibria, and phase transitions
836 55 Thermal properties of condensed matter
836 56 Transport properties of condensed matter (nonelectronic)
836 58 Surfaces and interfaces; thin films and whiskers
837 61 Electron states
837 62 Electronic transport in condensed matter
837 63 Electronic structure and electrical properties of surfaces, interfaces, and thin films
837 65 Magnetic properties and materials
837 66 Magnetic resonance and relaxation in condensed matter; Mössbauer effect
838 67 Dielectric properties and materials
839 68 Optical properties and condensed-matter spectroscopy
840 69 Electron and ion emission by liquids and solids; impact phenomena
840 71 Optics
840 74 Physical chemistry
840 75 Materials science and metallurgy

842 **Author index to volume 18**

This index is based on the 1974 *Physics and Astronomy Classification Scheme* developed by AIP. It is not a translation. It was produced by computer-aided photocomposition directly from the magnetic tapes of the AIP's Current Physics Information System. Suggestions for improvements as well as other comments are welcome and should be addressed to the Editor.

A new feature introduced in this index is the inclusion of microfilm reel and frame numbers for the convenience of those wishing to find articles in *Current Physics Microform* (CPM), the monthly microfilm edition of the complete set of journals of the American Institute of Physics. These numbers are given in the form **CPM-7201A0321**, where 72 refers to the year, 01 denotes the month (January in this example), A the cartridge (generally there are four cartridges every month: A,B,C,D), and 0321 the frame.

SUBJECT INDEX TO VOLUME 18

Papers are arranged in ascending page number order.

1. COMMUNICATION, EDUCATION, HISTORY, AND PHILOSOPHY

Teaching career of a great crystallographer —N. V. Belov. 18(2), 280–1 (Sep. 1973); CPM-7309D1482

Arkadii Sergeevich Shein (1912-1972) —18(3), 420 (Nov. 1973); CPM-7311E0552

3. CLASSICAL AND QUANTUM MECHANICS

Boundary conditions in the electrodynamics of optically active media —B. V. Bokut', A. N. Serdyukov, F. I. Fedorov, and N. A. Khilo. 18(2), 141–4 (Sep. 1973); CPM-7309D1343

29. EXPERIMENTAL METHODS AND INSTRUMENTATION FOR ELEMENTARY PARTICLE AND NUCLEAR PHYSICS

Monochromatization of neutrons in multiple Bragg scattering —A. A. Loshmanov, V. N. Sigaev, and I. I. Yamzin. 18(4), 530 (Jan. 1974); CPM-7401D0606

31. ATOMS

Laser based on Cr^{3+} ions in yttrium-aluminum garnet —B. K. Sevast'yanov, Kh. S. Bagdasarov, L. B. Pasternak, S. Yu. Volkov, and V. P. Orekhova. 18(2), 191–2 (Sep. 1973); CPM-7309D1393

32. MOLECULES

32.20.- Molecular structure and constants derived from experimental measurements

32.20.B General molecular conformation and symmetry; stereochemistry

Reflection intensity as a function of temperature during diffraction of slow electrons from (111) and (100) faces of germanium– B. Z. Ol'shanetskii, A. I. Volokitin, and S. M. Repinskii. 18(6), 815–6 (May 1974); CPM-7406X1259

32.20.D Interatomic distances and angles

X-ray study of potassium copper ethylenediaminetetraacetate trihydrate —M. A. Porai-Koshits, N. V. Novozhilova, T. N. Polynova, T. V. Filippova, and L. I. Martynenko. 18(1), 54–8 (Jul. 1973); CPM-7309D0304

Crystal and molecular structures of 4-chloroanthraquinonethiadiazole —O. A. Mikhno, Z. I Ezhkova, and G. S. Zhdanov. 18(1), 59–62 (Jul. 1973); CPM-7309D0309

Crystal structure of the potassium salt of 1,1-dinitroethane —O. V. Frank-Kamenetskaya, N. V. Grigor'eva, N. V. Margolis, and I. V. Tselinskii. 18(1), 108–9 (Jul. 1973); CPM-7309D0358

Zn-Mn isomorphism in Na_2ZnGeO_4 crystals —I. P. Kuz'mina, A. N. Lobachev, V. M. Vinokurov, N. M. Nizamutdinov, and L. A. Volkova. 18(1), 110–1 (Jul. 1973); CPM-7309D0360

Crystal structure of the coordination compound bis(pyridinaldehydethiosemicarbazonato)cobalt(III)nitrate —K. N. Akatova, T. N. Tarkhova, and N. V. Belov. 18(2), 162–5 (Sep. 1973); CPM-7309D1364

Crystal and molecular structures of the 1:2 complex of 1-methyl-3,3-dimethyl-2-(para-n-methyl-n-β-chloroethylstyryl)indole and 7,7,8,8-tetracyanoquinodimethane, $(C_{22}H_{26}N_2Cl)^+(C_{12}H_4N_4)(C_{12}H_4N_4)$ — R. P. Shibaeva, L. P. Rozenberg, and L. O. Atovmyan. 18(3), 326–9 (Nov. 1973); CPM-7311E0458

Crystal and molecular structure of phenyl phenoxtinium iodide —A. I. Gusev and Yu. T. Struchkov. 18(3), 330–2 (Nov. 1973); CPM-7311E0462

Crystal structure of 1,6-$[Coen_2Cl_2]Cl\cdot 3SC(NH_2)_2$ —Yu. A. Simonov, L. I. Landa, N. N. Proskina, T. I. Malinovskii, and A. V. Ablov. 18(3), 333–5 (Nov. 1973); CPM-7311E0465

Crystal structure of coumarin —R. M. Myasnikova, T. S. Davydova, and V. I. Simonov. 18(4), 454–6 (Jan. 1974); CPM-7401D0530

Crystal-chemical analysis of the structure of 1-I-substituted anthraquinone —N. L. Klimasenko, V. K. Bel'skii, V. K. Sarynin, and G. A. Gol'der. 18(4), 457–9 (Jan. 1974); CPM-7401D0533

X-ray diffraction study of naphthaloimide —A. N. Sobolev, L. A. Chetkina, G. A. Gol'der, Yu. G. Fedorov, and V. E. Zavodnik. 18 (6), 728–31 (May 1974); CPM-7406X1172

Crystal and molecular structures of octafluoroanthraquinone —L. A. Chetkina and E. G. Popova. 18(6), 732–5 (May 1974); CPM-7406X1176

32.20.G Bond strengths, dissociation energies, hydrogen bonding, molecular core binding energy, etc.

Structure of calcium-cobalt hexaborate $K_2Co[B_6O_7(OH)_6]_2\cdot 4H_2O$ —É. Ya. Silin', Ya. K. Ozol, and A. F. Levin'sh. 18(3), 317–9 (Nov. 1973); CPM-7311E0449

Proton magnetic resonance investigation of the localization of the protons in the crystal structures $Na_2Cr_2O_7\cdot 2H_2O$ and $Li_2Cr_2O_7\cdot 2H_2O$ —G. R. Bulka, V. M. Vinokurov, É. A. Kuz'min, Yu. A. Kharitonov, and N. V. Belov. 18(5), 617–9 (Mar. 1974); CPM-7403D0445

32.20.J Barrier heights (internal rotation, inversion); rotational isomerism

Atom-atom potentials and the coordinates of hydrogen atoms in methyl groups in the molecule and crystal —K. V. Mirskaya and L. V. Ivanova. 18(1), 101–2 (Jul. 1973); CPM-7309D0351

Spectroscopy of organic materials in the low-temperature, crystalline phases —G. N. Zhizhin. 18(4), 483–8 (Jan. 1974); CPM-7401D0559

32.60.- Molecular spectroscopy (measurement and phenomenology)

Spectroscopy of organic materials in the low-temperature, crystalline phases —G. N. Zhizhin. 18(4), 483–8 (Jan. 1974); CPM-7401D0559

Molecular scattering of light in a single crystal of hafnium dioxide — V. I. Aleksandrov, V. F. Kitaeva, I. V. Kozlov, V. V. Osiko, N. N. Sobolev, V. M. Tatarintsev, and I. L. Chistyi. 18(5), 682–4 (Mar. 1974); CPM-7403D0510

32.90.+ Other topics in molecular physics

Stable configurations of a bioctahedral complex with Jahn-Teller centers —I. B. Bersuker, B. G. Vekhter, and M. L. Rafalovich. 18 (1), 5–9 (Jul. 1973); CPM-7309D0255

Reflection intensity as a function of temperature during diffraction of slow electrons from (111) and (100) faces of germanium– B. Z. Ol'shanetskii, A. I. Volokitin, and S. M. Repinskii. 18(6), 815–6 (May 1974); CPM-7406X1259

34. COLLISION PROCESSES AND INTERACTIONS OF MOLECULES, ATOMS, OR IONS

Atomic scattering amplitudes for electrons at small scattering angles —A. N. Pilyankevich. 18(1), 103 (Jul. 1973); CPM-7309D0353

35. MACROMOLECULES AND POLYMERS

Evaluation of the heat effect during alkali halide monomer reorientation in an absorbed layer on a metal —Yu. N. Lyubitov and V. I. Mikhailov. 18(2), 266–7 (Sep. 1973); CPM-7309D1468

Calculation of the small-angle x-ray scattering intensity on a computer using a macromolecule model —Yu. A. Rol'bin, R. L. Kayushina, L. A. Feigin, and B. M. Shchedrin. **18**(4), 442–4 (Jan. 1974); CPM-7401D0518

51. STRUCTURE OF LIQUIDS AND SOLIDS; CRYSTALLOGRAPHY

51.10.- Techniques for determination of lattice and defect structures

One-dimensional models of the Patterson function —S. V. Borisov. **18**(5), 586–8 (Mar. 1974); CPM-7403D0414

Sharpening the peaks of the projection of the Patterson function by regularization —A. I. Kvitashvili, N. P. Zhidkov, B. M. Shchedrin, and A. E. Shvelashvili. **18**(5), 589–91 (Mar. 1974); CPM-7403D0417

Proton magnetic resonance investigation of the localization of the protons in the crystal structures $Na_2Cr_2O_7 \cdot 2H_2O$ and $Li_2Cr_2O_7 \cdot 2H_2O$ —G. R. Bulka, V. M. Vinokurov, É. A. Kuz'min, Yu. A. Kharitonov, and N. V. Belov. **18**(5), 617–9 (Mar. 1974); CPM-7403D0445

Statistical values of heavy atom weighted contributions (D_H) to the total structure amplitude —L. L. Shadyro and I. D. Feranchuk. **18**(6), 715–8 (May 1974); CPM-7406X1159

51.10.E Dynamical x-ray diffraction and scattering

Localization of heavy atoms in noncentrosymmetric crystals by single-wave anomalous x-ray scattering —L. L. Shadyro. **18**(1), 43–5 (Jul. 1973); CPM-7309D0293

X-ray diffraction by a cylindrical cavity in a crystal —A. F. Tsander. **18**(2), 151–3 (Sep. 1973); CPM-7309D1353

X-ray diffraction in crystals with deformation twins —D. A. Mirzaev and S. V. Rushchits. **18**(2), 204–6 (Sep. 1973); CPM-7309D1406

Dynamic theory of x-ray diffraction in crystals with modulated electron density —A. V. Kolpakov and Yu. P. Khapachev. **18**(3), 300–2 (Nov. 1973); CPM-7311E0432

Two-crystal spectrometer study of barium titanate single crystals —I. Ya. Nikoforov and Yu. F. Mal'tsev. **18**(3), 370–1 (Nov. 1973); CPM-7311E0502

Calculation of the small-angle x-ray scattering intensity on a computer using a macromolecule model —Yu. A. Rol'bin, R. L. Kayushina, L. A. Feigin, and B. M. Shchedrin. **18**(4), 442–4 (Jan. 1974); CPM-7401D0518

Applicability of Zachariasen's equations to calculations of the integral intensity scattered by a "thick" single crystal in the Bragg symmetry case for any dislocation density —A. V. Kuznetsov. **18**(5), 592–5 (Mar. 1974); CPM-7403D0420

Studies on ferroelectric crystals with a three-crystal x-ray spectrometer —I. Ya. Nikiforov, Yu. F. Mal'tsev, and V. Z. Borodin. **18**(5), 638–40 (Mar. 1974); CPM-7403D0466

"Spectral instability" of multiwave diffraction with coplanar x rays —A. D. Fofanov, A. V. Kuznetsov, and G. A. Karacheva. **18**(6), 711–4 (May 1974); CPM-7406X1155

Polarization and integrated intensity of x rays scattered by silicon crystals —N. M. Olekhnovich. **18**(6), 777–9 (May 1974); CPM-7406X1221

51.10.G Elastic-neutron diffraction and scattering

Monochromatization of neutrons in multiple Bragg scattering —A. A. Loshmanov, V. N. Sigaev, and I. I. Yamzin. **18**(4), 530 (Jan. 1974); CPM-7401D0606

51.10.N Inelastic-electron diffraction and scattering

Atomic scattering amplitudes for electrons at small scattering angles —A. N. Pilyankevich. **18**(1), 103 (Jul. 1973); CPM-7309D0353

Allowance for three-wave scattering in electron diffraction by face-centered metals —V. V. Udalova and Z. G. Pinsker. **18**(1), 136 (Jul. 1973); CPM-7309D0386

New method for determining the normalizing factor in electron diffraction studies of the structure of amorphous substances —Ya. I. Stetsiv. **18**(2), 158–61 (Sep. 1973); CPM-7309D1360

Effect of accelerating voltage on the intensity of the forbidden reflection 222 Ge in electron diffraction —A. S. Avilov, R. M. Imamov, Z. G. Pinsker, and A. F. Fedotov. **18**(4), 528–9 (Jan. 1974); CPM-7401D0604

Reflection intensity as a function of temperature during diffraction of slow electrons from (111) and (100) faces of germanium —B. Z. Ol'shanetskii, A. I. Volokitin, and S. M. Repinskii. **18**(6), 815–6 (May 1974); CPM-7406X1259

51.30.+ Liquid crystals

Structure of liquid crystals of the homologous series of n-alkoxyazoxybenzenes —I. G. Chistyakov and V. M. Chaikovskii. **18**(2), 181–3 (Sep. 1973); CPM-7309D1383

Theory of the electrodynamic effect in liquid crystals —S. A. Pikin and A. A. Shtol'berg. **18**(3), 283–7 (Nov. 1973); CPM-7311E0415

Phase transition in liquid crystals induced by an electric field —I. G. Chistyakov and L. K. Vistin'. **18**(4), 552–3 (Jan. 1974); CPM-7401D0628

Pretransition phenomena and optical activity of amorphous liquid phases of cholesteric liquid crystals —E. I. Ryumetsev, A. N. Cherkasov, V. G. Tishchenko, and M. M. Fetisova. **18**(5), 657–9 (Mar. 1974); CPM-7403D0485

X-ray investigation of some examples of a homologous series of cholesterol ethers in dicarboxylic acid —Ya. I. Dutchak and V. K. Burima. **18**(5), 677–9 (Mar. 1974); CPM-7403D0505

Determination of the degree of ordering in liquid crystals from the dichroism of dissolved dyes —V. G. Rumyantsev, L. M. Blinov, and V. A. Kizel'. **18**(5), 695–6 (Mar. 1974); CPM-7403D0523

Orientational order and molecular parameters of liquid crystals with a positive dielectric anisotropy —V. G. Rumyantsev, P. D. Berezin, L. M. Blinov, and I. N. Kompanets. **18**(5), 697–8 (Mar. 1974); CPM-7403D0525

Reflection intensity as a function of temperature during diffraction of slow electrons from (111) and (100) faces of germanium—B. Z. Ol'shanetskii, A. I. Volokitin, and S. M. Repinskii. 18(6), 815–6 (May 1974); CPM-7406X1259

51.40.- Amorphous and polymeric materials

Structure of liquid crystals of the homologous series of n-alkoxyazoxybenzenes —I. G. Chistyakov and V. M. Chaikovskii. **18**(2), 181–3 (Sep. 1973); CPM-7309D1383

Electron-diffraction analysis of amorphous films of carbon and boron —Yu. G. Poltavtsev, V. P. Zakharov, and V. M. Pozdnyakova. **18**(2), 270–1 (Sep. 1973); CPM-7309D1472

Theory of the electrodynamic effect in liquid crystals —S. A. Pikin and A. A. Shtol'berg. **18**(3), 283–7 (Nov. 1973); CPM-7311E0415

Determination of coordination numbers and mean-square displacements from the radial distribution curve —Ya. I. Stetsiv. **18**(3), 306–7 (Nov. 1973); CPM-7311E0438

Electron diffraction study of the structure of amorphous germanium telluride and selenide films —Yu. G. Poltavtsev and V. P. Zakharov. **18**(3), 379–80 (Nov. 1973); CPM-7311E0511

Crystallization of amorphous films of silicon nitride by ionic bombardment followed by annealing —P. V. Pavlov, É. V. Shitova, E. I. Zorin, and N. A. Genkina. **18**(3), 381–3 (Nov. 1973); CPM-7311E0513

Electron diffraction investigation of In_2S_3 films obtained by vacuum deposition —R. B. Shafizade, É. G. Éfendiev, and F. I. Aliev. **18**(3), 417–8 (Nov. 1973); CPM-7311E0549

Change in the structure of germanium and silicon during ion bombardment and subsequent annealing —P. V. Pavlov. **18**(4), 506–9 (Jan. 1974); CPM-7401D0582

Structure of amorphous indium monochalcongenide films —Yu. G. Poltavtsev, V. P. Zakharov, and T. V. Remizovich. **18**(5), 701–2 (Mar. 1974); CPM-7403D0529

51.50.- Crystalline state (including molecular rotation in solids)

Dislocation mechanism of growth with a low kink density —V. V. Voronkov. **18**(1), 19–23 (Jul. 1973); CPM-7309D0269

Internal stresses developing during crystal growth under a steady-state regime —V. L. Indenbom, I. S. Zhitomirskii, and T. S. Chebanova. **18**(1), 24–32 (Jul. 1973); CPM-7309D0274

Systematic analysis of Patterson functions on the basis of crystal symmetry. IV. Interpretation of the Patterson synthesis for crystals of lower systems —É. A. Kuz'min, V. P. Golovachev, V. V. Ilyukhin, and N. V. Belov. **18**(1), 33–8 (Jul. 1973); CPM-7309D0283

Localization of heavy atoms in noncentrosymmetric crystals by single-wave anomalous x-ray scattering —L. L. Shadyro. **18**(1), 43–5 (Jul. 1973); CPM-7309D0293

Refining the structure of crystals allowing for the anisotropy of the thermal vibrations of the atoms —L. A. Muradyan and V. I. Simonov. **18**(1), 46–9 (Jul. 1973); CPM-7309D0296

Statistical model of multiphase anisotropic crystallization —V. F. Dorfman. **18**(1), 93–8 (Jul. 1973); CPM-7309D0343

Stereographic projections of surfaces for the physical properties of crystals —Sh. M. Butabaev and Yu. I. Sirotin. **18**(1), 121–2 (Jul. 1973); CPM-7309D0371

Kinetics of motion of steps and rows of steps at smeared phase boundaries —D. E. Temkin. **18**(2), 145–50 (Sep. 1973); CPM-7309D1347

Structure-localizing sections of the duplicated Patterson function —V. N. Biyushkin. **18**(2), 154–7 (Sep. 1973); CPM-7309D1356

Proposed method for determining the coordinates of resonant nuclei using polarized Mössbauer spectroscopy —M. A. Andreeva and R. N. Kuz'min. **18**(2), 254–5 (Sep. 1973); CPM-7309D1456

Iteration method for calculating the intensity distribution in structural analysis —D. K. Khakimova, V. G. Nagornyi, and A. A. Smol'yaninov. **18**(3), 303–5 (Nov. 1973); CPM-7311E0435

Use of the methods of successive experiment planning with refining crystal-structure parameters —I. V. Igonina, B. I. Pokrovskii, A. K. Gapeev, P. I. Lazarev, and L. N. Komissarova. **18**(3), 308–13 (Nov. 1973); CPM-7311E0440

Sections of paired Patterson functions —V. N. Biyushkin and N. V. Belov. **18**(3), 311–3 (Nov. 1973)

Symmetries of functions for separating structures from a Patterson distribution of the triclinic, monoclinic, and orthorhombic systems —O. V. Frank-Kamenetskaya, N. V. Grigor'eva, and N. V. Margolis. **18**(3), 314–6 (Nov. 1973); CPM-7311E0446

Checking the cited mean parameters of oxide unit cells with the perovskite type structure —E. G. Fesenko and G. A. Geguzina. **18** (3), 336–8 (Nov. 1973); CPM-7311E0468

Laser detection of acentrism in crystals —V. D. Shigorin and G. P. Shipulo. **18**(3), 349–50 (Nov. 1973); CPM-7311E0481

Types of vector-localizing sections of the duplicated Patterson function —V. N. Biyushkin and N. V. Belov. **18**(3), 386–7 (Nov. 1973); CPM-7311E0518

Use of the methods of nonlinear optics in order to make a more accurate analysis of the structural characteristics of crystals associated with the absence of an inversion center —L. G. Koreneva, V. F. Zolin, B. L. Davydov, and V. I. Tsaryuk. **18**(3), 399 (Nov. 1973); CPM-7311E0531

Systematic analysis of patterson function on the basis of crystal symmetry. V. Regularities in the degeneracy of the rhombuses in vector sytems of crystals belonging to lower crystallographic systems —É. A. Kuz'min, R. I. Bochkova, Yu. N. Saf'yanov, V. P. Golovachev, and N. V. Belov. **18**(4), 429–33 (Jan. 1974); CPM-7401D0505

Vector-localizing cross section through a double Patterson function — V. N. Biyushkin. **18**(4), 434–6 (Jan. 1974); CPM-7401D0510

Primitive rotation regions of two Patterson syntheses —V. I. Burdina. **18**(4), 437–41 (Jan. 1974); CPM-7401D0513

Precision measurements of crystallographic parameters by the method of a widely divergent x-ray beam —V. V. Aristov, V. Sh. Shekhtman, and I. M. Shmyt'ko. **18**(4), 445–6 (Jan. 1974); CPM-7401D0521

Determination of the nature of the filling of positions by isomorphous elements —A. L. Kosoi and V. A. Frank-Kamenetskii. **18**(4), 464–6 (Jan. 1974); CPM-7401D0540

51.50.C Physics of crystal growth

Transformation of layer-spiral growth into normal growth on a basal face. I. Breadkdown of the elementary layers on the apices of the spiral hillocks —E. D. Dukova. **18**(4), 514–8 (Jan. 1974); CPM-7401D0590

Model of the controlled growth of macromolecular and crystalline structures —V. K. Bykhovskii. **18**(5), 575–7 (Mar. 1974); CPM-7403D0403

Simulation of a crystal surface equilibrium atomic structure for a single component system —V. O. Esin, V. I. Danilyuk, Yu. M. Plishkin, and G. L. Podchinenova. **18**(5), 578–81 (Mar. 1974); CPM-7403D0406

Phenomena arising on the arrest of crystal growth —V. N. Romanenko and V. S. Kheifets. **18**(5), 663–6 (Mar. 1974); CPM-7403D0491

Determination of the activation energy of forward and reverse reactions during crystal growth —E. B. Treivus. **18**(6), 788–90 (May 1974); CPM-7406X1232

51.50.E Crystal symmetry: models and space groups

Isolation of n points of the basic system from a vector system by use of the star of an (n-1) -dimensional simplex —R. V. Galiulin, M. I. Sirota, A. S. Naumov, and N. V. Belov. **18**(1), 39–42 (Jul. 1973); CPM-7309D0289

Symmetries of functions for separating structures from a Patterson distribution of the triclinic, monoclinic, and orthorhombic systems —O. V. Frank-Kamenetskaya, N. V. Grigor'eva, and N. V. Margolis. **18**(3), 314–6 (Nov. 1973); CPM-7311E0446

Kronecker product for the representations of the crystallographic pointgroups I —B. A. Men', A. N. Men', and V. I. Cherepanov. **18** (4), 421–4 (Jan. 1974); CPM-7401D0497

Loose packing of dense layers —P. I. Kripyakevich. **18**(4), 460–3 (Jan. 1974); CPM-7401D0536

Reduction of the Kronecker product of representations of the crystallogrphic groups. II —B. A. Men', A. N. Men', and V. I. Cherepanov. **18**(5), 567–9 (Apr. 1974)

Applicability of Zachariasen's equations to calculations of the integral intensity scattered by a "thick" single crystal in the Bragg symmetry case for any dislocation density —A. V. Kuznetsov. **18** (5), 592–5 (Mar. 1974); CPM-7403D0420

Reduction of the Kronecker product of representations of the crystallographic groups. III —B. A. Men', A. N. Men', and V. I. Cherepanov. **18**(6), 705–10 (May 1974); CPM-7406X1149

Statistical values of heavy atom weighted contributions (D_H) to the total structure amplitude —L. L. Shadyro and I. D. Feranchuk. **18** (6), 715–8 (May 1974); CPM-7406X1159

51.50.G Crystalline systems and crystalline classes

Homology and antihomology groups —P. A. Zabolotnyi. **18**(1), 1–4 (Jul. 1973); CPM-7309D0251

Chemical crystallography of mixed anion frameworks. I. Zirconium and scandium alkali sorosilicates —A. A. Voronkov, R. G. Sizova, V. V. Ilyukhin, and N. V. Belov. **18**(1), 67–72 (Jul. 1973); CPM-7309D0317

Unusual ion coordination numbers in the structure of garnet —B. V. Mill' and G. Ronniger. **18**(1), 76–9 (Jul. 1973); CPM-7309D0326

X-ray diffraction study of the tetrahydrates of the mesoperiodates of the rare earth elements and yttrium —M. B. Varfolomeev, N. B. Shamrai, B. G. Berenshtein, and V. E. Plyushchev. **18**(1), 106–7 (Jul. 1973); CPM-7309D0356

Vibrational spectrum and crystal structure of $TlNO_3$III —D. E. Pogarev and A. A. Shultin. **18**(2), 193–5 (Sep. 1973); CPM-7309D1395

New ions in the garnet structure —G. Ronniger and B. V. Mill'. **18** (3), 339–41 (Nov. 1973); CPM-7311E0471

Indexing of the crystallographic planes in rhombohedral crystals —V. A. Gerken, B. K. Kazurov, and G. M. Tsigel'nitskii. **18**(5), 674 (Mar. 1974); CPM-7403D0502

Key role of analysis of interaction distances in oxygen compounds containing heavy cations (high atomic numbers) —T. M. Polyanskaya, S. V. Borisov, and N. V. Belov. **18**(6), 719–27 (May 1974); CPM-7406X1163

Relationships of structure types. New representatives of the homologous classes corundum, spinel, and amesite —N. L. Smirnova, S. D. Polzikov, and N. A. Rebrova. **18**(6), 744–8 (May 1974); CPM-7406X1188

51.50.J Crystal morphology and crystal orientation

Determination of the arbitrary orientation of a crystal by proton diffraction —A. L. Fainshtein. **18**(2), 215–7 (Sep. 1973); CPM-7309D1417

Crystallographic orientation of dendrites of pure tin —V. O. Esin, G. N. Pankin, and R. Sh. Nasyrov. **18**(2), 246–9 (Sep. 1973); CPM-7309D1448

Two-crystal spectrometer study of barium titanate single crystals —I. Ya. Nikoforov and Yu. F. Mal'tsev. **18**(3), 370–1 (Nov. 1973); CPM-7311E0502

Epitaxial growth of AgCl on the thermoelectric polyvinylchloride films, copying the electrical properties of an NaCl surface —G. I. Distler and E. I. Tokmakova. **18**(3), 384–5 (Nov. 1973); CPM-7311E0516

Structural study of tochilinite. II. Acicular variety: Unusual diffraction patterns. —N. I. Organova, V. A. Drits, and A. L. Dmitrik. **18**(5), 606–9 (Mar. 1974); CPM-7403D0434

51.50.L Crystal binding

Stability of ionic crystals with an NaCl type lattice in the Born model —I. M. Ratner, N. A. Tenyakova, and A. I. Boiko. 18(1), 99–100 (Jul. 1973); CPM-7309D0349

Crystal-chemical analysis of the structure of 1-I-substituted anthraquinone —N. L. Klimasenko, V. K. Bel'skii, V. K. Sarynin, and G. A. Gol'der. 18(4), 457–9 (Jan. 1974); CPM-7401D0533

51.50.Q Specific structures: other inorganic materials

Crystal structure of ditrioctahedral chlorite —V. A. Aleksandrova, V. A. Drits, and G. V. Sokolova. 18(1), 50–3 (Jul. 1973); CPM-7309D0300

Crystal and molecular structures of 4-chloroanthraquinonethiadiazole —O. A. Mikhno, Z. I Ezhkova, and G. S. Zhdanov. 18(1), 59–62 (Jul. 1973); CPM-7309D0309

Electron-diffraction determination of the crystal structure of β-CuOHCl —A. A. Voronova and B. K. Vainshtein. 18(1), 63–6 (Jul. 1973); CPM-7309D0313

Chemical crystallography of mixed anion frameworks. I. Zirconium and scandium alkali sorosilicates —A. A. Voronkov, R. G. Sizova, V. V. Ilyukhin, and N. V. Belov. 18(1), 67–72 (Jul. 1973); CPM-7309D0317

Double cesium-rare earth molybdates of the composition $Cs_3Ln(MoO_4)_3$ (Ln=La, Pr, Nd) —P. V. Klevtsov, V. A. Vinokurov, and R. F. Klevtsova. 18(1), 73–5 (Jul. 1973); CPM-7309D0323

Crystal structure of a new modification, Bi_2Se_3II —É. Ya. Atabaeva, S. A. Mashkov, and S. V. Popova. 18(1), 104–5 (Jul. 1973); CPM-7309D0354

X-ray diffraction study of the tetrahydrates of the mesoperiodates of the rare earth elements and yttrium —M. B. Varfolomeev, N. B. Shamrai, B. G. Berenshtein, and V. E. Plyushchev. 18(1), 106–7 (Jul. 1973); CPM-7309D0356

Zn-Mn isomorphism in Na_2ZnGeO_4 crystals —I. P. Kuz'mina, A. N. Lobachev, V. M. Vinokurov, N. M. Nizamutdinov, and L. A. Volkova. 18(1), 110–1 (Jul. 1973); CPM-7309D0360

Gamma-resonance investigations of ferruginous tourmalines —V. F. Belov, T. A. Khimich, M. N. Shipko, I. E. Voskresenskaya, and E. N. Okulov. 18(1), 119–20 (Jul. 1973); CPM-7309D0369

Crystal structure of lithium bitungstate $Li_2W_2O_7$ —S. A. Magarill, R. F. Klevtsova, and V. V. Bakakin. 18(2), 166–70 (Sep. 1973); CPM-7309D1368

Crystal structure of the compound $EuMg_3Ge_3$ —O. F. Zmii, E. I. Gladyshevskii, and V. S. Bul'o. 18(2), 171–2 (Sep. 1973); CPM-7309D1373

Crystal structure of sodium hydrosilicate $Na_3HSiO_4{\cdot}5H_2O$ —Yu. I. Smolin, Yu. F. Shepelev, and I. K. Butikova. 18(2), 173–6 (Sep. 1973); CPM-7309D1375

Crystal structure of sodium ammonium selenate dihydrate $NaNH_4SeO_4{\cdot}2H_2O$ —A. I. Kruglik, V. I. Simonov, and V. I. Yuzvak. 18(2), 177–80 (Sep. 1973); CPM-7309D1379

Vanadates with a defect garnet structure —G. Ronniger and B. V. Mill'. 18(2), 187–90 (Sep. 1973); CPM-7309D1389

Change of the interplanar distances in deep layers of silicon during bombardment with medium-energy ions —G. I. Uspenskaya, V. M. Genkin, and D. I. Tetel'baum. 18(2), 224–5 (Sep. 1973); CPM-7309D1426

Crystal structure of lanthanum hypophosphite monohydrate —V. M. Ionov, L. A. Aslanov, V. B. Rybakov, and M. A. Porai-Koshits. 18 (2), 250–1 (Sep. 1973); CPM-7309D1452

Crystal structure of europium hypophosphite monohydrate —V. M. Ionov, L. A. Aslanov, M. A. Porai-Koshits, and V. B. Rybakov. 18 (2), 252–3 (Sep. 1973); CPM-7309D1454

Structure of calcium-cobalt hexaborate $K_2Co[B_6O_7(OH)_6]_2{\cdot}4H_2O$ —É. Ya. Silin', Ya. K. Ozol, and A. F. Levin'sh. 18(3), 317–9 (Nov. 1973); CPM-7311E0449

Crystal structure of langbanite —V. G. Rau and E. N. Kurkutova. 18 (3), 320–2 (Nov. 1973); CPM-7311E0452

Crystal structure of U_2MoO_8 —V. N. Serezhkin, L. M. Kovba, and V. K. Trunov. 18(3), 323–5 (Nov. 1973); CPM-7311E0455

Crystal structure of $CsNbO(SO_4)_2$ —A. A. Kashaev and G. V. Sokolova. 18(3), 388–9 (Nov. 1973); CPM-7311E0520

"Hexagonal YF_3" structure type and high-temperature modifications of rare-earth trifluorides isostructural with YF_3 —B. P. Sobolev and P. P. Fedorov. 18(3), 392 (Nov. 1973); CPM-7311E0524

New boride structural types in the homologous series based on the $CaCu_5$ and $CeCo_3B_2$ types —Yu. B. Kuz'ma and N. S. Bilonizhko. 18(4), 447–9 (Jan. 1974); CPM-7401D0523

Crystal structure of the compound $Ce_{15}Ni_4Si_{13}$ —M. G. Mys'kiv, O. I. Bodak, and E. I. Gladyshevskii. 18(4), 450–3 (Jan. 1974); CPM-7401D0526

Structure of Al_2O_3 in internally oxidized Cu-Al alloys —G. I. Kokhanchik and A. V. Serebryakov. 18(4), 467–70 (Jan. 1974); CPM-7401D0543

X-ray diffraction study of the system RbBr-TlBr —A. A. Haav and T. K. Muirsepp. 18(4), 471–2 (Jan. 1974); CPM-7401D0547

Crystal structure of the alkali titanosilicate labuntsovite —N. I. Golovastikov. 18(5), 596–9 (Mar. 1974); CPM-7403D0424

Crystal structure of zinc fluoride tetrahydrate, $ZnF_2{\cdot}4H_2O$ —B. V. Bukvetskii, S. A. Polishchuk, and V. I. Simonov. 18(5), 600–2 (Mar. 1974); CPM-7403D0428

Structure of the double oxide α-$U_3Mo_{20}O_{64}$ —V. N. Serezhkin, L. M. Kovba, and V. K. Trunov. 18(5), 603–5 (Mar. 1974); CPM-7403D0431

Structural study of tochilinite. II. Acicular variety: Unusual diffraction patterns. —N. I. Organova, V. A. Drits, and A. L. Dmitrik. 18(5), 606–9 (Mar. 1974); CPM-7403D0434

A group of synthetic cadmium germanates and their x-ray study —E. L. Belokoneva, M. A. Simonov, N. G. Duderov, A. N. Lobachev, and N. V. Belov. 18(5), 610–2 (Mar. 1974); CPM-7403D0438

Structure of nickel hydroxide containing potassium ions —P. N. Bityutskii, V. I. Khitrova, and Z. G. Pinsker. 18(5), 613–6 (Mar. 1974); CPM-7403D0441

Proton magnetic resonance investigation of the localization of the protons in the crystal structures $Na_2Cr_2O_7{\cdot}2H_2O$ and $Li_2Cr_2O_7{\cdot}2H_2O$ —G. R. Bulka, V. M. Vinokurov, É. A. Kuz'min, Yu. A. Kharitonov, and N. V. Belov. 18(5), 617–9 (Mar. 1974); CPM-7403D0445

Position of the hydroxyl groups in the structure of hydrosodalite —V. Yu. Galitskii, V. N. Shcherbakov, and S. P. Gabuda. 18(5), 620–2 (Mar. 1974); CPM-7403D0448

Crystal structure of $La_2Sr_3(BO_3)_4$ —G. K. Abdullaev, Kh. S. Mamedov, and S. T. Amirov. 18(5), 675–6 (Mar. 1974); CPM-7403D0503

Crystallochemical determination of the structure of $NaTl_3(SO_3)_2$ by means of the method of crystallograms —N. L. Smirnova. 18(5), 680 (Mar. 1974); CPM-7403D0508

Dislocation structure of $KMgF_3$ crystals —S. N. Bodrug. 18(5), 692–4 (Mar. 1974); CPM-7403D0520

Key role of analysis of interaction distances in oxygen compounds containing heavy cations (high atomic numbers) —T. M. Polyanskaya, S. V. Borisov, and N. V. Belov. 18(6), 719–27 (May 1974); CPM-7406X1163

Determination of the crystal structure of the hexagonal phase β^{III} in the copper-tellurium system by electron diffraction —R. V. Baranova, A. S. Avilov, and Z. G. Pinsker. 18(6), 736–40 (May 1974); CPM-7406X1180

Neutron-diffraction refinement of the structure of alpha lithium iodate —A. Émiraliev, A. G. Kocharov, I. I. Yamzin, and V. A. Lyubimtsev. 18(6), 741–3 (May 1974); CPM-7406X1185

Binary molybdates and tungstates of alkali metals with bismuth, $M^+Bi(TO_4)_2$ —P. V. Klevtsov, V. A. Vinokurov, and R. F. Klevtsova. 18(6), 749–51 (May 1974); CPM-7406X1193

Structures of leucophoenicite, $Mn_7[SiO_4]_2[(SiO_4)(OH)_2]$, and synthetic Cd orthogermanate, $Cd_3[GeO_4](OH)_2$ —E. L. Belokoneva, M. A. Simonov, and N. V. Belov. 18(6), 800–1 (May 1974); CPM-7406X1244

Crystal structures of $RbNbO(SO_4)_2$ and $NH_4NbO(SO_4)_2$ —A. A. Kashaev, G. E. Postoenko, and É. A. Zel'bst. 18(6), 802–3 (May 1974); CPM-7406X1246

Hydrothermal synthesis, x-Ray diffraction, and thermogravimetric study of rare-earth hydroxchlorides $Ln(OH)_2Cl$ —L. N. Dem'yanets, V. I. Bukin, E. N. Emel'yanova, and V. I. Ivanov. 18 (6), 806–8 (May 1974); CPM-7406X1250

Growth and investigation of binary cadmium oxides with structures of the perovskite type. II. Cadmium stannate and zirconate —R. I. Spinko, V. N. Lebedev, R. V. Kolesova, and E. G. Fesenko. 18(6), 809–10 (May 1974); CPM-7406X1253

51.50.S Specific structures: organic materials

X-ray study of potassium copper ethylenediaminetetraacetate trihydrate —M. A. Porai-Koshits, N. V. Novozhilova, T. N. Polynova, T. V. Filippova, and L. I. Martynenko. 18(1), 54–8 (Jul. 1973); CPM-7309D0304

Atom-atom potentials and the coordinates of hydrogen atoms in methyl groups in the molecule and crystal —K. V. Mirskaya and L. V. Ivanova. 18(1), 101–2 (Jul. 1973); CPM-7309D0351

Crystal structure of the potassium salt of 1,1-dinitroethane —O. V. Frank-Kamenetskaya, N. V. Grigor'eva, N. V. Margolis, and I. V. Tselinskii. 18(1), 108–9 (Jul. 1973); CPM-7309D0358

Crystal structure of the coordination compound bis(pyridinaldehydethiosemicarbazonato)cobalt(III)nitrate —K. N. Akatova, T. N. Tarkhova, and N. V. Belov. 18(2), 162–5 (Sep. 1973); CPM-7309D1364

Crystal and molecular structures of the 1:2 complex of 1-methyl-3,3-dimethyl-2-(para-n-methyl-n-β-chloroethylstyryl)indole and 7,7,8,8-tetracyanoquinodimethane, $(C_{22}H_{26}N_2Cl)^+(C_{12}H_4N_4)(C_{12}H_4N_4)$ —R. P. Shibaeva, L. P. Rozenberg, and L. O. Atovmyan. 18(3), 326–9 (Nov. 1973); CPM-7311E0458

Crystal and molecular structure of phenyl phenoxtinium iodide —A. I. Gusev and Yu. T. Struchkov. 18(3), 330–2 (Nov. 1973); CPM-7311E0462

Crystal structure of 1,6-$[Coen_2Cl_2]Cl\cdot 3SC(NH_2)_2$ —Yu. A. Simonov, L. I. Landa, N. N. Proskina, T. I. Malinovskii, and A. V. Ablov. 18(3), 333–5 (Nov. 1973); CPM-7311E0465

Crystal structure of coumarin —R. M. Myasnikova, T. S. Davydova, and V. I. Simonov. 18(4), 454–6 (Jan. 1974); CPM-7401D0530

Crystal-chemical analysis of the structure of 1-I-substituted anthraquinone —N. L. Klimasenko, V. K. Bel'skii, V. K. Sarynin, and G. A. Gol'der. 18(4), 457–9 (Jan. 1974); CPM-7401D0533

X-ray investigation of some examples of a homologous series of cholesterol ethers in dicarboxylic acid —Ya. I. Dutchak and V. K. Burima. 18(5), 677–9 (Mar. 1974); CPM-7403D0505

X-ray diffraction study of naphthaloimide —A. N. Sobolev, L. A. Chetkina, G. A. Gol'der, Yu. G. Fedorov, and V. E. Zavodnik. 18 (6), 728–31 (May 1974); CPM-7406X1172

Crystal and molecular structures of octafluoroanthraquinone —L. A. Chetkina and E. G. Popova. 18(6), 732–5 (May 1974); CPM-7406X1176

One-dimensional disorder in diazoaminobenzene —V. F. Gladkova. 18 (6), 783–7 (May 1974); CPM-7406X1227

Unit-cell parameters and space groups of several pyridino-anthraquinones —O. A. Mikhno, Z. I. Ezhkova, and M. I. Evstratova. 18(6), 804–5 (May 1974); CPM-7406X1248

51.70.- Defects in crystals

Rose channels —V. M. Finkel' and V. A. Fedorov. 18(3), 372–5 (Nov. 1973); CPM-7311E0504

51.70.B Thermodynamic processes (formation, annealing, etc.)

Influence of heat treatment on the structural perfection of single crystals of gallium arsenide alloyed with tellurium —M. G. Mil'vidskii, V. B. Osvenskii, A. G. Novikov, V. G. Fomin, and S. P. Grishina. 18(4), 519–20 (Jan. 1974); CPM-7401D0595

51.70.F Interstitials and vacancies

Vanadates with a defect garnet structure —G. Ronniger and B. V. Mill'. 18(2), 187–90 (Sep. 1973); CPM-7309D1389

Nature of the point defects in GaAs single crystals as a function of the composition of the melt during growth —V. T. Bublik, V. V. Karataev, R. S. Kulagin, M. G. Mil'vidskii, V. B. Osvenskii, O. G. Stolyarov, and L. P. Kholodnyi. 18(2), 218–9 (Sep. 1973); CPM-7309D1420

Interpretation of field-ion images. I. point defects —L. P. Potapov, T. L. Raznikova, and A. L. Suvorov. 18(2), 220–3 (Sep. 1973); CPM-7309D1422

Solid solutions of $BaTiO_3$ with barium niobates —I. N. Groznov and Yu. N. Venevtsev. 18(3), 395–6 (Nov. 1973); CPM-7311E0527

Vacancy concentration in relation to plastic deformation in NaCl crystals —N. A. Tyapunina and A. N. Tselebrovskii. 18(3), 410 (Nov. 1973); CPM-7311E0542

Short-range and long-range order in the arrangement of the interstitial atoms in (34%Ta66%Ti)D_x —N. F. Miron, V. I. Shcherbak, V. N. Bykov, and V. A. Levdik. 18(4), 532–3 (Jan. 1974); CPM-7401D0608

Nature of small etch pits in tellurium-alloyed GaAs single crystals —S. S. Shifrin, V. B. Osvenskii, M. G. Mil'vidskii, L. M. Morgulis, and S. P. Grishina. 18(6), 818–20 (May 1974); CPM-7406X1262

51.70.M Dislocations

Dislocation mechanism of growth with a low kink density —V. V. Voronkov. 18(1), 19–23 (Jul. 1973); CPM-7309D0269

Formation of a Debye-Hückel cloud around dislocations in LiF crystals —N. G. Politov, M. V. Galustashvili, and I. M. Paperno. 18(1), 125–6 (Jul. 1973); CPM-7309D0375

Focused laser-beam damage mechanism for CsI crystals —L. M. Belyaev, V. V. Nabatov, V. N. Rozhanskii, N. L. Sizova, and A. A. Urosovskaya. 18(2), 207–8 (Sep. 1973); CPM-7309D1409

Deformation dislocations in natural quartz crystals —V. F. Miuskov, L. I. Tsinober, and L. A. Gordienko. 18(2), 209–11 (Sep. 1973); CPM-7309D1411

Change of the interplanar distances in deep layers of silicon during bombardment with medium-energy ions —G. I. Uspenskaya, V. M. Genkin, and D. I. Tetel'baum. 18(2), 224–5 (Sep. 1973); CPM-7309D1426

Low-dislocation-density single crystals of corundum —Kh. S. Bagdasarov, E. R. Dobrovinskaya, V. V. Pishchik, M. M. Chernik, Yu. Yu. Kovalev, A. S. Gershun, and I. F. Zvyagintseva. 18(2), 242–5 (Sep. 1973); CPM-7309D1444

Dislocation networks formed during growth and annealing in the basal plane of a single crystal of zinc —N. A. Tyapunina, T. N. Pashchenko, and G. M. Zinenkova. 18(2), 264–5 (Sep. 1973); CPM-7309D1466

Growth dislocation distribution along a copper crystal and dislocation density as a function of mean diameter —A. G. Basariya, B. K. Kapanadze, and V. V. Sanadze. 18(3), 411 (Nov. 1973); CPM-7311E0543

Dislocation formed during the sintering of solids ("sintering rosettes") —Ya. E. Geguzin, A. S. Dzyuba, V. L. Indenbom, and N. N. Ovcharenko. 18(4), 502–5 (Jan. 1974); CPM-7401D0578

Charge on dislocations in sodium chloride crystals containing an anionic impurity —N. A. Tyapunina and A. I. Kolomiitsev. 18(4), 549–50 (Jan. 1974); CPM-7401D0625

Selective etching at dislocations in metals (Ni) —E. G. Popkova and A. A. Predvoditelev. 18(5), 647–50 (Mar. 1974); CPM-7403D0475

Dislocation structure of $KMgF_3$ crystals —S. N. Bodrug. 18(5), 692–4 (Mar. 1974); CPM-7403D0520

Domain boundaries, antiphase boundaries, and dislocations in gadolinium molybdate single crystals —V. A. Meleshina, V. L. Indenbom, Kh. S. Bagdasarov, and T. M. Polkhovskaya. 18(6), 764–8 (May 1974); CPM-7406X1208

51.70.P Stacking faults and other planar defects

Mechanical stability of small-angle growth boundaries in NaCl crystals —E. L. Pishchik and E. P. Kostyukova. 18(3), 414–5 (Nov. 1973); CPM-7311E0546

Temperature dependence of the rate of enlargement of the twinning layer in calcite crystals —V. P. Soldatov, V. I. Startsev, and N. M. Chaikovskaya. 18(5), 641–3 (Mar. 1974); CPM-7403D0469

51.70.R Crystal impurities, general

Nature of the impurity water in synthetic quartz crystals —L. I. Tsinober and V. E. Khadzhi. 18(5), 699–700 (Mar. 1974); CPM-7403D0527

51.70.T Doping methods and implantation

Alloying of epitaxial silicon layers with phosphorus and arsenic in a vacuum —V. A. Tolomasov, L. N. Abrosimova, T. N. Sergivskaya, and T. M. Zotova. 18(4), 558–9 (Jan. 1974); CPM-7401D0634

51.70.W Impurity concentration, distribution, and gradients

Distribution coefficients of divalent impurities in alkali halide crystals —O. L. Kreinin and K. M. Rozin. 18(2), 276–7 (Sep. 1973); CPM-7309D1478

Use of the luminescence polarization diagram method to investigate molecular crystals containing two impurities —G. S. Belikova, N. D. Zhevandrov, T. V. Il'inykh, L. E. Kraeva, and N. P. Sul'zhenko. 18(4), 489–91 (Jan. 1974); CPM-7401D0565

Influence of temperature gradient on the impurity distribution during growth of crystals form a melt —E. A. Krivandina and E. E. Kostyleva. 18(4), 560–1 (Jan. 1974); CPM-7401D0636

51.80.- Radiation damage and other irradiation effects

Determination of the arbitrary orientation of a crystal by proton diffraction —A. L. Fainshtein. 18(2), 215–7 (Sep. 1973); CPM-7309D1417

Change of the interplanar distances in deep layers of silicon during bombardment with medium-energy ions —G. I. Uspenskaya, V. M. Genkin, and D. I. Tetel'baum. 18(2), 224–5 (Sep. 1973); CPM-7309D1426

Some features of the action of penetrating radiation on the electrical properties of a quartz crystal —A. A. Fotchenkov and S. V. Kolodieva. 18(3), 366–9 (Nov. 1973); CPM-7311E0498

51.80.D X- and γ-rays

Phase transformations in $NaH_3(SeO_3)_2$ crystals irradiated with a large dose of gamma radiation —E. V. Peshikov and L. A. Shuvalov. 18 (4), 499–501 (Jan. 1974); CPM-7401D0575

Reconstruction of the phase of the electronic scattering amplitude from experiments on the diffraction of resonant γ quanta —I. P. Perstnev and F. N. Chukhovskii. 18(5), 582–5 (Mar. 1974); CPM-7403D0410

51.80.P Ion implantation

Change in the structure of germanium and silicon during ion bombardment and subsequent annealing —P. V. Pavlov. 18(4), 506–9 (Jan. 1974); CPM-7401D0582

Irradiation-induced phase transition in quartz —E. V. Kolontsova, É. E. Kulago, and N. A. Tomilin. 18(6), 752–4 (May 1974); CPM-7406X1196

52. MECHANICAL AND ACOUSTIC PROPERTIES OF CONDENSED MATTER

52.20.- Mechanical properties of solids

52.20.D Elasticity

Elastic properties of KDP and DKDP crystals of high temperatures —S. I. Chizhikov, N. G. Sorokin, I. Yu. Ledovskaya, and E. V. Makarevskaya. 18(4), 544–5 (Jan. 1974); CPM-7401D0620

52.20.F Deformation and plasticity, including yield, ductility, and superplasticity

Focused laser-beam damage mechanism for CsI crystals —L. M. Belyaev, V. V. Nabatov, V. N. Rozhanskii, N. L. Sizova, and A. A. Urosovskaya. 18(2), 207–8 (Sep. 1973); CPM-7309D1409

Vacancy concentration in relation to plastic deformation in NaCl crystals —N. A. Tyapunina and A. N. Tselebrovskii. 18(3), 410 (Nov. 1973); CPM-7311E0542

Mechanical stability of small-angle growth boundaries in NaCl crystals —E. L. Pishchik and E. P. Kostyukova. 18(3), 414–5 (Nov. 1973); CPM-7311E0546

Study of liquid inclusions in a rocksalt crystal crystal over the entire temperature range of their existence —Ya. E. Geguzin and A. S. Dzyuba. 18(4), 510–3 (Jan. 1974); CPM-7401D0586

Determination of the degree of bending of single crystals from the orientational scattering of β particles —A. Ya. Bobudaev, S. A. Vorob'ev, and V. V. Kaplin. 18(4), 551 (Jan. 1974); CPM-7401D0627

52.40.+ Anelasticity, internal friction, and mechanical resonances

Characteristic features of the internal friction of filamentary crystals of NaCl, KCl, and KBr at elevated temperatures —Lieh K'uang and V. N. Rozhanskii. 18(2), 260–2 (Sep. 1973); CPM-7309D1462

Internal friction and strength of germanium whiskers —V. S. Postnikov, S. A. Ammer, and A. I. Drozhzhin. 18(3), 416 (Nov. 1973); CPM-7311E0548

Relaxational internal friction in crystals of KH_2PO_4 without chromium added —S. A. Gridnev, L. N. Kamysheva, and N. F. Romanova. 18(6), 773–6 (May 1974); CPM-7406X1217

52.90.+ Other topics in mechanical and acoustical properties of condensed matter

Growth of diamond crystals in the form of needles and plates —Yu. A. Litvin, V. P. Butuzov, É. M. Nikoforova, and S. I. Futergendler. 18(2), 278–9 (Sep. 1973); CPM-7309D1480

Elastic properties of KDP and DKDP crystals of high temperatures —S. I. Chizhikov, N. G. Sorokin, I. Yu. Ledovskaya, and E. V. Makarevskaya. 18(4), 544–5 (Jan. 1974); CPM-7401D0620

53. LATTICE DYNAMICS

53.20.- Phonons and vibrations in crystal lattices

Vibrational spectrum and crystal structure of $TlNO_3III$ —D. E. Pogarev and A. A. Shultin. 18(2), 193–5 (Sep. 1973); CPM-7309D1395

53.70.- Thermal and statistical properties of lattices

Determination of the energy and thermodynamic characteristics of iron-aluminum alloys by the method of diffuse x-ray scattering —S. V. Semenovskaya, Zh. B. Sinyavskaya, and A. P. Senichkin. 18 (3), 344–8 (Nov. 1973); CPM-7311E0476

Short-range and long-range order in the arrangement of the interstitial atoms in $(34\%Ta66\%Ti)D_x$ —N. F. Miron, V. I. Shcherbak, V. N. Bykov, and V. A. Levdik. 18(4), 532–3 (Jan. 1974); CPM-7401D0608

One-dimensional disorder in diazoaminobenzene —V. F. Gladkova. 18 (6), 783–7 (May 1974); CPM-7406X1227

Reflection intensity as a function of temperature during diffraction of slow electrons from (111) and (100) faces of germanium —B. Z. Ol'shanetskii, A. I. Volokitin, and S. M. Repinskii. 18(6), 815–6 (May 1974); CPM-7406X1259

54. EQUATIONS OF STATE, PHASE EQUILIBRIA, AND PHASE TRANSITIONS

54.50.+ Phase equilibrium diagrams

Statistical model of multiphase anisotropic crystallization —V. F. Dorfman. 18(1), 93–8 (Jul. 1973); CPM-7309D0343

X-ray diffraction and dielectric studies of the system $Li(Ta_xSb_{1-x})O_3$ —V. I. Nesterenko and I. G. Ismailzade. 18(1), 112–3 (Jul. 1973); CPM-7309D0362

X-ray diffraction and dielectric studies of the $LiNbO_3$-$KNbO_3$ system —I. G. Ismailzade, V. I. Nesterenko, and É. A. Il'yasov. 18(1), 114–5 (Jul. 1973); CPM-7309D0364

The $PbZrO_3$-$SrCu_{1/3}Nb_{2/3}$ system —D. F. Dzhmukhadze, M. A. Ugryumova, Yu. N. Venevtsev, and G. S. Zhdanov. 18(1), 116–8 (Jul. 1973); CPM-7309D0366

Hydrothermal crystallization in the system CdO-GeO_2-$LiCl$-H_2O —L. N. Dem'yanets and N. V. Suvorova. 18(1), 133–4 (Jul. 1973); CPM-7309D0383

New ions in the garnet structure —G. Ronniger and B. V. Mill'. 18 (3), 339–41 (Nov. 1973); CPM-7311E0471

Solid solutions of $BaTiO_3$ with barium niobates —I. N. Groznov and Yu. N. Venevtsev. 18(3), 395–6 (Nov. 1973); CPM-7311E0527

Hydrothermal synthesis of a new crystalline modification of lithium lanthanum molybdate, α-$LiLa(MoO_4)_2$ —P. V. Klevtsov, V. I. Protasova, L. Yu. Kharchenko, and R. F. Klevtsova. 18(4), 523–4 (Jan. 1974); CPM-7401D0599

Preparation and preliminary investigation of cadmium phosphates —Yu. A. Ivanov, I. N. Ivanovskaya, V. I. Popolitov, M. A. Simonov, and N. V. Belov. 18(5), 671–3 (Mar. 1974); CPM-7403D0499

Phase diagram of the system $(HgI_2)_x(HgBr_2)_{1-x}$ and some optical properties of its single crystals —I. D. Turyanitsa and V. V. Khiminets. 18(5), 688–9 (Mar. 1974); CPM-7403D0516

54.70.- General studies of phase transitions and critical points

Phase transition in liquid crystals induced by an electric field —I. G. Chistyakov and L. K. Vistin'. 18(4), 552–3 (Jan. 1974); CPM-7401D0628

X-ray investigation of some examples of a homologous series of cholesterol ethers in dicarboxylic acid —Ya. I. Dutchak and V. K. Burima. 18(5), 677–9 (Mar. 1974); CPM-7403D0505

54.70.F Liquid-vapor transitions

Transport of boron from a source to an epitaxial layer during sublimation of silicon in vacuum —R. G. Loginova, R. A. Rubtsova, and M. I. Ovsyannikov. 18(2), 232–3 (Sep. 1973); CPM-7309D1434

54.70.H Solid-vapor transitions

Spatial distribution of particles during vaporization of a zinc single crystal —Yu. A. Gel'man, V. F. Vinogradov, and Yu. N. Lyubitov. 18(4), 556–7 (Jan. 1974); CPM-7401D0632

Some structural-morphological characteristics of the volatilization of single crystal of α-Al_2O_3 —E. M. Akulenok, Yu. K. Danileiko, V. V. Panteleev, E. A. Fedorov, and V. Ya. Khaimov-Mal'kov. 18(5), 654–6 (Mar. 1974); CPM-7403D0482

54.70.K Solid-solid transitions

Thermal properties of ammonium fluoroberyllate crystals over a wide temperature range —B. A. Strukov, T. L. Skomorokhova, V. A. Koptsik, A. A. Boiko, and A. N. Izrailenko. 18(1), 86–8 (Jul. 1973); CPM-7309D0336

Study of the structure and dielectric properties of solid solutions in the system $BaTiO_3$-$Pb(Fe_{1/2}Nb_{1/2})O_3$ —O. S. Didkovskaya, I. P. Kovalevskaya, V. G. Seryi, V. V. Klimov, and Yu. N. Venevtsev. 18(2), 184–6 (Sep. 1973); CPM-7309D1386

Relaxation of phase boundaries in SbSI single crystals —M. D. Volnyanskii, A. Yu. Kudzin, and A. N. Sukhinskii. 18(2), 202–3 (Sep. 1973); CPM-7309D1404

Effect of manganese on the transformation of the zinc sulfide cubic lattice to hexagonal —G. E. Arkhangel'skii, T. I. Voznesenskaya, and M. V. Fok. 18(3), 342–3 (Nov. 1973); CPM-7311E0474

Structural mechanism of the phase transition in erbium pyrosilicate, $Er_2Si_2O_7$ —Yu. I. Smolin and Yu. F. Shepelev. 18(3), 390–1 (Nov. 1973); CPM-7311E0522

Anisotropy of the growth rate of centers of the α modification in single crystals of high purity tin —V. B. Brik, L. N. Larikov, and V. M. Fal'chenko. 18(3), 412–3 (Nov. 1973); CPM-7311E0544

Effect of diffusion on the velocity of a break during the growth of an alloy crystal —D. E. Temkin. 18(4), 425–8 (Jan. 1974); CPM-7401D0501

Polmorphism and crystallographic properties of yttrium and rare-earth trifluorides —B. P. Sobolev, L. S. Garashina, P. P. Fedorov, N. L. Tkachenko, and K. B. Seiranyan. 18(4), 473–6 (Jan. 1974); CPM-7401D0549

Phase transformations in rubidium and cesium superoxides —V. Ya. Dudarev, A. B. Tsentsiper, and M. S. Dobrolyubova. 18(4), 477–9 (Jan. 1974); CPM-7401D0553

Electron-diffraction study of the kinetics of the $CuS \rightarrow Cu_{2-x}S$ transformation —M. M. Kazinets and R. B. Shafizade. 18(4), 480–2 (Jan. 1974); CPM-7401D0556

Spectroscopy of organic materials in the low-temperature, crystalline phases —G. N. Zhizhin. 18(4), 483–8 (Jan. 1974); CPM-7401D0559

Phase transformations in $NaH_3(SeO_3)_2$ crystals irradiated with a large dose of gamma radiation —E. V. Peshikov and L. A. Shuvalov. 18 (4), 499–501 (Jan. 1974); CPM-7401D0575

Characteristics of a diffusionless transformation in nonideal alloys —D. E. Temkin. 18(5), 570–4 (Mar. 1974); CPM-7403D0398

Estimation of texture of the bcc→fcc→bcc double phase transformation —I. P. Sorokin. 18(5), 627–9 (Mar. 1974); CPM-7403D0455

Irradiation-induced phase transition in quartz —E. V. Kolontsova, É. E. Kulago, and N. A. Tomilin. 18(6), 752–4 (May 1974); CPM-7406X1196

KIO_3: the first ferroelectric permitting just a 120° shift in the ferroelectric polarization —L. A. Shuvalov, N. R. Ivanov, O. A. Chikhladze, and A. N. Izrailenko. 18(6), 758–61 (May 1974); CPM-7406X1202

Phase transition, dielectric anomaly, and domain structure in hydrosodalite —N. R. Ivanov and V. Yu. Galitskii. 18(6), 762–3 (May 1974); CPM-7406X1206

Domain boundaries, antiphase boundaries, and dislocations in gadolinium molybdate single crystals —V. A. Meleshina, V. L. Indenbom, Kh. S. Bagdasarov, and T. M. Polkhovskaya. 18(6), 764–8 (May 1974); CPM-7406X1208

High-temperature phase transitions in crystals of $Rb(D_xH_{1-x})_2PO_4$ —V. A. D'yakov, V. A. Koptsik, I. V. Lebedeva, A. V. Mishchenko, and L. N. Rashkovich. 18(6), 769–72 (May 1974); CPM-7406X1213

54.80.- Other phase properties of systems

Simulation of a crystal surface equilibrium atomic structure for a single component system —V. O. Esin, V. I. Danilyuk, Yu. M. Plishkin, and G. L. Podchinenova. 18(5), 578–81 (Mar. 1974); CPM-7403D0406

54.80.C Solubility, segregation, and mixing

Zn-Mn isomorphism in Na_2ZnGeO_4 crystals —I. P. Kuz'mina, A. N. Lobachev, V. M. Vinokurov, N. M. Nizamutdinov, and L. A. Volkova. 18(1), 110–1 (Jul. 1973); CPM-7309D0360

Distribution coefficients of divalent impurities in alkali halide crystals —O. L. Kreinin and K. M. Rozin. 18(2), 276–7 (Sep. 1973); CPM-7309D1478

Determination of the energy and thermodynamic characteristics of iron-aluminum alloys by the method of diffuse x-ray scattering —S. V. Semenovskaya, Zh. B. Sinyavskaya, and A. P. Senichkin. 18 (3), 344–8 (Nov. 1973); CPM-7311E0476

X-ray diffraction study of the system RbBr-TlBr —A. A. Haav and T. K. Muirsepp. 18(4), 471–2 (Jan. 1974); CPM-7401D0547

Influence of heat treatment on the structural perfection of single crystals of gallium arsenide alloyed with tellurium —M. G. Mil'vidskii, V. B. Osvenskii, A. G. Novikov, V. G. Fomin, and S. P. Grishina. 18(4), 519–20 (Jan. 1974); CPM-7401D0595

Solubility of LnF_3 in lanthanum fluoride —O. V. Kudryavtseva, L. S. Garashina, K. K. Rivkina, and B. P. Sobolev. 18(4), 531 (Jan. 1974); CPM-7401D0607

Nature of the impurity water in synthetic quartz crystals —L. I. Tsinober and V. E. Khadzhi. 18(5), 699–700 (Mar. 1974); CPM-7403D0527

Use of the double-crystal neutron spectrometer to study the low-temperature decomposition in niobium single crystals saturated with hydrogen —M. Kalanov, S. Sh. Shil'shtein, and V. A. Somenkov. 18(6), 755–7 (May 1974); CPM-7406X1199

54.80.E Stoichiometry and homogeneity

Effective distribution constants of excess basic components during crystallization of gallium arsenide from a melt —V. V. Karataev, M. G. Mil'vidskii, V. B. Osvenskii, and O. G. Stolyarov. 18(4), 521–2 (Jan. 1974); CPM-7401D0597

54.80.G Microstructure

Micromorphology of epitaxial PbS films —R. V. Kudryavtseva and S. A. Semiletov. 18(2), 272–3 (Sep. 1973); CPM-7309D1474

Mechanical stability of small-angle growth boundaries in NaCl crystals —E. L. Pishchik and E. P. Kostyukova. 18(3), 414–5 (Nov. 1973); CPM-7311E0546

Estimation of texture of the bcc→fcc→bcc double phase transformation —I. P. Sorokin. 18(5), 627–9 (Mar. 1974); CPM-7403D0455

Nature of small etch pits in tellurium-alloyed GaAs single crystals —S. S. Shifrin, V. B. Osvenskii, M. G. Mil'vidskii, L. M. Morgulis, and S. P. Grishina. 18(6), 818–20 (May 1974); CPM-7406X1262

Formation of trigons at the }111{ faces of natural diamond during etching —O. N. Grigor'ev. 18(6), 821–2 (May 1974); CPM-7406X1265

55. THERMAL PROPERTIES OF CONDENSED MATTER

55.40.- Heat capacities of solids

Thermal properties of ammonium fluoroberyllate crystals over a wide temperature range —B. A. Strukov, T. L. Skomorokhova, V. A. Koptsik, A. A. Boiko, and A. N. Izrailenko. **18**(1), 86–8 (Jul. 1973); CPM-7309D0336

Heat capacity of single-crystal $BaTiO_3$ near the electrical critical point —B. A. Strukov and A. K. Ivanov-Shits. **18**(4), 548 (Jan. 1974); CPM-7401D0624

55.70.+ Thermal expansion and thermomechanical effects

Thermal properties of ammonium fluoroberyllate crystals over a wide temperature range —B. A. Strukov, T. L. Skomorokhova, V. A. Koptsik, A. A. Boiko, and A. N. Izrailenko. **18**(1), 86–8 (Jul. 1973); CPM-7309D0336

Focused laser-beam damage mechanism for CsI crystals —L. M. Belyaev, V. V. Nabatov, V. N. Rozhanskii, N. L. Sizova, and A. A. Urosovskaya. **18**(2), 207–8 (Sep. 1973); CPM-7309D1409

Anisotropy of certain physical properties of pyrargyrite and proustite crystals —N. I. Butsko, M. M. Pidorya, and T. D. Krushel'nitskaya. **18**(4), 540–1 (Jan. 1974); CPM-7401D0616

56. TRANSPORT PROPERTIES OF CONDENSED MATTER (NONELECTRONIC)

Study of liquid inclusions in a rocksalt crystal crystal over the entire temperature range of their existence —Ya. E. Geguzin and A. S. Dzyuba. **18**(4), 510–3 (Jan. 1974); CPM-7401D0586

Charge on dislocations in sodium chloride crystals containing an anionic impurity —N. A. Tyapunina and A. I. Kolomiitsev. **18**(4), 549–50 (Jan. 1974); CPM-7401D0625

Elastic-diffusion interaction of liquid inclusions in a NaCl single crystal —Ya. E. Geguzin and A. S. Dzyuba. **18**(5), 660–2 (Mar. 1974); CPM-7403D0488

Effect of the crystallization mechanism on boron diffusion in silicon-germanium solid-solution epitaxial films —K. L. Lyutovich, F. A. Gimel'farb, P. B. Orlov, and T. A. Ukhorskaya. **18**(6), 825–6 (May 1974); CPM-7406X1269

58. SURFACES AND INTERFACES; THIN FILMS AND WHISKERS

58.20.- Structure of surfaces and interfaces

58.20.D LEED

Investigation of the pure and cesium-coated (100) surface of germanium by slow-electron diffraction —A. Yu. Mityagin and V. P. Orlov. **18**(4), 554–5 (Jan. 1974); CPM-7401D0630

58.20.F Texture

X-ray diffraction in crystals with deformation twins —D. A. Mirzaev and S. V. Rushchits. **18**(2), 204–6 (Sep. 1973); CPM-7309D1406

Electron-diffraction investigation of the structure of thin $InTlS_2$ films —K. A. Agaev, V. A. Gasymov, and M. I. Chiragov. **18**(2), 226–7 (Sep. 1973); CPM-7309D1428

Study of the (111) surface of GaP by methods of Auger spectroscopy and slow-electron diffraction —A. Yu. Mityagin, V. P. Orlov, and N. Ya. Cherevatskii. **18**(2), 268–9 (Sep. 1973); CPM-7309D1470

Electron-diffraction analysis of amorphous films of carbon and boron —Yu. G. Poltavtsev, V. P. Zakharov, and V. M. Pozdnyakova. **18** (2), 270–1 (Sep. 1973); CPM-7309D1472

Micromorphology of epitaxial PbS films —R. V. Kudryavtseva and S. A. Semiletov. **18**(2), 272–3 (Sep. 1973); CPM-7309D1474

Determination of coordination numbers and mean-square displacements from the radial distribution curve —Ya. I. Stetsiv. **18**(3), 306–7 (Nov. 1973); CPM-7311E0438

Two-crystal spectrometer study of barium titanate single crystals —I. Ya. Nikoforov and Yu. F. Mal'tsev. **18**(3), 370–1 (Nov. 1973); CPM-7311E0502

Rose channels —V. M. Finkel' and V. A. Fedorov. **18**(3), 372–5 (Nov. 1973); CPM-7311E0504

Electron diffraction study of the structure of amorphous germanium telluride and selenide films —Yu. G. Poltavtsev and V. P. Zakharov. **18**(3), 379–80 (Nov. 1973); CPM-7311E0511

Electron diffraction investigation of In_2S_3 films obtained by vacuum deposition —R. B. Shafizade, É. G. Éfendiev, and F. I. Aliev. **18** (3), 417–8 (Nov. 1973); CPM-7311E0549

Simulation of a crystal surface equilibrium atomic structure for a single component system —V. O. Esin, V. I. Danilyuk, Yu. M. Plishkin, and G. L. Podchinenova. **18**(5), 578–81 (Mar. 1974); CPM-7403D0406

Temperature dependence of the rate of enlargement of the twinning layer in calcite crystals —V. P. Soldatov, V. I. Startsev, and N. M. Chaikovskaya. **18**(5), 641–3 (Mar. 1974); CPM-7403D0469

Etching of quartz and some features of the surface layer —E. I. Lazorina and V. V. Soroka. **18**(5), 651–3 (Mar. 1974); CPM-7403D0479

Structure of thin lead telluride films —E. V. Rakova and S. A. Semiletov. **18**(6), 797–9 (May 1974); CPM-7406X1241

58.35.+ Mechanical and acoustic properties of surfaces and interfaces

Internal friction and strength of germanium whiskers —V. S. Postnikov, S. A. Ammer, and A. I. Drozhzhin. **18**(3), 416 (Nov. 1973); CPM-7311E0548

Dislocation formed during the sintering of solids ("sintering rosettes") —Ya. E. Geguzin, A. S. Dzyuba, V. L. Indenbom, and N. N. Ovcharenko. **18**(4), 502–5 (Jan. 1974); CPM-7401D0578

58.40.- Chemical reactions and surface treatment

Kinetics of the polishing and etching of sodium chloride crystals. III —G. K. Baranova and É. M. Nadgornyi. **18**(5), 644–6 (Mar. 1974); CPM-7403D0472

Selective etching at dislocations in metals (Ni) —E. G. Popkova and A. A. Predvoditelev. **18**(5), 647–50 (Mar. 1974); CPM-7403D0475

Etching of quartz and some features of the surface layer —E. I. Lazorina and V. V. Soroka. **18**(5), 651–3 (Mar. 1974); CPM-7403D0479

Nature of small etch pits in tellurium-alloyed GaAs single crystals —S. S. Shifrin, V. B. Osvenskii, M. G. Mil'vidskii, L. M. Morgulis, and S. P. Grishina. **18**(6), 818–20 (May 1974); CPM-7406X1262

Formation of trigons at the }111{ faces of natural diamond during etching —O. N. Grigor'ev. **18**(6), 821–2 (May 1974); CPM-7406X1265

58.50.+ Thin film growth, structure, and epitaxy

Rate of whisker growth by the vapor-liquid-crystal mechanism and the role of surface energy —E. I. Givargizov and A. A. Chernov. **18** (1), 89–92 (Jul. 1973); CPM-7309D0339

Growth of smooth epitaxial germanium films by the iodide method in a through-flow system with diffusive mass transfer —G. M. Malkin, V. E. Grigor'ev, N. A. Lineva, and L. A. Malkina. **18**(1), 129–30 (Jul. 1973); CPM-7309D0379

Growth of pyrrhotite on nuclei of iron thiospinel —S. Yamaguchi. **18** (1), 135 (Jul. 1973); CPM-7309D0385

Anisotropy of growth and alloying for epitaxial germanium layers in the Ge-I_2 system —L. G. Lavrent'eva, I. S. Zakharov, I. V. Ivonin, N. P. Kolodeshnikova, and T. I. Opryshko. **18**(2), 228–31 (Sep. 1973); CPM-7309D1430

Transport of boron from a source to an epitaxial layer during sublimation of silicon in vacuum —R. G. Loginova, R. A. Rubtsova, and M. I. Ovsyannikov. **18**(2), 232–3 (Sep. 1973); CPM-7309D1434

Motion of a germanium-gold alloy droplet along a germanium surface under the action of a temperature gradient —S. A. Grinberg and E. I. Givargizov. **18**(2), 236–8 (Sep. 1973); CPM-7309D1438

Crystallographic orientation of dendrites of pure tin —V. O. Esin, G. N. Pankin, and R. Sh. Nasyrov. **18**(2), 246–9 (Sep. 1973); CPM-7309D1448

Growth of diamond crystals in the form of needles and plates —Yu. A. Litvin, V. P. Butuzov, É. M. Nikoforova, and S. I. Futergendler. 18(2), 278–9 (Sep. 1973); CPM-7309D1480

Mechanism of growth and etching of whisker crystals of aluminum nitride —K. I. Portnoi, V. N. Gribkov, B. V. Shchetanov, É. L. Umantsev, and V. A. Silaev. 18(3), 376–8 (Nov. 1973); CPM-7311E0508

Crystallization of amorphous films of silicon nitride by ionic bombardment followed by annealing —P. V. Pavlov, É. V. Shitova, E. I. Zorin, and N. A. Genkina. 18(3), 381–3 (Nov. 1973); CPM-7311E0513

Epitaxial growth of AgCl on the thermoelectric polyvinylchloride films, copying the electrical properties of an NaCl surface —G. I. Distler and E. I. Tokmakova. 18(3), 384–5 (Nov. 1973); CPM-7311E0516

Change in the structure of germanium and silicon during ion bombardment and subsequent annealing —P. V. Pavlov. 18(4), 506–9 (Jan. 1974); CPM-7401D0582

Effect of accelerating voltage on the intensity of the forbidden reflection 222 Ge in electron diffraction —A. S. Avilov, R. M. Imamov, Z. G. Pinsker, and A. F. Fedotov. 18(4), 528–9 (Jan. 1974); CPM-7401D0604

Alloying of epitaxial silicon layers with phosphorus and arsenic in a vacuum —V. A. Tolomasov, L. N. Abrosimova, T. N. Sergivskaya, and T. M. Zotova. 18(4), 558–9 (Jan. 1974); CPM-7401D0634

Electron-microscope investigation of thin film condensation kinetics —Yu. F. Komnik and V. V. Pilipenko. 18(5), 667–70 (Mar. 1974); CPM-7403D0495

Structure of amorphous indium monochalcongenide films —Yu. G. Poltavtsev, V. P. Zakharov, and T. V. Remizovich. 18(5), 701–2 (Mar. 1974); CPM-7403D0529

Structure of low-temperature "amorphous" bismuth films —Yu. F. Komnik, L. A. Yatsuk, A. A. Motornaya, M. L. Bolotina, and B. I. Belevtsev. 18(6), 791–6 (May 1974); CPM-7406X1235

Structure of thin lead telluride films —E. V. Rakova and S. A. Semiletov. 18(6), 797–9 (May 1974); CPM-7406X1241

61. ELECTRON STATES

61.50.- Level splitting and interactions

61.50.C Crystal and ligand fields

Calculation of the energy matrices for d^n configurations in intracrystalline fields with T(n=2,3,7,8) symmetry —E. F. Kustov. 18(1), 15–8 (Jul. 1973); CPM-7309D0265

Absorption spectra of $MgWO_4$ crystals activated with Cr^{3+} and Co^{2+} ions —O. N. Boksha and T. M. Varina. 18(3), 354–7 (Nov. 1973); CPM-7311E0486

61.50.E Spin-orbit coupling, Zeeman, Stark, and strain splitting

Stable configurations of a bioctahedral complex with Jahn-Teller centers —I. B. Bersuker, B. G. Vekhter, and M. L. Rafalovich. 18 (1), 5–9 (Jul. 1973); CPM-7309D0255

61.50.J Nuclear states and interactions

Proposed method for determining the coordinates of resonant nuclei using polarized Mössbauer spectroscopy —M. A. Andreeva and R. N. Kuz'min. 18(2), 254–5 (Sep. 1973); CPM-7309D1456

Magnetically nonequivalent cation positions in substituted ferrite garnets —I. S. Lyubutin, A. P. Dodokin, and L. M. Belyaev. 18(5), 623–6 (Mar. 1974); CPM-7403D0451

62. ELECTRONIC TRANSPORT IN CONDENSED MATTER

Some features of the action of penetrating radiation on the electrical properties of a quartz crystal —A. A. Fotchenkov and S. V. Kolodieva. 18(3), 366–9 (Nov. 1973); CPM-7311E0498

Electronic mechanism of the influence of radiation on the process of repolarization of ferroelectrics —A. A. Grekov, M. A. Malitskaya, and V. M. Fridkin. 18(4), 494–8 (Jan. 1974); CPM-7401D0570

63. ELECTRONIC STRUCTURE AND ELECTRICAL PROPERTIES OF SURFACES, INTERFACES, AND THIN FILMS

63.20.- Electronic surface states

Evaluation of the heat effect during alkali halide monomer reorientation in an absorbed layer on a metal —Yu. N. Lyubitov and V. I. Mikhailov. 18(2), 266–7 (Sep. 1973); CPM-7309D1468

Surface layer of barium titanate crystals —V. P. Dudkevich, I. N. Zakharchenko, V. S. Bondarenko, R. V. Kolesova, A. G. Stoinov, and E. G. Fesenko. 18(5), 690–1 (Mar. 1974); CPM-7403D0518

63.90.+ Other topics in electrical properties of surfaces, interfaces, and thin films

Epitaxial growth of AgCl on the thermoelectric polyvinylchloride films, copying the electrical properties of an NaCl surface —G. I. Distler and E. I. Tokmakova. 18(3), 384–5 (Nov. 1973); CPM-7311E0516

Effect of the crystallization mechanism on boron diffusion in silicon-germanium solid-solution epitaxial films —K. L. Lyutovich, F. A. Gimel'farb, P. B. Orlov, and T. A. Ukhorskaya. 18(6), 825–6 (May 1974); CPM-7406X1269

65. MAGNETIC PROPERTIES AND MATERIALS

65.30.- Magnetically ordered materials, intrinsic properties

Antiferromagnets with electric polarization —O. V. Kovalev. 18(2), 137–40 (Sep. 1973); CPM-7309D1339

Preparation of mixed single crystals of (Cr, Te) —É. A. Zavadskii and B. Ya. Sinel'nikov. 18(3), 419 (Nov. 1973); CPM-7311E0551

Magnetically nonequivalent cation positions in substituted ferrite garnets —I. S. Lyubutin, A. P. Dodokin, and L. M. Belyaev. 18(5), 623–6 (Mar. 1974); CPM-7403D0451

65.90.+ Other topics in magnetic properties and materials

Block conical ferromagnetic spiral in the hexagonal ferrite $BaGa_2Sc_{1.2}Fe_{8.8}O_{19}$ (M) —O. P. Aleshko-Ozhevskii, V. P. Cheparin, A. P. Cherkasov, and I. I. Yamzin. 18(3), 393–4 (Nov. 1973); CPM-7311E0525

Anisotropy of certain physical properties of pyrargyrite and proustite crystals —N. I. Butsko, M. M. Pidorya, and T. D. Krushel'nitskaya. 18(4), 540–1 (Jan. 1974); CPM-7401D0616

66. MAGNETIC RESONANCE AND RELAXATION IN CONDENSED MATTER; MOSSBAUER EFFECT

66.80.+ Mossbauer effect; other γ-ray spectroscopy

Gamma-resonance investigations of ferruginous tourmalines —V. F. Belov, T. A. Khimich, M. N. Shipko, I. E. Voskresenskaya, and E. N. Okulov. 18(1), 119–20 (Jul. 1973); CPM-7309D0369

Proposed method for determining the coordinates of resonant nuclei using polarized Mössbauer spectroscopy —M. A. Andreeva and R. N. Kuz'min. 18(2), 254–5 (Sep. 1973); CPM-7309D1456

Magnetically nonequivalent cation positions in substituted ferrite garnets —I. S. Lyubutin, A. P. Dodokin, and L. M. Belyaev. 18(5), 623–6 (Mar. 1974); CPM-7403D0451

66.90.+ Other topics in magnetic resonance and relaxation

Effect of manganese on the transformation of the zinc sulfide cubic lattice to hexagonal —G. E. Arkhangel'skii, T. I. Voznesenskaya, and M. V. Fok. 18(3), 342–3 (Nov. 1973); CPM-7311E0474
Proton magnetic resonance investigation of the localization of the protons in the crystal structures $Na_2Cr_2O_7$-$2H_2O$ and $Li_2Cr_2O_7$-$2H_2O$ —G. R. Bulka, V. M. Vinokurov, É. A. Kuz'min, Yu. A. Kharitonov, and N. V. Belov. 18(5), 617–9 (Mar. 1974); CPM-7403D0445

67. DIELECTRIC PROPERTIES AND MATERIALS

67.20.+ Permittivity

Dispersion of the dielectric constant in crystals of KH_2PO_4 —L. P. Pereverzeva, Yu. M. Poplavko, V. M. Petrov, E. V. Makarevskaya, and I. S. Rez. 18(3), 407–8 (Nov. 1973); CPM-7311E0539
Dispersion of the electric permittivity of triglycine suflate in the vicinity of the phase transition —L. P. Pereverzeva and Yu. M. Poplavko. 18(4), 492–3 (Jan. 1974); CPM-7401D0568
Thermooptical and dielectric properties of $(NH_4)_2$ BeF_4 in the neighborhood of the ferroelectric transition —A. T. Anistratov and S. V. Mel'nikova. 18(6), 811–2 (May 1974); CPM-7406X1255

67.30.+ Polarization: depolarization effects

Some features of the polarization of KH_2PO_4 in the phase transition region —E. V. Sidnenko and V. V. Gladkii. 18(1), 83–5 (Jul. 1973); CPM-7309D0333
Antiferromagnets with electric polarization —O. V. Kovalev. 18(2), 137–40 (Sep. 1973); CPM-7309D1339
Electret effect in n-azoxyanisole —A. P. Kapustin, Z. Kh. Kuvatov, and A. N. Trofimov. 18(2), 263 (Sep. 1973); CPM-7309D1465
Electronic mechanism of the influence of radiation on the process of repolarization of ferroelectrics —A. A. Grekov, M. A. Malitskaya, and V. M. Fridkin. 18(4), 494–8 (Jan. 1974); CPM-7401D0570

67.40.+ Dielectric loss and relaxation

The $PbZrO_3$-$SrCu_{1/3}Nb_{2/3}$ system —D. F. Dzhmukhadze, M. A. Ugryumova, Yu. N. Venevtsev, and G. S. Zhdanov. 18(1), 116–8 (Jul. 1973); CPM-7309D0366
Relaxation of phase boundaries in SbSI single crystals —M. D. Volnyanskii, A. Yu. Kudzin, and A. N. Sukhinskii. 18(2), 202–3 (Sep. 1973); CPM-7309D1404
Some features of the action of penetrating radiation on the electrical properties of a quartz crystal —A. A. Fotchenkov and S. V. Kolodieva. 18(3), 366–9 (Nov. 1973); CPM-7311E0498

67.70.+ Pyroelectric and electrocaloric effects

Dynamic pyroelectric effect —S. D. Pel'ts and A. E. Karpel'son. 18 (3), 360–2 (Nov. 1973); CPM-7311E0492
Heat effects in lithium metaniobate —I. A. Kleinman, T. A. Lyubimova, A. Z. Rabinovich, and M. B. Roitberg. 18(4), 546–7 (Jan. 1974); CPM-7401D0622
SbSI thin films with a ferroelectric phase transition —A. A. Agasiev, A. Kh. Zeinally, and V. G. Sil'vestrov. 18(6), 814 (May 1974); CPM-7406X1258

67.80.- Ferroelectricity and antiferroelectricity

67.80.B Transitions and Curie point

Effect of an electric field on phase transitions in $Na(D_xH_{1-x})_3(SeO_3)_2$ crystals. I. Induction of the β phase in crystals having $x \gtrsim 0.3$ by the field E_y—L. A. Shuvalov, A. M. Shirokov, N. R. Ivanov, and A. I. Baranov. 18(1), 80–2 (Jul. 1973); CPM-7309D0330
Study of the structure and dielectric properties of solid solutions in the system $BaTiO_3$-$Pb(Fe_{1/2}Nb_{1/2})O_3$ —O. S. Didkovskaya, I. P. Kovalevskaya, V. G. Seryi, V. V. Klimov, and Yu. N. Venevtsev. 18(2), 184–6 (Sep. 1973); CPM-7309D1386
Synthesis and ferroelectric properties of antimony orthoniobate —V. I. Popolitov, A. N. Lobachev, V. F. Peskin, L. N. Syrkin, and N. N. Feoktistova. 18(2), 258–9 (Sep. 1973); CPM-7309D1460
Solid solutions of $BaTiO_3$ with barium niobates —I. N. Groznov and Yu. N. Venevtsev. 18(3), 395–6 (Nov. 1973); CPM-7311E0527
Effect of a magnetic field on the Curie point of the ferroelectric semiconductor SbSI —S. V. Ivanova and V. A. Lyakhovitskaya. 18 (3), 404 (Nov. 1973); CPM-7311E0536
Phase transformations in $NaH_3(SeO_3)_2$ crystals irradiated with a large dose of gamma radiation —E. V. Peshikov and L. A. Shuvalov. 18 (4), 499–501 (Jan. 1974); CPM-7401D0575
Growth and study of crystals of double oxides of cadmium with structures of the perovskite type. I. Cadmium hafnate —R. I. Spinko, V. N. Lebedev, R. V. Kolesova, and E. G. Fesenko. 18(4), 536–7 (Jan. 1974); CPM-7401D0612
Heat capacity of single-crystal $BaTiO_3$ near the electrical critical point —B. A. Strukov and A. K. Ivanov-Shits. 18(4), 548 (Jan. 1974); CPM-7401D0624
Studies on ferroelectric crystals with a three-crystal x-ray spectrometer —I. Ya. Nikiforov, Yu. F. Mal'tsev, and V. Z. Borodin. 18(5), 638–40 (Mar. 1974); CPM-7403D0466
KIO_3: the first ferroelectric permitting just a 120° shift in the ferroelectric polarization —L. A. Shuvalov, N. R. Ivanov, O. A. Chikhladze, and A. N. Izrailenko. 18(6), 758–61 (May 1974); CPM-7406X1202
SbSI thin films with a ferroelectric phase transition —A. A. Agasiev, A. Kh. Zeinally, and V. G. Sil'vestrov. 18(6), 814 (May 1974); CPM-7406X1258

67.80.D Domain structure and effects; hysteresis

Some characteristics of the vibronic impurity spectra in ferroelectrics —N. N. Kristofeĺ. 18(1), 10–4 (Jul. 1973); CPM-7309D0260
Some features of the polarization of KH_2PO_4 in the phase transition region —E. V. Sidnenko and V. V. Gladkii. 18(1), 83–5 (Jul. 1973); CPM-7309D0333
X-ray diffraction and dielectric studies of the system $Li(Ta_xSb_{1-x})O_3$ —V. I. Nesterenko and I. G. Ismailzade. 18(1), 112–3 (Jul. 1973); CPM-7309D0362
X-ray diffraction and dielectric studies of the $LiNbO_3$-$KNbO_3$ system —I. G. Ismailzade, V. I. Nesterenko, and É. A. Il'yasov. 18(1), 114–5 (Jul. 1973); CPM-7309D0364
Morphology of the domain structure of SbSI crystals —L. A. Zadorzhnaya, V. A. Lyakhovitskaya, and L. M. Belyaev. 18(3), 363–5 (Nov. 1973); CPM-7311E0495
Surface tension of 180° domain boundaries and effects in triglycine sulfate and c-domain $BaTiO_3$ —É. S. Popov and L. A. Shuvalov.. 18(3), 405–6 (Nov. 1973); CPM-7311E0537
Electronic mechanism of the influence of radiation on the process of repolarization of ferroelectrics —A. A. Grekov, M. A. Malitskaya, and V. M. Fridkin. 18(4), 494–8 (Jan. 1974); CPM-7401D0570
Secondary effects accompanying movement of 180-decree α domains in $BaTiO_3$ —E. F. Dudnik and V. M. Duda. 18(4), 542–3 (Jan. 1974); CPM-7401D0618
Heat effects in lithium metaniobate —I. A. Kleinman, T. A. Lyubimova, A. Z. Rabinovich, and M. B. Roitberg. 18(4), 546–7 (Jan. 1974); CPM-7401D0622
Some features of the domain structure in lead titanate crystals —E. G. Fesenko, V. G. Gavrilyachenko, M. A. Martynenko, A. F. Semenchev, and I. P. Lapin. 18(5), 635–7 (Mar. 1974); CPM-7403D0463
Phase transition, dielectric anomaly, and domain structure in hydrosodalite —N. R. Ivanov and V. Yu. Galitskii. 18(6), 762–3 (May 1974); CPM-7406X1206
Domain boundaries, antiphase boundaries, and dislocations in gadolinium molybdate single crystals —V. A. Meleshina, V. L. Indenbom, Kh. S. Bagdasarov, and T. M. Polkhovskaya. 18(6), 764–8 (May 1974); CPM-7406X1208
Relaxational internal friction in crystals of KH_2PO_4 without chromium added —S. A. Gridnev, L. N. Kamysheva, and N. F. Romanova. 18(6), 773–6 (May 1974); CPM-7406X1217

67.90.+ Other topics in dielectric properties and materials

Thermodielectric effect at the phase transition between a liquid and solid crystal —A. P. Kapustin, Z. Kh. Kuvatov, and A. N. Trofimov. 18(3), 409 (Nov. 1973); CPM-7311E0541

68. OPTICAL PROPERTIES AND CONDENSED-MATTER SPECTROSCOPY

68.20.- Optical properties and materials

Interpretation of the dispersion of the rotatory power in the $LiIO_3$ crystal —Z. B. Perekalina, N. L. Smirnova, G. F. Dobrzhanskii, and I. A. Shpil'ko. **18**(4), 538–9 (Jan. 1974); CPM-7401D0614

68.20.D Optical constants and parameters

Optical activity in $Ba(NO_2)_2{\cdot}H_2O$ crystals —V. I. Burkov, V. A. Kizel', Z. B. Perekalina, N. L. Kozlova, and G. S. Semin. **18**(2), 196–7 (Sep. 1973); CPM-7309D1398

Dispersion of the optical activity in $(SrCa)S_2O_6{\cdot}4H_2O$ mixed crystals —A. Yu. Klimova, Z. B. Perekalina, and L. M. Belyaev. **18**(2), 198–9 (Sep. 1973); CPM-7309D1400

Growth of $KIO_3{\cdot}HIO_3$ crystals and investigation of some of their physical properties —N. R. Ivanov, A. N. Izrailenko, L. N. Rashkovich, and O. A. Chikhladze. **18**(3), 397–8 (Nov. 1973); CPM-7311E0529

Pretransition phenomena and optical activity of amorphous liquid phases of cholesteric liquid crystals —E. I. Ryumetsev, A. N. Cherkasov, V. G. Tishchenko, and M. M. Fetisova. **18**(5), 657–9 (Mar. 1974); CPM-7403D0485

Crystal optics of alkaline-earth metavanadates —M. P. Glazyrin, A. A. Ivakin, and V. A. Gurevich. **18**(5), 685–6 (Mar. 1974); CPM-7403D0513

Anisotropy of the molar refraction of liquid-crystal alkoxybenzoic acids —E. I. Ryumtsev, A. P. Kovshik, I. P. Kolomiets, and V. N. Tsvetkov. **18**(6), 780–2 (May 1974); CPM-7406X1224

68.20.F Birefringence (including stress birefringence, flow birefringence, etc.)

Thermooptical and dielectric properties of $(NH_4)_2$ BeF_4 in the neighborhood of the ferroelectric transition —A. T. Anistratov and S. V. Mel'nikova. **18**(6), 811–2 (May 1974); CPM-7406X1255

Optical activity in monoclinic sodium zincogermanate Na_2ZnGeO_4 —S. P. Kozyrev, A. B. Gil'varg, B. N. Grechushnikov, and N. V. Belov. **18**(6), 813 (May 1974); CPM-7406X1257

68.20.H Piezo-, elasto-, and acousto-optical effects

Characteristics of residual-stress relaxation in $LiNbO_3$ single crystals in the 20-200°C region —K. G. Belabaev, V. T. Gabrielyan, and V. Kh. Sarkisov. **18**(1), 123–4 (Jul. 1973); CPM-7309D0373

Scattering of light at elastic waves in optically biaxial crystals —Yu. V. Pisarevskii and I. M. Sil'vestrova. **18**(5), 630–4 (Mar. 1974); CPM-7403D0458

Temperature dependence of the elastooptical constants p_{11} and p_{12} of NaCl, KCl, Kbr, and Kl crystals —A. V. Pakhnev, S. S. Gorbach, and M. P. Shaskol'skaya. **18**(5), 687 (Mar. 1974); CPM-7403D0515

Influence of impurities on the photoelastic constants of potassium chloride crystals —M. P. Shaskol'skaya, A. V. Pakhnev, S. S. Gorbach, and N. M. Malikova. **18**(6), 817 (May 1974); CPM-7406X1261

68.20.J Electro-optical effects

Dynamic scattering with a memory effect in liquid-crystal mixtures —G. S. Chilaya, V. T. Lazareva, and L. M. Blinov. **18**(1), 127–8 (Jul. 1973); CPM-7309D0377

Proposed interference method for determining the signs of the electrooptical coefficients —V. I. Sokolov, D. B. Kushev, and V. K. Subashiev. **18**(2), 200–1 (Sep. 1973); CPM-7309D1402

Electrooptical properties of potassium dihydrogen phosphate crystals having different degrees of deuteration —E. N. Volkova and I. A. Velichko. **18**(2), 256–7 (Sep. 1973); CPM-7309D1458

Dynamic scattering of light in liquid crystals of the azocompound class —M. F. Grebenkin, G. S. Chilaya, V. T. Lazareva, K. V. Roitman, L. M. Blinov, and V. V. Titov. **18**(2), 274–5 (Sep. 1973); CPM-7309D1476

Calculation of the electrooptical constants in "ionic" crystals —L. B. Meisner and I. S. Rez. **18**(3), 288–90 (Nov. 1973); CPM-7311E0420

Nonlinear optical properties of paratellurite (TeO_2) crystals —Yu. V. Shaldin, S. P. Smirnov, L. M. Belyaev, and I. A. Shpil'ko. **18**(3), 358–9 (Nov. 1973); CPM-7311E0490

Growth of $KIO_3{\cdot}HIO_3$ crystals and investigation of some of their physical properties —N. R. Ivanov, A. N. Izrailenko, L. N. Rashkovich, and O. A. Chikhladze. **18**(3), 397–8 (Nov. 1973); CPM-7311E0529

68.20.L Magneto-optical effects and properties

Jones and Müller matrices of a phase-shifting slab with a rotating axis of the highest velocity —V. D. Tron'ko and G. P. Golovach. **18** (3), 291–4 (Nov. 1973); CPM-7311E0423

68.30.- Infrared and Raman spectra and scattering

68.30.G Infrared and Raman spectra in inorganic crystals

Double cesium-rare earth molybdates of the composition $Cs_3Ln(MoO_4)_3$ (Ln=La, Pr, Nd) —P. V. Klevtsov, V. A. Vinokurov, and R. F. Klevtsova. **18**(1), 73–5 (Jul. 1973); CPM-7309D0323

Vibrational spectrum and crystal structure of $TlNO_3$III —D. E. Pogarev and A. A. Shultin. **18**(2), 193–5 (Sep. 1973); CPM-7309D1395

Far infrared reflectance spectra of rubidium trihydro- and trideuterioselenite crystals —J. Petzelt, L. D. Kislovskii, and L. A. Shuvalov. **18**(3), 351–3 (Nov. 1973); CPM-7311E0483

Infrared spectra of manganese garnets containing a germanate tetrahedron —R. Hrichova. **18**(4), 534–5 (Jan. 1974); CPM-7401D0610

Molecular scattering of light in a single crystal of hafnium dioxide —V. I. Aleksandrov, V. F. Kitaeva, I. V. Kozlov, V. V. Osiko, N. N. Sobolev, V. M. Tatarintsev, and I. L. Chistyi. **18**(5), 682–4 (Mar. 1974); CPM-7403D0510

Nature of the impurity water in synthetic quartz crystals —L. I. Tsinober and V. E. Khadzhi. **18**(5), 699–700 (Mar. 1974); CPM-7403D0527

68.30.J Infrared and Raman spectra in organic crystals

Spectroscopy of organic materials in the low-temperature, crystalline phases —G. N. Zhizhin. **18**(4), 483–8 (Jan. 1974); CPM-7401D0559

68.45.+ Stimulated emission

Stimulated emission from $(Er,Lu)AlO_3$ crystals containing Ho^{3+} and Tm^{3+} ions —Kh. S. Bagdasarov, A. A. Kaminskii, A. M. Kevorkov, S. É. Sarkisov, and T. A. Tevosyan. **18**(5), 681 (Mar. 1974); CPM-7403D0509

68.50.- Impurity and defect absorption in solids

Some characteristics of the vibronic impurity spectra in ferroelectrics —N. N. Kristofel. **18**(1), 10–4 (Jul. 1973); CPM-7309D0260

Absorption spectra of $MgWO_4$ crystals activated with Cr^{3+} and Co^{2+} ions —O. N. Boksha and T. M. Varina. **18**(3), 354–7 (Nov. 1973); CPM-7311E0486

68.60.- Luminescence spectra and radiative recombination

Absorption spectra of $MgWO_4$ crystals activated with Cr^{3+} and Co^{2+} ions —O. N. Boksha and T. M. Varina. **18**(3), 354–7 (Nov. 1973); CPM-7311E0486

Luminescence of cuprous oxide single crystals —I. P. Kuz'mina, A. N. Lobachev, B. S. Predtechenskii, L. S. Starostina, V. B. Stopachinskii, and N. M. Khaidukov. **18**(3), 400–1 (Nov. 1973); CPM-7311E0532

Use of the luminescence polarization diagram method to investigate molecular crystals containing two impurities —G. S. Belikova, N. D. Zhevandrov, T. V. Il'inykh, L. E. Kraeva, and N. P. Sul'zhenko. **18**(4), 489–91 (Jan. 1974); CPM-7401D0565

68.70.- Other spectra and interactions between radiation and matter

Reconstruction of the phase of the electronic scattering amplitude from experiments on the diffraction of resonant γ quanta —I. P. Perstnev and F. N. Chukhovskii. 18(5), 582–5 (Mar. 1974); CPM-7403D0410

"Spectral instability" of multiwave diffraction with coplanar x rays —A. D. Fofanov, A. V. Kuznetsov, and G. A. Karacheva. 18(6), 711–4 (May 1974); CPM-7406X1155

Polarization and integrated intensity of x rays scattered by silicon crystals —N. M. Olekhnovich. 18(6), 777–9 (May 1974); CPM-7406X1221

69. ELECTRON AND ION EMISSION BY LIQUIDS AND SOLIDS; IMPACT PHENOMENA

Focused laser-beam damage mechanism for CsI crystals —L. M. Belyaev, V. V. Nabatov, V. N. Rozhanskii, N. L. Sizova, and A. A. Urosovskaya. 18(2), 207–8 (Sep. 1973); CPM-7309D1409

Interpretation of field-ion images. I. point defects —L. P. Potapov, T. L. Raznikova, and A. L. Suvorov. 18(2), 220–3 (Sep. 1973); CPM-7309D1422

Investigation of the pure and cesium-coated (100) surface of germanium by slow-electron diffraction —A. Yu. Mityagin and V. P. Orlov. 18(4), 554–5 (Jan. 1974); CPM-7401D0630

71. OPTICS

71.15.+ Propagation and transmission in homogeneous and anisotropic media

Relation between the radial and normal refraction vectors in anisotropic and gyrotropic media —L. M. Barkovskii. 18(3), 295–7 (Nov. 1973); CPM-7311E0427

Propagation of light in active absorbing crystals —A. F. Konstantinova and B. N. Grechushnikov. 18(3), 298–9 (Nov. 1973); CPM-7311E0430

Optimum spectral range for investigating double refraction by the modulation method —V. S. Chudakov. 18(3), 402–3 (Nov. 1973); CPM-7311E0534

71.20.- Propagation and transmission in inhomogeneous media

Boundary conditions in the electrodynamics of optically active media —B. V. Bokut', A. N. Serdyukov, F. I. Fedorov, and N. A. Khilo. 18(2), 141–4 (Sep. 1973); CPM-7309D1343

71.60.- Lasers

Laser based on Cr^{3+} ions in yttrium-aluminum garnet —B. K. Sevast'yanov, Kh. S. Bagdasarov, L. B. Pasternak, S. Yu. Volkov, and V. P. Orekhova. 18(2), 191–2 (Sep. 1973); CPM-7309D1393

Laser detection of acentrism in crystals —V. D. Shigorin and G. P. Shipulo. 18(3), 349–50 (Nov. 1973); CPM-7311E0481

71.65.- Nonlinear optics

Calculation of the electrooptical constants in "ionic" crystals —L. B. Meisner and I. S. Rez. 18(3), 288–90 (Nov. 1973); CPM-7311E0420

Jones and Müller matrices of a phase-shifting slab with a rotating axis of the highest velocity —V. D. Tron'ko and G. P. Golovach. 18 (3), 291–4 (Nov. 1973); CPM-7311E0423

Nonlinear optical properties of paratellurite (TeO$_2$) crystals —Yu. V. Shaldin, S. P. Smirnov, L. M. Belyaev, and I. A. Shpil'ko. 18(3), 358–9 (Nov. 1973); CPM-7311E0490

71.65.F Harmonic generation

Laser detection of acentrism in crystals —V. D. Shigorin and G. P. Shipulo. 18(3), 349–50 (Nov. 1973); CPM-7311E0481

Use of the methods of nonlinear optics in order to make a more accurate analysis of the structural characteristics of crystals associated with the absence of an inversion center —L. G. Koreneva, V. F. Zolin, B. L. Davydov, and V. I. Tsaryuk. 18(3), 399 (Nov. 1973); CPM-7311E0531

74. PHYSICAL CHEMISTRY

74.30.- Chemical reactions

Double cesium-rare earth molybdates of the composition Cs$_3$Ln(MoO$_4$)$_3$ (Ln=La, Pr, Nd) —P. V. Klevtsov, V. A. Vinokurov, and R. F. Klevtsova. 18(1), 73–5 (Jul. 1973); CPM-7309D0323

74.60.- Chemical thermodynamics

Dislocation mechanism of growth with a low kink density —V. V. Voronkov. 18(1), 19–23 (Jul. 1973); CPM-7309D0269

Kinetics of motion of steps and rows of steps at smeared phase boundaries —D. E. Temkin. 18(2), 145–50 (Sep. 1973); CPM-7309D1347

Motion of a germanium-gold alloy droplet along a germanium surface under the action of a temperature gradient —S. A. Grinberg and E. I. Givargizov. 18(2), 236–8 (Sep. 1973); CPM-7309D1438

Distribution coefficients of divalent impurities in alkali halide crystals —O. L. Kreinin and K. M. Rozin. 18(2), 276–7 (Sep. 1973); CPM-7309D1478

Determination of the energy and thermodynamic characteristics of iron-aluminum alloys by the method of diffuse x-ray scattering —S. V. Semenovskaya, Zh. B. Sinyavskaya, and A. P. Senichkin. 18 (3), 344–8 (Nov. 1973); CPM-7311E0476

Crystallization of amorphous films of silicon nitride by ionic bombardment followed by annealing —P. V. Pavlov, É. V. Shitova, E. I. Zorin, and N. A. Genkina. 18(3), 381–3 (Nov. 1973); CPM-7311E0513

Anisotropy of the growth rate of centers of the α modification in single crystals of high purity tin —V. B. Brik, L. N. Larikov, and V. M. Fal'chenko. 18(3), 412–3 (Nov. 1973); CPM-7311E0544

Electron-microscope investigation of thin film condensation kinetics —Yu. F. Komnik and V. V. Pilipenko. 18(5), 667–70 (Mar. 1974); CPM-7403D0495

74.65.- Surface processes

Wetting of faces of a single crystal in a melt —Yu. V. Naidich, V. M. Perevertailo, É. M. Lebovich, and L. P. Obushchak. 18(2), 234–5 (Sep. 1973); CPM-7309D1436

Evaluation of the heat effect during alkali halide monomer reorientation in an absorbed layer on a metal —Yu. N. Lyubitov and V. I. Mikhailov. 18(2), 266–7 (Sep. 1973); CPM-7309D1468

75. MATERIALS SCIENCE AND METALLURGY

75.20.- Methods of crystal growth and purification, including film deposition techniques

75.20.F Growth from melts and solutions

Double cesium-rare earth molybdates of the composition Cs$_3$Ln(MoO$_4$)$_3$ (Ln=La, Pr, Nd) —P. V. Klevtsov, V. A. Vinokurov, and R. F. Klevtsova. 18(1), 73–5 (Jul. 1973); CPM-7309D0323

Kinetics and structural aspect of the growth of single crystals of bismuthinite under hydrothermal conditions —V. I. Popolitov and A. N. Lobachev. 18(1), 131–2 (Jul. 1973); CPM-7309D0381

Hydrothermal crystallization in the system CdO-GeO$_2$-LiCl-H$_2$O —L. N. Dem'yanets and N. V. Suvorova. 18(1), 133–4 (Jul. 1973); CPM-7309D0383

Nature of the point defects in GaAs single crystals as a function of the composition of the melt during growth —V. T. Bublik, V. V. Karataev, R. S. Kulagin, M. G. Mil'vidskii, V. B. Osvenskii, O. G. Stolyarov, and L. P. Kholodnyi. 18(2), 218–9 (Sep. 1973); CPM-7309D1420

Reaction of foreign particles with a crystallization front —A. M. Zubko, V. G. Lobanov, and V. V. Nikonova. 18(2), 239–41 (Sep. 1973); CPM-7309D1441

Low-dislocation-density single crystals of corundum —Kh. S. Bagdasarov, E. R. Dobrovinskaya, V. V. Pishchik, M. M. Chernik, Yu. Yu. Kovalev, A. S. Gershun, and I. F. Zvyagintseva. 18(2), 242–5 (Sep. 1973); CPM-7309D1444

Synthesis and ferroelectric properties of antimony orthoniobate —V. I. Popolitov, A. N. Lobachev, V. F. Peskin, L. N. Syrkin, and N. N. Feoktistova. 18(2), 258–9 (Sep. 1973); CPM-7309D1460

Dislocation networks formed during growth and annealing in the basal plane of a single crystal of zinc —N. A. Tyapunina, T. N. Pashchenko, and G. M. Zinenkova. 18(2), 264–5 (Sep. 1973); CPM-7309D1466

Growth of $KIO_3 \cdot HIO_3$ crystals and investigation of some of their physical properties —N. R. Ivanov, A. N. Izrailenko, L. N. Rashkovich, and O. A. Chikhladze. 18(3), 397–8 (Nov. 1973); CPM-7311E0529

Growth dislocation distribution along a copper crystal and dislocation density as a function of mean diameter —A. G. Basariya, B. K. Kapanadze, and V. V. Sanadze. 18(3), 411 (Nov. 1973); CPM-7311E0543

Anisotropy of the growth rate of centers of the α modification in single crystals of high purity tin —V. B. Brik, L. N. Larikov, and V. M. Fal'chenko. 18(3), 412–3 (Nov. 1973); CPM-7311E0544

Preparation of mixed single crystals of (Cr, Te) —É. A. Zavadskii and B. Ya. Sinel'nikov. 18(3), 419 (Nov. 1973); CPM-7311E0551

Transformation of layer-spiral growth into normal growth on a basal face. I. Breakdown of the elementary layers on the apices of the spiral hillocks —E. D. Dukova. 18(4), 514–8 (Jan. 1974); CPM-7401D0590

Effective distribution constants of excess basic components during crystallization of gallium arsenide from a melt —V. V. Karataev, M. G. Mil'vidskii, V. B. Osvenskii, and O. G. Stolyarov. 18(4), 521–2 (Jan. 1974); CPM-7401D0597

Hydrothermal synthesis of a new crystalline modification of lithium lanthanum molybdate, α-$LiLa(MoO_4)_2$ —P. V. Klevtsov, V. I. Protasova, L. Yu. Kharchenko, and R. F. Klevtsova. 18(4), 523–4 (Jan. 1974); CPM-7401D0599

Study of crystallization in the hydrothermal system GeO_2-Sb_2O_3-KF-H_2O —M. N. Tseitlin, G. F. Plakhov, A. N. Lobachev, V. I. Popolitov, M. A. Simonov, and N. V. Belov. 18(4), 525–7 (Jan. 1974); CPM-7401D0601

Growth and study of crystals of double oxides of cadmium with structures of the perovskite type. I. Cadmium hafnate —R. I. Spinko, V. N. Lebedev, R. V. Kolesova, and E. G. Fesenko. 18(4), 536–7 (Jan. 1974); CPM-7401D0612

Influence of temperature gradient on the impurity distribution during growth of crystals form a melt —E. A. Krivandina and E. E. Kostyleva. 18(4), 560–1 (Jan. 1974); CPM-7401D0636

Synthesis of tourmaline in chloride media. I —I. E. Voskresenskaya and A. A. Shternberg. 18(4), 562–3 (Jan. 1974); CPM-7401D0638

Crystallization in the As-S-HI-H_2O system —V. I. Popolitov and A. N. Lobachev. 18(4), 564 (Jan. 1974); CPM-7401D0640

Growth of shaped germanium crystals having low dislocation density by the Bridgman method —L. A. Maslova and S. V. Tsivinskii. 18 (4), 565 (Jan. 1974); CPM-7401D0641

Crystallization apparatus for the growth of crystals at constant supersaturation of the solution —A. I. Munchaev. 18(4), 566 (Jan. 1974); CPM-7401D0642

Binary molybdates and tungstates of alkali metals with bismuth, $M^+Bi(TO_4)_2$ —P. V. Klevtsov, V. A. Vinokurov, and R. F. Klevtsova. 18(6), 749–51 (May 1974); CPM-7406X1193

Determination of the activation energy of forward and reverse reactions during crystal growth —E. B. Treivus. 18(6), 788–90 (May 1974); CPM-7406X1232

Hydrothermal synthesis, x-Ray diffraction, and thermogravimetric study of rare-earth hydroxchlorides $Ln(OH)_2Cl$ —L. N. Dem'yanets, V. I. Bukin, E. N. Emel'yanova, and V. I. Ivanov. 18 (6), 806–8 (May 1974); CPM-7406X1250

Growth and investigation of binary cadmium oxides with structures of the perovskite type. II. Cadmium stannate and zirconate —R. I. Spinko, V. N. Lebedev, R. V. Kolesova, and E. G. Fesenko. 18(6), 809–10 (May 1974); CPM-7406X1253

Forms of antimony crystal growth in alloys of the eutectic type —I. V. Salli, L. V. Samoilenko, and V. Z. Dolinskaya. 18(6), 823–4 (May 1974); CPM-7406X1267

75.20.M Semiconductor profile measurement

Wetting of faces of a single crystal in a melt —Yu. V. Naidich, V. M. Perevertailo, É. M. Lebovich, and L. P. Obushchak. 18(2), 234–5 (Sep. 1973); CPM-7309D1436

Preparation and preliminary investigation of cadmium phosphates —Yu. A. Ivanov, I. N. Ivanovskaya, V. I. Popolitov, M. A. Simonov, and N. V. Belov. 18(5), 671–3 (Mar. 1974); CPM-7403D0499

Simple method for preventing the formation of parasite crystals during the growth of crystals from solution —I. V. Isakov. 18(5), 703 (Mar. 1974); CPM-7403D0531

75.50.+ Amorphous and polymeric materials

Structure of amorphous indium monochalcongenide films —Yu. G. Poltavtsev, V. P. Zakharov, and T. V. Remizovich. 18(5), 701–2 (Mar. 1974); CPM-7403D0529

Structure of low-temperature "amorphous" bismuth films —Yu. F. Komnik, L. A. Yatsuk, A. A. Motornaya, M. L. Bolotina, and B. I. Belevtsev. 18(6), 791–6 (May 1974); CPM-7406X1235

75.55.+ Liquid and plastic crystals

Dynamic scattering with a memory effect in liquid-crystal mixtures —G. S. Chilaya, V. T. Lazareva, and L. M. Blinov. 18(1), 127–8 (Jul. 1973); CPM-7309D0377

Domain rotation in smectic liquid crystals —A. N. Chuvyrov and Z. Kh. Kuvatov. 18(2), 212–4 (Sep. 1973); CPM-7309D1414

Dynamic scattering of light in liquid crystals of the azocompound class —M. F. Grebenkin, G. S. Chilaya, V. T. Lazareva, K. V. Roitman, L. M. Blinov, and V. V. Titov. 18(2), 274–5 (Sep. 1973); CPM-7309D1476

Theory of the electrodynamic effect in liquid crystals —S. A. Pikin and A. A. Shtol'berg. 18(3), 283–7 (Nov. 1973); CPM-7311E0415

Thermodielectric effect at the phase transition between a liquid and solid crystal —A. P. Kapustin, Z. Kh. Kuvatov, and A. N. Trofimov. 18(3), 409 (Nov. 1973); CPM-7311E0541

Phase transition in liquid crystals induced by an electric field —I. G. Chistyakov and L. K. Vistin'. 18(4), 552–3 (Jan. 1974); CPM-7401D0628

Anisotropy of the molar refraction of liquid-crystal alkoxybenzoic acids —E. I. Ryumtsev, A. P. Kovshik, I. P. Kolomiets, and V. N. Tsvetkov. 18(6), 780–2 (May 1974); CPM-7406X1224

75.60.+ Granular materials and powders

Dislocation formed during the sintering of solids ("sintering rosettes") —Ya. E. Geguzin, A. S. Dzyuba, V. L. Indenbom, and N. N. Ovcharenko. 18(4), 502–5 (Jan. 1974); CPM-7401D0578

AUTHOR INDEX TO VOLUME 18

Papers are arranged in ascending page number order.

A

Abdullaev, G. K.—Crystal structure of $La_2Sr_3(BO_3)_4$ —G. K. Abdullaev, Kh. S. Mamedov, and S. T. Amirov. 18(5), 675–6 (Mar. 1974); CPM-7403D0503

Ablov, A. V.—Crystal structure of 1,6-$[Coen_2Cl_2]Cl \cdot 3SC(NH_2)_2$ —Yu. A. Simonov, L. I. Landa, N. N. Proskina, T. I. Malinovskii, and A. V. Ablov. 18(3), 333–5 (Nov. 1973); CPM-7311E0465

Abrosimova, L. N.—Alloying of epitaxial silicon layers with phosphorus and arsenic in a vacuum —V. A. Tolomasov, L. N. Abrosimova, T. N. Sergivskaya, and T. M. Zotova. 18(4), 558–9 (Jan. 1974); CPM-7401D0634

Agaev, K. A.—Electron-diffraction investigation of the structure of thin $InTlS_2$ films —K. A. Agaev, V. A. Gasymov, and M. I. Chiragov. 18(2), 226–7 (Sep. 1973); CPM-7309D1428

Agasiev, A. A.—SbSI thin films with a ferroelectric phase transition —A. A. Agasiev, A. Kh. Zeinally, and V. G. Sil'vestrov. 18(6), 814 (May 1974); CPM-7406X1258

Akatova, K. N.—Crystal structure of the coordination compound bis(pyridinaldehydethiosemicarbazonato)cobalt(III)nitrate —K. N. Akatova, T. N. Tarkhova, and N. V. Belov. 18(2), 162–5 (Sep. 1973); CPM-7309D1364

Akulenok, E. M.—Some structural-morphological characteristics of the volatilization of single crystal of α-Al_2O_3 —E. M. Akulenok, Yu. K. Danileiko, V. V. Panteleev, E. A. Fedorov, and V. Ya. Khaimov-Mal'kov. 18(5), 654–6 (Mar. 1974); CPM-7403D0482

Aleksandrov, V. I.—Molecular scattering of light in a single crystal of hafnium dioxide —V. I. Aleksandrov, V. F. Kitaeva, I. V. Kozlov, V. V. Osiko, N. N. Sobolev, V. M. Tatarintsev, and I. L. Chistyi. 18(5), 682–4 (Mar. 1974); CPM-7403D0510

Aleksandrova, V. A.—Crystal structure of ditrioctahedral chlorite —V. A. Aleksandrova, V. A. Drits, and G. V. Sokolova. 18(1), 50–3 (Jul. 1973); CPM-7309D0300

Aleshko-Ozhevskii, O. P.—Block conical ferromagnetic spiral in the hexagonal ferrite $BaGa_2Sc_{1.2}Fe_{8.8}O_{19}$ (M) —O. P. Aleshko-Ozhevskii, V. P. Cheparin, A. P. Cherkasov, and I. I. Yamzin. 18 (3), 393–4 (Nov. 1973); CPM-7311E0525

Aliev, F. I.—Electron diffraction investigation of In_2S_3 films obtained by vacuum deposition —R. B. Shafizade, É. G. Éfendiev, and F. I. Aliev. 18(3), 417–8 (Nov. 1973); CPM-7311E0549

Amirov, S. T.—Crystal structure of $La_2Sr_3(BO_3)_4$ —G. K. Abdullaev, Kh. S. Mamedov, and S. T. Amirov. 18(5), 675–6 (Mar. 1974); CPM-7403D0503

Ammer, S. A.—Internal friction and strength of germanium whiskers —V. S. Postnikov, S. A. Ammer, and A. I. Drozhzhin. 18(3), 416 (Nov. 1973); CPM-7311E0548

Andreeva, M. A.—Proposed method for determining the coordinates of resonant nuclei using polarized Mössbauer spectroscopy —M. A. Andreeva and R. N. Kuz'min. 18(2), 254–5 (Sep. 1973); CPM-7309D1456

Anistratov, A. T.—Thermooptical and dielectric properties of $(NH_4)_2$ BeF_4 in the neighborhood of the ferroelectric transition —A. T. Anistratov and S. V. Mel'nikova. 18(6), 811–2 (May 1974); CPM-7406X1255

Aristov, V. V.—Precision measurements of crystallographic parameters by the method of a widely divergent x-ray beam —V. V. Aristov, V. Sh. Shekhtman, and I. M. Shmyt'ko. 18(4), 445–6 (Jan. 1974); CPM-7401D0521

Arkhangel'skii, G. E.—Effect of manganese on the transformation of the zinc sulfide cubic lattice to hexagonal —G. E. Arkhangel'skii, T. I. Voznesenskaya, and M. V. Fok. 18(3), 342–3 (Nov. 1973); CPM-7311E0474

Aslanov, L. A.—Crystal structure of lanthanum hypophosphite monohydrate —V. M. Ionov, L. A. Aslanov, V. B. Rybakov, and M. A. Porai-Koshits. 18(2), 250–1 (Sep. 1973); CPM-7309D1452

—Crystal structure of europium hypophosphite monohydrate —V. M. Ionov, L. A. Aslanov, M. A. Porai-Koshits, and V. B. Rybakov. 18 (2), 252–3 (Sep. 1973); CPM-7309D1454

Atabaeva, É. Ya.—Crystal structure of a new modification, Bi_2Se_3II —É. Ya. Atabaeva, S. A. Mashkov, and S. V. Popova. 18(1), 104–5 (Jul. 1973); CPM-7309D0354

Atovmyan, L. O.—Crystal and molecular structures of the 1:2 complex of 1-methyl-3,3-dimethyl-2-(para-n-methyl-n-β-chloroethylstyryl)indole and 7,7,8,8-tetracyanoquinodimethane, $(C_{22}H_{26}N_2Cl)^+(C_{12}H_4N_4)(C_{12}H_4N_4)$ —R. P. Shibaeva, L. P. Rozenberg, and L. O. Atovmyan. 18(3), 326–9 (Nov. 1973); CPM-7311E0458

Avilov, A. S.–Investigation of the intensities of electron diffraction by NH_4Cl, NaCl, and TlCl films by using electrical recording and an electron filter–A. S. Avilov, R. M. Imamov, R. K. Karakhanyan, and Z. G. Pinsker. 18(1), 30–32 (Jul. 1973); CPM-7309D0280

—Effect of accelerating voltage on the intensity of the forbidden reflection 222 Ge in electron diffraction —A. S. Avilov, R. M. Imamov, Z. G. Pinsker, and A. F. Fedotov. 18(4), 528–9 (Jan. 1974); CPM-7401D0604

—Determination of the crystal structure of the hexagonal phase β^{III} in the copper-tellurium system by electron diffraction —R. V. Baranova, A. S. Avilov, and Z. G. Pinsker. 18(6), 736–40 (May 1974); CPM-7406X1180

B

Bagdasarov, Kh. S.—Laser based on Cr^{3+} ions in yttrium-aluminum garnet —B. K. Sevast'yanov, Kh. S. Bagdasarov, L. B. Pasternak, S. Yu. Volkov, and V. P. Orekhova. 18(2), 191–2 (Sep. 1973); CPM-7309D1393

—Low-dislocation-density single crystals of corundum —Kh. S. Bagdasarov, E. R. Dobrovinskaya, V. V. Pishchik, M. M. Chernik, Yu. Yu. Kovalev, A. S. Gershun, and I. F. Zvyagintseva. 18(2), 242–5 (Sep. 1973); CPM-7309D1444

—Stimulated emission from $(Er,Lu)AlO_3$ crystals containing Ho^{3+} and Tm^{3+} ions —Kh. S. Bagdasarov, A. A. Kaminskii, A. M. Kevorkov, S. É. Sarkisov, and T. A. Tevosyan. 18(5), 681 (Mar. 1974); CPM-7403D0509

—Domain boundaries, antiphase boundaries, and dislocations in gadolinium molybdate single crystals —V. A. Meleshina, V. L. Indenbom, Kh. S. Bagdasarov, and T. M. Polkhovskaya. 18(6), 764–8 (May 1974); CPM-7406X1208

Bakakin, V. V.—Crystal structure of lithium bitungstate $Li_2W_2O_7$ —S. A. Magarill, R. F. Klevtsova, and V. V. Bakakin. 18(2), 166–70 (Sep. 1973); CPM-7309D1368

Baranov, A. I.—Effect of an electric field on phase transitions in $Na(D_xH_{1-x})_3(SeO_3)_2$ crystals. I. Induction of the β phase in crystals having x—0.3 by the field E_y —L. A. Shuvalov, A. M. Shirokov, N. R. Ivanov, and A. I. Baranov. 18(1), 80–2 (Jul. 1973); CPM-7309D0330

Baranova, G. K.—Kinetics of the polishing and etching of sodium chloride crystals. III —G. K. Baranova and É. M. Nadgornyi. 18 (5), 644–6 (Mar. 1974); CPM-7403D0472

Baranova, R. V.—Determination of the crystal structure of the hexagonal phase β^{III} in the copper-tellurium system by electron diffraction —R. V. Baranova, A. S. Avilov, and Z. G. Pinsker. 18 (6), 736–40 (May 1974); CPM-7406X1180

Barkovskii, L. M.—Relation between the radial and normal refraction vectors in anisotropic and gyrotropic media —L. M. Barkovskii. 18(3), 295–7 (Nov. 1973); CPM-7311E0427

Basariya, A. G.—Growth dislocation distribution along a copper crystal and dislocation density as a function of mean diameter —A. G. Basariya, B. K. Kapanadze, and V. V. Sanadze. 18(3), 411 (Nov. 1973); CPM-7311E0543

Belabaev, K. G.—Characteristics of residual-stress relaxation in $LiNbO_3$ single crystals in the 20-200°C region —K. G. Belabaev, V. T. Gabrielyan, and V. Kh. Sarkisov. 18(1), 123–4 (Jul. 1973); CPM-7309D0373

Belevtsev, B. I.—Structure of low-temperature "amorphous" bismuth films —Yu. F. Komnik, L. A. Yatsuk, A. A. Motornaya, M. L. Bolotina, and B. I. Belevtsev. 18(6), 791–6 (May 1974); CPM-7406X1235

Belikova, G. S.—Use of the luminescence polarization diagram method to investigate molecular crystals containing two impurities —G. S. Belikova, N. D. Zhevandrov, T. V. Il'inykh, L. E. Kraeva, and N. P. Sul'zhenko. 18(4), 489–91 (Jan. 1974); CPM-7401D0565

Belokoneva, E. L.—A group of synthetic cadmium germanates and their x-ray study —E. L. Belokoneva, M. A. Simonov, N. G. Duderov, A. N. Lobachev, and N. V. Belov. 18(5), 610–2 (Mar. 1974); CPM-7403D0438

—Structures of leucophoenicite, $Mn_7[SiO_4]_2[(SiO_4)(OH)_2]$, and synthetic Cd orthogermanate, $Cd_3[GeO_4](OH)_2$ —E. L. Belokoneva, M. A. Simonov, and N. V. Belov. 18(6), 800–1 (May 1974); CPM-7406X1244

Belov, N. V.—Systematic analysis of Patterson functions on the basis of crystal symmetry. IV. Interpretation of the Patterson synthesis for crystals of lower systems —É. A. Kuz'min, V. P. Golovachev, V. V. Ilyukhin, and N. V. Belov. 18(1), 33–8 (Jul. 1973); CPM-7309D0283

—Isolation of n points of the basic system from a vector system by use of the star of an (n-1) -dimensional simplex —R. V. Galiulin, M. I. Sirota, A. S. Naumov, and N. V. Belov. 18(1), 39–42 (Jul. 1973); CPM-7309D0289

—Chemical crystallography of mixed anion frameworks. I. Zirconium and scandium alkali sorosilicates —A. A. Voronkov, R. G. Sizova, V. V. Ilyukhin, and N. V. Belov. 18(1), 67–72 (Jul. 1973); CPM-7309D0317

—Crystal structure of the coordination compound bis(pyridinaldehydethiosemicarbazonato)cobalt(III)nitrate —K. N. Akatova, T. N. Tarkhova, and N. V. Belov. 18(2), 162–5 (Sep. 1973); CPM-7309D1364

—Teaching career of a great crystallographer —N. V. Belov. 18(2), 280–1 (Sep. 1973); CPM-7309D1482

—Sections of paired Patterson functions —V. N. Biyushkin and N. V. Belov. 18(3), 311–3 (Nov. 1973); CPM-7311E0443

—Types of vector-localizing sections of the duplicated Patterson function —V. N. Biyushkin and N. V. Belov. 18(3), 386–7 (Nov. 1973); CPM-7311E0518

—Systematic analysis of patterson function on the basis of crystal symmetry. V. Regularities in the degeneracy of the rhombuses in vector sytems of crystals belonging to lower crystallographic systems —É. A. Kuz'min, R. I. Bochkova, Yu. N. Saf'yanov, V. P. Golovachev, and N. V. Belov. 18(4), 429–33 (Jan. 1974); CPM-7401D0505

—Study of crystallization in the hydrothermal system GeO_2-Sb_2O_3-KF-H_2O —M. N. Tseitlin, G. F. Plakhov, A. N. Lobachev, V. I. Popolitov, M. A. Simonov, and N. V. Belov. 18(4), 525–7 (Jan. 1974); CPM-7401D0601

—A group of synthetic cadmium germanates and their x-ray study —E. L. Belokoneva, M. A. Simonov, N. G. Duderov, A. N. Lobachev, and N. V. Belov. 18(5), 610–2 (Mar. 1974); CPM-7403D0438

—Proton magnetic resonance investigation of the localization of the protons in the crystal structures $Na_2Cr_2O_7 \cdot 2H_2O$ and $Li_2Cr_2O_7 \cdot 2H_2O$ —G. R. Bulka, V. M. Vinokurov, É. A. Kuz'min, Yu. A. Kharitonov, and N. V. Belov. 18(5), 617–9 (Mar. 1974); CPM-7403D0445

—Preparation and preliminary investigation of cadmium phosphates —Yu. A. Ivanov, I. N. Ivanovskaya, V. I. Popolitov, M. A. Simonov, and N. V. Belov. 18(5), 671–3 (Mar. 1974); CPM-7403D0499

—Key role of analysis of interaction distances in oxygen compounds containing heavy cations (high atomic numbers) —T. M. Polyanskaya, S. V. Borisov, and N. V. Belov. 18(6), 719–27 (May 1974); CPM-7406X1163

—Structures of leucophoenicite, $Mn_7[SiO_4]_2[(SiO_4)(OH)_2]$, and synthetic Cd orthogermanate, $Cd_3[GeO_4](OH)_2$ —E. L. Belokoneva, M. A. Simonov, and N. V. Belov. 18(6), 800–1 (May 1974); CPM-7406X1244

—Optical activity in monoclinic sodium zincogermanate Na_2ZnGeO_4 —S. P. Kozyrev, A. B. Gil'varg, B. N. Grechushnikov, and N. V. Belov. 18(6), 813 (May 1974); CPM-7406X1257

Belov, V. F.—Gamma-resonance investigations of ferruginous tourmalines —V. F. Belov, T. A. Khimich, M. N. Shipko, I. E. Voskresenskaya, and E. N. Okulov. 18(1), 119–20 (Jul. 1973); CPM-7309D0369

Bel'skii, V. K.—Crystal-chemical analysis of the structure of 1-I-substituted anthraquinone —N. L. Klimasenko, V. K. Bel'skii, V. K. Sarynin, and G. A. Gol'der. 18(4), 457–9 (Jan. 1974); CPM-7401D0533

Belyaev, L. M.—Dispersion of the optical activity in $(SrCa)S_2O_6 \cdot 4H_2O$ mixed crystals —A. Yu. Klimova, Z. B. Perekalina, and L. M. Belyaev. 18(2), 198–9 (Sep. 1973); CPM-7309D1400

—Focused laser-beam damage mechanism for CsI crystals —L. M. Belyaev, V. V. Nabatov, V. N. Rozhanskii, N. L. Sizova, and A. A. Urosovskaya. 18(2), 207–8 (Sep. 1973); CPM-7309D1409

—Nonlinear optical properties of paratellurite (TeO_2) crystals —Yu. V. Shaldin, S. P. Smirnov, L. M. Belyaev, and I. A. Shpil'ko. 18 (3), 358–9 (Nov. 1973); CPM-7311E0490

—Morphology of the domain structure of SbSI crystals —L. A. Zadorzhnaya, V. A. Lyakhovitskaya, and L. M. Belyaev. 18(3), 363–5 (Nov. 1973); CPM-7311E0495

—Magnetically nonequivalent cation positions in substituted ferrite garnets —I. S. Lyubutin, A. P. Dodokin, and L. M. Belyaev. 18(5), 623–6 (Mar. 1974); CPM-7403D0451

Berenshtein, B. G.—X-ray diffraction study of the tetrahydrates of the mesoperiodates of the rare earth elements and yttrium —M. B. Varfolomeev, N. B. Shamrai, B. G. Berenshtein, and V. E. Plyushchev. 18(1), 106–7 (Jul. 1973); CPM-7309D0356

Berezin, P. D.—Orientational order and molecular parameters of liquid crystals with a positive dielectric anisotropy —V. G. Rumyantsev, P. D. Berezin, L. M. Blinov, and I. N. Kompanets. 18(5), 697–8 (Mar. 1974); CPM-7403D0525

Bersuker, I. B.—Stable configurations of a bioctahedral complex with Jahn-Teller centers —I. B. Bersuker, B. G. Vekhter, and M. L. Rafalovich. 18(1), 5–9 (Jul. 1973); CPM-7309D0255

Bilonizhko, N. S.—New boride structural types in the homologous series based on the $CaCu_5$ and $CeCo_3B_2$ types —Yu. B. Kuz'ma and N. S. Bilonizhko. 18(4), 447–9 (Jan. 1974); CPM-7401D0523

Bityutskii, P. N.—Structure of nickel hydroxide containing potassium ions —P. N. Bityutskii, V. I. Khitrova, and Z. G. Pinsker. 18(5), 613–6 (Mar. 1974); CPM-7403D0441

Biyushkin, V. N.—Structure-localizing sections of the duplicated Patterson function —V. N. Biyushkin. 18(2), 154–7 (Sep. 1973); CPM-7309D1356

—Sections of paired Patterson functions —V. N. Biyushkin and N. V. Belov. 18(3), 311–3 (Nov. 1973); CPM-7311E0443

—Types of vector-localizing sections of the duplicated Patterson function —V. N. Biyushkin and N. V. Belov. 18(3), 386–7 (Nov. 1973); CPM-7311E0518

—Vector-localizing cross section through a double Patterson function —V. N. Biyushkin. 18(4), 434–6 (Jan. 1974); CPM-7401D0510

Blinov, L. M.—Dynamic scattering with a memory effect in liquid-crystal mixtures —G. S. Chilaya, V. T. Lazareva, and L. M. Blinov. 18(1), 127–8 (Jul. 1973); CPM-7309D0377

—Dynamic scattering of light in liquid crystals of the azocompound class —M. F. Grebenkin, G. S. Chilaya, V. T. Lazareva, K. V. Roitman, L. M. Blinov, and V. V. Titov. 18(2), 274–5 (Sep. 1973); CPM-7309D1476

—Determination of the degree of ordering in liquid crystals from the dichroism of dissolved dyes —V. G. Rumyantsev, L. M. Blinov, and V. A. Kizel'. 18(5), 695–6 (Mar. 1974); CPM-7403D0523

—Orientational order and molecular parameters of liquid crystals with a positive dielectric anisotropy —V. G. Rumyantsev, P. D. Berezin, L. M. Blinov, and I. N. Kompanets. 18(5), 697–8 (Mar. 1974); CPM-7403D0525

Bobudaev, A. Ya.—Determination of the degree of bending of single crystals from the orientational scattering of β particles —A. Ya. Bobudaev, S. A. Vorob'ev, and V. V. Kaplin. 18(4), 551 (Jan. 1974); CPM-7401D0627

Bochkova, R. I.—Systematic analysis of patterson function on the basis of crystal symmetry. V. Regularities in the degeneracy of the rhombuses in vector sytems of crystals belonging to lower crystallographic systems —É. A. Kuz'min, R. I. Bochkova, Yu. N. Saf'yanov, V. P. Golovachev, and N. V. Belov. 18(4), 429–33 (Jan. 1974); CPM-7401D0505

Bodak, O. I.—Crystal structure of the compound $Ce_{15}Ni_4Si_{13}$ —M. G. Mys'kiv, O. I. Bodak, and E. I. Gladyshevskii. 18(4), 450–3 (Jan. 1974); CPM-7401D0526

Bodrug, S. N.—Dislocation structure of $KMgF_3$ crystals —S. N. Bodrug. 18(5), 692–4 (Mar. 1974); CPM-7403D0520

Boiko, A. A.—Thermal properties of ammonium fluoroberyllate crystals over a wide temperature range —B. A. Strukov, T. L. Skomorokhova, V. A. Koptsik, A. A. Boiko, and A. N. Izrailenko. **18**(1), 86–8 (Jul. 1973); CPM-7309D0336

Boiko, A. I.—Stability of ionic crystals with an NaCl type lattice in the Born model —I. M. Ratner, N. A. Tenyakova, and A. I. Boiko. **18**(1), 99–100 (Jul. 1973); CPM-7309D0349

Boksha, O. N.—Absorption spectra of $MgWO_4$ crystals activated with Cr^{3+} and Co^{2+} ions —O. N. Boksha and T. M. Varina. **18**(3), 354–7 (Nov. 1973); CPM-7311E0486

Bokut', B. V.—Boundary conditions in the electrodynamics of optically active media —B. V. Bokut', A. N. Serdyukov, F. I. Fedorov, and N. A. Khilo. **18**(2), 141–4 (Sep. 1973); CPM-7309D1343

Bolotina, M. L.—Structure of low-temperature "amorphous" bismuth films —Yu. F. Komnik, L. A. Yatsuk, A. A. Motornaya, M. L. Bolotina, and B. I. Belevtsev. **18**(6), 791–6 (May 1974); CPM-7406X1235

Bondarenko, V. S.—Surface layer of barium titanate crystals —V. P. Dudkevich, I. N. Zakharchenko, V. S. Bondarenko, R. V. Kolesova, A. G. Stoinov, and E. G. Fesenko. **18**(5), 690–1 (Mar. 1974); CPM-7403D0518

Borisov, S. V.—One-dimensional models of the Patterson function —S. V. Borisov. **18**(5), 586–8 (Mar. 1974); CPM-7403D0414

—Key role of analysis of interaction distances in oxygen compounds containing heavy cations (high atomic numbers) —T. M. Polyanskaya, S. V. Borisov, and N. V. Belov. **18**(6), 719–27 (May 1974); CPM-7406X1163

Borodin, V. Z.—Studies on ferroelectric crystals with a three-crystal x-ray spectrometer —I. Ya. Nikiforov, Yu. F. Mal'tsev, and V. Z. Borodin. **18**(5), 638–40 (Mar. 1974); CPM-7403D0466

Brik, V. B.—Anisotropy of the growth rate of centers of the α modification in single crystals of high purity tin —V. B. Brik, L. N. Larikov, and V. M. Fal'chenko. **18**(3), 412–3 (Nov. 1973); CPM-7311E0544

Bublik, V. T.—Nature of the point defects in GaAs single crystals as a function of the composition of the melt during growth —V. T. Bublik, V. V. Karataev, R. S. Kulagin, M. G. Mil'vidskii, V. B. Osvenskii, O. G. Stolyarov, and L. P. Kholodnyi. **18**(2), 218–9 (Sep. 1973); CPM-7309D1420

Bukin, V. I.—Hydrothermal synthesis, x-Ray diffraction, and thermogravimetric study of rare-earth hydroxchlorides $Ln(OH)_2Cl$ —L. N. Dem'yanets, V. I. Bukin, E. N. Emel'yanova, and V. I. Ivanov. **18**(6), 806–8 (May 1974); CPM-7406X1250

Bukvetskii, B. V.—Crystal structure of zinc fluoride tetrahydrate, $ZnF_2{\cdot}4H_2O$ —B. V. Bukvetskii, S. A. Polishchuk, and V. I. Simonov. **18**(5), 600–2 (Mar. 1974); CPM-7403D0428

Bulka, G. R.—Proton magnetic resonance investigation of the localization of the protons in the crystal structures $Na_2Cr_2O_7{\cdot}2H_2O$ and $Li_2Cr_2O_7{\cdot}2H_2O$ —G. R. Bulka, V. M. Vinokurov, É. A. Kuz'min, Yu. A. Kharitonov, and N. V. Belov. **18**(5), 617–9 (Mar. 1974); CPM-7403D0445

Bul'o, V. S.—Crystal structure of the compound $EuMg_3Ge_3$ —O. F. Zmii, E. I. Gladyshevskii, and V. S. Bul'o. **18**(2), 171–2 (Sep. 1973); CPM-7309D1373

Burdina, V. I.—Primitive rotation regions of two Patterson syntheses —V. I. Burdina. **18**(4), 437–41 (Jan. 1974); CPM-7401D0513

Burima, V. K.—X-ray investigation of some examples of a homologous series of cholesterol ethers in dicarboxylic acid —Ya. I. Dutchak and V. K. Burima. **18**(5), 677–9 (Mar. 1974); CPM-7403D0505

Burkov, V. I.—Optical activity in $Ba(NO_2)_2{\cdot}H_2O$ crystals —V. I. Burkov, V. A. Kizel', Z. B. Perekalina, N. L. Kozlova, and G. S. Semin. **18**(2), 196–7 (Sep. 1973); CPM-7309D1398

Butabaev, Sh. M.—Stereographic projections of surfaces for the physical properties of crystals —Sh. M. Butabaev and Yu. I. Sirotin. **18**(1), 121–2 (Jul. 1973); CPM-7309D0371

Butikova, I. K.—Crystal structure of sodium hydrosilicate $Na_3HSiO_4{\cdot}5H_2O$ —Yu. I. Smolin, Yu. F. Shepelev, and I. K. Butikova. **18**(2), 173–6 (Sep. 1973); CPM-7309D1375

Butsko, N. I.—Anisotropy of certain physical properties of pyrargyrite and proustite crystals —N. I. Butsko, M. M. Pidorya, and T. D. Krushel'nitskaya. **18**(4), 540–1 (Jan. 1974); CPM-7401D0616

Butuzov, V. P.—Growth of diamond crystals in the form of needles and plates —Yu. A. Litvin, V. P. Butuzov, É. M. Nikoforova, and S. I. Futergendler. **18**(2), 278–9 (Sep. 1973); CPM-7309D1480

Bykhovskii, V. K.—Model of the controlled growth of macromolecular and crystalline structures —V. K. Bykhovskii. **18** (5), 575–7 (Mar. 1974); CPM-7403D0403

Bykov, V. N.—Short-range and long-range order in the arrangement of the interstitial atoms in (34%Ta66%Ti)D, —N. F. Miron, V. I. Shcherbak, V. N. Bykov, and V. A. Levdik. **18**(4), 532–3 (Jan. 1974); CPM-7401D0608

C

Chaikovskaya, N. M.—Temperature dependence of the rate of enlargement of the twinning layer in calcite crystals —V. P. Soldatov, V. I. Startsev, and N. M. Chaikovskaya. **18**(5), 641–3 (Mar. 1974); CPM-7403D0469

Chaikovskii, V. M.—Structure of liquid crystals of the homologous series of n-alkoxyazoxybenzenes —I. G. Chistyakov and V. M. Chaikovskii. **18**(2), 181–3 (Sep. 1973); CPM-7309D1383

Chebanova, T. S.—Internal stresses developing during crystal growth under a steady-state regime —V. L. Indenbom, I. S. Zhitomirskii, and T. S. Chebanova. **18**(1), 24–32 (Jul. 1973); CPM-7309D0274

Cheparin, V. P.—Block conical ferromagnetic spiral in the hexagonal ferrite $BaGa_2Sc_{1.2}Fe_{8.8}O_{19}$ (M) —O. P. Aleshko-Ozhevskii, V. P. Cheparin, A. P. Cherkasov, and I. I. Yamzin. **18**(3), 393–4 (Nov. 1973); CPM-7311E0525

Cherepanov, V. I.—Kronecker product for the representations of the crystallographic pointgroups I —B. A. Men', A. N. Men', and V. I. Cherepanov. **18**(4), 421–4 (Jan. 1974); CPM-7401D0497

—Reduction of the Kronecker product of representations of the crystallogrphic groups. II —B. A. Men', A. N. Men', and V. I. Cherepanov. 18(5), 567–9 (Mar. 1974); CPM-7403D0395

—Reduction of the Kronecker product of representations of the crystallographic groups. III —B. A. Men', A. N. Men', and V. I. Cherepanov. **18**(6), 705–10 (May 1974); CPM-7406X1149

Cherevatskii, N. Ya.—Study of the (111) surface of GaP by methods of Auger spectroscopy and slow-electron diffraction —A. Yu. Mityagin, V. P. Orlov, and N. Ya. Cherevatskii. **18**(2), 268–9 (Sep. 1973); CPM-7309D1470

Cherkasov, A. N.—Pretransition phenomena and optical activity of amorphous liquid phases of cholesteric liquid crystals —E. I. Ryumetsev, A. N. Cherkasov, V. G. Tishchenko, and M. M. Fetisova. **18**(5), 657–9 (Mar. 1974); CPM-7403D0485

Cherkasov, A. P.—Block conical ferromagnetic spiral in the hexagonal ferrite $BaGa_2Sc_{1.2}Fe_{8.8}O_{19}$ (M) —O. P. Aleshko-Ozhevskii, V. P. Cheparin, A. P. Cherkasov, and I. I. Yamzin. **18** (3), 393–4 (Nov. 1973); CPM-7311E0525

Chernik, M. M.—Low-dislocation-density single crystals of corundum —Kh. S. Bagdasarov, E. R. Dobrovinskaya, V. V. Pishchik, M. M. Chernik, Yu. Yu. Kovalev, A. S. Gershun, and I. F. Zvyagintseva. **18**(2), 242–5 (Sep. 1973); CPM-7309D1444

Chernov, A. A.—Rate of whisker growth by the vapor-liquid-crystal mechanism and the role of surface energy —E. I. Givargizov and A. A. Chernov. **18**(1), 89–92 (Jul. 1973); CPM-7309D0339

Chetkina, L. A.—X-ray diffraction study of naphthaloimide —A. N. Sobolev, L. A. Chetkina, G. A. Gol'der, Yu. G. Fedorov, and V. E. Zavodnik. **18**(6), 728–31 (May 1974); CPM-7406X1172

—Crystal and molecular structures of octafluoroanthraquinone —L. A. Chetkina and E. G. Popova. **18**(6), 732–5 (May 1974); CPM-7406X1176

Chikhladze, O. A.—Growth of $KIO_3{\cdot}HIO_3$ crystals and investigation of some of their physical properties —N. R. Ivanov, A. N. Izrailenko, L. N. Rashkovich, and O. A. Chikhladze. **18**(3), 397–8 (Nov. 1973); CPM-7311E0529

—KIO_3: the first ferroelectric permitting just a 120° shift in the ferroelectric polarization —L. A. Shuvalov, N. R. Ivanov, O. A. Chikhladze, and A. N. Izrailenko. **18**(6), 758–61 (May 1974); CPM-7406X1202

Chilaya, G. S.—Dynamic scattering with a memory effect in liquid-crystal mixtures —G. S. Chilaya, V. T. Lazareva, and L. M. Blinov. **18**(1), 127–8 (Jul. 1973); CPM-7309D0377

—Dynamic scattering of light in liquid crystals of the azocompound class —M. F. Grebenkin, G. S. Chilaya, V. T. Lazareva, K. V. Roitman, L. M. Blinov, and V. V. Titov. **18**(2), 274–5 (Sep. 1973); CPM-7309D1476

Chiragov, M. I.—Electron-diffraction investigation of the structure of thin $InTlS_2$ films —K. A. Agaev, V. A. Gasymov, and M. I. Chiragov. **18**(2), 226–7 (Sep. 1973); CPM-7309D1428

Chistyakov, I. G.—Structure of liquid crystals of the homologous series of n-alkoxyazoxybenzenes —I. G. Chistyakov and V. M. Chaikovskii. **18**(2), 181–3 (Sep. 1973); CPM-7309D1383

—Phase transition in liquid crystals induced by an electric field —I. G. Chistyakov and L. K. Vistin'. 18(4), 552–3 (Jan. 1974); CPM-7401D0628

Chistyi, I. L.—Molecular scattering of light in a single crystal of hafnium dioxide —V. I. Aleksandrov, V. F. Kitaeva, I. V. Kozlov, V. V. Osiko, N. N. Sobolev, V. M. Tatarintsev, and I. L. Chistyi. 18(5), 682–4 (Mar. 1974); CPM-7403D0510

Chizhikov, S. I.—Elastic properties of KDP and DKDP crystals of high temperatures —S. I. Chizhikov, N. G. Sorokin, I. Yu. Ledovskaya, and E. V. Makarevskaya. 18(4), 544–5 (Jan. 1974); CPM-7401D0620

Chudakov, V. S.—Optimum spectral range for investigating double refraction by the modulation method —V. S. Chudakov. 18(3), 402–3 (Nov. 1973); CPM-7311E0534

Chukhovskii, F. N.—Reconstruction of the phase of the electronic scattering amplitude from experiments on the diffraction of resonant γ quanta —I. P. Perstnev and F. N. Chukhovskii. 18(5), 582–5 (Mar. 1974); CPM-7403D0410

Chuvyrov, A. N.—Domain rotation in smectic liquid crystals —A. N. Chuvyrov and Z. Kh. Kuvatov. 18(2), 212–4 (Sep. 1973); CPM-7309D1414

D

Danileiko, Yu. K.—Some structural-morphological characteristics of the volatilization of single crystal of α-Al_2O_3 —E. M. Akulenok, Yu. K. Danileiko, V. V. Panteleev, E. A. Fedorov, and V. Ya. Khaimov-Mal'kov. 18(5), 654–6 (Mar. 1974); CPM-7403D0482

Danilyuk, V. I.—Simulation of a crystal surface equilibrium atomic structure for a single component system —V. O. Esin, V. I. Danilyuk, Yu. M. Plishkin, and G. L. Podchinenova. 18(5), 578–81 (Mar. 1974); CPM-7403D0406

Davydov, B. L.—Use of the methods of nonlinear optics in order to make a more accurate analysis of the structural characteristics of crystals associated with the absence of an inversion center —L. G. Koreneva, V. F. Zolin, B. L. Davydov, and V. I. Tsaryuk. 18(3), 399 (Nov. 1973); CPM-7311E0531

Davydova, T. S.—Crystal structure of coumarin —R. M. Myasnikova, T. S. Davydova, and V. I. Simonov. 18(4), 454–6 (Jan. 1974); CPM-7401D0530

Dem'yanets, L. N.—Hydrothermal crystallization in the system CdO-GeO_2-LiCl-H_2O —L. N. Dem'yanets and N. V. Suvorova. 18(1), 133–4 (Jul. 1973); CPM-7309D0383

—Hydrothermal synthesis, x-Ray diffraction, and thermogravimetric study of rare-earth hydroxchlorides $Ln(OH)_2Cl$ —L. N. Dem'yanets, V. I. Bukin, E. N. Emel'yanova, and V. I. Ivanov. 18 (6), 806–8 (May 1974); CPM-7406X1250

Didkovskaya, O. S.—Study of the structure and dielectric properties of solid solutions in the system $BaTiO_3$-$Pb(Fe_{1/2}Nb_{1/2})O_3$ —O. S. Didkovskaya, I. P. Kovalevskaya, V. G. Seryi, V. V. Klimov, and Yu. N. Venevtsev. 18(2), 184–6 (Sep. 1973); CPM-7309D1386

Distler, G. I.—Epitaxial growth of AgCl on the thermoelectric polyvinylchloride films, copying the electrical properties of an NaCl surface —G. I. Distler and E. I. Tokmakova. 18(3), 384–5 (Nov. 1973); CPM-7311E0516

Dmitrik, A. L.—Structural study of tochilinite. II. Acicular variety: Unusual diffraction patterns. —N. I. Organova, V. A. Drits, and A. L. Dmitrik. 18(5), 606–9 (Mar. 1974); CPM-7403D0434

Dobrolyubova, M. S.—Phase transformations in rubidium and cesium superoxides —V. Ya. Dudarev, A. B. Tsentsiper, and M. S. Dobrolyubova. 18(4), 477–9 (Jan. 1974); CPM-7401D0553

Dobrovinskaya, E. R.—Low-dislocation-density single crystals of corundum —Kh. S. Bagdasarov, E. R. Dobrovinskaya, V. V. Pishchik, M. M. Chernik, Yu. Yu. Kovalev, A. S. Gershun, and I. F. Zvyagintseva. 18(2), 242–5 (Sep. 1973); CPM-7309D1444

Dobrzhanskii, G. F.—Interpretation of the dispersion of the rotatory power in the $LiIO_3$ crystal —Z. B. Perekalina, N. L. Smirnova, G. F. Dobrzhanskii, and I. A. Shpil'ko. 18(4), 538–9 (Jan. 1974); CPM-7401D0614

Dodokin, A. P.—Magnetically nonequivalent cation positions in substituted ferrite garnets —I. S. Lyubutin, A. P. Dodokin, and L. M. Belyaev. 18(5), 623–6 (Mar. 1974); CPM-7403D0451

Dolinskaya, V. Z.—Forms of antimony crystal growth in alloys of the eutectic type —I. V. Salli, L. V. Samoilenko, and V. Z. Dolinskaya. 18(6), 823–4 (May 1974); CPM-7406X1267

Dorfman, V. F.—Statistical model of multiphase anisotropic crystallization —V. F. Dorfman. 18(1), 93–8 (Jul. 1973); CPM-7309D0343

Drits, V. A.—Crystal structure of ditrioctahedral chlorite —V. A. Aleksandrova, V. A. Drits, and G. V. Sokolova. 18(1), 50–3 (Jul. 1973); CPM-7309D0300

—Structural study of tochilinite. II. Acicular variety: Unusual diffraction patterns. —N. I. Organova, V. A. Drits, and A. L. Dmitrik. 18(5), 606–9 (Mar. 1974); CPM-7403D0434

Drozhzhin, A. I.—Internal friction and strength of germanium whiskers —V. S. Postnikov, S. A. Ammer, and A. I. Drozhzhin. 18 (3), 416 (Nov. 1973); CPM-7311E0548

Duda, V. M.—Secondary effects accompanying movement of 180-decree α domains in $BaTiO_3$ —E. F. Dudnik and V. M. Duda. 18 (4), 542–3 (Jan. 1974); CPM-7401D0618

Dudarev, V. Ya.—Phase transformations in rubidium and cesium superoxides —V. Ya. Dudarev, A. B. Tsentsiper, and M. S. Dobrolyubova. 18(4), 477–9 (Jan. 1974); CPM-7401D0553

Duderov, N. G.—A group of synthetic cadmium germanates and their x-ray study —E. L. Belokoneva, M. A. Simonov, N. G. Duderov, A. N. Lobachev, and N. V. Belov. 18(5), 610–2 (Mar. 1974); CPM-7403D0438

Dudkevich, V. P.—Surface layer of barium titanate crystals —V. P. Dudkevich, I. N. Zakharchenko, V. S. Bondarenko, R. V. Kolesova, A. G. Stoinov, and E. G. Fesenko. 18(5), 690–1 (Mar. 1974); CPM-7403D0518

Dudnik, E. F.—Secondary effects accompanying movement of 180-decree α domains in $BaTiO_3$ —E. F. Dudnik and V. M. Duda. 18 (4), 542–3 (Jan. 1974); CPM-7401D0618

Dukova, E. D.—Transformation of layer-spiral growth into normal growth on a basal face. I. Breadkdown of the elementary layers on the apices of the spiral hillocks —E. D. Dukova. 18(4), 514–8 (Jan. 1974); CPM-7401D0590

Dutchak, Ya. I.—X-ray investigation of some examples of a homologous series of cholesterol ethers in dicarboxylic acid —Ya. I. Dutchak and V. K. Burima. 18(5), 677–9 (Mar. 1974); CPM-7403D0505

D'yakov, V. A.—High-temperature phase transitions in crystals of Rb $(D_xH_{1-x})_2PO_4$ —V. A. D'yakov, V. A. Koptsik, I. V. Lebedeva, A. V. Mishchenko, and L. N. Rashkovich. 18(6), 769–72 (May 1974); CPM-7406X1213

Dzhmukhadze, D. F.—The $PbZrO_3$-$SrCu_{1/3}Nb_{2/3}$ system —D. F. Dzhmukhadze, M. A. Ugryumova, Yu. N. Venevtsev, and G. S. Zhdanov. 18(1), 116–8 (Jul. 1973); CPM-7309D0366

Dzyuba, A. S.—Dislocation formed during the sintering of solids ("sintering rosettes") —Ya. E. Geguzin, A. S. Dzyuba, V. L. Indenbom, and N. N. Ovcharenko. 18(4), 502–5 (Jan. 1974); CPM-7401D0578

—Study of liquid inclusions in a rocksalt crystal crystal over the entire temperature range of their existence —Ya. E. Geguzin and A. S. Dzyuba. 18(4), 510–3 (Jan. 1974); CPM-7401D0586

—Elastic-diffusion interaction of liquid inclusions in a NaCl single crystal —Ya. E. Geguzin and A. S. Dzyuba. 18(5), 660–2 (Mar. 1974); CPM-7403D0488

E

Éfendiev, É. G.—Electron diffraction investigation of In_2S_3 films obtained by vacuum deposition —R. B. Shafizade, É. G. Éfendiev, and F. I. Aliev. 18(3), 417–8 (Nov. 1973); CPM-7311E0549

Emel'yanova, E. N.—Hydrothermal synthesis, x-Ray diffraction, and thermogravimetric study of rare-earth hydroxchlorides $Ln(OH)_2Cl$ —L. N. Dem'yanets, V. I. Bukin, E. N. Emel'yanova, and V. I. Ivanov. 18(6), 806–8 (May 1974); CPM-7406X1250

Émiraliev, A.—Neutron-diffraction refinement of the structure of alpha lithium iodate —A. Émiraliev, A. G. Kocharov, I. I. Yamzin, and V. A. Lyubimtsev. 18(6), 741–3 (May 1974); CPM-7406X1185

Esin, V. O.—Crystallographic orientation of dendrites of pure tin —V. O. Esin, G. N. Pankin, and R. Sh. Nasyrov. 18(2), 246–9 (Sep. 1973); CPM-7309D1448

—Simulation of a crystal surface equilibrium atomic structure for a single component system —V. O. Esin, V. I. Danilyuk, Yu. M. Plishkin, and G. L. Podchinenova. 18(5), 578–81 (Mar. 1974); CPM-7403D0406

Evstratova, M. I.—Unit-cell parameters and space groups of several pyridino-anthraquinones —O. A. Mikhno, Z. I. Ezhkova, and M. I. Evstratova. 18(6), 804–5 (May 1974); CPM-7406X1248

Ezhkova, Z. I—Crystal and molecular structures of 4-chloroanthraquinonethiadiazole —O. A. Mikhno, Z. I Ezhkova, and G. S. Zhdanov. 18(1), 59–62 (Jul. 1973); CPM-7309D0309

—Unit-cell parameters and space groups of several pyridinoanthraquinones —O. A. Mikhno, Z. I. Ezhkova, and M. I. Evstratova. 18(6), 804–5 (May 1974); CPM-7406X1248

F

Fainshtein, A. L.—Determination of the arbitrary orientation of a crystal by proton diffraction —A. L. Fainshtein. 18(2), 215–7 (Sep. 1973); CPM-7309D1417

Fal'chenko, V. M.—Anisotropy of the growth rate of centers of the α modification in single crystals of high purity tin —V. B. Brik, L. N. Larikov, and V. M. Fal'chenko. 18(3), 412–3 (Nov. 1973); CPM-7311E0544

Fedorov, E. A.—Some structural-morphological characteristics of the volatilization of single crystal of α-Al_2O_3 —E. M. Akulenok, Yu. K. Danileiko, V. V. Panteleev, E. A. Fedorov, and V. Ya. Khaimov-Mal'kov. 18(5), 654–6 (Mar. 1974); CPM-7403D0482

Fedorov, F. I.—Boundary conditions in the electrodynamics of optically active media —B. V. Bokut', A. N. Serdyukov, F. I. Fedorov, and N. A. Khilo. 18(2), 141–4 (Sep. 1973); CPM-7309D1343

Fedorov, P. P.—"Hexagonal YF_3" structure type and high-temperature modifications of rare-earth trifluorides isostructural with YF_3 —B. P. Sobolev and P. P. Fedorov. 18(3), 392 (Nov. 1973); CPM-7311E0524

—Polmorphism and crystallographic properties of yttrium and rare-earth trifluorides —B. P. Sobolev, L. S. Garashina, P. P. Fedorov, N. L. Tkachenko, and K. B. Seiranyan. 18(4), 473–6 (Jan. 1974); CPM-7401D0549

Fedorov, V. A.—Rose channels —V. M. Finkel' and V. A. Fedorov. 18(3), 372–5 (Nov. 1973); CPM-7311E0504

Fedorov, Yu. G.—X-ray diffraction study of naphthaloimide —A. N. Sobolev, L. A. Chetkina, G. A. Gol'der, Yu. G. Fedorov, and V. E. Zavodnik. 18(6), 728–31 (May 1974); CPM-7406X1172

Fedotov, A. F.—Effect of accelerating voltage on the intensity of the forbidden reflection 222 Ge in electron diffraction —A. S. Avilov, R. M. Imamov, Z. G. Pinsker, and A. F. Fedotov. 18(4), 528–9 (Jan. 1974); CPM-7401D0604

Feigin, L. A.—Calculation of the small-angle x-ray scattering intensity on a computer using a macromolecule model —Yu. A. Rol'bin, R. L. Kayushina, L. A. Feigin, and B. M. Shchedrin. 18 (4), 442–4 (Jan. 1974); CPM-7401D0518

Feoktistova, N. N.—Synthesis and ferroelectric properties of antimony orthoniobate —V. I. Popolitov, A. N. Lobachev, V. F. Peskin, L. N. Syrkin, and N. N. Feoktistova. 18(2), 258–9 (Sep. 1973); CPM-7309D1460

Feranchuk, I. D.—Statistical values of heavy atom weighted contributions (D_H) to the total structure amplitude —L. L. Shadyro and I. D. Feranchuk. 18(6), 715–8 (May 1974); CPM-7406X1159

Fesenko, E. G.—Checking the cited mean parameters of oxide unit cells with the perovskite type structure —E. G. Fesenko and G. A. Geguzina. 18(3), 336–8 (Nov. 1973); CPM-7311E0468

—Growth and study of crystals of double oxides of cadmium with structures of the perovskite type. I. Cadmium hafnate —R. I. Spinko, V. N. Lebedev, R. V. Kolesova, and E. G. Fesenko. 18(4), 536–7 (Jan. 1974); CPM-7401D0612

—Some features of the domain structure in lead titanate crystals —E. G. Fesenko, V. G. Gavrilyachenko, M. A. Martynenko, A. F. Semenchev, and I. P. Lapin. 18(5), 635–7 (Mar. 1974); CPM-7403D0463

—Surface layer of barium titanate crystals —V. P. Dudkevich, I. N. Zakharchenko, V. S. Bondarenko, R. V. Kolesova, A. G. Stoinov, and E. G. Fesenko. 18(5), 690–1 (Mar. 1974); CPM-7403D0518

—Growth and investigation of binary cadmium oxides with structures of the perovskite type. II. Cadmium stannate and zirconate —R. I. Spinko, V. N. Lebedev, R. V. Kolesova, and E. G. Fesenko. 18(6), 809–10 (May 1974); CPM-7406X1253

Fetisova, M. M.—Pretransition phenomena and optical activity of amorphous liquid phases of cholesteric liquid crystals —E. I. Ryumetsev, A. N. Cherkasov, V. G. Tishchenko, and M. M. Fetisova. 18(5), 657–9 (Mar. 1974); CPM-7403D0485

Filippova, T. V.—X-ray study of potassium copper ethylenediaminetetraacetate trihydrate —M. A. Porai-Koshits, N. V. Novozhilova, T. N. Polynova, T. V. Filippova, and L. I. Martynenko. 18(1), 54–8 (Jul. 1973); CPM-7309D0304

Finkel', V. M.—Rose channels —V. M. Finkel' and V. A. Fedorov. 18(3), 372–5 (Nov. 1973); CPM-7311E0504

Fofanov, A. D.—"Spectral instability" of multiwave diffraction with coplanar x rays —A. D. Fofanov, A. V. Kuznetsov, and G. A. Karacheva. 18(6), 711–4 (May 1974); CPM-7406X1155

Fok, M. V.—Effect of manganese on the transformation of the zinc sulfide cubic lattice to hexagonal —G. E. Arkhangel'skii, T. I. Voznesenskaya, and M. V. Fok. 18(3), 342–3 (Nov. 1973); CPM-7311E0474

Fomin, V. G.—Influence of heat treatment on the structural perfection of single crystals of gallium arsenide alloyed with tellurium —M. G. Mil'vidskii, V. B. Osvenskii, A. G. Novikov, V. G. Fomin, and S. P. Grishina. 18(4), 519–20 (Jan. 1974); CPM-7401D0595

Fotchenkov, A. A.—Some features of the action of penetrating radiation on the electrical properties of a quartz crystal —A. A. Fotchenkov and S. V. Kolodieva. 18(3), 366–9 (Nov. 1973); CPM-7311E0498

Frank-Kamenetskaya, O. V.—Crystal structure of the potassium salt of 1,1-dinitroethane —O. V. Frank-Kamenetskaya, N. V. Grigor'eva, N. V. Margolis, and I. V. Tselinskii. 18(1), 108–9 (Jul. 1973); CPM-7309D0358

—Symmetries of functions for separating structures from a Patterson distribution of the triclinic, monoclinic, and orthorhombic systems —O. V. Frank-Kamenetskaya, N. V. Grigor'eva, and N. V. Margolis. 18(3), 314–6 (Nov. 1973); CPM-7311E0446

Frank-Kamenetskii, V. A.—Determination of the nature of the filling of positions by isomorphous elements —A. L. Kosoi and V. A. Frank-Kamenetskii. 18(4), 464–6 (Jan. 1974); CPM-7401D0540

Fridkin, V. M.—Electronic mechanism of the influence of radiation on the process of repolarization of ferroelectrics —A. A. Grekov, M. A. Malitskaya, and V. M. Fridkin. 18(4), 494–8 (Jan. 1974); CPM-7401D0570

Futergendler, S. I.—Growth of diamond crystals in the form of needles and plates —Yu. A. Litvin, V. P. Butuzov, É. M. Nikoforova, and S. I. Futergendler. 18(2), 278–9 (Sep. 1973); CPM-7309D1480

G

Gabrielyan, V. T.—Characteristics of residual-stress relaxation in $LiNbO_3$ single crystals in the 20-200°C region —K. G. Belabaev, V. T. Gabrielyan, and V. Kh. Sarkisov. 18(1), 123–4 (Jul. 1973); CPM-7309D0373

Gabuda, S. P.—Position of the hydroxyl groups in the structure of hydrosodalite —V. Yu. Galitskii, V. N. Shcherbakov, and S. P. Gabuda. 18(5), 620–2 (Mar. 1974); CPM-7403D0448

Galitskii, V. Yu.—Position of the hydroxyl groups in the structure of hydrosodalite —V. Yu. Galitskii, V. N. Shcherbakov, and S. P. Gabuda. 18(5), 620–2 (Mar. 1974); CPM-7403D0448

—Phase transition, dielectric anomaly, and domain structure in hydrosodalite —N. R. Ivanov and V. Yu. Galitskii. 18(6), 762–3 (May 1974); CPM-7406X1206

Galiulin, R. V.—Isolation of n points of the basic system from a vector system by use of the star of an (n-1) -dimensional simplex —R. V. Galiulin, M. I. Sirota, A. S. Naumov, and N. V. Belov. 18 (1), 39–42 (Jul. 1973); CPM-7309D0289

Galustashvili, M. V.—Formation of a Debye-Hückel cloud around dislocations in LiF crystals —N. G. Politov, M. V. Galustashvili, and I. M. Paperno. 18(1), 125–6 (Jul. 1973); CPM-7309D0375

Gapeev, A. K.—Use of the methods of successive experiment planning with refining crystal-structure parameters —I. V. Igonina, B. I. Pokrovskii, A. K. Gapeev, P. I. Lazarev, and L. N. Komissarova. 18(3), 308–13 (Nov. 1973); CPM-7311E0440

Garashina, L. S.—Polmorphism and crystallographic properties of yttrium and rare-earth trifluorides —B. P. Sobolev, L. S. Garashina, P. P. Fedorov, N. L. Tkachenko, and K. B. Seiranyan. 18(4), 473–6 (Jan. 1974); CPM-7401D0549

—Solubility of LnF_3 in lanthanum fluoride —O. V. Kudryavtseva, L. S. Garashina, K. K. Rivkina, and B. P. Sobolev. 18(4), 531 (Jan. 1974); CPM-7401D0607

Gasymov, V. A.—Electron-diffraction investigation of the structure of thin $InTlS_2$ films —K. A. Agaev, V. A. Gasymov, and M. I. Chiragov. 18(2), 226–7 (Sep. 1973); CPM-7309D1428

Gavrilyachenko, V. G.—Some features of the domain structure in lead titanate crystals —E. G. Fesenko, V. G. Gavrilyachenko, M. A. Martynenko, A. F. Semenchev, and I. P. Lapin. 18(5), 635–7 (Mar. 1974); CPM-7403D0463

Geguzin, Ya. E.—Dislocation formed during the sintering of solids ("sintering rosettes") —Ya. E. Geguzin, A. S. Dzyuba, V. L. Indenbom, and N. N. Ovcharenko. 18(4), 502–5 (Jan. 1974); CPM-7401D0578

—Study of liquid inclusions in a rocksalt crystal crystal over the entire temperature range of their existence —Ya. E. Geguzin and A. S. Dzyuba. 18(4), 510–3 (Jan. 1974); CPM-7401D0586

—Elastic-diffusion interaction of liquid inclusions in a NaCl single crystal —Ya. E. Geguzin and A. S. Dzyuba. 18(5), 660–2 (Mar. 1974); CPM-7403D0488

Geguzina, G. A.—Checking the cited mean parameters of oxide unit cells with the perovskite type structure —E. G. Fesenko and G. A. Geguzina. 18(3), 336–8 (Nov. 1973); CPM-7311E0468

Gel'man, Yu. A.—Spatial distribution of particles during vaporization of a zinc single crystal —Yu. A. Gel'man, V. F. Vinogradov, and Yu. N. Lyubitov. 18(4), 556–7 (Jan. 1974); CPM-7401D0632

Genkin, V. M.—Change of the interplanar distances in deep layers of silicon during bombardment with medium-energy ions —G. I. Uspenskaya, V. M. Genkin, and D. I. Tetel'baum. 18(2), 224–5 (Sep. 1973); CPM-7309D1426

Genkina, N. A.—Crystallization of amorphous films of silicon nitride by ionic bombardment followed by annealing —P. V. Pavlov, É. V. Shitova, E. I. Zorin, and N. A. Genkina. 18(3), 381–3 (Nov. 1973); CPM-7311E0513

Gerken, V. A.—Indexing of the crystallographic planes in rhombohedral crystals —V. A. Gerken, B. K. Kazurov, and G. M. Tsigel'nitskii. 18(5), 674 (Mar. 1974); CPM-7403D0502

Gershun, A. S.—Low-dislocation-density single crystals of corundum —Kh. S. Bagdasarov, E. R. Dobrovinskaya, V. V. Pishchik, M. M. Chernik, Yu. Yu. Kovalev, A. S. Gershun, and I. F. Zvyagintseva. 18(2), 242–5 (Sep. 1973); CPM-7309D1444

Gil'varg, A. B.—Optical activity in monoclinic sodium zincogermanate Na$_2$ZnGeO$_4$ —S. P. Kozyrev, A. B. Gil'varg, B. N. Grechushnikov, and N. V. Belov. 18(6), 813 (May 1974); CPM-7406X1257

Gimel'farb, F. A.—Effect of the crystallization mechanism on boron diffusion in silicon-germanium solid-solution epitaxial films —K. L. Lyutovich, F. A. Gimel'farb, P. B. Orlov, and T. A. Ukhorskaya. 18(6), 825–6 (May 1974); CPM-7406X1269

Givargizov, E. I.—Rate of whisker growth by the vapor-liquid-crystal mechanism and the role of surface energy —E. I. Givargizov and A. A. Chernov. 18(1), 89–92 (Jul. 1973); CPM-7309D0339

—Motion of a germanium-gold alloy droplet along a germanium surface under the action of a temperature gradient —S. A. Grinberg and E. I. Givargizov. 18(2), 236–8 (Sep. 1973); CPM-7309D1438

Gladkii, V. V.—Some features of the polarization of KH$_2$PO$_4$ in the phase transition region —E. V. Sidnenko and V. V. Gladkii. 18(1), 83–5 (Jul. 1973); CPM-7309D0333

Gladkova, V. F.—One-dimensional disorder in diazoaminobenzene —V. F. Gladkova. 18(6), 783–7 (May 1974); CPM-7406X1227

Gladyshevskii, E. I.—Crystal structure of the compound EuMg$_3$Ge$_3$ —O. F. Zmii, E. I. Gladyshevskii, and V. S. Bul'o. 18(2), 171–2 (Sep. 1973); CPM-7309D1373

—Crystal structure of the compound Ce$_{15}$Ni$_4$Si$_{13}$ —M. G. Mys'kiv, O. I. Bodak, and E. I. Gladyshevskii. 18(4), 450–3 (Jan. 1974); CPM-7401D0526

Glazyrin, M. P.—Crystal optics of alkaline-earth metavanadates —M. P. Glazyrin, A. A. Ivakin, and V. A. Gurevich. 18(5), 685–6 (Mar. 1974); CPM-7403D0513

Gol'der, G. A.—Crystal-chemical analysis of the structure of 1-I-substituted anthraquinone —N. L. Klimasenko, V. K. Bel'skii, V. K. Sarynin, and G. A. Gol'der. 18(4), 457–9 (Jan. 1974); CPM-7401D0533

—X-ray diffraction study of naphthaloimide —A. N. Sobolev, L. A. Chetkina, G. A. Gol'der, Yu. G. Fedorov, and V. E. Zavodnik. 18 (6), 728–31 (May 1974); CPM-7406X1172

Golovach, G. P.—Jones and Müller matrices of a phase-shifting slab with a rotating axis of the highest velocity —V. D. Tron'ko and G. P. Golovach. 18(3), 291–4 (Nov. 1973); CPM-7311E0423

Golovachev, V. P.—Systematic analysis of Patterson functions on the basis of crystal symmetry. IV. Interpretation of the Patterson synthesis for crystals of lower systems —É. A. Kuz'min, V. P. Golovachev, V. V. Ilyukhin, and N. V. Belov. 18(1), 33–8 (Jul. 1973); CPM-7309D0283

—Systematic analysis of patterson function on the basis of crystal symmetry. V. Regularities in the degeneracy of the rhombuses in vector sytems of crystals belonging to lower crystallographic systems —É. A. Kuz'min, R. I. Bochkova, Yu. N. Saf'yanov, V. P. Golovachev, and N. V. Belov. 18(4), 429–33 (Jan. 1974); CPM-7401D0505

Golovastikov, N. I.—Crystal structure of the alkali titanosilicate labuntsovite —N. I. Golovastikov. 18(5), 596–9 (Mar. 1974); CPM-7403D0424

Gorbach, S. S.—Temperature dependence of the elastooptical constants p$_{11}$ and p$_{12}$ of NaCl, KCl, Kbr, and Kl crystals —A. V. Pakhnev, S. S. Gorbach, and M. P. Shaskol'skaya. 18(5), 687 (Mar. 1974); CPM-7403D0515

—Influence of impurities on the photoelastic constants of potassium chloride crystals —M. P. Shaskol'skaya, A. V. Pakhnev, S. S. Gorbach, and N. M. Malikova. 18(6), 817 (May 1974); CPM-7406X1261

Gordienko, L. A.—Deformation dislocations in natural quartz crystals —V. F. Miuskov, L. I. Tsinober, and L. A. Gordienko. 18(2), 209–11 (Sep. 1973); CPM-7309D1411

Grebenkin, M. F.—Dynamic scattering of light in liquid crystals of the azocompound class —M. F. Grebenkin, G. S. Chilaya, V. T. Lazareva, K. V. Roitman, L. M. Blinov, and V. V. Titov. 18(2), 274–5 (Sep. 1973); CPM-7309D1476

Grechushnikov, B. N.—Propagation of light in active absorbing crystals —A. F. Konstantinova and B. N. Grechushnikov. 18(3), 298–9 (Nov. 1973); CPM-7311E0430

—Optical activity in monoclinic sodium zincogermanate Na$_2$ZnGeO$_4$ —S. P. Kozyrev, A. B. Gil'varg, B. N. Grechushnikov, and N. V. Belov. 18(6), 813 (May 1974); CPM-7406X1257

Grekov, A. A.—Electronic mechanism of the influence of radiation on the process of repolarization of ferroelectrics —A. A. Grekov, M. A. Malitskaya, and V. M. Fridkin. 18(4), 494–8 (Jan. 1974); CPM-7401D0570

Gribkov, V. N.—Mechanism of growth and etching of whisker crystals of aluminum nitride —K. I. Portnoi, V. N. Gribkov, B. V. Shchetanov, É. L. Umantsev, and V. A. Silaev. 18(3), 376–8 (Nov. 1973); CPM-7311E0508

Gridnev, S. A.—Relaxational internal friction in crystals of KH$_2$PO$_4$ without chromium added —S. A. Gridnev, L. N. Kamysheva, and N. F. Romanova. 18(6), 773–6 (May 1974); CPM-7406X1217

Grigor'ev, O. N.—Formation of trigons at the }111{ faces of natural diamond during etching —O. N. Grigor'ev. 18(6), 821–2 (May 1974); CPM-7406X1265

Grigor'ev, V. E.—Growth of smooth epitaxial germanium films by the iodide method in a through-flow system with diffusive mass transfer —G. M. Malkin, V. E. Grigor'ev, N. A. Lineva, and L. A. Malkina. 18(1), 129–30 (Jul. 1973); CPM-7309D0379

Grigor'eva, N. V.—Crystal structure of the potassium salt of 1,1-dinitroethane —O. V. Frank-Kamenetskaya, N. V. Grigor'eva, N. V. Margolis, and I. V. Tselinskii. 18(1), 108–9 (Jul. 1973); CPM-7309D0358

—Symmetries of functions for separating structures from a Patterson distribution of the triclinic, monoclinic, and orthorhombic systems —O. V. Frank-Kamenetskaya, N. V. Grigor'eva, and N. V. Margolis. 18(3), 314–6 (Nov. 1973); CPM-7311E0446

Grinberg, S. A.—Motion of a germanium-gold alloy droplet along a germanium surface under the action of a temperature gradient —S. A. Grinberg and E. I. Givargizov. 18(2), 236–8 (Sep. 1973); CPM-7309D1438

Grishina, S. P.—Influence of heat treatment on the structural perfection of single crystals of gallium arsenide alloyed with tellurium —M. G. Mil'vidskii, V. B. Osvenskii, A. G. Novikov, V. G. Fomin, and S. P. Grishina. 18(4), 519–20 (Jan. 1974); CPM-7401D0595

—Nature of small etch pits in tellurium-alloyed GaAs single crystals —S. S. Shifrin, V. B. Osvenskii, M. G. Mil'vidskii, L. M. Morgulis, and S. P. Grishina. 18(6), 818–20 (May 1974); CPM-7406X1262

Groznov, I. N.—Solid solutions of BaTiO$_3$ with barium niobates —I. N. Groznov and Yu. N. Venevtsev. 18(3), 395–6 (Nov. 1973); CPM-7311E0527

Gurevich, V. A.—Crystal optics of alkaline-earth metavanadates —M. P. Glazyrin, A. A. Ivakin, and V. A. Gurevich. 18(5), 685–6 (Mar. 1974); CPM-7403D0513

Gusev, A. I.—Crystal and molecular structure of phenyl phenoxtinium iodide —A. I. Gusev and Yu. T. Struchkov. 18(3), 330–2 (Nov. 1973); CPM-7311E0462

H

Haav, A. A.—X-ray diffraction study of the system RbBr-TlBr —A. A. Haav and T. K. Muirsepp. 18(4), 471–2 (Jan. 1974); CPM-7401D0547

Hrichova, R.—Infrared spectra of manganese garnets containing a germanate tetrahedron —R. Hrichova. 18(4), 534–5 (Jan. 1974); CPM-7401D0610

I

Igonina, I. V.—Use of the methods of successive experiment planning with refining crystal-structure parameters —I. V. Igonina, B. I. Pokrovskii, A. K. Gapeev, P. I. Lazarev, and L. N. Komissarova. 18(3), 308–13 (Nov. 1973); CPM-7311E0440

Il'inykh, T. V.—Use of the luminescence polarization diagram method to investigate molecular crystals containing two impurities —G. S. Belikova, N. D. Zhevandrov, T. V. Il'inykh, L. E. Kraeva, and N. P. Sul'zhenko. 18(4), 489–91 (Jan. 1974); CPM-7401D0565

Il'yasov, É. A.—X-ray diffraction and dielectric studies of the $LiNbO_3$-$KNbO_3$ system —I. G. Ismailzade, V. I. Nesterenko, and É. A. Il'yasov. 18(1), 114–5 (Jul. 1973); CPM-7309D0364

Ilyukhin, V. V.—Systematic analysis of Patterson functions on the basis of crystal symmetry. IV. Interpretation of the Patterson synthesis for crystals of lower systems —É. A. Kuz'min, V. P. Golovachev, V. V. Ilyukhin, and N. V. Belov. 18(1), 33–8 (Jul. 1973); CPM-7309D0283

—Chemical crystallography of mixed anion frameworks. I. Zirconium and scandium alkali sorosilicates —A. A. Voronkov, R. G. Sizova, V. V. Ilyukhin, and N. V. Belov. 18(1), 67–72 (Jul. 1973); CPM-7309D0317

Imamov, R. M.–Investigation of the intensities of electron diffraction by NH_4Cl, NaCl, and TlCl films by using electrical recording and an electron filter–A. S. Avilov, R. M. Imamov, R. K. Karakhanyan, and Z. G. Pinsker. 18(1), 30–32 (Jul. 1973); CPM-7309D0280

—Effect of accelerating voltage on the intensity of the forbidden reflection 222 Ge in electron diffraction —A. S. Avilov, R. M. Imamov, Z. G. Pinsker, and A. F. Fedotov. 18(4), 528–9 (Jan. 1974); CPM-7401D0604

Indenbom, V. L.—Internal stresses developing during crystal growth under a steady-state regime —V. L. Indenbom, I. S. Zhitomirskii, and T. S. Chebanova. 18(1), 24–32 (Jul. 1973); CPM-7309D0274

—Dislocation formed during the sintering of solids ("sintering rosettes") —Ya. E. Geguzin, A. S. Dzyuba, V. L. Indenbom, and N. N. Ovcharenko. 18(4), 502–5 (Jan. 1974); CPM-7401D0578

—Domain boundaries, antiphase boundaries, and dislocations in gadolinium molybdate single crystals —V. A. Meleshina, V. L. Indenbom, Kh. S. Bagdasarov, and T. M. Polkhovskaya. 18(6), 764–8 (May 1974); CPM-7406X1208

Ionov, V. M.—Crystal structure of lanthanum hypophosphite monohydrate —V. M. Ionov, L. A. Aslanov, V. B. Rybakov, and M. A. Porai-Koshits. 18(2), 250–1 (Sep. 1973); CPM-7309D1452

—Crystal structure of europium hypophosphite monohydrate —V. M. Ionov, L. A. Aslanov, M. A. Porai-Koshits, and V. B. Rybakov. 18 (2), 252–3 (Sep. 1973); CPM-7309D1454

Isakov, I. V.—Simple method for preventing the formation of parasite crystals during the growth of crystals from solution —I. V. Isakov. 18(5), 703 (Mar. 1974); CPM-7403D0531

Ismailzade, I. G.—X-ray diffraction and dielectric studies of the system $Li(Ta_xSb_{1-x})O_3$ —V. I. Nesterenko and I. G. Ismailzade. 18 (1), 112–3 (Jul. 1973); CPM-7309D0362

—X-ray diffraction and dielectric studies of the $LiNbO_3$-$KNbO_3$ system —I. G. Ismailzade, V. I. Nesterenko, and É. A. Il'yasov. 18 (1), 114–5 (Jul. 1973); CPM-7309D0364

Ivakin, A. A.—Crystal optics of alkaline-earth metavanadates —M. P. Glazyrin, A. A. Ivakin, and V. A. Gurevich. 18(5), 685–6 (Mar. 1974); CPM-7403D0513

Ivanov, N. R.—Effect of an electric field on phase transitions in $Na(D_xH_{1-x})_3(SeO_3)_2$ crystals. I. Induction of the β phase in crystals having $x \gtrsim 0.3$ by the field E_y–L. A. Shuvalov, A. M. Shirokov, N. R. Ivanov, and A. I. Baranov. 18(1), 80–2 (Jul. 1973); CPM-7309D0330

—Growth of KIO_3·HIO_3 crystals and investigation of some of their physical properties —N. R. Ivanov, A. N. Izrailenko, L. N. Rashkovich, and O. A. Chikhladze. 18(3), 397–8 (Nov. 1973); CPM-7311E0529

—KIO_3: the first ferroelectric permitting just a 120° shift in the ferroelectric polarization —L. A. Shuvalov, N. R. Ivanov, O. A. Chikhladze, and A. N. Izrailenko. 18(6), 758–61 (May 1974); CPM-7406X1202

—Phase transition, dielectric anomaly, and domain structure in hydrosodalite —N. R. Ivanov and V. Yu. Galitskii. 18(6), 762–3 (May 1974); CPM-7406X1206

Ivanov, V. I.—Hydrothermal synthesis, x-Ray diffraction, and thermogravimetric study of rare-earth hydroxchlorides $Ln(OH)_2Cl$ —L. N. Dem'yanets, V. I. Bukin, E. N. Emel'yanova, and V. I. Ivanov. 18(6), 806–8 (May 1974); CPM-7406X1250

Ivanov, Yu. A.—Preparation and preliminary investigation of cadmium phosphates —Yu. A. Ivanov, I. N. Ivanovskaya, V. I. Popolitov, M. A. Simonov, and N. V. Belov. 18(5), 671–3 (Mar. 1974); CPM-7403D0499

Ivanova, L. V.—Atom-atom potentials and the coordinates of hydrogen atoms in methyl groups in the molecule and crystal —K. V. Mirskaya and L. V. Ivanova. 18(1), 101–2 (Jul. 1973); CPM-7309D0351

Ivanova, S. V.—Effect of a magnetic field on the Curie point of the ferroelectric semiconductor SbSI —S. V. Ivanova and V. A. Lyakhovitskaya. 18(3), 404 (Nov. 1973); CPM-7311E0536

Ivanov-Shits, A. K.—Heat capacity of single-crystal $BaTiO_3$ near the electrical critical point —B. A. Strukov and A. K. Ivanov-Shits. 18 (4), 548 (Jan. 1974); CPM-7401D0624

Ivanovskaya, I. N.—Preparation and preliminary investigation of cadmium phosphates —Yu. A. Ivanov, I. N. Ivanovskaya, V. I. Popolitov, M. A. Simonov, and N. V. Belov. 18(5), 671–3 (Mar. 1974); CPM-7403D0499

Ivonin, I. V.—Anisotropy of growth and alloying for epitaxial germanium layers in the Ge-I_2 system —L. G. Lavrent'eva, I. S. Zakharov, I. V. Ivonin, N. P. Kolodeshnikova, and T. I. Opryshko. 18(2), 228–31 (Sep. 1973); CPM-7309D1430

Izrailenko, A. N.—Thermal properties of ammonium fluoroberyllate crystals over a wide temperature range —B. A. Strukov, T. L. Skomorokhova, V. A. Koptsik, A. A. Boiko, and A. N. Izrailenko. 18(1), 86–8 (Jul. 1973); CPM-7309D0336

—Growth of KIO_3·HIO_3 crystals and investigation of some of their physical properties —N. R. Ivanov, A. N. Izrailenko, L. N. Rashkovich, and O. A. Chikhladze. 18(3), 397–8 (Nov. 1973); CPM-7311E0529

—KIO_3: the first ferroelectric permitting just a 120° shift in the ferroelectric polarization —L. A. Shuvalov, N. R. Ivanov, O. A. Chikhladze, and A. N. Izrailenko. 18(6), 758–61 (May 1974); CPM-7406X1202

K

Kalanov, M.—Use of the double-crystal neutron spectrometer to study the low-temperature decomposition in niobium single crystals saturated with hydrogen —M. Kalanov, S. Sh. Shil'shtein, and V. A. Somenkov. 18(6), 755–7 (May 1974); CPM-7406X1199

Kaminskii, A. A.—Stimulated emission from $(Er,Lu)AlO_3$ crystals containing Ho^{3+} and Tm^{3+} ions —Kh. S. Bagdasarov, A. A. Kaminskii, A. M. Kevorkov, S. É. Sarkisov, and T. A. Tevosyan. 18(5), 681 (Mar. 1974); CPM-7403D0509

Kamysheva, L. N.—Relaxational internal friction in crystals of KH_2PO_4 without chromium added —S. A. Gridnev, L. N. Kamysheva, and N. F. Romanova. 18(6), 773–6 (May 1974); CPM-7406X1217

Kapanadze, B. K.—Growth dislocation distribution along a copper crystal and dislocation density as a function of mean diameter —A. G. Basariya, B. K. Kapanadze, and V. V. Sanadze. 18(3), 411 (Nov. 1973); CPM-7311E0543

Kaplin, V. V.—Determination of the degree of bending of single crystals from the orientational scattering of β particles —A. Ya. Bobudaev, S. A. Vorob'ev, and V. V. Kaplin. 18(4), 551 (Jan. 1974); CPM-7401D0627

Kapustin, A. P.—Electret effect in n-azoxyanisole —A. P. Kapustin, Z. Kh. Kuvatov, and A. N. Trofimov. 18(2), 263 (Sep. 1973); CPM-7309D1465•

—Thermodielectric effect at the phase transition between a liquid and solid crystal —A. P. Kapustin, Z. Kh. Kuvatov, and A. N. Trofimov. 18(3), 409 (Nov. 1973); CPM-7311E0541

Karacheva, G. A.—"Spectral instability" of multiwave diffraction with coplanar x rays —A. D. Fofanov, A. V. Kuznetsov, and G. A. Karacheva. 18(6), 711–4 (May 1974); CPM-7406X1155

Karakhanyan, R. K.–Investigation of the intensities of electron diffraction by NH_4Cl, NaCl, and TlCl films by using electrical recording and an electron filter–A. S. Avilov, R. M. Imamov, R. K. Karakhanyan, and Z. G. Pinsker. 18(1), 30–32 (Jul. 1973); CPM-7309D0280

Karataev, V. V.—Nature of the point defects in GaAs single crystals as a function of the composition of the melt during growth —V. T. Bublik, V. V. Karataev, R. S. Kulagin, M. G. Mil'vidskii, V. B. Osvenskii, O. G. Stolyarov, and L. P. Kholodnyi. 18(2), 218–9 (Sep. 1973); CPM-7309D1420

—Effective distribution constants of excess basic components during crystallization of gallium arsenide from a melt —V. V. Karataev, M. G. Mil'vidskii, V. B. Osvenskii, and O. G. Stolyarov. 18(4), 521–2 (Jan. 1974); CPM-7401D0597

Karpel'son, A. E.—Dynamic pyroelectric effect —S. D. Pel'ts and A. E. Karpel'son. 18(3), 360–2 (Nov. 1973); CPM-7311E0492

Kashaev, A. A.—Crystal structure of $CsNbO(SO_4)_2$ —A. A. Kashaev and G. V. Sokolova. 18(3), 388–9 (Nov. 1973); CPM-7311E0520

—Crystal structures of $RbNbO(SO_4)_2$ and $NH_4NbO(SO_4)_2$ —A. A. Kashaev, G. E. Postoenko, and É. A. Zel'bst. 18(6), 802–3 (May 1974); CPM-7406X1246

Kayushina, R. L.—Calculation of the small-angle x-ray scattering intensity on a computer using a macromolecule model —Yu. A. Rol'bin, R. L. Kayushina, L. A. Feigin, and B. M. Shchedrin. 18 (4), 442–4 (Jan. 1974); CPM-7401D0518

Kazinets, M. M.—Electron-diffraction study of the kinetics of the $CuS \rightarrow Cu_{2-x}S$ transformation —M. M. Kazinets and R. B. Shafizade. 18(4), 480–2 (Jan. 1974); CPM-7401D0556

Kazurov, B. K.—Indexing of the crystallographic planes in rhombohedral crystals —V. A. Gerken, B. K. Kazurov, and G. M. Tsigel'nitskii. 18(5), 674 (Mar. 1974); CPM-7403D0502

Kevorkov, A. M.—Stimulated emission from $(Er,Lu)AlO_3$ crystals containing Ho^{3+} and Tm^{3+} ions —Kh. S. Bagdasarov, A. A. Kaminskii, A. M. Kevorkov, S. É. Sarkisov, and T. A. Tevosyan. 18(5), 681 (Mar. 1974); CPM-7403D0509

Khadzhi, V. E.—Nature of the impurity water in synthetic quartz crystals —L. I. Tsinober and V. E. Khadzhi. 18(5), 699–700 (Mar. 1974); CPM-7403D0527

Khaidukov, N. M.—Luminescence of cuprous oxide single crystals —I. P. Kuz'mina, A. N. Lobachev, B. S. Predtechenskii, L. S. Starostina, V. B. Stopachinskii, and N. M. Khaidukov. 18(3), 400–1 (Nov. 1973); CPM-7311E0532

Khaimov-Mal'kov, V. Ya.—Some structural-morphological characteristics of the volatilization of single crystal of α-Al_2O_3 —E. M. Akulenok, Yu. K. Danileiko, V. V. Panteleev, E. A. Fedorov, and V. Ya. Khaimov-Mal'kov. 18(5), 654–6 (Mar. 1974); CPM-7403D0482

Khakimova, D. K.—Iteration method for calculating the intensity distribution in structural analysis —D. K. Khakimova, V. G. Nagornyi, and A. A. Smol'yaninov. 18(3), 303–5 (Nov. 1973); CPM-7311E0435

Khapachev, Yu. P.—Dynamic theory of x-ray diffraction in crystals with modulated electron density —A. V. Kolpakov and Yu. P. Khapachev. 18(3), 300–2 (Nov. 1973); CPM-7311E0432

Kharchenko, L. Yu.—Hydrothermal synthesis of a new crystalline modification of lithium lanthanum molybdate, α-$LiLa(MoO_4)_2$ —P. V. Klevtsov, V. I. Protasova, L. Yu. Kharchenko, and R. F. Klevtsova. 18(4), 523–4 (Jan. 1974); CPM-7401D0599

Kharitonov, Yu. A.—Proton magnetic resonance investigation of the localization of the protons in the crystal structures $Na_2Cr_2O_7{\cdot}2H_2O$ and $Li_2Cr_2O_7{\cdot}2H_2O$ —G. R. Bulka, V. M. Vinokurov, É. A. Kuz'min, Yu. A. Kharitonov, and N. V. Belov. 18(5), 617–9 (Mar. 1974); CPM-7403D0445

Kheifets, V. S.—Phenomena arising on the arrest of crystal growth —V. N. Romanenko and V. S. Kheifets. 18(5), 663–6 (Mar. 1974); CPM-7403D0491

Khilo, N. A.—Boundary conditions in the electrodynamics of optically active media —B. V. Bokut', A. N. Serdyukov, F. I. Fedorov, and N. A. Khilo. 18(2), 141–4 (Sep. 1973); CPM-7309D1343

Khimich, T. A.—Gamma-resonance investigations of ferruginous tourmalines —V. F. Belov, T. A. Khimich, M. N. Shipko, I. E. Voskresenskaya, and E. N. Okulov. 18(1), 119–20 (Jul. 1973); CPM-7309D0369

Khiminets, V. V.—Phase diagram of the system $(HgI_2)_x(HgBr_2)_{1-x}$ and some optical properties of its single crystals —I. D. Turyanitsa and V. V. Khiminets. 18(5), 688–9 (Mar. 1974); CPM-7403D0516

Khitrova, V. I.—Structure of nickel hydroxide containing potassium ions —P. N. Bityutskii, V. I. Khitrova, and Z. G. Pinsker. 18(5), 613–6 (Mar. 1974); CPM-7403D0441

Kholodnyi, L. P.—Nature of the point defects in GaAs single crystals as a function of the composition of the melt during growth —V. T. Bublik, V. V. Karataev, R. S. Kulagin, M. G. Mil'vidskii, V. B. Osvenskii, O. G. Stolyarov, and L. P. Kholodnyi. 18(2), 218–9 (Sep. 1973); CPM-7309D1420

Kislovskii, L. D.—Far infrared reflectance spectra of rubidium trihydro- and trideuterioselenite crystals —J. Petzelt, L. D. Kislovskii, and L. A. Shuvalov. 18(3), 351–3 (Nov. 1973); CPM-7311E0483

Kitaeva, V. F.—Molecular scattering of light in a single crystal of hafnium dioxide —V. I. Aleksandrov, V. F. Kitaeva, I. V. Kozlov, V. V. Osiko, N. N. Sobolev, V. M. Tatarintsev, and I. L. Chistyi. 18(5), 682–4 (Mar. 1974); CPM-7403D0510

Kizel', V. A.—Optical activity in $Ba(NO_2)_2{\cdot}H_2O$ crystals —V. I. Burkov, V. A. Kizel', Z. B. Perekalina, N. L. Kozlova, and G. S. Semin. 18(2), 196–7 (Sep. 1973); CPM-7309D1398

—Determination of the degree of ordering in liquid crystals from the dichroism of dissolved dyes —V. G. Rumyantsev, L. M. Blinov, and V. A. Kizel'. 18(5), 695–6 (Mar. 1974); CPM-7403D0523

Kleinman, I. A.—Heat effects in lithium metaniobate —I. A. Kleinman, T. A. Lyubimova, A. Z. Rabinovich, and M. B. Roitberg. 18(4), 546–7 (Jan. 1974); CPM-7401D0622

Klevtsov, P. V.—Double cesium-rare earth molybdates of the composition $Cs_3Ln(MoO_4)_3$ (Ln=La, Pr, Nd) —P. V. Klevtsov, V. A. Vinokurov, and R. F. Klevtsova. 18(1), 73–5 (Jul. 1973); CPM-7309D0323

—Hydrothermal synthesis of a new crystalline modification of lithium lanthanum molybdate, α-$LiLa(MoO_4)_2$ —P. V. Klevtsov, V. I. Protasova, L. Yu. Kharchenko, and R. F. Klevtsova. 18(4), 523–4 (Jan. 1974); CPM-7401D0599

—Binary molybdates and tungstates of alkali metals with bismuth, $M^+Bi(TO_4)_2$ —P. V. Klevtsov, V. A. Vinokurov, and R. F. Klevtsova. 18(6), 749–51 (May 1974); CPM-7406X1193

Klevtsova, R. F.—Double cesium-rare earth molybdates of the composition $Cs_3Ln(MoO_4)_3$ (Ln=La, Pr, Nd) —P. V. Klevtsov, V. A. Vinokurov, and R. F. Klevtsova. 18(1), 73–5 (Jul. 1973); CPM-7309D0323

—Crystal structure of lithium bitungstate $Li_2W_2O_7$ —S. A. Magarill, R. F. Klevtsova, and V. V. Bakakin. 18(2), 166–70 (Sep. 1973); CPM-7309D1368

—Hydrothermal synthesis of a new crystalline modification of lithium lanthanum molybdate, α-$LiLa(MoO_4)_2$ —P. V. Klevtsov, V. I. Protasova, L. Yu. Kharchenko, and R. F. Klevtsova. 18(4), 523–4 (Jan. 1974); CPM-7401D0599

—Binary molybdates and tungstates of alkali metals with bismuth, $M^+Bi(TO_4)_2$ —P. V. Klevtsov, V. A. Vinokurov, and R. F. Klevtsova. 18(6), 749–51 (May 1974); CPM-7406X1193

Klimasenko, N. L.—Crystal-chemical analysis of the structure of 1-I-substituted anthraquinone —N. L. Klimasenko, V. K. Bel'skii, V. K. Sarynin, and G. A. Gol'der. 18(4), 457–9 (Jan. 1974); CPM-7401D0533

Klimov, V. V.—Study of the structure and dielectric properties of solid solutions in the system $BaTiO_3$-$Pb(Fe_{1/2}Nb_{1/2})O_3$ —O. S. Didkovskaya, I. P. Kovalevskaya, V. G. Seryi, V. V. Klimov, and Yu. N. Venevtsev. 18(2), 184–6 (Sep. 1973); CPM-7309D1386

Klimova, A. Yu.—Dispersion of the optical activity in $(SrCa)S_2O_6{\cdot}4H_2O$ mixed crystals —A. Yu. Klimova, Z. B. Perekalina, and L. M. Belyaev. 18(2), 198–9 (Sep. 1973); CPM-7309D1400

Kocharov, A. G.—Neutron-diffraction refinement of the structure of alpha lithium iodate —A. Émiraliev, A. G. Kocharov, I. I. Yamzin, and V. A. Lyubimtsev. 18(6), 741–3 (May 1974); CPM-7406X1185

Kokhanchik, G. I.—Structure of Al_2O_3 in internally oxidized Cu-Al alloys —G. I. Kokhanchik and A. V. Serebryakov. 18(4), 467–70 (Jan. 1974); CPM-7401D0543

Kolesova, R. V.—Growth and study of crystals of double oxides of cadmium with structures of the perovskite type. I. Cadmium hafnate —R. I. Spinko, V. N. Lebedev, R. V. Kolesova, and E. G. Fesenko. 18(4), 536–7 (Jan. 1974); CPM-7401D0612

—Surface layer of barium titanate crystals —V. P. Dudkevich, I. N. Zakharchenko, V. S. Bondarenko, R. V. Kolesova, A. G. Stoinov, and E. G. Fesenko. 18(5), 690–1 (Mar. 1974); CPM-7403D0518

—Growth and investigation of binary cadmium oxides with structures of the perovskite type. II. Cadmium stannate and zirconate —R. I. Spinko, V. N. Lebedev, R. V. Kolesova, and E. G. Fesenko. 18(6), 809–10 (May 1974); CPM-7406X1253

Kolodeshnikova, N. P.—Anisotropy of growth and alloying for epitaxial germanium layers in the Ge-I_2 system —L. G. Lavrent'eva, I. S. Zakharov, I. V. Ivonin, N. P. Kolodeshnikova, and T. I. Opryshko. 18(2), 228–31 (Sep. 1973); CPM-7309D1430

Kolodieva, S. V.—Some features of the action of penetrating radiation on the electrical properties of a quartz crystal —A. A. Fotchenkov and S. V. Kolodieva. 18(3), 366–9 (Nov. 1973); CPM-7311E0498
Kolomiets, I. P.—Anisotropy of the molar refraction of liquid-crystal alkoxybenzoic acids —E. I. Ryumtsev, A. P. Kovshik, I. P. Kolomiets, and V. N. Tsvetkov. 18(6), 780–2 (May 1974); CPM-7406X1224
Kolomiitsev, A. I.—Charge on dislocations in sodium chloride crystals containing an anionic impurity —N. A. Tyapunina and A. I. Kolomiitsev. 18(4), 549–50 (Jan. 1974); CPM-7401D0625
Kolontsova, E. V.—Irradiation-induced phase transition in quartz —E. V. Kolontsova, É. E. Kulago, and N. A. Tomilin. 18(6), 752–4 (May 1974); CPM-7406X1196
Kolpakov, A. V.—Dynamic theory of x-ray diffraction in crystals with modulated electron density —A. V. Kolpakov and Yu. P. Khapachev. 18(3), 300–2 (Nov. 1973); CPM-7311E0432
Komissarova, L. N.—Use of the methods of successive experiment planning with refining crystal-structure parameters —I. V. Igonina, B. I. Pokrovskii, A. K. Gapeev, P. I. Lazarev, and L. N. Komissarova. 18(3), 308–13 (Nov. 1973); CPM-7311E0440
Komnik, Yu. F.—Electron-microscope investigation of thin film condensation kinetics —Yu. F. Komnik and V. V. Pilipenko. 18(5), 667–70 (Mar. 1974); CPM-7403D0495
—Structure of low-temperature "amorphous" bismuth films —Yu. F. Komnik, L. A. Yatsuk, A. A. Motornaya, M. L. Bolotina, and B. I. Belevtsev. 18(6), 791–6 (May 1974); CPM-7406X1235
Kompanets, I. N.—Orientational order and molecular parameters of liquid crystals with a positive dielectric anisotropy —V. G. Rumyantsev, P. D. Berezin, L. M. Blinov, and I. N. Kompanets. 18(5), 697–8 (Mar. 1974); CPM-7403D0525
Konstantinova, A. F.—Propagation of light in active absorbing crystals —A. F. Konstantinova and B. N. Grechushnikov. 18(3), 298–9 (Nov. 1973); CPM-7311E0430
Koptsik, V. A.—Thermal properties of ammonium fluoroberyllate crystals over a wide temperature range —B. A. Strukov, T. L. Skomorokhova, V. A. Koptsik, A. A. Boiko, and A. N. Izrailenko. 18(1), 86–8 (Jul. 1973); CPM-7309D0336
—High-temperature phase transitions in crystals of Rb $(D_xH_{1-x})_2PO_4$ —V. A. D'yakov, V. A. Koptsik, I. V. Lebedeva, A. V. Mishchenko, and L. N. Rashkovich. 18(6), 769–72 (May 1974); CPM-7406X1213
Koreneva, L. G.—Use of the methods of nonlinear optics in order to make a more accurate analysis of the structural characteristics of crystals associated with the absence of an inversion center —L. G. Koreneva, V. F. Zolin, B. L. Davydov, and V. I. Tsaryuk. 18(3), 399 (Nov. 1973); CPM-7311E0531
Kosoi, A. L.—Determination of the nature of the filling of positions by isomorphous elements —A. L. Kosoi and V. A. Frank-Kamenetskii. 18(4), 464–6 (Jan. 1974); CPM-7401D0540
Kostyleva, E. E.—Influence of temperature gradient on the impurity distribution during growth of crystals form a melt —E. A. Krivandina and E. E. Kostyleva. 18(4), 560–1 (Jan. 1974); CPM-7401D0636
Kostyukova, E. P.—Mechanical stability of small-angle growth boundaries in NaCl crystals —E. L. Pishchik and E. P. Kostyukova. 18(3), 414–5 (Nov. 1973); CPM-7311E0546
Kovalev, O. V.—Antiferromagnets with electric polarization —O. V. Kovalev. 18(2), 137–40 (Sep. 1973); CPM-7309D1339
Kovalev, Yu. Yu.—Low-dislocation-density single crystals of corundum —Kh. S. Bagdasarov, E. R. Dobrovinskaya, V. V. Pishchik, M. M. Chernik, Yu. Yu. Kovalev, A. S. Gershun, and I. F. Zvyagintseva. 18(2), 242–5 (Sep. 1973); CPM-7309D1444
Kovalevskaya, I. P.—Study of the structure and dielectric properties of solid solutions in the system $BaTiO_3$-$Pb(Fe_{1/2}Nb_{1/2})O_3$ —O. S. Didkovskaya, I. P. Kovalevskaya, V. G. Seryi, V. V. Klimov, and Yu. N. Venevtsev. 18(2), 184–6 (Sep. 1973); CPM-7309D1386
Kovba, L. M.—Crystal structure of U_2MoO_8 —V. N. Serezhkin, L. M. Kovba, and V. K. Trunov. 18(3), 323–5 (Nov. 1973); CPM-7311E0455
—Structure of the double oxide α-$U_3Mo_{20}O_{64}$ —V. N. Serezhkin, L. M. Kovba, and V. K. Trunov. 18(5), 603–5 (Mar. 1974); CPM-7403D0431
Kovshik, A. P.—Anisotropy of the molar refraction of liquid-crystal alkoxybenzoic acids —E. I. Ryumtsev, A. P. Kovshik, I. P. Kolomiets, and V. N. Tsvetkov. 18(6), 780–2 (May 1974); CPM-7406X1224
Kozlov, I. V.—Molecular scattering of light in a single crystal of hafnium dioxide —V. I. Aleksandrov, V. F. Kitaeva, I. V. Kozlov, V. V. Osiko, N. N. Sobolev, V. M. Tatarintsev, and I. L. Chistyi. 18(5), 682–4 (Mar. 1974); CPM-7403D0510
Kozlova, N. L.—Optical activity in $Ba(NO_2)_2{\cdot}H_2O$ crystals —V. I. Burkov, V. A. Kizel', Z. B. Perekalina, N. L. Kozlova, and G. S. Semin. 18(2), 196–7 (Sep. 1973); CPM-7309D1398
Kozyrev, S. P.—Optical activity in monoclinic sodium zincogermanate Na_2ZnGeO_4 —S. P. Kozyrev, A. B. Gil'varg, B. N. Grechushnikov, and N. V. Belov. 18(6), 813 (May 1974); CPM-7406X1257
Kraeva, L. E.—Use of the luminescence polarization diagram method to investigate molecular crystals containing two impurities —G. S. Belikova, N. D. Zhevandrov, T. V. Il'inykh, L. E. Kraeva, and N. P. Sul'zhenko. 18(4), 489–91 (Jan. 1974); CPM-7401D0565
Kreinin, O. L.—Distribution coefficients of divalent impurities in alkali halide crystals —O. L. Kreinin and K. M. Rozin. 18(2), 276–7 (Sep. 1973); CPM-7309D1478
Kripyakevich, P. I.—Loose packing of dense layers —P. I. Kripyakevich. 18(4), 460–3 (Jan. 1974); CPM-7401D0536
Kristofel, N. N.—Some characteristics of the vibronic impurity spectra in ferroelectrics —N. N. Kristofel. 18(1), 10–4 (Jul. 1973); CPM-7309D0260
Krivandina, E. A.—Influence of temperature gradient on the impurity distribution during growth of crystals form a melt —E. A. Krivandina and E. E. Kostyleva. 18(4), 560–1 (Jan. 1974); CPM-7401D0636
Kruglik, A. I.—Crystal structure of sodium ammonium selenate dihydrate $NaNH_4SeO_4{\cdot}2H_2O$ —A. I. Kruglik, V. I. Simonov, and V. I. Yuzvak. 18(2), 177–80 (Sep. 1973); CPM-7309D1379
Krushel'nitskaya, T. D.—Anisotropy of certain physical properties of pyrargyrite and proustite crystals —N. I. Butsko, M. M. Pidorya, and T. D. Krushel'nitskaya. 18(4), 540–1 (Jan. 1974); CPM-7401D0616
K'uang, Lieh—Characteristic features of the internal friction of filamentary crystals of NaCl, KCl, and KBr at elevated temperatures —Lieh K'uang and V. N. Rozhanskii. 18(2), 260–2 (Sep. 1973); CPM-7309D1462
Kudryavtseva, O. V.—Solubility of LnF_3 in lanthanum fluoride —O. V. Kudryavtseva, L. S. Garashina, K. K. Rivkina, and B. P. Sobolev. 18(4), 531 (Jan. 1974); CPM-7401D0607
Kudryavtseva, R. V.—Micromorphology of epitaxial PbS films —R. V. Kudryavtseva and S. A. Semiletov. 18(2), 272–3 (Sep. 1973); CPM-7309D1474
Kudzin, A. Yu.—Relaxation of phase boundaries in SbSI single crystals —M. D. Volnyanskii, A. Yu. Kudzin, and A. N. Sukhinskii. 18(2), 202–3 (Sep. 1973); CPM-7309D1404
Kulagin, R. S.—Nature of the point defects in GaAs single crystals as a function of the composition of the melt during growth —V. T. Bublik, V. V. Karataev, R. S. Kulagin, M. G. Mil'vidskii, V. B. Osvenskii, O. G. Stolyarov, and L. P. Kholodnyi. 18(2), 218–9 (Sep. 1973); CPM-7309D1420
Kulago, É. E.—Irradiation-induced phase transition in quartz —E. V. Kolontsova, É. E. Kulago, and N. A. Tomilin. 18(6), 752–4 (May 1974); CPM-7406X1196
Kurkutova, E. N.—Crystal structure of langbanite —V. G. Rau and E. N. Kurkutova. 18(3), 320–2 (Nov. 1973); CPM-7311E0452
Kushev, D. B.—Proposed interference method for determining the signs of the electrooptical coefficients —V. I. Sokolov, D. B. Kushev, and V. K. Subashiev. 18(2), 200–1 (Sep. 1973); CPM-7309D1402
Kustov, E. F.—Calculation of the energy matrices for d^n configurations in intracrystalline fields with $T(n=2,3,7,8)$ symmetry —E. F. Kustov. 18(1), 15–8 (Jul. 1973); CPM-7309D0265
Kuvatov, Z. Kh.—Domain rotation in smectic liquid crystals —A. N. Chuvyrov and Z. Kh. Kuvatov. 18(2), 212–4 (Sep. 1973); CPM-7309D1414
—Electret effect in n-azoxyanisole —A. P. Kapustin, Z. Kh. Kuvatov, and A. N. Trofimov. 18(2), 263 (Sep. 1973); CPM-7309D1465
—Thermodielectric effect at the phase transition between a liquid and solid crystal —A. P. Kapustin, Z. Kh. Kuvatov, and A. N. Trofimov. 18(3), 409 (Nov. 1973); CPM-7311E0541
Kuz'ma, Yu. B.—New boride structural types in the homologous series based on the $CaCu_5$ and $CeCo_3B_2$ types —Yu. B. Kuz'ma and N. S. Bilonizhko. 18(4), 447–9 (Jan. 1974); CPM-7401D0523

Kuz'min, É. A.—Systematic analysis of Patterson functions on the basis of crystal symmetry. IV. Interpretation of the Patterson synthesis for crystals of lower systems —É. A. Kuz'min, V. P. Golovachev, V. V. Ilyukhin, and N. V. Belov. 18(1), 33–8 (Jul. 1973); CPM-7309D0283

—Systematic analysis of patterson function on the basis of crystal symmetry. V. Regularities in the degeneracy of the rhombuses in vector sytems of crystals belonging to lower crystallographic systems —É. A. Kuz'min, R. I. Bochkova, Yu. N. Saf'yanov, V. P. Golovachev, and N. V. Belov. 18(4), 429–33 (Jan. 1974); CPM-7401D0505

—Proton magnetic resonance investigation of the localization of the protons in the crystal structures $Na_2Cr_2O_7{\cdot}2H_2O$ and $Li_2Cr_2O_7{\cdot}2H_2O$ —G. R. Bulka, V. M. Vinokurov, É. A. Kuz'min, Yu. A. Kharitonov, and N. V. Belov. 18(5), 617–9 (Mar. 1974); CPM-7403D0445

Kuz'min, R. N.—Proposed method for determining the coordinates of resonant nuclei using polarized Mössbauer spectroscopy —M. A. Andreeva and R. N. Kuz'min. 18(2), 254–5 (Sep. 1973); CPM-7309D1456

Kuz'mina, I. P.—Zn-Mn isomorphism in Na_2ZnGeO_4 crystals —I. P. Kuz'mina, A. N. Lobachev, V. M. Vinokurov, N. M. Nizamutdinov, and L. A. Volkova. 18(1), 110–1 (Jul. 1973); CPM-7309D0360

—Luminescence of cuprous oxide single crystals —I. P. Kuz'mina, A. N. Lobachev, B. S. Predtechenskii, L. S. Starostina, V. B. Stopachinskii, and N. M. Khaidukov. 18(3), 400–1 (Nov. 1973); CPM-7311E0532

Kuznetsov, A. V.—Applicability of Zachariasen's equations to calculations of the integral intensity scattered by a "thick" single crystal in the Bragg symmetry case for any dislocation density —A. V. Kuznetsov. 18(5), 592–5 (Mar. 1974); CPM-7403D0420

—"Spectral instability" of multiwave diffraction with coplanar x rays —A. D. Fofanov, A. V. Kuznetsov, and G. A. Karacheva. 18(6), 711–4 (May 1974); CPM-7406X1155

Kvitashvili, A. I.—Sharpening the peaks of the projection of the Patterson function by regularization —A. I. Kvitashvili, N. P. Zhidkov, B. M. Shchedrin, and A. E. Shvelashvili. 18(5), 589–91 (Mar. 1974); CPM-7403D0417

L

Landa, L. I.—Crystal structure of 1,6-$[Coen_2Cl_2]Cl{\cdot}3SC(NH_2)_2$ —Yu. A. Simonov, L. I. Landa, N. N. Proskina, T. I. Malinovskii, and A. V. Ablov. 18(3), 333–5 (Nov. 1973); CPM-7311E0465

Lapin, I. P.—Some features of the domain structure in lead titanate crystals —E. G. Fesenko, V. G. Gavrilyachenko, M. A. Martynenko, A. F. Semenchev, and I. P. Lapin. 18(5), 635–7 (Mar. 1974); CPM-7403D0463

Larikov, L. N.—Anisotropy of the growth rate of centers of the α modification in single crystals of high purity tin —V. B. Brik, L. N. Larikov, and V. M. Fal'chenko. 18(3), 412–3 (Nov. 1973); CPM-7311E0544

Lavrent'eva, L. G.—Anisotropy of growth and alloying for epitaxial germanium layers in the $Ge\text{-}I_2$ system —L. G. Lavrent'eva, I. S. Zakharov, I. V. Ivonin, N. P. Kolodeshnikova, and T. I. Opryshko. 18(2), 228–31 (Sep. 1973); CPM-7309D1430

Lazarev, P. I.—Use of the methods of successive experiment planning with refining crystal-structure parameters —I. V. Igonina, B. I. Pokrovskii, A. K. Gapeev, P. I. Lazarev, and L. N. Komissarova. 18(3), 308–13 (Nov. 1973); CPM-7311E0440

Lazareva, V. T.—Dynamic scattering with a memory effect in liquid-crystal mixtures —G. S. Chilaya, V. T. Lazareva, and L. M. Blinov. 18(1), 127–8 (Jul. 1973); CPM-7309D0377

—Dynamic scattering of light in liquid crystals of the azocompound class —M. F. Grebenkin, G. S. Chilaya, V. T. Lazareva, K. V. Roitman, L. M. Blinov, and V. V. Titov. 18(2), 274–5 (Sep. 1973); CPM-7309D1476

Lazorina, E. I.—Etching of quartz and some features of the surface layer —E. I. Lazorina and V. V. Soroka. 18(5), 651–3 (Mar. 1974); CPM-7403D0479

Lebedev, V. N.—Growth and study of crystals of double oxides of cadmium with structures of the perovskite type. I. Cadmium hafnate —R. I. Spinko, V. N. Lebedev, R. V. Kolesova, and E. G. Fesenko. 18(4), 536–7 (Jan. 1974); CPM-7401D0612

—Growth and investigation of binary cadmium oxides with structures of the perovskite type. II. Cadmium stannate and zirconate —R. I. Spinko, V. N. Lebedev, R. V. Kolesova, and E. G. Fesenko. 18(6), 809–10 (May 1974); CPM-7406X1253

Lebedeva, I. V.—High-temperature phase transitions in crystals of $Rb(D_xH_{1-x})_2PO_4$ —V. A. D'yakov, V. A. Koptsik, I. V. Lebedeva, A. V. Mishchenko, and L. N. Rashkovich. 18(6), 769–72 (May 1974); CPM-7406X1213

Lebovich, É. M.—Wetting of faces of a single crystal in a melt —Yu. V. Naidich, V. M. Perevertailo, É. M. Lebovich, and L. P. Obushchak. 18(2), 234–5 (Sep. 1973); CPM-7309D1436

Ledovskaya, I. Yu.—Elastic properties of KDP and DKDP crystals of high temperatures —S. I. Chizhikov, N. G. Sorokin, I. Yu. Ledovskaya, and E. V. Makarevskaya. 18(4), 544–5 (Jan. 1974); CPM-7401D0620

Levdik, V. A.—Short-range and long-range order in the arrangement of the interstitial atoms in (34%Ta66%Ti)D, —N. F. Miron, V. I. Shcherbak, V. N. Bykov, and V. A. Levdik. 18(4), 532–3 (Jan. 1974); CPM-7401D0608

Levin'sh, A. F.—Structure of calcium-cobalt hexaborate $K_2Co[B_6O_7(OH)_6]_2{\cdot}4H_2O$ —É. Ya. Silin', Ya. K. Ozol, and A. F. Levin'sh. 18(3), 317–9 (Nov. 1973); CPM-7311E0449

Lineva, N. A.—Growth of smooth epitaxial germanium films by the iodide method in a through-flow system with diffusive mass transfer —G. M. Malkin, V. E. Grigor'ev, N. A. Lineva, and L. A. Malkina. 18(1), 129–30 (Jul. 1973); CPM-7309D0379

Litvin, Yu. A.—Growth of diamond crystals in the form of needles and plates —Yu. A. Litvin, V. P. Butuzov, É. M. Nikoforova, and S. I. Futergendler. 18(2), 278–9 (Sep. 1973); CPM-7309D1480

Lobachev, A. N.—Zn-Mn isomorphism in Na_2ZnGeO_4 crystals —I. P. Kuz'mina, A. N. Lobachev, V. M. Vinokurov, N. M. Nizamutdinov, and L. A. Volkova. 18(1), 110–1 (Jul. 1973); CPM-7309D0360

—Kinetics and structural aspect of the growth of single crystals of bismuthinite under hydrothermal conditions —V. I. Popolitov and A. N. Lobachev. 18(1), 131–2 (Jul. 1973); CPM-7309D0381

—Synthesis and ferroelectric properties of antimony orthoniobate —V. I. Popolitov, A. N. Lobachev, V. F. Peskin, L. N. Syrkin, and N. N. Feoktistova. 18(2), 258–9 (Sep. 1973); CPM-7309D1460

—Luminescence of cuprous oxide single crystals —I. P. Kuz'mina, A. N. Lobachev, B. S. Predtechenskii, L. S. Starostina, V. B. Stopachinskii, and N. M. Khaidukov. 18(3), 400–1 (Nov. 1973); CPM-7311E0532

—Study of crystallization in the hydrothermal system $GeO_2\text{-}Sb_2O_3\text{-}KF\text{-}H_2O$ —M. N. Tseitlin, G. F. Plakhov, A. N. Lobachev, V. I. Popolitov, M. A. Simonov, and N. V. Belov. 18(4), 525–7 (Jan. 1974); CPM-7401D0601

—Crystallization in the $As\text{-}S\text{-}HI\text{-}H_2O$ system —V. I. Popolitov and A. N. Lobachev. 18(4), 564 (Jan. 1974); CPM-7401D0640

—A group of synthetic cadmium germanates and their x-ray study —E. L. Belokoneva, M. A. Simonov, N. G. Duderov, A. N. Lobachev, and N. V. Belov. 18(5), 610–2 (Mar. 1974); CPM-7403D0438

Lobanov, V. G.—Reaction of foreign particles with a crystallization front —A. M. Zubko, V. G. Lobanov, and V. V. Nikonova. 18(2), 239–41 (Sep. 1973); CPM-7309D1441

Loginova, R. G.—Transport of boron from a source to an epitaxial layer during sublimation of silicon in vacuum —R. G. Loginova, R. A. Rubtsova, and M. I. Ovsyannikov. 18(2), 232–3 (Sep. 1973); CPM-7309D1434

Loshmanov, A. A.—Monochromatization of neutrons in multiple Bragg scattering —A. A. Loshmanov, V. N. Sigaev, and I. I. Yamzin. 18(4), 530 (Jan. 1974); CPM-7401D0606

Lyakhovitskaya, V. A.—Morphology of the domain structure of SbSI crystals —L. A. Zadorzhnaya, V. A. Lyakhovitskaya, and L. M. Belyaev. 18(3), 363–5 (Nov. 1973); CPM-7311E0495

—Effect of a magnetic field on the Curie point of the ferroelectric semiconductor SbSI —S. V. Ivanova and V. A. Lyakhovitskaya. 18(3), 404 (Nov. 1973); CPM-7311E0536

Lyubimova, T. A.—Heat effects in lithium metaniobate —I. A. Kleinman, T. A. Lyubimova, A. Z. Rabinovich, and M. B. Roitberg. 18(4), 546–7 (Jan. 1974); CPM-7401D0622

Lyubimtsev, V. A.—Neutron-diffraction refinement of the structure of alpha lithium iodate —A. Émiraliev, A. G. Kocharov, I. I. Yamzin, and V. A. Lyubimtsev. 18(6), 741–3 (May 1974); CPM-7406X1185

Lyubitov, Yu. N.—Evaluation of the heat effect during alkali halide monomer reorientation in an absorbed layer on a metal —Yu. N. Lyubitov and V. I. Mikhailov. **18**(2), 266–7 (Sep. 1973); CPM-7309D1468
—Spatial distribution of particles during vaporization of a zinc single crystal —Yu. A. Gel'man, V. F. Vinogradov, and Yu. N. Lyubitov. **18**(4), 556–7 (Jan. 1974); CPM-7401D0632
Lyubutin, I. S.—Magnetically nonequivalent cation positions in substituted ferrite garnets —I. S. Lyubutin, A. P. Dodokin, and L. M. Belyaev. **18**(5), 623–6 (Mar. 1974); CPM-7403D0451
Lyutovich, K. L.—Effect of the crystallization mechanism on boron diffusion in silicon-germanium solid-solution epitaxial films —K. L. Lyutovich, F. A. Gimel'farb, P. B. Orlov, and T. A. Ukhorskaya. **18**(6), 825–6 (May 1974); CPM-7406X1269

M

Magarill, S. A.—Crystal structure of lithium bitungstate $Li_2W_2O_7$ —S. A. Magarill, R. F. Klevtsova, and V. V. Bakakin. **18**(2), 166–70 (Sep. 1973); CPM-7309D1368
Makarevskaya, E. V.—Dispersion of the dielectric constant in crystals of KH_2PO_4 —L. P. Pereverzeva, Yu. M. Poplavko, V. M. Petrov, E. V. Makarevskaya, and I. S. Rez. **18**(3), 407–8 (Nov. 1973); CPM-7311E0539
—Elastic properties of KDP and DKDP crystals of high temperatures —S. I. Chizhikov, N. G. Sorokin, I. Yu. Ledovskaya, and E. V. Makarevskaya. **18**(4), 544–5 (Jan. 1974); CPM-7401D0620
Malikova, N. M.—Influence of impurities on the photoelastic constants of potassium chloride crystals —M. P. Shaskol'skaya, A. V. Pakhnev, S. S. Gorbach, and N. M. Malikova. **18**(6), 817 (May 1974); CPM-7406X1261
Malinovskii, T. I.—Crystal structure of 1,6-$[Coen_2Cl_2]Cl \cdot 3SC(NH_2)_2$ —Yu. A. Simonov, L. I. Landa, N. N. Proskina, T. I. Malinovskii, and A. V. Ablov. **18**(3), 333–5 (Nov. 1973); CPM-7311E0465
Malitskaya, M. A.—Electronic mechanism of the influence of radiation on the process of repolarization of ferroelectrics —A. A. Grekov, M. A. Malitskaya, and V. M. Fridkin. **18**(4), 494–8 (Jan. 1974); CPM-7401D0570
Malkin, G. M.—Growth of smooth epitaxial germanium films by the iodide method in a through-flow system with diffusive mass transfer —G. M. Malkin, V. E. Grigor'ev, N. A. Lineva, and L. A. Malkina. **18**(1), 129–30 (Jul. 1973); CPM-7309D0379
Malkina, L. A.—Growth of smooth epitaxial germanium films by the iodide method in a through-flow system with diffusive mass transfer —G. M. Malkin, V. E. Grigor'ev, N. A. Lineva, and L. A. Malkina. **18**(1), 129–30 (Jul. 1973); CPM-7309D0379
Mal'tsev, Yu. F.—Two-crystal spectrometer study of barium titanate single crystals —I. Ya. Nikoforov and Yu. F. Mal'tsev. **18**(3), 370–1 (Nov. 1973); CPM-7311E0502
—Studies on ferroelectric crystals with a three-crystal x-ray spectrometer —I. Ya. Nikiforov, Yu. F. Mal'tsev, and V. Z. Borodin. **18**(5), 638–40 (Mar. 1974); CPM-7403D0466
Mamedov, Kh. S.—Crystal structure of $La_2Sr_3(BO_3)_4$ —G. K. Abdullaev, Kh. S. Mamedov, and S. T. Amirov. **18**(5), 675–6 (Mar. 1974); CPM-7403D0503
Margolis, N. V.—Crystal structure of the potassium salt of 1,1-dinitroethane —O. V. Frank-Kamenetskaya, N. V. Grigor'eva, N. V. Margolis, and I. V. Tselinskii. **18**(1), 108–9 (Jul. 1973); CPM-7309D0358
—Symmetries of functions for separating structures from a Patterson distribution of the triclinic, monoclinic, and orthorhombic systems —O. V. Frank-Kamenetskaya, N. V. Grigor'eva, and N. V. Margolis. **18**(3), 314–6 (Nov. 1973); CPM-7311E0446
Martynenko, L. I.—X-ray study of potassium copper ethylenediaminetetraacetate trihydrate —M. A. Porai-Koshits, N. V. Novozhilova, T. N. Polynova, T. V. Filippova, and L. I. Martynenko. **18**(1), 54–8 (Jul. 1973); CPM-7309D0304
Martynenko, M. A.—Some features of the domain structure in lead titanate crystals —E. G. Fesenko, V. G. Gavrilyachenko, M. A. Martynenko, A. F. Semenchev, and I. P. Lapin. **18**(5), 635–7 (Mar. 1974); CPM-7403D0463
Mashkov, S. A.—Crystal structure of a new modification, Bi_2Se_3II —É. Ya. Atabaeva, S. A. Mashkov, and S. V. Popova. **18**(1), 104–5 (Jul. 1973); CPM-7309D0354
Maslova, L. A.—Growth of shaped germanium crystals having low dislocation density by the Bridgman method —L. A. Maslova and S. V. Tsivinskii. **18**(4), 565 (Jan. 1974); CPM-7401D0641
Meisner, L. B.—Calculation of the electrooptical constants in "ionic" crystals —L. B. Meisner and I. S. Rez. **18**(3), 288–90 (Nov. 1973); CPM-7311E0420
Meleshina, V. A.—Domain boundaries, antiphase boundaries, and dislocations in gadolinium molybdate single crystals —V. A. Meleshina, V. L. Indenbom, Kh. S. Bagdasarov, and T. M. Polkhovskaya. **18**(6), 764–8 (May 1974); CPM-7406X1208
Mel'nikova, S. V.—Thermooptical and dielectric properties of $(NH_4)_2$ BeF_4 in the neighborhood of the ferroelectric transition —A. T. Anistratov and S. V. Mel'nikova. **18**(6), 811–2 (May 1974); CPM-7406X1255
Men', A. N.—Kronecker product for the representations of the crystallographic pointgroups I —B. A. Men', A. N. Men', and V. I. Cherepanov. **18**(4), 421–4 (Jan. 1974); CPM-7401D0497
—Reduction of the Kronecker product of representations of the crystallogrphic groups. II —B. A. Men', A. N. Men', and V. I. Cherepanov. **18**(5), 567–9 (Mar. 1974); CPM-7403D0395
—Reduction of the Kronecker product of representations of the crystallographic groups. III —B. A. Men', A. N. Men', and V. I. Cherepanov. **18**(6), 705–10 (May 1974); CPM-7406X1149
Men', B. A.—Kronecker product for the representations of the crystallographic pointgroups I —B. A. Men', A. N. Men', and V. I. Cherepanov. **18**(4), 421–4 (Jan. 1974); CPM-7401D0497
—Reduction of the Kronecker product of representations of the crystallogrphic groups. II —B. A. Men', A. N. Men', and V. I. Cherepanov. **18**(5), 567–9 (Mar. 1974); CPM-7403D0395
—Reduction of the Kronecker product of representations of the crystallographic groups. III —B. A. Men', A. N. Men', and V. I. Cherepanov. **18**(6), 705–10 (May 1974); CPM-7406X1149
Mikhailov, V. I.—Evaluation of the heat effect during alkali halide monomer reorientation in an absorbed layer on a metal —Yu. N. Lyubitov and V. I. Mikhailov. **18**(2), 266–7 (Sep. 1973); CPM-7309D1468
Mikhno, O. A.—Crystal and molecular structures of 4-chloroanthraquinonethiadiazole —O. A. Mikhno, Z. I Ezhkova, and G. S. Zhdanov. **18**(1), 59–62 (Jul. 1973); CPM-7309D0309
—Unit-cell parameters and space groups of several pyridinoanthraquinones —O. A. Mikhno, Z. I. Ezhkova, and M. I. Evstratova. **18**(6), 804–5 (May 1974); CPM-7406X1248
Mill', B. V.—Unusual ion coordination numbers in the structure of garnet —B. V. Mill' and G. Ronniger. **18**(1), 76–9 (Jul. 1973); CPM-7309D0326
—Vanadates with a defect garnet structure —G. Ronniger and B. V. Mill'. **18**(2), 187–90 (Sep. 1973); CPM-7309D1389
—New ions in the garnet structure —G. Ronniger and B. V. Mill'. **18** (3), 339–41 (Nov. 1973); CPM-7311E0471
Mil'vidskii, M. G.—Nature of the point defects in GaAs single crystals as a function of the composition of the melt during growth —V. T. Bublik, V. V. Karataev, R. S. Kulagin, M. G. Mil'vidskii, V. B. Osvenskii, O. G. Stolyarov, and L. P. Kholodnyi. **18**(2), 218–9 (Sep. 1973); CPM-7309D1420
—Influence of heat treatment on the structural perfection of single crystals of gallium arsenide alloyed with tellurium —M. G. Mil'vidskii, V. B. Osvenskii, A. G. Novikov, V. G. Fomin, and S. P. Grishina. **18**(4), 519–20 (Jan. 1974); CPM-7401D0595
—Effective distribution constants of excess basic components during crystallization of gallium arsenide from a melt —V. V. Karataev, M. G. Mil'vidskii, V. B. Osvenskii, and O. G. Stolyarov. **18**(4), 521–2 (Jan. 1974); CPM-7401D0597
—Nature of small etch pits in tellurium-alloyed GaAs single crystals —S. S. Shifrin, V. B. Osvenskii, M. G. Mil'vidskii, L. M. Morgulis, and S. P. Grishina. **18**(6), 818–20 (May 1974); CPM-7406X1262
Miron, N. F.—Short-range and long-range order in the arrangement of the interstitial atoms in $(34\%Ta66\%Ti)D_x$ —N. F. Miron, V. I. Shcherbak, V. N. Bykov, and V. A. Levdik. **18**(4), 532–3 (Jan. 1974); CPM-7401D0608
Mirskaya, K. V.—Atom-atom potentials and the coordinates of hydrogen atoms in methyl groups in the molecule and crystal —K. V. Mirskaya and L. V. Ivanova. **18**(1), 101–2 (Jul. 1973); CPM-7309D0351
Mirzaev, D. A.—X-ray diffraction in crystals with deformation twins —D. A. Mirzaev and S. V. Rushchits. **18**(2), 204–6 (Sep. 1973); CPM-7309D1406
Mishchenko, A. V.—High-temperature phase transitions in crystals of Rb $(D_xH_{1-x})_2PO_4$ —V. A. D'yakov, V. A. Koptsik, I. V. Lebedeva, A. V. Mishchenko, and L. N. Rashkovich. **18**(6), 769–72 (May 1974); CPM-7406X1213

Mityagin, A. Yu.—Study of the (111) surface of GaP by methods of Auger spectroscopy and slow-electron diffraction —A. Yu. Mityagin, V. P. Orlov, and N. Ya. Cherevatskii. 18(2), 268–9 (Sep. 1973); CPM-7309D1470
—Investigation of the pure and cesium-coated (100) surface of germanium by slow-electron diffraction —A. Yu. Mityagin and V. P. Orlov. 18(4), 554–5 (Jan. 1974); CPM-7401D0630
Miuskov, V. F.—Deformation dislocations in natural quartz crystals —V. F. Miuskov, L. I. Tsinober, and L. A. Gordienko. 18(2), 209–11 (Sep. 1973); CPM-7309D1411
Morgulis, L. M.—Nature of small etch pits in tellurium-alloyed GaAs single crystals —S. S. Shifrin, V. B. Osvenskii, M. G. Mil'vidskii, L. M. Morgulis, and S. P. Grishina. 18(6), 818–20 (May 1974); CPM-7406X1262
Motornaya, A. A.—Structure of low-temperature "amorphous" bismuth films —Yu. F. Komnik, L. A. Yatsuk, A. A. Motornaya, M. L. Bolotina, and B. I. Belevtsev. 18(6), 791–6 (May 1974); CPM-7406X1235
Muirsepp, T. K.—X-ray diffraction study of the system RbBr-TlBr —A. A. Haav and T. K. Muirsepp. 18(4), 471–2 (Jan. 1974); CPM-7401D0547
Munchaev, A. I.—Crystallization apparatus for the growth of crystals at constant supersaturation of the solution —A. I. Munchaev. 18 (4), 566 (Jan. 1974); CPM-7401D0642
Muradyan, L. A.—Refining the structure of crystals allowing for the anisotropy of the thermal vibrations of the atoms —L. A. Muradyan and V. I. Simonov. 18(1), 46–9 (Jul. 1973); CPM-7309D0296
Myasnikova, R. M.—Crystal structure of coumarin —R. M. Myasnikova, T. S. Davydova, and V. I. Simonov. 18(4), 454–6 (Jan. 1974); CPM-7401D0530
Mys'kiv, M. G.—Crystal structure of the compound $Ce_{15}Ni_4Si_{13}$ —M. G. Mys'kiv, O. I. Bodak, and E. I. Gladyshevskii. 18(4), 450–3 (Jan. 1974); CPM-7401D0526

N

Nabatov, V. V.—Focused laser-beam damage mechanism for CsI crystals —L. M. Belyaev, V. V. Nabatov, V. N. Rozhanskii, N. L. Sizova, and A. A. Urosovskaya. 18(2), 207–8 (Sep. 1973); CPM-7309D1409
Nadgornyi, É. M.—Kinetics of the polishing and etching of sodium chloride crystals. III —G. K. Baranova and É. M. Nadgornyi. 18 (5), 644–6 (Mar. 1974); CPM-7403D0472
Nagornyi, V. G.—Iteration method for calculating the intensity distribution in structural analysis —D. K. Khakimova, V. G. Nagornyi, and A. A. Smol'yaninov. 18(3), 303–5 (Nov. 1973); CPM-7311E0435
Naidich, Yu. V.—Wetting of faces of a single crystal in a melt —Yu. V. Naidich, V. M. Perevertailo, É. M. Lebovich, and L. P. Obushchak. 18(2), 234–5 (Sep. 1973); CPM-7309D1436
Nasyrov, R. Sh.—Crystallographic orientation of dendrites of pure tin —V. O. Esin, G. N. Pankin, and R. Sh. Nasyrov. 18(2), 246–9 (Sep. 1973); CPM-7309D1448
Naumov, A. S.—Isolation of n points of the basic system from a vector system by use of the star of an (n-1) -dimensional simplex —R. V. Galiulin, M. I. Sirota, A. S. Naumov, and N. V. Belov. 18 (1), 39–42 (Jul. 1973); CPM-7309D0289
Nesterenko, V. I.—X-ray diffraction and dielectric studies of the system $Li(Ta_xSb_{1-x})O_3$ —V. I. Nesterenko and I. G. Ismailzade. 18 (1), 112–3 (Jul. 1973); CPM-7309D0362
—X-ray diffraction and dielectric studies of the $LiNbO_3$-$KNbO_3$ system —I. G. Ismailzade, V. I. Nesterenko, and É. A. Il'yasov. 18 (1), 114–5 (Jul. 1973); CPM-7309D0364
Nikiforov, I. Ya.—Studies on ferroelectric crystals with a three-crystal x-ray spectrometer —I. Ya. Nikiforov, Yu. F. Mal'tsev, and V. Z. Borodin. 18(5), 638–40 (Mar. 1974); CPM-7403D0466
Nikoforov, I. Ya.—Two-crystal spectrometer study of barium titanate single crystals —I. Ya. Nikoforov and Yu. F. Mal'tsev. 18(3), 370–1 (Nov. 1973); CPM-7311E0502
Nikoforova, É. M.—Growth of diamond crystals in the form of needles and plates —Yu. A. Litvin, V. P. Butuzov, É. M. Nikoforova, and S. I. Futergendler. 18(2), 278–9 (Sep. 1973); CPM-7309D1480
Nikonova, V. V.—Reaction of foreign particles with a crystallization front —A. M. Zubko, V. G. Lobanov, and V. V. Nikonova. 18(2), 239–41 (Sep. 1973); CPM-7309D1441
Nizamutdinov, N. M.—Zn-Mn isomorphism in Na_2ZnGeO_4 crystals —I. P. Kuz'mina, A. N. Lobachev, V. M. Vinokurov, N. M. Nizamutdinov, and L. A. Volkova. 18(1), 110–1 (Jul. 1973); CPM-7309D0360
Novikov, A. G.—Influence of heat treatment on the structural perfection of single crystals of gallium arsenide alloyed with tellurium —M. G. Mil'vidskii, V. B. Osvenskii, A. G. Novikov, V. G. Fomin, and S. P. Grishina. 18(4), 519–20 (Jan. 1974); CPM-7401D0595
Novozhilova, N. V.—X-ray study of potassium copper ethylenediaminetetraacetate trihydrate —M. A. Porai-Koshits, N. V. Novozhilova, T. N. Polynova, T. V. Filippova, and L. I. Martynenko. 18(1), 54–8 (Jul. 1973); CPM-7309D0304

O

Obushchak, L. P.—Wetting of faces of a single crystal in a melt —Yu. V. Naidich, V. M. Perevertailo, É. M. Lebovich, and L. P. Obushchak. 18(2), 234–5 (Sep. 1973); CPM-7309D1436
Okulov, E. N.—Gamma-resonance investigations of ferruginous tourmalines —V. F. Belov, T. A. Khimich, M. N. Shipko, I. E. Voskresenskaya, and E. N. Okulov. 18(1), 119–20 (Jul. 1973); CPM-7309D0369
Olekhnovich, N. M.—Polarization and integrated intensity of x rays scattered by silicon crystals —N. M. Olekhnovich. 18(6), 777–9 (May 1974); CPM-7406X1221
Ol'shanetskii, B. Z.—Reflection intensity as a function of temperature during diffraction of slow electrons from (111) and (100) faces of germanium —B. Z. Ol'shanetskii, A. I. Volokitin, and S. M. Repinskii. 18(6), 815–6 (May 1974); CPM-7406X1259
Opryshko, T. I.—Anisotropy of growth and alloying for epitaxial germanium layers in the Ge-I_2 system —L. G. Lavrent'eva, I. S. Zakharov, I. V. Ivonin, N. P. Kolodeshnikova, and T. I. Opryshko. 18(2), 228–31 (Sep. 1973); CPM-7309D1430
Orekhova, V. P.—Laser based on Cr^{3+} ions in yttrium-aluminum garnet —B. K. Sevast'yanov, Kh. S. Bagdasarov, L. B. Pasternak, S. Yu. Volkov, and V. P. Orekhova. 18(2), 191–2 (Sep. 1973); CPM-7309D1393
Organova, N. I.—Structural study of tochilinite. II. Acicular variety: Unusual diffraction patterns. —N. I. Organova, V. A. Drits, and A. L. Dmitrik. 18(5), 606–9 (Mar. 1974); CPM-7403D0434
Orlov, P. B.—Effect of the crystallization mechanism on boron diffusion in silicon-germanium solid-solution epitaxial films —K. L. Lyutovich, F. A. Gimel'farb, P. B. Orlov, and T. A. Ukhorskaya. 18(6), 825–6 (May 1974); CPM-7406X1269
Orlov, V. P.—Study of the (111) surface of GaP by methods of Auger spectroscopy and slow-electron diffraction —A. Yu. Mityagin, V. P. Orlov, and N. Ya. Cherevatskii. 18(2), 268–9 (Sep. 1973); CPM-7309D1470
—Investigation of the pure and cesium-coated (100) surface of germanium by slow-electron diffraction — A. Yu. Mityagin and V. P. Orlov. 18(4), 554–5 (Jan. 1974); CPM-7401D0630
Osiko, V. V.—Molecular scattering of light in a single crystal of hafnium dioxide —V. I. Aleksandrov, V. F. Kitaeva, I. V. Kozlov, V. V. Osiko, N. N. Sobolev, V. M. Tatarintsev, and I. L. Chistyi. 18(5), 682–4 (Mar. 1974); CPM-7403D0510
Osvenskii, V. B.—Nature of the point defects in GaAs single crystals as a function of the composition of the melt during growth —V. T. Bublik, V. V. Karataev, R. S. Kulagin, M. G. Mil'vidskii, V. B. Osvenskii, O. G. Stolyarov, and L. P. Kholodnyi. 18(2), 218–9 (Sep. 1973); CPM-7309D1420
—Influence of heat treatment on the structural perfection of single crystals of gallium arsenide alloyed with tellurium —M. G. Mil'vidskii, V. B. Osvenskii, A. G. Novikov, V. G. Fomin, and S. P. Grishina. 18(4), 519–20 (Jan. 1974); CPM-7401D0595
—Effective distribution constants of excess basic components during crystallization of gallium arsenide from a melt —V. V. Karataev, M. G. Mil'vidskii, V. B. Osvenskii, and O. G. Stolyarov. 18(4), 521–2 (Jan. 1974); CPM-7401D0597
—Nature of small etch pits in tellurium-alloyed GaAs single crystals —S. S. Shifrin, V. B. Osvenskii, M. G. Mil'vidskii, L. M. Morgulis, and S. P. Grishina. 18(6), 818–20 (May 1974); CPM-7406X1262
Ovcharenko, N. N.—Dislocation formed during the sintering of solids ("sintering rosettes") —Ya. E. Geguzin, A. S. Dzyuba, V. L. Indenbom, and N. N. Ovcharenko. 18(4), 502–5 (Jan. 1974); CPM-7401D0578

Ovsyannikov, M. I.—Transport of boron from a source to an epitaxial layer during sublimation of silicon in vacuum —R. G. Loginova, R. A. Rubtsova, and M. I. Ovsyannikov. 18(2), 232–3 (Sep. 1973); CPM-7309D1434

Ozol, Ya. K.—Structure of calcium-cobalt hexaborate $K_2Co[B_6O_7(OH)_6]_2 \cdot 4H_2O$ —É. Ya. Silin', Ya. K. Ozol, and A. F. Levin'sh. 18(3), 317–9 (Nov. 1973); CPM-7311E0449

P

Pakhnev, A. V.—Temperature dependence of the elastooptical constants p_{11} and p_{12} of NaCl, KCl, Kbr, and Kl crystals —A. V. Pakhnev, S. S. Gorbach, and M. P. Shaskol'skaya. 18(5), 687 (Mar. 1974); CPM-7403D0515

—Influence of impurities on the photoelastic constants of potassium chloride crystals —M. P. Shaskol'skaya, A. V. Pakhnev, S. S. Gorbach, and N. M. Malikova. 18(6), 817 (May 1974); CPM-7406X1261

Pankin, G. N.—Crystallographic orientation of dendrites of pure tin —V. O. Esin, G. N. Pankin, and R. Sh. Nasyrov. 18(2), 246–9 (Sep. 1973); CPM-7309D1448

Panteleev, V. V.—Some structural-morphological characteristics of the volatilization of single crystal of α-Al_2O_3 —E. M. Akulenok, Yu. K. Danileiko, V. V. Panteleev, E. A. Fedorov, and V. Ya. Khaimov-Mal'kov. 18(5), 654–6 (Mar. 1974); CPM-7403D0482

Paperno, I. M.—Formation of a Debye-Hückel cloud around dislocations in LiF crystals —N. G. Politov, M. V. Galustashvili, and I. M. Paperno. 18(1), 125–6 (Jul. 1973); CPM-7309D0375

Pashchenko, T. N.—Dislocation networks formed during growth and annealing in the basal plane of a single crystal of zinc —N. A. Tyapunina, T. N. Pashchenko, and G. M. Zinenkova. 18(2), 264–5 (Sep. 1973); CPM-7309D1466

Pasternak, L. B.—Laser based on Cr^{3+} ions in yttrium-aluminum garnet —B. K. Sevast'yanov, Kh. S. Bagdasarov, L. B. Pasternak, S. Yu. Volkov, and V. P. Orekhova. 18(2), 191–2 (Sep. 1973); CPM-7309D1393

Pavlov, P. V.—Crystallization of amorphous films of silicon nitride by ionic bombardment followed by annealing —P. V. Pavlov, É. V. Shitova, E. I. Zorin, and N. A. Genkina. 18(3), 381–3 (Nov. 1973); CPM-7311E0513

—Change in the structure of germanium and silicon during ion bombardment and subsequent annealing —P. V. Pavlov. 18(4), 506–9 (Jan. 1974); CPM-7401D0582

Pel'ts, S. D.—Dynamic pyroelectric effect —S. D. Pel'ts and A. E. Karpel'son. 18(3), 360–2 (Nov. 1973); CPM-7311E0492

Perekalina, Z. B.—Optical activity in $Ba(NO_2)_2 \cdot H_2O$ crystals —V. I. Burkov, V. A. Kizel', Z. B. Perekalina, N. L. Kozlova, and G. S. Semin. 18(2), 196–7 (Sep. 1973); CPM-7309D1398

—Dispersion of the optical activity in $(SrCa)S_2O_6 \cdot 4H_2O$ mixed crystals —A. Yu. Klimova, Z. B. Perekalina, and L. M. Belyaev. 18(2), 198–9 (Sep. 1973); CPM-7309D1400

—Interpretation of the dispersion of the rotatory power in the $LiIO_3$ crystal —Z. B. Perekalina, N. L. Smirnova, G. F. Dobrzhanskii, and I. A. Shpil'ko. 18(4), 538–9 (Jan. 1974); CPM-7401D0614

Perevertailo, V. M.—Wetting of faces of a single crystal in a melt —Yu. V. Naidich, V. M. Perevertailo, É. M. Lebovich, and L. P. Obushchak. 18(2), 234–5 (Sep. 1973); CPM-7309D1436

Pereverzeva, L. P.—Dispersion of the dielectric constant in crystals of KH_2PO_4 —L. P. Pereverzeva, Yu. M. Poplavko, V. M. Petrov, E. V. Makarevskaya, and I. S. Rez. 18(3), 407–8 (Nov. 1973); CPM-7311E0539

—Dispersion of the electric permittivity of triglycine suflate in the vicinity of the phase transition —L. P. Pereverzeva and Yu. M. Poplavko. 18(4), 492–3 (Jan. 1974); CPM-7401D0568

Perstnev, I. P.—Reconstruction of the phase of the electronic scattering amplitude from experiments on the diffraction of resonant γ quanta —I. P. Perstnev and F. N. Chukhovskii. 18(5), 582–5 (Mar. 1974); CPM-7403D0410

Peshikov, E. V.—Phase transformations in $NaH_3(SeO_3)_2$ crystals irradiated with a large dose of gamma radiation —E. V. Peshikov and L. A. Shuvalov. 18(4), 499–501 (Jan. 1974); CPM-7401D0575

Peskin, V. F.—Synthesis and ferroelectric properties of antimony orthoniobate —V. I. Popolitov, A. N. Lobachev, V. F. Peskin, L. N. Syrkin, and N. N. Feoktistova. 18(2), 258–9 (Sep. 1973); CPM-7309D1460

Petrov, V. M.—Dispersion of the dielectric constant in crystals of KH_2PO_4 —L. P. Pereverzeva, Yu. M. Poplavko, V. M. Petrov, E. V. Makarevskaya, and I. S. Rez. 18(3), 407–8 (Nov. 1973); CPM-7311E0539

Petzelt, J.—Far infrared reflectance spectra of rubidium trihydro- and trideuterioselenite crystals —J. Petzelt, L. D. Kislovskii, and L. A. Shuvalov. 18(3), 351–3 (Nov. 1973); CPM-7311E0483

Pidorya, M. M.—Anisotropy of certain physical properties of pyrargyrite and proustite crystals —N. I. Butsko, M. M. Pidorya, and T. D. Krushel'nitskaya. 18(4), 540–1 (Jan. 1974); CPM-7401D0616

Pikin, S. A.—Theory of the electrodynamic effect in liquid crystals —S. A. Pikin and A. A. Shtol'berg. 18(3), 283–7 (Nov. 1973); CPM-7311E0415

Pilipenko, V. V.—Electron-microscope investigation of thin film condensation kinetics —Yu. F. Komnik and V. V. Pilipenko. 18(5), 667–70 (Mar. 1974); CPM-7403D0495

Pilyankevich, A. N.—Atomic scattering amplitudes for electrons at small scattering angles —A. N. Pilyankevich. 18(1), 103 (Jul. 1973); CPM-7309D0353

Pinsker, Z. G. –Investigation of the intensities of electron diffraction by NH_4Cl, NaCl, and TlCl films by using electrical recording and an electro filter–A. S. Avilov, R. M. Imamov, R. K. Karakhanyan, and Z. G. Pinsker. 18(1), 30–32 (Jul. 1973); CPM-7309D0280

—Allowance for three-wave scattering in electron diffraction by face-centered metals —V. V. Udalova and Z. G. Pinsker. 18(1), 136 (Jul. 1973); CPM-7309D0386

—Effect of accelerating voltage on the intensity of the forbidden reflection 222 Ge in electron diffraction —A. S. Avilov, R. M. Imamov, Z. G. Pinsker, and A. F. Fedotov. 18(4), 528–9 (Jan. 1974); CPM-7401D0604

—Structure of nickel hydroxide containing potassium ions —P. N. Bityutskii, V. I. Khitrova, and Z. G. Pinsker. 18(5), 613–6 (Mar. 1974); CPM-7403D0441

—Determination of the crystal structure of the hexagonal phase β^{III} in the copper-tellurium system by electron diffraction —R. V. Baranova, A. S. Avilov, and Z. G. Pinsker. 18(6), 736–40 (May 1974); CPM-7406X1180

Pisarevskii, Yu. V.—Scattering of light at elastic waves in optically biaxial crystals —Yu. V. Pisarevskii and I. M. Sil'vestrova. 18(5), 630–4 (Mar. 1974); CPM-7403D0458

Pishchik, E. L.—Mechanical stability of small-angle growth boundaries in NaCl crystals —E. L. Pishchik and E. P. Kostyukova. 18(3), 414–5 (Nov. 1973); CPM-7311E0546

Pishchik, V. V.—Low-dislocation-density single crystals of corundum —Kh. S. Bagdasarov, E. R. Dobrovinskaya, V. V. Pishchik, M. M. Chernik, Yu. Yu. Kovalev, A. S. Gershun, and I. F. Zvyagintseva. 18(2), 242–5 (Sep. 1973); CPM-7309D1444

Plakhov, G. F.—Study of crystallization in the hydrothermal system GeO_2-Sb_2O_3-KF-H_2O —M. N. Tseitlin, G. F. Plakhov, A. N. Lobachev, V. I. Popolitov, M. A. Simonov, and N. V. Belov. 18(4), 525–7 (Jan. 1974); CPM-7401D0601

Plishkin, Yu. M.—Simulation of a crystal surface equilibrium atomic structure for a single component system —V. O. Esin, V. I. Danilyuk, Yu. M. Plishkin, and G. L. Podchinenova. 18(5), 578–81 (Mar. 1974); CPM-7403D0406

Plyushchev, V. E.—X-ray diffraction study of the tetrahydrates of the mesoperiodates of the rare earth elements and yttrium —M. B. Varfolomeev, N. B. Shamrai, B. G. Berenshtein, and V. E. Plyushchev. 18(1), 106–7 (Jul. 1973); CPM-7309D0356

Podchinenova, G. L.—Simulation of a crystal surface equilibrium atomic structure for a single component system —V. O. Esin, V. I. Danilyuk, Yu. M. Plishkin, and G. L. Podchinenova. 18(5), 578–81 (Mar. 1974); CPM-7403D0406

Pogarev, D. E.—Vibrational spectrum and crystal structure of $TlNO_3III$ —D. E. Pogarev and A. A. Shultin. 18(2), 193–5 (Sep. 1973); CPM-7309D1395

Pokrovskii, B. I.—Use of the methods of successive experiment planning with refining crystal-structure parameters —I. V. Igonina, B. I. Pokrovskii, A. K. Gapeev, P. I. Lazarev, and L. N. Komissarova. 18(3), 308–13 (Nov. 1973); CPM-7311E0440

Polishchuk, S. A.—Crystal structure of zinc fluoride tetrahydrate, $ZnF_2 \cdot 4H_2O$ —B. V. Bukvetskii, S. A. Polishchuk, and V. I. Simonov. 18(5), 600–2 (Mar. 1974); CPM-7403D0428

Politov, N. G.—Formation of a Debye-Hückel cloud around dislocations in LiF crystals —N. G. Politov, M. V. Galustashvili, and I. M. Paperno. 18(1), 125–6 (Jul. 1973); CPM-7309D0375

Polkhovskaya, T. M.—Domain boundaries, antiphase boundaries, and dislocations in gadolinium molybdate single crystals —V. A. Meleshina, V. L. Indenbom, Kh. S. Bagdasarov, and T. M. Polkhovskaya. 18(6), 764–8 (May 1974); CPM-7406X1208

Poltavtsev, Yu. G.—Electron-diffraction analysis of amorphous films of carbon and boron —Yu. G. Poltavtsev, V. P. Zakharov, and V. M. Pozdnyakova. 18(2), 270–1 (Sep. 1973); CPM-7309D1472

—Electron diffraction study of the structure of amorphous germanium telluride and selenide films —Yu. G. Poltavtsev and V. P. Zakharov. 18(3), 379–80 (Nov. 1973); CPM-7311E0511

—Structure of amorphous indium monochalcongenide films —Yu. G. Poltavtsev, V. P. Zakharov, and T. V. Remizovich. 18(5), 701–2 (Mar. 1974); CPM-7403D0529

Polyanskaya, T. M.—Key role of analysis of interaction distances in oxygen compounds containing heavy cations (high atomic numbers) —T. M. Polyanskaya, S. V. Borisov, and N. V. Belov. 18(6), 719–27 (May 1974); CPM-7406X1163

Polynova, T. N.—X-ray study of potassium copper ethylenediaminetetraacetate trihydrate —M. A. Porai-Koshits, N. V. Novozhilova, T. N. Polynova, T. V. Filippova, and L. I. Martynenko. 18(1), 54–8 (Jul. 1973); CPM-7309D0304

Polzikov, S. D.—Relationships of structure types. New representatives of the homologous classes corundum, spinel, and amesite —N. L. Smirnova, S. D. Polzikov, and N. A. Rebrova. 18(6), 744–8 (May 1974); CPM-7406X1188

Popkova, E. G.—Selective etching at dislocations in metals (Ni) —E. G. Popkova and A. A. Predvoditelev. 18(5), 647–50 (Mar. 1974); CPM-7403D0475

Poplavko, Yu. M.—Dispersion of the dielectric constant in crystals of KH_2PO_4 —L. P. Pereverzeva, Yu. M. Poplavko, V. M. Petrov, E. V. Makarevskaya, and I. S. Rez. 18(3), 407–8 (Nov. 1973); CPM-7311E0539

—Dispersion of the electric permittivity of triglycine suflate in the vicinity of the phase transition —L. P. Pereverzeva and Yu. M. Poplavko. 18(4), 492–3 (Jan. 1974); CPM-7401D0568

Popolitov, V. I.—Kinetics and structural aspect of the growth of single crystals of bismuthinite under hydrothermal conditions —V. I. Popolitov and A. N. Lobachev. 18(1), 131–2 (Jul. 1973); CPM-7309D0381

—Synthesis and ferroelectric properties of antimony orthoniobate —V. I. Popolitov, A. N. Lobachev, V. F. Peskin, L. N. Syrkin, and N. N. Feoktistova. 18(2), 258–9 (Sep. 1973); CPM-7309D1460

—Study of crystallization in the hydrothermal system GeO_2-Sb_2O_3-KF-H_2O —M. N. Tseitlin, G. F. Plakhov, A. N. Lobachev, V. I. Popolitov, M. A. Simonov, and N. V. Belov. 18(4), 525–7 (Jan. 1974); CPM-7401D0601

—Crystallization in the As-S-HI-H_2O system —V. I. Popolitov and A. N. Lobachev. 18(4), 564 (Jan. 1974); CPM-7401D0640

—Preparation and preliminary investigation of cadmium phosphates —Yu. A. Ivanov, I. N. Ivanovskaya, V. I. Popolitov, M. A. Simonov, and N. V. Belov. 18(5), 671–3 (Mar. 1974); CPM-7403D0499

Popov, É. S.—Surface tension of 180° domain boundaries and effects in triglycine sulfate and c-domain $BaTiO_3$ —É. S. Popov and L. A. Shuvalov. 18(3), 405–6 (Nov. 1973); CPM-7311E0537

Popova, E. G.—Crystal and molecular structures of octafluoroanthraquinone —L. A. Chetkina and E. G. Popova. 18(6), 732–5 (May 1974); CPM-7406X1176

Popova, S. V.—Crystal structure of a new modification, Bi_2Se_3II —É. Ya. Atabaeva, S. A. Mashkov, and S. V. Popova. 18(1), 104–5 (Jul. 1973); CPM-7309D0354

Porai-Koshits, M. A.—X-ray study of potassium copper ethylenediaminetetraacetate trihydrate —M. A. Porai-Koshits, N. V. Novozhilova, T. N. Polynova, T. V. Filippova, and L. I. Martynenko. 18(1), 54–8 (Jul. 1973); CPM-7309D0304

—Crystal structure of lanthanum hypophosphite monohydrate —V. M. Ionov, L. A. Aslanov, V. B. Rybakov, and M. A. Porai-Koshits. 18(2), 250–1 (Sep. 1973); CPM-7309D1452

—Crystal structure of europium hypophosphite monohydrate —V. M. Ionov, L. A. Aslanov, M. A. Porai-Koshits, and V. B. Rybakov. 18(2), 252–3 (Sep. 1973); CPM-7309D1454

Portnoi, K. I.—Mechanism of growth and etching of whisker crystals of aluminum nitride —K. I. Portnoi, V. N. Gribkov, B. V. Shchetanov, É. L. Umantsev, and V. A. Silaev. 18(3), 376–8 (Nov. 1973); CPM-7311E0508

Postnikov, V. S.—Internal friction and strength of germanium whiskers —V. S. Postnikov, S. A. Ammer, and A. I. Drozhzhin. 18(3), 416 (Nov. 1973); CPM-7311E0548

Postoenko, G. E.—Crystal structures of $RbNbO(SO_4)_2$ and $NH_4NbO(SO_4)_2$ —A. A. Kashaev, G. E. Postoenko, and É. A. Zel'bst. 18(6), 802–3 (May 1974); CPM-7406X1246

Potapov, L. P.—Interpretation of field-ion images. I. point defects —L. P. Potapov, T. L. Raznikova, and A. L. Suvorov. 18(2), 220–3 (Sep. 1973); CPM-7309D1422

Pozdnyakova, V. M.—Electron-diffraction analysis of amorphous films of carbon and boron —Yu. G. Poltavtsev, V. P. Zakharov, and V. M. Pozdnyakova. 18(2), 270–1 (Sep. 1973); CPM-7309D1472

Predtechenskii, B. S.—Luminescence of cuprous oxide single crystals —I. P. Kuz'mina, A. N. Lobachev, B. S. Predtechenskii, L. S. Starostina, V. B. Stopachinskii, and N. M. Khaidukov. 18(3), 400–1 (Nov. 1973); CPM-7311E0532

Predvoditelev, A. A.—Selective etching at dislocations in metals (Ni) —E. G. Popkova and A. A. Predvoditelev. 18(5), 647–50 (Mar. 1974); CPM-7403D0475

Proskina, N. N.—Crystal structure of 1,6-$[Coen_2Cl_2]Cl \cdot 3SC(NH_2)_2$ —Yu. A. Simonov, L. I. Landa, N. N. Proskina, T. I. Malinovskii, and A. V. Ablov. 18(3), 333–5 (Nov. 1973); CPM-7311E0465

Protasova, V. I.—Hydrothermal synthesis of a new crystalline modification of lithium lanthanum molybdate, α-$LiLa(MoO_4)_2$ —P. V. Klevtsov, V. I. Protasova, L. Yu. Kharchenko, and R. F. Klevtsova. 18(4), 523–4 (Jan. 1974); CPM-7401D0599

R

Rabinovich, A. Z.—Heat effects in lithium metaniobate —I. A. Kleinman, T. A. Lyubimova, A. Z. Rabinovich, and M. B. Roitberg. 18(4), 546–7 (Jan. 1974); CPM-7401D0622

Rafalovich, M. L.—Stable configurations of a bioctahedral complex with Jahn-Teller centers —I. B. Bersuker, B. G. Vekhter, and M. L. Rafalovich. 18(1), 5–9 (Jul. 1973); CPM-7309D0255

Rakova, E. V.—Structure of thin lead telluride films —E. V. Rakova and S. A. Semiletov. 18(6), 797–9 (May 1974); CPM-7406X1241

Rashkovich, L. N.—Growth of $KIO_3 \cdot HIO_3$ crystals and investigation of some of their physical properties —N. R. Ivanov, A. N. Izrailenko, L. N. Rashkovich, and O. A. Chikhladze. 18(3), 397–8 (Nov. 1973); CPM-7311E0529

—High-temperature phase transitions in crystals of $Rb(D_xH_{1-x})_2PO_4$ —V. A. D'yakov, V. A. Koptsik, I. V. Lebedeva, A. V. Mishchenko, and L. N. Rashkovich. 18(6), 769–72 (May 1974); CPM-7406X1213

Ratner, I. M.—Stability of ionic crystals with an NaCl type lattice in the Born model —I. M. Ratner, N. A. Tenyakova, and A. I. Boiko. 18(1), 99–100 (Jul. 1973); CPM-7309D0349

Rau, V. G.—Crystal structure of langbanite —V. G. Rau and E. N. Kurkutova. 18(3), 320–2 (Nov. 1973); CPM-7311E0452

Raznikova, T. L.—Interpretation of field-ion images. I. point defects —L. P. Potapov, T. L. Raznikova, and A. L. Suvorov. 18(2), 220–3 (Sep. 1973); CPM-7309D1422

Rebrova, N. A.—Relationships of structure types. New representatives of the homologous classes corundum, spinel, and amesite —N. L. Smirnova, S. D. Polzikov, and N. A. Rebrova. 18(6), 744–8 (May 1974); CPM-7406X1188

Remizovich, T. V.—Structure of amorphous indium monochalcongenide films —Yu. G. Poltavtsev, V. P. Zakharov, and T. V. Remizovich. 18(5), 701–2 (Mar. 1974); CPM-7403D0529

Repinskii, S. M.—Reflection intensity as a function of temperature during diffraction of slow electrons from (111) and (100) faces of germanium —B. Z. Ol'shanetskii, A. I. Volokitin, and S. M. Repinskii. 18(6), 815–6 (May 1974); CPM-7406X1259

Rez, I. S.—Calculation of the electrooptical constants in "ionic" crystals —L. B. Meisner and I. S. Rez. 18(3), 288–90 (Nov. 1973); CPM-7311E0420

—Dispersion of the dielectric constant in crystals of KH_2PO_4 —L. P. Pereverzeva, Yu. M. Poplavko, V. M. Petrov, E. V. Makarevskaya, and I. S. Rez. 18(3), 407–8 (Nov. 1973); CPM-7311E0539

Rivkina, K. K.—Solubility of LnF_3 in lanthanum fluoride —O. V. Kudryavtseva, L. S. Garashina, K. K. Rivkina, and B. P. Sobolev. 18(4), 531 (Jan. 1974); CPM-7401D0607

Roitberg, M. B.—Heat effects in lithium metaniobate —I. A. Kleinman, T. A. Lyubimova, A. Z. Rabinovich, and M. B. Roitberg. 18(4), 546–7 (Jan. 1974); CPM-7401D0622

Roitman, K. V.—Dynamic scattering of light in liquid crystals of the azocompound class —M. F. Grebenkin, G. S. Chilaya, V. T. Lazareva, K. V. Roitman, L. M. Blinov, and V. V. Titov. 18(2), 274–5 (Sep. 1973); CPM-7309D1476

Rol'bin, Yu. A.—Calculation of the small-angle x-ray scattering intensity on a computer using a macromolecule model —Yu. A. Rol'bin, R. L. Kayushina, L. A. Feigin, and B. M. Shchedrin. 18(4), 442–4 (Jan. 1974); CPM-7401D0518

Romanenko, V. N.—Phenomena arising on the arrest of crystal growth —V. N. Romanenko and V. S. Kheifets. 18(5), 663–6 (Mar. 1974); CPM-7403D0491

Romanova, N. F.—Relaxational internal friction in crystals of KH_2PO_4 without chromium added —S. A. Gridnev, L. N. Kamysheva, and N. F. Romanova. 18(6), 773–6 (May 1974); CPM-7406X1217

Ronniger, G.—Unusual ion coordination numbers in the structure of garnet —B. V. Mill' and G. Ronniger. 18(1), 76–9 (Jul. 1973); CPM-7309D0326

—Vanadates with a defect garnet structure —G. Ronniger and B. V. Mill'. 18(2), 187–90 (Sep. 1973); CPM-7309D1389

—New ions in the garnet structure —G. Ronniger and B. V. Mill'. 18 (3), 339–41 (Nov. 1973); CPM-7311E0471

Rozenberg, L. P.—Crystal and molecular structures of the 1:2 complex of 1-methyl-3,3-dimethyl-2-(para-n-methyl-n-β-chloroethylstyryl)indole and 7,7,8,8-tetracyanoquinodimethane, $(C_{22}H_{26}N_2Cl)^+(C_{12}H_4N_4)(C_{12}H_4N_4)$ —R. P. Shibaeva, L. P. Rozenberg, and L. O. Atovmyan. 18(3), 326–9 (Nov. 1973); CPM-7311E0458

Rozhanskii, V. N.—Focused laser-beam damage mechanism for CsI crystals —L. M. Belyaev, V. V. Nabatov, V. N. Rozhanskii, N. L. Sizova, and A. A. Urosovskaya. 18(2), 207–8 (Sep. 1973); CPM-7309D1409

—Characteristic features of the internal friction of filamentary crystals of NaCl, KCl, and KBr at elevated temperatures —Lieh K'uang and V. N. Rozhanskii. 18(2), 260–2 (Sep. 1973); CPM-7309D1462

Rozin, K. M.—Distribution coefficients of divalent impurities in alkali halide crystals —O. L. Kreinin and K. M. Rozin. 18(2), 276–7 (Sep. 1973); CPM-7309D1478

Rubtsova, R. A.—Transport of boron from a source to an epitaxial layer during sublimation of silicon in vacuum —R. G. Loginova, R. A. Rubtsova, and M. I. Ovsyannikov. 18(2), 232–3 (Sep. 1973); CPM-7309D1434

Rumyantsev, V. G.—Determination of the degree of ordering in liquid crystals from the dichroism of dissolved dyes —V. G. Rumyantsev, L. M. Blinov, and V. A. Kizel'. 18(5), 695–6 (Mar. 1974); CPM-7403D0523

—Orientational order and molecular parameters of liquid crystals with a positive dielectric anisotropy —V. G. Rumyantsev, P. D. Berezin, L. M. Blinov, and I. N. Kompanets. 18(5), 697–8 (Mar. 1974); CPM-7403D0525

Rushchits, S. V.—X-ray diffraction in crystals with deformation twins —D. A. Mirzaev and S. V. Rushchits. 18(2), 204–6 (Sep. 1973); CPM-7309D1406

Rybakov, V. B.—Crystal structure of lanthanum hypophosphite monohydrate —V. M. Ionov, L. A. Aslanov, V. B. Rybakov, and M. A. Porai-Koshits. 18(2), 250–1 (Sep. 1973); CPM-7309D1452

—Crystal structure of europium hypophosphite monohydrate —V. M. Ionov, L. A. Aslanov, M. A. Porai-Koshits, and V. B. Rybakov. 18 (2), 252–3 (Sep. 1973); CPM-7309D1454

Ryumetsev, E. I.—Pretransition phenomena and optical activity of amorphous liquid phases of cholesteric liquid crystals —E. I. Ryumetsev, A. N. Cherkasov, V. G. Tishchenko, and M. M. Fetisova. 18(5), 657–9 (Mar. 1974); CPM-7403D0485

Ryumtsev, E. I.—Anisotropy of the molar refraction of liquid-crystal alkoxybenzoic acids —E. I. Ryumtsev, A. P. Kovshik, I. P. Kolomiets, and V. N. Tsvetkov. 18(6), 780–2 (May 1974); CPM-7406X1224

S

Saf'yanov, Yu. N.—Systematic analysis of patterson function on the basis of crystal symmetry. V. Regularities in the degeneracy of the rhombuses in vector sytems of crystals belonging to lower crystallographic systems —É. A. Kuz'min, R. I. Bochkova, Yu. N. Saf'yanov, V. P. Golovachev, and N. V. Belov. 18(4), 429–33 (Jan. 1974); CPM-7401D0505

Salli, I. V.—Forms of antimony crystal growth in alloys of the eutectic type —I. V. Salli, L. V. Samoilenko, and V. Z. Dolinskaya. 18(6), 823–4 (May 1974); CPM-7406X1267

Samoilenko, L. V.—Forms of antimony crystal growth in alloys of the eutectic type —I. V. Salli, L. V. Samoilenko, and V. Z. Dolinskaya. 18(6), 823–4 (May 1974); CPM-7406X1267

Sanadze, V. V.—Growth dislocation distribution along a copper crystal and dislocation density as a function of mean diameter —A. G. Basariya, B. K. Kapanadze, and V. V. Sanadze. 18(3), 411 (Nov. 1973); CPM-7311E0543

Sarkisov, S. É.—Stimulated emission from (Er,Lu)AlO_3 crystals containing Ho^{3+} and Tm^{3+} ions —Kh. S. Bagdasarov, A. A. Kaminskii, A. M. Kevorkov, S. É. Sarkisov, and T. A. Tevosyan. 18(5), 681 (Mar. 1974); CPM-7403D0509

Sarkisov, V. Kh.—Characteristics of residual-stress relaxation in $LiNbO_3$ single crystals in the 20-200°C region —K. G. Belabaev, V. T. Gabrielyan, and V. Kh. Sarkisov. 18(1), 123–4 (Jul. 1973); CPM-7309D0373

Sarynin, V. K.—Crystal-chemical analysis of the structure of 1-I-substituted anthraquinone —N. L. Klimasenko, V. K. Bel'skii, V. K. Sarynin, and G. A. Gol'der. 18(4), 457–9 (Jan. 1974); CPM-7401D0533

Seiranyan, K. B.—Polmorphism and crystallographic properties of yttrium and rare-earth trifluorides —B. P. Sobolev, L. S. Garashina, P. P. Fedorov, N. L. Tkachenko, and K. B. Seiranyan. 18(4), 473–6 (Jan. 1974); CPM-7401D0549

Semenchev, A. F.—Some features of the domain structure in lead titanate crystals —E. G. Fesenko, V. G. Gavrilyachenko, M. A. Martynenko, A. F. Semenchev, and I. P. Lapin. 18(5), 635–7 (Mar. 1974); CPM-7403D0463

Semenovskaya, S. V.—Determination of the energy and thermodynamic characteristics of iron-aluminum alloys by the method of diffuse x-ray scattering —S. V. Semenovskaya, Zh. B. Sinyavskaya, and A. P. Senichkin. 18(3), 344–8 (Nov. 1973); CPM-7311E0476

Semiletov, S. A.—Micromorphology of epitaxial PbS films —R. V. Kudryavtseva and S. A. Semiletov. 18(2), 272–3 (Sep. 1973); CPM-7309D1474

—Structure of thin lead telluride films —E. V. Rakova and S. A. Semiletov. 18(6), 797–9 (May 1974); CPM-7406X1241

Semin, G. S.—Optical activity in $Ba(NO_2)_2{\cdot}H_2O$ crystals —V. I. Burkov, V. A. Kizel', Z. B. Perekalina, N. L. Kozlova, and G. S. Semin. 18(2), 196–7 (Sep. 1973); CPM-7309D1398

Senichkin, A. P.—Determination of the energy and thermodynamic characteristics of iron-aluminum alloys by the method of diffuse x-ray scattering —S. V. Semenovskaya, Zh. B. Sinyavskaya, and A. P. Senichkin. 18(3), 344–8 (Nov. 1973); CPM-7311E0476

Serdyukov, A. N.—Boundary conditions in the electrodynamics of optically active media —B. V. Bokut', A. N. Serdyukov, F. I. Fedorov, and N. A. Khilo. 18(2), 141–4 (Sep. 1973); CPM-7309D1343

Serebryakov, A. V.—Structure of Al_2O_3 in internally oxidized Cu-Al alloys —G. I. Kokhanchik and A. V. Serebryakov. 18(4), 467–70 (Jan. 1974); CPM-7401D0543

Serezhkin, V. N.—Crystal structure of U_2MoO_8 —V. N. Serezhkin, L. M. Kovba, and V. K. Trunov. 18(3), 323–5 (Nov. 1973); CPM-7311E0455

—Structure of the double oxide α-$U_3Mo_{20}O_{64}$ —V. N. Serezhkin, L. M. Kovba, and V. K. Trunov. 18(5), 603–5 (Mar. 1974); CPM-7403D0431

Sergivskaya, T. N.—Alloying of epitaxial silicon layers with phosphorus and arsenic in a vacuum —V. A. Tolomasov, L. N. Abrosimova, T. N. Sergivskaya, and T. M. Zotova. 18(4), 558–9 (Jan. 1974); CPM-7401D0634

Seryi, V. G.—Study of the structure and dielectric properties of solid solutions in the system $BaTiO_3$-$Pb(Fe_{1/2}Nb_{1/2})O_3$ —O. S. Didkovskaya, I. P. Kovalevskaya, V. G. Seryi, V. V. Klimov, and Yu. N. Venevtsev. 18(2), 184–6 (Sep. 1973); CPM-7309D1386

Sevast'yanov, B. K.—Laser based on Cr^{3+} ions in yttrium-aluminum garnet —B. K. Sevast'yanov, Kh. S. Bagdasarov, L. B. Pasternak, S. Yu. Volkov, and V. P. Orekhova. 18(2), 191–2 (Sep. 1973); CPM-7309D1393

Shadyro, L. L.—Localization of heavy atoms in noncentrosymmetric crystals by single-wave anomalous x-ray scattering —L. L. Shadyro. 18(1), 43–5 (Jul. 1973); CPM-7309D0293

—Statistical values of heavy atom weighted contributions (D_H) to the total structure amplitude —L. L. Shadyro and I. D. Feranchuk. 18 (6), 715–8 (May 1974); CPM-7406X1159

Shafizade, R. B.—Electron diffraction investigation of In_2S_3 films obtained by vacuum deposition —R. B. Shafizade, É. G. Éfendiev, and F. I. Aliev. 18(3), 417–8 (Nov. 1973); CPM-7311E0549

—Electron-diffraction study of the kinetics of the $CuS \rightarrow Cu_{2-x}S$ transformation —M. M. Kazinets and R. B. Shafizade. 18(4), 480–2 (Jan. 1974); CPM-7401D0556

Shaldin, Yu. V.—Nonlinear optical properties of paratellurite (TeO_2) crystals —Yu. V. Shaldin, S. P. Smirnov, L. M. Belyaev, and I. A. Shpil'ko. 18(3), 358–9 (Nov. 1973); CPM-7311E0490

Shamrai, N. B.—X-ray diffraction study of the tetrahydrates of the mesoperiodates of the rare earth elements and yttrium —M. B. Varfolomeev, N. B. Shamrai, B. G. Berenshtein, and V. E. Plyushchev. 18(1), 106–7 (Jul. 1973); CPM-7309D0356

Shaskol'skaya, M. P.—Temperature dependence of the elastooptical constants p_{11} and p_{12} of NaCl, KCl, Kbr, and Kl crystals —A. V. Pakhnev, S. S. Gorbach, and M. P. Shaskol'skaya. 18(5), 687 (Mar. 1974); CPM-7403D0515

—Influence of impurities on the photoelastic constants of potassium chloride crystals —M. P. Shaskol'skaya, A. V. Pakhnev, S. S. Gorbach, and N. M. Malikova. 18(6), 817 (May 1974); CPM-7406X1261

Shchedrin, B. M.—Calculation of the small-angle x-ray scattering intensity on a computer using a macromolecule model —Yu. A. Rol'bin, R. L. Kayushina, L. A. Feigin, and B. M. Shchedrin. 18 (4), 442–4 (Jan. 1974); CPM-7401D0518

—Sharpening the peaks of the projection of the Patterson function by regularization —A. I. Kvitashvili, N. P. Zhidkov, B. M. Shchedrin, and A. E. Shvelashvili. 18(5), 589–91 (Mar. 1974); CPM-7403D0417

Shcherbak, V. I.—Short-range and long-range order in the arrangement of the interstitial atoms in (34%Ta66%Ti)D_x —N. F. Miron, V. I. Shcherbak, V. N. Bykov, and V. A. Levdik. 18(4), 532–3 (Jan. 1974); CPM-7401D0608

Shcherbakov, V. N.—Position of the hydroxyl groups in the structure of hydrosodalite —V. Yu. Galitskii, V. N. Shcherbakov, and S. P. Gabuda. 18(5), 620–2 (Mar. 1974); CPM-7403D0448

Shchetanov, B. V.—Mechanism of growth and etching of whisker crystals of aluminum nitride —K. I. Portnoi, V. N. Gribkov, B. V. Shchetanov, É. L. Umantsev, and V. A. Silaev. 18(3), 376–8 (Nov. 1973); CPM-7311E0508

Shekhtman, V. Sh.—Precision measurements of crystallographic parameters by the method of a widely divergent x-ray beam —V. V. Aristov, V. Sh. Shekhtman, and I. M. Shmyt'ko. 18(4), 445–6 (Jan. 1974); CPM-7401D0521

Shepelev, Yu. F.—Crystal structure of sodium hydrosilicate $Na_3HSiO_4 \cdot 5H_2O$ —Yu. I. Smolin, Yu. F. Shepelev, and I. K. Butikova. 18(2), 173–6 (Sep. 1973); CPM-7309D1375

—Structural mechanism of the phase transition in erbium pyrosilicate, $Er_2Si_2O_7$ —Yu. I. Smolin and Yu. F. Shepelev. 18(3), 390–1 (Nov. 1973); CPM-7311E0522

Shibaeva, R. P.—Crystal and molecular structures of the 1:2 complex of 1-methyl-3,3-dimethyl-2-(para-n-methyl-n-β-chloroethylstyryl)indole and 7,7,8,8-tetracyanoquinodimethane, $(C_{22}H_{26}N_2Cl)^+(C_{12}H_4N_4)(C_{12}H_4N_4)$ —R. P. Shibaeva, L. P. Rozenberg, and L. O. Atovmyan. 18(3), 326–9 (Nov. 1973); CPM-7311E0458

Shifrin, S. S.—Nature of small etch pits in tellurium-alloyed GaAs single crystals —S. S. Shifrin, V. B. Osvenskii, M. G. Mil'vidskii, L. M. Morgulis, and S. P. Grishina. 18(6), 818–20 (May 1974); CPM-7406X1262

Shigorin, V. D.—Laser detection of acentrism in crystals —V. D. Shigorin and G. P. Shipulo. 18(3), 349–50 (Nov. 1973); CPM-7311E0481

Shil'shtein, S. Sh.—Use of the double-crystal neutron spectrometer to study the low-temperature decomposition in niobium single crystals saturated with hydrogen —M. Kalanov, S. Sh. Shil'shtein, and V. A. Somenkov. 18(6), 755–7 (May 1974); CPM-7406X1199

Shipko, M. N.—Gamma-resonance investigations of ferruginous tourmalines —V. F. Belov, T. A. Khimich, M. N. Shipko, I. E. Voskresenskaya, and E. N. Okulov. 18(1), 119–20 (Jul. 1973); CPM-7309D0369

Shipulo, G. P.—Laser detection of acentrism in crystals —V. D. Shigorin and G. P. Shipulo. 18(3), 349–50 (Nov. 1973); CPM-7311E0481

Shirokov, A. M.—Effect of an electric field on phase transitions in $Na(D_xH_{1-x})_3(SeO_3)_2$ crystals. I. Induction of the β phase in crystals having $x \gtrsim 0.3$ by the field E_y—L. A. Shuvalov, A. M. Shirokov, N. R. Ivanov, and A. I. Baranov. 18(1), 80–2 (Jul. 1973); CPM-7309D0330

Shitova, É. V.—Crystallization of amorphous films of silicon nitride by ionic bombardment followed by annealing —P. V. Pavlov, É. V. Shitova, E. I. Zorin, and N. A. Genkina. 18(3), 381–3 (Nov. 1973); CPM-7311E0513

Shmyt'ko, I. M.—Precision measurements of crystallographic parameters by the method of a widely divergent x-ray beam —V. V. Aristov, V. Sh. Shekhtman, and I. M. Shmyt'ko. 18(4), 445–6 (Jan. 1974); CPM-7401D0521

Shpil'ko, I. A.—Nonlinear optical properties of paratellurite (TeO_2) crystals —Yu. V. Shaldin, S. P. Smirnov, L. M. Belyaev, and I. A. Shpil'ko. 18(3), 358–9 (Nov. 1973); CPM-7311E0490

—Interpretation of the dispersion of the rotatory power in the $LiIO_3$ crystal —Z. B. Perekalina, N. L. Smirnova, G. F. Dobrzhanskii, and I. A. Shpil'ko. 18(4), 538–9 (Jan. 1974); CPM-7401D0614

Shternberg, A. A.—Synthesis of tourmaline in chloride media. I —I. E. Voskresenskaya and A. A. Shternberg. 18(4), 562–3 (Jan. 1974); CPM-7401D0638

Shtol'berg, A. A.—Theory of the electrodynamic effect in liquid crystals —S. A. Pikin and A. A. Shtol'berg. 18(3), 283–7 (Nov. 1973); CPM-7311E0415

Shultin, A. A.—Vibrational spectrum and crystal structure of $TlNO_3III$ —D. E. Pogarev and A. A. Shultin. 18(2), 193–5 (Sep. 1973); CPM-7309D1395

Shuvalov, L. A.—Effect of an electric field on phase transitions in $Na(D_xH_{1-x})_3(SeO_3)_2$ crystals. I. Induction of the β phase in crystals having $x \gtrsim 0.3$ by the field E_y—L. A. Shuvalov, A. M. Shirokov, N. R. Ivanov, and A. I. Baranov. 18(1), 80–2 (Jul. 1973); CPM-7309D0330

—Far infrared reflectance spectra of rubidium trihydro- and trideuterioselenite crystals —J. Petzelt, L. D. Kislovskii, and L. A. Shuvalov. 18(3), 351–3 (Nov. 1973); CPM-7311E0483

—Surface tension of 180° domain boundaries and effects in triglycine sulfate and c-domain $BaTiO_3$ —É. S. Popov and L. A. Shuvalov. 18(3), 405–6 (Nov. 1973); CPM-7311E0537

—Phase transformations in $NaH_3(SeO_3)_2$ crystals irradiated with a large dose of gamma radiation —E. V. Peshikov and L. A. Shuvalov. 18(4), 499–501 (Jan. 1974); CPM-7401D0575

—KIO_3: the first ferroelectric permitting just a 120° shift in the ferroelectric polarization —L. A. Shuvalov, N. R. Ivanov, O. A. Chikhladze, and A. N. Izrailenko. 18(6), 758–61 (May 1974); CPM-7406X1202

Shvelashvili, A. E.—Sharpening the peaks of the projection of the Patterson function by regularization —A. I. Kvitashvili, N. P. Zhidkov, B. M. Shchedrin, and A. E. Shvelashvili. 18(5), 589–91 (Mar. 1974); CPM-7403D0417

Sidnenko, E. V.—Some features of the polarization of KH_2PO_4 in the phase transition region —E. V. Sidnenko and V. V. Gladkii. 18(1), 83–5 (Jul. 1973); CPM-7309D0333

Sigaev, V. N.—Monochromatization of neutrons in multiple Bragg scattering —A. A. Loshmanov, V. N. Sigaev, and I. I. Yamzin. 18 (4), 530 (Jan. 1974); CPM-7401D0606

Silaev, V. A.—Mechanism of growth and etching of whisker crystals of aluminum nitride —K. I. Portnoi, V. N. Gribkov, B. V. Shchetanov, É. L. Umantsev, and V. A. Silaev. 18(3), 376–8 (Nov. 1973); CPM-7311E0508

Silin', É. Ya.—Structure of calcium-cobalt hexaborate $K_2Co[B_6O_7(OH)_6]_2 \cdot 4H_2O$ —É. Ya. Silin', Ya. K. Ozol, and A. F. Levin'sh. 18(3), 317–9 (Nov. 1973); CPM-7311E0449

Sil'vestrov, V. G.—SbSI thin films with a ferroelectric phase transition —A. A. Agasiev, A. Kh. Zeinally, and V. G. Sil'vestrov. 18(6), 814 (May 1974); CPM-7406X1258

Sil'vestrova, I. M.—Scattering of light at elastic waves in optically biaxial crystals —Yu. V. Pisarevskii and I. M. Sil'vestrova. 18(5), 630–4 (Mar. 1974); CPM-7403D0458

Simonov, M. A.—Study of crystallization in the hydrothermal system GeO_2-Sb_2O_3-KF-H_2O —M. N. Tseitlin, G. F. Plakhov, A. N. Lobachev, V. I. Popolitov, M. A. Simonov, and N. V. Belov. 18(4), 525–7 (Jan. 1974); CPM-7401D0601

—A group of synthetic cadmium germanates and their x-ray study —E. L. Belokoneva, M. A. Simonov, N. G. Duderov, A. N. Lobachev, and N. V. Belov. 18(5), 610–2 (Mar. 1974); CPM-7403D0438

—Preparation and preliminary investigation of cadmium phosphates —Yu. A. Ivanov, I. N. Ivanovskaya, V. I. Popolitov, M. A. Simonov, and N. V. Belov. 18(5), 671–3 (Mar. 1974); CPM-7403D0499

—Structures of leucophoenicite, $Mn_7[SiO_4]_2[(SiO_4)(OH)_2]$, and synthetic Cd orthogermanate, $Cd_3[GeO_4](OH)_2$ —E. L. Belokoneva, M. A. Simonov, and N. V. Belov. 18(6), 800–1 (May 1974); CPM-7406X1244

Simonov, V. I.—Refining the structure of crystals allowing for the anisotropy of the thermal vibrations of the atoms —L. A. Muradyan and V. I. Simonov. 18(1), 46–9 (Jul. 1973); CPM-7309D0296

—Crystal structure of sodium ammonium selenate dihydrate $NaNH_4SeO_4 \cdot 2H_2O$ —A. I. Kruglik, V. I. Simonov, and V. I. Yuzvak. **18**(2), 177–80 (Sep. 1973); CPM-7309D1379

—Crystal structure of coumarin —R. M. Myasnikova, T. S. Davydova, and V. I. Simonov. **18**(4), 454–6 (Jan. 1974); CPM-7401D0530

—Crystal structure of zinc fluoride tetrahydrate, $ZnF_2 \cdot 4H_2O$ —B. V. Bukvetskii, S. A. Polishchuk, and V. I. Simonov. **18**(5), 600–2 (Mar. 1974); CPM-7403D0428

Simonov, Yu. A.—Crystal structure of 1,6-$[Coen_2Cl_2]Cl \cdot 3SC(NH_2)_2$ —Yu. A. Simonov, L. I. Landa, N. N. Proskina, T. I. Malinovskii, and A. V. Ablov. **18**(3), 333–5 (Nov. 1973); CPM-7311E0465

Sinel'nikov, B. Ya.—Preparation of mixed single crystals of (Cr, Te) —É. A. Zavadskii and B. Ya. Sinel'nikov. **18**(3), 419 (Nov. 1973); CPM-7311E0551

Sinyavskaya, Zh. B.—Determination of the energy and thermodynamic characteristics of iron-aluminum alloys by the method of diffuse x-ray scattering —S. V. Semenovskaya, Zh. B. Sinyavskaya, and A. P. Senichkin. **18**(3), 344–8 (Nov. 1973); CPM-7311E0476

Sirota, M. I.—Isolation of n points of the basic system from a vector system by use of the star of an (n-1) -dimensional simplex —R. V. Galiulin, M. I. Sirota, A. S. Naumov, and N. V. Belov. **18**(1), 39–42 (Jul. 1973); CPM-7309D0289

Sirotin, Yu. I.—Stereographic projections of surfaces for the physical properties of crystals —Sh. M. Butabaev and Yu. I. Sirotin. **18**(1), 121–2 (Jul. 1973); CPM-7309D0371

Sizova, N. L.—Focused laser-beam damage mechanism for CsI crystals —L. M. Belyaev, V. V. Nabatov, V. N. Rozhanskii, N. L. Sizova, and A. A. Urosovskaya. **18**(2), 207–8 (Sep. 1973); CPM-7309D1409

Sizova, R. G.—Chemical crystallography of mixed anion frameworks. I. Zirconium and scandium alkali sorosilicates —A. A. Voronkov, R. G. Sizova, V. V. Ilyukhin, and N. V. Belov. **18**(1), 67–72 (Jul. 1973); CPM-7309D0317

Skomorokhova, T. L.—Thermal properties of ammonium fluoroberyllate crystals over a wide temperature range —B. A. Strukov, T. L. Skomorokhova, V. A. Koptsik, A. A. Boiko, and A. N. Izrailenko. **18**(1), 86–8 (Jul. 1973); CPM-7309D0336

Smirnov, S. P.—Nonlinear optical properties of paratellurite (TeO_2) crystals —Yu. V. Shaldin, S. P. Smirnov, L. M. Belyaev, and I. A. Shpil'ko. **18**(3), 358–9 (Nov. 1973); CPM-7311E0490

Smirnova, N. L.—Interpretation of the dispersion of the rotatory power in the $LiIO_3$ crystal —Z. B. Perekalina, N. L. Smirnova, G. F. Dobrzhanskii, and I. A. Shpil'ko. **18**(4), 538–9 (Jan. 1974); CPM-7401D0614

—Crystallochemical determination of the structure of $NaTl_3(SO_3)_2$ by means of the method of crystallograms —N. L. Smirnova. **18**(5), 680 (Mar. 1974); CPM-7403D0508

—Relationships of structure types. New representatives of the homologous classes corundum, spinel, and amesite —N. L. Smirnova, S. D. Polzikov, and N. A. Rebrova. **18**(6), 744–8 (May 1974); CPM-7406X1188

Smolin, Yu. I.—Crystal structure of sodium hydrosilicate $Na_3HSiO_4 \cdot 5H_2O$ —Yu. I. Smolin, Yu. F. Shepelev, and I. K. Butikova. **18**(2), 173–6 (Sep. 1973); CPM-7309D1375

—Structural mechanism of the phase transition in erbium pyrosilicate, $Er_2Si_2O_7$ —Yu. I. Smolin and Yu. F. Shepelev. **18**(3), 390–1 (Nov. 1973); CPM-7311E0522

Smol'yaninov, A. A.—Iteration method for calculating the intensity distribution in structural analysis —D. K. Khakimova, V. G. Nagornyi, and A. A. Smol'yaninov. **18**(3), 303–5 (Nov. 1973); CPM-7311E0435

Sobolev, A. N.—X-ray diffraction study of naphthaloimide —A. N. Sobolev, L. A. Chetkina, G. A. Gol'der, Yu. G. Fedorov, and V. E. Zavodnik. **18**(6), 728–31 (May 1974); CPM-7406X1172

Sobolev, B. P.—"Hexagonal YF_3" structure type and high-temperature modifications of rare-earth trifluorides isostructural with YF_3 —B. P. Sobolev and P. P. Fedorov. **18**(3), 392 (Nov. 1973); CPM-7311E0524

—Polymorphism and crystallographic properties of yttrium and rare-earth trifluorides —B. P. Sobolev, L. S. Garashina, P. P. Fedorov, N. L. Tkachenko, and K. B. Seiranyan. **18**(4), 473–6 (Jan. 1974); CPM-7401D0549

—Solubility of LnF_3 in lanthanum fluoride —O. V. Kudryavtseva, L. S. Garashina, K. K. Rivkina, and B. P. Sobolev. **18**(4), 531 (Jan. 1974); CPM-7401D0607

Sobolev, N. N.—Molecular scattering of light in a single crystal of hafnium dioxide —V. I. Aleksandrov, V. F. Kitaeva, I. V. Kozlov, V. V. Osiko, N. N. Sobolev, V. M. Tatarintsev, and I. L. Chistyi. **18**(5), 682–4 (Mar. 1974); CPM-7403D0510

Sokolov, V. I.—Proposed interference method for determining the signs of the electrooptical coefficients —V. I. Sokolov, D. B. Kushev, and V. K. Subashiev. **18**(2), 200–1 (Sep. 1973); CPM-7309D1402

Sokolova, G. V.—Crystal structure of ditrioctahedral chlorite —V. A. Aleksandrova, V. A. Drits, and G. V. Sokolova. **18**(1), 50–3 (Jul. 1973); CPM-7309D0300

—Crystal structure of $CsNbO(SO_4)_2$ —A. A. Kashaev and G. V. Sokolova. **18**(3), 388–9 (Nov. 1973); CPM-7311E0520

Soldatov, V. P.—Temperature dependence of the rate of enlargement of the twinning layer in calcite crystals —V. P. Soldatov, V. I. Startsev, and N. M. Chaikovskaya. **18**(5), 641–3 (Mar. 1974); CPM-7403D0469

Somenkov, V. A.—Use of the double-crystal neutron spectrometer to study the low-temperature decomposition in niobium single crystals saturated with hydrogen —M. Kalanov, S. Sh. Shil'shtein, and V. A. Somenkov. **18**(6), 755–7 (May 1974); CPM-7406X1199

Soroka, V. V.—Etching of quartz and some features of the surface layer —E. I. Lazorina and V. V. Soroka. **18**(5), 651–3 (Mar. 1974); CPM-7403D0479

Sorokin, I. P.—Estimation of texture of the bcc→fcc→bcc double phase transformation —I. P. Sorokin. **18**(5), 627–9 (Mar. 1974); CPM-7403D0455

Sorokin, N. G.—Elastic properties of KDP and DKDP crystals of high temperatures —S. I. Chizhikov, N. G. Sorokin, I. Yu. Ledovskaya, and E. V. Makarevskaya. **18**(4), 544–5 (Jan. 1974); CPM-7401D0620

Spinko, R. I.—Growth and study of crystals of double oxides of cadmium with structures of the perovskite type. I. Cadmium hafnate —R. I. Spinko, V. N. Lebedev, R. V. Kolesova, and E. G. Fesenko. **18**(4), 536–7 (Jan. 1974); CPM-7401D0612

—Growth and investigation of binary cadmium oxides with structures of the perovskite type. II. Cadmium stannate and zirconate —R. I. Spinko, V. N. Lebedev, R. V. Kolesova, and E. G. Fesenko. **18**(6), 809–10 (May 1974); CPM-7406X1253

Starostina, L. S.—Luminescence of cuprous oxide single crystals —I. P. Kuz'mina, A. N. Lobachev, B. S. Predtechenskii, L. S. Starostina, V. B. Stopachinskii, and N. M. Khaidukov. **18**(3), 400–1 (Nov. 1973); CPM-7311E0532

Startsev, V. I.—Temperature dependence of the rate of enlargement of the twinning layer in calcite crystals —V. P. Soldatov, V. I. Startsev, and N. M. Chaikovskaya. **18**(5), 641–3 (Mar. 1974); CPM-7403D0469

Stetsiv, Ya. I.—New method for determining the normalizing factor in electron diffraction studies of the structure of amorphous substances —Ya. I. Stetsiv. **18**(2), 158–61 (Sep. 1973); CPM-7309D1360

—Determination of coordination numbers and mean-square displacements from the radial distribution curve —Ya. I. Stetsiv. **18**(3), 306–7 (Nov. 1973); CPM-7311E0438

Stoinov, A. G.—Surface layer of barium titanate crystals —V. P. Dudkevich, I. N. Zakharchenko, V. S. Bondarenko, R. V. Kolesova, A. G. Stoinov, and E. G. Fesenko. **18**(5), 690–1 (Mar. 1974); CPM-7403D0518

Stolyarov, O. G.—Nature of the point defects in GaAs single crystals as a function of the composition of the melt during growth —V. T. Bublik, V. V. Karataev, R. S. Kulagin, M. G. Mil'vidskii, V. B. Osvenskii, O. G. Stolyarov, and L. P. Kholodnyi. **18**(2), 218–9 (Sep. 1973); CPM-7309D1420

—Effective distribution constants of excess basic components during crystallization of gallium arsenide from a melt —V. V. Karataev, M. G. Mil'vidskii, V. B. Osvenskii, and O. G. Stolyarov. **18**(4), 521–2 (Jan. 1974); CPM-7401D0597

Stopachinskii, V. B.—Luminescence of cuprous oxide single crystals —I. P. Kuz'mina, A. N. Lobachev, B. S. Predtechenskii, L. S. Starostina, V. B. Stopachinskii, and N. M. Khaidukov. **18**(3), 400–1 (Nov. 1973); CPM-7311E0532

Struchkov, Yu. T.—Crystal and molecular structure of phenyl phenoxtinium iodide —A. I. Gusev and Yu. T. Struchkov. **18**(3), 330–2 (Nov. 1973); CPM-7311E0462

Strukov, B. A.—Thermal properties of ammonium fluoroberyllate crystals over a wide temperature range —B. A. Strukov, T. L. Skomorokhova, V. A. Koptsik, A. A. Boiko, and A. N. Izrailenko. **18**(1), 86–8 (Jul. 1973); CPM-7309D0336

—Heat capacity of single-crystal $BaTiO_3$ near the electrical critical point —B. A. Strukov and A. K. Ivanov-Shits. **18**(4), 548 (Jan. 1974); CPM-7401D0624

Subashiev, V. K.—Proposed interference method for determining the signs of the electrooptical coefficients —V. I. Sokolov, D. B. Kushev, and V. K. Subashiev. **18**(2), 200–1 (Sep. 1973); CPM-7309D1402

Sukhinskii, A. N.—Relaxation of phase boundaries in SbSI single crystals —M. D. Volnyanskii, A. Yu. Kudzin, and A. N. Sukhinskii. **18**(2), 202–3 (Sep. 1973); CPM-7309D1404

Sul'zhenko, N. P.—Use of the luminescence polarization diagram method to investigate molecular crystals containing two impurities —G. S. Belikova, N. D. Zhevandrov, T. V. Il'inykh, L. E. Kraeva, and N. P. Sul'zhenko. **18**(4), 489–91 (Jan. 1974); CPM-7401D0565

Suvorov, A. L.—Interpretation of field-ion images. I. point defects —L. P. Potapov, T. L. Raznikova, and A. L. Suvorov. **18**(2), 220–3 (Sep. 1973); CPM-7309D1422

Suvorova, N. V.—Hydrothermal crystallization in the system CdO-GeO_2-LiCl-H_2O —L. N. Dem'yanets and N. V. Suvorova. **18**(1), 133–4 (Jul. 1973); CPM-7309D0383

Syrkin, L. N.—Synthesis and ferroelectric properties of antimony orthoniobate —V. I. Popolitov, A. N. Lobachev, V. F. Peskin, L. N. Syrkin, and N. N. Feoktistova. **18**(2), 258–9 (Sep. 1973); CPM-7309D1460

T

Tarkhova, T. N.—Crystal structure of the coordination compound bis(pyridinaldehydethiosemicarbazonato)cobalt(III)nitrate —K. N. Akatova, T. N. Tarkhova, and N. V. Belov. **18**(2), 162–5 (Sep. 1973); CPM-7309D1364

Tatarintsev, V. M.—Molecular scattering of light in a single crystal of hafnium dioxide —V. I. Aleksandrov, V. F. Kitaeva, I. V. Kozlov, V. V. Osiko, N. N. Sobolev, V. M. Tatarintsev, and I. L. Chistyi. **18**(5), 682–4 (Mar. 1974); CPM-7403D0510

Temkin, D. E.—Kinetics of motion of steps and rows of steps at smeared phase boundaries —D. E. Temkin. **18**(2), 145–50 (Sep. 1973); CPM-7309D1347

—Effect of diffusion on the velocity of a break during the growth of an alloy crystal —D. E. Temkin. **18**(4), 425–8 (Jan. 1974); CPM-7401D0501

—Characteristics of a diffusionless transformation in nonideal alloys —D. E. Temkin. **18**(5), 570–4 (Mar. 1974); CPM-7403D0398

Tenyakova, N. A.—Stability of ionic crystals with an NaCl type lattice in the Born model —I. M. Ratner, N. A. Tenyakova, and A. I. Boiko. **18**(1), 99–100 (Jul. 1973); CPM-7309D0349

Tetel'baum, D. I.—Change of the interplanar distances in deep layers of silicon during bombardment with medium-energy ions —G. I. Uspenskaya, V. M. Genkin, and D. I. Tetel'baum. **18**(2), 224–5 (Sep. 1973); CPM-7309D1426

Tevosyan, T. A.—Stimulated emission from (Er,Lu)AlO_3 crystals containing Ho^{3+} and Tm^{3+} ions —Kh. S. Bagdasarov, A. A. Kaminskii, A. M. Kevorkov, S. É. Sarkisov, and T. A. Tevosyan. **18**(5), 681 (Mar. 1974); CPM-7403D0509

Tishchenko, V. G.—Pretransition phenomena and optical activity of amorphous liquid phases of cholesteric liquid crystals —E. I. Ryumetsev, A. N. Cherkasov, V. G. Tishchenko, and M. M. Fetisova. **18**(5), 657–9 (Mar. 1974); CPM-7403D0485

Titov, V. V.—Dynamic scattering of light in liquid crystals of the azocompound class —M. F. Grebenkin, G. S. Chilaya, V. T. Lazareva, K. V. Roitman, L. M. Blinov, and V. V. Titov. **18**(2), 274–5 (Sep. 1973); CPM-7309D1476

Tkachenko, N. L.—Polmorphism and crystallographic properties of yttrium and rare-earth trifluorides —B. P. Sobolev, L. S. Garashina, P. P. Fedorov, N. L. Tkachenko, and K. B. Seiranyan. **18**(4), 473–6 (Jan. 1974); CPM-7401D0549

Tokmakova, E. I.—Epitaxial growth of AgCl on the thermoelectric polyvinylchloride films, copying the electrical properties of an NaCl surface —G. I. Distler and E. I. Tokmakova. **18**(3), 384–5 (Nov. 1973); CPM-7311E0516

Tolomasov, V. A.—Alloying of epitaxial silicon layers with phosphorus and arsenic in a vacuum —V. A. Tolomasov, L. N. Abrosimova, T. N. Sergivskaya, and T. M. Zotova. **18**(4), 558–9 (Jan. 1974); CPM-7401D0634

Tomilin, N. A.—Irradiation-induced phase transition in quartz —E. V. Kolontsova, É. E. Kulago, and N. A. Tomilin. **18**(6), 752–4 (May 1974); CPM-7406X1196

Treivus, E. B.—Determination of the activation energy of forward and reverse reactions during crystal growth —E. B. Treivus. **18**(6), 788–90 (May 1974); CPM-7406X1232

Trofimov, A. N.—Electret effect in n-azoxyanisole —A. P. Kapustin, Z. Kh. Kuvatov, and A. N. Trofimov. **18**(2), 263 (Sep. 1973); CPM-7309D1465

—Thermodielectric effect at the phase transition between a liquid and solid crystal —A. P. Kapustin, Z. Kh. Kuvatov, and A. N. Trofimov. **18**(3), 409 (Nov. 1973); CPM-7311E0541

Tron'ko, V. D.—Jones and Müller matrices of a phase-shifting slab with a rotating axis of the highest velocity —V. D. Tron'ko and G. P. Golovach. **18**(3), 291–4 (Nov. 1973); CPM-7311E0423

Trunov, V. K.—Crystal structure of U_2MoO_8 —V. N. Serezhkin, L. M. Kovba, and V. K. Trunov. **18**(3), 323–5 (Nov. 1973); CPM-7311E0455

—Structure of the double oxide α-$U_3Mo_{20}O_{64}$ —V. N. Serezhkin, L. M. Kovba, and V. K. Trunov. **18**(5), 603–5 (Mar. 1974); CPM-7403D0431

Tsander, A. F.—X-ray diffraction by a cylindrical cavity in a crystal —A. F. Tsander. **18**(2), 151–3 (Sep. 1973); CPM-7309D1353

Tsaryuk, V. I.—Use of the methods of nonlinear optics in order to make a more accurate analysis of the structural characteristics of crystals associated with the absence of an inversion center —L. G. Koreneva, V. F. Zolin, B. L. Davydov, and V. I. Tsaryuk. **18**(3), 399 (Nov. 1973); CPM-7311E0531

Tseitlin, M. N.—Study of crystallization in the hydrothermal system GeO_2-Sb_2O_3-KF-H_2O —M. N. Tseitlin, G. F. Plakhov, A. N. Lobachev, V. I. Popolitov, M. A. Simonov, and N. V. Belov. **18**(4), 525–7 (Jan. 1974); CPM-7401D0601

Tselebrovskii, A. N.—Vacancy concentration in relation to plastic deformation in NaCl crystals —N. A. Tyapunina and A. N. Tselebrovskii. **18**(3), 410 (Nov. 1973); CPM-7311E0542

Tselinskii, I. V.—Crystal structure of the potassium salt of 1,1-dinitroethane —O. V. Frank-Kamenetskaya, N. V. Grigor'eva, N. V. Margolis, and I. V. Tselinskii. **18**(1), 108–9 (Jul. 1973); CPM-7309D0358

Tsentsiper, A. B.—Phase transformations in rubidium and cesium superoxides —V. Ya. Dudarev, A. B. Tsentsiper, and M. S. Dobrolyubova. **18**(4), 477–9 (Jan. 1974); CPM-7401D0553

Tsigel'nitskii, G. M.—Indexing of the crystallographic planes in rhombohedral crystals —V. A. Gerken, B. K. Kazurov, and G. M. Tsigel'nitskii. **18**(5), 674 (Mar. 1974); CPM-7403D0502

Tsinober, L. I.—Deformation dislocations in natural quartz crystals —V. F. Miuskov, L. I. Tsinober, and L. A. Gordienko. **18**(2), 209–11 (Sep. 1973); CPM-7309D1411

—Nature of the impurity water in synthetic quartz crystals —L. I. Tsinober and V. E. Khadzhi. **18**(5), 699–700 (Mar. 1974); CPM-7403D0527

Tsivinskii, S. V.—Growth of shaped germanium crystals having low dislocation density by the Bridgman method —L. A. Maslova and S. V. Tsivinskii. **18**(4), 565 (Jan. 1974); CPM-7401D0641

Tsvetkov, V. N.—Anisotropy of the molar refraction of liquid-crystal alkoxybenzoic acids —E. I. Ryumtsev, A. P. Kovshik, I. P. Kolomiets, and V. N. Tsvetkov. **18**(6), 780–2 (May 1974); CPM-7406X1224

Turyanitsa, I. D.—Phase diagram of the system $(HgI_2)_x(HgBr_2)_{1-x}$ and some optical properties of its single crystals —I. D. Turyanitsa and V. V. Khiminets. **18**(5), 688–9 (Mar. 1974); CPM-7403D0516

Tyapunina, N. A.—Dislocation networks formed during growth and annealing in the basal plane of a single crystal of zinc —N. A. Tyapunina, T. N. Pashchenko, and G. M. Zinenkova. **18**(2), 264–5 (Sep. 1973); CPM-7309D1466

—Vacancy concentration in relation to plastic deformation in NaCl crystals —N. A. Tyapunina and A. N. Tselebrovskii. **18**(3), 410 (Nov. 1973); CPM-7311E0542

—Charge on dislocations in sodium chloride crystals containing an anionic impurity —N. A. Tyapunina and A. I. Kolomiitsev. **18**(4), 549–50 (Jan. 1974); CPM-7401D0625

U

Udalova, V. V.—Allowance for three-wave scattering in electron diffraction by face-centered metals —V. V. Udalova and Z. G. Pinsker. **18**(1), 136 (Jul. 1973); CPM-7309D0386

Ugryumova, M. A.—The $PbZrO_3$-$SrCu_{1/3}Nb_{2/3}$ system —D. F. Dzhmukhadze, M. A. Ugryumova, Yu. N. Venevtsev, and G. S. Zhdanov. **18**(1), 116–8 (Jul. 1973); CPM-7309D0366

Ukhorskaya, T. A.—Effect of the crystallization mechanism on boron diffusion in silicon-germanium solid-solution epitaxial films —K. L. Lyutovich, F. A. Gimel'farb, P. B. Orlov, and T. A. Ukhorskaya. 18(6), 825–6 (May 1974); CPM-7406X1269

Umantsev, É. L.—Mechanism of growth and etching of whisker crystals of aluminum nitride —K. I. Portnoi, V. N. Gribkov, B. V. Shchetanov, É. L. Umantsev, and V. A. Silaev. 18(3), 376–8 (Nov. 1973); CPM-7311E0508

Urosovskaya, A. A.—Focused laser-beam damage mechanism for CsI crystals —L. M. Belyaev, V. V. Nabatov, V. N. Rozhanskii, N. L. Sizova, and A. A. Urosovskaya. 18(2), 207–8 (Sep. 1973); CPM-7309D1409

Uspenskaya, G. I.—Change of the interplanar distances in deep layers of silicon during bombardment with medium-energy ions —G. I. Uspenskaya, V. M. Genkin, and D. I. Tetel'baum. 18(2), 224–5 (Sep. 1973); CPM-7309D1426

V

Vainshtein, B. K.—Electron-diffraction determination of the crystal structure of β-CuOHCl —A. A. Voronova and B. K. Vainshtein. 18(1), 63–6 (Jul. 1973); CPM-7309D0313

Varfolomeev, M. B.—X-ray diffraction study of the tetrahydrates of the mesoperiodates of the rare earth elements and yttrium —M. B. Varfolomeev, N. B. Shamrai, B. G. Berenshtein, and V. E. Plyushchev. 18(1), 106–7 (Jul. 1973); CPM-7309D0356

Varina, T. M.—Absorption spectra of $MgWO_4$ crystals activated with Cr^{3+} and Co^{2+} ions —O. N. Boksha and T. M. Varina. 18(3), 354–7 (Nov. 1973); CPM-7311E0486

Vekhter, B. G.—Stable configurations of a bioctahedral complex with Jahn-Teller centers —I. B. Bersuker, B. G. Vekhter, and M. L. Rafalovich. 18(1), 5–9 (Jul. 1973); CPM-7309D0255

Velichko, I. A.—Electrooptical properties of potassium dihydrogen phosphate crystals having different degrees of deuteration —E. N. Volkova and I. A. Velichko. 18(2), 256–7 (Sep. 1973); CPM-7309D1458

Venevtsev, Yu. N.—The $PbZrO_3$-$SrCu_{1/3}Nb_{2/3}$ system —D. F. Dzhmukhadze, M. A. Ugryumova, Yu. N. Venevtsev, and G. S. Zhdanov. 18(1), 116–8 (Jul. 1973); CPM-7309D0366

—Study of the structure and dielectric properties of solid solutions in the system $BaTiO_3$-$Pb(Fe_{1/2}Nb_{1/2})O_3$ —O. S. Didkovskaya, I. P. Kovalevskaya, V. G. Seryi, V. V. Klimov, and Yu. N. Venevtsev. 18(2), 184–6 (Sep. 1973); CPM-7309D1386

—Solid solutions of $BaTiO_3$ with barium niobates —I. N. Groznov and Yu. N. Venevtsev. 18(3), 395–6 (Nov. 1973); CPM-7311E0527

Vinogradov, V. F.—Spatial distribution of particles during vaporization of a zinc single crystal —Yu. A. Gel'man, V. F. Vinogradov, and Yu. N. Lyubitov. 18(4), 556–7 (Jan. 1974); CPM-7401D0632

Vinokurov, V. A.—Double cesium-rare earth molybdates of the composition $Cs_3Ln(MoO_4)_3$ (Ln=La, Pr, Nd) —P. V. Klevtsov, V. A. Vinokurov, and R. F. Klevtsova. 18(1), 73–5 (Jul. 1973); CPM-7309D0323

—Binary molybdates and tungstates of alkali metals with bismuth, $M^+Bi(TO_4)_2$ —P. V. Klevtsov, V. A. Vinokurov, and R. F. Klevtsova. 18(6), 749–51 (May 1974); CPM-7406X1193

Vinokurov, V. M.—Zn-Mn isomorphism in Na_2ZnGeO_4 crystals —I. P. Kuz'mina, A. N. Lobachev, V. M. Vinokurov, N. M. Nizamutdinov, and L. A. Volkova. 18(1), 110–1 (Jul. 1973); CPM-7309D0360

—Proton magnetic resonance investigation of the localization of the protons in the crystal structures $Na_2Cr_2O_7 \cdot 2H_2O$ and $Li_2Cr_2O_7 \cdot 2H_2O$ —G. R. Bulka, V. M. Vinokurov, É. A. Kuz'min, Yu. A. Kharitonov, and N. V. Belov. 18(5), 617–9 (Mar. 1974); CPM-7403D0445

Vistin', L. K.—Phase transition in liquid crystals induced by an electric field —I. G. Chistyakov and L. K. Vistin'. 18(4), 552–3 (Jan. 1974); CPM-7401D0628

Volkov, S. Yu.—Laser based on Cr^{3+} ions in yttrium-aluminum garnet —B. K. Sevast'yanov, Kh. S. Bagdasarov, L. B. Pasternak, S. Yu. Volkov, and V. P. Orekhova. 18(2), 191–2 (Sep. 1973); CPM-7309D1393

Volkova, E. N.—Electrooptical properties of potassium dihydrogen phosphate crystals having different degrees of deuteration —E. N. Volkova and I. A. Velichko. 18(2), 256–7 (Sep. 1973); CPM-7309D1458

Volkova, L. A.—Zn-Mn isomorphism in Na_2ZnGeO_4 crystals —I. P. Kuz'mina, A. N. Lobachev, V. M. Vinokurov, N. M. Nizamutdinov, and L. A. Volkova. 18(1), 110–1 (Jul. 1973); CPM-7309D0360

Volnyanskii, M. D.—Relaxation of phase boundaries in SbSI single crystals —M. D. Volnyanskii, A. Yu. Kudzin, and A. N. Sukhinskii. 18(2), 202–3 (Sep. 1973); CPM-7309D1404

Volokitin, A. I.—Reflection intensity as a function of temperature during diffraction of slow electrons from (111) and (100) faces of germanium —B. Z. Ol'shanetskii, A. I. Volokitin, and S. M. Repinskii. 18(6), 815–6 (May 1974); CPM-7406X1259

Vorob'ev, S. A.—Determination of the degree of bending of single crystals from the orientational scattering of β particles —A. Ya. Bobudaev, S. A. Vorob'ev, and V. V. Kaplin. 18(4), 551 (Jan. 1974); CPM-7401D0627

Voronkov, A. A.—Chemical crystallography of mixed anion frameworks. I. Zirconium and scandium alkali sorosilicates —A. A. Voronkov, R. G. Sizova, V. V. Ilyukhin, and N. V. Belov. 18(1), 67–72 (Jul. 1973); CPM-7309D0317

Voronkov, V. V.—Dislocation mechanism of growth with a low kink density —V. V. Voronkov. 18(1), 19–23 (Jul. 1973); CPM-7309D0269

Voronova, A. A.—Electron-diffraction determination of the crystal structure of β-CuOHCl —A. A. Voronova and B. K. Vainshtein. 18(1), 63–6 (Jul. 1973); CPM-7309D0313

Voskresenskaya, I. E.—Gamma-resonance investigations of ferruginous tourmalines —V. F. Belov, T. A. Khimich, M. N. Shipko, I. E. Voskresenskaya, and E. N. Okulov. 18(1), 119–20 (Jul. 1973); CPM-7309D0369

—Synthesis of tourmaline in chloride media. I —I. E. Voskresenskaya and A. A. Shternberg. 18(4), 562–3 (Jan. 1974); CPM-7401D0638

Voznesenskaya, T. I.—Effect of manganese on the transformation of the zinc sulfide cubic lattice to hexagonal —G. E. Arkhangel'skii, T. I. Voznesenskaya, and M. V. Fok. 18(3), 342–3 (Nov. 1973); CPM-7311E0474

Y

Yamaguchi, S.—Growth of pyrrhotite on nuclei of iron thiospinel —S. Yamaguchi. 18(1), 135 (Jul. 1973); CPM-7309D0385

Yamzin, I. I.—Block conical ferromagnetic spiral in the hexagonal ferrite $BaGa_2Sc_{1.2}Fe_{8.8}O_{19}$ (M) —O. P. Aleshko-Ozhevskii, V. P. Cheparin, A. P. Cherkasov, and I. I. Yamzin. 18(3), 393–4 (Nov. 1973); CPM-7311E0525

—Monochromatization of neutrons in multiple Bragg scattering —A. A. Loshmanov, V. N. Sigaev, and I. I. Yamzin. 18(4), 530 (Jan. 1974); CPM-7401D0606

—Neutron-diffraction refinement of the structure of alpha lithium iodate —A. Émiraliev, A. G. Kocharov, I. I. Yamzin, and V. A. Lyubimtsev. 18(6), 741–3 (May 1974); CPM-7406X1185

Yatsuk, L. A.—Structure of low-temperature "amorphous" bismuth films —Yu. F. Komnik, L. A. Yatsuk, A. A. Motornaya, M. L. Bolotina, and B. I. Belevtsev. 18(6), 791–6 (May 1974); CPM-7406X1235

Yuzvak, V. I.—Crystal structure of sodium ammonium selenate dihydrate $NaNH_4SeO_4 \cdot 2H_2O$ —A. I. Kruglik, V. I. Simonov, and V. I. Yuzvak. 18(2), 177–80 (Sep. 1973); CPM-7309D1379

Z

Zabolotnyi, P. A.—Homology and antihomology groups —P. A. Zabolotnyi. 18(1), 1–4 (Jul. 1973); CPM-7309D0251

Zadorzhnaya, L. A.—Morphology of the domain structure of SbSI crystals —L. A. Zadorzhnaya, V. A. Lyakhovitskaya, and L. M. Belyaev. 18(3), 363–5 (Nov. 1973); CPM-7311E0495

Zakharchenko, I. N.—Surface layer of barium titanate crystals —V. P. Dudkevich, I. N. Zakharchenko, V. S. Bondarenko, R. V. Kolesova, A. G. Stoinov, and E. G. Fesenko. 18(5), 690–1 (Mar. 1974); CPM-7403D0518

Zakharov, I. S.—Anisotropy of growth and alloying for epitaxial germanium layers in the Ge-I_2 system —L. G. Lavrent'eva, I. S. Zakharov, I. V. Ivonin, N. P. Kolodeshnikova, and T. I. Opryshko. 18(2), 228–31 (Sep. 1973); CPM-7309D1430

Zakharov, V. P.—Electron-diffraction analysis of amorphous films of carbon and boron —Yu. G. Poltavtsev, V. P. Zakharov, and V. M. Pozdnyakova. 18(2), 270–1 (Sep. 1973); CPM-7309D1472

—Electron diffraction study of the structure of amorphous germanium telluride and selenide films —Yu. G. Poltavtsev and V. P. Zakharov. 18(3), 379–80 (Nov. 1973); CPM-7311E0511

—Structure of amorphous indium monochalcongenide films —Yu. G. Poltavtsev, V. P. Zakharov, and T. V. Remizovich. 18(5), 701–2 (Mar. 1974); CPM-7403D0529

Zavadskii, É. A.—Preparation of mixed single crystals of (Cr, Te) —É. A. Zavadskii and B. Ya. Sinel'nikov. 18(3), 419 (Nov. 1973); CPM-7311E0551

Zavodnik, V. E.—X-ray diffraction study of naphthaloimide —A. N. Sobolev, L. A. Chetkina, G. A. Gol'der, Yu. G. Fedorov, and V. E. Zavodnik. 18(6), 728–31 (May 1974); CPM-7406X1172

Zeinally, A. Kh.—SbSI thin films with a ferroelectric phase transition —A. A. Agasiev, A. Kh. Zeinally, and V. G. Sil'vestrov. 18(6), 814 (May 1974); CPM-7406X1258

Zel'bst, É. A.—Crystal structures of $RbNbO(SO_4)_2$ and $NH_4NbO(SO_4)_2$ —A. A. Kashaev, G. E. Postoenko, and É. A. Zel'bst. 18(6), 802–3 (May 1974); CPM-7406X1246

Zhdanov, G. S.—Crystal and molecular structures of 4-chloroanthraquinonethiadiazole —O. A. Mikhno, Z. I Ezhkova, and G. S. Zhdanov. 18(1), 59–62 (Jul. 1973); CPM-7309D0309

—The $PbZrO_3$-$SrCu_{1/3}Nb_{2/3}$ system —D. F. Dzhmukhadze, M. A. Ugryumova, Yu. N. Venevtsev, and G. S. Zhdanov. 18(1), 116–8 (Jul. 1973); CPM-7309D0366

Zhevandrov, N. D.—Use of the luminescence polarization diagram method to investigate molecular crystals containing two impurities —G. S. Belikova, N. D. Zhevandrov, T. V. Il'inykh, L. E. Kraeva, and N. P. Sul'zhenko. 18(4), 489–91 (Jan. 1974); CPM-7401D0565

Zhidkov, N. P.—Sharpening the peaks of the projection of the Patterson function by regularization —A. I. Kvitashvili, N. P. Zhidkov, B. M. Shchedrin, and A. E. Shvelashvili. 18(5), 589–91 (Mar. 1974); CPM-7403D0417

Zhitomirskii, I. S.—Internal stresses developing during crystal growth under a steady-state regime —V. L. Indenbom, I. S. Zhitomirskii, and T. S. Chebanova. 18(1), 24–32 (Jul. 1973); CPM-7309D0274

Zhizhin, G. N.—Spectroscopy of organic materials in the low-temperature, crystalline phases —G. N. Zhizhin. 18(4), 483–8 (Jan. 1974); CPM-7401D0559

Zinenkova, G. M.—Dislocation networks formed during growth and annealing in the basal plane of a single crystal of zinc —N. A. Tyapunina, T. N. Pashchenko, and G. M. Zinenkova. 18(2), 264–5 (Sep. 1973); CPM-7309D1466

Zmii, O. F.—Crystal structure of the compound $EuMg_3Ge_3$ —O. F. Zmii, E. I. Gladyshevskii, and V. S. Bul'o. 18(2), 171–2 (Sep. 1973); CPM-7309D1373

Zolin, V. F.—Use of the methods of nonlinear optics in order to make a more accurate analysis of the structural characteristics of crystals associated with the absence of an inversion center —L. G. Koreneva, V. F. Zolin, B. L. Davydov, and V. I. Tsaryuk. 18(3), 399 (Nov. 1973); CPM-7311E0531

Zorin, E. I.—Crystallization of amorphous films of silicon nitride by ionic bombardment followed by annealing —P. V. Pavlov, É. V. Shitova, E. I. Zorin, and N. A. Genkina. 18(3), 381–3 (Nov. 1973); CPM-7311E0513

Zotova, T. M.—Alloying of epitaxial silicon layers with phosphorus and arsenic in a vacuum —V. A. Tolomasov, L. N. Abrosimova, T. N. Sergivskaya, and T. M. Zotova. 18(4), 558–9 (Jan. 1974); CPM-7401D0634

Zubko, A. M.—Reaction of foreign particles with a crystallization front —A. M. Zubko, V. G. Lobanov, and V. V. Nikonova. 18(2), 239–41 (Sep. 1973); CPM-7309D1441

Zvyagintseva, I. F.—Low-dislocation-density single crystals of corundum —Kh. S. Bagdasarov, E. R. Dobrovinskaya, V. V. Pishchik, M. M. Chernik, Yu. Yu. Kovalev, A. S. Gershun, and I. F. Zvyagintseva. 18(2), 242–5 (Sep. 1973); CPM-7309D1444

BLANK
PAGE

Vol.
July 19
June 1

Soviet Physics—Crystallography Vol. 18, No. 1, July-August 1973
(Russian original: Kristallogr., Vol. 18, No. 1, pp. 1-216, January-February 1973)

1 (5) Homology and antihomology groups . . . P. A. Zabolotnyi
5 (11) Stable configurations of a bioctahedral complex with Jahn—Teller Centers . . . I. B. Bersuker, B. G. Vekhter, M. L. Rafalovich
10 (19) Some characteristics of the vibronic impurity spectra in ferroelectrics . . . N. N. Kristofel'
15 (26) Calculation of the energy matrices for d^n configurations in intracrystalline fields with T (n = 2, 3, 7, 8) symmetry. . . E. F. Kustov
19 (32) Dislocation mechanism of growth with a low kink density . V. V. Voronkov
24 (39) Internal stresses developing during crystal growth under a steady-state regime. . . V. L. Indenbom, I. S. Zhitomirskii, T. S. Chebanova
30 (49) Investigation of the intensities of electron diffraction by NH_4Cl, NaCl, and TlCl films by using electrical recording and an electron filter . . . A. S. Avilov, R. M. Imamov, R. K. Karakhanyan, Z. G. Pinsker
33 (54) Systematic analysis of Patterson functions on the basis of crystal symmetry. IV. Interpretation of the Patterson synthesis for crystals of lower systems. . . E. A. Kuz'min, V. P. Golovachev, V. V. Ilyukhin, N. V. Belov
39 (63) Isolation of n points of the basic system from a vector system by use of the star of an (n − 1)-dimensional simplex . . . R. V. Galiulin, M. I. Sirota, A. S. Naumov, N. V. Belov
43 (69) Localization of heavy atoms in noncentrosymmetric crystals by single-wave anomalous x-ray scattering . . . L. L. Shadyro
46 (75) Refining the structure of crystals allowing for the anisotropy of the thermal vibrations of the atoms . . . L. A. Muradyan, V. I. Simonov
50 (81) Crystal structure of ditrioctahedral chlorite. . . V. A. Aleksandrova, V. A. Drits, G. V. Sokolova
54 (89) X-ray study of potassium copper ethylenediaminetetraacetate trihydrate . . . M. A. Porai-Koshits, N. V. Novozhilova, T. N. Polynova, T. V. Filippova, L. I. Martynenko
59 (99) Crystal and molecular structures of 4-chloroanthraquinonethiadiazole . . . O. A. Mikhno, Z. I. Ezhkova, G. S. Zhdanov
63 (106) Electron-diffraction determination of the crystal structure of β-CuOHCl . . . A. A. Voronova, B. K. Vainshtein
67 (112) Chemical crystallography of mixed anion frameworks. I. Zirconium and scandium alkali sorosilicates . . . A. A. Voronkov, R. G. Sizova, V. V. Ilyukhin, N. V. Belov
73 (122) Double cesium—rare earth molybdates of the composition $Cs_3Ln(MoO_4)_3$ (Ln = La, Pr, Nd) . . . P. V. Klevtsov, V. A. Vinokurov, R. F. Klevtsova
76 (126) Unusual ion coordination numbers in the structure of garnet . . . B. V. Mill', G. Ronniger
80 (133) Effect of an electric field on phase transitions in $Na(D_xH_{1-x})_3(SeO_3)_2$ crystals. I. Induction of the β phase in crystals having $x \geqslant 0.3$ by the field E_y . . . L. A. Shuvalov, A. M. Shirokov, N. R. Ivanov, A. I. Baranov
83 (138) Some features of the polarization of KH_2PO_4 in the phase transition region . . . E. V. Sidnenko, V. V. Gladkii
86 (143) Thermal properties of ammonium fluoroberyllate crystals over a wide temperature range. . . B. A. Strukov, T. L. Skomorokhova, V. A. Koptsik, A. A. Boiko, A. N. Izrailenko
89 (147) Rate of whisker growth by the vapor—liquid—crystal mechanism and the role of surface energy . . . E. I. Givargizov, A. A. Chernov
93 (154) Statistical model of multiphase anisotropic crystallization. . . V. F. Dorfman

BRIEF COMMUNICATIONS

99 (165) Stability of ionic crystals with an NaCl type lattice in the Born model. . . I. M. Ratner, N. A. Tenyakova, A. I. Boiko

101 (168) Atom–atom potentials and the coordinates of hydrogen atoms in methyl groups in the molecule and crystal.... K. V. Mirskaya, L. V. Ivanova
103 (171) Atomic scattering amplitudes for electrons at small scattering angles.......................... A. N. Pilyankevich
104 (173) Crystal structure of a new modification, Bi_2Se_3II....... É. Ya. Atabaeva, S. A. Mashkov, S. V. Popova
106 (175) X-ray diffraction study of the tetrahydrates of the mesoperiodates of the rare-earth elements and yttrium . M. B. Varfolomeev, N. B. Shamrai, B. G. Berenshtein, V. E. Plyushchev
108 (178) Crystal structure of the potassium salt of 1,1-dinitroethane.......................... O. V. Frank-Kamenetskaya, N. V. Grigor'eva, N. V. Margolis, I. V. Tselinskii
110 (180) Zn–Mn isomorphism in Na_2ZnGeO_4 crystals.......... I. P. Kuz'mina, A. N. Lobachev, V. M. Vinokurov, N. M. Nizamutdinov, L. A. Volkova
112 (183) X-ray diffraction and dielectric studies of the system $Li(Ta_xSb_{1-x})O_3$ .... V. I. Nesterenko, I. G. Ismailzade
114 (185) X-ray diffraction and dielectric studies of the $LiNbO_3-KNbO_3$ system................... I. G. Ismailzade, V. I. Nesterenko, E. A. Il'yasov
116 (188) The $PbZrO_3-SrCu_{1/3}Nb_{2/3}$ system .... D. F. Dzhmukhadze, M. A. Ugryumova, Yu. N. Venevtsev, G. S. Zhdanov
119 (192) Gamma-resonance investigations of ferruginous tourmalines .... V. F. Belov, T. A. Khimich, M. N. Shipko, I. E. Voskresenskaya, E. N. Okulov
121 (195) Stereographic projections of surfaces for the physical properties of crystals........................ Sh. M. Butabaev, Yu. I. Sirotin
123 (198) Characteristics of residual-stress relaxation in $LiNbO_3$ single crystals in the 20-200°C region............. K. G. Belabaev, V. T. Gabrielyan, V. Kh. Sarkisov
125 (200) Formation of a Debye–Hückel cloud around fresh dislocations in LiF crystals..................... N. G. Politov, M. V. Galustashvili, I. M. Paperno
127 (203) Dynamic scattering with a memory effect in liquid-crystal mixtures .... G. S. Chilaya, V. T. Lazareva, L. M. Blinov
129 (206) Growth of smooth epitaxial germanium films by the iodide method in a through-flow system with diffusive mass transfer.......................... G. M. Malkin, V. E. Grigor'ev, N. A. Lineva, L. A. Malkina
131 (208) Kinetics and structural aspect of the growth of single crystals of bismuthinite under hydrothermal conditions . V. I. Popolitov, A. N. Lobachev
133 (211) Hydrothermal crystallization in the system $CdO-GeO_2-LiCl-H_2O$ .... L. N. Dem'yanets, N. V. Suvorova
135 (214) Growth of pyrrhotite on nuclei of iron thiospinel .... S. Yamaguchi

LETTER TO THE EDITORS

136 (215) Allowance for three-wave scattering in electron diffraction by face-centered metals............. V. V. Udalova, Z. G. Pinsker

Soviet Physics—Crystallography **Vol. 18, No. 2, Sept.-Oct. 1973**

(Russian original: Kristallografiya, Vol. 18, No. 2, pp. 217-440, March-April 1973)

137 (221) Antiferromagnets with electric polarization .... O. V. Kovalev
141 (227) Boundary conditions in the electrodynamics of optically active media .... B. V. Bokut', A. N. Serdyukov, F. I. Fedorov, N. A. Khilo
145 (234) Kinetics of motion of steps and rows of steps at smeared phase boundaries .... D. E. Temkin
151 (245) X-ray diffraction by a cylindrical cavity in a crystal .... A. F. Tsander
154 (251) Structure-localizing sections of the duplicated Patterson function .... V. N. Biyushkin
158 (257) New method for determining the normalizing factor in electron diffraction studies of the structure of amorphous substances .... Ya. I. Stetsiv
162 (263) Crystal structure of the coordination compound bis(pyridinaldehydethiosemicarbazonato)cobalt (III) nitrate .... K. N. Akatova, T. N. Tarkhova, N. V. Belov
166 (269) Crystal structure of lithium bitungstate $Li_2W_2O_7$ .... S. A. Magarill, R. F. Kievtsova, V. V. Bakakin
171 (277) Crystal structure of the compound $EuMg_3Ge_3$ .... O. F. Zmii, E. I. Gladyshevskii, V. S. Bul'o
173 (281) Crystal structure of sodium hydrosilicate $Na_3HSiO_4 \cdot 5H_2O$. Yu. I. Smolin, Yu. F. Shepelev, I. K. Butikova
177 (287) Crystal structure of sodium ammonium selenate dihydrate $NaNH_4SeO_4 \cdot 2H_2O$ .... A. I. Kruglik, V. I. Simonov, V. I. Yuzvak
181 (293) Structure of liquid crystals of the homologous series of n-alkoxyazoxybenzenes .... I. G. Chistyakov, V. M. Chaikovskii
184 (298) Study of the structure and dielectric properties of solid solutions in the system $BaTiO_3-Pb(Fe_{1/2}Nb_{1/2})O_3$ .... O. S. Didkovskaya, I. P. Kovalevskaya, V. G. Seryi, V. V. Klimov, Yu. N. Venevtsev
187 (303) Vanadates with a defect garnet structure .... G. Ronniger, B. V. Mill'
191 (308) Laser based on Cr^{3+} ions in yttrium–aluminum garnet... B. K. Sevast'yanov, Kh. S. Bagdasarov, L. B. Pasternak, S. Yu. Volkov, V. P. Orekhova
193 (311) Vibrational spectrum and crystal structure of $TlNO_3III$... D. E. Pogarev, A. A. Shultin
196 (315) Optical activity in $Ba(NO_2)_2 \cdot H_2O$ crystals.......... V. I. Burkov, V. A. Kizel', Z. B. Perekalina, N. L. Kozlova, G. S. Semin
198 (319) Dispersion of the optical activity in $(SrCa)S_2O_6 \cdot 4H_2O$ mixed crystals .... A. Yu. Klimova, Z. B. Perekalina, L. M. Belyaev
200 (322) Proposed interference method for determining the signs of the electrooptical coefficients.......... V. I. Sokolov, D. B. Kushev, V. K. Subashiev
202 (325) Relaxation of phase boundaries in SbSI single crystals ... M. D. Volnyanskii, A. Yu. Kudzin, A. N. Sukhinskii
204 (328) X-ray diffraction in crystals with deformation twins .... D. A. Mirzaev, S. V. Rushchits
207 (334) Focused laser-beam damage mechanism for CsI crystals. L. M. Belyaev, V. V. Nabatov, V. N. Rozhanskii, N. L. Sizova, A. A. Urusovskaya
209 (339) Deformation dislocations in natural quartz crystals..... V. F. Miuskov, L. I. Tsinober, L. A. Gordienko
212 (344) Domain rotation in smectic liquid crystals.......... A. N. Chuvyrov, Z. Kh. Kuvatov
215 (349) Determination of the arbitrary orientation of a crystal by proton diffraction.......... A. L. Fainshtein
218 (353) Nature of the point defects in GaAs single crystals as a function of the composition of the melt during growth... V. T. Bublik, V. V. Karataev, R. S. Kulagin, M. G. Mil'vidskii, V. B. Osvenskii, O. G. Stolyarov, L. P. Kholodnyi
220 (357) Interpretation of field-ion images. I. Point defects..... L. P. Potapov, T. L. Raznikova, A. L. Suvorov
224 (363) Change of the interplanar distances in deep layers of silicon during bombardment with medium-energy ions .. G. I. Uspenskaya, V. M. Genkin, D. I. Tetel'baum
226 (366) Electron-diffraction investigation of the structure of thin $InTlS_2$ films .... K. A. Agaev, V. A. Gasymov, M. I. Chiragov
228 (369) Anisotropy of growth and alloying for epitaxial germanium layers in the $Ge-I_2$ system.......... L. G. Lavrent'eva, I. S. Zakharov, I. V. Ivonin, N. P. Kolodeshnikova, T. I. Opryshko
232 (374) Transport of boron from a source to an epitaxial layer during sublimation of silicon in vacuum.......... R. G. Loginova, R. A. Rubtsova, M. I. Ovsyannikov

234 (377) Wetting of faces of a single crystal in a melt .... Yu. V. Naidich, V. M. Perevertailo, É. M. Lebovich, L. P. Obushchak
236 (380) Motion of a germanium–gold alloy droplet along a germanium surface under the action of a temperature gradient .... S. A. Grinberg, E. I. Givargizov
239 (385) Reaction of foreign particles with a crystallization front. . A. M. Zubko, V. G. Lobanov, V. V. Nikonova
242 (390) Low-dislocation-density single crystals of corundum .... Kh. S. Bagdasarov, E. R. Dobrovinskaya, V. V. Pishchik, M. M. Chernik, Yu. Yu. Kovalev, A. S. Gershun, I. F. Zvyagintseva
246 (396) Crystallographic orientation of dendrites of pure tin .... V. O. Esin, G. N. Pankin, R. Sh. Nasyrov

BRIEF COMMUNICATIONS

250 (403) Crystal structure of lanthanum hypophosphite monohydrate .... V. M. Ionov, L. A. Aslanov, V. B. Rybakov, M. A. Porai-Koshits
252 (405) Crystal structure of europium hypophosphite monohydrate .... V. M. Ionov, L. A. Aslanov, M. A. Porai-Koshits, V. B. Rybakov
254 (407) Proposed method for determining the coordinates of resonant nuclei using polarized Mössbauer spectroscopy. M. A. Andreeva, R. N. Kuz'min
256 (409) Electrooptical properties of potassium dihydrogen phosphate crystals having different degrees of deuteration .... E. N. Volkova, I. A. Velichko
258 (411) Synthesis and ferroelectric properties of antimony orthoniobate .... V. I. Popolitov, A. N. Lobachev, V. F. Peskin, L. N. Syrkin, N. N. Feoktistova
260 (413) Characteristic features of the internal friction of filamentary crystals of NaCl, KCl, and KBr at elevated temperatures .... Lieh K'uang, V. N. Rozhanskii
263 (416) Electret effect in n-azoxyanisole .... A. P. Kapustin, Z. Kh. Kuvatov, A. N. Trofimov
264 (418) Dislocation networks formed during growth and annealing in the basal plane of a single crystal of zinc .... N. A. Tyapunina, T. N. Pashchenko, G. M. Zinenkova
266 (421) Evaluation of the heat effect during alkali halide monomer reorientation in an absorbed layer on a metal .... Yu. N. Lyubitov, V. I. Mikhailov
268 (423) Study of the (111) surface of GaP by methods of Auger spectroscopy and slow-electron diffraction. .... A. Yu. Mityagin, V. P. Orlov, N. Ya. Cherevatskii
270 (425) Electron-diffraction analysis of amorphous films of carbon and boron .... Yu. G. Poltavtsev, V. P. Zakharov, V. M. Pozdnyakova
272 (427) Micromorphology of epitaxial PbS films .... R. V. Kudryavtseva, S. A. Semiletov
274 (429) Dynamic scattering of light in liquid crystals of the azocompound class .... M. F. Grebenkin, G. S. Chilaya, V. T. Lazareva, K. V. Roitman, L. M. Blinov, V. V. Titov
276 (432) Distribution coefficients of divalent impurites in alkali halide crystals .... O. L. Kreinin, K. M. Rozin
278 (435) Growth of diamond crystals in the form of needles and plates .... Yu. A. Litvin, V. P. Butuzov, É. M. Nikiforova, S. I. Futergendler
280 (437) Teaching career of a great crystallographer .... N. V. Belov

Soviet Physics—Crystallography Vol. 18, No. 3, Nov.-Dec. 1973

(Russian original: Kristallografiya, Vol. 18, No. 3, pp. 441-664, May-June 1973)

283 (445) Theory of the electrodynamic effect in liquid crystals ... S. A. Pikin, A. A. Shtol'berg
288 (454) Calculation of the electrooptical constants in "ionic" crystals ... L. B. Meisner, I. S. Rez
291 (459) Jones and Müller matrices of a phase-shifting slab with a rotating axis of the highest velocity ... V. D. Tron'ko, G. P. Golovach
295 (465) Relation between the radial and normal refraction vectors in anisotropic and gyrotropic media ... L. M. Barkovskii
298 (470) Propagation of light in active absorbing crystals ... A. F. Konstantinova, B. N. Grechushnikov
300 (474) Dynamic theory of x-ray diffraction in crystals with modulated electron density ... A. V. Kolpakov, Yu. P. Khapachev
303 (480) Iteration method for calculating the intensity distribution in structural analysis ... D. K. Khakimova, V. G. Nagornyi, A. A. Smol'yaninov
306 (484) Determination of coordination numbers and mean-square displacements from the radial distribution curve ... Ya. I. Stetsiv
308 (487) Use of the methods of successive experiment planning when refining crystal-structure parameters ... I. V. Igonina, B. I. Pokrovskii, A. K. Gapeev, P. I. Lazarev, L. N. Komissarova
311 (492) Sections of paired Patterson functions ... V. I. Biyushkin, N. V. Belov
314 (497) Symmetries of functions for separating structures from a Patterson distribution of the triclinic, monoclinic, and orthorhombic systems ... O. V. Frank-Kamenetskaya, N. V. Grigor'eva, N. V. Margolis
317 (503) Structure of calcium—cobalt hexaborate $K_2Co[B_6O_7(OH)_6]_2 \cdot 4H_2O$ ... E. Ya. Silin', Ya. K. Ozol, A. F. Ievin'sh
320 (508) Crystal structure of langbanite ... V. G. Rau, E. N. Kurkutova
323 (514) Crystal structure of U_2MoO_8 ... V. N. Serezhkin, L. M. Kovba, V. K. Trunov
326 (518) Crystal and molecular structures of the 1:2 complex of 1-methyl-3, 3-dimethyl-2-(para-n-methyl-n-β-chloroethylstyryl) indole and 7, 7, 8, 8-tetracyanoquinodimethane, $(C_{22}H_{26}N_2Cl)^+ (C_{12}H_4N_4)^{\dot{-}} (C_{12}H_4N_4)$ ... R. P. Shibaeva, L. P. Rozenberg, L. O. Atovmyan
330 (525) Crystal and molecular structure of phenyl phenoxtinium iodide ... A. I. Gusev, Yu. T. Struchkov
333 (530) Crystal structure of 1,6-$[Coen_2Cl_2]Cl \cdot 3SC(NH_2)_2$ ... Yu. A. Simonov, L. I. Landa, N. N. Proskina, T. I. Malinovskii, A. V. Ablov
336 (535) Checking the cited mean parameters of oxide unit cells with the perovskite type structure ... E. G. Fesenko, G. A. Geguzina
339 (539) New ions in the garnet structure ... G. Ronniger, B. V. Mill'
342 (544) Effect of manganese on the transformation of the zinc sulfide cubic lattice to hexagonal ... G. E. Arkhangel'skii, T. I. Voznesenskaya, M. V. Fok
344 (548) Determination of the energy and thermodynamic characteristics of iron—aluminum alloys by the method of diffuse x-ray scattering ... S. V. Semenovskaya, Zh. B. Sinyavskaya, A. P. Senichkin
349 (557) Laser detection of acentrism in crystals ... V. D. Shigorin, G. P. Shipulo
351 (560) Far infrared reflectance spectra of rubidium trihydro- and trideuterioselenite crystals ... J. Petzelt, L. D. Kislovskii, L. A. Shuvalov
354 (564) Absorption spectra of $MgWO_4$ crystals activated with Cr^{3+} and CO^{2+} ions ... O. N. Boksha, T. M. Varina
358 (570) Nonlinear optical properties of paratellurite (TeO_2) crystals ... Yu. V. Shaldin, S. P. Smirnov, L. M. Belyaev, I. A. Shpil'ko
360 (573) Dynamic pyroelectric effect ... S. D. Pel'ts, A. E. Karpel'son
363 (579) Morphology of the domain structure of SbSI crystals ... L. A. Zadorozhnaya, V. A. Lyakhovitskaya, L. M. Belyaev
366 (584) Some features of the action of penetrating radiation on the electrical properties of a quartz crystal ... A. A. Fotchenkov, S. V. Kolodieva

370 (590) Two-crystal spectrometer study of barium titanate single crystals .... I. Ya. Nikiforov, Yu. F. Mal'tsev
372 (593) Rose channels .... V. M. Finkel', V. A. Fedorov
376 (599) Mechanism of growth and etching of whisker crystals of aluminum nitride .... K. I. Portnoi, V. N. Gribkov, B. V. Shchetanov, É. L. Umantsev, V. A. Silaev
379 (605) Electron diffraction study of the structure of amorphous germanium telluride and selenide films .... Yu. G. Poltavtsev, V. P. Zakharov
381 (609) Crystallization of amorphous films of silicon nitride by ionic bombardment followed by annealing .... P. V. Pavlov, É. V. Shitova, E. I. Zorin, N. A. Genkina
384 (614) Epitaxial growth of AgCl on thermoelectric polyvinylchloride films, copying the electrical properties of an NaCl surface .... G. I. Distler, E. I. Tokmakova
386 (618) Types of vector-localizing sections of the duplicated Patterson function .... V. N. Biyushkin, N. V. Belov
388 (620) Crystal structure of $CsNbO(SO_4)_2$ .... A. A. Kashaev, G. V. Sokolova
390 (622) Structural mechanism of the phase transition in erbium pyrosilicate, $Er_2Si_2O_7$ .... Yu. I. Smolin, Yu. F. Shepelev
392 (624) "Hexagonal YF_3" structure type and high-temperature modifications of rare-earth trifluorides isostructural with YF_3 .... B. P. Sobolev, P. P. Fedorov
393 (626) Block conical ferromagnetic spiral in the hexagonal ferrite $BaGa_2Sc_{1.2}Fe_{8.8}O_{19}(M)$ .... O. P. Aleshko-Ozhevskii, V. P. Cheparin, A. P. Cherkasov, I. I. Yamzin
395 (629) Solid solutions of $BaTiO_3$ with barium niobates .... I. N. Groznov, Yu. N. Venevtsev
397 (631) Growth of $KIO_3 \cdot HIO_3$ crystals and investigation of some of their physical properties .... N. R. Ivanov, A. N. Izrailenko, L. N. Rashkovich, O. A. Chikhladze
399 (633) Use of the methods of nonlinear optics in order to make a more accurate analysis of the structural characteristics of crystals associated with the absence of an inversion center .... L. G. Koreneva, V. F. Zolin, B. L. Davydov, V. I. Tsaryuk
400 (635) Luminescence of cuprous oxide single crystals .... I. P. Kuz'mina, A. N. Lobachev, B. S. Predtechenskii, L. S. Starostina, V. B. Stopachinskii, N. M. Khaidukov
402 (638) Optimum spectral range for investigating double refraction by the modulation method .... V. S. Chudakov
404 (641) Effect of a magnetic field on the Curie point of the ferroelectric semiconductor SbSI .... S. V. Ivanova, V. A. Lyakhovitskaya
405 (642) Surface tension of 180° domain boundaries and effects in triglycine sulfate and c-domain $BaTiO_3$ .... É. S. Popov, L. A. Shuvalov
407 (645) Dispersion of the dielectric constant in crystals of KH_2PO_4 .... L. P. Pereverzeva, Yu. M. Poplavko, V. M. Petrov, E. V. Makarevskaya, I. S. Rez
409 (647) Thermodielectric effect at the phase transition between a liquid and solid crystal .... A. P. Kapustin, Z. Kh. Kuvatov, A. N. Trofimov
410 (649) Vacancy concentration in relation to plastic deformation in NaCl crystals .... N. A. Tyapunina, A. N. Tselebrovskii
411 (651) Growth dislocation distribution along a copper crystal and dislocation density as a function of mean diameter .... A. G. Basariya, B. K. Kapanadze, V. V. Sanadze
412 (653) Anisotropy of the growth rate of centers of the α modification in single crystals of high purity tin .... V. B. Brik, L. N. Larikov, V. M. Fal'chenko
414 (655) Mechanical stability of small-angle growth boundaries in NaCl crystals .... E. L. Pishchik, E. P. Kostyukova
416 (658) Internal friction and strength of germanium whiskers .... V. S. Postnikov, S. A. Ammer, A. N. Drozhzhin
417 (660) Electron diffraction investigation of In_2S_3 films obtained by vacuum deposition .... R. B. Shafizade, É. G. Éfendiev, F. I. Aliev
419 (662) Preparation of mixed single crystals of (Cr, Te) .... É. A. Zavadskii, B. Ya. Sinel'nikov
420 (664) Arkadii Sergeevich Shein (1912-1972) .... Arkadii Sergeevich Shein

Soviet Physics — Crystallography **Vol. 18, No. 4, Jan.-Feb. 1974**

(Russian original: Kristallografiya, Vol. 18, No. 4, pp. 665-896, July-August 1973)

421 (669) Kronecker product for the representations of the crystallographic point groups I. .... B. A. Men', A. N. Men', V. I. Cherepanov
425 (675) Effect of diffusion on the velocity of a break during the growth of an alloy crystal .... D. E. Temkin
429 (681) Systematic analysis of Patterson functions on the basis of crystal symmetry. V. Regularities in the degeneracy of the rhombuses in vector systems of crystals belonging to lower crystallographic systems... É. A. Kuz'min, R. I. Bochkova, Yu. N. Saf'yanov, V. P. Golovachev, N. V. Belov
434 (689) Vector-localizing cross section through a double Patterson function .... V. N. Biyushkin
437 (694) Primitive rotation regions of two Patterson syntheses ... V. I. Burdina
442 (701) Calculation of the small-angle x-ray scattering intensity on a computer using a macromolecule model .... Yu. A. Rol'bin, R. L. Kayushina, L. A. Feigin, B. M. Shchedrin
445 (706) Precision measurements of crystallographic parameters by the method of a widely divergent x-ray beam ...... V. V. Aristov, V. Sh. Shekhtman, I. M. Shmyt'ko
447 (710) New boride structural types in the homologous series based on the CaCu$_5$ and CeCo$_3$B$_2$ types .... Yu. B. Kuz'ma, N. S. Bilonizhko
450 (715) Crystal structure of the compound Ce$_{12}$Ni$_4$Si$_{13}$ .... M. G. Mys'kiv, O. I. Bodak, E. I. Gladyshevskii
454 (720) Crystal structure of coumarin .... R. M. Myasnikova, T. S. Davydova, V. I. Simonov
457 (725) Crystal-chemical analysis of the structure of 1-I-substituted anthraquinone.................. N. L. Klimasenko, V. K. Bel'skii, V. K. Sarynin, G. A. Gol'der
460 (730) Loose packing of dense layers .... P. I. Kripyakevich
464 (737) Determination of the nature of the filling of positions by isomorphous elements .... A. L. Kosoi, V. A. Frank-Kamenetskii
467 (741) Structure of Al$_2$O$_3$ in internally oxidize Cu−Al alloys .... G. I. Kokhanchik, A. V. Serebryakov
471 (747) X-ray diffraction study of the system RbBr−TlBr ...... A. A. Haav, T. K. Muirsepp
473 (751) Polymorphism and crystallographic properties of yttrium and rare-earth trifluorides.............. B. P. Sobolev, L. S. Garashina, P. P. Fedorov, N. L. Tkachenko, K. B. Seiranyan
477 (759) Phase transformations in rubidium and cesium superoxides .... V. Ya. Dudarev, A. B. Tsentsiper, M. S. Dobrolyubova
480 (764) Electron-diffraction study of the kinetics of the CuS → Cu$_{2-x}$S transformation.................. M. M. Kazinets, R. B. Shafizade
483 (769) Spectroscopy of organic materials in the low-temperature, crystalline phases .... G. N. Zhizhin
489 (779) Use of the luminescence polarization diagram method to investigate molecular crystals containing two impurities G. S. Belikova, N. D. Zhevandrov, T. V. Il'inykh, L. E. Kraeva, N. P. Sul'zhenko
492 (784) Dispersion of the electric permittivity of triglycine sulfate in the vicinity of the phase transition......... L. P. Pereverzeva, Yu. M. Poplavko
494 (788) Electronic mechanism of the influence of radiation on the process of repolarization of ferroelectrics.......... A. A. Grekov, M. A. Malitskaya, V. M. Fridkin
499 (796) Phase transformations in NaH$_3$(SeO$_3$)$_2$ crystals irradiated with a large dose of gamma radiation............ E. V. Peshikov, L. A. Shuvalov
502 (800) Dislocations formed during the sintering of solids ("sintering rosettes") .... Ya. E. Geguzin, A. S. Dzyuba, V. L. Indenbom, N. N. Ovcharenko
506 (807) Change in the structure of germanium and silicon during ion bombardment and subsequent annealing.......... P. V. Pavlov
510 (813) Study of liquid inclusions in a rocksalt crystal over the entire temperature range of their existence .... Ya. E. Geguzin, A. S. Dzyuba
514 (819) Transformation of layer-spiral growth into normal growth on a basal face. I. Breakdown of the elementary layers on the apices of the spiral hillocks .... E. D. Dukova

519 (826) Influence of heat treatment on the structural perfection of single crystals of gallium arsenide alloyed with tellurium . M. G. Mil'vidskii, V. B. Osvenskii, A. G. Novikov, V. G. Fomin, S. P. Grishina

521 (830) Effective distribution constants of excess basic components during crystallization of gallium arsenide from a melt . . . . V. V. Karataev, M. G. Mil'vidskii, V. B. Osvenskii, O. G. Stolyarov

523 (833) Hydrothermal synthesis of a new crystalline modification of lithium lanthanum molybdate, α-$LiLa(MoO_4)_2$ . . . . P. V. Klevtsov, V. I. Protasova, L. Yu. Kharchenko, R. F. Klevtsova

525 (836) Study of crystallization in the hydrothermal system $GeO_2-Sb_2O_3-KF-H_2O$ . . . . M. N. Tseitlin, G. F. Plakhov, A. N. Lobachev, V. I. Popolitov, M. A. Simonov, N. V. Belov

BRIEF COMMUNICATIONS

528 (840) Effect of accelerating voltage on the intensity of the forbidden reflection 222 Ge in electron diffraction . . . . . A. S. Avilov, R. M. Imamov, Z. G. Pinsker, A. F. Fedotov

530 (842) Monochromatization of neutrons in multiple Bragg scattering. . . . . A. A. Loshmanov, V. N. Sigaev, I. I. Yamzin

531 (843) Solubility of LnF_3 in lanthanum fluoride . . . . O. V. Kudryavtseva, L. S. Garashina, K. K. Rivkina, B. P. Sobolev

532 (845) Short-range and long-range order in the arrangement of the interstitial atoms in $(34\%Ta66\%Ti)D_X$ . . . . N. F. Miron, V. I. Shcherbak, V. N. Bykov, V. A. Levdik

534 (847) Infrared spectra of manganese garnets containing a germanate tetrahedron . . . . R. Hrichova

536 (849) Growth and study of crystals of double oxides of cadmium with structures of the perovskite type I. Cadmium hafnate . . . . R. I. Spinko, V. N. Lebedev, R. V. Kolesova, E. G. Fesenko

538 (852) Interpretation of the dispersion of the rotatory power in the $LiIO_3$ crystal . . . . Z. B. Perekalina, N. L. Smirnova, G. F. Dobrzhanskii, I. A. Shpil'ko

540 (855) Anisotropy of certain physical properties of pyrargyrite and proustite crystals . . . . N. I. Butsko, M. M. Pidorya, T. D. Krushel'nitskaya

542 (857) Secondary effects accompanying movement of 180-degree α domains in $BaTiO_3$ . . . . E. F. Dudnik, V. M. Duda

544 (860) Elastic properties of KDP and DKDP crystals at high temperatures . . . . S. I. Chizhikov, N. G. Sorokin, I. Yu. Ledovskaya, E. V. Makarevskaya

546 (863) Heat effects in lithium metaniobate . . . . I. A. Kleinman, T. A. Lyubimova, A. Z. Rabinovich, M. B. Roitberg

548 (866) Heat capacity of single-crystal $BaTiO_3$ near the electrical critical point. B. A. Strukov, A. K. Ivanov-Shits

549 (868) Charge on dislocations in sodium chloride crystals containing an anionic impurity. . . . . N. A. Tyapunina, A. I. Kolomiitsev

551 (871) Determination of the degree of bending of single crystals from the orientational scattering of β particles . . . . A. Ya. Bobudaev, S. A. Vorob'ev, V. V. Kaplin

552 (873) Phase transition in liquid crystals induced by an electric field. . . . . I. G. Chistyakov, L. K. Vistin'

554 (876) Investigation of the pure and cesium-coated (100) surface of germanium by slow-electron diffraction . . . . A. Yu. Mityagin, V. P. Orlov

556 (879) Spatial distribution of particles during vaporization of a zinc single crystal . . . . Yu. A. Gel'man, V. F. Vinogradov, Yu. N. Lyubitov

558 (882) Alloying of epitaxial silicon layers with phosphorus and arsenic in a vacuum . . . . V. A. Tolomasov, L. N. Abrosimova, T. N. Sergievskaya, T. M. Zotova

560 (885) Influence of temperature gradient on the impurity distribution during growth of crystals from a melt. . . . . E. A. Krivandina, E. E. Kostyleva

562 (888) Synthesis of tourmaline in chloride media. I . . . . I. E. Voskresenskaya, A. A. Shternberg

564 (891) Crystallization in the As–S–HI–H_2O system . . . . V. I. Popolitov, A. N. Lobachev
565 (892) Growth of shaped germanium crystals having low dislocation density by the Bridgman method . . . . L. A. Maslova, S. V. Tsivinskii
566 (894) Crystallization apparatus for the growth of crystals at constant supersaturation of the solution . . . . A. I. Munchaev

BLANK
PAGE

Soviet Physics – Crystallography   Vol. 18, No. 5, March-April 1974

(Russian original: Kristallografiya, Vol. 18, No. 5, pp. 897-1112, September-October 1973)

567 (901) Reduction of the Kronecker product of representations of the crystallographic groups. II. . . . . B. A. Men', A. N. Men', V. I. Cherepanov
570 (906) Characteristics of a diffusionless transformation in nonideal alloys. . . . . D. E. Temkin
575 (915) Model of the controlled growth of macromolecular and crystalline structures . . . . V. K. Bykhovskii
578 (920) Simulation of a crystal surface equilibrium atomic structure for a single component system . . . . V. O. Esin, V. I. Danilyuk, Yu. M. Plishkin, G. L. Podchinenova
582 (926) Reconstruction of the phase of the electronic scattering amplitude from experiments on the diffraction of resonant γ quanta . . . . I. P. Perstnev, F. N. Chukhovskii
586 (934) One-dimensional models of the Patterson function . . . . . S. V. Borisov
589 (939) Sharpening the peaks of the projection of the Patterson function by regularization . . . . A. I. Kvitashvili, N. P. Zhidkov, B. M. Shchedrin, A. E. Shvelashvili
592 (944) Applicability of Zachariasen's equations to calculations of the integral intensity scattered by a "thick" single crystal in the Bragg symmetry case for any dislocation density . . . . A. V. Kuznetsov
596 (950) Crystal structure of the alkali titanosilicate labuntsovite. . . . . N. I. Golovastikov
600 (956) Crystal structure of zinc fluoride tetrahydrate, $ZnF_2 \cdot 4H_2O$ . . . . B. V. Bukvetskii, S. A. Polishchuk, V. I. Simonov
603 (961) Structure of the double oxide α-$U_3Mo_{20}O_{64}$. . . . . V. N. Serezhkin, L. M. Kovba, V. K. Trunov
606 (966) Structural study of tochilinite. II. Acicular variety: Unusual diffraction patterns. . . . . N. I. Organova, V. A. Drits, A. L. Dmitrik
610 (973) A group of synthetic cadmium germanates and their x-ray study. . . . . E. L. Belokoneva, M. A. Simonov, N. G. Duderov, A. N. Lobachev, N. V. Belov
613 (978) Structure of nickel hydroxide containing potassium ions . P. N. Bityutskii, V. I. Khitrova, Z. G. Pinsker
617 (984) Proton magnetic resonance investigation of the localization of the protons in the crystal structures of $Na_2Cr_2O_7 \cdot 2H_2O$ and $Li_2Cr_2O_7 \cdot 2H_2O$ . . . . G. R. Bulka, V. M. Vinokurov, É. A. Kuz'min, Yu. A. Kharitonov, N. V. Belov
620 (988) Position of the hydroxyl groups in the structure of hydrosodalite. . . . . V. Yu. Galitskii, V. N. Shcherbakov, S. P. Gabuda
623 (992) Magnetically nonequivalent cation positions in substituted ferrite garnets. . . . . I. S. Lyubutin, A. P. Dodokin, L. M. Belyaev
627 (999) Estimation of texture of the bcc → fcc → bcc double phase transformation . . . . I. P. Sorokin
630 (1003) Scattering of light at elastic waves in optically biaxial crystals . . . . Yu. V. Pisarevskii, I. M. Sil'vestrova
635 (1014) Some features of the domain structure in lead titanate crystals . . . . E. G. Fesenko, V. G. Gavrilyachenko, M. A. Martynenko, A. F. Semenchev, I. P. Lapin
638 (1018) Studies on ferroelectric crystals with a three-crystal x-ray spectrometer . . . . I. Ya. Nikiforov, Yu. F. Mal'tsev, V. Z. Borodin
641 (1023) Temperature dependence of the rate of enlargement of the twinning layer in calcite crystals. . . . . V. P. Soldatov, V. I. Startsev, N. M. Chaikovskaya
644 (1028) Kinetics of the polishing and etching of sodium chloride crystals. III . . . . G. K. Baranova, É. M. Nadgornyi
647 (1033) Selective etching at dislocations in metals (Ni) . . . . E. G. Popkova, A. A. Predvoditelev
651 (1039) Etching of quartz and some features of the surface layer . . . . E. I. Lazorina, V. V. Soroka

654 (1044) Some structural–morphological characteristics of the volatilization of single crystals of α-Al_2O_3 . . . . E. M. Akulenok, Yu. K. Danileiko, V. V. Panteleev, E. A. Fedorov, V. Ya. Khaimov-Mal'kov
657 (1049) Pretransition phenomena and optical activity of amorphous liquid phases of cholesteric liquid crystals . E. I. Ryumtsev, A. N. Cherkasov, V. G. Tishchenko, M. M. Fetisova
660 (1053) Elastic-diffusion interaction of liquid inclusions in a NaCl single crystal . . . . Ya. E. Geguzin, A. S. Dzyuba
663 (1057) Phenomena arising on the arrest of crystal growth. . . . . V. N. Romanenko, V. S. Kheifets
667 (1063) Electron-microscope investigation of thin film condensation kinetics . . . . Yu. F. Komnik, V. V. Pilipenko
671 (1070) Preparation and preliminary investigation of cadmium phosphates . . . . Yu. A. Ivanov, I. N. Ivanovskaya, V. I. Popolitov, M. A. Simonov, N. V. Belov

BRIEF COMMUNICATIONS

674 (1074) Indexing of the crystallographic planes in rhombohedral crystals . . . . V. A. Gerken, B. K. Kazurov, G. M. Tsigel'nitskii
675 (1075) Crystal structure of $La_2Sr_3(BO_3)_4$ . . . . G. K. Abdullaev, Kh. S. Mamedov, S. T. Amirov
677 (1078) X-ray investigation of some examples of a homologous series of cholesterol ethers in dicarboxylic acid . . . . . Ya. I. Dutchak, V. K. Burima
680 (1082) Crystallochemical determination of the structure of $NaTl_3(SO_3)_2$ by means of the method of crystallograms . N. L. Smirnova
681 (1083) Stimulated emission from (Er, Lu) AlO_3 crystals containing Ho^{3+} and Tm^{3+} ions. . . . . Kh. S. Bagdasarov, A. A. Kaminskii, A. M. Kevorkov, S. É. Sarkisov, T. A. Tevosyan
682 (1085) Molecular scattering of light in a single crystal of hafnium dioxide . . . . V. I. Aleksandrov, V. F. Kitaeva, I. V. Kozlov, V. V. Osiko, N. N. Sobolev, V. M. Tatarintsev, I. L. Chistyi
685 (1088) Crystal optics of alkaline-earth metavanadates . . . . M. P. Glazyrin, A. A. Ivakin, V. A. Gurevich
687 (1090) Temperature dependence of the elastooptical constants p_{11} and p_{12} of NaCl, KCl, KBr, and KI crystals. . . . . . . A. V. Pakhnev, S. S. Gorbach, M. P. Shaskol'skaya
688 (1092) Phase diagram of the system $(HgI_2)_X(HgBr_2)_{1-X}$ and some optical properties of its single crystals . . . . I. D. Turyanitsa, V. V. Khiminets
690 (1095) Surface layer of barium titanate crystals . . . . V. P. Dudkevich, I. N. Zakharchenko, V. S. Bondarenko, R. V. Kolesova, A. G. Stoinov, E. G. Fesenko
692 (1098) Dislocation structure of $KMgF_3$ crystals. . . . . S. N. Bodrug
695 (1101) Determination of the degree of ordering in liquid crystals from the dichroism of dissolved dyes. . . . . . . V. G. Rumyantsev, L. M. Blinov, V. A. Kizel'
697 (1104) Orientational order and molecular parameters of liquid crystals with a positive dielectric anisotropy . . . V. G. Rumyantsev, P. D. Berezin, L. M. Blinov, I. N. Kompanets
699 (1107) Nature of the impurity water in synthetic quartz crystals . . . . L. I. Tsinober, V. E. Khadzhi
701 (1109) Structure of amorphous indium monochalcogenide films . Yu. G. Poltavtsev, V. P. Zakharov, T. V. Remizovich
703 (1111) Simple method for preventing the formation of parasite crystals during the growth of crystals from solution . . . . I. V. Isakov
704 (1112) Conference on anomalous scattering

Soviet Physics – Crystallography Vol. 18, No. 6, May–June 1974

(Russian original: Kristallografiya, Vol. 18, No. 6, pp. 1113-1336, November-December 1973)

705 (1117) Reduction of the Kronecker product of representations of the crystallographic groups. III . . . . B. A. Men', A. N. Men', V. I. Cherepanov
711 (1126) "Spectral instability" of multiwave diffraction with coplanar x rays . . . . A. D. Fofanov, A. V. Kuznetsov, G. A. Karacheva
715 (1134) Statistical values of heavy-atom weighted contributions (D_H) to the total structure amplitude . . . . L. L. Shadyro, I. D. Feranchuk
719 (1141) Key role of analysis of intercation distances in oxygen compounds containing heavy cations (high atomic numbers). . . . . T. M. Polyanskaya, S. V. Borisov, N. V. Belov
728 (1157) X-ray diffraction study of naphthaloimide . . . . A. N. Sobolev, L. A. Chetkina, G. A. Gol'der, Yu. G. Fedorov, V. E. Zavodnik
732 (1162) Crystal and molecular structures of octafluoroanthraquinone. . . . . L. A. Chetkina, E. G. Popova
736 (1169) Determination of the crystal structure of the hexagonal phase β^{III} in the copper–tellurium system by electron diffraction. . . . . R. V. Baranova, A. S. Avilov, Z. G. Pinsker
741 (1177) Neutron-diffraction refinement of the structure of alpha lithium iodate . . . . A. Émiraliev, A. G. Kocharov, I. I. Yamzin, V. A. Lyubimtsev
744 (1182) Relationships of structure types. New representatives of the homologous classes corundum, spinel, and amesite . . . . N. L. Smirnova, S. D. Polzikov, N. A. Rebrova
749 (1192) Binary molybdates and tungstates of alkali metals with bismuth, $M^+Bi(TO_4)_2$. . . . . P. V. Klevtsov, V. A. Vinokurov, R. F. Klevtsova
752 (1198) Irradiation-induced phase transition in quartz . . . . E. V. Kolontsova, É. E. Kulago, N. A. Tomilin
755 (1202) Use of the double-crystal neutron spectrometer to study the low-temperature decomposition in niobium single crystals saturated with hydrogen . . . . . M. Kalanov, S. Sh. Shil'shtein, V. A. Somenkov
758 (1207) KIO_3: the first ferroelectric permitting just a 120° shift in the ferroelectric polarization. . . . . L. A. Shuvalov, N. R. Ivanov, O. A. Chikhladze, A. N. Izrailenko
762 (1214) Phase transition, dielectric anomaly, and domain structure in hydrosodalite . . . . N. R. Ivanov, V. Yu. Galitskii
764 (1218) Domain boundaries, antiphase boundaries, and dislocations in gadolinium molybdate single crystals . . V. A. Meleshina, V. L. Indenbom, Kh. S. Bagdasarov, T. M. Polkhovskaya
769 (1227) High-temperature phase transitions in crystals of $Rb(D_xH_{1-x})_2PO_4$ . . . . V. A. D'yakov, V. A. Koptsik, I. V. Lebedeva, A. V. Mishchenko, L. N. Rashkovich
773 (1234) Relaxational internal friction in crystals of KH_2PO_4 with chromium added . . . . S. A. Gridnev, L. N. Kamysheva, N. F. Romanova
777 (1240) Polarization and integrated intensity of x rays scattered by silicon crystals . . . . N. M. Olekhnovich
780 (1246) Anisotropy of the molar refraction of liquid-crystal alkoxybenzoic acids . . . . E. I. Ryumtsev, A. P. Kovshik, I. P. Kolomiets, V. N. Tsvetkov
783 (1250) One-dimensional disorder in diazoaminobenzene . . . . . . V. F. Gladkova
788 (1258) Determination of the activation energy of forward and reverse reactions during crystal growth. . . . . E. B. Treivus
791 (1263) Structure of low-temperature "amorphous" bismuth films . . . . Yu. F. Komnik, L. A. Yatsuk, A. A. Motornaya, M. L. Bolotina, B. I. Belevtsev
797 (1272) Structure of thin lead telluride films . . . . E. V. Rakova, S. A. Semiletov

BRIEF COMMUNICATIONS

800 (1275) Structures of leucophoenicite, $Mn_7[SiO_4]_2[(SiO_4)(OH)_2]$, and synthetic Cd orthogermanate, $Cd_3[GeO_4](OH)_2$. . . . . E. L. Belokoneva, M. A. Simonov, N. V. Belov

802 (1278) Crystal structures of $RbNbO(SO_4)_2$ and $NH_4NbO(SO_4)_2$ . . . A. A. Kashaev, G. E. Postoenko, É. A. Zel'bst
804 (1281) Unit-cell parameters and space groups of several pyridino-anthraquinones . . . . O. A. Mikhno, Z. I. Ezhkova, M. I. Evstratova
806 (1283) Hydrothermal synthesis, x-ray diffraction, and thermogravimetric study of rare-earth hydroxychlorides $Ln(OH)_2Cl$ . . . . L. N. Dem'yanets, V. I. Bukin, E. N. Emel'yanova, V. I. Ivanov
809 (1287) Growth and investigation of binary cadmium oxides with structures of the perovskite type. II. Cadmium stannate and zirconate. R. I. Spinko, V. N. Lebedev, R. V. Kolesova, E. G. Fesenko
811 (1289) Thermooptical and dielectric properties of $(NH_4)_2BeF_4$ in the neighborhood of the ferroelectric transition . . . . A. T. Anistratov, S. V. Mel'nikova
813 (1292) Optical activity in monoclinic sodium zincogermanate Na_2ZnGeO_4 . . . . S. P. Kozyrev, A. B. Gil'varg, B. N. Grechushnikov, N. V. Belov
814 (1293) SbSI thin films with a ferroelectric phase transition . . . . A. A. Agasiev, A. Kh. Zeinally, V. G. Sil'vestrov
815 (1295) Reflection intensity as a function of temperature during diffraction of slow electrons from (111) and (100) faces of germanium . . . . B. Z. Ol'shanetskii, A. I. Volokitin, S. M. Repinskii
817 (1298) Influence of impurities on the photoelastic constants of potassium chloride crystals. . . . . M. P. Shaskol'skaya, A. V. Pakhnev, S. S. Gorbach, N. M. Malikova
818 (1299) Nature of small etch pits in tellurium-alloyed GaAs single crystals. . . . . S. S. Shifrin, V. B. Osvenskii, M. G. Mil'vidskii, L. M. Morgulis, S. P. Grishina
821 (1303) Formation of trigons at the $\{111\}$ faces of natural diamond during etching . . . . O. N. Grigor'ev
823 (1306) Forms of antimony crystal growth in alloys of the eutectic type . . . . I. V. Salli, L. V. Samoilenko, V. Z. Dolinskaya
825 (1309) Effect of the crystallization mechanism on boron diffusion in silicon–germanium solid-solution epitaxial films. . . . . K. L. Lyutovich, F. A. Gimel'farb, P. B. Orlov, T. A. Ukhorskaya
827 (1312) Lev Aleksandrovich Shuvalov (on his 50th birthday)

Homology and antihomology groups

P. A. Zabolotnyi
Kishinev State University

(Submitted September 8, 1971; resubmitted February 4, 1972)
Kristallografiya, 18, 5-10 (January-February 1973)

A new method for the derivation of V. I. Mikheev's crystallographic homology groups has been described. A. V. Shubnikov's concept of antisymmetry and V. I. Mikheev's concept of homology have been synthesized, leading to the derivation of 432 essentially new (minor) antihomology groups.

1. In 1961, Mikheev's work "The Homology of Crystals" appeared in a separate edition.[1] In it, the author examines a question to which attention was drawn at an early date by E. S. Fedorov: The question of homology or, in Fedorov's terminology, visible symmetry. After introducing the concept of homology transformations, the author gives the derivation of 218 crystallographic homology groups. The mathematical inaccuracies found in the presentation of the work cast doubt on the correctness of the final results. To verify these results, an attempt was made in the present work to repeat by a different method the derivation of the crystallographic homology groups.

2. The discrete group H of affine mappings of a finite figure F onto itself we shall call a homology group, and any transformation h of the group H we shall call a homology transformation. We subsequently proved: a) that any homology transformation is equiaffine; b) that the number of H-homologous points for any point $A \in F$ is finite; and c) that the homology group H of any finite figure F is finite.

In ref. 2, the following statement is made (following from Mashke's theorem): For a finite group H of affine transformations of a figure F it is always possible to choose an affine transformation σ, after the application of which the figure F is transformed into another figure $F' = \sigma(F)$, and the actual group H is transformed into the group G of symmetry transformations for the figure F'. By applying this statement to our case, we deduce that the homology group H of any finite figure F can be obtained from a given symmetry point group G of the finite figure F' by means of the affine transformation σ^{-1}, which transforms F' into F. This result is made the basis of the derivation of the crystallographic homology groups. The symmetry elements for all possible affine transformations we shall call homology elements. Simple arguments based on the properties of affine transformations make it possible to derive for finite figures the following homology elements (the notation makes use of V. I. Mikheev's symbols): a) the homology plane; in the general case this will be the plane of oblique reflection π, and in the particular case it will be the symmetry plane P; b) the center of inversion C; c) four types of homology axes of rotation of order k: λ_k, the oblique elliptical axis; $\lambda_{k'}$, the right elliptical axis; $\lambda_{k''}$, the oblique circular axis; and G_k, the right circular axis or axis of symmetry (it may be noted that two-fold homology axes can only be oblique λ_2 axes or axes of symmetry G_2); and d) four types of inversion–rotation homology axes of order k, which are described as oblique or right, and elliptical or circular, according to the simple homology axes of rotation, and which are denoted λ_{ki}, $\lambda_{ki'}$, $\lambda_{ki''}$, and G_{ki}. The two-fold inversion–rotation axis of symmetry G_{2i} is identical to the plane of symmetry P, and the two-fold inversion–rotation oblique homology axis λ_{2i} is identical to the plane of oblique reflection π.

It can be proved that after the application of an affine transformation σ to a figure F it is transformed into a figure F', and the symmetry group G of the figure F is transformed into the homology group H of the figure F' according to the law $H = \sigma G \sigma^{-1}$. The symmetry group G is called the parent group with respect to the homology group H if there exists an affine transformation σ such that $H = \sigma G \sigma^{-1}$. The parent symmetry group for any homology group is defined with an accuracy up to identity. The homology group H is called a crystallographic group if its parent symmetry group G is a crystallographic group. The homology group H is described as axial, central, or planar if its parent symmetry group G is axial, central, or planar, respectively.[3] The most difficult derivation is the derivation of the axial homology groups, since the central and planar groups are derived from the axial groups in the same way as the central and planar symmetry groups are derived from the axial symmetry groups.

3. We shall begin the derivation of the axial homology groups from the symmetry groups for the group of rotations of the cube 3/4 (the notation makes use of Shubnikov's symbols). It is necessary to examine the application of all possible affine transformations to the corresponding set of symmetry elements. Any transformation of the group 3/4 into the homology group H is accompanied by deformation of the cube into a parallelepiped. The face of any parallelepiped will be a square, or a rhomb of general form, or a rectangle of general form, or a parallelogram of general form; we shall denote these by the figures 1, 2, 3, and 4, respectively. If the basis for differentiating between the parallelepipeds is taken as a difference in the faces meeting at one apex, it is possible to

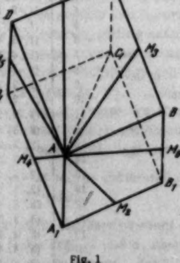

Fig. 1

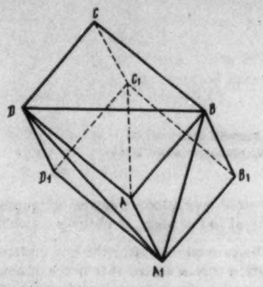

Fig. 2

have only 14 different parallelepipeds, which can be denoted conditionally by these sets of three faces: (1,1,1), (1,1,2), (1,2,2), (1,3,3), (1,3,4), (1,4,4), (2,2,2), (2,3,3), (2,3,4), (2,4,4), (3,3,3), (3,3,4), (3,4,4), (4,4,4).

Next, by selecting in turn all these parallelepipeds, it is necessary to determine the homology groups into which 3/4 can be transformed after the application to it, in accordance with the known law, of the affine transformation σ which transforms the cube into a given parallelepiped. For this purpose we make use of fairly obvious theorems.

1) A three-fold axis of symmetry passes through the apex A of a given parallelepiped if and only if three equal faces meet at the apex, the angle at the apex being equal.

2) In a parallelepiped $ABCDA_1B_1C_1D_1$, the three-fold homology axis AC_1 will be right, if and only if at least two of the following equalities apply: $AM_1 = AM_2$, $AM_3 = AM_4$, and $AM_5 = AM_6$, where M_1, M_2, M_3, M_4, M_5, and M_6 are, respectively, the centers of the edges DC, A_1B_1, BC, A_1D_1, DD_1, and BB_1 (see Fig. 1).

3) In the parallelepiped $ABCDA_1B_1C_1D_1$, the three-fold homology axis AC_1 will be circular if and only if the following condition is satisfied: $BD = DA_1 = A_1B$ (see Fig. 2).

These three criteria define the type of any three-fold homology axis in any parallelepiped. They lead to the following conclusions.

4) The only parallelepiped which allows simultaneously one oblique circular and one right elliptical three-fold homology axis is (2,4,4).

5) The only parallelepiped which allows simultaneously two oblique circular (or analogously two right elliptical) three-fold homology axes is (2,3,3).

The type of four-fold and, in particular, two-fold homology axis in a given parallelepiped is determined fairly simply. Detailed studies show that 21 homology groups are derived from the group 3/4. All these groups are written out in Table 1, where to the left of each homology group there is written the parallelepiped into which it is necessary to transform the cube in order to transform the group 3/4 into the given homology group, and on the right of each homology group there is written its corresponding number according to ref. 1. The derivation of the homology group from the parent symmetry group 3/4 then becomes trivial, since 3/2 is the only subgroup with index 2 in 3/4. After special examination of groups of the type k : 2 (k = 2, 3, 4, 6), the derivation of the axial homology groups is in fact complete, since the derivation of the homology groups from parent groups with symmetry 6, 4, 3, 2, 1 presents no difficulty. A total of 70 axial homology groups are derived from eleven axial symmetry groups.

All the central homology groups are derived by the addition of inversion as a generating element to each of the 70 axial groups. We use the symbol G^{**} to denote the planar symmetry group which is derived from the axial group G by the replacement of rotations about even axes by inversion rotations about axes of the same order. We shall examine all the axial homology groups for which the

TABLE 1

No.	Paral-lelepipeds	Homology elements			No. from ref. 1
		three-fold axes	four-fold axes	two-fold axes	
1	(1, 1, 1)	$G_3G_3G_3G_3$	$G_4G_4G_4$	$G_2G_2G_2G_2G_2G_2$	175
2	(1, 1, 2)	$\lambda_3\lambda_3\lambda_3\lambda_3$	$\lambda_4''\lambda_4''\lambda_4'$	$G_2G_2\lambda_2\lambda_2\lambda_2\lambda_2$	185
3	(1, 2, 2)	$\lambda_3\lambda_3\lambda_3\lambda_3$	$\lambda_4''\lambda_4\lambda_4$	$G_2\lambda_2\lambda_2\lambda_2\lambda_2\lambda_2$	189
4	(1, 2, 2)	$\lambda_3\lambda_3\lambda_3\lambda_3$	$\lambda_4''\lambda_4\lambda_4$	$\lambda_2\lambda_2\lambda_2\lambda_2\lambda_2\lambda_2$	195
5	(1, 3, 3)	$\lambda_3\lambda_3\lambda_3\lambda_3$	$G_4\lambda_4'\lambda_4'$	$G_2G_2\lambda_2\lambda_2\lambda_2\lambda_2$	176
6	(1, 3, 4)	$\lambda_3\lambda_3\lambda_3\lambda_3$	$\lambda_4''\lambda_4'\lambda_4$	$\lambda_2\lambda_2\lambda_2\lambda_2\lambda_2\lambda_2$	187
7	(1, 4, 4)	$\lambda_3''\lambda_3\lambda_3\lambda_3$	$\lambda_4''\lambda_4\lambda_4$	$G_2\lambda_2\lambda_2\lambda_2\lambda_2\lambda_2$	194
8	(1, 4, 4)	$\lambda_3'\lambda_3\lambda_3\lambda_3$	$\lambda_4''\lambda_4\lambda_4$	$G_2\lambda_2\lambda_2\lambda_2\lambda_2\lambda_2$	192
9	(2, 2, 2)	$G_3\lambda_3\lambda_3\lambda_3$	$\lambda_4\lambda_4\lambda_4$	$G_2G_2G_2\lambda_2\lambda_2\lambda_2$	177
10	(2, 2, 2)	$\lambda_3\lambda_3\lambda_3\lambda_3$	$\lambda_4\lambda_4\lambda_4$	$G_2\lambda_2\lambda_2\lambda_2\lambda_2\lambda_2$	180
11	(2, 2, 2)	$\lambda_3\lambda_3\lambda_3\lambda_3$	$\lambda_4\lambda_4\lambda_4$	$\lambda_2\lambda_2\lambda_2\lambda_2\lambda_2\lambda_2$	183
12	(2, 3, 3)	$\lambda_3''\lambda_3''\lambda_3\lambda_3$	$\lambda_4'\lambda_4\lambda_4$	$G_2G_2\lambda_2\lambda_2\lambda_2\lambda_2$	186
13	(2, 3, 3)	$\lambda_3'\lambda_3'\lambda_3\lambda_3$	$\lambda_4'\lambda_4\lambda_4$	$G_2G_2\lambda_2\lambda_2\lambda_2\lambda_2$	178
14	(2, 3, 3)	$\lambda_3\lambda_3\lambda_3\lambda_3$	$\lambda_4'\lambda_4\lambda_4$	$G_2G_2\lambda_2\lambda_2\lambda_2\lambda_2$	188
15	(2, 4, 4)	$\lambda_3''\lambda_3\lambda_3\lambda_3$	$\lambda_4\lambda_4\lambda_4$	$G_2\lambda_2\lambda_2\lambda_2\lambda_2\lambda_2$	190
16	(2, 4, 4)	$\lambda_3'\lambda_3\lambda_3\lambda_3$	$\lambda_4\lambda_4\lambda_4$	$G_2\lambda_2\lambda_2\lambda_2\lambda_2\lambda_2$	179
17	(2, 4, 4)	$\lambda_3''\lambda_3'\lambda_3\lambda_3$	$\lambda_4\lambda_4\lambda_4$	$G_2\lambda_2\lambda_2\lambda_2\lambda_2\lambda_2$	193
18	(3, 3, 3)	$\lambda_3\lambda_3\lambda_3\lambda_3$	$\lambda_4'\lambda_4'\lambda_4'$	$\lambda_2\lambda_2\lambda_2\lambda_2\lambda_2\lambda_2$	184
19	(3, 3, 4)	$\lambda_3\lambda_3\lambda_3\lambda_3$	$\lambda_4'\lambda_4\lambda_4$	$\lambda_2\lambda_2\lambda_2\lambda_2\lambda_2\lambda_2$	181
20	(3, 4, 4)	$\lambda_3''\lambda_3\lambda_3\lambda_3$	$\lambda_4\lambda_4\lambda_4$	$\lambda_2\lambda_2\lambda_2\lambda_2\lambda_2\lambda_2$	196
21	(3, 4, 4)	$\lambda_3'\lambda_3\lambda_3\lambda_3$	$\lambda_4\lambda_4\lambda_4$	$\lambda_2\lambda_2\lambda_2\lambda_2\lambda_2\lambda_2$	182

parent group is a given symmetry group G. If in each of these homology groups we carry out analogous replacements of rotations about even homology axes by inversion rotations about axes of the same order, we cover all planar homology groups G^{**} from the parent symmetry group. In this way, 75 planar homology groups are derived from 10 planar symmetry groups.

4. A total of 215 crystallographic homology groups have been derived: 70 axial, 70 central, and 75 planar. In ref. 1, under No. 191, there is listed the homology group $\{\lambda_4'', \lambda_4, \lambda_4, \lambda_3'', \lambda_3', \lambda_3, \lambda_3, G_2, \lambda_2, \lambda_2, \lambda_2, \lambda_2, \lambda_2\}$. According to point 4 in Sec. 3 of the present work, the only parallelepiped permitting simultaneously one oblique circular and one right elliptical three-fold homology axis is (2,4,4); this parallelepiped, however, does not have a square face, which is necessary if it is to allow a circular four-fold homology axis λ_4''. Thus group 191 according to ref. 1 cannot be accounted for in any of the 14 parallelepipeds, so that this homology group is extraneous. It is then clear that the group which in ref. 1 is listed under No. 213 is also extraneous, since it was derived from No. 191 by the addition of inversion as generating element. For a similar reason, the group listed under No. 164 in ref. 1 does not exist, since it is the planar group derived from 191. The other results obtained by Mikheev agree with our data.

5. After the derivation of the crystallographic homology groups there naturally arises the question of the transfer of Shubnikov's concepts of antisymmetry[4] to the case of homology. We assign to each point of a given finite figure F one of two possible signs (+ or –), which can be interpreted in any sense, after which the affine mapping of the figure F onto itself is called either a homology transformation, if it transforms every point of the figure F into a point with the same sign, or an antihomology transformation, if in the process each point of the figure F is transformed into a point with the opposite sign. Thus an antihomology transformation is the product of the mutually commutative homology transformation h and the antiidentity $\underline{e}$. We shall denote antihomology transformations by the underlined symbols for the corresponding homology transformations: $\underline{h}e = e\underline{h} = \underline{h}$.

Just as Shubnikov[4] defines antisymmetry elements and transformations on the basis of symmetry elements and transformations, it is possible to define antihomology elements and transformations on the basis of homology elements and transformations. The concepts of the homology antiplane $\underline{\pi}$, the homology rotationa antiaxis of order k, $\underline{\lambda}_k$, the inversion anticenter $\underline{C}$, and the homology inversion–rotation antiaxis of order k, $\underline{\lambda}_{ki}$, are derived in this way. A group which contains even one antihomology transformation is called an antihomology group. An antihomology group is called major or minor depending on whether it does or does not contain the antiidentity as an independent operation.[5] The antihomology group $\underline{H}$ will be called a crystallographic group if it can be obtained from a crystallographic homology group H by the replacement, in the latter, of some homology transformations by corresponding antihomology transformations. The group H is called the generating group with respect to $\underline{H}$. The generating homology group for any antihomology group is defined unambiguously. By the addition of inversion as a generating element to each of the 215 homology groups it is possible to cover all major antihomology groups. The number of such groups is also equal to 215. For the derivation of all minor antihomology groups it is necessary, in each of the 215 homology groups, to carry out all possible replacements of homology transformations by the corresponding antihomology transformations, bearing in mind that the antiidentity must not appear in the group as an independent operation. The antihomology group $\underline{H}$ is called axial, central, or planar, depending on whether it is derived from an axial, central, or planar generating homology group H.

6. For the derivation of the planar homology groups, we carried out, in each axial group, all possible replacements of rotations about even axes by inversion rotations about axes of the same order. If inversion is interpreted as the operation of transforming the signs of a figure, the derivation of the planar homology groups becomes the derivation of the minor axial antihomology groups. The number of the latter is therefore equal to 75.

Each minor central antihomology group $\underline{H}^*$ is obtained from a central homology group H^* by replacing in the latter certain homology transformations by the corresponding antihomology transformations. The group H^* in turn is obtained from an axial homology group H by adding to the latter inversion as a generating element $H^* = H \times \{c\}$, where $\{c\}$ is the cyclic group generated by inversion. This means that for the derivation of all minor central antihomology groups it is necessary to consider three cases: 1) $\underline{H}^* = H \times \{\underline{c}\}$, 2) $\underline{H}^* = \underline{H} \times \{c\}$; 3) $H^* = H \times \{\underline{c}\}$, where $\underline{H}$ is a minor axial antihomology group, and $\{c\}$ is a second-order cyclic group, generated by anti-inversion. Methods 1, 2, and 3 can be used to derive respectively 70, 75, and 75 minor central antihomology groups, that is, a total of 220 such groups.

Each minor planar antihomology group is derived from a planar homology group by the replacement of some homology transformation h in the latter by the corresponding antihomology transformation $\underline{h} = h\underline{e}$. Each planar homology group H^{**}, however, was in turn obtained from an axial homology group H by the replacement in this group of some rotations about even axes by inversion rotations about axes of the same order. We shall assume that all possible different replacements $\underline{\alpha}_1, \underline{\alpha}_2, \ldots, \underline{\alpha}_m$ of rotations by inversion rotations from the group H have been used to derive the corresponding planar groups H_1^{**}, $H_2^{**}, \ldots, H_m^{**}$. We use the symbols $\underline{\alpha}_1, \underline{\alpha}_2, \ldots, \underline{\alpha}_m$ to denote the analogous replacements, in each of the groups $H_1^{**}, H_2^{**}, \ldots, H_m^{**}$, of simple and inversion rotations about even axes by the corresponding antirotations. All minor antihomology groups from the generating group H_l^{**} are derived from the planar homology group H_l^{**} ($1 \leq l \leq m$) by the replacements $\alpha_1, \alpha_2, \ldots, \alpha_m$. Thus after the elimination of repeating groups we obtain all minor planar groups. 137 minor planar antihomology groups are derived from 75 planar homology groups.

The total number of minor antihomology groups derived is 75 + 220 + 137 = 432.

7. The next stage in the development of the theory of homology, judging from refs. 1 and 6, should be the derivation of homology space groups. Just as the deriva-

tion of the Fedorov groups was preceded by the derivation of the symmetry point groups,[7] the derivation of the homology space groups is preceded by the derivation of the homology point groups. The degree of similarity between the methods used in these two derivations depends on how broadly homology is understood. In the homology space groups we should encounter all 230 Federov groups.

The generalization of homology to include antihomology, begun in the present work, can be extended to space groups, and can also be extended further (multiple antihomology, color antihomology, etc.).

[1] V. I. Mikheev, The Homology of Crystals [in Russian], Gostoptekhizdat (1961).

[2] R. V. Galiulin, A Matrix-Vector Method for the Derivation of the Fedorov Groups [in Russian], Moscow (1969).

[3] A. V. Shubnikov, Kristallografiya, 10, 775 (1965) [Sov. Phys.—Crystallogr., 10, 655 (1966)].

[4] A. V. Shubnikov, The Symmetry and Antisymmetry of Finite Figures [in Russian], Izd. AN SSSR, Moscow (1951).

[5] A. M. Zamorzaev, Thesis [in Russian], Leningrad (1953).

[6] V. V. Nardov, Crystallographic Systems of Figures and Homology Space Groups. The Ideas of E. S. Fedorov in Modern Crystallography and Mineralogy [in Russian], Nauka, Leningrad (1970), pp. 65-74.

[7] B. Delone, N. Padurov, and A. Aleksandrov, Mathematical Principles of the Structural Analysis of Crystal [in Russian], Ob'edinen. Nauch. Tekh. Izd. (1934).

Stable configurations of a bioctahedral complex with Jahn–Teller centers

I. B. Bersuker, B. G. Vekhter, and M. L. Rafalovich
Institute of Chemistry, Academy of Sciences of the Moldavian SSR
(Submitted January 24, 1972)
Kristallografiya, 18, 11-18 (January-February 1973)

The equilibrium configurations of an M_2L_{11} bioctahedral complex, which govern the local symmetry of the corresponding crystal structures, were investigated while taking the Jahn–Teller effect into consideration. It was shown that if the octahedrally coordinated metal ions M possess a doubly degenerate electronic ground state, the complex is distorted with a decrease in symmetry to D_{2h} as a result of the electronic–vibrational interaction: The equatorial squares of the ligands L are converted into rhombuses. The number of distorted equilibrium configurations of the system was determined. Equations for the changes in the M–L distances were derived and the stabilization energies for the distortions were obtained. The latter are expressed through the normal coordinates and frequencies of the complex for whose determination the vibrational problem was preliminarily solved.

Jahn and Teller[1] formulated a theorem in 1937 according to which nuclear configurations which lead to a degenerate electronic ground state of the molecule are not stable. The inclusion of the electronic–vibrational interaction in such cases leads to the fact that the minima of the adiabatic potential correspond to the distorted configurations of the molecule for which the degeneracy is lifted. A large number of papers (see ref. 2) have recently been devoted to the investigation of the Jahn–Teller effect and, in particular, to finding the stable equilibrium configurations. With rare exceptions, isolated Jahn–Teller molecules or impurity centers have been analyzed in these papers.

Practially no investigations of the Jahn–Teller or pseudo-Jahn–Teller situations for interacting centers have been carried out up to the present. Meanwhile, the considerations concerning interacting dynamically unstable centers lie at the basis of a new evolving direction in the theory of stable configurations of crystal lattices and various phase transitions in them, including the ferroelectric ones.[3,4] Therefore, the problem concerning the stable configurations of polyatomic systems with several Jahn–Teller or pseudo-Jahn–Teller centers is quite urgent.

The simplest of such objects, a bioctahedral complex with two octahedral Jahn–Teller E centers[1)] with the common atom at the apices of the two octahedra (Fig. 1), is analyzed in this paper. A similar case was discussed by Lohr;[5] however, the assumption he made that the equilibrium configurations of the system are the various combinations of the equilibrium configurations of the individual octahedrons cannot be considered to be satisfactory because the theoretical effect of the interaction of the octahedra is thereby ignored. It is proposed to expand the discussion below to both other chain and crystal structures.

1. NORMAL COORDINATES

The solution of the problem concerning the stable configurations of a system requires knowledge of its normal coordinates and of the frequencies corresponding to them. The 33 normal vibrations for the system of 13 atoms with group symmetry D_{4h} which we are considering are transformed according to the following representation: $4a_{1g}$, $4a_{2u}$, a_{1u}, b_{1g}, $2b_{1u}$, $2b_{1g}$, b_{2u}, $4e_g$, and $5e_u$. Of them, only vibrations of the types a_{1g}, a_{2u}, b_{2g}, and b_{1u} are active in the electronic–vibrational interaction, as will be shown below. Using the standard theory of projection, it is not difficult to determine the mass-weighted symmetry coordinates $\eta_i(\Gamma)$ transformed with respect to these representations:

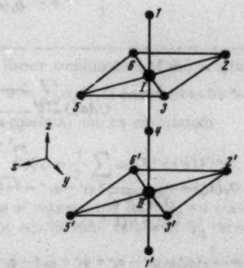

Fig. 1. Numbering of the ligands and choice of the coordinate axes of a bioctahedral complex. (The x, y, z coordinate system was chosen for all the atoms as the right set of three.)

$$\left.\begin{aligned}
&\eta_1(a_{2u})=q_4^z,\ \eta_2(a_{2u})=\frac{1}{\sqrt{2}}(q_7^z+q_{7'}^z),\\
&\eta_3(a_{2u})=\frac{1}{\sqrt{2}}(q_I^z+q_{II}^z),\\
&\eta_4(a_{2u})=\frac{1}{\sqrt{8}}(q_5^z+q_6^z+q_2^z+q_3^z+q_{5'}^z+q_{6'}^z+q_{2'}^z+q_{3'}^z),\\
&\eta_5(a_{1g})=\frac{1}{\sqrt{2}}(q_7^z-q_{7'}^z),\ \eta_6(a_{1g})=\frac{1}{\sqrt{2}}(q_I^z-q_{II}^z),\\
&\eta_7(a_{1g})=\frac{1}{\sqrt{8}}(q_5^x-q_2^x-q_6^y+q_3^y+q_{5'}^x-q_{2'}^x-q_{6'}^y+q_{3'}^y),\\
&\eta_8(a_{1g})=\frac{1}{\sqrt{8}}(q_5^z+q_6^z+q_2^z+q_3^z-q_{5'}^z-q_{6'}^z-q_{2'}^z-q_{3'}^z),\\
&\eta_9(b_{2g})=\frac{1}{\sqrt{8}}(q_5^x-q_2^x-q_3^y+q_6^y+q_{5'}^x-q_{2'}^x-q_{3'}^y+q_{6'}^y),\\
&\eta_{10}(b_{2g})=\frac{1}{\sqrt{8}}(q_5^z-q_6^z-q_3^z+q_2^z+q_{6'}^z+q_{3'}^z-q_{5'}^z-q_{2'}^z),\\
&\eta_{11}(b_{1u})=\frac{1}{\sqrt{8}}(q_5^x-q_2^x-q_3^y+q_6^y-q_{5'}^x+q_{2'}^x+q_{3'}^y-q_{6'}^y),\\
&\eta_{12}(b_{1u})=\frac{1}{\sqrt{8}}(q_5^z-q_6^z-q_3^z+q_2^z-q_{6'}^z-q_{3'}^z+q_{2'}^z+q_{5'}^z),
\end{aligned}\right\}\quad(1)$$

where $q_i^p=(m_i)^{1/2}p_i\ (p=x,\ y,\ z)$.

However, when several symmetry coordinates which are transformed with respect to the very same representation exist, the group-theoretical considerations only are inadequate for calculating their correct linear combinations, which are the normal coordinates. The determination of the normal coordinates in this case requires the solution of the vibrational problem within the framework of any model. One of the simplest models is used below for this purpose: It is assumed that the potential energy of the system contains quadratic terms with respect to the changes in the distances ΔR and angle $\Delta\varphi$, but does not contain mixed terms of the type $\Delta R\Delta\varphi$. This simple model even makes it possible to take the interaction of the octahedra, which is guaranteed by the existence of common atom 4 (Fig. 1), into consideration qualitatively correctly.

Upon writing the Lagrange equation, we obtain a system of equations in the usual way which define the mode of the vibrations and the corresponding frequencies.[6] In order to simplify the calculations, we will assume that the system being considered contains the heavy central ions I and II of a transition metal (mass M) and the lighter ligands (mass m), so that the expressions obtained can be expanded in a series with respect to parameter $\varkappa = m/M$ and retain in it only the terms of the order of $\varkappa$. Omitting the details of the calculations, we write the final expressions for the normal coordinates through the coordinates q_i^p and the frequencies corresponding to them:

$$Q_1(a_{2u}) = \sqrt{\frac{\varkappa}{2(2+\varkappa)}}\left(q_I^z + q_{II}^z - \frac{2}{\sqrt{\varkappa}}q_4^z\right),$$

$$\omega_1^2 = 2\alpha\left(1+\frac{\varkappa}{2}\right),$$

$$Q_2(a_{2u}) = \sqrt{\frac{\varkappa}{(2+\varkappa)(2+3\varkappa)}}\left[q_I^z + q_{II}^z + \sqrt{\varkappa}q_4^z - \frac{2+\varkappa}{2\sqrt{\varkappa}}(q_1^z + q_{1'}^z)\right],$$

$$\omega_2^2 = \alpha(1+\varkappa),$$

$$Q_3(a_{1g}) = \frac{1}{\sqrt{2(1+\varkappa)}}[q_1^z - q_{1'}^z - \sqrt{\varkappa}(q_I^z - q_{II}^z)],$$

$$\omega_3^2 = \alpha(1+\varkappa),$$

$$Q_4(a_{1g}) = \frac{1}{\sqrt{2(1+\varkappa)}}[\sqrt{\varkappa}(q_1^z - q_{1'}^z) + q_I^z - q_{II}^z],$$

$$\omega_4^2 = \alpha\varkappa(1-\varkappa),$$

$$Q_5(a_{1g}) = \frac{1}{\sqrt{8}}(q_3^x - q_2^x - q_6^y + q_5^y + q_{3'}^x - q_{2'}^x - q_{6'}^y + q_{5'}^y),$$

$$\omega_5^2 = \alpha,$$

$$Q_6(b_{2g}) = \frac{1}{\sqrt{8}}(q_3^x - q_2^x + q_6^y - q_5^y + q_{3'}^x - q_{2'}^x + q_{6'}^y - q_{5'}^y).$$

$$\omega_6^2 = \alpha,$$

$$Q_7(b_{1u}) = \frac{1}{\sqrt{8}}(q_3^x - q_2^x + q_6^y - q_5^y - q_{3'}^x + q_{2'}^x - q_{6'}^y + q_{5'}^y)$$

$$\omega_7^2 = \alpha. \tag{2}$$

where $\alpha = f/m$; f is the "rigidity" coefficient of the metal–ligand band.

2. INCLUSION OF THE ELECTRONIC–VIBRATIONAL INTERACTION

As has already been mentioned, the electronic states of the central ions of each octahedron are assumed to form the basis of the doubly degenerate E_g representation of the group O_h. The one-electron molecular orbitals $\psi^{s_I m_I}_{\Gamma_I \gamma_I}$, which are composed of these four functions u_I, v_I, u_{II}, v_{II} (u and v are the basis of the E_g representation in the octahedron), are transformed with respect to the representations A_{1g}, B_{2g}, A_{2u}, and B_{1u} of group D_{4h}. Let us construct the two-electron molecular orbitals, which take into consideration the rearrangements of the electrons and are eigenfunctions of the total spin operator $S = s_1 + s_2$ and its projection $M = m_1 + m_2$, according to the following equation:[7]

$$\Phi^{SM}(\Gamma\gamma) = \Sigma\langle\Gamma_1\gamma_1\Gamma_2\gamma_2|\Gamma\gamma\rangle\langle s_1m_1s_2m_2|SM\rangle|\psi^{s_1m_1}_{\Gamma_1\gamma_1}\psi^{s_2m_2}_{\Gamma_2\gamma_2}|. \tag{3}$$

In all, there are 28 electronic configurations possible in the problem considered; of them, 12 depict ionic states, i.e., the states in which both electrons exist at a single center. Because the energies of the ionic configurations increase by far the energies of the states in which a single electron exists on each center, due to the considerable interelectronic interaction of the electrons on the one center, we limited ourselves to investigate only the latter (states). The wave functions of the singlets and triplets (with M = 1) of the covalent states (the functions of the triplets with M = 0, −1 are easily obtained using the usual operations of lowering the spin) are given below:

$$\left.\begin{gathered}
\Phi_1^{00}(A_{1g}) = \frac{1}{\sqrt{2}}(|u_I\bar{u}_{II}| - |\bar{u}_I u_{II}|), \quad \Phi_1^{11}(A_{2u}) = |u_I u_{II}|, \\
\Phi_2^{00}(A_{1g}) = \frac{1}{\sqrt{2}}(|v_I\bar{v}_{II}| - |\bar{v}_I v_{II}|), \quad \Phi_2^{11}(A_{2u}) = |v_I v_{II}|, \\
\Phi_3^{00}(B_{2g}) = \frac{1}{2}(|u_I\bar{v}_{II}| - |\bar{u}_I v_{II}| + |v_I\bar{u}_{II}| - |\bar{v}_I u_{II}|), \\
\Phi_3^{11}(B_{2g}) = \frac{1}{\sqrt{2}}(|u_I v_{II}| - |v_I u_{II}|), \\
\Phi_4^{00}(B_{1u}) = \frac{1}{2}(|u_I\bar{v}_{II}| - |\bar{u}_I v_{II}| + |\bar{v}_I u_{II}| - |v_I\bar{u}_{II}|), \\
\Phi_4^{11}(B_{1u}) = \frac{1}{\sqrt{2}}(|u_I v_{II}| + |v_I u_{II}|).
\end{gathered}\right\} \tag{4}$$

Without accounting for the interelectronic interaction and on the assumption that the electrons interact only with the nearest ligands, the energies of all 16 covalent states coincide. A consideration of the electronic–vibrational interaction of the splittings introduced requires the solutions of the respective secular equation of the sixteenth order. It is broken down into four blocks of the fourth order, into respectively the singlet and triplet states with various values of M. Because the electronic–vibrational interaction does not depend on the spin state of the electrons, all four blocks turn out to be identical:

$$\begin{vmatrix} \frac{2B}{\sqrt{6}}(Q_5-Q_3-\sqrt{\varkappa}Q_4)-\varepsilon & 0 & -BQ_6 & BQ_7 \\ 0 & -\frac{2B}{\sqrt{6}}(Q_5-Q_3-\sqrt{\varkappa}Q_4)-\varepsilon & -BQ_6 & -BQ_7 \\ -BQ_6 & -BQ_6 & -\varepsilon & \frac{2B}{\sqrt{3}}\left(Q_1-\frac{Q_2}{\sqrt{2}}\right) \\ BQ_7 & -BQ_7 & \frac{2B}{\sqrt{3}}\left(Q_1-\frac{Q_2}{\sqrt{2}}\right) & -\varepsilon \end{vmatrix} = 0. \qquad (5)$$

The electronic–vibrational interaction was taken in the following form as a perturbation for which secular equation (5) was constructed:

$$V=\sum_n V_nQ_n(\Gamma,\gamma), \qquad (6)$$

where Γ, γ are respectively the representations and their rows for the vibrational coordinates Q_n obtained in Sec. 1. Coefficients V_n are expressed through the derivatives of the Hamiltonian with respect to Q_n. Knowing the representations with respect to which the electronic wave functions are transformed, it is not difficult to calculate the representations with respect to which their mixed vibrations are transformed: This will be vibrations of the a_{1g}, b_{2g}, b_{1u}, and a_{2u} types for the case being considered. The quantity B in Eq. (5) is an interaction constant between the E_g term and the e_g vibrations of the octahedron; the equilibrium positions of the ligands in the octahedron were chosen so that there was no interaction between the electrons and the completely symmetrical vibration. The overlap of the electronic functions of the various centers was neglected during the calculation of the matrix elements.

3. DETERMINATION OF THE EXTREME POINTS AND EQUILIBRIUM CONFIGURATIONS

The equilibrium configurations of the system are found from the conditions where the adiabatic potential $E(Q_n)$ is a minimum: $\partial E/\partial Q_n = 0$, $\partial^2E/\partial Q_n^2 < 0$. The adiabatic potential $E(Q_n)$ can be written in the form[2]

$$E(Q_n)=W(Q_n)+\varepsilon(Q_n), \qquad (7)$$

where $\varepsilon(Q_n)$ is the solution of the equation $\|V-\varepsilon\| = 0$, and $W(Q_n) = {}^1/_2\Sigma\omega_n^2Q_n^2$ is the elastic energy of the interaction between the ligands and the core of the central ion and with each other. The procedure for the direct minimization of $E(Q_n)$ in the case being considered is not practicable because we are not able to obtain simple analytical expressions for solving the electronic secular fourth-order equation (5). A somewhat different approach was developed by Öpik and Pryce for similar situations.[8] The electron wave function Ψ of the equilibrium configuration, which is the linear combination of the original degenerate functions Φ_i, $\Psi = \sum_i c_i\Phi_i$, is assumed to be known. Then, the adiabatic potential can be calculated:

$$E(Q_n)=\frac{1}{2}\sum_n\omega_n^2Q_n^2+\langle\Psi|V|\Psi\rangle. \qquad (8)$$

The condition of extremality $\partial E/\partial Q_n = 0$ makes it possible to express the equilibrium values of Q_n^0 through c_i:

$$\left.\begin{aligned} &Q_1^0=-\frac{2B}{\alpha\sqrt{3}}c_3c_4, \quad Q_4^0=-\frac{2B}{\alpha\sqrt{6\varkappa}}(c_1^2-c_2^2),\\ &Q_2^0=\frac{4B}{\alpha\sqrt{6}}c_3c_4, \quad Q_3^0=-\frac{2B}{\alpha\sqrt{6}}(c_1^2-c_2^2),\\ &Q_5^0=\frac{2B}{\alpha\sqrt{6}}(c_1^2-c_2^2), \quad Q_6^0=\frac{2B}{\alpha}c_3(c_1+c_2),\\ &Q_7^0=-\frac{2B}{\alpha}c_4(c_1-c_2). \end{aligned}\right\} \qquad (9)$$

Upon substituting these values of Q_n^0 into the electronic equation

$$V\Psi=\varepsilon\Psi, \qquad (10)$$

multiplying the left side by Φ_i, and integrating with respect to the electronic coordinates, we obtain the following system of equations relative to c_i and $\tilde{\varepsilon} = \varepsilon\alpha/B^2$:

$$\left.\begin{aligned} &c_1(1-2c_2^2)+c_2(c_3^2-c_4^2)=\tilde{\varepsilon}c_1,\\ &c_2(1-2c_1^2)+c_1(c_3^2-c_4^2)=\tilde{\varepsilon}c_2,\\ &c_3(c_1+c_2)^2+4c_3c_4^2/3=\tilde{\varepsilon}c_3,\\ &c_4(c_1-c_2)^2+4c_4c_3^2/3=\tilde{\varepsilon}c_4, \end{aligned}\right\} \qquad (11)$$

to which still another condition of normalization $\sum_i c_i^2 = 1$ should be added. The solutions of system (11) are given in Table 1.

The configurations given in Table 1 are characterized by the fact that $\partial E/\partial Q_n = 0$ for them. Consequently, they are extremes, but do not necessarily correspond to minima. In order for the configuration described by the function Ψ_0 to correspond to a minimum, it is necessary that the quadratic form

TABLE 1. Wave Functions, Stabilization Energies at the Extreme Points, and Equilibrium Values of the Coordinates of an M_2L_{11} Bioctahedral Complex

No.	Coefficients c_i of wave function Ψ_i	Equilibrium value of coordinates Q_n^0							Stabilization energy
	$[c_1\ c_2\ c_3\ c_4]$	Q_1^0	Q_2^0	Q_3^0	Q_4^0	Q_5^0	Q_6^0	Q_7^0	ε
1	$[1\ 0\ 0\ 0]$	0	0	$\frac{2B}{\alpha\sqrt{6}}$	$\frac{2B}{\alpha\sqrt{6\varkappa}}$	$\frac{-2B}{\alpha\sqrt{6}}$	0	0	$-\frac{B^2}{\alpha}\left(1-\frac{\varkappa}{3}\right)$
2	$[0\ 1\ 0\ 0]$	0	0	$-\frac{2B}{\alpha\sqrt{6}}$	$-\frac{2B}{\alpha\sqrt{6\varkappa}}$	$\frac{2B}{\alpha\sqrt{6}}$	0	0	$-\frac{B^2}{\alpha}\left(1-\frac{\varkappa}{3}\right)$
3	$\frac{1}{2}[-1\ 1\ 0\ \pm\sqrt{2}]$	0	0	0	0	0	0	$\pm\frac{B\sqrt{2}}{\alpha}$	$-\frac{B^2}{\alpha}$
4	$\frac{1}{2}[1\ 1\ \pm\sqrt{2}\ 0]$	0	0	0	0	0	$\pm\frac{B\sqrt{2}}{\alpha}$	0	$-\frac{B^2}{\alpha}$
5	$1/\sqrt{2}[0\ 0\ 1\ \pm 1]$	$\mp\frac{B}{\alpha\sqrt{3}}$	$\pm\frac{2B}{\alpha\sqrt{6}}$	0	0	0	0	0	$-\frac{2}{3}\frac{B^2}{\alpha}$

$$E(Q_n) = W(Q_n) - \sum_\nu{}' \frac{|\langle\Psi_\nu|V|\Psi_0\rangle|^2}{\varepsilon_\nu - \varepsilon_0} \tag{12}$$

be positively determined.[8] An examination of the solutions in Table 1 according to Eq. (12) shows that only the third and fourth ones correspond to minima. The corresponding equilibrium configurations are depicted in Fig. 2.

4. INCLUSION OF THE TETRAGONAL FIELD

As follows from Table 1, the energies of all four equilibrium configurations coincide. Consequently, the electronic–vibrational ground state of the complex by this approach proves to be quadruply degenerate and the electronic–vibrational functions for the minima can be written in the form

$$\left.\begin{aligned}
\Psi_{10} &= \frac{1}{2}(-\Phi_1 + \Phi_2 + \sqrt{2}\Phi_4)\chi_0\left(Q_7 - \frac{B\sqrt{2}}{\alpha}\right)\prod_{n\neq 7}\chi_0(Q_n),\\
\Psi_{20} &= \frac{1}{2}(\Phi_1 - \Phi_2 + \sqrt{2}\Phi_4)\chi_0\left(Q_7 + \frac{B\sqrt{2}}{\alpha}\right)\prod_{n\neq 7}\chi_0(Q_n),\\
\Psi_{30} &= \frac{1}{2}(\Phi_1 + \Phi_2 + \sqrt{2}\Phi_3)\chi_0\left(Q_6 - \frac{B\sqrt{2}}{\alpha}\right)\prod_{n\neq 6}\chi_0(Q_n),\\
\Psi_{40} &= \frac{1}{2}(\Phi_1 + \Phi_2 - \sqrt{2}\Phi_3)\chi_0\left(Q_6 + \frac{B\sqrt{2}}{\alpha}\right)\prod_{n\neq 6}\chi_0(Q_n).
\end{aligned}\right\} \tag{13}$$

This result was obtained while disregarding the splitting of the E levels of each octahedron due to the effect of the other octahedron. When this fact is taken into consideration, it leads to the lifting of the degeneracy mentioned above. If the splitting of the E states is small compared to the effects of the electronic–vibrational interaction, the secular equation for the functions of the vibrational ground state for each minimum has the form

$$\begin{vmatrix} -\varepsilon & 0 & -\frac{\Delta}{2}\gamma_0 & -\frac{\Delta}{2}\gamma_0 \\ 0 & -\varepsilon & \frac{\Delta}{2}\gamma_0 & \frac{\Delta}{2}\gamma_0 \\ -\frac{\Delta}{2}\gamma_0 & \frac{\Delta}{2}\gamma_0 & -\varepsilon & 0 \\ -\frac{\Delta}{2}\gamma_0 & \frac{\Delta}{2}\gamma_0 & 0 & -\varepsilon \end{vmatrix} = 0, \tag{14}$$

where Δ is the splitting of the E_g term of the individual octahedron, and the overlap integral of the vibrational functions of the neighboring minimum γ_0 is given by the expression

$$\gamma_0 = \exp\left(-B^2/\alpha\hbar\omega\right). \tag{15}$$

We find from Eq. (14) that when the splitting of the E term of the octahedra is accounted for, it leads to the following electronic–vibrational levels:

$$\varepsilon_1 = \varepsilon_2 = 0; \quad \varepsilon_3 = \Delta\gamma_0; \quad \varepsilon_4 = -\Delta\gamma_0. \tag{16}$$

The occurrence of the overlap integral in the expressions for the energies (16) is responsible for the suppresion effect described in refs. 9 and 10.

DISCUSSION OF THE RESULTS

It is evident from the results given above that the adiabatic potential surface of a bioctahedron has four minima within the extent of the normal coordinates $Q_1 \ldots Q_7$ in the approach we have discussed; the equilibrium configurations represented in Fig. 2 correspond to the latter. The symmetries of the two configurations of type a and of the two of type b mutually coincide, i.e., these configurations convert into each other during the symmetry conversions of the group. The energies of the configurations with the same symmetry should coincide; the agreement of the energies of all four configurations is evidently the consequence of taking the interaction of only the nearest neighbors into consideration.

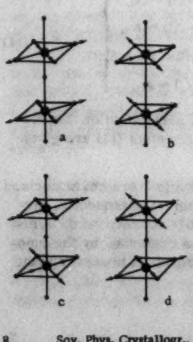

Fig. 2. Equilibrium configurations of a bioctahedral complex. a, b) Situations leading to stable configurations of type 3 (see Table 1); c, d) situations leading to a stable configuration of type 4.

Besides the four minima, the adiabatic potential surface, as is evident from Table 1, also possesses two types of saddle points 1, 2, and 5. Upon comparing these results with the results Lohr obtained,[5] it can be ascertained that they are entirely different. The account referred to showed that the qualitative treatment,[5] in which the mutual effect of the octahedra is neglected, is inaccurate: Not one of the proposed equilibrium configurations that Lohr offered is actually stable. Note that in our rough treatment, the interaction of the octahedra is taken into consideration in the vibrational problem and also by the introduction of the tetragonal component of the crystal field, which, apparently, is fully justified for ionic compounds. During an estimate of the covalency, the calculations are complicated because the inclusion of the overlapping of the electronic functions of the two centers requires the introduction of additional parameters. It is clearly evident from the results obtained how important the effect of the interaction of the Jahn–Teller centers is on their stable configurations. It is to be expected that this effect will be still greater with an increase in the number of interacting centers.

---

1) An E center in the sense of a doubly degenerate E_g electronic ground term.

---

[1] H. A. Jahn and E. Teller, Proc. Roy. Soc., A161, 120 (1937).
[2] I. B. Bersuker, The Structure and Properties of Coordination Compounds [in Russian], Khimiya, Leningrad (1971).
[3] I. B. Bersuker, Phys. Lett., 20, 589 (1966); I. B. Bersuker, B. G. Vekhter, and A. A. Muzalevskii, Phys. Status Solid, B45, K25 (1971).
[4] J. Kanomori, J. Appl. Phys. Suppl., 31, 14 (1960); R. Englman and B. Halperin, Phys. Rev., B2, 75 (1970).
[5] L. L. Lohr, Jr., Proc. Nat. Acad. Sci., 59, 720 (1968).
[6] E. Wilson, J. Decius, and P. Cross, Molecular Vibrations, McGraw-Hill (1955).
[7] S. Sugano, Y. Tanabe, and H. Kamimura, Theory of Multiplets of Transition-Metal Ions in Crystals, Academic Press, New York (1970).
[8] U. Öpik and M. H. L. Pyce, Proc. Roy. Soc., A238, 425 (1957).
[9] I. B. Bersuker, and B. G. Vekhter, Fiz. Tverd. Tela, 5, 2432 (1963) [Sov. Phys.–Solid State, 5, 1772 (1964)].
[10] F. S. Ham, Phys. Rev., A138, 1727 (1965).

Some characteristics of the vibronic impurity spectra in ferroelectrics

N. N. Kristofel'

Institute of Physics and Astronomy,
Academy of Sciences of the Estonian SSR

(Submitted June 5, 1971; resubmitted February 10, 1972)
Kristallografiya, 18, 19-25 (January-February 1973)

The likely features near T_C in the behavior of the purely electronic line and the one-phonon wing of the impurity absorption in ferroelectrics, which are caused by the existence of a soft vibrational branch, are qualitatively discussed and illustrated by a simple model.

A characteristic property of ferroelectrics is the existence in them of a soft vibrational branch whose frequencies decrease as the Curie temperature is approached. The dynamical instability and phase transition in a crystal are caused by the disappearance of the cutoff frequency of the soft mode. Besides the direct ferroelectric effects, the anomalous behavior of the soft branch should give rise to a number of characteristics in the physical processes which occur by means of the participation of the lattice vibrations in ferroelectrics. This fact in particular has been used in the investigations by the Mössbauer method of the ferroelectric phase transitions.[1] The Debye–Waller factor depends on the frequencies of the lattice vibrations, which govern the motion of the γ-active nucleus. When a more or less equilibrium distribution of the recoil momentum with respect to the ferroelectric branch of the vibrations exists, a decrease in the frequencies of its long-wave portion will take place as the Curie point is approached, because the Debye–Waller factor tends toward zero. The intensity of the Mössbauer line is again decreased with an increase in the frequencies of the soft mode after passing through the Curie point. Therefore, the Debye–Waller factor passes through a minimum at the Curie point on the background of the usual temperature dependence (on the vibrations which are inactive in the phase transition). This has been theoretically demonstrated for quite simple models in refs. 2 and 3; a more detailed theoretical investigation has been carried out in ref. 4.

A rather remotely operating analogy between the Mössbauer and the electronic–vibrational quasiline impurity spectra[5,6] exists, and is based on the symmetry of the Hamiltonian of the harmonic oscillator relative to the pulse and coordinate. It can be expected from general considerations and on the basis of this analogy that the investigation of the vibronic spectra of the impurity centers in ferroelectrics can furnish valuable information on the properties of the matrix crystal along with an explanation of curious spectral effects. Quasiline electronic–vibrational absorption and emission spectra are highly informative and have been extensively investigated for ordinary ionic crystals and a number of other systems. Unfortunately, the optical spectra of the impurity centers in ferroelectrics have not been investigated much. There is also practically no corresponding theory even at the level for calculating the energy levels of the impurity in a ferroelectric crystal.

It should be stressed that there is an important difference between the Mössbauer and electronic–vibrational spectra of the impurity centers which makes the investigation of the latter promising although difficult. It consists of the fact that a phonon wing, which is due to transition with the production of phonons, is also observed in the vibronic spectra along with a phononless line (the analog to the Mössbauer line). The one-phonon wing more or less bears direct information on the vibrational spectrum of the crystal. It practically is not seen in the Mössbauer spectra. The difficulty lies in the fact that the rather high Curie points of a number of common ferroelectrics dictate the employment of systems with an extremely small electron–phonon interaction in order that the quasiline spectra (including the phononless line) generally would be observable. Thereby, the topic of discussion can evidently only proceed with respect to the spectra linked with the transitions within the well-shielded electron shell of the impurity in systems with potentially low T_C. On the other hand, quite a difficult problem exists in the theory of vibronic spectra concerning the character of the distribution of the Stokes losses with respect to the frequencies of the active mode, i.e., in this case, the dependences of the interaction between the optical electrons of the impurity and the vibrations of the soft branch on the wave vector of the latter.

Vol. 18
July 1973
June 197

Some expected characteristics of the phononless line and the accompanying one-phonon spectrum of the impurity center in a ferroelectric crystal near the Curie temperature (T_C) are analyzed in this work using an extremely simple model.

The phononless and one-phonon optical spectra of the impurity center can be written in the following form correct to practically constant factors:[5]

$$I_0(T,\omega)=\Xi_0(T)\exp\Big\{-\sum_q \xi_q^2(2n_q+1)\Big\}\delta(E_0-\hbar\omega), \tag{1}$$

$$I_1(T,\omega)=\Xi_0(T)\exp\Big\{-\sum_q \xi_q^2(2n_q+1)\Big\}\Big\{\Xi_1(T,\omega)+\sum_q \xi_q^2[n_q\delta(E_0-\hbar\omega_q-\hbar\omega)+(n_q+1)\delta(E_0+\hbar\omega_q+\hbar\omega)]\Big\}, \tag{2}$$

where

$$\xi^2=\frac{A_q^2}{2M\omega_q^2}\frac{1}{\hbar\omega_q}. \tag{3}$$

In these equations, q denotes the wave vector and ω_q are the frequencies of the phonons of the ferroelectric soft branch of the vibrations; the contribution of the vibrations of the other branches is designated through the coefficients Ξ_0 and Ξ_1 (their detailed form is analogous to the one described for the active vibration); E_0 is the energy of the purely electronic transition, and ω is the frequency of the photon. The magnitude of A_q, which has the dimensions of energy/length, governs the distribution of the Stokes losses with respect to the active branch and M is the appropriate mass factor. Since the frequencies of the active branch are anomalously low when the temperature approaches T_C and the values of T_C themselves are usually fairly high, the phonon occupation numbers can be approximated by the expression $n_q = kT/\hbar\omega_q$, $2n_q + 1 = 2kT/\hbar\omega_q$; then the intensities of the Stokes (coefficient n_q+1) and anti-Stokes regions of the spectrum are the same. This approach is, of course, not obligatory. But, the equalization of the intensities of the Stokes and anti-Stokes regions of the phonon wing as T_C is approached (as the temperature is lowered) should be a characteristic feature of the systems being discussed. It is already evident from (1), (2), and (3) that the decrease in ω_q with small values of q as $T \to T_C$ should, generally speaking, contribute to a decrease in the intensity of the purely electronic line and of the regular portion (Ξ_1) of the one-phonon spectrum. "Quenching" of the portion of the one-phonon spectrum, which is linked with the ferroelectric mode, will take place in direct proximity to T_C, and with this, the low-frequency portion of the corresponding spectrum will be anomalously strengthened.1) This anomalous behavior will gradually disappear with the transition to the ferroelectric phase on the background of the usual temperature dependences, but more quickly than it developed in the paraphase because of the more rapid increase of ω_q with a decrease in temperature. The purely electronic line, which corresponds to the transition from the nondegenerate to the degenerate state, will be split as a result of the decrease in symmetry and the emergence of a spontaneous internal polarization field (the frequencies of the active branch of the vibrations will also be split).2) There will be no splitting within a single domain of the orientational degeneracy of these components, but the domain structure will lead to such. This makes it possible, in principle, to employ the usual methods of investigating the orientational degeneracy[9] in the components of the splitting of the purely electronic line for the study of the domain structure.

A model investigation of $I_0(T, \omega)$ and $I_1(T, \omega)$ for the ferroelectric phase is difficult, and we will limit ourselves to a more detailed consideration of them for the paraphase. First, let us convert from summation over the wave numbers of the active branch to integration with respect to the corresponding frequencies; then we have

$$g = \sum_q \xi_q^2(2n_q + 1) \approx \frac{2kT}{\hbar}\sum_q \frac{\xi_q^2}{\omega} = \frac{kT}{M\hbar^2}\int \frac{A^2(x)\,\rho(x)}{x^4}\,dx, \tag{4}$$

where $A^2(\omega_q) = N^{-1}A^2_{q|q=f(\omega_q)}$, and $\rho(x) = N^{-1}\sum_q \delta(\omega_q - x)$ is the density of the states in the active vibrational branch. For the Stokes portion of the one-phonon spectrum of the soft mode we obtain

$$I_{1s}(T, \omega) = \Xi_0(T)\,e^{-\varepsilon}\frac{kT}{2M\hbar^2}\frac{A^2(\omega, T)\,\rho(\omega, T)}{\omega^4}, \tag{5}$$

where it is assumed $E_0 = 0$. It is necessary to know the dependence of $\omega_q(T)$ for the soft mode for further calculations, and, in particular, to obtain $\rho(\omega, T)$.

Based on the results of the experimental investigation of $BaTiO_3$ for example,[10] it can be roughly assumed that beginning with the maximum value of q_m on the surface of the Brillouin zone to a certain value q_x ($q_x \sim 0.4q_m$), ω_q does not depend either on q or on T. When $q < q_x$, the frequencies decrease linearly with temperature from the beginning of the dispersion. As a result, the following approximation is obtained:

$$\begin{cases} 0 \leqslant q \leqslant q_*, & \omega_q^2(T) = a(T - T_c)\left[1 - \left(\dfrac{q}{q_*}\right)^2\right] + \nu^2\left(\dfrac{q}{q_*}\right)^2, \\ q_* \leqslant q \leqslant q_m, & \omega_q^2(T) = \nu^2, \end{cases} \tag{6}$$

in which the cutoff frequency reverts to zero when $T = T_C$. The density of the states corresponding to Eq. (6) has the form

$$\rho(\omega, T) = 3\left(\frac{q_*}{q_m}\right)^3 \omega \sqrt{\frac{\omega^2 - a(T - T_c)}{[\nu^2 - a(T - T_c)]^3}} + \left[1 - \left(\frac{q_*}{q_m}\right)^3\right]\delta(\omega - \nu), \tag{7}$$

where the values of ω are limited to the range $a(T - T_C) \leq \omega^2 \leq \nu^2$. According to ref. 10, $a = 1.66 \cdot 10^{22}\ \mathrm{sec^{-2} \cdot deg^{-1}}$, $\nu = 7.24 \cdot 10^{12}\ \mathrm{sec^{-1}}$, and $T_C = 393°K$ for $BaTiO_3$.

The choice of the dependence of A_q on q presents considerable difficulty. Its character has considerable importance for low values of q because the characteristics in Eqs. (4) and (5) will be compensated for when the increase of A with ω_q is too rapid, due to the presence of ω^4 in the denominators. The functional dependence of $A(\omega_q)$ has been successfully established in the theory of impurity centers only for a continuous model (see ref. 8, for example), or $A(\omega_q)$ has been successfully calculated numerically for relatively simple defects in bases where the dynamics of the lattice has been investigated in all details (eigenvectors of the vibrations exist over the whole Brillouin zone, for example NaCl-type crystals). And even in the latter case, it is not treated without a semiempirical element. At this level of the investigation for ferroelectrics, it is more accurate to raise the problem concerning the feasibility of explaining the character of the dependence of $A(\omega_q)$ on the basis of the experimental data; therefore, we will confine ourselves here to a consideration of a single simple variant of the dependence of $A(\omega_q)$.

Note that the cutoff optical vibrations (the soft ferroelectric branch exists among them) in systems with a center of inversion are odd. In connection with this, the coefficient of the electron–phonon interaction should become zero when q = 0. Further, let us consider that $A_q = -M\omega_q^2 y_{q0}$, where y_{q0} is the shift of the equilibrium value of the normal coordinate (a single active branch, whose index has been dropped, is considered) when the electronic state of the impurity is changed. According to ref. 11, we have

$$y_{q0} = -\frac{1}{\omega_q^2}\sum_{i,\alpha} F_i(\alpha) M_\alpha^{-1/2} B_i(\alpha|q), \tag{8}$$

where α enumerates the ions and i are the vector components; $F_i(\alpha)$ is the corresponding difference in the excess forces, which act laterally from the defect on the neighboring ions; $B_i(\alpha|q)$ is the transform matrix of the Cartesian shifts to y_q that have been given. It is evident from (8) that

$$A_q M^{-1} = \sum_{i,\alpha} F_i(\alpha) M_\alpha^{-1/2} B_i(\alpha|\mathbf{q}). \tag{9}$$

Let us represent $B_i(\alpha|q)$ in the form

$$B_i(\alpha|\mathbf{q}) = N^{-1/2} e_i(\alpha|\mathbf{q}) \begin{cases} \cos \mathbf{q}R_\alpha \\ \sin \mathbf{q}R_\alpha \end{cases}. \tag{10}$$

The polarization vectors $e_i(\alpha|0)$ correspond to the shift of the sublattices of the various atoms relative to each other, and after multiplying them by $F_i(\alpha)$, which are completely symmetrical about the impurity, the summation over i and α yields zero. In the case of an impurity without excess charge, it can be assumed that $F_i(\alpha) \neq 0$ only for its nearest neighbors. Then, it is easy to see that when the q are small, assuming $e_i(\alpha|q) \sim \text{const}$, $A_q \sim q$ from Eq. (9).

Consequently, for illustrative purposes, the following simple (parabolic) approximation was chosen:

$$\begin{cases} A_q^2 = 4A^2\left(1-\dfrac{q}{q_m}\right)^2\left(\dfrac{q}{q_m}\right)^2, \quad q \leqslant q_x; \\ A_q^2 = \dfrac{4A^2}{35}\left[1-21\left(\dfrac{q_x}{q_m}\right)^5+35\left(\dfrac{q_x}{q_m}\right)^6-15\left(\dfrac{q_x}{q_m}\right)^7\right], \end{cases} \tag{11}$$

$$q_x < q \leqslant q_m;$$

where simply the corresponding average value is taken for $q > q_x$, where $\rho(\omega) \sim \delta(\omega-\nu)$. The dependence of $A^2(\omega)$ is obtained from Eq. (11) with the assumption that according to Eq. (6) we have

$$\frac{q}{q_x} = \left[\frac{\omega^2 - a(T-T_c)}{\nu^2 - a(T-T_c)}\right]^{1/2} \tag{12}$$

for $q \leq q_x$.

Approximation (11) corresponds to the case when the increase of A with ω is so rapid that the magnitude of $A^2\rho/\omega^4$ in Eq. (5) remains finite when $\omega = 0$. However, at the same time $\sqrt{N} y_{q0}$ diverges when $q = 0$ (if $T = T_C$). Physically, this is connected with the fact that the lattice becomes infinitely easily deformed through the soft mode at the phase transition point. As a matter of fact, if the anharmonicity is taken into consideration, the values of $\sqrt{N} y_{q0}$ obtained are finite but anomalously high; one of the specific characteristics of ferroelectrics lies in this. As a result of this, a more accurate theory of the optical spectra of impurity centers in ferroelectrics should be evolved by taking the anharmonicity of the vibrations into consideration. However, when the known effect of anharmonicity in the spectra is taken into consideration,[5] it can be assumed it does not affect substantially the effects that have been discussed here. On the other hand, it must be kept in mind that the point where $T = T_C$ is not attained in the majority of ferroelectrics, since a transition of the first type takes place at a little higher temperature. This circumstance can to a certain extent interfere with the observation of the spectral anomalies discussed in this paper. It should also be noted that all the effects mentioned here could be more clearly manifested in crystals if "soft" behavior were to extend into the vibrations of the active branch with potentially large values of q (within the cutoff boundary of the zone).

The one-phonon spectrum is calculated directly from Eq. (5), and the integral in Eq. (4) can be taken analytically so that

$$\begin{aligned} g = \frac{4kTA^2}{M\hbar^2}\Bigg\{ & \frac{3(q_x/q_m)^3}{2[\nu^2 - a(T-T_c)]^2} \\ & \times\left[2+\frac{a(T-T_c)}{\nu^2} - 3\sqrt{\frac{a(T-T_c)}{\nu^2-a(T-T_c)}}\right. \\ & \left.\times \arccos\frac{\sqrt{a(T-T_c)}}{\nu} - 2\frac{q_x}{q_m}\right. \\ & \times\left[1-\frac{a(T-T_c)}{\nu^2-a(T-T_c)}\left(4\ln\frac{\nu}{\sqrt{a(T-T_c)}}\right.\right. \\ & \left.\left.\left.+\frac{a(T-T_c)}{\nu^2}-1\right)\right]+\left(\frac{q_x}{q_m}\right)^3\left[\frac{2}{3}\right.\right. \\ & +\frac{a(T-T_c)}{\nu^2-a(T-T_c)}\left(-4-\frac{a(T-T_c)}{\nu^2}\right. \\ & \left.\left.\left.+5\sqrt{\frac{a(T-T_c)}{\nu^2-a(T-T_c)}}\arccos\frac{\sqrt{a(T-T_c)}}{\nu}\right)\right]\right] \\ & +\frac{0.0258}{\nu^4}\left(1-\left(\frac{q_x}{q_m}\right)^3\right)\Bigg\}. \end{aligned} \tag{13}$$

The temperature dependence of the Debye–Waller factor e^{-g} (Fig. 1) and the contribution of the soft mode to the one-phonon spectrum $2I_{12}\Xi_0^{-1}e^{g}$ for four temperatures (Fig. 2) were calculated with the value A = 0.03 eV · Å^{-1}. It follows from Fig. 1 that the intensity of the purely electronic line near T_C remains practically constant (there is even a slight decrease in its intensity with temperature in direct proximity to T_C) instead of the usual exponential decrease. It can be presumed that such an anomalously slow change in the intensity of the purely electronic line in the vicinity of the phase transition temperature (the increase in the frequencies of the soft mode compensates for the increase in temperature) should be experimentally observable. Such an assumption is more characteristic for broad-gap ferroelectrics. The dependence of $\omega_q^2(T)$ for $T > T_C$ is different for broad- and narrow-gap systems from the point of view of the electron–phonon theory of the ferroelectric phase transitions.[12,13] In the first case, $\omega_q^2(T)$ simply increases with T as a result of strictly anharmonic contributions. For the narrow-gap sys-

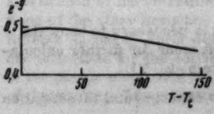

Fig. 1. Contribution of the soft mode to the intensity of the purely electronic line when $T > T_C$.

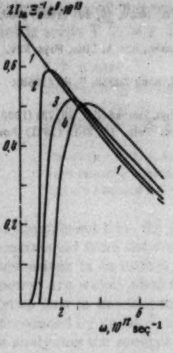

Fig. 2. Contribution of the soft mode to the Stokes portion of the one-phonon spectrum. 1) T − T_C = 0; 2) 10; 3) 40; 4) 100°C.

tems, $\omega_q^2(T)$ tends toward the high-temperature range (the harmonic frequency without any contribution of the interzonal electron−phonon renormalization), and the quenching action of the increase in temperature of e^{-g}, other conditions being equal, should show up earlier. The length of the "plateau" for $e^{-g(T)}$ will now be less, but it will probably be more clearly expressed.

When the increase in A_q with q is slower than in Eq. (11), e^{-g} near T_C will already tend toward zero in a way similar to the behavior of the Mössbauer line, and when the increase of A_q with q is faster, the anomalies in the behavior of e^{-g} will be quenched. An interesting possibility for the experimental determination of the rate of increase of A_q with q follows from this. Note also that $g \sim \omega_0^{-1} \cdot (1/\varepsilon_{opt} - 1/\varepsilon_{stat})$, where ω_0 is the frequency of the longitudinal optical vibrations, is obtained in the continuous theory.[8] If ω_0 were assumed to be constant (ferroelectrically active transverse branch), an effective intensification of the electron−phonon relation arises through $\varepsilon_{stat} \to \infty$, when $T \to T_C$, which causes quenching of the purely electronic line.

An interesting situation arises for the transitions forbidden with respect to parity in a rigid lattice. Their prohibition is lifted by the odd vibrations, which ensure the necessary "impurity" of the states of opposite parity to the excited (usual) state. The zero moment (integrated intensity) of the corresponding electronic−vibrational band depends on the temperature and is given by the following expression:

$$S_0 = \sum_q C_q^2 \frac{\hbar}{2M\omega} \coth \frac{\hbar\omega_q}{2kT} \qquad (14)$$

for the lowest order with respect to the vibronic interaction,[5] where C_q are the coefficients of the linear expansion term of the electronic matrix transition element with respect to the normal coordinates (the index of the branch of the vibrations is omitted for simplicity). It is not difficult to ascertain that C_0 is constant for the odd cutoff optical vibrations. Consequently, S_0 will contain a diverging (in the harmonic approximation) term like ω_0^{-2} when $\omega_0 \to 0$ for ferroelectrics for $T \to T_C$. As a result, when the temperature is lowered to T_C, the intensity of such an electronic−vibrational band will increase strongly, which is a clear anomalous effect (in ordinary systems, similar forbidden bands flare up with an increase in temperature).[3] This result will pertain to the purely electronic line, one-phonon wing, etc. For example, the intensity of the purely electronic line is given by the following expression under similar conditions:[5]

$$I_0 \sim \Big(\sum_q C_q y_{q0}\Big)^2 \exp\Big[-\sum_q \xi_q^2(2n_q+1)\Big],$$

and, as we mentioned, the Debye−Waller factor remains finite when T = T_C, although it behaves anomalously.[4]

Physically, this effect is caused by the strong increase in the low-symmetry fields, which lift the forbiddenness from the transition as a result of the considerable amplitudes of vibrations of the ions in the soft mode when ω_q decreases. The fairly large percentage of the impurity ions which are often used (among them, the rare-earth ions) in itself bears the possibility of similar "forbidden" transitions. The investigation of their temperature dependence in ferroelectrics is of considerable interest. The possibility that the above mentioned effect can also serve as a criterion of the "forbiddenness" of a transition is not to be excluded.

Turning to the one-phonon wing of the allowed transitions, we see from Fig. 2 that a strengthening of the low-frequency portion of the spectrum takes place with the approach to T_C [with the cutting off of the position of the purely electronic line when $a(T - T_C) \neq 0$]. It could be observed on the background of the regular portion of the spectrum[5] $\Xi_1(T, \omega)$. When A_q increases more slowly with q, this effect is much more clearly expressed. The constant portion of the soft branch yields a δ peak in this model at the cutoff frequency. This, of course, is a very rough approximation. Under actual conditions, an ordinary type of peak can be expected here.

We are confident that in spite of the experimental difficulties, the expected effects mentioned above could serve as a stimulus for investigating pertinent systems and their vibronic spectra near T_C.

The author thanks V. G. Vaks for his fruitful discussion and V. V. Khizhnyakov for discussing the paper.

---

[1] Since the value of ξ_q^2 as applied to the Mössbauer effect contains the additonal coefficient ω_q^2 in the denominator, the situation for observing similar anomalies there is much more favorable.

[2] The splittings, which can be present in connection with the Jahn−Teller effect in the impurity, can be neglected due to the weakness of the electron−phonon interaction.[7,8]

[3] In a low-symmetry phase, the corresponding band will already be resolved because a static, although temperature-dependent, drop in symmetry due to the equilibrium value $y_{q=0} \neq 0$ exists. The usual increase of S_0 with T can evidently appear only at lower temperatures, where spontaneous polarization (distortion of the lattice) begins and ω_0 is close to "saturation".

[4] We emphasize that for the purely electronic line, the forbiddenness is lifted by vibrations which simultaneously lead to a violation of the Condon approximation ($C_q \neq 0$) and interact with the electronic transition ($y_{q_0} \neq 0$).

[5] Which can be extended substantially beyond ν.

[1] G. A. Smolenskii, V. A. Bokov, V. A. Isupov, N. N. Krainik, R. E. Pasynkov, and M. S. Shur, Ferroelectrics and Antiferroelectrics [in Russian], Nauka, Leningrad (1971).

[2] C. Muzikář, V. Janovec, and V. Dvořák, Phys. Status Solidi, 3, K9 (1963).

[3] O. V. Dumbrais and B. N. Rolov, Izv. Akad. Nauk SSSR, 31, 1065 (1967).

[4] V. G. Vaks, V. M. Galitskii, and A. I. Larkin, Zh. Éksp. Teor. Fiz., 54, 1172 (1968) [Sov. Phys.–JETP, 27, 627 (1968)].

[5] K. K. Rebane, Elementary Theory of the Vibrational Structure of the Spectra of Impurity Centers in Crystals [in Russian], Nauka, Moscow (1968).

[6] A. A. Maradudin, Rev. Mod. Phys., 35, 417 (1964).

[7] M. D. Sturge, Solid State Phys., 20, 91 (1967).

[8] Y. Toyozawa, Tokyo Summer Lect. in Theor. Phys., Vol. 1, Syokaba, Tokyo (1967), p. 90.

[9] P. P. Feofilov and A. A. Kaplyanskii Usp. Fiz. Nauk, 76, 201 (1962) [Sov. Phys.–Usp., 5, 79 (1962)].

[10] G. Shirane, B. Frazer, V. Minkiewicz, J. Leake, and A. Linz, Phys. Rev. Lett., 19, 234 (1967).

[11] N. N. Kristofel', Tr. Inst. Fiz. Astron. Akad. Nauk EstSSR, 7, 85 (1958); 10, 3 (1959); 11, 180 (1960).

[12] N. Kristofel' (Kristoffel) and P. I. Konsin, Phys. Status Solidi, 28, 731 (1968).

[13] N. N. Kristofel' and P. I. Konsin, Fiz. Tverd. Tela, 13, 2513 (1971) [Sov. Phys.–Solid State, 13, 2113 (1972)].

Calculation of the energy matrices for d^n configurations in intracrystalline fields with T (n = 2, 3, 7, 8) symmetry

E. F. Kustov

Moscow Energy Institute

(Submitted July 19, 1971)
Kristallografiya, 18, 26-31 (January-February 1973)

The d^n (n = 2, 3, 7, 8) configurations are treated in intracrystalline fields with T symmetry. Proceeding from the wave functions constructed for the d^2 configuration, the matrices for the electrostatic interaction for this configuration are obtained and used to calculate the electrostatic interaction matrices for the $d^3(d^7)$ configurations.

At the present time the diagram of Tanabe and Sugano[1] constructed from the energy matrices for the d^n configurations in an intracrystalline field of octahedral symmetry[1] are widely used to analyze spectra from iron-group ions in intracrystalline fields, using the parameters introduced by Racah.[2] These matrices can also be used in analyzing the spectra from intracrystalline fields of tetrahedral symmetry with a symmetry group T_d isomorphous to the group O. For this it is necessary to change the sign of the intracrystalline field parameter Dq in the energy matrices of the corresponding configurations. However, in many crystals having four-fold coordination of the impurity center, the symmetry of the nearest neighbor surroundings belongs to the group T, which is not isomorphous to the octahedral group. Therefore, in the present paper we calculate the electrostatic interaction matrices for certain ion configurations in an intracrystalline field of symmetry T.

The basis functions for the irreducible representations of a group with symmetry T, according to ref. 3, can be taken as the following:

$$A - e_1,\quad E\ \begin{matrix} u' \\ v', \end{matrix}\quad F\ \begin{matrix} \alpha \\ \beta, \\ \gamma \end{matrix} \tag{1}$$

where e_1, u', v', α, β, and γ are linear combinations of spherical functions:

$$\left.\begin{aligned}
&e_1 = R(r)\,Y_{00} = \sqrt{\frac{1}{4\pi}}\,R(r),\\
&u' = \frac{1}{\sqrt{2}}(u+v) = \frac{1}{2\sqrt{2}}\sqrt{\frac{5}{4\pi}}\,R(r)\left[Y_{20} + \frac{1}{\sqrt{2}}(Y_{22} + Y_{2-2})\right],\\
&v' = \frac{1}{\sqrt{2}}(u-v) = \frac{1}{2\sqrt{2}}\sqrt{\frac{5}{4\pi}}\,R(r)\left[Y_{20} - \frac{1}{\sqrt{2}}(Y_{22} + Y_{2-2})\right],\\
&\alpha = -\frac{i}{\sqrt{2}}R(r)\,(Y_{21} + Y_{2-1}),\qquad \beta = -\frac{1}{\sqrt{2}}[R(r)\,(Y_{21} - Y_{2-1})],\\
&\gamma = \frac{i}{\sqrt{2}}R(r)\,(Y_{22} - Y_{2-2}).
\end{aligned}\right| \tag{2}$$

In order to obtain the electrostatic interaction matrices for two electrons we need to calculate the matrix elements for the following states:

$$\begin{array}{llllll}
{}^1A & t^2 & {}^1E & t^2 & {}^3Ft^2, & {}^1F^bet, \quad {}^3F^bet. \\
 & e^2, & & e^2, & & \\
{}^3A & e^2, & {}^1F & t^2 & {}^1F^aet, & {}^3F^aet.
\end{array} \tag{3}$$

Repeated states are denoted by indices *a* and b. This refers to the et configuration since the expansions of products of two irreducible representations of the T group contain repeated irreducible representations. Such indices are not introduced for t^2 configurations since the allowed states for these configurations differ in spin. The allowed states for each configuration are determined using the method developed in ref. 4, and for the mixed configurations in the intracrystalline field they are found with the aid of the multiplication rule introduced previously.[5]

Repeated irreducible representations, although they have identical characters, differ in the explicit form of the representation matrices for symmetry elements of the group T. This difference can be taken into account by calculating the Clebsch–Gordan coefficients for the products of the representations of the group of interest. For some of the representations these coefficients are determined using direct products of the representations of interest, written out in lexicographical order.[6]

The state functions for two electrons for the corresponding configurations of the intracrystalline field are as follows:

$$\left.\begin{array}{ll}
{}^1A\ t^2\ \dfrac{1}{\sqrt{3}}[\alpha\alpha + \beta\beta + \gamma\gamma], & {}^1Et^2u' - \dfrac{1}{\sqrt{3}}[\varepsilon^2\alpha\alpha + \varepsilon\beta\beta + \gamma\gamma], \\
\quad e^2\ \dfrac{1}{\sqrt{2}}[u'v' + v'u'], & \quad v' - \dfrac{1}{\sqrt{3}}[\varepsilon\alpha\alpha + \varepsilon^2\beta\beta + \gamma\gamma], \\
\quad {}^3Ae^2\ \dfrac{1}{\sqrt{2}}[u'v' - v'u'], & \quad e^2\ \dfrac{1}{\sqrt{2}}[u'u' - v'v'], \\
 & \quad \cdots\cdots\cdots\cdots \\
\quad {}^1F\ t^2\ \dfrac{1}{\sqrt{2}}[\alpha\beta + \beta\alpha], & {}^1F^aet\ \dfrac{1}{\sqrt{2}}[u'\gamma + \gamma u'], \\
\quad \dfrac{1}{\sqrt{2}}[\beta\gamma + \gamma\beta], & \quad \cdots\cdots\cdots\cdots \\
 & \quad \cdots\cdots\cdots\cdots \\
\quad \dfrac{1}{\sqrt{2}}[\gamma\alpha + \alpha\gamma], & {}^1F^bet\ \dfrac{1}{\sqrt{2}}[v'\gamma + \gamma v'], \\
 & \quad \cdots\cdots\cdots\cdots \\
 & \quad \cdots\cdots\cdots\cdots \\
\quad {}^3Ft^2\ \dfrac{1}{\sqrt{2}}[\alpha\beta - \beta\alpha], & {}^3F^aet\ \dfrac{1}{\sqrt{2}}[u'\gamma - \gamma u'], \\
 & \quad \cdots\cdots\cdots\cdots \\
 & \quad \cdots\cdots\cdots\cdots \\
\quad \dfrac{1}{\sqrt{2}}[\beta\gamma - \gamma\beta], & \\
\quad \dfrac{1}{\sqrt{2}}[\gamma\alpha - \alpha\gamma]. & {}^3F^bet\ \dfrac{1}{\sqrt{2}}[v'\gamma - \gamma v']. \\
 & \quad \cdots\cdots\cdots\cdots \\
 & \quad \cdots\cdots\cdots\cdots
\end{array}\right\} \tag{4}$$

Using the wave functions (4) we can calculate the matrix elements of the electrostatic interaction, which are expressed in terms of linear combinations of matrix elements for spherical functions according to Eqs. (2). The matrix elements for spherical functions were calculated using the tables of ref. 7. We used the Racah[8] notation for the matrix element values. In calculating the matrix elements it is convenient to proceed from the following relations:

$$\left.\begin{array}{r} J(u'v') = A + 2C, \\ K(u'v') = 8B + 2C, \\ J(u'\gamma) = A + C, \\ K(u'\gamma) = 2B + C, \\ K(v'\gamma) = K(u'\gamma), \end{array}\right| \quad \begin{array}{l} \langle\beta\alpha|v'\gamma\rangle = \langle\alpha\beta|\gamma v'\rangle \\ = \langle\alpha\beta|u'\gamma] = \dfrac{\sqrt{3}-3}{\sqrt{2}}B, \\ \langle\beta\alpha|u'\gamma\rangle = \langle\beta\alpha|\gamma v'\rangle = \langle\alpha\beta|\gamma u'\rangle \\ = \langle\alpha\beta|v'\gamma\rangle = \dfrac{\sqrt{3}+3}{\sqrt{2}}B, \\ \langle\beta\alpha|\gamma u'\rangle = \dfrac{\sqrt{3}-3}{\sqrt{2}}B. \end{array} \qquad (5)$$

$$\langle\gamma u'|v'\gamma\rangle = \langle u'\gamma|\gamma v'\rangle = 2B, \quad \langle\gamma u'|\gamma v'\rangle = \langle u'\gamma|v'\gamma\rangle = -4B,$$
$$\langle\alpha\alpha|u'v'\rangle = \langle\beta\beta|u'v'\rangle = \langle\gamma\gamma|u'v'\rangle = 2B + C, \quad \langle\alpha\alpha|v'u'\rangle =$$
$$\langle\alpha\alpha|u'v'\rangle, \quad \langle\beta\beta|v'u'\rangle = \langle\beta\beta|u'v'\rangle, \quad \langle\gamma\gamma|v'u'\rangle = \langle\gamma\gamma|u'v'\rangle,$$
$$\langle\gamma\gamma|u'u'\rangle = 2B + C, \quad \langle\beta\beta|u'u'\rangle = 2B + C - \sqrt{3}B, \quad \text{and}$$
$$\langle\alpha\alpha|u'u'\rangle = 2B + C + \sqrt{3}B.$$

In (5) we do not give all of the relations used in the calculations. The remaining relations can be easily found from (2) and the tables of Condon and Shortley.[7] Just as in ref. 7 and in ref. 1, the Coulomb and exchange matrix elements are denoted as follows:

$$J(a, b) = \langle ab|g|ab\rangle, \quad K(ab) = \langle ab|g|ba\rangle. \qquad (6)$$

For the ^1A, ^3A, and ^1E states the diagonal matrix elements coincide with the corresponding ones for the O group matrices. However, the matrix elements for the repeated states are different. For example the diagonal matrix elements of the electrostatic interaction for the $^1F^{a,b}$ states and $^3F^{a,b}$ states are calculated as follows:

$$\left.\begin{array}{l} \langle et\,^1F^a|g|et\,^1F^a\rangle = J(u'\gamma) + K(u'\gamma) = A + 2B + 2C, \\ \langle et\,^3F^a|g|et\,^3F^a\rangle = J(u'\gamma) - K(u'\gamma) = A - 2B, \\ \langle et\,^1F^b|g|et\,^1F^b\rangle = J(v'\gamma) + K(v'\gamma) = A + 2B + 2C, \\ \langle et\,^3F^b|q|et\,^3F^b\rangle = J(v'\gamma) - K(v'\gamma) = A - 2B. \end{array}\right\} \qquad (7)$$

In calculating the nondiagonal matrix elements there are additional nondiagonal elements connected with the repeated states. According to the selection rules for scalar quantities, the matrix elements for the electrostatic interaction are only nonzero between states which belong to the same irreducible representation. Therefore, in groups of T symmetry there is an interaction between F representations of the same type. In the O or T_d groups the irreducible F_1 and F_2 representations characterize substantially different states and the matrix elements between these states are zero. For a tetrahedral field with T symmetry the difference between the F_1 and F_2 states disappears, since some symmetry elements are absent in this group.

The nondiagonal matrix elements will be as follows in our case:

$$\langle t^2\,^1F|g|et\,^1F^a\rangle = \frac{1}{2}\langle\alpha\beta + \beta\alpha|g|\gamma u' + u'\gamma\rangle = \sqrt{6}B,$$
$$\langle t^2\,^1F|g|et\,^1F^b\rangle = \frac{1}{2}\langle\alpha\beta + \beta\alpha|g|\gamma v' + v'\gamma\rangle = \sqrt{6}B,$$
$$\langle t^2\,^3F|g|et\,^3F^a\rangle = \frac{1}{2}\langle\alpha\beta - \beta\alpha|g|\gamma u' - u'\gamma\rangle = 3\sqrt{2}B,$$
$$\langle t^2\,^3F|g|et\,^3F^b\rangle = \frac{1}{2}\langle\alpha\beta - \beta\alpha|g|\gamma v' - v'\gamma\rangle = -3\sqrt{2}B,$$
$$\langle et\,^1F^a|g|et\,^1F^b\rangle = \frac{1}{2}\langle\gamma u' + u'\gamma|g|\gamma v' + v'\gamma\rangle = -2B,$$
$$\langle et\,^3F^a|g|et\,^3F^b\rangle = \frac{1}{2}\langle\gamma u' - u'\gamma|g|\gamma v' - v'\gamma\rangle = -6B. \qquad (8)$$

Thus we can completely calculate the matrices for the electrostatic interaction for d^2 configurations in a field with symmetry T. In order to take account of the intracrystalline field one must add to this matrix the matrix for the intracrystalline field energy. It is necessary to take account of the fact that the sign of Dq for a tetrahedral field is opposite to the sign of Dq for an octahedral field. Therefore the energy matrix for the d^2 configuration contains the quantity Dq, taken as its absolute value. The constant A (as assumed) is identical for all diagonal terms and is not written. To obtain the matrices for the d^8 configuration it is necessary to change the sign of Dq. The matrices for the electrostatic interaction and the intracrystalline field for the $d^2(d^8)$ configuration are given in Table 1. The eigenvalues of these matrices with Dq = 0 give the energies of the d^2 configuration for the ion in the free state and in addition coincide with the eigenvalues of the matrix for an octahedral field (with Dq ≠ 0).

CALCULATIONS FOR THE $d^3(d^7)$ CONFIGURATIONS

Using the electrostatic interaction matrices for the d^2 configuration and parentage coefficients we can calculate the matrices for the electrostatic interaction for d^3 configurations in an intracrystalline field of symmetry T. For this calculation we use the generalized Racah method[7] given in ref. 1. The calculation is done directly from Eq. (3.1) of ref. 1. The parentage coefficients were calculated using Eq. (3.2) of ref. 1 and Eqs. (9) and (29) from ref. 9. The transformation matrices were calculated from a generalization of Eq. (6) of ref. 9 for point groups and using the corresponding equations from ref. 10. The vector coupling coefficients of the angular momentum, the 6j coefficients, were calculated using tables,[11] while the 6Γ coefficients were calculated using Eq. (3.9) of ref. 12 and the normalization relation (16) of ref. 13. When using the latter, it must be borne in mind that it is possible to have repeated representations in the expansion of the products of the irreducible representations. In the tetrahedral symmetry group T, in calculat-

TABLE 1. Energy Matrices for the d^2 Configuration

$^1A\,(^1S, {}^1G)$ $\qquad\qquad$ $^3A\,(^3F)$

$$\begin{array}{l|ll} t^2 & 10B + 5C + 8Dq & \sqrt{6}(2B + C) \\ e^2 & & 8B + 4C - 12Dq \end{array} \qquad\qquad \begin{array}{l|l} e^2 & -8B - 12Dq \end{array}$$

$^1F\,(^1G, {}^1D)$

$$\begin{array}{l|lll} t^2 & B + 2C + 8Dq & \sqrt{6}B & \sqrt{6}B \\ et\,(^1F^a) & & 2B + 2C - 2Dq & -2B \\ et\,(^1F^b) & & & 2B + 2C - 2Dq \end{array}$$

$^3F\,(^3P, {}^3F)$

$$\begin{array}{l|lll} t^2 & -5B + 8Dq & 3\sqrt{2}B & -3\sqrt{2}B \\ et\,(^3F^a) & & -2B - 2Dq & -6B \\ et\,(^3F^b) & & & -2B - 2Dq \end{array}$$

$^1E\,(^1G, {}^1D)$

$$\begin{array}{l|ll} t^2 & B + 2C + 8Dq & 2(1 - \varepsilon^*)B \\ e^2 & 2(1 - \varepsilon)B & 2C - 12Dq \end{array}$$

TABLE 2(a). Energy Matrices for the Electrostatic Interaction and the Intracrystalline Field for the d^3 Configuration

$^4A(^4F)$	t^3	$t^3(^4A)e^4$
	$-15B+12Dq$	

$^2A(^2G, ^2F)$

	$t^4(^1E)e^3A^a$	$t^4(^1E)e^3A^b$
$t^2(^1E)e\,^2A^a$	$-B+3C+2Dq$	$-10B$
$t^2(^1E)e\,^2A^b$		$-B+3C+2Dq$

$^4F(^4P, ^4F)$

	$e^2(^3A)t^5(^4F)$	$t^4(^3F)e^3(^4F^a)$	$t^4(^3F)e^3(^4F^b)$
$e^2(^3A)t\,^4F$	$-12B-8Dq$	$-3\sqrt{2}B$	$3\sqrt{2}B$
$t^2(^3F)e\,^4F^a$		$-9B+2Dq$	$-6B$
$t^2(^3F)e\,^4F^b$			$-9B+2Dq$

$^2E(^2D^a, ^2D^b, ^2G, ^2H)$

	t^3e^4	$t^4(^1A)e^3$	$t^4(^1E)e^3$	t^6e
t^3	$-6B+3C+12Dq$	$-6\sqrt{2}B$	$-3\sqrt{2}B$	0
$t^2(^1A)e$		$8B+6C+2Dq$	$10B$	$\sqrt{3}(2B+C)$
$t^2(^1E)e$			$-B+3C+2Dq$	$-2\sqrt{3}B$
e^3				$-8B+4C-18Dq$

TABLE 2(b)

$^2F(^2D^a, ^2D^b, ^2F, ^2G, ^2H, ^2P)$

		t^3e^4	$t^4(^1F)e^3$	$t^4(^3F)e^3$	$t^5e^2(^1E)$	t^3e^4	$t^4(^1F)e^3$	$t^4(^3F)e^3$	$t^5e^2(^1E)$	$t^5e^2(^3A)$	$t^5e^2(^1A)$
$^2F^a$	t^3	$6B+7C+12Dq$	$-\sqrt{3}B$	$3B$	0	0	$-\sqrt{3}B$	$3B$	0	0	0
	$t^2(^1F)e$		$-B+3C+2Dq$	$-2\sqrt{3}B$	$\sqrt{6}B$	$-\sqrt{3}B$	$-10B$	$-2\sqrt{3}B$	$-\sqrt{6}B$	$-\frac{3\sqrt{2}}{2}B$	$-\frac{\sqrt{3}}{2}B$
	$t^2(^3F)e$			$-3B+3C+2Dq$	$\frac{3\sqrt{3}}{2}B$	$3B$	$-2\sqrt{3}B$	$-6B$	0	$\frac{3\sqrt{2}}{2}B$	$\frac{3\sqrt{3}}{2}B$
	$te^2(^1E)$				$-2B+3C-8Dq$	0	$-\sqrt{6}B$	0	$-10B$	$2\sqrt{3}B$	$10B$
$^2F^b$	t^3					$6B+7C+12Dq$	$-\sqrt{3}B$	$3B$	0	0	0
	$t^2(^1F)e$						$-B+3C+2Dq$	$-2\sqrt{3}B$	$\sqrt{6}B$	$-\frac{3\sqrt{2}}{2}B$	$-\frac{\sqrt{3}}{2}B$
	$t^2(^3F)e$							$-3B+3C+2Dq$	$-\frac{3\sqrt{3}}{2}B$	$-\frac{3\sqrt{2}}{2}B$	$-\frac{3\sqrt{3}}{2}B$
	$te^2(^1E)$								$-2B+3C-2Dq$	$2\sqrt{3}B$	$10B$
^2F	$te^2(^3A)$									$-6B+3C-8Dq$	$-2\sqrt{3}B$
	$te^2(^1A)$										$10B+7C-8Dq$

ing the d^3 configuration, just as for the d^2 configuration, there are additional matrix elements for all F and A states. Thus for example if the energies of the $^2A_1$ and $^2A_2$ states in the O or T$_d$ groups are given by one-dimensional matrix elements, in our case the energy of the ^{2}A state must be found by solving a two-row matrix. This happens because there are additional nondiagonal matrix elements which couple A states of the T group of the same type. This also applies to the ^{4}F states. If in the O group the energies of these states are given by the two-row $^4F_1$ and one-row $^4F_2$ matrices, then in our case the energies of these states must be found from the eigenvalues of three-rowed matrices. A similar pattern is observed for F states with a multiplicity of 2.

The matrices for the electrostatic interaction and the intracrystalline field for T symmetry for the d^3 configuration are given in Tables 2a and 2b. As assumed, the coefficient 3A is not written in the diagonal terms of the matrices because it gives an identical shift to the energies of all states. The matrices take account of the change of sign of Dq in a tetrahedral field. When Dq = 0, the eigenvalues of these matrices give the energy of the free ion, from which we get the states in an intracrystalline field. The matrices for the d^7 configuration are obtained from those for the d^3 configuration by changing the sign of Dq.

It should be noted that the eigenvalues of the matrices for the d^3 configuration in a T field coincide with the eigenvalues of a matrix which corresponds to the configuration in a field with O or T$_d$ symmetry. Therefore, in analyzing the spectra of intracrystalline fields with T symmetry we can use the diagrams of Tanabe and Sugano using the following rules: For d^n configurations in a tetrahedral field we need to choose matrices for the d^{10-n} configuration in an octahedral field, and conversely. However, the explicit form of the matrix for the electrostatic interaction for a d^n configuration in a field with T symmetry is needed in calculating the intensity of the transitions and in taking account of the distortion of the basic symmetry of the intracrystalline field.

---

[1] Y. Tanabe and S. Sugano, J. Phys. Soc. Japan, 9, No. 5, 753 (1954).
[2] G. Racah, Phys. Rev., 76, 1352 (1949).
[3] V. Heine, Group Theory in Quantum Mechanics, Pergamon (1960).
[4] V. I. Cherepanov, A. N. Men', and D. T. Sviridov, Crystal Spectroscopy [in Russian], Nauka, Moscow (1966).
[5] I. G. Kaplan, The Symmetry of Multi-Electron Systems [in Russian], Nauka, Moscow (1969).
[6] M. Hamermesh, The Theory of Groups and Its Application to Physical Problems [Russian translation], Mir, Moscow (1966), p. 160.
[7] E. Condon and G. Shortly, Theory of Atomic Spectra, Cambridge Univ. Press (1935).
[8] G. Racah, Phys. Rev., 62, 438 (1942).
[9] G. Racah, Phys. Rev., 63, 367 (1943).

[10] Yu. F. Smirnov and D. T. Sviridov, Crystal Spectroscopy [in Russian], Nauka, Moscow (1966).

[11] A. F. Nikiforov, B. V. Uvarov, and Yu. L. Levitan, Tables of Racah Coefficients [in Russian], Vychis. Tsentr. Akad. Nauk SSSR, Moscow (1962).

[12] É. V. Mauza and I. B. Batarunas, Trudy Akad. Nauk LitSSSR, Ser. B, No. 3, 26, 27 (1961).

[13] D. T. Sviridov, Yu. F. Smirnov, and V. E. Troitskii, Kristallografiya, 9, 807 (1964) [Sov. Phys. – Crystallogr., 9, 684 (1965)].

Dislocation mechanism of growth with a low kink density

V. V. Voronkov

State Scientific-Research and Design Institute for the Rare Metal Industry

(Submitted November 2, 1971; resubmitted March 2, 1972)
Kristallografiya, 18, 32-38 (January-February 1973)

If the movement of a step over a face is limited by the attachment of atoms at kinks and the distance between the kinks L on a step with low indices is large, the dislocation growth spiral consists of almost linear sections oriented along the slowly growing steps with low indices. The dependence of the velocity of this section V on its length l for different relationships between L and the side of the critical nucleus l_{crit} has been analyzed. The qualitative course of $V(l)$ has been found to be fairly simple, and this has made it possible to find the form of the growth spiral and the velocity of the face R. For $l_{\text{crit}} \gg L$ (sufficiently small supersaturation s) the usual quadratic growth law $R \sim s^2$ applies. For low values of s, however, the opposite inequality $l_{\text{crit}} \ll L$ applies, and growth takes place according to the linear law $R \sim s$; the distance between the turns of the spiral becomes constant and of the same order of magnitude as L. This result applies for $s \ll 1$. In the region $s \gg 1$, the quantity L is not constant, and the growth law again becomes quadratic.

In the existing dislocation theory of growth[1-3] it is assumed that the rate of movement of a step is independent of its orientation. This is applicable if the velocity of the step is limited by the supply of material by diffusion (or the removal of heat) and not by the atomic processes at the actual step. The opposite case, where the velocity of the step is limited by the attachment of atoms at kinks in the step, is also of interest, however. We shall assume two further restrictions: 1) The step, generated on a dislocation face, is monatomic in height, and 2) the density of kinks in steps with low indices is small. Subsequently, we shall be interested only in steps with a small angle of inclination to the step with low indices (we shall denote the tangent of the angle of inclination by the symbol p). Thus, we require the equilibrium density of kinks $\rho(p)$ and the free energy of the step $\alpha(p)$ (both of these quantities will be related not to the unit length of the step, but to the unit length of its projection on the step with low indices). The function $\rho(p)$ is known,[1] and $\alpha(p)$ has been calculated for Kossel's cubic crystal,[1] but in our case for low values of ρ we can readily obtain a general expression. We shall use the symbol q_1 to denote the density of positions at which kinks may be situated on the step with low indices (that is, the linear density of the atoms in a close-packed row), and the symbol b to denote the distance between the neighboring close-packed rows. Since ρ is small, it is possible to consider only kinks with unit depth b. We let ρ_+ and ρ_- be the densities of the positive and negative kinks. The total density of kinks is $\rho = \rho_+ + \rho_-$, and the inclination of the step is $p = b(\rho_+ + \rho_-)$. The free energy of the step α is equal to

$$\alpha = q_1 W_1 + \rho W + kT[\rho_+ \ln(\rho_+ / eq_1) + \rho_- \ln(\rho_- / eq_1)], \quad (1)$$

where W_1 is the energy of the step with low indices without kinks for one edge atom, and W is the energy of the kink. The terms in brackets represent the usual configurational entropy determined by all possible arrangements of ρ_+ and ρ_- kinks over q_1 positions (the form of the entropy is exactly the same as for a dilute solution). The equilibrium values of ρ_+ and ρ_- are found from the condition for a minimum value of Eq. (1) for a given difference $\rho_+ - \rho_-$. For the step with low indices we obtain [introducing for convenience the symbol ρ_0 in place of $\rho(0)$] the familiar expression[1]

$$\rho_0 = 2q_1 \exp(-W/kT). \quad (2)$$

The fact that ρ_0 is small means that $W \gg kT$. This case is extremely probable for growth from the vapor and solution.[4] For a growing step the density of kinks is practically the same as the equilibrium value in Eq. (2) so long as the relative supersaturation is less than unity.[4]

For the sloping step, from the condition for a minimum value of Eq. (1), we obtain

$$\rho(p) = \sqrt{\rho_0^2 + (p/b)^2}. \quad (3)$$

The minimum free energy $\alpha(p)$ is

$$\alpha(p) = q_1 W_1 - kT\rho(p) + kTpb^{-1} \ln(\rho(p) + p/b)\rho_0^{-1}. \quad (4)$$

According to Eq. (3), even at very low values of p, the density of kinks $\rho(p)$ becomes much greater than ρ_0, so that the velocity of the linear step increases sharply with increase in its inclination p. Thus the dislocation growth spiral will consist chiefly of slowly growing, almost linear sections (Fig. 1a). The movement of the spiral is determined by the dependence of the velocity of the section V on its length l. The velocity V becomes zero at a certain length l_{crit}, equal to the side of the two-dimensional critical nucleus. According to Wulff's theorem, the distance r_{crit} from the center of a critical nucleus to its sides is equal to α_0 / fq_2, where the symbol α_0 is introduced in place of $\alpha(0)$, q_2 is the surface density of atoms in the layer bounded by the step, and f is the decrease in the bulk free energy on crystallization, calculated for one atom [in particular, for growth from a supersaturated medium with relative supersaturation s we have $f = kT\ln(1+s)$]. The quantity f has the significance of the driving force of the crystallization. The side of a m-angular critical nucleus l_{crit} can be expressed in terms of r_{crit}:

$$l_{\text{crit}} = 2r_{\text{crit}} \tan \pi/m = 2\alpha_0 (fq_2)^{-1}\,\mathrm{tg}\,\pi/m. \quad (5)$$

The velocity of the section for $l > l_{\text{crit}}$ is limited by the region of the step with low indices situated in the center of the section. The nature of the movement of this region depends on the ratio between its length l' and the average distance $L = \rho_0^{-1}$ between the kinks on the step with low indices. If $l' \gg L$, the region contains a large number of kinks, and it can be regarded from the macroscopic viewpoint as a curved line (Fig. 1a). In this case the boundary of the region, in accordance with Eq. (3), lies at $p \sim b\rho_0$. If, however, $l' \ll L$, the central region

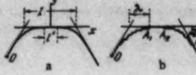

Fig. 1. Dislocation growth spiral for fairly low (a) and fairly high (b) supersaturation.

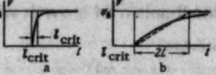

Fig. 2. Dependence of the velocity of a section of the spiral V on its length l. a, b) As in Fig. 1.

for a large part of the time does not contain kinks (Fig. 1b). To distinguish between these two cases it is necessary to know the length of the region l'_{crit}, on a critical nucleus. The element of a step with inclination p is situated on the critical nucleus at the point $x_{crit}(p)$ (the system of coordinates is indicated in Fig. 1a). It is known[3] that

$$x_{crit}(p) = -(fq_2)^{-1}\frac{d\alpha}{dp}(p). \tag{6}$$

The derivative $d\alpha/dp$ is found from Eq.(4):

$$d\alpha/dp = kTb^{-1}\ln(\rho(p) + p/b)\rho_0^{-1}. \tag{7}$$

From Eqs. (6), (7), and (3) we obtain $l'_{crit} = -2x_{crit}(p)$ at $p \sim b\rho_0$; this length is of the same order of magnitude as $2kT/bfq_2$. Comparison of this expression with Eq. (5) shows that l'_{crit} makes up a small constant fraction of the side of the critical nucleus l_{crit}, since the edge energy W_1 is of the same order of magnitude as W and is large compared with kT. We can now examine the movement of a section of the step for the two characteristic cases: $l'_{crit} \gg L$ and $l'_{crit} \ll L$.

a) Sufficiently low supersaturation, $l'_{crit} \gg L$ (Fig. 1a). We shall denote the velocity of the linear step by the symbol v(p), and the velocity of the step with low indices v(0) by the symbol v_0 (the velocity is measured along the y axis, and not along the normal to the step). The actual velocity of an element of the section with orientation p is less than v(p) as a consequence of the curvature of the step; the decrease in the velocity is proportional to the curvature dp/dx. Since all the elements of the section move at the same velocity V, we have the following relationship:

$$V = v(p)\left[1 - \frac{dp}{dx}\Big/\left(\frac{dp}{dx}\right)_{crit}\right], \tag{8}$$

where $(dp/dx)_{crit}$ is the curvature of the step on the critical nucleus. The velocity is limited by the curved region with low indices, that is, $V \leq v_0$. Since $v(p) \sim \rho(p)$ and increases rapidly with p [Eq. (3)], it follows that when $p \gg b\rho_0$ we have the inequality $V \ll v(p)$. In accordance with Eq. (8), this means that the curvature of the step is almost the same as that on the critical nucleus, that is, for $p \gg b\rho_0$ the step has the equilibrium form. The only part of the section which deviates from the equilibrium form is the central region with $|p| < p'$, where p' must be chosen to be several times greater than $b\rho_0$. The total increase in the length of the section $l - l_{crit}$ takes place because of this central region, and in accordance with Eq. (8), the relative increase in the length of an element of the step $(dx - dx_{crit})/dx_{crit}$ is greater, the smaller v(p). At equilibrium, the order of magnitude of the length of the central region $2x_{crit}(p')$, in accordance with Eqs. (6) and (7), is equal to that of the length of the section with low indices l'_{crit}. Thus the order of magnitude of the total increase in length $l - l_{crit}$ is equal to that of $l' - l'_{crit}$. As shown above, $l'_{crit} \ll l_{crit}$. Thus even a slight increase in $l - l_{crit}$ (of the same order of magnitude as l'_{crit}) brings about a perceptible increase in the length of the region with low indices l'. As a result, the curvature of the section (with order of magnitude equal to that of $b\rho_0/l'$) decrease significantly, and its velocity becomes close to v_0. Thus, the velocity of the section V increases sharply with increase in its length l (Fig. 2a). The actual curves of $V(l)$ can readily be obtained by solving Eq. (8) with respect to dx/dp, integrating, and equating the increase in the length of the central section to the total increase in length $l - l_{crit}$. For our purposes, however, the qualitative conclusion that $V(l)$ rapidly reaches saturation is sufficient.

b) Sufficiently high supersaturation (Fig. 1b). According to the estimate for l'_{crit} obtained above, this case is realized when the average distance between the kinks $L = \rho_0^{-1}$ is much greater than $2kT/fq_1$. As shown in ref. 4, with this condition the movement of the step with low indices involves the formation and growth of one-dimensional nuclei. The velocity of the finite section A_1A_2 (Fig. 1b) depends on its length. The extreme kink A_1 is situated at an average distance λ from the angle. This distance is determined by the statistical mechanics of the eroded angle and depends on the driving force f. Thus the section A_1A_2 has a length $l - 2\lambda$, which increases linearly with l. The approach and annihilation of the kinks A_1 and A_2 is associated with the overcoming of a free energy barrier $f(l - 2\lambda)q_1$. The probability of this process depends on l as $\exp(-f l q_1/kT)$. When the order of magnitude of $l - l_{crit}$ is equal to that of kT/fq_1 (that is, for a relatively small increase in the length of the section), the probability of annihilation becomes much less than that for the critical nucleus, since annihilation can be neglected compared with the formation of one-dimensional nuclei on the section A_1A_2. The effective critical size of a one-dimensional nucleus is equal[4] to kT/fq_1, so that the effective length at which a nucleus is produced is equal to $l_{eff} = l - 2\lambda - kT/fq_1$. So long as l_{eff} is sufficiently small, the section A_1A_2 moves by the successive deposition of rows of atoms. In accordance with ref. 4, the rate of growth V is given by the following expression:

$$V = v_0 l_{eff}/2L, \tag{9}$$

where, as above, v_0 is the velocity of the linear step with low indices, and L is the mean distance between the kinks on this step, which depends on the supersaturation s as $1/(1+s)^{1/2}$. The linear relationship given by Eq. (9) is applicable for $l_{eff} \ll L$. If, however, $l_{eff} \gg L$, the section A_1A_2 contains a large number of kinks, and its velocity is close to v_0. In accordance with Eq. (9), the velocity reaches saturation when l_{eff} is greater than its equilibrium value (small compared with L) by an amount ~2L, that is, when $l - l_{crit} \sim 2L$. The course of $V(l)$ is shown in Fig. 2b. In order to reach quantitative conclusions regarding the growth spiral, we can represent the course of $V(l)$ schematically, as shown by the dashed line in Fig. 2b.

The case represented in Fig. 2a is applicable for a sufficiently high value of l_{crit}/L (namely for $l'_{crit} \gg L$), and the case represented in Fig. 2b is applicable for a sufficiently low value of l_{crit}/L. In the intermediate range, when l'_{crit} and L are of the same order of magnitude, the ratio l_{crit}/L is large, so that the two $V(l)$ graphs coincide qualitatively: In both cases V rapidly reaches saturation. Thus the schematic relationship $V(l)$ in Fig. 2b is qualitatively correct for any values of l_{crit}/L. In accordance with Eqs. (2) and (5), the equality $l_{crit} = L$ is applicable for a very small value of f/kT (that is, at a very low relative supersaturation s), since $W \gg kT$. Thus for $s \ll 1$ the ratio l_{crit}/L may be either large or small.

We can now proceed to an analysis of the steady-state form of the growth spiral. We shall number the successive sections of the spiral, beginning from its center. We shall measure the time from the moment when the section l_1 adjoining the point of emergence of the dislocation 0 is equal to l_{crit}. At $t > 0$ the section l_1 begins to move, and a new section l_0 is produced at the point 0. After a certain time t its length reaches l_{crit}, and the spiral moves into a position which is completely equivalent to the original position: $l_k(t) = l_{k+1}(0)$. In this position the spiral is turned through an angle $2\pi/m$; the time required for a complete rotation of the spiral $\tilde{T}$ is equal to mt. The length of a section of the spiral l_k changes with time as a consequence of the movement of the section itself at a velocity V_k, and also as a consequence of the movement of the adjacent sections $k-1$ and $k+1$. The total rate of change in l_k is equal to

$$dl_k/dt = (\sin 2\pi/m)^{-1}(V_{k+1} + V_{k-1} - 2V_k \cos 2\pi/m). \tag{10}$$

In particular, for $k = 0$, only V_1 remains in Eq. (10). The most simple case is that for $L \ll l_{crit}$ (sufficiently small value of s), when the velocity V_1 almost instantly becomes equal to v_0 (Fig. 2b). From Eq. (10) for $k = 0$ we find immediately the time t after which l_0 increases from 0 to l_{crit}; a complete rotation of the spiral takes place in a time

$$T = l_{crit}\, v_0^{-1} m \sin 2\pi/m. \tag{11}$$

The normal rate of growth of the face R is equal to $h/\tilde{T}$, where h is the height of the step. Since v_0 is proportional to, and l_{crit} inversely proportional to the supersaturation s, it follows that R is quadratic with respect to s, as in the isotropic case.[1-3] The distance Y between neighboring turns of the spiral is equal to $v_0\tilde{T}$. By substituting $\tilde{T}$ from Eq. (11) and expressing l_{crit} from Eq. (5) in terms of the critical radius of a nucleus r_{crit}, we obtain $Y = r_{crit} m (2 \sin \pi/m)^2$. For m = 3, 4, and 6 the ratio Y/r_{crit} = 9, 8, and 6, that is, it differs slightly from the value 19 in the isotropic case.[2]

Let us now assume that the ratio L/l_{crit} is not small. We shall examine a spiral of special form, when the section $l_n(0)$ is exactly equal to $l_{crit} + 2L$, so that its velocity V_n is constant and equal to v_0. This situation is realized for a certain special ratio L/l_{crit}, which depends on n. For $k < n$ the velocity of the section is $V_k = v_0(l_k - l_{crit})/2L$ (see Fig. 2b), that is, it increases with increase in the number k. Thus the maximum contribution in Eq. (10) is made by the term V_{k+1}. For simplicity we shall subsequently take account of only this term (we shall see below that this approximation is fairly good). The solution of even these simplified equations is tedious and is carried out in the Appendix, where we find the period of rotation of the spiral $\tilde{T}$ as a function of the number n (and also the ratio L/l_{crit}, corresponding to a given n). This makes it possible to express $\tilde{T}$ in terms of L/l_{crit}:

$$T = 2\tau L v_0^{-1} m \sin 2\pi/m, \tag{12}$$

where the dimensionless parameter τ (for $L > 5l_{crit}$) is

$$\tau = e^{-1} + 2(\ln 4L/l_{crit})^{-2}. \tag{13}$$

For $L \gg l_{crit}$ the parameter τ is close to e^{-1} and depends little on L/l_{crit} (that is, on the supersaturation s). Thus the velocity of the face $R = h/\tilde{T}$ depends on s chiefly as a consequence of V_0, that is $R \sim s$. The distance between the turns of the spiral $Y = v_0\tilde{T}$ is almost independent of s and its order of magnitude is equal to that of L. The fact that $\tilde{T}$ is not sensitive to the parameter l_{crit} also means that the difference between the actual course and the schematic course of $V(l)$ close to l_{crit} is not significant (Fig. 2b).

The replacement of the quadratic law $R \sim s^2$ by the linear law with increase in s is also characteristic of the usual isotropic theory of dislocation growth.[1-3] The reason for the replacement in this case is that the face is so thickly covered with steps that it becomes an ideal sink, and the rate R is limited by the supply of material to the face. On the linear section, the kinetic coefficient R/s is independent of the kind of face. In our case, however, the change in the growth law is determined by the kinetics of the face itself, and R/s depends significantly on the kind of face.

At high values of s it is necessary to take account of the fact (ref. 4) that L depends on s as $1/(1 + s)^{1/2}$. This addition factor must also be introduced into the velocity of the step $v_0 \sim L^{-1}$. As a result, the velocity of the face R changes with s as $s(1 + s)$. For $s \gg 1$ we againain obtain a quadratic law.

APPENDIX

PERIOD OF ROTATION OF THE SPIRAL

We introduce in place of l_k the dimensionless quantities $u_k = (l_k - l_{crit})/2L$, and also the dimensionless time τ:

$$\tau = v_0 t (2L \sin 2\pi/m)^{-1}. \tag{14}$$

The equations of motion (10) (in which we keep only the maximum term V_{k+1}) are then written in the form

$$\dot{u}_k = u_{k+1}, \tag{15}$$

where the dot represents differentiation with respect to τ. Equations (15) are applicable for $0 \le k < n-1$. For the section with number $n-1$ we have $\dot{u}_{n-1} = 1$, since $V_n = v_0$. The initial values of the variables u_k will be represented by the symbols a_k. In our case $a_1 = 0$, $a_n = 1$, and $a_0 = -l_{crit}/2L$. By successive integration of the equations for $\dot{u}_k$, beginning with the number $n-1$, we obtain

$$u_k = \sum_{i=0}^{n-k} a_{k+i}\tau^i/i!. \tag{16}$$

$$\begin{pmatrix} \tau-1 & 1 & 0 & 0 & \ldots & 0 & 0 \\ \tau^2/2 & \tau-1 & 1 & 0 & \ldots & 0 & 0 \\ \ldots & \ldots & \ldots & \ldots & \ldots & \ldots & \ldots \\ \ldots & \ldots & \ldots & \ldots & \ldots & \ldots & \ldots \\ \tau^{n-1}/(n-1)! & \tau^{n-2}/(n-2)! & \ldots & \ldots & \ldots & \tau-1 & 1 \\ \tau^n/n! & \tau^{n-1}/(n-1)! & \ldots & \ldots & \ldots & \tau^2/2 & \tau-1 \end{pmatrix} \begin{pmatrix} a_n \\ a_{n-1} \\ \cdot \\ \cdot \\ a_2 \\ a_1 \end{pmatrix} = \begin{pmatrix} 0 \\ 0 \\ \cdot \\ \cdot \\ 0 \\ -a_0 \end{pmatrix}, \tag{17}$$

where $a_0 = -l_{crit}/2L$, and the index n for τ_n is omitted for the sake of simplicity. It is necessary to impose two conditions on the solution of the system of equations (17): $a_1 = 0$ and $a_n = 1$. The matrix of system (17) has a fairly simple structure: Each diagonal passing from the left downwards consists of identical elements of the form $\tau_k/k!$ (with the exception of the main diagonal, the elements of which are equal to $\tau - 1$). We denote the determinant of this matrix by the symbol $D_n(\tau)$. The solution of system (17) is written in terms of the minor of the last row: The quantity a_k is equal to the minor of the element with number $n-k+1$, multiplied by $-a_0$ and divided by D_n. The last column of the minor is zero, with the exception of the lowest element, which is equal to unity. Expansion of the minor with respect to this column gives a determinant for which the last column preserves its previous form. By carrying out this expansion $k-1$ times, we obtain a determinant of order $n-k$, situated in the upper left corner of the matrix. Thus the minor is equal to $(-1)^{k-1}D_{n-k}$. For convenience we introduce the symbol $B_n = (-1)^n D_n$; the solution of the system (17) is then written in the form

$$a_k = -(l_{crit}/2L)B_{n-k}/B_n. \tag{18}$$

This expression is applicable for all values of k from 1 to n, if we formally put $B_0 = 1$. The condition $a_1 = 0$ leads to the equation $B_{n-1}(\tau_n) = 0$, from which we also determine τ_n, the time required for the rotation of the spiral through an angle $2\pi/m$. Similarly, from the condition $a_n = 1$, we find the ratio L/l_{crit} for which the spiral is characterized by the number n. As a result, we obtain in parametric form (the parameter is the number n) the required dependence of the period of rotation of the spiral $\tilde{T}$ on L/l_{crit}. The problem of the motion of the spiral has been reduced to the analysis of the polynomials $B_n(\tau)$. By expansion of the determinant D_n with respect to the lower row, the minors of which were found above, we obtain the recursion relationship

$$B_{n-1} = \sum_{k=0}^{n} B_{n-k}\tau^k/k!. \tag{19}$$

We use the symbol τ_n to denote the time for the transformation of the spiral into an equivalent position, in which $u_k(\tau_n) = u_{k+1}(0) = a_{k+1}$.

With allowance for this condition, Eqs. (16) can be regarded as a system of n linear equations in n unknowns $a_n, a_{n-1}, \ldots, a_1$. In matrix form this system is written

For polynomials with small values of n we can readily establish the following equation:

$$B_n = \sum_{k=0}^{n} (-1)^k(n+1-k)^k\tau^k/k!. \tag{20}$$

This equation satisfies relationship (19), that is, it is applicable for any values of n. The polynomials B_n for n = 1-10 were constructed in the range of τ from 0 to 1 (in accordance with the first of Eqs. (17), $\tau_n = 1 - a_{n-1} \le 1$). In this range the polynomial has several roots, but it was found that only the smallest root satisfies the physical conditions $a_k > 0$ for $k > 1$ [that is, in accordance with Eq. (18), the inequalities $B_n(\tau_n) < 0$ and $B_i(\tau_n) > 0$ for $0 < i < n-1$]. The relative length of the section of the spirals a_k increases by a factor of 2-3 with increase in k by 1, that is, the velocity of the section $V_k \sim a_k$ increases significantly with increase in the number k; this justifies the approximation made above in Eq. (10). The time τ_n decreases very slowly with increase in n (for example, $\tau_4 = 0.482$, and $\tau_{11} = 0.383$), whereas $2L/l_{crit}$, for each increase in n by unity, increases by a factor of approximately 3 (changing from 35 for n = 4 to $6.4 \cdot 10^4$ for n = 11). For large values of n it is possible to obtain an analytical expression for τ_n. We differentiate Eq. (19) with respect to τ. The resulting series with coefficients B_{n-k}, by means of Eq. (19), can be reduced to B_{n-2}, so that we obtain

$$\dot{B}_{n-1} = B_{n-2} + \sum_{k=0}^{n} \dot{B}_{n-k}\tau^k/k! \tag{21}$$

By then differentiating Eq. (20) and separating one of the factors $(n+1-k)$ into terms n and $-(k-1)$, we obtain

$$\dot{B}_n = -nB_{n-1} + \tau\dot{B}_{n-1}. \tag{22}$$

The quantity $\dot{B}_{n-k}$ appearing in Eq. (21) can be expressed in terms of $\dot{B}_n$, by applying Eq. (22) successively k times:

$$\dot{B}_{n-k} = \tau^{-k}\dot{B}_n + \sum_{i=1}^{k} (n+1-i)B_{n-i}\tau^{i-k-1}. \tag{23}$$

The series in Eq. (21) converges rapidly as a consequence of k!, so that only the first terms in the series with small values of k are significant. The polynomial B_{n-i} becomes zero for $\tau = \tau_{n-i+1}$, and in a short range from τ_n to τ_{n-i+1} the dependence of B_{n-i} on τ can be regarded as linear. Thus, $B_{n-i}(\tau_n) \approx B_{n-i}(d\tau_n/dn)(i-1)$. We now assume that $nd\tau_n/dn \ll 1$ (this is justified by Eq. (25) obtained below). The series in Eq. (23) is then a small correction, so that

$$\hat{B}_{n-k} \approx \tau^{-k}\hat{B}_n. \tag{24}$$

The correction series in Eq. (23) is immediately summed by means of this relationship. After substitution of Eq. (23) in Eq. (21) we obtain series of the form $\sum 1/k! = e$, and Eq. (21) reduces to the equation: $nd\tau_n/dn = -2(\tau_n - e^{-1})$. By integrating, we obtain

$$\tau_n = e^{-1} + An^{-2}, \tag{25}$$

where A is a constant. In addition to τ_n, we are interested in the quantity $2L/l_{crit}$, which in accordance with Eq. (18) and the condition $a_n = 1$ is equal to $-B_n^{-1}(\tau_n) \approx (\dot{B}_n d\tau_n/dn)^{-1}$. According to Eq. (24), $\hat{B}_n$ depends on n approximately to $\tau^n \approx \exp(-n)$, so that $L/l_{crit} \sim \exp n$. With allowance for Eq. (25), this means that $1/(\tau_n - e^{-1})^{1/2}$ is linearly dependent on ln L/l_{crit}. The values of τ_n obtained by numerical calculation show very good agreement with this law for $n \geq 3$ (for $L/l_{crit} > 5$), and this makes it possible to find two constants characterizing the linear relationship. As a result we obtain Eq. (13). By expressing the actual time of rotation of the spiral t in terms of the dimensionless time τ from Eq. (14), we obtain Eq. (12) for the period of rotation of the spiral $\tilde{T} = mt$.

---

[1] W. Burton, N. Cabrera, and F. Frank, Phil. Trans. Roy. Soc. London, A243, 299 (1951).

[2] N. Cabrera and M. Levine, Phil. Mag., 1, 450(1956).

[3] A. A. Chernov, Usp. Fiz. Nauk, 73, 277 (1961) [Sov. Phys. – Usp., 4, 116 (1961)].

[4] V. V. Voronkov, Kristallografiya, 15, 13 (1970) [Sov. Phys. – Crystallogr., 15, 8 (1970)].

Internal stresses developing during crystal growth under a steady-state regime

V. L. Indenbom, I. S. Zhitomirskii, and T. S. Chebanova

Institute of Crystallography, Academy of Sciences of the USSR
Physicotechnical Institute of Low Temperatures, Academy of Sciences of the Ukrainian SSR
Khar'kov State University

(Submitted May 29, 1971; resubmitted January 25, 1972)
Kristallografiya, 18, 39–48 (January–February 1973)

We have demonstrated the dominant role of the axial temperature distribution T(z) in steady-state growth of tabular and cylindrical crystals from one end. Estimates of the thermoelastic stresses from the quantity d^2T/dz^2 are in good agreement with the results obtained in calculating the stresses in practical cases of crystal growth. We use the case of cylindrical crystals with a flat solidification front grown in an axially symmetric temperature field to consider the full series of solutions, which makes it possible to employ superposition to determine the temperature and stress field with an arbitrary pattern for cooling of the lateral crystal surface. A computer was used to devise characteristic examples of solutions in this series. Typical quantitative examples are used to analyze the reversal of the sign of the residual-stress curve.

The authors of a series of publications[1–6] have developed a method for solving problems regarding the temporary and residual stresses that develop during gradual solidification of solids with different shapes. In crystal growth, establishment of the dependence of the stresses on the crystallization conditions (particularly the manner in which the temperature field changes during crystallization and subsequent cooling) is of great practical interest for selection of the optimum crystal-growth regime yielding the minimum residual stresses or dislocation density, with the temporary stresses not exceeding a predetermined (safe) level.

These achievements in the production of ideal crystals of different types rest directly on progress made in the theory of internal stresses in crystals. In this connection, the present article summarizes the current state of the problem and gives detailed consideration to the theoretically very difficult, but practically most important case of stress development during crystal growth under a steady-state regime, which is characteristic of zone melting, controlled crystallization, and the Verneuil, Czochralski, Stockbarger, and Stepanov methods. The results of numerical calculations of the temperature and elasticity fields are given for crystals of cylindrical shape grown from one end.

The sources of the internal stresses developing during crystal growth include both temperature-induced deformations $\alpha_{ij}T$ (α_{ij} is the tensor of the coefficients of thermal expansion and T is the temperature) and residual deformations e_{ij}^0 associated with lattice defects (point defects, impurities, and dislocations). The contribution made by dislocations is usually decisive, and we will therefore henceforth treat e_{ij}^0 as the plastic deformation caused by dislocation formation and movement. The internal stresses always satisfy the equilibrium condition

$$\sigma_{ij,j}=0 \tag{1}$$

[the doubts raised by Tsivinskii[7] as to whether Eq. (1) is satisfied during crystal growth are not adequately grounded] and are related by Hooke's law

$$\sigma_{ij}=c_{ijkl}e_{kl} \tag{2}$$

to the elastic deformations

$$e_{kl}=[(u_{k,l}+u_{l,k})/2]-\alpha_{kl}T-e_{kl}^0, \tag{3}$$

where u_k is the displacement vector.

One of the two final terms in Eq. (3) can be used to segregate in the unified internal-stress field the temporary thermoelastic stresses corresponding to the temperature distribution at a given moment and the residual thermoplastic stresses caused by dislocations.

THERMOELASTIC STRESSES

Calculation of the thermoelastic stresses provides the basis for analysis of the dislocation formation and movement conditions[1)] and is itself of interest for establishing a safe crystal-cooling regime, since the temporary stresses are generally far greater than the residual stresses during cooling. Determination of the thermoelastic-stress field from the known temperature field T(x, y, z) theoretically presents only computational difficulties and can be carried out by the highly perfected methods of thermoelasticity theory. Specifically, successive exclusion of the stresses and elastic deformations from Eqs. (1)–(3) yields the basic permutational thermoelasticity equation:

$$c_{ijkl}(u_{k,lj}-\alpha_{kl}T_{,j})=0. \tag{4}$$

The boundary conditions for a specimen with a free surface are provided by the equation

$$\sigma_{ij}n_j|_S=0 \tag{5}$$

(n_j is the normal to the specimen surface S). These expressions can be permuted for Eqs. (2)–(3).

In the case of a constant temperature gradient, the total deformations $(u_{k,l}+u_{l,k})/2$ simply equal the thermal deformations and the elastic deformations in Eq. (3) vanish, i.e., no thermoelastic stresses develop.[2)] The source of the (static) thermoelastic stresses is the incompatibility tensor of the thermal deformations, expressed in terms of the second derivatives of the temperature field:

$$\eta_{ij}=\varepsilon_{ikm}\varepsilon_{jln}\alpha_{mn}T_{,kl}. \tag{6}$$

In the most interesting cases, it is possible to take into account only one component in the incompatibility tensor. For plates with isotropic thermal expansion ($\alpha_{ij}=\alpha\delta_{ij}$) and no temperature gradients over the specimen thickness, by selecting the z axis so as to be parallel to the pulling axis, the x axis parallel to the plate plane, and the y axis perpendicular to this plane, the sole essential component of the incompatibility tensor in coordinate form is written as

$$\eta_{yy} = \alpha(T_{,xx} + T_{,zz}). \tag{7}$$

The curvature of the temperature field in the pulling direction $T_{,zz}$ is usually more detrimental, since it far exceeds the curvature of the field in the transverse direction $T_{,xx}$, although more attention is traditionally paid to the latter, especially since it is clearly manifested in curvature of the growth front and isotherms. Morever, it follows from Eq. (7) that the temperature fields $T_1 = cx^2$ and $T_2 = cz^2$ produce the same thermoelastic stress field $\sigma_{ij}(x, z)$ in a plate of any shape.

For cylindrical specimens in an axially symmetric temperature field T = T(r, z), the incompatibility-tensor components are expressed in terms of the two independent quantities $\Delta T \equiv T_{,ii}$ and $T_{,zz}$. However, it follows from the thermal-conductivity equation for the usual low crystal-pulling speeds that ΔT is negligibly small in comparison with $T_{,zz}$ [see Eq. (22) below]. The thermoelastic field is consequently almost wholly governed by the distribution of the axial temperature gradients[3)] for both tabular and cylindrical specimens.

Proceeding from dimensionality considerations, one can write the following estimate for the thermoelastic stresses:

$$\sigma \approx \alpha E L^2 T_{,zz}, \tag{8}$$

where E is Young's modulus, while L is the characteristic length, which can be determined both by the transverse dimension of the crystal and by the geometry of the temperature field. If $T_{,zz}$ varies only slightly over distances of the order of the specimen width, one can use the estimates given previously[2,5] to determine the thermoelastic stresses at the crystallization front from Eq. (8), assuming the ratio of L to the specimen width to be 0.2 for normal stresses and 0.15 for tangential stresses. It is interesting to note that these simplified estimates are in satisfactory agreement with the results of computer calculations of the thermoelastic fields,[8] which took into account both the axial and radial temperature gradients for the temperature fields developing in practical cases of semiconductor-crystal growth.

If the axial temperature gradients vary rapidly over distances of the order of the crystal width, it is necessary to use an influence function that takes into account the difference in the contributions made by segments lying at different distances from the end of the crystal in estimating the stresses. We previously plotted such an influence function for plates in a one-dimensional temperature field on the basis of model experiments[2] and found it to agree with the results of subsequent analytic calculations.[10]

RESIDUAL (THERMOPLASTIC) STRESSES

If one knows the distribution of the residual (plastic) deformations e_{ij}^0, Eqs. (1)-(3) make it possible to plot the residual-stress field in precisely the same manner as the thermoelastic-stress field is plotted from the distribution of the temperature-related deformations $\alpha_{ij}T$. The main problem is to find the values of e_{ij}^0 themselves. For this purpose, Eqs. (1)-(3) must be supplemented by rheological equations of the type

$$\frac{\partial}{\partial t} e_{ij}^0 = f(\sigma_{kl}, T, e_{mn}^0, \ldots), \tag{9}$$

which describe the plastic flow of the material in the field formed by the total (transient and residual) stresses σ_{kl}.

In the general case, plastic flow can occur throughout the entire specimen volume. However, by taking into account the plastic properties of the crystal and the specific character of the temperature field, it is usually possible to isolate a comparatively small number of zones responsible for formation of the residual-stress field (and dislocation structure) of the crystal.[2,11] A narrow plastic zone adjoining the growth front is observed in low-plasticity high-melting crystals (e.g., ruby and leucosapphire grown by Verneuil's method or controlled crystallization) and in semiconductor crystals subjected to zone melting. Development of an anomalous stress diagram is characteristic of this case.[2,12] Dislocations develop in semiconductor crystals grown by the Czochralski method both at the growth front and at a considerable distance from it, where the rapid cooling of the lateral surface of the ingot results in formation of large radial temperature gradients, which lead to plastic flow and development of characteristic quenching stresses.[11,13]

It is easier to take into account the rheological properties of the crystal when the residual stresses are confined to a zone so narrow that it can be treated as a solidification front separating the plastic and elastic portions of the material. The solidification and crystallization fronts coincide during growth of nonplastic crystals. During growth of crystals whose yield strength varies sharply with temperature, the solidification front can be considered to lie along the isotherm corresponding to a relaxation period of the order of the characteristic variation time of the temperature field.

Calculation of the internal stresses for crystals with a distinct solidification front is substantially simpler and can be conducted by the well-developed methods of thermoelasticity theory. Taking into account the plastic properties of the crystal reduces to taking into account the boundary conditions at the solidification front. Unfortunately, such calculations can be made in analytic form only in the simplest cases (see, e.g., refs. 1-4). The problem in which we are interested, that of growth of cylindrical and tabular crystals from one end, specifically requires numerical determination of the thermoelastic field.

We will limit ourselves to the case of steady-state crystal growth, where the temperature and stress fields plotted on a stationary coordinate system are independent of time. The cooled end of the crystal is considered to lie at a distance from the solidification front far exceeding the specimen width.

The method for reducing the problem of development of residual deformations and stresses to the standard problem of determining the thermoelastic stresses reduces to the following: Since the residual deformations beyond the solidification front are already frozen and time-invariant, we differentiate the entire set of equations (1)-(3) for the coordinate z, which corresponds to the direction of the growth axis. Taking into account the fact that $e^0_{ij,z} \equiv 0$, we obtain the system of equations

$$\sigma_{ij,jz} = 0, \tag{1'}$$

$$\sigma_{ij,z} = c_{ijkl}e_{kl,z}, \tag{2'}$$

$$e_{kl,z} = [(u_{k,lz} + u_{l,kz})/2] - \alpha_{kl}T_{,z}, \tag{3'}$$

which is equivalent to the usual system of thermoelasticity equations with all the quantities replaced by their axial gradients. The boundary conditions (5) at the lateral surface of the specimen retain the usual form:

$$\sigma_{ij,z}n_j|_s = 0. \tag{5'}$$

As is usually supposed,[1,2,14] $z = z_0(r)$ at the solidification front and we set all six stress-tensor components equal to zero:

$$\sigma_{ij}|_{z=z_0} = 0 \tag{10}$$

[for different generalizations of Eq. (10), see refs. 2, 15, and 16], so that the boundary condition in Eq. (5') follows for all the axial stress gradients at the growth front.

We have thus obtained a simple rule as a special case of the general theorem given previously:[3] The axial gradients of the total (transient and residual) stresses for a steady-state crystallization regime are numerically equal to the thermoelastic stresses produced by the hypothetical temperature field numerically equal to the axial gradient of the temperature field in question, i.e.,

$$\frac{\partial}{\partial z}\sigma_{ij}(T(x, y, z)) = \sigma_{ij}^T\left\{\frac{\partial T}{\partial z}(x, y, z)\right\}, \tag{11}$$

where the symbol T represents the thermoelastic stresses.

It follows from Eqs. (10)-(11) that

$$\sigma_{ij}(T(x, y, z)) = \int_{z_0}^{z}\sigma_{ij}^T\left\{\frac{\partial T}{\partial z'}(x, y, z')\right\}dz', \tag{12}$$

which enables us to represent the residual stresses

$$\sigma_{ij}^*(x, y) = \lim_{z\to\infty}\sigma_{ij}(x, y, z) \tag{13}$$

in terms of the displacements u_i^0 at the crystallization front. Specifically, for tabular crystals with arbitrary anisotropy of the elastic yield tensor s_{ijkl} we have

$$\sigma_{zz}^* = (s_{zzzz})^{-1}(\alpha_{zz}T_0 - \overset{\circ}{u}_{z,z}), \tag{14}$$

while for elastically isotropic symmetrically stressed cylinders,

$$\sigma_{zz}^* - \nu(\sigma_{rr}^* + \sigma_{\varphi\varphi}^*) = E(\alpha T_0 - \overset{\circ}{u}_{z,z}), \tag{15}$$

$$r\frac{\partial}{\partial r}(\sigma_{rr}^* + \sigma_{\varphi\varphi}^* - \nu\sigma_{zz}^*) = E\frac{dz_0}{dr}\overset{\circ}{u}_{z,r}. \tag{16}$$

Here T_0 is the temperature at the solidification front (with respect to the temperature of the cooled end) and ν is Poisson's constant. In the case of a plane crystallization front, Eq. (16) yields the relationship

$$\sigma_{rr}^* + \sigma_{\varphi\varphi}^* = \nu\sigma_{zz}^*, \tag{17}$$

which corresponds to the presence in the residual-deformation tensor of only one component, $e_{zz}^0 = -(1 - \nu^2)E^{-1}\sigma_{zz}^*$. It should be noted that, during ordinary quenching of cylinders, when $e_{ij}^0 = \delta_{ij}e^0(r)$, the relationship

$$\sigma_{rr}^* + \sigma_{\varphi\varphi}^* = \sigma_{zz}^* \tag{18}$$

is satisfied, so that the ratio of the residual axial stresses to the residual dilatation can be used to determine the position of the solidification front. In terms of dislocation theory, the difference between the cases in Eqs. (17) and (18) is due to the different orientations of the superfluous dislocation planes: These planes are parallel to the crystal axes in the first case[17] and perpendicular to the lateral surface in the second.

NUMERICAL CALCULATION OF STRESSES FOR CIRCULAR CYLINDERS

As an illustration, we will give below the results of numerical solution of the problem of the stresses that develop in a circular cylinder with a plane solidification front. The temperature field was selected in such fashion that superposition of the solutions obtained made it possible to find the temperature and stress fields for arbitrary axially symmetric cooling of the lateral surface of the specimen. For this purpose, the temperature at the specimen surface was set in the following manner:

at the end (z = 0),

$$T(r, 0) = T_0, \tag{19}$$

at the lateral surface (r = R),

$$T(R, z, \zeta) = \begin{cases} T_0(1 - z/\zeta), & z < \zeta, \\ 0, & z > \zeta. \end{cases} \tag{20}$$

A complete set of solutions for the temperature field T(r, z, ζ) and stress field σ_{ij}(r, z, ζ) with different values of the parameter ζ theoretically makes it possible to plot the temperature and stress field with the arbitrary boundary condition T = T(R, z) by superposition:

$$\begin{aligned} T(r, z) &= \int_0^\infty \zeta\frac{\partial^2 T}{\partial\zeta^2}(R, \zeta)T(r, z, \zeta)d\zeta, \\ \sigma_{ij}(r, z) &= \int_0^\infty \zeta\frac{\partial^2 T}{\partial\zeta^2}(R, \zeta)\sigma_{ij}(r, z, \zeta)d\zeta. \end{aligned} \tag{21}$$

For practical purposes, one can obviously limit oneself to constructing a discrete set of standard solutions for values of ζ spaced at intervals corresponding to the characteristic length over which there is a change in the axial gradient at the crystal surface. In making the numerical calculations, we selected values of 0.5, 1.0, 2.0, and 2.5 for the parameter ζ/R.

The temperature field within the crystal was found by solving the thermal-conductivity equation with the boundary conditions in Eqs. (19)-(20). With a steady-state growth regime, the temperature field plotted on a coordinate system rigidly associated with the furnace is time-invariant and heat transfer from the moving crystal (during pulling) leads to a volume heat evolution proportional to the growth rate W and the axial temperature gradient. On this coordinate system, the thermal-conductivity equation has the form

$$a\Delta T = W\frac{\partial T}{\partial z}, \qquad (22)$$

where a is the thermal diffusivity of the specimen. The Peclet number Pe = WR/a, which defines the rate of heat transfer by the moving crystal, has a value not exceeding 10^{-2} in cases of practical interest. Comparison of the results of numerical calculations of the temperature fields and axial gradients for Pe = 0.01 and Pe = 0 showed that these fields virtually coincided at all points when $\zeta \sim R$ (the discrepancy did not exceed 1-2%). The thermoelastic fields were therefore calculated with the approximation Pe = 0.

The method described previously [see Eq. (11)] was used to determine the thermoelastic field for a fictitious temperature numerically equal to the axial gradient $T_{,z}(r, z)$. The thermoelasticity equations were selected as equivalent to the permuted expressions in Eq. (4):

$$(1-2\nu)\Delta u_{i,z} + u_{j,ijz} = 2(1+\nu)\alpha T_{,iz}. \qquad (23)$$

In contrast to Eq. (4), this equation takes into account the elastic-isotropic approximation and, in accordance with Eq. (11), all the quantities are replaced by their axial gradients. In making the numerical calculations, the Poisson constant ν was assumed to be 1/6 or 1/3. The boundary conditions were those in Eq.(5') and the natural boundary conditions at infinity:

$$\lim_{z\to\infty} u_{i,z} = 0. \qquad (24)$$

The axial displacement gradient and Eq. (2') were used to find the axial stress gradients. Further integration in accordance with Eq. (12), using the boundary condition in Eq. (10), permitted full reproduction of the stress distribution. The residual stresses were found from Eq. (13) and checked by comparison with the total deformations at the solidification front, using equations following from Eqs. (15) and (17) and the equilibrium equation

$$\sigma_{\varphi\varphi}^{*} = \frac{\partial}{\partial r}(r\sigma_{rr}^{*})$$

in particular (see also refs. 5 and 6)

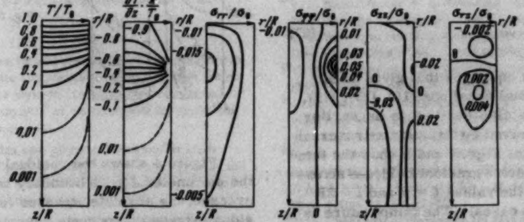

Fig. 1. Temperature and stress fields during growth of cylindrical crystal from one end. Boundary condition (20) with $\zeta = R$. The figures beside the isoline designate the temperature in T_0 units, the axial gradient in T_0/R units, and the stress in $\sigma_0 = \alpha E T_0/(1-\nu^2)$ units, respectively.

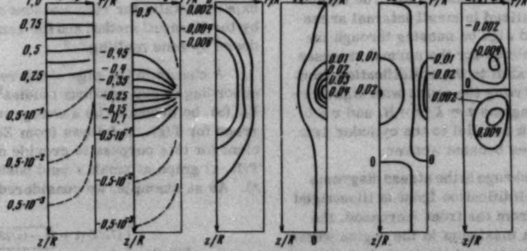

Fig. 2. Temperature and stress fields for boundary condition (20) with $\zeta = 2R$. Symbols are the same as in Fig. 1.

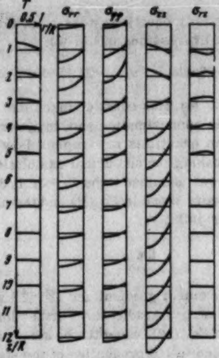

Fig. 3. Change in curves of radial temperature and stress distribution on moving away from solidification front for fields shown in Fig. 2. Temperature curves for cross sections $z/R = n$ ($n = 1, 2, 3, \ldots$); stress curves for cross sections $z/R = n + 1/2$.

$$(1-\nu^2)E^{-1}\sigma_{zz}^{*}=(2/R^2)\int\limits_0^R \overset{*}{u}_{z,z}(\rho)\rho\,d\rho-\overset{*}{u}_{z,z}(r), \tag{25}$$

$$\sigma_{rr}^{*}=(\nu/r^2)\int\limits_0^r \sigma_{zz}^{*}(\rho)\rho\,d\rho, \tag{26}$$

$$\sigma_{\varphi\varphi}^{*}=\nu\sigma_{zz}^{*}-\sigma_{rr}^{*}. \tag{27}$$

A system of difference equations that gives an approximation of the differential equations (19), (20), (22), (2'), (5'), (23), and (24) was also derived in an earlier study.[6] This system was solved by the matrix-traversal method.4) As an illustration, Figs. 1 and 2 show the temperature field, axial temperature gradient field, and stress-tensor component field for the values $\zeta = R$ and $\zeta = 2R$ (we assumed Pe = 0 in both cases). The temperature is in T_0 units, the temperature gradient in T_0/R units, and the stress in $\sigma_0 = \alpha E T_0/(1-\nu^2)$ units. The isotherms were almost straight lines when $z > \zeta$ and became concave when $z < \zeta$; the temperature decreases exponentially with increasing z near the cylinder axis. The level lines for the axial temperature gradient converged at the point $r = R$, $z = \zeta$ (a singularity of the nodal type). The tangential stresses $\sigma_{r\varphi}$ were localized in small internal areas of the specimen and changed sign on passing through the cross section $z = \zeta$. The isolines for the normal stresses σ_{rr}, $\sigma_{\varphi\varphi}$, and σ_{zz} were parallel to the solidification front at first and then curved, skirting the areas with high thermoelastic stresses in the regions $z = \zeta$, $r = R$, and $r = 0$ and being displaced to a path parallel to the cylinder axis as the thermoelastic stresses became weaker.

The overall trend of the change in the stress diagrams on moving away from the solidification front is illustrated in Fig. 3. As the distance from the front increased, the stresses rose and reached a maximum in the region where $z \sim \zeta$; the thermoelastic stresses subsequently became weaker and residual stresses appeared.

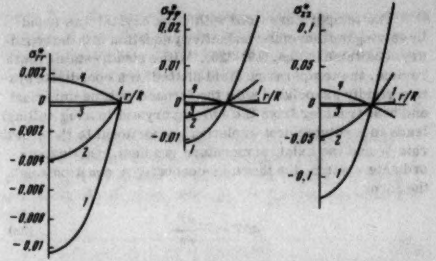

Fig. 4. Residual-stress curves for different field temperatures. 1) Boundary condition (20) for $\zeta = 0.5$ R; 2) the same for $\zeta = R$; 3) the same for $\zeta = 2R$; 4) boundary condition (28).

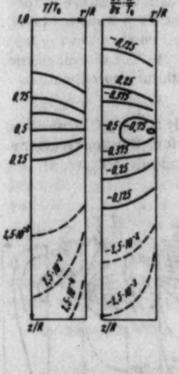

Fig. 5. Temperature field for boundary condition (28).

Figure 4 shows the residual stresses as a function of the parameter ζ with boundary condition (20). As ζ increased, the absolute stresses fell rapidly and all the residual-stress components reverted almost to zero when $\zeta > 2$. As was to be expected, an anomalous (reciprocal to that for hardening) stress curve was observed for all values of ζ: The stresses in the central portion of the specimen were negative (compression), while those at the periphery were positive (elongation). As was noted previously, such a stress distribution was actually observed experimentally for ruby and leucosapphire crystals grown by the Verneuil method and for semiconductor crystals produced by zone melting.[2,12]

A change in the sign of the residual-stress curve can, according to our previous studies[2,5] and the estimate in Eq. (8), be produced by a change in the curvature of the graph for T(z). It follows from Eq. (15) that it is sufficient for this purpose to provide negative curvature of the T(R, z) graph at small z (and positive curvature at large z). As an example, we considered the boundary condition

$$T(R,z)=\begin{cases}(T_0/2)\left(1+\sqrt{1-(z/2R)^2}\right), & z\leqslant 2R,\\ (T_0/2)\left(1-\sqrt{1-(z/2R)^2}\right), & 2R\leqslant z\leqslant 4R,\\ 0, & z>4R,\end{cases} \tag{28}$$

which corresponds to $T_{,zz}(R, z) < 0$ at $z < 2R$ and $T_{,zz}(R, z) \geq 0$ at $z > 2R$. Figure 5 illustrates the results of calculation of the temperature field for boundary condition (28). There is a change in the sign of the isotherm and axial-temperature-gradient isoline curvature in the cross section with $z = 2R$; the temperature (and gradient) decreases exponentially at $z > 4R$; the axial-gradient isoline has a singularity of the center type at the point $z = 2R$ and $r = R$. The corresponding residual-stress curve is shown in Fig. 4 and is actually a diagram of the hardening type.

It should be noted in conclusion that the solution obtained with boundary condition (20) can be used not only as a Green's function and employed in constructing a solution with Eq. (20) and an arbitrary boundary condition, but also as an approximation of the solution corresponding to the real temperature distribution at the lateral surface of the crystal.

The approximation of an abrupt solidification front, which we used in calculating the residual stresses, may be inadequate for crystals that are plastic in regions far from the front, where development of high thermoelastic stresses is possible, in conformity with Figs. 1 and 2. It is necessary to take into account the quenching in such crystals and to evaluate the residual stresses that develop during cooling (and the corresponding dislocation density) with the aid of relaxation equations of the type of Eq. (9). Simplified estimates for the hardening stresses and the dislocation density produced during quenching have already been proposed.[11,13]

[1)] Strictly speaking, dislocations are formed and displaced under the action of the overall field of thermoelastic and residual stresses, but there are no residual stresses in dislocation-free crystals. Successful use was recently made of this circumstance in an analysis[8] of the conditions for production of dislocation-free semiconductor crystals.

[2)] The estimate of the stresses in this case given by Tsivinskii[7] is inadequately grounded. We are actually dealing only with determination of the correlation between the stresses (or dislocation density) and the temperature gradients for fields that satisfy the similarity condition.

[3)] The neglect of the axial gradients in calculating the thermoelastic stresses in the studies by Avdonin et al.[9] is not permissible, as can be seen from the results of this work: The authors obtained a stress field in which the simplified equilibrium equation they adopted was not satisfied. This error was subsequently corrected.[8]

[4)] In order to determine the error in the finite-difference approximation, the variant corresponding to Pe = 0, $\zeta = 2$ was checked with different intervals for r and z. The deviation in the stress values was about 5-10%; the components σ_{zz} and σ_{rz} were found to have been calculated more accurately than σ_{rr} and $\sigma_{\varphi\varphi}$. Another method for checking the accuracy of the calculations was to determine the residual stresses by two different methods, from Eqs. (13) and (25)-(27); we took into account the fact that Eq. (13) yields a larger error, because of the cumulative error in integration of Eq. (12).

---

[1] V. L. Indenbom, Zh. Tekh. Fiz., 24, 925 (1954).

[2] V. L. Indenbom, Kristallografiya, 9, 74 (1964) [Sov. Phys.—Crystallogr., 9, 57 (1964)].

[3] I. S. Zhitomirskii, M. K. Likht, and T. S. Chebanova, in: Thermal Stresses in Structural Members [in Russian], Vol. 6, Naukova Dumka, Kiev (1966), p. 227.

[4] T. S. Chebanova, Mekh. Tverd. Tela, 3, 63 (1968).

[5] V. L. Indenbom, I. S. Zhitomirskii, and T. S. Chebanova, in: Growth of Crystals, Vol. 8, Consultants Bureau, New York (1969).

[6] V. L. Indenbom, I. S. Zhitomirskii, N. N. Morozovskaya, and T. S. Chebanova, in: Thermal Stresses in Structural Members [in Russian], Vol. 9, Naukova Dumka, Kiev (1970), p. 136.

[7] S. V. Tsivinskii, Fiz. Met. Metalloved., 25, 1013 (1968).

[8] S. S. Vakhrameev, V. B. Osvenskii, and V. A. Smirnov, in: Proceedings of the Fourth All-Union Conference on Crystal Growth: Growth and Structure of Crystals [in Russian], Izd. ArmSSR, Erevan (1972), Pt. II, p. 81.

[9] N. L. Avdonin, S. S. Vakhrameev, M. G. Mil'vidskii, V. B. Osvenskii, B. A. Sakharov, B. A. Smirnov, and Yu. F. Shchelkin, Dokl. Akad. Nauk SSSR, 200, 316 (1971) [Sov. Phys.—Dokl., 16, 772 (1972)]; Izv. Akad. Nauk SSSR, Ser. Fiz., 36, 554 (1972).

[10] V. L. Indenbom and V. I. Danilovskaya, Dokl. Akad. Nauk SSSR, 180, 1319 (1968) [Sov. Phys.—Dokl., 13, 613 (1968)].

[11] V. L. Indembom and V. I. Nikitenko, in: Stresses and Dislocations in Semiconductors [in Russian], Izd. Akad. Nauk SSSR, Moscow (1962), p. 8.

[12] V. L. Indenbom and G. E. Tomilovskii, Kristallografiya, 3, 593 (1958) [Sov. Phys.—Crystallogr., 3, 599 (1959)].

[13] V. I. Nikitenko and V. L. Indenbom, Kristallografiya, 6, 432 (1961) [Sov. Phys.—Crystallogr., 6, 341 (1961)].

[14] T. Hirone, Sci. Rep. Tohoku Univ., 1017 (1936); T. Mura, Res. Rep. Faculty Eng. Meiji Univ., 2, 10 (1957); G. Reider, Z. Angew. Math. Mech., 45, 153 (1965); É. A. Iodko, Inzh.-Fiz. Zh., 14, 674 (1968).

[15] B. Ya. Lyubov and B. N. Finkel'shtein, Zh. Tekh. Fiz., 16, 945 (1946); J. H. Weiner, J. Appl. Mech., 23, 397 (1956); H. G. Landau and J. H. Weiner, J. Appl. Mech., 25, 459 (1968); J. H. Weiner and B. A. Boley, J. Mech. Phys. Solids, 11, 145 (1963).

[16] T. S. Chebanova, Dissertation [in Russian], Khar'kovsk. Gos. Univ. (1969); B. A. Reznikov, Dissertation [in Russian], MGU (1970).

[17] V. L. Indenbom, Kristallografiya, 2, 594 (1957) [Sov. Phys.—Crystallogr., 2, 587 (1957)].

Investigation of the intensities of electron diffraction by NH_4Cl, NaCl, and TlCl films by using electrical recording and an electron filter

A. S. Avilov, R. M. Imamov, R. K. Karakhanyan, and Z. G. Pinsker
Institute of Crystallography, Academy of Sciences of the USSR
(Submitted December 28, 1971; resubmitted March 30, 1972)
Kristallografiya, 18, 49-53 (January-February 1973)

Polycrystalline films of NH_4Cl, NaCl, and TlCl, condensed in a 10^{-5} mm Hg vacuum, were investigated in an ÉR-100 electron-diffraction camera using electrical recording of scattered electrons at 50 and 100 kV in order to test the possibilities of this device in electron-diffraction structure analysis. It was shown that electrometric recording of intensities and the use of a filter to screen out inelastically scattered electrons increase the accuracy of measurement of reflection intensities. The accuracy of electrometric measurement of reflection intensities is substantially affected by faults of the recording system itself: low recording speed and insufficient stability of the high-voltage beam current and capacitor current.

In electron-diffraction structure investigations, the experimental material consists mainly of electron-diffraction photographs of polycrystalline masses and slanting textures, which always have a strong background of inelastic scattering. To eliminate this on the intensity curve plotted by microphotometric measurements, a smooth background line is usually drawn. Inelastic scattering increases the error in measuring the intensity of the maximum to 15-20%. It is well known that the accuracy of measurement of reflection intensities may be increased substantially by using electrometric recording and an electron filter to eliminate inelastically scattered electrons.

We investigated polycrystalline films of NH_4Cl, NaCl, and TlC in an ÉR-100 electron diffraction camera, recording the intensities of scattered electrons electrically in order to test the possibilities of this device in electron-diffraction structure analysis. The choice of substances for investigation was dictated by the fact that the atoms in the structures of these compounds lie in special positions without parameters, except for the H atoms in NH_4Cl. Owing to this, the effect of errors in atomic coordinates may be neglected when comparing experimental structure amplitudes with calculated values.

EXPERIMENTAL

The preparation of polycrystalline films of NH_4Cl, NaCl, and TlCl with no trace of preferred crystal orientation is a difficult problem. After a number of experiments, NH_4Cl and TlCl films were prepared by condensation in a vacuum of $\sim 10^{-5}$ mm Hg on a collodion base layer directly in the electron-diffraction camera. To prepare a NaCl film, a mesh bearing a 0.5% NaCl solution coated on the collodion was placed in a desiccator, and the latter was evacuated by a vacuum forepump. The absence of orientation was checked by examining diffraction patterns taken at different angles. The best diffraction pattern, practically free from orientation or strong background, was obtained in the case of NH_4Cl and NaCl films. The diffraction pattern from TlCl showed a slight degree of orientation.

The intensities of scattered electrons for NaCl and TlCl films were recorded at accelerating voltages of 50 and 100 kV. At 50 kV, an integral-type[1,2] electron-energy filter was used. To eliminate random errors in recording reflection intensities, the diffraction pattern was taken many times for each sample.

In order to record the entire diffraction pattern up to that value of $\sin \vartheta/\lambda$, at which the background merges with the useful signal, we went over to more sensitive scales and measured the intensity ratio at a given point. In diffraction patterns recorded at 100 kV, the intensities of the first two or three very strong reflections were substantially diminished. This was apparently due to some fault in the recording system. For this reason, the diffraction pattern at 100 kV was recorded with intensity decreased to a minimum for the first reflections and increased for the last. In this case, the reflection intensities were all converted to a common scale.

It would be noted that all the recordings, whether taken with or without an electron filter, showed a background (appreciably less in the former case), which, as in the case of photographic recording, was eliminated by drawing a smooth line. Diffraction patterns at 50 kV, whether taken with or without the electron filter, were recorded many times for each sample. The voltage applied to the filter [0-30 V (filter cutoff voltage)] was set to permit detection of the useful signal. Owing to inherent filter noise, it was necessary to record fewer reflections than in the case of recording without a filter.

In the present study, we also took patterns of NH_4Cl films at −50°C by using a low-temperature attachment to the ÉR-100 electron-diffraction camera. The films were cooled by liquid nitrogen. The patterns were taken at 50 kV both with and without a filter and at 100 kV without a filter.

In order to compare the results of measuring reflection intensities by electrometric recording with data of the photographic method, we took 10 diffraction photographs of NaCl with multiple exposures. All the plates were processed under the same conditions. Intensities in them were measured by plotting a density curve.

Experimental structure amplitudes of all compounds were calculated from the intensities by the equation of kinematic scattering.

DISCUSSION OF RESULTS

Comparison of experimental values of structure amplitudes, obtained from NH_4Cl films at 50 kV using a filter, with values calculated from a structure model[3] and the total temperature factor $B = 0.8$ Å^2 resulted in the dispersion $R = 10.8\%$. Further, a three-dimensional series was calculated from the experimental data. The intensities of reflections from planes crystallographically different but with identical interplanar distances (e.g., 300 and 221, 410 and 322) were distributed in proportion to the squares of the calculated structure amplitudes. In all, we used 30 amplitudes up to $\sin \vartheta/\lambda = 0.83$ Å^{-1}. All peaks of Cl, N, and H atoms were brought out in the cross section $\varphi(xxz)$ in the diagonal plane (110). From the fact that the four H atoms occupy a statistically 8-fold position, it follows that their peaks should correspond to half the potential of the H atom.

Experimental values of potential at the Cl, N, and H maxima with allowance for the average internal structure potential φ_{av} are 598, 251, and 42 V. In this case, the parameter x_H is assumed equal to 0.148, which is very close to the data of ref. 3 (see Table 1). The coordinates of x_H and the thermal parameters of the atoms were improved by the method of least squares according to programs of the Kristall group. Final data are given in Table 1. We obtained the value 0.155 for the parameter x_H: The corresponding interatomic distance N–H is 1.04 ± 0.02 Å, which agrees with the results of ref. 4 (see Table 1). The value of B for N is also close to the data of ref. 4, while B_{Cl} and B_H differ strongly.

After improving the hydrogen coordinates and the thermal parameters of the atoms, the dispersion was decreased[1)] to $R_2 = 7.2\%$. Further, the potentials at the centers of the Cl, N, and H atoms were calculated according to ref. 5 with allowance for improved thermal parameters of the atoms and breaking off of the series. These values were found to be 600, 254, and 43 V, respectively, for Cl, N, and H, i.e., they practically coincided with experimental values. The mean-square error in determining potentials, according to ref. 5, amounts to 3 V.

A comparison of experimental and calculated structure amplitudes is given in Fig. 1. Experimental amplitudes found at 50 and 100 kV without a filter are also plotted there. As the figure shows, the dispersion R is improved by using an electron filter (see Table 2).

The intensities of reflections from NH_4Cl were also recorded at −50°C. The diffraction pattern was taken only once, since, after cooling 30–35 min, residual water vapor condensed on the sample to form ice, which gave a strong incoherent background, and the maximum value of $\sin \vartheta/\lambda$ for recordable reflections was less than at room temperature. For measurements at 50 kV without a filter, the minimum value of R is 9.8% ($x_H = 0.155$; $B_{tot} = 0.6$ Å^2).

The dispersion R for NaCl at $B_{tot} = 0.8$ Å^2 is given in Table 2. Comparison of experimental and calculated structure amplitudes for this structure shows that the first strong reflections of NaCl must be corrected for extinction. The intensities of the (200) and (220) reflections, measured electrometrically at 100 kV, were corrected for an extinction calculated on the basis of a two-wave approximation[6,7] and an average crystal size $H_{av} \approx 250$ Å. In this case, R dropped from 9.8 to 8.5%.

As was noted above, the intensities of reflections from NaCl were also measured by plotting a density curve. In this case, the dispersion R = 12%. In the case of electrometric recording of intensities, R = 8.2% for the same reflections. This difference in values of R for the two methods is apparently due to the fact that, in the photographic method, the error of intensity measurement for weak and very strong reflections is large owing to nonlinearity of the density curve. In electrometric recording of reflection intensities, the error (with regard to reproducibility) amounts to 0.5% for strong, 4–5% for medium, and 15–20% for weak reflections.

The results of comparing the cross sections of the three-dimensional potential series $\varphi(xy0)_{el}$ and $\varphi(xy0)_p$ for the electrometric and photographic methods of measuring reflection intensities are given below. To allow for the effect of breaking off the series, we also plotted a synthesis of $\varphi(xy0)_c$ from calculated structure amplitudes (taken, as in experiment, up to $\sin \vartheta/\lambda = 0.815$ Å^{-1}) at B = 0.8 Å^2.

Values of the Cl potential in the cross sections $\varphi(xy0)_{el}$, $\varphi(xy0)_p$, and $\varphi(xy0)_c$ practically coincide. For Na (a relatively light element in the structure), there are discrepancies. Values of the Na potential in $\varphi(xy0)_{el}$ (394 V) and $\varphi(xy0)_p$ (374 V) differ from that in $\varphi(xy0)_c$ (402 V) by 8 and 28 V, respectively. However, these quantities lie within the upper and lower limits of the difference between calculated and experimental heights of maxima[8] (3–7%) in the photographic determination of intensities.

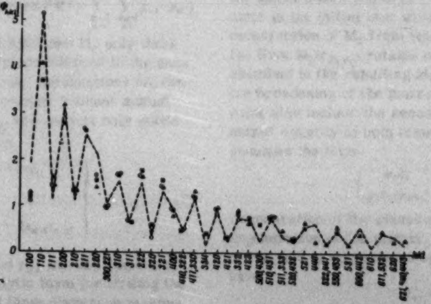

Fig. 1. Experimental and calculated structure amplitudes for NH_4Cl. Dashed line, Φ_c; filled triangles, Φ_e, 100 kV; filled squares, Φ_e, 50 kV, without filter; open circles, Φ_e, 50 kV, with filter.

TABLE 1

Parameters	Present study	Ref. 3	Ref. 4
r_H	0.155	0.146	0.154
B_{tot}, Å^2	0,75	1—2	
B_j, Å^2	$B_{Cl} = 0.63$ $B_N = 1.08$ $B_H = 1.60$		$B_{Cl} = 1.22$ $B_N = 1.33$ $B_H = 2.38$

TABLE 2

Compound	50 kV (without filter), R_1, %	50 kV (with filter), R_2, %	100 kV (without filter), R_3, %
NH_4Cl	14.5	7.2	11.0
NaCl	8.4	7.6	9.8

Since, despite numerous attempts, we were unable to prepare TlCl film wholly free from orientation, only preliminary results of investigating TlCl reflection intensities are given below. Values of the dispersion with allowance for the thermal factor (B = 1.8 Å^2) were R = 14.6, 14.8, and 13.4%, respectively, at 50 and 100 kV without the electron filter and at 50 kV with the filter. The relatively high value of the dispersion R for TlCl is also due in part to the fact that the diffraction pattern of TlCl changes appreciably during the exposure. In recording reflection intensities the action of the electron beam causes rings to appear, which we did not index.

The data set forth above show that electrometric recording of reflection intensities and the use of a filter to screen out inelastically scattered electrons substantially improve the agreement between experimental and calculated structure amplitudes. However, a counter-field cannot get rid of electrons scattered by numerous elastic collisions, or electrons which have lost a small part of their energy by thermal diffusion scattering and certain other processes contributing to the magnitude of the interference maximum. This is shown by the relatively high value of dispersion R for the simple structures of NH_4Cl and NaCl. Moreover, the measured intensity is affected by faults of the recording system in the ÉR-100, the elimination of which would increase considerably the accuracy of measurement of reflection intensities. Among these faults are low recording speed and insufficient stability of the high-voltage beam current and capacitor current. In electrometric recording, as a rule, the intensities of weak reflections turn out too high. This is the result of errors, due to various causes, which cannot be taken into account.

Thus, our investigation shows once more that scattering in polycrystalline films having crystallites from 200 to 300 Å in size is nearly kinematic. However, dynamic effects caused by two-wave as well as multiwave scattering are not ruled out.

---

1)According to ref. 3, R = 12% and the number of reflections is 28, whereas according to ref. 4, R = 10% and the number of reflections is 39. In these papers, reflection intensities were estimated visually and microphotometrically.

[1] A. G. Alekseev, L. G. Boyandina, I. A. Bul'ba, V. N. Vertsner, A. M. Gulyi, V. N. Kaplichnyi, G. D. Kisel', O. P. Ovchinnikov, A. S. Sur, M. I. Tregubov, and N. M. Shcherban', Izv. Akad. Nauk SSSR, Ser. Fiz., 34, 7, 1404 (1970).

[2] A. G. Alekseev, T. A. Verkhovskaya, and Yu. V. Vorob'ev, Izv. Akad. Nauk SSSR, Ser. Fiz., 34, 7, 1424 (1970).

[3] M. M. Stasova and B. K. Vainshtein, Tr. Inst. Kristallogr., Akad. Nauk SSSR, 12, 18 (1956).

[4] S. Kuwabara, J. Phys. Soc. Japan, 14, 9, 1205 (1959).

[5] B. K. Vainshtein, Structural Electronography [in Russian], Izd. Akad. Nauk SSSR, Moscow (1956).

[6] M. Blackman, Proc. Roy. Soc., A173, 68 (1939).

[7] G. G. Dvoryankina and Z. G. Pinsker, Kristallografiya, 3, 438 (1958) [Sov. Phys. – Crystallogr., 3, 439 (1958)].

[8] Z. G. Pinsker, Acta Geol. Geograph. Univ. Comenianae, Geol., 14, 125 (1968).

Systematic analysis of Patterson functions on the basis of crystal symmetry. IV. Interpretation of the Patterson synthesis for crystals of lower systems

É. A. Kuz'min, V. P. Golovachev, V. V. Ilyukhin, and N. V. Belov
Gor'kii State University
Institute of Crystallography, Academy of Sciences of the USSR

(Submitted August 2, 1972)
Kristallografiya, 18, 54-62 (January-February 1973)

An algorithm is given in analytic form for extracting the peak rhombuses, matching the fundamental and satellite rhombuses, and establishing the fundamental segment in the fundamental system for crystals of lower systems.

The effectiveness of the extracting of the fundamental system from the real Patterson function, in particular by superpositon methods,[1,2] depends substantially on the choice of the shift vectors – the vectors to the key peaks. One usually uses the geometric regularity in the arrangement of the maxima in the Patterson synthesis[3] to find them in symmetric crystals.1) The geometric approach, developed for vector systems[4-6] (predominantly in point form), namely, the search for peak rhombuses, can be generalized to apply to a continuous Patterson distribution. The basic aim of the algorithm is the extraction of the full system of peak rhombuses and thereby a check on the presence of the interatomic distances between 2k atoms (k is the order of the Federov group), and this is achieved in two steps: In the first step the peak rhombuses, which correspond to individual symmetry elements of the Fedorov group, are localized, and in the second step the fundamental rhombuses, which determine the initial segments relative to the origin of coordinates, are extracted.

In the most general case both ends of a segment in the fundamental system occupy general positions of a Fedorov group of order k; here the segments are not perpendicular or parallel to the symmetry elements (there are no degenerate rhombuses in the Patterson function). We also assume that the fundamental system contains no repeated (equal and parallel) segments other than those determined by the Fedorov group symmetries.

LOCALIZATION OF THE PEAK RHOMBUSES

We shall follow refs. 3 and 8 in representing the electron density distribution and the Patterson function as a set of atoms $\rho(\mathbf{r}) = \sum_{n}^{N}\sum_{k}^{k_0}\rho_n(\mathbf{r}_k)$ and peaks $P(\mathbf{r}) = \sum_{n,n'}\sum_{k,k'}p_{nn'}(\mathbf{r}_{kk'})$ respectively. In the extraction functions M_n only those maxima should be retained which correspond to the ends of the corresponding vectors,[7] i.e., the functions M_n constructed from the $(n-1)$ shift vectors (without mutual shift) $\mathbf{r}_{x_1y_1}, \mathbf{r}_{x_2y_2}, \ldots, \mathbf{r}_{x_{n-1}y_{n-1}}$ will contain only points $\mathbf{r}_{mn}$ which satisfy the conditions

$$\left.\begin{aligned}\mathbf{r}_{x_1y_1} &= \mathbf{r}_{mn} - \mathbf{r}_{k_1l_1},\\ &\;\vdots\\ \mathbf{r}_{x_{n-1}y_{n-1}} &= \mathbf{r}_{mn} - \mathbf{r}_{k_{n-1}l_{n-1}},\end{aligned}\right\} \tag{1}$$

where $\mathbf{r}_{xy}$ is the shift vector and $\mathbf{r}_{kl}$ are the vectors to any Patterson peaks. This analytic form for writing the results allows us easily to find those Patterson maxima which go over to the separation functions of any rank from the functions of the preceding rank.

We let M_3 be formed from two functions $M_2(\mathbf{r}_{x_1y_1})$ and $M_2(\mathbf{r}_{y_2x_2})$. Carrying out transformations similar to those in ref. 9 we find

$$\begin{aligned}\mathbf{r}_{x_1y_1} + \mathbf{r}_{k_1k_1} &= \mathbf{r}_{y_1} - \mathbf{r}_{k_1} + \mathbf{r}_{k_1} - \mathbf{r}_{x_1},\\ \mathbf{r}_{y_2x_2} + \mathbf{r}_{k_2k_2} &= \mathbf{r}_{x_2} - \mathbf{r}_{k_2} + \mathbf{r}_{k_2} - \mathbf{r}_{y_2}\end{aligned} \tag{2a}$$

or

$$\begin{aligned}\mathbf{r}_{x_1y_1} &= \mathbf{r}_{x_1k_1} - \mathbf{r}_{y_1k_1} = \mathbf{r}_{k_1y_1} - \mathbf{r}_{k_1x_1},\\ \mathbf{r}_{y_2x_2} &= \mathbf{r}_{y_2k_2} - \mathbf{r}_{x_2k_2} = \mathbf{r}_{k_2x_2} - \mathbf{r}_{k_2y_2}.\end{aligned} \tag{2b}$$

Comparing (1) and (2a, b) we see that M_3 only extracts those maxima which correspond to equality of two elements of the matrix (3) from different rows:

$$\begin{pmatrix} x_1k_1 & k_1y_1 \\ y_2k_2 & k_2x_2 \end{pmatrix} \tag{3}$$

The multiplicity of the initial shift vectors increases the number of elements in each row of the matrix, i.e., if $\mathbf{r}_{x_1y_1} = \mathbf{r}_{x_1'y_1'}$ and $\mathbf{r}_{y_2x_2} = \mathbf{r}_{y_2'x_2'}$ in the Patterson function the matrix (3) assumes the form

$$\begin{pmatrix} x_1k_1 & k_1y_1 & x_1'k_1 & k_1y_1' \\ y_2k_2 & k_2x_2 & y_2'k_2 & k_2x_2' \end{pmatrix}. \tag{4}$$

A similar analytical approach suffices for a simple extraction of the rhombuses from the Patterson synthesis. To localize the four vertices of the rhombus we need three functions M_2 and the total function M_4. However, the pairwise equality (and parallelness) of the sides of the rhombus are sufficient to construct two extraction functions: In $M_2(\mathbf{r}_{x_1y_1})$ rhombus sides are present among the set of points which are equal and parallel to a segment in the initial star which is easily found. Repeated construction of M_2 from this segment on the pattern of the first $M_2(\mathbf{r}_{x_1y_1})$ retains only one of the vertices of the rhombus in the resulting M_4. This fact is reflected in the broadening of the matrix (3): In its second row one must also include the second term from (2b) and "require" equality of both terms from (2b). The matrix (3) assumes the form

$$\begin{pmatrix} x_1k_1 & k_1y_1 \\ y_2k_2(x_2k_2) & k_2x_2(k_2y_2) \end{pmatrix}. \tag{5}$$

Degeneration of the rhombus into a line is reflected in a degeneration of the matrix. In this case for two segments $x_1 - y_1$ and $x_2 - y_2$ related by a center of symmetry we have

$$\mathbf{r}_{x_1y_1} = \mathbf{r}_{y_2x_2}, \tag{6}$$

i.e., a noncentrosymmetric vector corresponds to a double peak.

To extract the end of the line (see ref. 10) it is necessary to repeat the extraction from a single vector (the result is M_3) and all of the rows become identical in the corresponding matrix:

$$\begin{pmatrix} x_1k_1 & k_1y_1 & y_2k_2 & k_2x_2 \\ x_1k_1(y_1k_1) & k_1y_1(k_1x_1) & y_2k_2(x_2k_2) & k_2x_2(k_2y_2) \end{pmatrix}, \qquad (7)$$

i.e., in Eqs. (2a) and (2b) the first terms of the equation will be identical.[2)]

The general algorithm for extracting the rhombuses by constructing M functions can be made explicit for Fedorov groups of the monoclinic and rhombic classes in the following way: We separate them into five types from the features of the various fundamental and satellite rhombuses in the corresponding Patterson functions: a) monoclinic acentric (having a single symmetry element); b) monoclinic centrosymmetric; c) the rhombic "horseshoe" class (mm2); d) the rhombic hemisymmomorphic class with three two-fold axes; e) the rhombic "brick" class. In all of these groups the rhombuses are extracted from all of Patterson space (although it is sufficient to use a limited number of cross sections, different in each case). The problem consists of finding the fundamental rhombus and confirming its satellites.

A. EXTRACTION OF THE RHOMBUSES FOR MONOCLINIC ACENTRIC FEDOROV GROUPS

Two segments of the fundamental system (1−2 and 3−4 of Fig. 1a) are related by an arbitrary symmetry element such that $r_{12} \rightarrow r_{34}$. In the corresponding vector system (Fig. 1b), composed of the initial star and pairs of rhombuses, all of the vectors are single. In the initial star it is quite easy to localize the vector r_{34} connected with the initial r_{12} vector by symmetry operations of the given group and the r_{43} vector reciprocal to it. The first step is to construct $M_2(r_{12})$ and then $M_4 = M\{M_2(r_{43})[M_2(r_{12})]\}$.[3)] The points established by it are given by matrices analogous to[4)] Eq. (5):

$$\begin{pmatrix} 1k & k2 \\ 4k(3k) & k3(k4) \end{pmatrix} \qquad (8)$$

which results in only two of the points 13 and 42 (with the condition that points 1 and 4, and 2 and 3 do not coincide in the fundamental system), which give the position of the single symmetry element relative to the initial segment 1−2. Since

$$\begin{gathered} r_{13} + r_{34} = r_{14}, \\ r_{42} + r_{34} = r_{32}, \end{gathered} \qquad (9)$$

it is possible to have two versions of the set of points: 11, 12, 13, 14, and 22, 12, 42, 32; they represent images of two segments in different ends of the initial one (1−2).

B. EXTRACTION OF THE RHOMBUSES FOR GROUPS WITH MONOCLINIC HOLOHEDRY

In the vector system the rhombus from the center of symmetry will be fundamental (it establishes the position of the initial segment in a particular Fedorov group) while the rhombuses from the two-fold axis and the symmetry

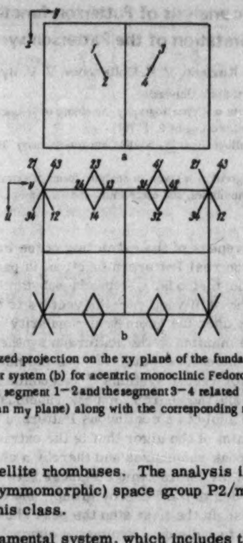

Fig. 1. Generalized projection on the xy plane of the fundamental system (a) and the vector system (b) for acentric monoclinic Fedorov groups. Extractions: initial segment 1−2 and the segment 3−4 related to it by a symmetry element (an m_y plane) along with the corresponding rhombuses.

plane are satellite rhombuses. The analysis is carried out for the (symmomorphic) space group P2/m, which falls within this class.

The fundamental system, which includes the initial segment 1-2 and segments related to it by symmetry elements, are 3−4 (m_y),[5)] 5−6 (2_y), 8−7 ($\bar{1}$) and are shown in Fig. 2a, which corresponds to the vector system (relative to the initial segment 1−2) of Fig. 2b. The twofold degeneracy of the interaction peaks and the bound peaks is determined by the relations

$$\begin{gathered} r_{12} = r_{87}, \quad r_{13} = r_{57}, \\ r_{43} = r_{56}, \quad r_{16} = r_{47}. \end{gathered} \qquad (10)$$

The vectors between the ends of segments which are related by the center of symmetry are nondegenerate. The general recipe for extracting the rhombuses is: minimization with respect to the initial vector r_{12} and then with respect to a vector from the initial star (related to the initial vector r_{12} by a given symmetry operation and taken with opposite sign), which is made explicit for the symmetry elements of the Fedorov group in the following way.

B. 1. To extract the rhombus from a plane we construct $M_4 = M\{M_2(r_{43} = r_{56}), [M_2(r_{12} = r_{87})]\}$. Fixing the points 13 = 57, 16 = 47, 52 = 83, and 42 = 86 we obtain the matrix

$$\begin{pmatrix} 1k & k2 & 8k & k7 \\ 4k(3k) & k3(k4) & 5k(6k) & k6(k5) \end{pmatrix}. \qquad (11)$$

All of the peaks are double.

B. 2. To extract the rhombus from a two-fold axis we need $M_4 = M\{M_2(r_{65} = r_{34})[M_2(r_{12} = r_{87})]\}$. The corresponding matrix (12),

$$\begin{pmatrix} 1k & k2 & 8k & k7 \\ 6k(5k) & k5(k6) & 3k(4k) & k4(k3) \end{pmatrix}, \qquad (12)$$

demonstrates that the extracted points 62 = 84, 32 = 85,

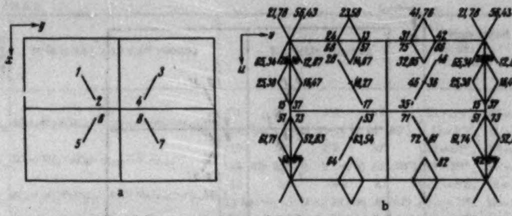

Fig. 2. Projection of the general picture of the fundamental (a) and vector (b) systems on the xy plane for groups with monoclinic holohedry (leading space group P2/m), the rhombic "horseshoe" class (leading space group Pmm2), and the hemisymmomorphic class 222 (leading space group P222). The numbers at the vertices of the rhombuses denote the ends of the corresponding vectors.

15 = 37, and 14 = 67 are also double.

B. 3. To extract the centrosymmetric line we construct $M_3 = M\{M_2(r_{12} = r_{87})[M_2(r_{12} = r_{87})]\}$. We extract the points 12 = 87, 17, 82 [see the matrix (13)]:

$$\begin{pmatrix} 1k & k2 & 8k & k7 \\ 1k(2k) & k2(k1) & 8k(7k) & k7(k8) \end{pmatrix}. \tag{13}$$

Thus the first step in extracting the vertices of the rhombuses (11 points in all including the zeroth, which remains fixed from the identity operation) is to construct M_4^4. In the second step it is necessary to match the fundamental (centrosymmetric) and satellite rhombuses. For this purpose in general M_4^4 accomplishes the extraction from any Harker peak, for example, the bound peaks from the m_y plane ($r_{13} = r_{57}$, $r_{42} = r_{86}$) are most easily localized due to the two fixed coordinates. The conditions for extraction from the vector r_{13} are written (by analogy with (2))

$$r_{13} = r_{1k} - r_{3k} = r_{k3} - r_{k1} = r_{5k} - r_{7k} = r_{k7} - r_{k5}. \tag{14}$$

This equation is satisfied by only two points, 13 = 57 and 17 ($r_{13} = r_{13} - r_{33}$ and $r_{13} = r_{57} - r_{77}$, and $r_{13} = r_{17} - r_{57}$), which are mutually related by a two-fold axis. Matching points 13 with 17 we find one point 17, which gives the origin in the given Fedorov group relative to the initial segment. If the extraction is done using the vector $r_{42} = r_{86}$, then we extract point 82, which also fixes an origin of coordinates (Fig. 2b).

The procedure written above does not change when the rotation axis and mirror plane are replaced by a screw axis and a slip plane.

C. EXTRACTION OF RHOMBUSES IN THE "HORSESHOE" CLASS mm2

In the Fedorov groups of the "horseshoe" class the origin of coordinates determines a two-fold axis, since it fixes two coordinates in a plane perpendicular to the axis (each of the symmetry planes is only fixed in one coordinate). Therefore the fundamental rhombus should be regarded as the one from the two-fold axis, and the rhombuses from the planes are satellites.

As the leading example we choose the (symmorphic) group Pmm2. The initial segment 1−2 is multiplied in the following way: 1 − 2 → 3 − 4(m_y); 1 − 2 → 5 − 6 (m_x); 1 − 2 → 8 − 7 (2_z) in Fig. 2a.[6] All of the interaction peaks are single, the bound peaks from planes are double, and those from binary axes are single, which is reflected in the conditions (15):

$$\begin{gathered} r_{13} = r_{57}, \quad r_{15} = r_{37}, \\ r_{24} = r_{68}, \quad r_{26} = r_{48}. \end{gathered} \tag{15}$$

We seek rhombuses corresponding to each symmetry element.

C. 1. To extract the rhombus from an m_y plane we need $M_4 = M\{M_2(r_{43})[M_2(r_{12})]\}$. The corresponding matrix is

$$\begin{pmatrix} 1k & k2 \\ 4k(3k) & k3(k4) \end{pmatrix}, \tag{16}$$

which fixes points 13 and 42.

C. 2. The analogous operation $M^4 = M\{M_2(r_{65})[M_2(r_{12})]\}$ extracts the vertices (15 and 62) of the rhombus corresponding to the m_x plane. The matrix (16) takes the form

$$\begin{pmatrix} 1k & k2 \\ 6k(5k) & k5(k6) \end{pmatrix}. \tag{17}$$

C. 3. To extract the rhombus from a two-fold (2_z) axis we construct $M_4 = M\{M_2(r_{87})[M_2(r_{12})\}$, in which we retain points 17 and 82 in agreement with the matrix condition (18):

$$\begin{pmatrix} 1k & k2 \\ 8k(7k) & k7(k8) \end{pmatrix}. \tag{18}$$

In this step the matching of the rhombuses of all seven localized points (including the initial one) is applied to the overall pattern of M_4^4, in which the extraction is done from any bound peak from the plane (r_{13}, r_{42}, r_{15}, r_{62}), for example from $r_{13} = r_{57}$ (from m_y).

The condition for extracting from this vector [see (14)] is fully satisfied only for the two points 13 = 57 and 17, which are related by a second plane m_x. In moving point 13 into point 17 there remains only point 17, which goes into the initial point 11 via the 2_z axis, which determines the position of the star in the given Fedorov group.

Similarly, if we take r_{42} or r_{62} in place of r_{13} for the initial vector in M_4^4 then point 82 is extracted, while for r_{15} point 17 is extracted; each of them also determines the position of an initial segment.

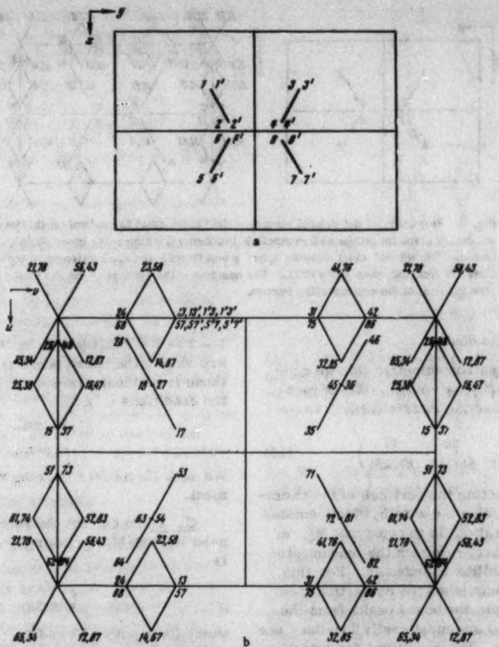

Fig. 3. Projection of the overall pattern of the fundamental (a) and vector (b) systems for the space group Pmmm ("brick" class) on the xy plane. At each point, for example 24, the four ends of the vectors 24, 2'4, 2'4' are projected, three of which are omitted in order not to clutter the picture.

TABLE 1

Symmetry element	M function	Matrix	Fixed points in M_4
2_x	$M_4 = M\{M_2(\mathbf{r}_{43})[M_2(\mathbf{r}_{12})]\}$	$\begin{pmatrix} 1k & k2 \\ 4k\,(3k) & k3\,(k4) \end{pmatrix}$	13 and 42
2_y	$M_4 = M\{M_2(\mathbf{r}_{65})[M_2(\mathbf{r}_{12})]\}$	$\begin{pmatrix} 1k & k2 \\ 6k\,(5k) & k5\,(k6) \end{pmatrix}$	15 and 62
2_z	$M_4 = M\{M_2(\mathbf{r}_{87})[M_2(\mathbf{r}_{12})]\}$	$\begin{pmatrix} 1k & k2 \\ 8k\,(7k) & [illegible]\,(k8) \end{pmatrix}$	17 and 82

The algorithm described does not change if the symmetry elements are modified by translational components.

D. EXTRACTION OF THE RHOMBUSES IN THE HEMISYMMOMORPHIC CLASS 222

It is characteristic of Fedorov groups of this class that all two-fold axes are equivalent and the origin is fixed not by one, but by two symmetry elements. Correspondingly, in the fundamental system the rhombuses are equivalent (there are no fundamental and satellite types) and the origin is fixed by two of three rhombuses.

In Fig. 2a, b we show the fundamental system and the vector system for the leading group P222 (the initial star 1−2 goes into 3−4 via the axis 2_x, into 5-6 via 2_y, and into 8−7 via 2_z). All of the vectors are single.

The extraction of the rhombuses is done in the following way: We initially construct $M_2(\mathbf{r}_{12})$ and then, depending on the directions of the 2_x, 2_y, or 2_z axes, for the second shift vector used to construct the function M_4 it follows to take $\mathbf{r}_{43}$ for the 2_x axis, $\mathbf{r}_{65}$ for the 2_y axis, and $\mathbf{r}_{87}$ for the 2_z axis. The relations of the corresponding M functions, matrices, and extracted points are illustrated in Table 1. We mark all seven points (including the initial one) on the overall pattern of M_4^4. At the step of matching the rhombuses we accomplish an extraction from any Harker peak, for example from $\mathbf{r}_{13}$ (from 2_x). The condition for extraction

$$\mathbf{r}_{13} = \mathbf{r}_{1k} - \mathbf{r}_{3k} = \mathbf{r}_{k3} - \mathbf{r}_{k1} \tag{19}$$

is only satisfied by the point 13. Then comes the extraction (from M_4^4) with respect to the vector connected with $\mathbf{r}_{13}$ by the 2_x axis but reciprocal in direction ($\equiv \mathbf{r}_{31}$). This vector is easily localized and will be related to the vector $\mathbf{r}_{13}$ of the Patterson plane by m_z. The condition for ex-

TABLE 2

symmetry element	M function (and shift vector)	Extraction matrix	Points fixed in the final M_n
m_x	$M_4=M\{M_3(r_{65}=r_{3'4'})[M_3(r_{12}=r_{8'7'})]\}$	$\begin{pmatrix} 1k & k2 & 8'k & k7' \\ 6k\,(5k) & k5\,(k6) & 3'k\,(4'k) & k4'\,(k3') \end{pmatrix}$	$62=8'4'$, $3'2=8'5$ $15=3'7'$, $14'=67'$
m_y	$M_4=M\{M_3(r_{43}=r_{5'6'})[M_3(r_{12}=r_{8'7'})]\}$	$\begin{pmatrix} 1k & k2 & 8'k & k7' \\ 4k\,(3k) & k3\,(k4) & 5'k\,(6'k) & k6'\,(k5') \end{pmatrix}$	$42=8'6'$, $5'2=8'3$, $13=5'7'$, $16'=47'$
m_z	$M_4=M\{M_3(r_{2'1'}=r_{78})[M_3(r_{12}=r_{8'7'})]\}$	$\begin{pmatrix} 1k & k2 & 8'k & k7' \\ 2'k\,(1'k) & k1'\,(k2') & 7k\,(8k) & k8\,(k7) \end{pmatrix}$	$2'2=8'8$, $72=8'1'$, $11'=77'$, $18=2'7'$
2_x	$M_4=M\{M_3(r_{4'3'}=r_{56})[M_3(r_{12}=r_{8'7'})]\}$	$\begin{pmatrix} 1k & k2 & 8'k & k7' \\ 4'k\,(3'k) & k3'\,(k4') & 5k\,(6k) & k6\,(k5) \end{pmatrix}$	$4'2=8'6$, $52=8'3'$ $13'=57'$, $16=4'7'$
2_y	$M_4=M\{M_3(r_{6'5'}=r_{34})[M_3(r_{12}=r_{8'7'})]\}$	$\begin{pmatrix} 1k & k2 & 8'k & k7' \\ 6'k\,(5'k) & k5'\,(k6') & 3k\,(4k) & k4\,(k3) \end{pmatrix}$	$6'2=8'4$, $32=8'5'$, $15'=37'$, $14=6'7'$
2_z	$M_4=M\{M_3(r_{87}=r_{1'2'})[M_3(r_{12}=r_{8'7'})]\}$	$\begin{pmatrix} 1k & k2 & 8'k & k7' \\ 8k\,(7k) & k7\,(k8) & 1'k\,(2'k) & k2'\,(k1') \end{pmatrix}$	$82=8'2'$, $1'2=8'7$, $17=1'7'$, $12'=87'$
$\bar{1}$	$M_8=M\{M_3(r_{12}=r_{8'7'})[M_3(r_{12}=r_{8'7'})]\}$	$\begin{pmatrix} 1k & k2 & 8'k & k7' \\ 1k\,(2k) & k2\,(k1) & 8'k\,(7'k) & k7'\,(k8') \end{pmatrix}$	$12=8'7'$, $17'$, $8'2$

traction

$$r_{57}=r_{5k}-r_{k7}=r_{7k}-r_{k5} \qquad (20)$$

is only satisfied by point 17.

We extract points 13 and 17, which are related by the 2_y axis. Shifting point 13 into point 17, we find only one point and thus these points uniquely determine the origin.

The steps in the algorithm remain the same when the two-fold rotational axis is replaced by a screw axis.

E. EXTRACTION OF THE RHOMBUSES IN THE "BRICK" CLASS mmm

In Fedorov groups of the "brick" class the fundamental rhombus is that of the center of symmetry; the remaining rhombuses from the three planes and three two-fold axes are satellites.

As an example of the extraction of the rhombuses we consider the leading symmomorphic space group Pmmm. The initial segment 1−2 in the fundamental system (Fig. 3a) is multiplied by symmetry elements from this group: 1−2 → 5−6 (m_x), 1−2 → 3−4 (m_y), 1−2 → 1'−2' (m_z), 1−2 → 3'−4' (2_x), 1−2 → 5'−6' (2_y), 1−2 → 8−7 (2_z), and 1−2 → 8'−7' ($\bar{1}$). All of the interaction peaks will be double, bound peaks from the symmetry planes will be four-fold degenerate, those from the two-fold axes will be double, while that from the center of symmetry is single.

The shift vectors for constructing the M function, and the rank and form of the extraction function itself, the form of the matrix, and the points fixed by the resulting M function are given in Table 2.

As previously, all of the extracted points are drawn on one total M_4^8. To check the mutual matching of the rhombuses the extraction is done for any Harker peak (from the plane), for example from $r_{13}=r_{1'3'}=r_{57}=r_{5'7'}$. The extraction condition

$$r_{13}=r_{1k}-r_{3k}=r_{k3}-r_{k1}=r_{1'k}-r_{3'k}=r_{k3'}-r_{k1'}$$
$$=r_{5k}-r_{7k}=r_{k7}-r_{k5}=r_{5'k}-r_{7'k}=r_{k7'}-r_{k5'} \qquad (21)$$

is only satisfied by points 13, 13', 17, and 17' (taking the multiplicity into account); of these points 13 and 13' and 17 and 17' are related pairwise to the m_z symmetry plane. If we shift these points by the vector $r_{33'}$ (since they are well localized on the w axis) then in the extraction function (taking account of the fact that $r_{33'}=r_{77'}$) two points 13' and 17' are preserved, which are mutually related by the m_x plane. We carry out the transposition 13' → 17' and only the one point 17' remains, which fully characterizes the position of the origin.

All of the steps in the procedure remain unchanged in the remaining groups of this class.

CONCLUSIONS

The algorithm which has been devised first of all allows us to check the presence of all peaks in the Patterson function (combined in rhombuses) generated by 2k atoms and to match the fundamental and satellite rhombuses with each other. The final step is the extraction of a single point, which fully determines the origin in the given particular Fedorov group relative to the initial segment. The necessary condition is the presence of all rhombus vertices. If one of the vectors (peaks) is absent, then the final point cannot be extracted precisely. In centered lattices several points are extracted, but they are mutually related by corresponding translations. If only the x-ray group is known, then the analysis is done within the framework of all of the Fedorov groups included within it, and the true group is establishing during the process of the analysis.

Since by extracting the rhombuses we obtain the position of the initial (basis) segment, then in all unit cells we establish the coordinates of 2k atoms. Their positions can be used to extract the whole structure using the minimization of functions of rank M_{2k}.

---

1) Here and in what follows we have in mind crystals with monoclinic or higher symmetry.

2) This is also valid for triclinic crystals with the space group P$\bar{1}$.

3) We use $M_2(r_{13})$ to construct the function $M_3(r_{48})$ but not $M_2(r_{34})$, in order to extract the vertex of a rhombus lying in the Harker cross section.

4) Here and in what follows in place of k_1, k_2, ... we have a running index

k, which can assume any independent value.

[5] The brackets show the symmetry element which relates the given segment to the initial segment; the subscript index refers to the direction of a two-fold axis or the normal to a plane.

[6] In the projection on the xy(uv) plane the general form of the arrangement of the segments and rhombuses does not change for the leading groups of the three classes 2/m, mm2, and 222, but with different third coordinates z(w), of course.

---

[1] M. Buerger, Structure of Crystals and Vector Spaces [Russian translation], IL, Moscow (1961).

[2] V. I. Simonov, Kristallografiya, 10, 155 (1965) [Sov. Phys.—Crystallogr., 10, 116 (1965)].

[3] S. V. Borisov, V. P. Golovachev, V. V. Ilyukhin, É. A. Kuz'min, and N. V. Belov, Zh. Strukt. Khim., 13, No. 1, 175 (1972).

[4] É. A. Kuz'min, V. P. Golovachev, and N. V. Belov, Kristallografiya, 16, 875 (1971) [Sov. Phys.—Crystallogr., 16, 762 (1972)].

[5] É. A. Kuzmin, V. P. Golovachev, and N. V. Belov, Kristallografiya, 17, 477 (1972) [Sov. Phys.—Crystallogr., 17, 419 (1972)].

[6] É. A. Kuz'min, V. P. Golovachev, and N. V. Belov, Dokl. Akad. Nauk SSSR, 192, 86 (1970) [Sov. Phys.—Dokl., 15, 427 (1970)].

[7] É. A. Kuz'min, V. V. Ilyukhin, and N. V. Belov, Zh. Strukt. Khimii, 12, No. 3, 447 (1971).

[8] N. P. Zhidkov, A. I. Kvitashvili, B. M. Shchedrin, and A. E. Shvelashvili, Soobshch. Akad. Nauk GruzSSR, 66, No. 1, 81 (1972).

[9] É. A. Kuz'min, V. V. Ilyukhin, and N. V. Belov, Dokl. Akad. Nauk SSSR, 196, 1080 (1971) [Sov. Phys.—Dokl., 16, 74 (1971)].

[10] É. A. Kuz'min, V. V. Ilyukhin, and N. V. Belov, Zh. Strukt. Khimii, 11, No. 5, 943 (1970).

Isolation of n points of the basic system from a vector system by use of the star of an (n − 1)-dimensional simplex

R. V. Galiulin, M. I. Sirota, A. S. Naumov, and N. V. Belov

Institute of Crystallography, Academy of Sciences of the USSR

(Submitted July 20, 1972)
Kristallografiya, 18, 63-68 (January-February 1973)

The n + 1 point of a basic system can always be considered to be the projection of an n-dimensional simplex on 3-dimensional space. Therefore, the vector system of these n + 1 points is the projection of an n-dimensional simplex on 3-dimensional space. The vector system of an n-dimensional simplex is obtained from the vector system of an (n − 1)-dimensional simplex by the addition of two (n − 1)-dimensional simplexes arranged centrosymmetrically. If a basic system consisting of k points is centrosymmetric, then it can be considered to be a projection of the vertices of a (k/2)-dimensional octahedron in 3-dimensional space, and the vector system is the projection of the vertices and centers of the edges of a (k/2)-dimensional octahedron on 3-dimensional space. Vector systems generated by vectors of multiplicity n can be considered to be the vector systems of two parallel n-dimensional simplexes.

I. It is convenient to consider two arbitrary points of a basic system[1] to be the vertices of a one-dimensional simplex (section). The vector system (star) of this simplex will be a triad of peaks, which form the corresponding point of the vector system along with the origin O and the point centrosymmetric with it (Fig. 1a), and such a triad in the basic system always corresponds to a one-dimensional simplex.

Three arbitrary noncollinear points of the basic system can always be considered to be the vertex of a two-dimensional simplex (triangle). The star of this simplex is a centrosymmetric hexagon (the Wrinch hexagon[1]) (Fig. 1b), from which the two-dimensional simplex is isolated with the accuracy of a centrosymmetric one. However, a triangle of the basic system does not correspond to every similar hexagon star, for such a hexagon is generated by any triad of vectors which are equal in pairs to the nonparallel sides of this hexagon (i.e., even those not having common vertices). It is essential that the star of a two-dimensional simplex be capable of being represented as the star of a one-dimensional simplex plus the two one-dimensional simplexes which generate this star and which are arranged centrosymmetrically relative to point O. Therefore, such a star is easily found in a vector system, and simply shifting an arbitrary section OA of the vector system parallel to itself is sufficient to find a section equal and parallel to section AO, but not lying on the same straight line with it. If the star found is not a random one, then any of the triangles with vertex at point O will become a simplex of the basic system, and for a direction not containing this vertex any edge of the hexagon can be taken as centrosymmetric to it.

We shall consider four arbitrary points of the basic system not lying in one plane to be the vertices of a three-dimensional simplex (tetrahedron). The affine shape of the cubooctahedron of Archimedes (Fig. 1c) becomes the star of this simplex.[2] For the isolation of this cubooctahedron from the vector system, upon shifting the section OA parallel to itself, we find two sections noncentrosymmetric relative to O, but equal and parallel to OA, and such that the vector joining their ends should be a vector of the given vector system. If the choice of this cubooctahedron is not fortuitous, then the tetrahedron made up of a triangular face of the cubooctahedron and point O or the one centrosymmetric to it will be a tetrahedron of the basic system. If four points lying in one plane had been chosen, then the star of such a group of four points would be the projection of the cubooctahedron on the plane.

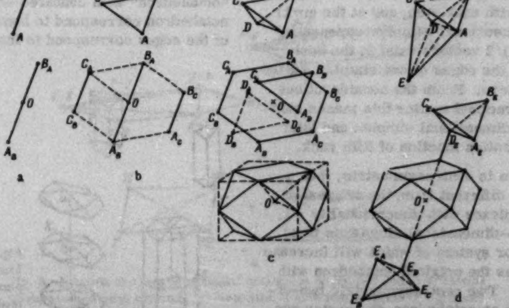

Fig. 1. Simplexes of different dimensions and the vector systems corresponding to them. a) n = 1; b) n = 2; c) n = 3; d) n = 4.

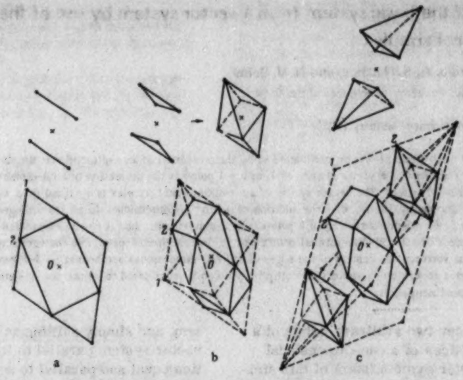

Fig. 2. Octahedra of different dimensionalities and the vector systems corresponding to them. a) n = 2; b) n = 3; c) n = 4.

In an analogous manner, five arbitrary points of the basic system can be considered to be the projection of a four-dimensional simplex ABCDE on three-dimensional space. The star of this simplex consists of the cuboctahedron described above and two tetrahedra $A_EB_EC_ED_E$ and $E_AE_BE_CE_D$ (Fig. 1d). Continuing in this same manner, all points of the vector system can be combined, since every basic system containing n points can conveniently be considered to be the projection of an (n−1)-dimensional simplex on three-dimensional space. A simple theorem holds true relative to the star of an n-dimensional simplex.

Theorem 1. The star of an n-dimensional simplex consists of the star of an (n−1)-dimensional simplex plus two (n−1)-dimensional simplexes arranged centrosymmetrically.

If a vector system is represented by only part of its vectors, then such a ladder naturally is broken at some step, for example, the k-th. But the minimalization function of k+1 rank can be constructed later.[3]

Now let us note that the probability of appearance of a random star decreases with each step, and at the (n−1) step the star of an n-dimensional simplex appears by chance only in case n(n+1)/2 vectors exist in the basic system which do not form the edges of one simplex and the sum of which is equal to zero. From the considerations outlined in Part II, as a practical matter this means stopping at the star of a four-dimensional simplex and later constructing the minimalization function of fifth rank.

II. If the basic system is centrosymmetric, then a centrosymmetric simplex different from the original one exists for each of its simplexes with dimensionality > 1. Two centrosymmetric one-dimensional simplexes form a parallelogram, the vector system of which will increase homothetically to two times the original octahedron with centered edges (Fig. 2a).[4] Two centrosymmetric two-dimensional simplexes form an octahedron, the vector system of which will increase homothetically to two times the original octahedron with centered edges (Fig. 3b). The centers of the edges of the octahedron form a cuboctahedron which does not correspond to the simplex of the basic system, since its vertices will be interaction peaks.[2]

Two centrosymmetric three-dimensional simplexes form a four-dimensional "octahedron." The ends of the interaction vectors of this "octahedron" are joined into a three-dimensional cuboctahedron plus two octahedra, the diagonals of which are equal and parallel to the diagonals of the rectangular faces of the cuboctahedron (Fig. 2c). Thus, the interaction peaks are not arranged according to the star of a four-dimensional simplex. This allows isolation of four pairs of centrosymmetric points of the basic vector system even for the absence of bonding peaks. Generalizing the results obtained for the case of n pairs of centrosymmetric points, which can always be considered to be the projection of an n-dimensional octahedron on three-dimensional space, we proceed to the following theorem.

Theorem 2. The star of two centrosymmetric (n−1)-dimensional simplexes becomes an n-dimensional "octahedron" with centered edges. The vertices of the octahedron correspond to bonding peaks, and the centers of the edges correspond to interaction peaks.

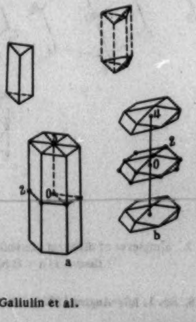

Fig. 3. Three-dimensional (a) and four-dimensional (b) prisms with simplex base and the vector systems corresponding to them.

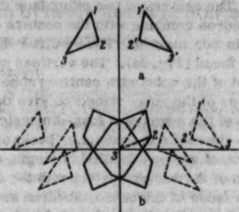

Fig. 4. Mirror-symmetrical triangles (a) and the vector system corresponding to them (b).

In this manner, triads of peaks of the vector system which corresponds to a basic system with n pairs of centrosymmetric points are joined into the projection of an n-dimensional octahedron on three-dimensional space.

III. Two centrosymmetric one-dimensional simplexes will also be parallel. Therefore, the vector system is the same for each of them.[6] But this is not the case for two-dimensional simplexes: Two parallel two-dimensional simplexes form a trigonal prism, the vector system of which becomes a hexagonal prism with centered bases and lateral edges (Fig. 3a). In an analogous manner, two parallel tetrahedra can be considered to be the projection of a four-dimensional prism with a simplex base onto three-dimensional space. The vector system of this prism consists of three cubooctahedra (Fig. 3b).

Let us now note that if n equal vectors exist in the basic system, then in a self-consistent manner the origin of these vectors, and also in a self-consistent manner their ends, form two parallel (n−1)-dimensional simplexes. The following theorem is rather obvious.

Theorem 3. The star of two parallel n-dimensional simplexes consists of the stars of an n-dimensional simplex with peaks of multiplicity 2 and with center at the origin of the vector system and two such stars located centrosymmetrically with respect to the origin of the vector system, the centers of which become peaks of multiplicity (n + 1).

Result 1. Peaks of multiplicity n are the centers of $(n^2-n)/2$ sections, the ends of which form the star of an n-dimensional simplex.

Result 2. Peaks of multiplicity 1 occur among those peaks of the vector system which are not the centers of sections joining any two points of the vector system.

In this manner, triads of peaks corresponding to vectors of multiplicity (n+1) are combined into the projection of an (n+1)-dimensional prism on three-dimensional space. The bases of this prism will be the star of an n-dimensional simplex, in the center of which are found peaks of multiplicity (n+1).

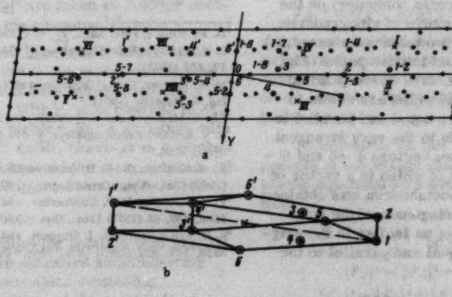

Fig. 5. Isolation of a four-dimensional octahedron on the real Patterson function of the vinogradovite structure. a) Projection of most intense peaks of eight unit cells of the Patterson function of vinogradovite; b) the cubooctahedron isolated by use of the 0−1 vector; c) octahedra found by use of diagonals of the cubooctahedron isolated; d) vertices of the four-dimensional octahedron.

IV. If the basic system has any sort of symmetry transformation different from inversion and the n-dimensional simplex chosen does not have this fixed transformation relative to it, then in the vector system are found two stars which are equivalent to each other in regard to the symmetry transformation given. On the Harker cross section, which corresponds to this symmetry transformation, there exist n + 1 points which have properties such that upon combination of a vertex of the simplex chosen with a definite point all the remaining vertices of the simplex are combined with points of the vector system. However, for isolation of such a pair of simplexes it is sufficient to fix one of them in the star corresponding to it and, shifting the equivalent simplex, to find this point. The vertices of a pair of n-dimensional simplexes so associated correspond to 2(n + 1) points of the basic system. This procedure has been worked out in detail (method of rhombs) by É. A. Kuz'min, V. P. Golovachev, and N. V. Belov[7] for one-dimensional simplexes (sections). A vector system of two mirror-symmetrical two-dimensional simplexes is shown in Fig. 4.

If the basic system has a few symmetry transformations, then combination even of equivalent one-dimensional simplexes gives a rather complex vector system. In this case, the characteristic details of specific isogons should be examined for the simplest of their combinations.[2]

V. The possibility of finding the projections of the vertices and centers of the edges of a four-dimensional octahedron on three-dimensional space was tested by use of programs (for the M-220 electronic computer) on the real Patterson function of the structure of vinogradovite, for which eight atoms of Ti form two tetrahedra arranged centrosymmetrically.[8] The 40 most intense peaks (Fig. 5a) were taken for isolation of the stars corresponding to the tetrahedra, the combinations of which are shown in Fig. 2. Having isolated the vectors equal and parallel to the 0 − 1 vector, which corresponds to the very strongest of the peaks chosen, we find the two vectors 4' − 5 and 6' − 2, the difference between the ends of which is a vector of the vector system. Thus the cubooctahedron was obtained (Fig. 5b). Taking any of the face diagonals of the cubooctahedron (for example, 6' − 5), let us isolate in the original vector system two vectors equal and parallel to the vector 6' − 5. The centers of two other face diagonals of the cubooctahedron combine with the centers of the vectors isolated in this manner. Thus a three-dimensional octahedron is found (Fig. 5c). The vertices of the octahedron found and of the octahedra centrosymmetric with it and the vertices of the cubooctahedron give the projection of the centers of the edges of a four-dimensional octahedron on three-dimensional space, i.e., peaks of multiplicity 2. The ends of vectors doubled in length, which combine the origin of the vector system with the centers of the parallelogram faces of the cubooctahedron and with the centers of the octahedra found, determine the projection of the vertices of the desired four-dimensional octahedron on three-dimensional space (Fig. 5d). The projection of the four-dimensional octahedron, which decreases homothetically by a factor of 2, gives eight points of the basic system. The algorithm described is comparatively difficult to do manually and research on its automatization is being carried out.

The authors thank B. N. Delaunay, V. I. Simonov, M. I. Shtorgin, V. I. Burdina, A. B. Tovbis, R. K. Rastsvetaeva, and A. M. Vaisberg for their help and for discussion of the results.

[1)] The term deals with the deciphering of the crystal structure. If it is created by a (three-dimensional) pattern with point atoms, then we consider this pattern to be the basic system. The corresponding pattern with interatomic distances – the Patterson function – we call the vector system.

[2)] According to S. V. Borisov,[5] the bonding peaks combine the points of one regular system, and the interaction peaks combine the points of different regular systems.

[1] D. M. Wrinch, Phil. Mag., 27, 98 (1936)

[2] R. V. Galiulin, Kristallografiya, 17, 701 (1972) [Sov. Phys. – Crystallogr., 17, 619 (1973)].

[3] M. A. Buerger, Crystal Structure and Vector Space [Russian translation], Izd. IL, Moscow (1961).

[4] Kh. S. Mamedov and N. V. Belov, Dokl. Akad. Nauk SSSR, 106, 462 (1956).

[5] S. V. Borisov, Kristallografiya, 9, 603 (1964) [Sov. Phys. – Crystallogr., 9, 515 (1965)].

[6] É. A. Kuz'min, V. V. Ilyukhin, and N. V. Belov, Kristallografiya, 14, 1059 (1969) [Sov. Phys. – Crystallogr., 14, 916 (1970)].

[7] É. A. Kuz'min, V. P. Golovachev, and N. V. Belov, Dokl. Akad. Nauk SSSR, 192, 86 (1970) [Sov. Phys. – Dokl., 15, 427 (1970)].

[8] R. K. Rastsvetaeva, V. I. Simonov, and N. V. Belov, Dokl. Akad. Nauk SSSR, 177, 832 (1967) [Sov. Phys. – Dokl., 12, 1090 (1968)].

Localization of heavy atoms in noncentrosymmetric crystals by single-wave anomalous x-ray scattering

L. L. Shadyro

Institute of Crystallography, Academy of Sciences of the USSR

(Submitted March 14, 1970; resubmitted December 27, 1970; June 7, 1972)
Kristallografiya, 18, 69-74 (January-February 1970)

The direct use of an anomalous scattering effect for isolating heavy-atom moduli F_H from total crystal scattering amplitudes was considered. In the proposed version, which represents a statistical solution to the problem, it was possible to avoid many substantial deficiencies inherent in the use of differential series. The new method of heavy-ion localization is compared with other series methods.

INTRODUCTION

In the function known from ref. 1, information on heavy atoms

$$P_s(\mathbf{u}) = \sum_{\mathbf{H}} |F_{\mathbf{H}}|^2 \sin 2\pi \cdot \mathbf{H} \cdot \mathbf{u} \tag{1}$$

in a noncentrosymmetric crystal is given in the form of two superimposed systems of positive and negative peaks, corresponding to the vectors between anomalous and normal scatterers. Such a situation is often difficult to interpret. A second deficiency in using a function like Eq. (1) is the total lack of information on the vectors between the anomalous scatterers themselves. These are very essential in determining heavy-atom positions. The procedures for utilizing (in a first approximation) the above information, using differential series in which terms of the type $|\Delta|F|_{H-\bar{H}}|^2$ or $|\Delta|F^2|_{H-\bar{H}}|^2$ are taken as Fourier coefficients, are known only for the albumins.[2,3]

This work proposes a new approach to heavy-atom localization based on single-wave anomalous scattering. More completely than before it uses information generally in the hands of researchers. With it, it is possible to obtain a general solution for a problem (for a structure with an arbitrary, not necessarily small, heavy-atom contribution to total scattering), and to avoid the many substantial deficiencies of differential anomalous series.

PROBLEM ASSIGNMENT

We first introduce the following notation (see Fig. 1):

F_H, $F_{\bar{H}}$ are the complete structure amplitudes for inverse reflections during anomalous scattering;

F_A is the effective component of the amplitude of anomalously scattering heavy atoms A;

F_A'' is an imaginary component of the amplitude of the atoms A;

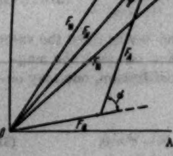

Fig. 1. Vector diagram for a noncentrosymmetric crystal during anomalous scattering of A atoms, leading to the development of a Bayfoot differential.

$k'' = \Delta f_A''/(f_A + \Delta f_A')$ is a corresponding anomalous correction;

F_Q is the structure amplitude of normal scatterers;

F_N is the complete structure amplitude for normal scattering;

Ψ is the phase angle between vectors of anomalous (F_A) and nonanomalous (F_Q) atoms;

θ is the angle between the imaginary component of anomalous scattering (F_A'') and the vector of normal scattering (F_N);

γ is the phase angle between vectors of anomalous atoms (F_A) and all atoms (F_N);

$A = \Delta I_{\bar{H}-H}/I_m = \Delta|F|^2_{\bar{H}-H}/|F_m|^2$ is the relative anomalous differential for reflections of a Bayfoot pair, $|F_m|^2 = {}^1/_2(F^2_H + F^2_{\bar{H}})$;

$D = |F_Q|/|F_A|$ is the ratio of the moduli of the amplitudes of normal and anomalous scatterers,

$\Sigma_A = m(f_A + \Delta f_A')^2$, $\Sigma_Q = \sum_{j=1}^{N-1} n_j f^2_{Qj}$, where $(f_A + \Delta f_A')$ and f_Q are the atomic scattering factors for anomalous and normal scatterers, m is the number of anomalous atoms, n_j is the number of normal scatterers of the species j, and N is the overall number of species of atoms in the structure.

Examination of the relationship between the components of the vector diagram (Fig. 1) leads to the following equations as starting points for further consideration:

$$|F_A''| = k''|F_A|, \tag{2}$$

$$|F_N|^2 = |F_A|^2 + |F_Q|^2 + 2|F_A||F_Q|\cos\Psi, \tag{3}$$

$$|F_H|^2 = |F_N|^2 + |F_A''|^2 - 2|F_N||F_A''|\cos(\pi-\theta), \tag{4}$$

$$|F_{\bar{H}}|^2 = |F_N|^2 + |F_A''|^2 + 2|F_N||F_A''|\cos(\pi-\theta), \tag{5}$$

$$\cos(\pi-\theta) = \{1 - [(|F_N|^2 + |F_A|^2 - |F_Q|^2)/2|F_N||F_A|]^2\}^{1/2}, \tag{6}$$

$$|F_N|\sin\gamma = |F_Q|\sin\Psi, \tag{7}$$

$$\cos\theta = \sin\gamma. \tag{8}$$

From (2), (3), (4), (5), and (6), with introduction of the parameter $D = |F_Q|/|F_A|$, it follows that

$$|F_A| = |F_N|/(1 + D^2 + 2D\cos\Psi)^{1/2}, \tag{9}$$

$$|F_A| = |F_H|/[k''^2 + 1 + D^2 + 2D(\cos\Psi - k''\sin\Psi)]^{1/2}, \tag{10}$$

$$|F_A| = |F_{\bar{H}}|/[k''^2 + 1 + D^2 + 2D(\cos\Psi - k''\sin\Psi)]^{1/2}, \tag{11}$$

$$|F_A| = |F_m|/(k''^2 + 1 + 2D\cos\Psi)^{1/2}, \tag{12}$$

$$|F_A| = |\Delta|F^2_{H-\bar{H}}/(4k''D\sin\Psi)^{1/2}. \tag{13}$$

The starting point for localization of the anomalous scatterers in the structure can be the set of moduli $|F_A|$, whose determination by (9)–(13) only involves the problem of finding values of the variables D and Ψ. The other values in (9)–(13) are considered to be known: in the numerator, k" from tabular values, *f* from curves and corrections of Δf' and Δf".

STATISTICAL DETERMINATION OF HEAVY-ATOM MODULI

We now show that Eqs. (10)–(13) contain sufficient information to determine the boundary conditions confining the values of $|F_A|$. The variables D and Ψ are related in another manner, as follows:

$$A = 4k''D\sin\Psi / (D^2 + 2D\cos\Psi + k''^2 + 1), \tag{14}$$

where

$$D_{1,2} = -\cos\Psi + \frac{2k''}{A}\sin\Psi \pm \left(\cos^2\Psi + \frac{4k''^2}{A^2}\sin^2\Psi - \frac{4k''}{A}\sin\Psi\cos\Psi - k''^2 - 1\right)^{1/2}. \tag{15}$$

The requirement for involvement of D leads to fulfillment of the condition

$$\cos^2\Psi + \frac{4k''^2}{A^2}\sin^2\Psi - \frac{4k''}{A}\sin\Psi\cos\Psi - k''^2 - 1 \geqslant 0. \tag{16}$$

Solving the inequality (16) with respect to Ψ, we get the interval of permissible Ψ values for a given A. Using the equation $\cos^2\Psi = (1 + \mathrm{tg}^2\Psi)^{-1}$, we obtain

$$1 + \frac{4k''^2}{A^2}\mathrm{tg}^2\Psi - \frac{4k''}{A}\mathrm{tg}\,\Psi - (k''^2 - 1)(1 + \mathrm{tg}^2\Psi) \geqslant 0, \tag{17}$$

$$\mathrm{tg}\,\Psi_{1,2} = k''A\{2 \pm [4 + 4k''^2 - (k''^2 - 1)A^2]^{1/2} / [4k''^2 - (k''^2 + 1)A^2]\}. \tag{18}$$

Consequently, from (15) and (18) we have for a given A,

$$(D_1)_A \leqslant (D)_A \leqslant (D_2)_A, \tag{19}$$

$$(\Psi_1)_A \leqslant (\Psi)_A \leqslant (\Psi_2)_A. \tag{20}$$

We are now interested in the span of D and Ψ values at a fixed A. First of all, we note that at $|A| = |A_{max}| = 2$, we have uniquely possible values of Ψ and D, whose values are determined only by the known parameter k", such that

$$\mathrm{tg}(\Psi)_{A_{max}} = 2k''|A|/[4k'' - (k''^2 + 1)A^2] = -k'', \tag{21}$$

$$(D)_{A_{max}} = -\cos\Psi + 2k''\sin\Psi/A = (1 + k''^2)^{1/2}. \tag{22}$$

Since $k'' \ll 1$, it is apparent from (21) and (22) that $(\Psi)A_{max} \to 180°$; usually $165° < (\Psi)A_{max} < 180°$, and $(D)A_{max} \simeq 1$.

It is easy to see that on decrease of |A| from $A = A_{max}$ to $A_{min} = 0$, the interval of $(\Psi)_A$ and $(D)_A$ values will gradually expand. The limiting span of the interval, at A = 0, corresponds to the maximum indeterminateness of solution for Eq. (14) with respect to variables D and Ψ.

For A values near A_{max}, the adequately narrow intervals with respect to Ψ and D allow a good approximation of the true values of $|F_A|$, if during computation values of D and Ψ are chosen in the middle of the ranges (19) and (20). However, the use of this procedure for computation of $|F_A|$ at small values of A is not possible in such a way. It is still necessary to carry out a preliminary evaluation of the D and Ψ values in the ranges (19) and (20), in a function of known Σ_A, Σ_Q. It is enough to trace the determination of the evaluated $(D)_A$ value since $(D)_A$ for the same A and k" sets the value of $(\Psi)_A$ by (14) in a well defined manner.

As additional illustration, we introduce a new characteristic D_T, which we define in the following way: $D_T = |F_A|/(|F_A| + |F_Q|)$. We now replace the parameter D by D_T.

The relationship between the latter is

$$D = (1 - D_T) / D_T, \tag{23}$$

$$D_T = 1 / (1 + D), \tag{24}$$

such that at A_{max} the value of D_T is ≃ 0.5, and at A_{min},

$$0 \leqslant D_T \leqslant 1. \tag{25}$$

We set the interval of (20) in the corresponding range of values of $(D_T)_A$:

$$(D_{T_1})_A \leqslant (D_T)_A \leqslant (D_{T_2})_A. \tag{26}$$

The width of the interval is

$$(\Delta D_T)_A = (D_{T_2})_A - (D_{T_1})_A. \tag{27}$$

Each value of $(D_T)_A$ in the interval (26) may be represented in the following form:

$$(D_T)_A = (D_{T_1})_A + W(\Delta D_T)_A, \tag{28}$$

where W is a weighting function, which assumes values W = 0.1 at boundaries of the interval (26), and 0 < W < 1 within that interval. In computing (25), it is natural to take the mathematically expected $\bar{D}_T$ as the weighting function in seeking out the desired weighted value of $(D_T)_A$ for the set of reflections from A to 0 (a majority of the reflections). It may be shown that for noncentrosymmetric crystal, in first approximation1) we have

$$\bar{D}_T \simeq \frac{1}{m}\left(\frac{\Sigma_A}{\Sigma_A + \Sigma_Q}\right)^{1/2} + \frac{m-1}{m}\frac{\Sigma_A}{\Sigma_A + \Sigma_Q}. \tag{29}$$

Consequently, in the same approximation,

$$(D_T)_A \simeq (D_{T_1})_A + \left[\frac{1}{m}\left(\frac{\Sigma_A}{\Sigma_A + \Sigma_Q}\right)^{1/2} + \frac{m-1}{m}\frac{\Sigma_A}{\Sigma_A + \Sigma_Q}\right](\Delta D_T)_A. \tag{30}$$

Having A from experiment and having fixed the value of $(D)_A$ by (30) and then (23), we now can seek the magnitudes of $(\Psi)_{A,D}$. With slight modification, one may obtain from (14) the equation

$$(a^2 - c^2)\mathrm{tg}^2\Psi - 2ab\,\mathrm{tg}\,\Psi + b^2 - c^2 = 0, \tag{31}$$

where $a = 4k''D$, $b = 2AD$, $c = A(1 + k''^2 + D^2)$. From (31), we obtain

$$\mathrm{tg}\,(\Psi_{1,2})_{A,D} = [ab \pm c(a^2 + b^2 - c^2)^{1/2}]\,/\,(a^2 - c^2). \qquad (32)$$

Evidently, $\tan(\Psi)_{A_{max}} = ab/(a^2 - c^2) = -k''$ in accordance with (21). The resulting solution for the general case has two values. However, it is easy to show that one of the solutions – the one with the minus before the radical sign in the numerator of (32) – can be rejected as improbable, giving $(\Psi_2)_{A,D}$ values always in the range

$$(\Psi)_{A_{max}} < (\Psi_2)_{A,D} < (\Psi_2)_A. \qquad (33)$$

The even greater probability (at $A \to 0$, $\Sigma_A \to 0$) of the values falling in the above range of Ψ angles by equalling $\arctan k''/\pi$ is very small, since usually $0.02 < k'' < 0.2$. Thus the most probable value of Ψ is determined from the equation

$$(\Psi)_{A,D} = \mathrm{arctg}\{[ab + c(a^2 + b^2 - c^2)^{1/2}]\,/\,(a^2 - c^2)\}. \qquad (34)$$

DISCUSSION OF RESULTS

The set of $|F_A|^2$ obtained by the method considered above may be used for direct localization of heavy atoms by way of construction and analysis of the corresponding Patterson functions. The extent of information from the above construction is actually more than that obtained on the basis of each of the set of $|F_N|^2$, $|F_m|^2$, $|\Delta|F|_{H-\bar{H}}|^2$, and $|\Delta|F^2|_{H-\bar{H}}|^2$. It is easy to see this by comparing this with the commonly known techniques using differential anomalous series. First of all, we should remember that the use of differentials, for example, of the type $|\Delta|F|_{H-\bar{H}}|$, also fulfills the goal of approximation, but use of $|F_A|$ values and of the directly associated (2) components $|2F_A''|$ does not. This means that in the equations for $|2F_A''|$, which can be easily obtained from (4), (5), and (8):

$$|2F_A''| = (F_H^2 - F_{\bar{H}}^2)/2F_N \sin\gamma, \qquad (35)$$

we should, for all Bayfoot pair reflections, assume $\sin\gamma = 1$ [in the approximation $F_N = (F_H + F_{\bar{H}})/2$].

In actuality, the $\sin\gamma$ values change very sharply from reflection to reflection, during which, as a rule, $\sin\gamma \simeq 0$–0.5 for the majority of the reflections.[2] It is easy to show that the problem of determining the $\sin\gamma$ values is identical to the previously solved problem of finding the values of $(D)_A$ and $(\Psi)_A$. From (35), considering (2), (7), (9), and (13), it follows that

$$\sin\gamma = D\sin\Psi\,/\,(1 + D^2 + 2D\cos\Psi)^{1/2}. \qquad (36)$$

Thus, the first and chief advantage of the new method of localizing heavy atoms is its differentiated approach, leading to determination of the most probable $\sin\gamma$ value for each actual reflection.

The use, as a basis for determination of $|F_A|$, of the relative anomalous difference in A also assures a second important advantage. This is the insignificant effect of several side factors which usually accompany the experiment on the accuracy of the above determination (absorption, extinction).[3] If the scattering volume of the crystal has a center of inversion, there is practically no necessity of considering absorption.

Finally, with a differential anomalous series, the possibility is excluded of using information on heavy-atom position corresponding to reflections with zero anomalous differential, when $|\Delta|F^2|_{H-\bar{H}} = 0$. In some space groups, especially those with centrosymmetric projections, the harm from this can be very pronounced. With the proposed method, according to Eq. (12), the possibility is in principle not excluded of using such reflections as a source of additional information. For this it is necessary to use the previously considered technique of fixing D, and to consider that with high probability,

$$\mathrm{sgn}(\cos\Psi) = \mathrm{sgn}(|F_N|\,/\,\overline{|F_N|}_{\Delta s} - 1). \qquad (s = \sin\theta/\lambda),$$

and not the reverse (at $|F_N| = |F_N|_{\Delta s}$, the average of the two possible values of $\cos\Psi = \pm 1$ is taken). The approximation for $|F_A|$ in this case will be rather rough, but not all information will be lost.

The present work provides the capability of simplifying solution of a phase problem for a wide class of compounds containing heavy atoms, occupying an intermediate position in complexity between albumins and low-molecular structures.

The author thanks N. S. Andreev, N. V. Belov, and D. M. Kheiker for preliminary discussion of the work and valuable comments.

---

[1] This follows from analysis of the D_T distributions, which will be given in a separate article for all cases of practical importance. The approximation (29) is computed for the region of optimal occurrence of the anomalous scattering effect, where $(\Sigma_A/\Sigma_Q) \to 1$.

[2] With the exception of albumins, where $\Sigma_A \to 0$.

[3] It is proposed in ref. 4 to use ratios of a somewhat different type, $|F_H|^2 \cdot |F_{\bar{H}}|^{-2}$, in order to avoid the side-factor effect when determining phase angles in the given experiment for two or more wavelengths, in the region of anomalous scattering.

---

[1] Y. Okaya and R. Pepinsky, Computing Methods and Phase Problems in X-Ray Crystal Analysis, Pergamon Press, Oxford (1961), p. 226.

[2] M. G. Rossman, Acta Crystallogr., 14, 383 (1961).

[3] S. Raman and W. N. Lipscomb, Z. Kristallogr., 116, 314 (1961).

[4] L. Unangst, E. Müller, J. Müller, and B. Keinert, Acta Crystallogr., 23, 898 (1967).

Refining the structure of crystals allowing for the anisotropy of the thermal vibrations of the atoms

L. A. Muradyan and V. I. Simonov

Institute of Crystallography, Academy of Sciences of the USSR

(Submitted April 5, 1972)
Kristallografiya, 18, 75-80 (January-February 1973)

The procedure for refining the structures of crystal by the method of least squares, allowing for the anisotropy of the thermal vibrations of the atoms, is considered, together with methods of representing the probability characteristics of these vibrations. The corresponding algorithms and programs realizing them in a computer of the M-220 (BÉSM-4) type are developed. The programs are written in the languages corresponding to these computers. A refinement of the structure of baddite allowing for the anisotropy of the thermal vibrations of the atoms is presented.

The accuracy of contemporary diffraction techniques is such that not only the coordinates of the basis atoms in the structure under consideration, but also the thermal motion of the atoms in the crystal lattice may be calculated in the anisotropic approximation.[1] General information pertaining to the use of the method of least squares in structural analysis may be obtained by consulting the appropriate sections of the computing handbook.[2] In this paper we shall set out a computing algorithm and also give a brief description of the potentialities of least-squares programs which have been developed for refining the coordinate and anisotropic-thermal parameters of the atoms in a crystal structure on the basis of diffraction data. The programs are written in the languages of the M-220 (BÉSM-4) computers and incorporated in the programming complex known as "Kristall".[3]

The parameters of the atomic structure of a crystal are refined on the least-squares principle by minimizing a function of the form

$$\Phi=\sum_{\mathbf{H}} w_{\mathbf{H}}(K|F_{\mathbf{H}}^{e}|-|F_{\mathbf{H}}^{c}|)^2, \tag{1}$$

where w_H is the weighting factor of the modulus of the experimental structure amplitude $|F_H^e|$ and K is a reduction factor for referring the set of $|F_H^e|$ to the absolute scale. In order to calculate the structure amplitudes we use the general equation

$$F_{\mathbf{H}}^{c}=\sum_{i=1}^{N} f_i^T(\mathbf{H})\exp(2\pi i\mathbf{H}\mathbf{r}_i), \tag{2}$$

in which the summation extends over all N atoms in the unit cell; $f_i^T(\mathbf{H}) = f_i(\mathbf{H})T_i(\mathbf{H})$ is determined by the isotropic atomic factor $f_i(\mathbf{H})$ of the atom in a state of rest and by the factor $T_i(\mathbf{H})$ allowing for the thermal motion.[4] The latter constitutes the Fourier transform of the probability density of the displacement of an atom from the equilibrium position during its thermal motion; in the system defined by the direct and reciprocal crystallographic axes it takes the form

$$T(\mathbf{H})=\exp\left\{-2\pi^2\sum_{i=1}^{3}\sum_{j=1}^{3}U^{ij}h_ih_j\right\}. \tag{3}$$

In this expression h_i are the covariant components of the vector H, i.e., the coordinates of the point in reciprocal space, while U^{ij} are the contravariant components of the symmetrical tensor U characterizing the vibrations of the atom in an anisotropic harmonic potential field.

The quantities U^{ii} are related to the mean-square displacements of the atoms along directions parallel to the reciprocal-lattice axes by the equation $u_i^2 = U^{ii}/(a_i^*)^2$. In general the components U^{ij} are used to calculate the orientations of the principal axes of the ellipsoids characterizing the thermal vibrations and the mean-square displacements of the atoms along these axes. In matrix form Eq. (3) may be expressed as

$$T(\mathbf{H})=\exp\{-2\pi^2\mathbf{H}\mathbf{U}\mathbf{H}^T\}, \tag{4}$$

where H and H^T are respectively the row and column of indices (h, k, l).

The anisotropy of the thermal vibrations prevents us from transforming in the usual way in Eq. (2) from a summation over all the atoms in the unit cell to a summation over the basis atoms of the structure. For the symmetry operation s, characterized by the rotation matrix A_s and the translational component t_s, the transformations of the coordinates and the contravariant tensor components of the basis atom i take the form $r_{is} = A_s r_i + t_s$ and $U_{is} = A_s U_i A_s^T$.

The summation over atoms related by the symmetry of a Fedorov group of multiplicity p may, on allowing for (4), be written

$$f_i(H)\sum_{s=1}^{p}\exp\{-2\pi^2(\mathbf{H}\mathbf{A}_s\mathbf{U}_i\mathbf{A}_s^T\mathbf{H}^T)\}\exp\{2\pi i\mathbf{H}(\mathbf{A}_s\mathbf{r}_i+\mathbf{t}_s)\}.$$

Of all crystallographic symmetry elements, only a center of inversion and translations centering a nonprimitive Bravais lattice leave the ellipsoids of the thermal vibrations of the symmetry-related atoms in the parallel position. If the crystal contains these symmetry elements, the terms in the above sum unite into groups, each of which consists of q identical terms. For acentric and centrosymmetric Fedorov groups q is equal to the number of lattice points associated with the unit cell, multiplied by 1 or 2, respectively.

Allowing for the foregoing considerations, the expression for the structure amplitude may be rewritten as

$$F_{\mathbf{H}}^{c}=\sum_{i=1}^{n}q_if_i(H)\sum_{s=1}^{p'}\exp\{-2\pi^2(\mathbf{H}\mathbf{A}_s\mathbf{U}_i\mathbf{A}_s^T\mathbf{H}^T)\}$$
$$\times\ \exp\{2\pi i\mathbf{H}(\mathbf{A}_s\mathbf{r}_i+\mathbf{t}_s)\}, \tag{5}$$

Vol. 18
July 1973–
June 1974

where n is the number of basis atoms in the structure and p' is the number of symmetry operations of the Fedorov group, without counting inversion centers and translations centering Bravais lattices.

The quantity q_i is given an index because, in the present case, it constitutes the product of q by the ratio of the multiplicity of the i-th position to the multiplicity of the general position in the particular symmetry group, and (in the case of defective structures) by the atomic occupation factor of the i-th position. In other words, the product $q_i p'$ equals the number of atoms in the unit cell of the crystal which are related by symmetry to the i-th basis atom.

Using the multiplication property of the transposed matrices $A_g^T H^T = [HA_g]^T$ and replacing the product HA_g by the row of equivalent indices $H_g = (h_g, k_g, l_g)$ and the scalar product $H \cdot t_g$ by τ_g, we may obtain a form of structure amplitude more economical from the point of view of calculations:[5]

$$F_H^c = \sum_{i=1}^{n} q_i f_i(H) \sum_{s=1}^{p'} \exp\{-2\pi^2 (H_s U_i H_s^T)\} \exp\{2\pi i (H_s r_i + \tau_s)\}. \quad (6)$$

In calculating each value of F_H^c from (6), independently of the number of basis atoms, rows of equivalent indices H_g should be obtained only once. The computing equation for the real part of the structure amplitude (built into the program) takes the form

$$A_H = \sum_{i=1}^{n} q_i f_i(H) \sum_{s=1}^{p'} \cos[2\pi(h_s x_i + k_s y_i + l_s z_i + \tau_s)] \exp\{-[B_i(11) h_s^2 + B_i(22) k_s^2 + B_i(33) l_s^2 + B_i(12) h_s k_s + B_i(23) k_s l_s + B_i(13) h_s l_s]\}. \quad (7)$$

Here we have retained all the nomenclatures and summation indices of Eq. (6), except for the thermal parameters, for which we have introduced the new variables B(ii) = $2\pi^2 U^{ii}$ and B(ij) = $4\pi^2 U^{ij}$. The imaginary part of the structure amplitude is calculated from an analogous equation, in which the cosine is replaced by a sine.

The programs so developed enable us to refine the coordinates of the basis atoms of the structure, the coefficients representing the extent to which various atoms occupy their positions in the lattice (atomic occupation factors) q_i, the individual isotropic and anisotropic parameters of the thermal vibrations of the atoms, and also the coefficients (both general and specific to particular layer lines) required for reducing the $|F_H^e|$ to the absolute scale. The absolute scale reduction coefficients of the layer lines are calculated once at the beginning of each stage if a corresponding indication is provided in the initial information. The general reduction coefficient is calculated every time (together with the average isotropic temperature factor) immediately after obtaining the corrections to any of the structural parameters undergoing refinement. By minimizing the function

$$\Phi = \sum_H w_H [K|F_H^e| - G|F_H^c| \exp\{-B_0 (\sin\theta/\lambda)^2\}]^2$$

we determine the parameters G and B_0, which are then immediately allowed for by using K/G instead of K and by including B_0 in the isotropic or anisotropic parameters of the thermal vibrations of the atoms.

The small operation memory of the computer employed necessitates limiting the number of parameters to be refined at the same time. In the program in question this number is no greater than 86 (the reduction factors are not included in this). Other limitations include: no more than 100 basis atoms in the structure, no more than 19 types of atom, no more than 4080 independent structure amplitudes. By analogy with the least-squares programs,[3] for the majority of Fedorov groups there is a distinct possibility of refining the dependent parameters of the atoms occupying particular positions in the structure. This possibility is realized by modifying the matrix of normal equations, using the Marquardt method.[6,3] For structures in which the number of parameters to be refined exceeds 86, provision is made for refining all the parameters in stages, in individual groups. The program incorporates one of the most economic algorithms, the so-called cascade block-diagonal algorithm, which realizes the Gauss–Seidel principle (see article by J. W. Shilling in ref. 2).

The results of the foregoing operations comprise the absolute-scale reduction coefficients of $|F|_e$ (general or specific to particular layer lines), the refined coordinates of the atoms, the atomic population factors for various lattice positions, and the characteristics of the anisotropic or isotropic thermal vibrations of the atoms, B(ij) or B(i). All these data may be preserved on magnetic tape in the computer and printed out by the machine in the form of tables convenient for further use. Provision is made for calculating the standard deviations of all the refined parameters of the structure.

An independent aspect of the work lies in providing various probability characteristics of the thermal vibrations of the atoms, calculated from the values of B(ij) and B(i). The mean-square displacement (dispersion) of an atom in the course of its thermal motion in the direction of an arbitrary vector I of unit length is calculated from the relation

$$\overline{u_l^2} = \sum_{i=1}^{3} \sum_{j=1}^{3} U^{ij} l_i l_j,$$

where l_i are the covariant components of the vector I and U^{ij} are the contravariant components of the tensor U [see Eq. (3)]. As a linear characteristic of the displacement of the atoms from the equilibrium position, the mean-square displacement $\sigma = (u^2)^{1/2}$ is calculated by means of the programs here developed. In order to secure a clear description of the anisotropic thermal vibrations of the atoms, the principal axes of the ellipsoid of thermal vibrations and their orientations relative to the crystallographic axes are calculated from the U^{ij}. If the reference is made to the principal axes, the probability density p(x, y, z) of the displacement of an atom from its equilibrium position (the "smearing" function), written in a system of coordinates related to the principal axes, takes the form

$$p(x, y, z) = (2\pi)^{-3/2} (\overline{u_1^2}\,\overline{u_2^2}\,\overline{u_3^2})^{-1/2} \times \exp\{-(x^2/\overline{u_1^2} + y^2/\overline{u_2^2} + z^2/\overline{u_3^2})/2\},$$

where $\overline{u_i^2}$ is the dispersion of the displacement of the atom along the i-th principal axis of the ellipsoid of thermal vibrations. The condition p(x, y, z) = const is realized on the surfaces

$$x^2/\overline{u_1^2} + y^2/\overline{u_2^2} + z^2/\overline{u_3^2} = \text{const}. \quad (8)$$

Equation (8) is the canonical form of a family of ellipsoids with semiaxes proportional to $\sigma_i = (\overline{u_i^2})^{1/2}$. By the ellipsoid of thermal vibrations we mean the surface corresponding to a constant probability density of the displacements of the center of the atom from its equilibrium position resulting from thermal vibration. In reciprocal space this corresponds to the ellipsoid of constant temperature factor T(H) = const.

An analysis and a comparison of various types of surfaces which might be used to describe the anisotropy of the thermal vibrations of the atoms were presented in ref. 7. For example, surfaces with a radius vector equal to the dispersion or mean-square displacement are respectively surfaces of the sixth and fourth order. Either of these exhaustively characterizes the thermal vibrations of the atoms, but neither is an ellipsoid.

In the program realized on the M-220 computer, the problem of finding the orientation of the principal axes of the ellipsoid of thermal vibrations and the dispersions along these axes is solved by tensor calculus.[8] A knowledge of the probability density of the displacement of an atom from its equilibrium position in the course of thermal motion enables us to calculate the volume within which the center of the atom lies to a specified probability. The probability characteristics of the thermal motion of the atoms are printed by the computer in the form of a table which calculates the following data for each atom: the principal axes of the ellipsoids within which the atom may be expected to lie with a probability of 0.5 and 0.9, respectively, the dispersion and mean-square displacement of the atom along the principal axes of the ellipsoid of thermal vibrations, the cosines of the angles (and the angles themselves) between the principal axes of the ellipsoid and the axes of the crystallographical coordinate system, and the dispersion along the crystallographic axes and along the direction leading from the atom under consideration to any specified atom in the structure. The programs are verified by reference to known structures. A new problem recently arising was that of calculating the structure of baotite allowing for the anisotropy of the thermal vibrations of the atoms. On refining baotite $Ba_4Ti_4(Ti_{0.48}Nb_{0.36}Fe_{0.16})_4[Si_4O_{12}]O_{16}Cl$; a = 19.99, c = 5.908 Å; space group $I4_1/a$; Z = 4 using an approximation based on the isotropic thermal vibrations of the atoms, the question as to the disposition of the isomorphic substituent Fe atoms remained undecided.[9] In the present investigation, we made due allowance for the anisotropy of the thermal vibrations of the atoms, and analyzed two hypothetical versions of the positions of the Fe atoms in baotite: 1) the version assumed in ref. 9, Ti_1, $(Ti_{0.48}Nb_{0.36}Fe_{0.16})_2$ and 2) $(Ti_{0.84}Fe_{0.16})_1$, $(Ti_{0.64}Nb_{0.36})_2$. As might be expected, the results obtained from these two versions were very similar. The final R factors of 3.41 and 3.31 indicate a slight preference for the second version. The weakness of this argument is emphasized by a crystal-chemical analysis of the structure.[9] The results of a refinement of the coordinates and the parameters of the anisotropic thermal vibrations of the atoms are presented in Table 1. An analysis of the ellipsoids of the anisotropic thermal vibrations of the basis atoms of baotite may conveniently be carried out on the basis of Table 2. A considerable anisotropy of the thermal vibrations (extending along the c axis of the ellipsoid of rotation) is found in the case of the Cl atom. In the equatorial plane of this ellipsoid, lying at the corners of a regular square, we find the four Ba cations closest to the Cl atom; in this plane the thermal vibrations of the Cl atom have their least amplitude. The anisotropy of the thermal vibrations of the cations in the structure is more weakly expressed. For all the cations, the maximum axis of the ellipsoid is closest in direction to the crystallographic c axis of the structure. The fact that the vibrations of the O_1 atom in a plane close to the bc plane have a greater amplitude than those in the direction perpendicular to this plane may be explained very simply. This oxygen atom closes the Si tetrahedra so as to make four-membered rings. The basis O_1 atom is situated in such a way that the bc plane is almost normal with respect to the Si–Si bond passing through the O_1 atom. We may assess the differences in the coordinates of the atoms obtained by the method of least squares allowing for the anisotropy of the thermal vibrations and simply allowing for the individual isotropic thermal vibrations of the atoms, respectively, by comparing the interatomic distances obtained from ref. 9 and from the present investigation. The differences in the cation–anion and anion–anion distances are limited to 0.02 and 0.03 Å, respectively. An exception is the $Ba-O_6$ distance, which differs by 0.06 Å.

The application of these programs to known structures and an analysis of the baotite data presented here

TABLE 1. Coordinates and Anisotropic Parameters $\exp\{-[B(11)h^2 + B(22)k^2 + B(33)l^2 + B(12)hk + B(23)kl + B(13)hl]\}$ of the Thermal Vibrations of the Basis Atoms of Baotite (all the parameters and standard deviations in brackets are multiplied by 10^5)

Atoms	x/a	y/b	z/c	$B(11)$	$B(22)$	$B(33)$	$B(12)$	$B(23)$	$B(13)$
Ba	2940(2)	9740(2)	62130(8)	24(1)	17(1)	411(13)	6(1)	3(6)	−18(6)
(Ti, Fe)	21273(6)	10800(6)	87002(25)	12(3)	22(3)	375(37)	2(4)	−2(20)	−6(21)
(Ti, Nb)	22167(4)	11779(4)	37247(17)	11(2)	11(2)	271(25)	6(3)	−23(13)	21(14)
Si	9284(9)	18531(9)	12502(42)	12(4)	12(4)	236(49)	10(6)	−20(27)	−8(27)
O_1	1671(26)	15631(30)	13125(125)	17(12)	65(13)	858(147)	−43(21)	78(91)	−84(83)
O_2	12705(27)	15954(26)	89767(107)	32(11)	26(11)	121(142)	18(18)	−104(66)	−42(72)
O_3	12809(27)	16255(27)	36082(124)	19(11)	46(12)	504(149)	14(18)	−15(80)	82(76)
O_4	18495(29)	5291(25)	12905(103)	53(13)	31(12)	211(136)	11(18)	9(90)	108(115)
O_5	18114(28)	5450(25)	62148(103)	43(12)	44(12)	205(137)	−8(18)	−22(89)	3(114)
O_6	24664(26)	16850(29)	12068(117)	39(12)	52(12)	472(141)	10(19)	194(108)	−14(93)
O_7	24111(25)	17050(27)	62939(109)	17(11)	45(12)	279(133)	48(18)	−7(102)	−28(85)
Cl	0	25000	62500	18	18	1029	0	0	0

TABLE 2. Ellipsoids of the Thermal Vibrations of the Basis Atoms of Baotite (ETV)

Atoms	Principal axes of the ETV, i = 1, 2, 3	σ in Å along the principal axes of the ETV	Angle (deg) between principal axes of ETV and crystallographic axes			Atoms	Principal axes of the ETV, i = 1, 2, 3	σ in Å along the principal axes of the ETV	Angle (deg) between principal axes of ETV and crystallographic axes		
			∠(ai)	∠(bi)	∠(ci)				∠(ai)	∠(bi)	∠(ci)
Ba	1	0,086	102	91	12	O_3	1	0,100	65	70	32
	2	0,071	25	68	78		2	0.098	93	157	67
	3	0,057	69	158	86		3	0,050	155	78	69
(Ti, Fe)	1	0,081	93	92	3	O_4	1	0.110	24	79	69
	2	0,067	85	6	88		2	0.078	81	169	84
	3	0.048	6	96	88		3	0.050	112	88	22
(Ti, Nb)	1	0.071	80	101	15	O_5	1	0.098	50	139	85
	2	0.053	44	46	89		2	0.090	140	130	85
	3	0.037	133	47	75		3	0.060	90	83	7
Si	1	0.067	107	113	29	O_6	1	0.124	86	40	51
	2	0.056	48	55	62		2	0,090	167	95	78
	3	0.037	133	44	84		3	0.058	78	129	43
O_1	1	0.135	108	53	43	O_7	1	0.109	120	149	85
	2	0,110	80	136	48		2	0.070	95	82	10
	3	0.040	20	71	83		3	0.024	30	119	62
O_2	1	0,095	130	130	66	Cl	1	0,135	90	90	0
	2	0.068	41	124	71		2	0.060	0	90	90
	3	0,015	89	59	31		3	0,060	90	0	90

indicate that the quality of the initial data employed has a considerable effect on the physical significance of the atomic thermal-vibration anisotropy characteristics so derived, and also on the degree of agreement between the refined parameters obtained by different refining procedures. It is essential that the integrated intensities of the reflections should be measured to a high accuracy, and also that these should be properly converted into the moduli of the structure amplitudes. Allowance for absorption, extinction, and anomalous-scattering corrections may make a considerable difference to the quantities B(ij). These parameters are sensitive to the atomic-scattering functions employed and to the system of weighting factors.

The authors wish to thank A. B. Tovbis for help in the execution of this work, and for valuable suggestions and comments in the course of discussion; they also thank V. I. Burdina for contributions in the initial stages of the work.

---

[1] H. Lipson and W. Cochran, The Determination of Crystal Structures, Bell, London (1966), p. 300.

[2] Crystallographic Computing, Munksgaard, Copenhagen (1970).

[3] A. B. Tovbis and B. M. Shchedrin, Kristallografiya, 15, 1127 (1970) [Sov. Phys.–Crystallogr., 15, 985 (1971)].

[4] B. K. Vainshtein, Kristallografiya, 1, 137 (1956) [Sov. Phys.–Crystallogr., 1, 103 (1956)].

[5] D. R. Fitzwater, Acta Crystallogr., 14, 1242 (1961).

[6] D. W. Marquardt, J. Soc. Industr. Appl. Math., 11, 2 (1963).

[7] R. J. Nelms, Acta Crystallogr., A25, No. 4, 523 (1969).

[8] S. Cerrini, Acta Crystallogr., A27, No. 2, 130 (1971).

[9] Yu. V. Nekrasov, V. I. Ponomarev, V. I. Simonov, and D. M. Kheiker, Kristallografiya, 14, 602 (1969) [Sov. Phys.–Crystallogr., 14, 508 (1970)].

Crystal structure of ditrioctahedral chlorite

V. A. Aleksandrova, V. A. Drits, and G. V. Sokolova

Geological Institute, Academy of Sciences of the USSR

(Submitted July 7, 1971; resubmitted February 1, 1972)
Kristallografiya, 18, 81-88 (January-February 1973)

A structure refinement is presented for Al−Mg ditrioctahedral chlorite, in which three-level dioctahedral layers alternate with one-level trioctahedral ones; it is shown that there is an ordered cation distribution in the octahedral and tetrahedral grids. The tetrahedra have a regular alternation of Si and Si, Al cations, while a one-level layer has a clear tendency for the Mg^{2+} cations to surround uniformly the Al^{3+} ones. The detailed distortions in the tetrahedra and octahedra are examined. The ordered cation distribution leads to minimization of cation repulsion when there is a repeat distance of two chlorite packets.

It has been shown[1−3] that there exist in nature Al−Mg ditrioctahedral chlorites, i.e., chlorites in which the three-level $Al_2(Si_3Al)O_{10}(OH)_2$ dioctahedral layers alternate with one-level $(Mg_2Al)OH)_6$ trioctahedral ones. Later, similar structures were described elsewhere.[4] At the present time, there are only two known localities of coarsely crystalline Al−Mg ditrioctahedral chlorite suitable for detailed structural analysis.[1,3] In other cases, these minerals occur in the finely divided state.[4]

A study has been made[4] of ditrioctahedral chlorite via the intensities of reflections on powder patterns; the model was a one-packet monoclinic cell, and only reflections with k = 3n were examined. Another study[3] employed single crystals of the chlorite and showed that the cell of the mineral is a two-packet one, being monoclinic with the parameters $a = 5.225 \pm 0.005$, $b = 9.058 \pm 0.005$, $c = 28.38 \pm 0.01$ Å, $\beta = 93°40'$, space group C2/c and the structural formula $(Si_{2.86}Al_{1.14})(Al_{2.98}Mg_{1.95}Fe^{3+}_{0.08}Fe^{2+}_{0.14})O_{16}(OH)_8$.

A geometrically ideal model for the chlorite was established by comparing the observed h0*l* and 0k*l* intensities with the calculated[5] $|F|^2$ for all possible polytypes of two-packet chlorites: The agreement was best for model II-I of Table 2 of ref. 5, in which the octahedra in the one-level and three-level layers are antiparallel, while the centers of the octahedra in the one-level layers coincide in normal projection with the vertices in the bases of octahedra in the three-level layers (Fig. 1). The chlorite packets are superimposed in such a way that their own planes of symmetry are parallel to the *a* axis but are displaced along the b axis in turn by ±b/3.

We refine the structure of the mineral via the intensities of 420 reflections derived from a single crystal (0.2 × 0.2 × 0.1 mm) used with Cu Kα radiation in a Weissenberg camera. The intensities were estimated via blackening marks, with no correction for absorption. The least-squares method was applied with a BÉSM-3M computer after several refinements to give r = 13.8%. Table 1 gives the values of the refined coordinates and the corresponding standard deviation σ, while Table 2 gives the interatomic distances calculated from them.

We consider the distortions in the three basic elements in the chlorite packets: the octahedral grids on the one- and three-level layers and the network of tetrahedra.

Octahedra in one-level layers. A characteristic feature of the one-level layers is the ordered distribution of the cations, in which two of the three independent positions are almost completely occupied by Mg, with one by Al, as is evident from the mean interatomic distances between cation and anion in each octahedron.

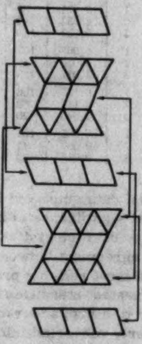

Fig. 1. Spatial superposition of one- and three-level layers in ditrioctahedral chlorite, projection along the b axis. The arrows show cations that coincide in normal projection on the *a* b plane.

TABLE 1. Atomic Coordinates

Atom	x/a	y/b	z/c	σ(x/a)	σ(y/b)	σ(z/c)
M_1	0.753	0.914	0	0.003	0.002	—
M_2	0.750	0.250	0	—	—	—
Al_1	0.500	0.251	0.250	—	0.002	—
Al_2	0.500	0.918	0.250	—	0.002	—
T_1	0.651	0.750	0.154_9	0.002	0.001	0.0007
T_2	0.651	0.418	0.154_2	0.002	0.002	0.0007
OH_1	0.435	0.264	0.035_7	0.003	0.003	0.001
OH_2	0,441	0.594	0.040_4	0.003	0.003	0.001
OH_3	0.419	0.902	0.036	0,004	0.003	0.002
OH_4	0.138	0.586	0.215_9	0.003	0.004	0.001
O_1	0.416	0.326	0.129_8	0.003	0.002	0.001
O_2	0.587	0.580	0.137_4	0.003	0.003	0.001
O_3	−0.092	0.350	0.133_4	0.003	0.003	0.001
O_4	0.672	0.412	0.212_0	0.004	0.002	0.001
O_5	0.672	0.756	0.216_7	0.003	0.002	0.001

For instance, the M_1 octahedron has $r_{av} = 2.075$ Å, while the M_2 octahedron has $r_{av} = 1.97$ Å. If we take[6] Mg−O = 2.10 and Al−O = 1.92 Å, then the compositions of the M_1 and M_2 octahedra are as follows: $Mg_{0.84}Al_{0.16}$ and $Al_{0.73} \cdot Mg_{0.27}$. The overall composition of the octahedra $Mg_{1.95} \cdot Al_{1.05}$ is very close to that deduced from chemical analysis.

The octahedral network in xanthophyllite[7] has the same cation composition and the same mean cation−anion separation (2.04 Å) as does a one-level layer in this chlorite, but the parameter b = 9.00 Å of xanthophyllite is less than that in the chlorite. Conversely, the height (2.15 Å) of the octahedra in xanthophyllite is greater than the height

TABLE 2. Interatomic Distances in Å

$M_1-OH_1^2$	1,92		$M_1-OH_1^3$	2.11	
$M_1-OH_2^2$	2.08		$M_1-OH_2^1$	2.02	
$M_1-OH_2^1$	2,18		$M_1-OH_2^3$	2.13	
	Average		$2,07_5$		
$OH_1^2-OH_2^2$	3.00		$OH_1^3-OH_2^1$	3.02	
$OH_1^3-OH_2^1$	2.97		$OH_1^3-OH_2^3$	3,28	
$OH_2^2-OH_2^1$	3,23		$OH_2^1-OH_2^3$	3,06	
$OH_1^2-OH_1^5$	2,73		$OH_2^3-OH_2^6$	2.88	
$OH_1^5-OH_2^1$	2,68		$OH_2^5-OH_2^1$	2,95	
$OH_2^6-OH_2^5$	2,79		$OH_2^1-OH_1^5$	2.63	
	Average		$2,93_5$		
$M_2^1-OH_1^1$	1.99	(2)	$OH_1^1-OH_2^2$	3.05	(2)
$M_2^1-OH_1^2$	2.04	(2)	$OH_1^1-OH_2^3$	2,82	(2)
$M_2^1-OH_2^2$	1,90	(2)	$OH_2^2-OH_2^5$	2.79	(2)
Average	1,98		$OH_2^2-OH_1^6$	2,68	(1)
			$OH_1^5-OH_2^2$	2.63	(1)
			$OH_2^3-OH_2^5$	2,79	(1)
			$OH_2^5-OH_1^1$	2,68	(1)
			$OH_1^1-OH_2^6$	2.63	(1)
			$OH_2^6-OH_2^2$	2.79	(1)
			Average	2.80	
$T_1-O_1^2$	1,74		$T_2-O_1^1$	1.61	
$T_1-O_2^1$	1.65		$T_2-O_2^1$	1.57	
$T_1-O_3^2$	1.64		$T_2-O_3^1$	1,62	
$T_1-O_3^1$	1.75		$T_2-O_4^1$	1.64	
Average	$1,69_5$		Average	1,61	
$O_1^2-O_4^1$	2,83		$O_1^1-O_2^1$	2,48	
$O_1^2-O_3^2$	2,67		$O_1^1-O_3^1$	2.57	
$O_2^1-O_3^2$	2,62		$O_2^1-O_3^1$	2,67	
$O_3^1-O_1^2$	2,92		$O_4^1-O_1^1$	2,73	
$O_3^1-O_2^1$	2.77		$O_4^1-O_2^1$	2.62	
$O_3^1-O_3^2$	2.79		$O_4^1-O_3^1$	2.73	
Average	$2,76_7$		Average	$2,63_3$	
$Al_1-O_4^1$	2.05	(2)	$Al_2-O_4^2$	1.98	(2)
$Al_1-O_5^2$	1.90	(2)	$Al_2-O_5^1$	1,96	(2)
$Al_1-OH_4^2$	1,93	(2)	$Al_2-OH_4^2$	1.97	(2)
Average	1,96		Average	1.97	
$O_4^1-O_5^2$	2.97	(2)	$O_4^2-O_5^1$	2.97	(2)
$O_4^1-OH_4^2$	2.95	(2)	$O_4^2-OH_4^2$	2.90	(2)
$O_4^1-O_5^2$	2.55	(2)	$O_5^1-OH_4^2$	3.00	(2)
$O_5^2-OH_4^2$	2.60	(2)	$OH_4^1-O_4^5$	2.71	(2)
$OH_4^2-OH_4^3$	2.48	(1)	$O_4^2-O_5^1$	2.55	(2)
$OH_4^4-O_4^1$	2.87	(1)	$O_5^1-O_5^4$	2,69	(1)
$O_5^2-OH_4^2$	2.88	(2)	$OH_4^2-OH_4^6$	2.48	(1)
Average	2.77		Average	$2,78_5$	

•Superscripts are as follows: 1) x, y, z; 2) $^1/_2$ + x, $^1/_2$ + y, z; 3) $^1/_2$ − x, $^1/_2$ + y, $^1/_2$ − z; 4) $\bar{x}$, y, $^1/_2$ − z; 5) $\bar{x}$, $\bar{y}$, $\bar{z}$; 6) $^1/_2$ − x, $^1/_2$ − y, $\bar{z}$.

of the one-level layers in the chlorite (2.12 Å). These values indicate that the one-level layers in the ditrioctahedral chlorite have been slightly compressed in the (001) planes on combination with the dioctahedral three-level layers.

Figure 2 shows in projection on the (001) plane the triangles for the top and the base of the octahedra, whose vertices are OH groups, and also the positions of the octahedral cations M. The arrows on this figure show the direction in which the anions are displaced from the positions of geometrically regular packing. Figure 2 shows that the anions forming the common edges M_1^1 and M_1^2 of the octahedra (for instance, OH_1^2 and OH_1^5, OH_2^1, and OH_2^5, etc.) are displaced along mutually opposite directions parallel to [110]. Conversely, the anions are the vertices of

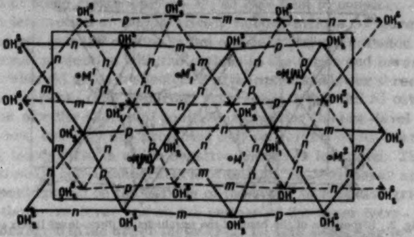

Fig. 2. Normal projection of a one-level layer. The arrows indicate the displacements of the anions from the positions with regular hexagonal packing.

M_2 octahedra, which are displaced in opposite directions (for instance, OH_1^4 and OH_2^5, OH_1^6 and OH_2^2, etc.) or towards the M_2 cations (for instance, OH_3^2 and OH_3^5). As a result, the edges common to the M_1 and M_2 octahedra (mean 2.70 Å) are shorter than the edges common to the M_1 octahedra (mean 2.85 Å) (Table 2). The displacement of the anions from the regular packing positions also causes the edges of the base triangles in the M_1 octahedra (mean 3.09 Å) to be substantially longer than the corresponding edges of the M_2 octahedra (mean 2.89 Å) (Table 2). A characteristic feature is that the triangles at the bases of the M_1 and M_2 octahedra have two short edges and one long one (Table 2).

If we assume that all the OH groups are displaced in the (001) plane by the same amount along the directions indicated by the arrows in Fig. 2, then in that case the slightly idealized planar nets for the top and base sections of the octahedra will be characterized by three different edge lengths, which are denoted in Fig. 2 by the letters m, n, and p, which form four slightly twisted isosceles triangles. The relationships between the edge lengths are such that m > n > p. The triangular faces have two short sides and one long side, and the tops of the M_1 octahedra have n and m as these (for instance, the triangle with vertices OH_1^1, OH_2^1, and OH_3^2), while in the M_2 octahedra these are p and n (Fig. 2). The empty triangles, on the other hand, have two long sides and one short one, and the large triangles (for instance the triangle with vertices OH_1^2, OH_2^1, and OH_3^2) are formed by m and n edges, while the smaller ones are formed by n and p edges.

This chlorite has a mean displacement of 0.13 Å for the OH groups, and in this case m = 3.25, n = 3.02, and p = 2.80 Å, which are very close to the measured distances between the anions forming the ends of the octahedra (Table 2).

The distortions in the octahedral grid are largely due to the ordered distributions of the octahedral cations; in fact, the M_1 cations are represented mainly by divalent Mg, while the M_2 cations are mainly trivalent Al, so the electrostatic repulsion between M_1 and M_2 should be greater than that between M_1 cations. The stronger interaction of the M_1 and M_2 cations leads to a need to screen off this effect by additional shortening of the common edges between the M_2 and M_1 octahedra relative to the edges common to the M_1 octahedra, which is attained via the above shifts in the OH groups. Simultaneously,

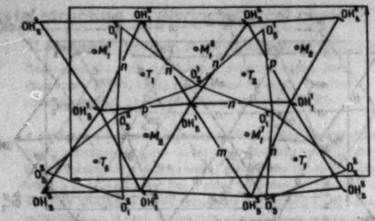

Fig. 3. Disposition of the bases of the tetrahedra in three-level layers and adjoining tops of the nearest octahedra in one-level layers.

one obtains normal mean interatomic distances between the anions and the Al and Mg cations.

Finally, we note that the basal hydroxyl groups do not lie in one plane; in particular, the OH_2 groups are displaced along c* towards the nearest anions O_2 in the tetrahedral grid.

Tetrahedral grid. The interatomic distances show that the Al replaces the Si in an ordered fashion; the T_2 tetrahedra have a mean cation–anion distance d_{av} = 1.61 Å, while the T_1 tetrahedra have d_{av} = 1.70 Å. The available evidence[8] indicates that the T_2 tetrahedra contain Si cations, while replacement of Si by Al occurs only in the T_1 tetrahedra.

Figure 1 shows that the tetrahedral grid has a prominent pseudoditrigonal pattern on account of rotation of the tetrahedral relative to the normal to the bases; the basal anions are displaced towards the hydroxyl groups of the adjacent one-level layer (Fig. 3) and towards the cations in the three-level layer [the latter practically coincide with the OH groups in projection on the (001) plane and so are not shown in Fig. 3]. The angle α of rotation of the tetrahedra is 8° on average. It has[9] been shown that α is determined by the relation between b_e and b_t, the parameters of the tetrahedral grid for $\alpha = 0$:

$$\cos\alpha = b_e / b_t. \quad (1)$$

Bailey[10] has found that b_t is defined by the following expression for layer silicates containing tetrahedra of composition $Si_{1-x}Al_x$:

$$b_t = 9.04 + 0.92\,x. \quad (2)$$

For a mean tetrahedron composition of $Si_{0.72}Al_{0.28}$ in this chlorite, we get from (2) that b_t should be 929 Å, while the result from (1) is α = 15°, which is almost twice α_e. This large discrepancy between the two values of α arises because the T_1 and T_2 tetrahedra are markedly elongated along the c* axis and their heights are 2.36 and 2.23 Å, respectively, whereas the heights of geometrically regular T_1 and T_2 tetrahedra for the same d_{av} would be 2.26 and 2.15 Å. As a result, the edges of the bases of the T_1 and T_2 tetrahedra (2.71 and 2.58 Å) are much shorter than the side edges (2.85 and 2.71 Å). Then the observed value is $b_t = 3(A + B)$ = 9.15 Å, where A and B are the mean lengths of the edges in the bases of the T_1 and T_2 tetrahedra,[10] while the result from (1) for this b_t is α = 8°. Then the anomalously large elongation of the tetrahedra in the di-trioctahedral chlorite substantially distinguishes the structure of these from the tetrahedra in most other layer-silicate structures that have been refined, for which (2) is met quite accurately.

The distortion of the tetrahedra in this chlorite is largely determined by the method of linking the one- and three-level layers; replacement of Si by Al in the tetrahedra produces a negative charge at the surface of the basal oxygen atoms in the three-level layers, and this charge is compensated by formation of hydrogen bonds between each pair of adjacent O and OH groups, and also by direct interaction between the basal oxygen atoms and the cations in the one- and three-level layers (Fig. 3). Under these conditions, each basal oxygen atom is acted on by two forces in opposite directions: one directed towards the nearest OH group and cation in the three-level layers, and the other towards the nearest cations in the one-level layers. For instance, Fig. 3 shows that approach of O_3^2 to OH_3^1 and the nearest cation in a three-level layer opposes the attraction to the M_2 cation in the one-level layer. The elongation along the c* axis and the reduction in α enable the basal oxygen atoms to lie at the minimum possible distances not only from the nearest OH groups, but also from the cations in the one-level layers, and this is also facilitated by the ordered disposition of the cations in the one-level layers and the resulting displacement of the OH groups, which in the main occurs in the direction of the nearest basal oxygen atoms (Fig. 3). Also, the triangles of OH groups (e.g., the triangle with the vertices OH_1^2, OH_2^1, and OH_3^1) are substantially smaller than the end faces of the M_1 octahedra and also than the triangles placed in Fig. 3 within the tetrahedral loops; this also allows the basal oxygen atoms to approach the OH groups by displacement along the c* axis and simultaneously to attain the closest approach to the cations in the one-level layers.

The observed values for the independent distances between pairs of adjacent O_{bas} and OH groups are 2.73, 2.74, and 2.81 Å, which are about 0.2 Å less than the corresponding bond lengths in trioctahedral chlorites, dickite, and nacrite.[10] All three hydrogen bond lengths are extremely similar, although the surface of the basal oxygen atoms is not a plane and, in particular, the O_2 atoms are pushed down along the normal into their layer as a result of the tilt in the tetrahedra.[7] The corresponding displacement of the $(OH)_2$ groups towards the O_2 atoms (Fig. 3) leads to coherent corrugation of the surfaces of the adjacent one- and three-level layers, with the ridges in one lying above the depressions in the other and vice versa. The short hydrogen bonds are the principal means of neutralizing the negative charge on the basal oxygen atoms.

The octahedral grid in a three-level layer has generally the distortions described for Al octahedra in other layer silicates.[10] The shared edges of the populated octahedra are substantially shortened, while the top and bottom of the octahedra are rotated in the (001) planes in opposite directions on average by 3°, while the cations have an ordered distribution and uniformly surround the empty octahedra. However, there are some distinctive features in the structure of the network of octahedra. First of all, the cation–anion distances are on the average 1.96 Å, which differs appreciably from the values usually encountered in Al octahedra for layer silicates (1.92 Å). The shared edges of the populated octahedra (2.53 Å) are approximately 0.1 Å longer than the corresponding edges in the structures of such minerals as paragonite, muscovite, and margarite.[10] Finally, there are very distinct variations in the z coordinates of the atoms forming the end faces of the octahedra.

These anomalous interatomic distances arise because the grid of octahedra is in a stressed state, because it is markedly elongated in the (001) plane as a result of linkage to the larger one-level layer; in fact, the usual parameters for layer silicates with Al octahedra do not exceed 8.97 Å, which is almost 0.1 Å less than in this chlorite. An Al−O distance of 1.92 Å and $b = 9.058$ Å will mean that the lengths of the shared edges should[6] be 2.37 Å, which would lead to strong repulsion between the anions; then the stretching of the Al octahedra in the (001) planes leads not to thinning of the octahedral grid by concentration of the shared edges, but it is accompanied by increase in the Al−O distances with the same height ($h = 2.09$ Å), such as is found in muscovite, paragonite, and margarite.[10] Part of the reason for the increase in the cation−anion distance is the presence of a small amount of Fe in the octahedra.

The ordered disposition of the Al replacing Si in the tetrahedra is responsible for the marked variations in the individual cation−anion distances; in fact, the z coordinates of the bases of the T_1 and T_2 tetrahedra are identical, and the two types of tetrahedron are elongated along the c* axis, so from (2) we see that population by cations different in size will lead to differences in height and consequently to differences in the z coordinates of the vertices, which simultaneously form the end faces of the octahedra.

Structure stability. The criteria proposed by Shirozu and Bailey[11] cause this structure to have a favorable disposition of the one- and three-level layers; in fact, in a normal projection there is no coincidence between the cations in the one-level layer and the nearest tetrahedral cations, while the OH and basal oxygen atoms are as close as possible to the cations in the one- and three-level layers, thereby forming short hydrogen bonds.

However, this structure has a repeat distance of two chlorite packets, and so the structural control extends out to large distances (> 14 Å), so it is best to consider the interaction of comparatively remote cations. Figure 1 shows that the cations in the one-level layers coincide in normal projection with the cations in the upper and lower tetrahedral grids respectively of the upper and lower three-level layers. The important point here is that the Al cations are the source of positive charge for the one-level layers, and they are projected only on cations of Al-bearing tetrahedra, in which negative charge is localized. The cations in the octahedral grid of each three-level layer are superimposed on the cations of the upper tetrahedral grid in the lower layer and on the cations of the lower tetrahedral grid in the upper layer (Fig. 1), this occurring in such a way that the cations in the Si tetrahedra are projected on the centers of the empty octahedra, and only the cations in the Si, Al tetrahedra coincide with the octahedral Al cations. This mutual disposition of the cations results in less electrostatic repulsion than when the more highly charged Si^{4+} cations are superimposed on the octahedral cations.

The cations in this chlorite are thus distributed so that the centers of the positive charges lie exactly above the centers of the negative charges, which provides minimal mutual repulsion between the cations; one may suppose that the distribution of the centers of one sign in an initial layer controls the distribution of the centers of the other sign in the next layer during growth, and this on the whole determines the periodicity of the structure.

---

[1] V. A. Drits, Acta Crystallogr., 21, 172 (1966).

[2] V. V. Vlasov and V. A. Drits, X-Rentgen. Miner. Syr'ya, 6, 114 (1967). 114 (1967).

[3] V. A. Drits and E. K. Lazarenko, Min. Sborn. L'vov. Geol. Obshch., 21, 40 (1967).

[4] R. A. Eggleton and S. W. Bailey, Amer. Mineralogist, 52, 673 (1967).

[5] V. A. Drits, Acta Crystallogr., B25, 632 (1969).

[6] G. Donnay, J. D. H. Donnay, and H. Takeda, Acta Crystallogr., 17, 1374 (1964).

[7] Y. Takeuchi, Clays and Clay Minerals, Proc. 13th Nat. Conf., Pergamon Press (1965), p. 3.

[8] J. V. Smith and S. W. Bailey, Acta Crystallogr., 16, 801 (1963).

[9] E. W. Radoslovich and K. Norrish, Amer. Mineralogist, 47, 599 (1962).

[10] S. W. Bailey, Clays and Clay Minerals, Proc. 14th Conf., Pergamon Press (1966), p. 1.

[11] H. Shirozu and S. W. Bailey, Amer. Mineralogist, 50, 868 (1965).

X-ray study of potassium copper ethylenediaminetetraacetate trihydrate

M. A. Porai-Koshits, N. V. Novozhilova, T. N. Polynova, T. V. Filippova, and L. I. Martynenko

M. V. Lomonosov Moscow State University

(Submitted May 4, 1971; resubmitted February 2, 1972)
Kristallografiya, 18, 89-98 (January-February 1973)

The structure of $K_2[CuA] \cdot 3H_2O$ (A is ethylenediaminetetraacetate) has been elucidated via the three-dimensional Patterson function and the electron density, followed by least-squares refinement to R = 0.124 via 909 independent reflections. The complex anions have the composition $[CuA]^{2-}$; A is a hexadentate ligand that forms five closed rings with Cu: the ethylenediamine ring E and four glycine rings G_1, G_2, G_1, and R_2. The copper polyhedron is unsymmetrically elongated as a tetragonal bipyramid; in the equatorial plane there lie two N atoms and two O atoms from rings E, G_1, and G_2, while the vertices have two O atoms from the rings R_1 and R_2. All the rings are nonplanar. The bending of the E and G rings is more pronounced than that of the R rings. Comparison with the $[CoA]^-$ complex indicates an increase in the radius of the metal by 0.12-0.15 Å, an increase in the angle between the rings (i.e., in the distances N...N and N...O), and consequently a change in the valence angles in the rings (reduction in the angles for the N and O atoms and increase for the C atoms). The $[CuA]^{2-}$ complexes form double layers in the structure, which are parallel to (110), between which are layers of K_I ions and $(H_2O)_I$ and $(H_2O)_{II}$ molecules. The K_{II} ions and the $(H_2O)_{III}$ molecules lie in the layers of the complexes and are additionally cross-linked.

INTRODUCTION

Compounds of the compositions $K_2[CuA] \cdot 3H_2O$ and $Cu_2A \cdot 4H_2O$ (A is ethylenediaminetetraacetate, EDTA) were obtained by ion-exchange separation of mixtures of the rare-earth elements; they differ in solubility, in their IR spectra, and in thermal stability. X-ray analysis indicates[1] that there are marked differences in the structure of these two copper complexes, a fact which has been confirmed by a preliminary structural study:[2,3] crystals of $K_2[CuA] \cdot 3H_2O$ contain the monomeric complexes $[CuA]^{2-}$, while crystals of $Cu_2A \cdot 4H_2O$ contain the binuclear complexes $[Cu_2A(H_2O)_2]$ (with bridge EDTA ligands), which are linked into layers by additional coordination of the Cu atoms in one complex to the O atoms in adjacent complexes.

Octahedral metal complexes with hexadentate EDTA have been found previously in the structures $NH_4[CoA] \cdot 2H_2O$, $Rb[CoA] \cdot 2H_2O$ (ref. 4), and $Rb[AlA] \cdot 2H_2O$ in the isostructural ammonium and potassium salt of Cr EDTA.[5] In all these compounds the ligand forms five rings involving the metal (Fig. 1a): the ethylenediamine E ring and four glycine rings, of which two form a common belt with the EDTA ring (the G rings in ref. 4), and also two approximately perpendicular to this belt and to one another (the R rings). The G rings are bent, while the R rings are nearly planar, from which it has been concluded[4] that the G rings are more stressed and should open more readily than the R rings. Data on $[Ni(H_2A)(H_2O)]$,[6] $[Ni(H_2O)_6][Ni(HA)(H_2O)]_2 \cdot 2H_2O$,[7] $[Cu(H_2A)(H_2O)]$,[8] confirm this: In these one of the G rings is open (Fig. 1b). In $[Ni(H_2A)(H_2O)]$, the bonds $Ni-O_G$ and Ni−N in the trans positions are appreciably longer than the analogous bonds (by 0.12 and 0.05 Å, respectively). They are even more elongated in $[Cu(H_2A)(H_2O)]$ (by 0.54 and 0.22 Å), which transforms the polyhedron into an elongated square bipyramid characteristic of Cu(II).

Also, $K_2[CuA] \cdot 3H_2O$ retains both G rings, and analogy with the deformation proposed for $[Cu(H_2A)(H_2O)]$ would require either nonequivalence in the two G rings (one $O_{G_1}-Cu-N_1$ coordinate along the axis of the bypyramid, the other $O_{G_2}-Cu-N_2$ in the equatorial plane), or else a transition to a shortened tetragonal bipyramid comparatively rare for Cu(II) (both O_G-Cu-N coordinates in the equatorial plane). On the other hand, the general symmetry of the $[CuA]^{2-}$ complex goes with the tendency of Cu(II) to weaken two bonds (not four), which makes it more likely that the structure of the complex has the weakened $Cu-O_R$ bonds in the trans position.

EXPERIMENTAL

The x-ray examination of $K_2[CuA] \cdot 3H_2O$ was performed with spherical specimens having d = 0.4 mm; the parameters of the orthorhombic unit cell (KFOR camera, NaCl standard) are $a = 12.93 \pm 0.02$, $b = 22.90 \pm 0.03$, $c = 11.45 \pm 0.02$ Å; $d_0 = 1.88$, $d_c = 1.90$ g/cm^3; N = 8, space group Pbca, which is confirmed by the negative result from tests for the piezoelectric effect (Physics Faculty of Moscow University).

We used the layer lines: hk0−hk8, h0l−h3l, and 0kl−3kl (KFOR camera, Mo radiation, $\sin\theta/\lambda \le 0.78$) to record 909 independent finite reflections; the intensities were estimated on blackening scales. The polarization and kinematic factors were incorporated, but no corrections were applied for absorption and extinction ($\mu r = 9.0$). The calculations were performed with an M-20 computer at the Computing Center, Moscow University, via programs written by Tarnopol'skii and Andrianov.

STRUCTURE INTERPRETATION

The three-dimensional Patterson function was used to determine the coordinates of the Cu atom and to obtain preliminary values for those of the six light atoms

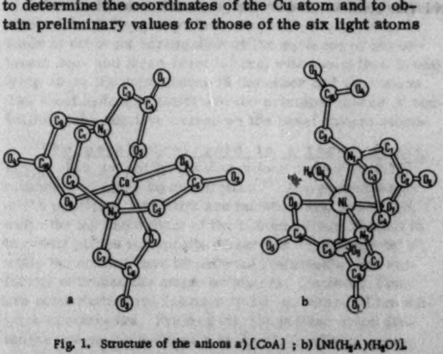

Fig. 1. Structure of the anions a) [CoA]; b) $[Ni(H_2A)(H_2O)]$.

TABLE 1. Coordinates and Individual Thermal Factors for the Basis Atoms

Atom	x/a	y/b	z/c	B, Å²	Atom	x/a	y/b	z/c	B, Å²
Cu	0.189_0	0.122_5	0.092_6	0.18	$(H_2O)_{III}$	0.247	0.387	0.152	3.8
K_I	0.152	0.497	0.158	2.23	N_1	0.036	0.140	0.074	1.0
K_{II}	0.382	0.407	0.325	2.02	N_2	0.211	0.208	0.151	1.3
O_1	0.141	0.038	0.093	1.3	C_1	0.018	0.200	0.126	0.5
O_2	0.338	0.117	0.083	3.2	C_2	0.118	0.230	0.091	1.3
O_3	0.188	0.141	−0.099	2.6	C_3	−0.006	0.093	0.156	1.3
O_4	0.205	0.110	0.298	1.8	C_4	0.056	0.037	0.152	2.7
O_5	0.018	−0.005	0.200	3.6	C_5	0.311	0.224	0.098	2.4
O_6	0.475	0.181	0.067	2.0	C_6	0.381	0.172	0.079	2.1
O_7	0.062	0.142	−0.239	4.1	C_7	−0.002	0.130	−0.055	1.7
O_8	0.279	0.165	0.436	2.0	C_8	0.091	0.143	−0.136	4.4
$(H_2O)_I$	0.245	0.001	0.400	3.9	C_9	0.216	0.214	0.277	2.0
$(H_2O)_{II}$	0.042	0.062	0.488	3.7	C_{10}	0.236	0.159	0.345	2.0

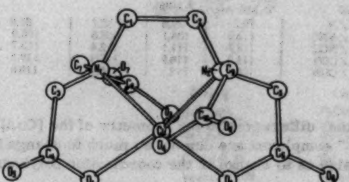

Fig. 2. Structure of $[CuA]^{2-}$.

TABLE 2. Valence Distances in Complexes, in Å

Cu − O_1	2.023	$C_1 - C_2$	1.52
Cu − O_2	1.933	$C_3 - C_4$	1.51
Cu − O_3	2.224	$C_5 - C_6$	1.51
Cu − O_4	2.381	$C_7 - C_8$	1.53
Cu − N_1	2.096	$C_9 - C_{10}$	1.50
Cu − N_2	2.094	$C_4 - O_1$	1.29
$N_1 - C_1$	1.51	$C_6 - O_2$	1.38
$N_1 - C_3$	1.52	$C_8 - O_3$	1.33
$N_1 - C_7$	1.47	$C_{10} - O_4$	1.31
$N_2 - C_2$	1.47	$C_4 - O_5$	1.21
$N_2 - C_5$	1.48	$C_6 - O_6$	1.25
$N_2 - C_9$	1.45	$C_8 - O_7$	1.24
		$C_{10} - O_8$	1.20

forming an octahedron round the Cu; the electron-density distribution was calculated from the Cu contributions, and this served to refine the coordinates of this atom and to confirm the octahedral coordination, as well as to reveal six EDTA atoms and two K atoms. The coordinates of these atoms were refined by least squares. The resulting electron-density distribution employed the atomic curves of nitrogen to reveal the remaining 11 light atoms, including the O atoms of all three water molecules. The final refinement of the coordinates and the isotropic temperature factors was done by least squares without weighting factors, which reduced R to 0.124. Table 1 gives the atomic coordinates and individual isotropic temperature factors. The probable errors averaged over the three coordinates were as follows: ε(Cu) 0.002, ε(K) 0.005, ε(O) 0.016, ε(N) 0.017, ε(C) 0.023 Å. The errors in the distances were similarly: ε(Cu−O) 0.016, ε(Cu−N) 0.017, ε(C − O) 0.028, ε(C−N) 0.029, ε(C−C) 0.032, ε(K −O) 0.017 Å; those in the valence angles were: ε(NCuN) 0.6, ε(OCuN) 0.6, ε(OCC) 2, ε(CCN) 2, ε(CuNC) 1.2, ε(CuOC) 1.2°. The mean errors in the temperature corrections were $\varepsilon(B_{Cu})$ 0.03, $\varepsilon(B_K)$ 0.1, $\varepsilon(B_N)$ 0.3, $\varepsilon(B_O)$ 0.3_5, $\varepsilon(B_C)$ 0.4_5 Å.

We found that the coordinates after least-squares refinement showed marked discrepancies from the final electron-density distribution as regards the position of O_2, which had a value of B larger than those for the equivalent atoms; the coordinates of O_2 have clearly been affected by fluctuations in the errors as well as errors in the distances and valence angles related to these, all of which substantially exceeded the above limits.

DISCUSSION

The crystals of $K_2[CuA] \cdot 3H_2O$ consist of $[CuA]^{2-}$ anions, K^+ cations, and H_2O molecules of crystallization. The configuration shown in Fig. 2 for the complex is the usual one for a six-coordinated complex of metal with EDTA; the EDTA forms five rings containing metal: the ethylenediamine ring $Cu-N_1-C_1-C_2-N_2-Cu$ and the four glycine rings $Cu-N_1-C_3-C_4-O_1-Cu(G_1)$, $Cu-N_2-C_5-C_6-O_2-Cu(G_2)$, $Cu-N_1-C_7-C_8-O_3-Cu(R_1)$, $Cu-N_2-C_9-C_{10}-O_4-Cu(R_2)$. The coordination polyhedron of copper is an unsymmetrical elongated tetragonal bipyramid. Of the three possible forms of the structure mentioned in the introduction, we found the third: On the axis of the bipyramid lie the oxygen atoms of the R glycine rings. The $Cu-O_3$ and $Cu-O_4$ distances are 2.22 and 2.38 Å; the $Cu-O_2$, $Cu-O_1$, $Cu-N_1$, and $Cu-N_2$ bonds lying in the equatorial plane are: 1.93, 2.02, 2.04, and 2.09 Å. Although the G rings are highly strained, they retain firm bonds to the metal at both ends, whereas the R rings are only partially closed.

The $[CuA]^{-2}$ complex probably shows two tendencies: 1) the tendency to form the strongest bonds with the N atoms (if possible with both); 2) a tendency to retain the structural equivalence of the chemically equivalent rings. Both tendencies are satisfied by stretching the octahedron along the $O_R \ldots Cu \ldots O_R$ coordinate.

The symmetry of the complex is C_2 in the first approximation: The dyad axis runs through the Cu atom and the middle of the C−C bond in the E rings. The N_1-C_3 bond in G_1 and the N_1-C_1 bond in ring E deviate to one side of the equatorial plane in the Cu bipyramid, while the N_2-C_5 bond in ring G_2 and the N_2-C_2 bond in ring E deviate to the other side. This makes it possible for the planes of the $Cu-N_1-C_7$ ring R_1 and the $Cu-N_2-C_1$ ring R_2 to set approximately perpendicular to the equatorial plane on opposite sides. The differences in the N−C, C−C, C−O, and C = O distances in the various rings only slightly exceed the probable errors (Table 2). There is a marked deviation for the C_6-O_2 distance, which is due to the low accuracy and the determination of the coordinates of O_2, so the distances C_6-O_2 1.38 and $Cu-O_2$ 1.93 Å are not particularly reliable; it would seem that the first is

TABLE 3. Mean Bond Lengths (Å)

	$[CuA]^{2-}$	$[Cu(H_2A)(H_2O)]$	$[CoA]^-$	$[AlA]^-$	$[Ni(H_2A)(H_2O)]$
$M-N$	2,065	2.178	1,925	2.03	$2,10_5$
$M-O$	1,975	2.086	1.900	1.96	2.08
$N-C$	1.48	1.478	1.49	1.47	1.49
$C-C$	1,51	1.518	1.53	1.52	1,52
$C-O$	1,33	1.258	1.30	1,30	1.26
$C=O$	1,22	1.261	1.22	1.22	1.22

TABLE 4. Valence Angles in Degrees

N_1-Cu-O_1	84.0	$O_5-C_4-O_1$	126.1
N_1-Cu-O_3	81.7	$O_5-C_4-C_3$	116.3
N_1-Cu-O_4	102.1	$Cu-N_2-C_5$	102.9
N_1-Cu-N_2	89.0	$N_2-C_5-C_6$	112.5
N_2-Cu-O_2	87.1	$C_5-C_6-O_2$	118.3
N_2-Cu-O_3	97.8	C_6-O_2-Cu	110.5
N_2-Cu-O_4	77.7	$O_2-C_6-O_6$	122.5
O_1-Cu-O_2	108.3	$C_5-C_6-O_6$	118.3
O_1-Cu-O_3	100.4	$Cu-N_1-C_7$	112.5
O_1-Cu-O_4	84.7	$N_1-C_7-C_8$	109.0
O_2-Cu-O_3	87.6	$C_7-C_8-O_3$	119.4
O_2-Cu-O_4	88.0	C_8-O_3-Cu	109.0
$Cu-N_1-C_1$	106.3	$O_7-C_8-O_3$	126.1
$N_1-C_1-C_2$	117.0	$O_7-C_8-C_7$	112.8
$C_1-C_2-N_2$	103.4	$Cu-N_2-C_9$	114.7
C_2-N_2-Cu	101.3	$N_2-C_9-C_{10}$	116.2
$Cu-N_1-C_3$	98.2	$C_9-C_{10}-O_4$	117.1
$N_1-C_3-C_4$	112.7	$C_{10}-O_4-Cu$	108.9
$C_3-C_4-O_1$	117.4	$O_8-C_{10}-O_4$	126.3
C_4-O_1-Cu	105.3	$O_8-C_{10}-C_9$	116.5

too great, while the second is too small. The mean bond lengths (neglecting these two) are Cu−N 2.07, Cu−O 2.02, N−C 1.48, C−C 1.51_5, C−O 1.33, C = O 1.22_5 Å, which are close to (but not the same as) the mean lengths in the structures of Co EDTA and Al EDTA (Table 3).

Table 4 gives the valence angles in the rings and the mean values; the angular distortions in the equatorial plane of the metal polyhedron are due to the rings and are approximately as in the octahedral Co and Al complexes. The valence angle of the metal in the E ring is almost undistorted, while in the G rings it is less than the ideal value by about 5°, while the O_2CuO_1 angle outside the ring is greater by about 13°. The other valence angles in the E and G rings in $[CuA]^{2-}$ and in $[CoA]^-$ are substantially different; the reason for the difference is easily established. A transition from Co(III) to Cu(II) involves increase in the M-ligand distances (the increase in the metal radius is 0.12–0.15 Å). If the valence angles at the metal atom remain unchanged, this would require an increase in the angle between the rings (i.e., the N . . . N distances in the E ring and the N . . . O distances in the G rings), i.e., reduction in the angles at the N and O atoms, with increase at the C atoms. Table 5 confirms both features: In ring E, the angles at the N are reduced by ~4°, while those at C increase by ~2°, whereas in the G rings the angles at N and O are reduced by 5-6°, with the ones at C_{met} increased by 6°; only the angles at C_{carb} are unaltered.

The pairs $[CoA]^- - [CuA]^{2-}$ and $[CoA]^- - [Ni(H_2A)(H_2O)]$ (Table 5) show that the ring shape is affected by the increase in distance on going from Co to Cu or Ni: In the first case, the angle between the rings increases with unaltered valence angles for the metal, while the ring angle also increases in the second, while the NMN and NMO angles are reduced. This difference is naturally ascribed to the greater rigidity of the system of four equatorial bonds in the Cu(II) complex relative to the system of octahedral (and more polar) bonds in the high-spin Ni(II).

TABLE 5. Mean Angles in Rings in $[MA]^{n-}$

	Complex			
	$[CuA]^{2-}$	$[CoA]^-$	$[Ni(H_2A)\cdot(H_2O)]$	$[Cu(H_2A)\cdot(H_2O)]$
	E ring			
∠*M*	89.0	89.7	86.5	84.6
∠*M*NC	103.8	107.5	104.3	103.6
∠NCC	110.3	108.1	109.8	111.0
	G rings			
∠*M*	85.2	83.2	79.4	75.0
∠*M*NC	100.5	105.9	104.5	110.9
∠NCC	112.6	106.4	111.7	112.4
∠CCO	117.8	115.1	119.8	123.5
∠CO*M*	107.9	112.9	109.5	105.2
	R rings			
∠*M*	79.7	88.5	82.7	82.8
∠*M*NC	113.6	108.1	108.8	106.0
∠NCC	112.7	111.1	112.4	113.7
∠CCO	118.2	116.9	117.9	118.1
∠CO*M*	109.0	113.1	116.6	118.5

The other differences in the geometry of the $[CoA]^-$ and $[CuA]^{2-}$ complexes are due not so much to change in metal atom size as to change in the coordination polyhedron.

The $Cu-O_4$ and $Cu-O_3$ bonds are weak, which is the reason for the flexibility of the angles at Cu in the R rings; there are no strict requirements as regards length and valence angles for the axial bonds in the bipyrimidal complexes of Cu(II), so the stress in the R rings can be relieved mainly by reducing the valence angles at the metal: by 9° relative to $[CoA]^-$ and by 12° relative to the ideal value. The deviations from the mean plane: $C_1(+0.25)$ and $O_2(-0.25)$, $N_1(-0.28)$ and $N_2(+0.29)$, represent a deformation of the ideal square in the flattened tetrahedron.

On the other hand, the relative freedom of the OR atoms (O_3 and O_4) alters the system of distortions in the tetrahedral angles at the N atoms; there is no force reducing the MNC angle in the R rings, and the stresses are redistributed: The angles at N are reduced in the E and G rings by increase in the angles at the N in the R rings. Relative to $[CoA]^-$, the valence angles at the N atoms in the R rings increase by 5.5°, while the other angles in these rings (apart from NMO and MOC) are practically unaltered.

Table 6 indicates that all five rings are essentially nonplanar; the bending in the E and G rings is somewhat greater than that in the R rings, but the differences are not as large as in the analogous structures for Co EDTA types described in ref. 4, where the R glycine rings are almost planar (sum of the angles 537.75°).

The following are the angles between the mean planes drawn through the atoms in the various rings: $(G_1)-(R_1)$ 66.7, $(G_2)-(R_2)$ 85.0, $(G_1)-(E)$ 149.0, $(G_2)-(E)$ 173.4, $(R_1)-(E)$ 86.2, $(R_2)-(E)$ 75.4, $(R_1)-(R_2)$ 81.7° and $(G_1)-(C_3C_4O_1O_5)$ 166.0, $(G_2)-(C_5C_6O_2O_6)$ 187.2, $(R_1)-(C_7C_8O_3O_7)$ 184.4, $(R_2)-(C_9C_{10}O_4O_8)$ 160.8°.

When Hoard and his co-workers discussed the stereochemistry of $[CoA]^-$ with hexadentate EDTA, they concluded that the R rings were less strained on the basis that in this case the R rings are practically planar; our results for $[CuA]^{2-}$ make this conclusion less convincing. In the copper complex, the Cu−O_R bonds are weak, so the R

Poraí-Koshits et al. 56

TABLE 6. Deviations of Atoms from Mean Planes in Rings

E ring		R_1 ring		G_1 ring	
$Cu-N_2-C_2-C_1-N_1-Cu$		$Cu-N_1-C_7-C_8-O_3-Cu$		$Cu-O_1-C_4-C_3-N_1-Cu$	
Cu	−0.09	Cu	−0.12	Cu	+0.27
N_2	+0.27	O_3	+0.07	O_1	−0.33
C_2	−0.38	C_8	+0.03	C_4	+0.16
C_1	+0.31	C_7	−0.18	C_3	+0.20
N_1	−0.10	N_1	+0.20	N_1	−0.30
Mean	0.23	Mean	0.12	Mean	0.25
Sum of angles	517.0°	Sum of angles	531.6°	Sum of angles	517.6°

R_2 ring		G_2 ring		Equatorial plane	
$Cu-N_2-C_9-C_{10}-O_4-Cu$		$Cu-O_2-C_6-C_5-N_2-Cu$		$N_1-N_2-O_1-O_2$	
Cu	+0.01	Cu	−0.18	N_1	−0.28
O_4	−0.09	O_2	+0.13	N_2	+0.29
C_{10}	+0.14	C_6	0.00	O_1	$+0.24_5$
C_9	−0.11	C_5	−0.18	O_2	−0.25
N_2	+0.05	N_2	+0.23	Deviation from plane	
Mean	0.08	Mean	0.14	Cu	−0.08
Sum of angles	534.6°	Sum of angles	531.3°	O_4	$+2.27_5$
				O_3	+1.68
				O_8	−0.43

Phase CCOO

G ring		R ring		G ring		R ring	
$O_1O_5C_3C_4$		$O_3O_7C_7C_8$		$O_2O_6C_5C_6$		$O_4O_8C_9C_{10}$	
O_1	−0.10	O_3	−0.03	O_2	+0.01	O_4	0.00
O_5	−0.05	O_7	−0.03	O_6	+0.01	O_8	0.00
C_3	−0.03	C_7	−0.02	C_7	−0.02	C_9	0.00
C_4	+0.18	C_8	+0.07	C_6	+0.00	C_{10}	−0.00
Mean	0.09	Mean	0.04	Mean	0.01	Mean	0.00

rings should be even less stressed than the cobalt rings, with the reservation as regards the angle at the N atom mentioned above; however, this does not reduce the bending of the R rings, but increases it relative to the $[CoA]^-$ complex. The fragment

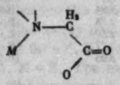

tends to be nonplanar (with the cis configuration relative to the methyl C atom), which may be due to van der Waals interaction for the pairs H...H, H...N, and H...C; if this is so, the flattening of the R rings in $[CoA]^-$ should be considered rather as a consequence of the need to tension this ring on the framework of the $N-Co-O_R$ angle, rather than a tendency to the most favorable mutual disposition of the atoms in this branch of the ligand.

The temperature constants given in Table 1 on the whole correctly reproduce the physical pattern of the thermal motion of the atoms in the structure, although the spread in the individual values is fairly large on account of the substantial errors; it is therefore of interest to analyze the B averaged over functionally identical atoms:

$B(Cu)$ 0.18
$\bar{B}(N)$ 1.2
$\bar{B}(-O_G-)$ 2.2
$\bar{P}(-O_R-)$ 2.2
$\bar{B}(C_{met\,E})$ 0.9
$\bar{B}(C_{met\,G})$ 1.8
$\bar{B}(C_{met\,R})$ 1.8
$\bar{B}(C_{carb\,G})$ 2.4
$\bar{B}(C_{carb\,R})$ 3.2
$\bar{B}(=O_G)$ 2.8
$\bar{B}(=O_R)$ 3.0
$\bar{B}(K)$ 2.12
$\bar{B}(H_2O)$ 3.8

The least B naturally occurs for the Cu central atom and low ones for the N atoms are on each side; the next in magnitude are the $\bar{B}$ for atoms directly adjoining the Cu and N: the hydroxyl O and the methyl C, while the maximal $\bar{B}$ occur for the peripheral atoms: the carboxyl C and the carbonyl O. Of course, the vibrations of these atoms effect also C_{met} in the glycine rings, increasing their $\bar{B}$ relative to the $\bar{B}$ for the same atoms in the E ring. The thermal vibrations of the molecules of water of crystallization are more pronounced than those of the potassium ions.

TABLE 7. Interatomic Distances (Å) in $K_2[CuA]\cdot 3H_2O$

I		III	
$O_2 \ldots C_9$	3.64	$O_4 \ldots C_4$	3.17
$O_6 \ldots C_9$	3.67	$O_8 \ldots C_3$	3.48
$O_6 \ldots C_{10}$	3.55	$C_5 \ldots C_{10}$	4.06
$O_6 \ldots C_1$	3.59	$C_9 \ldots C_8$	3.94
$O_8 \ldots N_1$	3.37	$C_9 \ldots C_4$	3.78
$O_8 \ldots C_1$	3.28	$C_{10} \ldots C_3$	3.92
$O_8 \ldots C_7$	3.20	IV	
$O_8 \ldots C_9$	3.39	$O_6 \ldots C_7$ (2)	3.38
$C_4 \ldots C_1$	3.87	$O_5 \ldots C_8$ (2)	3.54
$C_9 \ldots C_1$	4.08	$C_7 \ldots C_4$ (2)	4.08
$C_{10} \ldots C_1$	3.79		
$C_{10} \ldots C_9$	3.66		
II			
$O_8 \ldots C_9$	3.31		
$O_8 \ldots C_1$	3.55		
$C_6 \ldots C_1$	4.10		

Note: I is the link of the $a(\perp z)$ plane with two complexes, II is the link of the 2_1 axis ($\parallel x$) with two complexes, III is the link of the $c(\perp y)$ plane with two complexes, and IV is the link of the inversion center with one complex (double contacts)

Figure 3 gives a conception of the packing of the structural elements in the crystal: Each $[CuA]^{2-}$ anion is in contact with seven other anions, two K ions, and three H_2O. The interatomic distances in the contacts of the complexes with each other are given in Table 7 without allowance for the H atoms; we state all distances that do not exceed the sums of the van der Waals radii by 0.05 Å. As standard sums we assumed O...O 2.72, O...N 2.93, C...O 3.16, C...N 3.37, C...C 3.60 Å. The $a(\perp z)$ glide plane creates chains of complexes elongated along the x

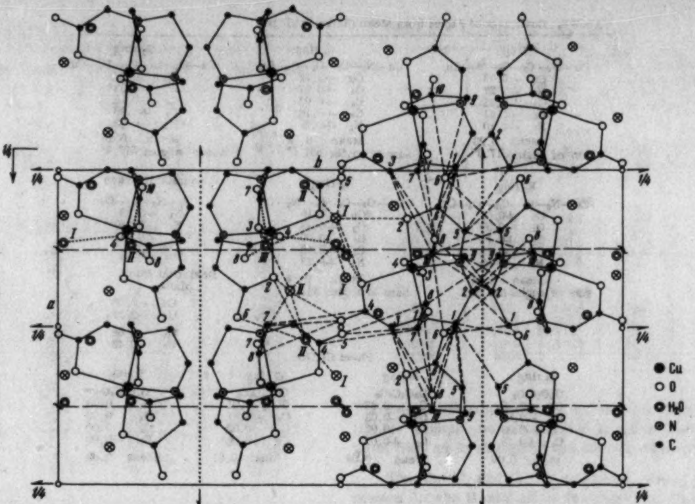

Fig. 3. Projection of structure of $K_2[CuA]\cdot 3H_2O$ on (001) plane.

TABLE 8. Coordination of Potassium Atoms (distances in Å)

$K_I \ldots (H_2O)_I$	3.07	$K_{II} \ldots (H_2O)_I$	2.84
$K_I \ldots (H_2O)_{II}$	2.77	$K_{II} \ldots (H_2O)_{II}$	3.05
$K_I \ldots (H_2O)_{III}$	2.80	$K_{II} \ldots O_3$	3.05
$K_I \ldots O_2$	2.87	$K_{II} \ldots O_6$	2.88
$K_I \ldots O_1$	2.90	$K_{II} \ldots O_7$	2.77
$K_I \ldots O_5$	2.75	$K_{II} \ldots O_5$	2.78

TABLE 9. Coordination of Water Molecules (distances in Å)

$(H_2O)_I \ldots K_I$	3.07	$(H_2O)_{II} \ldots O_2$	3.02
$(H_2O)_I \ldots K_{II}$	2.84	$(H_2O)_{II} \ldots O_6$	2.92
$(H_2O)_I \ldots O_4$	2.78	$(H_2O)_{III} \ldots K_I$	2.80
$(H_2O)_I \ldots O_1$	2.80	$(H_2O)_{III} \ldots O_3$	3.02
$(H_2O)_{II} \ldots K_I$	2.77	$(H_2O)_{III} \ldots O_8$	2.77
$(H_2O)_{II} \ldots K_{II}$	3.05	$(H_2O)_{III} \ldots O_7$	2.77

axis with the maximal number of contacts; the strongest one are $O_8 \ldots C_3$, $O_8 \ldots C_1$, $O_8 \ldots C_7$, $O_8 \ldots N$. The 2_1 ($\parallel x$) screw axes and the c ($\perp y$) glide plane transform the chains into double layers parallel to (010). The layers are held together by K_{II} ions and $(H_2O)_{III}$ molecules arranged in the cavities in the layer between the chains.

Adjacent layers are linked together by K_I ions and molecules $(H_2O)_I$ and $(H_2O)_{II}$; there are also contacts of complexes related by inversion centers at the cell nodes (the multiple contacts $O_5 \ldots C_7$ and $C_7 \ldots O_5$). Tables 8 and 9 indicate the contacts of the potassium ions and water molecules.

The coordination numbers of ions K_I and K_{II} are 6; their surroundings consist of O atoms from complexes and water molecules. The irregular K polyhedra have mean K–O distances of 2.88 Å.

The coordination numbers of all H_2O molecules are 4; for $(H_2O)_I$ and $(H_2O)_{II}$ we have two adjacent potassium ions (K_I and K_{II}), and also two oxygen atoms O_4, O_1 and O_2, O_6, respectively; the $(H_2O)_{III}$ molecule is coordinated to K_I, O_3, O_8, and O_7. The interatomic distances indicate that $(H_2O)_I$ and $(H_2O)_{III}$ molecules form two hydrogen bonds each with oxygen atoms: $(H_2O)_I \ldots O_4$ 2.78, $(H_2O)_I \ldots O_1$ 2.80, $(H_2O)_{III} \ldots O_8$ 2.77, $(H_2O)_{III} \ldots O_7$ 2.77 Å.

The hydrogen bonds of $(H_2O)_I$ bind adjacent layers of complexes, while the hydrogen bonds of $(H_2O)_{III}$ bind the complexes within layers that are placed one above the other translationally along the z axis.

---

[1] L. L. Martynenko, N. I. Pechurova, E. N. Efremov, and A. I. Grigor'ev, Zh. Neorg. Khim., 12, No. 2, 424 (1967).

[2] N. V. Novozhilova, T. N. Polynova, M. A. Porai-Koshits, and L. L. Martynenko, Zh. Strukt. Khim., 8, No. 3, 533 (1967).

[3] T. N. Polynova, T. V. Filippova, M. A. Porai-Koshits, and L. L. Martynenkc Zh. Strukt. Khim., 11, No. 3, 558 (1970).

[4] J. L. Hoard and H. A. Weakliem, J. Amer. Chem. Soc., 81, 549 (1959).

[5] T. N. Polynova, N. P. Bel'skaya, D. Turc de Garcia Baunus, M. A. Porai-Koshits, and L. L. Martynenko, Zh. Strukt. Khim., 11, No. 3, 164 (1970).

[6] G. S. Smith and J. L. Hoard, J. Amer. Chem. Soc., 81, 556 (1959).

[7] T. N. Polynova, D. Turc de Garcia Baunus, M. A. Porai-Koshits, L. L. Martynenko, and N. A. Luk'yanova, Zh. Strukt. Khim., 11, No. 3, 555 (1970).

[8] F. S. Stephens, J. Chem. Soc., A, 1723 (1969).

Crystal and molecular structures of 4-chloroanthraquinonethiadiazole

O. A. Mikhno, Z. I. Ezhkova, and G. S. Zhdanov

Organic Intermediates and Dyes Research Institute

(Submitted June 7, 1971; resubmitted January 19, 1972)
Kristallografiya, 18, 99-105 (January-February 1973)

X-ray methods have been used to determine the crystal and molecular structures of the compound; the structure has been derived from the Patterson function and has been refined by least squares and successive approximations to the electron-density distribution until R was 0.121. The C−C bond lengths in the end rings of the anthraquinone section are less nearly equal than those in anthraquinone itself; the angles are the most deformed in the ring adjoining the heterocyclic ring. The latter is planar, as are rings I and III. The central ring is not planar, since atom C_5 deviates by 0.09 Å. The Cl atom does not deviate from the plane of its ring. The molecule has a slight bend roughly along the line joining atoms C_9 and C_3.

Crystal and molecular structures have been given[1] for 4-chloroanthraquinoneoxadiazole. Here we report an x-ray study of the related but not isomorphous 4-chloroanthraquinonenthiadiazole, in order to compare the molecular conformations. The synthesis of the compound has been described.[2]

EXPERIMENT

The crystals of the compound

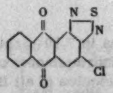

were made in the form of yellow needles by crystallization from solution in nitrobenzene; the cross section of the needles was 0.1 × 0.1 mm. The x-ray patterns gave a = 14.05, b = 11.55, c = 3.81 Å; α = 90°40', β = 96°30', γ = 109°; V = 580 Å^3; space group P$\bar{1}$, N = 2. The molecule lies in a general twofold position. The measured density (by flotation) was d_m = 1.71 g/cm^3, while the calculated density was d_x = 1.72 g/cm^3.

We used a Weissenberg x-ray goniometer with Cu radiation to record scans of the layer lines along the short c axis, which coincides with the axis of the needle. Each layer line was recorded with several exposures in the usual way with multiple films. We obtained 152 hk0 reflections, 302 hk1, and 261 hk2, making a total of 715 independent nonzero reflections. The intensities were estimated visually via blackening marks and were reduced to a common scale via another set of reflections obtained with h0l − h3l scans: 30 h0l, 35 h1l, 30 h2l, and 25 h3l, in all 120 independent nonzero reflections. In converting from the intensities to the structure factors we incorporated the Lorentz and polarization factors; no absorption correction was applied.

STRUCTURE INTERPRETATION

The P(uv) Patterson projection enabled us to establish the x and y coordinates of the Cl and S atoms; localization of these enable us to derive several forms for the projection of the molecule in the (001) plane. Here R for one of these was 0.33, and we refined this planar model by least squares to give R_{hk0} = 0.14.

The z coordinates of the chlorine and sulfur were found from the known x and y coordinates via the three-dimensional Patterson function; the z coordinates of all the other atoms were first of all calculated from geometrical considerations and were refined via linear sections of the three-dimensional electron-density series. The further refinement was based on the three-dimensional data and proceeded from R = 0.195 to R = 0.121 by alternation of least squares and successive approximations to the three-dimensional electron-density series. The final value for the general thermal-vibration constant was B_{tot} = 3.6 Å^2.

Table 1 gives the coordinates of the atoms from the last least-squares cycle, together with the individual isotropic temperature factors, the heights of the peaks in the observed electron-density distribution, and the ones obtained from Weinsteins's equation.[3] From these coordinates we calculated the interatomic distances and angles in the molecule (Fig. 1). The errors in the interatomic distances were calculated via standard equations:[2,4] ε(C−Cl) 0.009; ε(C−N) 0.011; ε(N−S) 0.008; ε(C−O) 0.011; ε(C−C) 0.013 Å. The errors in the angles were estimated via Darlow's equation,[5] and were for CCC, CCO, CCN, CNS ~ 0.7° and for CCCl and NSN ~ 0.5°.

DISCUSSION

Figure 1 shows that the distribution of the bonds in the central ring III of the anthraquinone section is as in anthraquinone itself;[6,7] the C_6-C_5 bond (1.53 Å) is somewhat longer than the analogous one in anthraquinone, but it is close

TABLE 1. Basis-Atom Coordinates, Peak Heights in Electron Density, and Individual and Isotropic Temperature Factors

Atom	x/a	y/b	z/c	ρ, el./Å^3 meas.	ρ, el./Å^3 calc.	D, Å^2
Cl	0.431	0.108	−0.036	19.4	28.2	3.6
S	0.103	−0.048	0.299	19.2	26.2	3.4
O(1)	0.430	0.556	0.264	7.9	11.2	3.8
O(2)	0.066	0.303	0.625	7.6	11.2	4.3
N(1)	0.215	−0.016	0.171	6.8	9.5	3.3
N(2)	0.096	0.087	0.406	7.1	9.5	3.2
C(1)	0.253	0.107	0.203	6.0	8.3	3.8
C(2)	0.351	0.180	0.130	5.8	8.3	2.7
C(3)	0.381	0.304	0.173	6.2	8.3	3.5
C(4)	0.313	0.360	0.315	5.7	8.3	3.7
C(5)	0.347	0.496	0.352	5.5	8.3	3.8
C(6)	0.284	0.562	0.516	5.2	8.3	3.7
C(7)	0.317	0.688	0.565	5.4	8.3	4.0
C(8)	0.257	0.746	0.677	4.5	8.3	4.4
C(9)	0.159	0.682	0.785	4.9	8.3	3.5
C(10)	0.128	0.557	0.735	5.0	8.3	3.7
C(11)	0.189	0.495	0.594	5.6	8.3	3.5
C(12)	0.150	0.362	0.552	5.2	8.3	4.0
C(13)	0.214	0.296	0.391	6.0	8.3	3.6
C(14)	0.188	0.168	0.329	5.5	8.3	3.4

TABLE 2. Geometrical Characteristics of Heterocyclic Parts

Compound	Bond lengths, Å;			Angles		
	C—C	C—N	N—S	CCN	CNS	NCN
1,2,5-thiadiazole[10]	1.420	1.328	1.631	113°46′	—	99°33′
1,2,5-thiadiazole[11]	1.400	1.329	1.628	—	—	99.4°
3,4-benzo-1,2,5-thiadiazole[12]	1.41	1.34	1.60	114°	105°	102°
4-chloroanthraquinonethiadiazole (our results)	1.44	1.34; 1.39	1.63; 1.64	113; 116°	103; 104°	103°

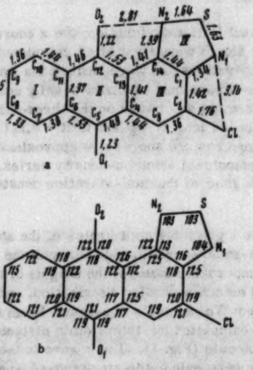

Fig. 1. a) Distances in Å; b) angles in degrees in the molecule.

TABLE 3. C−C and C−N Bond Lengths in Rings of Chlorinated Derivatives

Compound	Bond length, Å	
	C—C	C—N
7,10-dichloroanthraquinoneoxadiazole[4]	1.43	1.34; 1.37
4-chloroanthraquinoneoxadiazole[1]	1.38	1.36; 1.38
4-chloroanthraquinonethiadiazole (our results)	1.44	1.34; 1.39

to the value (1.52 Å) found for the quinoid ring of anthraquinoneoxadiazole.[8] The end rings I and III do not have the equal bond lengths characteristic of anthraquinone; we may note particularly the shortening of the C_7-C_8 bond to 1.33 Å. Some shortening of this bond is found also in 7, 10-dichloroanthraquinoneoxadiazole[9] and in 4-chloroanthraquinoneoxadiazole.[1]

The angles are also substantially different from those for anthraquinone;[6,7] the largest deformations occur in the ring adjoining the heterocyclic one, which is characteristic also of anthraquinoneoxadiazole,[8] 7,10-dichloroanthraquinoneoxadiazole,[9] and 4-chloroanthraquinoneoxadiazole.[1] It is of interest to compare the angles and bond lengths in the heterocyclic ring for this compound with those from other studies.

Table 2 gives the geometrical characteristics of the heterocyclic part in 1,2,5-thiadiazole as obtained by radiospectroscopy[10] and electron diffraction,[11] and also the values for 3,4-benzo-1,2,5-thiadiazole[12] (from x-ray studies), and for our compound. The molecules of the first two compounds are simpler and more symmetrical than is the molecule of our compound, and Table 2 shows good agreement between the results except for one of the C − N bonds, which in 4-chloroanthraquinonethiadiazole is increased to 1.39 Å.

The C − C and C − N bond lengths in the heterocyclic section also agree well with our results for the oxadiazole heterocyclic sections in 7,10-dichloroanthraquinoneoxadiazole[9] and 4-chloroanthraquinoneoxadiazole[1] (Table 3). It is clear that the molecules of all the compounds we have examined show an increase in the length of the C − N bond nearest to the carbonyl oxygen. The same asymmetry in the C − N bonds occurs also in anthraquinoneoxadiazole.[8]

This compound resembles 4-chloroanthraquinoneoxadiazole in having some steric hindrance between Cl and N_1 and also between N_2 and O_2; the distances are Cl... N_1 3.10, O_2... N_2 2.81 Å, while the sums of the van der Waals radii are, respectively, 3.35 and 2.93 Å; probably the steric hindrance between O_2 and N_2 explains the increase in the $C_{12}C_{13}C_{14}$ angle to 126°.

We examined the coplanarity in the molecule by deriving by least squares the equation for the planes through individual parts, together with the deviations of the atoms from these planes; Table 4 shows that rings I and III are planar, as is ring IV. The central ring is less planar, because atom C_5 deviates from the mean plane[2] through atoms C_4, C_6, C_{11}, C_{13} by 0.09 Å, while C_{12} deviates by 0.06 Å. Also, O_1 deviates by 0.18 Å from plane 2, but this is less than the deviation from this plane for the corresponding atom in 4-chloroanthraquinoneoxadiazole (0.34 Å). In terms of angles, these deviations are 4 and 10°, respectively. Atom O_2 deviates from the plane of the central ring by 0.09 Å, while the corresponding atom in the oxadiazole deviates by 0.02 Å. The deviation of Cl from the plane 3 of its ring (0.02 Å) is less than that in the diazole (0.09 Å) and is to the same side. We calculated the angles between the planes of individual rings as drawn through all atoms in each ring and found that they did not exceed 1-1.5°, i.e., they lie within the error of experiment. On the other hand, the oxadiazole has all the rings uniformly turned one relative to another, with the angles being approximately equal at 3-3.5°, and the angle between rings I and III being 6°30′.

The oxadiazole molecule has the boat form, whereas

TABLE 4. Deviations (0.01 Å) of Atoms from Mean Planes

Plane	Cl	S	O_1	O_2	N_1	N_2	C_1	C_2	C_3	C_4	C_5	C_6	C_7	C_8	C_9	C_{10}	C_{11}	C_{12}	C_{13}	C_{14}
1	+02	+08	+12	+03	+06	+09	+07	+02	+05	+03	+07	−01 *	−02 *	+04 *	−03 *	−01 *	+02 *	+02	+09	+11
2	−06	−13	+18	−09	−12	−09	−06	−06	+01	−01 *	+09	+01 *	+05	+10	+00	−03	−01 *	−06	+01 *	−02
3	+02	−05	+13	−11	−06	−05	−01 *	−01 *	+03 *	−02 *	+04	−07	−06	−03	−13	−12	−08	−07	+00 *	+01 *
4		+01 *			−00 *	−01 *	−00 *													+01 *
5	−05 *	+01 *	+09 *	−01 *	−02 *	+03 *	+01 *	−04 *	−01 *	−02 *	+04 *	−04 *	−04 *	+03 *	−03 *	−03 *	−01 *	−02 *	+04 *	+05 *
6	−06	−04	+12	−03	−06	−01	−02 *	−04 *	−00 *	−02 *	+06	−02 *	−01 *	+05 *	−02 *	−02 *	−01 *	−02 *	+03 *	+03 *

Note: Plane 1 through ring I(C_6-C_{11}). Plane 2 through ring II (C_4, C_5, C_{12}, C_{13}), $4.60x-2.809y+3.416z=1.501$. Plane 3 through ring III (C_1-C_4, C_{13}, C_{14}). Plane 4 through heterocyclic ring (Sn, N_1, N_2, C_1, C_{14}). Plane 5 through all atoms. Plane 6 through all C atoms except C_5. The asterisks denote the atoms through which the plane is drawn.

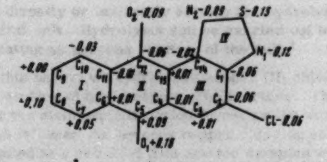
O_2−0.09
N_2−0.09
S−0.13
IV
−0.03
−0.06
−0.02
N_1−0.12
+0.00
C_{10}
C_{11}
−0.01
C_{12}
C_{13}
+0.01
C_{14}
C_1
−0.06
C_9
I
II
III
−0.10
C_8
C_7
C_6
+0.01
C_5
C_4
−0.01
C_3
C_2
−0.06
+0.05
+0.09
+0.01
Cl−0.06
O_1+0.18

Fig. 2. Deviations (Å) of atoms from the plane 2 passing through C_4, C_5, C_{11}, and C_{13}.

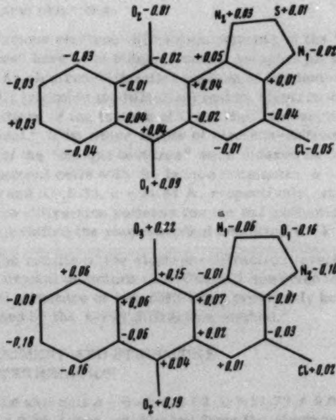
O_2−0.01
N_2+0.03
S+0.01
−0.03
−0.02
+0.05
N_1−0.02
−0.03
−0.01
+0.04
+0.01
+0.03
−0.04
+0.04
−0.02
−0.04
−0.04
−0.01
Cl−0.05
O_1+0.09
O_3+0.22
N_1−0.06
O_1−0.16
+0.06
+0.15
−0.01
N_2−0.10
−0.08
+0.06
+0.07
−0.01
−0.18
−0.06
+0.02
−0.03
−0.16
+0.04
+0.01
Cl+0.02
O_2+0.19

Fig. 3. Deviations (Å) from the mean planes in a) 4-chloroanthraquinonethiadiazole; b) 4-chloroanthraquinoneoxadiazole.

the thiadiazole has a small bend roughly along the line joining atoms C_9 and C_3, as Fig. 2 shows, which gives the deviations of the atoms from the plane of the central ring: C_5, O_1, C_7, C_8 deviate to one side from the mean plane, while atoms C_{10}, C_{12}, O_2, N_2, S, N_1, C_1, C_2 deviate to the other side. Figure 3 shows deviations of the atoms from the mean planes drawn through all the atoms in each of the molecules; it is clear that the thiadiazole is more planar than the oxadiazole.

We use the coordinates of Table 1 to calculate the intramolecular distances; some of them are shown in Fig.4,

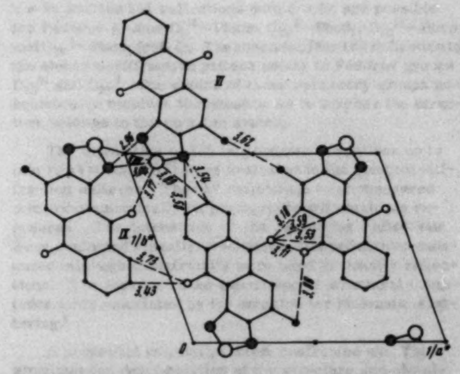
III
3.62
3.04
3.45
3.75
3.17
3.51
3.51
II
1/b*
3.73
3.43
3.18
3.59
3.53
3.17
3.88
0
1/a*

Fig. 4. Dispositions of molecules in projection on (001). Large open circles denote S, small open ones O, large filled ones Cl, small filled ones C, and hatched circles, N.

which shows the disposition of the molecules in projection on the (001) plane. Calculations indicate that the distance S VI... N(2) IX is 3.04 Å, i.e., is less than the sum of the intermolecular radii by 0.38 Å if we take the intermolecular radius of sulfur as[13] 1.85 Å (VI is the molecule in position x, 1 + y, z, while IX is the molecule in position −x, 1−y, 1 −z). The intermolecular S...S distance is reduced to about 3.45 Å in other compounds,[14,16] and it has been supposed[14] that the intermolecular radius of S is not 1.85 Å but 1.72–1.73 Å. That value for the intermolecular radius of S would make the shortening of the S...N distance in our structure 0.26 Å; there is also shortening in the N(2) VI...N(2) IX distance by 0.14 Å. These shortenings of the intermolecular distances do not exceed the values normally observed. All the other intermolecular distances are not less than the sums of the intermolecular radii.

The following conclusions are drawn from this study of the conformations of this oxadiazole and thiadiazole:

1. The molecules differ in conformation: The oxadiazole has the boat form, while the thiadiazole has a small bend.

2. The thiadiazole molecule is the more planar of the two.

3. The conformation is dependent not only on the steric

hindrance (much the same for the two molecules) but also on the nature of the atom in the heterocyclic part.

[1] O. A. Mikhno, Z. I. Ezhkova, L. A. Chetkina, S. L. Ginzburg, M. G. Neigauz, and L. A. Novakovskaya, Kristallografiya, 17, 1140 (1972) [Sov. Phys.–Crystallogr., 17, 1009 (1973)].

[2] M. V. Gorelik, S. B. Lantsman, and T. P. Kononova, Khim. Geter. Soed., 5, 808 (1968).

[3] B. K. Vainshtein, Zh. Eksp. Teor. Fiz., 27, 44 (1954).

[4] M. A. Porai-Koshits, A. Practical Textbook of X-Ray Structure Analysis [in Russian], Vol. 2, Izd. MGU (1960).

[5] S. F. Darlow, Acta Crystallgr., 13, 683 (1960).

[6] K. Lonsdale, H. J. Milledge, and K. El. Sayed, Acta Crystallogr., 20, 1 (1966).

[7] A. Prakash, Acta Crystallogr., 22, 439 (1967).

[8] L. A. Chetkina, S.L. Ginzburg, M. G. Neigauz, and G. A. Gol'der, Zh. Strukt. Khim., 13, No. 1, 91 (1972).

[9] O.A. Mikhno, L. A. Chetkina, and Z. I. Ezhkova, Kristallografiya, 17, 297 (1972) [Sov. Phys.–Crystallogr., 17, 251 (1972)].

[10] S. V. Dobyns and L. Pierce, J. Amer. Chem. Soc., 85, 3553 (1963).

[11] R. A. Bonham and F. A. Momany, J. Amer. Chem. Soc., 83, 4475 (1961).

[12] V. Luzzati, Acta Crystallogr., 4, 193 (1951).

[13] L. Pauling, Nature of the Chemical Bond, Cornell (1960).

[14] D. Van der Helm, A. E. Lessor, and L. L. Merritt, Acta Crystallogr., 15, 1227 (1962).

[15] R. E. Marsh, Acta Crystallogr., 8, 91 (1955).

[16] G. S. Zhdanov and Z. V. Zvonkova, Zh. Fiz. Khim., 24, 1339 (1950).

Electron-diffraction determination of the crystal structure of β-CuOHCl

A. A. Voronova and B. K. Vainshtein

Institute of Crystallography, Academy of Sciences of the USSR

(Submitted December 28, 1971; resubmitted April 23, 1972)
Kristallografiya, 18, 106-111 (January-February 1973)

The dimensions of the unit cell of β-CuOHCl are: $a = 6.45$, $b = 11.72$, $c = 11.75$ Å; Fedorov group $Pbn2_1$. The structure is a two-layered one. The Cu atoms are located in planes spaced $^1/_2$c from each other and parallel to (001), and have the coordination (4 + 2). The vertices of the coordination polyhedron of the Cu atom are occupied by three hydroxyl groups and three Cl atoms. Two hydroxyl groups and two Cl atoms form four short bonds with the Cu atom. The coordination polyhedra of the Cu atoms are linked in the layers edges, between which the hydrogen bonds O−H ... Cl are operative.

Basic salts can be obtained by various methods, which usually directly or indirectly employ the hydrolysis of the neutral salt. Hydrolysis can be carried out indirectly by heating an aqueous solution of the salt.[1]

In this paper, we hydrolyzed copper (II) chloride to obtain samples of basic copper (II) chlorides. The samples for the electron-diffraction investigation were prepared as follows: An aqueous copper chloride solution was applied to a celluloid film and the samples were dried at 50-80°C. After drying, the sample was coated on top with a second layer and again dried at the same temperature. All the samples were prepared only on a gold grid. The employment of brass grids made it possible to form basic zinc chlorides.

Various electron-diffraction patterns of the "oblique textures" have been obtained on the samples prepared this way: An electron-diffraction pattern of the texture of β-CuOHCl (rhombic modification) and an electron-diffraction pattern of the texture of $Cu_2(OH)_3Cl$ (monoclinic modification).[2] Two other forms of electron-diffraction patterns of the "oblique textures" were indexed on the basis of hexagonal cells with the lattice constants: $a = 6.74$, $c = 9.14$ Å and $a = 5.22$, $c = 24.62$ Å, respectively, whereby the electron-diffraction patterns for the hk*l* reflections of the latter satisfied the rhombohedral condition $h - k + l = 3n$.

The results of the electron-diffraction investigation of the crystal structure of β-CuOHCl are given below. The crystal structure of α-CuOHCl has previously been determined by the x-ray diffraction method.[3]

EXPERIMENT AND STRUCTURE DETERMINATION

The unit cell $a = 6.45 \pm 0.02$, $b = 11.72 \pm 0.02$, $c = 11.75 \pm 0.05$ Å was established from the electron-diffraction pattern of the "oblique texture". The axis of texture in our samples coincided with the c axis. It was impossible at this stage of the work to determine accurately the Fedorov symmetry group because of the overlapping of the reflections with equal or close values for d_{hkl}. The symmetry was fixed later during the interpretation of the structure. However, the absence of 0k*l* reflections with $k \neq 2n$ in the electron-diffraction pattern showed that a glide plane b exists. Among the h0*l* reflections, the 201, 203, and 205 reflections were cancelled out. We did not succeed in verifying the extinctions with respect to the other h0*l* reflections: the 10*l* reflections are located close to the primary beam, the 30*l* reflections coincide with the 24*l* reflections, and the 40*l* reflections coincide with the 17*l* reflections. Extinctions of the 0k*l* reflections with $k \neq 2n$ and the 20*l* reflections with $l \neq 2n$ are possible for Fedorov groups D_2^{16}−Pbnm, C_{2v}^9−$Pbn2_1$, D_{2h}^{11}−Pbcm, and C_{2v}^5−$Pbc2_1$ (ref. 4). The absence of the 100 reflection in the electron-diffraction pattern points to Fedorov groups D_{2h}^{16} and C_{2v}^9. The choice of these symmetry groups unequivocally resolves the question as to whether the structure belongs to the rhombic system.

The intensities of 135 independent reflections up to $(\sin \nu/\lambda) \leq 0.398$ Å^{-1} were evaluated in the electron-diffraction patterns. The hk0 reflections were measured microphotometrically on photographs with multiple exposures. The intensities of the remaining reflections were evaluated visually, whereupon the reflections measured microphotometrically were used as density reflections. The squares of the experimental structural amplitudes were calculated by the equation for kinematic scattering.[5]

A somewhat unusual problem confronted us: The simultaneous determination of the structure and chemical composition of the substance. The determination of the structure was begun by constructing a three-dimensional Patterson function. The nonequivalent reflections which coincided in the electron-diffraction pattern were excluded in the initial stage of the search for a model of the structure from the calculations. The structural factors of these reflections were brought into the calculation during the construction of three-dimensional Fourier series in the final stage during the refinement of the coordinates of the atoms.

The three-dimensional Patterson function made it possible to establish that the Cu atoms are located in planes spaced $^1/_2$c from each other and parallel to (001). The x and y coordinates of the Cu atoms were obtained from the location of the maxima in the P(u; v; 0) profile (Fig. 1a). The P(u; v; 0.5) profile determined the shift of the Cu atoms in the second plane relative to the first. The Cu atoms located in one plane form a distorted hexagonal network and contribute only to the hk*l* reflections with h = 2n.

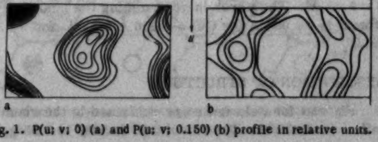

Fig. 1. P(u; v; 0) (a) and P(u; v; 0.150) (b) profile in relative units.

As Belov has shown,[6] the alternation of the populated layers with the unpopulated ones destroys the horizontal planes of symmetry. Therefore, all further calculations were carried out on the basis of the Fedorov groups $C_{2v}^9-Pbn2_1$ and $C_{2v}^5-Pbc2_1$.

From the chemical point of view, Wells[1] distinguishes among the following classes of anhydrous basic chlorides: $M^{II}OHCl$, $M^{II}(OH)_xCl_{2-x}$, and $M_2^{II}(OH)_3Cl$. The crystal structures of atacamite[7] and botallackite,[2,8] which possess the chemical composition $Cu_2(OH)_3Cl$, and the crystal structure of α-CuOHCl (monoclinic phase)[3] are known.

During the analysis of the three-dimensional Patterson function, we assumed that the compound investigated could have the chemical composition $Cu_2(OH)_3Cl$ or CuOHCl. If the compound investigated has the chemical composition $Cu_2(OH)_3Cl$ and the Cu atoms exist in the (4 + 2) coordination, then half of the Cu atoms are surrounded by four OH groups at distances of about 2 Å and by two Cl atoms at longer distances; the remaining Cu atoms also have four OH groups in the coordination plane and a Cl atom and OH group[1,7] occupy the axial positions. Because of the existence of the slip plane b, it proved to be impossible to construct a two-layer model of the structure corresponding to the chemical composition $Cu_2(OH)_3Cl$ in which the coordination polyhedra of the metal atoms would exhibit such a location for the ligands. Therefore, we proceeded to construct a structural model assigning the chemical composition CuOHCl to the compound investigated.

The coordinates of some of the Cl atoms were determined from the P(u; v; 0.150) profile (Fig. 1b). The maxima in the P(u; v; 0.350) profile corresponded to the interlayer distances between the Cu atoms of one layer and the Cl atoms of the adjacent layer. The coordinates of the Cl atoms were also determined from the three-dimensional Fourier synthesis constructed with respect to $|\Phi_{hkl}|$ with h = 2n and with the signs calculated on the basis of the position of the Cu atoms. The coordinates of the O atoms were determined from the three-dimensional Fourier synthesis constructed with respect to all values of Φ_{hkl}.

The magnitudes of the distances between the Cl atoms belonging to the two adjacent layers made it possible to select Fedorov group $C_{2v}^9-Pbn2_1$ unequivocally. In addition, the calculations carried out on the basis of this group led to the best agreement between $|\Phi_{exp}|$ and $|\Phi_{calc}|$. Based on Fedorov group $C_{2v}^9-Pbn2_1$, the smallest interlayer distances between the Cl atoms are: Cl(4)–Cl(2‴), 3.62 Å and Cl(1)–Cl(2″), 3.61 Å.

The coordinates were refined by the method of successive approximations. The relative coordinates of the atoms obtained from the final approximation of the three-dimensional potential series are given in Table 1. The discrepancy factor R = 19.5%, and the temperature factor B = 0.65 Å^2. The error in determining the positions of the atoms[5] is ±0,004 Å for Cu, ± 0.006 Å for Cl, and ± 0.011 Å for O.

DESCRIPTION OF STRUCTURE

Sixteen formula units are contained in the rhombic cell of β-CuOHCl. The calculated density is 3.35 g/cm^3.

The Cu atoms occupy four crystallographically independent positions and have the coordination (4 + 2). The apices of the coordination polyhedron of the Cu atom are occupied by three OH groups and three Cl atoms. Two of the OH groups and two of the Cl atoms form four short bonds with the Cu atom. Furthermore, the Cl atom and OH group located at the greatest distances from the Cu atom complete the coordination polyhedron of the Cu atom forming a distorted octahedron. The formation of a short Cu–Cl bond, while an OH group occupies the axial position in the coordination polyhedron of the Cu atom, is at odds with Orgel and Dunitz's assumption[9] that the long bonds should form ligands creating a weaker field. For example, when this assumption is not justified, it can lead to the compounds[10] $LiCuCl_3 \cdot 2H_2O$ and[11] $(CH_3)_2NNOCuCl_2$. The Cl atoms in the $LiCuCl_3 \cdot 2H_2O$ structure form four short bonds with the Cu atom (Cu–Cl 2.259–2.307 Å), and a water molecule (Cu–O 2.600 Å) and Cl atom (Cu–Cl 2.922 Å) occupy the axial positions in the coordination polyhedron of the Cu atoms. In the $(CH_3)_2NNOCuCl_2$ structure, four Cl atoms form the coordination square of the Cu atom (Cu–Cl 2.289 Å), and the O atom (Cu–O 2.29 Å) and N atom (Cu–N 3.0 Å) occupy the axial positions. However, it should be mentioned that the coordination polyhedra of the Cu atoms with the common edges in these structures are linked in dimers or chains, and the water molecule in the $LiCuCl_3 \cdot 2H_2O$ structure and the O and N atoms in the $(CH_3)_2NNOCuCl_2$ structure form only long bonds with the Cu atoms. The polyhedra of the Cu atoms with common edges in the β-CuOHCl structure are joined in a layer and the hydroxyl group is found at a short distance from one Cu atom at any rate.

The two OH groups, OH(1) and OH(2), in the coordination polyhedron of the Cu(2) atom are located at distances of 2.04 Å from the Cu atom, and the two atoms Cl(1) and Cl(2) at distances of 2.30 Å. Ligands OH(4) and Cl(4), which occupy the axial positions, are found at distances of 2.46 and 2.73 Å, respectively from the Cu(2) atom. The lines passing through the Cu(2) atom and the fifth ligand or the Cu(2) atom and the sixth ligand do not coincide with the normal to the coordination plane.

The interatomic distances in the coordination polyhedron of the Cu(1) atom are equal to the corresponding interatomic distances in the coordination polyhedron of the Cu(2) atom. The coordination polyhedra of the Cu(1′) and Cu(2′) atoms are equal to each other and are specularly equal to the coordination polyhedron of the Cu(2) atom.

TABLE 1. Coordinates of the Basis Atoms in the β-CuOHCl Structure

Atom	x/a	y/b	z/c
Cu(1)	0.950	0,052(5)	0
Cu(2)	0.450	0.052(5)	0
Cu(3)	0.250	0.302(5)	0
Cu(4)	0.750	0.302(5)	0
Cl(1)	0.700	–0.036	0.108
Cl(2)	0.200	0.141	–0.108
Cl(3)	0.950	–0.127(5)	–0.147
Cl(4)	0.450	0.232(5)	0.147
O(1)	0.200	–0.038	0.057
O(2)	0.700	0.143	–0.057
O(3)	0.950	0,228	0.108
O(4)	0.450	–0,123	–0.108

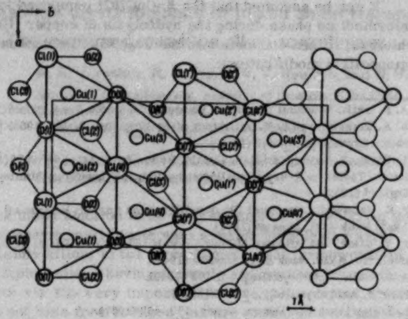

Fig. 2. Projection of one layer of the β-CuOHCl structure along the c axis.

The OH(2) and OH(3) groups and the Cl(1') and Cl(3') atoms in the coordination square of the Cu(4) atom are separated from the Cu atom by distances of 2.01, 2.01, 2.30, and 2.31 Å, respectively. The Cl(4) atom and OH(4') group form longer bonds with the Cu(4) atom: Cu(4)−Cl(4) 2.72 Å and Cu(4)−OH(4') 2.47 Å. The positions of the fifth and sixth ligands in the coordination polyhedron of the Cu(4) atom also do not coincide with the positions of the apices of the dipyramids. The interatomic distances in the coordination polyhedron of the Cu(3) atom are equal to the corresponding interatomic distances in the coordination polyhedron of the Cu(4) atom, and the coordination polyhedron of the Cu(3) atom is specularly equal to the coordination polyhedron of the Cu(4) atom and equal to the coordination polyhedron of the Cu(4') atom.

Two types of chains can be distinguished in the β-CuOHCl structure. The polyhedra of the Cu(1) and Cu(2) atoms are linked by the opposite sides of the OH(1)−Cl(2) and OH(2)−Cl(1) squares and form chains parallel to the *a* axis. The interatomic distances OH(1)−Cl(2) and OH(2)−Cl(1) are 2.86 Å. The common edges of the polyhedra are shortened in accordance with crystallochemical principles. However, it should be mentioned that the coordination polyhedra of the Cu atoms have the shortest common edges when they are joined through their opposite sides into dimers or chains. For example, the common sides of the squares in the[10] $LiCuCl_3 \cdot 2H_2O$ and[11] $(CH_3)_2NNOCuCl_2$ structures pass through the Cl atoms, the distances between which equal 3.11 and 3.13 Å, respectively; the common side of the two squares in the $Cu_3Cl_6(C_6H_7NO)_2 \cdot 2H_2O$ structure[12] passes through the O atoms, the distance between which is 2.32 Å.

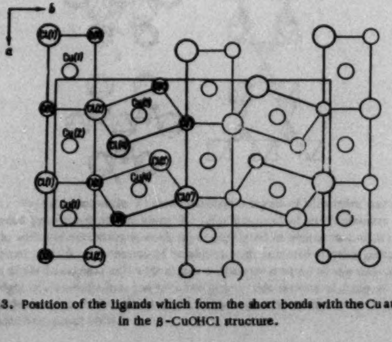

Fig. 3. Position of the ligands which form the short bonds with the Cu atoms in the β-CuOHCl structure.

The polyhedra of the Cu(3) and Cu(4) atoms are linked in chains through the common edges of the dipyramid, whereby the ligand, which is located at a short distance from one Cu atom, occupies the axial position in the coordination polyhedron of the neighboring Cu atom and vice versa.

Upon alternately staggering these two forms of the chains, which are linked by the common edges, a layer is formed. The projection of a single layer of the structure along the c axis with the Cu atoms lying in the plane z = 0 is given in Fig. 2. The arrangement of the ligands forming the short bonds with the Cu atoms in this layer is shown in Fig. 3.

The coordination squares of the Cu(1) and Cu(2) atoms are linked by opposite sides. The coordination squares of the Cu (3) and Cu(4) atoms are not connected to each other, but have one common angle with the two neighboring chains of squares. It is evident from Fig. 3 that all the ligands which enter into the coordination squares of the Cu(1) and Cu(2) atoms form short bonds with three Cu atoms. For example, the OH(2) group is located at short distances from three copper atoms: Cu(1), Cu(2), and Cu(4). However, the ligands which enter into the coordination squares of the Cu(3) and Cu(4) atoms form short bonds with three or with one Cu atom. The ligands which link the coordination squares of the Cu(3) and Cu(4) atoms with the coordination squares of the Cu(1), Cu(2), Cu(1'), and Cu(2') atoms are located at short distances from three Cu atoms [These are those ligands which form the coordination squares about the Cu(1) and Cu(2) atoms]. The remaining ligands are located at short distances only from one Cu(3) or Cu(4) atom.

The distances between the Cu atoms in a layer are: Cu(1)−Cu(2) and Cu(3)−Cu(4) 3.22(5) Å; Cu(1)−Cu(4) and Cu(2)−Cu(3) 3.20 Å; Cu(1)−Cu(3) and Cu(2)−Cu(4) 3.51 Å.

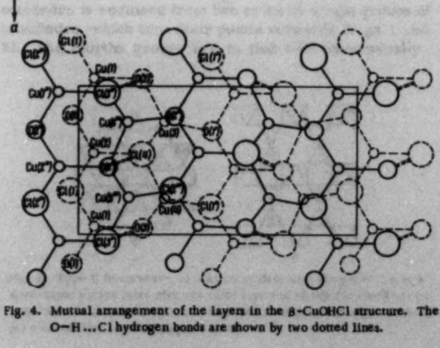

Fig. 4. Mutual arrangement of the layers in the β-CuOHCl structure. The O−H…Cl hydrogen bonds are shown by two dotted lines.

The mutual position of the layers is shown in Fig. 4. It is probable that O—H ... Cl hydrogen bonds exist between the layers. The interatomic distances corresponding to the hydrogen bonds in the β-CuOHCl structure amount to: Cl(3″)—OH(3) 3.18 Å, and Cl(4)—OH(4″) 3.22 Å.

Let us compare the arrangement of the ligands in a layer of the β-CuOHCl structure with the arrangement of the ligands in a layer of the $Cu_2(OH)_3Cl$ structure[2,8] (monoclinic modification). The Cl atoms and OH groups in the β-CuOHCl structure form short bonds with the Cu atoms. Only the OH groups in the $Cu_2(OH)_3Cl$ structure form short bonds with the Cu atoms. However, if the Cl(3) and Cl(4) atoms in a layer of the β-CuOHCl structure, which form one short bond with the Cu atoms, are replaced by hydroxyl groups, each of which forms a short bond with three Cu atoms (which is possible when the slip plane b is replaced by the plane of its mirror image), and the Cl(1) and Cl(2) atoms, each of which forms short bonds with three Cu atoms, are switched to the axial positions, then we will obtain a layer of the $Cu_2(OH)_3Cl$ structure.

It can be assumed that the β-CuOHCl compound is an intermediate phase during the hydrolysis of copper (II) chloride; it then converts into the $Cu_2(OH)_3Cl$ compound (monoclinic modification).

---

[1] A. F. Wells, Structural Inorganic Chemistry, Clarendon Press, Oxford (1962).

[2] A. A. Voronova and B. K. Vainshtein, Kristallografiya, 3, 444 (1958) [Sov. Phys.—Crystallogr., 3, 445 (1958)].

[3] Y. Iitaka, S. Locchi, and H. R. Oswald, Helv. Chem. Acta, 44, 2095 (1961).

[4] Intern. Tables for X-Ray Crystallography, Vol. 1, Kynoch Press, Birmingham, England (1952).

[5] B. K. Vainshtein, Structural Electron-Diffraction Analysis [in Russian], Izd. Akad. Nauk SSSR, Moscow (1956).

[6] N. V. Belov, The Structure of Ionic Crystals and Metallic Phases [in Russian], Izd. Akad. Nauk SSSR, Moscow (1947).

[7] A. F. Wells, Acta Crystallogr., 2, 175 (1949).

[8] F. Aebi, Acta Crystallogr., 3, 370 (1950).

[9] L. E. Orgel and J. D. Dunitz, Nature, 179, 462 (1957).

[10] P. H. Vossos, D. R. Fitzwater, and R. E. Rundle, Acta Crystallogr., 16, 1037 (1963).

[11] V. Klement, Acta Crystallogr., B25, 2460 (1969).

[12] R. S. Sager and W. H. Watson, Inorgan. Chem., 7, 2035 (1968).

Chemical crystallography of mixed anion frameworks.
I. Zirconium and scandium alkali sorosilicates

A. A. Voronkov, R. G. Sizova, V. V. Ilyukhin, and N. V. Belov
Institute of Crystallography, Academy of Sciences of the USSR
(Submitted August 12, 1972)
Kristallografiya, 18, 112-121 (January-February 1973)

The crystallochemical features are considered for stereometrically mixed frameworks by reference to the structures of alkali sorosilicates of Zr and Sc.

The anion function of an element may be judged from its tendency to participate with a major complexing agent (mainly silica) in the three-dimensional frameworks of complex anions having channels and cavities, in particular via the very important feature that complex anions do not have free vertices that are unshared with partners in the framework. Examples of replacements of Si^{4+} are the fairly characteristic tetrahedral cations Be^{2+}, Zn^{2+}, and B^{3+}, and especially Al^{3+}; the last participate in the widely occurring families of aluminosilicates[1] such as feldspars and feldspathoids and also zeolites with their three-dimensional frameworks and large cavities. See ref. 1 on the crystal chemistry of such purely tetrahedral mixed frameworks.

An octahedral arrangement is more characteristic of cations on the Fersman diagonals, such as the aluminum one (Be–Al–Ti), with the quadrivalent Ti^{4+}, or the parallel one with Sc^{3+} and Zr^{4+}; however, recent structural studies[2-13] have shown that there is a tendency for them to form planar and three-dimensional networks that can be called frameworks of mixed type, which have the same functional equivalence of the component frameworks for the stereometrically distinct elements, while maintaining the principal condition for a three-dimensional framework, namely the absence of free vertices in the complex anions. However, while Zr^{4+} enters on an equal footing with Si^{4+} into an octahedral environment, Ti^{4+} clearly shows a tendency to five-fold coordination, the most characteristic polyhedron for Ti^{4+} in planar titanosilicate oxygen nets being a tetragonal pyramid (half an octahedron).

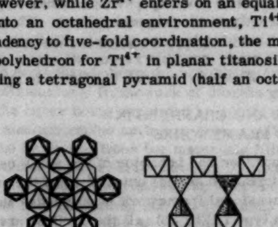

Fig. 1. Type I framework: a) three successive layers of octahedra mutually displaced by one polyhedron along the large diagonal of an elementary rhomb, with the octahedra in each layer populated in accordance with the antispinel law; b) combination of octahedra with centered diortho groups (basis of the hexagonal cell with a repeat distance *a* equal to the sum of the edges of an octahedron and tetrahedron); c) side section of array of octahedra and tetrahedra (three triple packets per c translation of the doubly centered hexagonal cell).

In this paper we consider the crystallochemical features of mixed frameworks (different coordination numbers in the basic elements), in particular, for the structures of the alkali sorosilicates of Zr and Sc.

TWO MODELS OF THE $[AB_2O_7]^{n-}$ FRAMEWORK

We take the following to be the distinctive features of the three-dimensional framework of octahedra and tetrahedra in all types of structures considered below: 1) insular character of the colored octahedra; 2) obligatory sharing of all vertices in the octahedra with tetrahedra in adjacent diortho groups; and 3) the $[Si_2O_7]$ anions are all parallel to a single direction.

Each octahedron is surrounded by six diortho groups, and each Si_2O_7 group is linked to six octahedra. Condition 2 defines the stoichiometry of the framework; in fact, if the numbers of neighbors are equal, to each A octahedron there corresponds one B diortho group, and to each A atom there is a group of $6 \times {}^1\!/_2 = 3$ O atoms, while to each B atom (incorporating the bridge) there are $4 \times {}^1\!/_2 = 2$ such atoms. Then we have the following as the equation for the framework radical: $A^{[6]}B_2^{[4]}O_{3+2+2} = AB_2O_7$.

Hexagonal or trigonal symmetry is obligatory in a three-dimensional array of regular octahedra and linear soro groups by virtue of the above conditions; simple analysis shows that steric difficulties do not occur for atoms in a mixed framework only when the axes of the diortho groups are parallel to the three-fold axes of the octahedra. The consequence of the first and third conditions is a layerwise disposition of the octahedra and tetrahedra: Along the single hexagonal axis (6 or 3) the layers of A octahedra should alternate with two-level layers of B tetrahedra (diortho groups). Formally, the entire framework consists of triple packets, in which a core of octahedra is enclosed from two sides by single groups of tetrahedra, which turn their points outwards (Figs. 1 and 2). The diortho groups are in that case conceptually

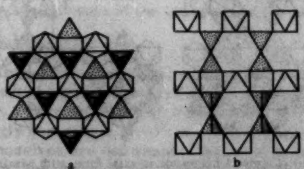

Fig. 2. Type II framework: a) plan coincident with the projection of a three-layer packet (core plus two outer layers of tetrahedra tuned to opposite sides); b) lateral section through two nonequivalent triple packets per c translation in the hexagonal cell.

broken up. The symmetry of such a group of regular polyhedra is P3m.

We get two distinct forms of the model in relation to the inherent symmetry of the diortho groups in the framework; in the first (type I), the two tetrahedra in a B_2O_7 group are mutually turned through 60° (180°), and this array is inscribed in an elongated centrosymmetric octahedron. In type II, the diortho group is inscribed in a trigonal prism, and the tetrahedra are related by a mirror plane. The $\bar{1}$ or m symmetry elements are retained when the packets are combined into a framework. The triple packets (core + layers of tetrahedra) are linked in a type I framework by inversion centers at the bridge vertices of the tetrahedra, while in type II they are related by a mirror plane (through the same vertices), which causes the octahedra in adjacent packets to lie on a single vertical line (parallel to the 6_3 axis) one above the other, but with antiparallel orientation, and translational repetition along the three-fold axis is attained only in the third packet. The holohedral symmetry of the construction corresponds to space group $P6_3/mmc$. The projection of this model along the 6_3 axis coincides with the projection of a single three-layer packet (Figs. 2 and 4a).[2]

The octahedra in a type I framework have identical orientations (parallel in all packets), but each successive octahedral layer is displaced along the major diagonal of the elementary rhomb relative to the preceding one by one octahedron, and a complete translation along the principal axis is attained in three triple packets (Fig. 1). The framework has rhombohedral symmetry $R\bar{3}m$, and the model is more complicated to represent on the printed page. Figure 1a shows the octahedral part, while the fragment shown in Fig. 1b and Fig. 3a illustrates the relationship between the octahedral and tetrahedral layers in the structure of $Na_2ZrSi_2O_7$ and its K analogs.

An additional condition (equality of the edges of the A octahedron and B tetrahedron in the ideal model) allows us to interpret the model in terms of close packing. The requirement for geometrical conformity with close-packed patterns makes the layers in such idealized models substantially defective; the most open layers, with 3/4 vacancies, are ones with bridge atoms in the diortho groups. In the two oxygen layers between them, which contain the triangular faces of octahedra and tetrahedra, only 1/4 of the positions are not filled (in relation to the total number of close-packed spheres); these vacancies are related to location of the alkali cations that fill the holes in the framework.

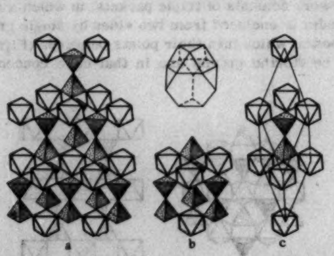

Fig. 3. a) Part of a type I framework in axial form, with parallel orientation of all octahedra; b) isolated cavity in polyhedron and point forms (the latter arises on linking the anions that participate in forming the cavity); c) six-sided and four-sided windows, with hexagonal section of a cavity and minimal rhombohedral cell characterizing the type I framework.

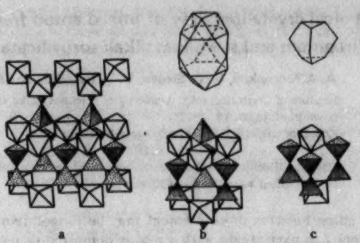

Fig. 4. a) Part of type II framework with antiparallel orientation of the octahedra in adjacent layers; b) large cavity in framework with two hexagonal sections; c) small cavity.

The difference in the geometry of the diortho groups results in different types of spherical packing for the models. The nine-layer tetradymite packing in the first[14] has the equation B/ABACACBCB/A and the symmetry $R\bar{3}m$, which persists in the two-color framework I. The basis of framework II is the B/AB/A hexagonal packing; in the colored framework, in spite of the defectiveness, the $P6_3/mmc$ symmetry is retained, but the translation along the z axis is tripled, to give six packing layers (Fig. 2b).

The two basic types of mixed framework can also be derived from the crystoballite and tridymite ones if we place A octahedra along the three-fold axis in each of the two levels of tetrahedra; but although the high-temperature cubic crystoballite is unique, the trigonal tridymites are now known to be numerous, because it is not essential for all packets to have Si_2O_7 groups either only in the octahedra or only in the trigonal prisms. When they alternate (via a varying law) we get a multiplicity of tridymites, and just as many possible zirconosilicates, although the probability of observing such polytypes is small.

CAVITIES AND CHANNELS IN MIXED FRAMEWORKS

The position and behavior of the alkali cations determine the form and spatial orientation of the cavities in the three-dimensional framework of octahedra and diortho groups; in type I (Fig. 3b), all the cavities are of a single elongated type with their axes along $\bar{3}$. The middle belt is bounded by three diortho groups, which are lined at the bottom via shared A octahedra (base of a cavity). Above the belt of diortho groups we have a triplet of octahedra attached to a tetrahedron that acts as the top cover. The height of the cavity is determined by the three close-packed layers: one octahderal layer and two tetrahedral layers. The belts of octahedra and diortho groups produce a hexagonal ring of diameter $\sim$5.5 Å; the centers of these rings are related to vacancies in the closest-packed layers of spherical packing. The symmetry of a cavity as an empty body corresponds to point group 3m. The cavity has three large six-sided windows in the belt region and three small square ones in the octahedron belt; the diameter of the first coincides with the diameter of the hexagonal section of the cavity. Via the windows, each cavity is in direct contact with six neighbors, in antiparallel orientation on account of the centers of symmetry. As a result, between the octahedral layers of the framework we get a system of broad (d ~ 5 Å) horizontal channels of pseudohexagonal cross section that intersect at 60°.

In a type II framework, the mirror relationship between the triple packets results in two forms of cavity (Fig. 4b, c), with the larger ones elongated along the 6 axis with $\bar{6}2m$ symmetry; these are similar to the cavities of framework I, but the upper and lower halves are identical on account of the horizontal m plane: Above and below the central belt of diortho groups lie triplets of octahedra with tetrahedra closing them. There are four packing layers, not three, in the height of the cavity. In the cavity there are two identical hexagonal cross sections with the same diameter of ~5.5 Å. The number of windows is increased to nine: three six-sided ones in the diortho group belt and three square ones in the two octahedral layers. The latter open into six adjacent cavities of the same type placed above and below the belt of diortho groups. To the six-sided windows are adjoined small cavities of the second type on 6_3 axes; these are isometric and occupy only two packing layers in height. A small cavity is bounded at the sides by three diortho groups, with single octahedra above and below (Fig. 4c). Each such cavity has three six-sided windows, which are shared with the larger cavities. The central sections of both types of cavity coincide with the most open layer in the anion packing and with three vacant nodes (for the closest packing), which occur for each one filled by bridge O atoms. Via the six-sided windows of the two types of cavity there run parallel to the packing layers channels in three horizontal directions, which are of pseudohexagonal cross section; the diameters are almost the same as those of the channels in the typical zeolite $(Ca, Na_2)[Al_2Si_4O_{12}] \cdot 6H_2O$.

POSITIONS FOR THE ALKALI CATIONS

We have considered above the population conditions for a three-dimensional framework of diortho groups and octahedra, the latter being populated by nonferrous atoms of small or medium radius acting as anions. These cavities should be likely positions for materials filling the framework, namely, large alkali cations. In framework I (the base of zirconosilicate phases) the surroundings of a cavity include four octahedra, and towards each octahedra there converge eight cavities of one kind, i.e., there are two cavities per octahedron. A simple calculation³⁾ shows that a cavity can accommodate only one large M^+ cation, so framework I can take alkali cations to the extent of only twice the number of color octahedra with the resultant equation $M_2AB_2O_7$ (this corresponds to the zirconosilicates $M_2ZrSi_2O_7$).

In a type II framework, each octahedron has two cavities, but here they are of different kinds, one being bulky and the other small, and the latter can accommodate only the large cation, while the large one can easily accommodate two cations, because its height is four packing layers (~8.5 Å). As a result, the number of sites that can take alkali cations is three times the number of nonferrous cations, and the possible stoichiometry in the structure of type II corresponds to $M_3AB_2O_7$ (characteristic of the scandium phase $Na_3ScSi_2O_7$). Then to each of the formulas $M_2AB_2O_7$ and $M_3AB_2O_7$ there corresponds a distinctive type of mixed framework. When the diortho groups are transferred from an octahedron to a triangular prism, space is released for the additional M cation without increasing the volume by one formula unit. In a type II framework, the isometric shape of a small cavity dictates that the M cation lies at the center, i.e., in the plane of the most open close-packed layer. The coordination number of this M_1 atom is 9 in the idealized model with M_1-O distances of 2.6-3.0 Å, the most remote ligands being bridge O atoms. Along the 6_3 axes the M_1 atoms alternate with A cations in octahedra. The most suitable positions for alkali cations in the large cavities are the centers of the two hexagonal cross sections; each M_2 cation replaces a deficient sphere in the close packing and is surrounded on its equator by six neighbors at distances of 2.6 Å and by three above or below in the adjacent end face. Such a cation is screened from its partner in the cavity by three bridge O atoms from the widest triangular section of the cavity; the corresponding M_2-O distances are ~3.0 Å.

In a type I framework there is a certain ambiguity as regards the filling of the cation positions; in one extreme case we have filling only of the M_2 position of framework II, while an alternative is an M_2 cation in triangular section in the plane of the bridge O atoms, and in this position the ideal number of nearest neighbors is 12, but the surroundings are less uniform: three anions on the equator, three below (at the base), and six above (hexagonal section), with M−O distances of 3.0, 2.6, and 3.5 Å. Then a M cation in a type I framework may lie at any point in the section joining the limiting positions.

Then even an idealized from for the frameworks (equality of the edges of the octahedron and tetrahedron) allows the cavities to accommodate large cations: K^+, Rb^+, and perhaps Cs^+. The actual sizes of the Zr(Sc) octahedra in the framework causes the volume of the cavities to increase, and they may appear excessive for a cation such as Na^+. The a priori incompatibility of distortion in the framework is largely eliminated, such distortions being the larger the smaller the radius of the alkali cation. The distortions 25 may extend to the diortho groups as well as to the octahedra, and any distortion of the former reduces the symmetry of the structure as a whole, because deformation displaces the Si^{4+} or the bridge O atoms from the three-fold axes, on which are fitted the diortho groups in the idealized models. We shall see below that deformations do not always reduce the symmetry, while the resulting adjustment sometimes can retain all the symmetry elements of the unperturbed framework.

REAL STRUCTURES

We turn now to real structures with mixed frameworks and large cations in the cavities: $Na_2ZrSi_2O_7$, $K_2ZrSi_2O_7$, and $Na_3ScSi_2O_7$. Here there are no surplus Si_2O_7 groups, which are strongly bent (angle Si−O−Si ~ 140°), while the tetrahedra themselves are deformed. The cavities are compressed and the channels are flattened when the symmetry is reduced to monoclinic or triclinic in the zirconosilicates, or to orthorhombic in the Sc silicate. The type I framework is very distorted in the Na, Zr silicate, the

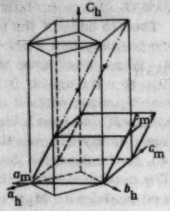

Fig. 5. The relation of the doubly centered hexagonal (rhombohedral) cell and the base-centered monoclinic cell: The first characterizes the undeformed I framework, while the second characterizes the real structure of $Na_2ZrSi_2O_7$ after small deformations of the angles α and β.

corresponding crystal has no visible signs of pseudosymmetry (large value for 2V, irregular habit, no apparent three-fold axes on Laue patterns). Replacement of the comparatively small Na^+ by the large K^+ straightens out the framework, which is reflected primarily in the expansion of the channels.[3,4] The greatest deviation from the ideal symmetry occurs in $Na_3ScSi_2O_7$, which has a mixed framework of type II. The hexagonal pseudosymmetry is seen in the habit of the six-faced crystal plates and also in x-ray patterns recorded along the six-fold pseudoaxis.

Although there are distortions in these real structures, there is a close correlation between framework geometry and lattice metric. Framework II (Fig. 2a, b) is based on a hexagonal unit cell with an a repeat distance equal to the sum of the edges of the octahedron and tetrahedron; the tabulated values for the edges of the Sc octahedron (~3.0 Å) and the Si tetrahedron (~2.6 Å) give us that $a = 5.6$ Å; the c translation is defined by two triple packets of thickness equal to the sum of the heights of octahedra lying on their faces (~ 2.4 Å) and two tetrahedra (2 × 2.15 Å), i.e., 6.7 Å (doubling this, we get the distance c = 13.4 Å). We have $b = a\sqrt{3} = 9.7$ for the orthohexagonal unit cell, and these figures (Table 1) agree well with the observed ones for the orthorhombic cell of $Na_3ScSi_2O_7$ (with deviations due to the distortions in the real structure).[15]

It is fairly simple to calculate the dimensions of the rhombohedral cell for framework I from the basic elements of the three-dimensional framework ($a_{rh} = 7.4$ Å and $\alpha = 44°$ for A = Zr and B = Si). Figure 3c shows a part of the structure within a cell, and this rhombohedron gives an idealized model for the structure of $Na_2ZrSi_2O_7$; the real triclinic cell of the Na zirconosilicate is seen in relation to the ideal rhombohedral cell more clearly if the latter is replaced by the equivalent doubly centered hexagonal cell, whose basis (Figs. 1 and 5) coincides with that described for the cell in framework II ($a = 5.6$ Å). However, the c repeat distance now has three packets: $c \simeq 6.7 \cdot 3 = 20.1$ Å. The corresponding orthohexagonal cell has $a = 5.6$, b = 9.7, c = 20.1 Å. We specify the two horizontal translations and direct the third along the doubly centered space diagonal, which gives us a monoclinic cell with the parameters $a = 5.6$, b = 9.7, c = 7.4 Å; $\alpha = 117°$. Small changes in the angles β and γ give us the triclinic actual cell of $Na_2ZrSi_3O_7$ (Table 1).[4)]

Then to a first approximation the lattice metric in these compounds is determined by the architectural features of the three-dimensional framework of octahedra and diortho groups; actually, the elementary cells deduced for unperturbed frameworks I and II without filling cations will have minimal volumes (the corresponding phases are $Na_2ZrSi_2O_7$ and $Na_3ScSi_2O_7$). Slight displacements of the atoms produce multiplication of the parameters, and in this way one can get superlattices, with the initial parallepiped acting as a subcell. Examples of such superlattices may be seen in the three forms of K zirconosilicate and the rare-earth analog of the Na, Sc phase, namely, $Na_3YSi_2O_7$ (and $Na_3YbSi_2O_7$). The cells of all modifications of $K_2ZrSi_2O_7$ are derived from that of $Na_2ZrSi_2O_7$ by doubling one or three of the linear parameters; for $K_2ZrSi_2O_7$ (I) $a_K = a_{Na} = 5.6$, $b_K = b_{Na} = 9.7$, $c_K = 2c_{Na} = 2 \cdot 7.4 = 14.8$ Å; for $K_2ZrSi_2O_7$ (II) $a_K = 2a_{Na} = 11.2$, $b_K = 2b_{Na} = 19.4$, $c_K = 14.8$ Å. We get the elementary parallelepiped for the rhombohedral $K_2ZrSi_2O_7$ (III) by doubling the edges of the minimal rhombohedron in the mixed framework of type I (Fig. 3b). It has been stated[17] that a further (triclinic) form can exist for $K_2ZrSi_2O_7$.

Similarly, $Na_3YSi_2O_7$ has one unit-cell period doubled ($a_Y = 2a_{Sc}$) while retaining the true hexagonal symmetry of the type II framework, as against the orthorhombic one for $Na_3ScSi_2O_7$.

We now relate the framework distortion on insertion of the alkali cations to the symmetry of the real structure; population of the cavities in the unperturbed framework by alkali cations displaces the bridge O atoms from the three-fold axes on which lie the Si_2O_7 groups in the ideal frameworks, and thus the 3 or $\bar{3}$ axes vanish within the framework of the minimal cells for each type:

TABLE 1. Basic Crystallographic Characteristics of the Alkali Diorthosilicates of Zr, Sc, and Y

Type of mixed framework	Formula	Symmetry	Space group	a, Å	b, Å	c, Å	α, deg	β, deg	γ, deg	Formula units in cell
I	$Na_2ZrSi_2O_7$	Tricl.	$P\bar{1}$	5,42	9.31	6.66	115.5	94	90.5	2
	$Na_2HfSi_2O_7$ *									
	$K_2ZrSi_2O_7$ (I)	Monocl.	$P2_1/b$	5.60	9.54	14,26 (7,13)	116,5	90	90	4
	$K_2ZrSi_2O_7$ (II)	Monocl.	$C2/m$	11,20 (5.60) **	19.10 (9,55)	14.26 (7.13)	116,5	90	90	16
	$K_2ZrSi_2O_7$ (III) ***	Trig.	$R3m$	14.26 (7.13)			46.3			
II	$Na_3ScSi_2O_7$	Orthorhombic	$Pbnm$	5.35	9,35	13.09	90	90	90	4
	$Na_3YSi_2O_7$	Hex.	Laue class $6/mmm$	10.83		13.63	90	90	120	16

*Powder patterns indicate that it is isostructural with $Na_2ZrSi_2O_7$.

** The distinct pseudorepeat distances are shown in parentheses.

***The cell parameters coincide with those of $K_2ZrSi_2O_7$ (II) in the monoclinic setting.

$Na_2ZrSi_2O_7$ and $Na_3ScSi_2O_7$. However, the deformed diortho groups (in general positions) may be related by one of the residual or three-fold axes in the framework, and on increasing the translations by an integer factor, the general hexagonal or rhombohedral symmetry is retained within the new enlarged unit cells. However, the identical adjacent polyhedra and diortho groups cease to be crystallochemically identical; all the same, in this case also the complex groups should remain three-fold axes, and the soro groups should have a linear shape (angle Si–O–Si = 180°) in order to retain the hexagonal or trigonal symmetry.

Table 1 illustrates the correlation of the parameters in this group of diorthosilicates, which is a regular consequence of the structural base, namely, the three-dimensional framework of diortho groups and octahedra. The two types of mixed framework represent different compositions: $M_2^+A^{4+}[B_2^{4+}O_7]$ and $M_3^+A^{3+}[B_2^{4+}O_7]$, which are characterized by cells with the same basis (in the hexagonal setting), which leads to identity (or multiplicity) of the *a* and b parameters no matter what the detailed cation composition of the phases. On the other hand, the c translations are distinctive for each framework type (I and II), and so they may be compared only within each family of structures. Also, the z axis in the monoclinic or triclinic setting chosen for the real Zr silicates is directed not along the three-fold pseudoaxis (edge of the hexagonal cell), but along the doubly centered space diagonal (edge of the distorted rhombohedron), so it is purely an accident if one finds coincidence of the c repeat distances for phases differing in composition.

There is satisfactory qualitative resemblance between these real structures and the a priori models, which implies active coordination of the alkali cations; the a priori coordination number of a M cation is 12 in framework I, whereas in the triclinic $Na_2ZrSi_2O_7$ the first coordination sphere of each of the two independent Na atoms includes only eight ligands with distances of ~2.40–2.97 Å. The Na_1 lies in a cavity close to the center of the broadest triangular section, and it draws towards itself the three surrounding bridge O atoms, causing a bend in the Si_2O_7 group and leaving no bridge for the Na_2 in the adjacent cavity, so Na_2 is displaced in its cavity towards the center of the hexagonal section, whose five oxygen vertices are linked to the central atom. The same environment occurs for the alkali ion in the monoclinic $K_2ZrSi_2O_7$ (I), where the active coordination of K^+ is 8 (with K–O ≃ 2.72–3.08 Å).

Now we consider the deviations from ideal coordination of the M cations in $Na_3ScSi_2O_7$; this example is particularly illustrated because in elucidating the structure one preserved the orthohexagonal setting for the crystal, and the coordinates of the Na atoms fitted almost exactly to the above positions for the alkali cations in the type II framework. The Na_1^+ ions were placed in the symmetry planes in the small cavities, which are too large for Na, and only five O atoms were directly linked to Na_1 out of the nine possible ligands in the real structure. Of these, the bridge atom lies in the m plane and is displaced towards Na_1 as a result of the bend in the diortho group. The Na_2 atom lies in pairs in the large cavities in positions close to the centers of the two hexagonal sections, but the active coordination of these Na_2 is only 4 instead of the 12 in the undistorted model for the framework (coordination of close-packed spheres).

Then the positions of the alkali atoms in the real structures are close to those calculated for the idealized model; the cations lie not simply in the channels in the structure but at the intersection of the channels in large cavities, which are characteristic of the ideal and distorted frameworks and which must be considered as the basis of the actual zirconium and scandium silicates of this composition.

There are thus three main causes of distortion in the three-dimensional framework of diortho groups and octahedra in the real crystal structures: 1) the difference in the edge lengths of the A octahedra and B tetrahedra, which distorts the close packing in the individual layers; 2) the specific shape of the large cavities, which is responsible for uneven surroundings for the alkali cations, with increased probability of bending in the diortho groups and hence the loss of the initial hexagonal or trigonal symmetry; and 3) the incompatibility between the cavity volumes and the size of the filling ion, the degree of distortion increasing as the ionic radius of the alkali cation decreases.

CONCLUSIONS

The crystallochemical features of structures having frameworks of mixed type fairly clearly reflect the interaction of the large alkali cations and smaller other cations during the structure formation, particularly the role of the large cations in subsequent structure modification when the mixed frameworks are stable. A resemblance to the characteristic aluminosilicates and zincosilicates is that a large alkali cation (K or Na) suppresses the initial cation function of Zr or Sc and forces it to pair up with silicon or to replace it: Zr octahedron in place of Si_2O_7 group,[4] this giving the architectural basis of the crystal.

The elementary size conditions mean that a large cation (e.g., K under hydrothermal conditions) can act as a transport agent for a mixed unit such as $\{[Zr]_6 + [Si_2O_7]\}$; once the framework has arisen, the alkali cation is taken up in the cavities in the latter. The strength of the structure is seen in its stability on removing (with appropriate compensation) the alkali cations, which relates these frameworks to those of molecular sieves. Once it has arisen, the framework of Zr octahedra and Si_2O_7 groups determines the metric of the lattice and the structural type of this class of compound.

Electrical neutrality in the three-dimensional framework of A octahedra and B diortho groups is a condition of possible existence of such frameworks as mixed acid anhydrides,5) i.e., without filling cations. If the framework has composition AB_2O_7, the oxygen compounds can be satisfied as regards valence by combinations such as $A^{2+}B_2^{6+}$ (where A = Mg, Ca; B = S, Se), $A^{4+}B_2^{5+}$ (A = Zr, Hf, Ti; B = P, As), and $A^{6+}B_2^{4+}$ (A = Cr, Mo, W; B = Si, Ge). However, when frameworks of types I and II are realized, Pauling's fifth principle is not obeyed, and this is probably why the pyrophosphates of quadrivalent cations (Ti, Zr, Sn, Hf), which fall in one of these combinations, have a different architecture.[14] The phase ZrP_2O_7 has a distinct Zr octahedron alternating with $[P_2O_7]$ diortho groups inscribed in elongated octahedra, but a difference from the alkali Zr diorthosilicates is that the P_2O_7 pyro group is oriented in space in a different way: It is parallel to the four nonintersecting three-fold axes of the cubic space group $T_h^6 = Pa3$ (pyrite type). This is to be contrasted with the alkali Zr diorthosilicates, where all the $[Si_2O_7]$ groups are parallel to the single three-fold axis of an octahedron.

---

1) Here one should point out that octahedral coordination of Zn and Al indicates a more cationic behavior.

2) This model is realized in the structure of $Na_3ScSi_2O_7$.

3) In fact, such a cavity in height involves three packing layers, which in an idealized model corresponds to ~6.5 Å. To avoid abnormally short M^+-O bonds, the M cation should stand off from the top or bottom of the cavity by not less than one packing layer. If two M atoms were placed in the cavity, the distance between them would equal the thickness of one layer, i.e., would be impermissibly small at 2.1-2.4 Å.

4) If the b axis of the resulting cell is directed along the short [110] diagonal, we get the cell given in ref. 16, but it reflects less well the structural features of the framework and therefore is less preferable.

5) Vernadskii considered that the kaolin nucleus $Al_2O_3 \cdot 2SiO_2$ should be considered as an example of this.

[1] N. V. Belov, Chemical Crystallography of Silicates with Large Cations [in Russian], Izd. AN SSSR, Moscow (1961).

[2] A. V. Nikitin, V. V. Ilyukhin, B. N. Litvin, O. K. Mel'nikov, and N. V. Belov, Dokl. Akad. Nauk SSSR, 157, 1355 (1964) [Sov. Phys.-Dokl., 9, 625 (1965)].

[3] A. A. Voronkov, N. G. Shumyatskaya, and Yu. A. Pyatenko, Zh. Strukt. Khim., 11, 933 (1970).

[4] A. N. Chernov, B. A. Maksimov, V. V. Ilyukhin, and N. V. Belov, Dokl. Akad. Nauk SSSR, 193, 1293 (1970) [Sov. Phys.-Dokl., 15, 711 (1971)].

[5] A. N. Chernov, V. V. Ilyukhin, B. A. Maksimov, and N. V. Belov, Kristallografiya, 16, 87 (1971) [Sov. Phys.-Crystallogr., 16, 65 (1971)].

[6] R. G. Sizova, A. A. Voronkov, N. G. Shumyatskaya, V. V. Ilyukhin, and N. V. Belov, Dokl. Akad. Nauk SSSR, 205, 90 (1972) [Sov. Phys.-Dokl., 17, 618 (1973)].

[7] A. A. Petrunina, V. V. Ilyukhin, and N. V. Belov, Dokl. Akad. Nauk SSSR, 198, 575 (1971) [Sov. Phys.-Dokl., 16, 338 (1971)].

[8] N. G. Shumyatskaya, V. V. Ilyukhin, A. A. Voronkov, and N. V. Belov, Dokl. Akad. Nauk SSSR, 185, 1289 (1969) [Sov. Phys.-Dokl., 14, 304 (1969)].

[9] R. K. Rastsvetaeva, V. I. Simonov, and N. V. Belov, Dokl. Akad. Nauk SSSR, 177, 832 (1967) [Sov. Phys.-Dokl., 12, 1090 (1968)].

[10] R. K. Rastsvetaeva, V. I. Simonov, and N. V. Belov, Dokl. Akad. Nauk SSSR, 197, 81 (1971) [Sov. Phys.-Dokl., 16, 182 (1971)].

[11] P. B. Moore and J. Louisnathan, Science, 156, 1361 (1967).

[12] P. J. Woodrow, Nature, 204, 375 (1964).

[13] N. G. Shumyatskaya, A. A. Voronkov, and N. V. Belov, Kristallografiya, 16, 492 (1971) [Sov. Phys.-Crystallogr., 16, 416 (1971)].

[14] N. V. Belov, Structures of Ionic Crystals and Metallic Phases [in Russian], Izd. AN SSSR, Moscow-Leningrad (1947).

[15] S. M. Skshat, V. I. Simonov, and N. V. Belov, Dokl. Akad. Nauk SSSR, 184, 337 (1969) [Sov. Phys.-Dokl., 14, 9 (1969)].

[16] V. Balashov, Acta Crystallogr., 9, 319 (1956).

[17] A. N. Chernov, B. A. Maksimov, V. G. Chukhlantsev, A. A. Voronkov, and V. V. Ilyukhin, Neorg. Mat., 7, No. 1, 180 (1971).

Double cesium—rare earth molybdates of the composition $Cs_3Ln(MoO_4)_3$ (Ln = La, Pr, Nd)

P. V. Klevtsov, V. A. Vinokurov, and R. F. Klevtsova

Institute of Inorganic Chemistry, Siberian Branch, Academy of Sciences of the USSR

(Submitted June 7, 1971)
Kristallografiya, 18, 122-125 (January-February 1973)

Double molybdates of the composition $Cs_3Ln(MoO_4)_3$ (where Ln = La, Pr, Nd) were prepared from a molten solution and by means of chemical reactions in the solid state. The compounds are isomorphous and their crystals belong in the rhombic symmetry class D_{2h}. The parameters of the unit lattice cells are : a = 26.05, b = 9.23, c = 6.40 Å for $Cs_3La(MoO_4)_3$; a = 25.97, b = 9.20, c = 6.39 Å for $Cs_3Pr(MoO_4)_3$; a = 25.91, b = 9.18, c = 6.38 Å for $Cs_3Nd(MoO_4)_3$. The unit cell contains four $Cs_3Ln(MoO_4)_3$ units. The density was determined [4.45 g/cm³ for $Cs_3Pr(MoO_4)_3$] and the infrared spectra of the compounds thus prepared were taken. The thermal stability was investigated. During heating, the double molybdate of the composition $Cs_3La(MoO_4)_3$ decomposes into cesium molybdate Cs_2MoO_4 and a double molybdate of the composition $CsLa(MoO_4)_2$. The decomposition mechanism is identical for all three compounds.

At present the double molybdates and tungstates of alkali and rare earth elements of the composition $M^+Ln^{3+}[Mo(W)\cdot O_4]_2$ and $M_5^+Ln^{3+}[Mo(W)O_4]_4$ are well known. No rare earth compound of the composition $M_3^+Ln^{3+}[Mo(W)O_4]$ is described in the literature. Neither has the formation of the double molybdates $Cs_3Ln(MoO_4)_3$ been detected in an investigation of the phase diagrams of the $CsLn(MoO_4)_2-Cs_2MoO_4$ system for Ln = La and[1] Nd.

References 2 and 3 report on the preparation of crystals of the double molybdates $CsLn(MnO_4)_2$ for the entire series of rare earth elements from molten solutions of cesium bimolybdate and on x-ray structure determinations. We also did experiments on the crystallization of $CsPr(MoO_4)_2$ from a molten solution in Cs_2MoO_4. The highest heating temperature equaled 1000°, and the solution was cooled to 700°C at a rate of 3 deg/h. Besides crystals of the main phase $CsPr\cdot(MoO_4)_2$, a small amount of $Cs_3Pr(MoO_4)_3$ crystals of needle-prism-shape were synthesized. The latter crystals are pale green compared with $CsPr(MoO4)_2$.

The $Cs_3Pr(MoO_4)_3$ crystals are characterized by the powder diffraction pattern reported in Table 1. According to the x-ray diffraction pattern of single crystals, $Cs_3Pr\cdot(MoO_4)_3$ belongs in the rhombic symmetry class sp. gr. $D_{2h}^{16}-Pbnm$. The parameters of the unit lattice cell were determined more accurately by applying the method of least squares to data on powder diffraction and using a special program on an electronic digital computer[4] (pattern recorded with URS-50I equipment, crystalline silicon being taken as the standard); the parameter values thus found are $a = 25.97 \pm 0.08$, $b = 9.20 \pm 0.03$, and $c = 6.39 \pm 0.02$ Å. The unit cell contains four units of the stochiometric formula. The density measured pycnometrically equals 4.45 ± 0.02 g/cm³ (d_x = 4.46 g/cm³.

The crystals prepared were identified by comparing the x-ray diffraction pattern and the infrared spectra taken in pulverized crystals with those of the double cesium—

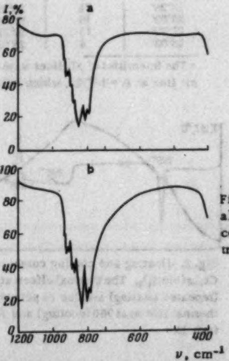

Fig. 1. Infrared spectra of $Cs_3Pr(MoO_4)_3$. a) Sintered compound; b) crystals. Recorded on a double-beam UR-10 spectrograph.

TABLE 1. X-Ray Diffraction Pattern of $Cs_3Pr(MoO_4)_3$*

hkl	d, Å	I	hkl	d, Å	I
120	4.53	6	041, 12.0.0., 141	2.153	11
220	4.33	4	332, 722, 241	2,136	8
411, 320	4.05	4	12.1.0., 540, 831	2,099	8
420	3,748	55	640	2.028	3
221	3,587	38	541, 931, 11.2.1	1,960	10
520, 321	3.432	79	12.2.0, 740, 13.1.0	1,948	4
611	3.333	7	922, 641, 023	1,935	8
701, 002	3.194	100	223, 732	1,911	8
130, 521	3,038	9	323, 840, 12.2.1., 11.3.0.	1,880	9
230, 112	2,987	5	613, 13.1.1., 142	1,866	12
720	2.882	11	14.0.0., 423, 242, 10.2.2.	1,844	25
131	2.746	2	13.2.0, 832, 250	1,817	4
820	2.648	2	841, 940	1,794	5
022	2,608	6	623, 13.2.1., 12.1.2., 542	1,752	5
10.0.0., 512	2.592	6	351, 941, 233	1,727	7
911	2,523	5	642, 333, 723, 903	1,710	3
422, 920	2.432	37	551, 15.0.1., 12.2.2., 13.1.2	1,664	3
730, 522, 631	2.337	10	842, 11.3.2	1,613	4
140, 11.1.0.	2.281	5	923, 751	1.598	6
240, 10.2.0	2.258	12	16.1.0.,14.0.2	1.594	9

*The intensities of the reflections in the Weisenberg diffraction patterns were taken into account in the assignment of indices to the reflections in the diffraction pattern.

TABLE 2 Parameters of the Unit Cell and Density

Compound	a, Å	b, Å	c, Å	d, g/cm³	
				x-ray	pycnometer
$Cs_3La(MoO_4)_3$	26.05	9.23	6.40	4.41	—
$Cs_3Pr(MoO_4)_3$	25.97	9.20	6.39	4.46	4.45±0.02
$Cs_3Nd(MoO_4)_3$	25.91	9.18	6.38	4.48	—

TABLE 3. Powder Diffraction (CuK_α) Pattern of the Decomposition Products of $Cs_3La(MoO_4)3$*

θ	I	$CsLa(MoO_4)_2$ [7]		Cs_2MoO_4 [5, 6]	
		θ	I	θ	I
11°08′	2			11°07′	9
11°30′	7			11°28′	17
12°30′	6			12°31′	8
13°06′	31			13°07′	100
13°21′	100	13°21′	100	13°21′	80
13°34′	76	13°35′	79	13°34′	46
14°44′	6			14°50′	9
15°38′	4			15°38′	10
16°16′	4			16°14′	11
16°32′	5	16°32′	14		
17°04′	1	17°03′	1		
17°43′	6			17°43′	22
17°58′	6	17°57′	13		
18°44′	11	18°43′	14	18°45′	11
18°58′	13			18°58′	24
19°25′	12	19°25′	38		
20°07′	3			20°07′	6
20°58′	5	20°55′	6	20°56′	9
21°13′	4	21°12′	6	21°14′	5
22°23′	2	22°23′	3	22°23′	6
22°48′	3			22°44′	8
23°28′	24	23°27′	59	23°27′	18
23°52′	46	23°53′	79	23°53′	14
27°32′	13	27°32′	42		
28°03′	4	28°03′	39		

* The intensities of all lines were estimated with reference to the strongest line at θ = 13°21′, which belongs to tetragonal $CsLa(MoO_4)_2$.

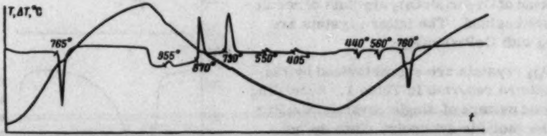

Fig. 2. Heating and cooling curves recorded during differential thermal analysis of $Cs_3La(MoO_4)_3$. The thermal effects at 550 and 405°C (cooling) and at 440 and 560°C (repeated heating) are due to polymorphic conversions in Cs_2MoO_4 (ref. 5), and the thermal effects at 730 (cooling) and 760°C (repeated heating) are due to the eutectic (ref. 1).

praseodymium molybdates of the assumed composition synthesized by reactions in the solid phase. Stoichiometric mixtures of the oxides were sintered at 500°C for 240 h and repeatedly ground at intervals during sintering. The x-ray diffraction patterns, the infrared spectra (Fig. 1), and the density point to the above-mentioned composition. From these spectra it can be concluded that the Mo atoms in the crystal structure are located in distorted oxygen tetrahedra.

The analogous La and Nd compounds were prepared by sintering the oxides $Cs_2O(Cs_2CO_3)$, Ln_2O_3, and MoO_3 in the stoichiometric ratio. The two compounds turned out to be isomorphous to the praseodymium compound; the parameters of their unit lattice cells are given in Table 2; they belong to the sp. gr. D_{2h}^{16}–Pbnm, Z = 4.

The thermal stability of the $Cs_3Ln(MoO_4)_3$ compounds was studied by differential thermal analysis (DTA). The curves referring to heating and cooling in air at a rate of 10 deg/min were taken in a NTR-62M equipment. The temperature was determined within ± 20°. These compounds decompose at 765 (La), 725 (Pr), and 710°C (Nd). After heating to above the melting point, the thermal effects produced by the decomposition products are revealed by the thermographic curves. The DTA curves for the lanthanum compound are shown in Fig. 2. Analysis of the powder x-ray diffraction pattern (Table 3) recorded after melting of the substance suggests the following conclusion: $Cs_3La \cdot (MoO_4)_3$ decomposes into a double molybdate of the composition $CsLa(MoO_4)_2$ and into Cs_2MoO_4, which agrees with the DTA data and the infrared spectra, the spectra being a superposition of the spectra of the decomposition products. $Cs_3Pr(MoO_4)_3$ and $Cs_3Nd(MoO_4)3$ decompose in an analogous way.

---

[1] M. V. Mokhosoev, I. F. Kokot and I. S. Kononenko, Zh. Neorgan. Khimii, 15, 271, 1648 (1970).

[2] V. A. Vinokurov and P. V. Klevtsov, Kristallografiya, 17, 127 (1972) [Sov. Phys.–Crystallogr., 17, 102 (1972)].

[3] R. F. Klevtsova, V. A. Vinokurov and P. V. Klevtsov, Kristallografiya, 17, 284 (1972) [Sov. Phys.–Crystallogr., 17, 240 (1972)].

[4] F. A. Brusentsev and A. N. Rebenko, Zh. Strukt. Khimii, 7, 136 (1966).

[5] R. Salmon and P. Caillet, Bull. Soc. Chim. France, No. 5, 1569 (1969).

[6] F. X. Kools, A. S. Koster, and G. D. Rieck, Acta Crystallogr., B26, No. 12, 1974 (1970).

Unusual ion coordination numbers in the structure of garnet

B. V. Mill' and G. Ronniger

M. V. Lomonosov Moscow State University

(Submitted July 7, 1971)
Kristallografiya, 18, 126-132 (January-February 1973)

Evidence is presented for sixfold coordination of Ca^{2+}, Cd^{2+}, Na^+, Ln^{3+}, Ge^{4+}, eightfold coordination of In^{3+}, Sc^{3+}, Li^+, and fourfold coordination of Cd^{2+} in garnet; the scope for occurrence of unusual coordination numbers is discussed for garnets containing isomorphous components.

The anion packing in garnet has holes with coordination numbers of 8, 6, and 4, which are usually populated by cations in accordance with their size, i.e., the larger ions take up cavities with higher coordination numbers, but there are exceptions, for instance1) Al^{3+} (0.39 Å), which has less preference for coordination number 4 than does the larger ion[2] Ga^{3+} (0.47 Å). In yttrium iron garnet, the smaller ion Cr^{3+} (0.62 Å) replaces Fe^{3+} (0.65 Å) only in the *a* positions.[3]

There are also ions with a marked preference for one particular coordination. We now have much evidence on the behavior of various ions in garnet, which has been surveyed.[3,4] A comparison with ref. 5 indicates how much evidence has accumulated on compounds with the garnet structure and ions in them and how much change there has been in our views on the scope for entry of ions into the various polyhedra.

Here we present new results on the entry of various ions into unusual positions in garnet and we show that the effect is sometimes very important.

Specimens were made by sintering in air with the temperatures and mixtures stated in the table, the components being always of purity at least 99.5%. The x-ray phase analysis was performed with a URS-50IM diffractometer (Co Kα radiation, SI-4R counter).

SIXFOLD COORDINATION OF Ca^{2+}, Cd^{2+}, Na^+, Ln^{3+}, AND Ge^{4+}

The scope for coordination number 6 in garnet has been demonstrated for Ca^{2+} (1.00 Å), Cd^{2+} (0.95 Å), and Ge^{4+} (0.54 Å) by the synthesis of tetragonal garnet-type phases at high pressures:2) $\{Ca_3\}[CaGe](Ge_3)O_{12}$ and $\{Cd_3\}[CdGe](Ge_3)O_{12}$.[5-7] Also, the garnet $\{Ca_3\}[CaZr]\cdot(Ge_3)O_{12}$ with $a = 12.716$ Å was[8] made at normal pressure, and this and its Hf analog (Table 1) were made independently by one of us[4] on the basis that Ca^{2+} would enter the *a* positions in pairs with sufficiently large tetravalent ions ($r_{Zr^{4+}} = 0.72$; $r_{Hf^{4+}} = 0.71$ Å). The smaller Sn^{4+} (0.69 Å) and Ti^{4+} (0.61 Å) do not form such garnets at atmospheric pressure, but in the systems $Ca_3[M^{3+}_{2-2x}Ca_xSn_x]Ge_3O_{12}$ with large M^{3+} ($r_{In^{3+}} = 0.79$; $r_{Yb^{3+}} = 0.86$ Å) a large fraction of the *a* positions (not less than 75%) can be taken by $Ca^{2+} + Sn^{4+}$ (Table 1 and Fig. 1). To synthesize $Ca_3[CaSn]\cdot Ge_3O_{12}$ requires a relatively low pressure, and it is very likely that this garnet would not have tetragonal distortion. From mixtures $Ca_{3+x}In_{2-2x}Ti_xGe_3O_{12}$ we were unable even at x = 0.5 to produce a single-phase ceramic of garnet, i.e., the small Ti^{4+} is a less convenient partner for Ca^{2+} than is Sn^{4+}. Sintering of $Ca_{3+x}In_{2-2x}Ge_{3+x}O_{12}$ mixtures resulted in the lattice parameter *a* of the garnet phase falling by at most 0.005 Å. We used the mean parameter for $Ca_3[CaGe]Ge_3O_{12}$ of[7] $a_{av} = \sqrt{a^2c} = 12.45$ Å to estimate that $x_{max} < 0.1$ in the latter system; we see that reduction in the size of M^{4+} hinders the entry of the large Ca^{2+} into the *a* positions. If Ca^{2+} (*a*) is to enter, the size of M^{3+} must also be sufficiently large. In the system $Ca_{3+x}Cr_{2-2x}Sn_x\cdot Ge_3O_{12}$ containing the small Cr^{3+} (*a*), one estimates from the change in *a* that there is only very restricted substitution; even at x = 0.25, the garnet is not a single-phase system. The *a* for $Ca_{3+x}Fe_{2-2x}Ge_{3+x}O_{12}$ does not alter (12.322 Å) and x = 0. When $Ca_{3+x}Fe_{2-2x}Sn_xGe_3O_{12}$ mixtures are sintered, the parameter of the garnet phase increases substantially with x, but the Fe^{3+} ions can take up d positions, so the substitution occurs via a different scheme: $\{Ca_3\}[Fe_{2-x}Sn_x](Ge_{3-x}Fe_x)O_{12}$, and the garnet $Ca_3Sn_2Fe_2\cdot GeO_{12}$ has $a = 12.61 \pm 0.01$ Å.

We have considered in detail the conditions for entry of Ca^{2+} into cavities with coordination number 6 in order

TABLE 1. Synthesis Conditions and Cell Parameters for Garnets

Formula	Synth. temp., °C	Cell parameter, Å
$Ca_3[CaZr]Ge_3O_{12}$	1350	12.719±4
$Ca_3[CaHf]Ge_3O_{12}$	1350	12.700±4
$Ca_3[Ca_{0.75}Sn_{0.75}In_{0.5}]Ge_3O_{12}$	1350	12.632±3
$Ca_3[Ca_{0.5}Sn_{0.5}In]Ge_3O_{12}$	1325	12.616±3
$Ca_3[Ca_{0.25}Sn_{0.25}In_{1.5}]Ge_3O_{12}$	1325	12.601±3
$Ca_3[Ca_{0.75}Sn_{0.75}Yb_{0.5}]Ge_3O_{12}$	1375	12.675±3
$Ca_3[Ca_{0.5}Sn_{0.5}Yb]Ge_3O_{12}$	1325	12.699±3
$Ca_3[Ca_{0.25}Sn_{0.25}Yb_{1.5}]Ge_3O_{12}$	1325	12.723±3
$Ca_3[Ca_{0.25}Ti_{0.25}In_{1.5}]Ge_3O_{12}$	1325	12.580±3
$NaPb_2[Cd_2]V_3O_{12}$	750	13.052±5
$NaCa_2[Cd_2]V_3O_{12}$	700	12.763±3
$NaCa_{2.2}Cd_{1.8}V_3O_{12}$	750	12.769±3
$Ca_3Na_{2/3}Zr_{4/3}Ge_3O_{12}$	1200	12.670±4
$Na_{0.8}Pb_{2.2}[Na_{0.2}Cd_{1.8}]V_3O_{12}$	750	13.075±10
$La_3[Lu_2]Ga_3O_{12}$	1375	13.038±3
$Pr_3[Lu_2]Ga_3O_{12}$	1325	12.935±4
$Nd_3[Lu_2]Ga_3O_{12}$	1400	12.883±4; 12.88[14]
$La_3[Yb_2]Ga_3O_{12}$	1350	13.052±2
$Pr_{2.92}Yb_{0.08}[Yb_{1.95}Ga_{0.05}]Ga_3O_{12}$	1325	12.940±5
$Ca_3[Fe_{1.5}Mg_{0.25}Ge_{0.25}]Ge_3O_{12}$	1225	12.307±3
$\{La_{2.8}In_{0.2}\}[In_2](Ga_3)O_{12}$	1300	12.934±4
$\{La_{2.8}In_{0.2}\}[In_{1.9}Ga_{0.1}](Ga_3)O_{12}$	1300	12.928±4
$\{La_{2.6}Sc_{0.4}\}[Sc_2](Ga_3)O_{12}$	1300	12.839+3
$(Pb_{2.53}Cd_{2.47}\}[Cd_2](Cd_{0.33}V_{2.67})O_{12}$	820	13.213±3

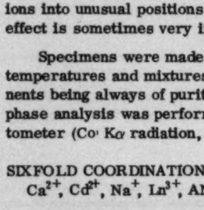

Fig. 1. Cell parameter *a* as a function of x for: 1) $Ca_3[Yb_{2-2x}Ca_xSn_x]\cdot Ge_3O_{12}$; 2) $Ca_3[In_{2-2x}Ca_xSn_x]Ge_3O_{12}$.

to show how our approach is used in solving such problems. Although Cd^{2+} is smaller than Ca^{2+}, garnets of the type $M^{2+}[CdZr]Ge_3O_{12}$ (M = Sr, Ca, Cd) are not formed under our conditions. On the other hand, Cd^{2+} vigorously enters the *a* positions in V^{5+} garnets.[9] Three such garnets are listed in Table 1, and in these all the octahedra are taken by Cd^{2+}, and in the last the Cd^{2+} partially fills also the c and d positions (see below). On the other hand, Ca^{2+} enters V garnets, and also germinates, only in the *a* positions and in restricted amounts.[9]

Na^+ (1.02 Å) is similar in radius to Ca^{2+}, but there is no information on the sixfold coordination of Na^+ in garnets. We made a garnet of composition[3] $Ca_3Na_{2/3}Zr_{4/3}\cdot Ge_3O_{12}$, but the x-ray pattern of the powder made it difficult to decide whether Ca^{2+} or Na^+ (or randomly both) enters the *a* positions. A similar problem arises for the garnet $NaCa_{2.2}Cd_{1.8}V_3O_{12}$, but in $NaPb_{2.2}Cd_{1.8}V_3O_{12}$ the *a* positions of course contain Na^+ (Table 1).[9] Thus Na^+ can have coordination number 6 in garnets.

We find the first indication of sixfold coordination for rare-earth elements (Ln^{3+}) and Y^{3+} in Ga garnets in refs. 11 and 12. Subsequently, Ge garnets were made in which all the *a* positions were taken by ions from Lu^{3+} (0.86 Å) to Dy^{3+} (0.91 Å).[13] It was recently stated that Ga garnets have been made in which the c and *a* positions have been completely filled[14] by Ln^{3+}. We would like to point out here that we made such garnets as long ago as 1967,[15] on the basis that sufficiently large Ln^{3+} in the c positions would enable the *a* positions to take up considerable amounts of small rare-earth ions; some of the synthetic garnets of this type are listed in Table 1. In the general case, the composition of such a garnet may be put as $\{Ln_{3-y}Ln_y'\} \times [Ln_x'Ga_{2-x}](Ga_3)O_{12}$, where $x_{max} = 2$ and usually $y < 1$ for $x = 2$. Only in certain cases does one attain compositions of the type $\{Ln_3\}[Ln_2'](Ga_3)O_{12}$, where $x = 2$ and $y = 0$ (Table 1). When ions larger than Lu^{3+} enter the *a* position, some of them simultaneously go also to the c position; for instance, the systems $Nd_2O_3-Ln_2'O_3-Ga_2O_3$ have given the single-phase garnets[14] $Nd_{2.7}Yb_{0.3}[Yb_2]\cdot Ga_3O_{12}$ and $Nd_{2.4}Tu_{0.6}[Tu_2]Ga_3O_{12}$.

There is an almost complete lack of such solid solutions with a garnet structure in the systems $Ln_2O_3-Fe_2O_3$ and most of the systems of the type $Ln_2O_3-Al_2O_3$, which is due to the existence of phases with the 1:1 perovskite structure, which take up the excess Ln_2O_3. In gallate systems, compounds with the perovskite structure are formed at normal pressure only with the largest Ln^{3+} ($La^{3+}-Nd^{3+}$); in the systems $Yb_2O_3-Al_2O_3$ and $Lu_2O_3-Al_2O_3$, in which there are no 1 : 1 compounds, the garnet structure will take up ~2 mole% of the excess Ln_2O_3, which is substantially less than in the corresponding Ga systems (up to 10 mole%).[12] It is clear that the Al garnets provide conditions for entry of large Ln^{3+} in pairs with the very small Al^{3+} (0.53 Å) less favorable than those found in the Ga garnets ($r_{Ga^{3+}} = 0.62$ Å).

There is no direct evidence for coordination number 6 for Ge^{4+} in garnets at normal pressure. Geller et al.[3] used magnetic measurements to deduce coordination number 6 for small amounts of Ge^{4+} in substituted ferrite garnets; to introduce small Ge^{4+} ions into the *a* positions, we used the system $Ca_3[M^{3+}_{2-2x}M_x^{2+}Ge_x]Ge_3O_{12}$ with the smallish ions Fe^{3+} and Mg^{2+} (0.72 Å). At x = 0.25, the garnet consisted of a single phase (Table 1), but at x = 0.5 the ceramic was not of single-phase composition, and from $a_{min} = 12.303 \pm 3$ Å one can estimate that $x_{max} \simeq 0.3$. Then Ge^{4+} can enter the *a* positions in restricted amounts at normal pressure also.

EIGHTFOLD COORDINATION OF In^{3+}, Sc^{3+}, AND Li^+

The ions In^{3+} (0.92 Å), Sc^{3+} (0.87 Å), and Li^+ are comparable in size with Mg^{2+} (0.89 Å), Co^{2+}, Zr^{4+} (0.84 Å) and Hf^{4+} (0.83 Å), for which coordination number 8 in garnets is known;[4] however, attempts to make garnets of the type $\{(In, Sc)_3\}B_5O_{12}$ (B = Al, Ga, Fe) at normal and elevated pressures have been unsuccessful.[16,17] It has recently been found that small amounts of Sc^{3+} will enter the c positions in Nd–Sc ferrite garnets.[18] Previously, we had reported[15] the synthesis of garnets of the type $La_3Ga_{5-x}(In, Sc)_xO_{12}$, but more careful examination showed that the composition of the resulting garnet phases was not as given: To obtain a single-phase sinter for the garnets, the c position must contain small amounts of In^{3+} and Sc^{3+} (Table 1).[4] Further increase in the contents of In^{3+} and Sc^{3+} again lead to a mixture of phases.

We observed coordination number 8 for Li^+ in examining the isomorphism in V^{5+} garnets,[9] and the Li^+ ions show much greater tendency to do this than do In^{3+}, Sc^{3+}, Mg^{2+}, or Co^{2+}. For instance, the garnet of composition $Ca_2Li_2ScV_3O_{12}$ is indicated by x-ray evidence to have the distribution $\{Ca_2Li\}[LiSc](V_3)O_{12}$. At normal pressure, one can introduce Li^+ ions up to 1/3 filling of the dodecahedral positions, which indicates that at high pressures one might make garnets in which all the c positions were filled by Li^+, for instance, $\{Li_3\}[Al_2](M_3^{5+})O_{12}$, where M = P, As, or V (a form of Li analog of pyrope).

FOURFOLD COORDINATION OF Cd^{2+}

In recent years, it has proved possible to introduce into the d positions in garnet ions large for coordination number 4 such as Mg^{2+} (0.58 Å), Co^{2+} (0.57 Å), Ni^{2+}, Zn^{2+} (0.60 Å), In^{3+}.[4,19] In yttrium aluminum garnet containing Mn^{2+}, it is found from ESR that the Mn^{2+}(c) and Mn^{2+}(*a*) are accompanied by very small amounts of Mn^{2+}(d).[20] In the system $PbO-CdO-V_2O_5$ we have observed a range of formation of garnets containing Cd^{2+} with coordination number 4, and one such composition is listed in Table 1, which contains Cd^{2+} in all three positions simultaneously. The system $PbO-CdO-V_2O_5$ gives a maximal lattice parameter for the garnet phases of 13.255 Å, but the composition $Pb_3Cd_{2.33}V_{2.67}O_{12}$ is not attained, and Pb^{2+} in the c positions is always diluted to a considerable extent by Cd^{2+}.

DISCUSSION

Garnet specialists may find it surprising that one gets coordination numbers 4 for Cd^{2+} and In^{3+}, 6 for Ca^{2+} and Na^+, and 8 for Li^+ and Sc^{3+}, etc., but for all these ions one can quote instances of such coordination numbers in other compounds. For instance, in spinels one finds Cd^{2+} ions and In^{3+} ions frequently preferring the A positions, which have fourfold coordination, while Ge^{4+}

enters into sixfold coordination;[21] for Li^+, eightfold coordination is known in the double tungstates $LiLn(WO_4)_2$, which have the scheelite structure,[22] etc.

In most of these instances of unusual coordination, one is concerned with restricted entry of ions into forbidden positions, and often in extremely specific instances; this might mean that one could neglect the probability of such replacements under ordinary circumstances, e.g., in studying substituted ferrite garnets or in growing single crystals. We know that even small changes in the composition and distribution of ions substantially influence magnetic properties, and the occurrence of magnetic ions in other positions alters the electronic and optical properties, while strongly influencing the magnetic anisotropy and other characteristics of the material. One should therefore be extremely cautious in interpreting the properties of single-crystal and polycrystalline garnets when the exact distribution of the ions is unknown.

Particularly great care is needed in research on single-crystal garnets of complex composition; for instance, in growing Ga garnet crystals, the composition may vary substantially on account of entry of Ln^{3+} into the *a* positions: $\{Ln_3\}[Ga_{2-x}Ln_x](Ca_3)O_{12}$ in the system $Y_2O_3-Ga_2O_3$ from $Y_3Ga_5O_{12}$ ($a = 12.274$ Å) to $Y_{3.74}Ga_{4.26}O_{12}$ ($a = 12.441$ Å).[3] A knowledge of the chemical composition is here obligatory, and considerable error can arise if the composition is deduced from the cell parameter. If we have two kinds of Ln^{3+} ions that differ appreciably in size, the composition of the garnet is expressed by the equation

$$\{Ln_{3-y}Ln'_y\}[Ln'_xGa_{2-x}](Ga_3)O_{12} \qquad (r_{Ln} > r_{Ln'}).$$

The smaller rare-earth ions in the c positions reduce the lattice parameter, while in the *a* positions they increase it, and as a result one cannot deduce the composition from the *a* parameter. Also, Ln^{3+} in Al and Fe garnets has a much lower tendency to take up coordination number 6 than it does in Ga garnets, but we cannot neglect this. Coordination number 6 is observed for Yb^{3+} in yttrium iron garnet containing[23] Yb^{3+}. One should take into account the scope for coordination number 6 for Ln^{3+} in growing the now very popular garnet crystals of complex composition for lasers and storage devices employing cylindrical domains.

Crystals of In- and Sc-bearing Ga and Fe garnets probably contain small amounts of In^{3+}(c) and Sc^{3+}(c) – $\{Ln_{3-y}(In, Sc)_y\}(Fe, Ga)_{5-x}(In, Sc)_xO_{12}$; further such examples might be quoted.

The composition problem is solved automatically for a polycrystalline garnet if this is composed of a single phase (provided there is no loss of components by evaporation), since the composition of the garnet is that of the initial mixture, but the ion-distribution problem remains. Measurements on single crystals of substituted ferrite-garnets have shown that even small amounts of ions such as Co^{2+} and Ni^{2+} in part enter into the d positions.[24,25] We have made the garnet $Y_3Ni_{2.2}Ge_{2.2}Fe_{0.6}O_{12}$, containing at least 9% of Ni^{2+}(d).[26] Geller[3] considered that coordination number 4 was possible for Co^{2+} in garnets, but that Ni^{2+} entered only polyhedra with sixfold coordination. In the systems $Y_3M_x^{2+}Fe_{5-x}M_x^{4+}O_{12}$($M^{2+} = Ni^{2+}$, Mg^{2+}; $M^{4+} = Si^{4+}$, Ce^{4+}), in all substitution ranges, there are small amounts of Ni^{2+}(d) and Mg^{2+}(d). The presence of such neglected small altered distribution factors may, in part, explain the observed differences in the influence of substituents on the magnetic properties of ferrite garnets;[27] of course, there remain differences due to change in the geometry of the exchange interactions when ions differing in size and valence enter the lattice.

It is meaningful to discuss the composition and ion distribution for polycrystalline garnets usually only if they are of single-phase type; if the sintering fails to produce a single-phase ceramic, this often means that the composition of the garnet phase differs from that laid down by the initial mixture. It is not always correct to attempt to determine the maximal degree of substitution by extrapolation from the single-phase region to the maximal or minimal lattice parameter of a multiphase solid solution, because the latter state may indicate a change in the mode of substitution. For instance, in the system $Y_3Fe_{5-2x}Mg_xSi_xO_{12}$, single phase specimens are obtained up to $x = 1.85$, while at higher Mg^{2+} contents the mixture is of several phases on account of entry of Mg^{2+} into the c positions: $\{Y_{3-y}Mg_y\}Fe_{5-2x-y}Mg_xSi_{x+y}O_{12}$, and x_{max} cannot be determined.[27]

These examples would seem to show that one should not neglect the scope for the occurrence of cations whose coordination appears unlikely.

There now remain comparatively few cations that enter only one position in the structure; these are, for example, the very large ions[9] La^{3+}, Nd^{3+}, Bi^{3+}, Sr^{2+}, Pb^{2+}, K^+, Ag^+, Tl^+, for which it is unlikely that one will get a transition from eightfold coordination to sixfold. Also, there are ions having a very strong preference for coordination number 6, such as Cr^{3+}, Mn^{3+}, Rh^{3+}, Sb^{5+}, Te^{6+}.

At normal pressure, it would seem that only minute amounts of Si^{4+} can enter the *a* positions, though such entry is observed at high pressures.[28] Most ions can enter two or three positions in the structure, while showing a preference for some one particular coordination; one finds Cd^{2+}, Mg^{2+}, Co^{2+}, In^{3+}, Li^+ in all three positions, but this list could probably be extended.

The following are some rules for the entry of ions into positions having coordination numbers unusual for them:

1. It is important to choose partners of suitable size in all three positions.

2. An ion can be displaced into other positions by blocking its usual positions with ions that show a strong preference for them; a good example is in the synthesis of garnets in which all the d positions have been taken up by large Zn^{2+} ions, and the *a* positions are blocked by Te^{6+} and Sb^{5+}.[29,30] However, this cannot always be done; attempts have been made to produce garnets in which the Sn^{4+} ions were present only in the d positions, with an attempt to block the *a* positions with[19] In^{3+}, but it was found that the Sn^{4+} in part displaced the In^{3+} into the d positions.

3. High pressures enable one to introduce small ions into the larger polyhedra; some predictions in this respect have been made,[4] and we merely add that it is extremely

likely that one can make garnets in which all c positions are taken up by Li^+.

4. New coordination numbers for ions can sometimes be observed in elucidating the reasons why a garnet ceramic is not of single-phase composition.

5. One can predict the scope for entry of new ions into a garnet or into a previously unknown coordination from the crystallochemical behavior of the ions in other structures.

---

1) We used the ionic radii for the corresponding coordination numbers as given in ref. 1.

2) Braces denote coordination number 8, square brackets denote coordination number 6, and parentheses denote coordination number 4.

3) The lattice parameter of $Ca_3Na_{2/3}Zr_{4/3}Ge_3O_{12}$ is 0.065 Å more than that[4] of $Na_2CaZr_2Ge_3O_{12}$. When a mixture of composition $Ca_3Na_{2/3}Sn_{4/3}Ge_3O_{12}$ is sintered, no single-phase garnet is formed, but the lattice parameter (12.58 ± 0.02 Å) is substantially increased relative to that for $Na_2CaSn_2 \cdot Ge_3O_{12}$, which is[10] 12.44 Å, i.e., the substitution is fairly extensive.

4) With Pr^{3+} we obtained garnets containing In^{3+} and Sc^{3+} only in the *a* positions: $Pr_3In_2Ga_3O_{12}$ (a = 12.829 Å) and $Pr_3Sc_2Ga_3O_{12}$ (a = 12.745 Å).

---

[1] R. D. Shannon and C. T. Prewitt, Acta Crystallogr., B25, No. 5, 925 (1969); B26, No. 7, 1046 (1970).

[2] M. Marezio, J. P. Remeika, and P. D. Dernier, Acta Crystallogr., B24, No. 12, 1570 (1968).

[3] S. Geller, Z. Kristallogr., 125 No. 1 (1967).

[4] B. V. Mill', in: Physical and Physicochemical Properties of Ferrites [in Russian], Izd. MGU (1971).

[5] S. Geller, J. Appl. Phys. Suppl., 31, 5, 30S (1960).

[6] A. E. Ringwood and M. Seabrook, J. Geophys. Res., 68, No. 15 4601 (1963).

[7] C. T. Prewitt and A. W. Sleight, Science, 163, No. 3865, 386 (1969).

[8] S. Geller and G. P. Espinosa, Inorg. Chem., 8, No. 1, 183 (1969).

[9] B. V. Mill' and H. Ronniger, in: Physics and Chemistry of Ferrites [in Russian], Izd. MGU, Moscow (1972).

[10] A. Durif and G. Maupin, Acta Crystallogr., 14, No. 4, 440 (1961).

[11] M. L. Keith and R. Roy, Amer. Mineralogist, 39, No. 1-2, 1 (1954).

[12] S. J. Schneider, R. S. Roth and J. L. Waring, J. Res. Nat. Bur. Standards, A65, No. 4, 345 (1961).

[13] B. V. Mill', Dokl. Akad. Nauk SSSR, 165, 555 (1965) [Sov. Phys.—Dokl., 10, 1015 (1966)].

[14] L. Suchow, M. Kokta, and V. J. Flynn, J. Solid State Chem., 2, No. 2, 137 (1970).

[15] B. V. Mill', Izv. AN SSSR, Inorg. Mat., 5, No. 9, 1604 (1969).

[16] M. A. Gilleo and S. Geller, Phys. Rev., 110, No. 1, 73 (1958).

[17] R. D. Shannon and C. T. Prewitt, J. Inorg. Nucl. Chem., 30, No. 6, 1389 (1968).

[18] J. Loriers, G. Villers, F. Clerc, and F. Lacour, Compt. Rend., B268, No. 24, 1553 (1969).

[19] L. M. Belyaev, I. S. Lyubutin, and B. V. Mill', Kristallografiya, 15, 174 (1970) [Sov. Phys.—Crystallogr., 15, 140 (1970)].

[20] J. A. Hodges, J. L. Dormann, and H. Makram, Phys. Status Solidi, 35, No. 1, 53 (1969).

[21] G. Blasse, Ferrospinel Chemical Crystallography [Russian translation], Metallurgiya, Moscow (1968).

[22] L. G. Sillen and K. Lundborg, Z. anorgan. und allgem. Chem., 252, No. 1, 2 (1943).

[23] J. F. Dillon, J. P. Remeika, and L. R. Walker, J. Appl. Phys., 38, 2235 (1967).

[24] M. D. Sturge, E. M. Gyorgy, R. C. Le Craw, and J. P. Remeika, Phys. Rev., 180, No. 2, 402, 413 (1969).

[25] R. Krishnan, Phys. Status Solidi, 18, No. 1, K53 (1966).

[26] K. P. Belov, B. V. Mill', V. I. Sokolov, and T. D. Khien, Fiz. Tverd. Tela, 13, 873 (1971) [Sov. Phys.—Solid State, 13, 721 (1973)].

[27] S. Geller, H. J. Williams, G. P. Espinosa, and R. C. Sherwood, Bell System Tech. J., 43, No. 2, 565 (1964).

[28] A. E. Ringwood, Earth Planet. Sci. Letters, 2, No. 3, 255 (1967).

[29] H. M. Kasper, Mater. Res. Bull., 3, No. 9, 765 (1968).

[30] B. V. Mill', Dokl. Akad. Nauk SSSR, 191, 86 (1970) [Sov. Phys.—Dokl., 15, 201 (1970)].

Effect of an electric field on phase transitions in $Na(D_xH_{1-x})_3(SeO_3)_2$ crystals. I. Induction of the β phase in crystals having $x \geqslant 0.3$ by the field E_y

L. A. Shuvalov, A. M. Shirokov, N. R. Ivanov, and A. I. Baranov

Institute of Crystallography, Academy of Sciences of the USSR
(Submitted November 3, 1971; resubmitted March 12, 1972)
Kristallografiya, 18, 133-137 (January-February 1973)

Optical and dielectric investigations were carried out which showed that, in $Na(D_xH_{1-x})_3(SeO_3)_2$ crystals with $x \geqslant 0.3$, which normally do not have a triclinic ferroelectric phase, this phase may be induced by applying an electric field along the Y axis. E_yT phase diagrams of the crystals were studied. It was concluded that different types of two-component electrical ordering, observed for the first time, occur in different ferroelectric phases.

INTRODUCTION

One of the most interesting peculiarities of ferroelectric $Na(D_xH_{1-x})_3(SeO_3)_2$ (SDHS) crystals is the dependence of the number and symmetry of the ferroelectric phases and the character of electrical order in them on the deuterium content x in the crystals (we call this new phenomenon isotopic anisomorphism[1-5]). In particular, SDHS crystals with[1)] $x \geqslant 0.3$ in the absence of external influences exhibit only one ferroelectric phase: the monoclinic γ phase (class m) with ferroelectric order in the m plane; in this case, the spontaneous polarization $P_{sm} \simeq P_{sx}$. At the same time, SDHS crystals with $x \leqslant 0.3$ also include a triclinic ferroelectric β phase (class 1) with ferroelectric order both in the m plane and along the Y axis (the Y axis is parallel to axis 2 of the paraphase).

It was shown in ref. 4 that the limiting concentration for existence of the β phase in SDHS crystals ($x \simeq 0.3$) may be shifted toward higher D concentrations by hydrostatic pressure. It was noted in ref. 2 that an electric field E_y also extends the concentration region of existence of the β phase in SDHS crystals.

In the present study, this effect, i.e., change in the character of electrical order in SDHS crystals with $x \geqslant 0.3$ by the field E_y, was investigated in detail by observing the behavior of dielectric characteristics and the optical indicatrix (see also ref. 4).

EXPERIMENTAL PROCEDURE. SAMPLES

We plotted curves of the Y component of the dielectric constant $\varepsilon_y(T)$ versus temperature, measured in weak fields at 1 kHz and various values of the steady field E_y, curves of the angle of rotation of the optical indicatrix around the Y axis versus the intensity of a very-low-frequency alternating field E_y, $\varphi_y(E_y)$, measured in a polarimeter,[6] and dielectric hysteresis loops $P_y(E_y)$, taken in the same very-low-frequency field.

The experiments were performed on SDHS crystals of various compositions with $x \geqslant 0.3$, mainly, crystals with $x \simeq 0.31$ and 0.50. The samples were Y-cut plates measuring $5 \times 4 \times 0.3$ mm. For dielectric measurements, they were coated with silver paste electrodes; for optical measurements, pieces of silica glass with transparent stannous oxide electrodes were placed in optical contact on the polished faces of the plates.

EXPERIMENTAL RESULTS

It is evident from Fig. 1 that the curve of $\varepsilon_y(T)$ for a SDHS crystal with $x \geqslant 0.3$ in the absence of a field E_y (curve 1) and at low values of the latter has, in accordance with the above, only one anomaly, which corresponds to phase transition from the paraelectric α phase to the ferroelectric γ phase. Application of a field $E_y > E_y^{crit}$, characteristic of the given x, produces a second anomaly on the curve of $\varepsilon_y(T)$, indicating a new phase transition (curve 2). Further increase in E_y shifts this transition toward higher temperatures (curve 3). At the same time, the temperature of the $\alpha \to \gamma$ transition $T_{\alpha\gamma}$ is not shifted by the field E_y. In this case, the new transition (like the old) has a distinct temperature hysteresis.

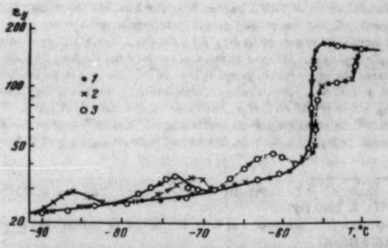

Fig. 1. Curves of dielectric constant ε_y versus temperature for $Na(D_{0.31}H_{0.69})_3 \cdot (SeO_3)_2$ crystal at various values of steady field E_y. 1) E = 0; 2) 19; 3) 29 kV/cm; solid lines denote cooling; dashed lines, heating.

The new anomaly on the curve of $\varepsilon_y(T)$ has qualitatively the same form as the anomaly in ε_y at the transition $\gamma' \to \beta$ in crystals[5] with $\leqslant 0.3$, and the same rate of shift

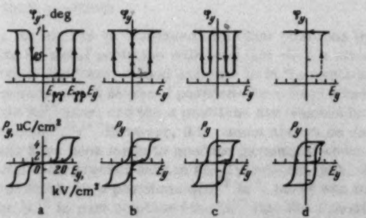

Fig. 2. Electrooptical (top) and dielectric (bottom) hysteresis loops for $Na \cdot (D_{0.31}O_{0.69})_3(SeO_3)_2$ crystal at various temperatures. a) 71; b) 82; c) 89; d) 102°C.

by the field E_y. Thus, even from these data, one may conclude that a steady field $E_y > E_y^{crit}$ induces the β phase in the γ phase of SDHS crystals with $x \geqslant 0.3$ at temperatures which approach $T_{\alpha\gamma}$ more closely with increasing E_y.

An analogous conclusion may be reached by analyzing the character of the $\varphi_y(E_y)$ curves obtained at $T < T_{\alpha\gamma}$ in a 0.01-Hz alternating field. Close to $T_{\alpha\gamma}$ (Fig. 2a) when E_y is small or zero, the orientation of the indicatrix corresponds to the γ phase. At a certain critical field $E_y = E_{\gamma\beta}$, regardless of its sign, φ_y changes abruptly, indicating transition of the crystal to the β phase [see the $\varphi_y(T)$ curves for SDHS crystals, given in ref. 8]. The β phase continues to exist even when E_y is increased further. The reverse transition $\beta \rightarrow \gamma$ on decrease of field takes place at $E_{\beta\gamma} < E_{\gamma\beta}$; hysteresis indicates a transition of the first kind. Thus, in this temperature region, the original γ phase reappears after removal of the field E_y.

On further cooling, the critical fields $E_{\gamma\beta}$ and $E_{\beta\gamma}$ decrease. At a certain temperature $E_{\beta\gamma}$ falls to zero (Fig. 2b) and then changes sign (Fig. 2c). In this temperature region, the field-induced β phase persists after removal of the field, and a field of opposite sign is required to reconvert the crystal to the γ phase.

Since $E_{\beta\gamma}$ continues to increase in absolute value on cooling, it reaches a value sufficient for induction of the β phase in a field of opposite sign, i.e., $|E_{\beta\gamma}| = |E_{\gamma\beta}|$, at a certain temperature (T_0 in Fig. 3). Beginning with this temperature, transition to the β phase in a field $E_\gamma \geq E_{\gamma\beta}$ becomes irreversible (Fig. 2d). On further cooling, $E_{\gamma\beta}$ increases, finally reaching breakdown values. The β phase can be obtained in this temperature region by inducing it at higher temperature and then cooling the crystal.

The form of the $P_y(E_y)$ dielectric loops (Fig. 2) qualitatively and even quantitatively supports conclusions drawn from study of the curves of $\varepsilon_y(T)$ and $\varphi_y(E_y)$. All three methods of determining the temperatures and fields of induction of phase transitions gave values which agreed well among themselves. The appearance of the β phase was also shown by direct observations of the domain structure, visible in the β phase and invisible in the γ phase, which were carried out by A. A. Askochenskii and V. A. Kirikov.

E_yT diagrams for SDHS crystals of two compositions are shown in Figs. 3 and 4. It is evident that $E_{\gamma\beta}$ increases with deuterium concentration x. It is practically impossible to induce the β phase at $x \geqslant 0.8$. The induced spontaneous polarization P_{sy} for crystals with $x \simeq 0.31$ and 0.50 amounts to about 3.5 $\mu C/cm^2$, which agrees well with its value for crystals[5] with $x < 0.3$.

Like the stable β phase in crystals with $x \leqslant 0.3$, the induced β phase in crystals with $x \geqslant 0.3$ vanishes at liquid-nitrogen temperatures. This fact was shown by the vanishing of the $P_y(E_y)$ loops (even in near-breakdown fields); it was not investigated in more detail.

Let us discuss certain temporal characteristics of the phenomena studied.

Field-induced $\gamma \rightarrow \beta$ transitions take place very slowly (for this reason, the field was varied under quasisteady conditions in the experiments). The critical field $E_{\gamma\beta}$ increases appreciably with the rate of change of E_y, whereas the critical field $E_{\beta\gamma}$ decreases appreciably, the transitions are spread out in time, and the $\varphi_y(E_y)$ and $P_y(E_y)$ loops deviate more and more from rectangular form. It should be remembered also that the change in slope of the $P_y(E_y)$ loops may be due to either phase transition or transition between multi- and single-domain states in a single phase.

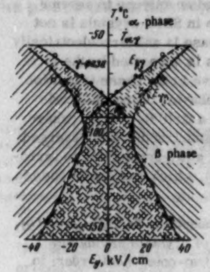

Fig. 3 E_yT phase diagram of an $Na \cdot (D_{0.31}H_{0.69})_3(SeO_3)_2$ crystal. ○ denotes measurements of $\varepsilon_y(T)$ in various bias fields; × denotes measurements of $P_y(E_y)$; ● denotes measurements of $\varphi_y(E_y)$.

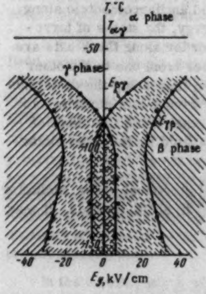

Fig. 4 E_yT phase diagram of an $Na \cdot (D_{0.50}H_{0.50})_3(SeO_3)_2$ crystal. ● denotes measurements of $\varphi_y(E_y)$ [to avoid cluttering the figure, measurements of $\varepsilon_y(T)$ and $P_y(E_y)$, which correlate with $\varphi_y(E_y)$ in the same way as in the case of the $Na(D_{0.31}H_{0.69})_3(SeO_3)_2$ crystal, are not plotted].

On cooling, the kinetics of the induced transitions $\gamma \rightarrow \beta$ and $\beta \rightarrow \gamma$ slows down, so that, at certain temperatures, loops taken at 50 Hz are not developed at all, although such loops taken at very low frequency have a saturated form at the same amplitudes of the field E_y.

The lifetime of the β phase in the absence of any inducing field E_y decreases rapidly with increasing deuterium concentration in the crystals and on cooling (from several hours, at least, to minutes).

DISCUSSION OF RESULTS

We noted earlier in a number of papers[1,2,4,5] that our concept of two components of spontaneous polarization in SDHS crystals is not simply a convenient form of description of the properties of these crystals, but corresponds to the different physical natures and different reactions of the components of P_s ($P_{sm} \simeq P_{sx}$ and P_{sy}) to change in such parameters as temperature, deuterium concentration in the crystals, and hydrostatic pressure.

The results of the present study provide one more clear proof of this assertion and enable one to assume that the situation in the γ phase in SDHS crystals is not simply $P_{sy} = 0$; instead, the phase is antiferroelectrically ordered along the Y axis. This is supported by the form of the anomaly in the $\varepsilon_y(T)$ curve in the phase transition at[5] $T_{\alpha\gamma}$ and the character of behavior of the dielectric properties of SDHS crystals in a field $E_y \geq E_{\gamma\beta}$ (where, it may be assumed, one of the substructures is reversed, and the crystal goes over from antiferroelectric to ferroelectric order along the Y axis), which was established in the present study.

Thus, according to our conception, $Na(D_xH_{1-x})_3(SeO_3)_2$ crystals are the first example of crystals having new types of electrical order, i.e., two-component order: in the β phase, ferroelectric in the m plane of the paraphase and ferroelectric along the Y axis, and in the γ phase, ferroelectric in the m plane and antiferroelectric along the Y axis. With regard to energy, the states of ferroelectric and antiferroelectric order along the Y axis are close together and easily go over from one to the other under certain conditions. Thus, increasing the deuterium concentration in the crystals[1-5] favors antiferroelectric order along the Y axis; on the other hand, the effect of hydrostatic pressure[4,9,10] and a field E_y favor ferroelectric order along the Y axis.

In principle, other types of electrical order, including two-component order, can exist in SDHS crystals. It may be supposed that the δ-phase, which exists in SDHS crystals only at high hydrostatic pressures,[4,9,10] has antiferroelectric order both along the Y axis and in the m plane.

The authors thank N. M. Shchagina for growing the crystals investigated in the present study.

---

1) In the present study, the same scale as in refs. 4 and 5 was used to determine the D concentration in SDHS crystals; x = 0.3 on this scale corresponds to x = 0.5 on the scale used in refs. 1 and 2.

[1] L. A. Shuvalov, N. R. Ivanov, L. F. Kirpichnikova, and N. M. Shchagina, ZhETF Pis. Red., 8, 235 (1968) [JETP Lett., 8, 143 (1968)].

[2] L. A. Shuvalov, N. V. Gordeeva (Gordeyeva), N. R. Ivanov, L. F. Kirpichnikova, A. M. Shirokov, and N. M. Shchagina (Schagina), J. Phys. Soc. Japan Suppl., 28, 75 (1970).

[3] H. Miki and Y. Makita, J. Phys. Soc. Japan, 28, 143 (1970).

[4] L. A. Shuvalov, A. M. Shirokov, N. R. Ivanov, A. I. Baranov, L. F. Kirpichnikova, and N. M. Shchagina (Schagina), J. Phys., 33, C2, 165 (1972).

[5] L. A. Shuvalov, V. N. Anisimova, N. R. Ivanov, and G. A. Velichko, Kristallografiya, 17, 1253 (1972) [Sov. Phys.—Crystallogr., 17, 1096 (1973)].

[6] N. R. Ivanov, L. A. Shuvalov, A. V. Mirenskii, and G. D. Shnyrev, Kristallografiya, 12, 307 (1967) [Sov. Phys.—Crystallogr., 12, 256 (1967)].

[7] L. A. Shuvalov, A. M. Shirokov, N. R. Ivanov, and L. F. Kirpichnikova, Kristallografiya, 18, (1973) (in press).

[8] N. R. Ivanov and L. A. Shuvalov, J. Phys. Soc. Japan Suppl., 28, 73 (1970).

[9] A. M. Shirokov, L. A. Shuvalov, and N. R. Ivanov, Phys. Lett., A29, 559 (1969).

[10] L. A. Shuvalov, A. M. Shirokov, N. R. Ivanov, and A. I. Baranov, Kristallografiya, 15, 1011 (1970) [Sov. Phys.—Crystallogr., 15, 879 (1971)].

Some features of the polarization of KH$_2$PO$_4$ in the phase transition region

E. V. Sidnenko and V. V. Gladkii

Institute of Crystallography, Academy of Sciences of the USSR

(Submitted December 27, 1971; resubmitted March 3, 1972)
Kristallografiya, 18, 138-142 (January-February 1973)

The results of an investigation of polarization and polarization reversal in KH$_2$PO$_4$ in slowly changing strong electric fields are given. In the paraelectric region near the phase transition dielectric hysteresis loops are observed whose existence cannot be explained by the phenomenological theories. It is proposed that the loops arise from the influence of crystal defects on the polarization relaxation processes. The nonlinearity of the polarization is analyzed from direct measurements of the temperature dependence of the equilibrium polarization P for various constant fields.

At the present time it is reliably established that the ferroelectric phase transition in KH$_2$PO$_4$ (KDP) is a first-order one. In contrast to earlier investigations, in several recent papers the observation of thermal hysteresis of the dielectric constant is reported,[1] as well as a jump and thermal hysteresis in the volume[2] characteristic of transitions of this kind, the appearance of the nonlinear polarization,[3,4] the temperature dependence of the reciprocal dielectric constant,[5] and the latent heat of the phase transition.[6] Recently precise measurements have been made of the thermal expansion,[7,8] electrocaloric effect,[9,10] and polarization reversal of KDP,[1] which support the initial data about a first-order phase transition. However, the quantitative disagreement of the parameters characterizing the transitions are so significant in some of the latter papers that they require further explanation.

We have investigated the nonlinearity of the polarization in KDP in the region of the phase transition from measurements of the pyroelectric effect in strong electric fields,[3,4] where it was shown that the observed features of the nonlinearity involve a first-order phase transition.

The aim of the present work is to investigate the polarization of KDP crystals having a maximum electric permittivity ε at the phase transition temperature T_C, which is usually related to the quality of the crystal. Pyroelectric measurements of the polarization have been carried out with a broad (in comparison to refs. 3 and 4) range of constant electric fields and supplemented by measurements of ε in weak alternating fields and investigations of polarization reversal in quasistatic electric fields.

The measurements of the polarization and electric permittivity were done by the method described in ref. 13 on two crystal samples of dimensions 5 × 5 × 1 mm with deposited gold electrodes. The crystals investigated had a Curie–Weiss temperature $\Theta = 123.56$°K, a maximum dielectric constant of $5.3 \cdot 10^4$ at $T_C = 123.62$°K, and a temperature coefficient for the Curie–Weiss law for the reciprocal dielectric constant which is $\alpha_\Theta = (3.8 \pm 0.1) \cdot 10^{-3}$ deg^{-1}. The value of α_Θ turns out to be close to the values of this coefficient which are most often encountered in the literature but is 1.5 times greater than that which we found previously.[3,4] The large differences in the α_Θ coefficients or the Curie–Weiss constants reciprocal to them for different samples of KDP crystals have been discussed in ref. 12, where the temperature dependence of the dielectric constant was determined for a large number of samples. It should also be noted that the crystals studied in the present work differ significantly from those used previously[3,4] in other parameters too, primarily in the shape of the temperature dependence and the polarization and polarizability in strong electric fields. The reason for such large quantitative differences of the polarization in KDP crystals has not been explained.

In KDP-group crystals the polarization in an electric field occurs so slowly that widely used measurement methods using alternating fields do not give correct information on the phase transition. For example in deuterated KDP crystals, according to our estimates after switching on a constant electric field the time for establishing the polarization is of the order of minutes.[14] Therefore, the only applicable method for studying polarization reversal in KDP is to make measurements in a slowly varying (quasistatic) field, especially since the low ohmic conductivity of these crystals hardly affects the results of the measurements.

In the investigations of polarization reversal in KDP the period of the field variation was 2 h, which corresponds to a frequency of the order of 10^{-4} Hz. As shown by the results of the measurements (Fig. 1) not only in the ferroelectric, but also in the paraelectric region the field dependence of the polarization takes the form of the usual hysteresis loop over an interval of about 1°. In an alternating electric field with a frequency of 50 Hz no hysteresis is observed in the paraelectric region. The appearance of ordinary polarization hysteresis in the paraelectric region does not follow from the phenomenological theory and evidently involves various defects of the crystal lattice.

One possible reason for the existence of a hysteresis loop could be directional ordering of the defects in a slowly varying strong electric field. Such ordering, as in Rochelle salt crystals for example,[15] can lead to creep of the polarization with time in an electric field, or in the terminology of ref. 15, to a certain stabilization of the polarization. The appearance of a hysteresis loop in our crystals in a comparatively broad temperature range above the transition evidently hinders the observation of double loops, which are characteristic of a first-order transition.

Since the polarization of KDP, as shown by our measurements, is established very slowly and substantially lags behind the field during polarization reversal, in making a quantitative analysis of the nonlinearity in addition to the values of the polarization closest to equilibrium one should consider experimental data which are obtained during a direct determination of the temperature dependence of the polarization (the pyroelectric method[13]). In this case the crystals are placed in a constant electric

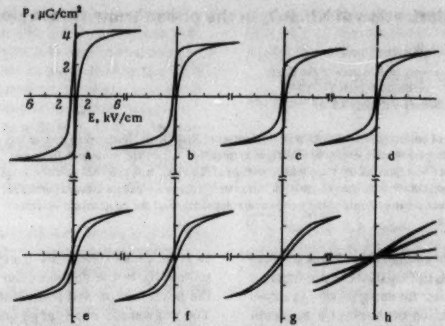

Fig. 1. Dielectric hysteresis loops in KH_2PO_4 crystals. T(°K): a) 120.00; b) 123.00; c) 123.60; d) 123.65; e) 123.70; f) 123.80; g) 124.10; h) 124.5, 125.0, 128.5.

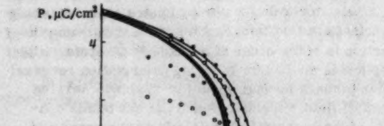

Fig. 2. Temperature dependence of the polarization in KH_2PO_4 for various strengths of the constant electric field. E(kV/cm): 1) 0.5; 2) 1; 3) 2; 4) 6; 5) 10. The curves were constructed from calculated data.

field for a long time (about 5 h). It should be noted that the pyroelectric measurements did not show an increase in the measured polarization. In strong electric fields, which correspond to branches of the saturation hysteresis loop, the values of the polarization measured by the pyroelectric method during polarization reversal or directly upon the application of a fixed field agreed within the limits of precision of the experiment. The results of our measurements of the temperature dependence of the polarization with various constant fields are shown in Fig. 2.

A quantitative analysis of the nonlinearity in the polarization leads to a check of the validity of the equation of state for a KDP crystal:

$$E = \alpha P + \beta P^3 + \gamma P^5 + \delta P^7 + \ldots, \qquad (1)$$

where $\alpha = \alpha_\Theta(T - \Theta)$, E is the electric field strength, P is the polarization, and to an estimate of the constant coefficients β, γ, and δ which enter (1). The phase transition is usually described using only the first three terms in the expansion (1). If such an approximation is sufficient, then we can get a quantitative estimate of the coefficients in Eq. (1) from a graph of the experimental relation $Y = (E - \alpha P)/P^3 = f(P^2)$, which represents, as follows from Eq. (1), a straight line. Figure 3 shows such a relation constructed from data on the polarization measurements of Fig. 2. The large scatter in the experimental points which lie close to the origin of coordinates is due to the decreased precision in the calculation of the difference $E - \alpha P$ for small values of P. If we approximate this relation by a straight line, then β and γ will be respectively $(-3.0 \pm 0.8) \cdot 10^{-11}$ and $(6.5 \pm 1.1) \cdot 10^{-19}$ cgs esu.

In ref. 9 it was reported that the temperature dependence of the spontaneous polarization in KDP determined from measurements of the electrocaloric effect obeys a relation which follows from the expansion (1) with $\beta < 0$, $\gamma = 0$, and $\delta > 0$. In this case, as one can easily see from (1), the relation $Y = f(P^2)$ should be parabolic, while $Y = f(P^4)$ should be linear. Actually our experimental data in Fig. 3 are closer to a parabolic law than to a linear law, while the experimental dependence on P^4 is linear within the limits of experimental error (Fig. 4). Thus for the crystals we studied the polarization (with comparatively large polarization values) in the phase transition region as in ref. 9 follows Eq. (1), including the first, second, and fourth terms in the expansion. Unfortunately the scatter in the experimental points for small polarizations in Fig. 4 is quite large, so that the coefficient β, which is the intersection point of the line on the ordinate axis, cannot be determined precisely for the crystals we studied. It can be seen from Fig. 4 that the value of β is small and equal to $-(5 \pm 3) \cdot 10^{-12}$ cgs esu. The coefficient δ given by the tangent of the slope of the line with respect to the abscissa is $(3.8 \pm 0.4) \cdot 10^{-27}$ cgs esu. The curves calculated from (1) for the coefficients α_Θ, Θ, β, and δ determined above for the dependence of the polarization are shown by solid lines in Fig. 2. The disagreement between the experimental data and the calculated

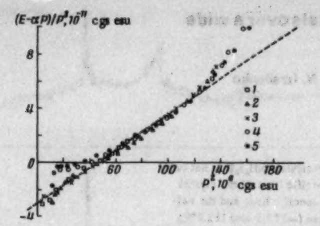

Fig. 3. Relation $(E-\alpha P)/P^3 = \beta + \gamma P^2$ for various values of E. E(kV/cm): 1) 2; 2) 4; 3) 6; 4) 8; 5) 10.

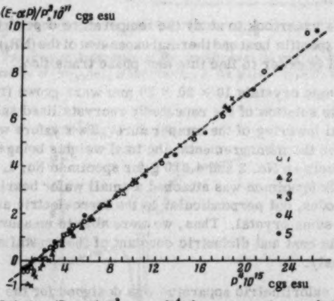

Fig. 4. Relation $(E-\alpha P)/P^3 = \beta + \delta P^4$ for various electric fields E. E(kV/cm): 1) 2; 2) 4; 3) 6; 4) 8; 5) 10.

data in the ferroelectric region for fields less than 6 kV/cm is due to the inability to produce a completely single-domain crystal; therefore these data in general are not taken into consideration in the graphs of Figs. 3 and 4.

We note in conclusion that investigations of KDP crystals which undergo phase transitions close to the critical point for transitions of the second order, in agreement with our estimates of the coefficients α_Θ, β, γ or α_Θ, β, and δ should have a jump in the spontaneous polarization at the transition point, $\Delta P_{\text{spon}} = (1.8 \pm 0.4)\ \mu C/cm^2$. The estimates made here for the jump in the polarization agree with the residual polarization determined directly from the hysteresis loop with $E = 0$ and T close to the transition temperature (Fig. 1c). All of the quantitative data given herein for the phase transition are close to the previous results of refs. 6, 9, and 10 and quite far from similar data in refs. 3 and 8. It is possible, however, that such differences are related to the differing degrees of perfection for the crystal samples studied.

The authors are grateful to R. Kh. Mamedov for analyzing the experimental data and formulating the results of this work.

---

[1] P. P. Craig, Phys. Lett., 20, 140 (1966).
[2] S. R. Garber and L. A. Smolenko, Zh. Eksp. Teor. Fiz., 55, 2031 (1968) [Sov. Phys.—JETP, 28, 1072 (1969)].
[3] V. V. Gladkii, I. S. Zheludev, and E. V. Sidnenko, Izv. Akad. Nauk SSSR, Ser. Fiz., 33, 300 (1969).
[4] V. V. Gladkii, I. S. Zheludev, and E. V. Sidnenko, J. Phys. Soc. Japan, Suppl., 28, 206 (1970).
[5] S. Tsunekawa, Y. Ishibashi, and Y. Takagi, J. Phys. Soc. Japan, 27, 919 (1969).
[6] W. Reese, Phys. Rev., 181, 2905 (1969).
[7] J. Kobayashi, Y. Uesu, I. Mizutani, and Y. Enomoto, Phys. Status Solidi, a3, 63 (1970).
[8] J. Kobayashi, Y. Uesu, and Y. Enomoto, Phys. Status Solidi, b45, 293 (1971).
[9] J. W. Benepe and W. Reese, Phys. Rev., B3, No. 9, 3032 (1971).
[10] B. A. Strukov, M. A. Korzhuev, A. Baddur, and V. A. Koptsik, Fiz. Tverd. Tela, 13, 1872 (1971) [Sov. Phys.—Solid State, 13, 1569 (1972)].
[11] K. Okada and H. Sugie, Phys. Lett., A37, No. 4, 337 (1971).
[12] L. N. Kamysheva, Dissertation, Voronezh University, Voronezh (1967).
[13] V. V. Gladkii and E. V. Sidnenko, Fiz. Tverd. Tela, 13, 1642 (1971) [Sov. Phys.—Solid State, 13, 1374 (1971)].
[14] V. V. Gladkii and E. V. Sidnenko, Fiz. Tverd. Tela, 13, 3092 (1971) [Sov. Phys.—Solid State, 13, 2592 (1972)].
[15] V. A. Yurin, Izv. Akad. Nauk SSSR, Ser. Fiz., 24, 1329 (1960).

Thermal properties of ammonium fluoroberyllate crystals over a wide temperature range

B. A. Strukov, T. L. Skomorokhova, V. A. Koptsik, A. A. Boiko, and A. N. Izrailenko

M. V. Lomonosov Moscow State University

(Submitted December 8, 1971)
Kristallografiya, 18, 143-146 (January-February 1973)

The temperature dependence of the specific heat and thermal expansion of single-crystal $(NH_4)_2BeF_4$ has been determined over the temperature range 70-300°K. The variation in the lattice specific heat of the crystal has been found to be essentially nonlinear in nature. The anomalies found in the specific heat and the volume coefficient of expansion indicate the existence of at least two phase transitions (~177.2 and 182.9°K), of which only the one at T = 177.2°K is accompanied by an anomaly in the dielectric constant. The results obtained are discussed from the viewpoint of the Levanyuk–Sannikov thermodynamic theory.

It is well known that the physical properties of certain ferroelectric crystals are not represented by the normal Ginzburg–Devonshire phenomenological theory. According to Indenbom,[1] the phase transition in such cases may be accompanied by a change in the number of atoms in the unit cell, while a corresponding change in the space symmetry is obtained by means of a characteristic parameter possessing the necessary transformation properties. Phase transitions in crystals of ammonium fluoroberyllate, gadolinium molybdate, and boracites would seem to belong to the "atypical" type of ferroelectric, in which polarization is not a characteristic parameter of the transition. So far it has not been completely clear whether the improved theory gives an adequate representation of the anomalies observed in "atypical" ferroelectrics.

Historically, ammonium fluoroberyllate is the first "atypical" ferroelectric.[2-7] Its characteristics are a low value for the Curie constant, an unusual shape of the double hysteresis loops, and an extremely low value for spontaneous polarization. As shown in ref. 3, the experimental value of the excess energy associated with the phase transition $\Delta Q = 310$ cal/mole, whereas a simple calculation by the Ginzburg–Devonshire theory gives $\Delta Q = 25.4$ cal/mole, i.e., a value more than 10 times lower. X-ray structural analysis has confirmed that a superstructure is formed, i.e., the number of atoms in the unit cell of $(NH_4)_2BeF_4$ is doubled at the point of the phase transition with a change in the space symmetry[4] $D_{2h}^{16} \rightarrow C_{2v}^{9}$. A group-theoretical analysis of this change in symmetry leads to the conclusion that in this case polarization is a "secondary" effect in the rearrangement of the structure, such that[8] $P_{sp} \sim (T - \Theta)$.

Levanyuk and Sannikov[9] proposed that the phase transition in $(NH_4)_2BeF_4$ crystals be represented by two characteristic parameters. On analyzing the experimental data pertaining to the phase transition in this crystal, they found that when two transition parameters exist two types of solution are possible, which correspond to phase transitions of the second type in different unsymmetrical phases of a substance (C_{2v}^{9} and C_{2h}^{5}). The experimental facts pertaining to the temperature dependence of the dielectric constant, spontaneous polarization, and the double hysteresis loops are represented very accurately by the theory if it is assumed that spontaneous polarization arises in the transition from one low-symmetry phase to the other. Since (as indicated above) it is now known that the space group of $(NH_4)_2BeF_4$ is D_{2h}^{16} at room temperature, it is to be expected (if the hypothesis in ref. 9 is correct) that another phase transition exists in this crystal.

We undertook to study the temperature dependence of the specific heat and thermal expansion of the $(NH_4)_2BeF_4$ crystal in order to find this new phase transition.

Single crystals 10 × 20 × 30 mm were grown from an aqueous solution of the repeatedly recrystallized salt by gradual lowering of the temperature. Two wafers were used for the measurements, the total weights being 6.740 g for specimen No. 2 and 4.610 g for specimen No. 1. To the bulk specimen was attached a small wafer bearing the electrodes, cut perpendicular to the ferroelectric axis b of the same crystal. Thus, we were able to measure the specific heat and dielectric constant of the crystal simultaneously.

A calorimetric apparatus was designed for the measurements which enabled the specific heat to be determined from liquid-helium temperature to 300°K for small single-crystal specimens. In the aneroid-type cryostat used the vacuum chamber in which the sample was placed was cooled by a primary refrigerant (in our measurements liquid nitrogen was used as the primary refrigerant, the vapor of which was pumped out by means of a mechanical vacuum pump). The exterior of the vacuum chamber was surrounded by an isothermal shield cooled by a secondary refrigerant, liquid nitrogen. The temperature of the system of adiabatic shields was controlled automatically by electronic circuits.[10] A platinum resistance thermometer and a heater were mounted on a mica backing plate placed between the crystal wafers.

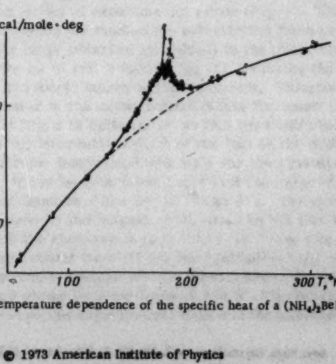

Fig. 1. Temperature dependence of the specific heat of a $(NH_4)_2BeF_4$ crystal.

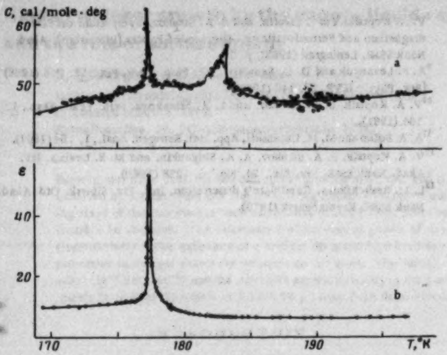

Fig. 2. Temperature dependence of the specific heat (a) and the dielectric constant (b) of $(NH_4)_2BeF_4$ in the vicinity of the phase transition points.

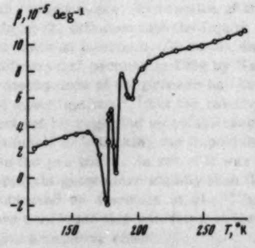

Fig. 3. Temperature dependence of the volume coefficient of expansion for $(NH_4)_2BeF_4$.

During the measurements the increase in temperature was varied from 0.30 to 0.05° in the phase transition regions. The measurements were conducted independently on two specimens cut from different crystals and the c(T) relationships obtained for these specimens were found to be completely identical. Thermal expansion was measured with an x-ray diffractometer having a low-temperature attachment with temperature stabilization[11] of the order of ± 0.1°.

The experimental curve for the temperature dependence of the specific heat of $(NH_4)_2BeF_4$ single crystal No. 2 is shown in Fig. 1. The curve has two maxima ($T_c' = 177.2°K$, $T_c'' = 182.9°K$) as well as a slight anomaly at 190°K. Because the measurements were carried out over a wide temperature range, we were able to show that the variation of the lattice specific heat is appreciably nonlinear in nature. The total excess heat associated with the phase transitions was found to be $\Delta Q = 200 \pm 20$ cal/mole (the error in determining ΔQ arising from difficulties in isolating the lattice specific heat in the region of a phase transition). This value is lower than that in ref. 3 (ΔQ = 310 cal/mole), where the variation in the lattice specific heat was approximated by a linear relationship, but higher than in ref. 12, where only part of the anomaly was considered.

The nature of the two specific heat maxima is different (Fig. 2). The low-temperature anomaly is almost symmetric with respect to the transition temperature, whereas for T_c'' there is a gradual increase in specific heat and then a small jump, which develops into a long "tail" extending over 20-30°. Another slight anomaly is observed on the "tail" at ~190°K, although the reproducibility of the experimental points within this region is poorer than outside it, as may be seen from Fig. 2. Only the specific heat maximum at T_c' is accompanied by an anomaly in the dielectric constant.

The phase transition at T_c' can evidently be considered as a phase transition of the first type; this is indicated by data for the temperature dependence of the spontaneous polarization, the symmetrical shape of the c(T) relationship, and the existeuce of a thermal hysteresis[4,5] for ε. The symmetrical peak for the specific heat would seem to be associated with the latent heat of transition, which is found to be equal to 2.5 cal/mole. The shape of the specific heat curve in the vicinity of the temperature T_c'' is typical of phase transitions of the second type. The existence of a transformation of the third type cannot be confirmed with absolute certainty from the results of the calorimetric measurements. In the x-ray dilatometric investigations anomalies in the thermal expansion were observed which agree well in temperature with the anomalies in specific heat. As may be seen from Fig. 3, at temperatures close to those indicated above anomalies are observed in the thermal expansion coefficient. However, the resolution with respect to temperature is not as high as in the calorimetric measurements and the data obtained require further refinement.

Nevertheless, from the data obtained it can be stated with certainty that there are at least two phase transitions in ammonium fluoroberyllate crystals. It can be assumed that at $T_c'' = 182.9°K$ there is a nonferroelectric second-type transition from the symmetry of the D_{2h}^{16} phase into the first nonsymmetrical phase, which is accompanied by the appearance of superstructuring (there is no dielectric anomaly). A similar transformation occurs in KMnF crystals at 184°K.[13]

At $T_c' = 177.2°K$ a ferroelectric phase transformation takes place which is accompanied by an anomaly in the dielectric constant. The latent heat associated with this jump is extremely low and the phase transition is accompanied by a small jump in polarization ($\Delta P_0 \sim 0.06$ mμ/cm² [see ref. 5]).

If we take into account that $T_k^{-1}(dT_k/dE) = \Delta P_0/\Delta Q_0$ and use the data presented in ref. 5 then, in fact, we obtained ΔQ ~ 3 cal/mole, which is in good agreement with the value obtained above by direct integration of the anomaly at $T = T_c'$.

In conclusion we may note that according to ref. 9 group-theory analysis of the possible changes in symmetry gives a space grouping C_{2h}^{5} for the intermediate nonferroelectric phase of ammonium fluoroberyllate. An experimental determination of the symmetry of this phase is undoubtedly very desirable.

We thank A. P. Levanyuk and D. G. Sannikov for fruitful discussion of the results of this investigation.

---

[1] V. L. Indenbom, Kristallografiya, 5, 115 (1960) [Sov. Phys.—Crystallogr., 5, 106 (1960)]; Izv. Akad. Nauk SSSR, Ser. Fiz., 24, 1180 (1960).

[2] R. Pepinsky and F. Jona, Phys. Rev., 105, 344 (1957).

[3] S. Hoshino, K. Vedam, J. Okaya, and R. Pepinsky, Phys. Rev., 112, 405 (1958).

[4] J. Okaya, K. Vedam, and R. Pepinsky, Acta Crystallogr., 11, 307 (1958).

[5] B. A. Strukov, N. D. Gavrilova, and V. A. Koptsik, Kristallografiya, 6, 780 (1961) [Sov. Phys.—Crystallogr., 6, 625 (1962)].

[6] B. A. Strukov and V. A. Koptsik, Kristallografiya, 7, 234 (1962) [Sov. Phys.—Crystallogr., 7, 182 (1962)].

[7] B. A. Strukov, Kristallografiya, 6, 635 (1961) [Sov. Phys.—Crystallogr., 6, 511 (1962)].

[8] V. A. Koptsik, Yu. I. Sirotin, and B. A. Strukov, Symposium on Ferromagnetism and Ferroelectricity, Abstracts of Papers [in Russian], Akad. Nauk SSSR, Leningrad (1963), p. 70.

[9] A. P. Levanyuk and D. G. Sannikov, Zh. Eksp. Teor. Fiz., 55, 256 (1968) [Sov. Phys.—JETP, 28, 140 (1969)].

[10] V. A. Koptsik, B. A. Strukov, and L. A. Ermakova, Prib. Tekh. Eksp., 1, 164 (1961).

[11] A. A. Boiko and M. M. Umanskii, App. Met. Rentgen. Anal., 1, 154 (1967).

[12] V. A. Koptsik, B. A. Strukov, A. A. Sklyankin, and M. E. Levina, Izv. Akad. Nauk SSSR, Ser. Fiz., 24, No. 10, 1228 (1960).

[13] L. M. Reshchikova, Candidate's dissertation, Inst. Fiz. Sibirsk. Otd. Akad. Nauk SSSR, Kransnoyarsk (1970).

Rate of whisker growth by the vapor–liquid–crystal mechanism and the role of surface energy

E. I. Givargizov and A. A. Chernov
Institute of Crystallography, Academy of Sciences of the USSR

(Submitted March 3, 1972)
Kristallografiya, 18, 147-153 (January-February 1973)

Experiments have been carried out on the growing of Si, Ge, and GaAs whiskers on a single-crystal substrate, initiated by Au particles as a liquid-forming impurity (vapor–liquid–crystal growth mechanism). The limiting stage of the process has been established qualitatively, phenomena at the liquid–crystal interface being found to be decisive. The dependence of the rate of growth of Si whiskers on their diameter has been studied quantitatively. The existence of a critical diameter (d_c) has been established below which (for a given supersaturation in the gas phase) the whiskers do not grow. The kinetic crystallization coefficient (found to be $\sim 3.7 \cdot 10^{-4}$ cm · sec^{-1}) and the effective supersaturations in the gas phase ($2.9 \cdot 10^{-2}$–$12.2 \cdot 10^{-2}$, which corresponds to critical diameters of 0.22–0.05 μ) have been determined.

INTRODUCTION

The present paper deals with a study of the growth of Si, Ge, and GaAs whiskers by the vapor–liquid–crystal mechanism. Growth by this mechanism evidently includes the following stages: (1) transport (including diffusion transport) in the gas phase; (2) reaction at the liquid–vapor interface; (3) diffusion into the liquid; (4) processes at the liquid–crystal interface. Since the discovery of the vapor–liquid–crystal process in 1964 by Wagner and Ellis[1,2] the mechanism of the process has been studied in a number of investigations,[3-7] but the relative role of these stages cannot yet be regarded as established. Wagner[7] restricted himself to indicating the importance of supersaturation in the gas phase. In ref. 4 it was established that thick crystals grow more rapidly than thin ones. This was also indicated by Bootsma et al.;[5,6] furthermore, these authors concluded that reactions at the liquid–vapor interface have a decisive effect.

In the present paper experiments are reported which have enabled the limiting stage of the vapor–liquid–crystal process to be established qualitatively (phenomena at the liquid–crystal interface were found to be decisive) and the dependence of the rate of growth on the diameter of the whiskers to be investigated quantitatively. The latter, as we attempt to show, is caused by the Gibbs–Thomson effect.

EXPERIMENT

Crystallization was carried out with a vertical quartz reactor by the method described previously,[8] the chloride–hydrogen process in a flow system being used. Silicon whiskers were grown on single-crystal substrates of silicon having (111) orientation, maintained at 850-1100°C (principally at 1000°C). The $SiCl_4$ concentration in H_2 was 0.01–0.05. Germanium whiskers were grown on Ge (111) substrates at 650-900°C and with $GeCl_4$ concentrations of 0.002–0.02 in H_2. GaAs whiskers were grown on GaAs substrates having B $(\bar{1}\bar{1}\bar{1})$ orientation in the gas-transport system $H_2 + AsCl_3 + Ga$ at 600-800°C.

In all cases Au was used as the impurity solvent initiating whisker growth. It was deposited on the substrate in the form of a continuous layer from 100 to 1000 Å thick by thermal vaporization. On heating, the layer melted with the substrate and, under the action of surface energy, divided into separate drops which also "extracted" the whiskers from the substrate. The thicker the layer, the wider was the range of diameter of the droplets. At 100°C a layer of Au 1000 Å thick divided into drops ranging from 300 Å to 10 μ in diameter.

The crystals grown were studied by means of an optical microscope and a JSM-2 scanning electron microscope.

RESULTS AND DISCUSSION

a) Limiting Stage of the Crystallization Process

Examination of a large number of Si, Ge, and GaAs whisker systems by optical and electron microscopy showed that relatively thick crystals grow more quickly than thin ones (Fig. 1). Hence certain qualitative conclusions can be drawn on the limiting stage of the process.

Transport in the gas phase. If the whiskers were distributed uniformly on the substrate, then the same amount of feed material in the gas phase should arrive at

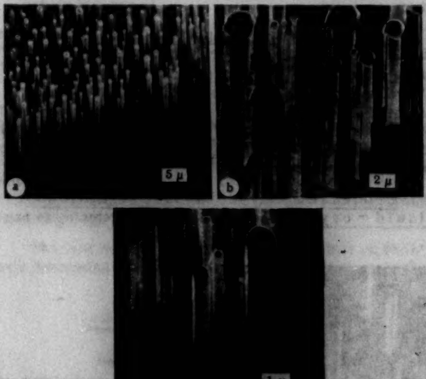

Fig. 1. Relative rates of growth of thick and thin whiskers. Crystals of a) Si; b) Ge; c) GaAs.

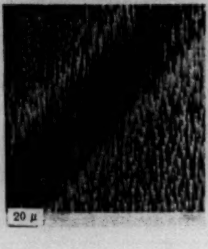

Fig. 2. "Cutting" in a thick system of Si whiskers.

each one. However, owing to the spontaneous dispersion of the initially uniformly thick liquid layer, drops of different sizes are formed, as indicated above. Since the shape of a drop is almost spherical, its diameter $d \sim V^{1/3}$; on the other hand, the volume V of a drop is proportional to the area from which the drop material has been collected. Consequently, for a larger drop the ratio of the volume of the gas phase from which it is supplied to the area of the growing surface is higher, i.e., the feed conditions for it are more favorable. To test the role of transport in the gas phase we should compare the rate of growth for whiskers having the same diameter which have been grown in "thick" and "rarefied" environments, i.e., with relatively lean and rich feeds. For this purpose we intentionally created a "cutting" by removing the gold layer from a narrow strip before growing the crystals (although still leaving a small amount of gold on the strip). Figure 2 shows the results of accumulation on a substrate of silicon whiskers so prepared. It was found that in spite of the rich feed the rate of whisker growth on the strip is the same as for crystals of corresponding diameter in the thick "forest", where the feed is appreciably leaner. On the other hand, the rate of growth on the strip is higher the larger the diameter (Fig. 3). Hence, it follows that stage (1) is not the limiting stage.

Diffusion in a drop. The drops at the ends of the Si, Ge, and GaAs whiskers wet the ends at a wetting angle close to 90°, i.e., they are almost hemispherical. Therefore, for thick crystals the diffusion resistance is higher than for thin crystals and if diffusion in the liquid did, in fact, limit the rate of growth then the thin crystals should grow more rapidly. Consequently, stage (3) is not the limiting stage either.

Processes at the vapor – liquid and liquid – crystal interfaces. It remains to examine the role of stages (2) and (4). For this purpose let us turn to Fig. 4, in which GaAs whiskers are shown. This material, which crystallizes with a sphalerite structure, has a tendency to twinning, twin (needle or ribbon) crystals having a ⟨211⟩ direction of growth being formed in the case of the vapor–liquid–crystal process, as has been shown.[9] It is well known that a twinning boundary serves as an active growth region, since the energy of nucleus formation at it is lowered. Consequently, of two whiskers, one of which has a twinning boundary at the growth front, the twinned crystal will grow more rapidly under otherwise equal conditions. In Fig. 4a inclined crystals growing in the ⟨211⟩ direction (indicated by an arrow) are seen, in addition to the crystals perpendicular to the substrate; see also Fig. 4b, which was obtained from a similar section of the substrate with a zero angle of incidence of the beam in the scanning microscope. Whereas the perpendicular crystals obey the general rules (i.e., thick crystals grow more rapidly than thin ones), the oblique ones surpass them markedly in growth, although their diameter is many times less than the thickest perpendicular crystals. This is seen especially clearly in Fig. 4b, where an oblique crystal is raised above a perpendicular crystal (marked with an arrow). Thus, it can be concluded that the structure of the crystallization front has a decisive effect on the rate of growth of whiskers, i.e., that state (4) is the limiting stage.

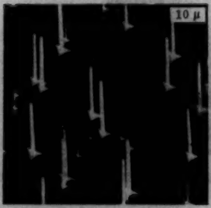

Fig. 3. Rate of growth of thick and thin Si whiskers under relatively intense feed conditions.

b) Dependence of the Rate of Growth on Diameter and the Role of Surface Energy

The experimental dependence of the rate of growth ν of silicon whiskers on their diameter d is shown in Fig. 5a, for a crystallization temperature of 1000°C and for the four concentrations of $SiCl_4$ in H_2 (consequently, four supersaturations in the gas phase) shown in Table 1. The range of diameters of the crystals studied was 0.05-5 μ and it is natural to assume that the increase in rate of growth with diameter is caused by the action of surface energy. Let us confirm the validity of this assumption by comparing the experimental relationship with the theoretical relationship.

It is readily seen that the driving force of the process (the effective difference $\Delta\mu$ between the chemical potentials of silicon in the gas phase1) and as a cylindrical crystal) is

$$\Delta\mu = \Delta\mu_0 - 4\Omega\alpha / d, \qquad (1)$$

where $\Delta\mu_0$ is the same difference in chemical potentials

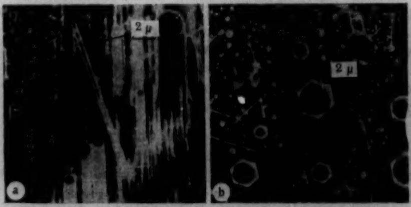

Fig. 4. Relative rates of growth of defect and nondefect whiskers of GaAs. a) Angle of incidence of scanning beam in microscope φ = 45°; b) φ = 0°.

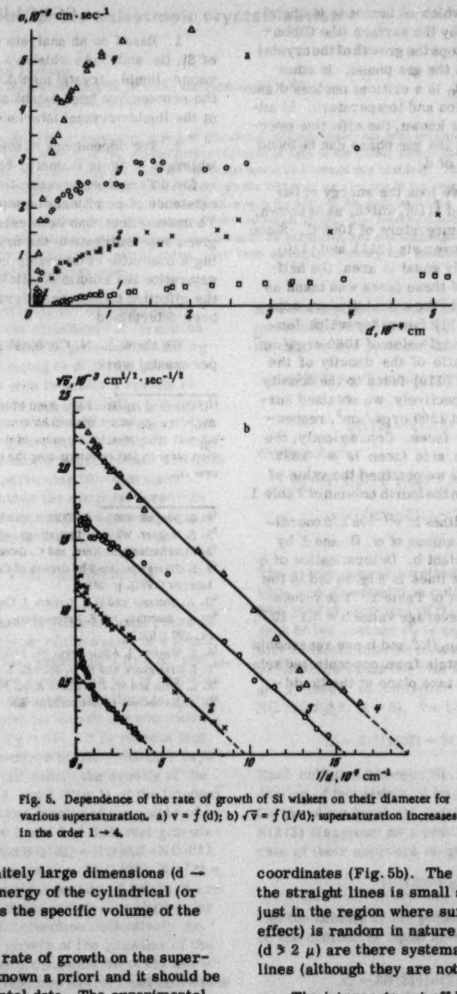

Fig. 5. Dependence of the rate of growth of Si wiskers on their diameter for various supersaturation. a) v = ƒ(d); b) $\sqrt{v} = f(1/d)$; supersaturation increases in the order 1 → 4.

at a plane boundary of infinitely large dimensions (d → ∞), α is the specific free energy of the cylindrical (or prismatic) surface, and Ω is the specific volume of the atom.

The dependence of the rate of growth on the supersaturation $v(\Delta\mu/kT)$ is unknown a priori and it should be determined from experimental data. The experimental curves in Fig. 5a are best approximated by the relationship

$$v = b(\Delta\mu/kT)^2, \tag{2}$$

i.e.,

$$\sqrt{v} = \Delta\mu_0\sqrt{b}/kT - 4\Omega\alpha\sqrt{b}/kTd, \tag{3}$$

where b is the kinetic coefficient of crystallization for the liquid–crystal interface. In fact, the experimental data given in Fig. 5a lie on straight lines in $v^{1/2}$ vs 1/d coordinates (Fig. 5b). The deviation of the points from the straight lines is small and in the region d < 2μ (i.e., just in the region where surface energy has the greatest effect) is random in nature. Only for the thick crystals (d ≫ 2 μ) are there systematic deviations from the straight lines (although they are not very large).

The intercepts cut off by the straight lines on the 1/d axis determine those crystal diameters d_c (shown in the

TABLE 1

No.	$SiCl_4/H_2$, %	Critical diameter d_c, 10^{-4} cm	Effective supersaturation, $\Delta\mu_0/kT$	Kinetic coefficient b, cm/sec
1	0.3	0,22	$2.9 \cdot 10^{-2}$	$4.0 \cdot 10^{-4}$
2	0.75	0.11	$6.0 \cdot 10^{-2}$	$3.9 \cdot 10^{-4}$
3	1.5	0.07	$9.8 \cdot 10^{-2}$	$3.3 \cdot 10^{-4}$
4	3.0	0.05	$12.2 \cdot 10^{-2}$	$3.6 \cdot 10^{-4}$

third column of Table 1) for which an increase in chemical potential under the curve by the surface (the Gibbs–Thomson effect) completely stops the growth of the crystal for a given supersaturation in the gas phase. In other words, each of the values of d_c is a critical nucleus diameter for a given supersaturation and temperature. In addition, if the surface energy is known, the effective overall supersaturation $\Delta\mu_0/kT$ in the gas phase can be found from the experimental values of d_c.

As the surface energy α we took the energy of the prismatic side faces {211} and {110}, which, as is known,[7] develop at a crystallization temperature of 1000°C. Since for our crystals it developed over six {211} and {110} faces, which are approximately equal in area, the half-sum of the surface energies of these faces was taken as the magnitude of the energy. In the calculation we commenced from the energy of {111} faces, for which Jaccodine[10] obtained an experimental value of 1060 $ergs/cm^2$. Taking into account that the ratio of the density of the broken bonds at the {211} and {110} faces to the density at {111} is 1.41 and 1.22, respectively, we obtained surface energy values of 1500 and 1290 $ergs/cm^2$, respectively, for the {211} and {110} faces. Consequently, the average surface energy of the side faces is $\alpha = 1395$ $ergs/cm^2$. Using this quantity we obtained the value of $\Delta\mu_0/kT$ which are presented in the fourth column of Table 1.

The slope of the straight lines in $v^{1/2}$ vs $1/d$ coordinates is determined for given values of α, Ω, and T by the value of the kinetic coefficient b. Determination of b from the slopes of the straight lines in Fig. 5b led to the values given in the last column of Table 1. The values are grouped around a certain average value $b \approx 3.7 \cdot 10^{-4}$.

The values obtained for $\Delta\mu_0/kT$ and b are reasonable for the laminar growth of crystals from concentrated solution, which would also seem to take place at the liquid–crystal interface.

CONCLUSIONS

1. Based on an analysis of experiments on the growth of Si, Ge, and GaAs whiskers from the gas phase by the vapor–liquid–crystal mechanism, the limiting stage of the process has been established qualitatively (phenomena at the liquid–crystal interface are found to be decisive).

2. The dependence of the rate of growth of silicon whiskers on their diameter has been studied quantitatively for different supersaturations in the gas phase. The existence of a critical diameter, caused by the Gibbs–Thomson effect, has been established below which (for a given supersaturation) the crystals do not grow. Assuming a quadratic relationship between growth and supersaturation the kinetic coefficient of crystallization and the effective total supersaturation in the gas phase have been determined.

We thank L. N. Obolenska for assistance in the experimental work.

---

1) If silicon is separated as a result of the overall reaction $\Sigma\nu_i A_i = 0$, then $\Delta\mu_0 = \Sigma\nu_i\mu_i$, where the stoichiometric coefficients are chosen such that $\nu_{Si} = 1$. The intermediate value of the chemical potential of silicon in a drop plays no part in determining the resulting driving force of the process $\Delta\mu$

---

[1] R. S. Wagner and W. C. Ellis, Appl. Phys. Letters, 4, 89 (1964).
[2] R. S. Wagner, Whisker Technology, Wiley, New York (1970), p. 47.
[3] B. Mutaftschiev, R. Kern, and C. Georges, Phys. Lett., 16, 32 (1965).
[4] E. I. Givargizov, in: The Growth of Crystals, Vol. 9 [in Russian], Nauka, Moscow (1972), p. 242.
[5] G. A. Bootsma and H. J. Gassen, J. Crystal Growth, 10, 223 (1971).
[6] G. A. Bootsma, W. F. Knippenberg, and G. Verspui, J. Crystal Growth, 11, 297 (1971).
[7] R. S. Wagner, J. Appl. Phys., 38, 1554 (1967).
[8] E. I. Givargizov and N. N. Sheftal, J. Crystal Growth, 9, 326 (1971).
[9] R. L. Barns and W. C. Ellis, J. Appl. Phys., 36, 2296 (1965).
[10] R. J. Jaccodine, J. Electrochem. Soc., 110, 524 (1963).

Statistical model of multiphase anisotropic crystallization

V. F. Dorfman

Institute of Electronic Control Machines

(Submitted March 12, 1971; resubmitted October 29, 1971, and February 23, 1972)
Kristallografiya, 18, 154-164 (January-February 1973)

The simultaneous random production and anisotropic growth of granules of different phases has been examined in terms of the partial degrees of covering of the original surface (volume) of each of the phases formed, the nonuniform (multicomponent) boundary of the granules, and the nodal points and lines of this boundary. The rates of normal growth for each type of granule and each crystallographic direction are assumed in the general case to be mutually independent, and allowance is made for the change in the habit of the granules during the growth process as far as the disappearance or reappearance of the individual apices. The mean-statistical dimensions of the filled regions (and pores, respectively), with allowance for anisotropy, and also the length of the total boundaries of the granules of each pair of phases, have been determined. Analytical solutions have been given for a number of particular cases.

In a number of cases, in particular for heteroepitaxy, there arises the problem of the simultaneous formation and competing anisotropic growth of granules exhibiting different orientations or belonging to different phases. The aim of the present work was to select a system of parameters and to derive equations describing this process. The method is based on the kinetic analysis of the complex boundary of all the granules, including its "nodal" elements: the apices and points of intersection. The first part of the paper examines particular two-dimensional cases, the second part examines the simplest three-dimensional cases, and the third part gives general equations for two-dimensional crystallization.

I. PARTICULAR CASES OF TWO-DIMENSIONAL CRYSTALLIZATION

1. We shall assume that a regular trigonal phase is produced. The rate of formation of the nuclei is g ($\mathrm{cm}^{-2}\cdot\mathrm{sec}^{-1}$), the rate of their normal growth is f(t) ($\mathrm{cm}\cdot\mathrm{sec}^{-1}$), and the total length of the free boundaries of the granules in each of the three crystallographic directions is $P_1 = P_2 = P_3$ ($\mathrm{cm/cm}^2$). These boundaries are the components of the generalized contour[1] $P_\Sigma = 3P_1$. It is obvious that the rate of covering of the surface by the substance crystallizing is $\dot{S} = fP_\Sigma$. We shall denote the density of the apices formed by the sides 1 and 2 (Fig. 1) of the trigonal granules N(1|02) cm^{-2}, and the density of the points of intersection between the sides 1 and 2 of different granules N(1|2) cm^{-2}. It is obvious that N(1|02) = N(2|03) = N(3|01), that the total density of apices is N_a = 3N(1|02), N(1|2) = N(2|3) = N(3|1), and that the total density of points of intersection is N_i = 3N(1|2). Subsequently, we shall refer to the apices and points of intersection collectively as "nodal points." During the growth of the granules of the components, P_1 increases as a consequence of the movement of the free apices N(1|02) and N(3|01) and decreases as a consequence of the "gliding" along it of the points of intersection N(1|2) and N(3|1). The rate of "gliding" of the apices and points of intersection along the contour is

$$\varphi(1|02)=\varphi(2|03)=\varphi(3|01)=\frac{f-f\cos 120^\circ}{\sin 120^\circ}=\sqrt{3}f=\varphi_1,$$

$$\varphi(1|2)=\varphi(2|3)=\varphi(3|1)=-\sqrt{3}f=\varphi_a.$$

We then have

$$\dot{P}_1=N(1|02)\varphi(1|02)+N(3|01)\varphi(3|01)+N(1|2)\varphi(1|2)$$
$$+N(3|1)\varphi(3|1)=2[N(1|02)-N(1|2)]\sqrt{3}f,$$
$$P_\Sigma=3\dot{P}_1=2[N_a-N_i]\sqrt{3f}. \tag{1a}$$

The apices appear together with the newly produced granules and disappear on collision with the free contour. The rate of approach of the apex N(1|02) and the component of the contour P_3 is equal to $3f$, and since the density of apices in a unit free surface is equal to N(1|02)/(1 − S), it follows that the rate of disappearance of these apices as a result of collision with the contour amounts to N(1|02)$P_3 3f$/(1 − S). We thus have

$$\dot{N}_a=3\dot{N}(1|02)=3(1-S)g-N_a\dot{S}/(1-S). \tag{1b}$$

Each collision between N(1|02) and P_3 leads to the production of two points of intersection N(3|1) and N(2|3). On the other hand, the points of intersection N(3|1) and N(2|3) disappear as a result of mutual collisions, and the rate of their approach on gliding along P_3 is equal to

$$|\varphi(1|3)+\varphi(2|3)|=2\sqrt{3f},$$

and the density of the points of intersection of each type on the contour is equal to N_i/P_Σ. We thus have

$$\dot{N}_i=3\dot{N}(3|1)=2\frac{N_a\dot{S}}{1-S}-2\sqrt{3}\frac{N_i^2}{P_\Sigma}f. \tag{1c}$$

By solving Eqs. (1)-(3) with allowance for the fact that $\dot{S}_\Sigma = P_\Sigma f$, we obtain

$$N_a=3(1-S)\int_0^t g\,dt, \tag{2a}$$

$$N_i=3P^2/\varkappa(1-S), \tag{2b}$$

$$P_\Sigma=\varkappa(1-S)\int_0^t f\left(\int_0^t g\,dt\right)dt, \tag{2c}$$

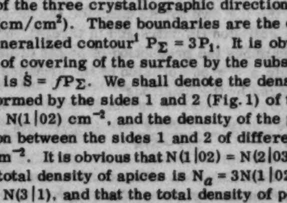

Fig. 1. Nodal points in the two-dimensional trigonal case. a) Reaction of an apex and a contour with the formation of two points of intersection; b) ternary annihilation of points of intersection.

$$S=1-\exp\left\{-\frac{\varkappa}{2}\int_0^t g\left(\int_\tau^t f\,dt\right)^2 d\tau\right\}, \tag{2d}$$

where $\varkappa = 6\sqrt{3}$. This last relationship is identical to the equation[2] for the two-dimensional case, and Eq. (2c) is identical to the equation[1] for the generalized contour. Equations (2a) and (2b) define N_a and N_i, that is the density of the nodal points of the boundaries of the granules, as a function of the degree of covering S and the length of the free boundaries P.

2. In the case of regular tetragonal granules, all the arguments are analogous to the foregoing, but the components of the contour also disappear as a consequence of mutual collisions (it is obvious that the components reacting are the parallel components P_1 with P_3 and P_2 with P_4; $\varphi_a = -\varphi_i = f$)

$$\dot{P}_\Sigma = 2(N_a - N_i)f - P^2 f/2(1-S). \tag{3}$$

Omitting the expressions for $\dot{N}_a$ and $\dot{N}_i$, we give the solution

$$N_a = 4(1-S)\int_0^t g\,dt;\quad N_i = 2P^2/\varkappa(1-S),$$

where $\varkappa = 8$. Equations (2c) and (2d) remain applicable.

3. A regular hexagonal phase is distinguished by the fact that in this case the initially formed points of intersection N_{120} interact not only with one another, but also with the apices (Fig. 2), since $\varphi_a + \varphi_{i_{120}} < 0$ ($\varphi_a = f/\sqrt{3}$; $\varphi_{i_{120}} = -\sqrt{3}f$). As a result of this interaction there is produced a new type of point of intersection N_{60} (here and subsequently the angles pertain to the vectors of the normal rates, and not the vectors of the sides). By arguments analogous to the preceding arguments, we find that

$$\dot{P} = \frac{2}{\sqrt{3}}f(N_a - N_{60} - 3N_{120}) - \frac{P\dot{S}}{3(1-S)}, \tag{4a}$$

$$\dot{N}_a = 6g(1-S) - \frac{2N_\nu S}{3(1-S)} + \frac{2N_{120}N_a}{P}\left(\frac{1}{\sqrt{3}} - \sqrt{3}\right), \tag{4b}$$

$$\dot{N}_{120} = \frac{2N_a S}{3(1-S)} + \frac{2f}{\sqrt{3}P}(N_{60}^2 - 3N_{120}^2 - 4N_{60}N_{120} - 2N_{120}N_a), \tag{4c}$$

$$\dot{N}_{60} = \frac{4f}{\sqrt{3}P}\{N_{120}N_a - N_{60}^2 - 2N_{60}N_{120}\}. \tag{4d}$$

From these we have

$$N_a = 6(1-S)\int_0^t g\,dt;\quad N(i|j) = \frac{P_i P_j}{1-S}\sin(i,j) \tag{4d}$$

(it may be noted that in this form the last expression is applicable for all single-phase cases), that is $N_{120} = N_{60} = 6N(i|j) = \sqrt{3}P_\Sigma^2/12(1-S)$ (here i, j, ..., n are the vectors of the six crystallographic directions). The equations for P and S are applicable in their earlier form ($\varkappa = 4\sqrt{3}$).

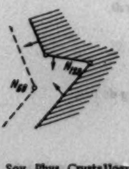

Fig. 2. Reaction of an apex with a point of intersection (for hexagons).

4. In the case of isotropic crystallization (growth of rounded granules) the number of "apices" n → ∞, and the components of the contour in the old representation are infinitely small. It is convenient to introduce the change $n \to n\,d\psi = 2\pi$; $N' = N_a = d\psi$. N' has the significance of the angular measure of the free boundary of the granules. We then have

$$\dot{P} = N'f + 2\int_0^\pi \varphi_\psi N_\psi\,d\psi - \frac{PN'f}{1-S}\frac{d\psi}{\pi} = N'f - 2\int_0^\pi |\varphi_\psi|\,d\psi, \tag{5a}$$

$$\dot{N}' = 2\pi g(1-S_\Sigma) + \frac{N'}{P}2\int_0^\pi N_\psi\varphi_\psi\,d\varphi - \frac{N'Pf}{\pi(1-S)}$$

$$= 2\pi g(1-S_\Sigma) + \frac{2N'}{P}\int_0^\pi N_\psi\varphi_\psi\,d\psi, \tag{5b}$$

$$\dot{N}_\psi = \frac{N'f}{P}\frac{\partial}{\partial\psi}N_\psi(|\varphi_\psi|) - \int_0^\pi \frac{N_\psi N_\gamma}{P}(|\varphi_\psi + \varphi_\gamma|)\delta_{\psi,\gamma}$$

$$+ \frac{1}{2}\int_0^\psi \frac{N_\gamma N_{(\psi-\gamma)}}{P}(|\varphi_\gamma + \varphi_{(\psi-\gamma)}|)\,d\gamma + \frac{N'Pf}{\pi(1-S)}\delta,$$

$$N = \int_0^\pi N_\psi\,d\psi;\quad \dot{N} = \int_0^\pi \dot{N}_\psi\,d\psi, \tag{5c}$$

where N is the total number of points of intersection, N_ψ is the number in the angle ψ, and

$$\delta_{\psi,\gamma} = \left|\begin{matrix} 1, & \text{if} & \psi+\gamma \leqslant \pi, \\ {}^1/_2, & \text{if} & \psi+\gamma > \pi, \end{matrix}\right. \qquad \delta = \left|\begin{matrix} 1, & \text{if} & \psi = \pi, \\ 0, & \text{if} & \psi \neq \pi. \end{matrix}\right.$$

In Eq. (5c) the first term describes the change in the angle ψ during the gliding of the points of intersection along the contour, the last two terms describe the change on their mutual collision (in pairs and in threes), and the last term describes the production of points of intersection with angle $\psi = \pi$ on collision of the granules. The solution is given by the functions

$$N_\psi = \int_0^{2\pi}\frac{P_\gamma P_{\gamma+\psi}}{1-S}\sin\psi\,d\gamma = \frac{P^2\sin\psi}{2(1-S)\pi},\quad N' = (1-S)2\pi\int_0^t g\,dt, \tag{5d}$$

analogous to Eqs. (2a)–(2d). The solutions for P and S are applicable in their previous form ($\varkappa = 2\pi$).

5. For an irregular trigonal phase (the three crystallographic directions i, j, and n form arbitrary angles), omitting intermediate transformations, we obtain the final result

$$N(i|0j) = \frac{N_a}{3} = (1-S)\int_0^t g\,dt;\quad N(i|j) = \frac{P_i P_j}{1-S}\sin(i,j)$$

$$= \frac{P^2}{2(1-S)}\operatorname{ctg}\left(\frac{i,j}{2}\right)\operatorname{ctg}\left(\frac{j,n}{2}\right)\operatorname{ctg}\left(\frac{n,i}{2}\right) = \frac{N_i}{3}. \tag{6}$$

For P_Σ, Eq. (2c) is applicable. Thus the solutions for the apices and the contour (and obviously for S) are preserved in their earlier form, and the densities of the three different points are equivalent, but other conditions being equal, they are lower than in the case of the regular phase (that is, merging of the nuclei begins more rapidly in the case of the regular phase).

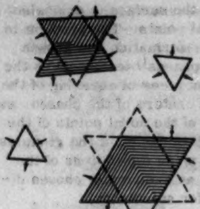

Fig. 3. Growth of twinned granules. The continuous line shows the actual part P of the visualized contour P* [since not all the visualized contour, passing over the free surface, is actually realized, it follows that the equation of ref. 1 P = P* (1 − S) and the equation in ref. 2 are inapplicable].

6. For two regular trigonal "phases" α and β in the twinned position, the derivation of the equations is analogous to that for the case of a single hexagonal phase. We give the result only for the apices (for $g_\alpha = g_\beta$ and $f_\alpha = f_\beta$):

$$\dot{N}_{\alpha\beta} = \dot{N}_{\alpha\alpha} = 3(1-S_\Sigma)g_\alpha - \frac{\dot{S}_\Sigma}{1-S_\Sigma}N_{\alpha\alpha} - \frac{\dot{S}_\Sigma}{6(1-S_\Sigma)}N_{\alpha\alpha},$$

from which we obtain

$$N_{\alpha\beta} = N_{\alpha\alpha} = 3(1-S_\Sigma)^{7/6}\int_0^t (1-S_\Sigma)^{-7/6} g_\alpha \, dt. \qquad (7)$$

It can be seen that this case does not reduce to the form given in ref. 1, so that it is not described by Kolmogorov's equations[2] (Fig. 3).

7. A phenomenon frequently encountered in crystallization practice is that in which, as a result of the action of impurities or other factors, the ratio of the rates of growth in different crystallographic directions changes with the passage of time. We can assume, for example, that at t = 0 the formation of a nucleus of a regular hexagonal phase has begun, that is $f_i = f_j = f_k = f_l = f_m = f_n$, and that at t = τ the rate of growth in the "odd" directions i, k, and n has decreased. If $f_i < f_j/2$, it follows that the apices (i|0j), (i|0k), (k|0l), (l|0m), (m|0n), (n|0i) begin to merge in pairs at a rate $|\varphi(i|0j) + \varphi(j|0k)| = (2/\sqrt{3})(2f_1 - f_2)$. After a period of time $\Delta t = \sqrt{3}\int_0^\tau f\,dt/2\int_\tau^t (2f_1 - f_2)\,dt$ (sec), all the old apices disappear as a result of merging in pairs (we shall call this process "degeneration"), and new apices (i|0k), (k|0m), (m|0i) are produced. This phenomenon, together with the opposite phenomenon – poisoning of the apices – is familar from experimental data (Fig. 4).

8. We can now examine the formation of a rectangular tetragonal phase, for which $f_1 = f_3$ and $f_2 = f_4$, with the assumption that all the nuclei G(cm^{-2}) have been formed during a small initial period of time. We then have

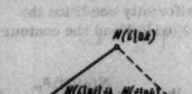

Fig. 4. "Degeneration" of apices.

$$\dot{P}_1 = \dot{P}_2 = \frac{f}{2}(N_a - N_1) - \frac{P_1^2}{1-S}2f_1;$$

$$\dot{P}_3 = \dot{P}_4 = \frac{f_1}{2}(N_a - N_1) - P_2^2\, 2f_2/(1-S);$$

$$N_a = -N_a S/(1-S); \quad N_1 = N_a S/(1-S) - SN^2/4P_1P_2.$$

By solving, we find that

$$P_1 : P_2 = \int_0^t f_2\,dt : \int_0^t f_1\,dt; \quad S = 1 - \exp\left\{-4G\left(\int_0^t f_1\,dt\right)\left(\int_0^t f_2\,dt\right)\right\}. \qquad (8)$$

It can be seen that if f_1 = const f_2, the last equation is converted into the form given in [2].

II. SIMPLEST THREE-DIMENSIONAL CASES

1. In the case of one cubic phase, the system of basic parameters is formed by the following: the filled volume V; the free surface area of the granules S (in the general case again multicomponent); the nodal lines, the edges of the granules P' and the lines of intersection of the faces of different granules P"; and the angular points, the apices N_a and the points of intersection of the nodal lines N' and N" (see Fig. 5a). In addition, there exist "virtual" points of intersection N‴, which are initially produced on the collision of granules, but which after small intervals of time dt "split" into pairs of points N' (see Fig. 5b). The absolute magnitude of N‴ vanishes at each given moment of time, but allowance must be made for their formation in the equation for $\dot{N}'$. We thus have

$$\dot{N}_a = 8(1-V)g - \frac{\dot{V}}{1-V}N_a;$$

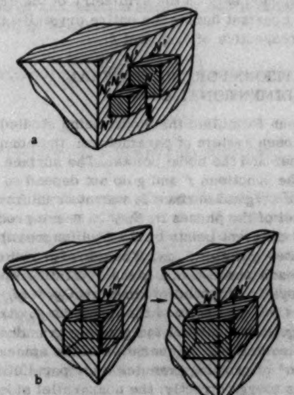

Fig. 5. Nodal points in the three-dimensional case. a) Basic nodal points N' and N"; b) the formation of a "virtual" nodal point N‴ and its splitting into two points N'.

$$\dot{N}' = N_a \frac{\dot{V}}{1-V} - 4\frac{N'P''f}{S} - \frac{(N')^2 f}{P'};$$

$$\dot{N}'' = \frac{2fN'P''}{S} - \frac{9(N'')^2 f}{P''};$$

$$\dot{P}'' = \frac{2P'\dot{V}}{3(1-V)} + f(2N' - 3N'') - \frac{2f(P'')^2}{S};$$

$$\dot{P} = 3f(N_a - N') - \frac{2P'\dot{V}}{3(1-V)}.$$

$$\dot{S} = 2f(P' - P'') - \frac{S\dot{V}}{3(1-V)}\cdot \quad \dot{V} = Sf. \tag{9}$$

By solving, we find that

$$N_a = 8(1-V)\int_0^t g\,dt; \quad N' = \frac{P'S}{3(1-V)}; \quad N'' = \frac{(P'')^2}{3S}.$$

$$P' = \varkappa(1-V)\int_0^t f\left(\int_0^t g\,dt\right)dt; \quad P'' = \frac{S^2}{3(1-V)};$$

$$S = 2\varkappa(1-V)\int_0^t g\left[\int_\tau^t f\,dt\right]^2 d\tau;$$

$$V = 1 - \exp\left\{-\frac{\varkappa}{3}\int_0^t g\left[\int_\tau^t f\,d\tau\right]^3 d\tau\right\}; \quad \varkappa = 24. \tag{10}$$

2. We give the final expression for the volume of a tetragonal phase:

$$V = 1 - \exp\left\{-\frac{\varkappa}{3}\int_0^t g\left[\left(\int_\tau^t f_1\,d\tau\right)\left(\int_\tau^t f_2\,d\tau\right)\left(\int_\tau^t f_3\,d\tau\right)\right]d\tau\right\}. \tag{11}$$

In conclusion we give the following fundamental result, which is general for the two-dimensional and three-dimensional cases examined: The relationship between the components of the free boundary and its nodal elements depends only on the symmetry of the crystal and remains constant during the entire crystallization process, irrespective of S, g, and f.

III. EQUATIONS FOR THE GENERAL TWO-DIMENSIONAL CASE

We can formulate the model being studied in terms of the chosen system of parameters: the components of the contour and the nodal points. The surface is uniform (that is, the functions f and g do not depend on the coordinates; the original surface is vacant or uniformly filled). The nuclei of the phases α, β, γ ... σ are produced randomly at different points on its free (ungrown) part ($1 - S_\Sigma$) at rates g_α, g_β, ..., g_σ. The rate of growth of the granules of each phase α in a given crystallographic direction i obeys an independent time law $v_{\alpha i} = i f_{\alpha i}(t)$, where $0 \leq f_{\alpha i} < \infty$. The ratio of the functions $f_{\alpha i}(t)$ determines the change in the habit of the growing granules and the above poisoning and degeneration of the apices. On the "collision" of growing granules their parallel i and i + n/2 sides merge directly; the nonparallel sides come into contact as a result of the "collision" of the apices with the sides. Subsequent merging of the granules takes place as a result of the "gliding" of the nodal points along the components of the contour and their collision with one another. Complete covering of the surface is equivalent to the disappearance of all nodal points. The problem is to use the given rates of nucleus formation and growth of the granules of the different phases[1] to determine the time dependence of the partial degrees of covering of the surface and the densities of the centers of the phases, and also to determine the densities of the nodal points of the contour, the length of the total boundaries of the granules of the different phases, and the mean dimensions of the filled sections of the surface in an arbitrarily chosen direction (that is, with allowance for anisotropy).

It is obvious that the rate of covering $\dot{S}_\Sigma$ of the surface of each of the phases is $\sum_i P_{\alpha i} f_{\alpha i}$, and $S_\Sigma = \sum_{\alpha=1}^{\sigma} \dot{S}_\alpha$; the rate of formation of new granules of the α phase is $\sigma_\alpha = (1 - S_\Sigma)g$. The total length of the boundaries of all the granules (the generalized contour) is $P_\Sigma = \sum_\alpha P_\alpha = \sum_\alpha \sum_i P_{\alpha i}$. For simplicity in presentation we shall assume that $f_{\alpha i}$ and g_α are given functions of time, and that the length of the contour and the area of the nuclei at the moment of production are equal to zero. With allowance for Eqs. (1)-(3) we obtain

$$P_{\alpha i} = \sum_{\beta=0}^{\sigma}\sum_{j=1}^{n} \varphi(\alpha i|\beta j) N(\alpha i|\beta j) - \sum_\beta \frac{f_{\alpha i} + f_{\beta(i+n/2)}}{1 - S_\Sigma} P_{\alpha i} P_{\beta(i+n/2)}. \tag{12}$$

Here the nodal points N(αi|βj) are formed by the i sides of the granules of the α phase and the j sides of the β phase, and in the particular case for $\beta = 0$ the symbol N(αi|0j) refers to the density of the apices formed by the i and j sides of the granules of the α phase. The rate of gliding of the nodal point N(αi|βj) along the component of the contour $P_{\alpha i}$ is

$$\varphi(\alpha i|\beta i) = (f_{\alpha i}\mathbf{i}\cdot\mathbf{j} - f_{\beta i})/\mathbf{i}\times\mathbf{j}.$$

Thus the chosen system of parameters makes it possible to transform the problem regarding the components $P_{\alpha,i}$ into a problem regarding the nodal points.

The dynamics of the nodal points are related to three types of process (see Table 1): 1) the nucleation of new centers; 2) the "collision" of apices with the contour; and 3) the "reaction" between the nodal points. Each process may take place if the condition defined for it is fulfilled; this is characterized by the function δ; $\delta = 1$ if the process is possible, and $\delta = 0$ if it is impossible. The rate of change in the density of each type of apex (for which the condition for existence is fulfilled) $\dot{N}$(αi|0j) and the points of intersection $\dot{N}$(αi|βj) is defined as the sum of the rates of all the reactions 1, 2, and 4-8 (see Table 1), taken with the sign "minus" if the given type of point is present in their left-hand part (as the original) and with the sign "plus" if it is present in the right-hand part (as the final). For the apices it is also necessary to take account of reaction 1. From the uniformity condition the rate of reaction 2 for the apices N(αi|0j) and the contour $P_{\beta k}$ is defined as

$$F\left(\frac{\alpha i|0j}{\beta k}\right) = \delta_2 |\{[\varphi(\alpha i|0j)\mathbf{P}_{i(j)} + \mathbf{v}_{\alpha i}]\mathbf{k} - f_{\beta k}\}| \frac{N(\alpha i|0j)P_{\beta k}}{1 - S_\Sigma}.$$

The rate of each of the reactions 4-8 for the pairs of nodal points N(αi|βj) and N(αi|γk) as a result of their

TABLE 1. Dynamics of the Nodal Points

No.	Process	Symbolic representation (reaction)	Conditions
1	A. The production of apices $N(\alpha i \mid 0j)$ from a set of the α phase by the nucleation of new α granules		$\delta_1(\alpha ij) = 1$, if reactions 3 and 4 with $N(\alpha i \mid 0j)$ in the left-hand side are not allowed
2	B. The collision of apices and components of the contour with the formation of points of intersection C. Reactions between nodal points C − 1. Reactions between apices	$N(\alpha i \mid 0j) \xrightarrow{P_{\beta k}} N(\alpha i \mid \beta k) + N(\alpha j \mid \beta k)$	$\delta_2(ijk) = 1$, if $<(-i, k) + (k, -j) \leq \pi$ for $j > i$ (and vice versa)
3	Poisoning of apices	$N(\alpha i \mid 0j) \to N(\alpha i \mid 0l) + N(\alpha l \mid 0j)$, где $i < l < j$	$\delta_3(\alpha i,\ j \mid l) = 1$, if $\varphi(\alpha i \mid 0l) + \varphi(\alpha l \mid 0j) > 0$
4	Degeneration of apices C − 2. Reactions of apices with points of intersection	$N(\alpha i \mid 0l) + N(\alpha l \mid 0j) \to N(\alpha i \mid 0j)$	$\delta_4(i, j, l) = 1$
5	With the production of a new point of intersection and a new apex	$N(\alpha i \mid 0l) + N(\alpha i \mid \beta j) \to N(\beta k \mid \alpha l) + N(\beta j \mid 0k)$, where $k > j$, if $l > i$ (and vice versa) and there does not exist a value of m from the set of α such that $j \leq m < k$	$\delta_5(i, j, l) = 1$, if $i < j < l$ or $i > j > l$
6	With the production of one point of intersection C − 3. Reactions of points of intersection	$N(\alpha i \mid 0l) + N(\alpha i \mid \beta j) \to N(\alpha l \mid \beta j)$	$\delta_6(i, j, l) = 1$, if $i < l < j$ or $j < l < i$
7	Paired reaction with the formation of a new point	$N(\alpha i \mid \beta j) + N(\alpha i \mid \gamma k) \to N(\beta j \mid \gamma k)$	$\delta_7(i, j, k) = 1$ if $\angle(i, j) + \angle(i, k) \geqslant \pi$
8	Triple annihilation	$N(\alpha i \mid \beta j) + N(\alpha i \mid \gamma k) + N(\beta j \mid \gamma k) \to 0$	$\delta_8 = {}^1\!/_2$, if $<(i, j) + <(i, k) < \pi$ (the factor ${}^1\!/_2$ is introduced so that one collision is not considered twice in the summation)

migration along the component of the contour $P_{\alpha i}$ is equal to [see Eq. (1c)]

$$\Phi[\alpha i(\beta i|\gamma k)] = \delta|[\varphi(\alpha i|\beta j)+\varphi(\alpha i|\gamma k)]|\frac{N(\alpha i|\beta j)\,N(\alpha i|\gamma k)}{P_{\alpha i}},$$

$$\begin{aligned}&\text{if}\quad \varphi(\alpha i|\beta j)+\varphi(\alpha i|\gamma k) \leqslant 0,\quad \Phi[\alpha i(\beta j|\gamma k)] = 0;\\ &\text{if}\quad \varphi(\alpha i|\beta j)+\varphi(\alpha i|\gamma k) \geqslant 0.\end{aligned}$$

We adopt the following notation:

$$\Phi[\alpha i(\beta j|\gamma k)] + \Phi[\alpha l(\beta m|\gamma s)] = \Phi[\alpha,\ i,\ l(\beta,\ j,\ m|\gamma,\ k,\ s)],$$

$$\Phi[\alpha i(\beta j|\gamma k)] - \delta\Phi[\theta l(\mu n|\varkappa s)] + \ldots = \Phi\left\|\begin{matrix}\alpha i(\beta j|\gamma k)\\ -\theta l'\mu n|\varkappa s)\end{matrix}\right\|.$$

We then have for the density of apices

$$\dot N(\alpha i/0j) = g_\alpha(1 - S_\Sigma)\,\delta_1(\alpha, i, j)$$

$$+\sum_{\beta,l}\left\{\Phi\left|\begin{matrix}\alpha l\,(0i\,|\,0j\\ \beta l\,(\alpha, i, j\,|\,0k)\\ -\alpha i, j\,(0, j, i\,|\,0l)\\ -\alpha i, j\,(0j, i\,|\,\beta l)\end{matrix}\right| + F\left(\frac{\alpha i\ \ 0j}{\beta l}\right)\right\}. \qquad (13)$$

For the density of the points of intersection we obtain

$$\dot N(\alpha i\,|\,\beta j) = \sum_k\left\{F\left(\frac{\alpha i\,|\,0k}{\beta j}\right)\right.$$

$$\left. + F\left(\frac{\beta j\,|\,0k}{\alpha i}\right) + \sum_{\gamma l}\Phi\left|\begin{matrix}\gamma k\,(\beta j\,|\,\alpha i)\\ \alpha k\,(\beta j,\ l\,|\,0i)\\ \beta k\,(\alpha i,\ l\,|\,0j)\\ -\alpha i\,(\beta j\,|\,0k)\\ -\beta j\,(\alpha i\,|\,0k)\\ -\alpha i\,(\beta j\,|\,\gamma k)\\ -\beta j\,(\alpha i\,|\,\gamma k)\end{matrix}\right\|\right\}. \qquad (14)$$

The system of equations (12)-(14) describes the kinetics of the processes within the framework of the crystallization model adopted. The structure of Eqs. (13) and (14) is very simple: The term associated with g_α corresponds to the production of new centers, that associated with the function F corresponds to the collision of the apices with the contour, and that associated with Φ corresponds to the collision of the nodal points with one another. [In Eq. (13) the first and third rows of indices in the column for Φ correspond to degeneration of the apices, and the second and fourth correspond to the collision of points of intersection with the apices. In Eq. (14) the first and the last two rows correspond to the mutual merging of the points of intersection, and the others correspond to the merging of the points of intersection with the apices.]

We can determine the rate of formation of the boundaries $L(\alpha|\beta)$ of the granules of the α and β phases. Each type of point of intersection $N(\alpha i|\beta j)$ will make a contribution to $\dot L(\alpha|\beta)$ equal to

$$N(\alpha i|\beta j)\left|\left[\frac{f_{\alpha i}\mathbf{P}_{i(j)} + f_{\beta j}\mathbf{P}_{j(i)}}{|\mathbf{i}\times\mathbf{j}|}\right]\right| = \theta(\alpha i|\beta j),$$

so that

$$L(\alpha|\beta) = \frac{1}{2}\sum_{ij}\theta(\alpha i|\beta j)\ \text{cm/cm}^2\cdot\text{sec}. \qquad (15)$$

To determine the mean dimensions of the filled regions we take account of the fact that if sections oriented in the direction i, with density P_i (cm/cm^2), are distributed uniformly over the surface, it follows that a straight line in the direction r intersects these sections at $P_i|\mathbf{i}\times\mathbf{r}|$ points in each centimeter of its length. (This also applies if sections of straight lines randomly distributed over the surface are drawn in the direction r.) The density of the points of intersection in the direction r with the free boundary of all the granules is

$$K(\mathbf{r}) = \sum_{\alpha,i} P_{\alpha i}|\mathbf{i}\times\mathbf{r}|, \qquad (16)$$

and the average dimensions of the filled regions is $\bar{R}(\mathbf{r}) = S_\Sigma/K(\mathbf{r})$ (cm) and that of the unfilled regions ("pores") is

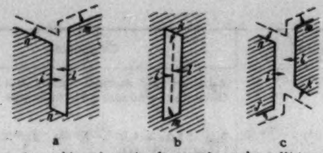

Fig. 6. Reactions taking place simultaneously on the collision of parallel components of the contour. a) $(i|n) + (n|l) \rightarrow 0$ and $(i|0n) + P_l \rightarrow (l|n)$, b) $(i|k) + (k|l) \rightarrow 0$ and $(i|m) + (m|l) \rightarrow 0$, c) $(n|i) + P_l \rightarrow (n|l)$ and $(l|k) + P_i \rightarrow (i|k)$.

$\overline{R}_0(r) = (1-S_\Sigma)/K(r)$ (cm). Since $(1 - S_\Sigma)$ and also S_Σ are not functions of the coordinates, the ratios of the mean dimensions of the pores in different directions are equal to the analogous ratios for the filled regions. The orientation of the vectors $\mathbf{P}_{i(j)}$ relative to the centers of the pores, however, is the opposite of the orientation relative to the centers of the granules, and the closed pores, mean-statistically, are twins of the granules (for trigonal granules this applies rigorously, and for tetragonal granules it applies only on the average; in both cases a pore is formed together with a granule of equivalent dimensions "parquet figure"). If two phases are formed successively, the second phase adopts the form of a pseudotwin of the first.

In conclusion it may be noted that all the parameters used in the derivation of the equations refer to observables and can be used, in particular, to verify the hypothesis that nucleus formation is random in character.

APPENDIX

1. All the expressions given for the rates of paired collisions are formally analogous to the equations of chemical kinetics. In particular, on the collision of parallel components of the contour (regular or irregular granules) there take place two paired reactions (see Fig. 6). The rate of approach of each pair of elements, however, is independent of the other paired interaction which takes place simultaneously with it. Thus it is not necessary to make special allowance for this effect, as can be illustrated by means of the observed analogy. The rate of transformation of the elements A, B, C, and D by the irreversible reactions: A + B = C; D + E = G; AD + BE = C + G, the rate constants of which are identical, is independent of the relative concentrations of the elements in the free state or in the associations AD and BE.

2. In the table the inequality $k < i < j$ has the following significance: The vector $\mathbf{i}$ lies between $\mathbf{k}$ and $\mathbf{j}$ on going along the smaller of the angles $\angle(\mathbf{k}, \mathbf{j})$ or $\angle(\mathbf{j}, \mathbf{k})$, or if they are equal, that is, $\mathbf{k} = -\mathbf{j}$, in the direction in which the indices are listed; if the order number i is greater than j, it follows that $i > j$ if $\angle(\mathbf{i}, \mathbf{j}) < \pi$; otherwise $i < j$, since $j + n = j$. It is also obvious that $N(\alpha i|\gamma k) \equiv 0$ if $\mathbf{i} = -\mathbf{k}$.

3. Of all the reactions between nodal points, only the third is monomolecular, and in view of the uniformity of the surface it defines the condition for the existence of the apices $N(\alpha i|0j)$; new apices of this type are not produced, and the old ones disappear, if $\delta_3 = 1$. When δ_3 jumps from 0 to 1, the density $N(\alpha i|0j) \rightarrow 0$, and $N(\alpha i|0l)$ and $N(\alpha l|0j)$ each increase by $N(\alpha i|0j)$. We assume that this process takes place instantaneously (where necessary, corresponding rate constants can be introduced). The vector $\mathbf{P}_{i(j)}$, which coincides with the component of the contour P_i, is directed towards the apex $(i|0j)$.

---

1) By "phase" we here mean the assembly of all granules which at a given moment of time are characterized by the same set of normal rates of growth and identical rates of nucleus formation.

---

[1] V. F. Dorfman, Kristallografiya, 15, 435 (1970) [Sov. Phys.—Crystallogr., 15, 370 (1970)].

[2] A. N. Kolmogorov, Izv. Akad. Nauk SSSR, Ser. Mat., 3, 355 (1937).

Stability of ionic crystals with an NaCl type lattice in the Born model

I. M. Ratner, N. A. Tanyakova, and A. I. Boiko

(Submitted July 7, 1971; resubmitted February 25, 1972)
Kristallografiya, 18, 165-167 (January-February 1973)

The energy of an ionic crystal can be described fairly well by Born's two-term equation[1]

$$U_i = \frac{1}{2}\sum_{j\neq i}\left(\frac{e_ie_j}{r_{ij}}+\frac{b}{r_{ij}^n}\right) = \frac{1}{2}\left(-\frac{e^2\alpha_0}{r}+\frac{b\beta_0}{r^n}\right), \qquad (1)$$

where e_i, e_j are the charges of the i-th and j-th ions, r_{ij} is their separation, U_i the specific energy, and r the minimum distance between the positive and negative ions. The repulsion index n is usually determined empirically from the elastic constants, and α_0 and β_0 are structural summations (α_0 being the Madelung constant). The constant b, which is determinable from the equilibrium condition, is given by the expression $b = e^2\alpha_0 r_0^{n-1}/n\beta_0$, where r_0 is the minimum ionic separation in the equilibrium position.

Let us find the forces which occur in the crystal during a uniaxial elongation along the X axis (the [100] direction). For this we use the energy expansion in a power series in $\xi = y^2/x^2 - 1$ near to the point $x = y = z = x_0$ (x, y, and z are the minimum ionic separations along the X, Y, and Z axes), $x_0 = r_0$. The specific energy then becomes

$$U_i = \frac{1}{2}\left[-\frac{e^2}{x}\left(\alpha_0+\sum_{l=1}^{\infty}c_l\alpha_l\xi^l\right)+\frac{b}{x^n}\left(\beta_0+\sum_{l=1}^{\infty}d_l\beta_l\xi^l\right)\right], \qquad (2)$$

where

$$\alpha_l = \sum_{\substack{m,k,p=-\infty\\ m^2+k^2+p^2\neq 0}}^{\infty}\frac{(-1)^{m+k+p+1}(k^2+p^2)^l}{(m^2+k^2+p^2)^{l+1/2}},$$

$$\beta_l = \sum_{\substack{m,k,p=-\infty\\ m^2+k^2+p^2\neq 0}}^{\infty}\frac{(k^2+p^2)^l}{(m^2+k^2+p^2)^{l+n/2}},$$

$$c_l = (-1)^l\frac{\Gamma(l+1/2)}{l!\Gamma(1/2)}, \qquad d_l = (-1)^l\frac{\Gamma(l+n/2)}{l!\Gamma(n/2)},$$

and $\Gamma(x)$ is a gamma function.

Using (2) we obtain the following expression for the forces:

$$F_x = -\frac{\partial U_i}{\partial x} = \frac{e^2}{2x_0^2}\left[\frac{1}{\eta^2}\left(\alpha_0'+\sum_{l=1}^{\infty}c_l'\alpha_l'\xi^l\right) - \frac{\alpha_0}{\beta_0\eta^{n-1}}\left(\beta_0'+\sum_{l=1}^{\infty}d_l'\beta_l\xi^l\right)\right],$$

$$F_y = F_z = -\frac{\partial U_i}{\partial y} = \frac{\eta e^2}{2x^2}\left[\left(\alpha_1+\sum_{l=1}^{\infty}c_l'\alpha_{l+1}\xi^l\right) - \frac{\alpha_0}{\beta_0\eta^{n-1}}\left(\beta_1+\sum_{l=1}^{\infty}d_l'\beta_{l+1}\xi^l\right)\right],$$

$$\alpha_l' = \alpha_l - \alpha_{l+1}, \qquad \beta_l' = \beta_l - \beta_{l+1},$$
$$c_l' = (2l+1)c_l, \qquad d_l' = (2l+n)d_l, \qquad \eta = z/x_0.$$

The crystal stability condition for a uniaxial elongation is

$$\left[\frac{d}{dx}\left(\frac{\partial U_i}{\partial x}\right)\right]_{\xi\to 0} > 0, \qquad \frac{\partial U_i}{\partial y} = 0, \qquad \frac{\partial U_i}{\partial z} = 0. \qquad (3)$$

The second and third terms of condition (3) lead to a relationship between η and ξ, that is, a relationship between the transverse compression and the longitudinal elongation:

$$\eta = \left[\alpha_0\left(\beta_1+\sum_{l=1}^{\infty}d_l'\beta_{l+1}\xi^l\right)\Big/\beta_0\left(\alpha_1+\sum_{l=1}^{\infty}c_l'\alpha_{l+1}\xi^l\right)\right]^{1/(n-1)}.$$

The first of the conditions (3) is equivalent to

$$\frac{d}{d\xi}\left(\frac{\partial U_i}{\partial x}\right) = \frac{d}{d\xi}(F_x) = \frac{\partial}{\partial\xi}\left(\frac{\partial U_i}{\partial x}\right)+\frac{\partial}{\partial\eta}\left(\frac{\partial U_i}{\partial x}\right)\frac{d\eta}{d\xi}$$
$$= \frac{e^2}{2x_0^2}\left\{c_1'\alpha_1' - \frac{\alpha_0}{\beta_0}d_1'\beta_1' + \frac{\alpha_0(d_1'\alpha_1\beta_2 - c_1'\alpha_2\beta_1)[(n+1)\alpha_0\beta_0' - 2\alpha_0'\beta_0]}{(n-1)\beta_0^2\alpha_1^2}\right\} < 0, \qquad (4)$$

because $\xi < 0$ for an elongation. The crystal stability condition during a uniaxial elongation then has the form

$$A_n < 0, \qquad (5)$$

where A_n stands for the only n-dependent factor inside the braces in Eq. (4). Table 1 shows the structural summations α_l and β_l calculated by Evjen's method.[2] The inequality (5) was solved numerically. It was found that $A_n > 0$ for $n \leq 6$ and $A_n < 0$ for $n \geq 7$. By dividing the segment (6.7) into two, the root of the equation $A_n = 0$ yields n = 6.1624. The solution of the inequality (5) is therefore

$$n > 6.1624. \qquad (6)$$

The values of n obtained from the elastic constant experimental data[3,4] (for NaF 7.03, NaCl 8.75, NaBr 8.79, NaI 8.87, KF 7.88, KCl 9.92, KBr 10.10, KI 10.65, RbF 7.89, RbCl 8.68, RbBr 8.75, and RbI 9.43) are confirmed by inequality (6).

It should be noted that all the constants and elastic moduli can be expressed in terms of the lattice summations α_l and β_l. For example, for S_{11}, S_{12}, and the compressibility χ we have

$$S_{11} = \frac{x_0^4}{e^2}\frac{6(d_1'\beta_2\alpha_0 - c_1'\alpha_2\beta_0)}{\alpha_0(n-1)(2c_1'\alpha_1'\beta_0 - 2d_1'\alpha_0\beta_1' + d_1'\beta_2\alpha_0 - c_1'\alpha_2\beta_0)}, \qquad (7)$$

$$S_{12} = \frac{x_0^4}{e^2}\frac{2[3(d_1'\beta_2\alpha_0 - c_1'\alpha_2\beta_0)+(n-1)\alpha_0\beta_0]}{\alpha_0(n-1)(2c_1'\alpha_1'\beta_0 - 2d_1'\alpha_0\beta_1' + d_1'\beta_2\alpha_0 - c_2'\alpha_2\beta_0)}, \qquad (8)$$

$$\chi = 3(S_{11}+2S_{12}) = \frac{x_0^4}{e^2}\frac{18}{\alpha_0(n-1)}. \qquad (9)$$

Table 2 shows the experimental values of S_{11}, S_{12}, and

TABLE 1

l	α_l	$\beta_l(n)$						
		$n=6$	$n=7$	$n=8$	$n=9$	$n=10$	$n=11$	$n=12$
$l=0$	1.74757	8.40046	7.46698	6.94580	6.62886	6.42612	6.29229	6,20215
$l=1$	1.16505	5.60031	4.97798	4.63053	4.41924	4.28408	4.19486	4.13477
$l=2$	1.628715	5.21752	4.73873	4.47413	4.31439	4.21271	4.14580	4.10081

TABLE 2

Crystal	Experimental values, 10^{-3} cm^2/dyn			Values calculated according to Eqs. (7)-(9), 10^{-13} cm^2/dyn		
	S_{11}	S_{12}	χ	S_{11}	S_{12}	χ
NaCl	22,9	—4.65	40.8	22.6	—5.25	36.3
NaBr	28.7	—5.8	51.3	28.4	—6.6	45.6
NaI	38.4	—8.1	66.6	38.1	—8,7	62.1
KCl	26.2	—3.5	57.6	25.7	—4.7	48.9
KBr	30,4	—4.4	64.8	30.0	—5.3	58.2
KI	39.2	—5.4	91.2	35,7	—6,0	71,1

and those calculated from Eqs. (7)-(9). It can be seen from the table that there is satisfactory agreement between the experimental and calculated values, the agreement being better for those crystals in which the deviation from the Cauchy relationship is least.

It should also be noted that the denominator in Eqs. (7) and (8) becomes 0 at the limiting value $n = 6.1624$, since $S_{11} \to \infty$ as $S_{12} \to -\infty$. For $n < n_0$, S_{11} and S_{12} change sign, which is physically absurd.

---

[1] M. Born and M. Geppert-Meier, Solid State Theory [Russian translation], Izd. IL, Moscow (1958).

[2] H. M. Evjen, Phys. Rev. 39, 675 (1932).

[3] G. Huntington, Usp. Fiz. Nauk, 74, 303, 461 (1961).

[4] A. A. Vorob'ev, Mechanical and Thermal Properties of Alkali Halide Single Crystals [in Russian], Vysshaya Shkola, Moscow (1968).

Atom–atom potentials and the coordinates of hydrogen atoms in methyl groups in the molecule and crystal

K. V. Mirskaya and L. V. Ivanova

Institute of Heteroorganic Compounds, Academy of Sciences of the USSR

(Submitted January 27, 1972)
Kristallografiya, 18, 168-170 (January-February 1973)

If the coordinates of the hydrogen atoms in an organic compound cannot be deduced from x-ray data, then they may be calculated from the known bond lengths and valence angles;[1] however, such a calculation cannot be performed completely for methyl groups, because even known bond lengths and valence angles leave undetermined the angle of rotation around the single C−C bond. In this case, the hydrogen coordinates can be calculated by means of atom−atom potentials[2,3] on the principle of minimum potential energy at equilibrium. Such calculations have been performed[4] for 4,12-dimethyl(2, 2)methacyclophane and 4-methylpentaleno-(6, 6a, 1, 2-def)heptalene.

Here we present calculations for the molecule and crystal of durol (1, 2, 4, 5-tetramethylbenzene).

The durol molecule has two pairs of CH_3 groups, which are joined to the benzene ring by single C−C bonds (Fig. 1). X-ray data[5] give the geometry of the hydrocarbon skeleton and the orientation of the molecule in the crystal at room temperature; the space group is $P2_1/a$, Z = 2, unit-cell parameters $a = 11.57$, $b = 5.77$, $c = 7.03$ Å, $\beta = 113.3°$. The molecule lies at an inversion center and has mmm symmetry with respect to the carbon atoms.

We assume that the C−H bonds have lengths of 1.08 Å, while the C−C−H valence angles in the methyl groups are tetrahedral and do not alter on rotation. If the methyl groups are rotated, only the torsion angles α_1 and α_2 are altered together with the distances between atoms not linked by valence bonds (there are only two independent torsion angles because the molecule has a center of symmetry).

One can calculate the energy of the nonvalent interactions for all possible values of α_1 and α_2 via the atom−atom approximation as the sum of the pairwise atom interactions.[2,3] See refs. 6 and 7 for the interaction potentials for C−C, C−H, and H−H.

Figure 2a shows the energy U_{mol} of the free molecule as a function of α_1 and α_2 (we have taken into account only the C−H and H−H interactions that alter on rotation of the CH_3 groups, while the energies have been calculated at 10° intervals). The $U_{mol}(\alpha_1, \alpha_2)$ energy map is symmetrical, in accordance with the symmetry of the carbon skeleton, and has two equivalent minima, both of which lie in the same valley, whose bottom is indicated by the dashed line (for each methyl group there is a root of least energy, but the two are completely symmetrical). Figure 3a shows the form of one of these curves and the coordinates of the minima. Figure 1 shows the disposition of the H atoms corresponding to minimum 1 (77°, 77°). Figures 2a and 3a show that the minima are separated by a small barrier (0.3 kcal/mole) and so the molecule allows torsional oscillations of the CH_3 group with large amplitudes, from one potential well to the other. Complete rotation of the single C−C bond from along the most favorable part involves overcoming a barrier of 1.2 kcal/mole, which is thus the minimal one of all the possible ones (it has been estimated[8] that the rotation barrier for CH_3 groups in durol is ~1.5 kcal/mole). In calculating the barrier we have neglected the so-called axial energy, but for molecules such as tol-

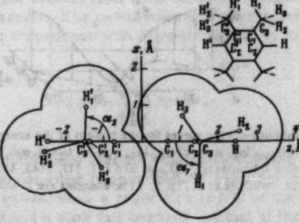

Fig. 1. Projection of the durol molecule on a plane perpendicular to the plane of the benzene ring: α_1 and α_2 are the angles of rotation of the CH_3 groups around the C_1-C_3 and $C_1'-C_3'$ bonds. The H atoms in the methyl groups have been shown with their van der Waals radii for clarity (r_H = 1.17 Å[1]).

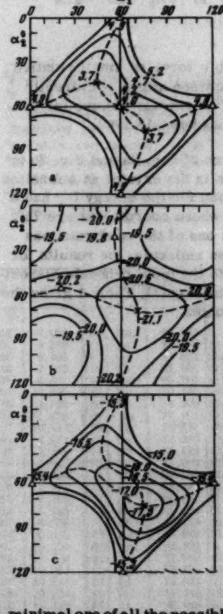

Fig. 2. Potential energy of the molecule and crystal of durol as a function of α_1 and α_2: a) $U_{mol}(\alpha_1, \alpha_2)$; b) $U_{lat}(\alpha_1, \alpha_2)$; c) $U_\Sigma(\alpha_1, \alpha_2)$. The energies on the equipotential lines are in kcal/mole. High-energy lines have been omitted; × represent minima, while Δ are saddle points.

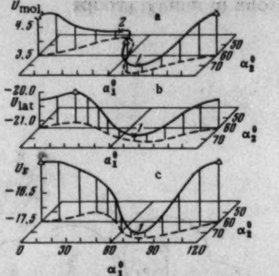

Fig. 3. Minimum-energy curves for the bottom of the energy valley on the surfaces: a) $U_{mol}(\alpha_1, \alpha_2)$; b) $U_{lat}(\alpha_1, \alpha_2)$; c) $U_\Sigma(\alpha_1, \alpha_2)$. The coordinates of the minima (given as α_1^0, α_2^0) are: a) 1 (77, 77), 2 (43, 43); b) (70, 70); c) 1 (75, 75). Symbols as in Fig. 2. The energies are in kcal/mole.

TABLE 1. Calculation of the Coordinates of the Hydrogen Atoms of the Methyl Group in the Crystal of Durol

Atom	x/a	y/b	z/c	Atom	x/a	y/b	z/c
H_1	0.148	0.484	0.259	H_1'	0.201	0.269	−0.173
H_2	0.219	0.249	0.424	H_2'	0.049	0.328	−0.358
H_3	0.267	0.323	0.224	H_3'	0.112	0.496	−0.130

uene, o-xylene, and durol, this term is small relative to the energy of interaction between atoms not directly connected by valence bonds.[8,9] A similar picture for the potential energy of o-xylene has been derived.[10]

We add the energy pictures of Fig. 2a and Fig. 2b to get the energy of the molecule in the crystal as a function of α_1 and α_2 (Fig. 2c). The map for the energy U_Σ has a single pronounced minimum, whose coordinates are 75°, 75°. Then the crystal selects one of the conformations that are equivalent for the free molecule; the results for α_1 and α_2 should correspond to the most probable disposition of the methyl groups in the crystal; Table 1 gives the corresponding H atom coordinates.

When the molecule is in a crystal, we have to consider the lattice energy, i.e., the energy of interaction of a given molecule with all the surrounding ones, again as a function of α_1 and α_2. We assume that the lattice parameters and carbon coordinates are known from experiments. Figure 2b shows the corresponding energy diagram. Here again there are two probable paths for rotation of the methyl groups, but they are not at all equivalent; the barrier due to intermolecular forces is 0.9 kcal/mole for one CH_3 group but 1.3 kcal/mole for the other. Figure 3b shows the shape of the first (more favorable) path; a difference from Fig. 2a is that Fig. 2b for $U_{lat}(\alpha_1, \alpha_2)$ has only one minimum instead of two, which is close to one of the minima for the free molecule.

Of course, the optimal molecular conformation in the crystal is the joint result of intramolecular and intermolecular forces, being determined by the minimum in the sum function $U_\Sigma = U_{mol} + U_{lat}$.

Figures 2c and 3c indicate that the smallest barrier to rotation of the methyl groups in the crystal is 1.9 kcal/mole, which agrees well with the observed activation barrier for rotation of CH_3 groups in solid durol (1.6 and 2.0 kcal/mole) as deduced by nuclear magnetic resonance and neutron scattering.[11]

We are indebted to Professor A. I. Kitaigorodskii for interest in the work and valuable advice.

---

[1] A. I. Kitaigorodskii, Organic Chemical Crystallography [in Russian], Izd. AN SSSR, Moscow (1955).

[2] A. I. Kitaigorodskii, Dokl. Akad. Nauk SSSR, 137, 116 (1961).

[3] A. I. Kitaigorodskii and K. V. Mirskaya, Kristallografiya, 6, 507 (1964) [Sov. Phys.–Crystallogr., 6, 408 (1962)].

[4] N. N. Afonina and P. M. Zorkii, Proceedings of the All-Union Conference on Research on the Structure of Organic Compounds by Physical Methods [in Russian], Izd. Kazan. Univ. (1971), p. 212.

[5] J. M. Robertson, Proc. Roy. Soc., A142, 659 (1933).

[6] A. I. Kitaigorodskii and K. V. Mirskaya, Kristallografiya, 9, 174 [Sov. Phys.–Crystallogr., 9, 137 (1964)].

[7] A. I. Kitaigorodskii, J. Chim. Phys. et Phys.-Chim. Biol., 63, No. 1, 9 (1966).

[8] K. C. Ingham and S. J. Strickler, J. Chem. Phys., 53, No. 11, 4313 (1970).

[9] H. D. Rudolph, H. Dreizler, A. Jaeschke, and P. Wendling, Z. Naturforsch., a22, 940 (1967).

[10] W. R. Woolfenden and D. M. Grant, J. Amer. Chem. Soc., 88, No. 7, 1496 (1966).

[11] P. S. Allen and A. Cowking, J. Chem. Phys., 49, No. 2, 789 (1968).

Atomic scattering amplitudes for electrons at small scattering angles

A. N. Pilyankevich

Institute of Materials-Science Problems, Academy of Sciences of the Ukrainian SSR

(Submitted February 14, 1972)
Kristallografiya, 18, 171-172 (January-February 1973)

One can calculate atomic scattering amplitudes for electrons via various atomic models and obtain satisfactory agreement for fairly heavy atoms at medium and large scattering angles ($\sin\theta/\lambda > 0.5$ Å^{-1}), but with substantial differences for small angles, especially zero. The reason is that the small-angle electron scattering is determined by the distribution of the potential at the edge of the scattering atom, where there are marked effects from the errors of approximation in the various methods.

The atomic amplitude for a zero scattering angle $f(0)$ may be expressed in terms of the mean-square radius of the scattering atom[1] $\langle r^2\rangle$:

$$f(0) = Z\langle r^2\rangle / 3a_0. \qquad (1)$$

For small scattering angles ($\sin\theta/\lambda = 0$–0.05 Å^{-1}), one obtains a good approximation via the equation of ref. 2, which also relates the electron scattering amplitude to the mean-square radius:

$$f(s) = f(0)\left[1 + \frac{s^2\langle r^2\rangle}{6}\right]^{-1}. \qquad (1a)$$

We now have tables of atomic weight functions calculated by the self-consistent field technique by variational methods (Hartree–Fock–Slater functions) for all atoms in the periodic system.[3] These results have been used to calculate the atomic scattering amplitudes of ref. 4 in the form of tables for values of the arguments s starting from 1.

Here we have used the Hartree–Fock–Slater wave function[3] to calculate the mean-square radii of the neutral isolated atoms $\langle r^2\rangle$ together with the atomic scattering amplitudes for electrons at zero scattering angle. Table 1 gives the results. The calculation was performed by integration in accordance with Simpson's rule by the equation

$$Z\langle r^2\rangle = \sum_{i=1}^{Z}\int_0^\infty P_i^2(r)\, r^2\, dr. \qquad (2)$$

The results show that the revised scattering amplitudes $f(0)$ do not alter in principle the basic periodic trends previously established: a rapid rise in $f(0)$ at the start of each period and a slow fall towards the end of the period with a general tendency for increase from period to period.[5,6] An interesting point is that good numerical agreement is obtained via these functions for all the inert gases and for the atoms of periods I and II.

The results allow one to calculate the electron-scattering amplitudes for small angles ($\sin\theta/\lambda = 0$–0.05 Å^{-1}) via (1a) or via the equivalent equation

$$f(s) = f(0)\left[1 + 0.2646\,(f(0)/Z)\,s^2\right]^{-1}. \qquad (3)$$

TABLE 1

Z	Atom	$\frac{Z\langle r^2\rangle}{a_0^2}$	$f(0)$	Z	Atom	$\frac{Z\langle r^2\rangle}{a_0^2}$	$f(0)$	Z	Atom	$\frac{Z\langle r^2\rangle}{a_0^2}$	$f(0)$
2	He	2.467	0.435	32	Ge	39.415	6.952	62	Sm	86.502	15.258
3	Li	17.596	3.104	33	As	39.050	6.888	63	Eu	84.976	14.989
4	Be	16.857	2.973	34	Se	38.360	6.766	64	Gd	82.820	14.609
5	B	15.843	2.795	35	Br	37.546	6.623	65	Tb	82.101	14.482
6	C	13.752	2.426	36	Kr	36.774	6.487	66	Dy	80.760	14.245
7	N	12.136	2.141	37	Rb	61.767	10.895	67	Ho	79.498	14.023
8	O	10.834	1.911	38	Sr	68.716	12.121	68	Er	78.202	13.794
9	F	9.657	1.703	39	Y	65.886	11.622	69	Tm	77.102	13.600
10	Ne	8.950	1.579	40	Zr	61.337	10.819	70	Yb	75.831	13.376
11	Na	25.160	4.438	41	Nb	56.529	9.971	71	Lu	74.360	13.116
12	Mg	27.794	4.903	42	Mo	53.547	9.445	72	Hf	72.483	12.785
13	Al	32.137	5.669	43	Tc	56.791	10.017	73	Ta	71.093	12.540
14	Si	30.923	5.455	44	Ru	50.390	8.888	74	W	69.505	12.260
15	P	29.066	5.127	45	Rh	48.440	8.554	75	Re	68.241	12.037
16	S	27.280	4.812	46	Pd	40.384	7.123	76	Os	66.952	11.810
17	Cl	25.675	4.529	47	Ag	46.122	8.135	77	Ir	65.723	11.593
18	Ar	24.201	4.269	48	Cd	49.087	8.658	78	Pt	60.129	10.606
19	K	46.630	8.225	49	In	57.109	10.079	79	Au	59.083	10.424
20	Ca	51.605	9.103	50	Sn	58.963	10.400	80	Hg	62.395	11.006
21	Sc	48.202	8.502	51	Sb	59.295	10.459	81	Tl	71.293	12.575
22	Ti	45.447	8.016	52	Te	59.097	10.424	82	Pb	73.989	13.051
23	V	42.863	7.561	53	I	58.627	10.341	83	Bi	75.034	13.235
24	Cr	36.629	6.461	54	Xe	58.018	10.234	84	Po	75.435	13.306
25	Mn	38.907	6.863	55	Cs	88.410	15.595	85	At	75.496	13.317
26	Fe	37.053	6.536	56	Ba	97.664	17.227	86	Ru	75.341	13.289
27	Co	35.397	6.244	57	La	93.970	16.575	87	Fr	108.491	19.137
28	Ni	34.041	6.004	58	Ce	93.945	16.465	88	Ra	119.277	21.039
29	Cu	29.447	5.194	59	Pr	91.585	16.155	89	Ac	116.640	20.574
30	Zn	31.551	5.565	60	Nd	89.729	15.827	90	Th	114.257	20.154
31	Ga	38.527	6.796	61	Pm	88.120	15.543				

---

[1] J. Ibers, Acta Crystallogr. 11, 178 (1958).
[2] F. Lenz, Z. Naturforsch., a9, 185 (1954).
[3] F. Herman and S. Skillman, Atomic Structure Calculations, Prentice-Hall, Englewood Cliffs, New Jersey (1963).
[4] E. Zeitler, Lab. Investig., 14, 36 (1965).
[5] A. N. Pilyankevich, Kristallografiya, 6, 341 (1961)[Sov. Phys.–Crystallogr., 6, 272 (1961)].
[6] B. K. Vainshtein, Structural Electron Diffraction [in Russian], Izd. AN SSSR, Moscow (1956).

Crystal structure of a new modification, Bi_2Se_3 II

É. Ya. Atabaeva, S. A. Mashkov, and S. V. Popova
Institute for High-Pressure Physics, Academy of Sciences of the USSR
(Submitted May 27, 1971; resubmitted March 2, 1972)
Kristallografiya, 18, 173-174 (January-February 1973)

A new phase, Bi_2Se_3II, which is metastable under normal conditions ($a = 11.62 \pm 0.03$ Å, $b = 11.83 \pm 0.01$ Å, $c = 4.09 \pm 0.02$ Å; space group Pbnm, Z = 4), obtained at high pressure and temperature and isostructural with Sb_2S_3, is described in ref. 1.

This work is devoted to determination of the atomic coordinates of the Bi_2Se_3II structure.

The crystal structure of[2] Sb_2S_3 is made up of ribbons parallel to the z axis and forming an angle of ~45° with the x and y axes. The bands are turned with respect to each other. Each of them consists of two infinite zigzag –Sb–S–Sb–S– chains with S and Sb atoms closely bound. In turn, the ribbons are combined into layers perpendicular to the y axis. Interaction between ribbons in the direction perpendicular to the z axis is considerably weaker. All atoms are located on planes of symmetry m in the 4(c) positions: $x, y, \frac{1}{4}$; $\bar{x}, \bar{y}, \frac{3}{4}$; $\frac{1}{2} - x, \frac{1}{2} + y, \frac{1}{4}$; $\frac{1}{2} + x, \frac{1}{2} - y, \frac{3}{4}$. Thus, determination of the structure is reduced to establishing the x and y coordinates of two Bi atoms and three Se atoms. The problem of determining these parameters was solved by the minimalization functions of numerous variables Φ, determined in the following manner: $\Phi = R + \alpha D$, where $R = \Sigma \| F_{exp}| - |F_{calc} \| / \Sigma |F_{exp}|$ and is the divergence factor, $D = \Sigma[(\rho_{ik} - r_{ik})/r_{ik})]\delta_{\rho r}$ is a function which depends on the interatomic distances, $\delta_{\rho r}$, ρ_{ik} is the minimum permissible distance between atoms i and k, r_{ik} is the distance between atoms i and k, $\delta_{\rho r} = 0$ if $r_{ik} \geq \rho_{ik}$, $\delta_{\rho r} = 1$ if $r_{ik} < \rho_{ik}$ and α is a numerical coefficient.

The x-ray diffraction pattern was taken by the Debye–Scherrer method on a DRON-1 diffractometer with filtered copper radiation, since the metastable Bi_2Se_3II phase could be obtained only in polycrystalline form. Values intermediate between the sum of the ionic and covalent radii were chosen for ρ_{ik}: $\rho_{Bi-Bi} = 2.16$ Å, $\rho_{Se-Se} = 3.44$ Å, $\rho_{Bi-Se} = 2.82$ Å. In this case the ionic radii of Bi and Se were taken as equal to 1.20 and 1.93 Å, and the covalent radii as 1.59 and 1.17 Å, respectively.[3,4]

The structure parameters[2] of Sb_2S_3 (see Table 1) were taken as starting values for the coordinates. Structure amplitudes, R factor, and the minimalization function Φ were calculated by successive choice of parameters to give the best agreement of $|F_{exp}|$ and $|F_{calc}|$ on a URAL-2 electronic computer by a specially compiled program.

TABLE 2. Interatomic Distances, in Å, in the Bi_2Se_3II Structure

Interatomic distances in ribbon		Interatomic distances between ribbons and layers	
$Bi_1 - Se_2$	2.82	$Bi_1 - Se_3$	3.14
$Bi_2 - Se_3$	2.83	$Bi_2 - Se_2$	3,41
$Bi_1 - Se_3$	2.85	$Se_2 - Se_3$	3,44
$Bi_2 - Se_1$	2.85	$Bi_1 - Se_3$	3,54
$Bi_2 - Se_1$	2.95	$Se_1 - Se_2$	3,67
$Bi_1 - Se_1$	3.26		
$Se_2 - Se_3$	3,69		
$Se_1 - Se_1$	3,87		
$Se_1 - Se_3$	3.93		
$Bi_2 - Bi_2$	4,31		
$Bi_1 - Bi_2$	4.33		

Final values of the coordinate parameters and of the R and D factors are given in Table 1. The parameters which we obtained differ from the starting parameters by not more than ± 0.018.

Interatomic distances in the Bi_2Se_3II structure are given in Table 2 and Fig. 1. Analysis of these values shows that the stronger bonds from 2.82 to 2.85 Å are formed inside the chain. The length of the bonding between chains in a ribbon is 2.95 Å. The ribbons form layers by means of the weaker interaction of 3.14 Å. Finally, the minimum distance between layers comes to 3.41 Å. Thus, the interatomic distances obtained agree well with the type of structure proposed for Bi_2Se_3II.

The authors consider it their pleasant duty to express their thanks to Academician L. F. Vereshchagin for continued attention to the work and discussion of the results,

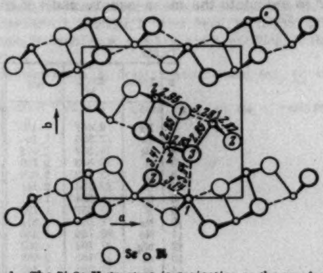

Fig. 1. The Bi_2Se_3II structure in projection on the xy plane.

TABLE 1. Starting Values and Values Obtained for Coordinate Parameters of the Bi_2Se_3II Structure

Structure parameters	Bi_1	Bi_2	Se_1	Se_2	Se_3	D	R, %
x_{start}	0.326	0.536	0.880	0.559	0.189		
y_{start}	0.030	0.351	0.055	0.869	0.214	0.958	44.9
x_{calc}	0.328	0,534	0.876	0,556	0.193		
y_{calc}	0.012	0.343	0.067	0.870	0.213	0.000	14.8

and to T. B. Zhukova for taking the x-ray diffraction patterns.

---

[1] L. F. Vereshchagin, E. S. Itskevich, É. Ya. Atabaeva, and S. V. Popova, Fiz. Tverd. Tela, 6, 2223 (1964) [Sov. Phys.–Solid State, 6, 1763 (1965)].

[2] S. Šćavničar, Z. Krist., 114, 85 (1960).

[3] V. G. Kuznetsov, Symposium on Chemical Bonding in Semiconductors and Solids [in Russian], Nauka i Tekhnika, Minsk (1965), p. 311.

[4] L. Pauling, Nature of the Chemical Bond, Cornell (1960).

X-ray diffraction study of the tetrahydrates of the mesoperiodates of the rare earth elements and yttrium

M. B. Varfolomeev, N. B. Shamrai, B. G. Berenshtein, and V. E. Plyushchev

Moscow Institute for Fine Chemical Technology

(Submitted December 14, 1971)
Kristallografiya, 18, 175-177 (January-February 1973)

The periodates of the rare earth elements belong to the comparatively little-studied compounds, and existing literature[1-3] deals only with the problem of synthesis of specific representatives of them. In a communication published recently,[4] results of calculation of the powder diffraction pattern of $YIO_5 \cdot 4H_2O$ are given which agree with the results which we obtained in ref. 5. On the basis of IR spectroscopic data, the formula $YH_2IO_6 \cdot 3H_2O$ is suggested for the compound.

The aim of this work was a systematic study of the crystallographic characteristics of $LnIO_5 \cdot 4H_2O$ compounds (where Ln are lanthanides in the series Pr−Lu and Y, in addition to Pm), clarification of the limits of isostructurality of these compounds, and also to establish the dependence of the unit cell dimensions of the crystals on the ionic radii of the elements in the isostructural series of compounds.

Crystals of the tetrahydrates of the rare earth periodates were prepared by the method described in ref. 4. Purity of the starting rare earth oxides amounted to not less than 99.5%, and the starting acids CH_3COOH and H_5IO_6 were "chemically pure." Analogous[4] to $YI_5 \cdot 4H_2O$, crystals of all compounds obtained were needle-like in shape, which allowed us to assume that they were isostructural. Powder x-ray diffraction patterns of the compounds, obtained on a Guinier−Wulff camera with Cu Kα radiation, had analogous sets of diffraction maxima, which confirmed the assumption of isostructurality of the $LnIO_5 \cdot 4H_2O$ compounds. To determine the symmetry of the compounds, systematic studies of single crystals of specific representatives of the family ($NdIO_5 \cdot 4H_2O$, $SmIO_5 \cdot 4H_2O$, and $HoIO_5 \cdot 4H_2O$) were carried out on RGNS-2 x-ray goniometers by the equiinclination method and on a KFOR-4 camera with Mo radiation. The hk0−hk8 layer lines, as well as the 0kl and ikl, were obtained.

The studies showed that the crystals of all the compounds belong to the monoclinic system, space group $P2_1/b$, for which the direction of the two-fold axis coincides with the elongation of the crystal. The lattice parameters *a* and b for the compounds $LnIO_5 \cdot 4H_2O$, obtained from the hk0 layer lines, were refined on a single-crystal attachment to the URS-50IM diffractometer for high-order reflections by means of the resolved α_1 and α_2 doublet of copper radiation. Cross sections of the crystals chosen for refinement of the lattice parameters *a* and b came to ~0.05 mm. The c parameter of the $LnIO_5 \cdot 4H_2O$ unit cell was refined from a diffraction pattern taken by the powder method (RKU-114M camera, Cr radiation) on the basis of the (008) reflection. Refined values of the lattice parameters are given in Table 1. The densities of the compounds, determined by the pycnometric method in toluene at 25°C, are also given in it. The monotonic character of the change of lattice parameters and pycnometric densities of the $LnIO_5 \cdot 4H_2O$ compounds point to the isostructurality of these compounds. We calculated the number of formula units in the unit cell, Z, which proved to be 4, which does not contradict the multiplicity of the true point system of space group $P2_1/b$, from the lattice parameters and pycnometric densities. The densities of the compounds as calculated for Z = 4 are in good agreement with experimental values (Table 1).

By use of single-crystal data, powder diffraction pat-

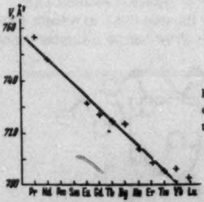

Fig. 1. Dependence of volume of unit cell V of $LnIO_5 \cdot 4H_2O$ compounds on the ionic radius of the lanthanide.

TABLE 1. Crystallographic Characteristics of Tetrahydrates of Rare Earth Mesoperiodates

Compound	Lattice parameters				d_{pycn}, g/cm³	$d_{x\text{-}ray}$, g/cm³
	a, Å	*b*, Å	*c*, Å	monoclinic angle		
$PrIO_5 \cdot 4H_2O$	7.635	10.53	10.72	118°30′	3.50	3.70
$NdIO_5 \cdot 4H_2O$	7.620	10.50	10.65	118°33′	3.58	3.77
$SmIO_5 \cdot 4H_2O$	7.580	10.48	10.63	118°23′	3.65	3.86
$EuIO_5 \cdot 4H_2O$	7.566	10.48	10.49	118°25′	3.71	3.93
$GdIO_5 \cdot 4H_2O$	7.553	10.46	10.46	118°27′	3.85	4.00
$TbIO_5 \cdot 4H_2O$	7.540	10.43	10.46	118°30′	3.86	4.03
$DyIO_5 \cdot 4H_2O$	7.529	10.42	10.43	118°33′	3.92	4.09
$HoIO_5 \cdot 4H_2O$	7.516	10.40	10.41	118°41′	3.97	4.15
$ErIO_5 \cdot 4H_2O$	7.510	10.38	10.36	118°40′	4.02	4.20
$TmIO_5 \cdot 4H_2O$	7.482	10.37	10.35	118°28′	4.07	4.23
$YbIO_5 \cdot 4H_2O$	7.492	10.39	10.37	118°51′	4.11	4.27
$LuIO_5 \cdot 4H_2O$	7.471	10.35	10.37	118°41′	4.16	4.31
$YIO_5 \cdot 4H_2O$	7.512	10.42	10.40	118°35′	3.34	3.44

Note: Accuracy of determination: *a*, ±0.007 Å; b, ±0.005 Å; c, ±0.07 Å; monoclinic angle, ±3′; d_{pycn}, ±0.01 g/cm³.

Vol. 18
July 1973–
June 1974

TABLE 2. Indexing of Powder Diffraction Patterns

Order number	$YIO_5 \cdot 4H_2O$		$PrIO_5 \cdot 4H_2O$		$NdIO_5 \cdot 4H_2O$		$SmIO_5 \cdot 4H_2O$		$EuIO_5 \cdot 4H_2O$		$GdIO_5 \cdot 4H_2O$		$TbIO_5 \cdot 4H_2O$		hkl	$DyIO_5 \cdot 4H_2O$		$HOIO_5 \cdot 4H_2O$		$ErIO_5 \cdot 4H_2O$		$TmIO_5 \cdot 4H_2O$		$YbIO_5 \cdot 4H_2O$		$LuIO_5 \cdot 4H_2O$		hkl
	I	d_{exp}	I	d_{exp}	I	d_{exp}	I	d_{exp}	I	d_{exp}	I	d_{exp}	I	d_{exp}		I	e_{exp}	I	e_{exp}	I	e_{exp}	I	e_{exp}	I	e_{exp}	I	e_{exp}	
1	2	6.85	2	6.99	2	6.95	2	6.87	2	6,99	2	6.98	2	6.89	011	2	6.88	2	6.87	2	6.84	2	6.88	2	6.83	2	6.83	011
2	5	6.57	5	6.79	5	6.66	5	6.68	5	6,75	5	6.72	5	6.56	100	5	6.57	5	6.56	5	6,57	5	6.56	5	6.54	5	6.53	100
3	5	5.96	5	5,98	4	6.04	5	5.99	4	6,05	4	6.05	5	5.97	$\bar{1}11$	5	5.96	5	5.97	4	5.93	4	5.94	4	5.93	4	5.91	$\bar{1}11$
4	2	5,57	2	5,65	2	5.70	2	5.63	2	5,68	2	5.67	2	5.65	$\bar{1}01$	2	5.63	2	5.59	2	5.57	2	5.58	2	5.56	2	5.55	101
5	2	5.04			2	5.14	2	5,09	2	5.13	2	5.14	2	5.09	$\bar{1}20$	2	5.09	2	5.06	2	5.02	2	5.06	2	5.04	2	5.01	$\bar{1}20$
6	5	4.58	5	4.63	5	4.67	5	4.64	5	4.66	5	4.67	5	4.61	020	5	4.62	5	4.61	5	4.58	5	4.57	5	4.59	5	4.56	020
7	4	4.21	4	4.31	4	4.28	4	4.27	4	4.29	4	4.28	4	4.24	021	4	4.24	4	4.23	4	4.23	4	4.21	4	4.23	4	4.19	021
8	4	4.08	4	4.15	4	4.17	4	4.15	4	4.16	4	4.15	3	4.10	111	4	4.11	3	4.11	3	4.09	4	4.08	3	4.09	4	4.08	111
9	4	3.63	4	3.68	5	3.69	4	3.67	5	3,69	5	3.68	4	3,65	$\bar{1}22$	5	3,66	4	3.64	4	3.62	4	3.62	4	3.62	4	3.61	$\bar{1}22$
10	1	3.52	1	3.51	1	3.52	1	3.57	1	3.58	1	3,57	1	3.55	$\bar{2}11$	1	3.53	1	3.52	1	3.52	1	3,52			1	3.50	$\bar{2}11$
11	1	3.43					1	3.50	1	3.39	1	3.44	1	3.48	022			1	3.45	1	3.44	1	3.44	1	3.44	1	3.44	022
12	1	3.38	1	3.38	1	3.39	1	3.38	1	3.32	1	3,34	1	3.37	200	1	3.33	1	3.34	1	3.32	1	3.33	1	3.33	1	3.33	200
13	5	3.14	5	3.18	5	3.20	5	3,18	5	3.19	5	3.18	5	3.15	120	5	3.16	5	3.14	5	3.14	5	3.14	5	3.14	5	3.13	120
14	4	3.03	4	3.02	4	3.02	4	3,02	3	3.02	4	3.02	4	3.00	$231/\bar{2}22$	4	3.05	4	3.01	4	3.03	4	3.03	4	3.04	4	3,02	$231/\bar{2}22$

terns of $LnIO_5 \cdot 4H_2O$ obtained on the RKU-114M camera (Cr Kα and Cr Kβ radiation) were indexed on the MIR-1 electronic computer. Results of indexing of the beginning lines are given in Table 2.[1)]

The series of isostructural compounds studied, which includes nearly all of the rare earth elements, allows tracing the lanthanide contraction phenomenon with great clarity. The dependence of the volume of the unit cell of $LnIO_5 \cdot 4H_2O$ compounds on the ionic radius of the lanthanide is shown in Fig. 1. From the data which we obtained for the periodates, $YIO_5 \cdot 4H_2O$ is placed in the series with $HoIO_5 \cdot 4H_2O$ and $ErIO_5 \cdot H_2O$, which agrees well with the location of yttrium in the series of rare earths for other classes of chemical compounds. The series of isostructural compounds which we synthesized once more supports the convention for division of the rare earth elements into subgroups.

[1)] Indexing data for the powder pattern of $YIO_5 \cdot 4H_2O$, unlike those in ref. 4, are presented in correspondence with the arrangement for $P2_1/b$.

[1] P. T. Cleve, Bull. Soc. Chim., 21, 196 (1874).
[2] R. C. Sahney, S. L. Aggarwal, and M. Singh, J. Indian Chem. Soc., 23, 177 (1946).
[3] R. K. Bahl and Surjit Singh, J. Indian Chem. Soc., 16, 375 (1939).
[4] M. B. Varfolomeev, N. B. Shamrai, I. F. Sgadova, and V. E. Plyushchev, Zh. Neorgan. Khim., 16, 1832 (1971).
[5] R. Kyrki Jukka and H. J. Lokio Ari, Suomen Kem., 44, 3, 105 (1971).

Crystal structure of the potassium salt of 1,1-dinitroethane

O. V. Frank-Kamenetskaya, N. V. Grigor'eva, N. V. Margolis, and I. V. Tselinskii

Leningrad State University

(Submitted April 23, 1972)
Kristallografiya, 18, 178-179 (January-February 1973)

Salts of 1,1-dinitroethane (DNE), which is a typical representative of the class of nitrocarbanions, are often used as starting materials for directed synthesis of various practically important compounds, and also as model substances for laboratory studies. The DNE anion is usually considered to be plane and its nitro groups equivalent.[1] The crystal structure of the potassium salt of DNE, $K^+[C(NO_2)_2CH_3]^-$, has been studied for confirmation of these assumptions. An attempt to determine this structure has been undertaken by Kosturkevich and Struchkov,[2] who did not go beyond the diffraction group symmetry and unit cell dimensions. They indicated that the deciphering of the structure was hindered by the small number of available measurements of diffraction reflections.

Among compressed elongated crystals, a specimen with transverse cross section of 0.08 mm² was selected for structure study. Eight formula units of the composition indicated above are contained in the monoclinic cell ($a = 12.59 \pm 0.03$ Å, $b = 12.54 \pm 0.03$ Å, $c = 7.28 \pm 0.02$ Å, $\beta = 101°30'$, space group C2/c, $\rho_{\text{calc}} = 1.87$). Integrated intensities of the reflections of CuKα radiation on the Weissenberg patterns were estimated microphotometrically, and very weak reflections were estimated visually. In all, 760 nonzero reflections were measured on the hk0–hk6 diffraction patterns.

The intensities were converted to values of $|F_{\text{exp}}|^2$ with the Lorentz and polarization factors and absorption being taken into account (the specimen approximated a cylinder with $\mu r = 1.3$). Reduction of $|F_{\text{exp}}|^2$ to unit scale was done by the Wilson method.

Coordinates of the K atoms on the basis of space group C2/c were established from a three-dimensional Patterson function. The coordinates of the light atoms were determined from a fourth-order minimization function constructed from the bonding vectors between K atoms.[3] Two successive approximations of a three-dimensional electron density synthesis and refinement of the coordinates of the heavy K atoms by the least-squares method,[4] reduction of coefficients of $|F_{\text{exp}}|$ to a common scale, and averaging of the temperature factor resulted in R = 0.24. Then, by use of the Cruickshank weighting scheme[5] for reflections measured photometrically, the coordinates and individual isotropic thermal parameters of all atoms of the structure were refined. A fixed weight equal to half the weight of $|F_{\min}|^2$ for those reflections measured by microphotometry was assigned to the reflections, which were estimated visually. The final value of the divergence factor, based on all reflections, was R = 0.14. Coordinates of the basis atoms of the structure are given in Table 1. The least-squares errors with regard to the coordinates of the K ions were $\varepsilon_x = 0.0003$, $\varepsilon_y = 0.0003$, $\varepsilon_z = 0.0005$; for the O atoms they were $\varepsilon_x \leq 0.0009$, $\varepsilon_y \leq 0.0010$, $\varepsilon_z \leq 0.0015$; and for the C atoms they were $\varepsilon_x \leq 0.0013$, $\varepsilon_y \leq 0.0014$, $\varepsilon_z \leq 0.0022$. The configuration of the DNE anion, interatomic distances, and valence angles are shown in Fig. 1. Errors in determination of the interatomic distances do not, with probability of 99.9%, exceed 0.03 Å, and errors in determination of the valence angles do not exceed 3°. The N–O bond lengths correspond to most of the charge distribution on one of the nitro groups ($O_2N_1O_1$). Very high multiplicity of the bond between the O_4 and N_2 atoms is observed. The distance of 2.57 Å between O atoms of neighboring nitro groups not bonded by valence is noticeably less than the sum of the intermolecular radii of oxygen [2.72 (ref. 6); 3.06 Å (ref. 7)], which is characteristic for most of the dinitrocarbanions studied.[8] The plane passed through the C_1, C_2, N_1, and N_2 atoms by the least-squares method has the form $0.7939x - 0.0838y - 0.6023z - 5.413 = 0$, where x, y, and z are the coordinates, in Å, of the atoms in an orthogonal cell with $c' = c \sin \beta$. The deviations of the atoms from this plane are shown in Fig. 1. The less highly charged ($O_4N_2O_3$) nitro group is rotated about the CN bond by an angle of 10°.

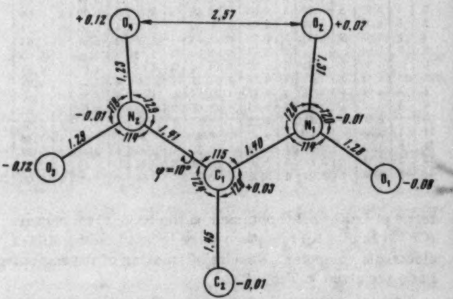

Fig. 1. Configuration of the anion in the structure of the potassium salt of 1,1-dinitroethane.

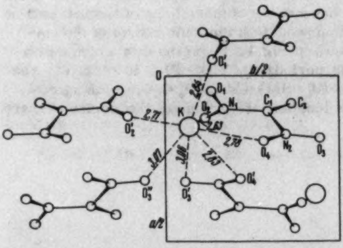

Fig. 2. Fragment of the structure of the potassium salt of 1,1-dinitroethane in projection on the ab plane.

The packing of the ions in the crystal and the distances between the K atom and its nearest neighbors are shown

TABLE 1. Coordinates of Basis Atoms of the Structure

Atoms	x/a	y/b	z/c
K	0.1580	0.0872	0.9652
O_1	0.0643	0.1403	0.5700
O_2	0.1316	0.1101	0.3119
O_3	0.3168	0.0701	0.6988
O_4	0.3115	0.2203	0.8425
N_1	0.1032	0.1767	0.4333
N_2	0.3351	0.1713	0.7101
C_1	0.3873	0.2120	0.5703
C_2	0.4214	0.1472	0.4277

in Fig. 2. The K – O_2 distance, which is 2.63 Å, is less than the sum of the ionic radii of potassium and oxygen. The values given in Fig. 2 confirm the inequality of distribution of charges on the atoms of the nitro groups and the presence of the main charge on the ($O_2N_1O_1$) nitro group.

---

[1] V. I. Slovetskii, S. A. Shevelev, V. I. Eroshko, A. A. Fainzil'ber, and S. S. Novikov, Izv. Akad. Nauk SSSR, Otd. Khim. Nauk, 1, 57 (1963).

[2] Z. S. Kosturkevich and Yu. T. Struchkov, Zh. Strukt. Khim., 5, 320 (1964).

[3] M. Buerger, Vector Space, Wiley, New York (1959).

[4] B. A. Tarnopol'skii and V. I. Andrianov, Zh. Strukt. Khim., 4, 433 (1963).

[5] D. W. J. Cruickshank, D. E. Pilling, A. Bujosa, F. M. Lovell, and M. E. Truter, Computing Methods and the Phase Problem in X-Ray Crystal Analysis, Pergamon Press, Oxford (1961), p. 32.

[6] A. I. Kitaigorodskii, Organic Crystal Chemistry [in Russian], Izd. Akad. Nauk SSSR, Moscow (1955).

[7] A. I. Kitaigorodskii, Molecular Crystals [in Russian], Nauka, Moscow (1971).

[8] N. V. Grigor'eva, N. V. Margolis, and I. V. Tselinskii, Zh. Strukt. Khim., 11, 562 (1970).

Zn—Mn isomorphism in Na_2ZnGeO_4 crystals

I. P. Kuz'mina, A. N. Lobachev, V. M. Vinokurov, N. M. Nizamutdinov, and L. A. Volkova

Institute for Crystallography, Academy of Sciences of the USSR

(Submitted May 11, 1971; resubmitted October 28, 1971)
Kristallografiya, 18, 180-182 (January-February 1973)

It was shown earlier in ref. 1 that reactions among GeO_2, ZnO, and NaOH (in regions of NaOH concentration above 15% by weight) at elevated temperatures and pressures result in the formation of germanate crystals of composition Na_2ZnGeO_4. Sodium zinc germanate is a stable phase within the wide range of temperatures and pressures studied (up to 500°C and 1500-2500 atm).

The formation of sodium zinc germanate under hydrothermal conditions can be represented in the following manner: Zinc oxide, dissolving in water solutions of caustic soda, forms the ZnO_2^{2-} zincate ion, the structure of which has not been established exactly. Perhaps it is more correctly represented in the form $[Zn(OH)_3H_2O]^-$, $[Zn(OH)_4]^{2-}$, $[Zn(OH)_3(H_2O)_3]^-$, or in the general form $[Zn(OH)_{n-x}(H_2O)_x]^{x-n+2}$, the value of x determining the pH of the medium, and n = 4 or 6. The complex $Zn(OH)_4^{2-}$ exists in strongly basic solutions, and in this case x = 0. Zincates[2,3] such as $NaZn(OH)_3$ and $Na_2Zn(OH)_4$ can be isolated in the solid state from concentrated solutions. Upon the dissolution of GeO_2 in water solutions of NaOH, evidently the formation of GeO_3^{2-} ions occurs in the form of the compound Na_2GeO_3, which, entering into reaction with zincate ions, forms the Na zinc germanate:

$$Na_2GeO_3 + Na_2Zn(OH)_4 \rightleftharpoons Na_2ZnGeO_4 + 2NaOH + H_2O,$$

or, in ionic form,[2]

$$GeO_3^{2-} + Zn(OH)_4^{2-} + 2Na^+ \rightleftharpoons Na_2ZnGeO_4 + H_2O + 2OH^-.$$

The appreciable solubility of sodium zinc germanate in water solutions of caustic soda at elevated temperatures and pressures allows its preparation in the form of coarse well-formed crystals, the sizes of which amount to some cubic centimeters. By use of the well-known temperature-jump method, this compound was successfully recrystallized from one temperature zone to another and crystallized on a seed crystal. The crystals obtained in this manner possessed prismatic, platelike, or isometric habit, depending on the conditions of synthesis, and were colorless, often transparent.

In most of the experiments which were carried out, the synthesis and crystallization of sodium zinc germanate were done in the presence of Mn^{2+} ions in the solution with the aim of preparing crystals activated by manganese. It is well known that manganese is widely used as an activator for the preparation of various zinc silicate phosphors.[4] Therefore, by activating the crystals mentioned by Mn^{2+} ions, we could be confident of preparing a new phosphor material. Such crystals were obtained. The presence of photo-, electro-, cathodo-, x-ray, and triboluminescence in them has been shown by special investigations.[1] Manganese compounds of various valences — $KMnO_4$, MnO_2, Mn_2O_3, etc. — were used as activators. At elevated temperatures and pressures, at which the synthesis of sodium zinc germanate also takes place, reducing conditions are created on account of the unavoidable corrosion of the steel autoclave by basic solutions. In this case, manganese ions of any higher degree of oxidation which may be present in the solution are reduced to Mn^{2+}.

This conclusion is confirmed by the fact that the colorless and transparent solutions recovered from autoclaves become dirty brown upon standing in air (15-30 min), and poorly soluble manganese hydroxides separate from them. This shows the presence of $Mn(OH)_2$, which forms in an alkaline medium from Mn^{2+}, in the solutions. Under normal conditions $Mn(OH)_2$ has weak amphoteric properties and under the action of hydroxides of the alkali metals can separate in the form of a gelatinous precipitate, which darkens rapidly in air as the result of oxidation:[5]

$$Mn(OH)_2 \rightarrow Mn_2O_3 \cdot xH_2O \rightarrow MnO_2 \cdot yH_2O.$$

At high temperatures and pressures, manganese in an alkaline medium is found in the form of Mn^{2+} and is partially entrapped by a growing crystal.

Na−Zn germanate crystals belong to the monoclinic system (space group $Pa - C_s^2$). Deciphering of its structure showed the Zn^{2+} and Ge^{4+} ions to occur in four-fold oxygen coordination.[6] The ZnO_4 and GeO_4 tetrahedra join with each other to form $ZnGeO_7$ mixed diorthogroups, which are arranged in space so that they form a three-dimensional framework. In the framework can be distinguished channels extending along the c_0 crystallographic axis. The coarse Na cations are located along the walls of these channels, occurring in two positions: five-fold and six-fold. The "tetrahedral" ZnO_4 and GeO_4 complexes are distorted so that their point group symmetry corresponds to C_1.

From literature data it is known that Mn^{2+} ions can occupy tetrahedral vacancies in some glasses, and can also replace zinc ions in crystals[5] of ZnO, spinels,[7] and other compounds. In the Na−Zn germanate which was studied, the more suitable of the crystal chemical positions for replacement by Mn^{2+} ions are the sites of the Zn^{2+} ions (isovalency and similar ionic radii: $R_{i\,Mn^{2+}} = 0.91$, $R_{i\,Zn^{2+}} = 0.83$, $R_{i\,Na^+} = 0.98$, $R_{i\,Ge^{4+}} = 0.44$ Å).[8] The green luminescence observed in the germanates under various modes of excitation is characteristic for luminescent zinc compounds in which part of the Zn^{2+} ions in four-fold coordination in the crystal lattice are replaced by Mn^{2+} ions.

The Na_2ZnGeO_4 crystals have been studied by the ESR method for confirmation of the $Zn^{2+} \rightarrow Mn^{2+}$ isomorphism in them. The ESR spectra of Mn^{2+} in Na−Zn germanate were studied at 300 and 77°K at frequencies of 10 and 37 MHz. The presence of two crystal chemically identical complexes (ZnO_4) in the unit cell of the germanate which are transformed one into the other by reflection from a plane of symmetry coinciding with (010) results in the

TABLE 1

Experimental values of angles			Angles calculated for ZnO_4				Angles calculated for GeO_4			
Z	Y	X	$Me-O_1$	$Me-O_2$	$Me-O_3$	$Me-O_4$	$Me-O_1$	$Me-O_2$	$Me-O_3$	$Me-O_4$
121	36	71	53	−72	68	−43	84.5	−45	−68	66
68.5	−85	−23	56	85	−22	80	8.5	−69	−63	−76
39	54	77	81	−55	−72	14	82	24	−64	−62

Note: Angles are calculated for an oblique cell.

formation of two $(Zn, Mn)O_4$ complexes which are magnetically nonequivalent with respect to the direction of the electric field. Study of the angular dependence of the spectrum showed the presence of two identical but magnetically nonequivalent Mn^{2+} spectra. The greatest scatter of spectral lines was observed in directions close to the c_0 axis. The following angles between like axes of the electric field have been found experimentally; $\angle Z_1, Z_2 = 43°$, $\angle X_1, X_2 = 134°$, $\angle y_1, y_2 = 10°$.

Angles between the X, Y, and Z axes of the electric crystal field and the a_0, b_0, and c_0 crystallographic axes, as well as the calculated angles between crystallographic axes of the cell and the directions of the $Me-O_{1,2,3,4}$ bonds for the ZnO_4 and GeO_4 complexes, respectively, are given in Table 1. From this table it can be seen that the experimentally obtained values of angles between the a_0, b_0, and c_0 axes and the X electric field axis agree well with the calculated angles between the crystallographic axes and the direction of the $Me-O_3$ bond in ZnO_4. The coincidence of the $Me-O_3$ bond with the X axis of the electric field for the zinc tetrahedron, as well as the value of the hyperfine structure (see below) may in some degree serve as confirmation of the $Zn^{2+}-Mn^{2+}$ isomorphism.

The spectrum is described as a spin Hamiltonian of orthorhombic symmetry for $g_z = g_x = g_y = 2.004 \pm 0.003$, $b_2^0 = 502 \pm 2$, $b_2^2 = 438 \pm 2$, $b_4^0 = 0 \pm 2$, $b_4^2 = 15 \pm 2$, $b_4^4 = -15 \pm 2$, and $A = B = C = 83 \pm 2$ G (the sign of b_2^0 is taken as positive).

At the present time ESR information about the iron group elements occurring in tetrahedral oxygen coordination is still small. Therefore their study has important theoretical and practical significance. ESR for Mn^{2+} ions in tetrahedral oxygen surroundings has been studied only in crystals[9] of ZnO, $ZnAl_2O_4$, and $MgAl_2O_4$. In connection with this, it is interesting to compare the hyperfine structure constant of the structures in the indicated matrices as a function of the $Me-O_4$ distance in them. These are given in Table 2, in which data for scheelite are also given. The nearest $Me-O_8$ surroundings in $CaWO_4$ can formally be looked upon as the combination of two tetrahedra.

TABLE 2

Crystal	Me−O distance, Å	$A, 10^{-4}$ cm^{-1}
ZnO	1.74	74.1
$ZnAl_2O_4$	1.88	74.9
$MgAl_2O_4$	1.92	75.4
Na_2ZnGeO_4	2.01	77.7
$CaWO_4$	2.46	88.9

From Table 2 it follows that the ionic character of the bonding of the environment of the Zn ion in Na_2ZnGeO_4 amounts to 80%, and the hyperfine structure constant A is found to be closely dependent on the metal−oxygen distance.

---

[1] I. P. Kuz'mina, O. K. Mel'nikov, and B. N. Litvin, Symposium on Hydrothermal Synthesis of Crystals [in Russian], Nauka, Moscow (1968), p. 141.

[2] I. P. Kuz'mina, B. N. Litvin, and V. S. Kurazhkovskaya, Symposium on the Study of Crystallization Processes under Hydrothermal Conditions [in Russian], Nauka, Moscow (1970), p. 164.

[3] F. A. Cotton and G. Wilkinson, Advanced Inorganic Chemistry, Interscience, New York (1966).

[4] V. V. Osiko, Izv. Akad. Nauk SSSR, Ser. Fiz., 23, 11, 1314 (1959).

[5] F. A. Cotton and G. Wilkinson, Advanced Inorganic Chemistry, Interscience, New York (1966).

[6] É. A. Kuz'min, V. V. Ilyukhin, and N. V. Belov, Kristallografiya, 13, 976 (1968) [Sov. Phys.−Crystallogr., 13, 848 (1969)].

[7] R. Stahe-Brada and W. Low, Phys. Rev., 116, 3, 561 (1959).

[8] G. B. Bokii, Crystal Chemistry [in Russian], Izd. MGU (1960).

[9] S. A. Al'tshuler and B. M. Kozyrev, Electron Paramagnetic Resonance [in Russian], Fizmatgiz, Moscow (1961).

X-ray diffraction and dielectric studies of the system $Li(Ta_xSb_{1-x})O_3$

V. I. Nesterenko and I. G. Ismailzade

Institute of Theoretical Problems in Chemical Technology,
Academy of Sciences of the Azerbaidzhan SSR
(Submitted April 28, 1971; resubmitted January 3, 1972)
Kristallografiya, 18, 183-184 (January-February 1973)

In the formation of various structure groups of ionic or predominantly ionic crystals, the geometrical dimensions of the ions which form the lattice often play a dominant role. However, cases are not rare where, regardless of the closeness of dimensions of the various sorts of ions which can occupy equivalent positions in the lattice, the construction symmetries of their lattices are substantially different. As an example, in lithium niobate (or tantalate) and lithium antimonate, $LiSbO_3$, the Nb^{5+} (or Ta^{5+}) and Sb^{5+} ions have practically the same sizes, 0.66 and 0.62 Å, respectively; however, lithium niobate (tantalate) has the pseudoilmenite type of structure (rhombohedral cell) whereas, according to Edstrand and Ingri,[1] $LiSbO_3$ crystallizes in an orthorhombic lattice: $a = 4.893$ Å, $b = 8.491$ Å, $c = 5.183$ Å, and the space group is the nonpolar D_{2h}^6-Pncn. Thus, $LiNbO_3$ ($LiTaO_3$) and $LiSbO_3$ belong to completely different structure types.

The aim of this work was the study of the phase diagrams of the system $xLiTaO_3-(1-x)LiSbO_3$ and the dielectric properties of the specimens of this system.

The specimens were synthesized by usual ceramic technology from "pure" Ta_2O_5, "c.p." Sb_2O_5, and "analytical grade" Li_2CO_3 for x = 0, 0.1, 0.2, 0.3, 0.4, 0.5, 0.6, 0.7, 0.8, 0.9, and 1.0. Preliminary heating was done at 900-1100°C for 2 h and the final heating at 1100-1350°C for 2 h, the heating temperature being raised with increase of Ta_2O_5 content in the specimens.

A phase analysis was made from x-ray diffraction patterns taken in RKU-114M cameras with Cu radiation. The cell parameters were determined by calculations based on the $1\bar{1}0$, 220, and 321 maxima for the pseudoilmenite phase and on the 123, 033, and 321 reflections for the phase with the lithium antimonate structure by plotting the error from points on a URS-50I x-ray diffractometer with Fe $K\alpha_1$ radiation.

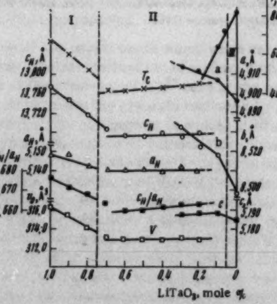

Fig. 1. Phase diagram of the $Li(Ta_xSb_{1-x})O_3$ system.

Owing to the high conductivity of the specimens, the dielectric susceptibility ε(T) was studied by the method suggested by Ismailzade and Nesterenko[2] at a frequency of 200 kHz.

The phase diagram of the system as constructed from x-ray data is shown in Fig. 1. Substitutional solid solutions with the lithium tantalate structure are formed for values of $x \geq 0.75$, while the lattice parameters of the cell (hexagonal description) a_H, c_H and the ratio c_H/a_H decrease monotonically with an increase in the concentration of Sb^{5+} ions. According to the x-ray method of determining the Curie temperature of hexagonal (or rhombohedral) ferroelectrics suggested by Ismailzade,[3] this should result in a lowering of the Curie temperature in accordance with the decrease in x, which was confirmed directly by the ε(T) curve of each specimen.

The lithium tantalate and lithium antimonate phases coexist in the concentration range $0.75 \geq x \geq 0.05$. The a_H cell parameter of the first phase remains practically unchanged in this interval, whereas the c_H period (polar direction) increases slightly with increase in x, i.e., the value of c_H/a_H increases slightly, which should result in some elevation of the Curie temperature. This actually occurs, as shown by the function ε(T). This elevation of T_C evidently is associated with some decrease in concentration of Sb^{5+} ions imbedded in the pseudoilmenite type lattice.

In the concentration range mentioned above, the *a* and b cell parameters of the second phase, which has the lithium antimonate structure type, decrease slightly with decrease in x. Only the lithium antimonate structure type is formed for $x < 0.05$.

Also shown in Fig. 1 is T_C as a function of the composition of the specimens. It is of special interest for the lithium antimonate phase. As can be seen, beginning with x = 0.2, T_C for the specimens rises sharply with increase in antimony ion content, and is ~740°C for $Li(Ta_{0.1}Sb_{0.9})O_3$. Extrapolation in the direction of $LiSbO_3$ gives $T_C \sim 825°C$ for lithium antimonate. An anomalous change in ε is observed at ~830°C on the curves of ε(T) obtained at frequencies of 200 kHz and 16.6 MHz (Fig. 2) for the $LiSbO_3$

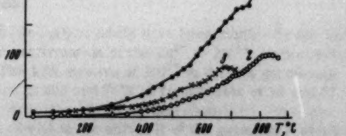

Fig. 2. The temperature function ε(T) of the dielectric susceptibility. 1) $LiSbO_3$, 200 kHz; 2) $LiSbO_3$, 16.6 MHz; 3) $Li(Ta_{0.1}Sb_{0.9})O_3$, 16.6 MHz.

crystal, which is characteristic for spontaneously polarized (or antipolarized) crystals. Since, according to ref. 1, the space group of lithium antimonate, D_{2h}^6–Pncn, is nonpolar, affiliation of $LiSbO_3$ with the group of ferroelectrics is precluded, and it is left to assume that the peak of ε at T ~ 830°C is associated with the presence of antiferroelectric properties in it. Thus, lithium antimonate is probably a new antiferroelectric with high T_C.

In the crystal lattice of $LiSbO_3$, each SbO_6 oxygen octahedron along the [001] axis is linked with two other such octahedra by its edges, forming a chain. These chains are linked among themselves by vertices of their octahedra. Each oxygen octahedron with a lithium ion, LiO_6, is linked with two similar octahedra by its faces, forming a chain along the [100] direction. Thus, although the small Li^{1+} and Sb^{5+} cations, like Li^{1+} and Ta^{5+} in $LiTaO_3$, are located inside oxygen octahedra in the $LiSbO_3$ crystal lattice, in principle the linking of the LiO_6 and SbO_6 octahedra in the cell of the $LiSbO_3$ structure is substantially different from that in the pseudoilmenite structure. The limiting solubility of $LiSbO_3$ in $LiTaO_3$ and the formation of a two-phase region within a wide concentration interval which we have established are caused by just this great difference in crystal structures of $LiTaO_3$ and $LiSbO_3$.

---

[1] M. Edstrand and N. Ingri, Acta Chem. Scand., 8, 1021 (1954).

[2] I. G. Ismailzade and V. N. Nesterenko, Kristallografiya, 12, 717 (1967) [Sov. Phys.–Crystallogr., 12, 625 (1968)].

[3] I. G. (I. H.) Ismailzade, Phys. Status Solidi, 46, K39 (1971).

X-ray diffraction and dielectric studies of the $LiNbO_3$–$KNbO_3$ system

I. G. Ismailzade, V. I. Nesterenko, and É. A. Il'yasov
Institute of Theoretical Problems of Chemical Technology,
Academy of Sciences of the Azerbaidzhan SSR

(Submitted April 28, 1971; resubmitted January 3, 1972)
Kristallografiya, 18, 185-187 (January 1973)

In crystal lattices of the pseudoilmenite type (ABO_3), cations A and B have small and almost identical dimensions (0.65–0.70 Å), and both types of ions are therefore located inside the oxygen polyhedra. Dense packing of the coordination polyhedra in such lattices is achieved by joining at the edges and faces.

When the A ions are substantially larger than the small cations of type B, they are not located inside the oxygen octahedra and occupy positions in the interoctahedral voids formed by oxygen octahedra joined at their vertices. This type of ion arrangement is known to occur in lattices of the perovskite type. Thus, these two types of crystals, both described by the general formula ABO_3, are totally different structurally and study of the phase diagram of the pseudoilmenite–perovskite system is therefore of definite scientific interest.

For this purpose, we synthesized specimens in the $(1-x)LiNbO_2-xKNbO_3$ system and made x-ray diffraction and dielectric studies of them. The synthesis was conducted by the usual ceramic technique, employing firing at 900-1000°C (1 h) and 1100°C (1.5 h). The starting materials are Li_2CO_3, Nb_2O_5, and K_2CO_3 (all chemically pure). The phase analysis was made from x-ray powder patterns determined in Cu radiation in RKU-114M chambers. The unit-cell parameters were found from the calculated maximum plotted by point-by-point determinations made in a URS-50I x-ray diffractometer in Fe radiation.

Figure 1 shows the phase diagram of the $LiNbO_3$ + $KNbO_3$ system plotted on the basis of the x-ray data. As can be seen from this diagram, diphasic regions are formed over the concentration ranges $0.1 = x < 0.6$ (I) and $0.6 < x = 0.9$ (II). A monophasic region exists only at $x = 0.6$ and consists of the potassium–tungsten bronze $Li_4K_6Nb_{10}O_{30}$ (KLN). Region (I) consists of lithium niobate and KLN; the content of the former gradually decreases with rising x and this phase totally disappears at $x = 0.6$. In region II, there is a decrease in the content of the tungsten-bronze phase as x increases and a corresponding increase in the content of the perovskite phase $KNbO_3$.

Thus, no solid solutions (substitution) are formed in this system on the part of the lithium niobate or potassium niobate. This is understandable, since the large K^{1+} cations cannot enter the oxygen octahedra and the small lithium cations Li^{1+} are too "loose" in the octahedral holes, which is responsible for the instability of such a structure. It can be hypothesized that these solid solutions are formed at low concentrations of Li^{1+} or K^{1+} ions. However, x-ray diffraction determination of the positions of the 110, 220, and 321 maxima showed that this is not the case (see Table 1). The phase $Li_4K_6Nb_{10}O_{30}$ is not a solid solution in this system, since it has the structure of neither system component. The crystal is a ferroelectric and the first representative of the "completely filled" tungsten-bronze structural type. The four trigonal, two tetragonal, and four pentagonal channels in its tetragonal cell are filled by $4Li^{1+}$, $2K^{1+}$, and $4K^{1+}$ cations, respectively.

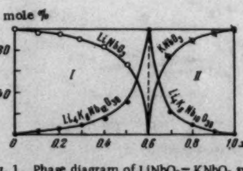

Fig. 1. Phase diagram of $LiNbO_3$– $KNbO_3$ system.

TABLE 1

Specimen	2θ		
	110	220	321
$LiNbO_3$	43°56′	61°55′	68°17′
$90LiNbO_3 - 10KNbO_3$	43°56′	61°56′	68°17′
$80LiNbO_3 - 20KNbO_3$	43°57′	61°56′	68°17′
$70LiNbO_3 - 30KNbO_3$	43°56′	61°57′	68°17′
$60LiNbO_3 - 40KNbO_3$	43°55′	61°56′	68°17′

The dielectric permeability of $Li_4K_6Nb_{10}O_{30}$ was investigated as a function of temperature by Van Uitert et al.,[1] who detected a highly diffuse peak in ε at 420°C; this is assumed to be the Curie temperature of this crystal. According to our measurements (at a frequency of 17 MHz), however, T_C = 475°C, which agrees with the results of Fukuda.[2] The discrepancy in the values of T_C was apparently due to a deficit of Nb_2O_5, the T_C of the specimen increasing as this deficit became layer.

Table 2 gives the unit-cell parameters of $Li_4K_6Nb_{10}O_{30}$ found by different authors.

A high-temperature x-ray diffraction study of this crystal was made by Fukuda.[3] However, the very large scattering of lattice-parameter values for a number of temperatures made it impossible for this author to detect the ferroelectric phase transition and to establish the character of the change in unit-cell parameters during it. Fukada did observe a gradual decrease in the unit-cell parameter along the [001] axis (the polar direction of the crystal) and an increase in that along the [100] axis with rising temperature.

Our high-temperature x-ray diffraction study of this crystal yielded results (Fig. 2) that differed from those of Fukuda.[3] As can be seen, the value of c gradually in-

TABLE 2

Constant, Å	According to ref. 2	According to ref. 1	Our data
a	12.56	12.59	12.63
c	4.03	3.97	3.97

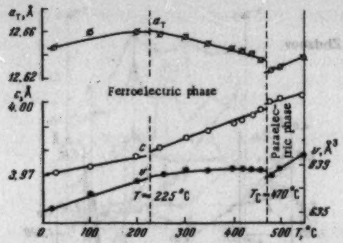

Fig. 1. Temperature dependence of the unit-cell parameters of $Li_4K_6Nb_{10}O_{30}$.

creased with rising temperature and underwent an abrupt jump at ~470°C, while a_T rose slightly until 225°C and then decreased monotonically, exhibiting a sharp drop at T ~ 470°C and a rise above this temperature. This type of function $a_T(T)$ can be explained by development of spontaneous polarization in this direction, its magnitude decreasing markedly above 255°C. On the basis of our x-ray data, we can therefore conclude that, as in the case of $Bi_4Ti_3O_{12}$, the spontaneous-polarization vector in the $Li_4K_6Nb_{10}O_{30}$ lattice is not directed exactly along the [001] axis but forms an angle with it. The absence of rhombic distortion of the unit cell when spontaneous polarization develops in the [100] ([010]) direction can be attributed to the equality of the spontaneous-polarization components along the [100] and [010] axes. The latter can occur when the spontaneous-polarization vector of the crystal lies in the plane passing through the [001] axis and the bisectrix of the angle x0y.

The direction of the spontaneous-polarization vector in solid solutions in the $Li_4K_6(Ta_xNb_{1-x})O_{30}$ system, particularly $Li_4K_6Nb_{10}O_{30}$, was studied by Fukuda.[2] The peak in ε characteristic of ferroelectrics was detected only in the direction parallel to the [001] axis of the crystal. Our results therefore indicate that it is necessary to conduct more thorough investigations of the functions $\varepsilon_{[001]}(T)$, $\varepsilon_{[100]}(T)$, and $\varepsilon_{[010]}(T)$ in single crystals.

---

[1] L. G. Van Uitert, H. J. Levinstein, J. J. Rubin, C. D. Capio, E. P. Dearborn, and W. A. Bonner, Mat. Res. Bull., 3, 47 (1968).

[2] T. Fukuda, Japan. J. Appl. Phys., 9, No. 6, 599 (1970).

[3] T. Fukuda, Japan. J. Appl. Phys., 8, 122 (1969).

Ismailzade et al. 115

The $PbZrO_3 - SrCu_{1/3}Nb_{2/3}$ system

D. F. Dzhmukhadze, M. A. Ugryumova, Yu. N. Venevtsev, and G. S. Zhdanov
L. Ya. Karpov Scientific-Research Physicochemical Institute
(Submitted April 1, 1972)
Kristallografiya, 18, 188-191 (January-February 1973)

According to our previous studies,[1-3] the perovskite $SrCu_{1/3}Nb_{2/3}O_3$ is a ferroelectric with a Curie temperature $T_C = 380°C$. The increased conductivity of this compound (even at room temperature) hampers the making of adequate dielectric measurements. The second component of the system, $PbZrO_3$, is a well-known perovskite antiferroelectric ($T_C = 235°C$) with low conductivity.[4,5]

In undertaking an investigation of solid solutions in the $PbZrO_3$(I)$-SrCu_{1/3}Nb_{2/3}O_3$(II) system, we expected that the solid solutions over a broad region from the compound I side would have low conductivity and this would permit us to study their dielectric properties, particularly to determine the trend of T_C in the system and to detect any possible similarity between the phase diagram of this system and that of the $PbZrO_3-PbTiO_3$ system.[6]

Preparation and investigation of specimens. The initial materials for synthesis of the specimens were the metal oxides PbO, ZrO_2, CuO, and Nb_2O_5 (chemically pure and analytically pure) and analytically pure strontium carbonate.

The specimens were produced by the usual ceramic technique with double firing. The temperature of the first firing was 900-1150°C (depending on composition), with holding at the maximum temperature for 2-2.5 h. The temperature of the second firing ranged from 1200 to 1350°C, with holding for 1 h. Both firings were conducted in covered alundum crucibles, in order to reduce the loss of volatile components.

For phase analysis, the x-ray diffraction patterns were determined in RKD-57 chambers; the patterns used for determination of the type of distortion and unit-cell parameters were determined in RKD-114 chambers with CoKα radiation. The parameters were calculated from the lines with $\Sigma h_i^2 = 18$ lying in the angle range $\theta = 70-75°$; the accuracy with which the parameters were determined was ± 0.003 Å. For the dielectric measurements, silver electrodes were applied to specimens in tablet form by fusion at $T \sim 600°C$. Study of the temperature functions of the dielectric permeability ε(t) and the tangent of the dielectric-loss angle tan δ(t) was conducted with E8-2 and MPP-300 bridges; an E9-4 chamber was used for the measurements at room temperature and a frequency of 11.6 MHz.

EXPERIMENTAL RESULTS

Results of x-ray diffraction analysis. Solid solutions were formed in the $PbZrO_3$(I)$-SrCu_{1/3}Nb_{2/3}O_3$ (II) system over the entire concentration range.

Figure 1 shows the unit-cell parameters of the solid solutions as functions of concentration and the analogous function for the values of ε and tan δ measured at room temperature.

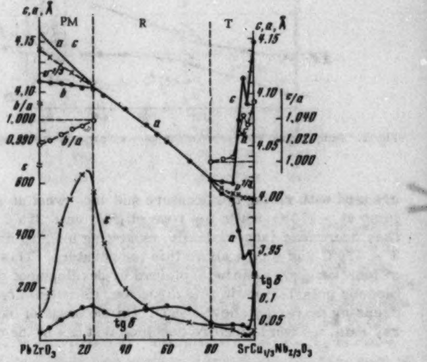

Fig. 1. Unit-cell parameters (a, c, $v^{1/3}$, and c/a), ε, and tan δ (at room temperature) as functions of concentration for solid solutions in the $PbZrO_3-SrCu_{1/3}Nb_{2/3}O_3$ system. PM) Pseudomonoclinic; R) rhombic; T) tetragonal modification.

The x-ray data on the subcell constants of the $PbZrO_3$ synthesized and investigated (a = c = 4.159, b = 4.111 Å) were similar to the results of Sawaguchi et al.[7] The unit-cell parameters of the perovskite $SrCu_{1/3}Nb_{2/3}O_3$ (a = 3.927, c = 4.144 Å) differed somewhat from the values given in the literature[1,2] and, as we established, depended on the synthesis conditions.

The solid solutions on the $PbZrO_3$ side (up to 25 mole % compound II) had a monoclinic distorted subcell and were characterized by the presence of a superstructure produced by antiparallel displacement of ions of the same type. In addition, the solid solutions on the compound II side had a tetragonal distorted unit cell (up to 80 mole % compound II). The x-ray diffraction patterns of these compositions, like that of compound II, exhibited additional weak lines, which were logically assumed to be superstructural (the intensity of these lines did not decrease with the angle θ). This superstructure was obviously produced by an ordered arrangement of type B cations (Cu^{2+}, Zr^{4+}, and Nb^{5+}) differing substantially in their valence and ionic radii (the latter ranging[8] from 0.65 to 0.82 Å).

The unit cell in solid solutions of intermediate composition (containing 25-80 mole % compound II) can be assumed to be rhombohedral. Actually, the corresponding x-ray diffraction patterns exhibited only slight diffusion of the lines at large angles, which usually masks distortion of a rhombohedral unit cell. In calculating the unit-cell parameters of these solid solutions, their unit cells were assumed to be cubic (in view of the lack of distinct splitting of the lines). The diffraction patterns also contained weak lines for specimens close to $SrCu_{1/3}Nb_{2/3}O_3$. These lines were obviously also superstructural, being produced by the ordered arrangement of the type B cations (they differed from the superstructural

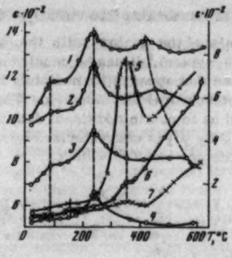

Fig. 2. Temperature functions of ε. 1-4) Specimens containing 20 mole % $SrCu_{1/3}Nb_{2/3}O_3$ measured at frequencies of 4, 12, 40, and 200 kHz; 5, 6, 7) specimens containing 80 mole % $SrCu_{1/3}Nb_{2/3}O_3$ measured at frequencies of 1, 10, and 200 kHz; scale at left for curves 1-4 and at right for curves 5-7.

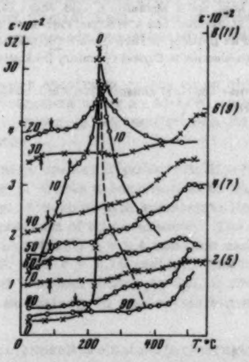

Fig. 3. Dielectric permeability as a function of temperature for solid solutions in the $PrZrO_3-SrCu_{1/3}Nb_{2/3}O_3$ system, measured at a frequency of 200 kHz. The numbers beside the curves represent the $SrCu_{1/3}Nb_{2/3}O_3$ content in mole %; curves 10 and 20 were plotted on the scale on the right side, the values for specimen 10 being given in parentheses; the scale for the peak of curve 0 is indicated at the top of the left-hand scale.

lines in the x-ray diffraction patterns of the solid solutions containing 0-25 mole % compound II). It must be noted that the unit-cell parameters of specimens containing 93-97 mole % compound II varied nonmonotonically with composition (Fig. 1). The causes of this phenomenon remain unclear.

Dielectric data. It must first be noted that the results of our study of ε and tan δ at a frequency of 11.6 MHz and room temperature for solid solutions with different compositions confirmed the presence of a transition from the pseudomonoclinic to the rhombohedral form at 25 mole % compound II (Fig. 1).

We measured the temperature functions of ε and tan δ for a number of specimens at different frequencies. The curves for a specimen containing 20 mole % compound II exhibited three anomalies (Fig. 2). The positions of two of them, those at lower temperatures, were independent of frequency, while the position of the third maximum depended on frequency, which indicated that it was relaxational in character. The displacement of this peak toward higher temperatures reached ~100°C. Only two peaks appeared in a specimen containing 80 mole % compound II and their positions were independent of frequency, which may indicate a ferroelectric or antiferroelectric character.

The temperature functions of ε for all the solid solutions in the system, measured at a frequency of 200 kHz (Fig. 3), exhibited three anomalies. The high-temperature maxima resembled the corresponding maximum for the specimen containing 20 mole % compound II, i.e., were relaxational in nature (Fig. 2). Of the other two anomalies (depending on composition), one was displaced in the low-temperature direction and the other in the high-temperature direction. A specimen containing 50 mole % compound II exhibited still another maximum at T = 350°C, which was independent of frequency. At this comparatively simple stoichiometric composition, the latter peak was apparently associated with formation of a specific atomic superstructure[9] (the circled point in Fig. 5 corresponds to this transition).

The maxima in the ε(T) curves measured at a frequency of 1 kHz for specimens with a high content of compound II (Fig. 4) were more pronounced than at a frequency of 200 kHz (compare Figs. 3 and 4). The curves for tan δ(T) also displayed anomalies at temperatures close to those for the anomalies in the ε(T) curves.

Phase diagram and discussion of results. The results of our x-ray diffraction and dielectric measurements were used to construct the phase diagram of the system (Fig. 5).

Among the maxima in the ε(T) curves for the solid solutions were some whose positions were independent of frequency. The temperatures of these maxima were naturally assumed to be the Curie points of the solid solutions. Anomalies were detected for almost all the solid solutions (up to 97 mole % compound II). If we extrapolate the trend of T_C to pure compound II, we obtain a temperature of ~380°C, which was previously taken as the T_C of this perovskite.[1-3]

In view of the fact that the solid solutions on the $PbZrO_3$ side were characterized by the presence of a migrational superstructure composed of monoclinically distorted subcells (similar to that in the antiferroelectric $PbZrO_3$) and that the tan δ of these specimens was low, we can conclude that solid solutions with compound II contents of up to 25 mole % have antiferroelectric properties.

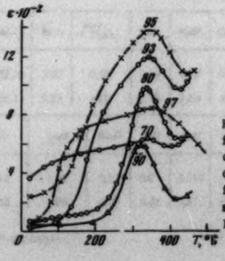

Fig. 4. Dielectric permeability as a function of temperature for specimens of solid solutions in the $PbZrO_3-SrCu_{1/3}Nb_{2/3}O_3$ system, measured at a frequency of 1 kHz. The numbers beside the curves represent the $SrCu_{1/3}Nb_{2/3}O$ content in mole %.

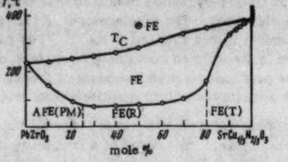

Fig. 5. Phase diagram of $PbZrO_3-SrCu_{1/3}Nb_{2/3}O_3$ system. FE) Ferroelectric; AFE) antiferroelectric; PM) pseudomonoclinic; R) rhombohedral; T) tetragonal.

As for the dielectric properties of compound II, we have no reason to doubt the conclusion previously drawn that they are ferroelectric in character.[1-3] Proceeding from the type of distortion (tetragonal and rhombohedral) of the unit cells of the solid solutions existing between the pseudomonoclinic modification and $SrCu_{1/3}Nb_{2/3}O_3$, taking into account our previous study,[10] we can state that they have ferroelectric properties.

The detection of a sequence of modifications (with changing composition), i.e., pseudomonoclinic–rhombohedral–tetragonal, indicates that the phase diagram of this system is similar to that of the $PbZrO_3-PbTiO_3$ system.[6]

On the basis of the analogy with the well-known $PbZrO_3-PbTiO_3$ system,[6] it can be concluded that the intermediate phase that appears immediately below T_C is obviously a rhombohedral ferroelectric. Thus, our investigation enabled us to obtain additional data definitely showing that $SrCu_{1/3}Nb_{2/3}O_3$ is characterized by a spontaneously polarized state and has $T_C \cong 380°C$.

---

[1] A. G. Kapyshev, V. V. Ivanova, and Yu. N. Venevtsev, Dokl. Akad. Nauk SSSR, 167, 564 (1966) [Sov. Phys.–Dokl., 11, 195 (1966)].

[2] Yu. N. Venevtsev, A. G. Kapyshev, and A. S. Viskov, Izv. Akad. Nauk SSSR, Ser. Fiz., 31, 1068 (1967).

[3] Yu. N. Venevtsev, A. G. Kapyshev, I. Yu. (J.) Shvorneva, Yu. Ya. Tomashpol'skii (Tomashpol'sky), A. S. Viskov, É. (Ye.) V. Zubova, V. V. Ivanova, D. G. Demurov, D. F. Dzmukhadze, D. Sal'nikov, and G. S. Zhadnov, J. Phys. Soc. Japan, 28, 139 (1970).

[4] S. Roberts, J. Amer. Ceram. Soc., 33, 63 (1950).

[5] G. A. Smolenskii, Zh. Tekh. Fiz., 20,137 (1950).

[6] B. Jaffe, R. S. Roth, and S. Marzullo, J. Appl. Phys., 25, 809 (1954).

[7] E. Sawaguchi, U. Maniwa, and S. Hoshino, Phys. Rev., 83, 1078 (1951).

[8] F. Galasso and W. L. Darby, J. Phys. Chem., 66, 131 (1962).

[9] G. B. Bokii, Introduction to Crystal Chemistry [in Russian], Izd. MGU (1954).

[10] Yu. N. Venevtsev and G. S. Zhdanov, Izv. Akad. Nauk SSSR, Ser. Fiz., 21, 275 (1957).

Gamma-resonance investigations of ferruginous tourmalines

V. F. Belov, T. A. Khimich, M. N. Shipko, I. E. Voskresenskaya, and E. N. Okulov
Institute of Crystallography, Academy of Sciences of the USSR
(Submitted December 31, 1971; resubmitted February 29, 1972)
Kristallografiya, 18, 192-194 (January-February 1973)

The iron ions in the tourmaline structure, whose formula can be written in the following way: $(NaCa)(MgLiFeAl)_3 \cdot (AlFeMg)_6 [(OH)_4(BO)_3Si_6O_{18}]$, can occupy two crystallographic positions whose symmetries differ markedly.[1,2] In connection with this, the overlaps of two doublets from the Fe^{57} nuclei located in these positions is to be expected in the Mössbauer spectra; this has previously been observed.[3,4] However, up to now, the population of these positions and the effect of the chemical composition on this population have remained unknown. For this purpose, we carried out Mössbauer and magnetic investigations of zinc-ferruginous and ferruginous elbaites (verdelites), and also ferruginous dravites from the cleavlanditic pegmatites of Central Asia. The chemical composition of the compounds investigated is given Table 1.

The Mössbauer spectra were run on an electrodynamic type of instrument using an AI-4096 multichannel analyzer. The radioactive isotope Co^{57} in a Pd matrix was used as the source.

The Mössbauer spectra of polycrystalline tourmalines are given in Fig. 1. Curve a corresponds to the zinc-ferruginous elbaite. A doublet with symmetric lines is observed in the spectrum of this compound. The magnitude of the quadrupole splitting $\Delta = 2.4$ mm/sec and of the isomeric chemical shift $\delta = 1.15$ mm/sec indicate that the spectrum of this tourmaline is due to divalent iron ions localized exclusively in one crystallographic position (A).

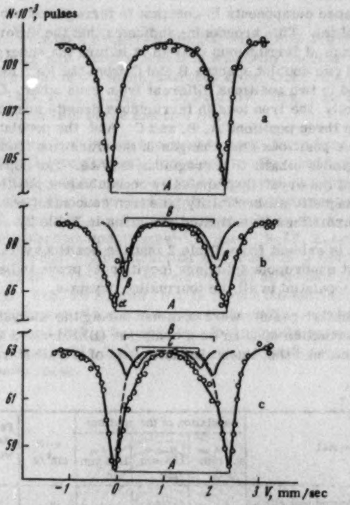

Fig. 1. Mössbauer spectra of ferruginous tourmalines. a) Zinc-ferruginous elbaite; b) ferruginous elbaite (verdelite); c) ferruginous dravite.

An interesting result is obtained for ferruginous elbaite (verdelite). A complex splitting pattern was observed in its Mössbauer spectrum (curve b): The right-handed absorption line is intensely broadened and the left-handed one consists of two components α and β. Upon normalizing the extreme components of the spectrum (dotted line) to a symmetrical form and subtracting the doublet with the symmetrical lines (A) from the overall spectrum, we obtain the difference spectrum B. The width of the components of the doublet is the same and is 0.35 mm/sec. Thus, the spectrum of verdelite is the superposition of the two doublets A and B from the nuclei of the Fe^{2+} ions located in the two somewhat different positions A and B. The valence of the ions in verdelite was determined by the magnitude of the isomeric chemical shift δ for the A and B spectra, which is 1.15 and 1.2 mm/sec, respectively. Such values for δ are possible only for Fe^{2+} ions in compounds with an ionic chemical bond. The quadrupole splittings for the Fe^{2+} ions located in positions A and B are 2.4 and 1.9 mm/sec, respectively.

The measurements of the Mössbauer spectrum of ferruginous dravite (curve c in Fig. 1) proved to be unexpected. The spectrum of ferruginous dravite consists of

TABLE 1

Components	SiO_2	TiO_2	Al_2O_3	B_2O_3	$FeO + Fe_2O_3$	MnO	MgO	CaO
Zinc-ferruginous elbaite (zinc verdelite)	37.3	0.15	37.35	9.92	6.93	0.39	0.15	0.21
Verdelite	40.05	0.50	35.1	9.23	4.58	0.28	1.50	0

Components	Na_2O	K_2O	Li_2O	Rb_2O	F_2O	ZnO	SnO
Zinc-ferruginous elbaite (zinc verdelite)	2.43	0.14	1.22	0.01	0.8	2.016	—
Verdelite	2.63	0.36	1.05	0.01	0.88	0.37	0.04

Note: Data of E. N. Okulov and I. E. Voskresenskaya.

a doublet, whose components have the same intensities. However, the inner slopes of the lines are less inclined than the outer ones. Upon normalizing the inner slopes of the doublet to a symmetrical form and subtracting the doublet with the symmetrical lines from the overall spectrum, we obtain a difference spectrum with strongly broadened components in contrast to ferruginous elbaite (verdelite). This broadening indicates that the difference spectrum of ferruginous dravite is in turn the superposition of two doublet spectra B and C from the Fe^{2+} ions located in two positions different from each other. Consequently, the iron ions in ferruginous dravite are localized in three positions A, B, and C. And the population of these positions also changes in the transition from zinc-ferruginous elbaite to ferruginous dravite. The populations of the crystallographically nonequivalent positions, paramagnetic susceptibility, and iron concentrations of the tourmalines investigated are given in Table 2.

It is evident from Table 2 that the positions with the largest quadrupole splittings (position A) prove to be the most populated in all the tourmaline crystals.

Similar results were obtained during the analysis of the tourmaline spectra on a computer (BÉSM-4). It should be mentioned that lines characteristic of trivalent iron ions were not detected in the tourmaline spectra given in Fig. 1. A comparison of the data from x-ray spectral analysis for the concentration of iron with the paramagnetic susceptibility given in Table 2 also indicates this.

TABLE 2

Crystal	Population of the positions			$\chi \cdot 10^6$ cm^3/g	Fe content, wt. %
	A, Δ = 2.4 mm/sec	B, Δ = 185 mm/sec	C, Δ = 1.35 mm/sec		
Zinc-ferruginous elbaite	1	—	—	12	6.93
Ferruginous elbaite (verdelite)	0.65	0.35	—	8.74	4.58
Ferruginous dravite	0.71	0.17	0.12	18.6	—

The ratio of the paramagnetic susceptibilities of the tourmaline crystals when iron ions of only one valence are present in them should correspond to the ratio of the concentration of these ions. As is evident from Table 2, the ratio $\chi_{\text{Zn-verdelite}}/\chi_{\text{verdelite}} = 1.38$ also agrees well with the ratio of the concentrations $n_{\text{Zn-verdelite}}/n_{\text{verdelite}} = 1.5$. The small discrepancies in these values could be due both to the different amounts of manganese (about 0.11%) and to the somewhat different average values of the magnetic moments of the Fe^{2+} ions in these samples.

Thus, the investigations carried out show that the iron ions in zinc-ferruginous elbaites (zinc verdelites) occupy exclusively one crystallographic position. The iron ions in ferruginous elbaite (verdelite) are localized in two crystallographic positions. The iron ions in ferruginous dravite are located in three somewhat different positions from each other. Up to this time, analogous effects have never been observed in tourmaline crystals.

The authors thank A. N. Lobachev and I. S. Zheludev for their interest in this effort.

---

[1] N. V. Belov, Synopses on Structural Mineralogy, Mineralogical Symposium of the L'vov Geological Society, No. 16, 14 (1962).

[2] M. J. Buerger, C. W. Burnham, and D. R. Peacor, Acta Crystallogr., 15, 6 (1962).

[3] I. S. Zheludev and V. F. Belov, Izv. Akad. Nauk SSSR, Ser. Fiz., 31, 7 (1967).

[4] M. DeCoster, H. Pollack, and S. Amelinckx, Phys. Status Solidi, 3, No. 2, 283 (1963).

Stereographic projections of surfaces for the physical properties of crystals*

Sh. M. Butabaev and Yu. I. Sirotin
Institute of Cybernetics, Academy of Sciences of the Uzbek SSR
M. V. Lomonosov Moscow State University
(Submitted July 5, 1971; resubmitted April 17, 1972)
Kristallografiya, 18, 195-197 (January-February 1973)

Indicative surfaces clearly indicate the anisotropy in the physical properties of crystals. Let F characterize a property and be dependent on direction, $F = F(n)$, where n is a unit vector. From an arbitrary point (the center of the indicative surface) we mark out in all possible directions of n quantities of length $|F(n)|$; the ends form the indicative surface for the corresponding property. The parts of the surface for which $F > 0$ are[1] considered as white (positive), while those where $F < 0$ are black (negative).

For instance, if we do this for all possible n via lines of length proportional to the relative expansion α in the direction of n on heating by 1 deg, we get the indicative surface from the thermal expansion: Clearly, $\alpha(n) = \alpha_{ij}n_i n_j$, where α_{ij} is the tensor for the expansion coefficients. Figure 1a shows the upper half of such a surface for an aragonite crystal (class mmm); the thermal-expansion coefficients were taken from ref. 2. Similarly, we construct the surface for the longitudinal piezoelectric effect via lines proportional to $d(n) = d_{ijk}n_i n_j n_k$, where d_{ijk} is the tensor for the piezoelectric coefficients.

Figure 1a shows that the surface clearly illustrates the anisotropy and symmetry of the property, but it is inconvenient for measurement of the property in any particular direction. It is simpler to construct and use a stereographic projection of this surface: For instance, Fig. 1b is such a projection for the surface of Fig. 1a. The lines here join directions of n in which the thermal expansion $\alpha(n)$ is the same, and they correspond to $\alpha(n) = 10.0;\ 11.5;\ 13.0;\ \ldots\ 32.5;\ 34.0;\ 35.0 \cdot 10^{-6}\ \mathrm{deg}^{-1}$, so these lines are levels of the function $\alpha(n)$.

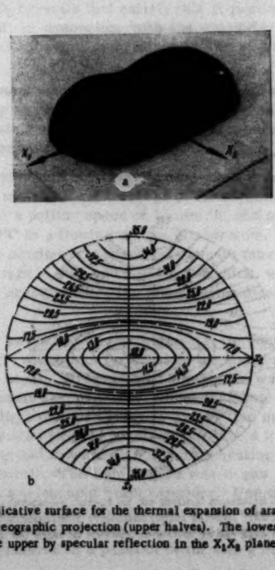

Fig. 1. a) Indicative surface for the thermal expansion of aragonite (10^{-6} deg^{-1}); b) stereographic projection (upper halves). The lower half is derived from the upper by specular reflection in the X_1X_2 plane.

Figure 2 shows stereographic projections for the surface for the longitudinal piezoelectric effect in tourmaline (class 3m); the values were taken from ref. 3. Figure 2a resembles Fig. 1b in showing the center of projection on the X_3 axis, while in Fig. 2b the center is on the X_1 axis (the standard choice of axes[2,4] is used: $X_3 \parallel 3$, $X_1 \perp m$). In the first case, the construction was based on a Boldyrev polar grid, while in the second we used an equatorial one (Wulff). The two figures clearly reveal the anisotropy and symmetry of the surface: a three-fold axis and a symmetry plane in Fig. 2a, and a two-fold antiaxis parallel to the X_1 axis in Fig. 2b.1) One can trace also the symmetry planes in these.

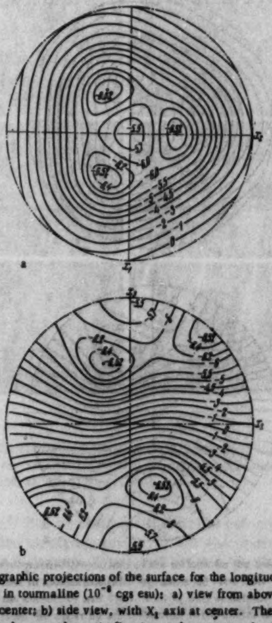

Fig. 2. Stereographic projections of the surface for the longitudinal piezoelectric effect in tourmaline (10^{-8} cgs esu): a) view from above, with the X_3 axis at the center; b) side view, with X_1 axis at center. The lower half is derived from the upper by antireflection at the center or by antirotation through 180° around the X_1 axis, and the rear half is derived from the front one by reflection in the X_2X_3 plane.

Such stereographic projections can be used as nomograms to determine properties in any direction or the directions in which a property has a given value, e.g., a turning-point value. Here one needs a polar grid of the same diameter as the projection, which is easily made on tracing paper.

Such surfaces and sections have long been used in books on crystallography and crystal physics, e.g., ref. 5, where we find surfaces for the extension coefficients of fluorite, quartz, and barite. Voigt[6] gives sections of the surfaces for this coefficient and for the torsion of a cylinder for fluorite, beryl, calcite, tourmaline, topaz, and barite, as well as sections of the surfaces for the longitudinal piezoelectric effect in quartz and tourmaline. Similar data have been given for various crystals by Wooster,[7] Cady,[8] and Kleber,[9] but none of these, nor other standard works[2,3,10-12] have stereographic projections, although these are much more obvious, as is clear from comparison of Fig. 2 with sections of the same surface in refs. 6 and 8 (Cady even slightly exaggerated the value of d_{22} in order to show more clearly the anisotropy of the surface). The stereographic projections clearly reveal the symmetry and antisymmetry of the corresponding property, which makes them valuable in courses on crystallography and crystal physics. They can also serve as nomograms, and a stereographic projection is equivalent in this respect to a whole series of sections (see Figs. 31-35 in ref. 8). The lack of such projections in textbooks is simply due to the laborious calculations needed to construct them.

We performed our calculations with a Minsk-2 computer. We are indebted to T. Koryagin, L. Markusov, and L. Yanusov for assistance in interpreting the machine results, plotting the surfaces, and making the drawings.

---

[*] Read at the Fedorov Meeting, Leningrad, 1971.

1) This is obtained by a combination of symmetry planes belonging to the crystal with the symmetry anticenter related to the piezoelectric effect; the antisymmetry group for the surface is thus $\bar{3}'m$ ($\underline{6}'m$ in Shubnikov's[1] notation).

---

[1] A. V. Shubnikov, Symmetry and Antisymmetry of Finite Figures [in Russian], Izd. AN SSSR (1951).

[2] J. Nye, The Physical Properties of Crystals, Oxford Univ. Press (1957).

[3] W. P. Mason, Crystal Physics of Interaction Processes, New York–London (1966).

[4] Proc. IRE, 37, 1378 (1949).

[5] P. Groth, Physical Crystallography and an Introduction to the Crystallographic Features of Major Compounds [Russian translation], Izd. Rikker, St. Petersburg (1897).

[6] W. Voigt, Lehrbuch der Kristallphysik, Teubner, Leipzig–Berlin (1928).

[7] W. A. Wooster, A Text-Book on Crystal Physics, Cambridge Univ. Press (1948).

[8] W. Cady, Piezoelectricity and Its Practical Application [Russian translation], Izd. IL (1949).

[9] W. Kleber, Einführung in die Kristallographie, Technik, Berlin (1969).

[10] A. V. Shubnikov, E. E. Flint, and G. B. Bokii, Principles of Crystallography [in Russian], Izd. AN SSSR (1949).

[11] S. Bhagavantam, Crystal Symmetry and Physical Properties, Academic Press, London–New York (1966).

[12] W. Kleber, K. Meyer, and W. Schoenborn, Einführung in die Kristallphysik, Akad. Verlag, Berlin (1968).

Characteristics of residual-stress relaxation in $LiNbO_3$ single crystals in the 20-200°C region

K. G. Belabaev, V. T. Gabrielyan, and V. Kh. Sarkisov

Institute of Physical Research, Academy of Sciences of the Armenian SSR;
Krivakan Chemical Combine

(Submitted September 6, 1971; resubmitted April 4, 1972)
Kristallografiya, 18, 198-199 (January-February 1973)

Numerous investigations of the optics of $LiNbO_3$ single crystals have made it possible to establish the dominant type of defect, which is manifested in an inhomogeneity of the refractive index. This inhomogeneity depends on the synthesis conditions, heat treatment, and application of the crystals.

It has been shown[1] that fluctuations in temperature during growth of $LiNbO_3$ crystals lead to a polydomain structure. The domain structure is in turn largely responsible for the electrophysical and optical properties of $LiNbO_3$ crystals and, together with other defects developing during crystal growth, leads to formation of local stresses and creates a complex internal-stress distribution pattern in the plane perpendicular to the Z axis of the crystal, in which birefringence should be absent in the case of a trigonal crystal.

This birefringence, which indirectly describes the internal-stress pattern, is characterized by the residual light flux at the output of an optical system consisting of the crystal and crossed polarizers. It is currently required that the residual light flux $I_{res} = I_{\times}/I_{\parallel}$, where $I_{\times}$ and $I_{\parallel}$ are the light intensities in the crossed and parallel polarizers respectively, not exceed[2] 0.005. Hence it follows that the maximum permissible anomalous birefringence should be no more than $9 \cdot 10^{-7}$. However, production of $LiNbO_3$ crystals that satisfy this requirement is very difficult, in connection with the characteristics of the optical behavior of crystals in the 20-200°C region.

The present investigation was conducted to study the processes by which internal stresses develop and are relaxed in crystals as a result of these characteristics of their behavior over the range 20-200°C.

The crystals for our investigation were grown by the Czochralski method from a charge of stoichiometric composition, with a pulling speed of 10 mm/h, and annealed at 1170-1180°C in a flowing oxygen atmosphere. The specimens were single-domain and polydomain tabular crystals 10 × 10 mm in size and 0.5-4.5 mm thick, which were cut from the crystals along the plane perpendicular to the Z axis.

In order to conduct the experiments, we constructed a polarimeter, which was installed on the coordinate table of an optical bench. Programmed adjustment was carried out with a contact thermometer, whose magnetic head bore a system of light pulleys driven by an electric motor. The temperature was held constant to within ± 0.25°C during holding and to within 0.5°C during heating (programmed control). The light source was a gas laser (LG-56) with a telescopic beam expander. Use of this source permitted visual observation of the conoscopic pattern in a converging beam. The anomalous birefringence was measured in a parallel beam with a Senarmon compensator.[3] The criterion of the stress pattern in the crystal was the birefringence Δn, which was determined from the path difference Γ per unit crystal length. The accuracy of the measurements of Δn was $\pm 4 \cdot 10^{-7}$.

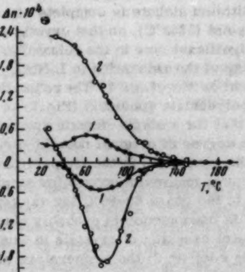

Fig. 1. Graph representing internal stresses as a function of temperature for single-domain (1) and polydomain (2) specimens.

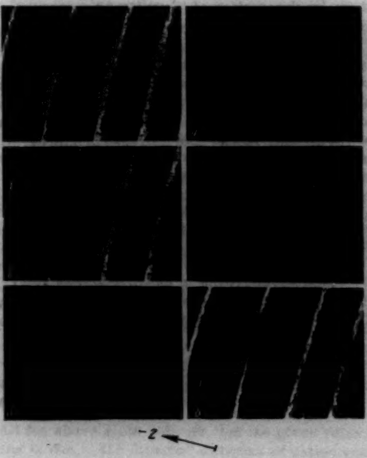

Fig. 2. Relaxation of striated structure in $LiNbO_3$ crystal as a function of temperature, × 40. Transmitted light, nicols crossed, XZ section. 1) T = 20°C; 2) 60; 3) 100; 4) 130; 5) 80; 6) 20°C.

Figure 1 shows typical internal-stress relationships for identical temperature rise and fall rates, as determined by measurements at the same points in single-domain and polydomain crystals. Comparing these curves with the data on stress relaxation in a typical dielectric, such as lithium fluoride[4] LiF, we can see both general similarities and material differences in the character of the relaxation. Thus, the temperatures at which nonisothermal stress relaxation was completed in both crystals were independent of the initial magnitude of the residual stresses and the heating rate. However, while relaxation is complete in a lithium fluoride crystal at 750°C, which is rather close to the melting point of LiF (870°C), relaxation in lithium niobate is complete at 150°C, far from its melting point (1253°C), so that crystal plasticity cannot play a significant role in the relaxation mechanism. The character of the relaxation in $LiNbO_3$ crystals also has other peculiarities, i.e.: 1) The relaxation-curve maximum for a polydomain specimen (Fig. 1) is substantially higher than that for a single-domain specimen, i.e., depends on the degree of original domain-structure unipolarity in the specimen; 2) the temperature at which the relaxation-curve maximum occurs for single-domain specimens lies in the range 60-80°C for any temperature-drop rate; this phenomenon is probably also responsible for the frequent cracking of crystals in this temperature region during cooling; 3) the temperature at which the stress-relaxation process is complete is independent of the extent to which the specimen has a single-domain structure.

The above characteristics were confirmed experimentally by observation of the optical behavior of growth layers with an induced domain structure as the temperature was varied. We were able to observe the growth layers as a result of the fact that they exhibited a refractive-index gradient caused by the stresses. The experimental results, which are given in Fig. 2, show that the striated structure disappeared from the crystals at 120°C, where there was already a noticeable decrease in internal stresses and subsequent development of this structure as the temperature was reduced (Fig. 1).

The observed characteristics of internal-stress relaxation in $LiNbO_3$ crystals over the range 20-200°C thus enable us to hypothesize the existence of a new relaxation mechanism in these crystals. It should be noted that the observed peculiarities in internal-stress relaxation and the disappearance of the striated structure in the 120-150°C region coincide with the appearance of pyrocoefficient anomalies,[5] the results of experiments on stimulated radiation in $LiNbO_3$ crystals activated by rare earths,[6] and the disappearance of optical defects[7] in $LiNbO_3$.

As was noted by Johnston,[8] the refractive-index inhomogeneity induced by a laser beam can be attributed to three-dimensional variation of the macroscopic-polarization density caused by defects of the double-acceptor type. It has been suggested that these are defects formed by excess niobium and, in conformity with the data of Meisner and Reis,[9] determine the optical properties of lithium niobate. We cannot preclude the possibility that this type of defect, but with a greater density, is also present in growth layers. Confirmation is provided by the changes we observed in the color of the bands (from light brown to black) with different heat-treatment regimes; they were apparently due to the heterovalence of uncontrollable impurities. Thus, the refractive-index inhomogeneity thermally induced in the crystal during growth and subsequent annealing is manifested in the same manner as optically induced changes in refractive index. In contrast to the latter, however, which disappears at 150°C, the development and disappearance of refractive-index inhomogeneity in our case was apparently associated with reversibility of the phase state of the defects in the crystal.

The authors wish to thank A. A. Kaminskii, I. M. Sil'vestrov, and Yu. V. Pisarevskii for their interest in this work and L. A. Shuvalov, B. A. Reznikov, and V. Ya. Khaimov-Mal'kov for their valuable advice.

---

[1] K. G. Belabaev, V. T. Gabrielyan, and V. Kh. Sarkisov, Abstracts of papers presented at the Seventh Scientific Conference on Ferroelectricity [in Russian], Voronezh (1970).

[2] A. L. Mikaélyan, N. M. Koblova, and É. A. Zasovin, Kvantovaya Elektron., 1, 120 (1971) [Sov. J. Quant. Electron., 1, 87 (1971)].

[3] A. V. Shubnikov, Principles of Optical Crystallography [in Russian], Izd. Akad. Nauk SSSR, Moscow (1958).

[4] N. E. Voropaeva, B. A. Reznikov, and Yu. I. Sirotin, Kristallografiya, 13, 487 (1968) [Sov. Phys.—Crystallogr., 13, 393 (1968)].

[5] M. B. Roitberg, V. K. Novik, and N. D. Gavrilova, Kristallografiya, 14, 938 (1969) [Sov. Phys.—Crystallogr., 14, 814 (1970)].

[6] A. A. Kaminskii, Phys. Status Sôlidi, a1, 573 (1970).

[7] A. Ashkin, G. D. Boyd, J. M. Dziedzic, R. G. Smith, A. A. Ballman, J. J. Levinstein, and K. Nassau, Appl. Phys. Lett., 9, 72 (1966).

[8] W. D. Johnston, Jr., J. Appl. Phys., 41, 3279 (1970).

[9] L. B. Meisner and I. S. Rez, Fiz. Tverd. Tela, 11, 2931 (1969) [Sov. Phys.—Solid State, 11, 2374 (1970)].

Formation of a Debye–Hückel cloud around dislocations in LiF crystals

N. G. Politov, M. V. Galustashvili, and I. M. Paperno
Institute of Physics, Academy of Sciences of the Georgian SSR
(Submitted July 1, 1971; resubmitted February 22, 1972)
Kristallografiya, 18, 200-202 (January-February 1973)

It is known that the plastic deformation of alkali halide crystals leads to the production of a potential difference between the surfaces of the specimen[1] (Stepanov effect). After the deformation, the potential difference gradually decreases.

The present paper describes a study of the time dependence of the decrease in the electrical signal. As in the earlier experiments,[2,3] the crystals were deformed by means of a concentrated load. We studied specimens of two types: LiFI (with cation vacancies predominating) and LiFII (with anion vacancies predominating). Specimens with dimensions 25 × 10 × 1.2 mm were cut along the cleavage planes from a single-crystal bar and annealed at 700°C for a period of 7 h. For this crystal thickness (1.2 mm) the load was chosen in such a way that the potential difference was a maximum.[2]

The electrical signal produced on deformation was passed to an IMT-66 electrometric amplifier (operating under current measurement conditions) and recorded by means of an electronic potentiometer, connected to the output from the amplifier. Since the input resistance of the instrument (10^{11} Ω) was much less than the resistance of the crystal (greater than 10^{15} Ω), the instrument recorded the discharge current, the duration of which was given by the time constant of the instrument RC ~ 30 sec. The area under the discharge current curve is equal to the charge Q passing through the instrument. On plastic deformation of the specimen (at the moment of impact of the indentor) the electrical circuit was opened. At the moment of measurement, after a given time interval from the deformation, the circuit was closed and the charge remaining on the surface of the crystal was recorded. The measurements were made for different temperatures of the specimen. The results of the measurements on the LiFI crystals are given[1)] in Fig. 1. For the curves recorded for three different temperatures we determined the relaxation time τ of the electric signal. It can be seen that with increase in temperature from room temperature to 310°K, τ decreases from 25 to min.

The decrease in the potential difference with time after the deformation can be explained as follows. The dislocations arising and moving through the crystal in the process of plastic deformation "sweep up" and transfer the charge, creating a nonequilibrium distribution of charge in the volume of the crystal. (In the case described for LiFI crystals, the cation vacancies were present in excess, so that the dislocations passing through the crystal were negatively charged.) With the passage of time the dislocations come into charge equilibrium with the point defects as a result of the diffusion of the latter toward or away from the dislocation.

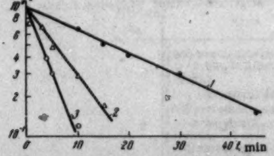

Fig. 1. Relative change in the charge Q/Q_0 with time after the deformation of LiFI crystals at different temperatures. 1) 294; 2) 300; 3) 310°K. Q_0 is the magnitude of the charge passing through the instrument at the moment of deformation of the crystal, and Q is the magnitude of the charge after a given time interval from the deformation.

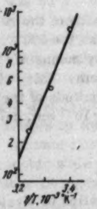

Fig. 2. Temperature dependence of the relaxation time of the electric signal τ for LiFI crystals.

For dielectric crystals the relaxation time of the nonequilibrium distribution of charges is given by the equation

$$\tau = \varepsilon / 4\pi\sigma, \tag{1}$$

where ε is the dielectric constant of the crystal, and σ is the ionic conductivity. The value of σ calculated from Eq. (1) shows good agreement with the conductivity values obtained by us from experiments involving the measurement of the electrical conductivity of the same crystals. Thus at room temperature, from the electrical conductivity measurements, $\sigma = 3.5 \cdot 10^{-16}\ \Omega^{-1} \cdot \mathrm{cm}^{-1}$, and by calculation from Eq. (1), $\sigma = 5 \cdot 10^{-16}\ \Omega^{-1} \cdot \mathrm{cm}^{-1}$. The activation energy of the relaxation process, determined from the slope of the curve giving the dependence of ln τ on 1/T (Fig. 2) and equal to 1 eV, also shows good agreement with the value of the activation energy of the current carriers (1.06 eV), determined from the slope of the curve giving the temperature dependence of the electrical conductivity in the temperature range 20-100°C.

All the above facts indicate that the given relaxation process is due to the directed diffusion of cation vacancies in the electric field of the dislocations. This diffusion process leads to the formation of a positively charged Debye–Hückel cloud, which screens the thermodynamically nonequilibrium negative charge of the dislocations. The relaxation time τ is related to the diffusion coefficient of the vacancies D by the following expression:[4]

$$\tau = \frac{1}{4}\left(\frac{\lambda^*}{\pi}\right)^2 \frac{1}{D}, \tag{2}$$

where λ^* is the radius of the region around the dislocation line in which the above diffusion process takes place. The diffusion coefficient of the cation vacancies can be calculated from the Einstein equation

$$\sigma / D = N\alpha e^2 / kT, \tag{3}$$

where e is the charge of the electron, N is the number of cations in unit volume, and α is the concentration of cation vacancies.

By substituting in Eq. (2) the value of the relaxation time τ, determined by experiment at T = 300°K, and the diffusion coefficient D, calculated by means of the Einstein equation, we obtained $\lambda^* = 2 \cdot 10^{-7}$ cm. This value of λ^* shows good agreement with the magnitude of the radius of the Debye–Hückel cloud $\lambda = 1.2 \cdot 10^{-7}$ cm, calculated from the relationship[5]

$$\lambda^2 = \varepsilon kT / 8\pi e^2 N\alpha. \tag{4}$$

(For T = 300°K, α = c, the concentration of divalent impurities, which according to spectral analysis is equal to 10^{-4} for the LiFI crystals.)

Thus $\lambda^* = \lambda$. It follows that the diffusion processes leading to charge equilibrium take place in a region bounded by the radius of the Debye–Hückel cloud.

We determined the relaxation time of the nonequilibrium distribution of charge in LiFI crystals irradiated with a γ-ray dose of 10^6 R. Since the diffusion coefficient in the crystals remains unchanged after irradiation, and the concentration of the ionic current carriers decreases (this last feature was confirmed experimentally by measuring the electrical conductivity of crystals with cation impurities, irradiated with γ rays), it follows that we should expect an increase in the relaxation time τ, which is observed experimentally (curve 2 in Fig. 3), and also an increase in the radius of the Debye–Hückel cloud.

Measurement of the relaxation time τ in LiFII crystals, in which the concentration of cation vacancies is much less than that in LiFI (the electrical conductivity of the LiFII crystals at 300°K is equal to $3 \cdot 10^{-17}\ \Omega^{-1} \cdot$ cm^{-1}) and the dislocations in their movement are positively charged and "sweep up" the excess anion vacancies, leads to the same conclusions. It follows from Fig. 3 (curve 3) that the relaxation time τ for LiFII at room temperature is ~5 h, which is greater by more than an order of magnitude than τ for LiFI. On the basis of the very large difference in the values of the mobilities of the cation and anion vacancies[6] at the temperatures of the experiment, it must be assumed that, as in the case of the LiFI crystals, the Debye–Hückel cloud in the LiFII crystals is formed around fresh dislocations as a consequence of the directed diffusion of cation vacancies. In the case of LiFII crystals (with positively charged dislocations), however, the cation vacancies move not away from, but towards the dislocations. In actual fact, the magnitude of the electrical conductivity σ, calculated from Eq. (1) ($4.5 \cdot 10^{-17}\ \Omega^{-1} \cdot \mathrm{cm}^{-1}$), in this case also agrees with the value of σ determined experimentally ($3 \cdot 10^{-17}\ \Omega^{-1} \cdot \mathrm{cm}^{-1}$). Since in LiFII crystals the concentration of cation vacancies is low, it follows that the formation of the cloud around the fresh dislocations must involve the participation of the cation vacancies from a large volume. The radius of the Debye–Hückel cloud calculated from Eq. (2) for the case of LiFII crystals is equal to $1.7 \cdot 10^{-6}$ cm.

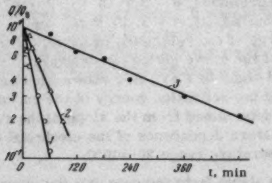

Fig. 3. Relative change in the charge with time after deformation. 1) Nonirradiated LiFI; 2) LiFI irradiated with γ rays (dose 10^6 R); 3) LiFII.

Thus the formation time and radius of the Debye–Hückel cloud around the thermodynamically nonequilibrium charge of the dislocations in LiF crystals is determined by the concentration and mobility of the cation vacancies. The determination of the relaxation time of the electrical signal makes it possible to estimate the ionic conductivity of LiF crystals in the range of temperatures in which the direct measurement of the electrical conductivity is impossible.

The authors thank D. D. Igitkhanashvili for assistance with the experiments involving the electrical conductivity measurements.

---

1) In all the figures, each point was obtained by averaging the results from 10 measurements.

[1] A. A. Urusovskaya, Usp. Fiz. Nauk, 96, 39 (1968).
[2] M. V. Galustashvili, Fiz. Tverd. Tela, 12, 1263 (1970) [Sov. Phys.–Solid State, 12, 987 (1970)].
[3] N. G. Politov, M. V. Galustashvili, and I. M. Paperno, Fiz. Tverd. Tela, 12, 2421 (1970) [Sov. Phys.–Solid State, 12, 1933 (1971)].
[4] Y. Haven, Rec. Trav. Chim., 69, 1471 (1950).
[5] J. S. Koehler, D. Langreth, and B. von Turkovich, Phys. Rev., 128, 573 (1962).
[6] C. Hubbert, J. Phys., 24, 543 (1963).
[7] M. Dubois, P. Berge, and G. Blanc, Discussions Faraday Soc., 31, 167 (1961).

Dynamic scattering with a memory effect in liquid-crystal mixtures

G. S. Chilaya, V. T. Lazareva, and L. M. Blinov

(Submitted December 15, 1971; resubmitted February 10, 1972)
Kristallografiya, 18, 203-205 (January-February 1973)

There are several papers[1-3] on dynamic scattering of light in nematic liquid crystals. A memory effect has been reported[4] in dynamic scattering by mixtures of nematic and cholesterol type liquid crystals (anilisidene-p-aminophenyl acetate with cholesteryl nonanoate). Here the scattering arises in the mixture when it is acted on by a steady or low-frequency alternating electric field, and it persists for a long time after the field has been removed. The mixture is restored to its initial state by an alternating electric field having a frequency above the critical value f_{cr} (erasure of the scattering). The temperature range for the dynamic-scattering effect in this case was[4] 77-97°C.

Here we report this effect for low-temperature mixtures of some nematic liquid crystals with cholesteryl decanoate, and also report a correlation between the electrical conductivity σ and the dielectric constant ε of the mixtures and the value of f_{cr}.

The method of observing the effect was as in ref. 4; we were also able to record the temperature dependence of the optical characteristics and the electrical conductivity for a layer of liquid crystal, whose thickness d in all cases was 50 μ. We characterized the scattering by the ratio of the light intensity transmitted by a layer of liquid crystal transparent before the steady voltage had been applied (I_0) to the intensity transmitted by the same crystal (I) after application, i.e., the contrast $K = I_0/I$.

Table 1 gives the names, chemical formulas, and temperature ranges Δt for the liquid-crystal state for our mixtures showing this effect. The effect is also seen in the supercooled state of these mixtures, i.e., 10-20° below the range Δt given in the table.

See refs. 1-3 for the dependence of the contrast K and the cell current I as functions of the steady voltage u for all the mixtures, as the results there were analogous to ours. There is a certain nonlinearity in the voltage-current characteristic near the region of marked change in contrast; to determine σ we used the initial (linear) part of I(u). This σ varied as between the mixtures and increased rapidly with temperature.

We found that f_{cr} also increased rapidly with temperature; Fig. 1 shows frequency characteristics for the contrast at various temperatures for mixture No. 1. Similar curves were recorded for the other mixtures.

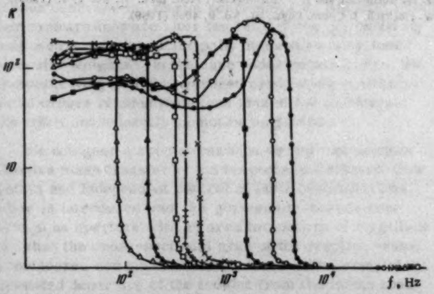

Fig. 1. Contrast as a function of frequency at various temperatures for mixture No. 1, 200 V: ●) 45; ○) 40; □) 32; ×) 22, +) 18; □) 15; ▲) 10; △) 5°C

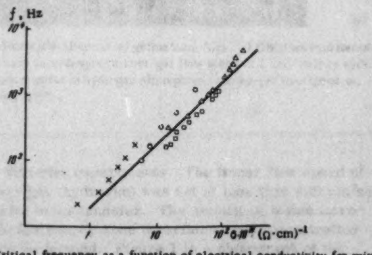

Fig. 2. Critical frequency as a function of electrical conductivity for mixtures: ○) No. 1; ×) No. 2; □) No. 3; △) No. 4.

TABLE 1

Mixture No.	Name	Chemical formula	Δt, °C
1	90% p-ethoxybenzylidene-p -n-butylaniline (EBBA) 10% cholesteryl decanoate	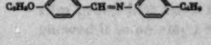 $C_2H_5O-C_6H_4-CH=N-C_6H_4-C_4H_9$	24 → 60
2	90% p-methoxygenzylidene-p'-n-butylaniline (MBBA) 10% cholesteryl decanoate	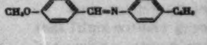 $CH_3O-C_6H_4-CH=N-C_6H_4-C_4H_9$	13 → 37
3	45% MBBA 45% EBBA 10% cholesteryl decanoate		−5 → +45
4	90% p-anisylidene-p'-aminophenyl acetate (APAPA) 10% cholesteryl decanoate	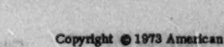 $CH_3O-C_6H_4-CH=N-C_6H_4-OCOCH_3$	67 → 80

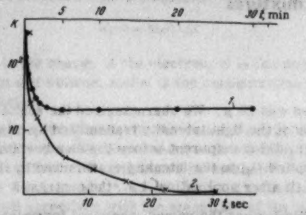

Fig. 3. Contrast as a function of time for mixture No. 1 at 25°C. The top abscissa scale represents the natural fall in K (curve 1) after the "write" voltage has been removed. The lower scale represents erasure (curve 2) of the scattering by 200 V ac at 1 kHz.

The conductivity is thus correlated with the critical frequency; as the latter we may take the frequency for which the contrast equals 10, and on that basis we perform the following experiment: The cell was heated until the material was isotropic and then was allowed to cool very slowly. At several temperature points we measured f_{cr} and σ. Figure 2 shows the dependence of f_{cr} on σ for all mixtures, which gives a linear relation ($f_{cr} = \alpha\sigma$), where α is the same for the various mixtures. We took the dielectric constant as being independent of temperature and as $\varepsilon = 4$ (this was verified with an R-568 bridge for mixture No. 1); then we get the approximate empirical expression for the critical frequency

$$f_{cr} \approx \frac{7}{\tau} = 7\frac{\sigma}{\varepsilon\varepsilon_0},$$

where τ is the time of dielectric relaxation and ε_0 is the dielectric constant of vacuum in the SI system, $\varepsilon_0 = 8.86 \cdot 10^{-12}$ F/m. A characteristic time for this effect is thus determined by the electrical characteristics of the liquid crystals. In our opinion, the erasure effect occurs at frequencies such that the space charge of the ions[5] is unable to follow the change in the electric field; the action of the field at frequencies $f > 1/\tau$ amounts to orienting the mixture and suppression of the scattering structure.

If technical use is to be made of such mixtures, it is important to know how the contrast varies with time; the K determined at u = 100 V varies from 300 to 1000. After the steady voltage has been switched off, K gradually falls to a steady value of 20-50, with Fig. 3 showing typical behavior for mixture No. 1. This stationary value of K persists for several days. We have found also that the switching times for mixture No. 1 at 25°C were respectively 50 and 30 msec for constant voltages respectively of 100 and 150 V. The same composition allowed the scattering to be erased in 1-2 sec (Fig. 3).

We are indebted to T. S. Plyusnin for assistance in the measurements and to V. V. Titov for valuable advice and discussions.

---

[1] I. G. Chistyakov, Liquid Crystals [in Russian], Nauka, Moscow (1966).

[2] G. H. Heilmeier, L. A. Zanoni, and L. A. Barton, Proc. IEEE, 56, No. 7, 24 (1968).

[3] D. Jones, L. Creagh, and S. Lu, Appl. Phys. Lett., 16, No. 2, 61 (1969).

[4] G. H. Heilmeier and J. E. Goldmacher, Proc. IEEE, 57, No. 1, 41 (1969).

[5] W. Helfrich, J. Chem. Phys., 51, No. 9, 4092 (1969).

Growth of smooth epitaxial germanium films by the iodide method in a through-flow system with diffusive mass transfer

G. M. Malkin, V. E. Grigor'ev, N. A. Lineva, and L. A. Malkina
Scientific-Research Institute of Chemistry, Gor'kii State University

(Submitted July 13, 1971; resubmitted January 24, 1972)
Kristallografiya, 18, 206-207 (January-February 1973)

The data in the literature[1-4] indicate that films grown by the iodide method in a through-flow system usually have an uneven surface. Thus, for example, macroscopic protuberances in the form of growth pyramids are observed on the (111) faces. It has been asserted[5] that a smooth film surface can be obtained when material is transferred to the base by diffusion, without forced transfer by a carrier gas; however, the role of irregularities and contaminants on the base surface was not taken into account.

It can be assumed that if the character of the film surface is governed by the mass-transfer mechanism in the reaction vessel, some irregularities on the base surface, including thin oxide layer, should not lead to the appearance of growth pyramids under conditions where gaseous-phase diffusion is limited.

Growth of films in a flowing carrier gas by screening of the base surface with a parallel surface separated from it by a distance of the order of 10 μ, as was done by Dorfman et al.,[6] makes it possible to reduce the carrier-gas flow speed above the base to a negligibly small level. The drawback of this method, however, is the simultaneous decrease in reagent concentration. Actually, small apertures are known to alter the ratio of the gas-mixture components, passing principally molecules with lower molecular weights.[7] In the case under consideration, the molecular weight of the hydrogen used as the carrier gas is two orders of magnitude less than of the iodides and this effect consequently cannot be neglected.

We designed a special reaction vessel that permits diffusive mass transfer of the reagents in a through-flow system and independent control of their concentrations. Iodine is introduced into the germanium-source zone through an aperture with an area two orders of magnitude less than the cross-sectional area of the reaction vessel in the source and crystallization zones. This completely prevented departure of the iodides from the iodine zone and provided diffusive mass transfer in the reaction zones at a low carrier-gas linear flow speed. The switch to forced reagent transfer (with carrier-gas linear flow speeds of 1 cm/sec or more) was made in the same reaction vessel by simply increasing the carrier-gas flow speed. The films were grown on a germanium base with a resistivity of 40 $\Omega \cdot$cm at the (111) surfaces. The dislocation density in the base was $2 \cdot 10^4$ cm^{-2}. Before film growth, the base surface was mechanically ground and polished to a finish of grade 14; it was then thoroughly degreased. Chemical etching was not conducted. The surface thus bore both an oxide film and a discontinuous layer. The thickness of the latter, according to our estimates, was about 1 μ. No gaseous-phase etching was conducted before deposition of this layer, for which the iodine zone was chilled to the temperature of liquid nitrogen. The source temperature during growth was 560°C, while that in the crystallization zone was varied from 360 to 410°C in different experiments. The linear flow speed of the carrier gas (hydrogen) was set at less than 0.01 cm/sec for diffusive mass transfer. The amount of iodine introduced into the source zone determined the concentration of the iodides formed. Figure 1 is a photograph of the surface of films obtained with the two aforementioned carrier-gas velocities. The film thicknesses, measured by the gravimetric method, were approximately identical and amounted to 4–5 μ. It can be seen from the photograph that the height of the irregularities on the film surface was small for diffusive mass transfer. The interference pattern of this surface showed that the irregularity height was less than 0.1 μ. The electron-diffraction pattern of a film grown with the diffusive reagent-transfer mechanism showed it to be single-crystal and highly ideal (Fig. 1).

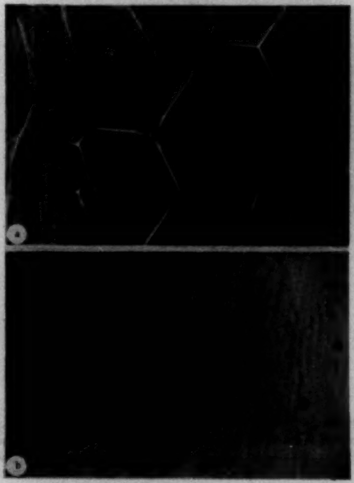

Fig. 1. Surface view of epitaxial germanium film. a) Obtained with forced reagent delivery in hydrogen (carrier-gas flow speed of 1 cm/sec); b) with diffusive mass transfer in hydrogen atmosphere (carrier-gas flow speed of 0.01 cm/sec). × 870.

Our experiment thus tended to support the hypothesis that films without growth pyramids can be produced on a base with a discontinuous surface layer and an oxide film by diffusive mass transfer in a through-flow system. In our opinion, this proves that the surface character of an epitaxial film is governed primarily by the mass-transfer mechanism.

The authors wish to thank G. Kh. Tachmuradov and Yu. A. Vandyshev for their assistance in the experimental work.

---

[1] H. S. Ingham and P. D. McDade, IBM J. Res. and Develop., 4, 302 (1960).

[2] J. C. Marinace, IBM J. Res. and Develop., 4, 248 (1960).

[3] G. A. Kurov and I. V. Filatova, Kristallografiya, 9, 575 (1964) [Sov. Phys.–Crystallogr., 9, 489 (1965)].

[4] M. Takabayashi, Japan. J. Appl. Phys., 1, No. 1, 22 (1962).

[5] V. F. Dorfman and M. S. Belokon', in: Growth of Crystals, Vol. 8, Consultants Bureau, New York (1969).

[6] V. F. Dorfman, K. A. Bol'shakov, and I. P. Kislyakov, Izv. Akad. Nauk SSSR, Neorgan. Mat., 1, 37 (1965).

[7] A. D. Frank-Kamenetskii, Diffusion and Heat Transfer in Chemical Kinetics [in Russian], Nauka, Moscow (1967).

Kinetics and structural aspect of the growth of single crystals of bismuthinite under hydrothermal conditions

V. I. Popolitov and A. N. Lobachev

Institute of Crystallography, Academy of Sciences of the USSR

(Submitted April 14, 1971; resubmitted September 22, 1971)
Kristallografiya, 18, 208-210 (January-February 1973)

The present paper gives the results of experimental studies of the dependence of the rates of growth of the (001) and (010) faces of Bi_2S_3 crystals on the temperature, composition, and concentration of the solvents NH_4Cl and NH_4Br. The experiments were carried out in autoclaves lined with titanium, with the following parameters: temperature 350–450°C, $\Delta T = 20°C$ ($H_{aut} = 400$ mm), pressure 600–1500 atm, duration of experiments from 24 to 120 h, concentration of aqueous NH_4Cl and NH_4Br solution from 2 to 12 wt.%. The procedure used to carry out the experiments and measure the rates of growth of the crystals was described in ref. 1. The dependence of the logarithms of the rates of growth of the (001) and (010) faces of Bi_2S_3 crystals on the logarithms of the concentrations of the solvents for temperatures in the range 350–450°C is shown in Fig. 1; the curves are approximated by linear equations of the following form:

$$\lg v_{(001)} = \lg K_1 + n \lg C, \qquad (1)$$

$$\lg v_{(010)} = \lg K_2 + n \lg C, \qquad (2)$$

where $v_{(001)}$ and $v_{(010)}$ are the rates of growth of the (001) and (010) faces in mm/day, K_1 and K_2 are the concentration kinetic coefficients for the (001) and (010) faces, n is the order of the crystallization process ($n \sim 2$), and C is the concentration of the solvents NH_4Cl and NH_4Br, in moles/liter. From the relationships given in Fig. 1, it can be seen that the rates of growth of the faces of Bi_2S_3 for the given solutions can be expressed by the inequality

$$v_{Bi_2S_3(NH_4Cl)} > v_{Bi_2S_3(NH_4Br)}. \qquad (3)$$

The activation energies, calculated from the slopes of the straight lines (Figs. 2 and 3) for the growth of the (001) face in aqueous NH_4Br and NH_4Cl solutions are 13 and 15 kcal/mole, respectively, and the activation energy for the (010) face in the same solutions has the values 3.5 and 3.0 kcal/mole, respectively. The data on the rates of growth of the Bi_2S_3 faces make it possible to reach certain conclusions concerning the growth mechanism. The Bi_2S_3 structure[2] is made up of infinite ... Bi–S–Bi ... chains arranged along the c axis and combined in $[Bi_4S_6]_n$ packets. The packets lie in the plane of the (010) face, which is the face with the highest reticular density. The bonding in the chain is predominantly covalent, and the bonding between the packets is by van der Waals forces, so that perfect cleavage is observed along the (010) face. Since the (010) face is made up of close-packed $[Bi_4S_6]_n$ packets, its growth is possible as a consequence of the van der Waals interaction between the packets, which can be regarded as the basis for the formation of two-dimensional nuclei. Unlike the (010) face, the (001) face exhibits free or uncompensated vacancies as a consequence of the constant unsaturation of the valence bonds in the [001] direction, that is, along the ... Bi–S–Bi ... chains. The existence of free valences is a prerequisite for the production of active centers[1] on the surface of the (001) face. The elementary act of separation of the crystallizing substance on the (001) face takes place on its active region centers and is accompanied by their annihilation with the simultaneous production of new active region centers. This process can apparently be represented schematically as follows:

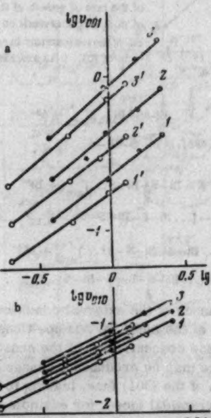

Fig. 1. Dependence of the logarithms of the rates of growth of the faces of single crystals of Bi_2S_3 on the logarithms of the concentrations of the solvents NH_4Cl and NH_4Br. a) (001) face; b) (010) face; 1,1') 350; 2,2') 400; 3,3') 450°C; 1,2,3) NH_4Cl; 1',2',3') NH_4Br.

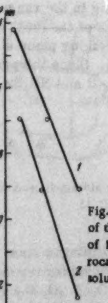

Fig. 2. Dependence of the logarithm of the rate of growth of the (001) face of Bi_2S_3 single crystals on the reciprocal of the temperature in aqueous solutions of NH_4Cl (1) and NH_4Br (2).

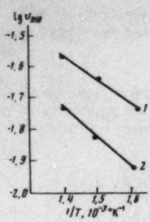

Fig. 3. Dependence of the logarithm of the rate of growth of the (010) face of Bi_2S_3 single crystals on the reciprocal of the temperature in aqueous solutions of NH_4Cl (1) and NH_4Br (2).

$$\left.\begin{aligned}&[\ldots \mathrm{Bi{-}S{-}Bi}\ldots]^{+}_{\mathrm{a.c.}} + S^{2-}\\ &\rightarrow [\ldots \mathrm{Bi{-}S{-}Bi{-}S}\ldots]^{-}_{\mathrm{a.c.}},\\ &[\ldots \mathrm{Bi{-}S{-}Bi{-}S}\ldots]^{-}_{\mathrm{a.c.}} + Bi^{3+}\\ &\rightarrow [\ldots \mathrm{Bi{-}S{-}Bi{-}S{-}Bi}\ldots]^{+}_{\mathrm{a.c.}},\\ &[\ldots \mathrm{Bi{-}S{-}Bi{-}S{-}Bi}\ldots]^{+}_{\mathrm{a.c.}} + nS_2^{2-}\\ &\rightarrow [\ldots \mathrm{Bi{-}S{-}Bi{-}S{-}Bi{-}S}\ldots]^{-}_{\mathrm{a.c.}}.\end{aligned}\right\} \quad (4)$$

Under the influence of the external conditions (pressure, adsorption, pH of the medium, compositions of the solution, mobility and concentration of the constructional species, etc.) there may be produced a change in the mechanism of growth of the (001) face, leading to the production of additional pyramidal faces, for example, (111), (113), etc. Even in this case, however, the basic principle of the Bi_2S_3 structural type is always clearly preserved. Thus the preferential growth of Bi_2S_3 single crystals along the c axis arises as a result of the difference in the mechanisms of growth of the (010) and (001) faces. In our experiments in aqueous NH_4Cl and NH_4Br solutions, needles always crystallize. The values of the activation energy of the growth of the (001) face, lying in the range 13-15 kcal/mole, indicate that the growth of the (001) face is controlled by a chemical reaction taking place at the crystal−solution surface of separation. Since the process of dissolution of Bi_2S_3 in aqueous NH_4Cl and NH_4Br solutions is accompanied by the formation of radicals of the type[3] $[BiCl_4]^-$ and $[BiBr_4]^-$, the growth of the (001) face can be regarded as a heterogeneous reaction. In our case these reactions will correspond to the decomposition of the radicals on the growing (001) face according to the scheme

$$[BiГ_4]^- \rightarrow Bi^{3+} + 4Г^-. \quad (5)$$

The decomposition of the radicals on the (001) face is naturally accompanied by the attachment of the constructional species (sulfur, bismuth) to the active regions of the surface in accordance with the scheme (4) examined above. The values of the activation energies indicate that the bulk diffusion from the solution in our case does not limit the rate of growth of the (001) face, that is, $K_d > K_g$. From this it is clear that the rate of the heterogeneous reaction on the surface of the (001) face in aqueous NH_4Cl and NH_4Br solutions will be determined by the rate of decomposition of the radicals. In actual fact, the displacement of the straight lines relative to one another (Fig. 1a) can only be due to a difference in the stabilities of the chloro and bromo radicals, that is, a difference in the activities of their decomposition. The calculated activation energies of growth of the (010) face for aqueous NH_4Cl and NH_4Br solutions amount to 3 and 3.5 kcal/mole, indicating that the growth of this face is limited by diffusion processes.

Analysis leads to the following conclusion: The anisotropy of the kinetics of growth of the (001) and (010) faces in Bi_2S_3 crystals is increased by the structural anisotropy of the chemical bonding, which is reflected specifically in the acicular form of the crystals obtained.

---

1)The active centers are the products of the hydrolysis and dissociation of the solvents

$$NH_4Cl(Br) + H_2O \rightleftarrows NH_4OH + HCl \rightleftarrows NH_4^+ + OH^- + H^+ + Cl^-$$

localized at the ends of the chains.

---

[1] V. I. Popolitov, Kristallografiya, 14, 545 (1969) [Sov. Phys.—Crystallogr., 14, 461 (1969)].

[2] W. Hofmann, Z. Krist., 86, 225 (1933).

[3] V. I. Popolitov, Thesis [in Russian], Institute of Crystallography, Academy of Sciences of the USSR, Moscow (1969).

Hydrothermal crystallization in the system $CdO-GeO_2-LiCl-H_2O$

L. N. Dem'yanets and N. V. Suvorova

Institute of Crystallography, Academy of Sciences of the USSR

(Submitted August 13, 1971)
Kristallografiya, 18, 211-213 (January-February 1973)

The nature of the reaction between oxides (or other compounds) under hydrothermal conditions is determined by the properties of the mineralizer introduced into the system. In a number of cases the mineralizer serves merely as a transporting agent, reacting in the dissolution zone to form complex compounds, which subsequently decompose in the growth zone. In other cases the cations (or anions) of the mineralizer take part in the construction of the crystal structure of the products of the hydrothermal reaction. In ref. 1 we studied crystallization in the $CdO-GeO_2-LiOH-H_2O$ system under conditions of increased temperatures and pressures. In order to determine the role of the mineralizer in the reaction of cadmium and germanium oxides, we studied phase formation in the $CdO-GeO_2-LiCl-H_2O$ system; the results of this last study are described in the present paper.

The experiments were carried out at a temperature of 450-500°C, and the degree of fill of the autoclave was 0.7-0.8. The LiCl concentration was varied from 0 to 25 wt.% (for a ratio $CdO:GeO_2 = 1:6$–45 wt.%) and the molar ratio of the original components of the charge $CdO:GeO_2$ was varied in the range 1 : 3–3 : 1. Crystallization in the $CdO-GeO_2-LiCl-H_2O$ system was studied by the temperature-drop method ($\Delta T = 20$–40°). The solid products obtained were identified by x-ray, spectral, and chemical analyses. We used the standard apparatus and procedures of hydrothermal synthesis; VT-1 grade titanium or ST-1 titanium alloy were used as lining material for the autoclaves. The results of the studies are given in Fig. 1.

Change in temperature in the range 450-500°C has practically no influence on the position of the boundaries of the stable crystallization of the individual phases; with decrease in T there is a slight decrease in the width of the range corresponding to the single-mineral crystallization of the germanate $Li_2O \cdot 10CdO \cdot 12GeO_2$ (Fig. 1, IV). The following main crystalline phases were synthesized in the system being considered: CdO, $Cd(OH)_2$, Cd_2GeO_4, $CdGe_2O_5$, Li_2GeO_3, $Li_2Ge_4O_9$, $Li_2O \cdot 10CdO \cdot 12GeO_2$. The results of the x-ray diffraction study are given in Fig. 2 (URS-50IM apparatus, CuKα radiation).

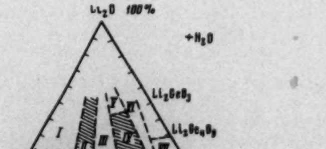

Fig. 1. Diagram of the crystallization fields in the $CdO-GeO_2-LiCl-H_2O$ system. The diagram gives the relationship between the composition of the charge and the composition of the solid phases synthesized. I) $CdO + Cd(OH)_2 + Cd_2GeO_4$; II) Cd_2GeO_4; III) $Cd_2GeO_4 + Li_2O \cdot 10CdO \cdot 12GeO_2$; IV) $Li_2O \cdot 10CdO \cdot 12GeO_2$; V) $Li_2GeO_3 + Li_2O \cdot 10CdO \cdot 12GeO_2$; VI) $Li_2GeO_4 + Li_2O \cdot 10CdO \cdot 12GeO_2$; VII) GeO_2 (tetragonal). The regions of single-mineral crystallization are hatched.

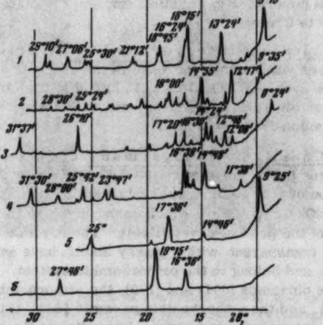

Fig. 2. X-ray diffraction patterns for the compounds synthesized. 1) Li_2GeO_3; 2) $Li_2Ge_4O_9$; 3) $Li_2O \cdot 10CdO \cdot 12GeO_2$; 4) Cd_2GeO_4; 5) $Cd(OH)_2$; 6) CdO.

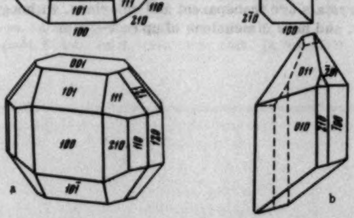

Fig. 3. Chief crystallographic forms of cadmium orthogermanate (a) and Li, Cd germanate (b).

Cadmium oxide CdO crystallizes with an excess of CdO in the charge, irrespective of the concentration of LiCl in the system. Crystals of octahedral habit, with colors varying from dark brown to black, and dimensions of 1-2 mm, were obtained.

Cadmium hydroxide $Cd(OH)_2$ crystallizes in accordance with the $CdO-H_2O$ phase diagram[2] when the autoclaves are cooled to temperatures below 300°C. The production of cadmium hydroxide also characterizes the experiments with a large excess of CdO ($CdO:GeO_2 > 2$). The crystals are obtained as hexagonal platelets with dimensions 3 × 3 mm.

Lithium germanate Li_2GeO_3 crystallizes with an excess of Ge in the system (ratio $CdO:GeO_2 \sim 2:3$) at LiCl concentrations greater than 20 wt.%. The crystals have a prismatic habit, are colorless, sometimes covered with a matte film, and have dimensions of up to 2 mm.

Lithium tetragermanate $Li_2Ge_4O_9$ crystallizes with further increase in the concentration of Ge in the system ($CdO:GeO_2 > 1:2$) and forms lamellar crystals or clusters, the dimensions of the individual crystals amounting to 0.5 mm.

Cadmium orthogermanate Cd_2GeO_4 crystallizes in the range of ratios $CdO:GeO_2 \sim 2:1-1:1$; the region of single-mineral crystallization lies in the range N ($CdO:GeO_2$) $\sim 2:1$, which corresponds to the composition of the product crystallizing. The crystals are colorless, transparent, with a glassy luster, have an isometric habit, and belong to the orthorhombic system. The faces of the pinacoids (001) and (100), the orthorhombic prism {101}, and the orthorhombic pyramid {111} (Fig. 3a) are most extensively developed. According to the x-ray diffraction data the product is isostructural with olivine. The crystals have dimensions of up to 4 mm. In the germanate with the composition $Li_2O \cdot 10CdO \cdot 12GeO_2$ (formula according to the results of the chemical analysis), the concentration of lithium varies slightly from one specimen to another. The crystals belong to the triclinic system, and exhibit a prismatic habit. The (010), (100), and (111) faces are most extensively developed (Fig. 3b). The crystals are transparent and colorless, with a glassy luster, and have dimensions of up to 1-4 mm.

Cadmium germanate $CdGe_2O_5$ crystallizes in dilute LiCl solutions (concentration less than 5%) with an excess of germanium (ratio $CdO:GeO_2 \sim 1:2-1:4$). The crystals are colorless and transparent, with a high refractive index, isometric habit, and dimensions less than 0.5 mm.

CONCLUSIONS

1. The composition of the stable solid phases crystallizing in the $CdO-GeO_2-LiCl-H_2O$ system correspond to the overall composition of the charge ($CdO + GeO_2$). CdO and $Cd(OH)_2$ crystallize in an excess of the first component, and lithium germanates crystallize in an excess of GeO_2.

2. The mineralizer added to the system acts as a transporting agent ($CdO:GeO_2 > 3:2$) or enters the composition of the final reaction products ($CdO:GeO_2 \sim 3:2-1:3$).

3. The chief crystalline phases are cadmium and lithium germanates; lithium enters the Cd germanate lattice in small quantities: $Li_2O:CdO = 0.1$ for the compound $Li_2O \cdot 10CdO \cdot 12GeO_2$.

4. The chief factor influencing phase formation in the $CdO-GeO_2-LiCl-H_2O$ system at T = 450-500°C is the ratio $CdO:GeO_2$; change in temperature (450-500°C) and concentration (in the range 5-25%) produces practically no change in the position of the boundaries of stable crystallization of the individual phases.

---

[1] N. S. Koryakina, N. V. Suvorova, L. N. Dem'yanets, B. A. Maksimov, V. V. Ilyukhin, and N. V. Belov, Dokl. Akad. Nauk SSSR, 200, 329 (1971) [Sov. Phys.-Dokl., 16, 700 (1972)].

[2] L. S. Dent Glasser and R. Roy, J. Inorg. Nucl. Chem., 17, 98 (1961).

Growth of pyrrhotite on nuclei of iron thiospinel

S. Yamaguchi

State Institute of Inorganic Materials, Japan

(Submitted April 14, 1972)
Kristallografiya, 18, 214 (January-February 1973)

A hydrothermal process has been used to increase the rate of growth of iron sulfide crystals. An aqueous-alkaline suspension of iron sulfide was obtained by mixing equal volumes of 0.1 M $(NH_4)_2SO_4FeSO_4 \cdot 6H_2O$ and 0.15 M Na_2S solutions. This suspension was heated hydrothermally at 190°C for a period of 10 h in a closed vessel. The vessel containing the suspension was then cooled slowly to room temperature. The electron-diffraction pattern of a specimen prepared in this way is shown in Fig. 1. Figure 1 proves that simultaneous precipitation of pyrrhotite and iron thiospinel takes place. The pyrrhotite was found to be polycrystalline, with particle size about 1 μ. The mean dimensions of the iron thiospinel particles, on the other hand, remain unchanged. After the suspension had been heated for a sufficiently long period at 190°C, only the grown crystals of pyrrhotite remained. Thus the iron thiospinel particles act as nuclei for the growth of pyrrhotite.

Figure 2 corresponds to a specimen of synthesized iron thiospinel, prepared by rapid cooling from 190°C to room temperature. The dimensions of the iron thiospinel particles obtained here amount to approximately 100 Å.

It is convenient to use this quenching process to suppress the crystal growth and conversion of iron thiospinel into pyrrhotite.[1] It has thus been found that the hydrothermal growth of iron thiospinel crystals is impossible. Iron thiospinel is stable only in the range of small crystal dimensions. In actual fact, natural iron thiospinel is always amorphous.[2,3]

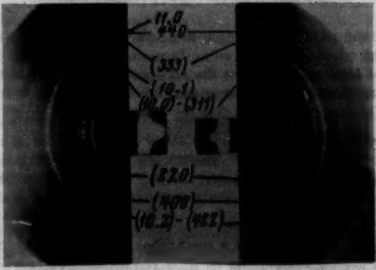

Fig. 1

Fig. 2

Fig. 1. Electron-diffraction pattern for iron sulfide obtained under hydrothermal conditions at 190°C. The polycrystalline specimens of hexagonal pyrrhotite were grown on nuclei of cubic iron thiospinel. The wavelength of the electron beam was 0.0406 Å, the distance from the specimen to the screen was 50 cm, and the positive was magnified by a factor of 2.3.

Fig. 2. Electron-diffraction pattern for synthesized iron thiospinel, prepared by quenching from 190°C to room temperature. Wavelength of the electron beam 0.0416 Å.

---

[1] S. Yamaguchi, Kristallografiya, 14, 752 (1969) [Sov. Phys.-Crystallogr., 14, 653 (1970)].
[2] R. A. Berner, Nature, 227, 700 (1970).
[3] S. Yamaguchi, M. Uda, and H. Wada, Chim. Anal., 52, 864 (1970).

Allowance for three-wave scattering in electron diffraction by face-centered metals

V. V. Udalova and Z. G. Pinsker

(Submitted February 17, 1972)
Kristallografiya, 18, 215 (January-February 1973)

It is comparatively simple to allow for multiwave scattering when there is a cubic face-centered or body-centered lattice, since then the structure amplitudes fall monotonically as $\sin\vartheta/\lambda$ increases.

For instance, in ref. 1 we used1) the Bethe dynamic potentials approximation[2] to allow for dynamic scattering in calculating structure amplitudes. This approximation is based on the assumption that there are only two strong beams (the primary beam and one of the diffracted ones).

Good agreement was obtained with experiment for the structure amplitudes for the higher orders of the (222) and (400) strong reflections by incorporating three terms in the series of systematic reflections: (111), (333), $(\bar{1}\bar{1}\bar{1})$ and (200), (600), $(\bar{2}00)$ respectively. The main contribution came from the term incorporating interaction of the (111) or (200) beam with the others.

The (0, g, 2g) three-wave case has been discussed[3] for the exact Bragg setting for 2g. A rigorous treatment via a dynamic matrix[4] was used, which gave the intensity of the 2g reflection and which showed that the three-wave approximation is adequate for systematic reflections in face-centered and body-centered cubic structures. There was only a small additional contribution to the intensity from five-wave scattering (3g and −g beams).

It has thus been shown[3] that our result[1] is of general significance, namely, that it is sufficient to incorporate three beams in the dynamic-potential approximation in considering dynamic effects in electron scattering for face-centered cubic metals.

In 3/3 the discussion related to electron scattering in a single crystal, whereas we employed multiwave scattering via Bethe potentials, which are applicable to polycrystalline aggregates as well as single crystals.

---

1)Paper 1 was submitted on August 18, 1970 and was returned in revised form on March 8, 1971; paper 3 was submitted on March 9, 1971.

[1] V. V. Udalova and Z. G. Pinsker, Kristallografiya, 17, 90 (1972) [Sov. Phys. – Crystallogr., 17, 70 (1972)].
[2] H. A. Bethe, Ann. Phys., 87, 55 (1928).
[3] R. Semeels and R. Gevers, Phys. Status, Solidi, 45b, 493 (1971).
[4] R. Semeels and R. Gevers, Phys. Status, Solidi, 33, 703 (1969).

Antiferromagnets with electric polarization

O. V. Kovalev

Physicotechnical Institute, Academy of Sciences of the Ukrainian SSR

(Submitted February 4, 1972)
Kristallografiya, 18, 221-226 (March-April 1973)

All structures in which electric polarization can exist alongside antiferromagnetism are found on the basis of Landau's theory of phase transitions of the second kind. The cases in which the coupling between the magnetic and the electric ordering has an exchange nature are established.

Much attention is presently being devoted to crystals with both magnetic and electric ordering.[1] On the basis of Landau's theory, we consider magnetic phase transitions from a magnetically and electrically unordered and even nonpyroelectric phase into an antiferromagnetic phase with spontaneous vector **P** of electric polarization under the condition that in the ordered phase the magnetic and the chemical cells coincide. We shall follow the method proposed in ref. 2 to calculate the magnetic structures; in this method, a magnetic transition is associated with an irreducible (or rather, physically irreducible) representation τ of the space group G of the unordered phase. The transitions are called magnetic because the density **M(r)** of the magnetic moment is expanded with respect to the functions of the representation τ and the coefficients c_l of these functions in the expansion of **M(r)** play the role of transition parameters. In the given case, all the τ are associated with **k** = 0, and the c_l can be represented as linear combinations of the components $m_{j\alpha}$ of the magnetic moments of the magnetic atoms of one cell ($\alpha = x, y, z$; j is the number of the atom in the cell). Since all transitions to an antiferromagnetic phase have been listed in ref. 3, our problem now reduces to establishing when such transitions may or must be accompanied by the appearance of the spontaneous vector **P**. We shall use the notation from refs. 2-4.

1. We show that if the cells coincide, a magnetic transition to a phase with $P \neq 0$ is impossible if G contains the inversion I; for the actual symmetry group of the unordered phase is the neutral group G1' = G × R, which consists of elements of G and their products with 1' = R, the operation of time reversal. Now R changes the signs of the magnetic moments, but it does not affect P or the density of the electric charge. When **k** = 0, in any representation of G × R the identity matrix corresponds to either I or IR. Therefore, one of these elements is conserved on the transition, but neither allows $P \neq 0$.

Magnetic transitions to a phase with $P \neq 0$ are also impossible from the classes 2221', 4221', 4321', and 6221'. In the case of 2221', this follows from the fact that the matrices of all representations of the group 222 are equal to 1 or −1. Such representations describe transitions under which the ordinary (nonmagnetic) symmetry is preserved. But this symmetry does not allow $P \neq 0$ in this case. With regard to the classes 4221', 4321', and 6221', transitions from them to a phase with $P \neq 0$ are again impossible on account of the singular properties of the representations of the corresponding groups. We shall not discuss these properties, but refer the reader to the list of transitions in ref. 3. It does not contain transitions to pyroelectric classes from these three classes.

Thus, the appearance of a spontaneous electric polarization can be expected only as a result of magnetic transitions from the classes $\bar{4}1'$, $\bar{4}2m1'$, 231', $\bar{4}3m1'$, $\bar{6}1'$, 321', $\bar{6}m21'$.

2. We must establish which terms in the expansion of the thermodynamic potential Φ with respect to the invariants of the group G × R give rise to a **P**. Clearly, such invariants must be of mixed form, i.e., consist of products of the components P_α and $m_{j\alpha}$ or, and this is the same thing, products of P_α and c_l. For brevity, we shall call these invariants PM invariants. Since Φ is invariant under R, $m_{j\alpha}$ (or c_l) can enter the PM invariants in even powers. Therefore, the PM invariants of lowest degree are the invariants of third degree: quadratic in $m_{j\alpha}$ and linear in P_α. (If G does not admit such invariants, it would seem that we must consider invariants of fourth degree: quadratic in $m_{j\alpha}$ and in P_α. Any group G admits these invariants; however, minimization of Φ shows, in accordance with Landau's theory, that they do not lead to the appearance of **P** as a result of a magnetic transition or the appearance of magnetic ordering in the case of a ferroelectric transition. The opposite conclusion is drawn in ref. 5, in which it is stated, in particular, that Landau's theory predicts transitions from the class m3m1' to classes allowing **P** and **M** simultaneously; **M** is the magnetic polarization vector.) In all that follows, PM invariants will mean only invariants of third degree.

We must prove that, first, under transitions from the above seven neutral classes to classes allowing $P \neq 0$, there are PM invariants of third degree that do not vanish in the ordered phase, and, secondly, these invariants do indeed give rise to a **P**.

We have failed to solved the first problem in a general form and we have therefore merely made a verification for all cases in accordance with the following specimen. In ref. 3 we find, for example, transitions from $\bar{6}m21'$ to the classes mm2 and mm'2'(σ_n), which allow $P \neq 0$. The transitions are described by the representation τ^5 (Table T33 from ref. 4). If it is assumed that c_1 and c_2 realize τ^5, then, as is readily verified, the quantities c_2^2 and c_1^2 realize τ^5, and c_1c_2 realizes τ^1. The quantities $P_x + iP_y$ and $P_x - iP_y$ are also transformed in accordance with τ^5, and also in accordance with the matrices given in T33 if the x axis is along a two-fold axis. Therefore, the group $\bar{6}m21'$ allows the invariant $I = c_2^2(P_x - iP_y) + c_1^2(P_x + iP_y)$. To the first transition there corresponds the solution $c_1 = c_2 = c$, to the second $c_1 = -c_2 = c$. In both cases $I = 2c^2P_x$ after the transition and also $I \neq 0$, $P_x \neq 0$.

The verification showed that in the case of all transitions from the seven neutral classes to phases with $P \neq 0$ there are PM invariants containing precisely those P_α that are allowed by the symmetry of the ordered phase and that, moreover, these invariants do not vanish in the ordered phase. We shall show that in the case of all transitions a spontaneous electric polarization must necessarily arise in the ordered phase; for the expansion of Φ always contains the invariant $\varepsilon[P_x^2 + P_y^2 + P_z^2]$, where 2ε is the permittivity of the unordered phase. Since the PM invariants are linear in P_α, minimization of Φ with respect to P_α leads to a system of equations whose solution cannot be $P = 0$. In particular, in the example given above the component P_x is proportional to the ratio of c^2 to 2ε. If there is a direct transition from a neutral class to a class allowing P, then

$$P \sim \Theta - T, \tag{1}$$

where Θ is the transition temperature. The relation (1) is a consequence of the assumption of the temperature dependences of the coefficients in the expansion of Φ of Landau theory. Of course, the results of symmetric nature given below do not depend on such assumptions.

3. In the case when the PM invariants are linear combinations of the products $m_j m_k P_\alpha$ and $m_j^2 P_\alpha$, i.e., they have an exchange nature, it is evident that the coupling between the magnetic and the electric ordering must be fairly strong. The form and the actual possibility of forming exchange PM invariants is determined by the group G and the group G(A) of the magnetic atom A; this is formed by the elements of G that leave atom A fixed. Since a general and exhaustive treatment of the question of exchange invariants would require much space, we shall here give without proof a rule that is sufficient in the case when the magnetic and the chemical cells coincide.

Using the irreducible representations τ of the point group $\hat{G}$ of the crystal in the unordered phase, one must form the so-called commutation representation, T_c, of the group $\hat{G}$ by including in T_c every representation τ as many times as the identity representation is contained in the matrices of the representation τ that correspond to the elements of G(A). The number of PM invariants containing the component P_α is equal to the number of times the representation with respect to which P_α transforms occurs in the symmetrized square, T^2_{cs}, of T_c.

(In the case under consideration the representation T_c arises as follows. The magnetic atoms of the crystal are split into as many sublattices as there are magnetic atoms in the cell; in one sublattice one includes all the atoms whose equilibrium positions differ by a period of the Bravais lattice. With the sublattice A_j corresponding to atom A_j we associate a certain quantity f_j, and in the space of the f_j we introduce the group of operators g, a homomorphic mapping of G, in accordance with this rule: If an element g of G carries the sublattice A_j into the sublattice A_k, then for the corresponding operator we set $\hat{g}f_j = f_k$. We have called the matrix form of the operators $\hat{G}$ the representation T_c. The dimensionality of T_c is equal to the number of sublattices. The representation T_c is unitary; we also assume that it can be transformed to a reduced form by means of a unitary matrix.)

Let us give some examples of the use of the rule.

Example 1. $\hat{G} = \bar{6}m2$, $G(A) = 32$. Using Table T33 in ref. 4, we establish that the identity representation contains the matrices of the representations τ^1 and τ^2 from T33 referred to the elements of the group 32 once (for each case). Therefore, $T_c = \tau^1 + \tau^2$. From the well-known equations, we find the symmetrized square of T_c: $T^2_{cs} = 2\tau^1 + \tau^2$. Since P_z transforms in accordance with τ^4 and P_x and P_y in accordance with τ^5 of the group $\bar{6}m2$, exchange PM invariants are impossible (but there are nonexchange invariants; see above.)

Example 2. $G = \bar{6}m2$, $G(A) = 3m$. We find that $T_c = \tau^1 + \tau^4$, $T^{c}_{2s} = 2\tau^1 + \tau^4$. Therefore, there is one exchange PM invariant and it contains P_z. However, this invariant does not give rise to a transition from the class $\bar{6}m21'$ to a structure with $P_z \neq 0$. This is most readily seen by referring to the list of transitions in ref. 3: It does not contain a transition to a structure admitting $P_z \neq 0$. This example shows that, by itself, the existence of PM invariants containing a certain component P_α by no means guarantees the existence of a transition to a structure with $P_\alpha \neq 0$.

Example 3. $\hat{G} = \bar{6}m2$, $G(A) = mm2$. To be specific, we shall assume that mm2 consists of the elements[4] h_1, h_8, h_{16}, and h_{23}. We find that $T_c = \tau^1 + \tau^5$ and $T^2_{cs} = 2\tau^1 + 2\tau^5$. In this case there are two exchange PM invariants with P_x and P_y.

What we have said in this section is valid in the case of one system of magnetic atoms that are equivalent in the unordered phase. Any of them may be taken as the original atom A. Our rule can be generalized to the case of two systems, A and B, of equivalent atoms with moments $m_j(A)$ and $m_j(B)$ as follows. For both systems one forms the corresponding commutation representations $T_c(A)$ and $T_c(B)$. The number of exchange PM invariants containing products of $m_j(A)$ and $m_k(B)$ and the component P_α is equal to the number of times the representation with respect to which P_α transforms occurs in the direct product $T_c(A) \times T_c(B)$.

Example 4. $\hat{G} = \bar{6}m2$, $G(A) = 32$, $G(B) = mm2$. In this case (Examples 1 and 3) $T_c(A) = \tau^1 + \tau^2$, and $T_c(B) = \tau^1 + \tau^5$ and the direct product of these representations is $\tau^1 + \tau^2 + \tau^5 + \tau^6$. Therefore, there is one exchange PM invariant containing the products $m_j(A)m_k(B)$ and the components P_x and P_y.

Finally, we give a further generalization of the rule (for the case of one system of equivalent magnetic atoms). If T^2_{cs} contains a certain irreducible representation τ^i, then there are exchange invariants that are linear combinations of the products of $m_j m_k$ and those components of the density of the displacements of the atoms from the equilibrium positions that transform in accordance with τ^i. These displacements accompany a magnetic transition if they do not vanish in the ordered phase on account of its symmetry.

4. In this section we list all transitions to an antiferromagnetic state with $P \neq 0$. As was shown in refs. 2 and 3, the list of representations that describe magnetic transitions is determined by the group G(A); namely, the irreducible representation τ of $\hat{G}$ can describe a transition from the class $\hat{G} \times R$ if τ is contained in $T_c \times \tilde{V}$, where $\tilde{V}$ is an axial vector representation. For every transition we give the representation τ that describes it and all the

groups G(A) when τ is contained in $T_c \times \tilde{V}$. In addition, we list the space groups in which each group G(A) can be realized (this last information can be obtained from ref. 5, but we have taken it from ref. 6). For example, for the transition II the statement d) G(A) = m, G = $D_{3h}^{1,3}$ means that the transition II is possible from the neutral space groups $D^1_{3h} \times R$ and $D^3_{3h} \times R$ if the crystal contains magnetic atoms with the intrinsic group G(A) = m in the unordered phase. The group G(A) = 1 is possible in any crystal and $T_c \times \tilde{V}$ contains every irreducible representation of $\hat{G}$. The data are not given for this case.

We should point out that structures to which a transition is described by a representation τ that is a part of $\tilde{V}$ or coincides with $\tilde{V}$ and is contained m ≥ 2 times in $T_c \times \tilde{V}$ are here called antiferromagnets with weak ferromagnetism. By antiferromagnets with weak ferromagnetism one generally understands a smaller class of structures, namely, only the case m = 2 and, in addition, when one can introduce an antiferromagnetic vector. Quite generally, for m ≥ 2 and m = 2 a magnetic moment's being small is an assumption that is indicated in a number of cases experimentally, but is not a consequence of symmetry. Therefore, all transitions to antiferromagnetic structures with weak ferromagnetism can be treated under other assumptions as transitions to ferromagnets with weak (or not weak) antiferromagnetism. These transitions become simply ferromagnetic transitions for m = 1. This last case is not considered here [we do not give the corresponding groups G(A)].

The number of types of domain in a single crystal that differ in the directions of the vectors **P** and **M** or the magnetic moments of atoms that are separated by lattice periods is equal in each case to the ratio of the orders of the original neutral point group and the final point group. Applying the symmetry operations of the neutral group to the vectors **P** and **M** and the magnetic moments of atoms that are present in a domain of a certain type, we can find the orientation of these vectors in the domains of the remaining types. As a rule, the structure data given in what follows refer to a domain of one type.

ANTIFERROMAGNETS

I. $\bar{4}3m1' \rightarrow 3m$, τ^4, F_2. A transition is possible for a) G(A) = 2, G = $T_d^{1,3-6}$; b) G(A) = m, G = T_d^{1-3}; c) G(A) = 222, G = T_d^4; d) G(A) = mm2, G = T_d^{1-3}; e) G(A) = $\bar{4}$, G = T_d^{3-6}; f) G(A) = $\bar{4}2m$, G = $T_d^{1,3}$; g) G(A) = 3, G = T_d^{4-6}; h) G(A) 3m, G = T_d^{1-3}; i) G(A) = 32, G = $T_d^{4,5}$. Exchange PM invariants exist in the cases G(A) = 1, 2, m, mm2, $\bar{4}'$, 3, 3m. In the ordered structure, the eight types of domain are naturally split into four pairs in accordance with the possible directions of the vector **P** along i + j + k, i − j − k, j − i − k, k − i − j. In one pair of types the vectors **P** are the same, but the magnetic moments of the corresponding atoms have opposite directions. In this connection we have several qualitatively different boundaries between the domains.

II. $\bar{6}m21' \rightarrow mm2$, τ^5, E'. A transition is possible for a) G(A) = 2, G = $D_{3h}^{2,4}$; b) G(A) = m(σ_h), G = D_{3h}^{1-4}; c) G(A) = m(σ_v); G = $D_{3h}^{1,3}$; d) G(A) = mm2, G = $D_{3h}^{1,3}$; e) G(A) = 3, G = D_{3h}^{2-4}; f) G(A) = 32, G = $D_{3h}^{2,4}$; g) G(A) = 3m, G = $D_{3h}^{1,3}$. Exchange PM invariants are present in the cases G(A) = 1, 2, m, mm2. The domains are split into three pairs of types in accordance with the three possible orientations of **P** along the two-fold axes. In the domains of one pair the vectors **P** are the same, but the magnetic moments of the corresponding atoms have opposite directions.

ANTIFERROMAGNETS WITH WEAK FERROMAGNETISM

Data for the vectors **P** and **M** are given for a domain of one type.

III. $\bar{4}1 \rightarrow 2'$, τ^{24}, E. A transition is possible in the groups $S_4^{1,2}$ when G(A) = 1, 2. In both cases, there are exchange PM invariants; **P** = (0, 0, P), **M** = (M_1, M_2, 0).

IV. $\bar{4}2m1' \rightarrow mm'2'$, τ^5, E. A transition is possible when: a) G(A) = m; G = $D_{2d}^{1,3,5,9,11}$; b) G(A) = 2(u_x), G = $D_{2d}^{1,2,5-12}$; c) G(A) = 2(C_4^2), G = D_{2d}^{1-12}; d) G(A) = mm2, G = $D_{2d}^{1,3,5,9,11}$; e) G(A) = 222; G = $D_{2d}^{1,2,6-8,10,11}$. Exchange PM invariants are present in the cases G(A) = 1, 2, m, mm2. **P** = (0, 0, P), **M** = (M_1, M_1, 0).

V. $231' \rightarrow 3$, τ^4, F and VI. $231' \rightarrow 2'$, τ^4, F. Transitions are possible when a) G(A) = 2, G = $T^{1,3,5}$; b) G(A) = 3, G = T^{1-5}; c) G(A) = 222, G = $T^{1,3}$. Exchange invariants are present in the cases G(A) = 1, 2, 3. After transition V we have **P** = (p, p, p), **M** = (m, m, m); after transition VI, **P** = (0, 0, P), **M** = (M_1, M_2, 0).

VII. $\bar{4}3m1' \rightarrow 3m'$, τ^5, F_1 and VIII. $\bar{4}3m1' \rightarrow mm'2'$, τ^5. Transitions are possible for a) G(A) = 2, G = $T_d^{1,3-6}$; b) G(A) = m, G = T_d^{1-3}; c) G(A) = mm2, G = T_d^{1-3}; d) G(A) = $\bar{4}$, G = T_d^{3-6}; e) G(A) = 3, G = T_d^{4-6}; f) G(A) = 3m, G = T_d^{1-3}. Exchange PM invariants are possible in the cases G(A) = 1, 2, m, mm2, $\bar{4}$, 3, 3m. After transition VII, **P** = (p, p, p), **M** = (m, m, m); after transition VIII, **P** = (0, 0, P), **M** = (M_1, M_2, 0).

IX. $\bar{6}1' \rightarrow m'$, τ^{46}, E_1. A transition is possible when G(A) = m. Exchange PM invariants exist in the cases G(A) = 1, m. In this case **P** is in the symmetry plane and **M** is perpendicular to it.

X. $321' \rightarrow 2$, τ^3, E and XI. $231' \rightarrow 2'$, τ^3. Transitions are possible when a) G(A) = 2, G = D_3^{1-7}; b) G(A) = 3, G = $D_3^{1,2,7}$. Exchange PM invariants exist in the cases G(A) = 1, 2. After transition X, **P** and **M** are along a two-fold axis; after transition XI, **P** is along a two-fold axis and **M** is perpendicular to it.

XII. $\bar{6}m21' \rightarrow mm'2'$, τ^6, E" and XIII. $\bar{6}m21' \rightarrow mm'2'$ (σ_h'), τ^6, E". Transitions are possible for a) G(A) = m(σ_h), G = D_{3h}^{1-4}; b) G(A) = m(σ_v), G = $D_{3h}^{1,3}$; c) G(A) = 2, G = $D_{3h}^{2,4}$; d) G(A) = mm2, G = $D_{3h}^{1,3}$; e) G(A) = 3, G = $D_{3h}^{2,4}$; f) G(A) = $\bar{6}$, G = D_{3h}^{2-4}.

Exchange PM invariants exist in the cases G(A) = 1, 2, m, mm2. After transition X, **P** and **M** are along the two-fold axis; after transition XIII, **P** is parallel to this axis and **M** is perpendicular to it and a three-fold axis.

ANTIFERROMAGNETS WITH SUPERWEAK FERROMAGNETISM

The transitions are described by a representation τ that is not contained in $\tilde{V}$, but the symmetrized cube of the representation contains irreducible representations that also belong to $\tilde{V}$. Ferromagnetism arises because of invariants that are cubic in the functions of the representation τ and linear in the components[8] M_α. Thus, **M** also appears in the second approximation if the symmetry group of the ordered phase allows the vector **M**. Note that the situation may be complicated by the presence of cubic PM invariants that are linear in the functions of the representation τ and the components M_α and P_α. It is possible that in a number of cases they are primarily responsible for the ferromagnetism.

XIV. $\bar{4}3m1' \rightarrow mm'2'$, τ^4, F_2. A transition is possible in the same cases as transition I, and the resulting structure has domains of the same type as are present after transition VIII.

XV. $\bar{6}1' \rightarrow m$, τ^{35}, E_1'. A transition is possible for G(A) = m, 3; exchange PM invariants exist in the cases G(A) = 1, m. The vector **P** is parallel and **M** is perpendicular to the symmetry plane.

XVI. $\bar{6}m21' \rightarrow mm'2'$, τ^5, E'. A transition is possible in the same cases as transition II. The vector **P** is parallel to a two-fold axis, **M** to a three-fold axis.

We believe that this list will be of greatest value in experimental searches for structures in which there is simultaneously magnetic and electric ordering, the more so because the list contains the space groups and groups G(A) when transitions are not forbidden on account of microscopic symmetry.

---

[1] G. A. Smolenskii and N. N. Krainik, Usp. Fiz. Nauk., 97, 657 (1969) [Sov. Phys.–Usp., 12, 271 (1969)].

[2] O. V. Kovalev, Fiz. Tverd. Tela, 5, 3156 (1963) [Sov. Phys.–Solid State, 5, 2309 (1964)].

[3] O. V. Kovalev, Kristallografiya, 9, 783 (1964) [Sov. Phys.–Crystallogr., 9, 665 (1965)].

[4] O. V. Kovalev, Irreducible Representations of the Space Groups, New York (1965).

[5] V. I. Lyubimov, Kristallografiya, 10, 520 (1965) [Sov. Phys.–Crystallogr., 10, 433 (1966)].

[6] International Tables for X-ray Crystallography, Vol. 1, Kynoch Press, Birmingham, England (1952).

[7] V. A. Koptsik, Shubnikov Groups [in Russian], Izd. MGU, Moscow (1966).

[8] O. V. Kovalev, Fiz. Met. Metalloved., 17, 498 (1964).

Boundary conditions in the electrodynamics of optically active media

B. V. Bokut', A. N. Serdyukov, F. I. Fedorov, and N. A. Khilo

Physics Institute, Academy of Sciences of the Belorussian SSR

(Submitted April 11, 1972)
Kristallografiya, 18, 227-233 (March-April 1973)

It is shown that the material relations customarily used for optically active crystals are not suitable for the description of spatially inhomogeneous media, including media with sharp separation boundaries. The material equation is generalized for nonabsorbing inhomogeneous optically active crystals, and the correct form of the boundary conditions in electrodynamics of such media is obtained on this basis. The boundary-value problems in the simplest case of isotropic medium are solved by way of illustration.

It is difficult to obtain the correct boundary conditions within the framework of the usual approach in the phenomenological theory of natural optical activity^1 (cf., e.g., the results of refs. 2 and 3). By starting from the possibility of a new formulation of the material equation$^{4-6}$ for optically active media, a corresponding analysis was performed in ref. 4 as well as in ref. 3.

In the present communication, the material equation [1] for nonabsorbing optically active crystals is generalized to include the case of inhomogeneous media, and the correct form of the boundary conditions is established on this basis. Their use is illustrated using as an example the boundary-value problems for an isotropic semiinfinite medium and a plane-parallel plate with normal incidence of the radiation.

1. Following ref. 1 (Sec. 83), we start from Maxwell's equations for the three vectors **E**, **D**, and **B**:

$$\operatorname{curl}\mathbf{E}=-\frac{1}{c}\frac{\partial\mathbf{B}}{\partial t},\qquad(1)$$

$$\operatorname{div}\mathbf{B}=0,\qquad(2)$$

$$\operatorname{curl}\mathbf{B}=\frac{1}{c}\frac{\partial\mathbf{D}}{\partial t},\qquad(3)$$

$$\operatorname{div}\mathbf{D}=0,\qquad(4)$$

without introducing the magnetic intensity vector, and assuming all the averaged currents induced in the medium to be incorporated in the definition of the electric induction **D**. A phenomenological description of optical activity is obtained in the case of homogeneous medium, as is well known, by introducing into the connection between the vectors **D** and **E** terms that are linearly dependent on the gradients of **E**. In the case of an inhomogeneous medium, the only possible generalization of such a connection is

$$D_i=\varepsilon_{ik}E_k+\alpha_{ikl}\partial_kE_l+\partial_k\beta_{ikl}E_l.\qquad(5)$$

We note that for a homogeneous medium, the last two terms in (5) can be unified in the form $(\alpha_{ikl}+\beta_{ikl})\partial_kE_l$ and the corresponding analysis reduces to that in ref. 1.

Let us see what limitations are imposed by the electromagnetic-field-energy conservation law on the properties of the tensors α_{ikl} and β_{ikl}, which characterize the optical activity, in the case of an inhomogeneous medium. To this end, using (5), we attempt to represent the relation

$$c\operatorname{div}[\mathbf{EB}]+\mathbf{B}\frac{\partial\mathbf{B}}{\partial t}+\mathbf{E}\frac{\partial\mathbf{D}}{\partial t}=0,\qquad(6)$$

which follows from (1) and (3), in the form of a continuity equation

$$\operatorname{div}\mathbf{S}+\frac{\partial w}{\partial t}=0.\qquad(7)$$

Substituting (5) in (6) and taking the symmetry ε_{ik} into account, we obtain

$$c\operatorname{div}[\mathbf{EB}]+\frac{1}{2}\frac{\partial}{\partial t}(\mathbf{E}\varepsilon\mathbf{E}+\mathbf{B}^2)+E_i\alpha_{ikl}\partial_k\dot{E}_l+E_i\partial_k\beta_{ikl}\dot{E}_l=0.\qquad(8)$$

It remains now to represent the last two terms in (8) $A=E_i\alpha_{ikl}\partial_k\dot{E}_l+E_i\partial_k\beta_{ikl}\dot{E}_l$ in the form of the sum of the time derivative of some scalar and the divergence of some vector. Account must be taken here of a possible dependence of the tensors α_{ikl} and β_{ikl} on the coordinates. Introducing the notation

$$\alpha_{ikl}=\alpha^s_{ikl}+\alpha^a_{ikl},\quad\beta_{ikl}=\beta^s_{ikl}+\beta^a_{ikl},$$

where

$$\alpha^s_{ikl}=(\alpha_{ikl}+\alpha_{ilk})/2=\alpha^s_{ilk},\ \beta^s_{ikl}=(\beta_{ikl}+\beta_{kil})/2=\beta^s_{kil},$$

$$\alpha^a_{ikl}=(\alpha_{ikl}-\alpha_{ilk})/2=-\alpha^a_{ilk}=e_{kln}\alpha_{in},$$

$$\beta^a_{ikl}=(\beta_{ikl}-\beta_{kil})/2=-\beta^a_{kil}=e_{ikn}\beta_{nl}$$

(e_{ijk} is the Levi–Civita pseudotensor), we transform the expression A into

$$A=\frac{\partial}{\partial t}(\mathbf{E}\alpha\operatorname{curl}\mathbf{E})+\operatorname{div}[\tilde{\alpha}\dot{\mathbf{E}},\mathbf{E}]+\mathbf{E}\operatorname{curl}(\beta-\tilde{\alpha})\dot{\mathbf{E}}$$
$$+E_i\alpha^s_{ikl}\partial_k\dot{E}_l+E_i\partial_k\beta^s_{ikl}\dot{E}_l,$$

where $\alpha=(\alpha_{ik})$, $\beta=(\beta_{ik})$ are certain pseudotensors of second rank. It is clear therefore that A can be represented in the required form if $\beta=\tilde{\alpha}$ and $\alpha^s_{ikl}=\beta^s_{ikl}=0$, i.e., if the material equation (5) takes the form

$$\mathbf{D}=\varepsilon\mathbf{E}+\alpha\operatorname{curl}\mathbf{E}+\operatorname{curl}\tilde{\alpha}\mathbf{E}.\qquad(9)$$

Relation (6) now takes the form of the continuity equation (7) with a Poynting vector

$$\mathbf{S}=\frac{c}{4\pi}[\mathbf{EB}]-\frac{1}{4\pi}[\mathbf{E},\tilde{\alpha}\dot{\mathbf{E}}]\qquad(10)$$

and with an energy density

$$w=\frac{1}{8\pi}(\mathbf{E}\varepsilon\mathbf{E}+\mathbf{B}^2+2\mathbf{E}\alpha\operatorname{curl}\mathbf{E}).\qquad(11)$$

For homogeneous optically active media, the energy conservation law was formulated in such a form earlier in ref. 3. Assuming in the latter case that α is independent of the coordinates, we can rewrite the material equation[9] in the form

$$\mathbf{D} = \varepsilon\mathbf{E} + [\gamma\nabla, \mathbf{E}], \tag{12}$$

where the second-rank optical-activity tensor γ is connected with the tensor α in (9) in the following manner:

$$\gamma = Sp\,\alpha - \tilde{\alpha}, \quad \alpha = Sp\,\gamma/2 - \tilde{\gamma}.$$

On the basis of the principle of symmetry of the kinetic coefficients, the material equation (12) was derived for a nonabsorbing homogeneous medium in ref. 1.

In must thus be emphasized that the material equation in the usual form (12) is valid for nonabsorbing optically active crystals only in the case of homogeneous media. For inhomogeneous media, with arbitrary coordinate dependence of the dielectric and optical-activity tensors, including the case when these quantitites change jumpwise (as on an interface between two media), relation (9) must be used in place of (12).

2. We investigate in this connection the question of the boundary conditions for the electromagnetic field in media with optical activity. The standard procedure of directly integrating Maxwell's equations (1)-(4) and using the connection (9) leads to the following boundary conditions (**q** is the normal to the interface between media 1 and 2):

$$[\mathbf{E}_1 - \mathbf{E}_2, \mathbf{q}] = 0, \tag{13}$$

$$(\mathbf{B}_1 - \mathbf{B}_2)\mathbf{q} = 0, \tag{14}$$

$$[\mathbf{B}_1 - \mathbf{B}_2, \mathbf{q}] = \frac{1}{c}\frac{\partial}{\partial t}[\tilde{\alpha}_1\mathbf{E}_1 - \tilde{\alpha}_2\mathbf{E}_2, \mathbf{q}], \tag{15}$$

$$(\mathbf{D}_1 - \mathbf{D}_2)\mathbf{q} = \operatorname{curl}\,(\tilde{\alpha}_1\mathbf{E}_1 - \tilde{\alpha}_2\mathbf{E}_2)\mathbf{q}, \tag{16}$$

which were obtained earlier in ref. 3.

It was noted in ref. 7 that the tangential components of the magnetic induction and the normal component of the electric inductions can be discontinuous on the interface between two media even in the absence of external surface sources. In the case of optically active media, however, the so-called indiced surface and charge densities

$$\mathbf{i} = -\frac{1}{4\pi}\int_1^2 dl\,\frac{\partial \mathbf{D}}{\partial t}, \quad \sigma = \frac{1}{4\pi}\int_1^2 dl[\mathbf{q}[\mathbf{D}\mathbf{q}]] \tag{17}$$

(the integration is over an infinitesimally small depth of the surface layer), which were obtained in ref. 7, were not evaluated, and such surface currents were omitted entirely in a solution of the boundary-value problems for a gyrotropic medium (ref. 8, Secs. 10.6 and 10.9).

It is easy to verify that **i** and σ differ from zero on the boundaries of optically active media by using an isotropic medium as an example. At scalar ε and α, the relation (9) can be written in the form

$$\mathbf{D} = \varepsilon\mathbf{E} + 2\alpha\,\operatorname{curl}\mathbf{E} + [\operatorname{grad}\alpha, \mathbf{E}].$$

If α changes jumpwise on the interface between two media, then the last term in **D** turns out to be proportional to a δ function and makes a finite contribution to **i** and σ. The use of (9) enables us to evaluate expressions (17) also in the general case of anisotropic media and obtain the boundary conditions (15) and (16).

It is possible to perform in the system of equations (1)-(4), (9) a procedure inverse to that used in ref. 3, of redefining the electric induction and magnetic intensity vectors. We introduce the quantities

$$\mathbf{D}^* = \mathbf{D} - \operatorname{curl}\,\tilde{\alpha}\mathbf{E} = \varepsilon\mathbf{E} - \frac{1}{c}\alpha\dot{\mathbf{B}}, \quad \mathbf{H}^* = \mathbf{B} - \frac{1}{c}\tilde{\alpha}\dot{\mathbf{E}},$$

for which Maxwell's equations remain in the forms (3) and (4):

$$\operatorname{curl}\mathbf{H}^* = \frac{1}{c}\frac{\partial \mathbf{D}^*}{\partial t}, \quad \operatorname{div}\mathbf{D}^* = 0.$$

We have in this case for (10) and (11) the simple expressions

$$\mathbf{S} = \frac{c}{4\pi}[\mathbf{E}\mathbf{H}^*], \quad w = \frac{1}{8\pi}(\mathbf{D}^*\varepsilon^{-1}\mathbf{D}^* + \mathbf{B}^2).$$

In addition, no fictitious surface currents and charges appear in the expressions for $\mathbf{H}^*$ and $\mathbf{D}^*$, $[\mathbf{H}_1^* - \mathbf{H}_2^*, \mathbf{q}] = 0$, $(\mathbf{D}_1^* - \mathbf{D}_2^*)\mathbf{q} = 0$, in the boundary conditions (15) and (16).

Thus, this approach, which is identical with the approach of refs. 5 and 6, results in an appreciable simplification of a number of relations in the electrodynamics of optically active media, and these relations are reduced to the usual form.

3. Proceeding now to the consideration of plane monochromatic electromagnetic waves, we assume all field vectors to be proportional to $\exp i\,(k_0\mathbf{m}\mathbf{r} - \omega t)$, where $k_0 = \omega/c$ is the wave number for vacuum, $\mathbf{m} = n\mathbf{n}$ is the refraction vector, **n** is the wave normal, and n is the refractive index. It follows then from Maxwell's equations (1) and (3) and from material equations, for regions where the medium is homogeneous, that

$$[\varepsilon + ik_0(\gamma\mathbf{m})^{\times} + \mathbf{m}^{\times 2}]\,\mathbf{E} = 0.$$

The lying cross denotes here an antisymmetric tensor of second rank, dual to the corresponding vector. The requirement that there exist nonzero solutions for **E** leads to the following equation for the normals:

$$\det(\varepsilon + ik_0(\gamma\mathbf{m})^{\times} + \mathbf{m}^{\times 2}) = 0, \tag{18}$$

which determines the values of the refractive indices n for a given direction **n** of propagation of a plane monochromatic wave in an optically active crystal of arbitrary symmetry. In the case of an isotropic medium, for scalar ε and $\gamma = 2\alpha$, Eq. (18) yields two values of the refractive index, corresponding to right- and left-circular polarized waves:

$$n_{\pm} = n_0 \pm k_0\alpha, \tag{19}$$

where $n_0 = \sqrt{\varepsilon}$.

Starting from (19) and neglecting the frequency dispersions of ε and α, we obtain an expression for the group velocity $\mathbf{v}_{\pm}^{\mathrm{gr}} = d\omega/d\mathbf{k}_{\pm}$ of circularly polarized waves

$$\mathbf{v}_{\pm}^{\mathrm{gr}} = cn/(n_0 \pm 2k_0\alpha),$$

with which it is easy to show that the quantities (10) and (11) are connected by the relation

$$\mathbf{S}_{\pm} = w_{\pm}\mathbf{v}_{\pm}^{\mathrm{gr}}.$$

4. Let us consider the reflection and refraction of a plane monochromatic wave normally incident on the boundary of an isotropic optically active medium. Assume that a wave

$$\begin{aligned} \mathbf{E}(z, t) &= \mathbf{E}\exp i(k_0nz - \omega t), \\ \mathbf{B}(z, t) &= n[\mathbf{qE}]\exp i(k_0nz - \omega t) \end{aligned} \tag{20}$$

is incident on a semiinfinite medium, along the z axis (which coincides with the direction of $\mathbf{q}$) from an isotropic inactive and nonmagnetic medium with refractive index n. We denote by

$$\begin{aligned} \mathbf{E}'(z, t) &= \mathbf{E}'\exp i(-k_0nz - \omega t), \\ \mathbf{B}'(z, t) &= -n[\mathbf{qE}']\exp i(-k_0nz - \omega t) \end{aligned} \tag{21}$$

the fields of the reflected wave, and by

$$\begin{aligned} \mathbf{E}_{\pm}(z, t) &= \mathbf{E}_{\pm}\exp i(k_0n_{\pm}z - \omega t), \\ \mathbf{B}_{\pm}(z, t) &= n_{\pm}[\mathbf{qE}_{\pm}(z, t)] = \mp in_{\pm}\mathbf{E}_{\pm}\exp i(k_0n_{\pm}z - \omega t) \end{aligned} \tag{22}$$

the fields of the circularly polarized waves propagating in the medium. The last equation takes into account the circular-polarization condition

$$[\mathbf{qE}_{\pm}] = \mp i\mathbf{E}_{\pm}. \tag{23}$$

In the case under consideration, the boundary conditions (13) and (15) can be written at z = 0 in the form

$$\mathbf{E} + \mathbf{E}' - \mathbf{E}_+ - \mathbf{E}_- = 0, \tag{24}$$

$$\mathbf{B} + \mathbf{B}' - \mathbf{B}_+ - \mathbf{B}_- = ik_0\alpha(\mathbf{E}_+ + \mathbf{E}_-). \tag{25}$$

Multiplying (25) vectorially by $\mathbf{q}$ and taking into account the Maxwell equations and the material equations for plane waves, as well as (19), we get

$$-n\mathbf{E} + n\mathbf{E}' + n_0\mathbf{E}_+ + n_0\mathbf{E}_- = 0. \tag{26}$$

From (24)-(26) and (21) and (22) we get the following expressions for the fields of the reflected and refracted waves:

$$\mathbf{E}'(z, t) = \frac{n - n_0}{n + n_0}\mathbf{E}\exp i(-k_0nz - \omega t), \tag{27}$$

$$\mathbf{B}'(z, t) = -\frac{n(n - n_0)}{n + n_0}[\mathbf{qE}]\exp i(-k_0nz - \omega t), \tag{28}$$

$$\mathbf{E}_{\pm}(z, t) = \frac{n}{n + n_0}(\mathbf{E} \pm i[\mathbf{qE}])\exp i(k_0n_{\pm}z - \omega t), \tag{29}$$

$$\mathbf{B}_{\pm}(z, t) = \mp i\frac{nn_{\pm}}{n + n_0}(\mathbf{E} \pm i[\mathbf{qE}])\exp i(k_0n_{\pm}z - \omega t). \tag{30}$$

Bearing in mind the fact that the flux of the electromagnetic energy in an optically active medium is defined by (10), and using (27)-(30), we obtain expressions for the energy flux densities of the reflected and refracted waves:

$$\mathbf{S}' = -\left(\frac{n - n_0}{n + n_0}\right)^2\mathbf{S}, \quad \mathbf{S}_1 = \frac{4nn_0}{(n + n_0)^2}\mathbf{S}, \tag{31}$$

where S is the flux density of the incident wave. The scalar factors preceding S in (31) are the reflection and transmission coefficients R and T, respectively. It is easy to verify that R + T = 1. Thus, the boundary conditions (13) and (15) and expression (10) for the Poynting vector agree with the balance conditions for the energy fluxes of radiation reflected and refracted at the boundary of a semiinfinite isotropic optically active medium.

Attention should also be called to the fact that the amplitudes of the electric intensity of the reflected and refracted waves, (27), (29), and also the reflection and transmission coefficients for the case of normal incidence are independent of the optical-activity parameter, whereas if one uses the boundary condition with the right-hand side discarded this does not take place (cf., e.g., the results obtained in ref. 8).

5. We now turn to the problem of the passage of a plane monochromatic wave through an isotropic optical active plane-parallel layer with normal incidence. Assume that the wave (20) is incident on a layer of thickness d. Two refracted waves of the type (22) and two circularly polarized waves

$$\begin{aligned} \mathbf{E}_{\pm}'(z, t) &= \mathbf{E}_{\pm}'\exp i(-k_0n_{\pm}z - \omega t), \\ \mathbf{B}_{\pm}'(z, t) &= \pm in_{\pm}\mathbf{E}_{\pm}'\exp i(-k_0n_{\pm}z - \omega t) \end{aligned} \tag{32}$$

reflected from the second boundary surface will then propagate in the layer . We represent the wave reflected from the layer in the form (21), and write for the wave passing through the layer

$$\begin{aligned} \mathbf{E}_1(z, t) &= \mathbf{E}_1\exp i(k_0nz - \omega t), \\ \mathbf{B}_1(z, t) &= n[\mathbf{qE}_1]\exp i(k_0nz - \omega t). \end{aligned} \tag{33}$$

The amplitudes of the reflected and transmitted waves, and also the amplitudes of the waves inside the layer, are determined from the boundary conditions

$$\begin{aligned} &\mathbf{E} + \mathbf{E}' - \mathbf{E}_+ - \mathbf{E}_- - \mathbf{E}_+' - \mathbf{E}_-' = 0, \\ &\mathbf{B} + \mathbf{B}' - \mathbf{B}_+ - \mathbf{B}_- - \mathbf{B}_+' - \mathbf{B}_-' = ik_0\alpha(\mathbf{E}_+ + \mathbf{E}_- + \mathbf{E}_+' + \mathbf{E}_-') \end{aligned} \tag{34}$$

for the first boundary (z = 0) and

$$\left.\begin{aligned} &\mathbf{E}_+\exp(i\varphi_+) + \mathbf{E}_-\exp(i\varphi_-) + \mathbf{E}_+'\exp(-i\varphi_+) \\ &\quad + \mathbf{E}_-'\exp(-i\varphi_-) - \mathbf{E}_1\exp(i\varphi) = 0, \\ &\mathbf{B}_+\exp(i\varphi_+) + \mathbf{B}_-\exp(i\varphi_-) + \mathbf{B}_+'\exp(-i\varphi_+) \\ &\quad + \mathbf{B}_-'\exp(-i\varphi_-) - \mathbf{B}_1\exp(i\varphi) \\ &\quad = -ik_0\alpha(\mathbf{E}_+\exp(i\varphi_+) + \mathbf{E}_-\exp(i\varphi_-) \\ &\quad + \mathbf{E}_+'\exp(-i\varphi_+) + \mathbf{E}_-'\exp(-i\varphi_-)) \end{aligned}\right\} \tag{35}$$

for the second boundary ($z = d$). Here $\varphi_\pm = k_0 n_\pm d$, $\varphi = k_0 n d$. Using Maxwell's equations, the circular-polarization conditions (23), and $[\mathbf{q}\mathbf{E}_\pm'] = \pm i\mathbf{E}_\pm'$ for the waves in the layer, and also expression (19), we obtain from (27), (28), and (35) the system of equations

$$\begin{gathered}
2n\mathbf{E} - (n_0 + n)(\mathbf{E}_+ + \mathbf{E}_-) + (n_0 - n)(\mathbf{E}_+' + \mathbf{E}_-') = 0,\\
2in[\mathbf{q}\mathbf{E}] - (n_0 + n)(\mathbf{E}_+ - \mathbf{E}_-) - (n_0 - n)(\mathbf{E}_+' - \mathbf{E}_-') = 0,\\
(n_0 - n)(\mathbf{E}_+ \exp(i\varphi_+) + \mathbf{E}_- \exp(i\varphi_-)) - (n_0 + n)(\mathbf{E}_+' \exp(-i\varphi_+)\\
+ (\mathbf{E}_-' \exp(-i\varphi_-)) = 0,\\
(n_0 - n)(\mathbf{E}_+ \exp(i\varphi_+) - \mathbf{E}_- \exp(i\varphi_-)) + (n_0 + n)(\mathbf{E}_+' \exp(-i\varphi_+)\\
- \mathbf{E}_-' \exp(-i\varphi_-)) = 0,
\end{gathered}$$

from which we get expressions for the electric intensities of the waves in the layer

$$\mathbf{E}_\pm(z, t) = \frac{n}{\xi}(n_0 + n)(\mathbf{E} \pm i[\mathbf{q}\mathbf{E}])e^{-i\varphi_0} \exp i(k_0 n_\pm z - \omega t), \quad (36)$$

$$\mathbf{E}_\pm'(z, t) = \frac{n}{\xi}(n_0 - n)(\mathbf{E} \mp i[\mathbf{q}\mathbf{E}])e^{i\varphi_0} \exp i(-k_0 n_\pm z - \omega t), \quad (37)$$

where $\xi = (n_0 + n)^2 \exp(-i\varphi_0) - (n_0 - n)\exp(i\varphi_0)$. Taking (36) and (37) into account, we determine from (34) and (35) also the electric intensities of the wave reflected from the layer and the wave transmitted through the layer:

$$\mathbf{E}'(z, t) = \frac{2i}{\xi}(n_0^2 - n^2)\sin\varphi_0 \mathbf{E} \exp i(-k_0 n z - \omega t), \quad (38)$$

$$\mathbf{E}_1(z, t) = \frac{4}{\xi} n_0 n e^{-i\varphi}(\mathbf{E}\cos\Delta\varphi - [\mathbf{q}\mathbf{E}]\sin\Delta\varphi)\exp i(k_0 n z - \omega t). \quad (39)$$

Here $\varphi_0 = k_0 n_0 d$, $\Delta\varphi = k_0^2 \alpha d$.

We introduce a unit vector of elliptic polarization of the incident wave $\mathbf{e} = (\mathbf{e}_1 + i\tau\mathbf{e}_2)/\sqrt{1 + \tau^2}$, with $\mathbf{E} = E\mathbf{e}$. Here τ is the ellipticity (the ratio of the polarization-ellipse axes), $\mathbf{e}_1$ and $\mathbf{e}_2$ are unit vectors of the principal axes of the ellipse, which form together with $\mathbf{q}$ a system of orthonormal vectors ($[\mathbf{e}_1\mathbf{e}_2] = \mathbf{q}$). It is easy to show here that the unit vector of polarization of the transmitted wave takes the form $\mathbf{e}' = (\mathbf{e}_1' + i\tau\mathbf{e}_2')/\sqrt{1 + \tau^2}$, where

$$\mathbf{e}_1' = \mathbf{e}_1 \cos\Delta\varphi - \mathbf{e}_2 \sin\Delta\varphi, \quad \mathbf{e}_2' = \mathbf{e}_1 \sin\Delta\varphi + \mathbf{e}_2 \cos\Delta\varphi.$$

The last relations mean that the ellipticity of the transmitted wave is equal to the ellipticity of the incident wave, and the axes of the polarization ellipse of the transmitted waves are rotated through the angle $\Delta\varphi = k_0^2 \alpha d$.

The average reflection and transmission coefficients are equal to

$$\begin{aligned}
R &= \frac{4(n_0^2 - n^2)^2 \sin^2\varphi_0}{(n + n_0)^4 - 2(n^2 - n_0^2)^2 \cos 2\varphi_0 + (n - n_0)^4}\\
T &= \frac{16 n_0^2 n^2}{(n + n_0)^4 - 2(n^2 - n_0^2)^2 \cos 2\varphi_0 + (n - n_0)^4}.
\end{aligned} \quad (40)$$

It is easy to verify that the obtained solutions satisfy the energy-flux balance condition $R + T = 1$ for reflection and transmission of radiation through the layer.

We present a brief analysis of the equations in (40). It should be noted, first, that the reflection and transmission coefficients do not depend on the ellipticity of the incident wave and are the same for either left- or right-circular polarized incident waves. Therefore, for example, in the case of linear polarization of the incident wave, the reflected and transmitted waves are polarized strictly linearly. Further, the reflection coefficient is equal to zero in the case when the refractive index n of the medium in which the optically active layer is placed coincides with the refractive index n_0 of the layer without the activity taken into account. Total transmission of the radiation through the plate (at arbitrary polarization), as seen from (40), is attained also in the case when $\varphi_0 = 0$, i.e., when the layer thickness d is a multiple of $\pi c/n_0\omega$.

---

[1] L. D. Landau and E. M. Lifshitz, Electrodynamics of Continuous Media, Addison-Wesley, 1959.

[2] B. V. Bokut' and B. A. Sotskii, Opt. Spektrosk., 14, 117 (1963).

[3] B. V. Bokut' and A. N. Serdyukov, Zh. Eksp. Teor. Fiz., 61, 1808 (1971) [Sov. Phys.—JETP, 34, 962 (1972)].

[4] R. M. Hornreich and S. Shtrikman, Phys. Rev., 171, 1065 (1968).

[5] B. V. Bokut', A. N. Serdyukov, and F. I. Fedorov, Kristallografiya, 15, 1002 (1970) [Sov. Phys.—Crystallogr., 15, 871 (1971)].

[6] V. N. Aleksandrov, Kristallografiya, 15, 996 (1970) [Sov. Phys.—Crystallogr., 15, 867 (1971)].

[7] V. P. Silin and A. A. Rukhadze, Electromagnetic Properties of Plasma and Plasmalike Media, Gordon and Breach.

[8] V. M. Agranovich and V. L. Ginzburg, Spatial Dispersion in Crystal Optics and the Theory of Excitons, Interscience (1966).

Kinetics of motion of steps and rows of steps at smeared phase boundaries

D. E. Temkin
Central Scientific Research Institute of Ferrous Metallurgy

(Submitted December 2, 1971; resubmitted April 3, 1972)
Kristallografiya, 18, 234-244 (March-April 1973)

An analysis is presented of a rectilinear step without kinks at a smeared phase boundary and the kinetics of its motion as a whole. The specific free energy and the step width l_s are calculated. Expressions are obtained for the dependence of the step velocity V_s on Δf, the deviation from equilibrium, for low and high velocities. The step moves as a whole with $\Delta f_s < \Delta f < \Delta f_1$, where Δf_s and Δf_1 are the critical values of Δf for the onset of step motion and planar boundary motion. With $\Delta f \to \Delta f_1$, V_s and l_s increase unboundedly and tangential motion of the step goes over to normal motion of the boundary. The tangential velocity V_t of a row of rectilinear steps is analyzed for a fixed distance d between steps. The relation between V_t and Δf for large V_t is obtained. With increasing Δf the contribution of the steps to the normal growth velocity decreases and V_n goes over to the growth velocity of the boundary without steps. The nature of the transition from tangential ($d \gg l_s$) to normal ($d \ll l_s$) motion during growth by a spiral mechanism and by two-dimensional nucleation is discussed.

A phenomenological description of the structure and kinetics of normal motion of a planar phase separation boundary having no steps has been given previously.[1,2] Here the boundary between two condensed phases α and β is regarded as a transition region, in which the parameter u, which characterizes the difference between the phases, varies from u = 0 corresponding to the β phase to u = 1 in the α phase. In describing the kinetics, the boundary structure is described by a set of functions $u_n(t)$ (t is the time and n is the number of the atomic plane parallel to the boundary). Normal motion of a boundary without steps is only possible with a deviation from equilibrium exceeding a certain critical value Δf_1. For smaller deviations the boundary moves due to the formation and tangential motion of steps. Without specifying the mechanism of formation, we consider the motion kinetics of single rectilinear steps and rows of steps.

The problem of a step at a smeared phase boundary was first discussed by Cahn.[3] He considered a rectilinear step of unit height *a*. In the presence of such a step part of the interfacial boundary (to the left of the step to be explicit) moves forward by one interplanar distance *a* relative to the other part of the boundary (Fig. 1). The step is a transition region in which the degree of motion of the boundary varies from *a* on the left, far from the step, to zero on the right. In the presence of a rectilinear step the parameter u depends on the two indices n and k, whose meaning is seen in Fig. 1, so that $u_{n,k}$ describes the state of a certain atomic row parallel to the step.

To describe the structure and kinetics we use the same model and approximations as in previous work.[1,2]

1. The free energy of a system with rectilinear steps is written in the form

$$F = a^2 \sum_{n,k=-\infty}^{\infty} \{f(u_{n,k}) + Ka^{-2}[(u_{n,k} - u_{n,k+1})^2 + (u_{n,k} - u_{n+1,k})^2]\}. \quad (1)$$

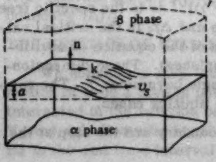

Fig. 1. Schematic representation of a step on a smeared phase-separation boundary.

Here F is the free energy per unit step length, $f(u_{n,k})$ are the excess free energies per unit volume of the homogeneous phase, which is characterized by the parameter $u_{n,k}$ [for the β phase we set $f(0) = 0$]; the second term in (1) describes the contribution involving the inhomogeneity of the system and K is a certain positive constant. In writing (1) we assume that the interplanar distances in n and k are set equal.

2. The function $f(0)$ is approximated by two parabolas which intersect at a point u° (see Fig. 2):

$$f(u) = \begin{cases} f_0 u^2, \ 0 \leqslant u < u^\circ & (\beta \text{ phase}), \\ -\Delta f + f_0(1-u)^2, \ u^\circ < u \leqslant 1 & (\alpha \text{ phase}), \end{cases} \quad (2)$$

where

$$u^\circ = {}^1/_2 - \Delta f / 2f_0. \quad (3)$$

Here Δf is the free energy difference between the β and α phases, which characterizes the deviation from equilibrium. For the β → α transition considered in what follows, $\Delta f > 0$.

3. The equation which describes the change in the state of the system with time is written in the form

$$\frac{du_{n,k}}{dt} = -\frac{D}{a}\frac{\partial F}{\partial u_{n,k}} \text{ for all n and k,} \quad (4)$$

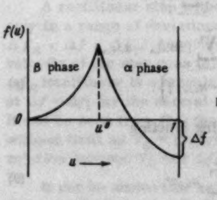

Fig. 2. Approximation of the relation f (u) by two parabolas.

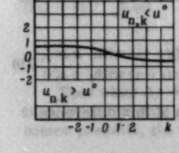

Fig. 3. Arbitrary position of the line $u_{n,k} = u^\circ$ in the (n, k) plane in the presence of a rectilinear step of unit height. In the region above this line $u_{n,k} < u^\circ$ and below it $u_{n,k} > u^\circ$.

where D is a certain kinetic coefficient. Equation (4) is written in agreement with the linear theory of irreversible processes with the additional assumption that all of the diagonal kinetic coefficients are equal to a constant D and the nondiagonal ones are equal to zero.

Using Eqs. (1-4) we find

$$V_j \frac{du_{n,k}}{d\tau} + 2(2+\gamma)u_{n,k} - u_{n+1,k} - u_{n-1,k} - u_{n,k+1} - u_{n,k-1}$$
$$= \begin{cases} 0 & \text{with } 0 \leqslant u_{n,k}(\tau) < u^\circ, \\ 2\gamma & \text{with } u^\circ < u_{n,k}(\tau) \leqslant 1. \end{cases} \quad (5)$$

Here $V_j = v_j/2DK$ is the dimensionless tangential velocity (in the direction of k), v_j is the dimensional tangential velocity, $\tau = v_j t/a$ is the dimensionless time, and $\gamma = f_0 a^2/2K$. For a single step we note $V_j \equiv V_s (v_j \equiv v_s)$ while for a row of steps: $V_j \equiv V_t (v_j \equiv v_t)$.

EQUILIBRIUM STRUCTURE AND FREE ENERGY OF A RECTILINEAR STEP

The equilibrium structure corresponds to a minimum in F. Setting $du_{n,k}/d\tau = 0$ in (5) we find the equations

$$2(2+\gamma)u_{n,k} - u_{n+1,k} - u_{n-1,k} - u_{n,k+1} - u_{n,k-1}$$
$$= \begin{cases} 0 & \text{with } n \geqslant 1,\ -\infty < k < \infty \text{ and } n = 0,\ k \geqslant 1, \\ 2\gamma & \text{with } n \leqslant -1,\ -\infty < k < \infty \text{ and } n = 0,\ k \leqslant 0. \end{cases} \quad (6)$$

It is here assumed that u° lies in the plane n = 0 between the points k = 0 and k = 1 (Fig. 3). Therefore,

$$u_{0,0} \geqslant u^\circ \geqslant u_{0,1};\ u_{0,k} > u^\circ > u_{1,k} \text{ with } k < 0;$$
$$u_{-1,k} > u^\circ > u_{0,k} \text{ with } k > 1. \quad (7)$$

The solution to Eq. (6) should satisfy the inequalities (7) and the boundary conditions $u_{-\infty,k} = 1$, $u_{\infty,k} = 0$, $u_{n,-\infty} = u_{n-1,\infty}$.

After a number of uncomplicated but tedious calculations we find the following expression for the free energy ε per unit step length from Eq. (1), using Eq. (5):

$$\varepsilon = \frac{a^2 f_0}{2\gamma}\Big\{u_{0,0} - u_{0,1} + \sum_{k=-\infty}^{0}\left[(u_{0,k} - u_{0,-\infty}) - (u_{1,k} - u_{1,-\infty})\right] + \sum_{k=1}^{\infty}\left[(u_{-1,k} - u_{-1,\infty}) - (u_{0,k} - u_{0,\infty})\right]\Big\}. \quad (8)$$

We introduce the generating function

$$Q_k(z) = \sum_{n=-\infty}^{\infty} u_{n,k} z^n. \quad (9)$$

for the solution of Eq. (5). After multiplying (5) by z^n and summing over n we find

$$\left(2 + \frac{\psi}{z}\right)Q_k(z) - Q_{k+1}(z) - Q_{k-1}(z) = \begin{cases} 2\gamma/(z-1) & \text{with } k \geqslant 1, \\ 2\gamma z/(z-1) & \text{with } k \leqslant 0, \end{cases} \quad (10)$$

where $\psi = 2\gamma z - (1-z)^2$. The solution of this difference equation is

$$Q_k(z) = \begin{cases} \dfrac{2\gamma z}{(z-1)\psi} + \dfrac{2\gamma z}{(1+\eta)\psi}\eta^k & \text{with } k \geqslant 0, \\ \dfrac{2\gamma z^2}{(z-1)\psi} - \dfrac{2\gamma z}{(1+\eta)\psi}\eta^{1-k} & \text{with } k \leqslant 1, \end{cases} \quad (11)$$

Here $\eta = 1 + \psi/2z - [(1 + \psi/2z)^2 - 1]^{1/2}$.

The quantities $u_{n,k}$ are coefficients of the Laurent expansion of the function $Q_k(z)$ and can be found using contour integration. By this means we find for $u_{0,0}$ and $u_{0,1}$

$$u_{0,1} = 1 - u_{0,0} = \frac{1}{2} - \frac{2\gamma}{\pi}\frac{\sqrt{ps}}{(1-ps)}K\left(\frac{s-p}{1-ps}\right), \quad (12)$$

where

$$s = 1 + \gamma - [(1+\gamma)^2 - 1]^{1/2},\ p = 3 + \gamma - [(3+\gamma)^2 - 1]^{1/2} \quad (13)$$

and K(k) is the complete elliptic integral of the first kind.

The solution to Eq. (6) which describes the structure of a metastable step exists only for those deviations from equilibrium for which the first inequality (7) is satisfied. For the $\beta \to \alpha$ transition setting $u_{0,1} = u^\circ$ we find the critical deviation Δf_s from equilibrium for which such a solution vanishes. Taking (12) and (3) into account, we find

$$\frac{\Delta f_s}{f_0} = \frac{4\gamma}{\pi}\frac{\sqrt{ps}}{(1-ps)}K\left(\frac{s-p}{1-ps}\right). \quad (14)$$

Calculation of ε leads to the expression

$$\varepsilon = \frac{4}{\pi}a^2 f_0 \frac{(1-s)s\sqrt{ps}}{(1+s)(1-ps)(s-p)}\left\{\frac{(1-ps)}{(1-s^2)}E\left(\frac{s-p}{1-ps}\right) - \frac{(p+s)}{2s}K\left(\frac{s-p}{1-ps}\right)\right\}. \quad (15)$$

Here E(k) is the complete elliptic integral of the second kind.

We now find the effective width l_s of the step. In the plane n = 0 the parameters $u_{0,k}$ decrease from $u_{0,-\infty}$ to $u_{0,\infty}$ with increasing k. Therefore l_s (in units of a) is defined as[1)]

$$l_s = [(u_{0,-\infty} - u_{0,\infty})/(u_{0,0} - u_{0,1})] - 1. \quad (16)$$

Since $(u_{0,-\infty} - u_{0,\infty}) = (1-s)/(1+s)$, taking (12) into account we have

$$l_s = \left[\pi(1-s)(1-ps)/4\gamma(1+s)\sqrt{ps}\,K\left(\frac{s-p}{1-ps}\right)\right] - 1. \quad (17)$$

It is interesting to compare the properties of the equilibrium step l_s, $\varepsilon/a^2 f_0$, and $\Delta f_s/f_0$ with the corresponding properties of a planar boundary,[1] $l_1 = 2s/(1-s)$, $\sigma/af_0 = s/(1-s^2)$, and $\Delta f_1/f_0 = [\gamma/(2+\gamma)]^{1/2}$ (σ is the specific free energy of the bounding surface and Δf_1 is the critical value of Δf for which the solution of the equation of equilibrium for a planar boundary vanishes). These dimensionless quantities depend on a single parameter γ. The comparison is carried out for two limiting cases.

1. For $\gamma \gg 1$ the phase boundary and the step at the

phase boundary are sharp.

For a rectilinear step we have

$$\left.\begin{aligned} l_s &\simeq \frac{1}{\gamma}\left(1-\frac{3}{2\gamma}\right), \\ \frac{\varepsilon}{a^2 f_0} &\simeq \frac{1}{2\gamma}\left(1-\frac{3}{\gamma}\right), \\ \frac{\Delta f_s}{f_0} &\simeq 1-\frac{2}{\gamma}, \end{aligned}\right\} \tag{18a}$$

and for a planar boundary,

$$\left.\begin{aligned} l_i &\simeq \frac{1}{\gamma}\left(1-\frac{1}{2\gamma}\right), \\ \frac{\sigma}{a f_0} &\simeq \frac{1}{2\gamma}\left(1-\frac{1}{\gamma}\right), \\ \frac{\Delta f_i}{f_0} &\simeq 1-\frac{1}{\gamma}. \end{aligned}\right\} \tag{18b}$$

With $\gamma \to \infty$, l_s and l_1 go to zero and $\varepsilon = a\sigma = K$. With γ finite, $\varepsilon < a\sigma$. The fact that $\Delta f_s/f_0$ and $\Delta f/f_0$ go to unity when $\gamma \to \infty$ is related to the approximation (2) which was used, according to which with $\Delta f/f_0 = 1$ the β phase loses stability.

2. With $\gamma \ll 1$ the phase boundary and the step are smeared.

For a rectilinear boundary we have

$$\left.\begin{aligned} l_s &\simeq \frac{\pi}{2\sqrt{2\gamma}\ln(2\gamma^{-1/2})}-1, \\ \frac{\varepsilon}{a^2 f_0} &\simeq \frac{1}{2\pi}\left[1-\frac{9(\sqrt{2}-1)\gamma}{4}\right], \\ \frac{\Delta f_s}{f_0} &\simeq \frac{2\gamma}{\pi}\ln(2\gamma^{-1/2}), \end{aligned}\right\} \tag{19a}$$

while for a planar boundary,

$$\left.\begin{aligned} l_i &\simeq \sqrt{\frac{2}{\gamma}}(1-\sqrt{2\gamma}), \\ \frac{\sigma}{a f_0} &\simeq \frac{1}{2\sqrt{2\gamma}}(1-\sqrt{2\gamma}), \\ \frac{\Delta f_i}{f_0} &\simeq \sqrt{\frac{\gamma}{2}}\left(1-\frac{\gamma}{4}\right). \end{aligned}\right\} \tag{19b}$$

Note that with decreasing γ the width of the step increases more slowly than that of the boundary and $\varepsilon/a^2 f_0$ goes to a limit of $^1/_2\pi$, while σ/af_0 grows without limit and $\Delta f_s/\Delta f_1$ goes to zero.

As we would expect, for any γ the critical deviation from equilibrium for a step (Δf_s) is greater than for a boundary (Δf_1).

THE KINETICS OF STEP MOTION

We consider a step without kinks. Thus stationary motion of such a step is possible with $\Delta f > \Delta f_s$. We are interested in the relation between the stationary velocity V_s and Δf. It can be found if we can find a solution of Eq. (5) in the unit time interval $0 \leq \tau \leq 1$ since $u_{n,k}(\tau + 1) = u_{n,k-1}(\tau)$. With

$$u_{0,0}(0) = u^\circ \tag{20}$$

the right-hand side of Eq. (5) coincides with the right-hand side of (6). Condition (20) itself is an additional equation for determining the unknown V_s.

We introduce the generating function

$$G(\tau; z, y) = \sum_{k=-\infty}^{\infty}\left[\frac{2\gamma z}{(z-1)\varphi} - Q_k(\tau; z)\right] y^k, \tag{21}$$

where

$$Q_k(\tau; z) = \sum_{n=-\infty}^{\infty} u_{n,k}(\tau) z^n.$$

In place of (5) we obtain the equation $V_s(dG/d\tau) + \varphi G = 2\gamma y/(y-1)$ and in place of the stationary condition $u_{n,k}(1) = u_{n,k-1}(0)$ we find the relation $G(1; z, y) = yG(0; z, y)$. Then

$$G(\tau; z, y) = \frac{2\gamma y}{\varphi}\left\{\frac{1}{(y-1)} + \frac{\exp(-\tau\varphi/V_s)}{\exp(-\varphi/V_s) - y}\right\}. \tag{22}$$

Here $\varphi = 2\gamma + 4 - z - (1/z) - y - (1/y)$.

To find the desired relation between V_s and Δf we need to calculate $u_{0,0}(0)$ and equate it to u°. To calculate $u_{0,0}(0)$ we must expand $G(0; z, y)$ in powers of z and y and find the coefficient of z and y in this expansion for the zeroth powers. Such an expansion will only be obtained in the limits of small and large V_s. Omitting the cumbersome calculations we write the final results. In the low-velocity region we have the expression

$$\frac{V_s}{2\pi}\exp\left(-\frac{2\gamma}{V_s}\right) \simeq \frac{\Delta f - \Delta f_s}{f_0}, \tag{23}$$

which describes the relation between V_s and Δf when $V_s \to 0$. In the high-velocity region, we have

$$\frac{2\gamma}{V_s^2} - \frac{8}{3}\frac{\gamma^2}{V_s^4} + \ldots = \frac{\Delta f_i - \Delta f}{f_0}. \tag{24}$$

A rectilinear step without kinks can move as a whole only in a range of deviations from equilibrium such that $\Delta f_s < \Delta f < \Delta f_1$. According to (23) when $\Delta f \to \Delta f_s$ the velocity of the step goes to zero while at the point $\Delta f = \Delta f_s$ itselfthere is a singularity similar to the singularity at $\Delta f = \Delta f_1$ for the normal motion of a planar boundary.[1] It can be seen from (24) that with $\Delta f \to \Delta f_1$, V_s grows without limit as $V_s \simeq [2\gamma f_0/(\Delta f_1 - \Delta f)]^{1/2}$. The schematic relation between V_s and $\Delta f/f_0$ is shown in Fig. 4.

It can be shown that as Δf increases, in addition to the velocity increase there is also an increase in the width l_s of the step. The calculation of l_s with $V_s \gg [8(1 + \gamma)]^{1/2}$ gives

$$l_s \simeq V_s / 2[\gamma(2+\gamma)]^{1/2}. \tag{25}$$

Thus when $\Delta f \to \Delta f_1$, i.e., upon approaching conditions where normal growth of the planar boundary becomes possible, the width of a step and the velocity of its motion grow without limit. At the point $\Delta f = \Delta f_l$ the step vanishes and the tangential motion of the step along the boundary changes into normal motion of the whole boundary (the velocity of boundary motion v_l is shown in Fig. 4). No such effect occurs in the molecular-kinetic description of the motion of a step[4-6] and the velocity of the step goes to infinity only for an infinitely large supersaturation. This is related to the fact that in refs. 4-6 a step at a sharp separation boundary was considered and no account was taken of the possibility of normal motion of the boundary as a whole.

THE KINETICS OF MOTION FOR A ROW OF STEPS

We consider a row of steps of unit height a, which are separated from each other by a distance d (Fig. 5). Such a structure is characteristic, for example, of crystal faces inclined relative to a singular direction. The kinetics of motion of a row is described by Eqs. (5), in which V_j equals V_t, the dimensionless tangential velocity. The dimensionless normal velocity (in the n direction) is given by $V_n = V_t/d$ (d in units of a). The analysis is done in the "continuum" approximation: In place of the discrete variable k we introduce the continuous variable x, and in place of $u_{n,k}(\tau)$ we use $u_n(x, \tau)$, and the second difference with respect to k in Eq. (5) is replaced by the second derivative with respect to x. Under stationary conditions $\partial u_n/\partial\tau = -V_t \partial u_n/\partial x$. Therefore in a coordinate system which moves together with the row, in place of (5) we have the equation

$$-V_t u_n'(x) - u_n''(x) + 2(1+\gamma)u_n(x) - u_{n+1}(x) - u_{n-1}(x) = \begin{cases} 0 \text{ with } 0 \leqslant u_n(x) < u^\circ, \\ 2\gamma \text{ with } u^\circ < u_n(x) \leqslant 1. \end{cases} \qquad (26)$$

and in addition we require that

$$u_{-\infty}(x) = 1, \quad u_\infty(x) = 0, \quad u_0(0) = u^\circ \qquad (27)$$

and we will seek a solution of Eq. (26) in the interval $0 \leq x \leq d$ which satisfies the following periodicity conditions at the ends of this interval:

$$u_n(0) = u_{n-1}(d), \qquad u_n'(0) = u_{n-1}'(d). \qquad (28)$$

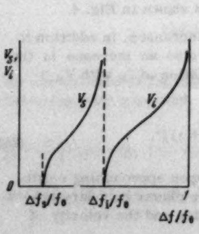

Fig. 4. Schematic relation between the velocity of step motion V_s and the deviation from equilibrium, $\Delta f/f_0$.

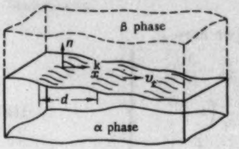

Fig. 5. Schematic illustration of a row of steps on a smeared phase-separation boundary.

If we introduce the generating function

$$Q(x; z) = \sum_{n=-\infty}^{\infty} u_n(x) z^n, \qquad (29)$$

then in addition to (26) and (28) we obtain an equation for Q and the auxiliary conditions

$$-V_t \frac{dQ}{dx} - \frac{d^2Q}{dx^2} + \frac{\psi}{z} Q = \frac{2\gamma}{z-1};$$

$$Q(0; z) = zQ(d; z); \quad \frac{dQ(0; z)}{dx} = z\frac{dQ(d; z)}{dx},$$

where $\psi = 2\gamma z - (1 - z)^2$. With $0 \leq x \leq d$ the solution takes the form

$$Q(x; z) = \frac{2\gamma z}{(z-1)\psi} - \frac{2\gamma z}{(s_1 - s_2)\psi} \times \left\{ \frac{s_2 \exp(s_1 x)}{1 - z\exp(s_1 d)} - \frac{s_1 \exp(s_2 x)}{1 - z\exp(s_2 d)} \right\},$$

$$s_{1,2} = -(V_t/2) \pm [(V_t^2/4) + (\psi/z)]^{1/2}. \qquad (30)$$

To determine V_t we need to find $u_0(0)$ as the coefficient of the zeroth power of z in the expansion of Q(0; z) in the series (29) in powers of z and set $u_0(0) = u^\circ \equiv (1/2) - \Delta f/2f_0$. With $d = \infty$, Q(0; z) goes over to the expression for a single step considered in the "continuum" approximation. Consequently when the density of steps goes to zero, V_t goes over to the velocity V_s for an isolated step. It is clear that $V_t \simeq V_s$ for such a density that the steps do not overlap, i.e., when the distance between steps d is much greater than the effective width l_s of an isolated step. Within the framework of the "continuum" approximation used, $l_s = \lim_{d \to \infty} [u_0(-d/2) - u_0(d/2)]/u_0'(0)$. Taking this into account, along with the solution (30) we can show that

$$l_s = \pi/2\sqrt{\gamma(2+\gamma)q}\,K(q), \qquad (31)$$

where

$$q = \frac{V_s^2}{8} + 1 + \gamma - \left[\left(\frac{V_s^2}{8} + 1 + \gamma\right)^2 - 1\right]^{1/2}.$$

With $V_s = 0$, Eq. (31) agrees with the expressions for the equilibrium step [see the footnote explaining Eq. (16)] while with $V_s \gg [8(1 + \gamma)]^{1/2}$ Eq. (31) agrees with Eq. (25). Since the width of the step increases with increasing velocity, with an increase of Δf the steps begin to interact even if the interaction is absent in equilibrium.

The expansion of Q(0; z) and the expression for $u_0(0)$ were obtained for large V_t retaining terms of order $1/V_t^2$ and d/V_t^3. Omitting the cumbersome calculations we write the relation obtained between the normal velocity V_n and Δf:

$$\frac{\Delta f}{f_0} \simeq \frac{\Delta f_0(V_n)}{f_0} - \frac{4\gamma}{d^2 V_n^2}[1 + \omega(V_n)]. \qquad (32)$$

Here $\Delta f_0(V_n)/f_0$ is determined by Eq. (29) from ref. 1 and is characterized by the deviation from equilibrium needed if the planar boundary without steps is to move with a given normal velocity V_n (in ref. 1 instead of V_n the quantity $V = V_n/2\sqrt{2\gamma}$ enters):

$$\frac{\Delta f_0(V_n)}{f_0} = \sqrt{\frac{\gamma}{2+\gamma}} + 2\sqrt{\frac{\gamma}{2+\gamma}}$$

$$\times \sum_{k=1}^{\infty} \exp\left[-\frac{2k(1+\gamma)}{V_n}\right]\left\{I_k\left(\frac{2k}{V_n}\right)\right.$$

$$\left. + \sum_{m=1}^{\infty} s^m \left[I_{k+m}\left(\frac{2k}{V_n}\right) + I_{k-m}\left(\frac{2k}{V_n}\right)\right]\right\}$$

[$I_n(x)$ is a modified Bessel function and s is determined by Eq. (13)]. The function $\omega(V_n)$ in Eq. (32) is given by

$$\omega(V_n) = \sum_{k=1}^{\infty} \exp\left[-\frac{2k(1+\gamma)}{V_n}\right]\left\{\left[1+k-\frac{2k(1+\gamma)}{V_n}\right] I_k\left(\frac{2k}{V_n}\right)\right.$$

$$\left. + \frac{2k}{V_n} I_{k+1}\left(\frac{2k}{V_n}\right)\right\}.$$

The function $\omega(x)$ has the following properties when $x \geq 0$: $\omega = 0$ when $x = 0$, x_0, and ∞; with $0 < x < x_0$, $\omega(x) < 0$ and it has a minimum at $x = x_m$; when $x_0 < x < \infty$, $\omega(x) > 0$ and passes through a maximum when $x = x_M$. Estimates in two limiting cases give: $x_m \sim 1.6\gamma$ when $\gamma \ll 1$ and $\omega_m \sim -0.08\sqrt{\gamma}$; with $\gamma \gg 1$ $x_m \sim 0.8\gamma$ and $\omega_m \sim -0.08/\gamma$, $x_M \sim 4.8\gamma$, and $\omega_m \sim 0.23/\gamma$. Consequently $|\omega_m|$ assumes its greatest values, of the order of 0.1, when $\gamma \sim 1$. Therefore the second term in (32) does not change sign and always increases the normal velocity of a row of steps in comparison to a planar boundary with the same Δf. As follows from (32), the contribution of a step to V_n decreases with increasing V_n and, as is natural, with decreasing step density. However, there is a most essential qualitative difference between the dependence of V_n on Δf for a row and V_l on Δf for a planar boundary. The latter is described by the function $\Delta f = \Delta f_0(V_n)$, which at the point $\Delta f_l/f_0 = [\gamma/(2+\gamma)]^{1/2}$ has a logarithmic singularity $V_l \approx -2\gamma/\ln[(\Delta f - \Delta f_l)/f_0]$. With $\Delta f \leq \Delta f_l$, $V_l = 0$. For a stepped surface this singularity is absent. The qualitative relation between V_n and Δf for various values of d is shown in Fig. 6. A planar boundary without steps corresponds to $d = \infty$.

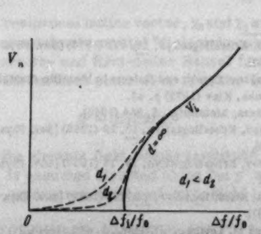

Fig. 6. Schematic normal velocity of motion V_n of a row of steps as a function of the deviation from equilibrium $\Delta f/f_0$ with various distances d between the steps. V_l is the velocity of normal motion of a planar boundary without steps ($d = \infty$).

AN ESTIMATE OF THE NATURE OF THE TRANSITION FROM TANGENTIAL GROWTH TO NORMAL GROWTH

On the basis of the results obtained we can qualitatively analyze the nature of the motion of a stepped surface and the transition from tangential motion to normal motion. One can speak of the tangential mechanism of motion for the surface when the steps on this surface are distinct, i.e., when $d \gg l_s$. In this case the steps do not overlap and the velocity V_t of a row is close to the velocity V_s of an isolated step. In the opposite case ($d \ll l_s$) the steps are indistinct and one must speak of the normal motion mechanism.

If the density of steps is low ($d \gg l_s$) with $\Delta f = 0$, then for small deviations from equilibrium we will observe tangential growth. With increasing Δf and an approach to the critical value of Δf_l for normal motion of a planar boundary, the width of a step increases [see (25) and (31)], becoming comparable to d and then even larger. Tangential growth goes over to normal growth in the neighborhood of $\Delta f = \Delta f_l$. This transition is the sharper the smaller the density of steps. With a further increase in Δf, as follows from (32), the normal velocity V_n of a row approaches the growth velocity V_l of a planar boundary without steps. If d is commensurate with or less than l_s with $\Delta f = 0$ then it is impossible for any Δf to distinguish a region of tangential growth.

In reality during the growth of a singular face the density of steps on it depends on the deviation from equilibrium and the growth mechanism which actually occurs. If we have in mind two-dimensional nucleation or spiral growth, then when $\Delta f \to 0$ the step density goes to zero and for low deviations from equilibrium tangential growth will always be observed. The transition to normal growth will be sharper the lower the density of steps near the critical Δf_l. The criterion for the sharpness of such a transition is the smallness of the correction in Eq. (32) involving the presence of steps in comparison to the first term $\Delta f_0(V_n)/f_0$ near $\Delta f = \Delta f_l$. For a planar boundary the relation between V_l and Δf can be described schematically as a jump by $\Delta V \sim \gamma/2$ at $\Delta f = \Delta f_l$ and a subsequent smooth variation.[1] Therefore as the criterion for the sharpness of the transition we use the smallness of the second term in (32) with[2)] $V_n = \Delta V$ in comparison to the first term, approximately setting $\Delta f_l/f_0 \equiv [\gamma/(2+\gamma)]^{1/2}$, i.e.,

$$A = 4\gamma/d^2(\Delta V)^2(\Delta f_l/f_0) \ll 1 \quad \text{or} \quad A \simeq \frac{16}{\gamma d^2}\left(\frac{2+\gamma}{\gamma}\right)^{1/2} \ll 1. \tag{33}$$

We will estimate d and A for the spiral growth mechanism and growth by two-dimensional nucleation. For such estimates we will, however, use the usual relations, obtained without considering the smeared nature of the boundary between phases, and rigorously speaking they are only applicable for sufficiently small Δf, where the radius of the critical two-dimensional nucleus r_c is much greater than the step width[3] l_s. Here $r_c \simeq \varepsilon/a^2\Delta f$ (r_c is in units of a). Here the approximation is such that for the specific free energy ε of a rectilinear step we use the expression obtained without considering kinks. For sharp boundaries ($\gamma \gg 1$) according to (18), $\varepsilon/a^2 f_0 \simeq 1/2\gamma$.

Therefore with $\Delta f = \Delta f_l$, $r_c \simeq 1/2\gamma \ll 1$, i.e., the critical size is much less than a. This means that already for Δf substantially less than Δf_l, namely, with $\Delta f/\Delta f_l \sim 1/2\gamma$ when r_c becomes of the order of unity, the planar boundary begins to move normally due to the nearly universal transition of the particles into the new phase at the interphase boundary. Therefore it makes sense to consider the nature of the transition from tangential to normal motion when $\Delta f \sim \Delta f_l$ for smeared and intermediate boundaries, i.e., with γ not exceeding a value of the order of unity.

For spiral growth[7] $d \simeq 19r_c$. Therefore with $\Delta f \sim \Delta f_l$ we have $d \simeq 19(\varepsilon/a^2 f_0)[(2+\gamma)/\gamma]^{1/2}$ and

$$A \simeq [22.6(\varepsilon/a^2 f_0)^2 \sqrt{\gamma(2+\gamma)}]^{-1}. \tag{34}$$

Calculations using this equation taking account of Eq. (15) for ε have shown that the minimum value of A (with $\gamma \simeq 2$) is ~1.5. For smeared boundaries $\varepsilon/a^2 f_0 \simeq {}^1/_2\pi$ and $A \simeq 1.23/\sqrt{\gamma} \gg 1$. Comparing this with the condition for sharpness, $A \ll 1$, we see that in the model used the transition from tangential spiral growth to normal growth need not be sharp. Taking kinks into consideration on the steps reduces ε and d and consequently makes the transition yet smoother.

For growth by the mechanism of two-dimensional nucleation, to estimate the step density 1/d we have used an expression for the normal growth velocity V_n of an infinite face obtained in ref. 8:

$$\frac{1}{d} \sim \frac{V_n}{V_s} = \left(\frac{L\Delta T}{RT_0^2}\right)^{-1/3} \exp\left(-\frac{W}{3kT}\right). \tag{35}$$

Here V_s is the velocity of motion of an isolated step, $W \simeq \pi\varepsilon^2/a\Delta f$ is the work required to form a two-dimensional critical nucleus, T_0 is the phase equilibrium temperature, ΔT is the supercooling, and L is the latent heat of the transition (per mole). The values of ΔT and Δf are related by $\Delta f = L\Delta T/v_m T_0$ where v_m is the molar volume. Taking (33) and (35) into account with $\Delta f = \Delta f_l$ we have

$$A \sim \frac{16}{\gamma}\left(\frac{2+\gamma}{\gamma}\right)^{2/3}\left(\frac{v_m f_0}{RT_0}\right)^{-1/3}$$
$$\times \exp\left[-\frac{2\pi p}{3}\left(\frac{v_m f_0}{RT}\right)\left(\frac{\varepsilon}{a^2 f_0}\right)^2\left(\frac{2+\gamma}{\gamma}\right)^{1/2}\right]. \tag{36}$$

Here p is the number of atoms in an elementary cube of volume a^3. The value of a is determined not only by the parameter γ, but also by the other parameter $v_m f_0/RT_0$. The value of f_0 characterizes the maximum change of free energy in going from one phase into the other due to a gradual change in the parameter u. According to (2) with $\Delta f = 0$ we have $f_{max} - f_{min} = f(^1/_2) - f(0) = f_0/4$.

With $\gamma \lessapprox 1$ we can estimate the dependence of A on the parameters, neglecting γ in comparison with 2 and the dependence of $\varepsilon/a^2 f_0$ on γ (with an increase of γ from 0 to 1, $\varepsilon/a^2 f_0$ decreases from ${}^1/_2\pi \simeq 0.16$ to 0.12). Here, in view of the expression $\gamma = a^2 f_0/2K$ we find that the preexponential factor and the exponent in (36) are proportional respectively to $K^{5/3}/f_0^2$ and $(f_0 K)^{1/2}$. For sufficiently large f_0 and K (but with $a^2 f_0/2K \lessapprox 1$) the parameter A can be small due to the exponential factor. In such systems the velocity of two-dimensional nucleation and the corresponding density of steps is small with $\Delta f \sim \Delta f_l$ and the transition from tangential growth to normal growth will be sharp.

CONCLUDING REMARKS

The analysis which has been given does not consider the presence of kinks on the steps. Consideration of kinks in analyzing the kinetics of a step would lead to their possible motion even in the region $0 < \Delta f < \Delta f_s$, in which they cannot move as a whole. This in turn would lead to a vanishing of the singularity in (23) just as consideration of step motion causes the singularity at the point $\Delta f = \Delta f_l$ to vanish. The formation and motion of the kinks is of a fluctuational nature, while the process considered here is directional and does not admit the possibility of fluctuational motion. It is clear that with $\Delta f < \Delta f_s$ the fluctuational processes play the decisive role while in going away from the point Δf_s in the direction of large Δf their effect decreases and the velocity of the step approaches a value which is determined taking account of only the directional motion. However, we do not have a theory which would take account of both of the aspects shown and which would give a single description which is valid not only for small $(\Delta f < \Delta f_s)$ but also for large $(\Delta f > \Delta f_s)$ deviations from equilibrium.

The "continuum" approximation, which is used in describing a row of steps, gives a linear relation between V_s (and V_t) for small Δf, i.e., a qualitatively more correct result than the "discrete" description. However, the proportionality coefficient between the velocity and Δf here has another meaning than during subsequent treatment of kinks on the steps.

---

1) A similar determination of the width of a planar boundary l_l in the notation of the present work gives $l_l = [1/(u_{0,-\infty} - u_{0,\infty})] - 1 = 2s/(1-s)$. This differs from that used in ref. 1, $l_l = 2\sqrt{s}/(1-s) = (2/\gamma)^{1/2}$, introduced on the basis of a "continuum" description. A similar "continuum" description of l_s obtained by replacing the discrete variable k by the continuous variable x and $u_{n,k}$ by $u_n(x)$ leads to an expression $l_s = [u_0(-\infty) - u_0(\infty)] \cdot [du_0(x)/dx]^{-1} = \pi(1-s)/2\gamma(1+s)\sqrt{s}K(s)$. Here the derivative $du_0(x)/dx$ is calculated at the point x for which $u_0(x) = u^*$.

Both definitions of l_l and l_s agree for $\gamma \ll 1$, where the width of the boundary and the step are much less than unity.

2) Since $|\omega(\gamma/2)| \ll 1$ in (32) we can neglect ω in comparison to unity. Actually with $\gamma \ll 1$, $\omega(\gamma/2) \sim \sqrt{2\gamma/\pi}\exp(-4)$, while with $\gamma \gg 1$, $\omega(\gamma/2) \sim -(4/\gamma)\exp(-4)$.

---

[1] D. E. Temkin, Kristallografiya, 15, 877 (1970) [Sov. Phys.-Crystallogr., 15, 767 (1971)].

[2] D. E. Temkin, in: Growth and Defects in Metallic Crystals [in Russian], Naukova Dumka, Kiev (1972) p. 45.

[3] J. W. Cahn, Acta. Metallurg., 8, 554 (1960).

[4] V. V. Voronkov, Kristallografiya, 13, 19 (1968) [Sov. Phys.-Crystallogr., 13, 13 (1968)].

[5] V. V. Voronkov, Kristallografiya, 15, 13 (1970) [Sov. Phys.-Crystallogr., 15, 8 (1970)].

[6] D. E. Temkin, Kristallografiya, 14, 227 (1969) [Sov. Phys.-Crystallogr., 14, 179 (1969)].

[7] N. Cabrera and M. Levine, Phil. Mag., 1, 450 (1956).

[8] H. B. Hillig, Acta Metallurg., 14, 1868 (1966).

X-ray diffraction by a cylindrical cavity in a crystal

A. F. Tsander

All-Union Electrotechnical Institute

(Submitted October 28, 1971; resubmitted April 25, 1972)
Kristallografiya, 18, 245-250 (March-April 1973)

The dynamic theory of x-ray propagation in a distorted crystal is used to treat x-ray diffraction from a sufficiently large cylindrical cavity inside a crystal. When the cavity is sufficiently far from the lower crystal planes, where the x-ray image is formed, approximate analytic expressions are obtained for the amplitude in the "center" of the x-ray image, where the theory used gives the largest amplitude deviations from those in an ideal crystal. A numerical integration was performed for the whole x-ray image. The results obtained are also applied to spherical cavities.

According to the dynamic theory of x-ray propagation in a distorted crystal,[1-3] an approximate solution of the Maxwell equations for a plane wave with an incidence angle close to the Bragg angle can be represented as a superposition of two waves with variable amplitudes. In this paper we apply this theory to x-ray diffraction by a sufficiently large cylindrical cavity inside a crystal ($kr_0 \gg 1$, where k is the wave number and r_0 is the smallest cavity size).

Consider the following problem. An x ray of wavelength $\lambda = 2\pi/k$ is incident, with an angle ϑ close to the Bragg angle, on the upper x'y' plane of a crystal (the x' axis points to the right, the y' axis to the reader, and the z' axis downward). Inside the crystal we have a cylindrical cavity with a base radius r_0 and with a generatrix parallel to the y' axis, and the distance from the upper plane to the cylinder axis is b. It is required to find the diffraction pattern at a distance ζ' from the cylinder axis at a point with a coordinate ξ' along the x' axis. We introduce the following notation, to be used in the sequel:

$$z=\frac{\chi_1 k}{2\cos\theta}z', \quad x=\frac{\chi_1 k}{2\sin\theta}x', \quad \zeta=\frac{\chi_1 k}{2\cos\theta}\zeta',$$

$$\xi=\frac{\chi_1 k}{2\sin\theta}\xi', \quad \xi_\zeta=\frac{\xi'}{\zeta'}, \quad \eta_\pm=\xi-x\pm(\zeta-z),$$

$$p_1=\frac{\chi_1 k}{2\cos\theta}r_0, \quad p_0=\frac{\chi_0 k}{2\cos\theta}r_0, \quad p_b=\frac{\chi_1 k}{2\cos\theta}b,$$

$$\alpha=(\mathbf{k}_1^2-\mathbf{k}^2)/\mathbf{k}^2, \ \mathbf{k}_1=\mathbf{k}+\mathbf{K}_1,$$

$$J_0=J_0\left(\sqrt{(\zeta-z)^2-(\xi-x)^2}\right), \quad i_1=\frac{J_1\left(\sqrt{(\zeta-z)^2-(\xi-x)^2}\right)}{\sqrt{(\zeta-z)^2-(\xi-x)^2}}\eta_-,$$

$$j_1=\frac{J_1\left(\sqrt{(\zeta-z)^2-(\xi-x)^2}\right)}{\sqrt{(\zeta-z)^2-(\xi-x)^2}}\eta_+, \tag{1}$$

where $\mathbf{K}_1$ is a reciprocal lattice vector, χ_0 and χ_1 are determined by the approximate crystal "dielectric constant", and J_0 and J_1 are zeroth- and first-order Bessel functions. We assume that the incident plane wave is of the form

$$E^i=\exp(i\mathbf{kr}'), \tag{2}$$

where E^i is the electric field, whose amplitude of magnitude unity is assumed directed along the y' axis. An approximate expression for the electric field is

$$E=E_0\exp\left[i\left(\mathbf{kr}'+(\chi_0/\chi_1)z\right)\right]+E_1\exp\left[i\left(\mathbf{k}_1\mathbf{r}'+(\chi_0/\chi_1)z\right)\right], \tag{3}$$

where E_0 and E_1 are variable amplitudes, coupled by the equations

$$i\left(\frac{\partial E_1}{\partial z}-\frac{\partial E_1}{\partial x}\right)=-E_0+\frac{\alpha}{\chi_1}E_1, \quad i\left(\frac{\partial E_0}{\partial z}+\frac{\partial E_0}{\partial x}\right)=-E_1. \tag{4}$$

In particular, for an ideal crystal with $\alpha = 0$ we have

$$E_1^{\mathrm{id}}=i\sin z=i\sin(\zeta+p_b), \quad E_0^{\mathrm{id}}=\cos z=\cos(\zeta+p_b). \tag{5}$$

The integral relations corresponding to the differential equations (4) are

$$\left.\begin{aligned}E_1^{\Delta}(\xi,\zeta)&=\int\left\{E_1\left(\frac{\partial G}{\partial x}+\frac{\partial G}{\partial z}\right)(dz+dx)+GiE_0(dz-dx)\right\},\\ E_0^{\Delta}(\xi,\zeta)&=\int\left\{E_0\left(\frac{\partial G}{\partial z}-\frac{\partial G}{\partial x}-i\frac{\alpha}{\chi_1}G\right)\right.\\ &\qquad\left.\times(dx-dz)-GiE_1(dz+dx)\right\},\end{aligned}\right\} \tag{6}$$

$$E_1^{\Delta}=E_1-E_1^{\mathrm{id}}, \quad E_0^{\Delta}=E_0-E_0^{\mathrm{id}},$$

where G is the Green's function, having in the present case the form

$$G=\begin{cases}G_0=\frac{1}{2}J_0\exp\left[\frac{i\alpha}{2\chi_1}\eta_-\right],\\ \qquad \text{if} \quad (\zeta-z)/\chi_1>|(\xi-x)/\chi_1|, \ (\zeta-z)/\chi_1>0\\ 0, \quad \text{if} \quad (\zeta-z)/\chi_1<|(\xi-x)/\chi_1|,\end{cases} \tag{7}$$

while $2G_0$ is the Riemann function.[2]

The integration in (6) is performed over a circle, the intersection of the cylinder surface with one of its planes, perpendicular to the y' axis. The direction of integration is clockwise. Introducing polar coordinates with an origin at the center of the circle, and taking into account (1), we obtain$^{1)}$

$$x=p_1\operatorname{ctg}\theta\cos\varphi, \quad z=p_1\sin\varphi+p_b \ (\text{or } z=p_1\sin\varphi). \tag{8}$$

The first of Eqs. (6) becomes

$$E_1^{\Delta}(\xi,\zeta)=\left\{\frac{p_1}{2\sin\theta}\left[i\int_{\varphi'}^{\varphi''}\sin(\varphi+\theta)J_0\exp\left[i\frac{\alpha}{2\chi_1}\eta_-\right]E_0\,d\varphi\right.\right.$$

$$\left.\left.+\int_{\varphi'}^{\varphi''}\sin(\varphi-\theta)i_1\exp\left[i\frac{\alpha}{2\chi_1}\eta_-\right]E_1\,d\varphi\right]+I\right\},$$

$$I=\Theta(-\xi)\left\{E_1(\varphi')\exp\left[-i\frac{\alpha}{\chi_1}(\zeta-p_1\sin\varphi')\right]-\right.$$

$$
-E_1(\varphi'')\exp\left[-i\frac{\alpha}{\chi_1}(\zeta-p_1\sin\varphi'')\right]\Bigg\}, \quad \Theta(x)=\begin{cases}1, & x>0,\\ 0, & x<0.\end{cases} \tag{9}
$$

The integration limits φ', φ'' are determined as follows for the regions AC, CD DB, respectively, in which the x-ray image is considered (Fig. 1):

$$
\begin{gathered}
\varphi'=\theta+\arccos w_-,\ 0(\pm\theta),\ 2\pi-\theta-\arccos w_+,\\
\varphi''=-\varphi'+2\theta+2\pi,\ 2\pi(2\pi\pm\theta),\ -\varphi'-2\theta+4\pi,\\
w_-=\frac{\zeta}{p_1}(\xi_\zeta\cos\theta+\sin\theta),\qquad w_+=\frac{\zeta}{p_1}(\xi_\zeta\cos\theta-\sin\theta).
\end{gathered} \tag{10}
$$

In what follows we consider the simplest case, when the angle of incidence of the plane wave (2) is the Bragg angle, and, consequently, $\alpha = 0$. In the region CD Eq. (9) is now of the form

$$
\begin{aligned}
E_1^\Delta(\xi,\zeta)=\frac{p_1}{2\sin\theta}\Bigg\{ & i\int_{-\pi-\theta}^{-\theta}\sin(\varphi+\theta)J_0(E_0)_{234}\,d\varphi\\
& +i\int_{-\theta}^{\pi-\theta}\sin(\varphi+\theta)J_0(E_0)_{412}\,d\varphi+\int_{-\pi+\theta}^{\theta}\sin(\varphi-\theta)i_1(E_1)_{341}\,d\varphi\\
& +\int_{\theta}^{\pi+\theta}\sin(\varphi-\theta)i_1(E_1)_{123}\,d\varphi\Bigg\}.
\end{aligned} \tag{11}
$$

The amplitudes $E_0(\varphi)$ and $E_1(\varphi)$, appearing in the right-hand side of Eqs. (9) and (11), are most complex to determine in the regions 23 and 41, respectively (Fig. 2). They are determined by the Volterra integral equations of the second kind:

$$
\begin{gathered}
E_0^\Delta(\varphi)=-\frac{p_1}{2\sin\theta}\Bigg\{i\int_{\varphi}^{\theta}\sin(\varphi'-\theta)J_0E_1^\Delta\,d\varphi'\\
+\int_{\varphi}^{\theta}\sin(\varphi'+\theta)j_1E_0^\Delta\,d\varphi'\Bigg\},\\
\varphi\geqslant-\theta,
\end{gathered} \tag{12}
$$

$$
\begin{gathered}
E_1^\Delta(\varphi)=\frac{p_1}{2\sin\theta}\Bigg\{i\int_{-\theta}^{\varphi}\sin(\varphi'+\theta)J_0E_0^\Delta\,d\varphi\\
+\int_{-\theta}^{\varphi}\sin(\varphi'-\theta)i_1E_1^\Delta\,d\varphi'\Bigg\}\\
\varphi\leqslant\theta.
\end{gathered} \tag{13}
$$

In the integral equation for $E_0^\Delta(\varphi)$ the integration is over the region 23 from the point Q to the point 3 ($\varphi = +\theta$), with the lowest possible limit of integration corresponding to the point 2 ($\varphi = -\theta$), and in the integral equation for $E_1^\Delta(\varphi)$ it is over the region 41 from the point 4 ($\varphi = -\theta$) to the point Q, with the uppermost possible limit of integration corresponding to the point 1 ($\varphi = +\theta$). The functions E_1^Δ and E_0^Δ on the right-hand sides of Eqs. (12) and (13), respectively, are determined by the "transport" method. For example, for the points P and Q (Fig. 2) we have, considering (3),

$$
\left[E_0\exp\left(i\frac{\chi_0}{\chi_1}z\right)\right]_P=\left[E_0\exp\left(i\frac{\chi_0}{\chi_1}z\right)\right]_Q.
$$

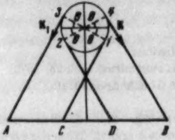

Fig. 1

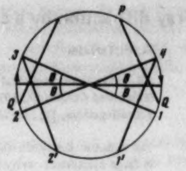

Fig. 2

A series solution was used for the integral equations (12) and (13), and its terms were estimated for the following parameter values:[2)]

$$
\begin{gathered}
p_1=-1,\quad p_0=-1.67,\quad \theta=0.2,\quad \zeta=-100,\\
p_b=-\zeta+\frac{\pi}{2}+2\pi n,\quad \text{n is an integer.}
\end{gathered} \tag{14}
$$

The estimate showed that it was sufficient to retain the first terms of the series only (the second term is less than $0.08 f_0$, where f_0 is the first term), i.e., the second terms on the right-hand sides of Eqs. (12) and (13) can be neglected. Account was also taken of the fact that the argument of the functions J_0, J_1, $\sin\varphi$, $\cos\varphi$ is small when φ varies from $-\theta$ to $+\theta$. Approximate analytic expressions were obtained, as a result, for $E_1^\Delta(\varphi)$, $E_0^\Delta(\varphi)$. As expected, the values of $E_1^\Delta(\varphi)$, $E_0^\Delta(\varphi)$ were noticeably different from zero close to the points 1 and 2, respectively. In these regions, however, the values of $\sin(\varphi-\theta)$, $\sin(\varphi+\theta)$, appearing in Eq. (9) for $E_1(\xi,\zeta)$, are small. Thus, the numerical estimates showed that the quantities E_1^Δ, E_0^Δ could be generally neglected for $|p_1| \leqslant 1$, $|p_0| \leqslant 1$, $\theta = 0.2$ due to the smallness of θ. The same refers also to the supplementary amplitudes E_1^δ, E_0^δ in the regions 11', 22' (Fig. 2), arising due to deviations of E_1^Δ, E_0^Δ from "ideal" amplitudes in the regions 41 and 23. Therefore the amplitudes $(E_1)_{341}$ and $(E_0)_{234}$ are assigned the amplitudes in an ideal crystal. $(E_1)_{123}$ and $(E_0)_{412}$ are determined by the "transport" method.[3,4] As a result we obtain

$$
\left.
\begin{gathered}
(E_1)_{341}=i\sin(p_1\sin\varphi+p_b),\\
(E_1)_{123}=i\sin[-p_1\sin(\varphi-2\theta)+p_b]\\
\times\exp\{-ip_0[\sin(\varphi-2\theta)+\sin\varphi]\},\\
(E_0)_{234}=\cos(p_1\sin\varphi+p_b),\\
(E_0)_{412}=\cos[-p_1\sin(\varphi+2\theta)+p_b]\\
\times\exp\{-ip_0[\sin(\varphi+2\theta)+\sin\varphi]\}.
\end{gathered}
\right| \tag{15}
$$

The dependence of $I - I^{id}$ on ξ_ζ, obtained by numerical integration, is shown in Fig. 3 for $|\sin(\zeta + p_b)| = 1$. It is seen that the largest amplitude oscillations around the background value, equal to unity, take place in the central region, and they are damped at the edges. This is easily explained by the fact that for sufficiently large ξ_ζ J_0 and J_1 are strongly oscillating functions of φ, and integrals of strongly oscillating functions are small. In particular, at the points C and D (Fig. 1) the arguments of J_0 and J_1 vanish for some values of φ, and for some other values they are

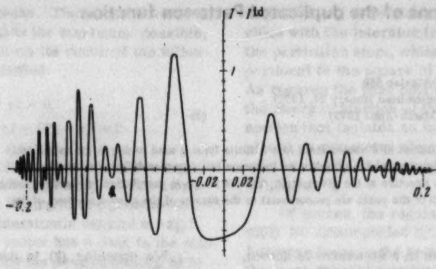

Fig. 3. Dependence of $I - I^{id}$ on ξ_ζ at $\sin(\zeta + p_b) = 1$ ($I^{id} = 1$).

comparatively large due to the large values of $|\zeta|$. It should be noticed that the values of $I - I^{id}$ are larger on the left than on the right. The curve describing the dependence of $I - I^{id}$ on ξ_ζ for $I^{id} = 0$ differs from the preceding curve by the smallness of $I - I^{id}$ and by its being fairly symmetric (Fig. 4). The value of the maximum, although positive, is never large.

The equations for $E_1^{\Delta}(\xi, \zeta)$, derived without considering absorption for small ξ_ζ, are valid also for x-ray absorption in the crystal, which corresponds to complex values of the coefficients χ_1, χ_0. An approximate analytic calculation of the relative diffracted wave intensity at $\xi_\zeta = 0$ was performed for complex values of χ_1, χ_0:

$$\frac{\operatorname{Im}\chi_1}{|\operatorname{Re}\chi_1|} = \frac{\operatorname{Im}\chi_0}{|\operatorname{Re}\chi_0|} = \frac{1}{50} > 0 \tag{16}$$

with the previous real parts p_1, p_0, ζ (14). In first approximation the imaginary parts of p_1, p_0 can be neglected, and $\cos p_b$, $\sin p_b$, J_0, J_1 can be represented as linear combinations of exponents, retaining only the largest exponents containing exponentially increasing factors. The following result is obtained:

$$(|E_1 + E_1^{id}|^2 - |E_1^{id}|^2) / |E_1^{id}|^2 \approx -0.59, \quad \xi_\zeta = 0,$$

i.e., the same order of magnitude and sign that were obtained without including absorption at $\xi_\zeta = 0$, $E_1^{id} = 1$ (in the latter case $I - I^{id} \approx -0.66$). In the simplest case, when $|p_1| \ll 1$, $|p_0| \ll 1$ (consequently, the cavity radius is significantly smaller than the extinction length), we have $E_1^{\Delta}(\xi, \zeta) = L + iN$,

$$L = \frac{p_1\pi}{2\operatorname{tg}\theta} p_0 (J_0^\circ \cos p_b + i_1^\circ \sin p_b),$$

$$N = \frac{p_1\pi}{2\operatorname{tg}\theta} p_1 (-i_1^\circ \cos p_b + J_0^\circ \sin p_b),$$

$$J_0^\circ = J_0(\sqrt{\zeta^2 - \xi^2}), \quad i_1^\circ = \frac{J_1(\sqrt{\zeta^2 - \xi^2})}{\sqrt{\zeta^2 - \xi^2}} (\zeta - \xi). \tag{17}$$

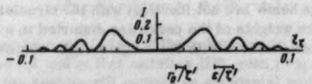

Fig. 4. Dependence of the intensity I on ξ_ζ at $\sin(\zeta + p_b) = 0$ ($I^{id} = 0$). ε is the extinction length; the intensity is not shown at the limits of the interval $-0.1 \leq \xi_\zeta \leq 0.1$ due to its smallness.

Eqs. (17) are interesting for comparing the dependence of $I - I^{id}$ on ξ_ζ for $|p_0| \sim 1$, $|p_1| \sim 1$ and for $|p_0| \ll 1$, $|p_1| \ll 1$. In particular, it is interesting to notice that a calculation of one term only, $2N\sin(\zeta + p_b)$, by Eq. (17) gives for $\sin p_b = 0$, $\cos p_b = 1$, $p_1 = -0.1$, $p_0 = -0.167$, $\zeta = -100$, $\theta = 0.2$ a curve similar to Fig. 3 but with an opposite sign, and for $\sin p_b = 1$, $\cos p_b = 0$ a symmetric curve is obtained with comparatively small positive ordinates in the center and neighboring negative minima.

Till now we have considered a cylindrical cavity. The results obtained above can be used also for diffraction by spherical cavities, but with restrictions to sphere edges located around the cavity axis parallel to the y′ axis, where the condition $kr_0 \gg 1$ remains satisfied.

The author is grateful to V. L. Indenbom and F. N. Chukhovskii for suggesting the problem and for discussing the results.

[1)] Wherever z appears in the combination $\zeta - z$.

[2)] p_b was chosen so as to satisfy the equality $\sin(\zeta + p_b) = 1$, giving, according to (5), $|E_1^{id}| = 1$.

---

[1] S. Takagi, Acta Crystallogr., 15, 1311 (1962).

[2] L. Sh. Slobodetskii, F. N. Chukhovskii, and V. L. Indenbom, ZhETF Pis. Red., 8, 90 (1968) [JETP Lett., 8, 55 (1968)].

[3] A. M. Afanas'ev (Afanse'ev) and V. G. Kohn, Acta Crystallogr., A27, 421 (1971).

[4] V. L. Indenbom and F. N. Chukhovskii, Usp. Fiz. Nauk, 107, 229 (1972) [Sov. Phys.−Usp., 15, 298 (1972)].

[5] G. Myunts, Integral Equations, Vol. 1 [in Russian], Gos. Tekhn. Teor. Izd., Leningrad−Moscow (1934).

Structure-localizing sections of the duplicated Patterson function

V. N. Biyushkin
Institute of Applied Physics,
Academy of Sciences of the Moldavian SSR
(Submitted October 6, 1971; resubmitted January 24, 1972)
Kristallografiya, 18, 251-256 (March-April 1973)

A relation containing the coordinates of a known atom in a definite form is used to derive the relationship between the vectors that are parameters of the duplicated Patterson function that defines the section. This section produces an image of a structure at the given atom, and the image is geometrically identical to the real structure, while the heights of the peaks are proportional to the squares of the atomic numbers of the corresponding atoms.

If the position of some one atom in a structure is known, one can construct a section of the duplicated Patterson function the peaks of which represent a geometrical image of the structure as seen at that atom. The sections we envisage below are not identical with the structure because the weights of the peaks are distorted in a definite way by comparison with the weights of the corresponding atoms.

To identify the sections that define the structure relative to the given atom (structure-localizing sections), we have to establish the following relationship between the variable vectors (parameters of the duplicated Patterson function):[1]

$$\mathbf{u}_2 = \vartheta(\mathbf{r}_0 + \mathbf{u}) - \mathbf{r}_0. \tag{1}$$

Here $\vartheta \equiv \{A|t\}$ is the operator for the symmetry transformation of the space group,[2] and A is the operator for the symmetry transformation of the point group, which in the standard crystallographic coordinate system is represented by a matrix A; t is parallel transfer of the $\{A|t\}$ transformation, while $\mathbf{r}_0$ is the position of the given atom, with $\mathbf{u}_2$ and $\mathbf{u}_1 = \mathbf{u}$ as variable vectors or parameters. The result from (1) is the section

$$DP_\vartheta(\mathbf{r}_0, \mathbf{u}) = \int_V \rho(\mathbf{r})\rho(\mathbf{r}+\mathbf{u})\rho(\mathbf{r}+[\vartheta(\mathbf{r}_0+\mathbf{u})-\mathbf{r}_0])\,dV, \tag{2}$$

where $\rho(\mathbf{r})$ is the electron-density distribution and V is the volume of the unit cell; we substitute for $\rho(\mathbf{r})$ into (2) in terms of Fourier series and perform the corresponding transformations to get

$$DP_\vartheta(\mathbf{r}_0, \mathbf{u}) = \frac{1}{V^2}\sum_{\mathbf{H}_1}\sum_{\mathbf{H}_2} F(-\mathbf{H}_2 - \mathbf{H}_1)F(\mathbf{H}_2)F(\mathbf{H}_1) \times \exp(-2\pi i(\mathbf{H}_2\mathbf{u} + \mathbf{H}_1[\vartheta(\mathbf{r}_0+\mathbf{u}) - \mathbf{r}_0])). \tag{3}$$

Vector $\vartheta(\mathbf{r}_0 + \mathbf{u})$ may be put as $\vartheta\,\mathbf{r}_0 + A\mathbf{u}$; further we put $(\mathbf{H}_2 + \mathbf{H}_1A)$ as H to transform (3) to

$$DP_\vartheta(\mathbf{r}_0, \mathbf{u}) = \frac{1}{V^2}\sum_{\mathbf{H}}\sum_{\mathbf{H}} F(-\mathbf{H} + \mathbf{H}_1A - \mathbf{H}_1)F(\mathbf{H} - \mathbf{H}_1A)F(\mathbf{H}_1) \times \exp(-2\pi i(\mathbf{H}_1(\vartheta\mathbf{r}_0 - \mathbf{r}_0)))\exp(-2\pi i\mathbf{H}\mathbf{u}). \tag{4}$$

To calculate this function we need to know the phases of the structure amplitudes; if the crystal has a center of symmetry, the problem is simplified, because the function may be calculated approximately via the moduli of the structure amplitudes if one uses the Sayre–Zachariasen relation[3-5] $S(\mathbf{H}) \approx S(\mathbf{H} - \mathbf{H}')S(\mathbf{H}')$.

We consider (2) to determine what structure information is contained in this section; this shows that $DP_\vartheta(\mathbf{r}_0, \mathbf{u})$ has a peak at the point u, if the summing triangle consisting of the point and defined by the arguments of the cofactors in the integrand has at least one position where each of its vertices rests on an atom. This position occurs whenever the variable of integration r coincides with the radius vector $\mathbf{r}_0$ of the specified j_0 atom, while parameter u coincides with one of the interatomic vectors drawn from atom j_0 to each atom in the structure, i.e., when $\mathbf{u} = \mathbf{r}_j - \mathbf{r}_0$ (Fig. 1). Then the third vertex of a summing triangle lies at the point $\vartheta\,\mathbf{r}_j$, where there is an atom related to atom j by the transformation ϑ. This configuration of the summing triangle corresponds to a peak in the function $DP_\vartheta(\mathbf{r}_0, \mathbf{u})$ at the point $(\mathbf{r}_j - \mathbf{r}_0)$; peaks of this type are regular ones for $DP_\vartheta(\mathbf{r}_0, \mathbf{u})$ and are generated by atom j_0 at point $\mathbf{r}_0$ as well as by pairs of equivalent atoms related one to another by the transformation ϑ, which defines the section of $DP_\vartheta(\mathbf{r}_0, \mathbf{u})$. To each atom, or rather triplet of atoms, there corresponds a peak in $DP_\vartheta(\mathbf{r}_0, \mathbf{u})$, and the set of these peaks gives the distribution of the atoms in the structure relative to atom j_0.

We substitute $F(\mathbf{H}) = \sum_{j=1}^{N} f_j(\mathbf{H})\exp(2\pi i\mathbf{H}\mathbf{r}_j)$ into (4) and use the fact that $A(\mathbf{r}_k - \mathbf{r}_j) = \vartheta(\mathbf{r}_k - \mathbf{r}_j)$, where $\vartheta \equiv \{A|t\}$, and denote $\mathbf{r}_0$ by $\mathbf{r}_{j_0}$ to get

$$DP_\vartheta(\mathbf{r}_0, \mathbf{u}) = \sum_{j,k,l}\Big(\frac{1}{V^2}\sum_{\mathbf{H}}\sum_{\mathbf{H}_1} f_j(-\mathbf{H} + \mathbf{H}_1A - \mathbf{H}_1) \times f_k(\mathbf{H} - \mathbf{H}_1A)f_l(\mathbf{H}_1)\exp\{-2\pi i\mathbf{H}_1[(\vartheta\mathbf{r}_k - \mathbf{r}_k) + (\vartheta\mathbf{r}_k - \mathbf{r}_l) - (\vartheta\mathbf{r}_j - \mathbf{r}_j)]\} \times \exp\{-2\pi i\mathbf{H}[\mathbf{u} - (\mathbf{r}_k - \mathbf{r}_j)]\}\Big). \tag{5}$$

The expression in the braces is the duplicated Patterson peak generated by the triplet of atoms j, k, and l; the duplicated Patterson function is defined in six-dimensional space and contains N^3 such peaks. The relevant section

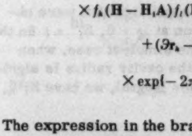
$\vartheta(\mathbf{r}_0+\mathbf{u})$
$\mathbf{r}_j$
$\mathbf{u}$
$\vartheta(\mathbf{r}_0+\mathbf{u})-\mathbf{r}_0$

Fig. 1. The production of a peak in $DP_\vartheta(\mathbf{r}_0, \mathbf{u})$ when a glide-reflection line is chosen as the specified symmetry element.

contains only some of these peaks. The contribution from a duplicated peak to $DP_\vartheta(\mathbf{r}_0, \mathbf{u})$ is the maximum possible, i.e., it enters into this section via its center if the following system of equations is satisfied:

$$\begin{gathered}\mathbf{u} - (\mathbf{r}_k - \mathbf{r}_j) = 0,\\ (\vartheta\mathbf{r}_{j_0} - \mathbf{r}_{j_0}) + (\vartheta\mathbf{r}_k - \mathbf{r}_l) - (\vartheta\mathbf{r}_j - \mathbf{r}_j) = 0.\end{gathered} \tag{6}$$

The left parts of these relationships enter into the arguments of the exponentials appearing in (5); the first equation implies that the peaks in $DP_\vartheta(\mathbf{r}_0, \mathbf{u})$ are possible at points corresponding to the interatomic vectors $\mathbf{u} = \mathbf{r}_k - \mathbf{r}_j$, but not every interatomic vector has a peak in the section $DP_\vartheta(\mathbf{r}_0, \mathbf{u})$; the condition for the section $DP_\vartheta(\mathbf{r}_0, \mathbf{u})$ to have a peak at the point $(\mathbf{r}_k - \mathbf{r}_j)$ is that the second equation in (6) is met, which we rewrite as follows:

$$(\vartheta\mathbf{r}_k - \mathbf{r}_l) = (\vartheta\mathbf{r}_j - \mathbf{r}_j) - (\vartheta\mathbf{r}_{j_0} - \mathbf{r}_{j_0}). \tag{7}$$

This equation is not correct for all atoms; it is essentially met if $j = j_0$ and $\vartheta\mathbf{r}_k = \mathbf{r}_l$. As subscripts k and l take values from unity up to N, where N is the number of atoms in the unit cell, one can always find two equivalent atoms related by the ϑ transformation, so atom j_0 taken with any pair of atoms related by transformation ϑ generates a peak in the $DP_\vartheta(\mathbf{r}_0, \mathbf{u})$ section, and these are regular peaks. The first equation in (6) implies that this kind of peak is produced at the points $\mathbf{u} = \mathbf{r}_k - \mathbf{r}_{j_0}$, whose radius vectors coincide with interatomic vectors drawn from atom j_0 to all the other atoms in the structure. Then geometrically the peaks in $DP_\vartheta(\mathbf{r}_0, \mathbf{u})$ coincide with the distribution of the atoms in the structure relative to atom j_0.

It follows from (5) that the height of peak jkl is defined by

$$\frac{1}{V^2}\sum_{\mathbf{H}}\sum_{\mathbf{H}_1} f_j(-\mathbf{H}+\mathbf{H}_1\mathbf{A}-\mathbf{H}_1)\, f_k(\mathbf{H}-\mathbf{H}_1\mathbf{A})\, f_l(\mathbf{H}_1) \tag{8}$$

or

$$\frac{1}{V^2}\sum_{\mathbf{H}}\sum_{\mathbf{H}_1} f_{j_0}(-\mathbf{H}+\mathbf{H}_1\mathbf{A}-\mathbf{H}_1)\, f_k(\mathbf{H}-\mathbf{H}_1\mathbf{A})\, f_k(\mathbf{H}_1).$$

We replace the curve $f_l(\mathbf{H})$ by $f_k(\mathbf{H})$ because atoms k and l, which generate the peak in question, are equivalent; if the structure consists of such atoms, then (8) may be put as

$$\frac{Z_{j_0}Z_k^2}{V^2}\sum_{\mathbf{H}}\sum_{\mathbf{H}_1} \hat{f}(-\mathbf{H}+\mathbf{H}_1\mathbf{A}-\mathbf{H}_1)\, \hat{f}(\mathbf{H}-\mathbf{H}_1\mathbf{A})\, \hat{f}(\mathbf{H}_1), \tag{9}$$

where $\hat{f}(\mathbf{H}) = f_j(\mathbf{H})/Z_j$ is unit atomic curve and Z is the atomic number of the atom. This means that peak j_0kl, which is obtained at point $\mathbf{u} = \mathbf{r}_k - \mathbf{r}_{j_0}$ and which coincides in position with atom k when the origin is taken at atom j_0, corresponds to atom k in the structure also in height. This height is proportional to the square of the atomic number. As subscript k is arbitrary, (9) must be true for all atoms, and so the heights of the regular peaks are proportional to the squares of the atomic numbers of the corresponding atoms. The cofactor in the coefficient of proportionality is the weight Z_{j_0} of the reference atom j_0.

Then to each atom in the structure there corresponds in the $DP_\vartheta(\mathbf{r}_0, \mathbf{u})$ section a peak whose radius vector coincides with the interatomic vector drawn from atom j_0 to the particular atom, while the height of the peak is proportional to the square of the atomic number of the latter. As regards the peak heights, this section is equivalent to the Buerger function of the product and is similar to the section that isolates an image of the structure of atoms placed on symmetry elements.[6] It is sufficient to take the square root in order to approximate $\rho(\mathbf{r})$ for each value of $DP_\vartheta(\mathbf{r}_0, \mathbf{u})$.

Of course, the regular peaks in $DP_\vartheta(\mathbf{r}_0, \mathbf{u})$ may possibly be accompanied by accidental ones. We give the following form to the second equation in (6), which gives the most general condition for a peak in the $DP_\vartheta(\mathbf{r}_0, \mathbf{u})$ section:

$$(\vartheta\mathbf{r}_j - \mathbf{r}_j) - (\mathbf{r}_m - \mathbf{r}_l) = (\vartheta\mathbf{r}_{j_0} - \mathbf{r}_{j_0}), \tag{10}$$

where we have $\mathbf{r}_m = \vartheta\mathbf{r}_k$; if there happens to be a triplet of atoms j, l and m that satisfies (10), with $j \neq j_0$ and $m \neq l$, then the section will contain an accidental peak, whose coordinates are defined by the difference $(\mathbf{r}_k - \mathbf{r}_j) = (\vartheta^{-1}\mathbf{r}_m - \mathbf{r}_j)$, where ϑ^{-1} is the symmetry transformation operator inverse to ϑ; the height of the accidental peak is shown by (5) to be given by

$$\frac{1}{V^2}\sum_{\mathbf{H}}\sum_{\mathbf{H}_1} f_j(-\mathbf{H}+\mathbf{H}_1\mathbf{A}-\mathbf{H}_1)\, f_k(\mathbf{H}-\mathbf{H}_1\mathbf{A})\, f_l(\mathbf{H}_1). \tag{11}$$

The height of an accidental jkl peak in a structure consisting of such atoms will be proportional to the product $Z_jZ_kZ_l$. The obvious geometrical meaning of the latter expression is made clear if the condition for a peak in the section is put in the form implied by (2): A maximum is obtained in the function when the parameters in the arguments of the cofactors are equal, these factors being for interatomic vectors drawn from a given atom:

$$\begin{gathered}\mathbf{u} = \mathbf{r}_k - \mathbf{r}_j,\\ (\vartheta\mathbf{r}_0 - \mathbf{r}_0) + \vartheta\mathbf{r}_k - \vartheta\mathbf{r}_j = \mathbf{r}_l - \mathbf{r}_j.\end{gathered} \tag{12}$$

In the above we have considered structures in which atom j_0 is unique in the sense that the structure has no other atoms placed relative to the symmetry element ϑ in the same way as j_0, but now we assume that atom j_0 has an associated atom disposed in the same way relative to ϑ, e.g., atom j_1. Analytically, this condition is put as the equation $(\vartheta\mathbf{r}_{j_1} - \mathbf{r}_{j_1}) = (\vartheta\mathbf{r}_{j_0} - \mathbf{r}_{j_0})$. Then the right side of (7) becomes zero not only for $j = j_0$, but also for $j = j_1$. The condition for a peak to arise is again $\vartheta\mathbf{r}_k = \mathbf{r}_l$, but peaks are now obtained at the points $\mathbf{u} = \mathbf{r}_k - \mathbf{r}_{j_1}$, and these consequently give the pattern in the atoms relative to atom j_1. The heights of these peaks are defined by

$$\frac{1}{V^2}\sum_{\mathbf{H}}\sum_{\mathbf{H}_1} f_{j_1}(-\mathbf{H}+\mathbf{H}_1\mathbf{A}-\mathbf{H}_1)\, f_k(\mathbf{H}-\mathbf{H}_1\mathbf{A})\, f_k(\mathbf{H}_1). \tag{13}$$

Here the atomic scattering curve for atom l is replaced by that of atom k, which is possible because atoms k and l are equivalent and are related by the transformation ϑ. For a structure of such atoms, the peak heights are proportional to $Z_{j_1}Z_k^2$, so the $DP_\vartheta(\mathbf{r}_0, \mathbf{u})$ function contains the images of the structure at the atom j_0 and at the atom j_1.

Both of these images correspond to a square-law dependence, but their weights are different: The image at atom j_0 is proportional to Z_{j_0}, while that at j_1 is proportional to Z_{j_1}. The images are superimposed in the section with the image of the atom j_0 at the origin for the first, while the origin contains j_1 for the second.

If the structure contains further atoms disposed relative to symmetry element Э as is j_0, then the $DP_Э(\mathbf{r}_0, \mathbf{u})$ section will contain images of the structure at these atoms also; the number of images is equal to the number of atoms identically disposed in relation to element Э . Atoms whose images contribute in this way to the section are called imaging atoms.

The section contains an image of the structure at, say, atom j_2 if this lies in the same way as atom j_0 but not relative to symmetry element Э , which corresponds to the transformation Э that specifies this section, but rather relative to an element $Э_R$, corresponding to the product of the transformation Э by the translation T_R, the latter being such that the parallel transfer additional to Э as applied to $Э_R$ is either zero or an integer multiple of a lattice translation. Geometrically, this requirement amounts to the following: A translation cofactor with a noninteger component must after its integer components have been eliminated be perpendicular to the initial symmetry element Э ; in that case one will have relative to $Э_R$ a set of atomic triplets that generate peaks in the section as though they were on element Э (Fig. 2). We can give the following analytic form to this disposition of atoms j_0 and j_2, each relative to its own symmetry element:

$$Э_R \mathbf{r}_{j_2} - \mathbf{r}_{j_2} = Э\mathbf{r}_{j_0} - \mathbf{r}_{j_0}. \tag{14}$$

To take (14) into account along with (6), we express the difference $(Э\mathbf{r}_j - \mathbf{r}_j)$ in terms of $(Э_R\mathbf{r}_j - \mathbf{r}_j)$; as $Э_R = T_R Э$, then $Э_R\mathbf{r} = Э\mathbf{r} + \mathbf{T}_R$, where the vector $\mathbf{T}_R$ characterizes the translation T_R. Then $(Э\mathbf{r}_j - \mathbf{r}_j) = (Э_R\mathbf{r}_j - \mathbf{r}_j) - \mathbf{T}_R$; we substitute the right part of the latter relationship in the second equation in (6), $(Э\mathbf{r}_{j_0} - \mathbf{r}_{j_0}) + (Э\mathbf{r}_k - \mathbf{r}_l) - (Э_R\mathbf{r}_j - \mathbf{r}_j) + \mathbf{T}_R = 0$. For $j = j_2$ this gives with (14) that $(Э\mathbf{r}_k - \mathbf{r}_l) + \mathbf{T}_R = 0$, which is equivalent to $Э_R\mathbf{r}_k - \mathbf{r}_l = 0$; consequently for $\mathbf{r}_l = Э_R\mathbf{r}_k$ the section $DP_Э(\mathbf{r}_0, \mathbf{u})$ contains a peak whose coordinates are defined by the difference $(\mathbf{r}_k - \mathbf{r}_{j_2})$, while the height for a structure of such atoms is proportional to $Z_{j_2}Z_k^2$. As subscript k takes all possible values from 1 to N, there will be such a peak for each atom in the structure. The feature common to all of these is that atom j_2 participates in their formation.

Then a function $DP_Э(\mathbf{r}_0, \mathbf{u})$ contains an image of the structure at atom j_2 if its disposition relative to $Э_R$ is similar to the disposition of j_0 relative to Э, while the symmetry element $Э_R$ corresponds to the product of the transformation Э by translation T_R such that it is perpendicular to the initial element Э after the integer components have been eliminated or is altogether zero.

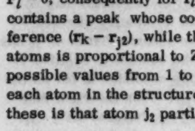

Fig. 2. Identity of atom configurations for similar symmetry elements on account of symmetry (crosses or filled circles) or of accidental atomic disposition (crosses and open circles).

As one cannot distinguish between the positions of the imaging atom relative to Э or $Э_R$, there is an ambiguity in the localization of the images of the structure relative to these symmetry elements; this is the implication ambiguity, which occurs in implication diagrams[7] and in certain other sections of the duplicated Patterson function in which symmetrical transformations are involved.[6,8]

This ambiguity is a consequence of the more general relationship between the functions $DP_Э(\mathbf{r}_0, \mathbf{u})$ for transformations differing in translational cofactor; consider the functions $DP_{Э_m}(\mathbf{r}_0, \mathbf{u})$ and $DP_{Э_n}(\mathbf{r}_0, \mathbf{u})$ with the common specified vector $\mathbf{r}_0$. We assume that transformation $Э_n$ is the product of $Э_m$ by an arbitrary translation T in the crystal, $Э_n = T\,Э_m$; we write the function for the $Э_n$ transformation in the form of (2) and use the fact that $Э_n(\mathbf{r}_0 + \mathbf{u}) = Э_m(\mathbf{r}_0 + \mathbf{u}) + \mathbf{T}$, while $\rho(\mathbf{r} + \mathbf{T}) = \rho(\mathbf{r})$, which gives

$$DP_{Э_n}(\mathbf{r}_0, \mathbf{u}) = \int\limits_V \rho(\mathbf{r})\rho(\mathbf{r}+\mathbf{u})\rho(\mathbf{r}+[Э_n(\mathbf{r}_0+\mathbf{u})-\mathbf{r}_0])\,dV$$

$$= \int\limits_V \rho(\mathbf{r})\rho(\mathbf{r}+\mathbf{u})\rho(\mathbf{r}+[Э_m(\mathbf{r}_0+\mathbf{u})-\mathbf{r}_0])\,dV = DP_{Э_m}(\mathbf{r}_0+\mathbf{u}).$$

This integral is the function $DP_Э(\mathbf{r}_0 + \mathbf{u})$ for the transformation $Э_m$, so the sections constructed by reference to the one common vector $\mathbf{r}_0$ are identical for symmetry transformations that differ in translational cofactors:

$$DP_Э(\mathbf{r}_0, \mathbf{u}) = DP_{TЭ}(\mathbf{r}_0, \mathbf{u}). \tag{15}$$

We have seen above that the section contains a number of images of the structure equal to the number of imaging atoms; to distinguish these images and localize a single one we need to know the mutual disposition of the imaging atoms, and information on this is contained in the geometry of the representations of the imaging atoms and can be extracted from the $DP_Э(\mathbf{r}_0, \mathbf{u})$ section itself. It can also be obtained in another way, e.g., by localizing known interatomic vectors in the structure. The positions of some of the imaging atoms equivalent to the desired one are unambiguously defined by the desired atom and the symmetry of the crystal; a further paper will be published on the methods of separating structure images isolated by the section.

This section of the duplicated Patterson function is very similar to Hoppe's section as regards method of specification, and the latter isolates an image of the structure proportional to the structure itself. In both cases one specifies an interatomic vector in defining the section; for a section that localizes the structure, this is reflected in the explicit form in the relationship of (1): $\mathbf{u}_2 = Э\mathbf{u} + (Э\mathbf{r}_0 - \mathbf{r}_0) = Э\mathbf{u} + \mathbf{u}_0$. In constructing a Hoppe section, one needs only one of the vectors of the duplicated function, $\mathbf{u}_2$ or $\mathbf{u}_1$, which is put equal to the interatomic vector $\mathbf{u}_0$. The structure image isolated by the Hoppe section is similar to the structure, which makes it possible to transfer the structural information contained in the section to the electron-density distribution without actually calculating the latter; the signs of the Fourier coefficients in the Hoppe section are simply ascribed to the corresponding structure amplitude.[10] However, this procedure needs to be carried out with care, because the Hoppe section isolates as many images as there are interatomic vectors equal to the specified one in the structure. Each of the images thereby produced makes its contribution to the coefficients of the series, but the resultant magnitudes of the latter are dependent also on the mutual displacement of the individual images. The Hoppe section isolates an image of the structure; in contrast, our localizing section isolates an image of the structure at the origin only for vectors equal to the given one that are disposed relative to the given symmetry element or similar elements in the same way as the given vector. This restriction of the permissible regions for the imaging vector involves in the general case a reduction in the number of images produced relative to the number for the Hoppe section.

---

[1] D. Sayre, Acta Crystallogr., 6, No. 5, 430 (1953).

[2] F. Seitz, Ann. Math., 37, 17 (1936).

[3] D. Sayre, Acta Crystallogr., 5, 1, No. 1, 60 (1952).

[4] W. Cochran, Acta Crystallogr., 5, No. 1, 65 (1952)

[5] W. H. Zachariasen, Acta Crystallogr., 5, 1, 68 (1952).

[6] V. N. Biyushkin, Kristallografiya, 17, 737 (1972) [Sov. Phys. – Crystallogr., 17, 647 (1973)].

[7] M. J. Buerger, Acta Crystallogr., 1, No. 5, 259 (1948).

[8] V. N. Biyushkin and N. V. Belov, Kristallografiya, 9, 771 (1964) [Sov. Phys. – Crystallogr., 9, 655 (1965)].

[9] W. Hoppe, Acta Crystallogr., 10, No. 12, 751 (1957).

[10] V. I. Simonov and A. V. Vaisberg, Dokl. Akad. Nauk SSSR, 191, 1050 (1970) [Sov. Phys. – Dokl., 15, 321 (1970)].

New method for determining the normalizing factor in electron diffraction studies of the structure of amorphous substances

Ya. I. Stetsiv
L'vov Polytechnic Institute
(Submitted July 19, 1971; resubmitted April 24, 1972)
Kristallografiya, 18, 257-262 (March-April 1973)

The width of the coordination peaks and the area under these peaks are shown to depend strongly on the normalizing factor and the upper integration limit s_2. From the dependence of the half-width of the coordination peaks on s_2, a new way is developed for determining a reliable value of the normalizing factor.

The radial distribution curve, which is obtained by Fourier transformation of the coherent scattered intensity of x rays, electrons, or neutrons, provides information about the structure of liquids and amorphous substances. From the radial distribution curves, this method permits the determination of the radii of the coordination spheres, the coordination numbers (c.n.), and the mean-square displacement of particles in the substance being investigated.

The radial distribution curves constructed in this way for many liquids, amorphous substances, and glasses from the data of different authors for a given substance are in poor agreement with each other. For example, from the data of ref. 1, the coordination number in molten germanium is equal to 8, while according to other data[2,3] it is between 5 and 6. No less contradictory are the results for many other molten and amorphous substances – for example, silicon[4,5] and antimony[6-8] (Table 1) even though the values of sin θ/λ of the maxima of the experimental curves of the intensity $I_e(s)$ all agree well (See Table 2, for example).

The question of the reliability of the results of diffraction investigations of the structures of amorphous substances and liquids has been repeatedly discussed in the literature,[9-14] and it has been established that the discrepancy mentioned above is due almost entirely to incorrect normalization of the $I_e(s)$ curve and the termination of the curve in the computation of the radial distribution.

We will now briefly discuss these two reasons for the disagreement.

1. Experimentally the intensity of the scattered radiation can be determined only for a finite interval of values of $s = (4\pi \sin\theta)/\lambda$. Therefore, the computation of the radial distribution always involves a termination of the intensity curve, thus causing a displacement and broadening of the coordination maxima, an increase in the area under these maxima, and the appearance of additional spurious maxima and minima. Typically, in their computations of the radial distribution curves for the same substance, many authors have used very different values of the upper limit of the integration and have completely neglected to correct for the termination effect. A method for calculating this correction is given in refs. 15 and 16.

2. The atomic distribution function is determined from the intensity of coherently scattered radiation, obtained from the experimental intensity curve after subtraction of the incoherent background. A procedure for computing the incoherent x-ray scattering is proposed in refs. 17 and 18. In ref. 19, different ways of computing the background in electron diffraction are considered and analyzed in detail.

It is necessary to note that at present, in the determination of the incoherent part of the intensity of electron scattering there always is some arbitrariness in the

TABLE 2. Values of $(\sin\theta/\lambda)_{\max}$ for Amorphous Antimony

X-ray data		Electron diffraction data		Computed from the function $\sin(r_k s)/(r_k s)$		
[8]	[6]	[7]	our data	$r_1 = 2{,}87$	$r_2 = 3{,}85$	$r_3 = 4{,}30$
0.167	0.166	0.168	0.157	—	0.160	0.143
0.263	0,260	0.265	0.262	0.215	0.290	0.261
0.334	0,35	0.34	0.35	—	—	0.378
0.404	0.395	0.412	0.405	0.390	0,420	—
0.495	—	0.510	0.50	—	—	0.495
0.568	—	0.57	0.567	0.565	0.552	0.680
0.735	—	0.74	0.745	0.740	0,680	0.727
—	—	—	0.835	—	0.816	0.845
0.910	—	—	0.925	0.915	0.945	0.960
—	—	—	1,07	1.09	1.07	1.08

TABLE 1. Radii of the Coordination Spheres (r) and the Coordination Number (c.n.) in Crystalline and Amorphous Antimony

Crystalline antimony		Amorphous antimony							
		x-ray data				electron diffraction data			
		[6]		[8]		[7]		our data	
r	c.n.	r	c.n.	r	c.n.	r	c.n.	r	c.n.
2,87	3	2,87	4	2.81--2.91	2.1—3.2	2.85	4	2.87	3
3,37	3	3.51	2	3.38—3.42	1.4—2.2	3.62	5	3.85	—
4.27	6	4.18	12	3.78--3.92	3.0—4.2	4.18	9	4.30	17
4.50	6	—	—	4.15—4.30	4.4—6.0	—	—	4.60	—
5.15	3	—	—	4.70—4.85	—	4.95	3	—	—
5.23	1	—	—	5.15—5.27	—	—	—	—	—
5,44	3	—	—	—	—	—	—	—	—
6,06	1	—	—	—	—	—	—	—	—
6.20	6	6.26	30	—	—	6.25	28	6.40	24

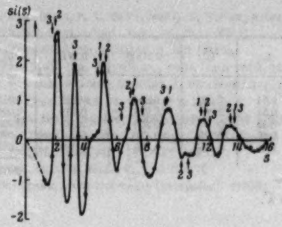

Fig. 1. The function si(s) for amorphous antimony.

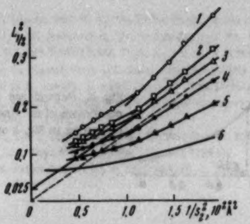

Fig. 3. The dependence of the half-width of the first coordination maximum of amorphous antimony on the upper integration limit s_2 for different values of the normalizing factor α. 1) α = 0.30; 2) 0.40; 3) 0.45; 4) 0.60; 5) 1.0; 6) ∞; the dotted straight line corresponds to $L_\infty = 0$.

calculation of the background. This uncertainty leads to an incorrect normalization of the experimental intensity curve and thus to inaccurate values of the normalizing factor.

We have proposed[20] a method for determining the intensity of the coherent scattering from the $I_e(s)/f^2(s)$ curves without a preliminary computation of the background. In this case, the radial distribution curves are calculated from the equation

$$4\pi r^2\rho(r) = 4\pi r^2\rho_0 + (2r/\pi)\alpha \int_0^{s_2} s i_1(s)\sin(sr)\,ds, \quad (1)$$

where α is the normalizing factor, and $i_1(s)$ is the unnormalized interference function. As is seen from (1), the height of the coordination peaks and their spatial resolution is determined by the factor α. Therefore, the question of the accuracy of the values of α becomes very important.

In this paper, for the example of amorphous antimony, we show that the width of the coordination peak and the area under it depend very strongly on the upper limit of integration s_2 and on α, and we will also demonstrate a new method of determining a reliable value of α, which we have developed from the relation between s_2 and the half-width of the coordination peak.

A layer of amorphous antimony was evaporated on fresh cystals of sodium chloride at liquid-nitrogen temperature and then removed on a distilled water surface. Electron diffraction patterns with different exposures were made at 80 kV with a rotating sector. This procedure permitted the function $I_e(s)/f^2(s)$ to be obtained directly. The normalized interference function was computed[20] and is shown in Fig. 1. The arrows show the positions of the theoretical interference maxima computed from the equation $\tan(r_k s) = r_k s$ for the first, second, and third interatomic distances, respectively.

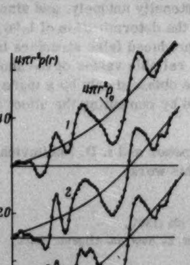

Fig. 2. Radial distribution curves for amorphous antimony, computed for different values of the upper limit s_2. 1) s_2 = 7.6; 2) s_2 = 11.6; 3) s_2 = 14.6 $\AA^{-1}$.

The integral in Eq. (1) was evaluated on a "Minsk-1" computer. The increments of the variables were $\Delta s = 0.1\ \AA^{-1}$ and $\Delta r = 0.1\ \AA$. The radial distribution curves were computed for different values of the upper limit s_2. Three of these curves are shown in Fig. 2.

The value of α was estimated by the method of ref. 20. In addition, the limits of the possible values of α were determined for different ways of drawing the background curve under $I_e(s)$. If the background line is drawn a short distance under the $I_e(s)$ curve, then by Vainshtein's method [21] we obtain α ≃ 0.1, while if the background is completely neglected, α ≃ 0.3. In connection with this, the effect of α on the half-width of the coordination maximum (Fig. 3) and on the area under this maximum (Fig. 4) must be studied for different values of s_2. Thus, if the correction for the termination effect is not considered, very different values of the coordination number – from 3 to 5 – can be obtained, depending on how the background curve is drawn (Fig. 4). This result can in some degree explain the differences in the experimental results shown in Table 1.

We will show that a reliable value of α can be determined from the behavior shown in Fig. 3. According to ref. 16, as a result of the termination effect, the half-

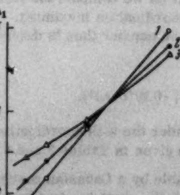

Fig. 4. The dependence of the area under the first coordination peak of the normalizing factor for different values of s_2. 1) s_2 = 14.6; 2) 9.4; 3) 7.2 $\AA^{-1}$.

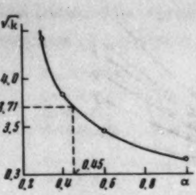

Fig. 5. Dependence of the angular coefficient of the linear portions of the curves in Fig. 3 on the normalization factor.

TABLE 3

s_2	$L_{1/2}$	$L^2_{1/2}$	$(3.71/s_2)^2$	$0.38\,L^2_\infty$	L^2_∞	L_∞
7.2	0.54	0.292	0.266	0.026	0.068	0.26
7.8	0.51	0.260	0.226	0.034	0.090	0.30
8.2	0.48	0.230	0.205	0.025	0.066	0.26
8.8	0.46	0.212	0.178	0.034	0.090	0.30
9.4	0.42	0.176	0.156	0.020	0.053	0.23
					0.073	0.27

$\overline{u_m^2} = 0.013$ Å².

TABLE 4

s_2	Δ_1	Δ_1'	$L_\infty s_2$	$(L_\infty s_2)^2$	z *	$0.18z$	$1 + 0.18z$	n_1	n_1'
7.2	3.6	3.4	1.94	3.76	0.68	0.122	1.122	3.2	3.0
8.2	3.55	3.3	2.22	4.93	0.61	0.110	1.110	3.2	3.0
9.4	3.5	3.25	2.54	6.45	0.52	0.094	1.094	3.2	3.0
11.6	3.4	3.15	3.13	9.80	0.37	0.067	1.067	3.2	3.0
14.6	3.3	3.1	3.94	15.52	0.21	0.038	1.038	3.2	3.0
								3.2	3.0

* $z = \exp[-0.10(L_\infty s_2)^2]$.

width $L_{1/2}$ of the coordination maximum is always too large. As s_2 increases, the true half-width L_∞ is approached. For low values of s_2, there is the relation

$$L^2_{1/2} = 0.38L^2_\infty + (3.71/s_2)^2. \qquad (2)$$

For coordination maxima described by a type of delta function, $L_\infty = 0$, and $L_{1/2} = 3.71/s_2$. This relation is shown in Fig. 3 by a dotted straight line. Since all real coordination groups are represented by coordination maxima with $L_\infty > 0$, when the curves in Fig. 3 drop into the region below the dotted straight line, the values of α have no meaning and must be rejected. From the straight lines located above the dotted line, the line must be selected for which the angular coefficient is $(3.71)^2$, as required by Eq. (2). From this line we obtain $\alpha \simeq 0.45$.

For a more precise determination of the value of α, the angular coefficients of the lines in Fig. 3 must be computed. Then, from a graph of the dependence of these coefficients on α, the correct normalization constant α is taken to be the value for which the angular coefficient is equal approximately to $(3.71)^2$ (Fig. 5). Consequently, α = 0.45.

After the best value of α is obtained, a series of radial distribution curves is constructed for this value of α for different values of s_2. From (2) we compute the true values of the half-width of the coordination maximum. The true value of the coordination number then is determined by use of the relation[16]

$$n_k = \Delta_k / 1 + 0.18 \exp[-0.10(L_\infty s_2)^2],$$

where $\Delta_k = \Delta_k(s_2)$ is the area under the k-th coordination maximum. All calculations are given in Tables 3 and 4.

For a maximum representable by a Gaussian curve, the mean-square displacement of the particles is determined from the half-width: $\overline{u_m^2} = 0.18\,L^2_\infty$.

For the first coordination group of amorphous antimony we obtain $r_1 = 2.87$ Å, $n_1 = 3.2$, $L_\infty = 0.27$ Å, and $\overline{u_m^2} = 0.013$ Å². The values of the coordination number for amorphous antimony are about 0.2 greater than in the crystalline state. This possibly can be explained by the fact that for calculations of the mean density of atoms in amorphous antimony we used density values for the crystalline state (6.69 g/cm³) which can be greater than the density for amorphous antimony. If we assume that the density of the amorphous state is 10% higher than for the crystalline form (as is true for selenium), we obtain the quantities Δ_1' (Table 4), and in this case the coordination number is 3. From these results it follows that in amorphous antimony the short-range order is the same as in the crystalline state.

To summarize our investigations of amorphous antimony, we conclude that the disagreement in the results of diffraction investigations of the structure of amorphous substance and liquids is due mainly to the termination effect and to an incorrect computation of the background. Since at present in electron diffraction it is not possible to determine the background intensity uniquely, and since regardless of the precision of the determination of $I_e(s)$, the termination effect always produced false structure in the radial distribution curves, reliable values of the short-range order parameters can be obtained only by a more precise determination of α and by computing the effect of the termination error.

The authors thank Z. G. Pinsker and I. D. Nabitovich for discussing the results of this work.

---

[1] H. Hendus, Z. Naturforsch., a2, No. 9, 205 (1947).

[2] H. Krebs, V. B. Lazarev, and L. Winkler, Z. Anorgan. Allgem. Chem., 252, 277 (1967).

[3] G. I. Batalin and V. P. Kazimirov, Kristallografiya, 15, 850 (1970) [Sov. Phys.–Crystallogr., 15, 739 (1971)].

[4] H. Richter and G. Breitling, Z. Naturforsch., a13, 988 (1958).

[5] I. A. Pavars, B. A. Baum, P. V. Gel'd, and G. S. Yur'ev, Kristallografiya, 16, 606 (1971) [Sov. Phys.–Crystallogr., 16, 514 (1971)].
[6] A. S. Lashko, Dop. Akad. Nauk UkrSSR, 6, 455 (1952).
[7] L. I. Tatarinova, Trudy Inst. Kristallogr., Akad. Nauk SSSR, 11, 104 (1955).
[8] H. Richter, H. Berckhemer, and G. Breitling, Z. Naturforschung, 29, 236 (1954).
[9] C. Finbak, Acta Chem. Scand., 3, 1279, 1293 (1949).
[10] T. Sugawara, Sci. Repts. Res. Inst. Tohoku Univ., B3, 39 (1951).
[11] J. Waser and V. Schomaker, Rev. Mod. Phys., 25, 671 (1953).
[12] V. N. Filipovich, Zh. Tekh. Fiz., 25, 1607 (1955).
[13] L. V. Radchenko, Usp. Fiz. Nauk, 61, 249 (1957).
[14] Ya. I. Stetsiv, Thesis, L'vov University [in Russian] (1968).
[15] R. Hosemann, K. Lemm, and H. Krebs, Zeits. Phys. Chem., 41, 121 (1964).
[16] A. I. Andrievskii, I. D. Nabitovich, Ya. I. Stetsiv, and Ya. V. Voloshchuk, Ukr. Fiz. Zh., 13, 1596 (1968) [Ukr. Phys. J., 13, 1137 (1969)].
[17] B. E. Warren and G. Mavel, Rev. Sci. Instr., 36, 196 (1965).
[18] B. E. Warren and R. L. Mozzi, J. Appl. Cryst., 2, 164 (1969); 3, 251 (1970).
[19] L. I. Tatarinova, Electron Diffraction by Amorphous Substances [in Russian], Nauka, Moscow (1972).
[20] I. D. Nabitovich, Ya. I. Stetsiv, and Ya. V. Voloshchuk, Kristallografiya, 12, 584 (1967) [Sov. Phys.–Crystallogr., 12, 513 (1968)].
[21] B. K. Vainshtein, Kristallografiya, 2, 29 (1957) [Sov. Phys.–Crystallogr., 2, 24 (1957)].

Crystal structure of the coordination compound bis(pyridinaldehydethiosemicarbazonato)cobalt (III) nitrate

K. N. Akatova, T. N. Tarkhova, and N. V. Belov

Gor'kii Research Physicotechnical Institute

(Submitted August 8, 1972)
Kristallografiya, 18, 263-268 (March-April 1973)

The crystal structure of the coordination compound bis(pyridinaldehydethiosemicarbazonato)cobalt (III) nitrate $Co(C_7H_7N_4S)_2 \cdot NO_3$ was determined by analysis of the three-dimensional Patterson function by the method of multiple peaks. The parameters of the triclinic cell are as follows: $a = 12.48$, $b = 8.76$, $c = 9.29$ Å; $\alpha = 92°$, $\beta = 103.2°$, $\gamma = 102.2°$, $Z = 2$, $P\bar{1}$. The structure was refined by the method of least squares in the isotropic approximation with $R_{hkl} = 17\%$. The planar structure and tridentate nature of the thiosemicarbazone were confirmed.

Information on the stereochemical difference in the chelates of metals with α-(N)-heterocyclic thiosemicarbazones is of interest in connection with attempts to determine the mechanism of antitumorigenic activity and the search for less toxic compounds.[1-3]

A series of crystals of the compounds of cobalt with α-pyridinecarbaldehyde thiosemicarbazone with the general formula $(CoL_2)X$, where L is a ligand with the molecular formula $C_7H_7N_4S$ (abbreviated as PAT) and X is the content of the outer sphere (I^-, Br^-, Cl^-, NO_3^-, ClO_4^-), have been synthesized at the Institute of Chemistry, Academy of Sciences of the Moldavian SSR, by the method described in ref. 4.

EXPERIMENT

Isometric clearly faceted cherry-red crystals of $[Co(PAT)_2]$ NO_3 were selected for x-ray investigation.

According to Laue and oscillating-crystal patterns and the long-range reflections of Weissenberg patterns the parameters of the triclinic cell are as follows: $a = 12.48(8)$, $b = 8.76(5)$, $c = 9.29(6)$ Å, $\alpha = 92°$, $\beta = 103.2°$, $\gamma = 102.2°$ on Delaunay apparatus; $V = 962.7$ Å^3, $M = 479$. For a pycnometric density ρ_p of 1.65 g/cm^3, $Z = 2$. The negative result from tests for the piezo effect (Department of Crystal Physics, Moscow State University) and statistical tests by the method of integral curves and intensity moments gave preference to the $P\bar{1}$ space group.

The experimental intensities were obtained from a $0.5 \times 0.5 \times 0.2$-mm crystal using multiple exposures. Molybdenum Kα radiation was used with $\sin\vartheta/\lambda \leq 0.68$. The intensities were evaluated against darkening standards with a step of $2^{1/4}$. Computer reduction of the hk0 – hk5 and h0l – hl$l$ scans to a single scale with correction for the LP factors and the form of the spot according to Phillips (beginning with the second layer) led to a set of 1570 unique nonzero F^2_{hkl} values, which were used to interpret the structure.

DETERMINATION OF STRUCTURE

The initial analysis of the three-dimensional Patterson function was performed for the supposed formula $[Co(PAT)_2]$ $Br \cdot 3H_2O$. Theoretical calculation of the weights of the P(uvw) function on the assumption of the presence of the heavy Br (Z = 35) and Co (Z = 27) atoms gave poor agreement with the experimental P(uvw) weights which had been normalized according to Burger. The three peaks of Mamedov and Belov[5] from these atoms did not appear and together with the significant discrepancy in the pycnometric (1.65 g/cm^3) and x-ray (1.90 g/cm^3) densities also indicated that the chemical formula was incorrect unless the absence of the expected details in the P(uvw) distribution was due to the complexity of the material being studied with the 49 atoms in a separate part of the cell. This made us turn to the method of multiple peaks,[6] which does not involve an a priori chemical formula in the initial stages of interpretation.

In Fig. 1 the three-dimensional P(uvw) function is given in point form. The vectors drawn to the five maximum (in "weight") peaks with numbers 7, 8, 11, 16, and 36 were chosen as reference points for the construction of the functions for minimizing the second rank of $M_2(xyz)$. In distinguishing the fundamental system from the vectorial system through superposition of the "point" maps of the real Patterson function each point was understood as some region with a dimension depending on the magnitude of the maximum.

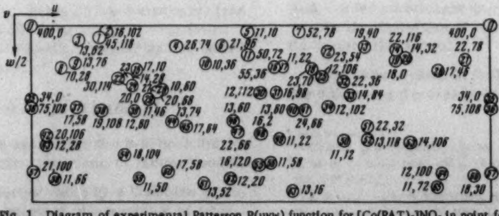

Fig. 1. Diagram of experimental Patterson P(uvw) function for $[Co(PAT)_2]NO_3$ in point form. The figures in circles represent the numbers of the peaks, and the figures beside them represent the "weight" and height of the peak in 120-ths of the v axis.

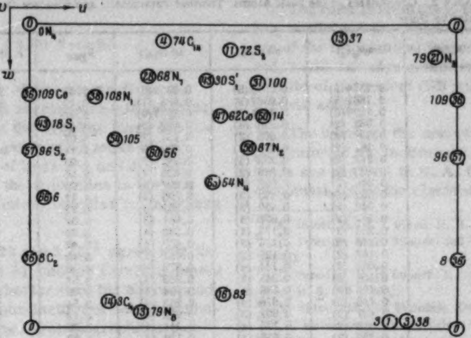

Fig. 2. The "statistical sum" obtained from P(uvw) with the origin of the coordinates at point No. 1.

TABLE 1. Coordinates of the Atoms of the Fundamental System in 120-ths of the Unit Cell

Atom No.	x	Y	z	Atom No.	x	Y	z
1	0	0	0	7	50	30	20
2	0	109	24	8	40	74	5
3	20	108	25	9	58	62	36
4	4	18	36	10	54	54	60
5	0	96	48	11	114	79	11
6	58	72	10				

The detailed procedure was described in ref. 6. Twelve different superposition functions with rank higher than second led to a "statistical sum" with 25 points, which is shown in Fig. 2 with indication of the chemical symbols of the atoms. The coordinates of 11 of the 25 points of the "sum" with better statistical confirmation (Table 1) formed the basis of the subsequent interpretation.

When it was impossible to differentiate between the atoms and to fix the position of the center of symmetry reliably at this stage, the structure was solved in the acentric variant with the origin of the coordinates at atom No. 1. Cycles of successive approximations of electron density with refinement by the method of least squares and crystal-chemical information made it possible to identify all the atoms of the inner coordination sphere of the cobalt and also to fix the center of symmetry. Subsequent calculation and refinement were carried out for the centrosymmetric model. In the final $\rho(xyz)$ the atoms of the outer sphere were fixed in the form of (NO_3) groups in place of the Br and $3H_2O$ in the initial formula. Recalculation gave values for the pycnometric and x-ray densities which coincided within the error limits of the measurement. An explanation was also obtained for the fact that the three peaks were absent from P(uvw).

TABLE 2. Experimental and Calculated Magnitudes of the Strongest P(uvw) Peaks

"Weight" of peak		Interatomic vectors
Experimental	Calculated	
150, 140	1242	2(Co — S), 2(Co — N)
111	1188	2(Co — S), 2(Co — C)
105	864	2(Co — S)
100	729	Co — Co
90	756	4(Co — N)

An a posteriori analysis of the Patterson function confirmed the multiple nature of the strongest peaks with satisfactory correlation of their experimental and theoretically calculated magnitudes (Table 2).

The 87 position parameters together with the standard

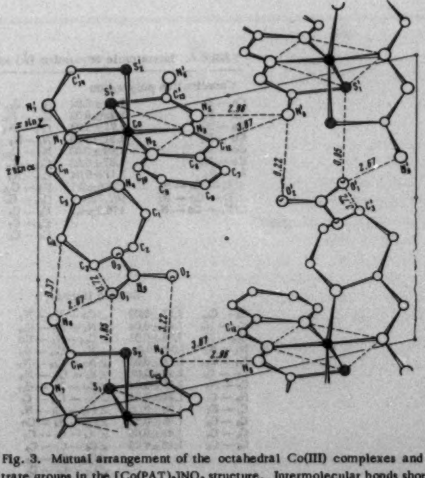

Fig. 3. Mutual arrangement of the octahedral Co(III) complexes and nitrate groups in the $[Co(PAT)_3]NO_3$ structure. Intermolecular bonds shorter than 4 Å are shown.

TABLE 3. Coordinates of the Basis Atoms, Thermal Parameters, and Electron Density in Relative Units

Atom	$x/a(\sigma_{x/a})$	$y/b(\sigma_{y/b})$	$z/c(\sigma_{z/c})$	B_{gen}	ρ, rel. units
Co	0.2354(3)	0.3015(5)	0.0490(5)	1.31	249
S_1	0.1861(5)	0.0567(9)	0.936 (1)	3.19	119
S_2	0.2328(6)	0.4021(9)	0.8333(9)	2.97	118
N_1	0.083 (2)	0.316 (3)	0.022 (3)	3.49	37
N_2	0.307 (2)	0.505 (3)	0.151 (3)	3.07	33
N_3	0.387 (2)	0.277 (3)	0.082 (3)	2.11	38
N_4	0.213 (2)	0.239 (3)	0.232 (3)	5.03	35
N_5	0.420 (2)	0.148 (3)	0.038 (3)	2.86	30
N_6	0.346 (2)	0.897 (3)	0.897 (3)	5.09	31
N_7	0.022 (2)	0.353 (3)	0.895 (3)	4.11	32
N_8	0.040 (2)	0.430 (3)	0.652 (3)	6.22	29
N_9	0.252 (2)	0.677 (3)	0.561 (3)	9.67	34
C_1	0.283 (2)	0.173 (4)	0.348 (4)	3.69	28
C_2	0.246 (2)	0.116 (3)	0.467 (4)	5.42	23
C_3	0.146 (2)	0.125 (3)	0.487 (4)	5.42	23
C_4	0.061 (2)	0.184 (4)	0.377 (4)	4.36	29
C_5	0.100 (2)	0.245 (3)	0.253 (4)	3.51	27
C_6	0.425 (2)	0.536 (4)	0.194 (4)	2.05	24
C_7	0.486 (2)	0.676 (4)	0.262 (4)	3.54	23
C_8	0.437 (2)	0.802 (3)	0.292 (4)	4.19	23
C_9	0.318 (2)	0.775 (4)	0.244 (4)	3.70	25
C_{10}	0.259 (2)	0.635 (4)	0.178 (4)	1.62	30
C_{11}	0.028 (2)	0.282 (4)	0.123 (4)	3.62	29
C_{12}	0.466 (2)	0.393 (4)	0.148 (4)	3.07	26
C_{13}	0.328 (2)	0.035 (3)	0.968 (4)	3.69	29
C_{14}	0.086 (2)	0.392 (3)	0.795 (4)	2.65	27
O_1	0.189 (2)	0.758 (3)	0.610 (3)	8.13	25
O_2	0.357 (2)	0.720 (4)	0.593 (4)	10.05	20
O_3	0.208 (2)	0.552 (4)	0.474 (4)	8.40	26

deviations and the isotropic thermal corrections are presented in Table 3. The "heights" of the electron density maxima for each of the atoms are also given. The final R_{hkl} value was 17%. The positions of the hydrogen atoms were not determined. The calculated interatomic separations and bond angles are given in Table 4.

DESCRIPTION OF THE STRUCTURE

Two molecules of bis-pyridinecarbaldehyde thiosemicarbazone, connected to the cobalt atom by the nitrogen atoms of the hydrazine residue, the nitrogen atom of the pyridine, and the sulfur atom, create a distorted octahedral coordination at the Co^{3+} ion and four five-membered chelate rings CoNCCN and CoNNCS. The five-membered rings, like the whole ligand, are flat. The equations of the planes drawn by the method of least squares through the $S_1C_{13}N_6N_5N_3C_{12}C_6N_2$ (first ligand) and $S_2C_{14}N_8N_7N_1C_{11}C_5N_4$ (second ligand) atoms are as follows:

$$2{,}203\,X + 3{,}649\,Y - 8{,}560\,Z = 1{,}199,$$

TABLE 4. Interatomic Separation (Å) and Bond Angles (deg)

Coordination polyhedron		First ligand			
$Co-S_1$	2.25±0.02	S_1-C_{13}	1.78±0.03	$\angle Co-N_3-N_5$	126.4±0.9
$Co-S_2$	2.22±0.02	$C_{13}-N_6$	1.40±0.04	$\angle N_3-N_5-C_{13}$	111±1
$Co-N_1$	1.91±0.03	$C_{13}-N_5$	1.30±0.04	$\angle C_{13}-S_1-Co$	94±1
$Co-N_2$	1.91±0.03	N_5-N_3	1.38±0.04	$\angle N_5-C_{13}-S_1$	122±2
$Co-N_3$	1.89±0.03	N_3-C_{12}	1.32±0.04	$\angle N_5-C_{13}-N_6$	119±2
$Co-N_4$	1.87±0.03	$C_{12}-C_6$	1.50±0.05	$\angle S_1-C_{13}-N_6$	118.5±2
S_1-S_2	3.17±0.04	C_6-N_2	1.40±0.04	$\angle Co-N_3-C_{12}$	117.2±0.8
$\angle S_1-Co-N_2$	169.6±0.1	N_2-C_{10}	1.43±0.04	$\angle N_3-C_{12}-C_6$	114.5±0.6
$\angle S_2-Co-N_4$	167.3±0.1	$C_{10}-C_9$	1.34±0.04	$\angle C_{12}-C_6-N_2$	109.7±0.8
$\angle N_1-Co-N_3$	176.2±0.1	C_9-C_8	1.41±0.04	$\angle C_6-N_2-Co$	115±1
		C_8-C_7	1.41±0.05	$\angle N_2-C_6-C_7$	121.1±0.9
		C_7-C_6	1.35±0.04	$\angle C_6-C_7-C_8$	123.3±0.5
				$\angle C_7-C_8-C_9$	116.5±0.9
				$\angle C_8-C_9-C_{10}$	119.3±0.9
				$\angle C_9-C_{10}-N_2$	124.8±0.5
				$\angle C_{10}-N_2-C_6$	114.8±0.9

Second ligand				Nitrate group	
S_2-C_{14}	1.77±0.03	$\angle Co-N_1-N_7$	123.2±0.8	N_9-O_1	1.31±0.05
$C_{14}-N_8$	1.40±0.04	$\angle N_1-N_7-C_{14}$	112±1	N_9-O_2	1.25±0.04
$C_{14}-N_7$	1.36±0.05	$\angle C_{14}-S_2-Co$	93±1	N_9-O_3	1.28±0.04
N_7-N_1	1.34±0.04	$\angle N_7-C_{14}-S_2$	124±2	$\angle O_1-O_2-O_3$	62±1
N_1-C_{11}	1.28±0.05	$\angle N_7-C_{14}-N_8$	122±2	$\angle O_2-O_1-O_3$	57±1
$C_{11}-C_5$	1.49±0.05	$\angle S_2-C_{14}-N_8$	113±2	$\angle O_1-O_3-O_2$	61±1
C_5-N_4	1.45±0.04	$\angle Co-N_1-C_{11}$	121.8±0.7		
N_4-C_1	1.44±0.04	$\angle N_1-C_{11}-C_5$	110.8±0.5		
C_1-C_2	1.38±0.05	$\angle C_{11}-C_5-N_4$	109.8±0.7		
C_2-C_3	1.35±0.05	$\angle C_5-N_4-Co$	116±1		
C_3-C_4	1.48±0.05	$\angle N_4-C_5-C_4$	122.1±0.7		
C_4-C_5	1.43±0.05	$\angle C_5-C_4-C_3$	114.5±0.6		
		$\angle C_4-C_3-C_2$	123.5±0.6		
		$\angle C_3-C_2-C_1$	121.9±0.7		
		$\angle C_2-C_1-N_4$	122.1±0.5		
		$\angle C_1-N_4-C_5$	115.7±0.7		

and

$$-0.478\,X+7.961\;Y+2.839\;Z=2.502.$$

The maximum departures of the atoms from the planes are 0.07 and 0.11 Å with averages of 0.03 and 0.04 Å, respectively. The planes of the pyridine rings are inclined to the planes of their ligands at an angle of ~5°. The angle between the planes of ligands 1 and 2 is 87°. Figure 3 shows the packing of the molecules in the unit cell in the XZ projection, and intermolecular contacts less than 4 Å are shown.

The Co−S distances of 2.22 and 2.25 Å agree with the sum of the covalent radii (2.26 Å), and the Co−N distances of 1.87-1.91 Å are somewhat shorter than the corresponding distances for octahedral coordination of cobalt in similar classes of compounds. The crystallographically unrelated sulfur atoms also exhibit their chemical nonequivalence in differences in environment and in the C−S distances of 1.77 and 1.78 Å, which are somewhat greater than those observed in free thiosemicarbazones (1.678 and[7] 1.695 Å and[8] 1.684 Å). A tendency towards increase in the C−S distance was also observed in the nickel complex of 1-isoquinolinecarbaldehyde thiosemicarbazone.[7]

The results from the x-ray investigation of $[Co(PAT)]_2 \cdot NO_3$ confirmed the planar structure and tridentate character of the thiosemicarbazone, which was established in ref. 7 and was also established for the barium salt of the chelate of chromium (III) with the thiosemicarbazone of pyruvic acid.[9]

The whole of the computation was performed with the programs of the Institute of Chemical Physics. The authors are grateful to E. A. Gladkikh for assistance in the computations on the electronic computer.

---

[1] F. A. French and E. J. Blanz, Jr., J. Med. Chem., 9, 585 (1966).

[2] H. G. Petering, H. H. Buskirk, and G. E. Underwood, Cancer Res., 24, 367 (1964).

[3] H. G. Petering, H. H. Buskirk, J. A. Crim, and G. J. Van Giessen, Pharmacologist, 5, 271 (1963).

[4] A. V. Ablov and N. I. Belichuk, Zh. Neorgan. Khim., 14, 179 (1969).

[5] Kh. S. Mamedov and N. V. Belov, Dokl. Akad. Nauk SSSR, 106, 462 (1956).

[6] V. P. Golovachev, Yu. N. Drozdov, É. A. Kuz'min, V. V. Ilyukhin, A. N. Chernov, and N. V. Belov, Kristallografiya, 16, 725 (1971) [Sov. Phys.−Crystallogr., 16, 631 (1972)].

[7] M. Mathew and Gus Palenik, J. Amer. Chem. Soc., 91, 6310 (1969).

[8] E. J. Gabe, M. R. Taylor, J. Pickworth Glusker, J. A. Minkin, and A. L. Patterson, Acta Crystallogr., B25, 1620 (1969).

[9] G. F. Volodina, G. A. Kiosse, N. V. Gérbéléu, and A. V. Ablov, Dokl. Akad. Nauk SSSR, 200, 1346 (1971).

Crystal structure of lithium bitungstate $Li_2W_2O_7$

S. A. Magarill, R. F. Klevtsova, and V. V. Bakakin

Institute of Inorganic Chemistry, Siberian Branch, Academy of Sciences of the USSR

(Submitted February 14, 1972)
Kristallografiya, 18, 269-276 (March-April 1973)

The structure of lithium bitungstate $Li_2W_2O_7$ (a = 8.26, b = 7.10, c = 5.06 Å, α = 95°, β = 78°, γ = 110°, Z = 2, space group $P\bar{1}$) was determined from two-dimensional projections of the Patterson function and electron density with allowance for the crystal-chemical relationships and refined by the method of least squares to R = 0.126 from a three-dimensional set of 1152 F_{hkl} values. The tungsten–oxygen motif is a new one for tungstates; it is composed of two chains of the wolframite type, which are connected by a common edge to form an isolated $[W_4O_{14}]^{4-}_{\infty}$ band in the [001] direction. The bands of the lithium polyhedra (in the same direction) from octahedra and semioctahedra repeat the configuration of the tungsten–oxygen chains.

In refs. 1 and 2 it was shown that three stable compounds are formed in the $Li_2WO_4-WO_3$ system, i.e., Li_2WO_4, $Li_2W_2O_7$, and $Li_2W_4O_{13}$. Crystal structure data[3] are only available for Li_2WO_4.

The present work gives the results from an x-ray diffraction and crystal-chemical investigation of lithium bitungstate $Li_2W_2O_7$, obtained as an additional phase (solvent) in experiments on the synthesis of lithium–rare-earth tungstates.[4,5] The synthesized $Li_2W_2O_7$ single crystals are colorless and have a long-prismatic habit. The direction of elongation is subsequently taken as the c axis. Preliminary investigations[5] had shown that they belong to the triclinic system. In accordance with these data, refined unit cell parameters were established from rotational x-ray patterns and three scans of the zero layer lines: a = 8.26, b = 7.10, c = 5.06 Å; α = 95°, β = 78°, γ = 110°, V = 272.7 Å^3, d_m = 6.05 g/cm^2, d_x = 6.04 g/cm^3, Z = 2. The experimental data for the structural determination comprised the intensities of 1152 unique nonzero reflections ($\sin\theta/\lambda \leq 0.7$ Å^{-1}) with scans of the $hk\bar{5}$ to $h\bar{k}5$ layer lines recorded with rotation of the crystal (0.1 × 0.1 × 0.8 mm) about the c axis (equiinclination Weissenberg goniometer, molybdenum radiation). One of the reflections of the zero layer hk0 was used to prepare darkening standards with a step of $2^{1/4}$ by means of which the intensities were evaluated. In view of the negative results from a test for the piezoeffect the structure was solved within the scope of the centrosymmetric $P\bar{1}$ space group.

To fix the heavy atoms it was sufficient to use two-dimensional projections of the Patterson function P(uv) and P(vw). The coordinates of the two tungsten atoms determined from them were used to calculate the signs of the structural amplitudes F_{hk0} and F_{0kl} and subsequently to construct ρ(xy) and ρ(yz) electron density maps. However, the resulting maps only revealed the same tungsten atoms distinctly. To make a correct selection of coordinates for the oxygen atoms even at this stage it was necessary to use certain crystal-chemical relationships characteristic of this class of compounds.

Practice in the interpretation of structures in the tungstate and molybdate series[6-8] has shown that the W–W distances are undoubtedly related to the types of tungsten coordination polyhedra and the method by which they are linked. These distances, calculated from the preliminary coordinates of the tungsten atoms, were therefore analyzed. The shortest distances, which do not exceed 3.30 Å and are of the greatest interest, were found to be between the two related basis atoms W_1 and W_2 and the two (through the center of symmetry) W_1 atoms. According to refs. 9 and 10, in such a structure it must be expected, firstly, that the coordination of the tungsten will be greater than 4 and, secondly, that the tungsten polyhedra will have common elements (edges). Being guided by this, we were able to distinguish on the electron-density maps five of the seven basis oxygen atoms controlling their positions by calculation of the W–O and O–O separations. The remaining two oxygen atoms were localized after refinement of the known part of the structure from the three-dimensional data. It should be noted that the stability of the refinement of the oxygen coordinates and the values of their temperature corrections were in this case found to be the most sensitive criterion of the accuracy of the selected position, for the R factor changed insignificantly.

From the foregoing it is clear that difficulties arose even during determination of the coordinates of the oxygen atoms owing to the presence of the heavy tungsten, which exceeded the oxygen atoms (in scattering power) by ~10 times. This applies to an even greater degree to fixing of the light lithium atom, to the presence of which the R factor and electron density distribution were almost insensitive. The locations of the lithium atoms were therefore obtained only from the crystal-chemical relationships revealed in the structure.

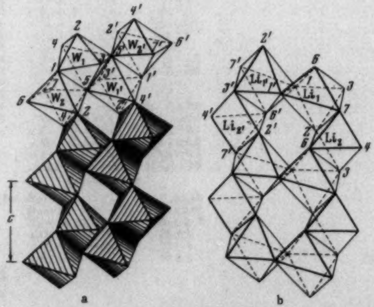

Fig. 1. Fragments of the $Li_2W_2O_7$ structure. a) Band with composition W_4O_{14} from tungsten–oxygen octahedra in projection on the (110) plane; b) motif of LiO_6 and LiO_5 polyhedra in the same projection.

The tungsten—oxygen motif (Fig. 1a) represents a band-like association of two chains of brookite—wolframite type from WO_6 octahedra with the characteristic lattice constant $c = 5.06$ Å. The band is, as it were, cut from the brookite structure (a two-level fragment in the ABC and CBA stacks of the layers of the general four-layer ABCBA packing of the anions). This provides grounds for supposing that the whole $Li_2W_2O_7$ structure conforms to a scheme of close packing in which the missing lithium atoms are easily located. With these aims and for comparative crystal-chemical analysis, it is convenient to represent the structure in the crystal-chemical aspect.[11] In our case the initial problem amounts to establishing the mutual arrangement of the bands of the tungsten—oxygen octahedra in a volume sufficient to isolate the "crystal-chemical cell" based on the translations characteristic of close packing. In the $Li_2W_2O_7$ structure one such translation, in the direction of the height of the face of the octahedron in the layer, i.e., the "level" of close packing (briefly, the "height" direction), is the c translation of the initial triclinic cell. Therefore, the projection of the structure along the c axis is convenient for further analysis.

Such a projection of the triclinic cell ABCD with the characteristically projecting ends of the idealized $(W_4O_{14})_\infty$ bands is presented at the top right of Fig. 2. Transfer of the beginning of the cell to another set of inversion centers such as that shown by the crosses conveniently places the band in the center of the cell but, at the same time, as it were, isolates it from the adjacent bands, reducing the external information on their mutual packing to zero. In such a cell it is difficult to see the crystal-chemical motif, especially as the close packing layers lie in a "complex" plane $(3\bar{2}0)$. Analysis of the combination of repeated translations of the cells makes it possible to establish that, firstly, the anions in the structure are arranged according to the law of three-layer close packing and, secondly, the shortest translation in the layer (apart from the reference c translation) is observed only in the projection through the 7,5 octahedra. In Fig. 2 it is denoted by DN. As follows from the nonintegral nature of the interval, the DN translation is not horizontal. Comparison of the relative heights of the points of the cell confirm that the point N occupies an intermediate level in relation to point D. Consequently, the elementary loop constructed on the two shortest translations in the layer is oblique-angled. Further extension of the motif to the left leads to the horizontal translation DK with an interval of 15 octahedra. This is the second standard crystal-chemical translation, perpendicular to the first "height" direction and coinciding in direction with the edge of the octahedra (or, briefly, the "edge" direction). The cell loop constructed on these translations is orthogonal.

Let us digress momentarily from the main problem, i.e., localization of the lithium atoms, and examine the few other possible cells, each of which is better according to crystal-chemical criteria than the reference cell constructed on the three shortest translations. First there is the primitive cell DACE. Compared with the reference "five-levels" cell it is located on only three levels, and with three-layer anion packing this makes it more convenient for comparison. It is related to the reference cell in the following way: $a' = 9.86$, $b' = b$, $c' = c$, $\alpha' = \alpha$, $\beta' = 83°$ (97°), $\gamma' = 61°$ (1190°). The figures in parentheses are the values for the standard cell with the origin of the coordinates at point D. The close-packing layers intersect it in the $(\bar{1}20)$ plane. In triclinic cells with translations AD and DN or CD and DN the two translations lie in the close-packing planes, but these cells are not primitive and contain one and two additional points.

In one of the minimal monoclinic cells DFGH there are already five additional points, and moreover the symbol for the close packing planes again has only one zero

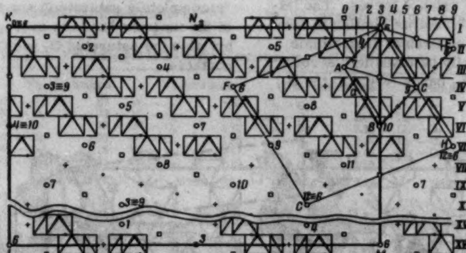

Fig. 2. Diagram of the packing of the bands of tungsten—oxygen octahedra in the $Li_2W_2O_7$ structure within the scope of close packing (height aspect). The roman numerals show the "levels" of packing by height in one octahedron. At the top right the vertical planes of concentration of the material units in close packing, separated by zones with a width of half an octahedron, are distinguished and numbered. The squares, crosses, and dark and light circles represent the four systems of inversion centers in the ab plane of the initial unit cell ABCD. The figures near the circles show their relative levels in thirds of the height of the octahedron face, which separate the sublevels of the horizontal "material" planes. The translation c is equal to six such sublevels. The various lines and letters distinguish several types of cells with common c translation: ABCD and DACE primitive triclinic; DFGH monoclinic; DKLM rhombic.

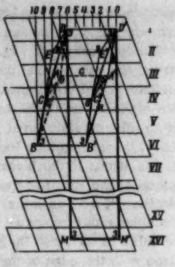

Fig. 3. Unit cells of $Li_2W_2O_7$ in close packing (edge aspect).

index (201). The other monoclinic cell with the same volume can be distinguished on the translations FD and DK; the symbol for the close-packing plane is (001). Finally, the minimal rhombic cell DKLM occupies 15 levels with a width of 15 octahedra. It is given here as an example of the standard crystal-chemical cell mainly for the methodical purposes of comparative analysis. A diagram of the reference and two derived unit cells in the edge aspect of the close packing is given in Fig. 3. Its translational depth is 15 octahedra. Their three-dimensional perception should be improved by parallel examination of the cells in two aspects.

Analysis of the arrangement of the W_4O_{14} bands in Fig. 2 leads to the establishment of a curious fact; while being located within the limits of the three-layer anion packing, some of the anionic positions (and indeed 1/15 of their total number) are "circumvented" by the bands and remain unoccupied. The conditions used for the synthesis of the given tungstate rule out the presence of water in it, and consequently these positions must be considered vacancies. In Figs. 2 and 4 they are shown by the squares.

To locate the lithium atoms we used the prepared scheme of free vacancies in close packing and, partly, the criterion of local balance of valence forces. The latter is not strictly observed in structures similar in composition with a wide range of "ponderable" interatomic separations, and it must primarily be taken into account in a qualitative way. In the W_4O_{14} bands (Fig. 1a) the O_3, O_6, and O_7 anions are combined with one tungsten atom, the O_1, O_2, and O_4 anions are combined with two tungsten atoms, and the O_5 anion is combined with one tungsten atom; the formal coordination of the tungsten atoms in respect of oxygen is 6. It is clear that the "supersaturated" O_5 will rather not enter into the coordination sphere of the lithium, while O_3, O_6, and O_7 must have a maximum of contacts with it.

A plan of the arrangement of the chains of WO_6 octahedra in one close packing level can be seen in the top part of Fig. 4. They form pairs of parallel arcs, having mirror reflections in the planes of symmetry DD' and NN' and "spoiled" by the vacancies before the pseudoplanes. This is the motif of the Debye pattern, of which the extended orthogonal loop DKK'D' is also reminiscent. The lithium polyhedra are located in a gap four to five octahedra wide between the pairs of tungsten arcs. An analysis of the possible positions suitable for lithium, the number of which is limited appreciably by the anionic vacancies, leads to two main crystallochemically reasonable variants. In one of them the lithium occupies the tetrahedral vacancies; as a result of 20–30 contemporary papers this coordination has become standard for it. The pyroxene-type chains of lithium tetrahedra, passing by the vacancies, link with the tungsten bands quite exquisitely. This variant is shown in the left half of Fig. 4. Its weak point can be considered the presence of a single contact between the lithium tetrahedron and one of the marginal O_7 anions with uniformly proportional distribution of the valence forces in the other "incompletely saturated" and "normally saturated" anions.

In the second variant the lithium is located in the octahedral vacancies lining the tetrahedral chains of the first variant (shown by the dashed line in Fig. 4). However, in half of the octahedra one apex is a vacancy, and the real coordination of the lithium is 5 while the coordination polyhedron is a semioctahedron. The distribution of the contacts between the lithium polyhedra and the "incompletely saturated" and "normally saturated" anions of the tungsten bands is averaged; each of the marginal, but also the saturated O_1 and O_2 atoms have two lithium contacts.

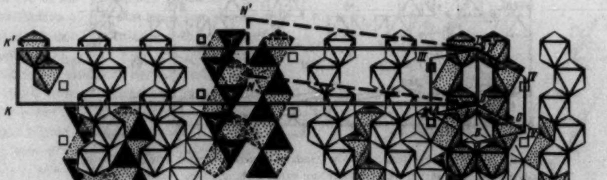

Fig. 4. Idealized structure of $Li_2W_2O_7$ in close packing (face aspect). One level of polyhedra is given in the top half and three levels (in part) are given in the bottom half. The actual variant of the location of the lithium atoms (the shaded octahedra and semioctahedra) are shown on the right and, in addition, the alternative hypothetical variant with the lithium atoms in tetrahedra (black) are shown on the left; the tungsten octahedra are not shaded. The squares show anionic vacancies in the two adjacent layers, and the roman numerals show the packing levels. Apart from the triclinic reference cell ABCDD'... with inclined translations (across one and two levels), the oblique-angled DD'N'N and right-angled DD'K'K loops on the two horizontal translations are distinguished.

TABLE 1. Coordinates of the Atoms and Standard Deviations in $Li_2W_2O_7$

Atoms	$x(\sigma_x)$	$y(\sigma_y)$	$z(\sigma_z)$	$B(\sigma_B)$
W_1	0.1654 (3)	0.9512 (4)	0.3156 (5)	0.09(2)
W_2	0.3217 (3)	0.2518 (4)	0.8030 (5)	0.10(2)
O_1	0.363 (9)	0.111 (10)	0.457 (15)	1.7(9)
O_2	0.244 (9)	0.937 (10)	0.973 (15)	1.8(9)
O_3	0.124 (8)	0.722 (10)	0.429 (14)	1.6(9)
O_4	0.203 (5)	0.244 (6)	0.150 (9)	0.1(5)
O_5	0.073 (7)	0.082 (9)	0.686 (13)	1.1(8)
O_6	0.535 (8)	0.312 (9)	0.862 (9)	1.3(9)
O_7	0.303 (12)	0.467 (15)	0.721 (19)	2.2(9)
Li_1*	0.37	0.80	0.55	—
Li_2*	0.23	0.58	0.05	—

*The coordinates of the lithium were determined by crystal-chemical methods.

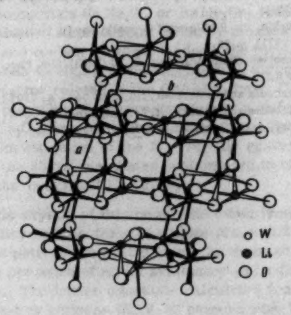

Fig. 5. The structure of $Li_2W_2O_7$ in projection along the c axis.

Calculation of the interatomic separations showed that the dimensions of the supposed lithium tetrahedra clearly exceed the standard dimensions; the edges are up to 3.9 Å with an average of 3.35 Å, and the Li–O distances are of the order of 2.15 Å. The lithium polyhedra of the second variant proved more compact with an average edge dimension of 3.2 Å and with reasonable approximate Li–O distances for six-fold and five-fold coordination. Detailed analysis of the interatomic separations gave new evidence in favor of this variant, within the scope of which the conclusion about the final coordinates for lithium was reached. The coordinates of the basis atoms, the isotropic temperature corrections, and the standard deviations obtained in the course of the refinement of the structure by the method of least squares[12] for all the atoms are presented in Table 1. They correspond to an R value of 0.126. The principal interatomic separations are given in Table 2.

The coordination polyhedra of the two tungsten atoms in the separate parts of the cell are distorted octahedra, and the observed spread in the W–O distances of 1.67-2.29 Å is typical of the structure of tungstates with coordination of this type in the tungsten. The main feature of the investigated structure is the projection of infinite isolated bands of tungsten octahedra parallel to the c axis (length) of the crystal (Fig. 1a). This band motif with the formula $[W_4O_{14}]^{4-}_{\infty}$, which has been described above in detail, is a new one for tungstates. The short W_1-W_2 distances of 3.26 and 3.29 Å given in Table 2 pertain to adjacent tungsten octahedra, which are connected through the common edges O_1-O_5 of 2.38 and O_2-O_4 of 2.39 Å and form a wolframite chain. Two chains are joined into a band through the common edge O_5-O_5' (2.44 Å) of two tungsten octahedra separated by a distance of 3.22 Å.

As clearly seen from Fig. 5, the oxygens of the individual tungsten bands do not have direct contacts between them, but are connected in the structure by means of the lithium cations. The motif of the lithium polyhedra is shown in Fig. 1b and, in conjunction with the tungsten–oxygen motif, in Fig. 4. At each given level the chains of octahedra and semioctahedra repeat the configuration of the tungsten–oxygen chains, joining into bands by their common edges with the marginal units in the pseudoplanes.

Alternation of motifs of M^{1+} polyhedra and Mo (or W) complexes is characteristic of the majority of structures in the investigated polymolybdates and polytungstates of

TABLE 2. The Principal Interatomic Separations in the $Li_2W_2O_7$ Structure

W_1 octahedron		W_2 octahedron		Li_1 octahedron		Li_2 semioctahedron	
W_1-O_3	1.67	W_2-O_7	1.68	Li_1-O_3	2.07	Li_2-O_7	1.86
W_1-O_2	1.73	W_2-O_6	1.75	Li_1-O_1	2.09	Li_2-O_6	1.90
W_1-O_1	1.88	W_2-O_4	1.82	Li_1-O_6	2.28	Li_2-O_3	2.26
W_1-O_5	1.90	W_2-O_1	1.96	Li_1-O_1'	2.35	Li_2-O_4	2.46
W_1-O_5'	2.13	W_2-O_5	2.17	Li_1-O_2	2.46	Li_2-O_2	2.58
W_1-O_4	2.21	W_2-O_2	2.29	Li_1-O_7	2.50		
Mean	1.92	Mean	1.93	Mean	2.29	Mean	2.21
*O_1-O_5	2.38	*O_1-O_5	2.38	**O_1-O_6	2.75	**O_4-O_7	2.62
*O_2-O_4	2.39	*O_2-O_4	2.39	$O_1'-O_3$	2.80	$O_6'-O_7$	2.75
*O_5-O_5'	2.44	O_4-O_7	2.62	O'_1-O_3	2.90	O_2-O_3'	2.77
O_3-O_5''	2.65	O_2-O_5	2.70	O_3-O_6	3.00	O'_3-O_6'	3.00
O_1-O_4	2.65	O_4-O_6	2.73	O_2-O_3	3.16	O_4-O_6'	3.15
O_4-O_5'	2.68	O_1-O_6	2.75	O_1-O_1'	3.31	O_3-O_6'	2.22
O_2-O_3	2.69	O_6-O_7	2.75	O_3-O_7	3.32	O_2-O_7	3.64
O_2-O_5''	2.79	O_5-O_7	2.76	O_6-O_7	3.37	$O_3'-O_4$	3.79
O_1-O_3	2.80	O_4-O_5	2.78	O_1-O_7	3.40	Mean	3.12
O_1-O_2	2.85	O_1-O_2	2.85	$O_1'-O_6$	3.58		
O_4-O_3	2.88	O_1-O_7	2.90	O_2-O_7	3.64		
O_3-O_5	2.89	O_2-O_6	2.92	O_1-O_3	3.65		
Mean	2.80	Mean	2.71	Mean	3.24		
$W_1-W'_1$	3.22	Li_1-Li_2	2.89				
W_1-W_2	3.29	$Li_1'-Li_2$	2.96				
W_1-W_2	3.26						
$W_1'-W_2$	3.94						

The primes denote the atoms related to the basis atoms by symmetry operations. One asterisk denotes edges common to two tungsten octahedra; two asterisks denote edges common to tungsten and lithium polyhedra.

the alkali metals. Their analysis, performed in ref. 13, has shown that the stability of the structural type depends on the structure of the molybdenum (or tungsten) complex itself. If it is sufficiently elastic, as occurs in the $K_2Mo_3O_{10}$ structure,[14] the structural type is retained when potassium is replaced by rubidium and cesium, while the more rigid complex in $K_2Mo_4O_{13}$ leaves the structure unchanged only when potassium is replaced by rubidium. By further comparing the bimolybdates of sodium and potassium,[8–15] we notice that the molybdenum–oxygen motif in them is similarly represented by chains of tetrahedra and octahedra. Replacement of sodium by potassium only leads to a change in the nature of the bond between the molybdenum polyhedra. A more radical rearrangement takes place when lithium and sodium are replaced in the bitungstates[15] $Li_2W_2O_7$ and $Na_2W_2O_7$. The tungsten–oxygen bands which have been recorded in $Li_2W_2O_7$ possess such a rigid configuration, little subject to deformation, that increase in the ionic radius of M^{1+} changes not only the nature of the bond of the tungsten polyhedra, as occurred in the previous case, but also the coordination of the tungsten atoms.

---

[1] F. Z. Hoermann, Z. Anorgan. Allgem. Chem., 177, 145 (1928).

[2] S. Sakka, Bull. Inst. Chem. Res. Kyoto Univ., 46, 6, 300 (1961).

[3] W. H. Zachariasen and H. A. Plettinger, Acta Crystallogr., 14, 229 (1961).

[4] P. V. Klevtsov and L. P. Kozeeva, Kristallografiya, 15, 57 (1970) [Sov. Phys. – Crystallogr., 15, 44 (1970)].

[5] P. V. Klevtsov, L. P. Kozeeva, and R. F. Klevtsova, Izv. Akad. Nauk SSSR, Neorgan. Materialy, 7, 8, 1461 (1971).

[6] S. V. Borisov and R. F. Klevtsova, Kristallografiya, 15, 38 (1970) [Sov. Phys. – Crystallogr., 15, 28 (1970)].

[7] R. F. Klevtsova and N. V. Belov, Kristallografiya, 15, 43 (1970) [Sov. Phys. – Crystallogr., 15, 32 (1970)].

[8] S. A. Magarill and R. F. Klevtsova, Kristallografiya, 16, 742 (1971) [Sov. Phys. – Crystallogr., 16, 645 (1972)].

[9] L. Kihlborg, Arkiv Kemi, 21, 44, 471 (1964).

[10] S. V. Borisov, Kristallografiya, 17, 5 (1972) [Sov. Phys. – Crystallogr., 17, 1 (1972)].

[11] V. V. Bakakin, in: Problems of Crystallology [in Russian], Izd. MGU, Moscow (1971), p. 50.

[12] F. A. Brusentsev, Kristallografiya, 8, 10 (1963) [Sov. Phys. – Crystallogr., 8, 7 (1963)].

[13] B. M. Gatehouse and P. Leverett, J. Chem. Soc., A, 2107 (1971).

[14] B. M. Gatehouse and P. Leverett, J. Chem. Soc., A, 1398 (1968).

[15] M. Seleborg, Acta Chem. Scand., 21, 2, 499 (1967).

Crystal structure of the compound $EuMg_3Ge_3$

O. F. Zmii, E. I. Gladyshevskii, and V. S. Bul'o
L'vov State University

(Submitted February 28, 1972)
Kristallografiya, 18, 277-280 (March-April 1973)

The structure of the compound $EuMg_3Ge_3$ (a = 4.485, b = 30.60, c = 4.485 Å, Z = 4, space group Cmcm) belongs to a new type derived from the AlB_2, $CeMg_2Si_2$, and CaF_2 types. The coordination numbers of the atoms are as follows: Eu 20; $Mg^{(1)}$ 11; $Mg^{(2)}$ 11; $Mg^{(3)}$ 10. The coordination polyhedra of the atoms with the smaller dimensions are trigonal prisms with additional apices, tetragonal antiprisms with additional apices, and cubes. The atomic parameters were refined by two-dimensional Fourier syntheses with R = 17.2% for 112 0kl reflections and R = 17.7% for 97 hk0 reflections.

In the Re–Me–Si and Re–Me–Ge systems, where Re is a rare-earth metal and Me is a metal of the iron group, there are compounds $ReMe_2Si_2$ or $ReMe_2Ge_2$ isostructural with $CeAl_2Ga_2$.[1,2] Replacement of Me by magnesium in the lanthanum and cerium systems leads to the formation of the compounds $CeMg_2Si_2$ and $LaMg_2Si_2$ with structures of the $CeMg_2Si_2$type related to the $CeAl_2Ga_2$ type. Compounds similar to composition but constructed on a different principle (the La_2O_2S type) have been found in the Re–Al–Si systems. Investigation of the Eu–Mg–Ge system by analogy with the above-mentioned systems led to the discovery of the compound $EuMg_3Ge_3$.

A single crystal of this compound taken from the $Eu_{20}\cdot Mg_{40}Ge_{40}$ alloy had the form of a plate (0.5 × 0.2 × 0.03 mm). Laue patterns recorded along the three directions showed the presence of mmm symmetry and a four-fold pseudoaxis. The lattice constants calculated from the rotational x-ray patterns (RKV-86 camera with Fe K radiation) and refined by the powder pattern (RKD-57.3 camera with Cr K radiation) have the following values: a = 4.485 ± 0.004, b = 30.60 ± 0.04, c = 4.485 ± 0.004 Å. The unit cell contains four formula units (ρ_m = 4.64 g · cm^{-3}, ρ_x = 4.80 g · cm^{-3}). By indexing the rotational and Weissenberg 0kl, 1kl, hk0, and hkl patterns, recorded on an equiinclination goniometer with Cu K radiation, it was possible to establish that the structure of the compound $EuMg_3Ge_3$ belonged to one of the following three space groups: Cmcm; $Cmc2_1$; C2cm. The location of the maxima on the projection of the interatomic function only at levels x = 0.00 and x = 0.50 (Fig. 1a) made it possible to choose the centrosymmetric group Cmcm. Analysis of the interatomic function showed that the europium atoms are in position 4 (c) 0y¼ with y = 0.06. The first Fourier synthesis was computed from the signs of the structural amplitudes with allowance for only the europium atoms. In all 112 0kl and 97 hk0 reflections, evaluated visually and corrected by introduction of the polarization and Lorentz factors, were used. Electron-density maps confirmed the accuracy of the coordinates of the europium atoms and made it possible to localize the remaining atoms of the structure (Fig. 1b). The positions of these atoms are as follows: Eu 4(c) 0y¼, y = 0.058; $Mg^{(1)}$ 4(c), y = 850; $Mg^{(2)}$ 4(c), y = 0.750; $Mg^{(3)}$ 4(c), y = 0.645; $Ge^{(1)}$ 4(c), y = 0.483; $Ge^{(2)}$ 4(c), y = 0.402; $Ge^{(3)}$ 4(c), y = 0.197. The divergence factors calculated for all the nonzero reflections are as follows: R_{0kl} = 17.2% (B = 1.0); R_{hk0} = 17.7% (B = 0.9).

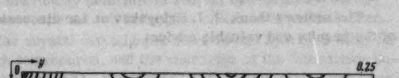

Fig. 1. Projection of the interatomic function (a) and electron density (b) of the structure of $EuMg_3Ge_3$ onto the XY plane.

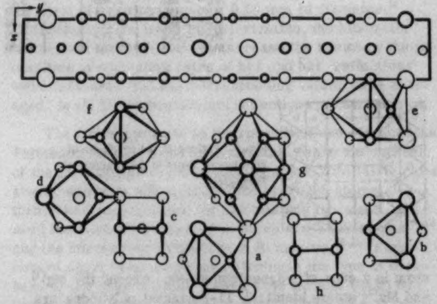

Fig. 2. Projection of the structure of $EuMg_3Ge_3$ onto the XY plane and the coordination polyhedra of the atoms. a) $Ge^{(1)}$; b) $Ge^{(2)}$; c) $Ge^{(3)}$; d) $Mg^{(1)}$; e) $Mg^{(2)}$; f) $Mg^{(3)}$; g) Eu; h) vacant cube. The light circles on the projection correspond to atoms with z = 0.25, and the heavy circles correspond to z = 0.75.

The projection of the unit cell of $EuMg_3Ce_2$ onto the XY plane and the coordination polyhedra of the atoms are presented in Fig. 2. The germanium atoms are characterized by coordination numbers of 8 and 9 and by coordination polyhedra of three types. The $Ge^{(1)}$ atom is at the center of a trigonal prism of europium atoms with additional germanium atoms opposite the center of the quadrangular faces, and the $Ge^{(2)}$ atom is at the center of a tetragonal antiprism of four europium atoms and four magnesium atoms with an additional germanium atom opposite the center of the larger face formed by the europium atoms. The coordination polyhedron of the $Ge^{(3)}$

TABLE 1. Interatomic Separations (δ) and Coordination Numbers (C.N.) of the Atoms in the Structure of $EuMg_3Ge_3$

Atoms	δ, Å	C.N.	Σr	Atoms	δ, Å	C.N.	Σr
Eu — 4Eu	4.435	20	4.04	$Mg^{(3)}$ — 4Mg	3.174	10	3.20
Eu — 2Eu	4.199		4.04	$Mg^{(3)}$ — Mg	3.213		3.20
Eu — 2Mg	3.599		3.62	$Mg^{(3)}$ — Mg	3.060		3.20
Eu — 2Mg	3.480		3.62	$Mg^{(3)}$ — 4Ge	2.767		2.99
Eu — 2Ge	3.208		3.41	$Ge^{(1)}$ — 4Eu	3.410	9	3.41
Eu — 4Ge	3.399		3.41	$Ge^{(1)}$ — 2Eu	3.208		3.41
$Mg^{(1)}$ — 2Eu	3.599	11	3.62	$Ge^{(1)}$ — 2Ge	2.472		2.78
$Mg^{(1)}$ — 4Mg	3.174		3.20	$Ge^{(1)}$ — Ge	2.479		2.78
$Mg^{(1)}$ — Mg	3.060		3.20	$Ge^{(2)}$ — 4Eu	3.399	9	3.41
$Mg^{(1)}$ — 2Ge	2.663		2.99	$Ge^{(2)}$ — 2Mg	2.749		2.99
$Mg^{(1)}$ — 2Ge	2.749		2.99	$Ge^{(2)}$ — 2Mg	2.664		2.99
$Mg^{(2)}$ — 2Eu	3.480	11	3.62	$Ge^{(2)}$ — Ge	2.479		2.78
$Mg^{(2)}$ — 4Mg	3.174		3.20	$Ge^{(3)}$ — 4Mg	2.767	8	2.99
$Mg^{(2)}$ — Mg	3.213		3.20	$Ge^{(3)}$ — 2Mg	2.749		2.99
$Mg^{(2)}$ — 2Ge	2.749		2.99	$Ge^{(3)}$ — 2Mg	2.664		2.99
$Mg^{(2)}$ — 2Ge	2.663		2.99				

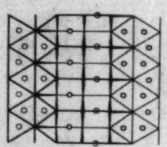

Fig. 3. Packing of the polyhedra of germanium atoms in the structure of $EuMg_3Ge_3$.

atom is a cube of magnesium atoms. Around the $Mg^{(1)}$ and $Mg^{(2)}$ atoms identical 11-cornered polyhedra are formed from two europium atoms, five magnesium atoms, and four germanium atoms; they are bounded by two quadrangular and 14 triangular faces. The coordination polyhedron of the $Mg^{(3)}$ atom is a 10-cornered polyhedron of six magnesium atoms and four germanium atoms; it differs from the 11-cornered polyhedra of the $Mg^{(1)}$ and $Mg^{(2)}$ atoms in that the two europium atoms are replaced by one magnesium atom, as a result of which it is bounded by 14 triangular faces. The europium atoms are characterized by a coordination number of 20 and a coordination polyhedron with mmm symmetry, containing six europium atoms, four magnesium atoms, and 10 germanium atoms; it has eight quadrangular and 20 triangular faces.

Altogether the structure of $EuMg_3Ge_3$ can be represented as packing of the following sorts of two-dimensional components parallel to the XZ planes: 1) walls[3] of $[EuGe_6]$ trigonal prisms; 2) layers of $[GeEu_4Mg_4]$ tetragonal antiprisms and vacant tetragonal pyramids; 3) layers of filled $[GeMg_8]$ and vacant cubes; the units are repeated in the order 1, 2, 3, 3, 2, 1, 2, 3 (Fig. 3). By examining the unit cell in the given aspect it is possible to break it down into fragments characteristic of known types of structures. The fragment from the trigonal prisms corresponds to the $EuGe_2$ structure,[4] but the Ge atoms form not corrugated but flat networks, as in the AlB_2 structure;[5] the height of the triangular base of the prism, parallel to the Y axis, is approximately equal to a_{EuGe_2}. The next fragment of the structure – it consists of a tetragonal antiprism and a vacant pyramid – can be regarded as half the unit cell of a structure of the $CeMg_2Si_2$ type,[6] i.e., the hypothetical compound $EuMg_2Ge_2$; the height of the tetragonal antiprism corresponds to $(\frac{1}{2})\,c_{CeMg_2Si_2}$. The double layer of cubes originates from the structure of Mg_2Ge (the CaF_2 type);[7] its thickness is approximately equal to a_{Mg_2Ge}. The sum of the dimensions of the described fractions in the appropriate multiples corresponds to the constant b of the $EuMg_3Ge_3$ structure. If the dimensions of the $EuMg_3Ge_3$ unit cell in the X and Z directions are considered, $a = b \approx a_{Mg_2Ge}/\sqrt{2} \approx a_{CeMg_2Si_2} \approx c_{EuGe_2}$.

Analysis of the interatomic separations in the $Eu\cdot Mg_3Ge_3$ structure (Table 1) shows that in each fragment there are the same deviations from the sums of the atomic radii as those which are typical of the respective structures. Thus, the δ_{Ge-Ge} distances are shortened in the layer of trigonal prisms, and the δ_{Mg-Mg} and δ_{Mg-Ge} distances are shortened in the layer of cubes.

The composition of the compound can also be represented in terms of the following "structural components": $2EuMg_3Ge_3 = EuGe_2 \cdot \text{"}EuMg_2Ge_2\text{"} \cdot 2Mg_2Ge$. The number of atoms in the unit cell (28) is equal to the sum of the numbers of the atoms of the separate fragments of the structure: $4EuMg_3Ge_3 = 2EuGe_2 + \text{"}EuMg_2Ge_2\text{"} + \frac{1}{2}(Mg_8Ge_4)$.

The authors thank P. I. Kripyakevich for discussion of the results and valuable advice.

---

[1] O. I. Bodak, E. I. Gladyshevskii, and P. I. Kripyakevich, Izv. Akad. Nauk SSSR, Neorgan. Mat., 2, 2151 (1966).

[2] Z. Ban and M. Sikirica, Acta Crystallogr., 18, 594 (1965).

[3] P. I. Kripyakevich, Zh. Strukt. Khim., 4, 2, 228 (1963).

[4] E. I. Gladyshevskii (Gladishevs'kii), Dopovidi Akad. Nauk URSR, 2, 209 (1964).

[5] W. Hofmann and W. Janicke, Z. Phys. Chem., 31, 3, 214 (1936).

[6] O. F. Zmii and E. I. Gladyshevskii, Kristallografiya, 15, 939 (1970) [Sov. Phys. – Crystallogr., 15, 817 (1971)].

[7] Strukturbericht, Vol. 1, Akad. Verlagges., Leipzig (1931), pp. 148, 185.

Crystal structure of sodium hydrosilicate $Na_3HSiO_4 \cdot 5H_2O$

Yu. I. Smolin, Yu. F. Shepelev, and I. K. Butikova
Institute of the Chemistry of Silicates, Academy of Sciences of the USSR

(Submitted March 16, 1972)
Kristallografiya, 18, 281-286 (March-April 1973)

The crystal structure of sodium hydrosilicate (a = 11.78, b = 10.94, c = 12.96 Å, Pbc$a$, Z = 8) was determined by direct methods. The intensities of 1180 reflections were measured by means of a diffractometer. The positions of the hydrogen atoms were determined. The coordinates of the atoms including the hydrogen were refined by the method of least squares to an R value of 0.05. It was shown that silicon–oxygen tetrahedra are linked in pairs by hydrogen bonds to form groups with the composition $Si_2O_6(OH)_2$. A crystallochemical description of the structure is given.

The existence of various hydrated sodium silicates has been established during investigation of the phase equilibria in the $Na_2O-SiO_2-H_2O$ system.[1-7] Preliminary x-ray data on compounds with the composition $Na_2O \cdot SiO_2 \cdot xH_2O$ (where x = 5, 6, 8, or 9) and also $3Na_2O \cdot 2SiO_2 \cdot 11H_2O$ were obtained by Jamieson and Dent-Glasser on crystals grown from aqueous solutions at room temperature.[8] Investigations into the infrared spectra of some compounds in this series by Ryskin, Stavitskaya, and Mitropol'skii showed the presence of Si–O–H and the absence of Si–O–Si bonds in these crystal hydrates.[9] The crystal structures of $Na_2O \cdot SiO_2 \cdot xH_2O$ compounds were subsequently determined by Jost and Hilmer for[10] x = 5 and by Jamieson and Dent-Glasser for x = 6 and[11,12] 9. All these crystals contain discrete SiO_4 tetrahedra. Although the hydrogen atoms were not localized, analysis of the interatomic separations made it possible to suppose the existence, in the structures of $Na_2H_2SiO_4 \cdot 4H_2O$ and $Na_2H_2SiO_4 \cdot 5H_2O$, of infinite chains of silicon–oxygen tetrahedra $SiO_2(OH)_2$, each of which is combined with the next by two hydrogen bonds. In a recent paper Williams and Dent-Glasser have refined the structure of $Na_2H_2 \cdot SiO_4 \cdot 5H_2O$ and determined the position of the hydrogen atoms by the neutron-diffraction method.[13] In this case the existence of chains of the above-mentioned type was demonstrated directly. In the $Na_2H_2SiO_4 \cdot 8H_2O$ crystal the $SiO_2(OH)_2$ groups form hydrogen bonds only with water molecules, and this was also established from analysis of the interatomic separations.

The present work was devoted to determination of the structure of $3Na_2O \cdot 2SiO_2 \cdot 11H_2O$. As stated above, all the previously determined sodium hydrosilicate structures contained two hydrogens on each SiO_4 tetrahedron. In the crystal investigated there is one hydrogen atom for each tetrahedron, and the character of the interaction between the SiO_4 tetrahedra, the water molecules, and the cations here must clearly differ from the previously described structures. Of special interest is the problem of localizing the hydrogen atoms from the x-ray data. The $Na_3HSiO_4 \cdot 5H_2O$ crystal, grown by crystallization from aqueous solution at room temperature, was investigated. The unit cell parameters (a = 11.780 ± 0.005, b = 10.940 ± 0.004, c = 12.958 ± 0.005 Å) were close to those previously determined by Jamieson and Dent-Glasser.[8] The observed systematic extinctions confirmed the space group Pbc$a$ with Z = 8 obtained by these authors. The intensities of the x-ray reflections were measured on a single-crystal diffractometer with a scintillation counter by a perpendicular beam system with monolayer recording and Mo Kα radiation monochromatized by reflection from a monochromator crystal. The crystal investigated was given the form of a polished sphere 0.28 mm in diameter.[14] Corrections were made for polarization, the kinematic factor, and absorption.[15] To increase the accuracy the intensities of equivalent pairs of hk$l$ and $\bar{h}$kl reflections were measured and the corresponding values were averaged. In all 1180 nonequivalent reflections were measured.

The initial attempts to interpret the three-dimensional Patterson function were unsuccessful. Since the unit cell of the investigated crystal contains atoms with fairly close atomic numbers (disregarding the hydrogen atoms), we turned to direct methods for determining the signs. We used the statistical equation of Sayre and Zachariasen[16-18] and the comparison procedure of Rumanova.[19,20] Eight sets of signs were compiled, differing in the type of evenness of the indices which included the largest U(hk$l$) between 0.15 and 0.4. In three chains of types 2n + 1, 2n, 2n; 2n, 2n + 1, 2n; and 2n, 2n, 2n + 1, including 91 of the U(hk$l$), the signs were placed arbitrarily, and this corresponded to choice of the origin of the coordinates at one of the eight centers of symmetry in the unit cell. Determination of the signs of the remaining sets, by means of Sayre–Zachariasen equation, increased the number of known signs to 227. The obtained group of U(hk$l$) was then used as reference, and the signs of a further 92 of the U(hk$l$) lying between 0.12 and 0.15 were determined on its basis by means of the statistical equation. In all, the signs of the 319 strongest unique F(hk$l$) values were determined in this way from the total number of 1180. Analysis of the three-dimensional electron density map plotted from the 319 amplitudes made it possible to determine the coordinates of all the atoms except the hydrogens. The structure was then refined in the complete F(hk$l$) set by the method of least squares[21] using the weighting system proposed by Cruickshank[22] to an R value of 0.085. The hydrogen atoms were determined from a three-dimensional difference synthesis which was then made. (All the obtained atoms were deducted.) The electron-density maxima corresponding to the hydrogen atoms were clearly distinguished against the background level if the two peaks stronger than hydrogen situated at the positions of the distant atoms were not considered.

The structure was then refined again by the method of least squares in all 1180 measured reflections using the Cruickshank weighting system. The atomic factors were used for the neutral atoms.[23] The position and thermal parameters of all the atoms, including hydrogen, were refined to an R value of 0.050. The final values for the parameters of the structure are presented in Table 1. The O_1, O_2, O_3, and O_4 atoms belong to the silicon–oxygen tetrahedra, and the others belong to the water. The errors

TABLE 1. Coordinates of the Atoms, Mean-Square Errors, and Temperature Factors

Atoms	x/a	σ_x/a	y/b	σ_y/b	z/c	σ_z/c	B, Å
Na_1	0.3265	0.0001	0.6329	0.0001	0.3705	0.0001	1.94
Na_2	0.1845	0.0001	0.6090	0.0001	0.5811	0.0001	1.90
Na_3	0.3395	0.0001	0.3787	0.0001	0.6792	0.0001	2.10
Si	0.47773	0.00006	0.62466	0.00006	0.63020	0.00008	0.95
O_1	0.3779	0.0002	0.5459	0.0002	0.5662	0.0002	1.39
O_2	0.4676	0.0002	0.7671	0.0002	0.5946	0.0002	1.48
O_3	0.6020	0.0002	0.5701	0.0002	0.6044	0.0002	1.50
O_4	0.4444	0.0002	0.5990	0.0002	0.7494	0.0002	2.00
O_5	0.3625	0.0002	0.5590	0.0002	0.1912	0.0002	1.79
O_6	0.2362	0.0002	0.6986	0.0002	0.7577	0.0002	1.86
O_7	0.2501	0.0002	0.7138	0.0002	0.0056	0.0002	2.27
O_8	0.5122	0.0002	0.7434	0.0002	0.3859	0.0002	2.24
O_9	0.3653	0.0002	0.4300	0.0002	0.8933	0.0002	2.39
H_1	0.423	0.004	0.512	0.004	0.222	0.004	1.4
H_2	0.402	0.004	0.625	0.004	0.155	0.003	0.8
H_3	0.304	0.004	0,655	0.004	0.757	0.004	1.5
H_4	0.188	0.004	0.652	0.004	0.794	0.004	1.3
H_5	0.318	0.004	0.693	0.004	0.022	0.004	2.2
H_6	0.209	0.004	0.650	0.004	0.022	0.004	1.5
H_7	0.480	0.004	0.810	0.004	0.341	0.003	1.2
H_8	0.505	0.004	0.765	0.005	0.453	0.004	2.1
H_9	0.417	0.006	0.365	0.005	0.900	0.005	4.5
H_{10}	0.402	0.005	0.494	0.005	0.852	0.004	2.9
H_{11}	0.393	0.005	0.494	0.005	0.498	0.004	4.2

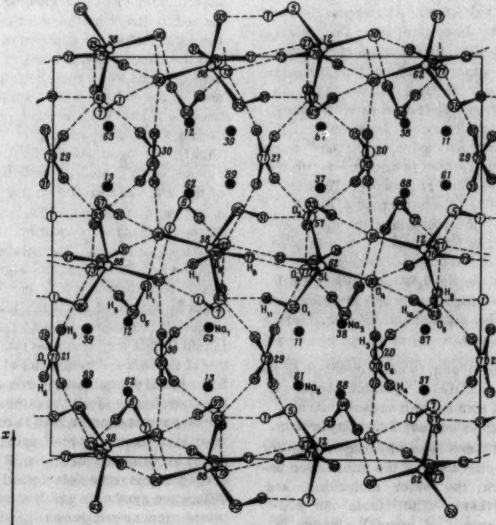

Fig. 1. Projection of the structure of sodium hydrosilicate $Na_3HSiO_4 \cdot 5H_2O$ onto the (010) plane. The figures give the y coordinates of the atoms in hundredths of the lattice constant.

in the determination of the temperature factors were 1–1.3 Å for hydrogen and less than 0.03 Å² for the other atoms. The structure obtained is presented in Fig. 1 in projection onto the (010) plane. The y coordinates of the atoms are given in the circles. The hydrogen bonds are shown as dashed lines.

The three independent sodium atoms have coordination numbers of 6, 7, and 7. Their coordination polyhedra are presented in Fig. 2a–c. In the surroundings of the sodium atoms only the O_1, O_3, and O_4 oxygen belong to the silicon–oxygen radicals, and the other oxygen atoms belong to the water molecules. The coordination polyhedra

TABLE 2. The Na−O Separations in the Sodium Polyhedra, Å

Na_1-O_1	2.776±0.003	Na_2-O_1	2.389±0.002	Na_3-O_1	2.386±0.003
Na_1-O_3	2.398±0.002	Na_2-O_5	2.392±0.003	Na_3-O_4	2.861±0.003
Na_1-O_5	2.496±0.003	Na_2-O_6	2.564±0.003	Na_3-O_5	2.480±0.003
Na_1-O_6	2.581±0.003	Na_2-O_7	2.305±0.003	Na_3-O_6	2.390±0.003
Na_1-O_7	2.587±0.003	Na_2-O_8	2.629±0.003	Na_3-O_7	3.682±0.003
Na_1-O_8	2.507±0.003	Na_2-O_9	2.540±0.003	Na_3-O_8	2.356±0.003
Na_1-O_9	2.380±0.003			Na_3-O_9	2.848±0.003

TABLE 3. Separations (Å) and Angles in the SiO_4 Tetrahedron

$Si-O_1$	1.677±0.002	O_1-O_2	2.666±0.003	O_1-Si-O_2	107°27′
$Si-O_2$	1.629±0.002	O_1-O_3	2.698±0.003	O_1-Si-O_3	110°02′
$Si-O_3$	1.616±0.002	O_1-O_4	2.568±0.003	O_1-Si-O_4	102°22′
$Si-O_4$	1.618±0.003	O_2-O_3	2.677±0.003	O_2-Si-O_3	111°10′
		O_2-O_4	2.731±0.003	O_2-Si-O_4	114°33′
		O_3-O_4	2.661±0.003	O_3-Si-O_4	110°46′

TABLE 4. Interatomic Separations (Å) and Angles in the Water Molecules and (OH) Group

H_1-O_5	0.96±0.04	$H_1-O_5-H_2$	104°07′
H_2-O_5	0.98±0.04		
H_3-O_6	0.93±0.05	$H_3-O_6-H_4$	105°42′
H_4-O_6	0.89±0.05		
H_5-O_7	0.86±0.05	$H_5-O_7-H_6$	112°47′
H_6-O_7	0.93±0.05		
H_7-O_8	1.01±0.04	$H_7-O_8-H_8$	109°22′
H_8-O_8	0.91±0.05		
H_9-O_9	0.94±0.06	$H_9-O_9-H_{10}$	107°36′
$H_{10}-O_9$	0.99±0.05		
$H_{11}-O_1$	1.06±0.06	$Si-O_1-H_{11}$	124°40′

TABLE 5. Lengths of Hydrogen Bonds (Å) and Angles of the Hydrogen Atoms

$H_1 \ldots O_4$	2.02±0.04	$O_5-H_1 \ldots O_4$	166°16′
$H_2 \ldots O_3$	1.61±0.04	$O_5-H_2 \ldots O_3$	179°27′
$H_3 \ldots O_4$	1.76±0.05	$O_6-H_3 \ldots O_4$	169°29′
$H_4 \ldots O_2$	1.89±0.05	$O_6-H_4 \ldots O_2$	167°00′
$H_5 \ldots O_2$	2.04±0.05	$O_7-H_5 \ldots O_2$	149°05′
$H_6 \ldots O_3$	1.86±0.05	$O_7-H_6 \ldots O_3$	159°00′
$H_7 \ldots O_4$	1.60±0.05	$O_8-H_7 \ldots O_4$	167°16′
$H_8 \ldots O_2$	1.89±0.05	$O_8-H_8 \ldots O_2$	163°14′
$H_9 \ldots O_2$	1.73±0.06	$O_9-H_9 \ldots O_2$	168°38′
$H_{10} \ldots O_4$	1.83±0.05	$O_9-H_{10} \ldots O_4$	165°18′
$H_{11} \ldots O_3$	1.51±0.05	$O_1-H_{11} \ldots O_3$	170°49′

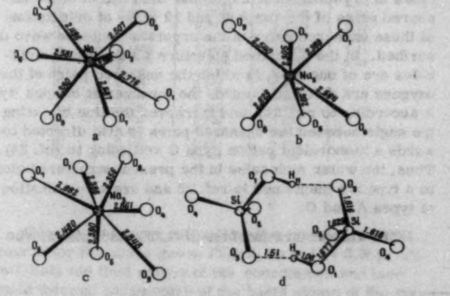

Fig. 2. Coordination polyhedra of sodium atoms (a–c) and the $Si_2O_6(OH)_2$ group (d).

of the sodium atoms are linked in the structure by their faces into four infinite columns extending along the direction of the c axis, and the common faces are $O_1O_7O_9$, $O_6O_7O_8$, and $O_5O_6O_9$. At these faces contacts are realized between the Na_1 and Na_2, Na_2 and Na_3, and Na_1 and Na_3 polyhedra, respectively. These columns are joined by common O_1 and O_5 apices into layers parallel to the (100) plane. The layers are in turn linked in the direction of the *a* axis by the O_8 apices and are drawn together by the silicon–oxygen tetrahedra situated between them. The interatomic separations in the coordination polyhedra of sodium atoms are presented in Table 2.

As mentioned above, in all the previously determined structures of the crystal hydrates of the acid silicates of sodium the silicon–oxygen tetrahedra $SiO_2(OH)_2$, linked by hydrogen bonds, formed infinite chains or discrete $SiO_2(OH)_2$ groups. In the structure described the $SiO_3(OH)$ tetrahedra are linked in pairs around the centers of symmetry by hydrogen bonds to form $Si_2O_6(OH)_2$ groups. This fragment of the structure is shown in Fig. 2d. The distances and angles in the tetrahedron are presented in Table 3.

Extremely high strength must be assigned to the hydrogen bond between the tetrahedra. The distance between the oxygens which it joins is 2.560 ± 0.003 Å and is less than the length of the edges of the SiO_4 tetrahedra. As seen from Table 3, the distance from the silicon to the oxygen forming the covalent O−H bond is appreciably greater than the remaining Si−O bonds of the tetrahedron. A decrease of this type in the order of the Si−OH bond has been observed many times.[8,13] Above it was mentioned that only the O_1, O_3, and O_4 oxygens of the SiO_4 tetrahedron are directly involved in the formation of the coordination polyhedra of sodium. The O_1 oxygen, which forms the OH bond, has three more sodium atoms in its environment. Each of the O_3 and O_4 atoms are in contact with only one sodium atom. The water molecules in the structure are contained in the coordination polyhedra of the cations, forming hydrogen bonds with the oxygens of the SiO_4 tetrahedra. The O_2 and O_4 atoms are each joined by four hydrogen bonds, while the O_3 atom is involved in three hydrogen bonds, two of which are formed with the hydrogens of the water molecules and one is formed with the OH group of the adjacent tetrahedron. The O−H separations and angles in the water molecules are given in Table 4. The lengths of the O ... H hydrogen bonds and O–H ... O angles are given in Table 5.

The average O–H separation in the water molecules is 0.94 ± 0.02 Å. The average H–O–H angle is 108°. These values agree very satisfactorily with the analogous values determined by neutron diffraction in the $Na_2H_2 \cdot SiO_4 \cdot 5H_2O$ structure,[13] i.e., 0.95 Å and 106.1°. Although the mean-square errors in the determination of the H–O interatomic distances were ≃0.05 Å, analysis of the lengths of the covalent O–H bonds and the corresponding H ... O hydrogen bonds makes it possible to establish a correlation between them with small deviations; shortening of the O–H bond, i.e., increase in its order, corresponds to a decrease in the order of the corresponding H ... O bond, and vice versa.

In ref. 24 it was proposed to classify the water molecules in crystals according to the orientation of the unshared pairs of the oxygens and 12 types of orientation of these unshared pairs in the crystal structures were described. In the described structure all the water molecules are of one type, in which the unshared pairs of the oxygens are directed towards the monovalent cations (type A according to ref. 24), and moreover the line bisecting the angle between the unshared pairs is also directed towards a monovalent cation (type C according to ref. 24). Thus, the water molecules in the present structure belong to a type not mentioned in ref. 24 and are a combination of types A and C.

The authors are indebted to G. P. Stavitskaya, who provided the crystals for the investigation.

---

[1] C. L. Baker and L. R. Jue, J. Phys. Chem., 54, 299 (1950).
[2] C. L. Baker, L. R. Jue, and I. H. Wills, J. Amer. Chem. Soc., 72, 5369 (1950).
[3] C. L. Baker, H. T. Woodward, and A. Pabst, Amer. Mineralogist, 18, 206 (1933).
[4] A. Grund, Bull. Soc. Franc. Minéral. et Crystallogr., 77, 775 (1954).
[5] A. Grund and M. M. Pizy, Acta Crystallogr., 5, 837 (1952).
[6] I. W. Howinson and H. F. W. Taylor, Mag. Concrete Res., 9, 13 (1957).
[7] H. Lange and M. von Stackelberg, Z. Anorgan. Chem., 256, 273 (1948).
[8] P. B. Jamieson and L. S. Dent-Glasser, Acta Crystallogr., 20, 373 (1966).
[9] Ya. I. Ryskin, G. P. Stavitskaya, and N. A. Mitropol'skii, Izv. Akad. Nauk SSSR, Ser. Khim., 3, 416 (1964).
[10] K. N. Jost and W. Hilmer, Acta Crystallogr., 21, 583 (1966).
[11] P. B. Jamieson and L. S. Dent-Glasser, Acta Crystallogr., 22, 507 (1967).
[12] P. B. Jamieson and L. S. Dent-Glasser, Acta Crystallogr., 20, 688 (1966).
[13] P. P. Williams and L. S. Dent-Glasser, Acta Crystallogr., B27, 11, 2269 (1971).
[14] Yu. I. Smolin and Yu. F. Shepelev, Kristallografiya, 13, 384 (1968) [Sov. Phys. – Crystallogr., 13, 315 (1968)].
[15] Internat. Tables for X-Ray Crystallography, Vol. 2, Kynoch Press, Birmingham, England (1959).
[16] D. M. Sayre, Acta Crystallogr., 5, 1, 60 (1952).
[17] W. Cochran, Acta Crystallogr., 5, 1, 65 (1952).
[18] W. H. Zachariasen, Acta Crystallogr., 5, 1, 68 (1952).
[19] I. M. Rumanova, Dokl. Akad. Nauk SSSR, 98, 3, 399 (1954).
[20] E. G. Fesenko, I. M. Rumanova, and N. V. Belov, Kristallografiya, 1, 171 (1956) [Sov. Phys. – Crystallogr., 1, 132 (1956)].
[21] B. L. Tarnopol'skii and V. I. Andrianov, Zh. Strukt. Khim., 4, 433 (1963).
[22] D. W. I. Cruickshank and D. E. Philling, Computing Methods and Phase Problem in X-Ray Crystal Analysis, Pergamon Press, Oxford (1961), p. 45.
[23] D. T. Cromer and I. T. Waber, Acta Crystallogr., 18, 104 (1965).
[24] R. Chidambaram, A. Secueira, and S. K. Silka, J. Chem. Phys., 41, 11, 3616 (1964).

Crystal structure of sodium ammonium selenate dihydrate $NaNH_4SeO_4 \cdot 2H_2O$

A. I. Kruglik, V. I. Simonov, and V. I. Yuzvak

Institute of Physics, Siberian Branch, Academy of Sciences of the USSR
Institute of Crystallography, Academy of Sciences of the USSR

(Submitted June 27, 1972)
Kristallografiya, 18, 287-292 (March-April 1973)

By x-ray diffraction the authors determine the atomic positions in the paraelectric phase of crystalline $NaNH_4SeO_4 \cdot 2H_2O$ (space group $P2_12_12_1$), which is isomorphous with the corresponding sulfate. The positions of the hydrogen atoms are unambiguously established by means of nuclear magnetic resonance (NMR) of H^1 and D^2 in the partly deuterated crystal. Information on the dynamics of water molecules in the structure is obtained from the NMR spectra of D^2.

The ferroelectric properties of sodium ammonium selenate dihydrate $NaNH_4SeO_4 \cdot 2H_2O$ were described for the first time in a paper by Aleksandrov et al.[1] A study of the electrooptical and dielectric properties, together with nuclear magnetic resonance (NMR) data,[2] reveals that the ferroelectric transition at 180°K is complex in character. Peculiar features were also found in the behavior of the NMR and certain physical properties near 177°K. To construct a model of the ferroelectric transition in this crystal it is necessary to determine the structures of the paraelectric and ferroelectric phases.

In this article we describe the results of a determination of the structure of $NaNH_4SeO_4 \cdot 2H_2O$ at room temperature. The similar chemical formulas, symmetry groups, lattice parameters, and many other properties show that, as confirmed by our present work, this crystal is isostructural with the corresponding sulfate $NaNH_4SO_4 \cdot 2H_2O$, the structure of which was described in ref. 3.

Sodium ammonium selenate dihydrate has a primitive unit cell with parameters $a = 8.405$, $b = 13.137$, $c = 6.287$ Å, and extinctions uniquely determine its space group as $P2_12_12_1$. The unit cell contains four formula units. An experimental set of structural factors $[F_{hkl}]^2$ was obtained from a spherical specimen (r = 0.8 mm) in a DARUM automatic diffractometer. Measurements were made on seven planes of the reciprocal lattice; 720 independent reflections were recorded. A correction was made for absorption ($\mu r = 6.7$).

TABLE 1. Coordinates and Isotropic Thermal Factors of Basis Atoms

Atoms	x/a	y/b	z/c	B
Se	0.0935	0.1284	0.3828	0.11
Na	0.2606	0.4894	0.9049	0.14
O_1	0.0783	0.2064	0.1873	1.75
O_2	0.0747	0.1907	0.6096	1.76
O_3	0.2642	0.0744	0.3730	1.98
O_4	0.0415	0.5410	0.1364	0.93
O_5	0.2050	0.6321	0.6749	0.53
O_6	0.0886	0.4042	0.6532	1.11
N	0.1596	0.8558	0.3772	0.91
H_1	0.382	0.200	0.867	
H_2	0.397	0.059	0.871	
H_3	0.217	0.160	1.024	
H_4	0.226	0.160	0.792	
H_5	0.027	0.922	0.858	
H_6	0.094	0.330	0.642	
H_7	0.281	0.688	0.679	
H_8	0.109	0.651	0.750	

The structure was refined by the method of least squares for the space group $P2_12_12_1$ up to R = 0.065. Table 1 lists the final values of the coordinates and isotropic thermal parameters of the basis atoms of the structure. Allowance for anisotropy of the thermal vibrations of the atoms did not appreciably reduce the R factor. The parameters of the anisotropic thermal vibrations of the atoms are listed in Table 2.

Figure 1 shows the projection of the structure on the xy plane. The SeO_4 group is a very regular tetrahedron

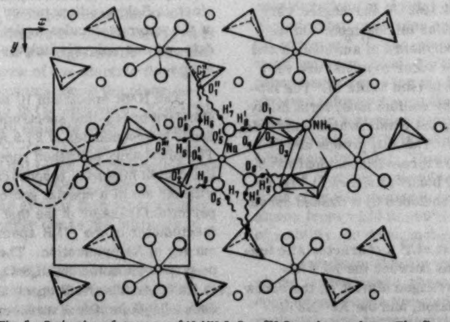

Fig. 1. Projection of structure of $NaNH_4SeO_4 \cdot 2H_2O$ on the xy plane. The figure delineates the SeO_4 tetrahedra and shows the bonds of the Na and NH_4 cations with their surrounding oxygens (straight lines) and the hydrogen bonds (wavy lines). A broken bond line means that instead of one of the two atoms joined by it, we must take one translationally identical along the projection axis. The dashed curve encloses one end of a band.

TABLE 2. Parameters of Anisotropic Thermal Vibrations of Basis Atoms of the Structure in the Form $\exp[-(B_{11}h^2 + B_{22}k^2 + B_{33}l^2 + B_{12}hk + B_{23}kl + B_{13}hl)]$

Atoms	B_{11}	B_{22}	B_{33}	B_{12}	B_{13}	B_{23}
Se	0.009	0.0036	0.017	—0.0014	—0.0002	0.0011
Na	0.009	0.0039	0.011	—0.0008	0.0019	0.0006
O_1	0.018	0.005	0.025	—0.001	0.008	—0.003
O_2	0.020	0.006	0.024	—0.005	—0.013	0.015
O_3	0.011	0.007	0.056	—0.004	—0.005	—0.005
O_4	0.121	0.006	0.015	0.001	0.000	0.000
O_5	0.129	0.005	0.014	0.002	—0.004	0.003
O_6	0.111	0.005	0.023	0.001	0.000	—0.002
N	0.015	0.005	0.021	0.000	0,002	0.004

TABLE 3. Main Interatomic Distances (Å) and Angles (deg)

Na — O_5'	2.23	Se — O_1	1.629	∠$O'_1NH_4O_2$	117
Na — O_4	2.37	Se — O_2	1.643	$O_1NH_4O_4'$	66
Na — O_5	2.41	Se — O_3	1.591	$O_1NH_4O_1$	115
Na — O_6	2.43	Se — O_4	1.636	$O_1'NH_4O_3'$	104
Na — O_4'	2.44			$O_1'NH_4O_3$	91
Na — O_6'	2.46	∠O_1SeO_2	110°09′	$O_1'NH_4O_3''$	98
		O_1SeO_3	110°00′	$O_2NH_4O_4'$	115
∠$O_5'NaO_4$	101	O_1SeO_4	108°53′	$O_2NH_4O_1$	78
$O_5'NaO_5$	157	O_2SeO_3	109°59′	$O_2NH_4O'_3$	73
$O_5'NaO_6$	103	O_2SeO_4	110°49′	$O_2NH_4O_3$	115
$O_5'NaO_4'$	99	O_3SeO_4	108°10′	$O_2NH_4O_3''$	53
$O_5'NaO_6'$	83			$O_4'NH_4O_1$	118
O_4NaO_5	81	NH_4 — O_1'	2.80	$O_4NH_4O_3'$	95
O_4NaO_6	83	NH_4 — O_2	2.87	$O_4NH_4O_3$	97
O_4NaO_4'	170	NH_4 — O_4'	2.99	$O_4'NH_4O_3''$	93
O_4NaO_6'	101	NH_4 — O_1	3.03	$O_1NH_4O_3'$	98
O_5NaO_6	82	NH_4 — O_3'	3.04	$O_1NH_4O_3$	49
O_5NaO_4	90	NH_4 — O_3	3.29	$O_1NH_4O_3''$	122
O_5NaO_6'	90	NH_4 — O_3''	3,38	$O_3'NH_4O_3$	100
O_6NaO_4'	86			$O_3'NH_4O_3''$	63
O_6NaO_6'	172			$O_3NH_4O_3''$	153
$O_4'NaO_6'$	81				

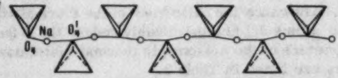

Fig. 2. Bands of SeO_4 tetrahedra linked by Na ions, projected on the yz plane.

with a mean Se–O distance of 1.62 Å and angles very nearly equal to those of a regular tetrahedron. On the other hand, the coordination polyhedra of ammonium and sodium (the latter includes the water oxygens) are very irregular in shape and distances (see Table 3). The isolated SeO_4 tetrahedra, linked by sodium ions, form fairly compact bands extending along the c axis, which is the axis of the columns of sodium ions. The NH_4 groups and hydrogen bonds join the bands into a three-dimensional structure. The configuration of the bands is shown in Fig. 2; the end of one of the bands is enclosed by a dashed curve in Fig. 1.

As remarked by Corazza et al.,[3] a characteristic feature of the structure is the link between the Na octahedra. The sodium ions are arranged almost on the screw axis parallel to the [001] direction, and the Na–Na distance is very small (3.163 Å) and almost equal to c/2. Apparently the smallness of this distance is the cause of the deformation of the sodium octahedra.

By the x-ray method we were able to pinpoint only the four hydrogen atoms belonging to the NH_4 group. The hydrogens belonging to the water molecules were not resolved on the electron density synthesis, and were localized in the structure by the NMR method. The NMR of protons was used to determine the lengths and orientations of the proton–proton (p–p) vectors of the water molecules relative to the crystallographic axes, and from an analysis of the NMR spectra of D^2 we determined the electric field gradient tensor at the localized sites of the deuterons. The orientations of the principal axes of the electric field gradient tensor characterize the positions of the water molecules in the structure. If we have these data, we can uniquely link the hydrogen atoms to the heavy atoms.

The NMR spectra of H^1 and D^2 were recorded on a nonstandard broad-line spectrometer with an autodyne transducer at frequencies of 27.9 and 6.2 MHz, respectively. The previously published results[4,5] of an investigation of the proton magnetic resonance spectra were refined by us with the aid of a special goniometric attachment which permitted transfer of the test crystal from the x-ray diffractometer to the NMR spectrometer without loss of accuracy of its orientation. The refined orientations of the p–p vectors in the $NaNH_4SeO_4 \cdot 2H_2O$ structure are listed in Table 4. The NMR spectra of D^2 in a crystal of $NaND_4 \cdot SeO_4 \cdot 2D_2O$ (~50% D) at room temperature consists of components with small splitting due to distorted tetrahedral ND_4 groups, reoriented relative to more than one axis of symmetry,[5] and two pairs of satellites with large splitting, due to heavy water molecules.

Analysis of the orientation dependences of the spec-

TABLE 4. Lengths and Orientations of p−p Vectors of Water Molecule

Molecule	r, Å ($\varphi_c \delta_c$)	$H\overset{(O-}{\underset{Å}{\cdot\cdot}}O)$ *,	(O − H) **, Å	$\angle OO_{H_2O}O$*	∠HOH
H_2O I	$(p-p) = 1.58\ (-50°;\ 0°)$	2.73	0.99	93	107
	$(O_2'' - O_3''')$ * $= 4.04\ (-50°;\ 2°)$	2.82	0.97		
HEO II	$(p-p) = 1.59\ (15°;\ -13°)$	2.79	0.98	109	109
	$(O_1'' - O_2)$ * $= 4.58\ (17°;\ -16°)$	2.84	0.96		

Errors in determination of lengths of p−p vectors, ±0.01 Å; angles φ_c and δ_c, ±1° for H_2O I, and ±3° for H_2O II.

*Calculated from atomic coordinates (Table 1).

**Estimated from Hamilton's empirical relation.[9]

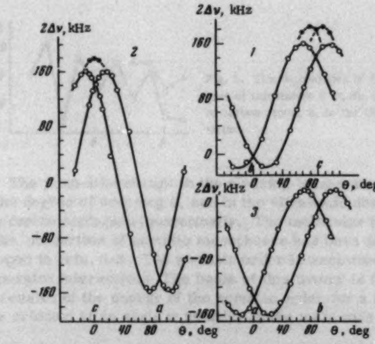

Fig. 3. Orientation dependences of quadrupole splitting 2Δν of NMR spectrum of D^2 in D_2O molecule at room temperature. 1, 2, 3) Rotation of crystal about a, b, and c axes, respectively.

tra reveals that each D_2O molecule of type II (notation same as in ref. 4) corresponds to one pair of lines with a maximum splitting of about 160 kHz. This type of spectrum is characteristic of a water molecule flipping relative to the bisectrix of the angle DOD with a frequency greater than that of quadrupole interaction.[6] As the temperature is reduced, the signal of D_2OII broadens and at −70°C it vanishes; this indicates a slowing down of the correlation frequency of flipping of the value $\nu_k \sim 10^5$ Hz. The lines of D_2OI are already broadened at room temperature, and are observed only at orientations corresponding to maximum splitting, $2\Delta\nu \sim 180$ kHz. At T ~ 15°C, the resonance of D_2OI completely disappears.

Figure 3 shows the orientation dependences of the quadrupole splitting $2\Delta\nu$ of the NMR spectra of D^2 in the D_2O molecule. We give the principal values and orientation of D_2OII, calculated from the orientation dependences of $2\Delta\nu$ by the method of Volkoff:[7] $eQ\Phi_{zz}/h = 123$ kHz ($\varphi_c = 129$, $\delta_c = 64°$), $eQ\Phi_{yy}/h = 113$ kHz ($\varphi_c = 15$, $\delta_c = -11°$), $eQ\Phi_{xx}/h = 10$ kHz ($\varphi_c = -102$, $\delta_c = 23°$). The position of the normal to the plane $O_1''O_6'O_2$ is determined by the angles $\varphi_c = 137°$, $\delta_c = 59°$, calculated from the atomic coordinates. The orientation of the axis $eQ\Phi_{zz}/h$ for D_2OI is $\varphi_a = 82°$, $\delta_a = 0$; the corresponding angles of the normal to the plane $O_2''O_5'O_3'''$ are $\varphi_a = 85°$, $\delta_a = 4°$, as calculated from the atomic coordinates (Table 1).

It is known (see, for example, ref. 6) that for a flipping water molecule, $eQ\Phi_{zz}/h$ is perpendicular to the plane DOD, $eQ\Phi_{yy}/h$ is parallel to D−D, and $eQ\Phi_{xx}/h$ is directed along the bisectrix of the angle DOD. Thus the directions of the principal axes of the electric field gradient tensor determine the orientation of the plane occupied by the water molecule in the structure. From Table 4 we see that these planes coincide with the planes $O_1''-O_5'-O_2$ (for H_2OII) and $O_2''-O_6'-O_3'''$ (for H_2OI), where $O_1''-O_2$ and $O_2''-O_3'''$ are parallel to the corresponding p−p vectors. The slight deviations of $eQ\Phi_{zz}/h$ from the normals n to these planes are no greater than those usually observed [8], and are apparently due to the influence of the positive sodium ions.

Knowing the lengths and orientations of the p−p vectors, the O−O distances, the lengths of the bonds O−H...O, O−H, and the valence angles of the water molecules (see Table 4), we can determine the coordinates of the protons (Table 1). Figure 1 shows the positions of the water molecules in the structure. Both water molecules have tetrahedral coordination. The "water" oxygens come into the Na octahedra, forming weak hydrogen bonds with the oxygens of the SeO_4 groups. The hydrogen bonds formed by the H_2OII molecules are linear. The H_2OI molecules form bent bonds (see Table 3), the angle OHO being 167°. The negative valences of the water molecules are directed towards the sodium cations. Our data agree with general considerations of crystal chemistry concerning the geometry of water molecules and their hydrogen bonds in crystal hydrates.[9-11] The structure contains another type of weak hydrogen bond, N−H ...O. From the temperature dependences found for the NMR spectra of D^2 and H^1 we obtained information on the dynamics of the water molecules. The activation energy of flipping, estimated in accordance with ref. 8, is 9-10 kcal/mole for D_2OII and 13-14 kcal/mole for D_2OI. These rather high values are characteristic of water molecules linked to cations. Investigations of proton magnetic resonance of water at temperatures from −120 to +60°C did not reveal any other types of mobility for these molecules.

As we have already remarked, to construct a model of the ferroelectric phase transition in the crystal under test we need a knowledge of the structures of the paraelectric and ferroelectric phases. We have solved this problem for the first time.

We consider that combination of the x-ray method with the nuclear magnetic resonance method can be very fruitful. This combination of methods can fairly reliably localize the hydrogen atoms in a structure, and can also yield conclusions on various dynamic processes in a crystal.

The authors thank K. S. Aleksandrov and I. P. Aleksandrova for discussing their results and making helpful observations.

---

[1] K. S. Aleksandrov, I. P. Aleksandrova, L. I. Zherebtsova, A. I. Rostuntseva, T. A. Leibovich, and M. P. Zaitseva, Fiz. Tverd. Tela, 11, 2027 (1969) [Sov. Phys. – Solid State, 11, 1639 (1970)].

[2] V. I. Yuzvak, I. P. Aleksandrova, and V. N. Shcherbakov, Fiz. Tverd. Tela, 13, 1932 (1971) [Sov. Phys. – Solid State, 13, 1620 (1972)].

[3] E. Corazza, C. Sabelli, and G. Guiseppetti, Acta Crystallogr., 22, 683 (1967).

[4] I. P. Aleksandrova, K. S. Aleksandrov, and V. P. Krupnaya, Fiz. Tverd. Tela, 12, 1024 (1970) [Sov. Phys. – Solid State, 12, 804 (1970)].

[5] I. P. Aleksandrova, V. I. Yuzvak, and V. N. Shcherbakov, Izv. Akad. Nauk SSSR, Ser. Fiz., 35, 1807 (1971).

[6] S. Ketudat and R. V. Pound, J. Chem. Phys., 26, 708 (1957).

[7] G. M. Volkoff, Canad. J. Phys., 31, 820 (1953).

[8] G. Soda and T. Chiba, J. Phys. Soc. Japan, 26, 249 (1969); G. Soda and T. Chiba, J. Chem. Phys., 50, 439 (1969).

[9] W. C. Hamilton, Annual Rev. Phys. Chem., 13, 28 (1962).

[10] Z. M. El Saffar, J. Chem. Phys., 45, 4643 (1966).

[11] I. D. Datt and R. P. Ozerov, Kristallografiya, 17, 437 (1972) [Sov. Phys. – Crystallogr., 17, 383 (1972)].

Structure of liquid crystals of the homologous series of n-alkoxyazoxybenzenes

I. G. Chistyakov and V. M. Chaikovskii
Institute of Crystallography, Academy of Sciences of the USSR
Ivanov Pedagogical Institute

(Submitted April 7, 1971; resubmitted February 4, 1972)
Kristallografiya, 18, 293-297 (March-April 1973)

The structure of liquid crystals of the first 10 homologs of the n-alkoxyazoxybenzene series has been studied. The degree of orientation S has been calculated and its dependence on the number of carbon atoms in the aliphatic chain has been found. The analysis of the cylindrical distribution functions of the molecular axes has made it possible to discover a regular change in the number of the nearest neighbors surrounding the molecules as a dependence on the serial number of the homolog. It is shown that molecules of liquid crystals of a given series in either the smectic or nematic state form layers sloping towards the texture axis. The extent of these layers has been estimated in the nematic state. The structure of the liquid crystals is related to their symmetry.

The study of a homologous series is of importance in that it enables us to form an opinion as to the character of the change in structure of the mesophase when there is an insignificant structural change in the molecular skeleton. At the same time we are interested in the sensitivity to small structural changes of the x-ray method we used in this study.

X-ray photographs were obtained for the first 10 terms of the series. Since the phase-transition points for this series change regularly with the change from the even to the next odd homolog and the temperature regions in which their mesophases exist are different, the x-ray photography was carried out at temperatures which were 3-5° above the melting point or the point at which the transition from the smectic to nematic state occurred. In order to produce oriented specimens a magnetic field of 17,200 G was used.

We must remember that the first six members of this series form only a nematic mesophase while Nos. 7-10 form both a nematic and smectic mesophase. The x-ray photographs of the odd homologs have more diffuse reflections, showing that their structures have a lower degree of orientation than the even homologs.

In order to find the quantitative features of this dependence, the degree of orientation $S = 1-3(\overline{\sin^2\alpha})/2$ was calculated for the nematic and smectic mesophases of each homolog: $\overline{\sin^2\alpha}$ was found from a study of the distribution of intensity along the arc of the main equatorial reflections of the x-ray photograph:[1]

$$\overline{\sin^2\alpha} = \int_0^{\pi/2} I(\theta)(\sin\theta)^3\,d\theta \Big/ \int_0^{\pi/2} I(\theta)(\sin\theta)\,d\theta. \qquad (1)$$

The dependence of S on the number of the homolog (the number of carbon atoms) is shown in Fig. 1; the dotted line joins the points corresponding to S for the smectic mesophases. The jump-like change in S with a change from odd to even terms of the series is clearly marked both for the nematic and smectic liquid crystals.

It should be noted that there is an analogous dependence of other properties of liquid crystals on the homolog number of the series. Thus, the clearing points undergo an analogous zigzag change in the n-alkoxyazoxybenzene series. An analogous form of dependence of ultrasonic absorption has been observed in ref. 2 for the same series.

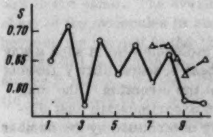

Fig. 1. The dependence of the degree of orientation S on the number of carbon atoms, n, in the aliphatic series.

The jump-like change in the clearing temperature T_{cl}, in the degree of ordering S, and in the ultrasonic absorption can be explained theoretically. The molecular theory of the properties of nematic mesophases has been developed in refs. 3-5. The nematic order is explained by dispersion interactions. The basis of this theory is the expression of the energy of the nematic order for a molecule oriented at an angle α relative to the main axis z:

$$E_i = -\frac{A}{V^2} S\left(1-\frac{3}{2}\sin^2\alpha\right), \qquad (2)$$

where A is a constant, and V is the molar volume. We should note that the theory considers S inside the microregion while the x-ray experiment provides information about the ordering of the specimen as a whole. As a result, however, of the significantly orienting field of 17,200 G, these values are the same or at the worst differ very little.

The theory leads to a relationship between the clearing temperature and the anisotropy of the high-frequency dielectric constant[6] $4.55\,kT_{cl} = c\Delta\varepsilon^2/V^2$. The change from an odd to an even number in the series is accompanied by an increase in $\Delta\varepsilon$ and therefore in T_{cl}. The decrease in the steps of T_{cl} as the homolog number increases is also understandable. This occurs as the result of an increase in the molar volume V.

We must also realize that the change in the homolog number in the series is accompanied by the addition of a C−C bond either almost parallel to the length of the molecular axis (even-numbered homolog) or at an angle of ~70° (odd-numbered homolog). Since the polarization of the C−C bond parallel to the molecular axis is significantly greater than that in the perpendicular direction, a polarization anisotropy appears which leads to the step-like change in T_{cl}.

It must also be noted that the long axes of the molecules lie parallel to the lines of force of the field. It has already been noted that such an orientation is caused by

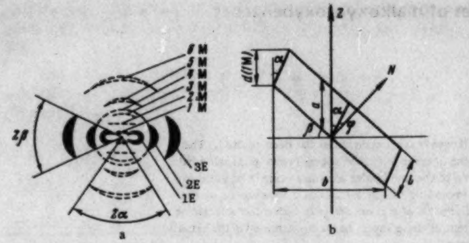

Fig. 2. Diagram of x-ray photograph of n-heptoxyazoxybenzene in a magnetic field (a) and the arrangement of the scattering region relative to the texture axis z (b).

diamagnetic anisotropy. The molecules lie in such a way that the direction of the greatest susceptibility χ (lowest diamagnetism) is the same as the direction of the magnetic field. It has been shown experimentally that diamagnetic anisotropy is mainly determined by the number of benzene rings in the molecule. It was recently established in ref. 7, however, that the dependence of $\Delta\chi$ in the homologous series of n-azoxyalkoxybenzenes indicates that the aliphatic groups also make a marked contribution to $\Delta\chi$. Clearly, this also determines the character of the change in S of liquid crystals of a given hmologous series.

Let us now consider the structural features of the nematic and smectic mesophases of this series. We may note that the x-ray photographs of the nematic mesophase of the third homolog resemble those of the n-azoxyanisole, in which the first meridian reflection appears as a diffuse layer. All the subsequent homologs have x-ray photographs which resemble those of the seventh homolog (n-heptoxyazoxybenzene) (Fig. 2). In the case of these, the form of the first meridian reflection is characteristic: It is in the shape of a figure 8 laid on its side (or of a "dumbbell"). This indicates that the nematic phase of these homologs (n = 2, 4-10) has a pseudolaminar structure. The molecular groups consist of pseudolayers in which the molecules slope at an angle normal to the surface of the layer and the layers themselves slope on average at an angle β (Fig. 2a, b) to the plane perpendicular to the texture axis z.

As for the first and third homologs, by using the data from ref. 8 it is possible to draw the conclusion that sloping pseudolayers of molecules are presented but to a lesser extent than in the homologs with n = 2, 4-10. The decisive factor in estimating the extent of the layer will be the value of the parameter $p = bt/a$ (Fig. 2b), which is determined by the form of the reflection[8] 1M. Here b is the width of the scattering region (layer), a is the size of the region along the texture axis, and t is $\tan\beta$, where β is the angle which the scattering region makes with the plane perpendicular to the texture axis. The estimate of the extent of b in the nematic pseudolayers of this series is given in Table 1.

It must also be noted that the 1M reflection which has the shape of a figure 8 on its side is also characteristic of the homologs with n = 2, 4-10, is blurred with a rise in the temperature, and acquires the form of the reflection appropriate to n-azoxyanisole and n-propoxyazoxybenzene (n = 1, 3). This indicates that there is a gradual fragmentation of the groups into finer groups as the temperature increases. Thus, the symmetry of the "cybotaxic" nematic mesophase can be described, as in ref. 1, by: $\tau_\infty^g W(xy)f(\psi)D(\alpha)\varphi(\widehat{lN})$. This symbol characterizes the fact that the aggregate consists of "skewed" molecular pseudolayers. Here τ_∞^g denotes the axis of the infinitely small translations of the molecular groups: W(xy) is the destruction function of the network; $f(\psi)$ is the rotation function of the molecules; $D(\alpha)$ is the function of the slope of the molecules relative to the z axis; $\varphi(lN)$ is the angle between the normal to the pseudolayer and the direction of orientation of the long molecular axes. The symmetry symbol of the "classical" nematic mesophases (n = 1, 3) will be: $\tau_\infty W(xy)f(\psi)D(\alpha)$.

It must be emphasized immediately that the classification of the nematic mesophases into "skewed cybotaxic," "classical," and "normally cybotaxic"[9,10] which we have used for the structural characteristics does not imply that they exist as independent thermodynamic phases. This is confirmed by the gradual transition of the structure observed for the homologs with n = 2,4-10:

$$\tau_\infty W(xy)f(\psi)D(\alpha)\varphi(\widehat{lN}) \rightarrow \tau_\infty W(xy)f(\psi)D(\alpha)$$

with an increase in the temperature of the nematic phase.

Photometric measurements around the circle of the main maximum 2E (Fig. 2) make it possible to construct the function $D(\alpha)$ and to calculate the mean-square value of the sin of the angle of slope of the molecules relative to the z axis.[1] For example, the function $D(\alpha)$ for n-azoxyanisole oriented by a magnetic field of 8000 G at

TABLE 1

Homolog No.	t, °C	α, °	β, °	φ, °	p	l_m, Å	d (1M), Å	$l-d/\cos\alpha$, Å	$a = l\cos\varphi/\cos\beta$, Å	b, Å
1	121	29	43	14	0.45	18.3	16.15	18.4	25	12.1
2	140	25	43	18	0.8	20.1	18.2	20.1	26.2	22.5
3	116	32	42.5	10.5	0.45	22.7	19.4	22.9	30.3	14.8
4	110	27	42	15	1.0	25.4	22.8	25.6	33.05	36.8
5	80	29	41	12	1.0	28.0	24.55	28.1	36.3	41.8
6	80	28	38	10	1.0	30.4	27.0	30.6	38	48.7
7	98	29	34	5	1.0	33.0	28.8	33.0	40.1	58.5
8	110	28	30	2	1.0	35.5	31.45	35.8	41	71
9	118	33	28	5	0.6*	38.0	32.2	38.4	43	48.5
10	120	34	26	8	0.6*	40.5	33.75	40.7	44.9	55.2

*The reflection is blurred due to its proximity to the clearing point.

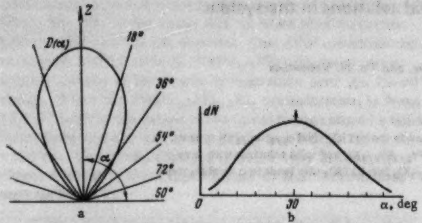

Fig. 3. The disorientation characteristics of molecules: a) the function D(α) for n-azoxyanisole at 118°C in a magnetic field of 8000 G; b) distribution of molecules with respect to the angles dN(α) obtained from the function D(α).

118°C is shown in Fig. 3a. In the expression $\overline{\sin^2 \alpha}$ the angle α is the average angle of slope of the molecules relative to the z axis. In fact, by definition the function[1] D(α) is the density of the traces of the long molecular axes on the unit sphere of the molecular orientations. Hence the number of molecules in the aggregate dN(α) lying in the angular range from α to $\alpha + d\alpha$ relative to the z axis is

$$dN(\alpha) = D(\alpha) \sin \alpha \, d\alpha. \tag{3}$$

The change in the value of dN as a function of α for $\Delta\alpha = 3°$ derived from the values of D(α) for n-azoxyanisole will be characterized by a Gaussian distribution (Fig. 3b). It is clear from Fig. 3 that most of the molecules slope towards the z axis at an angle $\alpha = 30°$. This value is in good agreement with the result obtained using Eq. (1).

Having the x-ray data for the whole homologous series, we verified the model data for the structure of the molecules. Naturally the statistical slope of the molecules must affect the values for the interplanar distances corresponding to the 1M reflection on the meridian of the x-ray photograph. The interplanar distance d calculated from the 1M reflection does not actually correspond to the length of a molecule l_m found from the model representations. If we calculate the length of the molecule $l_c = d/\cos \alpha$, then this value is in satisfactory agreement with the value for the length l_m of molecules for the whole series of n-alkoxyazoxybenzene (Table 1).

The behavior of the smectic mesophase of the 8th to 10th homologs in a magnetic field and the arrangement of the reflections on the x-ray photographs are the same as in the 7th homolog. The long molecular axes lie mainly in the direction of the magnetic field. The splitting of the first meridian reflection into two spotted patches shows the slope the molecular layers made with the plane perpendicular to the texture axis in the smectic state. The average slope of these layers is given by the angle β in the x-ray photographs. Moreover, the difference in the angle the average slope of the molecules make with the texture axis and the average slope the smectic layers make with the plane perpendicular to the texture axis indicates that the slope of the molecules in the smectic layers is the same. The average angle of this consistent slope of the molecules in smectic layers φ [average angle between the normal to the layer N and the long molecules l (Fig. 2b)] is determined by the difference between the angles β and α. We may thus conclude that all the smectic mesophases of the n-alkoxyazoxybenzene homologous series have a symmetry of the type: $C_N W(xy) f(\psi) D(\alpha) \varphi(\widehat{lN})$. We must remember here that C_N is the interlayer period in a direction normal to it.

The change in the degree of orientation S with the change from one homolog to another is analogous to the change in S for nematic mesophases. The only difference is that S has a higher value for the smectic phase (Fig. 1) than for the nematic (for a given homolog) phase.

In conclusion we must give our sincere thanks to B. K. Vainshtein for his constant interest in the work and for useful discussions of the results.

---

[1] B. K. Vainshtein, Diffraction of X-ray Beams by Chain Molecules [in Russian], Izd. Akad. Nauk SSSR, Moscow (1963).

[2] A. P. Kapustin and L. I. Mart'yanova, Kristallografiya, 14, 480 (1969) [Sov. Phys. – Crystallogr., 14, 394 (1969)].

[3] W. Maier and A. Saupe, Z. Naturforsch., 12, 668 (1957).

[4] W. Maier and A. Saupe, Z. Naturforsch., 14, 882 (1959).

[5] W. Maier and A. Saupe, Z. Naturforsch., 15, 287 (1960).

[6] I. V. Sushkin, in: The Structure and Properties of Liquid Crystals, Uch. Zap. Ivanovsk. Gos. Ped. Inst., 77, 65 (1970).

[7] V. N. Tsvetkov, E. I. Ryumtsev, and F. M. Aliev, Themes for the First Conference on Liquid Crystals [in Russian], Ivanovsk. Gos. Ped. Inst., Ivanovo (1970), p. 17.

[8] V. I. Gerasimov and D. Ya. Tsvankin, Vysokomolekul. Soedineniya, A11, 2652 (1969).

[9] A. de Vries, Molec. Cryst. and Liquid Cryst., 10, 31 (1970).

[10] A. de Vries, Molec. Cryst. and Liquid Cryst., 10, 219 (1970).

Study of the structure and dielectric properties of solid solutions in the system $BaTiO_3-Pb(Fe_{1/2}Nb_{1/2})O_3$

O. S. Didkovskaya, I. P. Kovalevskaya, V. G. Seryi, V. V. Klimov, and Yu. N. Venevtsev

(Submitted October 28, 1971; resubmitted April 7, 1972)
Kristallografiya, 18, 298-302 (March-April 1973)

It has been established that a continuous series of solid solutions is formed in the $BaTiO_3-Pb(Fe_{1/2}Nb_{1/2})O_3$ system. The Curie temperature passes through a minimum at 40-50 mole % $Pb(Fe_{1/2}Nb_{1/2})O_3$ and solid solutions with very diffuse phase changes are responsible. The introduction of $Pb(Fe_{1/2}Nb_{1/2})O_3$ into $BaTiO_3$ also leads to a displacement of the second and third phase changes into lower temperature regions.

Since the studies of the $PbTiO_3-Pb(Fe_{1/2}Nb_{1/2})O_3$ system produced results which were of scientific[1] and practical interest,[2] it seemed reasonable to study the related systems, $BaTiO_3-Pb(Fe_{1/2}Nb_{1/2})O_3$. Because there are no cations common to the components of the latter system, we could expect from ref. 1 that the Curie temperature would in this case change nonlinearly, in contrast to the $PbTiO_3-Pb(Fe_{1/2}Nb_{1/2})O_3$ system.

The experimental specimens were prepared by ceramic techniques, being twice fired first at 780-900°C (2 h) and then at 1050-1300°C (1.5 h). The following were used as the raw materials: $BaCO_3$ ("pure"); $PbCO_3$ ("pure"); TiO_2 ("extremely pure"); Fe_2O_3 ("analytically pure"); Nb_2O_5 ("first quality"); and Li_2CO_3 ("chemically pure").

The x-ray studies were carried out using the URS-50I equipment.

Disks ~10 mm in diameter and ~1 mm thick were used for measuring the electrical properties. The electrodes were applied by burning-in silver paste at 700°C. The measurements of the dielectric constant and dielectric loss were made with a MLE-1 bridge and the conductivity measurements with an E-6-3 device. A resonance method was used to measure the piezoelectric characteristics, which were calculated in accordance with the State Standard 12370-66. The specimens were polarized in a liquid polysiloxane at 50-110°C in a 3-kV/mm dc field.

When lead ferroniobate is added to the barium titanate, the ceramic sintering temperature is lowered. Its conductivity, however, is increased and its electrical strength deteriorates. We therefore added 5 mole % of lithium oxide to all the experimental compositions since this helps to lower the conductivity in the $PbTiO_3-Pb(Fe_{1/2}Nb_{1/2})O_3$ system.[2]

The x-ray studies showed that solid solutions with a perovskite type of structure are formed in the $BaTiO_3-Pb(Fe_{1/2}Nb_{1/2})O_3$ system over the whole range of concentrations. The solid solutions with a lead niobate concentration from 100 to 93 mole % exhibit a slight rhombohedral distortion (Fig. 1, R) of the unit cell at room temperature. The solid solutions containing from 0 to 10 mole % of lead ferroniobate have a unit cell with a tetragonal distortion (Fig. 1, T). The solid solutions containing 10-90 mole % $Pb(Fe_{1/2}Nb_{1/2})O_3$ have an undistorted cubic unit cell at room temperature.

Figure 1 shows the dependence on composition of the unit-cell parameters. It is clear that the *a* parameter increases with an increase in the $Pb(Fe_{1/2}Nb_{1/2})O_3$ concentration. This increase, however, is not monotonic. The breaks in the dependence of the cell parameters on the composition correspond to transitions from tetragonal to cubic and from cubic to rhombohedral phases. Moreover, a slight break inside the limits of the cubic phase is observed when the concentration of $Pb(Fe_{1/2}Nb_{1/2})O_3$ is ~50 mole %. The results of the dielectric measurements confirmed the data on the complexity of the phase diagram of this system. It is clear from Fig. 2, which shows the curves for ε (t) of various compositions, that the Curie temperature of the solid

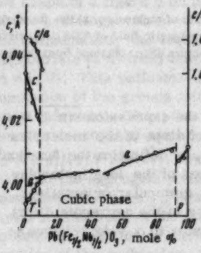

Fig. 1. Dependence on composition of the *a* and c parameters of the unit cells of solid solutions.

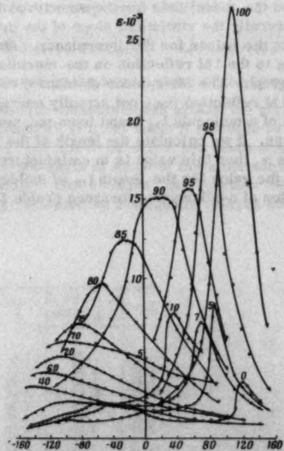

Fig. 2. Temperature dependence of the dielectric constant at 1 kHz of solid solutions. The figures on the curves denote the $Pb(Fe_{1/2}Nb_{1/2})O_3$ concentration in mole %.

solutions is lowered when $BaTiO_3$ is added to the $Pb \cdot (Fe_{1/2}Nb_{1/2})O_3$ in the same way as when lead ferroniobate is added to barium titanate. The solid solutions containing 90 and 10 mole % $Pb(Fe_{1/2}Nb_{1/2})O_3$ have very similar values of the Curie temperature over the 20-30°C range. When the $Pb(Fe_{1/2}Nb_{1/2})O_3$ concentration is from 10 to 90 mole %, the values of the Curie temperature lie below room temperature and reach fairly low values (down to −150°C). The phase changes become very diffuse the closer the ratio of barium titanate to lead ferroniobate approaches 1:1.

With a lead ferroniobate concentration of from 0 to 10 mole %, phase changes from tetragonal to orthorhombic and from orthorhombic to rhombohedral which occur in barium titanate are retained, but are displaced into the lower temperature region. The transition from the orthorhombic to the rhombohedral phase is particularly weakly expressed. With higher concentrations (>10 mole %) of lead ferroniobate, these phase changes become even more diffuse and are displaced into the low-temperature region, which makes it very difficult to identify them.

We also studied the electrical conductivity and the piezoelectric properties of the ceramic we produced. The measurements showed that the conductivity of the ceramic at room temperature lies in the range 10^{-10} to $10^{-12}\ \Omega^{-1} \cdot cm^{-1}$ and is weakly dependent on the composition. It is clear from the data in Fig. 3 that the curves of $\log \sigma = f(1/T)$ have a steep slope, i.e., the conductivity changes markedly with a change in temperature. The breaks in the curves correspond in some cases to the Curie temperature [e.g., in the case of the composition with 2 mole % $Pb(Fe_{1/2}Nb_{1/2})O_3$] and in others to the different character of the conductivity at different temperatures.

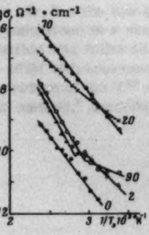

Fig. 3. Temperature dependence of the electrical conductivity of solid solutions. The figures on the curves denote the $Pb(Fe_{1/2}Nb_{1/2})O_3$ concentration in mole %.

The piezoelectric properties were studied at room temperature and only the composition with a Curie temperature above 30°C (Table 1) were included.

It is clear from Table 1 that the values of the electrophysical parameters for the $BaTiO_3$ and $Pb(Fe_{1/2}Nb_{1/2}) \cdot O_3$ ceramics correspond to the published data.[2,4] The highest values of ε, K_p, and d_{31} belong to the solid solution which contains 95 mole % $Pb(Fe_{1/2}Nb_{1/2})O_3$, which also has the lowest Curie temperature.

A provisional phase diagram of the experimental system (Fig. 4) was constructed. It is clear from this that in the $BaTiO_3-Pb(Fe_{1/2}Nb_{1/2})O_3$ system some ferroelectric phases occur below the Curie temperature: I with a tetragonal distortion; II with an orthorhombic; and III and IV with rhombohedral distrotions of the unit cell.

In some of the previously studied systems based on barium titanate, $BaTiO_3-BaHfO_3$ (ref. 5), $BaTiO_3-KNbO_3$ (ref. 6), and others, the lowering of the Curie temperature of barium titanate was accompanied by an increase in the temperature of the phase transitions from tetragonal to orthorhombic and from orthorhombic to rhombohedral. By contrast to these systems and the similarly well-known[7] $BaTiO_3-SrTiO_3$, a reduction in the temperature of all the phase changes of barium titanate can be fairly satisfactorily traced in our particular system. As a result, there is a displacement of the limits within which the tetragonal phase I can exist in the low-temperature region. The existence of the tetragonal phase at low temperatures and the presence of a break in the curve of the dependence of the unit-cell parameters on the composi-

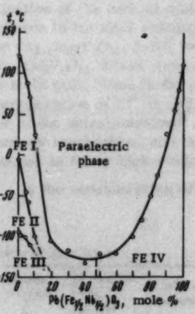

Fig. 4. Provisional diagram of the phase changes in the $BaTiO_3-Pb \cdot (Fe_{1/2}Nb_{1/2})O_3$ system.

TABLE 1. Electrophysical Properties of Some Ceramic Solid Solutions of $BaTiO_3-Pb(Fe_{1/2}Nb_{1/2})O_3$ with a 5 mole % Addition of Li_2O (at 20°C)

No.	$Pb(Fe_{1/2} \cdot Nb_{1/2})O_3$ concentration, mole %	Dielectric constant, ε	Dielectric constant after polarization ε_{33}	Electromechanical coupling coefficient K_p	Piezomodulus d_{31}, 10^{-6} cgs esu	Mechanical quality, Q	Curie temp., °C
1	100	2260	2280	0,27	2,3	160	100
2	95	7700	8000	0,33	5,5	190	55
3	7	2000	2000	0,15	1,0	330	70
4	2	1980	1860	0,31	2,9	220	95
5	0	1300	1350	0,28	1,7	340	120

tion at a $Pb(Fe_{1/2}Nb_{1/2})O_3$ concentration of ~40 to 50 mole % (Fig. 1) suggest that at this particular $Pb(Fe_{1/2} \cdot Nb_{1/2})O_3$ concentration and at temperatures below −120 to −130°C, there is probably a morphotropic tetragonal–rhombohedral boundary. The fact that it is also apparent in the higher temperature region is clearly associated with the following. Solid solutions of an intermediate concentration are characterized by very diffuse phase changes, indicating that a spontaneous-polarization state also exists above the temperatures of the maxima of the dielectric constants, conventionally the Curie temperature. Although above the Curie temperature (in our case at 20°C) the unit cells are taken to be cubic, the presence in the paraelectric phase of nuclei of a polarized state of tetragonal and rhombohedral phases can also clearly cause the breaks which are observed in the parameter curve. It cannot be ruled out that even in the paraelectric phase there are significant but still inconsistent displacements of ions along the four-fold axis in the region to the left of the anomaly and along the three-order axis in the region to the right. These displacements still do not lead to the emergence of distortions in the cells, but produce differences in the parameters of the cubic unit cells in the region of the boundary concentration.

The results obtained showed that the Curie temperature depends nonlinearly on the composition and passes through a minimum when the lead ferroniobate concentration is ~40 to 50 mole %. The existence of this minimum is in good agreement with the conclusions reached in refs. 3, 6, and 8, where it was shown that solid solutions of ferroelectrics which do not have cations in common have a minimum on the curve of the composition dependence of the Curie temperature.

It has already been noted above that the minima on the curves of ε (t) are very diffuse in the 10-90 mole % concentration region of lead ferroniobate and this is probably due to the large number of different ions arranged statistically in the B position.

Thus, as a result of our present study the phase diagram of solid solutions in the $BaTiO_3-Pb(Fe_{1/2}Nb_{1/2})O_3$ system has been investigated and solid solutions with 90 and 95 mole % $Pb(Fe_{1/2}Nb_{1/2})O_3$, etc., have been revealed. It is possible that these may have some practical importance.

---

[1] O. S. Didkovskaya, V. V. Klimov, and Yu. N. Venevtsev, Izv. Akad. Nauk SSSR, Neorgan. Mat., 3, 1243 (1967).

[2] O. S. Didkovskaya, T. P. Rudenko, V. V. Klimov, and Yu. N. Venevtsev, Elektron. Tekh., Ser. 14, No. 1, 6 (1969).

[3] T. V. Tien, E. C. Subbarao, and T. Hrizo, J. Amer. Ceram. Soc., 45, 572 (1962).

[4] I. A. Glozman, Peizoceramics [in Russian], Énergiya, Moscow (1967).

[5] W. H. Payne and V. J. Tennery, J. Amer. Ceram. Soc., 48, 413 (1965).

[6] Yu. I. Gol'tsov, I. N. Belyaev, S. A. Shilov, V. S. Filip'ev, and O. I. Prokopalo, Elektron. Tekh., Ser. 14, No. 5, 123 (1969).

[7] F. Jona and D. Shirane, Ferroelectric Crystals, Pergamon (1962).

[8] G. A. Smolenskii, A. I. Arganovskaya, and N. N. Krainik, Dokl. Akad. Nauk SSSR, 41, 55 (1953).

Vanadates with a defect garnet structure

G. Ronniger and B. V. Mill'

M. V. Lomonosov Moscow State University

(Submitted October 28, 1971; resubmitted February 15, 1972)
Kristallografiya, 18, 303-307 (March-April 1973)

In $MO-M'O-V_2O_5$ systems, ranges corresponding to the formation of defect garnets with the general formula $\square_{0.5}\cdot(M, M')^{2+}_{4.5}V^{5+}_3O_{12}$, where M = Pb or Ca and M' = Mg, Co, Ni, Zn, Mn, or Cd, and garnets $Pb_{3-x}Cd_{2.33+x}V_{2.67}O_{12}$, containing Cd^{2+} ions in four-fold coordination, have been detected. It has been shown that the cation vacancies in V garnets may occupy the c and *a* positions, with a preference for the former, and do not enter the d positions in significant quantities.

The garnet structure is regarded as extremely satisfactory as far as defects are concerned, although there are a number of reports that cation and anion vacancies are possible in this structure. In the preparation of Ge^{4+}-containing garnets at high temperatures (≥1200°C), loss of GeO_2 was observed as a consequence of its volatilization, accompanied by a change in the lattice parameter.[1] Defect garnets were obtained in attempts to prepare Ge garnets containing divalent iron.[1] In ferrite garnets at high temperatures (≥1400°C), Fe^{2+} is formed, and the garnets acquire oxygen defects.[2] We observed oxygen defects in the garnets $\{Ca_{3-x-y}Na_xLn_y\}Mn_2Ge_3O_{12}$. In a number of syntheses it has been impossible to obtain garnets without impurity phases, and this may also be an indication of defect structure.[3] In all these cases there are only small concentrations of defects, and the mechanism of their formation and their crystal-chemical character are not yet clear. In a study of isomorphism in vanadates with the garnet structure,[4] we obtained garnets with cation vacancies and general formula $\square_{0.5}\cdot(M, M')^{2+}_{4.5}V^{5+}_3O_{12}$, and determined the distribution of the vacancies in these materials.

The starting materials for the synthesis were the oxides, carbonates, and nitrates of at least "analytically pure" grade purity. Most of the compositions were sintered in air, but the low-temperature Pb−Mn mixtures were synthesized in a vacuum at 10^{-3} mm Hg. The phase composition was followed by x-ray diffraction studies with a URS-50IM diffractometer (Co Kα radiation). For the determination of the V^{4+} concentration we used the gravimetric method,[5] described below. The conditions for the formation of single-phase specimens and their characteristics are given in Table 1.

The presence of vacancies in garnets with the composition $(M, M')^{2+}_{4.5}V_3O_{12}$ requires proof, since they may be transformed into defect-free materials with the formation¹⁾ of $V^{4+}-(M, M')^{2+}_{4.8}V^{4+}_{1.6}V^{5+}_{1.6}O_{12}$. The loss in weight due to the O_2 liberated would then be 1-2.5 wt.% (depending on the composition), and for specimens weighting 2-3 g this makes it possible to detect 1-2% V^{4+} relative to the total concentration of vanadium. The gravimetric analysis was carried out for three garnets: $Ca_{2.5}Mg_2V_3O_{12}$, $Ca_{2.5}Ni_2V_3O_{12}$, and $Pb_{2.5}Cd_2V_3O_{12}$. For the first two we first prepared the vanadates $Ca_3V_2O_8$, $Mg_3V_2O_8$, and $Ni_3V_2\cdot O_8$, which were then used to prepare the garnets at the temperatures indicated in Table 1, according to the reaction $2.5Ca_3V_2O_8 + 2(Mg, Ni)_3V_2O_8 \rightarrow 3Ca_{2.5}(Mg, Ni)_2V_3O_{12}$. The garnet $Pb_{2.5}Cd_2V_3O_{12}$ was prepared directly from the oxides. Tablets of the components of the mixtures were heated at the same time as the garnet-forming mixtures.

According to the results of the gravimetric determination of the loss on sintering, the concentration of V^{4+} relative to the total quantity of vanadium amounts to 1.78% for $Ca_{2.5}Mg_2V_3O_{12}$, 2.36% for $Ca_{2.5}Ni_2V_3O_{12}$, and 1.65% for $Pb_{2.5}Cd_2V_3O_{12}$, which corresponds to less than 0.1 V^{4+} per formula unit. Thus in the garnets $(M, M')^{2+}_{4.5}V_3O_{12}$, the concentration of V^{4+} is negligibly small (close to the error of the determination)²⁾ and in actual fact there is a vacancy mechanism, and the concentration of cation vacancies is fairly high (~6%).

In the consideration of the problem of the distribution

TABLE 1. Conditions of Synthesis and Characteristics of the Garnets

Composition of garnet	Temp. of synthesis °C	Lattice constant, Å	X-ray density, g/cm³	Color of powder
$\{\square_{0.5}Ca_{2.5}\}Ni_2V_3O_{12}$	950	12,370±3	3.946	Yellow
$\{\square_{0.5}Ca_{2.5}\}Co_2V_3O_{12}$	950	12,429±3	3,893	Green
$\{\square_{0.5}Ca_{2.5}\}Mg_2V_3O_{12}$	950	12,431±3	3.413	White
$\{\square_{0.5}Ca_{2.5}\}Zn_2V_3O_{12}$	750	12,453±3	3,959	The same
$\{\square_{0.5}Ca_{2.5}\}Mn_2V_3O_{12}$	950	12,567±3	3,713	Brown
$\{\square_{0.25}Ca_{2.75}\}[\square_{0.25}Ni_{1.75}]V_3O_{12}$	950	12,387±3	3,897	Yellow
$\{\square_{0.25}Ca_{2.75}\}[\square_{0.25}Co_{1.75}]V_3O_{12}$	950	12,442±3	3,849	Green
$\{\square_{0.25}Ca_{2.75}\}[\square_{0.25}Mg_{1.75}]V_3O_{12}$	950	12,443±3	3,430	White
$\{\square_{0.25}Ca_{2.75}\}[\square_{0.25}Zn_{1.75}]V_3O_{12}$	750	12,456±3	3,913	The same
$\{\square_{0.25}Ca_{2.75}\}[\square_{0.25}Mn_{1.75}]V_3O_{12}$	950	12,550±3	3.703	Brown
$\{\square_{0.5}Pb_{2.5}\}Mn_2V_3O_{12}$	760 (in a vacuum)	12,974±5	5,915	The same
$\{\square_{0.5}Pb_{2.5}\}Cd_2V_3O_{12}$	760	13,164±5	6,331	Beige
$\{\square_{0.25}Pb_{2.75}\}[\square_{0.25}Cd_{1.75}]V_3O_{12}$	760	13,176±5	6,453	Yellowish
$\{Pb_{2.83}Cd_{0.17}\}[Cd_2](Cd_{0.33}V_{2.67})O_{12}$	820	13,213±3	6,719	The same
$\{Pb_{2.67}Cd_{0.33}\}[Cd_2](Cd_{0.33}V_{2.67})O_{12}$	820	13,230±10	6,769	»
$\{Pb_{2.5}Cd_{0.5}\}[Cd_2](Cd_{0.33}V_{2.67})O_{12}$	820	13,241±2	6,823	»

TABLE 2. X-Ray Standards for the Determination of the Distribution of Vacancies

Assumed distribution of the vacancies in the defect garnet and the composition of the standard	Atomic scattering factors		Lattice constant, Å	Temperature of synthesis of the standard, °C
	f_c^*	f_a^*		
$\{\square_{0.5}Ca_{2.5}\}[Co_2](V_3)O_{12}$	16.7	27.0	12.429±3	
$\{NaCa_2\}[Co_2](V_3)O_{12}$	17.0	27.0	12.431±3	900
$\{Ca_{2.5}Co_{0.5}\}[\square_{0.5}Co_{1.5}](V_3)O_{12}$	21.2	20.2	12.429±3	
$\{Na_{0.65}Ag_{0.35}Ca_2\}[Mg_{0.5}Co_{1.5}](V_3)O_{12}$	21.2	20.2	12.444±3	800
$\{\square_{0.5}Pb_{2.5}\}[Cd_2](V_3)O_{12}$	68.3	48.0	13.164±5	
$\{K_{0.40}Ag_{0.42}Tl_{0.18}Pb_2\}[Cd_2](V_3)O_{12}$	68.6	48.0	13.160±3	750
$\{Pb_{2.5}Cd_{0.5}\}[\square_{0.5}Cd_{1.5}](V_3)O_{12}$	76.3	36.0	13.164±5	
$\{Ag_{0.47}Pb_{2.53}\}[Li_{0.53}Cd_{1.47}](V_3)O_{12}$	76.5	36.1	13.079±4	700

TABLE 3. Line Intensities on the X-Ray Diffraction Patterns of the Defect Garnets and Their X-Ray Standards

hkl	Line intensities on the x-ray diff. patterns for the garnets					
	$\square_{0.5}Ca_{2.5}Co_2V_3O_{12}$	standard for c vacancies	standard for *a* vacancies	$\square_{0.5}Pb_{2.5}Cd_2V_3O_{12}$	standard for c vacancies	standard for *a* vacancies
211	22.2	21.0	4.9	18.6	21.8	26.8
220	7.4	6.4	—	—	—	2.9
321	9,3	10.1	1.3	18.6	18.6	30.5
400	46.3	45.3	52.2	37.2	37.0	29.7
420	100.0	101.5	149.1	100.0	100.4	112.9
332	12.9	19.7	19.5	—	—	2.6
422	90.7	94.2	53.7	81.4	84.1	47.5
431	12.0	10.0	15.4	2.3	1.9	1.8
521	3.7	3.2	4.2	14.0	13.8	15.6
611,532	6.0	6.4	9.1	18.2	17.0	22.2
620	5.1	5.1	2.1	0.8	—	0.6
631	2.3	2.7	—	3.7	3,1	3.5
444	6,5	7.3	13.3	6.2	6.2	8.1
640	26.8	22.9	32.1	20.9	19.3	17.8
721,633	1.4	1.4	1.3	6.6	5.4	9.7
552						
642	57,9	57.6	52.2	45.0	46.3	29.0
732,651	0.9	0.9	—	4.3	3.5	6.7
800	9.3	8.2	12.5	9.3	8.1	10.0
752	—	—	—	—	—	1.5
840	12.0	11.9	10.4	10.1	9.2	8.6
842	12.5	13.7	17.4	12.0	12.3	17.0
664	8.3	9.1	7.6	7.8	6.9	4.4
10 40,864	12.0	13.3	13.3	9.3	8.8	11.5
10 42	10.2	10.6	11.2	7.4	8,5	7.0
$R = \frac{\Sigma \lvert I_{\text{def}} - I_{\text{stand}} \rvert}{\Sigma I_{\text{def}}} \cdot 100$		4.6	35.0	—	4.8	30.0

of the vacancies in the c, *a*, and d positions (coordination numbers 8, 6, and 4, respectively), the latter can be eliminated immediately, since in the garnet structure V^{5+} has a strong preference for four-fold coordination and is not detected in *a* positions. For the compositions given in Table 1, the formation of d vacancies would require the transfer of V^{5+} into *a* positions, and this is unlikely. We tried to prepare a number of other compositions with d vacancies [$Ca_{2.75+x}M^{2+}_{2-x}V_{2.9}O_{12}$ (vacancies in all three positions), and $Ca_3M^{2+}_2V^{5+}_{2.8}O_{12}$], but we did not obtain a single-phase garnet, that is, d vacancies are not present in appreciable quantities in V garnets.

The concentration of vacancies in garnets of the type $\square_{0.5}M_{2.5}M'_2V_3O_{12}$ is sufficiently high for their distribution in the c and *a* positions to be estimated from the intensities of the x-ray diffraction patterns. Since the coordinates of oxygen in the V garnets are unknown (and apparently differ considerably from those determined in other garnets), we decided not to carry out the calculations for the x-ray diffraction patterns, but to prepare x-ray standards for the two opposite distributions of the vacancies. As standards, we prepared V garnets with known distribution of the cations, for which the lattice constants and atomic scattering factors for the c and *a* positions (f_c and f_a) were as close as possible to the value of a_0, f_c and f_a for the defect garnets (Table 2). The coordinates of the oxygen in these compositions are evidently sufficiently close to eliminate any influence on the ratio of the intensities.

It follows from a comparison of the intensities of the x-ray diffraction patterns of the defect garnets and the standards (Table 3) that in the garnets $\square_{0.5}Ca_{2.5}M_2V_3O_{12}$ and $\square_{0.5}Pb_{2.5}M_2V_3O_{12}$ the vacancies are concentrated in the c positions, that is, the distribution has the form $\{\square_{0.5}M_2\}[M'_2](V_3)O_{12}$. This is the distribution which we have assumed from the very beginning for $\square_{0.5}Ca_{2.5}M_2V_3O_{12}$, since in V garnets the Mg^{2+}, Co^{2+}, Mn^{2+} ions enter the c positions very reluctantly and in extremely small quantities, and the Ni^{2+} and Zn^{2+} ions do not enter these positions at all.[4] Sintering of the compositions $Ca_2M^{2+}_{2.5}V_3O_{12}$ (M = Mg, Co, Ni, Zn) did not give single-phase specimens, and the lattice constants are the same as a_0 for $Ca_{2.5}M_2V_3O_{12}$, again indicating that the small M^{2+} do not enter the c positions of the defect garnets. In the garnets

$\square_{0.5}Ca_{2.75}M^{2+}_{1.75}V_3O_{12}$, judging from the slight change in the parameter (the introduction of Ca^{2+} into the *a* positions would produce a marked increase[4] in a_0), the vacancies are present in the two positions in approximately equal quantities, that is, the large Ca^{2+} ions, which in V garnets exhibit a preference for eight-fold coordination, displace a corresponding number of vacancies into *a* positions. An analogous distribution of vacancies is observed in $\square_{0.5} \cdot Pb_{2.75}Cd_{1.75}V_3O_{12}$. The number of *a* vacancies is limited, however, and the compositions $(Pb, Ca)_3M^{2+}_{1.5}V_3O_{12}$ are not attained. Thus in V garnets the cation vacancies may be present in the c and *a* positions, with a preference for the former, and they are not detected in d positions.

The dimensions of the vacancies are determined by the dimensions of the cations with which they share the various positions in the structure. This can be clearly seen by comparing the lattice constants of the garnets $\{NaCa_2\}[M^{2+}_2](V_3)O_{12}$ (in which the c positions contain approximately equal quantities of Na^+ and Ca^{2+} ions), $\{\square_{0.5} \cdot Ca_{2.5}\}[M^{2+}_2](V_3)O_{12}$, and $\{\square_{0.25}Ca_{2.75}\}[\square_{0.25}M^{2+}_{1.75}](V_3)O_{12}$. In the lead garnets the lattice constant of the defect garnet is greater than a_0 for $NaPb_2Cd_2V_3O_{12}$, and smaller than a_0 for $KPb_2Cd_2V_3O_{12}$, and this corresponds to the ratio of the dimensions of Na^+, K^+, and Pb^{2+}. It is probable that when vacancies are present the metal–oxygen distances in the corresponding polyhedra are increased slightly, that is, in the garnets $\{\square_{0.25}Ca_{2.75}\}[\square_{0.25}M^{2+}_{1.75}](V_3)O_{12}$ the M–O distances are greater than those in $\{\square_{0.5}Ca_{2.5}\}[M^{2+}_2](V_3)O_{12}$, and, if the garnets $\{Ca_3\}[\square_{0.5}M^{2+}_{1.5}](V_3)O_{12}$ existed, the Ca–O distances in them would be less than those in $\{\square_{0.5}Ca_{2.5}\} \cdot [M^{2+}_2](V_3)O_{12}$.

The defect V garnets form continuous solid solutions with garnets of the type $M^+M^{2+}_2M'^{2+}_2V_3O_{12}$ (isomorphous replacement scheme $2M^+ \to \square^0 + M^{2+}$). In the systems $\square_{0.5}Ca_{2.5} \cdot Co_2V_3O_{12} - NaCa_2Co_2V_3O_{12}$ and $\square_{0.5}Pb_{2.5}Cd_2V_3O_{12} - M^+Pb_2 \cdot Cd_2V_3O_{12}$ (M = Na, Ag, K, Tl)[4] which we studied, the lattice constants obey Vegard's rule (see Fig. 1). It is obvious that other types of V garnets[4] may also contain appreciable quantities of cation vacancies. The presence of vacancies, and also the possibility of a change in the ratio of the cations (for example[4] $M^+Ca_{2\pm x}M^{2+}_{2\mp x}V_3O_{13}$) makes it necessary to exercise some care in the study of isomorphism in V garnets. In any case, the preparation of single-phase specimens is essential. We also observed appreciable concentrations of vacancies in the growth of single crystals of V garnets from solution in a melt; for example, instead of $NaCa_2M^{2+}_2V_3O_{12}$, we obtained crystals with the composition $Na_{1-2x}\square_xCa_{2+x}M^{2+}_2V_3O_{12}$.

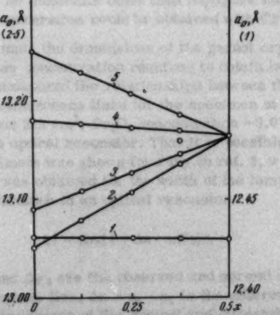

Fig. 1. Lattice constants a_0 for the solid solutions in the systems $\square_xNa_{1-2x}Ca_{2+x}Co_2V_3O_{12}$ (1) and $\square_xM^+_{1-2x}Pb_{2+x}Cd_2V_3O_{12}$, M = Na (2), Ag (3), K (4), and Tl (5).

In $MO - MO' - V_2O_5$ systems it is possible in principle to have the formation of defect-free garnets with the composition $(M, M')^{2+}_{3^{1/3}}V^{5+}_{2^{2/3}}O_{12}$; this assumes that the d positions contain simultaneously both M^{2+} ions (10% of the d positions) and V^{5+} ions (90%). We obtained garnets with an appreciable concentration of M^{2+} (d) only in the $PbO - CdO - V_2O_5$ system (Table 1), although for other M^{2+} (Mg^{2+}, Co^{2+}, Ni^{2+}, and Zn^{2+}), four-fold coordination in the garnet structure3) is known. An interesting feature is that the composition $Pb_3Cd_{2.33}V_{2.67}O_{12}$ is not attained, and the Pb^{2+} (c) is always slightly diluted by Cd^{2+}, that is, the Cd^{2+} is present simultaneously in all three positions. The introduction of the Cd^{2+} ion, which is very large for four-fold coordination,4) into the d position leads to a significant increase in the parameter compared with a_0 for $\square_{0.5}Pb_{2.5} \cdot Cd_2V_3O_{12}$. In the ternary systems $Pb_{3-x}Cd_{2.33+x}V_{2.67}O_{12} - \square_{0.5}Pb_{2.5}Cd_2V_3O_{12} - M^+Pb_2Cd_2V_3O_{12}$ there is complete solubility.

The defect vanadium garnets can be regarded as the first step towards a structure of the iron molybdate type $Fe_2(MoO_4)_3$, in which all dodecahedral positions are vacant, and the arrangement of the FeO_6 octahedra and MoO_4 tetrahedra is almost analogous to that in the garnet.[8] It is possible that compounds will be found with a garnet structure exhibiting a high concentration of defects. We tried to prepare garnets of this kind from mixtures of $Bi_{5/3}M^{2+}_2V_3O_{12}$ and $Ln_2M^{3+}_2(Si, Ge)_3O_{12}$ (Ln = La, Nd, Sm, Gd, Y, Yb; M = Y, Yb, In, Sc, Fe, Cr, Al), but without success.

These studies show the possibility of existence of appreciable concentrations of defects in the garnet structure and necessity for taking account of this phenomenon in the synthesis and the study of the isomorphism and properties of compounds with the garnet structure. The nature of the defects and their behavior in other types of garnet, however, may differ from those for the V garnets.

---

1) An extremely characteristic feature of the chemistry of pentavalent vanadium is the formation of "bronzes" containing V^{4+}. Tetravalent vanadium has been detected by EPR methods in single crystals of the garnet[5] $NaCa_2 \cdot Mg_2V_3O_{12}$.

2) The absence of appreciable quantities of V^{4+} is indicated by the fact that the colors of the vacancy-containing garnets and the corresponding Na garnets $NaM_2M'_2V_3O_{12}$ are identical, whereas V^{4+} produces deep colors in the components.

3) When $Ca_3M^{2+}_{2.33}V_{2.67}O_{12}$ mixtures were sintered, a single-phase ceramic was not obtained, and the parameters a_0 were the same as a_0 for the defect garnets.

4) Four-fold coordination for Cd^{2+} is known, for example, in silicates and spinels.

---

[1] S. Geller and C. E. Miller, Acta Crystallogr., 13, No. 3, 179 (1960).

[2] H. J. Van Hook, J. Am. Ceram. Soc., 45, No. 4, 162 (1962).

[3] S. Geller, H. J. Williams, R. C. Sherwood, and G. P. Espinosa, J. Phys. Chem. Solids, 26, No. 2, 443 (1965).

[4] B. V. Mill' and G. Ronniger, in: The Physics and Chemistry of Ferrites [in Russian], Vol. 2, Izd. MGU, Moscow (1972).

[5] D. Berham, Trans. Brit. Ceram. Soc., 64, No. 7, 419 (1965).

[6] V. Havlíček, P. Novak, and M. Vichr, Phys. Status Solidi, 44, 21 (1971).

[7] B. V. Mill', in: Physical and Physicochemical Properties of Ferrites [in Russian], Izd. MGU, Moscow (1971).

[8] L. M. Plyasova, S. V. Borisov, and N. V. Belov, Kristallografiya, 12, 33 (1967) [Sov. Phys. – Crystallogr., 12, 25 (1967)].

Laser based on Cr^{3+} ions in yttrium–aluminum garnet

B. K. Sevast'yanov, Kh. S. Bagdasarov, L. B. Pasternak, S. Yu. Volkov, and V. P. Orekhova
Institute of Crystallography, Academy of Sciences of the USSR

(Submitted December 25, 1972)
Kristallografiya, 18, 308-310 (March-April 1973)

A laser based on Cr^{3+} ions in yttrium–aluminum garnet ($Y_3Al_5O_{12}$) has been obtained. At liquid-nitrogen temperatures laser generation is obtained at a wavelength of 6874 Å. The threshold energy of the light flux incident on the surface of the crystal is ~300 J.

We have previously studied[1] the absorption and luminescence spectra of excited Cr^{3+} ions in yttrium–aluminum garnet ($Y_3Al_5O_{12}$) (YAG) and established the complete energy level scheme for Cr^{3+} in it.

Chromium-activated crystals of YAG absorb light in the wide bands at 433 and 606 nm caused by the transitions $^4A_2 \rightarrow {}^4T_2$ and $^4A_2 \rightarrow {}^4T_1$. The absorption cross sections for these transitions are $\sigma_{433} = 0.55 \cdot 10^{-19}$ and $\sigma_{606} = 0.35 \cdot 10^{-19}$ cm^2. Owing to the nonradiative transitions $^4T_1 \rightarrow {}^2E$ and $^4T_2 \rightarrow {}^2E$, population of the metastable level ^2E takes place, in which the lifetime of Cr^{3+} ions is 1.5 msec at room temperature and 9 msec at liquid-nitrogen temperature. The $^2E \rightarrow {}^4A_2$ transition is accompanied by an intense luminescence, the spectrum of which consists of two narrow lines R_1 and R_2 having maxima $\lambda_{R_1} = 6887$ Å and $\lambda_{R_2} = 6877$ Å at room temperature, and $\lambda_{R_1} = 6873$ Å and $\lambda_{R_2} = 6863$ Å at liquid-nitrogen temperature. The splitting of the ^2E level is 19.8 cm^{-1}. The half-widths of the R_1 and R_2 lines are 14 and 12 cm^{-1} at room temperature and 1.4 and 1.3 cm^{-1} at liquid-nitrogen temperature. Wide bands having a periodic structure caused by electron-vibrational transitions are observed at room temperature in the vicinity of the R lines, both in the long-wave and short-wave regions. At liquid-nitrogen temperature the short-wave luminescence band is destroyed by the cold. The luminescence lifetimes τ_{R_1} and τ_{R_2} coincide to an accuracy of ~0.1 msec, which indicates a sufficiently high rate of relaxation between the sublevels of the ^2E level.

The results in ref. 1 enabled us to assume that a laser operating on a three-level scheme can be made on the basis of YAG activated by chromium ions. It may be noted that according to recent data in the literature (see, e.g., ref. 2) no materials other than Al_2O_3 are known in which laser generation could be obtained with Cr^{3+} ions.

To estimate the dimensions of the garnet crystal and the chromium concentration required to obtain laser generation we measured the relationships between the widths of the R_1 luminescence lines for the specimen at our disposal (volume 2.3 cm^3, Cr_2O_3 concentration ~0.07 wt.%), placed in an optical resonator. That it is possible to make such an estimate was shown for ruby in ref. 3, where an expression was obtained for the width of the luminescence line of a substance in an optical resonator:

$$\Delta\nu = \Delta\nu_0[1 + \Delta n / n_0 K_l]^{1/2}, \qquad (1)$$

where $\Delta\nu$ and $\Delta\nu_0$ are the observed and normal widths of the luminescence line, $\Delta n = n_1 - n_2$ is the difference between the populations of the ground and metastable levels, n_0 is the total number of Cr^{3+} ions in 1 cm^3 of substance, and K_l is the loss coefficient,[4] which is equal to $[\rho + (1/l) \times (1/r_1r_2)^{1/2}]/\varkappa_R$. In this expression ρ represents the losses in the substance filling the resonator, referred to unit length, l the length of the specimen, r_1 and r_2 the reflection coefficients of the mirrors, and $\varkappa_R$ the absorption coefficient at the maximum of the R line.

From Eq. (1) it can be seen that for weak pumping ($\Delta n \simeq n_0$) the luminescence line undergoes broadening as a result of overabsorption. With an increase in pumping energy the linewidth decreases, being found equal to the normal width $\Delta\nu_0$ when there is equal population of the pair of levels between which luminescence is produced. With a further increase in pumping $\Delta\nu$ tends to zero, becoming zero (within the limits of such a consideration) when the generation threshold is reached.

Equation (1) was obtained in ref. 3 by considering the energy balance in a resonator, as was done in ref. 5. However, it should be noted that when solving the problem of the distribution of radiation in a long, uniformly excited rod the expression for $\Delta\nu$ has the same form.

Equation (1) enables K_l to be determined from the experimental value of $\Delta\nu/\Delta\nu_0$ for weak pumping. Since, as is known,[4] the generation threshold level can be written in the form $K_l = -\Delta n/n_0$, then the proposed generation threshold can be determined from K_l.

For the garnet specimen studied (l = 2 cm, d = 0.6 cm) K_l was found to be 2.75 ($\Delta\nu_{max} = 16.4$ cm^{-1}, $\Delta\nu_0 = 14.2$ cm^{-1}) and it was evidently impossible to obtain laser generation with it. The high losses in this specimen are explained by its poor optical quality.

Measurements conducted in ref. 1 of the population of the ^2E level indicated the possibility of obtaining values of $n_2/n_0 \approx 0.6$–0.7 over the available range of pumping. Hence it follows that for a specimen with which it was possible to expect generation, K_l should not exceed 0.3.

Crystals of chromium-activated YAG satisfying this condition were grown specially by horizontal directed crystallization.[6] The specimen with which generation was obtained had the shape of a cylinder 8.3 cm long and 1 cm in diameter. Its Cr_2O_3 concentration was 0.5 wt.%. The $\Delta\nu_{max}/\Delta\nu_0$ ratio for this specimen was 1.93 when mirrors were attached at its ends ($r_1 = 1$, $r_2 = 0.95$) and 1.4 without mirrors. These values of $\Delta\nu_{max}/\Delta\nu_0$ correspond to K_l values of 0.31 and 1.

We succeeded in achieving laser generation at liquid-nitrogen temperature at the wavelength of the R_1 line (λ = 6874 Å) in the apparatus described in ref. 1. The generation threshold was achieved with 300 J of light energy incident on the crystal surface, the energy being measured with the calorimeter described in ref. 7. The angle of divergence of the laser beam did not exceed 2°. The generation pulse had a clearly defined peak structure.

The high generation threshold and the appreciable divergence in the emission can be explained by the inadequate optical quality of the specimen and a nonoptimal relationship between its geometrical dimensions, its chromium concentration, and the transparency of the mirrors.

We thank E. A. Fedorov, V. A. Pavlov, and V. V. D'yachenko for assistance in preparing the specimen and B. K. Vainshtein for interest in the investigation.

---

[1] B. K. Sevast'yanov, D. T. Sviridov, V. P. Orekhova, L. B. Pasternak, R. K. Sviridova, and T. F. Veremeichik, in: Kvantovaya Elektron., 4, No. 10, 55 (1972) [Sov. J. Quant. Electron., 2, 339 (1973)].

[2] Yu. K. Voron'ko, V. V. Osiko, A. M. Prokhorov, and I. A. Shcherbakov, Trudy Fiz. Inst. Akad. Nauk SSSR, 60, 3, Nauka (1972).

[3] B. K. Sevast'yanov, L. B. Pasternak, and Yu. L. Remigailo, Zh. Prikl. Spektrosk., 18, 145 (1973).

[4] B. I. Stepanov, Methods of Laser Design, Vol. 1 [in Russian], Nauka, Minsk (1966), p. 103.

[5] T. H. Maiman, in: Optical Masers [Russian translation], Izd. Kazansk. Univ., Kazan' (1964), p. 120.

[6] Kh. S. Bagdasarov, L. M. Dedukh, I. A. Zhizheiko, A. M. Kevorkov, and V. I. Nikitenko, Kristallografiya, 15, 334 (1970) [Sov. Phys. – Crystallogr., 15, 278 (1970)].

[7] V. P. Orekhova, B. K. Sevast'yanov, and Yu. A. Sokolov, in: Methods and Instruments for the Quality Control of Ruby Crystals [in Russian], Nauka (1968), p. 98.

Vibrational spectrum and crystal structure of $TlNO_3$ III

D. E. Pogarev and A. A. Shultin

Leningrad State University

(Submitted February 13, 1972)
Kristallografiya, 18, 311-314 (March-April 1973)

The IR absorption spectrum and Raman spectrum of a $TlNO_3$III single crystal in polarized light at T = 295°K was investigated in the region where the ν_4, ν_2, and ν_1 internal vibrations of the nitrate ions occur. Davydov splitting of the bands and, also, interset splitting due to the presence in the unit cell of two sets of molecules not related by symmetry were detected. It was shown that the spectra observed correspond to the crystal space group D_{2h}^{16}−pbnm, where the nitrate ions occupy the site points C_s arranged in the σ_{xy} planes (set σ_h) and perpendicular to them (set σ_v).

According to the most complete results of x-ray structural investigations published up to now, the low-temperature phase of the $TlNO_3$III crystal (stable below 750°C) belongs either to space group D_{2h}^{16} − Pbnm or to C_{2v}^{9} − Pbn2_1 of the rhombic system.[1]

The unit cell for both groups should contain eight formula units. The sublattice formed by the Tl^+ ions is quite close to being tetragonal. The membership of the crystal to one or the other space group is governed only by the positions of the O atoms. A structure of the type Pbnm is shown in Fig. 1. In this case, the nitrate ions located in adjacent subcells are arranged alternately either normal to the rhombic z axis or almost normal to the y axis. Each Tl^+ ion is surrounded here asymmetrically by the O atoms. Their more symmetrical arrangement can be accomplished in a structure of the type Pbn2_1 through a turn of the four nitrate ions by approximately 15° along the N−O bonds, which are almost parallel to the x axis. However, refinement of the coordinates of these atoms is hindered as a result of the large discrepancy in the scattering factors.[1]

In order to obtain additional information, it was expedient to investigate the vibrational spectra of the single crystals in polarized light. The first such attempt was carried out in ref. 2, but for a number of reasons, the authors could not arrive at an unambiguous answer. The results of recent spectroscopic investigations of powdered $TlNO_3$III samples are contained in refs. 3-6.

The samples we investigated and which were oriented relative to their crystallographic alignments by the conoscopic method were cut from $TlNO_3$III single crystals which were grown from an aqueous solution (to which about 10% concentrated HNO_3 was added) by the temperature-drop method.[7] The scanning of the infrared spectra was carried out on a modified IKS-6 spectrometer.[8] The

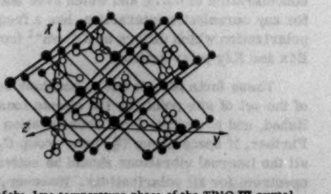

Fig. 1. Structure of the low-temperature phase of the $TlNO_3$III crystal based on space group Pbnm. The Tl ions are represented by the large black circles, the N atoms by the small (black) ones, and the O atoms by the open circles.

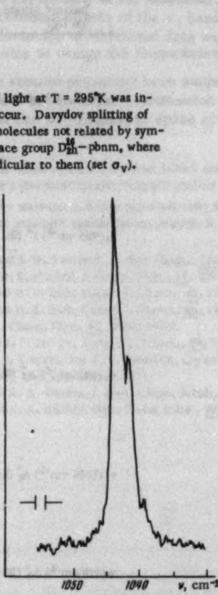

Fig. 2. Raman spectrum of a $TlNO_3$III single crystal in the ν_1 vibrational region at T = 295°K. Orientation x(zz)y.

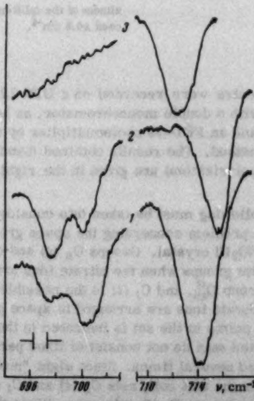

Fig. 3. Polarized infrared transmission spectrum of a $TlNO_3$III single crystal in the ν_4 vibrational region at T = 80°K. 1) E∥x; 2) E∥y; 3) E∥z. Spectra 1 and 3 were obtained for a sample with a thickness of 400 μ; spectrum 2 for a sample with a thickness of 250 μ.

TABLE 1. Correlation Diagrams and Observed Frequencies of the Internal Vibrations of the Nitrate Ions at T = 295°K in the $TlNO_3$III Crystal

Isolated nitrate ion D_{3h}	Site group C_s	Factor group D_{2h}	Observed frequency, cm^{-1}
		Set σ_h	
		$A_g (\alpha_{ii})$	701.7
		$B_{1g} (\alpha_{xy})$	701.7
ν_4 (720 cm^{-1}) E' (IR, Ra)	A'	$B_{2u} (T_y)$	698.0; 700.6 } 80°K
		$B_{3u} (T_x)$	698.0; 701.0 }
		Set σ_v	
		$A_g (\alpha_{ii})$	714.3
		$B_{1g} (\alpha_{xy})$	714.0
	A'	$B_{2u} (T_y)$	714.5
		$B_{3u} (T_x)$	713.1
ν_4 (720 cm^{-1}) E' (IR, Ra)			
		A_u (н. a.)	—
		$B_{1u} (T_z)$	711.6
	A''	$B_{2g} (\alpha_{xz})$	713.8
		$B_{3g} (\alpha_{yz})$	713.3
		Set σ_h	
		A_u (н. a.)	—
		$B_{1u} (T_z)$	819.5 (798.5 for $^{15}NO_3^-$)
ν_2 (825 cm^{-1}) A_2'' (IR)	A''	$B_{2g} (\alpha_{xz})$	$\sim$821
		$B_{3g} (\alpha_{yz})$	?
		Set σ_v	
		$A_g (\alpha_{ii})$	$\sim$821
		$B_{1g} (\alpha_{xy})$	?
ν_2 (1050 cm^{-1}) A_1' (Ra)	A'	$B_{2u} (T_y)$	821.7 (801.2 for $^{15}NO_3^-$)
		$B_{3u} (T_x)$	822.0 (801.2 for $^{15}NO_3^-$)
		Sets σ_h and σ_v	
		$A_g (\alpha_{ii})$	1043.0; 1041.2; 1039.2
		$B_{1g} (\alpha_{xy})$	1041.4
ν_1(825 cm^{-1}) A_2'' (IR)	A'	$B_{2u} (T_y)$	1040.5
		$B_{3u} (T_x)$	1041.0

Note: The ions belonging to the σ_h set lie in the σ_{xy} plane of reflection, whereas the planes of the nitrate ions of the σ_v set are perpendicular to σ_{xy}. The error in determining the absolute values of the infrared (IR) and Raman (Ra) spectral frequencies amounts to ±0.7 cm^{-1}, whereas the relative error in measuring the magnitudes of the splitting of the components of a single group of lines does not exceed ±0.2 cm^{-1}.

Raman spectra were recorded on a DFS-12 apparatus equipped with a double monochromator, an LG-36a laser (60 mW), and an FÉU-79 photomultiplier by the photon counting method. The results obtained (band frequencies and their polarization) are given in the right-hand side of Table 1.

The following must be taken into consideration when solving the problem concerning the space group realized for the $TlNO_3$III crystal. Groups C_s (4) and C_1 (8) are the possible site groups when the nitrate ions are arranged in space group D_{2h}^{16}, and C_1 (4) is the possible site group when the nitrate ions are arranged in space group C_{2v}^{9} (the number of points in the set is indicated in the parenthesis). The indicated sets do not consist of fixed parameters and can be filled several times. Since eight "molecules" are contained in the unit cell, sets C_s (4) and C_1 (4) should be filled twice and set C_1 (8) only once. When there is more than a single filling of a set, the site points of the nitrate ion can be exposed to the action of local fields of various magnitudes and can possess differing frequencies for their internal vibrations ("interset" splitting).[9]

As is evident from Fig. 2 and Table 1, maxima at 1043.0 and 1041.2 cm^{-1} are observed for the ν_1 vibration in the Raman spectrum of a $TlNO_3$III single crystal in the x(zz)y orientation.1) In addition, the ν_2 vibrational band of the $^{15}NO_3^-$ ions, which are present at a natural concentration of 0.37% and which have not been examined for any correlation interaction, has a frequency for E‖z polarization which differs by 2.7 cm^{-1} from those for the E‖x and E‖y polarizations.

These facts permit one to consider twofold filling of the set of site points by the nitrate ions to be established, and to exclude from consideration the set C_1 (8). Further, if space group C_{2v}^{9} [site group C_1 (4)] is realized, all the internal vibrations should be active in the infrared spectrum for all polarizations. However, as follows from Table 1, the ν_1 vibration is observed only in the spectra for the E‖x and E‖y polarizations, and the ν_4 vibration in the spectrum for the E‖z polarization has only one component (Fig. 3).[2]

Finally, the correspondence of the observed spectra to the case where the nitrate ions are arranged at the C_s site points of space group D_{2h}^{16} remains to be explained. On the basis of ref. 1, let us assume that the nitrate ions of one set lie in the σ_{xy} reflection planes, whereas the planes of the ions in the second set are perpendicular to them. The correlation scheme of the irreducible representations and types of symmetry of the vibrations for this case are given in the left-hand side of Table 1. Assignment of the observed frequencies of the nitrate ions to one or the other set is carried out unequivocally for the ν_2 vibration on the basis of the polarization of the bands. Assignment of the ν_4 vibrational frequencies can be accomplished due to the fact that the band with polarization $E \parallel z$ is attributed to the set σ_v, and Davydov splitting for the components with $E \parallel x$ and $E \parallel y$ equal to 1-4 cm^{-1} can be assumed.[5] It follows from this that "interset" splitting for this vibration amounts to about 14 cm^{-1}.

It is interesting to note that splitting of the ν_4 vibration (698-701 cm^{-1}) by the local field of the crystal for the σ_h set of the nitrate ions was detected as a result of careful experiments at 80°K, carried out for the purpose of proving the correctness of this correlation scheme.

In view of the identity of the selection rules concerning the spectroscopic effects of the ν_1 band for both sets of NO_3^- ions, inclusion of additional data on intensities is required in order to assign the frequencies.

Thus, the results presented here support the contention that the low-temperature modification of the thallium nitrate crystal can be assigned to space group D_{2h}^{16}.

---

[1] The origin of the weak maximum at about 1039.2 cm^{-1}, which was also noted in ref. 5 for a powdered sample, remains unclear as yet.

[2] The failure in the attempts to detect pyroelectricity in the $TlNO_3III$ crystal is an added argument against the realization of space group C_{2v}^{9}.

[1] S. W. Kennedy and J. H. Patterson, Z. Kristallogr., 116, 143 (1961).

[2] R. Newman and D. S. Halford, J. Chem. Phys., 18, 1276 (1950).

[3] M. H. Brooker and D. E. Irish, Canad. J. Chem., 48, 1183 (1970).

[4] M. H. Brooker and D. E. Irish, Canad. J. Chem., 48, 1198 (1970).

[5] M. H. Brooker, J. Chem. Phys., 53, 2670 (1970).

[6] D. W. James and J. P. Devlin, Austral. J. Chem., 24, 743 (1971).

[7] T. G. Petrov, E. B. Treivus, and A. P. Kasatkin, Crystal Growth from Solutions [in Russian], Nedra, Moscow (1967).

[8] S. V. Karpov and A. A. Shultin, J. Phys. Chem. Solids, 29, 475 (1968).

[9] S. V. Karpov and A. A. Shultin, Phys. Status Solidi, 39, 33 (1970).

Optical activity in $Ba(NO_2)_2 \cdot H_2O$ crystals

V. I. Burkov, V. A. Kizel', Z. B. Perekalina, N. L. Kozlova, and G. S. Semin

Institute of Crystallography, Academy of Sciences of the USSR

(Submitted April 11, 1972)
Kristallografiya, 18, 315-318 (March-April 1973)

The absorption spectra and dispersion of the optical activity have been recorded for $Ba(NO_2)_2 \cdot H_2O$ crystals; it is assumed that the optical activity in this case is determined by interaction of NO_2^- groups. This has been tested via various approximation equations for the dispersion of the optical activity, and it has been found that preference should be given to the equation $\varphi(\lambda) = \sum \frac{B_i\lambda^2}{(\lambda^2 - \lambda_i^2)^2}$, which characterizes the optical activity of the crystal.

Here we combine optical-activity curves with absorption spectra to elucidate the cause of optical activity in $Ba \cdot (NO_2)_2 \cdot H_2O$ crystals.

METHODS

The rotational dispersion curves were measured with a photoelectric spectropolarimeter;[1,2] the rotation of the plane of polarization was measured to $2\text{-}5 \cdot 10^{-2}$ deg. The spectra in absorption and diffuse reflection were recorded with a Hitachi EPS-3T spectrophotometer. The strong absorption meant that the spectrum could be recorded only over the range $0.39\text{-}0.5\,\mu$; the analogous spectrum of a solution of $Ba(NO_2)_2 \cdot H_2O$ was examined over the range $0.2\text{-}0.5\,\mu$, while the spectrum in diffuse reflection from the powder was recorded over the same wavelength range. The standard in the reflectance measurements was MgO.

The optical activity was examined on oriented specimens cut perpendicular to the optic axis, which were 1 cm^2 in area and 0.2-1.5 mm thick. The sections were oriented to better than 0.5°. The $Ba(NO_2)_2 \cdot H_2O$ crystal is hexagonal, and x-ray evidence[3,4] gives the unit cell parameters as $a = 7.05$, $c = 17.66$ Å, $Z = 6$, space group $P6_122(D_6^2)$ or $P6_522(D_6^3)$; however, it has been shown[5] that the space group is $P6_1(C_6^2)$ or $P6_5(C_6^3)$.

RESULTS AND DISCUSSION

The absorption spectrum in the near ultraviolet resembles that for solutions of most nitrides[6] in having three bands with peaks respectively at $\lambda_1 = 0.35$, $\lambda_2 = 0.28$, and $\lambda_3 = 0.21$ mm (Fig. 1).

The first band, peaking at about 0.35 μ, is[6-8] the allowed $n \rightarrow \pi^*$ transition of symmetry $^1A_1 \rightarrow {}^1B_1$ localized on the NO_2^- ion. The band near 0.21 μ is usually[8] assigned as an allowed $\pi \rightarrow \pi^*$ transition of symmetry $^1A_1 \rightarrow {}^1B_2$.

The third band, near 0.28 μ, is due to a forbidden $^1A_1 \rightarrow {}^1A_2$ transition.[6,9] Near 0.45 μ, the spectrum of $Ba(NO_2)_2 \cdot H_2O$ at high concentrations shows a very weak band, which occurs also for the crystal. This band is due to a forbidden S → T transition, which arises from spin-orbit interaction, which mixes the $^1B_2$ and $^3B_1$ states.[8] The diffuse-reflection spectrum of $Ba(NO_2)_2 \cdot H_2O$ crystals is in good agreement with the spectrum of the solution, so one can assign the absorption bands of the crystal to these electronic transitions.

The dispersion in the optical activity (Fig. 1b, curves 2 and 3) shows that the rotation rises rapidly near 0.4 μ, i.e., near the absorption band due to the $^1A_1 \rightarrow {}^1B_1$ transition localized on the NO_2^- group. Then one can say that the optical activity of the barium nitrite crystal is due to electronic transitions in the NO_2^- group. The symmetry of an isolated triatomic NO_2^- ion does not allow optical activity no matter what the deformation, because it always has a plane of symmetry, so one supposes that the optical activity in the crystal is due to interactions of the NO_2^- groups, which are appropriately disclosed in the unit cell.

The exact structure of $Ba(NO_2)_2 \cdot H_2O$ is not known, so the disposition of the NO_2^- groups in the unit cell can only be presumed; the space group is $P6_1$, and the Ba atoms lie on 6_1 axes,[3,5] so we assume that the O atoms in various NO_2^- groups lie around the Ba atoms to form a rectangle or a tetrahedron, while the interaction between the NO_2^- groups occurs via the 6_1 axis. This interaction results in the optical activity.

To test these assumptions we examined several empirical approximation equations for the optical-activity curve as recorded at room temperature and below; if the experimental evidence pertains only to points far from the absorption band, these approximations can be rough, particularly when there are several absorption bands, but they are sometimes useful.

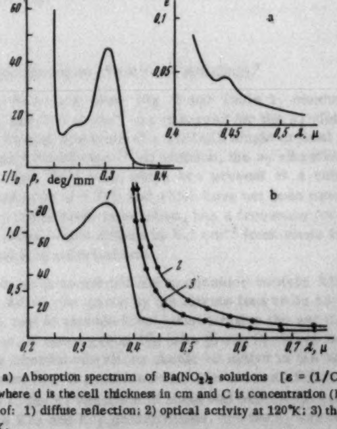

Fig. 1. a) Absorption spectrum of $Ba(NO_2)_2$ solutions $[\varepsilon = (1/Cd) \times \log (I_0/I)]$, where d is the cell thickness in cm and C is concentration (M); b) spectra of: 1) diffuse reflection; 2) optical activity at 120°K; 3) the same at 300°K.

TABLE 1. Approximation Equations and Results of Calculations

Quantity	Equation (1) $n=1$		(2) $f=1$		(3) $k=1$		(4) $i=1$		(1) $n=1,2$		(2) $f=1,2$	
A	2,003	3.98	1,340	3.21	1,034	2.76	0.785	1.49	0.238	5.25	0.885	1.593
B	—	—	—	—	—	—	0.820	2.12	1.764	−1.48	0.6520	2.019
λ_1, μ	0.3718	0.3520	0.3335	0.3019	0.3237	0.2850	0.3436	0.3202	0.3717	0.3660	0.3450	0.3174
λ_2, μ	—	—	—	—	—	—	—	—	0.3718	0.3795	0.2150	0.1959
g	22.41	13.72	9.79	12.06	24.71	32.08	4.882	4.74	22.41	3.026	5.15	4.73

The first column gives the results for 300°K and the second for 120°K.

The following equation is due to Drude[10,11] and is derived from the theory of intramolecular interactions:

$$\varphi(\lambda)=\sum_n \frac{A_n}{(\lambda^2-\lambda_n^2)}, \tag{1}$$

where $\varphi(\lambda)$ is the angle of rotation of the plane of polarization, A_n are the constants proportional to the rotational strength of the transitions, and λ_n are the wavelengths of the peaks giving rise to this dispersion. If the optical activity arises by intermolecular interaction, the expression for the dispersion becomes

$$\varphi(\lambda)=\sum_f \frac{B_f\lambda^2}{(\lambda^2-\lambda_f^2)^2}. \tag{2}$$

In other papers[12] the relationship proposed for this case is as follows:

$$\varphi(\lambda)=\sum_k \frac{C_k(\lambda^2+\lambda_k^2)}{(\lambda^2-\lambda_k^2)^2}. \tag{3}$$

A more general expression for the overall effect has been given:[11]

$$\varphi(\lambda)=\sum_i \left(\frac{D_i}{(\lambda^2-\lambda_i^2)}+\frac{k_i\lambda^2}{(\lambda^2-\lambda_i^2)^2}\right). \tag{4}$$

At first, our approximation was based on the one-term equation (1)-(3) with $i = k = f = n = 1$, i.e., on the assumption that the dispersion in this region is determined by a single transition; Table 1 gives the results. The calculations were performed with a BÉSM-4 computer by successive approximations; parameters A, B, C, and λ_1 were determined by least squares, by maximizing the function of $g=-\sum_k(\varphi_k^e-\varphi_k^c)^2$, where the number of experimental points was about 30. The value of $g \sim 5$ corresponded to a mean relative error $(\varphi^e-\varphi^c)/\varphi^e \sim 0.5\%$.

It is clear that an equation such as (2) is best for $Ba(NO_2)_2 \cdot H_2O$, as this describes the optical activity of the crystal, the more so since the characteristic value of λ_1 coincides with the peak at $\lambda = 0.35\ \mu$ in the diffuse-reflection spectrum.

If one uses an equation of the type of (4) ($i = 1$), one obtains a somewhat higher accuracy, which is due to the increased number of parameters; if one uses a two-term equation of type of (1) or (2) ($n = f = 1,2$), one gets an ambiguity that is largely a consequence of the method of calculation; in this case we narrowed the range of the parameters A_1, B_1, and λ_1 by employing the results from the one-term equations, and in this way we determined A_2, B_2, and λ_2. Calculation from (1) gave very close values for λ_1 and λ_2, and it is readily shown[13] that in this case we have effectively one optically active transition.

On the other hand, (2) gives values[13] of λ_1 and λ_2 that agree well with the absorption bands corresponding to allowed electronic transmissions in the nitrite ion.

Analogous approximations for the low-temperature data via (2) ($f = 1,2$) also led to the lowest value for g.

The shift in the results for λ_1 and λ_2 relative to the values for room temperature is not unexpected, and the actual values lie within reasonable limits, especially in view of the approximate character of the calculations.

It might appear logical to use three-term equations to describe the contribution from the third (forbidden) band at about $0.28\ \mu$, but it is even more likely that an ambiguity will arise when there are six parameters, so we did not refine the calculated values and used only the above results.

We can say that the nature of the optical activity in the barium nitrate crystal is due to intermolecular interaction of NO_2^- groups in the unit cell.

We are indebted to N. L. Smirnova for valuable advice on the structure of $Ba(NO_2)_2 \cdot H_2O$.

---

[1] V. A. Kizel', V. M. Kostrovskii, and V. N. Shamraev, Prib. Tekh. Eksp., 1, 160 (1967).

[2] V. A. Kizel' and V. N. Permogorov, Opt. Spektrosk., 10, 541 (1961).

[3] A. Ferrari and L. Cavalca, Period. Mineral., 17, 125 (1948).

[4] Landolt-Bornstein, 4, Springer-Verlag, Berlin (1955).

[5] G. Brink and M. Falk, Spectrochim. Acta, A27, 1811 (1971).

[6] S. T. Strickler and M. Kasha, J. Amer. Chem. Soc., 85, 2899 (1963).

[7] W. C. Allen and R. N. Dixon, Trans. Faraday Soc., 65, 1168 (1969).

[8] R. M. Hochstrasser and A. Marchette, J. Chem. Phys., 50, 1727 (1969).

[9] T. W. Sidman, J. Amer. Chem. Soc., 79, 2669 (1957).

[10] P. Drude, Theory of Optics, Dover (1902).

[11] V. M. Agranovich, Exciton Theory [in Russian], Nauka, Moscow (1968).

[12] Yu. A. Tsvirko, Zh. Eksp. Teor. Fiz., 38, 1615 (1960) [Sov. Phys. – JETP, 11, 1163 (1960)].

[13] S. Chandrasekhar, Proc. Indian Acad. Sci., A35, 103 (1952).

Dispersion of the optical activity in $(SrCa)S_2O_6 \cdot 4H_2O$ mixed crystals

A. Yu. Klimova, Z. B. Perekalina, and L. M. Belyaev

Institute of Crystallography, Academy of Sciences of the USSR

(Submitted December 15, 1971; resubmitted April 11, 1972)
Kristallografiya, 18, 319-321 (March-April 1973)

Results are given for $(SrCa)S_2O_6 \cdot 4H_2O$ mixed crystals grown from solution to have a $CaS_2O_6 \cdot 4H_2O$ concentration of 2.86 mole %. The optical activity of this material is less than that of $SrS_2O_6 \cdot 4H_2O$, but the materials in the mixed crystal show additivity in optical activity.

Papers on optical activity of crystals contain one dealing with the optical activity of a mixed crystal, for[1] $NaClO_3-NaBrO_3$.

We have examined how the dispersion for optical activity varies in salts of dithionic acid with divalent cation, $(SrCa)S_2O_6 \cdot 4H_2O$; the dispersion in the pure crystals of these compounds has already been examined.[2]

The $(SrCa)S_2O_6 \cdot 4H_2O$ mixed crystals were grown from water solution by temperature reduction; we used solutions with concentrations of 3, 5, 10, 20, and 30 mole % $CaS_2O_6 \cdot 4H_2O$, which gave transparent crystals 30 × 40 × 15 mm. The content of $CaS_2O_6 \cdot 4H_2O$ in the crystal was determined by plane photometry at the Institute of Geochemistry and Analytical Chemistry, Academy of Sciences of the USSR.1) This showed that crystals grown from solutions with 3, 5, 10, 20, and 30 mole % $CaS_2O_6 \cdot 4H_2O$ contained 0.072, 1.29, 2.86, 0.49, and 0.72 mole %, which indicates that these compounds do not form a continuous series of solid solutions under these conditions.

The phase composition was checked with an AEV-201 diffractometer (Toshiba); it was found that the Ca^{2+} isomorphously replaces Sr^{2+}.

There are two features that complicate measurement of the optical-activity dispersion for the $(SrCa)S_2O_6 \cdot 4H_2O$ crystals: 1) The maximum amount of Ca in the crystal is only 2.86 mole %; 2) the difference in optical activity between pure $SrS_2O_6 \cdot 4H_2O$ and pure $CaS_2O_6 \cdot 4H_2O$ is small. To minimize the errors, the measurements were made only in the ultraviolet and visible parts of the spectrum on thick specimens (3.4 to 9.9 mm) cut from four different crystals with $CaS_2O_6 \cdot 4H_2O$ contents of 2.86 mole %. We used a spectropolarimeter[3] with a DRSh-250 mercury lamp as source. The final results were taken as the means of all the measurements, and the error of measurement was calculated via $N = N_0 \pm 0.6745 \times \{[\Sigma(\Delta N)^2]/n(n-1)\}^{1/2}$, where N_0 is the arithmetic mean of all the measurements and n is the number of measurements.

The results show that the optical activity in $(SrCa) \cdot S_2O_6 \cdot 4H_2O$ is less than that in $SrS_2O_6 \cdot 4H_2O$ by an amount exceeding the mean error of experiment. The optical-activity dispersion for $(SrCa)S_2O_6 \cdot 4H_2O$ is described equally well by (1) and (2) (Table 1). The coefficients in the two equations are calculated by least squares with an M-220 computer. The rotational activity for the mixed crystal was calculated by measuring the density by weighing with immersion in carbon tetrachloride; the densities of $SrS_2O_6 \cdot 4H_2O$, $(SrCa)S_2O_6 \cdot 4H_2O$, and $CaS_2O_6 \cdot 4H_2O$ are, respectively, 2.377, 2.371, and 2.169 g/cm³. The measured density of $(SrCa)S_2O_6 \cdot 4H_2O$ and the density calculated via the concentrations of the components were in agreement, which indicates additive behavior in the density and indirectly confirms the determination of the Ca^{2+} content.

We used the calculated λ_0 and coefficient k with the measured density d for $(SrCa)S_2O_6 \cdot 4H_2O$ to calculate the rotational strength R, which was $7.97 \cdot 10^{-39}$ (R for $SrS_2O_6 \cdot 4H_2O$ is $8.1 \cdot 10^{-39}$). As expected, the rotational strength

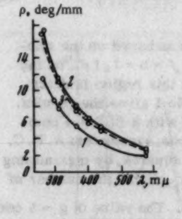

Fig. 1. Dispersion of the optical activity for crystals of: 1) $CaS_2O_6 \cdot 4H_2O$; 2) $SrS_2O_6 \cdot 4H_2O$; 3) $(SrCa) \cdot S_2O_6 \cdot 4H_2O$.

TABLE 1. Specific Rotation ρ (deg/mm) for Dithionates

λ, mμ	Measured			Calculated for $(SrCa)S_2O_6 \cdot 4H_2O$		
	$SrS_2O_6 \cdot 4H_2O$	$CaS_2O_6 \cdot 4H_2O$	$(SrCa)S_2O_6 \cdot 4H_2O$	(1) *	(2) *	(3) *
577.0	2.927	2.129	2.907±0.001	2.917	2.928	2.904
546.1	3.300	2.381	3.263±0.003	3.279	3.289	3.273
435.6	5.373	3.836	5.352±0.001	5.343	5.349	5.329
404.7	6.395	4.494	6.293±0.002	6.299	6.302	6.340
365.0	8.008	5.622	7.917±0.002	7.963	7.959	7.937
313.3	11.507	7.892	11.460±0.034	11.412	11.399	11.404
296.7	13.122	8.941	13.051±0.030	13.038	13.025	13.003
265.0	17.487	11.588	17.354±0.045	17.370	17.384	17.318

*1) $\rho = 0.9258\lambda^2/(\lambda^2 - 0.096^2)^2$; 2) $\rho = 0.9248/(\lambda^2 - 0.130^2)$; 3) $\rho = 0.9714\rho_1 + 0.0286\rho_2$, where ρ_1 and ρ_2 are the measured values for $SrS_2O_6 \cdot 4H_2O$ and $CaS_2O_6 \cdot 4H_2O$, respectively.

in the mixed crystal is somewhat below that for $SrS_2O_6 \cdot 4H_2O$.

Table 1 shows that the rotational activity of $(SrCa) \cdot S_2O_6 \cdot 4H_2O$, as calculated from (3),[1] agrees to within 0.3% with the observed values. It would seem that this result does not conflict with ref. 1, where this agreement was not observed, probably for the following reasons. The largest contribution to the optical activity comes from optically active absorption bands related to the anion,[4,5] so isomorphous replacement of the cations causes much less perturbation in the lattice and does not lead to fresh electronic transitions that contribute to the optical activity.

---

1) We are indebted to V. I. Lebedev for performing the chemical analysis.

[1] S. Chandrasekhar and M. S. Madhava, Mater. Res. Bull., 4, No. 8, 489 (1969).

[2] L. M. Belyaev and Z. B. Perekalina, Kristallografiya, 12, 291 (1967) [Sov. Phys. – Crystallogr., 12, 243 (1967)].

[3] Z. B. Perekalina, G. D. Shnyrev, A. V. Mirenskii, V. I. Permogorov, and V. A. Kizel', Kristallografiya, 10, 270 (1965) [Sov. Phys. – Crystallogr., 10, 221 (1965)].

[4] S. Chandrasekhar and M. S. Madhava, Acta Crystallogr., 23, No. 6, 911 (1967).

[5] Z. B. Perekalina and N. L. Smirnova, Kristallografiya, 14, 820 (1969) [Sov. Phys. – Crystallogr., 14, 708 (1970)].

Proposed interference method for determining the signs of the electrooptical coefficients

V. I. Sokolov, D. B. Kushev, and V. K. Subashiev

Institute of Semiconductors, Academy of Sciences of the USSR

(Submitted December 20, 1971; resubmitted April 25, 1972)
Kristallografiya, 18, 322-324 (March-April 1973)

The change of the refractive index of a plane-parallel plate in an external electric field shifts the interference transmission bands (electrointerference). To increase the sensitivity an alternating electric field is used. The present paper proposes the comparison of the interference and electrointerference spectra to determine the signs of the electrooptical coefficients r_{ij} for the linear electrooptical effect. The method is particularly convenient for thin films and layered crystals.

1. When an external electric field is applied to a plane-parallel plate, the interference bands in the transmission spectrum shift due to a change in the refractive index. We will refer to this as electrointerference. The electrointerference spectrum has been observed in amorphous Se films[1] and in ZnSe crystals,[2] in which the change of refractive index was proportional to the square of the field (quadratic electrooptical effect). In GaSe single crystals we first observed an electrointerference effect arising from a linear electrooptical effect. In addition to the change of refractive index Δn, the electrointerference effect can be used to determine the sign of this change, which was not discussed previously.[1,2] Note that the usual method for measuring the electrooptical effect (with the sample between crossed polarizers[3]) does not provide such a possibility. There are evidently no simple methods for determining the signs of the electrooptical coefficients (see ref. 4, Chap. 2).

In the transparent region the transmissivity T of a thin plane-parallel sample of thickness L taking account of multiple reflections takes the form

$$T = I / I_i = (1-R)^2 / (1+R^2-2R\cos\delta), \qquad (1)$$

where $\delta = 4\pi nL/\lambda$, $R = (n-1)^2/(n+1)^2$, n is the refractive index, λ is the wavelength, and I_i and I are the intensities of the incident and transmitted light.

The sign of Δn in principle can be determined from the shift of the T curve in a steady field, but due to its small value (it amounts to 0.04% of the period with $\Delta n = 10^{-5}$ and $L = 20\lambda$) one cannot use this method in practice.

We assume that an electric field of the form $F\cos\Omega t$ is applied to the sample. If the refractive index increases linearly with field then it will vary synchronously in phase with the field:

$$n(t) = n_0 + \Delta n\cos\Omega t, \qquad (2)$$

while if it decreases it is in the opposite phase, $n(t) = n_0 + \Delta n\cos(\Omega t + \pi) = n_0 - \Delta n\cos\Omega t$. We will use Eq. (2), ascribing to the amplitude a sign which is to be determined. The transmitted light will contain a harmonic of the same frequency Ω with an amplitude I_1. The change of the intensity will also occur with no phase lag, and this amplitude will be given a sign in the same sense as above. If this light is picked up by a detector which is connected to a narrow-band amplifier operating at frequency Ω and a phase-sensitive detector, then the signal V_1 measured at the detector output will be proportional to I_1:

$$V_1 = KI_1\cos\varphi,$$

where φ is the phase difference between the measured and reference signals and K is the positive calibration factor of the detection system.

Thus the sign of I_1 is uniquely related to the signs of V_1 and $\cos\varphi$. As for any dc signal, the sign of V_1 is known for each measurement. The sign of $\cos\varphi$ can be determined from the sign of V_1, for example, by measuring the electroabsorption below the intrinsic absorption edge E_g with the same phase difference; here the intensity of the light decreases with the application of a field, i.e., $I_1 < 0$.

To calculate I_1 we can use the fact that Δn is small (10^{-5}) and expand the transmission in a Taylor series. Here the amplitude of the first harmonic only makes contributions to the terms with odd derivatives of T with respect to n, which decrease rapidly. Therefore we can use its linear term in the Taylor expansion

$$T_1 = \frac{I_1}{I_i} \approx \left(\frac{dT}{dn}\right)_{n=n_0}\Delta n = \frac{8R_0T_0^2}{(1-R_0)^2}\left[\frac{(1+R_0)(\cos\delta_0-1)}{(1-R_0)(n_0^2-1)} - \frac{\pi L}{\lambda}\sin\delta_0\right]\Delta n. \qquad (3)$$

With the exception of a narrow region about the points $\delta_0 = (2m+1)\pi$, $m = 0, 1, 2, \ldots$, the term with $\sin\delta_0$ is dominant in (3). It can be seen that to determine the sign of Δn we must also know the sign of $\sin\delta_0$, which can be found from the spectrum of T_0. If T_0 decreases with a decrease in the light wavelength, then according to (1) δ_0 varies between 0 and π and in this energy range $\sin\delta_0 > 0$. Thus knowing T_1 and $\sin\delta_0$ we can determine the sign of Δn.

2. It is known that in an external electric field the change in the refractive index is of a tensor nature[3] and it must be related to particular electrooptical coefficients. For the same direction of the external electric field the electrointerference signal depends on the orientation of the electric vector of the incident light wave, which is illustrated using GaSe as an example. The linear electrooptical effect in the layered GaSe crystal (class $\bar{6}m2$) is characterized by three coefficients related by[3] $r_{61} = r_{12} = -r_{22}$. If the rectangular coordinate system is chosen such that the x axis is parallel to m, and the z axis is along the optical axis of the crystal and the external field runs along the y axis then the equation for the ellipsoid of wave normals (optical indicatrix) takes the form

$$(n_o^{-2} - r_{22}F)x^2 + (n_o^{-2} + r_{22}F)y^2 + n_e^{-2}z^2 = 1,$$

where n_ω and n_ε are the refractive indices of the ordinary and extraordinary rays and F is the amplitude of the applied electric field.

The crystals become biaxial and the cross section of the indicatrix in the plane z = 0 is an ellipse (Fig. 1) with principal axes along x and y equal to

$$n_x = n_\omega + 0.5 n_\omega^3 r_{22} F,$$
$$n_y = n_\omega - 0.5 n_\omega^3 r_{22} F,$$

and n_0 in (3) has the significance of n_ω. The experimental graphs of Fig. 2 show that $\Delta n_x < 0 < \Delta n_y$. According to a phenomenological description, $\Delta n_y = -\Delta n_x = -0.5 \times n_\omega^3 r_{22} F$, and thus r_{22} is negative while r_{61} and r_{12} are positive.

It is pointed out that the false electrooptical effect (the piezooptical effect via the inverse piezoelectric effect) for the class $\bar{6}m2$ cannot lead to a polarization dependence of T_1 in our configuration. The V_1 signal cannot arise from either electrostriction or the related piezooptical effect since it is quadratic in the field and should be observed at a frequency[3] 2Ω.

3. The electrointerference method allows one to determine both the magnitude and the sign of those electrooptical coefficients which represent deformation of the optical indicatrix,[5] i.e., r_{13} and r_{33} (classes mm, 3, 3m, 4, 4mm, 6, and 6mm), r_{22} (classes 2, 3m, and $\bar{6}m2$), r_{11} (class 32), r_{21} (class m), and r_{23} (classes m and mm). The method used in refs. 6 and 7 (polarizer – sample – analyzer; field parallel and propagation direction perpendicular to the optical axis with the light linearly polarized at an angle of 45° with respect to the field) does not give the coefficients r_{13} and r_{33} independently and only gives their combination $0.5(n_\omega^3 r_{13} + n_\varepsilon^3 r_{33})$. With electrointerference if the light is linearly polarized along and transverse to the field and propagates along the optical axis, r_{13} and r_{33} are obtained separately. In addition one can determine from electrointerference those coefficients (and their combinations) which in addition to deformation give rotation of the indicatrix by 45° (r_{41} for 23 and $\bar{4}3m$, r_{63} for $\bar{4}2m$, r_{61} for $\bar{6}m2$, $(r_{13}^2 + r_{63}^2)^{1/2}$ for $\bar{4}$, and $(r_{11}^2 + r_{22}^2)^{1/2}$ for 6).

Above we have had in mind the electrointerference due to the linear electrooptical effect. A similar treatment can be carried out for the quadratic electrooptical

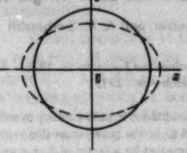

Fig. 1. Cross section of the optical indicatrix in the plane z = 0. The solid line is for F = 0 and the dashed line for F ∥ y.

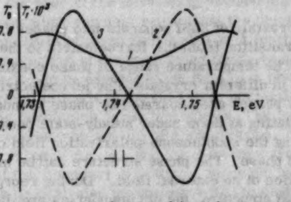

Fig. 2. T_0 (1) and T_1 (2, 3) as a function of the light quantum energy E = hc/λ. The light propagates along the optical axis and is linearly polarized parallel (2) and perpendicular (3) to the electric field (F = 10^4 V/cm; L = 10 μ).

effect. All of this permits us to regard the electrointerference effect as quite promising for studies of the electrooptical properties, especially for layered crystals and thin films.

---

[1] R. E. Drews, Appl. Phys. Lett., 9, 347 (1966); P. I. Petrov, L. A. Avdeeva, M. I. Elinson, and G. V. Stepanov, Fiz. Tekh. Poluprov., 3, 183 (1969) [Sov. Phys. – Semicond., 3, 153 (1969)].

[2] A. M. Andriesh, B. T. Kolomiets, and É. A. Senokosov, Fiz. Tekh. Poluprov., 4, 1160 (1970) [Sov. Phys. – Semicond., 4, 979 (1970)].

[3] I. S. Zheludev, Physics of Crystalline Dielectrics [in Russian], Nauka, Moscow (1970).

[4] A. S. Sonin and A. S. Vasilevskaya, Electrooptical Crystals [in Russian], Atomizdat, Moscow (1971).

[5] O. G. Vlokh and I. S. Zheludev, Kristallografiya, 5, 390 (1960) [Sov. Phys. – Crystallogr., 5, 368 (1960)].

[6] D. J. A. Gainon, J. Opt. Soc. America, 54, 270 (1964).

[7] V. S. Dneprovskii, V. N. Parygin, N. I. Kisil', L. A. Sysoev, and V. S. Solomatin, Kristallografiya, 13, 174 (1968) [Sov. Phys. – Crystallogr., 13, 141 (1968)].

Relaxation of phase boundaries in SbSI single crystals

M. D. Volnyanskii, A. Yu. Kudzin, and A. N. Sukhinskii

Dnepropetrovsk State University

(Submitted October 28, 1971; resubmitted February 15, 1972)
Kristallografiya, 18, 325-327 (March-April 1973)

We investigated the change in the dielectric permeability of an SbSI single crystal with time [$\Delta\varepsilon_{max} = f(t)$] under the action of a constant electric field $E_=$ in the phase-transition region. It was established that $\Delta\varepsilon_{max}$ tends toward saturation with increasing $E_=$ and decreases by a factor of 2 or more when the frequency is raised from 1 to 40 kHz. The time required for ε to decrease is shorter by a factor of 4-6 when the specimen is illuminated and it increases with the frequency. The relationships obtained can be attributed to the contribution made to ε by the newly formed phase boundaries, whose fixation time is several tens of seconds.

Single crystals of SbSI separate into phases in the vicinity of the transition from the ferroelectric to the paraelectric state. The temperature range of phase coexistence is 0.2-10° in different crystals. The ferroelectric and paraelectric phases are separated by phase boundaries, charges accumulating at them under steady-state conditions and screening the spontaneous-polarization field of the ferroelectric phase. The phase structure can be modified by application of an external field.[1] During reorganization of the phase structure, the old boundaries are displaced or new ones develop. Fixation of the boundaries then occurs over some definite time interval. There are currently no data on the properties of the phase boundaries and their fixation time.

The present investigation was conducted to study the dielectric properties of SbSI single crystals in the phase coexistence region, in order to obtain information on the behavior of the phase boundaries in ferroelectric crystals Our research was conducted with highly ideal SbSI crystals grown from the gaseous phase. We studied crystals with a phase-coexistence region covering a temperature interval of < 0.5°. Investigation of crystals over so narrow a temperature range while keeping their phase structure unaltered presents considerable difficulties, so that our basic experiments were conducted on compressed crystals. In this case, the phase structure remains unchanged over a broad temperature range.[2] Control measurements were also made on free crystals.

The dielectric permeability was determined with an E8-2 capacitance bridge and an S1-19B indicator connected into the circuit through a special amplifier. This made it possible to measure the change in capacitance with time. A constant electric field was simultaneously applied to the specimen. All the measurements were made with indium or Aquadag electrodes. Figure 1 shows the change in the dielectric permeability during rearrangement of the phase structure by a constant electric field [$\Delta\varepsilon = f(t)$]. It can be seen that $\Delta\varepsilon$ increases abruptly, reaches a maximum, and then returns slowly to its original value. The increase in dielectric permeability for individual specimens reaches 300%.

After application of a constant electric field, there is both a reorganization of the phase structure and repolarization, i.e., a change in the direction of the spontaneous-polarization vector. It is known that the dielectric permeability can also increase when repolarization occurs. We therefore measured $\Delta\varepsilon = f(t)$ in single-phase specimens both above and below the phase-transition temperature. No material change in ε was detected in this case. The increase in dielectric permeability on application of an electric field is thus related to the rearrangement of the phase structure.

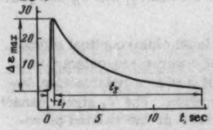

Fig. 1. Dependence of ε on time after reversal of field, $E_=$ = 180 V/cm.

The basic quantities characterizing the change in the dielectric permeability with time (Fig. 1) are the times t_1 and t_2 and the maximum change in ε ($\Delta\varepsilon_{max}$). These parameters were investigated as a function of certain experimental conditions. We varied the strength of the constant ($E_=$) and measuring ($E_\sim$) fields, the frequency, and the illumination. Microscopic observations were made of the change in phase structure under the action of the electric field. The constant electric field strength was varied from 40 to 240 V/cm, while the measuring-field frequency was varied from 1 to 40 kHz. Figure 2 shows the main parameters of the curve $\Delta\varepsilon = f(t)$ as functions of constant-field strength for illuminated and unilluminated specimens. As the field becomes stronger, $\Delta\varepsilon_{max}$ tends toward saturation and the time required for establishment of equilibrium decreases. The measuring field accelerates establishment of a steady-state dielectric permeability; t_2 decreases with increasing $E_\sim$ and increases with rising frequency. The dependence of $\Delta\varepsilon_{max}$

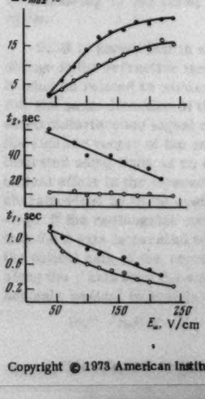

Fig. 2. Dependence of $\Delta\varepsilon_{max}$, t_2, and t_1 on repolarizing field. ●) Unilluminated specimen; ○) illuminated specimen; t = 20 kHz, $E_\sim$ = 20 V/cm.

on the measuring-field amplitude is nonlinear. There is a decrease by a factor of 2 or more in $\Delta\varepsilon_{max}$ as the frequency is increased from 1 to 40 kHz. Illumination of SbSI crystals reduces both $\Delta\varepsilon_{max}$ and the time t_2. Under illumination, t_2 decreases by a factor of 4-6 and t_1 decreases by a total factor of approximately 1.5. The specimen conductivity changes by two orders of magnitude under illumination.

Examination of the phase structure showed that new phase boundaries only appear 2-10 sec after reversal of the field. The developing boundaries are usually highly diffuse and become distinct only after a time close to t_2 has elapsed. This can be attributed to the fact that phase boundaries become visible in a microscope when space charges accumulate at them.[3,4] The latter can be produced by free carriers and by carriers bound in adhesion levels. It should be noted that the time required for phase-structure formation coincides with that required for establishment of a steady-state dielectric permeability.

Thus, the change in dielectric permeability when an electric field acts on the crystal can be accounted for by the contribution made by free phase boundaries.

The increase in $\Delta\varepsilon_{max}$, the simultaneous decrease in t_2, and the tendency of $\Delta\varepsilon_{max}$ toward saturation with increasing field strength (Fig. 2) may be due to a more severe change in structures. The time t_2 can be identified with the phase-boundary fixation time.

The contribution made by free phase boundaries to the dielectric permeability can be attributed to the fact that phase boundaries at which a depolarizing charge has not accumulated are unstable. They can readily be shifted by an electric field, which leads to a change in the total specimen polarization. After a depolarizing charge has accumulated at a boundary, it becomes electrically neutral and makes no contribution to the dielectric permeability. The time t_2 should then equal the screening time. According to Grekov et al.,[5] the screening of spontaneous polarization is governed by the dielectric relaxation time ($\tau = \rho\varepsilon$). The time τ in our experiments was several tenths of a second. Screening of a phase boundary during dielectric relaxation occurs for a stationary boundary. The phase boundaries for which we made our measurements were not in the steady state. A depolarizing charge accumulates at a boundary as it moves. This is apparently also responsible for the large value of t_2. It can also be concluded from the data of Mori and Sawaguchi[6] that screening of new phase boundaries in SbSI crystals occurs over a time materially exceeding the dielectric relaxation time.

Since, according to the data in Fig. 2, $\Delta\varepsilon_{max}$, t_1, and t_2 tend toward saturation for an illuminated specimen when $E_{=} > 200$ V/cm, it can be assumed that the overwhelming majority of boundaries develop and grow to their full extent within a time t_1 under these conditions. Since the phase-boundary fixation time (for $E_{=} = 240$ V/cm and $t_2 \approx 9$ sec) is substantially longer than the time required for development of the boundaries ($t_1 \approx 0.2$ sec), the leading edge of the $\Delta\varepsilon = f(t)$ curve reflects the dependence of the area of the developing boundaries on time, while the descending segment represents the change in the vibration amplitude of these boundaries as a function of time under the action of the measuring field. As an approximation, it can be assumed that $\Delta\varepsilon_{max}$ is produced by the contribution made to the dielectric permeability by all the newly developing phase boundaries. The boundaries are easily counted with the aid of a microscope. Thus, knowing the value of $\Delta\varepsilon_{max}$ and the boundary area, the amplitude of the boundary vibrations under the action of the field can be evaluated by analogy with the case of domain boundaries,[7] using the equation $\Delta x = \Delta\varepsilon_{max} E_{\sim} \times (4\pi S_0 P_s)^{-1}$, where S_0 is the phase-boundary area per unit specimen volume and P_s is the jump in the spontaneous polarization. With $S_0 = 240$ cm^{-2}, $P_s = 15$ μC/cm^2, and $E_{\sim} = 20$ V/cm, we obtain $\Delta x \approx 5 \cdot 10^{-6}$ cm.

The values of $\Delta\varepsilon_{max}$ exhibit considerable dispersion. As the frequency rises, $\Delta\varepsilon_{max}$ decreases rapidly. The drop in $\Delta\varepsilon_{max}$ with frequency may be related to a decrease in the vibration amplitude or an increase in the inertia of the phase boundary. The 90° domain boundary in $BaTiO_3$ single crystals displays similar behavior.[8]

---

[1] T. S. Travina, L. L. Golik, M. I. Elinson, V. I. Ignatskin, V. S. Lyakhovitskaya, Fiz. Tverd Tela, 11, 622 (1969) [Sov. Phys. – Solid State, 11, 500 (1969)].

[2] A. Yu. Kudzin, A. N. Sukhinskii, and M. D. Volnyanskii, Abstracts of papers presented at the Seventh Scientific Conference on Ferroelectricity [in Russian], Izd. Voronezh. Univ., Voronezh (1970).

[3] I. I. Groshik and V. M. Fridkin, Fiz. Tverd. Tela, 10, 2878 (1968) [Sov. Phys. – Solid State, 10, 2276 (1969)].

[4] T. Mori and E. Sawaguchi, Japan. J. Appl. Phys., 6, 792 (1967).

[5] A. A. Grekov, V. A. Lyakhovitskaya, A. I. Rodin, and V. M. Fridkin, Fiz. Tverd. Tela, 8, 2239 (1966).

[6] T. Mori and E. Sawaguchi, J. Phys. Soc. Japan, 25, 1195 (1968).

[7] A. S. Sonin and B. A. Strukov, Introduction to Ferroelectricity [in Russian], Vysshaya Shkola, Moscow (1970), p. 158.

[8] J. Fousek and B. Březina, Izv. Akad. Nauk SSSR, Ser. Fiz., 28, 717 (1964).

X-ray diffraction in crystals with deformation twins

D. A. Mirzaev and S. V. Rushchits

Chelyabinsk Polytechnic Institute

(Submitted April 10, 1972)
Kristallografiya, 18, 328-333 (March-April 1973)

The general problem of x-ray diffraction in a single crystal containing twins is considered. A general equation is derived for the intensity function in reciprocal space. Diffraction effects arising from twins in fcc and bcc lattices are analyzed.

Although the internal structures of growth and deformation twins are very similar, the theory of x-ray scattering in crystals containing growth defects[1-3] is inapplicable to the case of deformation twins, since it makes no allowance for the strictly specified thickness of the latter.

Until recently only particular cases had been considered; these pertained to deformation twins of thickness h = 1 in fcc[4] ("subtraction" stacking faults), hcp,[5] and bcc[3] crystals, h = 2 in fcc[6] (interstitial stacking faults) and hcp,[7] and h = 3 in fcc[8] crystals (h being the number of layers).

The problem of x-ray scattering in crystals containing deformation twins of any thickness h was first formulated in ref. 9, using Markov chain matrix representations. However, this method failed to yield any explicit expression for the desired x-ray intensity distribution, since it required the solution of equations of the h-th degree. In addition to this, the cumbersome mathematical apparatus hindered the derivation of even particular solutions.

In this paper we propose a simple method enabling us to find a general expression for the intensity distribution of rays scattered from translational crystals with deformation twins of any thickness h. The resultant expression includes the results of refs. 3, 4, 6, and 8 as particular cases.

It is well known that the intensity distribution of rays scattered in crystals with displacement defects is given by the function[10]

$$I(HKh_3)=C\sum_{m}(1-|m|/N_3)\exp(2\pi i\mathbf{S}\mathbf{r}_m). \tag{1}$$

In this expression C is the interference function for a two-dimensional crystal, **S** is the diffraction vector, $\mathbf{r}_m$ is the radius vector of the zeroth atom in the m-th layer:

$$\mathbf{r}_m=m\mathbf{d}+\boldsymbol{\delta}(m)+\boldsymbol{\delta}'(k), \tag{2}$$

where **d** is a vector perpendicular to the plane of displacement (in the present case the twinning plane) and equal to the interplane distance, $\boldsymbol{\delta}(m)$ is the relative displacement of the atoms due to the type of layer in the case of a perfect crystal, $\boldsymbol{\delta}'(k)$ is the relative displacement of the atoms due to the presence of k defective planes between the layers under consideration.

Allowing for (2), Eq. (1) takes the following form:

$$I(HKh_3)=C\sum_{m}(1-|m|/N_3)<\exp[2\pi i\mathbf{S}\boldsymbol{\delta}'(k)] \\ >\exp\{2\pi i[mdh_3b_3+\mathbf{S}\boldsymbol{\delta}(m)]\}. \tag{3}$$

Using the convolution theorem we may write

$$I(HKh_3)=C\left\{\sum_{m}(1-|m|/N_3)\exp(2\pi i[mdh_3b_3+\mathbf{S}\boldsymbol{\delta}(m)] \right. \\ \left. *\sum_{m}\langle\exp[2\pi i\mathbf{S}\boldsymbol{\delta}'(k)]\rangle\exp(2\pi i[mdh_3b_3+\mathbf{S}\boldsymbol{\delta}(m)])\right\}. \tag{4}$$

The first function in the convolution describes the case of a perfect crystal and constitutes a peak lying at a reciprocal lattice point, with a width inversely proportional to the crystal size. It is well known that, when one of the functions in the convolution has a fairly sharp peak (so that the second function remains relatively constant over the width of this peak), the value of the convolution equals the product of the area of this peak and the second function.[10] Thus, when the crystal is not too small and contains a fair number of imperfections, we have

$$I(HKh_3)=C'\sum_{m}\langle\exp[2\pi i\mathbf{S}\boldsymbol{\delta}'(k)]\rangle\exp\{2\pi i[mdh_3b_3+\mathbf{S}\boldsymbol{\delta}(m)]\}. \tag{5}$$

For lattices with translational symmetry in the normal sequence each layer is displaced from the previous one by a vector $\boldsymbol{\delta}_0$ in the projection on the twinning plane, so that $\boldsymbol{\delta}(m) = m\boldsymbol{\delta}_0$. The twinning sequence is obtained by the displacement of each plane through $-2\boldsymbol{\delta}_0$ relative to the previous one. Hence we obtain

$$2\pi\mathbf{S}\boldsymbol{\delta}(m)=\alpha_0 m,\quad 2\pi\mathbf{S}\boldsymbol{\delta}'(k)=-2\alpha_0 k, \tag{6}$$

where $\alpha_0 = 2\pi\mathbf{S}\boldsymbol{\delta}_0$ is the "normal" phase shift.

Equation (5), containing information pertaining to the phase shift, describes all the diffraction effects due to defects in this model. The expression for the averaged exponential $\langle\exp(2\pi i\mathbf{S}\boldsymbol{\delta}'(k))\rangle$ may be obtained by considering the corresponding probabilities for the appearance of a specific displacement $\boldsymbol{\delta}'(k)$ between the zeroth and m-th layers. Let us consider the following probability scheme. Let there be n defects with a thickness of h layers in a crystal containing N_3 planes. As in ref. 6 we define the transition probability β as the ratio of the number of single transitions into the layer constituting the twin origin to the total number of independent single transitions:

$$\beta=n/[N_3-n(h-1)]. \tag{7}$$

We introduce $U_{p,j}(m)$ to represent the probability that the layer m is completely free from the defect (j = 0), or that it constitutes its j-th layer, on condition that the zeroth layer is the p-th layer of the twin or is free from it (p = 0). Considering that the regular sequence in the stack of planes starts from the h-th layer of the defect [the shift $\boldsymbol{\delta}'(k)$ between the zero and m-th layers does not depend on whether these layers lie outside the defects or in their h-th layers], we combine the layers outside the defects with the h-th layers of the latter to form a group of "regular" layers.[1)] Then the probability that the m-th layer will be regular if the zeroth layer is regular equals q = (1 − β) if the (m − 1)th layer is regular, and β if the defect starts in the (m − h − 1)th layer. Hence,

$$U_{0,0}(m)=U_{0,0}(m-1)q+U_{0,0}(m-h)\beta. \tag{8}$$

We consider that the probabilities $U_{0,0}(m)$ are the coefficients of a certain generating function[11]

$$A_{0,0}(t)=\sum_{m=0}^{\infty}U_{0,0}(m)t^m. \tag{9}$$

In order to find it we multiply (8) by t^m and sum from m = h:

$$A_{0,0}(t)-1-qt-\ldots-q^{h-1}t^{h-1}$$
$$=qt[A_{0,0}(t)-1-qt-\ldots-q^{h-2}t^{h-2}]+\beta t^hA_{0,0}(t). \tag{10}$$

Hence,

$$A_{0,0}(t)=1/(1-qt-\beta t^h). \tag{11}$$

In order to find $U_{0,0}(m)$ we expand (11) in series:

$$A_{0,0}(t)=\sum_{m=0}^{\infty}\Big(\sum_n C^n_{m-nh}\beta^nq^{m-nh}\Big)t^m, \tag{11a}$$

where n is the number of defects in the segment [0, m]. It is easy to see that for the remaining versions of (p, j) we have

$$A_{0,j}(t)=\frac{\beta t^j}{1-qt-\beta t^h}=\sum_{m=0}^{\infty}\Big(\sum_n C^n_{m-nh-j}\beta^{n+1}q^{m-nh-j}\Big)t^m;$$

$$A_{p,0}(t)=\frac{t^{h-p}}{1-qt-\beta t^h}=\sum_{m=0}^{\infty}\Big(\sum_n C^n_{m-nh-(h-p)}\beta^nq^{m-nh-(h-p)}\Big)t^m;$$

$$A_{p,j}(t)=\frac{\beta t^{(h-p)+j}}{1-qt-\beta t^h}+t^{j-p}_{(j>p)}=\sum_{m=0}^{\infty}\Big(\sum_n C^n_{m-nh-(h-p)-j}\beta^{n+1}$$
$$\times q^{m-nh-(h-p)-j}+\delta_{m,j-p}\Big)t^m, \tag{12}$$

where $\delta_{m,j-p}$ is the Kronecker symbol. Each of the generating functions determines the probabilities of successive events in the (Markov) chains. The chains starting from a "regular" layer have a probability [N − n(h − 1)]/N = 1/[1 + β (h − 1)] (proportion of "regular" layers) and each of the others a probability n/N = β/ [1 + β (h − 1)]. Denoting $\xi = 2\pi dh_3b_3$ and allowing for (6), we obtain the following expression for $I(HKh_3)$:

$$I(HKh_3)=C'\sum_{m=-\infty}^{+\infty}\Big\{\frac{1}{1+\beta(h-1)}\Big[\sum_n C^n_{m-nh}\beta^nq^{m-nh}$$
$$\times\exp(-2i\alpha_0nh)+\beta\sum_{n,j}C^n_{m-nh-j}\beta^nq^{m-nh-j}\exp(-2i\alpha_0(nh+j))\Big]$$
$$+\frac{\beta}{1+\beta(h-1)}\Big[\sum_{n,p}C^n_{m-nh-(h-p)}\beta^nq^{m-nh-(h-p)}$$
$$\times\exp[-2i\alpha_0(nh+h-p)] \tag{13}$$
$$+\beta\sum_{n,j,p}C^n_{m-nh-(h-p)-j}\beta^nq^{m-nh-(h-p)-j}\exp[-2i\alpha_0(mh$$
$$+h-p+j)]+\delta_{m,j-p}\Big]\Big\}\exp(i\xi m).$$

In order to obtain the averaged exponential ⟨exp·[2πiSδ'(k)]⟩ we have to calculate the cumbersome sums in Eq. (13). However, it is easy to see that, on taking the expression

$$A(t)=\frac{1}{1+\beta(h-1)}\Big[A_{0,0}(t)+\beta\sum_jA_{0,j}(t)\Big]$$
$$+\frac{\beta}{1+\beta(h-1)}\Big[\sum_pA_{p,0}(t)+\sum_{p,j}A_{p,j}(t)\Big] \tag{14}$$

and making the substitutions $t=\exp[i(\xi-\alpha_0)]$ and $q=(1-\beta)\exp(2i\alpha_0)$ in this, we shall obtain

$$I(HKh_3)=A(t)+A^*(t)-1, \tag{15}$$

where A* (t) allows for the summation over m < 0 in (13). Hence

$$I(\xi)=\frac{\beta(1-\beta)}{1+\beta(h-1)}\times\{(1-\cos2\alpha_0)$$
$$\times[\sin^2h(\xi-\alpha_0)/2]/[\sin^2(\xi-\alpha_0)/2]\}/\{1-\beta$$
$$+\beta^2-(1-\beta)\cos(\xi+\alpha_0)+\beta(1-\beta)\cos[(h-1)\xi$$
$$-(h+1)\alpha_0]-\beta\cos h(\xi-\alpha_0)\}. \tag{16}$$

For certain values of α_0 and h the denominator of (16) may vanish at the corresponding points ξ_m. (For example, if α_0 = 120°, h = 3M, we have ξ_m = 240°.) Using the equation for the value of a polynomial close to a root[10]

$$P(x)=U(x)/V(x)_{x\to x_i}=-U(x_i)/V'(x_i)(x-x_i),$$

in the present case we obtain

$$\frac{(1-\beta)^2}{[1+\beta(h-1)]^2}\delta(\xi-\xi_m),$$

where $\delta(\xi-\xi_m)$ is the Dirac delta function.

The Laue function

$$\frac{(1-\beta)^2}{[1+\beta(h-1)]^2}\frac{\sin^2N_3[(\xi-\xi_m)/2]}{\sin^2[(\xi-\xi_m)/2]}$$

obtained after carrying out the convolution (4) must be used instead of the function (16) at these points.

Thus we have obtained a general expression for the intensity distribution of rays scattered from translational crystals with deformation twins of any thickness h. By appropriately choosing the values of ξ and α_0 we may analyze cases in which defects occupy various planes in a variety of crystal structures.

DEFORMATION TWINS IN THE {111} PLANES OF AN FCC LATTICE

For an appropriate choice of the hexagonal coordinate system[3] we obtain

$$\xi=\frac{2\pi}{3}h_3;\qquad \alpha_0=\begin{cases}2\pi/3 & \text{for } H-K=3N+1;\\ -2\pi/3 & \text{for } H-K=3N-1;\\ 0 & \text{for } H-K=3N.\end{cases}$$

It follows from (16) that for H − K = 3N ± 1 and h = 1 (subtraction-type stacking faults),

$$I(\xi) = 3\beta(1-\beta)\,/\,[2 - 3\beta + 3\beta^2 + \cos\xi \pm \sqrt{3}(1-2\beta)\sin\xi]$$

(Patterson equation[4]); for h = 2 (interstitial stacking faults),

$$I(\xi) = [3\beta(1-\beta)(2 - \cos\xi \pm \sqrt{3}\sin\xi)]\,/\,\{(1+\beta)[2(1-\beta+\beta^2) + (1+\beta-2\beta^2)\cos\xi + \sqrt{3}(1-\beta)\sin\xi + \beta\cos 2\xi \pm \sqrt{3}\beta\sin 2\xi]\}$$

(Johnson equation[6]); for h = 3,

$$I(\xi) = \frac{6\beta(1-\beta)(1-\cos\xi)}{(1+2\beta)[1 - 2\beta(1-\beta) - 2\beta(1+\beta)\cos(\xi \pm 60^\circ) + 4\beta\cos^2(\xi \pm 60^\circ)]} + \frac{(1-\beta)^2}{[1+\beta(h-1)]^2}\,\frac{\sin^2 N_3[(\xi-240^\circ)/2]}{\sin^2[(\xi-240^\circ)/2]}$$

(Sato equation[8]).

In order to compare the diffraction effects arising from twins of different thicknesses, it is convenient to introduce the concentration $f = nh/N_3 = \beta h/[1 + \beta(h-1)]$, i.e., the proportion of planes occupied by twins. Analysis of Eq. (16) and the intensity curves calculated from the latter in an electronic computer shows that, as regards their influence on the diffraction pattern, the deformation defects may be divided into three groups. Defects with h = 3M + 1 displace the main peak ($\xi = 240°$) in the small-angle direction, those with h = 3M − 1 in the large-angle direction, while those with h = 3M do not displace the main peak at all. The absolute displacement diminishes with increasing h (Fig. 1).

Defects of the third group (h = 3M) reduce the intensity of the main peak without widening it, while defects of the other two groups lead to asymmetrical widening; as f increases, the principal maximum degenerates and separates into two peaks. For h = 3M + 1 the new peak appears to the right, and for h = 3M − 1 it appears to the left of the main one (Fig. 2). The distance between these peaks increases with increasing f. The nature of the new peaks lies in the oscillation of the numerator of Eq. (16); the effect becomes more pronounced with increasing h.

For a certain value of f we find a "twin" peak at $\xi_{tw} > 120°$, independently of the type of defects. When $\beta \to 1$, $\xi_{tw} \to 120°$ (Fig. 1). The "twin" peak constitutes the symmetrically broadened (to a first approximation) principal maximum of the function $\sin^2 h[(\xi - \alpha_0)/2] \times \{\sin^2[(\xi - \alpha_0)/2]\}^{-1}$ in the numerator of (16), since the denominator of (16) varies comparatively monotonically close to 120°. The intensity of the "twin" peak $\sim \beta h^2$.

An exception to the general scheme is the case of h = 1, for which Eq. (16) has only one root, and hence one symmetrically broadened maximum, moving from $\xi = 240°$ ($\beta = 0$) to $\xi = 120°$ ($\beta = 1$).

DEFORMATION TWINS IN THE {211} PLANES OF A BCC LATTICE

For a corresponding choice of coordinate system[3]

$$\xi = \frac{2\pi}{3}h_3; \quad \alpha_0 = \begin{cases} 2\pi/3 & \text{for } K = 3N+1, \\ -2\pi/3 & \text{for } K = 3N-1, \\ 0 & \text{for } K = 3N. \end{cases}$$

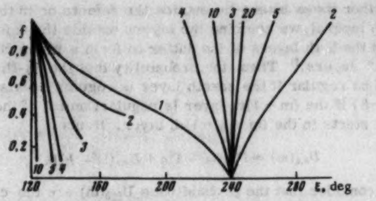

Fig. 1. Displacements of the principal and twin peaks in relation to the concentration of defective planes. The numbers on the curves correspond to the values of h.

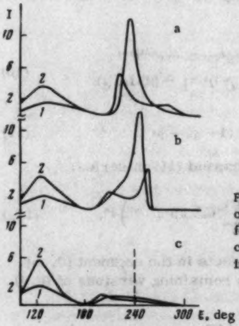

Fig. 2. Intensity distribution curves of reflected rays in the case of deformation twins. a) h = 4; b) h = 5; c) h = 6; 1) f = 0.3; 2) f = 0.6. The intensity is given in relative units.

The diffraction effects in this case are analogous to the effects arising from deformation twins in the {111} planes of the fcc lattice. This agrees with the results of Warren.

The method here proposed also enables us to describe diffraction effects arising from the presence of certain martensitic phases (particularly the ε phase). With a little complication the method may also be applied to the case of crystals with nontranslational lattices of the hcp type. The corresponding results will be considered in later publications.

---

1) It may be shown that the final expression (16) does not depend on the type to which the layer h belongs.

[1] A. J. C. Wilson, Proc. Roy. Soc., A180, 277 (1942).
[2] H. Jagodzinski, Acta Crystallogr., 7, 17 (1954).
[3] B. E. Warren, Progress in Metal Physics, Vol. 8, Pergamon Press, London (1959), p. 172.
[4] M. S. Paterson, J. Appl. Phys., 23, 8 (1952).
[5] J. W. Christian, Acta Crystallogr., 7, 415 (1954).
[6] C. A. Johnson, Acta Crystallogr., 16, 490 (1963).
[7] R. Sato, Acta Crystallogr., A25, 387 (1969).
[8] R. Sato, Acta Crystallogr., 20, 150 (1966).
[9] J. Kakinoki, Acta Crystallogr., 23, 875 (1967).
[10] A. Guinier, Theorie et Technique de la Radiocristallographie, Dunod, Paris (1956).
[11] W. Feller, Introduction to Probability Theory and Its Applications, Vol. 1, Wiley (1957).

Focused laser-beam damage mechanism for CsI crystals

L. M. Belyaev, V. V. Nabatov, V. N. Rozhanskii,
N. L. Sizova, and A. A. Urusovskaya
Institute of Crystallography, Academy of Sciences of the USSR

(Submitted March 17, 1972)
Kristallografiya, 18, 334-338 (March-April 1973)

A study has been made on the damage to CsI crystals by a free-running ruby laser at energies above and below threshold. A mechanism is proposed for production of the indentation figures.

Processes caused by localized loads are of considerable interest, as they give rise to normal stress gradients, especially in shock loading, which favor crowdion plasticity, prismatic slip, and other effects.[1-3] A focused laser beam produces localized stresses because of intense heating in a small region, and such stresses resemble, to a considerable extent, those produced by localized loads. A localized load[2] and a laser beam[4] produce effects ascribed to crowdion plasticity, but the mode of action of a laser beam is largely unexplained.

METHODS

We used a free-running ruby laser with a cavity containing two positive lenses, which produced a nearly Gaussian intensity distribution over the cross section. The beam was focused on the crystal with a lens of short focal length, the focal spot being 330 μ in diameter. The incident intensity was adjusted with calibrated filters at constant pumping. The occurrence of damage was deduced from the associated optical flash.[5]

The optically pure CsI crystal was oriented from impact figures and was cut into plates about 2 mm thick, which were polished in chemically pure methanol containing ferric chloride.

ENERGIES ABOVE THRESHOLD

The damage threshold in these crystals was about 130 J/cm^2; we used the range 170-250 J/cm^2. The flash oscillograms showed that the damage was not always caused by the first peak in the laser output. The flash intensity was also peaky, but with regions of constant intensity or a fall to zero, although the damage zone was still exposed to the laser. These effects are due to melting and ejection of molten material from the irradiated zone, or else to cracking. The damage focus was at the surface or at a certain depth, which was probably due not only to inexact focusing (because the beam contained many modes), but also to the surface state.[6]

At high intensities, the beam produced a crater with smooth melted walls; the diameter of this crater never exceeded that of the focal spot, while the depth was 0.3-2 mm, so it sometimes penetrated to the opposite side of the plate, with the exit hole also taking the form of an expanding crater. The damage area was much reduced at energy densities near the threshold. Crystal facets could be seen within the crater. The ejected material emerged along the slip direction and along ⟨100⟩ (the direction of identical ions), as Fig. 1a shows. The directional melt ejection was due to shear around the melt along ⟨100⟩. A dislocation rosette was produced around the damage focus, and the rays showed secondary slip lines at 45° to the compression direction. A similar effect is seen in indents produced in CsI at 77°K.[7] Pulse loading and low temperatures favor slip on the secondary {110}⟨110⟩ slip system, where the maximum shear stresses occur in this case. As in low-temperature indentation, the dislocation etch pits on this secondary system were larger and deeper than those in the basic system because the Burgers vectors are larger in the secondary system.

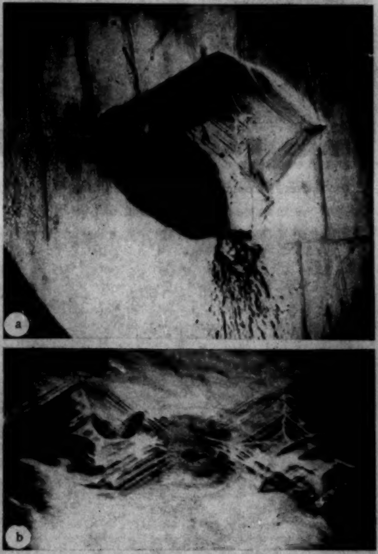

Fig. 1. Indentation figures in a CsI crystal, x200: a) {100} plane; b) {110}.

Facetted humps (impact figures) were produced on both surfaces when the damage focus lay within the crystal.[8,9] These lay outside the focal spot, and their symmetry was determined by the surface orientation (Fig. 1).

Etching of small such figures served to identify the defects (Fig. 2); at the corners of a square figure in the (100) plane there were clumps of etch figures. Successive etching stages showed that the figures in these clumps corresponded to long rectilinear dislocations perpendicular to the surface, whereas the etch-pit density at the center of an impact figure was much less and the pits corresponded to small dislocation loops, which could

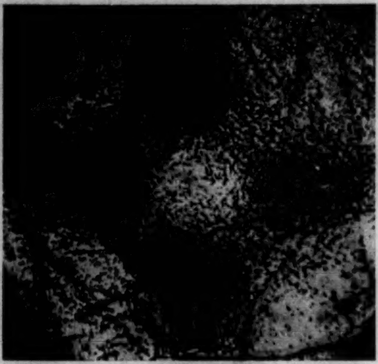

Fig. 2. Etch pattern of an indentation figure on a {100} plane of CsI, x500.

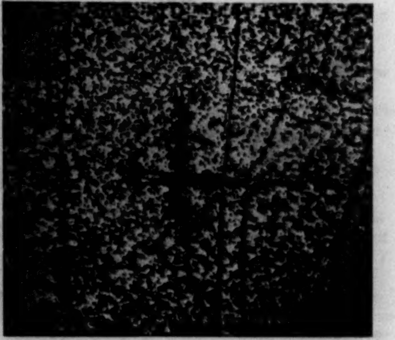

Fig. 3. Dislocation rosette at an inclination, x500; {100} plane, laser beam energy below threshold.

arise by accumulation of point defects, so one may assume that the impact figures were due in the main to slip involving a flow of interstitial ions along ⟨100⟩ to the center.

ENERGIES BELOW THRESHOLD

At ~110 J/cm^2 there were no visible effects at the surface, although etching revealed very small dislocation rosettes at certain points (Fig. 3). The center of such a rosette had an etch pit larger than the pits on dislocations, which evidently represented an inclusion; such rosettes probably are due to thermoelastic stresses around inclusions.[10,11]

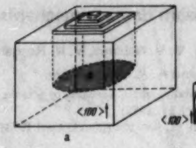

Fig. 4. a) Slip scheme for indentation; b) disposition of dislocation loops on slip surfaces. A is the zone of maximum heating.

CONCLUSIONS

A focused laser beam produces local heating in CsI and hence a focus of thermoelastic stresses, which are low at low intensities, so plastic deformation occurs only around inclusions. The dislocation rosettes show that these inclusions are sources of thermoelastic stresses on account of their different expansion coefficients. The stresses attain values sufficient for plastic deformation as the intensity is raised, and slip occurs on prisms, which results in facetted humps (pressure figures, Fig. 4), which involve translational slip and crowdion plasticity. Material is ejected when the material is softened by intense heating; the ejection direction coincides with the slip direction and the direction of disposition of identical ions.

---

[1] V. N. Rozhanskii (Rozshansky), M. P. Nazarova, I. L. Svetlov, and L. K. Kalashnikova, Phys. Status Solidi, 41, 549 (1970).

[2] V. N. Rozhanskii, N. L. Sizova, and A. A. Urusovskaya, Fiz. Tverd. Tela, 13, 411 (1971) [Sov. Phys. – Solid State, 13, 335 (1971)].

[3] T. Figielsky, Phys. Status Solidi, 4, 773 (1971).

[4] Yu. I. Boiko, Ya. E. Geguzin, and A. K. Emets, Fiz. Tverd. Tela, 13, 3096 (1971) [Sov. Phys. – Solid State, 13, 2596 (1972)].

[5] L. M. Belyaev, A. N. Golovistikov, and V. V. Nabatov, Fiz. Tverd. Tela, 10, 3733 (1968) [Sov. Phys. – Solid State, 10, 2972 (1969)].

[6] Yu. K. Danilenko, A. A. Manenkov, A. M. Khaimov-Mal'kov, and A. M. Prokhorov, Zh. Eksp. Teor. Fiz., 58, 31 (1970) [Sov. Phys. – JETP, 31, 18 (1970)]; A. F. Fersman and L. D. Khazov, Opt.-Mekh. Prom., No. 9, 69 (1970).

[7] N. L. Sizova, Kristallografiya, 17, 428 (1972) [Sov. Phys. – Crystallogr., 17, 374 (1972)].

[8] A. Smakula and M. Klein, J. Opt. Soc. America, 39, 445 (1949).

[9] M. V. Klassen-Neklyudova and A. A. Urusovskaya, Trudy Inst. Krist. AN SSSR, 11, 146 (1955).

[10] H. Kuzmann and G. J. Ritter, J. Appl. Phys., 41, 1683 (1970).

[11] V. I. Danilovskaya, V. L. Indenbom, and É. M. Shefter, in: Thermal Stresses in Structure Elements [in Russian], No. 8, Naukova Dumka, Kiev (1969), p. 134.

Deformation dislocations in natural quartz crystals

V. F. Miuskov, L. I. Tsinober, and L. A. Gordienko

Institute of Crystallography, Academy of Sciences of the USSR
All-Union Scientific-Investigation Institute of Mineral Resources

(Submitted March 27, 1972)
Kristallografiya, 18, 339-343 (March-April 1973)

The authors use x-ray topography to study dislocation aggregations of clear deformation origin (loops and three-dimensional Frank–Read sources) in a single crystal of natural quartz. Analysis of extinction of images of the dislocations revealed that the main slip planes in the specimen were $(10\bar{1}0)$, $(10\bar{1}1)$, and (0001); for most of the dislocations the Burgers vector is $[11\bar{2}0]$, but dislocations were also observed with the Burgers vectors $[11\bar{2}3]$ and $[0001]$.

The brittle behavior of crystalline quartz shows us that the motion, and hence the formation, of deformation dislocations in this substance at room temperature is difficult. In fact, investigations by the x-ray topography method[1,2] and the decoration method[3] showed that single crystals of quartz have a low dislocation density or contain no dislocations at all.[4] It was also found that dislocations in quartz are of the so-called growth type, which apparently do not owe their origin to deformation processes. The mechanism of formation of growth dislocations (found in many other crystals besides quartz) and the function which they fulfill in the real structure of the crystal remains as yet obscure. However, a high dislocation density ($\sim 10^9$ cm^{-2}) has been obtained artificially in quartz by deformations of the crystals at high pressures (above 15 kbars) and temperatures (above 500°C).[5] This would seem to leave us little hope of finding deformation dislocations in high-quality quartz crystals, which are formed at relatively low temperatures. Nevertheless, dislocations, clearly of the deformation type, have recently been discovered by the decoration method in a crystal of natural quartz.[6]

The relatively low density of the dislocations in this crystal permitted them to be studied by x-ray topography, which, of course, gives the most complete information on the geometry and main characteristics of dislocations in crystals with few of them. The main results of this investigation are given in this article.

Topograms were recorded by the Lang method in Ag $K\alpha_1$ radiation. We studied the same crystal which we described in ref. 6: Specimens were prepared from parts which had been shown by the decoration method to contain deformation dislocations. For topography we used plates 1-2 mm thick, oriented in the planes $(11\bar{2}0)$, (0001), and $(10\bar{1}1)$. Topograms were taken for all possible reflections of the types $10\bar{1}1$, $01\bar{1}1$, $20\bar{2}0$, and 0003. Some of the most characteristic topograms, necessary for illustration and discussion of our results, are shown in Figs. 1-4. From these we see that the overwhelming majority of the dislocations shown are of deformation origin. These dislocations differ from growth dislocations[1,2,7] in that they are either curved or consist of straight segments oriented at random, whereas the straight growth dislocations are oriented near the growth direction. In the topograms we can see complete loops or fragments of Frank–Read sources[3] (see especially Figs. 1 and 2). The field of the topograms in Figs. 1-3 is intersected (nearly horizontally) by a broad band, which consists of a series of parallel dislocations and is clearly resolved only in Fig. 3 in the $1\bar{1}01$ reflection. In appearance this resembles a slip band formed by plastic deformation. To compare them with deformation dislocations, let us turn our attention to the growth dislocations in these topograms. They are clearly seen in the lower parts of the topograms in Figs. 1-3 in the form of short straight streaks; in Figs. 1 and 2 their intensity is modulated owing to pendulum interference. These dislocations intersect the plane of the z section and form an angle of nearly 40° with it; it follows that the crystal has grown in the plane of the negative rhombohedron.

To judge by the sharply localized regions of high dislocation density, we can conclude that deformations took place in certain places: the sources. For convenience in describing the most interesting sources, these are numbered in Fig. 1. The "source" character of the deformation is especially clear and visible in Figs. 1-3. In these sources we see a high dislocation density, sometimes exceeding 10^5-10^6 cm^{-2}. The regions of high dislocation density are separated by gaps with low or zero dislocation

Fig. 1. z Section, $10\bar{1}0$ reflection. Plastic deformation and dislocation structure in basal plane. ×4.

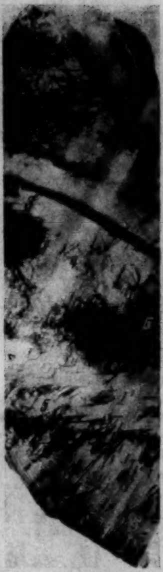

Fig. 2. Same plate as in Fig. 1 $(10\bar{1}0$ reflection). ×4. Dislocation structure in basal plane; some of the sources are extinguished; part of the dislocation structure remains in the plane of the small rhombohedron.

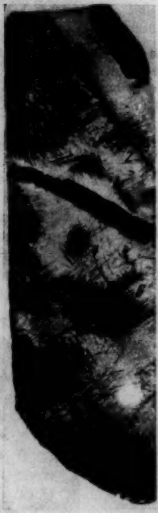

Fig. 3. Same plate as in Fig. 1 $(1\bar{1}01$ reflection). ×4.

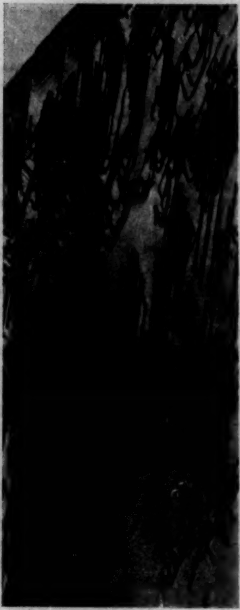

Fig. 4. y Section, $11\bar{2}0$ reflection. ×5.

density. The regions with zero dislocation density are so large that sometimes whole sections, 30 × 10 × 2 mm in size, were altogether without dislocations.

Investigations of the three-dimensional arrangement of dislocations on the topograms in Figs. 1–4 and stereoscopic pairs of photographs (not shown in this article) of these specimens and of a specimen with decorated dislocations[6] reveal that plastic deformation took place in the crystal in at least three systems of slip directions: these were in the basal, prism, and rhombohedron planes. The arrangement of dislocations in the basal plane is clearly seen in Figs. 1–3, which are topograms of a z section. In these we see that curved dislocations or straight fragments of Frank–Read source loops are mainly arranged parallel to the plane of the section (basal slip). Sometimes two or more loops are joined by dislocations lying nearly perpendicular to the basal plane.

The dislocation structure in the y section (Fig. 4), in the plane of the $(1\bar{1}00)$ prism, is somewhat different. Here the dislocation density is much less, and the dislocations themselves are peculiar loops. Segments of these loops are also visible in the z section (Fig. 2) in places where the images of the dislocations visible in Fig. 1 are extinguished (see sources 1, 4, and 5 and to the right above source 6). In each deformation source there are usually several slip systems. For example, in source 1 (Fig. 1), as well as basal slip dislocations with a Burgers vector of $\langle 11\bar{2}0\rangle$ there are dislocations of other slip systems, which are seen in the $01\bar{1}0$ reflection (source 1, Fig. 2). In this latter reflection the images of the basal dislocations have disappeared, but many fragments of Frank–Read sources have become visible. It is interesting that in the $1\bar{1}01$ reflection of source 1 (Fig. 3) there are a large number of dislocations of slip systems in the rhombohedron plane.

Thus we see that all three systems of slip deformation have operated simultaneously, and apparently for the same reason, namely, bulk stress or a nonuniform phase transition at fairly high temperatures.

The presence of prismatic and rhombohedral slip, characteristic of high-temperature processes in hexagonal crystals,[8] is an additional indication that deformation has occurred in the natural quartz specimen at high temperatures. The high-temperature character of the deformation is also confirmed by the presence of spiral dislocations seen in Fig. 3 (near source 1). These are known to be due to diffusion; they usually arise owing to slow deformations and elevated temperatures when the vacancy concentration is fairly high. The nonuniform distribution of deformation in source regions also indicates that deformation took place slowly at high temperatures.

The Burgers vectors of the dislocations were determined by analysis of the extinction of images in the reflections obtained from six prism planes $\{10\bar{1}0\}$ and six rhombohedron planes $\{10\bar{1}1\}$ for the z section; three of the twelve topograms taken are shown in Figs. 1-3. Usually any deformation source is wholly or partly extinguished.

The results of our analysis of the extinctions of the reflections of a section can be divided into three groups as follows.

1. We observed extinction of the images of dislocations in reflections from two neighboring planes of the rhombohedron $\{10\bar{1}1\}$ and the hexagonal prism $\{10\bar{1}0\}$. The Burgers vector of these dislocations lies along the direction of the intersection of these planes $\mathbf{b} = \mathbf{a}\langle 11\bar{2}0\rangle$.

2. We observed extinction of the images of dislocations only in two neighboring rhombohedra; in this case the direction of intersection of these planes is along $(\mathbf{a} + \mathbf{c})\langle 11\bar{2}3\rangle$, which is also the Burgers vector of these dislocations.

3. The images of the dislocations are not extinguished in any of the six reflections $\{10\bar{1}1\}$, but are extinguished in all six reflections $\{10\bar{1}0\}$. These dislocations have the Burgers vector $\mathbf{b} = \mathbf{c}\langle 0001\rangle$.

Analysis of the topograms showed that in the sources the most frequently encountered dislocations are those with Burgers vectors **a** (basal slip) and [**a** + **c**] (rhombohedral slip); only rarely do we find dislocations with vectors **c**. The high dislocation density in the individual sources made it difficult to analyze the Burgers vectors, and in turn this may have led to omission of some possible directions of these vectors.

Deformation dislocations have recently been discovered by x-ray topography in another specimen of natural quartz besides the crystal described above. Thus, we can reckon that minerals with plastic deformation are not as rare in nature as was suggested by Mokievskii et al.[9] The actual discovery of straight traces of plastic deformation in quartz crystals, which are difficult to deform, is an interesting detail, and must be taken into account in considering many geological, mineralogical, and geochemical problems for which exact solutions are of great practical importance.

CONCLUSIONS

1. A peculiar dislocation structure has been discovered in a specimen of natural quartz. It is due to plastic deformation.

2. There are several signs that deformation in this crystal occurred at high temperatures.

3. Three slip systems were found: basal, prismatic, and slip in the rhombohedron plane.

4. Possible Burgers vectors of the dislocations are $\mathbf{a}\langle 11\bar{2}0\rangle$, $\mathbf{c}\langle 0001\rangle$, and $(\mathbf{a} + \mathbf{c})\langle 11\bar{2}3\rangle$. The most frequently found slip systems have $\mathbf{a}\langle 11\bar{2}0\rangle$ and $(\mathbf{a} + \mathbf{c})\langle 11\bar{2}3\rangle$. Systems with the Burgers vector $\mathbf{c}\langle 0001\rangle$ are found relatively seldom.

---

[1] A. R. Lang and V. F. Miuskov (Miuscov), Growth of Crystals, Consultants Bureau, New York (1969).

[2] A. R. Lang and V. F. Miuskov (Miuscov), J. Appl. Phys., 38, 2477 (1967).

[3] E. V. Tsinzerling and Z. A. Mironova, Kristallografiya, 8, 117 (1963) [Sov. Phys. – Crystallogr., 8, 89 (1963)].

[4] L. A. Gordienko, V. F. Miuskov, V. E. Khadzhi, and L. I. Tsinober, Kristallografiya, 14, 539 (1969) [Sov. Phys. – Crystallogr., 14, 454 (1969)].

[5] A. C. McLaren, J. A. Retchford, D. T. Griggs, and J. M. Christie, Phys. Status Solidi, 19, 631 (1967).

[6] A. A. Shternberg, L. A. Gordienko, and L. I. Tsinober, Kristallografiya, 14, 845 (1969) [Sov. Phys. – Crystallogr., 14, 728 (1970)].

[7] V. F. Miuskov, Problems in Crystal Science [in Russian], Izv. MGU, Moscow (1971), p. 197.

[8] R. D. Baëta and K. H. G. Ashbee, Phil. Mag., 22, 177, 601, 625 (1970).

[9] V. A. Mokievskii, V. M. Titova, and Z. V. Bartoshinskii, Zap. Vses. Mineralog. Obshch., 91, No. 4, 381 (1962).

Domain rotation in smectic liquid crystals

A. N. Chuvyrov and Z. Kh. Kuvatov

Bashkir State University

(Submitted March 10, 1972)
Kristallografiya, 18, 344-348 (March-April 1973)

Helmholtz's first theorem for vortex tubes is applied. Molecular models are constructed for simple divergent and confocal textures.

A domain structure can arise in a smectic phase (and also in a nematic phase under certain conditions)[1] which has some specific properties, one of which is change in domain orientation in an electric field: domain rotation. This effect was first reported in ref. 2, but it has not been further examined.

Here we examine in more detail domain rotation and offer an explanation for it from the hydrodynamic model for domains adopted for nematic liquid crystals.[3,4] We use specimens 50 μ thick with a simple fan structure in smectic phase A of p-n-octylhydroxybenzoic acid.

The domain width and orientation were determined by light refraction, the light coming from an Ne–Ar laser (6327 Å); the diffraction pattern was photographed from a translucent screen. The domain width was determined from the shape of the diffraction peaks $2d \sin \varphi = k\lambda$; we also made polarization observations in parallel with photography of the structures.

The texture of a smectic liquid crystal of this substance is dependent on how it is made; for instance, if one allows the smectic phase to crystallize from a nematic phase in an electric field, one gets a confocal texture. A simple fan texture is obtained on crystallization in a temperature gradient in the plane of the specimen; the latter then consists of numerous grains with various directions for the optic axes.[2] In turn, each grain consists of individual smectic microcrystals, which may be represented approximately as confocal domains elongated in the plane of the preparation (Figs. 4 and 5). The boundaries between the individual microcrystals represent discontinuities in the molecular structure; the elongation axis of a microcrystal is always at 60–70° to the optic axis of the grain, and this angle is not dependent on the direction of a temperature gradient or the electric field at the moment of production of the texture.

RESULTS

A domain structure arises in a smectic liquid crystal, and also in a nematic one, for a certain threshold field, which is dependent on the frequency; Fig. 1 shows the dependence of the threshold field U_t on the frequency f, which is of the form $U_t \simeq kf + U_0$, where k is 0.04–0.05 and is a constant dependent on the properties of the mesophase, while U_0 is the threshold field for production of domains in steady fields, which is 16–18 V. In threshold fields, one gets domains of a quite definite nonzero width, while their elongation axes are parallel (within the grain) to the optic axis (Figs. 2 and 3). The domain width increases smoothly with the field, and at some critical field U_c, also dependent on f, the domains turn through about 60°; at the moment of rotation, the domain orientation changes sharply by 60°, with no intermediate positions being observed. Domains of the new orientation are always generated in layers, whose width gradually increases with the field (Fig. 3a-c). The rotation occurs at voltages of 20–30 V. As the voltage is reduced, there is a more marked rotation at about 20 V; the direction of the secondary domains coincides with the elongation direction of the microcrystals, i.e., these are oriented parallel to the lines of discontinuity in the molecular structure.

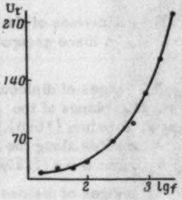

Fig. 1. Threshold field as a function of frequency.

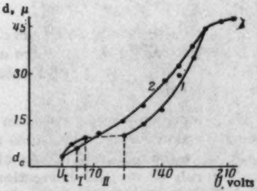

Fig. 2. Domain width as a function of electric field (f = 100 Hz): 1, 2) curves recorded on increasing and decreasing the field respectively; I) reverse rotation; II) rotation region.

The domain sizes before and after rotation are related by $d_2 = d_1(\sin \alpha \cot \theta + \cos \alpha)$, where d_1 and d_2 are the domain widths before and after rotation, α is the angle of rotation, and θ is the angle between the lines joining domains differing in orientation and the direction of the primary domains (Fig. 3).

The polarization direction in the diffraction peaks remains the same before and after domain rotation and coincides with the initial domain orientation, but the diffraction peaks themselves rotate through about 60° and take the form of rectangles oriented with their long sides perpendicular to the line of initial disposition of the centers of the diffraction peaks (Figs. 4 and 5). This means that: a) Domain rotation does not alter the molecular orientation, and this after-rotation constitutes 60° to the domain

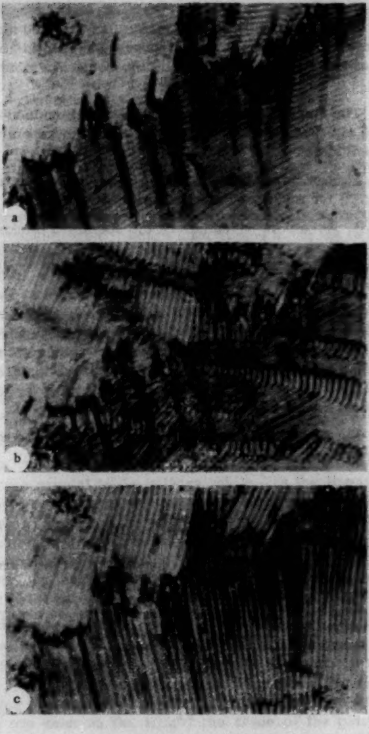

Fig. 3. Domain rotation.

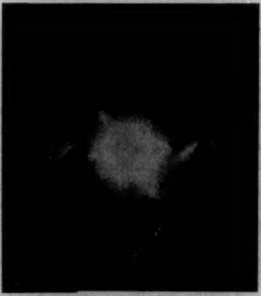

Fig. 4. Rotation of diffraction peaks.

elongation axis; b) the gradients in the refractive index within each domain are normal to the orientation direction; c) the molecules before domain rotation are parallel to the length of the latter (Fig. 3).

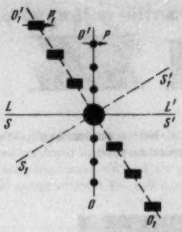

Fig. 5. Orientation of diffraction peaks relative to optic axis and elongation of microcrystals: SS' and S_1S_1' are the domain orientation directions before and after rotation, LL' is the optic axis, and OO' is the position of the diffraction peak, and P is the polarization direction.

Conclusions a and c were confirmed by polarization observations.

DISCUSSION

1. It has been shown[3] that periodic hydrodynamic flow eddies can rise in nematic liquid crystals under certain conditions, whose optical effect is a system of light and dark domain bands. A similar effect occurs in a smectic liquid crystal, but with the difference that the hydrodynamic instability at the threshold field arises at the center of the specimen. The threshold field for domain-structure production is dependent on various factors: viscosity, dielectric constant, conductivity, and elasticity, since these characteristics of the mesophase are approximately identical throughout the thickness in a nematic liquid crystal, so one gets a domain structure with well-defined areas $d \approx l$ (l is the specimen thickness), which is independent of the electric field. One can say (Fig. 2) that such a layer with uniform physical properties exists also in the smectic liquid crystal, where at U_t one gets a domain structure with a repeat distance of about 3 μ. We assume by analogy with nematic domains that $d = l$, which enables us to estimate the thickness at about 3 μ. The molecules are parallel to the length of the domains, which means that the layering in the molecular structure for the smectic case persists in the vortices and occurs after rotation of the domain. Here each domain may be represented as a set of distinct parallel vortices, whose thickness is a multiple of the smectic layer thickness (Fig. 6). One sees the domain pattern probably because of change in density of the mesophase at the instant when the hydrodynamic instability occurs.

2. The dark lines bounding the individual microcrystals correspond to the emergence of the Dupen hyperbolas and characterize the discontinuities in the molecular structure; we assume that these discontinuities extend to a depth Δ in the specimen, while the molecular orientation in the layer of thickness $l - 2\Delta$ is uniform, i.e., in this the director $\mathbf{n} = \text{const}$. As the electric field increases, the radius r of the domain vortices increases, and when $r > (l - 2\Delta)/2$ the surfaces of the domains at the points of emergence of the hyperbolas are deformed. We now consider how the strength of vortex tube (domain) is altered, this quantity for a liquid crystal being $\oint (\mathbf{v} + \mathbf{u})\,dx$ (v is the speed of the centers of inertia of the molecules, u is the linear velocity of the director, L is the circumference of a vortex tube).[5] Helmholtz's first

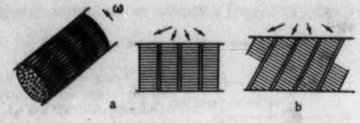

Fig. 6. Molecular structure of domains: a) before rotation; b) after (the arrows indicate the smectic layers).

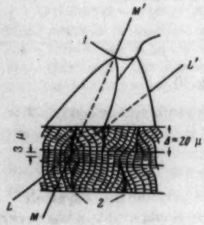

Fig. 7. Model of a simple divergent texture: 1) grain boundary; 2) structural discontinuities in liquid crystal. LL' is the optic axis and MM', the elongation of the microcrystal.

kinematic theorem gives

$$\Gamma=\oint_{L}(\mathbf{v}+\mathbf{u})\,d\mathbf{x}=\int_{\sigma}\omega\,d\sigma=\text{const}$$

where ω is angular velocity and σ is the cross-sectional area of a domain. This ω is determined primarily by the external electric field, and for a given field and frequency is the same at various points throughout the specimen. The vortex deformation at the points of emergence of the Dupen hyperboloids results in a change in cross section, i.e., in failure to satisfy the condition Γ = const. The latter may be met only if the domains are oriented along the elongation of the smectic microcrystals, i.e., in accordance with Helmholtz's theorem, the domains rotate through 60°.

The domain rotation enables one to determined Δ, which is $(l-d)/2$; Fig. 3 shows that $\Delta\approx 20\ \mu$ for specimens 50 μ thick.

This evidence has been used in a hypothetical model (Fig. 7) for a simple fan-type texture.

3. Here Δ is dependent on the specimen thickness, and preliminary evidence indicates that $\Delta/l\approx$ const, which would be interesting to test for smectic liquid crystals of other substances.

4. Studies similar to the above have been made on a confocal texture, and the following results were obtained: a) The optical axis of the texture lies at about 45° to the elongation axis of the individual microcrystals; b) Δ is 21-23 μ for a specimen with l = 50 μ; c) a layer with uniform molecular orientation is about 6-8 μ thick.

We are indebted to A. P. Kapustin and A. N. Trofimov for a discussion of the results.

---

[1] L. K. Vistin' and A. P. Kapustin, Kristallografiya, 13, 349 (1968) [Sov. Phys. – Crystallogr., 13, 284 (1968)].

[2] A. P. Kapustin, Z. Kh. Kuvatov, L. S. Mamaeva, and A. N. Trofimov, Izv. VUZ, Fizika, 9, 22 (1970).

[3] P. A. Penz, Phys. Rev. Lett., 24, 1405 (1970).

[4] S. A. Pikin, Zh. Eksp. Teor. Fiz., 60, 1185 (1971) [Sov. Phys. – JETP, 33, 641 (1971)].

[5] J. A. Geurst, Phys. Lett., A36, 1, 63 (1971).

Determination of the arbitrary orientation of a crystal by proton diffraction

A. L. Fainshtein
Khar'kov State University

(Submitted March 16, 1972)
Kristallografiya, 18, 349-352 (March-April 1973)

Proton diffraction is considered as a means of determining crystal orientation; the patterns are indexed by means of standard linear two-dimensional projections of the crystals. Analytical and graphical methods are considered for converting the diffraction pattern to a new projection plane. A determination has been made of the arbitrary orientation of an epitaxial film of Au relative to the direction of the proton beam for an energy of about 180 keV used in transmission.

1. The proton-diffraction pattern recorded in reflection[1] or in transmission[2–4] bears information about the orientation of the crystal via the geometry in the point reflexes and lines, which are traces respectively of crystallographic directions and planes, which arise on account of channeling and shadowing. Attempts have been made[5–8] to define or refine crystal orientations by proton diffraction when one can judge directly from the symmetry of the pattern what the orientation of the specimen is.

Here we consider how the patterns may be used to determine any orientation of the crystal although this cannot be judged directly from the pattern (Fig. 1).

2. The pattern in the case L ≫ d (L is the distance from the crystal to the pattern, while d is the linear dimension of the proton beam as measured at the surface of the specimen) coincides with the line two-dimensional projection of crystals using crystallography on the assumption that the projection center is the point where the photons leave the crystal and the projection is the plane of the pattern.

To determine the specimen orientation with a known geometry in the camera, it is sufficient to index the reflections and lines; in solving possible structure problems it may also be supposed that the plane of the recording film is perpendicular to the primary beam, whereupon one sees on the film[3,9] the trace of the primary beam, i.e., the axis of projection.

3. The method of indexing is based on trial and error: One indexes the pattern from a crystal with a known structure by transferring to another projection plane, which is carried out in such a way that the projection axis coincides with one of the basic close-packed crystallographic directions, in such a way that the most prominent point reflections on the pattern, i.e., the one having the greatest width, coincides with the trace of the primary beam. The resulting pattern must then be brought into coincidence with one of the standard linear projections constructed for projection axes coinciding with the principal close-packed directions in crystals of that structure, and one indexes directly the reflections and lines on the pattern. Standard projections should be constructed on the basis of the actual distance L from the projection center to the plane of projection. As an example, Fig. 2 shows the standard linear projection for the [011] axis of an fcc crystal, where the thickness of the lines or size of the points indicates qualitatively the angular width and intensity of the corresponding elements in the pattern.

Fig. 1. Proton pattern in transmission recorded from an epitaxial film of Au.

If we relate an x0y coordinate system for the plane of the proton-diffraction pattern in such a way that 0y joins the trace of the primary beam and the prominent reflection (dashed lines in Fig. 3a; see below on indexing of the reflections), then one can readily show as follows: When one passes to the new projection plane, this reflection moves along the line 0y, which corresponds to an imagined rotation of the crystal through an angle φ_0 such that $\tan \varphi_0 = y_0/L$, where y_0 is the coordinate of that particular reflection. The other reflections then move along hyperbolic paths whose equation is

$$(x^2/\mathrm{tg}^2\,\theta) - y^2 = L^2, \tag{1}$$

where θ is the angle between the crystallographic directions corresponding to the given reflections and the plane containing the direction of the primary beam and the 0y axis. Each reflection with its coordinates (x_1, y_1) on passing to the new projection plane moves to a point with coordinates (x_2, y_2):

$$\begin{gathered} x_2 = (Lx_1\sqrt{L^2 + y_0^2})/(y_0y_1 + L^2), \\ y_2 = [L^2(y_1 - y_0)]/(y_0y_1 + L^2) \quad \text{for} \quad y_0y_1 + L^2 > 0. \end{gathered} \tag{2}$$

The new positions of the lines in the pattern are defined by the straight lines joining the corresponding point reflections as referred to the new projection plane.

One can transform the coordinates of the reflections also by means of a grid consisting of a family of the hyperbolas of Eq. (1) and a family of the straight lines $y = L \tan \varphi$; it is readily seen that this grid is a linear projection of part of the projection sphere.

If the trace of the primary beam is brought to the center of the grid, while the most prominent reflection

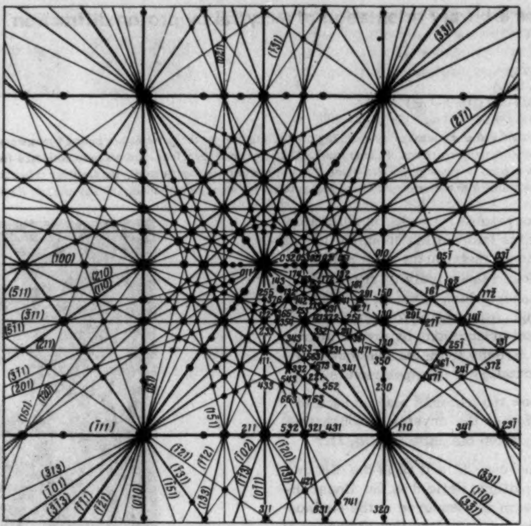

Fig. 2. Standard line projection for the [011] axis for fcc crystals.

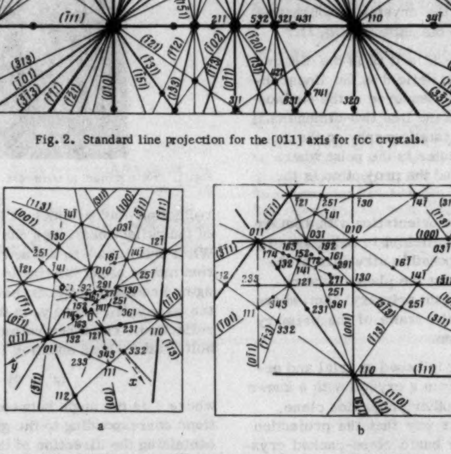

a

b

Fig. 3. Indexing of a proton-diffraction pattern for an epitaxial Au film: a) disposition of the reflections and lines in Fig. 1, with 0 the trace of the primary beam; b) proton pattern referred to a new projection plane and in agreement with the standard [011] projection.

lies on the equator of the latter, one can pass to the new projection plane without any calculations, for one simply reads off along the equator the angle for the imagined rotation of the crystal, and then one displaces each reflection in the pattern along the corresponding lines of latitude on the grid through this angular distance.

A single proton-diffraction pattern is not always sufficient to define the orientation of a crystal of low symmetry; in that case it may be necessary to record several patterns with the crystal in different positions and refer them to a single projection plane, then solving the orientation problem.

4. The above methods were tested for an epitaxial Au film of arbitrary orientation and thickness of about 5000 Å; the film was produced by condensation of a molecular beam under vacuum[8] on a (100) face of an NaCl single crystal. The proton-diffraction pattern in transmission recorded at a proton energy of 180 keV (collimated beam 1 mm in diameter, L = 40 mm) is shown in Fig. 1. The sketch of Fig. 3 shows the indexing sequence for the pattern; one passes to the new projection plane via (2) and the above net, whose latitudes and meridians are shown at intervals of two degrees with a maximum angle of deviation from the center of 65°. This net was used to measure the angles between the primary beam and the [010], [011], and [111] directions in the epitaxial film, which were respectively 23, 28, and 31°. This net can be used

in proton diffraction just as one uses a Wulff net in x-ray diffraction, in solving various crystallographic problems, which requires no special description.[10] For instance, the standard [011] projection (Fig. 2) was obtained by means of this net from the previously constructed [001] projection.

I am indebted to Ya. E. Geguzin for a valuable discussion of the results and to A. M. Markus for assistance in the experiments.

---

[1] A. F. Tulinov, Usp. Fiz. Nauk, 87, 585 (1965) [Sov. Phys. – Usp., 8, 864 (1966)].

[2] A. M. Markus, Ya. E. Geguzin, and A. L. Fainshtein, Fiz. Tverd. Tela, 13, 1476 (1971) [Sov. Phys. – Solid State, 13, 1232 (1971)].

[3] A. M. Markus, Yu. E. Geguzin, and A. L. Fainshtein, Zh. Eksp. Teor. Fiz., 61, 332 (1971) [Sov. Phys. – JETP, 34, 175 (1972)].

[4] A. M. Markus, Ya. E. Geguzin, and A. L. Fainshtein, Ukr. Fiz. Zh., 16, No. 8, 1369 (1971).

[5] R. S. Nelson, Phil. Mag., 15, 136, 845 (1967).

[6] J. U. Andersen, J. A. Davies, K. O. Nielsen, and S. L. Anderson, Nucl. Instr. Meth., 38, 210 (1965).

[7] G. Dearnaley and M. A. Wilkins, J. Scient. Inst., 44, 10, 1738 (1970).

[8] A. M. Markus and A. L. Fainshtein, Ukr. Fiz. Zh., 15, No. 10, 1738 (1970).

[9] C. S. Barrett, R. M. Mueller, and W. White, J. Appl. Phys., 39 (10), 4695 (1968).

[10] S. S. Gorelik, L. N. Rastorguev, and Yu. A. Skakov, X-ray and Electron-Optic Analysis [in Russian], Metallurgiya, Moscow (1970), p. 332.

Nature of the point defects in GaAs single crystals as a function of the composition of the melt during growth

V. T. Bublik, V. V. Karataev, R. S. Kulagin, M. G. Mil'vidskii, V. B. Osvenskii, O. G. Stolyarov, and L. P. Kholodnyi

State Scientific-Research and Design Institute of the Rare-Metal Industry

(Submitted September 9, 1971; resubmitted April 6, 1972)
Kristallografiya, 18, 353-356 (March-April 1973)

A study is made of the relation between the nature and concentration of point defects in GaAs single crystals and the melt composition during growth. In the course of the experiments a precision determination of the sample density was made and the lattice parameter and internal friction were measured. The results obtained indicate that single-phase GaAs crystals can be grown from melts with an As content between 46.7 and 53.5 at.% and crystals of stoichiometric composition can be made from a melt enriched in As with 50.5 at.% As in the melt.

The production of single crystals of decomposing semiconductor compounds (in particular of GaAs) having a definite and wide range of homogeneity with the stoichiometric composition is a complicated problem. Its successful solution depends on a number of factors. In the first place it is necessary to know the precise form of the microscopic phase diagram for Ga–As near the maximum melting point; in the second place it is necessary to have strict control of the growth conditions which allows one to reproducibly make single crystals with a given melt composition (in the case of growth from a melt). On the other hand, the difficulty of determining the deviation of the composition of the crystal from stoichiometry is aggrevated for GaAs in that the homogeneity region is very narrow and according to ref. 1 extends from 49.998 to 50.009 at.% As. Here it should be kept in mind that the homogeneity region was determined by measuring the lattice period and the density on several polycrystalline samples.

It is of undoubted interest to establish the relation between growth conditions, especially the composition of the melt, and the amount and nature of point structural defects which appear in the crystal. There is also great value in explaining the growth conditions which ensure the production of single-phase crystals and crystals of rigorously stoichiometric composition.

The investigations were done by several techniques. The densities of the samples were determined by a hydrostatic method[2] and the errors in the determination did not exceed $2 \cdot 10^{-5}$ g/cm^2 at 20°C. The lattice period was determined precisely using the Bond method[3] with a measurement precision of $\pm 3 \cdot 10^{-5}$ Å at 20°C. In addition we carried out investigations of the internal friction in samples by measurements of the damping decrement.

The point defect concentrations in the samples were calculated using the equation

$$\Delta N = (da^3 N_0 - 4M) / \bar{A}a^3, \tag{1}$$

where ΔN is the differential concentration of point defects, i.e., the difference between the concentrations of interstitial atoms and vacancies, d is the sample density in g/cm^3, a is the lattice parameter in Å, N_0 is Avogadro's number, M is the molecular weight of GaAs (144.650), and $\bar{A}$ is the mean atomic weight of GaAs (72.325).

The differential concentration ΔN of point defects calculated from (1) allows us to gauge the extent to which one form of defect prevails over the other; in other words if the number of interstitial atoms equals the number of vacancies per unit volume of crystal, then $\Delta N = 0$. If the number of interstitial atoms exceeds the number of vacancies per unit volume, then $\Delta N > 0$ while with $\Delta N < 0$ vacancies predominate in the crystal. The absolute error in the determination of ΔN amounts to 10^{17} cm^{-3}.

Measurements of the internal friction were made using a two-state vibrator[4] at a frequency of 100 kHz between 20 and 550°C. To eliminate the temperature dependence of the internal friction, buffer rods of fused quartz were placed between the crystals of piezoelectric quartz, which served as the transducer and detector of the vibrations, and the measured GaAs sample which was placed in a heater.

The investigations were carried out on undoped GaAs single crystals produced by floating zone melting with a molten zone traveling at ~0.5 km/min in which the As content in the melt varied from 43.6 to 54.7 at.%. The liquid phase content was determined from the temperature of As condensation. The absolute value of the temperature was measured within ±1%, while the As concentration in the melt was measured with a precision of 0.05 at.%. The total residual impurity content in the samples, according to mass spectroscopic analysis and the temperature dependence of the Hall effect, did not exceed 2 to $3 \cdot 10^{16}$ cm^{-3}.

Figure 1 shows the change in the density, lattice parameter, differential point defect concentration, and internal friction in a crystal as a function of the As content in the melt. It can be seen that as the As concentration varies from 46.7 to 53.5 at.% the densities of the samples (curve a) monotonically increase while beyond this region the behavior of the curve changes sharply to the opposite. The sharp growth of density with As content in the melt less than 46.7 at.% is evidently due to the formation of inclusions of excess Ga, whose density is greater than the density of GaAs. The sharp decrease in the density of GaAs with As content in the melt greater than 53.5 at.% is due to the formation of gaseous inclusions of As which condense during cooling of the crystal, leading to the appearance of holes.[5] This evidently indicates that the region of monotonic change in density corresponds to crystallization of GaAs from the melt within the homogeneity limits.

The results obtained suggest that within the homogeneity region of GaAs the densities of single crystals vary from 5.31650 to 5.31757 g/cm^3 with increasing As content in the melt. Note that in ref. 1 a drop in density

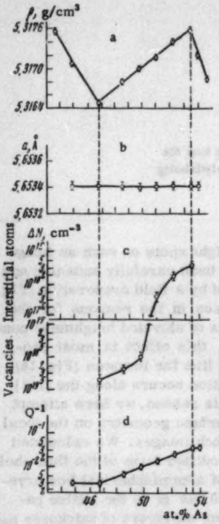

Fig. 1. Density (a), lattice parameter (b), defect concentration difference (c) and damping decrement (d) as functions of the As concentration in the melt.

from 5.3176 to 5.3157 g/cm³ was observed with an increase of the As content in the crystal. Such a discrepancy in the results can be related, evidently, to a quite low precision in the determination of the sample density in ref. 1 (the error of the measurements was, according to the authors, ± 0.0026 g/cm³), and in the second place these results were obtained on polycrystalline samples in which the impurity content was uncontrolled.

It can be seen from the data of Fig. 1 that in the entire concentration range of As in the melt which we studied, the lattice parameter remained unchanged within the limits of measurement, while the magnitude of the differential concentration of point defects and the damping decrement showed substantial changes.

With an As content of 50.5 to 53.5 at.% in the melt, interstitial atoms predominated in the crystals, while with an As content from 46.7 to 50.5 at.% vacancies predominated. Since the differential concentration of point defects in the crystals studied did not exceed $5.3 \cdot 10^{18}$ cm^{-3} (see Fig. 1c) which is substantially lower than the overall concentration of defects in GaAs,[6] it is evident that the crystals simultaneously contained defects of both types (vacancies and interstitials).

An As content of 50.5 at.% in the melt corresponds to the lowest differential concentration of point defects in the crystal. It is natural to assume that in the low-concentration region the energy of formation of point lattice defects does not depend on their concentration; therefore, the ratio of the concentrations of interstitial atoms and vacancies can be assumed constant over the whole homogeneity range (without considering the possible changes in the solubilities of the excess components during cooling of the crystals from the melting point). It follows from this that the lowest differential concentration of point defects corresponds to the lowest absolute values of their concentrations. Therefore we can assume that with As concentrations in the melt of 50.5 at.% the composition of the crystal is closest to stoichiometry. Evidently with an As content in the melt of more than 50.5 at.% the predominant interstitial atoms in the crystal are As atoms and with an As content in the melt less than 50.5 at.% As vacancies are predominantly formed in the crystal. Thus to produce GaAs single crystals of stoichiometric composition the melt should be enriched in As.

The nature of the changes in the differential concentration of point defects as a function of the As content in the melt and the results of ref. 7 indicate that the energy for forming arsenic vacancies, $U_{v_{As}}$ exceeds the energy of formation of gallium vacancies $U_{v_{Ga}}$ and allows us to write certain inequalities relating the energies of formation of point structural defects in GaAs: $U_{As_i} < U_{v_{Ga}} < U_{v_{As}} < U_{Ga_i}$.[1)] It follows from these equalities that the homogeneity region in this system is asymmetric with regard to the rigorous stoichiometric composition, i.e., the solubility of As is greater than the solubility of Ga in GaAs.

The measurements of the damping decrement reported here (Fig. 1d) show that the height of the 160° peak which, as shown previously,[8] characterizes the concentration of gallium vacancies in the crystal, increases smoothly with increasing As concentration in the belt between 46.7 and 53.5% and beyond this region remains constant. This fact, in addition to the previously noted characteristic change of the density as a function of the melt concentration, suggests that an As content in the melt between 46.7 and 53.5 at.% corresponds to the effective homogeneity region for GaAs crystals produced by floating-zone melting.

[1)] U_{As_i} and U_{Ga_i} are the energies for formation of interstitial As and Ga atoms, respectively.

---

[1] M. E. Straumanis and C. D. Kim, Acta Crystallogr., 19, 256 (1965).
[2] L. R. Weisberg and J. Blanc, J. Appl. Phys., 34, 1002 (1963).
[3] W. L. Bond, Acta Crystallogr., 13, 814 (1963).
[4] V. S. Postnikov, Internal Friction in Crystals [in Russian], Metallurgiya, Moscow (1969).
[5] B. D. Lainer, V. V. Rakov, and M. G. Mil'vidskii, Izv. Akad. Nauk SSSR, Neorgan. Mater., 5, No. 1, 25 (1969).
[6] J. Blanc, R. Bube, and L. Weisberg, Phys. Rev. Lett., 9, 252 (1962).
[7] M. G. Shumskii, V. T. Bublik, S. S. Gorelik, and M. A. Gurevich, Kristallografiya, 16, 779 (1971) [Sov. Phys. – Crystallogr., 16, 674 (1972)].
[8] V. B. Osvenskii, L. P. Kholodnyi, and M. G. Mil'vidskii, Proceedings of the All-Union Conference on Structural Defects in Semiconductors, Institute of Semiconductor Physics, Siberian Branch, Academy of Sciences of the USSR, Novosibirsk (1969), p. 125.

Interpretation of field-ion images.
I. Point defects

L. P. Potapov, T. L. Raznikova, and A. L. Suvorov
Central Ferrous Metallurgy Research Institute

(Submitted January 7, 1972)
Kristallografiya, 18, 357-362 (March-April 1973)

Possible forms of contrast are examined for these images, which can arise because of single interstitial atoms near the surface of the metal; the surface geometry is considered in relation to the observed decoration zone, the analysis being based on computer simulation of such images for ideal and defective bcc crystals.

The following is[1] the substance of existing views on the identification of interstitial atoms in such images from metal specimens. An interstitial atom in the first surface layer of atoms or under this layer increases the local curvature of the surface and thus produces a local increase in the field strength. This, in turn, increases the probability of ionization in the gas[2] over this part of the surface and thus increases the image current. Then near or directly above an interstitial atom one finds in the image a spot of increased intensity (Figs. 1b and 1d). However, there can be other causes of the same effect; increased contrast in the image may be due to adsorbed atoms or molecules, or to impurity atoms. Also, one needs to bear in mind a purely geometrical factor: the special position of an atom at the surface of the specimen.[3] A major problem in field-ion microscopy is to identify the causes of contrast increase. One approach is to use atom probe analysis,[4] while another is to bring to bear methods of computer simulation of such images for defect structures.

There are numerous bright spots on such an image even when the specimen has been carefully annealed and the surface has been cleaned by a field evaporation (Fig. 1a); particular interest arises in the reasons for the occurrence of chains of spots of elevated brightness zone (decoration[3]). In particular, this effect is most pronounced along the [001] zone line for tungsten (Fig. 1a), while less prominent decoration occurs along the $[1\bar{1}1]$ and $[\bar{1}11]$ zone lines. For this reason, we here attempt to elucidate the effects of surface geometry on the local brightness and contrast of such images. We calculated the image via a somewhat modified form of the thin-shell model.[5] The surface layer of a hemispherical bcc crystal of critical thickness $p_0 = 0.04a$ (a is the lattice parameter) was divided into four sublayers of thickness $p_0/4$, and then the calculation was performed in the usual way, for a model corresponding to crystal lattice nodes lying in the various sublayers; these were printed out by means

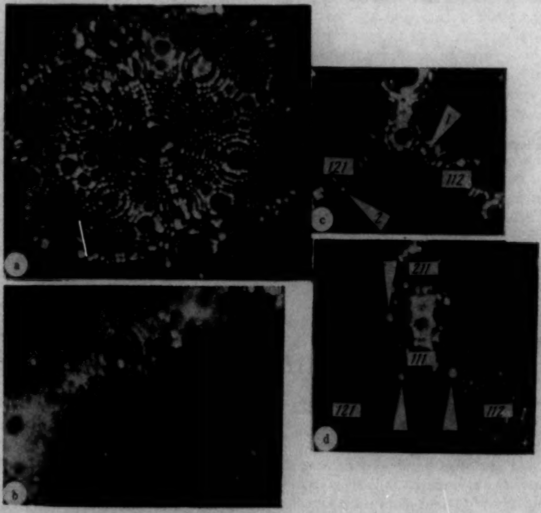

Fig. 1. Helium-ion images of tungsten specimens: a) decoration of zone lines in a field-cleaned surface; b) points of elevated brightness corresponding to atoms displaced to interstitial positions by α bombardment; c) typical example of elevated contrast (arrow 1) on a completed face and at the edge of a plane (arrow 2); d) local increase in contrast due to bombardment with 5-MeV deuterons.

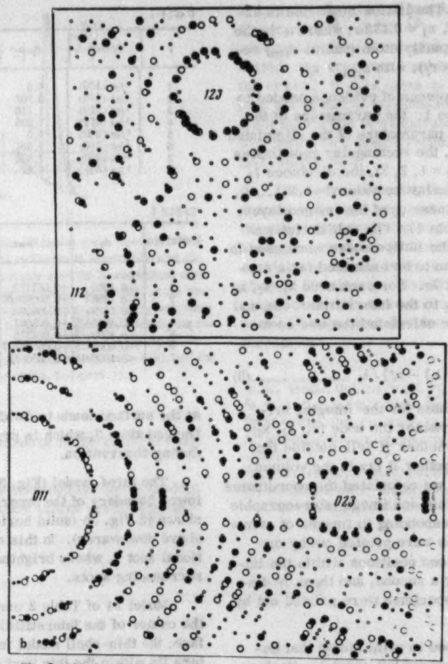

Fig. 2. Simulated models for two parts of the ion images from defect-free bcc specimens showing contrast variations due to surface geometry: $R_0 = 350$, $p_0 = 0.04$.

of various symbols.

The calculations were performed with a Razdan-3 computer with direct printout of the models on a line printer ATsPU-128; Fig. 2 shows the results for parts in the region of the (123) and (011) faces. Nodes lying in the top sublayer are represented in this figure by large filled circles (the brightest spots in the image). Then, in accordance with the brightness reduction, there follow the large open circles, the small filled circles, and the small open circles.

The result shows that the brightness of the atoms along the rings in the (011) planes varies somewhat; along the [001] zone lines, and also along $[1\bar{1}1]$ and $[\bar{1}11]$ lines, one observes a certain increase in contrast, so the decorated zones may be due, at least partly, to the geometrical disposition of the atoms near the surface, but this does not rule out the possible contribution from adsorption and displacement of atoms to metastable positions at the surface.

The models show that the conditions for image formation can result in pseudovacancies, including small groups of these; a good illustration is provided by the feature indicated by the arrow in Fig. 2a for a completely resolved face, where four atoms within this face (small open circles) are indistinguishable on an actual image and were thus erroneously interpreted as a group of vacancies. One can demonstrate this error here only by considering a set of images obtained by successive field evaporation of the surface atoms. One cannot draw conclusions on defects on the basis of a single photograph because such conclusions cannot be unambiguous.

We use the following assumptions in calculating models for images of bcc crystals containing interstitial) atoms: If the initial lattice is assumed to be an isotropic elastic continuum and we neglect bulk changes at distances $R \gg r_0$, where r_0 is the radius of a volume element damaged by elastic deformation, then the deformation may be written[6] in the form div $\mathbf{U}(\mathbf{r}) = 0$. The displacement vector $\mathbf{U}(\mathbf{r})$ under these conditions is always directed along the radius vector $\mathbf{r}$, so the following is the equation for the displacement in spherical coordinates:

$$\frac{d^2U(r)}{dr^2}+\frac{2}{r}\frac{dU(r)}{dr}-\frac{2}{r^2}U(r)=0. \tag{1}$$

This equation integrates to $U(r) = c_1/r^2 + c_2 r$, and the boundary conditions are $U(R) = 0$ and $U(r_0) = r_1 - r_0$ (r_1 is the radius of an interstitial atom), so we have

$$U(r) = (r_1 - r_0)(r_0/r)^2. \tag{2}$$

We consider two cases: 1) The lattice atom lies in an octahedral pore ($r_0 = 0.134a$, $r_1 = 0.433a$, where a is the lattice parameter); 2) an impurity atom (radius r_{im}) replaces a lattice atom (radius r_l), with $r_{im} > r_l$.

The following were the pieces of evidence needed to calculate the images for case 1: the parameters of the initial lattice (tungsten), the parameters of the stimulated area (around the ⟨123⟩ pole), the rectangular coordinates of the interstitial atom x_j^a (j = 1, 2, 3), the distances l_i from the dilatation center to the lattice nodes (i = 1, 2, ..., 8), the point radius R_0, the thickness p_0 of the imaged layer, and the ratio $\lambda_i = l_i/U_i$ (Table 1). The calculation was carried out as follows. All the lattice nodes were used in a set sequence within a region to be examined for a surface layer of thickness about 3a. For each node x_1, x_2, x_3 we calculated the distance d_x to the interstitial atom, and then, if d_x was equal to l_i, we calculated the new coordinates x_j' of this node:

$$x_j' = [x_j(1+\lambda_i) - x_j^a] / \lambda_i \tag{3}$$

and we examined the coordinates for the imaging criterion, i.e., we established whether the node (x_1', x_2', x_3') lay within the image layer, whether it fell outside the limits of the specimen, or whether it lay in the volume. In the first and second cases we calculated the coordinates φ and γ of this node in the field-ion image (stereographic projection). The points corresponding to images of atoms placed at normal lattice nodes were printed out by one symbol, while those in displaced positions within the image layer were printed out by a second, and those in displaced positions outside the specimen were printed out by a third (T = 1, 2, and 3).

The symbol T = 4 was used to print atoms that before displacement were not imaged but which by displacement entered the image layer; also we calculated the distances q of the displaced atoms from the (123) plane. The calculations were made for numerous different models (dispositions of the interstitial atom). Some of these are shown in Fig. 3. The maximum height q_{max} of the humps formed by displacement of the atoms is extremely small [Table 2: q_a is the distance of an interstitial atom from the (123) plane, while the minus sign corresponds to atoms under that plane]. Then the above model for the displacements means that one must take as extremely approximate the scheme for representing interstitial atoms usually used[1] for illustration. Nevertheless, the results for the displacements in the various cases may give quite definite effects in the images (Fig. 3, parts c–e). The first model (Fig. 3c) corresponds to the condition that R_0 = 349.76 (all numbers are given as fractions of the lattice parameter a) and p_0 = 0.085 (Fig. 3b). Then the chain of atoms denoted by the numbers 1 to 7 in Fig. 3 corresponds in the (123) plane to a hump as shown in Fig. 3a (Fig. 3 represents model 6 of Table 2). Although all the atoms in the displaced position and at the lattice nodes enter into layer p_0 and are imaged (Fig. 3b), the presence of an interstitial atom results in a hump, which may be the cause of increased contrast in the region of atoms 4 and 5, and which takes the form similar to that shown in Fig. 1c (arrow 1).

The second model (Fig. 3d) corresponds to R_0 = 349.694 and p_0 = 0.085; occurrence of an interstitial atom at the surface leads to field evaporation of the previously imaged atom 3, which is practically impossible to detect during observation.

TABLE 1

i	Vector	l_i, a	l_i, Å	U_i, Å	λ_i
1	$^1/_2a$ ⟨100⟩	0.5	1.58	0.01996	79.15
2	$^1/_2a$ ⟨110⟩	0,707	2.234	0.009985	223.735
3	$^1/_2a$ ⟨210⟩	1.118	3.5328	0.003928	884.79
4	$^1/_2a$ ⟨211⟩	1,225	3.871	0.0033256	1163,995
5	$^1/_2a$ ⟨300⟩	1,5	4.74	0.00221799	2137,066
6	$^1/_2a$ ⟨310⟩	1,581	4.9959	0.0019965	2502.211
7	$^1/_2a$ ⟨320⟩	1.802	5.6943	0,0015368	3705.135
8	$^1/_2a$ ⟨321⟩	1.87	5.9092	0.0014271	4140.654

TABLE 2

Model No.	q_a	q_{max}	Model No.	q_a	q_{max}
1	−0.1069	+0.001173	8	−0.5345	+0.0023853
2	−0.13363	+0.00059465	9	−0.5345	+0.002298
3	−0.13363	+0.000593	10	−0.668153	+0.00075902
4	−0.4008915	+0.005067	11	−0.668153	+0.000304678
5	−0.4008915	+0.003378	12	−0.8017	+0.0006895
6	−0.4008915	+0.00506727	13	−0.9354	+0.001061
7	−0.4008915	+0.0050672	14	+0.4008919	+0.4008915

The third model (Fig. 3e) is for the case where the lower boundary of the layer of thickness p_0 = 0.085 lies as shown in Fig. 3b (solid horizontal line with the arrow from above downwards). In this case the image has the additional spot 4, whose brightness is greater than that of the surrounding spots.

Model 14 of Table 2 corresponds to the case where the center of the interstitial atom lies above the (123) face; the thin-shell model indicates that atoms whose centers lie within the thin surface layer are imaged, while atoms whose centers lie outside the hemispherical surface are removed by the field, and from this we can draw the following conclusion. In the present case, the interstitial atom itself forms the hump on the surface, and when these atoms lie under the (123) plane, the height of the hump considerably exceeds the usual values of q_{max}, i.e., one obtains a spot of elevated brightness and large size. However, here one needs to bear in mind the scope for evaporation, since a large projection on the surface

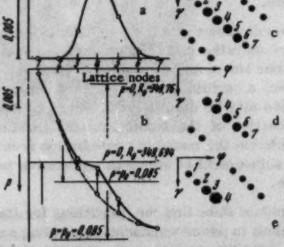

Fig. 3. Displacement of atoms from normal lattice nodes and changes in ion images due to a matrix atom in an octahedral hole.

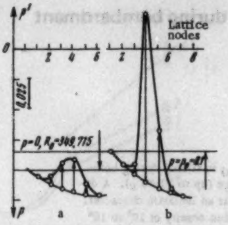

Fig. 4. Displacement of atoms from normal lattice nodes near a substitutional atom ($r_{su} > r_C$). Various effects can occur in accordance with the point radius R_0 and the distance of the atoms from the hemispherical section: 1) Atoms 3 and 4 (a) not seen for the clean metal (arrow at the center indicates the inner surface of the layer); 2) all atoms seen in both cases (a), but the impurity atom produces a hump that raised the intensity for two atoms (the arrow on the right indicates the outer surface of the layer); 3) the impurity atom produces field evaporation of matrix atom 4 (b), and the second effect corresponds to the image of Fig. 1c (arrow 1).

leads to a substantial local increase in the electric field over this atom.

An interesting result was obtained for these models when the bcc lattice had a proper lattice atom replaced by an impurity atom of much larger size [$(r - r_0) = 1.368$ Å, $C = (r_1 - r_0)r_0^2 = 2.739$ Å^3]. Figure 4b shows the results, where p' is the distance from the hemispherical surface outside the specimen, and p is the distance from this into the crystal; if p_0 is taken as 0.085, while $R_0 = 349.750$, then the result of substitution of a lattice atom under the (123) face leads to evaporation of atom 4 (Fig. 4b), i.e., production of a single vacancy on a completely cleaned and imaged face.

The above effects arise for crystals containing point defects and they represent a step towards more rigorous description of real cases; moreover, it is clear that even a simple model for an isotropic continuum leads to essential new details in the image. More rigorous consideration of the elastic characteristics of the crystal will make it possible to consider the effects on the image from sets of defects and also from anisotropy in the atomic displacements.

---

[1] E. W. Müller, Usp. Fiz. Nauk, 77, 481 (1962).

[2] E. W. Müller, and K. Bahadur, Phys. Rev., 102, 624 (1956).

[3] E. W. Müller, Usp. Fiz. Nauk, 92, 293 (1967).

[4] E. W. Müller, S. V. Krishnaswamy, and S. B. McLane, Surface Sci., 23, 112 (1970).

[5] A. J. W. Moore, J. Phys. Chem. Solids, 23, 907 (1962).

[6] F. McClintock and A. Argon, Deformation and Failure in Materials [Russian translation], Mir, Moscow (1970).

Change of the interplanar distances in deep layers of silicon during bombardment with medium-energy ions

G. I. Uspenskaya, V. M. Genkin, and D. I. Tetel'baum

Physicotechnical Research Institute, N. I. Lobachevskii Gor'kii State University

(Submitted May 27, 1971; resubmitted January 6, 1972 and March 21, 1972)
Kristallografiya, 18, 363-365 (March-April 1973)

A two-crystal spectrometer is used to find the change in the interplanar spacing $d_{(111)}$ in silicon during bombardment by argon and boron ions at depths up to many times the maximum ion range (up to 50-70 μ). A dependence of $(\Delta d/d)_{(111)}$ on the ion dose is found. It is shown that the deformation has an inelastic character. It has been established that the degree of deformation in the samples with a dislocation density of 10^3 to 10^4 cm^{-2} is greater than in low-dislocation samples.

It is known that the bombardment of silicon with ions of medium and high energies leads to great structural disruption (it can produce an amorphous structure) in the layer near the surface.[1-3] However, a change in the structure at depths exceeding the ion range (in the "sublayer") has hardly been studied. There are reports that the thickness of the disrupted layer can substantially exceed the ion range during bombardment of silicon by protons,[4] by nitrogen and boron ions at high energies,[5] and also diamond by lithium ions.[6] In contradiction to this, in ref. 7, where silicon was bombarded with nitrogen, boron, and phosphorus ions, it was concluded that no changes of structure occur beneath the amorphous layer (and consequently in the "sublayer" too).

The aim of the present work is to discover whether structural disruption leading to a change of interplanar spacings occurs in the "sublayer" of silicon during bombardment with medium energy ions and, if it arises, to study some of the features of this phenomenon.

EXPERIMENTAL METHOD

We used a two-crystal x-ray spectrometer[8] to detect changes in the interplanar spacing with parallel arrangements of the crystal monochromator and the sample to be studied. The rotation of the crystal as the measurements are carried out was done with a sine drive with micrometer actuation. The rotation angle was measured with an indicator, whose graduations (1 μ) corresponded to an angle of 0.5".

The method of measurement (the same as the method used in ref. 9) consisted of determining the position of the diffraction maximum during reflection of an x-ray beam (area 1.5 × 1 mm) alternately from two parts of the crystal, one of which is the investigated region and the other is the standard.[1)] The position of maximum reflection was established using a Geiger–Müller counter from the maximum counting rate. For the investigations we chose silicon crystals for which a rotation of not more than 0.5" from the position of the maximum led to a significant change of intensity. The measurements were done as follows. Using a screen fastened to the sample holder which overlaps the x-ray beam incident upon the upper (standard) part of the crystal, the sample is rotated to obtain the maximum counting rate. Then we cover the x-ray beam incident on the lower part of the crystal and again move the apparatus to the maximum and determine the rotation angle $\Delta\theta$ between the corresponding positions. Such a procedure was repeated not less than 10 times and the results averaged. The value of $\Delta\theta$ was determined for the very same parts of the crystal before irradiation and then after irradiation. Typical average values of $\Delta\theta$ before and after irradiation for five samples are given in Table 1. The nonzero $\Delta\theta$ before irradiation arises from the inhomogeneity of the initial samples.

The change in the Bragg angle resulting from the irradiation was determined from the formula $\delta\theta = \Delta\theta_1 - \Delta\theta$ where $\Delta\theta$ and $\Delta\theta_1$ are the displacements of the diffraction maxima before and after the irradiation respectively.

From the data obtained we calculated the change in the interplanar distance, $\Delta d/d = -\cot\theta\delta\theta$. The error in the determination of $\delta\theta$ arises in the first place from errors in fixing the reflection maximum and in the second place from a shift in the part of the sample struck by the x-ray beam during repeated positioning of the crystal (before and after irradiation). The mean-square error in the determination of $\Delta\theta$ due to the imprecise establishment of the maximum and the estimated scatter in the measurements amounts to 0.4" before irradiation and 0.5" after irradiation. The shift in the illuminated part of the sample during repeated setups did not exceed 0.5 mm. As shown by special measurements, upon scanning the x-ray beam over the sample before and after irradiation such a shift leads to an error of about 0.5". Thus the total mean-square error for $\delta\theta$ amounts to 1.3", while for $\Delta d/d$ it is $0.6 \cdot 10^{-5}$ for a (333) reflection and $2.6 \cdot 10^{-5}$ for the (111) reflection used.

The investigations were done with p-type silicon samples of grade KDB-20 with two dislocation densities N_d ($N_d \approx 10^2$ cm^{-2} and $N_d \approx 10^3$ cm^{-2}) cut from the (111) plane. The samples were lapped and polished with corundum powder and the disturbed layer removed by dynamic etching in a standard CP-4 etch. The ion irradiation was done in an accelerator with a magnetic analyzer at an ion en-

TABLE 1

Sample No.	$\overline{\Delta\theta'}$, before irradiation	$\overline{\Delta\theta''}$, after irradiation	$\overline{\delta\theta} = \overline{\Delta\theta_1} - \overline{\Delta\theta}$, "
1	1.5*	6.8	5.3
2	3.1	8.6	5.5
3	0.3	5.4	5.1
4	2.3	8.4	6.1
5	1.1	6.3	5.2

*Sample KDB-15 (111) with $N_d \leq 10^2$ to 10^3 cm^{-2} was irradiated with Ar^+; $D = 6.25 \cdot 10^{16}$ ion/cm², E = 50 keV.

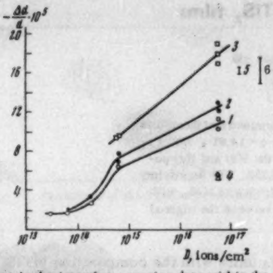

Fig. 1. Change in the interplanar spacing deep within the silicon as a function of the irradiation dose of argon and boron ions at 50 keV. 1) Ar$^+$, N$_d$ ≈ 10^2 cm^{-2}, (111) reflection; 2) Ar$^+$, N$_d$ ≈ 10^2 cm^{-2}, (333) reflection; 3) Ar$^+$, N$_d$ ≈ 10^3 to 10^4 cm^{-2} (111) reflection; 4) B$^+$, N$_d$ ≈ 10^2 cm^{-2}, (111) reflection; 5, 6) errors in the measurements for the (333) and (111) reflections, respectively.

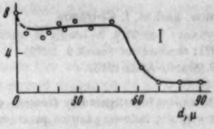

Fig. 2. $\delta\theta$ as a function of the thickness of the removed layer. The measurement error is shown to the right by a bar.

energy E = 50 keV and an ion current density of 5 μA/cm^2. The target was at room temperature during the irradiation.

RESULTS AND DISCUSSION

The experiments showed that ion bombardment with a sufficiently high dose shifts the (111) Bragg maximum toward increasing angle θ ($\Delta\theta > 0$), which corresponds to a decrease in the interplanar distance. The observed shift can arise not only from a change of d, but also from a rotation of the irradiated part of the crystal relative to the unirradiated part. In this case $\delta\theta$ should be the same for different orders of reflection.

Figure 1 shows the relative change in the interplanar distance $d_{(111)}$ as a function of the dose D when silicon is bombarded by argon ions for samples with different dislocation densities. The agreement (within the limits of measurement errors) of curves 1 and 2, which correspond to two orders of reflection, indicates a proportionality between $\delta\theta$ and tan θ [i.e., that the change of $\theta_{(111)}$ is due just to a decrease in $d_{(111)}$]. This figure shows the value of $\Delta d/d$ for low-dislocation samples irradiated with boron ions.

It should be noted that the diffraction pattern is nearly insensitive to the structure for a layer of thickness ≤ 1 μ (the "skin") in which the ions are stopped, since a layer of silicon with a thickness at least several microns participates in coherent scattering. Therefore the observed change in $d_{(111)}$ refers to the "sublayer."

In order to estimate the thickness of the disrupted layer we carried out successive etching of the sample, and determined $\delta\theta$ after each etch. Figure 2 shows the results for a low-dislocation sample irradiated with argon (D = 6.2 · 10^{16} ion/cm^2, E = 50 keV). It can be seen that $\delta\theta$ remains practically unchanged up to 50 μ and approaches zero after removing a layer of ~70 μ.

Since $\Delta d/d$ is nearly unchanged after etching off a layer of thickness 1 μ, the change in the interplanar distance cannot be ascribed to elastic deformation of the sublayer region under the action of a strongly disrupted (amorphous) surface layer. This phenomenon also cannot be explained as superdeep penetration of the implanted impurities since in this case one would expect that for argon and boron Δd would have opposite signs, i.e., compression for boron and expansion for argon.

The change in the interplanar distance evidently arises from penetration of radiation-produced defects into the "sublayer," for example vacancies, and trapping of them in this layer by formation of stable complexes. It is of interest that $(\Delta d/d)_{(111)}$ increases with increasing dislocation density (Fig. 1). The role of the latter must be explained by additional investigations.

[1)] By the position of the diffraction maximum we are to understand a position of the crystal for which with a given reflection we achieve the maximum intensity of the diffracted beam.

[1] D. J. Mazey, R. S. Nelson, and R. S. Barnes, Phil. Mag., 17, 150 (1968).
[2] A. I. Gerasimov, E. I. Zorin, P. V. Pavlov, and D. I. Tetel'baum, Dokl. Akad. Nauk SSSR, 192, 324 (1970) [Sov. Phys.–Dokl., 15, 430 (1970)].
[3] G. H. Schwuttke and K. Brack, Trans. Met. Soc. AIME, 245, No. 3 (1969).
[4] A. A. Autier and P. Lallemand, Compt. Rend., 255, 5 (1962).
[5] E. E. Gardner and G. H. Schwuttke, Bull. Am. Phys. Soc., 12, 1119 (1967).
[6] M. I. Guseva, L. M. Ershova, K. V. Kiseleva, V. V. Krasnopevtsev, and Yu. V. Milyutin, Kristallografiya, 15, 523 (1971) [Sov. Phys.–Crystallogr., 15, 441 (1970)].
[7] U. Bonse, M. Hart, and G. H. Schwuttke, Phys. Status Solidi, 33, 361 (1969).
[8] R. W. James, Optical Principles of the Diffraction of X Rays, Cornell (1948).
[9] R. Bubáková and Z. Szmid, Phys. Status Solidi, 8, No. 1, 93 (1965).

Electron-diffraction investigation of the structure of thin $InTlS_2$ films

K. A. Agaev, V. A. Gasymov, and M. I. Chiragov
Institute of Inorganic and Physical Chemistry, Academy of Sciences of the Azerbaidzhan SSR

(Submitted November 23, 1971; resubmitted March 9, 1972)
Kristallografiya, 18, 366-368 (March-April 1973)

The structure of thin $InTlS_2$ films was investigated by electron diffraction; it was determined that these films possessed a hexagonal lattice with the following lattice parameters: $a = 3.81 \pm 0.01$, $c = 14.91 \pm 0.02$ A. It was established that Tl occupies positions 1(*a*) and 1(d); In occupies the 2(i) and S the 2(h) and 2(g) positions in space group $P\bar{6}m2$ with the coordinates $z_{In} = 0.250$, $z_{S_1} = 0.167$, and $z_{S_2} = 0.333$. The uncertainty factor $R_{hkl} = 0.114$. The $InTlS_2$ structure is assigned to the structural class of the molybdenite MoS_2, with the difference being that in the case of the $InTlS_2$ the octahedra which are populated between the trigonal prisms prove to be occupied by trivalent indium.

The ternary chalcogenides of elements in groups II and III of the periodic system have been the objects of many investigations, in particular, electron-diffraction and X-ray investigations.[1] This paper is devoted to the electron-diffraction determination of the atomic structure of thin $InTlS_2$ films. It was established that the $InTlS_2$ structure differs from the structure of similar chalcogenides, which have been investigated by x-ray diffraction.[1]

We tested celluloid films and sodium chloride single crystals as a substrate for the vaporization of $InTlS_2$. The investigations showed that it was expedient to use sodium chloride substrates to obtain grain-oriented films of this compound, because celluloid films do not withstand the temperature necessary for the orientation of this film. The thin $InTlS_2$ films were prepared in vacuo at 10^{-5} mm Hg on a NaCl single crystal which was preliminarily annealed (10 min, T = 100°C). Then the films were aged for 4 h with heating to 250°C. This process yielded well-textured films suitable for the electron-diffraction investigation.

The indexing of the electron-diffraction pattern of the oblique-type texture was carried out on the basis of a hexagonal cell with the constants $a = 3.81 \pm 0.01$, $c = 14.91 \pm 0.02$ Å. The crystals were oriented with the basal face parallel to the plane of the substrate, i.e., the axis of texture enters into c. It should be mentioned that the powder pattern of $InTlS_2$ that was run was also indexed on the basis of the cell established by the electro-diffraction pattern of the oblique-type texture. The analysis of the electron-diffraction pattern showed that no systematic extinctions of the reflection are observed.

The intensities of the reflections located on the zero layer line were determined microphotometrically; the other reflections were evaluated visually by comparing them with the intensities of the hk0 reflections. The conversion from intensities to structural factors was accomplished through the kinematic scattering equations.[2]

About 80 reflections, the majority of which belonged to the h0*l* zone, were recorded in the electron-diffraction pattern of the oblique texture. For this reason, the analysis of the structure begins with plotting the projection of the interatomic vectors P(uw). The arrangement of the peaks on this projection showed that the x coordinates (and, consequently, the y coordinates too) of the atoms can only be multiples of 1/3 of the overall values of the z coordinates.

The dimensions of the unit cell and atoms which enter into the compound investigated permit one to arrange two formula units with the composition $InTlS_2$ in this cell, which agrees with the data that were obtained from the Patterson projection of P(uw). We selected four variations of the arrangement of the atoms, which satisfy the experimental projection of the interatomic vector function, for further analysis:

	A_1	B_1	C_1	A_2	B_2	A_2	C_2	B_2	A_1
1.	In	S	Tl	S	In	S	Tl	S	In
2.	Tl	S	In	S	Tl	S	In	S	Tl
3.	S	Tl	S	In	S	In	S	Tl	S
4.	S	In	S	Tl	S	Tl	S	In	S

In the other cases, either the nonmetallic atoms are arranged in succession or their respective packings are divided into two parts, indium and thallium, which is unlikely. A variation of the statistical arrangement of the metal atoms which we did not check out is also possible.

It was determined to a first approximation that the distances $A_1B_1 = A_2B_2 = 3.32$ and $B_1C_1 = C_1A_2 = 2.53$ Å from the projection of the interatomic vectors P(uw). Upon comparing these distances with the radii of the atoms entering into the structure, preference to the second of the four variations indicated can be given, i.e.,

Tl	S	In	S	Tl	S	In	S	Tl
a	*B*	*c*	*A*	*b*	*A*	*c*	*B*	*a*

We mentioned above the absence of any systematic extinctions of reflections in the electron-diffraction pattern. This leads to several allowable symmetry groups for the structure. However, the interpretation of the projection of the interatomic vector function made it possible to reduce the list of the possible symmetry groups to four: two trigonal ones P312, P3m1, and two hexagonal ones $P\bar{6}$ and $P\bar{6}m2$. The discrepancy factors R were calculated within the framework of each of these groups in order to obtain a model of the structure. The smallest value $R_{h0l} = 0.125$ proved to be for space group $P\bar{6}m2$. The discrepancy factor over all the experimental reflections R_{hkl} was 0.114. The projection of the Fourier potential $\varphi(xz)$ of the structure we investigated is shown in Fig. 1. The atoms within the framework of space group $P\bar{6}m2$ occupy the following positions:

1 Tl — 1 (*a*)	$\bar{6}$ *m*2	0	0	0
1 Tl — 1 (*d*)	$\bar{6}$ *m*2	$^1/_3$	$^2/_3$	$^1/_2$
2 In — 2 (*i*)	3 *m*	$^2/_3$	$^1/_3$	$\pm z_1$
2 S — 2 (*h*)	3 *m*	$^1/_3$	$^2/_3$	$\pm z_2$
2 S — 2 (*g*)	3 *m*	0	0	$\pm z_3$

where $z_1 = 0.250$, $z_2 = 0.167$, and $z_3 = 0.333$.

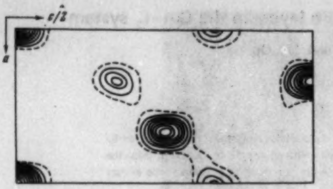

Fig. 1. Projection of the Fourier potential $\varphi(xz)$.

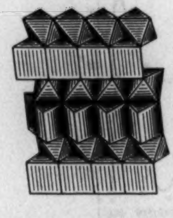

Fig. 2. Structure of $InTlS_2$.

The principal interatomic distances in the structure are: $Tl-S = 3.32$ Å; $In-S = 2.53$ Å; and $S-S = 3.32$–4.97 Å. It should be mentioned that both metal atoms are hexacoordinated. However, the polyhedra of these elements differ from each other in shape and dimensions: The Tl atoms exist within a trigonal prism (the sides of the base equal period a of the cell, and the height is 4.97 Å): In exists within a distorted octahedron (the sides of the octahedron are 3.31 Å and that of the translation a). Thus, the prism is elongated and the octahedron is compressed.

It is interesting to compare the interatomic distances obtained with known distances and the various radii of Tl, In, and S. The sums[3] of the ionic radii $Tl^{1+} + S^{2-} = 3.24$; $In^{3+} + S^{2-} = 2.65$; $S^{2-} + S^{2-} = 3.68$ Å are in accordance with the shortest distances we obtained. However, the observed distance of 2.53 Å for (In−S) is closest to the value of the sum of the covalent radii 2.46 Å (In + S) than the sum of their ionic radii (2.65 Å). Therefore, it can be assumed that the chemical bond in the $InTlS_2$ structure is ionic, in character with part of it being covalent in composition.

The $InTlS_2$ structure (Fig. 2) can be assigned to the molybdenite structure type.[4] The Mo atoms (small letters) in the MoS_2 structure ($a = 3.15$, $c = 12.30$ Å; $c/a = 3.81$; space group $P6_3/mmc$; |AbABaB|Ab ...) exist within the trigonal prisms, and the octahedra located between these prisms prove to be vacant. The trigonal prisms in the $InTlS_2$ structure are filled with Tl atoms and the octahedra with In atoms. A four-layer anionic packing lies at the basis of both structures.

All the calculations carried out during the interpretation of the structure were performed on the computer at the Institute of Cybernetics, Academy of Sciences of the Azerbaidzhan SSR.

---

[1] A. S. Avilov, K. A. Agaev, G. G. Guseinov, and R. M. Imamov, Kristallografiya, 14, 443 (1969) [Sov. Phys.–Crystallogr., 14, 364 (1969)].

[2] B. K. Vainshtein, Structural Electron-Diffraction Analysis [in Russian], Izd. Akad. Nauk SSSR, Moscow (1956).

[3] J. Chem. Ed., 9, 41 (1964).

[4] G. B. Bokii, Symposium: Crystal structure of arsenides, sulfides, arsenosulfides, and their analogs, Editorial Department, Siberian Branch, Academy of Sciences of the USSR, Novosibirsk (1964).

Anisotropy of growth and alloying for epitaxial germanium layers in the Ge$-$I$_2$ system

L. G. Lavrent'eva, I. S. Zakharov, I. V. Ivonin, N. P. Kolodeshnikova, and T. I. Opryshko

Siberian Physicotechnical Institute

(Submitted March 27, 1972)
Kristallografiya, 18, 369-373 (March-April 1973)

This article considers the anisotropy of growth rate and alloying conditions for autoepitaxial germanium in the Ge$-$I$_2$ system. It is shown that the degree of growth-discontinuity coagulation increases with the angle of deviation from the (111) and (100) faces. Formation of bounded growth discontinuities accompanied by a reduction in growth rate occurs at large angular deviations.

Little research has been done on anisotropy of growth and alloying in germanium during growth in vapor-transport systems. We know of only two studies[1,2] which dealt with anisotropy of growth and alloying for germanium iodide over the base-orientation range (111)$-$(100). A noticeable change in these quantities was observed over the orientation range in question. The results were explained on the basis of the Barton$-$Cabrera$-$Frank$-$Chernov model; it was necessary to assume that the efficiency of adsorbed-atom inflow to a discontinuity (jog) changes materially on making the transition from vicinal (0-10°) to diffusion (>10°) planes. We felt it necessary to consider the anisotropy of the growth rate of germanium at approximately the same crystallization temperatures in a system differing from that employed previously in the fact that it was possible to evaluate the generality of the observed patterns. For this purpose, we investigated the anisotropy of growth and alloying for germanium in the Ge$-$I$_2$ system.

EXPERIMENTAL METHOD

Autoepitaxial germanium films were grown in a closed iodide system containing iodine. The source temperature was 600°C, the base temperature was 400°C, the iodine concentration was 0.6 mg/cm^3, and the crystallization time was 4 h. The substrates were plates of single-crystal germanium (40 $\Omega \cdot$ cm), whose orientation was checked by x-ray diffraction analysis. The predetermined deviations from the (111) plane toward the (100) plane were 0, 2, 4, 10, 19.5, 29.5, 39, 45, 48, 52, and 54.7°. The substrates subjected to mechanical and chemical (in CP-4A for 2 min) polishing and gaseous-phase etching for 1.5 min. The source was p-type Ge ($7 \cdot 10^{-3}$ $\Omega \cdot$ cm).

We determined the growth rate (the film thickness was measured in fractured specimens) and degree of alloying (Hall effect and electrical conductivity) of the resultant specimens and studied their morphology by optical and electron microscopy. In the latter case, we employed carbon replicas preliminarily shadowed with platinum (with a shadowing angle of 15°). The resolving power of this method, with respect to relief height, was 20 Å.

ANISOTROPY OF GROWTH RATE AND ALLOYING LEVEL

Figure 1, curve 1, shows the growth rate as a function of orientation over the range investigated. It can be seen that the singular faces have the lowest growth rate. A deviation from these faces leads to an increase in growth rate, but there is a subsequent drop when the angular deviation is more than 10° and a deep minimum occurs in this factor in the vicinity of the (311) plane. The minimum alloying level (Fig. 1, curve 2) corresponds to the singular (111) and (100) faces. The impurity concentration increases with the deviation from these faces and there is a minimum in the alloying level near the (311) plane. The anisotropy of the growth rate and that of the degree of alloying are consequently similar.

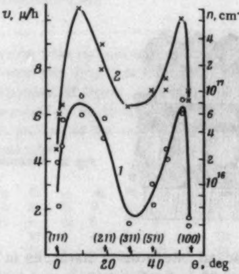

Fig. 1. Growth rate (1) and electron concentration in layer (2) as functions of base orientation.

If we compare the anisotropy of the growth rate for Ge in the Ge$-$HI$-$H$_2$ system[1,2] and in the Ge$-$I system, a noticeable difference can be seen. In the first case, the singular faces exhibit the maximum growth rate and the rate decreases with the deviation from them. Conversely, the growth rate increases with the angular deviation from the (111) and (100) faces in the latter case. The (311) planes correspond to the maximum growth rate in the first case and the minimum in the second. However, despite this qualitatively large difference in the form of the growth-rate curves, there is also something in common between them. If we assume that the growth of layers with nonsingular orientations is due in both cases to movement of jogs introduced by deviations from the (111) and (100) planes, it should be noted that there are some obstacles to movement of jogs in planes of the (h11) type. The Ge$-$HI$-$H$_2$ system also has obstacles to movement of jogs, causing a decrease in growth rate; these develop at small deviations from the (111) and (100) planes. At large deviations, they are to some extent compensated for by the high density of the jogs introduced, which leads to an increase in growth rate in the center of the crystallographic range. The growth rate in the Ge$-$I$_2$ system increases at small angles, in accordance with predictions following from the laminar-growth model; however, growth slows down when a certain angle (~5°) is reached and there is then an abrupt drop despite the fact that the angular deviation increases. The jogs introduced by this deviation obviously have little effect on growth. It should be noted that a similar phenomenon has been observed for GaAs

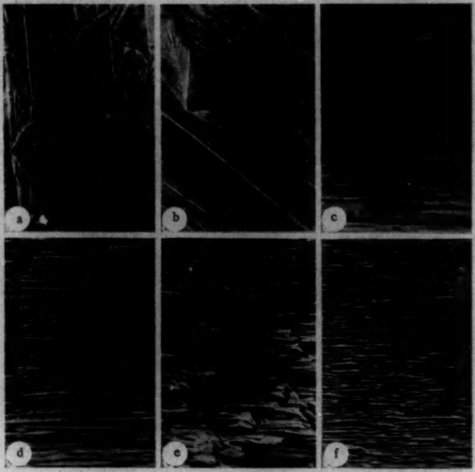

Fig. 2. Surface morphology of germanium layers with the following orientations: (×40); a) (111); b) 4°; c) 10°; d) (211); e) (311); f) (511).

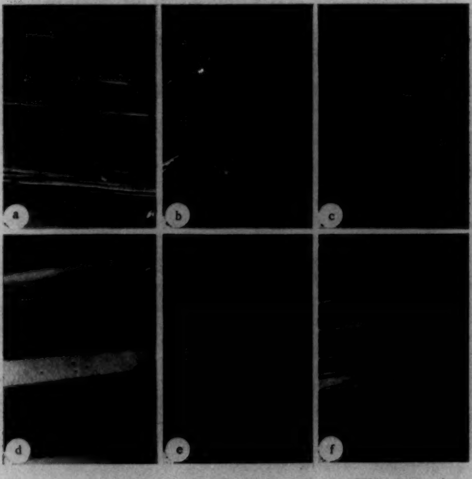

Fig. 3. Micromorphology of surface of germanium layers, ×7500. Orientations: a) (111); b) 4°; c) 10°; d) (211); e) (311); f) deviating from (211).

in the GaAs–$ZnCl_2$ system.[3] Its causes have not yet been established but it is assumed to be due to rearrangement of the surface as the angle θ increases. One factor responsible for this rearrangement may be the influence of impurities. In order to determine the validity of the surface-reorganization hypothesis, we conducted studies of surface morphology by optical and electron microscopy.

LAYER MORPHOLOGY

The phenomena observed when there are deviations from the (111) and (100) planes toward the (311) plane are qualitatively similar and we will therefore give data only for the (111)-(311) range.

Figure 2 shows the layer morphology observed at low magnifications by optical microscopy. A surface covered with vicinal pyramids of appropriate symmetry corresponds to the main faces. The pyramids are deformed in the presence of deviations and then disappear entirely when $\theta > 4°$. The surface is covered with parallel jogs. The size of the jogs varies somewhat with the deviation angle. Specifically, the jog height increases sharply as we move toward the (311) plane and the relief becomes far more discontinuous; the jog height then decreases once more.

The micromorphology (observed with the electron microscope) illustrates the same pattern of changes in the discontinuity system, but it is possible to see certain very important details related to the jog-rearrangement mechanism. As an illustration, we will consider the phenomena occurring in the (111)-(311) range.

The (111) plane exhibits almost no growth discontinuities, except for groups of figures clearly showing aggregates of jogs (kinematic waves, Fig. 3a). Similar aggregates are also present in two-degree specimens, although numerous small parallel jogs are visible on the main surface here. The size of the aggregates is greater in four-degree specimens (Fig. 3b). In ten-degree specimens, these aggregates (bundles) alternate with broad areas without visible jogs. Each "bundle" clearly shows a tendency toward enlargement of the jogs and appearance of faceting (Fig. 3c). Coagulation of jogs in the (211) plane leads to formation of elevated well-faceted jogs composed of (111) and (100) discontinuities, although "bundles" are also present (Fig. 3d). The highest best-faceted jogs are formed in the (311) plane. In direct proximity to the ribs of the large jogs are aggregates of small jogs (Fig. 3e). These jogs may attach to the large jog as the growth time increases. It is interesting to note that it is possible to observe very small jogs in the transverse direction at the ends of large jogs bounded by the (100) plane in some cases (Fig. 3e), which indicates that growth of such jogs can occur by movement over the surface of small jogs in both possible directions of the ⟨110⟩ type.

The following feature, which we feel to be important, should also be noted. If, in addition to the known angular deviation θ from the (111) plane toward the (100) plane, the specimen surface also has a small "lateral" deviation [i.e., toward the (010) plane], the jog coagulation is substantially weaker or totally absent. Where such a lateral disorientation occurs, e.g., at the edge of the specimen, the large jogs break up into smaller ones, as is illustrated in Fig. 3f for a specimen with the initial (211) orientation. The larger the lateral deviation, the more severe is this decomposition, i.e., there is a transition to a diffuse boundary. However, the laminar structure of such a surface is readily seen with small lateral deviations. The appearance of very small transverse jogs at the ends of the large jogs (Fig. 3e) is a sign of incipient decomposition produced by the very small lateral deviation that is hard to avoid in actually preparing a base for experimentation.

Thus, the data given above on surface morphology indicate that there is a material rearrangement of the superficial laminar structure when the angular deviation from a singular face increases. Slight deviations from a singular face lead to development of a surface with fine jogs, which efficiently utilizes the inflow of material, a phenomenon leading to a large increase in the growth rate. The jog coagulation is slight in this case. An increase in the deviation from a singular face leads to development of coagulation, to formation first of aggregated and then of faceted, i.e., "true" (in Chernov's terminology[4]) jogs, and to an increase in their size. This process is obviously advantageous in terms of energy, its basic "motive force" being the increase in superficial energy. This is supported by the fact that large jogs are unstable in the presence of lateral disorientation. The formation of a faceted jogs is accompanied by an abrupt decrease in the layer growth rate. It can be assumed that growth of a surface covered with large faceted jogs can occur by emergence of small jogs, as was observed by Chernov and Dukova[5] and by Lemmlein and Dukova.[6] The emission of such a jog requires a certain energy to break it free from the larger jog. In view of the fact that enlargement of the jogs leads to a decrease in the density of reentrant angles, which are the main sources of jogs, it can be assumed that the abrupt decrease in the growth rate over the range of θ from 20 to 40° is due to the small density of jogs, these being the principal collection points for adsorbed atoms.

Our data thus provide experimental confirmation of the hypothesis[4] that growth discontinuities of two types exist at the surface of growing crystals and that they undergo relative rearrangement under definite conditions.

Similar rearrangements of the jog system can occur in different ways in different crystallization systems. The temperature, alloying material, and type of transport agent can have a substantial influence on the process rate. In this connection, it can be assumed that the difference in the anisotropy of the growth rate of germanium in open and closed systems may be due to a difference in the rate of jog coagulation. Additional research should show whether this hypothesis is valid.

The observed dependence of the alloying level on the orientation, taking into account the surface structure under consideration, shows that the impurity atoms at the surface have low mobility and that their capture is governed by the growth-discontinuity density. It is possible that this is a manifestation of the individual characteristics of the impurity (gallium) in combination with the crystallization conditions (iodine in the system and a low crystallization temperature). The possible influence of an impurity with low mobility on jog coagulation requires detailed study.

The authors wish to thank A. A. Chernov for his helpful advice and L. M. Krasil'nikov and M. P. Yakuben' for their help in conducting the electron-microscope and x-ray diffraction studies.

---

[1] L. G. Lavrent'eva, I. S. Zakharov, and Yu. M. Rumyantsev, Kristallografiya, 15, 854 (1970) [Sov. Phys. – Crystallogr., 15, 744 (1971)].

[2] L. G. Lavrent'eva, I. S. Zakharov, and Yu. M. Rumyantsev, Kristallografiya, 16, 423 (1971) [Sov. Phys. – Crystallogr., 16, 348 (1971)].

[3] L. G. Lavrent'eva, L. G. Nesteryuk, and V. Sennikova, Izv. Vyssh. Ucheb. Zaved., Fiz., No. 6, 112 (1972).

[4] A. A. Chernov, Usp. Fiz. Nauk, 73, 277 (1961) [Sov. Phys. – Usp., 4, 116 (1961)].

[5] A. A. Chernov and E. D. Dukova, Kristallografiya, 5, 655 (1960) [Sov. Phys. – Crystallogr., 5, 627 (1961)].

[6] G. G. Lemmlein and E. D. Dukova, Kristallografiya, 1, 112 (1956) [Sov. Phys. – Crystallogr., 1, 84 (1956)].

Transport of boron from a source to an epitaxial layer during sublimation of silicon in vacuum

R. G. Loginova, R. A. Rubtsova, and M. I. Ovsyannikov
Gor'kii Research Physicotechnical Institute

(Submitted October 28, 1971; resubmitted April 3, 1972)
Kristallografiya, 18, 374-376 (March-April 1973)

The authors describe an experimental investigation of the transport coefficient of boron from boron-doped silicon sources to epitaxial silicon layers during sublimation in vacuum. They solve the diffusion equation, taking account of interactions of boron atoms on the surface of the source; the experimental values of the transport coefficient q lie closely on the theoretical graph of q vs boron concentration in the source, plotted by solving this equation.

In ref. 1 we showed that the steady-state transport coefficient of boron from strongly doped silicon sources into epitaxial layers grown by sublimation in vacuum is lower than unity, in contrast to that for sources with low boron concentrations.

In this article we give data on the transport of boron from sources with concentrations between $2.8 \cdot 10^{15}$ and $7 \cdot 10^{19}$ cm^{-3}. The boron concentrations in the sources and epitaxial layers were assumed to be equal to the hole concentrations, found by means of probe measurements of the Hall constant.

Figure 1 plots the steady-state transport coefficient q of boron vs the initial concentration N_∞ in the source. We see that $q < 1$ when $N_\infty > 2 \cdot 10^{18}$ cm^{-3}. This graph does not correspond to the predictions of the theory in ref. 2. We are of the opinion that the experimental results can be explained if we assume that diatomic or more complex boron molecules can be formed, together with chemical compounds involving silicon,[3] when the boron concentration in the source is high.

Let us calculate the transport coefficient, assuming the formation of diatomic molecules and a decrease in the flow of atomic boron, and consequently a fall in the concentration of electrically active boron in the epitaxial layer. We shall assume the flow of boron atoms to be proportional to their surface concentration in the source, which can be found by solving the equation of diffusion for a specimen with moving boundaries. For simplicity we shall consider the one-dimensional problem for a half-bounded specimen and a steady-state process.

Interaction of the atoms will occur mainly at the surface, in view of the large surface mobility of the atoms in comparison with the bulk mobility. The number of atoms associating in unit time is proportional to the concentration of atoms at the surface and the flow of atoms to the surface. The resultant flow of atoms to the surface is equal to the difference between two flows: accumulation due to evaporation of silicon, and diffusion within the crystal.

We shall take the origin at the moving boundary and the axis of abscissas along the interior normal to the specimen surface. After conversion to a system moving with the boundary, the equation of diffusion for a steady process becomes[2]

$$D\frac{d^2N}{dx^2}+v\frac{dN}{dx}=0 \tag{1}$$

with the following boundary and initial conditions:

$$D\frac{dN}{dx}=(k-v)N+\alpha\left(D\frac{dN}{dx}+vN\right)N \quad \text{at} \quad x=0, \tag{2}$$

and

$$N\to N_\infty \quad \text{as} \quad x\to\infty. \tag{3}$$

Here D is the coefficient of diffusion of boron in silicon, N is the volumetric concentration of boron, N_∞ is the initial (before evaporation) uniform volumetric concentration of boron, k and v are the rates of evaporation of boron and silicon respectively, and α is a coefficient independent of the concentration and characterizing the interaction of boron atoms leading to association in diatomic molecules.

Solving Eq. (1) with the aid of (2) and (3), we find the concentration distribution:

$$N(x)=N_\infty\left[1+\frac{v(1-\alpha N_\infty)-k}{k+\alpha vN_\infty}\exp\left(-\frac{vx}{D}\right)\right]. \tag{4}$$

Hence the volumetric concentration at the surface is

$$N(0)=vN_\infty/(k+\alpha vN_\infty). \tag{5}$$

When $N_\infty \to \infty$, $N(0) \to 1/\alpha$, i.e., α is the mean limiting volume belonging to one atom of boron in silicon. The density of the flow of boron atoms, $W = kN(0)$, from the silicon surface will be

$$W=kvN_\infty/(k+\alpha vN_\infty). \tag{6}$$

Assuming that the transport of boron is independent of the substrate temperature, and neglecting the influence of diffusion on the distribution of impurity at sufficient low substrate temperature, for the boron concentration in the layer we get

$$N_{\text{lay}}=kN_\infty/(k+\alpha vN_\infty). \tag{7}$$

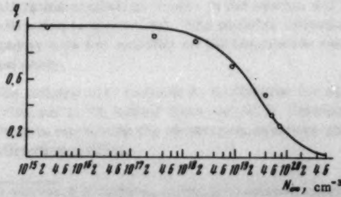

Fig. 1. Transport coefficient of boron vs initial boron concentration in source.

For the transport coefficient $q = N_{\mathrm{lay}}/N_\infty$, by (7) we have

$$q = k / (k + \alpha v N_\infty). \tag{8}$$

Hence $q \simeq 1$ at low values of N_∞ ($N_\infty \ll k/v\alpha$); q tends to a limiting value less than unity when $N_\infty \to N_{\infty\,\mathrm{lay}}$ (where $N_{\infty\,\mathrm{lay}}$ is the limit of the solubility of boron in silicon).

In Fig. 1 the solid curve plots $q(N_\infty)$, calculated from Eq. (8). (The value of $v\alpha/k = 3 \cdot 10^{-20}$ cm^3 was first found from the graph of $1/q$ vs N_∞.) Within the error of measurement the experimental data agree fairly well with the theoretical curve.

If we take[3] $N_{\infty\,\mathrm{lay}} \sim 6 \cdot 10^{20}$ cm^{-3} for a source temperature of 1380°C, then for the limiting value of the transport coefficient we get $q_{\mathrm{lim}} \sim 5 \cdot 10^{-2}$, and the limiting concentration of boron in the layer is about $3 \cdot 10^{19}$ cm^{-3}.

Metallographic examinations of the surfaces of silicon sources before and after evaporation revealed that a large number of pyramidal formations appear on the surfaces of strongly boron-doped sources after evaporation for several hours. The density of these formations reaches 10^5 cm^{-2}. Reflection electron diffraction patterns showed that a polycrystalline silicon structure appears on the surface of the single crystals. We can suppose that the morphological changes on the surfaces of such sources and the structural changes are due to the formation of inclusions of a second phase which may consist of complexes of atoms and chemical compounds of boron. However, the insufficient sensitivity of the electron diffraction method does not permit us to detect chemical compounds of boron.

It is of interest to estimate the activation energy of desorption of boron from the silicon surface. For this purpose we performed the following experiments. Silicon sources, boron-doped to a level of $4 \cdot 10^{19}$ cm^{-3}, were kept in vacuum at 1380°C (residual gas pressure $< 2 \cdot 10^{-7}$ mm) for at least 6 h. Then the source temperature was rapidly reduced to a given value and an epitaxial layer growth at this source temperature. We assumed that the surface boron concentration did not alter beyond the experimental error during the evaporation time, since it was close to the limit of solubility, which is nearly independent of the temperature in the range in question.[3] In this case, the boron concentration in the layers will be proportional to k/v and will depend exponentially on the source temperature in conformity with the temperature dependence of this ratio.

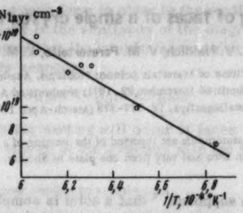

Fig. 2. Boron concentrations in layers vs source temperature.

Figure 2 is a semilogarithmic graph of N_{lay} vs the reciprocal of the absolute temperature. The proposed exponential dependence is satisfactorily obeyed. From the slope of the line we can find the activation energy of the process of transport of boron (26 kcal/g-atom). This energy must be equal to the difference between the activation energy of desorption of boron from the silicon surface and the heat of sublimation of silicon. If for the latter we assume the value[4] 111 kcal/g-atom, then the activation energy of desorption of boron is found to be 137 kcal/g-atom, which is quite realistic, as it is close to the heat of sublimation of boron which is[4] 130 kcal/g-atom.

We thank Yu. A. Romanov for his continual interest in our work and for helpful advice, T. N. Strizheva for recording the electron diffraction patterns, and N. N. Timina for helping in the work.

---

[1] M. I. Ovsyannikov, R. G. Loginova, and R. A. Rubtsova, Kristallografiya, 15, 1261 (1970) [Sov. Phys. – Crystallogr., 15, 1105 (1971)].

[2] V. P. Kuznetsov, R. G. Loginova, M. I. Ovsyannikov, and V. V. Postnikov, in: Growth Processes and Structure of Single-Crystal Layers of Semiconductors [in Russian], Nauka, Novosibirsk (1968), Sec. 1, p. 483.

[3] V. M. Glazov and V. S. Zemskov, Physicochemical Principles of Semiconductor Doping [in Russian], Nauka, Moscow (1967).

[4] V. I. Vedeneev, L. V. Gurvich, V. N. Kondrat'ev, V. M. Medvedev, and E. L. Frankevich, Handbook: The Rupture Energies of Chemical Bonds – Ionization Potentials and Electron Affinities [in Russian], Izd. AN SSSR, Moscow (1962).

Wetting of faces of a single crystal in a melt

Yu. V. Naidich, V. M. Perevertailo, É. M. Lebovich, and L. P. Obushchak

Institute of Materials Science Problems, Academy of Sciences of the Ukrainian SSR

(Submitted November 22, 1971; resubmitted April 11, 1972)
Kristallografiya, 18, 377-379 (March-April 1973)

Measurements are reported of the wetting of a salol crystal by its own melt; the contact angles are different from zero and vary from one plate to another.

It is often supposed[1-4] that a solid is completely wetted by its own melt; observations on solidification of liquids (menthol and salol) indicated[5] that the solid was highly wetted by the melt, and theoretical estimates[6] indicated a positive wetting coefficient.

On the other hand, there are some qualitative observations that some solids such as[7] Mg and Ga or[8,9] Cd are only incompletely wetted by their melts. There are a few recent quantitative studies, which also reveal a finite angle of contact in such cases: some organic substances,[10-13] ice,[14,15] and cadmium.[16] These results were for polycrystalline solids, with the liquid flowing over the surface; no allowance was made for possible hysteresis. In some cases the observations were made by indirect methods.

Here we consider the wetting in such a system with the liquid flowing off the solid surface; the angles of contact under such conditions are not zero, which indicates incomplete wetting. The experiments were done below the phase transition point, which eliminated effects from melting of the solid in response to temperature fluctuations. On the other hand, the supercooling was minimal. The purpose was to examine the wetting for various crystallographic faces of a single crystal; so far as we are aware, no such study has been published. We chose salol (phenyl salicate) as being convenient because the melt is transparent and the melting point is 41.5°C, while the entropy of melting is high, i.e., there is an appreciable difference in the properties of the solid and liquid phases. The material was of chemically pure grade.

The single crystals were grown by the method of ref. 17, the device consisting of a chamber fitted with double walls, between which there circulated distilled water supplied by a thermostat. This chamber had windows for observation of the growing crystal, as well as photography and measurement of contact angles by projection.

The melt temperature was 41°C, which is 0.5° below the melting point. At such supercooling, a salol crystal grows as a polyhedron with prominent (001), (111), and (110) faces, which were examined for wetting. The experiments were thus done under conditions for crystal growth, but at very low rates (less than 0.01 mm/min), so the face growth during a measurement, which lasted about a minute, was absolutely negligible, and this could not distort the results.

First we produced a small crystal, which was then used as a seed for growing a crystal with a horizontally oriented set crystallographic plane. This crystal had attained a size of 1-1.5 cm; a levelling device was used with table screws attached to the chamber to bring the required plane to the horizontal position. An argon bubble was inserted with a pipette under this face in the melt; a typical photograph is shown in Fig. 1.

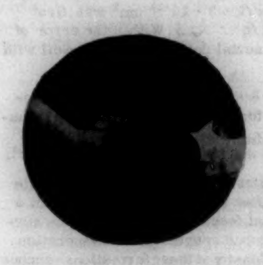

Fig. 1. Argon bubble under the (110) plane of salol crystal growing from the melt.

Under the argon bubble one obtained a dry face, as can be shown from the fact that the bubble was incorporated by growth into the crystal (this incorporation would not occur if there were a layer of melt between the bubble and the surface of the face). Formation of a dry face can also be observed in experiments of another type, which we also did to determine the contact angle. The oriented face is lifted above the melt and the residual melt left on the surface rapidly collected into a drop with a finite contact angle, leaving a dry surface behind. The contact angle was also measured by photoprojection in this case. The results for the contact angles (in the latter case the gas was air) agree well with the previous measurements. Table 1 gives the results on the wetting of the salol faces; we use these angles with Young's equation

$$W_A = \sigma_{\mathrm{liq}}(1 + \cos\theta) \qquad (1)$$

to determine the work of adhesion of salol to each face of the crystal (the surface tension of liquid salol at 41°C was taken[10] as 42.1 ergs/cm^2:) $W_{A(001)} = 82$, $W_{A(111)} = 80$, $W_{A(110)} = 78$ ergs/cm^2. The flow coefficient is defined as $K = W_A - W_K$, where W_K is the work of cohesion of the liquid, which equals $2\sigma_{\mathrm{liq}}$, and was $K_{(001)} = -2$, $K_{(111)} = -4$, $K_{(110)} = -6$ ergs/cm^2.

Table 1 shows that the contact angles were different from zero for all faces, and that the wetting of the various faces varied (Fig. 2).

The contact angles, work of adhesion, and flow coefficients run in the sequence

$$\theta_{(001)} < \theta_{(111)} < \theta_{(110)}, \qquad (2)$$

$$W_{A(001)} > W_{A(111)} > W_{A(110)}, \qquad (3)$$

$$K_{(001)} < K_{(111)} < K_{(110)}. \qquad (4)$$

The following relationship applies for the face growth rates on the basis of the lattice structure and the shape of the crystal:1)

$$V_{(001)} < V_{(111)} < V_{(110)} \ . \qquad (5)$$

TABLE 1. Wetting of Salol Crystal Faces by Melt

No.	(001), θ,deg	(111), θ,deg	(110), θ,deg
1	19.5	26	31
2	20.5	25	30
3	18.0	26	30
4	20.0	25,5	31
5	19.0	26	31
6	18.0	26,5	31
7	18.5	25	31.5
8	21.0*	26	31.5
9	19.0*	25	30
10	19.0*	24	31.5
11	21.0	25	31
Mean	19±1	25±1	31±1

*θ was measured on removing the crystal from the melt.

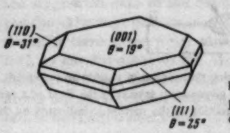

Fig. 2. Salol single crystal showing planes the wetting of which has been examined.

From (2)-(5) it follows that faces growing at the lowest rates are better wetted by the melt (mineral contact angle, high work of adhesion): Fast-growing faces are less well wetted (larger contact angles, lower work of adhesion). The faces we examined are evidently G faces, which belong to the equilibrium form; the growth-rate relationship of (5) and the corresponding growth forms (rhombic plates) persist approximately for microscopic salol crystals growing at very small supercoolings and minimal rates (less than 10^{-5} mm/min), when one can assume that the growth form is close to the equilibrium form[18] on account of the similarity of the diagrams. Wulff's theorem indicates that the interfacial energies of these faces run in the sequence

$$\sigma_{sl(001)} < \sigma_{sl(111)} < \sigma_{sl(110)} \qquad (6)$$

and then the better wetting will occur at faces with a lower interfacial energy at the boundary with the melt.

---

1) Relation (5) has been verified by experiment.

[1] G. Tammann, Z. Phys. Chem., 68, 205 (1910).

[2] A. S. Skapski, Acta Metallurg., 4, 576 (1956).

[3] A. S. Skapski, R. Phillips, and A. Rooney, J. Chem. Phys., 26, No. 5, 1350 (1957).

[4] C. Jackson, D. Uhlman, and J. Hunt, in: Crystal Growth Problems [Russian translation], Mir, Moscow (1968), p. 27.

[5] Ya. E. Geguzin and N. N. Ovcharenko, Surface Diffusion and Flow [in Russian], Nauka, Moscow (1969), p. 201.

[6] B. Ya. Pines, Zh. Tekh. Fiz., 22, 1985 (1952).

[7] M. Volmer and O. Schmidt, Z. Phys. Chem., 35, 467 (1937).

[8] I. N. Stranski and E. K. Paped, Z. Phys. Chem., 38, 451 (1938).

[9] I. N. Stranski, Ber. Dtsch. Chem. Ges., 72, 141 (1939).

[10] S. N. Zadumkin, M. P. Dokhov, and A. A. Karashaev, Dokl. Akad. Nauk SSSR, 189, 797 (1969).

[11] F. K. Gorskii, in: Liquid Crystallization [in Russian], Izd. VSSO Profobraz. BSSR, Minsk (1963).

[12] F. K. Gorskii and N. M. Sakevich, Kristallografiya, 12, 674 (1967) [Sov. Phys.—Crystallogr., 12, 586 (1968)].

[13] A. S. Mikulich, in: Crystallization and Phase Transitions [in Russian], Izd. AN BSSR, Minsk (1962).

[14] Ch. Knight, J. Colloid and Interface Sci., 25, 2 (1967).

[15] Ch. Knight., Phil. Mag., 23, No. 181, 153 (1971).

[16] B. Mutaftshiev and J. Zell, Surface Sci., 12, 317 (1968).

[17] R. Nacken, Neues Jahrb. Mineral., 11, 133 (1915).

[18] V. I. Danilov and V. I. Malkin, Zh. Fiz. Khim., 10, 1837 (1954).

Motion of a germanium—gold alloy droplet along a germanium surface under the action of a temperature gradient

S. A. Grinberg and E. I. Givargizov

Institute of Crystallography, Academy of Sciences of the USSR

(Submitted January 7, 1972; resubmitted February 15, 1972)
Kristallografiya, 18, 380-384 (March-April 1973)

The motion of a liquid germanium alloy droplet along a germanium surface under the action of a temperature gradient has been studied. The dependence of the migration rate on the diameter of the droplet indicates that atomic-kinetic processes taking place at the dissolution or crystallization front determine the overall rate under the conditions considered. The existence of a critical droplet size below which the droplet does not move has been detected. The threshold of the driving force of the process (the degree of supersaturation at the crystallization front, or the degree of unsaturation at the dissolution front) has been determined.

The method of liquid epitaxy finds extensive application in the technology of semiconductors; in particular, crystallization according to the vapor → liquid → solid phase scheme[1-3] makes it possible to control the growth of thread-like crystals.

In a study on the mechanism and kinetics of crystallization according to this scheme, valuable information can be drawn from experiments on zone melting under the action of a temperature gradient.[4-10]

The motion of an alloy droplet along a crystal surface noted in refs. 4, 11, and 12 may be used as one of the versions of zone melting.

In the present investigation we studied the motion of an alloy droplet along the surface of a germanium flake under the action of a longitudinal temperature gradient (Fig. 1). Such experiments make it possible to observe and simultaneously compare the velocity of a large number of droplets of different sizes and, consequently, to draw conclusions as to the kinetics of the processes over a broad range of driving forces. Moreover, the version in which a droplet is used makes it possible to follow in detail the recrystallization trail and draw some conclusions regarding the mechanism of the process from the micromorphology of this trail.

We intended to clarify in particular: a) Which of the two important stages (atomic-kinetic processes at the boundary of the droplet, or diffusion of the components of the solution through the bulk of the droplet) determines the migration rate of the droplet; b) what mechanism is responsible for the growth of germanium from the solution in the gold alloy under the given conditions, if the atomic-kinetic processes at the boundaries are essential?

The experiments were done in the following way: A thin (~50 to ~1000 Å) gold film was deposited by means of thermal evaporation in vacuo at ~10^{-5} mm Hg on the surface of single-crystal flakes of germanium with the orientation (111), (110), or (100). The underlayer with the film was mounted in a temperature apparatus (consisting, in particular, of a quartz tube heated by a resistance furnace), and the graphite holder was so constructed that thermal gradients in the direction perpendicular to the underlayer were excluded. Heating was done in vacuo at 10^{-5}-10^{-6} mm Hg pressure. Upon heating to above the eutectic temperature (~360°C for the Ge–Au system) the metal film alloyed with the underlayer; the liquid alloy film thus formed is unstable and splits up under the action of the surface tension into a large number of separate droplets ranging in size from ~10 to ~100 μ. The kinetics of formation of the liquid alloy (i.e., dissolution of Ge and Au until attainment of saturation along the branch in the phase corresponding to enrichment with germanium) is such that the solution in the various regions in the droplet is practically saturated right from the start. If the longitudinal temperature gradient (along the surface) is sufficiently high and the diameter of the droplet sufficiently large, the droplet shifts in the direction to the higher temperature.

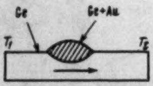

Fig. 1. Schematic drawing illustrating the motion of a germanium–gold alloy droplet along the surface of a germanium crystal in the field of a temperature gradient. $T_2 > T_1$; the direction of the motion is indicated by the arrow.

To simplify the picture by avoiding coalescence of different droplets, we used the following procedure. The gold film was deposited in strips, and the sample was so mounted in the holder that these strips were perpendicular to the direction of the gradient. By preliminary outgassing (usually at a temperature higher than the average temperature in the experiment) the droplets were displaced to regions in the underlayer where no gold had been deposited previously. By lowering the temperature to below the eutectic point near the trails of droplet migration we created marks there (in Fig. 2 these points are indicated by arrows), after which the temperature was raised to the fixed value and the flake was outgassed. After outgassing had been stopped, the samples cooled to room temperature were examined under an optical microscope with interference contrast. From the length of the recrystallization trail measured from the marks we determined the velocity of the droplet; moreover, some conclusions on the mechanism of the droplet motion could be drawn from the trail morphology.

The outgassing temperature ranged from 650 to 900°C, and the gradient G = (15-80) deg/cm.

In an analysis of the motion of spherical occlusions in crystals it was theoretically shown in refs. 7, 10, and 13 that two cases correspond to the diffusion regime: 1) When the transfer is determined by diffusion in the bulk,

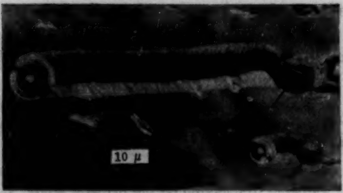

Fig. 2. Motion of a droplet along the surface of a germanium crystal. (111) surface, outgassing temperature T = 835°C, temperature gradient G = 35 deg/cm; the marks are indicated by arrows.

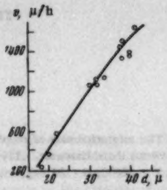

Fig. 3. The migration rate of droplets plotted versus their diameters. (111) surface, T = 870°C, C = 70 deg·cm^{-1}.

the migration rate of the droplet is independent of its size (as the diffusion path is prolonged, the driving force, which is here taken proportional to the temperature drop, i.e., to the diameter of the droplet, increases to the same extent); 2) when the transfer proceeds mainly by diffusion along the surface, the migration rate depends on the size of the occlusion according to the law $v \sim 1/l$. To the kinetic regime corresponds a rise of the velocity of the occlusion with increasing size. From the papers published on zone melting with a temperature gradient it is known[5,6,8–10] that under the normal experimental conditions (10–100 deg/cm) the thickness of the zone l = 10–100 μ (in our case the diameter of the droplet d should be regarded as the analog of the zone thickness) may correspond both to the diffusion regime (usually at larger values of l) and to the kinetic regime (usually at smaller values of l).

It has been established that over the interval of the conditions employed by us the migration rate of droplets increases with the droplet diameter (Fig. 2). This relationship was obeyed very distinctly in a large number of samples. The quantitative relationship is shown in Fig. 3. The data indicate that under the conditions considered the atomic-kinetic processes near the dissolution or the recrystallization front determine the migration rate. A certain leveling tendency in the dependence of the velocity on the diameter is noticed only in some samples of large diameter droplets, which can be explained by transition to the diffusion regime.

In several samples oriented with their surface along (110) and (100) we detected also the existence of a critical diameter, below which no migration of the droplet takes place. In Fig. 4 it can be seen that during outgassing at an average temperature lower than that during preliminary outgassing, only droplets of relatively large diameter, which are indicated by arrows (here, the diameters d_1, d_2, d_3 of droplets during preliminary outgassing are compared), migrate. From the curve in Fig. 5 we can estimate the critical (threshold) driving force during recrystallization of germanium from a solution in the alloy with gold. For example, at T = 650°C and G = 80 deg/cm the critical diameter d_c = 18 μ. The threshold of the driving force, i.e., the relative degree of supersaturation (near the crystallization front) or of unsaturation (near the dislocation front) for the droplet of critical diameter, is

$$\Delta C/C_e = \frac{dC}{dT}\Delta T_c \Big/ C_e = \frac{dC}{dT}\frac{dT}{dx} d_c \Big/ C_e,$$

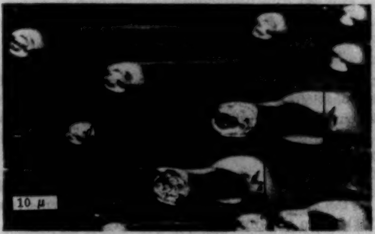

Fig. 4. The existence of a threshold for the motion of droplets along a germanium surface. (110) surface; temperature of preliminary outgassing T_1 = 840°C, G_1 = 85 deg/cm; temperature of subsequent outgassing T_2 = 650°C, G_2 = 80 deg/cm. During secondary outgassing only large-diameter droplets (d_1, d_2 during preliminary outgassing) migrate, whereas the droplet of the smallest diameter (diameter d_3 during preliminary outgassing) remains immobile.

where C_e denotes the germanium concentration in the solution corresponding to equilibrium at the temperature considered; dC/dT is the slope of the liquid curve in the phase diagram; dT/dx the temperature gradient along the surface of the crystal (and, as we suppose, near the boundary of the droplet). It was found that the absolute temperature drop ΔT_c = 0.15°C, and $\Delta C/C_e$ = 0.07%.

The existence of a threshold for zone melting under a temperature gradient was detected also in a study on the growth rate of SiC crystals from a solution in a Cr alloy by means of the method of a moving dissolution zone (see ref. 14), and in a study on the migration of a droplet of a salt solution through KCl crystals in the field of a temperature gradient (see ref. 15).

Kumagawa and his co-workers[14] relate the existence of a threshold to the circumstance that the motion of the relatively thin zone is blocked by the contaminants accumulated near the boundary, whereas in thicker zones the amount of molten substance suffices for dissolving these contaminations. Anthony and Cline[15] relate the shift of droplets to the effect of dislocations, and the existence of a threshold to the absence of dislocations intersecting the surface of droplets of sufficiently small size (the density of the dislocations in the samples examined in this study is about 10^6 cm^{-2}, and the critical droplet diameter is 10 μ).

To explain our data we can resort either to the first of the models mentioned (i.e., blocking of the dissolution

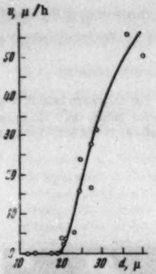

Fig. 5. The migration rate of droplets plotted versus their diameter. (110) surface, T = 650°C, G = 80 deg/cm.

or crystallization boundary) or to the second (the effect of dislocations). However, we note that the density of dislocations in the original crystals usually did not exceed 10^4 cm^{-2}, although the critical radius usually equalled ~30 μ.

Finally, it is not excluded that the critical radius is due to the existence of a barrier opposing two-dimensional nucleation on the dissolution boundaries consisting of various faces during crystallization (the authors of many papers, for example refs. 16-19, pointed out that these boundaries consist of various faces).

Further experiments are needed to find the actual mechanism responsible for the motion of droplets and the existence of a threshold.

CONCLUSIONS

1. It has been shown that during the motion of liquid germanium–gold alloy droplets in the field of a temperature gradient, the velocity of the droplets is limited by the atomic-kinetic processes at the boundary.

2. The existence of a critical droplet size below which no motion takes place has been detected. The critical driving force has been determined.

3. Statements are made as to the mechanisms which may be responsible for the motion of the droplets and the existence of a threshold.

The authors thank N. N. Sheftal' and A. A. Chernov for a valuable discussion on the present study, and P. D. Tkachev for his assistance in the experiments.

---

[1] R. S. Wagner and W. C. Ellis, Appl. Phys. Lett., 4, No. 5, 89 (1964).

[2] R. S. Wagner, Whisker Technology, Wiley, New York (1970), p. 47.

[3] E. I. Givargizov and N. N. Sheftal, J. Crystal Growth, 9, 326 (1971).

[4] W. G. Pfann, Zone Melting, Wiley, New York–London (1966).

[5] Tr. Novocherk. Inst. No. 170 (1967); No. 180 (1968); No. 208 (1970).

[6] V. N. Lozovskii and A. I. Udyanskaya, Kristallografiya, 13, 565 (1968) [Sov. Phys. – Crystallogr., 13, 477 (1968)].

[7] W. A. Tiller, J. Appl. Phys., 34, No. 9, 2757, 2763 (1963); 36, No. 1, 261 (1965).

[8] R. G. Seidensticker, J. Electrochem. Soc., 113, No. 2, 152 (1966).

[9] R. W. Hamaker and W. B. White, J. Appl. Phys., 39, No. 3, 1758 (1968); J. Electrochem. Soc., 116, No. 4, 478 (1969).

[10] Ya. E. Geguzin and M. A. Krivoglaz, Motion of Macroscopic Occlusions in Solids [in Russian], Metallurgiya, Moscow (1971).

[11] E. Biederman, J. Electrochem. Soc., 114, No. 2, 207 (1967).

[12] G. M. Gavrilov, Kristallografiya, 16, 834 (1971) [Sov. Phys. – Crystallogr., 16, 725 (1972)].

[13] A. A. Chernov, Zh. Eksp. Teor. Fiz., 31, 709 (1957) [Sov. Phys. – JETP, 4, 585 (1957)].

[14] M. Kumagawa, M. Ozeki, and S. Yamada, Japan. J. Appl. Phys., 9, No. 11, 1422 (1970).

[15] T. R. Anthony and H. E. Cline, J. Appl. Phys., 42, No. 9, 3380 (1971).

[16] J. W. Peterson, W. Glasson, and W. Hittinger, J. Metals, 9, No. 7, 823 (1957).

[17] A. P. Vyatkin and B. A. Selivanov, Izv. Vyssh. Ucheb. Zaved., Fizika, No. 5, 60 (1958).

[18] R. Dreiner and R. Garnache, J. Appl. Phys., 33, No. 3, 888 (1962).

[19] Tchang Il-Chung, J. Electrochem. Soc., 109, No. 3, 229 (1962).

Reaction of foreign particles with a crystallization front

A. M. Zubko, V. G. Lobanov, and V. V. Nikonova

Central Scientific-Research Institute of Ferrous Metallurgy
(Submitted October 14, 1971; resubmitted March 3, 1972)
Kristallografiya, 18, 385-389 (March-April 1973)

The reaction of foreign particles with crystals of naphthalene, tin, bismuth, and zinc being grown by the Bridgman method has been studied. The dependence of the rate of capture of the particles on their dimensions has been determined for particles of finely divided anthracite, broken glass, and fused glass. It has been shown that the ratio of the thermal conductivities of the particle and the melt has a significant influence on the behavior of the particle at the crystallization front.

The reaction of foreign particles with a crystal being grown from a melt was studied in refs. 1-4. The essential physical features of this phenomenon were studied in refs. 5-7. The results of studies carried out by different authors are contradictory, however, and this has led to fundamental differences in the explanation of the nature of the phenomenon. It has become necessary to obtain additional experimental data permitting an analysis of the causes and mechanism of the capture of foreign particles by a growing crystal.

In refs. 1 and 3 the conditions of capture of various particles by crystals of ice and readily fusible organic substances were studied. In refs. 1 and 2 the dependence of the probability of capture of the particles on their dimensions was obtained. Theoretical explanations of the experimental data were given in refs. 2 and 3. The theoretical schemes put forward were based on the following assumptions: 1) There is a thin film of melt between the foreign particle and the growing crystal; and 2) the rate of growth of the crystal under the particle is determined by the diffusion of the substance in this film, and the particle is captured when diffusion is unable to ensure growth of the crystal under the particle at the same rate as growth at a distance from it.

The first assumption was confirmed in refs. 8-10. The second assumption is reasonable for the interaction of a foreign particle with a crystal growing from solutions. In the case of the growth of a crystal from a melt, as was the case in refs. 1-3, the thin liquid film does not serve as a path for the diffusion of a dissolved substance, but is a direct source of supply for the crystal growing underneath it. Thus the formal agreement between the courses of the theoretical curves and the experimental curves obtained on crystallization from a melt cannot be regarded as a confirmation of the theory, since the theoretical scheme does not reflect the essential features of the phenomenon. Moreover, in refs. 2 and 3 there are significant differences in the explanation of the factors leading to the diffusion of the substance under the particle. The authors of ref. 2 assume that the diffusion under the particle arises as a result of the existence of an osmotic pressure and temperature gradient in the thin film of melt. In ref. 3 it was assumed that the diffusion arises as a result of a change in the magnitude of the surface energy of the film of the melt with change in its thickness.

The temperature field for the growth of a crystal from a melt in the presence of a spherical foreign particle situated at a fixed distance from the surface of the crystal was calculated in ref. 4. The authors cited examined the steady-state temperature distribution in a movable system of coordinates associated with the moving surface of the crystal, at a low growth rate, that is $vR/a \ll 1$, where v is the rate of growth of the crystal, R is the radius of the particle, and a is the thermal conductivity of the melt. The surface of the crystal had a steady-state form, the flow of heat to infinity in the melt was constant, and the removal of heat took place through the solid phase. The temperature distribution in the system was obtained for different ratios of the thermal conductivities of the particle, the solid phase, and the liquid phase. It was shown that when the thermal conductivity of the particle is less than the thermal conductivity of the melt, that is, for $\lambda_p/\lambda < 1$ (λ_p and λ represent the thermal conductivities of the particle and the melt, respectively), the rate of growth of the front situated under the particle increases, and the particle cannot be captured by the front of the growing crystal. If the thermal conductivity of the particle is greater than the thermal conductivity of the melt, that is, for $\lambda_p/\lambda > 1$, the rate of growth under the particle decreases, and a depression forms underneath it, as a result of which capture of the particle is possible.

The aim of the present work was to study the influence of the thermal parameters on the capture of particles by a crystal growing from a melt. We studied naphthalene and low-melting metals. The experiments were carried out by the Bridgman method[11] in long glass tubes. In contrast to ref. 3, this procedure ensured the production of a planar crystallization front throughout the entire range of rates of growth studied. The particles were wrapped in aluminum foil, placed in the melt, and kept there for a prolonged period. When the temperature had equalized and steady-state conditions of growth had been established, the foil was ruptured by means of a metal rod, and the particles were ejected onto the surface of the growing crystal. The behavior of the particles at the crystallization front was followed visually by means of an MB-1 microscope, and the moment of capture was recorded photographically. The observations were made only for particles which had not touched the walls of the tube.

We studied the reaction of a naphthalene crystal, growing at a rate varying in the range 0.14-5.6 μ/sec, with particles of finely divided anthracite, broken glass, fused glass, aluminum, and zinc, and also mercury droplets, with dimensions in the range 40-1000 μ.

The particles of aluminum and zinc and the mercury droplets, which have a much greater thermal conductivity than naphthalene, were captured even at the minimum rate of growth possible in our experiments: 0.14 μ/sec. For the particles of finely divided anthracite, broken glass, and

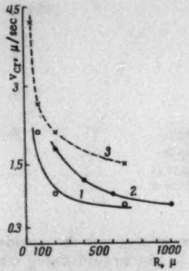

Fig. 1. Dependence of the critical rate of capture of particles by naphthalene on the particle dimensions: 1) broken glass; 2) fused glass; 3) finely divided anthracite.

fused glass, we established the dependence of the critical rate of capture on the dimensions of the particles. The critical growth rate was taken as the rate above which cases of the capture of the particles by the crystallization front were observed. The probability of capture increases with increase in the rate of growth of the crystal. Qualitatively, the dependence of the critical rate of capture on the dimensions of the particles (Fig. 1) is analogous to published results.[1,3] This relationship was observed, however, only for particles with a low thermal conductivity. As expected, one of the factors with a significant influence on the process of capture of the particles was found to be the ratio of the thermal conductivities of the particle and the melt λ_p/λ.

Let us examine the process of capture of a particle by a growing crystal. We shall assume that the thermal conductivity of the melt differs little from the thermal conductivity of the crystal, and that the crystallization front is isothermal. A spherical particle produces symmetrical curvature of the temperature field. The form of the isotherms close to a particle with a thermal conductivity greater than the thermal conductivity of the melt is represented schematically in Fig. 2a. In the process of crystal growth, the form of the crystal surface will be determined by the form of the isotherms. As the crystallization front approaches the particle, the surface of the front begins to bend, forming a depression under the particle. The degree of bending depends on the distance between the front and the particle and on the magnitude of λ_p/λ. The experiments showed that capture of the particle takes place only when it penetrates the crystal to a depth greater than half its diameter; otherwise, the particle is repelled by the growing crystal. When the particle penetrates into the crystal to a depth greater than half its diameter, a cylinder forms around the particle and subsequently envelopes it. This picture was observed for the capture of metallic particles by crystals of organic substances. A photograph illustrating the capture of a mercury drop by a crystal of naphthalene is shown in Fig. 3.

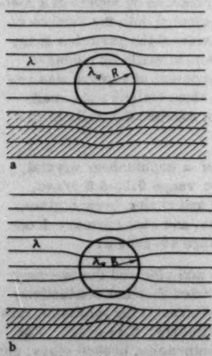

Fig. 2. Form of the isotherms close to particles placed in a melt. a) $\lambda_p/\lambda > 1$; b) $\lambda_p/\lambda < 1$.

For the case of the interaction of a crystal with a particle which has a lower thermal conductivity than the melt, the form of the isotherms close to the particle is shown in Fig. 2b. As the crystallization front approaches the particle, its surface begins to bend, forming a hillock under the particle; subsequently, the particle rolls off the hillock. On further growth of the crystal, the particle wanders over the surface of the front.

The experiments with the low-melting metals, like the experiments with naphthalene, were carried out by the Bridgman method. After the introduction of the particles and the subsequent movement of the crystallization front through a distance of 5-10 cm, the liquid was separated by decantation. The particles which had not been captured in the growth process were removed with the melt. When there were no particles in the melt, that is, when the particles were captured by the growing crystal, the grown piece of crystal was cut up and the pieces were remelted separately. When a particle was detected in the remelted piece, the position of its capture relative to the initial position of the front was fixed. For particles which were not wetted by the melt, the procedure used to detect the position of the particles was simplified. The strength of the crystal was much lower in the region of a particle surrounded by a gas envelope, and when the grown crystal was bent it broke at the point where the particle was situated.

As materials for study we chose bismuth, tin, and zinc. These metals have low melting points and widely different thermal conductivities, so that the conditions of the experiment can be varied. In the selection of the material for the particles, we had to satisfy the following requirements: 1) The particle must have a higher melting point than the growing crystal; 2) the specific gravity of the particle should be greater than the specific gravity of the melt, to avoid floating of the particle; and 3) the particle should be insoluble or at least have a low solubility in the crystallizing melt. On the basis of these requirements, we chose tungsten, iron, molybdenum, nickel,

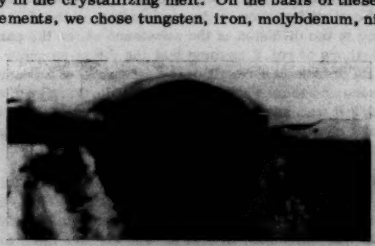

Fig. 3. Capture of a mercury drop by a crystal of naphthalene.

TABLE 1

Crystal	λ, cal/cm · sec · deg	Particle	λ_p, cal/cm · sec · deg	λ_p/λ	Predicted result	Result of experiment
Particle not wetted by the melt						
Zn	0.269	W	0.40	>1	Capture	Capture
		Ta	0.13	<1	Repulsion	Repulsion
Bi	0.02	W	0.40	>1	Capture	Capture
		Ta	0.13	>1	Capture	Capture
Sn	0.157	W	0.40	>1	Capture	Capture
		Ta	0.13	<1	Repulsion	Repulsion
		Mo	0.346	>1	Capture	Capture
Particle wetted by the melt						
Sn	0.157	Fe	0.20	>1	Capture	Capture
		Ni	0.198	>1	Capture	Capture
		Cr	0.07	<1	Repulsion	Repulsion

chromium, and tantalum. The diameter of the particles was 2–3 mm, and the rate of movement of the tube was varied in the range 5-100 cm/h. In the reaction of the growing crystal with insoluble particles, two cases are possible.

1. The particle is not wetted by the melt. This particle in the melt is surrounded by a gas envelope. Data on the interaction of these particles with growing crystals are given in Table 1. It may be assumed that the ratios λ_p/λ for room temperature are also applicable for the temperature of the interaction of the particle with the growing crystal. The nature of the interaction of the particles with the crystallization front confirmed this assumption. The presence of the gas envelope around the particles decreases slightly the ratio λ_p/λ, but does not alter the sign of the quantity $\lambda_p/\lambda - 1$.

An exception is provided by the interaction of tantalum particles with tin. As a consequence of the similarity in the values of their thermal conductivities at 20°C and the sharp change in the thermal conductivity of tin on fusion, it is found that at a temperature of 232°C the thermal conductivity of tantalum (0.13 cal/cm · sec · deg) becomes greater than the thermal conductivity of tin (0.08 cal/cm · sec · deg). It was thus expected that the tantalum particles would be captured. The experiments showed, however, that the tantalum particles are repelled by the growing crystal of tin, and this is possible only for the opposite ratio of the thermal conductivities. It may therefore be assumed that the thermal conductivity of the tantalum particle–gas envelope system is less than the thermal conductivity of liquid tin at the given temperature.

2. The particle is wetted by the melt. It can be seen from the experimental results given in Table 1 that all the particles for which the ratio $\lambda_p/\lambda > 1$ were captured during the experiment, and that all the particles for which $\lambda_p/\lambda < 1$ were repelled.

Thus the ratio of the thermal conductivities of the particle and the melt λ_p/λ is one of the chief factors determining the nature of the interaction of a particle with a crystal growing from the melt.

---

[1] A. E. Corte, J. Geophys. Res., 67, No. 3, 1085 (1962).
[2] P. Hoekstra and R. D. Miller, J. Colloid and Interface Sci., 25, 166 (1967).
[3] D. R. Uhlmann, B. Chalmers, and K. A. Jackson, J. Appl. Phys., 35, No. 10, 2986 (1964).
[4] A. A. Chernov and A. M. Mel'nikova, Kristallografiya, 10, 800 (1965) [Sov. Phys. – Crystallogr., 10, 672 (1966)].
[5] G. Correns and W. Steinborn, Z. Krist., A101, 117 (1939).
[6] A. V. Shubnikov, Tr. Lomonosov. Inst. Akad. Nauk SSSR, No. 6, 17 (1935).
[7] I. N. Fridlaynder and N. A. Vysotskaya, Dokl. Akad. Nauk SSSR, 62, 71 (1948).
[8] S. V. Nerten and B. V. Deryagin, Dokl. Akad. Nauk SSSR, 100, No. 1 (1955).
[9] A. N. Rusanov, Phase Equilibria and Surface phenomena [in Russian], Khimiya, Leningrad (1967), p. 273.
[10] D. M. Anderson and P. Hoekstra, Soil Sci. Soc. America Proc., 29, 498 (1965).
[11] P. W. Bridgman, Proc. Am. Acad. Arts and Sci., 47, 321 (1912).

Low-dislocation-density single crystals of corundum

Kh. S. Bagdasarov, E. R. Dobrovinskaya, V. V. Pishchik,
M. M. Chernik, Yu. Yu. Kovalev, A. S. Gershun,
and I. F. Zvyagintseva

All-Union Scientific-Research Institute for Single Crystals

(Submitted February 17, 1972; resubmitted May 26, 1972)
Kristallografiya, 18, 390-395 (March-April 1973)

The relationship between the conditions of growth and the degree of perfection of the structure of single crystals of corundum has been studied; the influence of the spatial orientation, the temperature gradient, and the stability of the thermal conditions on the formation of dislocations in corundum crystals grown by the directed crystallization method has been examined. The choice of appropriate orientations made it possible to reduce to a minimum the influence of defects in the structure of the seed crystal and to eliminate almost completely the inheritance of dislocations arising in the growth process. By studying and taking account of the influence of the spatial orientation and conditions of crystallization on structure perfection, it has been possible to obtain low-dislocation-density single crystals of leucosapphire without blocks.

In order to obtain perfect single crystals it is necessary to carry out a comprehensive study of the conditions of crystallization and to examine their influence on defects in the structure of the grown crystals. As a result of studies of this kind, it has been possible, for example, to obtain dislocation-free single crystals of germanium and silicon.[1] At the present time, the available data on the influence of the conditions of crystallization on the structural perfection of single crystals of corundum are limited and extremely contradictory. It is known that the density of dislocations in single crystals of corundum grown by different methods varies over a wide range of values from 10^2 to $4 \cdot 10^7$ cm^{-2}, and the most perfect single crystals are those grown by hydrothermal synthesis, by chemical transport reactions, and from solution in a melt.[2-6] An unsatisfactory feature common to most of the works cited is the absence of data on the distribution of defects throughout the volume of the crystal. The works cited give only data on the mean density of dislocations on the planes of the basis (0001) and the prism $(11\bar{2}0)$ and these data are frequently given without indication of the orientation of these planes relative to the direction of growth. In the study of the relationship between the conditions of crystallization and the structural perfection of crystals, however, it is necessary to have information not so much on the mean density of defects as on the regular features of the distribution of the density of dislocations in the volume of the crystal. The only exception is ref. 3, from which it follows that on the basal plane in crystals with 90° orientation (optical axis perpendicular to the direction of growth) the dislocation density is smaller by an order of magnitude than that on the same plane in crystals with 60° orientation. The dependence of the distribution of the dislocation density along one of the planes on the degree of perfection of the seed crystal was studied in ref. 7. Of particular interest are papers on the study of the block structure of corundum crystals,[8,9] where it was shown that with decrease in the angle between the axis of growth and the optical axis of the crystals, grown by the Verneuil method, the degree of perfection deteriorates sharply: The dimensions of the blocks decrease and the angle of disorientation increases. The same effect is observed in these crystals with increase in the distance from the single crystal used as seed crystal. Some information on the influence of the axial temperature gradient on the quality of crystals of ruby obtained by the Verneuil method is given in ref. 10.

The aim of the present work was to study the relationship between the conditions of growth and the structural perfection of single crystals of corundum. The problems of the influence of the spatial orientation, the temperature gradient, and the stability of the thermal conditions on the formation of dislocations in crystals of corundum grown by the directed crystallization method are discussed.

EXPERIMENTAL PROCEDURE

The materials studied were single crystals of corundum with dimensions 10 × 10 × 170 mm grown by the horizontal directed crystallization method. The starting material consisted of aluminum oxide with a total concentration of heavy metal impurities not exceeding $\sim 5 \cdot 10^{-3}$ wt.%. The single crystals used as seed crystals were oriented by means of a URS-50IM diffractometer, and were prepared in the form of rectangular parallelepipeds with dimensions 10 × 10 × 35 mm; they were then subjected to chemical polishing to remove the defect layer produced during the mechanical treatment. The deviation of the planes from those given in the seed crystals did not exceed 3°. The dislocation structure was revealed by selective etching on the (0001) and $(11\bar{2}0)$ planes.[4-6,11,12] The mean dislocation density in the seed crystals was $\sim 3 \cdot 10^4$ cm^{-2} on the basal plane and $\sim 6 \cdot 10^4$ cm^{-2} on the prism plane. We studied the distribution of the dislocations along the length of the crystals, and each point represented on the graphs corresponds to the value of the density of dislocations ρ, averaged over 5-25 fields of view; the area of the field of view was 1-4 mm^2.

The crystals were grown in series. Each series consisted of four crystals, grown in small boats arranged in parallel; this practically guaranteed identical crystallization conditions for the crystals in a given series.

INFLUENCE OF THE SPATIAL ORIENTATION OF THE SEED CRYSTALS

In the growth of crystals from a melt, various sources operate for the production of dislocations.[1] The chief of these is probably plastic deformation, arising behind the crystallization front under the influence of thermoelastic stresses. Plastic deformation and its associated effects may apparently also be responsible for the macroscopically nonuniform distribution of impurity. In addition to the formation of dislocations, processes involving the tapering out and inheritance of dislocations take place. Dislocations are inherited and taper out depending on the angle α between the dislocation line and the direction of growth. If the angle $\alpha = \pi/2$, inheritance does not take take place; if $0 < \alpha < \pi/2$, the dislocations taper out. Here, two cases are possible; in the first case, the creep of the dislocations in the growth process is slight, so that the dislocation comes out onto the lateral surface when the crystal has grown through a length $S = l \cot \alpha$ (where l is the distance from the dislocation on the crystallization front to the lateral surface at which the dislocation emerges); in the second case, the dislocations creep and are uniformly distributed over the cross section of the crystal. The inheritance of dislocations in the second case was examined in ref. 13. If the dislocation lines are arranged parallel to the direction of growth, they are inherited completely by the growing crystal.

In the present work we chose three orientations for the seed crystals: orientation I – direction of growth [0001], lateral surfaces $(11\bar{2}0)$ and $(10\bar{1}0)$; orientation II – direction of growth $[11\bar{2}0]$, lateral surfaces (0001) and $(10\bar{1}0)$; and orientation III – direction of growth $[10\bar{1}0]$, lateral surfaces (0001) and $(11\bar{2}0)$. These orientations were selected on the basis of the known glide systems and types of dislocation in single crystals of corundum[6,14,15] in such a way as, first, to decrease the density of dislocations arising during the growth process by weakening of the action of the main glide systems and, second, to reduce to a minimum the influence of defects in the structure of the seed crystal and to eliminate as far as possible the inheritance of dislocations produced in the growth process. In each series of crystals, one of the orientations was usually doubled in order to confirm that the thermal conditions in the direction perpendicular to the growth axis were identical. The distribution of the dislocation density was studied on planes parallel to and perpendicular to the direction of growth.

The distributions of the dislocation density along the length of crystals with orientations II and III are given in Figs. 1 and 2, respectively. Crystals with orientation I could not be grown, since usually this orientation was not preserved in the grown crystal.[16] It follows from the data given in the figures that the density of dislocations on the (0001) plane is much smaller than that for the seed crystal, since the dislocation lines emerging onto this plane lie in the prism planes, are perpendicular to the direction of growth, and are not inherited by the growing crystal, and the dislocation density formed under the influence of thermoelastic stresses is small, apparently, as noted above, due to the weakening of the action of the main glide systems.[14] The dislocation density of the prism planes in all cases is higher than that on the basal planes, as a consequence of the partial inheritance of dislocations. The dislocations lying in the (0001) plane with Burgers vectors $\langle 11\bar{2}0 \rangle$ and $\langle 1\bar{1}00 \rangle$ come out onto the $(11\bar{2}0)$ plane. If the $(11\bar{2}0)$ plane is parallel to the direction of growth (orientation III), the dislocation lines perpendicular to it are not inherited; the dislocation lines emerging at an angle of 60° are inherited, but they also gradually emerge onto the lateral surface. The observed tendency for the dislocation density to increase towards the end of the crystal may be due to increasing removal of heat from the crystallization zone or to an increase in the concentration of impurity as a result of its displacement by the growing crystal.

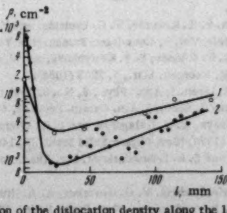

Fig. 1. Distribution of the dislocation density along the length of crystals of corundum with orientation II. 1) On the $(11\bar{2}0)$ plane; 2) on the (0001) plane.

None of the grown crystals with the given spatial orientations II and III contained block boundaries. The production of crystals free from blocks on seed crystals containing blocks may be due to a number of factors. In the first place, the single crystals used as seed crystals were chosen in such a way that the block boundaries either were perpendicular to the direction of growth or lay at angles from 30 to 60°. The boundaries perpendicular to the direction of growth are not inherited by the growing crystal; those lying at an angle, for a crystal width equal to 10 mm, emerge on the lateral surface at a length ≤14 mm, as can be seen from simple geometric considerations. In the second place, the density of single dislocations in the grown crystals does not reach the critical value, and new block boundaries are not produced.[17]

It may be noted that the quality of the seed crystal deteriorates sharply during the process of seeding and subsequent growth: There is an increase in the number of block boundaries and in the density of single dislocations, apparently due to thermal shock. Nevertheless, low-dislocation-density single crystals of corundum without blocks were still obtained on the defect seeds.

INFLUENCE OF THE THERMAL CONDITIONS ON THE DISLOCATION STRUCTURE OF THE SINGLE CRYSTALS

The production of perfect crystals, however, cannot

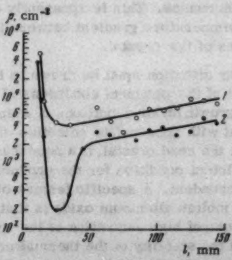

Fig. 2. Distribution of the dislocation density along the length of crystals of corundum with orientation III. a) On the $(11\bar{2}0)$ plane; 2) on the (0001) plane.

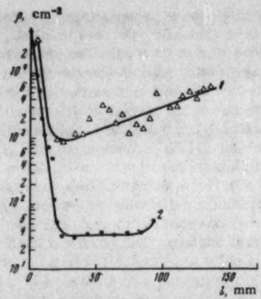

Fig. 3. Distribution of the dislocation density on the (0001) plane in crystals grown under different temperature gradient conditions (orientation II). 1) $\partial T_1/\partial x$; 2) $\partial T_2/\partial x$, $(\partial T_1/\partial x)/(\partial T_2/\partial x) \approx 2$.

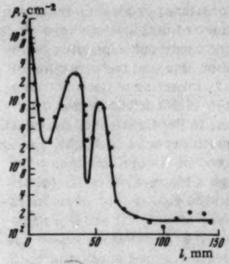

Fig. 4. Distribution of the dislocation density on the (0001) plane in a crystal grown with periodic breakdown of the stability of the thermal conditions.

be ensured simply by selection of the spatial orientation of the seed crystals. The dislocation density depends to a considerable extent on the magnitude of the axial temperature gradient.[18-20] The distribution of the dislocation density in crystals grown under different temperature gradient conditions is shown in Fig. 3. It can be seen from these data that decrease in the axial temperature gradient by a factor of 2 makes it possible to decrease sharply the dislocation density in the crystal. With growth under conditions of a small axial temperature gradient we obtained specimens with a density of dislocations ~30 cm^{-2}; large regions of these crystals (length ~15 mm) were completely free from dislocations.

It is obvious, however, that the influence of the axial temperature gradient is not the only significant factor in the production of perfect crystals. An important part is also played by the existence of temperature gradients in directions perpendicular to the direction of growth. Analysis of the distribution of the dislocation density along the length of the crystal in different cross sections showed that the dislocation density is not constant on the same planes in different cross sections of the crystal; for planes parallel to the direction of growth and for planes perpendicular to the direction of growth the minimum density of dislocations is characteristic of the central region of the crystal, and with increase in the distance away from the center towards the upper and lower surfaces the dislocation density increases. This is apparently due to the existence of a temperature gradient between the upper and lower surfaces of the crystal.

Particular attention must be drawn to the fact that the establishment of the optimum conditions of crystallization, that is, growth under conditions of a small temperature gradient with appropriate selection of the spatial orientation of the seed crystal, is a necessary condition but not a sufficient condition for the production of perfect crystals of corundum. A specific feature of the crystallization of molten aluminum oxide is that it takes place under conditions of high saturation of the melt with gas. Breakdown of the stability of the thermal conditions leads not only to the production of the structural inhomogeneity characteristic of directed crystallization but also to the capture of the gas bubbles which are formed in the melt at the boundary of separation between the phases and which are responsible for the production of pores in the crystal.[21] These pores, which are often facetted, act as stress concentrators and provide additional sources for the production of dislocations and low-angle boundaries.[22] The distribution of the dislocation density in a crystal grown under conditions of periodic breakdown of the stability of the thermal conditions (under stable conditions the accuracy of the stabilization of the voltage amounted to ~0.3% of the established value, and under unstable conditions the corresponding figure was greater than 2%) is shown in Fig. 4. It follows from these results that breakdown of the stability leads to a sharp increase in the dislocation density. On restoration of the normal conditions of crystallization, the dislocation density decreases rapidly. This decrease can be explained on the basis of the ideas put forward above regarding the relationship between the inheritance and tapering out of dislocations and the spatial orientation of the crystal.

Thus by studying and making allowance for the influence of the spatial orientation and conditions of crystallization on structure perfection it has been possible to obtain low-dislocation-density single crystals of leucosapphire.

---

[1] W. C. Dash, J. Appl. Phys., 30, 459 (1959).

[2] K. Janowski and H. Conrad, Trans. Metallurg. Soc. AIME, 230, 717 (1964).

[3] S. A. Medvedev, E. R. Kustov, and P. A. Arsen'ev, Kristallografiya, 10, 760 (1965) [Sov. Phys. – Crystallogr., 10, 640 (1966)].

[4] K. Sakhadzh'yan and M. Shiber, in: Growth of Crystals, Vol. 7, Consultants Bureau, New York (1969).

[5] J. A. Champion and M. A. Clemence, J. Mat. Sci., 2, 153 (1967).

[6] M. V. Klassen-Neklyudova, in: Methods and Apparatus for the Control of the Quality of Ruby Crystals [in Russian], Nauka, Moscow (1968), p. 19.

[7] E. R. Dobrovinskaya, A. N. Galagurya, L. A. Litvinov, V. V. Pishchik, and A. A. Burshtein, Kristallografiya, 16, 666 (1971) [Sov. Phys. – Crystallogr., 16, 583 (1971)].

[8] E. P. Kostyukova, B. K. Kazurov, V. G. Lyuttsau, and V. I. Sidenko, in: Growth of Crystals, Vol. 7, Consultants Bureau, New York (1969).

[9] B. K. Kazurov, I. G. Ganeev, E. P. Kostyukova, and V. G. Lyuttsau, Izv. Akad. Nauk SSSR, Neorgan. Mat., 5, 2203 (1968).

[10] Kenichi Shiroki, Japan. J. Appl. Phys., 8, No. 9, 1082 (1969).

[11] R. Scheuplein and P. Gibbs, J. Am. Ceram. Soc., 43, 458 (1960).

[12] E. R. Dobrovinskaya, A. N. Galagurya, and L. A. Litvinov, Fiz. Tverd. Tela, 12, 1839 (1970) [Sov. Phys. – Solid State, 12, 1460 (1970)].

[13] M. M. Chernik and E. R. Dobrovinskaya, Izv. Akad. Nauk SSSR, Ser. Fiz., 36, 570 (1972).

[14] M. V. Klassen-Neklyudova, V. G. Govorkov, A. A. Urusovskaya, N. M. Voinova, and E. P. Kozlovskaya, Phys. Status Solidi, 39, 679 (1970).

[15] M. V. Klassen-Neklyudova, E. P. Kozlovskaya, and A. A. Urusovskaya, Kristallografiya, 15, 1084 (1970) [Sov. Phys. – Crystallogr., 15, 947(1971)].

[16] E. R. Dobrovinskaya, V. V. Pishchik, A. S. Gershun, N. V. Mitina, and G. M. Tsigel'nitskii, in: Single Crystals and Technology [in Russian], Vses. N.-I. Inst. Monokrist., Khar'kov (1971), p. 12.

[17] S. V. Tsivinskii and L. A. Maslova, Izv. Akad. Nauk SSSR, Ser. Fiz., 35, No. 3, 514 (1971).

[18] V. L. Indenbom, Kristallografiya, 2, 594 (1957) [Sov. Phys. – Crystallogr., 2, 587 (1957)].

[19] V. L. Indenbom, in: Growth of Crystals, Vol. 3, Consultants Bureau, New York (1962).

[20] S. V. Tsivinskii, Fiz. Met. Metalloved., 25, 1013 (1968).

[21] V. V. Pishchik, E. R. Dobrovinskaya, B. I. Birman, A. S. Gershun, and I. F. Zvyagintseva, in: Single Crystals and Technology [in Russian], Vol.5, Vses. N.-I. Inst. Monokrist., Khar'kov (1971), p. 26.

[22] J. Friedel, Dislocations, Addison-Wesley (1964).

Crystallographic orientation of dendrites of pure tin

V. O. Esin, G. N. Pankin, and R. Sh. Nasyrov

Institute of Metal Physics, Urals Branch, Academy of Sciences of the USSR

(Submitted July 27, 1971; resubmitted April 10, 1972)
Kristallografiya, 18, 396-402 (March-April 1973)

The crystallographic orientation of dendrites developing on the surface of a supercooled melt of pure tin (99.9996 wt.% Sn) at different degrees of supercooling of the melt (0-18°) has been studied.

According to refs. 1 and 2, the crystallographic orientation of the direction of development of dendrite branches may vary, depending on the magnitude of the driving force of the phase transformation. This change in the anisotropy of the mobility of the interphase boundary is apparently responsible for the production of oscillations in the kinetic curve, recently detected in a study of the growth of dendrites in a supercooled melt of pure tin.[3]

PROCEDURE

The method used to determine the supercooling was for the most part analogous to that given in ref. 3. For the determination of the supercooling directly on the free surface we made an additional study of the temperature distribution in the melt; this made it possible to extrapolate the readings of the thermocouple to the surface of the melt. The studies were carried out in the range of supercooling 0-18°. To ensure reliable thermal contact, the working junction was immersed to a depth of 1.5-2 mm below the surface of the melt. As a consequence of the appreciable vertical temperature gradient in the melt, the magnitude of the minimum detectable supercooling for the method which we used amounted to 2.5°, for an overall accuracy of the measurement equal to ±0.3°C.[4] The primary nucleus of the solid phase was produced by bringing a fine steel needle into contact with the surface of the supercooled melt. The ingots obtained were generally single crystals, with crystallographic orientation of the lattice genetically related to the orientation of the primary nucleus of the solid phase. Figure 1 gives the crystallographic orientations of the plane of the free surface in a single-crystal ingot, corresponding to different original degrees of supercooling of the melt. In accordance with these results it may be assumed that the orientation of the primary nucleus of the solid phase relative to the surface of the melt was random. The studies which were carried out showed that it was only in isolated cases in a series of experiments corresponding to the same degree of supercooling that the primary branch developed directly along the surface of the melt; in most cases the direction of development of the primary branch is inclined to this surface at a certain angle. The crystallographic orientation of the dendrite branches forming a distinct relief on the free surface of the single-crystal ingot was determined by x-ray diffraction (by the Laue back-reflection method).

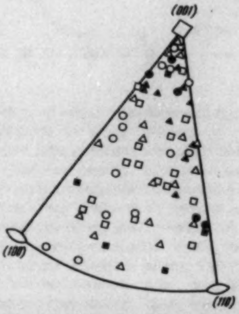

Fig. 1. Crystallographic orientation of the free surface of the melt for a single-crystal ingot. The blackened symbols ●, □, ▲ correspond to experiments in which the primary branch of the dendrite developed in the plane of the surface of the melt, and the open symbols correspond to experiments in which the primary branch of the dendrite developed at an angle to the surface: triangle) $0 < \Delta T < 10^\circ$; circle) $10 < \Delta T < 12^\circ$; square) $12 < \Delta T < 18^\circ$.

EXPERIMENTAL RESULTS

The crystallographic orientation of the primary branches of dendrites developing in the plane of the surface of the melt is given in Fig. 2. It was found that the orientation of the dendrites varies, depending on the magnitude of the supercooling of the melt. In the range of supercooling 0-10°, the change in the crystallographic orientation takes place along the (110)-(001) side of the stereographic triangle. In the range of small degrees of supercooling 0-2.5°, the point corresponding to the crystallographic orientation of the direction of development of the primary branch of the dendrite lies on the (110)-(001) side of the stereographic triangle, close to the (111) pole (Fig. 2). With increase in the supercooling of the melt to 10°, it is displaced along the side of the triangle in the direction of the (110) pole. In the range of supercooling from 10 to 12°, the opposite movement of the crystallographic orientation along the side of the stereographic triangle away from the (110) pole approximately as far as

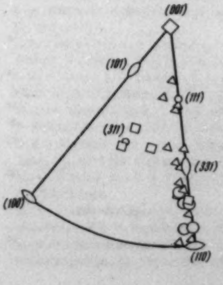

Fig. 2. Crystallographic orientation of the primary branches of dendrites developing directly along the free surface of the melt. The symbols for the temperature ranges are the same as those in Fig. 1.

the (331) pole is observed. With further increase in the supercooling of the melt, the orientation of the primary branches of the dendrites moves away into the interior of the stereographic triangle; for $\Delta T = 18°$ it lies on the region of the (311) pole.

The experimental procedure did not make it possible to determine the orientation of the dendrite branches developing at an angle to the surface of the melt. Analysis of the experimental results, however, indicates that the change in the crystallographic orientation of the direction of the development of the primary branches of these dendrites with change in the supercooling of the melt obeys the same laws (Fig. 2).

It was found that in the range of supercooling 0-12°C, the development of the primary branches of dendrites along the surface of the melt (Fig. 3a) is observed only in those cases where the crystallographic orientation of the directions of the nucleus of the solid phase lying in the plane of the surface of the melt is sufficiently close to the observed orientations of the corresponding dendrites situated on the (110)-(001) side of the stereographic triangle in Fig. 2. Figure 3b gives the stereographic projection of the plane of the surface of the ingot (the points give the crystallographic orientation of the primary branch and the secondary branches of the dendrite).

In the development of the primary branch of a dendrite at an angle to the surface of the melt, a distinct picture of the dendrite branch is not produced (Fig. 4a); information on the direction of growth of the primary branch can be obtained only from the local relief subsequently produced on the surface; this relief is formed by the secondary branches of the dendrite, emerging on the free surface of the melt (the development of the solidification process was recorded by means of high-speed cinematography[4]). This relief on the surface of the ingot (in the range of supercooling of the melt 0-12°C) is always produced when the crystallographic orientation of the directions lying in the plane of the surface of the melt is fairly far removed from the observed orientations of the primary branches of the corresponding dendrites lying on the (110)-(001) side of the stereographic triangle. The stereographic projection of the orientations of the directions of the nucleus of the solid phase, lying in the plane of the surface of the melt, for the development of this relief is given in Fig. 4b.

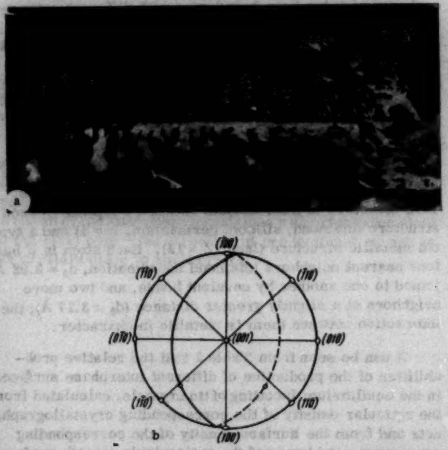

Fig. 3. Relief (×10) formed by a dendrite of the surface of an ingot for development of the primary branch along the free surface of the melt. a) Supercooling 3.6°; b) stereographic projection of the plane of the surface of the melt.

It may be noted that the analysis of the cine photographs, together with the x-ray diffraction studies, revealed the interesting fact that in the solidification process there are successively produced several dendrite systems which are genetically related to the primary nucleus of the solid phase, but which have different crystallographic orientations of the direction of development of the primary branches. It was found that the change in the crystallographic orientation of the dendrites produced directly after the seed is brought into contact with the surface of the melt, and the dendrites which develop after a certain time interval (which obviously corresponds to smaller degrees of supercooling of the melt), corresponds to the scheme given in Fig. 2.

DISCUSSION OF RESULTS

The crystallographic orientation of tin dendrites with comparatively low purity (99.98 wt.% Sn) was studied in ref. 5. The predominant orientation throughout the entire range of supercooling studied was bound to be ⟨110⟩. This result is apparently due to the influence of impurities,[6] which have been shown[2] to lead to the production of specific conditions of competitive growth, in which the ⟨110⟩ direction is preferred even when the crystal–melt system deviates considerably from equilibrium.

The change in the crystallographic orientation of the dendrites with change in the magnitude of the supercooling of a melt of pure tin, observed in the present work, shows qualitative agreement with familiar experimental results[2,7] and confirms the earlier suggestion that there is a change in anisotropy of the mobility of the crystal–melt interphase boundary (the direction of predominant growth of the crystal) as a function of the driving force of the phase transformation.[6,1] It can be apparently assumed that there are two limiting types of anisotropy of the mobility of the interphase boundaries: that close to equilibrium and that at a considerable distance from equilibrium, when the driving force of the phase transformation becomes greater than a certain critical value.

In the first case the direction of predominant growth of the crystal is given by the anisotropy of its equilibrium form, which is determined unambiguously by the mutual spatial arrangement of the interphase boundaries with the lowest relative mobility; in the second case this direction coincides with the orientation of the normals to the interphase surfaces of the equilibrium form of the crystal (exhibiting the lowest surface energy at equilibrium), which under these conditions acquire the greatest mobility. For intermediate values of the driving force the change in the crystallographic orientation of the direction of predom-

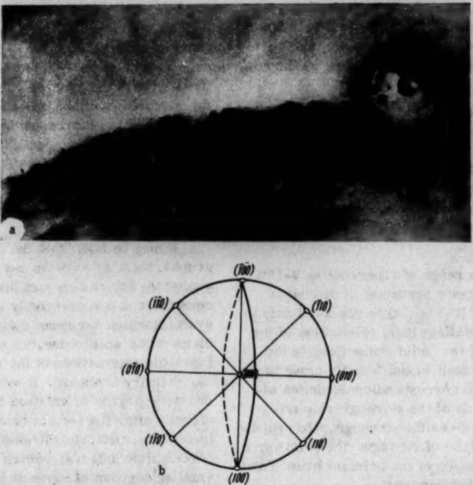

Fig. 4. Relief (×10) formed by a dendrite on the surface of an ingot for development of the primary branch at an angle to the surface of the melt (a) and the stereographic projection of the plane of the surface of the melt (b).

inant growth of the crystal can be found by a detailed analysis of the kinetics of the buildup of the interphase surfaces, which determine the equilibrium form of the crystal in contact with its own melt; an analogous calculation was carried out in ref. 8 for crystals with cubic symmetry.

At the present time there is no reliable information on the equilibrium form of tin crystals in their own melt, and prediction of the equilibrium habit of the crystal in accordance with the Gibbs–Curie–Wulff principle is impossible, since there are no experimental values or reliable methods for the calculation of the anisotropy of the surface energy of the corresponding interphase boundaries. For elements which crystallize with the formation of a close-packed lattice in which the bonds between the atoms are predominantly metallic, the planes of the equilibrium boundaries can readily be determined from the reticular density of the corresponding crystallographic nets. According to Bravais, these are parallel to the most closely packed planes of the crystal lattice.

In crystals with directed covalent bonds between the atoms, which are usually characterized by the highest coordination numbers Z, however, this rule does not apply. Thus for example for germanium, in the crystal lattice of which the bonds between the atoms are predominantly covalent (Z = 4, diamond coordination), the basal planes are arranged in order of decreasing reticular density as follows: (110), (111), (100) (0.0872, 0.0712, and 0.0616, respectively), whereas the planes of the equilibrium facetting, which determine the form of the crystal in equilibrium with its own melt, are planes of the (111) type.[9] For the purposes in which we are interested, the construction of the equilibrium form in accordance with the Gibbs–Curie–Wulff theorem can be carried out using the relative values of the specific surface density of the uncompensated bonds ρ of the molecularly smooth faces (see Table 1) instead of the corresponding values of the surface energy. The equilibrium form found in this way apparently reflects fairly accurately the anisotropy of the kinetics of atom exchange at interphase boundaries with different orientations at equilibrium. This calculation, carried out for germanium, showed that the lowest surface density of bonds is exhibited by the planes of type (111) ($\rho\{_{111}\}:\rho\{_{110}\}:\rho\{_{100}\} = 0.0712:0.0872:0.1233$), and the equilibrium form is a pure octahedron, in complete agreement with the experimental observations.[9]

Tin crystallizes with the formation of a tetragonal body-centered lattice with axial ratio $c/a = 0.545$, which can be described as a highly deformed diamond lattice. This structure is intermediate between a typical valence structure (diamond, silicon, germanium, Z = 4) and a typical metallic structure (lead, Z = 12). Each atom in it has four nearest neighbors (diamond coordination, $d_1 = 3.02$ Å) joined to one another by covalent bonds, and two more neighbors at a slightly greater distance ($d_2 = 3.17$ Å); the interaction between them is metallic in character.

It can be seen from Table 1 that the relative probabilities of the production of different interphase surfaces in the equilibrium facetting of tin crystals, calculated from the reticular density of the corresponding crystallographic nets and from the surface density of the corresponding noncompensated bonds of the molecularly smooth surfaces of the crystal, are different, and moreover depend to a significant extent on the energetic equivalence of the metallic and covalent bonds (for $\varphi_m \ll \varphi_c$, Z = 4, and for $\varphi_m = \varphi_c$, Z = 6).

TABLE 1. Anisotropy of the Specific Surface Density of Uncompensated Bonds (ρ) and Reticular Density of the Molecularly Smooth Surfaces of a Tin Crystal

(HKL)	Reticular density	Coordination No. 4		Coordination No. 6		$\varphi_m/\varphi_c = 0.6$	
		(HKL)	ρ	*(HKL)*	ρ	*(HKL)*	ρ
(100)	0.1082	(101)	0.0518	(100)	0.1082	(100)	0.1082
(110)	0.0765	(112)	0.0551	(110)	0.1531	(101)	0.1144
(112)	0.0550	(001)	0.0590	(101)	0.1555	(112)	0.1212
(101)	0.0518	(111)	0.0935	(112)	0.1653	(001)	0.1299
(001)	0.0295	(100)	0.1082	(001)	0.1771	(111)	0.1496
(111)	0.0234	(221)	0.1285	(441)	0.1820	(110)	0.1531
(221)	0.0164	(441)	0.1456	(111)	0.1870	(221)	0.1670
(441)	0.0091	(110)	0.1531	(221)	0.1927	(441)	0.1675

Observations made in a number of studies of the crystallography of layer growth in tin[10] indicate that the planes determining the habit of the crystal at equilibrium are apparently the (100) and (101) planes, with a relatively high probability for the (100) planes.

The results,[10] together with a preliminary analysis of the course of the change in the direction of predominant growth of tin crystals, carried out by us on the basis of the ideas developed earlier,[8] and comparison with the orientations of the primary branches of dendrites found in the present work make it possible to reach conclusions regarding the nature of the anisotropy of the mobility of the interphase crystal–melt boundaries close to equilibrium and, in particular, regarding the relative magnitudes of the surface density of the noncompensated bonds of various principal surfaces of the crystal with the assumption that these quantities are directly proportional to the mobility of the corresponding interphase boundaries (see the last column of Table 1). The resulting qualitative conclusion regarding the $\rho_{(hkl)}$ ratio for the four surfaces $\rho\,\{_{100}\} < \rho\,\{_{101}\} < \dots < \rho\,\{_{111}\} < \rho\,\{_{110}\}$) makes it possible to estimate the energetic equivalence of the metallic and covalent bonds between nearest atoms in the tin lattice ($0.54 < \varphi_m/\varphi_c < 0.64$).

The last column of Table 1 gives the relative arrangement of some of the interphase boundaries of a tin crystal in contact with its own melt close to equilibrium, in order of increasing mobility, for $\varphi_m/\varphi_c = 0.6$.

Analysis of the equilibrium form, constructed with the assumptions which we have made, indicates that the equilibrium facetting of the crystal should involve only the two types of plane $\{100\}$ and $\{101\}$, and the greatest mobility is shown by the interphase boundaries with orientation close to the (331) pole – the direction of predominant growth of tin crystals close to equilibrium.

For sufficiently strong deriving forces for the phase transformation, the greatest relative rate of movement will be shown by the interphase boundaries parallel to the $\{100\}$ planes of the crystal lattice, in accordance with the suggestions put forward in refs. 6 and 11 and confirmed experimentally in a study of the crystallography of competitive growth in the acicular zone of an ingot of pure tin.[2]

According to our estimates, even for a total supercooling of the tin melt greater than 30°, conditions should be established in which the primary branches of dendrites produced on solidification of the melt will develop in the $\langle 100 \rangle$ direction. Further increase in the driving force of the phase transformation (supercooling of the melt) does not alter the nature of the anisotropy of the mobility of the interphase boundaries. The $\langle 100 \rangle$ direction is the direction of predominant growth of the tin crystals under these conditions.

---

[1] M. Hill, H. Rau, and J. Schlipt, The Growth and Perfection of Crystals, Proceedings of the International Conference, Cooperstown, New York (1958), p. 325; Z. Elektrochem., 63, 283 (1959).

[2] V. O. Esin, Fiz. Met. Metalloved., 10, 233 (1960); 16, 509 (1963); 17, 269 (1964).

[3] V. O. Esin and G. N. Pankin, in: Crystallization and Phase Transformations [in Russian], Nauka i Tekhnika, Minsk (1971), p. 152.

[4] V. O. Esin, G. N. Pankin, and R. Sh. Nasyrov, Fiz. Met. Metalloved., 32, 1014 (1971).

[5] F. Weinberg and B. Chalmers, Can. J. Phys., 30, 488 (1952).

[6] A. Rosenberg and W. A. Tiller, Acta Metallurg., 5, 565 (1957).

[7] O'Hara, Acta Metallurg, 15, 231 (1967).

[8] V. O. Esin, Fiz. Met. Metalloved., 20, 226 (1965).

[9] S. A. Robinson, P. L. Ostapkovich, E. S. Schlegel, and C. P. Gazzara, Science, 116, 362 (1952).

[10] T. S. Plaskettt and W. C. Winegard, J. Inst. Metals, 88, 480 (1960); M. Koyama, J. Japan. Inst. Metals, 22, 40 (1958); V. O. Esin and A. A. Kralina, Fiz. Met. Metalloved., 9, 307 (1960).

[11] V. O. Esin and A. A. Kralina, Fiz. Met. Metalloved., 9, 305 (1960).

Crystal structure of lanthanum hypophosphite monohydrate

V. M. Ionov, L. A. Aslanov, V. B. Rybakov, and M. A. Porai-Koshits
M. V. Lomonosov Moscow State University

(Submitted December 14, 1971; resubmitted April 10, 1972)
Kristallografiya, 18, 403-404 (March-April 1973)

There is very little published information on the crystal structure of the compounds of rare-earth elements with phosphorus derivatives as ligands. We have made an attempt to investigate the crystal structures of the hypophosphites of the lanthanides. The first subject chosen for investigation was lanthanum hypophosphite monohydrate with the composition $La(H_2PO_2)_3 \cdot H_2O$.

Crystals 0.2 × 0.2 × 0.3 mm in size were examined on KFOR cameras with unfiltered molybdenum radiation. The unit-cell parameters (with an accuracy of ±0.3%) were as follows: a = 8.98, b = 8.08, c = 7.29 Å; α = 104.8°, β = 99.0°, γ = 109.7°, V = 464 Å^3, space group $P\bar{1}$, N = 2. Photographs were obtained of the 16 reciprocal lattice layers hk0−hk6, h0l−6hl, 0kl, and 1kl. For each layer six to nine films were recorded with multiple exposures, and the weighted mean I_{hkl} values were then obtained.

To interpret the structure by the heavy-atom method we used 948 reflections; ($\sin\theta/\lambda_{max} = 1.04$, F^2_{max}/F^2_{min}= 151. The coordinates of the heavy atom were obtained from the results from calculation of the interatomic function, and the coordinates of the phosphorus and oxygen atoms were obtained from the three-dimensional electron-density distribution. The position and thermal parameters of the atoms were refined by the method of least squares in isotropic approximation to an R value of 0.086. The final values of the parameters are given in Table 1.

The coordination number of the lanthanum atom in the investigated structure is 8. The metal atom is surrounded by the seven oxygen atoms of the three hypophosphite groups and one water molecule. Each of the three hypophosphite groups fulfills a specific function in the structure. The first group is a tridentate bridging group. the O_2 atom serves as a bridge between the two lanthanum atoms related by a center of symmetry 00½, while the O_1 is connected to the metal atom which is separated from one of the first two by a distance equal to the translation along the c axis (Fig. 1). The second hypophosphite group is a bidentate bridging group. The oxygen atoms of this group O_3 and O_4 are attached to two metal atoms between which there is a center of symmetry 000.

TABLE 1. Position and Thermal Parameters of the Atoms

Atom	x/a	y/b	z/c	B, Å^2
La	0.1300 (1)	0.1823 (1)	0.3408 (1)	2.2(0)
P_1	0.2679 (5)	0.1853 (7)	−0.1503 (7)	2.4(1)
P_2	0.1914 (6)	−0.2236 (7)	0.0330 (8)	2.7(1)
P_3	0.5907 (6)	0.3083 (7)	0.4655 (8)	2.9(1)
O_1	0.2037(16)	0.1618(19)	0.0198(21)	2.4(2)
O_2	0.1483(14)	0.0707(17)	−0.3457(18)	2.6(3)
O_3	0.1474(15)	−0.1343(18)	0.2069(19)	3.2(2)
O_4	0.0798(15)	−0.2657(18)	−0.1602(19)	1.4(2)
O_5	0.7237(17)	0.4752(20)	0.6146(22)	4.1(3)
O_6	0.4254(16)	0.2637(19)	0.4951(20)	3.5(3)
$O_{7(H_2O)}$	0.0430(16)	0.3636(19)	0.6113(20)	3.5(3)

TABLE 2. Interatomic Separation (Å) and Bond Angles (deg)

La — O_1	2.51(2)	La — $O_{7(H_2O)}$	2.53(2)	O_1 — P_1 — O_2	114.7
La — O_2''	2.66(1)	P_1 — O_1	1.48(2)	O_3 — P_2 — O_4	115.8
La — O_2'	2.65(1)	P_1 — O_2	1.49(1)	O_5 — P_3 — O_6	116.3
La — O_3	2.56(1)	P_2 — O_3	1.47(1)		
La — O_4	2.51(1)	P_2 — O_4	1.48(1)		
La — O_5	2.54(2)	P_3 — O_5	1.48(2)		
La — O_6	2.49(2)	P_3 — O_6	1.47(2)		

Note: The standard deviations of the angles lie between 0.8 and 0.9°.

TABLE 3. Dihedral Angles in the Coordination Polyhedron of Lanthanum

Angles	Atoms	Angles, deg
δ_1	O_2', O_1, O_4' and O_2, O_1, O_3	3.3
δ_2	O_6, O_7, O_2'' and O_6, O_7, O_5'	12.5
δ_3	O_1, O_6, O_3 and O_1, O_6, O_5'	44,4
δ_4	O_7, O_2', O_4' and O_7, O_2', O_2''	45.0
φ_1	O_1, O_7, $(O_3+O_2'')/2$ and O_3, O_2'', $(O_1+O_7)/2$	16.0
φ_2	O_2', O_6, $(O_4'+O_5')/2$ and O_4', O_5', $(O_2'+O_6)/2$	17.8
ω	O_7, O_2'', O_3, O_1 and O_6, O_5', O_4', O_2'	83.9

Note: The expression $(O_1 + O_7)/2$ denotes the point lying halfway between the O_1 and O_7 atoms.

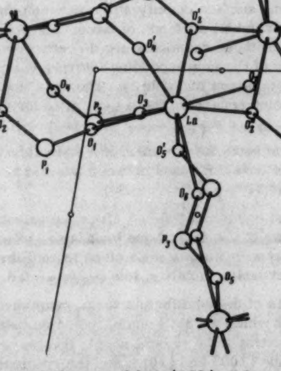

Fig. 1. Projection of a fragment of the $La(H_2PO_2)_3 \cdot H_2O$ structure onto the (010) plane.

By virtue of this method of adding the hypophosphite groups to the metal atoms a chain extended along the c axis is formed in the structure. These chains are linked to each other into layers parallel to the (110) plane by the third hypophosphite group $O_5P_3O_6$, which is also a bidentate bridging group.

The distance from the metal atoms to the bridging oxygen atoms O_2' and O_2'' is significantly longer than the lengths of the La–O bonds for all the other oxygen atoms (Table 2). The P–O bond lengths and O–P–O bond angles are close in value.

The coordination polyhedron of the lanthanum atom is a figure intermediate between a double-capped trigonal prism and a tetragonal antiprism. Table 3 gives the dihedral angles calculated in accordance with the criterion proposed in ref. 1. At the apices of one of the "four-cornered" faces of the polyhedron are the $O_1O_2'O_3O_4'$ atoms, and at the apices of the other are the $O_2''O_5'O_6O_7$ atoms.

The coordination polyhedra are joined in pairs by their common edge $O_2'-O_2''$. These pairs of polyhedra can be regarded as binuclear fragments of the chains mentioned above. When the chains are described in this way the bond between the binuclear fragments is realized by the $O_1P_1O_2$ and $O_3P_2O_4$ hydrophosphite groups. Analysis of the interatomic separations showed that the water molecules and hypophosphite ions do not form hydrogen bonds.

---

[1] M. A. Porai-Koshits and L. A. Aslanov, Zh. Strukt. Khim., 13, No. 2, 266 (1972).

Crystal structure of europium hypophosphite monohydrate

V. M. Ionov, L. A. Aslanov, M. A. Porai-Koshits, and V. B. Rybakov
M. V. Lomonosov Moscow State University

(Submitted February 17, 1972)
Kristallografiya, 18, 405-406 (March-April 1973)

During systematic investigation of the hypophosphites of rare-earth elements with the composition $Ln(H_2PO_2)_3 \cdot H_2O$ it was found that the crystal structures of the monohydrates of lanthanum and europium hypophosphites are very similar, but they cannot be considered isomorphous. The location of the reflections of the x-ray patterns of the equatorial layer lines recorded along the length of the crystals is almost the same in the two compounds, but the intensities of some of the reflections differ significantly. The difference increases on passing to the nonzero layer lines, and this indicates differences in the z coordinates of the individual atoms and similar values for the x and y coordinates.

Crystals 0.1 × 0.1 × 0.3 mm in size were examined on KFOR cameras with molybdenum radiation. The unit-cell parameters, determined with an accuracy of ±0.3%, were as follows: $a = 9.07$, $b = 8.30$, $c = 7.34$ Å; $\alpha = 115.5°$, $\beta = 94.2°$, $\gamma = 111.8°$, space group $P\bar{1}$, $N = 2$, $V = 443$ Å^3. The experiment included the nine layer lines hk0–hk5, 0kl, h0l; each of them was recorded on five to six films with multiple exposures. Weighted mean I_{hkl} values were obtained from the intensities evaluated on all the films; the absorption factor was not taken into account ($\mu = 72.1$).

The structure was determined by the heavy-atom method from 780 unique nonzero reflections; $\sin\theta/\lambda \leq 0.7$, $F^2_{max}/F^2_{min} = 140$. Refinement was accomplished by the method of least squares to an R value of 0.092 using individual isotropic temperature factors.

From comparison of the atomic coordinates in europium (Table 1) and lanthanum[1] hypophosphites it is seen that the x and y coordinates of the metal, P and O_3, and O_5 and O_6 atoms in the two structures are extremely close. For the convenience of comparing the structures the remaining atoms in europium hypophosphite on the (010) projection (Fig. 1) were renumbered in the same way as in lanthanum hypophosphite.[1] The z coordinates of the O_1 and O_2 atoms in the two structures are similar, and the values for the x and y coordinates of the O_1 and O_2 atoms in the structures have, as it were, changed plates. The difference is in the intensities of the hk0 reflections of the lanthanum and europian hypophosphites are mainly due to the significant difference in the x and y coordinates of the O_4 atoms and water molecules.

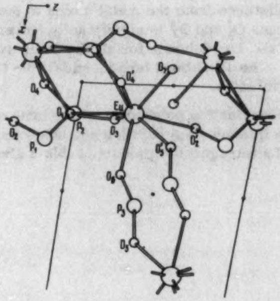

Fig. 1. Projection of the structure of $Eu(H_2PO_2)_3 \cdot H_2O$ on to the (010) plane.

In the crystal structure of the analyzed compound near the center of symmetry at the origin of the coordinates, it is possible to distinguish a pair of europium atoms joined by two bidentate bridging $O_2P_2O_4$ groups and two bridging O_1 atoms of the tridentate hypophosphite groups $O_1P_1O_2$ (Fig. 1). The latter form a link between the separate pairs of europium atoms, creating chains along the c axis. The bidentate bridging groups $O_5P_3O_6$ join the chains into pairs parallel to the (110) plane. The water molecule is in the inner coordination sphere of the metal atom. The lengths of the Eu–O bonds obey the same rules as in lanthanum hypophosphite; the distances from the europium atom to the bridging oxygen atom are significantly longer (2.60 and 2.47 Å) than the distances to most of the other oxygen atoms (Table 2). The coordination number of the europium atom is 8, and the coordination polyhedron is a tetragonal antiprism, where the europium polyhedra in the pair which we distinguished have a common edge O_1–O_1' and form a binuclear fragment of the chain. Thus, in europium hypophosphite compared with lanthanum hypophosphite the inner sphere of the lanthanide atom is reconstructed and as a result the eightfold inversion axis of the tetragonal antiprism in europium hypophosphite forms an angle close to a right angle with the analogous axis of the polyhedron in lanthanum hypophosphite.

TABLE 1. Position and Thermal Parameters of the Basis Atoms of the Structure

Atom	x/a	y/b	z/c	B, Å^2
Eu	0.1317 (2)	0.1947 (2)	0.3137 (2)	4.0(0)
P_1	0.2583 (8)	0.2021 (11)	−0.1512 (19)	3.8(2)
P_2	0.1484 (10)	−0.2543 (14)	−0.0088 (19)	4.0(2)
P_3	0.5628 (8)	0.3010 (11)	0.4211 (19)	3.8(2)
O_1	0.1369 (16)	0.0792 (22)	−0.0695 (37)	2.7(3)
O_2	0.1882 (27)	0.1775 (31)	−0.3577 (54)	5.9(5)
O_3	0.1590 (25)	−0.1015 (29)	0.2134 (49)	5.3(5)
O_4	0.0124 (22)	−0.3439 (25)	−0.2083 (41)	3.8(4)
O_5	0.7177 (23)	0.4693 (27)	0.4534 (45)	4.4(4)
O_6	0.4071 (19)	0.2847 (22)	0.3028 (42)	2.3(3)
O_7	−0.0746 (22)	0.2627 (27)	0.4937 (42)	4.1(4)

TABLE 2. Principal Interatomic Separations (Å) and Bond Angles (deg) in the Structure

$Eu-O_1$	2.60(2)	$Eu-O_7$	2.45(2)	$O_1-P_1-O_2$	116.4
$Eu-O_1'$	2.47(2)	P_1-O_1	1.55(2)	$O_3-P_2-O_4$	125.3
$Eu-O_2'$	2.47(3)	P_1-O_2	1.50(3)	$O_5-P_3-O_6$	116.9
$Eu-O_3$	2.36(3)	P_2-O_3	1.54(3)		
$Eu-O_4$	2.41(3)	P_2-O_4	1.53(3)		
$Eu-O_5$	2.29(3)	P_3-O_5	1.48(3)		
$Eu-O_6$	2.35(2)	P_3-O_6	1.53(2)		

Note: The standard deviations of the angles lie within 0.8-0.9°.

Comparison of the structures of lanthanum[1] and europium hypophosphites shows that the second hypophosphite group ($O_3P_2O_4$) has almost the same location in the crystals of the two compounds. However, its function in the structure changes on account of the fact that the oxygen atoms of the first hypophosphite group have a somewhat different location in the europium compound from that in lanthanum hypophosphite, and the bridging oxygen atom in europium hypophosphite is O_1 and not O_2, as in lanthanum hypophosphite. As a result the second hypophosphite group links the apices of two polyhedra having a common edge, whereas in lanthanum hypophosphite the same group connects the polyhedra of two adjacent binuclear fragments in the chain passing along the c axis.

The oxygen atoms of the third hypophosphite group in europium hypophosphite have z coordinates which differ greatly from the coordinates of the corresponding atom in lanthanum hypophosphite. This does not, however, change the role of the $O_5P_3O_6$ group in the structure.

---

[1] V. M. Ionov, L. A. Aslanov, V. B. Rybakov, and M. A. Poraï-Koshits, Kristallografiya, 18, 403 (1973) [Sov. Phys. – Crystallogr., 18, 250 (1973)].

Proposed method for determining the coordinates of resonant nuclei using polarized Mössbauer spectroscopy

M. A. Andreeva and R. N. Kuz'min
M. V. Lomonosov Moscow State University

(Submitted November 16, 1971; resubmitted April 30, 1972)
Kristallografiya, 18, 407-408 (March-April 1973)

The resolution of the energies of separate transitions between hyperfine resonant sublevels of nuclei which is achieved in Mössbauer spectroscopy allows one to carry out various polarization experiments with gamma rays. The Mössbauer polarimeter[1] at present is an effective method for studying the hyperfine interactions. In addition, the polarization of gamma radiation must be taken into account in interpreting a number of phenomena observed both in experiments on absorption of resonant radiation and in Mössbauer diffraction.

Here we consider the theory of the polarization of gamma radiation when it is diffracted by crystals containing Mössbauer nuclei in the presence of the hyperfine interaction. We consider the structure amplitude of the nuclear resonant scattering. If we neglect the electronic scattering, which is valid for high orders of reflection or for those maxima in which Rayleigh diffraction causes extinction (purely nuclear reflections), then the nuclear structure amplitude is written as

$$F(H)=\sum_j f_{r_j}\exp\{2\pi i(hx_j+ky_j+lz_j)\}, \tag{1}$$

where f_{r_j} is the scattering amplitude for the j-th Mössbauer nucleus with coordinates (x_j, y_j, z_j), while $H \equiv h, k, l$. It is known that in the presence of a hyperfine field at the Mössbauer nuclei the energy and angular dependences of f_{r_j} are determined by the magnitude and direction of the effective magnetic field or electric field gradient at each individual Mössbauer nucleus[2,3] and a dependence on the orientation of the axis for the hyperfine interaction exists not only for the absolute value of the scattering amplitude for one nuclear wave, but also for its polarization and for the initial phase of the scattered beam.

Thus if the effective magnetic field or electric field gradient has different directions at the nuclei in various positions in the unit cell, then within the limits of one unit cell there will be various directions which will produce interference of the waves of different polarizations scattered by resonant nuclei at different positions in the unit cell (these waves will be completely coherent if completely polarized resonant radiation is incident upon the crystal). The interference of waves of different polarizations is a physical feature of the Mössbauer diffraction process in the presence of a hyperfine interaction; this phenomenon leads to consequences of practical importance for structural analysis.

The structure factor for nuclear diffraction, $|F(H)|^2$, in the case of interest should be calculated in agreement with the general theory of interference of waves of various polarizations developed in crystal optics.[4] It follows from this theory, in particular, that for cases of two resonant nuclei in a unit cell with different hyperfine interactions, the structure factor for overlapping resonance can be calculated from

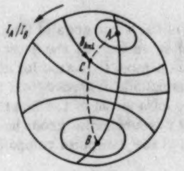

Fig. 1

$$|F(H)|^2=|f_{r_1}|^2+|f_{r_2}|^2+2|f_{r_1}|\,|f_{r_2}|\cos(c/2)\cos(\delta+\chi), \tag{2}$$

where $\delta = 2\pi[h(x_1-x_2)+k(y_1-y_2)+l(z_1-z_2)]$ is the spatial phase shift, while χ is the additional polarizational phase shift. It is important that in (2) the interference term which is of greatest interest for structural analysis is weakened by a "similarity of the polarization" factor which includes a wave cos(c/2). In the representation on the Poincare sphere[5] c is the arc length between points which represent the polarizations of the combined waves.

We consider explicitly the Mössbauer nucleus Fe^{57} (the spins of the ground and excited states are 1/2 and 3/2, respectively, with an M1 transition) and assume that the unit cell contains two such nuclei having the same magnetic splitting of the resonant levels, but with the effective magnetic fields at them antiparallel. In this case for transitions with $\Delta m = \pm 1$ in Eq. (2), we easily find

$$\begin{gathered}|f_{r_{1,2}}|^2\sim(1\pm M\Delta m\cos\beta)^2(1+\cos^2\beta'),\\ \cos(c/2)=(1-\cos^2\beta')/(1+\cos^2\beta'),\\ \chi=2\Delta m(\alpha'-\alpha),\end{gathered} \tag{3}$$

where $M = \pm 1$ represents right- and left-handed circular polarization of the incident radiation and β, β' and α, α' are the polar and azimuthal angles of the incident and scattered gamma quanta with an effective magnetic field $+H_{eff}$, respectively.

The polarization of the diffracted radiation can also be determined using the Poincare sphere. If A and B (see Fig. 1) are points on the sphere which represent the polarizations of wave scattered by nuclei at different positions in the unit cell, then the polarization of the total wave is represented by the point C which is determined from the relations

$$\begin{gathered}\sin(a/2)=(I_A/I)\sin^2(c/2),\\ \sin(b/2)=(I_B/I)\sin^2(c/2),\end{gathered} \tag{4}$$

where a, b, and c are the arc lengths $\widehat{BC}$, $\widehat{AC}$, and $\widehat{AB}$, respectively, $I_{A,B}$ is the intensity of the combined waves, and I is the total intensity determined from Eq. (2). It is most important that if we combine the nonidentical polarizations, then the resulting polarizations are not deter-

Vol.
July 19
June 1

mined uniquely by the intensities and polarizations of the combining waves, but depend essentially on the shifts in their phases. [The dependence on δ enters (4) through I]. In the Poincare-sphere representation, the points which represent the polarization of the total wave with different phase shifts and other parameters remaining the same, lie at the edge of a small circle with a center at the arc which joins points A and B (see Fig. 1). The position of this edge depends only on the ratio I_A/I_B.

For the case of interest, an antiferromagnetic unit cell, the polarization of the nuclear reflections is obtained in the form ($\tan\omega$ is the ellipticity, and λ is the azimuth of the principal axis of elliptical polarization)

$$\sin 2\omega = M\frac{4\cos\beta\cos\beta'}{(1+\cos^2\beta)(1+\cos^2\beta')+\sin^2\beta\sin^2\beta'\cos(\delta+\chi)},$$
$$\mathrm{tg}\,2\lambda = \frac{2\cos\beta'(1-\cos^2\beta)}{(1-\cos^2\beta\cos^2\beta')\,\mathrm{ctg}[(\delta+\chi)/2]+(\cos^2\beta-\cos^2\beta')\,\mathrm{tg}[(\delta+\chi)/2]} \qquad (5)$$

Similar treatment can be carried out for different orientations of the electric field gradient in the unit cell.

Thus there is a unique possibility for determining the coordinates of resonant nuclei in the unit cell from the polarizations of the components of the Mössbauer spectrum in the diffraction maxima of the nuclear scattering which has a definite analogy in optics (the polarization method for determining the thickness of a dichroic plate). The possibility of obtaining structural information from the polarization measurements is an inherent feature of Mössbauer spectroscopy. The actual possibilities of this method require further estimates. We only note that measurements of the parameters of the Mössbauer diffraction spectrum, the relation between the intensities and polarizations of the components of the spectrum, are of an independent nature, while other diffraction methods for studying the structures of crystals are based on the comparisons of the intensities of possibly a large number of reflections.

---

[1] H. Frauenfelder, D. E. Nagle, R. D. Taylor, D. R. F. Cochran, and W. M. Visscher, Phys. Rev., 126, No. 3, 1065 (1962).

[2] M. A. Andreeva and R. N. Kuz'min, Dokl. Akad. Nauk SSSR, 185, 1282 (1969) [Sov. Phys. – Dokl., 14, 298 (1969)]; Kristallografiya, 14, 708 (1969) [Sov. Phys. – Crystallogr., 14, 605 (1970)].

[3] V. A. Belyakov and Yu. M. Aivazyan, ZhETF Pis. Red., 7, 477 (1968) [JETP Lett., 7, 368 (1968)]; Zh. Eksp. Teor. Fiz., 54, 1162 (1968) [Sov. Phys. – JETP, 27, 622 (1968)].

[4] S. Pancharatnam, Proc. Indian Acad. Sci., A44, 247 (1956).

[5] F. A. Wright, J. Opt. Soc. America, 20, 529 (1930).

Electrooptical properties of potassium dihydrogen phosphate crystals having different degrees of deuteration

E. N. Volkova and I. A. Velichko
M. V. Lomonosov Moscow State University

(Submitted February 25, 1972)
Kristallografiya, 18, 409-410 (March-April 1973)

It was noted in ref. 1, in a comparison of the electrooptical constants of crystals of the KDP group, that the electrooptical coefficient r_{63} increases linearly with the Curie temperature T_C, each group of phosphates and arsenates having its own straight line. However, this assumption of linearity needs to be modified, since it contradicts the fact of nonlinear increase of r_{63} with T_C in[2] $Rb(D_xH_{1-x})_2PO_4$. For this purpose, we measured the electrooptical coefficients of isomorphous $K(D_xH_{1-x})_2PO_4$ crystals, grown by the method described in,[3] and compared the results with refs. 1 and 2.

Curie temperatures were measured for samples with x = 0.50, 0.90, and 0.98 by the method given in ref. 2, and the remaining values were taken from ref. 4; x is the calculated degree of deuteration of the solution.

The coefficient r_{63} was measured by the polarization method using z-cut crystals measuring 10 × 10 × 3 mm; the light ($\lambda = 0.633\ \mu$) and electric field ($\nu = 50$ Hz) were directed along the z axis. The coefficients r_{41} were measured with 45° x-cuts. In calculating r_{41} and r_{63}, we used linear relations between the refractive index and[2] T_C and employed the data of ref. 5 for $K(D_{0.9}H_{0.1})_2PO_4$. The dielectric constants ε_1 and ε_3 were measured by the bridge method at 2 kHz. The results are given in Fig. 1 and Table 1. Data from ref. 6 are given in the last column of Table 1.

As Fig. 1 shows, $V_{\lambda/2}$ (for the longitudinal effect) and ε_3^{-1} decrease linearly with increasing T_C (the temperature coefficients are equal to ~60 V · deg^{-1} and ~0.03 deg^{-1}, respectively). The nonlinearity of $r_{63}(T_C)$ and $\varepsilon(T_C)$ follows from this. Calculation by the method of least squares results in the following equations:

$$r_{63} = \frac{(1.8 \pm 0.1)}{T - T_C} \cdot 10^{-9}\ \text{m} \cdot \text{deg} \cdot \text{V}^{-1}, \tag{1}$$

$$\varepsilon_3 = (3800 \pm 200°) / (T - T_C), \tag{2}$$

where T = 295°K is the temperature at which the measurements were made.$^{1)}$

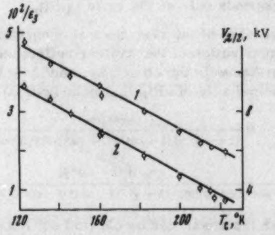

Fig. 1. Curves of inverse dielectric constant (1) and half-wave potential (2) versus Curie temperature for $K(D_xH_{1-x})_2PO_4$ crystals.

Since the Curie–Weiss law is symmetrical with respect to T_C and T, the explanation of Eqs. (1) and (2) would be obvious if the Curie–Weiss constants C for the crystals being studied were equal. It was shown in ref. 7 that C for $K(D_xH_{1-x})_2PO_4$ varies by ~30% (3200–4160°) as x varies from 0 to 0.96, which should result in nonlinearity of the functions $V_{\lambda/2}(T_C)$ and $\varepsilon_3^{-1}(T_C)$. Remote from the phase transition, however, as Fig. 2 in ref. 7 shows, the curve of ε_3^{-1} changes slope toward increased C. Since our measurements for concentrations x ≤ 0.50 were made far from the phase transition, the Curie–Weiss constants proved to be approximately equal. The above also applies to r_{63}, since $r_{63} \sim \varepsilon_3$ in both temperature changes[8] and isomorphous substitutions [it is evident from Table 1 that the ratio $r_{ij}/\varepsilon_0(\varepsilon_j - 1)$ is constant within the error of measurement]. The fact that the constants in Eqs. (1) and (2) agreed with the corresponding constants for $Rb(D_xH_{1-x})_2PO_4$ crystals is explained by the closeness of the C values for the two isomorphous series. According to our data, C changes from 3000 to 4500° on deuteration of RDP crystals.

The authors thank B. A. Strukov and L. N. Rashkovich for their assistance and a discussion of the results.

TABLE 1. Electrooptical Coefficients and Dielectric Constants of $K(D_xH_{1-x})_2PO_4$ Crystals

x	T_C, °K	r_{63}, 10^{-12} m/V	ε_3	$r_{63}/\varepsilon_0(\varepsilon_3 - 1)$, 10^{-2} m²/C	ε_1	r_{41}, 10^{-12} m/V	$r_{41}/\varepsilon_0(\varepsilon - 1)$, 10^{-2} m²/C
0	122.6	9.9±0,2	21.0±0,5	5.6±0.3	44±1	8.6±0.2	2.3±0.2
0.18	135.3	10.1±0.3	23.7±0.6	5.1±0.3			
0.30	145.6	11.7±0.3	25.6±0.7	5.4±0.3	45±1		
0.40	161.1	13.4±0.4	29.2±0.9	5.4±0.3			
0.50	160.2	12.8±0.4	27.2±0.4	5.5±0.2	48.3±1	9.3±0.3	2.2±0.2
0.70	182.0	16.0±0.6	33.4±0.9	5.5±0.3			
0.86	199.5	19.8±0.7	40.3±1.0	5.6±0.4	55.0±1.4	10.7±0.3	2.2±0.2
0.90	209.8	22.7±1.2	44.9±0.7	6.0±0.4	51.7±1.4	10.9±0.3	2.4±0.2
0.96	215.0	23.3±1.2	47.2±0.5	5.6±0.3	59.0±1.6		
0.98	216.3	25.8±0.2	49.0±1.0	6.1±0.4	55.2±1.4	10.7±0.3	2.2±0.2
0.998	222	26.4±0.7	50.0±2.0	6.1±0.3			

---

[1] The temperature varied by ±2° in the measurements; the corresponding error was taken into account in the constants of Eqs. (1) and (2).

---

[1] A. S. Vasilevskaya and A. S. Sonin, Kristallografiya, 14, 713 (1969) [Sov. Phys. – Crystallogr., 14, 611 (1970)].

[2] E. N. Volkova, B. M. Berezhnoi, A. N. Izrailenko, A. V. Mishchenko, and L. N. Rashkovich, Izv. Akad. Nauk SSSR, Ser. Fiz., 35, 1858 (1971).

[3] I. A. Velichko, Collection of Abstracts of the State Institute of Applied Chemistry on the Chemistry and Technology of Isotopes and Labeled Compounds for 1968 [in Russian], Leningrad (1970).

[4] A. Baddur, B. A. Strukov, I. A. Velichko, and V. N. Setkina, Kristallografiya, 17, 1065 (1972) [Sov. Phys. – Crystallogr., 17, 938 (1973)].

[5] R. Phillips, J. Opt. Soc. Am., 56, 629 (1966).

[6] T. R. Sliker and S. R. Burlage, J. Appl. Phys., 34, 7, 1837 (1963).

[7] B. A. Strukov, A. Baddur, V. A. Koptsik, and I. A. Velichko, Fiz. Tverd. Tela, 14, 1034 (1972) [Sov. Phys. – Solid State, 14, 885 (1972)].

[8] F. Jona and G. Shirane, Ferroelectric Crystals, Pergamon (1962).

Synthesis and ferroelectric properties of antimony orthoniobate

V. I. Popolitov, A. N. Lobachev, V. F. Peskin, L. N. Syrkin, and N. N. Feoktistova
Institute of Crystallography, Academy of Sciences of the USSR
(Submitted March 13, 1972; resubmitted May 22, 1972)
Kristallografiya, 18, 411-412 (March-April 1973)

The discovery[1] that natural crystals of the mineral stibiotantalate have pyro-piezoferroelectric properties lends interest to the preparation of pure (admixture-free) synthetic $A^VB^VO_4$ compounds (A^V = Sb or Bi, B^V = Nb or Ta).

This paper gives information on the synthesis and piezoferroelectric properties of single crystals of antimony orthoniobate, obtained by the hydrothermal method. The following initial substances were used for the synthesis: antimony trioxide and niobium pentoxide (both of "e.c.p." grade). The weight-to-weight ratios of the initial components Sb_2O_3 and Nb_2O_5 were varied from the stoichiometric value to 1:(1-3) and (1-3):1, respectively. As the crystallization medium we used aqueous solutions of caustic soda and potash ($C_{NaOH, KOH}$ = 10-50 wt.%), potassium fluoride (C_{KF} = 2-60 wt.%), and potassium carbonate ($C_{K_2CO_3}$ = 5-40 wt.%). The phases obtained were identified by x-ray phase analysis. Batch-type autoclaves holding 170 cm³ were used.

The principal crystallization parameters were as follows: temperature 500-650°C, temperature drop over the height of the autoclave 15-65 deg (autoclave height 300 mm), packing factor 0.6-0.65.

We shall now examine the crystallization conditions of antimony orthoniobate in certain solvents.

1. Crystallization of $SbNO_4$ in Aqueous Solutions of NaOH and KOH. As shown by experiments, formation of single crystals of $SbNbO_4$ in aqueous solutions of NaOH and KOH is accompanied by marked polymerization of niobium pentoxide and by formation of readily soluble compounds of the Na_3SbO_4 and K_2SbO_3 type and of single crystals of antimony trioxide. Polymerized solutions are observed when the autoclaves are opened. As shown by Lassner and Püschel,[2] the basic forms of existence of Nb_2O_5 in alkali solutions are hydroxyl complexes of the type $[Nb_6(OH)_{38}]^{8-}$. We added (CO_3^{2-}) anions[1)] to the NaOH and KOH solutions, which broke up these polymeric forms, but the required crystals were not obtained owing to formation of secondary phases of the $NaNbO_3$ and $KNbO_3$ type. It was only at high alkali and carbonate-anion concentrations ($C_{Na(K)OH}$ = 50 wt.% and $C_{K_2CO_3}$ = 40 wt.%) that we obtained, in addition to single crystals of Sb_2O_3, $NaNbO_3$, and $KNbO_3$, small amounts (1-2 wt.% of the initial charge) of small single crystals of antimony orthoniobate.

2. Crystallization of $SbNbO_4$ in aqueous solutions of KF + K_2CO_3 and KF. At 500-650°C and a temperature drop of 15-65°, the reaction of the initial charge of Sb_2O_3 and Nb_2O_5 with an aqueous solution of potassium fluoride is very nonuniform. At high (5-10 wt.%) KF concentrations, mainly antimony trioxide dissolves; it crystallizes with formation of Sb_2O_3 single crystals of different modifications, whereas Nb_2O_5 is retained in the initial form. At the same experimental parameters, an increase in the KF concentration from 10 to 45 wt.% increases the solubility of Nb_2O_5, which leads to formation of single crystals of Sb_2O_3, Nb_2O_5, and $Sb \cdot NbO_4$. However, at this KF concentration transfer of niobium pentoxide is negligibly small in comparison with that of antimony trioxide; this is reflected in the yield of Sb_2O_3, Nb_2O_5, and $SbNbO_4$ single crystals. The bulk of the Nb_2O_5 usually crystallizes in situ with formation of fine crystals of niobium pentoxide, and only a very small part is transferred to the upper zone, where, together with antimony trioxide, it forms single crystals of $SbNbO_4$, the yield of which is 1-3% of the weight of the initial charge. Thus the principal factor limiting crystallization of $Sb \cdot NbO_4$ for these KF concentrations is the poor solubility and slight transfer of niobium pentoxide. The different solubilities of Sb_2O_3 and Nb_2O_3 in KF lead to their nonsynchronous transfer to the solution, which largely explains their separate crystallization as single crystals of Sb_2O_3 and Nb_2O_5. A further increase in the KF concentration (45-60 wt.%) leads to an increase in its solvating capacity with respect to the initial charge; this is expressed in the formation of secondary complexes of the $K_xNb_yF_z$ type. Formation of such complexes is explained by the sharp increase in the reaction of Nb_2O_5 with KF, the result of which is splitting of the Nb–O bond and formation of fluoride forms of niobium. To break up the latter, we added potassium carbonate ($C_{K_2CO_3}$ = 5-40 wt.%) to the aqueous solution of potassium fluoride. The CO_3^{2-} anion competed with the fluoride ion, i.e., it practically prevented formation of fluoride forms of niobium and thus promoted crystallization of $SbNbO_4$. Thus the use of a mixed solvent KF + K_2CO_3 made it possible to avoid complex formation in the system $Sb_2O_3-Nb_2O_5-KF-H_2O$, thereby greatly increasing the rate of formation and the yield of antimony orthoniobate single crystals. To increase the yield of $SbNbO_4$ single crystals we also used several different procedures. In the first method the oxides were located in different zones of the reaction space. The more soluble Sb_2O_3 was placed in the colder upper zone, the less soluble Nb_2O_5 in the lower zone; this created the maximal pressure drop. Owing to the different temperatures in the upper and lower zones of the reaction space, the solubilities of Sb_2O_3 and Nb_2O_5 were to some extent equalized, which increased the yield of $Sb \cdot NbO_4$ single crystals. In the second method the niobium pentoxide solution was saturated and the readily soluble antimony trioxide was then dissolved in it. The anti-

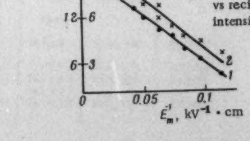

Fig. 1. Spontaneous polarization P_s (1) and coercive force E_c (2), plotted vs reciprocal of the alternating field intensity amplitude E_m^{-1}.

mony orthoniobate single crystals thus obtained were greenish brown plates, with {100}, {130}, {4, 12, 9}, and {209} as the principal forms. The maximal dimensions were as follows: length 2.5-3.5 mm, width 1.5-2.5 mm, and thickness 0.5-0.8 mm. To investigate the ferroelectric properties of $SbNbO_4$ single crystals, electrodes were soldered onto the (100) plane by means of silver paste. The synthesized $SbNbO_4$ single crystals have ferroelectric properties. The phase transition temperature T_C is 403 ± 2°C (for heating up). With T = 200°C, the graphs of P_s and E_c vs E^{-1} are practically linear (Fig. 1); from these we obtained the values $P_{s\infty} = 15\ \mu C/cm^2$ and 18 $\mu C/cm^2$, and $E_{C\infty} = 10$ and 11 kV/cm, respectively, for two specimens. Direct measurement of the hydrostatic piezoelectric modulus d_h at room temperature by the static method gave the value $0.8 \cdot 10^{-6}$ cgs esu. The combination of the low values of ε with the relatively high piezoelectric modulus d_h indicates the high piezoelectric sensitivity of $SbNbO_4$ crystals with respect to hydrostatic pressure.

---

1) Potassium carbonate was added to the solution of NaOH and KOH.

[1] N. D. Gavrilov, N. F. Koryakina, V. A. Koptsik, and V. K. Novik, Dokl. Akad. Nauk SSSR, 195, 823 (1970) [Sov. Phys.-Dokl., 15, 1075 (1971)].

[2] E. Lassner and R. Püschel, J. Less-Common Metals, 12, 146 (1967).

Characteristic features of the internal friction of filamentary crystals of NaCl, KCl, and KBr at elevated temperatures

Lieh K'uang and V. N. Rozhanskii
Institute of Crystallography, Academy of Sciences of the USSR
(Submitted February 14, 1972; resubmitted May 17, 1972)
Kristallografiya, 18, 413-415 (March-April 1973)

The curves giving the temperature dependence of the internal friction of crystals often show peaks associated with definite elementary mechanisms of scattering of the energy of the elastic vibrations. For massive alkali halide crystals there are only nonsystematic measurements, made at different frequencies.[1-4] There are no published data for filamentary alkali halide crystals.

Measurements in the temperature range 100-200°C showed internal friction peaks, which were interpreted as the manifestation of the formation and movement of kinks, the interaction of dislocations with point defects, the interaction of vacancies with impurity atoms, and other mechanisms. The measurements were made at different frequencies and with crystals with different compositions. It is not established whether the authors cited were dealing with peaks of different kinds or whether they have put forward different interpretations of the same phenomenon.

We measured the internal friction of the filamentary crystals in a vacuum assembly, which is illustrated diagramatically in Fig. 1. The filamentary crystals was firmly attached to the end of a mercury thermometer placed between two metal plate electrodes situated 10 mm apart. The tube containing the specimen was screened by means of a grounded copper screen. The crystal was heated by means of a small heater, and the temperature was measured from the thermometer readings. The measurements were made in a vacuum at 10^{-4}-10^{-5} torr in the temperature range from room temperature to 250°C. The bending vibrations were excited by applying an alternating voltage to the electrodes of the assembly. We used filamentary crystals of NaCl, KCl, and KBr with length 4-20 mm and thickness 3-20 μ, grown on cellophane[5] and silica gel,[6] and also filamentary crystals of NaCl and KBr, grown from solution with the addition of polyvinyl alcohol,[7] with axis parallel to [100].

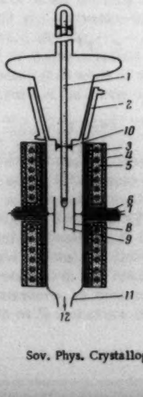

Fig. 1. Diagram of apparatus: 1) thermometer; 2) ground joint with water cooling; 3) heater winding; 4, 5) thermal insulation; 6) copper screen; 7) electrical insulation; 8) plate electrodes; 9) filamentary crystal; 10) centering wire ring; 11) glass tube; 12) side arm to vacuum sytem.

Figure 2 gives the temperature dependence of the internal friction of fibrous crystals of NaCl, KCl, and KBr, which were grown on silica gel and were not subjected to additional treatment after growth. All the curves show a clearly defined maximum A in the temperature range from 100 to 150°C for measurement at frequencies up to 500 Hz.

Some of the filamentary crystals showed a second maximum B in the range 30-70°C. Heating during the first measurement led to a decrease in the internal friction background and to disappearance of the maximum B, and the maximum A was displaced towards higher temperatures. On repeated heating the temperature of the maximum A changed little. Since the maximum B is very unstable, it was not studied in detail. Only the maximum A is dealt with below.

The results of the measurements on NaCl crystals are given in Fig. 2 (curve 4) in the form of the relationship between the logarithm of the frequency of the vibrations and the reciprocal of the absolute temperature of the position of the maximum A. A marked scatter is observed from one crystal to another, but the arrangement of the points in a sloping band indicates that the relaxation mechanism is activational in character. This scatter makes the determination of the activation energy unreliable, but an approximate estimate gives the values ~1 eV for the activation energy and $\tau_0 = 10^{15}$ $\sec^{-1}$ for the preexponential factor.

Annealing at 150°C for several hours leads to a decrease in the background, disappearance of the peak B, and a slight decrease in the height of the peak A. Annealing for 1 h at 200°C decreases the height of this maximum by 15-20%, and the temperature of the peak is displaced by 5-10° towards higher temperatures. In individual cases annealing at this temperature does not de-

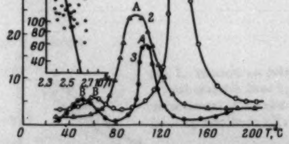

Fig. 2. Temperature dependence of the internal friction of filamentary crystals. 1) NaCl, frequency of the vibrations 315 Hz; 2) KBr, frequency of the vibrations 35 Hz; 3) KCl, frequency of the vibrations 66 Hz; 4) relationship between the temperature of the position of the internal friction peak A and the frequency of the vibrations for filamentary crystals of NaCl.

crease, but on the contrary increases, the height of the maximum. Annealing at 250°C for 1 hr leads to a further decrease in the height of the maximum A. After annealing at temperatures above 300°C for several hours, the peak A disappears completely.

Plastic deformation by twisting does not lead to restoration of the peak in annealed crystals. Only an increase in the overall background of internal friction is detected.

In nonannealed crystals, plastic deformation leads to an increase in both the level of the background and the magnitude of the internal friction peak (Fig. 3a). This gives grounds for assuming that the peak A is not only associated with processes of dislocation movement, but also determined by the interaction of dislocations with point defects, which may be removed from the crystal on annealing.

The amplitude dependence of the maxima A for the internal friction of filamentary NaCl crystals was studied for deformations in the range from 10^{-5} to $4 \cdot 10^{-4}$. For deformations from 10^{-5} to 10^{-4}, a dependence on amplitude was not observed, but in the range from 10^{-4} to $4 \cdot 10^{-4}$ a monotonic increase in the height of the peak with increase in the amplitude of the deformation was observed (Fig. 3c).

For the same amplitudes of bending, the magnitude of the maximum A for a given crystal depends markedly on the transverse dimensions of the crystal in the plane of the vibrations, and increases with increase in these dimensions. All these results indicate that in the range of deformations studied the internal friction shows a poorly defined amplitude dependence for a mechanism determined by the production of the peak A.

In the filamentary crystals, with increase in thickness there is an increase in the number of dislocations present. The height of the maximum A also increases with increase in the thickness of the crystal (Fig. 3b). Increase in the thickness of the crystal also leads to an increase in the amplitude of the deformation. The nature of the influence of the amplitude of the vibrations, studied on crystals with the same thickness, is slightly different, however. The dependence shown in Fig. 3c is much more regular than that shown in Fig. 3b. For a thickness greater than 5 μ, the scatter of the points in Fig. 3b is apparently related to the statistical irregularity of the concentration of dislocations in the filamentary crystals.

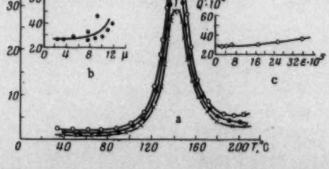

Fig. 3. Influence of plastic deformation on the height of the internal friction peak (a), dependence of the peak height on the thickness of the crystal (b), and the amplitude dependence (c) of the internal friction peak for a filamentary crystal of NaCl. a: 1) Nondeformed crystal; 2) crystal, deformed by twisting, 20°; 3) crystal, deformed by twisting, 30°, length of crystal 10.2 mm, frequency of the vibrations 82 Hz; c) length 3.8 mm, thickness 3 μ, frequency of the vibrations 110 Hz.

To alter the concentration of point defects, the crystals were subjected to irradiation by x rays at room temperature for a period of 10 min from a tube operating at a voltage of 45 kV and a current of 10 mA. After the irradiation, as in ref. 3, the height of the maximum decreased and the peak was displaced slightly towards higher temperatures (Fig. 4). This displacement continued for some time when the crystal was kept at room temperature. Restoration of the height of the internal friction peak of the irradiated crystal was not observed even after the crystal had been kept for 60 days at room temperature. The maximum A on the curve giving the temperature dependence of the internal friction was observed for all the crystals studied, irrespective of their composition and method of growth. It is probably produced by the same mechanism in all the crystals.

The dependence of the height of the peak on the amplitude of the vibrations and the thickness of the crystals makes it possible to relate it to the movement of dislocations. This peak disappears in well-annealed crystals. The introduction of new dislocations by plastic twisting, however, does not lead to its restoration. During the annealing, the crystal is freed from not only dislocation, but also point defects, which are not restored on subsequent deformation. It must therefore be assumed that the peak is due to the interaction of the dislocations with the point defects. These crystals also show another peak B, which disappears more rapidly when the crystal is heated. This is probably due to more mobile defects. It may be assumed, for example, that the peak B is due to the interaction of the dislocations with single point defects, and that the peak A is associated with complexes of point defects. In actual fact, irradiation, which leads primarily to a change in the structure and the concentration of complexes of point defects, influences the magnitude and position of the peak A. The peak is decreased slightly and displaced towards higher temperatures, probably due either to an increase in the points of attachment to the

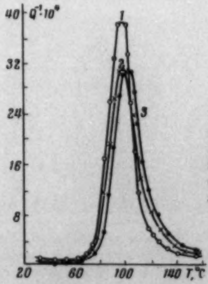

Fig. 4. Influence of irradiation with x rays on the internal friction of filamentary crystals of KCl. 1) Before irradiation; 2) after irradiation; 3) crystal kept for 15 h at room temperature after irradiation.

dislocations, or to an increase in the activation energy required to overcome these attachments. On annealing of the crystal, which is usually accompanied by the segregation of point defects on dislocations, the maximum is again decreased and is displaced towards higher temperatures. The nature of the internal friction peak is confirmed by the instability of its position and height for different filamentary crystals. This instability is apparently due to the statistical scatter in the concentration and strength of the points of attachment at the dislocations in different crystals.

The authors thank A. A. Predvoditelev for valuable discussion.

---

[1] A. Taylor, J. Appl. Phys., 32, 1799 (1961).

[2] A. A. Blistanov, Ya. I. Soifer, and M. P. Shaskol'skii, Fiz. Tverd. Tela, 10, 1968 (1968) [Sov. Phys. – Solid State, 10, 1549 (1969)].

[3] A. A. Botaki, Relaxation Phenomena in Solids [in Russian], Metallurgiya, Moscow (1968), p. 504.

[4] R. W. Dreyfus and R. B. Laibowitz, Phys. Rev., 135, A, 1413 (1964).

[5] S. Amelinckx, Physica, 24, 390 (1958).

[6] G. V. Berezhkova and V. N. Rozhanskii, Kristallografiya, 8, 420 (1963) [Sov. Phys. – Crystallogr., 8, 327 (1963)].

[7] B. Jeszenszky and E. Hartmann, Kristallografiya, 7, 433 (1962) [Sov. Phys. – Crystallogr., 7, 341 (1962)].

Electret effect in n-azoxyanisole

A. P. Kapustin, Z. Kh. Kuvatov, and A. N. Trofimov
Institute of Crystallography, Academy of Sciences of the USSR
Bashkir State University

(Submitted January 11, 1972; resubmitted March 24, 1972)
Kristallografiya, 18, 416-417 (March-April 1973)

The spontaneous polarization of an electret can be deduced from the depolarization current.[1,2]

In this way we have found that solid n-azoxyanisole made from the nematic phase in an electric field shows the electret effect, which persists for a long period. For instance, there is no appreciable polarization change on keeping a specimen with short-circuited electrodes for a day. There appears to be no paper on electrets from organic compounds that give liquid crystals.

We used a layer of area 1.72 cm² and 50 μ thick between flat electrodes. The device was heated and cooled in a thermostat. The polarized solid was produced from the nematic phase by cooling from 124°C to room temperature in an electric field over 10–15 min. Then the field was removed, the electrodes were connected to the measuring instrument, and the specimen was heated (curve 5 of Fig. 1).

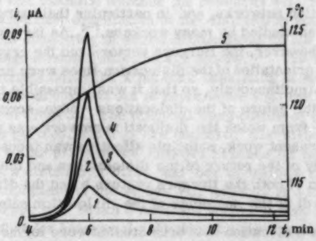

Fig. 1. Time dependence of: 1-4) depolarization current; 5) temperature for polarizing fields (V/cm) of: 1) 50; 2) 200; 3) 200; 4) 800.

A depolarization current flowed (Fig. 1) in the external circuit when the solid became a liquid crystal, because the polarization was thermally disrupted; this current was always in opposition to the polarization current, which indicates a frozen-in charge.

The depolarization current as a function of time (Fig. 1) gives this charge as $q = \int_0^\infty i\,dt$. Figure 2 shows that this was dependent on the polarizing field, and q = *f*(E) has a linear part and a saturation region. Electret theory shows that the specimen has only heterocharge in the linear region, but that this is accompanied by homocharge in the saturation region, i.e., charge begins to be injected in that region.[3]

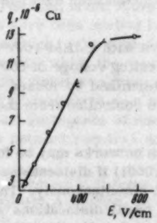

Fig. 2. Total frozen-in charge as a function of polarizing field.

Relatively weak polarizing fields are needed to make an electret from n-azoxyanisole, but the effective charge density is of the order of that found for ceramic electrets, which are the best as regards residual polarization.

We are indebted to V. M. Fridkin for discussions and valuable advice.

---

[1] B. Gross, J. Chem. Phys., 17, 10 (1949).
[2] L. I. Froiman and V. M. Fridkin, Kristallografiya, 1, 342 (1956) [Sov. Phys. – Crystallogr., 1, 263 (1956)].
[3] V. M. Fridkin and I. S. Zheludev, Photoelectrets and the Electrophotographic Process [in Russian], Izd. AN SSSR, Moscow (1960).

Dislocation networks formed during growth and annealing in the basal plane of a single crystal of zinc

N. A. Tyapunina, T. N. Pashchenko, and G. M. Zinenkova
M. V. Lomonosov Moscow State University

(Submitted October 22, 1971; resubmitted February 23, 1972)
Kristallografiya, 18, 418–420 (March-April 1973)

Dislocation networks, and in particular their structures, have been studied by many workers.[1–4] As far as we are aware, however, the Burgers vectors and the crystallographic orientation of the dislocation lines were not determined simultaneously, so that it was impossible to establish the nature of the dislocations – edge, screw, or mixed – from which the dislocation network was made up. In the present work, principle attention was focused on the study of the nature of the dislocations and the determination of both the Burgers vectors **b** and the direction vectors **dl** of the segments of the dislocation networks.

The dislocation networks studied were formed during the growth and annealing of single crystals of zinc, grown by the published method.[5] The specimens for the electron microscope studies were prepared by the method described in ref. 6. The crystallographic orientation of the Zn foil was determined from selected area electron diffraction data.

The studies were carried out with a JEM-100V electron microscope with an accelerating voltage of 100 kV. The Burgers vectors were determined by means of a goniometer attachment and were controlled from the dark-field image.

In zinc crystals, dislocation networks may be formed in the plane of ready cleavage (0001) if dislocations of two systems are generated in it simultaneously. The possible Burgers vectors for the basal dislocations are known; their moduli are equal and they lie along the direction of close packing $\langle 11\bar{2}0\rangle$.[7,8] To characterize completely the dislocation segments of the network, it is necessary to find the mutual orientation of the vectors **b** and **dl**.

Analysis of the photomicrographs obtained showed that the dislocation networks consist chiefly of mixed dislocations. We studied more than 20 networks, and in all cases it was found that the orientation of the segments of the dislocations was close to the edge orientation. The possibility of existence of networks of edge dislocations was examined theoretically in ref. 9.

The bright-field photomicrographs which formed the basis for the determination of the Burgers vectors of the dislocations are shown in Fig. 1. The photomicrographs were obtained by tilting the specimen by means of the goniometer, and the corresponding electron diffraction patterns from the section of the crystal being considered are given with allowance for the rotation of the image at the given magnification. Comparison of the photomicrographs and electron diffraction patterns shows that the dislocations in this network are edge dislocations.

The dislocation network shown in Fig. 2 consists of segments of mixed dislocations. The relationship between the magnitudes of the edge and screw components of the

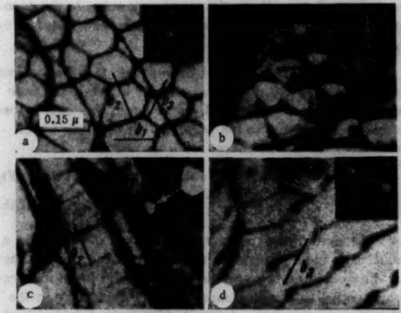

Fig. 1. Photomicrographs and selected area diffraction patterns for the determination of the Burgers vectors of the dislocations in a hexagonal dislocation network in the (0001) plane of zinc. The network consists of edge dislocation segments. a) All dislocations in contrast, image formed by several reflections; b) image of the family of dislocations with Burgers vector b_1 absent from the $10\bar{1}0$ reflection; c) image of the family of dislocations with Burgers vector b_2 absent from the $2\bar{2}00$ reflection; d) image of the family of dislocations with Burgers vector b_3 absent in the $02\bar{2}0$ reflection.

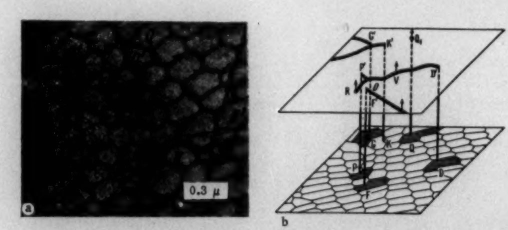

Fig. 2. Dislocation network (a) and a diagram of part of it (b). The network consists of mixed dislocations in the (0001) plane of zinc; the dislocations Q – Q', O – P', O– V, O – F', D' – V do not lie entirely in the plane of the network.

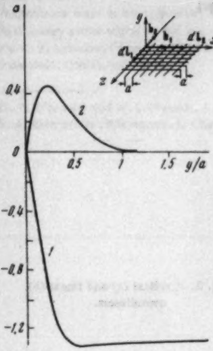

Fig. 3. Dependence of the components of the stress tensor σ_{xx}, σ_{yy}, and σ_{zz}, created by an orthogonal network of edge dislocations on the distance relative to the plane of the network along the line $x = z = a/2$. The stresses are given in units $Gb/a(1-\nu)$. 1) $\sigma_{zz} = \sigma_{xx}$; 2) σ_{yy}.

Burgers vector is different in different regions of the dislocation network. The angles between **b** and dl in the network have values between 65 and 90°.

It can be seen from the photomicrographs that some of the dislocations do not lie entirely in the plane of the network. A diagram of the three-dimensional dislocation structure, built up from the photomicrograph (Fig. 2a), is shown in Fig. 2b. The diagram shows how the dislocations at the sites D, Q, K, P, G, and F can emerge on to the plane parallel to it. Local change in the density of dislocations leads to the formation of expanded cells (these are hatched in the diagram) and unfinished "extra" rows of cells in the networks. Rearrangement of the rows of the network, brought about by the emergence of the dislocations from it, leads to changes in the orientation of dl. Thus in zinc the dislocation networks may consist of segments of practically all orientations. Networks consisting of screw segments bring about rotation of the regions of the crystal relative to an axis normal to the plane of the boundary, that is, they are boundaries of twist.[10] Networks consisting of edge segments do not lead to mutual disorientation of the blocks, but they bring about extension and compression of neighboring regions of the crystal. If, however, the dislocations in the network are mixed, there is rotation of the regions of the crystal, and also extension and compression. Networks of all three types may be formed from planar accumulations consisting of two systems of dislocations for which the Burgers vectors make an angle of 120°. Whether these segments in the network are edge, screw, or mixed is determined by the mutual orientation of the dislocations taking part in the reaction. Thus edge networks may result from the interaction of purely edge systems of dislocations or from mixed dislocations (for example, $\mathbf{b}_1$ and dl_1 make an angle of 60°, and $\mathbf{b}_2$ and dl_2 an angle of 120°).

We can examine whether the networks will be stable for an arbitrary orientation of the dislocation segments. Networks consisting of screw dislocations do not create long-range stress fields and are stable.[4,10] The analysis of the stress fields for a network consisting of edge dislocations was carried out in accordance with the square net model (Fig. 3). The diagonal components of the stress tensor σ_{xx}, σ_{yy}, and σ_{zz} are nonzero. The stress σ_{yy} normal to the plane of the network reaches its highest value at a distance of $0.25a$ and then decreases rapidly. The components of the stress σ_{xx} and σ_{zz} at a distance of the order of a reach a constant value. It may be assumed that for hexagonal networks the same components of the long-range stresses are preserved, and from this viewpoint, networks of edge dislocations are unstable. The presence of a screw component, in accordance with ref. 11, may stablize the dislocation boundary.

The fact, noted above, that most dislocation networks which have been studied had an orientation of the segments close to the edge orientation, can be related to the process by which the specimen was prepared, since dislocation structures from screw segments in thin foil can readily break down as a consequence of transverse gliding, and emergence of the edge segments from the plane of the network requires nonconservative movement.

[1] S. Amelinckx and W. Dekeyser, Solid State Phys., 8, 409 (1959).

[2] A. Berghezan, A. Fourdeux, and S. Amelinckx, Acta Metallog., 9, 464 (1961).

[3] W. Pfeiffer, Phys. Status Solidi, 2, 1727 (1962).

[4] G. M. Zinenkova and N. A. Tyapunina, Fiz. Met. Metalloved., 28, 637 (1969).

[5] F. F. Lavrent'ev, V. P. Soldatov, and Yu. G. Kazarov, Fiz. Met. Metalloved., 21, 793 (1966).

[6] V. N. Rozhanskii, A. A. Predvoditelev, and V. L. Indenbom, Fiz. Tverd. Tela, 9, 757 (1967) [Sov. Phys. – Solid State, 9, 593 (1967)].

[7] P. B. Price, J. Appl. Phys., 32, 1747 (1961).

[8] A. A. Predvoditelev, Kristallografiya, 7, 938 (1962) [Sov. Phys. – Crystallogr., 7, 759 (1963)].

[9] V. L. Indenbom, Kristallografiya, 2, 594 (1957) [Sov. Phys. – Crystallogr., 2, 587 (1957)].

[10] F. C. Frank, Defects in Crystalline Solids, Phys. Soc. L. (1955), p. 159.

[11] I. A. Kelareva and A. N. Orlov, Fiz. Met. Metalloved., 15, 824 (1963).

Evaluation of the heat effect during alkali halide monomer reorientation in an absorbed layer on a metal

Yu. N. Lyubitov and V. I. Mikhailov

Institute of Crystallography, Academy of Sciences of the USSR
(Submitted May 20, 1971; resubmitted January 4, 1972; March 17, 1972)
Kristallografiya, 18, 421-422 (March-April 1973)

It has already been established that in alkali halide salt pairs, in addition to monomeric MH molecules (M = metal, H = halide), which predominate at moderate temperatures, there exist the polymeric forms M_nH_n (n = 2,3) in a lower concentration, decreasing with decrease in temperature.

Only their orthorhombic modification was considered in refs. 1-5, which dealt with the structure of the alkali halide dimers M_2H_2. The analysis of Yarym-Agaev[6] has indicated that a linear dimer configuration is also possible. The calculations in refs. 1-6 were carried out in accordance with the usual equations for the electrostatic interaction energy of all ions in the dimer; Pauling's approximation[7] was used for the repulsion forces due to nonvalence electrons.

In ref. 6 the heats of transition are derived for the orthorhombic and linear modification; in all alkali halide dimers they range from 13 to 20 kcal/mole. We computed the potential barrier for transition from the linear to orthorhombic modification of Li_2F_2 to be 1.5-2 kcal/mole.[1)] From this data, the heat of activation for transition from the orthorhombic to linear modifications is about 20 kcal · mole^{-1}; here we use a heat of reaction for $(Li_2F_2)_{ortho} \rightleftharpoons (Li_2F_2)_{linear}$ of ~17 kcal/mole, in accordance[2)] with ref. 6. The basis for the computation performed consisted in a consideration of the nature of the change of the interaction potential of ions in the dimer for a smooth change of angles α and β from 0 to 100°. In this, our computation is distinct from that in ref. 6, where the same thing was done for only two pairs of angles: 1) $\alpha = \beta = 2$; 2) for the case of Li_2F_2: $\alpha \simeq 96$, $\beta \simeq 84°$ (Fig. 1). We will publish this very computation, which in general, does not differ from the one proposed in ref. 6. We note that deformation of the bonds 2−3 and 1−4 (Fig. 1) on change of temperature was not considered. The distance 1−2 changes very little even for transition from a monomer to a dimer.[5] The error introduced by this assumption does not exceed 20%.

Reference 8 gives the experimental confirmation of the calculations of ref. 6 for Li_2F_2, among the dimers of which the linear modification predominates above 1150°C, while the orthorhombic predominates below 1150°C. In view of the extreme complexity of the chemical properties of alkali halide compound pairs, it may be predicted that a similar phenomenon is characteristic of other compounds than Li_2F_2.

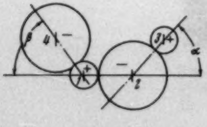

Fig. 1. Diagram of the linearization of a dimer: 1 and 3 are metal ions; 2 and 4 are halide ions.

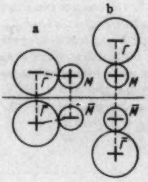

Fig. 2. Cyclical (a) and linear (b) quasidimers.

Let there be, at a relatively low temperature on the clean metal surface, an adsorbed layer of an alkali halide compound with a degree of surface cover less than unity. The monomers are usually more than the other polymers: in any case, we are considering only monomers.

The interaction of a monomer with the substrate, in spite of the presence of a surface energy barrier of a complex and yet unknown nature, may be imitated in some approximation, by the interaction of this monomer with its reflection relative to the surface in the illustration (see Fig. 2). During this, quasidimer complexes $ME\overline{MH}$ form, where $\overline{MH}$ are imaginary forms of M and H. The stability of these complexes is confirmed by the high (47.5 kcal/mole) desorption energy of CsI monomers: the only one of the alkali halide compounds whose heat of desorption from a metal (tungsten) was measured.[9] The heat of dissociation of Cs_2I_2 dimers to CsI is ~33 kcal/mole.[9] The concentration of the linear and orthorhombic modifications of Cs_2I_2 is unknown.

Quasidimeric complexes should therefore have a cyclical structure at lower temperatures ("monomers lie flat" – Fig. 2a); with increase of temperature the number of monomers forming a quasidimer complex should increase (the monomers rise at posts in Fig. 2b). A simple evaluation according to ref. 6 gives the heat of transition $M\overline{M}\overline{H}H \rightarrow HM\overline{M}\overline{H}$ for various alkali halide compounds to be in the limits of 10-25 kcal/mole, which is a reproducible value.

On occurrence of the proposed reaction, besides the above effect of the decrease in heat of desorption, a pseudoincrease in the adsorbing surface should be observed on increase in temperature, due to sites freed by the newly formed monomers. The experimental data available for systems other than that considered here at least do not contradict the proposed hypothesis. The crudeness of the model considered being admitted, it is impossible to pretend that it is the solution to the problem of the desorption mechanism of monomers from a metallic surface.

The authors are indebted to B. N. Grechushnikov, A. M. Mikhailov, N. I. Sosfenov, I. F. Shchegolev, and particularly to A. A. Chernov for discussion.

[1)] Experiment done at the suggestion of A. A. Chernov.

[2)] All energy terms which we use correspond with the text: G. M. Panchenkov and V. P. Lebedev, Chemical Kinetics and Catalysis [in Russian], Moscow State Univ. (1961), pp. 41-42.

---

[1] C. T. O'Konski and W. I. Higuchi, J. Chem. Phys., 23, 1174 (1955).

[2] S. A. Rice and W. Klemperer, J. Chem. Phys., 26, 618 (1957).

[3] S. A. Rice and W. Klemperer, J. Chem. Phys., 27, 573 (1957).

[4] S. A. Rice and W. Klemperer, J. Chem. Phys., 27, 643 (1957).

[5] T. A. Milne and D. Cubicciotti, J. Chem. Phys., 29, 846 (1958).

[6] N. L. Yarym-Agaev, Zhur. Fiz. Khim., 38, No. 11, 2579 (1964).

[7] L. Pauling, Proc. Nat. Inst. Acad. Sci. India, A25, Pt. 1 (1956).

[8] A. Snelson, J. Chem. Phys., 73, No. 6, 1919 (1969).

[9] B. Ya. Kolesnikov, A. M. Kolchin, and G. M. Panchenkov, Zh. Eksp. Teor. Fiz., 40, 858 (1970).

Study of the (111) surface of GaP by methods of Auger spectroscopy and slow-electron diffraction

A. Yu. Mityagin, V. P. Orlov, and N. Ya. Cherevatskii

(Submitted May 4, 1972)
Kristallografiya, 18, 423-424 (March-April 1973)

It is believed that the presence of free chemical bonds at the surface atoms of semiconducting crystals whose compensation depends on the method of surface treatment and on thermal conditions, leads to formation of the numerous atomic structures, observable by low-energy electron diffraction at different surfaces of semiconducting single crystals. However, thanks to the method of Auger electron spectroscopy, it has been possible to establish that a number of the atomic structures, in particular on the (111) surface of Si, are caused by impurity atoms.[1-3]

The present work considers the purification process of the (111) surface of GaP by thermal annealing in ~5 · 10^{-9} torr vacuum. Auger spectroscopy, low-energy electron diffraction, and mass spectrometry were used as methods of determination. It was observed that the atomic surface structure on the (111) of GaP (2 × 2) forming after medium-temperature annealing is due to surface contamination by C atoms. A high-temperature anneal leads to the desorption of C impurity atoms, and to formation of a (111) GaP structure (1 × 1), which appears to be the structure of an atomically pure (111) GaP surface.

The experiments were performed in a three-grid all-metal apparatus for low-energy electron diffraction. An apparatus for recording the Auger spectrum and a mass spectrometer were also used. When the crystal was heated to a temperature of 820°K, purification of the (111) GaP surface occurred. This was indicated by the low-energy electron diffraction patterns, the mass spectrograms of gas evolution, and by Auger spectroscopy of the surface under study. Figure 1a presents the Auger spectrum obtained from a (111) GaP surface after heating to 820°K. In addition to the Auger electron lines belonging to Ga and P atoms, the spectrum exhibits a line at 270 eV, corresponding to Auger electrons from C atoms. An increase in heating temperature in the range 820-870°K produced an increase in intensity of the Auger electron line due to C atoms at 270 eV. During this, formation was observed of a (111) GaP (2 × 2) atomic surface structure, the diffraction pattern of 65-eV electrons from which is shown in Fig. 2a. Further increase in annealing temperature to 920°K did not change the (111) GaP surface structure (2 × 2) or the intensity of the Auger spectrum lines. However, for annealing temperatures above 920°K, a sharp decrease was noted in the intensity of the (111) GaP (2 × 2) structure diffraction reflections. Also observed was a weakening of line intensities for Auger electrons from C atoms, and an increase in the structure of residual gases such as CO. A brief anneal at ~950°C completely removed the Auger electron line due to C atoms (Fig. 1b), and led to formation of a (111) GaP (1 × 1) atomic surface structure, whose diffraction pattern with 27-eV electrons is shown in Fig. 2b.

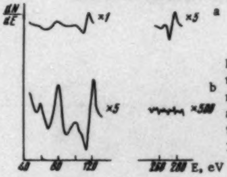

Fig. 1. Auger spectra obtained from the (111) surface of GaP: a) after annealing at a temperature of 820°K; b) after annealing at a temperature of 950°K. Energy of incident electrons = 1500 eV.

There are two possible causes of the contamination of the (111) GaP surface by C atoms: (1) adsorption on the surface of residual atmosphere from the working chamber and (2) diffusion from the volume during heating. In fact, adsorption of carbon from the volume, either in the form of CO molecules or by thermal decomposition of CO or CO_2, is possible at the crystal surface in our experiments. However, the absence of traces of O atoms in the Auger electron spectrum, the unchanged residual gas mass spectrum, and the stability, of the (111) GaP (1 × 1)

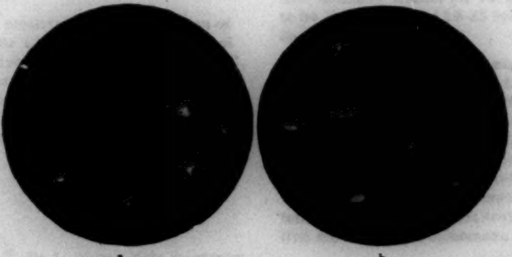

Fig. 2. Diffraction pattern of slow electrons. a) (111) GaP (2 × 2) atomic surface structure; electron energy 65 eV. b) (111) GaP (1 × 1) 27 eV.

atomic structure, indicated that the chief source of impurity was the crystal itself. Carbon atoms, being an electrically neutral impurity in GaP, can uncontrollably enter the crystal during growth. Heating at 820–920°C favors diffusion of C atoms from the volume to the crystal surface. The (111) GaP (2 × 2) atomic structure observed is probably formed by carbon domains of size (2 × 1), which are turned by 60° with respect to one another. An increase in crystal temperature leads to a "burning out" of the carbon, i.e., to chemical reaction with residual oxygen or, more probably, with carbon dioxide, and to formation of carbon monoxide which is evolved from the (111) surface of GaP. The process of complete purification occurs at the surface investigated, and the reduction of a (111) GaP (1 × 1) structure to an atomically pure (111) GaP surface.

It should be noted that prolonged storage of an atomically pure (111) GaP surface at room temperature, especially under an electron beam, leads to adsorption of an amorphous layer of C atoms, which, after corresponding heating, sometimes is reduced to a (111) GaP (2 × 2) structure.

---

[1] W. M. Mularie and T. W. Rusch, Surf. Sci., 19, No. 2, 469 (1970).
[2] J. M. Charly and D. K. Skinner, Surf. Sci., 19, No. 2, 283 (1970).
[3] N. J. Taylor, Surf. Sci., 15, No. 1, 169 (1969).

Electron-diffraction analysis of amorphous films of carbon and boron

Yu. G. Poltavtsev, V. P. Zakharov, and V. M. Pozdnyakova

(Submitted June 15, 1971; resubmitted January 27, 1972)
Kristallografiya, 18, 425-426 (March-April 1973)

In studying the graphitization kinetics of amorphous carbon films under the effect of powerful light pulses,[1] our attention was attracted by the fact that the short-range order of the films approaches the structure of graphite only when the films are irradiated with pulses of specific power. However, Boiko et al.[2] concluded that the short-range order in amorphous carbon films is the same as that in the structure of graphite. In our opinion, the question whether the structures of amorphous carbon films and graphite are similar or different may be correctly solved by comparing the corresponding radial atomic distributions, which Boiko et al.[2] did not do. Our paper gives such a comparison. Furthermore, we also give the results of investigations of the structure of amorphous films of boron, for which the literature gives no information.

Amorphous carbon films ~500 Å thick were obtained by evaporation in an arc of spectroscopically pure carbon rods; boron films were obtained by electron-beam sputtering of pressed tablets of a crystalline specimen. Table 1 gives the values of the $i_1(s)$ functions, from which we calculated, in accordance with ref. 1, the radial distribution curves of the atoms (Fig. 1).

Carbon. The radial distribution curve of the atoms in an amorphous carbon film with $r \leqslant 6$ Å exhibits marked deviations from the $4\pi r^2\rho_0$ parabola. The first structural maximum, located at $r_1 = 1.44$ Å, is isolated; the area beneath it $z_1 = 3.0$. The second and fourth structural maxima are located at $r_2 = 2.48$ and $r_4 = 3.7$ Å, the areas beneath them being $z_2 = 9.0$ and $z_4 = 12$ (the method used for resolution of the maxima is shown in Fig. 1). The third maximum is very diffuse; depending on the methods used to resolve the second and fourth maxima, its position is $r_3 = 3.3 \pm 0.2$ Å and $z_3 = 3\text{-}4.1$.

In the crystal lattice of graphite the atoms are located in layers, at the nodes of a regular hexagonal network; the distance between the layers is 3.34 Å.[4] Each atom in its layer at distances $r_1 = 1.42$, $r_2 = 2.45$, $r_3 = 2.83$, $r_4 = 3.75$ Å has three, six, three, and six neighboring atoms, respectively. Furthermore, at a distance of 3.34 Å, each atom has on the average one neighbor, and at a distance of 3.63 Å nine neighbors, located in the adjacent layers.

The radii of the first three coordination spheres and the coordination numbers of graphite are practically the same as those for an amorphous carbon film; the second and third coordination spheres of graphite fall within the region of the second maximum of the radial distribution curve of the atoms. Together with this similarity, we observe a marked difference between these structures, manifested in particular in a difference between the coordination numbers for $r \simeq 3.3$ Å.

Following Kaplow et al. [5], we calculated the radial distribution curves for two models: 1) The atoms were located in the nodes of a regular hexagonal network, the shortest distance between the nodes of which were taken as equal to the radius of the first coordination sphere in the amorphous film; 2) for the crystal lattice of graphite. The dispersions of the first three Gaussian curves were selected as $\sigma_1^2 = 0.03$, $\sigma_2^2 = \sigma_3^2 = 0.035$. It was found that the calculated curve for the first model agrees more closely with the experimental radial distribution curve than the curve calculated for the second model. However, even in this case, when $r > 3$ Å the calculated curve lies above the experimental curve.

Thus, according to our data, the only similarity between the structures of amorphous carbon films and graph-

TABLE 1

s	$i_1(s)_C$	$i_1(s)_B$	s	$i_1(s)_C$	$i_1(s)_B$	s	$i_1(s)_C$
1.8		−0.30	4.5	−2.60	2.30	7.2	−1.90
1.9		−0.40	4.6	−1.50	2,70	7.3	−2.00
2.0		−0.35	4.7	−0.02	3.20	7.4	−1.95
2.1		−0.05	4.8	1.70	3,40	7.5	−1.85
2.2		0.30	4.9	4.00	3.30	7.6	−1.70
2.3		0.35	5.0	6.50	2.80	7.7	−1.45
2.4	−1.00	0.40	5.1	9,30	2.00	7.8	−1.00
2.5	−0.30	0.42	5.2	12.00	0.50	7.9	−0.75
2.6	0,90	0.45	5.3	14.30	−0.60	8,0	−0.30
2.7	2.00	0.44	5.4	16.20	−1.20	8.1	0,20
2.8	3.20	0.43	5.5	17,40	−1.70	8.2	0.50
2.9	4.40	0.30	5.6	17,35	−1.90	8.3	0,80
3.0	5.00	0.02	5.7	16.20	−2.00	8.4	1.20
3.1	4.00	−0.20	5,8	14.21	−1.95	8.5	1.35
3.2	2.20	−0.40	5,9	12,00	−1.80	8,6	2.00
3.3	0.03	−0.70	6.0	10.30	−1.70	8.7	1,90
3.4	−1.50	−1.10	6.1	8.30	−1.70	8.8	1.70
3.5	−3.00	−1.30	6.2	6,40	−1.40	8.9	1.00
3.6	−4.00	−1.20	6.3	4,70	−1.20	9.0	0.60
3.7	−4.60	−0.80	6.4	3.30	−1.00	9.1	0.30
3.8	−4.80	−0.40	6.5	1,80	−0.80	9,2	0
3.9	−4.95	−0.20	6.6	0.70	−0.60		
4.0	−4.97	0.30	6.7	−0,02	−0.40		
4.1	−4.80	0.60	6.8	−0,08	−0.20		
4.2	−4.50	1,00	6.9	−1.30			
4.3	−4.10	1.40	7,0	−1.70			
4.4	−3.50	1.80	7.1	−1.80			

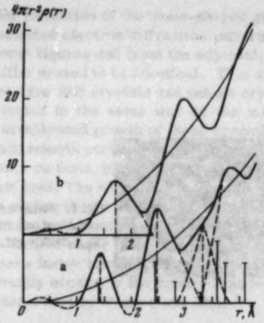

Fig. 1. Radial distribution curves of atoms in amorphous carbon (a) and boron (b) films.

ite is the similar location of the atoms in the first three coordination spheres.

Boron. On the radial distribution curve of the atoms in amorphous boron films the first two maxima are located at $r_1 = 1.75$ and $r_2 = 3.0$ Å, the values of the coordination numbers being $z_1 = 5.6$ and $z_2 = 17$.

Orthorhombic, rhombohedral, and tetragonal modifications of crystalline boron are known, but the unit-cell constants have been reliably determined only for the tetragonal modification, in which each atom has six bonds with its immediate neighbors, five of the interatomic spacings being equal to 1.805 and one equal to[6] 1.68 Å.

The mean radius of the first coordination sphere $r_1 = (5 \cdot 1.805 + 1.68)/6 = 1.784$ Å, and the coordination number for the tetragonal modification of crystalline boron are close to the experimentally determined values for amorphous films.

---

[1] Yu. G. Poltavtsev, V. P. Zakharov, and V. N. Chugaev, Kristallografiya, 16, 415 (1971) [Sov. Phys. – Crystallogr., 16, 341 (1971)].

[2] B. T. Boiko, L. S. Palatnik, and A. S. Derevyanchenko, Dokl. Akad. Nauk SSSR, Neorgan. Mat., 179, 2, 316 (1968).

[3] L. D. Nabitovich, Ya. M. Stetsiv, and Ya. V. Voloshchuk, Kristallografiya, 12, 584 (1967) [Sov. Phys. – Crystallogr., 12, 513 (1968)].

[4] Symposium: Chemical and Physical Properties of Carbon [Russian translation], Mir, Moscow (1969).

[5] R. Kaplow, S. L. Strong, and B. L. Averbach, Phys. Rev., 138, 5A, 1336 (1965).

[6] G. V. Samsonov, L. Ya. Markovskii, A. F. Zhigan, and M. G. Valyashko, Boron, Its Compounds, and Alloys [in Russian], Izd. AN SSSR, Kiev (1960).

Micromorphology of epitaxial PbS films

R. V. Kudryavtseva and S. A. Semiletov
Gor'kii Physicotechnical Research Institute
(Submitted July 19, 1971; resubmitted March 21, 1972)
Kristallografiya, 18, 427-428 (March-April 1973)

The growth of single-crystal films with an even, mirror-smooth surface free of growth figures, etch pits, and vicinal hillocks is quite a complex problem. A clarification of the causes and laws of formation of such elements of micromorphology is therefore very essential.

It was previously reported[1] that the shape of the growth figures on the surface of PbSe films strongly depends on the precipitation temperature. An analogous dependence was also observed in the case of PbS films. The present work reports results obtained during a study of dome-shaped growth figures which form on the surface of PbS films at the relatively high condensation temperatures of 300-450°C (Fig. 1).

The samples were prepared by molecular beam condensation at a pressure of $\sim 10^{-6}$ mm Hg on the cleavage faces of NaCl crystals. The intensity of the PbS molecular beam varied from 10^{14} to $6 \cdot 10^{15}$ $\text{cm}^{-2} \cdot \text{sec}^{-1}$; the condensation temperature varied from 300 to 450°C. The studies utilized the replica method and the method of diffraction contrast. Both the structure of transverse sections passing through the growth figures, and the structure of etch films were studied (3 h in a 10% aqueous solution of thiourea; 1 h in concentrated HCl, T = 60-80°C, etching time 10-15 sec). As a result of the investigations performed, the following points were established: 1) The dome-shaped growth figures form only on the surface of continuous films produced at a precipitation temperature, T_p, of 300-400°C; 2) their concentration is higher, the lower the substrate temperature, and the higher the condensation rate; 3) the growth figures are comprised of PbS crystals oriented the same as the adjacent, smooth portions of the film (established by selected area diffraction); 4) their solution rate is higher than the solution rate of the smooth film portions; 5) in diffraction contrast exposures, the dark spots correspond to the dome-shaped growth figures (Fig. 2); 6) round crystals are arrayed on the film surface (they do not extend into depth); however, there are small holes under them (Fig. 3).

We note that the dark spot picture was often previously observed in electron micrographs. It is assumed that such figures develop at point-defect accumulations which are too small to be directly resolved.[2,3]

Very often such accumulations come about during bombardment of the sample by the positive ions in the column of the microscope, i.e., radiation damage defects.[3] In our case, this defect formation mechanism is ruled out, since the dark spot concentration in the PbS films does not depend on time of exposure to the electron microscope, and depends only on conditions of film preparation.

In the case of binary or more complex compounds, formation of point defects may be associated with an excess (lack) of one of the components. Hall effect studies on PbS films revealed that they always display electron conductivity. This indicates that they have an excess of Pb atoms, which play the role of donor impurities in PbS group compounds.

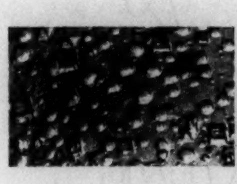
Fig. 1. Dome-shaped growth figures on the surface of epitaxial PbS films (T_p = 350°C) ×21,000.

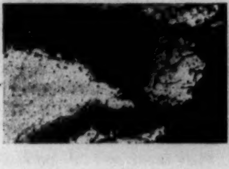
Fig. 2. Dark spots on electron micrographs of PbS layers, ×24,000.

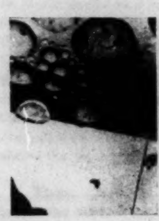
Fig. 3. Transverse section of a PbS surface: ×8500. The depression under the dome-shaped crystal is visible.

The formation of such atoms is apparently associated with the fact that during volatilization of PbS, the PbS molecules partially dissociated into Pb and S atoms.[4] According to the data of ref. 4, at T = 980°K the gaseous phase of PbS contains over 1% of free Pb atoms: ($\log P_{\text{PbS}} = -4.45$ atm, $\log P_{\text{Pb}} = -5.85$ atm). Part of the sulfur molecules apparently do not succeed in reacting with Pb atoms, and are desorbed from the substrate, resulting in accumulation of free Pb atoms on the surface of the growing film. Part of such atoms dissolve in the PbS lattice, and those remaining collect as accumulations distributed over the surface. Such accumulations should exist in the liquid state, since the growth of the films occurs at temperatures of 300-400°C, i.e., near or above the melting temperature of Pb (the melting temperature of small-size particles can be considerably below the melting temperature of macrosamples[5]).

Thus, during the growth of PbS films, liquid islands or microdroplets of lead form on the surface, which are the reason for formation of the dome-shaped growth figures. The selected electron diffraction patterns obtained from the growth figures and from the adjacent, flat portions of the film proved to be identical. This says that the growth figures are PbS crystals and not Pb crystals, since they are oriented in the same way as the matrix substrate. The accelerated growth of these crystals relative to the adjacent smooth portions of the film is explained by the presence on them of microdroplets, or of microfilms of liquid lead. The adhesion coefficient of PbS molecules in this region should be higher than the adhesion coefficient on the solid surface of the film; the region of the PbS film located under the liquid lead microdroplets therefore grows faster than the neighboring portions. Its growth apparently occurs by the vapor–liquid–solid mechanism once described by Wagner and Ellis.[6]

The decrease in concentration of the dark spots and dome-shaped growth figures on increase of substrate temperature is apparently associated with the revaporization of excess Pb atoms, or with the increase in probability of formation of PbS molecules on the reaction of Pb atoms with sulfur molecules.

The existence of holes under the dome-shaped crystals (Fig. 3) is not altogether clear. It can only be suggested that, after the evaporating equipment is shut off, the direction of the temperature gradient reverses itself, and the liquid droplet or film of Pb moves along the dome-shaped crystal from its top to the matrix where crystallization occurs.

---

[1] S. A. Semiletov, Seventh International Congress of Crystallographers, Theses of Proceedings [in Russian], Izd. Nauka, Moscow (1966), p. 297.

[2] L. C. DoJonghe and G. Thomas, J. Appl. Phys., 41, No. 12, 4885 (1970).

[3] P. Khirsh, A. Khovi, P. Nikolson, D. Peshli, and M. Uelan, Electron Microscopy of Thin Crystals [Russian translation], Izd. Mir (1968), p. 72.

[4] R. Colin and J. Drowart, J. Chem. Phys., 9, 354 (1954).

[5] M. Takagi, J. Phys. Soc. Japan, 37, 1120 (1962).

[6] R. S. Wagner and W. C. Ellis, Appl. Phys. Lett., 4, No. 5, 89 (1963).

Dynamic scattering of light in liquid crystals of the azocompound class

M. F. Grebenkin, G. S. Chilaya, V. T. Lazareva, K. V. Roitman,
L. M. Blinov, and V. V. Titov

(Submitted February 9, 1972)
Kristallografiya, 18, 429–431 (March–April 1973)

It is well known that the application of an electric field of sufficient strength to nematic liquid crystals with a negative dielectric anisotropy produces turbulent motions in the liquid,[1] which can cause dynamic scattering of light.[2–5] This effect has been studied in some detail in compounds related to Schiff bases. For liquid crystals of the azocompound type, results have been obtained for n-ethoxyphenyl-n'-azophenylheptanoate.[6]

The current interest in light scattering by liquid crystals is due largely to the successful application of this effect to alpha-numeric indicators and information display systems.[7,8] It has therefore become particularly important to investigate a wider range of materials in order to find compounds which have a low-temperature nematic interval and a high chemical stability, and also for practical purposes to study the way that the time response of this effect depends on external factors (temperature, electric field, viewing angle, etc.).

We have studied nematic liquid crystals of n-alkoxy-n'-acyloxybenzols which are azocompounds with the general formula

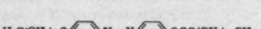

These compounds were obtained by the acylation of the corresponding n-alkoxy-n'-oxazobenzols with the acid chloranhydrates[9] which in turn were obtained by the diazo reaction of diazotized n-alkoxyanilines with phenol.[10] The substances were then purified by recrystallization. The specific conductivity in the nematic phase was found to be 10^{-8}–10^{-10} $\Omega^{-1}\cdot\text{cm}^{-1}$. The data below refer to n-ethoxyphenyl-n'-azophenylhexanoate which was the most extensively studied and which had a low-temperature nematic interval and other properties typical of the group.

In the practical application and experimental study of dynamic light scattering, the liquid-crystal cell can be operated in either a scattering[6] (I) or a transmission[4] (II) mode. Our experimental arrangement with two photodetectors permitted measurements to be made by both methods. In the transmission mode, the light passed twice through the liquid crystal, being reflected from a mirror electrode; this increased the effective thickness of the layer. The light source was an LG-55 laser and the detector was an FD-3 photodiode. A millivoltmeter or oscillograph was used as recorder. A dc voltage (0–200 V) was applied to the crystal and the voltage–contrast curves were derived. For mode I, the contrast K was taken to be the ratio of the detector signal with the electric field applied, I_E, to the signal without the field, I_0; for mode II, on the other hand, $K = I_0/I_E$.

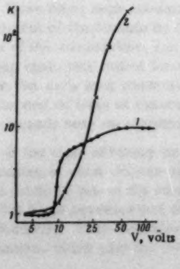

Fig. 1. Variation of contrast K with applied voltage. 1) Mode I; 2) mode II; cell thickness 10 μ, T = 68°C.

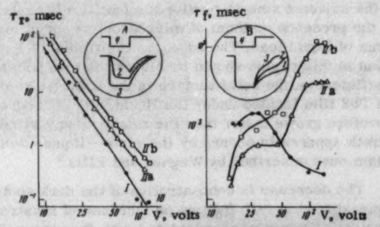

Fig. 2. Time response. I) Mode I, T = 120°C; IIa) mode II, T = 120°C; IIb) mode II, T = 70°C. Oscillogram A: 1) V = 10 volts; 2) V = 20 volts; 3) V = 40 volts; 4) pulse length 100 msec. Oscillogram B: 1) T = 68°C; 2) T = 105°C; 3) T = 125°C; 4) pulse length 100 msec, mode II, cell thickness 30 m.

The variation of K with applied voltage illustrated in Fig. 1 shows the difference both in the maximum values and the shape of the curves for the two modes. This difference can be explained by the changes in the scattering diagram with applied voltage given below. In order to find the way that the rise τ_r and fall τ_f times of the scattering effect depend on external factors, square pulses (0–

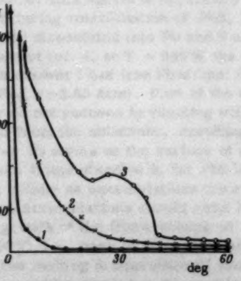

Fig. 3. Scattering diagram for a liquid-crystal cell. 1) V = 0; 2) V = 15 volts; 3) V = 50 volts; cell thickness 50 μ, T = 70°C. The ordinates are given in relative units: curve 1 tends to 15,000, curve 2 to 3000, and curve 3 to 1100 as the viewing angle tends to zero.

TABLE 1. Data on the Dynamic Scattering of Light in Liquid Crystals of the Azocompound Class

No.	Compound	ΔT_{nemat}, deg	T_{ch}, deg	d, μ*	K_{max}	$E = 10^4$ V/cm τ_r, msec	 τ_f, msec
1	$H_3C(CH_2)X^{**}CH_3$	110 → 130	108	30	1000	4	150
				10	500	4	15
2	$H_3C(CH_2)X(CH_2)_4CH_3$	68 → 128	77	30	450	8	350
				10	350	8	40
3	$H_3C(CH_2)X(CH_2)_5CH_3$	60 → 119	80	30	600	10	250
				10	700	8	30
4	$H_3C(CH_2)X(CH_2)_6CH_3$	81 → 118	97	30	500	10	300
				10	400	15	40
5	$H_3C(CH_2)X(CH_2)_8CH_3$	82 → 117	80	30	350	10	300
				10	400	10	50
6	H_3CXCH_3	108 → 119	112	30	500	10	200
7	$H_3C(CH_2)_2XCH_3$	109 → 115	112	30	600	8	250
8	$H_3C(CH_2)_3XCH_3$	88 → 105	100	30	550	12	300
9	$H_3C(CH_2)_4XCH_3$	88 → 102	95	30	450	10	350
10	$H_3C(CH_2)_7XCH_3$	95 → 105	97	30	400	8	300
11	$H_3C(CH_2)_2X(CH_2)_5CH_3$	82 → 104	90	30	500	8	350
12	$H_3C(CH_2)_4X(CH_2)_5CH_3$	72 → 106	90	30	600	10	200
13	$H_3C(CH_2)_7X(CH_2)_5CH_3$	90 → 108	100	30	550	6	250
14	$H_3C(CH_2)_7X(CH_2)_4CH_3$	82 → 109	95	30	650	6	300
15	50% № 2 + 50% № 5	53 → 120	59	30	310	4	400
16	50% № 10 + 25% № 13+ +25% № 14	47 → 97	50	30	400	6	400

*d is the cell thickness.

**X represents the group

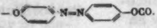

170 V) of different periods (1, 10, 100, 1000 msec) and with leading edges shorter than 20 μsec were applied to the cells.

The variation of τ_r with voltage shown in Fig. 2 does not indicate any real difference between the two modes, although it might be noted that the values are usually smaller in mode I. The recording A illustrates the variation obtained, which can be described by the equation $\tau_r \sim V^{-n}$, where n = 2–3 (although there is an suggestion in ref. 11 that n is exactly equal to 2). Figure 2 also shows how τ_f changes with the voltage. There is an obvious difference in the behavior of the two modes: In I, τ_f decreases with the applied voltage, but in II it decreases. This difference is due to the complex changes which occur in the shape of the scattering diagram of a liquid cell as the applied voltage is altered (Fig. 3).

Since one of the main parameters responsible for the shape of the diagram is the size of the scattering particles,[12] this variation with applied voltage seems to be caused by a change in the size of the scattering volume.

Oscillogram B in Fig. 2 gives an idea of the effect of temperature on τ_f. In general, an increase in temperature reduces both τ_r and τ_f: This is apparently due to the increase in electrical conductivity and hence the decrease in the dielectric relaxation time, and to a reduction in viscosity.

Tests with liquid-crystal cells of different thicknesses (10–50 μ) did not reveal any exact relationship between τ_r and τ_f and thickness, although it can be definitely stated that fairly thin cells must be used to obtain improved time response at higher operating temperatures and voltages. Thus for a thickness of 10 μ and a temperature of 125°C with a pulse amplitude of 150 V, τ_r = 90 μsec and τ_f = 10–15 μsec (mode I).

The complete data for the liquids we examined are given in Table 1. The values are nominal, as we did not attempt to find the optimum conditions for each compound. The observations all refer to mode II. Table 1 also shows data for some mixtures which were prepared with the idea of trying to reduce the temperature of the nematic interval. These mixtures do show the dynamic scattering effect and this justifies a further attempt to find lower temperature mixtures from the azocompound class. The greater chemical stability of these compounds in comparison, for example, with Schiff bases makes them look promising for future practical use.

The authors thank S. V. Belyaev for a number of preliminary measurements.

---

[1] V. Fredericks and V. Tsvetkov, Dokl. Akad. Nauk SSSR, 4(9), 123 (1935).

[2] G. H. Heilmeier, L. A. Zanoni, and L. A. Barton, Proc. IEEE, 56, 1162 (1968); IEEE Trans. ED-17, 22 (1970).

[3] V. M. Shoshin, Abstracts of Papers from the First Scientific Conference on Liquid Crystals [in Russian], Ivanovo Pedagogical Institute, Ivanovo (1970), p. 59.

[4] D. Jones, L. Creagh, and S. Lu, Appl. Phys. Lett., 16, 61 (1970).

[5] W. Helfrich, J. Chem. Phys., 50, 100 (1969); J. Chem. Phys., 51, 4092 (1969).

[6] G. Assouline and E. Leiba, Revue techn., Thomson-CSF, 1, 483 (1969).

[7] R. A. Soref, Appl. Optics, 9, 1323 (1970).

[8] J. A. Van Raalte, Proc. IEEE, 56, 2146 (1968).

[9] K. Weigand and G. Hilgetag, Experimenta. Methods in Organic Chemistry [Russian translation], Khimiya, Moscow (1968).

[10] Organic Chemistry Preparations [in Russian], Khimiya, Moscow–Leningrad (1964).

[11] H. Koelmans and A. M. Van Boxtel, Phys. Lett., A32, 32 (1970).

[12] H. van de Hulst, Light Scattering by Small Particles, Wiley, New York (1957).

Distribution coefficients of divalent impurities in alkali halide crystals

O. L. Kreinin and K. M. Rozin

Moscow Institute for Steel and Alloys

(Submitted December 16, 1971; resubmitted April 7, 1972)
Kristallografiya, 18, 432–434 (March–April 1973)

A correct estimate of the capability of one or another impurity to enter into the lattice of the base material during growth from the melt plays an important role in the task of preparing alkali halide crystals with prescribed properties, as well as the selection of media which allow control of the rate of entrance of impurities into the crystal in a prescribed direction. While it is expedient to use thermodynamic methods for the solution of the first problem, the second problem belongs basically in the realm of kinetics and is solved not only by calculation, but also by experiment. Obviously, a successful solution to this problem depends in substantial measure on finding more general methods for estimating the interaction of impurities within a crystal.

One of the more generally used criteria for replacement of an atom in the lattice of the base material by an atom of impurity is the sign difference Δr between the atomic or ionic radii of the impurity atoms and the atoms of the base material.[1–3] However, this criterion does not permit an answer to a multitude of important questions. In particular, an estimate of the difference between ionic radii in those cases where the ionic radii of the impurity and of the base material are close to each other or coincide may lead to an incorrect conclusion of the formation of a continuous series of base-impurity solid solutions down to complete replacement of one of the ions of the basic lattice by impurity.

Unlike this criterion, the influence of a different type of interaction between an ion of impurity and the matrix of base material surrounding it on the entrance of impurity into the crystal was established in ref. 4.

From calculations of the lattice energies of ionic crystals,[5,6] it follows that the most energetic contribution to the total change in lattice energy is made by the interaction of an impurity ion with the first coordination sphere. Upon entrance of a cation impurity into an alkali halide crystal, anions of the base material are found in the first coordination sphere about the impurity ion. If the entrance of the impurity is actually determined by the magnitude of the energy of distortion of the lattice, then the change in anionic surroundings in the first coordination sphere should react strongly on the entrance of impurities.

The aim of this work was the study of the entrance of cation impurities into alkali halide crystals as it depends on the anionic environment.

Single crystals of NaF, NaCl, NaBr, and NaI with Cd impurity were selected as subjects for study. The ionic radii of the impurity and the cation of the base material practically coincided (to within 1%).[7] In connection with this, starting from Hume-Rothery's rules,[1] the formation of isomorphous mixtures in the systems examined can be expected (experimental confirmation of this is contained in refs. 8 and 9), which is highly important for the possibility of application of the calculation method worked out in ref. 4. On the other hand, according to Andreev and Aleksandrov,[2,3] the entrance of Cd impurity into all crystals examined should be the same, so that the value of Δr is constant for all four systems. For estimation of the entrance of Cd impurity into the sodium halide crystals, we used the value of equilibrium distribution coefficient associated with the change in thermodynamic properties of the crystal and melt by the familiar equation:[10,4]

$$\ln K_0 = \frac{\Delta H^f - \Delta H^s}{RT} + \frac{\sigma - \Delta S^f}{R} + \ln \gamma, \qquad (1)$$

where ΔH^f and ΔS^f are the enthalpy and entropy of fusion of the impurity, ΔH^s is the heat of mixing, σ is the change of vibrational entropy of the system, and γ is the activity coefficient of the impurity in the melt.

The quantities ΔH^s, σ, and γ must be evaluated for estimation of K_0 according to (1). In this work, σ was calculated in a manner analogous to that in ref. 4, and the data obtained for cadmium in NaF, NaCl, NaBr, and NaI are given in Table 1. The Hildebrand equation for regular solutions[11] was used for calculation of the activity coefficient of the impurity in the melt, and the activity coefficients obtained for the impurity in melts of the salts are given in Table 1.

According to ref. 4, the quantity ΔH^s is the most difficult to calculate. We calculated the heat of mixing in accordance with the method in ref. 4, starting from the classical theory of lattice energy of ionic crystals.[5,6] As follows from ref. 4, the heat of mixing can be evaluated if the energies evolved during the formation of a vacancy and during substitution of one of the vacancies by an impurity ion are known. In both cases, the problem reduces to the determination of the work required for the formation of a point defect (impurity or vacancy) in the crystal lattice. For the calculation of this work in the lattice of an alkali halide crystal, two forms of interaction between ions are taken into account: electrostatic interaction and repulsion of electronic orbitals, which in turn can be found through the parameter ξ, which is the displacement of the ions nearest to the defect. The value of ξ is found by set-

TABLE 1. Calculation of ΔH^s and K_0 for Cd in NaF, NaCl, NaBr, and NaI and Experimental Values of K_0

Parameter	NaF	NaCl	NaBr	NaI
ξ_{CV-Me}	0.045	0.096	0.05	0.036
ξ_{Cd-Me}	0.022	0.018	0.06	0.036
$W_{CV(Na\ Hal)}$, eV	− 5.75	−4.3	− 3.64	− 3.65
$W_{Cd(Na\ Hal)}$, eV	−20.5	−16.9	−17.1	−15.0
g_i, eV	− 9.0	−8.3	− 9.71	− 7.7
ΔH^s, eV	0.9	0.8	0.5	0.4
σ, kcal/g·mole	0.78	1.48	2.35	2.93
$\ln \gamma$	0.033	0.173	0.17	2.93
K_0 (calculation)	0.006	0.014	0.10	0.38
K_0 (experiment)	0.007	0.017	0.09	—

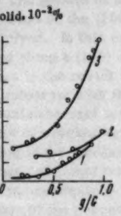

Fig. 1. Concentration of Cd impurity in NaCl single crystals grown by the Kyropoulos method as a function of the weight fraction of the crystallizing portion of the crystal. Rates of growth: 1) 6 mm/h; 2) 9 mm/h; 3) 25 mm/h.

ting equal to zero the sum of electrostatic and repulsive forces acting on an ion located in the first coordination sphere of the embedded defect.

We calculated the quantities mentioned above to a first approximation by the method of ref. 4, and the results obtained are given in Table 1. The following notations are used in Table 1: ξ is the displacement of ions of the first coordination sphere upon the introduction of a defect into the crystal (ξ_{Cd-Me} for a Cd ion, ξ_{CV-Me} for a cation vacancy), $W_{Cd(NaHal)}$ is the energy of distortion of the basic lattice of a single crystal of sodium halide upon the introduction of an impurity ion, $W_{CV(NaHal)}$ is the energy of distortion of the lattice upon the introduction of a vacancy, and $g_i = W_{Cd(NaHal)} - 2W_{CV(NaHal)}$ and is the energy evolved during the formation of two cation vacancies and upon replacement of one of the vacancies by an impurity ion.

Starting from the values of equilibrium distribution coefficients obtained, the conclusion can be drawn that the entrance of Cd impurity increases in the series from NaF to NaI (K_0 changes from 0.006 to 0.38), which correlates with the decrease of the heat of mixing in the series from NaF to NaI (see Table 1).

Thus, the data which we obtained allow us to conclude that the energy factor determines the efficiency of entrance of an impurity into a crystal lattice. The quantity ΔH^S depends on the difference between the ionic radii of the impurity and the base cation, as follows from the equations for calculation of refs. 4-6, but, in addition, the quantity ΔH^S is strongly dependent on the dielectric susceptibility of the medium, polarizability of the cations and anions, etc. It is evident that the relationship of all these parameters of the basic crystal and impurity determines the value of ΔH^S. In particular, it is evident that the sizes and polarizability of the anions exert great influences on the value of ΔH^S, by which, obviously, the difference of values of K_0 obtained for NaF, NaCl, NaBr, and NaI is also explained.

We have obtained experimental confirmation of the values of equilibrium distribution coefficients for the examples of the distribution of cadmium in single crystals of NaF, NaCl, and NaBr. The crystals were grown from melt by the Kyropoulos and Bridgman methods at growth rates from 6 to 45 mm/h. The starting concentration of impurity in the melt always remained constant at 0.1 wt.%. The method of growing the crystals is described in refs. 4 and 12. Typical curves of the distribution of cadmium in single crystals of NaCl grown by the Kyropoulos method are shown in Fig. 1.

The distribution curves obtained were interpreted with the aim of determining the effective distribution coefficients by the method of ref. 12. The kinetic functions of effective distribution coefficients of cadmium in NaF, NaCl, and NaBr were constructed later. Extrapolation of the kinetic functions allowed us to obtain the values of the equilibrium distribution coefficients (see Table 1). Comparison of calculated and experimental values of the equilibrium distribution coefficients of cadmium in NaF, NaCl, and NaBr shows good agreement.

CONCLUSIONS

1. The equilibrium distribution coefficients of Cd impurity in single crystals of NaF, NaCl, and NaBr have been found experimentally and by calculation.

2. It has been shown that the equilibrium distribution coefficient of Cd increases with decrease in the heat of mixing in the solid phase in the series NaF, NaCl, NaBr, and NaI.

3. It has been shown that the anionic environment in the first coordination sphere of the impurity ion exerts a noticeable influence on the entrance of the impurity into the crystal, which evidently is the result of change in the heat of mixing caused by polarization and anion size.

---

[1] W. Hume-Rothery, Elements of Structural Metallurgy, London, Institute of Metals (1966).

[2] G. A. Andreev and B. P. Aleksandrov, Fiz. Tverd. Tela, 7, 177 (1965) [Sov. Phys. – Solid State, 7, 135 (1965)].

[3] G. A. Andreev, Fiz. Tverd. Tela, 7, 1653 (1965) [Sov. Phys. – Solid State, 7, 1339 (1965)].

[4] O. L. Kreinin, L. E. Nikolaeva, K. M. Rozin, B. M. Telis, and M. P. Shal-kol'skaya, Symposium on Mechanisms and Kinetics of Crystallization [in Russian], Nauka i Tekhnika, Minsk (1969), p. 290.

[5] A. Lidyard, Ionic Conductivity of Crystals [Russian translation], Izd. IL, Moscow (1962).

[6] N. E. Mott and M. Littleton, Trans. Faraday Soc., 34, 485 (1938).

[7] C. Kittel, Introduction to Solid State Physics, Wiley, New York (1956).

[8] K. Suzuki, J. Phys. Soc. Japan, 10, 794 (1955).

[9] K. Suzuki, J. Phys. Soc. Japan, 16, 67 (1961).

[10] K. Weiser, J. Phys. Chem. Solids, 7, 118 (1956).

[11] K. Weiser, J. Phys. Chem. Solids, 7, 118 (1956).

[12] K. M. Rozin, O. L. Kreinin, and M. P. Shaskol'skaya, Izv. Akad. Nauk SSSR, Neorgan. Mat., 7, 1105 (1971).

Growth of diamond crystals in the form of needles and plates

Yu. A. Litvin, V. P. Butuzov, É. M. Nikiforova, and S. I. Futergendler

All-Union Scientific Research Institute for Mineral Synthesis
All-Union Scientific Research Institute for Abrasives and Polishes

(Submitted September 28, 1971; resubmitted March 13, 1972)
Kristallografiya, 18, 435-436 (March-April 1973)

B. V. Deryagin and co-workers[1] have reported the growth of whisker crystals of diamond up to 25 μ thick and up to a few millimeters long on the (111) faces of natural specimens of diamond in a medium of carbonaceous gas at subatmospheric pressures. They have also succeeded in obtaining spherical crystallites of diamond of sizes of, for example, 120 × 80 μ, which grow as whiskers in the initial stages.[2]

In the present work are presented facts on the formation of whisker crystals in metal–carbon systems under superhigh pressures. Diamonds have been grown in the form of needles up to 50 μ thick and a few hundred microns long, as well as plates of, for example, 50 × 200 × 600 μ. A single crystals of synthetic diamond served as a substrate, and conditions corresponded to the region of metastable supersaturation.[3] Needles and plates of diamond present themselves as singles of prismatic habit and are normally confined to dissolved curved surfaces of the substrate. They grow in the form of single crystallites (Fig. 1a), as a discrete linear series of crystals (Fig. 1b), or in groups.

The Laue method (type RKV-86 camera, Cu radiation) was used to study the specimens obtained. In the experimental set-up, the direction of the primary beam coincided with the [111] direction in the crystal and was perpendicular to a (111) face of the substrate and one of the planes of the needle or plate; the [110] direction of the substrate and the length of the needle were placed in the vertical camera together. A narrow diaphragm ~0.2 mm in diameter was used for taking local patterns of the needle and plate. A thin layer of substrate was also included in the beam with the base of the whisker crystal. An enlarged picture of the (111) Laue spot, where reflections from the needle are superimposed on the (111) reflection of the substrate (the specimen whose photograph is shown in Fig. 1b), is shown in Fig. 2. The protuberances on the Laue spot arise from the needle.

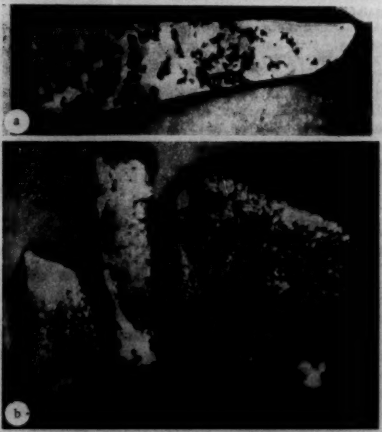

Fig. 1. Synthetic diamond crystals in the form of needles and plates. x300. a) Single needle; b) linear series of needles and plates.

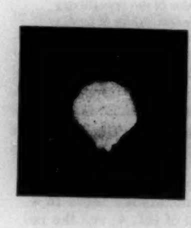

Fig. 2. Enlarged negative of a specific (111) spot of the Laue pattern. x 15.

It has been established that the needles and plates occur in parallel orientation with respect to the substrate and to each other, i.e., they grow following the orientation of the substrate. X-ray diffraction studies have confirmed the single-crystal nature of the needles and plates. The direction of their elongation coincides with the ⟨110⟩ directions, which is the direction of the C–C bonds in the diamond structure. The boundary and shape of the transverse cross sections of the needles and plates are shown in Fig. 3. During growth on a (110) plane, this "octahedron" is either greatly stretched out in the L_2 direction (needles) or compressed along the L_3 direction (plates). The boundary surfaces are (111) planes, although blunted (100) faces are also observed on the tips. The vertices of the needles and plates are terminated by an edge in a [110] direction. The lateral faces are usually strongly dissolved.

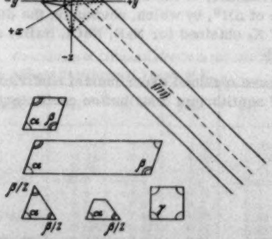

Fig. 3. Form and cross sections of needles and plates (pattern). Growth on (110) plane: α = 70°31'44", β = 109°28'16"; growth on (100) plane: γ = 90°.

The growth of needles usually occurs in groups and is observed on the (100) face of the substrate, which is also dissolved. In this case, the axes of the needles are oriented along a [100] direction. The growth of needles and plates is the result of a complex process of interaction of the substrate with the medium under conditions of strongly nonisothermal temperature fields. The local growth effect of whisker crystals arises on a solid front of interaction of the medium on the entire surface of the substrate. In this case, the transfer of dissolved carbon to the growth site is accomplished exclusively by diffusion. If the driving forces of the process of growth of needles and plates can, in general, be associated with the state of the medium, then the conditions for the start of growth are determined, in all probability, by the state of the substrate. It is not clear whether the case examined is a special case of normal growth proceeding to the formation of crystals of very small size and unusual shape, or whether the growth is associated with a dislocation mechanism.

---

[1] B. V. Deryagin, D. V. Fedoseev, V. M. Luk'yanovich, B. V. Spitsyn, V. A. Ryabov, and A. V. Lavrent'ev, Dokl. Akad. Nauk SSSR, 181, 1094 (1968) [Sov. Phys. – Dokl., 13, 783 (1969)].

[2] B. V. Deryagin, V. G. Lyuttsau, D. V. Fedoseev, and V. A. Ryabov, Dokl. Akad. Nauk SSSR, 190, 86 (1970) [Sov. Phys. – Dokl., 15, 58 (1970)].

[3] Yu. A. Litvin, G. N. Bezrukov, and V. P. Butuzov, Symposium on Mechanism and Kinetics of Crystallization [in Russian], Nauka i Tekhnika, Minsk (1969), p. 477.

Teaching career of a great crystallographer

N. V. Belov

Kristallografiya, 18, 437-439 (March-April 1973)

As of April 27 three years have elapsed since the day of Aleksei Vasil'evich Shubnikov's death, a period long enough for us to form a complete and unprejudiced estimate of the matchless scope of his favorite pursuit, crystallography, and that vigorous wave of creativity in the middle of the twentieth century on the crest of which was Aleksei Vasil'evich Shubnikov, our number-one crystallographer.

The author of these lines was in close contact with Aleksei Vasil'evich in 1937, as a member of a group of about 15 people, who, gathering every Wednesday as a scientific council, bore some resemblance to the present Scientific Council of the several-centuries-old Institute of Crystallography, which still meets every Wednesday. No candidate's or doctor's dissertations were dealt with, but rather printed novelties and original publications being prepared for the "Trudy Laboratorii (since 1944 Institute) Kristallografii" were issued over a period of one to two years. For honesty's sake, we state that among these papers there were many "N's Communications" on crystallographic measurements of some compounds with equations of little interest. At that time crystallography was concentrated in a small circle in the center of a triangle at whose vertices the powerful sciences of physics, chemistry, and mineralogy were located. We often jested that our science resembled an operetta among the three forms of the selective specific arts: drama, opera, and ballet.

But it was precisely in these years that the studies on the synthesis of large single crystals of saccharose were completed (?). Of course, the question mark in parentheses at the end of the preceding sentence is to be crossed out in the explanation of the main problem of this study: the construction of rather perfect equipment for the production of various perfect crystals important to science and technology. The "scientific technical workshop" in which Aleksei Vasil'evich, who perfected the methods of cutting and finishing crystals, participated in person, worked continuously. Already by that time quartz, which was needed in large amounts in radiotechnology, had been studied with particular thoroughness, perhaps not so much as regards its undoubted inherent advantages but rather as regards the abundance of defects, which, if not detected at the appropriate time, might put the high-power radio equipment out of commission.

The experience gathered by A. V. Shubnikov himself and by his co-workers over many years is reflected in his encyclopedia on quartz. At the same time he wrote the booklet on "How Crystals Grow," which in the first and last editions (published under different names) became the reference book in laboratories dealing with crystals, which have now vastly increased in number. At the same time "Bases of Crystallography" was composed by three authors under the supervision of Aleksei Vasil'evich; this book revolutionized the instruction on crystallography at high schools. "For the purpose of mental development," but certainly not only for that of the author, Aleksei Vasil'evich wrote the charming semiphilosophical book "Symmetry" with many illustrations taken from the field of applied art.

The fruits of this seemingly ineffective but unquestionably efficient creativity were to appear soon. The growth of large crystals of Seignette salt with a minimum number of defects, together with the encyclopedic data on quartz and slices of the latter substance, induced the Ministry of Electroindustry to create the Special Trust No. 13 for the exploitation of the progress achieved by the Laboratory of Crystallography. The laboratories of this trust were located inside the expanded areas of the academic Laboratory of Crystallography. A. V. Shubnikov was officially appointed technical manager of the ministerial institute. Corundum-ruby, the single crystals of which were soon produced in very good quality, were added to the trust's main points of interest: quartz and Seignette salt. Did Aleksei Vasil'evch at that time have any idea how many similar laboratories, institutes, and entire plants would in the 30 years now past spring from the academic Institute of Crystallography founded by him?

The Second World War broke out. The Institute of Crystallography (at that time still an independent academic laboratory) was moved to the Ural range. Here the knowledge and experience of the workers in the laboratory on quartz and Seignette salt enabled the laboratory to gain first place in the district among the factories working for defense. Since the task of the manager entailed only elementary operations for the competent crystallographer, much time was left for the more distracting semiphilosophic research to which Aleksei Vasil'evich was always inclined. At that time he was possessed by the idea of uniting, by symmetry reasoning, such contrasting concepts as white and black, positive and negative, plus and minus. Aleksei Vasil'evich Shubnikov's doctrine of antisymmetry, which is usually called black and white symmetry, was the recurrent main topic in his reports for over three years. With the aid of the mathematicians mobilized by him, this doctrine could afterwards be extended to apply also to the macro- and the microworld: the discontinuum. The Shubnikov groups, numbering 1651 and including as a particular case the well-known 230 classic Fedorov groups, were discovered. Their discoverer, who loved so much the technical application of crystallography, stated that 10 years would elapse before antisymmetry would become utilized in practice. Actually, this period was much shorter.

After the war, living a new life with a faster pulse, the Institute of Crystallography felt the need of an output of young leaders and, with its blacksmiths, in 1946 it was changed into the Physics Department of the Gor'kii University, where Aleksei Vasil'evich for three successive years taught his above-mentioned brilliant course on crystallography, and his co-workers continued educating new apprentices, although already by 1953 Aleksei Vasil'evich had received his own chair at the Moscow University. In Gor'kii the above-mentioned number "1651" was fixed, and it was shown almost simultaneously that the antisymmetry laws hold and control the statics of ferromagnetism, while the same was shown also for ferroelectricity. Shubnikov's group "descended onto the earth" and, provided with the letter "Sh", now occupy the largest area in a novel atlas of groups for structure analysis by means of x-ray, electron, and mainly neutron diffraction.

The last 25 years were marked by the realization of the dreams of the great crystallographer and in particular of the situation which seemed absurd to us, his co-workers of the thirties, viz., that the scientific workers constituted less than half the staff of the Institute of Crystallography, while the staff mainly consisted of production people who brought about the achievements of the crystallographic ideas. Nevertheless, it should be noted that it was precisely these scientific co-workers in the Institute of Crystallography who were the first to synthesize quartz single crystals of so large a size that a veto based on considerations of accident prevention was imposed on further production, and production had to be handed over to a specialized plant; among the technical diamonds manufactured industrially, those made by the procedure proposed to the "daughter" laboratory of the Institute are the best.

I wish to end with the Latin motto "Quod potui feci...," "he has done what he could, now it is your turn." However, much is contained in the five letters of the word "could."

BLANK PAGE

Theory of the electrodynamic effect in liquid crystals

S. A. Pikin and A. A. Shtol'berg

Institute of Crystallography, Academy of Sciences of the USSR

(Submitted May 29, 1972)
Kristallografiya, 18, 445-453 (May-June 1973)

A computer is used to calculate the dependence of the threshold potential difference and the period of the induced structural inhomogeneity as a function of the internal properties of a nematic liquid crystal and the external magnetic field. It is shown that the threshold for the appearance of stationary structure depends strongly on the anisotropy of the viscosity, and with a certain critical value of this anisotropy it becomes impossible.

INTRODUCTION

The theory of the electrohydrodynamic effect in liquid crystals has been the subject of much work,[1-4] in which the various aspects of this phenomenon observed optically in the form of bandlike ("domain") structure[5,6] have been treated. The appropriate hydrodynamics of a liquid crystal in combination with the properties of a poor conductor leads to instability in liquid crystals under the action of an electric field.[1,2] The inhomogeneous distribution of the director in the liquid crystal and the threshold electric field for which such a structure is formed can be found in the same way.[3,4] In general the threshold properties depend on the external conditions (the thickness of the liquid-crystal layer and the frequency of the electric field). The low-frequency region has important boundary conditions at the solid surfaces of the electrodes.[3,4]

Here a computer is used to calculate the dependence of the threshold voltage V_s and the period d_s of the structure on the internal properties of the liquid crystal (the anisotropy of the viscosity, elasticity, electric permittivity and conductivity) and also on the external magnetic field. The low-frequency electric-field case which is considered, where the electrical conductivity and the boundary conditions which occur determine the form of the dependence of V on d, corresponds to the formation of an instability.[3] V_s and d_s are found from the minimum of the low-lying branch of V(d). The anisotropy of the liquid crystal properties and the orienting magnetic field affect the form of the curve V(d) and the position of the minimum $V_s = V(d_s)$. With certain parameter values entering the problem the form of the relation V(d) can change in such a way that no instability of this kind ($d_s^{-1} \neq 0$) arises, and the minimum will correspond to $d_s^{-1} = 0$ and $V_s = 0$ or a uniform structure of the liquid crystal. It is stressed that we speak of the lower branch; under these conditions higher branches can have minima for various nonzero d_s^{-1} but the corresponding thresholds are substantially higher.

Analytical analysis of such behavior of the branches, unfortunately, is not possible. The use of a computer nevertheless allows us to reach a number of qualitative conclusions about the observation of the electrohydrodynamic effect in various liquid-crystal materials, which is the aim of this work.

EQUATIONS AND BOUNDARY CONDITIONS

We assume that in a layer of a nematic liquid crystal placed in a planar capacitor, in the absence of an electric field the director n is oriented along the x axis. This single-domain arrangement is sometimes achieved using a magnetic field H parallel to the x axis. When an electric field E is switched on parallel to the z axis a perturbation in the orientation of the director in the liquid-crystal layer arises. However at the solid planar surfaces of the capacitor, which are sometimes specially treated, the orientation of N remains unchanged. With the chosen geometry of the problem the small deviation θ of the director from the x axis lies in the xz plane. The system of linearized equations which describe the incompressible nematic liquid assumes the following form[3] in this case:

$$dv_x / dx + dv_z / dz = 0, \tag{1}$$

$$\frac{\partial}{\partial z}\left(\beta_1 \frac{\partial^2 v_x}{\partial x^2} + \beta_2 \frac{\partial^2 v_x}{\partial z^2}\right) - \frac{\partial}{\partial x}\left\{\beta_3 \frac{\partial^2 v_z}{\partial x^2} + \beta_4 \frac{\partial^2 v_z}{\partial z^2} + \frac{E}{4\pi}\left[\varepsilon_a E \frac{\partial \theta}{\partial x} - \varepsilon_\parallel \frac{\partial^2 \varphi}{\partial x^2} - \varepsilon_\perp \frac{\partial^2 \varphi}{\partial z^2}\right]\right\}, \tag{2}$$

$$\sigma_a E \frac{\partial \theta}{\partial x} - \sigma_\parallel \frac{\partial^2 \varphi}{\partial x^2} - \sigma \frac{\partial^2 \varphi}{\partial z^2} = 0, \tag{3}$$

$$\frac{\varepsilon_a}{4\pi} E\left(E\theta - \frac{\partial \varphi}{\partial x}\right) - \chi_a H^2 \theta + K_{11} \frac{\partial^2 \theta}{\partial z^2} + K_{33} \frac{\partial^2 \theta}{\partial x^2} = \alpha_3 \frac{\partial v_x}{\partial z} + \alpha_2 \frac{\partial v_z}{\partial x}. \tag{4}$$

Here V is the velocity of the liquid, φ is the deviation of the electric field potential from the value $-Ez = -V(z/l)$, where $|z| \leq l/2$, l is the thickness of the liquid-crystal layer, V is the electrode potential difference, $\varepsilon_a = \varepsilon_\parallel - \varepsilon_\perp$ is the anisotropy of the electric permittivity, $\sigma_a = \sigma_\parallel - \sigma_\perp$ is the anisotropy of the conductivity, χ_a is the anisotropy of the diamagnetic susceptibility, K_{11} and K_{33} are the elastic moduli of the liquid crystal, and dynamic viscosity coefficients β_i are related to the Leslie coefficients α_j by the relations

$$\beta_1 = \alpha_1 + \alpha_5 + (\alpha_3 + \alpha_4 + \alpha_6)/2, \quad \beta_2 = (\alpha_3 + \alpha_4 + \alpha_6)/2,$$

$$\beta_3 = (-\alpha_2 + \alpha_4 + \alpha_5)/2, \quad \beta_4 = (-\alpha_2 + \alpha_4 - \alpha_5)/2.$$

In the system treated, Eq. (1) is the continuity equation, Eq. (2) is a combination of the Navier–Stokes equations in an anisotropic liquid dielectric containing auxiliary charges, Eq. (3) describes the spatial distribution of the steady electric current, and Eq. (4) is the equation for equilibrium of the director, which includes the molecular field and friction forces.

Equations (1–4), which describe stationary flow of a nematic liquid and an inhomogeneous spatial distribution of the director in the liquid-crystal layer, determine unknown functions V, θ, and φ. The boundary conditions at the solid surface take the form

$$\varphi = 0, \quad v = 0, \quad \partial v_z / \partial z = 0, \quad \theta = 0, \tag{5}$$

where the condition $\partial v_z/\partial z = 0$ follows from the equation of continuity while the condition $\theta = 0$ follows from the statement of the problem (experiment).

Eliminating the functions V and θ from the equations obtained, we find that φ satisfies the equation

$$\sum_{m=0}^{4} \hat{a}_m \left(\frac{\partial^2}{\partial z^2}\right)^{4-m} \varphi = 0, \tag{6}$$

where

$$\hat{a}_0 = 1 - \eta_3,$$
$$\hat{a}_1 = \hat{a}_0 \hat{f} + (1 - 2\eta_2 - 2\eta_3)\frac{\partial^2}{\partial x^2},$$
$$\hat{a}_2 = \left[\hat{a}_0 \hat{g} + (1 - 2\eta_2 - 2\eta_3)\hat{f} - \eta_2 \frac{\partial^2}{\partial x^2} + \frac{1}{2}(1 - \eta_1)\zeta\lambda\right]\frac{\partial^2}{\partial x^2},$$
$$\hat{a}_3 = [(1 - 2\eta_2 - 2\eta_3)\hat{g} - \eta_2 \hat{f} - \eta_1\zeta\lambda]\frac{\partial^4}{\partial x^4},$$
$$\hat{a}_4 = -\left[\eta_2 \hat{g} + \frac{1}{2}(1 + \eta_1)\zeta\lambda\right]\frac{\partial^6}{\partial x^6},$$
$$\hat{f} = (\nu + \mu)\frac{\partial^2}{\partial x^2} - \frac{1}{l^2}(\delta - \varepsilon_a\lambda), \quad \hat{g} = \nu\left(\mu\frac{\partial^2}{\partial x^2} - \frac{\delta}{l^2}\right) + \frac{\varepsilon_a\lambda}{l^2},$$
$$\eta_1 = \frac{\alpha_2 - \alpha_3}{\alpha_2 + \alpha_3}, \quad \eta_2 = -\frac{\beta_2}{\alpha_2 + \alpha_3}, \quad \eta_3 = -\frac{\alpha_1}{2(\alpha_2 + \alpha_3)},$$
$$\nu = \frac{\sigma_\parallel}{\sigma_\perp}, \quad \mu = \frac{K_{33}}{K_{11}}, \quad \zeta = \nu\varepsilon_\perp - \varepsilon_\parallel,$$
$$\delta = \frac{\chi_a}{K_{11}}(lH)^2, \quad \lambda = \frac{V^2}{4\pi K_{11}}.$$

Using Eqs. (1–4) the boundary conditions (5) are now written in the form

$$\varphi = 0, \quad \frac{\partial^2\varphi}{\partial z^2} = 0, \quad \sum_{m=0}^{1} \hat{\Gamma}_m \left(\frac{\partial^2}{\partial z^2}\right)^{3-m} \varphi = 0,$$
$$\sum_{m=0}^{3} \hat{\Gamma}_m \left(\frac{\partial^2}{\partial z^2}\right)^{3-m} \frac{\partial\varphi}{\partial z} = 0, \tag{7}$$

where

$$\hat{\Gamma}_0 = \frac{1}{2}(1 - \eta_1^2)\hat{a}_0,$$
$$\hat{\Gamma}_1 = p\frac{\partial^2}{\partial x^2} + \hat{\Gamma}_0 \hat{f},$$
$$\hat{\Gamma}_2 = (p\hat{f} + \hat{\Gamma}_0 \hat{g} + q\lambda)\frac{\partial^2}{\partial x^2},$$
$$\hat{\Gamma}_3 = (p\hat{g} + q\lambda)\frac{\partial^4}{\partial x^4},$$
$$p = 1 + \eta_1 - 2\eta_2 - \eta_3(1 - \eta_1^2) + \frac{1}{2}\eta_2(1 - \eta_1)^2,$$
$$q = \frac{1}{4}(1 + \eta_1)(1 - \eta_1)^2\zeta.$$

THRESHOLD POTENTIAL DIFFERENCE

The solution of Eq. (6) is of the form

$$\varphi = \exp(ikx)\psi(z),$$

where $\psi(z)$ represents a linear combination of the functions

$$\operatorname{ch}(\xi_j^{1/2} z/l) \text{ and } \operatorname{sh}(\xi_j^{1/2} z/l). \tag{8}$$

The quantities χ_j (j = 1, ..., 4) are the roots of the algebraic equation obtained from Eq. (6) after the substitutions

$$\frac{\partial^2}{\partial x^2} \to -k^2, \qquad \frac{\partial^2}{\partial z^2} \to \frac{\xi_j}{l^2}.$$

With given parameters ν, μ, δ, ζ, η_1, η_2, η_3, and ε_a the root ξ_j is a function of $\varkappa = (kl)^2$ and λ.

The coefficients obtained for even and odd (relative to z) combinations of the functions (8) are determined by the boundary conditions (7). With $z = \pm(l/2)$) the conditions (7) lead to a system of algebraic equations whose matching conditions give the relation between λ and $\varkappa$.

The matching condition for the even branches is

$$\det \|c_{ij}\| = 0. \tag{9}$$

In the (4 × 4) matrix $\|c_{ij}\|$ the j-th column corresponds to the root ξ_j. If ξ_j is a real positive root then we have

$$c_{1j} = 1, \quad c_{2j} = \xi_j, \quad c_{3j} = \sum_{m=0}^{1} \Gamma_m \xi_j^{3-m},$$
$$c_{4j} = \sqrt{\xi_j}\,\operatorname{th}\left(\frac{\sqrt{\xi_j}}{2}\right)\sum_{m=0}^{3} \Gamma_m \xi_j^{3-m}. \tag{10}$$

If ξ_j is a real negative root then we have

$$c_{1j} = 1, \quad c_{2j} = \xi_j, \quad c_{3j} = \sum_{m=0}^{1} \Gamma_m \xi_j^{3-m},$$
$$c_{4j} = -\sqrt{|\xi_j|}\,\operatorname{tg}\left(\frac{\sqrt{|\xi_j|}}{2}\right)\sum_{m=0}^{3} \Gamma_m \xi_j^{3-m}. \tag{11}$$

If ξ_j is a complex root, i.e., $\xi_j = \xi_j' + i\xi_j''$, then $\xi_j^* = \xi_j' - i\xi_j''$ is also a root and these complex conjugate roots correspond to two columns (c_{ij}') and (c_{ij}'') of real elements:

$$c_{1j}' = 1, \; c_{2j}' = \xi_j', \; c_{3j}' = \Gamma_0[(\xi_j')^3 - 3\xi_j'(\xi_j'')^2] + \Gamma_1[(\xi_j')^2 - (\xi_j'')^2],$$
$$c_{4j}' = \frac{(\operatorname{sh} A_j)(A_j R_j + B_j I_j) + (A_j I_j - B_j R_j)\sin B_j}{\operatorname{ch} A_j + \cos B_j},$$
$$c_{1j}'' = 0, \; c_{2j}'' = \xi_j'', \; c_{3j}'' = \Gamma_0[3(\xi_j')^2\xi_j'' - (\xi_j'')^3] + 2\xi_j'\xi_j''\Gamma_1,$$
$$c_{4j}'' = \frac{(A_j I_j - B_j R_j)\operatorname{sh} A_j - (A_j R_j + B_j I_j)\sin B_j}{\operatorname{ch} A_j + \cos B_j}. \tag{12}$$

In (10–(12) the values of Γ_m are equivalent to $\hat{\Gamma}_m$, in which we have carried out the substitution $\partial^2/\partial x^2 \to -k^2$ while A_j, B_j, I_j, and R_j are given by the expressions

$$A_j = \sqrt{(\xi_j' + \sqrt{(\xi_j')^2 + (\xi_j'')^2})/2}, \quad B_j = -\xi_j''/2A_j,$$
$$R_j = [(\xi_j')^3 - 3\xi_j'(\xi_j'')^2]\Gamma_0 + [(\xi_j')^2 - (\xi_j'')^2]\Gamma_1 + \xi_j'\Gamma_2 + \Gamma_3,$$
$$I_j = [3(\xi_j')^2\xi_j'' - (\xi_j'')^3]\Gamma_0 + 2\xi_j'\xi_j''\Gamma_1 + \xi_j''\Gamma_2.$$

The matching conditions for the odd branches take a form similar to (9–12). Here the elements c_{1j}, c_{2j}, c_{3j} in (10–12) do not change while in the elements c_{4j} it is necessary to make the following substitutions: In (10),

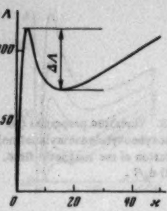

Fig. 1. Typical form of the relation $\Lambda(\varkappa)$.

$\tanh(\ldots) \to \coth(\ldots)$, in (11), $\tan(\ldots) \to -\cot(\ldots)$, while in (12), $\sin B \to -\sin B$ and $\cos B \to -\cos B$.

With given material parameters and $H = 0$ ($\delta = 0$) the transcendental equation (9) has in infinite sequence of solutions $\lambda_s^+(\varkappa)$ (even branches) and $\lambda_s^-(\varkappa)$ (odd branches), where $\varkappa = (kl)^2$ and $s = 1, 2, 3$.

As shown by the calculations, the lowest and thus energetically most favorable branch is $\Lambda \equiv \lambda_1^+$. The typical form of the relation $\Lambda(\varkappa)$ is shown in Fig. 1. The value of $\Lambda_s \equiv \Lambda(\varkappa_s)$ which corresponds to a minimum of $\Lambda(\varkappa)$ with a nonzero value of the wave number $k = k_s$ determines the threshold potential difference

$$V_s = \sqrt{4\pi K_{11}\Lambda_s},$$

for which an inhomogeneous distribution of the director occurs.

It is not hard to study the asymptote $\Lambda(\varkappa)$ with $\varkappa \ll 1$ and $\varkappa \gg 1$. As we see from Eq. (6), with $\delta = 0$ the roots ξ_j are proportional to $\varkappa$, multiplied by a certain function of the ratio $\lambda/\varkappa$. Therefore according to (10-12) with $\varkappa \ll 1$ and $\lambda \ll 1$ the determinant of the matrix $\|c_{ij}\|$ is a function of $\lambda/\varkappa$. The solution $\lambda/\varkappa = b > 0$ of the equation $\det\|c_{ij}\| = 0$ obeys the linear relation

$$\lambda = b\varkappa, \quad \varkappa \ll 1. \tag{13}$$

Similarly, with $\varkappa \gg 1$, $\lambda \gg 1$, and $\lambda/\varkappa \lesssim 1$ when Eq. (6) does not have a real negative root $\det\|c_{ij}\|$ also depends only on the ratio $\lambda/\varkappa$. The corresponding solution $\lambda/\varkappa = c > 0$ of Eq. (9) obeys the linear relation

$$\lambda \approx c\varkappa, \quad \varkappa \gg 1.$$

Calculations using a computer show that the coefficients b and c have the following orders of magnitude: $b \sim 10^2$ and $c \sim 1$.

To determine V_s and d_s in n-methoxybenzylidenebutylalinine (MBBA) we have used the following parameter values:

$$K_{11} \approx K_{33};\ \ K_{11}/\chi_a \approx 2.9,\ \ K_{33}/\chi_a \approx 6.9\ \text{cm}^2 \cdot \text{G}^2\ (\text{ref. } 7);$$
$$\chi_a \approx 1.25 \cdot 10^{-7}\ \text{erg} \cdot \text{cm}^{-3} \cdot \text{G}^{-2}\ (\text{ref. } 8);$$
$$\varepsilon_\parallel \approx 4.8,\ \ \varepsilon_\perp \approx 5.1,\ \ \sigma_\parallel/\sigma_\perp \approx 1.5\ (\text{ref. } 9);$$
$$\alpha_1 \approx 0.007,\ \ \alpha_3 \approx -0{,}078,\ \ \alpha_4/2 \approx 0.042,$$
$$\beta_2 \approx 0{,}024,\ \ \beta_3 \approx 0.104\ \text{g} \cdot \text{cm}^{-1} \cdot \text{sec}^{-1}\ (\text{ref. } 10).$$

Using these values the threshold voltage V_s and the period $d_s = \pi/k_s$ of the structure which appears turn out to be $V_s \approx 6.9$ V and $d_s \approx 0.7\,l$.

THE EFFECT OF ANISOTROPY IN THE VISCOSITY ON THE THRESHOLD PROPERTIES

It should be stressed that the form of the function $\Lambda(\varkappa)$ illustrated in Fig. 1 is due to the boundary conditions (5) and (7) if the material parameters do not have special values. It can be shown that the nature of the boundary conditions changes when $\eta_2 - 1 \to +0$. In this case the effect of the solid surfaces is only important in a thin layer near the walls having a thickness of the order of $(\eta_2 - 1)^{1/2} l \varkappa^{-1/2} \to 0$ and in the main part of the layer the relation $\varphi(z)$ is of the form $\varphi \sim \cos[(2s-1)\pi z/l]$ or $\varphi \sim \sin(2s\pi z/l)$. The corresponding relation $\Lambda(\varkappa) = \lambda_1^+(\varkappa)$ is given by the expression (with $\eta_1 = 1$)

$$\Lambda = \frac{\nu\mu\varkappa^3 + \pi^2(\nu + \mu + \nu\mu)\varkappa^2 + \pi^4(1 + \nu + \mu)\varkappa + \pi^6}{\zeta\varkappa^2 + \pi^2\zeta\varkappa + \pi^4\varepsilon_a}. \tag{14}$$

In this case with $\varkappa \ll \pi^2$, $\Lambda(\varkappa) \to \infty$, according to the law $\Lambda \simeq \pi^4/(\zeta\varkappa + \pi^2\varepsilon_a)$. However, for small deviations of η_2 from unity ($\eta_2 - 1 \gtrsim |\varepsilon_a|$) the asymptote (13) is valid.

The functional dependence $\Lambda(\varkappa)$ is substantially affected by the viscosity coefficient α_3. As is well known,[11] when $\alpha_3 < 0$ or $\eta_1 < 1$ (it is here taken into account that[12] $\alpha_2 + \alpha_3 = \alpha_6 - \alpha_5$) the molecules of a nematic liquid crystal are oriented in a flow with a constant velocity gradient at an angle $\theta = \arccos \eta_1/2$ with respect to the flow direction. If $\alpha_3 > 0$ or $\eta_1 > 1$ then no such orientation should be observed. Since the appearance of a periodic structure is due to orientation of the director in flows with a velocity gradient then the behavior of a liquid crystal when instabilities appear should depend strongly on the sign of α_3 or $\eta_1 - 1$. With a certain value of $\eta_1 = \eta_1^* > 1$ the minimum of the curve $\Lambda(\varkappa)$ at $\varkappa = \varkappa_s$ vanishes and an inflection point appears. With $\eta_1 > \eta_1^*$ the function $\Lambda(\varkappa)$ increases monotonically with increasing $\varkappa$. Thus when $\eta_1 \geq \eta_1^*$ there is no threshold for the appearance of stationary conditions involving the lower of the branches $\lambda_s^\pm$. The threshold involving the branch λ_1^-, which is closest to λ_1^+, does not vanish in a certain range of values $\eta_1 \gtrsim \eta_1^*$; however, the corresponding value $(\lambda_1^-)_s$ is substantially greater than Λ_s when $\eta_1 \lesssim \eta_1^*$.

Computer calculations showed that $\eta_1^* \simeq 1.12$ if the remaining parameters of the material are close to the parameters for p azoxyanisal (PAA); in this case $\lambda_1^-(\varkappa)$ has a minimum $(\lambda_1^-)_s \simeq \lambda_1^-(41) \simeq 227.3$. Note that if $\eta_1 \lesssim 1.12$ then $\Lambda_c \simeq \lambda_1^+(11) \simeq 64.7$. Figure 2 shows the calculated relations $\lambda_1^+(\varkappa)$, $\lambda_2^+(\varkappa)$, and $\lambda_1^-(\varkappa)$ for various values of η_1 in which the remaining parameters of the material remain unchanged and are: $K_{11} = 7 \cdot 10^{-7}$; $K_{33} = 1.7 \cdot 10^{-6}$ dyn, $\varepsilon_\perp = 5.83$, $\varepsilon_\parallel = 5.62$; $\sigma_\parallel/\sigma_\perp = 1.5$, $\alpha_1 = 0$ $\alpha_4/2 = 0.034$, $\beta_2 = 0.024$, and $\beta_3 = 0.092$ (here we have used the parameters[1] of PAA).

The quantity η_1^* depends weakly on the anisotropy of other parameters of the liquid crystal. Thus, if the viscosity coefficient α_1 is of the same order of magnitude as the remaining α_j ($\alpha_1 = 0.07$) then $\eta_1^* \simeq 1.10$; with a change of the anisotropy of the electric permittivity from $\varepsilon_a = 0$ to $\varepsilon_a = -0.4$, η_1^* varies within the range 1.07 to 1.16. This is related to the previously-cited fact that the form of the curve $\Lambda(\varkappa)$ depends strongly on the values of the paramters η_1 and η_2 and quite weakly on the other parameters of

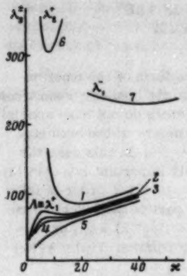

Fig. 2. The relation $\lambda_s \pm(\varkappa)$ calculated for various values of the parameter η_1. 1) $\eta_1 = 1$; 2) $\eta_1 = 1.1$; 3) $\eta_1 = 1.12$; 4) $\eta_1 = 1.13$; 5) $\eta_1 = 1.21$; 6) $\eta_2 = 1.12$; 7) $\eta_2 = 1.12$.

the material. Thus in searching for materials with a shallow trough $\Delta\Lambda(\varkappa)$ at the point $\varkappa = \varkappa_s$ one should pay primary attention to the parameters η_1 and η_2.

$\Lambda(\varkappa)$ has an absolute minimum when $\varkappa = 0$ and a localized minimum when $\varkappa = \varkappa_s$. The point $\varkappa = 0$ corresponds to the unperturbed state of the liquid crystal. At the point $\varkappa = \varkappa_s$ the amplitudes of θ, φ, and v are finite but small and are described by the linearized equations. Experiment has shown[13] that in the ranges of values $0 < \Lambda < \Lambda_s$ and $\Lambda_s < \Lambda < \Lambda_t$, where Λ_t is the threshold for turbulence, there can be stationary conditions with wave numbers $\varkappa = 0$ and $\varkappa = \varkappa_s$, respectively. The inhomogeneous structure with $\varkappa \neq 0$ or $\varkappa_s$ is consequently unstable. Evidently, in the neighborhood of the points $\varkappa = 0$ and $\varkappa = \varkappa_s$ the amplitudes of θ, φ, and v increase enough that the linear approximation becomes insufficient, while the possible stationary conditions should be found from a solution of the unlinearized problem.

With $\Lambda = \Lambda_s$ inhomogeneous structure with $\varkappa \neq \varkappa_c$ can arise due to fluctuations of the electric field. If $\Delta\Lambda$ (see Fig. 1) is not too large then such fluctuations can transform the liquid crystal at $\Lambda = \Lambda_s$ from a state with $\varkappa = \varkappa_s$ into a state with $\varkappa = 0$, i.e., with small $\Delta\Lambda$ the stationary conditions with $\varkappa = \varkappa_s$ become unstable. The corresponding values for the fluctuation of the electric field potential during the relaxation time of the bulk electric charge, $\tau_e \sim \varepsilon/4\pi\sigma$, should be of the order of $(\Delta\varphi)^2 \sim 4\pi K_{11}\Delta\Lambda$. On the other hand it is known[14] that the fluctuation $\overline{(\Delta\varphi)^2}$ at a temperature T is of the order of magnitude of

$$\overline{(\Delta\varphi)^2} \sim \tau_e^{-1} TR/\pi,$$

where $R = (l/\sigma\pi r^2)$ is a resistance of a liquid crystal layer of height l and radius r. The characteristic size r of the inhomogeneous structure is of the order of $r \sim \pi l \varkappa_s^{-1/2} \sim l$. As a result we find that the difference $\Delta\Lambda$ at least should not be greater than

$$(\Delta\Lambda)_{\max} \sim T/\varepsilon l K_{11}.$$

Consequently at the usual temperatures for the existence of a nematic mesophase we have $(\Delta\Lambda)_{\max} \sim 10^{-5}$. Since for $\eta_1 < \eta_1^*$ the value of $\Delta\Lambda$ is much greater than unity, then the probability τ^{-1} of the thermal fluctuations of interest is very small and the stationary inhomogeneous structure of the liquid crystal is stable. The times τ and τ_e become of the same order of magnitude and this structure ceases to be stable if $\Delta\Lambda \sim 10^{-5}$, i.e., with η_1 quite close to η_1^*.

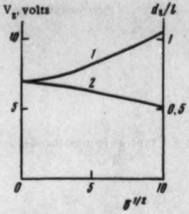

Fig. 3. Threshold properties (for n-methoxybenzylidenebutylanaline) as a function of the magnetic field. 1) V_s; 2) d_s/l.

THE EFFECT OF A MAGNETIC FIELD ON THE THRESHOLD PROPERTIES

The effect of a magnetic field parallel to the x axis changes the threshold properties such that the threshold voltage V_s increases with increasing H (or δ). Here the period d_s decreases, as shown by the calculations. Figure 3 shows the relations $V_s(\delta)$ and $d_s(\delta)$ calculated for MBBA. When ordinary liquid-crystal layers are used (thicknesses of several tens of microns), a magnetic field of the order of 10^3 G leads to a relative change of V_s and d_s of the order of 1%.

The effect of a magnetic field on the threshold properties Λ_s and $\varkappa_s$ becomes important when we have $\delta \gg \varkappa_s(\delta) \gg \pi^2$ in Eqs. (6) and (9). If this inequality is satisfied then the roots ξ_j of Eq. (6) have the following order of magnitude:

$$\xi_1 \sim \delta(\xi_1 > 0), \quad \frac{\xi_2}{\varkappa} \approx -\frac{\zeta\lambda - \eta_2\nu\delta - \eta_2\nu\mu\varkappa}{(\eta_2 + \eta_2\nu - \nu)\delta} \ll 1(\xi_2 < 0), \quad |\xi_3, \xi_4| \ll |\xi_2|,$$

where it is assumed for simplicity that $\eta_1 \simeq 1$, $\eta_3 \simeq 0$, and $\varepsilon_a \simeq 0$. In Eq. (9), the roots ξ_1 and ξ_2 correspond to columns (10) and (11), respectively, in which the coefficients of $\tanh(\sqrt{\xi_1}/2)$ in c_{41} are much larger in modulus than the coefficients of $\tan(\sqrt{|\xi_2|}/2)$ in c_{42}. Therefore by equating the determinant of the matrix $\|c_{ij}\|$ to zero we can estimate Λ from the condition

$$\frac{\sqrt{|\xi_2|}}{2} \simeq \frac{1}{2}\sqrt{\frac{(\zeta\Lambda - \eta_2\nu\delta - \eta_2\nu\mu\varkappa)\varkappa}{(\eta_2 + \eta_2\nu - \nu)\delta}} \simeq \frac{\pi}{2},$$

for which the contributions of the roots ξ_1 and ξ_2 to det $\|c_{ij}\|$ are comparable. From this we find that

$$\zeta\Lambda \simeq \nu\eta_2\delta + \nu\mu\eta_2\varkappa + [\pi^2(\eta_2 + \eta_2\nu - \nu)\delta]/\varkappa.$$

Thus, $\Lambda_s(\delta)$, $\varkappa_s(\delta)$, $V_s(H)$, and $d_s(H)$ with $\delta \gg \varkappa_s(\delta) \cdot \gg \pi^2$ are of the orders of magnitude $\Lambda_s(\delta) \sim (\nu\eta_2/\zeta)\delta$, $\varkappa_s(\delta) \sim \pi[(\eta_2 + \eta_2\nu - \nu)\delta/\nu\mu\eta_2]^{1/2}$, and

$$V_s(H) \sim \sqrt{\frac{4\pi\nu\eta_2\chi_a}{\zeta}}\, lH, \qquad d_s(H) \sim \left(\frac{\nu\mu\eta_2 K_{11}}{(\eta_2 + \eta_2\nu - \nu)\chi_a}\right)^{1/4}\left(\frac{l}{\pi H}\right)^{1/2}. \tag{15}$$

Note that with $\eta_2 = 1$, Eq. (15) is easily obtained from expressions similar to (14), in which we have assumed $\delta \neq 0$.

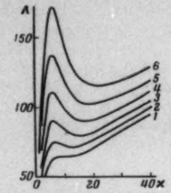

Fig. 4. Relation $\Lambda(\varkappa)$ calculated for various values of δ. 1) $\delta = 0$; 2) $\delta = 1$; 3) $\delta = 4$; 4) $\delta = 9$; 5) $\delta = 16$; 6) $\delta = 25$.

Another aspect of the magnetic field effect is of interest. A magnetic field of the indicated orientation stabilizes the instability of the inhomogeneous structure which appears when $\eta_1 \simeq \eta_1^*$. Figure 4 shows how the form of the functional relation $\Lambda(\varkappa)$ varies with a change of the parameter δ if $\eta_1 = \eta_1^*$ (the remaining parameters are those for PAA). Since $\Delta\Lambda \sim \delta$ with $\delta \ll \Lambda_g$ the condition $\Delta\Lambda \sim 10^{-5}$ corresponds to a magnetic field $H \sim 1$ G. With $H \gg 1$ G the stationary structural inhomogeneity of the liquid-crystal structure is stabilized.

CONCLUSIONS

The numerical calculations and qualitative considerations indicate a strong dependence of the threshold for forming a stationary inhomogeneous structure in a nematic liquid crystal on the anisotropy of its viscosity. Of greatest importance here are the parameters η_1 and η_2 [in the assumed notation from ref. 12, $\eta_1 = -\gamma_1/\gamma$, and $\eta_2 = (\alpha_1 - \alpha_4 - \alpha_5)/2\gamma_2$], which determine the form of the lower branch in the functional relation V(d) and correspondingly the possible threshold $V_g = V(d_g)$. It is shown that such a threshold vanishes if $\eta \geq \eta_1^* > 1$, where η_1^* is a certain critical parameter. The effect of a weak magnetic field with $0 \leq \eta_1 - \eta_1^* \ll \eta_1^*$ reduces the threshold region considered. Using the appropriate combination of electric and magnetic fields in nematic mesophases with $\eta_1 \gtrsim \eta_1^*$ (unfortunately we do not know of such a material but there is nothing forbidding its existence)[1] one can create a migrating threshold region. The corresponding turn-on time in a steady electric field should not exceed the order of magnitude of the relaxation time of the volume electric charge.

The inhomogeneity in the structure of a nematic mesophase (period d_g) can be changed by a magnetic field in which the magnetic field increases the distortion of the structure ($d_g \sim H^{-1/2}$) and the threshold for excitation ($V_g \sim H$). This fact is useful for diffracting systems with controllable grating periods.

These results are substantially related to the presence of solid surfaces, which bound the liquid-crystal layer and impose certain conditions on the behavior of the material in the layer near the wall.

The authors are grateful to V. L. Indenbom, B. V. Petukhov, and V. I. Al'shits for useful discussions.

---

[1] When the present work was in press, a report appeared[15] on synthesis of new liquid crystal with an anisotropy of the viscosity which changes substantially with temperature.

---

[1] W. Helfrich, J. Chem. Phys., 51, 4092 (1969).

[2] Orsay liquid-crystal group, Phys. Rev. Lett., 26, 1642 (1970).

[3] S. A. Pikin, Zh. Eksp. Teor. Fiz., 60, 1185 (1971) [Sov. Phys.–JETP, 33, 641 (1971)].

[4] S. A. Pikin, Zh. Eksp. Teor. Fiz., 61, 2133 (1971) [Sov. Phys.–JETP, 34, 1136 (1972)].

[5] L. K. Vistin' and A. P. Kapustin, Kristallografiya, 13, 349 (1968) [Sov. Phys.–Crystallogr., 13, 284 (1968)].

[6] L. K. Vistin' and A. P. Kapustin, Opt. Spektrosk., 24, 650 (1968).

[7] C. Williams and P. E. Cladis, Solid State Commun., 10, 357 (1972).

[8] T. W. Stinson and J. D. Litster, Phys. Rev. Lett., 25, 503 (1970).

[9] F. Rondelez, D. Diguet, and G. Durand, Molec. Crystals and Liquid Crystals, 8, 315 (1969).

[10] Ch. Gähwiller, Phys. Lett., A36, 311 (1971).

[11] F. M. Leslie, Quart J. Mech. and Appl. Math., 19, 357 (1966).

[12] O. Parodi, J. Phys., 31, 581 (1970).

[13] P. A. Penz, Phys. Rev. Lett., 24, 1405 (1970).

[14] L. D. Landau and E. M. Lifshitz, Electrodynamics of Continuous Media, Addison-Wesley (1960), Ch. 13.

[15] Ch. Gähwiller, Phys. Rev. Lett., 28, 1554 (1972).

Calculation of the electrooptical constants in "ionic" crystals

L. B. Meisner and I. S. Rez

(Submitted July 6, 1971; resubmitted June 12, 1972)
Kristallografiya, 18, 454-458 (May-June 1973)

The Born polarizable ion model is used to extend the Kelly model of the linear electrooptical effect in cubic crystals of the CuCl type to crystals with arbitrary symmetry. Equations are obtained for all of the components of the linear and quadratic electrooptical effect tensors. For a $BaTiO_3$ single crystal, using the crystal structure, the electric permittivity, and the degree of ionic nature, the temperature dependence of the "soft" vibration mode along the *a* and c axes is calculated, along with the temperature dependences of the electrooptical coefficients $r_{33} - r_{13}$, $R_{33} - R_{13}$, and $R_{11} - R_{21}$. The magnitude of the linear electrooptical effect is calculated for $PbTiO_3$ and $LiNbO_3$ crystals.

The microscopic theory and method of calculating the electrooptical constants of crystals presented in refs. 1-3 are of considerable interest. This approach allows us to explain the optical properties of individual ions,[3] to explain the temperature dependences of the electrooptical coefficients of ferroelectric materials,[2] and to estimate the magnitude of the effect using essentially only data on the crystal structure and its dielectric properties, i.e., parameters which can be determined using powder methods. The other parameters on which the electrooptical coefficients depend can be determined independently.

The aim of the present work is to obtain general equations for all of the components of the electrooptical effect tensors. Since the derivation of the equations does not differ in principle from the previous approach[1,2] we have not given it.

However, it should be noted that in the initial equation (1) of ref. 2 we consider the field due to the displacements of all of the ions by amounts u_i (ref. 4) and the nonlinearity in the polarization due to the medium beyond the limits of the Lorentz band will be taken into account as previously.[5]

After carrying out uncomplicated but cumbersome transformations similar to the previous work[1,2,5] we arrive at equations which relate the coefficients of the true linear (r) and quadratic (R) electrooptical effects to the crystal structure. These equations and the equations for the electric permittivity take the form

$$r_{\alpha\beta\gamma}=-\frac{4\pi}{2a^{\alpha}vn_{\alpha}^{2}n_{\beta}^{2}}\sum_{i=1}^{m}N_i\alpha_i(\omega)\sum_{k=1}^{m}f_{\alpha\beta\gamma ik}\{[D_k^{\beta}(\omega)A_k^{\gamma}+A_k^{\beta}D_k^{\gamma}(\omega)]$$
$$+a_k^{-1}[D_k^{\beta}(\omega)B_k^{\gamma}(0)+B_k^{\beta}(0)D_k^{\gamma}(\omega)]$$
$$+[D_k^{\beta}(\omega)D_k^{\gamma}(0)+D_k^{\beta}(0)D_k^{\gamma}(\omega)]a_k^{-1}\},\tag{1}$$

$$R_{\alpha\beta\gamma\eta}=-\frac{4\pi}{6a^{\alpha}vn_{\alpha}^{2}n_{\beta}^{2}}\sum_{i=1}^{n}N_i\alpha_i(\omega)\sum_{k=1}^{m}f_{\alpha\beta\gamma\eta ik}\{[D_k^{\beta}(\omega)A_k^{\gamma}A_k^{\eta}$$
$$+a_k^{-1}[A_k^{\beta}D_k^{\gamma}(\omega)(D_k^{\eta}(0)+B_k^{\eta}(0))$$
$$+A_k^{\beta}D_k^{\gamma}(\omega)A_k^{\eta}+A_k^{\beta}A_k^{\gamma}D_k^{\eta}(\omega)]$$
$$+A_k^{\beta}(D_k^{\gamma}(0)+B_k^{\gamma}(0))D_k^{\eta}(\omega)+(D_k^{\beta}(0)+B_k^{\beta}(0))A_k^{\gamma}D_k^{\eta}(\omega)$$
$$+D_k^{\beta}(\omega)A_k^{\gamma}(D_k^{\eta}(0)+B_k^{\eta}(0))+D_k^{\beta}(\omega)(D_k^{\gamma}(0)+B_k^{\gamma}(0))A_k^{\eta}$$
$$+(D_k^{\beta}(0)+B_k^{\beta}(0))D_k^{\gamma}(\omega)A_k^{\eta}]+a_k^{-2}[D_k^{\beta}(\omega)D_k^{\gamma}(0)B_k^{\eta}(0)$$
$$+D_k^{\beta}(\omega)B_k^{\gamma}(0)D_k^{\eta}(0)+D_k^{\beta}(\omega)B_k^{\gamma}(0)B_k^{\eta}(0)$$
$$+D_k^{\beta}(0)D_k^{\gamma}(\omega)B_k^{\eta}(0)$$
$$+B_k^{\beta}(0)D_k^{\gamma}(\omega)D_k^{\eta}(0)+B_k^{\beta}(0)D_k^{\gamma}(\omega)B_k^{\eta}(0)$$
$$+D_k^{\beta}(0)B_k^{\gamma}(0)D_k^{\eta}(\omega)+B_k^{\beta}(0)D_k^{\gamma}(0)D_k^{\eta}(\omega)$$
$$+B_k^{\beta}(0)B_k^{\gamma}(0)D_k^{\gamma}(\omega)]$$
$$+a_k^{-2}[D_k^{\beta}(\omega)D_k^{\gamma}(0)D_k^{\eta}(0)+D_k^{\beta}(0)D_k^{\gamma}(\omega)D_k^{\eta}(0)$$
$$+D_k^{\beta}(0)D_k^{\gamma}(0)D_k^{\eta}(\omega)]\},$$
$$(\alpha,\beta,\gamma,\eta=1,2,3),\tag{2}$$

$$\varepsilon(0)=1+\frac{4\pi}{v}\sum_{i=1}^{m}N_iD_i(0)+\frac{4\pi}{v}\sum_{i=1}N_i(B_i(0)+a_iA_i)$$
$$=\varepsilon_{\infty}(0)+\frac{4\pi}{v}\sum_{i=1}^{m}N_i(B_i(0)+a_iA_i).\tag{3}$$

Here $f_{\alpha\beta\gamma ik}$ and $f_{\alpha\beta\gamma\eta ik}$ are the structural coefficients of the quadrupole and octupole sublattices, $\alpha_i(\omega)$ is the high-frequency electronic polarizability of the i-th ion, N_i is the number of electrically equivalent ions of the i-th kind in volume v, m is the number of electrically distinct ions in the lattice, and a_k is the effective charge of the k-th ion. Other coefficients take the form

$$a^{\alpha}=1-\frac{\beta_{\alpha\alpha}}{v}\sum_{i=1}^{m}N_i\alpha_i(\omega),$$

$$n_{\alpha}^{2}=1+\frac{4\pi}{v}\sum_{i=1}^{m}N_iD_i^{\alpha}(\omega)$$

are the principal values of the refractive index,

$$D_k^{\alpha}(\omega)=\alpha_k(\omega)b_k^{\omega}(d^{\omega})^{-1},\ D_k^{\alpha}(0)=\alpha_k(0)b_k^{0}(d^{0})^{-1}$$

and

$$B_k^{\alpha}(0)=\alpha_k(0)\Big[\sum_{k'=1}^{m}d_{kk'}^{0}a_{k'}A_{k'}^{\alpha}$$
$$+\sum_{k'=1}^{m}Y_{kk'}^{0}A_{k'}^{\alpha}\Big(\sum_{k''=1}^{m}f_{\alpha\alpha k'k''}a_{k''}\Big)\Big](d^{0})^{-1},$$

where d^{ω} and d^{0} are determinants of the form

$$d^{\omega}=|g_{\alpha\alpha ik}\alpha_k(\omega)-\delta_{ik}|,\ \ d^{0}=|g_{\alpha\alpha ik}\alpha_k(0)-\delta_{ik}|,$$

$g_{\alpha\alpha ik}=\beta_{\alpha\alpha}+f_{\alpha\alpha ik}$ are the structure coefficients of the dipole lattice, $\beta_{\alpha\alpha}$ describes the field due to the medium beyond the limits of the Lorentz band, $f_{\alpha\alpha ik}$ describes the field of the dipoles located within the Lorentz band, b_k^{ω} and b_k^{0} are found respectively from the determinants d^{ω} and d^{0} by replacing the k-th column by −1, and $d_{kk'}^{0}$ is found from the determinant d^{0} by replacing the elements of the k-th column by the coefficients $\sum_{i,k}g_{\alpha\alpha ik}$. The determinant $Y_{kk'}$ is also obtained from the determinant d^{0} by successive substitution of +1 for elements of the k-th column. Other elements of the k-th column are zero. The

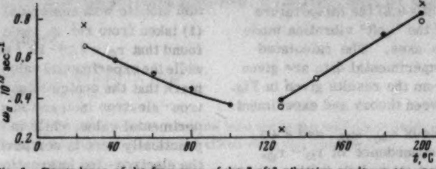

Fig. 1. Dependence of the frequency of the "soft" vibration modes on temperature for $BaTiO_3$ in the <100> direction. ●) calculation; ×) measurements of ref. 13; ○) measurements of ref. 9.

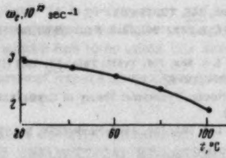

Fig. 2. Temperature dependence of the frequency of the "soft" vibration mode in the <001> direction for $BaTiO_3$.

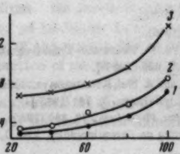

Fig. 3. Temperature dependence of $r_{33}-r_{13}$ for $BaTiO_3$. 1) Calculated from Eq. (4) of ref. 2 (displacements according to Frazer[14]); 2) calculated from Eq. (1); 3) experiment according to Johnston.[8]

superscripts α, β, γ, and η of the coefficients a, D_k, B_k, and A_k show the directions for which it is necessary to take structural sums of the dipole lattice (g_{ik}) during the calculation. In equations (1–3) the coefficients A_k remain indefinite. These coefficients are found by solving the equations of motion (1) from ref. 6. The solution of these equations assuming that the crystal has a transverse optical lattice vibration frequency ω_0, which gives the main contribution to the electric permittivity and the electrooptical coefficients of the crystal, can be written in the form

$$u_{\alpha k} = b_k^{\alpha} a_k (d^0 m_k \omega_0^2)^{-1} E_\alpha(0) = A_k^\alpha E_\alpha(0), \tag{4}$$

where m_k is the mass of the k-th ion and $E_\alpha(0)$ is the low-frequency electric field. Equation (4) is rigorously valid for a ferroelectric material with a displacive-type phase transition and is doubtful for application to nonferroelectric materials. However, if we eliminate ω_0 from Eqs. (1) and (2) using Eq. (3) for $\varepsilon(0)$, then evidently the errors in the calculation will be minimized. Good confirmation of this comes from the results on $LiIO_3$ (ref. 7), in which this approximation is not reflected in an analysis of the optical properties of individual ions in a lattice.

As a numerical example we give the results of calculations of the electrooptical constants for $BaTiO_3$, $PbTiO_3$, and $LiNbO_3$ single crystals.

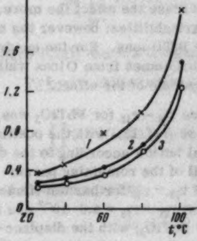

Fig. 4. Temperature dependence of $R_{33}-R_{13}$ for $BaTiO_3$. 1) Calculated from Eq. (2); 2) calculated from Eq. (5) of ref. 2; 3) experiment according to Johnston.[8]

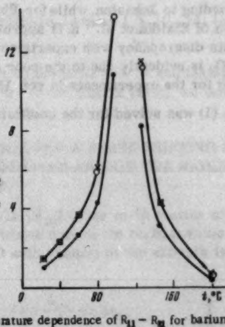

Fig. 5. Temperature dependence of $R_{11}-R_{12}$ for barium titanate. ●) Calculated from Eq. (5) of ref. 2; ×) calculated from Eq. (2); ○) measured.[8]

For $BaTiO_3$ the frequency of the "soft" mode of vibration gives an additional contribution to $\varepsilon(0)$. Then, knowing $\varepsilon(0)$ at 145°C (ref. 8) and ω_0 at the same temperature (ref. 9) we find[1] from Eq. (3) that $s = 0.56$ and from Eq. (3) of ref. 2 with the same parameters we find $s = 0.6$ (ref. 3), i.e., if in Eq. (1) of ref. 2 we take account of the field created by the dipoles when the ions are displaced by an amount $-u_1$, it hardly changes s.

It is a good approximation to assume temperature-independence of s (refs. 2 and 3). Then, knowing s at 145°C and the temperature dependence of $\varepsilon(0)$ along the c and a axes[8] we calculated from Eq. (3) (with $s = 0.56$)

and from Eq. (3) of ref. 2 (with s = 0.6) the temperature dependence of the frequence of the "soft" vibration mode in the directions of the c and a axes. The calculated values of ω_a and ω_c and the experimental data are given in Figs. 1 and 2. As we see from the results given in Fig. 1 there is good agreement between theory and experiment.

Using the theoretical values of ω_{0c}, ω_{0a}, and s we can calculate the temperature dependence of $r_{33} - r_{13}$, $R_{33} - R_{13}$, and $R_{11} - R_{21}$ from Eqs. (1) and (2) (with s = 0.56) and Eqs. (4) and (5) of ref. 2 (with s = 0.6). From the results of the calculation and the experimental data of Johnston[8] for $BaTiO_3$ given in Figs. 3, 4, and 5 we can see that there is good agreement between theory and experiment.

Analysis of the contributions of individual ions to r_{33} shows that the A(Ba) ions increase the effect the more, the greater their electronic polarizabilities; however the main contribution comes from the B(Ti) ions. For the quadratic effect the main contribution comes from O ions while the A ions decrease the magnitude of the effect.[3]

The coefficient difference $r_{33} - r_{13}$ for $PbTiO_3$ was calculated at 24°C with $\varepsilon = 30$ (ref. 15), with the positions of the atoms in the tetragonal lattice according to the data of ref. 14, s = 0.56, and all of the remaining parameters as in the calculation of $r_{33} - r_{13}$ for barium titanate. As a result we have found that $r_{33} - r_{13} = 4.6 \cdot 10^{-7}$ esu for $PbTiO_3$. This difference for $BaTiO_3$, with the displacements of the ions according to Frazer, equals $3.5 \cdot 10^{-7}$ esu, while with the atomic displacements of Känzig it is $7.8 \cdot 10^{-7}$ esu. The experimental value for $BaTiO_3$ is $6.9 \cdot 10^{-7}$ esu according to Johnston, while for $PbTiO_3$ according to the data of Shaldin et al.[15] it is approximately $0.3 \cdot 10^{-7}$ esu. This discrepancy with experimental data in the case of $PbTiO_3$ is evidently due to the poor quality of the crystals used for the experiments in ref. 15.

Equation (1) was solved for the coefficient r_{33} of lithium niobate with numerical values of the parameters in (1) taken from ref. 3. As a result of the calculation we found that $r_{33} = 2.05 \cdot 10^{-7}$ esu [$r_{33} = 2.1 \cdot 10^{-7}$ esu (ref. 3)] while the experimental value[3] is $9.2 \cdot 10^{-7}$ esu. Here we remark that the contribution to r_{33} arising from the electron–electron interaction amounts to only 5% of the experimental value, while in $BaTiO_3$ this contribution is practically zero in comparison to the contribution from the electron–ion interaction.

---

1) The structural coefficients and the electric polarizabilities were taken from refs. 10-12.

---

[1] L. Kelly, Phys. Rev., 151, 721 (1966).
[2] L. B. Meisner and I. S. Rez, Izd. Akad. Nauk SSSR, Ser. Fiz., 33, 222 (1969).
[3] L. B. Meisner and I. S. Rez, Fiz. Tverd. Tela, 11, 2931 (1969) [Sov. Phys.–Solid State, 11, 2374 (1970)].
[4] M. Bom and Kun Huang, Dynamical Theory of Crystal Lattices, Oxford Univ. Press (1954).
[5] L. B. Meisner and I. S. Rez, Izv. Akad. Nauk SSSR, Ser. Fiz., 35, 1802 (1971).
[6] L. B. Meisner and A. S. Sonin, Fiz. Tverd. Tela, 10, 557 (1968) [Sov. Phys.–Solid State, 10, 438 (1968)].
[7] I. S. Rez, L. B. Meisner, V. N. Nepomnyashchaya, E. A. Marchenko, A. A. Filimonov, and M. I. Kalitina, Izv. Akad. Nauk SSSR, Ser. Fiz., 34, 2567 (1970).
[8] R. Johnston, Appl. Phys. Lett., 7, 195 (1965).
[9] A. S. Barker, Phys. Rev., 145, A392 (1966).
[10] G. S. Zhdanov, S. P. Solov'ev, and Yu. N. Venevtsev, Kristallografiya, 2, 639 (1957) [Sov. Phys.–Crystallogr., 2, 630 (1957)].
[11] V. N. Lyubimov, Yu. N. Venevtsev, and E. Yu. Konstranskaya, Kristallografiya, 7, 949 (1962) [Sov. Phys.–Crystallogr., 7, 768 (1963)].
[12] J. Tessman, A. Kahn, and W. Shockley, Phys. Rev., 92, 890 (1953).
[13] T. M. Ballantyne, Proc. Intern. Meeting on Ferroelectricity, Vol. 1, Prague (1966), p. 55.
[14] F. Jona and G. Shirane, Ferroelectric Crystals, Pergamon (1962).
[15] Yu. V. Shaldin, M. L. Barsukova, V. A. Kuznetsov, and A. N. Lobachev, Kristallografiya, 16, 146 (1971) [Sov. Phys.–Crystallogr., 16, 114 (1971)].

Jones and Müller matrices of a phase-shifting slab with a rotating axis of the highest velocity

V. D. Tron'ko and G. P. Golovach

Kiev State University

(Submitted December 20, 1971; resubmitted April 10, 1972)
Kristallografiya, 18, 459-464 (May-June 1973)

Dividing the medium into infinitely thin layers, we determined the Jones and Müller matrices of media which give rise simultaneously to quadratic and linear magnetooptical effects which vary with time.

The method of Jones and Müller matrices is often used for the calculation of optical structure. These matrices are defined for the cases where the parameters of the medium through which the light passes change only slightly during the time needed for the light to pass through the object examined. In high-frequency and super-high frequency light modulators the finite propagation velocity of the light in matter has to be taken into account.

In the present papers several samples of practical interest are given.

FORMULATION OF THE PROBLEM. GENERAL THEORETICAL RELATIONSHIPS

Let us search for the elements of the matrix $a_{ij}(t, l)$ of the medium whose parameters vary with the time t and depend on the distance l travelled by the light through the medium. We divide the medium into n elementary sections[1] of thickness $l/n = \Delta x$. We suppose that the element of the matrix for an infinitely thin layer is given as a function of the time, the distance x and the layer thickness Δx: $a_{ij}(t, x, \Delta x) = a_{ij}(t, ml/n, l/n)$ where m = 0, n; m denotes the number of the layer. Consequently, the matrix for the entire sample can be written as follows:

$$[M(t,l)]=\lim_{n\to\infty}\prod_{m=1}^{n}\left[\bar{M}\left(t, m\frac{l}{n}, \frac{l}{n}\right)\right]. \tag{1}$$

For some class of problems considered here, the right-hand side of Eq. (1) can be written

$$\lim_{n\to\infty}\prod_{m=1}^{n}\left[\bar{M}\left(t, m\frac{l}{n}, \frac{l}{n}\right)\right]=\lim_{n\to\infty}\prod_{m=1}^{n}(I+[Q_{mn}]\Delta_n), \tag{2}$$

where I denotes the unit matrix; $[Q_{mn}]$ the matrix with the elements $Q(t, ml/n)$, $\Delta_n = l/n$.

The following theorem holds for the product in (2). If there exists a proper integral for the elements of the matrix $[Q_{mn}]$ with respect to x in the interval $[0, l]$, the following relationship holds:

$$\lim_{n\to\infty}\prod_{m=1}^{n}(I+[Q_{mn}]\Delta_n)=\exp\left(\int_0^l[Q(x)]dx\right), \tag{3}$$

where $[Q(x)]$ denotes the matrix with the elements $Q(t, x)$.

Proof: Utilizing the well-known identity

$$\prod_{m=1}^{n}(I+[Q_{mn}]\Delta_n)=\exp\left(\sum_{m=1}^{n}\ln(I+[Q_{mn}]\Delta_n)\right),$$

and also the equality

$$\ln(I+A)=A+o(A),$$

we get

$$\exp\left(\sum_{m=1}^{n}\ln(I+[Q_{mn}]\Delta_n)\right)=\exp\left(\sum_{m=1}^{n}[Q_{mn}]\Delta_n\right)\exp\left(o\left(\frac{1}{n}\right)\right).$$

Changing over to the limit n → ∞ and taking into account the integrability of the matrix $[Q(x)]$, we derive the equation (3).

JONES' MATRIX FOR A PHASE SHIFTING SLAB WITH A ROTATING AXIS OF THE HIGHEST VELOCITY

The matrix $[\bar{M}_m]$ of the m-th section of the phase-shifting slab whose axis of the highest velocity rotates at a frequency Ω with respect to the azimuth is

$$[\bar{M}_m]=[T(-\alpha_{mn})][P\delta_{mn}][T(\alpha_{mn})]=\begin{bmatrix}\cos\frac{\delta_{mn}}{2}+i\sin\frac{\delta_{mn}}{2}\cos 2\alpha_{mn} & i\sin\frac{\delta_{mn}}{2}\sin 2\alpha_{mn}\\ i\sin\frac{\delta_{mn}}{2}\sin 2\alpha_{mn} & \cos\frac{\delta_{mn}}{2}-i\sin\frac{\delta_{mn}}{2}\cos 2\alpha_{mn}\end{bmatrix}, \tag{4}$$

where $[P\delta_{mn}]$ denotes the matrix of the m-th phase shifting layer with an azimuth equal to zero; $[T(\alpha_{mn})]$ and $[T(-\alpha_{mn})]$ are the matrices of the direct and the reverse rotation,[2] respectively,

$$\delta_{mn}=\delta_0\frac{l}{n}f\left[\omega t+\frac{m-1}{n}l\left(\frac{\omega}{c}-k\right)\right],$$
$$\alpha_{mn}=\Omega t+\frac{\Omega}{c}\frac{(m-1)l}{n}, \tag{4a,b}$$

δ_{mn}, α_{mn} denote the phase shift and the azimuth shift of the m-th layer, respectively, in which the finite velocity of light in matter is taken into account; δ_0 denotes the specific phase shift created by matter; ω is the frequency with which the absolute phase shift varies with time; k is the wavenumber; f is a function which defines the dependence of δ_{mn} on time.

The matrix (4) can be written as follows:

$$[\bar{M}_m]=I\cos\frac{\delta_{mn}}{2}+i\begin{bmatrix}\cos 2\alpha_{mn} & \sin 2\alpha_{mn}\\ \sin 2\alpha_{mn} & -\cos 2\alpha_{mn}\end{bmatrix}\sin\frac{\delta_{mn}}{2}. \tag{5}$$

The matrix of a layer of thickness l is

$$[M]=\lim_{n\to\infty}\left\{\prod_{m=1}^{n}\cos\frac{\delta_{mn}}{2}\prod_{m=1}^{n}\right.$$

$$\left.\times\left(I+i\begin{bmatrix}\cos 2\alpha_{mn} & \sin 2\alpha_{mn}\\ \sin 2\alpha_{mn} & -\cos\alpha_{mn}\end{bmatrix}\operatorname{tg}\frac{\delta_{mn}}{2}\right)\right\}. \tag{6}$$

Since $|f|$ is bounded and $\lim\limits_{n\to\infty}\prod\limits_{m=1}^{n}\cos\frac{\delta_{mn}}{2}=1$, Eq. (6) can be transformed into

$$[\mathrm{M}]=\lim_{n\to\infty}\prod_{m=1}^{n}\left\{I+i\begin{bmatrix}\cos 2\alpha_{mn} & \sin 2\alpha_{mn}\\ \sin 2\alpha_{mn} & -\cos 2\alpha_{mn}\end{bmatrix}\frac{\delta_0}{2}f\left(t,\frac{ml}{n}\right)\Delta_n\right\}. \tag{7}$$

Utilizing Eq. (3), we derive

$$[M]=\exp\left\{\ i\frac{\delta_0}{2}\right.$$

$$\times\int_0^l\begin{bmatrix}\cos 2\left(\Omega t+\frac{\Omega x}{c}\right) & \sin 2\left(\Omega t+\frac{\Omega x}{c}\right)\\ \sin 2\left(\Omega t+\frac{\Omega x}{c}\right) & -\cos 2\left(\Omega t+\frac{\Omega x}{c}\right)\end{bmatrix}$$

$$\times f\left[\omega t+x\left(\frac{\omega}{c}-k\right)\right]dx$$

$$=\exp\left(i\frac{\delta_0}{2}\begin{bmatrix}q_{11} & q_{12}\\ q_{21} & q_{22}\end{bmatrix}\right)\quad(q_{11}=-q_{22},\ q_{12}=q_{21}). \tag{8}$$

We shall now consider the case when the absolute value of the phase shift varies according to the harmonic law $f=\cos[\omega t+x(\omega/c-k)]$, where

$$q_{11}=-q_{22}=\frac{\sin[\beta_1-\alpha_1+(\beta_2-\alpha_2)l]-\sin(\beta_1-\alpha_1)}{2(\beta_2-\alpha_2)}$$

$$+\frac{\sin[\beta_1+\alpha_1+(\beta_2+\alpha_2)l]-\sin(\alpha_1+\beta_1)}{2(\beta_2+\alpha_2)},$$

$$q_{21}=q_{12}=-\frac{\cos[\beta_1-\alpha_1+(\beta_2-\alpha_2)l]-\cos(\beta_1-\alpha_1)}{2(\beta_2-\alpha_2)}$$

$$-\frac{\cos[\beta_1+\alpha_1+(\beta_2+\alpha_2)l]-\cos(\alpha_1+\beta_1)}{2(\beta_2+\alpha_2)},$$

and $\alpha_1=\omega t$, $\alpha_2=[(\omega/c)-k]$, $\beta_1=2\Omega t$, and $\beta_2=2\Omega/c$.

Equation (8) can be expanded into the Taylor series

$$[M]=\cos\left\{\frac{\delta_0}{2}[c]\right\}+i\sin\left\{\frac{\delta_0}{2}[c]\right\}=I-\frac{(\delta_0/2)^2[c]^2}{2!}$$

$$+\frac{(\delta_0/2)^4[c]^4}{4!}+\ldots+i\left\{\frac{\delta_0}{2}[c]-\frac{(\delta_0/2)^3[c]^3}{3!}+\frac{(\delta_0/2)^5[c]^5}{5!}+\ldots\right\}, \tag{9}$$

where

$$[c]=\begin{bmatrix}q_{11} & q_{12}\\ q_{21} & q_{22}\end{bmatrix}.$$

Since matrix [c] has the following properties:

$$[c]^{2n}=P^nI,\ [c]^{2n+1}=P^n[c]\quad(n=0,1,2,\ldots), \tag{10}$$

where

$$P=q_{11}^2+q_{12}^2=\frac{1-\cos(\beta_2-\alpha_2)}{2(\beta_2-\alpha_2)^2}+\frac{1-\cos(\beta_2+\alpha_2)l}{2(\beta_2+\alpha_2)^2}$$

$$+\frac{\cos(2\alpha_1+\alpha_2l)(\cos\alpha_2l-\cos\beta_2l)}{\beta_2^2-\alpha_2^2} \tag{11}$$

(coefficient P varies with a frequency 2ω with time), matrix [M] can be finally written

$$[M]=I\cos\frac{\delta_0}{2}\sqrt{P}+i[c]\frac{\sin\delta_0\sqrt{P}/2}{\sqrt{P}}. \tag{12}$$

The shapes of Eqs. (5) and (12) are identical. Consequently, the phase shift generated by the rotated phase shifting slab is

$$\delta=\delta_0\sqrt{P}. \tag{13}$$

In the special case that the absolute value of the phase shift is independent of time $\alpha_1=\alpha_2=0$; $f=1$, Eq. (13) reads

$$\delta=\delta_0l\frac{\sin\Omega l/c}{\Omega l/c}. \tag{14}$$

Consequently, owing to the finite propagation velocity of light, the phase shift generated by a rotated phase-shifting slab is reduced by the factor (at small values of $\Omega l/c$)

$$\Delta_1=\delta_0l\left(1-\frac{\sin\Omega l/c}{(\Omega/c)l}\right)\approx\frac{\delta_0l}{3!}\left(\frac{\Omega l}{c}\right)^2. \tag{15}$$

If $[(\Omega l)/c]l=k\pi$ ($k=1, 2, \ldots,$), at $\delta_0=0$ the resulting phase shift $\delta=0$. When the axis of highest velocity is not rotated ($\Omega=0$), then

$$q_{11}=\frac{\sin(\alpha_1+\alpha_2l)-\sin\alpha_1}{\alpha_2},\ q_{12}=q_{21}=0.$$

and matrix [M] equals

$$[M]=\begin{bmatrix}\exp\left(i\frac{\delta_0l}{2}\frac{\sin\left(\frac{\omega}{c}-k\right)\frac{l}{2}}{\left(\frac{\omega}{c}-k\right)\frac{l}{2}}\cos\left[\omega t+\left(\frac{\omega}{c}-k\right)\frac{l}{2}\right]\right) & 0\\ 0 & \exp\left(-i\frac{\delta_0l}{2}\frac{\sin\left(\frac{\omega}{c}-k\right)\frac{l}{2}}{\left(\frac{\omega}{c}-k\right)\frac{l}{2}}\cos\left[\omega t+\left(\frac{\omega}{c}-k\right)\frac{l}{2}\right]\right)\end{bmatrix}.$$

The phase shift generated by the phase-shifting slab is

$$\delta=\delta_0l\frac{\sin\left(\frac{\omega}{c}-k\right)\frac{l}{2}}{\left(\frac{\omega}{c}-k\right)\frac{l}{2}}$$

It is obvious that if the velocity of light equals that of the steering electromagnetic waves, the phase shift attains the highest value δ_0l.

Finally, we note that Eq. (12) holds for any function f that can be integrated.

MÜLLER MATRIX OF A ROTATING PHASE-SHIFTING SLAB

Matrix [M] for the m-th element of the phase-shifting slab whose axis of highest velocity rotates at the frequency Ω with respect to the azimuth is

$$[\overline{M}_{mn}]^{(M)} = [T(-\alpha_{mn})]^{(M)}[P\delta_{mn}]^{(M)}[T(\alpha_{mn})]^{(M)} = \begin{bmatrix} & 0 & 0 & 0 \\ 0 & \cos^2 2\alpha_{mn} + \sin^2 2\alpha_{mn}\cos\delta_n & \sin 2\alpha_{mn}\cos 2\alpha_{mn}(1-\cos\delta_n) & -\sin 2\alpha_{mn}\sin\delta_n \\ 0 & \sin 2\alpha_{mn}\cos 2\alpha_{mn}(1-\cos\delta_n) & \sin^2 2\alpha_{mn} + \cos^2 2\alpha_{mn}\cos\delta_n & \cos 2\alpha_{mn}\sin\delta_n \\ 0 & \sin 2\alpha_{mn}\sin\delta_n & -\cos 2\alpha_{mn}\sin\delta_n & \cos\delta_n \end{bmatrix}. \quad (16)$$

where $[P\delta_{mn}]^{(M)}$ denotes Müller's matrix for the m-th phase shifting layer of zero azimuth; $[T(-\alpha_{mn})]^{(M)}$, $[T(\alpha_{mn})]^{(M)}$ denote Müller's matrices for the direct and reverse rotations, α_{mn} denotes the sequence defined by Eq. (6); $\delta_n = \delta_0(l/n)$ (ref. 2). The matrix (16) can be written as follows:

$$[\overline{M}_m]^{(M)} = \begin{bmatrix} 1000 \\ 0100 \\ 0010 \\ 0001 \end{bmatrix}$$

$$+\begin{bmatrix} 0 & 0 & 0 & 0 \\ 0 & 0 & 0 & -\sin 2\alpha_{mn} \\ 0 & 0 & 0 & \cos 2\alpha_{mn} \\ 0 & \sin 2\alpha_{mn} & -\cos 2\alpha_{mn} & 0 \end{bmatrix}\sin\delta_n + [\varepsilon_{mn}]\sin^2\frac{\delta_n}{2}. \quad (17)$$

Utilizing Eq. (3), we derive Müller's matrix for the phase-shifting slab from (17)

$$[M]^{(M)} = \exp\left(\delta_0\int_0^l \begin{bmatrix} 0 & 0 & 0 & 0 \\ 0 & 0 & 0 & -\sin 2\left(\Omega t + \frac{\Omega}{c}x\right) \\ 0 & 0 & 0 & \cos 2\left(\Omega t + \frac{\Omega}{c}x\right) \\ 0 & \sin 2\left(\Omega t + \frac{\Omega}{c}x\right) & -\cos 2\left(\Omega t + \frac{\Omega}{c}x\right) & 0 \end{bmatrix} dx\right) = \exp(\gamma[A]).$$

where

$$[A] = \begin{bmatrix} 0 & 0 & 0 & 0 \\ 0 & 0 & 0 & -\sin\left(2\Omega t + \frac{\Omega l}{c}\right) \\ 0 & 0 & 0 & \cos\left(2\Omega t + \frac{\Omega l}{c}\right) \\ 0 & \sin\left(2\Omega t + \frac{\Omega l}{c}\right) & -\cos\left(2\Omega t + \frac{\Omega l}{c}\right) & 0 \end{bmatrix}, \quad (18)$$

$$\gamma = \delta_0 l\,\frac{\sin\Omega l/c}{\Omega l/c}. \quad (19)$$

It is easily shown that

$$[A]^{2n+1} = (-1)^n[A],$$
$$[A]^{2n} = (-1)^{n+1}[A]^2 \quad (n = 1, 2, \ldots). \quad (20a,b)$$

Expanding matrix $[M]^{(M)}$ into the series

$$[M]^{(M)} = \exp(\gamma[A]) = I + \frac{\gamma[A]}{1!} + \frac{\gamma^2[A]^2}{2!} + \ldots + \frac{\gamma^n[A]^n}{n!} + \ldots$$

and utilizing relationships (20a, b), we find

$$[M]^{(M)} = I + [A]^2(1-\cos\gamma) + [A]\sin\gamma = \begin{bmatrix} 1 & 0 & 0 & 0 \\ 0 & -\sin^2\beta(1-\cos\gamma)+1 & \sin\beta\cos\beta(1-\cos\gamma) & -\sin\beta\sin\gamma \\ 0 & \sin\beta\cos\beta(1-\cos\gamma) & -\cos^2\beta(1-\cos\gamma)+1 & \cos\beta\sin\gamma \\ 0 & \sin\beta\sin\gamma & \cos\beta\sin\gamma & \cos\gamma \end{bmatrix}, \quad (21)$$

where $\beta = 2\Omega t + \Omega l/c$.

As regards shape, equations (16) and (21) are identical; consequently, both for Müller's matrices and for Jones' matrices the phase shift generated by a phase-shifting slab is determined by Eq. (14), and the shift of the axis of highest velocity with respect to the azimuth is

$$\Delta\beta = \Omega l/2c. \quad (22)$$

Generally, when δ_{mn} varies with time according to the law (4a, b), Müller's matrix is

$$[M]^{(M)} = I + \frac{[A]'}{\sqrt{P_1}}\sin(\delta_0 l\sqrt{P_1}) + \frac{([A]')^2}{P_1}(1-\cos(\delta_0 l\sqrt{P_1})), \quad (23)$$

where

$$P_1 = a_{24}^2 + a_{34}^2, \quad [A'] = \begin{bmatrix} 0 & 0 & 0 & 0 \\ 0 & 0 & 0 & -a_{24} \\ 0 & 0 & 0 & a_{34} \\ 0 & a_{24} & -a_{34} & 0 \end{bmatrix},$$

$$a_{24} = \frac{1}{l}\int_0^l \sin 2\left(\Omega t + \frac{\Omega x}{c}\right) f\left(\omega t + \left(\frac{\omega}{c} - k\right)x\right)dx,$$

$$a_{34} = \frac{1}{l}\int_0^l \cos 2\left(\Omega t + \frac{\Omega x}{c}\right) f\left(\omega t + \left(\frac{\omega}{c} - k\right)x\right)dx.$$

Consequently, Eq. (23) holds for any integrable function $f(x)$.

CONCLUSION

At present there exist several magnetic crytals which show a large Cotton–Mouton effect.[3] Placing such crystals in rotating magnetic fields, we get a phase-shifting slab whose axis of highest velocity can rotate at a frequency equal to several tens or hundreds of MHz. At these frequencies it is necessary to take into account the change produced in the phase shift by the final propagation rate of light. For example, at $\Omega/2\pi = 2\cdot 10^8$ Hz, $l = 1$ cm, n = 2.2 (refractive index), the relative phase shift changes by a factor $\Delta_1/\delta_0 l \approx 10^{-3}$. This large error is inadmissible in range finders, converters for changing the phase difference of two electric signals and rotating the polarization plane of light,[4] etc.

---

[1] V. D. Tron'ko, Opt. Spektrosk., 19, 354 (1970).

[2] U. Sherkliff, Polarized Light [in Russian], Mir, Moscow (1965).

[3] Z. V. Pisarev, I. S. Sinii, and G. A. Smolenskii, ZhETF Pis. Red., 9, 112 (1969) [JETP Lett., 9, 64 (1969)].

[4] V. D. Tron'ko, Radiotekh. Elektron., 17, 156 (1972).

Relation between the radial and normal refraction vectors in anisotropic and gyrotropic media

L. M. Barkovskii

Belorussian State University

(Submitted March 3, 1972; resubmitted June 19, 1972)
Kristallografiya, 18, 465-469 (May-June 1973)

A general covariant relation is established between the radial and normal refraction vectors of plane waves in homogeneous, nonmagnetic, transparent media with anisotropic and gyrotropic optical properties. The relation found allows one to study the behavior of light rays in the presence of various external effects with different orientations of the wave normal without finding new eigenvectors and eigenvalues of the dielectric tensor in the perturbed medium.

The development of methods for deflecting optical beams which combine a substantial deflection rate with a high resolving power has been stimulated by the appearance of laser technology. The majority of the fast deflection methods are based on a change in the optical properties of solid crystalline materials caused by directional external stimuli. This refers to electrooptical methods for discrete and continuous deflection,[1] acoustooptical methods[1,2] based on a change in the refractive index arising from the photoelastic effect, and many others. Because of the broad possibilities for application of deflecting structures for diverse purposes, it is necessary to make a universal theoretical analysis which allows us to find the orientations of the wave normal and the external effect for which the deflection angles of the rays in the crystal are greatest. The literature contains discussions of certain particular questions, but no general investigation of the behavior of rays with various orientations of the wave normal and the external effect, which is due to the cumbersome nature of the general relations using a coordinate description. The relation between the ray directions and the normals in crystals is usually studied in a system coinciding with the principal directions of the dielectric tensor ε (refs. 3, 4). A variable effect in general alters the orientation of the eigenvectors $\mathbf{u}_p$ ($p = 1, 2, 3$) of the tensor ε. Therefore in order to use the data given, for example, in refs. 3 and 4 it is first necessary to find new $\mathbf{u}_p$ so that in general one requires quite difficult calculations. There is no need for such calculations if the problem of the relation between the radial and normal refraction vectors is solved in covariant form. Such a problem has been solved for crystals with real ε in ref. 5.

Here we solve the analogous problem for a medium whose optical properties are characterized by a Hermitian dielectric tensor. From the Maxwell equations for plane waves it follows that[5]

$$\varepsilon\mathbf{E} = -\mathbf{m}^{\times}\mathbf{H},\ \mathbf{H} = \mathbf{m}^{\times}\mathbf{E},\ \tilde{\varepsilon} = \varepsilon^{*},\ \mu = 1, \tag{1}$$

where **E** and H are complex amplitudes for the electromagnetic wave fields, $\mathbf{m}^{\times}$ is an antisymmetric tensor dual to the normal refraction vector **m**, i.e., $(\mathbf{m}^{\times})_{ik} = \delta_{ikl}m_l$, where δ_{ikl} is the fully antisymmetric unit tensor. The wavy line and the asterisk denote the operations of transposition and complex conjugation. The normal refraction vector has the direction of the wave normal **n**, i.e., **m** = *n***n**. The general invariant expressions for n_+ and n_- of the two isonormal waves have been given previously[5] as functions of **n** and ε. The polarization state and the direction of energy propagation for a plane wave in a crystal are conveniently described using the beam tensor Φ introduced previously.[7] The tensor Φ in a crystal takes the form

$$\Phi = \mathbf{H}\cdot\mathbf{H}^{*} = \frac{1}{C}(\mathbf{m}\overline{\varepsilon^{-1}}\mathbf{m}\,\mathbf{m}^{\times 2} - \mathbf{m}^{\times}\varepsilon^{-1}\mathbf{m}^{\times}), \tag{2}$$

where C is a real constant, ε^{-1} is the inverse dielectric tensor, $\mathbf{H}\cdot\mathbf{H}^{*}$ denotes a dyad, and the bar above denotes a reciprocal tensor. For two elliptically polarized isonormal waves the constants C_+ and C_- have opposite signs, which is related to the opposite rotation of the field vectors. It is also convenient to introduce the "normalized" beam tensor $\rho = \Phi/\Phi_C = \mathbf{H}\cdot\mathbf{H}^{*}/\mathbf{H}\mathbf{H}^{*}$. The tensors $\rho_\pm$ for two waves can be represented in the form

$$\rho_\pm = \left(\frac{1}{n_\pm^2} - \frac{1}{n_\mp^2}\right)^{-1}\left(\frac{1}{n_\mp^2}\mathbf{n}^{\times 2} - \mathbf{n}^{\times}\varepsilon^{-1}\mathbf{n}^{\times}\right) \tag{3}$$

and have properties

$$\rho_\pm^2 = \rho_\pm = \rho_\pm^{+},\quad \rho_+ + \rho_- = -n^{\times 2}; \tag{4}$$

where the + sign denotes the Hermitian conjugation operation. The tensors $\rho_\pm$ are classical analogs of the density matrix for a quantum-mechanical description of wave polarization.[7,8]

We now find the general expression for the light refraction vector **p** as a function of **m** and ε using the properties of the beam tensor. The vector **p** is defined by the relation[5]

$$\mathbf{p} = \frac{\langle\mathbf{S}\rangle}{c\langle w\rangle} = \frac{1}{2\mathbf{H}\mathbf{H}^{*}}([\mathbf{E}\mathbf{H}^{*}] + [\mathbf{E}^{*}\mathbf{H}]),\quad \mathbf{m}\mathbf{p} = 1, \tag{5}$$

where ⟨S⟩ and ⟨w⟩ are respectively the time averages of the energy flux and density in the wave. The vector **p** has the direction of the ray and is equal in modulus to the inverse radial refractive index. Having expressed **E** in terms of **H** in (1), substituting it into (5) taking (2) and (3) into account we find that

$$\mathbf{p} = \frac{1}{2|\varepsilon|}((\varepsilon^{*}\rho)_e\varepsilon^{*}\mathbf{m} + (\varepsilon\rho^{*})_e\varepsilon\mathbf{m} - \varepsilon^{*}\rho\varepsilon^{*}\mathbf{m} - \varepsilon\rho^{*}\varepsilon\mathbf{m}). \tag{6}$$

After simple transformations using the equations for the normals, the Hamilton–Cayley identity for the ε tensor, and the explicit form of ρ we find finally

$$\mathbf{p} = \frac{1}{\mathbf{m}^2\mathbf{m}\overline{\varepsilon^{-1}}\mathbf{m} - 1}(\mathrm{Re}\,\varepsilon^{-1} + \mathbf{m}^2\,\mathrm{Re}\,\overline{\varepsilon^{-1}} + \mathbf{m}\overline{\varepsilon^{-1}}\mathbf{m} - \varepsilon_e^{-1})\mathbf{m}, \tag{7}$$

where Re $\varepsilon^{-1} = (\varepsilon^{-1} + \varepsilon^{-1*})/2$ denotes the real part of the tensor. For further calculations it is convenient to distinguish the real and imaginary parts

$$\varepsilon^{-1} = \varkappa + i\mathbf{G}^{\times}, \quad \varkappa = \tilde{\varkappa} = \varkappa^{*}, \quad \mathbf{G}^{\times} = -\tilde{\mathbf{G}}^{\times} = \mathbf{G}^{\times *}, \tag{8}$$

in the tensor ε^{-1}, where $\mathbf{G}^{\times}$ is an antisymmetric tensor dual to the G vector (the gyration vector). For waves propagating along $\mathbf{n}(\mathbf{n}^2 = 1)$ with $\mathbf{m}^+ = n_+\mathbf{n}$ and $\mathbf{m}^- = n_-\mathbf{n}$, after substituting the tensor ε^{-1} (8) and $\varepsilon^{-1} = \varkappa + i\mathbf{G}^{\times}$, found by the direct method[6] into (7) we find

$$\mathbf{p}^{\pm} = \frac{n_{\pm}}{1/n_{\mp}^2 - 1/n_{\pm}^2}\left(\frac{1}{n_{\pm}^2}(\varkappa - \varkappa_c) + \bar{\varkappa} + \mathbf{n}\bar{\varkappa}\mathbf{n} - \mathbf{G}\cdot\mathbf{G} - (\mathbf{nG})^2\right)\mathbf{n}. \tag{9}$$

To determine the angles $\delta_{\pm}$ between the rays and the normal it is necessary to multiply the unit vector of the normals by the unit vectors of the rays. It follows from Eq. (9) that

$$\cos\delta_{\pm} = \mathbf{ns}^{\pm} = \frac{\mathbf{np}^{\pm}}{|p^{\pm}|} = \mp\frac{\mathbf{n}\alpha_{\pm}\mathbf{n}}{\sqrt{\mathbf{n}\alpha_{\pm}^2\mathbf{n}}},$$
$$\alpha_{\pm} = \frac{1}{n_{\pm}^2}(\varkappa - \varkappa_c) + \bar{\varkappa} - \mathbf{G}\cdot\mathbf{G} - (\mathbf{nG})^2 + \mathbf{n}\bar{\varkappa}\mathbf{n}. \tag{10}$$

Equations (7), (9), and (10) give a general relation between the vectors of normal refraction $\mathbf{m}^{\pm}$ and the radial refraction $\mathbf{p}^{\pm}$ in homogeneous transparent media which have anisotropic and gyrotropic properties. Since crystals have special directions, optical axes (binormals) along which the wave velocity is identical in a nongyrotropic crystal (G = 0) it is interesting to treat the mutual relations between $\mathbf{p}^{\pm}$ and $\mathbf{m}^{\pm}$ with explicit account of these directions. For this purpose we used the representation of the tensor $\varkappa$ introduced previously[5] in biaxial crystals:

$$\varkappa = a + b(\mathbf{c}'\cdot\mathbf{c}'' + \mathbf{c}''\cdot\mathbf{c}'), \; a = 1/\varepsilon_2, \; b = (1/\varepsilon_1 - 1/\varepsilon_3)/2, \tag{11}$$

where $1/\varepsilon_1$, $1/\varepsilon_2$, and $1/\varepsilon_3$ $(1/\varepsilon_3 < 1/\varepsilon_2 < 1/\varepsilon_1)$ are the eigenvalues of $\varkappa$, and $\mathbf{c}'$ and $\mathbf{c}''$ are unit vectors along the optical axes of the crystal. Substituting $\varkappa$ (11) into (9) we find

$$\mathbf{p}^{\pm} = \frac{n_{\pm}}{2B}\Big\{\Big[2B(a + b\mathbf{c}'\mathbf{c}'') \pm b\Big([\mathbf{nc}']^2$$
$$+ [\mathbf{nc}'']^2 + \frac{1}{b^2}(\mathbf{nG})^2\Big)\Big]\mathbf{n} \mp b[(\pm B$$
$$- (\mathbf{nc}')(\mathbf{nc}''))\mathbf{nc}'' + \mathbf{nc}']\cdot\mathbf{c}'$$
$$\mp b[(\pm B - (\mathbf{nc}')(\mathbf{nc}''))\mathbf{nc}' + \mathbf{nc}'']\cdot\mathbf{c}'' \pm \frac{1}{b}\mathbf{nG}\cdot\mathbf{G}\Big\}, \tag{12}$$

where we have introduced the notation

$$B = \frac{1}{2b}\left(\frac{1}{n_+^2} - \frac{1}{n_-^2}\right) = \sqrt{[\mathbf{nc}']^2[\mathbf{nc}'']^2 + \frac{1}{b^2}(\mathbf{nG})^2}. \tag{13}$$

For uniaxial crystals, setting $\mathbf{c}' = \mathbf{c}'' = \mathbf{c}$, $a = a' = 1/\varepsilon_0$, and $2b = b' = 1/\varepsilon_e - 1/\varepsilon_0$ in (12) and (13) we find that

$$\mathbf{p}^{\pm} = \frac{n_{\pm}}{B'}\Big\{\Big[B'\Big(a' + \frac{1}{2}b'\Big) \pm \frac{b'[\mathbf{nc}]^2}{2} \pm \frac{(\mathbf{nG})^2}{b'}\Big]$$
$$\mp \mathbf{n}_{\mp}\frac{b'(B' + [\mathbf{nc}]^2)}{2}\mathbf{nc}\cdot\mathbf{c} \pm \frac{1}{b'}\mathbf{nG}\cdot\mathbf{G}\Big\}, \tag{14}$$

where

$$B' = \sqrt{[\mathbf{nc}]^4 + \frac{4}{b'^2}(\mathbf{nG})^2}. \tag{15}$$

For nongyrotropic crystals with $\mathbf{G} \equiv 0$ Eqs. (12) and (14) assume the form

$$\mathbf{p}^{\pm} = \frac{n_{\pm}}{2\sin\theta_1\sin\theta_2}([2\sin\theta_1\sin\theta_2(a + b\cos\beta)$$
$$\pm b(\sin^2\theta_1 + \sin^2\theta_2)]\mathbf{n}$$
$$\mp b\sin\theta_2\sin(\theta_2 \pm \theta_1)\cdot\mathbf{c}' \mp b\sin\theta_1\sin(\theta_1 \pm \theta_2)\cdot\mathbf{c}''), \tag{16}$$

$$\mathbf{p}^{+} = n_{+}((a' + b')\mathbf{n} - b'\cos\theta\cdot\mathbf{c}), \quad \mathbf{p}^{-} = n_{-}a'\mathbf{n}, \tag{17}$$

where the angles are determined from the relations

$$\mathbf{c}'\mathbf{c}'' = \cos\beta, \; |[\mathbf{nc}']| = \sin\theta_1, \; |[\mathbf{nc}'']| = \sin\theta_2, \; |[\mathbf{nc}]| = \sin\theta. \tag{18}$$

We assume that the light propagates in a gyrotropic biaxial crystal with $\mathbf{n}\|\mathbf{c}'$ when $\mathbf{c}'\mathbf{G} \neq 0$ and in a uniaxial crystal with $\mathbf{n}\|\mathbf{c}$ when $\mathbf{cG} \neq 0$. From (12) and (14) we find respectively for these two cases

$$\mathbf{p}^{\pm} = \frac{1}{2}n_{\pm}((2a + b\mathbf{c}'\mathbf{c}'' \pm \mathbf{c}'\mathbf{G})\mathbf{c}' - b\mathbf{c}'' \pm \mathbf{G}),$$
$$\mathbf{p}^{\pm} = \frac{1}{2}n_{\pm}((2a' \pm \mathbf{cG})\mathbf{c} \pm \mathbf{G}). \tag{19}$$

With $\mathbf{n}\|\mathbf{c}'$ and $\mathbf{c}'\mathbf{G} = 0$ or $\mathbf{G} = 0$ in biaxial crystals Eq. (12) gives the indefinite result 0/0. This is the case of conical refraction,[5] which will not be considered here.

We note that a medium in which the real part of the dielectric tensor is proportional to the unit tensor ($\varkappa_{ik} = 1/\varepsilon_0\delta_{ik}$) with $\mathbf{G} \neq 0$ is not isotropic since it contains a unique direction G. Indeed such a medium cannot be regarded as a uniaxial crystal. For $\mathbf{n} \parallel \mathbf{G}$ and $\mathbf{n} \perp \mathbf{G}$ the rays and normals coincide as in a uniaxial crystal. The difference, however, is that both of the normal refractive indices in such a medium depend on the directions of the wave normal n and therefore with an oblique direction n relative to G none of the rays coincides with n. From the general equations (12) and (13) for the case $\varkappa = 1/\varepsilon_0 = a$ it follows that

$$\mathbf{s}^{\pm} = [(2a \pm \mathbf{nG})\mathbf{n} \pm \mathbf{G}] / \sqrt{4a^2 \pm 8a\mathbf{nG} + 3(\mathbf{nG})^2 + \mathbf{G}^2},$$
$$\mathbf{nG} = \mathbf{G}\cos\theta. \tag{20}$$

We find the θ for which the rays $\mathbf{s}^+$ and $\mathbf{s}^-$ deviate maximally from n. Setting the derivative of $\cos\gamma^{\pm} = \mathbf{s}^{\pm}\mathbf{n}$ in (20) with respect to $\cos\theta$ equal to zero we find

$$\cos\theta_m^{\pm} = \pm G/a, \quad \operatorname{tg}\gamma_m^{+} = \operatorname{tg}\gamma_m^{-} = G/2\sqrt{a^2 - \mathbf{G}^2}. \tag{21}$$

The rays deviate from **n** by the same angle to the opposite side. In media with large **G** the splitting angle of the rays can be substantial. The equations obtained in this paper are exact and therefore usable for any **G**.

The covariant methods used for determining the ray refraction vectors are also applicable to a medium whose parameters change slowly in comparison to optical fields. Then in the Maxwell equations we can neglect time derivatives of the dielectric tensor. The external effect here is taken into account by expanding the reciprocal dielectric tensor in powers of the characteristic parameter. The reciprocal dielectric tensor of the perturbed crystal takes the general form

$$\varepsilon^{-1} = \varkappa + i\mathbf{G}^{\times}, \quad \varkappa = \varkappa^{0} + \varkappa', \quad \mathbf{G} = \mathbf{G}^{0} + \mathbf{G}', \tag{22}$$

where the incremental tensors $\varkappa'$ and $\mathbf{G}'^{\times}$ characterize the external effect. Their explicit forms are determined by the symmetry of the crystal and the nature of the external effect. For example for a transparent ($\varepsilon^{-1} = \varepsilon^{-1+}$), cubic ($\varkappa^{0} = 1/\varepsilon_{0}$), essentially nonactive ($\mathbf{G}^{0} = 0$) crystal in an external magnetic field $\mathbf{H}'$ we have $\mathbf{G} = \mathbf{G}' = k\mathbf{H}'$, where the constant k characterizes the Faraday effect. If the tensor $\varkappa'$ responsible for the Cotton–Mouton effect and the piezooptic effect arising from mechanical action of the field is small here then such a medium will be isotropic in $\varkappa = \varkappa^{0} = 1/\varepsilon_{0}$, but gyrotropic $k \neq 0$ with $\mathbf{nG} = \mathbf{nG}' = k\mathbf{nH}'$.

The covariant relations obtained provide a theoretical basis for solving various experimental and applied problems involving the behavior of light energy when parametric effects are present in nonlinear, transparent, homogeneous media with anisotropic and gyrotropic properties.

The author is grateful to F. I. Fedorov, B. V. Bokut, and B. A. Sotskii for discussions of the results and the remarks they have made.

---

[1] D. Holt, Optics Technology 2, 1-7 (1970).

[2] A. Korpel, R. Adler, P. Desmares, and W. Watson, Proc. IEEE, 54, 1429 (1966).

[3] L. D. Landau and E. M. Lifshitz, Electrodynamics of Continuous Media, Addison-Wesley (1960).

[4] M. Born and E. Wolf, Principles of Optics Pergamon (1966).

[5] F. I. Fedorov, Optics of Anisotropic Media [in Russian], Idz. Akad. Nauk Belorussian SSR, Minsk (1958).

[6] F. I. Fedorov, Theory of Elastic Waves in Crystals [in Russian], Nauka, Moscow (1965).

[7] F. I. Fedorov, Zh. Prikl. Spektroskopii, 2, 523 (1965).

[8] R. G. Newton, Scattering Theory of Waves and Particles, McGraw-Hill, N. Y. (1966).

Propagation of light in active absorbing crystals

A. F. Konstantinova and B. N. Grechushnikov

Institute of Crystallography, Academy of Sciences of the USSR

(Submitted March 16, 1972)
Kristallografiya, 18, 470-473 (May-June 1973)

Expressions are derived for the polarization of light transmitted through an active absorbing birefringent plate. The Müller matrix is obtained for such crystals.

A solution to the problem of light transmission through a plate made from an active uniaxial crystal was presented in refs. 1 and 2. An analogous solution to the problem using new coupling equations[3] was derived in ref. 4. Up to the present time, however, it was always been assumed in the solution of such problems that the plate has been cut from a nonabsorbing crystal. Although the problem of the passage of light through an absorbing plate was in fact solved in ref. 5, the complexity of the calculations has so far prevented the problem of the transmission of light through a plate cut from an optically active and absorbing crystal from being solved. Such a problem is nevertheless of very considerable interest.

TRANSMISSION OF LIGHT THROUGH A PLATE TAKEN FROM A UNIAXIAL ACTIVE ABSORBING CRYSTAL

In solving the problem of the transmission of light through an optically active plate, the authors of refs. 1, 2, and 4 made no assumptions as to the real nature of the dielectric permeability tensor ε. The specific form of the tensor ε is only required when studying the polarization of the transmitted wave. Hence the expressions for the amplitudes of the transmitted wave derived in refs. 1, 2, and 4 may also be used for active absorbing plates. It is only necessary to allow for the complex character of the dielectric constant ε (and correspondingly the refractive indices) by assuming that $n_1' = n_1 - i\varkappa_1$, $n_2' = n_2 - i\varkappa_2$. It is clear that the expressions for the polarization of the transmitted wave will differ from those obtained earlier for nonabsorbing crystals. Since the expressions for the amplitudes of the transmitted wave were earlier obtained in general form, i.e., for a plate cut at an arbitrary angle to the optic axis and for an arbitrary polarization of the incident light, they are also suitable for the general case of active absorbing crystals. As before, however, the greatest interest lies in the particular cases in which the wave passes through an inactive crystal without any change of polarization, i.e., when the incident wave is polarized parallel or perpendicular to the principal plane. In these cases the change in the polarization of the transmitted wave in active crystals is due solely to the existence of optical activity, while in absorbing crystals the light passes through the plate without any change of polarization. Let us consider what polarization light will have after transmission through a plate made from active and absorbing crystals. The exact expressions for the angle of rotation χ of the major axis of the polarization ellipse of the transmitted light and the ellipticity b/a are of a fairly cumbersome form, even for these particular cases of the polarization of the incident light when the new coupling equations are taken into account. However, for ordinary crystals, in which the birefringence is a small quantity, we obtain reasonably simple expressions for

$$\operatorname{tg} 2\chi_\parallel = -2k[e^{-\theta}\sin\Delta - p(1 - e^{-\theta}\cos\Delta)], \tag{1}$$

$$\operatorname{tg} 2\chi_\perp = -2k[e^{\theta}\sin\Delta + p(1 - e^{\theta}\cos\Delta)]. \tag{2}$$

For the same cases of polarization of the incident light, we have the following for the ellipticity of the transmitted light:

$$(b/a)_\parallel = |k[(1 - e^{-\theta}\cos\Delta) + pe^{-\theta}\sin\Delta]|, \tag{3}$$

$$(b/a)_\perp = |k[(1 - e^{\theta}\cos\Delta) - pe^{\theta}\sin\Delta]|, \tag{4}$$

where we have introduced the notation: k = ellipticity of the wave propagating in the crystals,[2] $\Delta = 2\pi d(n_2 - n_1)/\lambda$ = phase difference, $\theta = \varkappa_2 - \varkappa_1$, $p = (n_1 - n)\theta/n_1(n_1 + n)$. Equations (1)-(4) are valid for directions differing from that of the optic axis, i.e., for when k is a small quantity.

We see from the expressions for tan 2χ and b/a that the second term in the square brackets is small compared with the first, since for ordinary crystals the quantity $(n_1 - n)/n_1(n_1 + n) \sim 0.1$. This term is multiplied by the quantity $\theta = \varkappa_2 - \varkappa_1$, which in the majority of cases is also small. We may thus say that the quantities tan 2χ and b/a are principally described by the first term, and are

$$\operatorname{tg} 2\chi = -2ke^{\mp\theta}\sin\Delta, \tag{5}$$

$$(b/a) = k(1 - e^{\mp\theta}\cos\Delta). \tag{6}$$

Thus in these particular cases of polarization of the incident light the influence of absorption on the optical activity is mainly described by the term $e^{-\theta}$ or $e^{+\theta}$, i.e., there should be a change in the amplitude of the oscillations of the angle of rotation χ by a factor of $e^{\pm\theta}$ times.

THE MÜLLER MATRIX FOR ACTIVE ABSORBING CRYSTALS

Apart from the particular cases of the polarization of the incident light, it is interesting to know the polarization of the light passing through a plate cut from a uniaxial crystal for an arbitrary orientation of the optic axis and an arbitrary azimuth of the incident wave. Clearly, in such a general case, the expressions for tan 2χ and b/a will be extremely complicated and difficult to use in specific calculations. We therefore considered that it would be better to derive the Müller matrix for an active absorbing crystal and to study the polarization of the transmitted light by means of the Stokes vector.

Since we know the conversion factors relating the amplitudes of the incident (A_0, B_0) and transmitted (A_1, B_1) waves, we may use the general method of obtaining Müller matrices[6] to calculate all the components in the same way as in ref. 7, only for active crystals.

Vol. 18
July 1973
June 197

As in ref. 7 we shall consider the birefringence as small and shall now allow for reflection losses. For directions differing from that of the optic axis the value of k is small. In this case the Müller matrix for an active, absorbing, birefringent plate may be written in the form

$$\begin{vmatrix} {}^1/_2(e^{-2\varkappa_1}+e^{-2\varkappa_2}) & {}^1/_2(e^{-2\varkappa_1}-e^{-2\varkappa_2}) & 0 & -k(e^{-2\varkappa_1}-e^{-2\varkappa_2}) \\ {}^1/_2(e^{-2\varkappa_1}-e^{-2\varkappa_2}) & {}^1/_2(e^{-2\varkappa_1}+e^{-2\varkappa_2}) & 2ke^{-\varkappa_1-\varkappa_2}\sin\Delta & 2k\,[e^{-\varkappa_1-\varkappa_2}\cos\Delta-{}^1/_2(e^{-2\varkappa_1}+e^{-2\varkappa_2})] \\ kp(e^{-2\varkappa_1}-e^{-2\varkappa_2}) & -2k\,[(\sin\Delta+p\cos\Delta)e^{-\varkappa_1-\varkappa_2}-{}^1/_2p(e^{-2\varkappa_1}+e^{-2\varkappa_2})] & e^{-\varkappa_1-\varkappa_2}(\cos\Delta-p\sin\Delta) & e^{-\varkappa_1-\varkappa_2}(\sin\Delta+p\cos\Delta) \\ -k(e^{-2\varkappa_1}-e^{-2\varkappa_2}) & 2k\,[(\cos\Delta-p\sin\Delta)e^{-\varkappa_1-\varkappa_2}-{}^1/_2(e^{-2\varkappa_1}+e^{-2\varkappa_2})] & -e^{-\varkappa_1-\varkappa_2}(\sin\Delta+p\cos\Delta) & e^{-\varkappa_1-\varkappa_2}(\cos\Delta-p\sin\Delta) \end{vmatrix}$$

Clearly if we put k = 0 we obtain the expressions for an absorbing birefringent plate. For $\varkappa_1 = \varkappa_2 = 0$ we obtain the ordinary matrix for a birefringent plate. Using the Müller matrix, we may study the polarization of light passing through a plate with any arbitrary orientation of the optic axis, for any azimuth of the incident light.

COMPOUNDING OF TWO ELLIPTICAL VIBRATIONS IN ACTIVE ABSORBING CRYSTALS

Two elliptically polarized waves propagating in optically active crystals were compounded in refs. 2 and 8 to give approximate expressions for the orientation of the major axis of the polarization ellipse and for the ellipticity of light transmitted through the plate. Let us use the same technique to determine the polarization of the transmitted light when the plate is simultaneously active and absorbing.

The equations of the two ellipses should in this case be written

$$\begin{aligned} x_1 &= e^{-\varkappa_1}\cos\omega t, \quad x_2 = kme^{-\varkappa_2}\cos(\omega t-\Delta). \\ y_1 &= -ke^{-\varkappa_1}\sin\omega t, \quad y_2 = me^{-\varkappa_2}\sin(\omega t-\Delta), \end{aligned} \tag{7}$$

where k is the ellipticity of the two ellipses, m are the relative dimensions of the ellipses, determined by the azimuth of the polarization of the incident light, and Δ is the phase difference.

Adding the two elliptical vibrations, we obtain the following for the rotation of the major axis of the resultant ellipse:

$$\operatorname{tg} 2\chi_s = \frac{-2m(1+k^2)e^{-\varphi}\sin\Delta}{(1-k^2)(1-m^2e^{-2\varphi})+4kme^{-\varphi}\cos\Delta}. \tag{8}$$

In the case in which the incident light is linearly polarized parallel to the optic axis, m takes its minimum value and becomes equal to k. Then to an accuracy limited by terms of order k^2 (k is a small quantity) we obtain Eq. (5).

For the ellipticity of the resultant vibration ($b/a = \tan\gamma$) we have

$$\sin 2\gamma_s = -\frac{2[(k-me^{-\varphi}\cos\Delta)-kme^{-\varphi}(me^{-\varphi}-k\cos\Delta)]}{(1+k^2)(1+m^2e^{-2\varphi})}. \tag{9}$$

For k = m (k is small) we obtain Eq. (6).

It should be emphasized that, in compounding the two elliptic vibrations, we make no assumptions as to what kind of crystal (uniaxial or biaxial) is propagating the light waves. Hence the approximate expressions (5) and (6) are also valid for biaxial absorbing and active crystals.

CONCLUSIONS

We have thus obtained expressions for the polarization of light transmitted through a plate cut from a uniaxial active absorbing crystal. We have calculated the Müller matrix for such crystals. By compounding two elliptical vibrations propagating in the crystal we have obtained approximate expressions (5) and (6) for the angle of rotation of the major axis of the ellipse of polarization and for the ellipticity of the transmitted light. These expressions are also valid for biaxial crystals.

---

[1] F. I. Fedorov and A. F. Konstantinova, Opt. Spektrosk., 12, 407, 505(1962).

[2] A. F. Konstantinova, N. R. Ivanov, and B. N. Grechushnikov, Kristallografiya, 14, 283 (1969) [Sov. Phys.–Crystallogr., 14, 222 (1969)].

[3] B. V. Bokut', A. N. Serdyukov, and F. I. Fedorov, Kristallografiya, 15, 1002 (1970) [Sov. Phys.–Crystallogr., 15, 871 (1971)].

[4] B. V. Bokut', A. F. Konstantinova, and A. N. Serdyukov, Kristallografiya, 17, 812 (1972) [Sov. Phys.–Crystallogr., 17, 711 (1973)].

[5] A. M. Goncharenko, Opt. Spektrosk., 14, 94 (1963).

[6] H. van de Hulst, Scattering of Light by Small Particles, Wiley (1957).

[7] B. N. Grechushnikov and A. F. Konstantinova, Kristallografiya, 16, 448 (1971) [Sov. Phys.–Crystallogr., 16, 378 (1971)].

[8] V. A. Shamburov, A. F. Konstantinova, and B. N. Grechushnikov, Kristallografiya, 13, 273 (1968) [Sov. Phys.–Crystallogr., 13, 212 (1968)].

Dynamic theory of x-ray diffraction in crystals with modulated electron density

A. V. Kolpakov and Yu. P. Khapachev
M. V. Lomonosov Moscow State University

(Submitted May 14, 1971; resubmitted July 5, 1971; May 11, 1972)
Kristallografiya, 18, 474-479 (May-June 1973)

Dynamic x-ray diffraction in crystals with one-dimensional modulated electron density is discussed. Approximate expressions are obtained for the diffracted amplitudes in the Laue and Bragg cases for harmonic modulation, assuming that the modulation does not violate the crystal periodicity. It is shown that besides the fundamental maximum the diffracted amplitude contains satellites with overtone wave vectors.

A disturbance of an ideal crystal may occur due to two causes: deformation and displacement of atomic planes, and also a change in their scattering properties. Several problems related to the first cause are discussed in the literature.[1,2] Several problems which can be related to the second group are also discussed, such as the cavity image in defect packing.[3,4]

The problem of dynamic diffraction in a crystal, where the atomic planes are strictly ordered but the structure factor F(hk*l*) is a function of coordinates, belongs also to that group. A possible example is a crystal into whose surface impurity atoms are injected by diffusion, provided the impurity atoms are nonuniformly distributed in depth and they do not deform the unit cell. It was shown experimentally[5] that for not too high concentrations of point defects the dynamic diffraction properties of the crystal remain close to those of an ideal crystal.

In this paper we consider another possibility of a variable dielectric constant, a modulated structure. It will be assumed that the modulation does not change the phase relations between the radiation elements scattered toward various points of the crystal. Modulated structures occur, for example, in hardening and dissociation of alloys.[6] Such a structure can also be obtained by alternating thin crystal films having an ideal structure, or by applying an elastic wave.[7]

BASIC FIELD EQUATIONS IN THE CRYSTAL

We start by finding the equations for varying amplitudes of an electromagnetic field in a crystal with a dielectric constant arbitrarily deviating in shape from the ideal case, provided the deviation is not large.

We consider a plane-parallel layer crystal, in which the reflecting planes form some angle φ with the surface and we introduce a coordinate system following Fig. 1.

The diffracted field in the crystal is described by the wave equation

$$\nabla^2\mathbf{E}(\mathbf{r}) + (\omega/c)^2\varepsilon(\mathbf{r})\mathbf{E}(\mathbf{r}) = 0, \tag{1}$$

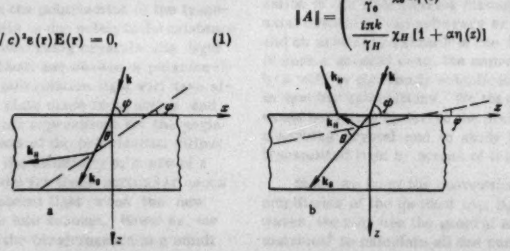

Fig. 1. The Laue (transmission) (a) and Bragg (reflection) (b) cases.

where $\varepsilon(\mathbf{r})$ is the dielectric constant of the medium, which can be represented as follows:

$$\varepsilon(\mathbf{r}) = 1 + \zeta(\mathbf{r})\chi(\mathbf{r}), \tag{2}$$

where $\chi(\mathbf{r})$ is the dielectric susceptibility of the crystal. In the general case $\zeta(\mathbf{r})$ appearing in (2) has the following form:

$$\zeta(\mathbf{r}) = 1 + \alpha\eta(\mathbf{r}), \quad \alpha \ll 1, \tag{3}$$

where $\eta(\mathbf{r})$ is a function describing the deviation of the dielectric susceptibility $\chi(\mathbf{r})$ from the ideal case.[1)] We note that $\eta(\mathbf{r})$ can be a function of not only the coordinates, but also of the field density.[8] In this case we pass to a nonlinear dynamic theory of diffraction. We write down the solution of (1) as a series in Bloch waves:

$$\mathbf{E}(\mathbf{r}) = \sum_n E_n(\mathbf{r})\exp[2\pi i(\mathbf{k}_n\cdot\mathbf{r})]. \tag{4}$$

Substituting this expansion in Eq. (1) and neglecting[9] second derivatives, we obtain, by (2), the system of equations

$$(i/\pi)\mathbf{k}_n\nabla E_n(\mathbf{r}) + (k^2 - k_n^2)E_n(\mathbf{r}) = -k^2\xi(\mathbf{r})\sum_m \chi_{n-m}E_n(\mathbf{r}), \tag{5}$$

where $|\mathbf{k}| = \omega/2\pi c$ is the wave vector of the incident wave outside the crystal. In what follows we restrict the discussion to two-ray problems. The system (5) consists then of two equations only. If $\eta(\mathbf{r})$ depends on the coordinate z only, the varying field amplitudes will be z-dependent only.[10] We thus find the following system of first-order linear differential equations determining the variation of the diffracted ray amplitudes:

$$d\|E_n(z)\|/dz = \|A\|\,\|E_H(z)\|. \tag{6}$$

The matrix $\|A\|$ is of the following form:

$$\|A\| = \begin{pmatrix} \dfrac{i\pi k}{\gamma_0}\chi_0\varkappa\eta(z) & \dfrac{i\pi k}{\gamma_0}\chi_{\bar{H}}[1+\alpha\eta(z)] \\ \dfrac{i\pi k}{\gamma_H}\chi_H[1+\alpha\eta(z)] & \dfrac{i\pi k}{\gamma_H}[\chi_0\varkappa\eta(z) - \beta_H] \end{pmatrix}, \tag{7}$$

where $\gamma_0 = \sin(\varphi + \theta)$, $\gamma_H = \sin(\varphi - \theta)$, and β_H is proportional to the deviation from the unmodified Bragg angle:[11]

$$\beta_H = -2\Delta\psi_0 \sin 2\theta - \chi_0(1 - \gamma_H/\gamma_0). \tag{8}$$

SOLUTION OF (6) FOR HARMONIC MODULATION

Approximate explicit solutions of the system (6) can be obtained in several particular cases by reducing it to well-known second-order equations with variable coefficients.

Substituting $\eta(z) = \cos \nu z$ in (6) and (7), where ν is not larger in order of magnitude than 10^5 cm^{-1} and retaining only first-order terms in α, we obtain the equation

$$d^2y(z)/dz^2 + \varkappa^2[1 + h_0 \cos \nu z + ih_1 \sin \nu z]y(z) = 0. \tag{9}$$

The function y(z) is related to the diffracted wave amplitude by

$$y(z) = E_H(z)\sqrt{1+\alpha\cos\nu z}\exp\left\{-\frac{i\pi k}{2\gamma_H}\beta_H z + \frac{i\pi k\chi_0}{2\nu}\left(\frac{1}{\gamma_0}+\frac{1}{\gamma_H}\right)\alpha\sin\nu z\right\} \tag{10}$$

By changing variables Eq. (9) can be reduced to the Mathieu equation in complex variables. The coefficient $\varkappa$ in (9) is the wave vector of the pendulum solution for fixed values of β_H:

$$\varkappa^2 = \frac{\pi^2k^2}{4\gamma_H^2}\left[\beta_H^2 + 4\chi_H\chi_{\bar{H}}\frac{\gamma_H}{\gamma_0}\right], \tag{11}$$

and the coefficients h_0 and h_1 are given by

$$h_0 = \frac{\alpha}{2\varkappa^2}\left\{\frac{\pi^2k^2}{\gamma_H^2}\left[4\chi_H\chi_{\bar{H}}\frac{\gamma_H}{\gamma_0} - \beta_H\chi_0\left(1-\frac{\gamma_H}{\gamma_0}\right)\right] - \nu^2\right\},$$
$$h_1 = \frac{\alpha\pi k\nu}{2\gamma_H}\,\frac{\beta_H + \chi_0(1-\gamma_H/\gamma_0)}{\varkappa^2}. \tag{12}$$

In what follows we assume that the crystal does not absorb, so that either χ_H and $\chi_{\bar{H}}$ have the same real parts or, if the crystal is centrosymmetric, their product with their complex conjugate $\chi_H\chi_{\bar{H}} = |\chi_H|^2$ is always positive.

Diffracted transmission. In case of Laue transmission we seek a solution of (9) in the form

$$y(z) = a(z)\cos(\varkappa + \delta/2)z + b(z)\sin(\varkappa + \delta/2)z, \tag{13}$$

where $a(z)$ and b(z) are slowly varying functions of coordinates (compared with the factors $\cos \varkappa z$ and $\sin \varkappa z$).

The quantity δ appearing in the assumed solution (13) is some small quantity satisfying the condition $\delta \ll \varkappa$. The selected form (13) is not an exact solution, since y(z) contains also terms with wave vectors differing from $\varkappa + \delta/2$ by integral multiples of $2\varkappa + \delta$. These terms are, however, of higher degree than h_1, and can therefore be neglected in the first approximation.[12,13] Consider the most interesting case of parametric resonance, when the relationship between the wave vectors is $\nu_{\beta_H} = 2\varkappa + \delta$. Substituting then (13) into (9) and using (10), we find for the diffracted wave amplitude $E_H(z)$ the expression

$$E_H(z) = \mathscr{E}(z)\exp\left\{-\frac{i\pi k}{2\gamma_H}\beta_H z + \frac{i\pi k\chi_0}{2\nu}\left(\frac{1}{\gamma_0}+\frac{1}{\gamma_H}\right)\alpha\sin\nu z\right\},$$

$$\mathscr{E}(z) = \sqrt{1+\alpha\cos\nu z}$$

$$\times\Bigg[\frac{b_2(\rho - ih_1\varkappa/4)\exp(-\rho z) + b_1(\rho + ih_1\varkappa/4)\exp(\rho z)}{(h_0\varkappa/2 - \delta)/2}$$

$$\times\cos(\varkappa + \delta/2)z + (b_1\exp(\rho z) + b_2\exp(-\rho z))\sin(\varkappa + \delta/2)z\Bigg], \tag{14}$$

where b_1 and b_2 are determined from the boundary conditions and have the values

$$b_1 = \frac{\rho - ih_1\varkappa/4}{\rho + ih_1\varkappa/4}b_2,$$
$$b_2 = \frac{E_0 i\pi k\chi_H(\rho + ih_1\varkappa/4)(h_0\varkappa/2 - \delta)\sqrt{1+\alpha}}{2\gamma_H\rho\{(\varkappa + \delta/2)(h_0\varkappa/2 - \delta) - 2[\rho^2 + (h_1\varkappa/4)^2]\}}, \tag{15}$$

where $\rho^2 = [(\varkappa^2/4)(h_0^2 - h_1^2) - \delta^2]/4$.

In transmission the quantity $h_0^2 - h_1^2$ is always negative, and consequently the solution (13) is stable.

The transmission coefficient corresponding to the diffracted amplitude (14) is, for $\delta = 0$,

$$D = \frac{2|\chi_H|^2}{\beta_H^2 + 4|\chi_H|^2|\gamma_H/\gamma_0|}\,\frac{h_1^2(1+\alpha)}{(h_1^2 - h_0^2)(1 - h_0^2/4)^2}. \tag{16}$$

Diffracted reflection. The form of the solution of (9) remains the same as for transmission. Therefore, omitting the exponentially growing solution, we obtain the following expression for the diffracted wave amplitude:

$$E_H(z) = \mathscr{E}(z)\exp\left\{-\frac{i\pi k}{2\gamma_H}\beta_H z + \frac{i\pi k\chi_0}{2\nu}\left(\frac{1}{\gamma_0}+\frac{1}{\gamma_H}\right)\alpha\sin\nu z\right\},$$

$$\mathscr{E}(z) = \exp(-\rho z)\left[\frac{\rho - ih_1\varkappa/4}{(h_0\varkappa/2 - \delta)/2}\cos\left(\varkappa + \frac{\delta}{2}\right)z\right.$$

$$\left.+\sin\left(\varkappa + \frac{\delta}{2}\right)z\right], \tag{17}$$

where b_2 is determined from the boundary conditions

$$b_2 = E_0 2\chi_H\sqrt{1+\alpha}\Bigg/\Bigg\{\Bigg[\beta_H + \chi_0\left(1 - \frac{\gamma_H}{\gamma_0}\right)\alpha$$

$$-\frac{2\gamma_H\rho}{i\pi k}\Bigg]\frac{\rho - ih_1\varkappa/4}{(h_0\varkappa/2 - \delta)/2}$$

$$+\frac{2\gamma_H}{i\pi k}\left(\varkappa + \frac{\delta}{2}\right)\Bigg\}. \tag{18}$$

The reflection coefficient corresponding to the diffracted amplitude (17) for fixed values of β_H and $\delta = 0$ is

$$R = 4|\chi_H|^2(1+\alpha)/[\beta_H^2 + (4|\chi_H|^2 - \beta_H^2)(1 + h_0/2)^2]. \tag{19}$$

The expressions obtained from the transmission and reflection coefficients are valid only in small neighborhoods of fixed values of β_H. Outside these neighborhoods the approximate method of this section is not valid and one should return to the general solution of (6) in the Floquet form.

Thus, an effective parametric transformation of wave vectors of diffracted waves with the periodic pendulum solution is possible for diffraction in an ideal crystal with modulated electron density.

Equations (14) and (17), determining together with (4) the amplitudes and propagation directions of the diffracted waves in the crystal, show that there appear in the crystal [due to the factor $1 + \alpha \cos \nu z)^{1/2}$] additional fields with wave vectors $\varkappa \pm \nu$, whose amplitudes are $\alpha/2$ times smaller. A diffracted beam is formed not by two wave fields, as in an ideal crystal, but by six.

Equations (14) and (17) contain the exponential factor $\exp\{(i\pi k \chi_0/2\nu)(1/\nu_0 + 1/\gamma_H)\,\alpha \sin \nu z\}$, which can be represented as a series expansion in Bessel functions:

$$\exp i\mu z = \sum_{n=-\infty}^{\infty} J_n(\mu)\exp(in\nu z), \tag{20}$$

where

$$\mu = \frac{\pi k \chi_0}{2\nu}\left(\frac{1}{\gamma_0} + \frac{1}{\gamma_H}\right)\alpha. \tag{21}$$

Substituting the expansion (20) in (14) and using (4), we find the form of the diffracted wave amplitude E(z):

$$E(z) = \mathscr{E}(z) \sum_{n=-\infty}^{\infty} J_n(\mu)\exp\left\{-\frac{i\pi k}{2\gamma_H}\beta_H z + in\nu z\right\}\exp[i(\mathbf{k}_H\mathbf{r})].$$

This formal solution shows that besides the fundamental maximum, corresponding to n = 0, there appear satellites with overtone wave vectors $k_H \pm |n|\nu$, whose amplitudes are related to each other as the coefficients of the series expansion (20). To estimate this ratio we note that the number μ, determined by Eq. (21) in the symmetric Laue case, equals for $\beta_H = 0$

$$\mu = \alpha\chi_0 / 2\chi_H.$$

Since $\alpha \ll 1$, we have for ordinary diffraction angles the inequality $\mu \ll 1$. The amplitude ratio of the fundamental maximum to the first satellite is then of the order of $J_0/J_1 = 1/2\mu$.

The angle $\Delta\theta$ between the fundamental maximum and the first satellite is determined by the following expression:

$$\Delta\theta = \frac{\nu}{k}\cos(\theta - \varphi).$$

In our case $\nu/k \sim 10^{-3}$. Consequently, $\Delta\theta$ is of the order of minutes, Since the angular width of the maximum can be smaller than this quantity, the central and secondary maxima can, in principle, be resolved by sectional x-ray topography.

---

1) The formal mathematical difference between the problem of modulated electron density and that of sinusoidal atomic displacements is that in the latter the dielectric susceptibility is given by $\chi(\mathbf{r}) = \sum_H \chi_H \exp[2\pi i(\mathbf{H}\mathbf{r}) \cdot \exp[2\pi i(\mathbf{H}\alpha \sin \nu z)]$ [sic].

---

[1] P. Penning and D. Polder, Phillips Res. Reps., 16, 419 (1964); Acta Crystallogr., 17, 950 (1964).
[2] D. Taupin, Acta Crystallogr., 23, 25 (1967).
[3] A. Authier and D. Simon, Acta Crystallogr., A24, 517 (1968).
[4] I. Sh. Slobodetskii, F. N. Chukhovskii, and V. L. Indenbom, ZhETF Pis. Red., 8, 90 (1968) [JETP Lett., 8, 55 (1968)].
[5] S. Maruyama, J. Phys. Soc. Japan, 20, 1399 (1965).
[6] T. Khachaturyan, Zh. Eksp. Teor. Fiz., 58, 175 (1970) [Sov. Phys.–JETP, 31, 98 (1970)].
[7] W. A. Wooster, Diffuse X-Ray Reflections from Crystals, Oxford (1962).
[8] J. Freud and B. F. Levin, Phys. Rev. Lett., 23, 854 (1969).
[9] S. Takagi, Acta Crystallogr., 15, 1311 (1962).
[10] A. V. Kolpakov, Vestn. Mosk. Univ., Ser. Fiz., 2, 130 (1970).
[11] R. W. James, Optical Principles of the Diffraction of X-Rays, Bell, London (1943).
[12] L. D. Landau and E. M. Lifshitz, Mechanics, Pergamon Press, Oxford (1960).
[13] C. Hayashi, Nonlinear Oscillations in Physical Systems, McGraw-Hill, New York (1964).

Iteration method for calculating the intensity distribution in structural analysis

D. K. Khakimova, V. G. Nagornyi, and A. A. Smol'yaninov

(Submitted December 30, 1971; resubmitted May 22, 1972)
Kristallografiya, 18, 480-483 (May-June 1973)

An iteration method for solving an integral equation of the convolution type is treated for structural analysis problems involving the search for a "true" reflection profile. The precision of this solution is estimated using the iteration method and the Stokes method.

In order to obtain the "true" profile of a diffraction reflection in structural analysis it is necessary to solve an integral equation of the form

$$h(x)=\int_a^b f(y)g(x-y)\,dy, \tag{1}$$

where h(x) is the experimental intensity distribution, whose range of definition is [*a*, b], *f* (x) is the required intensity distribution determined by the physical state of the material, and g(x) is an instrumental function. The first integral equation with a kernel depending on the difference of the arguments was studied by Weiner and Hopf.[1] At the present time a number of methods for solving Eq. (1) are known; it is a particular case of a first-order Fredholm equation.[2]

The solution of Eq. (1) using a Fourier transformation is based on the notion that the Fourier transform of the convolution of two functions is the product of the Fourier transforms of the two functions.[3] Such an approach to the solution of the structural analysis problem has been carried out by Stokes.[4] Below this problem is solved by an iteration method, which has been proposed by Friedman for solving a first-order Fredholm integral equation[5] and treated incompletely previously.[6,7] The paper concludes with a comparison of the Stokes and iteration methods and an estimate of the precision of the iteration method.

The usual iteration process consists of the following algorithm for searching for a solution:

$$f_n=f_{n-1}+(h-f_{n-1}*g), \tag{2}$$

where f_n is the n-th approximation to *f* (x), and $f_{n-1}*g$ is the direct convolution of the (n−1)-th approximation with the function g(x). Equation (2) is basic to the program. The most promising criterion for the choice of an approximation is the difference (relative or absolute) between the previous and present approximations, chosen taking account of the errors in the determination of the functions h(x) and g(x). A necessary condition for carrying out the iteration processes is the existence of a table of normalized values of the function g(x), for which $\int_c^d g(x) = 1$, where [c, d] is the range of definition of the function g(x). In addition, in determining the region where we search for the solution we should take account of the fact that during each subsequent convolution of the previous approximation with the function g(x) the range of the search increases by the extent of the interval in which the function g(x) is itself defined. For the step size of the tabulated distributions h(x) and g(x) and consequently also the step size used in carrying out the numerical summations, the requirements on it turn out to be the same as in carrying out the Fourier transformation.

In calculating *f* (x) by the iteration and Stokes methods we set up programs in the "Algol-60" language and translated them into code for a BÉSM-4 computer. The estimates for the iteration method and the comparison with the Stokes method were carried out on a test problem, where the determination of h(x) can be done by direct convolution of the known *f* (x) with the chosen instrumental function g(x). In this case the origins along the abscissa coincide for the functions h(x) and *f* (x). This avoids additional distortion of the shape of h(x), which is present in the Stokes method due to the mismatch of the origins[8] and there is no need for additional calculations which take account of the shift in the maximum h(x) relative to the zero point.[9,10] For the functions g(x) and *f*(x) we took distributions of the form $\exp(-x^2/100) + {}^1/_2 \exp[-(x-42)/100]$ and $\cos^2(\pi x/50)$, respectively. In carrying out the calculations we used the functions h(x) and g(x) tabulated with a step $\Delta x = 1$ and precision $\leq 0.1\%$. The nature of the distributions h(x), g(x), and *f* (x) is shown in Fig. 1. The instrumental function *f* (x) models the line of the standard at large diffraction angles, where it shows doublet nature due to the $K\alpha_1$, $K\alpha_2$ nature of the radiation.

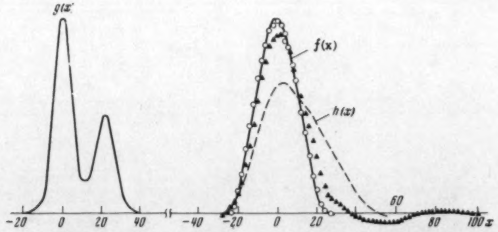

Fig. 1. Distributions g(x), h(x), and *f*(x) and two approximations to *f*(x) found by the iteration method. ▲) $f_2(x)$; ○) $f_5(x)$.

TABLE 1. "True" $f(x)$, Experimental Distribution h(x), and the Reflection Profiles f_2 and f_{10} Obtained by the Iteration Method

x	$f(x)$	$h(x)$	f_2	ε_2 *	f_{10}	ε_{10} *
−10	0.6547	0,4193	0,6174	5.65	0.6675	0.58
−9	0.7128	0.4521	0.6686	6.2	0.7162	0,48
−8	0,7678	0.4835	0.7166	6.6	0,7710	0,42
−7	0,8190	0.5131	0,7602	7.1	0,8212	0,37
−6	0,8640	0.5405	0,8005	7.3	0,8661	0,24
−5	0.9044	0.5655	0,8352	7.6	0,9051	0.08
−4	0,9379	0,5881	0.8646	7.8	0.9376	0.03
−3	0,9643	0.6079	0,8884	7,9	0,9633	0,10
−2	0,9841	0,6249	0.9064	7.9	0,9819	0.23
−1	0,9960	0.6390	0,9185	7.7	0.9932	0,28
0	1.0000	0.6502	0,9248	7.5	0.9969	0.31
1	0.9960	0,6585	0,9251	7.2	0.9930	0,30
2	0.9841	0,6638	0.9195	6.6	0.9816	0,26
3	0,9643	0.6662	0.9083	5.8	0.9625	0,19
4	0.9379	0,6658	0.8915	4.9	0.9364	0.16
5	0.9044	0.6626	0.8695	3.9	0.9032	0.13
6	0,8640	0.6568	0.8435	2.3	0.8635	0.59
7	0,8190	0.6484	0.8109	0,98	0.8179	0.14
8	0.7678	0.6376	0.7752	0,92	0.7671	0.10
9	0,7128	0.6247	0.7358	1,83	0.7119	0.13
10	0.6547	0.6098	0,6934	5,92	0.6533	0.22

---

* ε_i is the relative error in f_i.

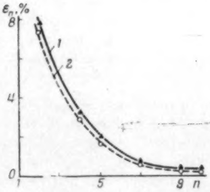

Fig. 2. Error ε_n in the intensity at the maximum (1) and over the whole shape (2) as a function of the order n of the approximation.

The geometric aberrations whose resulting profiles are described by the function g(x) decrease the intensity of the reflection $f(x)$ at the maximum (in the case of interest by ∼33%), smear the reflection, and shift its position (Table 1, Fig. 1). The results of a solution of the problem by the iteration method are shown in Table 1 for the interval near the maximum of the reflection and show the nature of the approximation in all of the region of interest. The forms of the distributions for the second and 10th approximations are given in Fig. 1. The convergence of the process is illustrated by the dependence of the intensity and the shift in the angular position of the reflection maximum on the order of the approximation (see Table 2 and Fig. 2). The second approximation, which requires in all one convolution of the distribution h(x) with the instrumental function g(x) in order to obtain it, determines the intensity distribution at points of the interval with errors not exceeding 8% and the whole shape with an error of 4.6%. For the 10th approximation the respective errors are 0.3 and 0.2% (Fig. 2). Here the "true" angular position of the maximum is already established from the fourth approximation.

In the Stokes method for calculating the Fourier transform of the distribution $f(x)$ in the Fourier series expansions of the functions h(x) and g(x) we used the interval [−60, 60]. The approximation f_N which is sought is synthesized from N Fourier coefficients, whose number varies from 10 to 40 with a step of 5. The comparison of the intensities obtained in this way for the chosen argument values (Table 3) shows quite high convergence of the process of search for a solution by the Fourier transform method. In order to estimate the precision of the solution we carried out a comparison of the "true" distribution with that synthesized after the additional normalization:

$$\int f(x)\,dx = K \int f_N(x)\,dx,$$

TABLE 2. Intensities of the Desired Approximations f_n at the Maximum and Angular Position of the Maximum

n	1	2	4	5	7	9	10
max f_n	0.6662	0.9251	0.9738	0,9833	0,9226	0.9961	0,9969
$x_{\max f_n}$	3	1	0	0	0	0	0

TABLE 3. Reflection Profiles Synthesized from N Fourier Coefficients

x	N						
	10	15	20	25	30	35	40
0	60.033	59.985	60,006	59.997	60.004	60,003	60.011
5	54.203	54.246	54.249	54.243	54.251	54.251	54.241
10	39.260	39.231	39.199	39.199	39.202	39,205	39.220
15	20,723	20.738	20.731	20,737	20.726	20.725	20.709
20	5.701	5.962	5,744	5.752	5.734	5.732	5.742
25	−0.015	−0.002	−0.001	0.004	0	0.003	0,001

where K is a normalization coefficient by which we should multiply the intensities of the synthesized approximations, and f_N is the approximation obtained from N Fourier coefficients. It turns out that 10-15 Fourier coefficients lead to a solution with a precision of 0.7%.

Thus in searching for the "true" reflection profile both methods can give a solution of Eq. (1) with high precision. However, in the iteration method the intensity of the sought distribution is obtained in the same scale as the experimental function h(x). In addition, one simultaneously establishes the "true" angular position of the profile $f(x)$ relative to h(x).

The authors are grateful to V. D. Krylov for his interest in the work and for the above remarks during discussions of it.

---

[1] History of Russian Mathematics [in Russian], 4, Book 1, Naukova Dumka Akad. Nauk SSSR, Akad. Nauk UkrSSR, Kiev (1970).

[2] S. G. Mikhlin, Integral Equations [in Russian], Gostekhizdat, Moscow–Leningrad (1949).

[3] E. Titchmarsh, Introduction to the Theory of Fourier Integrals, Oxford Univ. Press (1937).

[4] A. R. Stokes, Proc. Phys. Soc., A61, 382 (1948).

[5] V. M. Fridman, Usp. Mat. Nauk, 11, 233 (1956).

[6] W. C. Sauder, J. Appl. Phys., 37, 1495 (1966).

[7] S. Ergun, J. Appl. Crystallography, 1, 19 (1968).

[8] G. M. Vorob'ev, N. N. Turba, and T. Z. Gaivoronskaya, Apparatura i Metody Rent. Anal., 9, 51 (1971).

[9] V. V. Kukol', Zav. Labor., 31, 706 (1965).

[10] G. M. Vorob'ev, Zav. Labor., 27, 686 (1961).

Determination of coordination numbers and mean-square displacements from the radial distribution curve

Ya. I. Stetsiv

L'vov Polytechnic Institute

(Submitted February 1, 1972; resubmitted May 17, 1972)
Kristallografiya, 18, 484-486 (May-June 1973)

The effect of the upper limit of integration s_2 on the height of the coordination peaks in the radial distribution curve has been studied. From this dependence a new method has been developed for determining the coordination number and the mean-square displacement. We apply the method to amorphous antimony films.

Coordination numbers in amorphous materials and liquids are determined from the area under the coordination peaks in the radial distribution curves, which are obtained from the Fourier transform of the intensity of the coherent scattered radiation from the sample. Unfortunately, the coordination peaks for amorphous materials and especially for liquids are very diffuse and overlap each other, a fact which complicates the interpretation of the radial distribution curves. Depending on how the peaks are resolved, it is possible to obtain very different values for the coordination numbers.[1]

In this paper a new method is proposed for determining the coordination numbers and mean-square displacements, based on the functional dependence of the height of the coordination peak on the upper integration limit s_2.

The diffraction pattern for the radiation scattered by a system of particles with an interatomic spacing r_k can be represented by the interference function

$$i_k(s)=n_k\frac{\sin(r_ks)}{r_ks}\exp\left(-\frac{1}{2}\sigma_k^2s^2\right), \tag{1}$$

where n_k and σ_k are the coordination number and the mean square displacement.

Consequently, for the height of the coordination peak, we obtain

$$H_k=4\pi r^2\rho(r)\,|_{r=r_k}=\frac{2r_k}{\pi}\int_0^{s_2}si_k(s)\sin(r_ks)\,ds$$
$$=\frac{n_k}{\pi}\left[\int_0^{s_2}\exp\left(-\frac{1}{2}\sigma_k^2s^2\right)ds-\int_0^{s_2}\cos(2r_ks)\exp\left(-\frac{1}{2}\sigma_k^2s^2\right)ds\right]. \tag{2}$$

Here the term $4\pi r^2\rho_0$ is absent, since the integration is also carried out with the definite limits zero and s_2.

We denote the terms in (2) by H_{k1} and H_{k2} respectively and estimate their magnitudes:

$$H_{k1}=\frac{n_k}{\pi}\int_0^{s_2}\exp\left(-\frac{1}{2}\sigma_k^2s^2\right)ds=\frac{n_k}{\sqrt{2\pi}\,\sigma_k}\operatorname{erf}\left(\frac{\sigma_ks_2}{\sqrt{2}}\right). \tag{3}$$

Thus, the first term H_{k1} is a probability integral; with increasing s_2 it increases monotonically from zero to $n_k/\sqrt{2\pi}\sigma_k$.

By successive partial integrations of the second term and by taking account of the fact that $(\sigma_ks_2)^2 \ll 2r_ks_2$ for all values of s_2 accessible in practice, we obtain

$$H_{k2}=-\frac{n_k}{2\pi r_k}\sin(2r_ks_2)\exp\left(-\frac{1}{2}\sigma_k^2s_2^2\right). \tag{4}$$

According to (4), the term H_{k2} produces only small oscillations (Fig. 1) in the height of the coordination peak around the monotonic curve represented by the first term H_{k1}.

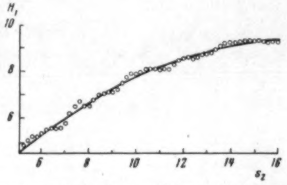

Fig. 1. The effect of the upper limit of integration in the height of the first coordination peak in the radial distribution of amorphous antimony. The solid curve shows the term H_{11}.

It must be noted that on a given peak there will always be superimposed spurious maxima and minima from neighboring coordination groups. These artifacts are due to the termination of the experimental intensity curve. Since[2] the position of the spurious maxima and minima changes with s_2, they, like the term H_{k2}, cause the height of the coordination peak to oscillate around the monotonic curve H_{k1}. Therefore it is easy to obtain the H_{k1} curve graphically from the experimental data by finding the average about which the height of the coordination peak oscillates (Fig. 1).

For $x < 1.7$, the function erf (x) can with high accuracy (with an error less than 0.5%) be analytically represented by $\varphi(x) = 2x/\sqrt{\pi}(1 + x^2/3)$. Therefore, for $(\sigma_ks_2)^2 < 6$, the term H_{k1} can always be expressed by

$$H_{k1}=\frac{n_k}{\pi}\,\frac{s_2}{1+(\sigma_ks_2)^2/6}. \tag{5}$$

It should be noted that the condition $(\sigma_ks_2)^2 < 6$ is in fact valid for all experimental intensities obtained in x-ray diffraction studies of amorphous materials and liquids.

From (5) we obtain

$$\frac{s_2}{H_{k1}\pi}=\frac{1}{n_k}+\frac{\sigma_k}{6n_k}s_2^2, \tag{6}$$

That is, the dependence of the quantity $s_1/H_{k1}\pi$ on s_2^2 will be represented by a straight line with an angular coefficient $K = \sigma_k^2/6n_k$ and with an intercept $b = 1/n_k$ on the ordinate. Consequently, we determine the coordination number from the value of the intercept b, and the square of the mean displacement is obtained from the angular coefficient K. That is, $\sigma_k^2 = 6n_kK$. We will use the example of amorphous antimony to demonstrate this meth-

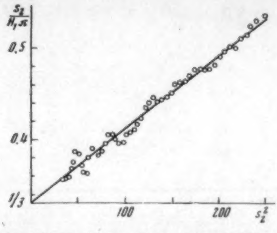

Fig. 2. The dependence of the quantity $s_2/(H_1\pi)$ on the upper limit of integration. The straight line shows $s_2/(H_{11}\pi)$.

od of determining the coordination number and the mean square displacement.

The height of the first coordination peak for amorphous antimony was computed from the expression

$$H_1 = 4\pi r_1^2\rho_0 + \frac{2r_1}{\pi}\int_0^{s_2} si(s)\sin(r_1 s)\,ds$$

and is shown in Fig. 1. For this calculation the interference function si(s) was used for the scattering data[3] for electrons with energy 80 keV. The value of the radius of the first coordination peak r_1 was determined from the radial distribution curve and was equal to 2.87 Å. For the mean density of amorphous antimony the value 6.02 g/cm^3 was used. This is 10% smaller than the value for crystalline antimony (6.69 g/cm^3). The calculation was done on a "Razdan-2" computer for the increments $\Delta s = 0.1$ and $\Delta s_2 = 0.2$ Å^{-1}. The H_{11} curve was obtained graphically. After finding the H_{11} values from the graph for different values of s_2, we compute the quantities $s_2/(H_{11}\pi)$ and plot them as a function of s_2^2. Thus we obtain the coordination number and σ_1. For this the values of the quantity $s_2/(H_1\pi)$ also can be used (Fig. 2). In this case the function $s_2/(H_{11}\pi)$ is represented by the straight line around which the $s_2/(H_{11}\pi)$ curve oscillates. From the intercept $b = 1/3$, obtained from the intersection of the line $s_2/(H_{11}\pi)$ and the ordinate, we find that $n_1 = 1/b = 3$, and from the angular coefficient, the mean-square displacement is given by $\sigma_1 = (6n_1k)^{1/2} = (6 \cdot 3 \cdot 0.2/250)^{1/2} = 0.12$ Å.

It is easy to show from the data of Fig. 2 that the accuracy of the determination of the coordination number and σ_1 depends on the manner in which the line $s_2/(H_{11}\pi)$ is drawn. But even if the $s_2/(H_{11}\pi)$ line is constructed only from the very low or the very high points of the $s_2/(H_1\pi)$ curve, the errors in the determination of the coordination number and σ_1 do not exceed 5% and 3%, respectively.

The values of the coordination number and σ_1 for amorphous antimony obtained by this procedure are in complete agreement with the results determined by other methods.[3]

The author thanks Z. G. Pinsker and I. D. Nabitovich for discussing the results of this work.

---

[1] P. G. Mikolaj and C. J. Pings, Phys. and Chem. of Liquids, 1, 93 (1968).

[2] I. D. Nabitovich, Ya. I. Stetsiv, and Ya. V. Voloshchuk, Visnik L'vovsk. Politekh. Inst., 28, 81 (1968).

[3] Ya. I. Stetsiv, Kristallografiya, 18, 257 (1973)[Sov. Phys.-Crystallogr., 18, 158 (1973)].

Use of the methods of successive experiment planning with refining crystal-structure parameters

I. V. Igonina, B. I. Pokrovskii, A. K. Gapeev, P. I. Lazarev, and L. N. Komissarova
M. V. Lomonosov Moscow State University

(Submitted November 22, 1971; resubmitted April 26, 1972)
Kristallografiya, 18, 487-491 (May-June 1973)

The problem of refining the parameters of the structural models of crystalline substances during x-ray structural analysis based on the powder method is considered. Using successive planning methods, the conditions governing the choice of an extra "optimum" experiment such as will improve the accuracy of the determination of the parameters to a specified extent are determined. The influence of any deviation of the theoretical atomic scattering factors from the experimental values on the ultimate accuracy of structure-parameter determination is considered. By way of example, the results of an x-ray structural analysis of magnesium ferrite are presented.

PRESENTATION OF THE PROBLEM AND PRINCIPLES OF ITS SOLUTION

X-ray structural analysis by the powder method often amounts to the refinement of the parameters characterizing a known atomic model. A serious failing of x-ray diffraction powder patterns is the limited amount of experimental data which they provide. In this case the accuracy of the determination of the structural parameters may be increased by carrying out an additional experiment in which the intensities of individual reflections are measured repeatedly. The choice of reflections for the extra experiment and the necessary number of measurements may be conveniently determined on the basis of the theory of optimum experiment planning.[1] The methods of this theory enable us to establish the minimum amount of work involved and the conditions of the experiment providing the desired accuracy in the estimation of the structural parameters. Consideration was given in refs. 2 and 3, in particular, to the application of optimum experiment-planning theory in problems of x-ray structural analysis when determining the time required to measure the reflections in computer-controlled diffraction cameras.

The refinement of the structural parameters by the method of least squares amounts to the minimization of a function $\Phi(x)$ in the space of the parameters x in the neighborhood of an already known initial value x^0:

$$\min \Phi(x) = \min_{x} \sum_{i=1}^{N} [I_i^e - I(\theta_i, x, k_i, f_i)]^2 W_i, \tag{1}$$

where I_i^e is the experimental and $I(\theta_i, x, k_i, f_i)$ the calculated value of the intensity of the i-th reflection, θ_i is the diffraction angle (or indices h, k, *l*), x is the vector of the parameters undergoing refinement, k_i is the vector of known constants, f_i is the atomic factor, $W_i = 1/\sigma_i^2$ is the weight of the i-th term in (1), which is associated with the random error in the intensity measurement ε_i by way of the equation $E(\varepsilon_i) = 0$, $E(\varepsilon_i^2) = \sigma_i^2$.

The direct application of the method of least squares to the problem (1) in this form is improper, since the atomic factors used in the calculations are not, strictly, speaking, precisely determined quantities, but are only known within a certain error. Hence, in addition to the random intensity-measuring error, the computing scheme must allow for errors associated with the approximate character of existing knowledge as to the form of the atomic scattering function in real crystals. In practical calculations we can only use certain estimates of these quantities, putting

$$f_j = f_j^0 + \delta_j, \tag{2}$$

where f_j is the atomic factor of the j-th atom in the real crystal, f_j^0 is the mean value of this factor obtained by various quantum-mechanical calculations, δ_j is the random error in estimating the atomic factor, with a mean value of $E(\delta) = 0$ and a mathematical expectation of $E(\delta_j^2) = \Delta_j^2$. According to ref. 4, the value of Δ_j in oxides, semiconductors, and metals is 3% for the cations and 5% for the oxygen atom relative to the corresponding values of f_j, i.e., $\Delta_j = \beta_j f_j^0$, where $\beta_j = 0.03$ and 0.05 respectively.

Using the method of error transfer[5] we may estimate the error in the intensity calculations due to errors in the atomic factors. For this purpose we express the function I in the following form:

$$I(\theta, x, k, f) = I(\theta, x, k, f^0) + \sum_{j=1}^{p} \frac{\partial I(\theta, x, k, f)}{\partial f_j}\bigg|_{x=\hat{x},\, f=f^0} \Delta_j + o(\Delta_j^2),$$

where p is the total number of atoms. We shall confine ourselves to terms of the first order in this expansion, since approximate estimates of the second-order correction give it a value equal to some 5% of the preceding term.

Then $I_i^e = I_i^0 + R_i + \varepsilon_i$, where

$$I_i^0 = I(\theta, x, k, f^0), \quad R_i = \sum_{j=1}^{p} \frac{\partial I(\theta, x, k, f)}{\partial f_j}\bigg|_{x=\hat{x},\, f=f^0} \Delta_j. \tag{3}$$

Thus problem (1) reduces to an ordinary regression problem. It follows from (3) that, in using the method of least squares for estimating the parameters, we must put the weight of the i-th measurement equal to

$$W_i = (R_i^2 + \sigma_i^2)^{-1}. \tag{4}$$

If r_i measurements are carried out at the i-th point, we must put

$$W_i = (R_i^2 + \sigma_i^2 / r_i)^{-1}. \tag{5}$$

in Eq. (4) when carrying out a least-squares calculation. Here $\sigma_i^2/r_i = \overline{\sigma}_i^2$ is the dispersion of the mean values of the r_i measurements at a single point, i.e., $\overline{\sigma}_i^2 = \sigma^2(\overline{I_i}^e)$, where

$$I_i^e = \Big(\sum_{s=1}^{r_i} I_{is}\Big) \Big/ r_i.$$

It is obvious that $\sigma_i^2/r_i \to 0$ as $r_i \to \infty$. For a known and constant experimental error, the error of the mean $\bar{I}_i^e$ may be made as small as desired by increasing the number of parallel measurements. However, the value of R_i will remain unaltered, since the errors Δ_j are determined in another experiment. Thus we encounter a certain specific limit for the quantities W_i, and it is fundamentally impossible to obtain estimations of the parameters more accurate than those obtained for $W_i = 1/R_i^2$.

Since the quantity R [Eq. (3)] depends on the unknown parameters, the solution of problem (1) has to be carried out by iteration, with a recalculation of $R_i(\hat{x})$ at each step. If the accuracy of the least-squares estimates of the parameters is unsatisfactory, the values of a certain set of parameters will have to be refined by means of an additional experiment. The planning of the additional experiment lies in disposing the possible measurements in such a manner that the final accuracy of our estimates of the unknown parameters may satisfy a particular "optimum" criterion. Usually this accuracy is characterized by a quantity F(D), constituting a certain function of the dispersion (error) matrix. Various currently employed optimum criteria may be found, for example, in ref. 1.

We choose

$$F(D) = \mathrm{Tr}_l D = \sum_{\alpha=1}^{l} D_{\alpha\alpha} = \sum_{\alpha=1}^{l} \sigma_\alpha^2, \tag{6}$$

where l is the number of parameters to be optimized, $\sigma_\alpha = \sigma(x_\alpha)$ is the error in the α-th parameter. The experiment should be set up in such a way as to obtain the least possible value of the mean dispersion of the parameters $\mathrm{Tr}_l D$. In this case the planning of the additional experiment amounts to the solution of a certain extremal problem:

$$\min_{\varepsilon} F(D), \tag{7}$$

where ε is the plan of the additional experiment.

In our particular case ε is the value of the angle θ_{N+1} (or the indices hk$l$) at which the (N + 1)-th additional measurement should be made. The choice of reflection for the (N + 1)-th measurement is determined after making the N-th measurement, by solving the equation

$$\max W f_N' D_N A D_N f_N, \tag{8}$$

where

$$f_N = \left. \frac{\partial I(\theta, x, k, f)}{\partial x} \right|_{x=\hat{x}_N},$$

$$D_N = M_N^{-1}, (M_N)_{\alpha\beta} = \sum_{i=1}^{N} W_i f_{N\alpha} f_{N\beta},$$

A is a diagonal numerical matrix (for $A_{\alpha\alpha} = 0$ the corresponding parameter x_α is not refined), the index N denotes the values of the corresponding functions after N measurements, and the prime denotes the operation of transposition.

By carrying out a measurement at the angle $\theta_{\max}$ obtained from (8) we obtain the greatest possible reduction in $\mathrm{Tr}_l D$ in one measurement. After the realization of each (N + 1)-th measurement $\hat{x}_{N+1}$ and D_{N+1} are calculated by the method of least squares. Then Eq. (8) is solved again, and so on, until the specified accuracy of $\mathrm{Tr}_l D$ has been reached.

We note that, for the linearly parametrized hypothesis (for which $f_N = f(\theta)$), Eq. (8) is independent of the estimates x_N, and we may therefore calculate a plan for a group of measurements of any volume a priori. In the case of nonlinear parametrization $f_N = f(\theta, x_N)$, Eq. (8) does depend on the unknown estimates $\hat{x}$. In this case a transition to group planning is only possible when the quantities f_N depend very little on x_N. In problems of x-ray structural analysis this condition is clearly satisfied.

EXPERIMENT

The foregoing considerations were employed when refining the structure of magnesium ferrite $MgFe_2O_4$. Magnesium ferrite has a spinel structure (space group Fd3m, $a = 8.378$ Å, Z = 8). The Mg and Fe cations are distributed over two crystallographic positions: the eightfold tetrahedral positions A and the 16-fold octahedral positions B.

The structural model of $MgFe_2O_4$ is completely characterized by the parameters y (the number of Mg atoms in the positions A) and z (the z coordinate of the basis O atom).

The effective atomic factors of the positions A and B are $f_A = y f_{Mg} + (1-y) f_{Fe}$, $f_B = [(1-y) f_{Mg} + (1+y) f_{Fe}]/2$.

In the calculations we take as basic the atomic factors of Fe, Mg, and O given$^{1)}$ in ref. 6, corrected for anomalous dispersion.[7]

X-ray powder diffraction photographs of $MgFe_2O_4$ were taken over a range of $\Sigma(h^2 + k^2 + l^2)$ values between 8 and 80, using a DRON-1 diffractometer (Co Kα radiation). The line intensities were determined on the basis of five independent measurements. Each of these measurements was carried out on a newly prepared sample, thus avoiding a whole series of systematic instrumental errors.[8] The mean intensities of thirteen reflections from the $MgFe_2O_4$ structure and the mean-square errors of their determination $\bar{\sigma}$ are presented in Table 1.

Applying the method of least squares to the experimental data$^{2)}$ in accordance with the scheme just discussed, we calculated the degree of inversion y of the magnesium ferrite, the oxygen coordinate z, the general tem-

TABLE 1. Experimental Intensities of $MgFe_2O_4$ Powder Diffraction Patterns

Serial No.	hk$l$	$\bar{I}$	$\bar{\sigma}$	Serial No.	hk$l$	$\bar{I}$	$\bar{\sigma}$
1	220	30402	912	8	444	2890	87
2	311	85595	1710	9	642	4754	142
3	400	21835	436	10	800	7853	234
4	422	9671	387	11	840	10007	400
5	440	37588	750	12	511 333	27402	510
6	620	3163	95	13	731 553	15076	450
7	533	7285	218				

TABLE 2. Changes in the Estimates of the Structural Parameters of the $MgFe_2O_4$ Model and Their Corresponding Errors during the Refinement Process

N*	hkl	I	$\frac{\chi^2}{N-m}$	K	$\sigma(K)$	B	$\sigma(B)$	y	$\sigma(y)$	z	$\sigma(z)$
13			0.55	0.0073	0.00031	0.54	0.15	0.118	0.0338	0.258	0.0011
14	220	30800	0.45	0.0072	0.00029	0.53	0.14	0.122	0.0320	0.258	0.0011
15	400	21500	0.42	0.0073	0.00027	0.54	0.13	0.127	0.0292	0.258	0.0011
16	400	21700	0.41	0.0073	0.00025	0.57	0.13	0.133	0.0275	0.258	0.0011
17	220	30900	0.38	0.0073	0.00025	0.57	0.12	0.134	0.0263	0.258	0.0011
25	220	28300	0.28	0.0073	0.00019	0.57	0.10	0.143	0.0199	0.258	0.0010

*N is the total number of measurements.

perature factor B, and the coefficient for reducing the structure factors to the absolute scale K.

The results of the calculations are presented in Table 2. The first line gives the values of the parameters calculated from the results of the main experiment. The subsequent lines give the results obtained by making use of the additional experiments. The table shows the indices of the reflections for which the intensities were measured additionally, together with the intensities themselves and the least-squares-refined estimates of the structural parameters. The adequacy of the model was estimated by reference to the χ^2 criterion; correspondingly, Table 2 gives the values of $\chi^2/(N-m) = [\sum_{i=1}^{N}(I_i^e - I_i)^2 W_i] / (N-m)$, where N is the total number of reflections and m is the number of parameters to be determined. As an initial approximation for the parameters we took the values given in ref. 10. For the majority of reflections $R_i \simeq \overline{\sigma}_i$. We see from Table 2 that the error in determining y from the results of the main experiment reaches a value as high as 0.034. However, when considering the mutual relationship between the magnetization of ferrospinels with Fe ions distributed over the A and B positions it is important to know the parameter y to an accuracy[11] of no lower than 0.02.

In order to refine the crystal structure we carried out successive experiment planning so as to refine the parameter y. From Eq. (8) with $x = \hat{x}_{13}$, we calculated a successive group plan to achieve an accuracy of $\sigma(y) = 0.020$. This calculation gave a rough estimate of the number of extra measurements required. We found that we had to carry out about 10 measurements of the intensities of the 220 and 400 reflection intensities with identical repetition frequency. Then we planned and performed four additional experiments, the results of which are presented in Table 2 (with N = 14-17). The points of the successive plan coincided with the points of the group plan, apart from the order of their alternation. This was because the possible values of θ_i lay a fairly long way from one another, and slight changes in the estimates $\hat{x}_N$ and $\hat{x}_{N+1}$ had no effect on the disposition of the points in the plan.

We found that after 17 measurements the quantities f_N and f_{N+1} changed very little. We therefore carried out a group planning of eight successive measurements. The resultant group plan consisted of the same alternating points, 220 and 400, i.e., in order to refine the parameter y, additional measurements had to be made on the intensities of only these two reflections. As a result of 12 additional experiments, we obtained a value of y = 0.143, with an error of $\sigma(y) = 0.0199$. Additional refinement calculations showed that a $\sigma(y)$ value of no better than $\sigma(y) = 0.019$ could in any case be obtained. This limitation follows directly from Eq. (5).

---

1)We used the atomic factors for the singly charged ionic state.

2)The calculations were carried out in the BÉSM-3M computer on the basis of standard programs.[9]

[1] V. V. Fedorov, Theory of the Optimum Experiment [in Russian], Nauka, Moscow (1971).

[2] D. P. Shoemaker, Acta Crystallogr., A24, 136 (1968).

[3] M. A. Shtremel', Kristallografiya, 14, 34 (1969) [Sov. Phys.—Crystallogr., 14, 24 (1969)].

[4] N. N. Sirota, Acta Crystallogr., A25, 223 (1969).

[5] D. Hudson, Statistics for Physicists [Russian translation], Mir, Moscow (1967).

[6] D. T. Cromer and J. T. Waber, Acta Crystallogr., 18, 104 (1965).

[7] D. T. Cromer, Acta Crystallogr., 18, 7 (1965).

[8] D. M. Kheiker and L. S. Zevin, X-Ray Diffractometry [in Russian], Fizmatgiz, Moscow (1963).

[9] I. M. Silin, "Standard program for solving problems by the method of least squares," Preprint D810, Dubna (1964).

[10] A. P. Erastova and Yu. G. Saksonov, in: Ferrites and Noncontact Cells [in Russian], Izd. AN SSSR, Minsk (1963), p. 163.

[11] T. Smit and H. P. G. Wijn, Ferrites Wiley, New York (1959).

Sections of paired Patterson functions

V. N. Biyushkin and N. V. Belov

Institute of Crystallography, Academy of Sciences of the USSR
Modrov State University

(Submitted December 2, 1972)
Kristallografiya, 18, 492-496 (May-June 1973)

Two independent symmetry transformations are used to specify the vector parameters of paired Patterson functions; these determine the section which contains the image or reflection of the structure at a fixed atom, and at other atoms distributed in a similar way with respect to the specified symmetry elements or pairs similar to them. When two elements are fixed, the admissible regions for the reflecting atoms are severely restricted in comparison with the sections of the first kind.

Sections of paired Patterson functions were considered in ref. 1; these sections localized, with respect to fixed symmetry elements, the image or reflection of the structure at the fixed atom. To construct such a section for vector parameters $\mathbf{u}_1$ and $\mathbf{u}_2$ of the paired function, the following relation must be established: $\mathbf{u}_2 = \text{Э}(\mathbf{u}_1 + \mathbf{r}_0) - \mathbf{r}_0$, where $\mathbf{r}_0$ are the coordinates of the given atom, and Э is the symmetry transformation. The section obtained in this way is similar to Hoppe's section in ref. 2; this section was constructed from the vector $\mathbf{u}_0 = \text{Э}\,\mathbf{r}_0 - \mathbf{r}_0$ and distinguished between the reflections of the structure at all atoms at the start of the interatomic vectors $\mathbf{u}_0$, as well as at the atom with coordinates $\mathbf{r}_0$. However, the sections localizing the structure do not distinguish the reflections at all atoms at the start of the interatomic vectors $\mathbf{u}_0$, but only these which are distributed or located, with respect to the symmetry element corresponding to the fixed transformation Э, in the same way as the given atom whose coordinates are $\mathbf{r}_0$. Nevertheless, there is still a large amount of freedom in the variation of the coordinates of the possible atoms whose structure reflections can be distinguished by actual sections of this type, providing that the inversion operation – either by itself or in combination with a rotation – cannot be used as the fixed symmetry transformation. In fact, the plane of symmetry implies determinacy only for one measurement, i.e., along the direction perpendicular to it. Atoms reflecting the structure, i.e., atoms whose structure reflections are distinguished by the section, must be located on the plane parallel to the fixed symmetry plane and passing through the given atom, or on another plane similarly located with respect to an element of symmetry corresponding to the fixed one. No other restrictions are imposed on the coordinates of the possible reflecting atoms, i.e., they can be at any point in the indicated planes. Rotational and screw axes require determinations through two measurements, viz., in the plane perpendicular to the axis, and so much more rigid conditions are imposed on the admissible coordinates of the reflecting atoms. The reflecting atoms must be on a line parallel to the fixed axis of symmetry and passing through the given atom, or on parallel lines similarly located with respect to other symmetry axes to that corresponding to the symmetry transformation which actualizes the section. The center of symmetry and the inversion axes fix the atom itself in three measurements, by removing all freedom of location from other atoms with respect to symmetry elements similar to them. For each such element, just as for the fixed one, there can be only one reflecting atom. When the center of symmetry or the inversion axis is the fixed element, the number of distinguishable reflections is minimal, all other things being equal. Therefore these elements of symmetry must be given preference over others. But since there are more centers of symmetry in the cell than there are axes of inversion (consider the number of singular points), the axes of inversion are the most desirable fixed elements.

More rigid restrictions – in comparison with those on the sections of ref. 1 – on the coordinates of possible reflecting atoms are imposed on the other type of structure-localizing sections; these restrictions are defined by the following vector parameters of the paired Patterson function:

$$\mathbf{u}_1 = \text{Э}_m(\mathbf{u} + \mathbf{r}_0) - \mathbf{r}_0, \quad \mathbf{u}_2 = \text{Э}_n(\mathbf{u} + \mathbf{r}_0) - \mathbf{r}_0. \tag{1}$$

In this equation $\text{Э}_m \equiv \{A_m \mid \mathbf{t}_m\}$ and $\text{Э}_n \equiv \{A_n \mid \mathbf{t}_n\}$ are symmetry transformation operators, $\mathbf{r}_0$ are the coordinates of the fixed atom, and $\mathbf{u}$ is a variable vector. In integral form the corresponding section takes the form

$$DP_{\text{Э}_m,\text{Э}_n}(\mathbf{r}_0, \mathbf{u}) = \int\limits_V \rho(\mathbf{r})\rho(\mathbf{r} + \text{Э}_m[\mathbf{u} + \mathbf{r}_0]$$

$$- \mathbf{r}_0)\rho(\mathbf{r} + \text{Э}_n[\mathbf{u} + \mathbf{r}_0] - \mathbf{r}_0)\,dV. \ (2) \tag{2}$$

Consider the peaks of this function. The function takes a nonzero value at $\mathbf{u}$ if the atoms at least once simultaneously fall on the vertices of the triangle of summation defined by the arguments of the integrands, as the variable $\mathbf{r}$ runs over the whole cell. The condition that peaks appear can be written in the form

$$\mathbf{r} = \mathbf{r}_i, \quad \mathbf{r} + \text{Э}_m(\mathbf{u} + \mathbf{r}_0) - \mathbf{r}_0 = \mathbf{r}_j, \quad \mathbf{r} + \text{Э}_n(\mathbf{u} + \mathbf{r}_0) - \mathbf{r}_0 = \mathbf{r}_k, \tag{3}$$

and after some elimination using the first equation we get the following pair of equations:

$$\text{Э}_m\mathbf{u} + \text{Э}_m\mathbf{r}_0 - \mathbf{r}_0 = \mathbf{r}_j - \mathbf{r}_i, \quad \text{Э}_n\mathbf{u} + \text{Э}_n\mathbf{r}_0 - \mathbf{r}_0 = \mathbf{r}_k - \mathbf{r}_i. \tag{4}$$

Since $\mathbf{r}_i$, $\mathbf{r}_j$ and $\mathbf{r}_k$ take values which are completely defined by each actual structure, and since $\mathbf{r}_0$, Э_m, and Э_n are fixed, the system of equations (4) cannot hold for all $\mathbf{u}$. Let us assume that $\mathbf{u} = \mathbf{r}_q - \mathbf{r}_p$ is the interatomic vector. Then (4) has an obvious solution for

$$\mathbf{r}_i = \mathbf{r}_p = \mathbf{r}_0. \tag{5}$$

The system (4) then becomes

$$\text{Э}_m\mathbf{r}_q = \mathbf{r}_j, \quad \text{Э}_n\mathbf{r}_q = \mathbf{r}_k. \tag{6}$$

The system (6) links equivalent atoms and is therefore consistent for every atom q.

Thus the function $DP_{\mathit{Э}_m, \mathit{Э}_n}$ $(\mathbf{r}_0, \mathbf{u})$ has peaks at the points $\mathbf{u} = \mathbf{r}_q - \mathbf{r}_0$. Each peak is generated by the fixed (specified) atom i_0 at the point $\mathbf{r}_0$ and by the atoms j and k which are equivalent to the atom q defining the coordinates of the actual peak, and which are related to the atom q by the fixed transformations $\mathit{Э}_m$ and $\mathit{Э}_n$ respectively. Each value of the vector parameter u which coincides with an interatomic vector drawn from the fixed i_0 atom to every other atom of the structure has its corresponding peak in the section or profile considered, i.e., the section $DP_{\mathit{Э}_m, \mathit{Э}_n}$ $(\mathbf{r}_0, \mathbf{u})$ contains the reflection of the structure at the atom with coordinates $\mathbf{r}_0$. Geometrically speaking, the reflection obtained is identical with the structure itself.

The section under consideration can be described by a Fourier series as follows:

$$DP_{\mathit{Э}_m, \mathit{Э}_n}(\mathbf{r}_0, \mathbf{u}) = \frac{1}{V^2} \sum_{\mathbf{H}_1} \sum_{\mathbf{H}_2} F(-\mathbf{H}_1 - \mathbf{H}_2) F(\mathbf{H}_1) F(\mathbf{H}_2)$$
$$\times \exp(-2\pi i(\mathbf{H}_1[\mathit{Э}_m(\mathbf{u} + \mathbf{r}_0) - \mathbf{r}_0] + \mathbf{H}_2[\mathit{Э}_n(\mathbf{u} + \mathbf{r}_0) - \mathbf{r}_0])), \qquad (7)$$

and this can also be written in the form:

$$DP_{\mathit{Э}_m, \mathit{Э}_n}(\mathbf{r}_0, \mathbf{u}) = \frac{1}{V^2} \sum_{i,j,k} \sum_{\mathbf{H}_1} \sum_{\mathbf{H}_2} f_i(-\mathbf{H}_1 - \mathbf{H}_2) f_j(\mathbf{H}_1) f_k(\mathbf{H}_2)$$
$$\times \exp(-2\pi i(\mathbf{H}_1[\mathit{Э}_m(\mathbf{u} + \mathbf{r}_0) - \mathbf{r}_0 - (\mathbf{r}_j - \mathbf{r}_i) \qquad (8)$$
$$+ \mathbf{H}_2[\mathit{Э}_n(\mathbf{u} + \mathbf{r}_0) - \mathbf{r}_0 - (\mathbf{r}_k - \mathbf{r}_i)])),$$

Whence it follows that if the atoms i, j, and k generate a paired Patterson peak, i.e., if the vector sums for $\mathbf{H}_1$ and $\mathbf{H}_2$ in the exponential function are zero, then the height of the peak is determined by the expression

$$\frac{1}{V^2} \sum_{\mathbf{H}_1} \sum_{\mathbf{H}_2} f_i(-\mathbf{H}_1 - \mathbf{H}_2) f_j(\mathbf{H}_1) f_k(\mathbf{H}_2). \qquad (9)$$

It has been proved above that the group of peaks forming the reflection of the structure at the specified atom with coordinates $\mathbf{r}_0$ is generated by the atom i_0 and by pairs of equivalent atoms. From (6), the atoms of these pairs are related by the transformation $(\mathit{Э}_n \mathit{Э}_m^{-1}) : \mathbf{r}_k = \mathit{Э}_n \mathit{Э}_m^{-1} \mathbf{r}_j$. Therefore the heights of the peaks forming the reflection of the structure at the i_0-th atom are given by the sum

$$\frac{1}{V^2} \sum_{\mathbf{H}_1} \sum_{\mathbf{H}_2} f_{i_0}(-\mathbf{H}_1 - \mathbf{H}_2) f_j(\mathbf{H}_1) f_j(\mathbf{H}_2). \qquad (10)$$

For the structure of similar atoms, when we can assume that $f(\mathbf{H}_j) = Z_j \hat{f}(\mathbf{H})$, the heights of the peaks are proportional to the atomic number of the atom and to the squares of the atomic numbers of the atoms corresponding to the peaks:

$$\frac{Z_{i_0} Z_j^2}{V^2} \sum_{\mathbf{H}_1} \sum_{\mathbf{H}_2} \hat{f}(-\mathbf{H}_1 - \mathbf{H}_2) \hat{f}(\mathbf{H}_1) \hat{f}(\mathbf{H}_2). \qquad (11)$$

We now show that, besides the reflection of the structure at the given atom i_0, the section also contains the reflections at other atoms which are located in a fashion similar to the i_0 atom or are similarly located with respect to the symmetry elements $\mathit{Э}_m$ and $\mathit{Э}_n$, which correspond to the fixed transformations $\mathrm{Э}_m$ and $\mathrm{Э}_n$, or are similarly located with respect to another combination of elements similar to the fixed ones. Suppose that the combination of fixed elements $\mathrm{Э}_m$ and $\mathrm{Э}_n$ is such that it is possible for not only one but several atoms to be similarly located with respect to them. Let us assume that i_0 and i_1 are similarly located with respect to $\mathrm{Э}_m$ and $\mathrm{Э}_n$. Then

$$\mathit{Э}_m \mathbf{r}_0 - \mathbf{r}_0 = \mathit{Э}_m \mathbf{r}_{i_1} - \mathbf{r}_{i_1}, \quad \mathit{Э}_n \mathbf{r}_0 - \mathbf{r}_0 = \mathit{Э}_n \mathbf{r}_{i_1} - \mathbf{r}_{i_1}. \qquad (12)$$

If we put u in (4) equal to the interatomic distance $(\mathbf{r}_q - \mathbf{r}_p)$, and if we take $\mathbf{r}_i = \mathbf{r}_p = \mathbf{r}_{i_1}$, then the above equations suffice to lead us to the system (6) once more. Therefore, along with the reflection of the structure at the given atom i_0, the section $DP_{\mathit{Э}_m, \mathit{Э}_n}$ $(\mathbf{r}_0, \mathbf{u})$ contains the reflection of thestructure at the atom i_1 providing this atom is in the structure.

In the elementary crystal cell, except for certain combinations in the hexagonal groups, there are other combinations of symmetry elements which are similar to the original combination of the elements and $\mathrm{Э}_n$,, and which correspond to the fixed transformations $\mathit{Э}_m$ and $\mathit{Э}_n$.. Let us assume that the elements $\mathrm{Э}_m{}^l$ and $\mathrm{Э}_n{}^l$ form such a pair. The combination $\mathrm{Э}_m{}^l$ and $\mathrm{Э}_n{}^l$ must be similar to the original one, both in the individual elements which form it, and in the geometry of their mutual location.

The symmetry elements $\mathrm{Э}_m{}^l$ and $\mathrm{Э}_n{}^l$ are similar to the original elements $\mathrm{Э}_m$ and $\mathrm{Э}_n$ only when the transformation $\mathit{Э}_m{}^l$, corresponding to the element $\mathrm{Э}_m{}^l$, can be written as the product of $\mathit{Э}_m$ by the translation T_{Rm}^l, and $\mathit{Э}_n{}^l = T_{Rn}{}^l \mathit{Э}_n$. The translations T_{Rm}^l and T_{Rn}^l must be such that the additional (with respect to the transformations $\mathit{Э}_m$ and $\mathit{Э}_n$) components of the parallel translation of the transformations $\mathit{Э}_m{}^l$ and $\mathit{Э}_n{}^l$ are equal, or zero, or are integer translations of the crystal lattice (among them, centering translations in nonprimitive cells). This means that a translation defined by each translation factor must be, after integer components have been removed from it, perpendicular to the corresponding element $\mathrm{Э}_m$ or $\mathrm{Э}_n$.

If the combination of the elements $\mathrm{Э}_m{}^l$ and $\mathrm{Э}_n{}^l$ differs from the original combination $\mathrm{Э}_m$ and $\mathrm{Э}_n$ by a vector $\mathbf{d}_l$, then each point r can be made to correspond to the point $\mathbf{r} + \mathbf{d}_l$ which is located with respect to $\mathrm{Э}_m{}^l$ and $\mathrm{Э}_n{}^l$ in the same way as r is located with respect to $\mathrm{Э}_m$ and $\mathrm{Э}_n$. Since the elements corresponding to these combinations are pairwise similar, the following equations hold for each r:

$$\mathit{Э}_m \mathbf{r} - \mathbf{r} = \mathit{Э}_m{}^l(\mathbf{r} + \mathbf{d}_l) - (\mathbf{r} + \mathbf{d}_l),$$
$$\mathit{Э}_n \mathbf{r} - \mathbf{r} = \mathit{Э}_n{}^l(\mathbf{r} + \mathbf{d}_l) - (\mathbf{r} + \mathbf{d}_l). \qquad (13)$$

Let us assume that, along with the given atom at the point $\mathbf{r}_0$, there is an atom at the point $(\mathbf{r}_0 + \mathbf{d}_l) = \mathbf{r}_l$. With $\mathbf{u} = \mathbf{r}_q - \mathbf{r}_p$ and $\mathbf{r}_i = \mathbf{r}_p = \mathbf{r}_l$, (13) reduces (4) to the form

$$\begin{matrix} \mathit{Э}_m \mathbf{r}_q + T_{Rm}^l = \mathbf{r}_j & & \mathit{Э}_m^l \mathbf{r}_q = \mathbf{r}_j \\ & \text{or} & \\ \mathit{Э}_n \mathbf{r}_q + T_{Rn}^l = \mathbf{r}_k & & \mathit{Э}_n^l \mathbf{r}_q = \mathbf{r}_k, \end{matrix} \qquad (14)$$

i.e., there is a solution for each atom q. Thus the section $\mathrm{DP}_{\text{Э}_m,\text{Э}_n}(\mathbf{r}_0, \mathbf{u})$ contains the reflection of the structure at the atom l with coordinates $\mathbf{r}_l$ and located similarly to the specified atom, but now with respect to the symmetry elements $\text{Э}_m'$ and $\text{Э}_n'$.

The reflection at the atom l will be distinguished in the section when the atom is not related with the given one by the relation $\mathbf{r}_0 + \mathbf{d}_l = \mathbf{r}_l$, but is located with respect to $\text{Э}_m'$ and $\text{Э}_n'$ just as the specified atom is related to Э_m and Э_n, i.e., when the following inequalities hold:

$$\vartheta_m \mathbf{r}_0 - \mathbf{r}_0 = \vartheta_m' \mathbf{r}_l - \mathbf{r}_l,$$
$$\vartheta_n \mathbf{r}_0 - \mathbf{r}_0 = \vartheta_n' \mathbf{r}_l - \mathbf{r}_l. \qquad (15)$$

This is possible for combinations of symmetry elements which permit the existence of definite regions all of whose points are related to the symmetry elements in identical fashion. Such combinations are combinations of planes of symmetry, of a plane and a parallel axis, and of two parallel axes, if at least one of them is not an axis of inversion.

So the function $\mathrm{DP}_{\text{Э}_m,\text{Э}_n}(\mathbf{r}_0, \mathbf{u})$ contains the reflection of the structure at the given atom with coordinates $\mathbf{r}_0$ and at all atoms similarly located to it either with respect to the original combination of symmetry elements Э_m and Э_n, which correspond to the fixed symmetry transformations, or with respect to another combination similar to the original one both in the individual elements forming it and in the geometry of their location. These reflections follow the rules for the section being considered and are equally valid. Reference of the peaks to this or that reflection is difficult in the general case, since the natural indicator as to which concrete or actual reflection a peak belongs is the weighting factor, and this can be assumed to be proportional to the atomic number of the reflecting atom. Besides, it is impossible to determine to which actual combination of symmetry elements – if there are several in the cell – to refer this or that reflection of the structure. Here, just as for sections of the first type which localize the structure (see ref. 1), there is an implicational or inferential or logical ambiguity (see ref. 3). However, because of the fact that two symmetry transformations are used to specify the vector parameters in the sections under consideration, there are substantial limitations – in comparison with sections of the first type – on the possible regions in which the atom giving the reflection of the structure in the actual section may be located. In fact, two planes define a line as the region for possible reflecting atoms; this line is parallel to both planes and passes through the specified atom. They do not define a plane as in the case of sections of the first type; two parallel planes as the fixed elements for the specification of the vector parameters which would define the plane of the reflecting atoms do not specify a section of the second type, since the points obtained by reflection in them of just one original point will be related by a translation. A line may be determined as an admissible region by two parallel axes which are not inversion axes. For sections of the first type, the symmetry axis permits reflecting atoms to be located along a line parallel to it, but the number of permissible lines is greater in the general case than for sections of the second type. For the remaining combinations, the possible regions are discrete points. In this respect, the sections localizing the structure considered here for the paired Patterson function have advantageous differences from the sections of the first type in ref. 1, since they impose more rigid limitations on the possible positions of the reflecting atoms, and at the same time they reduce the probability of distinguishing – by a section of the second type – the other reflections from the reflection at the specified atom. Besides the selection of atoms which coincide by chance in the admissible regions for reflecting atoms, sections of the second type curtail – in comparison with sections of the first type – the number of reflecting atoms among atoms cyrstallographically equivalent to the given atom. The sections we have considered have distinct advantages over the Hoppe sections of ref. 2, since the latter are constructed from the vectors between the specified atom and those equivalent to it.

---

[1] V. N. Biyushkin, Kristallografiya, 18, 251 (1973) [Sov. Phys.—Crystallogr., 18, 158 (1973)].

[2] W. Hoppe, Acta Crystallogr., 10, 751 (1957).

[3] M. J. Buerger, Vector Space and its Application in Crystal Structure Investigations, Wiley, New York (1959).

Symmetries of functions for separating structures from a Patterson distribution of the triclinic, monoclinic, and orthorhombic systems

O. V. Frank-Kamenetskaya, N. V. Grigor'eva, and N. V. Margolis

Leningrad State University

(Submitted July 27, 1972)
Kristallografiya, 18, 497-502 (May-June 1973)

The conditions and degree of symmetry exaggeration of the separation functions for groups of triclinic, monoclinic, and orthorhombic symmetry (constructed using one vector grouping) are compared with original space group symmetries. It was shown that the total number of solutions (of separable, fundamental systems) is 2^k, where k is the number of additional independent symmetry elements in the separation function which are absent in the crystal space group. A table is presented of the additional symmetry elements of separation functions, constructed for vector groupings at different positions of a reference atom in crystals of triclinic, monoclinic, and orthorhombic symmetry.

The role of the superposition method consists in localization of one fundamental point system (structure) from the N systems of a Patterson distribution.[1] It is generally accepted, in refining the functions resolving structure representations from pseudomaxima, to use the space group symmetry of the crystal, i.e., to construct a separation function of an order equal to the multiplicity of the space group. In this process, a group of vectors is used in the superposition which are generated by the spacings from the original atom to all other atoms connected to it by symmetry operations of the group. The systematic analysis of the symmetry dependence of second-order separation functions on the type of displacement vectors was first proposed by Subramanian.[2] Golyshev et al. continued this work and extended it to a symmetry analysis of separation functions whose order equalled the multiplicity of the space group.[3] The theory was set forth that the symmetry of such a separation function must of necessity conform with the symmetry of the space group, but it can also be higher (in particular for $\bar{1}$).

In the actual practice of interpreting structures by the superposition method, it is important to know the conditions and degree of symmetry exaggeration of the separation functions relative to the symmetry of the crystal space group. Symmetry exaggeration leads to the appearance in the separation functions of additional structure configurations.

In the structure determination of the potassium salt of β,β-dinitroethylacetamide in ref. 4, the maximizing function, constructed according to the vectors from a reference atom to those connected with it by the symmetry operations of the group $Pna2_1$, possessed a symmetry Pnmm, and a doubly shortened identity period along the x axis. Such a function symmetry led to separation on it of four structure configurations. From Fig. 1 it may be

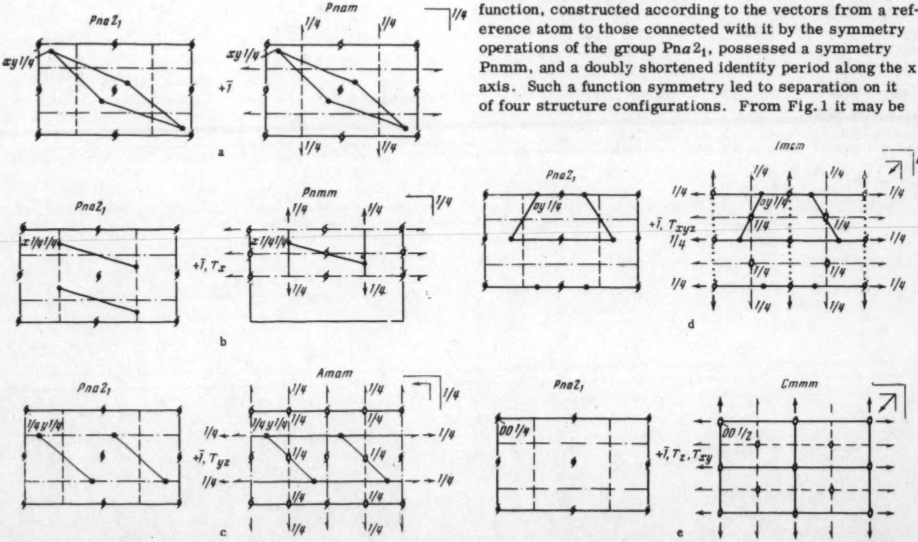

Fig. 1. Symmetry dependence of the separation function, constructed according to the vectors between the atoms of one rectilinear point system of the group $Pna2_1$, on reference atom position. Reference atom position: a) arbitrary relative to the symmetry element; b) on the plane a; c) on the plane n; d) equidistant from the two parallel planes n; e) at 2_1.

established that information on the symmetry of the Pnmm minimization function is contained in the vector grouping used for superposition (in a general rectilinear point system of the group $Pna2_1$, for an original reference atom situated on the surface of the glide reflection a).

This practical result led to the idea that information on the symmetry of separation functions constructed according to one grouping of vectors may be obtained from examination of the coordinates of atoms producing the grouping. The results of a symmetry analysis of a superpositional fourth-order matrix of a general rectilinear system of points of the group $Pna2_1$ are given in Table 1 for different reference atom positions and illustrated in Fig. 1. The analysis was performed by examination of the coordinates of the respective rectilinear point systems.

For each reference atom position relative to the symmetry elements of group $Pna2_1$ (Fig. 1), the separation function has a symmetry of at least Pn*a*m (vector grouping has an additional $\bar{1}$). This makes it impossible directly to resolve a structure of $Pna2_1$ symmetry on the Patterson distribution for a known position of only one reference atom. The minimum number of solutions obtained is two.

If the reference atom is situated on one of the open symmetry elements (Fig. 1b, c), or equidistant from two parallel symmetry elements in the plane passing through them, (Fig. 1d), the symmetry of the partition function then becomes greater than Pn*a*m. The corresponding vector groupings lead to a higher symmetry due to the appearance, (besides $\bar{1}$), of abbreviated (half-) translations. The number of resolvable structures becomes at least four. If the reference atom lies at the intersection of the special positions (Fig. 1e), the contribution of each of them to increasing the symmetry of the separation function remains as previously, but several additional symmetry elements (abridged translations) may prove to be reducible. The maximum number of structure configurations of the symmetry $Pna2_1$ functions is eight.

For groups of triclinic, monoclinic and orthorhombic symmetry, there occur the following laws of symmetry perfection for a separation function (constructed using one grouping of vectors), relative to the symmetries of the original space groups: 1) at $\bar{1}$ for each reference atom position in noncentrosymmetric space groups, belonging to the point groups 2, m, and mm2; 2) at a translation equaling the glide vector, if the reference atom is situated on the surface of a glide reflection or on a screw axis; 3) by a translation comprising the shortest distance between two parallel symmetry elements plus a component of their glide (it may equal zero), when the reference atom is situated equidistant from the two parallel symmetry elements in a plane passing through them.

Symmetry analysis also shows that the total number of solutions (of separable, fundamental systems) is 2^k, where k is the number of additional independent symmetry elements of the separation function which are absent in the crystal space group. Thus, each independent additional symmetry element increases the number of solutions by two times. If the separation function contains two additional (abridged) translations, then a third translation, reducible from them, does not produce an increase in the number of solutions. The maximum number of additional independent translations which a separation function may contain equals the number of independent symmetry elements in the original space group.

Table 2 gives the additional symmetry elements of separation functions constructed using a vector grouping for different reference atom positions in the framework of the space groups of triclinic, monoclinic, and orthorhombic systems.

Table 1 does not contain the reference atoms situated at the intersections of separate positions, since the result for these may be easily obtained by application of the symmetry of the separation functions which correspond to the special intersecting positions. An exception are the vector groupings for space groups which correspond to point group 222. In these groups, for reference atom positions producing two independent, abridged translations in the separation function, there arises an additional center of inversion, which again increases the number of solutions by two times.

The symmetry of a rectilinear system of points in space groups belonging to one point group obeys the same laws. An exception is the vector grouping Fdd2, which,

TABLE 1. Symmetry of a Superpositional Fourth-Order Matrix of a General Rectilinear Point System of the Group $Pna2_1$, for Different Reference Atom Positions

Reference atom position		Additional independent symmetry elements of the partition function	Partition function symmetry				Multiplicity of the general position in the cell $a \times b \times c$	Number of resolvable fundamental systems
relative to symmetry elements	coordinates		T_x	T_y	T_z	space group		
—	$xyz(^1/_4)$	$\bar{1}$	a	b	c	*Pnam*	8	2
At a	$x\,^1/_4\,^1/_4$	$\bar{1},\ T_x = {}^1/_2 a$	$^1/_2 a$	b	c	*Pnmm*	8×2=16	4
At a and halfway between n and 2_1	$0\,^1/_4\,^1/_4$	$\bar{1},\ T_x = {}^1/_2 a,\ T_{yz} = {}^1/_2(b+c)$	$^1/_2 a$	b	c	*Ammm*	16×2=32	8
At n	$^1/_4\,y\,^1/_4$	$\bar{1},\ T_{yz} = {}^1/_2(b+c)$	a	b	c	*Amam*	16	4
At n and halfway between a and 2_1	$^1/_4\,0\,^1/_4$	$\bar{1},\ T_{yz} = {}^1/_2(b+c),\ T_{xz} = {}^1/_2(a+c)$	a	b	c	*Fmmm*	32	8
At 2_1 and halfway between a and n	$0\,0\,^1/_4$	$\bar{1},\ T_z = {}^1/_2 c,\ T_{xy} = {}^1/_2(a+b)$	a	b	$^1/_2 c$	*Cmmm*	16×2=32	8
At intersection of n and a	$^1/_4\,^1/_4\,^1/_4$	$\bar{1},\ T_x = {}^1/_2 a,\ T_{yz} = {}^1/_2(b+c)$	$^1/_2 a$	b	c	*Ammm*	16×2=32	8
Halfway between a	$x\,0\,^1/_4$	$\bar{1},\ T_{xy} = {}^1/_2(a+b)$	a	b	c	*Ccmm*	16	4
Halfway between n	$0\,y\,^1/_4$	$\bar{1},\ T_{xyz} = {}^1/_2(a+b+c)$	a	b	c	*Imcm*	16	4

Note: a, b, and c are the unit-cell parameters of the crystal.

TABLE 2. Additional Symmetry Elements of Separation Functions Constructed for a Vector Grouping at Different Reference Atom Positions

Point group	Position of reference atom relative to symmetry elements							
	—	at				midway between		
		m	$m+T$ (a, b, c, n)	2	2_1	planes m or m + 2	axes 2 or 2_1	centers of symmetry
$\bar{1}$	No	—	—	—	—	—	—	T
2	1	—	—	*	$\bar{1}$, T	—	$\bar{1}$, T	—
m	$\bar{1}$	*	$\bar{1}$, T	—	—	$\bar{1}$, T	—	—
$2/m$	No	No	T	No	T	T	T	T
222	No	—	—	$\bar{1}$	T	—	T	—
$mm2$	$\bar{1}$	$\bar{1}$	$\bar{1}$, T	$\bar{1}$	$\bar{1}$, T	$\bar{1}$, T	$\bar{1}$, T	—
mmm	No	No	T	No	T	T	T	T

*The vector grouping reduces to a point.

in distinction to the groupings of other space groups of planar symmetry type in the orthorhombic system, contains an additional center of inversion only for a reference atom placement: a) equidistant from the two parallel planes d; b) at the intersection of two planes d. For reference atom positions on mirror planes or rotational symmetry axes, the separation functions, being of higher symmetry than the original space group, have the symmetry of the crystal or higher than it by $\bar{1}$.

For a known position of one reference atom, a direct separation of a unique structure configuration of low-symmetry crystals is possible from the Patterson distribution of centrosymmetric space groups, and also of orthorhombic space groups belonging to the point group 222, providing the reference atom does not fall in the special positions indicated in Table 2.

The authors thank Academician N. V. Belov, V. N. Blyushkin, V. M. Golyshev, and V. S. Fundamentskii for interest and discussion of results.

---

[1] M. J. Buerger, Vector Space and Its Application in Crystal Structure Investigation, Wiley, N. Y. (1959).

[2] E. Subramanian, Z. Kristallogr., 116, 182 (1961).

[3] V. M. Golyshev, V. I. Simonov, and N. V. Belov, Kristallografiya, 16, 703 (1971) [Sov. Phys. – Crystallogr., 16, 612 (1972)].

[4] I. I. Bannova, O. V. Frank-Kamenetskaya, N. V. Grigor'eva, N. V. Margolis, and I. V. Tselinskii, Proceedings of Third Seminar on Use of Structural Methods for Studying Materials in the Chemical Industry, Ministry of Chemical Industry, USSR, Moscow (1972), p. 61.

Structure of calcium–cobalt hexaborate $K_2Co\ [B_6O_7(OH)_6]_2 \cdot 4H_2O$

É. Ya. Silin', Ya. K. Ozol, and A. F. Ievin'sh

Institute of Inorganic Chemistry,
Academy of Sciences of the Latvian SSR

(Submitted April 29, 1972)
Kristallografiya, 18, 503-507 (May-June 1973)

The crystal structure of triclinic calcium–cobalt hexaborate is interpreted: $a = 10.86$, $b = 7.78$, $c = 7.42$ Å; $\alpha = 91°$, $\beta = 95°24'$, $\gamma = 108°26'$; $Z = 1$; space group $C_i^1 - P\bar{1}$. The structure was solved using a three-dimensional Fourier synthesis and was refined to $R = 0.125$, using the least squares method; the number of nonzero reflections was 1300. The calcium–cobalt hexaborate crystals consist of isolated boric anions $[B_6O_7(OH)_6]^{-2}$. The coordination polyhedron of the cobalt is an octahedron, and of the potassium, a distorted octahedron. The structure is stabilized by hydrogen bonds.

This particular borate was first produced by Keshan and Bimba[1] by crystallization from aqueous solution and was called a dodecaborate by them. On the basis of its structural features it would be more correct to call it a calcium–cobalt hexaborate.

The K_2Co hexaborate crystallizes in pink prisms in the triclinic system. The parameters of the unit cell (Co $K\alpha$, Weissenberg rotation) are as follows: $a = 10.86$, $b = 7.78$, $c = 7.42$ Å; $\alpha = 91°$, $\beta = 95°24'$, $\gamma = 108°26'$; $V = 591.4$ Å^3. There is one molecule of the hexaborate, density $d = 2.1$ g/cm^3 (ref. 1) in the cell. The space group $C_i^1 - P\bar{1}$ was selected[2] from the statistical values of F^2_{hk0}, F^2_{hki}, F^2_{h0l}.

The Weissenberg photographs hk0–hk6, h0l, and 0kl were obtained with Mo radiation. The intensities of the reflections were evaluated using a $2^{1/4}$ grey scale obtained from the same crystal. The number of nonzero hk0-hk6 reflections was ~1300. With the transition to structural factors the LP factors were taken into account and a Phillips correction was made for the shape of the spots. No corrections were made for absorption or excitation.

The structure was solved using the heavy-atom method. There is one Co atom in the unit cell at the center of symmetry (000). From projections of the electron density $\rho(x, y)$ and $\rho(x, z)$, the coordinates of the K and three O atoms surrounding the Co atom were found. The R factor calculated from the Co contribution was 0.42. Maxima corresponding to the K and 14 O atoms were clearly separated on the three-dimensional electron density distribution constructed with respect to $+F_{hkl}$. From the subsequent approximation of the three-dimensional electron density ($R_{hkl} = 0.31$), the coordinates of the remaining O and six B atoms were determined.

The divergence factor at this stage was $R = 0.22$. The projection of the structure along the z axis is shown in Fig. 1. The structure was refined by the least squares method in an isotropic approximation in the usual way and with the condition that $R = 0.125$. The coordinates and the individual thermal factors are shown in Table 1.

All the calculations were made on a BÉSM-3M computer using the "Roentgen" program of the Institute of Chemical Physics of the Academy of Sciences of the USSR.

The Co atom (000) is at the center of the octahedron on whose apices are two molecules of H_2O and four OH groups of boric anions joined at the center of symmetry. The cross section of the $O_{11}{}^*O_{14}{}^{**}O_{11}{}^{*\prime}O_{14}{}^{**\prime}$ octahedron (Fig. 1) is a square, within the limits of experimental error. The distance from Co to $O_{13}{}^*$ which plays a part in two hydrogen bonds is slightly shortened (Table 2).

TABLE 1. Atomic Coordinates, Individual Thermal Factors, and the Height of the Maxima of the Electron Densities

Atom	x/a	y/b	z/c	B, Å^2	ρ, el/A^3
Co	0	0	0	0.98	37.0
K	0.401	0.362	0.738	2.29	20.4
O_1	0.230	−0.134	0.223	1.11	8.1
O_2*	−0.036	−0.298	0.589	2.32	7.4
O_3	0.044	−0.359	0.320	1.50	8.0
O_4	0.167	−0.446	0.115	1.64	8.2
O_5*	0.334	−0.580	0.093	2.36	7.0
O_6	0.389	−0.265	0.134	1.28	7.8
O_7	0.460	0.044	0.238	2.04	7.8
O_8*	0.545	0.297	0.440	2.37	7.2
O_9	0.326	0.136	0.424	1.38	7.7
O_{10}	0.118	−0.065	0.467	1.08	8.0
O_{11}*	0.039	−0.249	0.027	1.12	8.3
O_{12}*	0.328	−0.050	−0.049	2.08	7.4
O_{13}*	0.145	0.117	0.210	0.88	8.0
O_{14}**	0.146	0.083	−0.182	1.62	8.0
O_{15}**	0.226	0.612	0.726	3.55	6.0
B_1	0.116	−0.296	0.171	0.86	4.7
B_2	0.354	−0.102	0.135	1.45	4.6
B_3	0.204	0.015	0.334	0.79	5.1
B_4	0.045	−0.238	0.454	1.66	4.2
B_5	0.295	−0.425	0.114	1.47	4.0
B_6	0.444	0.153	0.368	1.10	4.4

*O atom in OH group

**O atom in H_2O molecule

Every K atom is surrounded by six O atoms from the four boric anions (two O and four OH groups) and two water molecules (Table 2) forming a complex 12-sided figure with triangular faces. Five triangular faces meet at four of its vertices and four faces at four. The length of a side of the multifacetted figure varies within fairly wide limits (on average 3.71 Å). If, as is usually the case, we consider the six-fold $(BO)_3$ ring as the foundation of the borate radicals then there must be three of them in the K, Co hexaborate structure, joined by the common sides B–O (Fig. 2a) into the single $[B_6O_7(OH)_6]^{2-}$ anion (Fig. 2b). This particular configuration of the boric anion, but in the $[B_6O_9(OH)_2]^{2-}_{\infty}$ form, was found by Clark[3] in the laminar tanelite structure. The interatomic distances and bond angles in the anion, shown in Table 2, are in good agreement with those in the tanelite structure except for the B_1 tetrahedron where some distances have been slightly shortened. The insignificant distortion of the B_1 tetrahedron can clearly be explained by the tendency of $O_{11}{}^{*\prime}$ to form a hydrogen bond with O_4 (Fig. 1). The interatomic distances of the three-fold coordinated O_1–B are 1.48, 1.50, and 1.51 Å (average 1.50 Å) and are slightly greater than the average value for the B–O bond length of 1.47 Å. The respective distances in the tanelite structure are 1.48, 1.51, and 1.54 Å (average 1.51 Å). The

TABLE 2. Interatomic Distances (Å) and Valence Angles (deg)

$Co-O_{11}^{*}$	2.12	$O_{11}^{*}-O_{13}^{*}$	-2.96	$O_{11}^{*}-Co-O_{13}^{*}$	90	$K-O_{6}'$	2.72	$K-O_{8}^{*}$	2.95
$Co-O_{13}^{*}$	2.08	$O_{11}^{*}-O_{14}^{**}$	-3.01	$O_{11}^{*}-Co-O_{14}^{**}$	90	$K-O_{9}$	2.78	$K-O_{5}^{*'}$	2.98
$Co-O_{14}^{**}$	2.13	$O_{13}^{*'}-O_{14}^{**}$	-3.04	$O_{13}^{*}-Co-O_{14}^{**}$	88	$K-O_{5}^{*}$	2,87	$K-O_{14}^{**}$	3.05
		$O_{13}^{*}-O_{14}^{**}$	$-2,92$			$K-O_{8}^{*'}$	2.90	$K-O_{15}^{**'}$	3.12
								Average	2,92

B_1-tetrahedron		B_2-tetrahedron		B_3-tetrahedron	
B_1-O_1	1.48	B_2-O_1	1.50	B_3-O_1	1.51
B_1-O_3	1.42	B_2-O_6	1.43	B_3-O_9	1.45
B_1-O_4	1.51	B_2-O_7	1.48	B_3-O_{10}	1.44
$B_1-O_{11}^{*}$	1.42	$B_2-O_{12}^{*}$	1.46	$B_3-O_{13}^{*}$	1.47
Average	1.46	Average	1.47	Average	1.47
O_1-O_3	2.40	O_1-O_6	2.39	O_1-O_9	2.43
O_1-O_4	2.41	O_1-O_7	2.43	O_1-O_{10}	2.42
$O_1-O_{11}^{*}$	2.33	$O_1-O_{12}^{*}$	2.38	$O_1-O_{13}^{*}$	2.41
O_4-O_3	2.34	O_6-O_7	2.37	O_9-O_{10}	2,36
$O_4-O_{11}^{*}$	2.43	$O_6-O_{12}^{*}$	2.39	$O_9-O_{13}^{*}$	2.37
$O_3-O_{11}^{*}$	2.35	$O_7-O_{12}^{*}$	2.42	$O_{10}-O_{13}^{*}$	2,38
Average	2.38	Average	2.40	Average	2,40
$O_1-B_1-O_3$	112	$O_1-B_2-O_6$	109	$O_1-B_3-O_9$	110
$O_1-B_1-O_4$	107	$O_1-B_2-O_7$	109	$O_1-B_3-O_{10}$	110
$O_1-B_1-O_{11}^{*}$	107	$O_1-B_2-O_{12}^{*}$	107	$O_1-B_3-O_{13}^{*}$	108
$O_4-B_1-O_3$	106	$O_6-B_2-O_7$	109	$O_9-B_3-O_{10}$	109
$O_4-B_1-O_{11}^{*}$	112	$O_6-B_2-O_{12}^{*}$	111	$O_9-B_3-O_{13}^{*}$	109
$O_3-B_1-O_{11}^{*}$	112	$O_7-B_2-O_{12}^{*}$	111	$O_{10}-B_3-O_{13}^{*}$	110
Average	109.3	Average	109.3	Average	109.3

B_4-triangle		B_5-triangle		B_6-triangle					
						$O_{2}^{*}-O_3$	2.35	$O_{5}^{*}-O_4$	2.37
$B_4-O_{2}^{*}$	1.38	$B_5-O_{5}^{*}$	1.38	$B_6-O_{8}^{*}$	1.36	$O_{2}^{*}-O_{10}$	2.31	$O_{5}^{*}-O_6$	2.35
B_4-O_3	1.36	B_5-O_4	1.36	B_6-O_7	1.34	O_3-O_{10}	2.38	O_4-O_6	2.37
B_4-O_{10}	1.33	B_5-O_6	1.36	B_6-O_9	1.35	Average	2.35	Average	2.36
Average	1.36	Average	1.37	Average	1.35				

$O_{8}^{*}-O_7$	2.34	$O_{2}^{*}-B_4-O_3$	118	$O_{5}^{*}-B_5-O_4$	121	$O_{8}^{*}-B_6-O_7$	120
$O_{8}^{*}-O_9$	2.30	$O_{2}^{*}-B_4-O_{10}$	117	$O_{5}^{*}-B_5-O_6$	118	$O_{8}^{*}-B_6-O_9$	117
O_7-O_9	2.35	$O_3-B_4-O_{10}$	125	$O_4-B_5-O_6$	121	$O_7-B_6-O_9$	122
Average	2.33	Total	360	Total	360	Total	359

A dash indicates atoms whose coordinates were obtained from the original centers of inversion. The error in determining the interatomic distances was as follows: Co–O, 0.01; O–O, 0.02; and B–O, 0.03 Å.

TABLE 3. Characteristic Values of Boric Rings.

B_1-B_2	2,59	B_1-B_3	2,53	B_2-B_3	2.64	$B_1-O_1-B_2$	121
B_2-B_5	2,42	B_1-B_4	2.39	B_2-B_6	2.49	$B_1-O_4-B_5$	124
B_1-B_5	2.54	B_3-B_4	2.42	B_3-B_6	2.46	$B_2-O_6-B_5$	120
						$B_1-O_1-B_3$	116
				Average	2.50	$B_1-O_3-B_4$	119

$B_3-O_{10}-B_4$	122	I	$O_1-O_4-O_6$	$B_1+0.10$	II	$O_1-O_3-O_{10}$	$B_1+0.41$
$B_2-O_1-B_3$	122		$O_1-O_4-O_6$	$B_2+0.49$		$O_1-O_3-O_{10}$	$B_3+0.30$
$B_2-O_7-B_6$	125		$O_1-O_4-O_6$	$B_5-0.16$		$O_1-O_3-O_{10}$	$B_4-0.12$
$B_3-O_9-B_6$	123		$O_1-O_4-O_6$	$O_{5}^{*}-0.49$		$O_1-O_3-O_{10}$	$O_{2}^{*}-0.38$
Average	121.3		$O_1-O_4-O_6$	$O_{12}^{*}+1.95$		$O_1-O_3-O_{10}$	$O_{11}^{*}+1.81$

			Angles between planes			Equations for planes
III	$O_1-O_7-O_9$	$B_2+0.17$			I	$0.713x-1.193y+3.031z=0$
	$O_1-O_7-O_9$	$B_3+0.30$	I–II	146	II	$2.258x-1.266y+1.395z=0$
	$O_1-O_7-O_9$	$B_6-0.05$	I–III	157	III	$1.359x-1.920y+1.929z=0$
	$O_1-O_7-O_9$	$O_{8}^{*}-0.05$	II–III	155		
	$O_1-O_7-O_9$	$O_{13}^{*}+1.71$				

TABLE 4. Shortest Distances between O Atoms Not Belonging to the Same Anion

$O_{12}^{*}-O_{14}^{**}$	2.63	$O_{13}^{*}-O_{5}^{*}$	2.81
$O_{13}^{*}-O_{2}^{*'}$	2.63	$O_{12}^{*}-O_{15}^{**}$	2.93
$O_3-O_{2}^{*'}$	2.74	$O_3-O_{15}^{**}$	2.95
$O_{8}^{*}-O_{15}^{**}$	2.77	$O_4-O_{15}^{**'}$	3 03
$O_{10}-O_{14}^{**}$	2.78	O_6-O_{6}'	3.11
$O_{11}^{*'}-O_4$	2.80	$O_4-O_{2}^{*'}$	3.12
$O_7-O_{12}^{*'}$	2.80		

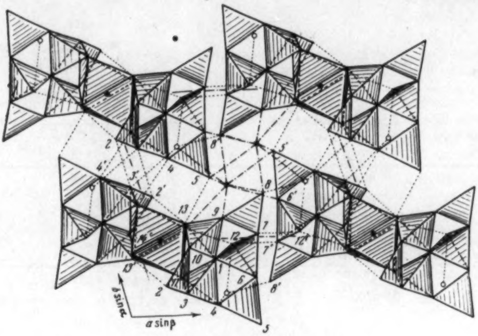

Fig. 2. Boric anion $[B_8O_7(OH)_6]^{2-}$.

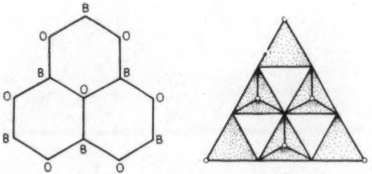

a b

Fig. 1. Projection of the K, Co hexaborate structure along the y axis.

three angles between B, O_1 and B (116, 121, and 122°) total 359° which places the O atom, within the limits of error, in the plane of the $B_1B_2B_3$ triangle. All the three-fold coordinated B atoms lie in the plane of the $BO_2(OH)$ triangle.

The values of the valence angles B−O−B and the B−B interatomic distances which characterize boric rings were calculated (Table 3). The minimum value for the angle $B_1-O_1-B_2$ between the tetrahedrally surrounded B atoms was 116°; the OH groups of these tetrahedra enter the coordination sphere of Co. The minimum B−B distances (2.39; 2.42 Å) are also slightly less than those found by Clark (2.46; 2.47 Å). In the laminar tenelite structure none of the six-membered boric rings lies in the same plane. Table 4 shows the distances of the atoms from the plane which was drawn through three O atoms of the boric ring in the K, Co hexaborate structure. The three-fold coordinated B_4, B_5, and B_6 atoms diverge least from the plane (maximum −0.16 Å); the four-fold coordinated B atoms diverge more significantly on the opposite side (maximum +0.49 Å). The angle between the I−I plane is 146°; between the I−III, 157°; and between the II−III, 155° (the corresponding angles in tanelite are 147, 152, and 153°).

The K, Co hexaborate structure consists of $Co[B_8O_7 \cdot (OH)_6]_2 \cdot 2H_2O$ islands and K ions. The water molecules O_{15}** lie in the tetrahedral cavities. In accordance with the clearly expressed isometricity of the external form of the crystal, their relative hardness, and the absence of cleavage, we can assume that the hydrogen bonds are distributed equally in all directions. Table 4 shows the shortest distances between the O atoms not belonging to the same coordination polyhedron. In the independent part of the unit cell 10 protons and 10 of the shortest distances were taken for the H bond. Each boric anion is joined directly by five H bonds to five neighboring anions; and the bonds with five anions are effected via the H_2O molecules.

---

[1] A. Keshan and S. Vimba, Izv. Akad. Nauk LatvSSR, 3, 115 (1954).

[2] E. R. Howells, D. C. Phillips, and D. Rogers, Acta Crystallogr., 3, 210 (1950).

[3] I. R. Clark, Amer. Mineralogist, 49, 1549 (1964).

Crystal structure of langbanite

V. G. Rau and E. N. Kurkutova
Vladimir Pedagogical Institute

(Submitted April 14, 1972; resubmitted June 12, 1972)
Kristallografiya, 18, 508-513 (May-June 1973)

A complete x-ray study has been made for langbanite; the structure has been used to revise the chemical formula, and a crystallochemical description of the mineral is given.

The mineral langbanite (longbanite), a manganese silicate, was discovered in 1888 by Flink and belongs to the obscure braunite group; morphological studies have led to it being assigned as hexagonal.[1-3] Varieties A, B, and C have been mentioned in the literature, which differ in crystal habit and chemical composition. The first x-ray study of langbanite[4] gave the parameters of the hexagonal cell as a = 11.54, c = 11.09 Å; in 1910 Flink[5] gave the best morphological ratio of the axes as c'/a' = 1.4407; if we take two thirds of c'/a', we get 0.9604, which agrees well with the x-ray data.[4] It has been concluded[4] that langbanite belongs to diffraction class 6 /mmm. There is no piezoelectric effect, and the systematic absences in the oscillation pattern gave the space group as[4,6,7] D_{6h}^1 = P6/mmm.

Densities and chemical analyses have been reported[2,3,6] for varieties A and B, which differ substantially. Most analyses indicate that langbanite contains not only Si and O but also, Mn, Fe, Sb, Ca, and Mg. Two chemical analyses show water. The SiO_2 contents vary from 8.75 to 12.82%, while the Fe_2O_3 contents vary from 4.75 to 13.98%, etc. Attempts have been made to derive the formula from the chemical analyses, making various assumptions about the valences and possible substitutions for the cations. For instance, it is said[3] that the mineral consists of the components $mSb_2O_3 + nFe_2O_3 + pR^{2+}R^{4+}$, where R^{2+} = Mn, Ca, Mg; R^{4+} = Mn, Si. It was assumed[4] that the possible formula is $(Mn_{42}^{2+}Ca_3)(Sb^{5+}Fe_{14}^{3+}Mg_3Mn_4^{3+}) \cdot (Si_{16}Mn_{11}^{7+})O_{159}(OH)_3$; Z = 1. Strunz[6,7] considered in more detail or more carefully the question of the chemical formula, and he used calculations to derive $(Mn^{2+}, Sb^{3+}, Ca)_4(Mn^{4+}, Fe^{3+}, Mg)_3[SiO_4/O_8]$; Z = 6; in simplified form we have $Mn_4^{2+}Mn_3^{4+}[SiO_4/O_8]$; Z = 6, with partial replacement of $2Mn^{2+}$ by Sb^{3+} + Ca and $2Mn^{4+}$ by Fe^{3+} + Mg. Strunz based his deductions on the assumption that the space group is P6/mmm.

We made our measurements on an opaque black specimen 0.3 × 0.1 × 0.1 mm from the Mineralogical Museum at the Leningrad Institute. The symmetry of the Laue pattern allowed the mineral to belong to the hexagonal system; the repeat distance along the principal direction was deduced from a rotation pattern, and later a 0kl Weissenberg pattern, which gave c = 11.12 ± 0.03 Å, which agrees satisfactorily with earlier values.[4,7] In the (0001) plane there were two identical repeat distances forming an angle $\gamma = 60°$: $a = b = 6.77 \pm 0.02$ Å, which are less by factors of $\sqrt{3}$ than the values given in refs. 4 and 7. The unit cell with these parameters then contains two formula units of composition $Mn_4^{2+}Mn_3^{4+}[SiO_4/O_8]$.

We used hk0−hk2, 0kl−4kl Weissenberg patterns with Mo radiation to conclude that the mineral is not hexagonal but trigonal (diffraction class $\bar{3}$m); there were no systematic absences, and the symmetry of the goniometer patterns indicated that the diffraction symbol is $\bar{3}$mP − − 1, with the three possible space groups P$\bar{3}$m1, P321, and P3m1. The statistics of the[8] F_{0kl}^2 and the disposition of the Patterson peaks on P(uvw) indicated that the space group is P$\bar{3}$m1.

The intensities were estimated on a $\sqrt[4]{2}$ scale with multiple exposures for the strong reflection; in converting to the structure factors we incorporated the Lorentz and polarization factors, but no absorption correction. In all we recorded 2170 nonzero (about 360 independent) reflections with $\sin\theta/\lambda \leq 1.2$ Å^{-1}.

The structure was established from the three-dimensional Patterson function and combinations with sequential three-dimensional electron-density syntheses. The P(uvw) pattern was interpreted by vector shift;[9] the positions for the heavy cations were at first interpreted as Mn atoms. The coordinates of the five independent manganese atoms were used in a ρ(xyz) electron-density synthesis; the R_{hkl} factor at this stage was 0.33. Several successive syntheses terminated with localization of the five basis O atoms and the Si atom, which give us a model for the structure.

The cations were identified as to type by comparing the peak heights on the ρ(xyz) distribution and also via crystallochemical regularities. The single-fold positions with coordinates (000) and (00$^1/_2$) are occupied respectively by Mn_4^{2+}(Ca) and $Mn^{4+}(Fe^{3+}, Sb^{5+})$; the two threefold positions at the centers of symmetry ($^1/_2$00) and ($^1/_2$0$^1/_2$) are populated by Mn_1^{2+} and Mn_2^{4+}, while the one sixfold position in the m plane is filled by Mn_3^{2+} atoms. The threefold axes ($^1/_3$ $^1/_3$z) and ($^2/_3$ $^2/_3$z) contain the Si atoms, while the 22 O atoms lie in m planes. The R_{hkl} factor was reduced to 0.24 when all the atoms identified in the synthesis were included.

The x-ray evidence indicates that the chemical formula may be written in the expanded form $Mn_9^{2+}Mn_3^{4+} \cdot Mn^{2+}(Ca)Mn^{4+}(Fe^{3+}, Sb^{5+})Si_2O_{22}$; Z = 1 or the simplified form $Mn_5^{2+}Mn_2^{4+}[SiO_4/O_7]$; Z = 2 with the substitutions $Mn^{2+} \rightarrow (Mn^{2+}, Ca)$, $Mn^{4+} \rightarrow (Fe^{3+}, Sb^{5+})$. It was impossible to establish more closely the type and de-

TABLE 1. Coordinates and Individual Temperature Factors for Basis Atoms

Atom and position multiplicity		x/a ($\sigma_{x/a}$)	y/b ($\sigma_{y/b}$)	z/c ($\sigma_{z/c}$)	B_j
Mn_1	(3)	0.500	0	0	0.36
Mn_2	(3)	0.500	0	0.500	0.89
Mn_3	(6)	0.173±0.001	0.173±0.001	0.232±0.001	1.22
Mn_4	(1)	0	0	0	0.21
(Fe, Sb)	(1)	0	0	0.500	0.53
Si	(2)	0.333	0.333	0.741±0.001	0.64
O_1	(2)	0	0	0.199±0.002	1.56
O_2	(2)	0.333	0.333	0.592±0.002	1.59
O_3	(6)	0.460±0.002	0.080±0.002	0.796±0.002	1.95
O_4	(6)	0.147±0.002	0.147±0.002	0.405±0.002	1.48
O_5	(6)	0.197±0.002	0.197±0.002	0.072±0.002	1.90

Note: Localization errors: for ε_{Mn}, ±0.0012; for ε_{Si}, ±0.0025; for ε_O, ±0.0054 Å.

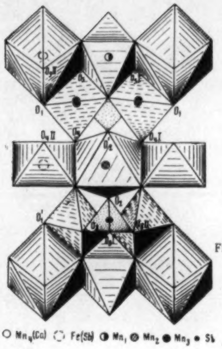

Fig. 1. Projection of the structure on the xz plane.

gree of substitution of the cations without an exact chemical analysis of the specimen; the total number of cations in the chemical formula is as in Strunz's formula,[6,7] but the number of oxygen atoms is smaller by 1. Also, the mode of substitution was somewhat different from that previously assumed.

The structure model was refined by least squares in the isotropic approximation; R_{hkl} taking all nonzero reflections was reduced to 0.17. Table 1 gives the coordinates and individual isotropic temperature factors for the basis atoms.

Figures 1 and 2 show the main features of the structure. The Mn atoms are of four crystallographic types: Mn_1^{4+} and Mn_2^{2+} at centers of symmetry with octahedral coordination, Mn_3^{2+} in m planes within a trigonal bipyramid, and Mn_4^{2+} within a figure having eight vertices. This trigonal bipyramid has previously been observed in the structure[10] of $Na_2Mn_2Si_2O_7$; the (Fe^{3+}, Sb^{5+}) polyhedron is of the type of the (Mn, Fe) octahedron found in the structure[11] of $(Mn, Fe)_2O_3$; Mn_4^{2+}(Ca) lies within a group of eight oxygen atoms with a large range of Mn_4^{2+}–O bond lengths, and six of these are close to 2.46 Å, while the other two are close to 2.22 Å; the Mn_4^{2+}(Ca) figure with eight vertices is a distorted rhombohedron with broken edges (scalenohedron).

The structure may be described as layered, with layers unbounded in two directions perpendicular to the c axis (Figs. 1 and 2). The most dense layer at height $z = {}^1/_2$ is formed by Fe and Mn_2 octahedra, which fill as closely as possible the entire two-dimensional space without gaps (Fig. 2a). Each Fe polyhedron is surrounded by six Mn_2 polyhedra (spinel pattern). The unit cell contains one (Fe, Sb) octahedron and three Mn_2 octahedra. The layer at height z = 0 consists of polyhedra of two types: elongated Mn_1 octahedra linked by vertices, which form a type of wall, whose hexagonal loops contain Mn_4^{2+}(Ca) polyhedra (Fig. 2b). Between the layers of this type lie hexagonal grids of Mn_3 bipyramids and Si tetrahedra (Fig. 2c). The unit cell is divided up by two grids mutually related by inversion, in which the vertices of the Si tetrahedra face towards the middle layer (Fig. 1). The layer at height z = 0 is more firmly linked to these grids, since the bipyramids are joined to it not only by vertices but also by edges.

Table 2 gives the interatomic differences; the six Fe–O distances in the octahedron are equal to 2.03 Å, while

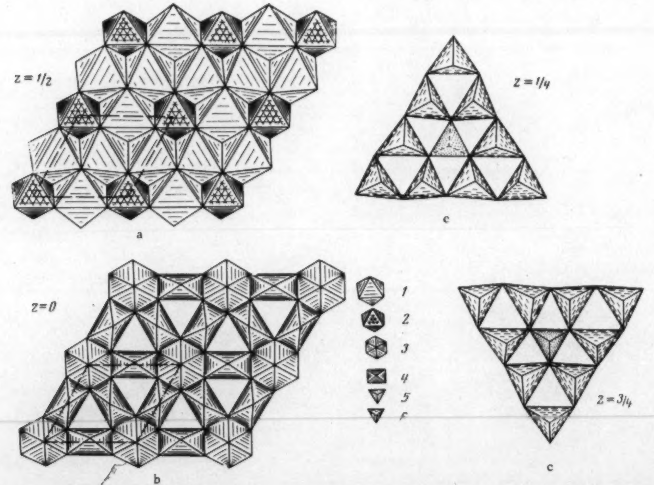

Fig. 2. Layers and grids: a) layer with the Fe octahedron; b) layer with Mn_4 polyhedron; c) grid for $[Mn_3SiO_{11}]_n^{2n-}$; 1) Mn_2^{2+} octahedron; 2) $Fe^{3+}(Sb^{5+})$ octahedron; 3) Mn(Ca) polyhedron; 4) Mn_1^{4+} octahedron; 5) Si tetrahedron; 6) Mn_3^{2+} trigonal bipyramid.

TABLE 2. Interatomic Distances in Å

Mn_1^{4+} octahedron	
Mn_1-O_3' (×2)	2.15
Mn_1-O_5 (×4)	1.99
Mean	2.05
$O_3'-O_5$	2.60
$O_3'-O_5'$	3.49
$O_3'-O_5'$ I	3.49
$O_3'-O_5$ I	2.60
O_5-O_5 I	2.78
O_5-O_5' I	2.85
Mean	2.97

(Fe^{3+}, Sb) octahedron	
$Fe-O_4$ (×6)	2.03
O_4-O_4 II (×3)	3.00
O_4-O_4' I (×3)	2.74
Mean	2.87

Mn_2^{2+} octahedron	
Mn_2-O_3 (×2)	2.25
Mn_2-O_4 (×4)	2.34
Mean	3.01
O_3-O_4	3.01
O_3-O_4'	3.02
O_4-O_4 I	3.77
O_4-O_4' I	2.74
Mean	3.21

Si-tetrahedron	
$Si-O_2$	1.66
$Si-O_3$ (×3)	1.61
Mean	1.62
O_2-O_3 (×3)	2.72
O_3-O_3 I	2.58
O_3-O_3 II	2.58
O_3I $-O_3$ II	2.58
Mean	2.65

Mn_3^{2+} trigonal bipyramid	
Mn_3-O_1	2.07
Mn_3-O_3' (×2)	2.23
Mn_3-O_4	1.96
Mn_3-O_5	1.92
Mean	2.04
O_1-O_4	2.88
O_1-O_5	2.71
O_1-O_3' I	3.43
O_1-O_3'	3.43
$O_3'-O_3'$ I	4.19
$O_3'-O_5$	2.61
O_4-O_3'	3.21
Mean	3.21

Mn_4^{2+} polyhedron	
Mn_4-O_1 (×2)	2.22
Mn_4-O_5 (×6)	2.46
Mean	2.43
O_5-O_5' I(×6)	2.85
O_1-O_5'	3.83
O_1-O_5' I	3.83
O_1-O_5' II	3.83
O_1-O_5	2.71
O_1-O_5 I	2.71
O_1-O_5 II	2.71

Errors (for O−O = ± 0.02)

Mn_1-O	±0.01	Mn_4-O	±0.01
Mn_2-O	±0.01	(Fe, Sb)−O	±0.01
Mn_3-O	±0.01₅	Si−O	±0.01

Subscripts I and II denote atoms derived from the basis atoms via the three-fold axis, while primes denote atoms related by the center of symmetry.

the O−O distances are of two values: 3.00 and 2.74 Å. The Mn−O distances for the Mn_1^{4+} and Mn_2^{2+} octahedra are correspondingly in the limits 1.99-2.15 Å with O−O of 2.60-3.49 Å and 2.25-2.34 Å with O−O of 2.74-3.77 Å. The Mn_3^{2+} trigonal bipyramid has Mn − O distances of 1.92-2.23 Å with O−O of 2.61-4.19 Å, while the Si−O bond lengths in the tetrahedron are 1.61-1.66 Å. The interatomic distances agree satisfactorily with analogous values for other compounds.

We are indebted to Academician N. V. Belov for valuable advice and discussions, and to our colleagues in the X-Ray Laboratories at the Institute of Crystallography and Gor'kii University for assistance in the computations.

---

[1] G. Flink, Z. Kristallogr., 13, 1 (1888).

[2] Hintze, Handbuch der Mineralogie, Vol. 2, Leipzig (1897), p. 445.

[3] C. Doelter, Handbuch der Mineralchemie, Vol. 3, Dresden−Leipzig (1918), p. 785.

[4] O. Kraus and F. Mussgnug, Zbl. Mineral., 12 (1942).

[5] G. Flink, Arkiv Kemi, Mineralogi Och Geol., 3, 1 (1910).

[6] H. Strunz, Zbl. Mineral., 133 (1942).

[7] H. Strunz, Mineralogische Tabeln, [Russian translation], Gosgortekhizdat, Moscow (1962).

[8] E. R. Howells, D. C. Phillips, and D. Rogers, Acta Crystallogr., 3, 210 (1950).

[9] M. Buerger, Crystal Structure and Vector Space [Russian translation], Izd. IL, Moscow−Leningrad (1961).

[10] L. P. Astakhova and V. I. Siminov, Kristallografiya, 14, 3 (1969) [Sov. Phys.−Crystallogr., 14, 1 (1969)].

[11] L. Pauling and M. D. Shappell, Z. Kristallogr., 75, 128 (1930).

Crystal structure of U_2MoO_8

V. N. Serezhkin, L. M. Kovba, and V. K. Trunov

M. V. Lomonosov Moscow State University

(Submitted May 12, 1972; resubmitted June 21, 1972)
Kristallografiya, 18, 514-517 (May-June 1973)

X-ray structural analysis of single crystals has been used to determine the structure of the binary oxide U_2MoO_8 (275 independent reflections, KFOR camera, Mo Kα radiation, R = 0.077), which crystallizes in a rhombic system having a = 6.734, b = 23.24, c = 4.115 Å, Z = 4, and space group $P2_12_12$. The structure contains $(UO_2)O_4$ and $(MoO_2)O_4$ octahedra interconnected at their vertices in the xy0 plane, all the $(MoO_2)O_4$ octahedra being connected in pairs by a common edge. Infinite −U−O−U−O− and −Mo−O−Mo−O− chains formed by the octahedra being connected at their vertices are located parallel to the z axis. The similarity between the ways in which the O atoms are coordinated about the U atoms in both the structure of U_2MoO_8 and the structure of α-U_3O_8 enables the structure of U_2MoO_8 (and of the isostructural U_2WO_8) to be considered as consisting of blocks having the α-U_3O_8 type of structure.

In studies of the systems[1] $UO_2-UO_3-MoO_3$ and[2] $UO_2-UO_3-WO_3$ the isostructural compounds U_2MoO_8 and U_2WO_8 were discovered. According to the data in those studies, both compounds crystallize in a rhombic system having a space group of $P22_12$. The unit-cell parameters are: a = 6.696 ± 0.003, b = 23.300 ± 0.008, and c = 4.120 ± 0.002 Å for[1] U_2MoO_8 and[2] a = 6.658 ± 0.006, b = 23.32 ± 0.04, c = 4.093 ± 0.001 Å for U_2WO_8. It was suggested that the structures of these binary oxides are derivatives of the α-U_3O_8 structure.[1]

In this paper the results are presented of an x-ray structural analysis of U_2MoO_8. Single crystals of U_2MoO_8 were prepared by the method described previously.[1] The x-ray pattern of U_2MoO_8, obtained by photographing with a Guinier monochromator camera (Cu Kα), was indexed (Table 1) taking account of the single-crystal data (RKOP, RKU cameras using CuKα, KFOR camera using MoKα). In spite of the good agreement between the interplanar distances and the line intensities we obtained[1] for U_2MoO_8, the results of indexing the x-ray pattern differed somewhat. The refined unit-cell parameters that we found for U_2MoO_8 were a = 6.734 ± 0.006, b = 23.24 ± 0.01, c = 4.115 ± 0.003 Å. The x-ray pattern of U_2WO_8, indexed similarly from the data in ref. 2, enabled the unit-cell parameters of U_2WO_8 to be determined: a = 6.711 ± 0.006, b = 23.28 ± 0.01, c = 4.091 ± 0.003 Å. For both compounds Z = 4, according to our data, and the space group is $P2_12_12$. The U_2MoO_8 and U_2WO_8 specimens which we studied contained U_4O_9 as an impurity. On the scans of the layer lines hk0−hk3, 0k*l*−2k*l*, and h0*l* the intensities of 275 independent nonzero reflections were estimated from the blackening using a $\sqrt[4]{2}$ scale. No correction for absorption was made. All the calculations were conducted on an M-20 computer and a BÉSM-4 computer, using the program of Tarnopol'skii and Andrianov.[3]

Analysis of the three-dimensional Patterson function showed that all its high maxima lie in the section P(uv0). For the space group $P2_12_12$ such a distribution of the maxima is possible if the z coordinates of all the metal

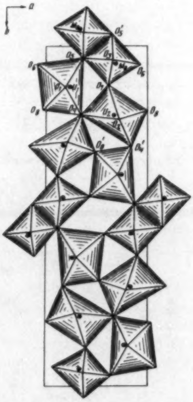

Fig. 1. Projection of the structure of U_2MoO_8 on the xy0 plane.

TABLE 1. Indexing of the X-Ray Pattern of U_2MoO_8 Powder

I	$10^4/d^2_{ex}$	$10^4/d^2_{calc}$	*hkl*	*I*	$10^4/d^2_{ex}$	$10^4/d^2_{calc}$	*hkl*
4	74	74	020	1	1404	1406	180
1	237	239	110	48	1477	1473, 1478	201, 161
7	294	295, 296	120, 040	5	1493	1491	211
3	516	517	140	2	1551	1547, 1549	221, 260
82	590	591	001	4	1720	1719, 1721	171, 190
5	664	665, 667	021, 060	1	1776	1769, 1776	241, 081
9	684	684	150	1	1856	1852	0.10.0
1	758	757	031	3	1998	1996	181
1	831	830	111	5	2060	2059, 2067	320, 280
100	884	882, 885, 887, 887	200, 121, 160, 041	20	2361	2362	002
				20	2446	2443, 2448	0.10.1 350
28	900	901	210	9	2667	2663, 2667	1.10.1. 0.12.0
1	958	956	220	1	2823	2825	052
1	1052	1049, 1064	230, 051	14	2890	2887, 2892	1.12.0, 370
2	1109	1107	141	7	3027	3029	062
8	1128	1128	170	7	3050	3046, 3052	152, 1.11.1
2	1181	1178, 1185	240, 080	4	3124	3123	2.11.0
5	1273	1274	151				

TABLE 2. Coordinates and Individual Thermal Corrections of the Basic Atoms in the Structure

Atom	x/a (σ_x)	y/b (σ_y)	z/c	B (σ_B)
U_1	0.20046(45)	0.12207(14)	0.0	1.62(0.05)
U_2	0.66956(48)	0.21512(13)	0.0	1.48(0.05)
Mo	0.6753(14)	0.04638(33)	0.0	2.49(0.16)
O_1	0 1958(85)	0.1227(25)	0.5	4.66(1.19)
O_2	0.7118(93)	0 2166(23)	0.5	3.05(1.26)
O_3	0.6452(92)	0.0409(23)	0.5	2.56(1.30)
O_4	0.3269(84)	0.2053(23)	0.0	2.56(1.05)
O_5	0.3707(73)	0.0335(18)	0.0	2.84(0.93)
O_6	0.9207(75)	0.0538(20)	0.0	3.19(0.90)
O_7	0.6057(87)	0.1159(24)	0.0	2.92(1.20)
O_8	0.9756(58)	0.1893(15)	0.0	—0.16(0.74)

TABLE 3. Basic Interatomic Distances (Å) in the Structure of U_2MoO_8

U_1-O_1	2.06	U_2-O_2	2.08	$Mo-O_3$	2.07
U_1-O_1'	2.06	U_2-O_2'	2.08	$Mo-O_3'$	2.07
U_1-O_4	2.11	U_2-O_4'	2.13	$Mo-O_5$	2.07
U_1-O_5	2.36	U_2-O_4	2.32	$Mo-O_5'$	1.88
U_1-O_6	2.46	U_2-O_7	2.35	$Mo-O_6$	1.66
U_1-O_7	2.73	U_2-O_8	2.15	$Mo-O_7$	1.68
U_1-O_8	2.18	U_2-O_8'	2 58	O_7-O_6	2.57
O_5-O_6	3.07	$O_4'-O_8$	2.65	O_6-O_5'	2.82
O_6-O_8	3.17	O_6-O_7	3.02	$O_5'-O_5$	2.34
O_8-O_4	2.40	O_7-O_4	2.80	O_5-O_7	2.48
		O_4-O_8'	2.65		
		$O_8'-O_4'$	2.40		

atoms are equal to zero. This simplified appreciably the problem of determining the x and y coordinates of the metal atoms.[4] The coordinates of the O atoms were determined from a difference three-dimensional synthesis of the electron density. Subsequent least-squares refinement of the structure, taking account of the individual thermal corrections in an isotropic approximation, enabled the divergence factor to be lowered to R = 0.077. The values for the atomic scattering functions of the neutral atoms and the corrections for anomalous dispersion were taken from ref. 5.

Table 2 shows the final coordinates and the individual thermal corrections for the basis atoms in the structure. Figure 1 shows the projection of the structure of U_2MoO_8 on the xy0 plane, while the principal interatomic distances are given in Table 3. The notations for all the atoms correspond with each other in Fig. 1 and Tables 2 and 3. The highly distorted octahedra are coordination polyhedra of U and Mo atoms. Infinite $-U-O-U-O-$ and $-Mo-O-Mo-O-$ chains formed by $(UO_2)O_4$ and $(M_0O_2)O_4$ octahedra joined at their vertices lie parallel to the c axis. In the xy0 plane the U octahedra are joined with each other and with the Mo octahedra only by their vertices, whereas the Mo octahedra are joined in pairs by a common edge. The Mo−Mo distance of 3.20 Å is in good agreement with data in the literature for such a joining mode of Mo octahedra.[6]

The connection between the structures of α-U_3O_8 and U_2MoO_8 requires special consideration. As is known, α-U_3O_8 also crystallizes in a rhombic system[7] (a = 6.717, b = 11.966, c = 4.148 Å). A comparison of the unit-cell parameters of α-U_3O_8 and U_2MoO_8 shows that the b constant is doubled for U_2MoO_8, whereas the magnitudes of the a and c constants are very close. This enables us to consider the cell for U_2MoO_8 as consisting of two α-U_3O_8 cells in which one third of the U atoms are replaced by Mo atoms. In the structures of α-U_3O_8 and U_2MoO_8, $-M-O-M-O-$ chains lie parallel to the c axis and in the xy0 plane the distribution of the O atoms around the U atoms

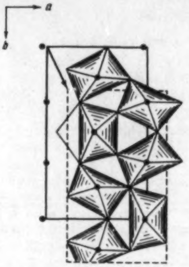

Fig. 2. Projection of the structure of α-U_3O_8 on the xy0 plane. Above each U atom (black dots) is situated an O atom having a coordinate $z = {}^1/_2$. The dashed line delineates the α-U_3O_8 structural block formed when the origin is displaced (as indicated by the arrow).

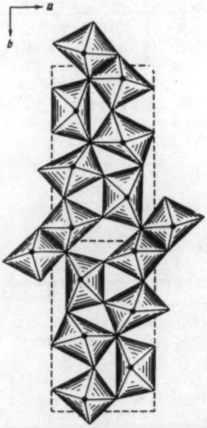

Fig. 3. Projection of the Mo_3O_8 structure consisting of two structural α-U_3O_8 blocks joined by a two-fold rotation axis ${}^1/_2$; ${}^1/_2$; z.

is very similar for the two compounds. In both cases the U atoms exhibit a tendency towards an increase in their coordination number to 7, owing to the seventh O atom, which is situated at a rather large distance. In the structure of α-U_3O_8 these O atoms are at distances of 2.71 and 2.58 Å from the crystallographically independent U atoms, whereas in the structure of U_2MoO_8 these distances are 2.73 and 2.58 Å, respectively.

It should be noted that in the structure of U_2MoO_8 the pseudohexagonal layers of metal atoms do not extend into the xy0 plane infinitely, as in the structure of α-U_3O_8, but only within the bounds of α-U_3O_8-type blocks. Each unit cell in U_2MoO_8 consists of two such blocks, which are formed by displacement of the origin in α-U_3O_8 and connected with each other by a two-fold rotation axis in ${}^1/_2$ ${}^1/_2$ z, as shown in Figs. 2 and 3.

In spite of the similarity between the structures of α-U_3O_8 and U_2MoO_8 the U−O distances in the equatorial plane differ markedly for the two compounds. For α-U_3O_8 these distances lie within the range 2.07-2.23 Å. As may be seen from Table 3 and Fig. 1, the increased U−O distances in the structure of U_2MoO_8 (compared with α-U_3O_8) belong to the O_5, O_6, and O_7 atoms, which participate in the formation of U−O−Mo bonds between adjacent $(UO_2)O_4$ and $(MoO_2)O_4$ octahedra. The replacement of the U atoms in the structure of α-U_3O_8 by Mo atoms leads to the replacement of relatively equivalent U − O − U bonds in the xy0 plane by U − O − Mo bonds with reduced Mo−O distances, which leads to a corresponding increase in the U−O distance. It must be noted that the average U−O distances in the xy0 plane do not differ greatly in either structure, being 2.20 and 2.17 Å respectively for α-U_3O_8 and 2.28 and 2.24 Å for U_2MoO_8.

Thus, it can be concluded from the x-ray structural analytical data for U_2MoO_8 that the isostructural binary oxides U_2MoO_8 and U_2WO_8 are made up of α-U_3O_8 structural blocks, in which one third of the U atoms are replaced by Mo or W atoms.

---

[1] V. K. Trunov, O. N. Pozanova, and L. M. Kovba, Zh. Neorgan. Khim., 10, 2576 (1965).

[2] O. N. Rozanova, V. K. Trunov, and L. M. Kovba, Izv. Akad. Nauk SSSR, Neorgan. Mat., 2, 319 (1966).

[3] B. L. Tarnopol'skii and V. I. Andrianov, Zh. Strukt. Khim., 4, 433 (1963).

[4] M. A. Porai-Koshits, A Practical Course in X-Ray Structural Analysis, Vol. 2 [in Russian], Izd. MGU (1960), p. 457.

[5] D. T. Cromer and J. T. Waber, Acta Crystallogr., 18, 104 (1965).

[6] L. Kihlborg, Arkiv kemi, 21, 471 (1963).

[7] V. O. Loopstra, Acta Crystallogr., 17, 651 (1964).

Crystal and molecular structures of the 1:2 complex of 1-methyl-3,3-dimethyl-2-(para-n-methyl-n-β-chloroethylstyryl)indole and 7,7,8,8-tetracyanoquinodimethane, $(C_{22}H_{26}N_2Cl)^+(C_{12}H_4N_4)\,(C_{12}H_4N_4)$

R. P. Shibaeva, L. P. Rozenberg, and L. O. Atovmyan

Branch of the Institute for Chemical Physics, Academy of Sciences of the USSR

(Submitted May 10, 1972)
Kristallografiya, 18, 518-524 (May-June 1973)

The structure of the molecular complex $(C_{22}H_{26}N_2Cl)^+(C_{12}H_4N_4)^-(C_{12}H_4N_4)$ (a = 17.97 Å, b = 8.23 Å, c = 26.67 Å, β = 92°13', space group $P2_1/n$, Z = 4) has been determined by the direct method and refined by the least squares method to R = 0.15. The presence of a tetrad of tetracyanoquinodimethane molecules is characteristic of the structure. The dye molecule is approximately planar, except for the chloroethyl and methyl groups.

Thanks to their unusual electrical and magnetic properties, molecular complexes based on 7,7,8,8-tetracyanoquinodimethane (TCQM) have recently attracted the attention of investigators. Analysis of the crystal structures of complexes of such types now allows conclusions to be drawn as to how such structural features are responsible for the presence of the good electrical conductivity of the complexes.[1]

We have carried out x-ray structure studies on a series of simple and complex salts of TCQM with various organic dyes. The results1) of an x-ray structure analysis of the 1 : 2 complex of 1-methyl-3,3-dimethyl-2-(para-N-methyl-N-β-chloroethylstyryl)indole and TCQM, $(C_{22}H_{26}N_2Cl)^+TCQM^-TCQM^0$, compound (1),

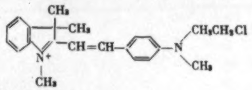

are reported in this work.

EXPERIMENTAL RESULTS

The basic crystallographic characteristics of compound (1) are: a = 17.97 ± 0.02 Å, b = 8.23 ± 0.03 Å, c = 26.67 ± 0.04 Å, β = 92°13' ± 03', V = 3941 Å³ space group $P2_1/n$. Formula $C_{46}H_{34}N_{10}Cl$, F(000) = 1588, M = 762.3, d_{calc} = 1.29 g/cm³, $\mu(CuK\alpha) = 12.4\ cm^{-1}$, Z = 4.

The unit-cell parameters were refined on a DRON-1 diffractometer. The intensities of ~3500 independent nonzero reflections from the h0l−h7l and 0kl−7kl layer lines were obtained on films, multiple exposures being taken on an equiinclination Weissenberg goniometer (Cu radiation) and estimated visually. Corrections for spot size were introduced in accordance with ref. 3.

DETERMINATION AND REFINEMENT OF THE STRUCTURE

The structure of the molecular complex, compound (1), was solved by the direct method.[4,5] Statistical means and distribution of the normalized structure amplitudes in comparison with the corresponding theoretical values for centrosymmetric and noncentrosymmetric space groups[6,7] are given in Table 1. From the total of 5150 reflections (allowance being made for reflections not observed, to which the value $F^2 = \frac{1}{2}F_{min}^2$ was assigned), 492 reflections were chosen with $|E| \geq 1.6$, and 1667 ternary products with $|TRP| \geq 14.8$ were compiled. In this case, the predicted values of estimates in accordance with refs. 4 and 5 amounted to R = 0.948 and ν = 109. For the structure of compound (1), the parameter is $\sigma = 0.0755$.

In the first test, six key reflections in addition to the three which determined the origin of the coordinates were chosen, and $2^6 = 64$ variants of the signs were checked off. However, a better system of signs was not successfully isolated in this case. Then, $12(3k + 9a_i)$ key reflections, a list of which is given in Table 2, were taken, and 512 variants of the signs (P_{min} = 0.97 and δ = 0.75) were obtained, from which was clearly isolated one variant with the estimates n = 390, R = 0.94, and ν = 121. A subsequent variant had the estimates n = 355, R = 0.91, and ν = 172.

The evaluation of signs was repeated with another $9a_i$ key reflections, which are given in Table 3. In this case, a single system was not isolated upon the calculations of signs with p_{min} = 0.97, but 13 close variants with R ~ 0.90 and ν ~ 180 were obtained. However, upon recalculation of signs with p_{min} = 0.99, one variant, the signs of which agreed with the signs of the best variant calculated earlier, was clearly isolated from these 13. In all, 452 signs were determined (390 + 12 key reflections + 50 determined for a small decrease in the criterion δ).

After refinement of the structure, the signs of 14 of these 452 reflections were changed. All 57 of the nonhydrogen atoms were localized from the E synthesis constructed from the 452 reflections. The F synthesis, analy-

TABLE 1

Quantity	Experimental values	$\bar{1}$	1	Quantity	Experimental values	$\bar{1}$	1
$\langle E^2\rangle$	1.040	1.000	1.000	$\|E\| > 1.4$	0.148	0.162	0.141
$\langle \|E^2-1\|\rangle$	1.073	0.968	0.736	$\|E\| > 1.6$	0.103	0.110	0.078
$\langle \|E\|\rangle$	0.790	0.798	0.886	$\|E\| > 1.8$	0.074	0.072	0.039
$\|E\| > 1.0$	0.275	0.320	0.368	$\|E\| > 2.0$	0.053	0.050	0.018
$\|E\| > 1.2$	0.200	0.230	0.237	$\|E\| > 3.0$	0.001	0.003	0.0001

TABLE 2

$\|E\|$	hkl	q*	$\|E\|$	hkl	q*
5.14	$\bar{3}17$	111	3.54	3.5.12	51
4.93	$\bar{3}16$	122	3.52	$\bar{3}$.0.7	40
3.22	14.1.10	25	3.41	2.4.4	50
7.10	$\bar{4}$.0.6	138	3.38	$\bar{3}$.1.5	44
3.59	7.5.6	54	3.20	$\bar{4}$.0.4	45
3.55	$\bar{7}$.1.12	54	3.08	10.6.5	38

---

*q denotes the number of ternary products into which a given reflection enters.

TABLE 3

$\|E\|$	hkl	q
3.33	475	34
3.22	$\bar{1}72$	38
3.19	345	32
3.08	10.6.5	38
3.14	$\bar{1}$.5.16	40
3.07	3.7.5	30
3.02	$\bar{7}$.1.11	31
2.81	3.1.8	31
2.76	3.2.17	36

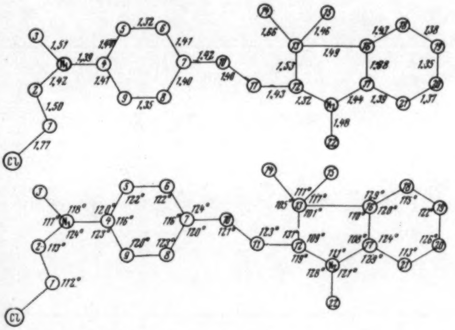

Fig. 1. Bond lengths (Å) and valence angles (deg) in the dye molecule.

sis of which showed that it did not differ in principle from the E synthesis, was also constructed. Calculation of the interatomic distances made it possible to identify the atoms and form three molecules: one molecule of the dye and two molecules of TCQM. The divergence factor R = 0.35 corresponded to this model of the structure. The electron density synthesis, constructed from the entire set of reflections, gave starting coordinates of the atoms for refinement of the structure by the least-squares method. Refinement was completed in two stages: an initial stage without calculation of a weighting function, and then with a weighting function of the type[8] $W_{hkl} = 1/\{1 + [(k|F| - b)/a]^2\}$, where k = 0.5, a = 12, and b = 7.5. The structure was refined[2)] to R = 0.15.

DESCRIPTION OF THE STRUCTURE

The bond lengths and valence angles in the dye molecule are shown in Fig. 1. Accuracy in the determination of these values amounts to $\Delta r = \pm 0.03$–0.04 Å and $\Delta\alpha = \pm 1.5$–$2°$.

If the chloroethyl and methyl groups are not taken into consideration, then the dye molecule is approximately flat. The angle between plane A, determined by atoms C(4), ..., C(10), and N(1), and plane B, passing through the atoms C(11), C(12), C(16), ..., C(21), and N(2) is ~4°. The methyl groups are located in a plane which is approximately perpendicular to plane B. The configuration of the bonds about the N(1) atom is nearly planar, and atom N(1) stands out from the plane of the three carbon atoms by a distance of 0.05 Å. The plane of the chloroethyl group makes an angle of 103° with the plane of atoms C(2), C(3), C(4), and N(1), the latter forming an angle of ~4° with plane A. The bond lengths and valence angles in the TCQM molecules are given in Figs. 2a and 2b. Unfortunately, the low precision in determination of the bond lengths did not allow us to identify TCQM⁻ and TCQM⁰, as was so brilliantly done, say, in the Cs_2TCQM_3 structure.[10]

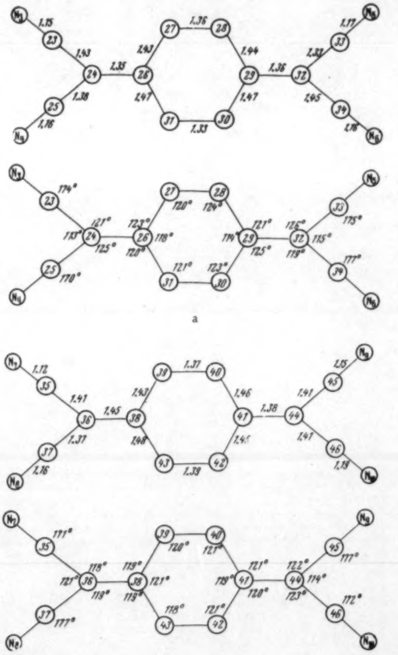

a

b

Fig. 2. Bond lengths (Å) and valence angles (deg) in the dye molecule of TCQM (1) (a) and TCQM (2) (b).

The projection of the structure of compound (1) on the (010) plane is shown in Fig. 3. The presence of a tetrad of TCQM molecules packed in a zig-zag manner along the a direction so that the two TCQM molecules 2 and 2" of the neighboring tetrad do not overlap appears

TABLE 4

Atom	x/a	y/b	z/c	B_j, Å^2	ρ, electrons/Å^3
Cl	0.133	−0.011	0.179	10.2	11.6
C(1)	0.132	−0.215	0.158	8.7	3.6
C(2)	0.204	−0.264	0.136	6.2	4.6
C(3)	0.268	−0.405	0.209	8.3	3.8
C(4)	0.316	−0.140	0.178	6.1	5.0
C(5)	0.315	−0.003	0.144	7.0	4.5
C(6)	0.363	0.117	0.149	7.2	4.6
C(7)	0.417	0.124	0.189	6.5	4.8
C(8)	0.418	−0.008	0.222	7.3	4.9
C(9)	0.372	−0.137	0.217	7.5	4.7
C(10)	0.467	0.257	0.197	7.2	4.7
C(11)	0.465	0.391	0.165	7.2	4.5
C(12)	0.512	0.529	0.172	6.6	4.8
C(13)	0.577	0.559	0.210	6.9	4.8
C(14)	0.539	0.570	0.265	7.2	4.2
C(15)	0.635	0.435	0.210	7.0	4.4
C(16)	0.600	0.727	0.196	5.8	5.1
C(17)	0.559	0.779	0.154	6.5	5.0
C(18)	0.658	0.827	0.217	7.6	4.3
C(19)	0.668	0.974	0.193	8.2	4.2
C(20)	0.624	1.020	1.154	8.2	4.4
C(21)	0.566	0.932	0.133	8.4	4.3
C(22)	0.451	0.674	0.098	8.1	4.2
N(1)	0.265	−0.265	0.172	8.0	6.1
N(2)	0.507	0.652	0.141	7.0	5.9
C(23)	0.984	0.108	0.095	6.9	4.7
C(24)	0.996	0.281	0.092	5.8	5.5
C(25)	1.051	0.336	0.125	7.0	4.8
C(26)	0.951	0.375	0.063	5.5	5.6
C(27)	0.892	0.311	0.031	6.1	4.9
C(28)	0.848	0.413	0.003	6.2	5.2
C(29)	0.859	0.586	−0.001	5.5	5.4
C(30)	0.924	0.645	0.030	6.2	4.9
C(31)	0.965	0.551	0.060	6.0	5.2
C(32)	0.814	0.680	−0.030	6.4	5.1
C(33)	0.757	0.628	−0.059	6.0	4.8
C(34)	0.831	0.852	−0.034	7.2	4.8
N(3)	0.969	−0.028	0.095	9.4	4.6
N(4)	1.102	0.389	0.146	8.0	5.0
N(5)	0.705	0.575	−0.082	8.5	4.8
N(6)	0.842	0.990	−0.039	8.7	5.0
C(35)	0.809	0.344	0.143	6.6	5.0
C(36)	0.828	0.510	0.137	6.5	5.0
C(37)	0.883	0.581	0.166	6.9	4.7
C(38)	0.777	0.612	0.107	6.0	5.3
C(39)	0.793	0.781	0.102	6.0	5.1
C(40)	0.748	0.876	0.072	6.3	4.8
C(41)	0.688	0.804	0.041	6.0	5.3
C(42)	0.672	0.633	0.046	6.3	5.0
C(43)	0.716	0.534	0.077	6.3	4.8
C(44)	0.640	0.901	0.012	7.1	5.1
C(45)	0.579	0.837	−0.017	8.1	4.1
C(46)	0.653	1.068	0.004	8.6	4.0
N(7)	0.804	0.209	0.146	8.1	5.1
N(8)	0.930	0.635	0.192	8.7	4.7
N(9)	0.528	0.786	−0.038	9.6	4.3
N(10)	0.670	1.206	0.001	10.7	3.9

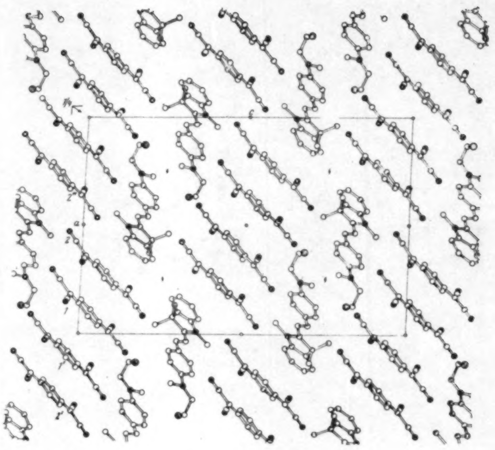

Fig. 3. Projection of the structure on the (010) plane.

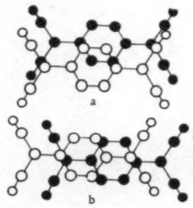

Fig. 4. Overlapping of TCQM molecules 1-1'(a), and of TCQM 1-2 and 1'-2'(b).

to be characteristic. Inside each tetrad, two modes of overlap of TCQM molecules are realized (Fig. 4) with interplanar distances of 3.40 Å for the 1-1' molecules and 3.18 Å for the 1-2 and 1'-2' molecules. Thus, while the tetrads consisting of TCQM molecules and occurring at the same distance from each other and with the same mode of overlapping form an infinite stack along the b axis in the $[CH_3As(C_6H_5)_3]^+TCQM_2^-$ structure,[11] in this structure the tetrads are presented as in an isolated structural unit. The planes of all TCQM molecules are parallel to each other and approximately perpendicular to the *ac* plane (angle of 99°). In addition, they are nearly parallel to the $(\bar{4}06)$ plane and make an angle of ~10° with it. This was revealed by the fact that the $\bar{4}06$ reflection is the strongest, with $F(\bar{4}06) = 524$ (i.e., ~1/3 of the total scattering power).

We have no data on the conductivity of this ion-radical salt, but on the basis of its crystal structure it should belong to the group of poorly conducting TCQM compounds.

The authors thank V. I. Andrianov for valuable advice during the determination of the structure and G. M. Mikhailova for help in setting up the work.

---

1) See ref. 2 for a brief communication on the structure of this complex.

2) It should be noted that the refinement process consumed quite a long time, since the "Roentgen" program[9] allows the recording of the coordinates of not more than 53 atoms in a coordinate field in the case of the least-squares method. V. I. Andrianov has found it possible to refine the structure with a large number of atoms by use of this program, but this procedure is associated with still more difficulties and inconveniences.

[1] R. P. Shibaeva and L. O. Atovmyan, Zh. Strukt. Khim., 13, 546 (1972).

[2] R. P. Shibaeva, L. O. Atovmyan, and L. P. Rozenberg, Tetrahedron Lett., 36, 3303 (1971).

[3] D. C. Phillips, Acta Crystallogr., 7, 746 (1954); 9, 819 (1956).

[4] V. I. Andrianov, B. L. Tarnopol'skii, and R. P. Shibaeva, Zh. Strukt. Khim., 10, 116 (1969).

[5] V. I. Andrianov, Dissertation, Inst. Khim., Fiz. Akad. Nauk SSSR, Chernogolovka (1969).

[6] I. L. Karle, K. S. Dragonette, and S. A. Brenner, Acta Crystallogr., 19, 713 (1965).

[7] F. Hanic, Acta Crystallogr., 21, 332 (1966).

[8] O. S. Mills and J. S. Rollett, Computing Methods and the Phase Problem in X-Ray Crystal Analysis, Glasgow (1961), p. 116.

[9] B. L. Tarnopol'skii and V. I. Andrianov, Zh. Strukt. Khim., 4, 434 (1963).

[10] C. J. Fritchie and P. Arthur, Jr., Acta Crystallogr., 21, 139 (1966).

[11] A. T. McPhail, G. M. Semenyuk (Semeniuk), and D. B. Chesnut, J. Chem. Soc., A13, 2174 (1971).

Crystal and molecular structure of phenyl phenoxtinium iodide

A. I. Gusev and Yu. T. Struchkov

Institute of Heteroorganic Compounds, Academy of Sciences of the USSR

(Submitted April 16, 1972; resubmitted June 12, 1972)
Kristallografiya, 18, 525-529 (May-June 1973)

A structural study of phenyl phenoxtinium iodide $[C_{18}H_{14}SO]^+I^-$ (a = 12.18, b = 16.58, c = 7.84 Å, γ = 90.0°, N = 4, space group $P2_1/n$) is presented. The structure is solved by the heavy-atom method and refined by the method of least squares to R = 10.6% by reference to 800 independent reflections. The phenyl substituent is connected to an S atom having a pyramidal configuration with a mean CSC valence angle of 104°, i.e., the compound is a sulfine. The organic cation is turned around the S... O line in such a way that the dihedral angle between the two plane fragments is 38°. The intracyclic C−S bond equals 1.78 Å, the S−C (phenyl) bond 1.83 Å. The cation and anion in the crystal form an ionic pair with an I^- ... S^+ distance of 3.85 Å.

Phenyl phenoxtinium iodide $[C_{18}H_{14}SO]^+I^-$ (I) was obtained[1)] when studying the cyclization of diazotized o-amino-o'-phenoxydiphenyl sulfide; the formation of an oxonium salt in which the phenyl substituent was connected to the oxygen atom had been expected. However, subsequent application of the ordinary method of synthesizing aromatic sulfonium salts yielded a salt completely identical in chemical behavior and spectral properties, which suggested that compound I had a sulfine structure.

In order to establish the structure of phenyl phenoxtinium iodide the latter was studied by x-ray diffraction.

EXPERIMENT

The compound I crystallizes in the monoclinic system. The lattice constants were determined from a calibrated hk0 Weissenberg photograph and a rotation photograph taken around the c axis: $a = 12.18 \pm 0.02$, $b = 16.58 \pm 0.03$, $c = 7.84 \pm 0.01$ Å, $\gamma = 90.0 \pm 0.2°$; V = 1583 Å^3; $d_{exp} = 1.66$, $d_{calc} = 1.71$ g/cm^3 for N = 4; space group $P2_1/n$.

Using an equiinclination Weissenberg x-ray goniometer with unfiltered radiation, we obtained developments of the hk0−hk4 layer lines (800 independent nonzero reflections). The intensities were estimated visually by reference to a photometric density scale and converted to structure factors using the Lp coefficients. No correction was made for absorption (the crystal dimensions were 0.2 × 0.3 × 0.5 mm; elongation along the c axis).

From a three-dimensional Patterson function we found the coordinates of the I atom. An electron-density series based on these (R = 34%) gave the S atom, on allowing for which the R factor fell to 26%. The next approximation of the electron-density distribution located the remaining atoms in the molecule (except for the hydrogen atoms), the specification of which reduced R to 17.5%. The structure was refined by the method of least squares, using certain obvious geometrical conditions in the initial stages (Waser[1]). At the final stages these conditions were dispensed with, and the Cruickshank weights[2] were taken into account. The final R factor was 10.6%; the corresponding coordinates and temperature factors are presented in Table 1.

All the calculations were based on programs composed by B. L. Tarnopol'skii, V. I. Andrianov, and Z. Sh. Safina (Branch of the Institute of Chemical Physics, Academy of Sciences of the USSR).

STRUCTURE OF THE COMPOUND

The crystals of compound I are made up of discrete $C_{18}H_{14}SO^+$ and I^- ions. The bond lengths and valence angles in the organic cation are shown in Fig. 1. The phenyl substituent C(1) ... C(6) is connected to the S atom, i.e., the compound has a sulfine rather than an oxonium structure. The S atom is characterized by a pyramidal configuration with a mean valence angle of 104°, very similar to the value of 102° found in another sulfonium compound[3] (fulfine), 1-acetonyl -1-thionyl-5-thiacyclooctane (II), in which the S atom is associated with three C atoms in a state of sp^3 hybridization.

The lengths of the intracyclic bonds S−C(7) and S−C(18) coincide with the normal length of the ordinary S−C(sp^3) bond,[4] 1.78 Å. The length of the extracyclic S−C(1) bond is increased by 0.05 Å; however, this difference is comparable with the accuracy of the determination (± 0.04 Å). The mean length of the S−C(sp^3) bond attached to the sulfonium atom in II is 1.82 Å, which practically coincides with the standard value[5] of 1.81 Å. The slight difference between the lengths of the C−S bonds in I and II is in conformity with the difference in the hybridization of the C atoms connected to the S atom.

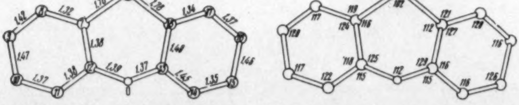

Fig. 1. Geometry of the organic cation. The probable errors in the S−C and O−C distances are 0.04 Å, in the remaining bonds 0.05-0.07 Å. The probable errors in the valence angles lie between 1.8 and 4.0°.

TABLE 1. Coordinates and Individual Isotropic Temperature Factors of the Basis Atoms of the Structure*

Atoms	x/a	y/b	z/c	B, Å²	Atoms	x/a	y/b	z/c	B, Å²
I	0.7624(2)	0.1085(2)	0.1777(4)	4.3(1)	C(9)	0.1599(36)	0.0622(27)	0.1658(62)	6.1(8)
S	0.4569(8)	0.1558(6)	0.2555(12)	4.1(2)	C(10)	0.0365(33)	0.1274(25)	0.2203(54)	4.7(8)
O	0.2847(19)	0.2778(14)	0.3491(36)	4.0(4)	C(11)	0.1355(33)	0.1957(25)	0.2815(54)	4.8(8)
C(1)	0.4805(29)	0.1370(21)	0.4831(52)	4.0(7)	C(12)	0.2478(25)	0.2053(19)	0.2770(44)	2.4(6)
C(2)	0.5713(31)	0.1824(23)	0.5364(62)	4.8(8)	C(13)	0.3783(31)	0.3047(24)	0.2710(49)	3.9(7)
C(3)	0.6015(32)	0.1659(23)	0.7200(58)	4.7(8)	C(14)	0.3828(32)	0.3913(24)	0.2447(49)	4.1(8)
C(4)	0.5417(28)	0.1099(21)	0.8146(57)	4.0(6)	C(15)	0.4752(34)	0.4201(25)	0.1701(66)	5.6(8)
C(5)	0.4515(40)	0.0634(29)	0.7451(63)	6.2(1)	C(16)	0.5692(35)	0.3719(26)	0.1137(54)	5.4(9)
C(6)	0.4174(33)	0.0843(25)	0.5752(60)	5.1(8)	C(17)	0.5611(32)	0.2908(24)	0.1426(52)	4.7(7)
C(7)	0.3127(30)	0.1408(23)	0.2384(48)	3.6(7)	C(18)	0.4703(33)	0.2610(24)	0.2165(49)	4.0(7)
C(8)	0.2759(29)	0.0730(22)	0.1721(55)	4.1(7)					

---

*The corresponding standard deviations are given in brackets.

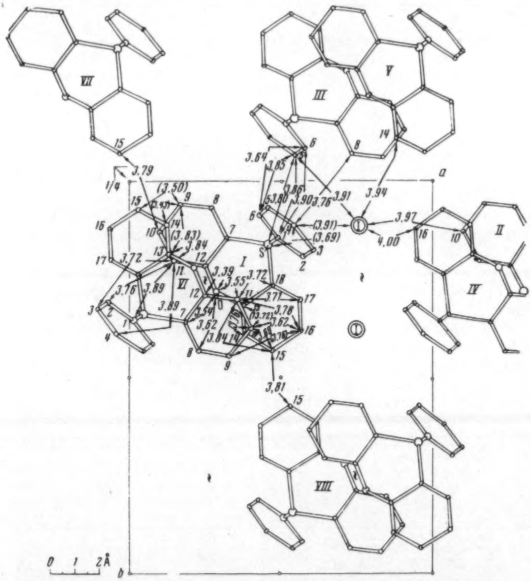

Fig. 2. Packing in the crystal, projected on the (001) plane. Molecule I lies at xyz (its atoms correspond to Table 1); I') $xy(z+1)$; II) $(x+1)yz$; III) $(1-x)\bar{y}(1-z)$; IV) $(^3/_2-x)(^1/_2-y)(^1/_2+z)$; V) $(^1/_2+x)(y-{}^1/_2)(^1/_2-z)$; VI) $(^1/_2-x)(^1/_2-y)(^1/_2+z)$; VI') $(^1/_2-x)(^1/_2-y)(-^1/_2+z)$; VII) $(-^1/_2+x)(-^1/_2+y)(^1/_2-z)$; VIII) $(1-x)(1-y)\bar{z}$. The brackets indicate the distances from the molecules derived by a translation 001 (these molecules are indicated by the primed numbers).

Thus in compound I the configuration of the S atom and the lengths of the C–S bonds are very similar to those found in II, in which there is no conjugation. It would appear that in compound I also the S atom does not appreciably participate in conjugation; this is confirmed by the nonplanar configuration of the cation, which is folded around the S...O line, the dihedral angle between the plane fragments C(13) ... C(18), S, O, and C(7) ... C(12), S, O being[2] 38°.

A very similar configuration was obtained for the phenothiazine[6] and N-methylphenothiazine[7] molecules, in which the bend angles respectively equalled 27 and 29° and the C–S bond lengths (1.770 and 1.82 Å) were similar to those found in I, the valence angles of the S atom (99.6 and 97°) being slightly smaller than in I (this may have been due to the greater steric hindrances in the latter owing to the presence of three substituents attached to the S atom). The nonplanar central heterocycle C(7), C(12), O, C(13), C(18), S has the conformation of a bath, the phenyl substituent C(1) ... C(6) in I occupying a quasi-equatorial position (the unshared pair of electrons of the S atom occupy a quasiaxial position), which is sterically more favorable.

TABLE 2. Coefficients of the Equations Ax + By + Cz + D = 0 Representing the Plane Fragments of the Molecule

Planes	Atoms	Coefficients of the equations of the planes *				Mean deviations of the atoms composing the plane, A	Deviations of the other atoms, Å	
		A	*B*	*C*	*D*		S	O
I	C(1)...C(6)	7.44	—12,05	—2.45	0.72	0.025	0.014	—
II	C(7)...C(12)	0.02	—6.03	7,30	0,84	0.031	0.093	0.036
III	C(13)...C(18)	5,13	1,91	7,05	4.44	0.003	0,006	0.017
IV	C(7), C(12), C(13), C(18)	2.70	—2,55	7.55	2.26	0.025	0,504	0.433
V	C(7)...C(12), S, O	—0.19	—6.09	7.29	0,80	0.032	—	—
VI	C(13)...C(18), S, O	5.16	1,93	7.04	4.46	0.004	—	—
VII	C(7), C(12), S, O	—0.59	—6.11	7.28	0.65	0.029	—	—
VIII	C(13), C(18), S, O	5.21	1.99	7.02	4.49	0.005	—	—

*The dihedral angles between the planes are: II/III 37.1°; V/VI 38.2°; VII/VIII 40.0°.

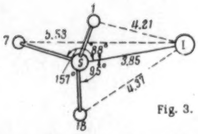

Fig. 3. The ionic pair $S^+ ... I^-$.

In the molecule[8] of 2,5-diphenyl-1,4-dithiine-1-oxide there is a similar six-membered cycle in bath conformation, but containing two S atoms. There is very little participation in conjugation in the case of one of the S atoms (which stands out of the plane of the four sp^2-hybridized C atoms by a distance of 0.64 Å), whereas the second S atom, which stands out from this plane by a distance of only 0.28 Å, exhibits substantial conjugation. In the molecule of compound I the S atom stands out 0.50 Å from the corresponding plane IV (Table 2) and evidently plays little part in conjugation.

The configuration of the bonds of the O atom is also unfavorable as regards participation in conjugation (this atom stands out 0.43 Å from plane IV). The C(12)OC(13) valence angle of 112° is even smaller[9] than in 1,4-dioxane, while the mean C–O bond length of 1.38 Å (allowing for the difference in the hybridization of the C atoms) is comparable with the value of 1.423 Å found in dioxane. At the same time, in[10] 1,2,3,7,8,9-hexachlordibenzo-p-dioxane, in which the central oxygen-containing cycle (and also the whole molecule) is approximately plane, the mean values of the COC valence angle and the C–O bond length are 117.5° and 1.36 Å.

We notice a regular distortion of the valence angles at the atoms C(7), C(12), C(18), and C(13) in the central heterocycle: The angles at C(7) and C(18), the atoms which lie closest to the large S atom, are reduced, while those at C(12) and C(13), which lie closest to the smaller O atom, are increased by comparison with the ideal value of 120°. These distortions of the valence angles in the heterocycle are compensated by a corresponding change in the two other valence angles, and as a result of this the atoms C(7), C(12), C(18), and C(13) retain their plane configuration, as indicated by the negligible (Table 2) departure of the S and O atoms from the planes of the rings C(7) ... C(12) and C(13) ... C(18) [an exception is the departure of the S atom from the plane of the cycle C(7) ... C(12)]. At the same time, in the structure of phenothiazine and N-methylphenothiazine the S atom stands out 0.18 Å from the planes of the two benzene rings.

PACKING IN THE CRYSTAL

The packing in the crystal and the short intermolecular distances are illustrated in Fig. 2. It is a characteristic feature that the I^- anion lies at the short distance of 3.85 Å from the S atom of only one cation, i.e., $S^+ ... I^-$ ionic pairs are formed in the structure. This distance is 0.3 Å shorter than the sum of the van der Waals distances and 1.43 Å greater than the sum of the covalent radii.[5] This fragment of the structure is shown in more detail in Fig. 3.

A similar (but apparently rather stronger) $Te^+ ... I^-$ interaction was observed in the $[Me_2Te]^+[MeTeI_4]^-$ structure.[11]

The authors wish to thank Academician A. N. Nesmeyanov for proposing the subject and for interest in the work, and also T. P. Tolstaya for discussing the results.

---

1) The compound was synthesized by Academician A. N. Nesmeyanov and T. P. Tolstaya in the organometallic laboratory of the Chemical Faculty of Moscow State University.

2) The equations of the plane fragments, the deviations of the atoms, and the dihedral angles between the planes are given in Table 2.

[1] J. Waser, Acta Crystallogr., 16, 1091 (1963).
[2] D. W. J. Cruickshank, D. E. Pilling, A. Bujosa, F. M. Lovell, and M. R. Truter, Computing Methods and the Phase Problem in X-Ray Crystal Analysis, Vol. 6, Pergamon Press, Oxford (1961).
[3] S. M. Johnson, C. A. Maier, and I. C. Paul, J. Chem. Soc., B, 1603 (1970).
[4] C. J. Fritchie, J. Chem. Soc., A, 1328 (1969).
[5] L. Pauling, The Nature of the Chemical Bond, Cornell Univ. Press, Ithaca, New York (1959).
[6] J. D. Bell, J. F. Blount, O. V. Briscoe, and H. C. Freeman, Chem. Commun., 1656 (1968).
[7] N. I. Nakayama, Bull. Chem. Soc. Japan, 44, 2847 (1971).
[8] G. Bandoli, C. Panattoni, D. A. Clemente, E. Tondello, A. Dandoni, and A. Mangini, J. Chem. Soc., B, 1407 (1971).
[9] M. Davis and O. Hassel, Acta. Chem. Scand., 17, 1181 (1963).
[10] J. S. Cantrell, N. C. Webb, and A. J. Mabis, Acta Crystallogr., B25, 150 (1969).
[11] F. Einstein, J. Trotter, and C. Williston, J. Chem. Soc., A, 2018 (1969).

Crystal structure of 1,6-$[Coen_2Cl_2]Cl \cdot 3SC(NH_2)_2$

Yu. A. Simonov, L. I. Landa, N. N. Proskina, T. I. Malinovskii, and A. V. Ablov

Institute of Applied Physics, Academy of Sciences of the Moldavian SSR

(Submitted May 4, 1972)
Kristallografiya, 18, 530–534 (May–June 1973)

An x-ray structural analysis is made of an addition compound of thiourea with 1,6-$[Coen_2Cl_2]Cl$, with the composition 1,6-$[Coen_2Cl_2]Cl \cdot 3SC(NH_2)_2$. The crystals are triclinic with a = 6.23, b = 9.23, c = 10.55 Å, α = 105.3°, β = 92.3°, γ = 109.5°, space group P1. The structure was solved by means of three-dimensional experimental data and refined by the method of least squares to R = 0.13. The authors suggest that the compound can be regarded as a channel adduct of the polycations $(1,6\text{-}[Coen_2Cl_2]^+)_\infty$ in the distorted structure of hexagonal thiourea.

The contradictory data[1–4] on the structure and even the composition of the addition product of thiourea with the chloride of 1,6-dichlorobis-(ethylenediamine) cobalt (III) have prompted us to make a complete x-ray structural investigation of the crystals 1,6-$[Coen_2Cl_2]Cl \cdot 3SC(NH_2)_2$. Preliminary data on the structure of this compound are given in ref. 5.

Crystals of $Coen_2Cl_3 \cdot 3SC(NH_2)_2$ were separated from a mixture of concentrated aqueous solutions of 1,6-$[Coen_2 \cdot Cl_2]Cl$ and thiourea in the molecular ratio 1:3. On slow evaporation, dark green crystals separated out with well formed faces.

By x-ray diffraction we found that the crystals are triclinic with the following unit-cell parameters: a = 6.23 ± 0.05, b = 9.23 ± 0.07, c = 10.55 ± 0.07 Å; α = 105.3 ± 0.5, β = 92.3 ± 0.5, γ = 109.5 ± 0.5°; ρ_{pycn} = 1.53, $\rho_{x\text{-}ray}$ = 1.51 g/cm³, with one formula unit $Coen_2Cl_3 \cdot 3SC(NH_2)_2$ per unit cell. The empirical formula $Coen_2Cl_3 \cdot 3SC(NH_2)_2$ with Z = 1 makes the noncentrosymmetrical space group P1 very probable. All our further calculations were performed in the framework of this space group. The experimental material consisted of a set of layer lines 0*kl*–4*kl* recorded in a KFOR x-ray goniometer in Mo radiation. In all, we recorded 748 independent nonzero reflections. The structure was determined from an analysis of the three-dimensional Patterson function by means of superposition methods. Refinement was performed by the method of least squares in the isotropic approximation to R(hk*l*) = 0.13. The coordinates and isotropic individual temperature factors of the basis atoms of the structure are listed in Table 1.

TABLE 1. Coordinates of Basis Atoms of Structure of [1,6-$[Coen_2Cl_2]Cl \cdot 3SC(NH_2)_2$]

Atom	*x/a*	*y/b*	*z/c*	σ, Å	*B*
Co	0	0	0	—	2.15
Cl_1	0.370	0.172	0.073	0.021	2.56
Cl_2	−0.370	−0.171	−0.010	0.021	2.39
Cl_3	0.304	0.174	0.505	0.019	2.90
S_1	−0.209	0.582	0.153	0.020	2.56
S_2	0.116	0.407	0.867	0.019	2.15
S_3	0.623	0.789	0.508	0.019	2.39
N_1	−0.025	−0.008	0.187	0.040	2.35
N_2	−0.111	0.180	0.052	0.043	1.39
N_3	0.026	0.046	−0.175	0.045	4.05
N_4	0.106	−0.179	−0.067	0.046	4.90
N_5	0.248	0.639	0.167	0.050	3.65
N_6	0.119	0.762	0.367	0.042	1.17
N_7	0.931	0.381	0.633	0.049	5.80
N_8	0.703	0.341	0.794	0.052	5.81
N_9	0.553	0.485	0.403	0.052	2.95
N_{10}	0.529	0.562	0.624	0.050	3.45
C_1	−0.179	0.079	0.236	0.054	2.38
C_2	−0.090	0.236	0.199	0.052	1.77
C_3	0.119	−0.070	−0.250	0.050	2.69
C_4	0.041	−0.224	−0.211	0.061	2.91
C_5	0.065	0.660	0.238	0.056	2.76
C_6	0.921	0.365	0.755	0.052	3.17
C_7	0.558	0.604	0.508	0.051	1.90

The structure is made up of complex cations 1,6-$[Coen_2Cl_2]^+$, Cl ions, and thiourea molecules. The complex cation is nearly centrosymmetric. Around the Co atom, the four N atoms of the two ethylenediamine molecules form a slightly distorted square with Co–N distances of 1.97–2.00 Å. The coordination of the cobalt is made up to six by two Cl atoms in transpositions. The Co–Cl bonds are perpendicular to the plane formed by the Co atom and the four N atoms. The Co–Cl distances are 2.29 and 2.30 Å. The complex cation is shown in Fig. 1. The main distances and valence angles in the complex anion are shown in Table 2.

Geometrically similar cations have already been found in the compounds [1,6-$[Coen_2Cl_2]Cl$ (ref. 6), 1,6-$[Coen_2Cl_2]$ $Cl \cdot HCl \cdot 2H_2O$ (ref. 7, and 1,6-$[Coen_2Cl] \cdot NO_3$ (ref. 8)] (Table 3). The molecules of ethylenediamine, which form a bidentate cyclic ligand, are of the "gauche" shape with KK' conformation, which was observed in all the above-mentioned compounds containing $[Coen_2Cl_2]^+$ ions.

The Co atom and the four N atoms of the two ethylenediamine molecules lie in the plane 4.77x + 2.53y + 1.26z = 0 with the following deviations from it: δ_{Co} = −0.003, δ_{N_1} = 0.004, δ_{N_2} = −0.03, δ_{N_3} = 0.004 and δ_{N_4} = −0.002 Å. The C atoms are separated from this plane by the distances δ_{C_1} = −0.38, δ_{C_2} = 0.40, δ_{C_3} = 0.06 and δ_{C_4} = −0.64 Å. Projections of the structure on the yz and xz planes are shown in Figs. 2 and 3.

A characteristic fragment of the structure is a chain of complex cations $[Coen_2Cl_2]^+$ lying along the x axis, which is seen particularly clearly in Fig. 3. The indi-

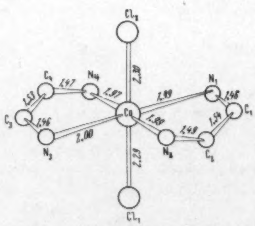

Fig. 1. Structure of complex cation 1, 6-$[Coen_2Cl_2]^+$.

TABLE 2. Interatomic Distances in Å and Valence Angles of the Complex Cation $[Coen_2Cl_2]^+$

$Co-Cl_1$	2.29±0.02	Cl_1CoCl_2	179°30′±0°50′
$Co-Cl_2$	2.30±0.02	Cl_1CoN_1	89°40′±1°20′
Cl_1-Cl_2	4.59±0.03	Cl_1CoN_2	89°50′±1°20′
$Co-N_1$	1.99±0.04	Cl_1CoN_3	90°00′±1°20′
$Co-N_2$	1.99±0.04	Cl_1CoN_4	90°20′±1°20′
$Co-N_3$	2.00±0.05	Cl_2CoN_1	90°40′±1°20′
$Co-N_4$	1.97±0.04	Cl_2CoN_2	89°50′±1°20′
N_1-C_1	1.46±0.07	Cl_2CoN_3	89°40′±1°20′
N_2-C_2	1.49±0.07	Cl_2CoN_4	89°50′±1°20′
N_3-C_3	1.46±0.07	CoN_1C_1	108°50′±3°10′
N_4-C_4	1.47±0.06	$N_1C_1C_2$	107°40′±3°30′
C_1-C_2	1.54±0.07	$C_1C_2N_2$	104°40′±4°20′
C_3-C_4	1.53±0.08	N_2CoN_1	85°20′±1°50′
		N_1CoN_3	170°10′±1°40′
		N_2CoN_4	174°50′±1°50′
		CoN_3C_3	103°00′±3°10′
		$N_3C_3C_4$	111°50′±4°20′
		$C_3C_4N_4$	105°50′±3°40′
		N_4CoN_3	90°00′±1°50′

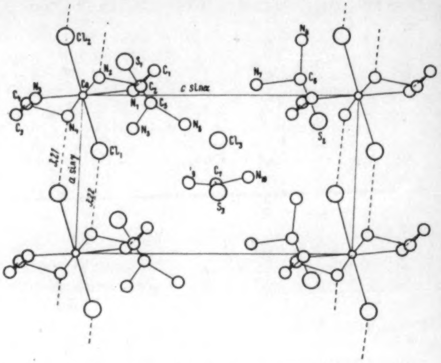

Fig. 3. Projection of structure of 1,6-$[Coen_2Cl_2]Cl\cdot 3SC(NH_2)_2$ on xz plane.

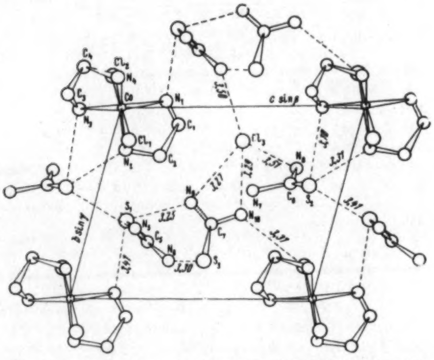

Fig. 2. Projection of structure 1,6-$[Coen_2Cl_2]Cl\cdot 3SC(NH_2)_2$ on yz plane.

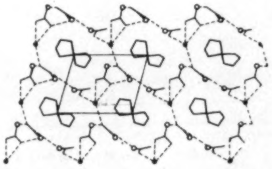

Fig. 4. Cross section of channels in thiourea, incorporating complex cations 1,6-$[Coen_2Cl_2]^+$.

TABLE 3. Co−Cl and Co−N Distances in Complex Cation $[Coen_2Cl_2]^+$

Compound	Co − Cl, Å	Co − N, Å	Symmetry	Comformation
$[Coen_2Cl_2]Cl\cdot 3SC(NH_2)_2$	2,29; 2,30	1,97; 1,99; 1,99; 2,00	1	KK′
$[Coen_2Cl_2]Cl$	2,22	1,98; 2,01	$\bar{1}$	KK′
$[Coen_2Cl_2]Cl\cdot HCl\cdot 2H_2O$	2,33	1,92; 2,00	$\bar{1}$	KK′
$[Coen_2Cl_2]NO_3$	2,26	1,99; 2,00	$\bar{1}$	KK′

TABLE 4. Interatomic Distances in Å and Valence Angles of Thiourea Molecules

S_1-C_5	1,72±0,06	$S_1C_5N_5$	123°00′±4°20′
S_2-C_6	1,72±0,05	$S_1C_5N_6$	124°00′±4°20′
S_3-C_7	1,72±0,05	$N_5C_5N_6$	113°00′±4°50′
C_5-N_5	1,35±0,06	$S_2C_6N_7$	124°20′±4°10′
C_5-N_6	1,37±0,07	$S_2C_6N_8$	121°20′±4°10′
C_6-N_7	1,33±0,07	$N_7C_6N_8$	113°00′±4°50′
C_6-N_8	1,40±0,07	$S_3C_7N_9$	125°30′±4°10′
C_7-N_9	1,34±0,08	$S_3C_7N_{10}$	120°20′±4°10′
C_7-N_{10}	1,38±0,07	$N_9C_7N_{10}$	113°50′±4°40′

vidual cations are linked together in a chain by strong hydrogen bonds of the type N−H ... Cl, with lengths of 3.21-3.22 Å, lying perpendicular to the rings formed by a metal atom and four N atoms. The thiourea molecules are not included in the complex. The main distances and valence angles in them are listed in Table 4. The thiourea molecules form a system of hydrogen bonds between themselves and the external Cl^- ion: This is shown in Fig. 2.

It is known that thiourea forms addition products of the channel adduct type;[9,10] the guest−host stoichiometric ratio is often[11] 1:3. Figure 4 shows a projection of some unit cells of the structure on the yz plane. We see that the crystal is actually a channel adduct of thiourea, where the infinite chains of complex cations $([Coen_2Cl_2]^+)_\infty$ are incorporated inside the channels in the distorted hexagonal thiourea. The thiourea molecules are somewhat separated in comparison with its channel adducts with branched paraffins and are also cemented by hydrogen bonds involving extraspherical Cl ions.

In the formation of the crystalline adducts, the complex cations in solution are organizing units around which the thiourea molecules are regularly arranged in a framework, forming close packing in the crystal.

Similar inclusion compounds of nickel iodide with urea, $NiI_2 \cdot 10\ OC(NH_2)_2$, were described by M. A. Porai-Koshits et al.[12]

Thus we can consider that the compound 1,6-[$Coen_2 \cdot Cl_2$] $Cl \cdot 3SC(NH_2)_2$ is a product of inclusion of trans-dichlorobis(ethylenediamine)cobalt (III) into hexagonal thiourea.

The authors are obliged to G. A. Kiosse and V. N. Biyushkin for helpful discussions during the preparation of this article for the press.

---

[1] M. A. Baker and F. M. Gaesser, J. Inorg. and Nucl. Chem., 25, 1161 (1963).

[2] S. S. Chan and K. K. Chan, Austral. J. Chem., 22, 12 (1969).

[3] P. V. Gogorishvili, L. R. Tsitsishvili, and M. V. Chrelashvili, Investigations in the Field of the Chemistry of Complex and Simple Compounds of Some Transition and Rare Metals [in Russian], Metsniereba, Tbilisi (1970).

[4] I. B. Baranovskii, G. S. Kovalenko, and A. V. Babaeva, Zh. Neorgan. Khim., 15, 954 (1970).

[5] A. V. Ablov, L. I. Landa, Yu. A. Simonov, N. N. Proskina, T. I. Malinovskii, and M. G. Gitel'man, Dokl. Akad. Nauk SSSR, 204, 1109 (1972).

[6] K. A. Backer, G. Grosse, and K. Plieth, Z. Kristallogr., 112, 375 (1951).

[7] A. Nakahara, T. Saito, and H. Kuroya, Bull. Chem. Soc. Japan, 25, 331 (1952).

[8] S. Ooi and H. Kuroya, Bull. Chem. Soc. Japan, 36, 9, 1083 (1963).

[9] Von H. I. Lenné Acta Crystallogr., 7, 1 (1954).

[10] L. Mandel'korn, Nonstoichiometric Compounds [in Russian], Khimiya, Moscow (1971).

[11] B. Angla, Ann. Chimie, Ser. 12, 4, 639 (1949).

[12] Kh. Suleimanov, M. A. Porai-Koshits, A. S. Antsyshkina, and K. Sulaimankulov, Zh. Neorgan. Khim., 16, 3394 (1971).

Checking the cited mean parameters of oxide unit cells with the perovskite type structure

E. G. Fesenko and G. A. Geguzina

Rostov State University

(Submitted March 27, 1972; resubmitted June 26, 1972)
Kristallografiya, 18, 535-538 (May-June 1973)

From a comparison of the mean parameters of the cited cells determined from the experimental data ($\bar{a}_{ex}$) and the calculated data ($\bar{a}_{th}$) from the equations, erroneous determinations of the parameters and incongruences between the assumed composition and the actual composition are discovered. The comparison was made for 675 compounds described in the literature. In 646 of these compounds the differences between $\bar{a}_{ex}$ and $\bar{a}_{th}$ was less than 1%. The causes of the divergence between $\bar{a}_{ex}$ and $\bar{a}_{th}$ are ascertained in those cases where the differences are > 1%.

Equations for the calculation of the average parameter $\bar{a}_{th}$ of the cited cells (containing an ABO_3 formula unit or its equivalent) of oxides with a perovskite-type structure were given in ref. 1. A system of unstrained cation–oxygen distances (bond lengths) were obtained, making it possible to use these equations for the calculations. By comparing $\bar{a}_{th}$ with the average parameter of the cited cell derived from the experimental data $\bar{a}_{ex}$, or by considering the corresponding morphotropic curves[2] it was possible to evaluate the correctness of the determination of $\bar{a}_{ex}$.

We used both methods of checking the parameters of 236 binary and 439 ternary (mainly of the composition $AB'_{1/2}B''_{1/2}O_3$) oxides with a perovskite-type structure which were known in the published literature, in order to find any errors in the determination of the parameters and any lack of correspondence between the assumed and actual composition. Those compounds for which there was a difference between $\bar{a}_{ex}$ and $\bar{a}_{th}$ of more than 1% or where there was a significant divergence from the morphotropic curves together with some calcium compounds are listed in Table 1.

TABLE 1

Group	Assumed composition	Experimental parameter $\bar{a}_{ex}$, Å	Calculated parameter $\bar{a}_{th}$, Å	Literature cited
1	$CdCeO_3$	3.82	4.19	[3,4]
	$CdThO_3$	4.37	4.31	[3]
	$CaCeO_3$	3.85	4.20	[3,4]
	$CaThO_3$	4.37	4.32	[3]
	$PbCeO_3$	3.81	4.33	[3,4]
	$PbThO_3$	4.48	4.44	[3]
	$BaVO_3$	4.39	3.96	[5]
	$YGe_{1/2}Mg_{1/2}O_3$	3.88	3.80	[6]
2	$PbSnO_3$	4.06	4.06	[7]
		3.97	4.06	[3]
	$CaTa_{1/2}Sc_{1/2}O_3$	4.00	3.92	[8]
	$BaTa_{1/2}Tl_{1/2}O_3$	4.21	4.14	[9]
3a	$La_{1/2}Li_{1/2}TiO_3$	3.86		[10]
	$La_{1/2}Na_{1/2}TiO_3$	3.86		[10,11]
	$La_{1/2}Ag_{1/2}TiO_3$	3.87		[10]
	$La_{1/2}K_{1/2}TiO_3$	3.90		[10,12]
	$La_{1/2}Tl_{1/2}TiO_3$	3.88		[10]
	$La_{1/2}Rb_{1/2}TiO_3$	3.90		[10]
	$SrNb_{1/2}La_{1/2}O_3$	4.16	4.21	[13]
b	$SrU_{1/2}Lu_{1/2}O_3$	4.32	4.23	[14]
	$SrU_{1/2}Gd_{1/2}O_3$	4.32	4.27	[14]
	$BaU_{1/2}La_{1/2}O_3$	4.37	4.44	[14]
c	$BaV_{1/2}Bi_{1/2}O_3$	4.34		[15]
	$BaTa_{1/2}Ga_{1/2}O_3$	4.10	4.04	[8]
	$BaU_{1/2}Be_{1/2}O_3$	4.41		[14]
d	$SrFeO_3$	3.87	3.92	[16]
	$PuMnO_3$	3.86	3.93	[17]
	$LaNiO_3$	3.84	3.97	[18]
	$LaRu_{1/2}Mn_{1/2}O_3$	3.92	3.98	[19]
e	$PbCrO_3$	4.00	3.86	[20,21]
	$BiCoO_3$	4.23	3.83	[22]
	$BiNiO_3$	4.17	4.00	[22]

The aim of our study was to establish the cause of the big differences between $\bar{a}_{ex}$ and $\bar{a}_{th}$ in these cases. The compounds included in Table 1 are divided into three groups.

1. Compounds in which the perovskite type of structure has not been confirmed: $CdCeO_3$, $CdThO_3$, $CaCeO_3$, $CaThO_3$, $PbCeO_3$, $PbThO_3$, $BaVO_3$, and $YGe_{1/2}Mg_{1/2}O_3$. We were not able to synthesize $BaVO_3$ and $YGe_{1/2}Mg_{1/2}O_3$ in a perovskite-type structure; moreover, neither we nor Keith et al.[23] were able to obtain the thorium compounds nor were we or the authors of refs. 5, 23, and 24 able to synthesize the cerium compounds. Moreover, Smith et al.[24] pointed out the unreliability of the data in ref. 3 from which these thorium and cerium compounds were first defined as having a perovskite-type structure.

2. Oxides with a perovskite-type structure where the parameters have been incorrectly determined: $CaTa_{1/2}Sc_{1/2}O_3$, $BaTa_{1/2}Tl_{1/2}O_3$, and $PbSnO_3$. The synthesis and x-ray determination which we carried out showed that in the first of these $\bar{a}_{ex}$ = 3.91 Å and in the second $\bar{a}_{ex}$ = 4.17 Å, which gives a difference of less than 1% between $\bar{a}_{ex}$ and $\bar{a}_{th}$. In the case of $PbSnO_3$ the parameters taken from two determinations are shown in Table 1. In ref. 7, $PbSnO_3$ was successfully synthesized in a perovskite-type structure (by contrast to ref. 3) only at high pressure and in this case $\bar{a}_{ex}$ was found to be equal to $\bar{a}_{th}$. Since it was confirmed in refs. 25 and 26 that it was impossible to obtain $PbSnO_3$ in a perovskite-type structure at atmospheric pressure, the value of $\bar{a}_{ex}$ from ref. 3 is incorrect.

3. Oxides with a perovskite-type structure whose actual composition does not correspond to the assumed composition.

a) Lanthanum compounds $La_{1/2}A''_{1/2}TiO_3$ (A" = Li, Na, K, Ag, Tl, Rb). Table 1 does not show the values of $\bar{a}_{th}$ for these compounds since the equation for calculating $\bar{a}_{th}$ given in ref. 1 are only for the AB'_{β}, $B''_{\beta_2}O_3$ compounds. It is clear, however, without calculating $\bar{a}_{th}$, that $\bar{a}_{ex}$ for these compounds is virtually independent of the size of the A" ion and does not fit the appropriate morphotropic curve. This may be explained by assuming that in many cases $La_{2/3}TiO_3$ ($\bar{a}_{ex}$ = 3.88 Å) is formed[27] with a small amount of impurity Li, Na, K, Ag, Tl, or Rb. Brous et al. suggested this in ref. 10 in the case of oxides containing Rb, after studying the chemical composition of the compounds produced in this way. It is also possible for

$SrNb_{4/5}O_3$ [$\bar{a}_{ex}$ = 4.13 Å (ref. 28)] to form analogously instead of $SrNb_{1/2}La_{1/2}O_3$.

b) Uranium oxides, $SrU_{1/2}Lu_{1/2}O_3$, $SrU_{1/2}Gd_{1/2}O_3$, and $BaU_{1/2}La_{1/2}O_3$ obtained with an impurity of rare-earth elements and obviously containing[31] a mixture of uranium of various degrees of oxidation (U^{IV}, U^{V}, U^{VI}). If we take this into account we can assume that the rare-earth ions do not in general enter into the structure and the composition of the first two oxides is close to $SrU_{1/2}Sr_{1/2}O_3$ [$\bar{a}_{ex}$ = 4.32 Å (ref. 30)] and of the barium, to $BaUO_3$ [$\bar{a}_{ex}$ = 4.39 Å (ref. 31)].

c) Compounds with small-sized B ions (V^{V}, Be^{II}, Ga^{III}), $BaV_{1/2}Bi_{1/2}O_3$, $BaU_{1/2}Be_{1/2}O_3$, $BaTa_{1/2}Ga_{1/2}O_3$. No values of $\bar{a}_{th}$ are given in Table 1 for the first two of these compounds. This is due to the lack of verified data in the literature on other compounds with a perovskite-type structure containing V^{V} and Be^{II} from which we could determine the $V^{V}-O^{II}$ and $Be^{II}-O^{II}$ interatomic distances, which are necessary for the calculation of $\bar{a}_{th}$. Comparatively high values of $\bar{a}_{ex}$ are found for $BaV_{1/2}Bi_{1/2}O_3$ and $BaU_{1/2}Be_{1/2}O_3$ in contradiction to the small ionic radii of V^{V} and Be^{II}. It is clear that in these cases the locations of the small ions are partially or fully filled by large ions and this produces the structural stability of the perovskite type. We can therefore assume that the composition of the first oxide is close to $BaBi_{1/2}{}^{V}Bi_{1/2}{}^{III}O_3$ [$\bar{a}_{ex}$ = 4.33 Å (ref. 32)], the second to $BaU_{1/2}Ba_{1/2}O_3$ [$\bar{a}_{ex}$ = 4.44 Å (refs. 30 and 33)], and in the third, part of the Ga is replaced by Ba.

d) Oxides containing ions in an untypical state of oxidation, $SrFe^{IV}O_3$, $LaRu_{1/2}Mn_{1/2}{}^{II}O_3$, $LaNi^{III}O_3$, and $Pu^{III}\cdot MnO_3$. Yakel[16] assumed that the first oxide was defective, and that the defectiveness of the second and third oxides followed from the fact that Ni and Mn are present in an unstable degree of oxidation and, moreover, in all those cases $\bar{a}_{ex} < \bar{a}_{th}$. We should note that this very defectiveness makes it impossible to calculate $\bar{a}_{th}$ from the equations given in ref. 1 for nondefective oxides with a perovskite structure. In relation to the last oxide it is necessary to point out that at a high temperature of synthesis (1500°C) and in an oxygen atmosphere[17] the degree of oxidation of Pu^{IV} is retained while that of Mn^{III} may be partially changed into the Mn^{II} state so that the fundamental composition is obviously close to $Pu^{IV}Mn^{II}O_3$ ($\bar{a}_{ex}$ = 3.86 Å).

TABLE 2

Group	Assumed composition	Experimental parameter $\bar{a}_{ex}$, Å	Calculated parameter $\bar{a}_{th}$, Å	Literature cited
1	$CaSb_{1/2}Tb_{1/2}O_3$	4.05	4.02	[34]
	$CaSb_{1/2}Gd_{1/2}O_3$	4.06	4.03	[34]
	$CaSb_{1/2}Sm_{1/2}O_3$	4.07	4.05	[34]
	$CaSb_{1/2}Nd_{1/2}O_3$	4.08	4.06	[34]
	$CaSb_{1/2}Pr_{1/2}O_3$	4.08	4.06	[34]
	$CaSb_{1/2}La_{1/2}O_3$	4.08	4.07	[34]
	$CaTa_{1/2}Tb_{1/2}O_3$	4.03	4.03	[35]
	$CaTa_{1/2}Gd_{1/2}O_3$	4.04	4.04	[35]
	$CaTa_{1/2}Sm_{1/2}O_3$	4.05	4.06	[35]
	$CaTa_{1/2}Nd_{1/2}O_3$	4.06	4.06	[35]
	$CaTa_{1/2}Pr_{1/2}O_3$	4.06	4.07	[35]
	$CaTa_{1/2}La_{1/2}O_3$	4.07	4.08	[35]
	$CaNb_{1/2}Tb_{1/2}O_3$	4.03	4.04	[35]
	$CaNb_{1/2}Gd_{1/2}O_3$	4.04	4.06	[35]
	$CaNb_{1/2}Sm_{1/2}O_3$	4.05	4.07	[35]
	$CaNb_{1/2}Nd_{1/2}O_3$	4.05	4.07	[35]
	$CaNb_{1/2}Pr_{1/2}O_3$	4.06	4.08	[35]
	$CaW_{1/2}Sr_{1/2}O_3$	4.06	4.07	[36, 37]
2	$BaPu_{1/2}Ti_{1/2}O_3$	4.03	4.18	[38]
	$BaU_{1/2}Ge_{1/2}O_3$	4.28	4.14	[14]
	$BaU_{1/2}Mn_{1/2}O_3$	4.24	4.16	[14]
	$BaU_{1/2}Ti_{1/2}O_3$	4.02	4.20	[14]
	$BaU_{1/2}Zr_{1/2}O_3$	4.18	4.30	[14]
	$BaU_{1/2}Hf_{1/2}O_3$	4.16	4.28	[14]
	$BaU_{1/2}Ce_{1/2}O_3$	4.44	4.39	[14]

e) Oxides of $PbCrO_3$, $BiCoO_3$, and $BiNiO_3$ were obtained at high pressure. Special studies are required to establish the reasons for the large differences between $\bar{a}_{ex}$ and $\bar{a}_{th}$ for these compounds.

Table 2 includes oxides with a perovskite-type structure where the composition has been incorrectly noted.

1. The compounds $CaB_{1/2}{}'B_{1/2}{}''O_3$ (B' = Sb^{V}, Ta^{V}, Nb^{V}; B" = Tb^{III}, Nd^{III}, Gd^{III}, Sm^{III}, Pr^{III}, La^{III}) and $CaW_{1/2}Sr_{1/2}O_3$ with an inverted perovskite structure. In accordance with crystal-chemical tradition, the formula should be written in the form: $(A_{1/2}B_{1/2}{}'')(B_{1/2}{}'A_{1/2})O_3$. Therefore in spite of the closeness of $\bar{a}_{ex}$ and $\bar{a}_{th}$ in these compounds, the values of $\bar{a}_{th}$ for these as given in Table 2 must only be considered as approximate.

2. The compounds $BaU_{1/2}{}^{IV}B_{1/2}{}^{IV}O_3$ (B^{IV} = Ge, Mn, Ti, Zr, Hf, Ce) and $BaPu_{1/2}Ti_{1/2}O_3$, which belong to the $BaUO_3-BaB^{IV}O_3$ and $BaPuO_3-BaTiO_3$ systems. The question of whether they are compounds or solid solutions is still an open one.

We must point out, in conclusion, that in the fundamental summary of the oxides with a perovskite-type structure,[39,40] all the oxides listed in the tables are classified in the perovskite family by incorrect structural characteristics or inaccurate composition. The uncritical attitude to this data may be the reason for the erroneous conclusion pertaining to the conditions under which oxides with a perovskite structure, bond lengths, etc., can exist.

---

[1] V. P. Sakhnenko, E. I. Fesenko, A. T. Shuvaev, E. T. Shuvaeva, and G. A. Geguzina, Kristallografiya, 17, 316 (1972) [Sov. Phys. – Crystallogr., 17, 268 (1972)].

[2] E. G. Fesenko, V. S. Filip'ev, and M. F. Kupriyanov, Ferroelectrics [in Russian], Izd. Rostovsk. Gos. Univ., Rostov (1968), p. 63.

[3] I. Naray-Szabo, Mülgyetemi Közlemenyck Budapest, 1, 30 (1947).

[4] I. Naray-Szabo, Naturwissenschaften, 31, 466 (1943).

[5] R. S. Roth, J. Res. Nat. Bur Standards, 58, 75 (1957).

[6] D. Reinen, Theor. Chim. Acta, 5, 312 (1966).

[7] F. Sugawara, Y. Syono, and S. Animoto, Mater. Res. Bull., 3, 529 (1968).

[8] B. V. Strizhkov and A. V. Lapitskii, Vestn. Moskovsk. Univ., Ser. 2, 43 (1964).

[9] A. W. Sleight and R. Ward, Inorgn. Chem., 3, 292 (1964).

[10] J. Brous, I. Fankuchen, and E. Banks, Acta Crystallogr., 6, 67 (1953).

[11] A. I. Agranovskaya, Izv. Akad. Nauk SSSR, Ser. Fiz., 24, 1275 (2960).

[12] R. Roy, J. Amer. Ceram. Soc., 37, 581 (1954).

[13] M. F. Kupriyanov, Dissertation [in Russian], Rostovsk. Gos. Univ., Rostov-on-Don (1968).

[14] S. K. Awasthi, D. M. Chackraburtty, and V. K. Tondon, J. Inorg. and Nucl. Chem., 29, 1225 (1967).

[15] A. S. Viskov, Yu. N. Venevtsev, and G. S. Zhdanov, Dokl. Akad. Nauk SSSR, 162, 323 (1965) [Sov. Phys. – Dokl., 10, 391 (1965)].

[16] H. L. Yakel, Acta Crystallogr., 8, 394 (1955).

[17] L. E. Russel and J. D. Harrison, J. Nucl. Mater., 2, 310 (1960).

[18] A. Wold, B. Post, and E. Banks, J. Amer. Chem. Soc., 79, 4911 (1957).

[19] F. Galasso and W. Darby, Inorg. Chem., 4, 71 (1965).

[20] R. C. de Vries and W. L. Roth, J. Appl. Phys., 38, 951 (1967).

[21] R. C. de Vries and W. L. Roth, J. Amer. Ceram. Soc., 51, 72 (1968).

[22] Yu. Ya. Tomashpol'skii, E. V. Zubova, K. P. Burdina, and Yu. N. Venevtsev, Kristallografiya, 13, 987 (1968) [Sov. Phys. – Crystallogr., 13, 859 (1969)].

[23] M. L. Keith and R. Roy, Amer. Mineralogist, 39, 1 (1954).

[24] A. J. Smith and A. J. E. Welch, Acta Crystallogr., 13, 653 (1960).

[25] W. W. Coffeen, J. Amer. Ceram. Soc., 36, 207 (1953).

LIBRARY
COLLEGE
PA. 17551

[26] B. Jaffe, R. S. Roth, and S. Marzullo, J. Res. Nat. Bur. Standards, 55, 239 (1955).

[27] M. Kestigian, J. G. Dickenson, and R. Ward, J. Amer. Chem. Soc., 79, 5598 (1957).

[28] L. Katz and R. Ward, Inorg. Chem., 3, 205 (1964).

[29] G. Remy, Inorganic Chemistry Course [Russian translation], Mir, Moscow (1966).

[30] A. W. Sleight and R. Ward, Inorg. Chem., 1, 790 (1962).

[31] S. M. Lang, F. P. Knudsen, C. J. Fillmore, and R. S. Roth, Nat. Bur. Standards Circ., 568, 20 (1956).

[32] E. G. Fesenko, E. T. Shuvaeva, and Yu. I. Gol'tsov, Kristallografiya, 17, 419 (1972) [Sov. Phys. – Crystallogr., 17, 362 (1972)].

[33] W. Rüdolff and F. Pfitzer, Z. Naturforsch., 9, 568 (1954).

[34] E. G. Fesenko, V. S. Filip'ev, M. F. Kupriyanov, R. U. Devlikanova, G. N. Zhavoronko, and V. A. Ochirov, Izv. Akad. Nauk SSSR, Neorgan. Mat., 6, 800 (1970).

[35] V. S. Filip'ev and E. G. Fesenko, Kristallografiya, 10, 297 (1965) [Sov. Phys. – Crystallogr., 10, 243 (1965)].

[36] I. N. Belyaev, V. S. Filip'ev, and E. G. Fesenko, Zh. Strukt. Khim., 4, 719 (1963).

[37] G. Steward and H. P. Rooksby, Acta Crystallogr., 4, 503 (1951).

[38] S. K. Awasthi, D. M. Chackraburtty, and V. K. Tondon, J. Inorg. Nucl. Chem., 30, 819 (1968).

[39] F. S. Galasso, Structure, Properties, and Preparation of Perovskite-Type Compounds, Pergamon Press, New York (1969).

[40] Landolt-Börnstein, 4a Numerical Data and Functional Relationships in Science and Technology, New Ser. Group III Crystal and Solid State Physics, Springer-Verlag, Berlin – New York (1969); J. B. Goodenough and J. R. Longo, Crystallographic and Magnetic Properties of Perovskites and Perovskite-Related Compounds, Springer, New York (1969).

New ions in the garnet structure

G. Ronniger and B. V. Mill'

M. V. Lomonosov Moscow State University

(Submitted January 12, 1972; resubmitted June 19, 1972)
Kristallografiya, 18, 539-543 (May-June 1973)

New vanadates have been synthesized with the garnet structure and the general formula $\{A^{+}B_2^{2+}\}[M_2^{2+}](V_3)O_{12}$, where A = Cu, Na, Ag, K, Tl; B = Ca, Sr, Pb; and M = Ni, Cu, Co, Mg, Zn, Mn, Cd. The ions, Cu^{+}, Ag^{+}, K^{+}, and Tl^{+} are described in the garnet structure for the first time. The Pb^{2+} ion has for the first time been introduced in the c position and the Cd^{2+} ion in the position. The field of stability of the garnet structure is shifted more towards larger c and *a* ions in the vanadates than in the case of the germanates.

Although it is more than 10 years since the discovery of vanadates with the garnet structure[1] they remain one of the most frequently investigated groups of garnets. Our study of isomorphism among vanadium garnets has made it possible to significantly increase their number and to extend the range of ions that it may be possible to introduce into the garnet structure. Isomorphism[1)] in garnets of the type, $\{A^{+}B_2^{2+}\}[M_2^{2+}](V_3)O_{12}$ is considered in this article.

For the raw materials for the syntheses we used Tl_2O_3, K_2CO_3, KNO_3, $AgNO_3$, $NaNO_3$, Na_2CO_3, Li_2CO_3, PbO, $Sr(NO_3)_2$, $SrCO_3$, $CaCO_3$, CdO, $CdCO_3$, $MnCO_3$, MgO, NiO, Co_3O_4, CuO, ZnO, NH_4VO_3 and V_2O_3, mainly of specially pure grades. The pressed mixtures were heated in air or in vacuum ($\sim 10^{-3}$ mm Hg) and kept at the specified temperature for 0.5 to 24 h. The experiments showed that at the optimum temperatures, the synthesis of the garnet occurs very rapidly and is virtually completed after a period of the order of 30 min. The differences in the starting components of the batch (oxides, carbonates, or nitrates) did not appear to have any marked effect on the reaction rate of garnet formation. The phase composition of the sintered products was determined by x-ray diffraction (URS-50IM electron-diffraction meter, Co, $K\alpha$ radiation). All the compositions given in Table 1, except for those specially mentioned, were single phase as determined by x-ray method.

The only known representatives[1] of garnets of this particular type were the V analogs of the mineral berzelite with the general formula $\{NaCa_2\}[M_2^{2+}](V_3)O_{12}$ where M = Mg, Co, Ni, Cu, Zn. We recently reported on the synthesis of the following garnets: $NaCa_2[Mn_2^{2+}]V_3O_{12}$ and $NaCd_2[Mn_2^{2+}]V_3O_{12}$ containing Mn^{2+} and Cd^{2+} ions which are new V garnets[2] (M = Ni, Co).

A further study has shown that Cd^{2+} can occupy the *a* position.[2)] The analysis of the intensity of the lines in the x-ray photography of $NaCa_2[Cd_2]V_3O_{12}$ confirms the six-fold coordination of the heavy Cd^{2+} ions. If we ignore the high-pressure garnet-like phase[5] of $\{Cd_3\}[CdGe](Ge_3)O_{12}$, we now have an example of a six-fold coordination of Cd^{2+} in garnets. To date, Cd^{2+} ions (0.95 Å) are[3)] the heaviest ions occupying all the *a* positions in the garnet structure. The dimensions of the *a* ions in the V garnets can be easily increased when Cd^{2+} is partially replaced by Ca^{2+}(1.00 Å) or Na (1.02 Å), for example[3,4,7] in $\{Na_{0.8}Pb_{2.2}\}[Na_{0.2}Cd_{1.8}](V_3)_{12}$, but such substitutions do not go far. The six-fold coordination of Ca^{2+} is well known in Ge garnets, but there the Ca^{2+} in the *a* position is always paired with a smaller ion, for example[8] $\{Ca_3\}[CaZr](Ge_3)O_{12}$, and the average size of the *a* ions is considerably smaller than the Cd^{2+}. If we compare the number of the $NaCd_2[M_2^{2+}]V_3O_{12}$ and the $A^{+}B_2^{2+}[Cd_2]V_3O_{12}$ garnets it is clear than in the V garnets, by contrast to the silicate or germanium garnets, the Cd^{2+} ions prefer six-fold coordination to eight-fold.

Of the divalent c ions known[9,10] in Ge garnets, Mg^{2+}, Co^{2+}, Cu^{2+}, Mn^{2+}, Cd^{2+}, Ca^{2+}, and Sr^{2+}, only the last three enter the c position in any significant numbers.[7] The Sr^{2+} has noticeable difficulty in entering the V garnets. The Sr−V garnets are only formed with Mn^{2+} (0.83 Å) and Cd^{2+} as the *a* ions, and when a mixture of the composition $NaSr_2Cd_2V_3O_{12}$ is sintered it is not possible to obtain a single-phase ceramic of the garnet. On the other hand the $NaPb_2[M_2]V_3O_{12}$ garnets were synthesized with all the divalent *a* ions apart from Cu^{2+} and if the size of the ions is increased in the order Ca^{2+} (1.12 Å)−Sr^{2+} (1.25 Å)−Pb^{2+} (1.29 Å), we should expect a smooth change in the isomorphic capacity.

The Pb^{2+} ions are new, in practice, in the garnet structure. Although lead compounds are widely used as solvents for growing crystals of yttrium iron garnet and its analogs, the concentration of lead in the crystals does not normally[11] exceed 1 wt.%. The attempts of one of the present authors to synthesize Pb−Ge garnets ended unsuccessfully.[12] It is only in V garnets that the Pb^{2+} readily occupies the c position. The Pb^{2+} ions are the largest divalent ions entering in significant quantities into the structure of nonaqueous oxygen garnets.[4)] Corresponding to the low melting point of lead oxide, the Pb garnets are lower temperature than their Ca analogs (Table 1).

Until the present study, Na^{+} was the only univalent c ion in the garnet structure. It was known from an x-ray study of the distribution of ions in the solid-solution systems $Ca_{3x}LiM_{1+x}^{2+}V_3O_{12}$, where M = Mg, Co, Ni, Zn, that Li^{+} can enter the c position.[3,4,7] In the $NaCa_2M_2V_3O_{12}$ garnets it is possible to have a partial replacement of the Na^{+} by Li^{+} (when M = Mg, the replacement is complete) and it is clear that Li^{+} occupies the c position. The role of the Na can also be played by Cu^{+}, Ag^{+}, K^{+}, and Tl^{+} ions which were the first to be introduced into a garnet structure.

The replacement of Na^{+} by Cu seems to be unique since their dimensions are almost the same (according to Ahrens the ionic radii are 0.97 and 0.96 Å, respectively) and the crystal chemistry of their oxide compounds is similar. The lattice constants of the Cu garnets are a little smaller than those of the sodium and this may possibly hinder the entry of the large $Cd^{2+}(a)$ ions. The $CuCa_2Cd_2V_3O_{12}$ garnet does not exist. The reaction, $CuO \rightarrow Cu_2O + {}^1/_2O_2$, occurs[14] above 1000°C and therefore the

TABLE 1. New Garnets of the $\{A^+B_2^{2+}\}[M_2^{2+}](V_3)O_{12}$ Type

Composition	Effective radius of ions[10] (Å), in the positions		Temperature of synthesis, °C	Lattice constant, Å	X-ray density, g/cm³	Color of powder
	c	a				
$NaCa_2Cd_2V_3O_{12}$	1.13	0.95	700	12.763±3	4.300	White
$NaSr_2Mn_2V_3O_{12}$	1.22	0.82	600*	12.792±5	4.142	Brown
$NaSr_2Cd_2V_3O_{12}$**		0.95	800	12.975±10	4.668	White
$NaPb_2Ni_2V_3O_{12}$	1.25	0.70	750	12.667±4	5.878	Yellow
$NaPb_2Co_2V_3O_{12}$		0.73	750	12.733±4	5.790	Green
$NaPb_2Mg_2V_3O_{12}$		0.72	750	12.742±4	5.333	White
$NaPb_2Zn_2V_3O_{12}$		0.74	650	12.752±4	5.847	White
$NaPb_2Mn_2V_3O_{12}$		0.82	650*	12.861±5	5.569	Brown
$NaPb_2Cd_2V_3O_{12}$		0.95	750	13.062±5	6.014	White
$LiCa_2Mg_2V_3O_{12}$***	1.08	0.72	900	12.378±4		White
$CuCa_2Ni_2V_3O_{12}$	1.13	0.70	1000*	12.362±3	4.259	Black
$CuCa_2Co_2V_3O_{12}$		0.73	1000*	12.423±3	4.190	Black
$CuCa_2Mg_2V_3O_{12}$		0.72	1000*	12.425±3	3,714	Black brown
$CuCa_2Zn_2V_3O_{12}$		0.74	700*	12.449±4	4.263	Black brown
$CuCa_2Mn_2V_3O_{12}$		0.82	900*	12.551±5	4.019	Black brown
$AgCa_2Ni_2V_3O_{12}$	1.18	0.70	650	12.441±3	4.517	Yellow
$AgCa_2Cu_2V_3O_{12}$		0.73	550	12.465±5	4.525	Dark brown
$AgCa_2Co_2V_3O_{12}$		0.73	650	12.470±3	4.456	Olive green
$AgCa_2Mg_2V_3O_{12}$		0.72	650	12.472±3	3.981	White
$AgCa_2Zn_2V_3O_{12}$		0.74	700	12.491±3	4.326	White
$AgCa_2Mn_2V_3O_{12}$		0.82	700*	12.596±5	4.271	Brown
$AgPb_2Co_2V_3O_{12}$	1.29	0.73	650	12.760±5	6.296	Muddy green
$AgPb_2Mg_2V_3O_{12}$		0.72	700	12.774±4	5.835	
$AgPb_2Zn_2V_3O_{12}$		0.74	600	12.785±5	6.341	Yellowish
$AgPb_2Mn_2V_3O_{12}$		0.82	700*	12.899±4	6.045	Brown
$AgPb_2Cd_2V_3O_{12}$		0.95	650	13.090±5	6.465	White
$KPb_2Mn_2V_3O_{12}$	1.36	0.82	650*	12.998±5	5.486	Brown
$KPb_2Cd_2V_3O_{12}$		0.95	650	13.180±5	5.934	White
$TlPb_2Cd_2V_3O_{12}$	1.39	0.95	750	13.250±3	6.790	Yellowish

---

*Anneal in vacuum: remainder of synthesis in air.

**Not obtained as single phase: garnet composition perhaps different from that quoted.

***Not obtained as single phase: composition of garnet phase determined by extrapolation to the minimum lattice parameter in the system.

formation of the Cu^+-containing garnets begins at comparatively high temperatures (>950°C). In this case a single-phase state is not achieved and the lattice constants "wander" significantly which may be due to a vacancy mechanism[15] or to the introduction of variable amounts of Cu^{2+} into the structure. The low-temperature Zn garnet could not be produced in air. The formation of the Cu^+ garnet is significantly easier with sintering in vacuum.

Unlike the copper oxide, Ag_2O dissociates markedly even at room temperature[14] but in complex oxide compounds the Ag^+ ion is partially stabilized. The Ag−V garnets have adequate thermal stability and are stable even with sintering in vacuum.

The introduction of large ions, Pb^{2+} (c), Cd^{2+} (*a*) and Mn^{2+} (*a*) into the V-garnet structure creates the conditions for an eight-fold coordination of the very large K^+ (1.51 Å) and Tl^+ (1.60 Å) ions. The lattice constant of $TlPb_2Cd_2 \cdot V_3O_{12}$ (13.250 Å) is the largest of the known[4] nonaqueous garnets (in hydrates it can rise[16] to 13.67 Å). The Rb^+ (1.60 Å) and Cs^+ (1.78 Å) do not form garnets of this particular type. Although there are garnet phases present in the sintered products, judging from the lattice constants they should obviously be classified as defect garnet phases,[15] possibly containing small quantities of Rb^+ and Cs^+. If we sinter mixtures of the composition $(Rb, Cs)_{1-2x}Pb_{2+x} \cdot Cd_2V_3O_{12}$, assuming that garnets with vacancies will form, it is impossible, even with low concentrations of Rb^+ and Cs^+ in the mixtures, to state unequivocally that the univalent ions enter the garnet structure since there is overlapping of the impurity- and garnet-phase lines in the x-ray photographs. While the Cs^+ is too big for an eight-fold coordination in garnets, Rb^+ and Tl^+ are almost the right size. The parallel with the behavior of $Sr^{2+} - Pb^{2+}$

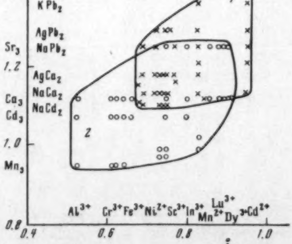

Fig. 1. The field of stability of vanadium (1) and germanium (2) garnets in coordinates of the effective radii, r_c and r_a, of the c and *a* ions.

pairs is automatically suggested. The difficulties involved in the introduction of Sr^{2+} and Rb^+ ions and the easier introduction of the Pb^{2+} and Tl^+ ions may possibly be associated with differences in the chemical bond formed between the ions. A tendency towards a purely ionic bond is characteristic of the first two and the covalency contribution is marked in the second two.

Figure 1 illustrates the stability field of Ge and V garnets at normal pressure in coordinates of the average effective radii of c and *a* ions.[5] The stability field of the Ge garnets was constructed from the data in refs. 9 and 10. On the right it is limited by the Dy^{3+} and Ho^{3+} ions [Ge garnets are not formed with Tb^{3+} (*a*)] and on the left by Al^{3+}, the smallest of the known trivalent octahedral ions. The upper boundary for the c ions may probably be raised by the partial replacement of Sr^{2+} by Ba^{2+}, but it is doubtful whether this substitution will occur further. The same can be said for the replacement of Mn^{2+}(c) (lower boundary) by Mg^{2+} since $Mg_3Al_2Ge_3O_{12}$ is not formed[17] at pressures under 200 kbar. The stability field of the V garnets was constructed on the basis of the data from our present paper and from refs. 2, 3, 4, 7, and 15. Its lower boundary is determined by the average size of the c ions in the $\{NaCd_2\}[M_2](V_3)O_{12}$, $\{LiCa_2\}[Mg_2](V_3)O_{12}$, and $\{LiCa_2\}[LiSc](V_3)O_{12}$ garnets.[6] The minimum dimensions of *a*-ion combination we observed was in the $\{Na_2Ca\}[MgFe](V_3)O_{12}$, $\{Ca_2Li\}[LiFe](V_3)O_{12}$, and $\{Ca_{2.2}Li_{0.8}\}[Cr_{0.9}Li_{1.1}](V_3)O_{12}$ garnets. The field is bounded at the top by the combination $TlPb_2$ and on the right the boundary goes slightly beyond Cd^{2+}, taking into account the limited entry of Ca^{2+} and Na^+ into the *a* position.

In comparing the stability fields of the garnet structure among vanadates and germanates, our attention is drawn to the shift of the field of the first type into the region of large c and *a* ions. If we compare the existing data for the V−O and Ge−O distances in orthovanadates and orthogermanates we can assume that the metal−oxygen distances in the tetrahedra of vanadium garnets are shorter. This conclusion is reached by extrapolating from $d-h = 1.88$ Å in the yttrium iron garnet[9] through $d-h = 1.80$ Å in[18] $Ca_{2.92}Bi_{0.08}Fe_{3.54}V_{1.46}O_{12}$ to a purely vanadium (d) garnet while[19] in $Mn_3Fe_2Ge_3O_{12}$, $Ge-O = 1.77$ Å. The shortening of the d−h distance means that there is a more rigid structure in the V garnets than in the Ge. This rigidity appears with respect to the entry of c and *a* ions which are small or have a large charge ("strong" ions)[2,3,4,7] into the structure of the V garnets. In the particular type of garnets considered here, the minimum size of c ions ($\{NaCd_2\}$ combination) is the result of the fact that there are no smaller divalent *a* ions than Ni^{2+} (0.69 Å). An analogous situation is found in other groups of garnets. For example among ermanates, the series, Mn^{2+}(c) garnets is interrupted at Fe^{3+} (0.64 Å) and beginning with Sc^{3+} (0.74 Å), Ge garnets are formed with Cd^{2+} and larger c ions. In silicate garnets the introduction of Cd^{2+} (c) is made difficult where there are *a* ions bigger[20] than Al^{3+} (0.53 Å).

We can see that by comparison with Ge garnets, the structure of the V garnets offers more possibilities for the introduction of large c and ions. In the garnet structure the oxygen octahedra and tetrahedra have no common edge but they do have edges in common with the dodecahedra. In our view, the congruence in size of the small tetrahedra and the large dodecahedra in the V garnets is achieved, primarily by the introduction of large ions into the octahedra, and secondarily by the "pliability" of the dodecahedra formed around the large, low-charge ("weak") ions. Clearly, structural studies will be necessary in order to understand the causes of the "anomalous" behavior of the vanadium garnets.

---

[1] The ions occupying the structural positions 24(c), 16(*a*), and 24(d) with coordination numbers 8, 6, and 4 are enclosed in curly, square, and round brackets, respectively.

[2] In V garnets Cd can also occupy up to 10% of the d positions, and we have synthesized garnets containing Cd^{2+} ions which occupy simultaneously all three positions.[3,4]

[3] The effective ionic radii according to ref. 6 for all the corresponding coordination numbers.

[4] The hydroxygarnet which has been described[13] as Ba^{2+} (c) is $Ba_3A_{12}(OH)_{12}$.

[5] It should be noted that the succession of the increase in the radii of the *a* ions in accordance with ref. 6 does not always agree with the sucession of lattice constants of lattice of the garnets (Table 1).

[6] The effective radius of Li^+ (c) is assumed to be 1.00 Å.

---

[1] A. Durif, Solid State Physics in Electronics and Telecommunications, Vol. 3, Academic Press, New York (1960), p. 500.

[2] B. V. Mill' and G. Ronniger, Kristallografiya, 16, 1035 (1971) [Sov. Phys.−Crystallogr., 16, 902 (1972)].

[3] B. V. Mill' and G. Ronniger, Kristallografiya, 18, 126 (1973) [Sov. Phys.−Crystallogr., 18, 76 (1973)].

[4] G. Ronniger, Author's Abstract of Dissertation [in Russian], Izd. Moskovsk. Univ. Moscow (1971).

[5] C. T. Prewitt and A. W. Sleight, Science, 163, No. 3865, 386 (1969).

[6] R. D. Shennon and C. T. Prewitt, Acta Crystallogr., B25, No. 5, 925 (1969).

[7] B. V. Mill' and G. Ronniger, in: The Physics and Chemistry of Ferrites [in Russian], Izd. Moskovsk Gos. Univ. Moscow (1973), p. 98.

[8] S. Geller and G. P. Espinosa, Inorg. Chem., 8, No. 1, 183 (1969).

[9] S. Geller, Z. Kristallogr., 125, No. 1 (1967).

[10] B. V. Mill', in: Magnetic and Crystal Chemical Studies of Ferrites Izd. Moskovsk. Gos. Univ. Moscow (1971), p. 56.

[11] A. B. Chase and J. A. Osmer, J. Crystal Growth, 5, No. 4, 239 (1969).

[12] B. V. Mill', Dokl. Akad. Nauk SSSR, 165, 555 (1965) [Sov. Phys.−Dokl., 10, 1015 (1966)].

[13] A. H. M. Ahmed and L. S. D. Glasser, Acta Crystallogr., B25, No. 10, 2169 (1969).

[14] N. A. Toporov, V. P. Barzakovskii, L. A. Bondar', and U. P. Udalov, Diagrams of States of Silicate Systems [in Russian], Vol. 2, Nauka, Leningrad (1970).

[15] G. Ronniger and B. V. Mill', Kristallografiya, 18, 303 (1973) [Sov. Phys.−Crystallogr., 18, 187 (1973)].

[16] J. Ito, Mater. Res. Bull., 3, 495 (1968).

[17] A. E. Ringwood and A. Major, Earth Planet Science Letters, 2, 331 (1967).

[18] E. L. Dukhovskaya and Yu. G. Saksonov, Fiz. Tverd. Tela, 10, 3308 (1968) [Sov. Phys.−Solid State, 10, 2613 (1969)].

[19] M. D. Lind and S. Geller, Z. Kristallogr., 129, 427 (1969).

[20] B. V. Mill', Izv. Akad. Nauk SSSR, Neorgan. Mat., 5, 1604 (1969).

Effect of manganese on the transformation of the zinc sulfide cubic lattice to hexagonal

G. E. Arkhangel'skii, T. I. Voznesenskaya, and M. V. Fok

Physics Institute, Academy of Sciences of the USSR

(Submitted June 26, 1972)
Kristallografiya, 18, 544-547 (May-June 1973)

It was shown by using EPR spectra that introduction of manganese by diffusion at 1170°C promotes transformation of the zinc sulfide cubic lattice to hexagonal. However, the hexagonal phase is not formed when cubic crystals already containing manganese are fired under analogous conditions.

It is well known that in the heat treatment of zinc sulfide either the cubic or hexagonal modification of its lattice can be obtained at a given temperature. The studies of a number of authors showed that a major role in this is played by impurities: activators, coactivators, etc. Thus, small amounts of oxygen and aluminum impurities cause formation of the hexagonal modification,[1] whereas addition of copper, silver,[2] and europium ions results in formation of the cubic lattice. In some cases, this effect may be connected with the lattice structure of the corresponding sulfides (or zinc oxide in the case of oxygen impurity). This effect is apparently explained by the fact that the free energies of the two modifications of zinc sulfide are nearly the same. Hence, even a slight increase in the difference between these free energies, caused by adding an impurity, may strongly diminish the stability of a modification at the given temperature. This is apparently the reason that refiring at another temperature usually does not change the crystal modification of an already-formed sulfide lattice (unless, of course, sublimination is carried out, in which event the crystal lattice is completely disrupted). In the latter case, for instance, the presence of manganese favors the appearance of the hexagonal modification at a lower temperature.[3]

The purpose of the present study was to investigate the effect of manganese on the formation of the hexagonal phase in already-formed cubic crystals of zinc sulfide. The amount of each phase present was determined by comparing intensities of the EPR spectra of Mn^{2+} ions isomorphously replacing zinc ions, which are characteristic of the hexagonal and cubic environments. The central line of the fine structure in this spectrum (slit into components of hyperfine structure) is isotropic, which permits work with powdered material. This line is quite distinct in both modifications of zinc sulfide (Fig. 1). The presence of a number of additional rather intense lines, apparently due to forbidden transitions between hyperfine splitting levels, is typical of the spectrum of the hexagonal modification. These transitions become possible under the influence of the axial field present in the hexagonal lattice. The positions of two of these lines on the scale of the magnetic field coincide with $|\Delta m| = 1$, calculated according to a general expression for magnetic levels of the Mn^{2+} ion.[4] Values of the field H were derived from the equations

$$H = H_0 - \frac{1}{2}A'(2m-1) + \frac{A'^2}{2H_0}\left(m^2 - m + \frac{1}{4}\right)$$

for the transition $M = -{}^1/_2,\ m - 1 \rightarrow M = {}^1/_2,\ m$ and

$$H = H_0 - \frac{1}{2}A'(2m-1) + \frac{A'^2}{2H_0}\left(m^2 - m - \frac{67}{4}\right)$$

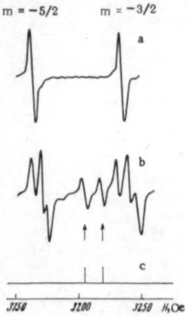

Fig. 1. Part of electron paramagnetic resonance spectrum of ZnS−Mn luminophor. Transition $M = -{}^1/_2 \rightarrow M = +{}^1/_2$; $\Delta m = 0$; a) cubic modification; b) hexagonal modification; c) lines of transition $|\Delta m| = 1$ (calculated values).

for the transition $M = -{}^1/_2,\ m \rightarrow M = {}^1/_2,\ m - 1$, where $H_0 = h\nu/g\beta$; $A' = A/g\beta$. The constants A and g are taken from ref. 5. Figure 1 shows values of the field H for the transitions $m = -{}^3/_2 \rightarrow -{}^5/_2$ and $m = -{}^5/_2 \rightarrow -{}^3/_2$. Evidently, they correspond quite well to the EPR lines.

We also used the ratio of intensities of these additional lines to those of lines of allowed transitions as a measure of the quantity of hexagonal phase in the sample.

The samples were prepared by pulverizing the coarser of the nonactivated cubic crystals grown from the vapor phase in a sealed ampoule at T = 1380°C in a H_2S or NH_3 atmosphere. The velocity of passage of the ampoule through the temperature maximum of the furnace was 0.18 mm/h.

The microcrystals so prepared were activated by manganese from $MnCl_2$ at 1170°C for 30 min in the presence of 1% of a chloride flux under dried ammonia. Then the mixture was divided by sifting into three fractions having average grain radii of 20, 40 and 100 μ. The relative

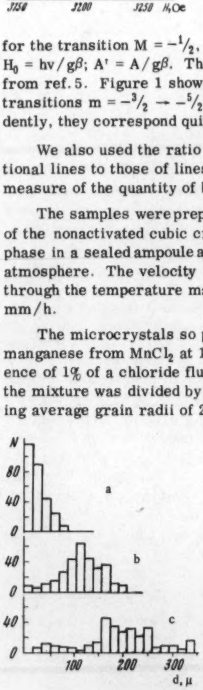

Fig. 2. Relative granulometric composition of fine (a), medium (b), and coarse (c) fractions.

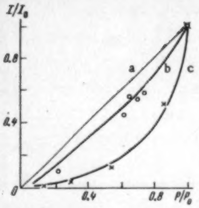

Fig. 3. Relative quantity of manganese remaining after partial solution. P_0 and P) Sample weight before and after solution; ×) coarse fraction; ○) medium fraction; solid curves are calculated: a) for uniform distribution; b, c) for medium and coarse fractions, respectively.

granulometric composition was determined for each fraction by counting the particles in the microscope field and measuring their diameters (Fig. 2). The EPR spectra of each fraction were taken from samples having the same weight. They showed lines belonging to both the hexagonal and cubic modifications.

In order to determine the relative quantity of each phase and to find out how it is distributed throughout the volume of the microcrystals, it was necessary to know the distribution of manganese ions throughout this volume. For this, we used the method of successive solution of each fraction and measured the total intensity I of EPR lines of a weighed portion of this fraction. The results of these measurements are shown in Fig. 3. It is evident from the latter that Mn^{2+} ions are distributed quite uniformly in the medium fraction, whereas there is a concentration gradient in the coarse fraction. The distribution of manganese in the fine fraction is, no doubt, more uniform than in the medium one.

Figure 3 also shows those theoretical curves, characterizing the quantity of manganese remaining in microcrystals of the coarse and medium fractions after partial solution, which agree best with experimental data. Their points were calculated for a diffusion coefficient $D = 2.2 \cdot 10^{-9}$ cm²/sec. The dispersion of the experimental points corresponds to a variation of D by a factor of 1.5-2.

Together with this, it was found that lines characteristic of the hexagonal modification become weaker as the surface portions of the microcrystals dissolve (Fig. 4). This means that the hexagonal phase lies on the surface. Knowing the percentage of volume occupied by the hexagonal phase and the granulometric composition of the fractions, one could estimate the effective thickness of the layer of hexagonal phase on the crystals. It proved to be 6-10 μ.

Moreover, it was noted that the intensity ratio I_c/I_h of the cubic and hexagonal EPR spectra of Mn^{2+} in the

TABLE 1

Fraction	d_c, μ	I_c/I_h	Δr, μ	$(I_c/I_h)/(I_c/I_h)_{soln}$	Δr, μ
a	25	0.16	10.5	0.03	9.6
b	80	2.75	5.9	0.25	10.7
c	210	8.8	4	—	—

original (undissolved) samples of the three fractions under consideration varied, being 10 times as large for the coarse fraction as for the fine (Fig. 4). This enabled us to determine the indicated intensity ratios with the calculated ratio of volumes of the surface layer for the internal cubic part of the microcrystal, for each fraction. The hexagonal-layer thickness calculated in this way is independent of microcrystal size within the error of measurement and amounts to 9.5-11 μ (see Table 1).

Formation of the hexagonal phase on the surface of a ZnS crystal during firing of the sample at T = 1170°C may occur, generally speaking, not only because of the introduction of Mn, but also simply because rearrangement begins in the more disturbed surface layer of the crystal.

In the principal experiments, the average manganese concentration was 10^{-4} mole per mole of ZnS. To determine the role of manganese in the formation of the hexagonal layer, analogous experiments were performed with different manganese concentrations. It was found that, as the manganese concentration decreases from 10^{-4} to 10^{-7} mole per mole of ZnS in samples fired under identical conditions, the percentage of the hexagonal phase decreases. However, neither replacement of the NH_3 atmosphere by H_2S nor elimination of the chloride flux changed the amount of hexagonal phase in the samples.

It follows that manganese plays an active role in transformation of the cubic zinc sulfide lattice to hexagonal. However, if the manganese was introduced into the cubic lattice at the instant of its formation, refiring at 1170°C does not produce the hexagonal phase. An experiment was performed on a zinc sulfide crystal grown from the melt and activated by manganese during growth. After pulverizing the crystal and firing it with and without flux, even the finest fraction did not go over to hexagonal despite the high manganese content (over 10^{-3} g/g).

A manganese-free crystal, grown analogously and then activated by manganese by diffusion in the manner described above, goes over to the hexagonal phase from the surface. This shows that in formed cubic ZnS crystals, the hexagonal phase is produced in appreciable quantity at 1170°C only during diffusion of the impurity (Mn). Hence, the mechanism of formation of the hexagonal phase in the formed cubic ZnS lattice differs substantially from that of formation of stacking faults during crystal growth.

The authors thank N. A. Gorbacheva and I. V. Shtambur for kindly supplying the crystals.

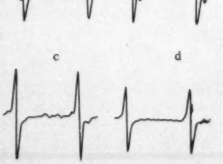

Fig. 4. Electron paramagnetic resonance spectra of finely crystalline ZnS–Mn. a) Fine fraction; b) medium fraction; c) coarse fraction; d) medium fraction after partial solution.

---

[1] A. I. Ryskin and G. I. Khil'ko, in: Spectroscopy of Crystals [in Russian], Nauka, Moscow (1970), p. 330.

[2] M. Aven and J. A. Pardoni, J. Phys. Chem. Solids, 13, 56 (1960).

[3] S. A. Kostylev and B. N. Sherstyak, Kristallografiya, 8, 456 (1963) [Sov. Phys.—Crystallogr., 8, 357 (1963)].

[4] S. P. Keller, I. L. Geller, and W. V. Smith, Phys. Rev., 110, 850 (1958).

[5] J. Schneider, S. R. Sircar, and A. Räuber, Z. Naturforsch., 18, 980 (1963).

Determination of the energy and thermodynamic characteristics of iron–aluminum alloys by the method of diffuse x-ray scattering

S. V. Semenovskaya, Zh. B. Sinyavskaya, and A. P. Senichkin

Moscow Institute of Steel and Alloys

(Submitted May 29, 1972)
Kristallografiya, 18, 548-556 (May-June 1973)

The diffuse scattering of x rays by single crystals of disordered Fe–Al solid solutions (with 9, 12, 16, 19, and 22 at.% Al) was used to study the concentration and temperature dependence of the Fourier components of the energy of mixing V(**k**). It was found that: 1) The magnetic energy and the energy of the conduction electrons contributed a major proportion of the energy of mixing; 2) in calculating the magnetic energy attention could be confined to the approximation involving the exchange interaction of only the nearest neighboring Fe atoms; 3) the approximation of the self-consistent field was satisfactorily fulfilled and could be used in analyzing the thermodynamics of the alloys. From experimentally determined values of V($\mathbf{k}_1$) and V($\mathbf{k}_2$) the equilibrium parameters of long-range order were calculated and an equilibrium Fe–Al diagram was constructed (without considering the possibility of phase separation). The magnetic energy was found to have a considerable influence on the thermodynamics of the ordering processes.

It is well known[1] that when the approximation of the self-consistent field is used in order to determined the free energy of a solid solution, the latter may be expressed in terms of a number of energy constants constituting the Fourier components of the energy of mixing V(**k**) associated with the structural wave vectors (those with **k** = 0) and the superstructural vectors (those which differ from one another by an amount not equal to the structural vector of the reciprocal lattice).

In ref. 2 a specific expression was given for the free energy of alloys with a bcc lattice undergoing ordering of the Fe_3Al type. For such alloys the free energy is determined by three Fourier components of the energy of mixing, V(0), V($\mathbf{k}_1$), and V($\mathbf{k}_2$) and two long-range ordering parameters η_1 and η_2 expressed in terms of the same quantities V($\mathbf{k}_1$) and V($\mathbf{k}_2$) using the equations

$$\ln\frac{(1-c-\eta_1/4+\eta_2/2)(c+\eta_1/4+\eta_2/2)}{(1-c-\eta_1/4-\eta_2/2)(c+\eta_1/4-\eta_2/2)}=-\eta_2\frac{V(\mathbf{k}_2)}{T\varkappa},\quad(1)$$

$$\ln\frac{(1-c+\eta_1/4)^2(c+\eta_1/4+\eta_2/2)(c+\eta_1/4-\eta_2/2)}{(c-\eta_1/4)^2(1-c-\eta_1/4-\eta_2/2)(1-c-\eta_1/4+\eta_2/2)}=-\eta_1\frac{V(\mathbf{k}_1)}{T\varkappa}\quad(2)$$

where c is the atomic proportion of Al, T is the absolute temperature, $\varkappa$ is Boltzmann's constant, the superstructural wave vectors $\mathbf{k}_1$ and $\mathbf{k}_2$ are given by $\mathbf{k}_1 = 2\pi\mathbf{a}_1^*$ and $\mathbf{k}_2 = \pi(\mathbf{a}_1^* + \mathbf{a}_2^* + \mathbf{a}_3^*)$ ($\mathbf{a}_1^*$, $\mathbf{a}_2^*$, and $\mathbf{a}_3^*$ are reciprocal-lattice vectors). The energy of mixing for all the coordination spheres enters into V($\mathbf{k}_1$), V($\mathbf{k}_2$), and V(0).

Thus, on the approximation of the self-consistent field, all the thermodynamic properties of alloys undergoing ordering of the Fe_3Al type are determined by the three Fourier components of the energy of mixing: V(0) (for **k** = 0), V($\mathbf{k}_1$), and V($\mathbf{k}_2$).

On allowing for correlation,[3] Eqs. (1) and (2) become more complicated, the right-hand sides constituting polynomials in η_1 and η_2 with coefficients containing integrals of V(**k**).

The results obtained in refs. 1 and 2 open new possibilities for achieving a more accurate theoretical construction of phase equilibrium diagrams, since the theory developed in these papers differs from that employed in refs. 4-7 in making no a priori assumptions as to the radius of action of the potential of the interatomic interaction.

We accordingly set ourselves two problems: 1) to make an independent experimental determination of the energy parameters V(0), V($\mathbf{k}_1$), and V($\mathbf{k}_2$) by the diffusion scattering of x rays in single crystals prepared from disordered Fe–Al solid solutions; 2) to achieve a theoretical construction of the Fe–Al equilibrium diagram in the range 0–50 at.% Al by using the energy parameters so determined.

Up to the present time the diffuse scattering method has never been employed for an experimental determination of the energy structure of a solid solution. The first attempt in this direction was made in ref. 2 by one of the present authors for the case of an Fe–16 at.% Al alloy.

It was shown in ref. 2 that the quantities V($\mathbf{k}_1$) and V($\mathbf{k}_2$) determined from the intensity of diffuse scattering in an equilibrium system existing in a state of short-range order only led to the correct values of the order–disorder phase-transition temperatures (Kurnakov points) on allowing for the magnetic-energy contribution to the energy of mixing (the magnetic energy of mixing). A method was proposed in ref. 2 for estimating the Fourier component of the magnetic energy of mixing $V_{\text{mag}}(\mathbf{k})$ on the assumption that exchange interaction only existed between the nearest neighboring Fe atoms. Since $F_{\text{mag}}(\mathbf{k})$ depends on both the temperature and the composition of the alloy, in order to study the temperature and concentration dependences of the energy characteristics under consideration we carried out experiments on a series of five Fe–Al single crystals, containing 9, 12, 16, 19, and 22 at.% Al, over a wide temperature range (320–850°C).

The experimental procedure and the method of calculating the V(**k**) were the same as before.[2] In contrast to ref. 2, in the present investigation we greatly increased the intensity-measuring accuracy and the accuracy of the V(**k**) determination by using BSV-10 x-ray tubes, in conjunction with a bent germanium monochromator, and measuring the intensity of at least four equivalent points (differing from one another by an amount equal to the reciprocal-lattice vector) for the wave vectors $\mathbf{k}_1$ and $\mathbf{k}_2$; for $\mathbf{k}_1$ – (120), (210), (201), and (021); for $\mathbf{k}_2$ – $({}^1/_2\;{}^3/_2\;{}^1/_2)$, $({}^1/_2\;{}^1/_2\;{}^3/_2)$, $({}^3/_2\;{}^1/_2\;{}^1/_2)$, $({}^{\bar{1}}/_2\;{}^3/_2\;{}^1/_2)$. At each of the four points the measurement was repeated two or three times.

In a single measurement 1000 pulses were recorded. The final values of $V(\mathbf{k}_1)$ and $V(\mathbf{k}_2)$ were obtained as the means of the values pertaining to the four equivalent points.

In order to determine V(0) the intensity was measured for small values of k at six to eight points on both sides of the structural points (020) and (200) in the [010] and [100] directions, respectively, and around the (220) point in the [110] direction.

The investigation was carried out with the URS-50IM diffractometer, using Co Kα radiation at a voltage of 45 kV and a current of 17 mA; the radiation was made monochromatic by means of a germanium single crystal bent into a radius of ~500 mm. Recording was effected with MST-17 and Si-3B Geiger counters. The single crystals were cut along the (110) plane, the accuracy of setting this plane being ~20-30'.

The thermal and Compton scatterings were allowed for more precisely than in ref. 2. The intensity of the thermal one-phonon scattering was determined by using the frequencies of normal vibrations in pure Fe and Fe_3Al, obtained in ref.8 by inelastic slow neutron scattering, at the same time allowing for the change in the elastic constants of Fe on dissolving Al in the latter.[9] The intensity of two-phonon thermal scattering (not allowed for in ref. 2) was calculated as in ref. 10. The intensity of the Compton scattering of Al and Fe was determined as in ref. 11.

The Fourier components of the total energy of mixing $V(\mathbf{k}_1)$ and $V(\mathbf{k}_2)$ were determined from the diffuse scattering intensity obtained under equilibrium short-range order conditions $I(2\pi\mathbf{H} + \mathbf{k})$, the scattering being measured at points of reciprocal space lying at a distance equal to the vector $\mathbf{k}_1$ (or $\mathbf{k}_2$) from the nearest structural reciprocal lattice point $2\pi\mathbf{H}$, using the equation[12]

$$I(2\pi\mathbf{H}+\mathbf{k})=\frac{|\varphi(2\pi\mathbf{H}+\mathbf{k})|^2c(1-c)}{1+c(1-c)V(\mathbf{k})/\varkappa T}, \qquad (3)$$

where $\varphi(2\pi\mathbf{H} + \mathbf{k})$ is the effective structure amplitude, depending on the difference $(f_{\mathrm{Al}} - f_{\mathrm{Fe}})$ between the atomic factors of Al and Fe and the value of the static distortions.[13] For reciprocal lattice points corresponding to $\mathbf{k}_1$ and $\mathbf{k}_2$, the contribution of the static distortions is identically equal to zero and $\varphi(2\pi\mathbf{H} + \mathbf{k}) = f_{\mathrm{Al}} - f_{\mathrm{Fe}}$. Equation (3) was obtained in ref. 12 on the approximation of the self-consistent field and is valid for single-phase solid solutions.

The quantity V(0) was calculated by extrapolating the experimental data for small k to k = 0, using the equation[14]

$$\frac{|\varphi(2\pi\mathbf{H}+\mathbf{k})|^2}{I(2\pi\mathbf{H}+\mathbf{k})}=\frac{1}{c(1-c)}+\frac{V(0)}{\varkappa T}+\frac{1}{\varkappa T}\left(\frac{\partial^2 V}{\partial \mathbf{k}^2}\right)_{\mathbf{k}=0}k^2. \qquad (4)$$

The quantities $V(\mathbf{k}_1)$, $V(\mathbf{k}_2)$, and V(0) determined from the intensity $I(2\pi\mathbf{H} + \mathbf{k})$ using Eqs. (3) and (4) respectively constitute the Fourier components of the total energy of mixing. Hence in the case of magnetic alloys these are equal to

$$V(\mathbf{k}) = V_{\mathrm{mag}}(\mathbf{k}) + V_{\mathrm{chem}}(\mathbf{k}), \qquad (5)$$

where $V_{\mathrm{mag}}(\mathbf{k})$ and $V_{\mathrm{chem}}(\mathbf{k})$ are the Fourier components of the magnetic and chemical components of the energy of mixing respectively.

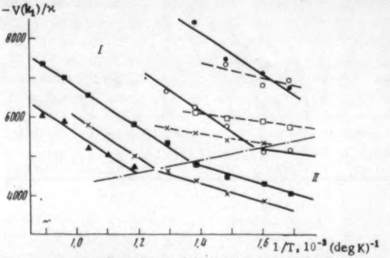

Fig. 1. Temperature dependence of the Fourier component of the total energy of mixing $V(\mathbf{k}_1)$ (continuous lines) and the Fourier component of the chemical energy of mixing $V_{\mathrm{chem}}(\mathbf{k}_1)$ (dashed lines) for Fe–Al alloys. 9; ○) 12; ■) 16; ×) 19; ▲) 22 at.% Al.

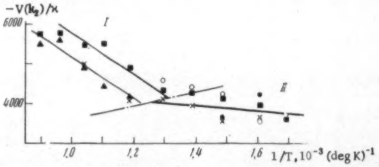

Fig. 2. Temperature dependence of the Fourier component of the total energy of mixing $V(\mathbf{k}_2)$ for Fe–Al alloys ●) 9; ○) 12; ■) 16; ×) 19; ▲) 22 at.% Al.

It was shown in ref. 2 that, on the approximation of exchange interaction between nearest Fe neighbors only, we obtain

$$V_{\mathrm{mag}}(\mathbf{k}_2) = 0 \text{ and } V(\mathbf{k}_2) = V_{\mathrm{chem}}(\mathbf{k}_2), \qquad (6a)$$

$$V_{\mathrm{mag}}(\mathbf{k}_1) = -V_{\mathrm{mag}}(0). \qquad (6b)$$

If this approximation is valid, the experimentally determined values of $V(\mathbf{k}_2)$ based on Eq. (3) should not depend on temperature or the composition of the alloy. On the other hand $V(\mathbf{k}_1)$, which contains the magnetic component $V_{\mathrm{mag}}(\mathbf{k}_1)$, should depend on both of these.

Figures 1 and 2 show the experimental values of $-V(\mathbf{k}_1)/\varkappa$ and $-V(\mathbf{k}_2)/\varkappa$ as functions[1)] of 1/T.

We see from Fig. 2 that, in the low-temperature range (section II), $V(\mathbf{k}_2)$ is in fact almost independent of temperature and alloy composition, while $V(\mathbf{k}_1)$ depends very substantially on both, even in this temperature range.

The appearance of a temperature dependence of $V(\mathbf{k}_2)$ and $V(\mathbf{k}_1)$ in the high-temperature range (section I) is due to the fact that quenching (in water) from high temperatures cannot "fix" the state of high-temperature short-range order quite perfectly, since a redistribution by diffusion of the atoms takes place even in the course of quenching.

The temperature corresponding to the boundary between the steep (I) and gradual (II) sections evidently corresponds to that diffusion rate of the slower Fe atoms, for which the time required for them to jump through the shortest interatomic distance τ is of the order of the quench time. If we accept that the quench time is ~1 sec and $\tau = x_0^2 \exp(Q/RT)/12D_0$ (x_0 is the shortest distance between the atoms, D_0 is the pre-exponential factor, equal to ~1, $x_0^2/12D_0 \sim 0.5 \cdot 10^{-16}$ sec^{-1}), we may use the data of Fig. 1 to calculate the activation energy of diffusion Q: ~49, 54, and 58 kcal/g-mole for alloys containing 12, 16, and 19 at.% Al, respectively. These results agree closely with independent experiments.[15,2]

Thus the true temperature dependence of $V(\mathbf{k}_1)$ and $V(\mathbf{k}_2)$ is represented by the gradual (II) section.

Subsequently we shall analyze and use simply the values of $V(\mathbf{k}_1)$ and $V(\mathbf{k}_2)$ obtained in this range of temperatures.

The fact that $V(\mathbf{k}_2)$ does not depend on temperature and concentration (for all the alloys and temperatures studied, $V(\mathbf{k}_2)$ varies between −4000 and −3500°C, and subsequently[2)] we use the mean value, or −3700 ± 200°) while $V(\mathbf{k}_1)$ does so very considerably indicates that the approximation based on exchange interaction between the nearest neighboring Fe atoms only, for which conditions (6) are satisfied, is perfectly adequate.

The observed temperature dependence of $V(\mathbf{k}_1)$ (Fig. 1, continuous lines) is evidently mainly due to the temperature dependence of its magnetic component $V_{\mathrm{mag}}(\mathbf{k}_1)$. This is confirmed by the fact that the resultant values of $V_{\mathrm{chem}}(\mathbf{k}_1)$ (dashed lines in Fig. 1)[3)] depend less strongly on temperature than $V(\mathbf{k}_1)$.

We see from Fig. 1 that the quantity $V_{\mathrm{chem}}(\mathbf{k}_1)$ depends on the amount of Al in the alloy, i.e., the observed concentration dependence of $V(\mathbf{k}_1)$ is only slightly due to the concentration dependence of its magnetic component $V_{\mathrm{mag}}(\mathbf{k}_1)$. The concentration dependence of $V_{\mathrm{chem}}(\mathbf{k}_1)$ may be attributed to the contribution of the conduction electrons to the chemical energy of mixing. It was shown in ref. 17 that a concentration dependence of the Fourier component of the energy of mixing $V(\mathbf{k})$ might arise in those cases in which the position of the Cohen singularity was close to the point $\mathbf{k}$ (the position of the Cohen singularity is determined by the relation $|\mathbf{k} + 2\pi\mathbf{H}| = 2k_F$, where k_F is the Fermi momentum). The Cohen construction for pure iron showed that, in the case of Fe, spheres of radius k_F (the value of k_F is determined from the number of electrons per atom, equal[18] to 2.9) pass through points of the type $\{\mathbf{k}_1\}$ but not $\{\mathbf{k}_2\}$, i.e., $|\mathbf{k}_1 + 2\pi\mathbf{H}| = 2k_F$. Clearly when Al atoms dissolve in Fe the position of the Cohen singularity is displaced with respect to the points $\{\mathbf{k}_1\}$, and this should lead to a concentration dependence of $V(\mathbf{k}_1)$.

The assumption as to the existence of Cohen singularities agrees with the observed increase in intensity and hence $|V(\mathbf{k})|$ at points of the type $\{\mathbf{k}_1\}$ for alloys with a low Al content (9 and 12 at. % Al).

An analogous type of Cohen singularities in the form of a number of additional diffuse maxima was observed earlier in the systems[19,21] Cu−Au and[20] Ti−O. In view of the fact that, when constructing the equilibrium diagrams, we are chiefly interested in those ranges of composition in which the effect of the Cohen singularities does not appear, in subsequent calculations the values of $V_{\mathrm{chem}}(\mathbf{k}_1)$ for alloys with 9 and 12 at.% Al will not be used. The values of $V_{\mathrm{chem}}(\mathbf{k}_1)$ obtained for alloys with 16 and 19 at.% Al at various temperatures (in section II) differ very little from one another; we therefore average them and subsequently use the mean value of $V_{\mathrm{chem}}(\mathbf{k}_1)/\varkappa = -5700 \pm 200$°K. Thus in the concentration range of present interest (c > 12 at.% Al) we assume that $V_{\mathrm{chem}}(\mathbf{k}_1)$ and $V_{\mathrm{chem}}(\mathbf{k}_2) = V(\mathbf{k}_2)$ are independent of temperature and concentration, while the whole temperature and concentration dependence of $V(\mathbf{k}_1)$ is associated with the analogous dependence of $V_{\mathrm{mag}}(\mathbf{k}_1)$, i.e.,

$$\frac{V(\mathbf{k}_1, T, c)}{\varkappa} = -5700° + \frac{V_{\mathrm{mag}}(\mathbf{k}_1, T, c)}{\varkappa}; \tag{7a}$$

$$V(\mathbf{k}_2)/\varkappa = -3700°. \tag{7b}$$

The quantity $V_{\mathrm{mag}}(\mathbf{k}_1, T, c)/\varkappa$ was calculated (using the Minsk-32 computer) for any temperature and concentration using the equation given in ref. 2. Here we employed experimental data pertaining to the Curie temperatures obtained from ref. 22, the saturated magnetizations from ref. 23, and the temperature dependences of the magnetization curves of Fe−Al alloys obtained by Z. N. Bulycheva.

Using the intensity measurements close to the structural nodes together with Eq. (4) we determined V(0), from which, after calculating $V_{\mathrm{mag}}(0)$, we found $V_{\mathrm{chem}}(0)$. The value of $V_{\mathrm{chem}}(0)$ was also calculated from the chemical activities of aluminum a_{Al} in Fe−Al alloys at 900°C obtained by a physicochemical method in ref. 24, using the equation[14]

$$\frac{1}{1-c}\,\frac{1}{a_{\mathrm{Al}}}\,\frac{da_{\mathrm{Al}}}{dc} = \frac{1}{c(1-c)} + \frac{V(0)}{\varkappa T}. \tag{8}$$

All the values of V(0) are shown[4)] in Table 1.

We see from Table 1 that the values of $V_{\mathrm{chem}}(0)$ calculated from the thermodynamic data of ref. 25 agree closely with those derived in the present investigation.

It should be noted that the experimental error committed in determining V(0) is much greater than that in determining $V(\mathbf{k}_1)$ and $V(\mathbf{k}_2)$, since V(0) is determined from the intensity of diffuse scattering close to the structural points; there is thus a distinct probability of measuring the intensity in a direction not passing through the center of the reciprocal-lattice point (this probably occurred for the alloy containing 19 at.% Al). This latter difficulty cannot be eliminated if the single crystal has a severely mosaic structure.

TABLE 1. Fourier Components of the Energy of Mixing V(0) (in °K)

c, at. % Al	T, °C	$V(0)/\varkappa$	$V_{\mathrm{mag}}(0)/\varkappa$	$V_{\mathrm{chem}}(0)/\varkappa$	$V_{\mathrm{chem}}(0)/\varkappa$ at 900°C (ref. 24)
16	570	5220	780	6000	5740
19	570	6000	630	6630	5800
22	630	6180	0	6180	5810
22	690	5280	0	5280	5810
22	770	5630	0	5630	5810

The agreement between the x-ray and thermodynamic values of $V_{\mathrm{chem}}(0)$ indicates the possibility of using the x-ray method to determine $V_{\mathrm{chem}}(0)$. The values of $V_{\mathrm{chem}}(0)$ obtained by measuring the activity a_{Al} of aluminum[24] at 900°C over a wide range of compositions are practically constant (they vary by ~3% over the range 12-23 at.% Al) and agree closely with our present x-ray values for the low-temperature range (570-770°C). All this [as well as the constancy of $V(\mathbf{k}_2)$] indicates that the approximation of the self-consistent field is excellently satisfied, and may be regarded as adequately reliable in determining the Fourier components of the energy of mixing from Eqs. (3) and (4).

The resultant values of $V(\mathbf{k}_1)$ and $V(\mathbf{k}_2)$ [see Eq. (7)] were used to calculate the equilibrium values of the long-range order parameters η_1 and η_2 from (1) and (2) and the temperatures of the order–disorder phase transition (Kurnakov points). The calculation was carried out in the Minsk-32 computer for temperatures of 0-1423°K and compositions of 0-50 at.% Al, using two versions. In the first allowance was made in (7a) for the magnetic energy $V_{\mathrm{mag}}(\mathbf{k}_1)$; in the second $V_{\mathrm{mag}}(\mathbf{k}_1)$ was assumed to be zero.

For alloys with different Al contents we plotted the temperature dependences of the long-range order parameters of types $\mathrm{FeAl}(\eta_1)$ and $\mathrm{Fe_3Al}(\eta_2)$ and also the temperature dependences of the quantities $\eta_1/\eta_1(0°\mathrm{K})$ and $\eta_2/\eta_2(0°\mathrm{K})$, where $\eta_1(0°\mathrm{K})$ and $\eta_2(0°\mathrm{K})$ are the maximum values of the long-range order parameters for the composition in question. All the relationships were plotted for the two versions (with and without allowing for the magnetic energy).

Analysis of the resultant relationships leads to the following conclusions.

1. At temperatures below the magnetic Curie temperature, the contribution of the magnetic energy to the total energy of mixing leads to a considerable reduction in order of the $\mathrm{FeAl}(\eta_1)$ and $\mathrm{Fe_3Al}(\eta_2)$ types. At the magnetic Curie temperature the $\eta_1(T)$ and $\eta_2(T)$ curves suffer an inflection.

2. The long-range order of the $\mathrm{FeAl}(\eta_1)$ type reaches a maximum in an alloy containing 50 at.% Al, and that of the $\mathrm{Fe_3Al}(\eta_2)$ type in one containing 25 at.% Al.

3. At all temperatures except those in the immediate neighborhood of the Kurnakov point the quantity $\eta_1/\eta_1(0°\mathrm{K})$ is a maximum for the alloy containing 40 at.% Al and falls in the following sequence: c = 0.5, 0.3, 0.25, and 0.2 (atomic proportion of Al). Analogously $\eta_2/\eta_2(0°\mathrm{K})$ is a maximum for the alloy containing 30 at.% Al and falls in the sequence c = 0.25, 0.20, and 0.40.

The latter characteristics are evidently associated with the mutual influence of the two types of long-range order. The same circumstance probably leads to the asymmetrical disposition of the line of Kurnakov points for the FeAl → $\mathrm{Fe_3Al}$ phase transition: The maximum temperature is displaced from the composition corresponding to the alloy $\mathrm{Fe_3Al}$ in the sense of greater Al concentrations.

The concentration dependences of the long-range order parameters $\eta_1(c)$ and $\eta_2(c)$ were plotted at all temperatures from 0 to 1423°K at intervals of 50° by means of an electronic computer.

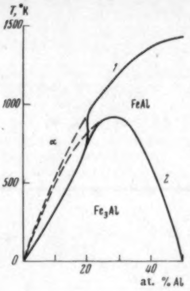

Fig. 3. Equilibrium diagrams of the Fe–Al system plotted by means of the energy parameters $V(\mathbf{k}_1)$ and $V(\mathbf{k}_2)$ (without allowing for the possibility of phase separation). The continuous lines correspond to the real case, in which the magnetic energy of the alloys is taken into account, the dashed lines to the case in which magnetic energy is neglected. The ranges of solid solutions ordered in the B2(1) and $\mathrm{DO_3}$(2) manner are indicated as FeAl and $\mathrm{Fe_3Al}$, respectively.

Those concentrations (at any specified temperature) for which nonzero values of η_1 and η_2 arise [branch points of Eqs. (1) and (2)] correspond to the Kurnakov points T_{B2} and $T_{\mathrm{DO_3}}$ respectively on the equilibrium diagram. These two temperatures are the Kurnakov points, corresponding to the formation of ordered phases with the structure of FeAl(B2) and $\mathrm{Fe_3Al(DO_3)}$, respectively.

The lines of Kurnakov points T_{B2} and T_{DO3} are shown in Fig. 3 (curves 1 and 2, respectively) as continuous lines for version I [$V_{\mathrm{mag}}(\mathbf{k}_1) \neq 0$] and dashed lines for version II[$V_{\mathrm{mag}}(\mathbf{k}) = 0$]. We see from Fig. 3 that ferromagnetism leads to a reduction in the stability of the ordered phases – i.e., to a reduction in the regions with long-range order on the T-c diagram – and a fall in the temperatures of the phase transitions. Hitherto the only attempt at allowing for the contribution of the magnetic energy to order–disorder phase transitions in the Fe–Al system was made in ref. 7. However, the approximation used in that paper was so coarse that no allowance was made for the leading features of the phenomenon, the concentration and temperature dependence of the magnetic energy. The magnetic energy was not taken into account at all in refs. 4-6, which were devoted to a theoretical calculation of the Fe–Al equilibrium diagram. In all these cases[4-7] the Fe–Al diagram was plotted on the assumption that the atoms only interacted in the first two coordination spheres. The energies of mixing in these spheres, W and w, were chosen in such a way as to obtain the experimentally determined phase-transition temperatures (i.e., W and w were simply matching parameters in the theory of plotting the equilibrium diagrams).

Our own diagram (Fig. 3, continuous lines) was plotted by means of the energy parameters $V(\mathbf{k}_1)$ and $V(\mathbf{k}_2)$ determined from independent experiments on diffuse scattering. In plotting the diagram we did not use any additional published data pertaining to the Kurnakov points, nor did we make any assumptions regarding the radius of interatomic interaction. Owing to the temperature and concentration dependence of the magnetic energy $V_{\mathrm{mag}}(\mathbf{k}_1)$, at a certain temperature and concentration the quantities $V(\mathbf{k}_1)$ and $V(\mathbf{k}_2)$ become equal to one another, and then on reducing the temperature, $|V(\mathbf{k}_2)| > |V(\mathbf{k}_1)|$. As a result of this

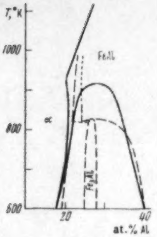

Fig. 4. Comparison between the Fe–Al equilibrium diagram derived from x-ray data pertaining to V($\mathbf{k}_1$) and to V($\mathbf{k}_2$) (allowing for magnetic energy) and the diagram plotted in ref. 25 on the basis of transmission electron microscopy (shown by the dashed lines).

the disordered α solid solution transforms directly into the ordered phase Fe_3Al, without any intermediate stage $\alpha \rightarrow FeAl \rightarrow Fe_3Al$. This latter fact was apparently not noted earlier.

The equilibrium diagram presented in Fig. 3 was obtained without allowing for the possibility of phase separation (for constructing the diagram allowance would in this case have to be made for the concentration dependence of the magnetic component of the entropy in the expression for the free energy. A theoretical calculation of the Fe–Al phase diagram was carried out in ref. 5 on the free-energy curves, and the two-phase regions were plotted (the calculation was carried out without allowing for the magnetic energy, using an approximation restricted to the interaction of atoms in two coordination spheres, with two parameters W and w). It was shown in ref. 5 that the lines T_{B2} and T_{DO3} practically coincided with the outer boundaries of the two-phase regions (i.e., with the outer boundaries of the ranges of existence of the ordered phases on the equilibrium diagram). This offers the possibility of comparing our own diagram with existing experimental data. Figure 4 illustrates a comparison with the results of one of the later investigations, based on transmission electron microscopy.[25] We see from Fig. 4 that the outer boundaries of the two-phase regions do indeed agree with the lines of Kurnakov points obtained in our own investigation. A more accurate allowance for the magnetic free energy carried out on the molecular-field approximation later enabled us to plot the Fe–Al equilibrium diagram with due allowance for phase separation.[26]

The authors wish to thank V. Z. Pogosov for kindly providing the Fe–Al alloy single crystals, thus enabling the present investigation to be carried out.

---

1) The choice of reciprocal temperature as variable is due to the fact that, on allowing for correlation,[3] the first and largest-in-magnitude correction term to V(**k**) in Eqs. (3) and (4) takes the form $[(1-2c)^2/2\varkappa T](1/N) \times \sum_{\mathbf{k}'} V(\mathbf{k}-\mathbf{k}')V(\mathbf{k}')$.

2) Here and subsequently the Fourier components of the energies of mixing are given in energy degrees, in units of $\varkappa$.

3) To obtain $V_{chem}(\mathbf{k}_1)$ we calculated the value of $V_{mag}(\mathbf{k}_1)$. The calculation was carried out by two methods: by the equations of ref. 2 and from the energy of spin waves for Fe at various temperatures.[16] The values of $V_{mag}(\mathbf{k}_1)$ obtained by the two methods differed from one another by no more than 20%.

4) In contrast to the points $\mathbf{k}_1$ and $\mathbf{k}_2$, quenching from 570-770°C fixes the intensity of the diffuse scattering close to the point $\mathbf{k} = 0$ at the quench temperature. This is due to the fact that the evolution of diffuse scattering close to $\mathbf{k} = 0$ is associated with diffusion through greater distances $\sim 2\pi/k$, and this is effected more slowly than the evolution, which leads to the establishment of equilibrium diffuse scattering at the points $\mathbf{k}_1$ and $\mathbf{k}_2$.

---

[1] A. G. Khachaturyan, Fiz. Tverd. Tela, 5, 26 (1963) [Sov. Phys.–Solid State, 5, 16 (1963)]; Zh. Eksp. Teor. Fiz., 69, 1421 (1972).
[2] M. M. Naumova and S. V. Semenovskaya, Fiz. Tverd. Tela, 13, 381 (1971) [Sov. Phys.–Solid State, 13, 312 (1971)].
[3] D. A. Badalyan and A. G. Khachaturyan, Fiz. Tverd. Tela, 12, 439(1970) [Sov. Phys.–Solid State, 12, 346 (1970)].
[4] V. V. Geichenko, V. M. Danilenko, and A. A. Smirnov, Fiz. Met. Metalloved., 13, 321 (1962).
[5] I. L. Aptekar', Fiz. Met. Metalloved., 12, 197 (1961).
[6] R. S. Rudman, Acta Metallurg., 8, 321 (1960).
[7] C. R. Houska, J. Phys. Chem. Solids, 24, 95 (1963).
[8] C. Van Dijk and J. Bergsma, Neutron Inelastic Scattering, 1, 233 (1968).
[9] H. J. Leamy, E. D. Gibson, and F. X. Kayser, Acta Metallurg., 15, 1827 (1967).
[10] C. B. Walker, Phys. Rev., 13, 547 (1956).
[11] A. J. Freeman, Phys. Rev., 113, 176 (1959); Acta Crystallogr., 13, 618 (1960).
[12] M. A. Krivoglaz, Zh. Eksp. Teor. Fiz., 32, 1368 (1957) [Sov. Phys.–JETP, 5, 1115 (1957)].
[13] M. A. Krivoglaz, Zh. Eksp. Teor. Fiz., 34, 204 (1958) [Sov. Phys.–JETP, 7, 139 (1958)].
[14] M. A. Krivoglaz, Theory of the Scattering of X Rays and Thermal Neutrons by Real Crystals [in Russian], Fizmatgiz, Moscow (1967).
[15] S. D. Gertsriken, I. Ya. Dekhtyar, N. P. Plotnikova, L. F. Slastnikova, and T. K. Yatsenko, Study of Heat-Resistant Alloys, Vol. 3 [in Russian], Izd. Metallurgiya, Moscow (1958), p. 68.
[16] H. Bjerrum Møller, Neutron Inelastic Scattering, 2, 3 (1968).
[17] M. A. Krivoglaz and Tyu Khao, Naukova Dumka, 24, 84 (1968) (sic).
[18] S. Wakon and J. Yamashita, J. Phys. Soc. Japan, 21, 1721 (1966).
[19] S. C. Moss, Phys. Rev. Lett., 22, 1108 (1969).
[20] J. B. Castles, J. M. Cowley, and A. E. Spargo, Acta Crystallogr., A27, 376 (1971).
[21] S. Hashimoto and S. Ogawa, J. Phys. Soc. Japan, 29, 710 (1970).
[22] L. Rimlinger, Compt. Rend., 261, 4090 (1965).
[23] A. Arrott and H. Sato, Phys. Rev., 114, 1420 (1954).
[24] J. Eldridge and L. L. Kamarek, Trans. Met Soc. AIME, 230, 226 (1964).
[25] H. Warlimont, Z. Metallkunde, 60, 195 (1969).
[26] S. V. Semenovskaya, Dokl. Akad. Nauk SSSR, 210, 1056 (1973).

Laser detection of acentrism in crystals

V. D. Shigorin and G. P. Shipulo

Physics Institute, Academy of Sciences of the USSR

(Submitted March 17, 1972)
Kristallografiya, 18, 557-559 (May-June 1973)

Laser frequency doubling provides a simple way of detecting acentrism in crystals; numerous organic compounds have been used to compare the results from this method with ones from x-ray and piezoelectric measurements.

Detection of acentrism in crystals is often an important auxiliary task in structure analysis by diffraction; an inversion center cannot be observed directly from the diffraction pattern, and a correct deduction of the space group often requires additional evidence, some of it difficult to obtain.[1] Crystals lacking a center of symmetry can produce a second harmonic from laser radiation,[2,3] and we have examined the practical value of this as a method of detecting acentrism by means of a relatively simple apparatus applied to some dozens of organic compounds for which the lattice symmetry was known or else for which piezoelectric measurements were available, since this effect is described by a tensor of the same form as that for frequency doubling.

The experiments were done with crystals in the most readily available (finely divided) form; we used a neodymium laser ($\lambda_1 = 1.06\ \mu$) in preference to a ruby laser ($\lambda_1 = 0.69\ \mu$) to produce the second harmonic; the reason is that the second harmonic for ruby ($\lambda_2 = 0.35\ \mu$) is less intense, because organic molecules absorb strongly in the ultraviolet region, and the light cannot be seen directly by eye, whereas there is often inherent or impurity luminescence of the specimen.[4]

The emission from a solid caused by high-power laser radiation often falls in the second-harmonic region; this undesirable background may be the short-wave edge of the fluorescence spectrum resulting from two-photon excitation if the emission and absorption bands of the crystal overlap considerably. This means that photoelectric detection of second-harmonic generation is unreliable even with narrow-band filters, and one needs to examine the spectrum of the scattered light near the harmonic frequency. For this reason, we used the following scheme for identifying the second harmonic: The neodymium laser radiation scattered by the crystal was examined to detect the second-harmonic line via a high-aperture spectrometer for the visible region that can be used as a spectroscope or spectrograph.1) If the material does not fluoresce in response to laser radiation or gives a continuous spectrum, one can use an instrument with low dispersion; such a method is very simple and enables one to examine acentrism in crystals at various temperatures, pressures, etc.

In our experiments, the neodymium laser radiation (medium power) was passed through a KS-15 filter and directed by a long-focus lens2) on to the specimen ($P \sim 100$ MW/cm^2). The scattered light was collected by a two-lens condenser, whose optic axis lay at about 30° to the laser beam, and this fed an ISP-51 spectrograph. The camera in this system had F = 120 mm, and its focal plane can be fitted with an eyepiece, a scattering screen, or a photographic plate to record the single green line. To identify this as the second-harmonic line one can use a powder of some familiar nonlinear material, e.g., potassium dihydrogen phosphate or lithium niobate, or else the light of a filament lamp passed through an interference filter having $\lambda_2 = 530$ nm. If all the parts of the apparatus other than the laser are placed in a light-tight unit, the instrument can be operated even in a lit room. The microscopic crystals may for convenience be poured into narrow thin-walled glass test tubes, and the grain size can be from 10^{-2} to 1 mm.

The substances can be divided into four groups in accordance with the observations on second-harmonic generation.

Compounds in the first group have acentrism established by x-ray methods,3) and this was confirmed by the second-harmonic generation. The materials were benzophenone, xanthone, phthalic anhydride, triphenylmethane, p-toluidine, m-nitrobenzene, m-aminophenol (all of which are piezoelectric),[6,7] and also diphenylurea, salicylindeneaniline, etc. There was no case where x-ray or piezoelectric measurements indicated acentrism and second-harmonic generation was absent.4) On the other hand, 4-aminopyridine, xanthone, and p-nitrodimethylaniline gave quite strong second harmonics (stronger than potassium dihydrogen phosphate), while the piezoelectric effect is weak.[7] This indicates comparatively high sensitivity for the method.

Compounds in the second group have centers of symmetry in the crystal, and they gave no second harmonics for various powder grain sizes,5) although most of them have a polar structure of the molecules characteristic of such generation.[4] Examples of this are acetanilide, azobenzene, *a*-nitrochlorobenzene, o-dinitrobenzene, pyrocatechol, p-phenylenediamine, p-nitrophenol, p-nitrotoluene, p-nitroaniline, 1-nitronaphthalene, and benzoic acid, none of which show the piezoelectric effect,[6] and also phthalimide, dibenzoylmethane, 4,5-dichloronaphthalic anhydride, naphthalimide, 1-bromonaphthaloxene, anthraquinoneoxadiazole, and anthraquinonethiadiazole.6)

The third group includes p,p'-dibromodibenzoylmethane (from chloroform), p-aminoazobenzene (from ethanol), p-anisidine (from ethanol), and m-nitrophenol (from benzene); all of these generate readily visible green second harmonics, in conflict with the previously established centers of symmetry. Second-harmonic generation, but with efficiencies lower by factors of hundreds,[10-12] can arise from local symmetry reduction near lattice defects, or from magnetic-dipole or electric-quadrupole interactions. Here we may note the very strong second-harmonic generation by powders of p,p'-dibromodibenzoylmethane and p-aminoazobenzene, as well as the piezoelectric p-anisidine and m-nitrophenol,[6] which indicates erroneous determination of the space groups of these crystals as being centrosymmetric. This aspect requires further examination.

In the last groups (p-aminophenol, p-chlorobenzene, nickel diacetylacetonate, etc.), the second-harmonic generation enabled one to choose from the various proposed structure types that which most correctly describes the structure, which provides a considerable simplification. For instance, the correct alternative can be chosen for the space group ($P2_1$ or $P2_1/m$) for crystals of o-nitrobenzaldehyde,[13] which required a very complex analysis in order to determine the structure. The intense second harmonic indicates at once that the crystals do not have a center of symmetry.

We also examined the second-harmonic generation in phase transitions in thiourea and triglycine sulfate, whose Curie points are about 173 and 322°K, respectively. The observed second-harmonic generation reflects accurately the symmetry changes in these crystals with temperature. The effect was not recorded at room temperature for thiourea, but on lowering the tube containing the crystals into a vessel containing liquid nitrogen, the green harmonic line was clearly visible at the output of the spectrograph, in accordance with the $P2_1ma$ symmetry of the ferroelectric phase. The opposite effect occurs on plunging tubes containing triglycine sulfate into a vessel containing hot water, which gives the crystals the symmetry $P2_1/m$.

This laser method of detecting acentrism is thus very simple and allows one to work with materials in readily available powder form, while requiring only small quantities of material and providing good sensitivity. The second-harmonic method may be very valuable as an accessory one in determining space groups, examining phase transitions, and studying ordering in textures.

We are indebted to A. M. Prokhorov for direction in this work.

---

1)With some experience, the reasonably strong green emission of the second harmonic from a neodymium laser can be recognized by the unaided eye.

2)The degree of focusing by this lens controls the efficiency in second-harmonic generation and also the damage threshold for the material; the optimal relationship between second-harmonic intensity and specimen damage is provided by lasers with very short pulses.[5]

3)See Structure Report for the original work on crystal structure.

4)Exceptions are provided by the acentric crystals of alternate hydrocarbons, where there is no generation of the harmonic on account of the electronic structure of the molecules.[4]

5)The extent of second-harmonic generation in the powder may fall considerably as the mean grain size increases.[3]

6)It has recently been shown[8,9] that these last five compounds have centers of symmetry.

---

[1] P. J. Wheatley, Determination of Molecular Structure, Oxford Univ. Press (1959).

[2] V. S. Suvorov and A. S. Sonin, Kristallografiya, 11, 832 (1966)[Sov. Phys.—Crystallogr., 11, 711 (1967)].

[3] S. K. Kurtz and T. T. Perry, J. Appl. Phys., 39, 3798 (1968).

[4] V. D. Shigorin and G. P. Shipulo, Opt. Spektrovsk., 34, 151 (1973).

[5] A. J. DeMaria, W. H. Glenn, and M. E. Mack, Phys. Today, 24, 19(1971).

[6] A. Hettich and H. Steinmetz, Z. Phys., 76, 688 (1932).

[7] V. A. Koptsik, K. A. Minaeva, A. A. Voronkov, A. F. Solov'ev, A. N. Izrailenko, E. G. Popkova, and G. I. Kozlova, Vestnik Mosk. Univ., 6, 91 (1958).

[8] Le Nguyen Shok and G. A. Gol'der, Zh. Strukt. Khim., 11, 939 (1970).

[9] L. A. Chetkina, O. A. Mikhno, and Z. I Ezhkova, Zh. Strukt. Khim., 12, 187 (1971).

[10] T. P. Belikova and E. A. Sviridenkov, ZhETF Pis. Red., 5, 29 (1967) [JETP Lett., 5, 22 (1967)].

[11] I. I. Kondilenko, P. A. Korotkov, and V. I. Malyi, in: Quantum Electronics [in Russian], issue 3, Naukova Dumka, Kiev (1969), p. 120.

[12] H. Rabin, Radiat. Effects, 4,167 (1970).

[13] P. Coppens and G. M. J. Schmidt, Acta Crystallogr., 17, 222 (1964).

Far infrared reflectance spectra of rubidium trihydro- and trideuterioselenite crystals

J. Petzelt, L. D. Kislovskii, and L. A. Shuvalov

Physical Institute, Czechoslovakian Academy of Sciences
Institute of Crystallography, Academy of Sciences of the USSR

(Submitted May 30, 1972)
Kristallografiya, 18, 560-563 (May-June 1973)

The infrared spectra in the 30-430 cm^{-1} region of $RbH_3(SeO_3)_2$ and $RbD_3(SeO_3)_2$ crystals in their paraelectric and ferroelectric phases were investigated. No differences between the spectra of the H and D salts were detected in the two phases.

Shuvalov et al.[1] established that the $RbH_3(SeO_3)_2$ (RHS) crystal undergoes a 222 ⟶ 2 phase transition at $T_C = -115°C$ ($T_C = -119°C$ according to refined data[2]) and is a ferroelectric below the transition point. The extremely slight anomaly[1] of the dielectric constant $\varepsilon_y = \varepsilon_b$ in the vicinity of T_C and a number of other characteristics[3] of the physical properties of RHS indicate that the polarization P cannot be a parameter of the transition in RHS; in other words, RHS belongs among the improper ferroelectrics[4-6] similar to $Gd_2(MoO_4)_3$. It was also established in refs. 2 and 3 that when the hydrogen is replaced by deuterium in the $Rb(D_xH_{1-x})_3(SeO_3)_2$ (RHDS) crystals, there is almost no shift in T_C, but the ferroelectric polarization P_s and dielectric anomaly decrease with an increase in the deuterium concentration and practically disappear when $x \simeq 0.9$. It was concluded in refs. 2 and 3 on the basis of these data that the low-temperature phases of the RDHS crystals with $x \leqslant 0.9$ and with $x \geqslant 0.9$ have different point symmetries. The structure of the paraelectric phase of RHS (space group D_2^4, Z = 4) was recently determined by x-ray diffraction analysis.[7] As before, there are no data on the structure of the low temperature phase of the RDHS crystals in the literature.

The results of an investigation of the reflectance spectra of $RbH_3(SeO_3)_2$ and $RbD_3(SeO_3)_2$ (RDS) crystals in the far infrared region (30–430 cm^{-1}) at temperatures corresponding to the high temperature and low temperature phases are reported in this paper.

The measurements were carried out on an RIIC FS620 Fourier spectrometer adapted to measure small samples.[8] It should be mentioned that spatial instability of the discharge of the radiation source could show up noticeably during work with the adaptation.[8] In addition, the stabilization of the source with respect to the overall flux, which has been been structurally provided for in the FS620 instrument, generally speaking does not guarantee its stabilization with respect to the spectrum. Therefore, the photometric results presented below should be considered to be only qualitative in a rigorous treatment (especially in the long-wave portion of the spectrum) without a special investigation of the spatial and time stability of the radiation source. However, this observation does not change the overall conclusions obtained below from the experimental data.

In order to avoid the effect of the possible replacement of D by H on the surface of the RDS samples, the measurements were carried out on RDS wafers with a surface freshly pickled in D_2O.

Group analysis (Table 1) shows that 23 external vibrations active in the far infrared region can be expected for each of the orientations $\mathbf{E}\parallel x$, $\mathbf{E}\parallel y$, and $\mathbf{E}\parallel z$ for the paraelectric phase of RHS and RDS, and if the motions of hydrogen are not taken into account, then 14 can be expected. (It can be assumed that the frequencies of the internal vibrations lie in the high-frequency portion of the spectrum, because these frequencies lie above 370 cm^{-1}

TABLE 1. Classification of the Long-Wave Lattice[1] Vibrations of the RHS and RDS Crystals in the Paraphase

Type of symmetry	No. of external vibrations		No. of external vibrations without account of motion of hydrogen		Activity in infrared spectrum
	optical	acoustic	optical	acoustic	
A	24	—	15	—	—
B_1	23	1	14	1	$\mathbf{E}\parallel z$
B_2	23	1	14	1	$\mathbf{E}\parallel y$
B_3	23	1	14	1	$\mathbf{E}\parallel x$

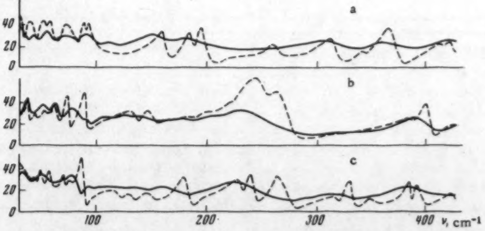

Fig. 1. Far-infrared spectra of the $RbH_3(SeO_3)_2$ crystal. a) $\mathbf{E}\parallel x$; b) $\mathbf{E}\parallel y$; c) $\mathbf{E}\parallel z$; solid curve, T = 25°C; dashed curve, T = −170°C.

in the dynamics of the phase transitions in RHS and RDS (as has already been mentioned in refs. 2 and 3). Therefore, it can be assumed in accordance with Table 1 during the interpretation of the spectra that there are 14 external vibrations for each orientation of **E** which are active in the infrared region for the paraelectric phase of RHS. As is evident from Table 2, the number of them found is a little lower than the group analysis provides. Therefore, the existence of still lower frequency vibrations ($\nu < 30\ \text{cm}^{-1}$) can be expected. A comparison of the calculated values of ε_y with the static values[1] also does not contradict the fact that the region where ε_y is dispersed should lie below 30 cm^{-1}. The considerable increase in the number of active vibrations below T_C indicates the emergence of a superstructure in the low-temperature phase of RHS.

The question concerning the detection of a soft mode remains open. Accurate measurements of the temperature dependence of the low-frequency portion (10-100 cm^{-1}) of the $E \parallel y$ spectrum in the low temperature phases of RHS and RDS are needed.

The authors thank N. V. Gordeeva for the crystals grown for the investigations and I. Maierova for help during the experiment.

---

[1] L. A. Shuvalov, N. R. Ivanov, N. V. Gordeeva, and L. F. Kirpichnikova, Kristallografiya, 14, 658 (1969) [Sov. Phys.—Crystallogr., 14, 554 (1970)].

[2] L. A. Shuvalov, N. R. Ivanov, L. F. Kirpichnikova, and N. V. Gordeeva (Gordeyeva), Phys. Lett., 33, 490 (1970).

[3] N. R. Ivanov, I. T. Tukhtasunov, and L. A. Shuvalov, Kristallografiya, 15, 752 (1970) [Sov. Phys.—Crystallogr., 15, 647 (1971)].

[4] A. P. Levanyuk and D. G. Sannikov, Fiz. Tverd. Tela, 12, 2997 (1970) [Sov. Phys.—Solid State, 12, 2418 (1971)].

[5] V. Dvorak, Phys. Status Solidi, B45, 147 (1971).

[6] J. Petzelt and V. Dvorak, Phys. Status Solidi, B46, 413 (1971); J. Petzelt, Solid State Commun., 9, 1485 (1971).

[7] A. V. Tovbis, T. S. Davydova, and V. I. Simonov, Kristallografiya, 17, 103 (1972) [Sov. Phys.—Crystallogr., 17, 81 (1972)].

[8] L. Novak and J. Petzelt, Ceskosl. Casop. Fys., A20, 482 (1970).

[9] K. Nakamoto, Infrared Spectra of Inorganic and Coordination Compounds [Russian translation], Moscow (1966), p. 125.

[10] V. Dvorak, Phys. Status Solidi, B51, K129 (1972).

[11] L. A. Shuvalov, N. R. Ivanov, A. A. Boiko, L. F. Kirpichnikova, A. Fouskova, N. V. Gordeeva, V. S. Ryabkin, V. A. Babayants, and S. Kh. Aknazarov, Kristallografiya, 18, (1973) [Sov. Phys.—Crystallogr., 18, (1973)].

Absorption spectra of $MgWO_4$ crystals activated with Cr^{3+} and Co^{2+} ions

O. N. Boksha and T. M. Varina

Institute of Crystallography, Academy of Sciences of the USSR

(Submitted November 16, 1971; resubmitted June 14, 1972)
Kristallografiya, 18, 564-569 (May-June 1973)

The absorption spectra of $MgWO_4-Cr^{3+}$ and $MgWO_4-Ca^{2+}$ were investigated. The location of the Cr and Co ions on the large oxygen octahedra governed the low value of the crystal field strength parameter for these ions in $MgWO_4$. The broad band in the red region in the spectrum of Cr^{3+} in $MgWO_4$ is the superposition of several bands due to the transitions to the closely lying $^4T_2$, ^2E, and $^2T_1$ levels. The group of bands observed for $MgWO_4-Co^{2+}$ in the 16,000-15,000 cm^{-1} region was attributed to transitions to the $^2T_1$ and $^4T_1$ levels in the Co^{2+} ion which are split, as in the case of the Cr^{3+} ion, by the low-symmetry crystal field. Splitting of the ground state of the Co^{2+} ion amounting to ~ 200 cm^{-1} was established.

The $MgWO_4$ crystals are assigned to the 2/m monoclinic system.[1] Geometrically equivalent zig-zag chains of populated and empty octahedra alternate in the two-layer (hexagonal) packing of the tungstate. Two types of cations alternate along the two layers of packing. When Cr and Co ions enter into $MgWO_4$, they occupy the site of the Mg^{2+} ion which enters into the field of the deformed octahedron formed by the oxygen ions.[2,3] The Me–O distances in these octahedrons are as follows:[1] 2.043, 2.116, and 2.125 Å (an average of 2.094 Å).

Investigations of the optical spectra have been carried out at room and low temperatures (down to 4.2°K) in polarized light on samples cut parallel and perpendicular to the plane of the optical axes from the crystals grown by the authors.[4]

The absorption spectrum of $MgWO_4-Cr^{3+}$ measured at room temperature on an SF-4 spectrophotometer has broad absorption bands in the 18,860-19,600 and 12,500-14,300 cm^{-1} regions (Fig. 1) which are connected with the $^4A_2 \rightarrow {}^4T_1$, and $^4T_2$ transitions for Cr^{3+} ions in a field of octahedral symmetry and which are allowed with respect to spin (Table 1).

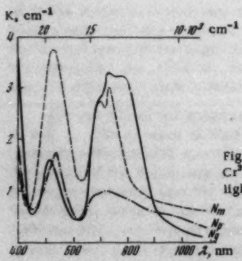

Fig. 1. Absorption spectrum of $MgWO_4-Cr^{3+}$ at room temperature in polarized light.

The parameter of the crystal field intensity is equal to ~ 1400 cm^{-1}, whereas this parameter ~ 1800 cm^{-1} for Cr^{3+} in Al_2O_3 and MgO. When $Dq \sim 1400$ cm^{-1}, the quartet $^4T_2$ state, close to which lie the doublet ^2E and $^2T_1$ states, should be the first excited state, according to the diagram of the energy levels of the $3d^3$ configuration.[5] The absorption band of $^4A_2 - {}^4T_1$ for waves with vibrations with respect to N_m and N_p has a maximum at 18,860 cm^{-1}, and for the wave with vibrations with respect to N_g at 19,600 cm^{-1}. This indicates that the $^4T_1$ electron energy level is split by 740 cm^{-1} by the low symmetry field of $MgWO_4$. An additional weak and narrower absorption band was observed at 19,860 cm^{-1} at low temperatures for the N_m wave; it is evidently connected with the transition to the $^2T_2$ state (analog to the B lines of ruby).

The band in the 12,500-14,300 cm^{-1} region is complex even at room temperature and possesses considerable pleochroism. Its structure at 4.2°K for the three polarizations is given in Fig. 2 from the measurements on a DFS-12 spectrometer.

An analysis of the temperature changes in the spectrum in the 12,000-15,000 cm^{-1} region showed that the bands have different temperature shifts. The band at 12,600 cm^{-1} is shifted in the N_g and N_m spectra in the low-frequency region with a drop in temperature, whereas in the N_p spectrum it has the usual shift in the high-frequency region. It is possible that the band at 12,600 cm^{-1} in the N_g and N_m spectra is not a fundamental one and the observed shift is in fact connected with a change

TABLE 1. Location of the Absorption Bands of Cr^{3+} in $MgWO_4$ in the Regions Where the $^4A_2 \rightarrow {}^4T_2$, ^2E, and $^2T_1$ Transitions Occur

Direction	Temp., °K	Absorption bands, cm^{-1}						
		I	II	III	IV	V	VI	VII
N_p	290		14750			14080		
	77		14750			14080		12620
	4.2		14750			14080		12650
N_g	290		14750				13730	12790
	77		14780	14520	14310		13800	12650
	4.2		14790	14520	14340		13800	12600
N_m	290		14700		14330		13580	
	77	15220	14730		14360		13660	12650
	4.2	15240	14740		14380		13690	12600

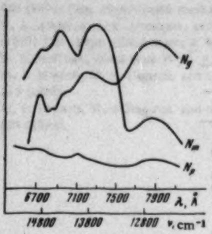

Fig. 2. Structure of the absorption bands of Cr^{3+} in $MgWO_4$ in the 12,000-15,000 cm^{-1} region at 4.2°K in polarized light. The absorption on the ordinates is plotted in relative units.

in the ratio of the intensities of its components when the temperature is lowered. All the remaining bands are shifted in the high-frequency region, but the magnitudes of their shifts differ. The broader bands in the 12,600-13,800 cm^{-1} region are shifted more strongly ($\delta \sim 60$-180 cm^{-1}); the bands in the 14,340-15,240 cm^{-1} region are slightly shifted with temperature ($\delta \sim 20$-50 cm^{-1}).

The differences in the width of the bands and in the magnitude of their temperature shift make it possible to assign them to transitions to the quadruplet and doublet states. The bands in the 12,000-13,800 cm^{-1} region are evidently connected with the transitions to the components of the $^2T_1$ electron energy level which is split by 1000 cm^{-1} by the low symmetry field of $MgWO_4$. Further, the transition to the components of the ^2E electron energy level is situated in the 14,340 to 15,240 cm^{-1} region, and the transitions to the components of the $^2T_1$ electron energy level lie in the 14,500 to 15,240 cm^{-1} region. The ^2E and $^2T_1$ levels are located close to the $^4T_2$ level, which also evidently leads to an increase in the intensity of the transitions to these levels and to their broadening through spin-orbital coupling. Thus, absorption bands similar to the R, R′, and B lines of Cr^{3+} in oxides are located in those same spectral regions for $MgWO_4-Cr^{3+}$, but have high intensities and broad half-widths.

A broad band with a maximum at 10,750 cm^{-1} was observed at room temperature in the luminescence spectrum of $MgWO_4-Cr^{3+}$. The intensity of the luminescence increases with a decrease in temperature, and the maximum shifts to 10,520 cm^{-1}.

The existence of a broad emission band for $MgWO_4-Cr^{3+}$, in contrast to the majority of compounds containing Cr^{3+} in the octahedrons of oxygen ions and which have narrow luminescence lines, indicates that the luminescence is connected with the transition from the $^4T_2$ electron energy level to the $^4A_2$ ground state, and not with the transition $^2E_1, {}^2T_1 \rightarrow {}^4A_2$. This confirms the interpretation of the absorption spectrum given above, according to which $^4T_2$ is the lowest of the excited states of Cr^{3+} in $MgWO_4$ and is in agreement with the spectrum of Cr^{3+} in other tungstates.[6-8]

The $MgWO_4$ crystals containing Co that were investigated had a blue color, whereas a rose coloration is characteristic for crystals with hexacoordinated Co^{2+}. The blue coloration of $MgWO_4-Co^{2+}$ is evidently connected with the large Me–O distances in the octahedrons.

The absorption spectrum of $MgWO_4$–Co at room temperature contains three broad absorption bands (6,250, 13,000 cm^{-1}, and a band with a triple maximum in the 16,000-19,000 cm^{-1} region).[9] These bands are characteristic for crystals containing Co^{2+} in octahedral locations and correspond to the $^4T_1(^4F) \rightarrow {}^4T_2(^4F)$, $^4A_2(^4F)$, and $^4T_1(^4P)$ transitions in an octahedral field when the ratio of the parameters $Dq/B \sim 0.8$.

A broad absorption band with a maximum in the 16,000-17,000 cm^{-1} region and narrower bands at 18,800-19,300 cm^{-1} are observed in the 16,000-19,000 cm^{-1} region at room temperature. The detailed structure of these bands was investigated on a DFS-12 spectrometer. A band at 17,360 cm^{-1} and a band in the 16,000 cm^{-1} region, which has a complex structure at 4.2°K (maxima at 16,310, 16,160, and 16,020 cm^{-1}), are observed at low temperatures for all three directions of the vibrations. The broad band in the N_m spectrum in the 17,240 cm^{-1} region at

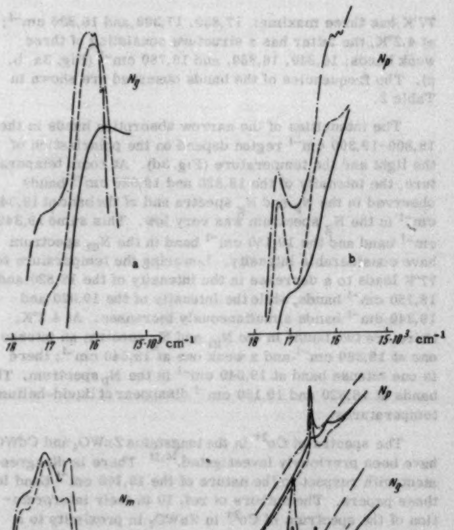

Fig. 3. Absorption spectrum of $MgWO_4-Co^{2+}$ at various temperatures in the 16,000-17,000 cm^{-1} spectral region (a, b, c) and in the 18,000-19,000 cm^{-1} region (d) in the N_g, N_p, and N_m directions. Solid line, 290; dashed line, 77; dot–dash line, 4.2°K.

TABLE 2. Location of the $MgWO_4-Co^{2+}$ Absorption Bands in the 16,000-19,000 cm^{-1} Region

Frequency of the absorption band, cm^{-1}								
$E \parallel N_p$			$E \parallel N_m$			$E \parallel N_g$		
290	77	4.2	290	77	4.2	290	77	4.2
		16020		16020	16020			16020
	16120					16120		
		16160			16160			16160
		16310		16200	16310		16200	16310
					16780			
				16830	16860			
					16940			
	17300	17360	17240	17300	17360	17120	17240	17360
				17850	17920			
18820	18820					18820	18820	
19020	19040	19040		19040	19040	19020	19040	19040
			19150	19150				
			19340	19340	19360	19340	19360	19360

Note: Temperature in °K.

77°K has three maxima: 17,850, 17,300, and 16,830 cm^{-1}; at 4.2°K, the latter has a structure consisting of three weak bands; 16,940, 16,860, and 16,780 cm^{-1} (Fig. 3a, b, c). The frequencies of the bands observed are shown in Table 2.

The intensities of the narrow absorption bands in the 18,800-19,300 cm^{-1} region depend on the polarization of the light and the temperature (Fig. 3d). At room temperature, the intensity of the 18,820 and 19,020 cm^{-1} bands observed in the N_p and N_g spectra and of the band at 19,340 cm^{-1} in the N_g spectrum was very low. This same 19,340 cm^{-1} band and the 19,150 cm^{-1} band in the N_m spectrum have considerable intensity. Lowering the temperature to 77°K leads to a decrease in the intensity of the 18,820 and 19,150 cm^{-1} bands, while the intensity of the 19,020 and 19,340 cm^{-1} bands simultaneously increases. At 4.2°K, there are two bands in the N_m and N_g spectra; an intense one at 19,360 cm^{-1} and a weak one at 19,040 cm^{-1}; there is one intense band at 19,040 cm^{-1} in the N_p spectrum. The bands at 18,820 and 19,150 cm^{-1} disappear at liquid-helium temperatures.

The spectra of Co^{2+} in the tungstates $ZnWO_4$ and $CdWO_4$ have been previously investigated.[10,11] There is disagreement with respect to the nature of the 19,100 cm^{-1} band in these papers. The authors of ref. 10 in their interpretation of the spectrum of Co^{2+} in $ZnWO_4$ in proximity to a trigonal field attribute this band to the transition to the $^2A_1$ electron energy level, and those of ref. 11 to one of the components $[^4T_1(B_3)]$ of the splitting of the $^4T_1$ electron energy level in a field of rhombic symmetry.

As was shown above, the $MgWO_4-Co^{2+}$ spectra investigated in this paper contain a system of bands in the 19,100 cm^{-1} region which are relatively narrow (their half-width ~30-100 cm^{-1}) compared to the half-widths of the bands in the 16,000-17,000 cm^{-1} region (~300 cm^{-1}) which are slightly shifted with a drop in temperature and are weak compared to the bands in the 16,000-17,000 cm^{-1} region. The difference in the character of the bands in the 19,100 cm^{-1} region from the bands in the 16,000-17,000 cm^{-1} region does not permit one to assign them to the transition to one of the components of the $^4T_1$ electron energy level as in ref. 11. On the other hand, two bands at 19,040 and 19,360 cm^{-1} are distinctly observed in the spectrum at liquid-helium temperatures; this does not permit one to assign the transition in the 19,100 cm^{-1} region to the orbital singlet $^2A_1$ as in ref. 10. The absorption in the 19,100 cm^{-1} region in $MgWO_4-Co^{2+}$ can be connected with the transition to the components of the $^2T_1$ doublet level whose splitting in the low symmetry field of $MgWO_4$ amounts to ~300 cm^{-1} according to our data.

In addition to the two bands at 19,040 and 19,360 cm^{-1}, there are another two bands at 18,820 and 19,150 cm^{-1}, which are spaced ~200 cm^{-1} from the first ones and disappear when the temperature is lowered to that of liquid helium, in the spectrum at 290-77°K. Such a temperature dependence of the components in this region indicates that four levels participate in the transition: Two correspond to the split $^4T_1$ ground state, and two to the components of the excited $^2T_1$ state. A decrease in temperature leads to a decrease in the population of the upper sublevel of the ground state which leads to the disappearance of the bands corresponding to the transitions from it to the components of the $^2T_1$ level. The splitting of the ground state of Co^{2+} in $MgWO_4-Co^{2+}$ thus amounts to ~200 cm^{-1}.

The bands in the 16,000-17,000 cm^{-1} region are connected with the transitions allowed with respect to spin from the ground level to the excited $^4T_1(P)$ level which is split into two components by the low symmetry field.

The equidistant bands in the 16,000-16,300 and 16,700-16,900 cm^{-1} regions are evidently the electronic-vibrational structure, and their frequency intervals of 140 and 80 cm^{-1} are the natural frequencies of the vibrations of the $MgWO_4$ lattice.

As has already been mentioned by the authors who investigated the spectra of Co^{2+} in tungstates, the correctness of the interpretation can be definitely established only by rigorous calculations.

The authors thank E. G. Valyashko for supervising this work.

---

[1] O. S. Filipenko, E. A. Pobedimskaya, V. I. Ponomarev, and N. V. Belov, Kristallografiya, 13, 1073 (1968) [Sov. Phys.–Crystallogr., 13, 933 (1969)].

[2] V. A. Atsarkin, É. A. Gerasimova, I. G. Matveeva, and A. V. Fratsesson, Zh. Eksp. Teor. Fiz., 43, 1272 (1962) [Sov. Phys.–JETP, 16, 903 (1963)].

[3] A. A. Bugai, V. M. Maksimenko, and A. B. Roitsin, Fiz. Tverd. Tela, 12,

659 (1970) [Sov. Phys.—Solid State, 12, 511 (1970)].

[4]V. A. Atsarkin, S. K. Morshnev, and L. A. Potkin, Fiz. Tverd. Tela, 9, 3 (1967) [Sov. Phys.—Solid State, 9, 1 (1967)].

[5]D. S. McClure, Solid State Phys., 9, 399 (1959).

[6]M. L. Reynols, W. E. Hagston, and G. F. J. Garlick, Phys. Status Solidi, 30, 113 (1968).

[7]M. L. Reynols, W. E. Hagston, and G. F. J. Garlick, Phys. Status Solidi, 30, 507 (1968).

[8]A. E. Nosenko, Author's abstract of doctoral dissertation, L'vov (1970).

[9]T. M. Varina and O. N. Boksha, Symposium on the spectroscopy of crystals activated by rare earth and transition metal ions, State Optical Institute Publishing House, Leningrad (1970).

[10]M. L. Reynols, W. E. Hagston, and G. F. J. Garlick, Phys. Status Solidi, 30, 735 (1968).

[11]A. E. Nosenko, M. V. Pashkovskii, and D. L. Futorskii, Opt. Spektrosk., 28, 297 (1970).

Nonlinear optical properties of paratellurite (TeO_2) crystals

Yu. V. Shaldin, S. P. Smirnov, L. M. Belyaev, and I. A. Shpil'ko

Institute of Crystallography, Academy of Sciences of the USSR

(Submitted May 4, 1972)
Kristallografiya, 18, 570-572 (May-June 1973)

The problem of calculating the nonlinear refractive index of TeO_2 crystals from curves of intensity of the composite wave ($\nu \pm \nu_0$) vs angle was solved within the scope of crystal optics; the calculated value of the nonlinear refractive index is $\delta n = (56 \pm 6) \cdot 10^{-8}$ cgs esu. It was shown that the coefficients of the tensor of nonlinear susceptibility (for the linear electrooptical effect) in crystals of this class are equal in magnitude and have opposite signs.

From the viewpoint of the investigator concerned with nonlinear optics and, in particular, electrooptics, paratellurite (TeO_2) crystals are rather unusual. The individuality of compounds of this class (tetragonal system, point group[1] 422) consists of the fact that, being optically anisotropic, their nonlinear (electrooptical) properties are described by one linearly independent coefficient $\varkappa_{14}(r_{41})$.

It is known from independent measurements that TeO_2 crystals are characterized by high values of electronic ($\varepsilon_\infty \sim 5$) and ionic ($\varepsilon_0 \sim 25$) polarizability.[2] Hence, it is quite reasonable to assume that substantial nonlinear (electrooptical) properties may be present.

1. We shall consider the general case of the action of a quasistatic electric field of frequency ν_0 on the optical properties of paratellurite crystals. If the symmetry of the tensor for the linear electrooptical effect[3] is taken into account, the equation of the optical indicatrix in generalized spherical coordinates has the form

$$\rho^2[1 + n_o n_e r_{41} E \sin 2\theta (\cos \varphi - \sin \varphi)] = 1, \tag{1}$$

ρ is the refractive index in generalized spherical coordinates, E is the amplitude of the field of frequency ν_0, n_o, and n_e are the refractive indices for the ordinary and extraordinary rays, and θ and φ are angular coordinates. When E = 0, Eq. (1) is identical with the equation of the unit sphere. From Eq. (1), an expression for refractive index may be derived which has the form

$$\rho^{\pm} = 1 \pm {}^1/_2\, n_o n_e r_{41} E \sin 2\theta (\cos \varphi - \sin \varphi). \tag{2}$$

Multiplication of the latter by n_{ij} gives the equation

$$\rho_{ij}^{\pm} = n_{ij} \pm {}^1/_2\, n_o n_{ij} n_e r_{41} E \sin 2\theta (\cos \varphi - \sin \varphi), \tag{3}$$

which determines the refractive index of the crystal in spherical coordinates. The second term corresponds to an effective nonlinear refractive index δn_{ij} of the medium, whose value wholly determines the degree of interaction of waves of frequencies ν and ν_0, resulting in waves of the sum and difference frequencies having nonzero intensity $I_\sim(\nu \pm \nu_0)$. After employing ref. 4, assuming that $I_0(\nu) \gg I_\sim(\nu \pm \nu_0)$, we may calculate the intensity of the mixed wave:

$$4I_\sim(\nu \pm \nu_0) = k l_{\text{eff}} I_0(\nu) n_o n_{32} n_e r_{41} E \sin 2\theta (\cos \varphi - \sin \varphi); \tag{4}$$

l_{eff} is the effective sample length, k is the wave vector, and n_{32} is the refractive index in the ⟨011⟩ direction.

Most interesting from our viewpoint is the case (to be investigated experimentally) where the field intensity vector coincides with the ⟨110⟩ direction, whereas the light is $\langle\bar{1}10\rangle$ (and conversely). Contrary to the analogous geometry of the experiment in $\bar{4}3m$, 23 cubic crystals, the intensity of the mixed wave with this orientation of the paratellurite sample is zero, as follows from Eq.(4).

The degree of mixing of the two waves in the crystal plate, with allowance for the fact that the effective path length depends on the refraction angle φ according to a $\cos^{-1} \varphi$ law,[5] is determined by the equation

$$4I_\sim(\nu \pm \nu_0) = \sqrt{2}\, k l_0 I_0 n_o n_{32} n_e r_{41} E \sin 2\theta \operatorname{tg} \varphi, \tag{5}$$

where l_0 is the geometrical thickness of the plate. The factor $\sqrt{2}$ is obtained on passing to a new coordinate system, rotated by 45° in the yz plane, in which the angle $\varphi = 0$ corresponds to normal incidence of the light ray. This equation is valid only for the series of discrete values of refraction angle, corresponding to phase shifts equal to multiples of $\lambda/4$ between the ordinary and extraordinary rays.

2. TeO_2 crystals were grown from the melt under elevated oxygen pressure. Our method enabled us to obtain large (up to several cubic centimeters) crystals of sufficiently high optical quality.

To investigate the anisotropy of δn_{32}, we prepared crystalline samples in the form of rectangular plates. Their planes coincided with either ⟨110⟩ or $\langle\bar{1}10\rangle$; accordingly, the narrow faces coincided with $\langle\bar{1}10\rangle$ and ⟨110⟩. This sample orientation was achieved by cutting the original preparation, oriented along the ⟨100⟩ cleavage plane and with respect to the conoscopic pattern in the form of a cube with ⟨110⟩ and $\langle\bar{1}10\rangle$ faces, with a corundum saw. The plates were then polished with diamond paste on pitch very carefully in order to avoid partial decomposition due to heating during the work. The electrode material was silver paste. The sample, with electrodes applied, was mounted on a goniometer stage, which enabled one to vary the angle of incidence of the light beam from a helium–neon laser ($\lambda \sim 6328$ Å). An electric field of frequency $\nu_0 = 1$ kHz was produced by an oscillator having an output voltage of 2 kV. The experimental results were treated by the method described in ref. 4.

The curve of the change of intensity of the mixed wave $I_\sim(\nu \pm \nu_0)$ versus angle of incidence (specific rotation $\rho \sim 145°$) is shown in Fig. 1. The angle of incidence $\varphi' = 0$ corresponds to the crystallographic direction $\langle\bar{1}10\rangle$. The intensity $I_\sim(\nu \pm \nu_0)$ varies nearly according to a tan φ law, where the refraction angle $\varphi = \arcsin\ (n_{32}{}^{-1} \sin \varphi')$. Knowing the angle of incidence and the refractive index[5] $n_{32} \sim 2.35$, we used Eq. (5) to calculate $|\delta n_{41}| = n_O n_{32} n_C r_{41} =$

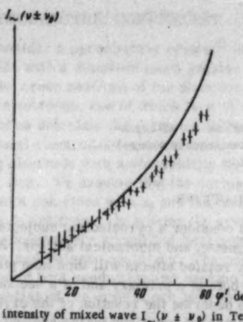

Fig. 1. Curve of intensity of mixed wave $I_\sim(\nu \pm \nu_0)$ in TeO_2 crystals versus angle of incidence of light beam. Curve denotes theoretical values.

$-2\pi m_{32}^{-1}\varkappa_{14}$, which proved equal to $(56 \pm 6) \cdot 10^{-8}$ cgs esu. This value of δn coincides with data for synthetic ZnS crystals.[6]

An analogous study of the anisotropy of $I_\sim(\nu \pm \nu_0)$ was carried out in crystalline samples whose orientation relative to the first was diametrically opposed (specific rotation $\rho \sim 131°$). Treatment of the experimental data gives the value $\delta n_{32} = (28 \pm 3) \cdot 10^{-8}$ cgs esu. The considerable discrepancy between this value and the above data cannot be explained by experimental error or crystal quality,[1)] but is evidently due to neglect of the gyrotropy of TeO_2 crystals. This observation calls for special consideration of the phenomenon in gyrotropic media.

It follows from the above experimental data that the coefficients of the tensor $\varkappa_{ijk}(r_{ijk})$, to which values of the nonlinear refractive index $\delta n_{42}\delta n_{41}$ correspond, are equal in magnitude but have opposite signs.

An attempt to measure the dispersion of δn_{41} in TeO_2 crystals was unsuccessful owing to insufficient spectral resolution of the SPM-2 monochromator and the large value of the parameter $\partial\Delta n/\partial\lambda$ (rate of change of double refraction Δn with wavelength), which caused the interference pattern to smooth out on scanning over the spectrum.

The authors thank V. M. Nesterova for her assistance in preparing the samples.

[1)] The effect of optical imperfections was eliminated by the fact that, in Eq. (5), a value of $I_0(\nu)$ was used which corresponded to the amplitude of interference of the light beams with changing angle of incidence.

[1] J. Liebertz, Kristal und Technik, 4, 221 (1969).
[2] N. Uchida, Phys. Rev., 4, 3736 (1961).
[3] J. F. Nye, Physical Properties of Crystals, Oxford Univ. Press (1957).
[4] Yu. V. Shaldin, Yu. V. Pisarevskii, and Yu. A. Mel'nikov, Zh. Prikl. Spektrosk., 3, 463 (1965).
[5] M. Born and E. Wolf, Principles of Optics, Pergamon (1966).
[6] Yu. V. Shaldin, Author's Abstract of Dissertation, Moscow Institute of Steel and Alloys, Moscow (1967).

Dynamic pyroelectric effect

S. D. Pel'ts and A. E. Karpel'son

(Submitted April 20, 1972)
Kristallografiya, 18, 573-578 (May-June 1973)

A system of equations describing the phenomenon of the dynamic pyroelectric effect is derived. An expression is obtained for the potential on the electrodes of the crystal. It is shown that the direction of the maximum of the dynamic pyroeffect may not coincide with the maximum of the static effect.

INTRODUCTION

The dynamic pyroelectric effect lies in the development of an alternating electric signal on the electrodes of a pyroelectric crystal after irradiating the latter with a time-modulated thermal flux. The effect finds practical application in thermal radiation receivers, infrared image converters, and also in studying ferroelectrics.

The dynamic pyroeffect was first considered by Chynoweth,[1] who proposed that the time-periodic change in the spontaneous polarization P_s was equivalent to a current i flowing in an external circuit, and wrote down the following expression for the pyroelectric current:

$$i = \frac{\partial P_s}{\partial t} = \frac{\partial P_s}{\partial T}\frac{\partial T}{\partial t}, \tag{1}$$

where T is the temperature, t is the time, basic for all calculations associated with the study and practical application of the dynamic pyroeffect. Kremenchugskii et al. developed the dynamic method,[2-5] and, working on the basis of Eq. (1), derived the value of the dynamic pyroelectric coefficient. The results of measurements of the dynamic pyrocoefficients (γ_d) of triglycine sulfate crystals and barium titanate ceramics of various compositions showed that the dynamic pyrocoefficients were usually smaller than the static (γ_{st}) by a factor of 2-4. Attempts at "matching" these two by measuring γ_d in the infrasonic region of frequencies[4] were unsuccessful.

Let us return to Eq. (1). Although the use of this equation gave some success in applied calculations associated with pyroelectric infrared radiation receivers, it does not describe the phenomenon completely. First, Eq. (1) only allows for the temperature dependence of the polarization, whereas mechanical stress and electric field ought also to be taken into account. Second, Eq. (1) is only valid if all the charge formed as a result of the change in P_s is evolved at the electrodes; this requirement corresponds to a change in crystal temperature uniform throughout the whole thickness of the crystal.

In actual fact there is an extremely nonuniform temperature (and hence polarization) distribution in the crystal. The nonuniform distribution of polarization in the crystal leads under certain conditions to the field effects considered in refs. 6 and 7, which cannot be explained on the basis of Eq. (1) alone. Furthermore, these effects may serve as a basis for the perfection of pyroelectric radiation detectors and the construction of fundamentally new devices, such as those described in refs. 8 and 9.

The aim of the present investigation is to provide a phenomenological description of the dynamic pyroeffect and an illustration of this approach.

BASIC EQUATIONS

Let us consider a pyroelectric subjected to thermal, electromagnetic, and mechanical actions. A whole series of mutually related effects will then take place simultaneously, both of a primary and of a secondary nature.[10] In order to describe the reaction of the crystal we construct a system of equations taking account of all the effects. We write:

1. Maxwell's equations for a dielectric:

$$\operatorname{div}\mathbf{D} = \operatorname{div}\mathbf{B} = 0,\ \operatorname{curl}\mathbf{H} = \partial\mathbf{D}/\partial t,\ \operatorname{curl}\mathbf{E} = -\partial\mathbf{B}/\partial t, \tag{2}$$

where **E** and **H** are the electric and magnetic fields, **D** is the electric displacement, and **B** is the magnetic induction.

2. The equations of motion of an element of the medium, allowing for both elastic and electric forces:

$$\frac{\partial\sigma_{ij}}{\partial x_j} + f_i = \rho\frac{\partial^2 u_i}{\partial t^2}, \tag{3}$$

where σ_{ij} are the mechanical stresses, x_j are the coordinates, u_i are the displacements, ρ is the density, and f_i are the electromagnetic forces.[11]

3. The heat-conduction equation, with due allowance for secondary effects:

$$C\frac{\partial T}{\partial t} + T\alpha_{ij}\frac{\partial\sigma_{ij}}{\partial t} + T\gamma_i^{\sigma}\frac{\partial E_i}{\partial t} = \chi_{ij}\frac{\partial^2 T}{\partial x_i\,\partial x_j}, \tag{4}$$

where C is the specific heat, α_{ij} is the thermal expansion, χ_{ij} is the thermal conductivity, γ_i is the pyroelectric coefficient at constant stress, allowing for the primary and secondary pyroeffects as in ref. 10.

4. The coupling equations for the various parameters for the pyroelectric material:

$$\begin{gathered} D_i = \varepsilon_{ij}E_j + d_{ijk}\sigma_{jk} + \gamma_i^{\sigma}T, \\ u_{ik} = \lambda_{iklm}\sigma_{lm} + d_{lik}E_l + \alpha_{ik}T, \end{gathered} \tag{5}$$

where ε_{ij} is the dielectric constant, λ_{iklm} are the elastic moduli, d_{lik} are the piezomoduli, and u_{ik} are the deformations.

By solving the system (2)-(5) with the corresponding boundary conditions, we may in principle derive the temperature, deformation, and electric field strength at any point of the pyroelectric material.

We studied the potential distribution on the surface of pyro- and piezoelectric plates irradiated with a sharply focused thermal flux earlier[6,7] by solving a simplified system of equations. The results were supported experimentally.

DYNAMIC PYROELECTRIC COEFFICIENT

Let us consider a pyroelectric crystal[1)] in the form of a round plate with a diameter much greater than its thickness. The cross sections of the plate are entirely covered with electrodes, one of which ($x_3 = 0$) absorbs radiation. Let us calculate the potential difference between the crystal electrodes for a uniform irradiation of the absorbing electrode with a sinusoidally time-modulated thermal flux. We assume that the normal to the cut (cross section) **n** coincides with x_3 and the direction of the polar axis is arbitrary. In solving the system (2)-(5) we consider successively simplified heat-conduction, thermoelastic, and Poisson equations. The one-dimensional equation of heat conduction (we assume that the thermal properties of the crystal are isotropic) takes the form

$$\frac{\partial^2 T}{\partial x_3^2} = a^{-1}\frac{\partial T}{\partial t}$$

with the boundary conditions

$$\left.\frac{\partial T}{\partial x_3}\right|_{x_3=0} = \left(A\exp(-i\omega t) + \frac{4\sigma T_0^3}{k}T\right)\mathbf{n},\qquad \left.\frac{\partial T}{\partial x_3}\right|_{x_3=d} = \frac{4\sigma T_0^3}{k}T\mathbf{n}; \tag{6}$$

it does not allow for the constant component of the incident radiation and the transient process. Here a is the thermal diffusivity, A is a constant associated with the intensity of the incident flux, ω is the cyclical modulation frequency, T_0 is the temperature of the external medium, k is the thermal conductivity, and σ is Boltzmann's constant. We obtain

$$T = (C_1\cos\mu x_3 + C_2\sin\mu x_3)\exp(-i\omega t),$$

$$C_1 = \frac{A[\mu\cos\mu d - 4\sigma T_0^3\sin\mu d/k]}{\mu[\mu\sin\mu d + (4\sigma T_0^3)^2\sin\mu d/k^2]},$$

$$\mu = \sqrt{i\omega/a},$$

$$C_2 = \frac{A}{\mu} + \frac{4\sigma T_0^3 A[\mu\cos\mu d - 4\sigma T_0^3\sin\mu d/k]}{\mu^2 k[\mu\sin\mu d + 4\sigma T_0^3\sin\mu d/k]}. \tag{7}$$

If in (7) we neglect the terms corresponding to the radiation of the sample, we obtain

$$T = \frac{A\cos\mu(d - x_3)}{\mu\sin\mu d}\exp(-i\omega t). \tag{8}$$

The error so committed, for example, in the case of triglycine sulfate (T_0 = 300°K, ω = 150 rad/sec), is less than 1% and diminishes with increasing frequency.

Let us turn to the thermoelastic equation. By virtue of the fact that the temperature falls quite rapidly with thickness, while ∇T is the stimulating force, we may replace the thermoelastic equation by equations representing the small vibrations of a thin isotropic plate, on the surface of which a uniformly distributed stimulating force, varying periodically with time, is acting.[12] The equation for the longitudinal vibrations of a disk clamped at the edges with corresponding boundary conditions takes the form

$$\frac{\partial^2 u_r}{\partial t^2} - b_1\frac{\partial^2 u_r}{\partial r^2} = 0,\qquad u_r|_{r=R} = \left.\frac{\partial u_r}{\partial r}\right|_{r=R} = 0, \tag{9}$$

where u_r are the displacements along the radius of the plate, $r = (x_1^2 + x_2^2)^{1/2}$, R is the radius of the plate, and b_1 is a constant. The equation for bending waves in a disk with corresponding boundary conditions is

$$\frac{\partial^2 u_{x_3}}{\partial t^2} + b_2\Delta^2 u_{x_3} = b_3\frac{\partial T}{\partial x_3},\qquad u_{x_3}|_{r=R} = \left.\frac{\partial u_{x_3}}{\partial r}\right|_{r=R} = 0, \tag{10}$$

where u_{x_3} is the displacement along x_3; b_2, b_3 are constants, Δ is the two-dimensional Laplace operator. Solving (9) and (10) with the aid of ref. 13 we find u_{x_3} and u_r. Using the generalized Hooke's law, we obtain the stress in the form

$$\sigma_{ii} = -f\alpha T\delta_{ii},\quad \sigma_{12} = 0,$$

$$\sigma_{13} = -[B_1 J_1(r) + B_2 I_1(r)]\frac{x_1}{r}f\exp(-i\omega t),$$

$$\sigma_{23} = [-B_1 J_1(r) + B_2 I_1(r)]\frac{x_2}{r}f\exp(-i\omega t), \tag{11}$$

where $J_1(r)$ is a Bessel function of the first order, $I_1(r)$ is a modified Bessel function of the first order, B_1 and B_2 are constants, δ_{ij} is the Kronecker symbol, and f is Young's modulus.

Let us turn to the determination of the electric potential. Neglecting the magnetic field, we obtain the D'Alembert equation for the scalar potential. Neglecting the delay effect and considering that $(\mathrm{Re}\ \mu)^2 \gg \omega^2/c^2$ for any real modulation frequencies, where c is the velocity of light, we arrive at the Poisson equation. Let us analyze the charge terms $d_{ijk}(\partial\sigma_{jk}/\partial x_i)$ and their influence on the potential in this. We note that for i = 1, 2 these take the form $f(r)x_1x_2$. Hence in view of the sign antisymmetry of the charge relative to the center of the disk these have no effect on the potential of the electrodes. The remaining charge terms depend solely on x_3; hence the Poisson equation reduces to one-dimensional form:

$$\varepsilon\frac{\partial^2\varphi}{\partial x_3^2} = d_{mp}\frac{\partial\sigma_p}{\partial x_m} + \gamma_m^\sigma\frac{\partial T}{\partial x_m}, \tag{12}$$

where ε is the dielectric constant in the direction of the normal **n**. We consider that the electrodes are connected to one another through a load resistance and write down the boundary conditions accordingly. We ground one electrode and put $\varphi(0) = 0$. For the second electrode we have

$$D_{n1} - D_{n2} = \frac{4\pi}{SZ}\int_{-\infty}^{t}[\varphi(0) - \varphi(d)]\,dt_1,$$

where D_{n1} and D_{n2} are the normal components of the induction vector from the two sides of the crystal electrode, S is the area of the electrode, and Z is the total complex load impedance. Solution of (12) gives

$$\varphi(d) = B\cos(\omega t + \delta),$$

$$B = \frac{4\pi A a(\gamma_m{}^\sigma - f\alpha\, d_{mik}\delta_{ik})n_m\theta}{\varepsilon\omega\sqrt{1+(\theta+\theta_1)^2}},$$

$$\delta = -\operatorname{arctg}(\theta+\theta_1),$$

$$\theta = \frac{\varepsilon SR\omega}{4\pi d} = RC\omega, \qquad \theta_1 = R\omega C_1, \tag{13}$$

where R, C_1 are the resistance and capacity of the load and C is the capacity of the crystal.

Analysis of the resultant expression for the signal amplitude shows that it is similar to the expression derived in ref. 14. The dependences of the potential on ω, d, S, R, and ε are identical. The dependence on C_1 is different. The expression $(\gamma_m{}^\sigma - f\alpha d_{mik}\delta_{ik})n_m = \gamma_3{}^\sigma - f\alpha(d_{31} + d_{32} + d_{33})$ in (13) is according to ref. 10 the projection of the primary pyroelectric coefficient for constant deformation γ^ε on x_3. This may be explained by the rigid fixing of the crystal around the perimeter and the approximate replacement of the thermoelastic equation by the equation of elastic vibrations with a stimulating force.

The dynamic pyrocoefficient γ_d was derived in ref. 2. Since γ^ε and γ_d describe exactly the same phenomenon, it is natural to compare them for two limiting cases. For $\theta \ll 1, \gamma^\varepsilon/\gamma_d = 1$, and for $\theta \gg 1$, $\gamma^\varepsilon/\gamma_d = 1 + C_1/C$.

In refs. 2 and 3 the introduction of the dynamic pyrocoefficient is based on the observed difference between the experimental values of the pyroelectric coefficient measured under static and dynamic conditions.

It should be noted that in these papers γ_d was compared with the $\gamma_{st}{}^\sigma$ of a free crystal, not a particularly well-based choice, since in dynamic measurements a certain fixing of the crystal always occurs. In addition to this, the pyrocoefficients in the static and dynamic modes may differ considerably even if the crystal is fixed in the same way, since an additional term proportional to ∇T appears in the thermoelastic equation under dynamic conditions: See Eqs. (3) and (5). Equation (13) is not suitable for the case of infrasonic frequencies, since in this range the foregoing approximation is inadequate. It is essential to allow for the effects of the resorption of the coupled space charges and the neutralization of the surface charges.

In contrast to the static pyroeffect, which appears as a change in the polarization vector, the dynamic pyroeffect appears in the form of a periodic potential difference determined from the foregoing equations. In view of this the boundary conditions (thermal, mechanical, and electrical) may have an effect on the potential. For example, if the crystal is fixed asymmetrically relative to the origin of coordinates, shear piezomoduli enter into the expression for the potential, and this may be one reason for the development of a dynamic pyrocoefficient in cuts perpendicular to the polar axis, as observed in ref. 5.

We may now show that, by changing the boundary conditions in the Poisson equation, we may change the direction of the maximum of the dynamic pyroeffect in an arbitrarily cut crystal.

1. Let $(\theta + \theta_1) \ll 1$. $B = Aa\gamma^\varepsilon nSR/d$. In this case the direction of the maximum dynamic pyroeffect coincides with that of the maximum static effect.

2. Let $(\theta + \theta_1) \gg 1$. We assume that $\theta_1 = q(T)\theta$. Usually in dynamic measurements the coefficient $q < 1$. Then $B = 4\pi Aa\gamma^\varepsilon n/\varepsilon\omega(1 + q)$. Since $\gamma^\varepsilon n$ and ε change in different ways on rotating the coordinate axes, the direction of the maximum of the dynamic pyrocoefficient does not necessarily coincide with the polar axis. Studying the extreme condition of the function

$$\gamma_m l_m / (\varepsilon_{11}l_1^2 + \varepsilon_{22}l_2^2 + \varepsilon_{33}l_3^2 + 2\varepsilon_{13}l_1l_3), \tag{14}$$

we may find the direction cosines l_1, l_2, and l_3 in the crystal-physical system of coordinates corresponding to the maximum of the ratio $\gamma n/\varepsilon$. Applying this procedure to triglycine sulfate, we have the following result: If the normal to the cut is set at an angle of 60° to the polar axis in the yx plane, the signal may be increased by a factor of 1.3. In the practical application of Eq. (14) one should remember the dependence of the components of tensor ε on the thickness of the crystal.

---

1) Here and subsequently we shall not consider pyroelectric crystals belonging to classes 1 and m, in which a change in the direction of the polarization with temperature may take place.

[1] A. G. Chynoweth, J. Appl. Phys., 27, 78 (1956).

[2] L. S. Kremenchugskii and V. V. Samoilov, Kristallografiya, 12, 1077 (1967) [Sov. Phys.–Crystallogr., 12, 940 (1968)].

[3] L. S. Kremenchugskii, A. K. Mal'nev, and V. V. Samoilov, In: Electrical and Optical Properties of Dielectrics [in Russian], Naukova Dumka, Kiev (1966), p. 65.

[4] L. S. Kremenchugskii and M. A. Kladkevich, Summaries of Contributions to the All-Union Conference on Ferroelectricity [in Russian], Riga (1968), p. 135.

[5] L. S. Kremenchugskii, G. A. Danil'chuk, and M. S. Itskovskii, Ukr. Fiz. Zh., 14, 975 (1967).

[6] S. D. Pel'ts, Fiz. Tverd. Tela, 12, 3648 (1970) [Sov. Phys.–Solid State, 12, 2973 (1971)].

[7] S. D. Pel'ts and A. E. Karpel'son, Fiz. Tverd. Tela, 13, 3104 (1971) [Sov. Phys.–Solid State, 13, 3079 (1972)].

[8] S. D. Pel'ts, Soviet Patent No. 277315, Byull. Izobr., 24 (1970).

[9] S. D. Pel'ts, Soviet Patent No. 302992, Byull. Izobr., 29 (1971).

[10] J. Nye, Physical Properties of Crystals, Oxford Univ. Press (1957).

[11] L. D. Landau and E. F. Lifshitz, Electrodynamics of Continuous Media, Addison-Wesley (1960).

[12] L. D. Landau and E. F. Lifshitz, Theory of Elasticity, Addison-Wesley (1959).

[13] B. V. Korenev, Introduction to the Theory of Bessel Functions [in Russian], Nauka, Moscow (1970).

[14] L. S. Kremenchugskii, Opt.-Mekhan., Prom., 10, 17 (1966).

Morphology of the domain structure of SbSI crystals

L. A. Zadorozhnaya, V. A. Lyakhovitskaya, and L. M. Belyaev

Institute of Crystallography, Academy of Sciences of the USSR
(Submitted February 24, 1972; resubmitted June 7, 1972)
Kristallografiya, 18, 579-583 (May-June 1973)

A combination of etching and electronphotographic development methods has made it possible to elucidate the morphology of the domain structure of SbSI on the (101) faces close to the ferroelectric cuts to determine the sign of the domains, and to establish the effect of heat and an external electric field on the domain configuration and on the local stability of the domain boundaries.

The morphology of SbSI crystals is determined by the characteristic internal structure of this compound.[1] The presence of a double chain ($Sb_2S_2I_2$) extended along the c axis is responsible for the fact that the growing faces are predominantly grouped around the vertical zone (hk0). The crystal habit produced by the chain structure is acicular. The needle axis is the same as the crystal axis c (Fig. 1).

A study of the morphology of the crystals[2] has shown that crystals grown from the gas phase are imperfect, with traces of skeletal growth, gas inclusions, etc. The presence of defects is largely explained by the small flexibility of the pair of SbSI molecules which produce the crystal growth and the fact that it is necessary to carry out the crystallization with high supersaturation in order to accelerate the process.

It was possible to obtain crystals which were optically uniform with well-developed faces of the orthorhombic prism (101) which normally does not appear on SbSI crystals [dimensions of (101) face were 3 × 4 mm] by a modification of the method used to grow crystals from the gas phase, namely: a) by reducing the supersaturation (as a result of a reduction in the temperature gradient to 5-10°); b) by decreasing the number of nucleation centers by preliminary heating of the crystallization zone; and c) by a stabilization of the temperature.

The spontaneous polarization vector P in SbSI crystals is in the direction of the c axis. The very perfect cleavage along [110] and the softness of the crystals made it impossible to prepare the ferroelectric shear (001). The domain structure of SbSI was first studied on the nonferroelectric shear planes,[3] using methods of selective crystallization and etching. When crystals were produced which had an orthorhombic prism (101), the plane of the faces of which sloped towards the polar axis at an angle of 67°56′, i.e., close to the ferroelectric cuts, it became possible to study more fully the domain structure. Later in the study of the dynamics of the domain structure we used these particular crystal faces.

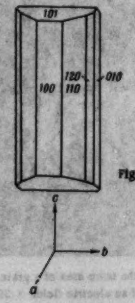

Fig. 1. The form of the SbSI crystal (from the goniometric data).

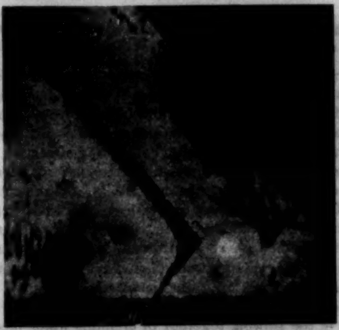

Fig. 2. The domain faces parallel to the (110) planes × 200.

The SbSI crystals are formed at a temperature at which the nonpolar phase is stable. The division into domains occurs in the growing crystal at 20-22°C, i.e., with the transition through the Curie point.

The domains were revealed by using the sensitivity of charged powder to the electrostatic state of oppositely charged surfaces of the antiparallel domains and an

Fig. 3. Elliptical domains in an SbSI crystal; × 200.

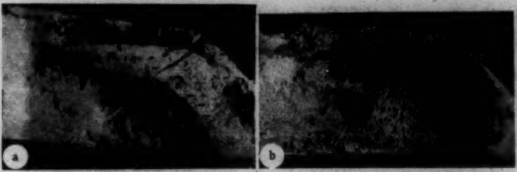

Fig. 4. Pattern of the domain structure; × 200: a) electrophotographic development; b) etching. The signs "+" and "−" denote the charge at the surface of the blocks.

etching method based on the differential solubility of these surfaces.

The SbSI crystals with mirror-smooth faces were carefully washed in dilute hydrochloric acid and alcohol, cooled to 14-16°C, and etched in cold 50% HIO_3. Since the domain structure depends on the growth conditions, the orientation of the domains is associated of course with the growth zones in the crystals which had not been acted on by electrical and mechanical fields. Domains, bounded by walls which had exact crystallographic indices (Fig. 2) were observed in the crystals. In some growth zones the domain boundaries are subordinate to the growth layers and in the intervals between these layers occupy the orientation normal for elliptical domains (Fig. 3). The complex relief of the domain boundaries arises as the result of the flowing together of domains which have different dimensions but neighboring centers.[4] When the crystals are heated slightly above the phase-transition temperature the domain structure does not disappear completely. Only significant heating of the crystals (to 50 or 60°C) can eliminate the domain structure.

The oppositely charged surface of the antiparallel 180° domains can also be shown by an electrophotographic development[5] method. A liquid electrophotographic developer obtained from black printing ink dispersed in CC14 was used.

The specimens were placed in the very dilute electrophotographic developer (0.1 mg/cm^3) at 16-17°C for 20-30 sec, after which the specimens were removed, the solvent evaporated, the pattern of the powder distribution remaining on the surface of the crystal. Particles of powder settled on the domains of the same sign and on the domain boundaries. A clear image is retained on the surface of the crystal for an unlimited period and this makes it possible to study the domain structure. The developer can easily be removed from the surface of the crystal.

Fig. 5. Partial shift of the domain walls as a result of heating; × 300.

The combination of etching and electrophotographic methods made it possible to determine the domain sign (Fig. 4). The particles of black printing ink dispersed in CC14 are negatively charged and are deposited on the sections of the crystal which have a positive charge at the surface (Fig. 4a). It is clear from Fig. 4b that the etch pattern is the reverse of the pattern obtained by the charged-powder method and therefore we may conclude that the positive domains are not etched or are only etched very slowly while the domains with the negative sign are intensely etched (dark regions in Fig. 4b). The negative domains on the matrix of a positive domain are etched into wells which are 3-4 μ deep.

At the center of the face the domains have a highly developed surface while the edge of the (101) face often appears as a single-domain block (up to 100 μ in width) with boundaries which are strictly parallel to the crystallographic direction [100], [110], [120]. Figure 5 illustrates an interesting case where part of the boundary of the positive domain exposed by etching does not coincide with the boundary exposed by the negative electrophotographic developer. This situation is clearly due to the fact that during the experiments the domain walls have been displaced by heat. The displacement did not occur along the whole boundary: Part of the wall remained in the same place.

The movement of the domain walls under the action of a dc field was observed. A dc field (E ≥ 300 V/cm) was applied to the crystal along the c axis. The distance between the contacts was ~1.5-2.0 mm. The field on the

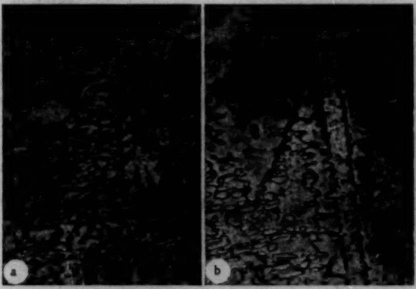

Fig. 6. Picture of the selection etching of the same area of a grain (101) before (a) and after (b) application of an electric field. × 300.

specimen in the ferroelectric state was maintained for 12 h. The field was then removed and the crystal etched.

The presence in the crystal of internal stresses associated with defect in the crystal resulted in some domains retaining their sign of polarization under the action of an external field. A dc voltage moves the domain boundaries and changes the size of the domains (Fig. 6). As a result of the coalescing and restructuring of the domains, the dimensions of the negative component are increased.

Thus, the use of the combined etching and electrophotographic development methods has made it possible to expose the morphology of the SbSI domain structure and to establish the effect of heat and an external field on the configuration of the domains and the local stability of the domain boundaries.

---

[1] A. Kijuchi, Y. Oka, and E. Sawaguchi, J. Phys. Soc. Japan, 23, 337 (1967).
[2] L. A. Zadorozhnaya, V. A. Lyakhovitskaya, and L. M. Belyaev, Vest. Moskovsk. Univ., Ser. Geolog., No. 6, (1971).
[3] M. O. Kliya and V. A. Lyakhovitskaya, Kristallografiya, 15, 75 (1970) [Sov. Phys.–Crystallogr., 15, 59 (1970)].
[4] V. A. Meleshina, Diss. Institute Crystallography [in Russian], Akad. Nauk SSSR, Moscow (1966).
[5] L. G. Yuskeselieva and A. S. Antonov, Dokl. Akad. Nauk SSSR, 164, 1260 (1965) [Sov. Phys.–Dokl., 10, 956 (1966)].

Some features of the action of penetrating radiation on the electrical properties of a quartz crystal

A. A. Fotchenkov and S. V. Kolodieva

All-Union Scientific-Research Institute for the Synthesis of Raw Materials

(Submitted December 2, 1971; resubmitted May 3, 1972)
Kristallografiya, 18, 584-589 (May-June 1973)

The temperature dependence of the specific resistance and the dielectric loss of crystals of natural and synthetic quartz has been measured. The crystals were irradiated by fast neutrons, electrons, protons, and gamma quanta. The results have been analyzed in terms of the generation of two types of radiation defects in these crystals.

As a result of the numerous studies carried out recently on the interaction between radiation and materials, it has been established that isotropic materials have a higher radiation resistance than anisotropic[1,2] materials and, in the case of crystals, the radiation resistance of the physical properties increases with an increase in the degree of perfection.[3,4]

The effect of radiation on the electrical properties of quartz crystals has been studied by several authors from the change in the specific resistance ρ, the dielectric constant ε, and the dielectric loss $\tan\delta$ measured at room temperature.[2,5-7] Data on the effect of radiation on such sensitive electrical characteristics of quartz as TKε and the activation energy of the conduction process have been published only in refs. 8-10. These authors, however, did not examine the effect of the degree of perfection of the crystal structure on the value of the radiation changes in the electrical properties and there was an inadequate range of doses and types of radiation.

We have studied the change in ρ and $\tan\delta$ over the temperature range 20-550°C for crystals of natural and synthetic quartz with varying degrees of perfection of the crystal structure, under the action of reactor radiation and irradiation by gamma quanta, protons, and electrons of various energies.

The natural quartz crystals selected for the study were from the Ukraine seam. The artificial crystals were of two types: S-7 and S-5. Both types of crystals were grown by a hydrothermal method, but the growth parameters were different: The crystallization temperature of the S-5 crystals was lower and the growth rate significantly higher than for the S-7. This produced a higher concentration of nonstructural impurities[11] in the S-5 crystals, which led to the milk-white coloring of the control specimens during annealing.[12] The S-7 slices, annealed under the same conditions, remained transparent (i.e. the concentration of nonstructural impurity did not exceed 10^{-4} wt. %).

The resistivity ρ was measured by an electrometric method. The values of the activation energy U of the electrical conduction process were calculated from the temperature dependence of ρ in accordance with the Rash–Henricson equation: $\rho = \rho_0 \exp(U/kT)$. The temperature dependence of $\tan\delta$ of the experimental specimens was normalized with respect to the temperature T_m of the maximum[13] of $\tan\delta$ measured at a fixed frequency of 1 kHz using an MLE-1 bridge.

The specimens were flat-ground disks, 15 mm in diameter and 1.5-2 mm thick, oriented perpendicular to the x axis to an accuracy of 5'.

The results of the study are shown in Table 1 and Figs. 1-3. It is clear from Table 1 and Fig. 1 that with low doses (10^4-10^5 R in the case of the radiation and 10^{12}-$3\cdot10^{12}$ particles/cm^2 in the case of particle radiation) the

TABLE 1. Dependence of the Activation Energy U of the Electrical Conduction Process in Quartz on the Type and Dose of Radiation

Type of quartz	Integrated dose of radiation in the reactor (neutron with energies > 0,1 MeV), neutrons/cm^2	Integrated dose of accompanying γ radiation with irradiation in a reactor, R	U, kcal/mole	Integrated dose γ radiation (Co^{60} source), R	U, kcal/mole	Integrated dose of radiation by electrons with energy of 10 MeV, electrons/cm^2	U, kcal/mole	Integrated dose of radiation by protons with energy of 22.5 MeV, protons/cm^2	U, kcal/mole
Artificial, S-7	Before irradiation		28	Before irradiation	28	Before irradiation	28	Before irradiation	28
	$0.8\cdot10^{12}$		30	10^4	28	$3.2\cdot10^{12}$	33,5	10^{12}	30.5
	$1.4\cdot10^{14}$	$1.2\cdot10^8$	34	10^5	30.5	$3.2\cdot10^{13}$	32	10^{13}	30.5
	$2.2\cdot10^{14}$		33	10^6	32	$3.2\cdot10^{15}$	40	10^{15}	35
	$5.7\cdot10^{15}$	$2.4\cdot10^8$	51	$5\cdot10^6$	36.5				
	$1.6\cdot10^{17}$	$6.7\cdot10^9$	95	10^7	39				
				10^8	44				
				$5\cdot10^8$	61				
Natural, from the Ukrainian seam	Before irradiation		24	Before irradiation	24	Before irradiation	24	Before irradiation	24
	$0.8\cdot10^{12}$		24	10^4	24	$3,2\cdot10^{12}$	24	10^{12}	24
	10^{13}		26	10^5	24	$3.2\cdot10^{13}$	24	$3.2\cdot10^{13}$	37.5
	$1.4\cdot10^{14}$	$1.2\cdot10^8$	40	$3,7\cdot10^5$	26	$3.2\cdot10^{15}$	43	10^{15}	47
	$5.7\cdot10^{15}$	$2.4\cdot10^8$	45	10^6	34				
				10^7	40				
				$5\cdot10^8$	48				

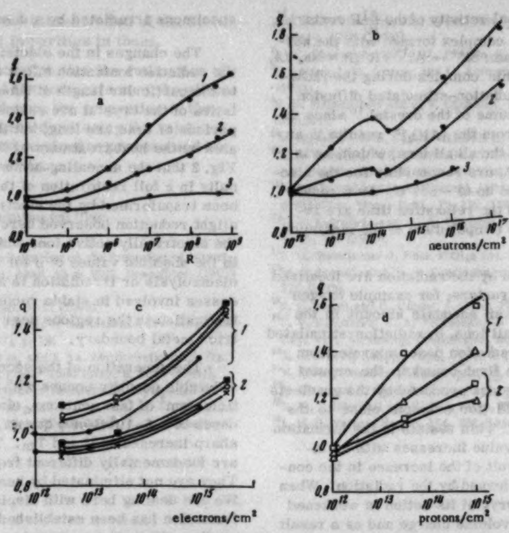

Fig. 1. The relative change ($q = T_{m,\mathrm{irr}}/T_{m,\mathrm{nonirr}}$) of the temperature of the maximum of tan δ of quartz crystals measured at a frequency of 1 kHz as a function of the radiation dose by (a) γ quanta, (b) in reactor, (c) electrons, and (d) protons: 1) Ukrainian quartz; 2) synthetic quartz S-7; 3) synthetic quartz, S-5; ●, ×, O, □ are electron energies of 3, 10, 35, and 110 MeV; □, △ are proton energies of 22.5 and 680 MeV, respectively.

values of U and T_m either do not change by comparison with the measurements made on the unirradiated specimens or the change is insignificant and, depending on the original state of the specimen, there may be either an increase in U and T_m or a decrease. With high doses of 10^5-10^9 R for γ radiation, 10^{13}-$3 \cdot 10^{15}$ particles/cm² for electron and proton radiation, and 10^{13}-10^{17} neutron/cm² for radiation in the nuclear reactor (accompanying γ radiation,1) 10^5-$7 \cdot 10^9$ R) a monotonic increase in U and T_m is observed except for the clearly expressed minimum in the region of doses of $\sim 2 \cdot 10^{14}$ n/cm² in the case of the reactor radiation. It should be noted that for both the natural and artificial quartz, the values of U and T_m increase with an increase in the electron energy from 3 to 110 MeV at isodose radiation (Fig. 1c); an increase in the proton energy from 22.5 to 680 MeV results, as is clear from Fig. 1d, in an increase in the degree of the radiation-induced change in U and T_m.

By analyzing the changes in the electrical properties of quartz under the effect of the irradiation, we were led to assume that they are caused by two types of radiation-generated defects, which differ in energy spectrum and thermal stability.

The first type of defect is generated by doses of γ radiation up to $5 \cdot 10^8$ R and by doses of fast neutrons, protons, and electrons up to $2 \cdot 10^{14}$ particles/cm². At such doses, the ionization mechanism of the radiation effect predominates for all forms of irradiation. The changes in the electrical properties of quartz are produced

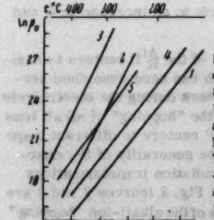

Fig. 2. The temperature dependence of the specific volume resistance of S-7 quartz crystals: 1) unirradiated, U = 28 kcal/mole; 2) after γ irradiation with a dose of 10^8 R, U = 43.5 kcal/mole; 3) after electrolysis with T ≈ 450°C for 2 h, U = 43 kcal/mole; 4, 5) after annealing of irradiated and electrolyzed specimens, respectively, U = 28.5 kcal/mole.

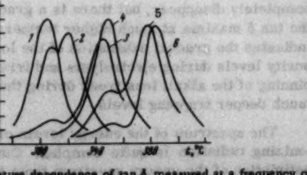

Fig. 3. The temperature dependence of tan δ measured at a frequency of 1 kHz for S-7 crystals: 1) unirradiated; 3, 4, 6) after γ irradiation at doses of $8 \cdot 10^6$, 10^7, $5 \cdot 10^8$ R respectively; 2) after electrolysis at 450°C and field strength of 50 V/cm for 15 min; 5) after electrolysis at 500°C and field strength of 1.5 kV/cm for 20 h.

in this case by the electrical activity of the ${}^{Al}_{R}P$ centers[14], representing the $[AlO_4]-R$ complex formed with the heterovalent microisomorphism: $Si^{4+} \rightarrow Al^{3+} + R^{+}$(R = Na, Li, K, ...). The ionization of this complex during the radiation process produces a radiation-stimulated diffusion of the alkali ions in the volume of the crystal,[15] since the removal of the electrons from the $[AlO_4]^{5-}$ results in an increase in the mobility of the alkali ions, which, as is known from refs. 16 and 17, are responsible for the electrical conductivity of quartz up to ~800°C. As a result the activation energies and the relaxation time are reduced and consequently the temperature of the maximum of tan δ is lowered.

The electrons released by the radiation are localized at various defects of the structure, for example oxygen vacancies,[18] which exist in an adequate amount in the original crystals. The alkali ions, by radiation-stimulated diffusion enhanced by the radiation dose, migrate from the places where they were first bound in the crystal lattice and are trapped at nodes produced by the gradients of the intracrystalline field (for example close to the electron-trapping centers). This results in the formation of a volume charge, whose value increases with an increase in the dose as a result of the increase in the concentration of alkali ions released by the radiation. When a field E is applied to the crystal its action is weakened by the reverse field of the volume charge and as a result the "effective" conductivity is reduced. With an increase in the temperature of the specimen a gradual dissipation of the volume charge occurs as a result of the thermally activated restoration of the ${}^{Al}_{R}P$ centers, which leads at ~400°C to the complete disappearance of the charge which has been generated and to the restoration of the equality of the values of ρ for nonirradiated and irradiated specimens. This process also leads to an increase in U and T_m.

The radiation destruction of the ${}^{Al}_{R}P$ centers is analogous to the destruction, which has been described several times,[16,17,19] of these centers during the electrolysis of quartz crystals, producing the "hopping" of alkali ions freed by the field from the ${}^{Al}_{R}P$ centers to different traps with a higher bond energy. The generality of the character of the electrolytic and radiation transformations of the ${}^{Al}_{R}P$ centers is shown in Fig. 2 (curves 2 and 3 are parallel). The process kinetics of the alkali-ion "hopping" from one center to another during electrolysis and irradiation are shown in Fig. 3, from which it is clear that as the radiation dose and the electrolysis parameters E−T−t increase there is a redistribution of the tan δ maxima: The lower-temperature tan δ maxima are lowered and then completely disappear, but there is a gradual increase in the tan δ maxima at much higher temperatures. This indicates the gradual exhaustion of the low-energy impurity levels during electrolysis and irradiation and the pinning of the alkali ions freed during these processes at much deeper trapping levels.

The spectrum of the energy levels created by the ionizing radiation is quite complex. Our quantitative estimation of the energy spectrum from the Cole−Cole diagram[20] showed that the parameter α which characterizes the width of the set of relaxation times is 0.14 and 0.21 for unirradiated specimens of C-7 crystals and for specimens irradiated by a dose of 10^7 R, respectively.

The changes in the electrical characteristics under the radiation ionization effect are reversible: According to the particular length of time, the primary characteristics of the crystal are restored. It is true that these periods of time are long, but the process can be accelerated by the heat treatment of the crystal. It is clear from Fig. 2 that the annealing of the specimens at ~450°C results in a full restoration of the ${}^{Al}_{R}P$ centers which had been transformed by the electrolysis or irradiation. The slight reduction observed here in the concentration of the electrically active ions which produce the increase in the absolute values of ρ for specimens annealed after electrolysis or irradiation is associated with the processes involved in stable recombination and charge neutralization in the regions near the electrode at the dielectric−metal boundary.

The generation of the second type of defects in considerable quantity occurs with the flow of $\geq 2 \cdot 10^{14}$ particles/cm^2 of fast neutrons, electrons, or protons and at doses of $\geq 5 \cdot 10^8$ R of γ quanta. In this case there is a sharp increase in U and T_m. The second type of defects are fundamentally different from those of the first type. They are not eliminated by heat treatment at ~450°C. We are dealing here with displaced oxygen atoms, whose formation has been established in ref. 21 in the optical studies of quartz irradiated in a reactor with doses higher than 10^{15} neutrons/cm^2. As a result of the Varley mechanism[22] the displacement of the atoms occurs where there is irradiation by large doses of γ quanta, electrons, and protons, which also produce the stable changes in U and T_m. The significant increase in U and T_m accompanying the formation of the displaced oxygen atoms may be taken as being the result of a decrease in the mobility of the alkali ions during their migration along the structural channels blocked by these displaced atoms.[9]

The increase in U and T_m as a result of the formation of the second type of radiation defects is preceded by the above-noted decrease in these values at doses of $\sim 2 \cdot 10^{14}$ neutrons/cm^2. This decrease is clearly associated with the prevailing contributory effect at these doses of the increase in the mobility of the electrically active alkali ions caused by the weakening of the bond between the latter and the oxygen atoms which have been displaced into the interstices during irradiation.[21]

It should be noted that the presence of the structural channels leads to an increase in the radiation resistance of the electrical characteristics of quartz crystals with an increase in the concentration of the nonstructural impurity, which is electrically inactive[13] up to ~600°C. It is clear from Table 1 and Fig. 1 that the biggest changes in the electrical properties occurred in our experimental natural quartz crystal, in which nonstructural impurity is absent; the electrical properties of the artificial quartz crystals, S-7 and S-5, which contain, as was noted previously, varying amounts of nonstructural impurity which suppress the radiatively stimulated diffusion of alkali ions, change to a lesser extent on irradiation.

We can assume that in the case of other crystals which also contain electrically active impurity ions, the radiation resistance of the electrical properties will increase with an increase in the concentration of the electrically inactive interstitial impurities in them.

It must be noted in conclusion that the estimation of the radiation resistivity and the comparison of the effects of various types of irradiation on the properties of the crystals (Table 1) can be carried out using the values of the activation energies of the conduction process and the temperature of the tan δ maxima.

---

1) Hot neutrons were cut off by a cadmium foil filter.

[1] A. A. Vorob'ev, in: The Effect of Radiation on the Properties of Materials [in Russian], Izd. Sibirsk. Otdel. Akad. Nauk SSSR, Novosibirsk (1963) p. 133.

[2] G. I. Potakhova, Izv. VUZ. Fiz., No. 3, 71 (1963).

[3] S. V. Starodubtsev, in: Radiation Physics of Nonmetallic Crystals [in Russian], Naukova Dumka, Kiev (1967), p. 19.

[4] M. I. Ignat'eva, E. K. Zavodovskaya, and I. Ya. Melik-Gaikazyan, Fiz. Tverd. Tela, 5, 2775 (1963) [Sov. Phys.—Solid State, 5, 2031 (1964)].

[5] G. I. Potakhova, in: Radiation Physics of Nonmetallic Crystals [in Russian], Naukova Dumka, Kiev (1967), p. 371.

[6] V. M. Nesterov, E. S. Nesmelova, N. I. Ol'shanskaya, T. G. Mikhailova, and G. I. Potakhova, Fiz. Tverd. Tela, 4, 3010 (1962) [Sov. Phys.—Solid State, 4, 2206 (1963)].

[7] V. K. Zhuravlev, Izv. VUZ. Fiz., No. 3, 79 (1958).

[8] J. Volger, J. M. Stevels, and C. Amerongen, Philips Res. Repts., 10, 260 (1955).

[9] S. V. Starodubtsev and L. B. Chubarov, Dokl. Akad. Nauk UzbekSSR, 5, 16 (1967).

[10] R. Kiryama and S. Kawai, Mineral. J., 3, 19 (1960).

[11] L. I. Tsinober, V. E. Khadzhi, L. A. Gordienko, and M. I. Samoilovich, in: Growth of Crystals [in Russian], Vol. 6, Nauka, Moscow (1965), p. 22.

[12] I. P. Khadzhi and V. E. Khadzhi, Dokl. Akad. Nauk SSSR, 172, 1321 (1967) [Sov. Phys.—Dokl., 12, 122 (1967)].

[13] S. V. Kolodieva and A. A. Fotchenkov, Elektron. Tekh., Radiokomponenty, No. 6, 117 (1970).

[14] J. M. Stevels and A. Kats, Philips Res. Repts., 11, 103 (1956).

[15] M. I. Samoilovich, L. A. Gordienko, and L. I. Tsinober, Radiokhimiya, 12, 125 (1970).

[16] R. C. Vogel and G. Gibson, J. Chem. Phys., 18, 490 (1950).

[17] S. V. Kolodieva, A. A. Fotchenko, É. M. Tashker, and L. N. Khetchikov, Zap. Vses. Mineralog. Obshchestva, No. 2, 216 (1971).

[18] R. A. Weeks, J. Appl. Phys., 27, 1376 (1956).

[19] H. E. Wenden, Amer. Mineralogist, 42, 859 (1957).

[20] H. Cole and R. Cole, J. Chem. Phys., 4, 341 (1941).

[21] E. W. J. Mitchell and E. G. I. Paige, Phil. Mag., 1, 1085 (1956).

[22] J. H. O. Varley, Nature, 174, 886 (1956).

Two-crystal spectrometer study of barium titanate single crystals

I. Ya. Nikiforov and Yu. F. Mal'tsev
Rostov State University

(Submitted April 4, 1972; resubmitted May 26, 1972)
Kristallografiya, 18, 590-592 (May-June 1973)

A two-crystal x-ray spectrometer has been used to show that the angles between blocks at the surface of $BaTiO_3$ lie in the range 50-180". The specific features of $BaTiO_3$ are responsible for the discrepancy between the theoretical shape of the diffraction peak and the one observed for an individual block.

Various structural features of ferroelectric crystals can be elucidated via two-crystal x-ray spectrometers;[1] they provide information on the shapes of diffraction peaks, which can also be found theoretically using the dynamical theory of x-ray diffraction. Comparison of the two indicates the degree of perfection of the crystals and the structure of the surface layer.

We have examined barium titanate crystals with a two-crystal spectrometer as previously described,[2] which enables one to measure relative diffraction angles to 1".

The crystals were examined with Cu Kα and Fe Kα radiation in the parallel position (2, −2) and also with Ag Kα radiation in the (3, −3) position. The x rays from tubes with anodes of Fe, Cu, and Ag were reflected in sequence from the two crystals and recorded by a Geiger counter. The double-reflection curve was recorded by automatic rotation of the second crystal and charting on a pen recorder the intensity reaching a fixed counter with a wide input slit. Rotation of the second crystal through an angle φ corresponds to a change in the Bragg angle by $\varphi/2$. It takes 15 min to record the curve from one double reflection. The crystals were cut from a single crystal of $BaTiO_3$ 2.5 cm^2 in area, grown by Remeika's method.

The polarizing microscope showed that this was a defective crystal of type *a*, i.e., the vector for the spontaneous polarization was parallel to the plane of the plate; there were inclusions of the parent solution and growth steps due to screw dislocations on the internal faces of the crystal.

The double-reflection curves were recorded from various parts of the outer faces of the crystal and for various points on the cross section of the primary beam before and after etching the crystals in phosphoric acid.

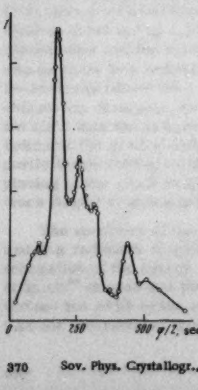

Fig. 1. Double reflection of Cu Kα radiation from two $BaTiO_3$ crystals in positions (2, −2) for an x-ray beam of cross section 20 mm^2.

We recorded the shape of the reflections from the (200) planes (Fe Kα and Cu Kα radiation) and from (300) planes (Ag Kα radiation). Figure 1 shows the double-reflection curve for Cu Kα radiation as recorded from two $BaTiO_3$ crystals with a beam cross section of 20 mm^2; the curve consists of one prominent peak, with weaker peaks on both sides. The width of the prominent peak at half-height was about 50", while those of the secondary peaks were 50-100". The distances between the peaks were from 50 to 200" on the various curves. The shape of the curve was very much dependent on the point of incidence of the radiation on the second crystal; there was a redistribution of the intensity between the peaks, and the number of peaks changed. If the area of the x-ray beam was reduced to 1.2 mm^2, the number of double-reflection peaks fell to 1 or 2, the point of incidence being the decisive feature, and each such peak had a symmetrical shape of width 35" (Fig. 2). Analogous curves were recorded for Fe Kα radiation. Etching of the crystal did not affect the character of the curves. The shape of the curves, however, was very much affected when Ag Kα radiation was used (Fig. 3). The double-reflection curve from (300) consisted of only one peak of width about 130", and its shape did not alter when the point of incidence and the beam cross section were varied.

The large number of double-reflection peaks for Cu Kα and Fe Kα radiation arise from reflections from the various blocks exposed on the surfaces; the crystal is divided into blocks mainly on account of uneven development of the growth step below[3] 1000°C, and also dislocations and point defects. The short-wave Ag Kα radiation gave a very different curve because deeper layers are involved in the reflection. The curves for the various wavelengths indicate that large angles between blocks

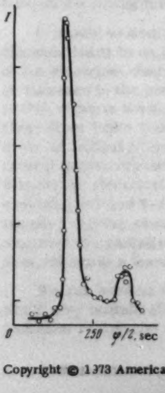

Fig. 2. Double reflection of Cu Kα radiation from two $BaTiO_3$ crystals in positions (2, −2) for an x-ray beam of cross section 1.2 mm^2.

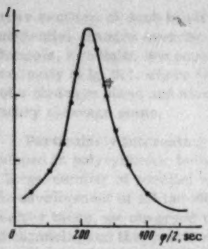

Fig. 3. Double reflection of Ag Kα radiation by $BaTiO_3$ crystals in the (3, – 3) position.

arise from thin surface layers; further in the angles between the blocks become small. The reflections from the individual blocks are superimposed to give a curve consisting of a single broad peak.

We used the dynamical theory to calculate the shape of the peaks for (200) and (300) planes for Cu Kα and Ag Kα radiation; the theoretical calculation was performed by the method of refs. 4 and 5 and defined the width of a diffraction peak as 10.5" for Cu Kα and 1" for Ag Kα. Experiment gives the convolution of two diffraction peaks, so the theoretical curve was convoluted, and the width of the double-reflection curve was attained as 14.7" for Cu Kα and 1.4" for Ag Kα. These values are roughly half the observed diffraction width for a single block for Cu Kα, and the difference from the observed one may be due to: a) displacement of the Ti ion in the oxygen octahedron; b) the presence of vacancies, replacement of individual atoms in the unit cell of $BaTiO_3$ by impurity atoms, and interstitial impurity atoms; c) the presence of a spontaneous-polarization vector;[6-8] and d) nonuniformity in the crystals due to variation in the degree of tetragonality with depth.[3]

The calculations showed that displacement of Ti did not give an appreciable change in the width of the double-reflection curve; replacement of individual atoms in the unit cells by other atoms also had no marked effect. For instance, replacement of Ti by Fe, and of O by F gives widths of 11.5" for Cu Kα, which exceeds by only 1" the width for pure $BaTiO_3$. There is an appreciable change in width if one assumes that the impurity atoms are introduced into the unit cell; the width of each diffraction peak becomes 14", with 20" for the convolution, but the actual impurity concentrations were too small to have an appreciable effect. It has been reported in certain papers that the integrated intensity of x-ray reflections is dependent on the spontaneous polarization; as the integrated intensity of the reflection is closely related to the peak width, the latter is also dependent on the spontaneous polarization.

We also calculated the coefficients of integrated reflection for Cu Kα radiation with a $BaTiO_3$ crystal for two limiting cases: ideal crystal ($55.3 \cdot 10^{-6}$ rad) and a mosaic crystal ($96.3 \cdot 10^{-6}$ rad). Direct measurement of this coefficient with a two-crystal spectrometer gave $74.1 \cdot 10^{-6}$ rad, and this may be taken with other evidence to show that for $BaTiO_3$ single crystals consist of individual blocks, each of which is close to being ideal.

We are indebted to E. G. Fesenko for kindly making available the crystals and for valuable discussions.

---

[1] F. Brown and W. Todt, J. Appl. Phys., 35, 5 (1964).

[2] M. A. Blokhin, A. B. Gilvarg, I. Ya. Nikoforov, and V. P. Savchenko, Izv. AN SSSR, Ser. Fiz., 26, 397 (1962).

[3] O. I. Prokopalo, E. G. Fesenko, V. G. Gavrilyachenko, R. I. Spinko, and V. S. Bondarenko, Barium Titanate [in Russian], Izd. Rostov. Univ. (1971).

[4] R. James, Optical Principles of the Diffraction of X Rays, Cornell Univ. Press (1948).

[5] M. Renninger, Acta Crystallogr., 8, 597 (1955).

[6] E. F. Bertaut, Solid State Commun., 5, 173 (1967).

[7] N. Niizeki and M. Hasegawa, J. Phys. Soc. Japan, 19, 550 (1964).

[8] B. Morlon, Compt. Rend., B226, 863 (1968).

Rose channels

V. M. Finkel' and V. A. Fedorov
Tambov Chemical Engineering Institute

(Submitted January 6, 1972; resubmitted May 3, 1972)
Kristallografiya, 18, 593-598 (May-June 1973)

Microscopic investigation has shown that there are several variants in the formation of Rose channels of the first type, and that these are different from the scheme proposed by Rose himself. The existence of elastic Rose channels has been observed. When calcite crystals were deformed, among the developing parallel bands there were some which grew towards each other and which interacted freely when they came close, and so formed elastic Rose channels in their initial stages. Local investigation of the cross section of these twins has shown that a channel of the second type is a region of broken or crumbled material and is not a band.

It is known that when Iceland spar is deformed, it is possible to see the formation of crystallographically oriented planes called Rose channels (see ref. 1). It has been said that two morphologically different forms exist: channels of the first type which arise from the interaction of parallel twinned layers, and channels of the second type which arise from the interlacing of the intersecting twins. There are very few publications on Rose channels in either Russian or foreign journals (see refs. 2-6).

Crystals of optically transparent Iceland spar were used in the experiments. The specimens were pricked out of large single crystals as prisms either 10 × 10 × 30 or 15 × 15 × 15 mm, along the $\{100\}$ planes. Practically no glide takes place in calcite under normal conditions, and changes in the form of the material occur only by twinning along (100), (101), and (011). The crystals were deformed by static compression in clamps with grooved surfaces along the large diagonal of the cross section. Fairly many twins with the one orientation were produced. The evolution of parallel layers which approached each other was carried out so that they interacted to form Rose channels of the first type. These occurred in a plane perpendicular to the displacement when twinning took place along the directions [110], [101], [011]. The specimens in which Rose channels of the second type were formed were alternately deformed in any two perpendicular directions; the twins so formed intersected along $[\bar{1}11]$, $[1\bar{1}1]$, $[11\bar{1}]$.

Fig. 1. Large-scale formation of first type Rose channels.

1. The channel of the first type so generated went into the depths of the material and came out on the opposite side in a similar rhombic form. The geometry of its section was completely determined by the dimensions of the conflicting layers and their mutual spacing. Thus the channels of the first type were hollow, inclined prisms. Their permeability was checked by forcing liquid through them. Formation of these channels frequently occurs on a large scale (see Fig. 1).

Chemical etching in a 10% aqueous solution of tartaric acid gave dislocated boundaries of the twins forming the channels; the edges of the first type channels were almost untouched by the chemical action. Only individual dislocations of the same density as the dislocations in the matrix were observed when the interior surface of the channels was etched.

Microscopic investigation showed that there are several variants in the formation of first type channels, and that these variants differed from the scheme adopted by Rose. Figure 2a shows a channel which corresponds to Rose's scheme in its form and its method of production, but has this difference, that it lies in the twinned mass and owes its existence to the untwinning elements wedging into the twin. Disturbance of the continuity during the formation of these channels occurs on a cleavage plane oriented across the material. Similar bands are encountered at the base of high-energy twins which are the result of fusion of layers of polysynthetics. The appearance of "twin channels" has been observed in microlayers.

The channels can arise between continuous twinned layers of variable thickness and discontinuous layers ending at a first type channel (Fig. 2b). An irregularity is formed where the layer thickness changes. The incomplete twin has cross section equal to the reduction in the area of the basic layer and thus would be the part split off from the parent high-energy twin.

Several channels were observed to have irrationalities in their configuration; these appeared as partial openings in the material but not along the cleavage plane. The

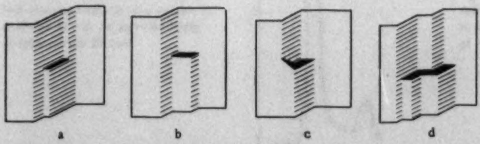

Fig. 2. Schemes for the formation of Rose channels.

cross sections of such bands were unstable, and underwent substantial changes over the whole range. For several channels, a definite law could be found as they lost their continuity (Fig. 2c), where the opening occurred on a plane not a cleavage plane and also did not correspond to a secondary cleavage plane.

Particularly interesting were the channels which developed in polysynthetic twins. In a system composed of a large number of parallel twinned layers, we observed the development of all the channels described above. But besides these, we observed the junction of different types of channels, and this junction created a Rose channel of complex configuration (Fig. 2d). In the polysynthetic twin such bands were predominant and were free to reach large size. In the calcite, it was possible for such channels to exist, and their behavior could explain the partial and even complete reversibility which occurs.

When he investigated twinning in calcite, Garber encountered the reversibility of this process (see ref. 7), and postulated it on the basis of observations on elastic Rose channels. Several loading regimes were used. In the first of these, the deformation was done in clamps with a grooved surface. Among the parallel layers which developed, there were some which grew into each other and freely interacted when they got close, so that they formed an elastic Rose channel in the initial stages. This went from the surface where it was generated into the depths of the material and had the appearance of an air wedge, this being easily observable under a light interferometer. When the load was removed, the elastic twins and the channel vanished simultaneously. No optical changes of any kind could be observed where the channel had been.

The process described above could be irreversible, depending on the jamming of the twins; this sticking or jamming was related to the disintegration of the material on the surface where the twin was generated. Two methods were used to ensure reversibility. First, the whole crystal was subjected to bending stresses so as to make the process reversible; the second method was to remove by cracks those particles which blocked reversibility. Then on the surface of one half of the crystal the Rose channel was stable, on the other it was reversible (Fig. 3). The formation of elastic Rose channels as in the experiments can be expected not only when elastic twins meet, but also when a stationary layer and an elastic twin come into conflict.

One method of observing the reversibility of Rose channels can also serve as a method of generating a plentiful supply of parallel twinned layers. Moreover, a set of channels is produced. The mechanism for closing the channels during polysynthetic twinning is unusual and is not an elastic process. In the initial stages of the deformation the twins and the channels appear, and then the subsequent loading of the crystal displaces the boundary of the twins, unites the separate layers, and forms a single dislocated mass. Thus the Rose channels come and go during the deformation process and are essentially an organic part of the complete process of changing the shape of the crystal.

The possibilities of observing elastic Rose channels we have given above have a fairly random character because the channels can occur in quite arbitrary places, and are not generally formed. In order to get some control over the production of the elastic channels a device was constructed which gave some hope that these channels would appear at a fixed point in the field of view of the microscope and thus the kinetics of their formation could be watched. Garber's experiment in ref. 7 is based on this method. Our arrangement allows us to produce two individual elastic twins which intersect. As their vertices converge, a vacuum band or elastic channel of the first type is formed. Unloading removes both twins and channel. As it disappears, the elastic Rose channel slows down the disappearance of the elastic twins to some extent.

When the crystal cracks where the elastic Rose channel appeared, steps remain in the face. Etching brings out the short dislocation lines. When elastic channels lying completely inside the crystal are produced, since there is no contact with the atmosphere the process is completely reversible without the formation of steps and dislocations during the subsequent unloading. Etching of the polysynthetic conglomerate mentioned above – formed of a finite number of macrotwins – makes the old layer boundaries reappear and, what is more interesting, produces short dislocation lines which jut out from these boundaries (Fig. 4). By their form and orientation, these correspond to the dislocation chart obtained by etching the surfaces of the block with the elastically closed channels. Some data lead us to suppose that in this case the Rose channels are free to open and shut without reaching the surface. Irreversible channels are also observed in the body of the twin, and these do not close up for any reason.

2. When a crystal containing Rose channels of the second type is examined under the microscope, the material lying close to them is permeated with a large number

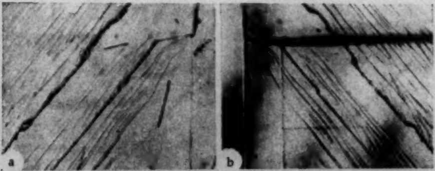

Fig. 3. Two half crystals. a) shows reversible channels, while b) shows channels which have gone into stable form, as the shadows under the light attest.

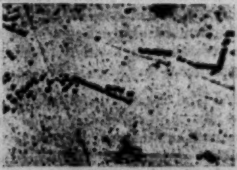

Fig. 4. Etching of a face with reversible Rose channels closed during polysynthetic twinning.

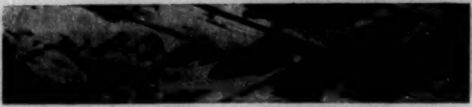

Fig. 5. Generating a Rose channel of the second type: The dark spots are cracks along the cleavage of the crystal.

of cracks, and these cracks are all around the channels and are intimately connected with them. Moreover, the region surrounding these channels and the material around them are permeated with fine, often wedge-shaped channels of the first type starting in the zone of the channel of the second type. Some of these terminate inside the crystal. When the point where the channel of the second type meets the crystal surface is investigated, it is seen that this is generally not a hollow formation, but is usually filled with deformed material: This differs from Rose's scheme, which presumes that a hollow is formed. Subsequent study of the development of channels of the second type enabled the following stages in their evolution to be distinguished.

The first stage is the growth of the twin and its attack on the stationary layer. When the primary twin reaches the surface, the mobile twin is slowed down and its front is distributed along the boundary of the blocking twin and the matrix. As the load is increased further, up to the appearance of the second type Rose channel, cracks begin to appear along the cleavage surface and their development leads to disintegration in the specimen, as noted in ref. 8. At this stage the active twin does not go across to the opposite side of the stable layer. The external form and the mutual orientation of the expanding "petal cracks" (Fig. 5) allows us to assert that they grow only on the active or attaching side of the twinning barrier and that they do not grow through it; we may assert further that they are distributed along the boundary between the mobile twin and the matrix. The initial batch of developing cracks severely restricts the dimensions of the cracks after the active twin breaks through the transverse twin. The breakthrough itself generates the channel of the second type, and it is accompanied by the appearance of a set of new cracks in the body of the crystal; these cracks are oriented in all directions and are developed further by loading.

An experiment was carried out to find out the change in the form of the material inside the second type channel. The test was set up so that the directions of displacement of the material in the conflicting twins were in the plane of observation. As the attacking twin became clogged up, it caused the material at the point of contact to disintegrate and swell, and this was observed by a photointerferometer. The number of cracks grew as the load increased. The breakthrough led to disorientation in the disintegrating material and to crumpling (Fig. 6).

As a second type channel develops, i.e., as its dimensions grow, the pulverization spreads out into the surrounding volume and leads to an increase in the stresses localized at such a channel. For an approximate determination of the level of fragmentation, material taken from the channel was investigated under a microscope. The size of some of the particles did not exceed $1.2\ \mu$, which means that there can be no cracks in these fragments. Such intense fragmentation guarantees that the stress concentration around the Rose channel of the second type is high. A comparison of the admissible displacement directions of the material in the second type channel with displacements which have actually occurred disclosed their obvious differences. As a result of this discrepancy, there must be either a high-energy localized plastic flow or drastic pulverization of the material at the core of the Rose channels of the second type. Since practically no sliding or glide takes place in calcite under normal conditions, drastic pulverization of the material must take place. Undoubtedly this lead to very high stress concentrations. These concentrations are the obvious explanation of the appearance of the main cracks which start in the zone of the second type channels (Fig. 6).

Thus the intersection of twinned layers in calcite does not form crystallographic hollow Rose channels of the second type; the intersection is a region of disintegrated, disoriented material which is highly fragmented. Under certain conditions, irreversibility can occur during disturbances of this kind. An experiment was done as follows. Crystals of Iceland spar which had twins produced in them were ground off normal to one of the twinning planes to obtain a surface which cut the layers already generated. In the immediate neighborhood of the stationary layer in this surface, the crystal was statically loaded by pressing on it with a spherical steel punch 1.6

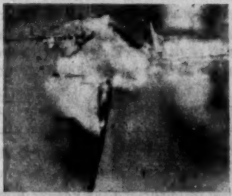

Fig. 6. Changes in the form of the material near a Rose channel of the second type.

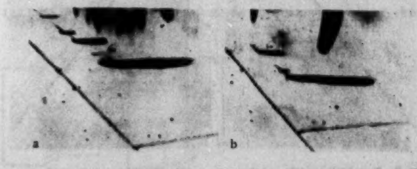

Fig. 7. The reversible stage in the production of a Rose channel of the second type. a) cleavage cracks produced by the load; b) shows how the second loading produces new cracks.

mm in diameter. This produced a twinned elastic petal. When this reached the surface of the deformed zone, a system of parallel cracks began to develop along the cleavage. When the load was removed, they shrank and then vanished completely (Fig. 7). A new attack on the stable twin was made with an elastic twin after some time had elapsed; this led to the appearance of new cracks whose positions did not depend on the previous breaks in the continuity of the material. Thus the visible breaks had healed. This is obviously possible because all the interaction occurred inside the crystal and the bands formed remained vacuums. The freshly opened surfaces set together easily when they were brought into contact. It must be noted however that this occurs in the early stages of the formation of Rose channels of the second type, when the attacking twin has not yet broken through the static twin.

---

[1] G. Rose, Physik. Abhandl. kön. Akad. Wiss. Berlin, 57-79 (1968).

[2] M. V. Klassen-Neklyudova, Mechanical Twinning of Crystal [in Russian], Akad. Nauk SSSR, Moscow (1960).

[3] J. Czochralski, Moderne Metallkunde, Berlin (1924).

[4] R. I. Garber, I. A. Gindin, V. S. Kogan, and B. G. Lazarev, Dokl. Akad. Nauk SSSR, 110, 64 (1956).

[5] G. B. Rais, Izv. Vyssh. Ucheb. Zaved., Fizika, 4, 79 (1962).

[6] É. S. Yakovela and M. V. Yakutovich, Zh. Tekh. Fiz., 20, 420 (1950).

[7] R. I. Garber, Dokl. Akad. Nauk SSSR, 21, 233 (1938).

[8] V. I. Startsev, V. M. Kosevich, and Yu. S. Tomlenko, Kristallografiya, 1, 425 (1956) [Sov. Phys. – Crystallogr., 1, 336 (1956)].

Mechanism of growth and etching of whisker crystals of aluminum nitride

K. I. Portnoi, V. N. Gribkov, B. V. Shchetanov, É. L. Umantsev, and V. A. Silaev

(Submitted March 31, 1972; resubmitted June 7, 1972)
Kristallografiya, 18, 599-604 (May-June 1973)

The mechanism of the influence of iron impurity on the growth of whisker crystals of aluminum nitride by the reduction of aluminum oxide by carbon in a nitrogen atmosphere according to the equation $Al_2O_3 + 3C + N_2 = 2AlN + 3CO$ has been investigated. It has been established that the presence of iron is a decisive factor in the growth of the crystals. Not participating in the process of reduction of aluminum oxide, iron makes possible the growth of whisker crystals by the vapor–liquid–solid phase mechanism, playing the role of solvent for aluminum and nitrogen. It is shown that, for a deficiency of aluminum in the gas phase, the reverse process of evaporation of nitride crystals by the solid phase–liquid–vapor mechanism can occur with participation of iron as a solvent.

Notwithstanding the large number of works on the preparation of whisker crystals of aluminum nitride,[1–5] the mechanism of their growth remains unclear. The possibilities of action of a diffusion-dislocation mechanism[3] and the mechanism of growth of an ideal crystal[2] have been examined, and in ref. 5 a two-stage model is proposed, according to which the formation of the crystal in the beginning stage goes by means of extrusion of a rapidly nitriding melt of aluminum oxide through pores in the surface crust of the nitride, and in the second stage precipitation onto the naturally rough surface occurs directly from the gas phase to the solid state with two-dimensional nucleation or condensation. At the same time, in many works[1,2,5–7] indications of a determining influence on growth are cited or the presence of impurities of a series of elements – silicon, molybdenum, cobalt, or tungsten – in the experiments is ascertained, without any explanation. According to Gribkov, Isaikin, Umantsev, and Shchetanov,[8] and an analysis of the diagrams of state of these elements with aluminum and nitrogen, they could promote the condensation of aluminum nitride by the vapor–liquid–solid phase mechanism[9,10] through drops of liquid solutions of the impurity element with aluminum and nitrogen.

The influence of iron impurity on the growth of whisker crystals of aluminum nitride was studied in this work. It was assumed that the use of iron as a solvent for aluminum and nitrogen, since it does not interact with aluminum, has a low vapor pressure, and is not inclined toward the formation of volatile compounds under the conditions of growth, allows the action of the vapor–liquid–solid phase mechanism to be revealed more clearly without complication by secondary effects.

Crystals of AlN were grown by reduction of aluminum oxide by carbon in an atmosphere of nitrogen[4] in accordance with the reaction $Al_2O_3 + 3C + N_2 = 2AlN + 3CO$. The process was carried out in the temperature range 1800–2050°C in a furnace with a horizontal tubular graphite heating element, a graphite boat with a charge of a mixture of Al_2O_3 + Fe powders being reduced in the isothermal zone of the furnace. The total impurity content of the graphite did not exceed 0.01%, while the aluminum oxide had a purity of 99.8% and the iron a purity of 99.99%.

Curve 1 in Fig. 1 demonstrates the influence of the iron content in the initial charge on the weight yield of whisker crystals of AlN per unit area of surface of the charge at a temperature of 1900°C, the time of holding being 20 min and the flow rate of nitrogen being 6 liters/h–cm². Without the introduction of iron and for iron contents up to 2% by weight, growth occurred only upon fusion of the charge. The density of growth of crystals (in cm^{-2}) as a function of iron content (curve 2 in Fig. 1) was computed on the basis of the dispersion curves of the crystals formed, plotted on the basis of length and diameter according to the method described in ref. 4.

Thus, the presence of iron proved to be a decisive factor in the growth of the crystals. This effect cannot be explained by the reduction of aluminum oxide by iron, since it is thermodynamically impossible in the presence of carbon and carbon monoxide. To confirm whether or not iron promotes the intensification of the reduction of aluminum oxide by carbon as the result of dissolution of carbon in the liquid phase and possible improvement of its contact with oxygen, the carrying away of aluminum oxide from the charge as a function of iron content was determined. The amount carried away proved to be constant for all concentrations of iron within limits up to 20%. The ac-

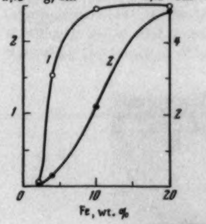

Fig. 1. Number of AlN crystals as a function of iron content in charge.

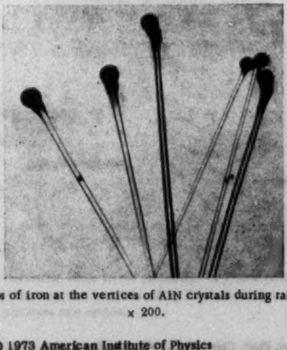

Fig. 2. Drops of iron at the vertices of AlN crystals during rapid cooling. × 200.

tivation energy for the transport of aluminum oxide as the result of reaction with carbon[4] agreed with the activation energy as calculated on the basis of the weight yield of crystals in the presence of iron for the temperature range 1800-1940°C. This fact also negates the participation of iron in the chemical transformations which take place during growth.

The crystals obtained in the presence of iron looked as shown in Fig. 2 for high rates of buildup of the vertices. The opaque metallic drops possessed magnetic properties and, from the results of local x-ray spectral analysis, consisted predominantly of iron. Often the transformed portions of the crystals had noticeable broadened regions, inside which were observed cavities filled with iron. An analogous effect was noted earlier[11] during the rapid cooling of silicon crystals grown by the vapor–liquid–solid phase mechanism. In some cases, intermittent channels filled with iron were found along the entire length in crystals of $\langle 10\bar{1}1\rangle$ orientation, which gave unambiguous evidence of the presence of drops on the vertices in the course of the entire growth period. Sharp but slight cooling to temperatures at which growth could still proceed, in agreement with ref. 10, resulted in the homogeneous formation of nuclei in the liquid phase, to breaking down of the drop at the vertex, and to growth of a bundle of finer crystals from it (Fig. 3a). Just such bundles of crystals were formed from drops condensed on the lateral faces (Fig. 3b).

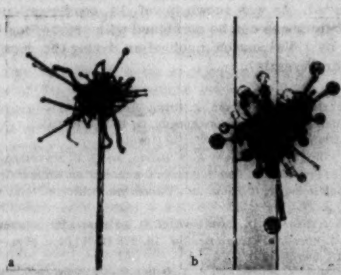

Fig. 3. Formation of bundles of AlN crystals from drops. × 150. a) At vertex; b) on a lateral face.

Depending on the cooling schedule, crystallographic orientation of the crystal, and other conditions, different variants of the behavior of the drop, including the breaking away of drops from the vertices, gradual evaporation of drops, and etching of the crystal near the vertices by evaporation through an intermediate liquid phase were observed during slow cooling.

Successive stages of transformation during the cooling of a vertex drop of iron and the $\langle 0001\rangle$ vertex of the crystal itself, which we observed at magnifications of 50-80 directly in a camera by time exposures, are shown in Fig. 4. The photographs were obtained with a selected specimen. Retention of the shape of the drop and the vertex, which is characteristic for each of the stages, was attained by rapid cooling, the time for complete cooling not exceeding 1-2 sec. A crystal at the time of growth at a temperature of 1900°C, the crystal growing vertically upward, is shown in Fig. 4a. Upon cooling, the angle of wetting of the drop continued to increase and the area of the face portion of the drop–crystal contracted, forming an apical cone. At 1800°C, the angle of wetting approached 180° and the drop gathered into a sphere on the most sharply pointed vertex (Fig. 4b). At this stage, the growth of the crystal is completely stopped, since the reaction of formation of the nitride from aluminum oxide practically does not go at all below 1800°C. Beginning with 1800°C, the drop started to decrease in volume, lost stability at 1700°C, and shifted from the vertex and fastened onto a lateral face of the vertex of the pyramid (Fig. 4c). In most cases, especially on crystals growing obliquely and vertically downward, the drops breaking away from the vertex were not held on the crystal and disappeared without a trace.

Upon sufficiently long holding at temperatures below 1800°C, where the pressure of aluminum in the gas phase with respect to reduction of the oxide proves to be below the equilibrium pressure above the nitride, the etching of crystals by drops according to the reverse solid phase–liquid–vapor mechanism was observed. Successive stages of etching of the pre-vertex portion of a $\langle 10\bar{1}1\rangle$ crystal at 1750°C are shown in Fig. 5. On this portion, the drop, moving from the vertex upon cooling, shifted within bounds limited by the vertex and curvature of the crystal. As can be seen from Fig. 5, the drop disappeared in the later stages, and the pre-vertex portion greatly decreased in diameter and lost a regular boundary.

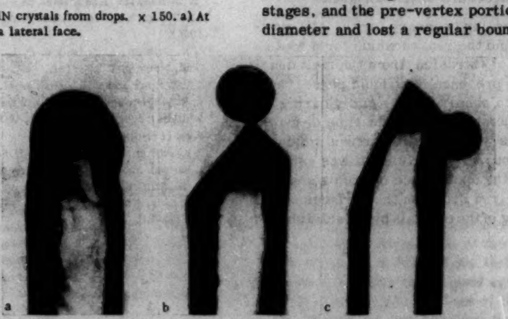

Fig. 4. Successive transformations of a drop at the <0001> vertex of a crystal during slow cooling. × 300. a) 1900; b) 1800; c) 1700°C.

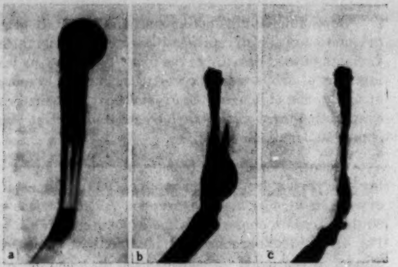

Fig. 5. Successive stages of etching of the pre-vertex portion of a crystal by drops at 1750°C. × 200. a) At starting moment; b) at 3 min; c) at 6 min.

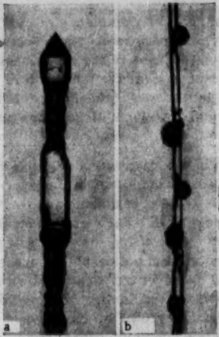

Fig. 6. Etching of lateral faces of AlN crystals by drops. a) Final stage (× 150); b) intermediate stage (× 100).

Thus, the results obtained give evidence that, in the process investigated, the condensation of AlN proceeded in accordance with the vapor–liquid–solid phase mechanism. They confirm the belief that such a mechanism of condensation could also occur in refs. 1, 2, 5-7, in which the participation of silicon, molybdenum, cobalt, and other impurities in growth was noted. The fact that drops were not always observed on the vertices of the crystals after cooling cannot serve as a contradiction of condensation through the liquid phase. As was shown above, drops can disappear as the result of loss of stability upon change of the angle of wetting or etching of the crystal, and also as the result of gradual entrapment of the solvent by the crystal, upsetting of dynamic equilibrium, evaporation of the solvent, formation of volatile compounds of the solvent with components of the gaseous phase, or other causes analyzed in refs. 8, 12, and 13. For aluminum nitride crystals growing at extremely high temperatures, decrease in volume and disappearance of the drop for any of the reasons mentioned can proceed with high speed. It should be especially intense if solvents inclined toward the formation of volatile compounds, silicon or molybdenum for example, are used. Upon cooling, in the low-temperature region the rate of formation of SiO and MoO_3 as the result of reaction with oxygen and moisture impurities in the nitrogen can greatly exceed the rate of supply of silicon and molybdenum to the drop from the charge, which rapidly decreases with decrease in temperature.

The absence of a regular boundary for the AlN crystals observed in ref. 5 and the reason which for a while favored the mechanism of extrusion from the melt can also be explained by the presence of a liquid phase. In the process studied, we often observed, especially during noticeable temperature fluctuation within the time of growth, the formation of crystals with periodic portions which did not possess a regular boundary (Fig. 6a). It was established that the cause of the appearance of such a shape was the condensation of iron drops on the surfaces of the lateral faces and etching of the crystals by the solid phase–liquid–vapor mechanism. A crystal in an intermediate stage of etching is shown in Fig. 6b. The destruction of the regular boundary about the drop is quite noticeable. As in ref. 5, the absence of a regular boundary was observed predominantly in the lower portions of crystals. Evidently this was associated with the fact that they were found close to the charge, which is the source of the drops, and the probability of condensation of a drop on these portions was greatest.

Condensation through a liquid phase and the axial dislocations observed in aluminum nitride crystals[3] are not precluded. As was shown in ref. 14, condensation through the liquid phase can be combined with crystallization of drops by a dislocation mechanism during the growth of whisker crystals.

---

[1] W. Kleber and H. D. Witzke, Z. Krist., 116, 126 (1961).

[2] H. D. Witzke, Freiberger Forschungsh., C, 195, 44 (1965).

[3] C. M. Drum, J. Appl. Phys., 36, 816 (1965).

[4] K. I. Portnoi, V. N. Gribkov, A. S. Isaikin, and B. V. Shchetanov, Abstracts of Proceedings, First Scientific Conference on Whisker Crystals and Nonferromagnetic Films, Izd. Voronezhsk. Politekhn. Inst., Voronezh, (1970), p. 27.

[5] G. V. Berezhkova, I. N. Tsvetkova, N. D. Zakharov, V. N. Rozhanskii, and V. I. Koryukin, Kristallografiya, 16, 978 (1971) [Sov. Phys.–Crystallogr., 16, 848 (1972)].

[6] K. I. Portnoi, V. N. Gribkov, A. S. Isaikin, B. V. Shchetanov, and M. Kh. Levinskaya, Izv. Akad. Nauk SSSR, Neorgan. Mat., 6, 1762 (1970).

[7] J. A. Kohn, R. G. Cotter, and R. A. Potter, Am. Mineralogist, 55, 355 (1956).

[8] V. N. Gribkov, A. S. Isaikin, É. L. Umantsev, and B. V. Shchetanov, Izv. Akad. Nauk SSSR, Neorgan. Mat., 8, 1249 (1972).

[9] R. S. Wagner and W. C. Ellis, Appl. Phys. Lett., 4, 89 (1964).

[10] R. S. Wagner and W. C. Ellis, Trans. Met. Soc. AIME, 233, 1053 (1965).

[11] Whisker Technology, A. Levitt William and Sons, New York–London–Paris (1970), pp. 92-93.

[12] J. K. Arthur and R. S. Wagner, U.S. Patent No. 3,505,127 (April 7, 1970).

[13] J. Berman and C. E. Ryan, J. Crystal Growth, 9, 314 (1971).

[14] V. N. Gribkov, V. A. Silaev, B. V. Shchetanov, É. L. Umantsev, and A. S. Isaikin, Kristallografiya, 16, 982 (1971) [Sov. Phys.–Crystallogr., 16, 852 (1972)].

Electron diffraction study of the structure of amorphous germanium telluride and selenide films

Yu. G. Poltavtsev and V. P. Zakharov

(Submitted December 9, 1971; resubmitted April 14, 1972)
Kristallografiya, 18, 605-608 (May-June 1973)

The short-range order in amorphous GeTe films obtained by thermal and laser sputtering of the samples has been studied by electron diffraction. It has been shown that the structure of films obtained by laser sputtering of the samples can be well described by a model with the ZnS crystal structure. In films obtained by thermal sputtering of the samples, there exist "crystal-like" groupings of atoms and groups with predominantly covalent character of the interatomic bonds. The structure of amorphous GeSe films is better described by a model with the ZnS crystal lattice than by a model with octahedral arrangement of the atoms.

References 1-3 describe an electron diffraction investigation of the structure of the short-range order of amorphous GeTe and GeSe films obtained by thermal sputtering. The smallest interatomic distance r_1 in GeSe is 2.6 Å. This distance is nearly equal to the radius of the first coordination sphere in the crystal. The first coordination number is equal to 5.8; and the ratio $r_2/r_1 = 1.54$. In the authors' opinion,[1] these results indicate an octahedral arrangement of the atoms analogous to the arrangement of nearest neighbors in the crystal.

The data on the GeTe structure are contradictory. The values of 6 for the coordination number Z_1 and 2.75 Å and 4.05 Å for the radii r_1 and r_2 of the first two coordination spheres indicate an octahedral arrangement of the nearest neighbors, according to ref. 1. However, in ref. 2, $Z_1 = 4$, $r_1 = 2.65$ Å, and the atomic configuration is concluded to be tetrahedral. In ref. 3, a complex model of the structure is proposed, in which, along with a tetrahedral arrangement of the neighbors of the Ge atoms, a coordination number of 2 is allowed around the Te atoms. This large difference in the experimental data and the models of the GeTe structure evidently indicates that the structure depends strongly on the conditions of preparation of the films. Therefore it is desirable to study the structure of amorphous GeTe films obtained under very different sputtering conditions, but always using the same material as a substrate. Germanium selenide has been studied only once; a second determination of its structure would also be of interest.

In this work amorphous GeTe and GeSe films are studied by electron diffraction. The GeTe films were obtained by thermal and laser (ruby laser) sputtering of single crystals in a vacuum of 10^{-5} torr; the GeSe films were prepared by thermal sputtering. Glass plates at 300°K served as substrates. The curves of the scattered intensity were constructed by the method of ref. 4, and the background was calculated according to ref. 5. For monitoring the composition, the amorphous films were irradiated by strong light pulses,[6] and during this process the films crystallized. The electron diffraction patterns from the polycrystalline films contain no Debye–Scherrer lines not characteristic of GeTe and GeSe. This confirms the conclusion[7] that when sputtered on a hot substrate, chalcogenide films are obtained without deviation from stoichiometry.

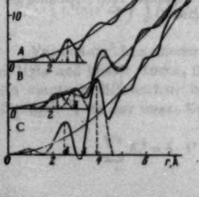

Fig. 1. The atomic radial distribution functions in amorphous GeTe, obtained by laser (A)(S_{max} = 7.7 Å^{-1}) and thermal (B) (the thin line and the dotted curve correspond respectively to S_{max} = 8.0 and 4.5 Å^{-1}) sputtering of the sample, and in amorphous GeSe (C) (S_{max} = 8.0 A^{-1}).

RESULTS AND DISCUSSION

Figure 1 shows the atomic radial distribution functions (ARDF) for amorphous GeTe and GeSe films. The values of S_{max} are also indicated.

Germanium telluride: laser sputtering of the sample (see Fig. 1A). On the ARDF for GeTe there are maxima for r_1 = 0.5, 1.6, 2.6, 4.15, 5.0, and 6.0 Å; on the left side of the maximum for r = 4.15 Å there is a shoulder at r = 3.6 Å. The maxima at r = 0.5 and 1.6 Å and the shoulder at 3.6 Å are due[8] to the "termination effect." The radius r_1 of the first coordination sphere thus is 2.6 Å. This value is near the result obtained in ref. 2 but smaller than the r_1 value given in ref. 1.

In crystalline GeTe (the low temperature modification) the first interatomic distance r_{1c} is 3.01 Å, which lies between the sum of the covalent (2.54 Å) and the ionic (3.14 Å) radii of the components.[9] The nearness of the value of r_1 in the film to the sum of the covalent radii of Ge and Te indicates the predominantly covalent character of the interatomic bonds in the amorphous film, in contrast to the ionic–covalent character in the crystal. From the area under the first maximum in the ARDF, the first coordination number Z_1 is 3.5. Since Z_1 is so close to 4, there is evidence for a tetrahedral arrangement of the nearest neighbors in the film, unlike the octahedral structure in the crystal. To find a model for the structure of amorphous GeTe, we compared the positions of the maxima of the ARDF with the radii of the coordination spheres constructed from tetrahedra. It was found that the ratios r_i/r_1 = 1, 1.6, 1.92, and 2.31 agree with the corresponding values for a structure of the ZnS type, which is characteristic for a number of semiconducting compounds.[9] The poor resolution of the second and higher-order maxima in the ARDF does not permit a detailed comparison of the distribution of different kinds of atoms in amorphous GeTe and in the ZnS lattice. However, because of the good agreement of the value of Z_1 and of the relative values of the radii of the coordination spheres, we can consider the two atomic distributions to be analogous in their principal features.

Germanium telluride: thermal sputtering of the sample. (see Fig. 1B). On the ARDF for GeTe computed for $S_{max} = 8\ Å^{-1}$, there are structural maxima for $r = 2.15$, 2.90, 4.2, 6.0, and 7.8 Å; the maximum for $r = 1.0$ Å is spurious. An ARDF is also computed for $S_{max} = 4.5\ Å^{-1}$ – that is, with exclusion of the part of the information about the structure that is contained in the intensity curve for $S > 4.5\ Å^{-1}$. On this curve the maxima are very washed out, but their positions are near the values given above. Here the washed-out maximum at 2.55 Å corresponds to the first two maxima in the ARDF for $S_{max} = 8\ Å^{-1}$. The position of the washed-out maximum is in good agreement with the average position (2.15 + 2.90)/2 Å of the maxima in the $S_{max} = 8\ Å^{-1}$ curve. The presence of two closely spaced maxima in the ARDF indicates the presence of atomic groupings with different characteristic interatomic interactions. Since the value $r_1' = 2.9$ Å is so near the radius of the first coordination sphere in the crystal, we can assume that there are "crystal-like" groupings of atoms: that is, groupings with short-range order like the short-range order in the crystal. An ionic–covalent bond such as exists in the crystal is characteristic for these atomic groupings. In groups of a second type, there is a primarily covalent bond, as shown by the fact that $r_1'' \ll 3.01$ Å. The values of the coordination numbers in these groups of atoms cannot be found with acceptable accuracy, since for this it is necessary to know the relative number of groups of different type and to make an unambiguous determination of the area under the corresponding maxima in the ARDF's. However, as a confirmation of the presence of "crystal-like" groupings of atoms, in addition to the fact that $r_1' \simeq r_{1C}$, there is the result that $r_2/r_1'' \simeq \sqrt{2}$, as is characteristic of an octahedral arrangement of atoms.

Germanium selenide (see Fig. 1C). On the ARDF for amorphous GeSe there are maxima at $r = 2.5$, 3.85, 5.1, 6.0, and 7.2 Å. The first two coordination numbers Z_1 and Z_2 are 4.8 and 12.5; the ratios r_i/r_1 are 1, 1.54, 2.08, 2.4, and 2.88. In crystalline GeSe there are one, two, two, and one atoms at distances of 2.56, 2.59, 3.32, and 3.37 Å, respectively. The first two interatomic distances, with a total coordination number of 3, fall in the region of the first maximum. The radii of the third and fourth coordination spheres in the crystal correspond approximately to the deep minumum in the ARDF. Thus the radial distribution of atoms in crystalline GeSe is different from the ARDF in the amorphous state.

In amorphous GeSe the values of Z_2 and r_2/r_1 are near 12 and $\sqrt{2}$, respectively, and the value of Z_1 is somewhat less than 6. These data suggest a "loose" octahedral atomic arrangement for a model of the short-range order. The large difference in the ratios r_i/r_1 for $i \geq 3$ for the film and the crystal, however, show the unsuitability of this model of the structure of amorphous GeSe. Another possibility for a model is the ZnS crystal structure, for which $Z_1 = 4$, $Z_2 = 12$, $r_i/r_1 = 1$, 1.6, 1.92, 2.31, and 2.52. For this model there is significantly better agreement of the values of Z_1, Z_2, and r_i/r_1 with the experimental results. This evidently indicates a "looser" packing of atoms in the amorphous state than in the crystal, as a result of the predominantly covalent character of the interatomic bonds. Evidence for this also comes from the result that $r_1 > 2.56$ Å. It is interesting to note that the first maximum on the ARDF is broader on the small-r side. This asymmetry reflects the fact that interatomic distances smaller than r_1 occur more often than distances somewhat exceeding r_1.

CONCLUSION

This investigation has shown that the structure of amorphous GeTe films depends on the conditions of preparation. Thus, the structure of films obtained by laser sputtering of the sample is different from the structure of the crystal and can be well described by a model assuming a tetrahedral arrangement of the nearest neighbors. In films obtained by thermal sputtering of the sample, there exist "crystal-like" groupings of atoms and groupings with interatomic bonds which have a predominantly covalent character. Apparently one cannot exclude the possibility that films of amorphous GeTe with different structure can be obtained by thermal sputtering of the sample by selection of the proper conditions. From this point of view, the different experimental results and the different models of the structure of GeTe mentioned previously are quite natural. The structure of amorphous GeSe films is different from the structure of the crystal. The ZnS crystal is a better model of the structure of amorphous germanium selenide than an octahedral arrangement of atoms. This result, one with the broadening of the first maximum of the experimental ARDF on the small-r side and the fact that the value of the radius of the first coordination sphere in the amorphous state is smaller than in the crystal, indicates that the interatomic bonds have a predominantly covalent character.

---

[1] A. G. Mikolaichuk and A. N. Kogut, Kristallografiya, 15, 353 (1970) [Sov. Phys.–Crystallogr., 15, 294 (1970)].

[2] D. B. Done, M. B. Heritage, K. L. Chopra, and S. K. Bahl, Appl. Phys. Lett., 16, No. 3, 138 (1970).

[3] F. Betts, A. Bienenstock, and S. R. Ovshinsky, J. Non-Crystalline Solids, 4, 554 (1970).

[4] L. I. Tatarinova, Tr. Inst. Kristallogr. AN SSSR, 11, 104 (1955).

[5] I. D. Nabitovich, Ya. M. Stetsiv, and Ya. V. Voloshchuk, Kristallografiya, 12, 584 (1967). [Sov. Phys.–Crystallogr., 12, 513 (1968)].

[6] Yu. G. Poltavtsev, V. P. Zakharov, and V. N. Chugaev, Kristallografiya, 16, 415 (1971) [Sov. Phys.–Crystallogr., 16, 341 (1971)].

[7] Lyu Tsyun'-khua, A. S. Pashinkin, and A. V. Novoselova, Zh. Neorgan. Khimii, 7, 963 (1962).

[8] R. Hosemann, L. Lemm, and H. Krebs, Z. Phys. Chem., 41, 121 (1964).

[9] N. Kh. Abrikosov, V. F. Bankina, L. V. Poretskaya, E. V. Skudnova, and L. E. Shelimova, Semiconducting Compounds–Their Preparation and Properties [in Russian], Nauka, Moscow (1967).

Crystallization of amorphous films of silicon nitride by ionic bombardment followed by annealing

P. V. Pavlov, É. V. Shitova, E. I. Zorin, and N. A. Genkina

Gor'kii Physicotechnical Reseach Institute

(Submitted July 23, 1971; resubmitted May 22, 1972)
Kristallografiya, 18, 609-613 (May-June 1973)

Electron diffraction is used to study the structural changes in silicon nitride films bombarded with Ar^+, P^+, and B^+ ions followed by annealing. This treatment forms the polycrystalline alpha phase of Si_3N_4. The present authors investigate the influence of the type of bombarding ions on the degree of disordering of the structure of the Si_3N_4 films before thermal annealing, and determine the critical temperature and dose for the onset of crystallization. A theoretical estimate of the dimensions of the crystallites which constitute the "amorphous" phase is made and an experimental test of the results is carried out.

In work on ion-beam doping of semiconducting materials, it is necessary to know what happens to the dielectric films which act as masks when impurity atoms are locally implanted in them. It has previously been shown[1] that amorphous SiO_2 films which have been subjected to ion bombardment crystallize on annealing.

We have used electron diffraction to investigate the structural changes occurring in amorphous Si_3N_4 films made by the plasma–chemical method when they are bombarded and subsequently annealed with B^+, P^+, and Ar^+ ions with an energy of 40 keV; the dose was varied between $6.2 \cdot 10^{12}$ and $6.2 \cdot 10^{16}$ ions/cm².

The short-range structures of the films were determined by means of Fourier analysis.[2] To construct the experimental intensity curve, on a single photographic plate we photographed five electron diffraction patterns with short exposures. As a rule, the diffraction patterns had two diffuse rings corresponding to interplanar distances of $d_1 = 3.9$ Å ($\sin\theta/\lambda = 0.14$); $d_2 = 1.35$ Å ($\sin\theta/\lambda = 0.36$), and from photomicrometric data we calculated the radial distribution curves by means of the expression

$$4\pi r^2 \sum_i K_i\rho(r) = 4\pi r^2 \sum_i K_i\rho_0 + \frac{2r}{\pi}\int_0^\infty si(s)\sin sr\,ds, \qquad (1)$$

where $4\pi r^2 \sum_i K_i\rho(r)$ characterizes the radial distribution of nearest neighbors around each atom, ρ_0 is the mean number of atoms per unit volume, and $s = 4\pi\sin\theta/\lambda$,

$$i(s) = \sum_i K_i^2\left\{I_n \Big/ \Big[\sum_i f_i^2(s)\Big] - 1\right\},$$

where f_i is the atomic scattering factor of the electrons of the i-th atom, K_i is the effective number of electrons in the atom, which, for substances consisting of several species of atoms, is given by

$$K_i^2 = \int f_i^2(s)s^2\,ds \Big/ \int f_l^2(s)s^2\,ds = \sum_i f_i^2(s)s^2 \Big/ \sum_i f_l^2(s)s^2.$$

Vainshtein[3] has shown that, for a substance consisting of light and heavy atoms, it is simplest to calculated K_i (in electron diffraction) by means of the relation $K_i = (Z_i/Z_l)^{0.75}$. In our case, $K_{Si} = 1.68$; thus we have

$$\sum_i K_i^2 = 4 \cdot 1^2 + 3 \cdot 1.68^2 = 12.47,$$

$$\text{and } i(s) = 12.47\left(I_n \Big/ \sum_i f_i^2(s) - 1\right),$$

where I_n is the normalized value of the experimental intensity. Values of r were taken over the range from 1 to 7 Å at 0.1 Å intervals. From an analysis of the radial distribution curves of the atomic density (Fig. 1), we see that, both for the original Si_3N_4 film and after irradiation with Ar^+, P^+, and B^+ ions, we observe a first sharply-resolved peak at r = 1.75 Å, corresponding to the distance between the Si and N atoms in the SiN_4 tetrahedron. The numbers of N atoms surrounding each Si atom at a distance of 1.75 Å were calculated from the areas under the first maxima of the curves: They range between 4.0 and 4.3, which coincides with the tetrahedral configuration in crystalline Si_3N_4. For the number of Si atoms around an N atom, calculations give 3-3.3 (the coordination number in crystalline silicon nitride is 3). The second maximum, lying at a distance r = 2.95 Å, is asymmetrical and is composed of the distances N_I-N_I (r = 2.97 Å is the edge of the SiN_4 tetrahedron) and Si_I-Si_I (r = 3.0 Å in the three tetrahedra linked via vertices at an angle of 120° to one another). The coordination numbers, obtained by subdivision of the total area under the second peak in proportion to the theoretical areas, were found to be $K_{N-N} = 11$ and $k_{Si-Si} = 8$, in agreement with ref. 4. The third peak, at a distance of 3.8 Å, (the Si_I-N_{II} bond) is not clearly evident for the untreated Si_3N_4 films. For films irradiated with B^+, P^+, and Ar^+ ions, this peak gets even more diffuse as

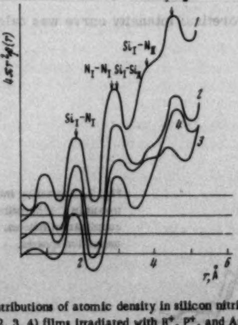

Fig. 1. Radial distributions of atomic density in silicon nitride films. 1) Untreated film; 2, 3, 4) films irradiated with B^+, P^+, and Ar^+ ions, respectively.

TABLE 1. Values of h/ω before and after Bombardment by Various Ions

No. of maximum	Before irradiation	After bombardment		
		B+(Z = 11)	P+(Z = 31)	Ar+(Z = 40)
I	4.00	3.90	2.81	2.55
II	4.50	3.88	3.64	3.25

TABLE 2. Temperature of Onset of Crystallization in deg C

Dose, μC/cm²	After bombardment		
	Ar+	P+	B+
1·10³	650	675	750
5·10³	550	600	650
1·10⁴	400	550	600

the mass of the bombarding ion increases, and for Ar^+ it totally disappears. Hence it follows that the group of three SiN_4 tetrahedra joined via their vertices, which is a characteristic element in the structure of Si_3N_4 in the crystalline state, is retained in amorphous films obtained by the plasma–chemical method. On bombardment, apparently owing to rupture of $Si_I - N_{II}$ bonds, this structural element is only partly preserved. At $r > 5$ Å the radial distribution curve rapidly levels out, showing that the SiN_4 tetrahedra are randomly oriented.

In our investigation of the influence of the type of bombarding ions on the degree of short-range order, as a measure of ordering we chose the quantity h/ω, which characterizes the sharpness of the first and second maxima on the radial distribution curves (h being the height of the peak at its maximum, and ω the width of peak at the level $h = 0$). Table 1 lists the values of h/ω in relative units: From this we see that the heavier the ion, the more disorderly is the structure (other conditions being constant).

By comparing the theoretical and experimental scattering intensity curves, we estimated the dimensions of the regions within which short-range order, characteristic of crystalline silicon nitride, is preserved.

The theoretical intensity curve was calculated on the assumption that there is strict short-range order within two, and then four, coordination spheres, according to the equation[2]

$$I(s) = Nf^2\left\{1 + 4\pi\int r^2(\rho(r) - \rho_0)\frac{\sin sr}{sr}dr\right\}. \quad (2)$$

To determine the experimental intensity curve we used the method of blackening curves.[5] From the blackening curves we determined the relative intensities at various points on the microphotometric curves with various values of sin θ/λ, and from these we found the experimental intensity curve, which we then normalized[6] by means of the expression

$$\int_0^\infty I_n(s)S^2\,ds = \sum_{i=1}^{n}\int_0^\infty f_i^2(s)\,ds. \quad (3)$$

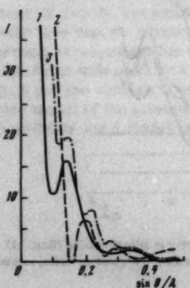

Fig. 2. Scattering intensities (in electron units). 1) Experimental; 2) for two coordination spheres; 3) for four coordination spheres.

Figure 2 plots the experimental and theoretical intensity curves. The curve calculated on the assumption of short-range order within four coordination spheres is the closest to the experimental curve. Hence we can assume that short-range order is preserved in at least four coordination spheres. The dimension of the region corresponding to four coordination spheres is about 13 Å. If the dimension of the region in which short-range order is preserved is calculated directly from the electron diffraction patterns by means of the half-width of the intensity maximum [see (4)], the value obtained is 10 Å.

The diffraction patterns from films bombarded with Ar^+, P^+, and B^+ ions and then annealed at 400–900°C were rather different. At certain temperatures, depending on the dose and type of ions, the electron diffraction patterns contained a considerable number of rings characteristic of a polycrystalline substance. The temperatures of onset of crystallization are given in Table 2.

Table 3 lists the interplanar distances of the alpha and beta phases,[7] and also the interplanar distances determined by the present authors from electron diffraction patterns for Si_3N_4 films subjected to irradiation with Ar^+ followed by annealing. From a comparison of the interplanar distances we see that the crystal structure of the films corresponds to that of the low-temperature α phase, which ought to arise, because on heating it is energetically more stable in the given temperature range.

As the annealing temperature is raised, the intensity of the Debye rings falls and against them as a background

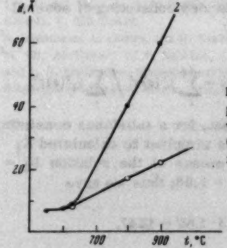

Fig. 3. Grain size vs annealing temperature, for Si_3N_4 film. Irradiation with Ar^+ ions, energy 50 keV. 1) Dose $6.2 \cdot 10^{15}$ ions/cm²; 2) dose $3 \cdot 10^{16}$ ions/cm².

TABLE 3. Interplanar Spacings and Indices of Reflections for Si_3N_4 Films

α phase[7]		β phase[7]		d, Å our data	α phase[7]		β phase[7]		d, Å, our data
(hkl)	d, Å	(hkl)	d, Å		(hkl)	d, Å	(hkl)	d, Å	
100	6.65	100	6.59	6.66	112	2.27	211	1.89	—
101	4.32	100	3.79	4.26	300	2.24	310	1.83	—
110	3.88	200	3.29	—	202	2.15	310	1.75	—
200	3.36	101	2.66	3.51	301	2.08	—	—	2.07
201	2.88	210	2.49	2.87	220	1.93	—	—	—
002	2.81	111	2.31	2.75	212	1.88	—	—	—
102	2.59	300	2.19	—	310	1.86	—	—	1.89
210	2.54	201	2.18	—	103	1.80	—	—	—
211	2.31	220	1.90	2.35	311	1.77	—	—	—

there arise reflections indicating the growth of crystal grains. To estimate the dimensions of the crystallites we used the equation[8]

$$\varepsilon = L\lambda / B, \tag{4}$$

where ε is the dimension of the scattering crystallite in a given direction, B is the corresponding half-width of the maximum, and L is the distance from the specimen to the photographic plate.

When reflections appear on the electron diffraction patterns (enlargement of the crystallites), the grain dimensions are found[9] from the relation

$$q = Q\alpha \cos\theta / 2n_{hkl}, \tag{5}$$

where Q is the volume participating in scattering of the electron beam, α is the angle of convergence of the electron beam, θ is the Bragg angle, and n_{hkl} is the number of reflections forming a ring with indices hkl.

Figure 3 plots the crystallite dimensions vs the annealing temperature. We see that as the radiation dose increases, the crystallite dimensions decrease, and the number of crystallization centers increases. Thus when the dose is increased from $6.2 \cdot 10^{15}$ to $3 \cdot 10^{16}$ ions/cm^2, the number of crystallization centers rises from $3 \cdot 10^{18}$ to 10^{20} cm^{-3}; this is quite natural, because when the dose is increased, there is a large number of broken bonds, and consequently of crystallization centers.

Thus ion bombardment leads to marked changes in the short-range order structure of amorphous Si_3N_4 films (rupture of bonds, previously existing in amorphous films before irradiation); the heavier the ion, the more marked are the changes. Furthermore, whereas the original amorphous films do not crystallize on annealing up to 1100°C, the bombarded films crystallize at lower temperatures (see Table 2). This is apparently because the original film contains ordered regions which after irradiation act on annealing as seeds of the crystal phase, which grow at the expense of the imperfect disorderly regions, the number of which is markedly increased by irradiation, and where the mobility of the atoms is greater than before irradiation.

---

[1] P. V. Pavlov, É. V. Shitova, and E. L. Zorin, Dokl. Akad. Nauk SSSR, 192, 559 (1970) [Sov. Phys.–Dokl., 15, 433 (1970)].

[2] A. I. Kitaigorodskii, X-Ray Structural Analysis of Finely Crystalline and Amorphous Bodies [in Russian], Izd. Tekh.-Teor. Lit., Moscow–Leningrad (1952).

[3] B. K. Vainshtein, Kristallografiya, 2, 29 (1957) [Sov. Phys.–Crystallogr., 2, 24 (1957)].

[4] M. V. Coleman and D. Thomas, Phys. Status Solidi, 25, 1 (1968).

[5] L. I. Tatarinova, Kristallografiya, 2, 260 (1957) [Sov. Phys.–Crystallogr., 2, 251 (1957)].

[6] P. V. Pavlov and É. V. Shitova, Kristallografiya, 12, 119 (1967) [Sov. Phys.–Crystallogr., 12, 95 (1967)].

[7] D. Hardie and K. H. Jack, Nature, 180, 332 (1957).

[8] Z. G. Pinsker, Electron Diffraction [in Russian], Izd. AN SSSR, Moscow–Leningrad (1949).

[9] Ya. S. Umanskii, X-Ray Diffraction of Metals and Semiconductors [in Russian], Metallurgiya, Moscow (1969).

Epitaxial growth of AgCl on thermoelectric polyvinylchloride films, copying the electrical properties of an NaCl surface

G. I. Distler and E. I. Tokmakova

Institute of Crystallography, Academy of Sciences of the USSR
(Submitted January 9, 1972; resubmitted May 25, 1972)
Kristallografiya, 18, 614-617 (May-June 1973)

The crystallization characteristics of silver chloride during vacuum deposition onto the surface of thermoelectric polyvinylchloride (PVC) films copying NaCl crystal surfaces were studied as a function of the previous heating temperature of the PVC films on the crystal substrate and the film temperature during AgCl deposition. The previous heatings of the PVC films at 160 and 220°C led to highly oriented AgCl films only when the PVC films were correspondingly heated to 40-50 and 40-70°C during AgCl deposition. Heating the PVC films to 270°C caused a sharp crystal orientation deterioration and at 290°C the AgCl crystals became randomly arranged. The AgCl crystallization characteristics are explained by the PVC film formation and thermoelectric state thermal stability conditions and by the fact that the nuclei and AgCl particles can migrate, depending on the film-substrate temperature. It is concluded that plastic films can be used during epitaxy as electric copies of crystal substrates.

INTRODUCTION

It has been shown[1-2] that diffraction-amorphous polyvinylchloride (PVC) films have the property of copying, via a thermoelectric mechanism, the electric microrelief of the crystal-substrate surface on which they are produced. Oriented crystallization occurs on the surface of such electric copies when the latter are used as substrates.

The aim of this investigation was to study the AgCl oriented crystallization characteristics as a function of the thermoelectric state formation conditions in the PVC films and the temperature of the latter during the AgCl deposition.

EXPERIMENTAL METHOD

A few drops of 0.3% PVC solution in butyl acetate were placed on a freshly air-cleaved NaCl crystal surface, and the solution residue removed after 3-5 minutes with filter paper. The crystals covered with PVC film were then placed in a vacuum chamber and the outer side of the PVC film reinforced with a 70-100 Å thick carbon layer. The thermoelectric state was induced by heating the PVC films on the NaCl crystals for one minute at 160, 220, 270, and 290°C, the temperature being measured with a chromel—alumel thermocouple. After air cooling the specimens to room temperature the PVC films were separated from the NaCl crystals by dissolving the latter away in water, and were placed on the electron microscope grid. The side which had been in contact with the NaCl crystal was then covered with silver chloride at a rate of 2 Å/sec in a 10^{-5} torr vacuum. The AgCl film thickness was of the order of 100 Å. The deposition rate and film thickness were controlled with a quartz microbalance, and the PVC film temperature during AgCl deposition was measured in the range 20-160°C.

RESULTS AND DISCUSSION

AgCl oriented crystallization occurs on the surface of PVC films previously heated to 160°C on NaCl crystals, but to obtain well oriented films the substrate should be heated to 40-50°C. Under these conditions the AgCl crystallization kinetics are generally similar to those for AgCl on PVC films at room temperature if the latter are previously heated on an NaCl surface at 110°C for one minute.[2] At first, in both cases unoriented[1)] AgCl nuclei form, followed by bridges between the nuclei, and then oriented nuclei coalescence begins with quite large particles. The appearance of bridges between the nuclei, reflecting the presence on the crystal-substrate surface of real-crystal linearly polarized lattice structure elements,[2,5,6] shows that the copying of the NaCl surface electric structure occurs generally at an elementary level. A further increase in PVC film temperature during AgCl deposition leads to a sharp deterioration in the AgCl crystal orientation. Debye rings appear on the AgCl film diffraction pattern and the point reflections gradually smear out. The AgCl crystal orientation completely vanishes at PVC film temperatures above 90°C.

On the surface of PVC films previously heated on NaCl crystals to 220°C, the general AgCl crystallization characteristics are preserved, but highly oriented AgCl films then form (see Fig. 1a) at higher substrate temperature (40-70°C) than in the previous case, and over a wide temperature range. Debye rings and a gradually smearing texture appear on the AgCl film diffraction pattern (Fig. 1b) when the PVC films are heated to 80-130°C. The NaCl crystal orientation completely vanishes at substrate temperatures above 140°C (Fig. 1c).

The substrate temperature change also produces a morphological variation in the AgCl crystals. During AgCl condensation onto PVC heated to ~60°C, a network structure forms, consisting of AgCl particles and islands between them (Fig. 1a) on whose elements further AgCl oriented crystallization occurs, similar to that observed for PbS crystallization on the outer side of a carbon bounded film.[5] A further substrate temperature rise to ~70°C causes the AgCl particles to become round and the bridges between the individual particles to disappear gradually (Fig. 1b, c).

Thus, preliminary heating of PVC films at high temperatures increases the thermal stability of their thermoelectric memory. This is possibly due to the formation of cross links between the polyvinylchloride chain molecules which stabilize the film thermoelectric structure.

Rather badly oriented AgCl films form on PVC specimens previously heated to 270°C. Clearly expressed Debye rings can be seen on the diffraction pattern from such films. Increasing the previous heating temperature to 290°C causes AgCl crystals to form randomly. This

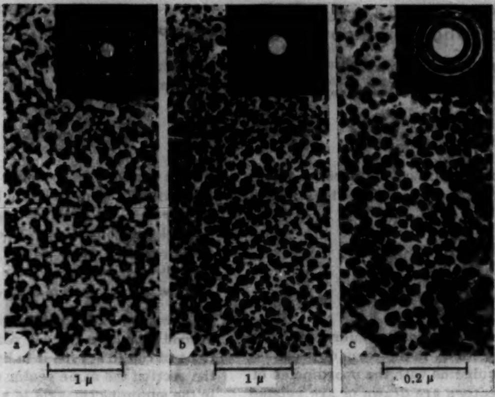

Fig. 1. Silver chloride crystallization on polyvinylchloride films previously heated to 220°C on an NaCl crystal. a) Polyvinylchloride film temperature during silver chloride deposition 65; b) 90; c) 150°C.

TABLE 1

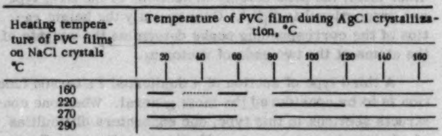
Heating temperature of PVC films on NaCl crystals °C
Temperature of PVC film during AgCl crystallization, °C
20
40
60
80
100
120
140
160
160
220
270
290

Notation: —— Debye diffraction pattern from AgCl; .... texture with angular arc length not greater than 20°C; ══ mixed diffraction (texture and Debye rings).

means that at high working temperatures no thermoelectric structure forms in PVC films copying the NaCl electrostatic relief, obviously because of the thermal destruction processes taking place in the films.[7]

The dependence of the orientation characteristics of the silver chloride films on the preparation of the PVC substrate film and the AgCl deposition conditions is shown in Table 1.

As can be seen from the table the AgCl film optimum orientation occurs only under certain mutually dependent PVC film preparation and AgCl deposition conditions.

Epitaxy on the PVC film surface is governed by the stability of the thermoelectric state copying the electrical properties of the crystal-substrate surface on the one hand, and by the migration facility of the depositing atoms, ions, or molecules (which is highly dependent on substrate temperature) on the other. The complex interdependence of these factors and the possible directed flow of AgCl molecules from the gaseous phase to the more electrically active film surface elements can explain the quite narrow temperature range over which the optimum degree of AgCl film orientation is observed at the given deposition rate. At lower PVC film temperatures a nucleus and fairly large particle migration rate, suitable for oriented coalescence, is not reached and at too high PVC film temperatures depolarization occurs, that is, the electrical memory is lost.

The narrow "epitaxial temperature" range indicates that the governing factor in AgCl epitaxy is the electrical (thermoelectric) relief of the PVC film surfaces and not their structure due to the effect of the NaCl crystals, since such a structuring occurs over a very narrow temperature range. The destruction by light of the memory in amorphous photoelectric selenium films separated from the surface of NaCl crystals[8] also shows that it is the electrical (and not atomic) structure of these films which is the governing factor in such heterogeneous processes as epitaxy. The presence on the PVC film surfaces of NaCl crystal "splinters" undissolved during the detachment of the PVC films can be practically ruled out, since crystal "splinters" and larger NaCl single crystals should also have a strong effect on the AgCl epitaxy over a wide temperature range.

Thus, plastic films prepared under specific conditions from materials with thermoelectric properties can be used during epitaxy as electrical copies of crystal substrates.

---

1) As was shown in refs. 3 and 4 during epitaxy nuclei usually form randomly and orientation does not occur until the coalescence stage is reached.

[1] G. I. Distler and S. A. Kobzareva, Dokl. Akad. Nauk SSSR, 188, 811 (1969) [Sov. Phys.–Dokl., 14, 935 (1970)].
[2] G. I. Distler and E. I. Tokmakova, Thin Solid Films, 6, 203 (1970).
[3] A. Masson, J. J. Metois, and R. Kern, J. Crystal Growth, 3-4, 196 (1968).
[4] V. P. Vlasov and G. I. Distler, Kristallografiya, 16, 663 (1971) [Sov. Phys.–Crystallogr., 16, 578 (1971)].
[5] G. I. Distler and E. I. Tokmakova, Kristallografiya, 16, 212 (1971) [Sov. Phys.–Crystallogr., 16, 171 (1971)].
[6] G. I. Distler and E. I. Tokmakova, Kristallografiya, 17, 634 (1972) [Sov. Phys.–Crystallogr., 17, 545 (1972)].
[7] N. Grassie, Chemistry of High Polymer Degradation Processes, Butterworth (1956).
[8] G. I. Distler and V. G. Obronov, Dokl. Akad. Nauk SSSR, 191, 584 (1970) [Sov. Phys.–Dokl., 15, 213 (1970)].

Types of vector-localizing sections of the duplicated Patterson function

V. N. Biyushkin and N. V. Belov

Institute of Crystallography, Academy of Sciences of the USSR
Moscow State University

(Submitted December 2, 1972)
Kristallografiya, 18, 618-619 (May-June 1973)

We have[1] considered vector-localizing sections of the duplicated Patterson function that are defined by a function of the form

$$DP_{\vartheta_m,\vartheta_n}(\mathbf{u}_0,\mathbf{u}_0,\mathbf{r})=\int_V \rho(\mathbf{r}')\rho(\mathbf{r}'+\vartheta_m[\mathbf{r}+\mathbf{u}_0]-\mathbf{r})\rho(\mathbf{r}'+\vartheta_n[\mathbf{r}+\mathbf{u}_0]-\mathbf{r})\,dV. \tag{1}$$

Such a section contains transforms of the interatomic vectors equal to the chosen vector $\mathbf{u}_0$ in the form of peaks whose coordinates either coincide with the coordinates of atoms from which these vectors are drawn or are related to those coordinates by a law that is defined by the specific symmetry transformations ϑ_m and ϑ_n. The peak height may be taken as proportional to: 1) the atomic number Z of the atom from which the vector originates (the origin of it) and the square of the atomic number of the atom at the end of the vector, $Z_iZ_j^2$. Each pair of symmetry transformations of the space group of the crystal corresponds to a definite section of the duplicated Patterson function; for a given vector $\mathbf{u}_0$, all of these isolate images of the equivalent atomic vectors.

These are not the only possible sections of the duplicated Patterson function; there is a second type, which, as for the first, can be constructed by specifying only one particular interatomic vector.

Sections of the second type for some transformations ϑ_m and ϑ_n are obtained if the parameter vectors in the duplicated Patterson function are specified as

$$\mathbf{u}_1=\vartheta_m\mathbf{r}-\mathbf{r},\qquad \mathbf{u}_2=\vartheta_m(\mathbf{r}+\mathbf{u}_0)-\mathbf{r}. \tag{2}$$

The specified vector appears in only one of the parameter vectors; the other parameter vector, in this case the first, is constructed with a zero specified vector. The method of specification makes it completely coincident with the parameter vectors used in constructing symmetrical sections of the duplicated Patterson function.[2,3]

The following Fourier series describes the section of the duplicated function that corresponds to the vector combination of (2):

$$DP_{\vartheta_m,\vartheta_n}(0,\mathbf{u}_0,\mathbf{r})=\frac{1}{V^2}\sum_{\mathbf{H}_1}\sum_{\mathbf{H}_2}F(-\mathbf{H}_1-\mathbf{H}_2)F(\mathbf{H}_1)F(\mathbf{H}_2)\times\exp\{-2\pi i[\mathbf{H}_1(\vartheta_m\mathbf{r}-\mathbf{r})+\mathbf{H}_2(\vartheta_n\mathbf{r}-\mathbf{r}+\vartheta_n\mathbf{u}_0)]\}. \tag{3}$$

We take all possible combinations of the symmetry transformations that make up the symmetry groups for the particular structure to get all forms of vector-localizing sections of the second type for a particular crystal; if instead of (2) we use the combination

$$\mathbf{u}_1=\vartheta_m(\mathbf{r}+\mathbf{u}_0)-\mathbf{r},\qquad \mathbf{u}_2=\vartheta_n\mathbf{r}-\mathbf{r}$$

we get nothing new, because these combinations are identical with (2) if by ϑ_n in the latter we understand ϑ_m, and ϑ_m for ϑ_m. But each such type combines sections of all possible combinations of the symmetry transforms for the particular group, so the vectors of that type must already contain among their combinations ones that define the second type of section.

Sections of the duplicated Patterson function of the second type have regular peaks at the same points as sections of the first type if in both cases one uses to construct the section the same vector $\mathbf{u}_0$; but as the third vertex in the summing triangle is a point equivalent to the initial one in sections of the second type, the peak heights are proportional to the square of the atomic number of the origin atom, as multiplied by the Moseley number of the atom at the end of the vector, namely $Z_i^2Z_j$. On the other hand, the peak heights in sections of the first type are proportional to $Z_iZ_j^2$. Consequently the height ratios of the corresponding peaks determine the weights of the atoms at the two ends of vector $\mathbf{u}_0$.

A third type of section of a duplicated Patterson function is to be considered the most general. When one constructs sections in this type, one encounters difficulties of a basic character; to specify these sections we first have to define two interatomic vectors arising from a common origin, and neither of these vectors should be zero.

The parameter vectors that define sections of this third type are represented in the form

$$\mathbf{u}_1=\vartheta_m(\mathbf{r}+\mathbf{u}_{01})-\mathbf{r},\qquad \mathbf{u}_2=\vartheta_n(\mathbf{r}+\mathbf{u}_{02})-\mathbf{r}, \tag{4}$$

where $\mathbf{u}_{01}$ and $\mathbf{u}_{02}$ are interatomic vectors generated by atoms i, j, and k, while $\mathbf{u}_{01}=\mathbf{r}_j-\mathbf{r}_i$, $\mathbf{u}_{02}=\mathbf{r}_k-\mathbf{r}_i$. The corresponding section is described by the function

$$DP_{\vartheta_m,\vartheta_n}(\mathbf{u}_{01},\mathbf{u}_{02},\mathbf{r})=\frac{1}{V^2}\sum_{\mathbf{H}_1}\sum_{\mathbf{H}_2}F(-\mathbf{H}_1-\mathbf{H}_2)F(\mathbf{H}_1)F(\mathbf{H}_2)\times\exp\{-2\pi i[\mathbf{H}_1(\vartheta_m\mathbf{r}-\mathbf{r}+\vartheta_m\mathbf{u}_{01})+\mathbf{H}_2(\vartheta_n\mathbf{r}-\mathbf{r}+\vartheta_n\mathbf{u}_{02})]\}. \tag{5}$$

The peak heights for sections of this type may be taken as proportional to the product $Z_iZ_jZ_k$ subject to the reservation that such proportionality actually is characteristic of the structure consisting of atoms with a similar scattering curve.

If sections of all three types are based on the same interatomic vector $\mathbf{u}_0$, one gets regular peaks at the same points in the sections for identical combinations of the symmetry transformations. Analogous coincidences of the regular peaks in such sections of all three types occur also when they are constructed via different atomic vectors but ones such that they all have a common origin in some one atom. However, to each section there differs from the other types; one consequence of this is that one gets random peaks, which should appear at different points if they occur in sections of the different types; therefore, noncoincidence peaks in the sections of the different types constructed from the same symmetry transformations may be discarded and considered as accidental. This increases the probability of isolating the regular peaks.

---

[1] V. N. Biyushkin, Kristallografiya, 18, 689 (1973) [Sov. Phys.–Crystallogr., (in press)].

[2] V. N. Biyushkin and N. V. Belov, Kristallografiya, 9, 771 (1964) [Sov. Phys.–Crystallogr., 9, 655 (1965)].

[3] V. N. Biyushkin, Kristallografiya, 17, 729 (1972) [Sov. Phys.–Crystallogr., 17, 641 (1973)].

Crystal structure of $CsNbO(SO_4)_2$

A. A. Kashaev and G. V. Sokolova

Irkutsk Pedagogical Institute
Geological Institute, Academy of Sciences of the USSR
(Submitted March 2, 1972; resubmitted May 26, 1972)
Kristallografiya, 18, 620-621 (May-June 1973)

The double cesium niobium sulfate and rubidium niobium sulfate have compositions which can be expressed as: $Cs_2O \cdot Nb_2O_5 \cdot 4SO_3$ and $Rb_2O \cdot Nb_2O_5 \cdot 4SO_3$. The crystal habit, the data from the chemical analysis, and the Debye powder photographs of these materials are close to the corresponding characteristics of the rarely studied[1] compound $NH_4NbO(SO_4)_2$. Although this formula has not been proved by structural studies, analogous formulae were attributed in this study to cesium and rubidium sulfates. The subsequent study has confirmed the correctness of this choice.

The crystals of the experimental sulfates are thin white fibers not exceeding 0.1-0.2 mm in cross section. The Laue diffraction patterns indicated that they belong to the orthorhombic system. The parameters of the unit cell, determined by an oscillation method, are given in Table 1. The cell contains four formula units.

Scanning of the layer lines h0*l*, h1*l*, and hk0–hk4 was performed (Weissenberg goniometer, Mo radiation). The analysis of the regular extinctions of the reflections showed the possible space groups of the sulfates to be P*nam* and P*na*2_1. The unequivocal choice of symmetry group was based on the projection of the Patterson function of all three sulfates. The heavy Cs and Nb atoms in any of these groups must lie in fourfold positions. In the P*nam* space group, the Cs–Cs, Nb–Nb, and Cs–Nb peaks can only be at fixed levels along the c axis, while in the P*na*2_1 group the large Cs–Nb peaks may generally have any values of the z coordinate. By taking these circumstances into account, it is then possible to choose in favor of the P*nam* group, a choice which has been confirmed by the results of the structural interpretation.

In this group the fourfold positions correspond to the positions of atoms in the mirror plane and in the two systems of centers of symmetry. The absence on the xy projection of the Patterson function of all three compounds of large peaks at the points $0\frac{1}{2}$, $\frac{1}{2}0$, and $\frac{1}{2}\frac{1}{2}$ suggested that the Cs and Nb atoms lie on mirror planes of symmetry. If we compare the xy projection of different compounds we can separate the peaks of the alkali cation and niobium cation family of peaks. By analyzing the coordinates of the strong peaks of the general position (peaks of interaction) it was possible to find the mutual disposition of the Cs (Rb, NH_4) and Nb.

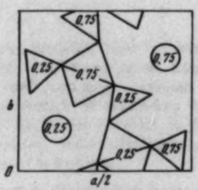

Fig. 1

TABLE 1. Parameters of the Unit Cells of Sulfates

Compound	a, Å	b, Å	c, Å	$\rho_{x\text{-ray}}$	ρ_e
$CsNbO(SO_4)_2$	17.55	8.82	5.17	3.64	3.60
$RbNbO(SO_4)_2$	16.96	8.76	5.16	3.38	3.23
$NH_4NbO(SO_4)_2$	17.01	8.69	5.13	2.80	2.70

The approximated coordinates of the heavy atoms were used to determine the structure of the cesium sulfate. The coordinates of all the atoms of the structure were determined and refined by constructing a few approximate projections of the electron density and the structural model was subsequently refined using a least-squares method. The extreme dispersion factor calculated from 520 independent reflections was 15%. The atomic coordinates corresponding to this are given in Table 2. The main interatomic distances of the structure are summarized in Table 3. The representation of the cesium and niobium sulfate structures is shown in Fig. 1. The Cs cations are represented by circles. The numbers in Fig. 1 denote the relative z coordinates of the corresponding cations.

The basic $CsNbO(SO_4)_2$ structure is represented by undulating layers of Nb octahedra and S tetrahedra ori-

TABLE 2. The Coordinates of the Atoms in the $CsNbO(SO_4)_2$ Structure

Atoms	x/a	y/b	z/c	B
Cs (4)	0.0674	0.1512	0.25	1.21
Nb (4)	0.3145	0.0633	0.25	0.88
S_1 (4)	0.2943	0.4573	0.25	1.33
S_2 (4)	0.4348	0.1300	0.75	1.33
O_1 (8)	0.2286	0.0403	–0.0190	1.33
O_2 (8)	0.3819	0.1561	–0.0195	1.33
O_3 (4)	0.2634	0.3098	0.25	1.33
O_4 (4)	0.4718	–0.0130	0.75	1.33
O_5 (4)	0.4846	0.2568	0.75	1.33
O_6 (4)	0.3827	0.4746	0.25	1.33
O_7 (4)	0.1537	0.3982	0.75	1.33

The multiplicity of the atomic positions is given in brackets.

TABLE 3. The Main Interatomic Distances in the Structure, Å

S_1 tetrahedron		S_2 tetrahedron		Nb octahedron	
S_1-O_1	1.46 (2)	S_2-O_2'	1.53 (2)	$Nb-O_1$	2.06 (2)
S_1-O_3	1.41	S_2-O_4	1.42	$Nb-O_2$	2.00 (2)
S_1-O_6	1.56	S_2-O_5	1.42	$Nb-O_3$	2.35
$S-O_{av}$	1.47	$S-O_{av}$	1.48	$Nb-O_7$	1.56
$O_1'-O_1''$	2.38	$O_2'-O_2''$	2.39	O_1-O_1'	2.78
$O_1''-O_3$	2.36 (2)	$O_2''-O_4$	2.48 (2)	O_2-O_2'	2.79
O_1-O_6	2.36 (2)	$O_2''-O_5$	2.34 (2)	O_3-O_2	2.84 (2)
O_3-O_6	2.55	O_4-O_5	2.39	O_2-O_7	2.75 (2)
Cs polyhedron				O_1-O_7'	2.78 (2)
$Cs-O$	3.04–3.78			O_1-O_2	2.88 (2)
				$O_1'-O_3$	2.82 (2)

ented parallel to the bc plane. The layers are joined together by the Cs cations. All the anions of the octahedra, with the exception of the O_7, are joined to the S cations. The O_7 oxygen are only joined to the Nb. It is clear that under these conditions the $Nb-O_7$ bond is stronger than the remaining Nb–O bonds and this also causes the displacement of a cation from the center of the octahedron along a direction parallel to the free apex. The corresponding $Nb-O_7$ distance is shortened to 1.56 Å and the $Nb-O_3$ distance to the opposite apex of the octahedron is increased (2.35 Å) with insignificant variations in the lengths of the sides of the octahedron and the remaining Nb–O distances. The absence of a bond between the O_7 anion and the S ion is reflected in the notation of the structural formula.

The structural motif explains the observed individuality in the *a*c and bc planes of the $CsNbO(S_4)_2$ single crystals and their extension along the c axis. The established structure of the twin cesium and niobium sulfate conforms completely to the scheme for the classification of sulfates proposed by G. B. Bokii and L. I. Gorotskii.[2]

We should like to thank Academician N. V. Belov for his interest in the work, V. A. Drits for his help in the research, and L. S. Perepelitsa for the supply of sulfate specimens.

---

[1] Ya. G. Goroshchenko, Zh. Neorgan. Khim., 1, 909 (1956).

[2] G. B. Bokii and L. I. Gorotskaya, Zh. Strukt. Khim., 10, 624 (1969).

Structural mechanism of the phase transition in erbium pyrosilicate, $Er_2Si_2O_7$

Yu. I. Smolin and Yu. F. Shepelev

Institute of Silicate Chemistry, Academy of Sciences of the USSR

(Submitted April 24, 1972)
Kristallografiya, 18, 622-623 (May-June 1973)

Polymorphism in a number of rare-earth pyrosilicates has been studied as a function of two parameters, the size of the cation and the synthesis temperature, by infrared spectroscopy[1] and x rays.[2-4] It has been established that between 1000 and 1600°C the pyrosilicates of rare-earth elements undergo a whole series of phase transformations going from one structure type to another, in which each of the subsequent crystal modifications with a larger cation is a high-temperature phase for preceding cations with smaller sizes.

Here we consider the probable structural mechanism of the phase transition between monoclinic modifications in $Er_2Si_2O_7$. According to previous work[3-5] this compound exists in three modifications, a triclinic low-temperature phase ($P\bar{1}$, $a = 6.583$, $b = 6.609$, $c = 12.000$ Å, $\alpha = 94°34$, $\beta = 90°34'$, $\gamma = 91°45'$, ref. 4), a monoclinic modification ($B2/m$, $a = 6.85$, $b = 4.72$, $c = 8.94$ Å, $\gamma = 101°36'$, ref. 3), and a high-temperature monoclinic modification ($P2_1/a$, $a = 5.556$, $b = 4.683$, $c = 10.79$ Å, $\gamma = 96°$, ref. 5). The transitions between these phases occur at 1050 and 1400°C.

The triclinic modification, which also corresponds to the low-temperature forms of the Eu and Er pyrosilicates, also includes the α form of the natural mineral yttrialite and is a structural analog of the rare-earth germanates having the composition $TR_2Ge_2O_7$ with La–Nd cations. We have established this by comparing the Debye patterns of the corresponding compounds and confirmed the parameter values and the unit cell symmetries. The structure of $La_2Ge_2O_7$ was determined and it was established that this compound, which formally agrees with the pyrogermanate composition, contains two types of germanium–oxygen radicals: triortho groups and isolated tetrahedra.[6] The structural similarities found allow us to assert that the low-temperature form of $TR_2Si_2O_7$ with Eu–Er cations is a pyrosilicate in composition only, but contains the triortho groups Si_3O_{10} and isolated SiO_4 tetrahedra.

The monoclinic modification, which is stable for $Er_2Si_2O_7$ between 1050 and 1400°C, is isostructural to the natural mineral thortveitite ($Sc_2Si_2O_7$). Its structure has been determined by Zachariasen[7] and refined by Cruickshank et al.[8] We also confirmed this modification in a $Yb_2Si_2O_7$ crystal with unit cell parameters which differ little from $Er_2Si_2O_7$ ($B2/m$, $a = 6.802$, $b = 4.703$, $c = 8.875$ Å, $\gamma = 102°7'$, ref. 9).

The thortveitite structure is characterized by layers of subgroups having a linear configuration ($< Si-O-Si = 180°$). The pyrogroups are parallel to each other in the layers. The cations lie between these layers and their coordination polyhedra have the forms of distorted octahedra consisting of the end oxygens of the pyrogroups.

We have determined the high-temperature form of erbium pyrosilicate for an $Er_2Si_2O_7$ single crystal.[5] We have also established a similar structural motif for $Y_2Si_2O_7$ (ref. 10). This form, like the thortveitite modification, is constructed of layers of centrosymmetric pyrogroups, whose end oxygens form distorted octahedra surrounding the Er atoms. However, while in the low-temperature form the pyrogroups in the layers are translationally equivalent and therefore parallel, in the high-temperature form the layer is constructed from pyrogroups which repeat through one translation-equivalence row. The neighboring rows of pyrogroups are rotated with respect to each other by about 60°.

Figure 1 shows the schematic crystal structures for the monoclinic modifications of $Er_2Si_2O_7$, which transform into each other at 1400°C. The high-temperature structure is the one with darkened bonds. For the low-temperature form we have taken the atomic coordinates of its close structural analog, $Yb_2Si_2O_7$. The unit cells of these modifications are projected on each other such that the directions of the nearly equal b axes coincide (4.72 and 4.68 Å) and the atomic displacements should be of minimal size. The y coordinates of the atoms are given in the circles.

The mechanism of the phase transformation is quite obvious. As we see from Fig. 1 the substantial changes in going from one structure to the other only affect the rows of pyrogroups. At the transformation temperature

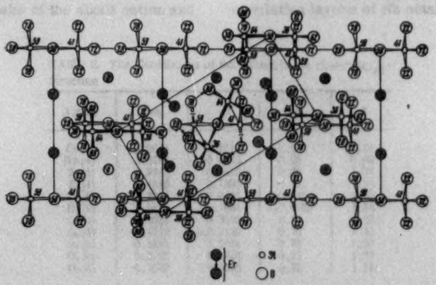

Fig. 1. Schematic phase transformation in $Er_2Si_2O_7$.

the cations, whose effective radii increase, move away from the zero plane, evidently in the direction of least resistance. Here one group of pyrogroups is shifted somewhat but does not undergo any significant changes. The rearrangement of the pyrogroups in the other row probably occurs in the following way. One of the end bonds is disrupted. As a result, a Si ion is now bonded to only three O atoms and is not rigidly attached at its site; going through the face of the tetrahedron, it forms a new tetrahedron, which captures the nearest O atom belonging to another tetrahedron of the pyrogroup. The previously existing bond of this O atom with a second Si is disrupted. In a like manner this Si ion migrates in a direction opposite to the first Si through the face of a SiO_4 tetrahedron and combines with a "free" one. A new tetrahedron is also formed about it. Thus the pyrogroups occupy new centrosymmetric positions. It should be noted that the maximum shift of the O and Er atoms is of the order of 1 Å, while the Si ions in the rearranged pyrogroups are shifted by distance of 2 Å. This mechanism for the phase transformation in $Er_2Si_2O_7$ largely corresponds to one of the mechanisms for phase transformations in calcium hydrosilicates proposed by Dent Glasser, Glasser, and Taylor.[11] Recently Ponomarev, Kheiker, and Belov described a structural transformation mechanism for dehydration of tetracalcium trihydroaluminate which also involves migration from a tetrahedron of aluminum ions.[12]

We note in conclusion that a number of pyrosilicates of the rare-earth elements have transitions similar to those described above, which also occur in $Y_2Si_2O_7$ and $Ho_2Si_2O_7$.

---

[1] A. N. Lazarev, Vibrational Spectra and Structure of Silicates [in Russian], Nauka, Leningrad (1968), p. 251.

[2] I. Warshaw and R. Roy, Progress in the Science and Technology of the Rare Earths, Vol. 1, Pergamon Press (1964), p. 203.

[3] J. Ito and H. Jonson, Amer. Mineralogist, 53, 1940 (1968).

[4] J. Felshe, J. Less-Common Metals, 21, 1 (1970).

[5] Yu. I. Smolin and Yu. F. Shepelev, Izv. Akad. Nauk SSSR, Neorgan. Mater., 4, 1133 (1968).

[6] Yu. I. Smolin, Yu. F. Shepelev, and T. V. Upatova, Dokl. Akad. Nauk. SSSR, 187, 322 (1969) [Sov. Phys.–Dokl., 14, 630 (1970)].

[7] W. H. Zachariasen, Z. Kristallogr., 74, 139 (1930).

[8] D. W. J. Cruickshank, H. Lynton, and G. A. Barclay, Acta Crystallogr., 15, 491 (1962).

[9] Yu. I. Smolin, Yu. F. Shepelev, and I. K. Butikova, Zh. Strukt. Khim., 12, 272 (1971).

[10] N. G. Batalieva and Yu. A. Pyatenko, Zh. Strukt. Khim., 8, 548 (1967).

[11] L. S. Dent Glasser, F. P. Glasser, and H. F. W. Taylor, Quart. Revs. Chem. Soc., London, 16, 343 (1962).

[12] V. I. Ponomarev, D. M. Kheiker, and N. V. Belov, Izv. Akad. Nauk SSSR, Neorgan. Mat., 7, 1783 (1971).

"Hexagonal YF_3" structure type and high-temperature modifications of rare-earth trifluorides isostructural with YF_3

B. P. Sobolev and P. P. Fedorov
Institute of Crystallography, Academy of Sciences of the USSR
(Submitted April 29, 1972)
Kristallografiya, 18, 624-625 (May-June 1973)

The isomorphism of the trifluorides of the rare-earth elements has been studied several times by x-ray diffraction and thermographic methods.[1-5] The most reliable information about the structure of high-temperature modifications of LnF_3 compounds (where Ln is a lanthanide) was obtained in ref. 3, where the polymorphic transitions of YF_3 and a series of LnF_3 compounds were studied by high-temperature diffraction. The use of this method is required by the fact that the α modifications of most LnF_3 compounds cannot be successfully quenched. The possibility of stabilization of tysonite α-LnF_3 structures by heterovalent isomorphic replacement of Ln^{3+} by M^{2+} ions in binary systems was examined in refs. 6-8.

In ref. 3 it was shown that the trifluorides of the rare-earth elements crystallize in three structural types: tysonite (LaF_3, space group P$\bar{3}$c1), orthorhombic β YF_3 (Pnm*a*), and "hexagonal α YF_3." The first two are known for the rare-earth trifluorides from refs. 1, 9. An x-ray diffraction pattern for α YF_3, a representative of the structure type called "hexagonal YF_3" by the authors, was presented for the first time in ref. 3. According to the results of ref. 3, the trifluorides of yttrium and the rare-earth elements from erbium to lutetium, inclusively, crystallize in this structure type. No assumption as to a possible structure type for α LnF_3 (where Ln = Er−Lu) was expressed in ref. 3, other than an indication that α YbF_3 belongs to the hexagonal system and is different from LaF_3. The indices presented for the x-ray diffraction pattern of α YbF_3 correspond to the parameters of a hexagonal unit cell with a = 6.99 Å and c = 8.32 Å with retention of the tysonite Z = 6. The x-ray diffraction patterns of the rest of the α LnF_3 compounds of this type have been indexed on this basis.

During the search for a structural analog of α YF_3 we observed that, among the oxides, α UO_3 (space group C$\bar{3}$m1) is one of them. Diagrams of the x-ray diffraction patterns of α YbF_3 according to ref. 3 and α UO_3 according to ref. 10 are shown in Fig. 1 (the α UO_3 structure has been refined recently[11]). The results of indexing the x-ray powder diffraction pattern of α YbF_3 are given in Table 1.

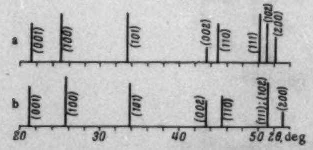

Fig. 1. Diagrams of powder x-ray diffraction patterns of α YbF_3 (a) and α UO_3 (b); Cu Kα radiation.

TABLE 1. Indexing of the Powder Diffraction Pattern of α YbF_3

I/I_0	*d*, Å	*hkl*	$1/d^2_{exp}$	$1/d^2_{calc}$
80	4.145	001	0.0582	0.0579
100	3.496	100	0.0818	0.0819
100	2 677	101	0.1395	0.1398
30	2,079	002	0.2314	0.2314
80	2.017	110	0.2458	0.2458
100	1.816	111	0.3032	0.3036
90	1.785	102	0.3139	0.3133
50	1.747	200	0.3277	0.3277

TABLE 2. Unit-Cell Parameters of α-(Y, Ln)F_3 Compounds (α UO_3 structure type, c/a = 1.03)

Compound	*a*, Å	*c*, Å
YF_3	4.12	4.23
ErF_3	4.02	4.14
TmF_3	4.05	4.17
YbF_3	4.03	4.16
LuF_3	4.02	4.15

Thus, "hexagonal α YF_3" and the high-temperature modifications of the trifluorides of the rare-earth elements from erbium to lutetium, inclusively, crystallize in the α-UO_3 structure type. The parameters of the respective hexagonal unit cells, recalculated from the data of ref. 3, are given in Table 2. The ratio of parameters c/a for α (Y, Ln)F_3 is less than the analogous value for α UO_3 (c/a = 1.05). This leads to the conclusion that in α UO_3 the reflection with indices (102) merges with the (111) reflection and the diagrams of the x-ray diffraction patterns of α UO_3 and α YbF_3 are slightly different (see Fig. 1).

---

[1] A. Zalkin and D. H. Templeton, J. Am. Chem. Soc., 75, 2453 (1953).
[2] F. H. Spedding and A. H. Daane, The Rare Earths, Wiley, New York (1961).
[3] R. E. Thoma and G. D. Brunton, Inorg. Chem., 5, 1937 (1966).
[4] D. A. Jones and W. A. Shand, J. Crystal Growth, 2, 361 (1968).
[5] F. H. Spedding and D. C. Henderson, J. Chem. Phys., 54, 2476 (1971).
[6] M. Mansmann, Z. Krist., 122, 375 (1965).
[7] O. E. Izotova, L. S. Garashina, and B. P. Sobolev, Kristallografiya, 15, 580 (1970) [Sov. Phys.—Crystallogr., 15, 496 (1970)].
[8] L. S. Garashina and B. P. Sobolev, Kristallografiya, 16, 307 (1971) [Sov. Phys.—Crystallogr., 16, 254 (1971)].
[9] I. Oftedal, Z. Phys. Chem., B5, 272 (1929).
[10] X-ray Diffraction Data Cards, ASTM, No. 12-43 (1950).
[11] S. Siegel and H. R. Hoekstra, Inorg. Nucl. Chem. Lett., 7, 497 (1971).

Block conical ferromagnetic spiral in the hexagonal ferrite $BaGa_2Sc_{1.2}Fe_{8.8}O_{19}$ (M)

O. P. Aleshko-Ozhevskii, V. P. Cheparin, A. P. Cherkasov, and I. I. Yamzin
Institute of Crystallography, Academy of Sciences of the USSR
(Submitted May 12, 1972)
Kristallografiya, 18, 626-628 (May-June 1973)

The hexagonal ferrites have been successful subjects for magnetic and neutron diffraction studies in recent years. The unusual behavior of magnetic anisotropy, observed weak exchange interactions, the presence of critical values of magnetic field, and the open existence of block noncollinear magnetic structures have substantially enlarged our knowledge of the mechanism of exchange interactions in ferrimagnets.

Single crystals of the type M ferrite with double replacement of trivalent iron ions by ions of gallium and scandium were grown from solution in $NaFeO_2$ melt, having the form of truncated hexagonal pyramids with height 0.2-2 mm and base cross section 2-3 mm. The unit-cell parameters ($a = 5.95$ Å, $c = 23.63$ Å) were determined by x-ray diffraction. The single-phase nature of the crystals was confirmed by neutron diffraction measurements.

The atomic structure of the hexagonal type M ferrite was first determined in ref. 1 and has later been refined several times. The values of coordinates from ref. 2 and the method of calculation in ref. 3 were used in this study. The purpose of the study was to determine the magnetic structure and the sites of placement of the gallium and scandium ions.

The neutron diffraction patterns, taken at liquid-nitrogen and room temperatures and above the Curie point, proved to be similar to those of $BaSc_{1.2}$(M) in ref. 4. At 293°K, only reflections with even values of l, resulting from nuclear scattering, were present in the neutron diffraction pattern for the series of basal reflections (Fig. 1).

TABLE 1. Calculated (I_{calc}) and Experimental (I_{exp}) Values of Intensities for the Basal Series of Reflections of a Single Crystal of $BaGa_2Sc_{1.2}Fe_{8.8}O_{19}$ at 78°K

00l	I_{calc}	I_{exp}	00l	I_{calc}	I_{exp}
002	45.14	65.29	008+ 009−	7.31	8.40
002+ 003−	1.69	1.81	009+ 0010−	5.17	5.30
003+ 004−	5.91	5.98	0010	108.55	98.70
004	53.01	58.63	0010+ 0011−	0.58	1.68
004+ 005−	19.37	20.35	0011+ 0012−	0.26	0.36
005+ 006−	17.23	18.25	0012	1.27	6.58
006	37.35	22.47	0012+ 0013−	0.02	0
006+ 007−	2.01	0	0013+ 0014−	0.08	0
007+ 008−	2.87	2.16			
008	88.30	80.09			

At 78°K, pairs of magnetic reflections forbidden by the atomic space group of the crystal, $P6_3/mmc$, appeared in the space between the basal reflections. Their locations corresponded to a period of the magnetic structure of ~33 Å, equal to one and one-half times the c parameter of the chemical unit cell.

During examination of the various models, the best results were obtained for the case of the block conical ferromagnetic spiral (Fig. 2). In this case, collinear ordering of spins in accordance with the scheme of Gorter and Néel remains within the limits of the spinel block (S_4). Repetition of spins occurs during the transition from one block to another along the hexagonal axis. In this case,

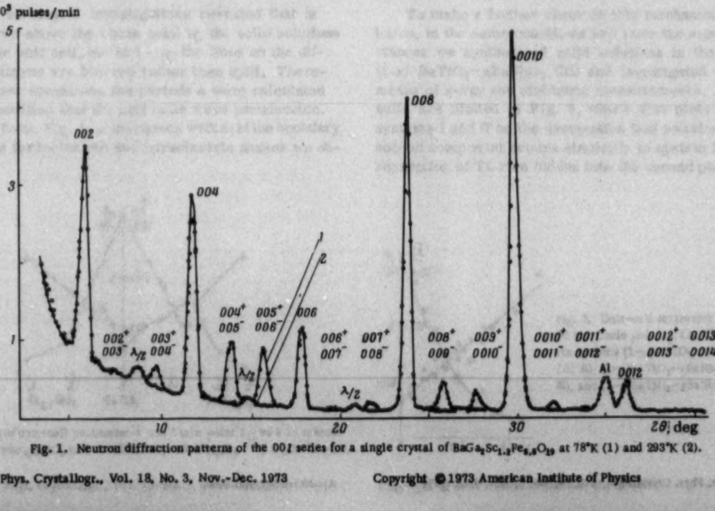

Fig. 1. Neutron diffraction patterns of the 00l series for a single crystal of $BaGa_2Sc_{1.2}Fe_{8.8}O_{19}$ at 78°K (1) and 293°K (2).

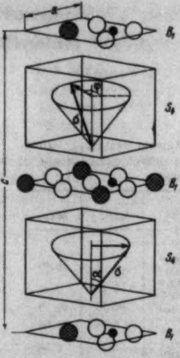

Fig. 2. Model of the block conical ferromagnetic spiral for a hexagonal type M ferrite.

the summed magnetic moments σ of the blocks are arranged so as to form a cone with half-aperture angle α of the cone, and are rotated about the axis of the cone by a constant angle. For our case, the angle of rotation of the projection of the total magnetic moment on the base plane is $\varphi = 120°$, and the half-aperture angle of the cone is $\alpha = 20°$. A comparison of calculated and experimental values of intensities for the series of basal reflections at 78°K is given in Table 1. The divergence factor is R = 0.17.

In view of the closeness of the nuclear scattering amplitudes for gallium, iron, and scandium (respectively $0.72 \cdot 10^{-12}$, $0.95 \cdot 10^{-12}$, and $1.18 \cdot 10^{-12}$ cm), the nuclear scattering pattern in this case is only slightly sensitive to the distribution of cations among the crystallographic positions of the unit cell. On the other hand, the magnetic scattering patterns should differ substantially upon the replacement of iron ions of the various positions by nonmagnetic ions. This difference is especially noticeably pronounced in the cases in which reflections of purely magnetic scattering exist and the crystal is a ferrimagnet. The calculations done showed the sites of the predominant locations of the scandium ions to be positions with fivefold coordination (the filling coefficient of scandium is K = 0.7) and the 12k positions (K = 1/12). The gallium and iron ions are statistically distributed among the rest of the crystallographic positions.

The creation of the block noncollinear magnetic structure in the specimen studied, as in a series of earlier cases, can be explained by weakening of the magnetic interactions at the boundaries of the spinel blocks owing to the preferred location of the scandium ions in the B_1 bond and the formation of a nonmagnetic interlayer. The appearance of statistically distributed gallium ions in the unit cell does not result in a change in the model of the magnetic structure, but shows up in an increase in the angle of deviation of the spins from the hexagonal axis. This evidently is the result of decrease of magnetic interactions in the unit cell upon dilution of the iron ions by a nonmagnetic ion. Calculations on the neutron diffraction patterns for $BaSc_{1.2}(M)$ and $BaGa_2Sc_{1.2}(M)$ at 78°K, carried out by a similar method and for similar values of extinction parameters, gave values of 15° and 20°, respectively, for the angle α.

---

[1] V. Adelsköld, Arkiv Kemi, Mineral., et Geol., A12, 29 (1938).

[2] W. D. Townes, J. H. Fangs, and A. J. Porrotta, Z. Krist., 125, 437 (1967).

[3] O. P. Aleshko-Ozhevskii and I. I. Yamzin, Zh. Eksp. Teor. Fiz., 56, 1217 (1969) [Sov. Phys.–JETP, 29, 655 (1969)].

[4] O. P. Aleshko-Ozhevskii, R. A. Sizov, I. I. Yamzin, and V. A. Lyubimtsev, Zh. Eksp. Teor. Fiz., 55, 820 (1968) [Sov. Phys.–JETP, 28, 425 (1969)].

Solid solutions of $BaTiO_3$ with barium niobates

I. N. Groznov and Yu. N. Venevtsev
L. Ya. Karpov Scientific-Research Physicochemical Institute
(Submitted February 4, 1972; resubmitted April 24, 1972)
Kristallografiya, 18, 629-630 (May-June 1973)

Research on solid solutions with stoichiometric vacancies based on $BaTiO_3$ (refs. 1, 2), $PbTiO_3$ (refs. 3-5), and $SrTiO_3$ (refs. 6, 7) has revealed that they are of great scientific and practical interest. In this connection we have studied similar solid solutions in the systems $(1-x) \cdot BaTiO_3-xBa_{0.5}NbO_3$ (I) up to x = 0.2, $(1-x)$ $BaTiO_3-xBaNb_{0.8}O_3$ (II) up to x = 0.3, and, for comparison, $(1-x) \cdot BaTiO_3-BaNbO_3$ (III) up to x = 0.2. System I has been studied before, and our results wholly agree with those of Subbarao and Shirane.[2]

The specimens were synthesized by the usual ceramic technology by threefold annealing in the ordinary atmosphere with a sintering temperature of 1300-1400°C, in conditions similar to those for obtaining specimens of the system $(1-x)$ $BaTiO_3-xSrNb_{0.8}O_3$, which was studied by us.[8] As the starting material we used TiO_2 (rutile) and $BaCO_3$ of cp grade, together with first-grade Nb_2O_5. We made x-ray investigations at room temperature in a URS-50IM diffractometer and an RKD-57 camera. We also used an ordinary bridge method at 100 kHz to study the temperature dependence of the dielectric constant ε.

X-ray phase analysis revealed that, within the limits of error of the photographic method, the specimens of system II are single-phase up to x = 0.30, while in system I for the specimens with x = 0.16 and 0.20 weak additional lines were visible, evidently showing that they were not single-phase. When we studied similar solid solutions with $Ca_{0.5}NbO_3$ and $Sr_{0.5}NbO_3$, the x-ray diffraction patterns of the specimens with x = 0.16 and 0.20 showed the same lines.[9] This gives grounds for supposing that, with deficit of Ba ions, these lines belong to oxides of Ti and Nb or their mixed oxide.

X-ray structural investigations revealed that at temperatures above the Curie point t_C the solid solutions have a cubic unit cell, but at $t < t_C$ the lines on the diffraction patterns are blurred rather than split. Therefore for these specimens the periods a were calculated on the supposition that the unit cells were pseudocubic. As we see from Fig. 1, a increases with x; at the boundary between the ferroelectric and paraelectric phases we observe a bend on the $a(x)$ graph. In system II at x = 0.15 there is a sudden decrease in a, apparently due to a change in the mechanism of solution of the second component (see below). Similar changes in the $a(x)$ graphs were observed[3,4] in a study of other, similar solid solutions.

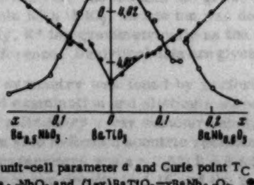

Fig. 1. Graphs of unit-cell parameter a and Curie point T_C vs x in systems $(1-x)BaTiO_3-xBa_{0.5}NbO_3$ and $(1-x)BaTiO_3-xBaNb_{0.8}O_3$. ●) $a(x)$; ○) $t_C(x)$.

In studying the dielectric constant, on the $\varepsilon(t)$ curves we observed marked maxima at temperatures corresponding to the phase transitions from the ferroelectric to the paraelectric phase. By correlating the results of the dielectric measurements we were able to plot t_C vs x (Fig. 1). We see that t_C sharply falls as x rises, but in system II at x = 0.15 there is a sudden jump in t_C towards higher temperatures, which is undoubtedly due to a sudden change in the structure parameters. In all the specimens studied we observed hysteresis loops at $t < t_C$.

It is known that the presence of vacancies leads to a decrease in the unit-cell volume in compounds with the perovskite structure.[10] The increase in a with x, despite the stoichiometric vacancies entailed by the composition of the mixture, and the similarity between the $a(x)$ graphs in systems I and II indicate that the formation of solid solutions does not follow a given stoichiometry, but occurs without vacancies according to the pattern of $BaTiO_3-BaNbO_3$. Part of the Ti or Nb oxides in system I and Ba in system II must be separated in the form of a second phase, and the requirement of electrical neutrality of the crystal will be satisfied by reduction of the valence of some of the Ti^{4+} ions or Nb^{5+} ions to Ti^{3+} or Nb^{4+}. The latter actually occurs in compounds with the perovskite structure[11,12] and leads to the manifestation of semiconducting properties in $BaTiO_3$ crystals.[13]

To make a further check on this mechanism of solution, in the same conditions and from the same substances we synthesized solid solutions in the system $(1-x)$ $BaTiO_3-xBaNbO_3$ (III) and investigated them by means of x-ray and dielectric measurements. The results are plotted in Fig. 2, which also plots data for systems I and II on the assumption that solution of the second component occurs similarly to system III with separation of Ti-rich oxides into the second phase in

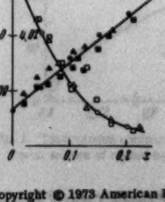

Fig. 2. Unit-cell parameter a (▲, ■, ●) and Curie point t_C (△, □, ○) in the systems $(1-x)BaTiO_3-xBa_{0.5}NbO_3$ (△, ▲), $(1-x)BaTiO_3-xBaNb_{0.8}O_3$ (□, ■), and $(1-x)BaTiO_3-xBaNbO_3$ (○, ●).

system I, and Ba-rich oxides in system II. With these assumptions, the data on $a(x)$ and $t_C(x)$ agree among themselves for all three systems. The steeper $a(x)$ curve in system II at $x > 0.15$ and the absence of a second phase on the x-ray diffraction patterns show that the excess Ba ions are distributed partly among the B positions in the perovskite-type structure ABO_3. This is quite possible, because we know of compounds with a similar structure: $Sr(Sr_{0.5}Ta_{0.5})O_{2.75}$ and $Ba(Sr_{1/3}Ta_{2/3})O_3$ (see refs. 14 and 15), where the large Sr^{2+} ions occupy B positions.

In conclusion, we would remark that the hypotheses put forward in this article concerning the character of the solution of the second components have enabled us to explain the shapes of the graphs of the structure parameters and Curie points in the systems $(1-x)\,BaTiO_3-xA_{0.5}\cdot NbO_3$, $(1-x)\,BaTiO_3-xANb_{0.8}O_3$, and $(1-x)\,BaTiO_3-xANbO_3$, where A denotes a Ca or Sr ion.

---

[1] G. A. Smolenskii, V. A. Isupov, and A. I. Agranovskaya, Fiz. Tverd. Tela, 1, 1573 (1959) [Sov. Phys.—Solid State, 1, 1438 (1960)].

[2] E. G. Subbarao and G. Shirane, J. Amer. Ceram. Soc., 42, 279 (1959).

[3] A. S. Viskov and Yu. N. Venevtsev, Kristallografiya, 14, 460 (1969) [Sov. Phys.—Crystallogr., 14, 379 (1969)].

[4] A. S. Viskov, Izv. Akad. Nauk SSSR, Neorgan. Mat., 5, 105 (1969).

[5] A. S. Viskov and A. N. Abramova, "New piezoelectric and ferroelectric materials and their applications," in: Symposium from Moscow House of Scientific-Technical Propaganda [in Russian], Moscow (1969), p. 97.

[6] G. I. Skanavi, Ya. M. Ksendzov, V. A. Trigubenko, and V. G. Prokhvatilov, Zh. Eksp. Teor. Fiz., 33, 320 (1957) [Sov. Phys.—JETP, 6, 250 (1958)].

[7] T. Y. Tien and L. E. Cross, Japan. J. Appl. Phys., 6, 459 (1967).

[8] I. N. Groznov, A. S. Viskov, and V. M. Petrov, Izv. Akad. Nauk SSSR, Neorgan. Mat., 7, 1216 (1971).

[9] I. N. Groznov and Yu. N. Venevtsev, in: Physics and Chemistry of the Solid State, Vol. 2, [in Russian], N. Fiz.-Khim. Inst., Moscow (1971); Vol. 3, (1972).

[10] Shin-ichi Shirasaki, Solid State Commun., 9, 1217 (1971).

[11] M. Restingian, J. G. Dickinson, and R. Ward, J. Amer. Chem. Soc., 79, 5598 (1957).

[12] P. Ridgley and R. Ward, J. Amer. Chem. Soc., 77, 6132 (1955).

[13] O. I. Prokopalo, Izv. Akad. Nauk SSSR, Ser. Fiz., 35, 1956 (1971).

[14] L. Brixner, J. Amer. Chem. Soc., 80, 3214 (1958).

[15] F. Galasso and J. Pyle, J. Phys. Chem., 67, 1561 (1963).

Growth of $KIO_3 \cdot HIO_3$ crystals and investigation of some of their physical properties

N. R. Ivanov, A. N. Izrailenko, L. N. Rashkovich, and O. A. Chikhladze

Institute of Crystallography, Academy of Sciences of the USSR
M. V. Lomonosov Moscow State University
Institute of Cybernetics, Academy of Sciences of the Georgian SSR

(Submitted June 6, 1972)
Kristallografiya, 18, 631-632 (May-June 1973)

It is well known that crystals of iodic acid α HIO_3 and its salts AIO_3 (A = Li, Na, K, Rb, Cs, NH_4) are promising materials for second-harmonic generation, electrooptical modulation of light, etc. It was found that most crystals of this group have different symmetries: 222 (HIO_3), 6 ($LiIO_3$), mmm ($NaIO_3$), 1 (KIO_3), mm2 ($RbIO_3$ and NH_4IO_3), and 3m ($CsIO_3$). This explains the failure of attempts to grow crystals of binary solid solutions. However, $KIO_3 \cdot HIO_3$ crystals can be obtained.

Data in the literature on $KIO_3 \cdot HIO_3$ crystals are very contradictory, even with regard to their point symmetry. Kemper and Vos[1] give space group $P2_1/c$ but note that this is unreliable, since the crystal has an appreciable piezoelectric effect. In ref. 2, the same group $P2_1/c$ was found, the unit-cell parameters were measured ($a = 7.028$, $b = 8.203$, $c = 21.841$ Å, $\beta = 98.03°$), and the structure was established, but a correctional note was added in which second-harmonic generation and the piezoelectric effect were explained by departure from centrosymmetry, apparently due to hydrogen bonds. Finally, in ref. 3, Kemper and Vos insisted on group $P2_1/c$ and explained the piezoelectric effect and second-harmonic generation by the presence of a layer of KIO_3 or HIO_3 on the crystal surface. In the present note, we report the growth of $KIO_3 \cdot HIO_3$ crystals and give the results of a preliminary investigation of them.

Colorless isometric $KIO_3 \cdot HIO_3$ crystals having volumes up to 3 cm^3 were grown from aqueous solution by cooling from 45 to 30°C while stirring the solution vigorously. The starting materials were ultrapure-grade KIO_3 and cp-grade HIO_3. At 50°C, the saturated solution contained 10.5 wt.% KIO_3 and 2.45 wt.% HIO_3 (molar ratio $KIO_3/HIO_3 = 3.54$). After mixing, the solution was filtered to remove a small amount of precipitated white powder. The seeds were spontaneously grown crystals having linear dimensions of the order of 2 mm. The seed was oriented and mounted by pyramid faces in a holder. The growth rate was ~ 0.3 mm/day. We note that the crystal grows upward on the basal (001) face, vertical-prism and rhombic-pyramid faces also being well developed.

Chemical analysis showed that the grown crystals had the formula $KIO_3 \cdot HIO_3$. Iodate ion was determined iodometrically, K^+ ion gravimetrically as the sulfate, and H^+ by difference. Analytical data are given in Table 1.

TABLE 1. Chemical Composition of Grown Crystals

Ion	Content, wt.%	
	calc.	chem. analysis
K^+	10.028	9.867
IO_3^-	89.740	89.90
H^+	0.232	0.233
Sum	100.00	100.00

Rhombic symmetry was found by performing a morphological examination and plotting a stereographic projection. Preliminary x-ray structure analysis of these crystals also indicated acentric rhombic symmetry; the unit-cell parameters are $a = 7.52$; $b = 8.55$, $c = 19.40$ Å, Z = 8. The x-ray density is 4.15 and the measured density 4.10 g/cm^3.

Thermal analysis was carried out in a Thermoflex differential scanning calorimeter at a heating rate of 5 deg/min. The thermogram shows that the sample remains unchanged from room temperature to 180°C. At 180 ± 0.5°C, the sample weight decreases by 2.25 ± 0.3%. Since $KIO_3 \cdot HIO_3$ contains 2.46% H_2O, one may presume that all the water is lost at 180°C. Decomposition of the sample, accompanied by evolution of iodine, begins at 350°C; slightly below this temperature (beginning at 322°C), a number of solid-phase transformations take place in the sample along with absorption of heat.

Figure 1 shows polarization transmission spectra of an X-cut sample, measured on a Hitachi spectrophotometer, which demonstrate considerable dichroism. The cross section of the crystal by the (001) basal plane and the choice of crystallographic axes are also shown there.

$KIO_3 \cdot HIO_3$ crystals are optically biaxial (2V = 56°), negative, and have weak rhombic dispersion of the angle of optic axes of the form $r > v$; ac is the plane of optic axes, and a is the bisector of the acute angle of the optic axes. The dispersion of the three principal refractive indices, measured by the prism method, and the dispersion of double refraction ($n_z - n_y$), determined more precisely by using the band spectrum, are shown in Fig. 2.

Values of the dielectric constant, measured at room temperature, are: $\varepsilon_a = 38$, $\varepsilon_b = 52$, and $\varepsilon_c = 21$. It was

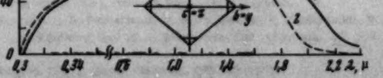

Fig. 1. Transmission spectrum of $KIO_3 \cdot HIO_3$ crystal (d = 0.86 mm) and cross section of crystal by (001) basal plane. 1) E ∥ c; 2) E ∥ b.

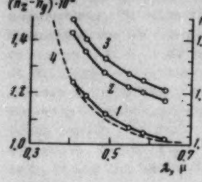

Fig. 2. Dispersion of three refractive indices n_x (1), n_y (2), and n_z (3) and dispersion of double refraction $n_z - n_y$ (4).

found that the crystals have a linear electrooptical effect due to rotation of the optical indicatrix in an electric field (the rotation of the indicatrix was measured with ± 6" accuracy). The corresponding electrooptical coefficients of the mechanically free crystal proved to be: $r_{41} = 1.6 \pm 0.2$, $r_{52} = 0.7 \pm 0.7$, and $r_{63} = (2.2 \pm 0.7) \cdot 10^{-11}$ cm/V.

Evidently, our data on the unit-cell parameters and symmetry groups of $KIO_3 \cdot HIO_3$ crystals differ substantially from those of Kemper and Vos[1,3] and Chan and Einstein.[2] Since chemical analysis showed that our crystals had the formula $KIO_3 \cdot HIO_3$, it may be assumed that we are dealing with a different crystal modification. Electrooptical measurements conclusively show the absence of a center of symmetry and indicate that the 222 group is probable. Possibly, however, the true symmetry of the crystal may prove to be lower.

The authors sincerely thank L. M. Belyaev, L. A. Shuvalov, and G. F. Dobrzhanskii for posing the problem, a discussion of the results, attention, and support, M. P. Golovei for measuring the refractive indices, L. V. Soboleva for performing the chemical analyses, and V. V. Ilyukhin for setting up the x-ray structure investigation.

---

[1] G. Kemper and A. Vos, Acta Crystallogr., B26, 302 (1970).
[2] L. J. J. Chan and F. W. Einstein, Can. J. Chem., 49, 468 (1971).
[3] G. Kemper and A. Vos, Acta Crystallogr., B27, 2286 (1971).

Use of the methods of nonlinear optics in order to make a more accurate analysis of the structural characteristics of crystals associated with the absence of an inversion center

L. G. Koreneva, V. F. Zolin, B. L. Davydov, and V. I. Tsaryuk

(Submitted February 10, 1972; resubmitted May 3, 1972)
Kristallografiya, 18, 633-634 (May-June 1973)

The principal method of studying the symmetry of crystals is that of x-ray structural analysis. However, about half the space groups can only be determined in an ambiguous manner by x-ray methods, the accuracy of these methods being insufficient to decide on whether or not an inversion center exists in the crystal.[1]

In this paper we shall use a number of examples to show that the question as to the existence of an inversion center may be solved by the methods of nonlinear optics. The simplest method of nonlinear optics enabling the absence of an inversion center to be detected is the generation of a second harmonic. The existence of a signal at twice the frequency immediately indicates the absence of an inversion center in the crystal under examination.[2] It is easiest to detect the doubling of the frequency of radiation with a wavelength of $1.06\,\mu$, since the converter radiation falls in the optical region. The conversion effect may be observed in powders prepared from the compounds under consideration.[3] We shall now illustrate the use of the method.

The authors observed the generation of a second harmonic in samples of three substances which, according to published data, crystallized with an inversion center. We studied a number of samples of phthalic anhydride,1) methanyl acid, and paraanisidine2) obtained under different conditions. Crystals of these substances were earlier assigned to the space groups $\mathrm{Pnm}a$ (ref. 5) and $\mathrm{Pn}a\mathrm{m}$ (ref. 6), and $\mathrm{P2_1/c}$. All three groups were determined in an ambiguous manner on using the extinction rules.[1] The generation of a second harmonic in these crystals clearly indicated that their space groups had been determined incorrectly; actually they crystallize in the groups $\mathrm{Pn}a2_1$, $\mathrm{Pn}a2$, and $\mathrm{P2_1}$, respectively.

On the other hand, in certain samples of the ethyl ester of paraaminobenzoic acid (anestezine) we found no second harmonic generation, although according to published data anestezine crystallizes without any inversion center in the $\mathrm{P2_12_12_1}$ space group.[5] The infrared spectra of all the anestezine samples (whether these gave a nonlinear conversion or not) were completely identical. Evidently different crystal forms of anestezine were being studied on different occasions. The forms giving generation were obtained from the melt and from solution in alcohol. The forms not giving generation were obtained by crystallization from solution in acetone, benzene, ether, and mixtures of these. So far as we know, forms of anestezine with an inversion center have never yet been described.

A considerable amount of information has now been obtained in relation to second harmonic generation in organic crystals,[8,9] the space groups of which have never been determined. These data may clearly be used later in determining space groups.

Interesting results were obtained when studying racemic mixtures of optically active compounds. It is well known[10] that the majority of racemic mixtures of amino acids crystallize with an inversion center. An exception is DL-glutamino acid, the crystals of which belong to the $\mathrm{P2_12_12_1}$ group. We only detected second harmonic generation in powders of optically active isomers, and also DL-glutamino acid and DL-ornithine. This indicates that in ornithine the mirror-image isomers crystallize separately, by analogy with DL-glutamino acid.

A racemic mixture of mirror isomers of 1-phenethyl-3-p-nitrophenyl-2-thiourea undergoes partial separate crystallization. This is indicated by the doubling of the frequency in the powdered racemate of this compound. The effectiveness of the doubling is several times lower than in the powder of the optically active substance.

Finally, second-harmonic generation may reveal phase transitions accompanied by the loss of an inversion center. An example is the observed generation of a second harmonic in thiourea at liquid-nitrogen temperature. At room temperature there is no nonlinear conversion.

These examples illustrate the applicability of the methods of nonlinear optics in order to improve our knowledge of crystal structure. The method is quite simple and reliable. All that is required is a fine-crystalline powder of the material under test and a standard apparatus for producing powerful coherent radiation.

The authors are grateful to N. S. Andreeva for valuable consultations regarding problems of x-ray structural analysis.

---

1) Crystals obtained by (slow) evaporation from a solution of phthalic anhydride in water and a mixture of water with acetone did not yield any second harmonic generation. However, their infrared spectra showed partial or complete hydrolysis of the anhydride.

2) The generation of a second harmonic in paraanisidine was also observed in ref. 4, but interpreted as a random disruption of symmetry in some of the crystals.

---

[1] Intern. Tables for X-Ray Crystallography, Vol. 1, Kynoch Press, Birmingham, England (1952).
[2] N. Bloembergen, Nonlinear Optics, Benjamin (1965).
[3] S. K. Kurtz and T. T. Perry, J. Appl. Phys., 39, 3798 (1968).
[4] V. D. Shigorin and G. P. Shipulo, Brief Communications on Physics [in Russian], Physics Institute, Academy of Sciences of the USSR, Vol. 10 (1971), p. 34.
[5] R. Wyckoff, Crystal Structures, Vols. 5 and 6, Interscience, New York (1969).
[6] S. R. Hall and E. N. Maslen, Acta Crystallogr., 18, 301 (1965).
[7] M. Y. Khan and J. Misra, Indian J. Phys., 40, 271 (1966).
[8] B. L. Davydov, L. D. Derkacheva, V. V. Dunina, M. E. Zhabotinskii, V. F. Zolin, L. G. Koreneva, and M. A. Samokhina, Opt. Spektrosk., 30, 503 (1971).
[9] J. Jerphagnon, IEEE J. Quant. Electron., QE7, 42 (1971).
[10] G. G. Gurskaya, Structure of Amino Acids [in Russian], Nauka, Moscow (1967).

Luminescence of cuprous oxide single crystals

I. P. Kuz'mina, A. N. Lobachev, B. S. Predtechenskii, L. S. Starostina, V. B. Stopachinskii, and N. M. Khaidukov

Institute of Crystallography, Academy of Sciences of the USSR

(Submitted December 31, 1971; resubmitted July 5, 1972)
Kristallografiya, 18, 635–637 (May–June 1973)

For a long time, the only method of preparing cuprite crystals was by oxidation and subsequent annealing of copper plates in air.[1] Under these conditions, the Cu is oxidized, and a polycrystalline Cu_2O plate is obtained having grains enlarged by annealing. This process is difficult to control. Crystals prepared by this method are nonstoichiometric (they contain a considerable amount of CuO and Cu) and are under considerable stress. Attempts to grow crystals from the melt in a crucible were unsuccessful, since no crucible material could be found that would not react[2] with Cu_2O. The recently developed method of hydrothermal growth of cuprite single crystals gives more perfect crystals, but as yet they are small.

As is well known, Cu_2O is the compound in whose absorption spectrum series of narrow lines of the exciton spectrum were first found.[3] A number of properties of the exciton were studied[4] in Cu_2O. However, luminescence on recombination of excitons was not obtained in cuprite crystals. The less perfect the crystal is (impurities, departures from stoichiometry, structure defects), the more probable nonradiative recombinations are. In 1968, E. F. Gross and F. I. Kreingol'd first observed luminescence in exciton lines in Cu_2O crystals grown hydrothermally.

In order to conduct a number of investigations (study of the collective interaction of excitons and the possibility of building a cuprite laser), it was necessary to prepare large, perfect Cu_2O crystals, which would give intense, narrow luminescence lines of recombination of free excitons; this was done by the following method.

The starting material consists of polycrystalline Cu_2O samples. The Cu_2O sample is placed in special clamps of the working cell and subjected to zone crystallization.[5] The zone is heated by bombarding the sample with an electron beam. The sample is grounded, and a high negative voltage is applied to the tungsten-loop cathode and focusing plates. The zone is held suspended by surface tension.[6]

The crystals are grown under conditions slightly outside the region of stability of Cu_2O (point B in the Cu–O_2 phase diagram,[7] Fig. 1). To bring the working point closer to the region of stability of Cu_2O, the melting is carried out in a measured oxygen atmosphere. Part of the oxygen is formed by decomposition of cupric oxide: $4CuO \rightleftharpoons 2Cu_2O + O_2$.

The copper formed by decomposition of Cu_2O (only a small amount of Cu_2O, about 1%, decomposes) is eliminated owing to the high vapor pressure at the melting point of Cu_2O and the zone mechanism of purification. Other impurities present in the original sample are eliminated analogously.

After traversal by the zone, the sample usually consists of two or three crystals, whose boundaries lie in the direction of the rod axis. This is apparently due to low anisotropy of growth rates in Cu_2O. To grow a single crystal, the crystallization is carried out on a seed prepared from one of the crystals obtained.

Cu_2O single crystals grown by the above method differ substantially from cuprite crystals grown by other methods. They are large, transparent crystals of cylindrical shape (diameter up to 10 and length up to 100 mm). The degree of perfection of the resulting samples was investigated by x-ray methods and chemical etching. Before etching, the samples were ground, and the resulting plane was polished mechanically and chemically. After this treatment, the sample was etched in a solution of $Cu \cdot (NO_3)_2$ in HNO_3. No block boundaries were found in single crystals grown on seeds. Laue patterns taken from these crystals give distinct single spots.

As was mentioned above, the purpose of the present study was to grow large Cu_2O single crystals giving luminescence in exciton lines. Such luminescence can be detected only in sufficiently perfect single crystals. Defect and impurity levels in the forbidden gap increase the probability of nonradiative transitions, and luminescence in exciton lines does not occur. Until recently, Cu_2O crystals showed only long-wave luminescence. The long-wave luminescence lines make up two broad bands having maxima at 7200, 8200 and 9100, 10,100 Å. The 7200, 8200 Å band corresponds to levels of oxygen vacancies, and the 9100, 10,100 Å band, to levels of copper vacancies.[8] In samples whose composition departs from stoichiometric, evidently radiative recombination of carriers proceeds mainly through these levels.

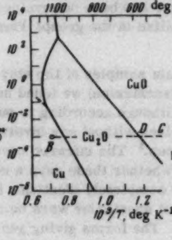

Fig. 1. Phase diagram of copper–oxygen system.

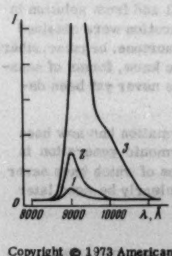

Fig. 2. Luminescence lines at 9100–10, 100 Å for three cuprite samples, grown at various velocities of traversal by zone.

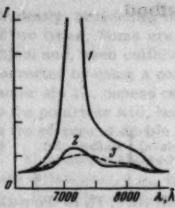

Fig. 3. Luminescence lines at 7200–8200 Å for three cuprite samples. 1) Growth in vacuum; 2, 3) in residual oxygen atmosphere.

The luminescence of a number of grown crystals was investigated at 4.2 and 1.5°K. Luminescence was excited by a type LG-106 argon laser (λ = 4880 Å). The luminescence spectra of the grown crystals contained a weak line corresponding to copper vacancies. The luminescence lines at λ = 9100, 10,100 Å for three Cu_2O crystals (1, 2, 3), grown at correspondingly reduced velocities of traversal by the zone, are shown in Fig. 2. It is evident from Fig. 2 that the line intensity increases markedly with decreasing velocity of traversal of the sample by the zone. Evidently, decreasing this velocity increases the residence time of the sample at temperatures corresponding to the region of stability of CuO (segment DC of line BC in Fig. 1).

Luminescence lines at λ = 7200, 8200 Å, corresponding to oxygen vacancies, were almost wholly absent in the case of samples grown in an oxygen atmosphere. This is evident from Fig. 3, where the 7200, 8200 Å luminescence lines are plotted for three samples.

By correctly choosing the conditions of growth (number and velocities of zone traversals, oxygen pressure, orientation of seeds), one can obtain crystals which give intense lines of exciton luminescence. Crystals prepared with a large number of traversals by the zone give only the free exciton line and its phonon replica. The width of the exciton lines is small, only a few angstroms. Luminescence lines of the free exciton (n = 1) are shown for two samples in Fig. 4.

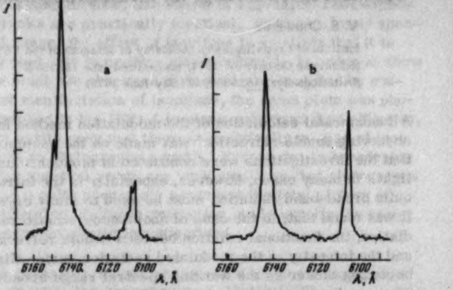

Fig. 4. Luminescence of two cuprite samples in exciton line. a) λ 6104 Å, recombination of excitons n = 1; b) λ 6144 Å, recombination of excitons n = 1 with emission of phonon.

Thus, thanks to luminescence in exciton lines, large (diameter ~1 cm and length ~100 mm) grown single crystals may be used to investigate a number of new properties of excitons (interaction of excitons, the possibility of creating levels with inverse population, etc.).

---

[1] Ya. I. Kushnir, Author's Abstract of Dissertation, Chernovtsy State University (1970).

[2] R. S. Zucker, J. Electrochem. Soc., 112, 117 (1965).

[3] E. F. Gross and N. A. Karryev, Dokl. Akad. Nauk SSSR, 84, 471 (1952).

[4] E. F. Gross, Usp. Fiz. Nauk, 76, 433 (1962) [Sov. Phys.—Usp., 5, 195 (1963)].

[5] N. A. Brilliantov, L. S. Starostina, and O. P. Fedorov, Kristallografiya, 6, 261 (1961) [Sov. Phys.—Crystallogr., 6, 202 (1961)].

[6] O. P. Fedorov and L. S. Starostina, Prib. Tekh. Eksp., 2, 195 (1963).

[7] W. S. Brover and H. S. Parker, J. Crystal Growth, 8, 227 (1971).

[8] J. Bloem, A. J. Van der Houven, Van Oordt, and F. A. Kröger, Physica, 22, 1254 (1956).

Optimum spectral range for investigating double refraction by the modulation method

V. S. Chudakov

Institute of Crystallography, Academy of Sciences of the USSR

(Submitted October 29, 1971; resubmitted June 19, 1972)
Kristallografiya, 18, 638-640 (May-June 1973)

A fundamental calculation of the modulation method for observing double refraction[1] was made on the assumption that the investigations were conducted in monochromatic light. In many cases, however, especially in the infrared, quite broad-band radiation must be used to study crystals. It was found that, in the case of nonmonochromatic radiation, the functional relation between double refraction and the intensity of the modulated radiation varies slightly, becoming closer as the working spectral range broadens. Thus, an increase in the spectral half-width of the light filter causes additional errors in the visualization and measurement of double refraction.

In order to estimate these errors and thereby to determine the optimum spectral width of the light filter, one must first obtain the transmission function of the polariscope and rotating analyzer for nonmonochromatic radiation and determine just how it differs from the transmission function for monochromatic radiation, which, as was shown earlier,[1] has the form

$$I \sim \sin \delta, \tag{1}$$

where I is the intensity of modulated radiation at the analyzer exit, and δ is the phase difference produced by the object. Using Müllers method of calculation,[2] one can show that the intensity of modulated monochromatic radiation beyond the analyzer will be described by the following expression:

$$\begin{aligned} I \sim \sin \delta \sin \Delta \sin (2\omega t - 2\alpha) - \cos \delta \cos \Delta \sin 2\alpha \sin (2\omega t - 2\alpha) \\ + \cos \Delta \cos 2\alpha \cos (2\omega t - 2\alpha), \end{aligned} \tag{2}$$

where Δ is the phase difference of the phase plate located ahead of the object, α is the angle between the axis of the highest velocity of light in the object and the direction of highest transmission of the polarizer, and ω is the angular frequency of rotation of the analyzer. To simplify the calculation, we shall consider that, in the frequency range $\nu_1 - \nu_2$ under investigation, the polariscope and object do not have appreciable spectral selectivity, whereas the dispersion of double refraction of the object and that of the phase plate are negligibly small. We shall assume that the path difference of the phase plate is such that there is no modulation of radiation in the polariscope with the object removed. Then the functional relation between the modulated light flux and double refraction takes the form

$$\Phi \sim \int_{\nu_1}^{\nu_2} \sin \delta \sin \Delta d\nu - \int_{\nu_1}^{\nu_2} \cos \delta \cos \Delta \sin 2\alpha \, d\nu. \tag{3}$$

After integration, we obtain the following expression for the modulated flux Φ:

$$\begin{aligned} \Phi \sim \frac{1}{2\pi} \sin \pi \Gamma (\nu_1 + \nu_2) \cdot 10^{-4} \Bigg[\frac{\sin \pi (\Gamma_p - \Gamma) (\nu_2 - \nu_1) \cdot 10^{-4}}{(\Gamma_p + \Gamma)} (1 - \sin 2\alpha) \\ + \frac{\sin \pi (\Gamma_p + \Gamma) (\nu_2 - \nu_1) \cdot 10^{-4}}{(\Gamma_p + \Gamma)} (1 + \sin 2\alpha) \Bigg] \sin (2\omega t - 2\alpha), \end{aligned} \tag{4}$$

where Γ is the measured path difference, Γ_p is the path difference of the phase plate in μ, and ν is the spectral frequency in cm^{-1}. If $\Gamma \leq \Gamma_p$, it may be considered with sufficient accuracy that

$$\begin{aligned} \Phi \sim (\nu_2 - \nu_1) \cdot 10^{-4} \sin \pi \Gamma (\nu_2 - \nu_1) \cdot 10^{-4} \Bigg[1 - \frac{\pi^2}{6} (\nu_2 - \nu_1)^2 \cdot 10^{-8} (\Gamma_p^2 + \Gamma^2) \\ - \frac{\pi^2}{3} (\nu_2 - \nu_1)^2 \cdot 10^{-8} \Gamma_p \Gamma \sin 2\alpha \Bigg]. \end{aligned} \tag{5}$$

It follows from expression (5) that the relative error due to broadening of the spectral range is

$$\gamma \sim \frac{\pi^2}{6} (\nu_2 - \nu_1)^2 \cdot 10^{-8} (\Gamma_p^2 + \Gamma_2) + \frac{\pi}{3} (\nu_2 - \nu_1)^2 \cdot 10^{-8} \Gamma_p \Gamma \sin 2\alpha. \tag{6}$$

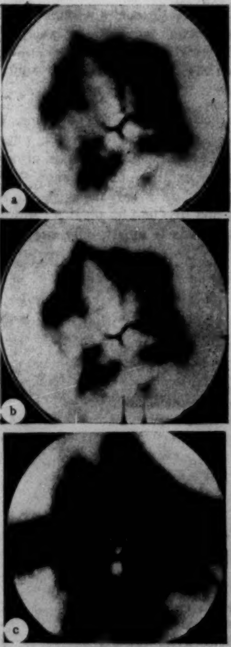

Fig. 1. Pictures of double refraction, taken in cross section of silicon single crystal by modulation method. a) Width of spectral range less than 1000 cm^{-1}; b) about 5000 cm^{-1}; c) plane-polarized light.

Evidently, broadening of the spectral range causes errors of two types. Some are independent of the position of the object and, when calibrating an instrument, can easily be corrected by using a compensator. Others, containing the factor sin 2α, depend on the position of the object relative to the polarizer and, hence, should be manifested primarily in the picture of double refraction.

Calculation showed that, in the measurement of small path differences, i.e., under the condition that $\Gamma_p \gg \Gamma$, even for quite broad spectral ranges of the order of 3000 cm^{-1}, the total error does not exceed a few percent. This was confirmed by an experimental check during an investigation of high-resistance silicon plates in an FPD-1 polariscope constructed in the special Design Office, Institute of Crystallography, Academy of Sciences of the USSR. Photographs of one of the plates, taken in the infrared spectral intervals 1.75-2.05 and 1.1-2.5 μ by the modulation method, are shown in Fig. 1a,b. The two photographs are practically identical. Even in a broad spectral range, the effect of isoclines is so slight that it is detected only in precise measurements. In order to show how much the observed picture can be modified by contrast manifestation of isoclines, the same plate was photographed in the FPD-1 in plane-polarized light (Fig. 1c). It is easily seen that there is practically no sign of isoclines in photographs a and b. Errors due to broadening of the spectral range are very small, so that photographs a and c quite accurately represent the total picture of distribution of double refraction, as is usually the case in monochromatic investigations.

---

[1] V. S. Chudakov, B. N. Grechushnikov, and G. G. Prave, Kristallografiya, 16, 939 (1971) [Sov. Phys.–Crystallogr., 16, 813 (1972)].

[2] W. A. Shurcliff, Polarized Light. Production and Use. Harvard Univ. Press (1962).

Effect of a magnetic field on the Curie point of the ferroelectric semiconductor SbSI

S. V. Ivanova and V. A. Lyakhovitskaya
M. V. Lomonosov Moscow State University;
Institute of Crystallography, Academy of Sciences of the USSR
(Submitted August 26, 1971; resubmitted May 11, 1972)
Kristallografiya, 18, 641 (May-June 1973)

Attempts have been made in refs. 1–6 to explain the reason for the phase transitions brought about by the electron–phonon interaction which occurs under conditions of the pseudo-Jahn–Teller effect. Such a micromechanism, in particular, permits one quantitatively to determine the shift in the Curie point in ferroelectric semiconductors under the effect of a magnetic field.[7–9] According to the equation reported in ref. 10, the authors have reckoned that shifts in T_C of 0.1–1°C in fields of $\sim 10^4$–$5 \cdot 10^4$ Oe should be expected when the width of the forbidden band changes by 10^{-4} eV.

We investigated the shift in the Curie point with respect to the temperature variation of the capacitance of an SbSI sample. The measurements were conducted on a polycrystalline sample with the dimensions 0.3 × 0.14 × 0.085 cm. The capacitance was measured with a Sullivan bridge at a 20 kHz frequency. Silver paste electrodes were applied onto the ends of the sample. The sample was placed in a thermostatted chamber mounted between the poles of a magnet. The value of the capacitance in the region of the phase transition was measured each time in the absence of a field and with an applied magnetic field of $1.1 \cdot 10^4$ Oe. The field was applied along the polar axis and in a perpendicular direction. The temperature was varied in the range 17–50°C and was stabilized at each point for 45 min. Measurements with an accuracy of $\sim$0.025°C were carried out with a copper – constantan thermocouple. Because the transition in SbSI is of the first type, it was naturally assumed that the curve of the dependence of the capacitance on temperature would be shifted progressively along the temperature axis with a shift in the Curie point. The left front of the curve, which is the most sensitive to a shift (see Fig. 1), has a slope of $25 \cdot 10^{-12}$ F/deg. The accuracy to which the capacitance was measured was $0.25 \cdot 10^{-12}$ F. Therefore, a shift in the front of the curve could be noted and, consequently, a shift in the Curie point by 0.01°C also.

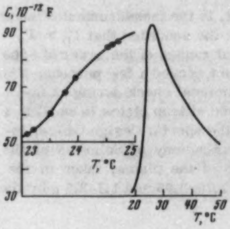

Fig. 1. Temperature dependence of the dielectric constant of the SbSI crystals: +) In the absence of an external magnetic field; ○) H = $1.1 \cdot 10^4$ Oe.

Thus, it follows from our experiments that a magnetic field of the magnitude indicated above does not shift the Curie point within the accuracy of our measurements. The discrepancy between experiment and theory could be caused by excessive simplification of the latest band structure of the SbSI crystals.

The authors thank B. A. Strukova for suggesting the topic and for interest in the work, and V. A. Koptsika for her discussion of the results and interest in the work.

---

[1] N. N. Kristofel', Tr. Inst. Fiz. Astron. Akad. Nauk EstSSR, No. 27, 85 (1964); Fiz. Tverd. Tela, 6, 3266 (1964) [Sov. Phys.–Solid State, 6, 2613 (1965)].
[2] J. Birman, Phys. Rev., 125, 1959 (1962); 127, 1013 (1962).
[3] K Sinha and A. Sinha, Indian J. Pure and Appl. Phys., 2, 91 (1964).

Surface tension of 180° domain boundaries and effects in triglycine sulfate and c-domain BaTiO$_3$

É. S. Popov and L. A. Shuvalov
Volgograd City Engineers Institute
Institute of Crystallography, Academy of Sciences of the USSR
(Submitted May 24, 1972; resubmitted October 11, 1972)
Kristallografiya, 18, 642-644 (May-June 1973)

Any phase interface in a thermodynamic system has a surface free energy, which is responsible for the specific properties of the interface, in particular, the surface tension, which for 180° domain boundaries in ferromagnets can be observed via a Laplace pressure[1] and which must be taken into account in calculating the forces acting on the domain wall.[2] Measurement of this pressure enables one to determine the surface energy density for the domain wall.[1,3]

One naturally assumes that the surface tension of the domain walls plays a decisive part in ferroelectric crystals; effects due to domain-wall surface tension are often masked by more prominent effects, but one can formulate the conditions that favor observation of the surface tension. For this to be so, the energy due to the bulk mechanical stresses arising by domain-wall displacement must be small; in other words we need crystals that are not piezoelectric in the paraelectric state,[4] and they must not contain any domain configurations that are not 180° ones, since these produce considerable change in the elastic energy of the crystal (for instance, 90° domains in barium titanate single crystals). Also, the domain walls should have sections with high curvature, where the Laplace pressure can become sufficient for observation.

On this basis, we have restricted consideration to 180° domain walls in crystals of triglycine sulfate (TGS) and c-domain barium titanate. We assume that the walls take the form of cylinders (in the general sense), whose generators are parallel to the axis of the spontaneous polarization P_s. Laplace's equation for the pressure on a curved phase interface gives the pressure at a cylindrical domain wall as

$$p = \sigma_w / R, \tag{1}$$

where σ_w is the energy of a unit area of walls and R is the radius of curvature. Strictly speaking, one should take into account[2] the anisotropy in σ_w, but this anisotropy is low for walls of this type, so we assume that p is directed normal to the wall and tends to displace it towards the center of curvature. The Laplace pressure at the walls is conveniently represented as an electric field, which we call the equivalent field. To determine this, we express[5] the pressure at the wall in the presence of an external electric field parallel to P_s as

$$p = 2P_sE. \tag{2}$$

It follows from (1) and (2) that the Laplace pressure on a cylindrical wall is equivalent to the action of an electric field

$$E_{eq} = \sigma_w / 2P_sR. \tag{3}$$

We now turn to the experimental results; detailed studies[6-8] on the domain structure of TGS have been published, as have studies for barium titanate.[9,10] It is clear that the 180° domain boundaries in TGS and barium titanate arise when the crystal becomes ferroelectric, and they have much in common and constitute sets of numerous narrow and highly elongated domains of both signs in sections perpendicular to P_s. As time passes, and if the external conditions are unchanged, the domain structure becomes of larger scale, but the reasons for this have not been established, so far as we are aware. It has been observed[8] that TGS has longitudinal extension of very narrow domains, which we consider to be characteristic of the action of surface-tension forces.

Photographs[7-10] for domain structures in TGS and barium titanate have been used to determine the radii of curvature at the ends of the domains, and then from (3) we calculated the equivalent field; Table 1 gives the results for the most curved parts of the wall at room temperature.

The equivalent fields under actual conditions are sufficient to produce slow polarization reversal via lateral motion of the 180° domain walls; these fields correspond to the part of the exponential dependence of the domain-wall boundary on the field for these crystals.[13] It is likely that the equivalent fields arising from the Laplace pressure may be considered as one of the components of the inherent field in the ferroelectric.

An example where surface tension may be responsible for an effect is the gradually decreasing dielectric constant of a ferroelectric in response to a weak low-frequency electric field.[14] The accelerated aging in this case may be ascribed to accelerated elongation of the domains in the weak external field, because the equivalent field and the external field act together for half a period and substantially increase the speed of domain wall displacement.

Low-frequency dielectric relaxation and dispersion has[15,16] been reported for TGS single crystals, where it is described by Coule's equation. This dispersion is related to the domain dynamics,[16] which indicates a possible mechanism for the restoring forces at the domain walls. If these walls are fixed at certain points by dislocations,[17,18] it is readily shown that the restoring force due to surface tension will be quasielastic when the wall bends. Also, the differential equation for the wall motion

TABLE 1

Compound	P_s, μC/cm^2	σ_w, erg/cm^2	R, μg	E_{eq}, V/cm
TGS	2,8 [11]	1 [12]	6.2 [7, 8]	29
BaTiO$_3$	26 [11]	7 [11]	0.5 [9, 10]	270

contains a negligible inertial term (see ref. 19 on the neglect of the inertial term in description of the motion of domain walls in ferromagnets), which automatically results in relaxation of the required type. The relaxation frequency is dependent on the period of the dislocation network, and the rigidity of the domain walls increases as this period falls.

It is possible to determine the surface energy of 180° domain walls via the spontaneous motion of the latter in response to the Laplace pressure; we use (3) together with the exponential law for the lateral motion of 180° walls:

$$v = v_\infty \exp(-\delta / E). \qquad (4)$$

The speed of spontaneous wall displacement for a curvature R may be measured, and we assume that this occurs in response to an equivalent field E_{eq} via the law of (4); then we have

$$\sigma_w = 2P_s R\delta / \ln(v_\infty / v). \qquad (5)$$

The quantities in (5) are determined from experiments of two types: δ and v_∞ are found from polarization reversal by lateral displacement of 180° walls in weak fields,[13] while v and R are determined from observation of the spontaneous displacement of the domain walls. It is possible that in practice there may be difficulties due to defects in real crystals, in which case additional information may be obtained by observing the wall motion in the total field constituted by the external field and the equivalent Laplace field.[3]

This method of determining the energy of 180° domain walls in a ferroelectric with a centrosymmetric paraelectric phase avoids the need to set up an equilibrium domain structure in the crystal (the concept of an equilibrium domain structure in a ferroelectric does not have the rigorous physical sense that it has for a ferromagnet, because the depolarizing field is balanced by electric charges, while the degree of compensation varies in time); in principle, the method is applicable over a wide temperature range, so spontaneous motion of the domain walls in response to surface tension should be observable.

---

[1] H. Williams and M. Goertz, J. Appl. Phys., 23, 316 (1952).
[2] E. Della Torre, IEEE Trans. Mag., 6, 822 (1970).
[3] Yu. L. Danilevskii and A. A. Seleznev, Physics of Magnetic Films: Proceedings of the International Symposium, June 8-16, 1968 [in Russian], Inst. Fiz. SO AN SSSR, Irkutsk, p. 154.
[4] L. A. Shuvalov, J. Phys. Soc. Japan, Suppl., 28, 75 (1970).
[5] A. S. Sonin and B. A. Strukov, Introduction to Ferroelectricity [in Russian], Vysshaya Shkola, Moscow (1970), p. 159.
[6] F. Moravets and V. P. Konstantinova, Kristallografiya, 13, 284 (1968). [Sov. Phys.—Crystallogr., 13, 221 (1968)].
[7] J. Fousek and M. Šafrankova, Japan. J. Appl. Phys., 4, 403 (1965).
[8] Ya. Stankovskaya and V. P. Konstantinova, Kristallografiya, 16, 158 (1971) [Sov. Phys.—Crystallogr., 16, 123 (1971)].
[9] S. L. Rapoport and L. I. Dontsova, in: Physics of Dielectrics and Semiconductors [in Russian], Vol. 29, Izd. Volgograd. Ped. Inst. (1970), p. 61.
[10] S. L. Rapoport and L. I. Dontsova, Kristallografiya, 15, 384 (1970) [Sov. Phys.—Crystallogr., 15, 327 (1970)].
[11] F. Jona and J. Shirane, Ferroelectric Crystals, Pergamon (1962).
[12] H. F. Kay and J. W. Dunn, Phil. Mag., 7, 207 (1962).
[13] R. C. Miller and A. Savage, Phys. Rev., 113, 755 (1958).
[14] J. Kalisz, Acta Phys. Polon., 26, 77 (1964).
[15] M. Ida and S. Kawada, Sci. Repts. Kanazawa Univ., 8, 39 (1962).
[16] A. V. Shil'nikov, Thesis, Voronezh Polytechnical Institute (1971).
[17] T. Nakamura and H. Nakamura, Japan. J. Appl. Phys., 1, 253 (1962).
[18] V. A. Meleshina, Kristallografiya, 16, 557 (1971) [Sov. Phys.—Crystallogr., 16, 475 (1971)].
[19] C. Kittel and J. Galt, Solid State Phys., 3, 337 (1956).

Dispersion of the dielectric constant in crystals of KH_2PO_4

L. P. Pereverzeva, Yu. M. Poplavko, V. M. Petrov, E. V. Makarevskaya, and I. S. Rez

Kiev Polytechnic Institute; Moscow Steel and Alloy Institute

(Submitted June 19, 1972)
Kristallografiya, 18, 645-646 (May-June 1973)

Data on the frequency–temperature variations in the dielectric constant ε and loss factor tan δ of potassium dihydrophosphate are given in refs. 1-9 and other sources. The results are, however, incomplete since the studies were carried out at comparatively low frequencies[1,2] or quite far from the phase transition region[3,6] or the measurements were only indirect.[4] In particular, there is insufficient information on the dispersion of the domain polarization mechanism.

The study of KH_2PO_4 single crystals described in this paper was carried out in the frequency range $10^3 - 4 \cdot 10^{10}$ Hz at temperatures from −196 to +180°C. The microwave measurements were made in the neighborhood of the phase transition. The relative error in ε was 2-5% and in tan δ was 10-30% (the higher values refer to measurements near T_C). For the low and radio frequencies, standard bridges and Q meters were used. At microwave frequencies, a coaxial measuring line[10] was used for 1-6 GHz and a waveguide resonance method[11] for 9-40 GHz. The crystals were commercially produced and grown by the temperature reduction technique. The dislocation density was not greater than 10^2 cm^{-2}. For the low-frequency measurements, the samples were in the form of plates about 1 mm thick; in the decimeter region they were disks 2-3 mm in diameter and in the centimeter region, slugs of standard waveguide dimensions. Silver electrodes (gold for microwaves) were plated by vacuum sputtering. The main experimental results are shown in Fig. 1.

In the paraelectric region, the variation of ε_3 at microwave frequencies near the transition point closely follows the Curie–Weiss law with $C_1 = 2800 \pm 50$, $\theta_1 = -154$°C, and $\varepsilon_{\infty_1} = 5.5$. It is interesting to note that after "piezoelectric pressure" (at frequencies of 10^4-10^7 Hz) there is no noticeable dispersion in $\varepsilon_3(T)$ in the paraelectric phase (within the limits of error) even at millimeter wavelengths and the maximum value of $\varepsilon_3 = 650 \pm 50$ at $T_C = -150.3$°C. However, the approach to the dispersion frequency is shown by the sharp drop in $\tan\delta_3$ which is particularly clear above 10 GHz and where $T - \theta < 10°$. In the paraelectric phase, the temperature variation of $\tan\delta_3$ for microwave frequencies has been described in ref. 12 by the expression $(T - \theta \tan\delta = \alpha + \beta T + \gamma T^2$, which follows from an application of the dynamic theory of phase transitions.[13] It appeared in our experiments that this equation is only valid far from T_C). At least, when $T - \theta < 20°$, there are considerable deviations from the equation. It seems that there must be other mechanisms which were not taken into account in refs. 7 and 13 and which dominate in producing the value of $\tan\delta_3$. These mechanisms are probably connected with the particular features of the phase transition in KH_2PO_4.

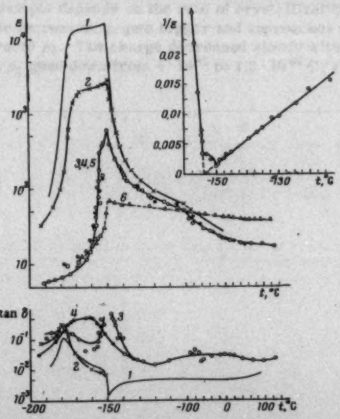

Fig. 1. Temperature variation of the dielectric constant ε_3 and of the loss factor tan δ_3 at various frequencies. 1) 10^3 Hz (thin line); 2) $2 \cdot 10^4$ Hz (×); 3) 9.3 GHz (○); 4) 3 GHz (●); 5) 6 GHz (□); 6) 9.4 GHz (△).

In the ferroelectric region in the immediate neighborhood of T_C there is a plateau in the $\varepsilon_3(T)$ curves at low frequencies where ε_3 varies little with temperature and is equal to ~10^4. It can be seen from Fig. 1 that the length of this plateau and the value of ε_3 decrease with frequency. At centimeter wavelengths below T_C, ε_3 has already begun to decrease rapidly with temperature so that below −152°C at microwave frequencies the $\varepsilon_3(T)$ curve can be described by the parameters $C_2 = 110 \pm 10$, $\theta_2 = -153$°C and $\varepsilon_{\infty_2} = 2.6$. At the place where $\varepsilon_3(\omega)$ falls sharply in the ferroelectric phase, $\tan\delta_3$ has a maximum which shifts towards higher temperatures as the frequency is increased. The nature of the variation in ε_3 and $\tan\delta_3$ shows that the dispersion of KH_2PO_4 is related to the dynamics of domain walls. If it is assumed that the dispersion is of the relaxation type, then the temperature variation of the appropriate activation energy needs to be investigated. In fact, the graph of relaxation frequency against inverse temperature is not a straight line, and this shows that the activation energy of the domain walls[14] changes as the Curie point is approached.

Near the phase transition, there is a sharp drop in $\varepsilon_3(T)$ which is very clear at microwave frequencies when the effect of the comparatively low-frequency domain processes is weaker. This jump is evidence in favor of the suggestion that the phase transition in KH_2PO_4 is of the first order type.[15]

---

[1] G. Busch, Helv. Phys. Acta, 11, 269 (1938).

[2] P. Bornarel. A. Fouskowa, P. Guyon, and J. Lajzerowicz, Proc. Intern. Meeting Ferroelectricity, 2, Prague (1966), p. 81.

[3] L. M. Belyaev, G. S. Belikova, G. F. Dobrzhanskii, G. B. Netesov, and Yu. V. Shaldin, Fiz. Tverd. Tela, 6, 2526 (1964) [Sov. Phys.–Solid State, 6, 2007 (1965)].

[4] E. Litov [illegible]nd E. Uehling, Phys. Rev., B1, 3713 (1970).

[5] L. A. Shuvalov, I. S. Zheludev, A. V. Mnatsakanyan, Ts. Zh. Ludupov and

I. Fiala, Izv. Akad. Nauk SSSR, Ser. Fiz., 31, 1919 (1967).

[6] N. M. Barkla and D. M. Finlayson, Phil. Mag., 44, 349 (1953).

[7] I. P. Kaminov and G. O. Harding, Phys. Rev., 129, 1562 (1963).

[8] I. P. Kaminov, Phys. Rev., 138, A1539 (1965).

[9] A. V. Shil'nikov, E. S. Popov, and S. L. Rapoport, Papers from the Seventh Conference on Ferroelectricity, Voronezh University, Voronezh (1970), p. 92.

[10] V. M. Petrov, Prib. Tekh. Eksp., 4, 118 (1960).

[11] L. P. Pereverzeva, B. Ya. Yazytskii, and Yu. M. Poplavko, Vest. Kievsk. Politekh. Inst. Ser. Radioelektron., 9, 35 (1972); Yu. M. Poplavko and B. Ya. Yazytskii, Prib. Tekh. Eksp., 4, 144 (1967).

[12] I. P. Kaminov and T. C. Damen, Phys. Rev. Lett., 20, 1105 (1968).

[13] K. K. Kobayashi, J. Phys. Soc. Japan, 24, 497 (1968).

[14] V. M. Petrov, Izv. Akad. Nauk SSSR, Ser. Fiz., 35, 1113 (1971).

[15] J. Kobayashi, Y. Uesu, and Y. Enomoto, Phys. Status Solidi, b45, 293 (1971).

Thermodielectric effect at the phase transition between a liquid and solid crystal

A. P. Kapustin, Z. Kh. Kuvatov and A. N. Trofimov
Crystallography Institute, Academy of Sciences of the USSR
Bashkir State University

(Submitted January 11, 1972; resubmitted May 26, 1972)
Kristallografiya, 18, 647-648 (May-June 1973)

During phase transition between an isotropic liquid and a solid dielectric, the solid phase usually grows with a net electric charge. This phenomenon, which has been called the thermodielectric effect (Costa Ribeiro effect) can be explained by an unequal affinity of the solid phase for charges of different signs.[1-3]

We first discussed a similar effect which occurs at phase transitions from liquid to solid crystals. In our experiments, a small drop (m = 0.05 g) of a nematic melt of n-azoxyanisol was crystallized on a grounded plate at a cooling rate of 5 deg/min. At the instant of crystallization an induced charge was observed on a measuring electrode 3 (Fig. 1) placed near the sample. This can be explained by charge separation occuring during nucleation and growth of the solid phase. Figure 2 shows a graph of the variation in the charge; t_a and t_b are the times corresponding to the beginning and end of the crystallization process. When the sample was placed in a Faraday cylinder, it was found that the charge was positive.

Even individual crystallites within the main sample acquire a charge. This fact, taken together with the long relaxation time, shows that the charge is distributed throughout the volume of the solid phase. The magnitude of the total charge Q can then be found as Q = 2q, where q is the maximum charge induced on the measuring electrode when it is brought right up to the free surface of the sample. The average value of the specific charge for the solid phase of n-azoxyanisol, measured directly after crystallization, was $\rho = 1.2 \cdot 10^{-8}$ C/g.

The experiments showed that the specific charge of the solid sample depends on the rate of crystallization. As the rate increases, ρ gets bigger and approaches some constant value ρ_0. The charge decreases slowly with time; after 24 h ρ_0 goes down from $4 \cdot 10^{-8}$ to $1.3 \cdot 10^{-8}$ C/g.

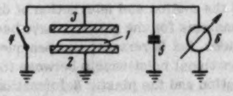

Fig. 1. Basic circuit for charge measurement. 1) Sample; 2, 3) electrodes; 4) switch; 5) shunt capacity; 6) electrometer.

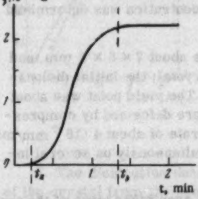

Fig. 2. Variation in charge during crystallization of a nematic melt.

This decrease is apparently due to absorption of ions from the air on the surface of the sample.

Preliminary studies show that a solid crystal obtained from a smectic liquid crystal also possesses an uncompensated electric charge.

The authors are grateful to A. M. Mel'nikova for considerable help in the literature selection.

---

[1] I. Costa Ribeiro, Anais. Acad. Brasil. Cienc., 22, 3 (1950).
[2] A. D. Tavares, Anais. Acad. Brasil. Cienc., 31, 3 (1959).
[3] A. M. Mel'nikova, Kristallografiya, 14, 548 (1969) [Sov. Phys.—Crystallogr., 14, 464 (1969)].

3

Vacancy concentration in relation to plastic deformation in NaCl crystals

N. A. Tyapunina and A. N. Tselebrovskii

M. V. Lomonosov Moscow State University

(Submitted May 22, 1972)
Kristallografiya, 18, 649-650 (May-June 1973)

Point defects arise in crystals during plastic deformation as a result of the motion and interaction of dislocations; several mechanisms for the process have been proposed for alkali halides, but it remains an open question as to what is the functional relationship between the point-defect concentration and the plastic deformation.[1-3] Only a few experiments have been done on this.[3-5]

We have examined the relation of plastic deformation to vacancy concentration for NaCl single crystals at room temperature; the vacancy concentration was determined by reference coloring.[6]

The NaCl specimens were about 7 × 5 × 2 mm, and were cleaved from a single crystal; the initial dislocation density was $3 \cdot 10^5$ cm^{-2}. The yield point was about 250 gf/mm^2. The crystals were deformed by compression along [001] at a constant rate of about $4 \cdot 10^{-2}$ mm/min. This caused slip to occur simultaneously on several intersecting planes.

The deformed and control specimens were of the same thickness and were exposed also to x rays (Mo, 45 kV, 14 mA). The irradiation time was chosen such that the F-center concentration was proportional to the concentration of anion vacancies existing in the crystal before irradiation (first coloring stage); this set of irradiation conditions allowed us to assume that the concentration change for the F centers is due to the change in concentration of the anion vacancies during plastic deformation. The optical absorption spectra of the crystals were recorded with SF-4A and SF-10 spectrophotometers. The concentration of F centers was determined from the absorption coefficient at the peak of the F band via Smakula's[7] equation.

The half-width of the F-center absorption line was unaltered by deformation and was 0.5 eV; the anion-vacancy concentration in the deformed specimens was higher than that in the control specimens, and the relative change Δn/n for the deformed specimens is shown in Fig. 1 as a function of the degree of plastic deformation ε. The vacancy concentration increases nonlinearly with ε, and there was no observable increase in vacancy concentration at ε < 2%. The nonlinear dependence agrees with results obtained by flotation under similar loading conditions for LiF single crystals.[3]

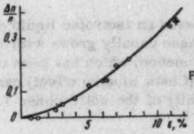

Fig. 1. Proportion of anion vacancies in relation to plastic deformation.

If one assumes a power function for the vacancy concentration as a function of the plastic deformation,[1] one gets the exponent p in this power relationship as 3/2, so the relationship in the above mode of loading is

$$\Delta n / n = A\varepsilon^{3/2}, \tag{1}$$

and the graph of this is indicated by the solid line in Fig. 1. The observed points fit closely to the curve of (1) to 8% deformation, but above this there is a tendency for Δn /n to be less than that given by (1). One expects the deviation from (1) at high ε on account of the dynamic equilibrium between the production and absorption of point defects by interaction with dislocations, as well as by formation of complexes. In the deformation of LiF single crystals by slip on one system of (011) planes,[3] there was a linear relationship between Δn /n and ε up to 20% deformation; it is stated[8] for copper that one can obtain values of p between 3/2 and 1 by varying the deformation conditions, so the above value for p is related to the conditions of plastic deformation rather than to the material and the structure.

---

[1] Van Bueren, Imperfections in Crystals, North-Holland, Amsterdam (1960).
[2] A. H. Cottrell, in: Vacancies and Other Point Defects in Metals and Alloys [Russian translation], Gos. Izd. Lit. Chem. Tsvet. Met., Moscow (1961), p. 7.
[3] G. A. Andreev and B. I. Smirnov, Fiz. Tverd. Tela, 10, 1693 (1968)[Sov. Phys.—Solid State, 10, 1336 (1968)].
[4] R. Davidge and P. Pratt, Phys. Status Solidi, 3, 665 (1963).
[5] C. Bauer and R. Gordon, Phys. Rev., 126, 73 (1962).
[6] M. A. Élango, in: Radiation Physics [in Russian], Izd. AN LatvSSR, Riga (1964), p. 35.
[7] D. L. Dexter, Phys. Rev., 101, 48 (1956).
[8] H. R. Peiffer, J. Appl. Phys., 34, 298 (1963).

Growth dislocation distribution along a copper crystal and dislocation density as a function of mean diameter

A. G. Basariya, B. K. Kapanadze, and V. V. Sanadze
Georgian Polytechnical Institute

(Submitted November 2, 1971; resubmitted November 22, 1972)
Kristallografiya, 18, 651-652 (May-June 1973)

There are several theoretical and experimental studies[1-9] on the origin of dislocations during crystal growth from melts, which relate to materials such as Si, Ge, and Al. There are two published papers[10,11] on growth dislocations in copper single crystals.

We grew almost perfect single crystals of copper by the Czochralski method at growth rates of 0.5 and 0.7 mm/min; the seeds were made from a single crystal with a sharp end, with [111] orientation. This was kept 3-4 cm above the melt for 20-25 min, after which it was lowered into the superheated melt and raised rapidly until the diameter of the contact between the seed and the melt was 0.3-0.8 mm; then the temperature of the melt was reduced to just above the crystallization point and was kept there for 1-1.5 h before the start of pulling. The growing crystal during pulling remained within the thermal screen, where the cooling was very slow. These screens consisted of a vessel made of tantalum and two vessels of graphite, one within the other. Appropriate choice of the thermal screening of the melt and growing crystal made it possible to control the cooling rate of the crystal surface without using special heaters, and this eliminated thermal stresses that facilitate dislocation multiplication.

The single crystals were examined by selective etching and by x-ray methods; the main results were as follows:

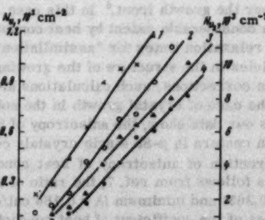

Fig. 1. Distribution of dislocation density along a crystal at various growth rates: 1, 2) v_1 = 0.5; 3, 4) v_2 = 7.5 mm/min; 1-4) are for crystal diameters of 10, 6, 8, and 6 mm, respectively.

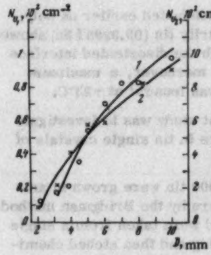

Fig. 2. Dislocation density as a function of diameter for copper crystals grown at speeds: 1) v_1 = 0.5 mm/min; 2) v_2 = 7.5 mm/min.

1. The dislocation density is proportional to the length of the crystal from the seed to the far end (Fig. 1), because the dislocations at the start are inherited from the seed, and subsequently they multiply on account of the thermal stresses set up at the crystal–melt interface.

2. The dislocation density increases monotonically with the crystal diameter no matter what the growth rate (Fig. 2); this may occur because the heat is lost more rapidly from the surface as the diameter increases, relative to the axial part, which sets up a radial temperature gradient that facilitates dislocation multiplication. The dislocation density determined by x-ray topography exceeded by 3.5% the number of dislocations revealed by selective etching.

---

[1] F. C. Frank, Deformation and Flow of Solids, Berlin (1956), p. 73.

[2] S. Howe and G. Elbaum, Phil. Mag., 6, 1227 (1961).

[3] W. C. Dash, J. Appl. Phys., 30, 459 (1959).

[4] E. Billig, Proc. Roy. Soc., A235, 37 (1956).

[5] P. Penning, Philips Res. Repts., 13, 79 (1958).

[6] S. V. Tsivinskii, Fiz. Met. Metalloved., 25, 1013 (1968).

[7] E. Yu. Kokrish and N. N. Sheftal', in: Growth of Crystals, Consultants Bureau, New York (1962).

[8] V. V. Sanadze, B. K. Kapanadze, and A. G. Basariya, Izv. VUZ, Fizika, 7, 127 (1970).

[9] F. D. Rosi, RCA Rev., 19, 349 (1958).

[10] W. Uelhoff, Intern. Simpos. Reinststoffe in Wissenshaft unde Techniki., Dresden, 1965, 3, Tegunsber, Berlin (1967), p. 261.

[11] M. C. Wittels, F. A. Sherrill, and W. Young, Appl. Phys. Lett., 1, 1, 22 (1962).

Anisotropy of the growth rate of centers of the *α* modification in single crystals of high purity tin

V. B. Brik, L. N. Larikov, and V. M. Fal'chenko

Institute of Metal Physics, Academy of Sciences of the Ukrainian SSR

(Submitted January 14, 1972; resubmitted May 30, 1972)
Kristallografiya, 18, 653-654 (May-June 1973)

The results of investigations conducted earlier on polycrystalline samples of high-purity tin (99.9995% Sn) showed that α-Sn centers grow through the disoriented interface by a dislocation mechanism; moreover, a maximum growth rate equal to 3 mm/h was found[1,2] at −23°C.

The purpose of the present study was to investigate the growth rate of α-Sn centers in tin single crystals of the same degree of purity.

Single crystals of OVCh-000 tin were grown in ampoules in a protective atmosphere by the Bridgman method. The samples to be investigated were taken from a single crystal by electric-spark cutting and then etched chemically. The crystallographic orientation of the samples was determined by the Laue back-scattering method. To produce α-Sn centers, the samples were kept beforehand at −50°C in contact with gray tin powder. The growth rate of the α-Sn centers was determined in various crystallographic planes (see Table 1) at −21°C by the method described in ref. 1. As follows from Table 1, the growth rate of α-Sn centers is markedly anisotropic in certain crystallographic directions. In this case, the gray tin centers become elliptical. The degree of anisotropy was defined as the ratio a/b, where a and b are the major and minor axes of the ellipsoidal α-Sn center. For all centers in a given plane, the anisotropy of the growth rate has the same direction, whereas the growth rate is constant. A cyclic temperature change near the point of phase equilibrium T_0 does not affect the direction of anisotropy of the growth rate of α-Sn centers. As the number of cycles is increased, the existing gray tin centers grow further. Owing to the large volume effect in the $\beta \rightarrow \alpha$ transformation, which upsets the crystallographic correspondence at the interface, this fact evidently cannot be explained by the orienting effect of the matrix of original β-Sn phase on the growth of the α-Sn crystals, which, for instance, was investigated in refs. 3-5 in a study of polymorphic transformations in single-crystal platelets of organic compounds. The x-ray photographs taken in the present study show that a slightly textured polycrystalline structure is present in regions where the $\beta \rightarrow \alpha$ transformation has occurred.

The maximum anisotropy is noted in planes having two-fold symmetry axes: (100), (010), and, on the average, amounts to 2.25 (see Table 1). The direction of the maximum growth rate (3 mm/h) coincides with the crystallographic direction [100] or [010], whereas the minimum coincides with the [001] direction. For the rest of the crystallographic planes investigated, the degree of anisotropy of growth has smaller values, from 1.05 to 1.78. For planes of the [001] zone, the anisotropy of the growth rate decreases at first with increasing angle with the (100) or (010) plane, reaching a maximum value of 1.25 in the (110) plane, and then increases again to the earlier value at 90°.

TABLE 1

Crystallographic indices of samples plane (hk*l*)	Average degree of observed anisotropy of growth of α Sn, *a*/b	Direction of anisotropy of growth [uvw]		Growth rate in direction of major axis of ellipse V, mm/h
		a	*b*	
100	2.25±0,05	010	001	3,0±0,05
001	1,0±0,05	—	—	3.0±0.05
110	1.25±0.05	$1\bar{1}0$	001	2.8±0.05
011	1.05±0.05	—	—	—
112	1.4±0.1	$1\bar{1}0$	—	1.8±0.05
301	1.45±0.05	010	103	2.8±0.05
311	1,70±0,05	130	—	1,5±0,05

For planes of the [100] or [010] zones, the anisotropy of the growth rate decreases continuously with increasing angle with the (010) or (100) planes, respectively; in the (001) plane, which has a four-fold symmetry axis, there is no anisotropy: The α-Sn centers in this plane are circular. The practically identical maximum growth rates of α-Sn centers ($V \simeq 3$ mm/h in both single-crystal and polycrystalline β-Sn matrices) show, in fact, that the new phase grows in the single crystal through a disoriented interface, similar in structure to the region between grains. This is supported by the fact that the growth rate of α-Sn centers on passing through the $\beta \rightarrow \alpha$-Sn interface does not vary from one grain to another.[1] Under these conditions, α-Sn crystals may grow by a dislocation mechanism.[1] In the case of layered growth of crystals from the melt on dislocations, the normal growth rate of a spiral mound is determined by the temperature distribution near the growth front.[6] In this case, growth is limited to a considerable extent by heat conduction processes and relaxation times for "assimilation" of individual particles in the structure of the growing crystal. With certain corrections, such calculations also may be applied to the case of crystal growth in the solid phase. Actually, as our data show, the anisotropy of the growth rate of α-Sn centers in β-Sn single crystals coincides with the direction of anisotropy of heat conductivity.[7] However, as follows from ref. 7, the ratio of the maximum ($\lambda = 0.265$) and minimum ($\lambda = 0.160$ cal/cm · sec · deg C) values of the coefficient of heat conductivity, equal to 1.60, is slightly less than the degree of anisotropy of growth of α-Sn centers in the corresponding directions, equal to 2.25. Since the growth of α-Sn centers is determined to a considerable extent[1,2] by the value of boundary self-diffusion D_{bd}, it is of interest to compare our results with data on the anisotropy of the coefficient of self-diffusion in single-crystal tin.[8] The degree of anisotropy of the coefficient of volume self-diffusion at 177-220°C is equal to about 2.5, which is close to the experimentally observed anisotropy of the growth rate. D_a/D_c increases slightly on cooling; however, this increase is far less in the case of boundary self-diffusion than in that of volume self-diffusion.[9]

---

[1] A. I. Bykhovskii, L. N. Larikov, and V. M. Fal'chenko, in: Growth of

Metallic Crystals and Imperfections in Them [in Russian], Naukova Dumka, Kiev (1966), p. 68.

[2] A. I. Bykhovskii, L. N. Larikov, and V. M. Fal'chenko, Kristallografiya, 12, 528 (1967) [Sov. Phys.—Crystallogr., 12, 460 (1967)].

[3] A. I. Kitaigorodskii, Yu. V. Mnyukh, and Yu. G. Asadov, Dokl. Akad. Nauk SSSR, 148, 1065 (1963) [Sov. Phys.—Dokl., 8, 127 (1963)].

[4] Yu. V. Mnyukh, N. I. Musaev, and A. I. Kitaigorodskii, Dokl. Akad. Nauk SSSR, 174, 345 (1967) [Sov. Phys.—Dokl., 12, 409 (1967)].

[5] N. I. Musaev and Yu. V. Mnyukh, Kristallografiya, 15, 555 (1970) [Sov. Phys.—Crystallogr., 15, 468 (1970)].

[6] A. A. Chernov, Usp. Fiz. Nauk, 73, 277 (1961) [Sov. Phys.—Usp., 4, 116 (1961)].

[7] A. Misnar, Heat Conductivity of Solids, Liquids, and Gases and Their Compositions [in Russian], Mir, Moscow (1968).

[8] J. D. Meakin and E. Klokholm, Trans. Met. Soc. AIME, 218, 463 (1960).

[9] L. N. Larikov, V. M. Fal'chenko, and L. F. Chernaya, in: Metal Physics, No. 31 [in Russian], Naukova Dumka, Kiev (1970), p. 75.

Mechanical stability of small-angle growth boundaries in NaCl crystals

E. L. Pishchik and E. P. Kostyukova
State Machine Science Research Institute

(Submitted July 4, 1972)
Kristallografiya, 18, 655-657 (May-June 1973)

Small-angle boundaries are among the most common defects in crystals; they divide a crystal into blocks differing in orientation, and they are sites of lattice distortion, so they substantially influence the mechanical properties of crystals.[1–5]

We have examined the behavior of the small-angle boundaries in the deformation of sodium chloride crystals, both those produced by growth and those resulting from deformation and annealing.

The sodium chloride crystals 20 × 10 × 0.2 mm were cut on cleavage planes. Polygonal small-angle boundaries were produced by deforming some of the crystals in sign-varying bending and straightening on a cylinder with a radius of curvature of 28 mm, which was followed by annealing at 700°C for 7 h. The small-angle boundaries in the initial state (after polygonization or cleaving and subsequent annealing) were compared with those after bending around the [010] axis on the cylinder. X-ray topography[6] was used to reveal the boundaries.

Figure 1 shows the 200 diffraction spots from a sodium chloride crystal annealed after sign-varying deformation (Fig. 1a), while Fig. 1b shows the same for one bent on [100], and Fig. 1c does the same for [010]. Figure 1a shows clearly the small-angle boundaries, which intersect the surface along [010]. The 020 spot does not reveal these boundaries, so the rotation axis for the blocks is [010], which lies in the planes of the boundaries. Then these boundaries are simple inclined ones; their behavior on deformation is dependent on the direction of the applied load, i.e., on the disposition of the slip elements relative to the crystallographic elements for the boundaries (plane of boundary and axis of block rotation. Bending of a polygonized crystal on [100] preserves the boundaries, as this axis is perpendicular to the rotation axis of the polygonal blocks. Bending around [010] causes the images of the boundaries in the spots to vanish almost completely (Fig. 1c), and one gets a picture analogous to that from deforming a crystal lacking a previous system of small-angle boundaries. The mechanical stability of the boundaries is thus dependent on the load direction. The small-angle polygonal boundaries are eliminated if the deformation involves dislocations of the type that produced the boundaries. A similar effect has been reported[7] during high-temperature creep in sodium chloride crystals.

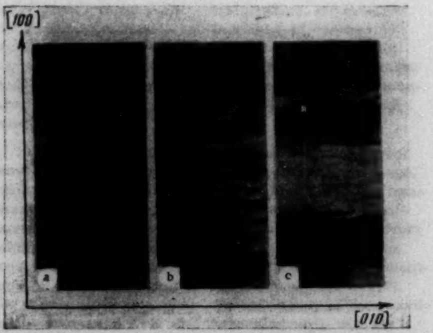

Fig. 1. Type 200 diffraction spots from sodium chloride: a) Polygonized crystal; b) crystal polygonized and bent around [100]; c) polygonized and bent around [010].

A different picture is observed on deforming a crystal with growth boundaries; Fig. 2 shows the 200 diffraction spots from a single crystal in the initial state (Fig. 2a) and after bending around [010] (Fig. 2b). The arrow in Fig. 2a indicates a growth boundary intersecting a (001) surface along [010]; the axis of block rotation is also [010], because there is no image of this boundary in the spot from the (010) plane. This growth boundary is therefore a simple inclined boundary. The images in the spots remain as sharp as those for the undeformed crystal on bending on directions perpendicular or parallel to the block rotation axis. Growth boundaries thus differ from polygonal ones of the same type in being mechanically stable (they persist on deformation). Also, asterism occurs only on one side of the boundaries. Figure 2b shows that the radial extent of the diffraction peak above a small-angle boundary is roughly as for the undeformed crystal, so these small-angle growth boundaries present effective barriers to deformation.

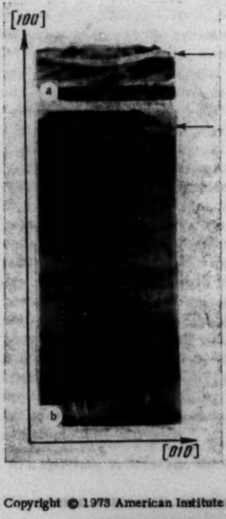

Fig. 2. Type 200 diffraction spots from sodium chloride: a) initial crystal; b) bent around [010].

[1] S. Amelinckx, in: Dislocations and the Mechanical Properties of Crystals, I. C. Fisher (ed.), Wiley, New York (1957).

[2] A. A. Predvoditelev, in: Dislocation Dynamics [in Russian], Fiz.-Tekh. Inst. Niz. Temp. AN UkrSSR, Khar'kov (1968).

[3] J. J. Gilman, Micromechanics of Flow in Solids, McGraw-Hill (1969).

[4] S. Weissmann, M. Hirabayashi, and H. Fujita, J. Appl. Phys., 32, 1156 (1961).

[5] V. M. Finkel', Z. A. Maslovskaya, and V. V. Vakhonin, Fiz. Tverd. Tela, 9, 1213 (1967) [Sov. Phys.–Solid State, 9, 945 (1967)].

[6] E. P. Kostyukova, Kristallografiya, 15, 769 (1970) [Sov. Phys.–Crystallogr., 15, 660 (1971)].

[7] Ya. E. Geguzin and V. P. Matsokin, Fiz. Tverd. Tela, 8, 2558 (1966) [Sov. Phys.–Solid State, 8, 2048 (1967)].

Internal friction and strength of germanium whiskers

V. S. Postnikov, S. A. Ammer, and A. I. Drozhzhin
Voronezh Polytechnical Institute

(Submitted May 20, 1972)
Kristallografiya, 18, 658-659, (May-June 1973)

A study has been made of the effects of transverse size on the strength and internal friction Q^{-1} for germanium whiskers. The crystals were prepared by chemical transport reaction.[1] We selected p-type crystals with ⟨111⟩ as the growth axis, the diameters being 2-50 μ and the working length about 1.5 mm. The surfaces were either smooth or defective. The measurements of Q^{-1} and strength were made at room temperature and at about 760°C at a pressure of about $5 \cdot 10^{-5}$ mm Hg by the method of ref. 2.

Figure 1 shows that there was a considerable spread in Q^{-1} and strength for the initial crystals, as is characteristic of whiskers.

In spite of the spread, we found that at room temperature and at 760°C there was a decrease in the strength with increasing thickness; high strength occurred only in thin whiskers with perfect surfaces. The highest strength at about 760°C was about 50 kgf/mm^2 = G/100 for crystals of thickness 3 μ and at 20°C was about 210 kgs/mm^2 = G/25 for thickness of 2.5 μ. The strength of large whiskers (d > 40 μ) was close to that of ordinary single crystals. Surface defects (growth steps, cracks, etc.) usually caused the crystals to break at the defect point, and the strength was invariably low.

The Q^{-1} at room temperature were independent of the diameter and were quite small; at 760°C, Q^{-1} increased with the diameter; and crystals more than 40 μ in diameter had internal friction of the same order as large single crystals. The minimum Q^{-1} occurred in crystals of diameter less than 10 μ, which usually showed high strength and a sharp yield point in mechanical tests.

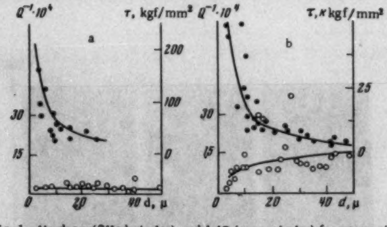

Fig. 1. Hardness (filled circles) and 1/Q (open circles) for germanium whiskers at: a) Room temperature; b) 760°C.

If one assumes that Q^{-1} for a whisker at about 760°C is of dislocation character, then the dependence of d may be due only to the dislocation density; the more perfect the crystal, other things being equal, the lower the Q^{-1}. Some whiskers with d < 10 μ, although of small Q^{-1}, had low strength; this discrepancy is due to the statistical nature of the strength in whiskers,[3] which allows random defects in crystals with perfect lattices. These defects make little contribution to the internal friction, but they can reduce the strength considerably.

We found that whiskers with defective surfaces were always weak,[4-6] but the damping was not always high.

This means that defects at the surface or in the bulk of the crystal differ in their effect on the strength and energy dissipation; the strength is most affected by surface defects, which in platy crystals begin to generate dislocations at lower stresses than do defects within the bulk.[7] Surface defects in brittle crystals are efficient stress concentrators, which lead to crack nucleation and failure.[8]

The effects of dislocations on internal friction were examined by deforming thin crystals (d < 10 μ) at 760°C to the stage of ready slip; Q^{-1} at room temperature was little affected by this, which indicates low mobility for dislocations at this temperature. On the other hand, Q^{-1} at 760°C was raised by a factor of 20-50. This marked increase in the damping was due to accumulation of mobile dislocations. Subsequent annealing at 850°C for 1 h greatly reduced Q^{-1}, and the shape of the whisker was entirely restored. The annealing effect is due to escape of dislocations from the surface in response to the force distributions set up by the dislocations themselves.[5]

---

[1] A. V. Sandulova, P. S. Bovoyavlenskii, and M. I. Dronyuk, Fiz. Tverd. Tela, 5, 2580 (1963) [Sov. Phys.—Solid State, 5, 1883 (1964)].

[2] V. S. Postnikov, A. T. Kosilov, V. K. Belonogov, and S. A. Ammer, Izv. VUZ, Chern. Met., 9, 124 (1967).

[3] V. N. Geminov and I. M. Kop'ev, Trudy Inst. Met. AN SSSR, 10, 202 (1962).

[4] I. A. Oding and I. M. Kop'ev, Trudy Inst. Met. AN SSSR, 8, 252 (1961).

[5] S. S. Ammer, A. T. Kosilov, and V. S. Postnikov, Fiz. Tverd. Tela, 7, 2242 (1965) [Sov. Phys.—Solid State, 7, 1808 (1966)].

[6] S. Z. Bokshtein, S. T. Kishkin, M. P. Nazarova, and I. L. Svetlov, Fiz. Tverd. Tela, 9, 1987 (1967) [Sov. Phys.—Solid State, 9, 1488 (1968)].

[7] M. A. Adams, Acta Metallurg., 6, 327 (1958).

[8] D. M. Marsh, Fracture of Solids, Wiley, N. Y., (1963), p. 119.

[9] L. V. Tikhonov, in: Metal Failure Mechanisms [in Russian], Naukova Dumka, Kiev (1966), p. 83.

Electron diffraction investigation of In_2S_3 films obtained by vacuum deposition

R. B. Shafizade, É. G. Éfendiev, and F. I. Aliev

Institute of Physics, Academy of Sciences of the Azerbaidzhan SSR

(Submitted May 10, 1972)

Kristallografiya, 18, 660-661 (May-June 1973)

Among the phases of the system In−S, the most thorough structural research has been carried out on In_2S_3, though even for this phase some of the literature data are contradictory. The first x-ray study of In_2S_3 was made by Klemn and Vogel.[1] The crystal structure of In_2S_3 was investigated by Hahn and Klingler.[2] They found that the compound crystallizes in two different modifications. The low-temperature modification α In_2S_3 has a cubic structure with $a = 5.36$ Å. However, the diffraction pattern shows three weak reflections, which cannot be indexed on the basis of the assumed cell. Therefore Hahn and Klingler[2] consider that this phase has a superlattice structure with double the parameter, $2a_{\text{cub}} = 10.72$ Å. The formation of a superlattice was explained by them[2] by supposing that the positions of the S atoms undergo changes. They also claimed the existence of a low-temperature modification β In_2S_3, with the spinel structure with $a = 10.72$ Å. Despite the coincidence between the lattice parameters of the superlattice and the phase β In_2S_3, the different intensities of some of the lines led Hahn and Klingler[2] to the conclusion that the phases have different structures.

Roymans[3] describes β In_2S_3 on the basis of a tetragonal cell with $a = 7.62$, $c = 32.32$ Å, with symmetry $I4_122$; King[4] gives the same parameters but assumes the space group $I4_1/amd$. By thermal analysis, others[5,6] have found a high-temperature phase transition in β In_2S_3 at 750°C.

This article describes an electron diffraction investigation of the conditions for formation of In_2S_3 films with amorphous and crystalline structures. The In_2S_3 films were obtained by evaporating synthetic In_2S_3 in a vacuum of 10^{-5} mm onto freshly cleaved rocksalt crystals. The substrates were at various temperatures from room temperature to 400°C.

The films deposited on substrates at room temperature were amorphous. An electron diffraction pattern from such a film is shown in Fig. 1a. We see three haloes corresponding to interplanar distances of 2.98, 1.85, and 1.17 Å. Annealing of these films for 10-15 min at about 200°C causes their crystallization; the corresponding electron diffraction pattern is shown in Fig. 1b. It can be indexed on the basis of a tetragonal unit cell with the parameters $a = 7.61$, $c = 32.24$ Å, in agreement with Roymans.[3]

When In_2S_3 is deposited on heated substrates, mosaic crystals are formed. At substrate temperatures of ~ 100°C, together with diffuse lines from amorphous In_2S_3, the electron diffraction patterns display point reflections (spots). At 200°C these spots become sharper, but the amorphous haloes remain (Fig. 2a). Further rise of substrate temperature to 400°C leads to complete disappearance of the haloes. Such an electron diffraction pattern is shown in Fig. 2b. It can also be indexed on the basis of the above-mentioned tetragonal cell. The crystals lie with the (001) faces parallel to a cube face of the NaCl (strong spots). Together with reflections of type hk0, the electron diffraction pattern displays spots due to the twinning effect and double diffraction.[7]

Thus between substrate temperatures of 100 and 400°C we observe a transition from an amorphous to a single-crystal structure, the polycrystalline state being omitted.

Specimens obtained by crystallization of amorphous films give two types of electron diffraction pattern according to the heat treatment conditions. On diffraction patterns of the first type, for values of $\sin \theta/\lambda$ between 0.228 and 0.264 $Å^{-1}$ we observe a relatively strong background. If we ignore this fact, all the lines can be indexed on the basis of a cubic unit cell with $a = 10.72$ Å (ref. 2). The diffraction lines on the patterns of the second type are not continuous but are formed from many discrete spots. This shows that these films have a more perfect structure (Fig. 1b). On the diffraction patterns of the second type, the total number of reflections is greater. The extra lines, which are mainly formed in the region of intense background, compel us to index the pattern as a whole on the basis of the above-mentioned tetragonal unit cell.

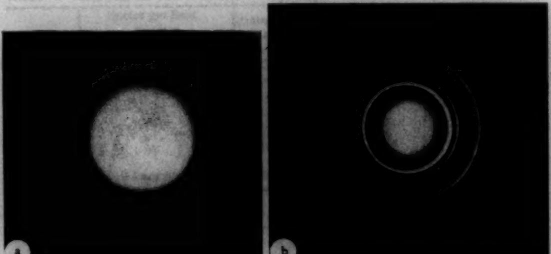

Fig. 1. Electron diffraction patterns of amorphous phase of In_2S_3 (a) and polycrystalline In_2S_3 (b).

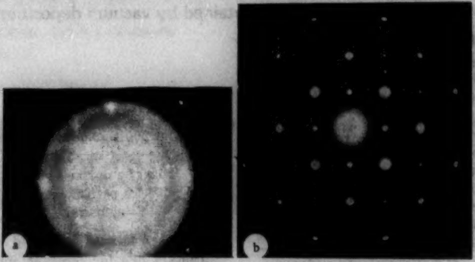

Fig. 2. Selected area electron diffraction pattern of In_2S_3 in mixture with amorphous phase (a) and electron diffraction pattern of mosaic crystal of In_2S_3 (b).

Thus our results show that In_2S_3 has a tetragonal structure. If we work with In_2S_3 specimens in which for some reason the crystallization process has not gone to completion, i.e., where not all the diffraction lines are manifested, then the diffraction patterns from these specimens may be mistakenly indexed on the basis of a cubic cell. This apparently explains the discrepancies in the literature data (refs. 2 and 3).

The authors thank M. I. Zargarova, who kindly lent the test specimens, and also Prof. Z. G. Pinsker for discussing the results.

---

[1] W. Klemm and H. Vogel, Z. Anorgan. und Allgem. Chem., 219, 45 (1934).

[2] H. Hahn and W. Klingler, Z. Anorgan. und Allgem. Chem., 260, 97 (1949).

[3] C. Roymans, J. Inorg. and Nucl. Chem., 11, 78 (1959).

[4] C. King, Acta Crystallogr., 15, 512 (1962).

[5] J. M. Gulles, H. Hatwell, G. Offerfeld, and J. Van Cakenberghe, Phys. Status Solidi, 2, K-73 (1962).

[6] H. Hatwell, G. Offerfeld, G. Hernickx, and J. Van Cakenberghe, Compt. Rend., 252, 3586 (1961).

[7] P. B. Hirsch et al., Electron Microscopy of Thin Crystals, Butterworths, Wash. (1965).

Preparation of mixed single crystals of (Cr, Te)

É. A. Zavadskii and B. Ya. Sinel'nikov

Donets Physicotechnical Institute,
Academy of Sciences of the Ukrainian SSR

(Submitted March 16, 1972; resubmitted April 18, 1972)
Kristallografiya, 18, 662-663 (May-June 1973)

Investigations of the physical properties of the system chromium–tellurium have remained urgent for some time. The attention of investigators has been attracted by the electrical and magnetic properties[1,2] and the crystal structure,[3,4] and also by the effect of pressure and magnetic field on the magnetic properties.[5-7] Unfortunately, most measurements have been made on imperfect polycrystalline specimens.

In this article we describe methods of preparing various single crystals of the system with between 50 and 60 at.% of Te, and we give the results of an analysis of these crystals.

Our starting materials for the preparation of the single crystals were electrolytic chromium (99.9%) and tellurium (99.98%). Chromium and tellurium powders in the necessary proportions were sintered in an evacuated quartz capsule at temperatures from 1000 to 1100°C for 36 h. After crushing, the charge was subjected to a second sintering. The charge thus obtained was used to grow single crystals by the Stockbarger method. The capsule was prepared from a quartz tube, one end of which was finished in the shape of a cone. After crystallization, the crystals were slowly cooled to room temperature. Table 1 lists the optimum characteristics of the crystal growth process.

X-ray investigations reveal that all compounds in the system in the investigated range of concentrations can be represented by a unified formula $Cr_{1-x}\square_xTe$, where $\square$ denotes vacancies in a-type points of the CrTe lattice. From the results of structural investigations, listed in Table 2, it also follows that only in CrTe is a hexagonal lattice of type $B8_1$ realized. All the other crystals have a lattice of type C6. For convenience of comparison, the unit cell parameters a and c for the monoclinic crystals are halved.

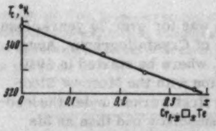

Fig. 1. Magnetic transition temperatures of single crystals from the system chromium–tellurium vs chemical composition.

We have grown single crystals not only by the Stockbarger method, but also by the Bridgman and Obreimov–Shubnikov methods. However, the most perfect crystals were those obtained by the Stockbarger method. This is revealed to some extent by the results of measurements of the dislocation densities in specimens obtained by various methods. Thus the dislocation density of crystals grown by the Bridgman method was 10^5 cm^{-2}, whereas the Stockbarger method gives only half this density.

All the crystals were ferromagnetic. The magnetic transition temperature falls smoothly as the Te concentration rises (see Fig. 1). Specimens of all compositions displayed marked anisotropy of the electric and magnetic properties. It is also noteworthy that all the tested crystals have a marked anomaly in the temperature dependence of the unit-cell volume near the Curie point. This feature of the thermal expansion properties is apparently due to the marked dependence of the exchange interactions in the crystals on the interatomic distance, and therefore crystals from the chromium–tellurium system can be used to study the origins and variations in the exchange interactions.

TABLE 1. Conditions for Growth of Mixed Single Crystals of CrTe

Crystal	Heater gradient, deg/cm		Heater temperature ahead of growth zone, deg C	Velocity of heater, mm/h	Cone angle of capsule in growth zone, deg
	axial	radial			
CrTe	15	> 0.5	1350 ± 1	15.00	70
Cr_7Te_8	15	> 0.5	1300 ± 1	14.06	70
Cr_5Te_6	15	> 0.5	1280 ± 1	10.00	60
Cr_3Te_4	12	> 0.5	1250 ± 1	7.03	50
Cr_2Te_3	10	> 0.5	1200 ± 1	5.00	40

TABLE 2. Unit-Cell Parameters of Mixed Single Crystals of CrTe

Crystal	a, Å	b, Å	c, Å	β	V, Å^3
CrTe	4.0150	—	6.267	—	87.49
Cr_7Te_8	3.4524	3.9797	6.231	90°41′00″	85.61
Cr_5Te_6	3.4502	3.9663	6.210	90°49′00″	84.92
Cr_3Te_4	3.4450	3.9397	6.179	91°11′00″	83.85
Cr_2Te_3	3.4388	3.9048	6.128	91°37′00″	82.17

---

[1] I. G. Fakidov, N. P. Grazhdankina, and A. K. Kikoin, Dokl. Akad. Nauk SSSR, 68, 491 (1949).

[2] A. F. Anderson, Acta Chem. Scand., 17, 1335 (1963).

[3] H. Haraldsen and A. Neuber, Z. Anorgan. Chem., 234, 353 (1937).

[4] C. Guillaud and S. Barbezat, Compt. Rend., 222, 386 (1946).

[5] N. P. Grazhdankina, Izv. Akad. Nauk SSSR, Ser. Fiz., 30, 990 (1966).

[6] A. A. Galkin (O. O. Galkin), É. A. Zavadskii (E. A. Zavads'kii), and B. Ya. Sinel'nikov, Dopovidi Akad. Nauk UkrRSR, 9, 837 (1971) [in Ukrainian].

[7] A. A. Galkin, É. A. Zavadskii, and B. Ya. Sinel'nikov, Fiz. Tverd. Tela, 14, 157 (1972) [Sov. Phys.–Solid State, 14, 125 (1972)].

Arkadii Sergeevich Shein (1912-1972)

Kristallografiya, 18, 664 (May-June 1973)

On November 18, 1972, just a month before his sixtieth birthday, Doctor of Mathematical Physics Arkadii Sergeevich Shein died. He was an important Soviet specialist in applied crystallography, and a tireless researcher and innovator.

The career of A. S. Shein was for over 30 years closely connected with the Institute of Crystallography, Academy of Sciences of the USSR, where he started in 1940 after terminating his association with the Moscow Electrotechnical Institute. Having first worked under the leadership of Academician A. V. Shubnikov and then as his constant colleague, the basis of the career of A. S. Shein lay in a love for the creation of the new: new things needed for practical application. Innovation was always present in the creativity of A. S. Shein; he is responsible for many inventions, most of which he himself accomplished. All of these were based on A. S. Shein's indepth knowledge of radiotechnology and the physical properties of crystals (particularly ferroelectrics).

The principal area of his research was the creation and application of new piezoelectric converters. He did very much to prepare and apply large Seignette salt crystals, several important new properties of which he established. Thus, already during the first years of World War II, A. S. Shein became director-chief engineer of an experimental factory for piezoelectric devices, and actually carried out his ideas for making highly sensitive piezoelements for communications and defense technology.

Since 1949, A. S. Shein was a co-worker of the All-Union Scientific Research Institute for the Fish Industry and Oceanography (VNIRO), where he founded the Laboratory of Hydroacoustic Fishing Devices. He remained director of this laboratory until the end of his life. During the 1950's, A. S. Shein founded the Scientific-Experimental Hydroacoustic Base of VNIRO. The laboratory and base represent the only contemporary hydroacoustic complex.

A. S. Shein always solved the real problems of the fish industry on the basis of his original development of hydroacoustic converters. The results of these developments in many cases departed far from the framework of the needs of the fish industry, and were in themselves important stages in the development of domestic hydroacoustic science and technology.

Twice during the 1950-1960's A. S. Shein reported to the Presidium of the Academy of Sciences of the USSR on the results of his development of new converters. The high appraisal of these works resulted in A. S. Shein's being awarded, in 1961, the honorary degree of Doctor of Mathematical Physics.

A tireless innovator, energetic, and not knowing rest from study, A. S. Shein did much for the national economy, and to a considerable degree facilitated the development of hydroacoustics and applied crystallography. His services were acknowledged by six government awards.

He will long be remembered in the hearts of those who knew him and worked with him.

Kronecker product for the representations of the crystallographic point groups I

B. A. Men', A. N. Men', and V. I. Cherepanov
Metallurgical Institute of the Ural Scientific Center
Ural State University
(Submitted February 7, 1972; resubmitted July 6, 1972)
Kristallografiya, 18, 669-674 (July-August 1973)

The identification of repeated representations is considered for the decomposition of the Kronecker product of the representations. A procedure is given whereby the functions of the required symmetry may be constructed for any number of spaces, where the factors are trigonal or tetragonal. As an example, the sixth-order invariant is constructured for functions transformed by the representation Γ_3 of the group D_3.

In this article we consider the question of the identification and the genealogy of repeated representations in the Kronecker product decomposition

$$\Gamma = \Gamma_i \times \Gamma_2 \times \ldots \times \Gamma_r \tag{1}$$

of the irreducible representations Γ_i of the crystallographic point group G for the irreducible representation Γ_j of this group

$$\Gamma = \Sigma a_j \Gamma_j, \tag{2}$$

and we also consider the decomposition of the tensor space attached to the products of basis functions for the spaces of factors.

When there are two factors Γ_i for the simply reducible groups,[1] this problem may be solved through the Clebsch–Gordan coefficients. When there are several factors for the simply reducible groups, it may be solved by step-by-step combination of the factors. Such methods will not work for the remaining groups.

In ref. 2 the question of the identification and genealogy of the repeated representations in the decomposition (2) was considered; introduction of intermediate subgroups or sequential descent was the method used. For simply reducible groups, the combination of the factors is one form of descent. When the groups are not simply reducible, the method of descent offers new possibilities. In ref. 2 there is a proof of the feasibility of solving this problem for all crystallographic point groups. Here we pose the problem of finding the most economical descents, i.e., those with the least number of intermediate subgroups. If, when the factors are combined in simply reducible groups, the number of intermediate subgroups (and thus the number of additional quantum numbers or intermediate moments) is equal to the number of factors minus 2, and if the actual decomposition of the tensor space is difficult to carry out (generally speaking it cannot be done for groups which are not simply reducible), then the method of descent gives at most one or two additional numbers corresponding to the one or two intermediate subgroups.

We do not give only the mathematical theory of the

TABLE 1

S_3	e	(12) (13) (23)	(123) (132)	A_3	e	(123)	(132)
Γ_1	1	1	1	Γ_1	1	1	1
Γ_2	1	−1	1	Δ	1	ω	ω^2
Γ_3	2	0	−1	∇	1	ω^2	ω

TABLE 2

Decomposition of r	Initial selection	α_1	α_2	α_3	$\delta = \alpha_1 + \alpha_2 - \alpha_3$ (mod 3)	Initial and conjugate selections	Form of the functions ψ_1 and ψ_2	Form of the functions* $(\alpha_1\alpha_2\alpha_3)$ $\psi = \prod_{i=1}^{k} \psi_i^{(1)} \prod_{j=1}^{l} \psi_j^{(2)}$
1	2		3		4	5	6	7
3=3	ΔΔΔ	3	0	0	0	$\begin{pmatrix}\Delta\Delta\Delta\\ \nabla\nabla\nabla\end{pmatrix}$	$\psi_1 = \psi\psi_{11}^{(3)}\psi_{21}^{(3)}\psi_{31}^{(3)}$ $\psi_2 = \psi\psi_{12}^{(3)}\psi_{22}^{(3)}\psi_{32}^{(3)}$	$\psi_{\Gamma_1}(\Delta\Delta\Delta) = \frac{1}{\sqrt{2}}[(-1)^l\psi_1 + \psi_2]$ $\psi_{\Gamma_2}(\Delta\Delta\Delta) = \frac{1}{\sqrt{2}}[(-1)^{l+1}\psi_1 + \psi_2]$
3=2+1	ΔΔ∇	2	1	0	1	$\begin{pmatrix}\Delta\Delta\nabla\\ \nabla\nabla\Delta\end{pmatrix}$	$\psi_1 = \psi\psi_{11}^{(3)}\psi_{21}^{(3)}\psi_{32}^{(3)}$ $\psi_2 = \psi\psi_{12}^{(3)}\psi_{22}^{(3)}\psi_{31}^{(3)}$	$\psi_{\Gamma_3}(\Delta\Delta\nabla) = \begin{cases}\psi_1\\ (-1)^l\psi_2\end{cases}$
3=1+2	Δ∇∇	1	2	0	2	$\begin{pmatrix}\Delta\nabla\nabla\\ \nabla\Delta\Delta\end{pmatrix}$	$\psi_1 = \psi\psi_{11}^{(3)}\psi_{22}^{(3)}\psi_{32}^{(3)}$ $\psi_2 = \psi\psi_{12}^{(3)}\psi_{21}^{(3)}\psi_{31}^{(3)}$	$\psi_{\Gamma_3}(\Delta\nabla\nabla) = \begin{cases}(-1)^l\psi_2\\ \psi_1\end{cases}$
3=1+1+1	Δ∇Δ	1	1	1	1	$\begin{pmatrix}\Delta\nabla\Delta\\ \nabla\Delta\nabla\end{pmatrix}$	$\psi_1 = \psi\psi_{11}^{(3)}\psi_{22}^{(3)}\psi_{31}^{(3)}$ $\psi_2 = \psi\psi_{12}^{(3)}\psi_{21}^{(3)}\psi_{32}^{(3)}$	$\psi_{\Gamma_3}(\Delta\nabla\Delta) = \begin{cases}\psi_1\\ (-1)^l\psi_2\end{cases}$

---

* $\alpha_i = \left\{\frac{\Delta}{\nabla}, (\alpha_1\alpha_2\alpha_3)\right.$ is the characteristic of the wave functions of the given representation.

problem, but go on to give a procedure for constructing the functions with the required symmetry for any number of spaces of factors.

1. TRIGONAL TYPE $D_3 \cong C_{3V} \cong S_3$

We write down the character table for the permutation group S_3 (isomorphic to D_3 and C_{3V}) and its subgroup A_3 (containing the even permutations) in Table 1. We choose the basis so that the matrices of the reduced representation Γ_3 have the form (3):

$$\begin{array}{cccccc} e & (12) & (13) & (23) & (123) & (132) \\ \begin{pmatrix}1&0\\0&1\end{pmatrix} & \begin{pmatrix}0&1\\1&0\end{pmatrix} & \begin{pmatrix}0&\omega^2\\\omega&0\end{pmatrix} & \begin{pmatrix}0&\omega\\\omega^2&0\end{pmatrix} & \begin{pmatrix}\omega&0\\0&\omega^2\end{pmatrix} & \begin{pmatrix}\omega^2&0\\0&\omega\end{pmatrix}. \end{array} \quad (3)$$

Consider the tensor product of the representations and the functions corresponding to them:[1)]

$$\begin{array}{c} \overbrace{\Gamma_1\times\ldots\times\Gamma_1}^{k}\times\overbrace{\Gamma_2\times\ldots\times\Gamma_2}^{l}\times\overbrace{\Gamma_3\times\ldots\times\Gamma_3}^{r} \\ \Big| \qquad\quad \Big| \quad \Big| \qquad\quad \Big| \quad \Big|\!\!-\!\!-\!\!\Big| \quad \Big|\!\!-\!\!-\!\!\Big| \\ \underbrace{\psi_1^{(1)}\ \ldots\ \psi_k^{(1)}\ \psi_1^{(2)}\ \ldots\ \psi_l^{(2)}}_{\psi=\prod\limits_{i=1}^{k}\psi_i^{(1)}\prod\limits_{j=1}^{l}\psi_j^{(2)}}\ \psi_{11}^{(3)},\ \psi_{12}^{(3)}\ldots\psi_{r1}^{(3)}\ \psi_{r2}^{(3)} \end{array}$$

$$= {}^1\!/_3[2^{r-1}+(-1)^r](\Gamma_1+\Gamma_2)+{}^1\!/_3[2^r-(-1)^r]\Gamma_3. \qquad (4)$$

To construct the functions which transform under the representations on the right of (4), we proceed as follows.

1. Split the number r into the sum of positive integers in all possible ways, allowing for their order (see column 1 of Table 2).

2. To each decomposition we attach a set of Δ and ∇, beginning with Δ (see column 2 of Table 2).

3. For each composition we find a δ mod 3

$$\delta = d_1 - d_2 \qquad d_1 = a_1 + a_3 + a_5 + \ldots, \qquad (5)$$
$$d_2 = a_2 + a_4 + a_6 + \ldots,$$

where a_1 is the number of Δ starting from the beginning, a_2 the number of ∇ starting after Δ, a_3 the number of Δ starting after ∇, and so on (see column 3 of Table 2).

4. For each decomposition we write down the corresponding pair of functions ψ_1 and ψ_2 by the following rule: For each state as defined by a selection of Δ and ∇ we assign a conjugate state by interchanging $\Delta \rightleftarrows \nabla$. The initial state gives the function ψ_1 and the conjugate state gives the function ψ_2, if one takes ψ for $\Gamma_1 \times \ldots \times \Gamma_1 \times \Gamma_2 \times \ldots \times \Gamma_2$; and for Γ_3 each Δ has its corresponding function $\psi_{t1}^{(3)}$ and each ∇ its function $\psi_{t2}^{(3)}$ (t denotes the ordinal number of Δ or ∇ in the selection) (see columns 5 and 6 in Table 2).

5. The explicit form of the functions for each of the representations (4) can be rewritten as a function of δ (column 7 of Table 2) as follows:[2)]

$$\left.\begin{array}{ll} \delta=0 \pmod 3, & \Gamma_1\to\dfrac{1}{\sqrt{2}}[(-1)^l\psi_1+\psi_2], \\ & \Gamma_2\to\dfrac{1}{\sqrt{2}}[(-1)^{l+1}\psi_1+\psi_2], \\ \delta=1 \pmod 3, & \Gamma_3\to\psi_1,\ (-1)^l\psi_2, \\ \delta=2 \pmod 3, & \Gamma_3\to(-1)^l\psi_2,\ \psi_1. \end{array}\right\} \qquad (6)$$

For the trigonal type, only one intermediate group need be inserted; the functions characterized by the initial selection of Δ and ∇ are obtained with its help, i.e., by the decomposition of r (see column 2 of Table 2). In Table 2 the construction of functions for the tensor product of the following type is given as an example:

$$\underbrace{\Gamma_1\times\ldots\times\Gamma_1}_{k}\times\underbrace{\Gamma_2\times\ldots\times\Gamma_2}_{l}$$
$$\times\underbrace{\Gamma_3\times\Gamma_3\times\Gamma_3}_{r=3}=\Gamma_1+\Gamma_2+3\Gamma_3. \qquad (7)$$

2. TETRAGONAL TYPE $D_4 \cong C_{4V} \cong D_{d2} \cong R$

We write down the character table for the permutation group R (isomorphic to D_4, C_{4V}, and D_{2d}) and its subgroup V_4 (Table 3). We choose the basis so that the matrices of the reduced representation Γ_5 have the form (8):

$$\begin{array}{cccc} e & (12) & (34) & (12)\,(34) \\ \begin{pmatrix}1&0\\0&1\end{pmatrix} & \begin{pmatrix}0&1\\1&0\end{pmatrix} & \begin{pmatrix}0&-1\\-1&0\end{pmatrix} & \begin{pmatrix}-1&0\\0&-1\end{pmatrix} \\ (13)\,(24) & (14)\,(23) & (1423) & (1324) \\ \begin{pmatrix}1&0\\0&-1\end{pmatrix} & \begin{pmatrix}-1&0\\0&1\end{pmatrix} & \begin{pmatrix}0&-1\\1&0\end{pmatrix} & \begin{pmatrix}0&1\\-1&0\end{pmatrix}. \end{array} \qquad (8)$$

Consider the tensor product of the representations and their corresponding functions for $r \neq 0$:

$$\begin{array}{c} \overbrace{\Gamma_1\times\ldots\times\Gamma_1}^{k}\times\overbrace{\Gamma_2\times\ldots\times\Gamma_2}^{l}\times\overbrace{\Gamma_3\times\ldots\times\Gamma_3}^{u}\times\overbrace{\Gamma_4\times\ldots\times\Gamma_4}^{t} \\ \Big| \qquad\quad \Big| \quad \Big| \qquad\quad \Big| \quad \Big| \qquad\quad \Big| \quad \Big| \qquad\quad \Big| \\ \underbrace{\psi_1^{(1)}\ \ldots\ \psi_k^{(1)}\ \psi_1^{(2)}\ \ldots\ \psi_l^{(2)}\ \psi_1^{(3)}\ \ldots\ \psi_u^{(3)}\ \psi_1^{(4)}\ \ldots\ \psi_t^{(4)}}_{\psi=\prod\limits_{i_1=1}^{k}\psi_{i_1}^{(1)}\prod\limits_{i_2=1}^{l}\psi_{i_2}^{(2)}\prod\limits_{i_3=1}^{u}\psi_{i_3}^{(3)}\prod\limits_{i_4=1}^{t}\psi_{i_4}^{(4)}} \end{array}$$

$$\begin{array}{c} \times\overbrace{\Gamma_5\times\ldots\times\Gamma_5}^{r} \\ \Big|\!\!-\!\!-\!\!\Big| \quad \Big|\!\!-\!\!-\!\!\Big| \\ \psi_{11}^{(5)}\ \ \psi_{12}^{(5)}\ldots\psi_{r1}^{(5)}\ \ \psi_{r2}^{(5)} \end{array} = \begin{cases} 4^{\frac{r}{2}-1}(\Gamma_1+\Gamma_2+\Gamma_3+\Gamma_4)\ (r\ \text{even}), \\ 2^{r-1}\Gamma_5\,(r\ \text{odd}); \end{cases} \qquad (9)$$

TABLE 3

R	e	(12) (36)	(13) (26) (16) (23)	(12) (36)	(1623) (1362)		V_4	e	(12) (34)	(13) (24)	(14) (23)
Γ_1	1	1	1	1	1		A	1	1	1	1
Γ_2	1	1	1	−1	−1		B	1	1	−1	−1
Γ_3	1	1	−1	1	−1	(Δ)	C	1	−1	1	−1
Γ_4	1	1	−1	−1	1	(∇)	D	1	−1	−1	1
Γ_5	2	−2	0	0	0						

TABLE 4

Decomposition of r	Initial selection	a_1	a_2	a_3	$r\equiv 1 \pmod 2$, $d_2 \equiv a_2 \pmod 2$, $u+t+d_2 \equiv 1+d_2 \pmod 2$		Initial and conjugate selections	Form of the functions ψ_1 and ψ_2	Form of the functions $\psi_{\Gamma_1}(\alpha_1\alpha_2\alpha_3)$ $\psi=\prod_{i_1=1}^{k}\psi^{(1)}_{i_1}\prod_{i_2=1}^{2}\psi^{(2)}_{i_2}\psi^{(4)}_{1}$
					d_2	$u+t+d_2$			
3=3	ΔΔΔ	3	0	0	0	1	$\begin{pmatrix}\Delta\Delta\Delta\\ \nabla\nabla\nabla\end{pmatrix}$	$\psi_1=\psi\psi^{(5)}_{11}\psi^{(5)}_{21}\psi^{(5)}_{31}$ $\psi_2=\psi\psi^{(5)}_{12}\psi^{(5)}_{22}\psi^{(5)}_{32}$	$\psi_{\Gamma_5}(\Delta\Delta\Delta)=\begin{cases}-\psi_2\\ \psi_1\end{cases}$
3=2+1	ΔΔ∇	2	1	0	1	0	$\begin{pmatrix}\Delta\Delta\nabla\\ \nabla\nabla\Delta\end{pmatrix}$	$\psi_1=\psi\psi^{(5)}_{11}\psi^{(5)}_{21}\psi^{(5)}_{32}$ $\psi_2=\psi\psi^{(5)}_{12}\psi^{(5)}_{22}\psi^{(5)}_{31}$	$\psi_{\Gamma_5}(\Delta\Delta\nabla)=\begin{cases}\psi_1\\ -\psi_2\end{cases}$
3=1+2	Δ∇∇	1	2	0	0	1	$\begin{pmatrix}\Delta\nabla\nabla\\ \nabla\Delta\Delta\end{pmatrix}$	$\psi_1=\psi\psi^{(5)}_{11}\psi^{(5)}_{22}\psi^{(5)}_{32}$ $\psi_2=\psi\psi^{(5)}_{12}\psi^{(5)}_{21}\psi^{(5)}_{31}$	$\psi_{\Gamma_5}(\Delta\nabla\nabla)=\begin{cases}-\psi_2\\ \psi_1\end{cases}$
3=1+1+1	Δ∇Δ	1	1	1	1	0	$\begin{pmatrix}\Delta\nabla\Delta\\ \nabla\Delta\nabla\end{pmatrix}$	$\psi_1=\psi\psi^{(5)}_{11}\psi^{(5)}_{22}\psi^{(5)}_{31}$ $\psi_2=\psi\psi^{(5)}_{12}\psi^{(5)}_{21}\psi^{(5)}_{32}$	$\psi_{\Gamma_5}(\Delta\nabla\Delta)=\begin{cases}\psi_1\\ -\psi_2\end{cases}$

and if r = 0, then

$$\overbrace{\Gamma_1\times\ldots\times\Gamma_1}^{k}\times\overbrace{\Gamma_2\times\ldots\times\Gamma_2}^{l}\times\overbrace{\Gamma_3\times\ldots\times\Gamma_3}^{u}$$

$$\times\overbrace{\Gamma_4\times\ldots\times\ldots\Gamma_4}^{t}=\begin{cases}\Gamma_1\ (l,\ u,\ t \text{ even or } l,\ u,\ t \text{ odd});\\ \Gamma_2\ (l \text{ even, } u,\ t \text{ odd, } l \text{ odd, } u,\ t \text{ even});\\ \Gamma_3\ (u \text{ even, } l,\ t \text{ odd, } u \text{ odd, } l,\ t \text{ even});\\ \Gamma_4\ (t \text{ even, } l,\ u \text{ odd, } t \text{ odd } l,\ u \text{ even}).\end{cases}\qquad(10)$$

To construct the functions which transform under the representation on the right of (9), we proceed just as in the trigonal case of the previous section, with the omission of points 3 and 5, however. For point 3 we operate as follows in the tetragonal case:

3. For each decomposition we find values for the numbers r, $d_2 = a_2 + a_4 + \ldots$, $u + t + d_2 \bmod 2$ (see column 6 of Table 4).

5. We write the explicit form of the functions for each representation (9) as a function of r and $u + t + d_2$ (see column 9 of Table 4):

$$\left.\begin{array}{l} r\equiv 0 \pmod 2 \begin{cases} u+t+d_2\equiv 0 \pmod 2 \begin{cases}\Gamma_1\to\dfrac{1}{\sqrt{2}}[(-1)^{l+t}\psi_1+\psi_2]\\ \Gamma_2\to\dfrac{1}{\sqrt{2}}[(-1)^{l+t+1}\psi_1+\psi_2]\end{cases}\\ u+t+d_2\equiv 1 \pmod 2 \begin{cases}\Gamma_3\to\dfrac{1}{\sqrt{2}}[(-1)^{l+t}\psi_1+\psi_2]\\ \Gamma_4\to\dfrac{1}{\sqrt{2}}[(-1)^{l+t+1}\psi_1+\psi_2]\end{cases}\end{cases}\\ r\equiv 1 \pmod 2 \left[\begin{array}{l} u+t+d_2\equiv 0 \pmod 2,\ \Gamma_5\to\psi_1,\ (-1)^{l+t}\psi_2,\\ u+t+d_2\equiv 1 \pmod 2,\ \Gamma_5\to(-1)^{l+t}\psi_2,\ \psi_1.\end{array}\right.\end{array}\right\}\qquad(11)$$

In Table 4 we give an example of the construction of the functions for the tensor product of the form (12) (l = 0, u = 2, t = 1, r = 3):

$$\underbrace{\Gamma_1\times\ldots\times\Gamma_1}_{k}\times\underbrace{\Gamma_3\times\ldots\times\Gamma_3}_{u=2}$$

$$\times\underbrace{\Gamma_4}_{t=1}\times\underbrace{\Gamma_5\times\Gamma_5\times\Gamma_5}_{r=3}=4\Gamma_5.\qquad(12)$$

We have explained the procedure for constructing the appropriate functions for the groups D_3 and D_4. It must be noted that each point group has its own intermediate subgroup, and therefore the procedure is quite different for each group. The method of constructing the appropriate functions for the tetrahedral and octahedral type groups, and for the remaining groups will be explained elsewhere. Let us now illustrate the power of the above method by calculating an invariant. In ref. 3

a sixth-order invariant I is given; this invariant is constructed from the quantities γ_x and γ_y which are transformed under the representation Γ_3 of the group D_3. This invariant

$$I = (\gamma_x + i\gamma_y)^6 + (\gamma_x - i\gamma_y)^6 \tag{13}$$

comes into the expression for the thermodynamic potential characterizing crystals of the type α-Fe_2O_3.

We obtain this invariant by the method of sequential descent. The matrices of the representation for the second-order elements of the group D_3 have the form

$$\begin{pmatrix} 1 & 0 \\ 0 & -1 \end{pmatrix}, \begin{pmatrix} -\frac{1}{2} & -\frac{\sqrt{3}}{2} \\ -\frac{\sqrt{3}}{2} & \frac{1}{2} \end{pmatrix}, \begin{pmatrix} -\frac{1}{2} & \frac{\sqrt{3}}{2} \\ \frac{\sqrt{3}}{2} & \frac{1}{2} \end{pmatrix}. \tag{14}$$

It is easy to show that the matrices (14) take the form of the corresponding matrices (3) if certain linear combinations of γ_x and γ_y are chosen as the basis, in particular, $\psi_1^{(3)} = \gamma_x + i\gamma_y$, $\psi_2^{(3)} = \gamma_x - i\gamma_y$. Consider the product $\Gamma_3 \times \Gamma_3 \times \Gamma_3 \times \Gamma_3 \times \Gamma_3 \times \Gamma_3$. Since the invariant corresponds to combinations which transform under the representation Γ_1, from all the decompositions of the number r = 6 one must choose that one for which $\delta = 0$ [see (6)]. Take the decomposition 6 = 6 (see Table 2), and then obviously $\delta = 0$, and so according to (6) we get (for $l = 0$)

$$\psi_{\Gamma_1}(\Delta\Delta\Delta\Delta\Delta\Delta) = \frac{1}{\sqrt{2}}(\psi_1 + \psi_2) = \frac{1}{\sqrt{2}}[\psi_{11}^{(3)}\psi_{21}^{(3)}\psi_{31}^{(3)}\psi_{41}^{(3)}\psi_{51}^{(3)}\psi_{61}^{(3)}$$

$$+ \psi_{12}^{(3)}\psi_{22}^{(3)}\psi_{32}^{(3)}\psi_{42}^{(3)}\psi_{52}^{(3)}\psi_{62}^{(3)}] = \frac{1}{\sqrt{2}}[(\gamma_x + i\gamma_y)^6 + (\gamma_x - i\gamma_y)^6]. \tag{15}$$

Other decompositions for which $\delta = 0$ are possible, e.g., 6 = 3 + 3, etc. They give other invariants not studied in ref. 3.

---

1) If r = 0, then $\Gamma_1 \times \ldots \times \Gamma_1 \times \Gamma_2 \times \ldots \times \Gamma_2 = \begin{cases} \Gamma_2 \ (l \text{ odd}) \\ \Gamma_1 \ (l \text{ even}) \end{cases}$

2) The order of the functions is essential here and is related to the choice of the matrices of the representations in (3).

---

[1] M. Hamermesh, Group Theory and Its Application to Physical Problems, Addison–Wesley (1962).

[2] B. A. Men', A. N. Men', and V. L. Cherepanov, Dokl. Akad. Nauk SSSR, 203, 776 (1972) [Sov. Phys.–Dokl., 17, 330 (1972)].

[3] I. Dzyaloshinskii, J. Chem. Phys. Solids, 4, 241, 255 (1958).

Effect of diffusion on the velocity of a break during the growth of an alloy crystal

D. E. Temkin

Central Scientific-Research Institute of Ferrous Metallurgy

(Submitted April 20, 1972; resubmitted July 17, 1972)
Kristallografiya, 18, 675-680 (July-August 1973)

Using a model with an isolated break, the effect of the diffusion of the components on the velocity of the break during a phase transformation in the alloy is analyzed. It is shown that in the two-phase region the steady-state velocity is limited by lateral diffusion, while in the one-phase region there is a velocity component not dependent on lateral diffusion.

When analyzing a purely diffusionless transformation in an ideal alloy (a diffusionless transformation being one in which the phase boundary moves, but the atoms of the components do not execute any diffusion jumps or exchange places), it was shown earlier on the basis of a one-dimensional model that, under conditions corresponding to the two-phase region of the phase diagram, the velocity of the phase boundary diminished with time and tended toward zero, while in the one-phase region it tended toward a steady-state value.[1] This is associated with the fact that, as it moves forward, the phase boundary encounters fluctuations of composition which are more and more difficult to overcome. In the two-phase region the motive force of the transformation is insufficient to overcome these fluctuations, and the velocity tends to zero. An analysis of the diffusionless motion of a rectilinear step confirms the existence of an analogous situation in the two-dimensional case (the results of this analysis will be presented elsewhere). The effect in question is thus not specifically one-dimensional but should also appear in two- and three-dimensional systems (in the motion of phase-interface surfaces).

In two cases, however, the situation will be qualitatively different, and the effect of the velocity falling to zero will not appear.

a) In the presence of diffusion, the fluctuations which are proving difficult to overcome will be resorbed, and the obstacles will thus be removed from the path of the moving boundary. Even in the two-phase region the interface (a break in the one-dimensional and a step in the two-dimensional case) will move at a certain steady-state velocity, determined by the rate of removal of the obstacles, i.e., by the diffusion. For this possibility to be realized, it is essential that the "dimensionality" of the diffusion should be higher than that of the boundary motion. Hence, allowing for diffusion will not lead to the vanishing of the effect under consideration in the case of the motion of a plane phase boundary.

b) If the moving boundary is able to pass around an obstacle by changing its direction of motion (for example, if a step passes around an obstacle by moving out of the specified plane of motion), the effect under consideration will also be absent, and the steady-state velocity will be determined by the probability of the "bypass" effect.

It is interesting to consider how a diffusionless transformation will develop when an (on average) rectilinear step or plane boundary cannot move with the steady-state velocity. Evidently the step (or surface), encountering regions difficult to overcome, loses stability, throwing out "tongues" with a view to passing around the obstacles, and no steady-state shape of the moving phase boundary will occur. An example of such a "tongue" may be seen in Fig. 5 of ref. 2: For a force less than the critical value, a dislocation moving through a system of obstacles has thrown out a "tongue" embracing a region with a comparatively low content of obstacles; the length of the "tongue" is much greater than the mean distance between these obstacles. Possibly the "purest" answer to the problem may be obtained by simulating a diffusionless transformation on an electronic computer.

In this paper we shall consider the motion of an isolated break for case a and shall show how the diffusion of the atoms influences the velocity for a transformation in the two- and one-phase regions.

Let us consider the same model of an isolated break (Fig. 1) as was considered in ref. 3, in which the capture of an impurity was analyzed. Phases α and β constitute substitutional solutions of the components A and B and have simple cubic lattices with the same period; the phase interface is the (100) plane; on this boundary is a [10] step with one break. The A and B atoms only pass from one phase to the other at the break. Let ν_{+A} and ν_{+B} be the frequencies with which the A and B atoms in the β phase immediately in front of the break pass into the α, ν_{-A} and ν_{-B} be the frequencies of the reverse transitions from α to β. In the model under consideration diffusion takes place by virtue of a change of places between neighboring atoms. Let two neighboring A and B atoms situated in the atomic row along which the break is being displaced change places with a frequency ν_β in the β phase and ν_α in the α; for other positions of A and B the frequencies are respectively ν_β', and ν_α' (Fig. 1).1) No diffusion takes place through the interface (i.e., through the surface, step, and break).

Let us assume that, before the onset of the transformation, the distribution of components A and B in the two phases is completely random, and the concentration of B is equal to C. The motion of the break leads to the creation of an inhomogeneous distribution of the components around it. In order to find this distribution, which

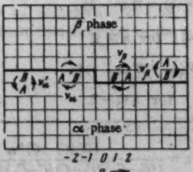

Fig. 1. Schematic representation of a step with a break.

also determines the velocity of the break, we must consider the diffusion of the atoms and the motion of the break in terms of random walks. This problem simplifies considerably and becomes one-dimensional in the case of small ν_α' and ν_β'. Everywhere, apart from in the nodes of the atomic row along which the break is moving, the concentrations are such that their difference from C is proportional to ν_α' and ν_β'. Hence to a first approximation these concentrations may be put equal to C, the concentration a long way from the break.

Let us number the nodes of the atomic row along which the break is moving in such a way that the nodes situated in the β phase in front of the break are represented by $n = 0, 1, \ldots$, and those in the α phase behind the break by $n = -1, -2, \ldots$. In order to describe the distribution of the components in this row we introduce a sequence of distribution functions W(n; t), W(n, k; t), etc., having the following meaning: W(n;t) is the probability of observing a B atom in the n-th node relative to the break at the moment of time t, W(n, k; t) is the probability of observing B atoms in nodes n and k at time t, and so on. The fluxes of A and B atoms from the β into the α phase, respectively, equal $j_{+A} = \nu_{+A}[1 - W(0; t)]$, $j_{+B} = \nu_{+B}W(0; t)$ and from the α into the β phase $j_{-A} = \nu_{-A}[1 - W(-1; t)]$, $j_{-B} = \nu_{-B}W(-1; t)$. Equating the fluxes $j_{+A} = j_{-A}$ and $j_{+B} = j_{-B}$, we find the concentrations $C_\alpha = W(-1)$, $C_\beta = W(0)$ of the α and β phases in equilibrium:

$$C_\alpha = \frac{\nu_{+B}(\nu_{+A} - \nu_{-A})}{\nu_{+A}\nu_{-B} - \nu_{-A}\nu_{+B}}, \quad C_\beta = \frac{\nu_{-B}(\nu_{+A} - \nu_{-A})}{\nu_{+A}\nu_{-B} - \nu_{-A}\nu_{+B}}. \tag{1}$$

Let us consider the case in which $\nu_{+A} > \nu_{-A}$, $\nu_{+B} < \nu_{-B}$. Here $0 < C_\alpha < C_\beta < 1$. The velocity of the break v(t) (in units of reciprocal time) equals the resultant flux from the β to the α phase:

$$\begin{aligned} v(t) = j_{+A} + j_{+B} - j_{-A} - j_{-B} = \nu_{+A} - \nu_{-A} + (\nu_{+B} - \nu_{+A})W(0; t) \\ - (\nu_{-B} - \nu_{-A})W(-1; t). \end{aligned} \tag{2}$$

For the $\beta \to \alpha$ transformation $v > 0$.

The distribution functions satisfy an infinite system of "linked" equations, so that the equation for W(n; t) contains the binary functions W(n, k; t) and so on. However, we "split" these equations by making the additional assumption of no correlation, as in ref. 1:

$$W(n, k; t) = W(n; t)W(k; t). \tag{3}$$

The equations for W(n; t) are then analogous to Eqs. (10)-(12) in ref. 1. The difference lies in allowance for lateral diffusion from the atomic row under consideration and leads to terms in ν_β' and ν_α':

$$dW(n; t)/dt = j_+[W(n+1) - W(n)] + j_-[W(n-1) - W(n)] + \left\{ \begin{array}{l} \nu_\beta[W(n+1) - 2W(n) + W(n-1)] \\ \quad + 2\nu_\beta'[C - W(n)] \ \text{for} \ n \geqslant 1, \\ \nu_\alpha[W(n+1) - 2W(n) + W(n-1)] \\ \quad + 2\nu_\alpha'[C - W(n)] \ \text{for} \ n \leqslant -2, \end{array} \right. \tag{4}$$

$$\begin{aligned} dW(0; t)/dt = j_+W(1) - j_-W(0) - \nu_{+B}W(0) + \nu_{-B}W(-1) \\ + \nu_\beta[W(1) - W(0)] + 2\nu_\beta'[C - W(0)], \end{aligned} \tag{5}$$

$$\begin{aligned} dW(-1; t)/dt = j_-W(-2) - j_+W(-1) + \nu_{+B}W(0) - \nu_{-B}W(-1) \\ + \nu_\alpha[W(-2) - W(-1)] + 2\nu_\alpha'[C - W(-1)], \end{aligned} \tag{6}$$

$$W(n; 0) = W(-\infty; t) = W(\infty; t) = C. \tag{7}$$

Here $j_+ = j_{+A} + j_{+B}$, $j_- = j_{-A} + j_{-B}$ are the fluxes from the β to the α and from the α to the β phase in the break:

$$\begin{aligned} j_+ = \nu_{+A} + (\nu_{+B} - \nu_{+A})W(0; t), \\ j_- = \nu_{-A} + (\nu_{-B} - \nu_{-A})W(-1; t). \end{aligned} \tag{8}$$

The solution of the steady-state equations (4) [dW(n; t)/dt = 0] subject to conditions (7) takes the form

$$W(n) = \begin{cases} C + [W(0) - C]s_\beta^{\,n} & \text{for } n \geqslant 0, \\ C + [W(-1) - C]s_\alpha^{\,n+1} & \text{for } n \leqslant -1, \end{cases} \tag{9}$$

where

$$\begin{aligned} s_i = \{j_+ + j_- + 2(\nu_i + \nu_i') \pm [(j_+ + j_- + 2\nu_i + 2\nu_i')^2 \\ - 4(j_+ + \nu_i)(j_- + \nu_i)]^{1/2}\} / 2(j_+ + \nu_i) \end{aligned} \tag{10}$$

and $i = \alpha, \beta$. For $i = \alpha$ we take the plus sign in front of the radical and for $i = \beta$ the minus sign. After substituting (8)-(10) into (5) and (6), we obtain a system of two nonlinear equations for determining the unknowns W(0) and W(−1). According to (2), the steady-state velocity is determined in terms of these quantities. Regarding ν_i' as small, we shall seek W(0) and W(−1) in the form

$$W(0) = W_0(0) + \varepsilon, \quad W(-1) = W_0(-1) + \delta, \tag{11}$$

where $W_0(0)$ and $W_0(-1)$ are the corresponding quantities for $\nu_\alpha' = \nu_\beta' = 0$, while ε and δ are small corrections.

Allowing for (2) and (11), we have the following for the velocity of the break:

$$v = v_0 + \varepsilon(\nu_{+B} - \nu_{+A}) - \delta(\nu_{-B} - \nu_{-A}). \tag{12}$$

Here and subsequently the zero subscript indicates that the quantities are found for $\nu_\alpha' = \nu_\beta' = 0$. Let us find v separately for the two-phase $(\alpha + \beta)$ and the one-phase α region.

1. In the two-phase region $C_\alpha < C < C_\beta$. In this case for $\nu_\alpha' = \nu_\beta' = 0$ the following picture is realized in the steady-state mode:[1] In the atomic row under consideration, in front of the break and behind it, the equilibrium concentrations $W_0(n) = C_\beta$ for $n \geq 0$ and $W_0(n) = C_\alpha$ for $n \leq -1$ are established, so that $j_+^0 = j_-^0 = j_0$, and the velocity of the break equals zero. We find the velocity v from the equation obtained by summing (5) and (6), after expanding all the terms in it in powers of ε and δ. In this expansion we retain the terms proportional to ε, δ, and $(\nu_i')^{1/2}$ in the first degree [ε and δ are proportional to $(\nu_i')^{1/2}$]. Omitting the simple but cumbersome calculations, we may write the final expression for the velocity

$$v \simeq \frac{\sqrt{2}[(C_\beta - C)^2\nu_\beta'(j_0 + \nu_\beta) - (C - C_\alpha)^2\nu_\alpha'(j_0 + \nu_\alpha)]}{\{(C_\beta - C_\alpha)(C_\beta - C)(C - C_\alpha)[(C_\beta - C)\nu_\beta'(j_0 + \nu_\beta) + (C - C_\alpha)\nu_\alpha'(j_0 + \nu_\alpha)]\}^{1/2}}. \tag{13}$$

Here $j_0 = \nu_{+A} + (\nu_{+B} - \nu_{+A})C_\beta$. The denominator of (13) in the two-phase region is always positive, while the numerator changes sign for

$$C = C^* = [C_\alpha\sqrt{\nu_\alpha'(j_0+\nu_\alpha)} + C_\beta\sqrt{\nu_\beta'(j_0+\nu_\beta)}]\,/\,[\sqrt{\nu_\alpha'(j_0+\nu_\alpha)} + \sqrt{\nu_\beta'(j_0+\nu_\beta)}].$$

For $C_\alpha < C < C^*$, $v > 0$, and we have the $\beta \to \alpha$ transformation, while for $C^* < C < C_\beta$, $v < 0$ ($\alpha \to \beta$ transformation). In the two-phase region the steady-state velocity of the break is determined by the lateral diffusion and vanishes for $\nu_\alpha' = \nu_\beta' = 0$. Roughly speaking, v is proportional to $(\nu_i')^{1/2}$, which may easily be seen for $\nu_\alpha = \nu_\beta$ and $\nu_\alpha' = \nu_\beta'$. Equation (13) is valid for $\nu_i'/(j_0 + \nu_i) \ll 1$ and concentrations C fairly well removed from the equilibrium C_α and C_β, when $|v/(j_0 + \nu_i)| \ll 1$.

2. Let us consider the $\beta \to \alpha$ transformation in the one-phase α region ($0 < C < C_\alpha$). In this region, in the absence of lateral diffusion, there is a steady-state mode of motion of the break, as considered in ref. 1. The velocity v_0 and the concentration $W_0(0)$ are described by the following relationships [see Eqs. (4) and (15) from ref. 1]:

$$v_0 = \nu_{+A}\nu_{+B}\left[1 - C\frac{\nu_{-B}}{\nu_{+B}} - (1-C)\frac{\nu_{-A}}{\nu_{+A}}\right] \Big/ [C\nu_{+A} + (1-C)\nu_{+B}], \tag{14}$$

$$W_0(0) = C + C(1-C) \times (\nu_{+A} - \nu_{-A} - \nu_{+B} + \nu_{-B})/[C\nu_{+A} + (1-C)\nu_{+B}]. \tag{15}$$

In the α phase behind the break the distribution is uniform: $W_0(n) = C$ for $n \leq -1$. Using these relationships as the zero approximation, after substituting (8)-(10) and the expansion with respect to ν_α' and ν_β' in Eqs. (5) and (6) we obtain the following, in an approximation linear with respect to these parameters:

$$v \simeq v_0\left\{1 + 2\nu_\beta'(j_+^0 + \nu_\beta)C(1-C) \times \frac{\nu_{+A}\nu_{+B}(\nu_{+A} - \nu_{-A} - \nu_{+B} + \nu_{-B})^2}{v_0^2[C\nu_{+A} + (1-C)\nu_{+B}]^2}\right\}. \tag{16}$$

Here $j_+^0 = \nu_{+A} + (\nu_{+B} - \nu_{+A})W_0(0)$. In the linear approximation v does not depend on the diffusion parameters in the α phase. We see from (16), that, for any relationships of the parameters, lateral diffusion leads to an increase in velocity. Equation (16) was obtained for $\nu_i'/(j_+^0 + \nu_i) \ll 1$, and is valid provided that the correction associated with ν_β' in (16) is small compared with unity. The latter condition, and hence Eq. (16), cease to be satisfied when C approaches C_α, since then v_0 tends to zero. The neighborhood of the boundaries between the one- and two-phase regions, in which the expansions (13) and (16) are not satisfied, requires special attention.

Figure 2 gives a schematic picture of the relationship between the steady-state velocity of the break and the concentration of the alloy, with or without allowing for the lateral diffusion (the dashes indicate the range of concentrations not studied). In the two-phase region the velocity of the break is limited by lateral diffusion. In the one-phase region there is a velocity component not depending on lateral diffusion.

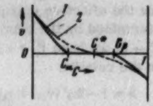

Fig. 2. Schematic relationship between the velocity of the break and the concentration of the alloy, without allowing for lateral diffusion (1), and after allowing for lateral diffusion (2).

In order to illustrate the influence of diffusion, we have here considered a somewhat arbitrary presentation of the problem, in which the concentrations in the original and developing phases are the same and equal to C a long way from the break [Eq. (7)]. This presentation is similar to that considered in ref. 1, and arises when we are interested in the direction and velocity of the transformation after α and β phases of composition C have been brought into contact. Another presentation of the problem, however, is more realistic.

We have an initial β phase of composition C. What will the steady-state velocity of the transformation $\beta \to \alpha$ and the composition of the developing α phase then be in relation to the conditions (i.e., C and the set of frequencies) if the transformation is due to the scanning of one break along the interphase boundary? In this case the concentration $W(-\infty)$ in the α phase a long way from the break is not prespecified, as was done earlier, but is determined by the conditions of the transformation. In the remaining atomic rows of the α phase the concentration is also equal to $W(-\infty)$. On allowing for this, we may replace C by $W(-\infty)$ in Eqs. (4) (for $n \leq -2$) and (6); we shall also have a uniform distribution in the α phase $W(n) = W(-\infty)$ (for $n \leq -1$) instead of (9). Owing to the homogeneity of the developing α phase, the steady-state velocity of the break depends solely on the diffusion frequencies in the original β phase.

In the two-phase region, instead of (13) we have the following:

$$v \simeq \sqrt{2(j_0 + \nu_\beta)\nu_\beta'}\,(C_\beta - C)\,/\,\sqrt{(C_\beta - C_\alpha)(C - C_\alpha)}. \tag{17}$$

The composition of the α phase is determined by the expression

$$W(-\infty) \simeq C_\alpha\left[1 - \frac{v\nu_{+A}(\nu_{+A} - \nu_{-A} - \nu_{+B} + \nu_{-B})}{(\nu_{+A} - \nu_{-A})(\nu_{+A}\nu_{-B} - \nu_{-A}\nu_{+B})}\right], \tag{18}$$

from which we see that the deviation of the composition from the equilibrium value C_α is proportional to the velocity of the break. As we should expect, $v = 0$ for $C = C_\beta$. As $C \to C_\alpha$ the solution (17) loses validity, as indicated by the tendency of v toward ∞.

In the one-phase α region the expression considered for the velocity in the approximation linear with respect to ν_β' coincides with (16), while the composition of the α phase is described by the expression

$$W(-\infty) \simeq C\left\{1 - 2\nu_\beta'(j_+^0 + \nu_\beta) \times (1-C)\frac{(\nu_{+A} - \nu_{-A} - \nu_{+B} + \nu_{-B})}{v_0^2[C\nu_{+A} + (1-C)\nu_{+B}]}\right\}. \tag{19}$$

If we introduce the effective capture coefficient[3] k = W(−∞)/C, k is determined by the expression in the braces in Eq. (19). As C → 0, we have $j_+^0 = \nu_{+A}$ and $v_0 = \nu_{+A} - \nu_{-A}$ and we obtain the relation

$$k \simeq 1 - 2v_\beta{}'(v_{+A} + v_\beta)$$
$$\times (v_{+A} - v_{-A} - v_{+B} + v_{-B}) / [v_{+B}(v_{+A} - v_{-A})^2],$$

coinciding (for $\nu_\beta = 0$) with Eq. (12) of ref. 3.

---

[1] For these assumptions regarding the frequencies the α and β solutions are regarded as ideal.[1]

[1] D. E. Temkin, Kristallografiya, 17, 77 (1972) [Sov. Phys. – Crystallogr., 17, 60 (1972)].

[2] A. J. Foreman and M. J. Makin, Phil. Mag., 14, 911 (1966).

[3] D. E. Temkin, Kristallografiya, 17, 461 (1972) [Sov. Phys. – Crystallogr., 17, 405 (1972)].

Systematic analysis of Patterson functions on the basis of crystal symmetry. V. Regularities in the degeneracy of the rhombuses in vector systems of crystals belonging to lower crystallographic systems

É. A. Kuz'min, R. I. Bochkova, Yu. N. Saf'yanov, V. P. Golovachev, and N. V. Belov
Gor'kii Physicotechnical Research Institute

(Submitted March 13, 1973)
Kristallografiya, 18, 681-688 (July-August 1973)

The regularities in the degeneracy of peak rhombuses in the vector systems of crystals of the lowest systems with a particular position of the initial segment are treated.

The theoretical a priori rhombus diagrams[1] which arise from representing a vector system as a vector system of segments have been constructed for crystals of the lowest systems for a general position of the basis segment. If the segment is parallel or perpendicular to symmetry elements and if one or both of its ends lie on symmetry elements or both ends are related by a symmetry operation, i.e., for a particular position of the segment in the basis system, the rhombus pattern changes. Analysis (and construction) of the a priori diagrams corresponding to degenerate rhombuses is of interest in solving the inverse problem of analysis of Patterson functions, especially for crystals with obvious pseudosymmetries.

Below we will consider degeneracy of rhombuses which correspond to various such versions of particular positions of the segments, for Fedorov groups of crystals of the lowest systems having three and seven symmetry elements. The degeneracy of the peak rhombuses for Fedorov groups with one symmetry element has been discussed previously.[2] The results obtained here can also be extended to groups with several symmetry elements.

In the basis system of any Fedorov group with a multiplicity k for the general positions, we should find k segments involving (k − 1) basic symmetry operations. In the lowest systems the order of each symmetry element ($2, \bar{2}, \bar{1}$) is 2 and all k of the segments of the basis system can be divided into k/2 pairs connected by the same symmetry operations. If it turns out that two of the segments of a single pair are connected by several pseudosymmetry elements then the latter act on each of the pairs.

In the "little" groups with three symmetry elements (classes C_{2h}, C_{2v}, and D_2) the multiplicity of a general position is 4. In the vector systems of 16 rhombuses, four are grouped in the initial star while the other 12 are arranged as four on each of the symmetry elements. In Fedorov groups of class C_{2h} all of the Patterson peaks other than the centrosymmetric peaks are double; the rhombuses created by a two-fold axis or a symmetry plane are superimposed pairwise and thus these elements are characterized by two rhombuses. In the class C_{2v} only the bound Patterson peaks from symmetry planes are doubled and the corresponding rhombuses are connected in rhombic bipyramids. In considering these differences, the regularities are the same in the degeneracy of the rhombuses in the vector systems of these Fedorov groups; therefore we will treat the details of the Patterson patterns using the Fedorov groups of class C_{2h} as an example.

In Fedorov groups of the holohedral brick class D_{2h}, the multiplicity of a general position is 8. Of the 64 rhombuses corresponding to the vector system, eight form the initial star and the remaining 56 are distributed among seven symmetry elements (with eight on each). Since all of the interaction peaks in the primitive Fedorov groups of this class are double, the bound peaks from the symmetry planes are fourfold degenerate while those from the twofold elements are double, and the eight rhombuses which correspond to a single symmetry plane are connected in the form of two bipyramids while the peaks which correspond to two-fold axes are connected in four rhombuses.

The eight segments of the basis system can, in three versions, be divided into four pairs, in each of which the segments involve the same symmetry element.[1)] For example, $r_0 - r_{m_x}$, $r_{m_z} - r_{2_y}$, $r_{m_y} - r_{2_z}$, $r_{2_x} - r_1$ are all segments connected in pairs by the m_x plane. A similar separation of $r_0 - r_{2_x}$, $r_{m_z} - r_{m_y}$, $r_{2_y} - r_{2_z}$, $r_{m_x} - r_1$ reflects combinations of pairs by the 2_x axis while $r_0 - r_1$, $r_{m_z} - r_{2_z}$, $r_{m_y} - r_{2_y}$, $r_{m_x} - r_{2_x}$ correspond to a center of symmetry.

To obtain the diagrams of rhombuses which correspond to particular arrangements of segments in the basis system we proceed from the standard diagrams[1] constructed for segments at a general position. Since the coordinates of all of the peaks of the rhombuses are determined by the coordinates of the ends of the basis segment $(x_1y_1z_1)$ and $(x_2y_2z_2)$ then with a particular position of the segment the independent coordinates become either dependent or fixed. The corresponding economy in the co-

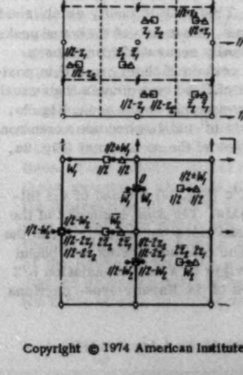

Fig. 1. Space group Pbca, basis segment parallel to the b plane.

ordinates of rhombus vertices in the standard diagrams[1] allows one to obtain easily the diagrams of the degenerate rhombuses.

We turn to the pseudosymmetry elements, which arise for a particular position of the basis segment and which are determined by the rhombus degeneracies for Fedorov groups in crystals of low syngonies with three and seven symmetry elements.

1. If the initial (basis) segment r_0 is parallel (perpendicular) to a symmetry element, then in the basis system the segment is pairwise related not only to the given element, but also to a pseudocenter, and in the vector system the corresponding peak rhombuses degenerate into lines. Figure 1a shows the basis and vector systems for the Pbc*a* space group (the group D_{2h}^{15} with nonintersecting two-fold screw axes);[2] the basis segment r_0 is parallel to the b plane (=g_x). The segments of the basis system which involve the b plane (=g_x) are $r_0-r_{g_x}$, $r_{g_y}-r_{2_{1z}}$, $r_{g_z}-r_{2_{1y}}$, and $r_{2_{1x}}-r_i$, and also for the 2_{1x} axis, $r_0-r_{2_{1x}}$, $r_{g_y}-r_{g_z}$, $r_{g_x}-r_i$, and $r_{2_{1z}}-r_{2_{1y}}$, which are pairwise parallel (connected by a pseudocenter) and the peak rhombuses corresponding to them degenerate into lines in the vector system. The rhombuses from g_y and 2_{1z}, and g_z and 2_{1y}, the lines from 2_{1x} and i, g_x and segments of the basis star [i.e., rhombuses in whose creation segments connected with the b plane (=g_x) participate] are pairwise parallel.

In Fedorov groups of the class C_{2h} there is only one axis and planes perpendicular to it; therefore the parallel or perpendicular nature of the basis segment of any symmetry element makes all of the segments of the basis system mutually parallel (connected by a pseudocenter) and in the vector system all of the rhombuses degenerate into lines.

2. If one end of the initial segment lies on a symmetry element (in the general case with glide), then for all segments related pairwise to it there are points (ends) mutually separated by a half-translation along the glide direction. As a consequence all rhombuses of the vector system are connected in pairs mutually distant at the same distance (independent sides of the rhombuses). Moreover all of the rhombuses which correspond to the given symmetry element have a common vertex, whose bound peak is separated from the origin of coordinates by the corresponding half-translation. This peak is easily established in the Harker cross sections. Since one of the bound peaks from each rhombus is mutually separated from others by a half-translation, then certain of them can fall in positions with a larger number of fixed coordinates than usual (for example, for a centrosymmetric bound peak, Fig. 2a, there are two fixed coordinates)[3] and thus become a common vertex for several rhombuses of the same form (Fig. 2a, d).[4]

In the space group p2_1/c (Fig. 2a) the end of the initial segment falls on a 2_1 axis. The four segments of the basis system are divided into pairs: $r_0-r_{2_1}$, r_c-r_i; in the corresponding rhombuses the common vertex is a bound peak separated from the origin by a half-translation b/2 and lying at the intersection of the Harker cross sections (all three coordinates are fixed); two sides of these rhombuses are parallel to segments of the initial star. In rhombuses generated by a c plane two sides are also parallel to centrosymmetric lines, while the common bound peak of the latter is separated from the corresponding bound peaks of the rhombuses (from the c plane) by b/2 and takes up a particular position (two fixed coordinates).

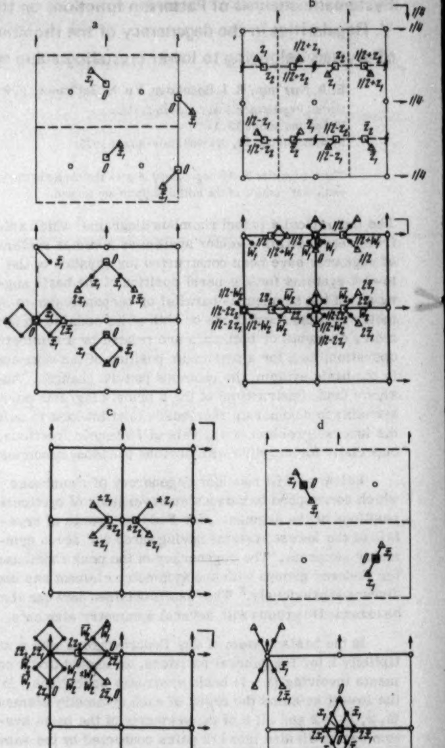

Fig. 2. Space group P2_1/c, the end of the basis segment lies on the 2_1 axis (a space group Pbc*a*, one of the ends of the basis segment falls in the b plane (b space group Pmmm, the basis segment lies at one end of the m_x plane (c); space group P2_1/c with the end of the initial segment at the center of symmetry.

For the space group Pbc*a* (Fig. 2b) one end of the basis segment lies in the b (=g_x) plane and in the corresponding pairs at one end of the segment we have a half-translation b/2. In the vector system all of the rhombuses from the b plane have a common bound peak, which is separated from the origin by b/2 and lies in the intersection of three Harker cross sections and two sides of the rhombuses parallel to segments of the initial star. Correspondingly the bound peaks of the rhombuses from $c = g_y$ and 2_{1_z}; from 2_{1_x} and $\bar{1}$, and from $a = g_z$ and 2_{1_y} are mutually separated by a half-translation b/2 and both sides of the rhombuses in the enumerated pairs are mutually parallel. If the end of the initial segment in the space group P2/m falls on a two-fold axis, then within each pair of segments connected by this axis there is a common point at which the two-fold axis does not act. The two common points are mutually connected by two symmetry elements m and $\bar{1}$. The two rhombuses of the vector system which are associated with a 2 axis have a common bound peak at the origin of the unit cell and the two rhombuses which come out from its sides coincide with the rays of the initial star. Simultaneously the centrosymmetric lines have a common side with the rhombuses from the plane (common peaks: one is bound and the second is an interaction peak).

Figure 2c shows the basis and vector systems for the space group Pmmm; the basis segments lie at one end of the m_x plane. The segments within each pair are $r_0 - r_{m_x}$, $r_{m_z} - r_{2_y}$, $r_{m_y} - r_{2_z}$, and $r_{2_x} - r_{\bar{1}}$ and have a common point. In the vector system two sides of the rhombuses from m_x merge with the rays of the initial star with a common bound peak falling at the origin. For rhombuses from m_x and 2_y, 2_x, and $\bar{1}$, and m_y and 2_z there is characteristically a collectivization for one bound peak and one interaction peak (i.e., along one side of the rhombus). The common bound peaks lie at the intersection of Harker cross sections (the bound peaks from m_x have all three coordinates fixed, those from m_z and 2_y or m_y and 2_z have two fixed, and those from 2_x and $\bar{1}$ have one coordinate fixed).

If one of the ends of the segment falls at a center of symmetry (Fig. 2d) for space group $P2_1/c$, then the common point occurs for the pairs $r_0 - r_{\bar{1}}$ and $r_{2_1} - r_c$. In the vector system four centrosymmetric rhombuses (lines) merge at the origin and coincide with the rays of the initial star along one side of the rhombuses. The four other rhombuses from 2_1 and c also exist on one common side.

3. If one of the ends of the segment lies at the intersection of two symmetry elements then all k of the segments divide into different groups of pairs, within which their pseudosymmetry elements are preserved; therefore in the vector system two sides of each rhombus are separated by various half-translations from two sides of the other rhombuses. In the case where the end of the segment falls on the intersection of n symmetry elements then in the vector system the side of each rhombus is separated by the corresponding half-translation from the other rhombuses. Here for rhombuses of the same form (of the number noted) as previously one common vertex is characteristic and it is a bound peak. If the symmetry elements do not contain translational components then such a common bound peak located at the origin of the unit cell extends to yet another side of each rhombus.

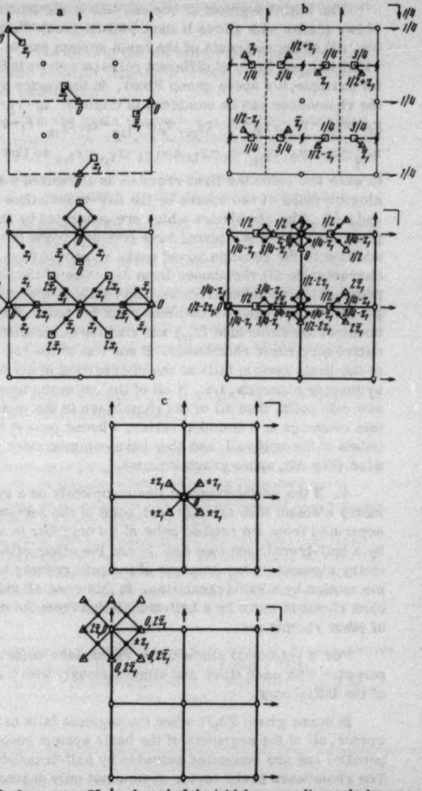

Fig. 3. Space group $P2_1/c$; the end of the initial segment lies at the intersection of 2_1 and c (a); space group Pbca, one end of the basis segment lies at the intersection of two elements, the planes b and a (b); space group Pmmm, the end of the segment lies at the intersection of all seven symmetry elements (c).

In the space group $P2_1/c$ we let one end of the initial segment fall at the intersection of the 2_1 axis and the c plane (Fig. 3a). The segments can be divided simultaneously into two pairs $r_0 - r_{2_1}$ and $r_c - r_{\bar{1}}$, which are connected with b/2 and $r_0 - r_c$ and $r_{2_1} - r_{\bar{1}}$, which are connected with c/2. In the vector system the rhombuses from 2_1 and c have common bound peaks, which are separated respectively by b/2 and c/2 from the origin of coordinates, while the bound peak for the centrosymmetric rhombus (line) falls at the intersection of the Harker cross sections and will be the common point for all four centrosymmetric lines. If one end of the initial segment lies simultaneously on three symmetry elements (in Fedorov group P2/m, at the intersection of axis 2, plane m, and the point $\bar{1}$, common to the four intercepts, in the reference system), then in the vector system we will have a bound peak at the origin common to all rhombuses, which also merges along two sides of each rhombus with the sides of the three others, including also the rays of the initial star.

The initial segment of one end lies at the intersection of two planes with glides b and *a*, space group Pbc*a*, Fig. 3b. All of the segments of the basis system can be divided into two kinds of different pairs (see above in Sec. 2, for example, for space group Pbc*a*). In the vector system the rhombuses can be combined in triplets: $r_0-r_b-r_a$, $r_c-r_{2_{1z}}-r_{2_{1x}}$, $r_b-r_0-r_{2_{1y}}$, $r_a-r_{2_{1y}}-r_0$, $r_{2_{1x}}-r_i-r_c$, $r_{2_{1y}}-r_a-r_b$, $r_{2_{1z}}-r_c-r_i$, and $r_i-r_{2_{1x}}-r_{2_{1z}}$ so that within each two sides the first rhombus is connected with analogous sides of two others by the half-translations b/2 and *a*/2. The rhombuses which are generated by the b plane (and also the *a* plane) have common bound peaks in addition to the common bound peaks related to them, which characterize all rhombuses from 2_{1z}. One of the bound peaks of the rhombus from 2_{1z} and i falls in a particular position and becomes a common point for pairs of rhombuses of the same kind (2_{1z}) and also for quadruplets of centrosymmetric rhombuses. If one end of the segment in the basis system falls at the intersection of all seven symmetry elements, i.e., if all of the segments have a common point, then all of the rhombuses in the vector system converge at a common vertex, a bound peak at the origin of the unit cell, and they have common sides pairwise (Fig. 3c, space group Pmmm).

4. If the initial segment lies completely on a symmetry element then already each point of the segment is separated from the related point of its neighbor in a pair by a half-translation (see Sec. 2) and the effect of the symmetry element on any segment of the pair reduces to simple motion by a half-translation. In this case all sides of each rhombus move by a half-translation from the sides of other rhombuses.

For a rotational element the rhombuses coincide pairwise with each other and simultaneously with the rays of the initial star.

In space group $P2_1/c$ when the segment falls in the c plane, all of the segments of the basis system become parallel and are connected pairwise by half-translations. The rhombuses in the vector system not only degenerate into lines, but also are separated from each other by c/2. In Fig. 5a, space group Pbc*a*, the initial star lies in the b plane (we can assume that this particular case is version 1). All of the segments in the basis system are pairwise related by the half-translation b/2 and the same half-translation separates the corresponding rhombuses in the vector system. The rhombuses which correspond to the b plane and a 2_{1x} axis degenerate into lines.

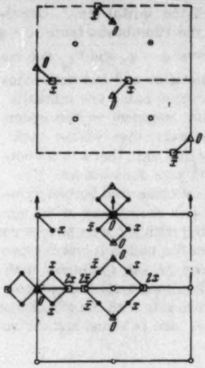
Fig. 4. The space group $P2_1/c$; the segments lie on two ends of the symmetry elements 2_1 and c.

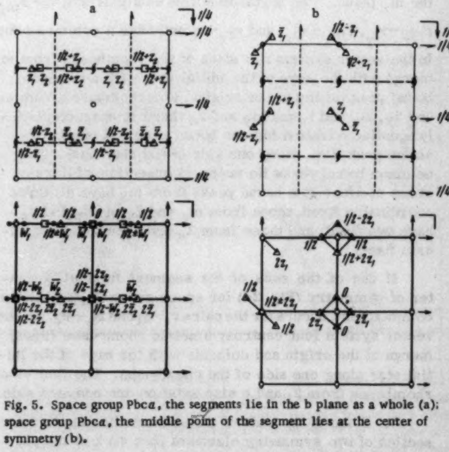

Fig. 5. Space group Pbc*a*, the segments lie in the b plane as a whole (a); space group Pbc*a*, the middle point of the segment lies at the center of symmetry (b).

If the ends of the segment are connected to symmetry elements, i.e., the segment carries this element into itself, the rhombuses corresponding to other symmetry elements are mutually superimposed and the vertices of the common rhombus will be bound peaks while its center turns out to be at the intersection of the Harker cross sections. The rhombuses from this symmetry element come in to the rays of the initial star. In Fig. 5b, space group Pbc*a*, the center of inversion divides the segment into halves, i.e., the segment is carried into itself by the inversion center: $r_0 \rightarrow r_i$, $r_b \rightarrow r_{2_{1x}}$, $r_c \rightarrow r_{2_{1y}}$, and $r_a \rightarrow r_{2_{1z}}$. In the vector system all of the rhombuses which correspond to the coincidence of segments have at their vertices only bound peaks, while the centers of the rhombuses lie at the intersections of the Harker cross sections.

5. If the ends of the basis segments lie on two different symmetry elements, then the results previously obtained[2] for each of the ends of the segments are superposed. Each rhombus corresponds to two related ones; for the four sides of the first rhombus there are two adjoining sides lying at a half-translation from the two sides of the second while the two others are at a half-translation from two sides of the third rhombus. Here all of the rhombuses which correspond to symmetry elements at which the ends of segments rest should (individually) have a common bound peak (Fig. 4, $P2_1/c$, the segment rests its ends on the 2_1 axis and the c plane). The segments are divided into two pairs in the basis system, $r_0-r_{2_1}$ and r_c-r_i, in which the ends are related by half-

translations b/2 plus two pairs $r_0 - r_c$ and $r_{2_1} - r_1$, where the other ends are already related by the glide c/2. In the corresponding vector system each pair of rhombuses from 2_1 and c have a bound peak in common; for a centrosymmetric rhombus (line) it is characteristic to have a separation of one bound peak and an interaction peak by c/2 from the sides of the 2_1 rhombus and another bound peak and the same interaction peak separated by b/2 from the sides of the rhombus which is generated by the c plane. Since both bound peaks of each centrosymmetric rhombus lie in Harker cross sections (both 2_1 and c), then one should be common for pairs of centrosymmetric rhombuses. The case where the basis segment lies in the symmetry planes b and *a* at both ends in the space group Pbc*a* is close to that considered in Sec. 3 (Fig. 3b). In this version the segment can be located in two ways, either the ends of the segments are connected with the translations b/2 or the other ends of the segments are connected with translations *a*/2.

The regularity in the arrangement of the rhombuses in the vector system is similar to that considered in Sec. 3 (Fig. 3b), only previously we had $W_1 = {}^1\!/_4 - z_1$, $W_2 = {}^3\!/_4 - z_1$, and in the present case we have $W_1 = z_2 - {}^1\!/_4$, $W_2 = {}^1\!/_4 + z_2$.

We give a brief recapitulation of what has been said:

a) The particular position of the basis segment leads to the appearance of pseudosymmetry (additional), either a center of symmetry or translations, or identity operations which relate the basis segment with derived ones.

b) When the initial segment is parallel or perpendicular to a symmetry element, the rhombus corresponding to the symmetry element degenerates into a line.

c) If the segment at one end (ends) or as a whole lies on a symmetry element, then the corresponding rhombuses of the vector system are pairwise connected and either are separated from each other by a half-translation (symmetry elements with glide) or have a common vertex (there is no glide).

d) If the ends of the segments are connected to a symmetry element, then the vertices of the rhombuses will be bound peaks.

e) With the basis segment in a particular position the rhombuses are mutually superimposed and correspondingly there is a drop in the number of independent peaks which characterize this symmetry element; this also substantially complicates localization of the rhombuses.

f) In groups with centered lattices there is no new (in principle) version of the degeneracy in comparison with that considered in the primitive lattice.

g) Diagrams of degenerate rhombuses are easily obtained from the standard ones by simply relating the hitherto independent coordinates of the vertices of rhombuses for each particular explicit arrangement of the basis segments in the basis system.

The authors thank V. V. Ilyukhin for participation in the discussion of the results.

---

1) We denote the initial segment by r_0 and those derived from it by symmetry operations by r_2 or r_{2_1} when they come from rotational or screw axes, by r_m, r_c, etc., for symmetry planes, and by r_1 for an inversion center.

2) For clarity the diagrams show both the independent and some dependent rhombuses in the whole Patterson unit cell.

3) In the general case in a centrosymmetric rhombus (line) there are no fixed coordinates; the bound peaks from an axis exist along one fixed coordinate while those from a plane exist along two fixed coordinates.

4) The rhombuses of the same form correspond to symmetry elements of the same order, for example, twofold 2, m, or 1.

---

[1] É. A. Kuz'min, V. P. Golovachev, and N. V. Belov, in: Patterson Methods of Structure Analysis [in Russian], Shtiintsa, Kishinev (1972).

[2] É. A. Kuz'min, V. P. Golovachev, and N. V. Belov, Dokl. Akad. Nauk SSSR, 207, 1340 (1972) [Sov. Phys. – Dokl., 17, 1136 (1973)].

Vector-localizing cross section through a double Patterson function

V. N. Biyushkin

Institute of Applied Physics, Academy of Sciences of the Moldavian SSR

(Submitted January 17, 1972; resubmitted July 27, 1972)
Kristallografiya, 18, 689-693 (July-August 1973)

When a fixed interatomic vector and vectors found by calculation of the radius vector of some point from the vector sum of the radius vector of the same point after application of a symmetry transformation are used as parameters of a double Patterson function, the maxima in the cross section thus constructed represent atoms forming the starting points of interatomic vectors equal to the fixed vector.

Interpretation of an interatomic function usually reduces to analysis of the multiple peaks. The more complicated the structure, the higher will be the multiplicity of the peaks still emerging from the general background of the Patterson function. This makes it necessary to start from the multiple peaks. For successful deciphering of the structure it is desirable to know the arrangement of those atom pairs which generate the original peak. In particular, information on the arrangement of those atom pairs may suffice for sorting out the structure mappings distinguished by Buerger functions[1] and obtaining a single mapping. Such information is used also in the multiple peak method.[2,3]

The cross section through the double Patterson function considered in the present paper may be used for singling out interatomic vectors equal to the fixed vector. This procedure makes it possible to localize with some definiteness (or, rather, some indefiniteness) precisely those atom pairs in the structure which generate the maximum of the Patterson function taken as the starting peak, i.e., to localize the interatomic vectors which are equal to the fixed vector. This feature explains why we call these cross sections vector-locating cross sections.

To construct a vector-locating cross section we define the parameter vectors $\mathbf{u}_1$ and $\mathbf{u}_2$ in the double Patterson function[4]

$$DP(\mathbf{u}_1, \mathbf{u}_2) = \int_V \rho(\mathbf{r})\rho(\mathbf{r}+\mathbf{u}_1)\rho(\mathbf{r}+\mathbf{u}_2)\,dV \tag{1}$$

as follows:

$$\begin{aligned} \mathbf{u}_1 &= \mathbf{u}_m = \vartheta_m(\mathbf{r}+\mathbf{u}_0) - \mathbf{r}, \\ \mathbf{u}_2 &= \mathbf{u}_n = \vartheta_n(\mathbf{r}+\mathbf{u}_0) - \mathbf{r}. \end{aligned} \tag{2}$$

Here, $\mathbf{u}_0$ denotes the fixed (given) interatomic vector: According to ref. 5, the symbol ϑ denotes a transformation operator of the space symmetry group $\{A|\mathbf{t}\}$ and $\mathbf{r}$ the radius vector of the point. The cross section considered will be described by the function

$$\begin{aligned} DP(\mathbf{u}_0, \mathbf{r}) = \int_V &\rho(\mathbf{r}')\rho(\mathbf{r}' + [\vartheta_m(\mathbf{r}+\mathbf{u}_0) - \mathbf{r}]) \\ &\times \rho(\mathbf{r}' + [\vartheta_n(\mathbf{r}+\mathbf{u}_0) - \mathbf{r}])\,dV \end{aligned} \tag{3}$$

or by the following Fourier series:

$$\begin{aligned} DP(\mathbf{u}_0, \mathbf{r}) = \frac{1}{V^2} \sum_{\mathbf{H}_1} \sum_{\mathbf{H}_2} &F(-\mathbf{H}_1 - \mathbf{H}_2) F(\mathbf{H}_1) F(\mathbf{H}_2) \\ \times \exp(-2\pi i (&\mathbf{H}_1[\vartheta_m(\mathbf{r}+\mathbf{u}_0) - \mathbf{r}] + \mathbf{H}_2[\vartheta_n(\mathbf{r}+\mathbf{u}_0) - \mathbf{r}])). \end{aligned} \tag{4}$$

If the crystal has a symmetry center, the series (4) can be calculated approximately from the modulus of the structural amplitude, provided that Sayre–Zachariasen's[6-8] sign relationship $S(\mathbf{H})S(\mathbf{K}) \approx S(\mathbf{H}+\mathbf{K})$ is employed. Consequently, the cross section $DP(\mathbf{u}_0, \mathbf{r})$ can be constructed also for some crystals of unknown structure; this cannot be done for any crystal, but only for a crystal having an inversion center and a symmetry not lower than monoclinic.

We shall consider what atom combinations in what points generate peaks in a vector-locating cross section. From (3) it follows that peaks appear in the function $DP(\mathbf{u}_0, \mathbf{r})$ if there exists an arrangement – albeit a single one – in which all apices of the summation triangle defined by the arguments of the factors in the function under the integral sign are simultaneously occupied by atoms. The condition for a maximum can be written as follows:

$$\begin{aligned} \mathbf{r}' &= \mathbf{r}_j, \\ \mathbf{r}' + \vartheta_m(\mathbf{r}+\mathbf{u}_0) - \mathbf{r} &= \mathbf{r}_k, \\ \mathbf{r}' + \vartheta_n(\mathbf{r}+\mathbf{u}_0) - \mathbf{r} &= \mathbf{r}_l, \end{aligned} \tag{5}$$

where j, k, and l denote the numbers of atoms in the structure. This condition reduces to the following set of two equations:

$$\begin{aligned} \mathbf{r}_j + \vartheta_m(\mathbf{r}+\mathbf{u}_0) - \mathbf{r} &= \mathbf{r}_k, \\ \mathbf{r}_j + \vartheta_n(\mathbf{r}+\mathbf{u}_0) - \mathbf{r} &= \mathbf{r}_l. \end{aligned} \tag{6}$$

Supposing that the fixed vector $\mathbf{u}_0$ is formed by the atoms p and q, $\mathbf{u}_0 = \mathbf{r}_q - \mathbf{r}_p$, we get the final system defining the coordinates $\mathbf{r}$ of a possible jk$l$-th peak

$$\begin{aligned} \vartheta_m\mathbf{r} - \mathbf{r} &= \mathbf{r}_k - \mathbf{r}_j - \vartheta_m(\mathbf{r}_q - \mathbf{r}_p), \\ \vartheta_n\mathbf{r} - \mathbf{r} &= \mathbf{r}_l - \mathbf{r}_j - \vartheta_n(\mathbf{r}_q - \mathbf{r}_p). \end{aligned} \tag{7}$$

Since the coordinates of the atoms in the various structures cover only a completely defined set of values, the set of equations can certainly not be satisfied by any combination of atoms. It is obvious that the set has the solution $\mathbf{r} = \mathbf{r}_j = \mathbf{r}_p$. Substitution of this solution transforms the set (7) into the very simple set

$$\begin{aligned} \mathbf{r}_k &= \vartheta_m\mathbf{r}_q, \\ \mathbf{r}_l &= \vartheta_n\mathbf{r}_q. \end{aligned} \tag{8}$$

Since k and l take all possible values from unity to the total number N of atoms in the structure, it is always possible to find two atoms k and l which satisfy (8).

Consequently, a peak of the function $DP(\mathbf{u}_0, \mathbf{r})$ appears at the point whose radius vector $\mathbf{r}$ coincides with the radius vector of the atom p forming the starting point of the fixed interatomic vector $\mathbf{u}_0$. The peak is generated by the atoms p, k, and l. The two latter atoms are equivalent to the atom q, which is the end point of the fixed vector $\mathbf{u}_0$. The atom k is related to q by the transformation $Э_m$, the atom l by the transformation $Э_n$.

If the structure contains another interatomic vector equal to $\mathbf{u}_0$, a peak of the function $DP(\mathbf{u}_0, \mathbf{r})$ will correspond to the latter vector and occur at the point whose radius vector coincides with the radius vector of the atom forming the starting point of the second interatomic vector, which is equal to $\mathbf{u}_0$. The same holds for other similar vectors. Corresponding to each interatomic vector equalling the fixed $\mathbf{u}_0$ is a peak of the function $DP(\mathbf{u}_0, \mathbf{r})$, and the coordinates of the peak are equal to the coordinates of the atom forming the starting point of the fixed vector.

Consequently, a regular peak in the cross section localizes the starting point of an interatomic vector which equals $\mathbf{u}_0$ and refers to the fixed origin or, in other words, refers to the symmetry elements $Э_m$ and $Э_n$, corresponding to the given transformations $Э_m$ and $Э_n$. The unit cell contains, besides $Э_m$ and $Э_n$ the identical element combinations $Э_m'$ and $Э_m'$, which correspond to the product of $Э_m$ or $Э_n$ and a translation of the crystal lattice.[9] Let

$$Э_m' = T_1 Э_m = \{A_m | \mathbf{t}_m + \mathbf{T}_1\} \text{ and } Э_n' = T_2 Э_n = \{A_n | \mathbf{t}_n + \mathbf{T}_2\}.$$

For $\mathbf{r}$ we shall now choose the radius vector of the point oriented in the same way with respect to $Э_m'$ and $Э_n'$ as the atom p forming the starting point of one of the interatomic vectors equal to $\mathbf{u}_0$ is oriented with respect to $Э_m$ and $Э_n$. This implies that the following equalities hold:

$$\begin{aligned} Э_m \mathbf{r}_p - \mathbf{r}_p &= Э_m' \mathbf{r} - \mathbf{r}, \\ Э_n \mathbf{r}_p - \mathbf{r}_p &= Э_n' \mathbf{r} - \mathbf{r}. \end{aligned} \tag{9}$$

Then $Э_m(\mathbf{r} + \mathbf{u}_0) - \mathbf{r} = Э_m'(\mathbf{r} + \mathbf{u}_0) - \mathbf{T}_1 - \mathbf{r} = Э_m(\mathbf{r}_p + \mathbf{u}_0) - \mathbf{r}_p - \mathbf{T}_1$ and $Э_n(\mathbf{r} + \mathbf{u}_0) - \mathbf{r} = Э_n(\mathbf{r}_p + \mathbf{u}_0) - \mathbf{r}_p - \mathbf{T}_2$. When $\mathbf{r}' = \mathbf{r}_p$, the summation triangle defined by the $\mathbf{r}$ vectors chosen transforms into a single product of the following values of the electron density: $\rho(\mathbf{r}_p)\rho(\mathbf{r}_p + Э_m[\mathbf{r}_p + \mathbf{u}_0] - \mathbf{r}_p - \mathbf{T}_1)\,\rho(\mathbf{r}_p + Э_n[\mathbf{r}_p + \mathbf{u}_0] - \mathbf{r}_p - \mathbf{T}_2) = \rho(\mathbf{r}_p)\rho(Э_m \mathbf{r}_q - \mathbf{T}_1)\rho(Э_n \mathbf{r}_q - \mathbf{T}_2)$. Each factor corresponds to a value of the electron density in the center of an atom: the first with the electron density in the center of atom p forming the starting point of the interatomic vector pq, which is equal to $\mathbf{u}_0$, and to the second and third with the electron densities in the centers of the atoms k and l, which are identical but for a translation and equivalent to the atom q forming the end point of the vector pq. Consequently, the radius vector $\mathbf{r}$ of a point oriented in the same way with respect to $Э_m'$ and $Э_n'$ as atom p is oriented with respect to $Э_m$ and $Э_n$ defines a configuration of the summation triangle which also warrants a peak of the function. The peak appears in the point $\mathbf{r}$, which is removed from the point $\mathbf{r}_p$ by the vector $\mathbf{d}'$, equal to the displacement of the element pair $Э_m$ and $Э_n$ with respect to the similar configuration of the elements $Э_m'$ and $Э_n'$. The peaks at the points $\mathbf{r}_p$ and $\mathbf{r} = \mathbf{r}_p + \mathbf{d}'$ are indistinguishable in the synthesis of $DP(\mathbf{u}_0, \mathbf{r})$ and are of equal magnitude, since the first of them is generated by the atoms p, k, and l, and the second by the same atom p and the atoms k' and l', which, but for a translation, are identical to the atoms k and l, respectively.

If the symmetry of the crystal is such that the lattice cell contains g element pairs which not only are similar to the elements $Э_m$ and $Э_n$ corresponding to the symmetry transformation yielding the cross section, but also form configuration pairs similar to the configuration of the elements $Э_m$ and $Э_n$, then g peaks of the function $DP(\mathbf{u}_0, \mathbf{r})$ will correspond to every interatomic vector which equals $\mathbf{u}_0$. The coordinates of these peaks are defined by the equations $\mathbf{r} = \mathbf{r}_p + \mathbf{d}_i$, $i = 1, 2, \ldots, g$, where $\mathbf{d}_i$ are the vectors which represent the displacement of the identical combinations of elements similar to $Э_m$ and $Э_n$ with respect to these elements, $\mathbf{d}_1 = 0$. All these peaks are of identical height and it is impossible to conclude from the cross section what peak corresponds to the original position of the interatomic vector equal to $\mathbf{u}_0$. As a result difficulties arise in the assignment of a given peak to a given combination of the symmetry elements $Э_m'$ and $Э_n'$. This problem becomes particularly great when peaks from different sets of equivalent peaks corresponding to different interatomic vectors all equal to $\mathbf{u}_0$ are to be localized. This is the so-called implicative indefiniteness, which is analogous to the indefiniteness of implicative diagrams[1] and also to that of cross sections through a double Patterson function when symmetry transformations are used in the construction of the double Patterson function.[10-12] In particular, this indefiniteness is identical to the implicative indefiniteness of symmetrical cross sections through a double Patterson function.[10]

Let the structure contain not a single interatomic vector equal to $\mathbf{u}_0$, but several vectors, say, h. Then, g regular peaks will correspond to each interatomic vector in the cross section. We shall call such peaks "main peaks." gh main peaks will correspond to the h vectors. For certain combinations of the transformations $Э_m$ and $Э_n$ yielding the cross section there may appear so-called satellite peaks, whose positions can be derived from the positions of the main peak by means of definite rules. The appearance of satellite peaks, if in principle admitted by the symmetry of the crystal, further depends on the actual orientation of the fixed vector $\mathbf{u}_0$.

In (4) we substitute, instead of the structural amplitudes themselves, their expression in the atomic scattering factors and the coordinates of the atoms. This yields

$$\begin{aligned} DP(\mathbf{u}_0, \mathbf{r}) = \frac{1}{V^2} \sum_{jkl} \sum_{\mathbf{H}_1} \sum_{\mathbf{H}_2} & f_j(-\mathbf{H}_1 - \mathbf{H}_2) f_k(\mathbf{H}_1) f_l(\mathbf{H}_2) \\ & \times \exp\{-2\pi i \mathbf{H}_1 [Э_m(\mathbf{r} + \mathbf{u}_0) - \mathbf{r} - \mathbf{r}_k + \mathbf{r}_j]\} \\ & \times \exp\{-2\pi i \mathbf{H}_2 [Э_n(\mathbf{r} + \mathbf{u}_0) - \mathbf{r} - \mathbf{r}_l + \mathbf{r}_j]\}. \end{aligned} \tag{10}$$

The function has a maximum when the sum in the exponents of the exponential factor is zero:

$$\vartheta_m \mathbf{r} - \mathbf{r} + \vartheta_m \mathbf{r}_q - \vartheta_m \mathbf{r}_p - \mathbf{r}_k + \mathbf{r}_j = 0,$$
$$\vartheta_n \mathbf{r} - \mathbf{r} + \vartheta_n \mathbf{r}_q - \vartheta_n \mathbf{r}_p - \mathbf{r}_l + \mathbf{r}_j = 0.$$

This set is identical to the set (7) derived above for a maximum. Here, too, it is assumed that $\mathbf{u}_0 = \mathbf{r}_q - \mathbf{r}_p$. It has been shown that this set yields a solution when $\mathbf{r} = \mathbf{r}_j = \mathbf{r}_p$. The regular main peak corresponding to this solution appears in the point $\mathbf{r} = \mathbf{r}_p$. It is generated by the atom $j = p$ and the atoms k and l, which are equivalent to q and related to q by the transformations ϑ_m and ϑ_n, respectively.

The height of the main separate jkl-th peak is given by the sum

$$\frac{1}{V^2}\sum_{\mathbf{H}_1}\sum_{\mathbf{H}_2} f_j(-\mathbf{H}_1-\mathbf{H}_2) f_k(\mathbf{H}_1) f_l(\mathbf{H}_2)$$

$$= \frac{1}{V^2}\sum_{\mathbf{H}_1}\sum_{\mathbf{H}_2} f_p(-\mathbf{H}_1-\mathbf{H}_2) f_q(\mathbf{H}_1) f_q(\mathbf{H}_2). \tag{11}$$

If the structure contains similar atoms, Eq. (11) can be transformed into

$$\frac{Z_p Z_q^2}{V^2}\sum_{\mathbf{H}_1}\sum_{\mathbf{H}_2} \hat{f}(-\mathbf{H}_1-\mathbf{H}_2) \hat{f}(\mathbf{H}_1) \hat{f}(\mathbf{H}_2), \tag{12}$$

where $\hat{f}(\mathbf{H}) = f_j(\mathbf{H})/Z_j$ denotes the atomic factor, Z the sequence number of the atom. Consequently, the height of a main peak for a structure consisting of similar atoms is proportional to the sequence number of the atom forming the starting point of the interatomic vector equal to $\mathbf{u}_0$ and to the squared sequence number of the atom forming the end point of this vector.

Since the equalities $T\vartheta\mathbf{r} = \vartheta\mathbf{r} + \mathbf{T}$ and $\rho(\mathbf{r} + \mathbf{T}) = \rho(\mathbf{r})$ hold, it is easily shown that the cross section defined by the symmetry transformations ϑ_m and ϑ_n for a given fixed vector $\mathbf{u}_0$ is identical to the cross section defined for the same vector by the products of the transformations and a translation of the crystal lattice (the products $T_i\vartheta_m$ and $T_j\vartheta_n$):

$$DP_{T_i\vartheta_m, T_j\vartheta_n}(\mathbf{u}_0, \mathbf{r}) = DP_{\vartheta_m, \vartheta_n}(\mathbf{u}_0, \mathbf{r}).$$

Another method, viz., separation of parallel peak lines in the Patterson function, can also be used for determining the arrangement of the interatomic vectors which equal a fixed vector.[3] In the application of this method a Patterson synthesis yields the original distribution. This explains why the method offers definite advantages: Only the modulus of the structural amplitudes is needed for the synthesis, the method is applicable to crystals of any symmetry, and does not lead to implicative indefiniteness. On the other hand, the method is sensitive to undesirable characteristics of the function itself, i.e., to the intensive background, the accidental and inaccurate superposition of peaks, and the "smearing" of the maxima. The method of separating peak lines, and that of vector-locating cross sections may complement each other as regards the results. Therefore, the efficiency of the search for equal interatomic vectors and the reliability of the results will be improved if both methods are used.

---

[1] M. Buerger, Vector Space and Its Application in Crystal Structure Investigation, Wiley, New York (1959).

[2] E. A. Kuz'min, V. V. Ilyukhin, and N. V. Belov, Dokl. Akad. Nauk SSSR, 189, 774 (1969) [Sov. Phys. – Dokl., 14, 1136 (1970)].

[3] E. A. Kuz'min, V. V. Ilyukhin, and N. V. Belov, Zh. Strukt. Khim., 11, 778 (1970).

[4] D. Sayre, Acta Crystallogr., 6, 430 (1953).

[5] F. Seitz, Ann. Math., 37, 17 (1936).

[6] D. Sayre, Acta Crystallogr., 5, 60 (1952).

[7] W. Cochran, Acta Crystallogr., 5, 65 (1952).

[8] W. H. Zachariasen, Acta Crystallogr., 5, 68 (1952).

[9] N. V. Belov, Tr. Inst. Kristallogr., No. 6, 25 (1951).

[10] V. N. Biyushkin and N. V. Belov, Kristallografiya, 9, 771 (1964) [Sov. Phys. – Crystallogr., 9, 655 (1965)].

[11] V. N. Biyushkin, Kristallografiya, 17, 729 (1972) [Sov. Phys. – Crystallogr., 17, 641 (1973)].

[12] V. N. Biyushkin, Kristallografiya, 17, 737 (1972) [Sov. Phys. – Crystallogr., 17, 647 (1973)].

Primitive rotation regions of two Patterson syntheses

V. I. Burdina

Institute of Crystallography, Academy of Sciences of the USSR

(Submitted February 23, 1972; resubmitted July 14, 1972)
Kristallografiya, 18, 694–700 (July–August 1973)

A method is described for isolating the primitive rotation regions of two syntheses P_1 and P_2 of interatomic vector functions, with respect to rotation groups of the latter. Tables are presented with 66 symmetry groups, which describe radial rotation regions by denoting the limits of change of axial direction and angles of rotation.

The symmetry of the component rotations of two syntheses P_1 and P_2 of interatomic vector functions is described in refs. 1 and 2 by the direct product $G_1 \times G_2$ of the rotation groups G_1 and G_2 of the interatomic vector functions. Since only the relative position of the syntheses is important, one may consider the synthesis P_1 as fixed and the synthesis P_2 as rotating. The product $S \times T$ of the rotations S and T of groups G_1 and G_2 will then be related to the equivalent rotations ρ and ρ' of refs. 3 and 4:

$$\rho' = S\rho T. \tag{1}$$

In the rotation function of ref. 3,

$$R(\rho) = \int_{\bullet} P_1(u) P_2(\rho^{-1}u)\, du,$$

representing an integral taken about a spherical region from the product $P_1(u)$ to the value of P_2 at the point $\rho^{-1}u$ (made coincident with u by a rotation ρ), the equivalence (1) reduces to the equality $R(\rho) = R(\rho')$.

Representation of the rotations by quaternions,[5] in distinction from known descriptions,[2,4] permits construction of a geometric model of a variety of rotations in the form of points of a single three-dimensional sphere S^3 in four-dimensional Euclidean space R^4, with linear orthogonal transformations as symmetry conversions. Besides this, representation by quaternions allows a simple transition to be described with representation of the rotations by their axis and angle of rotation. Primitive or fundamental rotation regions comprising nonequivalent rotations may be obtained as radial regions by specifying the directions of the l rotation axis and the limits of the rotational angles φ from $\varphi = 0$ to some $\varphi_{\max}(l)$, using the "principle of the maximum" (see, for example, ref. 6). A rotation of ρ with the rotation axis along the direction

$$\mathbf{l} = l_1\mathbf{i} + l_2\mathbf{j} + l_3\mathbf{k}, \quad l_1^2 + l_2^2 + l_3^2 = 1$$

and a rotation angle φ may be described by the unit quaternion:

$$\mathbf{u} = \cos\varphi/2 + \sin(\varphi/2)\,(l_1\mathbf{i} + l_2\mathbf{j} + l_3\mathbf{k}) = u_0 + u_1\mathbf{i} + u_2\mathbf{j} + u_3\mathbf{k}, \tag{2}$$

where $u_0 = \cos\varphi/2$, $u_i = l_i \sin\varphi/2$, $i = 1, 2, 3$. On substitution of $\varphi + 2\pi$ for φ, the rotation does not change; however the quaternion u changes sign. The quaternion-rotations thus have a center of inversion.

The equivalence (1) obeys the quaternion relationship:

$$\mathbf{u}' = \mathbf{s}\mathbf{u}\mathbf{t}. \tag{3}$$

Operations with quaternions are analogous to operations with complex numbers, during which: $\mathbf{i}^2 = \mathbf{j}^2 = \mathbf{k}^2 = -1$, $\mathbf{ij} = \mathbf{k}$, $\mathbf{jk} = \mathbf{i}$, $\mathbf{ki} = \mathbf{j}$, $\mathbf{ij} = -\mathbf{ji}$, $\mathbf{jk} = -\mathbf{kj}$, $\mathbf{ki} = -\mathbf{ik}$.

After conversion to the component form of notation, the equivalence (3) assumes the form

$$\left.\begin{aligned} u_0' &= z_{00}u_0 + z_{01}u_1 + z_{02}u_2 + z_{03}u_3, \\ u_1' &= z_{10}u_0 + z_{11}u_1 + z_{12}u_2 + z_{13}u_3, \\ u_2' &= z_{20}u_0 + z_{21}u_1 + z_{22}u_2 + z_{23}u_3, \\ u_3' &= z_{30}u_0 + z_{31}u_1 + z_{32}u_2 + z_{33}u_3 \end{aligned}\right\} \tag{3a}$$

or in matrix form

$$\mathbf{u}' = \mathbf{Z}\mathbf{u}, \tag{3b}$$

where the orthogonal 4×4 matrix $\mathbf{Z} = \| z_{ij} \|$ is equal to the product of commuting matrices S and T:

$$\mathbf{Z} = \mathbf{ST} = \mathbf{TS}, \tag{4}$$

during which

$$\mathbf{S} = \begin{pmatrix} s_0 & -s_1 & -s_2 & -s_3 \\ s_1 & s_0 & -s_3 & s_2 \\ s_2 & s_3 & s_0 & -s_1 \\ s_3 & -s_2 & s_1 & s_0 \end{pmatrix}, \quad \mathbf{T} = \begin{pmatrix} t_0 & -t_1 & -t_2 & -t_3 \\ t_1 & t_0 & t_3 & -t_2 \\ t_2 & -t_3 & t_0 & t_1 \\ t_3 & t_2 & -t_1 & t_0 \end{pmatrix}$$

The matrices of the left and right rotations S and T are determined by the quaternions $\mathbf{s} = s_0 + s_1\mathbf{i} + s_2\mathbf{j} + s_3\mathbf{k}$ and $\mathbf{t} = t_0 + t_1\mathbf{i} + t_2\mathbf{j} + t_3\mathbf{k}$.

Table 1 enumerates (ref. 5) the equivalent points of the left and right quaternion conversions $\mathbf{u}' = \mathbf{su}$ and $\mathbf{u}'' = \mathbf{ut}$, associated with the principal rotational axes:

$$2_{001},\ 2_{010},\ 2_{100},\ 4_{001},\ 4_{010},\ 4_{100},\ 3_{001},\ 6_{001},\text{and } 3_{111}. \tag{5}$$

Each of the conversions associated with the axes in (5) decays to R^4 over two rotations, with a doubly reduced rotation angle. This occurs in two orthogonal planes, one of which contains the direction u_0 and the direction l of the rotation axis.

We note that the overall transformation (3) does not change the coordinate u_0 of the longitudinal point $\mathbf{u} = (u_0, u_1, u_2, u_3)$. It only does this in the case where it has the form $\mathbf{u}' = \mathbf{sus}^{-1}$, and reduces to a rotation of S in three-dimensional space $R^3(u_1, u_2, u_3)$.

In actuality, in this case the first line of (3a) reduces to the equality $u_0' = u_0$; consequently $z_{00} = 1$, $z_{01} = z_{02} = z_{03} = 0$. Bearing in mind that $z_{00} = s_0t_0 - s_1t_1 - s_2t_2 - s_3t_3$ is equal to the scalar product of the unit vectors $\mathbf{s}^{-1} = (s_0, -s_1, -s_2, -s_3)$ and $\mathbf{t} = (t_0, +t_1, +t_2, +t_3)$, we assume an equality of the vectors $\mathbf{s}^{-1}$ and t, i.e., $s_0 = t_0$, $s_1 = -t_1$, $s_2 = -t_2$, and $s_3 = -t_3$. Consequently, the "rotations" s and t differ in the signs of the directions, $\mathbf{l}(\mathbf{t})$ and $-\mathbf{l}(\mathbf{s})$, and is the reciprocal of $\mathbf{t} = \mathbf{s}^{-1}$.

Considering the latter circumstance, we conclude that in symmetry groups $G_i \times G_i$ not containing like comultipliers (except for the trivial 1×1, one may pick out rota-

TABLE 1. Elementary Transformations in a Quaternion Space

Axis of rotation	Direction	$u' = gu$	$u'' = ug$
1	—	$\pm(u_0,\ u_1,\ u_2,\ u_3)$	$\pm(u_0,\ u_1,\ u_2,\ u_3)$
2	001	$\pm(-u_3,\ -u_2,\ u_1,\ u_0)$	$\pm(-u_3,\ u_2,\ -u_1,\ u_0)$
	010	$\pm(-u_2,\ u_3\ u_0,\ -u_1)$	$\pm(-u_2,\ -u_3,\ u_0,\ u_1)$
	100	$\pm(-u_1,\ u_0,\ -u_3,\ u_2)$	$\pm(-u_1,\ u_0,\ u_3,\ -u_2)$
4	001	$\pm\frac{\sqrt{2}}{2}(u_0-u_3,\ u_1-u_2,\ u_1+u_2,\ u_0+u_3);$	$\pm\frac{\sqrt{2}}{2}(u_0-u_3,\ u_1+u_2,\ -u_1+u_2,\ u_0+u_3);$
		$\pm(-u_3,\ -u_2,\ u_1,\ u_0);$	$\pm(-u_3,\ u_2,\ -u_1,\ u_0);$
		$\pm\frac{\sqrt{2}}{2}(u_0+u_3,\ u_1+u_2,\ -u_1+u_2,\ -u_0+u_3)$	$\pm\frac{\sqrt{2}}{2}(u_0+u_3,\ u_1-u_2,\ u_1+u_2,\ -u_0+u_3)$
	010	$\pm\frac{\sqrt{2}}{2}(u_0-u_2,\ u_1+u_3,\ u_0+u_2,\ -u_1+u_3);$	$\pm\frac{\sqrt{2}}{2}(u_0-u_2,\ u_1-u_3,\ u_0+u_2,\ u_1+u_3);$
		$\pm(-u_2,\ u_3,\ u_0,\ -u_1);$	$\pm(-u_2,\ -u_3,\ u_0,\ u_1);$
		$\pm\frac{\sqrt{2}}{2}(u_0+u_2,\ u_1-u_3,\ -u_0+u_2,\ u_1+u_3)$	$\pm\frac{\sqrt{2}}{2}(u_0+u_2,\ u_1+u_3,\ -u_0+u_2,\ -u_1+u_3)$
	100	$\pm\frac{\sqrt{2}}{2}(u_0-u_1,\ u_0+u_1,\ u_2-u_3,\ u_2+u_3);$	$\pm\frac{\sqrt{2}}{2}(u_0-u_1,\ u_0+u_1,\ u_2+u_3,\ -u_2+u_3)$
		$\pm(-u_1,\ u_0,\ -u_3,\ u_2);$	$\pm(-u_1,\ u_0,\ u_3,\ -u_2);$
		$\pm\frac{\sqrt{2}}{2}(u_0+u_1,\ -u_0+u_1,\ u_2+u_3,\ -u_2+u_3)$	$\pm\frac{\sqrt{2}}{2}(u_0+u_1,\ -u_0+u_1,\ u_2-u_3,\ u_2+u_3)$
3	001	$\pm\frac{1}{2}(u_0-\sqrt{3}\,u_3,\ u_1-\sqrt{3}\,u_2,\ \sqrt{3}\,u_1+u_2,\ \sqrt{3}\,u_0+u_3);$	$\pm\frac{1}{2}(u_0-\sqrt{3}\,u_3,\ u_1+\sqrt{3}\,u_2,\ -\sqrt{3}\,u_1+u_2,\ \sqrt{3}\,u_0+u_3);$
		$\pm\frac{1}{2}(u_0+\sqrt{3}\,u_3,\ u_1+\sqrt{3}\,u_2,\ -\sqrt{3}\,u_1+u_2,\ -\sqrt{3}\,u_0+u_3)$	$\pm\frac{1}{2}(u_0+\sqrt{3}\,u_3,\ u_1-\sqrt{3}\,u_2,\ \sqrt{3}\,u_1+u_2,\ -\sqrt{3}\,u_0+u_3)$
6	001	$\pm\frac{1}{2}(\sqrt{3}\,u_0-u_3,\ \sqrt{3}\,u_1-u_2,\ u_1+\sqrt{3}\,u_2,\ u_0+\sqrt{3}\,u_3);$	$\pm\frac{1}{2}(\sqrt{3}\,u_0-u_3,\ \sqrt{3}\,u_1+u_2,\ -u_1+\sqrt{3}\,u_2,\ u_0+\sqrt{3}\,u_3);$
		$\pm\frac{1}{2}(u_0-\sqrt{3}\,u_3,\ u_1-\sqrt{3}\,u_2,\ \sqrt{3}\,u_1+u_2,\ \sqrt{3}\,u_0+u_3);$	$\pm\frac{1}{2}(u_0-\sqrt{3}\,u_3,\ u_1+\sqrt{3}\,u_2,\ -\sqrt{3}\,u_1+u_2,\ \sqrt{3}\,u_0+u_3);$
		$\pm(-u_3,\ -u_2,\ u_1,\ u_0);$	$\pm(-u_3,\ u_2,\ -u_1,\ u_0);$
		$\pm\frac{1}{2}(u_0+\sqrt{3}\,u_3,\ u_1+\sqrt{3}\,u_2,\ -\sqrt{3}\,u_1+u_2,\ -\sqrt{3}\,u_0+u_3);$	$\pm\frac{1}{2}(u_0+\sqrt{3}\,u_3,\ u_1-\sqrt{3}\,u_2,\ \sqrt{3}\,u_1+u_2,\ -\sqrt{3}\,u_0+u_3);$
		$\pm\frac{1}{2}(\sqrt{3}\,u_0+u_3,\ \sqrt{3}\,u_1+u_2,\ -u_1+\sqrt{3}\,u_2,\ -u_0+\sqrt{3}\,u_3)$	$\pm\frac{1}{2}(\sqrt{3}\,u_0+u_3,\ \sqrt{3}\,u_1-u_2,\ u_1+\sqrt{3}\,u_2,\ -u_0+\sqrt{3}\,u_3)$
3	111	$\pm\frac{1}{2}(u_0-u_1-u_2-u_3,\ u_0+u_1-u_2+u_3,\ u_0+u_1+u_2-u_3,\ u_0-u_1+u_2+u_3);$	$\pm\frac{1}{2}(u_0-u_1-u_2-u_3,\ u_0+u_1+u_2-u_3,\ u_0-u_1+u_2+u_3,\ u_0+u_1-u_2+u_3);$
		$\pm\frac{1}{2}(u_0+u_1+u_2+u_3,\ -u_0+u_1+u_2-u_3,\ -u_0-u_1+u_2+u_3,\ -u_0+u_1-u_2+u_3)$	$\pm\frac{1}{2}(u_0+u_1+u_2+u_3,\ -u_0+u_1-u_2+u_3;\ -u_0+u_1+u_2-u_3,\ -u_0-u_1+u_2+u_3)$

tions to the primitive region according to the principle of the largest coordinate u_0, i.e., requiring fulfillment of the inequality

$$|u_0^{(k)}| \leqslant |u_0^{(1)}|, \qquad k = 1, \ldots, n$$

in a system of equivalent points $u^{(k)}$. If we omit the signs of the moduli, as can always be done, bearing in mind the equivalent character of u and −u and using expressions (2) and (3), we get the inequality

$$z_{00}^{(k)} \cos \varphi/2 + (z_{01}^{(k)} l_1 + z_{02}^{(k)} l_2 + z_{03}^{(k)} l_3) \sin \varphi/2 \leqslant \cos \varphi/2$$

or if we divide both parts as $\cos \varphi/2 \geq 0$ (the rotation angle φ is considered to be within the limits $0 \leq \varphi \leq \pi$), we get

$$\operatorname{tg} \varphi/2 (z_{01}^{(k)} l_1 + z_{02}^{(k)} l_2 + z_{03}^{(k)} l_3) \leqslant 1 - z_{00}^{(k)}, \qquad (6)$$

$k = 1, 2, \ldots, n$. The system of inequalities (6) at fixed l_1, l_2, and l_3 defines the limits of change of the angle φ from 0 to some $\varphi_{\max}(l_1, l_2, l_3)$.

We note that the primitive rotation regions on a unit sphere S^3 of four-dimensional quaternion space R^4, chosen on the principle of the maximum, are not much different from the generalized regions of Voronov[7] or the stereohedra of Delone,[8] with a center at the point $u^*(1, 0, 0, 0)$, i.e., they are the geometric loci of points nearest to u^* in a system of equivalent u^* points.

The addition of the transformations of type $S \times S^{-1}$ forming a rotation subgroup $R^3(u_1, u_2, u_3)$, permits a further decrease in the region of change of the directions $l = (l_1, l_2, l_3)$, according to the rules of manipulation for the usual rotation space groups.

Table 2 describes the primitive regions of 66 symmetry groups $G_i \times G_j$ with $i \geq j$. The original groups G_i corresponding to the Laue point groups[9] are given in Ta-

TABLE 2. Primitive Rotation Regions

No.	Group	Group order	Conditions at a rotation angle φ	Conditions at direction of rotations l	Symmetry of primitive region
1	{1} × {1}	1	$0<\operatorname{tg}\frac{\varphi}{2}<\infty$	—	$P_\infty(l_1, l_2, l_3)$
2	{2} × {1}	2	$0<\operatorname{tg}\frac{\varphi}{2}<\frac{1}{\|l_3\|}$	—	$P_\infty(0,0,1)/m$
3	{222} × {1}	4	$0<\operatorname{tg}\frac{\varphi}{2}<\min\frac{1}{\|l_{1,2,3}\|}$	—	$m3m$
4	{4} × {1}	4	$0<\operatorname{tg}\frac{\varphi}{2}<\frac{\sqrt{2}-1}{\|l_3\|}$	—	$P_\infty(0,0,1)/m$
5	{422} × {1}	8	$0<\operatorname{tg}\frac{\varphi}{2}<\min\left(\frac{1}{\|l_1\|}, \frac{1}{\|l_3\|}, \frac{\sqrt{2}}{\|l_1\|+\|l_2\|}, \frac{\sqrt{2}-1}{\|l_3\|}\right)$	—	$P_\infty(0,0,1)/mm$
6	{3} × {1}	3	$0<\operatorname{tg}\frac{\varphi}{2}<\frac{\sqrt{3}}{3\|l_3\|}$	—	$P_\infty(0,0,1)/m$
7	{32} × {1}	6	$0<\operatorname{tg}\frac{\varphi}{2}<\min\left(\frac{1}{\|l_3\|}, \frac{2}{\sqrt{3}\|l_1\|+\|l_2\|}, \frac{1}{\sqrt{3}\|l_3\|}\right)$	—	$6/mmm$
8	{6} × {1}	6	$0<\operatorname{tg}\frac{\varphi}{2}<\frac{2-\sqrt{3}}{\|l_3\|}$	—	$P_\infty(0,0,1)/m$
9	{622} × {1}	12	$0<\operatorname{tg}\frac{\varphi}{2}<\min\left(\frac{1}{\|l_{1,2}\|}, \frac{2-\sqrt{3}}{\|l_3\|}, \frac{2}{\sqrt{3}\|l_{1,2}\|+\|l_{2,1}\|}\right)$	—	$P_{12}(0,0,1)/mm$
10	{23} × {1}	12	$0<\operatorname{tg}\frac{\varphi}{2}<\frac{1}{\|l_1\|+\|l_2\|+\|l_3\|}$	—	$m3m$
11	{432} × {1}]	24	$0<\operatorname{tg}\frac{\varphi}{2}<\min\left(\frac{\sqrt{2}-1}{\|l_{1,2,3}\|}, \frac{1}{\|l_1\|+\|l_2\|+\|l_3\|}\right)$	—	$m3m$
12	{2} × {2}	4	As in gr. 2	$l_1 \geq 0$	
13	{222} × {2}	8	" " 3	$l_1 \geq 0$	
14	{4} × {2}	8	" " 4	$l_1 \geq 0$	
15	{422} × {2}	16	" " 5	$l_1 \geq 0$	
16	{3} × {2}	6	" " 8	—	$P_\infty(001)/m$
17	{32} × {2_{010}}	12	" " 7	$l_1 > 0$	
18	{6} × {2}	12	" " 8	$l_1 > 0$	
19	{622} × {2}	24	" " 9	$l_1 \geq 0$	
20	{23} × {2}	24	" " 10	$l_1 > 0$	
21	{432} × {2}	48	" " 11	$l_1 > 0$	
22	{222} × {222}	16	" " 3	$l_1 > 0,\ l_2 > 0$	
23	{4} × {222}	16	" " 5	$l_1 \geq 0$	
24	{422} × {222}	32	As in gr. 5	$l_1 \geq 0,\ l_2 \geq 0$	
25	{3} × {222}	12	" " 9	—	
26	{32} × {222}	24	" " 25	$l_1 \geq 0$	
27	{6} × {222}	24	" " 9	$l_1 \geq 0$	
28	{622} × {222}	48	" " 27	$l_1 \geq 0,\ l_2 \geq 0$	
29	{23} × {222}	48	" " 10	$l_1 \geq 0,\ l_2 \geq 0$	
30	{432} × {222}	96	" " 11	$l_1 > 0,\ l_2 > 0$	
31	{4} × {4}	16	" " 4	$l_1 > 0,\ l_2 > 0$	
32	{422} × {4}	32	" " 5	$l_1 > 0,\ l_2 > 0$	
33	{3} × {4}	12	$0<\operatorname{tg}\frac{\varphi}{2}<\frac{\operatorname{tg}\pi/24}{\|l_3\|}$	—	$P_\infty(0,0,1)/m$
34	{32} × {4}	24	$0<\operatorname{tg}\frac{\varphi}{2}<\min\left(\frac{1}{\|l_{1,2}\|}, \frac{\operatorname{tg}\pi/24}{\|l_3\|}, \frac{2}{\sqrt{3}\|l_{1,2}\|+\|l_{2,1}\|}, \frac{\sqrt{2}}{\|l_1\|+l_2\|}, \frac{2\sqrt{2}}{\sqrt{3}(\|l_1\|+\|l_2\|)+\|\|l_1\|-\|l_2\|\|}\right)$	—	$P_{24}(0,0,1)/mm$
35	{6} × {4}	24	As in gr. 33	$l_1 > 0$	
36	{622} × {4}	48	" " 34	$l_1 > 0$	
37	{23} × {4}	48	" " 11	$l_1 > 0$	
38	{432} × {4}	96	" " 11	$l_1 > 0,\ l_2 \geq 0$	
39	{422} × {422}	64	" " 5	$l_1 \geq 0,\ l_2 > 0, l_3 \geq 0$	
40	{3} × {422}	24	" " 34	—	
41	{32} × {422}	48	" " 40	$l_1 \geq 0$	
42	{6} × {422}	48	" " 40	$l_1 \geq 0$	
43	{622} × {422}	96	" " 40	$l_1 > 0,\ l_2 > 0$	
44	{23} × {422}	96	" " 37	$l_1 > 0,\ l_2 > 0$	
45	{432} × {422}	192	" " 11	$l_1 > 0, l_2 > 0, l_3 > 0$	
46	{3} × {3}	9	" " 6	$\|l_2\| < \sqrt{3}\ l_1$	
47	{32} × {3}	18	" " 7	$\|l_2\| < \sqrt{3}\ l_1$	
48	{6} × {3}	18	" " 8	$\|l_2\| < \sqrt{3}\ l_1$	
49	{622} × {3}	36	" " 9	$\|l_2\| < \sqrt{3}\ l_1$	
50a	{22} × {3}	36	If $l_1 l_2 l_3 > 0$, then $0<\operatorname{tg}\frac{\varphi}{2}<\min\left(\frac{2-\sqrt{3}}{\|l_3\|}, \frac{\sqrt{3}}{\|l_1\|+(2+\sqrt{3})\|l_2\|+\|l_3\|}, \frac{\sqrt{3}}{(2+\sqrt{3})\|l_1\|+\|\|l_2\|-\|l_3\|\|}\right);$	—	422

Table 2 (continued)

No.	Group	Group order	Conditions at rotation angle φ	Conditions direction of rotations l	Symmetry of primitive region
			If $l_1 l_2 l_3 < 0$, then $0 \leqslant \mathrm{tg}\frac{\varphi}{2} \leqslant \min\left(\frac{2-\sqrt{3}}{\lvert l_3\rvert},\right.$ $\frac{\sqrt{3}}{(2+\sqrt{3})\lvert l_1\rvert+\lvert l_2\rvert+\lvert l_3\rvert},$ $\left.\frac{\sqrt{3}}{(2+\sqrt{3})\lvert l_2\rvert+\lVert l_1\rvert-\lvert l_3\rVert}\right)$		
50b	$\{23\}\times\{3_{111}\}$		As in gr. 10	$l_2 \leqslant l_1,\ l_3 \leqslant l_1$	422

51a	$\{432\}\times\{3\}$	72	If $l_1 l_2 l_3 > 0$, then
			$0 \leqslant \mathrm{tg}\frac{\varphi}{2} \leqslant \min\left(\frac{\mathrm{tg}\,\pi/24}{\lvert l_3\rvert},\right.$
			$\frac{\sqrt{2}-1}{\lvert l_{1,2}\rvert},$
			$\frac{\sqrt{3}}{\lvert l_1\rvert+(2+\sqrt{3})\lvert l_2\rvert+\lvert l_3\rvert},$
			$\left.\frac{\sqrt{3}}{(2+\sqrt{3})\lvert l_1\rvert+\lVert l_2\rvert-\lvert l_3\rVert}\right);$
			If $l_1 l_2 l_3 < 0$, then
			$0 \leqslant \mathrm{tg}\frac{\varphi}{2} \leqslant \min\left(\frac{\mathrm{tg}\,\pi/24}{\lvert l_3\rvert},\right.$
			$\frac{\sqrt{2}-1}{\lvert l_{1,2}\rvert},$
			$\frac{\sqrt{3}}{(2+\sqrt{3})\lvert l_1\rvert+\lvert l_2\rvert+\lvert l_3\rvert},$
			$\left.\frac{\sqrt{3}}{(2+\sqrt{3})\lvert l_2\rvert+\lVert l_1\rvert-\lvert l_3\rVert}\right)$		

516	$\{432\}\times\{3_{111}\}$	72	As in gr. 11	$l_2 \leqslant l_1,\ l_3 \leqslant l_1$	
52	$\{32\}\times\{32\}$	36	" " 7	$\lvert l_2\rvert \leqslant \frac{\sqrt{3}}{3} l_1$	
53	$\{6\}\times\{32\}$	36	" " 9	$\lvert l_2\rvert \leqslant \sqrt{3}\, l_1$	
54	$\{622\}\times\{32\}$	72	" " 9	$\sqrt{3}\,\lvert l_2\rvert \leqslant l_1$	
55	$\{23\}\times\{32\}$	72	" " 50a	$l_1 \geqslant 0$	
56	$\{432\}\times\{32\}$	144	" " 51a	$l_1 \geqslant 0$	
57	$\{6\}\times\{6\}$	36	" " 8	$\lvert l_2\rvert \leqslant \frac{\sqrt{3}}{3} l_1$	
58	$\{622\}\times\{6\}$	72	" " 9	$\lvert l_2\rvert \leqslant \frac{\sqrt{3}}{3} l_1$	
59	$\{23\}\times\{6\}$	72	" " 50a	$l_1 \geqslant 0$	
60	$\{432\}\times\{6\}$	144	" " 51a	$l_1 \geqslant 0$	
61	$\{622\}\times\{622\}$	144	" " 9	$0 \leqslant l_2 \leqslant \frac{\sqrt{3}}{3} l_1$	
62	$\{23\}\times\{622\}$	144	" " 50a	$l_1 \geqslant 0,\ l_2 \geqslant 0$	
63	$\{432\}\times\{622\}$	288	" " 51a	$l_1 \geqslant 0,\ l_2 \geqslant 0$	
64	$\{23\}\times\{23\}$	144	" " 10	$0 \leqslant l_2 \leqslant l_1, \lvert l_3\rvert \leqslant l_1$	
65	$\{432\}\times\{23\}$	288	" " 11	$0 \leqslant l_2 \leqslant l_1,$ $\lvert l_3\rvert \leqslant l_1$	
66	$\{432\}\times\{432\}$	576	" " 11	$0 \leqslant l_2 \leqslant l_1,$ $0 \leqslant l_3 \leqslant l_1$	

TABLE 3. Groups Corresponding to Laue Point Groups

i	G_i	Directions of axes	i	G_i	Directions of axes
1	{1}		7	{32}	001, 010
2	{2}	001	8	{6}	001
3	{222}	001, 010, 100	9	{622}	001, 010
4	{4}	001	10	{23}	001, 111
5	{422}	001, 010	11	{432}	001, 111
6	{3}	001			

ble 3, which also gives directions of the principal axes in Cartesian coordinates.

For each group are indicated: the multiplicity n of points of an overall position, equal to the product $n_i n_j$ of group orders and comultipliers G_i and G_j; the inequalities defining the limits of change of $\tan\varphi/2$; and the directions of rotations **l**. For regions containing a complete set of directions **l**, the type of external symmetry of the region is described with notation similar to that generally accepted.[9] By $P_\infty(l_1, l_2, l_3)$ is meant an infinite rotational axis, in the direction **l**, by $m(l_1, l_2, l_3)$ is meant a mirror plane with a normal in the direction $\mathbf{l} = (l_1, l_2, l_3)$. Such an expression as $1/|l_{1,2}|$ is equivalent to the notation $1/|l_1|, 1/|l_2|$.

For the case of a nonstandard distribution different from that in Table 3, the axial direction is identified by indices.

The primitive regions of the other 55 $G_i \times G_j$ groups with $i < j$ may be obtained from the regions of the isomorphous groups $G_j \times G_i$, which differ in order of comultiplier sequence by means of substituting l_1, l_2, and l_3 for $-l_1$, $-l_2$, and $-l_3$ in describing the regions. This corresponds to a transition from rotations of $\varphi(\mathbf{l}, \varphi)$ to inverse rotations $\rho^{-1} = \rho(-\mathbf{l}, \varphi) = \rho(\mathbf{l}, -\varphi)$ (see ref. 2). Since in the representations the majority of the regions have only absolute values of $|l_1|$, $|l_2|$, and $|l_3|$, the isomorphous groups, as a rule, receive the same treatment for the change limits of the notation angles in the primitive regions.

---

[1] G. Korn and T. Korn, Handbook on Mathematics for Scientists and Engineers [in Russian], Izd. Nauka, Moscow (1970), p. 397.

[2] V. I. Burdina, Kristallografiya, 15, 623 (1970) [Sov. Phys. – Crystallogr., 15, 545 (1971)].

[3] M. S. Rossman and D. M. Blow, Acta Crystallogr., 15, 24 (1962).

[4] P. Tollin, P. Main, and M. G. Rossman, Acta Crystallogr., 20, 404 (1966).

[5] V. I. Burdina, Dokl. Akad. Nauk SSSR, 203, 338 (1972) [Sov. Phys. – Dokl., 17, 428 (1972)].

[6] L. S. Pontryagin, V. G. Boltyanskii, R. V. Gamkrelidze, and E. F. Mishchenko, Mathematical Theory of Optimal Processes [in Russian], Fizmatgiz, Moscow (1961).

[7] B. N. Delone, N. Padurov, and A. Aleksandrov, Mathematical Foundations of Crystal Structure Analysis [in Russian], Izd. Ob'edin. Nauchno-Tekh., Moscow, Leningrad (1934), p. 154.

[8] B. N. Delone and N. I. Sandakova, Trudy Matem. Inst. Akad. Nauk SSSR, 64, 28 (1961).

[9] International Tables for X-Ray Crystallography, Vol. 1, Kynoch Press, Birmingham (1952), p. 30.

Calculation of the small-angle x-ray scattering intensity on a computer using a macromolecule model

Yu. A. Rol'bin, R. L. Kayushina, L. A. Feigin, and B. M. Shchedrin

Institute of Crystallography,
Academy of Sciences of the USSR
M. V. Lomonosov Moscow State University

(Submitted December 19, 1972)
Kristallografiya, 18, 701-705 (July-August 1973)

A method has been developed for calculating the small-angle x-ray scattering intensity on a computer using models homogeneous in electron density and models with two values of the electron density, by dividing the model into a definite number (up to 1364) of scattering regions. A comparison is made (over a broad range of variation of the scattering intensity) of theoretical curves and curves calculated according to the approximate method for a homogeneous ellipsoid and for a system of two contacting spheres of different electron densities. Near the main maxima the discrepancy does not exceed a fraction of a percent and with increasing scattering angle the error gradually increases.

In determining the shapes of macromolecules by small-angle x-ray scattering (we have in view the resolution of a system of identical particles where we can neglect the intermolecular interference) two mutually complementary approaches are used; the direct method and the model methods.[1-3] The difficulty of extracting structural information from small-angle x-ray scattering data by direct methods and the limited nature of such information are naturally related to the fact that experimentally one obtains a scattering curve of individual particles averaged over all spatial orientations. Well-known progress in the development of direct methods has been made in Stuhrmann's work.[4,5] At the present time due to the development of x-ray experimental technique there is a real possibility of obtaining precision scattering curves over a "broad" range of small angles. The situation is now such that experimental data often remain in a certain sense "evidence in itself", from which one cannot extract fundamental information on structure. Therefore the possibility of constructing models and comparing their scattering with experiment over a broad angular range, the appropriate small-angle transposition of the "method of trial and error" of structural crystallography, is one possible route to a more complete use of the data on small-angle x-ray scattering experiments.

However, it should be borne in mind that the realization of these possibilities involves the fast setting-up of computer models and a high rate of calculation of the scattering intensities from such a model since the number of models to be studied is in general quite large and increases sharply with an increase in spatial resolution. The treatment of an approximate (practical, quite accurate, and comparatively fast) method for calculating the small-angle scattering by models is the subject of the present work.

We calculate the intensity from the general Debye equation[6]

$$I(s)=\sum_j\sum_k f_j f_k(\sin s r_{jk})/s r_{jk}, \qquad (1)$$

(where f_j and f_k are the atomic scattering amplitudes, r_{jk} is the distance between two arbitrary atoms, $s = 4\pi \cdot \sin\theta/\lambda$, and θ is half the scattering angle), which is not always possible since usually for the objects studied we do not know the number of atoms, their kind, or their positions. But even if all of these parameters were known the number of atoms could be so large that the calculations would become quite lengthy. Individual calculations using (1) have been done in a number of cases; for example, theoretical curves have been calculated from structural analysis data for single crystals of myoglobin,[7,8] hemoglobin,[9] and lysozyme.[10] However in searching for models of large proteins, nucleic acid, and viruses it is not possible to use Eq. (1) directly. A modification of the computation of Eq. (1) on a computer has been developed[11] in which a method of approximate calculation of the small-angle x-ray scattering intensity was proposed for bodies of any shape with an arbitrary distribution of electron density, i.e., the calculation was to be done using the equation

$$I(s)=g(s)\sum_j\sum_k W_j W_k(\sin s r_{jk})/s r_{jk}, \qquad (2)$$

where W_j and W_k are the numbers of electrons in the j-th and k-th regions, into which the body is divided respectively and g(s) is the shape function of the region averaged over all orientations and depending only on the modulus of the vector **s**. However in this form already for 200 to 300 scattering regions the computation time (on a computer with an average rate of 20,000 operations/sec) was too long.

In most cases the analysis of the experimental curves for small-angle scattering can be limited to approximating the structure of the particles by models with uniform electron density or models with two values of the electron density. We first consider uniform models, for which the electron density $\rho(\mathbf{r}) = 1$ within the surface $S(\mathbf{r})$ which bounds the given model [$S(\mathbf{r})$ in general is a multiply connected surface]. The model is approximated by a system of identical regions, whose centers form a lattice (face-centered cubic or simple cubic). We consider how to solve the whole modeling problem which arises for small-angle x-ray scattering: the setting up of the computer model (with division into ~1000 regions this becomes quite difficult), the search for a rapid method of calculating on a computer using the specific details of the problem, and finally, an estimate of the errors in the magnitude of the intensity for various values of the scattering angle.

The constancy of the electron density and the use of a lattice for the arrangement of the centers of the subdivision regions allows one to avoid the introduction into the machine of the coordinates of those centers which do not lie at the surface S(r). Therefore by giving a system of parallel cross sections on a certain scale we define the model by a quite small number of surface centers. The coordinates of the internal regions needed for calculating the intensity are computed by the machine. For a broad class of particles with constant electron density this allows us to simplify the setup of computer models. Here the amount of information given to the machine about the shape of the object is almost independent of the shape whether the model has 100 to 200 subdivision regions or 1000 to 1500 of them.

In making a direct calculation of the intensity it should be assumed that since $W_1 = W_2 = W$ (in view of the homogeneity of the model and the identical nature of the subdivision regions) and the centers of the subdivision regions form a lattice then r_{jk} in Eq. (2) forms a bounded often-repeating set of values from zero to L, where L is the greatest distance in the model. Then calculating the frequency A_k with which we encounter the distance r_k in the model we can represent Eq. (2) in the form

$$i(s)=\frac{I(s)}{I(0)}=g(s)\frac{n+2\sum_{l=1}^{m}A_l\frac{\sin sr_l}{sr_l}}{n^2},\qquad(3)$$

where i(s) is the intensity normalized to I(0), I(0) is the scattering intensity at zero angle, n is the number of subdivision regions, A_l is the number of distances r_l, and m is an integer which gives the maximum distance L.

This allows us to cut down the computation time using Eq. (3) by a factor of 200 relative to Eq. (2) with 1000 to 1300 subdivision regions and this coefficient increases with an increasing number of subdivision regions in the model, i.e., spatial resolution.

We now consider the case of a model with two electron densities. Then Eq. (3) changes its form somewhat since it is necessary to consider not only the distance between centers of subdivision regions but also the electron density in these regions:

$$i(s)=g(s)\left[\frac{n_1W_1^2+n_2W_2^2+2W_1^2\sum_{l=1}^{m}A_l^{(1)}\frac{\sin sr_l}{sr_l}}{(n_1W_1+n_2W_2)^2}+\frac{2W_2^2\sum_{l=1}^{m}A_l^{(2)}\frac{\sin sr_l}{sr_l}+2W_1W_2\sum_{l=1}^{m}A_l^{(3)}\frac{\sin sr_l}{sr_l}}{(n_1W_1+n_2W_2)^2}\right],\qquad(4)$$

where n_1 and n_2 are the numbers of subdivision regions containing W_1 and W_2 electrons respectively, $A_l^{(1)}$, $A_l^{(2)}$, $A_l^{(3)}$ are the numbers of distances r_l between centers of subdivision regions containing respectively W_1 and W_1, W_2 and W_2, and W_1 and W_2 electrons. Naturally it is now necessary to give the coordinates of the scattering centers located at the boundaries of the regions with different electron densities which would lead (for not too broken a boundary) to an increase in the information introduced by about a factor of 2.

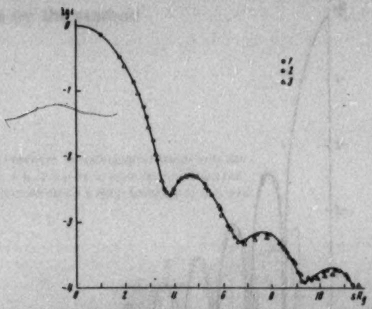

Fig. 1. Scattering intensity of an elongated ellipsoid of rotation with a ratio *a* : b : c = 1 : 1 : 1.4 of the semiaxes. The solid curve is a calculation according to an analytical expression[12] and 1, 2, and 3 are approximate computer calculations for various ways of dividing the ellipsoid into scattering regions (see the text). R_g is the radius of gyration of the ellipsoid.

The appropriate programs have been constructed to calculate the scattering intensity i(s) for a homogeneous model using Eq. (3) and models with two values of the electron density according to Eq. (4). These programs also allow one to calculate the radius of gyration of the model and its volume, which are invariants of small-angle scattering found from experiment by direct methods (without assumptions about the form of the model). Since the radius of gyration of the hypothetical model is not known precisely in the program the scattering intensity is calculated for a model similar to the given one but having beforehand fixed the radius of gyration, determined, for example, from experimental data. The number of scattering regions in the model studied should not exceed 1364, which in the given case involves the amount of usable machine memory (8 k).

We will now consider the possibilities of the proposed modeling method. In Fig. 1 we show the scattering curve for a uniform ellipsoid of rotation, *a* : b : c = 1 : 1 : 1.4, calculated from the analytical expression.[12] Here we also give the intensity values (symbols 1, 2, and 3) obtained in calculating the intensity using a computer according to the proposed method with ~1300 subdivision regions. The quantities 1, 2, and 3 differ in the way the ellipsoid is fixed; in the first case the ellipsoid has circular cross sections perpendicular to the c axis and in the second place it has elliptical cross sections perpendicular to the *a* axis, while in the third case we have elliptical cross sections rotated by 45° in the bc plane. From the data given in Fig. 1 we can see that until the intensity falls by three orders of magnitude the intensities for the models almost completely agree with the exact curve. The discrepancy in the neighborhood of the main maximum does not exceed a fraction of a percent and then gradually the deviation increases, but while $sR_g < 7$ the discrepancy does not exceed 2%, which with regard to a comparison with experiment can be considered complete agreement. For large angles $(-3 > \lg i(s) > -4)$ the agreement also is fully sat-

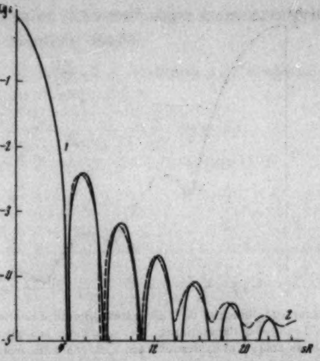

Fig. 2. Scattering intensity from two touching spheres with different electron densities. $W_1 = 1, W_2 = 2$. 1) Calculated from Eq. (5); 2) calculated using our approximate method.

isfactory: The shapes and positions of the maxima are very close to theoretical. However, here we observe a certain sensitivity of the scattering curve of the model to the imprecise specification of the shape, which involves the use of a finite network formed of centers of scattering regions. Just this error source – nonuniqueness in the specification of the model for the system of scattering regions – is evidently a fundamental error for the given method. Note that the range of variation i(s) is sufficient to bring out the shape and individual details of the folding structure of a number of biopolymers.

We turn to analysis of nonuniform models, the case of two electron densities. For the model nonuniform in electron density we chose a system of two touching spheres, one of whose electron densities was unity and the other two. The theoretical curve was calculated from the following relation:

$$i(s) = \Phi(sR)\,\frac{W_1^2 + W_2^2 + 2W_1W_2\,\dfrac{\sin 2sR}{2sR}}{(W_1 + W_2)^2}, \qquad (5)$$

where r is the radius of the sphere, $\Phi(sR) = [3(\sin sR - sR\cos sR)/(sR)^3]^2$, W_1 and W_2 are the numbers of electrons lying within the first and second spheres, respectively. An approximate calculation of the scattering intensity was carried out using Eq. (4), subdividing each sphere into 624 regions. The calculation was done up to an sR of 24 (Fig. 2). The approximate scattering curves show all the maxima in the shape up to the sixth subsidiary maximum and the agreement of the position and shape of the first three maxima can be regarded as complete. It is to be understood that the curve calculated using Eq. (4) does not convey the depths of the minima, although their positions are conveyed with the same precision as the positions of the maxima. The small error in the shape given by the model, the deviation from two touching ideal spheres, is especially pronounced at the theoretical minima i(s) = 0. In this sense the model considered is evidently one of the most unfavorable cases for checking the effectiveness of this method.

Using the method discussed here the computation time for the scattering intensity for a model with 1300 subdivision regions on a computer with a speed of 20,000 operations/sec is 15 min. This allows us to easily compute i(s) for 10 to 20 versions in seeking models closest to experimental scattering curves.

The authors thank B. K. Vainshtein for discussions of the results.

---

[1] A. Guinier and G. Fournet, Small-Angle X-Ray Scattering, Wiley, New York (1955).
[2] R. Hosemann and S. N. Bagchi, Direct Analysis of Diffraction by Matter, North-Holland, Amsterdam (1962).
[3] B. K. Vainshtein, Diffraction of X-Rays by Chain Molecules [in Russian], Izd. Akad. Nauk SSSR, Moscow (1963).
[4] H. B. Stuhrmann, Acta Crystallogr., A26, 297 (1970).
[5] H. B. Stuhrmann, Z. Phys. Chem., Neue Folge, 72, 177 (1970).
[6] R. W. James, Optical Principles of the Diffraction of X Rays, Cornell (1948).
[7] H. C. Watson, Small-Angle X-Ray Scattering, Gordon and Breach, New York (1967), p. 267.
[8] R. G. Kirste and H. B. Stuhrmann, Z. Phys. Chem., Neue Folge, 56, 338 (1967).
[9] R. Schneider, A. Mayer, W. Schmatz, J. Schelten, R. Franzel, and H. Eicher, Europ. J. Biochem., 20, 179 (1971).
[10] W. R. Krigbaum and F. R. Kügler, Biochemistry, 9, 1216 (1970).
[11] Yu. A. Rol'bin, L. A. Feigin, and B. M. Shchedrin, Apparat. Metody Rentgen. Anal., 9, 46 (1971).
[12] P. Mittelbach and G. Porod, Acta Phys. Austriaca, 14, 405 (1961).

Precision measurements of crystallographic parameters by the method of a widely divergent x-ray beam

V. V. Aristov, V. Sh. Shekhtman, and I. M. Shmyt'ko

Institute for Solid State Physics, Academy of Sciences of the USSR

(Submitted March 16, 1972; resubmitted July 21, 1972)
Kristallografiya, 18, 706-709 (July-August 1973)

A method is suggested for determination of lattice parameters and angles between crystallographic planes from the borders of the shadows at breaks of pseudo-Kossel lines. For calculation, it is necessary to have the coordinates of not less than three breaks on one line. A screen of thick copper wire is used to obtain a sharp boundary for the break.

The method of taking patterns in a widely divergent beam, suggested in 1962, opens a new series of possibilities for x-ray diffraction studies of crystals.[1-5] In particular, such a scheme, like the Kossel method, allows determination of structure parameters with a precision not attainable by other methods used for photographic recording.

Regardless of their outward similarity, notable differences between the interpretations of x-ray patterns obtained by the widely divergent beam method and Kossel diffraction patterns should be emphasized. Actually, when the point source is removed from the crystal to a macroscopic distance, the beams diffracted by one system of crystallographic planes form a figure which is more complex than the usual cone. Therefore, diffraction lines on x-ray patterns obtained in a widely divergent beam should not be looked upon as true conic sections.[3-5]

Thus, the familiar methods of calculation based on measurements along the major axes of a diffraction line, which may be mistaken for an ellipse,[1,6] result in systematic error. This shortcoming is removed by the use of semitransparent screens when taking x-ray patterns with multiple exposures.[5] However, as the authors themselves indicated, the precision of the method is limited by the fact that it is associated with a large error in the determination of the coordinates of the point of discontinuity.

A method of precision measurements of interplanar spacings and angles between crystallographic planes from multiple-exposure x-ray diffraction patterns with the use of thick opaque screens to create sharp breaks on the diffraction lines is explained in this work. It is shown that preliminary orientation of the specimen is not required in this case, but an arbitrary orientation of the working surface is obtained and open diffraction lines can be used.

A diffraction line on a pattern obtained in a widely divergent beam can be looked upon as the result of intersection of the plane of the film with some surface formed by rays diffracted by a given system of planes. Without considering a mathematical description of this diffraction surface, let us say that the angle between the plane so formed and the normal to a crystallographic plane is equal to (90° − θ). From this it follows that, for an arbitrary diffracted beam, we obtain

$$\cos(90^\circ - \theta) = \sin\theta = \alpha_{n_1}\alpha_{s_i} + \beta_{n_1}\beta_{s_i} + \gamma_{n_1}\gamma_{s_i}, \tag{1}$$

where θ is the diffraction angle, α, β, and γ are directional cones, and n_1 and s_i are the indices of the normal to the crystallographic plane $(h_1k_1l_1)$ and the i-th diffracted beam, respectively.

Taking account of the familiar condition

$$\alpha_{n_1}^2 + \beta_{n_1}^2 + \gamma_{n_1}^2 = 1, \tag{1a}$$

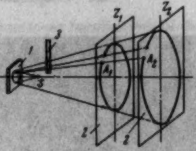

Fig. 1

we see that the problem of finding the angle θ and the directional cones of the normal is reduced to determination from experiment of the directional cones of three diffracted beams. A diagram of the experiment is shown in Fig. 1. A widely divergent beam of x rays falls on crystal 1. Screen 3, of strongly absorbing material, is placed in the path of the diffracted beams. As a result, breaks appear on the diffraction lines. The diffraction pattern is recorded by successive exposures on the same film 2, which lies in the two planes Z_1 and Z_2. Points A_1 and A_2 at the edges of the breaks of the lines determine the diffracted beam, which glides along the surface of the screen.

The coordinates $x_{1,i}$, $y_{1,i}$, and $x_{2,i}$, $y_{2,i}$ of points A_1 and A_2, as well as $\Delta x_i = x_{2,i} - x_{1,i}$ and $\Delta y_i = y_{2,i} - y_{1,i}$, can be obtained by measurement of the x-ray pattern of a double exposure, and $\Delta z = z_2 - z_1$ is given by the fixed displacement of the cassette. The direction cosines are calculated from the equations

$$\alpha_{s_i} = \Delta x_i / \sqrt{\Delta x_i^2 + \Delta y_i^2 + \Delta z^2}, \qquad \beta_{s_i} = \Delta y_i / \sqrt{\Delta x_i^2 + \Delta y_i^2 + \Delta z^2},$$
$$\gamma_{s_i} = \Delta z / \sqrt{\Delta x_i^2 + \Delta y_i^2 + \Delta z^2}.$$

The values obtained from measurements of the coordinates of the three discontinuities on one line are used to solve the system of equations (1) and (1a), i.e., to determine the scalar quantity sin θ and n, the vector of the normal.

Let us emphasize that, since measurements on the diffraction pattern are done on the basis of arbitrary X and Y coordinate axes lying in the plane of the film, the direction cosines of the normal calculated in this manner are tied to the rational coordinate system of the crystal. However, if measurements are made for a few diffraction lines in the same (arbitrary) system of X and Y coordinate axes, the calculated values of the direction cosines allow determination of the angles between the respective crystallographic planes $(h_1k_1l_1)$ and $(h_2k_2l_2)$ according to the equation

$$\cos\varphi_{n_1,n_2} = \alpha_{n_1}\alpha_{n_2} + \beta_{n_1}\beta_{n_2} + \gamma_{n_1}\gamma_{n_2}. \tag{2}$$

An analysis of the method has been carried out on specimens of silicon single crystals of high purity. The

TABLE 1. Values of Interplanar Spacings d(hk*l*)/n and Angles $\varphi(h_1k_1l_1)/(h_2k_2l_2)$ between Planes $(h_1k_1l_1)$ and $(h_2k_2l_2)$

HKL	Interplanar spacings, in Å		$\varphi(hkl)/(110)$		$\varphi(hkl)/(310)$		$\varphi(hkl)/(111)$	
	experimental values	ref. 7	experimental values	calculated values for cubic cell	experimental values	calculated values for cubic cell	experimental values	calculated values for cubic cell
440	0.9600 ± 0.0002	0.9600	—	—	—	—	—	—
620	0.8584 ± 0.0002	0.8586	26°32′	26°34′	—	—	—	—
533	0.8273 ± 0.0003	0.8281	30°33′	30°41′	29°47′	29°56′	14°25′	14°21′
444	0.7839 ± 0.0004	0.7839	35°16′	35°16′	43°08′	43°05′	—	—

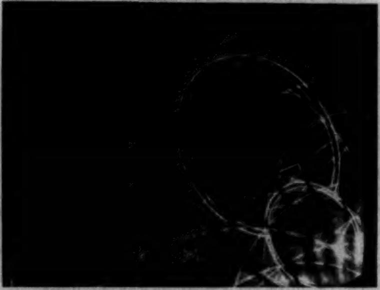

Fig. 2

x-ray diffraction patterns (by reflection) were obtained on "Microflex" apparatus with a copper anode. The distance from the surface of the crystal to the tube focus was 3 mm. A screen in the form of a radial net of copper wires ~1 mm in diameter was placed between the specimen and cassette at a distance of about 15 mm. Displacement of the cassette during double exposure was fixed by use of an end gauge (Johanson block).

Type RT-5 film and type MK photographic plates were used as photographic materials. The form of one of the x-ray patterns, a double exposure with breaks, is shown in Fig. 2. A pair of points which correspond to the "trail" of one diffracted beam for the two positions of the cassette may be noted on the x-ray pattern.

Measurements on the film were made on a type UIM-21 instrument microscope. The edges of the breaks were sharp enough that precision of measurements of not less than 5 μ was secured. The values obtained were introduced into a "Nairi" computer.

The results obtained for four reflections are given in Table 1. It can be seen that the method guarantees an error Δd/d of not less than 0.0005 and allows determination of angles between the arbitrary planes with an error of a few minutes.1) As in other photographic methods, the chief source of error is shrinkage of the emulsion. In the proposed scheme, calculation of shrinkage of the photographic material can be done if Δx in Eq. (1) is replaced by $(\Delta x)' = \Delta x(1 + \delta m)$ and Δy by $(\Delta y)' = \Delta y(1 + \delta m)$, where δm characterizes the shrinkage of the emulsion, which is taken to be isotropic.2)

It is in order to say that the precision in determination of the crystallographic parameters can be increased if necessary. Increase in the number of exposures, of the number of breaks on the lines, or increase of the interval Δz, as well as special mathematical treatment, can be used for this purpose.

We note that similar precision for d is also attained in diffractometry, where, however, stiff requirements as to orientation of the specimen are present and the familiar difficulties in the determination of interplanar spacings for arbitrary reflections exist.

To this it must be added that the possibility of precise calculation of angles between arbitrary planes marks the scheme outlined as an effective x-ray goniometric method which allows one to obtain a rather complete description of the crystal lattice from a limited number of photographs from stationary specimens. In this case, since measurements can be made from portions of the diffractions, the method is also suitable for the determination of differences in orientations of blocks. In conclusion, it can again be emphasized that the advantages noted for the method, in conjunction with the simplicity of the experimental completion, obviously allow consideration of its wide use for the study of single crystals on a par with earlier known methods.

---

1)Calculation of experimental error in the determination of angles is cumbersome. In the text, the error is considered the difference between the calculated and experimental values of the angles.

2)In this work, δm was determined experimentally and was equal to 0.0004.

[1] T. Imura, S. Weissmann, and J. J. Slade, Jr., Acta Crystallogr., 15, 786 (1962); T. Ellis, L. F. Nanni, A. Shrier, S. Weissmann, G. E. Padawer, and N. Hosokawa, J. Appl. Phys., 35, 3364 (1964).

[2] V. N. Rozhanskii, V. V. Lider, and V. G. Lyuttsau, Kristallografiya, 11, 701 (1966) [Sov. Phys. – Crystallogr., 11, 603 (1967)].

[3] D. M. Vasil'ev and S. A. Ivanov, Zavodskaya Lab., 37, 1099 (1971).

[4] V. Sh. Shekhtman, I. M. Shmyt'ko, L. G. Shabel'nikov, and V. G. Rostiashvili, Dokl. Akad. Nauk SSSR, 205, 834 (1972) [Sov. Phys. – Dokl., 17, 738 (1973)].

[5] B. A. Newman, J. Appl. Cryst., 3, 191 (1970); B. A. Newman and A. Shrier, J. Appl. Cryst., 3, 280 (1970).

[6] V. V. Lider and V. N. Rozhanskii, Fiz. Tverd. Tela, 9, 3539 (1967) [Sov. Phys. – Solid State, 9, 2787 (1968)].

[7] W. B. Pearson, Handbook of Lattice Spacings and Structure of Metals, Vol. 2, Pergamon Press, Oxford–London (1967).

New boride structural types in the homologous series based on the $CaCu_5$ and $CeCo_3B_2$ types

Yu. B. Kuz'ma and N. S. Bilonizhko

L'vov State University

(Submitted March 20, 1972)
Kristallografiya, 18, 710-714 (July-August 1973)

We determined the crystal structures of the compounds $ReCo_4B$, $Re_3Co_{11}B_4$, and $Re_2Co_7B_3$ (Re is a rare earth). They form a homologous series based on the $CaCu_5$ and $CeCo_3B_2$ types. In the structures of $CeCo_4B$, $Ce_3Co_{11}B_4$, and $Ce_2 \cdot Co_7B_3$, $CeCo_5$ layers of the $CaCu_5$ type alternate with one, two, or three $CeCo_3B_2$ layers, respectively.

Determination[1] of the crystal structure of the compound $CeCo_3B_2$ showed that it consists of a superstructure of the $CaCu_5$ type with a greatly reduced c/a ratio; the position of the dodecagon $[Cu^{(1)}Cu_6^{(2)}Cu_3^{(1)}Ca_3]$ is occupied by a trigonal prism with the additional atoms opposite the centers of the $[BCo_6Ce_3]$ lateral faces. Further investigation of the Ce–Co–B system established that the compositions of three compounds containing approximately 17, 22, and 25 at.% B lie in the $CeCo_5$–$CeCo_3B_2$ section. The similarity of the x-ray diffraction patterns of the new compounds to those of $CeCo_5$ and $CeCo_3B_2$ indicates that their structures are related.

The crystal structure of the $Ce(Co, B)_5$ compounds containing ~17 and 22 at.% B ($CeCo_4B$ and $Ce_3Co_{11}B_4$) were determined with tabular single crystals taken from ingots of alloys with the above compositions. The structures were evaluated with Laue powder patterns, rotary diffraction patterns, and scanning of the reciprocal-lattice layer lines (KFOR, Mo Kα radiation). The reflection intensities were evaluated visually and corrected for the Lorentz and polarization factors (the absorption factor was not taken into account). Both compounds are characterized by a hexagonal symmetry and space group P6/mmm; $a = 5.01$, $c = 6.93$ Å, $N \approx 12$ for $CeCo_4B$ and $a = 5.02$, $c = 9.85$ Å, $N \approx 18$ for $Ce_3Co_{11}B_4$. Analysis of the interatomic-function projections on the XZ plane for the two structures showed that the heavy Ce and Co atoms were located in layers perpendicular to the c axis; the interlayer distance was approximately $c/4$ for $CeCo_4B$ and $c/6$ for $Ce_3Co_{11}B_4$. Proceeding from these data and assuming the new structures to be related to those of the $CaCu_5$ and $CeCo_3B_2$ types, we constructed models and verified them by using electron-density projections; localization of the maxima by the method of least squares was employed to refine the coordinates of the Ce and Co atoms and the B atoms were positioned on the basis of geometric considerations. The lattice constants of the compounds, calculated from the powder patterns (with a camera diameter of 142.25 mm and Cr K radiation), are given in Table 1. The divergence factors, taking into account the secondary-extinction corrections[2] for the $CeCo_4B$ and $Ce_3Co_{11}B_4$ structures respectively were 13.6 and 13.8% (93 and 101 observed $h0l$ reflections), 14.7 and 17.4% (from 118 and 156 possible $h0l$ reflections), and 11.4 and 14.1% (from 64 and 59 observed hll reflections). The high divergence-factor values were apparently due to the fact that the form factor was not taken into account for single crystals with a tabular habit. Table 2 gives the positions of the basis atoms.

The unit cell of the compound $CeCo_4B$ contains 12 atoms ($\rho_e = 8.37$, $\rho_c = 8.49$ g/cm³) arranged in four layers perpendicular to the c axis (Fig. 1). If the layer sequence in structures of the $CaCu_5$ and $CeCo_3B_2$ types is described[3] by the formulas $c_{Co}C$ and c_BC, the structure of $CeCo_4B$ corresponds to the formula $c_{Co}Cc_BC$ (Fig. 2). The constant c of the $CeCo_4B$ structure is almost equal to the sum of the constants c of the $CeCo_5$ and $CeCo_3B_2$ structures ($4.02 + 3.04 = 7.06$). The coordination polyhedra of the Ce in the $CeCo_4B$ structure are the same as in the $CaCu_5$ and $CeCo_3B_2$ structures; the Co atoms have two types of coordination (one related to icosahedral and one typical of the $Cu^{(1)}$ atoms in $CaCu_5$); the B atoms are arranged in $[BCo_6]$ trigonal prisms with three additional Ce atoms opposite the centers of the orthogonal faces (Fig. 1). In contrast to the $CeCo_3B_2$ structure, where the trigonal

TABLE 1. Lattice Constants and Unit-Cell Volumes of Compounds with Structures of $CeCo_4B$, $Ce_3Co_{11}B_4$, and $Ce_2Co_7B_3$

Re	$ReCo_4B$			$Re_3Co_{11}B_4$			$Re_2Co_7B_3$		
	$a \pm 0.003$ Å	$c \pm 0.004$ Å	V, Å³	$a \pm 0.003$ Å	$c \pm 0.006$ Å	V, Å³	$a \pm 0.003$ Å	$c \pm 0.02$ Å	V, Å³
Sc	*			*			*		
Y	5.005	6.864	148.90	5.086	9.810	219.78	5.045	12.88	283.96
La	5.172	6.860	158.92	*			*		
Ce	5.005	6.932	150.38	5.045	9.925	218.74	5.053	12.97	286.80
Pr	5.100	6.777	152.65	5.145	9.784	224.24	5.150	12.75	292.82
Nd	5.102	6.788	153.01	5.132	9.808	223.72	5.134	12.78	291.74
Sm	5.078	6.871	153.43	5.092	9.799	220.04	*		
Eu	*			**			**		
Gd	5.053	6.854	151.55	5.079	9.842	219.90	5.078	12.85	286.88
Tb	4.998	6.864	148.49	5.058	9.823	217.60	5.061	12.83	284.88
Dy	4.991	6.863	148.05	5.048	9.839	217.10	5.046	12.84	283.10
Ho	4.976	6.873	147.38	5.030	9.846	215.72	5.033	12.88	282.53
Er	4.968	6.858	146.58	5.022	9.845	215.02	5.006	12.87	279.30
Tm	4.948	6.862	145.49	5.004	9.853	213.66	5.002	12.85	278.43
Yb	*			**			**		
Lu	4.940	6.867	145.12	4.982	9.867	212.08	*		

*This compound could not be produced.

**Compound not investigated.

TABLE 2. Atomic Positions in Structures of Compounds $CeCo_4B$, $Ce_3Co_{11}B_4$, and $Ce_2Co_7B_3$ (P6/mmm Space Group)

Compound	Atoms and regular point system	x/a	y/b	z/c
$CeCo_4B$	Ce 1(a)	0	0	0
	Ce 1(b)	0	0	1/2
	Co 2(c)	1/3	2/3	0
	Co 6(i)	1/2	0	0.287
	B 2(d)	1/3	2/3	1/2
$Ce_3Co_{11}B_4$	Ce 1(a)	0	0	0
	Ce 2(e)	0	0	0.333
	Co 2(c)	1/3	2/3	0
	Co 3(g)	1/2	0	1/2
	Co 6(i)	1/2	0	0.200
	B 4(h)	1/3	2/3	0.350
$Ce_2Co_7B_3$	Ce 1(a)	0	0	0
	Ce 1(b)	0	0	1/2
	Ce 2(e)	0	0	0.250
	Co 2(c)	1/3	2/3	0
	Co 6(i_1)	1/2	0	0.150
	Co 6(i_2)	1/2	0	0.375
	B 2(d)	1/3	2/3	1/2
	B 4(h)	1/3	2/3	0.262

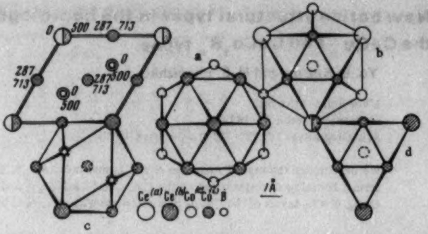

Fig. 1. Projection of structure of $CeCo_4B$ type on ab plane. Coordination polyhedra: a) $[Ce^{(b)}B_6Co_{12}Ce_2]$; b) $[Co^{(c)}Co_9Ce_3]$; c) $[Co^{(i)}B_2Co_6Ce_4]$; d) $[BCo_6Ce_3]$; z coordinates expressed in thousandths of the constant c.

prisms are joined by their lateral edges and bases and form hexagonal channels, the trigonal prisms in the $CeCo_4B$ structure are joined only by their lateral edges and form six-member rings. As can be seen from Table 3, the interatomic distances δ_{Ce-Ce}, δ_{Ce-Co}, and δ_{Co-B} are markedly less than the sums of the atomic radii of the components: $2r_{Ce} = 3.66$, $r_{Ce} + r_{Co} = 3.08$, and $r_{Co} + r_B = 2.13$ Å.

The unit cell of the $Ce_3Co_{11}B_4$ structure (Fig. 2) contains 18 atoms ($\rho_e = 8.32$, $\rho_c = 8.39$ g/cm^3) and $c(Ce_3 \cdot Co_{11}B_4) \approx c(CeCo_5) + 2c(CeCo_3B_2)$. The layer sequence in this compound is $c_{Co}Cc_BCc_BC$. The coordination numbers and coordination polyhedra of the atoms are the same as in the $CeCo_4B$ structure, while the six-member rings of trigonal $[BCo_6]$ prisms in the $Ce_3Co_{11}B_4$ structure are joined in pairs at the prism bases. The reduction in interatomic distances in the $Ce_3Co_{11}B_4$ structure is of the same order as in the $CeCo_4B$ structure (Table 3).

The third compound in the $Ce(Co, B)_5$ section (containing 25. at.% B) is formed only after prolonged annealing and we were unable to obtain single crystals. In view of the similarity between the x-ray powder patterns of this compound and $Ce_3Co_{11}B_4$ and $CeCo_3B_2$ and that of the boron contents, we assumed that its structure belongs to the homologous series[4,5] based on the $CaCu_5$ and $CeCo_3B_2$ types and can be represented as a combination of one unit cell of the $CaCu_5(CeCo_5)$ type and three cells of the $Ce \cdot Co_3B_2$. In this case, the composition of the compound is represented by the formula $Ce_2Co_7B_3$ (which agrees with the experimental composition); the structure conforms to the P6/mmm space group and, with similar constants a, has $c(Ce_2Co_7B_3) \approx c(CeCo_5) + 3c(CeCo_3B_2) \approx 13.1$ Å. This analogy made it possible to interpret the diffraction pattern of $Ce_2Co_7B_3$ and to obtain the lattice constants given in Table 1. The layer sequence $c_{Co}Cc_BCc_BCc_BC$ (Fig. 2) and the positions of the 24 atoms shown in Table 2 correspond to these constants; the number of atoms in the $Ce_2Co_7B_3$ unit cell was confirmed by comparison of densities ($\rho_e = 8.18$, $\rho_c = 8.35$ g/cm^3). Calculation of the intensities in the x-ray powder patterns proved the validity of our structural model: The divergence factor for the 26 observed lines was 10.4%, while that for all 68 possible lines in the diffraction pattern was R = 15.9% (Cr Kα ra-

TABLE 3. Interatomic Distances (δ) and Coordination Numbers (c.n.) in Structures of $CeCo_4B$ and $Ce_3Co_{11}B_4$

$CeCo_4B$				$Ce_3Co_{11}B_4$			
central atom	surrounding atoms	δ, Å	c.n.	central atom	surrounding atoms	δ, Å	c.n.
$Ce^{(a)}$	$2Ce^{(b)}$	3.47		$Ce^{(e)}$	$2Ce^{(a)}$	3.31	
	$12Co^{(i)}$	3.20	20		$6Co^{(g)}$	3.02	20
	$6Co^{(c)}$	2.89			6B	2.92	
$Ce^{(b)}$	$2Ce^{(a)}$	3.47			$6Co^{(i)}$	2.85	
	$12Co^{(i)}$	2.91	20	$Co^{(c)}$	$3Ce^{(a)}$	2.91	
	6B	2.89			$3Co^{(c)}$	2.91	12
$Co^{(c)}$	$3Ce^{(a)}$	2.89			$6Co^{(i)}$	2.46	
	$3Co^{(c)}$	2.89	12	$Co^{(g)}$	$4Ce^{(e)}$	3.02	
	$6Co^{(i)}$	2.46			$4Co^{(g)}$	2.52	12
$Co^{(i)}$	$2Ce^{(a)}$	3.20			4B	2.08	
	$2Ce^{(b)}$	2.91		$Co^{(i)}$	$2Ce^{(a)}$	3.21	
	$4Co^{(i)}$	2.50	12		$2Ce^{(e)}$	2.85	
	$2Co^{(c)}$	2.46			$4Co^{(i)}$	2.52	12
	2B	2.07			$2Co^{(c)}$	2.46	
B	$3Ce^{(b)}$	2.89	9		2B	2.08	
	$6Co^{(i)}$	2.07		B	$3Ce^{(e)}$	2.91	
$Ce^{(e)}$	$2Ce^{(e)}$	3.31			$3Co^{(g)}$	2.08	
	$12Co^{(i)}$	3.21	20		$3Co^{(i)}$	2.08	9
	$6Co^{(c)}$	2.91					

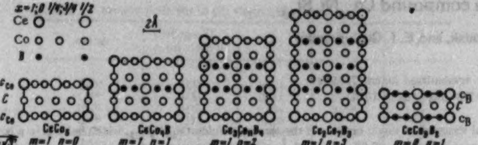

Fig. 2. Structural projections of homologous series based on $CaCu_5$ and $CeCo_3B_2$ types on bc plane. Orthohexagonal arrangement; see the text for the meaning of the quantities m and n.

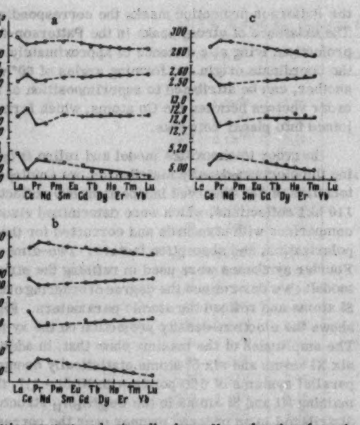

Fig. 3. Lattice constants and unit-cell volumes V as a function of atomic number of Re component for compounds of $ReCo_4B$ (a), $Re_3Co_{11}B_4$ (b), and $Re_2Co_7B_3$ (c) types.

diation, with the structural, repeatability, Lorentz, and polarization factors taken into account).

The coordination characteristics of the $Ce_2Co_7B_3$ structure are similar to those of the $CeCo_4B$ and $Ce_3 \cdot Co_{11}B_4$ structures: Three six-member rings of $[BCo_6]$ prisms are joined at their bases and form channel fragments. The reduction in the interatomic distances in the $Ce_2Co_7B_2$ structure is the same as in the $CeCo_4B$ and $Ce_3 \cdot Co_{11}B_4$ structures.

Our investigation established the existence of a homologous series of structures based on the $CaCu_5$ and $Ce \cdot Co_3B_2$ types; Fig. 2 shows the projections of these structures in comparison with the initial structural types. The structures of this series exhibit alternation of layers with structures of the $CaCu_5(ReX_2^{\prime}$ and $X_3^{\prime})$ and $CeCo_3B_2$ $(ReX_2^{\prime\prime}$ and $X_3^{\prime})$ types. The compositions of all members of the series are described by the formula $Re_{m+n}X^{\prime}_{5m+3n} \cdot X^{\prime\prime}_{2n}$: m = 1 and n = 0 for $CeCO_5$, and m = 1, n = 1 for $Ce \cdot Co_4B$; m = 1, n = 2 for $Ce_3Co_{11}B_4$, m = 1, n = 3 for $Ce_2Co_7 \cdot B_3$, and m = 0, n = 1 for $CeCo_3B_2$. We can assume the existence of the hypothetical structures $Re_3X^{\prime}_{13}X^{\prime\prime}_2$ (m = 2, n = 1), $Re_5X^{\prime}_{17}X^{\prime\prime}_8$ (m = 1, n = 4), etc. Formation of homologous series is quite characteristic of boride structures: In addition to the aforementioned series, there are other series based on α-Fe and AlB_2 (refs. 5, 6), Al_2Cu and $U_3 \cdot Si_2$ (ref. 7), and CsCl and AlB_2 (ref. 8) types.

Investigation of the Re−Co−B system, where Re = Sc, Y, La, Pr, Nd, Sm, Eu, Gd, Tb, Dy, Ho, Er, Tm, Yb, and Lu, led to discovery of a series of new ternary compounds with structures of the $CeCo_4B$, $Ce_3Co_{11}B_4$, and $Ce_2Co_7B_3$ types (Table 1; the specimens were smelted from rare earths with a purity of no less than 99%, 99.87% pure cobalt, and 99.3% boron; annealing was conducted in evacuated quartz ampoules at 800°C for no less than 50 h). As can be seen from Fig. 3, the variation of the lattice constants *a* and c was in opposite directions in all the series (the same relationship was observed for the $Re \cdot Co_5$ and $ReCo_3B_2$). The minima in the curves representing the variation of the constant *a* and the unit-cell volume for the cerium compounds indicates that the cerium is in the tetravalent state. The absence of $ReCo_4B$, $Re_3Co_{11}B_4$, and $Re_2Co_7B_3$, where Re = Eu, Yb, or La (particularly the latter), is apparently due to the overly large atomic radii of these rare earths.

The authors wish to thank P. I. Kripyakevich for discussing this work.

---

[1] Yu. B. Kuz'ma, P. I. Kripyakevich, and N. S. Bilonizhko, Dopovidi Akad. Nauk URSR, Ser. A, No. 10, 939 (1969).

[2] C. B. Shoemaker and D. P. Shoemaker, Acta Crystallogr., 23, 231 (1967).

[3] P. I. Kripyakevich, Zh. Strukt. Khim., 4, 282 (1963).

[4] A. Magnéli, Acta Chem. Scand., 6, 495 (1953).

[5] P. I. Kripyakevich, Kristallografiya, 15, 690 (1970) [Sov. Phys. – Crystallogr., 15, 596 (1971)].

[6] R. Kiessling, Acta Chem. Scand., 4, 209 (1950).

[7] M. V. Chepiga, Yu. B. Kuz'ma, and P. I. Kripyakevich, Abstracts of Papers Presented at the All-Union Conference on the Crystal Chemistry of Intermetallic Compounds [in Russian], Izd. L'vovsk. Univ., L'vov (1971), p. 31.

[8] Yu. B. Kuz'ma, P. I. Kripyakevich, and N. F. Chaban, Dopovidi Akad. Nauk URSR, Ser. A, No. 12, 1118 (1972).

Crystal structure of the compound Ce$_{15}$Ni$_4$Si$_{13}$

M. G. Mys'kiv, O. I. Bodak, and E. I. Gladyshevskii

L'vov State University

(Submitted June 22, 1972; resubmitted August 7, 1972)
Kristallografiya, 18, 715-719 (July-August 1973)

We determined the crystal structure of single crystals of the ternary silicide Ce$_{15}$Ni$_4$Si$_{13}$, which belongs to a new structural type (P6$_3$/m$-C_{6h}^2$ space group, a = 20.27, c = 4.306 Å, N = 64). The atomic parameters were refined by two-dimensional Fourier syntheses: R = 16.3% for 270 possible hk0 reflections; R = 17.2% for 190 hkl reflections. The distribution in the Ni and Si atoms is partially disorderly and corresponds to the formula Ce$_{15}$NiX$_6$Si$_{10}$, where X = Ni$_{0.5}$ · Si$_{0.5}$. The structure of Ce$_{15}$Ni$_4$Si$_{13}$ belongs to the same homogeneous series as the previously investigated Ce$_2$NiSi and Ce$_6$Ni$_2$Si$_3$ structures.

The present article describes a structure investigation of the compound Ce$_{15}$Ni$_4$Si$_{13}$, which belongs to the comparatively cerium-rich portion of the Ce−Ni−Si system.

An alloy with the composition Ce$_{15}$Ni$_4$Si$_{13}$ was prepared in an arc furnace in an argon atmosphere from the compact metals: 99.56% pure cerium, 99.98% pure electrolytic nickel, and single-crystal silicon with a purity of 99.99%. The Laue patterns determined from a single crystal in the form of a well-facetted acicular rod indicate that the Ce$_{15}$Ni$_4$Si$_{13}$ structure belongs to the 6/m diffraction class. The lattice constants were determined from the rotary x-ray diffraction patterns (RKV-86a camera and Cu Kα radiation) and refined on the basis of the powder patterns (RKD and VRS-3 cameras with diameters of 57.3 and 143.2 mm respectively and Cr Kα radiation): a = 20.27 ± 0.01, c = 4.306 ± 0.005 Å, c/a = 0.212. The unit cell contains two Ce$_{15}$N$_{14}$Si$_{13}$ formula units (ρ_e = 5.89, ρ_C = 5.90 g/cm^3). Interpretation of the rotary diffraction patterns in the [100] and [001] directions and the Weissenberg hk0, hk1, and hk2 patterns determined in an equi-slope goniometer (Cu Kα radiation) yields the P6$_3$ and P6$_3$/m space groups. The constant intensity ratio of the reflections obtained in scanning the zero and second layer lines gives us grounds for assuming the presence of an m plane perpendicular to the 6$_3$ axis and indicates that the structure under investigation has a "bilaminar" character. Proceeding from the projection of the interatomic function P(uv0) (Fig. 1), the number of atoms in the unit cell (N = 64), and the centrosymmetric space group (P6$_3$/m), we constructed a model with the atoms in the following positions: 30 Ce in the 5×6 (h) positions and 34 Ni and Si in the 5×6(h), 2(c), and 2(b) positions; the latter orthogonal point system was taken a priori, since the original maximum in the Patterson projection masks the corresponding detail. The existence of strong peaks in the Patterson-function projection, lying at a distance of approximately 4 Å from the coordinate origin and forming angles of 60° with one another, can be attributed to superimposition of the second-order vectors between the Co atoms, which form triangles joined into planar networks.

In order to check this model and refine it by calculating the electron-density distribution, we employed the intensities of 180 observed independent hk0 reflections and 110 hk1 reflections, which were determined visually by comparison with standards and corrected for the Lorentz, polarization, and absorption factors. Two-dimensional Fourier syntheses were used in refining the structural model: We determined the degree of ordering of the Ni and Si atoms and refined the atomic parameters. Figure 2 shows the electron-density projection on the xy plane. The amplitudes of the maxima show that, in addition to six Ni atoms and six Si atoms statistically occupying two parallel systems of 6(h) points with Ni:Si = 1:1, the remaining Ni and Si atoms in the Ce$_{15}$Ni$_4$Si$_{13}$ structure are distributed in an ordered manner over the corresponding positions. Hence the formula for the structural type is Ce$_{15}$NiX$_6$Si$_{10}$, where X = Ni$_{0.5}$Si$_{0.5}$.

Table 1 gives the results obtained in refining the x and y parameters of the Ce, Ni, and Si atoms. The divergence factor was reduced to 15.4% for the 180 observed hk0 reflections, 16.3% for all 270 possible independent hk0 reflections, and 17.2% for the 190 possible independent hk1 reflections. Table 2 gives the interatomic distances.

The structure of Ce$_{15}$Ni$_4$Si$_{13}$, whose projection and atomic coordination polyhedra are shown in Fig. 3, is similar

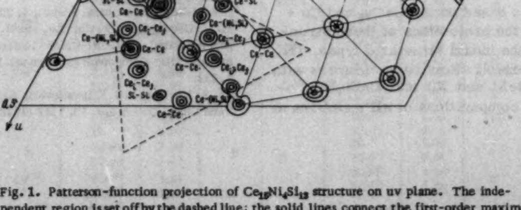

Fig. 1. Patterson-function projection of Ce$_{15}$Ni$_4$Si$_{13}$ structure on uv plane. The independent region is set off by the dashed line; the solid lines connect the first-order maxima of the Ce atoms.

TABLE 1. Atomic Positions in the $Ce_{15}Ni_4Si_{13}$ Structure

Atoms	Orthogonal point system	x	y	z
$Ce^{(1)}$	6(*h*)	0.144	0.143	¼
$Ce^{(2)}$	6(*h*)	0.112	0.317	¼
$Ce^{(3)}$	6(*h*)	0.074	0.496	¼
$Ce^{(4)}$	6(*h*)	0.030	0.675	¼
$Ce^{(5)}$	6(*h*)	0.290	0.537	¼
Ni	2(*b*)	0	0	0
$Si^{(1)}$	6(*h*)	0.794	0.715	¼
$Si^{(2)}$	6(*h*)	0.860	0.558	¼
$Si^{(3)}$	6(*h*)	0.797	0.408	¼
$Si^{(4)}$	2(*c*)	0.667	0.333	¼
$(Ni_{0.5}Si_{0.5})^{(1)}$	6(*h*)	0.897	0.374	¼
$(Ni_{0.5}Si_{0.5})^{(2)}$	6(*h*)	0.828	0.245	¼

$B = 1.1$

TABLE 2. Interatomic Distances δ (Å) in the $Ce_{15}Ni_4Si_{13}$ Structure

Atoms	δ	c.n.	Atoms	δ	c.n.
$Ce^{(1)} - 4\ Ce^{(1)}$	3.62		$Ce^{(4)} - 2\ X^{(1)}$	3.02	17
$Ce^{(1)} - 2\ Ce^{(1)}$	4.31		$Ce^{(4)} - 2\ X^{(2)}$	3.27	
$Ce^{(1)} - 2\ Ce^{(2)}$	3.76				
$Ce^{(1)} - 1\ Ce^{(2)}$	3.89		$Ce^{(5)} - 1\ Ce^{(2)}$	4.10	
$Ce^{(1)} - 1\ Ce^{(4)}$	4.02	14	$Ce^{(5)} - 1\ Ce^{(3)}$	3.99	
$Ce^{(1)} - 2$ Ni	3.10		$Ce^{(5)} - 1\ Ce^{(3)}$	4.03	
$Ce^{(1)} - 2\ Si^{(1)}$	3.30		$Ce^{(5)} - 1\ Ce^{(4)}$	4.09	
$Ce^{(1)} - 1\ Si^{(1)}$	3.68		$Ce^{(5)} - 2\ Ce^{(5)}$	4.01	20
			$Ce^{(5)} - 2\ Ce^{(5)}$	4.31	
$Ce^{(2)} - 2\ Ce^{(1)}$	3.76		$Ce^{(5)} - 2\ Si^{(2)}$	3.42	
$Ce^{(2)} - 1\ Ce^{(1)}$	3.89		$Ce^{(5)} - 2\ Si^{(3)}$	3.19	
$Ce^{(2)} - 2\ Ce^{(2)}$	4.31		$Ce^{(5)} - 2\ Si^{(3)}$	3.00	
$Ce^{(2)} - 1\ Ce^{(3)}$	4.07		$Ce^{(5)} - 2\ Si^{(4)}$	3.16	
$Ce^{(2)} - 2\ Ce^{(4)}$	3.66		$Ce^{(5)} - 2\ X^{(1)}$	3.33	
$Ce^{(2)} - 1\ Ce^{(4)}$	3.99	17	$Ce^{(5)} - 2\ X^{(2)}$	3.03	
$Ce^{(2)} - 1\ Ce^{(5)}$	4.10				
$Ce^{(2)} - 1\ Si^{(1)}$	3.37		Ni $- 6\ Ce^{(1)}$	3.10	8
$Ce^{(2)} - 2\ Si^{(1)}$	3.15		Ni $-$ 2 Ni	2.15	
$Ce^{(2)} - 2\ Si^{(3)}$	3.15				
$Ce^{(2)} - 2\ X^{(2)}$	3.25		$Si^{(1)} - 2\ Ce^{(1)}$	3.30	
			$Si^{(1)} - 1\ Ce^{(1)}$	3.68	
$Ce^{(3)} - 1\ Ce^{(2)}$	4.07		$Si^{(1)} - 2\ Ce^{(2)}$	3.15	9
$Ce^{(3)} - 2\ Ce^{(3)}$	3.72		$Si^{(1)} - 1\ Ce^{(2)}$	3.37	
$Ce^{(3)} - 1\ Ce^{(4)}$	4.15		$Si^{(1)} - 2\ Ce^{(4)}$	3.01	
$Ce^{(3)} - 2\ Ce^{(4)}$	3.71		$Si^{(1)} - 1\ X^{(2)}$	2.38	
$Ce^{(3)} - 1\ Ce^{(5)}$	3.99				
$Ce^{(3)} - 1\ Ce^{(5)}$	4.03		$Si^{(2)} - 2\ Ce^{(3)}$	3.04	
$Ce^{(3)} - 2\ Ce^{(3)}$	4.31	17	$Si^{(2)} - 2\ Ce^{(3)}$	3.01	
$Ce^{(3)} - 2\ Si^{(2)}$	3.01		$Si^{(2)} - 1\ Ce^{(4)}$	3.05	9
$Ce^{(3)} - 2\ Si^{(3)}$	3.19		$Si^{(2)} - 2\ Ce^{(5)}$	3.42	
$Ce^{(3)} - 2\ X^{(1)}$	3.22		$Si^{(2)} - 1\ Si^{(3)}$	2.64	
$Ce^{(3)} - 1\ X^{(1)}$	3.18		$Si^{(2)} - 1\ X^{(2)}$	2.42	
$Ce^{(4)} - 1\ Ce^{(1)}$	4.02		$Si^{(3)} - 2\ Ce^{(3)}$	3.19	
$Ce^{(4)} - 1\ Ce^{(2)}$	3.99		$Si^{(3)} - 2\ Ce^{(5)}$	3.31	9
$Ce^{(4)} - 2\ Ce^{(2)}$	3.66		$Si^{(3)} - 2\ Ce^{(5)}$	3.00	
$Ce^{(4)} - 1\ Ce^{(3)}$	4.15		$Si^{(3)} - 1\ Si^{(2)}$	2.64	
$Ce^{(4)} - 2\ Ce^{(3)}$	3.71		$Si^{(3)} - 1\ Si^{(4)}$	2.29	
$Ce^{(4)} - 2\ Ce^{(4)}$	4.31	17	$Si^{(3)} - 1\ X^{(1)}$	2.44	
$Ce^{(4)} - 1\ Ce^{(5)}$	4.09				
$Ce^{(4)} - 2\ Si^{(1)}$	3.01		$Si^{(4)} - 4\ Ce^{(2)}$	3.17	9
$Ce^{(4)} - 1\ Si^{(2)}$	3.05		$Si^{(4)} - 2\ Ce^{(5)}$	3.15	
			$Si^{(4)} - 2\ Si^{(3)}$	2.29	
			$Si^{(4)} - 1\ Si^{(3)}$	2.31	
$X^{(1)} - 2\ Ce^{(3)}$	3.22		$X^{(2)} - 2\ Ce^{(2)}$	3.26	
$X^{(1)} - 1\ Ce^{(3)}$	3.20		$X^{(2)} - 2\ Ce^{(4)}$	3.30	
$X^{(1)} - 2\ Ce^{(4)}$	3.05		$X^{(2)} - 2\ Ce^{(5)}$	3.03	
$X^{(1)} - 2\ Ce^{(5)}$	3.33	9	$X^{(2)} - 1\ Si^{(1)}$	2.38	9
$X^{(1)} - 1\ Si^{(3)}$	2.45		$X^{(2)} - 1\ Si^{(2)}$	2.42	
$X^{(1)} - 1\ X^{(2)}$	2.27		$X^{(2)} - 1\ X^{(1)}$	2.27	

$X^{(1)} = (Ni_{0.5}Si_{0.5})$; $X^{(2)} = (Ni_{0.5}Si_{0.5})$.

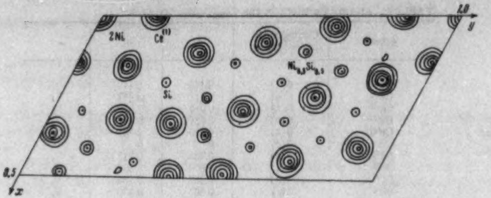

Fig. 2. Electron-density projection of $Ce_{15}Ni_4Si_{13}$ structure on xy plane. The isolines are drawn at equal intervals (in relative units).

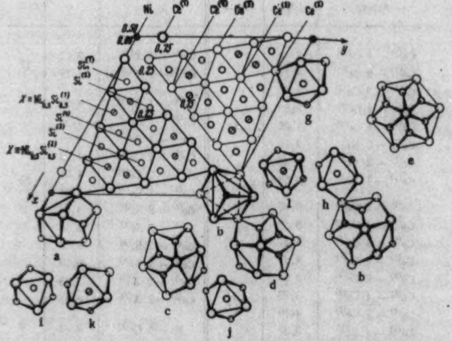

Fig. 3. Projection of unit cell and coordination polyhedra of atoms in structure of compound $Ce_{15}Ni_4Si_{13}$. a) $[Ce^{(1)}Ce_{10}NiSi_9]$; b) $[Ce^{(2)}Ce_{10}X_2Si_5]$; c) $[Ce^{(3)}Ce_{10}X_2Si_5]$; d) $[Ce^{(4)}Ce_{10}X_4Si_6]$; e) $[Ce^{(5)}Ce_8X_4Si_2]$; f) $[NiCe_6Ni_2]$; g) $[Si^{(1)}Ce_8X]$; h) $[Si^{(2)}Ce_7XSi]$; i) $[Si^{(3)}Ce_6XSi_2]$; j) $[Si^{(4)}Ce_6Si_3]$; k) $[X^{(1)}Ce_7XSi]$; l) $[X^{(2)}Ce_6XSi_2]$.

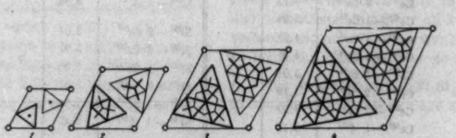

Fig. 4. Projections of unit cells on xy plane in structures of homologous series $Ce_6Ni_2Si_3$–$Ce_{15}Ni_4Si_{13}$. 1) n = 1, R_6X_4; 2) n = 2, $Ce_{12}(Ni_{0.4}Si_{0.6})_{10}$; 3) n = 3, $Ce_{20}(Ni_{0.4}Si_{0.6})_{20}$; 4) n = 4, $Ce_{30}(Ni_{0.23}Si_{0.77})_{34}$.

in the relative arrangement of the Ce, Ni, and Si atoms to that of the previously investigated[1] ternary silicide $Ce_2 \cdot NiSi$.

The Ce atoms form fragments with simple hexagonal packing (complex prisms), each of which consists (within the limits of the constant c) of 16 simple prisms. The unit cell contains two complex prisms; each of these fragments is surrounded by similar prisms displaced with respect to one another by c/2. Within each simple prism is an Si atom or $Ni_{0.5}Si_{0.5}$ group. These atoms form fragments of a network having the form of hexagons joined at their sides. Along the 6_3 axis, i.e., among six complex prisms and joined to them, is a column of trigonal antiprisms (fused octahedra) of $[NiCe_6]$. The coordination characteristics of the atoms are the same as in the $Ce_2 \cdot NiSi$ structure, i.e., c.n. (Ce) = 14, 17, or 20, c. n. (Ni) = 8 (a trigonal antiprism with two atoms opposite the centers of the faces perpendicular to the 6_3 axis), and c.n. (Si) = 9 (a trigonal prism with three additional vertices opposite the centers of the lateral faces).

Together with the previously investigated structures of Ce_2NiSi (a = 16.12, c = 4.309 Å, $P6_3/m$ space group) and $Ce_6Ni_2Si_3$ (a = 12.11, c = 4.323 Å, $P6_3/m$ space group),[2] the $Ce_{15}Ni_4Si_{13}$ structure forms a homologous series of structures constructed of fragments of the AlB_2, AsNi, and α-Fe types. The members of this series differ in the area of the prism cross section (Fig. 4); the cell composition can be represented by the formula $Ce_{n^2+3n+2}(Ni, Si)_{2n^2+2}$, where n is the number of simple prisms forming the complex prism (n = 4 for $Ce_{15}Ni_4Si_{13}$, n = 3 for Ce_2NiSi, and n = 2 for $Ce_3Ni_2Si_3$); when n = 1, we obtain the composition R_6X_4, which corresponds to a structure of the Cl_3U type with additional X atoms in the 2(b) positions.

The members of this homologous series are completed-shell analogs[3] of the series $S_{12}Th_7 - Rh_{20}Si_{13}$ or the series of hypothetical "S_2Th" – "Rh_5Si_3" structures, which lack atoms on the 6_3 axes and are based on the Cl_3U and WC types.[4]

The authors wish to thank P. I. Kripyakevich for discussing this work.

---

[1] O. I. Bodak, E. I. Gladyshevskii, and M. G. Mis'kiv, Kristallografiya, 17, 502 (1972) [Sov. Phys. – Crystallogr., 17, 439 (1972)].

[2] O. I. Bodak, E. I. Gladyshevskii, and O. I. Kharchenko, Abstracts of papers Presented at the All-Union Conference on the Crystal Chemistry of Intermetallic Compounds [in Russian], Izd. L'vovsk. Univ. (1971), p. 11.

[3] I. Engstrom, Acta Chem. Scand., 19, 1930 (1965).

[4] P. I. Kripyakevich, Kristallografiya, 15, 690 (1970) [Sov. Phys. – Crystallogr., 15, 596 (1971)].

Crystal structure of coumarin

R. M. Myasnikova, T. S. Davydova, and V. I. Simonov

Institute of Heteroorganic Compounds, Academy of Sciences of the USSR
Institute of Crystallography, Academy of Sciences of the USSR

(Submitted August 29, 1972)
Kristallografiya, 18, 720-724 (July-August 1973)

Three-dimensional diffractometer data and superimposition methods were used to establish the atomic structure of coumarin $C_9H_6O_2$ (a = 15.500, b = 5.664, c = 7.915 Å; Pc$a2_1$ space group, Z = 4). The structure was refined by the method of least squares, taking into account the isotropic individual thermal factors for 539 independent nonzero structural amplitudes, bringing the divergence factor to R = 10.4%. We have considered the molecular geometry and analyzed the intermolecular contacts. The molecular packing is such that the natural dipole moments of the molecules in the crystal remain uncompensated.

A. I. Kitaigorodskii's laboratory has been conducting a systematic study of the structure and properties of molecular-solid-solution crystals of organic compounds at the nonvalence-interaction level.[1,2] Substances with a "model" molecular form that can be described geometrically (naphthalene, anthracene, acridine, diphenyl, tolane, etc.) are used to establish the mechanisms of solid-solution formation. From this standpoint, coumarin is interesting for the fact that, in addition to having a "model" form very similar to that of the naphthalene molecule, its molecules have a considerable intrinsic dipole moment[3] with p = 4.51 D. The crystal structure of coumarin has not been previously studied. The first investigations of this compound were therefore of the mechanisms of solid solution formation, which were necessary for establishment of its structure.

Coumarin (1,2-benzopyrone) is an aromatic substance with the aroma of fresh hay; it is quite common in the plant world and is used in the perfume industry. The coumarin molecule, $C_9H_6O_2$, has the structural formula shown in Fig. 1. The arrow indicates the approximate direction of the molecular dipole moment. Single crystals were obtained by double recrystallization of coumarin with a melting point of 68.5°C from ethanol. The coumarin crystals for the structural investigation were grown from aqueous-alcoholic solution by slow evaporation of the solvent.

X-ray diffraction analysis of the single crystals confirmed that coumarin has a rhombic habit.[4] The lattice parameters were measured in a DRON-1 diffractometer and found to be a = 15.500, b = 5.664, and c = 7.915 Å. The natural volume of the coumarin molecule[5] is V_{cou} = 133.3 Å^3. With the volume occupied by this molecule and the usual packing factor $k \approx 0.7$ for organic crystals, the unit cell should contain four formula units ($Z = kV_{\mathrm{ce}}/V_{\mathrm{cou}}$ = 3.6). The actual packing factor for the molecules in the structure in this case is 0.77. This is a rather high packing density for an organic crystal. The density of coumarin calculated from the x-ray diffraction data is ρ = 1.405 g/cm^3.

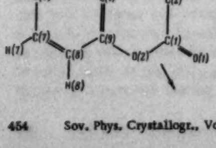

Fig. 1. Structural formula of coumarin molecule. The arrow indicates the approximate direction of the molecular dipole moment.

In order to obtain three-dimensional diffraction data, we used a coumarin single crystal in the form of an orthogonal prism elongated along the b axis (0.35 × 0.90 × 0.70 mm in size). The experimental data (539 independent $|F_H| \neq 0$ reflections from the h0l − h6l layers) were obtained in Cu radiation in a computer-controlled DAR-UM automatic diffractometer.[6] The absorption correction, μ = 6.42 cm^{-1} was not taken into account.

Analysis of the regular reflection extinction yielded the mmmPca −diffraction symmetry group for coumarin, which corresponds to the two Fedorov groups Pcam and Pc$a2_1$. With four molecules in the unit cell, the Pcam space group can be realized only if the planar coumarin molecules are arranged in mirror symmetry planes. Such an arrangement contradicts the theory of dense packing of organic molecules.[5] Analysis of the three-dimensional Patterson function conclusively refuted the hypotheses of a holohedral symmetry group and made it necessary to assume coumarin to belong to the acentric Pca_2 space group with one independent molecule in the asymmetric region of the unit cell.

With an idealized molecular size and shape (C−C and C−O valence bonds of approximately 1.4 Å and valence angles of about 120°), the structural determination reduces to establishment of the orientation of the molecular plane and the position of its center of gravity in the unit cell. Analysis of the three-dimensional Patterson function made it possible to establish the orientation of the coumarin molecule with respect to the crystallographic axes; the numerous multiple peaks in the Patterson function aided in this, corresponding to approximately equal and parallel intramolecular vectors of the type C(3)−C(5), O(2)−C(8), etc.; O(1)−C(2), C(1)−C(3), etc.; and others (see Fig. 1).

Superimposition synthesis[7,8] was used to localize the molecule with respect to the symmetry elements of the Pc$a2_1$ group. A coumarin molecule of known form and orientation was placed with its C(7) atom at the coordinate origin. The C(7) atom was selected as the initial atom because it is one of the most remote from the O(1) and O(2) atoms, which distort the ideal form of the molecule. The interatomic vectors from the C(7) atom to the other atoms of the molecule were used to plot the Burger minimization function $M_{10}(\mathbf{r})$. Fourier inversion of this function, preliminarily modified by removal of the background, enabled us to calculate the structural-amplitude phases and construct a superimposition synthesis within the framework

TABLE 1. Coordinates and Individual Isotropic Thermal Parameters of Basis Atoms of Coumarin

Atoms	x/a	y/b	z/c	B, Å^2
O(1)	0.2832(2)*	0.6008(6)	0.2757(5)	4.98
O(2)	0.1545(2)	0.5025(4)	0.3670(4)	3.60
C(1)	0.2408(3)	0.4568(6)	0.3537(6)	3.56
C(2)	0.2727(2)	0.2417(7)	0.4274(6)	3.89
C(3)	0.2211(3)	0.0947(7)	0.5125(6)	3.52
C(4)	0.1294(2)	0.1430(7)	0.5245(5)	3.04
C(5)	0.0706(3)	0.0014(6)	0.6100(5)	3.73
C(6)	—0.0154(3)	0.0617(8)	0.6168(7)	4.35
C(7)	—0.0447(3)	0.2676(8)	0.5368(6)	4.21
C(8)	0.0130(3)	0.4141(7)	0.4550(6)	3.61
C(9)	0.0995(2)	0.3500(5)	0.4499(5)	3.00
H(2)	0.342**	0.199	0.414	3.64
H(3)	0.247	—0.064	0.569	3.64
H(5)	0.094	—0.161	0.665	3.64
H(6)	—0.062	—0.053	0.674	3.64
H(7)	—0.113	0.313	0.539	3.64
H(8)	—0.003	0.574	0.395	3.64

*The standard deviations are given in parentheses.

**The coordinates of the H atoms were found geometrically.

of the P1 space group, which gave us an approximation of the electron-density distribution in the crystal. Like the $M_{10}(x)$ function, the superimposition synthesis was calculated for the full crystal cell, without taking into account the symmetry elements of the $Pca2_1$ group, whose location with respect to the C(7) atom selected as the coordinate origin had to be determined. Visual analysis of the electron-density distribution thus obtained was sufficient for localization of all the symmetry elements of the $Pca2_1$ space group. After conversion to the standard coordinate origin for the $Pca2_1$ group, the structure was refined by the usual method of least squares.

Refinement was conducted with all 539 independent $|F_{hkl}| \neq 0$ with weighted experimental multipliers.[9] We refined the factors used to reduce the layer lines to an absolute scale and the coordinate and isotropic thermal parameters of all the O and C atoms; no geometric conditions were introduced in the refinement procedure for the bond lengths and valence angles. During the final stage, we took into account the H atoms, whose coordinates were determined from the usual geometric rules (the H atoms lie on the diagonals of the ring and the C–H bond length is 1.08 Å). The average thermal factor was determined for all the H atoms; their coordinates were not refined.

Table 1 gives the coordinates and isotropic thermal factors of all the basal atoms in the structure. The final value of the divergence factor was R = 0.104.

It must be pointed out that, in refining the coumarin structure, we attempted to take into account the anisotropy of the thermal vibrations of the O and C atoms, using the program devised by L. A. Muradyan. The R factor of the structure was reduced to 0.063 in this case; when all three reflections were not taken into account, R = 0.047. However, the scattering of the C–C bond lengths in the aromatic ring of the coumarin molecule had no physical sense in this situation. Because the absorption was not taken into account for this substantial deviation of the coumarin crystal used from an isometric shape, the experimental values of $|F_{hkl}|$ were obviously systematically distorted. For this reason, the final atomic coordinates in Table 1 were obtained with the approximation of isotropic individual atomic thermal vibrations, particularly since the values for different atoms in the molecule have an explicit physical sense.

Figure 2 gives the bond lengths and valence angles in the coumarin molecule. The standard deviations $\sigma(l)$ and $\sigma(\theta)$ calculated by the method described in refs. 10 and 11 were better than 0.01 Å for the bonds and 0.5° for the angles.

Despite the presence of a heterocyclic ring, the form of the coumarin molecule differs little from the geometrically regular form for condensed aromatic molecules. The average C–C bond length in the aromatic ring is 1.389 ± 0.006 Å (in naphthalene, it ranges from 1.391 to 1.396 Å, according to the data of various authors[12]). The C–C distances between alternate atoms not valence-bonded is 2.38–2.43 Å, i.e., close to the standard value of 2.4 Å. There is almost complete agreement for the distances O(2)–C(4) = 2.42, O(2)–C(2) = 2.40, and O(1)–C(2) = 2.37 Å. The ring diagonals vary little from 2.8 (2.82–2.76 Å); analogously, O(2)–C(3) = 2.78 Å. Other interatomic distances are O(1)–O(2) = 2.19 and O(1)–H(2) = 2.68 Å.

The coumarin molecule is planar in the crystal. The equation for the median plane, derived by the method of least squares for six atoms in the atomatic ring [C(4)–C(9)], is 2.5288x + 2.8687y + 6.7009z = 4.2641 (I), while the equation for the median plane passing through all nine atoms of the molecule is 2.5346x + 2.8491y + 6.7167z = 4.2692 (II). Table 2 gives the deviations of the coumarin-molecule atoms from median planes I and II.

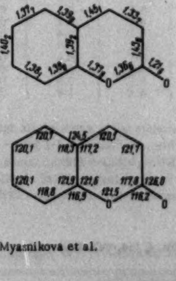

Fig. 2. Valence bonds in Å and angles in deg in the coumarin molecule.

TABLE 2. Deviation of Atoms in Coumarin Molecule from Median Planes I and II (Å)

Atoms	Deviation from plane		Atoms	Deviation from plane	
	I	II		I	II
O(1)	0.023	0.012	C(5)	0.006	0.010
O(2)	0.027	0.019	C(6)	0.007	0.010
C(1)	0.025	0.018	C(7)	−0.012	−0.014
C(2)	−0.018	−0.019	C(8)	0.006	−0.000
C(3)	0.001	0.003	C(9)	0.007	0.002
C(4)	−0.012	−0.011			

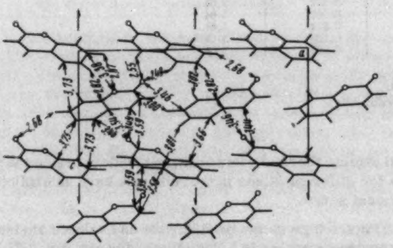

Fig. 3. Projection of coumarin structure on *a*c plane. Shortest intermolecular distances in Å.

The molecular packing in the coumarin structure is very unusual. This type of packing occurs among organic structures when polar molecules are joined in pairs by their inversion centers with their dipole moments directed in antiparallel, so that the pair packing is dictated principally by van der Waals interaction forces. There are no inversion centers in the coumarin structure. The molecules are "strung" along their 2_1 axes and there is no compensation of the vector component of the dipole moment parallel to the 2_1 axis. This is apparently responsible for the very high molecular packing factor in the structure, although dispersion interaction forces prevent the dipoles from being arranged "head to tail."

As is to be expected in this situation, the intermolecular distances include some that are a bit lower than the sum of the van der Waals radii R_i. The two shortest C−C distances (Fig. 3) are 3.39 and 3.44 Å (the generally accepted values of R_C range from 1.72 to 1.80 Å). One C−H distance is reduced to 2.82, in comparison with the usual 2.97 Å. The most interesting examples are the two markedly shortened contacts O(1)−H(3) = 2.55 and O(1)−H(5) = 2.49 Å, as against the sum of the intermolecular radii $R_O + R_H = 1.51 + 1.17 = 2.68$ Å. It might be assumed that hydrogen bonds of the C−H ... O type are formed in the structure, but we would then expect[13] the C−O distances to be reduced to 3.2 Å. The corresponding distances in coumarin, O(1)−C(3) = 3.49 and O(1)−C(5) = 3.46 Å, exceed the sum of the intermolecular radii. The other shortest intermolecular contacts are also shown in Fig. 3.

The authors wish to thank Prof. A. I. Kitaigorodskii for his consistent interest and valuable advice.

---

[1] A. I. Kitaigorodskii and R. M. Myasnikova, Kristallografiya, 16, 1253 (1971) [Sov. Phys. – Crystallogr., 16, 1096 (1972)].

[2] A. I. Kitaigorodskii, Molecular Crystals [in Russian], Nauka, Moscow (1971).

[3] O. A. Osipov, V. I. Minkin, and A. D. Garnovskii, Handbook of Dipole Moments [in Russian], Vysshaya Shkola, Moscow (1971).

[4] Ramaswamy, Current Sci., 10, 197 (1941); Chem. Abst., 35, 7261 (1941).

[5] A. I. Kitaigorodskii, Organic Crystal Chemistry [in Russian], Izd. Akad. Nauk SSSR, Moscow (1955).

[6] M. E. Andrianova, I. A. Kudryashov, and D. M. Kheiker, Kristallografiya, 16, 899 (1971) [Sov. Phys. – Crystallogr., 16, 781 (1972)].

[7] V. I. Simonov, Acta Crystallogr., B25, 1 (1969).

[8] A. B. Tovbis and V. I. Simonov, Kristallografiya, 16, 1131 (1971) [Sov. Phys. – Crystallogr., 16, 994 (1972)].

[9] É. L. Lube and D. M. Kheiker, in: Equipment and Methods for X-Ray Diffraction Analysis [in Russian], Vol. 3, SKB Rent. Apparat., Leningrad (1968), p. 162.

[10] F. R. Ahmed and D. W. J. Cruickshank, Acta Crystallogr., 6, 385 (1953).

[11] S. F. Darlow, Acta Crystallogr., 13, 683 (1960).

[12] D. W. J. Cruickshank, Acta Crystallogr., 10, 504 (1957).

[13] W. C. Hamilton and J. A. Ibers, Hydrogen Bonding in Solids, W. A. Benjamin, Inc., New York–Amsterdam (1968).

Crystal-chemical analysis of the structure of 1-I-substituted anthraquinone

N. L. Klimasenko, V. K. Bel'skii,
V. K. Sarynin, and G. A. Gol'der
L. Ya. Karpov Scientific-Research Physicochemical Institute
(Submitted April 30, 1972; resubmitted July 12, 1972)
Kristallografiya, 18, 725-729 (July-August 1973)

We determined the molecular and crystal structure of 1-I-substituted anthraquinone by x-ray diffraction (R = 0.130). Some distortion of the valence angles in the molecular plane was noted and there was a reduction in the intramolecular distance between the non-valence bound I and O atoms in comparison with the equilibrium distance and a shortening of the intermolecular I...I contact in comparison with the sum of the van der Waals radii. Proceeding from energy calculations and geometric analysis, we compared the packing of the 1-I-substituted anthraquionone molecules in the crystal with that of compounds isomorphic to it (1-Cl- and 1-Br-substituted anthraquionone).

We previously gave the results of a complete x-ray diffraction analysis of 1-Br and 1-Cl-anthraquinone.[1,2] The present article describes the results obtained for the isomorphic 1-I-substituted anthraquinone. The unit cell of 1-I-anthraquinone has the constants a = 7.90, b = 4.24, c = 17.04 Å; β = 92°, Z = 2, $P2_1 - C_2^2$ space group, d_c = 1.94 g/cm³, d_e = 1.99 g/cm³. The crystals are yellow needles with an orange tint; they are elongated along the b axis when grown from solution in hexane.

The structure was established from a set of intensities determined while rotating the crystal about its shortest axis (using a Weissenberg equislope goniometer and Cu radiation), which yielded 1021 nonzero reflections. The intensities were evaluated visually from the blackening, using a scale with steps of $2^{1/4}$; the Lorentz and polarization factors were taken into account in converting to structural amplitudes. Refinement of the structure, which was plotted on the same coordinates as the isomorphic bromine compound, began at R = 29%. Alternate use of the method of least squares (MLS), the Wasser modification[3] of the MLS (the superposition condition was completely eliminated in the final stages) in the full-matrix isotropic approximation, and successive approximation of the three-dimensional electron-density series led to a final R-factor value of 13%.

Table 1 gives the basis-atom coordinates, the individual temperature factors $B_j = B_{tot} + u_j$ (B^{tot} = 3.5 Å²), the amplitudes of the maxima (as determined from a three-dimensional electron-density synthesis and calculated by Vainshtein's method[4]), and the probable errors in the atomic coordinates (in parentheses) obtained during refinement by the MLS.

Assuming the error in the coordinates to be isotropic, the error in determining the interatomic distances is estimated at 0.04–0.05 Å and that in determining the valence angles at 3°.

DISCUSSION OF RESULTS

The geometric parameters of the 1-I-anthraquinone molecule are given in Fig. 1. The length of the C–I bond (2.13 Å) is close to the standard value for aromatic structures.[5] The two C=O bonds (1.21 and 1.22 Å) and the C–C bond at the carbonyl groups (1.49–1.55 Å) correspond precisely to the standard distances.[5] The C–C bonds in the two terminal rings can, within the limits of experimental error (0.04–0.05 Å), be considered aromatic.

The result of the steric interaction of the nonvalence-bound I and O atoms (which produces a tendency for the latter to separate to the equilibrium distance, while the

TABLE 1. Basis-Atom Coordinates, Maximum Amplitudes, and Individual Isotropic Temperature Factors

Atoms	x	y	z	ρ_0, el · Å³	ρ_C, el · Å³	B, Å²
I	0.1776(03)	0.8199(05)	0.0489(01)	99.5	114	4.0
O_1	0,063 (3)	0.431 (6)	0.193(1)	9.1	11.0	4.6
O_2	0.634 (3)	0.242 (6)	0.370(1)	9.4	11.0	5.7
C_1	0,373 (4)	0.686 (9)	0.131(2)	6.4	7.8	4.1
C_2	0.537 (4)	0.785 (11)	0.109(2)	5.8	7.8	4.6
C_3	0.673 (4)	0.758 (9)	0.156(2)	5.9	7.8	5.0
C_4	0,671 (4)	0.598 (11)	0.229(2)	6.0	7.8	5.1
C_5	0.342 (4)	−0.017 (10)	0.422(2)	5.9	7.8	4.2
C_6	0.189 (4)	−0.109 (11)	0.445(2)	5.7	7.8	5.6
C_7	0.040 (4)	−0.100 (9)	0.399(2)	5.9	7.8	5.7
C_8	0,050 (4)	0.068 (11)	0.329(2)	5.8	7.8	5.5
C_9	0.196 (4)	0,402 (9)	0.230(2)	6.9	7.8	3,9
C_{10}	0,507 (3)	0.278 (21)	0.328(2)	6.0	7.8	4.3
C_{11}	0.510 (4)	0.481 (12)	0,252(2)	6.8	7.8	3.8
C_{12}	0,361 (4)	0.529 (11)	0.202(2)	6.2	7.8	3.0
C_{13}	0.197 (4)	0.200 (9)	0,306(2)	6.0	7.8	4.8
C_{14}	0.341 (4)	0.150 (9)	0.353(2)	6.1	7.8	5.0

Note: The equations for the planes passed through all the atoms in the molecule and the form $0.1913x - 0.8464y - 0.5033z + 3.0658 = 0$ for 1-I-anthraquinone, with the molecule having an inclination of 32° to the xz plane; $0.2425x - 0.8800y - 0.4281z + 2.7471 = 0$ for 1-Br-anthraquinone, with the molecule having an inclination of 28° to the xz plane; $0.2557x - 0.8869y - 0.4093z + 2.6063 = 0$, with the molecule having an inclination of 27° to the xz plane.

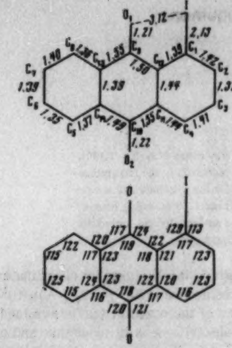

Fig. 1. Interatomic distances in Å and angles in deg in 1-I-anthraquinone molecule.

valence angles retain their normal value of 120° each) is manifested in a reduction in the length obtained for the I...O bond (3.12 Å) in comparison with the sum of the van der Waals radii[6] (3.48 Å) (by 0.36 Å) and a slight increase in the characteristic C−C−Hal angle (to 129°). A similar reduction in the Hal ... O distance is observed in 1-Cl-substituted (0.37 Å) and 1-Br-substituted anthraquinone (0.37 Å); the C−C−Hal angles in these molecules are 122 and 124°, respectively.[1,2]

In order to make a quantitative estimate of the coplanarity of the molecules of these compounds, we derived the mean square equations for the planes passing through all the atoms (Table 2). Both oxygen atoms in all three anthraquinone halogen derivatives deviate from the median plane in the same direction and, within the limits of experimental error, by the same distance in each compound, not deviating very much from the O_1-O_2 line, so that there is probably a tendency for the central portion of the molecule to acquire a dish-like shape. This tendency is most clearly manifested in 1-Cl-anthraquinone[1)] and is less distinct in molecules containing heavy atoms.

Within the limits of experimental accuracy, the halogen atoms lie in the molecular planes, deviating by −0.03, −0.02, and +0.02 Å respectively for I, Br, and Cl.

The intermolecular-interaction energy was calculated in order to arrive at a physically grounded interpretation of the characteristics of molecular packing in the crystal (choice of chain, layer, etc.).

It seemed expedient to use the results of this calculation and of geometric analysis to elucidate the factors responsible for the retention of isomorphism in the series 1-Cl-, 1-Br-, and 1-I-substituted anthraquinones.

The intermolecular-interaction energy was calculated by the method described previously,[7,8] i.e., that of atom−atom approximation, using the semiempirical "6-exp" potential.

The parameters A, B, and α for interactions involving Cl and Br atoms were taken from ref. 9, while those for the interaction involving the I atom were taken from ref. 10; the parameters for all other interactions were calculated from the universal curve given by Mirskaya.[11] The parameters for interactions of the Cl ... O, Br ... O, and I ... O types were found with the aid of Dashevskii's combination rules.[10] We employed the following values for the van der Waals radii: 1.17 for H, 1.72 for C, 1.36 for O, 1.95 for Br, 2.10 for[6] I, and[12] 1.86 Å. The energies obtained represent the sum of the dispersion attraction and repulsion. The lack of parameters in the literature for calculating the σ charges on the halogen atoms made it impossible to take into account the electrostatic contribution.

According to our calculations for 1-I-anthraquinone, for example, the interaction energy of the original molecule (x, y, z) with a molecule separated from it by the translation distance (x, y + 1, z) is −4.85 kcal/mole; the energy for other molecules composing the short-range environment of the original molecule is smaller (on a modulus basis). Thus, the energies of the interaction with the (x + 1, y, z) and (1 − x, y + 1/2, 1 − z) molecules are −1.24 and −0.91 kcal/mole respectively.

A similar pattern occurs for 1-Cl- and 1-Br-anthraquinone. Thus these structures exhibit distinct P_C1 symmetry chains (z' = 1) elongated along the y axis: A, B, C, D, E, and F chains (Fig. 2). This figure shows the arrangement of the molecules along the y axis in the structure of 1-I-anthraquinone and certain intermolecular distances less than 4 Å. The coordination number, determined by the method described previously,[13] is 14.

Although, as was pointed out above, the contribution made by the electrostatic forces was not taken into account in the energies obtained, the interaction of the x, y, z)

TABLE 2

Atom	Deviation of atoms (d) from median planes, Å			Atom	Deviation of atoms (d) from median planes, Å		
	1-I-anthraquinone	1-Br-anthraquinone	1-Cl-anthraquinone		1-I-anthraquinone	1-Br-anthraquinone	1-Cl-anthraquinone
C_1	0.04	0.04	0.01	C_{11}	−0.06	−0.03	−0.01
C_2	0.11	0.02	−0.00	C_{12}	−0.03	−0.03	−0.03
C_3	0.02	0.06	0.03	C_{13}	0.02	0.00	−0.01
C_4	−0.04	0.06	0.04	C_{14}	0.01	−0.02	0.01
C_5	0.02	0.01	0.00	O_1	−0.05	−0.04	−0.07
C_6	−0.07	0.03	0.04	O_2	−0.02	−0.07	−0.06
C_7	0.06	0.05	0.02	I	−0.03	—	—
C_8	0.07	0.02	0.03	Br	—	−0.02	—
C_9	−0.05	−0.01	−0.02	Cl	—	—	+0.02
C_{10}	0.01	−0.04	−0.02				

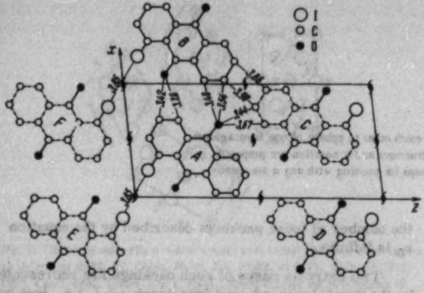

Fig. 2. Arrangement of molecules in 1-I-anthraquinone crystals (view along y axis).

molecule with the (x, y + 1, z) molecule is so much stronger than any other that taking into account these forces should have no effect on unambiguous chain selection.

The chain structure is identical in all three compounds: In order to compare them, we calculated the angle between the chain axis and the molecular plane φ, the distance between the molecular planes n, and the relative center displacement m (Table 3).

The results obtained in calculating the chain-interaction energies are given in Table 4. It follows from these data that there are no distinct layers in crystals of 1-Cl-, 1-Br-, and 1-I-substituted anthraquinone.

Analysis of the shortest intermolecular contacts2) enables us to conclude that there are no short distances (close to the sum of the van der Waals radii) in these structures, particularly for the halogen atoms.

There is one short contact in the structure of 1-Cl-anthraquinone, formed by Cl atoms ($\Delta R_{Cl-Cl} = -0.02$ Å). When the Cl is replaced by Br, the chain-superimposition mode remains the same and there is a slight increase in $|\Delta R|$ ($\Delta R_{Br-Br} = -0.02$ Å). When iodine is introduced, ΔR is 0.35 Å. It is known that Br—Br and particularly I—I contacts are often shorter than the sum of the van der Waals radii.[14-16] There is no unanimity of opinion in accounting for the causes of this type of short contact. There is no doubt, however, that the interactions in such cases are stronger than the usual van der Waals interaction.

In view of this fact, it can be assumed that, when the Cl atom in this structure is replaced by Br and then by I, the intermolecular interaction becomes somewhat stronger, which accordingly stabilizes the packing mode.

Thus, on one hand, the lack of short contacts involving the halogen atoms within the chains (short contacts between the halogen and other atoms might be unfavorable) and, on the other hand, the presence of Cl—Cl, Br—Br, and I—I contacts between chains and the nature of the contacts formed by heavy halogens (the possibility of interactions between them, especially in the case of iodine, that are stronger than the ordinary van der Waals interactions) apparently explain the existence of isomorphism in the series of 1-Cl-, 1-Br-, and 1-I-substituted anthraquinones.

TABLE 3. Comparison of Molecular-Chain Structures in 1-Monohalogen-Substituted Anthraquinone

Parameter	Cl	Br	I
φ, °	61.22	61.72	61.02
n, Å	3.50	3.56	3.72
m, Å	1.94	1.92	2.06

TABLE 4. Chain-Interaction Energies in Structures of 1-Monohalogen-Substituted Anthraquinone

Pairs of interacting chains	−U, kcal/mole		
	Cl	Br	I
A — B	2.38	2.50	1.83
A — C	1.94	1.96	2.03
A — D	1.66	1.71	1.50
A — E	1.18	1.17	0.22
A — F	2.35	2.64	1.64

The authors wish to thank P. M. Zorkii for his interest in this work and his discussion of the results.

---

1) The accuracy with which the distances were determined was estimated at 0.020-0.025 Å for 1-Cl-anthraquinone and 0.030 Å for 1-Br-anthraquinone.

2) The criterion in this case was the quantity $\Delta R = r_{ij} - (\rho_i + \rho_j)$, where r_{ij} is the distance between atoms of different molecules and ρ_i and ρ_j are the van der Waals radii.

---

[1] N. L. Klimasenko, G. A. Gol'der, and G. S. Zhdanov, Kristallografiya, 14, 266 (1969) [Sov. Phys. – Crystallogr., 14, 207 (1969)].

[2] N. L. Klimasenko and G. A. Gol'der, Kristallografiya, 14, 694 (1969) [Sov. Phys. – Crystallogr., 14, 586 (1970)].

[3] J. Wasser, Acta Crystallogr., 16, 1091 (1963).

[4] B. K. Vainshtein, Zh. Eksp. Teor. Fiz., 27, 44 (1954).

[5] Tables of Interatomic Distances and Configurations in Molecules and Ions, London (1958).

[6] A. I. Kitaigorodskii, Organic Crystal Chemistry [in Russian], Izd. Akad. Nauk, Moscow (1955).

[7] A. I. Kitaigorodskii and K. V. Mirskaya, Kristallografiya, 6, 507 (1961) [Sov. Phys. – Crystallogr., 6, 408 (1962)].

[8] P. M. Zorkii, V. K. Bel'skii, S. G. Lazareva, and M. A. Porai-Koshits, Zh. Strukt. Khim., 8, 312 (1967).

[9] M. A. Davydova and Yu. T. Struchkov, Zh. Strukt. Khim., 6, 113 (1965).

[10] V. G. Dashevskii, Zh. Strukt. Khim., 7, 594 (1966).

[11] K. V. Mirskaya, Dissertation [in Russian], Inst. Kristallogr. Akad. Nauk SSSR, Moscow (1967).

[12] P. M. Zorkii, L. M. Prezman, M. A. Porai-Koshits, and G. P. Murav'eva, Zh. Strukt. Khim., 10, 633 (1969).

[13] V. K. Bel'skii, Dissertation [in Russian], Khim. Fak. MGU (1969).

[14] V. K. Bel'skii, L. A. Chetkina, P. M. Zorkii, and G. A. Gol'der, Kristallografiya, 15, 262 (1970) [Sov. Phys. – Crystallogr., 15, 220 (1970)].

[15] A. I. Kitaigorodskii, T. L. Khotsyanova, and Yu. T. Struchkov, Zh. Fiz. Khim., 27, 780 (1953).

[16] T. L. Khotsyanova, A. I. Kitaigorodskii, and Yu. T. Struchkov, Zh. Fiz. Khim., 27, 1330 (1953).

Loose packing of dense layers

P. I. Kripyakevich
L'vov State University

(Submitted June 9, 1972; resubmitted August 27, 1972)
Kristallografiya, 18, 730-736 (July-August 1973)

Structures consisting of closely packed layers loosely superimposed on each other (a sphere of one layer against two neighboring spheres) are considered. A method of deriving such structures and a notation are proposed. Packing numbers and equations for n = 2-10 and the possible space groups for packing with any n are established.

A planar layer in which spheres of identical size are closely packed is in most cases a fragment of various three-dimensional close-packed layers,[1,2] being the basis of a large number of generated structures (superlattices, interstitials, etc.).[1] Dense layers of loose packing [the amount of space filling is $(2\pi/9)\cdot 100 = 69.8\%$, i.e., higher than α-Fe packing type], in which a sphere of a definite layer is above (under) the center of a segment joining the centers of two spheres of neighboring layers, is much more rare. As shown by Smirnova and Belov[3] there are two well-known series of such generated packings: the $MoSi_2-CrSi_2-TiSi_2$ series with superlattice packing (number of layers[4] in a period is n = 2, 3, 4), and the $Al_2Cu-Mg_2Ni-Mg_2Cu$ series, in which the packing considered is formed by the centers of empty hexagonal bipyramids located between slabs of the tetragonal $[CuAl_8]$, $[NiMg_8]$, $[CuMg_8]$ antiprisms (with the same number of layers per period).[1)] Each of these series may contain an infinite number of representations. Nevertheless, until recently only the three enumerated above were known for each of them. In particular, the problem of the possible number, types, and symmetries of packings with n > 4 did not attract the attention of investigators. The discovery of a 12-layer analog of the Al_2Cu-type structure[6] focuses attention on this problem.

It is possible to characterize the loose packing of dense layers by the four letters α, β, γ, δ (Fig. 1) in the same way that one characterizes the positions of the spheres in close packing by equations comprised of three symbols—the letters A, B, C. Four letters are necessary in the general case because the number of spacings in which the spheres of a neighboring layer may be located is three times greater than the number of spheres in any one layer. The general features of both series are the following: 1) Each letter in the equation should be surrounded by letters, different from itself; 2) these two letters surrounding the original one can be either the same or different letters. It hence follows that two types of multiple-face coordinates are possible in each of the series, a cubo-octahedral (c) and hexagonal analog of cubo-octahedral (h) in the first, and a 10-vertex 222 rhombic symmetry (r) and tetragonal 4/mmm symmetry (t) in the second.

Unlike the equations for h and c, the equations for r and t do not characterize the packing uniquely. This is mostly related to the fact that an r layer of a definite symbol (for example, γ) can be surrounded by different pairs of layers ($\alpha\gamma\beta$, $\alpha\gamma\delta$, $\beta\gamma\delta$). As a result the sequence of letters r can contain rr pairs (for example, $\beta\gamma$) surrounded by identical ($\alpha\beta\gamma\alpha$, $\delta\beta\gamma\delta$) or different ($\alpha\beta\gamma\delta$, $\delta\beta\gamma\alpha$) Greek letters. Consequently, when only a single close packing of single c layers (ccc = ABC) is possible, the number of loose packings described by the equation r_n is infinite.

Two extreme cases of such packings are represented by the three-layer $\alpha\beta\gamma$ and four-layer $\alpha\beta\gamma\delta$, i.e., just by packings with nonidentical surrounding layers, whose representation is sufficiently well known. In the equation for four-layer packing C (the prime between two letters denotes corresponding pairs) we notice the pairs surrounded by different letters: It seems that the equation can be decomposed into components along the layer width ($\alpha'\beta'\gamma'\delta'$). This packing is denoted by the symbol $\bar{1}1\bar{1}1$, where the numbers contain information on the component lengths (similarly to the Zhdanov symbols for close packing[7,1] and to the symbols applied by Smirnova in describing several superlattices of cubic close packings[8]) and the sign on the direction of rotation (a minus is counterclockwise rotation, and the centers of rotation are centers of equilateral triangles, of which the rhombs in Fig. 1 consist) in passing from the left-hand-side letters of the layer to those on the right-hand side ($\alpha'\beta'\gamma = \gamma'\delta'\alpha = 1$, $\beta'\gamma'\delta = \delta'\alpha'\beta = \bar{1}$). The three-layer packing equation cannot be decomposed ($\alpha\beta\gamma$); therefore the numerical symbol of the given packing is ∞. The symbols of all other packings r_n (for example, $'\alpha\beta\gamma'\alpha\delta\gamma' = 3\bar{3}$, $'\alpha'\beta'\gamma'\delta\alpha\gamma\delta' = \bar{1}1\bar{1}4$) contain a number of large units; consequently, it is advisable to consider them as combinations of $\bar{1}1\bar{1}1$ and ∞ packings.

Numerical symbols can also be assigned to packings containing t layers. In each case the number 1, i.e., the letter between the primes, will be responsible for a t layer. Since this letter is located relative to the neighbors (see Fig. 1) not on a spiral, but in a domain lying in one plane, we introduce for it a new symbol, $\underline{1}$. Therefore the second 4-layer packing $\alpha'\beta'\alpha'\gamma'$, whose equation also consists of four components but contains letters of three sorts, will be described by the symbol $1\underline{1}\bar{1}\underline{1}$, differing from the packing symbol $'\alpha'\beta'\gamma'\delta'$.

From what has been said it follows that the loose packing equations of dense layers consist of elements corresponding (if the sign is not taken into account) to the numbers $\underline{1}$, 1, and $p \geq 2$, i.e., of the packing fragments $\alpha\beta = 11$, $'\alpha'\beta'\gamma'\delta'$, and $\alpha\beta\gamma$ (examples are given below). In the presence of $'\alpha'\beta'\gamma'\delta'$ fragments not only does the symbol 1 occur, but also connections of the numbers p (for example, in $'\alpha\beta\gamma'\alpha\delta\gamma' = 3\bar{3}$).

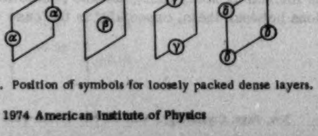

Fig. 1. Position of symbols for loosely packed dense layers.

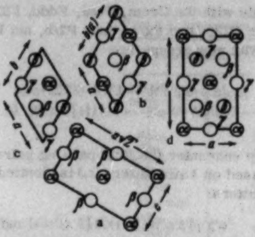

Fig. 2. Choice of unit cells of substructures with loosely packed dense layers. a) I4/mmm; b) P2, B2, P2/m, B2/m, $P6_2$, $P6_222$; c) P2/b, B2/b, d) C222, F222, Ccc2, Fdd2, Cccm, Ccca, Fddd. Small circles are projections of sphere locations, and letter notation is the conventional one.

The number of loose packings of dense layers with $n \geq 4$ is for each n larger than the number of close packings (for n = 3 these numbers are equal since we include only one αβγ packing and neglect the existence of enantiomorphous modification). To each n there corresponds a number of packings from α, β, γ, equal to the number of close packings (with the replacement of A, B, C by α, β, γ; concerning a change in symmetry see below) and determined (being usually larger) by the number of packings from α, β, γ, δ.

To derive the packings of a definite n we first write down all possible equations from the letters r and t. For each equation we then investigate all combinations of the letters α, β, γ and α, β, γ, δ, excluding those combinations already arising by translation ('α'β'α'γδ' → 'γ'δ'γ'·αβ'), by rotation around a vertical axis ('α'β'α'γδ' → 'β'δ'β'γα' = 'γ'δ'γ'αβ'), and also by enantiomorphous modification.[2] As a control we used numerical symbols: All packings (at least all with $n \leq 10$) possessing different equations with respect to the Greek letters but the same numerical symbols would be considered identical.

The minimum symmetry of any loose packing of dense layers corresponds to the P2 complex (and the pseudohexagonal unit cell $a = b$, $\gamma = 120°$, $c = n(\sqrt{3}/2)a$; Fig. 2b, c). To this complex we may combine the horizontal (perpendicular to the Z axis) m, b, or *a* planes (vertical m planes are excluded), c planes (vertical), and also the 3_1 axes passing through the centers of the triangles constituting the elementary rhombs (vertical axes of types 2_1, 3, 6, 6_1, 6_3 are not allowed), and the horizontal binary axes at 90 or 60° to each other. As a result packings appear of symmetries P2/m, P2/b, Ccc2, $P6_2$, C222, Cccm, Ccc*a*, $P6_222$. Rhombic packing (for which $b = a\sqrt{3}$, $c = n(\sqrt{3}/2)a$; Fig. 2d) is clearly base-centered (two atoms per layer). Alignment of monoclinic packings by the lateral face and of rhombic packings by the sides generates packings with B2, B2/m, B2/b, Fdd2, F222, and Fddd symmetries. Thus, 16 space groups are possible (if enantiomorphous groups[3] are not considered and packing with I4/mmm symmetry is possible[4] only for n = 2) for loosely packed dense layers.

The packing symmetries were established by analyzing the symbol positions (letters) or the numerical symbols. We restrict the discussion to the second property.

To determine the space groups according to numerical symbols it is necessary to investigate whether the equation decomposes by periods [identical or differing from each other only in the signs of the numbers and whether it has line symmetry (dividing it into mirrorlike equal parts) or "antisymmetry" (a reflected part with numbers of opposite signs)]. The results are given in Table 1. The 6_2 axis indicates the presence of three, and the F or B lattices the presence of two identical periods in the equation. If each period consists of two semiperiods differing from each other by signs of numbers there are two series of vertical d or c planes in the packing. The symmetry lines correspond to horizontal binary axes and the "antisymmetry" lines to centers of symmetry located in horizontal m planes (if the lines pass through $\underline{1}$) or d, n, *a*, b planes (lines between digits).

TABLE 1. Symmetry Determination of Loosely Packed Dense Layers by Numerical Symbol Analysis

Number of period repetition*	Number of symmetry lines			Space group	Example	
	with no sign variation	with sign variation				
		in $\underline{1}$	between digits			
3	6	0	0	$P6_222$	$1\bar{2}1\bar{2}1\bar{2}$	= 'α'βδ'α'δγ'α'γβ'
3	0	0	0	$P6_2$	$\bar{1}12\bar{1}12\bar{1}12$	= 'α'β'αδ'β'γ'βδ'γ'α'γδ'
2 (4)	4	0	4	*Fddd*	$\bar{1}1\bar{1}1$	= 'α'β'γ'δ'
2 (4)	0	0	0	*Fdd2*	$12\bar{1}1\bar{2}112\bar{1}1\bar{2}1$	= 'α'βγ'α'δ'αβ'δ'γ'δα'γ'β'γδ'β'
2	4	0	0	*F222*	1313	= 'α'βγα'β'αδβ'
2	0	2	2	*B2/m*	$11\bar{1}11\bar{1}$	= 'α'β'γ'δ'γ'β'
2	0	0	4	*B2/b*	$11\bar{1}111\bar{1}1$	= 'α'β'γ'δ'γ'δ'α'β'
2	0	0	0	*B2*	$14\bar{1}14\bar{1}$	= 'α'βγαβ'γ'δ'γβδγ'β'
1 (2)	2	2	0	*Cccm*	$11\bar{1}1$	= 'α'β'α'γ'
1 (2)	2	0	2	*Ccca*	33	= 'αβγ'αδγ'
1 (2)	0	0	0	*Ccc2*	$1112\bar{1}11\bar{2}$	= 'α'β'α'βγ'α'δ'α'δγ'
1	2	0	0	*C222*	$11\bar{3}$	= 'α'β'αγβ'
1	0	2	0	*P2/m*	$1111\bar{1}1$	= 'α'β'α'β'α'γ'
1	0	0	2	*P2/b*	$11\bar{1}1\bar{1}1$	= 'α'β'γ'δ'α'β'
1	0	0	0	*P2*	$111\bar{1}3$	= 'α'β'γ'β'αδβ'

*The number of semiperiods is in parentheses (see text).

The numerical symbols have the following features. In symbols of centrosymmetric groups the algebraic sum of the numbers (except for $\underline{1}$, i.e., t layers) always vanishes, and in noncentrosymmetric groups it either vanishes or is a multiple of three. The signs of numbers responsible for r layers, and not differing by t layers, alternate; a t layer and t layer groups can be combined with both identical and sign differing numbers. The signs in the equations of enantiomorphous modification are opposite to each other, for example, $'\alpha'\beta'\alpha'\gamma\delta' = \bar{1}\underline{1}\bar{1}2$, $'\alpha'\beta'\alpha'\delta\gamma' = 1\underline{1}1\bar{2}$.

We provide a list of packings for n ≤ 6.

For n = 2 and 3 we have by single packing:
n = 2. $'\alpha'\beta' = tt = \underline{1}\underline{1}$ (I4/mmm);
n = 3. $\alpha\beta\gamma = rrr = \infty$ ($P6_222$).

Two four-layer packings;
n = 4: 1) $'\alpha'\beta'\gamma'\delta' = rrrr = \bar{1}\underline{1}\bar{1}1$ (Fddd);
2) $'\alpha'\beta'\alpha'\gamma' = rtrt = 1\underline{1}\bar{1}\underline{1}$ (the appearance of horizontal m planes and vertical c planes; Cccm). Additional packings cannot occur.

For n = 5 there are also double packings, three- and four-letter, but both of the same C222 symmetry (a single additional symmetry element with respect to P2, a horizontal binary axis under 90°):

1) $'\alpha'\beta'\alpha\gamma\beta' = ttrrr = \underline{1}\underline{1}\bar{3}$;
2) $'\alpha'\beta\alpha'\gamma\delta' = rtrrr = \bar{1}\underline{1}\bar{1}2$;

There exist seven packings for n = 6 and each has its own symmetries. We have already encountered the $P6_222$, Cccm, and C222 groups for n = 3, 4, 5; the remaining, among them the monoclinic, appear first.

n = 6. Three-letter packings:

1) $'\alpha'\beta\gamma'\alpha'\gamma\beta' = 121\bar{2}$ (*Cccm*);
2) $'\alpha'\beta'\alpha'\beta'\alpha'\gamma' = 1111\bar{1}1$ (*P2/m*).

Four-letter packings:

3) $'\alpha'\beta'\gamma'\beta'\delta'\beta' = \bar{1}11111$ ($P6_2/22$);
4) $'\alpha\beta\gamma'\alpha\delta\gamma' = 3\bar{3}$ (*Ccca*);
5) $'\alpha'\beta\gamma'\alpha'\gamma\delta' = \bar{1}212$ (*C222*);
6) $'\alpha'\beta'\gamma'\delta'\gamma'\beta' = 11\bar{1}11\bar{1}$ (*B2/m*);
7) $'\alpha'\beta'\gamma'\delta'\alpha'\beta' = 11\bar{1}1\bar{1}1$ (*P2/b*).

It is not hard to evaluate the equations from t and r letters by numerical symbols. Packings 1 and 6 with a different choice of Greek letters have the same equation (trrtrr).

Packing symbols with n = 7-10 are not given due to lack of space.

There are 10 seven-layer packings, three three-letter (all C222) and seven four-letter, including four C222 and three new P2 groups of minimum symmetry (one example is $'\alpha'\beta'\gamma'\beta\alpha'\gamma\delta' = \bar{1}1\underline{1}\bar{2}2$). Two packings, the three-letter $'\alpha'\beta'\gamma'\beta\alpha\gamma\beta' = \underline{1}1\underline{1}\bar{4}$ (C222) and the four-letter $'\alpha'\beta'\gamma\beta'\alpha\delta\beta' = \underline{1}1\underline{1}\bar{1}3$ (P2), have the same t and r equations.

There are 28 eight-layer packings, six three-letter (two with the Cccm, C222, and P2/m groups) and 22 four-letter (single with the Cccm, Ccc*a*, Fddd, F222, and B2/b groups, five C222, two P2/m, four P2/b, six P2). Packing examples with new groups are

$'\alpha'\beta\gamma\alpha'\beta'\alpha\delta\beta' = 1313$ (*F222*) and
$'\alpha'\beta'\gamma'\delta'\gamma'\delta'\alpha'\beta' = 11\bar{1}111\bar{1}1$ (*B2/b*).

For n = 8 we encounter the first packing pairs where the equation based on Latin letters (r_8) is identical to that based on Greek letters:

$'\alpha'\beta'\gamma\delta'\beta'\alpha'\gamma\delta' = \bar{1}1\bar{2}1\bar{1}2$ (*Ccca*) and
$'\alpha\beta'\gamma\delta'\beta\alpha'\delta\gamma' = 2\bar{2}2\bar{2}$ (*Fddd*);

The second of these equations was foreseen by Smirnova and Belov.[3]

There are 56 nine-layer packings, among which are seven three-letter (one with $P6_222$, three with C222, three with P2) and 44 four-letter packings (the respective packing groups are 2, 13, 34 in quantity). As seen, new groups do not appear and the assortment of groups is not large, just as for the other odd values of n.

There are 156 10-layer packings, among which are 16 three-letter (three Cccm, five C222, six P2/m, two P2) and 140 four-letter packings of various symmetries (one Cccm, four Ccc*a*, two Ccc2, 26 C222, two F222, 10 P2/m, four B2/m, 12 P2/b, 79 P2). We first encounter the Ccc2 group ($'\alpha'\beta'\alpha'\beta\gamma'\alpha'\delta'\alpha'\delta\gamma' = 1\underline{1}\underline{1}2\bar{1}\underline{1}\underline{1}\bar{2}$).

At the same time for n = 11, as for n = 7, only two space groups are possible (let us cite examples of three-letter packings):

$'\alpha'\beta'\alpha\gamma\beta\alpha\gamma\beta\alpha\gamma\beta' = 119$ (*C222*) and
$'\alpha'\beta\gamma'\alpha'\gamma'\alpha'\gamma\beta\alpha\gamma\beta' = 12111\bar{5}$ (*P2*).

For n = 12 we note for the record their number, 13 (for $P6_222$, Cccm, Ccc2, C222, P2/m, and P2 three-letter packings are given; new groups are $P6_2$ and B2):

$'\alpha'\beta'\alpha\gamma'\beta'\gamma'\beta\alpha'\gamma'\alpha'\gamma\beta' = 11\bar{2}11\bar{2}11\bar{2}$ ($P6_222$);
$'\alpha'\beta'\alpha\delta'\beta'\gamma'\beta\delta'\gamma'\alpha'\gamma\delta' = \bar{1}12\bar{1}12\bar{1}12$ ($P6_2$);
$'\alpha'\beta\gamma\alpha\beta\gamma'\alpha'\gamma\beta\alpha\gamma\beta' = 151\bar{5}$ (*Cccm*);
$'\alpha'\beta'\alpha'\beta'\gamma\delta'\beta'\alpha'\beta'\alpha'\gamma\delta' = \bar{1}111\bar{2}111\bar{1}2$ (*Ccca*);
$'\alpha'\beta'\alpha'\beta'\gamma'\beta'\gamma'\delta'\gamma'\delta'\alpha'\delta' = \bar{1}11111\bar{1}11111$ (*Fddd*);
$'\alpha'\beta'\gamma'\beta'\gamma\alpha'\beta'\alpha'\gamma'\alpha'\gamma\beta' = 111121\bar{1}11\bar{2}$ (*Ccc2*);
$'\alpha'\beta'\gamma'\beta'\alpha'\beta'\gamma'\delta'\alpha'\delta'\gamma'\delta' = \bar{1}11\bar{1}11\bar{1}11\bar{1}11$ (*F222*);
$'\alpha'\beta'\alpha'\beta'\alpha'\beta'\alpha\gamma\beta\alpha\gamma\beta' = 111111\bar{6}$ (*C222*);
$'\alpha'\beta\gamma\alpha\beta'\gamma'\beta'\gamma'\beta\alpha\gamma\beta' = 14111\bar{4}$ (*P2/m*);
$'\alpha'\beta\gamma'\alpha\delta'\gamma'\delta'\gamma\beta'\delta\alpha'\beta' = 12\bar{2}112\bar{2}1$ (*B2/b*);
$'\alpha'\beta'\gamma'\beta'\alpha'\beta'\alpha'\beta'\alpha'\delta'\alpha'\beta' = 111\bar{1}111111\bar{1}1$ (*P2/b*);
$'\alpha'\beta\gamma\alpha\beta'\gamma'\delta'\gamma\beta\delta\gamma'\beta' = 14\bar{1}14\bar{1}$ (*B/2*);
$'\alpha'\beta'\gamma'\beta'\gamma'\beta\alpha\gamma\beta\alpha\gamma\beta' = 111117$ (*P2*).

The entire set of groups is impossible even for one value of n (even if I4/mmm is not taken into account) since the conditions for the occurrence of the groups Fddd and Fdd2 (n is divisible by 4) and of the group B2/m (an even number n is not divisible by 4) are contradictory. Close packing of the group set (besides Fm3m) is first achieved for n = 24.

TABLE 2. Symmetries of Close Packings and Their Related Loose Packings

Space group		Number of layers (n), at which first occurs	
close packing	loose packing	close (A, B, C) or loose (α, β, γ) packing	loose packing (α, β, γ, δ)
$P3m1$	$P2$	9	7
$R3m$	$P6_2$	21*	12
$P\bar{3}m1$	$C222$	5	5
$P\bar{6}m2$	$P2/m$	6	8
$P6_3mc$	$Ccc2$	12	10
$P6_3/mmc$	$I4/mmm$ $Cccm$	2 (A,B) 2 (α, β) 4 (α, β, γ)	— 8
$R\bar{3}m$ $Fm3m$	$P6_222$	9 (A, B, C) 3 (A, B, C) 3 (α, β, γ)	6

* 'α'γ'α'γ'β'γα'β'α'β'α'γ'αβ'γ'β'γ'β'α'β'γ' — $111\bar{1}12111\bar{1}12111\bar{1}12$.

As seen from the data, for each n there are one or more packings not containing in their position equations the letter δ. Indeed, the number of such packings with definite n equals the number of close packings with the same number of layers. The analogy between close and loose packing is not yet exhausted: There exists also a correlation between the packing symmetries of both classes (see Table 2). In passing from close to loose packing the c, n, and horizontal m planes are conserved, and the vertical m and *a* planes disappear. Replacing a simple triple axis by inversion in close packing corresponds to two horizontal binary axes in loose packing. The only exceptions to the single-valuedness are the correspondence of the $P6_3/mmc$ group to two groups (I4/mmm to αβ only, Cccm to the rest) and of the Fm3m and $R\bar{3}m$ groups (related, incidentally, to each other[1]) to one group, $P6_222$. It should be added that three of the three-letter packings given in Table 2 (P2, Ccc2, and $P6_2$) first occur at four-letter packings of lower n (i.e., they have no analog in close packing).

The symmetries of four-letter packings vary significantly compared with three-letter packings. Besides those indicated in Table 2 (with the exception of I4/mmm), four-letter packings with n ≤ 12 can be characterized by the following groups (the parentheses give the n for which the group occurs first): Fddd (n = 4), Ccc_a, B2/m, P2/b (all at n = 6), F222, B2/b (both at n = 8), B2 (n = 12). Each of these groups is body- or face-centered or has a horizontal *a* (b) plane. The indicated lattices and planes are incompatible with the three-letter set. The last possible group, Fdd2, is encountered at n = 16 ('α'βγ'α'δ'αβ'δ'γ'· δα'γ'β'γδ'β = $\underline{1}2\bar{1}\underline{1}\bar{2}1\underline{1}2\bar{1}\underline{1}\bar{2}1$). Thus, in loose packing the new groups are exhausted earlier than in close packing, where this occurs at n = 21 only.[1]

We consider now the following features of four-letter packings compared to three-letter packings. The number of the former increases much more rapidly with n. If at n = 5 their number is equal, at n = 10 the number of four-letter packings is almost nine times that of three-letter packings. Each three-letter packing contains only an even number of t layers (not exceeding n − 2, in analogy with close packing). Four-letter packings can contain any number, not exceeding, however, n − 3 for even n or n − 4 for odd n. The high contents of t layers prevent the formation of four-letter packings to a large extent. The thicker the t layers, the harder it is to place between them an r layer responsible for two additional positions (instead of one). In distinction from three-letter packings (besides αβγ) four-letter packings can consist of single r layers. For n = 4–10, 14 such packings are known, with the $P6_222$, Fddd, Cc*a*, F222, C222, P2/b groups, i.e., groups deprived of m planes are excluded.

The symmetry variation of loose packings and the measure of their unit cells in passing to any structure will be considered in a separate paper.

The author is deeply grateful to I. I. Zalutskii and É. V. Mel'nyk for careful reading of the manuscript and particularly for remarks and discussions which helped to improve the notation of this paper.

---

1) Shubert[5] has also noticed the connection between the $MoSi_2-CrSi_2-TiSi_2$ and $Al_2Cu-Mg_2Ni-Mg_2Cu$ series.

2) Examples of enantiomorphous modification are 'α'β'α'γδ' → α'β'α'δγ' (reflection in a vertical plane) and 'α'β'α'γδ → 'γ'β'γ'αδ' = 'α'β'α'δγ' (reflection in a horizontal plane).

3) Enantiomorphous pairs besides $P6_2-P6_4$ and $P6_222-P6_422$ are possible in the P2, B2, C222, and F222 groups.

4) For two-layer packing (Fig. 2a) we have $a = a_{hex}\sqrt{3}/2$, $c = a_{hex}$.

---

[1] N. V. Belov, Structure of Ionic Crystals and of Metallic Phases [in Russian], Izd. AN SSSR (1947), p. 8-38.

[2] V. V. Bakakin and N. V. Belov, Kristallografiya, 1, 491 (1956) [Sov. Phys.—Crystallogr., 1, 391 (1956)].

[3] N. L. Smirnova and N. V. Belov, Kristallografiya, 7, 671 (1962) [Sov. Phys.—Crystallogr., 7, 544 (1963)].

[4] H. J. Wallbaum, Z. Metallkunde, 33, 378 (1941).

[5] K. Schubert, Crystal Structures of Two-Component Phases, Springer-Verlag, Berlin (1964), p. 288.

[6] P. I. Kripyakevich and É. V. Mel'nyk, All-Union Conference on Crystal Chemistry of Intermetallic Compounds, Thesis, L'vov State University, (1971), p. 28.

[7] G. S. Zhdanov, Dokl. Akad. Nauk SSSR, 48, 40 (1945).

[8] N. L. Smirnova and R. N. Sheftal', Vestn. Mosk. Univ. Ser. Geol., 6, 85 (1968).

Determination of the nature of the filling of positions by isomorphous elements

A. L. Kosoi and V. A. Frank-Kamenetskii

Leningrad State University

(Submitted June 28, 1972; resubmitted October 5, 1972)
Kristallografiya, 18, 737-740 (July-August 1973)

It has been shown that it is appropriate to use different weighting schemes in the refinement, by the method of least squares, of structural parameters of different types: the coordinates of atoms, thermal constants, and the population of positions. For the example of the Mg–Fe replacement in orthorhombic pyroxenes, methods have been proposed for the refinement of the population of structural positions and thermal constants, taking account of the strong correlation coupling between these parameters. The possibilities provided by rapid methods for estimating the population of positions for known structures on the basis of accurate measurements of a limited number of reflections have been examined.

In many structures which are members of isomorphous series, the contents of various regular systems of points are not accurately known at the start of the refinement, so that the multiplicity of the positions (in the case where they are partly filled) or the ratios of isomorphous elements with different scattering powers must be refined together with the positional and thermal parameters.

The strong correlations between individual thermal constants B_i and the way in which the positions in the structure are populated have been noted many times in the literature (see, for example, ref. 1). When abnormally large (or on the contrary, negative) values of B_i are obtained in refinement by the method of least squares, the results are of assistance in estimating approximately the filling of the positions by heavy and light atoms. The estimate from the height of the electron density peak and from different syntheses is also fairly approximate.

At the same time, the correlations between B_i and the population of the positions prevent a more accurate determination of both the multiplicities and the thermal constants, since if the B_i are refined before the multiplicities, the error in the setting of the original multiplicities will be compensated by the B_i, and vice versa. When any of the weighting schemes at present in use are employed, the simultaneous refinement of the thermal constants and the filling of the positions is not appropriate, since the strong correlations may lead to some distortions of the true relationships between the multiplicities and the B_i. In the successive refinement of the thermal constants and multiplicities, the standard errors obtained by the method of least squares are clearly too low, since they are in fact the errors of the determination of the total influence of the B_i and the multiplicities.

The reasons for the strong correlations are clear: With increase in $s = (\sin\theta/\lambda)$, the number of sites of the reciprocal lattice increases as s^3, so that the great majority of the reflections taking part in the refinement consists of those which have s values close to the maxima of the changing values. For these reflections the addition of a heavy atom or a decrease in the B_i produces identical changes in the structure factors.

Table 1 gives an example of the relationships arising as a consequence of the strong correlations, revealed in the refinement of the structure of an orthorhombic pyroxene with the composition $Mg_{1.12}Fe_{0.88}Si_2O_6$ (1100 reflections with s values reaching 0.9 were measured on a diffractometer by the perpendicular beam method with Mo radiation and Y–Zr balanced filters). The refinement of the coordinates and the thermal constants was carried out by means of the programs of Tarnopol'skii and Andrianov[2] with Cruickshank's weighting scheme[3] for four versions of the distribution of Mg and Fe in the octahedral positions M1 and M2. In these versions the coordinates also change within a range of 2σ. Refinement of the filling of the positions, carried out after the refinement of the thermal constants, did not significantly alter the original distributions, and the standard errors obtained were of the order of 0.2% Fe.

To overcome these difficulties, two schemes are proposed, which make it possible to obtain independent estimates of the filling of the positions and the individual thermal constants, and also a real estimate of the errors in their determination.

1. Strong correlation coupling between B_i and the multiplicities takes place only at sufficiently large values of s. At low values of s the influence of the indeterminate nature of B_i and the coordinates on the determination of the multiplicity is small. We can estimate the dependence of the error in the determination of the filling of the position x on s. We shall assume that only the values of x and B for one atom are indeterminate, and that all the other parameters of the structure have been determined accurately. We shall assume for the sake of simplicity that the filling of the position is equivalent to the multiplicity and that x is a dimensionless parameter, $0 \le x \le 1$. From the theory of the method of least squares it is known that

TABLE 1

Fe conc., %		$B(M1)$	σ	$B(M2)$	σ	R, %
$M1$	$M2$					
4	84	0.48	0.012	0.72	0.007	4.62
6	82	0.58	0.011	0.69	0.006	4.56
8	80	0.66	0.011	0.67	0.006	4.55
10	78	0.73	0.012	0.65	0.006	4.63

for any parameter, including x,

$$\sigma^2(x) \sim K/(n-m) \sim K/n \sim K_1/s^3 \tag{1}$$

(n is the number of equations, that is, reflections, and m is the number of parameters; we shall assume that n ≫ m and we shall replace n by s^3, with the assumption that all sites of the reciprocal lattice within a sphere of radius s have been measured).

On the other hand, as a consequence of the indeterminate nature of B, the error in the determination of the contribution of the atom being considered to the total sum for the structure factor will be greater, the greater σ(B) and the greater s. We shall assume in a first approximation that this error is determined by the value of s for the last reflections measured. (This assumption is fairly well-founded, if it is assumed that all sites up to s are measured, so that the total number of sites is proportional to s^3). By estimating the relative error of the contribution of the atom, related to σ(B), we obtain

$$\sigma^2(x) \sim K\frac{\sigma^2[\exp(-Bs^2)]}{[\exp(-Bs^2)]^2} \sim K\frac{s^4[\exp(-Bs^2)]^2\sigma^2(B)}{[\exp(-Bs^2)]^2} \sim K_2s^4. \tag{2}$$

Combination of Eqs. (1) and (2) gives

$$\sigma^2(x) \approx K_1/s^3 + K_2s^4, \tag{3}$$

where the first term reflects the decrease in the error with increase in the number of measurements, and the second reflects the increase in the error due to the indeterminate nature of B. The minimum error is obtained for

$$s \approx (3K_1/4K_2)^{1/7}. \tag{4}$$

For the estimation of K_1 we assume that the thermal constant B is known and for the estimation of x a large number of measurements have been made, for example, as far as s = 1. Published data[4] and our experience show that it is possible to attain an error in x ~ 0.2-0.3% in favorable cases, or 3-4% in unfavorable cases (isomorphism of elements with similar scattering power). If we take account of the fact that these results were obtained in the refinement of x together with several tens of other parameters, it is appropriate to estimate the error in x (with the condition that a large number of accurate measurements are made and with the assumption that x is the only unknown parameter) from 0.01 to 0.001 and hence from 10^{-4} to 10^{-6} for K_1.

For the estimation of K_2 we assume that for values of B_l equal to 0.5-1 (for example, for silicates), the indeterminacy in B_l amounts to between ±0.1 and ±0.2 Å². We shall now assume that σ(x) is determined entirely by σ(B); by assuming that s = 1, we obtain the relative error in the contribution of the atom from 0.2 to 0.4 and hence the estimate from 0.04 to 0.16 for K_2. From these estimates for K_1 and K_2 we obtain the estimate from 0.2 to 0.35 for s_0.

In accordance with this estimate it is possible to put foward the following scheme for the refinement of the structural parameters in the case of indeterminacy in the filling of the positions: a) An arbitrary distribution of the isomorphous elements with different scattering power is taken, and the coordinates and thermal constants are refined with respect to a complete hk*l* set with weighting according to Cruickshank or with weighting which takes account of the experimental errors in the intensities; b) using the parameters obtained, the filling of the positions is refined with respect to a "truncated" experimental block with s < 0.30, with unit weighting; c) the refinement of the coordinates and thermal constants is repeated with new multiplicities, etc.

In the example mentioned above, this procedure after two repetitions converged to concentrations of Fe in M1 6.7 ± 0.8% and in M2 80.5 ± 0.8%; B(M1) = 0.62 ± 0.02, B(M2) = 0.68 ± 0.01. The concentrations of Fe in M1 and M2 were regarded as two independent parameters, although for a known overall chemical composition one of these parameters is linearly dependent on the other. When s_0 = 0.4-0.5 is used in the procedure described, it converges much more slowly and the final result shows poor agreement with the overall chemical composition.

2. Simultaneous refinement of the B_l and the multiplicities is possible if the reflections with small values of s are given the same weighting as the reflections with large values of s. If several atoms with identical coordinates are taken and their multiplicities and thermal constants are refined, the summation can give a good approximation to the experimental scattering curve for a given position (in the form of the sum of exponents). In the case of two atoms with different scattering power, distributed between two positions, these curves can be expressed as follows in terms of the theoretical scattering factors and thermal constants:

$$\begin{aligned} f_{e1}(s) &= [f_l(s) + x(f_h(s) - f_l(s))]\exp(-B_1s^2),\\ f_{e2}(s) &= [f_l(s) + (k-x)(f_h(s) - f_l(s))]\exp(-B_2s^2), \end{aligned} \tag{5}$$

where f_{e1} and f_{e2} are the experimental values of the scattering for positions 1 and 2, f_l and f_h are the theoretical scattering factors for the light and heavy atoms, x and (k − x) are the concentrations of the heavy atom in positions 1 and 2 (that is, the restrictions on the overall composition of the crystal, proposed by Finger,[5] are introduced), and B1 and B2 are the individual thermal constants of the atoms in positions 1 and 2. We shall assume that x_0 is the initial approximation for the distribution parameter. We use the symbols

$$\begin{aligned} f_{01} &= f_l(s) + x_0(f_h(s) - f_l(s)),\\ f_{02} &= f_l(s) + (k-x_0)(f_h(s) - f_l(s)). \end{aligned}$$

Taking logarithms of Eq. (5), we expand the expressions obtained in a Taylor series in the region of x_0 and reject all the terms of the expansion except the first:

$$\begin{aligned} \ln f_{e1}(s) &\approx -B_1s^2 + \ln f_{01}(s) + \Delta x(f_h(s) - f_l(s))/f_{01}(s),\\ \ln f_{e2}(s) &\approx -B_2s^2 + \ln f_{02}(s) - \Delta x(f_h(s) - f_l(s))/f_{02}(s). \end{aligned} \tag{6}$$

By writing out Eqs. (6) for different values of s within the range in which the measurements were made, we obtain a linear system for the estimation of the parameters B1, B2, and Δx. It is appropriate to repeat the calculations two or three times, until the values of the parameters remain unchanged.

The use of this procedure in the case of the orthorhombic pyroxene being considered gave the following results: Fe in M1 6.9 ± 0.2%, and in M2 81.1 ± 0.2%; $B1 = 0.615 \pm 0.006$, $B2 = 0.686 \pm 0.004$. The errors must be increased by a factor of two to three, since the values given do not reflect the errors in the determination of f_{e1} and f_{e2}.

The errors in the determination of the filling of the positions depend on several factors: a) the relationships between the number of nonequivalent reflections with $s < 0.3$ and the number of parameters for the filling of the positions, and also the total number of varying structural parameters. The number of reflections increases with increase in the cell dimensions and with decrease in its symmetry but there is a simultaneous increase in the number of parameters of the structure, so that in a first approximation their ratio remains constant; b) the number of elements replacing one another in the nonequivalent positions, and the relative differences in their scattering power; c) the errors in the determination of the intensities, including the errors associated with absorption, extinction, multiple reflections, etc.

On the basis of the foregoing, it is possible to reach the following conclusions.

1. The refinement of the coordinates and thermal constants of atoms, on the one hand, and the filling of the positions, on the other hand, require significantly different weighting systems in the refinement of the structure by the method of least squares: The greatest weighting must be given to the reflections with maximum s in the first case, and to the reflections with minimum s in the second case. In the simultaneous refinement of the thermal constants and multiplicities it is desirable to use the weighting scheme to take account of the difference in the volume of experimental material for different values of s.

2. For known structures the refinement of the filling of the positions is possible without significant loss of accuracy with respect to several tens of reflections with $s < 0.2$–0.3 (without the refinement of the coordinates and thermal constants).

The authors thank Yu. I. Smolin for valuable discussion of the problems examined here.

---

[1] S. Ghose, Z. Kristallogr., 122, 81 (1965).

[2] B. L. Tamopol'skii and V. I. Andrianov, Zh. Strukt. Khim., 4, 434 (1963).

[3] D. W. J. Cruickshank, Errors in Least Squares Methods, Computing Methods in Crystallography, Pergamon Press, Oxford (1965).

[4] C. W. Burnham, Y. Ohashi, S. S. Hafner, and D. Virgo, Am. Mineralogist, 56, 850 (1971).

[5] L. W. Finger, Determination of Cation Distribution by Least Squares Refinement of Single-Crystal X-Ray Data, Carnegie Inst. Wash. Year Book, 67, 216 (1969).

Structure of Al_2O_3 in internally oxidized Cu–Al alloys

G. I. Kokhanchik and A. V. Serebryakov

Institute of Solid-State Physics, Academy of Sciences of the USSR

(Submitted August 17, 1972; resubmitted November 23, 1972)
Kristallografiya, 18, 741-746 (July-August 1973)

Individual particles of the oxide formed by the internal oxidation of a Cu–0.29% Al alloy are studied by electron diffraction and microscopy. The particles give at least five different types of electron-diffraction patterns. The difference between these types is associated with the different dispositions of the cations in the tetrahedral vacancies of the spinel lattice of aluminum oxide.

Information as to the structures of the oxides formed by the internal oxidation of alloys is of particular interest in connection with understanding the mechanisms of the processes involved in internal oxidation and the laws governing the structure formation of the compounds. No detailed investigations have yet been made into this field. Data at present existing in the literature are often of a contradictory nature. Thus, on the basis of the diffraction pattern obtained from a large set of particles, the oxide formed by the internal oxidation of Cu–Al alloys was assigned the structure of $\varkappa$-Al_2O_3 in ref. 1, while in refs. 2 and 3 it was asserted that γ- and α-Al_2O_3 were formed in these alloys.

In this paper we shall analyze the results of an electron-diffraction and electron-microscope study of individual oxide particles extracted from an internally oxidized Cu–Al alloy. We shall see that in this alloy at least five types of aluminum oxides with different crystal structures are formed.

EXPERIMENTAL RESULTS

Plane Cu–0.29% Al samples 3 mm thick were oxidized in a $Cu_2O + Al_2O_3$ packing at 950°C. The particles of oxide so formed were extracted on carbon replicas previously evaporated on to the sample cross sections. These particles constituted plates with an angle of 120° between the side faces. Characteristic electron-microscope images of the particles appear in Fig. 1.

We studied particles with large linear dimensions of between 0.1 and several microns. All the electron-diffraction patterns obtained from these particles may be divided into four different types. The first three of these (Fig. 2, a, b, and c) are simple in the sense that each type of electron-diffraction pattern corresponds to one type of structure and hence to a particle having a homogeneous structure throughout its volume. The fourth type comprises "composite" electron-diffraction patterns constituting the result of the superposition of two or several simple patterns, each of which corresponds to different elements within the volume of one and the same particle. On analyzing the various electron-diffraction patterns, two more simple types may be distinguished in addition to the three mentioned. The five simple patterns are illustrated schematically in Fig. 3. The composite pattern obtained by superimposing the simple patterns of Fig. 3, c and d, is shown in Fig. 2d.

Semiquantitative spectral analysis of the oxide powders separated from the samples showed that the amount of copper in them was no greater than 1% and was approximately the same for particles lying at various different depths.

DISCUSSION OF RESULTS

The spectral analysis data suggest that, in the course of internal oxidation, aluminum oxide Al_2O_3 is formed rather than double copper–aluminum oxides of the $CuAl_2O_4$ or $CuAlO_2$ types. The small amount of copper found in the separated powder may be associated with the presence of residual copper dissolution products, a copper-rich intermediate transitional region between the particle and the matrix, and the dissolution of copper oxides in the Al_2O_3. However, the small proportion of copper present justifies us in ignoring any effects of the latter two processes (if indeed they occur) on the form of the diffraction patterns.

The electron-diffraction patterns shown in Fig. 2 may be explained by assuming that the oxide Al_2O_3 created during internal oxidation forms a lattice, in which the disposition of the anions and the cations occurring in the octahedral spaces exactly coincides with that of the ordinary (2-3 type) spinel.

The spinel forms[4] a cubic lattice. The reflections arising from x-ray or electron diffraction in spinel crystals belong to the set which is allowed to exist in an fcc cell (their indices have the same parity). The unit cell of the spinel contains 32 oxygen atoms forming 64 tetrahedral and 32 octahedral positions (called A and B sites),

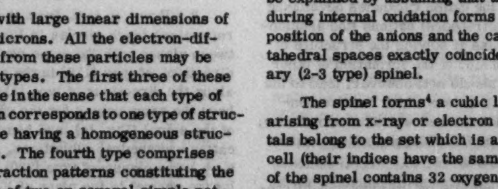

Fig. 1. Electron-microscope images of Al_2O_3 particles. a) ×36,000; b) ×82,000.

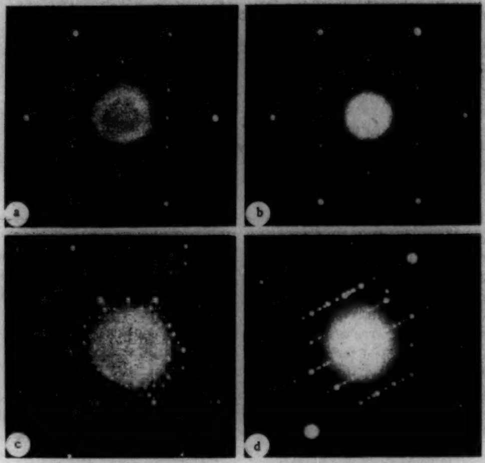

Fig. 2. Characteristic electron-diffraction patterns of Al_2O_3 particles.

of which eight of the A sites are occupied by divalent atoms and sixteen of the B sites by tervalent atoms. The oxygen forms a lattice with a fcc unit cell and a parameter $a_0/2$ (half that of the spinel lattice). The cation sublattices have a parameter a_0.

When Al_2O_3 crystallizes with the formation of oxygen sublattices and octahedral cations of the spinel type, only $5\frac{1}{3}$ of the 64 possible vacancies will be occupied in the tetrahedral sublattice (in this case the unit cell contains $21\frac{1}{3}$ tervalent instead of the 24 di- and tervalent cations of the spinel). It is quite clear that, with this abundance of vacant sites, there is a fundamental possibility not only of the ordering of the cation vacancies developing in the spinel sublattice of tetrahedral cations (the assumption usually made[4] in attempts at solving the structure of various forms of Al_2O_3), but also of the formation of other types of sublattices. This should not, however, lead to the vanishing of those spinel reflections which receive contributions from the anion and octahedral cation sublattices, particularly those reflections for which the indices acquire identical parity after dividing by 2.

The position of the reflections on the electron-diffraction patterns of Fig. 2 suggests that the patterns may be regarded as the images of planes of the (111) type in the reciprocal space of the spinel with "superstructural" lattice points (light circles in Fig. 3). The appearance of various systems of additional reflections we associate in the present investigation with different arrangements of the cations in the tetrahedral vacancies.

The projection of the tetrahedral cation sublattice of the spinel on the (111) plane is shown in Fig. 4 (the scale of the projection is indicated by the segments corresponding to distances d_{110} and d_{221}). The arrangement of the (111) planes along the [111] direction over a distance corresponding to the space diagonal of the spinel cell is indicated in Fig. $4b_1$. The strokes indicates the unoccupied planes of the tetrahedral sublattice. The ordering of the plane is characteristic of an fcc cell (ABCABC).

Since in the case of Al_2O_3 the number of cations in the tetrahedral vacancies is one third less than in the case of the spinel, for the same method of filling the (111) planes in Al_2O_3 there will be four cations instead of six. The first type of electron-diffraction pattern in Fig. 3a may be explained by the ordering of the tetrahedral vacancies, leading to the vanishing of one plane of type B and one of type C (three versions of such ordering are possible: Fig. $4b_2$, b_3, b_4).

It follows, in fact, from the positions of the spinel reflections (dark circles in Fig. 3) that the distances between planes with the same scattering power along the directions of type [110] in the spinel are equal to d_{220}, and along the directions of type [211] to d_{422}. These distances have the same values for the cation tetrahedral sublattice of the spinel (Fig. 4a), and hence for the set of anion and cation–octahedral sublattices. After ordering (Fig. $4b_2$, b_3, b_4), the planes of type (220) of the tetrahedral sublattice normal to the plane of Fig. 4a will have the same scattering power; however, planes with $d = 3d_{422}$ in the direction of type [211] in the plane of Fig. 4a will differ in scattering power from planes with d_{422}; this will naturally lead to the appearance of superstructural reflections, dividing the distance from the nodes of type (422) in the (111) plane of reciprocal space into three parts. The electron-diffraction pattern corresponding to this case and its schematic representation are respectively shown in Fig. 2a and Fig. 3a.

The space group for the cases represented in Fig. $4b_2$, b_3 will be $P\bar{3}m1(D_{3d}^3)$, for the case corresponding to Fig. $4b_4$ it will be $P3m1(C_{3v}^1)$. For all cases of ordering (Fig. $4b_2$, b_3, b_4) the dimensions of the unit cell in hexagonal axes

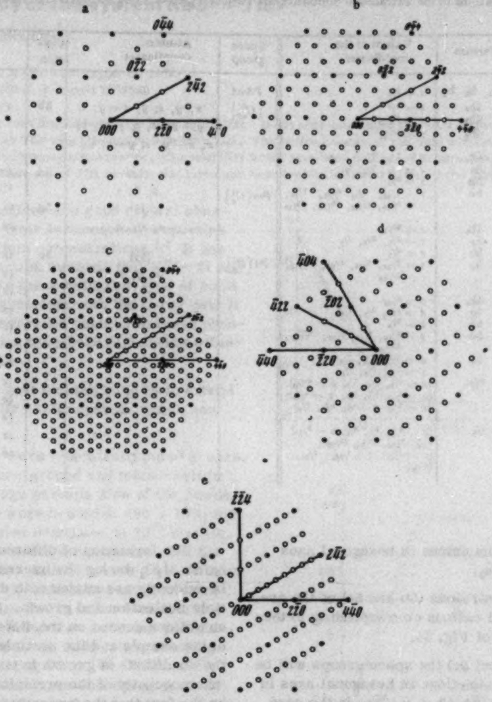

Fig. 3. Electron-diffraction paterns (schematic). a, b, c) correspond to Fig. 2a,b,c; d, e) corresponds to Fig. 2d when superimposed.

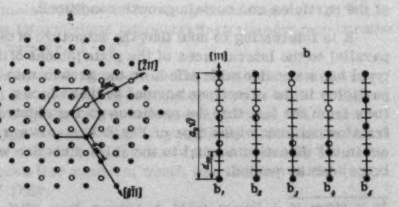

Fig. 4. Arrangements of the aluminum cations in the tetrahedral sublattice of the oxide corresponding to Fig. 3a.

will be $a = b = \sqrt{2}a_0/2, c = \sqrt{3}a_0$.

A higher symmetry in the arrangement of the tetrahedral cations may be achieved, without changing the position of the reflections in the schematic representation of the electron-diffraction pattern of Fig. 3a, by disposing the (111) planes as in Fig. 4b$_5$. The position of the atoms in the (111) planes corresponds to the spinel case; only the sequence of their alternation in the [111] direction of the spinel is altered. The dimensions of the unit cell remain the same as in the case of ordering. The space group of the oxide structure is $P\bar{3}m1(D_{3d}^3)$.

None of the three remaining electron-diffraction schemes (Fig. 3,b,c,d, and e) can be explained by the ordering of the tetrahedral vacancies in the spinel lattice. In all these cases agreement with the schematic representations of the electron-diffraction patterns (as regards the position of the reflections) can only be achieved while still preserving the stoichiometry of the oxide by changing the arrangement of the atoms in the (111) planes of the spinel and the order of alternation of the occupied and unoccupied planes.

Possible versions of arrangements of the tetrahedral cations corresponding to the schematic electron-diffraction patterns of Fig. 3,b,c,d, and e, are given in Table 1.

The disposition of the tetrahedral cations 5a in the table corresponds to the electron-diffraction pattern of Fig. 3b. The space group of the oxide in this case is

TABLE 1. Disposition of the Al Atoms in the Tetrahedral Sublattices of Various Types of Al_2O_3 Formed in the Internal Oxidation of a Cu–Al Alloy

Space group	Atomic coordinates	Version	Values of the coordinates
$P\bar{3}m1$ (D^3_{3d})	(2c) $0, 0, z; 2/3, 1/3, \bar{z}$ (2d) $1/3, 2/3, z; 2/3, 1/3\ \bar{z}$	$4b_2, b_3, b_4$	$z = 1/8$
		$4b_5$	$z = 5/8$
		$4b_1$	$z = 13/24$
		$4b_3$	$z = 19/24$
	(1a) $0, 0, z$	$4b_6$	$z = 1/8, 7/8$
		5a	$z = 1/8, 3/8, 7/8$
		5b	$z = 3/8$
		5c	$z = 1/16, 3/16, 5/16, 7/16, 9/16, 11/16, 13/16, 15/16$
	(1b) $1/3, 2/3, z$	$4b_4$	$z = 19/24$
		5a	$z = 1/8, 3/8, 7/8$
		5b	$z = 3/8$
		5c	$z = 3/16, 5/16, 9/16, 13/16, 15/16$
$P3m1$ (C^1_{3v})	(1c) $2/3, 1/3, z$	$4b_1$	$z = 5/24$
		5a	$z = 1/8, 3/8, 7/8$
		5b	$z = 3/8$
		5c	$z = 3/16, 5/16, 9/16, 13/16, 15/16$
	(3d) $x, \bar{x}, z; x, 2x, z;$	5a	$x = 1/6, 1/2, 5/6;$ $z = 1/8, 3/8, 7/8$
		5b	$(x = 1/9, 4/9, 7/9; z = 19/24);$ $(x = 2/9, 5/9; 8/9; z = 5/24);$ $(x = 1/3; z = 1/8, 3/8, 7/8)$
	$2x, \bar{x}, z$	5c	$(x = 1/6, 1/2, 5/6; z = 3/16, 5/16, 9/16, 13/16, 15/16);$ $(x = 1/3; z = 1/16, 7/16, 11/16)$
$P3m1$ (C^1_{3v})	(6e) $x, y, z; \bar{y}, x-y, z;$ $y-x, \bar{x}, z; \bar{y}, \bar{x}, z;$ $x, x-y, z; y-x, y, z$	5b	$x = 1/6; y = 1/3; z = 3/8$
$Pm(C^1_s)$	(1a) $x, 0, z$	5d	$(x = 1/6; z = 1/8); (x = 3/6; z = 3/8, 17/24); (x = 7/6; z = 7/8, 13/24)$
	(1b) $x, 1/2, z$	5d	$(x = 5/6; z = 1/8); (x = 3/6; z = 13/24);$ $(x = 7/6; z = 17/24)$
$P1(C^1_1)$	(1a) x, y, z	5e	$(x=0; 1/3; 2/3; y = 15/16; z = 1/16);$ $(x = 1/3; y = 19/48; z = 3/16);$ $(x = 0; y = 13/16; z = 3/16)$ $(x = 1/9; 4/9; 7/9; y = 7/16; z = 11/48);$ $(x = 2/9; 5/9; 8/9; y = 15/16; z = 19/48);$ $(x = 1/3; y = 9/16; z = 7/16)$ $(x = 0; y = 1/16; z = 7/16);$ $(x = 0; 1/3; 2/3; y = 7/16; z = 9/16);$ $(x = 1/3; y = 5/16; z = 11/16)$ $(x = 2/9; 5/9; 8/9; y = 29/48; z = 35/48);$ $(x = 1/9; 4/9; 7/9; y = 37/48; z = 43/48);$ $(x = 1/3; y = 9/16; z = 15/16)$

$P3m1(C^1_{3V})$. The unit cell dimensions in hexagonal axes are $a = b = 3\sqrt{2}a_0/2$; $c = \sqrt{3}a_0$.

Analysis indicates two versions (5b and 5c) of the arrangement of the tetrahedral cations corresponding to the electron-diffraction pattern of Fig. 3c.

For both versions (5b and 5c) the space groups will be $P3m1(C^1_{3V})$. The unit cell dimensions in hexagonal axes in the case of 5b are $a = b = 3\sqrt{2}a_0/2$, $c = \sqrt{3}a_0$; in the case of 5c they are $a = b = 3\sqrt{2}a_0/2$, $c = 2\sqrt{3}a_0$.

As indicated earlier, the electron-diffraction pattern of Fig. 2d constitutes the superposition of two patterns: Fig. 3, d and e. Table 1 presents dispositions of the cations 5d and 5e capable of explaining the patterns of Fig. 3,d and e respectively. For version 5d the space group will be $Pm(C^1_S)$ and the unit cell dimensions (monoclinic) $a = \sqrt{6}a_0/2$, $b = \sqrt{2}a_0/2$; $c = 3\sqrt{2}a_0/2$; $\alpha = \gamma = 90°$, $\beta = 125°16'$.

The cation tetrahedral lattice in the second case (5e) lowers the symmetry of the oxide lattice to $P1(C^1_1)$. The dimensions of the triclinic unit cell in this case are $a = 3\sqrt{2}a_0/2$; $b = \sqrt{2}a_0/2$; $c = 5\sqrt{2}a_0/2$; $\alpha \simeq 101°32'$; $\beta \simeq 95°44'$; $\gamma = 120°$.

The orientational relationships between the spinel cell and the cell of the Al_2O_3 take the following form in every case (versions $4b_2$–5e in Table 1): $(111)_{\text{spinel}} \parallel (001)_{Al_2O_3}$; $[0\bar{1}1]_{\text{spinel}} \parallel [010]_{Al_2O_3}$.

The formation of different structural types of the oxide Al_2O_3 during the internal oxidation of Cu–Al alloys is evidently associated with different conditions of particle nucleation and growth. In the present case these conditions depend on the distance from the free surface of the sample and the particle growth time. A change in the conditions of growth in time may lead to structural inhomogeneity of the precipitate. This view is supported by the fact that the majority of electron-diffraction patterns obtained constitute the result of the superposition of two or several "simple" patterns of the kind shown in Fig. 3. It is later proposed to conduct further experiments in order to discover the relationship between the structure of the particles and certain growth conditions.

It is interesting to note that the structure of the planes parallel to the lateral faces of the plate [planes of the (211) type] has a considerable effect on the growth rate of the particles in the directions normal to these faces. This follows from the fact that the particles giving electron-diffraction patterns of the type of Fig. 2d are always drawn out in the direction normal to the [211] direction with a large identity period.

---

[1] F. N. Rhines, W. A. Johnson, and W. A. Anderson, Trans. AIME, 147, 205 (1942).

[2] M. F. Ashby and G. C. Smith, J. Inst. Metals, 91, 182 (1962-1963).

[3] O. Preston and N. J. Grant, Trans. Metallurg. Soc. AIME, 221, 164 (1961).

[4] R. W. G. Wyckoff, Crystal Structures, Vol. 3, Interscience, New York (1963).

X-ray diffraction study of the system RbBr − TlBr

A. A. Haav and T. K. Muirsepp
Tartu State University

(Submitted April 14, 1972; resubmitted August 22, 1972)
Kristallografiya, 18, 747-750 (July-August 1973)

The system RbBr−TlBr has been studied by powder x-ray diffraction. It has been established that substitution-type solid solutions are formed by TlBr with RbBr and by RbBr with TlBr. The lattice constant of the solid solutions varies linearly with an increase in impurity concentration. The solubility limits have been studied. The lattice constants of RbBr having a CsCl structure and of TlBr having a NaCl structure have been calculated by linear extrapolation.

Thallium-activated alkali halides are good crystal phosphors. For some of them their luminescent properties are retained with high thallium concentrations.[1,2] It has been proved by x-ray diffraction methods that KCl−Tl and KBr−Tl phosphors belong to the substitution type of solid solutions.[3,4] In complete agreement with the x-ray data it is considered that the luminescence centers in these phosphors are thallium ions which have been replaced by potassium ions at the lattice nodes.[5]

The purpose of the present investigation is to extend the x-ray studies to the RbBr−TlBr system, which has not yet been so studied.

The starting materials were "chemically pure" grades. Mixtures of the powders were ground and mixed well in an agate mortar. The average particle size of the powder was 5-10 μ. The mixtures were heated at 400 ± 10°C for 30-50 h sealed glass ampoules evacuated to 10^{-2} mm Hg. The samples were cooled to room temperature over the course of 2-3 min. The x-ray patterns were taken with an RKU-114 camera at 22 ± 1°C. Different radiation were used to record the x-ray patterns in order to determine the lattice constant with the maximum accuracy possible. For example, Ni Kα radiation was used when studying RbBr−TlBr mixtures containing 16 mole% TlBr, while pure TlBr and TlBr−RbBr mixtures containing up to 20 mole% RbBr were studied by using Cr Kα radiation. For the intermediate concentrations Cu Kα and Cr Kα radiations were used. The absolute error in determining the lattice constant using Ni Kα radiation is not greater than $\pm 6 \cdot 10^{-4}$ Å, while for studies using Cr Kα radiation (up to 20 mole% RbBr) it is not greater than $\pm 4 \cdot 10^{-4}$ Å. For the intermediate concentrations the accuracy is rather lower, namely $\pm 1 \cdot 10^{-3}$ Å.

Phase analysis showed that the x-ray patterns recorded for specimens containing up to 14 mole % TlBr exhibit only the lines corresponding to the NaCl structural type in which RbBr crystallizes under normal conditions. For concentrations of 16 and 20 mole %, a new very weak line appears, which was indexed as the (110) line of TlBr.

Figure 1 shows the relationship between the lattice constant of RbBr and the TlBr concentration. It is seen that the lattice constant decreases linearly with an increase in TlBr concentration. Beyond a concentration of 30 mole % TlBr the lattice constant shows no further change. It can also be seen from the figure that under the given conditions the solubility limit of TlBr in RbBr is ≈27 mole %. The existence of lines from TlBr on the x-ray patterns at lower concentrations than the limiting concentration is evidently caused by the free TlBr phase which may be produced by the partial breakdown of the solid solution. However, the amount of the free phase should be small because of the strongest (110) line from TlBr on the x-ray patterns is very weak, while the lattice constants calculated for these concentrations lie satisfactorily on the straight line.

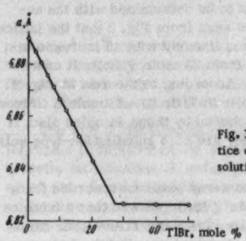

Fig. 1. Relationship between the lattice constant of the RbBr−TlBr solid solution and the TlBr concentration.

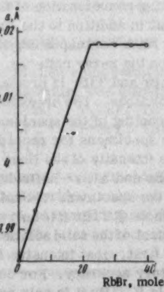

Fig. 2. Relationship between the lattice constant of TlBr−RbBr solid solution and the RbBr concentration.

On the x-ray patterns obtained for specimens containing 20 mole % or more of TlBr there are lines having an odd sum of (hkl) indices, which are absent on the x-ray pattern for pure RbBr, because the atomic factors for the Rb^+ and Br^- ions are almost equal. However, since the atomic factor of the Tl^+ ion is greater than that of the Rb^+ ion, when some of the Rb^+ ions are replaced by Tl^+ ions at the lattice nodes of RbBr, the difference between the atomic factors for reflections having odd indexes is increased with an increase in TlBr concentration, which also causes the appearance of appropriate reflections on the x-ray patterns with a sufficiently high impurity concentration. Taking into account also that the lattice constant in the RbBr−TlBr system follows Vegard's law, it may be concluded that we had substitution-type solid solutions.

On the x-ray patterns recorded from specimens of TlBr–RbBr (up to 20 mole % RbBr) only the lines belonging to the CsCl structure in which TlBr crystallizes are observed. Figure 2 shows the relationship between the lattice constant of TlBr and the RbBr concentration. Here it is pertinent to note that on the x-ray patterns recorded for TlBr–RbBr specimens immediately after their preparation the latter lines were comparatively weak and broad and it was found difficult to measure them accurately. After annealing the specimens for 2-3 h at 200°C the sharpness of the lines referred to was restored, which enabled the lattice constant to be determined with the accuracy noted above. It is seen from Fig. 2 that the lattice constant of TlBr increases linearly with an increase in RbBr concentration, but from 25 mole % RbBr it undergoes no further change. According to the data in Fig. 2 the solubility limit of RbBr in TlBr is ≈22 mole%. Since Vegard's law is closely obeyed by these samples also, it may be concluded that they are also substitution-type solid solutions.

Phase analysis of the x-ray patterns recorded for a sample containing 50 mole % RbBr showed that a mixture of the solid solutions RbBr–TlBr and TlBr–RbBr exists chiefly in this specimen. Determination of the lattice constants for these solid solutions showed that their composition corresponds to the limiting concentration of the components. It must be noted that in addition to the lines from the solid solutions, the weak lines corresponding to pure RbBr and TlBr still appear on the x-ray patterns. In our opinion, the free phase of RbBr and TlBr is produced by the breakdown of the solid solutions. The breakdown may take place either during the cooling of the specimens or during the preparation of the specimens for recording the x-ray patterns. The relative intensity of the lines from the solid solutions RbBr–TlBr and TlBr–RbBr depends on their relative amounts in the specimen. Therefore, for concentrations of 30 and 40 mole % TlBr it is only possible to determine the lattice constant of the solid solution TlBr–RbBr–TlBr and observe the first, most intensive lines of RbBr and TlBr with satisfactory accuracy. For concentrations of 60, 70, and 75 mole % TlBr it is only possible to determine the lattice constant of the solid solution TlBr–RbBr and establish the presence of the lines of TlBr and RbBr.

By linear extrapolation the lattice constant of TlBr having the NaCl structure can be calculated from the data in Fig. 1 and the lattice constant of RbBr having the CsCl structure can be calculated from the data in Fig. 2. For TlBr (NaCl structure) a = 6.656 Å and for RbBr (CsCl structure) a = 4.134 Å.

Slater[6] was the first to establish that at high pressure RbBr undergoes a polymorphic transition from the phase having the NaCl structure to a phase having the CsCl structure. Jacobs[7] used the Born–Mayer theory to calculate the distance r_0 between closest ions at the pressure of the polymorphic transition ($4.5 \cdot 10^8$ N/m^2). Subsequently Tosi and Fumi[8] conducted similar calculations and obtained a result agreeing with Jacobs' result. More recently Weir and Piermarini[9] determined r_0 by x-ray diffraction at the pressure of the polymorphic transitions. According to the data of ref. 10 RbBr sublimed on a silver film also crystallizes with a CsCl structure. From our data r_0 = 3.580; from the data in refs. 7 and 8 r_0 = 3.54; from ref. 9 r_0 = 3.54 and 3.55; from ref. 10 r_0 = 3.55 Å.

On the basis of ref. 9 we have calculated two values for r_0. The first of the values presented corresponds to the average value of the lattice constant (a = 4.09 Å), while the second is obtained from two recent values of the lattice constant (a = 4.10 Å). In our view, the latter value of r_0 should be the more accurate (the diffraction angle being greater). The value of r_0 we found differs markedly from the result given in ref. 10, although they were both determined at atmospheric pressure. However, the experimental and calculated values of r_0 at the pressure of the polymorphic transition are in good agreement with each other.

The compressibility of RbBr having the CsCl structure can be estimated from the lattice constant at atmospheric pressure and at the pressure of the polymorphic transition. As is well known, the isothermal compressibility $K = -(1/V_0)(\Delta V/\Delta p)$, where V_0 is the initial volume (proportional to r_0^3) taken at atmospheric pressure, and Δp corresponds in the present case to the pressure of the polymorphic transition. To calculate ΔV we used the value of r_0 we had determined and the corresponding data from ref. 9. All the values of r_0 are referred to room temperature.

The compressibility calculated from the r_0 values of 3.54 and 3.55 Å for RbBr having the CsCl structure was found to be 6.6 and $5.0 \cdot 10^{-11}$ m^2/N respectively, which agrees satisfactorily with its experimental value[8] of $5.3 \cdot 10^{-11}$ m^2/N. From this result it may be concluded that the strong stresses which distort the distance between ions are absent in the solid solution TlBr–RbBr. However, films of RbBr deposited on silver films should be highly compressed because the value of r_0 is even lower for them than its value at the pressure of the polymorphic transition.

In ref. 4 the lattice constant of TlBr having the NaCl structure was calculated (6.672 Å) and determined by extrapolation (6.711 Å), whereas we obtain a value of 6.656 Å (see above). Hence, it is seen that a decreases for TlBr if a compound having a heavier cation is used as the base. It seems to us that the decrease in a is associated with an increase in the polarizability of the Rb$^+$ ions compared with the K$^+$ ions.

---

[1] R. I. Gindina, A. A. Élango, A. A. Maarooz, and A. A. Haav, Proceedings of the 19th Conference on Luminescence, Vol. 1 [in Russian], Latvian State University, Riga (1970), p. 71.

[2] R. I. Gindina, A. A. Maaroos, and A. A. Haav, Abstracts of Proceedings, Sixth All-Union Conference on the Synthesis, Production and Use of Scintillators [in Russian], All-Union Scientific Research Institute for Single Crystals, Khar'kov (1971), p. 30.

[3] W. Runciman and E. Steward, Proc. Phys. Soc., A66, 484 (1953).

[4] A. A. Haav, Kristallografiya, 13, 1078 (1968) [Sov. Phys. – Crystallogr., 13, 938 (1969)].

[5] C. Luschchik, R. Gindina, S. Zazubovich, and N. Lushchik, Czech. J. Phys., B20, 585 (1970).

[6] J. Slater, Phys. Rev., 23, 488 (1924).

[7] R. Jacobs, Phys. Rev., 54, 468 (1938).

[8] M. Tosi and F. Fumi, J. Phys. Chem. Solids, 23, 359 (1962).

[9] C. Weir and G. Piermarini, J. Res. Nat. Bur. Standards, A68, 105 (1964).

[10] Landolt-Börnstein, Zahlenwerte und Funktionen. Atom und Molekularphysik, Vol. 4, Kristalle, Springer, Berlin–Göttingen–Heidelberg (1955).

Polymorphism and crystallographic properties of yttrium and rare-earth trifluorides

B. P. Sobolev, L. S. Garashina, P. P. Fedorov, N. L. Tkachenko, and K. B. Seiranyan
Institute of Crystallography, Academy of Sciences of the USSR
(Submitted June 9, 1972)
Kristallografiya, 18, 751-758 (July-August 1973)

By stabilizing the tysonite structure type (LaF_3) by isomorphous substitution new data have been obtained on the size of the unit cell for the unquenched high-temperature modifications α-LnF_3 (Ln = Sm to Ho) for standard conditions. The crystallographic properties given in the literature for various modifications of LnF_3 and YF_3 are analyzed and a summary tabulation of the most reliable values is given. Using the refined and newly found unit cell parameters for LnF_3 compounds, the regularities in their variation in the series of various modifications of the rare-earth trifluorides have been traced.

The polymorphism, structure, and crystallographic properties of rare-earth and yttrium trifluorides have been the subject of much work.[1-13] The most complete data on polymorphism in LnF_3 has been obtained[9] by high-temperature x-ray work and it was there shown that LnF_3 crystallizes not in two structure types, as assumed previously, but in three.

The tysonite structure of LaF_3 and the rhombic β-YF_3 structure have been discovered previously.[1,2] The new "hexagonal YF_3" structure type in which the high-temperature modifications of α-LnF_3 crystallize (Ln = Er to Lu) was not identified by Thomas and Brunton.[9]

Both types of high-temperature α-LnF_3 (tysonite and "hexagonal YF_3") are not quenched from the melt and their properties cannot be studied at room temperature (other than α-SmF_3, according to Jones and Shand[12]). Because of this, the literature contains hardly any crystallographic information on the unit cell parameters of α-LnF_3 for standard conditions. The high-temperature measurements of the unit cell parameters of α-LnF_3 (ref. 9), as we will show below, turn out to be divergent from the properties of the other LnF_3.

Refinements of the unit cell parameters of the rare-earth and yttrium trifluorides have been carried out repeatedly,[5,10-14] depending on whether it appears possible to make measurements on purer reactants. All of the refinements were done for modifications of LnF_3 which are stable at room temperature.

The aim of the present paper is to obtain the crystallographic properties of the high-temperature (unquenched) tysonite modification of α-LnF_3 under standard conditions, which are absent in the literature, and also to analyze the properties of α- and β-LnF_3 found in the literature and choose the most reliable values on the basis of their agreement with the general course of the variation of the unit cell parameters, molar volumes, and other properties in the series of polymorphic modifications of LnF_3.

EXPERIMENTAL METHOD

We studied solid solutions formed on the basis of the high-temperature (not quenched in pure form) tysonite modifications of α-LnF_3 (Ln = Sm to Ho) in the systems LnF_3-CaF_2, LnF_3-SrF_2, LnF_3-BaF_2, and LnF_3-LaF_3 (refs. 15-17).1)

The samples were obtained by sintering the corresponding fluorides, which were first melted in an HF atmosphere, at temperatures from 800 to 1050°C for 2 to 10 days. The heat treatment was done in hermetically

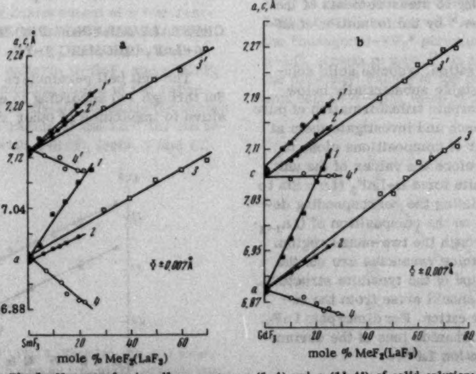

Fig. 1. Hexagonal unit cell parameters a (1-4) and c (1'-4') of solid solutions formed from α-SmF_3 (A) and α-GdF_3 (B). A: 1, 1') $Sm_{1-x}Ba_xF_{3-x}$; 2, 2') $Sm_{1-x}Sr_xF_{3-x}$; 3, 3') $Sm_{1-x}La_xF_3$; 4, 4') $Sm_{1-x}Ga_xF_{3-x}$; B: 1, 1') $Gd_{1-x}Ba_xF_{3-x}$; 2, 2') $Gd_{1-x}Sr_xF_{3-x}$; 3, 3') $Gd_{1-x}La_xF_3$; 4, 4') $Gd_{1-x}Ca_xF_{3-x}$.

sealed nickel vessels in a fluorine atmosphere and quenched in running water. The amount of oxygen in the samples of the LnF_3-MeF_2 systems after sintering was determined by vacuum melting and was between 0.01 and 0.015 wt.%.

X-ray phase analysis and determination of the unit cell parameters was carried out using an AFV-202E diffractometer–spectrometer from the Toshiba company (Japan) using Cu $K\alpha,\beta$ radiation. The precision of the determination for the solid solutions amounted on the average to ±0.007 Å and the error in the parameters of pure $\alpha-LnF_3$ obtained by the extrapolation basically did not exceed ±0.01 Å. Figure 1, a and b, shows examples of the extrapolation of the parametric dependence to the pure LnF_3 ordinate[2)] for SmF_3 and GdF_3. The validity of the extrapolation through a two-phase region has been determined from the satisfactory approximation of the experimental values of the lattice parameters to linear equations over a broad concentration range. The coefficients of the equations for the lines of Fig. 1 were calculated by the least squares method.

STABILIZATION OF THE LaF_3 STRUCTURE TYPE IN THE BINARY SYSTEMS LnF_3-MeF_2 (Me = Ca, Sr, Ba) AND LnF_3-LaF_3

The possibility of experimentally obtaining the crystallographic properties of the unquenched modification $\alpha-LnF_3$ is based on the stabilization of the tysonite structure type by isomorphous substitution.

In the theoretical discussion of stabilization of the LaF_3 structure type by anion vacancies given previously[6] the conclusion is based on energy considerations. More recently we have experimentally confirmed the validity of the proposal of Mansmann;[6] in the binary systems LnF_3-CaF_2 and LnF_3-BaF_2 based on $\alpha-LnF_3$ with the tysonite structure below the temperature of a polymorphic transition $\alpha \rightarrow \beta-LnF_3$ there is a broad series of solid solutions. We have found such a series in the systems LnF_3-SrF_2. Heterovalent isomorphous substitution of Me^{2+} for Ln^{3+} is accompanied, according to measurements of the densities of the solid solutions,[16] by the formation of anion vacancies.

As a result of the stabilization, tysonite solid solutions in binary systems are stable substantially below the temperature of the polymorphic transformation of pure LnF_3 and it is possible to quench and investigate them at room temperature. A number of compositions close to LnF_3 were not quenched; therefore the values of the unit cell parameters for the tysonite form $\alpha-LnF_3$ (Ln = Sm to Ho) were obtained by extrapolating the corresponding dependences of these quantities on the composition of $(Ln_{1-x}\cdot Me_x)Fe_{3-x}$ solid solutions through the two-phase region. In the systems LnF_3-MeF_2, anion vacancies are not the only reason for the stabilization of the tyosinite structure. Additional stabilizing effects should arise from the replacement of Ln^{3+} by a larger cation. For dimorphic LnF_3, promising substituents are lanthanide ions of the cerium subgroup, especially the large ion La^{3+}.

An experimental investigation of LnF_3-LaF_3 systems (Ln = Sm, Gd, Tb, and Ho) confirmed this idea. More detailed results of the investigation of these systems have been given in ref. 17; here we limit our consideration to solid solutions based on the high-temperature modification $\alpha-LnF_3$ stabilized by the replacement of Ln^{3+} by La^{3+}. The compositions of the solid solutions $(Ln_{1-x}La_x)F_3$ with greatest content of LnF_3 which could be quenched were different for different LnF_3, but all of them (the quenching conditions are the same) are characterized by the same average ionic radius of the cation, which turns out to be close in size to Nd^{3+}. In the series of rare-earth trifluorides, NdF_3 is the last fluoride having one modification of the tysonite type over the whole temperature range and forming a continuous (at all temperatures) series of solid solutions with LaF_3. Thus in the systems LnF_3-LaF_3 the cation size in the "stabilized" component is less than the "stabilizing" cation and isovalent isomorphous replacement of Ln^{3+} in the tysonite structure by a larger cation increases the ratio of the average cation ionic radius to the radius F, shifting it into the range of values for a stable tysonite-type structure.

CRYSTALLOGRAPHIC PROPERTIES OF $\alpha-LnF_3$ (LaF_3 STRUCTURE TYPE)

The methods described above were used to find the unit cell parameters for six tysonite modifications of $\alpha-LnF_3$ from SmF_3 to HoF_3 inclusively. For GdF_3, TbF_3, and DyF_3 these quantities were not previously known under standard conditions. A comparison of the crystallographic properties for the remaining $\alpha-LnF_3$ structures with those in the literature[2] has shown that the difference is quite substantial.

The variation in the unit cell parameters for the tysonite form of $\alpha-LnF_3$ (Fig. 3) with a change in the ionic radius of the Ln^{3+} (ref. 20) suggests the preferability of our measurements for $\alpha-SmF_3$, $\alpha-EuF_3$, and $\alpha-HoF_3$ as giving the most satisfactory overall linear character to the dependence (the numerical values of a and c for six $\alpha-LnF_3$ compounds are given in Table 1). It apparently follows from these considerations that we should prefer the data[12] of Jones and Shand[3)] for CeF_3 and refine the characteristics for PmF_3.

CRYSTALLOGRAPHIC PROPERTIES OF $\beta-LnF_3$ (RHOMBIC $\beta-YF_3$ TYPE)

The unit cell parameters of rhombic $\beta-LnF_3$ (Ln = Sm through Lu) according to existing data[12,13] is little sensitive to impurities of other rare-earth elements or oxy-

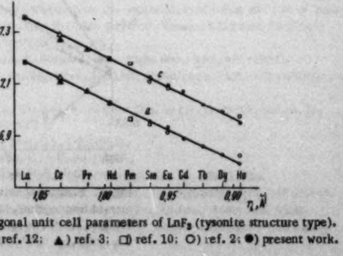

Fig. 2. Hexagonal unit cell parameters of LnF_3 (tysonite structure type). ■) ref. 4; △) ref. 12; ▲) ref. 3; □) ref. 10; ○) ref. 2; ●) present work.

TABLE 1. Crystallographic Properties of Rare-Earth and Yttrium Trifluorides

LnF_3	LaF_3 structure type*				β-YF_3 structure type†					α-UO_3 (α-YF_3) structure type‡				references
	unit cell parameters, Å		V_{mol}, Å³	$\rho_{x\text{-ray}}$, g/cm³	unit cell parameters, Å			V_{mol}, Å³	$\rho_{x\text{-ray}}$, g/cm³	unit cell parameters, Å		V_{mol}, Å³	$\rho_{x\text{-ray}}$, g/cm³	
	a	c			a	b	c			a**	c**			
LaF_3	7.186	7.352	54.79	5.94	—	—	—	—	—	—	—	—	—	[9, 13]
CeF_3	7.125	7.292	53.43	6.13	—	—	—	—	—	—	—	—	—	[12]
PrF_3	7.078	7.239	52.34	6.28	—	—	—	—	—	—	—	—	—	[9, 13]
NdF_3	7.030	7.200	51.36	6.51	—	—	—	—	—	—	—	—	—	[9, 13]
PmF_3	6.970	7.150	50.41	6.72	—	—	—	—	—	—	—	—	—	[10]
SmF_3	6.962	7.128	49.87	6.90††	6.669	7.059	4.405	51.84	6.64	—	—	—	—	[2, 12]
EuF_3	6.940	7.100	49.35	7.03††	6.622	7.019	4.396	51.08	6.79	—	—	—	—	[2, 13]
GdF_3	6.890	7.076	48.48	7.34††	6.570	6.984	4.393	50.39	7.06	—	—	—	—	[2, 12, 13]
TbF_3	6.865	7.026	47.79	7.50††	6.513	6.949	4.384	49.61	7.23	—	—	—	—	[2, 12]
DyF_3	6.836	7.009	47.27	7.71	6.460	6.906	4.376	48.81	7.47	—	—	—	—	[2, 12]
HoF_3	6.802	6.961	46.42	7.83*****	6.404	6.875	4.379	48.20	7.64	—	—	—	—	[2, 12, 13]
ErF_3	—	—	—	—	6.354	6.846	4.380	47.63	7.82	4.024	4.125	57.84	6.44	[2, 12, 21]
TmF_3	—	—	—	—	6.283	6.811	4.408	47.16	7.95	4.059	4.175	59.57	6.30	[2, 12, 21]
YbF_3	—	—	—	—	6.216	6.786	4.434	46.76	8.17	4.036	4.160	58.68	6.51	[2, 12, 21]
LuF_3	—	—	—	—	6.145	6.761	4.472	46.45	8.29	4.018	4.150	58.02	6.64	[13, 21]
YF_3	—	—	—	—	6.367	6.859	4.394	47.97	5.05	4.117	4.225	62.02	3.91	[13, 21]

*Trigonal class, space group $P\bar{3}c1 = D_{3d}^4$, Z = 6, 11 Ln^{3+} particles (ref. 6).

†Rhombic class, space group $Pnma = D_{2h}^{16}$, Z = 4, 9 Ln^{3+} particles (ref. 2).

‡Trigonal class, space group $C\bar{3}m1 = D_{3d}^3$, Z = 1, 8 Ln^{3+} particles (ref. 22).

**For a temperature of 10 to 15 degrees above the transition $\beta \rightarrow \alpha$-LnF_3.

††Present work.

gen. The most important difference from the earlier data[2] was noted by Spedding and Henderson[13] for β-YF_3 and β-LuF_3. Table 1 gives the later measurements.

Figure 3 shows the change of the unit cell parameters of β-LnF_3 as a function of the atomic number of the lanthanide. The curves consist of two nearly linear regions which join in the region of HoF_3 and ErF_3. The change in the behavior of curves a, b, and c involves a maximum in the thermal stability in the isostructural series of β-LnF_3 (according to the data of refs. 5, 9, 13 the highest temperature for the transformation of β-LnF_3 into α-LnF_3 is observed for HoF_3, YF_3, and ErF_3). The change in the behavior of the parameters and the stability between HoF_3 and ErF_3 reflects a definite change in the structure of the rhombic form of β-LnF_3 which requires individual discussion.

Simultaneously with the achievement of a low-temperature β-LnF_3, the maximum thermal stability in the series of high-temperature α-LnF_3 compounds is observed to have the opposite pattern, α-HoF_3 and α-ErF_3 turn out to have the lowest melting points of the rare-earth trifluorides.[5,9,12,13] The instability again decreases with a variation of the ionic radius of the Ln^{3+} for the tysonite structure beginning with α-ErF_3 (refs. 9 and 12).

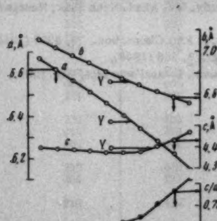

Fig. 3. Rhombic unit cell parameters for LnF_3 (β-YF_3 structure type).

This second morphotropic transition in the series of rare-earth trifluorides is due to the regular variation of the cation ionic radius. Thus the variation in the unit cell parameters divides the series of rhombic β-LnF_3 compounds into two subgroups, in complete agreement with the position of the second morphotropic transition in the series of high-temperature modifications (between α-HoF_3 and α-ErF_3 according to ref. 9) and changes in the thermal stability of α- and β-LnF_3. Anomalous behavior of the parameters in the isostructural series of β-LnF_3 was not remarked previously.

CRYSTALLOGRAPHIC PROPERTIES OF α-LnF_3 (α-UO_3 STRUCTURE TYPE)

Thomas and Brunton[9] first discovered a new structure type in the rare-earth elements called "hexagonal YF_3" in which the high-temperature modifications of α-LnF_3 crystallize (Ln = Er to Lu). We have shown[21] that the "hexagonal-YF_3" structure is the previously known α-UO_3 structure type.[22] In agreement with this, in ref. 21 the previous[9] values of the parameters of the hexagonal unit cell of α-LnF_3 were recalculated for a temperature

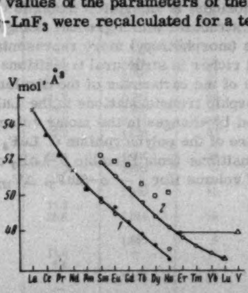

Fig. 4. Change of the molar volume in the LnF_3 series as a function of the atomic number of the lanthanide. 1) LaF_3 structure type: ☐) according to ref. 9; x) ref. 4; ▲) ref. 3; ■) ref. 10; ○) ref. 2; ●) present work; 2: β-YF_3 structure type; ○) ref. 2; △) ref. 13.

of 10 to 15° above the polymorphic transition temperature. The parameters of α-LnF_3 (Ln = Er to Lu) reduced to a hexagonal unit cell of the α-UO_3 type (Z = 1) are given in Table 1. This is also the structure type in which α-YF_3 crystallizes.

The transition from the low-temperature β-LnF_3 into an α modification of the α-UO_3 type is accompanied by a sharp increase in the molar volume. The molar volumes of α-LnF_3 and α-YF_3 are substantially higher than the analogous properties of the tysonite and rhombic modifications of LnF_3. Their changes in the LnF_3 series are not of a regular nature due to the large errors in the high-temperature measurements; therefore this data is not shown on the graphs of the changes in molar volume (Fig. 4).

DISCUSSION OF THE RESULTS

The experimental determination of the parameters of the unit cells and other crystallographic properties of six unquenched tysonite α-LnF_3 (Ln = Sm through Ho) structures under standard conditions has permitted us to analyze their changes in the series of rare-earth fluorides. The previously existing data for α-LnF_3 produced[2] by thermal decomposition of complex salts[4)] and direct high-temperature measurements[9] are shown in Fig. 4, where the variation in the molar volumes of tysonite and rhombic modifications of LnF_3 is shown as a function of the atomic number of the lanthanide. We see the incompatibility of the existing data and its uselessness for analyzing the changes in the properties in the series of polymorphic modifications.

Using the general regularities in the variation of the unit cell parameters and the molar volume of LnF_3 we can estimate the measured crystallographic properties of LnF_3 existing in the literature and choose those which best correspond to the overall behavior of the changes in the properties within the series.

Table 1 gives crystallographic data for LnF_3 chosen on this basis. It is divided into three groups of LnF_3 according to the number of structure types in which the different modifications of LnF_3 crystallize. The α-UO_3 structure type corresponds to the least dense structure.

The series of rare-earth trifluorides (like that of their sesquioxides) is an explicit example of the regular variation of structure with a gradual change in the cation ionic radius (morphotropy) more representative (16 compounds) and richer in structural transitions than the classical example of the carbonates of the divalent metals.[23] The polymorphic transformations in the LnF_3 series are accompanied by changes in the molar volume. An interesting feature of the polymorphism of LnF_3 is the fact that the transitions from rhombic β-LnF_3 occur with a decrease of volume (for $\beta \rightarrow \alpha$-SmF_3, $\Delta V_{mol} = -3.3\%$ relative to β-SmF_3). This difference should evidently decrease during the transition $\beta \rightarrow \alpha$-HoF_3, whose transformation heat is negligibly small.[13] The second morphotropic transition from the LaF_3 structure type to the hexagonal α-UO_3 type occurs with a large increase in the molar volume; in going from α-HoF_3 to α-ErF_3 the increase in volume amounts to 15% (relative to α-HoF_3). This value is obtained by comparing values of the unit cell parameters measured at high temperatures.[9] High-temperature α-LnF_3 (Ln = Er to Lu) cannot be stabilized by isomorphous substitutions in any of the LnF_3−MeF_2 (Me = Ca, Sr, Ba) or LnF_3−LaF_3 systems studied.

The authors thank V. B. Aleksandrov for valuable discussions on the questions considered here.

[1)] The hexagonal phases in the systems CaF_2−GdF_3 and CaF_2−DyF_3 are not compounds, as shown by Gogadze et al.,[18] but solid solutions based on α-LnF_3.

[2)] The tysonite solid solutions in the system BaF_2−GdF_3 were quenched and subjected to x-ray analysis despite the assertions of Zhigarnovskii and Ippolitov.[19]

[3)] Recalculated for a unit cell with Z = 6.

[4)] Zalkin and Templeton[2] obtained tysonite modifications of SmF_3, EuF_3, HoF_3, and TmF_3 by precipitation from a solution of complex compounds and their thermal decomposition. Possible reasons that their tysonite forms of LnF_3 were stable have been discussed by Mansmann[6] in relation to a change in chemical composition.

---

[1] J. Oftedal, Z. Phys. Chem., B5, 272 (1929); B13, 190 (1931).
[2] A. Zalkin and D. H. Templeton, J. Am. Chem. Soc., 75, 2453 (1953).
[3] H. E. Swanson, Nat. Bur. Standards Circ. 5 (1955); 7 (1957); 8 (1959).
[4] E. Staritzki and L. B. Asprey, Analyt. Chem., 29, 855 (1957).
[5] F. H. Spedding and A. H. Daane, The Rare Earths, Wiley, New York (1961).
[6] M. Mansmann, Z. Kristallogr., 122, 375 (1965).
[7] R. E. Thoma, Progress in the Science and Technology of the Rare Earths, 2, Pergamon Press, New York (1966).
[8] A. Zalkin, D. H. Templeton, and T. E. Hopkins, Inorg. Chem., 5, 1466 (1966).
[9] R. E. Thoma and G. D. Brunton, Inorg. Chem., 5, 1937 (1966).
[10] F. Weigel and V. Sherer, Radiochim. Acta, 7, 40 (1967).
[11] D. Brown, Halides of Lanthanides and Actinides, Wiley, New York (1968).
[12] D. A. Jones and W. A. Shand, J. Cryst. Growth, 2, 361 (1968).
[13] F. H. Spedding and D. C. Henderson, J. Chem. Phys., 54, 2476 (1971).
[14] L. P. Batsanova, Usp. Khim., 40, 945 (1971).
[15] O. E. Izotova, L. S. Garashina, and B. P. Sobolev, Kristallografiya, 15, 580 (1970) [Sov. Phys. – Crystallogr., 15, 496 (1970)].
[16] L. S. Garashina and B. P. Sobolev, Kristallografiya, 16, 307 (1971) [Sov. Phys. – Crystallogr., 16, 254 (1971)].
[17] O. V. Kudryavtseva, L. S. Garashina, K. K. Rivkina, and B. P. Sobolev, Kristallografiya, 18, 843 (1973) [Sov. Phys. – Crystallogr., 18, 531 (1974)].
[18] N. G. Gogadze, E. G. Ippolitov, and B. M. Zhigarnovskii, Zh. Neorgan. Khimii, 17, 576 (1972).
[19] B. M. Zhigarnovskii and E. G. Ippolitiv, Izv. Akad. Nauk SSSR, Neorgan. Mater., 6, 1598 (1970).
[20] D. H. Templeton and C. H. Dauben, J. Am. Chem. Soc., 76, 5237 (1954).
[21] W. H. Zachariasen, Acta. Crystallogr., 1, 265 (1948).
[22] G. B. Bokii, Crystallography [in Russian], Izdatel'stvo Mos. Gos. Univ., Moscow (1960).

Phase transformations in rubidium and cesium superoxides

V. Ya. Dudarev, A. B. Tsentsiper, and M. S. Dobrolyubova

L. Ya. Karpov Physicochemical Scientific-Research Institute
Institute of General and Inorganic Chemistry, Academy of Sciences of the USSR

(Submitted April 11, 1972; resubmitted July 13, 1972)
Kristallografiya, 18, 759-763 (July-August 1973)

The graphical dependence of the lattice parameters of RbO_2 on temperature in the range from −170 to +200°C has been given. For RbO_2 (and CsO_2) a phase transformation, analogous to the transformation in KO_2, from the tetragonal (I4mmm) into the cubic (Fm3m) modification (NaCl structural type) has been detected by x-ray diffraction. In RbO_2 the transformation takes place in the range from 130 to 150°C, and in this range both phases are recorded simultaneously. The cubic face-centered lattice constant is a = 6.35 ± 0.01 Å (at 150°C). The transformation in CsO_2 is assumed to take place in the range from 130 to 200°C. The cubic face-centered lattice constant is a = 6.62 ± 0.01 Å (200°C). The O_2^- ion in the structure of the β phases of rubidium and cesium superoxides (as in β-NaO_2 and β-KO_2) does not have a preferred orientation (or rotates).

It was previously established[1,2] that crystalline potassium superoxide (KO_2) undergoes a phase transformation in the temperature range from 110 to 150°C, and is converted from a low-temperature tetragonal α modification (I4 mmm) into the cubic β modification (Fm3m). The heating curves for RbO_2 at 150°C showed a small reproducible endothermic effect,[3] which was attributed to the polymorphic transformation. The authors cited, however could not obtain proof of the change in structure by direct x-ray diffraction methods. In the temperature range from room temperature to −195°C, a phase transformation in RbO_2 was detected by neutron diffraction methods,[4] and the heat capacity curve at −94.7°C showed an anomaly,[5] apparently corresponding to this transition. Since thermographic analysis[5] did not detect the latent heat of the transformation, the latter was classified as a phase transformation of the second kind. There is no published information on structural changes in CsO_2.

We carried out a phase analysis of crystalline RbO_2 and CsO_2 by x-ray diffraction methods, in the range from −170 to +200°C for the first compound, and at 20 and 200°C for the second compound. All the operations with the superoxides were carried out in an atmosphere of dry nitrogen. The fine powder was packed into a special container, after which the specimen was covered with an air-tight terylene film with a thickness of 6 μ. The specimens were placed in a universal temperature camera attachment on a URS-50IM diffractometer, in which the specimen was flushed with nitrogen vapor heated to the temperature of the experiment. The x-ray diffraction patterns were recorded after the specimen had been kept for 20 min at the temperature of the recording. Each diffraction pattern was

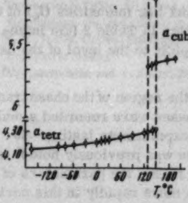

Fig. 1. Temperature dependence of the lattice constants of RbO_2. At 20°C, c_{tetr} = 7.01, a_{tetr} = 4.22 Å; at 150°C, a_{cub} = 6.35 Å. The broken lines show the temperature range in which both phases are recorded simultaneously.

TABLE 1. Data from the X-Ray Diffraction Patterns of the Low-Temperature Tetragonal α Phases of Potassium, Rubidium, and Cesium Superoxides at Room Temperature (Cu Kα)

hkl, body-centered cell	hkl, face-centered cell*	α-KO_2 [*], a = 4.03, c = 6.75 Å			α-RbO_2, a = 4.224, c = 7.013 Å			α-CsO_2, a = 4.462, c = 7.326 Å		
		d_e, Å	I_e	I_c	d_e, Å	I_e	I_c [6]	d_e, Å	I_e	I_c [6]
101	111	—	—	7.3	3.612	61	61.8	3.811	100	100
002	002	3.367	40	34.0	3.500	51	52.6	3,666	29	53
110	200	2.855	100	100	2.980	100	100	3.158	97	94
112	202	2.183	70	65.0	2.269	68	61.8	2.388	59	71
200	220	2.022	60	53.0	2,108	35	36.0	2.230	39	33
103	113	1.961	50	46.0	2.044	45	40.0	2.141	32	43
211	311			8.4	1.820	29	25.2	1.926	35	36
		1,734	60							
202	222			43.0	1.806	31	29.6	1.907	28	31
004	004	—	—	1.5	1.751	5	3.0	1.828	5	4
114	204	—	—	4.9	1.510	9	—			—
								1.580	15	
220	400	1.428	30	26.0	1.491	8	11.2			9
213	313	1.410	40	47.0	1.466	21	28,6	1.544	16	29
301	331			33.0	1.377	5	—			—
		1.315	30					1.456	6	
222	402			25.0	1,372	8	11,4	—	—	12
204	224	—	—	4.0	1.346	5	5.4			7
								1.413	10	
310	420			41.0	—	—	—			—
		1.276	60		1.331	14				
105	115			40.0			13,0	1.391	6	11
312	422	1,196	30	42.0	1.245	10	16.0	1.316	10	17
303	333	1.157	10	17.0	1.203	4	7.4	1.269	6	7
006	006	—	—	0.8	—	—	—	—	—	—

recorded over a period of 30 min.

The dependence of the lattice constants of RbO_2 on temperature is shown in Fig. 1. The constant a of the tetragonal body-centered cell corresponds to a value which is smaller by a factor of $\sqrt{2}$ than that given in ref. 6, since in the work cited the RbO_2 cell (like the CsO_2 cell in the same paper, and the KO_2 cell in corresponding papers) was taken as face-centered, which does not agree with the assignment of all these isomorphous superoxides to I4mmm (correspondingly $Z = 2$). The new values of the constants and the indices of the lines for the old and new choice of cell are given in Table 1. The line intensities for RbO_2 and CsO_2, measured by us at room temperature, are compared with the corresponding calculated values given in ref. 6. The comparison shows good agreement between these values.

It can be seen from Fig. 1 that in the range from −170 to +120°C the lattice constants of RbO_2 change monotonically within the limits of accuracy of the measurements, and do not show any phase transformations. Thus the structural transformation corresponding to the anomaly on the heat capacity curve[5] at −94.7°C and apparently detectable by neutron diffraction[4] could not be detected by us by x-ray diffraction methods.

At 130–150°C, RbO_2 undergoes a phase transformation with the production of a face-centered cubic lattice with $a = 6.35 \pm 0.01$ Å (at +150°C). The experimental values of the interplanar spacings (d_e) and line intensities (I_e) of the high-temperature phase are given in Table 2 (the intensities of the lines decrease rapidly to the level of the background with increase in hkl).

On heating and cooling in the region of the phase transformation (130–150°C), both phases were recorded simultaneously in x-ray diffraction experiments lasting ~50 min. An analogous phenomenon was previously noted[2] for KO_2. A characteristic feature is that the parameters of both RbO_2 phases change much more rapidly in this period than in the range of existence of only one phase. At the same time the difference in the volumes of the face-centered cells (tetragonal in the published version[6] and cubic) in the phase transformation is small.

Thus the anomaly previously observed[3] on the heat capacity curve for RbO_2 at 150°C does in fact correspond to a structural phase transformation (of the first kind), which with increase in temperature leads to the transformation of the tetragonal form of the superoxide into a cubic form.

Comparison of the x-ray diffraction patterns recorded for CsO_2 at 20 and 200°C also indicates a structural phase transformation in this range. At 20°C, a tetragonal lattice (I4mmm) with a constants $a = 4.46 \pm 0.01$ and $c = 7.32 \pm 0.01$ Å was detected. The value of c is greater by 0.08 Å than that given in ref. 6. This difference lies outside the range of error of our measurements. The value of a (Table 1) shows good agreement with that given in ref. 6 (with an accuracy up to a decrease by a factor of $\sqrt{2}$ for the correct choice of this constant). At 200°C (heating for 50 min), the x-ray diffraction pattern obtained showed only lines due to the face-centered cubic lattice with $a = 6.62 \pm 0.01$ Å (Table 2). Qualitative extrapolation of the properties of the alkali metal superoxides indicates that this phase transformation for CsO_2 takes place in the range between 130 and 200°C.

The extinction law observed on the x-ray diffraction patterns for the powders (Table 2) is the same for the face-centered cubic cells of RbO_2 and CsO_2, and leads initially to the choice of five space groups: F23, Fm3, F432, F$\bar{4}$3m, and Fm3m.

Since it is extremely unlikely that with the slight increase in the relative volume there should be an almost two-fold increase in the density of the high-temperature phases of RbO_2 and CsO_2 (the true values of which cannot be measured) compared with the low-temperature phases, we assume that the number of molecules in the face-centered cubic cell is the same as in the tetragonal face-centered cell,[6] that is $Z = 4$.

For the placing of four Rb^+ (Cs^+) ions and four O_2^- ions with fixed positions of the oxygen nuclei in the face-centered cubic cell, only four-fold positions a, b, c, and d of any of the above space groups can be taken into account.[7] The placing of "fixed" O atoms is impossible, however, as a consequence of the geometric factor. In actual fact, the distances between the nearest positions indicated in the face-centered cubic cells of RbO_2 and CsO_2 (and KO_2), equal to $a/2$ and $a\sqrt{3}/4$, are too large (for example 3.18 and 2.75 Å for RbO_2) to accommodate two oxygen atoms of the O_2^- ion with O–O distance approximately 1.30 Å.

Since the structure of the high-temperature cubic phases, for KO_2, RbO_2, and CsO_2 at least, does not make it possible to fix the oxygen nuclei in the special positions indicated, it must be assumed that only the centers of gravity of O_2^- ions which have no preferred orientation are

TABLE 2. Data from the X-Ray Diffraction Patterns of the Low-Temperature Cubic β Phases of Sodium, Potassium, Rubidium, and Cesium Superoxides (Cu Kα)

hkl	β-NaO_2, a = 5,49 Å (20° C)				β-KO_2, a = 6,00 Å (150° C)				β-RbO_2, a = 6,39 Å (200° C)				β-CsO_2, a = 6,62 Å (200° C)			
	d_e	I_e (ref. 1)	I_1	I_2	d_e (ref. 2)	I_e (ref. 2)	I_1	I_2	d_e	I_e	I_1	I_2	d_e	I_e	I_1	I_2
111	3.17	—	0.4	100	3.50	13	7,3	100	3,633	47	45	100	3.814	57	75	100
200	2.74	100	100	1.10	3.04	100	100	5.0	3.195	100	100	23	3.302	100	100	31.4
220	1.94	41	33	35.3	2.16	34	51	46.1	2,259	57	59	49.3	2.342	57	68	49,7
311	1.65	11	11	19,3	1.83	11	16	28.6	1,926	24	40	44.9	1.993	31	52	47.1
222	1.58	9,2	8.6	3.1	1.76	11	11.4	5.2	1,843	17	18,5	9.6	1.910	17	22	11.4
400	1.37	1.3	2.6	2.4	—	—	4.3	4.0	1.598	2	8,2	6.8	—	—	10	7,2
331	1.26	4.9	7.7	6,1	1,40	8	9,8	9.7	1.466	6	19.8	17.9	—	—	25	19.7
420	1.23	3,6	5.4	6.6	1,36	8	10.1	8.6	—	—	20,2	15.3	—	—	25	16.8

I_1 represents the calculated values of the intensity for the NaCl structural type; I_2 represents the calculated values of the intensity for the ZnS (sphalerite) structural type.

fixed in these positions. A randomly oriented O_2^- ion can formally be replaced by a model consisting of a group rotating within a sphere of radius ρ. This spherically symmetrical ion[1] with $\rho \approx 1.70$ Å in the face-centered cubic cells of RbO_2 and CsO_2 (and KO_2) can be placed in any fourfold special positions of the five possible space groups, assuming the radii $Rb^+ \approx 1.50$ Å and $Cs^+ \approx 1.65$ Å ($K^+ \approx 1.33$ Å). The different combinations of ways of filling these positions with alkali metal and O_2^- ions, however, lead either to the ZnS sphalerite structural type ($F\bar{4}3m$) or to the NaCl structural type ($Fm3m$).

Both of these possibilities were tested by appropriate calculation of the intensities of the reflections. The scattering factor of the O_2^- ion, regarded as a group rotating about its center of gravity, was calculated in the form taken from ref. 8: $f_{O_2^-} = (f_O + f_{O^-}) \sin \varphi_0/\varphi_0$, where $\varphi_0 = 4\pi \rho_s \sin \theta/\lambda$; and ρ_s is the distance from the center of rotation to each of the atoms of the rotating group. We took $\rho_s = 0.66$ Å, that is, half the O–O distance in the O_2^- ion. A correction for the temperature factor was not introduced, and we restricted ourselves to a qualitative comparison of the dependence of the line intensities on the angle θ.

The calculated and experimental relative values of the intensities of the reflections for RbO_2 and CsO_2 are given in Table 2. It can readily be seen that good agreement with experiment is given only by the version corresponding to the NaCl structural type ($Fm3m$). With the assumption that this structural type is common to all four superoxides, we repeated the calculation of the line intensities for β-KO_2 and β-NaO_2, previously carried out[1,2] by the same method of calculation but with different values of ρ_s. The corresponding experimental values in Table 2 were taken from the papers cited. The good agreement between the experimental data and our calculated data, for these substances also, indicates that the approximate value of ρ_s used in our calculations is acceptable, and that the interpretation of the structure of the β phases is correct.

It has thus been established that there is a structural analogy between the high-temperature phases of RbO_2 and CsO_2 and the corresponding β-KO_2 and β-NaO_2 phases. By analogy, we have called the previously studied[6] rubidium and cesium superoxide phases stable at room temperature α-RbO_2 and α-CsO_2 respectively, and their high-temperature modifications β-RbO_2 and β-CsO_2.

---

[1] G. S. Zhdanov and Z. V. Zvonkova, Dokl. Akad. Nauk SSR, 82, 743 (1952).

[2] G. F. Carter, J. L. Margrave, and D. H. Templeton, Acta Crystallogr., 5, 581 (1952).

[3] A. B. Tsentsiper and M. S. Dobrolyubova, Izv. Akad. Nauk SSSR, Ser. Khim., 1, 175 (1968).

[4] H. G. Smith, R. M. Nicklow, L. J. Raubenheimer, and M. K. Wilkinson, Summaries of Papers Presented at the Seventh International Congress and Symposium on the Growth of Crystals [in Russian], Nauka, Moscow (1966), p. 194.

[5] I. E. Paukov, F. S. Rakhmenkulov, M. S. Dobrolyubova, and A. B. Tsentsiper, Izv. Akad. Nauk SSSR, Ser. Khim., 9, 2135 (1970).

[6] A. Helms and W. Klemm, Z. Anorg. Allgem. Chem., 241, 97 (1939).

[7] International Tables for X-Ray Crystallography, Vol. 1, Kynoch Press, Birmingham, England (1965), pp. 306-346.

[8] R. W. James, Optical Principles of the Diffraction of X Rays, Cornell Univ. Press (1948).

[9] V. Kasatochkin and V. Kotov, Zh. Tekh. Fiz., 7, 1668 (1937).

Electron-diffraction study of the kinetics of the CuS—$Cu_{2-x}S$ transformation

M. M. Kazinets and R. B. Shafizade

Institute of Physics, Academy of Sciences of the Azerbaidzhan

(Submitted May 29, 1972; resubmitted July 20, 1972)
Kristallografiya, 18, 764-768 (July-August 1973)

We made an electron-diffraction study of the kinetics of the CuS → $Cu_{2-x}S$ transition. The constancy of primary-peak intensity was monitored with the aid of a standard (NaCl). The data obtained in analyzing the series of kinematic electron-diffraction patterns were used to plot conversion isotherms: the transition rate was determined at different temperatures and the activation energy of this process was found to be Q = 8.3 kcal/mole. The present article discusses the conversion mechanism.

According to phase-diagram data,[1,2] the Cu−S system contains the phases Cu_2S, $Cu_{2-x}S$, and CuS. It has been shown[3] that, by adding sulfur to Cu_2S, it is possible to shift it into the pure CuS region of the phase diagram. Reversal of this process, i.e., removal of sulfur atoms from CuS, requires a definite time (from minutes to hours) at a temperature of from 100 to 300°C, depending on the specimen thickness and the degree of sulfur removal. On the other hand, Djurle[4] has noted that CuS is stable up to 500°C. In an electron-diffraction study of thin films in the Cu−S system,[5,6] we observed concentration-related CuS → $Cu_{2-x}S$ → Cu_2S transitions due to evaporation of sulfur during vacuum heat treatment of CuS.

All the aforementioned studies dealt with the well-known hexagonal modification of the compound CuS. We have reported[7] the existence of a cubic modification of analogous composition, which was investigated at temperatures of 20-600°C and found to be stable over this range.

The present investigation was conducted to study the kinetics and mechanism of the conversion of the hexagonal modification of CuS to the fcc $Cu_{2-x}S$ phase (Fig. 1). The further transformations of $Cu_{2-x}S$ were studied previously.[8]

Our investigation was conducted by kinematic electron-diffraction analysis,[9,10] which permits continuous recording on a moving photographic plate of the reduction of the original phase and the formation of the new one. Investigation of process kinetics by this method is based on the relationship between the line intensities in the electron-diffraction pattern and the irradiated volume of the material being tested:[11]

$$I_{hkl} = I_0\lambda^2 \left| \frac{\Phi_{hkl}}{\Omega} \right|^2 V \frac{d_{hkl}^2}{4\pi L\lambda} \Delta p,$$

where I_{hkl} is the local Debye-ring intensity over a small segment Δ, Φ_{hkl} is the structural amplitude, Ω is the unit-cell volume, p is the repeatability factor, and 2Lλ is the instrument constant. With I_0 and 2Lλ constant, the intensity I_{hkl} of the hkl line is proportional to the irradiated volume V and, since V = Sh, where S is the cross-sectional area of the beam and h is the film thickness, $I_{hkl} \sim h$ for a flat subject when S = const. This relationship holds when scattering has a coherent and kinematic character. These conditions are satisfied for CuS films 100-300 Å thick.

The main steps in the procedure are production of a series of isothermal kinematic electron-diffraction patterns for the phase transition under investigation, photometry of individual segments of these diffraction patterns, use of the data from the microphotometric curves to plot conversion isotherms, and determination of the conversion rate for each temperature, as well as the process activation energy.

Study of phase-transition kinetics is only possible when the primary-beam intensity I_0 remains constant. However, experimentation has shown that I_0 varies during an exposure. Such fluctuations make it impossible to obtain an unambiguous correlation between the deviations in the intensities of the analytic lines and the changes in thickness for the layers of the original and new phases. In order to evaluate the influence of primary-beam intensity fluctuations, exposures are made with a standard.[6]

The standard is selected in such fashion that its quantity remains constant during the exposure when subjected to heat treatment over the temperature range chosen. Its lines should therefore retain constant intensity. Changes in the intensities of the standard lines are produced solely by fluctuations in I_0, while the line intensities for the test substance are affected by two factors: the change in I_0 and the change in the thickness of the layers of the original and growing phases. The changes in the standard lines can thus be used to evaluate the influence of fluctuations in I_0 and to make an appropriate correction in the line intensities for the test substance.

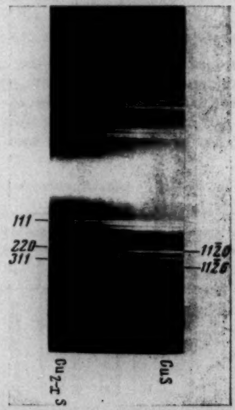

Fig. 1. Kinematic electron-diffraction pattern of CuS → $Cu_{2-x}S$ transition obtained at 200°C.

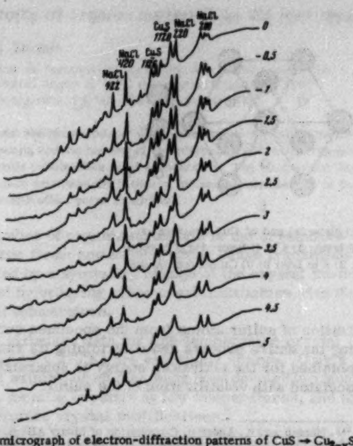

Fig. 2. Photomicrograph of electron-diffraction patterns of CuS → $Cu_{2-x}S$ transition. Exposure made with NaCl standard; the figures at the right correspond to the heating time (in min) at 200°C.

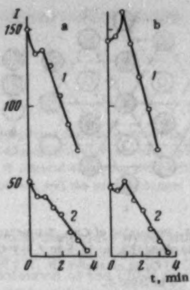

Fig. 3. Intensities of 11$\bar{2}$0 and 11$\bar{2}$6 lines (curves 1 and 2) of CuS as a function of heat-treatment time at 200°C. a) Without correction; b) with correction.

We employed NaCl as the standard in investigating the kinetics of the CuS → $Cu_{2-x}S$ transition. The vapor tension of NaCl over the temperature range 100-200°C, where our study was made, is low and this ensured a constant line intensity during heat treatment. The similarity of the unit-cell constants of the NaCl (5.63 Å) and the growing $Cu_{2-x}S$ phase (5.60 Å) led to coincidence of the nearby lines, so that the course of the conversion process was investigated solely from the change in the line intensities for the original phase. In a previous study, where we did not use a standard,[5] we considered both the decrease in intensity for the original phase and the increase in intensity for the growing phase.

The CuS films, which were produced by vacuum deposition of synthetic CuS on NaCl crystals at room temperature, were transferred to a grid-type furnace for the kinematic exposures. The standard was applied to the back of the specimen in such fashion that there was a layer of celluloid between the CuS and NaCl. The subject was placed in an electron-diffraction apparatus and investigated at the temperatures selected. Figure 2 shows a photomicrograph of the kinematic electron-diffraction pattern obtained for the CuS → $Cu_{2-x}S$ transition with an NaCl standard at 200°C. This transition was evaluated from the decrease in the intensities of the 11$\bar{2}$0 and 11$\bar{2}$6 CuS lines. The standards were the 420 and 422 reflections of NaCl.

Isothermal kinematic electron-diffraction patterns of the CuS → $Cu_{2-x}S$ phase transition were obtained at 140, 160, 180, and 200°C. Photomicrographs of different sections of the electron-diffraction patterns made at definite intervals were then used to determine the intensities of the 11$\bar{2}$0 and 11$\bar{2}$6 lines for the CuS and the 420 and 422 lines for the NaCl. The fluctuations in I_0 during the exposures were found from the NaCl and an appropriate correction was introduced into the intensities of the CuS 11$\bar{2}$0 and 11$\bar{2}$6 lines. Figure 3 gives graphs representing the intensities of the 11$\bar{2}$0 and 11$\bar{2}$6 lines as a function of the heat-treatment time at 200°C without these fluctuations taken into account (Fig. 3a) and after the correction was introduced (Fig. 3b). Comparison of the graphs obtained at all four temperatures showed that the CuS → $Cu_{2-x}S$ transition did not begin at the very start of heat treatment and that the delay in its onset increased as the temperature decreased; the line intensity for the initial CuS phase increased at first, which can be attributed to enlargement and structural improvement of the crystals. However, this process lasted only a short time and destruction of the original phase soon began to predominate.

If we assume that there was no decomposition of the original compound during the initial stage of the process, the maximum intensity can be correlated with the maximum layer thickness of 200 Å (the layer thickness was calculated[12]) and we can plot a graph representing the layer thickness as a function of the annealing time at different temperatures. The decrease in layer thickness follows the linear rule $h = h_0 - vt$, where v is the conversion rate, which depends on temperature. We obtained the following rates for the temperatures selected: v = 60 Å/min at t = 200°C, 40 Å/min at 180°C, 25 Å/min at 160°C, and 17 Å·min^{-1} at 140°C. These data were employed to determine the process activation energy, yielding Q = 8.3 kcal/mole.

The physical sense of this factor can be seen by considering the transition mechanism. When thin CuS films are subjected to vacuum heat treatment, some sulfur atoms are vaporized from the specimen surface. The free copper atoms left behind diffuse into the specimen, where they create a concentration corresponding to the compound $Cu_{2-x}S$, whose structure is produced by rearrangement of the CuS lattice.

The sulfur atoms in the CuS structure are arrayed in layers, which alternate in the sequence $\ldots A\dot{\underset{.}{}}ABAABA\dot{\underset{.}{}}A\ldots$.

The copper atoms have triangular (in layers B) or tetrahedral (between layers A and B and layers B and A) coordination.[13,14] The sulfur atoms in the structure of $Cu_{2-x}S$ form the densest cubic packing ...ABCABC... . Four copper atoms are located in the tetrahedral voids at the midpoints of the cube edges.[7] Figure 4a shows the projection of the $Cu_{2-x}S$ structure on the (111) plane. For purposes of comparison, Fig. 4b shows the projection of the CuS structure on the (0001) plane. As can be seen

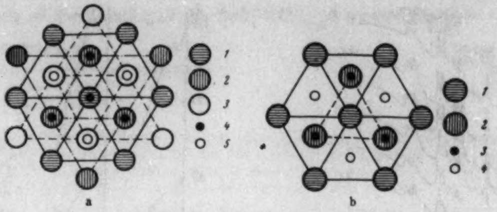

Fig. 4. Projection of $Cu_{2-x}S$ structure on (111) plane (a) and of CuS structure on (0001) plane (b). a: 1) S in A layer; 2) S in B layer; 3) S in C layer; 4) Cu in tetrahedra; 5) Cu in octahedra; b: 1) S in layer A; 2) S in later B; 3) Cu between A and B; 4) Cu in layer B.

from a comparison of the layer sequences in these structures,

$$\begin{array}{llll} \mathrm{CuS} & \ldots A & AB\underset{\downarrow}{A}AB\underset{\downarrow}{A} & A\ldots \\ \text{и } \mathrm{Cu_{2-x}S} & \ldots & ABCABC & \ldots, \end{array}$$

the CuS → $Cu_{2-x}S$ phase transition can be represented geometrically in the following manner. One of the A layers in the CuS structure is converted to a C layer of the $Cu_{2-x}S$ structure as a result of displacement in the same plane over a distance of a 3/3; the S−S linkages of the AA layers separate under the influence of the intervening copper atoms.[15] During the transition, there is an increase in the S−S and Cu−S distances both within and between layers. The S−S distance in the (0001) plane is 3.80 Å in the CuS structure and 3.95 Å in the $Cu_{2-x}S'$ structure. For the copper in the tetrahedra, Cu−S = 2.35 Å for CuS and 2.41 Å for $Cu_{2-x}S$.

The CuS → $Cu_{2-x}S$ phase transition is thus a complex process consisting of various stages: evaporation of sulfur atoms, diffusion of copper, and reorganization of the lattice framework.

Experiments with CuS specimens coated with a layer of celluloid to prevent evaporation of sulfur showed that the decisive stage of the CuS → $Cu_{2-x}S$ transition is vaporization of sulfur atoms from the specimen surface, limiting the entire process and determining its rate. The value obtained for the activation energy is apparently also associated with volatilization of the sulfur.

---

[1] M. Hansen and K. Anderko, Constitution of Binary Alloys, McGraw-Hill (1958).

[2] V. Webefritz, Z. Phys. Chem., 26, 339 (1960).

[3] L. Eisenmann, Ann. Phys., 10, 129 (1952).

[4] S. Djurle, Acta Chem. Scand., 12, 1415 (1958).

[5] G. A. Éfendiev and M. M. Kazinets, Dokl. Akad. Nauk AzerbSSR, 25, 12 (1969).

[6] M. M. Kazinets, Dissertation [in Russian], Inst. Fiz. Akad. Nauk AzerbSSR, Baku (1968).

[7] M. M. Kazinets, Kristallografiya, 14, 704 (1969) [Sov. Phys. – Crystallogr., 14, 607 (1971)].

[8] M. M. Kazinets, Izv. Akad. Nauk SSSR, Neorgan. Mat., 8, 1011 (1972).

[9] A. Boettcher and R. Thun, Optik, 11, 22 (1954).

[10] G. A. Éfendiev and R. B. Shafizade, Prib. Tekh. Eksp., No. 1, 142 (1963).

[11] B. K. Vainshtein, Structural Electron-Diffraction Analysis [in Russian], Izd. Akad. Nauk, Moscow (1956).

[12] S. A. Vekshinskii, A New Method for Metallographic Analysis of Alloys [in Russian], Moscow (1944).

[13] G. B. Bokii, Introduction to Crystal Chemistry [in Russian], Izd. MGU (1954).

[14] N. V. Belov and E. A. Pobedimskaya, Kristallografiya, 13, 969 (1968) [Sov. Phys. – Crystallogr., 13, 843 (1969)].

[15] N. V. Belov and E. A. Pobedimskaya, Mineral. Sb. L'vov. Geol. Obshch., 20, 326 (1966).

Spectroscopy of organic materials in the low-temperature, crystalline phases

G. N. Zhizhin

Institute of Spectroscopy, Academy of Sciences of the USSR

(Submitted August 3, 1971; resubmitted February 7, 1972)
Kristallografiya, 18, 769-778 (July-August 1973)

Infrared absorption spectra of low-temperature crystal phases are used to determine position symmetries, factor groups, and the number of molecules in a unit cell. The number of components of Davydov band splitting and their polarizations serve as indicators. The temperature dependence of infrared absorption bandwidths allows us to determine the barrier to molecular reorientation in the plastic phases, and the sudden changes in bandwidth affect phase transitions.

A large number of organic materials in the crystalline state undergo first- and second-order phase transitions,[1] accompanied by a symmetry change of the crystal modification and by ordering of the crystal structure with the lowering of temperature.

X-ray structure data for low-temperature crystal modifications (< 273°K) are extremely scarce. Only a very small number of studies have been devoted to organic materials, forming crystals at low temperatures, and to low-temperature crystal modifications.[2]

The vibrational spectra of molecules, the infrared absorption spectrum and Raman light scattering, which are indicators of phase transitions in molecular crystals, are of large interest in this connection. The crystal field symmetry (static effects), the amount of crystal ordering, and the molecular resonance interactions in a unit cell (dynamic effects) change the selection rules for optical transitions and lead to frequency shifts and splittings, to a change in band intensities and widths of infrared absorption and Raman scattering lines, and to a change in the nature of their polarization. In most cases these spectral changes can be successfully related to features of the crystal structure up to and after the transition.

These possibilities of crystal spectroscopy have been known for a long time,[3-6] but their realization became possible only in the last five to seven years with the appearance of instruments capable of achieving resolutions of 0.5-1 cm^{-1} under low-temperature experimental conditions (high-sensitivity infrared radiation detectors and the use of gas lasers to excite Raman scattering spectra[7]). Progress in this area was also assisted by the improved experimental low-temperature techniques in the broad infrared spectral region[8,9] (1-25 μ).

Systematic studies of infrared absorption spectra of molecular crystals at low temperatures (about 100 organic materials were studied), initiated in 1964 in the Komissii Spectroscopy Laboratory of the Academy of Sciences of the USSR and later extended in the Laboratory of Crystal Spectroscopy of the Spectroscopy Institute of the Academy of Sciences of the USSR, have shown that the information obtained from vibrational spectra can be utilized to establish the crystal symmetry of a unit cell, the number of molecules in it, and the position[1)] symmetry of molecules under conditions such that molecular vibrational spectra can be reliably interpreted.[8,10-12] In case of reliable x-ray data the peculiar features of the spectrum of a molecular crystal allow one to identify the symmetry of vibrational transitions.[4,13]

In this paper examples are given of the use of infrared spectral data to determine the crystal symmetry of unit cells by the number of components of Davydov splitting and their polarizations, to determine the barrier to molecular reorientation in low-temperature crystal modification, and also to discover unknown phase transitions in organic materials.

SYMMETRY DETERMINATION OF CRYSTAL UNIT CELLS BY THE NUMBER OF COMPONENTS OF DAVYDOV SPLITTING AND THEIR POLARIZATION

The number and polarization of Davydov splitting components can be established by knowing the position symmetry of a site occupied by a molecule in the crystal (position symmetry), the factor groups[2)] of the unit cells, and the number of molecules in them.[14,15] The number of components n_l^α into which a band of position symmetry class l is split relative to a factor group of class α is determined by the relation

$$n_l^\alpha = \frac{\sigma}{F} \sum_R \chi_\alpha(R) \chi_l(R),$$

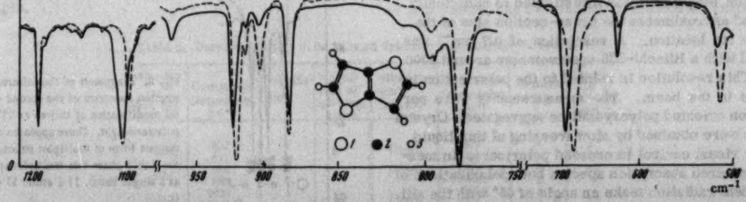

Fig. 1. Fragment of infrared spectrum of crystalline thiophthene in polarized radiation. T) Transmission: dashed and solid lines are two mutually perpendicular polarizations; 1) S atom; 2) C; 3) H.

where σ is the number of molecules in a unit cell (in a primitive repetitive parallelepiped), F is the order of the factor group, R is a symmetry operation common to the position group and to the factor group (the summation is over them), $\chi_l(R)$ is the character of irreducible representation of operation R in the position symmetry class l, and $\chi_\alpha(R)$ is the character of irreducible representation of operation R in the factor group of symmetry class α. The activity of each multiplet component and its polarization in a crystal infrared spectrum are determined by the factor group's belonging to different symmetry classes.

For known unit-cell symmetries, multiplet analysis can be used to interpret symmetry types of vibrational transitions. However, the study of fine structure of infrared absorption bands, Raman scattering lines, the polarization of split components in the crystal spectrum, and also the analysis of the change in selection rules in passing from gases and liquids to a crystal allow one to solve also the inverse problem, that is, to establish position symmetries, factor groups, and the number of molecules in a crystal unit cell. For a successful solution it is necessary first of all to assume a reliable interpretation of the molecular vibrational spectrum. The membership of an infrared band in the various molecular symmetry classes can be established from the infrared spectrum of a gas, from infrared and Raman scattering spectra of a liquid,[16,17] from the vibrational spectra of a number of related substances, and also from calculations.[18,19]

In the presence of such an interpretation one can follow the change in the selection rules when passing to the crystalline state. From this comparison one can draw conclusions concerning the molecular position symmetry[6] in the crystal, and then start the analysis of Davydov multiplets. Of course, they must first be observed in the spectrum in a large number of bands, and then their belonging to Davydov multiplets can be ascertained.[20] For those problems it is necessary to have the highest possible resolution and to use polarized light and single crystal samples. The relation of multiplets and their polarizations with unit cell symmetry was systematically pointed out in spectroscopic investigations by Halford and coworkers,[11] and was recently discussed in detail by Fialkovskaya and Nefedov.[21]

For reliable determination of multiplet components we performed low-temperature measurements at high resolution. The crystals employed by us practically exclude vignetting of the radiation beams since the sample size of the single crystals investigated is sufficiently large and approximates the cross-section size of the beam in its location. A resolution of 0.7 cm^{-1} was achieved with a Hitachi-225 spectrometer around 1000 cm^{-1}. This resolution is related to the polarization introduced in the beam. The measurements were performed on oriented polycrystalline aggregates. Crystal samples were obtained by slow freezing of thin liquid films by visual control in crossed polarizers. In measuring infrared absorption spectra both polarizations of the incident radiation make an angle of 45° with the slit, which eliminates the polarizing action of the instrument. In small splitting measurements (~ 1-2 cm^{-1}) particular attention was devoted to reproducibility of the spectra, which for the Hitachi-225 spectrometer can achieve 0.04 cm^{-1} and fully satisfies experimental requirements. The splitting of many bands can be established only relative to the band displacement of the spectrum for two mutually perpendicular polarizations of the incident radiation, while in nonpolarized radiation such bands often appear single.

A large number of Davydov doublets were first observed by us in the infrared spectrum of thiophthene: thieno-3, 2-b-thiophene (Fig. 1), whose crystal structure is well known.[22] Assuming the detailed interpretation of its vibrational spectrum,[23] one can draw some unique conclusions about its unit-cell symmetry, which can be obtained only from spectral data. C_{2h} and D_{2h} were considered as possible factor groups and C_1 and C_{2h} as position symmetry groups for Z = 4 and 2. The choice of the position symmetry group is detailed by the conservation of alternate exclusion in the infrared and Raman scattering crystal spectra. Among all possible variants the infrared spectrum obtained can be explained only by the unit-cell factor group D_{2h}, Z = 4 with position symmetry group C_1, which coincides with data of x-ray structure analysis.[22]

A similar approach was later applied to materials crystallizing at low temperatures and to low-temperature crystalline modifications, which could be obtained in the form of oriented polycrystalline aggregates.

Thiiran (thioxide ethylene).[3]) In the infrared spectrum of the low-temperature, crystalline modification of thiiran, giving rise to a phase transition (166°K) noted in ref. 24, quartets replacing several single (liquid) bands are of particular interest. A study of the polarization of the components revealed that two of the quartet components close to 824 cm^{-1} have opposite polarizations (Fig. 2). It is known that this multiplet arises from the band reliably related[24] to a vibration of class B_2. It is not ideal, but sufficiently clear, separated into four split component bands at 668, 1050, and 1435 cm^{-1}, related[24] to the B_1 class. The bands 1033 (A_1), 1109 (A_1), 1173 (A_2), and 1456 (A_1) cm^{-1} are doublets with single polarization components (Table 1).

Considering the selection rules for components of Davydov splitting, we verified that multiplets with such

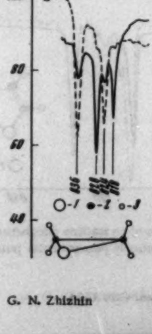

Fig. 2. Fragments of the infrared absorption spectrum of the second crystal modification of thiiran at 77°K in polarized light. There appears a clear, distinct form of multiplet structure (in the liquid phase this multiplet appears as a single band). 1) S atom; 2) C; 3) H.

TABLE 1. Davydov Multiplets in the Infrared Spectrum in Crystalline Thiiran

Vibration ν, cm^{-1} (gas)	Component frequency, intensity	Polarization	Magnitude of splitting, cm^{-1}
620	600 av 604 s	a* b	4
627 A_1	608 s 614 av	b a	6
668 B_1	634 sh 641 av 644 av 646 av	a a b b	12
824 B_2	818 av 824 av 828 av 836 av	a b a b	18
890 A_2	899 w 901 w 904 w 910 w	b b a a	11
944 B_2	940.5 sh 946 av 952 av	b* a b	11.5
1033 A_1	1028 v.s. 1030 v.s.	a a	2
1050 B_1	1044.5 av 1052 av 1058 av 1063 av	a b b a	19.5
1109 A_1	1114.5 av 1118 w	a a	3.5
1173 A_2	1171 av 1174.5 av	a a	3.5
1435 B_1	1423.5 s 1427 av 1429 s 1436 av		7.7
1456 A_1	1438.5 1445		6.6

*a corresponds to the full curve of Fig. 2, b to the dashed curve; s) strong; av) average; w) weak; sh) shoulder; vs) very strong.

TABLE 2

Molecular symmetry C_2	Position symmetry C_2	Elementary unit cell, factor group C_{2v}, Z = 4	
A_1	$\longrightarrow A \longrightarrow$	$N_{A_1}=2, \mu_z^*$, $N_{A_2}=2$ $N_{B_1}=0$ $N_{B_2}=0$	Doublets, infrared inactive
A_2	$\longrightarrow A \longrightarrow$	The same	
B_1	$\longrightarrow B \longrightarrow$	$N_{A_1}=0$ $N_{A_2}=0$ $N_{B_1}=2, \mu_x$ $N_{B_2}=2, \mu_y$	Quartz
B_2	$\longrightarrow B \longrightarrow$	The same	

*μ_x, μ_y, μ_z is the transition moment of an elementary unit cell, directed along its axes (the z axis coincides with C_2)

component polarizations are possible only for position symmetry C_2, factor group C_{2v}, and four molecules per unit cell (see Table 2). In this case, in fact, bands related to the molecular classes B_1 and B_2 should each represent in the crystal a quartet with pairs of opposite polarization components μ_x and μ_y. Bands related to the molecular classes A_1 and A_2 represented doublets with single polarization components μ_z. The appearance of all three moment components μ in the spectrum is related to the arbitrary orientation of the single crystal film sample.

The low-temperature crystal modification of thiiran can thus be related to rhombic systems[6] with possible space groups Cmm2, Ama2, Aba2, Ima2.

Thiophane[4)] forms an anisotropic crystal in freezing (~168°K), as infrared dichroism clearly indicates. As for thiiran, x-ray structure data are not available for this substance.[2]

Many bands in the infrared spectrum of crystalline thiophane are doublets, while in a crystalline CCl_4 solution many bands are singlets.[25] On this basis the resonance nature of band splitting was determined, as detailed in Table 3. We note that the doublet components are oppositely polarized.

It has been noticed[25] that a number of bands related to class A_2 vibrations, which are forbidden for isolated molecules, appear in the infrared spectrum of the crystal. This implies symmetry lowering in the crystal toward C_2, C_s, or C_1 (position symmetry). However, the fact that bands related[25] to A_1 and B_1 classes represent doublets with oppositely polarized components in the crystal allows one to conclude that the position symmetry is C_s, the unit-cell factor group is C_{2v}, and there are two molecules per unit cell (see the correlation in Table 4). The thiophane crystal can thus be related to rhombic systems[6] with space groups Pmm2, Pmc2_1, Pma2, Pmn2_1.

The conclusions on the unit-cell symmetry must be considered as upper limits. Higher unit-cell symmetry is impossible, and the number of molecules cannot ex-

TABLE 3. Davydov Splitting in the Infrared Spectrum of Crystalline Thiophane

vibration, cm^{-1} (ref. 20)	Component frequencies, cm^{-1}	Polarization	Magnitude of splitting, cm^{-1}
820A_1	822 827	a b	5
882A_1	884 888	a b	4
1035A_2	1035 1039.5	a b	4.5
1194B_1	1189 1196	a b	7
1256B_1	1259 1261	a b	2
1272A_1	1269 1274.5	a b	5.5
1322A_1	1319.5 1324	a b	4.5

TABLE 4

Molecular symmetry C_{2v}	Position symmetry C_s	Elementary unit cell, factor group C_{2v}, Z = 2	
A_1	$\longrightarrow A' \longrightarrow$	$N_{A_1} = 1, \mu_z$	Doublets
		$N_{A_2} = 0$	
		$N_{B_1} = 1, \mu_x$	
		$N_{B_2} = 0$	
B_1	$\longrightarrow A' \longrightarrow$	The same	
		$N_{A_1} = 0$	
A_2	$\longrightarrow A'' \longrightarrow$	$N_{A_2} = 1$	Infrared, inactive
		$N_{B_1} = 0$	
		$N_{B_2} = 1, \mu_y$	Singlets
B_2	$\longrightarrow A'' \longrightarrow$	The same	

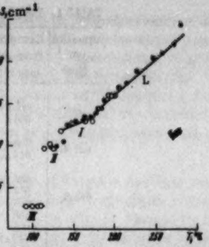

Fig. 3. Temperature dependence of the 546 cm^{-1} bandwidth of cyclopentane in the liquid (L), of the plastic crystal phases (I and II), and of the anisotropic crystal (III). The light and dark circles correspond to samples of different widths.

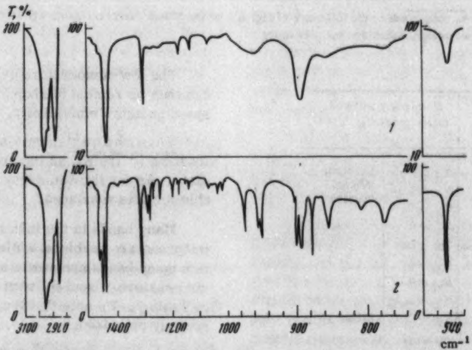

Fig. 4. Infrared absorption spectrum of crystalline cyclopentane. 1) Crystal II; 2) crystal III.

ceed that obtained from group theoretical analysis. Such spectral information can in some cases significantly supplement data of x-ray structure analysis of molecular crystals. So far simultaneous crystallographic and spectroscopic studies are extremely rare,[26,27] but it can be expected that the increasing role of molecular crystals in creating new materials will intensify such efforts.

The accuracy of spectral data on crystal symmetry depends to a large extent on the possibility of establishing the multiplet structure of infrared absorption bands. Obviously, the smaller the intrinsic component width (low temperature, and consequently, the advantage of studying low-temperature crystal modifications) and the lower the instrumental distortion (high resolution), the sharper are the multiplets.

SPECTROSCOPY OF PLASTIC CRYSTALS AND PHASE TRANSITIONS IN THEM

A number of organic materials with "spherical" molecules have a high-temperature plastic crystal modification.[1] It is well known that the molecules in them, overcoming a certain barrier U, can "jump over" from one orientation to another at a time τ, where $1/\tau = A \exp(-U/RT)$ (according to Frenkel[28,29]). Similar reorientation leads to broadening of infrared absorption bands and of Raman scattering lines. The barrier to reorientation can be determined from the temperature dependence of the widths.

Similar studies were performed by us on the vibrational spectrum of cyclopentane and cyclohexane.[30] The measurements showed single infrared absorption bands of cyclopentane (546 and 1315 cm^{-1}) and cyclohexane (523, 864, 906 cm^{-1}) in the interval 77–350 °K. In this interval cyclopentane crystallizes (179.6°K) and has two phase transitions (138.1 and 122.4°K), and cyclohexane crystallizes (279°K) and has a second-order phase transition (186°K).

Since an infrared absorption bandwidth is determined also by other causes besides rotational reorientation, we considered each band shape as a spectrum (superposition) of shapes determined by distinct mechanisms. Following ref. 31 we assumed that reorientation leads to a Lorentzian line shape. A study of line shapes in a wide temperature interval, including all crystal modifications, showed that they can be described by a convolution of a Lorentzian and a Gaussian (the Voigt function). With lowering of temperature the line shape is closer to a Gaussian.

Assuming that the Lorentzian component of the line shape is completely explained by rotational reorientation of molecules, one can put S_L equal to $1/\tau$ and determine the barrier to reorientation from the temperature dependence.[30] For the plastic phases of cyclopentane and cyclohexane they were close to those of the liquid, about 0.4–0.5 kcal/mole. The preexponential factors (A) were close[32] to the crystal librational frequencies (20–30 cm^{-1}).

Besides the jump in infrared absorption bandwidths at phase transitions (for example, the 546 cm^{-1} band of cyclopentane, Fig. 3), there occurs a sudden change in the band shape. We notice that the general shapes of the cyclopentane spectrum of crystals I and II are practically identical and phase transitions are noticeable only as small jumps in the 546 cm^{-1} bandwidths (Fig. 3).[30]

In the low-temperature crystal modifications of both substances (crystal III of cyclopentane and crystal II of cyclohexane) the bandwidths are practically temperature independent, the shape is close to Gaussian, and sharp infrared dichroism is observed. This allows one to conclude that there is no rotational reorientation of molecules in these anisotropic crystal modifications, i.e., there exists a large barrier preventing it (> 10 kcal/mole). In the transition of the low-temperature modification the infrared and Raman spectra of both substances undergo radical changes. Many bands are split and a large number of new bands appear (Fig. 4).

For cyclopentane we have related these changes with the tight configuration of a five-term cycle in a shape of C_s symmetry,[33] so that besides Davydov splitting of the bands, the number of bands is increased still more due to lowering of molecular symmetry. For cyclohexane the combined nature of the splitting of several bands (Davydov and Bethe) was shown in studies[34] of solid solutions of cyclohexane and cyclohexane d_{12}. The bands, split into two components after a phase transition in a weak solution of cyclohexane and cyclohexane d_{12}, belong to a doubly degenerate molecular vibration (E_u). The degeneracy in crystal II is removed by the lowering[35] of position symmetry to C_i.

Nortricyclene (tricyclo- (2, 2, 1, 0)- heptane) can also be considered a spherical molecule. Changes in the infrared spectrum can be related[36] to a previous unknown phase transition at (174 ± 2) °K. The study of crystalline cyclohexane spectra with a varying amount of nortricyclene impurity enabled us to observe a new crystal phase of cyclohexane, whose temperature interval widens with higher impurity concentration.[37]

A previously unknown phase transition was discovered[38] in accordance with field splitting in infrared absorption in the spectrum of cis-1,4-dimetoxicyclohexane at about 140°K.

The conclusions obtained from the vibrational spectra could be more detailed and accurate if the studies described above were supplemented by data of Raman scattering spectra at resolutions comparable with those obtained in the infrared spectrum. This, obviously, will be accomplished in the near future by using powerful gas lasers to excite Raman scattering spectra. The contemporary spectral instruments with cryogenic techniques will soon allow a spectroscopic study of the kinetics of phase transitions, which is obviously of great interest.[39]

---

1) In the crystallographic literature, position symmetry. In this sense spectroscopists use the term "local symmetry" to translate the English "site symmetry."

2) Having in mind the symmetry point group, isomorphic to the crystal factor group.

3) Investigated as in ref. 24.

4) Investigated as in ref. 25.

---

[1] Collection: Solid State Physics and Chemistry of Organic Compounds [in Russian], Mir, Moscow (1967).
[2] V. Bel'skii, Thesis, Moscow State University (1969).
[3] A. S. Davydov, Theory of Molecular Excitons, McGraw-Hill (1962).
[4] J. P. Mathieu, J. Phys. Rad., 16, 219 (1955).
[5] A. M. Vergnoux, Cahiers Phys., 11, 40 (1957).
[6] R. S. Halford, J. Chem. Phys., 14, 8 (1946).
[7] M. Ito and T. Shigeoka, Spectrochim. Acta, 22, 1029 (1966).
[8] G. N. Zhizhin, Thesis, Institute of Physics, Academy of Sciences of the USSR, Moscow (1965).
[9] N. L. Bagdanskis, M. O. Bulanin, and Yu. V. Fadeev, Opt. Spektrosk., 29, 687 (1970).
[10] G. N. Zhizhin, G. M. Kuz'yants, M. A. Moskaleva, and A. Usmanov, Opt. Spektrosk., 33, 903 (1972).
[11] C. Brecher, E. Krikorian, J. Blanc, and R. S. Halford, J. Chem. Phys., 35, 1097 (1961).
[12] V. Schettino, M. P. Marzochi, and S. Califano, J. Chem. Phys., 51, 5264 (1969).
[13] Ya. M. Kimel'feld, M. A. Moskaleva, G. N. Zhizhin, and V. T. Aleksanyan, Zh. Strukt. Khim., 11, 656 (1970).
[14] A. S. Davydov, Theory of Molecular Excitons, Plenum, New York (1971).
[15] R. M. Hochshtrasser, Molecular Aspects of Symmetry, Benjamin (1966).
[16] R. M. Badger and J. R. Zumwalt, J. Chem. Phys., 6, 711 (1938).
[17] V. T. Aleksanyan, Ya. M. Kimel'fel'd, N. N. Magdesiev, and Yu. K. Yur'ev, in: Optics and Spectroscopy [in Russian], 3, Nauka, Leningrad (1967), p. 168.
[18] L. M. Sverdlov, M. A. Kovner, and E. P. Krainov, Vibrational Spectra of Polyatomic Molecules [in Russian], Nauka, Moscow (1970).
[19] L. S. Mayants, Theory and Calculation of Molecular Vibrations [in Russian], Izd. Akad. Nauk SSSR, Moscow (1960).
[20] G. N. Zhizhin, M. A. Moskaleva, and E. B. Perminov, Opt. Spektrosk., 30, 1047 (1971).
[21] O. V. Fialkovskaya and A. V. Nefedov, Opt. Spektrosk., 26, 847 (1969).
[22] A. L. Kitaigorodskii, Organic Chemical Crystallography, Consultants Bureau (1961).
[23] Ya. M. Kimel'fel'd, M. A. Moskaleva, G. N. Zhizhin, V. P. Litvinov, S. A. Ozolin', and Ya. L. Gol'dfarb, Opt. Spektrosk., 28, 1112 (1970).
[24] V. T. Aleksanyan and G. M. Kuz'yants, Zh. Strukt. Khim., 12, 266 (1971).
[25] Ya. M. Kimel'fel'd, A. Usmanov, and G. N. Zhizhin, Zh. Strukt. Khim., 11, 864 (1970).
[26] R. Kahn, R. Fourm, D. Andre, and M. Renaud, Comt. Rend., B271, 1078 (1970).
[27] Ch. Menard and A. Meller, Compt. Rend., B271, 1181 (1970).
[28] L. Darmon and C. Brot, Molec. Crystals, 2, 301 (1967).
[29] A. V. Rakov, Trudy Fiz. Inst. Akad. Nauk SSSR, 27, 111 (1964).
[30] G. N. Zhizhin and A. Usmanov, Fiz. Tverd. Tela, 13, 1538 (1971) [Sov. Phys.–Solid State, 13, 1289 (1971).
[31] K. A. Valiev and A. Sh. Agishev, Opt. Spektrosk., 16, 881 (1964).
[32] E. G. Brutan and A. V. Sechkarev, Izv. Vyssh. Ucheb. Zaved. Fizika, 2, 48 (1967).
[33] G. N. Zhizhin, Yu. E. Lozovik, M. A. Moskaleva, and A. Usmanov, Dokl. Akad. Nauk SSSR, 190, 301 (1970) [Sov. Phys.–Dokl., 15, 36 (1970)].
[34] G. N. Zhizhin, M. A. Moskaleva, and Kh. E. Sterin, in: Solid State Spectroscopy [in Russian], 3, Nauka, Leningrad (1969), p. 146.
[35] G. N. Zhizhin and Kh. E. Sterin, Opt. Spektrosk., 19, 55 (1965).

[36]G. N. Zhizhin, M. A. Moskaleva, Kh. E. Sterin, and E. M. Mil'vitskaya, Zh. Strukt. Khim., 12, 928 (1971).

[37]G. N. Zhizhin, M. A. Moskaleva, and Kh. E. Sterin, Zh. Strukt. Khim., 10, 52 (1969).

[38]A. Usmanov, G. N. Zhizhin, Kh. E. Sterin, O. V. Bragin, V. N. Tatarinova, and A. L. Liberman, Zh. Strukt. Khim., 11, 1061 (1970).

[39]V. L. Ginzburg, Usp. Fiz. Nauk, 77, 621 (1962) [Sov. Phys.–Usp., 5, 649 (1963)].

Use of the luminescence polarization diagram method to investigate molecular crystals containing two impurities

G. S. Belikova, N. D. Zhevandrov, T. V. Il'inykh, L. E. Kraeva, and N. P. Sul'zhenko

Physics Institute, Academy of Sciences of the USSR
Institute of Crystallography, Academy of Sciences of the USSR

(Submitted April 30, 1972; resubmitted August 4, 1972)
Kristallografiya, 18, 779-783 (July-August 1973)

Comparison of the experimental and calculated luminescence polarization diagrams for two different impurities, lumogen and anthracene, was used to determine the manner in which their molecules are incorporated into and oriented in the lattice of the same naphthalene single crystal. Comparison of the results with the polarization diagrams of the corresponding single-impurity crystals and studies made at different concentrations showed that the molecules of different impurities enter the naphthalene lattice in a statistically independent fashion and that there is no tendency toward incorporation in pairs.

The polarization-diagram method, i.e., study of the three-dimensional distribution of luminescence polarization, was developed in earlier studies[1–4] and employed to investigate the manner in which one impurity is incorporated into and oriented in a base lattice for concentrations of up to 10^{-7} g/g.

Structural investigations of two-impurity molecular crystals are of great interest, since energy transfer from the base to different impurities and from molecules of one impurity (donor) to those of the other (acceptor) depends strongly on the orientation and relative arrangement of the molecules of these impurities in the base lattice. It is very important to determine how the impurity molecules are incorporated into the base lattice, i.e., in pairs or singly.

A whole series of experimental data tend to support statistically independent incorporation of single impurity molecules. These data were presented in an earlier article.[5] A direct proof of the single incorporation of impurity molecules was the discovery[5] that there is no energy migration between impurity molecules (lumogen A) incorporated into the naphthalene lattice in small concentrations (up to $8 \cdot 10^{-6}$ g/g).

In the present investigation, we attempted to solve the problem of paired or individual incorporation of molecules of two different impurities into the base lattice with the aid of luminescence polarization diagrams.

Our work was conducted with naphthalene single crystals with impurities of lumogen A and anthracene. Two-impurity single crystals were grown from a melt by the method described previously.[4] It was found that, with the substances selected, the presence of a second impurity had no effect on the growth of single crystals. We grew and investigated single crystals with the same concentrations for both impurities (10^{-4} and 10^{-5} g/g) and with different concentrations: 10^{-5} g/g anthracene and 10^{-3} g/g lumogen A; $5 \cdot 10^{-4}$ g/g anthracene and 10^{-6} g/g lumogen A.

We obtained single crystals of poor quality with large concentrations of lumogen A and anthracene (starting at 10^{-3} g/g), apparently as a result of development of strong lattice stresses leading to breakdown of the lattice.

Determination of the polarization diagrams is itself a check on the quality and purity of the single crystals. If they contain a foreign impurity that prevents growth of high-quality single crystals, regular polarization diagrams are not obtained for the crystals. Moreover, the polarization-diagram method permits checking for the absence of foreign impurities that luminesce in the visible region of the spectrum, down to a concentration of 10^{-7} g/g.

The substances selected for our investigation are very convenient for use of the polarization-diagram method for a number of reasons. First of all, use of this method requires precise isolation with appropriate filters of the luminescence region first of one impurity and then of the other. This was easily done in the case in question, since the luminescence spectra of naphthalene, anthracene, and lumogen A hardly overlap at all (Fig. 1). The luminescence spectrum of lumogen A was isolated with a ZhZS-9 filter, while that of anthracene was isolated with an SS-14 filter.

Secondly, the radiative oscillator in the lumogen A molecule is known to be directed parallel to the longitudinal axis of the molecule, while that in anthracene is directed perpendicular to this axis; it was therefore possible to obtain fundamentally different polarization diagrams for the differently oriented radiative oscillators of the two impurities in the same crystals. This basic difference in the overall trend of the diagrams for the two impurities in the same base, each of which was in good agreement with the corresponding calculations, greatly increased the reliability of the results obtained.

The method employed was considered in detail previously.[1–4] Knowing the crystal structure of naphthalene and the orientations of the radiative oscillators in the impurity molecules and having made definite assumptions regarding the orientation of the impurity molecules in the lattice, we can calculate the polarization diagrams for selected crystal sections and for the crystal orientations with extremal polarization. These diagrams are given in Fig. 2. Experimental measurements are then made of the corresponding polarization diagrams. The crystal

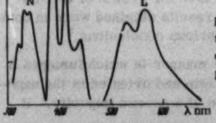

Fig. 1. Luminescence spectrum of two-impurity naphthalene crystal (N) containing anthracene (A) and lumogen A (L).

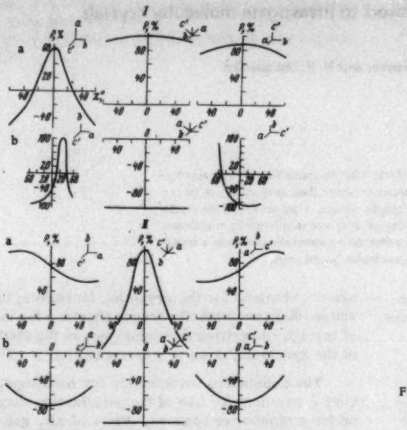

Fig. 2. Calculated polarization diagrams of naphthalene for oscillator directed parallel to longitudinal (I) and transverse (II) molecular axes. a) Positive diagrams; b) negative diagrams; χ) observation angle; P) degree of polarization of luminescence. The appropriate crystal orientation is indicated near each diagram.

positions with extremal polarization (positive represented by curves a in Figs. 2 and 3 and negative represented by curves b in Figs. 2 and 3) are found by preliminary measurement of the azimuthal function of the degree of polarization, i.e., the dependence of the degree of luminescence polarization on the angle through which the crystal is rotated about its horizontal axis, which coincides with the optical axis of the polarimeter. Comparison of the experimental and calculated diagrams for each impurity makes it possible to determine which is the correct hypothesis regarding the orientation of its molecules in the base lattice.

We have shown[2] that the anthracene molecules in single-impurity naphthalene molecular crystals isomorphically replace naphthalene molecules. However, such substitution is difficult, since the anthracene molecule differs by one benzene ring from the napthalene molecule and causes substantial local deformation of the lattice. This is indicated by some distortion of the trend of the experimental diagrams in comparison with the calculated diagrams. The development of crystal-lattice distortions is confirmed by qualitative observations showing appearance of a second cleavage plane at an angle of the order of 60° to the first.

In the present investigation, we repeated the measurements for anthracene-containing naphthalene single crystals grown from the same reagents in the same concentrations as subsequently used for growth of two-impurity single crystals. The results obtained were in complete agreement with our previous conclusions.[2]

We have determined the manner in which lumogen A molecules are incorporated into and oriented in the naphthalene lattice in the absence of a second impurity.[4] It was found that incorporation of lumogen A molecules into the naphthalene lattice occurs by replacement of two adjacent naphthalene molecules running parallel to the c axis by one impurity molecule. This results in formation of a substitution solution; this type of substitution occurs rather readily and does not involve large lattice deformations, as is indicated by the good agreement between the experimental and calculated diagrams. However, local lattice deformation around the incorporated impurity molecules still occurs. In the present study, comparison of the experimental and calculated diagrams was used to determine the manner in which lumogen A and anthracene are incorporated into and oriented in the lattice of a single two-impurity naphthalene single crystal.

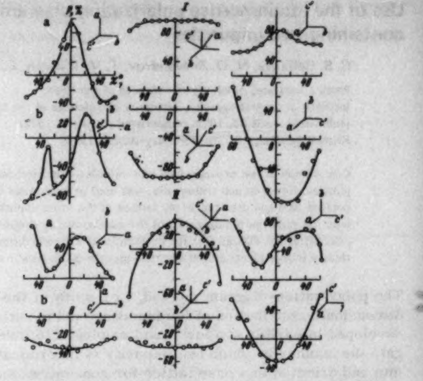

Fig. 3. Experimental polarization diagrams of lumogen A (I) and anthracene (II) in naphthalene. a) Positive diagrams; b) negative diagrams.

Our experiments were conducted with spherical specimens, using excitation in the center of the sphere to avoid errors associated with birefringence.[4] The spheres were cut into hemispheres along the same crystallographic planes as for the one-impurity single crystals: 1) along the (001) *ab* cleavage plane; 2) along the (010) *ac* optic-axis plane; 3) along the plane perpendicular to the *ac* and *ab* planes, i.e., the bc' plane. Excitation was conducted in the center of the hemisphere with light having a wavelength of 313 nm from a PRK-4 mercury bulb. The polarization was measured visually with an improved Korn polarimeter.[4]

The experimentally obtained positive and negative diagrams for all the aforementioned sections of naphthalene crystals containing lumogen A and anthracene are shown in Fig. 3; each diagram indicates the corresponding crystal orientation. It must be noted that, for sections along the *ab* and bc' planes, the crystal position with maximum positive polarization for lumogen A coincides with that of maximum negative polarization for anthracene; for sections along the *ac* plane, the positions with maximum positive (or negative) polarization for anthracene and lumogen A coincide, which is in agreement with our calculations. In definite optical measurements, this permits isolation of the luminescence of each impurity in the two-impurity crystal by both the spectral and polarization methods. Using crystal sections for which the polarization diagrams are antibatic, the luminescence of the second impurity can be blocked out with a polarization filter.

Comparison of the experimental and calculated diagrams shows that the polarization diagrams of lumogen A in naphthalene are in good agreement with the calculated diagrams for an oscillator parallel to the longitudinal axis (compare Fig. 2, curve I, and Fig. 3, curve I), while those for anthracene are in agreement with the calculated diagrams for an oscillator parallel to the transverse axis (Fig. 2, curve II, and Fig. 3, curve II). The "gap" in the experimental diagram in Fig. 3, curve I, for a section along the *ab* plane corresponds to the direction of the optical axis and is due to the appearance of conical internal reflection and is readily extrapolated (dashed line).[4]

The incorporation of lumogen A and anthracene into two-impurity crystals based on naphthalene is therefore such that the longitudinal axes and benzene-ring planes of the naphthalene and impurity molecules are close to parallel. Comparison of the molecular dimensions shows that one lumogen A molecule replaces two naphthalene molecules in the direction parallel to the c axis, while the anthracene molecule replaces one naphthalene molecule.

Thus, the impurity molecules in two-impurity molecular crystals of the type investigated are oriented in the base lattice in the same manner as in the corresponding one-impurity crystals. The good agreement between the polarization diagrams of the two-impurity crystals and the corresponding diagrams of single-impurity crystals enables us to conclude that the presence of one impurity has no effect on the manner in which the other is incorporated and oriented, since the presence of a second impurity does not lead to noticeable deformation of the polarization diagrams of the first impurity.

This result indicates that the molecules of two different impurities do not have a tendency toward arrangement in pairs when incorporated into a base (naphthalene), i.e., there is no tendency toward replacement of base molecules in the same or adjacent unit cells. If there were such a tendency, the presence of local deformation created by molecules of one impurity would undoubtedly lead to noticeable distortion of the polarization diagrams of the second impurity.

We measured the polarization diagrams of two-impurity crystals containing identical and different impurity concentrations: 10^{-5} g/g anthracene and 10^{-3} g/g lumogen A; $5 \cdot 10^{-4}$ g/g anthracene and 10^{-6} g/g lumogen A. The good agreement of the experimental diagrams obtained in all cases with the calculated diagrams indicates independent incorporation and orientation of one impurity with respect to the concentration of the other.

The experimental data obtained enable us to conclude that the molecules of different impurities are incorporated into the naphthalene lattice in a statistically independent manner and that there is no tendency toward incorporation in pairs.

---

[1] N. D. Shevandrov, Tr. Fiz. Inst. Akad. Nauk, 25, 3 (1965).

[2] G. S. Belikova, V. N. Varfolomeeva, and N. D. Zhevandrov, Kristallografiya, 13, 129 (1968) [Sov. Phys.–Crystallogr., 13, 98 (1968)].

[3] G. S. Belikova, V. N. Varfolomeeva, and N. D. Zhevandrov, Kristallografiya, 13, 267 (1968) [Sov. Phys.–Crystallogr., 13, 209 (1968)].

[4] G. S. Belikova, N. D. Zhevandrov, T. V. Il'inykh, L. E. Kraeva, and N. V. Khromeeva, Kristallografiya, 17, 366 (1972) [Sov. Phys.–Crystallogr., 17, 310 (1972)].

[5] N. D. Zhevandrov and T. V. Il'inykh, Izv. Akad. Nauk SSSR, Ser. Fiz., 36, 370 (1972).

Dispersion of the electric permittivity of triglycine sulfate in the vicinity of the phase transition

L. P. Pereverzeva and Yu. M. Poplavko

Kiev Polytechnic Institute

(Submitted July 21, 1972; resubmitted November 26, 1972)
Kristallografiya, 18, 784-787 (July-August 1973)

The temperature and frequency dependences of the electric permittivity ε of triglycine sulfate between 5 and 40 GHz have been studied. It has been shown that in this frequency region the dispersion of ε in TGS crystals can only be described by taking account of resonant polarization processes (in addition to the relaxation mechanism which gives the main contribution to ε in the initial dispersion region up to 3 GHz).

Dispersion of the electric permittivity ε in ferroelectric triglycine sulfate (TGS) in the region of the phase transition has been observed[1] at frequencies from 0.1 to 2.5 GHz and has subsequently been studied in refs. 2–8. Quantitative data on the dispersion of ε given in those papers differ and there are differences in the method of describing the dispersion spectra. In ref. 4, for example, the relation $\varepsilon(\nu)$ was described assuming a nearly normal distribution of relaxation times; the authors of ref. 6 attempted to include the distribution of relaxing entities by the Cole–Cole method, leading to a dependence of ε'' on ε' taking the form of the arc of a circle. In ref. 7 it was confirmed that the ε'' versus ε' diagram is close to a lemniscate arc, which is obtained in the case of mutual influence of the relaxing entities. Finally, the authors of ref. 8 proposed that the dispersion of ε in TGS can be described by a single relaxation time in the neighborhood of the critical temperature T_C. In the majority of these papers the measurements were carried out in the microwave region up to 3 GHz or up to 10 GHz.

In the present paper we report a detailed study of the dispersion spectra of TGS crystals between 5 and 40 GHz in the neighborhood of the phase transition and show that in this higher-frequency region the dispersion of ε can only be described taking account of resonant polarization mechanisms whose frequencies depend on the temperature in a critical way. As a model mechanism which agrees with our results, it is appropriate to use the representations of pendulum vibrations of the glycine I ion whose frequency at T_C has been estimated by Galanov et al.[9] to be ~0.36 cm^{-1} (12 GHz).

The measurements were done using a shorted waveguide[10] in which the electrical length of the sample was close to a quarter wavelength (this condition produces least error). We used modern waveguide equipment for centimeter and millimeter waves. The method chosen is marked by comparative simplicity and reliability and also allows a simple analysis of the measurement errors.[11] With $\varepsilon'' < \varepsilon'$ the error in the determination of ε' and ε'' amounts to 3 to 10% depending on the magnitude of the loss. In the vicinity of the transition where $\varepsilon'' \geq \varepsilon'$ the absolute value of the error in the measurement of ε' amounted to ±10% and the relative error in the determination of ε'' did not exceed 20%. These errors, however, are systematic and do not preclude the occurrence of some fine details in the temperature dependence of ε' and ε''.

The samples to be measured were prepared in the form of rectilinear plates of dimensions 35 × 15 mm to 7.2 × 3.6 mm (in agreement with the sizes of the standard waveguides) from the very same large single crystal[1)] with a dislocation density no more than 10^3 cm^{-2}. The thermal conditions for the measurements, which are

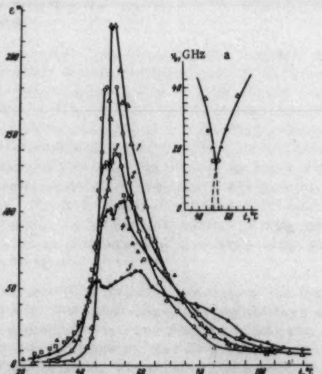

Fig. 1. Temperature dependence of the dielectric loss in triglycine sulfate crystals at various frequencies. 1) 10.2; 2) 5.5; 3) 16.6; 4) 20.4; 5) 26.2 GHz; a) temperature dependence of the frequency of the resonant polarization mechanism.

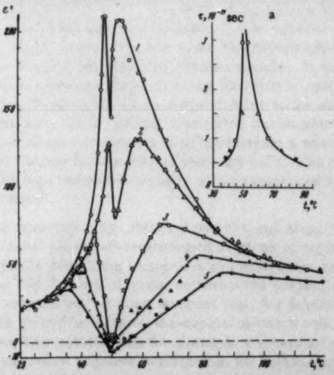

Fig. 2. Temperature dependence of the electric permittivity of a triglycine sulfate crystal. 1) 5.5 GHz; 2) 10.2 GHz; 3-5) frequencies the same as for Fig. 1. a) Temperature dependence of the characteristic relaxation time $\tau = B/2\pi A(T-\theta)$.

very important for obtaining reproducible results, were the same during investigations in different microwave apparatus; the samples were first heated to 120°C and held at this temperature for not less than 1/2 h; then the measurements were done during cooling at a rate no more than 30 deg/h.

The experimental data are given in Figs. 1 and 2. As previously indicated above, the temperature and frequency dependence of ε'' and ε' which were obtained cannot be explained assuming a purely relaxation mechanism for the polarization. This can be seen, for example, from the temperature dependence of ε' (Fig. 2). The sharp minimum of $\varepsilon'(T)$ which is found in the microwave range at the top of the temperature maximum of ε' beginning at frequencies of about 2.5 GHz with $\nu \geq 15$ GHz falls lower than the infrared contribution to the permittivity ($\varepsilon_\infty \approx 10$). It is just this anomaly in the neighborhood of the maximum of $\varepsilon''(T)$ (Fig. 1) at high frequencies which can only be explained assuming dielectric resonances. The effects of resonant polarization mechanisms can be included as usual by using the equations for a dispersed oscillator. Both above and below T_C the relation $\varepsilon^*(\nu, T)$ is well described by the expression

$$\frac{\varepsilon_0-\varepsilon_\infty}{\varepsilon^*(\nu,T)-\varepsilon_\infty}=1+i\Gamma\frac{\nu}{\nu_0}-\frac{\nu^2}{\nu_0^2}, \tag{1}$$

within the limits of measurement error, where

$$\varepsilon_0-\varepsilon_\infty=C/(T-\theta),\quad \nu_0=A\sqrt{T-\theta},\quad \Gamma=B/\sqrt{T-\theta}.$$

The results of the measurements in the microwave range shown in Figs. 1 and 2 above 50°C can be described by the following parameters: Curie–Weiss constant C = 2600°C, a Curie–Weiss temperature θ = 48.5°C, a temperature coefficient of the frequency A = 8.5 GHz/deg$^{1/2}$, a temperature coefficient of the damping B = 10 deg$^{1/2}$, and ε_∞ = 10. Below T_C in the ferroelectric region Eq. (1) describes the dispersion of ε assuming $C_C = 1000°$, $\theta_C = 53°C$, $A_C \approx 12$, and $B_C \approx 6$. In Fig. 1a we show the temperature dependence of the frequency ν_0 calculated from A and A_C. The experimental points correspond to the temperatures and frequencies for which there is a maximum of $\varepsilon''(T)$, and the positions of these maxima, as follows from an analysis of Eq. (1), should correspond to the frequency $\nu_0(T)$. The very low value of the frequency at the phase transition point for the crystal studied should lie between 14 and 16 GHz in good agreement with the calculations carried out previously[9] for pendulum vibrations of glycine I molecules. Thus our experimental data confirm the molecular model[9] of the phase transition mechanism in TGS crystals.

It should be noted that in another lot of TGS crystals which evidently had larger defect concentrations, the parameters C, θ, A, and B differed; above T the dispersion of ε was described by C = 3100°, θ = 47°C, A = 6 GHz · deg$^{-1/2}$, and B = 9 deg$^{1/2}$. It has been established that there is a substantial effect on these parameters from changes in the thermal conditions for measurement in addition to differences in technique, since the electrical properties of TGS crystals near T_C are unusually sensitive to thermal and electrical history. It is known, for example, that in these crystals domain formation can persist[12] even substantially above T_C if they are not given a preliminary "annealing."

In order to compare our results on the dispersion of ε in TGS with data of earlier work we assume that in the initial region of dispersion of ε for a comparatively low frequencies the latter term in Eq. (1) can be neglected ($\nu^2/\nu_0^2 \ll 1$). In this approximation it is easy to arrive at the Debye dispersion equation which is characteristic of polarization relaxation

$$\frac{\varepsilon_0-\varepsilon_\infty}{\varepsilon^*(\nu,T)-\varepsilon_\infty}\approx 1+i\frac{B\nu}{A(T-\theta)}=1+i\omega\tau, \tag{2}$$

where

$$\tau=\tau_0/(T-\theta),\ B/A=2\pi\tau_0,\ \omega=2\pi\nu,\ \varepsilon_0-\varepsilon_\infty=C/(T-\theta).$$

With these values of C and θ the dispersion in ε can now be described by only a single parameter τ_0. Above T_C (Figs. 1 and 2) $\tau_0 = 2 \cdot 10^{-10}$ sec · deg, while below T_C $\tau_0 = 7.5 \cdot 10^{-11}$. Figure 2a gives the curve $\tau(T)$ calculated for these parameters and in the experimental points corresponding to the maxima of $\varepsilon'(T)$ are shown to the left and right of the critical region of minimum $\varepsilon'(T)$ from an analysis of Eq. (1).

Using Eq. (2) to describe the experimental data on the dispersion of ε in TGS obtained previously[4] we find τ_0 = 2–3.3 · 10^{-10} sec · deg, while from ref. 5 we find $\tau_0 \sim 3.3 \cdot 10^{-10}$ sec · deg. These results should be regarded as agreeing approximately with our data since there are large effects due to differences in crystal quality and the thermal conditions for measuring the dispersion of ε in TGS in the neighborhood of the phase transition.

---

1)The crystals were kindly provided by I. S. Rez.

[1] A. Lurio and E. Stern, J. Appl. Phys., 31, 1125 (1960).
[2] E. Nakamura and J. Furuichi, J. Phys. Soc. Japan, 15, 2101 (1960).
[3] V. M. Petrov, Kristallografiya, 6, 632 (1961); V. M. Petrov and O. I. Kagan, Kristallografiya, 15, 1018 (1970) [Sov. Phys. – Crystallogr., 6, 508 (1962); 15, 885 (1971)].
[4] R. M. Hill and S. K. Ichiki, Phys. Rev., 128, 1140 (1962); R. M. Hill and S. K. Ichiki, Phys. Rev., 132, 1603 (1963).
[5] Yu. M. Poplavko and L. P. Solomonova, Izv. Akad. Nauk SSSR, Ser. Fiz., 31, 1771 (1967); M. M. Nekrasov, Yu. M. Poplavko, and V. I. Molchanov, in: Ferroelectric Materials and Their Applications in Radio Electronics [in Russian], Gosplan UkrSSR, Kiev (1966), pp. 59-63.
[6] K. Yoshimitsu and T. Matsubara, Prog. Theor. Phys., 37, 634 (1967).
[7] K. Ishibashi, A. Sawada, and V. Takagi, J. Phys. Soc. Japan, 28, 1488 (1970).
[8] G. Luther and H. E. Müser, Z. Naturforsch., a24, 389 (1969); G. Luther and H. E. Müser, Z. Angew. Phys., 29, 231 (1970).
[9] E. K. Galanov, L. D. Kislovskii, L. A. Shuvalov, and N. R. Ivanov, Izv. Akad. Nauk SSSR, Ser. Fiz., 33, 246 (1969).
[10] Yu. M. Poplavko, Izv. Kievsk. Politekh. Inst., 40, 42-58 (1962).
[11] A. Ya. Brok, in: Methods for Investigating Polycrystalline Ferroelectrics [in Russian], Izdatel'stvo Latv. Gos. Univ. Riga (1970), pp. 116-142.
[12] E. J. O'Brien and T. A. Litovitz, J. Appl. Phys., 35, 180 (1964).

Electronic mechanism of the influence of radiation on the process of repolarization of ferroelectrics

A. A. Grekov, M. A. Malitskaya, and V. M. Fridkin
Rostov State University
Crystallography Institute, Academy of Sciences of the USSR

(Submitted June 21, 1972; resubmitted August 28, 1972)
Kristallografiya, 18, 788-795 (July-August 1973)

It is shown that irradiation of a ferroelectric in the already-polarized and unpolarized states affects the ferroelectric polarization and repolarization processes in various ways for the example of photoconductive ferroelectrics of the $A^{V}B^{VI}C^{VII}$ type with a low-temperature phase transition. Photoelectric studies have allowed investigation of the role of electronic processes in the mechanism of unipolarity and ferroelectric polarization and the suggestion of this mechanism as an explanation of earlier known results on the influence of radiation on repolarization processes.

INTRODUCTION

The existence of photoconductivity in ferroelectrics of the $A^{V}B^{VI}C^{VII}$, $BaTiO_3$, and other types lies at the basis of a series of new photoferroelectric phenomena, such as shift of the Curie temperature upon irradiation, change of temperature hysteresis and a series of parameters of the ferroelectric crystal near the phase transition,[1-3] and the influence of irradiation on domain structure.[4] One of the methods of investigation of the distribution of internal fields in a ferroelectric crystal is photoconductivity; this method has recently been used for the study[5] of Känzig layers (surface shielding layers) in SBSI and $BaTiO_3$. Finally, photoconductivity results in a change in the conditions of spontaneous polarization shielding in a ferroelectric, in a change of kinking of zones in the surface region, and also in optical recharging of levels in the body and on the surface, which open additional possibilities in the study of the mechanism of recharging of domains and repolarization. These possibilities have already been foreseen by Känzig when he wrote that "the nucleation of domains begins everywhere with a surface ...; probably extremely interesting effects could be found during the irradiation of a surface by light."[6] Some of these effects were actually observed in this work and are used for study of the role of nonequilibrium electrons in the mechanism of ferroelectric repolarization.

In previous works,[7-8] we have shown that two forms of polarization can coexist in $A^{V}B^{VI}C^{VII}$ solid solutions with low-temperature phase transitions: spontaneous (ferroelectric) and electronic (photoelectret), which arises during photoconductivity and is stable due to the large value of u/kT, where u is the energy of activation of the local levels responsible for the photoelectret polarization. In this work, the formation of photoelectret polarization in crystals of $A^{V}B^{VI}C^{VII}$ solid solutions during their irradiation by natural light in the ferroelectric region, as well as the influence of photoelectret polarization on the ferroelectric properties, is investigated. In this case it proved to be possible to draw a series of new conclusions as to the influence of nonequilibrium carriers on the mechanism of ferroelectric polarization and repolarization.

RESULTS OF MEASUREMENTS

As in previous works,[7,8] single crystals of $SbSI_{0.35}Br_{0.65}$, which had a phase transition temperature of $T_C \simeq 170°K$, Curie–Weiss temperature $T_0 \simeq 165.5°K$, and spontaneous polarization $P_s \sim 20\ \mu C/cm^2$, were studied. Other parameters of these crystals, as well as the method of ferro- and photoelectric measurements in a vacuum cryostat, have been reported earlier.[7,8]

Study of the photoelectret polarization, which is formed upon shielding of ferroelectric polarization by nonequilibrium carriers, and its influence on the ferroelectric polarization was done in the following manner. The crystal was polarized by cooling and transition from the paraelectric to the ferroelectric phase under an external field. After removal from the field and short-circuiting of the electrodes, the ferroelectric was irradiated in the natural spectral region. As was established earlier,[7] this resulted in shielding of P_s by nonequilibrium carriers and the formation of a photoelectret charge caused by localization of shielding charge on deep-lying levels. The density of photoelectret charge Q_f could be measured by heating the crystal and its transition to the paraelectric phase, and repeated irradiation and measurement of the depolarization current.[7] In our work, in addition to this measurement we studied the influence of the photoelectret polarization created in this manner on the ferroelectric polarization of the crystal. For this, a crystal previously polarized in a field of high coercive force and irradiated was transformed by heating in the paraelectric region; at the phase transition temperature a pyroelectric current was observed, which corresponded to a pyroelectric charge density of $q \sim 20\ \mu C/cm^2$ (saturation pyroelectric charge). Later the crystal was cooled in the absence of the external field and transformed to the ferroelectric phase, after which it was heated again, a pyroelectric current corresponding to $q \sim 18\ \mu C/cm^2$ being observed at the phase transition temperature. It was found that this same crystal, upon one-time cooling and heating, showed the same pyroelectric charge density of $q \sim 18\ \mu C/cm^2$, which was close to the value of P_s. (We note that a crystal not previously polarized showed $q \sim 0.4\ \mu C/cm^2$ as the result of unipolarity.) The result obtained was evidence that the internal field of a photoelectret causes ferroelectric polarization of the crystal below the Curie point T_C. Since the photoelectret was stable in the temperature region investigated, such a ferroelectric electret is the analog of a pyroelectric material. We had studied this phenomenon earlier by the formation of photoelectret polarization under the action of an external field in the paraelectric phase of the crystal.[8] Study of this phenomenon under conditions of shielding P_s showed a series of peculiarities.

1. The quantity P_s, estimated from the pyroelectric charge, was studied as a function of Q_f. It had been found

TABLE 1

Transparency of light filter, %	Pyroelectric charge density q in forward direction, μC/cm²	Pyroelectric charge density q in reverse direction, μC/cm²
0	2	0.15
0.6	3.3	0.2
1	6.2	1
2	8.4	0.6
3	10	0
100	18	0

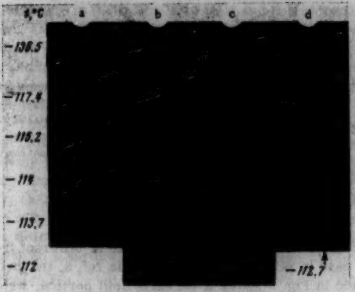

Fig. 1. Influence of irradiation of a ferroelectric on the ferroelectric repolarization process.

earlier that Q_f in the crystals studied can rise from 0 to $\sim 2\ \mu C/cm^2$ with increase in the intensity of the light used for screening (see ref. 7, Figs. 2 and 5). The dependence of the pyroelectric charge density on the transparency of the neutral light filters used to change the intensity of the light and, accordingly, Q_f, is given in Table 1. The maximum light intensity corresponded to a density of $Q_f \sim 2\ \mu C/cm^2$. As can be seen from the values in Table 1, and as already noted above, the presence of $Q_f \sim 2\ \mu C/cm^2$ caused a pyroelectric current in the forward direction and, accordingly, $P_s \sim 18\ \mu C/cm^2$, which corresponded to almost complete saturation of the polarization (see ref. 8 for the determination of forward and reverse directions of current). Along with this the photoelectret charge created in the paraelectric phase by irradiation of the crystal in an external field, which is the same in value, resulted in a value of P_s which was less by an order of magnitude.[8] As can be seen from the data of Table 1, not only did the pyroelectric charge decrease with decrease in Q_f, but the nature of the pyroelectric current also changed: A second maximum of the pyroelectric current, of reverse direction, appeared, which was comparable with the forward pyroelectric current. Let us keep in mind that an analogous structure of the pyroelectric current was observed for a photoelectret created in the paraelectric phase.[8]

2. The influence of the internal field of the photoelectret on the process of ferroelectric repolarization was studied by use of the dielectric hysteresis loop. The photoelectret was formed by the method described above. A crystal previously polarized in an external field with short-circuited electrodes was irradiated by natural light at a temperature below T_C. After this, the crystal was transformed to the paraelectric phase by heating and again cooled below T_C. The dielectric hysteresis loops were later observed by use of the usual method. Hysteresis loops for a crystal in which the photoelectret charge is absent (without preliminary irradiation in the polarized state) are shown in Fig. 1a. Hysteresis loops for this same crystal with $Q_f \sim 2\ \mu C/cm^2$ are shown in Figs. 1b and 1c for the two opposite directions of photoelectret polarization. The influence of the field of the photoelectret on repolarization shows up in the asymmetry of the loops. In addition, from Fig. 1 the shift of T_C in the high-temperature direction, caused by the field of the photoelectret and observed earlier by use of pyroelectric measurements,[7] is clearly seen. Depolarization of the photoelectret by repeated irradiation of the crystal with natural light in the paraelectric phase reduces the symmetrical form of the hysteresis loops (transition from the loop of Fig. 1b or 1c to the loops of Fig. 1a) and raises T_C to the original equilibrium value. Reduction of the symmetrical form of the hysteresis loop also occurs if the crystal is irradiated with natural light in the process of observation of the hysteresis loop. This is illustrated in Fig. 2. Measurements have shown that the time of reduction of a hysteresis loop is close to the Maxwellian value of $\tau = \varepsilon/4\pi\sigma$. Thus, at a temperature of −119°C the dielectric susceptibility is $\varepsilon \simeq 4 \cdot 10^4$ and the photoconductivity is $\sigma \simeq 1.4 \cdot 10^{-10}\ \Omega^{-1} \cdot cm^{-1}$ for $\tau \simeq 25$ sec, which is in good agreement with the values for Fig. 2. With an increase in intensity of the light and therefore the photoconductivity, the time of reduction of the loop decreases. A photoelectret charge of this same value, created in the paraelectric region by irradiation of the crystal in an external electric field, did not change the form of the hysteresis loop, which is in agreement with the values of pyroelectric measurements given above.

Fig. 2. Influence of natural illumination on the asymmetric hysteresis loops and their reduction in the repolarization process. 1) 0 sec; 2) 3 sec; 3) 7 sec; 4) 10 sec; 5) 30 sec; 6) 50 sec. $\sigma = 14 \cdot 10^{-11}\ \Omega^{-1} \cdot cm^{-1}$.

3. From the preceding analysis it follows that the internal field of a photoelectret influences the ferroelectric polarization in various ways, depending on the conditions of formation of photoelectret polarization in the crystal. This indicates that the ferroelectric polarization process is determined not only by the value of charge of the photoelectret, but also by the distribution of its internal field. The distribution of the internal field has been investigated earlier by use of a light probe (ref. 8, Fig. 1) for the case of a photoelectret formed in an external field in the paraelectric phase. In this work, the distribution of the internal field of a photoelectret formed by shielding of P_s by nonequilibrium carriers was studied by this same method. The distribution obtained is shown

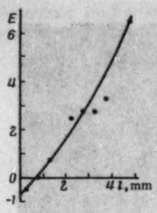

Fig. 3. Distribution of internal field (in relative units) formed in the paraelectric region of a crystal as the result of shielding of spontaneous polarization by nonequilibrium carriers.

in Fig. 3 and actually shows a character different from the case in ref. 8. Unlike the case in ref. 8, the distribution in Fig. 3 shows a forward-field portion, which evidently determines the ferroelectric polarization and therefore the forward direction of the pyroelectric current. Another difference lies in the unsymmetrical character of the distribution of the internal field.

4. Finally, it was found that irradiation of an unpolarized ferroelectric in the ferroelectric phase by natural light also strongly influences the process of ferroelectric polarization and repolarization. An unpolarized ferroelectric at a temperature below T_C was irradiated in its region of inherent photosensitivity. After this, the dielectric hysteresis loop shown in Fig. 1d was taken in darkness. Comparison of the shapes of the loops for the unirradiated (Fig. 1a) and irradiated (Fig. 1d) crystals shows that previous irradiation of an unpolarized ferroelectric hinders the process of ferroelectric repolarization, which is equivalent to a sharp increase in coercive field during irradiation. Data from pyroelectric measurements also tell of this. An unpolarized and irradiated ferroelectric was transformed to the paraelectric phase and after this was cooled below T_C under a field higher than the dark coercive force. Upon subsequent heating, the crystal showed $q \sim 1\ \mu C/cm^2$. At the same time, a saturation pyroelectric charge of $q \sim 20\ \mu C/cm^2$ was always measured for an unirradiated crystal under these same conditions. The pyroelectric charge rose slightly with rise of polarizing field, but was much less than saturation pyroelectric charge in the region of attainable fields. In addition, as can be seen from Fig. 1d, irradiation of the crystal in the ferroelectric phase near T_C results in the appearance of a double hysteresis loop. If an unpolarized crystal previously irradiated in the ferroelectric phase is again irradiated in the paraelectric phase, its coercive field falls to the dark value: The saturated form of the hysteresis loop is reduced, the pyroelectric charge grows and reaches saturation, and the double hysteresis loops disappear. Irradiation of the crystal with natural light during the process of observing the hysteresis loop also reduces the shape of the hysteresis loop. This is illustrated in Fig. 4, which shows the kinetics of reduction of the hysteresis loop for three different intensities of light and the three corresponding values of photoconductivity σ at a temperature of −119°C (the value of σ was measured near the phase transition to the paraelectric phase for these same intensities of light). The Maxwellian time for the three values of σ amounts to 25, 75, and 180 sec, respectively, which is in agreement with the measurement data shown in Fig. 4. Specific observations showed that distortion and reduction of the hysteresis loop occur only upon irradiation of the entire volume of the crystal, and irradiation of only the end surfaces does not affect the shape of the loops and does not result in any noticeable unipolarity.

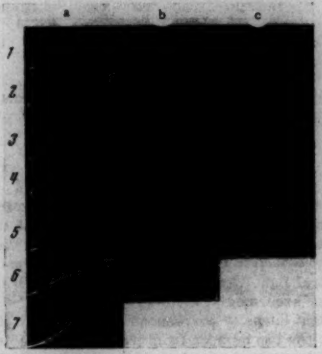

Fig. 4. Influence of natural illumination on double hysteresis loops and their reduction in the repolarization process. 1) t = 0; 2) t = 3 sec; 3) t = 7 sec; 4) t = 10 sec; 5) t = 30 sec; 6) t = 60 sec; 7) t = 84 sec. a) $\sigma = 2 \cdot 10^{-11}\ \Omega^{-1} \cdot cm^{-1}$; b) $\sigma = 5 \cdot 10^{-11}\ \Omega^{-1} \cdot cm^{-1}$; c) $\sigma = 14 \cdot 10^{-11}\ \Omega^{-1} \cdot cm^{-1}$.

DISCUSSION

Combining the results presented above shows that irradiation of a ferroelectric material by natural light in the ferroelectric phase strongly influences the processes of ferroelectric polarization and repolarization, while the character of this influence is different for the already polarized and unpolarized states.

In the unpolarized state, kinking of zones at the surface of a ferroelectric is determined by the charge of the surface levels. This leads to the result that fields of opposite direction exist along the length of the shielding for opposite facial surfaces of the crystal perpendicular to the direction of spontaneous polarization. According to the confirming ideas in ref. 6, these fields lead to the appearance of nuclei of antiparallel domains, and the difference of charges of opposite surfaces, and therefore the fields, can be one of the causes of unipolarity of the ferroelectric.[9] Under conditions where the ferroelectric polarization process is determined by nucleation, change in the charges of the surface levels during irradiation of the ferroelectric should affect the process of ferroelectric polarization and repolarization. Therefore, the influence of irradiation on the repolarization of a multidomain crystal could be explained by starting from the model outlined above. This, however, is in contradiction to the entire combination of experimental facts presented above, which point to the volume nature of this phenomenon: the necessity for irradiation of the entire volume of the crystal and the agreement of the time of reduction of the shape of the loop with Maxwellian time.

It is therefore natural to conclude that the influence of irradiation on the repolarization of a multidomain crystal is associated with the process of shielding of the domain walls in the body of the crystal, and therefore their fixation, by nonequilibrium carriers. In this case, domain walls should be understood to include both walls of wedge-shaped domains and other possible domain walls not parallel to the c axis, which have been observed earlier in SbSI. In this case the fact of reduction of shape of the hysteresis loop during irradiation of the crystal in the paraelectric phase or in the process of repolarization becomes acceptable, since in these cases the disappearance or rearrangement of domain structure makes possible the disappearance of the shielding charges localized on the levels of attachment as the result of photoconductivity. It is natural that in this case the kinetics of reduction of the hysteresis loops should be described by a time close to the Maxwellian time.

The surface-region kinking of zones in the polarized state is determined both by the charge of the surface levels and by the charge shielding the spontaneous induction D_0. On the strength of the large values of D_0, the shielding charge appears to be the determining one for typical ferroelectrics, and therefore the fields corresponding to opposite polar surfaces have the same direction, which corresponds to unipolarity of a polarized crystal. In addition, the large value of surface-region shielding field causes the appearance of the so-called surface layers (Känzig layers), which play the role of a dielectric gap.[7] The problem of shielding of the spontaneous induction of a single-domain crystal with the surface layer being taken into account is examined in ref. 7. Following the notation accepted in ref. 7, we have

$$4\pi Q_f = l/\varepsilon_l (D_0 - 4\pi Q_p)/(l/\varepsilon_l + d/\varepsilon_s), \tag{1}$$

$$D_l^s = \left(\frac{d}{\varepsilon_s} \Big/ \frac{l}{\varepsilon_l}\right) 4\pi Q_f \tag{2}$$

where Q_f is the volume shielding charge at the boundary of the surface layer of the crystal, Q_p is the surface charge at this same boundary (numerically equal to the pyroelectric charge, since $Q_f \ll Q_p$), D_l^S is the induction in the surface layer in the ferroelectric phase, l and ε_l are, respectively, the thickness of the surface layer and its dielectric susceptibility in the ferroelectric phase, and d and ε_s are, respectively, the length of the shielding and the dielectric susceptibility in the volume of the crystal. According to (1), irradiation of an already polarized ferroelectric leads to an increase of the shielding charge Q_f localized on low-lying levels of attachment and therefore stable both in the ferroelectric and paraelectric phases of the crystal photoelectret charge). If, in accordance with ref. 7, it is accepted that $Q_p = 0$ above the Curie temperature, then in the paraelectric region the charge Q_f localized on the shielding length d sets up an induction D_l in the surface layer such that

$$D_l^p = -4\pi Q_f \tag{3}$$

if $L \gg 2\varepsilon_s l/\varepsilon_l$, where L is the dimension of the crystal in the polar direction. From (3) it can be seen that in the paraelectric phase the photoelectret charge Q_f sets up an induction in the reverse direction of value $D_l^P = -[(l/\varepsilon_l) \cdot (d/\varepsilon_s)^{-1}] D_l^S$ in a surface layer of the crystal of thickness l. With increase in the intensity of light and therefore the concentration of nonequilibrium carriers, the length d of screening decreases, the charge Q_f and induction $|D_l^P|$ rise, and the induction $|D_l^S|$ falls, accordingly. In the limiting case, where $d/\varepsilon_s \ll l/\varepsilon_l$, saturation photoelectret charge $4\pi Q_f \simeq D_0 - 4\pi Q_p$ occurs and, therefore, $|D_l^S| \ll |D_l^P|$. Thus, a photoelectret saturation charge of $Q_f \simeq 2$ $\mu C/cm^2$(ref. 7) corresponds to a ferroelectric phase of relatively low field $|E_l^S|$ (corresponding to the conditions of shielding of spontaneous induction), and the field is $|E_l^P| = 4\pi Q_f/\varepsilon_l \simeq 2 \cdot 10^5$ V/cm if it is accepted, in accordance with ref. 10, that $\varepsilon_l = 10$. Such a significant reverse field is evidently shielded by the injection of carriers from a surface layer or from electrodes in the body of the crystal, which also results in the nature of distribution of internal field shown in Fig. 3. In this case, the determining role of the forward field near the surface and its strong influence on the ferroelectric polarization is naturally associated with the fact that this field is concentrated at the surface layer–crystal boundary and determines both the processes of nucleation and domain growth. The low effectiveness of the photoelectret created by shielding of the external field in the paraelectric region is explained by the fact that in this case the strong forward field is concentrated in the surface layer, the thickness of which is much less than l. The unsymmetrical nature of the distribution of the internal field in Fig. 3 corresponds to the asymmetry in the distribution of the injected ground-state and nonground-state carriers. The presence of an internal field of both directions in the short-circuited electret results in the two maxima of the pyroelectric current in the forward and reverse directions. However, unlike the situation in ref. 8, a maximum for the reverse pyroelectric current is observed only for low light intensities (corresponding to low values of Q_f and the field $|E_l^P|$), which is also associated with the determining influence of the field on the ferroelectric polarization in the surface layer.

In conclusion, let us note that the stable character of the phenomena described above is associated with the large value of u/kT, and therefore these phenomena are weakly pronounced or in general are not observed in SbSI at room temperatures, although the influence of irradiation on the "shaping" of the hysteresis loop in SbSI was observed earlier in ref. 11. On the other hand, in such wide-zone ferroelectrics as $BaTiO_3$ these phenomena can also be observed in the region of a high-temperature phase transition, which has been confirmed experimentally.[12] Finally, it can be assumed that the analogous influence of hard radiation on the hysteresis loop and the repolarization processes in seignette salt, triglycine sulfate,[13] and barium titanate,[14] observed earlier, are associated not only with the appearance of radiation defects, as was suggested earlier, but also with the shielding of domain boundaries by nonequilibrium carriers. This does not contradict the possible absence of noticeable conductivity for seignette salt and triglycine sulfate due to the short lifetime and low mobility of the carriers in these crystals.

---

[1] V. M. Fridkin, ZhETF Pis. Red., 3, 252 (1966) [JETP Lett., 3, 161 (1966)].
[2] R. E. Pasynkov, Izv. Akad. Nauk SSSR, Ser. Fiz., 34, 2466 (1970).
[3] V. M. Fridkin, L. M. Belyaev, A. A. Grekov, and A. I. Rodin, J. Phys. Soc.

Japan, Suppl., 28, 448 (1970).

[4] V. M. Fridkin, Ferroelectrics, 2, 119 (1971).

[5] V. M. Fridkin, A. A. Grekov, E. A. Savchenko, and T. R. Volk, Phys. Status Solidi, A8, K55 (1971).

[6] W. Känzig, Ferroelectrics and Antiferroelectrics, Academic Press, New York, Ch. 5.

[7] A. A. Grekov, M. A. Malitskya, V. D. Spitsyna, and V. M. Fridkin, Kristallografiya, 15, 500 (1970) [Sov. Phys.–Crystallogr., 15, 423 (1970)].

[8] A. A. Grekov, M. A. Malitskaya, and V. M. Fridkin, Kristallografiya, 17, 581 (1972) [Sov. Phys.–Crystallogr., 17, 504 (1972)].

[9] N. M. Bezdetnyi, A. Kh. Zeinally, G. A. Gorbatov, and M. K. Sheinkman, Fiz. Tekh. Poluprov., 5, 1016 (1971) [Sov. Phys.–Semicond., 5, 904 (1971)].

[10] F. Jona and G. Shirane, Ferroelectric Crystals, Pergamon (1962).

[11] A. Yu. Kudzin and A. N. Sukhinskii, Fiz. Tverd. Tela, 11, 1389 (1969) [Sov. Phys.–Solid State, 11, 1126 (1969)].

[12] T. R. Volk, A. A. Grekov, N. A. Kosonogov, and V. M. Fridkin, Fiz. Tverd. Tela, 14, 3219 (1972) [Sov. Phys.–Solid State, 14, 2744 (1973)].

[13] V. A. Yurin, A. S. Baberkin, É. N. Kornienko, and L. V. Gavrilova, Izv. Akad. Nauk SSSR, Ser. Fiz., 24, 1334 (1960).

[14] G. A. Smolenskii, V. A. Bokov, V. A. Isupov, N. N. Krainik, R. E. Pasynkov, and M. S. Shur, Ferroelectrics and Antiferroelectrics [in Russian], Nauka, Moscow (1971), p. 259.

Vol.
July 19
June 1

Phase transformations in $NaH_3(SeO_3)_2$ crystals irradiated with a large dose of gamma radiation

E. V. Peshikov and L. A. Shuvalov

Institute of Nuclear Physics, Academy of Sciences of the Uzbek SSR
Institute of Crystallography, Academy of Sciences of the USSR

(Submitted July 27, 1972; resubmitted October 19, 1972)
Kristallografiya, 18, 796-799 (July-August 1973)

It is shown that in ferroelectric sodium trihydroselenite crystals irradiated with a large dose of gamma radiation a γ phase with a different form of electric ordering is realized immediately below the Curie point rather than the usual triclinic β phase. The new phase is monoclinic. This confirms that gamma irradiation may change the character of the electric ordering in crystals.

Earlier papers written by one of the authors and various colleagues[1-8] indicated that the number and sequence of the phase transitions in ferroelectric $Na(D_xH_{1-x})_3(SeO_3)_2$ crystals (SDHS) might vary with the deuterium concentration,[1,3,5,6,9] the hydrostatic pressure,[2-5] and the electric fields[5,7,8] E_y and[8] E_x. All this indicates the lability of the structure of SDHS crystals and the small difference between the internal energies of their ferroelectric phases.

In this paper we shall show that the γ irradiation of sodium trihydroselenite crystals (SHS) may also change the character and symmetry of the ferroelectric phase realized below the Curie point T_C.

We studied the $\varepsilon_y(T)$ relationships in weak fields, using an E-12-2 bridge at a frequency of 1 kHz, and the $P_y(E_y)$ relationships, using a Sawyer–Tower system at a frequency of 100 Hz. The measurements were carried out on Y-cut plates of SHS (the Y axis being parallel to the two-fold axis of the para-phase) ~0.5 mm thick with sprayed-on aluminum electrodes. The samples were irradiated with Co^{60} γ quanta at a dose rate of $4 \cdot 10^3$ R/sec at T = 60°C.

We see from the experimental results (Fig. 1, curves 1-3) that after moderate doses of irradiation the T_C of the SHS crystal moves in the low-temperature direction in the usual manner of a ferroelectric, while the ε_y anomaly at T_C is gradually suppressed and there is a general fall in the value of ε_y in the ferroelectric phases, as mentioned in ref. 10.

On irradiating the samples with a dose of D = 120 MR, the Curie point T_C was displaced still further, and there was also a sharp change in the character of the ε_y anomaly at T_C and the whole $\varepsilon_y(T)$ relationship in the ferroelectric phase, both on lowering and on raising the temperature (Fig. 1, curves 4). The temperature hysteresis of the transition contracted slightly. On passing the crystal repeatedly through the T_C point after this, the new form of the $\varepsilon_y(T)$ curve remained intact.

On comparing the form of the $\varepsilon_y(T)$ curves in Fig. 1 with each other and with the form of the analogous curves relating to nonirradiated SDHS crystals having various deuterium contents,[6] we may draw the following conclusions. The properties of the paraelectric α phase of the SHS crystal remain qualitatively the same after any dose of γ irradiation, including D = 120 MR. Immediately below T_C, after irradiation with a dose of $D \leq 30$ MR, the triclinic ferroelectric β phase (class 1) appears, as in

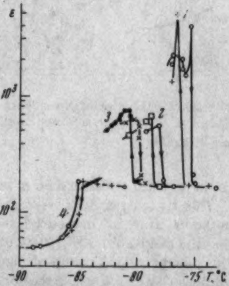

Fig. 1. Temperature dependences of the dielectric constant ε_y of $NaH_3 \cdot (SeO_3)_2$ crystals after receiving various doses of γ radiation, 1) 0; 2) 15; 3) 30; 4) 120 MR.

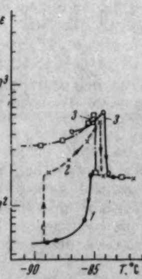

Fig. 2. Changes in the temperature dependence of the ε_y of an $NaH_3 \cdot (SeO_3)_2$ crystal γ irradiated with a dose of 120 MR under the independent influence of the field E_y and time. 1) Before the action (3 h after irradiation); 2) after the action of the field; 3) three days after plotting curves 1 (without the action of the field).

nonirradiated SHS crystals. After irradiation with a dose of 120 MR, another phase (which we may call γ*) is realized in the SHS crystals immediately below T_C; this is evidently identical with the monoclinic ferroelectric phase γ' (class m) arising just below T_C in nonirradiated SDHS crystals with a deuterium concentration[6] of $x \geq 0.05$. These conclusions are supported by the fact that, in the first case (with $D \leq 30$ MR), $P_y(E_y)$ loops appear below T_C, whereas in the second case (with D = 120 MR) the $P_y(E_y)$ relationship remains linear if the fields are not too strong.

Further investigations showed that the γ* phase was metastable: The application of a strong alternating field

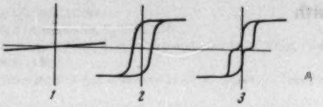

Fig. 3. The $P_y(E_y)$ relationships observed in an $NaH_3(SeO_3)_2$ crystal γ irradiated with a dose of 120 MR. 1) Linear relationship; 2) transitional loop; 3) steady-state loop (the scale along the axes in oscillogram 1 is five times as great as in oscillograms 2 and 3).

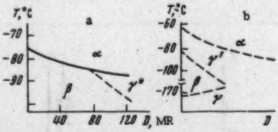

Fig. 4. Qualitative form of the proposed phase diagrams in coordinates of temperature and dose of γ irradiation for the crystals $NaH_3(SeO_3)_2$ (a) and $Na(D_{0.2}H_{0.8})_3(SeO_3)_2$ (b).

$E_y > E_y^{crit}$ to the crystal transformed it from the γ^* to the β phase. This transition is proved, firstly, by the sharp rise in the value of ε_y measured in a weak field after removing the field $E_y > E_y^{crit}$ (by comparison with its initial value), and the qualitative change in the whole $\varepsilon_y(T)$ curve below T_C, which takes the form characteristic of the β phase (Fig. 2). Secondly, in the field $E_y > E_y^{crit}$ the initially linear $P_y(E_y)$ relationship (Fig. 3a) changes sharply into the ordinary hysteresis loop (Fig. 3b), with the value of P_{sy} characteristic of the β phase; this rapidly changes into a split loop (Fig. 3c) typical of the β phase of the γ irradiated crystal.[10] The latter is readily explicable, since the internal bias field responsible for the splitting of the loop, which is itself due to structural defects created by the γ irradiation, only arises in the presence of the macroscopic P_{sy}, which is absent from the γ^* phase but present in the β phase.

Although the $\gamma^* \to \beta$ transition initiated by the field E_y is irreversible (for T = const), after heating the crystal above T_C and starting a new cycle of heating and cooling the $\alpha \to \gamma^*$ and $\gamma^* \to \alpha$ transitions appear once again. Thus immediately after irradiation with a dose of $D \geq 120$ MR the following scheme of phase transitions is realized:

$$\begin{tikzcd}
 & \alpha \arrow[dl, dash, "T"'] \arrow[dr, shift right] & \\
\beta & & \gamma^* \arrow[ll, "E_y"] \arrow[ul, shift right, "T"']
\end{tikzcd}$$

The γ^* phase is unstable, and the following happens as time progresses: In the sample irradiated with a dose of D = 120 MR, which initially experienced the $\alpha \rightleftharpoons \gamma^*$ transitions, after three days storage at T = 25°C the ordinary $\alpha \rightleftharpoons \beta$ phase transitions appear (Fig. 2). This may be explained by the partial annealing of the radiation defects. This assertion is supported by the fact that slight additional irradiation ($D \simeq 10$ MR) again restores the $\alpha \rightleftharpoons \gamma^*$ transitions.

The present results, together with those presented in refs. 1–8, lead to the following conclusions. In SDHS crystals, below the T_C point, a two-component state of electrical ordering is realized: In the β phase there are two components of spontaneous polarization ($P_{sx} \simeq P_{sm}$ and P_{sy}), but in the γ phase (γ' and γ^*) only one (P_{sx}), while along the Y axis we may assume that the ferroelectric ordering is replaced by antiferroelectric. The foregoing experimental data indicate that, like the other factors (deuterium concentration, hydrostatic pressure, and external electric field),[1-8] γ irradiation affects the stability of the existence of P_{sx} and P_{sy} in different ways.1) The ferroelectric ordering in the m plane of the paraelectric phase is comparatively stable with respect to the action of the factors in question and is realized in all phases below T_C (apart from the δ phase, which only exists at high hydrostatic pressures[2-5]). However, the electric ordering along the Y axis is capable of changing its character quite easily under the influence of the same factors; this reflects the closeness between the energies of the states with ferro- and antiferroelectric ordering along the Y axis.

We see in particular from the results of the present investigation that γ irradiation favors antiferroelectric ordering along the Y axis. (The same effect is created on replacing hydrogen by deuterium, which may thus be likened to the introduction of defects.) For a hypercritical dose of γ irradiation, antiferroelectric rather than ferroelectric ordering along the Y axis appears in SHS crystals directly below T_C.

We may even predict the qualitative form of the phase diagrams in coordinates of temperature and dose of γ irradiation for SDHS crystals with different deuterium contents (Fig. 4). We see from Fig. 4a that by irradiating SHS crystals at fairly low temperatures we may obtain two radiation-induced phase transformations at T = const, the first involving a change in the character of the electrical ordering along the Y axis, and the second involving the complete breakdown of electrical ordering. Radiation-induced phase transitions of the second type had already been observed in a number of ferroelectric crystals, but so far not those of the first type. In SDHS crystals with a deuterium concentration of x < 0.3 (but not too far from 0.3), irradiation with a fairly heavy dose should lead to a situation in which the development of the β phase, which exists stably between the γ' and γ phases in nonirradiated crystals (Fig. 4b), is quite impossible.

Finally, we may foresee that not only relation, but other structural defects also, including impurities, may lead to a change in the character of the electrical ordering in SDHS crystals.

The authors wish to thank N. M. Shchagina, who grew the crystals studied in the present investigation.

---

1)This effect was predicted by one of the authors.[11]

[1] L. A. Shuvalov, N. R. Ivanov, L. F. Kirpichnikova, and N. M. Shchagina, ZhETF Pis. Red., 8, 235 (1968) [JETP Lett., 8, 143 (1968)].

[2] A. M. Shirokov, L. A. Shuvalov, and N. R. Ivanov, Phys. Lett., A29, 559 (1969).

[3] L. A. Shuvalov, N. V. Gordeyeva, N. R. Ivanov, L. F. Kirpichnikova, A. M. Shirokov, and N. M. Shchagina, J. Phys. Soc. Japan, Suppl., 28, 75 (1970).

[4] L. A. Shuvalov, A. M. Shirokov, N. R. Ivanov, and A. I. Baranov, Kristallografiya, 15, 1011 (1970) [Sov. Phys. – Crystallogr., 15, 879 (1971)].

[5] L. A. Shuvalov, A. M. Shirokov, N. R. Ivanov, A. R. Baranov, L. F. Kirpichnikova, and N. M. Shchagina, J. Phys., 33, C2, 165 (1972).

[6] L. A. Shuvalov, N. R. Ivanov, L. E. Kirpichnikova, and N. M. Shchagina, Kristallografiya, 17, 966 (1972) [Sov. Phys. – Crystallogr., 17, 851 (1973)].

[7] L. A. Shuvalov, A. M. Shirokov, N. R. Ivanov, and A. I. Baranov, Kristallografiya, 18, 133 (1973) [Sov. Phys. – Crystallogr., 18, 80 (1973)].

[8] L. F. Kirpichnikova, Candidate's Dissertation, Inst. Crystallography, Academy of Sciences of the USSR (1972).

[9] N. Miki and Y. Makita, J. Phys. Soc. Japan, Suppl., 28, 143 (1970).

[10] E. V. Peshikov, Izv. Akad. Nauk SSSR, Ser. Fiz., 35, 1936 (1971).

[11] L. A. Shuvalov, Doctor's Dissertation, Institute of Crystallography, Academy of Sciences of the USSR (1971).

Dislocations formed during the sintering of solids ("sintering rosettes")

Ya. E. Geguzin, A. S. Dzyuba, V. L. Indenbom, and N. N. Ovcharenko

Khar'kov State University
Institute of Crystallography, Academy of Sciences of the USSR

(Submitted February 28, 1973)
Kristallografiya, 18, 800-806 (July-August 1973)

The dislocation structure ("sintering rosettes") formed by sintering polycrystalline LiF granules on an LiF single crystal (001) plane was observed. A linear relationship between the contact area radius and the length of the dislocation rosette ray was established. The observed effect is explained in terms of the forming and relaxation of a lattice mismatch between the granules and the crystal over the contact area. An estimate is made of the stress and deformation in the contact zone from the sintering rosette dimensions, and of the total energy of all the rosette dislocations. The strict solution of the field stress calculation for the sintering of flat particles to a crystal surface is given in a mathematical appendix.

INTRODUCTION

The question of the role of dislocations in sintering processes has not been considered seriously for a number of years because, according to Herring,[1] the Laplace stresses occurring in the contact neck area are insufficient to cause dislocation motion.

The "dislocation and sintering" problem was revived after the publication of Morgan's articles,[2-4] which, although describing the dislocation formation close to fluorite granules sintered to a fluorite single crystal, did not give any practical explanation of this phenomenon.

It should be emphasized that information about the contact region dislocation structure is important for the correct description of high-temperature intersolid contact formation processes. Such information becomes even more important when dealing with small dimension granules, whose contact region is practically the same size as that of the corresponding granule.

The present investigation was devoted to the study of dislocation formation laws in the contact zone between a granule and a macroscopic crystal of the same material. In our experiments we used LiF crystals for which reliable dislocation detection methods are available. For quantitative measurements we used single crystal and almost spherical LiF granules, produced by dropping mechanically pulverized powders through an electric arc flame. Spherical powders prepared in this way were polycrystalline, as confirmed from an x-ray analysis of an individual granule. It should be noted that the sintering of spheres to planes has previously been used in many model mechanisms during sintering (see ref. 5).

BASIC OBSERVATIONS

The experimental method was as follows. Almost spherical granules with radii from 10 to 250 μ were randomly scattered over a lithium fluoride natural cleavage surface with initial dislocation density not exceeding $5 \cdot 10^4$ cm^{-2}. Before carrying out an isothermal anneal under specially controlled conditions, we checked that none of the procedures to which the specimens were subjected lead to the formation of a dislocation structure around the granules. This structure did appear, however, after isothermally annealing the specimens for various times in the range 600–750°C. To avoid any doubt in identifying the observed dislocation structures the chosen assembly of granules were photographed before and after annealing and after the normal dislocation structure revealing treatments of etching, washing, and drying. In discussing the results we consider only those granules which remained undisplaced after the various treatments and required a certain force to move them. A typical dislocation structure on an LiF single crystal (001) surface around a presintered granule is shown in Fig. 1. The region around the sintered granule will be characterized by the two linear parameters in the subsequent discussion: the radius of the contact zone r_0 and the length L of the "dislocation rosette" ray.

We shall list and describe the basic observations made in the described experiments.

1. "Dislocation rosettes" form around all the sintered granules whose external appearance is similar to that observed around an indenter impression.[6] Around a sintered sphere the rays which form contain mainly edge dislocations. By analogy with the mechanical case we shall refer to these below as "sintering rosettes."

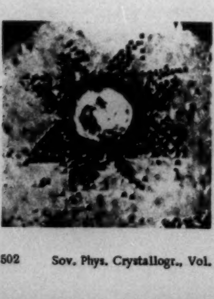

Fig. 1. Dislocation structure (sintering rosette) on an LiF single crystal (001) surface around a sintered LiF granule (T = 740°C, t = 1 h), ×250.

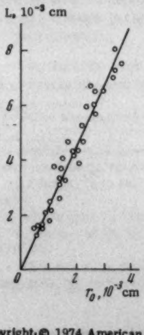

Fig. 2. Dependence of dislocation rosette ray length on radius of presintered granule (T = 740°C, t = 1 h).

2. The contact zone structure appears to be inhomogeneous (spotted), that is, the sphere joins to the single crystal at several separate places.

3. The length of the dislocation ray and the radius of the contact area are related linearly, $L \sim r_0$ (Fig. 2).

4. By successive polishing the dislocation distribution with depth in the precontact zone under the sintered granule could be studied. Typical contours, bounding the deformation zone, are shown in Fig. 3, from which it is easy to see that a proportional change in the deformation zone characteristic dimensions takes place with a change in the linear dimension of the presintered zone.

THE MECHANISM OF THE EFFECT

As already noted in the introduction, capillary stresses due to surface strains are insufficient to explain the observed effect, according to Herring's calculation.[1] It is reasonable to consider in the explanation those stresses in the contact zone which are caused by the lattice mismatch along the plane joining the granule and the single crystal. The existence of such stresses was experimentally demonstrated in 1955 by Erdman-Jesnitser and others,[7,8] who did not study the sintering zone dislocation structure but did conclude, however, that the occurring stresses, whose presence was revealed by x rays, were not connected with the generation and motion of dislocations.

We shall calculate the contact zone stresses caused by the lattice mismatch between joining single crystals (a similar calculation is given in the Appendix). We assume that some dislocation network forms over the contact surface, giving rise to long range stresses. It is obvious that an abrupt change in the stress over the boundary depends only on the degree of mismatch of the joining lattices and can be characterized quantitatively by the mismatch factor $\varepsilon \approx \Delta a/a$ (where a is the lattice parameter), which is governed by the dislocation network boundary geometry and not by the size or shape of the sintering region and granule. Thus a granule having the same shape and contact region geometry will cause in the crystal a similar stress field, differing only in scale, $\sigma = \sigma_p f(x/r_0)$, where r_0 is the characteristic size of the sintering particle (or contact region). As a result the dislocation rosette around a contact region under stress σ should have dimensions which are proportional to the radius of the contact zone. This is indeed observed experimentally (Fig. 2).

For a local crystal surface loading (indentation) the stress decays according to an R^{-2} law for distances R large in comparison with the dimensions of the contact area. It follows from the internal stress equilibrium conditions that the principal vector for stresses lying in the sintering contact area is zero and that the stress decays according to the R^{-3} law, characteristic of dipole type local perturbations.

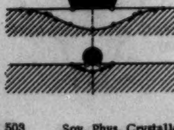

Fig. 3. Dislocation rosette contours formed under presintered granules of various sizes (T = 740°C, t = 1 h).

Bearing in mind the above remarks we can perform a simple calculation to establish a relationship between the contact stresses in the indentation (σ_0^i) and sintering (σ_0^s) zones and the corresponding dislocation rosette characteristics. Assuming that the contact areas in both cases are equal ($r_i^2 = r_s^2$) and that the stresses at the ends of the dislocation rays in the rosette are equal, we obtain

$$\sigma_0^s \simeq \sigma_0^i \left(\frac{L_s}{L_i}\right)^2 \frac{L_s}{r_s}, \tag{1}$$

where the indices i and s pertain respectively to indentation and sintering. It follows from the special indentation experiments which we performed on the same specimens as used for sintering that the quantity $(L/r)_i$ is constant over a wide loading range and equal to 13, and that $\sigma_0^i = 6 \cdot 10^9$ dyn/cm^2. As can be seen in Fig. 2, $(L/r)_s \approx 2$, so that $(L_s/L_i) = 2/13$. Thus, according to (1), $\sigma_0^s \approx \sigma_0^i/20 \approx 3 \cdot 10^8$ dyn/cm^2 and the stress at the end of the dislocation rays $\sigma^s = \sigma_0^s (r_s/L_s)^3 \approx 4 \cdot 10^7$ dyn/cm^2, which is approximately the elastic limit for LiF.

Knowing σ_0^s, we can find the lattice mismatch factor using the expression $\sigma_0^s = \varepsilon E/(1-\nu)$ (where E is Young's modulus and ν Poisson's ratio). For $E = 5 \cdot 10^{11}$ dyn · cm^{-2} and $\nu = 0.3$ we obtain $\varepsilon \approx 4 \cdot 10^{-4}$. Correspondingly the elastic energy density in the contact zone reaches a value of the order $\sigma_0^s \varepsilon \approx 10^3$ erg/cm^3. For simplicity, assuming that the sintering granule is a circular platelet of radius r_0 and height h, we obtain

$$W = \pi r_0^2 h \sigma_0^s \varepsilon \simeq \pi r_0^2 h \varepsilon^2 E / (1-\nu) \tag{2}$$

for the total elastic energy W in the granules.

It is interesting to compare W with the total dislocation energy in the rosette

$$W_s = \rho T_0 V \simeq \pi L_s^3 G b^2 / 3, \tag{3}$$

where ρ is the dislocation density, $V \approx 2\pi L_s^3/3$ is the rosette volume, $T_0 = Gb^2\pi 2$ is the dislocation linear energy, G is the shear modulus, and b is the Burgers vector. Equating (2) and (3) we obtain an independent estimate of

$$\varepsilon \simeq b\left(\frac{\rho L_s^3}{6hr_0^2}\frac{1-\nu}{1+\nu}\right)^{1/2}. \tag{4}$$

In our case, $L_s \approx 2r_0$ and $h \approx r_0$, so that

$$\varepsilon \simeq b\left(\frac{4\rho}{3}\frac{1-\nu}{1+\nu}\right)^{1/2} \simeq b\rho^{1/2}. \tag{5}$$

Our experimental mean value of the rosette dislocation density is $\rho = 6 \cdot 10^{17}$ cm^{-2} so it follows from (5) that $\varepsilon \approx 3 \cdot 10^{-4}$, which agrees well with the value of ε obtained above from the rosette dimensions. Thus an analysis of the sintering rosette formation conditions both from the stress field and the energy balance conditions give comparable values[1)] of the required mismatch factor $\varepsilon \sim (3\text{–}4) \cdot 10^{-4}$. There remains, however, the open question of the origin of this mismatch since in our case both the original lattice parameters and the granule and single crystal coefficients of expansion were practically the same.

Apparently the mismatch is connected with the polycrystalline nature of the granules causing the above indicated contact zone inhomogeneity: Initially the sinterable crystals touch one another at individual points, but after a high-temperature anneal "contact rods" form due to mass transfer towards these points. Since these "rods" join crystals mutually oriented at some angle φ, strains arise in them, governed by the obvious equation

$$\sigma \simeq E\frac{r}{\lambda}\frac{\varphi}{2}, \tag{6}$$

where r is the radius and λ the length of a rod. For $r \sim 2\lambda$ and $\varphi \sim 0.1$ we obtain $\sigma \sim 10^{10}$ dyn/cm², corresponding to a local mismatch $\varepsilon \sim \sigma/E \sim 2 \cdot 10^{-2}$, which completely guarantees the above average value of the order 10^{-3}–10^{-4}. It should be emphasized that the total grain boundary energy in a polycrystalline granule $W_s \simeq r_0^3\alpha/d$ (where $\alpha \approx 10^2$ erg/cm² is the intergrain energy and d the grain diameter) is larger than W and W_g even for $d \leqslant 10\ \mu$. Recrystallization in the granule may therefore be the reason for the lattice mismatch between sinterable crystals and the cause of the formation of the elastic field and sintering rosettes.

CONCLUSIONS

The formation of dislocations in a solid contact zone can in its essential features influence many processes, particularly the sintering process.

The described experiments involved the study of the dislocation structure in a single crystal. It may be assumed, however, that at the contact zone stress levels in question, there will be dislocations in the granules, an assembly of randomly oriented interconnected particles. In particular, the dislocation formation in granules at their point of contact during sintering has been observed by Hall and Morgan.[9] In this connection the formation of sintering rosettes which influence the sintering crystal defectivity degree acts as a unique controller of their "activity." Taking into account sintering rosette formation, it can be confirmed that free surfaces in an assembly of contacting granules govern the tendency to contract, while the intergrain contact area, although it does not completely determine, nevertheless contributes to the "activity" during mass transfer during the contraction process.

The stress field detected in our experiments can be considered as an example of long range stresses occurring in the contact zone between similar or different crystalline materials. Such stresses can essentially determine many of the characteristics of epitaxial films, which have an island character during the early growth stages. As the above example shows, contact stresses caused by each of the islands can be so large that they would easily cause not only the elastic, but also plastic deformation of the crystal substrate in regions comparable in size with the island diameter, leading to the corresponding "long range action."

APPENDIX

Let a thin planar particle sinter with some mismatch $\varepsilon = \Delta a/a$ to a crystal surface lying along the $z = 0$ plane. In the elastic isotropic approximation the stress discontinuities σ_{xx} and σ_{yy} at the separation boundary will be governed by the quantity $\sigma_0 = \varepsilon E/(1-\nu)$. Stresses caused by particles in the crystal at distances large in comparison with the particle thickness h can arise as a result of the application to the specimen surface of tangential forces $F = \varepsilon Eh/(1-\nu)$ distributed around the particle contour and directed normally to this contour. The stress field can be calculated directly by integrating the known expressions for the field caused by a concentrated tangential load, but it is more convenient to construct the stress function. Using Indenbom's result[10] and going from a contour integration to a particle area integration, we obtain the following simple expressions for the stress functions:

$$\Psi_{xx} = \Psi_{yy} = \frac{Fz^3}{2\pi}\int\frac{dS}{R^3}, \tag{A.1}$$

$$\Psi_{zz} = \frac{F}{2\pi}\left[z^2\int\frac{dS}{R^3} - 2(1-\nu)\int\frac{dS}{R}\right], \tag{A.2}$$

where R is the distance from the observation point to a point moving across the area of contact. At distances large in comparison with the particle dimensions, the integration can be replaced by the multiplication of the subintegral expressions over the particle area S.

All the stress tensor components are obtained from (1) and (2) by twofold differentiation:

$$\sigma_{xx} = \Psi_{zz,yy} + \Psi_{yy,zz}; \qquad \tau_{xy} = -\Psi_{zz,xy} \tag{A.3}$$

(for the components σ_{ij} the expressions are obtained by cyclically rearranging the indices in (3)). For axial symmetry (for a circular area of contact) in cylindrical polar coordinates r, φ, z we obtain

$$\sigma_{rr} = \frac{\partial^2}{\partial z^2}\Psi + \frac{1}{r}\frac{\partial}{\partial r}\Psi_{zz},$$

$$\sigma_{\varphi\varphi} = \frac{\partial^2}{\partial z^2}\Psi + \frac{\partial^2}{\partial r^2}\Psi_{zz},$$

$$\sigma_{zz} = \left(\frac{\partial^2}{\partial r^2} + \frac{1}{r}\frac{\partial}{\partial r}\right)\Psi,$$

$$\sigma_{rz} = -\frac{\partial^2}{\partial r\,\partial z}\Psi,$$

where $\Psi = \Psi_{xx} = \Psi_{yy}$.

In the experimentally considered case of dislocation sintering rosette formation on an LiF single crystal (001) surface, the slip in edge type systems $(110)[1\bar{1}0]$ and $(1\bar{1}0)[\bar{1}10]$ is governed by the tangential stress $\tau_1 = (\sigma_{xx} - \sigma_{yy})/2$, whereas slip in screw systems of the type $(101)[10\bar{1}]$, $(10\bar{1})[101]$, $(01\bar{1})[011]$, and $(011)[01\bar{1}]$ by tangential stresses $\tau_2 = (\sigma_{xx} - \sigma_{zz})/2$ and $\tau_3 = (\sigma_{yy} - \sigma_{zz})/2$. It may be supposed that the edge dislocation density is governed by the stress field τ_1 and the screw dislocation density by stress fields τ_2 and τ_3. According to ref. 11 the total dislocation density may be compared with the mean-square tangential stress:

$$\bar{\tau} = \sqrt{(\tau_1^2 + \tau_2^2 + \tau_3^2)/3}. \tag{A.5}$$

Transposing to a cylindrical coordinate system we have

$$\bar{\tau} = (2\sqrt{3})^{-1}\left[(\sigma_{rr} - \sigma_{\varphi\varphi})^2\left(\cos^2 2\varphi - \frac{1}{2}\sin^2 2\varphi\right) + \right.$$

$$+(\sigma_{rr}-\sigma_{zz})^2+(\sigma_{\varphi\varphi}-\sigma_{zz})^2\Big]^{1/2} \qquad \text{(A.6)}$$

It is not difficult to show that the expression for all the stress tensor components (4) and for all the quoted tangential stresses τ_1, τ_2, and τ_3, in agreement with ref. 3, takes the form

$$\sigma_{ij}=A_{ij}FSR^{-3}, \qquad \text{(A.7)}$$

where A_{ij} is a numerical factor of the order unity, constant at distances R, considerably larger than the area of contact radius r_0.

Figure 4 shows corresponding τ_1 and $\bar{\tau}$ rosettes constructed for equal tangential stresses when $R \gg r_0$. A Poisson's ratio value $\nu = 0.25$ was assumed in the calculation. As can be seen in Fig. 4a, the stress τ_1 plays a dominant role on the crystal surface in determining the dislocation density in edge type slip planes. Under the contact area within the crystal, however, the tangential stresses τ_2 and τ_3 predominate, and these are comparable for slip along screw type planes (see Fig. 4b).

In comparing Fig. 4 with Figs. 2 and 3 we must bear two facts in mind. First, dislocation rays will move out from regions of high stress to low original stress regions, so that the rosette shape for equal stresses in Fig. 4a is quite different from the Fig. 2 dislocation rosette shape. Second, near the contact area it is already impossible to calculate the integrals in (1)-(2) on average, and the integration must be carried out over the contact area. This is equivalent to averaging an expression of the type (7) with A_{ij} = const over an area equal and parallel to the contact area. It can be easily seen that such an averaging according to Fig. 3 will lead to a flattening of the rosette in Fig. 4b and to an increase in its dimensions parallel to the crystal surface.

In particular, for Ψ_{zz} on the specimen surface for a particle in the form of a circular disk of radius r_0 we obtain

$$\Psi_{zz}(r,0)=-\frac{F(1-\nu)}{\pi}\int\frac{dS}{r'}$$

$$=\begin{cases}-\dfrac{4r_0}{\pi}(1-\nu)FE\left(\dfrac{r}{r_0}\right), & r<r_0,\\[2ex] -\dfrac{4r}{\pi}(1-\nu)F\left[E\left(\dfrac{r_0}{r}\right)-\left(1-\dfrac{r_0^2}{r^2}\right)K\left(\dfrac{r_0}{r}\right)\right], & r>r_0.\end{cases} \qquad \text{(A.8)}$$

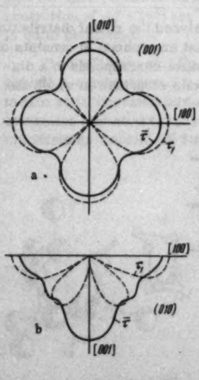

Fig. 4. Tangential stress field remote from the contact area. Equal tangential stress rosettes τ_1 and $\bar{\tau}$ constructed for the crystal surface (a) and for a cross section of the rosette (b) in the (010) plane.

In this case r is the distance in the boundary plane and E and K the full elliptical integrals of the second and first type, respectively. From (8) we can find the tangential stress total distribution in the boundary plane:

$$\sigma_{xx}(r,0)=\left[-(1-\nu)^{-1}+\sin^2\varphi\frac{\partial^2}{\partial r^2}+\cos^2\varphi\left(\frac{1}{r}\frac{\partial}{\partial r}\right)\right]\Psi_{zz}(r,0),$$

$$\sigma_{yy}(r,0)=\left[-(1-\nu)^{-1}+\cos^2\varphi\frac{\partial^2}{\partial r^2}+\sin^2\varphi\left(\frac{1}{r}\frac{\partial}{\partial r}\right)\right]\Psi_{zz}(r,0),$$

$$\tau_1=\frac{1}{2}(\sigma_{xx}-\sigma_{yy});\qquad \tau_2=\frac{1}{2}\sigma_{xx};\qquad \tau_3=\frac{1}{2}\sigma_{yy}, \qquad \text{(A.9)}$$

and also the boundary displacements u_r, which according to ref. 10 are governed in our case by the radial derived Ψ_{zz} function:

$$u_r=-\frac{1}{2G}\frac{\partial}{\partial r}\Psi_{zz}(r,0). \qquad \text{(A.10)}$$

Expression (10) can be used to calculate the elastic energy concentrated in the crystal and equal to the work of the forces F in displacing the crystal surface. Since the field (8) diverges logarithmically at points on the particle contour, this work must be calculated from the displacement at a distance h from the particle contour. The calculation indicates that for thin disks with $r_0/h > 10^2$ the elastic energies within the crystal amount to only a small fraction of the general energy of the specimen concentrated almost completely in the weak link sintering the particle to the crystal.

Our case of sintered thin planar particles allows all the calculations to be performed exactly. For particles of other shapes, for example, the experimentally observed isometric particles, calculation of the stress field is considerably more difficult. However, it should be noted that the stress distribution over the contact area should always correspond to a self-compensated dipole system of forces of a type similar to those arising in a planar particle. Therefore at distances large in comparison with the contact area size we again obtain an expression of the type (7) for the stress field, where FS acts as the effective strength of the dipole force.

[1)] That is, sintering rosette formation can be regarded as a result of the relaxation of the elastic stresses (W_g increases due to a decrease in W).

[1] C. Herring, Structure and Properties of Solid Surfaces, Univ. Chicago Press (1952).

[2] C. S. Morgan and C. S. Yust, J. Nucl. Mater., 10, 182 (1963).

[3] C. S. Morgan, C. J. McHarque, and C. S. Yust, Proc. Brit. Ceram. Soc., 3, 177 (1965).

[4] C. S. Morgan and C. S. Yust, Trans. Met. Soc., AIME, 236, 1504 (1966).

[5] Ya. E. Geguzin, Sintering Physics [in Russian], Nauka, Moscow (1967).

[6] A. A. Predvoditelev, V. N. Rozhanskii, and V. M. Stepanova, Kristallografiya, 7, 418 (1962) [Sov. Phys. – Crystallogr., 7, 330 (1962)].

[7] F. Erdman-Jesnitser, and M. May, Z. Metallkunde, 46, 756 (1955).

[8] F. Erdman-Jesnitzer and F. Gunter, Z. Metallkunde, 46, 801 (1955).

[9] L. L. Hall and C. S. Morgan, J. Amer. Ceram. Soc., 54, 55 (1971).

[10] V. L. Indenbom, Kristallografiya, 9, 74 (1964) [Sov. Phys. – Crystallogr., 9, 57 (1964)].

[11] V. I. Nikitenko and V. L. Indenbom, Kristallografiya, 6, 432 (1961) [Sov. Phys. – Crystallogr., 6, 341 (1961)].

Change in the structure of germanium and silicon during ion bombardment and subsequent annealing

P. V. Pavlov

Gor'kii Scientific-Research Physicotechnical Institute

(Submitted April 20, 1972; resubmitted July 10, 1972)
Kristallografiya, 18, 807-812 (July-August 1973)

An electron-diffraction study of the short-range structure of amorphous Ge films obtained by bombardment with N^+, Ar^+, and Xe^+ has been made. The structure consists of pentagonal rings. Amorphous Si has the same structure. The present article discusses possible amorphization mechanisms during bombardment, preference being given to the mechanism involving amorphization through accumulation of radiation induced point defects. It has been shown that vaporization of the surface atoms can cause amorphization of the surface layer. Experiments on the diffusion of In^{114} and Ge^{71} in Si previously subjected to bombardment with a dose of $6 \cdot 10^{15}$ ions/cm^2 of Ar^+ ions established that complete annealing of defects during crystallization of the amorphous layer does not occur even at a temperature of 1000°C.

Study of the structure of solids subjected to ion bombardment and subsequent annealing is of both theoretical and practical interest. Despite the fact that many researchers are occupied with these problems, the amorphization mechanism is still unclear and it is not known what specifically constitutes the amorphous state of a semiconductor after ion bombardment.

In the present investigation, we made an electron-diffraction analysis of the short-range structure of amorphous Ge obtained by ion bombardment. Analysis of the structure of Ge and Si before and after annealing and of the dependence of the "amorphization dose" on the defect concentration is used as a basis for considering the amorphization mechanism during bombardment.

Fourier analysis[1] was employed to calculate the radial atomic-density distribution curves for amorphous Ge films obtained by vacuum deposition on a cold NaCl base and bombardment of polycrystalline Ge films (applied to bases heated to 400°C) with N^+, Ar^+, and Xe^+ ions. The ion energy was $E = 50$ keV and the dose was $6 \cdot 10^{15}$ ions $\cdot$ cm^{-2}. The dose for the Xe^+ ions was $6 \cdot 10^{12}$ ions/cm^2. The vacuum in the target region was no less than $2 \cdot 10^{-5}$ torr. The films were irradiated directly on the bases. The film thickness was 200-500 Å.

It can be seen from an analysis of the radial distribution curves (Fig. 1 and Table 1) that the curves were almost totally identical regardless of the method used to produce the amorphous films. Thus, the first and second peaks lie at distances close to those for crystalline Ge (2.45 and 3.97 Å). The areas under the first two peaks indicate that the coordination numbers in the first and second coordination spheres are approximately 4 and 12, i.e., the same as in crystalline Ge. This shows that the short-range structure of amorphous Ge remains the same as in crystalline Ge. There is no such complete correspondence between the atomic positions in the crystalline and amorphous phases for other coordination spheres. For example, the radial distribution curves (see Table 1) contain no peak corresponding to the 4.65 Å distance in crystalline Ge, but there is a peak for the 5.03-5.07 Å distance, which is absent in crystalline Ge. Hence it follows that amorphous Ge is composed of material with a diamond-type structure and distances identical to those in crystalline Ge; a similar situation is observed for amorphous Si (see ref. 3) produced by different methods. However, the radial distribution curve for Si contains no peak corresponding to the 4.5 Å distance for crystalline Si, although there is a peak for 4.65 Å, which is absent for crystalline Si.

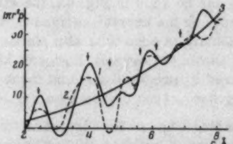

Fig. 1. Radial distribution curves for amorphous germanium films. 1) Films obtained by vacuum deposition; 2) films produced by ion bombardment, the arrows indicating the interatomic distances in crystalline germanium; 3) $4\pi r^2\rho_0$.

Coleman and Thomas[4] analyzed the radial distribution curves for Si and concluded that amorphous Si consists of 60% of a material whose structure corresponds to a diamond-type structure and 40% of a structure in which the

TABLE 1

Positions of maxima in radial distribution curve for amorphous Ge, Å					Inelastic distances in crystalline Ge
sublimation		ion bombardment			
our data	data from ref. 2	Ar^+	N^+	Xe^+	
2.47	2.41—2.54	2.45	2.43	2.49	2.43
4.09	3.95—4.14	4.12	3.96	4.05	3.97
—	—	—	—	—	4.65
5.03	—	5.07	5.05	5.05	—
—	5.60	—	5.74	—	5.62
5.92	5.95—6.16	5.95	—	6.00	6.12
6.80	6.80	—	—	—	6.87
7.60	7.30	7,15	7.25	7.60	7.31

atoms are arranged in a pentagonal dodecahedron. The same structure has been postulated for amorphous Ge.

Proceeding from an analysis of the diffraction patterns and electron micrographs of amorphous Ge deposited in a vacuum on an NaCl base, Mader[6] showed that an amorphous Ge film is a conglomerate of particles ranging in size from 50 to 100 Å. These particles consist of different numbers of primary and secondary twins. The twins are oriented around the common [110] direction and form pentagonal rings. Formation of pentagonal rings has been found[7] to be facilitated by the presence of defects (clusters, microvoids, etc.).

The probability of pentagonal-ring formation apparently increases during ion bombardment of a semiconductor into which a sufficiently large number of defects has been introduced. Figure 2 is a diagram showing the formation of pentagonal rings from the hexagonal rings characteristic of structures of the diamond type. When atom A is knocked out of a lattice point by an incoming ion, the atoms located in positions B draw as close together as is permitted by the rigidity of their bonds. This approximation naturally becomes easier as defects accumulate, since rotation of the tetrahedra of Ge atoms becomes possible. The formation of pentagonal rings and their adaptation to an architecture with a basic hexagonal motif evidently leads to appearance of a new Ge–Ge (Si–Si) distance of about 5 Å (4.65 Å) in the structure of amorphous Ge (Si); this distance is observed in all radial distribution patterns, regardless of the method used to produce the amorphous Ge. Bombardment leads to disappearance of the 4.65 and 6.87 Å distances between the Ge atoms in positions A and C and positions A and D (see Figs. 1 and 2 and Table 1).

We can thus state that the structure of amorphous germanium films produced by vacuum deposition consists of a mixture of hexagonal rings (i.e., a structural characteristic of the diamond type, which is retained) and pentagonal rings; the structure of amorphous germanium produced by ion bombardment at the "amorphization dose" consists predominantly of pentagonal rings. This means that an average of one atom is knocked out of each hexagon during amorphization, which corresponds to a concentration of ~17 at.%. It follows from the data obtained in a theoretical calculation of the vacancy distribution curves[8] that the amorphization dose corresponds to a vacancy concentration of ~$7 \cdot 10^{21}$ cm^{-3} or 16 at.%, i.e., the agreement is quite satisfactory.

The literature usually considers two possible amorphization mechanisms. In the first mechanism, the crystalline state becomes unstable at a certain critical concentration and structural reorganization occurs. The other mechanisms consist of ion-decelerating regions of local melting (thermal peaks), which solidify within a very short time (10^{-11}–10^{-12} sec). Crystallization cannot occur over so short a time, so that the structure of the liquid or some intermediate state becomes fixed (partial crystallization). This mechanism was proposed by the present authors[9] and later by Parsons.[10]

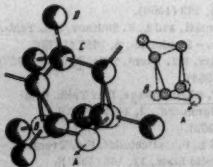

Fig. 2. Diagram representing formation of pentagonal rings in diamond-like structure during ion bombardment.

In order to decide which mechanism is preferable, we established the short-range structure of amorphous Ge films produced by bombardment with Ar^+ ions.[11] It was found that, as for crystalline Ge, the first coordination sphere has a radius of 2.45 Å in this case and is characterized by a tetrahedral configuration, in contrast to the octahedral configuration in liquid Ge (with r = 2.7 Å). Similar results were obtained when polycrystalline Ge films were bombarded with N^+ and Xe^+ ions (see above).

Thus, if we assume that amorphization occurs through local melting in thermal-peak regions, we must also assume that there is time during the existence of a thermal peak (10^{-11}–10^{-12} sec) for the atomic regrouping necessary to reduce the coordination number from 8 to 4, which is improbable. The only serious argument in favor of this mechanism is the appearance of individual amorphous inclusions preceding formation of a continuous amorphous layer. However, the inclusions in question may be associated not with thermal peaks, but with coagulation of radiation defects, e.g., at impurity atoms.

If we assume amorphization to be associated with accumulation of radiation defects, there must be a relationship between the parameters characterizing amorphization and those characterizing defect formation. We have demonstrated[12] that such a relationship exists for bombardment of Ge and Si with boron and phosphorus. It was also found that, within rather wide limits, the "amorphization dose" corresponding to formation of a continuous amorphous layer is inversely proportional (for both Ge and Si) to the vacancy concentration n_0 at the surface resulting from 1 ion/cm². This indicates that amorphization of Ge and Si begins after a definite defect concentration has accumulated, being to some extent independent of the irradiation conditions.

Thus, our experimental data support the first mechanism, i.e., amorphization apparently proceeds primarily through accumulation of defects, and show that the main patterns observed during ion bombardment can be accounted for within the framework of theories of point defect formation, without calling on the thermal-peak hypothesis. In connection with the foregoing, it should be noted that, in speaking of amorphization as proceeding through accumulation of point defects, we have always, in opposition to Pridachin and Smirnov,[13] kept in mind that defect accumulation need not necessarily occur in the form of Frenkel defects (see, for example, ref. 14); the latter are very mobile even at low temperatures and can exist for only a short time,[15] after which they associate into more complex, stable defect aggregates (divacancies, trivacancies, microvoids, etc.[16,17] No matter what the formation mechanism of complex defects and their form (VV centers,[18] in which uncompensated vacancies or other types of defects play the dominant role) immediately before amorphization, their numbers should depend on the initial concentration on Frenkel defects formed during bombardment. It follows from the above that accumulation of a large defect concentration, sufficient for amorphization of the crystal, is quite possible. The assertion made by Pridachin and Smirnov[13] is apparently based on the fact that, in calculating the distribution of radiation induced point defects by the Monte Carlo method,[8] we did not take into account their recombination, the probability of which can be rather high, despite the existence of a repulsion barrier in some cases.[19,20]

Taking into account the recombination would scarcely alter the qualitative ratio between the defect concentrations in different cases. The situation is different if the calculations do not take into account, for example, the vaporization of the target under the action of the incident ion beam. The occurrence of vaporization can in some cases lead to a rather high defect concentration at the surface and can cause amorphization to take place not only in the region of the vacancy-distribution maximum,[12] but also in the layer of the crystal directly beneath the surface. During vaporization, vacancies not compensated by interstitial atoms accumulate near the surface. Vaporization alone cannot account for formation at the surface of an amorphous layer whose thickness reaches several hundred angstroms, since the detached atoms penetrate to a depth of the order of several angstroms.[21] However, formation of vacancies at the surface during atomization (and other processes as well) leads to development of additional elastic stresses in the lattice[22] and causes the uncompensated vacancies in the interior of the specimen to move into the stressed layer below the surface.[23]

We also made an electron-diffraction analysis of Ge and Si layers made amorphous by ion bombardment and annealed. It was found that crystallization of Ge occurs at 400-500°C and crystallization of Si at 600-700°C (with an annealing time of 0.5 h). This is in agreement with the data in the literature.[24]

Crystallization becomes somewhat more difficult as the irradiation dose and ion mass increase, although the difference in crystallization temperature is small (~50°). The dependence on ion mass is understandable. We previously showed[12] that the degree of short-range ordering decreases with increasing mass, so that there is a decrease in the number of sufficiently large, highly ordered regions that can serve as crystallization centers.

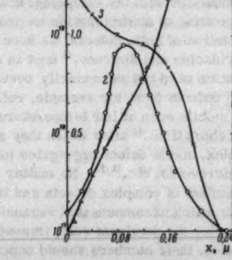

Fig. 3. Dimensionless parameter $\eta = x/2(Dt)^{1/2}$ for In^{114} (1), vacancy distribution (2), and In^{114} distribution (3) as functions of depth x.

The delay in crystallization at large doses indicates that, as the dose increases, the amorphous layer undergoes accumulation of an excess concentration of vacancies, comparatively large defects of the cluster type, or micropores, some of which form ordered aggregates (manifested as dislocations) during annealing. These defects serve as obstacles to crystallization. This is responsible for the fact that the amorphous layer retains a larger number of defects after crystallization at large doses than at small doses,[25] i.e., the structure does not return to its original state even with very high annealing temperatures. This is illustrated by our experiments on the diffusion of Ge^{71} and In^{114} in Si preliminarily subjected to bombardment with Ar^+ ions having an energy E = 100 keV in a dose of $6 \cdot 10^{15}$ ions/cm^2. Diffusion was conducted at 1000°C for 1 h. Figure 3 shows the dimensionless parameter $\eta = x/2(Dt)^{1/2}$ as a function of x for In^{114}. The quantity η was determined from the experimental data obtained in calculating the diffusion constants by the method of Gruzin et al.[26] This figure also shows the defect distribution after ion bombardment with Ar^+ and the In^{114} distribution after diffusion in the irradiated layer.

It can be seen from Fig. 3 that accelerated diffusion can occur in the vicinity of the defect-distribution maximum. This also indicates that, despite recrystallization of the amorphous layer, complete annealing up of defects does not take place even at high temperatures.

---

[1] L. I. Tatarinova, Tr. Inst. Kristallogr. Akad. Nauk SSSR, 11, 104 (1955).
[2] H. Richter and G. Breitling, Z. Naturforsch., a13, 988 (1959).
[3] S. C. Moss and J. F. Graczyk, Phys. Rev. Lett., 23, 1167 (1969).
[4] M. V. Coleman and D. J. D. Thomas, Phys. Status Solidi, 24, K111 (1967).
[5] R. Grigorovici and R. Manaila, Thin Solid Films, 1, 343 (1967/68).
[6] S. Mader, J. Vacuum Technol., 9, 247 (1971).
[7] M. H. Brodsky, J. Vacuum Technol., 9, 125 (1971).
[8] P. V. Pavlov, D. N. Tetel'baum, E. I. Zorin, and V. I. Alekseev, Fiz. Tverd. Tela, 8, 2679 (1966) [Sov. Phys. – Solid State, 8, 2141 (1967)].
[9] P. V. Pavlov, E. I. Zorin, D. I. Tetel'baum, and Yu. S. Popov, Fiz. Tverd. Tela, 6, 3222 (1964) [Sov. Phys. – Solid State, 6, 2577 (1965)].
[10] J. P. Parsons, Phil. Mag., 12, 1159 (1965).
[11] P. V. Pavlov and D. I. Tetel'baum, Dokl. Akad. Nauk SSSR, 175, 823 (1967) [Sov. Phys. – Dokl., 12, 746 (1968)].
[12] A. I. Gerasimov, E. I. Zorin, P. V. Pavlov, and D. I. Tetel'baum, Dokl. Akad. Nauk SSSR, 192, 324 (1970) [Sov. Phys. – Dokl., 15, 430 (1970)].
[13] A. B. Pridachin and L. S. Smirnov, Fiz. Tekh. Poluprov., 5, 166 (1971) [Sov. Phys. – Semicond., 5, 142 (1971)].
[14] P. V. Pavlov, E. I. Zorin, and D. I. Tetel'baum, Proc. Conf. Radiation Effects on Semiconductor Components, Toulouse, France, March, 1967: J. d'Electronique.
[15] J. Mackey and E. Klontz, Proc. Santa Fe Conf. Radiation Effects in Semiconductors, October 1967, Plenum Press, New York (1968); C. D. Watkins, Proc. Conf. Radiation Effects on Semiconductor Components, Toulouse, France, March 1967, J. d'Electronique.
[16] K. L. Brower, F. V. Vook, and J. A. Border, Appl. Phys. Lett., 16, 108 (1970).
[17] K. L. Merkle, Phys. Status Solidi, 18, 173 (1966).
[18] N. N. Gerasimenko, A. V. Dvurechenskii, and L. S. Smirnov, Fiz. Tekh. Poluprov., 5, 1700 (1971) [Sov. Phys. – Semicond., 5, 1487 (1972)].
[19] V. V. Khainovskaya and L. S. Smirnov, Fiz. Tverd. Tela, 9, 2043 (1967) [Sov. Phys. – Solid State, 9, 1603 (1968)].
[20] L. S. Smirnov, V. F. Stas', and V. V. Khainovskaya, Fiz. Tekh. Poluprov., 3, 1760 (1969) [Sov. Phys. – Semicond., 3, 1491 (1970)].
[21] P. Sigmund, Phys. Rev., 184, 283 (1969).
[22] V. M. Koshkin, Yu. A. Freiman, and L. P. Gal'chinskii, Fiz. Tverd. Tela, 11, 212 (1969) [Sov. Phys. – Solid State, 11, 165 (1969)].

[23] B. K. Bokshtein, S. Z. Bokshtein, Yu. S. Nechaev, A. A. Zhukhovitskii, S. T. Kishkin, and L. G. Kornelyuk, Dokl. Akad. Nauk SSSR, 183, 1280 (1968) [Sov. Phys. – Dokl., 13, 1231 (1969)].

[24] J. W. Mayer, L. Eriksson, and J. A. Davies, Ion Implantation in Semiconductors, Academic Press, New York–London (1970).

[25] L. N. Large and R. W. Bicknell, J. Mater. Sci., 2, 589 (1967).

[26] P. L. Gruzin, Yu. D. Zharov, S. V. Zemskii, and Yu. N. Polikarpov, Transactions of the Third All-Union Conference on Diffusion in Metals and Alloys [in Russian], Sovet Fiz. Tverd. Tela Akad. Nauk SSSR, Tul'sk. Politekhn. Inst., Tula (1968).

Study of liquid inclusions in a rocksalt crystal over the entire temperature range of their existence

Ya. E. Geguzin and A. S. Dzyuba
Khar'kov State University

(Submitted April 14, 1972; resubmitted September 18, 1972)
Kristallografiya, 18, 813-818 (July-August 1973)

We have investigated the behavior of a saturated aqueous solution of the matrix material in natural NaCl single crystals as a function of inclusion-crystallization temperature to levels exceeding the temperature of the critical state, at which the inclusion material enters the gaseous phase.

INTRODUCTION

Liquid and solid inclusions in minerals have been a subject for research by geologists for almost 150 years.[1-3] During the past two decades, gas–liquid inclusions in crystals have been investigated by crystal physicists,[4-6] whose studies have established certain patterns in the behavior of such inclusions under conditions where the crystal temperature varies and when the crystal is subjected to an external force field.

Our experiments were undertaken as a systematic investigation of the behavior of inclusions of a saturated solution of the matrix material in water over the entire temperature range of their existence, i.e., from the crystallization temperature of the inclusions to a temperature above the critical-state level, where the inclusion material is driven into the vapor state. We considered it wise to conduct such experiments in connection with the purely physical aspect of the problem of "inclusion–matrix" equilibrium conditions, taking into account the influence of the stresses that must develop in the matrix with varying temperature, and in connection with the practical interest which the results of such experiments hold for consideration of many problems arising in attempts to reproduce the previous history of a mineral on the basis of information gained in studying liquid and gaseous inclusions.

Our research subjects were single crystals of natural rocksalt from the Artemovskii deposit, which contained liquid inclusions. The main advantages of these crystals are the fact that the inclusions in them are rather large (10^{-3}–10^{-1} cm) and therefore convenient for experimentation, while the slight inhomogeneity of chemical composition for the natural inclusions does not make any fundamental difference in the establishment of general patterns.

EXPERIMENTAL METHOD

We made continuous observations of the liquid inclusions during heating and cooling, taking frame-by-frame motion pictures of the subject. The specimen was heated in an electric furnace and cooling was conducted on a metal stage connected to a copper rod, which was immersed in a Dewar flask of liquid nitrogen; the observations were made with an optical microscope.

The experiments in which the specimen was heated or cooled from room temperature will be described separately.

Heating. In the experiments where the specimen was monotonically and continuously heated at a rate of 1 deg/min, i.e., a sufficiently slow rate to permit establishment of thermal equilibrium in the specimen, we found that the inclusion volume increased slightly at first. At 370°C, a gas bubble developed within the inclusion and the inclusion and bubble volumes increased rapidly on further heating. At T > 395°C, enlargement of the bubble occurred as a result of attachment of numerous small gas bubbles, which developed throughout the entire inclusion volume. The inclusion was wholly filled with gas at 410°C. These observations are illustrated by a series of photographs (Fig. 1) and curves (Fig. 2).

In order to determine the deformation of the cavity containing the liquid inclusion, we conducted experiments in which the specimen was cooled to room temperature after heating to a temperature T. The volume of the gas

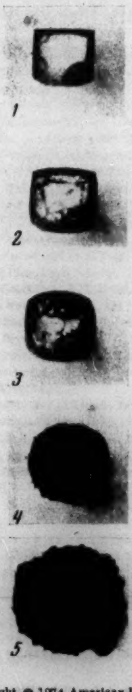

Fig. 1. Sequence of movie frames obtained during continuous heating of rocksalt specimen with inclusion liquid in original state, x25. 1) 24; 2) 320; 3) 370; 4) 390; 5) 410°C.

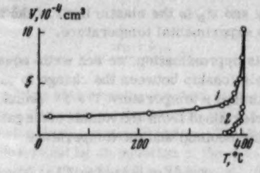

Fig. 2. Volume of inclusion cavity (1) and of gas bubble developing in it (2) as a function of temperature.

bubble that developed in this case was a precise quantitative measure of the change in cavity volume resulting from deformation of the matrix (Fig. 3). Figure 4 shows the dependence of the quantity $\Delta T_i = T - T_i$ on the temperature T in these experiments (T_i was the temperature at which the gas bubble developed). It is noteworthy that ΔT_i tended monotonically toward zero at the temperature where a gas bubble developed in the inclusion as a result of boiling of the solution.

The procedure described above was used to conduct experiments under ordinary atmospheric conditions and in an autoclave under an inert-gas pressure P = 120 atm (Fig. 5). The fact that a limiting value of ΔT (ΔT*) was detected in these experiments, no gas bubble developing after cooling from this level, was a natural consequence of the fact that the stresses produced during heating did not exceed the elastic limit of the crystal material.

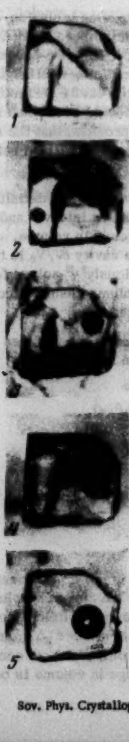

Fig. 3. Deformation of liquid-inclusion cavity during heating, x60. The size of the gas bubble in the inclusion was determined quantitatively after cooling of the crystal to room temperature. 1) 24; 2) 64; 3) 94; 4) 124; 5) 174°C.

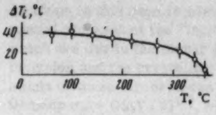

Fig. 4. Supercooling ΔT_i necessary for detachment of liquid within inclusion as a function of temperature.

Cooling. Experiments in which crystals were cooled revealed that crystallization of the inclusion material, which occurred over the temperature range from −40 to −50°C (the crystallization process was clearly detected from the blackening of the inclusion region resulting from diffusive scattering of transmitted light in the crystallized solution), led to an abrupt increase in cavity volume, which was accompanied by cracking of the matrix (Fig. 6). It was noted in these experiments that even inclusions located near one another crystallized at temperatures differing by a few degrees, which apparently indicates a difference in the chemical compositions of the solutions in the inclusions.

According to data obtained in experiments with a large number of inclusions, the change in cavity volume during crystallization of the inclusion material was $\delta V/V_0 = 1.4 \cdot 10^{-2}$. This value was found from the volume of the gas bubble formed after heating of the specimen.

CALCULATIONS

Heating of an inclusion-containing crystal is accompanied by a change in pressure at the "matrix–inclusion" boundary, as a result of the difference in the volumetric thermal coefficients of expansion for the inclusion and matrix materials and the dependence of the solubility of the matrix material in the inclusion on the temperature and pressure. Assuming that the temperature scale starts at $T = T_0$, where the pressure on the "inclusion–matrix" boundary is zero, and that the inclusion material is insoluble in the matrix material, we can write the following equations:

$$\delta_k = \frac{\Delta V}{V_0 \Delta T}\bigg|_k = \alpha_k + \omega_k \left(\frac{\partial n}{\partial T}\right)_P + \left[\omega_k \left(\frac{\partial n}{\partial P}\right)_T + \gamma_k\right]\left(\frac{\partial P}{\partial T}\right)_n, \tag{1}$$

$$\delta_i = \frac{\Delta V}{V_0 \Delta T}\bigg|_i = \alpha_i + \omega_i \left(\frac{\partial n}{\partial T}\right)_P + \left[\omega_i \left(\frac{\partial n}{\partial P}\right)_T - \gamma_i\right]\left(\frac{\partial P}{\partial T}\right)_n,$$

where $\alpha = (1/V)(\partial V/\partial T)_{P,n}$ is the coefficient of volume expansion, $\omega = (1/V)(\partial V/\partial n)_{T,P}$ is the atomic volume, $\gamma = (1/V)(\partial V/\partial P)_{T,n}$ is the compressibility factor, n is the number of matrix-material particles per unit inclusion volume, and the subscripts k and i refer to the materials of the matrix and inclusion respectively.

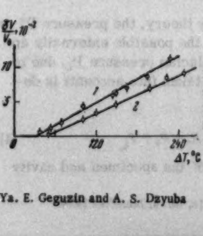

Fig. 5. Deformation of liquid-inclusion cavity in rocksalt $\delta V/V_0$ as a function of degree of heating ΔT from room temperature. 1) P = 1; 2) 120 atm.

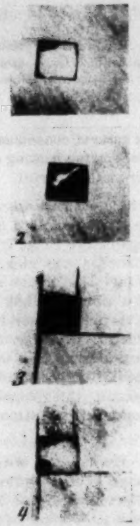

Fig. 6. Sequence of photographs obtained in the experiment involving cooling of NaCl crystal to the crystallization temperature of the solution filling the inclusion cavity, ×20. 1) 24; 2) 45.5; 3) 46; 4) 24°C.

The condition $\delta_k = \delta_l$, which means that there is no discontinuity at the inclusion–matrix boundary, yields an expression defining the temperature function of the pressure at this boundary before initiation of possible stress relaxation in the matrix and inclusion:

$$\left(\frac{\partial P}{\partial T}\right)_n = \frac{\Delta\alpha + \Delta\omega(\partial n/\partial T)_P}{\gamma_l + \gamma_k - \Delta\omega(\partial n/\partial P)_T} = \psi, \tag{2}$$

where $\Delta\alpha = \alpha_l - \alpha_k$, $\Delta\omega = \omega_l - \omega_k$.

Assuming that the constants defining $\partial P/\partial T$ vary only slightly with temperature, Eq. (2) can be used to estimate the minimum heating ΔT^* at which irreversible deformation of the matrix begins:

$$\Delta T^* = T^* - T_0 = P^* / \psi, \tag{3}$$

where P^* has the sense of the pressure applied to the inner surface of the cavity such that the entire crystal is in a state of plastic flow. Strictly speaking, the cavity can be deformed when part of the matrix remote from the cavity is in a state of quasiviscous flow.[7] However, as experimentation has shown, the pressure relaxes so rapidly in the case of a liquid inclusion and not overly high temperatures that the basic mechanism is apparently plastic rather than quasiviscous flow.

As follows from plasticity theory, the pressure P^* in which we are interested (with the possible externally applied pressure P_0 and the Laplacian pressure P_L, due to the curvature of the boundary taken into account) is defined by the relationship[8]

$$P^* = 2\sigma_s \ln R / R_0 + P_0 + P_L, \tag{4}$$

where R and R_0 are the radii of the specimen and cavity respectively and σ_s is the elastic limit of the matrix material at the experimental temperature.

With this approximation, we can write equations defining the relationship between the change in cavity volume on heating to a temperature $T > T^*$ (which can be precisely determined from the volume of the gas bubble, v, formed during cooling) and the temperature

$$v = \delta V = V_0 \psi \gamma_l (T - T^*). \tag{5}$$

Equation (5) expresses the obvious fact that the pressure in the liquid drops to zero when the cavity volume increases to an extent equal to the decrease in liquid volume due to the pressure.

Equations (4) and (5) can be used to make an independent determination of the constant ψ from data on the shift in ΔT^* under pressure and from data on $\delta V/V_0$ as a function of temperature (see Fig. 5). Assuming $P_L = 0$ and $\gamma_l = 4 \cdot 10^{-11}$ cm²/dyn, both methods yield the same value, $\psi = 8 \cdot 10^6$ dyn/cm² · deg.

Direct calculation of ψ from Eq. (2), using the tabulated data on the constants for the H_2O–NaCl system ($\omega_l = 3.3 \cdot 10^{-23}$ cm³, $\omega_k = 4.1 \cdot 10^{-23}$ cm³; $\gamma_l = 4 \cdot 10^{-11}$ cm²/dyn, $\gamma_k = 8 \cdot 10^{-12}$ cm²/dyn; $\alpha_l = 4.14 \cdot 10^{-4}$ deg⁻¹, $\alpha_k = 1.21 \cdot 10^{-4}$ deg⁻¹; $\partial n/\partial T = 6.54 \cdot 10^{18}$ cm⁻³ · deg⁻¹, and $\partial n/\partial P = 13.2 \cdot 10^{12}$ dyn⁻¹ · cm⁻¹), yields $\psi = 5 \cdot 10^6$ dyn/cm² · deg, which is close to the value we obtained.

Let us now consider the cooling of an inclusion-containing crystal to the crystallization temperature. Cooling is accompanied by development of negative pressure in the inclusion, its magnitude determining whether the liquid undergoes detachment from the cavity surface or internal separation. A gas bubble should be formed in the cavity in both cases, obviously provided that the required negative pressure in the liquid is achieved before the liquid crystallizes.

Assuming that crystallization occurs at a definite temperature and not over a temperature interval and that it is accompanied by an abrupt increase in volume, we can calculate the deformation of the cavity $\delta V/V_0$ in this case. A similar problem was previously[9,10] solved for the case in which the increase in volume resulted from local melting rather than crystallization.

Using the equality of the changes in the volumes of the cavity and the liquid crystallizing in it,

$$\begin{aligned} \frac{\Delta V}{V_0}\bigg|_{k} &= (1 - \delta_k \Delta T)\gamma_k P(\varkappa), \\ \frac{\Delta V}{V_0}\bigg|_{l} &= (1 - \delta_l \Delta T)[\varkappa - \gamma_{lk} P(\varkappa)], \end{aligned} \tag{6}$$

we readily obtain an expression defining the quantity $P(\varkappa)$:

$$P(\varkappa) = \frac{b}{a\gamma_k + b\gamma_{lk}}\varkappa. \tag{7}$$

In Eqs. (6) and (7), $T = T_0 - T_C$ (T_C is the crystallization temperature), $\varkappa = (V_t - V_L)/V_L$ is the change in volume during crystallization, γ_{lk} is the compressibility factor of the crystallized phase, i.e., ice, $a = 1 - \delta_k \Delta T$, and $b = 1 - \delta_l \Delta T$. Plastic deformation of the crystal occurs only when $P(\varkappa) > P^*$ or, if the change in volume is positive, $\varkappa > \varkappa^*$:

$$\varkappa^* = \frac{a\gamma_h + b\gamma_m}{b} P^*. \tag{8}$$

The deformation of the cavity consists of two components in this case: the compression during cooling and the abrupt expansion during crystallization. The first component is described by an equation of the type of Eq. (5) and the second is determined from Eqs. (6)-(8). The resultant change in volume is

$$\left.\frac{\delta V}{V_0}\right|_h = \frac{ab\gamma_h}{a\gamma_h + b\gamma_m}(\varkappa - \varkappa^*). \tag{9}$$

Calculation of the value of $\delta V/V_0$ from Eqs. (8) and (9) yields excellent agreement with experimental data.

It should be noted that this calculation was made without including the fact that crystallization is not instantaneous but involves movement of the crystallization front. Taking account of this factor can introduce corrections into the calculation, since the relaxation conditions for the stresses produced may be different.

CONCLUSIONS

Our experiments with NaCl single crystals indicate that, when a crystal containing a liquid inclusion located far from the outer surface of the crystal and various internal defects is heated, no macroscopic cracks through which part of the liquid phase might escape are formed in the deformed matrix. We observed that relaxation of the resultant pressure is accompanied by high-temperature creep of the matrix at a rate that decreases with time. This is naturally explained by the character of the stress pattern and the high crystal plasticity at temperatures of 300-400°C.

A somewhat different situation is created during crystallization of a liquid inclusion. The stress pattern that develops in this case is complicated by additional tangential stresses at the "inclusion–matrix" boundary, which are due to the planar junction of the crystallized inclusion and the crystalline matrix. The order of magnitude of these stresses can be estimated from the relationship $\sigma_T \sim G(\Delta V/V)^{1/3}$, where G is the shear modulus of the crystal and $(\Delta V/V)^{1/3}$ is the linear dilatation at the boundary resulting from crystallization of the inclusion. Since $G \simeq 10^{11}$ dyn/cm^2 and $\Delta V/V \simeq 3 \cdot 10^{-2}$, $\sigma_T \simeq 5 \cdot 10^{10}$ dyn/cm^2. We became convinced of the actuality of these stresses in conducting experiments in which a liquid drop was crystallized on a flat crystal surface. Microcracks and an enormously high dislocation density were detected beneath the crystallized drop. At temperatures between −20 and −50°C, where the matrix plasticity is low, these stresses lead to cracking. Under our experimental conditions, these cracks did not absorb a noticeable amount of the liquid phase after heating to room temperature.

It should be emphasized that these conclusions are not universal and apply principally to cases in which the ratio of the inclusion and matrix constants is such that cracks develop in the matrix when the crystal is heated.

---

[1] N. P. Ermakov, Investigation of Mineral-Forming Solutions [in Russian], Izd. Khar'kovsk. Univ. (1950).

[2] F. G. Smith, Geological Thermometry based on Inclusions in Minerals [Russian translation], Izd. IL, Moscow (1956).

[3] D. N. Khitarov, in: Mineral Microinclusions [in Russian], Nauka, Moscow (1965), p. 74.

[4] G. G. Lemmlein, Dokl. Akad. Nauk SSSR, 72, 775 (1950); 78, 685 (1951); 85, 325 (1952); 87, 957 (1952).

[5] T. R. Anthony and H. E. Cline, Phil. Mag., 22, 893 (1970); 24, 695 (1971); J. Appl. Phys., 42, 3380 (1971).

[6] H. E. Cline and T. R. Anthony, Acta Metallurg., 19, 175 (1971); 19, 491 (1971).

[7] Ya. E. Geguzin, A. S. Dzyuba, and A. M. Kosevich, Fiz. Tverd. Tela, 5, 2219 (1963) [Sov. Phys. – Solid State, 5, 1615 (1964)].

[8] L. M. Kachanov, Principles of Plasticity Theory [in Russian], Moscow (1969), p. 103.

[9] I. M. Lifshits and L. S. Gulida, Dokl. Akad. Nauk SSSR, 87, 377 (1952).

[10] L. S. Gulida and I. M. Lifshits, Dokl. Akad. Nauk SSSR, 87, 522 (1952).

Transformation of layer-spiral growth into normal growth on a basal face.
I. Breakdown of the elementary layers on the apices of the spiral hillocks

E. D. Dukova

Institute of Crystallography, Academy of Sciences of the USSR

(Submitted August 10, 1972)
Kristallografiya, 18, 819-825 (July-August 1973)

The change in the slopes of spiral growth hillocks at different layer heights with change in supersaturation on crystals of p-toluidine has been studied experimentally. It has been found that for each spiral layer there is a characteristic limiting angle of slope, after which breakdown of the layer at the apex and transformation of the cone-shaped hillock into a hillock with a flat top take place. The limiting angle for the elementary spiral has been found, and the surface energy of the edge of the step has been estimated; the value found is $2 \cdot 10^{-3}$ ergs/cm^2, which confirms the possibility of breakdown of the elementary layers at the apices of the spiral hillocks.

INTRODUCTION

The growth of a close-packed face by the dislocation mechanism should lead to the formation of layer-spiral growth hillocks, the slope of which increases with increase in the supersaturation.

It has been found,[1] however, that in the growth of diphenyl from the gaseous phase close to the melting point at supersaturations $\sigma > 10^{-3}$, the growth of the (001) face took place without the deposition of layers visible in the optical microscope and with kinetic parameters corresponding to normal growth. At $\sigma < 10^{-3}$, growth hillocks appeared on the face, but steps either did not appear at all or appeared as concentric microsteps on the slopes of the hillocks. A spiral center formed at even smaller supersaturations. According to dislocation theory, the curvature of the hillock is related to the rate of rotation of the step around the dislocation, which should increase with increase in supersaturation, but the state of the microstep should also change at the same time.

The present paper describes a study of the behavior of spiral hillocks from the viewpoint of the change in their slopes and the heights of their components layers with change in the supersaturation.

PUBLISHED DATA

A fairly large amount of material on the observation and measurement of growth spirals on the faces of crystals of different substances, growing from the gaseous phase, solution, or solution in melts, has now accumulated. In a review of the literature devoted to spiral growth, we examined work in which the heights h of the spiral layers were measured and photographs of these spirals were given, together with the magnification. From the photographs we measured the average distance between the turns of the spiral y_0. The ratio h/y_0 was used to determine the angle of slope of the spiral hillock. The spiral hillocks for the substances listed in Table 1 were measured in this way. A total of approximately 80 hillocks were measured. The graph in Fig. 1 gives the dependence of the angle of slope of the spiral hillocks $\tan \varphi = h/y_0$ on the height of the component step. It can be seen that the flattest hillocks are those with elementary steps $h < 20$ Å ($\tan \varphi = h/y_0$ has values between $\sim 10^{-5}$ and $\sim 4 \cdot 10^{-3}$ for different substances). On the whole there is a tendency for the angle of slope of the hillocks to increase with increase in the height of the step. This fact in itself is rather curious. If it is assumed that the elementary steps represent the final product of the breakdown of thick steps and that they exist unchanged on the basal face, the slopes of the elementary hillocks should not be the most flat. The slopes of the end faces of the steps also differ considerably from 90°, however. It has been shown by multiple-beam interferometry that in $BaTiO_3$ crystals,[8] steps with height ~200 Å have a slope of 1/300, that is $\tan \varphi \sim 3 \cdot 10^{-3}$. In the diamond crystal,[9] a step with height ~100 Å occupies an extended range of $\sim 5 \cdot 10^{-4}$ cm, so that its slope is $\tan \varphi \sim 2 \cdot 10^{-3}$. With increase in the supersaturation the distance between the turns of the spiral should decrease, and its slope will become steeper, but the thick steps will break down into thinner steps. Is it then possible for steep dislocation hillocks with an angle of slope much greater than the slope of the end face of the step to be produced?

Spiral hillocks in which the elementary layers are at the same time monomolecular (unit cell dimension along the c axis equal to one molecule) have been observed[7] on crystals of the paraffin $C_{39}H_{80}$. The authors cited present electron micrographs. These hillocks are also the steepest for the given layer heights ($h = 45$ Å, $\tan \varphi \sim 6 \cdot 10^{-3}$). Together with these hillocks there are photographs of steeper hillocks ($h/y_0 > 10^{-2}$), but hillocks of this last kind with flat tops, and not cone-shaped apices, are not

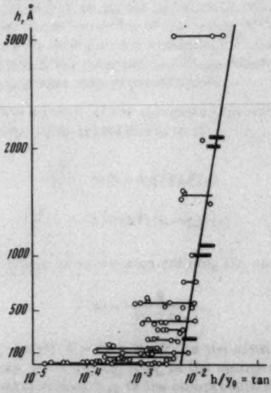

Fig. 1. Dependence of the angle of slope of the spiral hillocks on the height of the component step for the substances listed in Table 1.

TABLE 1

Substance, crystallization conditions, and references	Height of step h, 10^{-8} cm	Distance between turns y_0, 10^{-4} cm	$\frac{h}{y_0}$, 10^{-4}
Silicon carbide SiC, vapor (mixture)[2,3]	~5	7	~0.1
	51.9	8,2	~0,6
	375	14	2,6
	381	30	1,2
	485	68	7.1
	378	32	1.1
	376	53	1.4
	1493	50	30
	2191	115	14
	15	50	0.03
	15	20	~0.1
	620	42	1.5
	165	30	0,53
	15	10	0.15
Hematite Fe_2O_3, vapor[3,4]	14	10	0.14
	65	19	0,32
	1600	20	8
	12.4	20	0.06
	17.2	10	0.172
	11.5	0.8	~1
Silver, vapor[5]	5	8	~0.1
Beryllium, solution[6]	5	4	0.11
	20	4	0.5
	7.9	38	0.02
	20	4	0.2
Paraffin $C_{29}H_{60}$, solution[7]	45	0.7	6
	45	5	8
	45	0.8	5.6
	45	0.33	14
	45	2	22
Stearic acid $C_{17}H_{35}COOH$, solution[7]	47	5	9
	47	1	4.5
$BaTiO_3$, solution in melt[8]	204	50	0.4
	482	50	0.9
			3
Diamond, solution in melt[9]	100	15	0.66
	100	5	2
Sodium niobate, solution in melt[10]	137	100	0.137
	589	60	0.9
	~140	7	2
Synthetic ruby, mixture[11]	12.9	22	0.058
	5.62	0.2	2.81
NaCl, vapor[12,13]	2.81	0.25	1.13
	5,62	0.17	3.30
	5,62	0.16	3.40
Graphite, mixture[14]	500	~4	~10
Titanium, electrocrystallization from solution[15]	340	4	8
	340	7,5	11.5
	340	10	3.4
	240	4	6,0
	240	7,5	3.2
	240	10	2.4
	140	4	3,5
	140	7,5	1.6
	140	10	1.4
CdI_2 (refs. 16 and 17)	756	9	8
	756	7	10.9
CdI_2(ref. 18)	294	4	7.3
	246	2.3	~10
	1000	10	~10
Magnesium, sublimed in a stream of Ar[19]	10—20	12	0.1—0.16
Magnesium, vapor[19]	20	5	0.4
Cadmium, vapor[19]	5	3	0.17
Zinc, vapor[19]	~100	7	1.7
Gold, growth from a mixture[20] with conc. HCL	400±100	~3	~10
	100	1.3—1.5	~6
Platinum, on muscovite from $PtCl_4$ solution[21]	10	5	0.2
Lithium sulfate, solution[22]	3000	44	6.8
	3000	22	13.6
	3000	11	2,72
Magnetoplumbite, solution in melt[23]	48	5.4	~0.8
	163	~5.4	~3
ZnS, natural[24]	~500	12	4,2
Synthetic quartz, solution[25]	20	8	0.25
Cu_2O on a Cu crystal, copper surfate solution[26]	5	0.5	~1
	100	11	~9
Glass, corrosion[27]	500	27	1.8

Table 1 (continued)

Substance, crystallization conditions, and references	Height of step h, 10^{-8} cm	Distance between turns y_0, 10^{-4} cm	$\frac{h}{y_0}$, 10^{-4}
AlB_2, mixture[28]	200	11	1.70
β-Methylnaphthalene, solution[29]	55.2	8	0.65
SbSI, vapor	10	10	~0.1

present. It is found that spiral hillocks appear during the growth of crystals by evaporation of a solution at room temperature. If the temperature of the solution is increased by 10-15°C (so that the rate of evaporation and the supersaturation are increased), the spiral hillocks disappear, and hillocks with flat tops and rounded contours appear. This means that the production of a flat top is associated with the production of rounded contours, that is nonsingular surfaces, and this possibly leads to the disappearance of the dislocations.

CRITICAL SLOPE OF A SPIRAL HILLOCK AND THE FORMATION OF A FLAT TOP

We carried out experiments with p-toluidine to investigate the change in the spiral growth hillocks under conditions of a slight increase in vapor pressure. The rate of growth at the center of the spiral hillocks on these crystals was studied earlier, and it was found that in the range where the dependence of the rate of growth on the supersaturation is nonlinear, the rate of growth is higher at the center of a hillock with a higher spiral layer, so that the spiral cone is steeper in this case.[30] In the present work this process was studied from the point of view of the change in the slopes of the spiral hillocks and the heights of the component layers with further increase in the supersaturation, by means of color cinematography under conditions in which the crystals exhibit first- or second-order interference colors. The observations showed that the spiral growth hillocks do not retain a constant cone-shaped form with increase in the vapor pressure. At first the spiral increases its rate of rotation around the center, after which it breaks down into thinner layers, and finally in the center the layers become imperceptible, forming an almost flat surface. The thin spiral layers break down first, followed by the thicker layers. Frames from a color motion-picture film* demonstrating this process are shown in Fig. 2a-d. The following quantities were measured from the frames of the color motion-picture-film: the height H of the spiral hillock at its center, the radius of the base of the hillock l, the angle of slope H/l, the number of layers n making up a spiral hillock, and the average height of a layer h. The method described made it possible to measure spiral layers with a height from 200 Å (~10 elementary parameters) to 3000 Å. Table 2 gives as an example the successive measurements for two spiral hillocks for five increasing values of the supersaturation.

If the formation of a visually flat top with radius l_1 were associated simply with the disappearance of visible layers around the center of the hillock with preservation of the cone

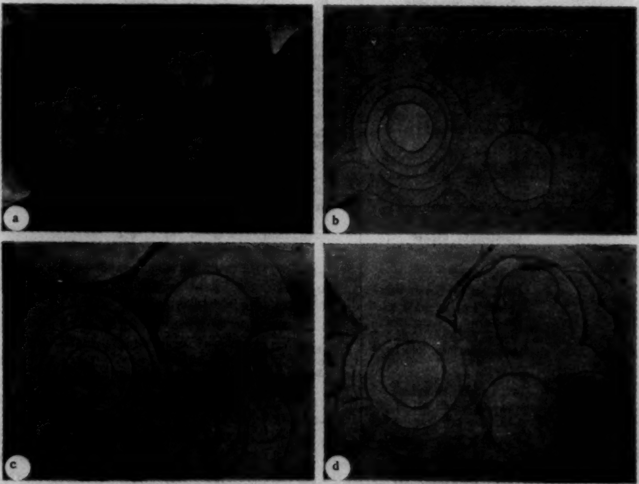

Fig. 2. Transformation of spiral hillocks into hillocks with flat tops on crystals of p-toluidine (frames from a cinematographic film.*) x 400).

TABLE 2

No.	H, μ	l, μ	ΔH, μ	H/l, 10^{-3}	l_1	l_1H/l	n	h, Å
1	0.22	60	0.2	3.8	—	—	10	220
2	0.34	60	0.2	5.6	—	—	15	220
3	0.53	60	0.2	8.9	—	—	—	680
4	0.68	46	0.1	1.4	14	1.96	10	680
5	0.68	36	0.1	1.9	26	5.00	8	800
1	2.03	138	0.1	1.48	—	—	9	2900
2	2.62	151	0.2	1.73	—	—	10	2600
3	3.35	157	0.25	2.11	—	—	15	2200
4	3.35	125	0.4	2.68	40	1.18	10	3350
5	3.35	108	0.4	3.14	60	1.88	9	3700

formed by elementary steps invisible in the microscope, the change in color around the apex of the hillock would be appreciable. In actual fact, the change in the heights within a flat region would amount to l_1H/l, which, as can be seen from Table 2, is much greater than the minimum in thickness ΔH detected from a change in color. After the formation of the limiting spiral cone (measurement 3 for both spirals) a new process – flattening of the apex – in fact begins (measurement 4). This flattening of the apex is accompanied by the disappearance of the macrosteps in the center and an increase in the average thickness of the remaining layers with increase in the angle of slope of the hillock with the flattened apex.

A photomicrograph of a spiral hillock with layer thickness ~3000 Å, and its transformation into a hillock with a relatively flat top, constructed from the data in Table 1, are represented in Fig. 3a. The scale used increases the height of the hillock by a factor of 10 relative to the magnitude of the base. A diagram illustrating the process of increase in the size of the layers after breakdown of the spiral in the center of the hillock and the formation of a flat top is shown in Fig. 3b.

The measurements given in Table 1 were made for spirals with different layer thicknesses. They can be represented in the form of a graph (Fig. 4). The graph gives the dependence of the average layer thickness h on tan φ, the angle of slope of the spiral hillock for each spiral. The hatched rectangles denote the angles of slope of spiral hillocks with the corresponding layer height. With increase in the vapor pressure (tan $\varphi \sim \sigma$), each spiral hillock (mean result from three or four measurements) attains a maximum angle and a minimum layer thickness (this is shown by the black rectangles in Fig. 4). A flat top then appears, and subsequently, as it grows, the angle of slope of the hillock with the flat top becomes steeper, and the average layer thickness increases (empty rectangles on the graph).

The limiting angle of the spiral hillock is linearly dependent on the corresponding step height (black rectangles). Transfer of these data to the graph in Fig. 1 indicates that the values of the limiting spiral angles for p-toluidine show satisfactory agreement with the highest values of the spiral cones of the crystals of other substances. The equation giving the dependence of the angle of slope of the critical spiral hillock on the height of its component step has the following form:

$$h = 3.12 \cdot 10^{-3}(h/y_0 - 7.5 \cdot 10^{-3}), \qquad (1)$$

where h is the height of the spiral layer, y_0 is the distance between the turns of the spiral, and $\tan\varphi = h/y_0 \sim 7.5 \cdot 10^{-3}$ is the critical slope of the elementary spiral. For p-toluidine crystals, solution of the kinetic problem[31] gives approximately the supersaturation at which spiral growth takes place when the method is used: $\sigma = \Delta P/P \sim 10^{-5}$. From this it is possible to estimate the surface energy of the edge of the elementary step when the spiral attains the critical angle according to the Frank–Barton–Cabrera theory:[32]

$$\gamma = kTa\sigma/4\pi \tan\varphi_1\Omega \sim 2 \cdot 10^{-3}\,\mathrm{erg/cm^2},$$

$$k = 1.38 \cdot 10^{-16}\ \mathrm{erg/deg},\quad T = 310°\,\mathrm{K},\quad a = 23.65 \cdot 10^{-8}\,\mathrm{cm},$$

$$\sigma \sim 10^{-5},\ \tan\varphi = 7.5 \cdot 10^{-3},\ \Omega = 1.57 \cdot 10^{-22}\,\mathrm{cm^3}.$$

From this estimate it can be seen that the surface energy of the step is extremely small for the step to be preserved[33] (for growth from the gaseous phase $\gamma \sim 40$–50 ergs/cm²). The step is apparently spread out and essen-

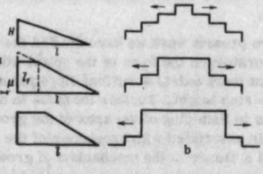

Fig. 3. Successive stages in the change in the shape of a spiral hillock with increase in the supersaturation (a) and a diagram illustrating the process of increase in the size of the layers after breakdown of the spiral in the center of the hillock (b).

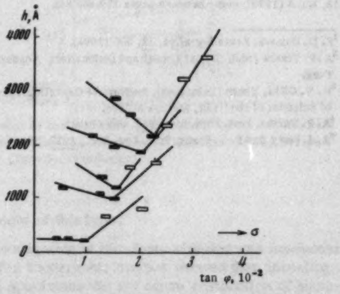

Fig. 4. Dependence of the average layer thickness on the angle of slope of the spiral hillock for crystals of p-toluidine.

tially begins to break down. Subsequently, growth of the hillock begins, and its apex now grows not by rotation of the step around the dislocation, but by a different mechanism, most probably normal.[34]

At the same time such low values of the linear energy of the steps may lead to a very low work of formation of the nuclei and the critical supersaturation for nucleus formation. In this case, nuclei of only the liquid phase on the end faces of the steps are apparently possible. The formation of an intermediate liquid phase may also influence the spreading of the steps and facilitate flattening of the apex. We shall examine this problem in the next part of the work.

In the present work we have studied the influence of supersaturation on the form of the spiral hillocks and have shown that there exists a critical slope for a hillock with a definite step height. Further increase in supersaturation leads to flattening of the apex of the growth hillocks, and this is associated with breakdown of the elementary steps and a change in the mechanism of growth.

The author thanks A. A. Chernov for discussion of the results of this work.

---

*Publisher's note: Figure 2 is reproduced here in black and white. Those wishing to inspect the color original are referred to Kristallografiya, Vol. 18, No. 4 (1973), insert between pages 820 and 821.

[1] E. D. Dukova, Kristallografiya, 12, 200 (1971).

[2] A. R. Verma (ed.), Crystal Growth and Dislocations Academic Press, New York.

[3] N. V. Gliki, Thesis [in Russian], Institute of Crystallography, Academy of Sciences of the USSR, Moscow (1953).

[4] A. R. Verma, Proc. Phys. Soc., B65, 806 (1952).

[5] A. J. Forty and F. C. Frank, Proc. Roy. Soc., A217, 262 (1953).

[6] L. J. Griffin, Phil. Mag., 41, 196, 199 (1950).

[7] N. G. Anderson and J. M. Dawson, Proc. Roy. Soc., A218, 255 (1953).

[8] N. V. Gliki and V. A. Timofeeva, Kristallografiya, 4, 908 (1959) [Sov. Phys. – Crystallogr., 4, 861 (1960)].

[9] S. Tolansky and I. Sunagawa, Nature, 184, 4698, 1593 (1959).

[10] N. V. Gliki and V. A. Timofeeva, Kristallografiya, 5, 105 (1960) [Sov. Phys. – Crystallogr., 5, 96 (1960)].

[11] S. Amelinckx, Compt. Rend., 234, 1793 (1952).

[12] M. Bethge, K. W. Keller, and E. Zieybr, J. Cryst. Growth, 3-4, 184 (1968).

[13] H. Bethge, Crystal Growth, Oxford (1966), p. 623.

[14] F. H. Horn, Nature, 170, 581 (1952).

[15] M. A. Steinberg, Nature, 170, 1119 (1952).

[16] A. J. Forty, Phil. Mag., 42, 670 (1951).

[17] A. J. Forty, Phil. Mag., 43, 72 (1952).

[18] A. J. Forty, Phil. Mag., 43, 377 (1952).

[19] A. J. Forty, Phil. Mag., 43, 949 (1952).

[20] S. Amelinckx, Phil. Mag., 43, 562 (1952).

[21] E. Votava, Naturwissenschaften, 40, 437 (1953).

[22] H. Rae and A. E. Robinson, Proc. Roy. Soc., 222, 558 (1954).

[23] R. A. Lefever and A. B. Chase, Nature, 190, 4772, 255 (1961).

[24] E. Votava, S. Amelinckx, and W. Dekeyser, Physica, 12, 1163 (1953).

[25] M. S. Joshi and S. Tolansky, Proc. Roy.Soc., 260, 1303, 475 (1961).

[26] F. W. Young, J. Appl. Phys., 27, 554 (1956).

[27] R. M. Tichane and L. B. Winson, J. Appl. Phys., 35, 2537 (1964).

[28] F. H. Horn, E. F. Fullam, and I. S. Kasper, Nature, 169, 927 (1952).

[29] M. I. Kozlovskiĭ and G. G. Lemmlein, Kristallografiya, 3, 351 (1958) [Sov. Phys. – Crystallogr., 3, 352 (1958)].

[30] A. A. Chernov and E. D. Dukova, Kristallografiya, 5, 655 (1960) [Sov. Phys. – Crystallogr., 5, 627 (1961)].

[31] E. D. Dukova and D. Nenov, Kristallografiya, 17, 1210 (1972) [Sov. Phys. – Crystallogr., 17, 1059 (1973)].

[32] Collection, Elementary Processes of Crystal Growth [Russian translation], Izd. IL, Moscow (1959).

[33] V. V. Voronkov and A. A. Chernov, Kristallografiya, 11, 662 (1966) [Sov. Phys. – Crystallogr., 11, 571 (1967)].

[34] A. A. Chernov, Physicochemical Problems of Crystallography [in Russian], Alma-Ata (1969), pp. 8-40.

Influence of heat treatment on the structural perfection of single crystals of gallium arsenide alloyed with tellurium

M. G. Mil'vidskii, V. B. Osvenskii, A. G. Novikov, V. G. Fomin, and S. P. Grishina

State Scientific-Research and Planning Institute of the Rare Metals Industry

(Submitted February 22, 1972; resubmitted August 7, 1972)
Kristallografiya, 18, 826-829 (July-August 1973)

Selective chemical etching, measurement of the Hall effect, a twin-crystal spectrometer, diffraction topography, and precise measurement of the lattice constant were employed to study the influence of heat treatment of gallium arsenide alloyed with tellurium on certain of its physical properties. It was shown that the observed structural transformations during different types of heat treatment were due to decay of a supersaturated solid solution accompanied by formation of second-phase pre-precipitation and precipitation regions.

Preliminary investigations[1] showed that crystals of gallium arsenide highly alloyed with tellurium exhibit a number of specific structural characteristics. These include the presence of small nondislocation etch pits, natural decoration of dislocations, and development of disoriented areas and stresses in crystals with carrier concentrations $n \geq 5 \cdot 10^{18}$ cm^{-3}. In addition, electron-microscope examination of such crystals revealed very small prismatic loops and areas of precipitation.[2,3] These experimental data enabled us to hypothesize that partial decay of a supersaturated solid solution occurs in such crystals when they are cooled from the crystallization temperature.

The present investigation was conducted to study the influence of heat treatment on certain physical properties of gallium arsenide crystals with a tellurium concentration N of more than 10^{19} atoms/cm^3.

Our research methods were selective chemical etching, measurement of the Hall effect, twin-crystal spectrometry, diffraction topography, and precise measurement of the lattice constant with reference to a standard.[4] The x-ray diffraction experiments were conducted with Cu Kα radiation and the 440 (twin-crystal spectrometer), 220 (diffraction topography), and 444 (precision lattice-constant measurement) reflections. The twin-crystal spectrometer was used to measure the width of the oscillation curves at 1/2, 1/4, and 1/8 of their height. The diffraction topograms were determined with $\mu t \geq 10$.

The specimens used in these investigations were cut along the (111) and (110) planes from crystals grown in the [111] direction by the Czochralskii method under a layer of flux; the dislocation density did not exceed 10^3 cm^{-2}, the Hall carrier concentration was $1 \cdot 10^{19}$ cm^{-3}, the oscillation-curve width and integrated reflection constant were higher than for the standard,[1)] and the 220 and $20\bar{2}$ topograms exhibited growth bands, whose contrast was independent of the indices of the reflection planes. The lattice constant was 5.65435 Å.

In order to drive the maximum amount of the alloying impurity into the solid solution, the crystals were subjected to homogenization treatment at 1100°C for 15 min and quenched in ethylene glycol. After this heat treatment, the specimens no longer exhibited anomalous transmission of x rays and there was an increase in the width of the oscillation curves (by a factor of almost 2) and in the integrated reflection constant for x rays; the lattice constant decreased to a = 5.65423 Å. The current-carrier concentration increased in this case (Fig. 1). Quenching of control (unalloyed) gallium arsenide specimens did not produce effects of this type.

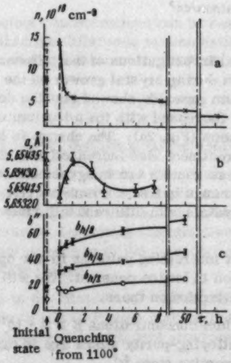

Fig. 1. Influence of heat treatment on the current-carrier concentration (a), the lattice constant (b), and the oscillation-curve width (c) of gallium arsenide alloyed with tellurium.

Our investigation of the decay kinetics was conducted at 700°C. The topographic studies showed that annealing of quenched specimens did not cause restoration of anomalous x-ray transmission, regardless of the annealing time.

As can be seen from Fig. 1, an increase in annealing time led to a monotonic decrease in the free current-carrier concentration and to a rise in the oscillation-curve width in comparison with the quenched state. We observed the largest increases in the width of the reflection curves at 1/8 and 1/4 of their height. It must be noted that the largest changes occurred during the initial period of the experiment.

In contrast to the oscillation-curve width and free-carrier concentration, the lattice constant exhibited a rather complex dependence on time (Fig. 1b). During the first hour, there was a material increase in the lattice constant in comparison with the quenched state and the value of a approached that of the original crystal. Further annealing led to a decrease in the lattice constant; after 3.5 h, a level close to that for the quenched state was reached and a remained virtually constant as the annealing time was further prolonged (to 7.5 h).

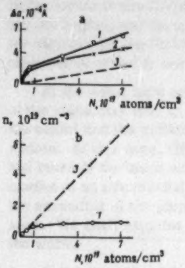

Fig. 2. Influence of alloying with tellurium on certain properties of gallium arsenide single crystals. a) The change in lattice constant; b) current-carrier concentration; 1) initial state; 2) quenching from t = 110°C; 3) calculated values of Δa.

Additional investigations of the influence of alloying with tellurium during crystal growth on the lattice constant of gallium arsenide showed that the deviation from Vegard's law increased with the tellurium concentration in the specimens (Fig. 2a). The change in lattice constant during heat treatment also increased with the degree of alloying. These results are in agreement with the patterns of the change in free current-carrier concentration in the crystals with different tellurium concentrations (Fig. 2b).

The most interesting patterns in our opinion are those of the variation in lattice constant. We will concentrate most of our attention on these.

At tellurium concentrations $N \geq 2 \cdot 10^{18}$ atoms/cm^3, some of the alloying-purity atoms are in crystals in an electrically inactive state.[5,6]

The difference in the character of the kinetic curves representing the changes in the concentration of electrically active tellurium and the lattice constant (Fig. 1) indicate that inactive tellurium can be present in the crystal in several forms. These forms of electrically inactive tellurium can include interstitial atoms, short-range complexes with atoms of the main component or structural defects, and regions of second-phase pre-precipitation or precipitation.

The following model of the behavior of Te atoms during heat treatment can be proposed to account for the experimental data. If all the Te atoms are statistically distributed in the arsenic sublattice and form only a substitutional solution, then the atomic concentration N equals the carrier concentration n and Vegard's law should be satisfied. In our case, N > n and there was a large positive deviation from Vegard's law (Fig. 2a). This indicates that inactive tellurium has a far stronger influence on the lattice constant than active tellurium in the substitutional solution (despite the fact that the latter has a large tetrahedral radius). A similar effect is apparently possible as a result of formation of injection-type defects in the crystal, which can be detected by electron-microscope examination.[2] Such defects are formed during decay and can be regarded as tellurium-enriched regions of the gallium arsenide lattice, similar to the well-known Guinier–Preston zones.

The crystal contains a substantial amount of such defects in its original state. During annealing at 1100°C (a temperature close to that of the maximum solubility of tellurium in gallium arsenide), some injection-type defects are destroyed and some of the Te atoms return to the substitutional solution (electrically active state), as indicated by an increase in current-carrier concentration and a decrease in lattice constant.

The fact that the n < N ratio and the positive deviation from Vegard's law remain the same after such heat treatment indicates that injection-type defects are still present in the crystal, although in lower concentration. This can be attributed to the fact that the resolution process is not completed during the holding time and that quenching does not fix the high-temperature state.

Rapid decay of the supersaturated solid solution occurs during annealing at 700°C. During the early stage (the first hour of annealing), the concentration of injection-type defects, associated with formation of the pre-precipitation regions in the crystal, again increases substantially, as indicated by a large increase in the lattice constant. A state close to that in the growing crystal is apparently achieved in this case.

When the holding time is further increased, the decay process continues at a reduced rate but, as before, there is a decrease in the current-carrier concentration and broadening of the oscillation curves. However, the character of the change in the lattice constant is greatly altered. The decrease in lattice constant during the latter stages of annealing indicates that coagulation processes begin to play a greater role in decay.

The results obtained made it possible to conclude that the electrical properties and structure of gallium arsenide crystals highly alloyed with tellurium, in both the as-grown state and after various types of heat treatment, are materially affected by decay of supersaturated solid solutions to form second-phase precipitation and pre-precipitation regions and convincingly indicated that a composite approach to study of this type of phenomenon is best.

[1)] The standard was unalloyed gallium arsenide with a current-carrier concentration of $1 \cdot 10^{17}$ cm^{-3} and a dislocation density of $\sim 5 \cdot 10^3$ cm^{-2}.

[1] N. S. Belyatskaya, S. P. Grishina, E. V. Lopatin, M. G. Mil'vidskii, V. B. Osvenskii, and V. G. Fomin, Kristallografiya, 17, 158 (1972) [Sov. Phys. – Crystallogr., 17, 126 (1972)].
[2] L. M. Morgulis, V. B. Osvenskii, M. G. Mil'vidskii, and S. P. Grishina, Proceedings of an All-Union Conference on Structural Defects in Semiconductors [in Russian], Inst. Fiz. Poluprovod. Sib. Otd. Akad. Nauk SSSR, Novosibirsk (1970), Pt. II, p. 121.
[3] H. Kressel and H. Nelson, J. Appl. Phys., 40, 3720 (1969).
[4] V. G. Fomin and A. G. Novikov, Zavod. Lab., 3, 303 (1972).
[5] M. G. Mil'vidskii, V. B. Osvenskii, V. I. Fistul', É. M. Omel'yanovskii, and S. P. Grishina, Fiz. Tekh. Poluprov., 1, 969 (1967) [Sov. Phys. – Semicond., 1, 813 (1968)].
[6] S. P. Girshina, M. G. Mil'vidskii, V. B. Osvenskii, and V. I. Fistul', Fiz. Tekh. Poluprov., 4, 294 (1970) [Sov. Phys. – Semicond., 4, 240 (1970)].

Effective distribution constants of excess basic components during crystallization of gallium arsenide from a melt

V. V. Karataev, M. G. Mil'vidskii, V. B. Osvenskii, and O. G. Stolyarov

State Scientific-Research and Planning Institute of the Rare Metals Industry

(Submitted March 27, 1972; resubmitted July 24, 1972)
Kristallografiya, 18, 830-832 (July-August 1973)

We calculated the total concentration of the excess basic components in GaAs single crystals grown from a melt with various deviations from stoichiometric composition. The available experimental data were used to make an analytic calculation of the equation of the solidus. It was shown that the maximum melting point of the compound did not precisely correspond to the stoichiometric composition. We found the effective distribution constants of the excess basic components during crystallization of GaAs from the molten state. These coefficients were shown to be independent of the excess-component concentration over the range investigated.

Gallium arsenide is a decomposable compound of variable composition with a narrow homogeneity region (from 0.011 to 0.022 at.% according to the data of refs. 1 and 2 respectively). The type and concentration of the point defects, which are governed by the deviation of the composition from stoichiometry, have a material influence on the properties of the crystals.[3]

In order to produce crystals with a given component ratio under controlled melt-composition conditions, it is necessary to know the effective distribution coefficients for the basic components during crystallization of GaAs. These factors can be determined from the effective phase microdiagram of GaAs in the immediate vicinity of the composition with the maximum melting point.

The present article describes the calculation of the effective distribution coefficients of Ga and As during growth of GaAs single crystals by noncrucible zone melting, using melts with different deviations from stoichiometry. The total residual-impurity content in the crystals investigated did not exceed 10^{17} cm^{-3}.

The calculations were based on experimental data obtained in measuring the differential point-defect concentration,[2] which showed the differential defect concentrations corresponding to the boundaries of the GaAs homogeneity region to be $4.2 \cdot 10^{18}$ and $5.3 \cdot 10^{18}$ cm^{-3} for excess As and Ga, respectively. The maximum total point-defect concentration in GaAs resulting from the deviation from stoichiometry during crystallization from the molten state[4] can reach ~10^{19} cm^{-3}. Assuming the total defect concentration to correspond to the phase boundaries, the differential point-defect concentrations can be used to find the absolute values at the boundaries of the homogeneity region. In the case of excess As, $c_{i_{As}} = 7.1 \cdot 10^{18}$ cm^{-3} and $c_{v_G} = 2.9 \cdot 10^{18}$ cm^{-3}; in the case of excess Ga, $c_{v_{As}} = 7.65 \cdot 10^{18}$ cm^{-3}, and $c_{i_{Ga}} = 2.35 \cdot 10^{18}$ cm^{-3}. It should be noted that, according to data obtained in internal-friction measurements, the maximum concentration of gallium vacancies in the single crystals investigated was $4.7 \cdot 10^{18}$ cm^{-2} for growth from a melt enriched in As.

In view of the fact that the energy of point-defect formation is independent of the concentration when the latter is small, the ratio of the numbers of interstitial atoms and vacancies within the regions where defects of the same types exist can be assumed to be constant: $\alpha_1 = c_{i_{As}}/c_{v_{Ga}} = 2.448$ and $\alpha_2 = c_{v_{As}}/c_{i_{Ga}} = 3.255$. In this case the absolute point-defect concentrations can be expressed in terms of the absolute difference concentrations $|\Delta N|$. The total point-defect concentration is then

$$c_\Sigma = |\Delta N|(\alpha_i + 1)/(\alpha_i - 1), \tag{1}$$

where i can be 1 or 2, depending on the notation adopted.

In order to find the effective distribution coefficient with any excess-component concentration in the vicinity of the stoichiometric composition, it is necessary to have analytic expressions describing the effective liquidus and solidus in direct proximity to the composition with the maximum melting point.

According to the literature,[5,6] the liquidus in the immediate vicinity of the maximum melting point of GaAs can be approximated with sufficient accuracy of the expression

$$T = T_m - c_1^2/7.0, \tag{2}$$

where $c_1 = 50 - c_L$, c_L is the As concentration in the melt (at. %), T_m is the maximum melting point of GaAs (deg C), and T is the melt temperature (deg C). Under conditions where the solid phase partially dissociates, the solidus can be described by a similar function relationship.[7] Since the maximum melting point can, strictly speaking, fail to correspond to the exact stoichiometric composition of the compound, $c_1 = c_m - c_L$, where c_m is the composition of the compound with the maximum melting point. We then obtain for the effective solidus

$$T = T_m - Ac_2^2/7.0, \tag{3}$$

where A is the coefficient of parabola curvature and $c_2 = c_m - c_S$ (c_S is the total excess-component concentration in the crystal). Knowing the values of c_S (see Table 1) for two different single crystal compositions, we can write the equation system

$$T_1 = T_m - A(c_m - c_{S1})^2/7.0, \tag{4a}$$

$$T_2 = T_m - A(c_m - c_{S2})^2/7.0. \tag{4b}$$

The unknown quantities T_1 and T_2 can be found from Eq. (2). Since the As vapor pressure over the melt from which the crystals are produced is known, we can calculate[6-8] the corresponding As concentrations in the melt c_L. Then,

$$c_m = (c_{L2}c_{S1} - c_{L1}c_{S2}) / (c_{L2} - c_{S2} - c_{L1} + c_{S1}), \tag{5}$$

$$A = (c_m - c_{L1})^2/(c_m - c_{S1})^2. \tag{6}$$

TABLE 1. Values of c_L and c_S for Crystals Obtained with Various Deviations from Stoichiometry

Crystal characteristics	c_L, at.%	c_S, at.%	c_E, 10[illegible] cm^{-3}
Grown from melt enriched in As	53.4±0.1	50.022	42
	51.0±0.1	50.002	4.0
Grown from melt enriched in Ga	49.8±0.1	49.996	9.0
	46.7±0.1	49.977	53

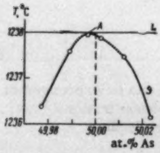

Fig. 1. T−x projection of GaAs phase diagram. A) 1238°C, 49.996 at.% As.

Substituting in the values of c_L and c_S (see Table 1), we obtain the following values for the quantities sought: c_m = 49.994 at.% and A = 13759.700 for growth from a melt enriched in As and c_m = 49.997 at.% and A = 27005.430 for growth from a melt enriched in Ga. Since the values of c_m obtained in calculations for the left and right sides of the microdiagram differed only slightly, subsequent calculations were conducted with the average value $\overline{c}_m$ = 49.9960. The equations for the effective solidus near the composition corresponding to the maximum melting point then take the form:

$$T = T_m - 27005{,}430(49.996 - c_s)^2/7.0, \qquad (7a)$$

for excess Ga and

$$T = T_m - 13759.700(49.996 - c_s)^2/7.0. \qquad (7b)$$

for excess As.

Figure 1 shows the T−x projection of the GaAs phase diagram.

The effective distribution coefficients can be calculated from the equation

$$K = |c_m - c_s| \,/\, |c_m - c_L|. \qquad (8)$$

When the melt is enriched in Ga, k = 6.1 · 10^{-3}; when the melt is enriched in As, k = 8.5 · 10^{-3}.

In connection with the fact that growth of GaAs crystals from a melt by noncrucible zone melting is conducted at a low rate (0.5 mm/min) with vigorous agitation of the melt and rapid cooling of the crystal from the melting point (which makes it possible to ignore the possible influence of decay processes), the values obtained for the effective distribution coefficients can be considered sufficiently close to the equilibrium values.

---

[1] M. E. Straumanis and C. D. Kim, Acta Crystallogr., 19, 256 (1965).

[2] V. T. Bublik, V. V. Karataev, M. G. Mil'vidskii, V. B. Osvenskii, O. G. Stolyarov, and L. P. Kholodnyi, Kristallografiya, 18, 353 (1973) [Sov. Phys.− Crystallogr., 18, 218 (1973)].

[3] E. V. Solov'eva, V. V. Karataev, M. G. Mil'vidskii, V. B. Osvenskii, and O. G. Stolyarov, Fiz. Tverd. Tela, 14, 528 (1972) [Sov. Phys.− Solid State, 14, 441 (1972)].

[4] J. Blanc, R. Bube, and L. Weisberg, J. Phys. Chem. Solids, 25, 225 (1965).

[5] C. Wagner, Acta Metallurg., 6, 309 (1958).

[6] B. D. Lainer, A. V. Berkova, M. G. Mil'vidskii, and V. V. Rakov, Kristallografiya, 14, 867 (1969) [Sov. Phys. − Crystallogr., 14, 743 (1970)].

[7] F. A. Kröger, The Chemistry of Imperfect Crystals, North Holland Publ. Co., Amsterdam, Interscience, New York (1964).

[8] V. V. Rakov, Yu. D. Lainer, and M. G. Mil'vidskii, Zh. Fiz. Khim., 44, 1641 (1970).

Hydrothermal synthesis of a new crystalline modification of lithium lanthanum molybdate, α-$LiLa(MoO_4)_2$

P. V. Klevtsov, V. I. Protasova, L. Yu. Kharchenko, and R. F. Klevtsova
Institute of Inorganic Chemistry, Siberian Branch, Academy of Sciences of the USSR
(Submitted June 7, 1972; resubmitted July 31, 1972)
Kristallografiya, 18, 833-835 (July-August 1973)

$LiLa(MoO_4)_2$ single crystals in a rhombic modification, hitherto unknown, were prepared in lithium molybdate solutions at 500-575°C with unit cell parameters: $a = 9.92$, b = 10.09, and c = 13.58 Å; Z = 8, sp. gp. $D_{2h}^{15} = Pcab$. On heating, the rhombic modification transforms irreversibly to a scheelite-type tetragonal modification at about 730°C.

Double molybdates $LiLn(MoO_4)_2$ are known for every series of rare-earth elements (Ln = La—Lu, Y). They are prepared by crystallization from solution in the melt[1-4] and solid-phase synthesis, i.e., sintering of the component oxides.[5-7] The entire series of compounds is isostructural to the tetragonal scheelite $CaWO_4$.

In a study of the conditions for hydrothermal synthesis of rare-earth molybdates, we prepared $LiLa(MoO_4)_2$ single crystals in a new polymorphic modification. The experiments were performed in stainless steel autoclaves having self-sealing doors, provided with titanium inserts. Crystallization was carried out under isothermal conditions at 500-575°C, the autoclave being 55-70% full. The working solvent was aqueous lithium molybdate solution. The initial charges were mechanical mixtures of lanthanum and molybdenum oxides in the molar ratios La_2O_3: MoO_3 = 1:3, 1:4, and 1:5 as well as sintered masses of these oxides in the same ratios. Each experiment lasted 180-200 h.

It was found experimentally that, at synthesis temperatures below 525°C, the yield of crystals of the double molybdate is diminished, and lanthanum hydroxymolybdate crystallizes as the main phase.

The habit and size of the $LiLa(MoO_4)_2$ crystals depend on the initial charge and the synthesis temperature: Mechanical mixtures of the components result in the formation mainly of acicular prismatic crystals up to 10 mm long and 0.3-0.4 mm across; when the charge consists of sintered masses, the bulk of the crystals are relatively isometric and have the form of short, slightly flattened prisms. From the increase in size and total yield of the crystals with crystallization temperature and charge, one may conclude that the solubility of this compound increases with temperature. The maximum size of the isometric crystals obtained at 575°C was 3 mm.

Single crystals faceted on all sides were used to determined the symmetry by optical goniometry. Results of the measurements are given in Table 1.

The crystals were referred to the rhombic system, rhombobipyramidal class D_{2h}. The two unit-cell parameters (a, b) lying in the plane of the pinacoid {001} on which the crystals are flattened are nearly the same (equal within the error of measurement of the angles). The ratio of parameters, calculated from goniometric (optical) data, is a:b:c = 0.99:1:1.37. The tetragonal symmetry is formally satisfied by a combination of pinacoids and the bipyramids {112} and {111}. With regard to morphological importance, the pinacoid {001} is followed by the simple forms {012}, {111}, {010}, and {112}. The prisms and the pinacoid {100}, which is perpendicular to the direction of extension of the crystals, are only slightly developed.

The preliminary results of x-ray structure analysis confirm the data of optical goniometry. The unit-cell parameters, determined from oscillation and rotation photographs and improved (with ±0.02 Å accuracy) by using a powder pattern (Table 2), are as follows: $a = 9.92$, b = 10.09, and c = 13.58 Å. The density, measured pycnometrically, is 4.55 g/cm³; this corresponds to a content of eight formula units of $LiLa(MoO_4)_2$ in the unit cell (x-ray density 4.57 g/cm³). Weissenberg photographs showed the extinctions: h = 2n + 1 in the h0l zone, k = 2n + 1 in hk0, and l = 2n + 1 in the 0kl zone; they unambiguously determine the sp.gp. $D_{2h}^{15} = Pcab$. Based on the infrared spectrum (Fig. 1), one should expect tetrahedral coordination of the Mo atoms in the structure of this crystalline modification.

The composition $LiLa(MoO_4)_2$ was confirmed by chemical analysis for lithium, rare-earth elements, and molybdenum; we found La 28.8% (29.2% from calculation), Mo 39.9% (41.2%), Li 1.5% (1.5%).

Thermographic and x-ray investigations showed that, on heating in air, our crystalline modification of $LiLa \cdot (MoO_4)_2$ goes over irreversibly to the known scheelite form at about 730°C. Heating curves for α-$LiLa(MoO_4)_2$ are shown in Fig. 2.

TABLE 1. Forms of Growth of α-$LiLa(MoO_4)_2$

hkl	Angles of normals with axes, deg			No. of faces	Growth form
	$\vec{x}$	$\vec{y}$	$\vec{z}$		
001	90	90	0	2	Pinacoid
010	90	0	90	2	The same
100	0	90	90	2	" "
120	63.7	26.3	90	4	Rhombic prism
012	90	55.5	34.5	4	The same
101	35.5	90	54.5	4	" "
122	68.5	42	57	8	Rhombic bipyramid
112	60	61	46	8	The same
111	51	51.4	63	8	" "

TABLE 2. Powder Diffraction Pattern of α-LiLa$(MoO_4)_2$*

hkl	*d*, Å	*I*	*hkl*	*d*, Å	*I*	*hkl*	*d*, Å	*I*
111	6.30	20	042	2.364	6	441 326	1.755	3
020	5.05	13	331 134	2.325	5	253 344	1.728	20
200	4.97	13	006	2.265	7	060	1.680	5
120	4.50	10	332	2.229	10	146	1.662	3
211	4.25	20	016	2.208	7	317	1.650	10
022	4.06	25	403	2.174	4	336	1.631	2
113	3.816	20	116 324	2.151	30	028	1.607	10
122	3.753	10	422	2.114	4	260 237	1.594	4
212	3.721	4	333	2.089	4	128	1.588	8
220	3.533	5	206 315	2.056	3	515 261	1.583	6
221 004	3.430	100	126 243	2.016	10	163 451	1.559	4
203	3.347	45	340	2.003	25	541	1.545	3
014	3.219	50	235	1.942	25	255	1.538	2
213	3.180	25	052 511	1.931	20	354 613	1.536	3
131	3.110	8	152	1.899	8	038	1.515	4
114	3.061	20	512	1.872	12	056	1.507	6
032	3.016	55	424	1.861	10	263	1.503	6
312	2.856	25	251 520 136	1.852	10	361 164	1.489	5
024	2.815	25	316 521	1.833	5	631 543	1.475	8
320	2.769	12	207	1.808	4	355	1.454	2
231	2.728	7	217	1.776	5	209	1.444	5
133	2.603	3	440	1.769	10	129	1.429	3
313 322	2.581	12						
115	2.538	12						
400	2.482	5						
141	2.406	4						
233 411	2.374	5						

*The powder pattern was recorded on a URS-50I diffractometer in filtered Cu radiation, crystalline germanium being added to the sample as an internal standard.

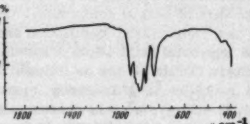

Fig. 1. Infrared spectrum of α-LiLa$(MoO_4)_2$ (UR-10 spectrometer).

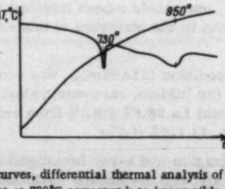

Fig. 2. Heating curves, differential thermal analysis of α-LiLa$(MoO_4)_2$. Endothermic effect at 730°C corresponds to irreversible transformation of rhombic modification to tetragonal; effect at 950°C is due to melting of the compound.

In order to determine more precisely the conditions of formation of the low-temperature modification, we prepared this compound from mixtures of $Li_2MoO_4 + La_2 \cdot (MoO_4)_3$ by solid-phase reactions. Annealing was carried out at 450°C for 10 h and then at 550–600°C for 140 h, the mixture being ground many times during the interval. The compound LiLa$(MoO_4)_2$ was obtained, as under hydrothermal conditions, in the rhombic modification, as is shown by the identity of powder patterns taken from sintered masses and ground single crystals.

The authors thank G. M. Rylov for control measurements of the unit-cell parameters in a DRON instrument and Z. A. Grankina for taking the infrared spectrum.

---

[1] L. G. Van Uitert, J. Chem. Phys., 37, 981 (1962).
[2] L. G. Van Uitert, J. Electrochem. Soc., 110, 46 (1963).
[3] M. M. Schieber, Inorg. Chem., 4, 762 (1965).
[4] P. V. Klevtsov and L. P. Kozeeva, Izv. Akad. Nauk SSSR, Neorgan. Mat., 5, 1842 (1969).
[5] M. V. Mokhosoev, E. I. Get'man, and F. P. Alekseev, Dokl. Akad. Nauk SSSR, 185, 361 (1969).
[6] V. K. Rybakov and V. K. Trunov, Zh. Neorgan. Khim., 14, 2889 (1969).
[7] M. V. Savel'eva, I. V. Shakhno, and V. E. Plyushchev, Izv. Akad. Nauk SSSR, Neorgan. Mat., 6, 1665 (1970).

Study of crystallization in the hydrothermal system GeO_2–Sb_2O_3–KF–H_2O

M. N. Tseitlin, G. F. Plakhov, A. N. Lobachev, V. I. Popolitov, M. A. Simonov, and N. V. Belov

M. V. Lomonosov Moscow State University
Institute of Crystallography, Academy of Sciences of the USSR

(Submitted December 2, 1972)
Kristallografiya, 18, 836-839 (July-August 1973)

Crystallization in the $GeO_2-Sb_2O_3-KF-H_2O$ system is studied at 400, 450, 500, and 550°C in relation to the concentration of the aqueous solution of potassium fluoride and the molar ratio of the original components of the mixture. It is shown that the phase composition of the system is determined by the concentration of the solvent and the temperature. A new single-crystal compound is obtained: Antimony germanate $Sb_2Ge_2O_7$; x-ray phase and optical analyses are applied to this compound and the results are presented.

The hydrothermal method of synthesizing single crystals is widely employed in producing a great variety of inorganic substances, including simple and complex germanates. By studying the conditions of crystallization of such systems as $ZnO-GeO_2-R-H_2O$ (ref. 1), $Bi_2O_3-GeO_2-R-H_2O$ (ref. 2), where R is the solvent, a number of single crystals with interesting physical properties have been obtained. As a result of a systematic study of the systems formed between germanium dioxide and the oxides of various other elements in the periodic table, extremely broad prospects may well be opened for producing germanates of various compositions, structures, and properties, not having any analogs in nature, and hence offering considerable interest in connection with various aspects of solid-state physics and inorganic chemistry.

This investigation is devoted to a study of the conditions of crystallization in the $GeO_2-Sb_2O_3-KF-H_2O$ system by the hydrothermal method. Apart from the desire to fill the gap in our knowledge as to the chemistry of the interaction beteen germanium dioxide and antimony trioxide in the presence of a solvent at high temperatures and pressures, it also appeared interesting to produce a wide variety of single crystals not having any analogs in nature and therefore potentially being of great interest as regards their structural and physical properties.

The experimental study of the $GeO_2-Sb_2O_3-KF-H_2O$ system was carried out in standard copper-lined autoclaves of periodic action. The mixture was prepared from germanium dioxide and antimony trioxide of the very-high purity type. The principal crystallization parameters in the $GeO_2-Sb_2O_3-KF-H_2O$ system were: 400-550°C, temperature drop 20-45° (height of autoclave 400 mm), autoclave occupation factor 0.86-0.65. The crystallization medium was an aqueous solution of KF; the concentration was varied from 0 to 60 wt.%. The GeO_2/Sb_2O_3 molar ratios were varied from 0.5 to 8. Each experiment lasted 192 h. The resultant phases were identified by optical, x-ray, and chemical methods.

Let us consider the crystallization conditions in the $GeO_2-Sb_2O_3-KF-H_2O$ system for each temperature region separately.

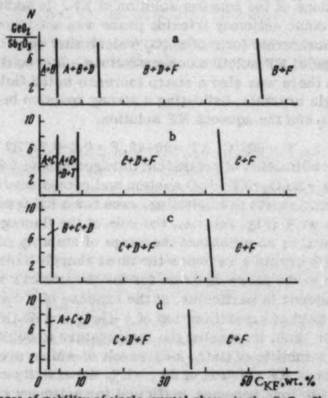

Fig. 1. Ranges of stability of single-crystal phases in the $GeO_2-Sb_2O_3-KF-H_2O$ system. A) β-GeO_2; B) α-Sb_2O_3; C) α-S_2O_3 + β-Sb_2O_3; D) $Sb_2 \cdot Ge_2O_7$: T) $K_2Ge_4O_9$; F) K_2GeF_6; a) T = 400; b) 450; c) 500; d) 550°C.

1. T = 400°C, $\Delta T = 20-45$, $F = 0.75-0.85$. Experiments with these parameters enabled us to establish the boundaries of the ranges of crystallization of various single-crystal phases in coordinates of composition and KF concentration (Fig. 1a). We see from these data that, for solvent concentrations of 0-5 wt.%, germanium dioxide single crystals (cubic senarmontite) are formed. This separate crystallization of β-GeO_2 and α-Sb_2O_3 may be explained by the different solubilities of the original components (GeO_2 and Sb_2O_3), the different rates at which these pass into solution, and the individual manner in which the single crystals in question are formed. For aqueous KF solutions of 5-14 wt.% the β-GeO_2 and α-Sb_2O_3 crystals are accompanied by the formation of antimony germanate single crystals (chemical analysis gives the formula of these as $Sb_2Ge_2O_7$) and also single crystals of potassium tetragermanate $K_2Ge_4O_9$. On further increasing the KF concentration ($C_{KF} > 14$ wt.%) the field of $K_2Ge_4O_9$ vanishes and single crystals of potassium fluorogermanate K_2GeF_6 appear. The formation of this phase indicates unambiguously that, as the KF concentration increases, so does the activity of the F ion, which completely expels the oxygen from GeO_2, and the germanium is transferred into solution in the form of the fluorogermanate radical $[GeF_6]^{2-}$, as confirmed by the results of ref. 3. For aqueous KF solutions stronger than 50 wt.% only single crystals of α-Sb_2O_3 and K_2GeF_6 are formed. Summarizing the laws governing crystallization in the $GeO_2-Sb_2O_3-KF-H_2O$ system, we may note that the ranges of stability of the different single phases do not depend on the molar ratio GeO_2/Sb_2O_3, but are simply determined by the concentra-

tion of the aqueous KF solution. However, as indicated in Fig. 1, the slopes of the boundary lines separating the ranges of stability of the single phase do depend on the molar ratio GeO_2/Sb_2O_3.

2. T = 450°C, ΔT = 20–45, F = 0.7–0.8. Raising the temperature to 450°C increased the reactivity of the $GeO_2-Sb_2O_4-KF-H_2O$ system, and thus also the growth rate and yield of the various single crystals. As regards the composition of the precipitating single crystals and the sequence of their formation, there was hardly any difference from the series of experiments at 400°C, although the boundaries of the single-phase fields (Fig. 1b) were shifted relative to those at 400°C in the direction of lower concentrations of the aqueous solution of KF. In addition to this, the cubic antimony trioxide phase was accompanied by an orthorhombic form of Sb_2O_3 (valentinite) over the whole range of KF solution concentrations. It should be noted that there was also a sharp increase in the field of K_2GeF_6 single crystals, indicating a strong reaction between the GeO_2 and the aqueous KF solution.

3. T = 500°C, ΔT = 20–45, F = 0.6–0.7. At 500°C the crystallization of potassium tetragermanate ceases in the $GeO_2-Sb_2O_3-KF-H_2O$ system and potassium fluorogermanate starts precipitating, even for a KF concentration of 4 wt.% (Fig. 1c), i.e., the role of the fluorogermanate radical is so great that the range of stability of the K_2GeF_6 single crystals becomes the most sharply expressed feature in the phase diagram for the parameters specified; it extends in particular, at the expense of a contraction in the field of crystallization of β-GeO_2 and $Sb_2Ge_2O_7$. On the other hand, increasing the temperature to 500°C increases the solubility of GeO_2, as a result of which, even for an aqueous KF solution of 0–1 wt.%, the activity of the germanate ions becomes sufficient for antimony germanate to crystallize. These two features sharply distinguish crystallization in the system at 500°C from crystallization at 400 and 450°C.

4. T = 550°C, ΔT = 20–45, F = 0.5–0.6. Raising the temperature to 550°C still further contracted the range of stability of β-GeO_2 and $Sb_2Ge_2O_7$ and expanded the range of K_2GeF_6 (Fig. 1d). However, the association of the phases remained similar to that in the case of 500°C. One characteristic of crystallization at this temperature is an increase in the yield of valentinite single crystals. By varying the occupation factor of the linings, we varied the pressure in our experiments on crystallization in the $GeO_2-Sb_2O_3-KF-H_2O$ system from 500 to 1800 atm. However, pressure had no serious effect on the range of formation of the single-crystal phase at any of the temperatures studied. As regards the temperature drop, varying this also had no marked effect on the dimensions of the single crystals so formed.

Thus phase formation in the $GeO_2-Sb_2O_3-KF-H_2O$ system depends on the concentration of the aqueous solution of KF and the temperature; it does not depend on the pressure or the temperature drop. The molar ratio of the original components GeO_2/Sb_2O_3 has hardly any effect on the range of stability of the single phases, but affects the slopes of the boundaries between them.

Our study of hydrothermal crystallization in the $GeO_2-Sb_2O_3-KF-H_2O$ system enabled us to produce six single-crystal phases, α-Sb_2O_3, β-Sb_2O_3, β-GeO_2, $K_2Ge_4O_9$, $Sb_2 \cdot Ge_2O_7$, K_2GeF_6. The hydrothermal method had already been used to produce α-Sb_2O_3, β-Sb_2O_3 (ref. 4), β-GeO_2 (ref. 5) crystals, and we need therefore not dwell on these in detail. We note that the tetragonal variety of germanium dioxide crystals obtained by other authors took the form of a fine crystalline powder with dimensions of hundredth parts of a millimeter. In our own experiments at 500–550°C β-GeO_2 crystallized in the form of short transparent prisms up to 0.7 mm in size.

We were the first to produce potassium fluorogermanate hydrothermally. The K_2GeF_6 crystals are hexagonal with lattice parameters[3] a = 5.71, c = 9.27 Å. These crystallize both in the cold and in the hot zone of the autoclave in the form of hexagonal transparent colorless (to

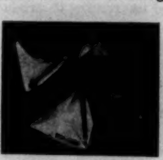

Fig. 2. Antimony germanate crystals. ×10.

TABLE 1

K_2GeF_6				$Sb_2Ge_2O_7$			
I	d/n	I	d/n	I	d/n	I	d/n
7	5,005	4	1.757	50	4.27	2	1.359
100	4.604	8	1.740	64	3.30	2	1.349
80	4.387	3	1.704	100	2.79	5	1.328
2	4.167	8	1.673	16	2.61	7	1.285
2	3.789	8	1.491	3	2.339	2	1.247
62	3.401	3	1.469	2	2.227	7	1.232
3	3.211	5	1.452	29	2.135	7	1.216
3	3.104	3	1.436	10	2.049	5	1.185
30	2.894	3	1.386	20	1.909	1	1.169
30	2.623	5	1.365	5	1.847	2	1.155
9	2.451	5	1.325	16	1.793	5	1.127
7	2.421	2	1.281	30	1.696	8	1.103
7	2.390	2	1.273	5	1.653	4	1.057
18	2.317	1	1.212	17	1.614	6	0.999
39	2.207	2	1.161	16	1.541	3	0.949
6	2.102	1	1.153	7	1.509		
16	1.947	1	1.137	15	1.479		
2	1.861	1	1.130	5	1.450		
1	1.833			6	1.422		
4	1.811			9	1.398		

Note: The recordings were made in a URS-50IM diffractometer with Cu Kα radiation and an Ni filter.

white) plates. Basal cleavage is perfect. In the crystals are some regions containing charge materials which have not reacted completely, and these lose their transparency. The maximum dimensions are 2-3 mm. The interplane distances of K_2GeF_6 are given in Table 1.

We were also the first to produce antimony germanate crystals $Sb_2Ge_2O_7$ (Fig. 2). X-ray diffraction indicated cubic symmetry with[1] $a = 10.478 \pm 0.004$ Å. The maximum yield of $Sb_2Ge_2O_7$ occurs at 500°C for a 10-12 wt.% concentration of the aqueous KF solution. The crystallization of this phase takes place mainly in the upper zone of the reaction space. For a low concentration of the solvent the $Sb_2Ge_2O_7$ crystals grow in the form of small trigonotritetrahedra ($0.5 \times 0.5 \times 0.5$ mm). With increasing KF concentration the antimony germanate crystallizes in the form of druses with sharp trigonotritetrahedral vertices, although there are also individual trigonotritetrahedra as well. The druses have dimensions of 3×4 mm and the individual $Sb_2Ge_2O_7$ crystals reach 1.5-2 mm. The crystals are transparent, colorless, or in some cases colored (from light yellow to orange). Cleavage is perfect perpendicular to the b axis and imperfect perpendicular to the two-fold axis. The luster is the same as diamond, the specific gravity 4.80. Viewed in immersion liquids under the microscope, a slight anisotropy is observed; twins also occur. According to the refractive indices, the crystals are optically uniaxial,[2] $N_g = 1.990 \pm 0.003$, $N_p = 1.980 \pm 0.003$ ($\lambda = 589$ nm). The table gives a set of interplane distances for antimony germanate crystals.

CONCLUSIONS

1. Our study of crystallization in the $GeO_2-Sb_2O_3-KF-H_2O$ system has shown that under hydrothermal conditions there is a vigorous interaction between the original components of the mixture present in solution and the solvent, so that crystals of both the original oxides and the low-solubility antimony and potassium germanates precipitate, together with potassium fluorogermanate.

2. The ranges of stability of the various single-crystal phases depend on the concentration of the solvent as well as the temperature, but not on the pressure or temperature differential (drop).

3. We obtained six single-crystal phases, of which potassium fluorogermanate K_2GeF_6 was obtained for the first time hydrothermally, and antimony germanate $Sb_2 \cdot Ge_2O_7$ was obtained for the first time altogether.

We have given a description of antimony germanate and presented certain results obtained by x-ray diffraction.

---

[1] The cubic lattice parameters of $Sb_2Ge_2O_7$ were determined in the automatic R1 diffractometer of the "Sintex" company.

[2] The refractive indices were determined by the immersion method in the Mineralogy Department of Moscow State University by T. N. Ivanova.

[1] Hydrothermal Synthesis of Germanates [in Russian], Nauka, Moscow (1968).

[2] V. S. Kurazhkovskaya, Dissertation, Moscow State University (1971).

[3] I. V. Tananaev and M. Ya. Shpirt, Chemistry of Germanium [in Russian], Khimiya, Moscow (1967).

[4] V. I. Popolitov, A. N. Lobachev, and V. F. Peskin, Kristallografiya, 17, 435 (1972) [Sov. Phys. – Crystallogr., 17, 382 (1972)].

[5] I. P. Kuz'mina, Dissertation, Institute of Crystallography, Academy of Sciences of the USSR (1968).

Effect of accelerating voltage on the intensity of the forbidden reflection 222 Ge in electron diffraction

A. S. Avilov, R. M. Imamov, Z. G. Pinsker, and A. F. Fedotov
Institute of Crystallography, Academy of Sciences of the USSR

(Submitted July 3, 1972)
Kristallografiya, 18, 840-841 (July-August 1973)

The conditions under which the 222 reflection of Si and Ge single crystals (forbidden for the diamond type of structure) might be made to appear in x-ray diffraction patterns were considered in refs. 1-4. It is well known[3,4] that this effect is due to asymmetry in the distribution of the electron cloud around the atomic nucleus (i.e., to the covalence factor), which reaches a maximum in the [111] direction of the crystal for a structure of the diamond type.

The structure amplitude of the 222 reflection of Si was determined experimentally in refs. 5-7, using electron diffraction, with an accelerating voltage of 70 kV. The results of refs. 5 and 6 agree closely with the x-ray data.[8] However, it is important to note that the best agreement between the x-ray and electron-diffraction data is obtained when the systematic and unsystematic multiple-wave scattering of the electrons is duly allowed for in the latter case when calculating Φ_{222}.

The problem of the present investigation was to study the changes taking place in the intensities of the forbidden 222 reflection in polycrystalline Ge films on diffracting electrons with energies of 100-400 keV.

TABLE 1

Intensity ratio	Voltage, kV			
	100	200	300	400
I_{222}/I_{311}	0,13	0.07	0.05	0.03
I_{222}/I_{331}	0.40	0,26	0.19	0.10

The thin Ge films for electron-diffraction analysis were prepared by evaporation in a vacuum of ~10^{-5} mm Hg. The polycrystalline samples were obtained by evaporating Ge onto NaCl substrates heated to 320°C. Using these films, we recorded electron-diffraction patterns with multiple exposures at voltages of 100, 200, 300, and 400 kV. We checked for the absence of orientation by making microphotometer recordings of patterns taken at an angle of ~ 45°.

We used a microphotometric method to measure the intensities. For quantitative analysis we used only those reflections on the electron-diffraction patterns recorded at different voltages, whose intensities could be measured reliably with a microphotometer. The intensities of the 511 and 333 reflections, which merged into a single ring, were determined with due allowance for the multiplicity factor. Experiments in which the reflection curves were obtained by rotating the scattering crystal[9] indicated the existence of two-wave electron scattering in Si and Ge, so that allowance would have to be made for extinctions in the 111 and 220 reflections; the intensity of the forbidden 222 reflection was therefore compared with the intensities of the comparatively distant orders of reflections 311 and 331.

Table 1 gives the ratio of the intensity I_{222} to I_{311} and I_{331}. Comparison between these quantities shows that the intensity of the forbidden 222 reflections is 4.0-4.4 times smaller for an electron energy of 400 keV $[(I_{222}/I_{311})^{100\ \mathrm{kV}} \cdot [(I_{222}/I_{311})^{400\mathrm{kV}}]^{-1} \approx 4.4$ and $(I_{222}/I_{331})^{100\mathrm{kV}}/(I_{222}/I_{331})^{400\ \mathrm{kV}} \approx 4.0]$ than for an electron energy of 100 keV. This reduction is evidently associated with the fact that, for the rela-

TABLE 2. Theoretical and Experimental Values of the Structure Amplitudes in V

hkl	100 kV		200 kV		300 kV		400 kV	
	ΦT	ΦE	ΦT	ΦE	ΦT	ΦE	ΦT	ΦE
111	9.31	8.54	10,84	10.81	12.37	12,85	13.89	14.16
220	8,66	9,20	10.07	11.42	11.49	12.80	12.91	13.71
311	5.13	4.98	5.97	6.12	6.81	6.83	7,65	7,73
222*	0,05	3.24	0,068	2,95	0.067	2.76	0.075	2,38
400	5.68	5.01	6.61	5,69	7.54	6.48	8,47	7.11
331	3.65	3,73	4.24	4.17	4.84	4.67	5.44	5.34
422	4.24	4.56	4.94	4.97	5.63	5,49	6,33	6.43
511	2.71	3.02	3.16	3,10	3.60	3,49	4.05	3.86
333	2.71	3.02	3.16	3.10	3.60	3.49	4,05	3.86
440	3.38	2.75	3.94	3.14	4.49	3,70	5,05	4.34
531	2.22	2.69	2,59	2,73	2.95	2,94	3.32	3.40
620	2.64	2.84	3,08	3.02	3.51	3,47	3.94	3.60
533			2.17	2.20	2.48	2.36	2.78	2.67
444			2.89	2.21	3.30	3,05	3.71	3.74
551			1,86	2.64	2.13	2,96	2,39	3.04
642			2.41	2.59	2.75	2,90	3.08	3.14
553							2.03	2.98
R_1 (from all the reflections), %	8.8		7.9		7.2		6.8	
R_2 (from the first 11 reflections), %	8.8		6.3		6.4		6.2	

---

* The structure amplitude Φ_{222} was calculated from ref. 4.

tively higher electron energies, a greater part is played by the inner electrons of the atoms in the crystal; this also is associated with the weakening of the multiple-wave effects.

It is interesting to compare the experimental structure amplitudes of all the reflections observed with electron energies of 100, 200, 300, and 400 keV, calculated on the basis of the kinematic theory, with the amplitudes calculated after allowing for the relativistic correction and a temperature factor of B = 0.54 Å^2 (which corresponds to the characteristic temperature of Θ = 296°). The experimental structure amplitudes were normalized with respect to all the reflections except the forbidden 222. Table 2 also shows the variance factors R for all four sets of experimental amplitudes, calculated from all the reflections (R^1), and from the first eleven (R^2), the 222 not being considered. As the energy of the scattered electrons increases from 100 to 400 keV, the value of R falls slightly (from 8.8 to 6.8%); this may also be associated with the weakening of the dynamic effects.[10]

---

[1] H. Hattori, H. Kuriyama, T. Katagava, and N. Kato, J. Phys. Soc. Japan, 20, 988 (1965).

[2] H. Hattori, H. Kuriyama, and N. Kato, J. Phys. Soc. Japan, 20, 1047 (1965).

[3] B. Dawson, J. Proc. Roy. Soc., A298, 379 (1967).

[4] B. Dawson, J. Proc. Roy. Soc., A298, 395 (1967).

[5] M. Kreutle and G. Meyer-Ehmsen, Phys. Status Solidi, 35, K17 (1969).

[6] M. Kreutle and G. Meyer-Ehmsen, Phys. Status Solidi, a8, 111 (1970).

[7] J. M. Cowley, Acta Crystallogr., A25, 129 (1969).

[8] J. J. De Marco and R. J. Weiss, Phys. Rev., A137, 1869 (1965).

[9] G. Meyer-Ehmsen, Z. Phys., 218, 352 (1969).

[10] A. S. Avilov, R. M. Imamov, and Z. G. Pinsker, Kristallografiya, 16, 628 (1971) [Sov. Phys. – Crystallogr., 16, 533 (1971)].

Monochromatization of neutrons in multiple Bragg scattering

A. A. Loshmanov, V. N. Sigaev, and I. I. Yamzin
Institute of Crystallography, Academy of Sciences of the USSR

(Submitted June 19, 1972)
Kristallografiya, 18, 842 (July-August 1973)

Multiple Bragg scattering in single crystals can under certain circumstances lead to the appearance of intense reflections at places which are forbidden by the extinction laws of the given space group. Kottwitz[1,2] has considered the possibility of obtaining highly monochromatic neutrons by multiple Bragg scattering from perfect single crystals belonging to the space groups F$\bar{4}$3m and C6/mmc and has calculated the orientation of the single crystals relative to the primary monochromatic beam at which at least two reciprocal space angles occur on the Ewald sphere. He estimates that the intensity of the "forbidden" reflections for Be and Ge single crystals can be as high as 20% of the intensity of the strongest allowed reflections.[3]

We might expect that an increase in the mosaic structure of a crystal which would broaden the reciprocal space angles should increase the intensity in the "forbidden" reflections and produce the familiar randomness in the orientations required to obtain this monochromatization effect. If the incident radiation is "white," the beam which is monochromatized by the Bragg reflection contains neutrons with wavelengths $\lambda/2$, $\lambda/3$, ...; 2λ, 3λ; ..., which makes it difficult to analyze the resultant diffraction data especially in methods which use several wavelengths over a narrow range, such as the introduction of extinction corrections and extrapolation to zero wavelength, the anomalous scattering method, and the use of the same crystal monochromator for obtaining several wavelengths by rotating the crystal about the zone axis.

We have made an experimental study of the wavelength distribution of a neutron beam obtained from a zinc monochromator (mosaicity ~30') cut parallel to a (0001) plane. An analysis of the beam was made with a diamond powder neutron-diffraction pattern since the absence of (222) and (622) reflections in diamond made it possible to determine quite clearly the diffraction peaks from λ and 2λ neutrons. The results for λ = 0.60, 0.65, 0.73, and 0.77 Å (Fig. 1) lead to values for $I_0^{2\lambda}/I_0^{\lambda}$, where I_0^{λ} and $I_0^{2\lambda}$ are the intensities of the reflections from the zinc monochromator for λ and 2λ neutrons. We transform Eq. (4.6) of ref. 4 to

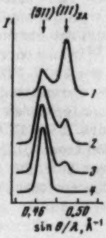

Fig. 1. Neutron-diffraction patterns of diamond powder. 1) λ = 0.6; 2) λ = 0.65; 3) λ = 0.73; 4) λ = 0.77 Å.

$$\frac{I_{111}^{\lambda}}{I_{311}^{\lambda}+I_{111}^{2\lambda}}=\frac{K_{111}^{\lambda}}{K_{311}^{\lambda}+\sqrt{2}\,(I_0^{2\lambda}/I_0^{\lambda})\,K_{111}^{2\lambda}}.$$

Here $K_{hkl}^{\lambda} = \lambda^3 j F_{hkl}^2 D_{hkl}/L_{hkl}$, where j is the repetition factor, F_{hkl} is the structure factor, D_{hkl} is the Debye–Waller factor, L_{hkl} is the Lorentz factor, and the $\sqrt{2}$ appears as a result of the inverse proportionality of the counter efficiency on the neutron velocity.

Estimates of $I_0^{2\lambda}/I_0^{\lambda}$ gave the values 1.60, 0.21, and 0.10 for λ = 0.60, 0.65, and 0.73 Å, respectively. No contribution from 2λ neutrons was found at λ = 0.77 Å (the random experimental error did not exceed 5%).

Thus the 2λ neutrons occur in the beam over a wavelength interval of at least 0.15 Å. When mosaic monochromators of the above space groups are used, it is therefore necessary to take into account the azimuthal orientation of the "monochromatizing" plane relative to the scattering vector in order to avoid contamination of the monochromatic beam by neutrons of greater wavelength.

---

[1] D. A. Kottwitz, Acta Crystallogr., A24, 117 (1968).
[2] D. A. Kottwitz, Acta Crystallogr., A25, 459 (1969).
[3] D. A. Kottwitz, Phys. Rev., 175, 1056 (1968).
[4] G. E. Bacon, Neutron Diffraction, Clarendon Press, Oxford (1962).

Solubility of LnF_3 in lanthanum fluoride

O. V. Kudryavtseva, L. S. Garashina, K. K. Rivkina, and B. P. Sobolev

Institute of Crystallography,
Academy of Sciences of the USSR

(Submitted April 29, 1972; resubmitted August 31, 1972)
Kristallografiya, 18, 843-844 (July-August 1973)

There is only one paper which deals with the solubility of the rare-earth trifluorides in LaF_3 on crystallization from the melt.[1] In their investigation the authors of ref. 1 considered the possibility of obtaining single crystals of the solid solutions to be the criterion from which the solubility limit was determined. The limiting solubilities of LnF_3 in LaF_3 calculated from a graph[1] were found to be extremely low for the LnF_3 series (Ln = Sm−Yb). It is also known[2] that LnF_3 (Ln = Sm−Ho) have a high-temperature modification isostructural with LaF_3, which would seem to form a continuous series of solid solutions with LaF_3 at fairly high temperatures.

The too-low values obtained in ref. 1 for the solubility of LnF_3 in LaF_3 are explained by the tendency of the tysonite (LaF_3) α modifications of the rare earth fluorides to undergo a transition to a rhombic modification (β-YF_3 type), which was favored by the slow cooling conditions in the experiments.[1]

The purpose of the present investigation was to study the solubility of LnF_3 in LaF_3. To maintain the high-temperature equilibrium state the specimens were quenched in flowing water. We found that the replacement of Ln^{3+} (Ln = Sm−Er) in LnF_3-LaF_3 systems by the large La^{3+} ion has a stabilizing action and enables tysonite solid solutions $(La_{1-x}Ln_x)F_3$ having an appreciably higher LnF_3 content than in the determinations in ref. 1 to be obtained by quenching.

The specimens were prepared by sintering the rare-earth trifluorides at 800-950°C in sealed nickel vessels in a fluorinating atmosphere. The results of measuring the unit cell parameters of the $(La_{1-x}Ln_x)F_3$ solid solutions are shown in Fig. 1. In spite of the high rate of quenching, partial breakdown of the solid solutions on cooling was observed for all the LnF_3-LaF_3 systems (in the two-phase region the unit cell parameters of the tysonite phases continue to change). Thus, our determinations of the solubility of LnF_3 in LaF_3 do not characterize the high-temperature equilibrium state either, although they are appreciably closer to it than the data in ref. 1. Taking the extreme single-phase compositions to be the limit of quenchability of the tysonite solid solutions, we obtained values for the solubility of LnF_3 in LaF_3 from which the graph in Fig. 2 was plotted. Calculation of the average ionic radii of the cations for the limiting concentrations of the $(La_{1-x}\cdot Ln_x)F_3$ solid solutions showed that in all cases (including ErF_3 and YF_3, which do not have tysonite modifications) they vary between 0.99 and 1.00 Å, being 0.996 Å on average, which virtually coincides with the radius of Nd^{3+} (0.995 Å)[3]. From this it follows that the quenchability of tysonite solid solutions of LnF_3 in LaF_3 is determined by the stabilizing action of replacing Ln^{3+} by the larger La^{3+} cation, which leads to the average radius of the cation in the solid solution being increased to values at which an LaF_3-type structure is stable over the whole temperature range from room temperature to the melting point, as also occurs with NdF_3 (SmF_3, which follows it, is already dimorphous).

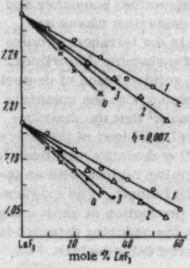

Fig. 1. Variation in the unit cell parameters of solid solutions of LnF_3 in LaF_3. 1) SmF_3; 2) GdF_3; 3) YF_3; 4) ErF_3; T = 945°C. The a and c parameters are first-order quantities.

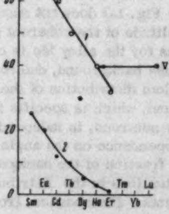

Fig. 2. Solubility of LnF_3 in LaF_3. 1) This investigation; 2) data from ref. 1; T = 867°C.

---

[1] D. A. Jones and W. A. Shand, J. Crystal Growth, 2, 361 (1968).
[2] R. E. Thomas and G. D. Brunton, Inorg. Chem., 5, 1937 (1966).
[3] D. Templeton and C. Dauben, J. Amer. Chem. Soc., 76, 5237 (1954).

Short-range and long-range order in the arrangement of the interstitial atoms in $(34\%Ta66\%Ti)D_x$

N. F. Miron, V. I. Shcherbak, V. N. Bykov, and V. A. Levdik

(Submitted February 4, 1972; resubmitted August 21, 1972)
Kristallografiya, 18, 845-846 (July-August 1973)

In a study of monodeuterides of transition metals of the vanadium subgroup by neutron diffraction, Somenkov and co-workers[1] established that the deuterium atoms are distributed in an ordered fashion in the tetrahedral holes of the metal lattice and create orthorhombic distortions in it. In a study of an interstitial solid solution of deuterium in an alloy of titanium and niobium with the composition $(34\%\ Nb\ 66\%\ Ti)D_{0.35}$ it was found[2] that the distribution of deuterium in the tetrahedral positions of the body-centered cubic structure of the alloy deviates significantly from the random distribution, forming regions with an increased concentration of interstitial atoms. The existence of these regions is related to the production of short-range order, which apparently precedes the ordering detected in the monodeuterides of body-centered cubic metals.

The present paper gives the results of a neutron-diffraction study of a 34% Ta—60% Ti alloy, and also specimens of this alloy deuterated to a composition $MeD_{0.35}$ and $MeD_{0.70}$ (where Me = 34% Ta—66% Ti). The experimental procedure and the preparation of the specimens were analogous to those described earlier.[2]

The neutron-diffraction patterns of the original alloy (see Fig. 1a) does not show coherent maxima (the mean amplitude of the coherent elastic scattering of slow neutrons for the alloy Me is close to zero). It shows only a diffuse background, due to the spin incoherence and the random distribution of the isotopes. This diffuse background, which is specific for the case of the scattering of slow neutrons, is independent of the angle of scattering. A dependence on the angle of scattering is shown only by that fraction of the background which is associated with fluctuations in the distribution of the atoms of the components. The absence, from the neutron-diffraction pattern of the alloy, of the part of the diffuse background which depends on the angle of scattering indicates an almost random distribution of atoms in the lattice sites, that is, the contribution to the diffuse background due to the difference in the scattering power of the Ti and Ta atoms is determined in this case by the Laue equation.[3]

Deuteration of the alloy leads to significant changes in the picture for the scattering of slow neutrons. The neutron-diffraction pattern for the specimen $MeD_{0.35}$ (Fig. 1b) shows a number of coherent reflections, and in the range of angles 20-40° and 52-72° (2ϑ) diffuse maxima are observed. The regular reflections are indexed in a body-centered cubic lattice with constant $a = 3.31$ Å (x-ray diffraction studies showed that the original alloy has a body-centered cubic structure with $a = 3.30$ Å). Calculation shows that good agreement between the calculated and experimental intensities is obtained for a model of the structure with distribution of deuterium in the tetrahedral holes of the lattice of the alloy. The preservation of the structure of the original alloy on deuteration up to a concentration D/Me = 0.35 indicates the existence of a wide range of primary interstitial solid solutions of deuterium in Me. It was previously generally assumed that in primary interstitial solid solutions deuterium is distributed randomly in the sites of the metal lattice. As shown earlier[2] and confirmed in the present work, however, the deuterium distribution deviates from a random distribution. For a random distribution the contribution to the diffuse background due to the penetration of deuterium into the lattice of the alloy is described by the Laue equation. Experiment shows, however, that this contribution depends to a significant extent on the angle of scattering, on the basis of which it is concluded that the distribution deviates from a random distribution.

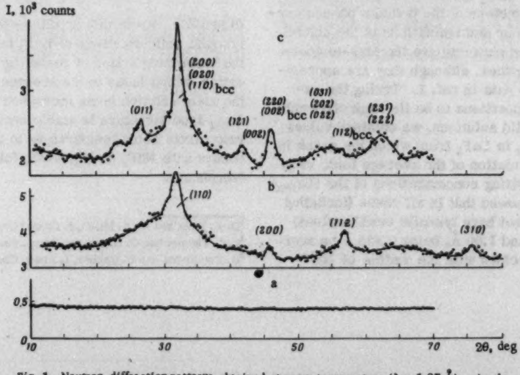

Fig. 1. Neutron-diffraction patterns obtained at room temperature ($\lambda = 1.27$ Å): a) original alloy Me = 34% Ta 66% Ti; b) $MeD_{0.35}$; c) $MeD_{0.70}$.

The following suggestion may be put forward regarding the nature of the distribution of deuterium in the interstitial solid solution. At low concentrations in the interstitial solid solution, regions with an increased concentration of deuterium are formed. In these there is a high degree of ordering of the interstitial atoms. The dimensions of these regions are insufficient to give a diffraction pattern, and the neutron-diffraction pattern shows a diffuse maximum. The regions with increased concentration can be regarded as the nuclei of a new phase. Increase in the concentration of deuterium leads initially to an increase in the number of nuclei, and after a certain concentration has been reached, increase in the dimensions of the nuclei begins. When the dimensions of the nuclei reach values sufficient for the production of an interference pattern, indistinct diffraction maxima, corresponding to the structure of this phase, appear on the neutron-diffraction pattern (Fig. 1c). Judging from the position of the additional reflections on the neutron-diffraction pattern of MeD$_{0.7}$, the ordered phase is isostructural with the monodeuterides of transition metals of group V. The MeD$_{0.7}$ specimen consisted of two phases. In addition to the reflections of the new phase there are also present lines due to the interstitial solid solution, which are marked by the letters bcc in Fig. 1. It should be emphasized that according to the x-ray diffraction data, throughout the entire range of concentrations of deuterium the alloy Me remains disordered, and the observed changes in the diffraction patterns are due to changes in the distribution of the interstitial atoms.

On the basis of the data obtained it is possible to reach the following conclusions: a) The original alloy is a disordered substitutional solid solution; b) the deuterium atoms in MeD$_{0.35}$ and MeD$_{0.70}$ are distributed in the tetrahedral holes of the lattice of the alloy; c) deuterium dissolves in Me, forming a wide range of interstitial solid solutions up to a concentration D/Me = 0.35; d) in the interstitial solid solution the distribution of deuterium deviates from a random distribution, forming regions with an increased concentration of deuterium, the dimensions of which in MeD$_{0.35}$ are insufficient for an interference pattern to be obtained.

---

[1] V. A. Somenkov, A. V. Gurskaya, M. A. Zemlyanov, M. E. Kost, N. A. Chernoplekov, and A. A. Chertkov, Fiz. Tverd. Tela, 10, 1355 (1968) [Sov. Phys. – Solid State, 10, 1076 (1968)].

[2] N. F. Miron, V. I. Shcherbak, L. E. Fykin, V. N. Bykov, V. A. Levdik, and S. P. Solov'ev, ZhETF Pis. Red., 13, 686 (1971) [JETP Lett., 13, 485 (1971)].

[3] M. A. Krivoglaz, The Theory of the Scattering of X Rays and Slow Neutrons by Nonideal Crystals [in Russian], Nauka, Moscow (1968).

Infrared spectra of manganese garnets containing a germanate tetrahedron

R. Hrichova

Higher School of Chemical Technology, Prague, Czechoslovakia

(Submitted April 17, 1972; resubmitted August 28, 1972, December 14, 1972)
Kristallografiya, 18, 847-848 (July-August 1973)

Garnets $Mn_3R_2Ge_3O_{12}$ (R^{3+} = Al, Cr, Ga, or Fe) prepared by the ceramic method have been described in the literature.[1,2]

We used the methods of ceramic technology to prepare garnets of the types $Mn_3Ga_xR_{2-x}Ge_3O_{12}$, where R^{3+} = Al, Cr, or Fe, and $Mn_3Al_xCr_{2-x}Ge_3O_{12}$, $Mn_3Cr_xFe_{2-x}Ge_3O_{12}$, and $Mn_3Al_xFe_{2-x}Ge_3O_{12}$, where x = 0, 0.5, 1.0, 1.5, or 2.0. The original components of the charge were $MnCO_3$, Al_2O_3, Cr_2O_3, Fe_2O_3, and Ga_2O_3, and GeO_2 ("analytically pure" grade). Compressed mixtures (after heating at 750°C for a period of 5 h) were heated in air for a period of 6–8 h. The phase composition of the products of the synthesis was studied by x-ray diffraction methods (Rigaku Denki diffractometer, Co Kα and Cu Kα radiation); the lattice constants a_0 of the single-phase products (see Table 1) were determined with an accuracy of ±0.005 Å. The x-ray diffraction method developed by Mill was used to confirm that the specimens obtained consisted of single phases. Table 1 gives the conditions of the synthesis and the characteristics of the single-phase garnet ceramic.

The specimens for the recording of the infrared spectra were obtained by compressing the material being studied with KBr. The spectra were recorded on a Perkin–Elmer 325 instrument in the range 200–1200 cm^{-1} with an accuracy of ±5 cm^{-1}. The vibrational spectra of the garnets were used to determine the positions of the maxima due to the stretching vibration ν_3 of the germanate tetrahedra. We studied the dependence of the frequency of the triplet ν_3 of the stretching vibration of the GeO_4 tetrahedra on the cell parameters (see Fig. 1).

In agreement with the results obtained by other workers, it was found that the frequency of the stretching vibration ν_3 decreases with increase in the cell parameter.[3,4]

It can be seen from Fig. 1 that the plot of the frequencies of the stretching vibration of the GeO_4 tetrahedron of garnets not containing gallium, with change in a_0, is close to a continuous curve. The frequencies of the gallium garnets are displaced from this curve towards higher values.

In an earlier paper[5] it was suggested that the anomalous decrease in the lattice constant a_0, found in the case of d^{10} ions, is due to the participation of the d electrons in π bonding. It was also found[6] from a structural study that in the garnets $Y_3Al_{5-x}Ga_xO_{12}$, Ga^{3+} enters the tetrahedron before the Al^{3+} ion, the radius of which is smaller than that of Ga^{3+}.

The data from the infrared spectra of the manganese garnets, obtained in the present work, are in agreement with the previously observed[7] anomalous displacements of ν_3 for calcium and cadmium garnets (with a germanate tetrahedron) containing d^{10} ions (Cd^{2+}, In^{3+}, Ga^{3+}), where the displacement of ν_3 is equal to ~10 cm^{-1} for every d^{10} atom in the formula of the garnet.

The increase in the frequencies of the stretching vibration of the GeO_4 tetrahedra can apparently be interpreted as a consequence of an increase in the stability of the lattice as a result of the participation of d electrons

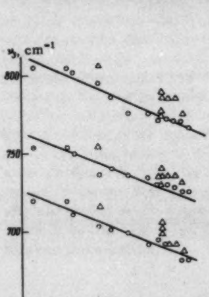

Fig. 1. Dependence of the frequency of the triplet ν_3 of the GeO_4 stretching vibration on the unit cell parameter (see Table 1). △) $Mn_3Ga_xR_{2-x}\cdot Ge_3O_{12}$; ○) other garnets.

TABLE 1

Garnet	a_0, Å	ν_3, cm^{-1}			T, °C
$MnFe_2Ge_3O_{12}$	12.084	765	725	680	1200
$Mn_3Fe_{1.5}Al_{0.5}Ge_3O_{12}$	12.037	775	735	690	1200
$Mn_3Fe_1Al_1Ge_3O_{12}$	11.989	785	740	700	1150
$Mn_3Fe_{0.5}Al_{1.5}Ge_3O_{12}$	11.942	802	750	710	1150
$Mn_3Al_2Ge_3O_{12}$	11.896	805	755	720	1100
$Mn_3Fe_{1.5}Cr_{0.5}Ge_3O_{12}$	12.075	770	725	680	1200
$Mn_3Fe_1Cr_1Ge_3O_{12}$	12.067	770	729	690	1200
$Mn_3Fe_{0.5}Cr_{1.5}Ge_3O_{12}$	12.058	771	730	692	1200
$Mn_3Cr_2Ge_3O_{12}$	12.049	770	730	695	1250
$Mn_3Fe_{1.5}Ga_{0.5}Ge_3O_{12}$	12.077	775	732	685	1180
$Mn_3Fe_1Ga_1Ge_3O_{12}$	12.068	785	735	690	1150
$Mn_3Fe_{0.5}Ga_{1.5}Ge_3O_{12}$	12.060	785	735	690	1150
$Mn_3Ga_2Ge_3O_{12}$	12.053	790	740	705	1150
$Mn_3Al_1Ga_1Ge_3O_{12}$	11.975	807	755	716	1130
$Mn_3Al_{1.5}Cr_{0.5}Ge_3O_{12}$	11.935	805	755	720	1150
$Mn_3Al_1Cr_1Ge_3O_{12}$	11.973	796	737	702	1150
$Mn_3Al_{0.5}Cr_{1.5}Ge_3O_{12}$	12.010	775	736	699	1150
$Mn_3Ga_{1.5}Cr_{0.5}Ge_3O_{12}$	12.053	785	735	702	1150
$Mn_4Ga_1Cr_1Ge_3O_{12}$	12.051	777	735	700	1170
$Mn_3Ga_{0.5}Cr_{1.5}Ge_3O_{12}$	12.050	772	730	698	1170

and the associated increase in electron density close to the Ge atoms.

---

[1] A. Tauber, C. G. Whinfrey, and E. Banks, J. Phys. Chem. Solids, 21, 25 (1961).

[2] A. Tauber, E. Banks, and H. Kedesdy, J. Appl. Phys., 29, 385 (1958).

[3] K. A. Wickersheim, R. A. Lefever, and B. M. Hankins, J. Chem. Phys., 32, 271 (1960).

[4] R. K. Moore, A. B. White, and T. V. Long, Am. Mineralogist, 56, 54 (1971).

[5] R. Hrichova and J. Feixova, Collected Reports of the 26th Congress of the Czechoslovak Chemical Society [Russian translation], Cheske Budeiovitse, Czechoslovak SSR (1970).

[6] M. Marezio, J. P. Remeika, and P. D. Dernier, Acta Cryst., B24, 1670 (1968).

[7] R. Hrichova and R. Lastovka, Sbornik VSCHT-G-15.

Growth and study of crystals of double oxides of cadmium with structures of the perovskite type.

I. Cadmium hafnate

R. I. Spinko, V. N. Lebedev, R. V. Kolesova, and E. G. Fesenko
Rostov State University

(Submitted May 17, 1972)
Kristallografiya, 18, 849-851 (July-August 1973)

It was previously shown[1] that the dielectric constant of $CdHfO_3$ passes through maxima at 15 and 605°C. These and other indications suggested that the phase transformations in $CdHfO_3$ are antiferroelectric or ferroelectric.

The aim of the present work was to prepare and study single crystals of $CdHfO_3$. The x-ray diffraction data and the results of the study of the dielectric and optical properties indicate that $CdHfO_3$ exhibits antiferroelectric properties.

GROWTH OF CRYSTALS

Since $CdHfO_3$ melts incongruently, we used a method involving growth of the crystals from solutions in molten salts and oxides. Attempts were made to obtain $CdHfO_3$ crystals from systems containing potassium, lead, and cadmium fluoride, cadmium borates, and their mixtures. The best crystals were obtained using the system $CdO - B_2O_3 - PbF_2 - HfO_2$, after some study of this system.

On the basis of the results of a study of the $CdO - B_2O_3$ system[2] and our studies, the components of the system were taken in the molar ratio (10-13):7:12:1.

The experiments were carried out in a platinum crucible with a volume of 10 cm^3. The crucible containing a mechanical mixture of the components was placed in a furnace at a maximum temperature of the experiment equal to 1100-1150°C, the melt was kept at this temperature for 5-10 h, cooled at a rate of 4-6 deg/h to 800°C, and then poured off, after which the crystals were annealed by slow cooling to room temperature. Traces of the flux were removed comparatively readily with 10-20% aqueous acetic acid solution. Under these conditions we obtained lamellar and acicular colorless or slightly yellowish $CdHfO_3$ crystals.

OPTICAL OBSERVATION OF THE PHASE TRANSFORMATIONS, AND DIELECTRIC MEASUREMENTS

Thin (10-100 μ) crystalline platelets of $CdHfO_3$ are optically uniform (Fig. 1a) and in polarized light show systematic extinctions at 90° intervals. Thicker crystals (300 μ and above) showed twinning (Fig. 1b) in the form of alternating light and dark regions. We characterized these as domains – regions with different directions of the antipolarization vector, in agreement with the results of further study of the crystals.

On passing through the Curie point (~600°C), a sudden change in the interference color of the crystal is observed, but the nature of the extinctions remains unchanged. The domain structure becomes simpler, the dimensions of the light and dark regions increasing (Fig. 1c). On further heating (above 700°C), gradual extinction of the light regions is observed, accompanied by breakdown of the crystal (Fig. 1d). The crystal becomes optically isotropic at a temperature of 720°C.

In thin crystals, both phase transformations appear only in the form of sudden changes in the interference color. This indicates an appreciable sudden change in volume in the transformation; sudden changes of this kind are characteristic of ferroelectric and antiferroelectric transitions.

For the dielectric measurements we used thin and

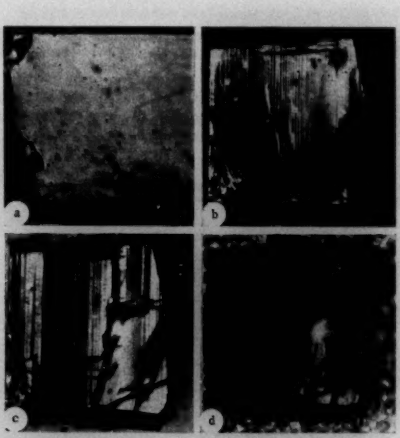

Fig. 1. Crystals of $CdHfO_3$ in polarized transmitted light. ×10. a) Optically uniform crystal; b, c, d) twinned crystal at temperature of 20, 610, and 750°C, respectively.

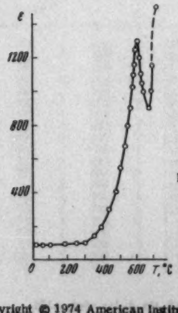

Fig. 2. ε(T) curve for a $CdHfO_3$ crystal (1 kHz).

thick crystals. The dielectric constant of the optically uniform crystals is slightly greater than that of the twinned crystals, and at room temperature does not exceed 90. In a study of the temperature dependence of ε, the first high-temperature phase transformation was clearly detected at 605 ± 3°C (Fig. 2). Above 700°C, however, in addition to the increase in ε, a rapid increase in the dielectric losses was observed, and the second transformation could not be fixed. A dielectric hysteresis loop was not observed. The linear dependence of the polarization on the applied field was followed up to 200 kV/cm.

X-RAY DIFFRACTION STUDY

The structural difference between the ferroelectric and antiferroelectric crystals is defined by the superstructure of the latter. The x-ray diffraction patterns (RKV-86N camera) obtained by rotation about the *a*, b, and c axes of the reduced perovskite cell showed layer lines, the reflections of which were indexed according to a doubled lattice constant. On the x-ray rotation photographs recorded with twinned crystals, the layer lines contain double reflections, which were indexed with respect to the parameters *a* and b, confirming the twinning.

The x-ray diffraction study of the phase transformations was carried out with polycrystalline specimens on a URS-50IM diffractometer by means of a high-temperature attachment, with Fe Kα radiation. The parameters were measured from the structure-sensitive reflections with $h^2 + k^2 + l^2 = 10$ and 12.

The temperature dependence of the parameters of $CdHfO_3$ is given in Fig. 3, and confirms the existence of two high-temperature phase transformations at 600 ± 15 and 720 ± 5°C. The first transformation from the orthorhombic phase I into the orthorhombic phase II is characterized by an appreciable increase in the volume of the reduced perovskite cell. The second phase transformation is also accompanied by a sharp change in the volume of the perovskite cell and a change in its symmetry. We did not observe[1] a low-temperature phase transformation at 15°C.

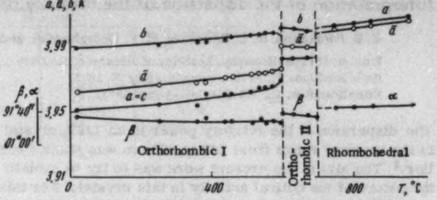

Fig. 3. Temperature dependence of the parameters of $CdHfO_3$.

CONCLUSIONS

The familiar criteria of the ferroelectric state of oxides with structures of the perovskite type do not make it possible to predict whether $CdHfO_3$ will be ferroelectric: Cd^{2+}, according to the formal oxidation number, is an s element, and its polarizability is low, and Hf^{4+} exhibits a weak tendency to form directed bonds and is not considered ferroactive.

To explain the properties of $CdHfO_3$, we estimated the perturbation of the oxygen atoms on the valence orbitals of the Cd atoms[3] and found that they are weakly perturbed. As a consequence, the directed character of the bonds resulting from the use of hybrid sp orbitals in bonding may be considerable, and this explains[3] the ferroelectric state of $CdHfO_3$.

A noteworthy feature is the tendency, previously observed in many cases (see, for example, ref. 4), for Cd atoms to form directed bonds as a consequence of the participation of d electrons in bonding. The number of such electrons unfortunately has not been established accurately, so that it is impossible to calculate the parameter of the directed character of the Cd–O bonds and to use the semiquantitative criterion developed by Fesenko.[3]

---

[1] L. N. Aver'yanova, I. N. Belyaev, Yu. I. Gol'tsov, L. A. Solov'ev, R. I. Spinko, and O. I. Prokopalo, Fiz. Tverd. Tela, 10, 3416 (1968) [Sov. Phys. – Solid State, 10, 2698 (1969)].

[2] W. D. Hand and J. Krogh-Moc, J. Am. Ceram. Soc., 45, 197 (1962).

[3] E. G. Fesenko, The Perovskite Family and Ferroelectricity [in Russian], Atomizdat, Moscow (1972).

[4] V. K. Grigorovich, Mendeleev's Periodic Law and the Electronic Structure of Crystals [in Russian], Nauka (1966), p. 228.

Interpretation of the dispersion of the rotatory power in the $LiIO_3$ crystal

Z. B. Perekalina, N. L. Smirnova, G. F. Dobrzhanskii, and I. A. Shpil'ko

Institute of Crystallography, Academy of Sciences of the USSR

(Submitted June 27, 1972; resubmitted July 20, 1972)
Kristallografiya, 18, 852-854 (July-August 1973)

The dispersion of the rotatory power in an $LiIO_3$ crystal in the spectral range from 290 to 600 nm was studied earlier.[1] The aim of the present work was to try to explain the nature of the optical activity in this crystal. For this purpose we carried out additional studies of the dispersion of the rotatory power in the range from 600 to 925 nm, and the absorption spectra in the ultraviolet range.

The absorption spectra were studied on a Hitachi EPS-3T spectrophotometer. In the region from 290 to 400 nm in the range of relative transparency of $LiIO_3$ we used plane-parallel plates, prepared from $LiIO_3$ crystals, as specimens for the measurement of the absorption spectra. In the shorter wavelength range, where the crystal absorbs strongly, the absorption spectrum was measured from the diffuse reflectance from powders prepared from the same crystals. The measurements were made by means of a special attachment to the spectrophotometer. LiF powder was used as standard reflector. For the treatment of the reflectance spectra we used the Kubelka–Munk function[2]

$$F = (1 - R)^2 / 2R, \qquad (1)$$

where R is the reflectance coefficient, and F is a quantity characterizing the absorption. The results of the measurements and the calculations are given in Fig. 1, from which it can be seen that the absorption spectrum of $LiIO_3$ contains two bands: one intense, with maximum at 253 nm, and the other weak ($\sim$3.7 cm^{-1}), with maximum at 320 nm. Similar absorption bands were also observed experimentally[3] for $NaIO_3$. It was shown theoretically[4,5] that both absorption bands are due to electronic transitions in IO_3^-. The intense absorption band at 253 nm is due to allowed transitions with symmetry $A_1 \leftarrow {}^1A_1$, and the weak band at $\lambda \sim 320$ nm is due to a forbidden $n \to \pi^*$ transition with symmetry ${}^1A_1 \to {}^1A_2$. These results were obtained with allowance for the fact that IO_3^- has C_{3v} symmetry.

From the smooth course of the curve giving the dispersion of the rotatory power in $LiIO_3$, obtained earlier,[1] it can be seen that the band with $\lambda \sim 320$ nm does not make a significant contribution to the rotation. The rotatory power increases sharply in the region of 300 nm, that is, close to the electronic transition in IO_3^-, associated with the band at $\lambda = 253$ nm. To determine the nature of the optical activity in $LiIO_3$ we calculated the dispersion of the rotatory power according to different empirical equations.[6–8] We used the single-term and two-term equations of Chandrasekhar

$$\rho = \sum_i \frac{K_i'\lambda^2}{(\lambda^2 - \lambda_{0i}^2)^2} \qquad (2)$$

and Drude

$$\rho = \sum_i \frac{K_i''}{(\lambda^2 - \lambda_{0i}^2)}, \qquad (3)$$

and also the Born–Vyšin equation

$$\rho = \frac{K_1'\lambda^2}{(\lambda^2 - \lambda_{01}^2)^2} + \frac{K_1''}{(\lambda^2 - \lambda_{01})^2}. \qquad (4)$$

In these equations K_i' and K_i'' are constants, and λ_{0i} is the characteristic wavelength.

Equation (2) characterizes the optical activity arising due to the structure of the crystal. Equation (3) characterizes the optical activity arising due to the asymmetric structure of the molecule. Equation (4) shows the extent to which the two mechanisms are involved in the phenomenon. The applicability of the equations was estimated from the magnitude of $\Sigma(\rho_e - \rho_c)^2$ and the agreement between the calculated λ_{0i} and the experimental λ.

The calculations were carried out on an M-220 computer by means of two programs. In the single-term equations we used a direct method[9] of calculating the parameters K and λ_0 from the minimum sum of squares of the deviations $\Sigma(\rho_e - \rho_c)^2 = 0$. The calculation with the two-term equations was carried out by means of the standard program for searching for the minimum of a function of many variables.[10] The results of the calculation using the single-term equations (2) and (3) and Eq. (4) are given in Table 1.

The calculations using the two-term equations (2) and (3) showed that they reduce essentially to one-term equations. It can be seen from Table 1 that Eq. (3) gives the smallest value of $\Sigma(\rho_e - \rho_c)^2$, and the calculated λ_0 is found to be close to the absorption band with maximum at $\lambda = 253$ nm. It can be seen from the calculation according to Eq. (4) that the term of type (3) makes a decisive contribution to the dispersion of the rotatory power of $LiIO_3$.

From all the above it may be concluded that Eq. (3) is the most suitable for the description of the dispersion of the rotatory power in $LiIO_3$; this means that the optical activity in this crystal is determined by the structure of the molecule.

Crystal-chemical analysis of the structure of $LiIO_3$ confirms this conclusion. $LiIO_3$ belongs to the pyramidal class 6 of the hexagonal system.[11] The space group is $P6_3$, and the unit cell parameters are $a = 5.478$, $c = 5.170$, $Z = 2$.

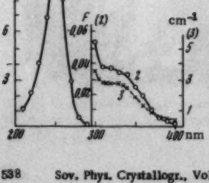

Fig. 1. Spectral characteristics of $LiIO_3$ crystals. 1, 2) Absorption spectra, determined from the diffuse reflectance [from Eq. (1)]; 3) absorption spectrum of $LiIO_3$, measured in transmission.

TABLE 1

Parameters	Equation			
	(2)	(3)	(4)	Eq. (4) with parameters taken from ref. 13
K_1'	26.6	—	—0.6	46.6
K_1''		29.4	29.9	—20.0
λ_{01}	0.191	0.232	0.234	0.169
$\Sigma(\rho_e - \rho_c)^2$	1627	607	608	12433
$\sqrt{\frac{\Sigma(\rho_e - \rho_c)^2 *}{n}}$	6.9	4.2	4.2	19.1

*n is number of experimental points.

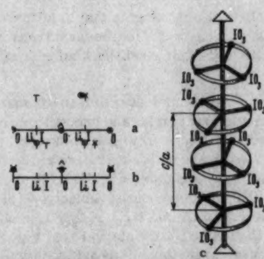

Fig. 2. LiIO$_3$ structure. Line diagram of LiIO$_3$ for the cases where the IO$_3^-$ group has symmetry C_{3v} (a) and 3 (b); c) schematic arrangement of the IO$_3^-$ groups related by the 6_3 axis in the LiIO$_3$ crystal.

The analysis was carried out by the line diagram method.[12] It was established (Fig. 2) that with a 6_3 axis present and two molecules in the unit cell, the IO$_3^-$ groups must lie in planes and the structure does not have screw character. Each IO$_3^-$ group, however, on entering the crystal structure, decreases its symmetry from C_{3v} in solution to 3 in the crystal.[11] It is as a consequence of the asymmetrization of IO$_3^-$ in the LiIO$_3$ crystal that the optical activity arises.

The results which we obtained do not agree with the conclusions reached in ref. 13, in which it was proposed that the dispersion of the rotatory power in LiIO$_3$ be described by means of Eq. (4), but with other parameters K and λ_0 (see Table 1). It can be seen from Table 1 that when these parameters are used, Eq. (4) gives the highest value of $\Sigma(\rho_e - \rho_c)^2$, and λ_0 does not coincide with the value of λ obtained experimentally.

---

[1] Z. B. Perekalina, G. F. Dobrzhanskii, and I. A. Shpil'ko, Kristallografiya, 15, 1252 (1970) [Sov. Phys. – Crystallogr., 15, 1095 (1971)].

[2] G. Kortum, W. Braun, and G. Herzog, Usp. Fiz. Nauk, 85, 365 (1965).

[3] S. P. Tandon and J. P. Gupta, Opt. Commun., 3, 248 (1971).

[4] A. D. Walsh, J. Chem. Soc., 2301 (1953).

[5] S. P. McGlynn and M. Kasha, J. Chem. Phys., 24, 481 (1956).

[6] S. Chandrasekhar, Proc. Indian. Acad. Sci., A39, 243 (1954).

[7] P. Drude, Theory of Optics, Dover (1902).

[8] V. Vyšín, Proc. Phys. Soc., 87, 55 (1966).

[9] B. N. Grechushnikov and Z. B. Perekalina, Zh. Prikl. Spektrosk., 8, No. 5 (1973).

[10] B. T. Polyak and V. A. Skokov, Standard Program for the Minimization of a Function of Many Variables [in Russian], Izd. MGU (1967).

[11] I. L. de Bouer, F. van Bolhuis, R. Olthof-Hazekamp, and A. Vos, Acta Crystallogr., 21, 841 (1966).

[12] Z. B. Perekalina and N. L. Smirnova, Kristallografiya, 14, 820 (1969) [Sov. Phys. – Crystallogr., 14, 708 (1970)].

[13] V. Janku and V. Vyšín, Opt. Commun., 3, 308 (1971).

Anisotropy of certain physical properties of pyrargyrite and proustite crystals

N. I. Butsko, M. M. Pidorya, and T. D. Krushel'nitskaya

L'vov Polytechnic Institute

(Submitted June 16, 1972; resubmitted August 23, 1972)
Kristallografiya, 18, 855-856 (July-August 1973)

In this study, we investigated the anisotropy of the magnetic susceptibility, coefficient of linear expansion, microhardness, and electrical resistivity of pyrargyrite and proustite single crystals grown by the Bridgman method.[1,2] The crystals belong to the trigonal system; the symmetry type is bitrigonal-pyramidal. Samples in the form of regular parallelepipeds 5-10 mm long were cut out of the bars.

The anisotropy of the magnetic susceptibility χ was studied at room temperature in a uniform 3000-Oe magnetic field. The absolute value of magnetic susceptibility was measured according to ref. 3. The investigations showed that pyrargyrite and proustite samples of any form are oriented in a steady magnetic field in such a way that the c axis is parallel to the field intensity vector, and are diamagnetic. The c axis either coincided approximately with the long edge of the sample or formed some angle up to 30° with it.

Experimental values of magnetic susceptibility in the direction of the c axis were $\chi_{\parallel c(p)} = -0.316 \cdot 10^{-6}$ cm^3/g for pyrargyrite and $\chi_{\parallel c(pr)} = -0.332 \cdot 10^{-6}$ cm^3/g for proustite.

For directions perpendicular to the c axis, the values of the anisotropy, measured by the vibration method,[4] were $\chi_{\perp c(p)} = -0.401 \cdot 10^{-6}$ cm^3/g for pyrargyrite and $\chi_{\perp c(pr)} = -0.481 \cdot 10^{-6}$ cm^3/g for proustite. If the sample is oriented so that the line of suspension coincides with the c axis, no anisotropy of magnetic susceptibility is observed. Our results are consistent with data on the chemical structure of pyrargyrite and proustite.

The structural chemical formula of proustite with covalent and ionic bonds indicated[5] has the form $\mathrm{As}_3^{1+} \cdot [\mathrm{As}^{\downarrow\downarrow\downarrow} \mathrm{S}_3^{\uparrow -}]^{3-}$. Here, the As atom forms covalent bonds through p electrons, directed along the edges of a trigonal pyramid, whereas the S atoms assume the form $\mathrm{S}^{\uparrow -}$, having one covalent and one ionic bond. The radical $[\mathrm{As}^{\downarrow\downarrow\downarrow} \mathrm{S}_3^{\uparrow -}]^{3-}$ has the form of a low trigonal pyramid, where the S atoms make up an equilateral triangle.

The results of our measurements of magnetic susceptibility are quite consistent with the above structural concepts. The covalent bonds have an orientation which does not give diamagnetic components of χ in the direction of the symmetry axis C, but they are symmetrical with respect to this axis in the plane perpendicular to it. Hence, the diamagnetism due to covalent bonds is developed only in directions perpendicular to the c axis.

The considerable flattening of the pyramid in the direction of the c axis will, obviously, give rise to a paramagnetic component due to deformation of the electron shells. The indicated factors determine the anisotropy of magnetic susceptibility of proustite (and pyrargyrite, since they are isostructural). As a result, the diamagnetic component in the direction of the c axis is much less than the component perpendicular to this axis.

The direction of the c axis in pyrargyrite and proustite samples suspended in a uniform magnetic field is easily determined from their orientation. For this, it is sufficient to determine the orientation relative to two arbitrarily chosen directions of suspension of the sample. These conclusions were verified by x-ray analysis.

The well-known hypothesis that Van Vleck paramagnetism must decrease with increasing strength of a single covalent bond[6] (all other conditions being equal) explains why $\chi_{pr} > \chi_p$.

Curves of the coefficient of linear expansion α versus temperature for pyrargyrite and proustite were taken between 20 and 360°C on an IZV-1 dilatometer. The measurements were made with single crystals in the direction of the c axis ($\alpha_{\parallel c}$) and perpendicular to it ($\alpha_{\perp c}$). In the case of the indicated compounds, anisotropy of the coefficient of thermal expansion $\alpha_{\perp c} > \alpha_{\parallel c}$ was observed throughout the temperature interval (see Fig. 1). In the structures of pyrargyrite and proustite, therefore, the energy of bonds in the direction perpendicular to c is less than in that parallel to c.

Our results are supported by measurements of the microhardness of Ag_3SbS_3 and Ag_3AsS_3 crystals (PMT-3 instrument, polished planes, temperature interval 20-150°C). At a 50-g load, the microhardness is practically constant. In the direction of the c axis at room temperature and a 50-g load, the microhardness was found to be $H_{\parallel c(p)} = 93$ kg/mm^2 for pyrargyrite and $H_{\parallel c(pr)} = 146$ kg/mm^2 for proustite. Values perpendicular to the c axis are $H_{\perp c(p)} = 71$ kg/mm^2 for pyrargyrite, and $H_{\perp c(pr)} = 107$ kg/mm^2 for proustite. In the given temperature interval, both compounds have anisotropy of the first kind, $H_{\parallel c} > H_{\perp c}$. Comparison of coefficients of linear expansion α and of values of microhardness H showed that these quantities are correlated: $\alpha_{\perp c} > \alpha_{\parallel c}$ and $H_{\parallel c} > H_{\perp c}$.

The resistivity of the Ag_3SbS_3 and Ag_3AsS_3 samples was measured with ac (10 kHz) at room temperature. For the direction along the c axis, the resistivity amounts to: $\rho_{\parallel c(p)} = 3.37 \cdot 10^4$ $\Omega \cdot$ cm for pyrargyrite and $\rho_{\parallel c(pr)} = 1.88 \cdot 10^5$ $\Omega \cdot$ cm for proustite. For the direction perpendicular to the c axis, the resistivity is: $\rho_{\perp c(p)} = 1.66 \cdot 10^4$ $\Omega \cdot$ cm for pyrargyrite and $\rho_{\perp c(pr)} = 0.82 \cdot 10^5$ $\Omega \cdot$ cm for proustite.

Data on the coefficients of anisotropy of magnetic sus-

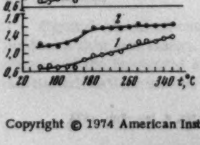

Fig. 1. Curves of the coefficients of linear expansion $\alpha_{\parallel c}$ (1, 3) and $\alpha_{\perp c}$ (2, 4) of pyrargyrite (3, 4) and proustite (1, 2) versus temperature.

TABLE 1

Compound	$K_1 = \frac{\chi_{\perp c}}{\chi_{\parallel c}}$	$K_2 = \frac{\alpha_{\perp c}}{\alpha_{\parallel c}}$ (150° C)	$K_3 = \frac{H_{\parallel c}}{H_{\perp c}}$	$K_4 = \frac{\rho_{\parallel c}}{\rho_{\perp c}}$
Ag_3SbS_3	1.27	1.48	1.32	2.03
Ag_3AsS_3	1.45	1.58	1.36	2.30

ceptibility K_1, linear expansion K_2, microhardness K_3, and resistivity K_4 are given in Table 1.

When pyrargyrite and proustite samples are heated from 20 to 400°C in a TU-1M thermal apparatus, the weight is decreased by 1.5% between 160 and 400°C as a result of dissociation of the material.

---

[1] N. I. Butsko, Ukr. Fiz. Zh., 9, 686 (1964).

[2] N. I. Butsko, E. G. Moroz, and I. O. Osipishin, Ukr. Fiz. Zh., 12, 2055 (1967).

[3] N. G. Shul'ga, M. M. Pidorya, and B. E. Bandrivskii, Proceedings of the Third All-Union Conference on Ferromagnetic Alloys [in Russian], Izd. L'vovskogo Univ., L'vov (1971).

[4] W. A. Wooster, Experimentalle Kristallphysik, Berlin (1958), p. 55.

[5] D. P. Grigor'ev, Dokl. Akad. Nauk SSSR, 167, 1123 (1966).

[6] Ya. G. Dorfman, Diamagnetism and the Chemical Bond [in Russian], Izd. Fiz.-Mat. Lit., Moscow (1961).

Secondary effects accompanying movement of 180-degree α domains in $BaTiO_3$

E. F. Dudnik and V. M. Duda

Dnepropetrovsk State University

(Submitted December 2, 1972; resubmitted February 29, 1972; January 17, 1973)
Kristallografiya, 18, 857-859 (July-August 1973)

It is known that the 180° domains in barium titanate become visible during repolarization, as a result of the presence of pseudomonoclinic distortions in the boundary regions separating these domains.[1] As we previously demonstrated,[2] if the boundary regions terminate within an a-domain crystal, they clearly delineate the wedge-shaped 180° α domains and make it possible to observe the latter without application of any external factors, by use of a polarization microscope. In the extinction position, the two 180° boundary regions forming the wedge appear light-colored. When the microscope stage is turned to a slight angle from the extinction position, it is possible to obtain extinction of one boundary region and transmission through the other. This indicates that the polar axes and hence the optical indicatrices in the boundary regions are rotated through a small angle with respect to their orientation in the a domain. In investigating the movement of the 180° cuneate a domains under the action of an electric field, we noted that a visible track remained in the area traversed by the 180° boundary region. The present investigation was conducted to study the behavior of this track.

Our investigation was made with $BaTiO_3$ single crystals grown by the Remeika method and having an $a-a$ domain structure,[1] which was obtained by the method described previously.[3] The electric field was applied perpendicular to the 90° walls (Fig. 1). The observations were made in the (001) plane with an MIN-8 polarization microscope set to a position close to the extinction position. In $a-a$ domain crystals, the wedge-forming 180° boundaries pass in a zig-zag manner through the 90° walls (Fig. 2a). If an electric field with a strength of 300–400 V/cm is applied to such a crystal, the 180° wedges begin to shift. As the field strength is increased to 1 kV/cm, they gradually exit from the crystal (Fig. 2b and c). Tracks remain at the old sites of the 180° domain boundary regions (Fig. 2d); they can be seen especially clearly after the electric field is discontinued.

If a $BaTiO_3$ single crystal containing a track is subjected to a sufficiently large field strength (~8 kV/cm), which causes displacement of the 90° domain wall, the track retains an inflection at the prior site of the crystal, i.e., the inflection lies not at the displaced 90° wall but within the a domain (Fig. 3). This indicates that the phenomenon we observed is actually the track.

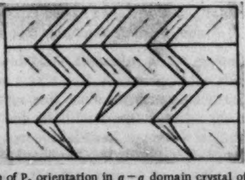

Fig. 1. Diagram of P_s orientation in $a-a$ domain crystal of $BaTiO_3$. The external electric field is directed vertically upward.

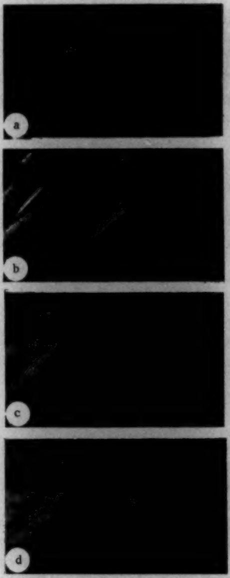

Fig. 2. Change in domain structure of $BaTiO_3$ single crystals containing 180° cuneate a domains under the action of an electric field applied in the [110] direction, ×200. a) E = 0; b) 1.2; c) 1.6; d) 3.1 kV/cm.

Fig. 3. Position of track after displacement of 90° $a-a$ domain wall under the action of an electric field (~8 kV/cm), ×350.

Numerous observations have established the following properties of the track.

1. In positions close to the extinction position, the track behaves like a 180° boundary region, although the transmission and extinction are less pronounced in this case.

2. The time for which the track exists increases with

the wedge lifetime and reaches a constant level of 3-4 h if the wedge is present in the crystal for 9-12 h. No track is observed if the 180° wedge exists in the crystal for less than 20-30 sec.

3. If a 180° wedge exits from the crystal under the action of the field and then reappears before the track disappears, it develops at the same point where it exited and quite often "enters" its track, i.e., an unusual "memory" effect is observed.

One of the main conditions for stability of 180° cuneate domains is compensation of the polarization charges at the wall by conductivity charges. It can therefore be assumed that the track we observed is a residual distortion maintained by the compensation-charge field after a 180° cuneate domain has exited under the action of an external field.

This hypothesis is supported by the aforementioned track properties and by our subsequent investigations. We expected that an increase in the conductivity of $BaTiO_3$ caused by heating of the crystal, addition of certain impurities, or irradiation with light having a wavelength corresponding to the absorption edge would lead to a decrease in track life. Actually, if a crystal in which a track has existed at room temperature for 3-4 h is rapidly heated to 100°C and then quickly cooled to room temperature, no track was usually detected. Track disappearance was 10-12 times as rapid in single crystals of a $BaTiO_3-ZnO$ solid solution, in which the conductivity at $t = 20°C$ is markedly greater than in pure barium titanate. There was a substantial decrease in track life after irradiation with ultraviolet light.

The unusual "memory" effect, i.e., the return of the wedge to its track, may have the following causes. Any imperfect ferroelectric crystal contains sites that "trap" domain walls.[4] In our case, these "traps" might be regions with residual distortions, i.e., tracks. As soon as a wedge enters a track in its movement, the polarization charges are compensated by the conduction charges and the wall becomes stable.

Our investigations thus enable us to conclude that a track is a region with residual stresses maintained by the compensation-charge field after a 180° wedge has exited under the action of an external field.

The authors wish to thank L. A. Shuvalov and E. V. Sinyakov for their interest in this work and their discussion of our results.

[1)] The domain structure of a crystal containing 90° walls separating the a domains will be termed an $a-a$ domain structure.

---

[1] J. Kabayashi, W. Yamada, and F. Nakamura, Phys. Rev. Lett., 11, 410 (1963).
[2] E. V. Sinyakov, V. M. Duda, E. F. Dudnik, and S. I. Yakunin, Fiz. Tverd. Tela, 13, 2558 (1971) [Sov. Phys. – Solid State, 13, 2149 (1972)].
[3] E. V. Sinyakov, E. F. Dudnik, and V. Fonduroko, Kristallografiya, 13, 10 (1968) [Sov. Phys. – Crystallogr., 13, 7 (1968)].
[4] W. Känzig, Ferroelectrics and Antiferroelectrics, Academic Press.

Elastic properties of KDP and DKDP crystals of high temperatures

S. I. Chizhikov, N. G. Sorokin, I. Yu. Ledovskaya, and E. V. Makarevskaya

Moscow Institute of Steel and Alloys

(Submitted April 14, 1972; resubmitted July 19, 1972)
Kristallografiya, 18, 860-862 (July-August 1973)

The elastic constants and absorption of elastic waves in KDP and DKDP crystals have been studied quite adequately at temperatures from −150 to +20°C. However, there are no data at all for high temperatures. The elastic constants and the coefficient of absorption of elastic waves are structure-sensitive parameters; hence, the result of this type of investigation of KDP and DKDP crystals is of interest, especially in a discussion of the nature of the high-temperature phase transitions whose presence was established in refs. 1-5. The nature of these transitions in crystals isomorphous with KDP is not yet clear. According to refs. 1, 2, and 6, they are due to rupture of hydrogen bonds, whereas in refs. 3 and 4, they are attributed to disordered rotation of the H_2PO_4 group around all three axes.

In the present study, we took curves of the elastic constants and coefficients of absorption of elastic waves versus temperature for KDP and DKDP crystals between 20 and 200°C. The measurements were made by a pulsed interference method at frequencies from 20 to 70 MHz. The method used enables one to measure the elastic constants of the crystals with an error not exceeding 0.5%, a sensitivity to relative changes in elasticity equal to 0.05%, and an absorption coefficient of 10% or better.[7,8]

The experimental curves of the elastic constants C_{11}, C_{33}, C_{44}, and C_{66} for KDP and DKDP crystals versus temperature are shown in Figs. 1 and 2. On heating from room temperature to 158°C for DKDP crystals and 187°C for KDP crystals, the elastic constants decrease linearly (see Table 1).

It is remarkable that substitution by deuterium changes only those elastic constants and corresponding temperature coefficients which are connected with elastic-wave velocities v_{11} and v_{12} [the vectors of the directions of propagation and displacement of the waves lie in the (x, y) plane]; the hydrogen bonds also lie in this plane. This shows that the O−H−O bond is weakened on substitution of hydrogen by deuterium. The increased coefficient of absorption of elastic waves α_{11} (Figs. 3, 4) in the DKDP crystal as compared with the KDP also supports the above.

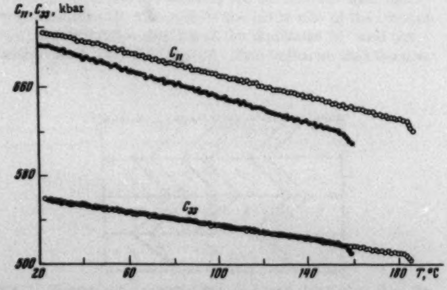

Fig. 1. Curves of elastic constants C_{11} and C_{33} versus temperature. ○) KH_2PO_4, ●) KD_2PO_4

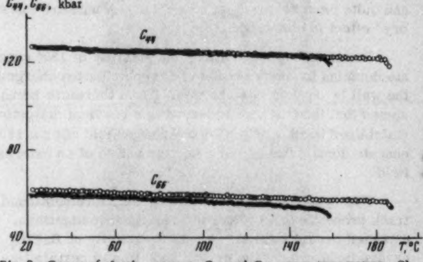

Fig. 2. Curves of elastic constants C_{44} and C_{66} versus temperature. ○) KH_2PO_4, ●) KD_2PO_4

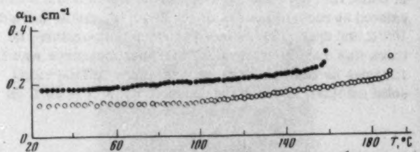

Fig. 3. Curves of coefficient of absorption of elastic wave α_{11} versus temperature. ○) KH_2PO_4, ●) KD_2PO_4, 10 MHz.

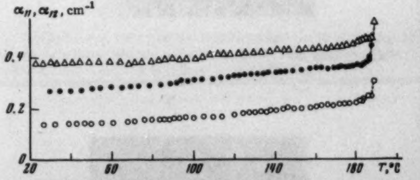

Fig. 4. Curves of coefficients of absorption of elastic waves α_{11} and α_{12} versus temperature for KH_2PO_4 crystals. ○) α_{11}, 30 MHz, ●) α_{11}, 70 MHz, △) α_{12}, 60 MHz.

TABLE 1. Temperature Dependence of Elastic Constants (kbar)

KDP	DKDP
$C_{11}(T) = 711-0.50(T-20°)$ $C_{33}(T) = 560-0.30(T-20°)$ $C_{44}(T) = 127-0.036(T-20°)$ $C_{66}(T) = 62.2-0.036(T-20°)$	$C_{11}(T) = 690-0.52(T-20°)$ $C_{33}(T) = 560-0.30(T-20°)$ $C_{44}(T) = 127-0.036(T-20°)$ $C_{66}(T) = 60.4-0.047(T-20°)$

A thorough investigation of elastic constants and coefficients of absorption of elastic waves between 20 and 190°C did not reveal any anomalies within the limits of sensitivity up to 187°C for KDP and 158°C for DKDP. Since anomalies of elasticity and absorption coefficients are observed in any type of phase transition, the slight changes in ε and $\tan\delta$ in the region of uhf and linear expansion, pointed out in refs. 5 and 9, cannot be due to a high-temperature phase transition, the occurrence of which we did not confirm.

The departure of the elastic constants from linearity and the increase in the absorption coefficient at 187-189°C for the KDP crystal and 158-160°C for the DKDP are due to irreversible transformation of the crystals at these temperatures. The crystals become white. At these temperatures, evidently, the hydrogen bonds, being the weakest in the crystal, are ruptured. Since the O−D−O bond is weaker than the O−H−O, irreversible changes in elasticity and elastic-wave absorption in the DKDP crystal take place at a lower temperature.

---

[1] J. Grinberg, S. Levin, I. Pelah, and E. Wiener, Solid State Commun., 5, 863 (1967).

[2] N. O'Keeffe and C. Perrino, J. Phys. Chem. Solids, 28, 211 (1967).

[3] R. Blinc, D. Reilly, E. Peterson, and I. Williams, J. Chem. Phys., 50, 5400 (1969).

[4] R. Blinc, V. Dimic, D. Kolar, G. Lahajnar, J. Stepišnik, S. Žumer, N. Vene, and D. Hadži, J. Chem. Phys., 49, 4996 (1968).

[5] L. P. Pereverzeva, N. Z. Pogozskaya, Yu. M. Poplavko, V. I. Pakhomov, I. S. Rez, and G. B. Sil'nitskya, Fiz. Tverd. Tela, 13, 3199 (1971) [Sov. Phys.−Solid State, 13, 2690 (1972)].

[6] Y. Imry, I. Pelah, and F. Wiener, J. Chem. Phys., 43, 2332 (1965).

[7] H. McSkimin, J. Acoust. Soc. Am., 34, 404 (1962).

[8] V. M. Korolev, S. I. Chizhikov, and P. G. Sorokin, Obmen Opytom v Élektronnoi Promyshlennosti, 3, 83 (1969).

[9] Yu. M. Poplavko, I. S. Rez, N. V. Gorbokon', and E. N. Dimarova, Kristallografiya, 17, 680 (1972) [Sov. Phys.−Crystallogr., 17, 595 (1972)].

Chizhikov et al. 545

Heat effects in lithium metaniobate

I. A. Kleinman, T. A. Lyubimova, A. Z. Rabinovich, and M. B. Roitberg
Scientific-Research Institute of Chemical Reagents and Ultrapure Chemical Compounds
Moscow Institute of Steel and Alloys

(Submitted March 7, 1972; resubmitted May 29, 1972, July 20, 1972)
Kristallografiya, 18, 863-865 (July-August 1973)

In a ferroelectric crystal located in a steady electric field, a number of thermal phenomena occur: an electrocaloric effect, i.e., evolution of Joule heat Q_j as a result of the finite conductivity of the crystal, Peltier heat Q_p appearing at the electrodes, and a heat effect[1] of change in the macroscopic unipolarity Q_m. Usually, only the electrocaloric effect is noted, the others being either neglected or eliminated as far as possible.

The purpose of the present study was to estimate the ratios of the heat effects on application of a steady electric field to a real ferroelectric crystal, e.g., lithium metaniobate.

The change in crystal temperature is related to the amount of heat evolved or absorbed on account of the electrocaloric effect Q_{ec} by the equation[2]

$$dQ_{ec} = c\rho V\Delta T = c\rho V q dE, \tag{1}$$

here ρ is the crystal density, c is its heat capacity, V is its volume, T is its temperature (°K), E is electric field intensity, and q is the electrocaloric coefficient.

Owing to the anisotropy of ferroelectrics, the regions near the electrodes on the crystal are not identical;[2] this may result in the evolution or absorption of heat on account of the difference in magnitude of the Peltier effects in these regions. The Peltier heat at the electrode Q_p is determined from the equation[3]

$$dQ_p = \Pi E h \sigma d\tau = \alpha T E h \sigma d\tau, \tag{2}$$

where Π is the Peltier coefficient equal to αT; α is the thermo-emf, h is the crystal thickness, σ is its electrical conductivity, and τ is time.

According to ref. 3, we assume that the scattering factor p is equal to 3/2, i.e., that scattering takes place at impurity ions, and find

$$\sigma = ke\left({}^5/_2 + p - \Delta E_D / 2kT\right), \tag{3}$$

where ΔE_D is the distance from the impurity level to the bottom of the conduction band of the ferroelectric $LiNbO_3$, calculated according to ref. 4 and equal to 1.7 eV, k is Boltzmann's constant, and e is the electronic charge. A calculation by Eq. (3) for $LiNbO_3$ at room temperature gives $\alpha \cong 2.125 \cdot 10^{-3}$ V/deg. From this, dQ_p/dt is equal to $2.4 \cdot 10^{-9}$ W at 10^3 V and a crystal conductance of $10^{-13}\ \Omega^{-1}$.

Q_m was found by considering[1,5] the change in entropy S of the crystal with its unipolarity M

$$dQ_m = dST = T\left(\frac{c_e}{T} dT + t dM\right), \tag{4}$$

where t is the heat of single domain formation.

The heat effects appearing in lithium niobate on application of a steady electric field were measured in a Calvet differential microcalorimeter[6] by using samples of polished single-crystal $LiNbO_3$ plates. Plates ~120 mm^2 in area and ~1 mm thick were cut out of the middle of a single bar, perpendicular to the c axis with ±1° accuracy. We used ultrapure Cu and Bi electrodes, deposited by vacuum evaporation. The electrode thickness, controlled by a silica balance,[7] amounted to ~1300 Å, the area being 64 mm^2. Moreover, palladium was applied to a number of samples by burning in.

DISCUSSION OF RESULTS

For all samples investigated, measurements at room temperature showed that the main contribution to Q_Σ comes from the electrocaloric effect. In this case, the quantity q, calculated by Eq. (1), is equal to $(5 \pm 0.5) \cdot 10^{-7}$ deg·cm/V, which agrees well with the value calculated from the pyroelectric coefficient for the same samples.[4,5]

The difference in absolute values of the temperature increments caused by turning the field on and off amounts to $0.15 \cdot 10^{-3}$ deg C and is due to the contribution Q_j, corresponding to $\sigma = 10^{-13}\ \Omega^{-1}$, which is supported by direct measurements of resistance of the samples under the

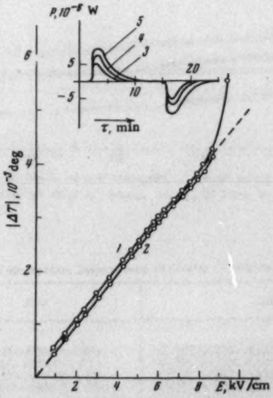

Fig. 1. Curves of $\Delta T(E)$ at 25°C for samples bearing palladium electrodes. Direction of field is opposite to that of spontaneous-polarization vector of crystal; 1) on turning on field; 2) on turning it off; dashed line is curve of $\Delta T(E)$, calculated from pyroelectric coefficient. Diagrams of the rate of evolution and absorption of heat on turning field off and on are shown at top: 3) 4.5; 4) 6.8; 5) 8.0 kV/cm.

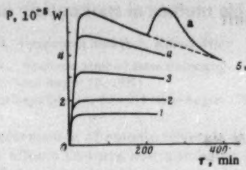

Fig. 2. Diagrams of rate of evolution of heat at T = 110°C for samples bearing copper electrodes. Direction of field is same as that of spontaneous-polarization vector; a) this curve illustrates case of reversal of field at $\tau \approx 200$ min. Dashed line shows saturation of process of change in crystal conductivity on prolonged action of field. 1) E = 1.9; 2) 2.8; 3) 3.8; 4) 5.7; 6) 6.6 kV/cm.

same conditions in weak fields (Fig. 1).

Departure from linearity of the curve of $\Delta T(E)$ in fields stronger than 6 kV/cm may be explained by increase in the influence of the heat of change in macroscopic unipolarity due to lateral motion of domain walls. Calculation of this effect at E = 7.5 kV/cm gives $Q_m = 1.05 \cdot 10^{-4}$ W · sec.

At elevated temperatures, owing mainly to the increase in conductivity[4] of $LiNbO_3$, Joule-effect heating of the samples at the instant the electric field is turned on exceeds the heat development due to the electrocaloric effect, and Q_Σ above 40°C is determined almost entirely by evolution of Joule heat (Fig. 2).

The rate of Joule heating increases with the electric field intensity, but its value, calculated from the equation $P_j = E^2\sigma$, is slightly larger than that observed. This is due to nonlinearity of the voltage–current characteristic of $LiNbO_3$ in strong fields, which is generally characteristic of ferroelectrics.[8]

At field intensities larger than a certain fixed value for each temperature, the rate of heat evolution decreases with time. Thus, in samples bearing copper electrodes at 110°C, this effect appears in fields above 2.8 kV/cm, whereas in samples bearing Cu–Bi electrodes, it appears above 1.4 kV/cm. The effect may be explained hypothetically: by change in volume resistivity of the ferroelectric crystal with time in a strong electric field,[2,8] by absorption of heat as a result of repolarization due to motion of the domain walls, and by change in resistivity of the electrode regions on account of formation of surface levels or barrier layers.[9,10]

On prolonged application of an electric field parallel to the polar axis of the crystal, the concentration of carriers injected into the crystal from the cathode increases, which produces a contact potential difference in the electrode region, thus decreasing the conductivity. On reversal of the electric field, the opposite process takes place, and the barrier layer becomes an antibarrier layer. As is evident from curve a in Fig. 2, this results in a certain increase in sample conductivity. In this case, however, prolonged application of the field changes the unipolarity of the sample, which, in turn, makes the electrode region a barrier.

Analysis of the heat effects characteristic of $LiNbO_3$ shows that, at room temperature, the largest contribution to the total heat effect (Q_Σ) comes from Q_{ec}, whereas Q_j predominates at higher temperatures. In strong fields, however, Q_Σ is appreciably affected by Q_m and the change in crystal conductivity due to the formation of barrier or antibarrier layers in the electrode regions.

The authors thank V. K. Novik and N. D. Gavrilova for their interest and a discussion of the results.

---

[1] J. Nye, Physical Properties of Crystals, Oxford Univ. Press, New York (1956).

[2] I. S. Zheludev, Physics of Crystalline Dielectrics [in Russian], Nauka, Moscow (1968).

[3] P. S. Kireev, Semiconductor Physics [in Russian], Vysshaya Shkola, Moscow (1969).

[4] M. B. Roitberg, V. K. Novik, and N. D. Gavrilova, Kristallografiya, 14, 938 (1969) [Sov. Phys.–Crystallogr., 14, 814 (1970)].

[5] M. B. Roitberg, Dissertation, Moscow Institute of Steel and Alloys, Moscow 1970.

[6] E. Calvett and H. Prat, Recent Progress in Microcalorimetry, Pergamon (1963).

[7] G. A. Ivanov, Dissertation, Moscow Institute of Steel and Alloys, Moscow (1972).

[8] V. M. Gurevich, Electrical Conductivity of Ferroelectrics [in Russian], Izd. Komiteta Standartov, Mer i Izmeritel'nikh Priborov, Moscow (1969).

[9] V. F. Krapivin and E. V. Chenskii, Fiz. Tverd. Tela, 12, 597 (1970) [Sov. Phys.–Solid State, 12, 454 (1970)].

[10] B. G. Vekhter, Sh. N. Gifeisman, L. S. Kremenchugskii, Yu. E. Perlin, and V. B. Samoilov, Fiz. Tverd. Tela, 13, 94 (1971) [Sov. Phys.–Solid State, 13, 74 (1971)].

Heat capacity of single-crystal $BaTiO_3$ near the electrical critical point

B. A. Strukov and A. K. Ivanov-Shits
M. V. Lomonosov Moscow State University
(Submitted June 9, 1972; resubmitted September 28, 1972)
Kristallografiya, 18, 866-867 (July-August 1973)

It is well known that continuous transition between different phases of a material is possible in the case where the curve of phase equilibrium X(T) ends in a critical point (X is the generalized thermodynamic force, and T is temperature). The latent heat of transition vanishes at the critical point, whereas the heat capacity approaches infinity. There is a well-known critical point on the curve of phase transitions in the liquid–vapor system, where the external generalized force is pressure.

In the present study, it was shown experimentally for the first time that ferroelectric crystals with a phase transition of the first kind near the critical Curie point have a critical point on the E(T) diagram (E is the external electric field). Earlier, the phenomenon was predicted theoretically in refs. 1 and 2.

We shall consider a ferroelectric whose equation of state[2] is

$$E = \alpha(T - T_C)P + \beta P^3 + \gamma P^5,$$

where $\alpha, \gamma > 0$, $\beta < 0$ (phase transition of the first kind), and P is the electric polarization. The coordinates of the electrical critical point may be determined from the conditions $(\partial E/\partial P)_p = 0$, $(\partial^2 E/\partial P^2)_p = 0$:

$$P_{cr} = \pm\left(-\frac{3\beta}{10\gamma}\right)^{1/2}, \quad E_{cr} = \pm\frac{6\beta^2}{25\gamma}\left(-\frac{3\beta}{10\gamma}\right)^{1/2}, \quad T_{cr} - T_C = \frac{9\beta^2}{20\gamma}. \tag{1}$$

Calculation by Eqs. (1) gives $E_{cr} = 9 \cdot 10^3$ V/cm for values of the thermodynamic coefficients $\beta = -8.1 \cdot 10^{18}$ $V \cdot cm^5/C^3$ and $\gamma = 16.2 \cdot 10^{27}$ $V \cdot cm^9/C^5$, taken from ref. 3.

We investigated the heat capacity of the $BaTiO_3$ crystal in an external electric field by the method of pulsed heating.[4] One of the large surfaces of a thermostatted sample measuring 6 × 6 × 1 mm was heated by a $3 \cdot 10^{-3}$ sec light pulse from an IFK-120 pulse lamp. The temperature change of the other surface was used to determine the heat capacity $c = Q/\rho l \Delta T_{max}$, where Q is the amount of heat absorbed by the sample, ρ is density, l is thickness, and ΔT_{max} is the maximum change in temperature of the rear surface. We note that the latent heat of phase transition cannot be determined by this method. The accuracy of measurement of the relative heat capacity is ~5%.

The electric field was applied to electrodes coated on the large surfaces of the sample, directly before the light pulse was delivered ($\Delta t \sim 5$ msec), since the problem of determining the "true" field intensity within the sample arises in the region of the phase-transition temperature ($T_C = 116.2$°C) owing to the increasing electrical conductivity of the crystal.[5,6] The electrocaloric effect was carefully taken into account in the measurements.

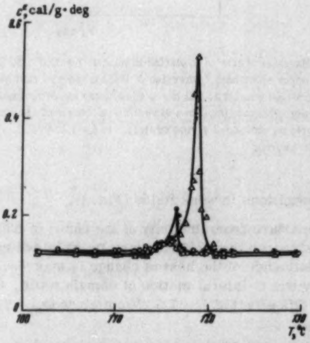

Fig. 1. Curves of heat capacity versus temperature for single-crystal $BaTiO_3$. ○ – E = 0, ● – $3.5 \cdot 10^3$, △ – $5.9 \cdot 10^3$ V/cm.

In our experiments, the maximum field intensity was of the order of $6 \cdot 10^3$ V/cm, since the crystals cracked in stronger fields. Data obtained at E = 0, $3.5 \cdot 10^3$, and $5.9 \cdot 10^3$ V/cm are shown in Fig. 1, from which it is evident that the heat capacity of the $BaTiO_3$ crystal at E = 0 changes very slightly near the Curie point (transition of the first kind; the latent heat evolved could not be determined in our experiment) and reaches a maximum at $T_C = 116.2$°C. When an electric field is applied, the heat-capacity maximum is shifted toward higher temperatures, and the phase transition becomes critical in type: Excess heat capacity appears on both sides of the phase-transition point, and the maximum value of heat capacity is markedly increased. The shifts in phase-transition temperature (0.4 and 3.1°C), observed by us, show that the field in the sample is subcritical (for $BaTiO_3$, from Eq. (1), $T_{cr} - T_C = 7.5$°C). Nevertheless, it is obvious that the conclusions of the theory regarding the character of transformation of the curve of heat capacity versus temperature on approach to the electrical critical point are qualitatively confirmed.

The authors thank E. V. Sinyakov, who supplied the $BaTiO_3$ single crystals for the experiments.

---

[1] Y. Le Corr and L. Ben Guigui, Phys. Let., A24, 419 (1967).
[2] V. Kh. Kozlovskii, in: Mechanism and Kinetics of Crystallization [in Russian], Nauka i Tekhnika, Minsk (1969), pp. 25-34.
[3] B. M. Kulwick, J. Appl. Phys., 40, 3118 (1969).
[4] W. Parker and B. Jenkins, J. Appl. Phys., 32, 1679 (1962).
[5] S. Triebwasser, Phys. Rev., 118, 100 (1960).
[6] M. Scholjet, Phys. Status Solidi, 4, 639 (1964).

Charge on dislocations in sodium chloride crystals containing an anionic impurity

N. A. Tyapunina and A. I. Kolomiitsev

M. V. Lomonosov Moscow State University

(Submitted August 18, 1972)
Kristallografiya, 18, 868-870 (July-August 1973)

Plastic deformation of anionic crystals is accompanied by electrical effects that are now attributed to movement of charged dislocations.[1] The sign and magnitude of the charge on dislocations in ionic crystals depend to a substantial extent on the impurity composition, concentration, and state. It has been established that divalent impurity cations intensify the negative charge on dislocations in the original crystal, while divalent anions reduce the charge on these dislocations and, when present in large concentrations, make them positive.[2-7] However, there are very few quantitative experimental data on the influence of impurities, especially anionic impurities, on the dislocation charge.

In the present investigation, we studied the linear dislocation-charge density in NaCl crystals as a function of the content of a divalent anionic impurity, sulfur being used for this purpose. The sulfur was introduced into the crystals by the Soifer diffusion method.[8]

In order to detect changes in the electrical properties of the impure NaCl crystals, we determined their electrical conductivity. This factor is known to be independent of the impurity concentration and state. The influence of a divalent anionic impurity on the conductivity of ionic crystals with an NaCl structure has been noted in the literature.[10-16]

18
973–
974

The electrical conductivity of NaCl crystals doped with sulfur was measured with an F507 teraohmmeter over the range from 100 to 550°C. The sulfur concentration in the specimens varied from $2.2 \cdot 10^{-4}$ to $2.3 \cdot 10^{-2}$ mole%. As was shown by analysis, the initial crystal without sulfur contained divalent cations in a total concentration of about $3 \cdot 10^{-3}$ mole%.

The conductivity σ of all the specimens containing the anionic impurity was lower at all temperatures than that of the original specimen (at the same temperature). The change in σ with varying impurity concentration was nonmonotonic. This can be seen from Fig. 1, which shows the conductivity isotherms. All the curves in Fig. 1 passed through a minimum at the same anionic impurity concentration, $\sim 3.1 \cdot 10^{-3}$ mole%. This quantity is close to the figure given above for the total concentration of all divalent cations in the crystal under investigation.

The results obtained are in agreement with the Kessler theory,[16] which predicted the appearance of a minimum in the isotherms when the concentrations of cationic and anionic impurities are equal. The increase in σ with large anionic-impurity concentrations was apparently due to participation in conductivity of anionic vacancies of impurity origin.

Thus, the electrical-conductivity data indicate changes in the vacancy system of NaCl crystals when sulfur impurities are introduced into them.

The linear dislocation-charge density in NaCl crystals with sulfur present as an impurity was measured by the method described previously.[17] The specimens used in the measurements were cut from single crystals to which sulfur was added as an impurity (the same ones used for measurement of the electrical conductivity σ). The temperatures at which the linear dislocation-charge density q was determined ranged from room temperature to 500°C.

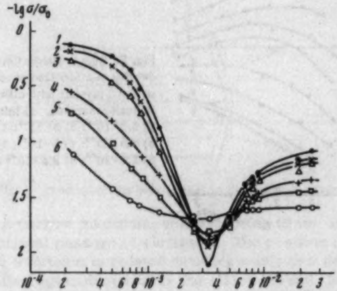

Fig. 1. Electrical conductivity of NaCl crystals as a function of impurity-sulfur concentration. σ_0) Conductivity of initial crystal; 1) t = 215; 2) 255; 3) 300; 4) 370; 5) 430; 6) 525°C.

The experimental results are presented in Fig. 2. Each point in this figure corresponds to the average of four to six measurements of q made with specimens having the same impurity content at the same temperature. The results obtained for different specimens under these conditions differed by 30–40%. For purposes of comparison, Fig. 2 also gives a graph of the dependence of q on temperature for the original crystal.

We observed a number of interesting peculiarities in the behavior of q as a function of the sulfur content and temperature. At small sulfur concentrations c, the sign of the charge induced at the crystal surface by the dislocations was negative at all temperatures (curves 2 and 3). The absolute value of q increased with rising temperature. This increase was linear at low temperatures but, starting at t ≈ 200°C, we observed a deviation from linearity. Specimens containing sulfur in a concentration of $5.0 \cdot 10^{-4}$ mole% (curve 3) exhibited a decrease in the absolute value of q at t ≈ 300°C. As the impurity concentration increased, the maximum in q was shifted toward lower temperatures.

The sulfur-containing NaCl crystals studied displayed the important phenomenon of inversion of the sign of the charge carried by the dislocations. A strong dependence of q on concentration existed over the entire temperature range, including room temperature. It can be seen from Fig. 2 that, when c was increased at room temperature, the sign on q changed from negative to positive when c reached 10^{-3} mole%. A further increase in the sulfur

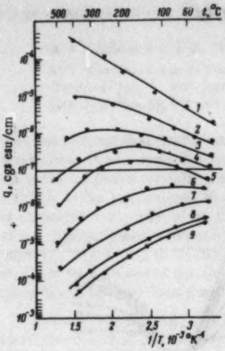

Fig. 2. Linear dislocation-charge density as a function of temperature in NaCl crystals with different sulfur-impurity contents. 1) Initial crystal; 2) $2.2 \cdot 10^{-4}$; 3) $5 \cdot 10^{-4}$; 4) $9 \cdot 10^{-4}$; 5) $2.3 \cdot 10^{-3}$; 6) $5 \cdot 10^{-3}$; 7) $8 \cdot 10^{-3}$; 8) $1.8 \cdot 10^{-2}$; 9) $2.4 \cdot 10^{-2}$ mole% S.

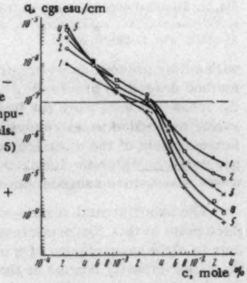

Fig. 3. Linear dislocation-charge density as a function of sulfur-impurity concentration in NaCl crystals. 1) t = 60; 2) 130; 3) 200; 4) 270; 5) 340°C.

concentration led to a rise in the absolute value of q, whose sign remained positive.

Curves 4 and 5 reflect the temperature-related changes in q, a tendency toward which was seen in curves 2 and 3. In curve 4, q increased in absolute value with rising temperature but remained negative, passing through a maximum at t = 160°C and then decreasing. The sign of q was inverted at 440°C. The form of curve 5, which represents the temperature function for specimens with $c = 2.3 \cdot 10^{-3}$ mole%, was the same as that of curve 4. However, q changed sign twice in this case: first from positive to negative at t = 65°C and then in the opposite direction at t = 280°C. For specimens with $c > 5 \cdot 10^{-3}$ mole%, q was positive at all temperatures. There was a smooth increase in q with rising temperature for all these specimens.

Figure 3 shows the linear charge density q as a function of concentration for several temperatures. These curves permit more graphic representation of the patterns in the behavior of q, some of which were described above. It must be emphasized that inversion of the dislocation-charge sign occurred at roughly the same sulfur concentration where the electrical-conductivity isotherms exhibited minima.

The aggregate of the experimental data presented above can be explained on the basis of the theory that dislocations increase the number of vacancies.[17,18] In order for the electrical-neutrality condition to be satisfied in a crystal containing an excess of a negatively charged divalent impurity (S^{2-} in our case), a compensating number of anionic vacancies carrying an effective positive charge is formed. Transfer of these vacancies by dislocations also leads to inversion of the sign of the charge carried to the surface during plastic deformation.

The increase in the absolute magnitude of the negative charge on the dislocations in crystals with a small impurity content (Fig. 2, curves 2-5) at sufficiently low temperatures can be attributed to the participation of cationic vacancies in the process,[17] their presence resulting from a cationic impurity in the original material. It is interesting to note that this phenomenon occurs against a background of a decrease in the absolute value of q (with rising sulfur content). At higher temperatures, the anionic vacancies are included in the process, and q shifts in the positive direction. Only the anionic vacancies play a significant role at large impurity-sulfur concentrations (Fig. 2, curves 6-9).

The results presented in this article indicate the importance of the anionic impurity with respect to the sign and magnitude of the linear dislocation-charge density, and the latter has been found to depend on the temperature and the impurity concentration.

---

[1] A. A. Urusovskaya, Usp. Fiz. Nauk, 96, 39 (1968) [Sov. Phys.–Usp., 11, 631 (1969)].

[2] F. Rueda and W. Dekeyser, J. Appl. Phys., 32, 1799 (1961).

[3] S. Sonoike, J. Phys. Soc. Japan, 24, 1019 (1968).

[4] F. Rueda and W. Dekeyser, Acta Metallurg., 11, 35 (1963).

[5] F. Froelich and D. Suisky, Phys. Status Solidi, 4, 151 (1964).

[6] L. L. Kushsh, Author's Abstract of Dissertation [in Russian], MGU, Moscow (1966).

[7] T. Yoshi-yama, M. Mannami, and K. Tanaka, J. Phys. Soc. Japan, 24, 1019 (1968).

[8] L. M. Soifer, in: Single Crystals and Technology [in Russian], Izd. Vses. Nauchn.-Issled. Inst. Monokristallov, Khar'kov (1970), p. 108.

[9] A. Lidiard, Ionic Conductivity of Crystals [Russian translation], Izd. IL, Moscow (1962).

[10] R. M. Gruzensky and A. B. Scott, Phys. Chem. Solids, 21, 128 (1961).

[11] M. V. Pashkovskii, N. A. Tsal', and A. D. Tkachuk, Fiz. Tverd. Tela, 5, 1167 (1963) [Sov. Phys.–Solid State, 5, 853 (1963)].

[12] A. B. W. Redfern and P. L. Pratt, Proc. Brit. Ceram. Soc., 173 (1964).

[13] J. Rolfe, Canad. J. Phys., 42, 2195 (1964).

[14] A. Kessler and E. Mariani, Czechoslovak J. Phys., B17, 178, 786 (1967).

[15] M. M. Tagieva, Author's Abstract of Dissertation [in Russian], Mosk. Inst. Stali i Splavov, Moscow (1972).

[16] A. Kessler, Casop. Ceskosl. Fyz., 18, 23 (1968).

[17] A. L. Kolomiitsev, Fiz. Tverd. Tela, 13, 1487 (1971) [Sov. Phys.–Solid State, 13, 1244 (1971)].

[18] R. W. Whitworth, Phil. Mag., 15, 305 (1967).

Determination of the degree of bending of single crystals from the orientational scattering of β particles

A. Ya. Bobudaev, S. A. Vorob'ev, and V. V. Kaplin
Tomsk Scientific-Research Institute for Nuclear Physics, Electronics, and Automation

(Submitted July 25, 1972)
Kristallografiya, 18, 871-872 (July-August 1973)

When a collimated beam of β particles passes through a single crystal, orientational scattering effects are observed if the direction of the incident beam coincides with the crystallographic axis of the single crystal.[1-3] The orientational effects of the scattering of positrons, attributed to the effect of channeling, are revealed in the form of a decrease in the magnitude of the scattering at large angles, whereas for electrons, as a consequence of their focusing on the chains of nuclei of the crystal lattice, the scattering at large angles increases. Electrons which have passed through thin single crystals show a narrow output maximum, related to the anomalous orientational passage of the electrons along the atomic rows.[4] The observed sensitivity of the process of elastic scattering of β particles to the structure of a single crystal may find application in crystallographic studies.

The aim of the present work was to measure the angle of bending of a single crystal from the orientational scattering of electrons. The experimental assembly was described earlier.[3] As a target we used a KCl single crystal of 100-200 μ thickness. The specimens were pricked out from crystalline rods grown from a melt by the Kyropoulos method. During the pricking of the thin plate, the single-crystal specimen undergoes a certain amount of bending as a consequence of internal mechanical stresses. The dependence of the count rate of back-scattered electrons from a KCl single crystal with thickness 115 μ on the angle of orientation of the crystal is shown in Fig. 1. The distributions obtained were normalized to the magnitude of the output of the back-scattered electrons in the case of a disoriented crystal. The electron beam from the $(Sr-Y)^{90}$ radioactive source had an angular divergence of ±0.5° and spot diameter on the target 5 mm.

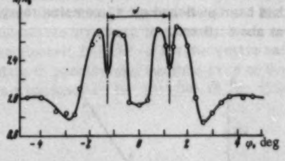

Fig. 1. Orientational dependence of the output of back-scattered electrons on the angle of rotation of the KCl single crystal.

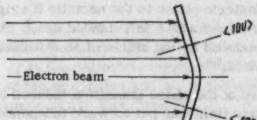

Fig. 2. Position of the bent crystal in the beam of particles.

The central region of the back-scattering maxima shows a narrow minimum, corresponding to the anomalous orientational passage of electrons. The position of the central minimum is related unambiguously to a definite crystallographic direction in the single crystal, in our case the ⟨100⟩ axis. The explanation for the production of two symmetrically arranged maxima in the back scattering of the electrons is that the dimensions of the beam at the surface of the crystal were greater than the magnitude of the deformed bent zone in the crystal (Fig. 2). Rotation of the single crystal relative to the incident quasiparallel beam in this case leads to the successive coincidence of the axis of the beam with the ⟨100⟩ axis passing through each plane of the single crystal on either side of the band. In the bent zone, which has a deformed crystal structure, the normal output of scattered electrons, the same as that for the disoriented crystal, is observed. Thus the distance between the central minima of the orientational peaks of the back scattering of the electrons corresponds to the angle of bending of the single crystal, in our case equal to $\theta \simeq 2.46°$.

It should be noted that positrons can also be used to determine the degree of bending of single crystals. The use of electron beams, however, ensures a higher angular resolution for the proposed method, since the orientational maxima for electrons are narrower than those for positrons,[1] and the central minimum of the anomalous orientational passage is even narrower.

The authors thank Professor A. A. Vorob'ev for direction of this work.

[1] E. Uggerhoj and J. U. Andersen, Can. J. Phys., 46, 543 (1968).
[2] H. H. A. Ok, Z. Phys., 240, 314 (1970).
[3] A. A. Vorob'ev (Vorobiev), A. N. Didenko, S. A. Vorob'ev (Vorobiev), and I. A. Tsekhanovskii (Tsekhanovski), Phys. Status Solidi, 6A, 389 (1971).
[4] H. J. Kreiner, F. Bell, R. Sizmann, D. Harder, and W. Hüttl, Phys. Lett., A33, 135 (1970).

Phase transition in liquid crystals induced by an electric field

I. G. Chistyakov and L. K. Vistin'

Institute of Crystallography, Academy of Sciences of the USSR

(Submitted July 6, 1972; resubmitted September 4, 1972)
Kristallografiya, 18, 873-875 (July-August 1973)

It is a well-known fact that a liquid crystal can go over from the cholesteric phase to the nematic if a right-handed cholesteric is mixed with a left-handed one.[1] The transition can be produced by the action of an external electric or magnetic field.[2,3]

The theory of the phase transition induced by a magnetic or electric field was put forward independently by de Gennes[4] and Meyer[5] and was experimentally confirmed by the change in the pitch length of the helical cholesteric structure as a function of the applied electric field.[6,7]

Experimental studies on the induced cholesteric–nematic phase transition have been made on plane-parallel samples consisting of a homogeneous mixture of several cholesteric and nematic components.

In this paper we consider electrically induced phase transitions in samples of varying concentration. A melt of cholesteryl chloride and cholesteryl myristate was introduced between glass plates coated with a thin conducting layer of SnO_2. When the preparate is cooled to room temperature, a band of nematic phase 20-30 μ wide forms at the merging point. Studies with polarized light showed that in the nematic region the long axes of the molecule were roughly parallel with the plates. To the right and left of the nematic region (Fig. 1a) zones of planar or Grandjean texture are observed with colors varying across the whole spectrum. Beyond this are sections where the material has crystallized.

A number of conclusions can be drawn from these facts: 1) A nematic phase can be obtained at any temperature, including room temperature, by mixing two cholesteric oppositely rotating compounds; 2) it is possible to obtain a mixture with a uniform color with two different values of concentration at the same temperature; 3) it is possible to prepare mixtures which traverse the whole spectrum twice for a continuous variation in temperature.

We have studied the effect of homogeneous dc and ac electric fields on the nematic phase and on the adjacent Grandjean texture. For dc fields at the threshold value of E_c = 4000-10,000 V, the nematic phase band is completely extinguished (Fig. 1b). It is not possible to alter this situation by turning the microscope table. This shows that the optic axes of the molecules are oriented parallel to the field lines and perpendicular to the glass plates. Further increase in the field strength produces a broadening of the nematic region with the molecules stretched out along the field; a normal layer is formed and the Grandjean texture changes color (Fig. 1c). Since with increase in field strength the nematic band extends equally into both the right-handed and left-handed regions, the total width of the band has been measured in all cases.

The straight line 1 in Fig. 2 shows the variation of the width d of the nematic phase band with the value of the electric field E.. It can be seen that d is directly proportional to E, $d = kE$. When the field is turned off, d returns to its initial value.

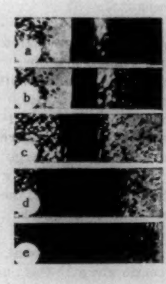

Fig. 1. Broadening of the nematic phase for various applied voltages. a) V = 0; b) V = 7.5 V; c) V = 15 V; d) V = 30 V; e) V = 60 V.

From 10 kHz upwards, the critical field value E_c (for a sample thickness of 20 μ) begins to vary rapidly with frequency in a direct relationship (see Table 1 and Fig. 2). Finally, at 25-27 kHz, the effect of nematic phase extinction by the field increases to exist (Fig. 3a).

Between 27-30 kHz, there was some kind of resonance effect in that the nematic region was destroyed and the sample took on a more or less uniform appearance (Fig. 3b). Above 30 kHz, the field acted equally on all phases, brightening up the preparate in crossed Nicols and giving it a uniform planar Grandjean texture (Fig. 3c). We can thus see that an ac field at frequencies above a certain threshold brings about a reverse transition from the nematic to the cholesteric phase.

The transition time from cholesteric to nematic phase τ_1 has been studied in ref. 8. Our observations are in agreement with the results of that paper and show that τ_1 decreases rapidly with field values above the threshold level. The time for the reverse transition to occur after the field has been switched off τ_2 remains more or less constant at about 10 sec.

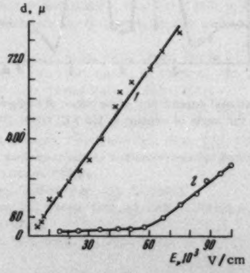

Fig. 2. Variation of the width of the nematic phase with the value of the electric field. 1) dc field; 2) ac field at 20 kHz.

TABLE 1

Threshold voltage, V	Alternating current frequency, Hz
7—8	20
7—8	200
7—8	500
9—10	1000
15—20	1500
30—35	2000
—	2500—28000

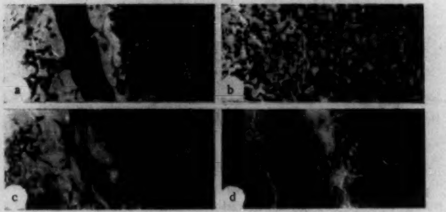

Fig. 3. Action of an ac longitudinal electric field on the nematic phase of a cholesteric mixture. a) f = 26 kHz, u = 60 V; b) f = 28 kHz, u = 60 V; c) f = 50 kHz, u = 60 V; d) f = 50 kHz, u = 100 V.

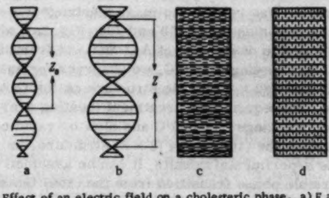

Fig. 4. Effect of an electric field on a cholesteric phase. a) $E = 0$, b) $0 < E < E_C$; c) $E_C < E$; d) $E > E_C$.

Our experimental results are in good agreement with the usual theoretical ideas on the phase transition from a cholesteric structure to a nematic one under the effect of an electric field.[4,5] If the dielectric anisotropy of the system is positive and the long axes of the molecules have a tendency to lie parallel to the field, the twisted cholesteric structure becomes unstable above some critical value of the electric field E_C and the transition to the nematic phase occurs. Meyer[5] showed that under certain conditions the value of E_C could be expressed as

$$E_C = \frac{2\pi}{Z_0}\left(\frac{K_{22}}{\varepsilon_{\parallel} - \varepsilon_{\perp}}\right)^{1/2}, \tag{1}$$

where Z_0 is the pitch of the helical cholesteric structure in the absence of external fields, K_{22} is the torsional elastic constant, $\varepsilon_{\parallel}$ is the dielectric constant measured along the long axes of the molecules and $\varepsilon_{\perp}$ is the dielectric constant perpendicular to this direction.

Since the width of the nematic phase band varies linearly with E, the ratio $K_{22}/(\varepsilon_{\parallel} - \varepsilon_{\perp})$ should not change very much the concentration and we can write

$$E_C = \alpha / Z_0, \tag{2}$$

where α is a constant. Thus the value of E_C is determined mainly by the pitch of the helical structure and is in fact inversely proportional to this quantity. In the absence of any field, the pitch is Z_0 (Fig. 4). The action of a field smaller than E_C is to unwind the spiral and increase the pitch. At the limiting value of E, the helix is completely unwound and the nematic phase starts to form. For higher fields the molecules become oriented along the field lines. A normal layer of liquid crystal is thus obtained. During the transitions in one direction or the other, the concentrations of the various components change.

The experiments show that a decrease of the concentration of one phase in the other is accompanied by a reduction in pitch Z_0. In fact, the wider the nematic phase band, the less the concentration of one substance in the other and hence the smaller the pitch near the phase boundary; this also means from (1) that the value of the threshold field must increase.

---

[1] M. G. Friedel, Ann. Phys., 18, 273 (1922).
[2] J. J. Wysocti, J. Adams, and W. Haas, Phys. Rev. Lett., 20, 1024 (1968).
[3] G. Durand, L. Leger, F. Rondelez, and M. Veyssic, Phys. Rev. Lett., 22, 227 (1969).
[4] P. G. de Gennes, Solid State Commun., 6, 163 (1969).
[5] R. B. Meyer, Appl. Phys. Lett., 12, 281 (1968).
[6] F. J. Kahn, Phys. Rev. Lett., 24, 209 (1970).
[7] H. Baessler and M. M. Labes, Physica, 1846 (1969).
[8] J. W. Shelton and Y. R. Shen, Phys. Rev., A5, 1867 (1972).

Investigation of the pure and cesium-coated (100) surface of germanium by slow-electron diffraction

A. Yu. Mityagin and V. P. Orlov

(Submitted January 7, 1972; resubmitted July 6, 1972)
Kristallografiya, 18, 876-878 (July-August 1973)

Study of the surfaces of semiconductors of the $A^{III}B^{V}$ type in pure form and when coated with alkali-metal atoms is of great importance for establishment of the crystal-physical and crystal-chemical patterns displayed by the surface structures, which are vital for interpretation of surface phenomena and for production of effective photoemitters.

In the present investigation, we employed low-energy electron diffraction, mass spectrometry, and Auger spectroscopy to study the (100) surface of GaAs and the adsorption of Cs atoms. Our experiments were conducted in a composite all-metal three-grid apparatus for diffraction of low-energy electrons, which included a system for recording the Auger-electron spectrum, an MSKh-3A mass spectrometer, a Cs source, and a system for measuring the change in work function. The specimens were GaAs single crystals and epitaxial films (pure and alloyed with Sn and Zn). The (100) surface of the GaAs was purified by heating in a vacuum of $1 \cdot 10^{-9}$ torr.

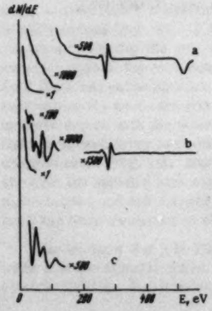

Fig. 1. Auger spectra of (100) GaAs. a) Without heating of crystal, after achievement of working vacuum in apparatus; b) after heating for 5 h at 300°C; c) during vaporization of Cs.

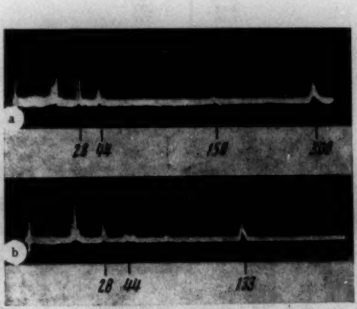

Fig. 2. Mass spectrograms obtained during heating of (100) GaAs, T = 400°C (a) and operation of Cs source (b).

Figure 1a shows the Auger spectrum of (100) GaAs obtained without heating of the crystal after the working vacuum was reached in the instrument. The 270 and 510 eV Auger lines indicate the presence of a layer of C and O impurity atoms on the surface. The adsorbed layer was so thick that there were no low-energy Auger lines for the Ga and As atoms. Prolonged heating (5 h) at 300°C removed the O atoms, but the C atoms remained at the surface (Fig. 1b). Since the presence of C atoms affected the intensity ratio of the diffraction reflections and the background during diffraction of low-intensity electrons, it can be assumed that the C atoms formed amorphous structures, which were present on the surface in the form of isolated islands. Other researchers[1-3] have noted similar behavior for C atoms not affecting the superficial atomic structure of semiconductors of the $A^{II}B^{V}$ type. Prolonged heating at 300°C, in addition to removing the oxide and adsorbed layers, promoted ordering of the surface layer and formation of a superficial atomic structure of the (100) GaAs (8 × 2) type. A rise in heating temperature to above 300°C led to irreversible rearrangement of the surface atomic structure, as was indicated by a number of the observed diffraction patterns. As the heating temperature was raised, the mass spectrograms exhibited appearance of masses of 150 and 300 (Fig. 2a), which can be attributed to desorption of As2 and As4 from the surface. After heating at 600°C, we observed formation of an (100) GaAs (2 × 8) atomic structure on the GaAs (100) surface. Subsequent heat treatment (heating over the temperature range 300-600°C and slow or rapid cooling) did not alter the (100) GaAs (2 × 8) structure. In analyzing the experimental results, it can be assumed that the irreversible phase transition from the (100) GaAs (8 × 2) surface structure to the (100) GaAs (2 × 8) was due to impoverishment of the subsurface layer in As atoms. Proceeding from the usual rules for interpretation of the diffraction patterns produced by low-energy electrons, we can propose the following model for the (2 × 8) superficial atomic structure: The free bonds of the surface-plane atoms interact, displacing the atoms in the direction of these bonds. The displacement of surface atoms and formation of dumbbell-type pairs has also been observed[4] in studying the structure of the (100) surface of Si and Ge. In contrast to Si and Ge, the ionic type of bonding between

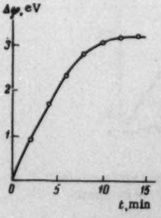

Fig. 3. Curve representing change in work function of (100) GaAs + Cs system as a function of Cs deposition time.

Fig. 4. Diffraction pattern of electrons with energy of 12 eV from (100) GaAs (2 × 8)−Cs structure.

the (100) Ga and As layers in GaAs prevents full displacement of each surface atom, which leads to a long-period (2 × 8) structure.

The Cs was deposited in a vacuum of $1 \cdot 10^{-9}$ torr from a glass ampoule containing metallic Cs distilled in the working vacuum. Figure 2b shows the mass spectrogram obtained during operation of the Cs source. The temperature of the (100) GaAs was varied from −200 to +300°C. The adsorption processes were monitored by diffraction of low-energy electrons, Auger-electron spectroscopy, and determination of the change in the work function of the (100) GaAs + Cs system. Figure 1c shows the low-energy portion of the Auger spectrum of the (100) GaAs + Cs. The appearance and intensification of a maximum in the 47 eV Auger line, which corresponds to the $N_{IV,V}O_{II,III}O_{II,III}$ Auger transition for Cs atoms, during deposition indicates a gradual increase in the surface concentration of adsorbed Cs atoms.

Figure 3 shows a curve representing the change in the work function of the (100) GaAs (p-type, alloyed with Zn in a concentration of $3.6 \cdot 10^{19}$ cm^{-3}) + Cs system as a function of the Cs deposition time. In the low-energy electron diffraction patterns, the initial stages of Cs adsorption were characterized by appearance of diffraction bands of half-integral and integral orders in the $\{0, y\}$ directions. An increase in coverage led to gradual weakening of the diffraction-reflection intensities. However, brief heating at 150°C restored the diffraction pattern of the (100) GaAs (2 × 8) structure and there was a large increase in the intensity of the diffraction reflections of the $\{1/2, 2n+1\}$ type (Fig. 4). Further changes in the crystal temperature, the annealing time and temperature, and the superficial Cs concentration did not lead to material changes in the diffraction patterns of low-energy electrons. It can be assumed that adsorbed Cs atoms fill the voids between chains of surface base atoms. The shortest Cs−Cs distance in the [110] direction is ~8Å. The appearance of diffraction bands indicates relative disordering of the Cs−Cs distances in the $[\bar{1}10]$ direction. An increase in the adsorbed Cs concentration or additional annealing promoted ordering of the surface (100) GaAs (2 × 8)−Cs structure, as was indicated by the characteristic increase in the intensity of the diffraction reflections of the $\{1/2, 2n+1\}$ type. Actually, the severe asymmetry of the atomic scattering of Ga−Ga or As−As pairs in the [110] and $[\bar{1}10]$ directions for the (100) GaAs structure in the (2 × 8) form is responsible for the low intensity of the $\{1/2, 2n+1\}$ diffraction reflections. During formation of the (100) GaAs (2 × 8)−Cs structure, the main contribution to the intensity of the low-energy electron diffraction reflections is made by the Cs atoms, whose atomic scattering factor is greater than that for Ga and As and basically symmetric. Simple calculations of the theoretical intensities, even within the framework of the kinematic structural model, shows that the intensities of reflections of the $\{m/2, 2n+1\}$ and $\{m, 2n\}$ types are similar, as was observed in the low-energy electron diffraction patterns for the (100) GaAs (2 × 8)−Cs structure.

---

[1] J. T. Grant and T. W. Haas, Surf. Sci., 26, 669 (1971).

[2] N. J. Taylor, J. Vacuum Sci. and Technol., 6, 41 (1969).

[3] J. J. Uebbing, J. Appl. Phys., 41, 802 (1970).

[4] J. J. Lander and J. Morrison, J. Chem. Phys., 37, 729 (1962).

Spatial distribution of particles during vaporization of a zinc single crystal

Yu. A. Gel'man, V. F. Vinogradov, and Yu. N. Lyubitov

Institute of Crystallography, Academy of Sciences of the USSR

(Submitted July 22, 1972)
Kristallografiya, 18, 879-881 (July-August 1973)

The literature contains numerous data on different types of thermal etch pits on different faces,[1–8] on the faceting of spherical single crystals during vaporization in a vacuum[3,9–15] and on the different vaporization rates of different faces.[16,17] The factors that cause this anisotropy are believed to be anisotropy of vaporization rate (refs. 1-8, 12, 13, 16, 17), anisotropy of surface diffusion (refs. 9-11, 14, 15), and anisotropy of O_2 adsorption (refs. 8-10). Other factors may include anisotropic distribution of impurities[13,18] or some other type of disruption of crystal ideality and anisotropy of parameters of the condensation-factor type.

The vaporization of a Zn single crystal by the Knudsen method has been described.[19] The authors detected a large difference in vapor pressure and activation energy in those cases where different faces of the Zn single crystal were turned toward the effusion aperture.1) These results are unprecedented with respect to the magnitude of the anisotropy detected. Strictly speaking, they could not have been obtained in an ideal Knudsen cell, but detailed investigation of the effusion properties of Knudsen cells (see, e.g., refs. 20, 21) showed that measurements with real cells yield results that depend strongly on the specimen shape, cell-cavity geometry, and the interaction between the cell material and the substance being vaporized. The deviation of Knudsen cells from ideality might have enabled the above authors[19] to observe anisotropy of vaporization. The vaporization of Zn has also been investigated by the Langmuir torsion method,[22] but return flow from the hot walls to the evaporating crystal surface was not excluded. No anisotropy of vaporization was recorded in this investigation.

The above factors, as well as the large anisotropy of the lattice parameters[23] (c/a = 1.8555), impelled us to study the anisotropy of Zn vaporization.

EXPERIMENTAL RESULTS AND METHOD

Our investigation was conducted in a mass spectrometer whose basic characteristics were described previously.[24] Figure 1 shows the physical sense of the experiment. The Zn crystal was held in a two-channel ceramic mount with the aid of a thermocouple 1. The ceramic mount itself was fixed in a mechanism that permitted rotation of the crystal by 180°. The specimen was heated with radiation from tantalum foil 3; Screen 2 was installed to reduce the power consumed by heating element 3. We preliminarily studied the temperature distribution over the specimen 4. The temperature difference between the center of the crystal and its edges did not exceed ± 1.5° at temperatures of 450-650°K. The temperature was therefore subsequently measured only at the center of the crystal. The molecular beam entered the detector and was cut off by collimator 5. Screens 6 and 9 and collimator 5 were cooled by tube 10, which was filled with liquid nitrogen. The temperature of screen 6 was monitored with a copper–constantan thermocouple. At the maximum heater power of 3-50 W, the crystal temperature was 750°K, the temperature of screen 6 was ~ 100°K, and all the Zn striking the screen was condensed. Without screen 6, the ionic current increased sharply as the temperature was raised, but it remained almost unchanged when the molecular beam was intercepted by slide 8, since the chamber walls were at room temperature and the Zn was reflected from them and entered the ionization chamber both at the molecular-beam inlet and through other slits in the chamber. Cooling of screen 9 and collimator 5 to the temperature of liquid nitrogen did not eliminate this phenomenon. After screen 6 was installed, the ionic current was reduced to 0.5-1% of the signal amplitude when the molecular beam was intercepted by slide 8. The collimator was selected in such fashion that the cutoff beam passed through the ionization chamber without touching its walls and the ion-production region had a clear path only to the crystal surface; in addition, it permitted study of the evaporation indicatrices.

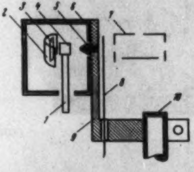

Fig. 1. Diagram of experiment. 1) Ceramic; 2) screen; 3) heating element; 4) specimen; 5) collimator; 6) screen; 7) ionization chamber; 8) slide; 9) screen; 10) tube.

Overall analysis of the dependence of the signal on the geometric characteristics of the emitter–collimator–detector system is quite cumbersome.[25,26] The situation is somewhat simpler in the two limiting cases: 1) an infinitely narrow collimator; 2) an infinitely small (infinitely elongated, point) specimen. Our experimental setup was close to the first case, where, with particle vaporization following the Knudsen rule, the signal from the detector remained constant when the inclination of the specimen to the collimator axis was varied, down to a slip angle commensurate with the detector aperture. In order to satisfy the above conditions, we selected a

TABLE 1

Specimen No.	Composition of Zn single crystals, at.% · 10^4													
	Cu	Ag	Mg	Ca	Cd	Sn	Pb	Sb	Bi	Cr	Mn	Fe	Co	Ni
1	—	0.25	0.20	0.40	60	1	20	0.40	0.30	1	20	30	20	30
2	50	—	—	—	100	30	2000	300	100	7	0.3	100	—	—

collimator with a diameter of 0.5 mm and a length of 7 mm.

Our specimens were single crystals grown by the Bridgman method or by zone melting. The crystal composition is given in Table 1.

The specimens had the form of cylinders 2.5 mm in diameter and 2-2.5 mm long. The (0001) plane was perpendicular to the specimen axis. In order to obtain a (0001) basal plane, the single crystal was cooled to the temperature of liquid nitrogen and split. The $(10\bar{1}0)$ prism planes were located parallel to the cylinder generatrices. Before being placed in the mass spectrometer, the specimens were etched in weak hydrochloric acid to remove the oxide. The vaporization rate was monitored from the ionic current of the Zn^{64} isotope.

Figure 2 presents the results obtained for the vaporization rates from the basal and prismatic faces and faces at an angle of 30 and 50° to the basal plane. As can be seen, there was no dependence on the crystallographic orientation or the angle of inclination. The points for angles of 20 and 60°, which are not given in Fig. 2, lay on the same line. The fact that there was no dependence on the angle of inclination indicates that the vaporization indicatrix followed the rule of cosines. Since the collimation was rather strict, we were able to investigate the vaporization only at relatively high temperatures, corresponding to pressures of 10^{-2}-10^{-5} torr. This temperature range overlaps that investigated by other researchers.[19,22] Higher temperatures were employed in the latter study.[22]

In the present investigation, we attempted to determine the dependence of the Zn vaporization rate (specimen 2) on the partial oxygen pressure over the range 10^{-8}-10^{-5} torr. We did not record the systematic dependence of the vaporization of different facets of Zn on the partial O_2 pressure over this range.

The difference in the heats of vaporization activation for different zinc facets and different directions with respect to these faces, determined under what we believe to be the most correct conditions, did not exceed ± 1.0 kcal/mole, i.e., the experimental error. It is difficult to conceive that the anisotropy observed by Tsvetaev et al.[19] was due to inhibited superficial diffusion. It can sooner be attributed to the anisotropy of inclusions of one sort or another that influence the vaporization rate. The fact that we did not observe any effect of oxygen on the vaporization rate can be explained by the fact that the original specimen was not highly purified and addition of oxygen changed nothing.

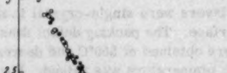

Fig. 2. Vaporization rate of Zn at different temperatures. ○) (0001) basal plane; ●) $(10\bar{1}0)$ prismatic plane; □) 30° to basal plane; □) 50° to basal plane.

Comparison of our data with those of Mar and Searey[22] enables us to conclude that there is no anisotropy of the condensation coefficient of zinc, since such anisotropy would lead to a different type of coiling for cases in which reverse flow occurs. The alternative, proportionality of the condensation coefficient to the flux, is improbable.

The heat of vaporization activation obtained, H^0_{298} = 29.6 ± 1.0 kcal/mole, is in rather good agreement with the data in the literature[27] (30.05 ± 0.42 kcal/mole).

The authors wish to thank V. G. Govorkov and A. A. Predvoditelev for furnishing the single crystals, D. V. Kormilitsin for analyzing the specimens, and V. I. Mikhailov for assisting in this work.

---

[1] The activation energy of vaporization was 16.3 ± 0.6 kcal/mole from the (0001) base plane and 41.2 ± 3.0 kcal/mole from the $(10\bar{1}0)$ prism plane.

[1] J. P. Hirth and L. Vassamillet, J. Appl. Phys., 29, 595 (1958).
[2] J. C. Danko and A. J. Griest, J. Metals, 8, 515 (1956).
[3] F. W. Young and A. T. Gwathmety, J. Appl. Phys., 31, 225 (1960).
[4] E. N. Andrade and R. F. Y. Randall, Proc. Phys. Soc., B63, 198 (1950).
[5] A. W. Ruff, Jr., J. Chem. Phys., 41, 1204 (1964).
[6] G. B. Rais and M. L. Bromberg, Kristallografiya, 4, 594 (1965) [Sov. Phys.-Crystallogr., 4, 555 (1960)].
[7] Yu. P. Pshenichnikov, Dokl. Akad. Nauk SSSR, 174, 821 (1967) [Sov. Phys.-Dokl., 12, 633 (1967)].
[8] B. Ya. Pines and L. G. Ivanov, Kristallografiya, 11, 802 (1966) [Sov. Phys.-Crystallogr., 11, 680 (1967)].
[9] E. Menzel, B. Schichler, and U. Jeschkowski, Surface Sci., 7, 482 (1967).
[10] A. Ponslet and D. Barlaux, Acta Metallurg., 12, 593 (1964).
[11] B. E. Sundquist, Acta Metallurg., 12, 67 (1964); 12, 585 (1964).
[12] B. Mutaftschiew, Phys. Status Solidi, 8, 223 (1965).
[13] V. N. Voitsekhovskii, Kristallografiya, 13, 563 (1968)[Sov. Phys.-Crystallogr., 13, 474 (1968)].
[14] P. I. Lukirskii, Dokl. Akad. Nauk SSSR, 46, 300 (1945).
[15] Superficial Diffusion and Flow [in Russian], Nauka, Moscow (1969).
[16] F. R. Rideal and P. M. Wiggins, Proc. Roy. Soc., A210, 291 (1952).
[17] C. B. Alcock, Bull. Soc. Franc. Ceram., 72, 25 (1966).
[18] G. G. Lemmlein, Sectorial Structure of Crystals [in Russian], Izd. Akad. Nauk SSSR, Moscow-Leningrad (1948).
[19] A. A. Tsvetaev, M. P. Glazunov, V. A. Kiselev, L. A. Alekseev, and R. K. Chuzhko, Zh. Fiz. Khim., 35, 2800 (1961).
[20] Yu. N. Lyubitov, Calculation of the Interaction of Molecular Fluxes with Containers Enclosing Them [in Russian], Nauka, Moscow (1964).
[21] J. W. Ward, N. R. Mulford, and R. L. Biving, J. Chem. Phys., 47, 1718 (1967).
[22] R. W. Mar and A. W. Searey, J. Chem. Phys., 53, 3076 (1970).
[23] S. S. Gorelik, L. N. Rastorguev, and Yu. A. Skakov, X-Ray Diffraction and Electron-Diffraction Analysis of Metals [in Russian], Metallurgiya, Moscow (1963).
[24] Yu. N. Lyubitov, Yu. A. Gel'man, A. M. Zatselyapin, V. M. Mikhailov, and L. V. Sumin, Prib. Tekh. Eksp., No. 3, 218 (1969); Dep. VINITI, No. 525-69.
[25] N. F. Ramsey, Molecular Beams, Oxford Univ. Press (1956).
[26] Yu. A. Gel'man, A. M. Zatselyapin, and V. M. Mikhailov, Prib. Tekh. Eksp., No. 3, 207 (1970).
[27] A. N. Nesmeyanov, Vapor Pressure of Chemical Elements [in Russian], Izd. Akad. Nauk SSSR, Moscow (1961).

Alloying of epitaxial silicon layers with phosphorus and arsenic in a vacuum

V. A. Tolomasov, L. N. Abrosimova, T. N. Sergievskaya, and T. M. Zotova
Gor'kii Scientific-Research Physicotechnical Institute

(Submitted July 21, 1971; resubmitted September 27, 1971, May 29, 1972)
Kristallografiya, 18, 882-884 (July-August 1973)

Use of elemental phosphorus and arsenic for alloying of silicon films produced in a vacuum involves considerable technical difficulties. Both elements react vigorously with the atmosphere (during loading of the apparatus) and have a high vapor tension at temperatures of 200-450°C, which are necessary for preliminary annealing in the high-vacuum apparatus used to produce silicon films.

In order to avoid these difficulties in working with phosphorus and arsenic, we generated fluxes of these elements by vaporization of their compounds with gallium, GaP and GaAs. Both compounds are stable in air, decomposing only at rather high temperatures; moreover, the vapor tension of gallium is several orders of magnitude lower than the vapor tension of phosphorus or arsenic. Golyshev et al.[1] used GaAs as an impurity source for growth of silicon films from the gaseous phase. However, alloying proceeded through a number of intermediate chemical reactions and the suitability of these compounds for alloying of films produced in a vacuum was not immediately obvious.

The epitaxial silicon layers were produced by sublimation, using the method described previously[2] and a residual gas pressure of $<10^{-7}$ mm Hg. The source and base disks were fabricated from type KDB-20 silicon. The GaP and GaAs were vaporized from a tungsten crucible heated with a tantalum coil. The alloyed silicon layers were produced over the growth-temperature range 500-700°C at a growth rate of 2-4 μ/h.

The layer structure was investigated by electron-diffraction analysis, electron microscopy, and metallographic methods. The packing defects and dislocations were made visible by etching with Sirtle's reagent, the layer thickness was determined from the packing defects and the position of the p–n transition, the current-carrier concentration was found from the voltage–capacitance curve for the rectifying mercury–silicon contact, and the current-carrier mobility was determined from probe measurements of the Hall emf and resistivity.

When vaporization of the alloying impurities was not conducted, the silicon layers had p-type conductivity and a current-carrier concentration of $5 \cdot 10^{14}$ cm^{-3}. When the crucible containing GaAs or GaP was heated to 500-800°C, the layers acquired n-type conductivity. The dependence of the current-carrier concentration n on the crucible temperature T is shown in Fig. 1. As can be seen from this figure, ln n was proportional to the temperature of the evaporator containing the alloying impurity, i.e., to the flux of arsenic or phosphorus molecules.

According to the data in Fig. 1, the activation energy of the dissociation of the GaP and GaAs was 15-17 kcal·mole. This is substantially lower than the activation energy of vaporization of pure phosphorus, arsenic, or gallium.

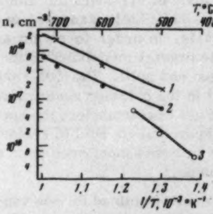

Fig. 1. Electron concentration in epitaxial silicon layers as a function of reciprocal temperature of crucible containing alloy. 1) Layer alloyed from GaP, T_g = 500°C, V_g = 3 μ/h; 2) layer alloyed from GaAs, T_g = 620°C, V_g = 4 μ/h; 3) layer alloyed with Sb, T_g = 620°C, V_g = 3.5 μ/h (ref. 2).

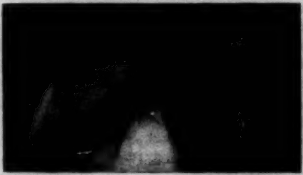

Fig. 2. "Transmission" electron-diffraction pattern of thin silicon film alloyed with GaAs to electron concentration of $5 \cdot 10^{17}$ cm^{-3} (T_g = 620°C).

Investigation of the current-carrier concentration distribution over the thickness of the epitaxial silicon layer (T_g = 570°C and V_g = 2.5 μ/h) showed that the impurities were distributed rather uniformly (over the range from 0 to 7 μ), the scattering around the value of 10^{17} cm^{-3} not exceeding the experimental error. Low epitaxy temperatures made it possible to obtain large variations in concentration. The current-carrier mobility in the epitaxial layers equalled that in massive single crystals with the same carrier concentration.

All the layers were single-crystal in structure and had a mirror surface. The packing defect density was 10^5-10^6 cm^{-2} in layers obtained at 500°C and decreased as the condensation temperature was raised. Figure 2 shows the "transmission-type" electron-diffraction pattern obtained from a thin silicon specimen alloyed with arsenic in a concentration of $5 \cdot 10^{17}$ cm^{-3}. The electron-diffraction pattern contained only Kikuchi lines for silicon and no reflections from other phases were detected; the presence of such phases was to be expected when there was a substantial amount of adsorbed GaAs.

Electron photomicrographs of thin specimens made by the "transmission" method (Fig. 3) showed that the structure of silicon layers alloyed from GaP and GaAs resembled the structure of unalloyed layers obtained at the same low growth temperatures (500-700°C). In addition to packing defects, point defects with a density of $\sim 1 \cdot 10^{10}$ cm^{-2} were observed in both cases. Some of them resembled small dislocation loops. No point defects were

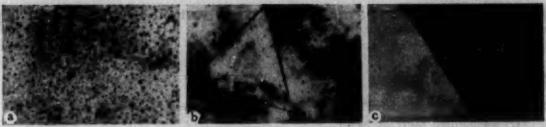

Fig. 3. "Transmission" electron photomicrographs of thin silicon layers. a) Layer alloyed by vaporization of GaP to electron concentration of 10^{17} cm^{-3}, $T_g = 620$°C, $V_g = 4$ μ/h, $N_{ar} = 4 \cdot 10^4$ cm^{-2}, × 30,000; b) unalloyed layer grown at $T_g = 500$°C, $V_g = 3.4$ μ/h, and $N_{ar} = 2 \cdot 10^5$ cm^{-2}, × 30,000; c) unalloyed layer grown at $T_g = 1100$°C and $N_{ar} = 10^{-2}$, × 70,000.

detected in photomicrographs made with unalloyed silicon specimens obtained at temperatures above 1000°C.

Our investigation showed that use of GaP and GaAs as independent sources can yield alloyed epitaxial layers of n-type silicon with a sufficiently ideal crystal structure.

The authors wish to thank R. A. Rubtsov, L. M. Prokhorov, and E. A. Rozanov for their assistance in this work.

---

[1] V. I. Golyshev, V. I. Ivanov, R. N. Kruglov, E. S. Lyubimov, L. V. Sazonov, B. A. Sukhodaev, and U. N. Stepanov, Elektron. Prom., No. 1, 94 (1971).

[2] V. A. Tolomasov, L. N. Abrosimova, and G. N. Gorshenin, Kristallografiya, 15, 1233 (1970) [Sov. Phys–Crystallogr., 15, 1076 (1971)].

Influence of temperature gradient on the impurity distribution during growth of crystals from a melt

E. A. Krivandina and E. E. Kostyleva

Institute of Crystallography, Academy of Sciences of the USSR

(Submitted January 13, 1972; resubmitted April 24, 1972)
Kristallografiya, 18, 885-887 (July-August 1973)

The KI−TII system has been used as an example[1] to study the influence of the furnace temperature on mass transfer during crystal growth in a melt by controlled crystallization. It was shown that the transfer mechanism is convective for the case of large gradients (~ 10 deg/cm for KI) and diffusive for that of small gradients (< 10 deg/cm for KI).

In order to obtain a more general characterization of this pattern, we conducted experiments on a system composed of the isomorphic organic compounds dibenzyl $C_{14}H_{14}$ (T_m = 51.2 ± 0.05°C) and tolane $C_{14}H_{10}$ (T_m = 61.5 ± 0.05°C), which have a rhomboprismatic monoclinic habit.[2,3]

Single crystals of $C_{14}H_{14}$ with an admixture of $C_{14}H_{10}$ (2 wt. %) were grown by the Stockbarger method on dibenzyl seed crystals oriented with the (001) cleavage plane perpendicular to the growth front. An unusual feature of the crystallization furnace employed was the fact that the test tube containing the material remained stationary, while the heating element moved upward at a predetermined rate. The furnace temperature gradient was preset by using different numbers of turns in the heating coil and regulated by varying the rate of heat removal through the condenser. The temperature at the crystallization front was measured with a differential copper − constantan microthermocouple (with a diameter of 0.1 mm) facing toward the crystal; the measurement accuracy was ± 0.4°.

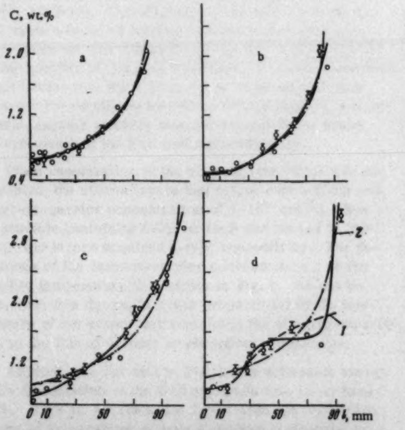

Fig. 1. Distribution of impurity tolane over length of dibenzyl crystal. The dashed lines are the theoretically calculated curves, while the solid lines are the experimental curves. Temperature gradients: a) 30; b) 10; c) 5; d) 2.5 deg/cm. The ordinate represents the impurity content in wt.%.

We employed the following growth regimes: a crystallization rate V = $6.0 \cdot 10^{-6}$ cm/sec and temperature gradients at the crystallization front dT/dl = 2.5, 5.0, 10, and 30 deg/cm.

In order to determine the impurity-tolane content of the single crystals thus produced, we employed optical absorption analysis. Tolane in toluol solution exhibits a pronounced absorption band at λ = 302 nm. Single crystals 10 mm in diameter and 90-110 mm long grown in glass test tubes were cut into tablets 10-15 mm long. A weighed sample of material was taken from the entire surface of each section and dissolved in toluol. The transmission spectra of the resultant solutions were determined and the impurity content of the crystal was found from a standard curve. The accuracy of the procedure used to determine the tolane in the composite dibenzyl−tolane crystals was ±2%. The impurity distribution over the crystal diameter was not studied.

The results obtained are presented in Fig. 1. Thus, the impurity distribution over the length of the crystal had a monotonic character with temperature gradients of from 30 to 5 deg/cm (Fig. 1a, b, and c). The situation was different for the graph representing the impurity distribution in a crystal grown at dT/dl = 2.5 deg/cm (Fig. 1d). This graph contained a linear segment, which enables us to assume that impurity transfer takes place by a diffusion mechanism in this case.[1,4]

Proceeding from the equation generally employed to describe the convective transfer mechanism,[5] we calculated the theoretical curves for k = 0.28, 0.22, 0.44 and the distribution constants given below by the finite-difference method. It can be seen from these graphs that there was complete agreement between the experimental and theoretical curves in the first two cases (Fig. 1a and b), while the theoretical curve differed somewhat from the experimental curve.

Equations describing the diffusive transfer mechanism[4,6] were employed[7] to calculate the theoretical curve (1), using D = $2 \cdot 10^{-5}$ cm²/sec and k = 0.001. It can be seen from Fig. 1d that a purely diffusive transfer mechanism did not occur in this case.[4,6] On the other hand, the theoretical curve (curve 2 in Fig. 1d) calculated for k = 0.48 from the equation for the convective transfer mechanism does not fully correspond to the experimental results. It should be noted that the process can be described by either a diffusive or convective mechanism at dT/dl = 2.5 deg/cm, although the latter apparently governs the distribution constant.

We obtained an interesting relationship between the distribution constant k and the temperature gradient. It can be seen from Fig. 2 that k decreased as the temperature gradient increased, tending toward saturation at large gradients. A transition region from impurity capture

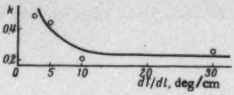

Fig. 2. Impurity-distribution constant as a function of furnace-temperature gradient.

described by a diffusive mechanism to a process described by a convective mechanism may be reflected by the interval $2.5 < dT/dl < 10$ deg/cm.

The following conclusions can thus be drawn.

1. The character of the impurity distribution in the crystal depended to a material extent on the temperature gradient: a) At large gradients (for $C_{14}H_{14} \geq 5$ deg/cm), the process is described by a convective impurity-transfer mechanism; b) at small gradients (< 5 deg/cm for $C_{14}H_{14}$), it is described by a diffusive mechanism.

2. The transition from a convective to a diffusive mechanism occurs over a rather narrow temperature-gradient range, which is in agreement with the results in the literature.[1]

3. The impurity-distribution constant decreases with the axial furnace temperature gradient, tending toward a constant value (starting at $dT/dl = 10$ deg/cm for $C_{14}H_{14}$).

In conclusion, it must be noted that, although the character of the impurity distribution over the length of the crystal (Fig. 1a, b, and c) is described by the equation for a convective transfer mechanism, its actual manifestation requires special proof, particularly since the overall crystallization-method geometry does not itself involve convection.

The authors wish to thank G. S. Belikov and V. Ya. Khaimov-Mal'kov for their consistent interest in this work and their valuable advice.

---

[1] V. Ya. Khaimov-Mal'kov and V. A. Perl'shtein, Kristallografiya, 4, 904 (1959) [Sov. Phys. – Crystallogr., 4, 857 (1960)].

[2] A. I. Kitaigorodskii, Organic Crystal Chemistry [in Russian], Izd. Akad. Nauk SSSR, Moscow (1955).

[3] P. Groth, Chemische Krystallographie, Vol. 5, Leipzig (1919), pp. 191-194.

[4] A. I. Landau, in: Crystal Growth [in Russian], Izd. Akad. Nauk SSSR, Moscow (1957), p. 74

[5] W. G. Pfann, Trans. AIME, 194, 747 (1952).

[6] O. W. Memelink, Philips Res. Repts., 3, 183 (1956).

[7] J. N. Sherwood, Crystal Growth, Pergamon Press, Oxford (1967).

Synthesis of tourmaline in chloride media. I

I. E. Voskresenskaya and A. A. Shternberg

Institute of Crystallography, Academy of Sciences of the USSR

(Submitted February 20, 1972; resubmitted June 20, 1972)
Kristallografiya, 18, 888-890 (July-August 1973)

Our previous investigations of the synthesis and growth of tourmaline crystals $NaR_3Al_6[Si_6O_{18}] \cdot (BaO_3)_3(OH, F)_4$ (where R is Li, Al, or Fe) and studies by other authors[1,2] dealt with the formation of tourmaline in boron chloride, boron fluoride, and composite boron chloride–fluoride systems. The syntheses were conducted at temperature of 500-700°C and pressures of up to 3 kbar, through reaction of aqueous solutions with a series of aluminum silicates.

The highest tourmaline-phase yield occurred[3] in boron chloride systems,1) obviously as a result of the absence of nonreactive complexes of the $[AlF_6]^{3-}$. An undesirable aspect of tourmaline formation in boron chloride systems was development of a number of secondary phases, primarily crystalline phases in the $Al_2O_3-SiO_2-FeO$ system.

In order to find the conditions for maximum tourmaline yield, we employed a TM-1 apparatus,2) which permitted synthesis at higher temperatures. This apparatus was previously used for synthesis of another aluminum silicate, spodumene.[4]

The experiments to determine the conditions for maximum tourmaline yield were conducted in welded copper or platinum ampoules with a capacity of 0.5-0.8 ml, which were filled with oxides or hydroxides having a composition corresponding to the desired tourmaline variety. At 750 and 800°C and a pressure of 5-8 kbar, experiments lasting 2-3 h yielded basic tourmalines (aluminum–lithium, magnesium, and iron) in the form of a mass of conical nodules of fine prismatic crystals 0.5-1.5 mm in size. It follows from analysis of the charge diagrams in Fig. 1 that mullite was synthesized together with tourmaline in a number of ampoules (specimens C3I and C3II). In its basic composition, the material synthesized was a monomineral tourmaline fraction.

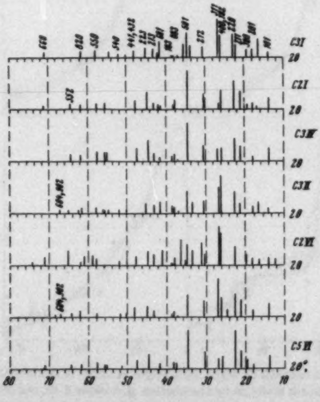

Fig. 1. X-ray diffraction patterns of synthetic tourmaline varieties obtained.

In order to obtain larger crystals and slow down the synthesis reaction, alumina and silica were added in low-solubility form (crystal aggregates or single-crystal rods of quartz and corundum), while the other components were in reagent form: boric acid, sodium chloride, and crystal hydrates of other chlorides. Each ampoule (with a capacity of 3-4 ml) contained two or three seed crystals of the appropriate tourmaline. In order to ensure free growth of tourmaline crystals in the liquid phase, the amount of chlorides in the ampoule was two or three times the volume of the expected solid phases. Thus, when corundum and quartz were introduced into the ampoule in the form of separate single-crystal rods and the solvent was crystalline hydrated magnesium chloride ($MgCl_2 \cdot 6H_2O$), synthesis at 750°C and a pressure of 5-8 kbar yielded a colorless single-crystal material up to 3 mm thick on one side of a monohedral magnesium tourmaline (dravite)3) seed (the growth rate being up to 1 mm/day) and traces of growth in a prismatic habit, as well as crystallization of isolated large (up to 1.5-2 mm) parasitic crystals of colorless tournaline. The crystals were transparent and well-faceted (Fig. 2), having a thick prismatic appearance. Their structure was uniaxial and negative; $N_o = 1.633-1.634$, $N_e = 1.609-1.610$, and $N_o - N_e = 0.024$.

When lithium chloride was used as the medium, we obtained negative results: Despite the fact that the composition of the other components corresponded to the stoichiometric composition of lithium tourmaline, we observed massive crystallization of eucryptite.

In addition to lithium and magnesium chlorides, ferrous chloride was also used as a solvent, in the form of $FeCl_2 \cdot 4H_2O$. It is curious that growth of a light brown tourmaline, almost colorless in individual experiments, occurred on seeds of iron tourmaline (schorl); corundum fragments or rods were coated with light brown, fine prismatic crystals of tourmaline up to 1 mm in size. The crystals were uniaxial and negative: $N_o = 1.668-1.667$, $N_e = 1.636-1.635$, and $N_o - 0.032$.

Since it was difficult to achieve a pressure of 5-8 kbar, we attempted in a subsequent series of experiments to find the minimum pressure at which the reaction would take place, reducing the H_2O content of the system as far as possible for this purpose. It was established in this series of experiments that, with a temperature of 750°C and a medium containing 70% $MgCl_2$ and 30% H_2O, the pressure could be reduced by a factor of 8, from 8 to 1 kbar. In growing layers of homogeneous tourmaline on seeds in these experiments, we were able to almost completely avoid parasitic crystals. In experiments with $P < 800$ bar, dravite seeds decomposed, becoming coated with an opalescent light blue layer.

Thus, using the complex silicate tourmaline as an

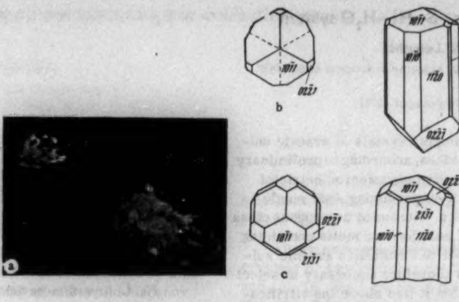

Fig. 2. Crystals of synthetic colorless magnesium tourmaline (10 ×) (a) and their orthogonal (b, c) and axonometric (d, e) projections.

example, we were able to show that synthesis from spatially separated low-solubility components in highly concentrated chloride media makes it possible to obtain homogeneous colorless single crystals at relatively low pressures; these crystals are suitable for investigation of physical properties.

The authors wish to thank N. A. Kovyzhenko for his assistance in diagnosing the tourmaline phases.

---

[1] The chloride concentration in the systems in question did not exceed 2-3%.

[2] An autoclave with an internal heating element in the form of a corrugated tube, designed by A. A. Shternberg.

[3] Seeds of lithium tourmaline (elbaite) decomposed under the conditions investigated, becoming coated with fine scales of light blue sapphire.

[1] C. Frondel and R. L. Collette, Am. Mineralog., 42, 11 (1957).

[2] E. N. Emel'yanova and T. A. Zigareva, Kristallografiya, 5, 955 (1960) [Sov. Phys. – Crystallogr., 5, 910 (1961)].

[3] I. E. Voskresenskaya and M. L. Varsukova, in: Hydrothermal Synthesis of Crystals [in Russian], Nauka, Moscow (1968).

[4] A. A. Shternberg, V. A. Kuznetsov, and T. K. Ivanova, Transactions of the Eighth Conference on Experimental and Technical Mineralogy and Petrography [in Russian], Nauka, Moscow (1971).

Crystallization in the As–S–HI–H_2O system

V. I. Popolitov and A. N. Lobachev

Institute of Crystallography, Academy of Sciences of the USSR

(Submitted July 24, 1972)
Kristallografiya, 18, 891 (July-August 1973)

The problem of producing single crystals of arsenic sulfoiodide is a pressing one, since, according to preliminary data, it is a photosemiconductive piezoferroelectric of the SbSi type.[1] The difficulty in producing AsSI single crystals lies in the fact that a vitreous or amorphous mass is formed during cooling of solutions or melts containing arsenic and sulfur.[2] In order to crystallize arsenic sulfoiodide from solution, it is therefore necessary to select a temperature range such that it lies above the vitrification temperature and below the melting point. Experimental investigations showed this temperature range to be 325-346°C. Below this temperature, a solution containing arsenic, sulfur, and iodine is converted to a vitreous or amorphous mass. Crystallization was conducted in standard periodic-action autoclaves lined with Teflon. The temperature gradient over the height of the autoclave was 5-21° (400 mm) and the liquid pressure was 595-640 atm. The crystallization medium was an aqueous solution of hydroiodic acid with a concentration of 5-55 wt.%. The initial charge components were elemental arsenic, semiconductor-grade sulfur, and natural crystals of orpiment As_2S_3. The gravimetric ratio of the arsenic to the sulfur was varied from stoichiometric to 1 : 2 or 2 : 1. The volumetric ratio of the solid and liquid phases was held constant at 1 : 6. Study of the crystallization conditions in the As–S–HI–H_2O system showed that (see diagram) the single-crystal phases AsSI, As_2S_3, AsI_3, and As were formed over the HI concentration range from 3 to 55 wt.% at a temperature of 325-346°C, depending on the component ratio in the charge. The monophasic arsenic sulfoiodide region occurred with a stoichiometric arsenic-to-sulfur ratio and with a ratio of 1 : 1. Single crystals of AsSI were formed in the upper zone of the reaction vessel and their yield increased with the hydroiodic acid concentration. At an As : S ratio of 2 : 1, both AsSI and single crystals of orpiment As_2S_3 were formed, the field for the latter being replaced by that for single crystals of arsenic triiodide at HI concentrations above 43 wt.%. Crystallization of the above phases was accompanied by formation of arsenic single crystals. An excess of sulfur with respect to the arsenic led to disappearance of the arsenic crystals and an increase in the yield of orpiment (yellow arsenic) single crystals. The charge composition had a considerable influence on the AsSI crystallization rate. Use of a charge with the composition As_2S_3 in a number of experiments showed that it was driven into the hydroiodic acid solution more rapidly than elemental arsenic, which provided a higher crystallization rate (yield of AsSI single crystals per unit time) for arsenic sulfoiodide, all other conditions being equal. The AsSI crystals obtained had the form of dark-red needles elongated along the c axis. The composition of these single crystals was confirmed by x-ray diffraction analysis.

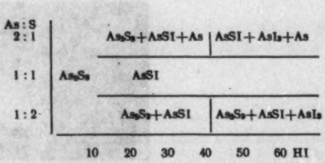

Fig. 1. Crystallization field in the As–S–HI–H_2O system.

---

[1] V. I. Popolitov and B. N. Litvin, in: Investigation of Crystallization Processes under Hydrothermal Conditions [in Russian], Nauka, Moscow (1970), p. 65.

[2] S. A. Dembovskii and A. A. Chernov, Izv. Akad. Nauk SSSR, Neorgan. Mat., 4, 1229 (1968).

Growth of shaped germanium crystals having low dislocation density by the Bridgman method

L. A. Maslova and S. V. Tsivinskii

Physicotechnical Institute of Low Temperatures,
Academy of Sciences of the Ukrainian SSR

(Submitted July 14, 1972)
Kristallografiya, 18, 892-893 (July-August 1973)

As was shown in ref. 1, the main cause of dislocation formation in the growth of crystals in a solid crucible by the Bridgman method is plastic deformation due to adhesion of the crystal to the crucible walls and the differences in their coefficients of linear expansion. If adhesion is eliminated, dislocations will be produced by temperature gradients, as in the Czochralski and Stepanov methods and in zone melting without a crucible.[2] When the transverse dimensions are small, the thermal stress will not exceed the critical shear stress, and the crystals will grow without dislocations.[2]

In the present study, crystals were grown in demountable graphite molds as described in ref. 3. Adhesion was eliminated by sooting up the inner surface of the crucible (a layer of soot ≈ 10 μ thick was deposited). The growth rate was 8.5 cm/h, whereas the direction of growth coincided with [111]. Growth was carried out in a $(1\text{-}2)\cdot 10^{-2}$ torr vacuum. The temperature gradient of the furnace in the crystallization zone was 60 deg/cm.

The crystals were grown in the form of round rods 0.7 cm in diameter and 5 cm long and as rods with a square cross section of 0.3×0.3 cm and about 6-9 cm long. The crystals were cut transversely into pieces 0.5-2 cm long. The dislocation density was determined from etch pits on the ends corresponding to the (111) planes. Alkaline potassium ferricyanide solution was used as the etchant.[4]

The dislocation density in the round crystals was small and varied very slightly along the length ($N = 1\text{-}5 \cdot 10^2\ \mathrm{cm}^{-2}$).

There were no small-angle boundaries. In the single crystals of square cross section, N lay between $6 \cdot 10^4$ and $1.6 \cdot 10^5\ \mathrm{cm}^{-2}$ for the first 1.5-2 cm of length. Beyond this, the dislocation density fell rapidly, and the last portion, ≈ 2 cm long, was dislocation-free. The distribution of dislocations in various cross sections of the crystals is shown in Fig. 1.

Germanium crystals were grown in the form of plates in demountable graphite forms earlier.[5] However, the crystals had a dislocation density of $10^3\text{-}10^4\ \mathrm{cm}^{-2}$ and contained small-angle boundaries. Evidently, that is the reason this method did not come into use.

The results of the present study show that perfect shaped crystals of semiconductors can be grown.

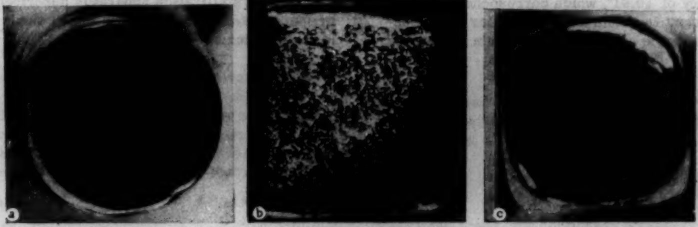

Fig. 1. Distribution of etch pits in crystals having round (a) and square cross sections (b is first portion; c is dislocation-free portion of same crystal).

---

[1] S. V. Tsivinskii, L. A. Maslova, and B. N. Aleksandrov, Fiz. Met. Metalloved., 28, 487 (1969).
[2] S. V. Tsivinskii, Fiz. Met. Metalloved., 25, 1013 (1968).
[3] L. A. Maslova, S. V. Tsivinskii, and B. N. Aleksandrov, Tr. Fiz.-Tekh. Inst. Nizkikh Temperatur, Akad. Nauk UkrSSR, Fizika Kondensirovannogo Sostoyaniya, 10, 65 (1970).
[4] E. Yu. Kokorish and E. V. Myakinenkova, in: Growth of Crystals, Vol. 3, Consultants Bureau, New York (1962).
[5] W. Bosenberg, Z. Angew. Phys., 9, 347 (1957).

Crystallization apparatus for the growth of crystals at constant supersaturation of the solution

A. I. Munchaev

Institute of Crystallography, Academy of Sciences of the USSR

(Submitted June 21, 1972; resubmitted August 22, 1972)
Kristallografiya, 18, 894-895 (July-August 1973)

The present paper describes the design of a crystallization apparatus for the growth of crystals from solution, which makes it possible to carry out the crystallization process at a given value of the supersaturation for substances with either low or high solubility.

The crystallization apparatus, with a volume of approximately 2.5 dm^3 (see Fig. 1), consists of two vessels, a saturation vessel and a growth vessel, made of heat-resistant glass. The vessels have double walls, between which (T_1-T_1 and T_2-T_2) water at different temperatures is circulated. The saturation vessel contains a beaker with holes, containing the substance being crystallized, and a centrifugal pump; the rate of circulation of the solution can be controlled by changing the rate of rotation of the pump. One end of the beaker is firmly attached by means of packing in the saturation vessel, to ensure the supply of solution with constant concentration to the growth vessel. The saturated solution passes from the saturation vessel into the growth vessel through a thermostated coil, and the nonsaturated solution is returned to the saturation vessel. The sloping position of the tube, and also the special geometry of the growth vessel (the smooth decrease in width in the lower part) and the additional heating of the walls of the joint, are chosen in such a way that the "parasitic" crystals formed in the growth vessel are transferred without hindrance to the saturation vessel by the stream of solution.

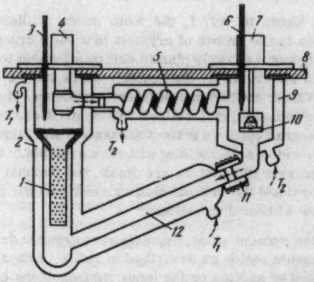

Fig. 1. Diagram of the crystallization apparatus: 1) quartz beaker; 2) saturation vessel; 3, 6) control thermometers; 4) pump; 5) coil; 7) electric motor; 8) plate; 9) growth vessel; 10) crystal holder; 11) additional heater; 12) tube.

The crystallization apparatus has been used to grow crystals of potassium sodium tartrate containing traces of copper; the temperature in the vessels was kept constant with an accuracy of ±0.01°, which corresponded to a concentration constant to within ±0.08%. Under these conditions, perfect single crystals of potassium sodium tartrate weighing up to 50 g, with different copper contents, were obtained. The rate of growth of these crystals is 10 g/day. It was established experimentally that in the growth of crystals of potassium sodium tartrate at rates of ~0.2 mm/h in the [001] direction, complete saturation of the solution in the saturation vessel takes place at rates of circulation up to 0.1 liter/min. It was also observed that at values of the relative supersaturation up to 15%, extensive formation of "parasite" crystals does not take place in the growth vessel.

The crystallization apparatus described is reliable in operation and makes it possible to obtain large crystals in small volumes.

Reduction of the Kronecker product of representations of the crystallographic groups. II

B. A. Men', A. N. Men', and V. I. Cherepanov
Metallurgical Institute of the Ural Scientific Center

(Submitted July 25, 1972; resubmitted November 9, 1972)
Kristallografiya, 18, 901-905 (September-October 1973)

A procedure is given for the construction of functions of lower symmetry for any number of spaces of factors for the group of the tetrahedron.

In ref. 1 we considered the reduction of the Kronecker product of representations of the crystallographic groups of trigonal ($D_3 \simeq C_{3v} \simeq S_3$) and tetragonal types ($D_4 \simeq C_{4v} \simeq D_{2d}$).

In this article we present a procedure for constructing functions of lower symmetry for any number of factors when the group is the tetrahedral group $T \simeq A_4$.

We write down the character tables of A_4 and V_4 (Table 1) and choose a basis such that the matrices of the degenerate representation (Γ_4) have the form (1):

$$\overset{e}{\begin{pmatrix}1&0&0\\0&1&0\\0&0&1\end{pmatrix}}\overset{(12)\quad(34)}{\begin{pmatrix}1&0&0\\0&-1&0\\0&0&-1\end{pmatrix}}\overset{(13)\,(24)}{\begin{pmatrix}-1&0&0\\0&1&0\\0&0&-1\end{pmatrix}}\overset{(14)\,(23)}{\begin{pmatrix}-1&0&0\\0&-1&0\\0&0&1\end{pmatrix}}$$

$$\overset{(134)}{\begin{pmatrix}0&0&1\\1&0&0\\0&1&0\end{pmatrix}}\overset{(123)}{\begin{pmatrix}0&0&1\\-1&0&0\\0&-1&0\end{pmatrix}}\overset{(243)}{\begin{pmatrix}0&0&-1\\-1&0&0\\0&1&0\end{pmatrix}}\overset{(142)}{\begin{pmatrix}0&0&-1\\1&0&0\\0&-1&0\end{pmatrix}}$$

$$\overset{(143)}{\begin{pmatrix}0&1&0\\0&0&1\\1&0&0\end{pmatrix}}\overset{(132)}{\begin{pmatrix}0&-1&0\\0&0&-1\\1&0&0\end{pmatrix}}\overset{(234)}{\begin{pmatrix}0&-1&0\\0&0&1\\-1&0&0\end{pmatrix}}\overset{(124)}{\begin{pmatrix}0&1&0\\0&0&-1\\-1&0&0\end{pmatrix}}. \quad (1)$$

Consider the tensor product of the representations and the functions corresponding to it:

$$\overbrace{\Gamma_1\times\ldots\times\Gamma_1}^{k}\times\overbrace{\Gamma_2\times\ldots\times\Gamma_2}^{l}\times\overbrace{\Gamma_3\times\ldots\times\Gamma_3}^{r}\times\overbrace{\Gamma_4\times\ldots\times\Gamma_4}^{n}=\sum_i\Gamma_i, \quad (2)$$

$$\underbrace{\psi_1^{(1)}\ \ldots\ \psi_k^{(1)}\ \ \psi_1^{(2)}\ \ldots\ \psi_l^{(2)}\ \ \psi_1^{(3)}\ \ldots\ \psi_r^{(3)}}\ \ \psi_{11}^{(4)}\psi_{12}^{(4)}\psi_{13}^{(4)}\ldots\psi_{n1}^{(4)}\psi_{n2}^{(4)}\psi_{n3}^{(4)}$$

$$\psi=\prod_{i_1}^{k}\psi_{i_1}^{(1)}\prod_{i_2=1}^{l}\psi_{i_2}^{(2)}\prod_{i_3=1}^{r}\psi_{i_3}^{(3)}.$$

To construct the functions which transform under the representations Γ_1 and which appear on the right of (2), we proceed as follows.[1)]

1. We partition the number n in all possible ways into the sum of positive numbers n_i, allowing for their order $\left(n=\sum_i n_i\right)$. Each such partition obtained is written down in the form $n_1 \pm n_2 \pm n_3 \pm \ldots$.

2. For each partition we choose a certain set of signs (e.g., $n_1 + n_2 - n_4 + \ldots$), and we put each partition in correspondence with matrices containing n columns and three rows; the elements of such a matrix will be 0(B), + (C), and −(D). The elements of the first row of the matrix are filled according to the following rule.

a) n_1 columns in the first row are filled with zeros:

$$3\begin{pmatrix}\overbrace{0\ldots0}^{n_1}\ldots\\ \underbrace{\ldots\qquad\ldots}_{n}\end{pmatrix}.$$

b) The next n_2 columns in the first row have the sign + (if a plus sign appears between n_1 and n_2 in the partition) or the sign − (if there is a minus sign between these numbers in the partition).

In the example given in this section, there will be n_2 plus signs:

$$\begin{pmatrix}\overbrace{0\ldots0}^{n_1}&\overbrace{+\ldots+}^{n_2}&\ldots\\ \ldots&\ldots&\ldots\\ \ldots&\ldots&\ldots\end{pmatrix}.$$

c) The next n_3 columns are written down according to the sign between n_2 and n_3 according to the following change rules:

$$\begin{aligned}&n_2+n_3\rightarrow(0\rightarrow+),\ (+\rightarrow-),\ (-\rightarrow0)\\&n_2-n_3\rightarrow(0\rightarrow-),\ (-\rightarrow+),\ (+\rightarrow0)\end{aligned} \quad (3)$$

and so the procedure continues.

In the example used above, the minus sign appears between n_2 and n_3, so that after the n_2 plus signs we have n_3 minus signs, and so on:

TABLE 1

A_4	e	(12) (34) (13) (24) (14) (23)	(123) (142) (134) (243)	(132) (124) (143) (234)
Γ_1	1	1	1	1
Γ_2	1	1	ω	ω^2
Γ_3	1	1	ω^2	ω
Γ_4	3	−1	0	0

V_4	e	(12) (34)	(13) (24)	(14) (23)
A	1	1	1	1
(0) B	1	1	−1	−1
(+) C	1	−1	1	−1
(−) D	1	−1	−1	1

TABLE 2

n	Form of the matrix	$\delta_1\equiv\delta_2\equiv\delta_3\equiv(\mathrm{mod}\,2)$	Form of the function $\psi_{\Gamma_j}\begin{pmatrix}\alpha_{11}&\alpha_{12}&\alpha_{13}\\\alpha_{21}&\alpha_{22}&\alpha_{23}\\\alpha_{31}&\alpha_{32}&\alpha_{33}\end{pmatrix}$; $\psi=\prod_{i_1=1}^{k}\psi_{i_1}^{(1)}\psi_{1}^{(2)}\psi_{2}^{(3)}$
$n_1n_2n_3$ ψ $3+0+0$	$\begin{pmatrix}0&0&0\\+&+&+\\-&-&-\end{pmatrix}$	1 0 0	$\psi_{\Gamma_4}\begin{pmatrix}0&0&0\\+&+&+\\-&-&-\end{pmatrix}\to\psi\psi_{11}^{(4)}\psi_{21}^{(4)}\psi_{31}^{(4)}$; $\omega\psi\psi_{12}^{(4)}\psi_{22}^{(4)}\psi_{32}^{(4)}$; $\omega^2\psi\psi_{13}^{(4)}\psi_{23}^{(4)}\psi_{33}^{(4)}$
$2+1+0$	$\begin{pmatrix}0&0&+\\+&+&-\\-&-&0\end{pmatrix}$	0 1 0	$\psi_{\Gamma_4}\begin{pmatrix}0&0&+\\+&+&-\\-&-&0\end{pmatrix}\to\omega^2\psi\psi_{13}^{(4)}\psi_{23}^{(4)}\psi_{31}^{(4)}$; $\psi\psi_{11}^{(4)}\psi_{21}^{(4)}\psi_{32}^{(4)}$; $\omega\psi\psi_{12}^{(4)}\psi_{22}^{(4)}\psi_{33}^{(4)}$
$2-1+0$	$\begin{pmatrix}0&0&-\\+&+&0\\-&-&+\end{pmatrix}$	0 0 1	$\psi_{\Gamma_4}\begin{pmatrix}0&0&-\\+&+&0\\-&-&+\end{pmatrix}\to\omega\psi\psi_{12}^{(4)}\psi_{22}^{(4)}\psi_{31}^{(4)}$; $\omega^2\psi\psi_{13}^{(4)}\psi_{23}^{(4)}\psi_{32}^{(4)}$; $\psi\psi_{11}^{(4)}\psi_{21}^{(4)}\psi_{33}^{(4)}$
$1+2+0$	$\begin{pmatrix}0&+&+\\+&-&-\\-&0&0\end{pmatrix}$	1 0 0	$\psi_{\Gamma_4}\begin{pmatrix}0&+&+\\+&-&-\\-&0&0\end{pmatrix}\to\psi\psi_{11}^{(4)}\psi_{22}^{(4)}\psi_{32}^{(4)}$; $\omega\psi\psi_{12}^{(4)}\psi_{23}^{(4)}\psi_{33}^{(4)}$; $\omega^2\psi\psi_{13}^{(4)}\psi_{21}^{(4)}\psi_{31}^{(4)}$
$1-2+0$	$\begin{pmatrix}0&-&-\\+&0&0\\-&+&+\end{pmatrix}$	1 0 0	$\psi_{\Gamma_4}\begin{pmatrix}0&-&-\\+&0&0\\-&+&+\end{pmatrix}\to\psi\psi_{11}^{(4)}\psi_{23}^{(4)}\psi_{33}^{(4)}$; $\omega\psi\psi_{12}^{(4)}\psi_{21}^{(4)}\psi_{31}^{(4)}$; $\omega^2\psi\psi_{13}^{(4)}\psi_{22}^{(4)}\psi_{32}^{(4)}$
$1+1+1$	$\begin{pmatrix}0&+&-\\+&-&0\\-&0&+\end{pmatrix}$	1 1 1	$\psi_{\Gamma_5}\begin{pmatrix}0&+&-\\+&-&0\\-&0&+\end{pmatrix}\to\frac{1}{\sqrt{3}}\psi\,[\psi_{11}^{(4)}\psi_{22}^{(4)}\psi_{33}^{(4)}$ $+\omega\psi_{12}^{(4)}\psi_{23}^{(4)}\psi_{31}^{(4)}+\omega^2\psi_{13}^{(4)}\psi_{21}^{(4)}\psi_{32}^{(4)}]$; $\psi_{\Gamma_5}\to\frac{1}{\sqrt{3}}\psi\,[\psi_{11}^{(4)}\psi_{22}^{(4)}\psi_{33}^{(4)}+\psi_{12}^{(4)}\psi_{23}^{(4)}\psi_{31}^{(4)}$ $+\psi_{13}^{(4)}\psi_{21}^{(4)}\psi_{32}^{(4)}]$; $\psi_{\Gamma_5}\to\frac{1}{\sqrt{3}}\psi\,[\psi_{11}^{(4)}\psi_{22}^{(4)}\psi_{33}^{(4)}$ $+\omega^2\psi_{12}^{(4)}\psi_{23}^{(4)}\psi_{31}^{(4)}+\omega\psi_{13}^{(4)}\psi_{21}^{(4)}\psi_{32}^{(4)}]$
$1-1+1$	$\begin{pmatrix}0&-&0\\+&0&+\\-&+&-\end{pmatrix}$	0 0 1	$\psi_{\Gamma_4}\begin{pmatrix}0&-&0\\+&0&+\\-&+&-\end{pmatrix}\to\omega\psi\psi_{12}^{(4)}\psi_{21}^{(4)}\psi_{32}^{(4)}$; $\omega^2\psi\psi_{13}^{(4)}\psi_{22}^{(4)}\psi_{33}^{(4)}$; $\psi\psi_{11}^{(4)}\psi_{23}^{(4)}\psi_{31}^{(4)}$
$1+1-1$	$\begin{pmatrix}0&+&0\\+&-&+\\-&0&-\end{pmatrix}$	0 1 0	$\psi_{\Gamma_4}\begin{pmatrix}0&+&0\\+&-&+\\-&0&-\end{pmatrix}\omega^2\psi\psi_{13}^{(4)}\psi_{21}^{(4)}\psi_{33}^{(4)}$; $\psi\psi_{11}^{(4)}\psi_{22}^{(4)}\psi_{31}^{(4)}$; $\omega\psi\psi_{12}^{(4)}\psi_{23}^{(4)}\psi_{32}^{(4)}$
$1-1-1$	$\begin{pmatrix}0&-&+\\+&0&-\\-&+&0\end{pmatrix}$	1 1 1	$\psi_{\Gamma_5}\begin{pmatrix}0&-&+\\+&0&-\\-&+&0\end{pmatrix}\to\frac{1}{\sqrt{3}}\psi\,[\psi_{11}^{(4)}\psi_{23}^{(4)}\psi_{32}^{(4)}$ $+\omega\psi_{12}^{(4)}\psi_{21}^{(4)}\psi_{33}^{(4)}+\omega^2\psi_{13}^{(4)}\psi_{22}^{(4)}\psi_{31}^{(4)}]$; $\psi_{\Gamma_5}\begin{pmatrix}0&-&+\\+&0&-\\-&+&0\end{pmatrix}\frac{1}{\sqrt{3}}\psi\,[\psi_{11}^{(4)}\psi_{23}^{(4)}\psi_{32}^{(4)}$ $+\psi_{12}^{(4)}\psi_{21}^{(4)}\psi_{33}^{(4)}+\psi_{13}^{(4)}\psi_{22}^{(4)}\psi_{31}^{(4)}]$; $\psi_{\Gamma_5}\begin{pmatrix}0&-&+\\+&0&-\\-&+&0\end{pmatrix}\to\frac{1}{\sqrt{3}}\psi\,[\psi_{11}^{(4)}\psi_{23}^{(4)}\psi_{32}^{(4)}$ $+\omega^2\psi_{12}^{(4)}\psi_{21}^{(4)}\psi_{33}^{(4)}+\omega\psi_{13}^{(4)}\psi_{22}^{(4)}\psi_{31}^{(4)}]$

$$\begin{pmatrix}\overbrace{0\ldots0}^{n_1}\overbrace{+\ldots+}^{n_2}\overbrace{0\ldots0}^{n_3}\overbrace{-\ldots-}^{n_4}\cdots\\ \vdots\qquad\vdots\qquad\vdots\qquad\vdots\qquad\vdots\end{pmatrix}. \tag{4}$$

The elements of the second row in (4) are obtained from those of the first row by the following change rules:

$$(0\to+),\quad(+\to-),\quad(-\to0). \tag{5}$$

The third row is obtained from the second by the same change rule (5).

For the example we have been considering, the change

rule (5) turns (4) into

$$\begin{pmatrix} 0 \ldots 0 + \ldots & + 0 \ldots & 0 - & \ldots - \ldots \\ + \ldots + - \ldots & - + \ldots & + 0 & \ldots 0 \ldots \\ - \ldots - 0 & \ldots 0 - \ldots & - + & \ldots + \ldots \end{pmatrix}. \tag{6}$$

The matrix (6) will be the characteristic representation.

3. We count up the number of zeros, pluses, and minuses in the first row of (6), and denote them by δ_1, δ_2 and δ_3, respectively.

4. To each of the three rows i, i = 1, 2, 3, we assign a function ψ_i as follows: The function ψ_i is the product of functions $\psi_{pj}^{(4)}$ where p is the ordinal number of the column in the matrix, and j takes the value 1 for a zero, 2 for a plus, and 3 for a minus.

Thus for the matrix in (6) we get

$$\begin{aligned} \psi_1 = {} & \psi_{11}^{(4)}\, \psi_{21}^{(4)} \ldots \psi_{n_1 1}^{(4)}\, \psi_{n_1+1,2}^{(4)} \psi_{n_1+2,2}^{(4)} \ldots \psi_{n_1+n_2,2}^{(4)} \psi_{n_1+n_2+1,1}^{(4)} \ldots \\ & \ldots \psi_{n_1+n_2+n_3,1}^{(4)} \psi_{n_1+n_2+n_3+1,3}^{(4)} \ldots \psi_{n_1+n_2+n_3+n_4,3}^{(4)} \ldots, \\ \psi_2 = {} & \psi_{12}^{(4)} \ldots \psi_{n_1 2}^{(4)} \psi_{n_1+1,3}^{(4)} \ldots \psi_{n_1+n_2,3}^{(4)} \psi_{n_1+n_2+1,2}^{(4)} \ldots \psi_{n_1+n_2+n_3,2}^{(4)} \\ & \times \psi_{n_1+n_2+n_3+1,1}^{(4)} \ldots \psi_{n_1+n_2+n_3+n_4,1}^{(4)} \ldots, \\ \psi_3 = {} & \psi_{13}^{(4)} \ldots \psi_{n_1,3}^{(4)} \psi_{n_1+1,1}^{(4)} \ldots \psi_{n_1+n_2,1}^{(4)} \psi_{n_1+n_2+1,3}^{(4)} \ldots \psi_{n_1+n_2+n_3,3}^{(4)} \\ & \times \psi_{n_1+n_2+n_3+1,2}^{(4)} \ldots \psi_{n_1+n_2+n_3+n_4,2}^{(4)} \ldots \end{aligned} \tag{7}$$

5. We write down the explicit form of the functions for each of the representations in the partition (2) according to the theorem [where l is the number of the representations Γ_2, and r the number of representations of Γ_3 in (2)]:

a) $\delta_1 \equiv \delta_2 \equiv \delta_3 \pmod 2$,

$$\begin{aligned} \Gamma_1 &\to \frac{1}{\sqrt{3}}(\psi_1 + \omega^{l-r}\psi_2 + \omega^{2(l-r)}\psi_3)\psi, \\ \Gamma_2 &\to \frac{1}{\sqrt{3}}(\psi_1 + \omega^{l-r+2}\psi_2 + \omega^{2(l-r)+1}\psi_3)\psi, \\ \Gamma_3 &\to \frac{1}{\sqrt{3}}(\psi_1 + \omega^{l-r+1}\psi_2 + \omega^{2(l-r+1)}\psi_3)\psi, \end{aligned} \tag{8}$$

b) $\delta_1 \equiv \delta_2 \not\equiv \delta_3 \pmod 2$,

$$\Gamma_4 \to \omega^{l-r}\psi_2\psi,\ \omega^{2(l-r)}\psi_3\psi,\ \psi_1\psi,$$

c) $\delta_1 \equiv \delta_3 \not\equiv \delta_2 \pmod 2$,

$$\Gamma_4 \to \omega^{2(l-r)}\psi_3\psi,\ \psi_1\psi,\ \omega^{l-r}\psi_2\psi,$$

d) $\delta_2 \equiv \delta_3 \not\equiv \delta_1 \pmod 2$,

$$\Gamma_4 \to \psi_1\psi,\ \omega^{l-r}\psi_2\psi,\ \omega^{2(l-r)}\psi_3\psi.$$

Consider the example

$$\underbrace{\Gamma_1 \times \ldots \times \Gamma_1}_{k} \times \underbrace{\Gamma_3 \times \Gamma_3}_{r=2} \times \underbrace{\Gamma_4 \times \Gamma_4 \times \Gamma_4}_{n=3} = 2(\Gamma_1 + \Gamma_2 + \Gamma_3) + 7\Gamma_4.$$

The results of the calculations according to the method outlined above are shown in Table 2.

[1)] The mathematical basis for this procedure is given in ref. 2.

---

[1] B. A. Men', A. N. Men', and V. I. Cherepanov, Kristallografiya, 18, 669 (1973) [Sov. Phys.–Crystallogr., 18, 421 (1974)].

[2] B. A. Men', A. N. Men', and V. I. Cherepanov, Dokl. Akad. Nauk SSSR, 203, 776 (1972) [Sov. Phys.–Dokl., 17, 330 (1972)].

Characteristics of a diffusionless transformation in nonideal alloys

D. E. Temkin
Central Scientific-Research Institute of Ferrous Metallurgy

(Submitted September 26, 1972)
Kristallografiya, 18, 906-914, (September-October 1973)

The diffusionless $\alpha \rightleftharpoons \beta$ transformation of nonideal phases α and β is analyzed for a one-dimensional model from the kinetic point of view. The $C_{\alpha,k}(T)$ and $C_{\beta,k}(T)$ lines on which the steady-state velocity v of the phase boundary vanishes during the $\beta \to \alpha$ and $\alpha \to \beta$ transformations, respectively, are determined in the (T, C) plane. In general these lines do not coincide with the phase-equilibrium lines $C_\alpha(T)$ and $C_\beta(T)$. Coincidence of $C_{\alpha,k}$ and $C_{\beta k}$ with C_α and C_β respectively only occurs if the energies of mixing of the two phases are the same. The lines v = 0 for the transformation in a completely ordered system are also found. For equal energies of mixing, these lines coincide with the line C_0 on which the free energies of the α and β phases are equal. The effect of the diffusion of the components on the relationship between v and the conditions of the transformation is also discussed. For nonzero diffusion coefficients, in particular, the steady-state velocity vanishes on the equilibrium lines C_α and C_β.

In our earlier papers[1-4] we studied the kinetic characteristics of the motion of the phase boundary during a diffusionless transformation in a binary system. By diffusionless transformation we mean one in which the atoms are unable to change places by the diffusion mechanism for a certain characteristic transformation time.[1,2] In the strict sense a transformation will only be diffusionless in a model system in which the phase boundary moves but there is no diffusion of the atoms at all. An analysis of the steady-state mode of a transformation of this kind shows that this can only occur under conditions corresponding to the single-phase regions of the equilibrium (phase) diagram of the phases under consideration.[1,2] The following situation may be envisaged.

Let us consider the mutual transformation of phases α and β (α is the low-temperature phase) in a binary system comprising the components A and B, while C_α and C_β are the concentrations of the components A and B corresponding to the equilibrium lines of these phases on the phase diagram (Fig. 1a).[1)] During the $\beta \to \alpha$ transformation the phase boundary may travel at a velocity v independent of the time if the concentration C in the original β phase and the temperature of the transformation correspond to the $\alpha \to \beta$ region (Fig. 1b); the situation is analogous for the $\alpha \to \beta$ transformation. On the lines C_α and C_β, v = 0 for the $\beta \to \alpha$ and $\alpha \to \beta$ transformations respectively.

Subsequent analysis of a purely diffusionless transformation in the two-phase ($\alpha + \beta$) region[3] showed that in this case a transient transformation occurred: For large t (t = time), the velocity of the boundary v fell as $t^{-1/2}$.

The foregoing characteristics of a purely diffusionless transformation may be visualized by considering the following simple model: 1) The transformation takes place in an infinite one-dimensional chain (or a model in which a step with a single break occurs at the phase boundary and the transformation takes place by virtue of the motion of this break); 2) the α and β phases are ideal solutions of the components and hence basically contain no short- or long-range order. Consideration of point 1 leads to the conclusion[4] that any results obtained for a one-dimensional system should remain qualitatively intact if the plane surface separating the phases moves in a three-dimensional system. As yet there is no rigorous proof of this. Here we shall devote more detailed consideration to point 2 and shall discuss the special features of the kinetic characteristics in the case of nonideal phases.

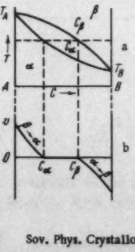

Fig. 1. Phase equilibrium diagram (ideal solutions) (a) and concentration dependence of the steady velocity of the phase boundary (b).

In a diffusionless transformation, the phase being formed has nonequilibrium properties (for example, short- and long-range order) reflecting the state of the original, phase and the manner in which the atoms change places without diffusion. It is by analyzing such properties of the new phase (and not simply by considering the similarity between its composition and that of the original phase) that we may establish the diffusionless[1,2,5] character of the transition.

The main problem in which we shall be interested is as follows. Let $C_{\alpha,k}(T)$ and $C_{\beta,k}(T)$ be the lines in the T, C plane (T = temperature) on which the steady velocity of the boundary vanishes for the purely diffusionless $\beta \to \alpha$ and $\alpha \to \beta$ transformation respectively (here it is assumed that the original phase β or α possesses equilibrium properties for the temperature and composition under consideration). Do these lines coincide with the equilibrium $C_\alpha(T)$ and $C_\beta(T)$, as occurred in the earlier-considered case of ideal solutions[1-3] (Fig. 1) ? We shall show that in nonideal cases these lines do not in general coincide.

Let us consider the $\beta \rightleftharpoons \alpha$ transformation for the model of a one-dimensional chain. In an infinite chain the α- phase lies to the left of the interface and the β phase to the right. The atoms are only able to pass from one phase to the other at the phase boundary. Let ν_{+ij} (i and j = A, B) be the frequency with which an atom of type i in the β phase at the boundary transforms into α if the place immediately to its right is occupied by a j atom. (In a transition of this kind the phase boundary moves by one interatomic distance to the right.) Analogously ν_{-ji} is the frequency for the transition of an i atom from i to α if the nearest place in the β phase is occupied by a j atom. This definition of the frequencies corresponds to an allowance for interaction between nearest-neighbor atoms only (in refs. 1–4 this interaction was not taken into account and the case of $\nu_{+ij} = \nu_{+i}$ and $\nu_{-ji} = \nu_{-i}$ was considered). The set of specified frequencies and the concentration C in the original phase completely determines the steady-state kinetics of the motion of the phase boundary during the diffusionless transition of this phase into the new one. At the same time, by using these quantities, we may construct the diagram giving the equilibrium between phases α and β, and hence compare the equilibrium lines $C_\alpha(T)$, $C_\beta(T)$ with the kinetic lines $C_{\alpha,k}(T)$ $C_{\beta,k}(T)$.

Let ε_{ij}^γ be the interaction energy of neighboring atoms i and j in the phase $\gamma (= \alpha, \beta)$ and $w_\gamma = \varepsilon_{AB}^\gamma - (\varepsilon_{AA}^\gamma + \varepsilon_{BB}^\gamma)/2$ be the energy of mixing. We use μ_i^γ to denote the chemical potential of component i in phase γ, and $\mu_{i,0}^\gamma$ the chemical potential in the case in which the γ phase contains only the i component. The following relations hold between the specified transition frequencies:[6]

$$\nu_{-ii}/\nu_{+ii} = \exp(\Delta\mu_{i,0}/kT);$$
$$\nu_{-ii}/\nu_{-ji} = \exp[(\varepsilon_{ii}^\alpha - \varepsilon_{ji}^\alpha)/kT];$$
$$\nu_{+ii}/\nu_{+ij} = \exp[(\varepsilon_{ii}^\beta - \varepsilon_{ij}^\beta)/kT];$$
$$\nu_{-BA}\nu_{-AB}/\nu_{-AA}\nu_{-BB} = \exp(2w_\alpha/kT) = y_\alpha;$$
$$\nu_{+AB}\nu_{+BA}/\nu_{+AA}\nu_{+BB} = \exp(2w_\beta/kT) = y_\beta. \tag{1}$$

Here

$$\Delta\mu_{i,0} = \mu_{i,0}^\alpha - \mu_{i,0}^\beta \text{ and } y_\gamma = \exp(2w_\gamma/kT).$$

The thermodynamic properties of a one-dimensional two-component phase are well known.[7] Thus the chemical potential μ_i^γ is given by

$$\mu_i^\gamma(C) = \mu_{i,0}^\gamma + kT\ln C_{ii}^\gamma/C_i, \tag{2}$$

in which $C_B = C$ is the concentration of component B, $C_A = 1 - C$, and C_{ii}^γ is the equilibrium proportion of the ii pairs, determined by the relations

$$C_{AA}^\gamma C_{BB}^\gamma/(C_{AB}^\gamma)^2 = y_\gamma,\ C_{AA}^\gamma = C_A - C_{AB}^\gamma,\ C_{BB}^\gamma = C_B - C_{AB}^\gamma. \tag{3}$$

From (3) we obtain

$$C_{AB}^\gamma(C) = [\sqrt{1 + 4(y_\gamma - 1)C(1-C)} - 1]/2(y_\gamma - 1). \tag{4}$$

In an ideal solution $w_\gamma = 0$ ($y_\gamma = 1$) and $C_{AB}^\gamma = C(1-C)$. Using Eqs. (2)–(4) and the equilibrium condition $\mu_i^\alpha(C_\alpha) = \mu_i^\beta(C_\beta)$, we may find the equilibrium concentrations C_α and C_β, and on allowing for (1) we may express these concentrations in terms of the transition frequencies. After some easy transformations we obtain the following two equations:

$$\left[1 - \frac{\nu_{-AA}}{\nu_{+AA}}\frac{C_{AA}^\alpha(C_\alpha)}{(1-C_\alpha)}\right]\left[1 - \frac{\nu_{-BB}}{\nu_{+BB}}\frac{C_{BB}^\alpha(C_\alpha)}{C_\alpha}\right] = \frac{\nu_{-BA}\nu_{-AB}}{\nu_{+AB}\nu_{+BA}}\frac{[C_{AB}^\alpha(C_\alpha)]^2}{C_\alpha(1-C_\alpha)}, \tag{5}$$

$$\left[1 - \frac{\nu_{+AA}}{\nu_{-AA}}\frac{C_{AA}^\beta(C_\beta)}{(1-C_\beta)}\right]\left[1 - \frac{\nu_{+BB}}{\nu_{-BB}}\frac{C_{BB}^\beta(C_\beta)}{C_\beta}\right] = \frac{\nu_{+AB}\nu_{+BA}}{\nu_{-BA}\nu_{-AB}}\frac{[C_{AB}^\beta(C_\beta)]^2}{C_\beta(1-C_\beta)}. \tag{6}$$

On the basis of Eqs. (1)–(4) we also find the concentration C_0 for which the free energies of the α and β phases referred to one particle are equal. The concentration C_0 satisfies the equation $C_0\mu_B^\alpha(C_0) + (1 - C_0)\mu_A^\alpha(C_0) = C_0\mu_B^\beta(C_0) + (1 - C_0)\mu_A^\beta(C_0)$, which, after substituting (1)–(4) into it, takes the form

$$C_0 \ln\frac{\nu_{-BB}C_{BB}^\alpha(C_0)}{\nu_{+BB}C_{BB}^\beta(C_0)} + (1-C_0)\ln\frac{\nu_{-AA}C_{AA}^\alpha(C_0)}{\nu_{+AA}C_{AA}^\beta(C_0)} = 0. \tag{7}$$

Here $C_{ii}^\alpha(C_0)$ and $C_{ii}^\beta(C_0)$ are the equilibrium values of the proportions of ii pairs in the α and β phase, determined by Eqs. (3) and (4) for $C = C_0$.

Let us now find the concentration $C_{\alpha,k}$ in the original β phase for which the steady-state velocity v of the phase boundary equals zero in the $\beta \to \alpha$ transformation. For this we may use the method proposed by Chernov.[6,8] Although the frequencies of the transition of atoms from the β to the α phase are defined rather differently in the model here under consideration from the way in which they were defined[2)] in refs. 6 and 8, the final expression determining $C_{\alpha,k}$ is the same as that obtained by Chernov (see Eq. (4.17)[3)] from ref. 6). Hence, omitting the corresponding calculations, we may write the final expression

$$\left[1 - \frac{\nu_{-AA}}{\nu_{+AA}}\frac{C_{AA}^\beta}{(1-C_{\alpha,k})}\right]\left[1 - \frac{\nu_{-BB}}{\nu_{+BB}}\frac{C_{BB}^\beta}{C_{\alpha,k}}\right] = \frac{\nu_{-BA}\nu_{-AB}}{\nu_{+AB}\nu_{+BA}}\frac{(C_{AB}^\beta)^2}{C_{\alpha,k}(1-C_{\alpha,k})}. \tag{8}$$

In this equation C_{ij}^β is the proportion of ij pairs in the original β phase for a concentration of the B component equal to $C_{\alpha,k}$ in this. When the short-range order in the β phase takes the equilibrium value for the concentration and temperature under consideration, C_{ij}^β is given by Eqs. (3). It is precisely this case which we shall subsequently consider. We simply note that Eq. (8) is also valid for the transformation of the nonequilibrium $\alpha \to \beta$ phase. The expression analogous to (8) for the $\alpha \to \beta$ transformation takes the form

$$\left[1 - \frac{\nu_{+AA}}{\nu_{-AA}}\frac{C_{AA}^\alpha}{(1-C_{\beta,k})}\right]\left[1 - \frac{\nu_{+BB}}{\nu_{-BB}}\frac{C_{BB}^\alpha}{C_{\beta,k}}\right] = \frac{\nu_{+AB}\nu_{+BA}}{\nu_{-BA}\nu_{-AB}}\frac{(C_{AB}^\alpha)^2}{C_{\beta,k}(1-C_{\beta,k})} \tag{9}$$

and determines the concentration $C_{\beta,k}$ in the original α phase for which the steady velocity of the $\alpha \to \beta$ transformation is equal to zero.

Comparing Eq. (5) with (8) and (6) with (9), we see that the kinetic lines $C_{\alpha,k}$ and $C_{\beta,k}$ do not respectively coincide with the equilibrium lines C_α and C_β. Coincidence only occurs if $C_{ij}^\alpha(C_\alpha) = C_{ij}^\beta$ and $C_{ij}^\beta(C_\beta) = C_{ij}^\alpha$, i.e., when the short-range order of the original phase coincides with the equilibrium short-range order of the new phase (the one being formed). In the case of an equilibrium original phase this is realized for $w_\alpha = w_\beta$, and in particular for ideal solutions when $w_\alpha = w_\beta = 0$.

It was shown in ref. 3 for a very simple model corresponding to the particular case of ideal α- and β phases were equal. Let us consider this question in relation to nonideal solutions. In this case the concentration C_0 determined from thermodynamics is given by Eq. (7). Let r be the period of the structure in the infinite chain. For a concentration $C_{0,k}$, among the whole set of r atoms there are $rC_{0,k}$ B and $r(1 - C_{0,k})$ – A atoms. If the short-range order is such that, among the r bonds, there are rC_{ij} ij bonds, then it may easily be shown that the velocity of the phase boundary in a chain of this kind will vanish independently of r if

$$\sum_{ij} C_{ij} \ln(\nu_{-ij}/\nu_{+ij}) = 0. \tag{10}$$

This expression coincides with those given in refs. 6 and 8, despite the different definition of the frequencies. Since $C_{BB} = C_{0,k} - C_{AB}$, $C_{AA} = 1 - C_{0,k} - C_{AB}$, Eq. (10) may be written in the form

$$C_{0,k} \ln\frac{\nu_{-BB}}{\nu_{+BB}} + (1 - C_{0,k}) \ln\frac{\nu_{-AA}}{\nu_{+AA}} + C_{AB}\left[\ln\frac{\nu_{-AB}\nu_{-BA}}{\nu_{-AA}\nu_{-BB}} - \ln\frac{\nu_{+AB}\nu_{+BA}}{\nu_{+AA}\nu_{+BB}}\right] = 0. \tag{11}$$

If we consider the transformation of an equilibrium β phase into α, then $C_{AB} = C_{AB}^\beta(C_{0,k})$ and Eq. (11) determines the concentration $C_{0',k}$ at which the velocity of the β – α transformation in the periodic chain vanishes. The analogous concentration $C_{0'',k}$ for the α→β transformation is obtained from (11) for $C_{AB} = C_{AB}^\alpha(C''_{0,k})$. In the general case, the kinetic lines $C_{0,k}$ and $C_{0'',k}$ do not coincide with each other or with the thermodynamic line C_0 in the (T, C) plane. For $w_\alpha = w_\beta$ the expression in the square brackets in (11) vanishes. Remembering that in this case $C_{ij}^\alpha = C_{ij}^\beta$, we thus have the following from (7) and (11):

$$C'_{0,k} = C''_{0,k} = C_0 = \frac{\ln(\nu_{-AA}/\nu_{+AA})}{\ln(\nu_{-AA}\nu_{+BB}/\nu_{+AA}\nu_{-BB})}. \tag{12}$$

For a diffusionless transformation the new phase inherits the shortrange order of the original phase. We might therefore expect that the kinetic lines would coincide with the equilibrium lines of the metastable diagrams reflecting the deviation of the short-range order from equilibrium in the phase being formed. Let us consider the transformation of the equilibrium β phase into α. The kinetic line $C_{\alpha,k}$ will in this case be determined by Eq. (8) for $C_{AB}^\beta = C_{AB}^\beta(C_{\alpha,k})$ (the latter quantity is given by Eq. (4)). Let us construct the equilibrium lines C_α and C_β for the equilibrium phase β, the short-range order in which is characterized by the quantities C_{ij}^β (and not by the equilibrium values C_{ij}^α). The chemical potentials in the β phase are given by Eq. (2), while in the α phase instead of (2) we have

$$\mu_i^\alpha(C) = \mu_{i,0}^\alpha + kT \ln\frac{C_{ii}^\beta}{C_i} + \frac{2(w_\alpha - w_\beta)C_{AB}^\beta}{CC_{AA}^\beta + (1-C)C_{BB}^\beta} \times \begin{cases} C_{BB}^\beta & \text{for } i = A, \\ C_{AA}^\beta & \text{for } i = B. \end{cases} \tag{13}$$

Equating μ_i^α from (13) and μ_i^β from (2) we obtain two equations for $C_{\alpha,M}$ and $C_{\beta,M}$. Without actually writing these out we note that $C_{\alpha,k}$ does not coincide with the $C_{\alpha,M}$ determined in this way, except for the case $w_\alpha = w_\beta$ when $C_\alpha = C_{\alpha,M} = C_{\alpha,k}$. Using (13) and (2) we find the concentration $C'_{0,M}$, for which the free energies of the α and β phases are equal. For $C'_{0,M}$ we have

$$C'_{0,M}\Delta\mu_{B,0} + (1 - C'_{0,M})\Delta\mu_{A,0} + 2(w_\alpha - w_\beta)C_{AB}^\beta(C'_{0,M}) = 0. \tag{14}$$

Allowing for Eq. (1), it is easy to see that (14) agrees with (11) if in the latter we put $C_{AB} + C_{AB}^\beta$. Hence the concentration $C'_{0,k}$ for which the velocity of the diffusionless transformation of the equilibrium β phase into the α phase vanishes in the periodic chain coincides with the $C'_{0,M}$ of the metastable diagram. It may be shown in an analogous manner that $C''_{0,k}$ coincides with $C''_{0,M}$ at which the free energies of the equilibrium α and the nonequilibrium β phases, the latter with a short-range order inherited from the α phase, are equal. Since the free energy of the nonequilibrium phase is higher than that of the equilibrium phase, on the (T, C) diagram the $C'_{0,k}$ line always lies below and the $C''_{0,k}$ above the C_0 line[9] (we remember that β is the high-temperature phase). We note that for C → 0 and C → 1, when the solutions are ideal, the corresponding lines (for example, C_0, $C'_{0,k}$ and $C'_{0,M}$, C_α, $C_{\alpha,k}$ and $C_{\alpha,M}$) have common tangents.

The reason for the disagreement between the C_α and $C_{\alpha,k}$ lines is as follows. The $C_{\alpha,M}$ line reflects the equilibrium of the α with the β phase for the same short-range order, which is only equilibrium (order) for the β phase. At the same time, the kinetic line $C_{\alpha,k}$ reflects dynamic equilibrium between the α phase with the short-range order indicated and the β phase in which short-range order differing from equilibrium arises in front of the phase boundary (the equilibrium order is only preserved in the β phase a long way from the phase boundary). This effect arises from the "interaction" of the phase boundary with the structure of the chain. The existence of this effect may be demonstrated by using the method developed in refs. 6 and 8.

Let W(n) be the probability of observing a B atom in the chain point lying in the n-th position relative to the phase boundary (in the β phase to the right of the boundary, n = 0, 1, 2, ..., and in the α phase n = –1, –2, ...); W(n, k) is the probability of observing B atoms in the n-th and k-th points. The ternary and subsequent distribution functions may be defined analogously. Let us consider the particular case in which $\nu_{+AA} = \nu_{+AB} = \nu_{+A}$, $\nu_{+BA} = \nu_{+BB} = \nu_{+B}$. Here the solution β is ideal, there is no short-range order in the equilibrium, $C_{AB}^\beta = C(1 - C)$. Omitting the cumbersome calculations, we shall simply give the expressions for the first distribution functions in the case of the β → α transformation with a boundary velocity tending to zero (i.e., for $C = C_{\alpha,k}$).

$$W(n)=\begin{cases} C & \text{for} \quad n\leqslant -2, \\ C\dfrac{\nu_{+B}[\nu_{+A}+(1-C)(\nu_{-BA}-\nu_{-AA})]}{\nu_{+A}\nu_{+B}+C(1-C)[\nu_{+A}(\nu_{-AB}-\nu_{-BB})+\nu_{+B}(\nu_{-BA}-\nu_{-AA})]} & \text{for} \quad n=-1, \\ W(0)=W(-1)[(1-C)(\nu_{-AB}/\nu_{+B})+C(\nu_{-BB}/\nu_{+B})] & \text{for} \quad n\geqslant 0, \\ & \text{for} \quad n=\infty. \end{cases} \tag{15}$$

$$W(n,n+1)=\begin{cases} C^2 & \text{for} \quad n\leqslant -2, \\ W(-1)C\nu_{-BB}/\nu_{+B} & \text{for} \quad n=-1, \\ W(0)C\nu_{-BB}/\nu_{+B} & \text{for} \quad n\geqslant 0, \\ C^2 & \text{for} \quad n=\infty. \end{cases} \tag{16}$$

From this we see that in the β phase in front of the boundary there is a correlation $W(n, n+1) \neq W(n)W(n+1)$, although in the original β phase there is none even at an infinite distance from the boundary. At the same time in the β phase inheriting the short-range order of the α phase no correlation exists. It may furthermore be shown that in the case under consideration only pair correlations arise around the boundary, i.e., for example, $W(0, 1, 2) = W(0, 1)\,W(1, 2)/W(1)$.

The position of the kinetic lines $C_{\alpha,k}$ and $C_{\beta,k}$ relative to the equilibrium lines C_α and C_β is not so definite as the position of $C'_{0,k}$ and $C''_{0,k}$ relative to C_0. For example, the line $C_{\alpha,k}$ may lie below C_α, in the one-phase α region, above C_α in the two-phase $(\alpha+\beta)$ region, and may also intersect C_α, i.e., lie partly in the one- and partly in the two-phase region. This may be seen most easily by considering the path of these lines in the neighborhood of the temperatures T_A and T_B for small C or $(1-C)$. At $T = T_A$, $\nu_{-AA} = \nu_{+AA}$. By way of deviation from T_A we take the quantity $\sigma = 1 - \nu_{-AA}/\nu_{+AA} = 1 - \exp(\Delta\mu_{A,0}/kT)$. Let $\sigma_\gamma(C)$ and $\sigma_{\gamma,k}(C)$ describe the dependence of σ on C along the equilibrium line C_γ and the kinetic line $C_{\gamma,k}$ $(\gamma = \alpha, \beta)$. Expanding Eq. (4) in series we have

$$C_{AB}{}^{\gamma}=C(1-C)[1-(y_\gamma-1)C(1-C) + 2(y_\gamma-1)^2C^2(1-C)^2-\ldots]. \tag{17}$$

Taking account of this and limiting ourselves in the expansion of (5) and (8) to terms quadratic in σ and C, we obtain

$$\sigma_\alpha(C)\simeq C\left[\frac{\nu_{-BA}\nu_{-AB}}{\nu_{+AB}\nu_{+BA}}-1\right]+C^2\left[\mathring{y}_\alpha-2-\frac{2(\mathring{y}_\alpha-1)}{\mathring{k}}+\frac{\mathring{y}_\beta}{\mathring{k}^2}\right], \tag{18}$$

$$\sigma_{\alpha,k}(C)\simeq C\left[\frac{\nu_{-BA}\nu_{-AB}}{\nu_{+AB}\nu_{+BA}}-1\right]+C^2\left[\mathring{y}_\beta-2-\frac{2(\mathring{y}_\beta-1)}{\mathring{k}}+\frac{\mathring{y}_\beta^2}{\mathring{y}_\alpha\mathring{k}^2}\right]. \tag{19}$$

Here the index ° indicates that the corresponding quantity relates to the temperature T_A (i.e., to $\sigma = 0$). The quantity $\mathring{k}$ is the equilibrium distribution coefficient at $T = T_A$

$$\mathring{k}=\frac{C_\beta}{C_\alpha}=\frac{\mathring{\nu}_{+AB}\mathring{\nu}_{+BA}}{\mathring{\nu}_{-BA}\mathring{\nu}_{-AB}}=\frac{\mathring{\nu}_{+BB}}{\mathring{\nu}_{-BB}}\frac{\mathring{y}_\beta}{\mathring{y}_\alpha}. \tag{20}$$

In Eqs. (18) and (19) the C terms coincide, which indicates a common tangent, while the C^2 terms only coincide for $y_\alpha = y_\beta$. The kinetic curve $\sigma_{\alpha,k}$ lies in the single-phase α region close to T_A if $\sigma_{\alpha,k}(C) > \sigma_\alpha(C)$, or on allowing for (18) and (19) when

$$(\mathring{y}_\beta-\mathring{y}_\alpha)[\mathring{k}^2-2\mathring{k}+\mathring{y}_\beta/\mathring{y}_\alpha]>0. \tag{21}$$

Condition (21) is satisfied (and hence the line $C_{\alpha,k}$ lies in the α region) for any $\mathring{k}(>0)$, if $\mathring{y}_\alpha < \mathring{y}_\beta$, and for

$$1-\sqrt{1-\mathring{y}_\beta/\mathring{y}_\alpha}<\mathring{k}<1+\sqrt{1-\mathring{y}_\beta/\mathring{y}_\alpha}, \tag{22}$$

if $y_\alpha > y_\beta$. If these conditions are not satisfied, the $C_{\alpha,k}$ line (close to T_A) lies in the two-phase $(\alpha+\beta)$ region. An analogous consideration may be applied to C_β and $C_{\beta,k}$. The line $C_{\beta,k}$ lies in the single-phase β region on satisfying the condition

$$(\mathring{y}_\alpha-\mathring{y}_\beta)[1/\mathring{k}^2-2/\mathring{k}+\mathring{y}_\alpha/\mathring{y}_\beta]>0, \tag{23}$$

derived from (21) by the cyclic replacement of $\mathring{y}_\alpha$ by $\mathring{y}_\beta$ and k by $1/\mathring{k}$. For $\mathring{y}_\beta < \mathring{y}_\alpha$ condition (23) is satisfied for any $\mathring{k}$, and for $\mathring{y}_\beta > \mathring{y}_\alpha$ if

$$1-\sqrt{1-\mathring{y}_\alpha/\mathring{y}_\beta}<1/\mathring{k}<1+\sqrt{1-\mathring{y}_\alpha/\mathring{y}_\beta}. \tag{24}$$

Thus there are three possible versions of the disposition of lines $C_{\alpha,k}$ and $C_{\beta,k}$: It is possible for one of the lines to lie in the one-phase and the other in the one-phase or two-phase region, but the lines never both lie in the two-phase region. For $\mathring{y}_\alpha < \mathring{y}_\beta$ (i.e., $w_\alpha < w_\beta$), the kinetic line $C_{\alpha,k}$ has to lie in the α-region, and for $\mathring{y}_\beta < \mathring{y}_\alpha$ – $C_{\beta,k}$ in the β-region. In other words, the line corresponding to the formation of the phase with the lower energy of mixing must necessarily lie in the one-phase region. We see from (22) and (24) that whether the other line falls into the one- or two-phase region depends on the width of the latter; if it is wide enough, then this line will lie within it. Thus for example the $C_{\alpha,k}$ line lies in the two-phase region for $\mathring{y}_\alpha > y_\beta$ if the distribution coefficient $\mathring{k}$ is sufficiently small ($\mathring{k} < 1 - \sqrt{1-\mathring{y}_\beta/\mathring{y}_\alpha}$) or large ($\mathring{k} > 1 + \sqrt{1-\mathring{y}_\beta/\mathring{y}_\alpha}$).[4]

So far we have considered a purely diffusionless transformation in which the diffusion coefficients D_α and D_β in the α and β phase are equal to zero. An analysis of the effect of diffusion on the kinetics of the transformation lies outside the scope of this article and will be carried out elsewhere. Here we shall simply consider the main qualitative aspects of this problem.

The inclusion of diffusion, i.e., the mechanism based on the relaxation of short-range order, which was absent from the purely diffusionless transformation, has the effect that, for a fairly low velocity of the transformation, the short-range order in both the original and the new phase will differ little from the equilibrium values around the interface (and even more so a long way from the boundary), while at v = 0 it will exactly coincide with them. This in turn has the effect that the lines on which the steady velocity of the $\beta \to \alpha$ and $\alpha \to \beta$ transformations vanishes will coincide with the equilibrium lines C_α and C_β in the presence of diffusion. This latter is valid for arbitrarily small diffusion coefficients. Thus the position

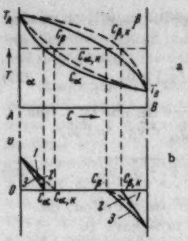

Fig. 2. Phase-equilibrium diagram (nonideal solutions) and kinetic lines of zero velocity of a diffusionless transformation (1); steady velocity of the phase boundary as a function of concentration for various diffusion coefficients (b) 1) D = 0, 2) 0 < D < ∞, 3) D = ∞.

of the kinetic lines under consideration, treated as dependent upon the diffusion coefficients, is not an analytical function, but takes only two values: $C_{\alpha,k}$ and $C_{\beta,k}$ for $D_\alpha = D_\beta = 0$, C_α and C_β for D_α and/or $D_\beta > 0$. Let us consider qualitatively how the steady velocity will then depend on the conditions of the transformation and the diffusion coefficient D (by D we understand a certain combination of D_α and D_β, which has to be discovered by subsequent analysis). Let us consider the dependence of v on C for a fixed temperature and various D (Fig. 2). In order to consider each of the two possible cases, we here assume that one of the kinetic lines ($C_{\beta,k}$) in the two-phase part of the phase diagram. In the first case (in which the kinetic line lies in the one-phase region) the velocity of the diffusionless transformation is less than in the case of D ≠ 0; with decreasing D, v and the slope of the curve v(C) at the point C_β also diminish, while as $D \rightarrow 0$ the v(C) curve tends toward a broken straight line with a break at the point $C_{\beta,k}$: v(C) = 0 for $C_\beta \leq C \leq C_{\beta,k}$ and coincides with curve 1 (for D = 0) when $C > C_{\beta,k}$. In the second case, however, a fall in D leads to an increase in v and the slope of the curve v(C) at the point C_α. In the limit $D \rightarrow 0$ the curve v(C) jumps at the point C_α to a value of v corresponding to D = 0, while at $C < C_\alpha$ it coincides with the v value for D = 0. In this case in the range $C_\alpha < C < C_{\alpha,k}$ the broken part of curve 1 (for D = 0) is not realized at all, and v = 0. We arrive, in fact, at a peculiar nonanalytical situation: For $C_\alpha < C < C_{\alpha,k}$, v is described by curve 1 if D is exactly equal to zero, and v = 0 if D > 0 but is arbitrarily small. This and all the other nonanalytical characteristics are associated with the fact that we are considering the steady-state stage of the transformation in an infinite system. These characteristics do not appear if we consider a finite system or the transient period in an infinite system. For example, we may picture the transient stage of the transformation under conditions in which $C_\alpha < C < C_{\alpha,k}$.

Let us suppose that, at the initial instant of time, there is a semiinfinite β chain of composition C at the end of which there is a nucleus of the α phase. If we had D = 0, then, during the course of a certain characteristic time τ_1, over which the phase boundary would move through a fair distance away from the end of the chain, a steady state would become established, with a certain velocity v and with a corresponding distribution of the components relative to the phase boundary. For D = 0 this situation would continue to last for an arbitrarily long time. However, if D ≠ 0, but still small, then a spatial redistribution of the components would indeed take place, albeit slowly, during the transformation. The effect of this will be that, starting from a certain instant τ_2, at which the changes in concentration at the phase boundary become appreciable, the velocity of the boundary will start falling, and will subsequently tend to zero as the effect of diffusive redistribution develops. Without going into details as to the calculation of τ_1 and τ_2, we note that for small D the time τ_1 will hardly depend on D at all, while τ_2 will be inversely proportional to D. Hence if for small D we consider instants of time t lying in the range $\tau_1 < t < \tau_2$, the velocity of the transformation will be similar to the velocity for D = 0. If we are interested in $t \gg \tau_2$, then in the case under consideration the velocity will be close to zero.

A large-scale $\beta \rightarrow \alpha$ transformation in a Cu−38 at.% Zn alloy was studied in ref. 10, and the rate of growth of the α phase was determined at various temperatures. The transformation could only be observed in the one-phase α region. However, it was found that the growth rate did not vanish at the boundary between the one- and two-phase regions. This may have been because, in the system under consideration, the kinetic line $C_{\alpha,k}$ lay within the two-phase region. Then for small D the dependence of v on T will be similar to curve 1 (for $C \leq C_\alpha$) in Fig. 2b.

---

1) We emphasize that C_α and C_β are the lines on the equilibrium phase diagram, although we are considering a diffusionless transformation in which the metastable phase equilibrium is described by the line C_β.

2) Here ν_{+ij} is the transition frequency of the i atom when a j atom lies to the right of it in the j phase. In refs. 6 and 8 ν_{+ij} is the transition frequency of the j atom from β to α on condition that an i atoms lies to the left of it in the α phase.

3) There was actually an error in Eq. (4.17). Instead of $(x_{AB}/x_A x_B)^2$ this should have had $x_{AB}^2/x_A x_B$. In the nomenclature taken here $x_{AB} = C_{AB}$, $x_A = C_A = 1 - C$, $x_B = C_B = C$.

4) If for $y_\alpha < y$ the two-phase region close to T_A is sufficiently narrow and wide close to T_B, the line C_α will lie in the one-phase region close to T_A and in the two-phase region close to T_B, so that the lines C_α and $C_{\alpha,k}$ will intersect.

---

[1] D. E. Temkin, J. Crystal Growth, 5, 193 (1969).
[2] D. E. Temkin, Kristallografiya, 14, 423 (1969)[Sov. Phys.−Crystallogr., 14, 349 (1969)].
[3] D. E. Temkin, Kristallografiya, 17, 77 (1972) [Sov. Phys.−Crystallogr., 17, 60 (1972)].
[4] D. E. Temkin, Fiz. Tverd. Tela, 15, 888 (1973) [Sov. Phys.−Solid State, 15, 610 (1973)].
[5] D. E. Temkin, Kristallografiya, 15, 884 (1970) [Sov. Phys.−Crystallogr., 15, 773 (1971)].
[6] A. A. Chernov, Usp. Fiz. Nauk, 100, 277 (1970) [Sov. Phys.−Usp., 13, 101 (1970)].
[7] T. Hill, Statistical Mechanics, McGraw−Hill (1956).
[8] A. A. Chernov, Biofizika, 12, 297 (1967).
[9] D. E. Temkin, Kristallografiya, 15, 428 (1970) [Sov. Phys.−Crystallogr., 15, 365 (1970)].
[10] D. A. Karlyn, J. W. Cahn, and M. Cohen, Trans. Met. Soc. AIME, 245, 197 (1969).

Model of the controlled growth of macromolecular and crystalline structures

V. K. Bykhovskii

Institute of Control Problems, Academy of Sciences of the USSR

(Submitted June 4, 1970; resubmitted September 20, 1971; July 1, 1972)
Kristallografiya, 18, 915-919 (September-October 1973)

It has been suggested that in the process of growth, a crystal is in a nonstationary coherent electronic state and emits coherent photons, modulated by the structure of the crystal lattice. By exciting the atoms of the gaseous phase, these photons ensure the preferential resonance attraction of those atoms of which the crystal is made up. A simplified selection ("recognition") model, formulated in terms of the theory of scattering, has been developed, and the results of numerical calculations of the selectivity parameters are presented. A more realistic model of the crystal–atom interaction, which takes account of the possibility of electronic transitions with the emission of the modulated photons controlling the recognition and attachment of the atoms of the gaseous phase, has been analyzed qualitatively.

1. Although considerable progress has been made in the theory of the growth of crystals (see, for example, ref. 1), the role of the electronic subsystem in the growth process is still not sufficiently clear. In particular, it is necessary to find an answer to the question of whether the choice or selection of the atoms (or molecules) being attached in the process of growth from the gaseous (or liquid) phase is random during attachment and removal, or whether the actual possibility of attachment is determined by a long-range interaction of the electron clouds of the crystal and the atom.

The present paper sets out the hypothesis that in the growth process, a crystal A is in a nonstationary coherent electronic state and emits photons, the frequency spectrum of which is modulated by the structure of the crystal. These photons subsequently reach the atoms B of the gaseous phase and excite them into a corresponding electronic state with the transfer of their modulation state to these atoms. The phenomenon being considered is analogous to the familiar phenomenon of the optically controlled orientation of the nuclear spins of atoms (see for example ref. 2) and also to the Schwarz – Hora effect, which was recently detected experimentally[3] and has been studied theoretically (see, for example, ref. 4); this effect consists of the modulation, by monochromatic laser radiation, of an electron beam passing through a thin crystal (SiO_2). On excitation of the atom B, information on the structure of the radiating crystal [coded by the complex coefficients $c_n(t)$ – the weights of the stationary states $\psi_n(x, t)$ in the coherent state $\psi(x, t)$] is transferred to the electron cloud of the B atom. If the crystal A and the aton B are of the same kind (A = B), the interaction $A-A^*$, where * symbolizes electronic excitation, has resonance character[5] and is an attraction, which is significantly stronger than that for A ≠ B. Thus the crystal A "recognizes" its own atoms A.

The development of the concept requires that account be taken of all the quantum numbers of A and B, and not merely the identical character of the nuclei of A and B; thus in the interaction of identical atoms with spin S = 1/2, only the singlet state ($^1\Sigma$) has a suitable phase structure and leads to attraction, whereas the triplet state is characterized by repulsion. This also means that, for example, the NaCl crystal will "recognize" Na(^2S) and Cl(^2P) atoms and will interact weakly with other atoms (or with the same atoms in other electronic states). The "recognition" or selection being considered is based on the phenomenon of interference of quantum states, for which phase properties (coherence properties), and not merely the energy of the state, are significant. This is a consequence of the fact that each quantum state is an oscillator, and the interaction of oscillators depends, in particular, on their phase properties. The most general case of an $A-B^*$ interaction is a resonance multipole–multipole interaction, in which B^* is in a superpositional coherent state (which does not have definite quantum numbers).

2. For a specific illustration of the role of quantum effects, we can examine a simplified model of the interaction of two atoms – a stationary atom A (modeling the crystal) and a moving atom B. We shall assume that both atoms are in ^1S states, so that the interaction between them can be described by a potential $V_{AB}(R)$ of radially symmetric form. A qualitative discussion of the model of the interaction of atoms in arbitrary electronic states is given in Sec. 3.

The wave function $\psi(R)$ of the atom B (in the field of A) has the asymptotic form

$$\lim_{R\to\infty}\psi(R)=\exp(ikz)+q(\theta,E)\exp(ikR)/R,\quad k^2=2mE/\hbar^2,$$
$$I(\theta,E)=|q(\theta,E)|^2,\quad \sigma(E)=2\pi\int_0^\pi d\theta\sin\theta I(\theta,E),\qquad (1)$$

where k is the momentum, E is the energy, $q(\theta, E)$ and $I(\theta, E)$ are the amplitude and intensity of the scattering of the atom B in the direction θ (relative to the vector k), and $\sigma(E)$ is the total intensity of scattering. To find $q(\theta, E)$, which gives a complete description of the A–B interaction, we carried out the numerical integration of the three-dimensional Schrödinger wave equation. It can be seen from Eq. (1) that $q(\theta, E)$ controls the interference of the incident wave exp (ikz) (adsorption wave) and the scattered wave q exp(ikR)/R (desorption wave) and in this way makes a contribution to the process of crystal growth. We carried out the calculation for the sorption of an He^4 atom on an He^4 "center;" for the potential $V_{AB}(R)$ we used the Lennard-Jones 6-12 potential with parameters v_0 (the depth of the well) and c_V (characteristic dimension). The results obtained are shown in Figs. 1-3. The existence of narrow resonances on the $\sigma(E)$ and $\sigma(v_0)$ curves, which are clearly revealed on differentiation with respect to the argument, is a manifestation of the high selectivity of the sorption with respect to the parameters of the A–B pair. A small change in the parameters of the A–B pair – the energy E (or de Broglie wavelength $\lambda = 1/k$) of the atom B being sorbed and the parameters of $V_{AB}(R)$ – is accompanied by a marked change (by two to three orders of magnitude) in the intensity of scattering σ. It should be noted that the form of $V_{AB}(R)$ is determined by the structure of the electronic state of the system A–B.

Thus the phase properties or coherence properties of the wave function play an extremely important role in the dynamics of the A–B interaction. In particular, for suitable conditions of interference of the adsorption and desorption waves, "its own" B atom "adheres" to the center A, but a small shift of the phases of these waves (displacement of the parameters of the pair AB) is sufficient to "detune" the resonance.

3. We can now discuss a more general model of the A–B interaction. We shall assume that the "center" A is in a nonstationary electronic state $\psi(x, t)$, which is a coherent superposition (packet) of substrates $\psi_n(x, t)$ $(n \equiv E, \alpha)$ with definite energy E and other (permitted by the symmetry of the center) quantum numbers α. The mechanism of excitation of this state is the subject of a separate examination. In the process of relaxation of the nonstationary electronic state $\psi(x, t)$, photons may be omitted, and nonradiative transitions leading to the excitation of vibrational–rotational degrees of freedom of the "center" A may take place. Here it is significant that in both the radiative process and the nonradiative relaxation there is transfer of the parameters of the electronic coherence $c_n(t)$, coding information on the structure of the "center" A, outside and inside the "lattice of the center." It is assumed that these coherence parameters control the process of selective attraction of B atoms.

The control mechanism is as follows. On excitation of the electron cloud of the B atom by a coherent photon modulated by the structure of the "center" A, modulation of the electronic state of the B atom takes place (analogous to the Schwarz–Hora effect[3,4]: see Sec. 1). The coherence properties of the excited atom B are controlled both by its coherence in the original state and by the coherence parameters of the electron cloud of the "center" A. At large distances ($R \gg 1$ atomic unit), the interaction W_{AB} between A and B can be described as a multipole–multipole interaction.[5] Thus in the dipole–dipole approximation there is an attraction $W_{AB} \sim R^{-6}$. If however, the "center" A and the atom B are of the same kind (A = B), the long-range interaction A–A* has resonance character[5] and follows the law $W_{AA} \sim R^{-3}$, that is, it is significantly stronger than in the case where $A \neq B$. Depending on the structure of the electronic states A and B (that is on the properties of the electronic coherence of A and B), the interaction W_{AB} may be strong or weak, A and (or) B are in a coherent superpositional state $(c_n \neq 0, n = 1, 2, ..)$, $W_{AB}^{nn'}$ has the form of a matrix with elements which depend on the spatial coordinates and on time (quantum beats), and the form of W_{AB} is determined by the ratio of the phases of the different substrates in the nonstationary state of A and (or) B.

Thus attraction of atom B to the "center" A is possible only for a definite ratio of the phases of the modulated photon emitted by the "center" and for a definite electronic state of the atom B. In other words, the attraction carries resonance character (with respect to the coherence parameters), and the actual long-range forces A–B are determined by the electromagnetic interference effects.

If the atom B is attracted to the "center" A to the distances corresponding to electron tunneling (0.1–1 nm), that is to a distance corresponding to chemical bonding, interference between the electronic states of A and B, which is controlled by the same coherence parameters as the electromagnetic interference, becomes possible. For constructive (in-phase) interference, the amplitude of the electron in the range of A–B binding increases, leading to the formation of a chemical bond, that is, to growth of the "center." In the case of destructive interference, the amplitude of the electron in the binding range decreases, leading to the formation of a weak chemical bond or to the repulsion of B from the "center" A.

Thus it is the coherence properties of the electronic states of A and B which control the selection, that is, the "recognition" and subsequent attachment of the proper atom to the "center." At large distances the effective forces are electromagnetic forces, and at small distances they are the exchange forces due to the interference of the electronic states. The interference spatial control of the forces acting on the nuclei of the system AB from its electron cloud (Gell–Mann–Feynman forces) is achieved in the same way. Because of the metastable nature of the original state of the system AB (relative to its state for the existence of a chemical bond A–B), growth of the "center" takes place without the supply of energy from outside, and this interference mechanism of control of the interatomic forces merely "allows" (or "forbids") the transition, and in its action it is analogous to the "selection rules" controlling transitions which are energetically possible but which do not necessarily take place.

4. We can attempt to extend the qualitative results obtained to processes of crystal growth, with the assumption that the role of the "center" A is played by the crystal.

a) The growth of crystals, that is, the attachment of new atoms (or molecules), is apparently controlled by the coherence parameters of the electronic states of the crystal–atom system (AB). At large distances A–B the transfer of coherence (that is, the information controlling the selection) is brought about by modulated photons emitted by the growing crystal in a nonstationary coherent electronic state.

b) In the growth of crystalline and macromolecular structures we should expect the generation of coherent photons modulated by the structure of the lattice of the growing crystal.

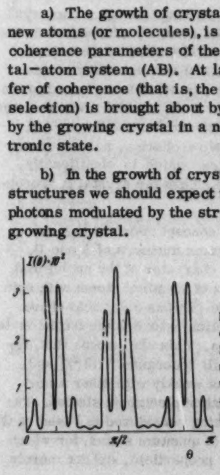

Fig. 1. Angular distribution I(θ, E) of the desorbed atoms (scattering of He^4 atoms on an He^4 "crystal," atomic units, Lennard-Jones 6-12 potential with parameters: $v_0/k = 15°K$, $R_0 = 5.32$ atomic units, $E/k = 1.5°K$, and k is the Boltzmann constant).

c) A magnetic field may have an influence on the growth parameters, since the coherence parameters controlling growth, for example the phase of the electronic wave function, are directly dependent on the vector potential of the magnetic field.

d) Under conditions of ordered preparedness (for example solid-phase crystallization or polymerization), the rate of propagation of the growth front is apparently controlled by electromagnetic factors (in particular the rate of propagation of the modulated photons in a dispersion medium with resonance absorbing characteristics).[7] This rate can be decreased considerably (possibly to 10^2-10^4 m/sec, compared with a photon velocity in a vacuum equal to $3 \cdot 10^8$ m/sec).

e) By means of sources of electromagnetic radiation with controlled coherence properties it is possible to alter artificially the "genetic" coherence parameters of the electronic states of a crystal and the phase of growth, and hence to control the growth of the crystal. The phenomenon of the optically controlled growth of crystalline and macromolecular structures can apparently be used to create molecular optoelectronic functional schemes for future-generation computers.

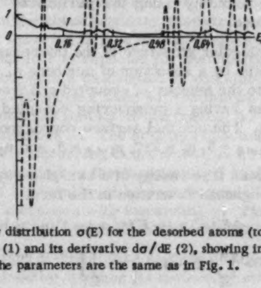

Fig. 2. Energy distribution σ(E) for the desorbed atoms (total "desorption cross section") (1) and its derivative dσ/dE (2), showing inhomogeneities (resonances); the parameters are the same as in Fig. 1.

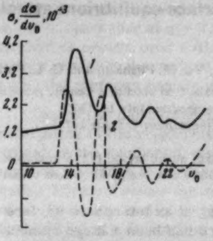

Fig. 3. Dependence of the desorption cross section σ (1) on the depth of the potential well v_0 and its derivative $d\sigma/dv_0$ (2), showing resonances (cross section and its derivatives in atomic units, depth of the well in °K); the parameters are the same as in Fig. 1.

The author thanks L. P. Pitaevskii, A. A. Chernov, and L. A. Shuvalov for useful and constructive criticism, which led to significant clarification of the basic aspects of this work.

---

[1] D. R. Frankl and J. A. Venable, Adv. Phys., 19, 409 (1970).

[2] K. Kastler, J. Phys. et Radium, 11, 250 (1951).

[3] H. Schwarz and H. Hora, Appl. Phys. Lett., 15, 349 (1969).

[4] H. Schwarz, Appl. Phys. Lett., 19, 148 (1971).

[5] L. D. Landau and E. M. Lifshits, Quantum Mechanics, Oxford Univ. Press (1965).

[6] P. H. Geil, Polymer Single Crystals, Wiley (1963).

[7] G. L. Lamb, Rev. Mod. Phys., 43, 99 (1971).

Simulation of a crystal surface equilibrium atomic structure for a single component system

V. O. Esin, V. I. Danilyuk, Yu. M. Plishkin, and G. L. Podchinenova

Institute for the Physics of Metals, Ural Scientific Center, Academy of Sciences of the USSR

(Submitted March 13, 1972; resubmitted July 10, 1972)
Kristallografiya, 18, 920-925 (September-October 1973)

A computer was used to simulate an fcc crystal {111} interphase surface and to determine the molecular structure corresponding to minimum surface free energy for various values of a parameter α.

Molecular processes occurring at an interphase surface depend on its structure. There has been a large number of experimental and theoretical publications on the study of crystal–vapor separation boundaries, most of them highly successful. A more complicated problem, because of experimental and theoretical difficulties, is the study of a crystal–melt surface. A knowledge of the molecular structure of a crystal–melt surface is necessary for the understanding of the crystal growth mechanism and kinetics.

The aim of the present investigation was the study of the molecular structure of a crystal–melt surface for fcc metals using a computer simulation. At such a surface the atoms are continually interchanging between the neighboring phases. The intensity of the atomic interchange depends on the molecular structure and the development degree of the phase boundary, which is a function of its orientation in the crystal lattice.

In the interphase-surface (a Kossel' crystal {100} face) models considered to date a limit to the surface development has been applied: The formation of "overhang" type configuration has been forbidden.[1,2] This limitation can distort the equilibrium molecular structure of an interphase surface and affect its displacement kinetics during crystal growth. In our model such a limitation is removed.

An fcc crystal interphase surface in the nearest neighbor approximation can be simulated as follows. It is assumed that the phase boundary surface consists of two layers of ideal crystal lattice. The first layer sites are occupied by atoms situated on the crystal surface, and the second layer, directly touching the first, consists of sites at which the isotropic phase atoms possibly join to the crystal surface. We will call this a layer of free sites. In this case there is no kind of limitation on the surface development, that is, either in the number of surface atoms or in the surface width, expressed as the number of interplanar separations occupied by the crystal-to-melt transition region.

A two-dimensional model of a phase boundary surface is shown in Fig. 1. A crystal surface atom and a free site, depending on the surface position, are characterized by an index i equal to the number of nearest neighbors on the crystal side. Atoms situated within the crystal have i = 12. For atoms and free sites belonging to the surface, i can range from 1 to 11.

In its initial state an element of an atomically smooth phase boundary surface is considered parallel to a {111} face containing 217 occupied and 217 free sites. The parameters characterizing the equilibrium surface are determined from the minimum free energy condition for the system.

The basic act in this model of changing the surface configuration is to remove an atom from the occupied site layer or to place an atom in the free layer.

The following boundary conditions were used: Basic acts outside the limits of the considered surface element are forbidden, and the number of atomic neighbors at the boundary is found by using the peripheral layer of the smooth surface.

The molecular structure of the interphase surface will be denoted by a spectrum of numbers n_i' and n_i corresponding to the number of occupied and free crystal surface sites having i neighboring occupied sites (i = 1, 2, ..., 11). The original surface corresponds to the spectrum $n_{i\neq 9}' = 0$, $n_9' = 217$, $n_{i\neq 3} = 0$, and $n_3 = 217$.

The excess free energy of a two-phase system due to boundary roughness is written in the form

$$\Delta F^*(n_i', n_i) = F^*(n_i', n_i) - F^*(n_9', n_3) = \sum_{i=1}^{11} (12-i)\, n_i' - \alpha \ln \prod_{i=1}^{11} \frac{(n_i' + n_i)!}{n_i'!\, n_i!}, \tag{1}$$

where $\Delta\varphi$ is the excess free energy due to the presence of the boundary without allowing for the configurational entropy associated with a single surface bond, $\alpha = kT/\Delta\varphi$, and ΔF^* is expressed in units of $\Delta\varphi$.

The second term in (1) is the change in the configurational entropy caused by the surface roughness. The number of ways in which the given molecular structure can exist can be written, to a sufficiently good approximation, in the form

$$W = \prod_{i=1}^{11} (n_i' + n_i)!/n_i'!\, n_i!$$

In this case, rearrangements between different types of sites are not taken into consideration, since this would

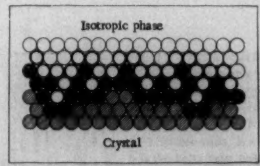

Fig. 1. Two-dimensional phase boundary surface model. ●) Crystal surface atoms; O) sites at which isotropic phase atoms can join to the crystal.

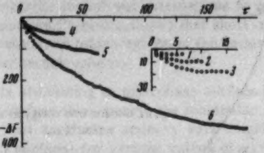

Fig. 2. Change in system free energy when the interphase boundary approaches the equilibrium state for various α. 1) $\alpha = 1.4$; 2) 1.6; 3) 1.8; 4) 2.2; 5) 2.6; 6) 3.2; τ) the number of essential basic acts.

produce a marked change in the molecular structure due to the bonds existing between crystal surface atoms.

Minimizing $\Delta F^*(n_i', n_i)$ we find the equilibrium surface configuration corresponding to different values of α. The minimization of $\Delta F^*(n_i', n_i)$ was programmed as follows. All possible surface configurational changes are considered for a single basic act and the corresponding free energy changes calculated. Out of all the possible basic acts on the phase boundary, there is one which causes the greatest lowering in free energy of the system. After this, the procedure is repeated for the changed surface configuration. Such a calculation is continued until the system does not reach a state with minimum free energy. Figure 2 shows the results of minimizing $\Delta F^*(n_i', n_i)$ for various parameters α. The abscissa denotes the number of basic acts τ occurring in the model, as a result of which the system approaches thermodynamical equilibrium. It is clear that the number of basic acts needed to reach equilibrium increases with increasing α. This confirms that the surface development increases with increasing α.

A complete picture of the surface development can only be obtained by studying its molecular structure, diffusivity, and roughness spectra. The molecular structure spectrum changes with increasing α (Fig. 3). If there is a small number of vacancies and adsorbed atoms on the surface when $\alpha = 1.4$, then this number sharply increases when $\alpha = 2.2$. Such surfaces, although they are not smooth, can be thought of as being molecularly rough. Further surface development ($\alpha > 2.6$) occurs via the formation of vacancies and adsorbed atoms in the following layers. At $\alpha = 3.2$ the surface is strongly developed (Fig. 4). Its molecular structure is characterized by a complete set of numbers n_i'. Such surfaces are considered to be completely rough.

Figure 5 shows the concentration of solid phase atoms (n/N_s) along the layer surface as a function of parameter α. It is clear that at $\alpha = 3.2$ the transition from one phase to another occurs over a distance of four to five atomic layers, and that the surface is diffuse; at $\alpha < 2.2$, however, the surfaces remain molecularly sharp.

One of the most important surface development characteristics is the roughness, definable as the relative increase in the number of surface bonds for the development of a surface in comparison with the atomically smooth case. Figure 6 shows the surface roughness as a function of α. Over the studied range of this parameter, no discontinuities are detected on the roughness curve, as is the case in the purely analytical solution of the structure problem for an fcc crystal $\{111\}$ face with two levels, given by Wannier and Onsager.[3] They found $\alpha_c = 1.82$ ($kT/2\Delta\varphi = 0.91$) corresponding to a critical temperature T_c at which there is a transition from a planar (molecularly smooth) surface to a fairly rough one. In our model the transition occurs without any features over a wide parameter range ($1.4 < \alpha < 2.6$).

The specific surface free energy α calculated in the model can be determined from the free energy of the separation boundary $F^*(n_i', n_i)$:

$$\sigma S_a / kT = F^* / N_s \alpha,$$

where S_a is the area associated with an atom in the $\{111\}$ plane. Figure 7 shows the dependence of the dimensionless quantity $\sigma S_a/kT$ on α.

Comparing the free surface energy calculated from the model with the experimental values of the interphase surface tension for fcc metals on the boundary of a crystal with a particular melt[4] ($\sigma_{SL} S_a / kT \approx 0.55$) or with a vapor ($\sigma_{SV} S_a / kT \approx 5.5$) at the melting point allows the value of parameter α corresponding to a real system to be determined ($kT/\Delta\varphi_{SL} \approx 3.0$; $kT/\Delta\varphi_{SV} \approx 0.5$). In this case the interphase crystal–melt boundary ($\alpha = 3.0$) is quite rough and diffuse (in this model the transition from one phase to another occurs over four to five atomic layers), while the crystal–vapor boundary ($\alpha = 0.5$) even at the melting point remains practically atomically smooth and sharp.

As can be seen in Fig. 7, for $\alpha > 4$ the surface free energy decreases to zero and becomes negative. This should be accompanied by a loss in stability of the interphase surface, whose roughness would apparently increase to an unlimited extent on approaching the critical value

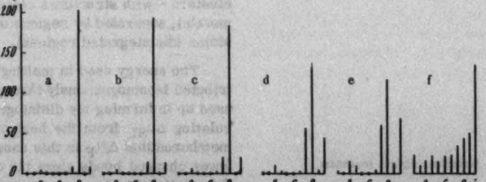

Fig. 3. Spectrum of numbers n_i' for various α. a) $\alpha = 1.4$; 2) 1.6; c) 1.8; d) 2.2; e) 2.6; f) 3.2.

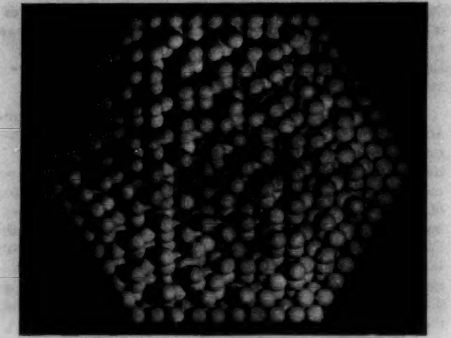

Fig. 4. Model of an fcc crystal (111) interphase surface molecular structure with $\alpha = 3.2$.

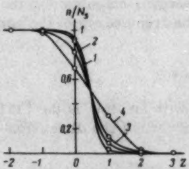

Fig. 5. Concentration of solid phase atoms along the layer on an interphase boundary for various α. 1) α = 1.8; 2) 2.2; 3) 2.6; 4) 3.2. n is the number of solid phase atoms in the layer Z; N_s is the total number of sites in the layer Z (N_s = 217).

corresponding to $\sigma = 0$.

Jackson[2,5] and Temkin[1] have studied surface roughness as a function of the parameter α using the quantity $kT/\Delta u_{SL}$, where T is the equilibrium temperature and Δu_{SL} is the heat of fusion occurring in a single bond, calculated assuming that the energy expended upon melting is equally distributed among the melt atoms.

Recently Nasson and Tiller[6] calculated the surface free energy for a Jackson[5] and Temkin[1] rough surface model.

They showed that the excess crystal–melt ($F = F_s + \Delta F_r$) surface energy for metallic systems is negative if it is assumed that the idealized atomically smooth surface from energy F_s includes the excess enthalpy due to the presence of a solid–melt phase, and that the corresponding entropy change is negligibly small (where ΔF_r is the lowering in free surface energy due to surface roughness). It is thereby assumed that this enthalpy change is due to the presence on the surface of $\frac{1}{2}(Z - Z_l)N_s$ displaced bonds, each of which has an enthalpy $\Delta u_{SL} = \Delta H_F/NZ$ (where N is Avogadro's number, ΔH_F is the molar heat of fusion, Z the full coordination number, Z_l the nearest-neighbor number in a plane parallel to the surface, and N_s the number of atoms on a smooth crystal surface).

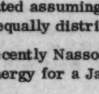

Fig. 6. Interphase surface roughness.

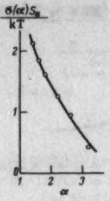

Fig. 7. Surface free energy as a function of α.

Jackson[7], in reply to Nason and Tiller, did not analyze the reasons for the negative crystal–melt free energy for metals. In fact such a representation means that the free energy for a crystal–melt surface must be negative for metals. This was noted by Temkin[8] in reply to Nason and Tiller.

The equilibrium structure of a {100} Kossel' crystal surface was recently computed by Jackson.[2] He also obtained a negative free surface energy value ($\sigma < 0$ when $kT/\Delta u > 2$) and concluded that it was impossible to calculate the free surface energy roughness from its energy. We consider this conclusion to be somewhat premature.

For a crystal–melt surface in fcc metals, in calculating u_{SL} from the heat of fusion ΔH_F, the parameter $\alpha' = kT/\Delta u_{SL} \approx 10$, which also corresponds to a negative free energy in our model (Fig. 7).

We conclude therefore that the parameter Δu_{SL}, calculated assuming a homogeneous distribution of heats of fusion among the melt atoms, cannot be used in determining σ_{SL} for a crystal–melt surface. Comparing α' with α calculated from the crystal–melt surface model indicates that $\Delta\varphi_{SL}$ should be approximately three times larger than Δu_{SL}.

We assume that the discrepancy is connected with neglecting the real melt structure in calculating Δu_{SL}. It may be supposed that close to the melting point a metallic melt contains microregions of short-range order – clusters – with structures close to crystalline (for fcc metals), separated by regions of disordered arrays of atoms (disintegrated regions).

The energy used in melting a crystal ΔH_F is distributed inhomogeneously through the melt and is basically used up in forming the disintegration regions. In calculating Δu_{SL} from the heat of fusion, it must be remembered that ΔH_F in this case is distributed among fewer changed bonds along the cluster boundaries. From the relationship $\Delta\varphi_{SL} > 3\Delta u_{SL}$ the minimum cluster size can be calculated to be of the order of 50 atoms. This value lies between those found from neutron-diffraction studies of metallic melts[9] and calculations of radial distribution functions,[10] which indicate that short-range order in liquids extends to microregions of the order of three to four coordination spheres.

Thus, in simulating an interphase surface by minimizing the surface free energy, the molecular structure, diffusivity, and roughness spectra were found for fcc metal $\{111\}$ surfaces for various values of α. The value of the parameter α for materials with fcc lattices allowed the phase boundary free surface energy to be derived from the model. The α value at which a loss in stability of such a surface is to be expected was also obtained. It was shown that in choosing the α for calculating the surface free energy for the surface roughness, the melt structure must be taken into consideration.

---

[1] D. E. Temkin, Growth and Imperfection of Metallic Crystals [in Russian], Naukova Dumka, Kiev (1966), p. 15; Mechanism and Kinetics of Crystallization [in Russian], Nauka i Tekhnika, Minsk (1964), p. 86.
[2] H. J. Leamy and K. A. Jackson, J. Appl. Phys., 42, 2121 (1971).
[3] V. Barton, N. Cabrera, and F. Frank, Elementary Processes in Crystal Growth [Russian translation], Izd. IL, Moscow (1959), p. 11.
[4] D. Turnbull, J. Appl. Phys., 21, 1022 (1950); J. H. Hollomon and D. Turnbull, Progr. Metal Phys., 4, 333 (1953).
[5] K. A. Jackson, Liquid Metals and Their Solidification [Russian translation], Metallurgizdat, Moscow (1962), p. 200; Problems in Crystal Growth [Russian translation], Mir, Moscow (1968), p. 27.
[6] D. Nason and W. A. Tiller, J. Crystal Growth, 10, 117 (1971).
[7] K. A. Jackson, J. Crystal Growth, 10, 119 (1971).
[8] D. E. Temkin, J. Crystal Growth, 10, 190 (1971).
[9] K. C. Turberfield, Proc. Phys. Soc., 80, 395 (1962).
[10] I. Z. Fisher, Statistical Theory of Metals [Russian translation], Gos. Izd. Fiz.-Matem. Lit., Moscow (1961), p. 86.

Reconstruction of the phase of the electronic scattering amplitude from experiments on the diffraction of resonant γ quanta

I. P. Perstnev and F. N. Chukhovskii

Crystallography Institute, Academy of Sciences of the USSR

(Submitted January 12, 1973)
Kristallografiya, 18, 926-933 (September-October 1973)

Consideration is given to the problem of the reconstruction of the phase of the electronic scattering amplitude for resonant Bragg scattering of γ quanta. An exact solution is given to the integral equation relating the spectral scattering coefficient to the experimental interference reflection coefficient. A detailed analysis is given of scattering at mosaic crystals for the general case of hyperfine splitting of the Mössbauer line in the crystal. Analytical expressions are obtained for determining the phase from the asymptote of the solution of the integral equation. The theory is compared with experimental results.

INTRODUCTION

Theoretical and experimental work[1,2] has recently been done on the determination of the phase $\varphi^{(e)}$ of the electronic scattering amplitude in Mössbauer γ spectroscopy. The method is based on the interference of nuclear resonant and electronic Rayleigh scattering channels in the diffraction of γ quanta in crystals.[3-6] Thus in ref. 2 the phases were found for scattering from the (020) and (040) planes of a potassium ferricyanide crystal $K_3Fe(CN)_6$ and it was shown that the results obtained were in good agreement with the existing x-ray data on the structure of this compound.

The idea of using the interference of nuclear and electronic scattering for reconstructing the phase of the electronic scattering amplitude was suggested in refs. 7-9. The general theory of resonant diffraction scattering of γ quanta in regular crystals was developed in refs. 10-11. In particular, ref. 11 gives a full analysis of the effect of the dynamic nature of the scattering in a thick crystal on the Bragg reflection picture when there is interference between the electronic and nuclear scattering. The inverse problem of reconstructing the phase of the electronic scattering amplitude from experiments on the Bragg reflection of γ quanta for the case of unsplit Mössbauer lines is considered in detail in ref. 12.

This paper gives an analysis of the problem of reconstructing the phase of the electronic scattering amplitude in the general case of the diffraction of resonant γ quanta. Particular attention is paid to the scattering at mosaic crystals, since this is important in practice. An exact solution is given to the integral equation which relates the spectral scattering coefficient $r(\omega)$ with the experimental interference reflection coefficient $R(v)$ (v is the velocity of the Mössbauer source relative to the scattering crystal and ω is the frequency of the γ quanta). It is shown that the problem of determining the phase $\varphi^{(e)}$ can be very efficiently solved by using the asymptotic solution of the integral equation far from the exact resonance of the nuclear scattering amplitude. A comparison of this theory with experiment is presented.

CALCULATION OF THE SPECTRAL SCATTERING COEFFICIENT $r(\omega)$ OF A MOSAIC CRYSTAL FOR A MÖSSBAUER LINE WITH SPLITTING

Suppose that a plane monochromatic wave $\mathbf{E}(\omega, \mathbf{r}) = \mathbf{e}_0 \exp(i\varkappa_0\mathbf{r})$ is incident on a crystal in the shape of a plane-parallel plate of thickness t. If the orientation of the crystal as a whole is close to one of the Bragg positions with reflection vector K_1, the field $\mathbf{E}(\omega, \mathbf{r})$ in the crystal is the superposition of a transmitted and a diffracted wave:

$$\mathbf{E}(\omega, \mathbf{r}) = \mathbf{E}_0 \exp(i\mathbf{k}_0\mathbf{r}) + \mathbf{E}_1 \exp(i\mathbf{k}_1\mathbf{r}), \qquad \mathbf{k}_1 = \mathbf{k}_0 + \mathbf{K}_1,$$

where the eigenwave vectors $\mathbf{k}_{0,1}$ and the amplitudes $\mathbf{E}_{0,1}$ are determined from the Maxwell equations in the momentum representation:[10]

$$\left(\frac{\mathbf{k}_h^2}{\varkappa_0^2} - 1\right)\mathbf{E}_h = \sum_{h'} \hat{\chi}_{hh'}\mathbf{E}_{h'} \quad (h = 0,1). \tag{1}$$

Here $\hat{\chi}_{hh'} = \hat{\chi}^{(e)}_{hh'} + \hat{\chi}^{(n)}_{hh'}$; $\hat{\chi}^{(e)}_{hh'}, \hat{\chi}^{(n)}_{hh'}$ are the Fourier components of the polarization tensor for the electronic and nuclear subsystems of the crystal, respectively, and $\hat{\chi}^{(e)}_{hh'} = \chi^{(e)}_{h-h'}\delta^{ij}$ ($i, j = 1, 2, 3$). The form of the tensor $\hat{\chi}^{(n)}_{hh'}$ is determined by the multiplicity of the transition (M1, E1, or E2) and the internal fields at the resonance nuclei:[13-15]

$$\hat{\chi}^{(n)}_{hh'} = -\frac{\Gamma_c}{2}\sum_{\xi} \frac{\hat{T}_{hh'\xi}}{\omega - \omega_c - \Delta_\xi + i\Gamma_c/2}, \tag{2}$$

where the index ξ numbers the resonance nuclei in the unit cell and the sublevels of the nuclear multiplet, and Δ_ξ is the value of the nuclear hyperfine splitting. The tensor $\hat{T}_{hh'\xi}$ depends very much on the polarization properties of the ξ resonance.

With arbitrary orientation of the internal fields at the resonance nuclei relative to the scattering plane ($\mathbf{k}_0$, $\mathbf{k}_1$), Eq. (1) represents a system of four homogeneous equations for the amplitudes $\mathbf{E}_{h\lambda}$ (λ is the polarization index). The natural values of the wave vectors $\mathbf{k}_{h\lambda}$ are found from a fourth-order dispersion equation, whose solution is very cumbersome and quite unsuited for practical analysis.

Fortunately, the majority of crystals used in the experiments are highly mosaic and this enables the problem to be greatly simplified. The intensity of the diffracted wave $I_1(z)$ at a depth z from the crystal surface is given simply by the summation over the thickness of the intensities $|\mathbf{E}_1(z, z')|^2$ of the γ radiation singly scattered through an angle $2\theta_B = \mathbf{k}_0, \mathbf{k}_1$:

$$I_1(z) = \int_0^t dz' |\mathbf{E}_1(z, z')|^2 \theta[\gamma_1(z - z')], \tag{3}$$

where $\mathbf{E}_1(z, z')$ is the amplitude of the diffracted wave at the point z scattered from an infinitesimally thin layer of crystal at a depth z'; $\theta(z)$ is a step-wise function with $\theta(z) = 0$ for $z < 0$ and $\theta(z) = 1$ for $z > 0$; the parameter

γ_1 determines the scattering geometry, $\gamma_1 > 0$ for Laue diffraction and $\gamma_1 < 0$ for Bragg diffraction.

In what follows we limit ourselves to the scattering of γ quanta at mosaic crystals. When the Mössbauer line of the nuclei is split, we have to take into account not only the attenuation of the transmitted $I_0(z)$ and diffracted $I_1(z)$ intensities but also the change in the polarization vectors of the appropriate waves through the thickness of the crystal.[15] We therefore introduce polarization vectors for the waves in the crystal $\mathbf{e}_{0\lambda}$ and $\mathbf{e}_{1\lambda}$ propagating in the directions $\varkappa_0$ and $\varkappa_1 = \varkappa_0 + \mathbf{K}_1$ and the corresponding eigenvalues

$$\mathbf{k}_{h\lambda} = \varkappa_h + \frac{\varepsilon_{h\lambda}}{\gamma_h}\mathbf{n} \quad (h = 0, 1;\ \lambda = 1, 2)$$

[n is the internal normal to the crystal surface $\gamma_h = \cos(\widehat{\varkappa_h, \mathbf{n}})$].

We then have the following expression for the wave field in a mosaic crystal:

$$\mathbf{E}_0(\mathbf{r}) = \mathbf{E}_0(z)\exp(i\varkappa_0\mathbf{r}),\ \mathbf{E}_0(z) = \sum_\lambda a_{0\lambda}\mathbf{e}_{0\lambda}\exp\left(i\frac{\varkappa_0}{\gamma_0}\varepsilon_{0\lambda}z\right), \tag{4}$$

$$\mathbf{E}_1(\mathbf{r}, \mathbf{r}') = \mathbf{E}_1(z, z')\exp(i\varkappa_1\mathbf{r}),\ \mathbf{E}_1(z, z') = \sum_\lambda a_{1\lambda}\mathbf{e}_{1\lambda}\exp\left(i\frac{\varkappa_0}{\gamma_1}\varepsilon_{1\lambda}(z - z')\right). \tag{5}$$

The coefficients $a_{0\lambda}$ and $a_{1\lambda}$ are given by the boundary conditions

$$\mathbf{E}_0(0) = \mathbf{e}_0, \tag{6}$$

$$\mathbf{E}_1(z, z) = \left(\frac{\pi\varkappa_0\Delta\theta}{2\gamma_0\,\delta\sin 2\theta_B}\right)^{1/2}(\hat{\chi}_1^{(\sigma)} + \hat{\chi}_{10}^{(\pi)})\mathbf{E}_0(z). \tag{7}$$

The constant factor $(\pi\varkappa_0\Delta\theta / 2\gamma_0\delta\sin 2\theta_B)^{1/2}$ in (7) ($\Delta\theta$ is the collimation angle of the incident beam and δ is the effective disorientation angle of mosaic blocks, $\Delta\theta < \delta$) can be most simply determined from the condition that $r(\omega)$ (see Eq. (10) below) goes over to the corresponding expression for the spectral scattering coefficient in the case where the Mössbauer line is not split.[11]

The eigenvalues $\varepsilon_{h\lambda}$ and the eigen polarization vectors $\mathbf{e}_{h\lambda}$ in a mosaic crystal are found from (1) with $\hat{\chi}_{h,1-h} = 0$ and have the form

$$\varepsilon_{h\lambda} = \frac{1}{4}\{\chi_{hh}^{\sigma\sigma} + \chi_{hh}^{\pi\pi} \pm [(\chi_{hh}^{\sigma\sigma} - \chi_{hh}^{\pi\pi})^2 + 4\chi_{hh}^{\sigma\pi}\chi_{hh}^{\pi\sigma}]^{1/2}\}, \tag{8}$$

$$\mathbf{e}_{h\lambda} = \frac{\chi_{hh}^{\sigma\pi}\mathbf{e}_h^{(\sigma)} + (2\varepsilon_{h\lambda} - \chi_{hh}^{\sigma\sigma})\mathbf{e}_h^{(\pi)}}{(|\chi_{hh}^{\sigma\pi}|^2 + |2\varepsilon_{h\lambda} - \chi_{hh}^{\sigma\sigma}|^2)^{1/2}},\ \chi_{hh}^{ss'} = \mathbf{e}_h^{(s)}\hat{\chi}_{hh}\mathbf{e}_h^{(s')}. \tag{9}$$

In deriving (8) and (9), we used the standard directions of π and σ polarizations $\mathbf{e}_h^{(s)}$; the index s takes the two values π and σ; by definition $\mathbf{e}_h^{(s)}\varkappa_0\varkappa_1 = 0$, $\mathbf{e}_h^{(\pi)}\mathbf{e}_h^{(\sigma)} = 0$.

Using (3)-(9), we find for the spectral scattering coefficient $r(\omega) = I_1(\omega, t)/|\mathbf{e}_0|^2$

$$r(\omega) = \frac{\pi\Delta\theta}{2\delta\sin 2\theta_B}$$

$$\times\sum_{\lambda,\lambda',\mu,\mu'}\frac{(\mathbf{e}_{1\mu'}^{*}\mathbf{e}_{1\mu})(\tilde{\mathbf{e}}_{1\mu}\hat{\chi}_{10}\mathbf{e}_{0\lambda})(\tilde{\mathbf{e}}_{1\mu'}\hat{\chi}_{10}\mathbf{e}_{0\lambda'})^{*}}{i\left[\varepsilon_{0\lambda'}^{*} - \varepsilon_{0\lambda} - \frac{\gamma_0}{\gamma_1}(\varepsilon_{1\mu'}^{*} - \varepsilon_{1\mu})\right]}\frac{(\tilde{\mathbf{e}}_{0\lambda}\mathbf{e}_0)(\tilde{\mathbf{e}}_{0\lambda'}\mathbf{e}_0)^{*}}{|\mathbf{e}_0|^2}$$

$$\times\begin{cases}1 - \exp\left[i\varkappa_0 t\left(\frac{\varepsilon_{0\lambda} - \varepsilon_{0\lambda'}^{*}}{\gamma_0} - \frac{\varepsilon_{1\mu} - \varepsilon_{1\mu'}^{*}}{\gamma_1}\right)\right], & \gamma_1 < 0,\\ \exp\left[i\varkappa_0 t\left(\frac{\varepsilon_{1\mu} - \varepsilon_{1\mu'}^{*}}{\gamma_1}\right)\right] - \exp\left[i\varkappa_0 t\left(\frac{\varepsilon_{0\lambda} - \varepsilon_{0\lambda'}^{*}}{\gamma_0}\right)\right], & \gamma_1 > 0,\end{cases} \tag{10}$$

where $\tilde{\mathbf{e}}_{h\lambda}$ are vectors inverse to the eigen polarization vectors $\mathbf{e}_{h\lambda}$, $\mathbf{e}_{h\lambda}\tilde{\mathbf{e}}_{h\lambda} = \delta_{\lambda\lambda'}$, and equal to

$$\tilde{\mathbf{e}}_{h\lambda} = \frac{\mathbf{e}_{h\lambda}^{*} - (\mathbf{e}_{h\lambda}^{*}\mathbf{e}_{h,3-\lambda})\mathbf{e}_{h,3-\lambda}^{*}}{1 - |\mathbf{e}_{h\lambda}^{*}\mathbf{e}_{h,3-\lambda}|^2}. \tag{11}$$

Equation (10) is a generalization of the spectral scattering coefficient obtained in ref. 11 in the case of arbitrary splitting of the Mössbauer nuclear line in a mosaic crystal.

DETERMINATION OF THE PHASE OF THE ELECTRON SCATTERING AMPLITUDE

The experimentally measured quantity is the interference reflection coefficient of the γ quanta $R(v)$ for a given source velocity v. $R(v)$ is related to $r(\omega)$ by the integral equation

$$R(v) = f_s\int_{-\infty}^{\infty} d\omega\, I_s(v, \omega)\overline{r(\omega)} + (1 - f_s)\overline{r(\infty)}, \tag{12}$$

where f_s is the Mössbauer factor of the source and the bar over $r(\omega)$ denotes averaging of the coefficient (10) over the polarizations $\mathbf{e}_0$ of the incident radiation. The energy distribution of the source γ quanta $I_s(v, \omega)$ has the Lorentz form

$$I_s(v, \omega) = \frac{\Gamma_s/2\pi}{[\omega - \omega_s(1 + (v/c))]^2 + \Gamma_s^2/4}, \tag{13}$$

where ω_s and Γ_s are the center and width of the line and c is the velocity of light. Equation (13) assumes that the source line is not split and that self-absorption in the source can be neglected; $r(\infty)$ corresponds to the reflection coefficient when $2v\omega_c/c\Gamma_c \to \infty$ (ω_c and Γ_c are the center and width of the Mössbauer line in the crystal). It is clear that there is then no nuclear scattering and $r(\infty)$ is determined by the electron Rayleigh scattering.

Expression (12) is an integral relationship for determining the phase $\varphi^{(e)}$, which enters as a parameter in $\overline{r(\omega)}$. Thus the problem of reconstructing the phase of the electron scattering amplitude from the experimental values of $R(v)$ reduces to the solution of the integral equation (12) with the kernel (13). In the dimensionless variables

$$u = \frac{\omega_s(1 + (v/c)) - \omega_c}{\Gamma_c/2},\quad \Gamma = \frac{\Gamma_s}{\Gamma_c} \tag{14}$$

the solution has the form[12]

$$\overline{r(u)} - \overline{r(\infty)} = f_s^{-1}\cos\left(\Gamma\frac{\partial}{\partial u}\right)[R(u) - R(\infty)] +$$

$$+\pi f_s^{-1}\sin\left(\Gamma\frac{\partial}{\partial u}\right)\int_{-\infty}^{\infty}du'\frac{R(u')-R(\infty)}{u-u'}. \qquad (15)$$

Here $\begin{smallmatrix}\cos\\ \sin\end{smallmatrix}\left(\Gamma\frac{\partial}{\partial u}\right)$ denotes symbolically the series of appropriate trigonometric functions in powers of the differential operator $\Gamma\partial/\partial u$.

Using the asymptotic solution (15) far from the nuclear scattering amplitude resonance, we can obtain equations for the direct determination of the phase $\varphi^{(e)}$. In fact putting $|u| \gg 1$ formally into (15) and using (2), (8)-(10), we find

$$\overline{r(u)}=\overline{r(\infty)}\left[1+\frac{A}{u}+\frac{B}{u^2}+O\left(\frac{1}{u^3}\right)\right], \qquad (16)$$

$$\frac{A}{u}+\frac{B}{u^2}\approx f_s^{-1}\left[\frac{R(u)}{R(\infty)}-1\right]-\frac{\Gamma f_s^{-1}}{\pi u^2}\int_{-\infty}^{\infty}du'\left[\frac{R(u')}{R(\infty)}-1\right]. \qquad (17)$$

The coefficients A and B depend on the phase $\varphi^{(e)}$ of the nuclear scattering amplitude and are equal to

$$A=\frac{2\delta_{11}^{ij}\delta_{00}^{jk}}{(1+\cos^2 2\theta_B)|\chi_1^{(e)}|}\operatorname{Re}(\exp(-i\varphi^{(e)})T_{10}^{ik}), \qquad (18)$$

$$B=\frac{1}{1+\cos^2 2\theta_B}\left\{\frac{\delta_{11}^{ij}\delta_{00}^{kl}T_{10}^{ik}T_{10}^{jl*}}{|\chi_1^{(e)}|^2}\right.$$

$$+\frac{2\delta_{11}^{ij}\delta_{00}^{jk}\operatorname{Re}[\exp(-i\varphi^{(e)})(\Delta_{10}^{ik}-iT_{10}^{ik})]}{|\chi_1^{(e)}|}$$

$$\left.-\frac{\varkappa_0 t}{2}\delta_{11}^{ij}\delta_{00}^{jk}\left(\frac{T_{00}^{ik}}{\gamma_0}+\frac{T_{11}^{ik}}{|\gamma_1|}\right)\right\}, \qquad (19)$$

where we use the notation

$$\chi_1^{(e)}=-|\chi_1^{(e)}|\exp(i\varphi^{(e)}),\qquad T_{hh'}^{ik}=\sum_l T_{hh'l}^{ik},$$

$$\Delta_{hh'}^{ik}=\sum_l\frac{2\Delta_l}{\Gamma_c}T_{hh'l}^{ik},\qquad \delta_{hh'}^{ik}=\frac{1}{\varkappa_0^2}((\varkappa_h\varkappa_{h'})\delta^{ik}-\varkappa_{h'}^{i}\varkappa_h^{k}). \qquad (20)$$

For simplicity, expression (19) was obtained for a crystal which is thin as regards electronic absorption, so that $\varkappa_0 t\ \mathrm{Im}\ \chi_0^{(e)} \ll 1$. We note that (19) retains its form when $\gamma_0=\gamma_1$ (symmetric Laue diffraction) for any electronic absorption thickness. For the case of Bragg diffraction in a thick crystal, when $\varkappa_0 t\ \mathrm{Im}\ \chi_0^{(e)} \gg 1$, the last term in the braces on the right side of (19) must be replaced by

$$\delta_{11}^{ij}\delta_{00}^{jk}\left(\frac{T_{00}^{ik}}{\gamma_0}-\frac{T_{11}^{ik}}{\gamma_1}\right)\Big/\mathrm{Im}\,\chi_0^{(e)}\left(\frac{1}{\gamma_0}-\frac{1}{\gamma_1}\right). \qquad (21)$$

Equations (17)-(21) represent a complete solution to the problem of reconstructing the phase of the electronic scattering amplitude from the experimental values of the interference reflection coefficient R(u). The coefficient A is universal and does not depend on the magnitude and direction of the internal fields at the nuclei; it is determined simply by the asymptote of the experimental R(u) curve far from the nuclear resonant point. In order to determine $\varphi^{(e)}$ uniquely (except when $\varphi^{(e)}=0$ and $\varphi^{(e)}=\pi$), it is essential to use the value of the coefficient B which is determined not only by the asymptote of R(u), but also by the area of the experimental curve $R(u)-R(\infty)$. The form of B depends to a large extent on the parameters of the Mössbauer line splitting. We may note that the area of the experimental reflection curve can be expressed in terms of the integral (over frequency) of the scattering coefficient. It follows from (12) and (13) that with (14) we have

$$\int_{-\infty}^{\infty}du[R(u)-R(\infty)]=f_s\int_{-\infty}^{\infty}du[\overline{r(u)}-\overline{r(\infty)}].$$

Then (17) transforms to ($|u| \gg 1$)

$$\frac{A}{u}+\frac{B}{u^2}\approx f_s^{-1}\left[\frac{R(u)}{R(\infty)}-1\right]-\frac{\Gamma}{\pi u^2}\int_{-\infty}^{\infty}du'\left[\frac{\overline{r(u')}}{R(\infty)}-1\right], \qquad (22)$$

from which in principle it is possible to determine the phase of the electronic scattering amplitude by using only the asymptote of the experimental function R(u). However, the integral in (22) now also depends on the phase $\varphi^{(e)}$. It can easily be seen that for an unsplit Mössbauer line it is better to use (22) for finding the coefficients A and B.

COMPARISON WITH EXPERIMENT

We now apply (17)-(19) to determine the phase of the electronic scattering amplitude for Bragg scattering of resonant γ quanta from the (020) and (040) planes[2] of potassium ferricyanide $K_3Fe(CN)_6$. An analysis of the Mössbauer-effect data on this substance has shown that there is an electric field gradient at the Fe nuclei which produces a splitting of the excited state of Fe^{57} into two levels. Since the crystallographic structure of the unit cell of potassium ferricyanide is quite complicated [the unit cell contains two molecules of $K_3Fe(CN)_6$] it is not possible to make an a priori statement about the direction of the electric field gradient.

Assuming that the gradient is axial, we have the following expression for the tensor $\Delta_{hh'}^{ik}$, [see (20)]:

$$\Delta_{hh'}^{ik}=\frac{E_Q}{\Gamma_c}\left\{T_{hh'}^{ik}-\frac{4\pi\eta(f_hf_{h'})^{1/2}}{\varkappa_0^3V_0(1+\alpha)}\right.$$

$$\left.\times\sum_l 3\frac{[\mathbf{v}_l\varkappa_h]^i[\mathbf{v}_l\varkappa_{h'}]^k}{\varkappa_0^2}\exp(i(\varkappa_{h'}-\varkappa_h)\rho_l)\right\}, \qquad (23)$$

$$T_{hh'}^{ik}=\chi_{hh'}^{(n)}\delta_{hh'}^{ik},\qquad \chi_{hh'}^{(n)}=\frac{4\pi\eta(f_hf_{h'}^*)^{1/2}}{\varkappa_0^3V_0(1+\alpha)}\sum_l\exp(i(\varkappa_{h'}-\varkappa_h)\rho_l), \qquad (24)$$

where E_Q is the magnitude of the quadrupole splitting, ν_l is the unit vector in the direction of the axis of the electric field gradient at the l-th nucleus, f_h is the Mössbauer factor of the crystal, α is the conversion coefficient, V_0 is the volume of the unit cell, and η is the concentration of the resonant isotope Fe^{57}. The summation in (23) and (24) is over the nuclear coordinates ρ_l.

Using (23) and (24) and remembering that for the (020) and (040) reflections the phase factor $\exp[i(\varkappa_{h'}-\varkappa_h)\rho_l]$ is exactly equal to unity, we can reduce (18) and (19) for A and B to the form

$$A=\frac{4\cos 2\theta_B}{1+\cos^2 2\theta_B}\left|\frac{\chi_{10}^{(n)}}{\chi_1^{(e)}}\right|\cos\varphi^{(e)}, \qquad (25)$$

$$B=\left|\frac{\chi_{10}^{(n)}}{\chi_{1}^{(e)}}\right|^{2}-\frac{4\cos 2\theta_{B}}{1+\cos^{2}2\theta_{B}}\left|\frac{\chi_{10}^{(n)}}{\chi_{1}^{(e)}}\right|\sin\varphi^{(e)}$$

$$-\frac{\varkappa_{0}t}{2\gamma_{0}}(\chi_{00}^{(n)}+\chi_{11}^{(n)})-\frac{2}{1+\cos^{2}2\theta_{B}}\left|\frac{\chi_{10}^{(n)}}{\chi_{1}^{(e)}}\right|\frac{E_{Q}}{\Gamma_{0}}$$

$$\times\left[\frac{3}{2\varkappa_{0}^{2}}(\mathbf{v}_{1}\boldsymbol{\varkappa}_{1})(\mathbf{v}_{1}\boldsymbol{\varkappa}_{0})+\frac{3}{2\varkappa_{0}^{2}}(\mathbf{v}_{2}\boldsymbol{\varkappa}_{1})(\mathbf{v}_{2}\boldsymbol{\varkappa}_{0})-\cos 2\theta_{B}\right]\cos\varphi^{(e)}. \qquad (26)$$

Substituting into (25) and (26) the numerical values of the parameters corresponding to the conditions of the experiment,[2] we find

$$A_{020}^{(t)}=3.08\cos\varphi_{020}^{(e)},\qquad A_{040}^{(t)}=1.02\cos\varphi_{040}^{(e)}, \qquad (27)$$

$$\left.\begin{aligned} B_{020}^{(t)}&=-1.79-3.08\sin\varphi_{020}^{(e)}-2.50[{}^{3}/{}_{2}(\mathbf{v}_{1}\mathbf{n})^{2}\\ &\quad+{}^{3}/{}_{2}(\mathbf{v}_{2}\mathbf{n})^{2}-1]\cos\varphi_{020}^{(e)},\\ B_{040}^{(t)}&=-3.90-1.02\sin\varphi_{040}^{(e)}-0.83[{}^{3}/{}_{2}(\mathbf{v}_{1}\mathbf{n})^{2}\\ &\quad+{}^{3}/{}_{2}(\mathbf{v}_{2}\mathbf{n})^{2}-1]\cos\varphi_{040}^{(e)}. \end{aligned}\right\} \qquad (28)$$

It can be seen from (28) that the theoretical value of B depends very much on the direction of the axes of the electric field gradient and in principle it is conversely possible to judge these directions from the values of B.

The experimental values of A and B obtained from (17) by a least squares fit to the R(v) interference curves[2] are given in Table 1.

TABLE 1

N	10	12	13	14
$A_{020}^{(e)}$	2.89	2.81	2.63	2.31
$B_{020}^{(e)}$	−6.56	−6.32	−5.78	−7.05
$\cos\varphi_{020}^{(e)}$	0.94	0.91	0.85	0.75
$A_{040}^{(e)}$	1.20	1.18	1.13	1.03
$B_{040}^{(e)}$	−3.93	−3.64	−2.76	−3.51
$\cos\varphi_{040}^{(e)}$	1.18	1.16	1.11	1.01

The first row of Table 1 shows the number of experimental points on the left "tail" of the R(v) interference curve. The points on the right "tail" were chosen symmetrically about the exact resonance $[v = c(\omega_c - \omega_s)/\omega_s]$. The third and sixth rows give the values of $\cos\varphi_{020}^{(e)}$ and $\cos\varphi_{040}^{(e)}$ calculated over $A^{(e)}$.

It can be seen that the values of $A^{(e)}$ and $\cos\varphi_{h}^{(e)}$ obtained from R(v) are stable and almost real ($\cos\varphi_{h}^{(e)} = 1$), while for B the scatter in the values is very big although the sign and order of magnitude are correct. It should be noted that the statistics of the experiment[2] were insufficient to make a comparison of $B^{(e)}$ and $B^{(t)}$. Moreover, the fact that the direction of the axes of the electric field gradient are undetermined means that the values of $B^{(t)}$ are uncertain to a degree comparable with the value of the coefficient itself [see (28)].

It must be emphasized that in the present case ($\varphi^{(e)} = 0$) the phase of the electronic scattering amplitude is sufficiently well defined by the coefficient $A^{(e)}$ alone and $\Delta\varphi^{(e)} \sim \pm 20°$.

The authors wish to thank B. K. Vainshtein for his constant interest in this work and F. Parak for valuable advice in the reduction of the experimental data.

---

[1] F. Parak, R. L. Mossbauer, and W. Hoppe, Ber. Bunsengesellschaft Phys. Chem., 74, 1207 (1970).

[2] F. Parak, R. L. Mössbauer, U. Biebl, H. Formanek, and W. Hoppe, Z. Phys., 244, 456 (1971).

[3] P. J. Black, D. E. Evans, and D. A. O'Connor, Proc. Roy. Soc., A270, 168 (1962).

[4] P. J. Black, G. Longworth, and D. A. O'Connor, Proc. Phys. Soc., 83, 925 (1964).

[5] D. A. O'Connor and P. J. Black, Proc. Phys. Soc., 83, 925 (1964).

[6] V. K. Voitovetskii, I. L. Korsunskii, A. I. Novikov, and Yu. F. Pazhin, Zh. Eksp. Teor. Fiz., 54, 1361 (1968) [Sov. Phys. – JETP, 27, 729 (1968)].

[7] R. S. Raghavan, Proc. Indian Acad. Sci., A53, 265 (1961).

[8] P. B. Moon, Nature, 185, 427 (1961).

[9] G. S. Zhdanov and R. N. Kuz'min, Acta Crystallogr., B24, 10 (1968).

[10] A. M. Afanas'ev and Yu. Kagan, Zh. Eksp. Teor. Fiz., 48, 327 (1965) [Sov. Phys. – JETP, 21, 215 (1965)].

[11] Yu. Kagan, A. M. Afanas'ev, and I. P. Perstnev, Zh. Eksp. Teor. Fiz., 54, 1530 (1968) [Sov. Phys. – JETP, 27, 819 (1968)].

[12] F. N. Chukhovskii and I. P. Perstnev, Acta Crystallogr., A28, 405 (1972).

[13] V. A. Belyakov, Fiz. Tverd. Tela, 13, 2170 (1971) [Sov. Phys. – Solid State, 13, 1824 (1972)].

[14] A. M. Afanas'ev, Thesis, Crystallography Institute, Academy of Sciences of the USSR, Moscow (1972).

[15] M. Blume and O. C. Kistner, Phys. Rev., 171, 417 (1968).

One-dimensional models of the Patterson function

S. V. Borisov

Inorganic Chemistry Institute, Siberian Branch, Academy of Sciences of the USSR

(Submitted September 5, 1972)
Kristallografiya, 18, 934-938 (September-October 1973)

An algorithm for the extraction from the Patterson function of maxima, corresponding to the edges of equal segments in the presence of peaks of multiplicity 3 and higher, is considered by matrix superposition. A procedure for interpreting the Patterson function for two multiple peaks is also discussed.

The complicated problems of analyzing Patterson functions require intuitive geometric or adequate mathematical models, based on a minimum number of clear rules and properties. In considering model structures (point systems) with more than 10 atoms the geometric representation of Patterson functions becomes difficult, and the penalty is that they can no longer be represented by simple figures. It is customary to describe the Patterson functions by square matrices, each of whose elements is a vector equal in magnitude and direction to an interatomic distance, indicated by the index of this vector.[1,2] Moreover, it was shown by Buerger[2] that the specific magnitudes and directions of the interatomic vectors are not very meaningful for the explanation of many properties of Patterson functions, in particular, superposition properties.

Following ref. 2 we determine a formal model of Patterson functions as a matrix, each of whose elements is a combination of two digits or letters. All atoms of the structure are marked in advance by letters or digits in arbitrary order. It is agreed that the matrix element mn corresponds to the interatomic distance from atom m to atom n. Each matrix row corresponds then to successive distances from the atom whose number equals the row number to all remaining atoms in the order of their enumeration. Naturally, no information on the magnitudes and directions of interatomic distances is contained in such matrices, nor can they be made similar to a one-dimensional projection of the vector matrices on some arbitrary direction in space.

We notice one property, common both to vector elements and to any of their projections. The sum of interatomic vectors, comprising a closed contour, vanishes:

$$\mathbf{r}_{12} + \mathbf{r}_{23} + \mathbf{r}_{34} + \ldots + \mathbf{r}_{n1} = 0. \qquad (1)$$

Passing to the elements of the one-dimensional projection matrices, the so-called superposition matrices, this implies that the sum of superposition matrices of Patterson functions, corresponding to a closed contour, vanishes:

$$ab + bc + cd + \ldots + na = 0. \qquad (2)$$

The simplest consequence of this property is the vanishing of elements consisting of single numbers:

$$aa = bb = \ldots = nn = 0. \qquad (3)$$

Indeed, such elements, being the shortest contours, start and end at the same point. Since atoms superposable in each other are not possible in the structure, all remaining elements are nonvanishing.

Two elements can consist of a closed contour if they differ by the permutation of the numbers: $ab + ba = 0$, $ab = -ba$. The presence of mutually inverse elements in the pair matrix reflects, as well known, the centrosymmetry of the Patterson function. A nontrivial conclusion is obtained from a four-term contour: For two matrix elements one can find two more, such that the sum of the first two equals the sum of the second two. The four elements associated by their sum are located on vertices of a rectangle in the superposition matrix, while any two occupying one of the diagonals determine the rectangles:

$$ab + bc + cd + da = 0, \quad ab + cd = ad + cb. \qquad (4)$$

Quadruplets associated by their element difference are obtained by the permutations

$$ab - dc = ad - bc \quad \text{or} \quad cd - ba = cb - da. \qquad (5)$$

Deficient pairs of associated elements can always be found by performing the permutations indicated by the arrows:

$$a\underset{\curvearrowright}{\overset{\curvearrowleft}{b+c}}d = ad + cb, \quad a\underset{\curvearrowright}{\overset{\curvearrowleft}{b-c}}d = ac - bd \qquad (6)$$

If two superposition matrix elements are equal to each other (a peak of multiplicity 2 on the Patterson function), the two elements associated by their difference are also equal to each other: $ab = cd$, but $ab - cd = ac - bd$, i.e., $ac = bd$. Atoms a, b, c, d are located in this case on the vertices of a parallelogram, since opposite edges are pairwise equal.

In the vector matrix from any one row one can obtain another one, adding to all elements the corresponding interatomic distance. It is easy to verify that the superposition matrix conserves this property: The difference of corresponding elements of two fixed rows (columns) equals always the same matrix elements, which is easily determined from those pairs, for which the vanishing element of the main diagonal is subtracted. It follows, then, that on the superposition matrix one can model the displacement operation of two or more duplicates of the Patterson function. An element determining the displacement is added to all elements of the superposition matrix. If an element of the original matrix is obtained as a result of the summation, it is written down in the same place it occupied in the original matrix. The remaining places remain empty. It is clear from the preceding discussion that the result of matrix superposition by some element mn represents the element of row m and column n. Indeed, all elements of row n are changed into the elements of row m after summation with mn: $na + mn = nn + ma = ma$, $nb + mn = nn + mb = mb$, and so on. Column n is similarly obtained from column m: $am + mn = an + mm = an$, $bm + mn = bn + mm = bn$, and so on.

TABLE 1. Result of Matrix Superposition $\begin{pmatrix} aa\cdots\cdots \\ \cdots\cdots\cdots \\ \cdots\cdots gg \end{pmatrix}$ by the Element ab = cd = ef*

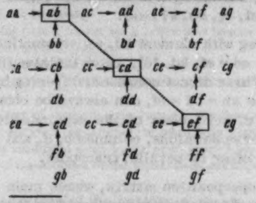

aa →	$\boxed{ab}$	ac →	ad	ae →	af	ag
	↑		↑		↑	
	bb		bd		bf	
ca →	cb	cc →	$\boxed{cd}$	ce →	cf	cg
	↑		↑		↑	
	db		dd		df	
ea →	ed	ec →	ed	ee →	$\boxed{ef}$	eg
	↑		↑		↑	
	fb		fd		ff	
	gb		gd		gf	

*The equal elements are framed and joined to each other by lines. The arrows show element permutations with the repeated superposition ab = cd = ef.

TABLE 2. Results of the Repeated Superposition M(0, M_2(0, ab = cd = ef) + ab = cd = e)*

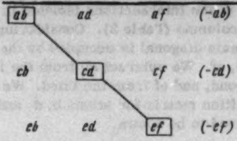

$\boxed{ab}$	ad	af	(-ab)
cb	$\boxed{cd}$	cf	(-cd)
eb	ed	$\boxed{ef}$	(-ef)

*The elements which must be substrated from the row elements, so as to obtain zero on the main diagonal, are shown at the right.

TABLE 3. Result of Subtraction, the Superposition Matrix of Elements b, d, f

0	bd	bf
ab	0	df
fb	fd	0

A row of the superposition matrix represent a solution; the structure is given by the distances from one atom to all remaining atoms, and the column is the inverse solution. To obtain a unique solution it is necessary to increase the superposition rank n. This can be done by a parallel superposition method, by which n elements of one row (or one column) are added to the elements of the superposition matrix, and only those recovered at all displacements are written down. It is easily verified that this is general for all rows (columns) of the matrix. We write such a superposition as M_n (0, ab, ac, ad, ..., an).

A successive superposition is also possible: The result of superposition by the first element (ab) is transposed by the second element (bc), then this result is transposed by the third (cd), and so on. The sequence of such superpositions is conventionally written down as M_2(0, ab), M_3(0, M_2(0, ab) + bc); M_4(0, M_3(0, M_2(0, ab) + bc) + cd),... . It can be shown that the inverse matrix solution is extracted only when the set of displacement elements obeys the rule of contour cycle: ab, bc, cd, ... Choosing from the sequence of displacements the inverse elements in the same order: ba, cd, dc, ... , we obtain the direct matrix solution. If the displacement elements form a closed contour, including all atoms, we extract from the Patterson function n n-corners whose centers give, as is well known,[2] the inverse solution.

We show on the superposition matrix that the presence of a peak of multiplicity 3 or higher enables us to extract peaks from the Patterson function, belonging to edges of equal segments.[3] Let ab = cd = ef. Due to this basic equality we have three more: 1) ac = bd (from ab − cd = ac − bd); 2) ae = bf (from ab − ef = ae − bf); 3) ce = df (from cd − ef = ce − df). The number of additional equalities determines the number of atomic parallelograms in the structure.[4]

Superpositions in ab are at the same time superpositions in cd and ef. Consequently, we add to the matrix elements all three elements and fix all the originally obtained elements. In complete agreement with theory there remain three rows and three columns in M_2(0, ab = cd = ef), in whose intersections ab, cd, and ef (Table 1) are located. In performing again a second successive superposition by ab = cd = ef it is necessary to bear in mind that row a contains elements which are found in row b in

TABLE 4. Result of Matrix Superposition $\begin{pmatrix} aa\cdots\cdots am \\ \cdots\cdots\cdots\cdots \\ ma\cdots\cdots mm \end{pmatrix}$ by the Element ab = cd = ef*

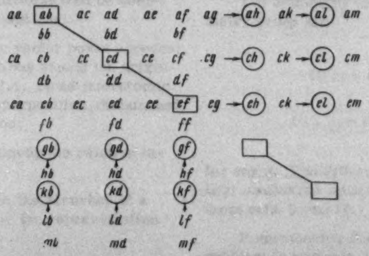

aa	$\boxed{ab}$	ac	ad	ae	af	ag →	$\textcircled{ah}$	ak →	$\textcircled{al}$	am
	bb		bd		bf					
ca	cb	cc	$\boxed{cd}$	ce	cf	cg →	$\textcircled{ch}$	ck →	$\textcircled{cl}$	cm
	db		dd		df					
ea	eb	ec	ed	ee	$\boxed{ef}$	eg →	$\textcircled{eh}$	ek →	$\textcircled{el}$	em
	fb		fd		ff					
	$\textcircled{gb}$		$\textcircled{gd}$		$\textcircled{gf}$		$\boxed{\;}$			
	↑		↑		↑					
	hb		hd		hf					
	$\textcircled{kb}$		$\textcircled{kd}$		$\textcircled{kf}$				$\boxed{\;}$	
	↓		↓		↓					
	lb		ld		lf					
	mb		md		mf					

*Circles indicate the elements remaining after successive superpositions M_4(0, M_2(0, ab = cd = ef) + gh = kl). The empty frames are the positions of the elements gh = kl in the matrix.

$M_2(0, ab = cd = ef)$, row c contains elements of row d, and so on. Nine elements remain in $M_3(0, M_2(0, ab = cd = ef) + ab = cd = ef)$ in the intersections isolated in the first stage of rows and columns (Table 2). Considering them as a matrix, its main diagonal is occupied by the equal elements *a*b, cd, ef. We subtract *a*b from the first row, cd from the second, and ef from the third. We are left with the superposition matrix for atoms b, d, and f (Table 3), as was required to be shown.

Using the superposition matrix, we discuss the algorithm for interpreting Patterson functions with doubly multiple peaks.[5] Let $ab = cd = ef$ and $gh = kl$. The first stage $M_2(0, ab = cd = ef)$, omits from the matrix rows *a*, c, e, and columns b, d, f (Table 4). A successive superposition by $gh = kl$ cannot give a solution, since these two elements have no common row (column) with the first three. Only 12 intersections of rows g and k and columns h and *l* with those earlier separated (the equation for $2N_1N_2$ of ref. 5) remain. Choosing any of the remaining elements, for example, *a*h, and recovering on the known segment $gh = kl$ one element of column *a* $(ah - gh\ (=kl) = ag - hh = ag)$, we obtain together with the well-known *a*b (= cd = ef) a "quadrangle" of atoms *a*, b, g, h. A superposition by three elements of row *a*, $M_4(0, ab, ag, ah)$, gives a theoretically unique matrix solution. The absence of the "reduced" element *a*g would remain in superposing *a*b and *a*h with the "superfluous" elements ch and eh. Such an exact result should be obtained by starting with the element $al - M_4(0, ab = cd = ef, al, ak)$. Convincing oneself of that, one may confirm the superposition solution by the hexagon of atoms *a*, b, g, h, *l*, k: $M_6(0, ab = cd = ef, ag, ah, al, ak)$.

Starting with element kd, we automatically obtain $M_4(0, ab = cd = ef, kd, ld)$, which isolates the d matrix column. Three direct solutions, differing by parallel displacements $ab = cd = ef$, can always be obtained. Those are the *a*, c, and *l* rows of the superposition matrix. Three inverse solutions, columns b, d, and f, also differ from each other by parallel transport.

The superposition matrix, whose main merit is the possibility of replacing operations with three-dimensional vectors by operations with numbers, is useful in solving new problems and smoothly illustrating problems already solved in analyzing Patterson functions.

---

[1] A. I. Kitaigorodskii, Usp. Fiz. Nauk, 46, 23 (1952).

[2] M. J. Buerger, Vector Space and Its Application in Crystal Structure Investigation, Wiley (1959).

[3] É. A. Kuz'min, V. V. Ilyukhin, and N. V. Belov, Zh. Strukt. Khim., 12, 643 (1971).

[4] É. A. Kuz'min, V. V. Ilyukhin, and N. V. Belov, Kristallografiya, 14, 1059 (1969) [Sov. Phys. – Crystallogr., 14, 916 (1970)].

[5] É. A. Kuz'min, V. V. Ilyukhin, and N. V. Belov, Zh. Strukt. Khim., 9, 820 (1968).

Sharpening the peaks of the projection of the Patterson function by regularization

A. I. Kvitashvili, N. P. Zhidkov, B. M. Shchedrin, and A. E. Shvelashvili
Scientific Research Institute for Applied Mathematics
Tbilisi State University
Computing Center for the M. I. Lomonosov Moscow State University
Gruzin Polytechnic Institute
(Submitted March 23, 1973)
Kristallografiya, 18, 939-943 (September-October 1973)

The problem of sharpening the Patterson distribution is reduced to the problem of solving the inverse heat conduction problem and then regularizing the solution by Tikhonov's method. The solution algorithm for this problem under the boundary conditions given by the pmm group is applied to sharpen the projection of the function of the interatomic vectors of the structure of the crystal $(NH_4)_2Ni(SO_4)_2 \cdot 6H_2O$.

Practical application of the various methods of inferring crystal structure from the Patterson distribution comes up against the low contrast provided by the function of the interatomic vectors: The maxima which characterize the interatomic vectors overlap and give rise to new peaks which are unrelated to the vector spacings. Therefore, beginning with Patterson in ref. 1, the question of increasing the contrast in the interatomic vector function P(r) has been raised.

It is known that P(r) may be represented as the superposition of N^2 bell-shaped finite functions $P_{ij}(r)$, each of which is a packet of the electron densities of the i-th and j-th atoms:

$$P(\mathbf{r})=\sum_{i,j=1}^{N} P_{ij}(\mathbf{r}-\mathbf{r}_{ij}), \tag{1}$$

where r_{ij} are the coordinates of the interatomic spacing vector. The functions $P_{ij}(r)$ can be approximated by Gaussian exponents, as in ref. 2, with good accuracy.

But it is also well known that the analogous distribution for point atoms can be represented as a sum of δ functions; this sum is transformed into a real distribution by a packet with Gaussian exponent functions as in ref. 3. This allows us to reformulate the problem of sharpening the peaks as the solution of an inverse heat conduction problem as in ref. 4. Although the latter is not well posed, its solution can be obtained by means of the regularization procedure proposed by A. N. Tihonov in refs. 5 and 6. The distribution P(r) is taken to be the solution of the heat conduction equation for a certain time value T, and the sharpened distribution P'(r) will be sought at some time value $t = T - \Delta T$. The sharpening process will be completed according to the following conditions:

a) a basic group of interatomic vector peaks appears; for these, some preliminary reductions among the original group of atoms can be obtained, i.e., those interatomic vectors which can be obtained by superposition, the bunched peaks for the heavy atoms, and so on;

b) there is no sharp division among the relative intensities of the separated peaks;

c) the peaks are localized up to the accuracy of a grid step, the latter being chosen for the representation of the Patterson distribution;

d) there are no reduction peaks as in ref. 7.

Naturally one cannot ask whether all the peaks $P_{ij}(r)$ have appeared, since, on the one hand, some peaks intersect completely and others intersect within the accuracy of the chosen tabulation grid P(r); and on the other hand, at some definite instant the effect of the change in order (the boundedness of the experiment with respect to $\sin\theta/\lambda$) begins to be felt, which must inevitably show itself by the appearance of parasitic peaks. The boundary conditions for the heat conduction problem are completely determined by the symmetry of the Patterson distribution. The solution is sought in the independent region of a unit cell.

In this form we tested the sharpenening problem on one-dimensional distributions as in ref. 8, and we then applied it to the analysis of two-dimensional distributions with group pmm. The heat conduction equation

$$\partial u / \partial t = \partial^2 u / \partial x^2 + \partial^2 u / \partial y^2 \tag{2}$$

can be transformed, by the introduction of the difference operator, to a system of linear algebraic equations:

$$\begin{aligned} U_{i,j,k-1} &= (1+4\alpha)U_{i,j,k} - \alpha(U_{i+1,j,k} + U_{i-1,j,k}) \\ &\quad - \alpha(U_{i,j+1,k} - U_{i,j-1,k}), \quad 0 \leqslant i, j \leqslant n, \end{aligned} \tag{3}$$

where $U_{i,j,k-1}$ is the desired solution at the current stage, and $U_{i,j,k}$ is the solution at the previous stage, $\alpha = \tau / h^2$ (τ is the step in t, and h is the step in the spatial variable). The initial value U_{ijk} is specified by the original Patterson distribution. For a grid, 60 × 60, n is 30, and this corresponds to the boundary of the independent part of the unit cell for the group pmm.

The symmetry conditions imposed by the chosen symmetry group are

$$\begin{gathered} U_{i,j,k} = U_{-i,j,k}; \quad U_{i,j,k} = U_{i,-j,k}; \\ U_{n+1,j,k} = U_{n-1,j,k}; \quad U_{i,n+1,k} = U_{i,n-1,k} \end{gathered} \tag{4}$$

for any k. The difference equation (3) approximates the heat conduction equation (2) with an accuracy $O(h^2 + \tau)$ from refs. 9 and 10.

Remembering that the solution of the inverse heat problem is unstable, we introduce the regularization. As the solution of (3) we take those $\{U_{i,j,k-1}\}$ which realize the minimum of the functional

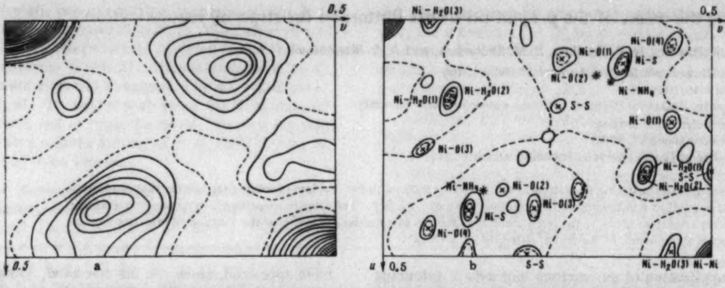

Fig. 1. Patterson distribution of the projection P(u, v) (a) and the results of the sharpening of the Patterson distribution (b). The dotted line indicates the zero level of the original Patterson distribution; the crosses denote interatomic vectors, Ni denote other atoms, and S−S denote those appearing under the sharpening, while the asterisks denote vectors of this group which have not appeared.

$$\Phi=\sum_{i,j=0}^{n}\{U_{i,j,k-1}-[(1+4\alpha)U_{i,j,k}-\alpha(U_{i+1,j,k}+U_{i-1,j,k})$$
$$-\alpha(U_{i,j+1,k}+U_{i,j-1,k})]\}^2+\gamma\sum_{i,j=0}[(U_{i,j,k-1}-U_{i-1,j,k-1})^2$$
$$+(U_{i,j,k-1}-U_{i,j-1,k-1})^2]+\beta\sum_{i,j=0}(U_{i,j,k-1})^2,$$

where γ and β are the regularization parameters. If we now apply the extremal and boundary conditions, we obtain a system of linear algebraic equations, which can be written in matrix form as follows:

$$\begin{gathered}A\mathbf{U}_{0,k-1}-2\gamma\mathbf{U}_{1,k-1}=\mathbf{F}_{0,k},\\ -\gamma\mathbf{U}_{i+1,k-1}+A\mathbf{U}_{i,k-1}-\gamma\mathbf{U}_{i-1,k-1}=\mathbf{F}_{i,k}\\ (i=1,2,\ldots,n-1),\\ A\mathbf{U}_{n,k-1}-2\gamma\mathbf{U}_{n-1,k-1}=\mathbf{F}_{n,k},\end{gathered}\tag{5}$$

where

$$\mathbf{U}_{i,k-1}=(U_{i,0,k-1},\ldots,U_{i,n,k-1});\ \mathbf{F}_{i,k}=(F_{i,0,k},\ldots,F_{i,n,k}),$$

and

$$A=\begin{pmatrix}1+\beta+4\gamma & -2\gamma & 0 & 0\ldots & 0 & 0 & 0\\ -\gamma & 1+\beta+4\gamma & -\gamma & 0\ldots & 0 & 0 & 0\\ \cdot & \cdot & \cdot & \cdot\cdot\cdot\cdot & \cdot & \cdot & \cdot\\ \cdot & \cdot & \cdot & \cdot\cdot\cdot\cdot & \cdot & \cdot & \cdot\\ 0 & 0 & 0 & 0\ldots-\gamma & 1+\beta+4\gamma & -\gamma & \\ 0 & 0 & 0 & 0\ldots 0 & -2\gamma & 1+\beta+4\gamma & \end{pmatrix}.$$

The stability of the difference scheme has been proved. The system obtained is solved by iterative methods as in refs. 9 and 10.

For the role of test distributions for trying out this sharpening method and for selecting actual values of the parameters α, β, and γ, several theoretical Patterson syntheses were constructed; the peaks of these were specified by Gaussian exponents. The parameters were selected by the scanning method. The optimality criterion for the parameters obtained was taken to be the satisfaction of the four conditions formulated above. The solution of each variant of the sharpening problem took approximately 10 to 12 minutes on an M-220 computer.

The efficiency of the method set out above was tested on the known crystal structure of $(NH_4)_2Ni(SO_4)_2 \cdot 6H_2O$ of ref. 11, Federov group $P2_1/a$; the cell parameters are a = 9.181, b = 12.459, c = 6.239 Å, β = 106°57'; Z = 2.

The sharpening was carried out for the two-dimensional projection P(u, v) having symmetry pmm. The number of independent reflections hk0 is 178.

Table 1 shows the values of the coordinates of the atoms taken from ref. 11 and used to construct the vector diagram; the sharpened Patterson distribution is compared with this below. Figure 1 shows the Patterson distribution obtained for F^2_{hk0} as Fig. 1a; Fig. 1b shows the final distribution obtained as a result of the application of the method proposed in this article, the sharpening being done on a grid 60 × 60. The values of the parameters under which the sharpening was done were γ = 0.1, τ = 0.01, and β = 13. Three t steps were made for the sharpening, and the individual peaks appeared sequentially.

When these are compared with the vector diagram, it is clear that all the Ni−O peaks have been faithfully distinguished along with the Ni−Ni and Ni−S peaks, all except one of the Ni−O peaks; the Ni−O_{H_2O} peaks are more definitely separated out than the Ni−N_{NH_4} peaks. The Ni−N_{NH_4} vectors do not appear in the required positions. When one compares the original distribution with the

TABLE 1. Coordinates of Atoms in the Crystal $(NH_4)_2Ni(SO_4)_2 \cdot 6H_2O$

Coordinates	S	NH_4	O(1)	O(2)	O(3)	O(4)	$H_2O(1)$	$H_2O(2)$	$H_2O(3)$
x/a	0.091	0.133	0.089	0.117	0.220	−0.051	−0.167	0.161	0.006
y/b	0.636	0.347	0.729	0.679	0.570	0.573	0.106	0.110	−0.065

sharpened distribution, the clearer localization of three peaks in the sharpened diagram should be noted; these peaks correspond to S−S vectors. There is some distortion of the relative heights of the Harker peaks. The highest peaks in general position are the Ni−S peaks and the S atom is fairly accurately localized by them.

The next highest group of peaks consists of two Ni−H_2O peaks which intersect within the grid step (these are in general position) and three peaks in special position; two Ni−H_2O peaks and one S−S peak.

The third group of peaks is formed by vectors corresponding to spacings Ni−O, S−S and by concentrations of peaks of the type S−O and O−O, which intersect within the grid steps. It should be noted that all the peaks obtained are at the required positions and there is not one peak which cannot be explained from the vector diagram.

A general comparison of the original Patterson distribution and that obtained from the sharpening shows how effective the above method is for heightening the contrast in the Patterson function.

We have recently applied the above method deciphering several actual structures.

---

[1] A. L. Patterson, Z. Kristallogr., A90, 543 (1935).

[2] V. I. Simonov and B. M. Shchedrin, Kristallografiya, 11, 536 (1966) [Sov. Phys. – Crystallogr., 11, 475 (1967)].

[3] R. Hosemann and S. N. Bagchi, Direct Analysis of Diffraction by Matter, North-Holland, Amsterdam (1962).

[4] H. S. Carslaw and J. C. Jaeger, Conduction of Heat in Solids, Oxford (1959).

[5] A. N. Tikhonov, Dokl. Akad. Nauk SSSR, 151, 501 (1963).

[6] A. N. Tikhonov, Dokl. Akad. Nauk SSSR, 153, 49 (1963).

[7] M. A. Porai-Koshits, A Practical Course in X-Ray Analysis [in Russian], Vol. 2, Izd. MGU (1960).

[8] N. P. Zhidkov, A. I. Kvitashvili, B. M. Shchedrin, and A. E. Shvelashvili, Soobshch. Akad. Nauk GruzSSR, 66, 81 (1972).

[9] I. S. Berezkin and N. P. Zhidkov, Computation Methods [in Russian], Vol. 2, Fizmatgiz, Moscow (1962).

[10] A. N. Tikhonov and A. A. Samarskii, Equations of Mathematical Physics [in Russian], Nauka, Moscow (1972).

[11] N. W. Grimes, H. F. Kay, and M. W. Webb, Acta Crystallogr., 16, 823 (1963).

Applicability of Zachariasen's equations to calculations of the integral intensity scattered by a "thick" single crystal in the Bragg symmetry case for any dislocation density

A. V. Kuznetsov

Petrozavodsk State University

(Submitted April 24, 1972; resubmitted November 15, 1972)
Kristallografiya, 18, 944-949 (September-October 1973)

An equation which describes the integral intensity scattered by a "thick" crystal in Bragg geometry as a function of the dislocation density was derived on the basis of ideas regarding dislocations and Zachariasen's theory of a real crystal. At high and low dislocation densities the equation thus derived yields equations for ideal and ideally mosaic crystals. Experimental data published in the literature satisfactory obey the theoretical relationship.

In 1967 Zachariasen published a paper[1] in which equations were derived for calculating the integral intensity by taking into account the effects of primary and secondary extinction in crystals for which $\mu\overline{T} < 1$ (μ is the linear absorption coefficient, $\overline{T}$ the mean path length of the beam in the crystal). By means of these equations, the effects of extinction are calculated in a novel way, and the effects which disorientation as well as the linear sizes of the mosaic blocks have on secondary extinction are taken into account.

According to Zachariasen's theory,[1] the experimental integral intensity R_e can be represented by

$$R_e = R_{\mathrm{id.mos}}y, \tag{1}$$

where $R_{\mathrm{id.mos}}$ denotes the integral intensity calculated from the equation for an ideally mosaic crystal; y is the extinction parameter.

The theoretical equation for the extinction parameter y reads

$$y = (1+2x)^{-1/2}, \tag{2}$$

where

$$x = \frac{2}{3}\frac{\bar{t}_\perp}{\lambda}Q_0\left\{\bar{t} + (\bar{T}-\bar{t})\left[1+\left(\frac{2}{3}\frac{\bar{t}_\perp}{\lambda g}\right)^2\right]^{1/2}\right\}. \tag{3}$$

Here, $\overline{T}$ and $\overline{t}$ denote the mean path length of the beam in the crystal and in a mosaic block, respectively; g is a coefficient related to the effect of secondary extinction; parameter $\bar{t}_\perp$ has a less defined physical meaning, and its value under actual conditions will be given below.

Besides Eq. (2), Zachariasen gave several other equations for the extinction parameter, in particular

$$y = \operatorname{th}\sqrt{3x}\,/\,\sqrt{3x}, \tag{4}$$

and the conclusion as to what equation gives the best agreement with the experimental data was left to depend on the outcome of the experiment. This is because several simplifications had to be made in the derivation of Eq. (2).

An experimental check of Eq. (2) was carried out in papers by Zachariasen[2] and several other authors,[3-5] and it was shown that the theoretical values agree fairly well with the experimental data on crystals with a very strong extinction. It should be noted that the reverse view is also advocated. For example, Werner[6] draws attention to his own study regarding the calculation of secondary extinction, and criticized that part of Zachariasen's paper in which a calculation is carried out for an ideal crystal on the basis of kinematic theory. However, Zachariasen's calculation is restricted to a very small mosaic block, in which absorption can be neglected, and where the dynamic theory yields results differing only slightly from those resulting from the kinematic theory. Moreover, both in the former paper and in later papers Zachariasen points out that the theory refers to crystals in which the size of a mosaic block is much smaller than the crystal size.

In ref. 7 Zachariasen extended his theory to crystals with an arbitrary value for the product $\mu\overline{T}$. The main idea is that (according to conclusions drawn from the dynamic theory) it is not a single wave with the absorption coefficient μ_0 which is propagated in a crystal, but four waves with the absorption coefficients $\mu = \mu_0[1 \pm k_pP\exp(-M)]$. The coefficient k_p is determined by the degree of perfection of the crystal, and tends to unity as the size of the mosaic blocks is reduced (increasing dislocation density).

According to this paper the extinction parameter should read

$$y = \frac{A_{+1}y_{+1} + A_{-1}y_{-1} + P^2(A_{+P}y_{+P} + A_{-P}y_{-P})}{2A_0(1+P^2)}; \tag{5}$$

here, $A_{\pm P}$ denotes the absorption factor for the absorption coefficient $\mu = \mu_0[1 \pm k_PP\exp(-M)]$; $y_{\pm P}$ corresponds to the extinction parameters in Eqs. (2) or (4), but in a calculation of x it is necessary to take into account the polarization factor P and the absorption coefficient $\mu = \mu_0[1 \pm kpP\exp(-M)]$ if the absorption coefficient occurs in the corresponding equation.

The value of parameter k_P should be calculated from the equation

$$k_P = \frac{z}{\pi\sqrt{1-z^2}}\ln\frac{1+\sqrt{1-z^2}}{1-\sqrt{1-z^2}}, \tag{6}$$

where

$$z = \frac{4}{3}\bar{t}_\perp\left[1+\left(\frac{2}{3}\frac{\bar{t}_\perp}{\lambda g}\right)^2\right]^{-1/2}\frac{e^2}{mc^2}\frac{\lambda}{\sin 2\theta}FN\exp(-M)P. \tag{7}$$

Although in Zachariasen's papers it is stated that the theory is applicable when the size of the mosaic blocks is much smaller than the crystal size, Eq. (2) can be applied to an ideal crystal, too. In fact, for an ideal crystal $\overline{T} = \overline{t}$, so that in Eq. (3) for x the second term, related to the effect of secondary extinction, disappears and only the first term, related to the effect of primary extinction, i.e., to the effect inherent in an ideal crystal, remains.

Therefore, the aim of the present study was to check how close the predictions of Zachariasen's equations at $\overline{T} = \overline{t}$ come to those resulting from the dynamic theory. It is further attempted to derive an equation for the integral intensity scattered by a "thick" single crystal in the Bragg symetry case as a function of the dislocation density, starting from Zachariasen's theory and ideas on dislocations. The following aims are pursued: First, at high dislocation densities the equation derived should yield the same dependence as follows from the equations derived by Zachariasen; second, at a dislocation density equal to zero the equation derived should be identical to that following from the dynamic theory. The Bragg symmetry case was chosen because the literature contains several papers[8–11] in which the dependence of the integral intensity on the dislocation density was measured. This makes it possible to check the equation derived against experimental evidence. Moreover, the Bragg case is simpler than the Laue case, for in the Bragg case the extinction parameter y can vary from zero to unity, whereas in the Laue case the variation goes from zero to infinity. In the Bragg symmetry case $\overline{T} = T_0/\sin\vartheta$, where T_0 denotes the size of the crystal measured at right angles to the surface. Similarly we take that for a mosaic block $\overline{t} = t/\sin\vartheta$. Parameter $\overline{t}_\perp = t_0 \cos\vartheta$. Strictly speaking, the two last equations hold for a mosaic block having the shape of a plane-parallel slab. It is supposed here that these equations hold also for a mosaic block having the shape of a parallelepiped with edge t_0, which according to several papers, in particular ref. 6, can be represented by

$$t_0 = 1/\rho^{1/2}. \tag{8}$$

The equation turned out to hold at high dislocation densities, but not at low ones: At $\delta \to 0$, t_0 should tend to T_0. This can be achieved by replacing Eq. (8) by

$$t_0 = T_0/(1 + T_0\rho^{1/2}). \tag{9}$$

Equation (9) was chosen because it is quite simple and yields correct results at $\rho = 0$ and high dislocation densities. If $\overline{t}$ and $\overline{t}_\perp$ are replaced by t_0, and t_0 in its turn is expressed by the dislocation density according to Eq. (9), we get the following equations for x and z:

$$x = \frac{1}{3}\frac{Q_0 \sin 2\theta}{\lambda}\left(\frac{T_0}{\sin\theta}\right)^2 \frac{(1 + \alpha T_0\rho^{1/2})}{(1 + T_0\rho^{1/2})^2}, \tag{10}$$

$$z = \frac{2}{3}\frac{T_0}{(1 + T_0\rho^{1/2})}\alpha\frac{e^2}{mc^2}\frac{\lambda}{\sin\theta}NF\exp(-M)P. \tag{11}$$

In an analogous way the parameter

$$\alpha = \left[1 + \left(\frac{2}{3}\frac{\overline{t}_\perp}{\lambda g}\right)^2\right]^{-1/2} \tag{12}$$

can be expressed by the dislocation density. According to ref. 12 we have

$$g = t_0/3\sqrt{\pi}b, \tag{13}$$

where b is the modulus of the Bragg vector.

Moreover, in the calculation of α it is convenient to take $t_\perp = t_0$. This assumption is based on the following facts: In the calculation of x at low values of ρ, parameter α does not play a role, and at high dislocation densities Zachariasen's approximation $\overline{t}_\perp = \overline{t} = t_0$ can be used.

In the latter case

$$\alpha = [1 + (2\sqrt{\pi}b/\lambda)^2]^{-1/2} \approx \lambda/2\sqrt{\pi}b. \tag{14}$$

For the crystals to be considered in this paper, $b = \sqrt{2}a/2$.

The crystal size T_0 at right angles to the surface of the sample occurs in the equations for x and z. For a 'thick' crystal in the Bragg symmetry case $\overline{T} = 1/\mu$, and hence $T_0 = \sin\vartheta/\mu$.

Starting from Eq. (5) and bearing in mind the above considerations, we can represent the extinction parameter y in the following way:

$$y = \frac{1}{2(1 + \cos^2 2\alpha\cos^2 2\theta)}\sum_P \{[1 + k_P P\exp(-M)]^2 + 2x_P\}^{-1/2}, \tag{15}$$

$$x_P = \frac{P^2}{3}\frac{Q_0\sin 2\theta}{\mu_0^2\lambda}\frac{\left(1 + \frac{\lambda}{\sqrt{2\pi}a}\frac{\sin\theta}{\mu_0[1 + k_P P\exp(-M)]}\rho^{1/2}\right)}{\left(1 + \frac{\sin\theta}{\mu_0[1 + k_P P\exp(-M)}\rho^{1/2}\right)^2}. \tag{16}$$

Parameter P takes the four values: ± 1 and $\pm|\cos\alpha \cdot \cos 2\vartheta|$; the equation for z, which is needed for calculating k_P, reads

$$z = \frac{2}{3}\frac{1}{\{\mu_0[1 + k_P P\exp(-M)] + \sin\theta\rho^{1/2}\}} \times \frac{\lambda^2}{\sqrt{2\pi}a}\frac{e^2}{mc^2}NF\exp(-M)P. \tag{17}$$

Calculating the extinction parameter should be done as follows: Calculate z from Eq. (17) for the four values of P, which makes it possible to calculate k_P from Eq. (6), and thus find the extinction parameter y. However, since z depends on k_P, this creates a situation resembling a vicious circle. Nevertheless, the question as to whether at $\rho = 0$ y yields the correct value for the $R_{dyn}/R_{id.mos}$ ratio can be answered unambiguously.

The extinction parameter y at $\rho = 0$ was calculated for the (200), (400), and (800) lines of KCl from the Mo Kα radiation passed through a LiF(200) monochromator. The square $[1 + k_P P\exp(-M)]^2 < 2.7$ for the maximum value of k_P according to ref. 7 equals $2/\pi$. For all lines mentioned above $2x_P \gg [1 + k_P P\exp(-M)]^2$. For example $2x_{P=\pm1} = 660$ for the Mo Kα (200) KCl line, $2x_{P=\pm1} = 226$ for the (400) line, and $2x_{P=\pm1} = 30$ for the (800) line. Therefore, the result of the calculation varies only slightly, and hardly depends on what k_P value is chosen from the possible range between 0 and $2/\pi$. Application of Eq. (15) yields the following y values for the above-mentioned lines at $\rho = 0$: 0.042, 0.066, and 0.21. An accurate value of $y = R_{dyn}/R_{id.mos}$ at $\rho = 0$ can be calculated on the basis of ref. 13. Calculated values of R_{dyn} yield the following y values: 0.055, 0.091, 0.25. Although the relative difference between the data calculated from

Zachariasen's equation and the accurate values is quite noticeable, it should be kept in mind that y tends to unity as the dislocation density increases. A correction for the small absolute difference can be easily made, as will be shown below.

The example demonstrates that the product $k_pP\exp^{\circ}(-M)$ can be neglected in the case of strong interference lines, since it is small compared with $2x_p$. In the case of weak interference lines, for which $2x_p$ is much smaller, the product $k_pP\exp(-M)$ can also be neglected, because z, and consequently also k_p, is small, moreover, the product $k_pP\exp(-M)$ decreases becuase the thermal factor $\exp(-M)$ is reduced. These conclusions are confirmed by an analysis of the interference lines of a NaCl crystal irradiated with Mo Kα radiation and a Ge crystal irradiated with Cu Kα radiation.

Summing up, it can be taken that for all four polarization states of a "thick" crystal in the Bragg symmetry case $\mu=\mu_0$, and that the following equation can be employed for the extinction parameter:

$$y=\frac{1}{1+P^2}[(1+2x)^{-1/2}+P^2(1+2xP^2)^{-1/2}], \tag{18}$$

where

$$x=\frac{1}{3}\frac{Q_0\sin 2\theta}{\mu_0^2\lambda}\frac{\left(1+\frac{\lambda}{\sqrt{2\pi}\,a}\frac{\sin\theta}{\mu_0}\rho^{1/2}\right)}{\left(1+\frac{\sin\theta}{\mu_0}\rho^{1/2}\right)^2}, \tag{19}$$

$$P^2=\cos^2 2\alpha\cos^2 2\theta.$$

In order that the equation for the extinction parameter y yield correct values at $\rho=0$, too, it is necessary to replace the function $(1+2x)^{-1/2}$ by another function which will yield correct values also at small values of ρ (large values of x in Zachariasen's notation). This hint was given by Zachariasen himself and applied in ref. 5 to a crystal of cylindrical shape. The function $(1+nx)^{-1/n}$ comes closest to the function $(1+2x)^{-1/2}$ and satisfies the requirements mentioned. At small x values this function represents the same dependence as that following from the functions proposed by Zachariasen. The parameter n must be chosen so that y equals $R_{\mathrm{dyn}}/R_{\mathrm{id.mos}}$ at $\rho=0$. When the polarization factor is taken into account, the expression for the extinction parameter y reads

$$y=\frac{1}{1-P^2}[(1+nx)^{-1/n}+P^2(1+nxP^2)^{-1/n}]. \tag{20}$$

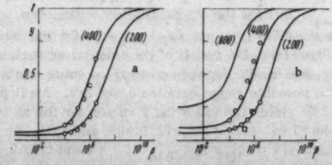

Fig. 1. Plots of the extinction parameter y versus the dislocation density in NaCl (a) and KCl (b) crystals. Mo Kα radiation, LiF (200) monochromator, experimental values: ○) data from ref. 10; □) data from ref. 11.

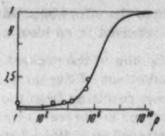

Fig. 2. Plot of the extinction coefficient y for the (333) line of Ge versus the dislocation density. Cu Kα radiation, Ge (333) monochromator; ○) experimental values derived from data in ref. 8.

As before, parameter x is found from Eq. (19). Parameter n is close to 2, so that the y values come close to those which follow from Zachariasen's equation, whatever the dislocation density. For example, for the (200)KCl line n = 2.25, for the (400) line n = 2.26, for the (800) line n = 2.35.

In Figs. 1 and 2 the theoretical values of the extinction parameter y for single crystals of NaCl, KCl, and Ge are shown and compared with experimental data from refs. 8, 10, and 11. In ref. 11 Mo Kβ radiation was used, but the theoretical values of the extinction parameter y for the (200)KCl lines of Mo Kα and Mo Kβ radiation are quite close to each other.

As can be seen in Figs. 1 and 2, the agreement between the theoretical and experimental data is quite satisfactory. Of course, Eq. (20) must be checked against other lines, other crystals, other radiations, but it seems quite improbable that the agreement between the experimental data of three papers and the theoretical values is accidental. This suggests that in the present stage Eq. (20) can be used for estimating dislocation densities in the range from 10^2 to 10^{10} cm^{-2}.

Of course, an accurate expression for the integral intensity as a function of the dislocation density can be derived only on the basis of the dynamic theory, and several studies in this field can be mentioned, for example refs. 14-16, but it is uncertain whether specific equations enabling the diffraction pattern to be determined for any dislocation density will be derived in the nearest future.

---

[1] W. H. Zachariasen, Acta Crystallogr., 23, 588 (1967).

[2] W. H. Zachariasen, Acta Crystallogr., A24, 212 (1968); A24, 324 (1968); A24, 425 (1968); A25, 102 (1969).

[3] S. Chandrasekhar, S. Ramaseshans, and A. K. Singh, Acta Crystallogr., A25, 140 (1969).

[4] M. J. Cooper, K. D. Rouse, and B. T. M. Willis, Acta Crystallogr., A24, 484 (1968).

[5] M. J. Cooper and K. D. Rouse, Acta Crystallogr., A26, 214 (1970).

[6] S. A. Werner, Acta Crystallogr., A25, 639 (1969).

[7] W. H. Zachariasen, Acta Crystallogr., A24, 421 (1968).

[8] S. Sh. Shil'shtein, Kristallografiya, 9, 727 (1964) [Sov. Phys.–Crystallogr., 9, 610 (1965)].

[9] T. V. Kuskova, E. L. Raikhel's, L. V. Smushkov, and T. V. Tetyunnikova, Fiz. Tverd. Tela, 9, 926 (1967).

[10] E. L. Raikhel's, L. V. Smushkov, and V. M. Trembach, Fiz. Tverd. Tela, 10, 1684 (1968) [Sov. Phys.–Solid State, 10, 1330 (1968)].

[11] É. F. Chaikovskii and L. B. Zagarii, Fiz. Tverd. Tela, 12, 1534 (1970) [Sov. Phys.–Solid State, 12, 1205 (1970)].

[12] J. A. Larson and C. L. Corey, J. Appl. Phys., 40, 2708 (1969).

[13] A. M. Afanas'ev and J. P. Perstnev, Acta Crystallogr., A25, 520 (1969).

[14] I. M. Dubrovskii, V. B. Molodkin, L. V. Tikhonova, and E. A. Tikhonov, Fiz. Met. Metalloved., 27, 21 (1969).

[15] M. Kuriyama and T. Miyakawa, Acta Crystallogr., A26, 667 (1970).

[16] É. D. Okun', Izv. Akad. Nauk BSSR, Ser. Fiz.—Matem. Nauk, No. 1, 107 (1970).

Crystal structure of the alkali titanosilicate labuntsovite

N. I. Golovastikov

Institute of Crystallography, Academy of Sciences of the USSR

(Submitted January 12, 1973)
Kristallografiya, 18, 950-955 (September-October 1973)

The crystal structure of labuntsovite $(K, Ba, Na, Ca)_8(Ti, Nb)_8(O, OH)_{16}[Si_4O_{12}]_4 \cdot nH_2O$ (Fedorov group I2/m, a = 14.18, b = 15.48, c = 13.70 Å, γ = 117°, Z = 2) is determined. The structure is solved by minimizing the three-dimensional Patterson function, with successive approximations to the electron density distribution, the parameters then being refined by the method of least squares. The two halves of the unit cell of this crystal (along the b axis) are very similar to each other, the difference being of the nature of a partial lack of order.

Labuntsovite was first discovered by A. N. Labuntsov in the Khibinsk and Lovozersk alkali massifs (Kol'sk peninsula) in 1926 and described under the name of titanoelipidite.[1] In 1955 Semenov and Burova[2] showed that titanoelpidite was a new mineral with a chemical formula of $(K, Na, Ba, Ca, Mn)(Ti, Nb)[Si_2(O, OH)_7] \cdot 0.6H_2O$, and called it labuntsovite. Later Semenov[3] described several varieties of labuntsovite with considerably differing chemical compositions; he suggested that these varieties formed an isomorphic series together with another titanium–niobium silicate, nenadkevichite, although nenadkevichite and labuntsovite had different unit cells. The two extreme representatives of the proposed series (on the labuntsovite side) are characterized by the following compositions: brown labuntsovite $(K_{0.43}Na_{0.29}Ba_{0.16}Ca_{0.06}Mn_{0.09})(Ti_{0.89} \cdot Nb_{0.03}Fe_{0.05}Mg_{0.03})[Si_{1.83}Al_{0.07}O_{5.79}(OH)_{1.21}] \cdot 0.6H_2O$, and light-brown labuntsovite $(K_{0.16}Na_{0.22}Ba_{0.11}Ca_{0.18})(Ti_{0.77} \cdot Nb_{0.19}Fe_{0.07})[Si_{1.54}Al_{0.07}O_{4.48}(OH)_{2.52}] \cdot 0.38H_2O$.

Our own labuntsovite samples were obtained from E. I. Semenov, and we assumed that they belonged to the brown variety. Oscillation and rotation x-ray diffraction photographs gave the parameters of the monoclinic cell of labuntsovite as: a = 14.18, b = 7.74, c = 13.70 Å, γ = 117°. For a density of 2.96–2.90 g/cm^3 the cell contains about eight formula units of labuntsovite. The systematic extinctions of the reflections indicated a centered B face of the cell, so that the labuntsovite crystals belonged to one of the three Fedorov groups B2/m, B2, or Bm.

Semenov received a private communication from C. Milton, who was studying American labuntsovite samples; the unit cell parameters in this case were a = 14.27, b = 15.57, c = 13.75 Å, γ = 116°55' with a fixed Fedorov group of I2/m. These parameters are quoted in the Mineralogical Tables of H. Strunz,[4] with a mention of ref. 2, although the parameters of the labuntsovite cell were not given in the latter paper. Attempts at detecting any intermediate layer lines on the x-ray rotation and Weissenberg photographs which would represent a doubling of the 7.74 Å spacing failed, although in the last stage of the structural analysis these layers did appear in oscillation x-ray photographs taken with a long exposure; they consisted not of spots but of weak, diffuse strokes, thus indicating a partial loss of order by the crystal structure.

The x-ray diffraction pattern of the labuntsovite was recorded photographically in a Weissenberg goniometer (Mo radiation, layer lines h0l–h6l, hk0–hk2, and 0kl). The intensities of 1450 independent, nonzero reflections were measured with the aid of a photometric density scale.

In the P(xyz) Patterson function there were no sharply expressed "bundles" of peaks corresponding to 2/m symmetry; together with the weak piezoeffect, this led us to exclude the B2/m group from the class of possible Fedorov groups in the initial stages. However, a statistical analysis of the h0l and hk0 reflections indicated that the corresponding projections of the crystal structure had centrosymmetrical properties, and in the course of the structural determination we finally chose the B2/m group, with a center of symmetry.

The results obtained by minimizing the Patterson function with respect to two interatomic vectors were used as a basis for a series of approximations of the three-dimensional electron-density distribution, first in the Bm and B2 Fedorov groups, then in the B2/m. As a result of several approximations, Ti octahedra and four-fold silicon–oxygen rings were clearly revealed in the structure (Figs. 1 and 2). The K(Ba) and Na(Ca) atoms were located less reliably, a number of difficulties arising in connection with the disposition of the K_1 atoms. Among the electron-density peaks identified with the O atoms forming the environment of the Ti_1 atom, two were sharply distinguished by their height. The distances from these peaks to the closest O atoms corresponded to the generally accepted distances between K and O atoms. Attempts at eliminating the Ti_1 atom from the calculations (this atom being superfluous with respect to the formula) and putting K atoms instead of the O atoms at the vertices of the Ti_1 octahedron made the R factor less favorable. However, on simultaneously specifying a Ti_1 atom and K atoms in place of the O atoms, the R factor fell by 5%. Furthermore, a strong peak at a distance of about 2.1 Å from the origin corresponded to the Ti_1–K_1 interatomic vector in the Patterson function, creating perplexity. One way out

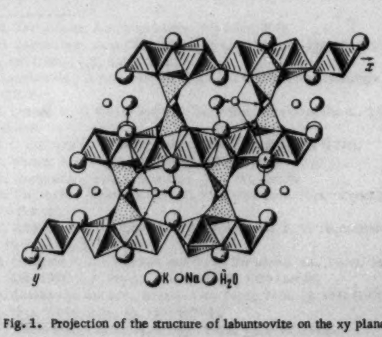

Fig. 1. Projection of the structure of labuntsovite on the xy plane.

TABLE 1. Coordinates of the Atoms (in the Half Cell) and Individual Temperature Parameters

Atom	x/a	y/b'	z/c	Multiplicity of atom	B
Ti_1	0	0	0	1.50	0.935
Ti_2	0	0	0.2291	3.80	1.065
Ti_3	0.2500	0	0.2500	3.92	1.025
Si_1	0.1806	0.2506	0.3889	8	0.889
Si_2	0.2077	0.3028	0.1105	8	0.787
$K_1(+OH)$	0.0892	0.8464	0	4.21	1.712
K_2	0.0807	0.8025	0.5000	2.61	2.328
Na	0.0889	0.4907	0.2355	2.74	2.084
O_1	0.0979	0.8379	0.2262	8	1.584
O_2	0.0815	0.1718	0.1188	8	0.874
O_3	0.0819	0.1957	0.3212	8	1.179
O_4	0.2365	0.1127	0.3739	8	1.804
O_5	0.2331	0.5246	0.1287	8	1.516
O_6	0.2271	0.7630	0.3182	8	0.997
O_7	0.2456	0.2836	0	4	1.100
O_8	0.1373	0.2287	0.5000	4	1.149
$(H_2O)_1$	0.0182	0.5092	0.1161	3.34	2.448
$(H_2O)_2$	0.0231	0.5061	0.3444	3.51	2.572

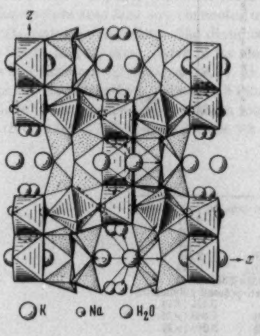

Fig. 2. Projection of the labuntsovite structure in the direction of the y axis.

of this apparently unacceptable situation (the Ti and K atoms with a mutual distance of 2.09 Å, not separated in any way) was that of doubling the b period, i.e., passing to the Milton cell. In half of the positions initially fixed as Ti_1 these atoms may then not be present at all, while the pair of O ligands is replaced by K cations in 11-pointed polyhedra, connected by a two-fold axis, with one common face.

Suitable positions for the Na atoms were found not far from the two-fold axis passing through the middle of the A face of the cell; the two O atoms separating the pair of Na atoms could then only lie on the two-fold axis, whereupon the Na–O distances would be shorter than normal. The transition to the double cell eliminated this two-fold axis, reduced the number of positions for the Na atoms by a factor of 2, and provided more suitable positions for the O atoms.

On passing to the double cell, the need arose for additional information as to the intermediate (odd) layers of the reciprocal lattice. An electron density synthesis calculated from the existing even layers only gave a superposition of the two halves of the double cell, with a number of indeterminacies, arising primarily on account of the fact that one set of equivalent points in the half cell (Fedorov group B2/m) transformed into two different sets of equivalent points on doubling the cell (Fedorov group I2/m). Thus the Na atom, together with two O atoms from its environment, may be sited in two different ways on different sides of the vanishing two-fold axis. The K_2 atoms, which, in the half cell, only partly fill one set of equivalent points, occupy two sets of equivalent points in the double cell, and the question arises as to the distribution of the K_2 between these two positions. The K_1 atoms and the O atoms from the Ti_1 octahedron merge on superposition, and we can only establish their average position, whereas in actual fact their coordinates may be slightly different. These ambiguities are hard to resolve simply from crystal-chemical considerations, since the alternative positions have very little crystal-chemical differences. As already mentioned at the beginning of the article, the odd layer lines in the present case indicate a state of disorder in the structure. This state of disorder, and also the very considerable difference in the K, Ba, Na, and Ca content of different samples of labuntsovite are evidently attributable to the considerable degree of freedom which exists in the disposition of the atoms of these elements, whence also the possibility of the replacement of tetravalent Ti by pentavalent Nb.

The least-squares refinement was only carried out by reference to the even layers of the reciprocal lattice (along the b* axis), since it was assumed that the atoms might lie arbitrarily close to the two-fold axes, which are obligatory in the half cell (Fedorov group B2/m), but vanish on doubling it. Apart from the coordinates of the atoms, their individual isotropic temperature parameters and the multiplicities of the Ti, K, and Na atoms were also refined, as well as the two O atoms from the Na polyhedron, later taken as water molecules. As a result of successive approximations of the electron-density distribution, the R factor based on the three-dimensional set $|F_{hkl}|$ fell to 0.178. The least-squares refinement reduced this factor to 0.132. Table 1 gives the coordinates of the atoms in the half cell derived from this refinement, their multiplicities, and their individual isotropic temperature parameters. Although the diffuseness of the odd layer lines indicates structural disorder, to a first approximation the structure may nevertheless be regarded as or-

TABLE 2. Coordinates of the Atoms in the Double Cell

Atom	x/a	y/b	z/c	Multiplicity of position	Multiplicity of position (from MLS refinement)
Ti_1	0	0	0	2	3.06
Ti_2	0	0	0.2291	4	3.80
Ti_2'	0	0.5	0.2291	4	3.80
Ti_3	0.25	0	0.25	4	3.92
Ti_3'	0.25	0.5	0.25	4	3.92
Si_1	0.1806	0.1253	0.3889	8	
Si_1'	0.1806	0.6253	0.3889	8	
Si_2	0.2077	0.1514	0.1105	8	
Si_2'	0.2077	0.6514	0.1105	8	
K_1	0.0892	0.4232	0	4	6.74
K_2	0.0807	0.4013	0.5	4	2.61
K_2'	0.0807	0.9013	0.5	4	2.61
Na	0.0889	0.7453	0.2355	8	5.47
O_1	0.0979	0.4440	0.2262	8	
O_1'	0.0979	0.9440	0.2262	8	
O_2	0.0815	0.0859	0.1188	8	
O_2'	0.0815	0.5859	0.1188	8	
O_3	0.0819	0.0979	0.3212	8	
O_3'	0.0819	0.5979	0.3212	8	
O_4	0.2365	0.0564	0.3739	8	
O_4'	0.2365	0.5564	0.3739	8	
O_5	0.2331	0.2623	0.1287	8	
O_5'	0.2331	0.7623	0.1287	8	
O_6	0.2271	0.3815	0.3182	8	
O_6'	0.2271	0.8815	0.3182	8	
O_7	0.2456	0.1418	0	4	
O_7'	0.2456	0.6418	0	4	
O_8	0.1373	0.1144	0.5	4	
O_8'	0.1373	0.6144	0.5	4	
OH	0.0892	0.9232	0	4	
$(H_2O)_1$	0.0182	0.2546	0.1161	8	6.67
$(H_2O)_2$	0.0231	0.2530	0.3444	8	7.03

TABLE 3. Interatomic Distances in Å

Ti octahedron	
$Ti_1 — O_2$	2.082 (×4)
$Ti_1 — OH$	2.082 (×2)
Average 2.082	
Ti_2 octahedron	
$Ti_2 — O_1$	1.940 (×2)
$Ti_2 — O_2$	1.933 (×2)
$Ti_2 — O_3$	1.899 (×2)
Average 1.944	
Ti_3 octahedron	
$Ti_3 — O_1$	1.954 (×2)
$Ti_3 — O_4$	1.953 (×2)
$Ti_3 — O_6$	1.935 (×2)
Average 1.947	
Si_1 tetrahedron	
$Si_1 — O_3$	1.570
$Si_1 — O_4$	1.599
$Si_1 — O_5$	1.615
$Si_1 — O_6$	1.621
Average 1.601	
Si_2 octahedron	
$Si_2 — O_2$	1.611
$Si_2 — O_5$	1.590
$Si_2 — O_6$	1.578
$Si_2 — O_7$	1.636
Average 1.604	
Na five-pointed polyhedron	
$Na — O_3$	2.511
$Na — O_5$	2.432
$Na — O_6$	2.401
$Na — (H_2O)_1$	2.240
$Na — (H_2O)_2$	2.340
Average 2.385	
K_1 eleven-pointed polyhedron	
$K_1 — O_1$	3.112 (×2)
$K_1 — O_2$ (1)	2.868 (×2)
$K_1 — O_2$ (2)	3.019 (×2)
$K_1 — O_4$	2.917 (×2)
$K_1 — O_7$	3.062 (×1)
$K_1 — (H_2O)_1$	2.816 (×2)
Average 2.957	
K_2 eleven-pointed polyhedron	
$K_2 — O_3$	3.360 (×2)
$K_2 — O_4$	2.957 (×2)
$K_2 — O_6$	3.340 (×2)
$K_2 — O_7$	2.829 (×1)
$K_2 — O_8$ (1)	2.990 (×1)
$K_2 — O_8$ (2)	2.994 (×1)
$K_2 — (H_2O)_2$	2.950 (×2)
Average 3.003	

dered, within the framework of the doubled unit cell and the Fedorov I2/m, and the atoms will then have the coordinates indicated in Table 2. Table 3 gives the interatomic distances.

The balance of valences led to the conclusion that the two vertices of the Ti_1 octahedron contained not O atoms but OH groups (these were linked to only a single Ti_1 cation), while two H_2O molecules took part in the environment of the Na atoms (one of these also entered into the polyhedron around the K_1 atom, the other into the environment of the K_2 atom). The replacement of some of the O_1 atoms by OH groups was also quite possible.

The refinement of the multiplicities of the Ti, K, and Na cations revealed an excess multiplicity for the Ti_1 atom (1.5, for a multiplicity of the position in the half cell equal to unity), which might have been due to the partial replacement of Ti by Nb atoms. The multiplicity of the K_1 atoms (together with the OH groups) was found to be 4.2, or 3.4 without the OH groups, for a multiplicity of the position equal to two. Here the increase in multiplicity may be explained as being due to the replacement of K by Ba atoms. The multiplicities of the K_2 and Na (Table 2) show that the corresponding positions are only partly occupied by the atoms. We see from a comparison of the multiplicities of the atoms obtained by the refinement of the structure with the number of these in the formula of brown labunstovite that niobium (which is practically absent from the formula) plays a considerable part in the crystal under consideration, while the actual amount of sodium is lower than the formula would imply.

Projections of the structure of labuntsovite are shown in Figs. 1 and 2. In the direction of the *a* edge of the cell, infinite chains of Ti_2 and Ti_3 octahedra, connected by their vertices, stretch along the whole structure. The chains are connected into strips (lying in planes parallel to the B face of the cell) by octahedra containing Ti_1 atoms. Neighboring strips are linked by four-fold silicon–oxygen rings $[Si_4O_{12}]$, the planes of these being parallel to the c axis. The K atoms lie in m symmetry planes, in eleven-pointed figures of three types. The K_1 polyhedron touches the symmetrical K_1 polyhedron and the Ti_2 octahedron along the faces, and the Ti_3 octahedra and Si_2 tetrahedra along the edges. The K_2 and $K_2^{\prime}$ atoms lie in only slightly differing eleven-pointed polyhedra (owing to the different positions of the H_2O molecules relative to the K_2 and $K_2^{\prime}$ atoms). These eleven-pointed polyhedra have no faces in common with the other polyhedra; they are connected by their edges to the Na, Ti_3, and Si_1 polyhedra. The distances from the K_2 atom to the O_3 and O_8 atoms lying in its eleven-pointed polyhedron are rather long (3.34 and 3.36 Å). Without these atoms the K_2 polyhedron transforms into a heptahedron with very long edges (most of them longer than 4 Å). In the five-pointed polygon around the Na atom, two vertices are occupied by H_2O molecules. The sixth O atom (O_2), close to the Na atom, lies at 2.884 Å from the latter, as is often the case, this being greater than the ordinary Na–O distance (2.25–2.78 Å). On the basis of the foregoing structural data, the approximate formula of labuntsovite may be written: $(K, Ba, Na, Ca)_8(Ti, Nb)_9(O, OH)_{10} \cdot [Si_4O_{12}]_4 \cdot nH_2O$, in which $n \sim 7$ for our own sample.

As already mentioned, the disorder of the structure, indicated by the diffuse character of the odd layer lines in the oscillation photograph taken around the b axis, may evidently be attributed to the irregular replacement of Ti_1 octahedra by pairs of K_1 polyhedra, the ambiguous disposition of the Na atoms and the water molecules entering into their environment, and the different dispositions of the K_2 atoms with respect to their two positions in the I2/m space group found in the different subcells. Refinement of these "errors" in the structure awaits further research.

---

[1] A. N. Labuntsov, Dokl. Akad. Nauk SSSR, A, 39 (1926).

[2] E. I. Semenov and T. A. Burova, Dokl. Akad. Nauk SSSR, 101, 1113 (1955).

[3] E. I. Semenov, Tr. Inst. Mineralog., Geokhim. Kristallokhim. Redkozem. Elementov, 2, 102 (1959).

[4] H. Strunz, Mineralogische Tabellen, Akad. Verl.-Ges., Leipzig (1970).

Crystal structure of zinc fluoride tetrahydrate, $ZnF_2 \cdot 4H_2O$

B. V. Bukvetskii, S. A. Polishchuk, and V. I. Simonov

Institute of Crystallography, Academy of Sciences of the USSR

(Submitted April 18, 1972)
Kristallografiya, 18, 956-960 (September-October 1973)

From three-dimensional diffraction data, obtained at room temperature, the atomic structure of $ZnF_2 \cdot 4H_2O$ (a = 12.630, b = 5.288, c = 7.540 Å; $Pca2_1$, Z = 4) is determined. The structure is analyzed with the aid of the Burgers minimization function, and refined by the method of least squares to R = 5.06%. The atomic structure of $ZnF_2 \cdot 4H_2O$ and the possible hydrogen bonds in this compound are discussed.

The varied viewpoints on the atomic structures of the crystal hydrates of metal fluorides are due to the limited structural data on these compounds. By investigating the dihydrates of cadmium and mercury difluorides and the tetrahydrate of zinc difluoride, using infrared spectroscopy and NMR, Polishchuk and Khmeleva[1] were able to postulate that the water molecules in these crystal hydrates are in the coordination spheres of the metals and that the structures contain hydrogen bonds of the types O–H...O or O–H...F. However, Patil and Secco[2] do not regard the water molecules in $ZnF_2 \cdot 4H_2O$ as bound to the Zn atoms. A definite solution to this problem can be expected only from a complete structural determination of the compound. A group of Indian authors have tried to establish the atomic structure of $ZnF_2 \cdot 4H_2O$, but their first brief report[3] in 1965, in which they gave the unit-cell dimensions and found the symmetry group of the crystals to be acentric orthorhombic, was not followed by further publications.

Our experimental material – crystals of zinc fluoride tetrahydrate $ZnF_2 \cdot 4H_2O$ – was obtained by evaporation of zinc carbonate, dissolved in 40% HF, at room temperature, followed by further recrystallization from a weakly acid solution. X-ray diffraction of single crystals of $ZnF_2 \cdot 4H_2O$ obtained in this way confirmed that they are orthorhombic. The parameters of the primitive unit cell, found with a DRON-1 diffractometer, were a = 12.630 ± 0.002, b = 5.288 ± 0.01, c = 7.540 ± 0.001 Å; these are close to the values found by the Indian authors.[3] To obtain experimental three-dimensional diffraction data, we used a single crystal turned to a sphere 0.29 mm in diameter. The intensities of 443 independent nonzero reflections from six layer lines, $h0l - h5l$, were measured in Cu radiation with a Ni filter in a computer-controlled DAR-UM automatic diffractometer.[4] In converting the intensities to structure amplitudes, we made a correction for absorption of x rays in the specimen, $\mu R = 1.01$.

Analysis of the systematic extinctions led to the diffraction symmetry group $mmmPca-$, which corresponds to the two Fedorov groups $Pcam$ and $Pca2_1$. As the density is[3] d = 2.307 g · cm^{-3}, in this unit cell there must be four formula units $ZnF_2 \cdot 4H_2O$. Arranged in any fashion in the space group $Pca2_1$, the four Zn atoms will obey the symmetry of the orthorhombic holohedron $Pcam$. For this reason, localization of the Zn atoms by means of the three-dimensional Patterson function was performed with the symmetry $Pcam$. The vectors from the basis Zn atom to the three atoms linked with it by the symmetry enabled us to construct the Burgers minimization function of the fourth rank. The symmetry of this function was[5] $Pcam$. With marked deviation in the arrangement of the F and O atoms from the centrosymmetrical law for $M_4(r)$ there would be doubling of the number of light atoms in the unit cell. However, the number of maxima on $M_4(r)$ strictly corresponded to the chemical formula. The first steps in refining the structure were taken in the framework of the group $Pcam$ without differentiation of the F and O atoms. One basis Zn atom and two light atoms were localized on the mirror plane m, and two other light atoms in general positions for the group $Pcam$. All attempts to distinguish the F and O atoms with the symmetry $Pcam$ led to physically meaningless individual isotropic temperature parameters of the atoms, though the discrepancy factor was reduced to R = 6.7%. At this stage we rejected the centrosymmetrical Fedorov group and for further refinement of the structure used the space group $Pca2_1$. The new available set of positions of the F and O atoms rapidly led to arrangements of these atoms which are forbidden by the group $Pcam$. The method of least squares in the isotropic approximation of the thermal vibrations of the atoms (without allowing for H atoms) reduced the discrepancy factor to R = 5.4%. The final values of the coordinates and individual isotropic temperature factors of the basis atoms of the structure (without the H atoms) are listed in Table 1.

The electron density synthesis constructed from these coordinates confirmed the chosen positions of the F and O atoms and revealed a series of weak peaks, by means of which we tried to localize the H atoms. Further information on the positions of the H atoms was obtained from the general architecture of the atomic structure of $ZnF_2 \cdot 4H_2O$, which clearly showed that the F and O atoms are linked by hydrogen bonds.

The structure is based on fairly regular Zn octahedra, made up of four O atoms and two F atoms, in "trans" positions in the octahedron. Figures 1 and 2

TABLE 1. Coordinates and Isotropic Thermal Factors of Basis Atoms in $ZnF_2 \cdot 4H_2O$

Atoms	x/a	y/b	z/c	B	Atoms	x/a	y/b	z/c	B
Zn	0.124_8	0.203_1	0.250_0	0.81	O_2	0.283_7	0.337_1	0.257_7	1.38
F_1	0.101_7	0.450_8	0.041_4	0.85	O_3	0.466_0	0.917_9	0.243_0	1.63
F_2	0.147_4	0.946_8	0.446_9	0.44	O_4	0.092_3	0.473_9	0.438_9	0.76
O_1	0.162_4	0.930_2	0.060_0	1.22					

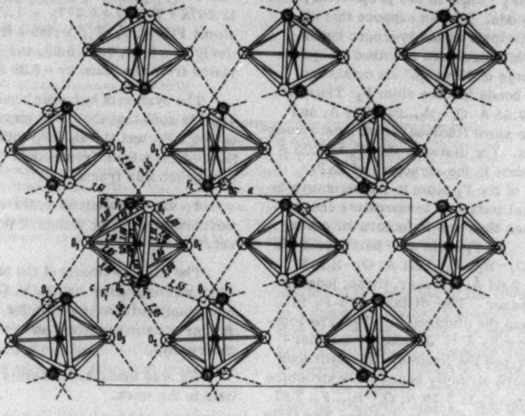
O3
O2
F1
F2
a
c
Zn
2.65
2.67

Fig. 1. Crystal structure of $ZnF_2 \cdot 4H_2O$, ac projection.

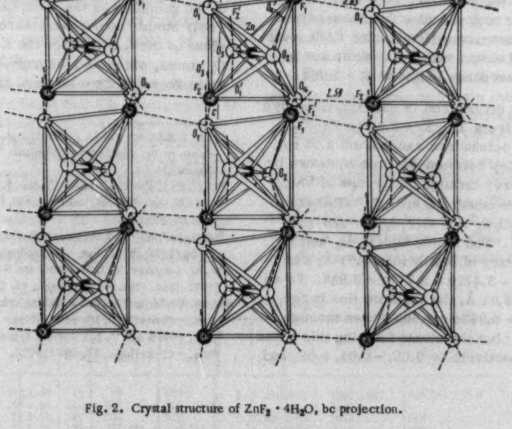
O3'
O2
O4'
F1
F2
F2'
Zn
O3
O1
O4
b
c
2.65
2.59

Fig. 2. Crystal structure of $ZnF_2 \cdot 4H_2O$, bc projection.

TABLE 2. Approximate Coordinates of Basis H Atoms in $ZnF_2 \cdot 4H_2O$

Atoms	x/a	y/b	z/c	Atoms	x/a	y/b	z/c
H_1	0.24	0.92	0.01	H_5	0.33	0.35	0.38
H_2	0.12	0.70	0.42	H_6	0.12	0.70	0.05
H_3	0.42	0.90	0.07	H_7	0.42	0.85	0.44
H_4	0.00	0.55	0.50	H_8	0.33	0.32	0.13

show the structure of $ZnF_2 \cdot 4H_2O$ in two projections, with the probable hydrogen bonds. We can suppose that all eight basis H atoms participate in the hydrogen bonds. Each of the F atoms in this structure is linked by hydrogen bonds to three O atoms of "foreign" Zn octahedra. The strongest hydrogen bonds involve atom F_2: The distances are $O_1-H_1...F_2$, 2.55 Å; $O_4-H_2...F_2$, 2.59 Å; and $O_3-H_3...F_2$, 2.66 Å. The same fluorine is also most strongly bound to the Zn atoms. The distance $Zn-F_2$ is 2.03 Å and is the shortest distance in the structure of $ZnF_2 \cdot 4H_2O$. This rigid fixing of the F_2 atom in the structure is reflected in the individual isotropic temperature factors: $B_{F_2} = 0.44$ Å^{-2}, much less than the B factors of other atoms in the structure. The F_1 atom also participates in three hydrogen bonds: $O_4-H_4...F_1$, 2.61 Å; $O_1-H_6...F_1$, 2.65 Å; and $O_2-H_5...F_1$, 2.65 Å; however, these, judging by the distances, are weaker. The distance $Zn-F_1$ is 2.07 Å, much greater than the distance $Zn-F_2$. The temperature factor is $B_{F_1} = 0.85$ Å^{-2}. Judging by the thermal vibration parameter and the lengths of the hydrogen bonds, the atom O_4 is more strongly bound in the structure than the atom F_1: $O_4-H_2...F_2$ is 2.59 Å; $O_4-H_4...F_1$, 2.61 Å; and $O_2-H_8...O_4$, 2.95 Å, whereas the distance $Zn-O_4$ is 2.06 Å. We can postulate an eighth hydrogen bond in the structure, between the atoms $O_3-H_7...O_1$, with a length of 2.88 Å. The above probable hydrogen bonds enabled us, on the above electron density distribution, to choose maxima which might be identified with the H atoms. Table 2 lists the rough coordinates of the H atoms, taken from the electron density synthesis. We did not refine the coordinates of the H atoms. We give them here only so as to indicate the region of the unit cell in which these atoms should be sought by the neutron diffraction or NMR method. Allowance for the H atoms with the coordinates in Table 2 reduces the discrepancy factor to R = 5.06%.

Distortion of the Zn octahedron is characterized by a scatter of the distances from $Zn-F_2 = 2.03$ to $Zn-O_2 = 2.14$ Å; the edges of the octahedron range from 2.85 to 3.04 Å; the dihedral angles between the planes, drawn by the method of least squares through the groups of four equatorial atoms of the octahedron, are: 71° ($F_1O_1O_4F_2$ and $O_1O_2O_3O_4$); 84° ($O_1O_2O_3O_4$ and $O_3F_2O_2F_1$); and 113° ($F_1O_1O_4F_2$ and $O_3F_2O_2F_1$). The atoms O_1, O_2, O_3, and O_4 are coplanar to an accuracy of better than 0.01 Å, and lie in the plane $-2.564x - 3.472y + 5.477z = 0.988$. To an accuracy of better than 0.01 Å, the Zn atom lies in the plane $-3.186x + 3.737y + 4.983z = 1.609$ drawn through the atoms O_3, F_2, O_2, F_1; but the atoms forming this plane are spaced from it respectively by 0.05, −0.05, 0.05, and −0.05 Å. The third equatorial plane of the octahedron, $12.207x + 1.342y + 0.277z = 1.877$, drawn through the atoms F_1, O_1, O_4, F_2, deviates from these atoms respectively by −0.03, 0.03, 0.03, and −0.03 Å; the Zn atom deviates from the plane by −0.02 Å.

The system of hydrogen bonds in the structure of $ZnF_2 \cdot 4H_2O$ is such that the three strongest ones ($O_1-H_1...F_2$, $O_4-H_2...F_2$, and $O_4-H_4...F_1$) join the Zn octahedra into a three-dimensional framework. The other hydrogen bonds strengthen this framework.

All the calculations on the structure of $ZnF_2 \cdot 4H_2O$ were carried out by means of programs of the "Kristall" set.[6,7]

The work to interpret the atomic structure of $ZnF_2 \cdot 4H_2O$ was suggested by Yu. V. Gagarinskii. We take this opportunity of thanking him for suggesting the theme and for his constant interest and very helpful discussion of the results.

We also thank A. B. Tovbis and L. V. Gorbatti for help in the work.

Note added in proof. Some months after the manuscript was submitted to the editors, we became acquainted with a paper by Martine Nierlich, Pierette Charpin, and Paulette Herpin [Compt. Rend. Acad. Sci., B272, 448 (1971)] on the structure of the above-described compound. These French authors interpreted the structure by means of projections and did not solve the question of the distribution of the O and F atoms in the structure or of the geometry of the possible system of hydrogen bonds. Their atomic coordinates were, to a first approximation, close to ours, except for the z coordinates of the F_1 and O_4 atoms, which they interchange. This is apparently why their Zn octahedron is more distorted than ours.

---

[1] S. A. Polishchuk and M. G. Khmeleva, Proc. of Second All-Union Symposium on the Chemistry of Inorganic Fluorides [in Russian], Nauka, Moscow (1970).

[2] K. C. Patil and E. A. Secco, Canad. J. Chem., 50 (2), 567 (1970).

[3] K. V. K. Rao, S. V. N. Naidu, and A. P. V. Rao, Indian J. Pure and Appl. Phys., 3, 68 (1965).

[4] M. E. Andrianova, I. A. Kudryashov, and D. M. Kheiker, Kristallografiya, 16, 54 (1971) [Sov. Phys. – Crystallogr., 16, 39 (1971)].

[5] V. M. Golyshev, V. I. Simonov, and N. V. Belov, Kristallografiya, 16, 703 (1971) [Sov. Phys. – Crystallogr., 16, 612 (1972)].

[6] A. B. Tovbis and B. M. Shchedrin, Kristallografiya, 15, 1127 (1970) [Sov. Phys. – Crystallogr., 15, 985 (1971)].

[7] A. B. Tovbis and V. I. Simonov, Kristallografiya, 16, 1131 (1971) [Sov. Phys. – Crystallogr., 16, 994 (1972)].

Structure of the double oxide α-$U_3Mo_{20}O_{64}$

V. N. Serezhkin, L. M. Kovba, and V. K. Trunov

M. V. Lomonosov Moscow State University

(Submitted October 14, 1972)
Kristallografiya, 18, 961-965 (September-October 1973)

By means of x-ray structural analysis of single crystals (KFOR camera, Mo Kα, 640 independent reflections, R = 0.155), the authors have established the structure of the double oxide α-$U_3Mo_{20}O_{64}$, which is orthorhombic with unit-cell parameters a = 8.246, b = 28.76, c = 19.78 Å, Z = 4, sp. gr. Cccm. Perpendicular to the c direction there are infinite layers with the composition Mo_2O_7 (the "thickness" of a layer corresponds to two MoO_6 octahedra linked by a common vertex). The U, Mo, and O atoms, lying between the layers, are joined into infinite metal—oxygen chains running parallel to the a direction. The coordination polyhedra of the U atoms are hexagonal bipyramids; those of the Mo atoms are octahedra. These results enable us to regard the double oxide α-$U_3Mo_{20}O_{64}$ as the result of replacing some of the U atoms by Mo atoms in the structure of the double β-UMo_2O_8.

In a study of the system β-UMo_2O_8—MoO_2—MoO_3 it was found that there are two double oxides $UMo_{10}O_{32}$, and α-, β-, and γ-$U_3Mo_{20}O_{64}$, which, according to preliminary results,[1] have structures based on that of β-UMo_2O_8. The present article describes an x-ray structural investigation of α-$U_3Mo_{20}O_{64}$.

The single crystals of α-$U_3Mo_{20}O_{64}$ were synthesized by the method described in ref. 1. Indexing the powder patterns of α-$U_3Mo_{20}O_{64}$ (Table 1, photographed in monochromator camera, in Cu Kα radiation), we found that this compound crystallizes in the orthorhombic system with [a = 8.246(7), b = 28.76(2), c = 19.78(2) Å, Z = 4] space group Cccm. On expansions of the layer lines hk0—hk8 and h0l—h2l we used the blackenings to estimate the intensities of 640 independent nonzero reflections. No correction was made for absorption. All the computations were made on a BÉSM-4 computer by means of the "Roentgen" set of programs.[2]

On analyzing the three-dimensional distribution of the interatomic function we found that the arrangement of the metal atoms in the structure of α-$U_3Mo_{20}O_{64}$ is similar to that found[3,4] in β-UMo_2O_8, and therefore the appearance of superlattice lines on the x-ray diffraction pattern of α-$U_3Mo_{20}O_{64}$ was regarded by us as a consequence of the ordered arrangement of U and Mo atoms and vacancies[1)] over positions which are occupied only by U atoms in the structure of β-UMo_2O_8. Despite multiple superimpositions of the Me—Me maxima in P(u, v, w), analysis of the heights of the maxima of the interatomic function led us to some conclusions on possible variants of the alternation of U and Mo atoms. In our determination of the structure of α-$U_3Mo_{20}O_{64}$, together with refinement of the atomic coordinates, we obtained better values for the population of the regular systems of points which could be occupied by U and Mo atoms. The fact that the results of our refinement of the populations of these positions were practically independent of the original variant of the alternation and of the results of refinement of the coordinates of all the metal atoms shows that ordering of the positions of the metal atoms is the only cause of the appearance of superlattice reflections in α-$U_3Mo_{20}O_{64}$.

The coordinates of the O atoms were found from the three-dimensional electron density difference distribution. Subsequent refinement of the atomic coordinates by the method of least squares, with individual thermal corrections in the isotropic approximation, led to the value R = 0.155. In Tables 2 and 3 we give the corresponding atomic coordinates and main interatomic distances, and in Fig. 1 we show a zone projection ($-1/4 \le x \le 1/4$, y, z) of the structure of α-$U_3Mo_{20}O_{64}$.

According to these results, the structure of α-$U_3Mo_{20}O_{64}$ contains infinite layers with the composition Mo_2O_7, perpendicular to the c axis. These layers are formed by MoO_6 octahedra which are linked only by five common vertices (the "thickness" of the layer corresponds to two octahedra with a common vertex). Between neighboring

TABLE 1. Indices of Diffraction Pattern of α-$U_3Mo_{20}O_{64}$

I	d, Å	$10^4/d^2$	$10^4/d^2_c$	hkl	I	d, Å	$10^4/d^2$	$10^4/d^2$	hkl
11	14.49	48	48	020	2	2.334	1836	1829,1841, 1844	048,334, 0.12.2
9	9.94	101	102	002	5	2.197	2072	2070	068
5	8.19	149	150	022	1	2.121	2222	2223	208
2	6.21	259	258,261	130,112	1	2.097	2274	2272,2276	228,266
1	5.29	358	360	132	7	2.062	2353	2352,2353, 2356	336,400, 2.12.1
1	4.67	459	457	024	13	2.039	2406	{2401,2406 {2409,2413	420,392 068,248
1	4.31	539	538	026	5	1.979	2554	2547,2555, 2560	440, 0.0.10, 2.12.3
67	4.13	587	588	200	7	1.898	2775	2779	0.14.4
3	3.884	663	663	221	4	1.873	2850	2844,2852	0.10.8, 249
9	3.598	772	774	080	9	1.827	2997	2990,2997	0.6.10, 288
7	3.520	807	807	241	27	1.737	3097	3094,3096	269, 0.16.0
100	3.383	874	876	082	27	1.733	3328	3321,3329	426, 0.8.10
100	3.300	919	920	006	1	1.682	3536	3536	484
23	3.144	1012	1012	243	27	1.649	3679	3679,3680 3684	0.0.12, 2.0.11 2.16.0
80	2.910	1181	1178,1183	136,084					
19	2.617	1460	1464	282					
19	2.576	1507	1508	206					
1	2.471	1637	1635	008					
1	2.424	1702	1702	246					
16	2.378	1768	1771	284					

TABLE 2. Atomic Coordinates in the Structure of α-$U_3Mo_{20}O_{64}$ (σ values for coordinates given in parentheses)

Atom		x	y	z	B_j	σ_B
U_1	4 (*c*)	0	0	0	0.2	0.4
U_2	4 (*d*)	0	0.5	0	0.9	0.5
Me_1*	8 (*l*)	0.9832(7)	0.25	0	—0.4	0.2
Mo_1	16 (*m*)	0.054 (1)	0,0623(4)	0.1474(8)	0.5	0.2
Mo_2	16 (*m*)	0.954 (1)	0.1881(4)	0.1677(8)	0.3	0.3
Mo_3	16 (*m*)	0.040 (1)	0.3124(4)	0.1511(8)	0.6	0.3
Mo_4	16 (*m*)	0.956 (1)	0.4375(4)	0.1717(8)	—0.1	0.2
Mo_5	8 (*l*)	0.958 (1)	0.3743(4)	0	2.4	0.7
Mo_6	8 (*l*)	0.046 (1)	0.1262(4)	0	—0.2	0.2
O_1	16 (*m*)	0.25	0.060 (3)	0.136 (9)	1.5	1.8
O_2	16 (*m*)	0.75	0.062 (2)	0.180 (7)	—0.4	1.0
O_3	16 (*m*)	0.25	0.186 (2)	0.154 (6)	—1.3	0.5
O_4	16 (*m*)	0.75	0.187 (4)	0.198 (8)	2.6	2.6
O_5	16 (*m*)	0	0.036 (2)	0.067 (7)	—0.7	0.7
O_6	16 (*m*)	0	0.124 (3)	0.180 (7)	0.2	0.7
O_7	16 (*m*)	0	0 168 (2)	0.065 (8)	0.7	1.0
O_8	16 (*m*)	0	0.250	0.123 (6)	2.3	1.4
O_9	16 (*m*)	0	0.325 (2)	0.065 (7)	0.1	1.1
O_{10}	16 (*m*)	0	0.375(2)	0.174(6)	—0.2	0.6
O_{11}	16 (*m*)	0	0.423(2)	0.060(7)	0.9	1.5
O_{12}	8 (*h*)	0	0.049(4)	0.25	0.5	1.6
O_{13}	8 (*h*)	0	0.204(3)	0.25	—0.5	1.2
O_{14}	8 (*h*)	0	0.307(2)	0 25	—1.0	0.8
O_{15}	8 (*h*)	0	0.450(4)	0.25	1.0	2.1
O_{16}	8 (*l*)	0.25	0,120(2)	0	—1.7	0.7
O_{17}	8 (*l*)	0.75	0,135(3)	0	3.6	2.8
O_{18}	8 (*i*)	0	0	0.137(8)	—2.0	1.0
O_{19}	8 (*j*)	0	0.5	0.127(9)	1.6	1.7
O_{20}	8 (*l*)	0.25	0	0	2.2	1.4
O_{21}	4 (*e*)	0.25	0,25	0	0.4	1.6
O_{22}	4 (*f*)	0.75	.0,25	0	2.3	1.4

*Me_1 = 0,5 U + 05□ (□ is a vacancy).

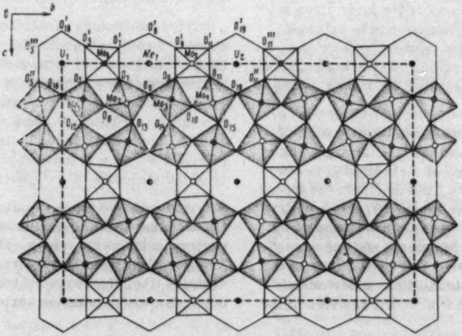

Fig. 1. Zone projection (−1/4≤ x≤ 1/4, y, z) of the structure of α-$U_3Mo_{20}O_{64}$.

layers are the remaining Mo and O atoms and all the U atoms. Between the layers of metal atoms are oxygen atoms in infinite linear uranium−oxygen and molybdenum−oxygen chains stretching parallel to the *a* axis.

The coordination polyhedra of the U atoms in the structure are hexagonal bipyramids $(UO_2)O_6$. The O atoms on the principal axis of a bipyramid are incorporated in uranium−oxygen chains, whereas all the O atoms in the equatorial plane belong to neighboring Mo_2O_7 layers (Fig. 1). The distances U−O = 2.06 Å in the chains, like the mean distances $U-O_{equ}$ = 2.44-2.54 Å, agree with the literature data for this type of coordination of U atoms. Note that statistical arrangement of the U atoms (Tables 2 and 3) means inequality of the U−O distances in the chain (1.92 and 2.20 Å).

In contrast with uranium−oxygen chains, inequality of the distances in molybdenum−oxygen chains, due to shifting of the Mo atoms towards one of the neighboring O atoms in the chain, is the rule rather than the exception. Thus in the MoO_6 octahedra we can distinguish one short distance (about 1.70 Å), one long distance (aobut 2.50 Å), and four intermediate distances (about 1.80-2.00 Å) between Mo and O. The mean Mo−O distance in the octahedra varies over a relatively narrow range, from 1.94 to 2.04 Å.

Comparison of the structures of α-$U_3Mo_{20}O_{64}$ and β-UMo_2O_8 reveals that the structural difference between these compounds is governed by the alternation of U and Mo atoms and vacancies among U sites in the structure of β-Umo_2O_8. The structural affinity of these double

TABLE 3. Main Interatomic Distances (Å) and Valence Angles (deg) in the Structure of α-$U_3Mo_{20}O_{64}$. O−O Distances Shown Are Those Which Do Not Exceed 2.70 Å

U_1-2O_{20}	2.06	Mo_1-O_1	1.63	Mo_4-O_2'	1.71
U_1-4O_5	2.31	Mo_1-O_2	2.59	Mo_4-O_1'	2.53
U_1-2O_{18}	2.71	Mo_1-O_{18}	1.80	Mo_4-O_{10}	1.83
O_5-O_5'	2.65	Mo_1-O_5	1.66	Mo_4-O_{11}	2.28
O_5-O_{18}	2.34	Mo_1-O_6	1.94	Mo_4-O_{19}	2.04
$O_5-U_1-O_5'$	68°	Mo_1-O_{12}	2.11	Mo_4-O_{15}	1.63
$O_5-U_1-O_{18}$	56°	O_1-O_{18}	2.69	O_1-O_{11}	2.60
U_2-2O_{20}'	2.06	O_1-O_5	2.48	$O_1'-O_{19}$	2.69
U_2-4O_{11}	2.51	O_2-O_{12}	2.51	$O_2'-O_{15}$	2.51
U_2-2O_{19}	2.52	O_6-O_{12}	2.56	$O_{10}-O_{11}$	2.64
$O_{11}-O_{11}'$	2.37	$O_{12}-O_{18}$	2.64	$O_{15}-O_{10}$	2.63
$O_{11}-O_{19}$	2.58	Mo_2-O_4	1.79	$-O_{1,70}$	1.74
$O_{11}-U_2-O_{11}'$	56°	Mo_2-O_3	2.47	Mo_5-O_{16}'	2.41
$O_{11}-U_2-O_{19}$	68°	Mo_2-O_6	1.90	Mo_5-2O_9	1.95
Me_1-O_{22}	1.92	Mo_2-O_7	2.09	Mo_5-2O_{11}	1.87
Me_1-O_{21}	2.20	Mo_2-O_8	2.02	$O_{11}-O_{16}'$	2.68
Me_1-2O_8	2.43	Mo_2-O_{13}	1.73	$O_{17}'-O_9$	2.69
Me_1-2O_9	2.51	O_4-O_{13}	2.36	Mo_6-O_{16}	1.69
Me_1-2O_7	2.68	O_6-O_7	2.55	Mo_6-O_{17}	2.45
O_7-O_7'	2.57	O_8-O_{13}	2.69	Mo_6-2O_5	2.21
O_9-O_9'	2.57	Mo_3-O_3'	1.73	Mo_6-2O_7	1.84
O_8-O_9	2.44	Mo_3-O_4'	2.57	$O_{17}-O_7$	2.64
O_8-O_7	2.60	Mo_3-O_8	1.91		
$O_7-\mathit{Me}_1-O_7'$	57°	Mo_3-O_9	1.77		
$O_9-\mathit{Me}_1-O_9'$	61°	Mo_3-O_{10}	1.89		
$O_8-\mathit{Me}_1-O_9$	59°	Mo_3-O_{14}	1.99		
$O_8-\mathit{Me}_1-O_7$	62°	O_9-O_{10}	2.59		
		$O_4'-O_{14}$	2.31		
		$O_{10}-O_{14}$	2.47		

oxides is most clearly seen if we compare their crystallochemical formulas: β-UMo_2O_8 corresponds to $[UO]\cdot[Mo_2O_7]$, and α-$U_3Mo_{20}O_{64}$ to $[U_2(U+\square)Mo_4O_8][Mo_2O_7]_8$.

Together with this, ordered replacement of part of the U atoms in the structure of β-UMo_2O_8 by Mo atoms leads to certain structural changes. The most marked of these are the formation of vacancies in the cation sublattice and the difference between the types of coordination polyhedra of the metal atoms in the structure of α-$U_3Mo_{20}O_{64}$ in positions corresponding to those of U atoms in the structure of β-UMo_2O_8. In β-UMo_2O_8 the U atoms form one type of polyhedra (according to Pailleret,[3] distorted hexagonal bipyramids, but according to Kovba,[4] pentagonal bipyramids), whereas the coordination polyhedra of the metal atoms between Mo_2O_7 layers in α-$U_3Mo_{20}O_{64}$ are different: The Mo atoms have octahedra while the U atoms have hexagonal bipyramids. Comparison of the structures of the above double oxides of uranium and molybdenum reveals that octahedral coordination of Mo atoms between Mo_2O_7 layers in α-$U_3Mo_{20}O_{64}$ is realized on account of distortion of neighboring layers of Mo_2O_7, as a result of which two O atoms become separated from the equatorial plane and the remaining four atoms are slightly displaced, leading to conversion of the hexagonal bipyramids $(Mo_2)O_8$ to octahedra $(Mo_2)O_4$.

On the basis of the above results we can state that α-$U_3Mo_{20}O_{64}$ belongs to the group of double oxides of uranium and molybdenum and structures based on that of β-UMo_2O_8.

---

1) If the structure of α-$U_3Mo_{20}O_{64}$ is derived from that of β-UMo_2O_8, then the replacement of some of the U atoms by Mo must be accompanied by simultaneous formation of vacancies in the cation sublattice.[1]

[1] V. N. Serezhkin, G. N. Ronami, L. M. Kovba, and V. K. Trunov, Zh. Neorgan. Khim., 18, 11 (1973).

[2] B. L. Tarnopol'skii and V. I. Andrianov, Zh. Strukt. Khim., 4, 433 (1963).

[3] P. Pailleret, Compt. Rend., C265, 85 (1967).

[4] L. M. Kovba, Radiokhimiya, 13, 909 (1971).

Structural study of tochilinite.
II. Acicular variety: Unusual diffraction patterns

N. I. Organova, V. A. Drits, and A. L. Dmitrik
Institute of the Geology of Ore Deposits, Petrography, Mineralogy,
and Geochemistry, Academy of Sciences of the USSR
Geological Institute, Academy of Sciences of the USSR
(Submitted July 3, 1972; resubmitted October 30, 1972)
Kristallografiya, 18, 966-972 (September-October 1973)

Powder patterns and acicular textures have been recorded with x rays for the acicular variety of tochilinite, and electron-diffraction studies have been made on microcrystals in the electron microscope. The material is found to consist of a set of two regularly oriented phases, one of which has a structure analogous to that of the isometric tochilinite I, while the second (tochilinite II) differs from the I variety in having a different distribution of the vacancies in the sulfide component; the sulfide and brucite components of type II are described in different sublattices: the sulfide has P1, $a = 8.34$; $b = 8.54$; $c = 10.74$ Å, $\alpha = 87° 20'$, $\beta = 94°30'$, $\gamma = 92°$ and the brucite has C1, $a = 5.42$; $b = 15.65$; $c = 10.74$ Å, $\alpha = \gamma = 90°$, $\beta = 95°$. The chemical formula is $6Fe_{0.9}S \cdot 5[Mg_{0.7}Fe_{0.3}(OH)_2]$. The isometric and acicular varieties have been examined by microdiffraction in the electron microscope, and some unusual diffraction patterns have been observed, which are ascribed to features of the structure.

It has been shown[1,2] that the recently discovered mineral tochilinite (isometric variety) consists of an alternation of layers of iron sulfide and brucite; the sulfide layers have an iron deficiency and contain an ordered disposition of the vacancies, while the brucite layers contain not only magnesium but also iron. The adjacent layers of the same type are displaced one relative to another by $a/6$. The crystallographic characteristics of the isometric variety are space group C1, $a = 5.37$; $b = 15.60$; $c = 10.70$ Å, $\alpha = \gamma = 90°$, $\beta = 95°$; chemical formula $6Fe_{0.9}S \cdot 5[Mg_{0.7} \cdot Fe_{0.3}(OH)_2]$.

The isometric and acicular morphologic varieties of the mineral have similar powder patterns and similar compositions, so their structures must be similar or identical.[1,2] However, the acicular variety has been found to contain macroscopic needles, whose x-ray patterns show that they consist of an acicular texture. The basal $(00l)$ reflections on the zero layer line for rotation patterns have been used to show that tochilinite is a hybrid structure, from which the z coordinates of the atoms have been deduced.[1,2] The hk0 point electron-diffraction patterns for the two varieties indicate that the acicular one consists of two phases; there is a set of peaks with cmm symmetry, and also reflections arranged in accordance with a pseudosquare pattern. We find that $a_{sq} = 8.34$, $b_{sq} = 8.54$ Å, $\gamma = 92°$, with the angle between the x^*_{sq} and y^*_0 axes being 21°. Figure 1 shows an idealized scheme for the hk0 diffraction pattern of the acicular variety; the orthorhombic variety in this pattern is represented by a pattern analogous to that of the isometric variety. In what follows we call the structure responsible for the latter system of reflections tochilinite I. The additional pseudosquare network of reflections indicates that the variety I is accompanied by a second component with a regular orientation with respect to the first. We have examined numerous electron-diffraction patterns and found that the geometrical relationship between the two parts of the pattern is the same in every case, as is the intensity ratio between the two sets of reflections, but with individual intensities varying from one pattern to another, which indicates variation in the quantitative relationships between the two phases.

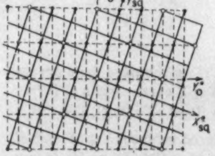

Fig. 1. An idealized scheme for the point electron-diffraction pattern of the acicular variety of tochilinite.

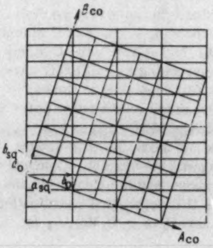

Fig. 2. An idealized relation between the orthorhombic and pseudosquare unit cells.

The reflections from the orthorhombic and pseudosquare components coincide in part (Fig. 1), which enables us to describe the entire set of reflections within a single unit cell; Fig. 2 shows the idealized relationship between the corresponding unit cells in ordinary space. The relation between the coordinate axes can be found in vector form from Fig. 2: $a_o + b_o = 2a_{sq}$, $9a_o + b_o = 6b_{sq}$; for the common unit cell $A_{co} = 6a_{sq}$, $B_{co} = 6b_{sq}$.

The structure responsible for the pseudosquare pattern was interpreted by measuring the intensities; in all we measured 166 independent reflections for the pseudosquare system, of which 39 coincided with the orthorhombic pattern. The maximum $\sin \vartheta/\lambda = 0.66$, while the measurements were made by the method of ref. 2. We converted from the intensities to the structure amplitudes via the equation $\Phi \sim \sqrt{I}$.

TABLE 1. Atomic Coordinates for a Sulfide Layer in Tochilinite II

Atom	x	y	z	Atom	x	y	z
Fe_1	0.29	0.092	0	S_2	0.790	0.107	−0.129
Fe_2	0.582	0.206	0	S_3	0.093	0.201	0.129
Fe_3	0.906	0.287	0	S_4	0.386	0.307	−0.129
Fe_4	0.226	0.411	0	S_5	0.692	0.387	0.129
Fe_5	0.774	0.589	0	S_6	0	0.5	−0.129
Fe_6	0.418	0.794	0	S_7	0.210	0.893	−0.129
Fe_7	0.094	0.713	0	S_8	0.907	0.799	0.129
Fe_8	0.774	0.589	0	S_9	0.614	0.693	−0.129
S_1	0.5	0	0.129	S_{10}	0.308	0.611	0.129

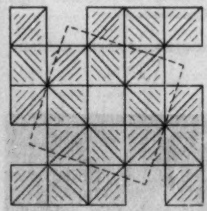

Fig. 3. Idealized model of a sulfide layer in the second phase in the acicular variety of tochilinite.

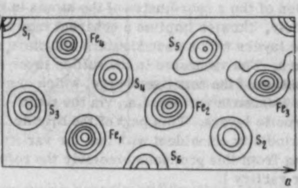

Fig. 4. Final potential synthesis for the sulfide part of tochilinite II.

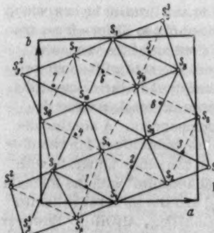

Fig. 5. Normal projection of a sulfide layer in tochilinite II.

The Patterson synthesis constructed with all the measured intensities had the peaks lying on slightly distorted squares, with their heights corresponding in magnitude and geometry to the makinawite sulfide pattern (as in the layered iron sulfide makinawite[3] FeS), each layer containing Fe tetrahedra with a four-fold environment. The intensities were distributed in the pseudosquare pattern in such a way that as a rule reflections with hk0 indices for which h + k = 2n were usually stronger than those with h + k = 2n + 1, which indicates pseudocentering of the cell. This indicates a possible form for the structure as shown idealized in Fig. 3. We used the ideal model with the planar symmetry group p2 to calculate the R for various degrees of population of the tetrahedra shown empty in Fig. 3. The agreement was best (R = 40%) when the empty tetrahedra were not populated at all. The atomic coordinates could not be revised via potential syntheses because some of the reflections for the two systems coincided, but least-squares refinement with the intensities for the pseudosquare set gave R = 29.9% when we assumed that the coincident reflections had zero intensity. We derived the theoretical structure amplitudes from the coordinates found after refinement, which showed that the strongest structure amplitudes are ones corresponding to the reflections in common with the orthorhombic pattern, which agreed with experiment. We replaced the coincident reflections by the theoretical intensities, which improved R to 21.6%; the corresponding potential synthesis showed small displacements of the atoms. A further application of least squares with zero intensities for the coincident reflections gave R = 25%. The complete set of intensities with theoretical values for the superimposed ones gave a final R of 18.4%.

Table 1 gives the coordinates of the atoms in the sulfide layer of the second phase for the acicular variety; as in the case of the isometric variety, the symmetry of the projection is higher than that of the structure as a whole, the center of symmetry being lost in passing to the three-dimensional coordinates.

Figure 4 gives the final potential synthesis, while Fig. 5 gives the normal projection of the sulfide layer from the second phase in the acicular variety.

The mean Fe−S interatomic distance was 2.34 Å (as against 2.32 Å for the isometric variety), with a range from 2.10 to 2.54 Å. The unshared edges had lengths from 3.68 to 3.94 Å with a mean of 3.78 Å, while the shared edges had from 3.67 to 4.10 Å with a mean of 3.84 Å. The mean interatomic distances in the sulfide layer of the second phase in the acicular variety are somewhat larger than those in the isometric variety. The mode of distortion of the sulfur tetrahedra is similar to that in the isometric variety.[2]

We used the equations of ref. 4 to estimate the level of error in the atomic coordinates, which gave $\Delta x = \Delta y = 0.022$ Å for the iron and $\Delta x = \Delta y = 0.035$ Å for the sulfur with b = 0.2; the error in determining the interatomic distances was at least 0.05 Å.

These sulfide layers are responsible for the pseudosquare reflection pattern in electron diffraction, and they are intercolated with brucite layers, as in the isometric variety; this was deduced as follows. First of all, if the specimen contained only the sulfide phase, it would be unlikely that the dimensions of the unit cell would be an exact multiple of the thickness of a tochilinite layer. If the agreement were not exact, the even order of the basal reflections would be split into pairs, since the thickness of a makinawite layer is 5.046 Å, and the strongest reflection in the powder pattern of makinawite itself has a (001) index and the corresponding reflection would always be present on the zero layer line in the rotation pattern. Besides, a satisfactory value of the R factor, equal to 9.4% according to the x-ray data, resulting from the calculation of the z coordinates of the atoms in the acicular variety, likewise implies a coherent intercalation of sulfide layers with a pseudosquare structure and brucite layers. The vacancies in the sulfide layer require compensation of the negative charge, which is provided as in the isometric variety, i.e., via the positive charge on the brucite layers. This part of the brucite layers has a periodicity coincident with that for variety I, so the scattering from this produces precisely the reflections found for variety I.

The acicular variety thus consists of two phases: The first phase has a structure analogous to that for tochilinite I, while the second phase has a hybrid structure also,^{5} with alternation of sulfide and brucite layers, which we call tochilinite II. The second phase differs from the first in having a different distribution of the vacancies in the sulfide layer, which alters the size of the unit cell for the sulfide component of variety II in the plane of the layer and implies also a separate crystallographic description for each of the two components. A similar division of a single crystal into two sublattices for two distinct components occurs also in two other minerals with hybrid structures: the mineral kenenite^6 with the formula $(Na, Mg)Cl_2 \cdot 1.78[Mg, Al(OH)_2]$ and the mineral valleriite^5 with the formula $2(Cu, Fe)S \cdot 1.524[Mg, Al(OH)_2]$. However, these structures have only the basal 00l reflections common in reciprocal space, whereas tochilinite II has some of the reflections of general hk$l$ type in coincidence, which indicates that the structure of tochilinite II can be described within a single large unit cell. However, it is clear that the structural investigation is considerably facilitated by separate consideration of the nonoverlapping reflections.

If we assume that adjacent sulfide layers in variety II have a mutual disposition analogous to that in variety I, we can determine all the dimensions of the sulfide sublattice: a = 8.34; b = 8.54; c = 10.74 Å, α = 87°20', β = 94.5°, γ = 92° with space group P1. Calculation of the theoretical structural formula for tochilinite II gives the relationship between the number of sulfide and brucite molecules found for tochilinite I, but with a different value for the coefficient of the iron atom in the sulfide layer: $6Fe_{0.8}S \cdot 5[Mg_{0.7}Fe_{0.3}(OH)_2]$.

When we come to describe and interpret the unusual diffraction patterns of the two varieties of the mineral, one should begin with the explanation of the distribution of the hk0 reflections of high intensity on the electron-diffraction point patterns; some of these fit a pseudosquare net, while the others form a pseudohexagonal pattern, whose distribution is close to that of the reflections for a brucite structure. We calculated the theoretical intensities for the isometric variety separately for the sulfide and brucite parts, which showed that the strongest reflections were determined mainly either by the sulfide component or by the brucite one. For instance, the main contribution to the strong (350) and (0.10.0) reflections comes from the brucite layers, and the same applies to the weaker (200) and (150) reflections. Conversely, the (260) and (0.12.0) reflections, and also (400), arise mainly from the sulfide layers. Figure 6 shows the hk0 reciprocal lattice plane for the isometric variety; the circles denote the brucite reflections, and the triangles the sulfide ones. The first set of reciprocal-lattice points corresponds to a_h = 3.13 Å (a = 3.12 for brucite), while the second has a_{sq} = 1.87 Å, which is the makinawite subcell of the sulfide layer, which corresponds to projection of the Fe—S distance in the sulfur tetrahedron.

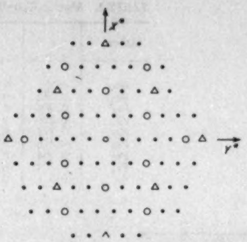

Fig. 6. Cross section in kh0 for the reciprocal lattice of isometric tochilinite.

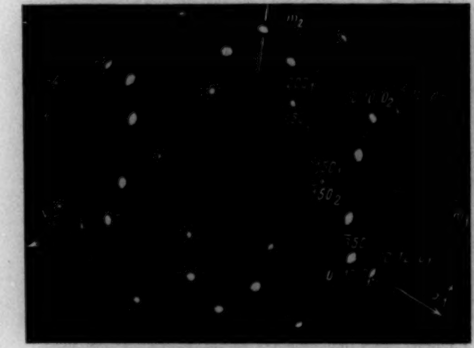

Fig. 7. Electron-diffraction pattern of a twinned microcrystal of tochilinite (m_1 and m_2 are symmetry planes).

The electron microscope revealed unusual diffraction patterns of four types for both varieties; each of these could be explained in terms of the above features in the distribution of the hk0 reflection intensities.

Type 1. Figure 7 shows the electron-diffraction spot pattern from the isometric variety, and similar patterns were observed for the other variety; the reflections

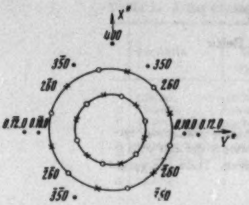

Fig. 8. Scheme for the electron-diffraction pattern of isometric tochilinite containing a valeriite component.

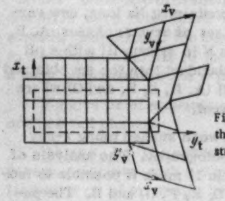

Fig. 9. Likely mutual disposition of the tochilinite and valeriite-type structures within a sulfide layer.

seen on the plate constitute an ensemble of two tochilinite patterns, one turned relative to the other through 120°. Figure 7 shows the Y_1^* and Y_2^* axes of the reciprocal lattice for each of the components. The diffraction pattern has two mutually perpendicular symmetry planes, which are absent in each of the components, i.e., the diffracting volume is a twin. This twin is formed by error in superposition of adjacent sulfide layers; the pseudotrigonal symmetry of a brucite layer causes one part of the scattering volume to be turned relative to the other through 120°. The volumes turned one relative to the other are approximately equal, so the point electron-diffraction pattern contains additional symmetry elements (Fig. 7 shows the indices for some of the reflections, among which are also the brucite ones).

Type 2. This occurs in both varieties. The tochilinite pattern is accompanied by a series of additional reflections, among which one can distinguish ones derived from the strongest reflections of tochilinite, namely (260) and (2$\bar{6}$0). The geometry and intensity of the pattern shown in Fig. 8 indicate that there are 12 reflections at identical distances from the primary electron beam, half of which are related via a six-fold axis to the (260) reflection, while the other half are related to the (2$\bar{6}$0) reflection of tochilinite. A similar system lies on a circle at a distance less by a factor $\sqrt{3}$ (Fig. 8). The intensities and the distances from the primary beam enable one to assign these reflections to the sulfide component of the valleriite-type structure.[5] The essential difference between the structures of tochilinite and valleriite lies in the disposition of the atoms in the sulfide layer; in tochilinite, the sulfide layer $Fe_{1-x}S$ consists of tetrahedra lying on the side edges, while in valleriite the sulfide layer $Cu_{2-x}Fe_xS_2$ is constructed from tetrahedra standing on their bases and has a three-fold symmetry axis. Figure 9 shows a scheme for the most probable mode of coexistence of parts with tochilinite and valleriite atomic dispositions within a single sulfide layer, the latter having two equally probable orientations. The elementary squares shown in the figure are tochilinite tetrahedra,[1,2] while the rhombs are unit cells of the sulfide part with the valleriite type of structure.[5] The disposition of the reflections on the point electron-diffraction pattern agrees with this mutual disposition of the squares and rhombs, in which the diagonals of the squares coincide with the small diagonals of the rhombs. This gives us two orientations of the valleriite atomic ray in the sulfide layer.

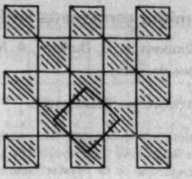

Fig. 10. Vacancy redistribution in a sulfide layer in tochilinite, type 3.

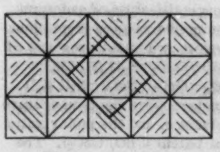

Fig. 11. Vacancy redistribution in a sulfide layer in tochilinite, type 4.

Types 3 and 4. When specimens were made from an aqeuous suspension in which isometric tochilinite particles had been left for a month, there was a considerable redistribution of the intensities in the corresponding point electron-diffraction patterns; this concerned mainly reflections arranged in the square pattern, which indicates a change in the sulfide part of the structure. One of these unusual patterns had high-intensity reflections corresponding to a square subcell in reciprocal space of side $\sqrt{5.37^2 + (15.65/3)^2}/2 = 3.74$ Å, while a second corresponded to $a = 5.37/2 = 2.68$ Å, $b = 15.65/6 = 2.6$ Å; the most probable explanation of this observed intensity redistribution is a change in the vacancy distribution in the sulfide layer of tochilinite I, where the vacancies are distributed in a centered rhombic pattern.[1,2] The treatment in aqueous suspension provides for a more equilibrium location of most of the vacancies with respect to the squares; Fig. 10 shows the vacancy distribution in a sulfide layer corresponding to one type of these diffraction patterns, while Fig. 11 does the same for the other type. In the first case, the vacancies are arranged in a chessboard pattern, while in the second they are uniformly distributed over all tetrahedra.

---

[1] N. I. Organova, A. D. Genkin, V. A. Drits, A. L. Dmitrik, and O. V. Kuz'mina, Zap. Vses. Min. Obshch., series 2, No. 4, 477 (1971).

[2] N. I. Organova, V. A. Drits, and A. L. Dmitrik, Kristallografiya, 17, 761 (1972) [Sov. Phys.—Crystallogr., 17, 667 (1973)].

[3] R. A. Berner, Science, 137, 669 (1962).

[4] B. K. Vainshtein, Structural Electron Diffraction [in Russian], Izd. AN SSSR (1956).

[5] H. T. Evans, Jr., and R. Allmann, Z. Kristallogr., B127, 73 (1968).

[6] R. Allmann, H. H. Lohse, and E. B. Hellner, Z. Kristallogr., B126, 7 (1968).

A group of synthetic cadmium germanates and their x-ray study

E. L. Belokoneva, M. A. Simonov, N. G. Duderov, A. N. Lobachev, and N. V. Belov

M. V. Lomonosov Moscow State University

(Submitted January 11, 1973)
Kristallografiya, 18, 973-977 (September-October 1973)

Hydrothermal crystallization in $CdO-GeO_2-H_2O$, $CdO-GeO_2-NaOH-H_2O$, and $CdO-GeO_2-NaCl-H_2O$ systems has been studied. Eight phases have been revealed by x-ray studies. The parameters of the unit cells refined in a DRON-1 diffractometer and an R1 "Syntex" automatic diffractometer are given. There is a marked structural affinity between the synthetic cadmium germanates and calcium silicates.

A study of the hydrothermal crystallization of cadmium germanates was carried out in media ranging from close to neutral to alkali, in pure water, and in the presence of Na ions. We studied[1,2] the $CdO-GeO_2-H_2O$ (I), $CdO-GeO_2-NaOH-H_2O$ (II), and $CdO-GeO_2-NaCl-H_2O$ (III) systems. The variable parameters were the temperature T, the concentration of the solvent c, and the molar ratio N of the original oxides (in the batch) (CdO/GeO_2). The ranges of variation in the parameters were: T = 300-500°C; c_{NaOH} = 0-60 wt.%; N = 1:6 to 6:1. The pressure was kept constant. It was found that the phase formation depends on all the above parameters. The crystallization of Cd germanates is affected not only by the presence of the large Na cation in the solution, but also by the pH of the medium and the various anions of the solvent. When the pure water of system I, in which three Cd germanates (A, B, and C) dependent on N can be formed, is replaced by systems containing Na ions, new germanates crystallize and the set of crystal phases (A, B, E, F, G, and H) dependent on N in system III with a pH close to neutral, are more abundant than the set obtained in the strong alkali system II (A, B, D, E, and G) where sodium hydroxide is the solvent.

The phases we obtained were studied using x-ray powder and single crystal photography. The analysis of the diffraction patterns (Table 1) made it possible to isolate eight phases: A, B, C, D, E, F, G, and H. The parameters of their unit cells were established from oscil-

TABLE 1. The Interplanar Spacings in Cd Germanates*

A		*B*		*C*		*D*		*E*		*F*		*G*		*H*	
d	I	d	I	d	I	d	I	d	I	d	I	d	I	d	I
5.61	7	3.87	10	7.76	3	7.14	3	9.35	4	7.50	28	4.80	6	7.02	5
4.72	4	3.48	65	4.53	18	5.50	4	8.04	14	7.08	28	4.35	5	6,24	10
4.27	8	3.14	100	3.83	10	5.25	4	7.25	20	5.04	14	4.04	4	4,82	50
3.83	35	3.04	25	3.56	8	4.67	2	5.54	6	3.74	30	3.38	6	4.23	5
3.28	13	2.98	10	3.28	3	4.31	2	5.04	4	3.53	28	3.25	48	3.53	70
3.04	93	2.85	18	3.02	100	4.27	2	4.85	4	3.31	74	3.16	100	3.28	60
2.85	51	2.65	90	2.90	18	3.83	18	4.73	4	3.24	53	2.98	90	3.10	100
2.80	28	2.64	18	2.88	35	3.33	10	3.96	30	3.14	100	2.80	34	3.03	40
2.75	85	2.58	10	2.76	9	3.02	68	3.82	6	3.04	61	2.64	61	2.98	90
2.71	100	2.49	20	2.68	2	2.93	60	3.57	16	2.87	65	2.58	71	2.81	70
2.61	29	2.48	7	2.62	2	2.75	44	3.36	100	2.75	70	2.53	22	2.73	6
2.56	19	2.25	6	2.52	30	2.69	15	3.18	85	2.64	78	2.40	22	2.68	40
2.45	4	2.24	15	2.48	5	2.66	13	3.05	35	2.56	37	2.33	8	2.64	50
2.37	4	2.20	20	2.44	35	2.58	26	3.00	68	2.52	50	2.30	8	2.54	4
2.22	3	2.03	5	2.30	6	2.52	12	2.86	20	2.34	28	2.26	6	2.49	5
2.13	4	2.01	5	2.10	2	2.42	1	2.73	72	2.31	28	2.25	4	2.45	40
2.08	5	1.95	7	2.08	5	2.30	2	2.63	60	2.18	14	2.16	19	2.43	50
1.99	7	1.94	20	2.00	2	2.24	2	2.56	18	2,10	8	2.10	4	2.40	10
1.96	5	1.93	35	1.90	56	2.12	1	2.49	18	1.96	14	2.08	6	2,30	10
1.92	56	1.82	4	1.90	56	2.12	1	2.48	18	1,91	14	2.05	4	2.26	30
1.83	11	1.78	10	1.79	3	1.98	6	2.31	20	1.76	62	2.01	29	2.07	5
1.79	22	1,74	5	1.76	6	1.91	55	2.22	6	1.68	14	1.94	3	2.01	5
1.78	21	1,70	35	1.69	10	1.85	5	2.18	8	1.62	14	1.87	5	1,87	15
1.74	16	1,67	40	1.66	20	1.78	18	2.08	12	1.58	14	1.85	4	1,84	10
1.72	5	1.65	13	1.55	16	1.69	4	2.01	8	1.55	18	1.83	12	1,76	30
1.63	9	1.61	20	1.53	12	1,64	100	1,97	2	1.53	6	1.77	8	1.72	5
1.65	33	1.56	7	1.50	2	1.53	12	1.93	40	1.51	41	1.73	3	1.71	5
1.62	18	1.53	25	1.45	2	1.47	6	1.85	3	1.46	10	1.70	29	1.55	5
1.58	7			1.43	4	1.39	7	1.81	20	1.41	10	1.69	23	1.49	5
1.52	25			1.39	10	1.29	5	1.77	40	1.40	8	1.65	14	1.44	5
1.48	8			1.34	2	1.28	4	1.75	4	1.36	8	1.62	16	1.42	5
1.44	13			1.28	3	1.24	4	1.72	20			1.58	24		
1.41	4			1.26	3	1.23	3	1.65	22			1.53	22		
1.39	9			1.25	3	1.21	2	1.59	4			1.48	13		
1.37	8			1.23	4	1,20	2	1.57	12			1.47	10		
1.30	3					1.18	11	1.55	16			1.45	18		
1.28	2					1.16	3	1.52	17			1.42	13		
1.27	5					1.13	3	1.51	23			1.41	12		
1.24	5							1.44	8			1.40	8		
1.21	4							1.42	12			1.39	16		
1.18	2							1.39	9			1.37	10		
								1.38	4			1.36	13		
								1.34	5			1.32	8		
								1.32	3			1.31	5		
								1.30	5			1.29	5		
								1.28	2			1.27	11		
								1.27	4			1.25	5		
								1.25	1			1.23	1		
												1.21	4		

*Urr-50IM, scintillation counter, Cu Kα radiation

TABLE 2. X-Ray Characteristics of Cd Germanates

	Formula	Crystal system	a (Å)	b (Å)	c (Å)	α, °	β, °	γ, °	d, (g/cm³)	Z	Fedorov group
A	Cd_2GeO_4	orthorhombic	5.190	6.570	11.12	90	90	90	6.4	4	$D_{2h}^{16} = Pnma$
B	$Cd_2Ge_2O_6$	monoclinic	5.253	9.64	9.96	90	102.91	90	5.7	4	$C_{2h}^{6} = A2/a$
C	$Cd_3GeO_4(OH)_2$	orthorhombic	9.89	5.784	5.036	90	90	90	5.8	2	$C_{2v}^{7} = Pm2_1n$
D	$Cd_9Ge_4O_{16}(OH)_2$	monoclinic	11.052	5.194	14.818	90	100.35	90	6.0	2	$C_{2h}^{5} = P2_1/a$
E	$NaCdGe_3O_8(OH)$	triclinic	7.090	8.036	7.224	103.02	90.52	93.53	5.3	2	$P1$, $P\bar{1}$
F	$NaCd_4Ge_5O_{14}(OH)$	the same	7.078	8.023	12.618	111.46	84.43	94.28	5.2	2	$P1$, $P\bar{1}$
G	$CdGe_2O_5$	"	5.325	5.686	7.254	116.86	82.80	114.16	6.0	2	$P1$, $P\bar{1}$
H	$Cd_2Ge_2O_7$	"	7.081	8.069	7.559	108.90	84.46	117.40	5.3	2	$P1$, $P\bar{1}$

lation x-ray photographs (RKOP camera) and were refined in a DRON-1 (A, B, C, D) diffractometer and an $R\bar{1}$, "Syntex" automatic diffractometer (E, F, G, and H). The densities were determined by a hydrostatic weighing method. Research at the Department of Crystal Physics in the Physics Faculty of Mosocw State University showed a weak piezoeffect in the C phase.

We give brief accounts of the characteristics of the synthesized phases.

Phase A. The crystals in this phase are transparent, colorless, with a vitreous glint on fracture, either isometric or of prismatic habit, 0.1–1.0 mm in size (sometimes up to 4 mm) and have significant photosemiconductivity. The parameters of the orthorhombic cell (Table 2) and the interplanar spacings (Table 1) indicate fairly well the relationship between the experimental compounds and γ-$Ca_2[SiO_4]$. The accepted formula Cd_2GeO_4 is confirmed by more recent chemical analysis (Table 3) and the structural interpretation.[4] The olivine-type motif, consisting of Cd octahedra encrusted with isolated $[GeO_4]$ tetrahedra, is repeated in the $Cd_2[GeO_4]$ crystal structure.

Phase B. The crystals of this phase are transparent, colorless, and 3 mm long. The parameters of the monoclinic cell and the interplanar spacings showed a probable analogy with diopside $CaMg\ Si_2O_6$.[5] The formula assumed for phase B, $Cd_2[Ge_2O_6]$, was confirmed by a later chemical analysis and structural interpretation.[6] In the structure of $Cd_2[Ge_2O_6]$ as in diopside, the layers made of zigzag strips of Cd octahedra alternate with laminar units of $[Ge_2O_6]_\infty$ meta-chains.

Phase C. The crystals are transparent, colorless, isometric, and measure 0.1–0.4 mm. The chemical formula $Cd_3[GeO_4](Oh)_2$ was based on the data from chemical analysis which gave a Cd:Ge ratio of 3:1 using x-ray microanaylsis (by I. D. Shevaleevskii). The IR spectroscopic analysis (made by I. I. Plyusina) showed a hydrogen bond in the structure and a germanium orthoradical $[GeO_4]$. The structural interpretation[7] like the later microchemical analysis (Table 3) confirmed the assumed formula. In the $Cd_3[GeO_4]\ (Oh)_2$ structure the Cd octahedra form endless chains along b with the units made from the structural octahedra with a common edge. The strips of filled octahedra alternating with the analogous strips of empty octahedra are interlaid by $[GeO_4]$ tetrahedra.

Phase D. The crystals are transparent, colorless, of various habits (laminar, prismatic), frequently cloudy with visible skeletal forms, and measuring 0.2–10 mm. The parameters of the monoclinic cell and the interplanar spacings indicated that there is an analogy between the experimental compounds and the mineral clinohumite, $Mg_9[Si_4O_{16}(OH)_2]$, of the chondrodite group.[8] From this analogy, the chemical analysis and the IR spectroscopy data (I. I. Plyusina) which established the hydrogen bonds in the structure, the following formula was taken for phase D: $Cd(OH)_2 \cdot 4Cd_2[GeO_4] = Cd_9[Ge_4O_{16}(OH)_2]$.

Phase E. The crystals are transparent, colorless, acicular, and sometimes in the form of intergrowths. The needles measure up to 8 mm in length with a cross section of 0.1–1.0 mm. Immediately it was noted that Phase E was analogous to wollastonite, $Ca_3[Si_3O_9]$. The latter chemical analysis, however, and the refinement of the parameters indicated a structural relationship with pectolite,[9] $NaCa_2[Si_3O_8(OH)]$ which belongs to the wollastonite group. Thus the chemical formula of the E phase should be $NaCdGe_3O_8(OH)$. The Fedorov Group is P1 or $P\bar{1}$.

Phase F. The crystals are transparent, extended, colorless or yellowish, show intergrowths, and the needles measure up to 6 mm in length with a cross section of 0.1–2.0 mm. The parameters of the triclinic cell (Table 2), the interplanar distances, and the data from the chemical analysis, favor the assumption that we are dealing with a new synthetic analog of the pyroxenoid rhodonite[10] $CaMn_4[Si_5O_{15}]$ – $NaCd_4Ge_5O_{14}(OH)$ in which the Ca position is occupied by Na, Mn by Cd, and Si by Ge.

TABLE 3. The Chemical Analysis of Cd Germanates *

Components (wt. %)	A	B	C	D	E	F	G	H
Na_2O	0.02	—	—	0,13	4.42	2.82	—	—
CdO	71.02	55.11	78.00	73.90	45.37	45.80	45.70	43.38
GeO_2	28.44	45.50	19.75	26.42	48.75	50.84	54.00	56.64
H_2O	—	—	2.75	—	1.98	0.80	—	—
Σ	99.48	100.61	100.50	100.45	100.52	100.26	99.70	100.02

*The chemical analyses were made at the Institute of Crystallography, Academy of Sciences of the USSR (analyst E. N. Emel'yanova) and at the Institute of the Geology of Ore Deposits, Petrography, Mineralogy, and Geochemistry, Academy of Sciences of the USSR (analyst G. A. Aranova).

To compensate the valency in the anionic group, part of the O atoms is replaced by OH groups as is characteristic for the pectonite $NaCA_2[Si_3O_8(OH)]$ by contrast to the wollastonite $Ca_3[Si_3O_9]$. The Fedorov group is P1 or P1.

Phase G. The crystals are transparent, either isometric with well-developed faceting or in the form of a rhombus, and measure 0.1–3.0 mm. The parameters of the triclinic cell, the interplanar spacings, and the chemical analysis data, confirmed the structural analogy[11] with titanite–sphene $CaTi[SiO_5]$ and the position of the Ca atom is clearly occupied by Cd, Ti by Ge, and Si by Ge, corresponding to the formula $CdGe_2O_5CdGe(GeO_5)$. We have here an illustration of the extensive structural role of Ge entering both the anionic and cationic part of the expanded formula. The Federov groups is P1 or P$\bar{1}$.

Phase H. The crystals are transparent, almost isometric, well-faceted, and measure 0.1–2.0 mm. From the chemical analysis data, the phase H formula is $Cd_2 \cdot Ge_3O_8$. The Fedorov group is P1 or P$\bar{1}$.

The results of the study can be considered as establishing the close structural relationship between the synthetic cadmium germanates and the calcium silicates. Out of the eight phases we have studied, six were analogs of well known minerals: olivine γ-$Mg_2[SiO_4]$; pyroxene $CaMg[Si_2O_6]$; clinohumite $Ca_9[Si_4O_{16}(OH)_2]$; pectolite $NaCa_2[Si_3O_8(OH)]$; rhodonite $CaMn_4[Si_5O_{15}]$; and sphene $CaTi[SiO_5]$. Analogies have previously been noted[12] in the case of the Ca silicates: $CdSiO_3$ phase with β-$Ca \cdot [SiO_3]$ wollastonite; Cd_3SiO_5 with the well-known cement mineral tricalcium silicate, $C_3S = Ca_3SiO_5$; $NaCd_2[Si_3O_8 \cdot (OH)]$ and $Cd_5[SiO_4]_2(OH)_2$ with pectolite and chondronite; only when large amounts of Na are introduced are original structures formed[13] (phases M, K, R, L). The synthetic calcium silicate[14] $Na_2Ca_3[Si_3O_{10}]$ which is rich in sodium was found to be a structural analog of phase L, $Na_2Cd_3 \cdot [Si_3O_{10}]$. In the case of the Ca germanates, analogies have also been observed with the Ca silicates:[15] Ca_3GeO_5 with Ca_3SiO_5; $Ca_2[GeO_4]$ with $Ca_2[SiO_4]$; $CaGe_2O_5$ with $CaTi[SiO_5]$; $CaGe_4O_9$ with $BaTi[Si_3O_9]$; $Ca[GeO_3]$ with $Ca[SiO_3]$; and $Ca_3[Ge_2O_7]$ with $Ca_3[Si_2O_7]$ (rankinite). This series of examples can be taken as positive confirmation of the main assumption in the second chapter of "The Crystal Chemistry of Silicates"[16] that the large cations play a dominating – "steering" – role in the structure of silicates and their analogs.

---

[1] N. G. Duderov, L. N. Dem'yanets, E. L. Belokoneva, A. N. Lobachev, and N. V. Belov, Kristallografiya, 17, 1044 (1972) [Sov. Phys.–Crystallogr., 17, 916 (1973)].

[2] E. L. Belokoneva, B. N. Litvin, M. A. Simonov, and N. V. Belov, Izv. Akad. Nauk SSSR, Neorgan. Mat., 8, 1675 (1972).

[3] D. K. Smith, A. Majumdar, and F. Ordway, Acta Crystallogr., 18, 787 (1965).

[4] E. L. Belokoneva, Yu. A. Ivanov, M. A. Simonov, and N. V. Belov, Kristallografiya, 17, 217 (1972) [Sov. Phys.–Crytsallogr., 17, 177 (1972)].

[5] B. E. Warren and W. L. Bragg, Z. Kristallogr., 69, 168 (1928).

[6] E. L. Belokoneva, M. A. Simonov, and N. V. Belov, Vestn. Moskovsk. Universitet., Ser. Geol., No. 6, 36 (1971).

[7] E. L. Belokoneva, M. A. Simov, and N. V. Belov, Dokl. Akad. Nauk SSSR, 207, 850 (1972) [Sov. Phys.–Dokl., 17, 1124 (1973)].

[8] W. H. Taylor and J. West, Z. Kristallogr., 70, 461 (1929).

[9] C. T. Prewitt, Z. Kristallogr., 125, 298 (1967).

[10] D. R. Peacor and N. Niizeki, Z. Kristallogr., 119, 98 (1963).

[11] W. H. Zachariasen, Z. Kristallogr., 73, 7 (1930).

[12] L. Dent Glasser and F. P. Glasser, Inorg. Chem., 3, 1228 (1964).

[13] M. A. Simonov, Yu. K. Egorov-Tismenko, and N. V. Belov, Vestn. Moskovsk. Univ. Ser. Geol., No. 6, 16 (1971).

[14] E. N. Treushnikov, V. V. Ilyukhin, and N. V. Belov, Kristallografiya, 16, 76 (1971) [Sov. Phys.–Crystallogr., 16, 56 (1971)].

[15] A. K. Shirvinskaya, R. G. Grebenshchikov, and N. A. Toropov, Izv. Akad. Nauk SSSR, Neorgan Mat., 2, 332 (1966).

[16] N. V. Belov, Crystal Chemistry of Large-Cation Silicates, Consultants Bureau, New York (1964).

Structure of nickel hydroxide containing potassium ions

P. N. Bityutskii, V. I. Khitrova, and Z. G. Pinsker
Institute of Crystallography, Academy of Sciences of the USSR

(Submitted June 28, 1972; resubmitted August 4 and September 20, 1972)
Kristallografiya, 18, 978-983 (September-October 1973)

By electron-diffraction structural analysis, in a vacuum of about $5\cdot10^{-4}$ mm, the authors have studied the structure of the higher hydroxide of nickel, γ-NiOOH, stabilized by small amounts of K^+ ions. This compound was obtained from potassium nickelate ($K_{\sim0.23}NiO_2$) by washing from an alkaline cell. By analogy with clays, they suggest that exchange of K^+ for H^+ and H_3O^+ ions occurs during washing. From the electron-diffraction analysis it follows that the most probable variant is the arrangement of hydroxonium ions H_3O^+ between the layers in the nickel hydroxide.

We have previously published[1,2] the results of an electron-diffraction investigation of the structures of nickel hydroxides containing potassium ions (potassium nickelates). We found that in the hydrated crystalline phase, the alkali metal cations are arranged together with the water molecules in the spaces between layers in the structure of γ-NiOOH. On dehydration, a comparatively small content of alkali metal (about 0.14 per formula unit in the structure of potassium nickelate II, $K_{0.14}NiO_2$) does not affect the structure of γ-NiOOH: The structure is unchanged and the K^+ ions are arranged in the spaces between layers statistically over all positions in a layer — near the centers of the trigonal prisms which cover the interlayer spaces.[2] If the structure of the higher hydroxide of nickel contains large amounts of potassium (about 0.23 per formula unit in the structure of potassium nickelate I, $K_{0.23}\cdot NiO_2$), dehydration leads to relative displacement of the nickel—oxygen octahedral layers, and as a result the K^+ ions lie, not at the centers of the oxygen prisms, but at the centers of distorted octahedra;[1] the structural type changes γ-NiOOH to $LiNiO_2$. In some experiments with high K^+ contents, dehydration was accompanied by (partial) ordering of potassium ions in the layers: The K^+ ions then occupied only one third of the positions in a layer, but with three times the probability (about 0.70).

Among minerals, we can distinguish montmorillonite and the hydromicas as analogs of the alkali nickelates under investigation. It is usually accepted that the interlayer spaces in the hydromicas are populated by small amounts of alkali metal atoms and hydroxonium ions H_3O^+. It is supposed that the hydroxonium occupies the same positions as the alkali metal atoms.

On p. 124 of his article,[2] Belov observes in a footnote that hydroxonium ions may perhaps be present in the structures of the alkali metal nickelates studied by us, though in small amounts; with this in mind, we made an electron-diffraction structural investigation of specimens from which K^+ ions had been additionally washed, supposing that with an even further reduction in the content of alkali metal atoms we should succeed in detecting hydroxonium ions in the structure. Potassium, of course, is relatively easily removed from hydroxides. After intensive washing of potassium nickelate I ($K_{0.23}NiO_2$), chemical analysis data indicated the phase composition to be $K_{0.1}NiO_{1.77}\cdot 0.56H_2O$.

In preparing the specimen for electron diffraction, we washed a further amount of alkali metal cations out of the substance, and as a result, in the structure of potassium nickelate the probability of occurrence of a K^+ ion at any vacancy in a layer was apparently reduced to below about 0.05. (In potassium nickelate II with about 0.14 of K^+ per molecule, the vacancies in a layer were occupied with a probability[2] of about 0.07). From additionally washed specimens we obtained electron diffraction patterns of the oblique texture type and x-ray diffraction (powder) patterns from which it follows that the unit cell is rhombohedral. The cell dimensions are given in Table 1 in hexagonal axes; for comparison we also give the dimensions of potassium nickelates I and II and γ-NiOOH. The difference between the lattice parameters c of the potassium nickelates found from electron and x-ray dif-

TABLE 1

Formula	Electron diffraction data, Å		X-ray diffraction data, Å	
	a	c	a	c
$K_{0.22}NiO_2$ [1]	2.82	19.12	2.82	21.65
$K_{0.14}NiO_2$ [2]	2.82	19.15	2.82	27.15
$K_{<0.10}NiO_2$*	2.82	19.90	2.82	20.20
γ-NiOOH [3]	—	—	2.82	20.65

*The phase studied in this article.

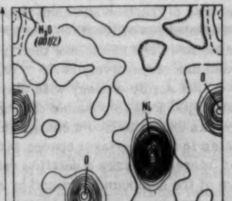

Fig. 1. Section of three-dimensional Fourier potential series in $\bar{1}10$ plane, in structure under investigation.

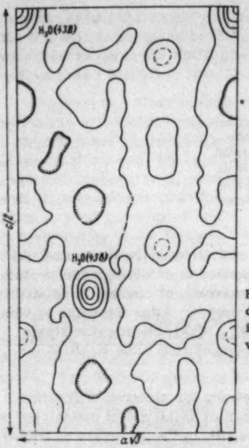

Fig. 2. Differential section of three-dimensional Fourier potential series in $\bar{1}10$ plane, for structure under investigation.

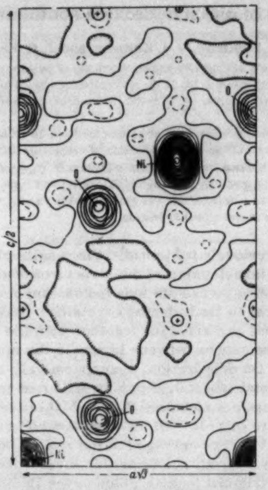

Fig. 3. Section of three-dimensional Fourier potential series in $\bar{1}10$ plane, for structure of potassium nickelate II.

fraction are due to separation of interlayer water in the chamber of the electron diffraction camera (pressure $5 \cdot 10^{-5}$ mm). From Table 1 we see that the parameter c of the cell increases from 19.15 to 19.90 Å after additional washing, in comparison with the period c of the cell of potassium nickelate II according to electron diffraction data.

From x-ray diffraction patterns (obtained at atmospheric pressure), the parameter c conversely decreases from 21.15 to 20.70 and becomes close to the parameter c of the higher hydroxide of nickel γ-NiOOH (20.65 Å) (all the cited formulas except γ-NiOOH were established by us by electron diffraction and confirmed by chemical analysis). The changes of length of the hydrated and anhydrous phases are here much less than in potassium nickelate I and are respectively 20.70 − 19.90 = 0.80 and 21.15−19.12 ≃ 2.03 Å. By analogy with clays, exchange of K^+ for H^+ and H_3O^+ ions is possible during washing, and therefore we can expect to find a change in the positions of the particles in the interlayer space. In this connection it seemed of interest to make a detailed determination of the structure of the compound obtained by additional washing. This was done by means of electron diffraction. From the substance we obtained electron diffraction patterns of the oblique texture type. The line intensities were estimated visually with the aid of photomicrometric measurements of some of the reflections to serve as standards. We found that the intensities of the reflections from the phase under test were close to those of potassium nickelate II, so that we can suppose that their structures must be almost the same. We used the signs of the structure amplitudes of the potassium nickelate II phase to calculate the Fourier sections of the structure. Figures 1 and 2 show the (110) section for the phase under investigation. Let us compare these figures with Figs. 3 and 4 for analogous sections of the structure of potassium nickelate II. From a comparison of these figures, it follows that the positions of nickel and oxygen (z_0 = 0.382) are the same in the two structures. However, in Fig. 2 the peak corresponding to a K atom in the position 00 ± z at z = 0.17_5 is absent, but there is a peak in the position $00^1/_2$. We shall return to this point later. At this stage we can calculate the principal interatomic distances in the structure: Ni−O = 1.90 Å; O−O = 2.82 Å (in basal plane); O−O = 4.68 Å (along edge of prism).

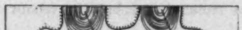

Fig. 4. Differential section of three-dimensional Fourier potential series in $\bar{1}10$ plane, for structure of potassium nickelate II.

TABLE 2

hkl	$\|\Phi_{exp}\|$	$\|\Phi_{cal}\|$	*hkl*	$\|\Phi_{exp}\|$	$\|\Phi_{cal}\|$	*hkl*	$\|\Phi_{exp}\|$	$\|\Phi_{cal}\|$
101	8.79	4.77	11.18	5.31	4.86	$21.\overline{10}$	3.39	3.99
$\bar{1}02$	13.17	12.72	11.21	5.10	4.05	$21.\overline{11}$	1.71	3.18
104	3.63	3.93	$\bar{2}.01$	2.22	2.04	21.13	4.20	4.05
$\bar{1}05$	13.41	15.42	202	8.04	5.94	21.16	3.27	3.54
107	4.94	5.10	$\bar{2}04$	2.34	1.83	300	4.71	4.77
$\bar{1}08$	11.76	14.49	205	8.16	7.83	303	4.14	3.60
10.10	8.25	9.90	$\bar{2}07$	2.64	2.85	306	3.24	2.34
$\bar{1}0.11$	6.78	7.50	208	7.32	7.95	220	3.45	3.54
10.13	8.94	10.29	20.10	3.84	5.82	223	3.06	2.70
$\bar{1}0.14$	2.91	3.45	20.11	4.02	4.62	226	2.31	1.83
10.16	6.48	7.50	20.13	4.92	5.94	312	3.12	2.19
110	14.28	11.58	212	5.58	3.93	315	3.00	2.70
113	9.54	8.43	214	1.20	1.35	318	2.85	2.88
116	5.31	4.74	215	5.01	5.01	$31.\overline{10}$	1.86	2.28
11.12	1.38	2.10	217	1.50	1.98	31.11	1.89	1.9^5
11.15	4.32	3.15	218	4.89	5.28	31.13	2.37	2.43

The potential peak at $00^1/_2$ cannot correspond to the position of a K atom, because there are no grounds for supposing that when the quantity of K in the structure of potassium nickelate II is reduced, the K^+ ion will shift from the center to the edge of a prism to a position with coordination number two. To find the nature of the peak with coordinates $00^1/_2$, we can conveniently analyze two assumptions: Either it corresponds to a hydrogen atom, or to a hydroxonium ion H_3O^+. According to the chemical analysis data, the test phase has the composition $K_{0.1}\cdot NiO_{1.77}\cdot 0.56H_2O$. This formula can be rewritten, taking hydrogen away from the water: $K_{0.1}H_{0.46}NiO_2\cdot 0.33H_2O$. From the formula we see that the ratio of the atomic concentrations of hydrogen and nickel is equal to 0.46 (~0.5), not allowing for hydrogen combined in the water. The multiplicity of the position corresponding to the peak with coordinates $00^1/_2$ in the space group R3m is three (c), i.e., the same as in nickel 3(a). Hence it follows that hydrogen occupies the position with a probability of about 0.5. Correspondingly the height of the peak must be equal to half the height of the potential peak of a hydrogen atom. The height of the potential peak of a hydrogen atom is about 40 V, whence it follows that in the synthesis (Fig. 2) the peak with coordinates $00^1/_2$ must have a height of about 20 V. However, the height of this peak is about 43 V, much higher than expected. Furthermore, the distance between the oxygen atoms along an edge of the prism, equal to about 4.68 Å, is too great to allow a symmetrical hydrogen bond. Thus the structural data contradict the hypothesis that the peak belongs to hydrogen at $00^1/_2$.

More convincing is the hypothesis that it is the H_3O^+ ion which is present between the layers. In this case the potential peak might correspond to the oxygen of the hydroxonium. The distance of 2.34 Å between the peak at $00^1/_2$ and the peak corresponding to oxygen from the octahedral environment of the nickel corresponds to the distance between two oxygen atoms with a hydrogen bond between them.

The third proton from the hydroxonium ion H_3O^+ is apparently located near the center of a trigonal prism; this is natural, since when K ions are washed out of nickelate the alkali metal cations can exchange with hydrogen during washing out. Further support for the idea that the peak with Z = 0.5 corresponds to a hydroxonium ion (or more precisely, the oxygen from a hydroxonium ion) is provided by its energy of formation[3,4] from H^+ and H_2O (169 kcal/g-ion), which is much greater than the energy of hydration of potassium (81 kcal/g-ion). Whereas the bond of K^+ and H_2O is insufficiently strong to retain water in a vacuum, since the binding energy between H^+ and H_2O is over twice as great as that between K^+ and H_2O, dissociation of H_3O^+ may fail to occur in a vacuum.

From the chemical formula it follows that the height of the peak with coordinates $00^1/_2$ should correspond to about half the height of the potential peak of oxygen; however, its height (about 43 V) corresponds to about 1/5 of the oxygen peak (about 260 V). This reduction may be due to two circumstances, as follows. 1) Only part of the hydrogen in the compound is bound in water molecules. The rest is bound to oxygen from octahedral coordination of Ni, forming the hydroxyl group OH^-; correspondingly not all the water revealed by chemical analysis will be bound in hydroxonium ions. Thus the amount of hydroxonium per molecule of the compound will not be about 0.46 but much less. 2) It is thought that the H_3O^+ ion has a large temperature factor.

On the basis of structural analysis in the phase obtained by intensive washing of potassium nickelate, the atoms are in the following crystallographic positions (space group $R\bar{3}M$) K 3(a): 000; O_I 6(c): 00z; $00\bar{z}$, $z_{O_I} = 0.38_2$; O_{II} (H_3O^+) 6(c): 00z, $00\bar{z}$, $z_{O_{II}} = 0.5$ (plus multiplication by the lattice R). The hydroxonium ions occupy the vacancies with a probability of about 0.2.

Table 2 lists the experimental and calculated values of the amplitudes R = 16.1%, for the composition $(H_3O)_{0.2}\cdot NiO_2$. Finally, taking account of all the interlayer water, the composition of the phase can be expressed as $K_{0.1}\cdot (H_3O)_{0.2}NiO_{1.72}(OH)_{0.26}\cdot 0.13H_2O$. Water in the phase, not bound to hydrogen, is lost during electron diffraction. As a result, the lattice parameter c, as we remarked above, is reduced from 20.70 to 19.90 Å. Now let us return to the question of the potassium content of the phase. According to the chemical analysis data, the K atom content of additionally washed potassium nickelate suspension is less than that of potassium nickelate II. If we assume that extra potassium is lost at the moment of preparation of the specimens for electron diffraction analysis, we can suppose that K ions are present in the structure in insufficient quantities for detection by electron diffraction. Nevertheless, we can suppose that in this structure they will lie near their former positions in the structure of potassium nickelate II, i.e., within the trigonal prisms rather than on their edges.

We can thus draw conclusions on the structure of the interlayer space of the higher hydroxide of nickel, γ-NiOOH, when in a vacuum[1] of about 10^{-4} mm. So far the literature has not contained a complete representation of the atomic structure of this compound as a whole. It is known that the unit cell contains three identically repeating layers of oxygen octahedra (filled with nickel) with interlayer distances (along prism edges) of 5.08 Å (in our results, 4.68 Å approx.) – in general features, similar[5,6] to CoOOH, except that in CoOOH the prism edge of the interlayer space, equal to 2.4 Å, is half as long as in γ-NiOOH, and is close to the value characteristic of the linear $O-H-_0$ bond.

According to the literature data in the structure of the higher hydroxide of nickel, the interlayer space contains 1/3 of a molecule of γ-NiOOH. Let us return to our own results. From the electron diffraction analysis, the most probable variant is that in which H_3O^+ ions are arranged between the layers of the higher hydroxide of nickel; then with the oxygen of the hydroxonium located at the center of a prism edge, the O–(H)–O distance will be 2.34 Å, though this is somewhat less than the usual distance for this type of bond (linear bond).

The authors would like to thank Academician N. V. Belov for suggesting that hydroxyl ions are present in these structures.

---

[1] We are supposing that γ-NiOOH can be obtained in a vacuum (of about 10^{-4} mm) only because of the presence of K ions as impurity in the higher hydroxide of Ni, apparently playing the part of a structure stabilizer.

---

[1] P. N. Bityutskii and V. I. Khitrova, Kristallografiya, 13, 53 (1968) [Sov. Phys.–Crystallogr., 13, 40 (1968)].
[2] P. N. Bityutskii and V. I. Khitrova, Kristallografiya, 14, 122 (1969) [Sov. Phys.–Crystallogr., 14, 99 (1969)].
[3] B. V. Nebrasov, Principles of General Chemistry [in Russian], Vol. 1, Khimiya, Moscow (1969), p. 213.
[4] N. A. Izmailov, Electrochemistry of Solutions [in Russian], Izd. Khar'kovsk. Univ., Khar'kov (1959).
[5] P. N. Bityutskii and V. I. Khitrova, Zh. Strukt. Khim., 9, 1035 (1968).
[6] Yu. D. Kondrashov and N. M. Fedorova, Dokl. Akad. Nauk SSSR, 94, 229 (1954).
[7] O. Clemser and J. Einerhand, Z. anorgan. Chem., 261, 26, 43 (1950).

Proton magnetic resonance investigation of the localization of the protons in the crystal structures $Na_2Cr_2O_7 \cdot 2H_2O$ and $Li_2Cr_2O_7 \cdot 2H_2O$

G. R. Bulka, V. M. Vinokurov, É. A. Kuz'min, Yu. A. Kharitonov, and N. V. Belov

Kazan State University, Institute of Crystallography, Academy of Sciences of the USSR

(Submitted October 27, 1972)
Kristallografiya, 18, 984-987 (September-October 1973)

The crystal structures of Na and Li dichromates are fully deciphered; the coordinates of the basal hydrogen atoms (30 position parameters) are presented. The question concerning the hydrogen bonds is discussed.

Among the salts composed of dichromic acid and the alkali metals (ordinarily the so-called dichromates), only two contain water in their composition: $Li_2Cr_2O_7 \cdot 2H_2O$ and $Na_2Cr_2O_7 \cdot 2H_2O$. An x-ray diffraction investigation of the former salt[1] showed that it crystallizes in space group C2/c, a_0 = 13.30, b_0 = 7.51, c_0 = 7.67 Å; β = 93°30', and Z = 4. On the basis of an analysis of the interatomic distances and infrared spectra, the authors of ref. 1 proposed that the chemical formula of lithium dichromate can be depicted in the form $Li_2H_4Cr_2O_9$. Space group $P2_1/m$, a_0 = 6.05, b_0 = 10.5, c_0 = 12.6 Å; β = 94.9°, and Z = 4 was assumed in the initial x-ray diffraction investigation of sodium dichromate crystals.[2] It was shown in later papers[3,4] that this salt crystallizes into the noncentrosymmetric group $P2_1$ (a_0 = 6.21, b_0 = 10.90, c_0 = 12.94 Å; β = 95°, and Z = 4), which was confirmed by its considerable piezoelectric effect.

Polycrystalline and single-crystal samples of lithium dichromate and sodium dichromate were investigated by the proton magnetic resonance (PMR) method in order to establish unambiguously the chemical formula of the former and the group symmetry of the latter. The PMR spectra were obtained on a wide line NMR spectrometer under the following scanning conditions: frequency of the autodyne generator 17.45 MHz, amplitude of the modulating field 0.5 G, rate at which the spectrum was transmitted 0.0486 G/sec, time constant of the phase detector 4 sec, and temperature 300°K. The shape of the PMR line for the polycrystalline samples (Fig. 1) of the salts investigated is normal for two-spin systems,[5] which immediately contradicts the existence of the $[HCrO_4]^{1-}$ anions in these compounds and confirms the results of refs. 3 and 4. This permits one to adopt quite unambiguously the formula $Li_2Cr_2O_7 \cdot 2H_2O$ for lithium dichromate. The narrow peak in Fig. 1 is explained by the presence of free water both sorbed by the surface of the polycrystalline sample and as inclusions of the mother liquor, which were confirmed by visual observations. The magnitude of the doublet splitting 2α = 10.36 G for sodium dichromate and 11.38 G for lithium dichromate, which leads to a proton–proton distance in the water molecules of 1.585 and 1.550 Å respectively.

The single-crystal samples used for the investigation were obtained by the slow evaporation of the aqueous dichromate solutions in a desiccator over concentrated H_2SO_4 in a nitrogen atmosphere. The average dimensions of the sodium dichromate samples were 4 × 1.5 × 0.8 cm and those for lithium dichromate 3 × 0.8 × 0.8 cm.

The angular dependences of the PMR spectra of the $Li_2Cr_2O_7 \cdot 2H_2O$ single crystals were investigated by rotating the crystal about [010] and [001] (Fig. 2). Their character indicates that there are just two orientations of the proton–proton vector in the unit cell, which are defined relative to the crystallographic axes by the following angles: $\alpha = \widehat{a_0 r} = 120°$, $\beta = \widehat{b_0 r} = 90 \pm 17°$, $\gamma = \widehat{c_0 r} = 23°30'$, where $\mathbf{r}$ is the proton–proton vector. This unambiguously leads to space group C2/c along with the presence of eight molecules in the unit cell. An analysis of the lithium dichromate structure indicates that with the orientation of the interproton vectors found, a hydrogen bond can be formed with just one of the oxygen atoms belonging to the $Cr_2O_7^{2-}$ diortho group. Each such O atom participates in two hydrogen bonds, which evidently also leads to a slight isotropic temperature correction for this atom, 0.17 (the average with respect to the structure is 1.97).

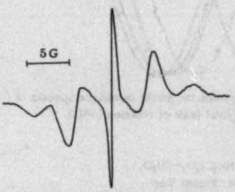

Fig. 1. Proton magnetic resonance spectrum of a polycrystalline sample of $Na_2Cr_2O_7 \cdot 2H_2O$.

The angular dependence of the PMR spectra of the sodium dichromate single crystal was investigated by rotating the crystal about the [010], [001], and two other axes, which lie in the (001) plane and form angles of 43 and 60° respectively with the b_0 axis (Fig. 3). This aggregate of experimental points can be explained by the existence of eight proton–proton senses, which are linked by an element of symmetry not higher than L_2 or P, in the $Na_2Cr_2O_7 \cdot 2H_2O$ unit cell. These eight senses are defined by angles φ and ρ (Table 1).

The experimental set of the interproton vectors obtained confirms the results of refs. 3 and 4 and permits one to select space group $P2_1$ for sodium dichromate.

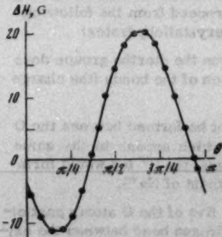

Fig. 2. Angular dependence of the proton magnetic resonance spectra of a lithium dichromate single crystal (axis of rotation [010]).

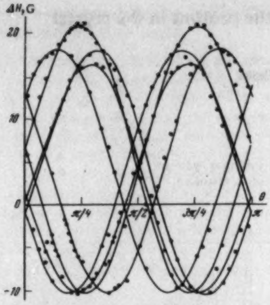

Fig. 3. Angular dependence of the proton magnetic resonance spectra of a sodium dichromate single crystal (axis of rotation [001]).

TABLE 1. $Na_2Cr_2O_7 \cdot 2H_2O$. Eight Proton−Proton Vectors

No. of H atoms	φ, deg	ρ, deg
1	30*	35
2	30	215
3	137	0
4	137	180
5	55	33
6	55	213
7	57	22
8	57	202

*φ is reckoned from the positive direction of the b_0 axis, and ρ from the positive direction of the a_0 axis in the a_0c_0 plane.

The investigation of the sodium dichromate structure indicates that the principal cause of its structure is created by the distorted sodium polyhedra, which are aligned in chains in the (010) plane. These chains are linked to each other by the Cr_2O_7 diortho groups. The O atoms from the water molecules and the diortho groups form nonuniform staggered (010) layers; the four water oxygens and four oxygens of the diortho groups lie in one layer, the second layer consists of 10 O atoms belonging only to the diortho groups. An analysis of the structure shows that the inhomogeneity of these planar networks can be moderated only through hydrogen bonds between the layers. In order to derive the pattern of the hydrogen bonds in the crystal, let us proceed from the following usual assumptions made for crystallohydrates:

a) The bridge O atom from the diortho groups does not participate in the formation of the bonds (the charge on the bridge O atom > + 3);

b) a hydrogen bond cannot be formed between the O atoms of the diortho group which appear in the same sodium polyhedron (in this case, the H^+ ion would form a part of the nearest environment of Na^+).

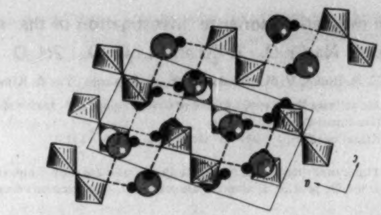

Fig. 4. Crystal structure of lithium dichromate. Projection on (010). The black spheres are H atom; the large shaded ones are the O atoms in the water. The spheres represented by the dotted lines are the Li atoms.

TABLE 2. Coordinates of the H Atoms in the Two Dichromates

Compound	Atom	x	y	z
$Na_2Cr_2O_7 \cdot 2H_2O$	H_1	−0.080	0.715	0.250
	H_2	−0.177	0.589	0.286
	H_3	0.375	0.603	0.054
	H_4	0.201	0.710	0.054
	H_5	0.104	0.558	0.577
	H_6	0.292	0.637	0.535
	H_7	0.494	0.591	0.835
	H_8	0.692	0.674	0.780
$Li_2Cr_2O_7 \cdot 2H_2O$	H_I	0.206	0.772	0.305
	H_{II}	0.153	0.712	0.469

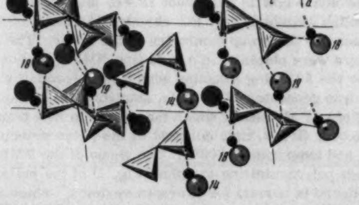

Fig. 5. Crystal structure of sodium dichromate. Projection on (010). Only one diortho group is depicted in the lower layer, the remaining details of the layer are easily obtained by the treatment of axis 2_1. The black spheres are the H atoms (the small ones are the unobservable protons hidden by the oxygen atom), the large shaded ones are the O atoms of the water (the numbers denote the heights with respect to the b axis in hundredth parts of the cell).

With these assumptions, five of the O atoms participate in the formation of a hydrogen bond between the oxygen layers, and the remaining three form hydrogen bonds within the water−oxygen layer.

The coordinates of the hydrogen atoms in the crystal lattice can be calculated on the basis of this scheme for the hydrogen bonds and also from the results of refs. 6 and 7. The data obtained substantially supplement the description of the crystal structures of lithium and sodium dichromates[1–4] and permit one to look at them in a new way. If it is assumed that the hydrogen bond is no less strong than the Li−O and Na−O bonds, then both structures are represented as a collection (a bundle) of small chains $[Cr_2O_7 \cdot nH_2O]_\infty$ connected to each other through the cations (Figs. 4, 5). The coordinates of the hydrogen atoms are given in Table 2.

The small chains in $Li_2Cr_2O_7 \cdot 2H_2O$ $\{[Cr_2O_7] \cdot 2H_2O\}_\infty$ extend along [101] (Fig. 4).

The $\{[Cr_2O_7] \cdot H_2O\}_\infty$ chain in sodium dichromate passes through the center of the selected cell parallel to the *a* axis. The infinite two-dimensional undulating layer $\{[Cr_2O_7] \cdot 3H_2O\}_{\infty\infty}$ passes through the origin of the cell (also parallel to *a*, see Fig. 5) and is put together with similar $[Cr_2O_7] \cdot H_2O$ chains, which are strengthened with additional H_2O molecules.

---

[1] I. D. Datt, I. V. Rannev, G. G. Balicheva, and R. P. Ozerov, Kristallografiya, 15, 949 (1970) [Sov. Phys.—Crystallogr., 15, 826 (1971)].

[2] J. A. Campbell, Acta Crystallogr., 9, 192 (1956).

[3] Ya. A. Kharitonov, É. A. Kuz'min, and N. V. Belov, Kristallografiya, 15, 942 (1970) [Sov. Phys.—Crystallogr., 15, 820 (1971)].

[4] Yu. A. Karitonov, É. A. Kuz'min, and N. V. Belov, Dokl. Akad. Nauk SSSR, 186, 96 (1969) [Sov. Phys.—Dokl., 14, 403 (1969)].

[5] G. E. Pake, J. Chem. Phys., 16, 327 (1948).

[6] Z. M. Elsaffar, J. Chem. Phys., 45, 4653 (1966).

[7] G. R. Bulka, S. V. Vedenin, V. M. Vinokurov, T. A. Zakharchenko, N. M. Nizamutdinov, and R. S. Tukhvatullin, Kristallografiya, 16, 138 (1971) [Sov. Phys.—Crystallogr., 16, 107 (1971)].

Position of the hydroxyl groups in the structure of hydrosodalite

V. Yu. Galitskii, V. N. Shcherbakov, and S. P. Gabuda

Institute of Crystallography, Academy of Sciences of the USSR
Institute of Physics, Siberian Branch, Academy of Sciences of the USSR
(Submitted October 22, 1971; resubmitted October 25, 1972)
Kristallografiya, 18, 988-991 (September-October 1973)

By applying the method of nuclear magnetic resonance to ^{23}Na, the quadrupole coupling constants of the sodium nuclei in hydrosodalite were measured between −140 and +350°C. The two OH groups associated with the unit cell lay with equal statistical probability in the eight-fold positions 8(e), with coordinates (x, x, x) where $x = -0.15a_0$. At room and higher temperatures, diffusion of the OH groups occurred in the cavities of the structure, while at temperatures above +120°C the sodium atoms diffused as well. On reducing the temperature from room to −80°C, the diffusion of the OH groups was retarded, but they remained in disordered positions right down to −120°C. At lower temperatures the ordered disposition of the OH groups lowered the symmetry of the hydrosodalite.

Hydrosodalite $Na_8[Al_6Si_6O_{24}](OH)_2 \cdot 6H_2O$ is an aluminosilicate belonging to the cubic system and resembling the zeolites (space group[1] $P\bar{4}3m$, $a_0 = 8.88$ Å). The structure is formed by an isomeric framework, with large spaces occupied by sodium atoms, water molecules, and hydroxyl groups. Proton magnetic resonance (PMR) was earlier employed in order to determine the orientation of the p−p vectors of the water molecules, thus revealing the manner in which the hydrogen entered into the structure, and in particular indicating the position of the H_2O in hydrosodalite.[2]

The question as to the location of the OH groups remained open, since in the presence of water molecules the PMR spectra were usually insensitive to variations in the coordinates of the "isolated" protons in the composition of the hydroxyl.

In order to discover the position of the OH groups in hydrosodalite, we explored the NMR spectra of ^{23}Na. The existence of quadrupole moments on the sodium nuclei (spin 3/2) has the effect that the NMR spectra depend in a very sensitive manner on the way in which the charges are disposed in the lattice, including the position of the negatively charged $[OH]^-$ ion. It is clear, in particular, that a knowledge of even the symmetry of the electrical environment of the sodium atom will enable us to solve the fundamental question as to whether the hydroxyls lie in the centers of the cavities, isomorphically replacing the chlorine in chlorosodalite (which is isostructural with respect to hydrosodalite[3]). The ^{23}Na NMR data also enable us to study the mobility of the sodium atoms, as well as the possible mobility of the hydroxyl groups.

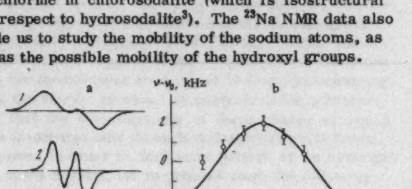

Fig. 1. Nuclear magnetic resonance (NMR) spectra of ^{23}Na in hydrosodalite at high temperatures (a) and angular dependence of the shifts in the spectral components on rotating the crystal around the [001] axis (b). The curves were calculated in accordance with ref. 6 in the second order of perturbation theory for $e^2Qq/h = 420$ kHz (the principal axes of the axial tensors are oriented along directions of the [111] type): 20° (1), 100° (2), 275°C (3); b) $\nu_0 = 4170$ kHz, T = 100°C.

We studied hydrosodalite samples grown by the hydrothermal method.[4] The NMR spectra of ^{23}Na were taken in a modified RYa-2301 spectrometer, in fields between 4 and 10 kOe. We studied the shape and the angular dependence of the shifts of the central components of the NMR spectra of ^{23}Na corresponding to the transitions $+\frac{1}{2} \rightleftharpoons -\frac{1}{2}$; no side satellites ($\pm\frac{3}{2} \rightleftharpoons \pm\frac{1}{2}$ transitions) occurred in our samples. We analyzed the resultant relationships by examining the quadrupole splittings and shifts of the NMR spectra, using the Pound[5] and Vokoff[6] methods. As a result of this analysis, we obtained the quadrupole coupling constants determining the energy of the interaction between the quadrupole moments of the nuclei and the electric-field gradients, and also further information regarding the symmetry and orientation of the principal axes of the electric-field gradient tensor at the sites of the sodium nuclei.

First we studied the spectra at room temperature. We found that at room temperature the NMR line of ^{23}Na was very wide. On raising the temperature the line contracted slightly, and above 60°C it decomposed into two identical components (Fig. 1). The angular dependence of the shifts of these components relative to the NMR signal of ^{23}Na in an aqueous solution of NaCl is shown in Fig. 1. Simple analysis of these relationships on the basis of refs. 5 and 6 shows that the electric-field gradient tensors at the ^{23}Na nuclei in hydrosodalite are axially symmetrical, with the orientation of their principal axes along the space diagonals of the cube, i.e., along the [111] type of direction. The value of the quadrupole coupling constant at +100°C equals 420 ± 20 kHz. These data agree with the fact (already known from the structure of the crystal) that the sodium lies on the space diagonals of the cubic lattice of sodalite, in the 8(e) positions, while the charges of the hydroxyl do not disrupt the axial symmetry of the electrical environment of the sodium ion. This is entirely possible if the OH lies in the center of the cavity in the 2(a) positions, or if the OH executes rapid motion around the center of the cavity, so that the average charge distribution at +50-100°C is centrosymmetrical.

In order to resolve this dilemma we studied the NMR spectra over a wide temperature range (Figs. 1 and 2). We found that on raising the temperature above +120°C the shifts of the central component diminshed, and at 275°C they vanished for all orientations of the crystal. It follows[6] that the quadrupole coupling constant of ^{23}Na is equal to zero at 275°C. This is only possible if the sodi-

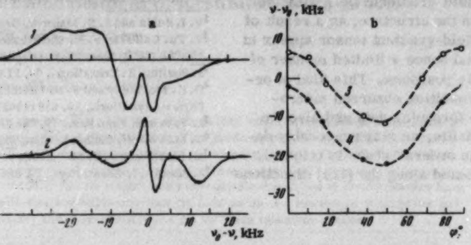

Fig. 2. NMR spectra of ^{23}Na in hydrosodalite (a) at −100°C (1), −130°C (2), and angular dependences (b) of the shifts in the points of maximum curvature lying on the high (3) and low (4) frequency side. The spectrum always contains a weak narrow line, the frequency of which coincides with the Larmor frequency for the ^{23}Na nuclei and is independent of the orientation of the crystal; 3, 4) ν_0 = 6800 kHz, T = −85°C.

um ions diffuse in the structure; from ordinary considerations[7] we may estimate the height of the diffusion barrier as U_0 = 18 kcal/mole. On reducing the temperature below +20°C the width and shifts of the NMR line increase, and at −80°C they reach a maximum value of 20 kHz at ν_0 = 6.8 MHz. Further reducing the temperature does not lead to any increase in the shifts, but at −(100-120)°C the NMR signal of ^{23}Na splits into several components (Fig. 2).

We attempted to determine the quadrupole coupling constants and the orientation of the electric-field gradient tensor at low temperatures. To this end we studied the angular dependence of the shifts (Fig. 2) in the NMR lines of ^{23}Na at −85°C. Analysis of the resultant relationship showed that it could not be represented by any one electric-field gradient tensor, or a single value of the quadrupole coupling constant. In other words, the wide diffuse NMR line of ^{23}Na at −85°C is due to the superposition of a large number of individual, closely spaced lines, the angular dependences of these not being capable of individual determination, owing to their mutual superposition. At −120°C the number of these components evidently diminishes, since fine structure appears in the spectrum; however, it still remains too large to allow the behavior of each individual one to be followed, in view of the cubic symmetry of the crystal.

We may thus only conclude from the observed angular dependence that the electric-field gradient tensor at the sodium nuclei at −85°C is nonaxial, since, if axial symmetry were preserved, the angular dependence of the shifts would remain constant as the temperature fell from +100 to −85°C (regardless of its amplitude). We found from the maximum shift of the central line[5,6] that the quadrupole coupling constant of ^{23}Na at temperatures below −85°C equalled 1.7 ± 0.3 MHz (the limits of error are determined by the indeterminacy of the asymmetry parameter).

The temperature dependence of the NMR spectra of ^{23}Na may be associated with the annular diffusion of water, and possibly of the OH groups. The temperature at which the effect of annular diffusion begins may be estimated[7] from the condition that the frequency of the motion $\nu_c = \nu_0 \exp(-U_0'/kT)$ should be greater than or equal to the quadrupole coupling constant of ^{23}Na at low temperature. The value[2] of $\nu_0 = 10^{12}$ Hz, U_0' = 5 kcal/mole. Hence the temperature at which ν_c = 1.7 ± 0.3 MHz is 80 ± 5°C, which practically coincides with the observed temperature at which the NMR spectra start changing.

Thus the retardation of internal mobility in hydrosodalite is accompanied by an increase in the quadrupole coupling constant of ^{23}Na from 420 kHz to 1.7 MHz. From this change we may determine the source of the change in the electric-field gradient. We note that, in calculating the jump in field gradient and the quadrupole coupling constant, there is no need to allow for the contributions from the stationary lattice charges, since these contributions are the same whether motion occurs or not. Using the Bersohn method[8] we thus calculate the changes taking place in the corresponding contributions from the OH groups in the cavities of the sodalite structure (Table 1) when these moved out of the 2(a) and 8(e) positions and when the diffusion of the water molecules and OH groups with respect to the 8(e) positions was retarded. We see that a change in the mobility of the molecules can only explain part of the jump in the quadrupole coupling constant. The statistical displacement of the OH groups from position 8(e) to position 2(a) increases this constant, fusion of OH groups with respect to the 8(e) positions completely explains the observed change in the quadrupole coupling constant of ^{23}Na.

It thus follows from the ^{23}Na NMR data that the OH groups in hydrosodalite lie in the 8(e) positions. The diffuseness of the ^{23}Na NMR line for temperatures from −85 to −120°C indicates the disordering of this position. The observed decomposition of the spectrum into several components at −120° may be associated with a sharp reduction in the number of Na positions which are not equiv-

TABLE 1. Calculated Change in the Quadrupole Coupling Constants of the ^{23}Na Nuclei in Hydrosodalite in kHz

Theoretical value			Experimental value of the change in the constant on reducing the temperature from +20 to −80°C
displacement of OH from 2(a) to 8(e)	retardation of the diffusion of OH through the 8(e)	retardation of the diffusion of H_2O through the 8(e)	
−1200	1590	380	1285 ± 300

alent as regards electric-field gradient, i.e., with the ordering of the OH groups in the structure, as a result of which a limited number of field-gradient tensor appear at the Na nucleus at −120°C, and hence a limited number of structurally nonequivalent Na positions. This kind of ordering signifies the phase transition observed macroscopically. Considering the foregoing data and also the known structure of hydrosodalite, we may reasonably deduce that the structure of the ordered phase is trigonal, polar, and with the axes oriented along the [111] directions of the original cubic crystal.

---

[1] V. I. Bukin and E. S. Makarov, Geokhimiya, 1, 31 (1967).

[2] V. Yu. Galitskii, V. N. Shcherbakov, and S. P. Gabuda, Kristallografiya, 17, 788 (1972) [Sov. Phys. – Crystallogr., 17, 691 (1973)].

[3] L. Pouling, Z. Kristallogr., 74, 213 (1930).

[4] O. K. Mel'nikov and B. N. Litvin, Kristallografiya, 10, 266 (1965) [Sov. Phys. – Crystallogr., 10, 216 (1965)].

[5] R. V. Pound, Phys. Rev., 79, 685 (1950).

[6] G. M. Volkoff, Canad. J. Phys., 31, 820 (1952).

[7] M. Bloembergen, E. M. Purcell, and R. V. Pound, Phys. Rev., 73, 679 (1948).

[8] R. Bersohn, J. Chem. Phys., 29, 326 (1958).

Magnetically nonequivalent cation positions in substituted ferrite garnets

I. S. Lyubutin, A. P. Dodokin, and L. M. Belyaev
Institute for Crystallography, Academy of Sciences of the USSR
(Submitted November 9, 1972)
Kristallografiya, 18, 992-998 (September-October 1973)

By use of γ-resonance Mössbauer spectroscopy it has been observed that magnetically nonequivalent states of Fe atoms in the d sublattice, caused by the different number of magnetic neighbors, are formed in the ferrite garnet system $Y_{3-x}Ca_xFe_{5-x}Sn_xO_{12}$. The temperature curve of the magnetic moments of Fe^{3+} ions has been determined for each type of nonequivalent d position. The intersublattice exchange interaction integrals of magnetization of the *a* sublattice and of various magnetically nonequivalent positions of the d sublattice have been made. An equation has been obtained which describes the field on tin as a function of temperature and concentration, with the magnetically nonequivalent states of the Fe^{3+} ions taken into account.

INTRODUCTION

The replacement of magnetic atoms by nonmagnetic atoms in ferrite garnets results in weakening of the basic *a*–d exchange interaction, change in magnetic properties, and lowering of the ferrimagnetic transition temperature T_N. If the nonmagnetic ions in such garnets are statistically distributed about a sublattice, then magnetically nonequivalent positions, associated with the presence of a different number of magnetic and nonmagnetic neighbors in the closest environment of an Fe^{3+} ion, can be formed for the Fe^{3+} ions.

The study of substituted ferrite garnets by means of the Mössbauer effect has allowed the experimental observation of the nonequivalent positions.[1–5] Upon the replacement of the Fe^{3+} ions in a d sublattice by nonmagnetic ions, the number of nonequivalent positions for *a*-type Fe^{3+} ions is 7. Upon the substitution of nonequivalent ions in an *a* sublattice, from the point of view of nearest environment there should be only five positions for d-type Fe^{3+} ions.[5] Therefore a garnet system in which the substituent nonmagnetic ions are located in the *a* sublattice is presented as being more simple and convenient for the study of the statistics of magnetically nonequivalent states of Fe^{3+} ions.

From x-ray and Mössbauer studies of the garnet system $Y_{3-x}Ca_xFe_{5-x}Sn_xO_{12}$ it follows that tin replaces iron in the octahedral *a* sites.[6,5] The distribution of ions about the sublattices is as follows: $\{Y_{3-x}Ca_x\}[Fe_{2-x}Sn_x](Fe_3)O_{12}$.

The probability that ions of the *a* and d sublattices will have a given number of magnetic ions in their nearest environment upon substitution in the *a* sublattice is shown in Table 1. P_a^{nd} is the probability of an *a*-type iron ion having n magnetic ions in the nearest d environment (n = 6 for the $Y_{3-x}Ca_x[Fe_{2-x}Sn_x](Fe_3)O_{12}$ system). P_d^{na} is the probability of a d-type Fe^{3+} ion having n nearest *a*-type Fe^{3+} ions in the *a* sublattice (n = 0, 1, ... 4). P_a^{na} is the probability of an *a*-type Fe^{3+} ion having n nearest ions in the *a* sublattice (n = 0, 1, ... 8). P_d^{nd} is the probability of a d-type Fe^{3+} ion having n nearest ions in the d sublattice (n = 4).

Calculations were carried out in accordance with the equation

$$P_j^{ni} = \frac{z_j^i!}{n!\,(z_j^i - n)!}\, m^n (1-m)^{z_j^i - n}, \tag{1}$$

where i, j = *a*, d; z_j^i is the number of nearest i-th neighbors of the j-th ion examined: $z_d^a = 4$ for calculation of the probability P_d^{na}, $z_a^d = 6$ for P_a^{nd}, and $z_a^a = 8$ for P_a^{na}; and m = 2 − x/2.

EXPERIMENT

We studied the temperature dependence of the Mössbauer spectra of Fe^{57} and Sn^{119} in garnets $Y_{3-x}Ca_xFe_{5-x}\cdot Sn_xO_{12}$ (x = 0, 0.3, and 0.5) from 78 to 600°K. Measurements were carried out on apparatus described earlier.[7] The garnet specimens were simultaneously enriched with the isotopes Fe^{57} and Sn^{119} and carefully controlled in regard to phase composition. The lattice parameters for garnets with x = 0.0, 0.3, and 0.5, respectively, are as follows: a_0 = 12.374 ± 0.002 Å, 12.411 ± 0.003 Å, and 12.437 ± 0.003 Å.

Values of the Néel temperature T_N which we obtained for these specimens were 555, 500, and 450°K, respectively.

RESULTS AND DISCUSSION

1. Lines corresponding to the d sublattice in the Mössbauer spectrum of Fe^{57} nuclei in the substituted garnets were found to be greatly broadened and even split (Fig. 1). This is evidence of the presence of a few mag-

TABLE 1

(1a) First coordination sphere

x	P_d^{4a}	P_d^{3a}	P_d^{2a}	P_d^{1a}	P_d^{0a}	P_a^{6d}
0	1	0	0	0	0	1
0.3	0.52	0.37	0.1	0.01	0	1
0.5	0.32	0.415	0.21	0.05	0.005	1

(1b) Second coordination sphere

x	P_a^{8a}	P_a^{7a}	P_a^{6a}	P_a^{5a}	P_a^{4a}	P_a^{3a}	P_a^{2a}	P_a^{1a}	P_a^{0a}	P_d^{4d}
0	1	0	0	0	0	0	0	0	0	1
0.3	0.272	0.385	0.238	0.084	0.018	0.003	—	—	—	1
0.5	0.100	0.267	0.311	0.208	0.087	0.023	0.004	—	—	1

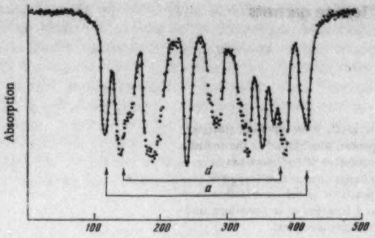

Fig. 1. Mössbauer spectrum of Fe^{57} nuclei in the garnet $Y_{2.7}Ca_{0.3}Fe_{4.7}$·$Sn_{0.3}O_{12}$ at 340°K.

netically nonequivalent positions in the d sublattice. The three most intense components were successfully isolated upon resolution of the experimental spectrum. Comparison of the relative intensities of these components with calculated values (Table 1) showed them to correspond to d-type Fe^{3+} ions having four, three, and two magnetic neighbors in the *a* sublattice in the nearest environment.

For all specimens, the widths of the Mössbauer lines belonging to the *a* sublattice differed but little from one another (Fig. 1). This indicates that nonequivalence of *a*-type ions caused by the difference in magnetic environment is small. It shows the weakness of the *a*–*a* exchange interaction (i.e., only their second coordination sphere changes upon substitution). In Fig. 2 is shown the temperature dependence of effective magnetic fields on the nuclei of the iron atoms for the *a* sublattice (Fig. 2a) and for the different nonequivalent sites of the d sublattice ($H_4{}^d$, $H_3{}^d$, and $H_2{}^d$, where the lower index corresponds to the number of nearest magnetic neighbors) (Fig. 2b). Values of effective fields H^a and $H_n{}^d$ as extrapolated to 0°K were also obtained, and fields for the *a* and d sublattices as functions of temperature and reduced coordinates [$\widetilde{H}^a \equiv H^a(T)/H^a(0)$, $\widetilde{T} \equiv T/T_N$, $\widetilde{H}_n{}^d \equiv H_n{}^d(T)/H_n{}^d(0)$], were plotted (Fig. 3). We used the NMR results of ref. 8 for extrapolation of the H(T) curves to 0°K, and calculated the correction to the effective field for the *a* and d sublattices for the change from liquid-nitrogen to liquid-helium temperature.

Having plotted the temperature function of the effective field for the *a* sublattice in reduced coordinates, we observed that the $\widetilde{H}^a(T)$ curves coincide for all substitutions (Fig. 3).

At the present time it is taken for granted that the effective magnetic field on the nucleus of an Fe^{3+} ion in any sublattice as a function of temperature is proportional to the magnetic moment of the ion.[9,10] If the magnetization is expressed through the effective magnetic field on the nucleus, the molecular field equation for the *a* sublattice is written in the following form:

$$H^a(T) = B_{5/2}\left[\frac{I_0^2}{T_N(x)NkT}\left(n_{aa}(x)\rho_a(x)H^a(T) + n_{ad}(x)\rho_d H^d(x,T)\right)\right], \tag{2}$$

where $B_{5/2}$ is the Brillouin function for spin 5/2, I_0 is the magnetic moment of a gram-ion of Fe^{3+} at 0°K, N is Avogadro's number, k is Boltzmann's constant, n_{ij} is the molecular field coefficient, and ρ_j is the fraction of magnetic ions in the j-th sublattice. The first term in the brackets describes the influence on the *a* sublattice of the nearest *a* ions (second coordination sphere). It differs considerably for *a*-type ions which differ in nearest *a*-type environment (Table 1). If the role of this term is important, then a set of magnetic fields should exist on the nuclei of the *a*-type Fe^{3+} ions, which is contradictory to experiment. Consequently, this term is small in comparison with the second, which describes the *a*–d intersublattice interaction.

The second term in the brackets describes the influence on the *a* sublattice of the six nearest d-type iron ions (first coordination sphere). Since the nearest environment of the *a*-type Fe^{3+} ion consists of magnetically nonequivalent d-type iron ions, then the second term in (2) represents the sum of contributions from these nonequivalent ions:

$$n_{ad}\rho_d H^d(x,T) = \frac{2z_a{}^d}{Ng^2\mu_B^2} J_{ad} \frac{\sum_{n=1}^{4} P_d{}^{na}(x) H_n{}^d(x,T)}{\sum_{n=1}^{4} P_d{}^{na}(x)}, \tag{3}$$

where $z_a{}^d = 6$ is the number of nearest d-type iron ions in the environment of an *a*-type ion, g is the g factor of the

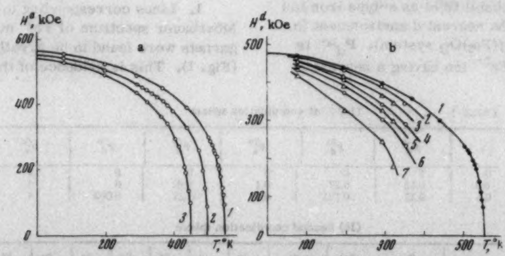

Fig. 2. Effective magnetic fields on nuclei of Fe^{3+} ions in $Y_{3-x}Ca_xFe_{5-x}Sn_xO_{12}$ garnets. a) *a* sublattice: 1) x = 0; 2) x = 0.3; 3) x = 0.5. b) Various magnetically nonequivalent sites in the d sublattice: 1) x = 0; 2, 4, 6) x = 0.3; 3, 5, 7) x = 0.5; 2, 3) H_4; 4, 5) H_3; 6, 7) H_2.

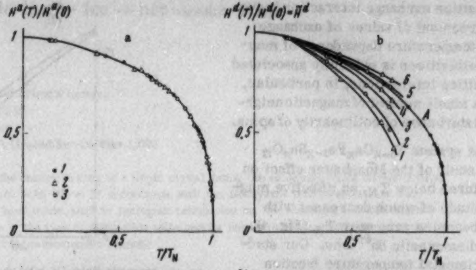

Fig. 3. Magnetic fields on nuclei of Fe^{3+} ions as functions of temperature for $Y_{3-x}Ca_xFe_{5-x}Sn_xO_{12}$ garnets with reduced coordinates H(T)/H(O) and T/T_N. a) *a* sublattice: 1) x = 0; 2) x = 0.3; 3) x = 0.5. b) Various magnetically nonequivalent positions in the d sublattice: A) x = 0; 2, 3, 5) x = 0.3; 1, 4, 6) x = 0.5; 1, 2) $\tilde{H}_2$; 3, 4) $\tilde{H}_3$; 5, 6) $\tilde{H}_4$.

Fe^{3+} ion, μ_B is the Bohr magneton, and J_{ad} is the intersublattice exchange integral. Here it is assumed that J_{ad} is the intersublattice exchange integral. Here it is assumed that J_{ad} = const. The summation is carried out from 1 to 4, since all d-type Fe^{3+} ions surrounding an *a*-type Fe^{3+} ion have not less than one magnetic neighbor.

The condition of invariance of $\tilde{H}^a(T)$ with respect to the degree of substitution of x should indicate that the argument of the Brillouin function [Eq. (2)] depends only on the corrected temperature:

$$\sum_{n=1}^{4} P_d^{na}(x)\tilde{H}_n^d(x,T) \Big/ T_N(x)\sum_{n=1}^{4} P_d^{na}(x) = M^d(T). \qquad (4)$$

The value of $M^d(\tilde{T})$ so determined is proportional to the algebraic sum of the magnetizations of the ions of the d sublattice with number of nearest magnetic *a*-type neighbors equal to 4, 3, 2, and 1. In this case the number of d-type ions of each type is considered. Condition (4) is the expression of the invariance of $\tilde{H}^a(\tilde{T})$ with respect to x under the conditions $J_{aa}/J_{ad} \ll 1$ and J_{ad} = const.

Now, using the experimental curves of $\tilde{H}_n^d$ and knowing the probability P_d^{na}, we can confirm the relationship in (4). It was found out that, with the temperature $\tilde{T}$ fixed and the quantity M^d being evaluated for the various substitutions x = 0, 0.3, and 0.5, this quantity did not remain constant, but increased with increase in x. The dependence of M^d on concentration indicates either that the condition J_{ad} = const is not met, i.e., the dual exchange integral J_{ad} depends on the concentration of diamagnetic ions in the ferrite garnet and perhaps on temperature, or else this is evidence of the disturbance of the collinearity of the magnetic moments in the d sublattice. In this case, a vector summation should be carried out in Eq. (4).

2. Making use of the functions $\tilde{H}^a(\tilde{T})$ and $\tilde{H}_n^d(\tilde{T})$ (Fig. 3) in collinear molecular field theory, we could estimate the values of the intersublattice exchange integrals, the magnetically nonequivalent positions in the d sublattice being taken into account. We evaluated the exchange integrals individually from the temperature function of magnetization for the *a* sublattice (J_{ad}) and for the various magnetically nonequivalent positions of the d sublattice (J_{da}).

The molecular field equation for the *a* sublattice, with magnetically nonequivalent states in the d sublattice taken into account, is written in the following manner on the assumption of J_{aa} = 0:

$$\tilde{H}^a(T) = B_{5/2}\left[\frac{2S^2 z_a^d J_{ad}}{kT} M^d(T,x)\right], \qquad (5)$$

where S = 5/2 and is the spin of the Fe^{3+} ion.

By use of this equation we calculated the values of the J_{ad} exchange integrals from the experimental curves of $\tilde{H}^a(\tilde{T})$ and the function $M^d(\tilde{T}, x)$. The values of J_{ad} are given in Table 2 and show some tendency toward decrease with increase in substitution.

The molecular field equation for the d sublattice, on the assumption of J_{dd} = 0, is written

$$\tilde{H}_n^d(T) = B_{5/2}\left(\frac{2z_d^a S^2 J_{da}}{kT}\tilde{H}^a(T)\right). \qquad (6)$$

We found the values of the J_{da} exchange integrals for the nonequivalent d-type Fe^{3+} ions for various substitutions (Table 2) from comparison of the function (6) with the experimental curves of Fig. 3.

The J_{da} exchange parameters obtained in this manner were found to be constant within experimental error. In the end, the values of exchange integrals given in Table 2 can serve only as estimates, since they were obtained for

TABLE 2. Values of Exchange Integrals, °K (error ± 0.8°)

x	J_{da}			J_{ad}
	number of nearest magnetic neighbors			
	4	3	2	6
0	21.4	—	—	17.6
0.3	21.5	21.3	22.3	17.1
0.5	20.4	21.9	20.3	16.4

the condition of intrasublattice exchange interaction being equal to zero. The disagreement of values of exchange integrals found from the temperature dependence of magnetization of the *a* and d sublattices is evidently associated with this. The intrasublattice interactions, in particular, were done for ions with a small number of magnetic neighbors and may result in disturbance of collinearity of spins.

3. The ferrite garnet system $Y_{3-x}Ca_xFe_{5-x}Sn_xO_{12}$ was quite convenient for study of the Mössbauer effect on Sn^{119} nuclei. At temperatures below T_N, an effective magnetic field H^{Sn}, the magnitude of which decreases with rise in temperature and becomes zero near T_N (Fig. 4), acts on the nuclei of the diamagnetic Sn^{4+} ions. Our studies showed that the experimental temperature function $\widetilde{H}^{Sn}(T) \equiv H^{Sn}(T)/H^{Sn}(0)$ does not agree with any one of the curves of $\widetilde{H}_n{}^d(T)$ and $\widetilde{H}^a(T)$.

In ref. 11 we have proposed a simple statistical model, which allows a description of the field on the tin nuclei as a function of concentration and temperature, $H^{Sn}(x, T)$. We have based it on the fact that the effective magnetic field on the Sn nuclei is determined mainly by the closest environment, which consists of six nonequivalent d-type iron ions. It can be assumed that the contribution of each type of nonequivalent d-type Fe^{3+} ion to the effective magnetic field H^{Sn} is proportional to the average value of magnetic moment I_n of the given d-type ion and the probability of finding this type of ion in the closest environment of tin. The total average field on tin is the vector sum of all contributions from the six neighboring d-type ions and agrees with the direction of the total magnetic moment of the d sublattice. The projections of the I_n vectors on this direction are set by the coefficients of $\cos\theta_n$, where θ_n is the angle between the direction of the magnetic moment of a d-type Fe^{3+} ion with number of magnetic neighbors equal to n and the direction of the total magnetization of the d sublattice. The equation which sets the value of the magnetic field on tin for any concentration x and temperature T can then be written in the form

$$H^{Sn}(x,T)=H^{Sn}(0,0)\sum_{n=0}^{3} a_n \cos\theta_n P(n)\widetilde{I}_n(T). \qquad (7)$$

Here

$$P(n)=\frac{P_d{}^{na}}{P_d{}^{3a}+P_d{}^{2a}+P_d{}^{1a}+P_d{}^{0a}}, \quad \sum_{n=0}^{3} P(n)=1.$$

The a_n coefficients can be set equal to unity.[11] Assuming, as above, that $\widetilde{I}_n(T) \equiv I_n(T)/I_n(0) = \widetilde{H}_n{}^d(T)$, we constructed the theoretical field on tin as a function of temperature from Eq. (7) for specimens with x = 0.3 and 0.5 by use of the experimental $\widetilde{H}_n{}^d(T)$ curves (Fig. 4). In this case, the $\cos\theta_1 P(1)\widetilde{H}_1{}^d + \cos\theta_0 P(0)\widetilde{H}_0{}^d$ terms were neglected, since the statistical weight of these contributions is small and the magnetic moments of these ions obviously deviate strongly from the collinear configuration, as follows from analysis of $H^{Sn}(x)$ as a function of concentration.[11]

From Fig. 4 it can be seen that the theoretical curves agree very well with experiment. This confirms the validity of our statistical model. The proposed model also explains why the experimental function $\widetilde{H}^{Sn}(T)$ does not agree with any of the curves of $\widetilde{H}_n{}^d(T)$ and $\widetilde{H}^a(T)$. The temperature function of $\widetilde{H}^{Sn}(T)$ is a linear combination of $\widetilde{H}_n{}^d(T)$ with the corresponding terms [see (7)].

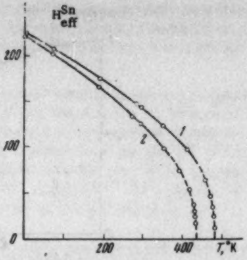

Fig. 4. Magnetic fields (in kOe) on nuclei of tin ions in $Y_{3-x}Ca_xFe_{5-x}\cdot Sn_xO_{12}$ garnets. Points denote experimental values. A solid line denotes an experimental curve obtained from Eq. (7). 1) x = 0.3; 2) x = 0.5.

At low temperatures, the d-type ions for which nearest magnetic neighbors are absent should have their direction of magnetization nearly antiparallel with respect to the total magnetic moment of the d sublattice due to d–d antiferromagnetic intrasublattice interaction.[12] Therefore, the contribution of these d-type ions to the field on tin should be negative. With elevation of temperature, the antiparallel ordering of these d-type ions should be disturbed, and at temperatures of ~ 50°K they become practically disordered.[13] This should lead to the presence of a maximum on the temperature function of the effective field on the tin nuclei. The position of the maximum should correspond approximately to the temperature of disordering of d-type Fe ions which do not have magnetic neighbors in the *a* sublattice.

The maximum associated with this very effect has been observed on curves of magnetic moment as functions of temperature in ferrite garnets substituted by silicon.[12]

The authors thank B. V. Mill' for help in preparation of the specimens.

---

[1] I. S. Lyubutin, E. F. Makarov, and V. A. Povitskii, Zh. Eksp. Teor. Fiz., 53, 65 (1967) [Sov. Phys.—JETP, 26, 44 (1968)].

[2] I. S. Lyubutin, E. F. Makarov, and V. A. Povitskii, Fiz. Tverd. Tela, 10, 534 (1968) [Sov. Phys.—Solid State, 10, 419 (1968)].

[3] V. A. Bokov, G. V. Popov, and S. I. Yushchuk, Fiz. Tverd. Tela, 11, 593 (1969) [Sov. Phys.—Solid State, 11, 479 (1969)].

[4] V. A. Bokov, G. V. Popov, and S. I. Yushchuk, Fiz. Tverd. Tela, 11, 1994 (1969) [Sov. Phys.—Solid State, 11, 1607 (1970)].

[5] I. S. Lyubutin, Proc. Conf. Application Mössbauer Effect, Tihany, Hungary (1969), p. 467.

[6] S. Geller, R. Bozorth, M. Gilleo, and C. Miller, J. Phys. Chem. Solids, 12, 111 (1960).

[7] I. S. Lyubutin, L. M. Belyaev, Yu. S. Vishnyakov, T. V. Dmitrieva, A. P. Dodokin, V. Ya. Dubossarskaya, and L. P. Shlyakhina, Zh. Eksp. Teor. Fiz., 58, 1204 (1970) [Sov. Phys.—JETP, 31, 647 (1970)].

[8] R. Gonano, E. Hunt, and H. Meyer, Phys. Rev., 156, 521 (1967).

[9] V. Jaccarino, Magnetism, Vol. II-A; Academic Press, New York (1965).

[10] J. J. van Loef, Physica, 32, 2102 (1966).

[11] I. S. Lyubutin and A. P. Dodokin, ZhETF Pis. Red., 15, 339 (1972) [Sov. Phys.—JETP Lett., 15, 239 (1972)].

[12] S. Geller, H. J. Williams, G. P. Espinosa, and R. C. Sherwood, Bell System Tech. J., 43, 565 (1964).

[13] A. P. Dodokin, I. S. Lyubutin, B. V. Mill', and V. P. Peshkov, Zh. Eksp. Teor. Fiz., 63, 1002 (1972) [Sov. Phys.—JETP, 36, 526 (1973)].

Estimation of texture of the bcc → fcc → bcc double phase transformation

I. P. Sorokin
Institute for Metal Physics, Ural Science Center,
Academy of Sciences of the USSR

(Submitted November 1, 1972)
Kristallografiya, 18, 999-1002 (September-October 1973)

An analytical calculation of the texture arising in a single crystal during the successive phase transformations bcc → fcc and fcc → bcc, which take place in accordance with the Nishiyama relationships, has been carried out. Comparison has been made, with an analogous calculation for the Kurdjumov–Sachs relationships. It is shown that change in the type of orientation relationships results in considerable change in the shape of the pole figures (double-tranformation texture).

The phase transformation textures which form in single crystals during crystallographically ordered transformations are well known.[1-4] An ordered transformation taking place in a polycrystalline textured structure results in the formation of a new, more complex structure.[5] A double-transformation texture, which as a rule is associated with the orientation of the primary crystal, is created in single-crystal material which undergoes two successive ordered transformations. When the bond orientation of the crystal lattices is known for specific transformations, it is possible to establish the nature of this regularity for a double transformation also. If the bond orientation for one of the transformations has not been established experimentally, then some sort of model can be assumed in order to analyze the crystallographic possibilities resulting from the model, to compare calculation with experimental data for successive transformations, and to estimate the plausibility of the model in this manner.

It is convenient to make use of the matrix form of writing the bond orientations.[6,7] Then the rule for reorganization of coordinates for successive phase transformations is given by the product of the reorganized matrix coordinates for each transformation.

Thermal cycles through the temperature (or temperature interval) of transformation are examples of heat treatment which include successive phase transformations. The double-transformation texture during a thermal cycle can be calculated on the assumption that the same bond orientation exists between crystal lattices for both transformations which make up the cycle. Experiments carried out on an iron–nickel alloy[8] agree with this assumption.

In the present work, the rule for reorganization of coordinates during the bcc → fcc → bcc successive phase transformations is evaluated for the case of orientation relationships between lattices described in accordance with Nishiyama: $(111)_{\mathrm{fcc}} \parallel (101)_{\mathrm{bcc}}$; $[\bar{1}\bar{1}2]_{\mathrm{fcc}} \parallel [\bar{1}01]_{\mathrm{bcc}}$.

The matrix representation of the orientation relationships is taken from refs. 7 and 9. The different variants of the same orientation relationships, which correspond to different possible positions of the crystal lattice forming the phase with respect to the lattice of the primary phase, are obtained by symmetrical rotation of the primary phase (superimposing it upon itself, but translating the lattice of the phase formed to another position in space). The regular rearrangement of matrix elements and the change of signs of some of them correspond to this rotation. For the Nishiyama relationships, 12 different matrices of reorganized coordinates were taken, in accordance with the number of variants of the orientation relationships.

Let us call one of the transformations making up the cycle the "forward" transformation and the other the "reverse." If the matrices of reorganization of coordinates are known for the forward transformation, then the reverse transformation is described by the inverse matrix. In the case of cubic symmetry, both lattices of the reverse transformation matrix are obtained by simple transposition of the matrices of the forward transformation. The rule for reorganization of coordinates for the complete bcc → fcc → bcc cycle is described by the product of the matrices for reorganization of coordinates during the forward and during the reverse transformations. Twelve such matrix products are given in Table 1. Operating on each of these matrices by the matrices for the symmetrical rearrangement of the cube, we obtained all the rest of the matrices for reorganization of coordinates for the bcc → fcc → bcc cycle.

The matrices for reorganized coordinates obtained in this manner allow the calculation of the position of any vector of the primary lattice in the new coordinate system associated with one of the crystal lattices appearing during the bcc → fcc → bcc cycle. This is equivalent to calculation of the possible positions of the crystallographic axes of the new crystals in the coordinate system associated with the lattice of the primary crystal. The complete pole figures characteristic of the double transformation texture can be constructed in this manner.

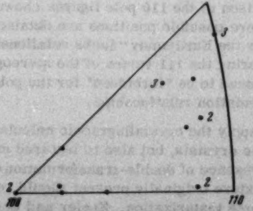

Fig. 1. Possible positions of 100 poles after the bcc → fcc → bcc cycle (Nishiyama orientation relationships).

TABLE 1. Matrices for Reorganization of Coordinates (bcc → fcc → bcc, Nishiyama orientation relationships)

$\begin{pmatrix} 1 & 0 & 0 \\ 0 & 1 & 0 \\ 0 & 0 & 1 \end{pmatrix}$	$\begin{pmatrix} 0.943 & 0 & 0.333 \\ 0 & -1 & 0 \\ 0.333 & 0 & -0.943 \end{pmatrix}$
$\begin{pmatrix} 0.250 & -0.612 & 0.750 \\ 0.612 & -0.500 & -0.612 \\ 0.750 & 0.612 & 0.250 \end{pmatrix}$	$\begin{pmatrix} 0.250 & 0.612 & 0.750 \\ -0.612 & -0.500 & 0.612 \\ 0.750 & -0.612 & 0.250 \end{pmatrix}$
$\begin{pmatrix} 0.486 & -0.612 & -0.624 \\ -0.373 & 0.500 & -0.781 \\ 0.790 & 0.612 & 0.014 \end{pmatrix}$	$\begin{pmatrix} 0.486 & 0.612 & -0.624 \\ 0.373 & 0.500 & 0.781 \\ 0.790 & -0.612 & 0.014 \end{pmatrix}$
$\begin{pmatrix} 0.486 & -0.373 & 0.790 \\ -0.612 & 0.500 & 0.612 \\ -0.624 & -0.781 & 0.014 \end{pmatrix}$	$\begin{pmatrix} 0.486 & 0.373 & 0.790 \\ 0.612 & 0.500 & -0.612 \\ -0.624 & 0.781 & 0.014 \end{pmatrix}$
$\begin{pmatrix} -0.721 & -0.373 & 0.583 \\ -0.373 & -0.500 & -0.781 \\ 0.583 & -0.781 & 0.221 \end{pmatrix}$	$\begin{pmatrix} -0.721 & 0.373 & 0.583 \\ 0.373 & -0.500 & 0.781 \\ 0.583 & 0.781 & 0.221 \end{pmatrix}$
$\begin{pmatrix} 0.029 & 0.986 & -0.167 \\ -0.986 & 0 & -0.169 \\ -0.167 & 0.169 & 0.971 \end{pmatrix}$	$\begin{pmatrix} 0.029 & -0.986 & -0.167 \\ 0.986 & 0 & 0.169 \\ -0.167 & -0.169 & 0.971 \end{pmatrix}$

A stereographic triangle (1/24 part of the complete pole figure) in which the possible positions of the 100 poles are noted is shown in Fig. 1. Some positions coincide (or are very close together) for calculation by use of different matrices. The of the stereographic for these coincident positions is indicated.

Possible positions of 110 poles (with multiplicity of points indicated) are noted in the stereographic triangle in Fig. 2.

It is interesting to see how the choice of these or other orientation relationships influences the form of the "theoretical" pole figure arising after the bcc → fcc → bcc cycle. The results of calculation for the Nishiyama relationships are compared with the results of calculation for the Kurdjumov–Sachs relationships[10] in Fig. 3. A substantial difference can be seen in the results obtained for the orientation relationships examined. First of all, the Kurdjumov–Sachs relationship results in a considerably greater number of possible 100 poles. Increase in the number of poles results in greater filling of the stereographic triangle. Poles appear for the Kurdjumov–Sachs relationships in many regions of the triangle which are free from poles for the Nishiyama relationships. But nearly all positions calculated for the Nishiyama orientation relationships lie in regions occupied by poles for the Kurdjumov–Sachs relationships.

Let us turn our attention to the existence of "forbidden" regions for the 100 poles. The region lying at an angle of separation of 21-32° from the 100 vertex of the stereographic triangle is "forbidden" for poles of both types of orientation relationships.

Comparison of the 110 pole figures shows that considerably more possible positions are obtained in this case also for the Kurdjumov–Sachs relationships.[10] The region bordering the 111 vertex of the stereographic triangle is found to be "forbidden" for the poles for both types of orientation relationships.

Let us apply the crystallographic calculations not only to single crystals, but also to textured material in which the presence of double-transformation texture on top of the texture originally present should result in retention of some texturization. Keeler and Geisler carried out a similar calculation to plot the pole figures of titanium after the hcp → bcc → hcp double transformation in material with initial recrystallization texture.[11] The experimental pole figures agreed satisfactorily with those calculated.

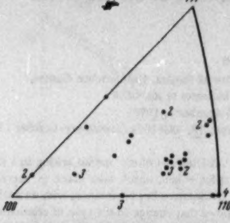

Fig. 2. Possible positions of 110 poles after the bcc → fcc → bcc cycle (Nishiyama orientation relationships)

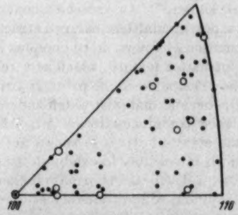

Fig. 3. Possible positions of 100 poles after the bcc → fcc → bcc cycle. ●) For Kurdjumov–Sachs orientation relationships;[10] ○) for Nishiyama orientation relationships.

The mathematical apparatus used for calculation of the diffuse axial ⟨111⟩ texture as the result of the bcc → fcc → bcc cycle is explained in ref. 12 on the assumption of equal probability of all crystallographically possible variants for the Nishiyama orientation relationships. It was found, in particular, that 110 poles should not be near the direction of the texture axis. Hu showed this result to be in good agreement with the values which he obtained[10] for double transformation for the Kurdjumov–Sachs orientation relationships. As the analysis done shows (Fig. 2), agreement of the results is caused by the fact that in both cases the 111 direction is found near a region which is free from 110 poles. In the general case itself, different results can be obtained for different orientation relationships.

For comparison of experimental results with those calculated it should be kept in sight that the different crystallographically possible variants are equally probable only in an ideal lattice. In real structures, factors operate which can segregate one or another variant, so that normally not nearly all possibilities are realized. In the limiting case, the complete "reduction" of the original texture[11] or orientation[13,14] can be observed after a thermal cycle.

The author is grateful to V. O. Esin for help during calculation of the matrices for reorganization of coordinates.

---

[1] G. Kurdjumov and G. Sachs, Z. Phys., 64, 325 (1930).

[2] V. I. Arkharov, Crystallography of the Tempering of Steel [in Russian], Metallurgizdat, Sverdlovsk–Moscow (1951).

[3] A. Kochendoerfer and G. Otto, Arch. Eisenhuettenwesen, 29, 775 (1958).

[4] L. I. Lysak and B. I. Nikolin, Fiz. Met. Metalloved., 21, 873 (1966).

[5] V. D. Sadovskii and L. P. Sorokin, Symposium on Structure and Properties of Textured Metals and Alloys [in Russian], Nauka, Moscow (1969), p. 171.

[6] M. A. Jaswon and J. A. Wheeler, Acta Crystallogr., 1, 216 (1948).

[7] A. Kochendoerfer and G. Otto, Arch. Eisenhuettenwesen, 30, 227 (1959).

[8] H. Kessler and W. Pitsch, Acta Metallurg., 13, 871 (1965).

[9] L. P. Sorokin, Fiz. Met. Metalloved., 22, 239 (1966).

[10] H. Hu, Trans. Met. Soc. AIME, 233, 1071 (1965).

[11] J. H. Keeler and A. H. Geisler, J. Metals, Trans. Sect., 8, 80 (1956).

[12] A. S. Kagan and L. P. Sorokin, Fiz. Met. Metalloved., 20, 889 (1965).

[13] V. D. Sadovskii, Izv. Akad. Nauk SSSR, Ser. Met., 1, 40 (1969).

[14] A. V. Ozhiganov, D. P. Rodionov, V. D. Sadovskii, L. V. Smirnov, and V. M. Schastlivtsev, Fiz. Met. Metalloved., 32, 1326 (1971).

Scattering of light at elastic waves in optically biaxial crystals

Yu. V. Pisarevskii and I. M. Sil'vestrova
Crystallography Institute, Academy of Sciences of the USSR

(Submitted October 4, 1972)
Kristallografiya, 18, 1003-1013 (September-October 1973)

The effect of optical anisotropy on the scattering geometry for light at elastic waves is considered for biaxial crystals. The variations of the angles of incidence and diffraction with elastic wave frequency are quite different from the normal curves for an isotropic medium and are not exactly the same as those for uniaxial crystals. It is shown that the most characteristic features for this case occur when the plane of scattering is close to the optic axes. It is also shown that differences from the isotropic case arise when the scattering is associated with a rotation of the plane of polarization.

There has recently been great interest in optical–acoustic interactions and in this connection special attention has been paid to the study of such interactions in crystals. This is due both to the richness of the possibilities which result from the anisotropic properties of crystals and to the great advantages enjoyed by instruments and devices which make use of optical–acoustic interactions.[1]

It is well known[2] that the wave synchronism condition is of great importance in optical–acoustic and indeed in all nonlinear waveinteractions. When this condition is satisfied the interaction takes place most effectively.

The existence of optical anisotropy means that there is a considerable difference in the interaction (scattering) geometry of the light and elastic waves to produce phase synchronism. When the interest is in an interaction with a coherent sound wave, a knowledge of the scattering geometry as a function of the elastic-wave frequency becomes extremely important.

The first analysis of the frequency variation of the synchronism conditions is given in ref. 3, which considers the comparatively simple but indicative case of optically uniaxial crystals. References 4-6 deal with the particular scattering geometries of a number of special crystallographic systems. A thorough treatment of the conditions of phase synchronism in uniaxial crystals is given in ref. 7.

The aim of the present paper is to give a detailed study of the scattering geometry corresponding to phase synchronism (Bragg condition) in optically biaxial crystals.

It is shown in ref. 3 that the phase synchronism condition, together with the fact that the change in the frequency in the scattered light is negligible ($\sim 10^{-6}$), leads to the following relationship:

$$\begin{aligned} \sin\theta_{\text{inc}} &= \frac{\lambda}{2v}\frac{\nu}{n_{\text{inc}}}\left[1+\left(\frac{v}{\lambda\nu}\right)^2 (n^2_{\text{inc}}-n^2_{\text{dif}})\right], \\ \sin\theta_{\text{dif}} &= \frac{\lambda}{2v}\frac{\nu}{n_{\text{dif}}}\left[1+\left(\frac{v}{\lambda\nu}\right)^2 (n^2_{\text{dif}}-n^2_{\text{inc}})\right], \end{aligned} \tag{1}$$

where λ is the wavelength of the light in vacuum, ν and v are the frequency and velocity of the elastic wave, n_{inc} and n_{dif} are the refractive indices of the incident and diffracted light waves. The angles of incidence and refraction are measured, as usual, from the normal to the propagation direction of the sound. The directions are shown in Fig. 1. They are the same as those in refs. 4 and 7 but differ from those in ref. 3.

The main features of the scattering geometry in biaxial crystals are related to the change in the refractive indices with the direction of propagation. The variation can be depicted as a self-intersecting, two-valued surface (Fig. 2), which is best described in a coordinate system[8] where the axis coincides with the principal axes of the dielectric permittivity tensor at optical frequencies ε_{ik}. These axes are usually called the principal dielectric axes X, Y, and Z (and the planes XY, YZ, and XZ are the principal dielectric planes).

The expression for the refractive indices of light propagating in an arbitrary direction has the form[9]

$$(n_1)^{-2} = \alpha + \beta\{[\mathbf{lc}_1][\mathbf{lc}_2] + ([\mathbf{lc}_1]^2[\mathbf{lc}_2]^2)^{1/2}\}, \tag{2}$$

$$(n_2)^{-2} = \alpha + \beta\{[\mathbf{lc}_1][\mathbf{lc}_2] - ([\mathbf{lc}_1]^2[\mathbf{lc}_2]^2)^{1/2}\}, \tag{3}$$

where $\alpha = 1/n_y^2$, $\beta = (n_z^2 - n_x^2)/2n_z^2n_x^2$, c_1 and c_2 are unit vectors in the directions of the optic axis, l is a unit vector in the direction of propagation of the light, n_x, n_y, and n_z are the refractive indices corresponding to the principal dielectric axes X, Y, and Z (for the sake of being definite, we take $n_x > n_y > n_z$).

When the refractive indices of the incident and diffracted waves belong to the same group [for example to (2)], the interaction process is one of scattering without rotation of the plane of polarization. If, however, they belong to different systems [(2) and (3)] the process is known as scattering with rotation of the plane of polarization.

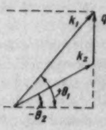

Fig. 1. Vector synchronism for scattering of light at an elastic wave in an optically anisotropic crystal and the directions for measuring the angles θ_1 and θ_2.

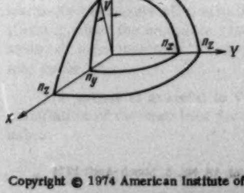

Fig. 2. Section of the refractive index surface by the coordinate planes.

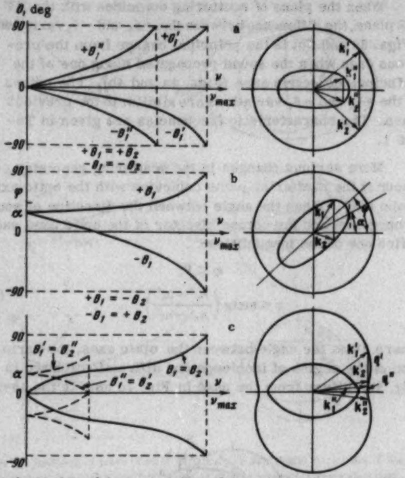

Fig. 3. Sections of the wave-vector surfaces and schematic plots of the variation of θ_1 and θ_2 with the frequency of the elastic waves. Scattering without rotation of the plane of polarization. a) Direction of sound propagation coincides with the axis of symmetry of the section of the wave-vector surface; b) arbitrary direction of sound propagation; c) one of the optic axes lies near the scattering plane.

We assume below that both types of scattering are always possible, as is in fact true for triclinic crystals. (In biaxial crystals belonging to the rhombic and monoclinic systems, the form of the photoelastic tensor[10] implies that under certain conditions scattering is impossible.)

VARIATION OF THE ANGLES OF INCIDENCE AND DIFFRACTION WITH FREQUENCY FOR SCATTERING WITHOUT ROTATION OF THE PLANE OF POLARIZATION

This group is characterized by the fact that the variations of $n_{\text{inc}}(\theta)$ and $n_{\text{dif}}(\theta)$ are identical. However, only in particular cases, when $n_{\text{inc}}(\theta) = n_{\text{dif}}(\theta) = \text{const}$, does this type of scattering lead to the normal isotropic equation

$$\sin\theta_1 = \sin\theta_2 = \lambda\nu / 2vn. \qquad (4)$$

This relationship holds for biaxial crystals when the scattering plane coincides with one of the principal dielectric planes and the plane of polarization of the incident and diffracted waves is perpendicular to the scattering plane.

The picture becomes more complicated if the plane of polarization of the incident and diffracted waves coincides with the scattering plane (say, the XY plane). If the sound wave is propagating along one of the principal dielectric axes (X, say) and $n_{\text{inc}} = n_{\text{dif}}$, but varies with the frequency of the elastic wave, the variation can be written from (2) as

$$n^2(\theta) = n_x^2 n_y^2 / (n_x^2\cos^2\theta + n_y\sin^2\theta). \qquad (5)$$

From (5) and (1) we can obtain the connection between the angles of incidence and diffraction and the frequency of the elastic wave:

$$\sin\theta_1 = \sin\theta_2 = a n_y / [4n_x^2 n_y^2 + a^2(n_x^2 - n_y^2)]^{0.5}, \qquad (6)$$

where $a = \lambda\nu/v$. This relationship, together with the curve for the isotropic case, is shown in Fig. 3a and it can be seen that despite the fact that (6) is a more complex equation than (4), the two variations are almost identical.

A more serious complication of the scattering geometry arises when the direction of propagation of the elastic wave does not coincide with any of the principal dielectric axes. The variations of $\sin\theta_1(\nu)$ and $\sin\theta_2(\nu)$ can again be derived from (1) and (2), but the form of the equations is very cumbersome and so we do not quote them here but only give the graph of Fig. 3b. The principal feature of this case is that the variations of $n_{\text{inc}}(\theta)$ and $n_{\text{dif}}(\theta)$ are not identical. In addition, there is an asymmetry between positive and negative angles of incidence, i.e., a difference between measurement of the angles of incidence in the direction of the X axis and measurement in the direction of the Y axis. The following relationships then hold: $\sin[-\theta_1(\nu)] = \sin[+\theta_2(\nu)]$ and $\sin[+\theta_1(\nu)] = \sin[-\theta_2(\nu)]$. The angle of incidence corresponding to zero sound frequency is given by the equation

$$\sin(\varphi - \alpha) = n_x \operatorname{tg}\varphi / (n_y^2 + n_x^2 \operatorname{tg}^2\varphi)^{0.5}, \qquad (7)$$

where φ is the angle between the x axis and the normal to the direction of the elastic wave (for the sake of being definite we choose the XY plane as the scattering plane).

For an arbitrary scattering plane the variation of $n_1(\theta)$ and $n_2(\theta)$ can no longer be described by circles or ellipses.[8] The equation for the variation of incidence and scattering angles with elastic-wave frequency become even more complicated. However, the nature of the variations is close to that depicted in Figs. 3a and 3b. Special attention must be given to the case when the scattering plane passes near the optic axis (in the limits $\varphi = (\tan^{-1} V - \tan^{-1}[n_x/n_z \tan V])$, where 2V is the angle between the optic axes). This region (see Fig. 2) has the peculiar section of the wave vector surface shown in Fig. 3c. It can be seen that at low frequencies the $\sin\theta(\nu)$ variation splits into two branches. This extremely complex variation of θ_1 and θ_2 with frequency is possible when the scattering takes place without rotation of the plane of polarization.

VARIATION OF THE ANGLES OF INCIDENCE AND DIFFRACTION WITH FREQUENCY FOR SCATTERING WITH ROTATION OF THE PLANE OF POLARIZATION

We noted above that this group corresponds to a difference in the variations of $n_{\text{inc}}(\theta)$ and $n_{\text{dif}}(\theta)$. We consider first the situation where the scattering plane coincides with one of the principal dielectric planes. The $n_1(\theta)$ and $n_2(\theta)$ variations then have the shape of a circle enclosed in an ellipse (the YZ scattering plane), an ellipse enclosed in a circle (XY scattering plane), and an intersecting ellipse and circle (ZX scattering plane) (Fig. 2).

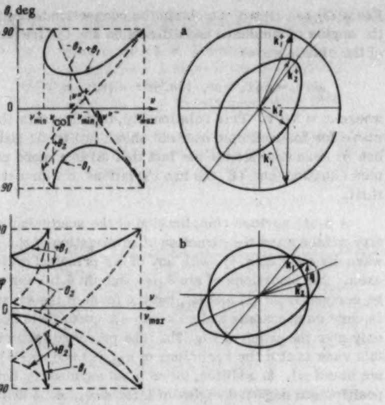

Fig. 5. Sections of the wave-vector surfaces and schematic variations of the angles θ_1 and θ_2 with the frequency of the elastic waves for scattering with rotation of the plane of polarization and for arbitrary sound-wave direction. a) XY or YZ scattering plane; b) XZ.

pressions for these frequencies and the corresponding angles are also given in Table 1.

It should be noted that the form of the variation in angles of incidence and diffraction (8) is similar to that obtained in ref. 1 for oblique sections in uniaxial crystals. This is because the sections of the wave-vector surfaces by the XY plane correspond to an "oblique" cut of optically negative crystals and sections by the YZ plane to an oblique cut in optically positive uniaxial crystals. The section by the XZ plane has no analog in uniaxial crystals.

2. Direction of sound propagation inclined to the principal dielectric axes (the scattering plane coincides with one of the principal dielectric axes). The scattering geometry is considerably more complicated when the sound wave propagates at an angle to the principal dielectric axes. Although the procedure for calculating the variation of the angles of incidence and scattering is the same as before, the equations themselves become very cumbersome. We therefore limit ourselves to the graphs and equations for the characteristic frequencies ν_{col}, ν_{max}, and ν^*.

The necessary graphs are given in Figs. 5 and 6 together with the appropriate sections of the wave-vector surfaces by the plane of scattering. The sections, as can be seen from the figures, are asymmetric about the direction of sound propagation. The synchronism condition is therefore satisfied at different angles of incidence for the same sound frequency corresponding to measurement of the angle of incidence from the normal to the sound direction towards the semimajor axis of the ellipse and towards the semiminor axis ($-\theta_1$). Thus in contrast to the cases where the sound wave propagates along any of the principal dielectric axes, there are two different variations for the angles of incidence and diffraction with the elastic wave. One corresponds to $+\theta_1$ and $+\theta_2$ and the other to $-\theta_1$ and $-\theta_2$.

When the plane of scattering coincides with the XY or YZ plane, the difference between the $+\theta_1$ and $-\theta_2$ variations (Figs. 5a and 5b) is the principal change from the previous case when the sound propagated along one of the principal dielectric axes (Figs. 4a and 4b). The nature of the $+\theta_1$ and $-\theta_1$ variations are similar to the previous case. The characteristic frequencies are given in Table 1.

More serious changes in the scattering geometry can occur if the scattering plane coincides with the optic axis plane (XZ). When the angle between the direction of sound propagation and the obtuse bisector of the optic axes satisfies one of the inequalities

$$\varphi < V,$$

$$\varphi < \operatorname{arctg}\left(\frac{n_y^2 - n_x^2}{n_z^2 - n_y^2}\right)^{0.5}, \qquad (9)$$

where 2V is the angle between the optic axes, the variation of the angles of incidence and diffraction (shown in Fig. 5b) differs from the case in Fig. 4c only in the asym-

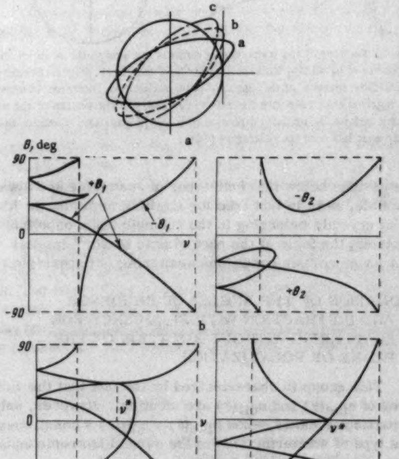

Fig. 6. Sections of the wave-vector surface by the XZ plane and schematic variations of the angles θ_1 and θ_2 with the elastic-wave frequency for scattering with rotation of the plane of polarization and for three directions (a, b, c) of sound propagation satisfying inequality (10).

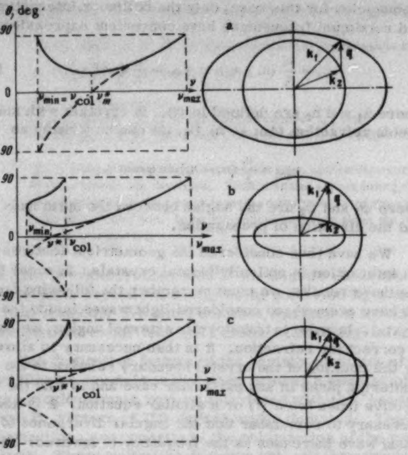

Fig. 4. Sections of wave-vector surfaces and schematic variations of the angles θ_1 and θ_2 with the frequency of elastic waves for scattering with rotation of the plane of polarization and for sound directions coinciding with one of the principal dielectric axes. a) YZ scattering plane; b) XY; c) ZX.

1. Sound wave directed along one of the dielectric axes. The simultaneous solution of (1)-(3) gives the following equation for the angles:

$$\sin\theta_1 = \frac{-an_i^2 \pm [a^2 n_i^2 n_j^2 - n_j^2 (n_j^2 - n_i^2)(n_i^2 - n_k^2)]^{0.5}}{n_k (n_j^2 - n_i^2)} \qquad (8)$$

$$\sin\theta_2 = \left(\frac{n_i^2 n_j^2 - n_k^2 n_j^2 \cos^2\theta_1}{n_k^2 n_j^2 - n_k^2 \cos^2\theta_1 (n_j^2 - n_k^2)} \right)^{0.5},$$

where $a = \lambda\nu/v$, n_k is the refractive index along the dielectric axis k perpendicular to the plane of scattering, n_i is the refractive index of the dielectric axis i along which the elastic wave is traveling, and n_j is the refractive index along the axis j, perpendicular to i and k. The variations corresponding to (8) are shown in Fig. 4 for the three interaction planes. It should be noted that the form of these curves depends not only on the scattering plane, but also along which of the axes the sound is propagated, i.e., the number of curves in Fig. 4 should be doubled. However, the cases we have already described cover the possible qualitative differences.

It can be seen from the diagrams that the variations of the angles of incidence and scattering with the sound frequency are quite different from the isotropic case. As for uniaxial crystals,[3,7] it is possible to find a number of frequencies which are characteristic of just anisotropic diffraction. This refers in particular to the frequency at which a collinear interaction becomes possible. This type of interaction is possible only when the scattering occurs with rotation of the plane of polarization in an anisotropic medium. Another characteristic frequency is the minimum frequency below which effective scattering (with phase synchronism) is impossible. These frequencies and the corresponding angles are given in Table 1. For scattering in the XY and YZ planes and propagation along the Y axis the minimum frequency with small double refraction differs from the collinear frequency but it approaches it as the difference in refraction increases and coincides when $(n_y^2 - n_x^2)^{1/2}/n_x \geq 1$ and $(n_z^2 - n_y^2)^{1/2}/n_z \geq 1$. This condition cannot be satisfied for an overwhelming number of the crystals.

Yet another characteristic frequency, confined to anisotropic diffraction, is the frequency ν^* at which one of the angles reaches its minimum value. Since at this frequency one angle varies much more rapidly and the other much more slowly than in the isotropic case, it can prove useful in practice and in experimental studies. The ex-

TABLE 1. Characteristic Frequencies of the Optical–Acoustic Interaction in Biaxial Crystals for Scattering Planes Perpendicular to Any of the Principal Dielectric Axes

Scattering plane	Sound direction	Minimum frequency $\nu_{\min}\frac{\lambda}{v}$	$\sin\theta_1$	Frequency $\nu^*\frac{\lambda}{v}$	$\sin\theta_1$	$\nu_{\text{col}}\frac{\lambda}{v}$
XY	X	$n_z - n_y$	1	$(n_z^2 - n_x^2)^{0.5}$	$\frac{(n_z^2 - n_x^2)^{0.5}}{n_z}$	$n_z - n_y$
XY	Y*	$\frac{(n_x^2 - n_y^2)^{0.5}(n_y^2 - n_z^2)^{0.5}}{n_y^2}$	$\frac{(n_y^2 - n_x^2)}{n_x}$	$(n_z^2 - n_y^2)^{0.5}$	$\frac{(n_z^2 - n_y^2)^{0.5}}{n_z}$	$n_z - n_x$
ZX	Z	0	$\frac{n_z}{n_y}\left(\frac{n_z^2 - n_y^2}{n_z^2 - n_x^2}\right)^{0.5}$	$\frac{n_x}{n_z}(n_z^2 - n_y^2)^{0.5}$	$\frac{n_x}{n_z}\frac{(n_z^2 - n_y^2)^{0.5}}{n_y}$	$n_y - n_x$
ZX	X	0	$\frac{n_z}{n_y}\left(\frac{n_y^2 - n_x^2}{n_z^2 - n_x^2}\right)^{0.5}$	$(n_y - n_x^2)^{0.5}$	$\frac{(n_y^2 - n_z^2)^{0.5}}{n_y}$	$n_z - n_y$
YZ	Y**	$\frac{(n_z^2 - n_y^2)^{0.5}(n_y^2 - n_x^2)^{0.5}}{n_y^2}$	$\frac{(n_z^2 - n_y^2)}{n_z}$	$\frac{n_y}{n_z}(n_z^2 - n_x^2)^{0.5}$	$\frac{n_y}{n_z}\frac{(n_z^2 - n_x^2)^{0.5}}{n_x}$	$n_z - n_x$
YZ	Z	$(n_y - n_x)$	1	$\frac{n_z}{n_y}(n_y^2 - n_x^2)^{0.5}$	$\frac{n_z}{n_y}\frac{(n_y^2 - n_x^2)^{0.5}}{n_x}$	$n_y - n_x$
YZ ***	At an angle φ to z	—	—	$n_x\left(\frac{2(a^2 - b^2 + ac) + u}{b^2 + 2ac + u}\right)^{0.5}$	$\frac{2(a^2 - b^2 + ac) - u}{2a^2 - b^2}$	$n_x - \frac{n_y n_z}{[n_y^2\cos^2\varphi + n_z^2\sin^2\varphi]^{0.5}}$
XY ****	At an angle φ to x	—	—	$d\cos^2\varphi + l\cos\varphi + f\cos^2\varphi\sin\varphi$		$n_z - \frac{n_x n_y}{[n_y^2\cos^2\varphi + n_x^2\sin^2\varphi]^{0.5}}$

---

*For crystals in which $n_y - n_x < 0.5$, $n_z - n_y < 0.5$.

**For crystals in which $n_z - n_y < 0.5$, $n_y - n_x < 0.5$.

metry of the $+\theta_1$ and $-\theta_1$ branches. When the above angle satisfies

$$V < \varphi < \operatorname{arctg}\left(\frac{n_y^2 - n_z^2}{n_x^2 - n_y^2}\right)^{0.5}, \tag{10}$$

the variations acquire a very special form, shown in Fig. 6. The main feature is the presence of several points where the curve crosses itself. These points correspond to frequencies at which two light waves incident on the crystal are scattered in the same direction. Also, two scattered waves can appear simultaneously as in the scattering of a beam of sound with a large angular divergence in the so-called Raman–Hutt diffraction.

The characteristic frequencies for scattering in the plane of the optic axes are given by equations similar to those quoted for the XY and YZ planes but with n_z replaced by n_y, n_x by n_z, and n_y by n_x. The equation for ν^* can be obtained from the corresponding equation for XY if the angle between the obtuse bisector and the direction of the sound lies within the limit

$$|\sin\varphi| \leqslant \frac{n_z}{n_y}\left(\frac{n_x^2 - n_y^2}{n_x^2 - n_z^2}\right)^{0.5}. \tag{11}$$

If, however, the angle φ is such that (11) is not satisfied, then the expression for ν^* is derived from the equation for the YZ plane given in Table 1 with n_x replaced by n_y and n_y by n_x.

One other characteristic frequency appears when the angle between the sound direction and the obtuse bisector becomes equal to the angle between this bisector and the biradial. The $+\theta_1$ and $-\theta_2$ branches then merge (Fig. 6b) at the frequency given by

$$\nu = \frac{v}{\lambda}\left(\frac{n_y^2 n_z^2 + n_y^2 n_x^2 + n_z^2 n_x^2 - n_y^2}{n_y^2}\right)^{0.5}, \tag{12}$$

with the angles θ_1 and θ_2 equal to

$$\theta_1 = \operatorname{arctg}\left(\frac{n_y^2 - n_x^2}{n_z^2 - n_y^2}\right)^{0.5} + \operatorname{arctg}\frac{n_z^2}{n_x^2}\left(\frac{n_y^2 - n_x^2}{n_z^2 - n_y^2}\right)^{0.5}, \quad \theta_2 = 0. \tag{13}$$

If the scattering plane is arbitrarily oriented with respect to the principal dielectric planes, the $n_{\mathrm{inc}}(\theta)$ and $n_{\mathrm{dif}}(\theta)$ variations are of a very cumbersome form and the angle of incidence and diffraction curves are even more difficult. However, the shapes of the $\theta_1(\nu)$ and $\theta_2(\nu)$ variations are qualitatively similar to those shown in Fig. 4 and Fig. 5b if the angle between the scattering plane and the optic axes γ is smaller than $\operatorname{arctg}\frac{n_z}{n_x}\left(\frac{n_y^2 - n_x^2}{n_z^2 - n_y^2}\right)^{0.5}$. If $\gamma < \operatorname{arctg}\frac{n_z}{n_x}\left(\frac{n_y^2 - n_x^2}{n_z^2 - n_y^2}\right)^{0.5}$, the shape is similar to those shown in Figs. 5b and 6. Of the characteristic frequencies for this case, only the collinear interaction and maximum frequencies have convenient expressions:

$$\nu_{\min} = \frac{v_s}{\lambda}(n_1 - n_2), \quad \nu_{\max} = \frac{v_s}{\lambda}(n_1 + n_2), \tag{14}$$

where n_1 and n_2 are defined in (2). In crystals with small double refraction ($\Delta n_i \ll n$) Eq. (2) can be written as

$$\nu_{\mathrm{col}} = \frac{v_s}{\lambda}(n_z - n_x)\sin\varphi_1 \sin\varphi_2,$$

where φ_1 and φ_2 are the angles between the optic axes and the direction of propagation.

We have thus considered the geometrical features of the interaction in optically biaxial crystals. In order to use these results, we must remember the following facts. We have everywhere considered light waves inside the crystal. In order to transform to external angles, we have to correct for refraction. It is then necessary to allow for the position of the crystal boundary relative to the scattering plane in any particular case and to find the refractive index from (2) or a similar equation. It is also necessary to remember that the angular divergence of the sound wave increases as the frequency is lowered. The uncertainty in the direction of the sound-wave vector increases and effective optical–acoustic interaction becomes possible even when the Bragg condition is not exactly fulfilled.

At low frequencies the relationships we have derived will "smear out." For inclined scattering planes it is also necessary to bear in mind that the polarization orientation of the incident and diffracted wave varies with frequency in the same way for both of them.

The laws for anisotropic optical–acoustic interaction that we have given above can be used in studying these interactions themselves and related phenomena in solid bodies.

---

[1] R. W. Damon, W. T. Maloney, and O. H. McMahon, Physical Acoustics, Vol. 7, Academic Press, New York–London (1970).

[2] N. B. Bloembergen, Nonlinear Optics, Benjamin, New York (1965).

[3] R. W. Dixon, IEEE J. Quant. Electronics, QE-3, 85 (1967).

[4] M. S. Kharusi and G. W. Farnell, Canad. J. Phys., 47, 2719 (1969).

[5] M. S. Kharusi and G. W. Farnell, Proc. IEEE, 58, 275 (1970).

[6] V. V. Lemanov and O. V. Shakin, ZhETF Pis. Red., 13, 549 (1971) [JETP Lett., 13, 392 (1971)].

[7] V. V. Lemanov and O. V. Shakin, Fiz. Tverd. Tela, 14, 229 (1972) [Sov. Phys. – Solid State, 14, 184 (1972)].

[8] L. D. Landau and E. M. Lifshitz, The Electrodynamics of Continuous Media, Pergamon Press, Oxford–New York (1960).

[9] F. I. Fedorov, Optics of Anisotropic Bodies [in Russian], Izd. AN BSSR, Minsk (1958).

[10] J. F. Nye, Physical Properties of Crystals, Clarendon Press, Oxford (1964).

[11] A. N. Winchell and H. Winchell, The Microscopic Characters of Artificial Inorganic Solid Substances: Optical Properties of Artificial Minerals, Academic Press, New York–London (1964).

Some features of the domain structure in lead titanate crystals

E. G. Fesenko, V. G. Gavrilyachenko, M. A. Martynenko,

A. F. Semenchev, and I. P. Lapin

Rostov State University

(Submitted May 10, 1972; resubmitted October 5, 1972)
Kristallografiya, 18, 1014-1017 (September-October 1973)

The method of observation, localization sites, and configurations of reversed domains, and their formation in $PbTiO_3$ crystals are described. These domains appear during the phase transition. The concentration of reversed domains in the crystal depends on the velocity of the phase front and is smallest for a velocity of the order of 0.1 mm/min. Some suggestions are made about the role of such domains in the screening of the spontaneous polarization.

We have previously described[1-3] the domain structure of lead titanate crystals ($PbTiO_3$) using polarized light and etching methods. We noted common features of the domain structures for lead and barium titanate crystals.

One distinctive feature of the domain structure of lead titanate crystals is that they basically consist of large single-domain regions interlaced with the "heads" of the P_s vectors of 180-degree wedge domains. Their polarizations are opposite to the polarization of the main volume. These wedgelike domains (we call them reversed) inhibit polarization reversal in the crystal and retain their stability under heating up to the Curie point.

METHODS OF OBSERVATION, SHAPE, AND LOCALIZATION SITES OF THE REVERSED DOMAINS

To study the shape and determine the size of the reversed domains we etched transverse cross sections of c-domain crystals. The crystals were cut, polished, and then etched for 3-5 sec in a mixture of hydrofluoric and hydrochloric acids.

It turned out that the boundaries of the antiparallel domains in these cross sections and in the domains themselves, evidently due to a deviation of the intersecting plane from the normal to the (001) direction, etched intensely, bringing out the domain boundaries.

The etching method was used to observe the different reversed domains which interpenetrate the free surface of the crystal. These are needle-shaped with a small wedge angle at the vertex (Fig. 1a), or wedge-shaped domains with an angle up to 20° (Fig. 1b), and combinations of several wedge-shaped domains. Often the boundaries of the latter form a continuous sawtooth surface within the crystal dividing mutually opposed single-domain regions. The depth to which the reversed domains penetrate depends on the conditions of the phase transition and varies from 3-5 up to 100 μ and more. It has been established that they also appear at cracks and inclusions (Fig. 1b; the dark region above is a gaseous inclusion).

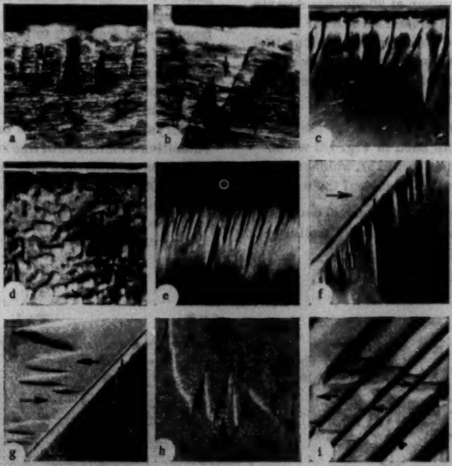

Fig. 1. Reversed domains in lead titanate crystals. a) × 1100; c) × 500; d) × 360; e) × 500; f) × 360; g) × 360; h) × 250; i) × 360.

In thin crystals (150 to 200 μ) as a rule, the polarization P_s of the reversed domains is such that the direction of the "head" of the vector is into the crystal. In thicker crystals we observed small (5 to 10 μ) wedge-shaped domains with a reversed polarization direction.[3]

In addition to reversed domain boundaries, etching revealed a system of parallel stripes (and sometimes lines) oriented perpendicular to P_s as in Fig. 1b, for example, where we can clearly see a transition of the stripes into *a* domains (the darker bands pass at an angle of 45°). The nature of these lines varies from crystal to crystal, from one internal point of a crystal to another, and even within the same domain. The presence of the streaks creates additional contrast.

Reversed domains can also be observed using a polarizing microscope; they are clearly seen in *a*-domain crystals in crossed Nicols near the position of parallel extinction (Fig. 1c) and in c-domain crystals one sees weak light outlines of wedge domains (Fig. 1d), which has been established from a comparison with photographs of etch figures. Upon rotation of an *a*-domain crystal one observes alternating brightening and extinction of the wedge boundaries. The rotation angle between the positions of the greatest brightness of the left and right boundaries amounts to about 3° while the parallel extinction of the whole crystal lies in the middle of this interval. Similar phenomena at the boundaries of wedge domains are observed in investigations of barium titanate crystals,[4,5] where the brightening of the domain boundaries is explained by rotation of P_s to different sides from the forming wedge.

In *a*-domain crystals the reversed domains as a rule are larger than in c-domain crystals. Wedges up to 1 mm and larger have been observed.

Reversed domains also appear at 90-degree domain boundaries, where the twinning plane is a mirror plane and not dark—light. In Fig. 1e we see such domains in a c-domain layer, in Fig. 1f we see them at 90° boundaries in *a*-domain crystals, and in Fig. 1g we see them on both sides of a 90-degree boundary.

In large *a*-domain crystals in addition to the reversed domains at the faces (as seen in Fig. 1c) we observe other sawtooth boundaries (Fig. 1h), which indicate the repeated rotation of P_s along the axis of the c crystal.

In layered *a* and c domain crystals and *a* domain crystals the reversed domains are bent at 90° walls, which enter the bulk of the crystal. This can be illustrated by the wedge domains in an *a*-domain layer crystal shown in Fig. 1i.

FORMATION OF REVERSED DOMAINS

In investigations of the phase transition in lead titanate crystals we observed the formation of reversed domains in *a*-domain crystals. The crystals studied were placed in a special heater attached to the stage of the polarizing microscope, which created the required temperature gradient and made observations in the position of "parallel" extinction.

Figure 2a shows schematically the formation of the reversed domains. The direction of motion of the phase front is indicated by an arrow. The lower part of the crystal has transformed into the ferroelectric phase. In the right-hand part far from the front the reversed domains which are formed appear. They are formed in the region where the front and the crystal face intersect. The wedge domains which are largely attached to the face of the crystal are elongated by the phase front inside, and then are cut off from it.

The reversed domains with P_s pointing into the crystal occupy the free surface during the phase transition. In the rest of the crystal P_s lies such that a "tail" moves behind the phase front. This has been established by the etching method and measurements of the piezoelectric and pyroelectric effects.

Depending on the velocity of the front there is a change in the amount and size of the reversed domains. In Fig. 2b an etch figure is shown for an *a*- and c-domain crystal which was transformed into the ferroelectric phase in such a way that the phase front velocity changes over a broad range. The closed regions are the emergence of reversed domains at the crystal surface while the longitudinal stripes are *a* domains. The planar phase front moved from left to right from section AA at a velocity of the order of 50 μ/min. In the part of the crystal between sections AA and BB the phase front passed with acceleration. From the etch figures of the surface and also from longitudinal and transverse cross sections of this crystal we established that for large phase front velocities a multitude of fine reversed domains are formed, and as the velocity decreases they become larger and extend deeper into the crystal. With phase front velocities less than 0.1 μ/min reversed domains are only rarely encountered and conditions are created for producing single-domain crystals reproducibly.

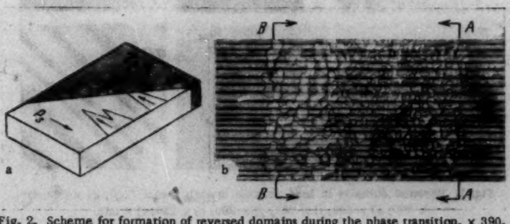

Fig. 2. Scheme for formation of reversed domains during the phase transition. × 390.

CONCLUSIONS

We have established that in lead titanate crystals the main elements of 180-degree domain configurations are coarse single-domain regions, wedge-shaped reversed domains which appear at free surfaces, and 90-degree domain boundaries at which the conditions for zero charge are not satisfied. Domain walls normal to (001), i.e., parallel to $\mathbf{P}_s$, as in barium titanate are not observed; one only observes sawtooth boundaries. In our opinion this feature of the domain structure can be explained by the high conductivity of the crystal during the phase transition ($\sigma \simeq 10^{-3}$ to 10^{-4} ohm/cm).

The existence of stable single-domain regions in real ferroelectric crystals is usually related to screening of $\mathbf{P}_s$ by the following mechanisms:[6] 1) Ions settling on the crystal surface; 2) formation of bulk charge near the crystal surface due to free carriers; 3) formation of *a* domains at the surface which close the polarization flux. Of these mechanisms, in ferroelectric materials with high conductivity the second is of the least importance during the phase transition. Screening of $\mathbf{P}_s$ by bulk charge can be explained by the existence of various stable boundaries between domains in the crystal which do not satisfy the condition of zero charge. In order to be certain that the boundaries of the reversed domains are sites where bulk charge is localized we used the light probe method and investigated several thin *a*-domain crystals with such domains. The crystals were placed on the stage of a polarizing microscope and illuminated with a light beam of diameter 0.2 mm.

We applied a voltage to the ends of the crystal, perpendicular to $\mathbf{P}_s$, using liquid electrodes of saturated water solution of LiCl; the current was measured using a F116/2 instrument. The dark current was beyond the sensitivity of the apparatus. Upon illumination of the parts of the crystal near the domain walls a significant photocurrent flowed in the circuit. Just as the light probe touched the boundary of the reversed domain we observed a scintillation and a current pulse. This was an indication that carriers are freed from traps in the domain boundary.

The reversed domains in lead titanate crystals can be regarded as elements of a developed antiparallel domain structure. The surfaces at which the "head" of the $\mathbf{P}_s$ vector is compensated by negative bulk charge are rearranged within the crystal and substantially increase their area.

---

[1] E. G. Fesenko, V. G. Gavrilyachenko, and E. V. Zarochentsev, Izv. Akad. Nauk SSSR, Ser. Fiz., 34, 2541 (1970).

[2] E. G. Fesenko, V. G. Gavrilyachenko, R. I. Spinko, M. A. Martynenko, E. A. Grigor'eva, and A. D. Feronov, Kristallografiya, 17, 153 (1972) [Sov. Phys.–Crystallogr., 17, 122 (1972)].

[3] E. G. Fesenko and V. G. Gavrilyatchenko (Gavrilyachenko) J. Phys. Suppl., 33, C2-169 (1972).

[4] E. V. Sinyakov, V. M. Duda, E. F. Dudnik, and S. I. Yakunin, Fiz. Tverd. Tela, 13, 2558 (1971) [Sov. Phys.–Solid State, 13, 2149 (1972)].

[5] J. Kobayashi, Phys. Status Solidi, 21, 151 (1967).

[6] I. I. Ivanchik, Fiz. Tverd. Tela, 3, 373 (1961) [Sov. Phys.–Solid State, 3, 271 (1961)].

Studies on ferroelectric crystals with a three-crystal x-ray spectrometer

I. Ya. Nikiforov, Yu. F. Mal'tsev, and V. Z. Borodin

Rostov State University

(Submitted July 7, 1972; resubmitted October 11, 1972)
Kristallografiya, 18, 1018-1022 (September-October 1973)

Methods are presented for examining ferroelectric crystals with a three-crystal x-ray diffractometer and spectrometer. The true diffraction peaks are deduced for single-domain crystals, which are compared with theoretically calculated ones. Temperature effects for the diffraction peak shape are examined; above the Curie point one gets reflections that indicate that the surface has regions differing in degree of tetragonal structure.

X-ray diffraction topography has an important place among the various methods of examining single crystals.[1-3] When a ferroelectric crystal is examined by the Lang technique, which has been used[4] to observe dislocations in $BaTiO_3$, one can make a comparison of this method[5,6] with the Berg–Barrett method[7,8] in relation to the domain structures and the 90° domains of the material. Anomalous dispersion can be used to observe 180° domain walls.[9] A major disadvantage of existing methods of x-ray topography is that the results are qualitative; quantitative information can be obtained with a diffraction apparatus that enables one to examine the true form of the diffraction peak in order to determine lattice defects, angles between domains in ferroelectrics, and simultaneous recording of interplanar distances and lattice distortions introduced by domain walls.

The best such instruments for the latter purpose are the present two-crystal[10-12] and three-crystal[13-15] x-ray spectrometers; if a two-crystal spectrometer is used in the parallel position (n, −n), the double reflection curve is then a convolution of the two diffraction peaks, and so one obtains a picture that is extremely difficult to interpret if each diffraction maximum itself contains a series of subordinate peaks. This is precisely the situation encountered with ferroelectrics on two-crystal spectrometers.[16,17] Also, the two crystals should have the same lattice constant. Major difficulties arise in examining the effects of electric fields and temperature on the properties of crystals when a two-crystal system is used. A three-crystal spectrometer is free from all these difficulties, but as yet it has not been employed with ferroelectrics.

The present three-crystal x-ray spectrometer–diffractometer was based upon a two-crystal x-ray spectrometer described elsewhere;[11] the first two perfect quartz crystals were cut on $(11\bar{2}0)$ planes and used as monochromators for the x radiation, which in conjunction with a collimator enabled us to examine the third crystal with radiation having $\Delta\lambda = 16 \cdot 10^{-5}$ Å for its wavelength range, the cross section of the beam being 0.7×1.5 mm and the angular divergence 4". The third crystal could be set to 0.5".

The crystals were used in the Bragg setting (1, 1-2) with Cu Kα radiation. The reflection from the third crystal was recorded with a scintillation counter, and the discriminator enabled us to suppress the background to the level of 0.1 sec^{-1}. The intensity at the peak in the curves was 50-500 sec^{-1} with an anode current in the demountable x-ray tube of 20 mA at 45 kV. The crystal was fastened to a PTFE plate by insertion in a groove, which made it possible to scan the x-ray beam over almost all the surface. The crystal was initially set up by x-ray methods.

We made room-temperature measurements on single-domain crystals of $BaTiO_3$ grown by the Remeika method, the polarization being parallel to the plane of the plate (type-*a* crystals) or perpendicular to it (type-c crystals). Table 1 gives results on five crystals of each type, it gives the observed and theoretical values for the three basic parameters of the diffraction peak for the *a* and c crystals. We calculated the theoretical form for the diffraction peak and the integrated reflection coefficient for the (200) and (002) planes by means of the dynamical theory[18,19] with an ODRA-1204 computer.

There is a spread in the experimental results on account of differences in perfection of the crystals; Table 1 shows that the basic parameters of the peak for c-type crystals are very close to the theoretical ones, whereas those for the *a*-type crystals deviate more markedly.

The results have to be interpreted on the basis of the effects on the reflections from 180° and 90° walls. The *a*-domain crystal showed more marked deviation of the experimental parameters than the c-domain one did, which arises because the 90° walls have more effect on the structure and optical uniformity of the crystal than do 180° walls. This interpretation is confirmed by published evidence on the wall thickness in the two cases. Tables[20] of these thicknesses indicate that the thickness of a 180° wall is several cell parameters, whereas that

TABLE 1

Crystal type	hk*l*	ω*		ρ, 10^{-6} rad		I_{max}, sec^{-1}
		exp.	theor.	exp.	theor.	
c	002	16.5—30	12	40—55	55.3	120—500
a	200	38—51	12	13—15	55.3	50—60

---

*ω is the width of the diffraction peak at half-height (in angular seconds), while ρ is the integrated reflection coefficient and I is the peak intensity for crystals of *a* and c types.

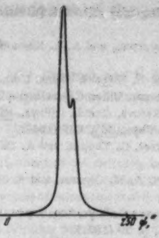

Fig. 1

of a 90° wall may be hundreds or even thousands of Å.

When the diffraction peaks were recorded from the two types of crystals, we were able to detect a splitting of the beam into two or sometimes more peaks at certain points; in the c-domain crystal, the angular separation between these peaks might be 10-30", as against 17-50" for an *a*-domain one. Figure 1 shows the diffraction peak from a c-domain crystal recorded with a slit in front of the counter of 0.05 mm. It may be that these angles indicate domain disorientation as a result of large stresses at the boundaries between 180° and 90° domains. Sometimes we found angles of 100-200" between diffraction peaks, which is probably due to macroscopic orientation difference between blocks in the crystal on account of various types of defects.

We made a detailed study of c-type crystals with single *a*-domain wedges; it was of great interest that the (001) and (100) planes of adjacent c and *a* domains formed angles lying within limits of 0 and 10' for various orientations of the crystals relative to the normals to the reflecting planes. Etching caused the reflection curves to become sharper, and reduced the number of weak peaks, but the angles between the c and *a* domains still remained within the limits 0 to 10'.

This method involves examining the crystal in two stages. In the first stage, the crystal is rotated, while the counter with a broad slit remains fixed, the positions of the individual peaks being determined by two factors: the angular orientation difference between the blocks in the corresponding domain and the interplanar distance in this. These factors can be distinguished by making a fresh measurement (second stage) on the diffraction profile with an apparatus where the counter has a narrow slit and rotates at twice the speed of the crystal. The difference between the Bragg angles corresponding to the different interplanar distances was determined from the expression $\Delta\vartheta = (\delta_1 - \delta_2)/2$, where δ_1 and δ_2 are readings made on the counter scale to ±36". The block disorientation angles for the different types of domains were calculated from $\varphi = \pm[\Psi_1 - \Psi_2 - (\delta_1 - \delta_2)/2]$, where Ψ_1 and Ψ_2 are the angles of rotation of the specimen in the apparatus with the counter fixed, which were determined to 0.5". Figure 2 shows the shape of the diffraction profile for one of the numerous crystals we examined at various temperatures. The profiles were recorded with a fixed counter and the third crystal rotating.

The Curie point of this specimen (a crystal containing a small quantity of iron) was 107°C. These profiles show how the shape changes abruptly as one passes through the Curie point; the c and *a* peaks on the profiles for the ferroelectric phase pertain correspondingly to reflections from c and *a* domains, while peak b corresponds to reflections on a c-domain region with a somewhat lower degree of tetragonality. Peak *f* on curves recorded above the Curie point corresponds to a reflection from a para region, while the residual peaks m, h, g, and d are related to regions with elevated or reduced tetragonality, which persists above the phase transition point. Table 2 gives the differences in the interplanar distances and the angular discrepancy between the domain regions relative to the c peak for diffraction profiles recorded for the ferroelectric state, or relative to the *f* peak for the paraelectric state. It is clear from Table 2 that the c and b peaks preserve a constant small difference in the interplanar distances as the temperature increases, while there is a monotonic decrease in the angle between them from 8' to zero. On the other hand, the c and *a* peaks show a monotonic reduction in the difference between the

TABLE 2

T, °C	Peak	φ, '	Δd, Å
26	*a*	0.2	0.042
	b	8.0	0.009
89	*a*	—0.6	0.031
	b	3.3	0.011
104	*a*	—1.3	0.025
	b	0.3	0.011
106	*a*	—0.1	0.018
	b	0.0	0.010
108	*m*	2.5	0.020
	h	2.1	0.014
	d	0.7	0.008
129	*m*	3.2	0.020
	h	2.6	0.014
	g	1.9	0.009
	d	1.0	0.008
Error		±0.5	±0.0015

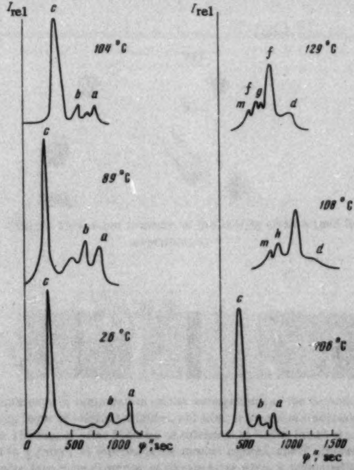

Fig. 2

interplanar distances for only small changes in the mutual orientation. These results reveal the analogy in the change in the spontaneous polarization and the angular disorientation of the domains for the c and b peaks as functions of temperature; we can therefore give the following interpretation for the diffraction profile. One can assume that an a-domain wedge in a crystal is surrounded by a c-domain region with reduced tetragonality relative to the main c-domain region and having a considerable angular disorientation relative to the latter. Therefore there is a small transitional film between the a-domain wedge and the c-domain part of the crystal. Traces of domain structure were observed in most of the crystals above the Curie point; they were observed also after etching the crystal in orthophosphoric acid above the phase transition point, which agrees with the assumption that there is a special surface layer in a ferroelectric that persists above the Curie point.[21,22]

This method is of value in examining a variety of domain structures; an advantage of the method is that it enables one to determine not only the presence or absence of domains and the quantitative relation between their areas, but also the angles between the domains and the interplanar distances, which define the perfection of the structure.

---

[1] L. B. Bersuker, B. G. Vekhter, and A. A. Muzalevskii, Abstrs. Second European Conf. on Ferroelectricity, Dijon, France (1971).

[2] Ya. S. Umanskii, X Radiography of Metals [in Russian], Metallurgizdat, Moscow (1967).

[3] B. M. Rovinskii, V. G. Lyuttsau, and A. A. Khanonkin, App. Met. Rent. Anal., 9, 3 (1971).

[4] H. Toyoda, S. Waku, and N. Niizeki, Abstrs. Communs. Sixth Internat. Congr. and Sympos. Internat. Union Crystallography, Rome, Italy (1963).

[5] J. Caslavsky and M. Polkarova, Czech. J. Phys., B14, 454 (1964).

[6] M. Polkarova, Czech. J. Phys., B19, 657 (1969).

[7] M. Lambert, A. M. Quettet, C. Taupin, and A. Guinier, J. Phys., 25, 345 (1964).

[8] C. Bousquet, M. Lambert, A. M. Quettet, and R. Guinier, Acta Crystallogr., 16, 989 (1963).

[9] N. Niizeki and M. Hasegava, J. Phys. Soc. Japan, 19, 550 (1964).

[10] G. Brogren, Arkiv Phys., 3, 29 (1951).

[11] M. A. Blokhin, A. B. Gil'varg, L. Ya. Nikiforov, and V. P. Sachenko, Izv. AN SSSR, Ser. Fiz., 26, 397 (1962).

[12] J. Backovsky, J. Hrdy, and B. Novakova, Czech. J. Phys., B19, 1607 (1969).

[13] R. Bubacova, Czech. J. Phys., B12, 695 (1958).

[14] H. B. Hammar and G. Brogren, Kullagertidningen, 4, 85 (1961).

[15] K. Kohra and S. Kikuta, J. Phys. Soc. Japan, 8, 1565 (1966).

[16] F. Braun and W. H. Todt, J. Appl. Phys., 35, 5 (1964).

[17] Yu. F. Mal'tsev and L. Ya. Nikiforov, Abstracts for the 10th Conference on the Application of X Rays to Examination of Materials [in Russian], Inst. Krist. AN SSSR, Moscow (1971), p. 130.

[18] R. W. James, The Optical Principles of the Diffraction of X Rays, Cornell Univ. Press (1948).

[19] M. Renninger, Acta Crystallogr., 8, 597 (1955).

[20] G. A. Smolenskii, V. A. Bokov, V. A. Isupov, N. N. Krainik, R. E. Pasynkov, and M. S. Shur, Ferroelectrics and Antiferroelectrics [in Russian], Nauka, Leningrad (1971).

[21] H. Motegi, J. Phys. Soc. Japan, 29, 524 (1970).

[22] H. Motegi, J. Phys. Soc. Japan, 32, 202 (1972).

Temperature dependence of the rate of enlargement of the twinning layer in calcite crystals

V. P. Soldatov, V. I. Startsev, and N. M. Chaikovskaya

Physicotechnical Institute of Low Temperatures, Academy of Sciences of the Ukrainian SSR

(Submitted July 24, 1972)

Kristallografiya, 18, 1023-1027 (September-October 1973)

The rate of enlargement of the twinning layer in calcite crystals with a density of dislocations ~ 10^3 cm^{-2} has been measured in the range of shearing stresses 130-190 g/mm^2 at temperatures 153-473°K. It has been shown that the process of enlargement of the layer within a definite range of temperatures in the range studied, which depends on the magnitude of the applied stress, is controlled by thermally activated nucleation (multiplication) of the twinning dislocations. The activation energy and activation volume of the process of nucleation of the twinning dislocations, and their dependence on temperature and the shearing stress, have been determined. It has been shown that within the range of shearing stresses studied, at a definite temperature, there is a change in the controlling mechanism; with decrease in temperature, this change takes place more rapidly, the smaller the magnitude of the shearing stress.

As shown earlier,[1] the rate of enlargement of the twinning layer in calcite crystals with a density of total dislocations ~ 10^3 cm^{-2} depends both on the rate of movement of the twinning dislocations along the boundary of separation between the twin and the mother crystal and on the rate of their nucleation at this boundary. The controlling role of each of these processes is determined by the magnitude of the shearing stress, under the influence of which the enlargement of the twin takes place. At room temperature and low shearing stresses, the enlargement of the twinning layer is limited by the rate of movement of the twinning dislocations. At high stresses, as a consequence of the high rate of movement of the dislocations, their emergence from the crystal is determined by the nucleation of new dislocations, and the controlling process becomes the nucleation of the twinning dislocations. The rate of this process, according to earlier work[1] (assuming a thermally activated mechanism of dislocation nucleation) should be described by an equation of the type

$$\dot{n}(\tau, T) = \dot{n}_0 \exp\left(-\Delta H(\tau) / kT\right) = \dot{n}_0 \exp\left[-(u_0 - \gamma\tau / kT)\right], \quad (1)$$

where $\dot{n}(\tau, T)$ is the rate of nucleation of the twinning dislocations on unit length of the twinning boundary, $\Delta H(\tau)$ is the activation energy of the nucleation process, and γ is its activation volume. Thus for the thermodynamic description of the process of nucleation (multiplication) of twinning dislocations, and also to obtain information on the specific mechanism of this process, it is necessary to know such parameters of Eq. (1) as $\Delta H(\tau)$, γ, and their dependence on the stress, temperature, and structural state of the crystals. The possibility of determining these parameters arises as a consequence of the experimental confirmation of the suggestion that the nucleation of the twinning dislocations takes place by a thermally activated mechanism, so that its description by means of Eq. (1) is justified. For this purpose, in the present work we studied the temperature dependence of the rate of enlargement of the twin layer in the range of shearing stresses in which this process is controlled by the nucleation of the twinning dislocations.

EXPERIMENTAL PROCEDURE

The experiments were carried out with colorless transparent calcite crystals with an emergent density of total dislocations not exceeding 10^3 cm^{-2}. The characteristic dislocation structure of these crystals is shown in Fig. 1. Since the rate of enlargement of the twinning layer is extremely sensitive to the structure of the crystal, the constancy of this rate for fixed shearing stress and temperature was required, in addition to the requirement of identical emergent density of dislocations, in the selection of the crystals. From the crystals selected, we cut specimens with dimensions 3 × 10 × 15 mm, in which isolated twinning layers with thickness approximately 5–10 μ were produced. The subsequent increase in the thickness of these layers and the procedure used in the measurement of the rate of this process at room temperature has been described in detail.[1,2] The same procedure (after slight modifications) was used in the present work for the temperature range 150–470°K. Above room temperature, this was achieved by placing the deformation aparatus in a special heater, in which the specimen, heated to the required temperature, was kept for 1-1.5 h under isothermal conditions and then deformed under a definite shearing stress. Temperatures below 0°C were obtained by cooling the specimen with the vapor from liquid nitrogen, which was blown at a controlled rate through the working

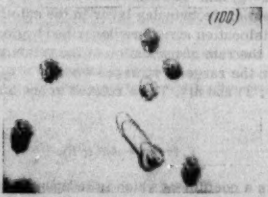

Fig. 1. Typical dislocation structure of the calcite crystals used in the experiments.

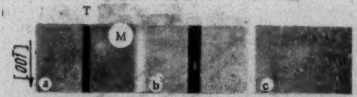

Fig. 2. Influence of temperature on the enlargement of the twinning layer; a) twinning layer of original thickness; b) after increase in thickness at 173°K for 150 sec; c) after increase in thickness at 253°K for 10 sec; τ = const = 170 g/mm^2, M represents the mother crystal, and T represents the twinning layer; the direction of the shearing stress is indicated by the arrow.

volume containing the specimen. In both cases the temperature was kept constant to within ± 0.5°, and measured with a thermocouple.

RESULTS OF THE MEASUREMENTS AND DISCUSSION

The influence of temperature on the process of enlargement of the twinning layer in calcite is shown in Fig. 2. The specimens shown in the photograph were cut from the same previously twinned crystal, that is, they had original twinning layers of the same thickness. One of the specimens was subsequently not deformed (Fig. 2a), while the twins in the other two crystals were enlarged at the same shearing stress $\tau = 170$ g/mm^2 and temperatures of 173°K (Fig. 2b) and 253°K (Fig. 2c). Comparison of these photographs shows the existence of a strong temperature dependence, and the appropriate calculation shows that the rate of enlargement of the twinning layer (subsequently denoted by the symbol V) is greater by almost four orders of magnitude at 253°K than at 173°K.

To establish the nature of the $V_n(T)$ relationship, we measured the rates of enlargement of the twinning layer in the range 153–473°K for shearing stresses of 130, 150, 170, and 190 g/mm^2. It can be seen from the data in Fig. 3 that for any shearing stress these relationships are linear only within a definite temperature range, after which deviation from linearity begins, and the $V_n(T)$ dependence becomes much less marked. It can also be seen that the deviation begins at a higher temperature, the smaller the magnitude of the applied stress. For the stresses studied (in increasing order) the corresponding temperatures are 278, 232, 189, and 174°K. The linear shape of the relationships shown in Fig. 3 indicates directly that the enlargement of the twinning layer takes place by a thermoactivated mechanism in the corresponding range of stresses and temperatures. It was previously shown[1] that when a certain (critical) shearing stress $\tau \sim 110$–120 g/mm^2 at room temperature is reached, the enlargement of the twinning layer in the calcite crystals with the dislocation structure described begins to be controlled by the rate of nucleation of the twinning dislocations $\dot{n}$. In the range of stresses where $\tau > \tau_{cr}$, the quantities $V_n(\tau, T)$ and $\dot{n}(\tau, T)$ are related to one another by the equation

$$V_n(\tau, T) = A\dot{n}(\tau, T), \tag{2}$$

where A is a coefficient which is independent of temperature and stress. From this equation it follows that the temperature dependence $\dot{n}(T)$ in the corresponding range of stresses should be equivalent to the temperature dependence $V_n(T)$.

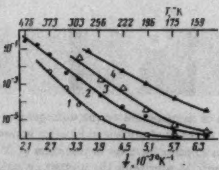

Fig. 3. Temperature dependence of the rate of enlargment of the twinning layer. 1) $\tau = 130$; 2) 150; 3) 170; 4) 190 g/mm^2.

The $V_n(T)$ relationships given in Fig. 3 were obtained in the range of stresses above the critical stress of change in mechanism at room temperature. This stress may change with change in temperature, however, as a consequence of the difference in the temperature dependence for the processes of movement and multiplication of the twinning dislocations controlling the enlargement of the twinning layer before and after the attainment of the critical stress. The nature of this displacement will be determined by the relative role of each of the above processes in the enlargement of the twin layer with change in temperature. According to ref. 1, the change in this mechanism takes place on the section of the $V_n(\tau)$ curve corresponding to viscous movement of the twinning dislocations. The rate of movement of the dislocations in this region, which is determined by the mechanisms of viscous retardation, increases with decrease in temperature according to a power law. This should lead to a slight displacement of the critical stress towards higher stresses, at which, with decrease in temperature, the start of intensive multiplication of dislocations may be achieved. The experimental data obtained indicate that this displacement of the critical stress does in fact take place. This can clearly be seen from the data in Fig. 3 on the deviation from the linear ln $V_n(1/T)$ relationship. It can readily be seen that the deviation increases more rapidly with a decrease in temperature, the smaller the magnitude of the shearing stress applied to the crystal. An analogous tendency is observed in the course of the $V_n(\tau)$ curves, shown in Fig. 4.

The dependence of the activation energy of the process of enlargement of the twin layer, constructed from the data in Fig. 3, is shown in Fig. 5. The process of thermally activated enlargement of the twinning layer corresponds in this figure to the sections of the curves (for a given τ) where the activation energy is independent of temperature. It can readily be seen that for each shearing stress there is a temperature at which a change is observed in the nature of the temperature dependence of the activation energy, indicating a change in the mechanism controlling the enlargement of the twin layer. The upper corner of Fig. 5 shows the dependence of the activation energy of the enlargement of the twin layer on the shearing stress for the temperature range above 278°K, that is, for the range where this process is controlled by the nucleation of the twin dislocations.

According to this relationship, the activation energy decreases linearly with increase in the shearing stress from a value of 0.43 eV ($\tau = 130$ g/mm^2) to 0.2 eV ($\tau = 190$ g/mm^2). Extrapolation of the $\Delta H(\tau)$ curve to the point where $\tau = 0$ gives the value of the energy required for the nucleation of dislocations by a purely fluctuation process. The magnitude of this energy was found to be

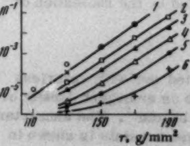

Fig. 4. Dependence of the rate of enlargement of the twin layer on the shearing stress at different temperatures: 1) (crosses) 298; 2) 273; 3) 253; 4) 223; 5) 198; 6) 173°K; open circles – data obtained in ref. 1.

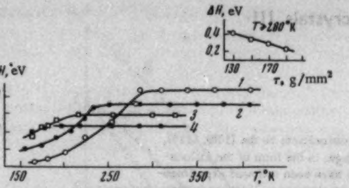

Fig. 5. Temperature dependence of the activation energy of the process of enlargement of the twin for different shearing stresses: 1) τ = 130; 2) 150; 3) 170; 4) 190 g/mm².

equal to 1 eV. Since according to Fig. 5 the thermal fluctuations carry from 20 to 40% of this energy, the rest is provided by mechanical activation resulting from the external shearing stresses, under the influence of which the enlargement of the twin layer takes place. The magnitude of the activation volume γ, constructed from the data in Fig. 4, for $\tau > 150$ g/mm² in the range from 225 to 300°K is independent of temperature and equal to $5 \cdot 10^{-20}$ cm³.

Thus the accumulated experimental data obtained at the present time provide evidence that the nucleation of the twin dislocations is a thermally activated process and is controlled by the transverse rate of twinning at high shearing stresses. An analogous conclusion was reached earlier[3] on the basis of a study of the temperature dependence of the transverse rate of twinning in single crystals of bismuth.

The activation energy of the nucleation of dislocations has been determined[4] from data on the enlargement of the twinning layers in the β and β'' structures of an AuCd alloy. The value found was ~ 0.1 eV. According to Cooper,[5] the activation energy of the enlargement of a single twin layer in single crystals of zinc lies in the range 0.12–0.25 eV. The corresponding value for bismuth,[6] at a fairly high (~400 g/mm²) shearing stress, was found to be ~0.03 eV. If the $\Delta H(\tau)$ curve obtained in the present work is extrapolated to a stress of 400 g/mm², that is if the activation energies are compared for the same value of τ in the morphologically similar crystals of calcite and bismuth, the value obtained is $\Delta H \sim 0.09$ eV, the order of magnitude of which is close to that of the value obtained for bismuth. Thus, judging from data obtained from different sources, the activation energy of the nucleation of twinning dislocations varies in the range 0.03–0.2 eV.

The activation energy of the nucleation of the twinning dislocations in calcite for enlargement of the twin layer at a constant fixed rate (active deformation) has been estimated.[7] The value found was ~ 1 eV. Since the energy of mechanical activation provided by external stresses was smaller by four orders of magnitude than that required, the authors concluded that the nucleation of the dislocations takes place on local defects which ensure a concentration of stresses equal to ~ 10⁴. From this it was concluded that the nucleation of the twinning dislocations in calcite is heterogeneous in character; this was convincingly confirmed[7] in experiments with calcite crystals with different degrees of perfection.

Thus the results of the present work, together with earlier results,[1,3,8] indicate that the model of the cavity mechanism is not applicable to the real process of enlargement of the twinning layer in bismuth and calcite crystals. The specific physical mechanism of nucleation of the twinning dislocations controlling the process of transverse enlargement of the twinning layer is not yet clear, but in the construction of possible models it is necessary to take account of not only thermal and mechanical activation but also the stress concentration factor, determined by the presence of structural imperfections (heterogeneities) in the crystal.

---

[1] V. P. Soldatov, V. I. Startsev, and N. M. Chaikovskaya, Fiz. Tverd. Tela, 13, 3153 (1971) [Sov. Phys.—Solid State, 13, 2653 (1972)].

[2] V. P. Soldatov, V. I. Startsev, N. M. Chaikovskaya, and T. O. Danilevich, Fiz. Tverd. Tela, 12, 79 (1970) [Sov. Phys.—Solid State, 12, 62 (1970)].

[3] V. I. Startsev, V. P. Soldatov, and M. M. Brodskii, Fiz. Met. Metalloved., 25, 1111 (1968).

[4] H. K. Birnbaum and T. A. Reed, Trans. Met. Soc. AIME, 218, 662 (1960).

[5] B. E. Cooper, Acta Metallurg., 15, 639 (1967).

[6] V. B. Pariiskii and A. Tret'yak, Fiz. Tverd. Tela, 9, 2457 (1967) [Sov. Phys.—Solid State, 9, 1933 (1968)].

[7] S. N. Komnik, V. Z. Bengus, and V. I. Startsev, Fiz. Tverd. Tela, 7, 127 (1965) [Sov. Phys.—Solid State, 7, 96 (1965)].

[8] V. I. Startsev, V. P. Soldatov, and M. M. Brodsky, Phys. Status Soldi, 18, 863 (1966).

Kinetics of the polishing and etching of sodium chloride crystals. III

G. K. Baranova and É. M. Nadgornyi

Institute of Solid State Physics, Academy of Sciences of the USSR

(Submitted January 10, 1972; resubmitted September 18, 1972)
Kristallografiya, 18, 1028-1032 (September-October 1973)

The kinetics of the formation of etch pits around the points of emergence of dislocations on the (100), (110), and (111) surfaces of single crystals of NaCl have been studied. The changes in the form of the dislocation pits under conditions of simultaneous etching and polishing of the crystal have been followed experimentally. On the basis of the results obtained for homologous series of acids and alcohols, three schemes have been proposed for the dissolution process, which make it possible to describe all the cases from etching to polishing characteristic of the action of these solvents.

INTRODUCTION

The points of emergence of dislocations onto the crystallographic surfaces of alkali metal halide crystals are usually detected by means of aliphatic acids and alcohols of the homologous series.[1-5] The process of formation of the etch pits is always accompanied by appreciable dissolution of the entire surface of the crystal. Thus the possibility of revealing the etch pits, and also their dimensions and constants, is determined by a combination of a number of dissolution and etching processes.[1-5] Until recently, however, no experimental data on the simultaneous measurement of the rates of these processes had been published. Recently, a detailed study of the kinetics of the etching and dissolution (polishing) of the surfaces of NaCl crystals in various acids and alcohols was undertaken.[6,7] It was found that the rates of polishing and normal etching are comparable with one another in all cases, so that in the examination of the origin of an etch pit it is essential to take account of the entire dissolution process, including possible differences in the rates of dissolution of the surface of the crystal (outside the pit), and the walls and foot of the pit.[7] At the same time, a direct relationship between the rates of etching and polishing was not detected. Frequently, the same rate of polishing corresponded to pits with different dimensions and slopes, and sometimes pits were absent altogether. This was observed both on going from one crystallographic plane to another and in different solvents.[6,7] Thus the nature of the local kinetics of formation of the dislocation pits under the conditions of intensive dissolution of the surface remained unknown.

In the present work, which is a continuation of earlier work,[6,7] we studied the nature of the relationship between the processes of polishing and etching of the (100), (110), and (111) planes of NaCl crystals in organic acids (formic, acetic, and propionic) and alcohols (methanol, ethanol, and propanol).

EXPERIMENTAL PROCEDURE AND RESULTS

We used a method involving the successive repeated etching of the surface of the crystal. It was established that the interruption of the etching under the conditions used in the experiments did not produce changes in the kinetics of the process. Thus the form of the pits and their dimensions are determined exclusively by the total duration of etching. The action of solvents was examined both for freshly broken or polished crystals and for specimens carrying previously produced so-called "primary" dislocation pits of definite dimensions L_1 and h_1 (2L is the width of the pit, and h is the depth of the pit). After repeated etching, interferometry[4] was used to determine the dimensions L_2 and h_2 of the pits newly produced around the dislocations at new points ("secondary" pits), and also the dimensions of the remaining "combined" pits L and h and the dimensions of the "internal" pits L_{int} and h_{int}, which appear in the center of the "combined" pits. Simultaneously, chemical analysis of the solution was used[6] to determine the average thickness H of the layer of substance removed from the surface of the crystal into the solution during the repeated etching.

This series of experiments, with fixation of the original state of the surface, made it possible to follow the change in the form of the pit with time in the etching agents studied, including those cases where etching as such did not take place at all, to compare the action of different solvents, and to investigate the part played by etching and polishing in the process of formation of the dislocation pits.

It was found that the acids and alcohols can be divided into three groups according to the nature of their action on the surface. Figure 1 shows graphs giving the changes in L and h with time, and Fig. 2 gives the "instantaneous" profile of the pits and Fig. 3 their interference pattern after repeated etching in specific solvents of each group. As origin of coordinates in Fig. 2 we took the point of emergence of the dislocation onto the surface at a given moment of time, in order to record correctly measured pit dimensions, since during dissolution the point of emergence of the dislocation is displaced along the h axis by an appropriate amount.

The solvents of the first group give pits with equal slopes, which are characterized by constant values of $\partial L/\partial t$ and $\partial h/\partial t$, and also by the fact that all the steps

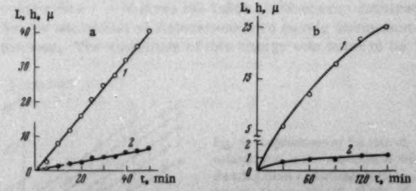

Fig. 1. Dependence of the width L (1) and depth h (2) of the pits on the duration of etching; a) acetic acid, 22°C; b) propionic acid, 22°C.

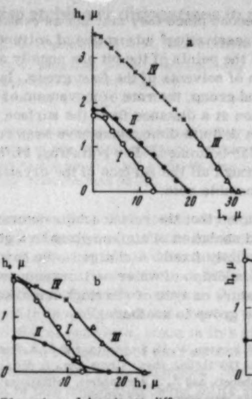

Fig. 2. Dimensions of the pits at different moments during etching: I) "primary" pits (acetic acid, 22°C, 15 min); II) "secondary" pits; III) "combined" pits; IV) "internal" pits. Conditions of repeated etching: a) acetic acid, 22°C, 6 min; b) propionic acid, 22°C, 1.5 h; c) ethanol, 22°C, 3 min.

of the echelon forming the side of the pit have the same velocity in a tangential direction. This can be clearly seen from Figs. 2a and 3b. On repeated etching, the sloping sides of the "primary" pit were displaced in such a way that its slope and dimensions remained unchanged (straight lines I and III are parallel). In the center of the pit, around the point of emergence of the dislocation line, there was formed an "internal" pit (IV), with dimensions equal to those of the "secondary" pit (II), that is, $L = L_1 + L_2$ and $h = h_1 + h_2$. The two pits (II) and (IV) have a constant slope, which is determined by the conditions of the repeated etching. The etching is accompanied by simultaneous polishing, in which a layer of substance approximately equal to the height of the "primary" pit ($H = 1.25$ μ) is removed from the surface, but the conditions for preservation of similarity are observed throughout. This indicates that the polishing takes place at equal rates on the surface, on the sloping side of the pit, and on the foot of the pit, without altering its dimensions. The etch pits on the (100) and (111) planes in formic and acetic acids are produced according to the same scheme.

In etching agents of the second group, the kinetics of formation of the pits is slightly different. The rates of etching $\partial L/\partial t$ and $\partial h/\partial t$, and also their ratio $\partial h/\partial L$, decrease with time, as shown in Figs. 1b. Under these conditions, pits with irregular slopes, which are indistinct at the periphery, are produced. When the widths of the pits reaches 40-50 μ, their growth into the interior stops completely, and they become flat-bottomed and continue to expand at an appreciable rate. From this it may be concluded that the movement of the echelon changes relative to that in the first case in such a way that the steps in positions closer to the foot of the pit, in their tangential movement, lag behind the steps situated in positions closer to the surface of the crystal. This is also indicated by the results of the repeated etchings (Figs. 2b and 3c), in which the primary pit is eroded, its width increases, and the slope $\partial h/\partial L$ decreases with increase in L (III). An analogous dependence of $\partial h/\partial L$ is observed for the "internal" and "secondary" pits, the dimensions of which in this case do not coincide; here, $L_2 > L_{int}$ and $h_2 > h_{int}$, so that $L < L_1 + L_2$ and $h < h_1 + h_2$. Polishing ($H = 1.80$ μ for the moment of time indicated in Fig. 2b) also takes place slightly more rapidly at the surface of the crystal than on the sloping side and foot of the pit, as indicated by the decrease in the height of the "primary" pit after repeated etching. The pits on the (100) and (111) planes in propionic acid and methanol, and also on the (110) plane in formic acid and methanol, are formed in this way.

The third group consists of solvents in which etch pits are not formed at all. If a crystal with "primary" pits is placed in one of these solvents, the width and the slope of the walls of the pits remain almost unchanged, and the height decreases with time until the pit disappears completely (Figs. 2c and 3d). This means that the points of emergence of the dislocations onto the surface do not now act as preferential dissolution centers, and the echelon of steps forming the sloping side of the pit, in contrast to the preceding cases, is no longer displaced as a whole; the polishing of the pit and the formation of a flat bottom in the center take place as a consequence of the fact that the surface of the crystal dissolves much more rapidly than the sloping sides and foot of the pit. For example, for the (100) plane in ethanol the rates of dissolution of the surface and the foot are equal to 0.9 and 0.5 μ/min respectively. It was found that all the planes studied in ethanol and propanol, and also the (110) plane in acetic and propionic acids, dissolve in this way.

DISCUSSION OF RESULTS

Thus the process of formation of an etch pit around a dislocation is determined by the ratio of the normal and tangential rates of etching and the change in this ratio with time. In those cases where $\partial L/\partial t$ and $\partial h/\partial t$ are constant and all the steps of the echelon forming the sloping wall of the pit are displaced in the tangential direction at the same rate, pits with constant slope are formed. If, however, $\partial L/\partial t$ and $\partial h/\partial t$ decrease with time and the rate of movement of the steps of the echelon depends on their

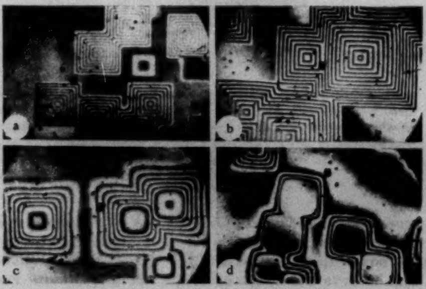

Fig. 3. Form of etch pits. × 570. a) Primary etching, acetic acid, 22°C, 15 min; repeated etching: b) acetic acid, 40°C, 6 min; c) propionic acid, 22°C, 1.5 h; d) ethanol, 22°C, 3 min.

position relative to the surface of the crystal, the pits are eroded and their slopes decrease. Although the dissolution of the surface of the crystal, which takes place independently of the presence of a dislocation at a given point, accompanies the etching processes, it influences the dimensions of the pits only in those cases where it takes place at a higher rate on the surface of the crystal outside the pit than on the sloping sides and foot of the pits. In polishing solvents, $\partial L/\partial t = 0$ and $\partial h/\partial t = 0$, that is, pits are not formed, since the dislocation does not act as a preferential dissolution center and an echelon of steps cannot exist (or be displaced).

It can be seen that a change from etching to polishing (from the first scheme to the third) takes place in the homologous series with increase in the length of the chain from HCOOH to CH_3-CH_2-COOH and from H_3COH to $CH_3-CH_2-CH_2OH$, and in analogous pairs from the acids to the alcohols, that is, with decrease in the mobility and polarity of the molecules of the solvent. The rates of etching and polishing decrease in the same direction.[7] This may be related to the fact that with decrease in the mobility and polarity of the solvent molecules there is a decrease in their ability to form solvate complexes, and the removal of the reaction products from the surface is hindered. It is also known that with increase in the chain length in homologous series there is an increase in their tendency to undergo molecular adsorption.[8] Both of these factors produce a decrease chiefly in the rate of etching in the tangential and normal directions, since in the first place the points of emergence of the dislocations and the steps of the echelon are slightly removed from the surface, and in the second place they may act as centers for the preferential "passivating" adsorption of solvent molecules. Thus all the points of the pit are equally accessible to the action of solvents of the first group. In solvents of the second group, the rate of movement of the steps of the echelon at a distance from the surface is decreased, and when definite dimensions have been reached the pits become flat-bottomed. For polishing, $\partial L/\partial t = 0$ and $\partial h/\partial t = 0$, although all the surface of the crystal dissolves at an appreciable rate.

It should be noted that the relationships determining the conditions of dissolution of a given plane in a given solvent are not strictly fixed. A change in the conditions of dissolution (the addition of water or inorganic salts, change in temperature or rate of stirring) may transfer a solvent from one group to another.

---

[1] V. N. Rozhanskii, E. V. Parvova, V. M. Stepanova, and A. A. Predvoditelev, Kristallografiya, 6, 704 (1961) [Sov. Phys.–Crystallogr., 6, 564 (1962)].

[2] N. F. Kostin, S. V. Lubenets, and K. S. Aleksandrov, Kristallografiya, 6, 737 (1961) [Sov. Phys.–Crystallogr., 6, 588 (1962)].

[3] É. Yu. Gutmanas and É. M. Nadgornyi, Kristallografiya, 13, 114 (1968) [Sov. Phys.–Crystallogr., 13, 85 (1968)].

[4] G. K. Baranova and É. M. Nadgornyi, Kristallografiya, 13, 836 (1968) [Sov. Phys.–Crystallogr., 13, 722 (1969)].

[5] É. Yu. Gutmanas and É. M. Nadgornyi, Fiz. Tverd. Tela, 11, 1179 (1969) [Sov. Phys.–Solid State, 11, 959 (1969)].

[6] G. K. Baranova and É. M. Nadgornyi, Kristallografiya, 16, 596 (1971) [Sov. Phys.–Crystallogr., 16, 506 (1971)].

[7] G. K. Baranova and É. M. Nadgornyi, Kristallografiya, 17, 875 (1972) [Sov. Phys.–Crystallogr., 17, 772 (1973)].

[8] V. V. Kuznetsov, Physical and Colloid Chemistry [in Russian], Vysshaya Shkola, Moscow (1968), p. 289.

Selective etching at dislocations in metals (Ni)

E. G. Popkova and A. A. Predvoditelev
M. V. Lomonosov Moscow State University

(Submitted November 27, 1972)
Kristallografiya, 18, 1033-1038 (September-October 1973)

The process of selective chemical etching at dislocations in nickel single crystals has been investigated. A series of new etching reagents has been developed for the {100} and {111} faces and also for the {110} face, no reagent for which had previously been known. The kinetics of selective etching on the individual faces of the crystal has been studied.

The present authors have previously expressed the view[1,2] that the development of etchants for the selective etching of metal single crystals is determined by the way they oxidize and to a considerable extent by the position of the metal in the electromotive series. Consequently it is important to investigate metals having a normal potential close to that of hydrogen, since in this case certain peculiarities in the nature of the reaction between the metal and the etchant are to be expected. Nickel is of particular interest in this connection owing to its specific chemical properties and also on account of its wide application in technology. Nickel has a tendency to form spontaneously protective oxygen-containing films on its surface, and this creates certain experimental difficulties. It is for this reason that very little research has been devoted to the selective chemical etching of nickel and that no analysis at all has been made of the mechanism of this process. Moreover, the information available in the literature, with the exception of refs. 3 and 4, is concerned with questions of the electrolytic etching of polycrystalline[5,6] and single-crystal[7-10] specimens. This fact, and also the presence of the oxide films which have to be destroyed in the course of etching, arouse additional interest in the study of the effect of individual properties of the metal on possible types of etchant for revealing the dislocation structure.

Single crystals of nickel (99.99% pure), grown by the Czochralski method, were orientated by means of x rays, and then subjected to mechanical treatment and to electropolishing in a 60% H_2SO_4 solution at a strictly constant and controlled anode potential, using a P-5827 potentiostat. The etching process was studied on the {100}, {110}, and {111} faces by an experimental method similar to that already described by the authors in ref. 11. The experimental results are summarized in Table 1. Analysis of this table shows that all the etchants for nickel can be divided into a small number of groups.

Acid etchants. The presence of an oxide film on the nickel surface means that its rate of solution, with evolution of hydrogen, is extremely small in the majority of acid solutions, and hence the latter cannot be used as etchants. However, according to data given in refs. 12 and 13, efficient protective films are not formed on nickel in solutions containing nitric, sulfuric, acetic, and certain other acids. Consequently it is to be expected that solutions of this type are suitable for the selective etching of nickel. In fact, in etching nickel single crystals in mixtures containing nitric acid and other acids such as acetic, formin, etc., clear well-faceted pits are formed at both "old" and "new" dislocations on the {100} and {111} planes and also on the {110} plane (Fig. 1a-c). The shape of the pits conforms to the crystallography of the face on which they are formed. According to the results of x-ray structural analysis, pits on the {110} plane are greatly extended in the ⟨110⟩ direction, their shape being very sensitive to the extent to which the crystal face accurately coincides with {110}.

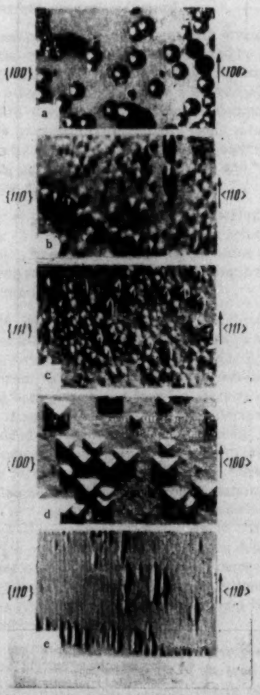

Fig. 1. Etch pits at dislocations in nickel single crystals: a) (100) face, etchant 5 ml HNO_3 + 5 ml CH_3COOH + 1 ml H_2O, ×650; b) (110) face, etchant 5 ml HNO_3 + 5 ml CH_3COOH + 1 ml H_2O, ×650; c) (111) face, etchant 5 ml HNO_3 + 5 ml HCOOH + 1 ml H_2O, ×650; d) (100) face, etchant 1 ml H_2O_2 + 1 ml H_3PO_4 + $BaCl_2$, ×1000; e) (110) face, etchant 1 ml H_2O_2 + 1 ml H_3PO_4 + $NiCl_2$, ×650.

The rate of etching in the reagents concerned depends on the HNO_3 concentration and also on that of other

TABLE 1. Composition and Characteristics of Etchants for Nickel

Reagent	Solvent	Concentration, volume, ml (or mole, M)	Time and character of etching		
			{100}	{110}	{111}
HNO_3 (d = 1.36)	H_2O	1 + 1	–	20 min, old	–
	C_2H_5OH	1 + 1	–	1-2 min, new and old	–
HNO_3 + HCl (d = 1.18)		1 + 1	1-2 min, new and old	–	15 min, new and old
HNO_3 + HCOOH	H_2O	5 + 5 + 1	1-2 min, new and old	1-2 min, new and old	1-5 min, new and old
HNO_3 + CH_3COOH (glac.)	H_2O	5 + 5 + 1	10 min, new and old	3-5 min, new and old	10 min, old
HNO_3 + H_3PO_4 + $FeCl_3$	H_2O	1 + 5*	10-20 min, new and old	–	10-20 min, new and old
HNO_3 + H_3PO_4 + $BaCl_2$	–	1 + 1**	3-10 min, new and old	–	3-10 min, new and old
$FeCl_3$	H_2O	1 M	1-5 min, new and old	–	–
	C_2H_5OH	1 M		–	Polishing
$FeCl_3$ + HCl (or H_2SO_4, H_3PO_4, HCOOH, CH_3COOH	C_2H_5OH	1 M	1-5 min, new and old	–	1-5 min, old
$(NH_4)_2S_2O_8$ + HCl (or H_3PO_4)	H_2O	1-2 M***	5 min, new and old	–	–
$(NH_4)_2S_2O_8$ + H_2SO_4	H_2O	1-2 M***	5 min, old	–	–
H_2O_2 + HCl	–	Optimally 1 + 1	1 min, new and old	1 min, old	Polishing
H_2O_2 + HF (or + HI)	–	1 + 1	1 min, old	–	–
H_2O_2 + H_2SO_4	–	1 + 1	1 min, old	–	–
H_2O_2 + HCOOH	–	1 + 1	–	–	Polishing
H_2O_2 + H_3PO_4	–	1 + 1	20 h, new and old	–	–
H_2O_2 + H_3PO_4 + $FeCl_3$	–	1 + 1*	1 min, new and old	–	Polishing
H_2O_2 + H_3PO_4 + NH_4Cl		1 + 1**	2 min, new and old	5-10 min, old	–
H_2O_2 + H_3PO_4 + $MNCl_2$	–	1 + 1**	2 min, new and old	3-5 min, old	–
H_2O_2 + H_3PO_4 + $BaCl_2$	–	1 + 1**	1-5 min, new and old	3-5 min, old	–
H_2O_2 + H_3PO_4 + $NiCl_2$	–	1 + 1**	5-6 min, new and old	5-10 min, old	–
I_2	C_2H_5OH	1 M	5 min, old	–	–
I_2 + HCl	KI + H_2O	I M (I)***	20 min, new and old	–	–
Br_2 + HCl	C_2H_5OH	1 + 1 + 10	10-20 min, new and old	10-20 min, old	Polishing

Notation: "old" and "new" refer to the dislocations.

* Concentration of $FeCl_3$ in the etchant is 0.1-0.2 mole.

** Salt added until the solution is saturated.

***Acid added until pH ≤ 3.

components, e.g., CH_3COOH. Dilution of the solutions leads to a reduction in the etching rate and in some cases to an improvement in the faceting of the pits. Since the potential of nickel is displaced in the positive direction as the pH of the solution is reduced,[14] the resistance of nickel increases considerably in dilute etchants, and nickel is practically insoluble in weak acid media. Hence acid solutions with pH ≤ 3 should be used for the selective etching of nickel.

A study of the kinetics of selective etching carried out on the {100} plane of nickel single crystals in a mixture of nitric and acetic acids showed (Fig. 2, curves 1–3) that the rate of selective etching remains constant over the whole range of concentrations chosen. The kinetics of selective etching was also studied on the {110} plane in a solution of nitric and acetic acids, and in this case the rate of selective etching is again constant (Fig. 3). The ratio of rates $v_{T\langle 110\rangle}/v_{T\langle 100\rangle}$ is about 2.

Etchants containing a cation (or anion) of variable valence. In the selective etching of nickel, it is possible to use oxidation–reduction systems, such as $FeCl_3$ solutions which contain a cation with variable valence, ammonium persulfate $(NH_4)_2S_2O_8$ containing an anion with variable valence, and others (see Table 1). It has been found that in the selective etching of nickel in aqueous and also alcoholic solutions of $FeCl_3$ pits are

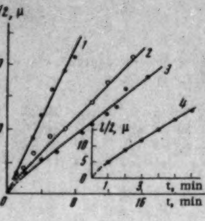

Fig. 2. Size of etch pits on the (100) face in various etchants as a function of time: 1) 5 ml HNO_3 + 5 ml CH_3COOH; 2) 5 ml HNO_3 + 5 ml CH_3COOH + 1 ml H_2O; 3) 5 ml HNO + 5 ml CH_3COOH + 3 ml H_2O; 4) 1 ml H_2O_2 + 1 ml H_3PO_4 + $BaCl_2$ (saturated).

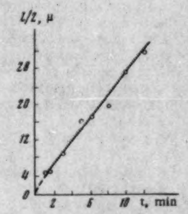

Fig. 3. Size of etch pits on the (110) face as a function of time. Etchant: 5 ml HNO_3 + 5 ml CH_3COOH + 3 ml H_2O.

formed at both "old" and "new" dislocations on the {100} face. Nickel is known not to be resistant to acid solutions when they contain an oxidizing agent.[12,15] In fact, if any kind of acid – hydrochloric, phosphoric, etc. – is added to an alcoholic solution of $FeCl_3$, the rate of etching increases and the faceting of the pits improves. In these solutions the ionization of nickel is evidently accompanied by the formation of nickel oxides of variable composition Ni_xO_y, which are converted by the acids into soluble nickel salts. After etching, the residues of these salts are removed from the surface of the crystal by washing the specimen in distilled water and alcohol.

Similar results are obtained on etching the {100} face of a nickel single crystal in aqueous solutions of ammonium persulfate containing additions of HCl, H_3PO_4, or H_2SO_4. In these solutions oxidation of the nickel takes place as a result of the reduction of S^{6+} to S^{2+}. Both "new" and growth dislocations are revealed. Optimum results are obtained in the presence of HCl, apparently because of the activating effect of the Cl ion.

Etchants containing "internal" oxygen. As already stated, nickel is characterized by a high capacity for the chemisorption of oxygen. If it is possible to destroy the oxide films formed in this way, the nickel should dissolve. This is achieved by adding to the etchant a suitable solvent as well as the oxidizing agent. Experiments have in fact shown that nickel can be selectively etched in solutions of hydrogen peroxide mixed with various acids, e.g., H_3PO_4, etc. Dislocation pits are formed in this way, but they are of poor quality, indicating that the means used to dissolve the oxide films were inadequate. The efficacy of the etchants in question is considerably increased by adding activating agents, which bring about dissolution of the surface oxides. According to current ideas, such an agent may be the Cl^{1-} ion, which breaks down the passive oxide film.[16] Addition of various chlorides to the etchant does in fact markedly change the character of the etching process, the pits becoming more sharply faceted. The introduction into the etchant of heavy-metal chlorides such as $BaCl_2$ and $MnCl_2$ has a particularly beneficial effect on the process of dislocation-pit formation. Thus, on adding $BaCl_2$ to an etchant composed of equal volumes of H_2O_2 and H_3PO_4, clear well-faceted etch pits are formed on the {100} surface of a nickel single crystal (Fig. 1d). Figure 1e shows the pits produced on etching the {110} face in an H_2O_2 + H_3PO_4 + $NiCl_2$ solution. Etching does not lead to the formation of pits on the {111} plane, general polishing of the surface occurring instead.

The creation of an acid medium with simultaneous addition of the chlorine ion can be achieved by adding a single component – HCl – to the etchant. It may be noted that ions of other halides also have a beneficial effect from the point of view of the quality of selective etching. Experiments have shown that on this basis it is possible to make up etchants with a wide range of etching times, thus enabling us to distinguish both "old" and "new" dislocations (see Table 1).

A study of the kinetics of selective etching on the {100} plane of nickel single crystals in a solution of H_2O_2+ H_3PO_4 + $BaCl_2$ has shown that in this case also a constant rate of selective etching is maintained over a fairly considerable time interval (Fig. 2, curve 4).

Halide solutions. Nickel single crystals can also be selectively etched in iodine and bromine solutions, although pit formation takes place more easily at dislocations in bromine solutions. Alcoholic solutions of bromine reveal both growth and "new" dislocations on the {100} face if an activating agent – the chlorine ion (e.g., HCl) – is added to the etchant. In the absence of the chlorine ion, these solutions only reveal growth dislocations, and the pits formed are not well faceted. "New" dislocations are also revealed by an aqueous solution of iodine in KI. After etching, the crystals must be carefully washed to remove halide salts of nickel. As in the previous case, the rate of etching in these solutions depends on the concentration of the etching component, increasing with rise in the latter. The optimum concentrations of etching reagents whose principal component is a halide are given in Table 1.

Conclusions. In the electromotive series nickel lies among the "non-noble" metals of the iron group and, having a negative potential, it should easily react with acids, displacing hydrogen. Hence, one would expect the types of etchant discovered in ref. 17 to be also suitable for nickel. However, it follows from what has been said above that etchants suitable for metals having a positive potential[11,18] are suitable for nickel too. Nickel is known to have a relatively high chemical affinity for oxygen,[12,19] and hence the ionization stage in nickel is inhibited by other, more rapid processes, which lead to the formation of adsorbed protective oxygen-containing films on the surface.[20,21] It is for this reason that nickel is characterized by an exceptionally high resistance to alkaline solutions and displays a well-marked resistance to acid solutions too. This means that nickel is mainly etched by oxidation followed by dissolution of the oxides formed, i.e., in the manner typical of "noble" metals. In other words, the presence of the oxide film "ennobles" nickel in acid etching reagents. Moreover, it is known that with a fairly well-developed passivation process the potential of nickel becomes positive.[12] This explains why etchants suitable for metals with a positive normal potential are also suitable for nickel.

Another peculiarity of nickel single crystals is that, in contrast to other metals,[11] experiments have shown that selective etching takes place most readily not on the $\{111\}$ plane, but on the cube face. It proved possible to devise for this face a considerable number of different etching reagents which give rise to well-faceted etch pits at the points where dislocations emerge at the surface. The information available in the literature on the selective etching of nickel[4,9,10] also pertains mainly to the $\{100\}$ face. Under the same conditions pits of considerably poorer quality are formed on the $\{111\}$ face or no pits are formed at all. The reason for this is evidently the difference in oxidation rate of the individual faces of nickel single crystals. According to ref. 22, the oxidation rate of nickel is greatest on the cube face, decreasing in the following order: $\{100\} \to \{110\} \to \{111\}$. Since, as has already been shown, etching takes place through an intermediate stage of oxide formation, it follows that the $\{100\}$ face should have the highest reactivity in selective etching. The very low tendency for the $\{111\}$ face to oxidize means that only a very limited number of etching reagents can be recommended for it. This fact explains why some authors[5-10] have used electrolytic etching in the selective etching of nickel. There are data in ref. 12 to show that oxide passivating films may be removed during electrolytic etching.

Nickel, like copper, has an fcc lattice, and so all that we have noted for copper[11] in regard to the morphology of etch pits and their orientation is applicable also to nickel.

---

[1] E. G. Popkova and A. A. Predvoditelev, in: Physicochemical Problems of Crystallization [in Russian], Vol. 2, Izd. Kazakhsk. Gos. Univ., Alma-Ata (1971), p. 138.

[2] E. G. Popkova and A. A. Predvoditelev, Growth and Defects of Metallic Crystals [in Russian], Naukova Dumka, Kiev (1972), p. 293.

[3] P. Feltham, J. Inst. Metals, 86, 237 (1957-1958).

[4] J. Echigoya, S. Haydshi, and M. Jamamoto, Japan. J. Appl. Phys., 8, 964 (1969).

[5] M. B. Guterman and A. S. Trekalo, Zavod. Lab., No. 7, 822 (1968).

[6] B. A. Movchan and T. A. Molodkina, Fiz. Met. Metalloved., 27, 1124 (1969).

[7] R. W. Guard, Trans. Met. Soc., AIME, 218, 573 (1960).

[8] L. Garz and G. Gerth, Prakt. Metallogr., 7, 417 (1970).

[9] W. Schatt and H. Worch, Prakt. Metallogr., 7, 483 (1970).

[10] W. Schatt and H. Worch, Corros. Sci., 11, 629 (1971).

[11] E. G. Popkova and A. A. Predvoditelev, Kristallografiya, 17, 612 (1972) [Sov. Phys.–Crystallogr., 17, 528 (1972)].

[12] F. Todt, Corrosion and Corrosion Protection [Russian translation], Khimiya, Moscow – Leningrad (1966).

[13] I. I. Kornilov, Nickel and Its Alloys [in Russian], Izd. Akad. Nauk SSSR, Moscow (1958).

[14] V. I. Shatalov and V. A. Khitrov, Izv. Voronezhsk. Gos. Ped. Inst., 47, 46 (1964).

[15] H. Remy, Treatise on Inorganic Chemistry [Russian translation], Vol. 2, Mir, Moscow (1966).

[16] N. P. Zhuk, Course in the Corrosion and Protection of Metals [in Russian], Metallurgiya, Moscow (1968).

[17] E. G. Popkova and A. A. Predvoditelev, Kristallografiya, 14, 53 (1969) [Sov. Phys.–Crystallogr., 14, 40 (1969)].

[18] E. G. Popkova and A. A. Predvoditelev, Kristallografiya, 15, 91 (1970) [Sov. Phys.–Crystallogr., 15, 72 (1970)].

[19] The Oxidation of Metals [in Russian], Vol. 1, Metallurgiya, Moscow (1968).

[20] R. Piontelli and C. Serravalle, Z. Elektrochem., 62, 758 (1958).

[21] P. D. Dankov, D. V. Ignatov, and N. A. Shishakov, Electron-Diffraction Study of Oxide and Hydroxide Films on Metals [in Russian], Izd. Akad. Nauk SSSR, Moscow (1953).

[22] K. R. Lawless, F. W. Young, and A. T. Gwathmey, J. Chem. Phys., 53, 667 (1956).

Etching of quartz and some features of the surface layer

E. I. Lazorina and V. V. Soroka

Leningrad Institute of Aircraft Instrumentation

(Submitted July 13, 1971; resubmitted January 21, July 17, and November 14, 1972)
Kristallografiya, 18, 1039-1043 (September-October 1973)

The effect of structural defects, temperature, and etching time on the etching rate of quartz crystals has been studied. From the dependence of the etching rate on time it has been established that on quartz crystals there is a surface layer with an enhanced etching rate which is formed during mechanical treatment and irradiation. Possible mechanisms involved in the formation of the surface layer are considered.

In order to determine the etching rate v_s at an arbitrary point on the surface, Cabrera[1] introduced an expression of the type

$$v_s = a\nu_s \exp(-\Delta E_s / kT), \tag{1}$$

where v_s is the frequency factor characterizing the frequency of nucleation, a is the height of the step ($\sim 10^{-8}$ cm), ΔE_s is the activation energy of formation of a nucleus, k is Boltzmann's constant, and T is the absolute temperature.

By studying the temperature dependence of the etching rate v_s it is possible to check the validity of Eq. (1) and to evaluate the parameters v_s and ΔE_s. Figure 1 shows the temperature dependence of the etching rate of a quartz crystal along the x, y, and z axes. The measurements were made on quartz crystal specimens in the form of small cubes with a length of side of 10 mm, whose polished faces were perpendicular, respectively, to the x, y, and z axes. The etchant was 40% HF. Two identical Teflon vessels were placed in the thermostat: one containing water and the other HF. The specimen was first kept in the water until the required temperature was reached and then quickly transferred into the vessel with the acid. The temperature of the acid was assumed to be the same as that of the water in the neighboring vessel. After a specified interval (normally ~ 1 h) the specimen was quickly transferred back into the vessel with the water. After cooling, the size of the specimen was measured and the etching rate along each direction calculated.

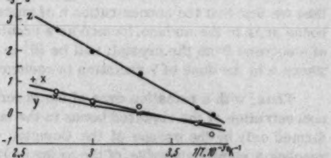

Fig. 1. The dependence of the etching rate v_s (μ/h) on the temperature of the etch (40% HF).

TABLE 1

Direction of etching	ΔE_s, eV	ν_p, sec^{-1}
+x	0.22±0.03	$5.6 \cdot 10^3$
y	0.16±0.03	$3.2 \cdot 10^2$
z	0.50±0.05	$1.8 \cdot 10^9$

ν_s,

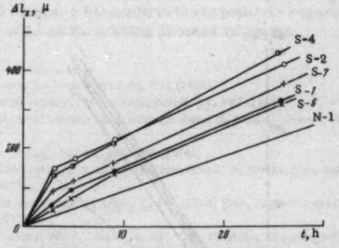

Fig. 2. The dependence on the etching time of the decrease in length along the optical axis of several quartz crystals (S, synthetic; N, natural quartz) during etching.

It is clear from Fig. 1 that the dependence of log v_s on 1/T is close to linear and therefore in good agreement with Eq. (1). Assuming the height of the step to be 5 Å we can determine v_s and ΔE_s for various directions from the graphs (Table 1). The etching rate in either direction along the y and z axes was assumed to be equal to half the rate of decrease in the size of the specimens during etching along these directions. In the +x direction the etching rate was significantly higher than in the opposite direction and therefore the rate of decrease in the length of the specimen after etching along the x axis was assumed to be the rate of etching in the +x direction.

Thus, the low etching rate of the quartz in a direction perpendicular to the optical axis was mainly caused by the low probability of nucleation.

Our studies of the etch figures on polished surfaces of the x, y, and z slices of quartz have indicated that most of the etch pits on the polished surfaces of the quartz specimens are due to dislocations formed in a thin surface layer of the specimens during mechanical treatment (slicing, grinding, polishing).

Figure 2 shows the graphs for the reduction in the length of several quartz crystals along the optical axis as a function of the etching time. In order to eliminate the effect of any nonuniformity in the composition of the etch, the temperature, or other factors, all the specimens were etched simultaneously in the same solution. It is clear from the graphs that all the experimental crystals had a surface layer with an enchanced etching rate and the thickness of the layer depended on the state of the surface. On the ground specimens (crystals S-1 to S-7), the thickness of the surface layer on each side of the slice varied from 30 to 80 μ, but on the polished specimens (N-1) it was < 1 μ. The etching rate was lower after the sur-

TABLE 2. The Concentration of the Main Impurities in the Experimental (Fig. 2) Crystals (wt.%)

Crystal	Impurity				
	Al	Fe	Na	K	Other
N-1	$3\cdot10^{-3}$	$1\cdot10^{-4}$	$1.6\cdot10^{-3}$	$1.6\cdot10^{-3}$	$3\cdot10^{-4}$
S-1	$1\cdot10^{-3}$	$1\cdot10^{-4}$	?	?	$3\cdot10^{-4}$
S-2	$1\cdot10^{-2}$	$1\cdot10^{-4}$	$1.8\cdot10^{-2}$	$5.7\cdot10^{-4}$	$3\cdot10^{-4}$
S-4	10^{-3}—10^{-4}	$3\cdot10^{-2}$	$1.4\cdot10^{-3}$	$5\cdot10^{-2}$	$1\cdot10^{-3}$
S-6	$1\cdot10^{-3}$	10^{-3}—10^{-2}	$1.2\cdot10^{-2}$	$17\cdot10^{-2}$	$1\cdot10^{-3}$
S-7	$3\cdot10^{-3}$	$1\cdot10^{-4}$	$5\cdot10^{-4}$	—	$1\cdot10^{-4}$

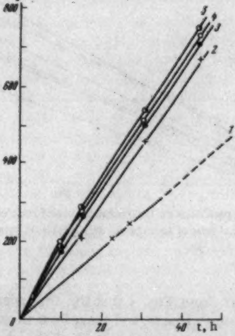

Fig. 3. The effect of γ radiation on the dependence on the etching time of the reduction in length along the optical axis of a natural quartz crystal N-1: 1) unirradiated crystal; 2) 10^6; 3) 10^8; 4) $6.3\cdot10^8$; 5) 10^7 R.

face layer had been etched away and could be taken as the etching rate of the crystal. In Figure 2 the graphs do not show any experimental points for t = 1 h since these points overlap for various crystals. If they are plotted, however, the dependence of Δl_z on t remains linear within the limits of experimental error when $t \to 0$. Table 2 shows the concentration of the main impurities in the experimental crystals.

Figure 3 shows the dependence of the extent of the etching of polished cubes (10 × 10 × 10 mm) cut from the natural quartz crystals N-1 as a function of the etching time and the dose of Co^{60} γ radiation. By the graphs in Fig. 3 and the results of additional studies it is possible to draw the following conclusions: 1) When the natural quartz crystal N-1 is γ-irradiated, a surface layer is formed which has an enhanced rate of etching; 2) the thickness of the layer is close to the mean free path length of the fast Compton electrons and is reduced when the dose of γ radiation is increased; 3) the etching rate of the γ-irradiated quartz beyond the surface layer is considerably greater than the etching rate of the unirradiated quartz crystal; 4) on heating (annealing) to 200°C the changes in the etching rate of the N-1 crystal caused by the γ radiation beyond the surface layer disappear in the course of several hours (Table 3), while the surface layer with the higher etching rate is retained even after annealing at 600°C; 5) after etching away the surface layer formed under γ irradiation, the surface layer can be restored by a repeat irradiation.

TABLE 3. The Effect of Annealing on the Ratio of v to v_0 *

Dose of γ radiation (R)	Before annealing	After annealing for 3 h at a temperature of	
		200° C	300° C
10^6	1.66	0.81	1.0
10^7	1.73	1.06	1.15
10^8	1.66	0.96	1.10

*v is the rate of etching of the γ-irradiated N-1 crystal; v_0 is that of the unirradiated N-1 crystal.

These features of the etching of a γ-irradiated N-1 crystal can be explained on the basis of the mechanisms involved in the interaction of the γ radiation with the material[2,4] and the quartz-etching mechanism.[3] An increase in the etching rate after irradiation indicates that the bonds between the Si and the structural O atoms are weakened, i.e., that ionizing radiation produces an increased number of ruptured Si−O bonds. Moreover, the rapid Compton-emission electrons formed in a surface layer of thickness less than their mean free path can escape beyond the boundaries of the crystal, thus causing some of the features of this layer. When the dose is increased, the number of electron traps increases, the mean free path of the Compton electrons is reduced, and consequently the thickness of the surface layer is also reduced. If we assume that the Compton-scatter cross section[4] of the γ photons with an energy of 1.25 MeV is 0.3 b, then we find that the concentration n of ruptured chemical bonds near to the surface, formed as a result of the escape of electrons from the crystal, will be 10^8 to 10^9 Φ (cm^{-3}), where Φ is the dose of γ radiation in roentgens.

Thus, with a radiation dose of the order of 10^8 R, the concentration of the ruptured bonds in the surface layer, formed only by the escape of the Compton electrons, reaches a significant value, of the order of 10^{16}–10^{17} cm^{-3}. These calculations support the suggested mechanism for the formation of the surface layer during the γ irradiation of a quartz crystal.

The increase in the etching rate beyond the surface layer in irradiated quartz is probably due to other processes. The saturation of the change in etching rate with dose (all the specimens irradiated with a dose of 10^6 R and above have roughly the same etching rate) indicates that these changes are caused by defects whose number is virtually unchanged during irradiation but which change into another state. Heating to 200°C produces the inverse

TABLE 4

Etchant composition	Δl_z, μ
40% HF	49±5
40% HF + 0.01% LiCl	33±5
40% HF + 1% LiCl	35±5
40% HF + HCl	53±5

process, in which the defects are returned to their original state, i.e., the change in etching rate caused by irradiation is annealed out. The analysis of the published data shows that after the irradiated quartz crystals have been heated to 200°C there is a sharp rise in the traps associated with the Li impurity.[5,6] Moreover, it has been established in ref. 7 that an increase in the Li concentration in the solution from which the crystal was grown leads to a significant reduction in the rate of growth. On the basis of the laminar growth theory, the effect of the Li can be explained by the fact that Li "poisons" the growth step, thus slowing down the growth rate. Analogous processes can also occur during etching. Therefore, the increase in the etching rate of the N-1 crystal after γ irradiation can be explained by the change in the state of the Li impurity in the crystal. The radiation-stimulated diffusion in the quartz may lead to the formation of atomic complexes containing Li and as a result some Li may pass into the solution in the bonded state. In this case the effect of the Li on the etching rate will be reduced, i.e., the etching rate increases. In order to verify this hypothesis, the etching rate of quartz was studied in etchant solutions to which LiCl, which dissociates into Li^+ and Cl^- ions, had been added. A small quantity of hydrochloric acid was added to one of the solutions in order to identify the effect of the Cl^- ions on the etching rate. The results of this experiment, shown in Table 4 (etching time for all etches, 5 h), confirm the hypothesis regarding the effect of Li on the etching process in quartz.

---

[1] N. Cabrera, J. Chem. Phys., 53, 675 (1956).

[2] F. M. Ernsberger, J. Phys. Chem. Solids, 13, 347 (1960).

[3] Physical Encyclopedic Dictionary [in Russian], Vol. 4, Moscow (1965), p. 231.

[4] J. H. O. Varley, Nature, 174, 886 (1954).

[5] L. G. Chentsova, B. N. Grechushnikov, and E. N. Batrak, Opt. Spektrosk., 3, 619 (1957).

[6] E. N. Batrak, Kristallografiya, 3, 627 (1958) [Sov. Phys.—Crystallogr., 3, 635 (1958)].

[7] M. M. Lukina, M. V. Lelekova, and V. E. Khadzhi, Kristallografiya, 15, 607 (1970) [Sov. Phys.—Crystallogr., 15, 530 (1970)].

Some structural–morphological characteristics of the volatilization of single crystals of α-Al_2O_3

E. M. Akulenok, Yu. K. Danileiko, V. V. Panteleev, E. A. Fedorov,
and V. Ya. Khaimov-Mal'kov

Institute of Crystallography, Academy of Sciences of the USSR

(Submitted July 19, 1972; resubmitted December 11, 1972)
Kristallografiya, 18, 1044-1048 (September-October 1973)

The temperature dependence of the morphology and rate of Langmuir volatilization of the faces of leucosapphire has been studied. It has been found that the rates of volatization of the faces decrease in the order $(10\bar{1}0) > (2\bar{1}\bar{1}0) > (0001)$. The morphology of the volatilization of the first two faces corresponds to a layer mechanism, and that of the $(10\bar{1}0)$ face to a monolayer or normal mechanism. The energy of volatilization has been determined, the value found being (210 ± 20) kcal/mole. The results obtained have been compared with the theory of structural morphology.

A fairly large number of papers have been published on the problems of studying the characteristics of the volatilization of corundum crystals. They are mostly devoted to purely physicochemical aspects of the problem: the determination of the composition and pressure of the vapor (mass-spectroscopic methods),[1,2] and the determination of the volatilization coefficients (by gravimetric methods).[3-6] At the same time, various crystallographic aspects of this problem, for example, the comparison of the morphology of the volatilization of different faces of the crystals and their rates of volatilization, are of interest. The present paper gives the chief results of a study of the structural–morphological characteristics of the volatilization of α-Al_2O_3 crystals.

MORPHOLOGY OF THE VOLATIZING FACES

Procedure. The morphology of the surface of volatilization was studied for crystals of leucosapphire (purity 99.99%) grown by the Verneuil method and by directional crystallization. We used specimens in the form of parallelepipeds with dimensions 5 × 5 × 15 mm, the surfaces of which were treated according to the 14th class. The principal crystallographic directions were determined by means of an x-ray goniometer to within several minutes of arc. To obtain natural faces, crystal growth from the vapor phase was carried out. The volatilization was carried out in a vacuum furnace at a reduced pressure of 10^{-5} torr in a special chamber illustrated diagramatically in Fig. 1. The specimen was suspended freely from a tungsten/tungsten–rhenium thermocouple, which controlled its temperature with an accuracy of 2000 ± 10°C. The apparatus made it possible to vary both the temperature of the heater, which was maintained automatically to within ± 5°, and the duration of volatilization. The gradient at the point of attachment of the specimen did not exceed 5 deg/cm. The morphological study of the surfaces was carried out on an optical microscope with interference contrast.

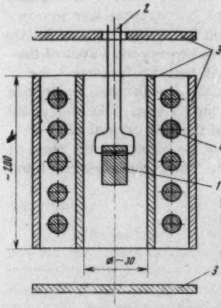

Fig. 1. Diagram of the heating chamber: 1) specimen; 2) thermocouple; 3) system of tungsten screens; 4) tungsten heater.

Experimental results. Photomicrographs of the volatilization surfaces of the (0001), $(2\bar{1}\bar{1}0)$, and $(10\bar{1}0)$ faces are shown in Fig. 2. The first two faces (Fig. 2, a and b) show clearly the layer structure of the surfaces, whereas the $(10\bar{1}0)$ (Fig. 2, c) and $(10\bar{1}1)$ faces show only

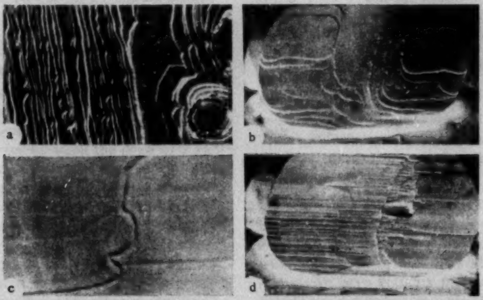

Fig. 2. Photomicrographs of the surfaces of the volatilizing faces. a) (0001); b, d) $(2\bar{1}\bar{1}0)$; c) $10\bar{1}0)$. × 320.

block boundaries. The difference in the morphological pictures for these faces are independent of the duration and temperature of volatilization. The direct volatilization of mechanically treated surfaces, the orientations of which were close (to within one deg) to the orientations of the faces studied showed that the microrelief of these surfaces [in the sense of "layer" or "nonlayer" (see Fig. 2)], even in the initial stage of the volatilization, is analogous to the volatilization relief of the corresponding faces. A noteworthy feature is the specific change in the morphology of volatilization of the $(2\bar{1}\bar{1}0)$ face with change in temperature: At temperatures close to 1900°C the volatilization takes place in layers parallel to the actual face (Fig. 2, b), whereas at temperatures close to 1700°C the layers volatilizing are those parallel to the faces (14, 14, $\overline{28}$, 3) which are produced either at the edge of the crystal or at the relief steps (Fig. 2, d).

ANISOTROPY OF THE RATES OF VOLATILIZATION

Procedure. In the study of the anisotropy of the rates of volatilization, the experimental procedure was analogous to that previously described for the study of the morphology of the volatilizing faces, except that the experiments were carried out using specimens without blocks detectable on the x-ray goniometer.

The rates of volatilization were calculated by measuring the thickness of the volatilizing layer in a given crystallographic direction after a definite time interval at a definite temperature. The accuracy of the measurement was $\pm 10^{-4}$ cm. The absolute values of the size of the volatilizing layers were determined in the range $2 \cdot 10^{-3}$–$2 \cdot 10^{-2}$ cm, depending on the duration of treatment. For example, for a temperature of ~1650°C the time was of the order of 12 days. In the calculation we took account of only the faces turned towards the heated screen (Fig. 1). The same specimen was usually employed for the study of the time and temperature dependence.

The treatment of the experimental data involved the determination of the "Langmuir" pressure P as a function of temperature. The pressure P for each face was calculated from the familiar relationship

$$P_{\text{atm}} = (V/44.33)(T/M)^{1/2},$$

where V, $g/cm^2 \cdot sec$, is the measured rate of volatilization of the face, T is the absolute temperature of the specimen, and M is the effective molecular weight.

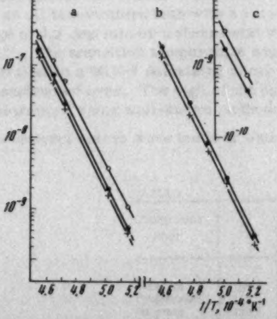

Fig. 3. Pressure as a function of the reciprocal of the temperature (for explanation see text). ○) $(10\bar{1}0)$; ●) $(2\bar{1}\bar{1}0)$, + (0001).

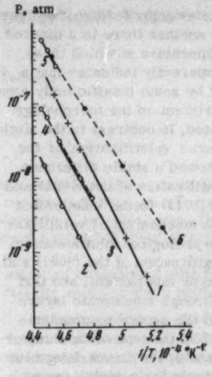

Fig. 4. Dependence of the pressure on the reciprocal of temperature for tungsten cells; 1) present work; 2,3) Langmuir volatilization, gravimetric method;[5,6] 4) Knudsen volatilization, gravimetric method;[6] 5, 6) Knudsen volatilization, mass-spectrometric method.[1,2]

In the measurement of the rate of volatilization, the density of $\alpha-Al_2O_3$ was taken as equal to 3.99 g/cm^3. The effective molecular weight was calculated from the corresponding partial pressures, measured[1] by the mass-spectrometer method (tungsten cell). From the calculation of the vapor pressure of O, Al, AlO, and Al_2O, M = 24, in agreement with published data.[6]

Experimental results. The logarithmic dependence of the magnitude of the pressure on the reciprocal of the temperature for the (0001), $(2\bar{1}\bar{1}0)$, and $(10\bar{1}0)$ faces is shown in Fig. 3. Figure 3a corresponds to the volatilization of two specimens: For one we measured the rates of volatilization of the (0001) and $(10\bar{1}0)$ faces, and for the other the rate for the $(2\bar{1}\bar{1}0)$ face. Figure 3, b and c, corresponds to the volatilization of different specimens in different series of experiments; specimen 3, c, was prepared from the same crystal as the specimen in experiment 3, a. According to these relationships, anisotropy of the rates of volatilization is observed in each experiment. The faces can be arranged in the following order of decreasing rates of volatization: $V_{(10\bar{1}0)} > V_{(2\bar{1}\bar{1}0)} > V_{(0001)}$. It can be seen from the graphs, however, that the absolute values of the rates may differ significantly even for crystals of similar quality. This difference in many cases is greater than the difference due to the anisotropy of volatilization. At the same time, as expected, the energy of volatilization, equal to 210 ± 20 kcal mole^{-1}, is independent of the quality of the specimens used and the indices of the face being volatilized.

DISCUSSION

We shall leave open the question of the change in the nature of the layer volatilization of the $(2\bar{1}\bar{1}0)$ face with change in temperature (Fig. 3, b and c), which may be due to the intrinsic kinetics of volatilization or to the conditions of volatilization (for example, the presence of tungsten oxides in the vapor).[1] A noteworthy feature, however, is that from one experiment to another there is a marked scatter in the values of the temperature at which these changes begin. This scatter apparently indicates that a significant influence is exerted by some insufficiently controlled parameters of the experiment on the morphology of the surfaces. As already noted, in contrast to the slight change in the nature of the layer volatilization of the $(2\bar{1}\bar{1}0)$ face, the experiments showed a stable difference between the morphology of volatilization of the (0001) and $(2\bar{1}\bar{1}0)$ faces and the $(10\bar{1}0)$ and $(10\bar{1}1)$ faces, independent of temperature. If we judge the mechanism of volatilization of the faces from their morphological manifestation, it may be assumed that the volatilization of the (0001) and $(2\bar{1}\bar{1}0)$ faces takes place by a layer mechanism, and that of the $(10\bar{1}0)$ and $(10\bar{1}1)$ faces through monatomic layers or normally. Both the first and the second mechanisms of volatilization are determined by the type of face undergoing volatilization.[7] Unfortunately, the direct determination of the type of face, particularly for complex ionic structures, involves considerable difficulties. The most convenient method for determining the type of face was found to be that proposed by Hartman,[8] who carried out a calculation[9] for the structure of α-Al_2O_3, according to which corundum can have only seven simple forms of type F, that is, seven simple face forms, each of which is parallel to two or more atomic chains with intensive bonds (PBC). The other faces belong to type S (each of which is parallel to one chain PBC) or to type K (which are not parallel to any chain PBC). According to Hartman, the faces (0001) and $(2\bar{1}\bar{1}0)$ which we studied in the present work belong to type F, and the $(10\bar{1}0)$ and $(10\bar{1}1)$ faces belong to type S. Comparison of the above data on the volatilization with Hartman's calculation shows that the PBC theory for α-Al_2O_3 agrees with the observed morphology of volatilization. Qualitatively, according to the number of free bonds in unit surface area, the PBC theory also agrees with the observed order of rates of voltailization of the faces: $V_{(10\bar{1}0)} > V_{(2\bar{1}\bar{1}0)} > V_{(0001)}$ (Fig. 3). It seems to us, however, that in spite of the above discussion, there are at present insufficient data to permit a reliable comparison of experimental and theoretical results. This is particularly true of data on the measurement of the absolute values of the rate of volatilization, for which the scatter in the values obtained by different authors reaches an order of magnitude (Fig. 4). This scatter is evidently due to differences in the specimens used, for example, in the presence of impurities,[6] bulk defects, etc. The same factors are probably responsible for the discrepancies in the determination of volatilization coefficients (0.15–0.8), whereas the values of the energies of volatilization in these cases differ comparatively little (Fig. 4).[1,2,5,6]

The authors thank Kh. S. Bagdasarov and Yu. N. Lyubitov for discussion of the procedure and experimental results.

---

[1] J. Drowart, G. De Marie, R. P. Burns, and M. G. Ingram, J. Chem. Phys., 32, 1566 (1960).

[2] M. Farber, R. D. Srivastava, and O.M. Uy, J. Chem. Soc., Faraday Trans., 2, 249 (1972).

[3] E. G. Wolf and C. B. Alcock, Trans. Brit. Ceram. Soc., 61, 667 (1962).

[4] C. B. Alcock and M. Peleg, Trans. Brit. Ceram. Soc., 66, 217 (1967).

[5] C. B. Alcock, Bull. Soc. Franc. Ceram., 72, 25 (1966).

[6] T. Sasamoto and T. Sata, J. Chem. Soc. Japan, Industr. Chem. Sect., 74, 578 (1971); 74, 832 (1971).

[7] J. P. Hirth and G. M. Pound, Condensation and Evaporation, Pergamon (1963).

[8] P. Hartman and W. G. Perdok, Acta Crystallogr., 8, 521 (1951).

[9] P. Hartman, Zap. Vses. Mineralog. Obshchestva, 91, 672 (1962).

Pretransition phenomena and optical activity of amorphous liquid phases of cholesteric liquid crystals

E. I. Ryumtsev, A. N. Cherkasov, V. G. Tishchenko, and M. M. Fetisova

Physics Institute, Leningrad State University
Khar'kov Institute of Single Crystals

(Submitted July 10, 1972; resubmitted September 19, 1972)
Kristallografiya, 18, 1049-1052 (September-October 1973)

The temperature dependence of the optical activity of a number of complex esters of cholesterol has been studied. It has been shown that above the transition temperature where the cholesteric phase goes over to an isotropic liquid (T_c) fluctuational nuclei of the mesophase have internal structure of the nematic type. The sharp increase in the optical activity below T_c arises from the appearance of a homotropic cholesteric state in the esters studied.

In studies of the temperature dependence of the electrical birefringence of cholesteric liquid crystals near the temperature of the transition into the cholesteric phase, T_c, it has been found that there are fluctuational nuclei of a liquid crystal phase in the isotropic melt for a number of complex esters of cholesterol.[1] The formation of larger-than-molecular clusters in amorphous liquids at temperatures above T_c is accompanied by a sharp temperature dependence of the electrical birefringence upon approaching T_c.

The aim of the present work is to study the structure of the observed nuclei in the same samples of cholesteric liquid crystals. One of the basic properties of the cholesteric mesophase is its enormous optical activity due to the details of the supermolecular arrangement of cholesteric liquid crystals, a systematic "corkscrew" type of structure. Therefore in order to solve the problem of interest it is natural to study the temperature dependence of the optical activity near the temperature of the isotropic liquid ⇌ cholesteric phase transition.

The studies of the optical activity were carried out using a Pepol-60 spectropolarimeter (English) at 546 nm. The samples were placed in a hermetically sealed glass cell with a length (along the beam path) of 5.5 mm. The samples were heated in an oven of length 150 mm with two windows. The temperature was determined using a chromel–nickel thermocouple with a precision of ± 0.2°. The temperature for the cholesteric phase → isotropic liquid transition was determined in a thin-walled capillary of diameter between 0.8 and 3 mm. The measurements were done using an oil temperature bath with a rate of temperature change of 0.2 deg/min or a thermostat with a precision of 0.2°. The transition temperature was determined in parallel in a MIN-8 polarizing microscope in a specially constructed oven. The sign of the optical rotation was determined using well-known methods.[2,3]

The cholesterol esters were made by ester condensation of cholesterol with the corresponding monocarboxylic acids or their acid chlorides.

The temperature T_c for the transition from the cholesteric phase into an isotropic liquid was determined during heating of the sample and is shown in the second column of Table 1. For some esters the formation of a cholesteric homeotropic state was observed.[4-7] This state appears during cooling of the isotropic melts of a number of cholesterol esters below T_c in the form of a transparent blue–violet fog.

Upon further cooling the homeotropic state goes over to a nontransparent one (with the use of thick samples) of the cholesteric mesophase. In the third column of Table 1 we show the temperature range for the existence of the cholesteric homeotropic state Δt_Γ for various esters.

For temperatures above the transition from the cholesteric phase into an isotropic liquid the specific rotations of the cholesterol esters and the sample of basic cholesterol remain nearly constant and amount to about 0.5 deg/mm. These values of $[\alpha]$ are shown in the fourth column of Table 1. They are three or four orders of magnitude less than the corresponding values of $[\alpha]$ for the cholesteric mesophase in the same materials.[8] In order

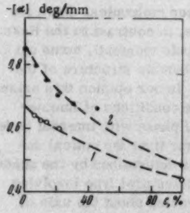

Fig. 1. Specific rotation angle of the polarization plane for cholesterol (1) and cholesteryl acetate (2) solutions in CCl_4 as a function of the concentration.

TABLE 1

Cholesterol ester	T_c	Δt_Γ	$[\alpha]$, deg/mm	Cholesterol ester	T_c	Δt_Γ	$[\alpha]$, deg/mm
Acetate	107		—0.50	Decanoate	88.7	8.2	
Propionate	111	0	—0.30	Laurate	87.9	6.9	
Butyrate	110.2	2.3	—0.48	Myristate	84.7	6.1	
Valerate	94	2.8		Tetradecanoate	83.2	5.9	
Hexanoate	98	2.8					
Nonanoate	91	8	—0.42	Palmitate	81.7	5.4	—0.35
				Cholesterol	142		—0.42

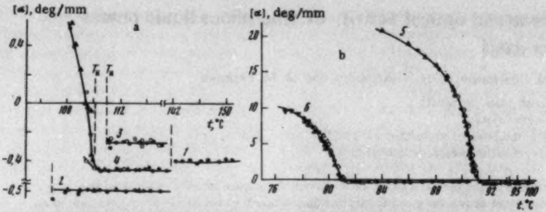

Fig. 2. Specific rotation angle of the polarization plane as a function of the temperature for various cholesterol derivatives. a: 1) cholesterol; 2) cholesteryl acetate; 3) cholesteryl propionate; 4) cholesteryl butyrate; b: 5) cholesteryl nonanoate; 6) cholesteryl palmitate; the dark symbols are cooling data and the light symbols are heating data. The symbols of various shapes correspond to different runs.

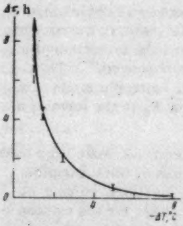

Fig. 3. Time for the existence of a cholesteric homeotropic state as a function of the degree of supercooling of cholesteryl nonanoate.

to show that [α] corresponds to a molecular rotation of the polarization plane we studied the concentration dependence of [α] for solutions of cholesterol and cholesteryl acetate in CCl_4. The results obtained are shown in Fig. 1. It can be seen that the curve for the concentration dependence of [α] upon extrapolation to 100% leads to [α] values which agree with the [α] values measured in the melt with $t > T_c$.

Thus these investigations indicate that when $t > T_c$ the rotation of the polarization plane arises from the intrinsic optical activity of the ester molecules. Here the rotation of the polarization plane, in contrast to the Kerr effect (optical anisotropy and dipole moment), turns out to be insensitive to the supermolecular structure of the melt at temperatures above T_c. In our opinion this arises from the appearance under these conditions of fluctuational nuclei of the liquid crystal phase with internal order of the nematic form.[1] At the same time the optical activity of the mesophase in turn is determined by the supermolecular organization of the cholesterol type involving systematic rotations of the molecules about the axis of cholesteric order. The formation of fluctuation nuclei with cholesteric internal structure at temperatures above T_c is evidently impossible, which is indicated by the absence of a temperature dependence of [α] above T_c. This is indicated by the negative sign of the molecular optical activity and the opposite signs of [α] in the cholesteric mesophase for the esters studied.

Upon lowering the temperature below T_c, investigation of the optical activity in the samples of cholesteryl acetate and propionate turned out to be impossible due to the great cloudiness of the preparation (the thickness of the layer along the light beam was 5.5 mm) (Fig. 2ab). For the samples of cholesteryl butyrate, nonanoate, and palmitate for which $\Delta t_\Gamma \neq 0$ (see Table 1) we observed a sharp increase of the specific rotation with $t < T_c$ with a change of the sign of [α] (Fig. 2). This growth of [α] involves the appearance of a transparent cholesteric homeotropic state with a sign of the optical activity which agrees with the sign of [α] for the cholesteric mesophase.

The temperature dependence of the optical activity of the cholesteric homeotropic state is opposite. Thus in the curves for the dependence of [α] on t (Fig. 2) we show points obtained during sequential cooling and heating of samples at a constant rate within Δt_Γ.

It is important to notice that the observed cholesteric homeotropic state is metastable and goes into a stable mesophase with external influences on the preparation such as shocks and motion of the cover glass. Similar effects appeared with the imposition of a pulsed electric field when formation of a cholesteric homeotropic state was not observed during investigations of the electrical birefringence of the same ester samples.[1] The nonequilibrium nature of this state also appears in the limited time Δτ for its existence, which depends strongly on the degree of supercooling of the sample studied. This is illustrated by the experimental data of Fig. 3, where as an example we show graphs of the relation between Δτ and ΔT, the deviation of the sample temperature from T_c, for cholesteryl nonanoate.

Gray[8] has considered the reason for the appearance of a cholesteric homeotropic state to be the orienting action of the glass surface. However, since the size of the cuvette of the spectropolarimeter is quite large such an explanation could hardly be valid. We have determined the existence range of this state for the esters studied in capillaries with various surface to volume ratios and between cover glasses with gaps of the order of 0.02 mm. In all cases the temperature range for the existence of the homeotropic state remained the same.

Evidently it is possible that there are at least two reasons for the appearance of a cholesteric homeotropic state. One of them may be the suggestion set forth first by Gray[8] that this state is none other than the supercooled isotropic state of cholesteric liquid crystals. Such an assumption is favored by the reversible temperature dependence of the optical activity of a cholesteric homeotropic state, its metastable character, and the tendency toward crystallization under external influences. In this case the increase of the optical activity of a cholesteric homeotropic state arises from the appearance of nuclei of the cholesteric phase whose dimensions increase with decreasing temperature as long as the critical temperature is not reached, which allows initiation of the transition of the isotropic liquid into the cholesteric phase. However, it is also possible that the effect comes from microscopic impurities in the ester samples, which extend the temperature range of this transition and give rise to the appearance of microscopic regions of cholesteric phase in the melt below T_c. The presence of microscopic impurities may involve the use of esters of natural cholesterol for the synthesis.

---

[1] E. I. Ryumtsev, M. V. Mykhina, and V. N. Tsvetkov, Dokl. Akad. Nauk SSSR, 204, 397 (1972).

[2] O. Lehman, Ann. Physik, 4, 2, 649 (1900).

[3] O. Lehman, Ann. Physik, 4, 18, 796 (1905).

[4] O. Lehman, Ann. Physick, 4, 12, 311 (1903).

[5] O. Lehman, Ann. Physik, 4, 19, 1 (1906).

[6] G. Friedel, Ann. Phys., 19, 273 (1922).

[7] G. W. Gray, J. Chem. Soc., 10, 3733 (1956).

[8] G. W. Gray, Molecular Structure and Properties of Liquid Crystals, London – New York (1962).

Elastic-diffusion interaction of liquid inclusions in a NaCl single crystal

Ya. E. Geguzin and A. S. Dzyuba
Khar'kov State University

(Submitted July 10, 1972)
Kristallografiya, 18, 1053-1056 (September-October 1973)

The reaction of the faceted liquid inclusions in natural single crystals of NaCl, which takes place when the crystal is heated and an internal pressure is produced in the volume of the inclusion, has been studied experimentally. It has been shown that the rate of approach of the inclusions situated in the (100) plane increases with increase in the angle φ between the [100] direction and the straight line joining the centers of the inclusions. The experimental results have been compared with the Krivoglas–Osinovskii theory, and qualitative agreement between theory and experiment has been established.

1. The mechanism and kinetics of the elastic–diffusion interaction of pores situated in a single crystal have been the subject of theoretical studies.[1,2] It was found that, in contrast to pores situated in an isotropic medium, where their approach may take place chiefly as a consequence of mirror–image forces on the surface of the pore with which the interaction is taking place, in the case of an elastic–anisotropic crystal, forces are produced which are significantly greater than mirror–image forces. These forces determine the rate of approach of the pores, which depends on their orientation relative to the elements of symmetry of the crystal. Application to a crystal with cubic symmetry[1] gave the following orientational dependence for the rate of approach of pores in a direction parallel to the straight line joining the centers of the interacting pores:

$$\begin{aligned} \mathbf{v} &= -\mathbf{v}_0\mathbf{e} \quad \text{for} \quad \mathbf{e} \parallel [100], \\ \mathbf{v} &= \mathbf{v}_0\mathbf{e}/4 \quad \text{for} \quad \mathbf{e} \parallel [110], \\ \mathbf{v} &= 2\mathbf{v}_0\mathbf{e}/3 \quad \text{for} \quad \mathbf{e} \parallel [111]. \end{aligned} \tag{1}$$

In Eq. (1), $\mathbf{e}$ is the unit vector in the direction of the straight line joining the centers of the pores, $\mathbf{v}_0$ is the rate of movement of a pore with radius R_2 in the field of the stresses created by a pore of radius R_1, to the surface of which a pressure P_1 is applied. The magnitude of $\mathbf{v}_0$ depends on the mechanism of the mass transfer responsible for the movement and on the distance between the pores, and can be represented in the form[2]

$$v_0 \simeq -\tilde{D}\frac{P_1\omega_k}{kT}\frac{R_1^3}{L^4}\frac{1+\nu}{1-2\nu}\zeta. \tag{2}$$

When the mass transfer is determined by the mechanism of diffusion in the volume of the crystal (D_k) we have

$$\tilde{D} = D_k, \tag{3}$$

and in the case of surface diffusion (D_s)

$$\tilde{D} = D_s a / R_2. \tag{4}$$

In Eq. (2), $L = R_1 + R_2 + l$ is the distance between the centers of the pores (l is the minimum distance between the surfaces of the interacting pores), $\omega_k = a^3$ is the atomic volume in the crystalline phase, ν is the Poisson coefficient, and $\zeta = (c_{11} - c_{12} - 2c_{44})/c_{11}$ is the anisotropy coefficient, which in theory is assumed to be small ($\zeta \ll 1$).

It is easy to understand that the general physical considerations forming the basis of the theory of the interaction of pores can also be used to describe the interaction of material (in particular, liquid) inclusions in a crystal. It should be borne in mind that the diffusion streams responsible for the approach of inclusions may arise not only in the volume of the matrix or along the "matrix–inclusion" interphase boundary, but also in the volume of the inclusion.

We considered it of interest to study the behavior of liquid inclusions situated close together in a crystal, having in mind the importance of this effect both in the examination of specific situations arising during the growth of crystals from solution and in the study of liquid inclusions in natural minerals.

The present paper gives the results of experiments carried out with specimens of NaCl single crystals containing liquid inclusions.

2. In order to obtain an equation describing the relative movement of liquid inclusions, we turned our attention to the fact that, as follows from calculations,[1,2] the effective diffusion coefficient $\tilde{D}$ for the case where the movement is due to streams in the volume of the inclusion can be written in the following form:

$$\tilde{D} \simeq \frac{1}{2}\frac{\omega_k}{\omega_i}\frac{\beta R_2 c_i D_i}{\beta R_2 + n_i D_i}, \tag{5}$$

where β is a kinetic coefficient, with the dimensions $\text{cm}^{-2} \cdot \text{sec}^{-1}$, which describes the ability of the boundary to give up or absorb the atoms of the material of the matrix, c_i and D_i are respectively the equilibrium concentration of the atoms of the material of the matrix in the inclusion and their diffusion coefficient, $n_i = 1/\omega_i$, and ω_i is the volume corresponding to one atom of the material of the matrix in the volume of the inclusion. By substituting this coefficient in Eq. (2) we obtain an equation giving the rate of approach of liquid inclusions for the case where the process is determined by the streams in the volume of the inclusion.

It can readily be seen that the coefficient $\tilde{D}$ takes account of the fact that the stream of the atoms of the matrix in the volume of the inclusion may be determined both by processes at the boundary and intrinsically by diffusion in the volume of the inclusion. It is of interest to estimate $\tilde{D}$ for those limiting cases where the approach is due to the processes at the "inclusion–matrix" boundary or to streams in the volume of the matrix. These estimates have the following form: a) $\beta R_2 \ll n_i D_i$; in this case the kinetics of approach are determined by processes at the boundary,

$$\tilde{D} \simeq \beta R_2 c_i \omega_k / 2; \tag{6}$$

b) $\beta R_2 \gg n_i D_i$; in this case the kinetics of approach are determined by the diffusion streams in the volume of the inclusion,

$$\tilde{D} \simeq \frac{1}{2}\frac{\omega_k}{\omega_i} c_i D_i. \tag{7}$$

The set of equations (1)–(5) describes the effect of the interaction of the liquid inclusions which we are examining. They indicate, in particular, that throughout the entire temperature range of existence of inclusions of a saturated solution of the salt in water in NaCl crystals[3] (that is, from −42 to 410°C), their interaction will be determined by the streams in the volume of the inclusion, since for a reasonable value of the constants the quantities D_k and $D_s a/R_2$ are known to be smaller than $\tilde{D}$, defined by Eq. (5).

It may be noted that for $R^* = n_i D_i/\beta$ there is a change in the "bottleneck" determining the stream in the volume of the inclusion: For $R < R^*$ the decisive factors are the processes at the "inclusion–matrix" boundary, and for $R > R^*$ the decisive factor is diffusion in the volume of the inclusion.

3. The following experiments were carried out. From a crystal of rock salt from the Artemov deposit we took specimens containing pairs of closely situated ($\sim 10^{-2}$–10^{-3} cm) faceted liquid inclusions with approximately equal dimensions ($\sim 10^{-2}$ cm) lying in the (100) plane and oriented relative to one another in such a way that the angle φ between the straight line joining their centers varied from zero to $\pi/4$ (Fig. 3). We studied the reaction between the inclusions under conditions of prolonged isothermal treatment at a temperature of 48 ± 0.02°C. In the process a hydrostatic pressure directed outwards was created in the volume of the inclusions; the magnitude of this pressure was calculated from the equation[3]

$$P = \frac{\alpha_i - \alpha_k + (\omega_i - \omega_k)(\partial n/\partial T)}{\gamma_i + \gamma_k - (\omega_i - \omega_k)(\partial n/\partial P)}\Delta T, \tag{8}$$

where α is the thermal coefficient of volume expansion, γ is an isothermal compressibility factor, and the subscripts k and i refer to the matrix and the material of the inclusion respectively. The magnitude of the pressure acting inside the inclusions was $P = 1.6 \cdot 10^8$ dyn/cm^2. Special control experiments established that at the chosen temperature of isothermal treatment, this pressure, during the period studied, did not deform the inclusion, so that their interaction was not distorted by a change in shape.

We made observations on pairs of inclusions, the mutual orientation of which was defined by the following values of the angle φ: 0, $\pi/8$, and $\pi/4$. As an example, the time sequence of the relative positions of pairs of inclusions corresponding to $\varphi = 0$ and $\pi/4$ is shown in Fig. 1. The $l(t)/l_0$ relationship is shown in Fig. 2.

We can compare the results obtained with the arguments and equations put forward earlier. The approach predicted by theory for inclusions oriented in such a way

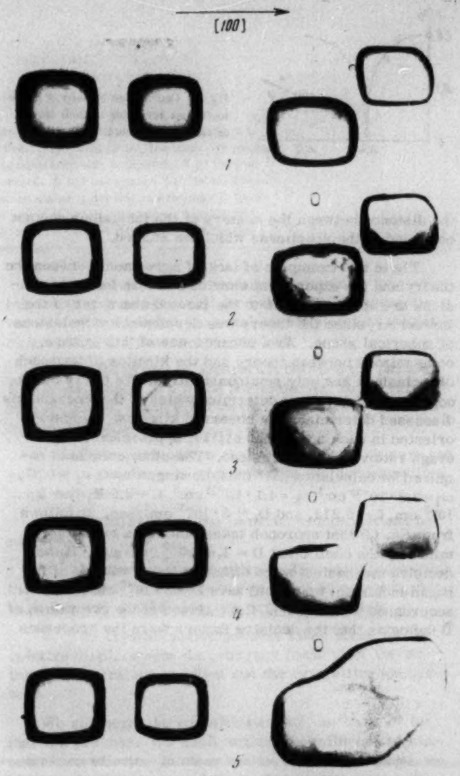

Fig. 1. Sequence of relative arrangements of the inclusions during isothermal treatment. × 185. 1) t = 0; 2) 50; 3) 100; 4) 300; 5) 600 h. The two pairs of inclusions were situated in the same crystal.

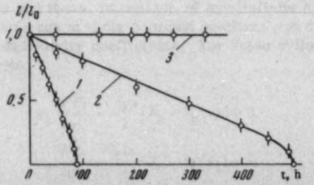

Fig. 2. Time dependence of the distance between the surfaces of pairs of interacting inclusions. 1) $\varphi = \pi/4$; 2) $\pi/8$; 3) 0.

that e ∥ [110] is observed experimentally, whereas we did not observe repulsion of inclusions for e ∥ [100]: It was found that the corresponding pairs of inclusions did not interact. Another noteworthy feature is that the relationship predicted by theory between the rate of approach and

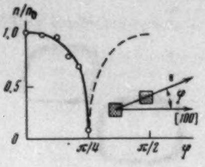

Fig. 3. Distribution of pairs of liquid inclusions according to their mutual orientation in natural rocksalt.

the distance between the centers of the inclusions was not observed in the specimens which we studied.

These two examples of lack of agreement between the theory and the experiment carried out with faceted inclusions are apparently due to the faceted character of the inclusions, since the theory was developed for inclusions of spherical shape. As a consequence of this feature, comparisons between theory and the kinetics of approach of inclusions are only semiquantitative. We carry out the comparison in order to determine which of the mechanisms discussed determines the observed kinetics. Inclusions oriented in such a way that $e \parallel [110]$ approached at an average rate $v = 8 \cdot 10^{-9}$ cm/sec. The other constants required for calculation have the following values: $c_i = 0.37$, $\omega_i = 3.3 \cdot 10^{-23}$ cm^3, $\omega_k = 4.1 \cdot 10^{-23}$ cm^3, $L \approx 2.5$ R, $R \simeq 2 \cdot 10^{-3}$ cm, $\zeta = 0.212$, and $D_i \approx 5 \cdot 10^{-5}$ cm^2/sec. It follows from Eq. (2) that approach takes place at a rate determined by the coefficient $D = 1.6 \cdot 10^{-8}$ cm^2/sec. If the decisive mechanism were diffusion in the volume of the liquid inclusion, we should have $\tilde{D} = 3 \cdot 10^{-6}$ cm^2/sec, in accordance with Eq. (7). Comparison of the two values of $\tilde{D}$ indicates that the decisive factors were the processes at the boundary, with the value $\beta = 10^{18}$ cm^{-2}/sec, which follows from Eq. (6). We cannot compare the estimated value of β directly with the value obtained from these experiments or experiments of a different type. It appears reasonable, however, if we have in mind an indirect comparison. In particular, the same value of β was obtained from the movement of the cavities in single crystals of NaCl in the field of a temperature gradient.[4]

4. A curious consequence of the above angular dependence of the rate of approach was observed in a study of the random orientations of pairs of inclusions in natural crystals of salt from the Artemov deposit. It was found (Fig. 3) that orientations corresponding to $\varphi = 0$ are encountered most frequently, and those corresponding to $\varphi = \pi/4$ least frequently. In the construction of the curve in Fig. 3 we took into account only those pairs of identical inclusions with dimensions R for which $L \leq 3r$. It may be noted that this feature indicates directly that in its geological period of existence, the salt of the Artemov deposit was subjected to heating – the cause of the production of internal pressure in the inclusions – which determines the kinetics of their approach.

We thank T. I. Tarapunets for assistance with the experiments.

---

[1] M. A. Krivoglaz and M. E. Osinovskii, Fiz. Met. Metalloved., 24, 805 (1967).

[2] Ya. E. Geguzin and M. A. Krivoglaz, The Movement of Macroscopic Inclusions in Solids [in Russian], Metallurgiya, Moscow (1971).

[3] Ya. E. Geguzin and A. S. Dzyuba, Kristallografiya, 18, 813 (1973) [Sov. Phys.–Crystallogr., 18, 510 (1974)].

[4] Ya. E. Geguzin, S. S. Simeonov, and V. M. Mostovoi, Fiz. Tverd. Tela, 13, 100 (1971) [Sov. Phys.–Solid State, 13, 79 (1971)].

Phenomena arising on the arrest of crystal growth

V. N. Romanenko and V. S. Kheifets

Leningrad Marine Engineering Higher School

(Submitted May 26, 1972; resubmitted December 11, 1972)
Kristallografiya, 18, 1057-1062 (September-October, 1973)

The processes taking place in a crystallization system when the movement of the external temperature gradient is suddenly stopped, that is, on so-called thermal arrest, have been examined. It has been shown that after this arrest, the crystal undergoes additional growth through a certain length. This additional growth is determined by thermal and concentration factors. The theory of this phenomenon has been presented. It has been shown that measurement of the magnitude of the additional growth of the crystal after thermal arrest makes it possible to determine a number of important quantities characterizing the system. An illustration is provided by the determination of the distribution coefficient of indium in gallium arsenide. Experiments on the determination of this quantity by the thermal arrest method gave the value 0.1, in good agreement with published data.

Changes in the external conditions of crystallization leads to the production of phenomena, the nature of which depends to a marked extent on the parameters of the crystallization system.[1,2] The most marked change in the external conditions is the sudden interruption of the relative movement of the heater and the crystallization system, that is, interruption of the external temperature gradient G_h responsible for growth.

The aim of the present work was to examine the phenomena arising in a binary system in this sudden interruption of growth, which we have called thermal arrest.

We shall examine the crystallization of the binary substance – impurity system. For simplicity we shall assume that we are dealing with the Bridgman method. Under the conditions of steady-state growth, two gradients – temperature and concentration – will exist in the liquid close to the boundary of separation between the phases. The first of these ensures the removal, into the melt, of part of the latent heat of fusion, and the second ensures the removal of the impurity, with distribution coefficient k less than unity, which is displaced into the melt during crystallization. (For $k > 1$ the second gradient ensures the supply of impurity to the boundary.) We shall assume that the conditions do not correspond to the production of constitutional (diffusion) supercooling in the melt.[1] We now assume that the movement of the external temperature field responsible for growth is interrupted. The liberation of the latent heat of fusion and the displacement of impurity then stop. Thus after a certain interval, a steady state characterized by the absence of temperature and concentration gradients close to the growth front will again be established.

We can examine how this influences the position of the boundary of separation between the phases. We make the following assumptions.

1. The thermal arrest takes place under conditions in which growth of the crystal continues for a time interval sufficient for steady-state temperature and concentration fields to be established close to the boundary of separation between the phases.

2. Mixing in the layers of the liquid phase being studied takes place only by diffusion, and heat transfer takes place only by conduction.

3. Diffusion in the solid phase is so slight that it can be neglected.

4. The crystal – melt system consists of a long cylinder with a constant small diameter. This assumption automatically includes the usual assumption that the densities of the two phases are constant.

5. The boundary of separation between the phases (the growth front) is a plane perpendicular to the direction of growth, which coincides with the axis of the crystal – melt cylinder.

6. All the parameters characterizing the system are constant in the range of temperatures and concentrations being considered.

7. Volatilization of the impurity component can be neglected.

8. The temperature gradient of the heater from which the crystal and melt are being removed is constant, that is, it does not change along the axis of the system.

9. The crystallization process takes place by the relative displacement (in arbitrary fashion) of the external temperature gradient and the crystallization system.

We can begin the examination with the case of the thermal process. We shall neglect the influence of concentration effects. In other words, in the first stage, we shall study the process of thermal arrest in a pure (impurity-free) substance.

The temperature field under steady-state growth conditions is found by solving the heat conductance equation for the two end faces, in contact, of semiinfinite cylinders with heat sources at their common boundary and different thermal conductivity coefficients. For these cylinders we can write

$$\begin{aligned} &\varkappa_l \frac{d^2T_l}{dx^2} - \frac{q_l p}{s}[T_l - T_h(x)] = 0, \\ &\varkappa_s \frac{d^2T_s}{dx^2} - \frac{q_s p}{s}[T_s - T_h(x)] = 0. \end{aligned} \quad (1)$$

Here, ϰ, T, p, and s represent respectively the thermal conductivity coefficients, temperatures perimeters, and cross-sectional areas. Since p and s are assumed to be the same for the two phases, we shall omit the phase subscripts for these quantities. $T_h(x)$ denotes the temperature of the external medium. The transfer of heat to the medium is taken into account by introducing the heat output coefficients q. The fact that the heat output is directed towards the heater, the temperature of which differs little from the temperature of the crystal–melt system, makes it possible to assume that the coefficients q are not very large and, as we have already assumed, constant. Billing's data[3] show that even with the large deviations from real conditions, these simplifications make possible a fairly good description of the principal features of the process. Strictly speaking, Eqs. (1) are written not for a stationary system of coordinates, but for a system of coordinates moving together with the growth front. For low rates of crystallization f and for the examination of only the two limiting cases as in the present work, however, this feature can be neglected.

We shall assume that the point x = 0 coincides with the surface of separation of the phases. Positive values of x will correspond to the liquid phase, and negative values of the solid phase. As boundary conditions it is natural to write

$$\begin{aligned} &[T_l - T_h(x)]_{x\to\infty} \to 0, \\ &[T_s - T_h(x)]_{x\to-\infty} \to 0. \end{aligned} \tag{2}$$

In this case, for $T_h(x) = T_0$ = const, the solution of Eqs. (1) will be

$$\begin{aligned} (T_l - T_0) &= (T_m - T_0)\exp\left(-\frac{q_l p}{\varkappa_l s}\right)^{1/2} x, \\ (T_s - T_0) &= (T_m - T_0)\exp\left(\frac{q_s p}{\varkappa_s s}\right)^{1/2} x. \end{aligned} \tag{3}$$

The temperature at the surface of separation of the phases for the crystallization of a pure substance coincides with its melting point T_m. This is taken into account in Eq. (3). At the boundary of separation between the phases, it is obvious that

$$-\varkappa_l \frac{dT_l}{dx} + \varkappa_s \frac{dT_s}{dx} = H\rho f, \tag{4}$$

where H is the heat (enthalpy) of fusion, and ρ is the density of the substance. By substituting Eq. (3) in Eq. (4), we obtain$^{1)}$

$$(T_m - T_0) = \frac{H\rho f}{(p/s)^{1/2}[(\varkappa_l q_l)^{1/2} + (\varkappa_s q_s)^{1/2}]}. \tag{5}$$

Substitution of Eq. (5) into Eq. (3) makes it possible to find the final temperature distribution in the phases for the case of a constant temperature of the external medium. Under real conditions it is necessary to take account of the change in this temperature. Usually in this case, as we have assumed, the external temperature gradient is constant, G_h = const, and

$$T_h(x) = T_h^0 + G_h x. \tag{6}$$

The symbol T_h^0 denotes the temperature of the external heater at the point where the boundary of separation between the phases is situated, that is, at x = 0. The solution of Eqs. (1) with allowance for Eq. (6) (see, for example, ref. 4) for the case of the liquid phase in which we are interested has the form

$$(T_l - T_h^0) = (T_m - T_h^0)\exp\left(-\frac{q_l p}{\varkappa_l s}\right)^{1/2} x + G_h x. \tag{7}$$

Thus the actual course of the change in temperature is the sum of two temperature curves. The first of these is the external temperature field of the heater, that is, the partial solution of the nonhomogeneous equation in the absence of liberation of heat at the boundary. The second is the temperature field created by thermal conductivity and radiation into space at a constant temperature, that is, the total solution of a homogeneous differential equation for the function $T_l - T_h^0$. We can now obtain the temperature gradient in the melt, equal to

$$G_l = \frac{dT_l}{dx} = G_h - (T_m - T_h^0)\left(\frac{q_l p}{\varkappa_l s}\right)^{1/2} \exp\left(-\frac{q_l p}{\varkappa_l s}\right)^{1/2} x. \tag{8}$$

Close to the boundary of separation between the phases, that is, for x = 0, we have

$$(G_l)_{x=0} = G_l^0 = G_h - \frac{H\rho f (q_l/\varkappa_l)^{1/2}}{(\varkappa_l q_l)^{1/2} + (\varkappa_s q_s)^{1/2}}. \tag{9}$$

Thus, as follows from analysis of Eq. (7), thermal conductivity transfers to the melt only part of the heat of fusion liberated. The radiation of this heat into the heater space is so slight, however, that it does not influence the temperature conditions in the external medium. This may be the case only for sufficiently small values of f, as we have already stipulated. The condition of small values of f is effectively satisfied in practice.

Equation (9), which relates the external temperature gradient to the temperature gradient in the melt close to the growth front G_l^0, is useful, for example, in the calculations of the critical growth rates f_{cr}, above which structural imperfections are produced in the crystal. In actual fact, the quantity G_h in the sense of the process is positive. The quantity G_l^0 is smaller than this by an amount proportional to the growth rate f. At low growth rates, G_l^0, although smaller than G_h, nevertheless remains positive. If, however, we have

$$f > f_{cr} = \frac{G_h^0[(\varkappa_l q_l)^{1/2} + (\varkappa_s q_s)^{1/2}]}{H\rho (q_l/\varkappa_l)^{1/2}}, \tag{10}$$

the temperature gradient in the melt becomes negative, and conditions are produced for the creation of a strongly supercooled layer. By analogy with concentration (diffusion) supercooling, this supercooling can be described as thermal. It is obvious that Eq. (10) must define the critical growth rates for the pure substance, that is, for those cases where the theory of concentration supercooling begins to give values of the critical rate which are too high.[5] We previously carried out estimates of this kind for pure germanium.[6] The results obtained were found to be quite reasonable. This in turn confirms the applicability of Eq. (9) to real processes.

We can now turn to thermal arrest. After the establishment of a new stationary state, the difference between the temperature gradients in the heater and in the two phases of the system disappear. The temperature at the point where the growth boundary was situated becomes lower than the temperature of the substance T_m. This means that the crystal undergoes additional growth through a certain length l_t, which depends on the difference between T_m and the temperature T_{cr} which is finally established at the point where the boundary of separation of the phases was situated at the moment of the thermal arrest. It is obvious that

$$l_t = (T_m - T_{cr}) / G_h = \Delta T_t / G_h. \tag{11}$$

When Eq. (11) and all subsequent equations are being used, it is necessary to make allowance for the fact that the quantity G_h is usually measured in the heater from which the crystal has been removed. Its presence may change G_h slightly.[2)] For sufficiently powerful heaters and long narrow boats, however, this difference can be neglected.

From Eqs. (9) and (11) we can obtain

$$G_l{}^{\circ} = G_h\left[1 - l_t\left(\frac{q_l p}{\varkappa_l s}\right)^{1/2}\right]. \tag{12}$$

Thus by measuring l_t experimentally it is possible to estimate the values of the temperature gradient in the melt directly at the growth front. With the same assumptions it is possible to express the heat of fusion H in terms of l_t and other parameters of the system

$$H = \{G_h l_t (p/s)^{1/2}[(\varkappa_l q_l)^{1/2} + (\varkappa_s q_s)^{1/2}]\} / f\rho. \tag{13}$$

The values of H obtained by measurement in this way cannot be very accurate. Moreover, they are not very simple, and require the estimation of the quantities q_l and q_s. Thus, Eq. (13) can hardly be recommended for investigational purposes.

We can now examine thermal arrest for the case where the melt contains an impurity. In this case, in contrast to the case examined above, a "diffusion wave" of the impurity component is produced in front of the growth front (see, for example, ref. 1). Thus for steady-state growth the temperature at the boundary of separation T_b, that is, the temperature which is required for the crystallization of the layers of liquid adjoining the front, will be lower than the temperature of the start of the crystallization of the deep layer of the melt. When a stationary state is established after the thermal arrest, the diffusion wave is dissipated, and T_b is found to be lower than the temperature of the start of the crystallization of the established composition of the melt. Thus the crystal should undergo additional growth through a certain length l_{cr}, corresponding to the arrival of the boundary of separation at the point with the temperature T_m^c of the start of the crystallization of the mass of the melt with the composition C_l. It is obvious that

$$l_{cr} = \frac{\Delta T_{cr}}{G_h} = \frac{T_m{}^c - T_h}{G_h}. \tag{14}$$

It is convenient to rewrite Eq. (14) in the form

$$T_b = T_m{}^c - G_h l_{cr}. \tag{15}$$

For high dilutions it may be assumed that the change in the temperature of the start of crystallization with change in composition ΔT_m^c is proportional to the concentration of impurity in the melt C_l

$$\Delta T_m{}^c = mC_l, \tag{16}$$

where m is the slope of the tangent to the liquidus curve, drawn through the melting point of the pure main component. Since the composition of the melt close to the boundary of separation of the phases C_l^0 differs from its composition in the deep layers C_l, we can write, on the basis of the last two equations,

$$C_l{}^{\circ} = (G_h l_{cr} + mC_l) / m. \tag{17}$$

Thus l_{cr} can be used to estimate the quantity C_l^0. If the growth process continues for a sufficiently long time, we have[1]

$$C_l{}^{\circ} = C_l / k. \tag{18}$$

Thus

$$k = mC_l / (G_h l_{cr} - mC_l) \approx mC_l / G_h l_{cr}. \tag{19}$$

At sufficiently low concentrations of impurity it is possible to neglect the second term in the denominator.

In the general case the length corresponding to the additional growth of the crystal is determined by both effects. If it is assumed that these effects are additive, it is necessary for their separation to carry out two experiments with thermal arrests: one with the pure substance and one with the substance containing the impurity. Experiment and numerical calculations show, however, that l_{cr} is usually significantly greater than l_t, so that no special complications arise in the determination of l_{cr}.

The experimental verification of the effect described above was carried out with gallium arsenide. The studies were carried out not only for the growth of bulk crystals, but also for the preparation of films in the process of liquid epitaxy, carried out by the method of forced cooling. In the last case we established a number of interesting characteristic features, but their examination lies outside the scope of the present paper. The thermal arrest in the case of bulk crystals was studied not only to obtain fundamental confirmation of the effect, but also to verify that the equations obtained are reasonable, since these equations may be used for investigational purposes. From this viewpoint it is most convenient to verify Eq. (19), since the values of the distribution constants of impurities are usually sufficiently well known. We selected this equation for experimental verification.

In our experiments, small quantities of indium were added to gallium arsenide. The crystals were grown in a small horizontal quartz boat. Growth was arrested after 2.5 h at a distance of 9 cm from the start of the solid. (According to the available data, the steady-state region was established under the conditions of the experiment at a distance of 3 cm from the start of crystal growth.) The additional growth section could usually be distinguished clearly on the surface of the crystal. Its length under our conditions was close to 0.4 cm. In order to use Eq. (19) it was necessary to estimate the proportion of this length corresponding to the quantity l_t. For this purpose we carried out additional experiments to estimate l_t. Experiments with stainless-steel rods made it possible to find the upper limit of this quantity and hence to show that the temperature drop at the boundary of separation between the phases did not exceed 0.5°. For the gradient $G_h = 8$ deg/cm which we used, this meant that the magnitude of the thermal additional growth is very small. Thus, all the additional growth of the crystal took place as a consequence of the concentration effect. The value of m for the system studied[7] is equal to 7.7 deg/at.%. The value of C_l in our experiments was $4 \cdot 10^{-2}$ at.%, so that neglect of the second term in the denominator of Eq. (19) gives for the distribution constant of indium in gallium arsenide a value of about 0.1, in agreement with published data.[8,9]

CONCLUSIONS

1. As a consequence of the temperature and concentration gradients existing in a melt close to the growth front, additional growth of a crystal takes place to a certain length on arrest of the movement of the external heating assembly (thermal arrest). It is possible to separate the effect of additional growth into two effects – thermal and concentration.

2. The principles of the theory of the additional growth of the crystal after thermal arrest have been described. It has been shown that the measurement of the magnitude of the additional growth can be used for investigational purposes.

3. It has been shown that, by analogy with the familiar concentration (diffusion) supercooling of the melt, another form of supercooling, which has been called thermal supercooling, may arise in the system at sufficiently high rates of growth. This supercooling imposes a definite limit on the attainable rates of growth of pure crystals.

4. The effect of concentration additional growth has been used to determine the magnitude of the distribution coefficient of indium in gallium arsenide. The value found was 0.1, which shows fairly good agreement with published values.

---

[1] Here and in all subsequent equations it would be possible instead of the ratio p/s to write 2/r, where r is the radius of the crystal. This is not quite accurate, however, since it implies that the radiation is emitted equally in all directions, that is, into the heater space and into the boat. In the case where we write p/s, however, it is possible to speak of the effective area of radiation s. The latter is clearer and is therefore preferred.

[2] For this reason, instead of G_h, we can write, as was done in ref. 2, the value of the temperature gradient in the crystal, having in mind, however, the gradient which is established after the thermal arrest. The form of notation which we have proposed appears more convenient.

---

[1] B. Chalmers, Principles of Solidification, Wiley (1964).

[2] E. T. Abdukarimov, V. A. Ermolaev, V. N. Romanenko, and V. S. Kheifets, Izv. Akad. Nauk UzbekSSR, Ser. Fiz.-Mat. Nauk, 2, 47 (1972).

[3] E. Billig, Proc. Roy. Soc., A229, 346 (1955).

[4] E. Kamke, Reference Book of Ordinary Differential Equations [Russian translation], Fizmatgiz, Moscow (1961), p. 419.

[5] G. V. Mikitin and V. N. Romanenko, Teor. Osnovy Khim. Tekhnol., 4, 839 (1970).

[6] G. V. Nikitina, K. V. Ostanina, V. N. Romanenko, and V. S. Kheifets, Summaries of papers Presented at the Third Symposium on the Processes of Growth and the Synthesis of Semiconducting Crystals and Films [in Russian], Izd. Inst. Yad. Fiz. SO AN SSSR, Novosibirsk (1972), p. 28.

[7] V. N. Vigdorovich, A. Ya. Nashel'skii, L. I. Marina, and N. Ya. Zakharova, Scientific papers of the State Scientific-Research Institute for the Rare Metals Industry [in Russian], Vol. 10, Metallurgizdat, Moscow (1963), p. 264.

[8] M. G. Mil'vidskii and O. V. Pelevin, Izv. Akad. Nauk SSSR, Neorgan. Mat., 3, 1159 (1967).

[9] J. M. Whelan, Conf. 5, Properties of Elemental and Compound Semiconductors, Met. Soc. Interscience, New York (1960), p. 245.

Electron-microscope investigation of thin film condensation kinetics

Yu. F. Komnik and V. V. Pilipenko

Physicotechnical Institute for Low Temperatures, Academy of Sciences of the Ukrainian SSR

(Submitted May 22, 1972; resubmitted September 19, 1972)
Kristallografiya, 18, 1063-1069 (September-October 1973)

An electron microscope was used to study the formation kinetics for the condensation of molecular beams of bismuth, antimony, silver, and gold onto neutral substrates. For several specimen series, differing within a given series only in the condensation times, the following kinetic parameters were determined: the time dependence of the condensation center numerical density, the particle growth rate in the substrate plane, and the fraction of the area occupied by the condensate. The time variation of the latter is compared with the two-dimensional crystallization process kinetic curves, constructed using the experimental data on the nucleation and particle growth rates. Several types of kinetic curve were obtained and it was also found that coalescence had a strong influence on the thin film formation process.

The thin film formation kinetics for molecular beam condensation under vacuum can be described by the following parameters: $b(\tau)$ the particle nucleation rate, $c(\tau, r)$ the particle growth rate, $\sigma(\tau)$ the fraction of the area occupied by the condensate at an instant τ, and $\omega(\tau)$ the volume of condensate arriving over unit area of substrate [or the effective thickness $L(\tau)$].

The kinetics of the condensate covering the substrate can be followed with an electron microscope, that is, information on the two-dimensional process of forming a condensed phase from a two-dimensional vapor of adsorbed atoms and the molecular beam can be derived. For this, the particle growth on the substrate plane is recorded: Processes in the third dimension lead only (in comparison with the purely two dimensional process) to a change in the nature of the τ dependence of parameters such as the nucleation rate $b = \partial n/\partial\tau$ and the particle growth rate in the substrate plane $c = \partial r/\partial\tau$ where n is the numerical density of centers, and r the mean radius of particle half-size dimension).

Two-dimensional crystallization kinetics can be described by a two-dimensional modification[1] of Kolmogorov's equation,[2]

$$\sigma(\tau) = 1 - \exp(-a\Omega), \quad \Omega = \int_0^\tau b(\tau') \left[\int_{\tau'}^{\tau} c(\tau'')\, d\tau''\right]^2 d\tau', \qquad (1)$$

where a is a coefficient allowing for the particle shape (for spheres $a = \pi$, for cubes $a = 4$, etc.). A similar form is also considered in ref. 3.

An analysis of thin film electron micrographs produced for various times τ at constant molecular beam density generally allows information on all the parameters in expression (1) to be obtained, and also allows the experimentally found $\sigma(\tau)$ dependence to be compared with the one calculated from (1) using experimental data on $b(\tau)$ and $c(\tau)$. Such an analysis was the principal aim of this investigation.

The studied specimens were films of bismuth, antimony, silver, and gold. These metals were condensed at a pressure of 10^{-7}–10^{-6} torr onto varnish or amorphous carbon thin films at various temperatures (for Bi and Sb, room temperature and higher up to 150°C, for Ag and Au 500–600°C). By keeping all the condensation parameters constant in a given experiment series of specimens were prepared which differed only in their condensation times. The electron micrographs for such a series were taken with a UEMV-100 instrument (see, for example, Fig. 1), and then subjected to various analyses, as a result of which data on the time variations of the fraction of the area σ occupied by the condensate, the center numerical density n, and the mean particle radius r (from the histogram for nonspherical particles calculated from σ and n) could be obtained. Parameters σ and r were determined from the electronmicrographs by attaching a fine graticule.

BISMUTH

Figure 2 shows the time dependence of the size and number of particles of bismuth for various deposition conditions. The feature of the $n(\tau)$ curves is a noticeable fall in n after some time from the start of condensation. This drop in n is caused by coalescence which starts even in the early condensation stages for effective thicknesses of less than 10 Å.

The covering of the substrate surface by the condensate is shown in the curves of Fig. 3a (to bring curves relating to different condensation rates to the same scale, the quantity $\nu\tau$ which is proportional to the calculated effective thickness, is marked off along the abscissa). The shape of these curves is similar to that expected from Eq. (1), but at low τ they do not extrapolate to $\sigma = 0$, rather to some value σ_0; this can also be seen on the $r(\tau)$ dependences (Fig. 2). A possible explanation of this fact

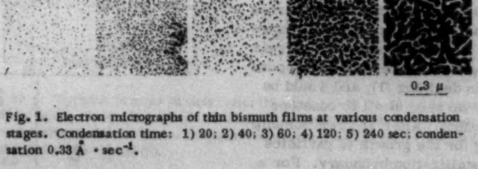

Fig. 1. Electron micrographs of thin bismuth films at various condensation stages. Condensation time: 1) 20; 2) 40; 3) 60; 4) 120; 5) 240 sec; condensation 0.33 Å · sec⁻¹.

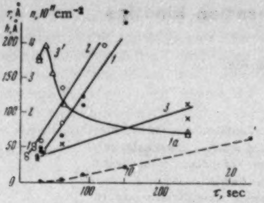

Fig. 2. Change in mean radius r (1, 2, 3) height h (curve 1a), and numerical density n (3') of bismuth particles during the condensation process. Condensation rates (Å · sec^{-1}): 1, 1a) 2.1; 2) 0.33; 3, 3') 0.24; substrate temperatures: 25, 80, and 80°C respectively. For curves 1 and 1a the time scale is 0-25 sec.

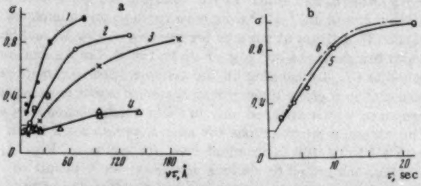

Fig. 3. Time dependence of relative area occupied by bismuth condensate (or effective thickness dependence). a) The notation for curves 1, 2, and 3 is as in Fig. 2; curve 4 is for $\nu = 0.24$ Å · sec^{-1}, substrate temperature 96°C; b) comparison of experimental curve 5 with curve 6, calculated from relations (1) and (3).

could be the effective increase in particle size for all the observed specimens due to the formation of an oxide layer. However, no trace of bismuth oxide could be detected in the microscope using electron diffraction. Moreover, this proposal was also tested for gold for which σ_0 was also detected. It must be supposed that the initial condensate formation period is characterized by considerably higher nucleation and particle growth rates than in the stages recorded later. This would also guarantee a small time ($\leqslant \tau_c$) to reach some relatively large σ values. All the characteristic properties of the kinetic curve ought to be present in the initial period (see below for Sb), but it is technically difficult to study them for bismuth since only observations on particles larger than 30 Å can be considered reliable.[4] By comparing the experimental curves for times $\tau \geqslant \tau_c$ with Eq. (1), we can understand the presence of an initial period by introducing some additional time τ_0, such that, after a period $\tau_0 + \tau_c$, a coverage σ_0 is reached for all the kinetic parameters characteristic of the condensation stages recorded in the experiment.

A more complex question apparently arises in connection with the effect of coalescence on the kinetic curves $\sigma(\tau)$. Taking into account the particle number decreases during coalescence directly in the center nucleation rate (that is, by introducing a negative b) does not correspond to the physical model used in deriving (1), and would be inaccurate. In fact, there is no need at all to consider coalescence as a separate effect: After all, relationship (1) was obtained by allowing for the growth of particles and the decrease in the crystallization boundary. For a purely two-dimensional process, during particle growth, the area occupied by them remains constant, for coalescence it decreases as the particle height increases. Coalescence therefore slows particle development in the substrate plane and decreases the mean growth rate. To compare with theory, it is necessary to consider a negative particle growth rate component as being due to coalescence, but the number of particles is taken to be fixed and equal to the maximum number of centers $n_{\max}$, recorded before the coalescence mechanism set in. For bismuth the particle growth rate negative component did not change over a wide time range (up to the continuous condensate formation stage), so that the $r(\tau)$ dependence appears linear (Fig. 2).

Under these conditions, Eq. (1) simplifies. For a constant number of particles

$$\Omega = n\left[\int_0^{\tau} c(\tau')\,d\tau'\right]^2, \tag{2}$$

and for a constant growth rate

$$\Omega = nc^2\tau^2. \tag{3}$$

Figure 3b shows the experimental points and the calculated $\sigma(\tau)$ curve, constructed for the experimentally found $n_{\max} = 3.7 \cdot 10^{11}$ cm^{-2}, $c \simeq 9$ Å·sec^{-1}, and the calculated extrapolation $\tau_0 = 4$ sec. The agreement between the calculated curve and experimental points is quite good.

The extent to which coalescence affects the condensate substrate covering kinetics is governed by how much the particle height increases during merging and therefore how much the occupied area decreases. From Fig. 3a it can be seen that a temperature rise causes the $\sigma(\tau)$ curve to slope. Figure 4 pertains to the case[5] when the condensate exists in a liquid phase for temperatures $T > T_l$. The particles then can flow like a liquid easing their coalescence into spherical drops.

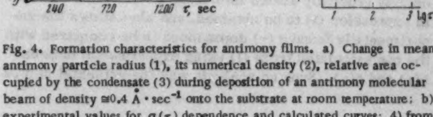

Fig. 4. Formation characteristics for antimony films. a) Change in mean antimony particle radius (1), its numerical density (2), relative area occupied by the condensate (3) during deposition of an antimony molecular beam of density ≅0.4 Å · sec^{-1} onto the substrate at room temperature; b) experimental values for $\sigma(\tau)$ dependence and calculated curves: 4) from relationships (1) and (4); 5) from (1) and (3).

TABLE 1

T, °C	$v = \frac{d\omega}{d\tau}$, Å/sec	$c = \frac{dr}{d\tau}$, Å/sec	$c' = \frac{dh}{d\tau}$, Å/sec
20	2.1	9	1.3
80	0.33	1.6	0.22

If we consider the $L(\tau)$ dependence in addition to $\sigma(\tau)$, that is, the characteristic growth of the effective film thickness, we can determine the time variation of the mean particle height $h = L(\tau)/\sigma(\tau)$. If we assume a linear rise of effective thickness, that is, assume a constant condensation coefficient, the calculation gives an absurd result: The particle frequency decreases with time. We shall assume, as in ref. 1, that the optical density S in a bismuth island film is related linearly to the effective thickness L, that is, the dependence $S(\tau) \sim (\nu\tau)^{\alpha}$ (where[1] $\alpha \geqslant 2$) reflects the kinetics for the growth of the amount of metallic material on the substrate. Thus, from the $\sigma(\tau)$ and $S(\tau)$ dependences and assuming $L \simeq \beta S$ (for Bi, $\beta = 2 \cdot 10^2$ Å), we can find the mean particle height. An example of the $h(\tau)$ dependence for one of the specimen series is shown in Fig. 2 (curve 1a). It can be seen that a constant particle growth rate perpendicular to the substrate is established after some initial period.

It should be noted that the feature of bismuth thin film formation kinetics derived from a quantitative treatment of our results is that the particle growth rate in the substrate plane, notwithstanding coalescence, exceeds the condensation rate, whereas the particle growth rate normal to the substrate is considerably smaller than the latter (see Table 1). As a result, the bismuth crystallites develop mainly in the substrate plane and adopt the shape of flat particles.

ANTIMONY

The feature of antimony is that island and very thin films produced on a substrate at room temperature are amorphous. Moreover, it appears that the numerical density of amorphous nucleating particles in antimony condensates is extremely small. This prevents the early occurrence of a coalescence process. In fact the $n(\tau)$ dependence shows an initial rise in particle numbers followed by a fall due to the coalescence process (Fig. 4a). When coalescence occurs, the initial growth rate sharply falls which appears graphically as a discontinuity in the particle dimension dependence on τ. [The $r(\tau)$ dependence cannot, unfortunately, be continued to the high thickness region because amorphous antimony particles at the coalescence stage take on a rosette shape, so that they can no longer be characterized by their mean radius.] Incidentally it should be noted that the interaction and merging of the antimony particles occur at quite considerable interparticle separations (~1000 Å). A possible explanation of this might be the presence of electrostatic attractions between the amorphous particles and their possible ability to migrate.[6]

The main difference in the $\sigma(\tau)$ dependences for antimony (Fig. 4) is that they do extrapolate to $\sigma = 0$ as $\tau \to 0$. The appearance of two kinetic stages on the $n(\tau)$ and $r(\tau)$ curves and also the nonmonotonic experimental $\sigma(\tau)$ curve make it necessary to carry out separate analyses for the different antimony film formation stages. The first stage is characterized by a constant particle nucleation rate b and a constant growth rate c. In this case

$$\Omega = \frac{1}{3} bc^2\tau^3. \qquad (4)$$

The second stage should be described, as in bismuth, by relationships (1) and (3) with c constant and $n = n_{\max}$.

Figure 4b shows the experimental points and calculated $\sigma(\tau)$ curves for a given specimen series. Curve 4 corresponds to the initial stage and is calculated from relationships (1) and (4) for the following parameters found from the $n(\tau)$ and $r(\tau)$ dependences: $b = 2.7 \cdot 10^7$ cm^{-2} · sec^{-1}, c = 4.4 Å · sec^{-1}; curve 5 was constructed for parameters $n_{\max} = 5.75 \cdot 10^9$ cm^{-2}, c = 0.75 Å · sec^{-1}, and $\tau_0 = 200$ sec (to reflect better the situation at low thicknesses a log–log graph is plotted). It can be seen in Fig. 4 that the initial period is characterized by a cubic time dependence for σ (the slight deviation for the initial stage between the experimental points and calculated curve can be eliminated by moving the latter in a parallel direction, that is, by inserting a correction to the kinetic parameters b and c).

SILVER AND GOLD

The characteristic of silver and gold films is that coalescence becomes effective at the stage preceding that at which a significant amount of metal can be recorded. Starting with very thin specimens, there is normally observed a decrease in the number of particles (Fig. 5), and the $\sigma(\tau)$ dependence extrapolates to some σ_0, as with bismuth.[1)]

From the start of coalescence, the mean particle growth rate does not stabilize for silver as for bismuth or antimony, but continuously decreases, that is, with increasing amounts of condensed metal the coalescence has

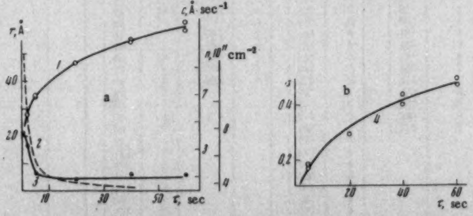

Fig. 5. a: Variation in mean particle radius (1), mean growth rate (2), numerical particle density (3); b: fraction of area occupied by condensate (4), for condensation of a silver molecular beam. Substrate temperature 500°C, curve 4 calculated from relationships (1) and (5).

a more rapidly growing effect and it slows the substrate covering process. Figure 5a shows an example of one of the $r(\tau)$ curves and the $c(\tau)$ curve obtained by differentiating graphically the latter. This dependence was quite well described by the approximate expression $c \sim C_0\tau^{-1}$ for all our observations.

In this case

$$\Omega = nc_0^2[\ln \tau]^2. \tag{5}$$

Figure 5b compares the experimental points and the calculated $\sigma(\tau)$ curve obtained for the following derived parameters: $C_0 = 10$ Å, $n_{\max} = 1.2 \cdot 10^{12}$ cm^{-2}, and $\tau_0 = 4$ sec. Thus, the detected unusual "convex" kinetic $\sigma(\tau)$ curve for silver is explained by the fact that the silver particle growth rate under coalescence conditions noticeably falls with time.

The kinetic curve characteristics were the same for gold as for silver.[2]

CONCLUSIONS

1. The initial formation period of condensed films and the coalescence stage can be described by expression (1), together with the aid of the function Ω, the fraction of the area occupied by the condensate σ, and the kinetic parameters b (particle nucleation rate) and c (particle growth rate).

For antimony, the initial condensate formation stage, predominated by coalescence, is characterized by a constant nucleation and particle growth rate, as a result of which $\Omega \sim \tau^3$.

2. During the coalescence stage particle merging leads to a braking in their growth along the substrate surface. A constant particle growth rate is established during the condensation of bismuth films during the coalescence stage; in this case $\Omega \sim r^2$. During silver and gold condensation a continuous slowing down of the particle growth rate under the influence of coalescence is observed. In many cases the particle growth rate is described well by the expression $c \sim \tau^{-1}$, which corresponds to $\Omega \sim (\ln \tau)^2$ Such a description of the substrate surface condensate covering kinetics is quite successful in comparisons with the experimental $\sigma(\tau)$ curves.

---

[1] We were only able to record the initial part of the kinetic curves for those cases in which a discontinuity in $\sigma(\tau)$, $r(\tau)$ and the area of maximum for $n(\tau)$ was detected; a substrate temperature rise therefore leads to shift in the discontinuity to larger effective thicknesses.

[2] For gold two sharp maxima were found on the histograms, making calculations difficult since the kinetic analysis has to be carried out separately for the two groups of particles.

---

[1] L. S. Palatnik and Yu. F. Komnik, Dokl. Akad. Nauk SSSR, 129, 74 (1959).
[2] A. N. Kolmogorov, Izv. Akad. Nauk SSSR, Ser. Matem., 3, 355 (1937).
[3] L. N. Aleksandrov and Yu. G. Sidorov, Crystal Growth, 8, Nauka, Moscow (1968), p. 241.
[4] V. N. Trofimov and V. M. Luk'yanovich, Fiz. Tverd. Tela, 14, 228 (1972).
[5] Yu. F. Komnik, Fiz. Tverd. Tela, 6, 2897 (1964) [Sov. Phys. – Solid State, 6, 2309 (1965)].
[6] A. A. Chernov and L. I. Trusov, Kristallografiya, 14, 218 (1969) [Sov. Phys. – Crystallogr., 14, 172 (1969)].

Preparation and preliminary investigation of cadmium phosphates

Yu. A. Ivanov, I. N. Ivanovskaya, V. I. Popolitov, M. A. Simonov, and N. V. Belov

M. V. Lomonosov Moscow State University
Institute of Crystallography, Academy of Sciences of the USSR
(Submitted January 16, 1973)
Kristallografiya 18, 1070-1073 (September-October 1973)

A study has been made of hydrothermal crystallization in the system $CdO-(NH_4)_2HPO_4-NaCl-H_2O$ at 400-500°C for aqueous NaCl solution concentrations of 0-60 wt.% and molar $CdO:(NH_4)_2HPO_4$ ratios of 1:2 at 400 and 500°C and 1:2, 1:6, and 1.5:1 at 450°C. The stability regions of five single-crystal phases have been established, and their chemical compositions, Laue symmetries, and unit-cell dimensions determined.

The few crystal chemical studies of Cd phosphates and their promising physical properties stimulated these studies concerning their preparation.

When the present investigation was undertaken, cadmium phosphates had not been found to occur naturally, but information was available in the literature on the preparation of cadmium phosphates in powder form by precipitation from solutions,[1-4] using the reactions of Cd salts, oxides, or hydroxides with phosphoric acid. In addition, a method is described in refs. 3 and 5 for obtaining cadmium fluoroapatite $Cd_5(PO_4)_3F$ from powdered $Cd_3(PO_4)_2$ and CdF_2 which had been pressed into tablets and heated to 900°C. Cadmium hydroxylapatite $Cd_5(PO_4)_3\cdot OH$ has been obtained by a hydrothermal method[4,6] and by the hydrolysis[5] of $Cd_5H_2(PO_4)_4\cdot 4H_2O$. In none of these investigations did the problem arise of establishing the conditions and other characteristics of crystallization in CdO–phosphate–solvent systems.

When studying the chemical reaction in the system $CdO-(NH_4)_2HPO_4-NaCl-H_2O$ we wanted to prepare single crystals of various cadmium phosphates suitable for physical and x-ray structural investigations. The crystallization conditions for the cadmium phosphates were studied with batch-type autoclaves having different linings. The principal crystallization parameters were: 400-500°C, liquid pressure 800-1400 atm (filling factor = 0.7 – 0.75), temperature gradient 0.5 – 1.1 deg/cm. The charge consisted of cadmium oxide and a high purity grade of diam-

TABLE 1. Interplanar Distances* of Cadmium Phosphates

Phase A		Phase B		Phase C		Phase D		Phase E	
d	*I*	*d*	*I*	*d*	*I*	*d*	*I*	*d*	*I*
13,0	3	8.93	23	5,16	8	5.39	53	4.83	5
8.92	100	7.90	10	4,03	54	4.57	22	4,19	22
4.90	1	5.57	25	3.80	7	3.70	100	3,88	21
4.42	10	4.44	3	3,03	70	3.23	90	3,54	6
3.83	1	3.93	27	2.76	46	2,93	70	3.26	17
3.51	4	3.80	17	2.67	100	2,78	34	3,17	40
3,21	1	3.50	15	2.32	3	2.67	80	3.04	30
2,93	8	3,24	100	2,23	11	2.50	23	2.83	100
2.89	10	2.97	100	2,18	2	2.52	28	2,79	80
2.78	2	2.92	66	2,01	11	2,39	4	2,70	65
2.54	2	2.83	66	1.90	9	2,29	16	2,58	10
2.44	1	2.78	34	1,85	17	2.16	8	2,32	5
2,33	3	2.72	32	1,78	18	2,17	9	2.27	5
2,20	2	2.61	15	1,76	35	1,99	23	2,19	4
2,07	2	2.49	6	1,72	9	1.95	36	2,09	5
1,91	2	2.38	6	1,66	2	1,90	10	1.98	10
1,82	1	2.34	9	1,55	3	1.87	50	1.94	31
1,76	2	2.30	17	1,52	10	1.85	14	1,92	15
1,68	2	2.24	5	1,51	5	1,77	23	1.89	29
		2.19	2	1,482	1	1.74	48	1,84	25
		2.14	4	1.447	9	1.69	22	1.82	29
		2.10	11	1,412	10	1.62	30	1,79	25
		2,06	3	1,290	3	1,58	4	1.76	33
		1.99	18	1,266	4	1,55	3	1.63	8
		1.96	19	1,246	2	1,53	5	1,58	8
		1.90	10	1,229	6	1.483	18	1,56	5
		1.87	18	1 220	6	1,432	12	1,52	4
		1,85	19	1,163	6	1,422	6	1,500	4
		1.81	5	1,115	2	1,404	4	1.487	4
		1.79	5	1,088	3	1.384	8	1,460	13
		1,76	10	1,068	3	1,365	5	1.435	8
		1,72	3	1,004	3	1,347	4	1,405	7
		1.68	15	0,985	2	1.325	6	1,337	5
		1.66	7			1.247	7	1.276	6
		1.63	3			1.231	6	1,264	8
		1,56	3			1.215	6	1,236	9
		1.53	20			1,188	6	1,204	8
		1.51	6			1,171	8		
		1,492	8			1 149	4		
		1,437	6			1.140	4		
		1,410	5			1.130	3		
		1.394	5			1,102	5		
		1,385	5			1.083	4		
		1,357	5			1.075	3		
		1,328	4			1,062	3		
		1.298	3			1,051	3		
		1.291	5						
		1,187	5						

---

*URS-50IM diffractometer, Cu Kα radiation.

TABLE 2. Results from Chemical Analysis

Composition	Content wt.%				
	A	B	C	D	E
CdO	51.43	67.51	65.29	60.97	69.41
Na_2O	—	3.2	—	11.12	0.50
P_2O_5	31.25	27.5	28.71	28.00	26.14
Cl	—	traces	—	—	3.02
$\pm H_2O$	17.50	0.84	5.55	0.45	0.80
Σ	100.18	99.05	99.55	100.54	99.87

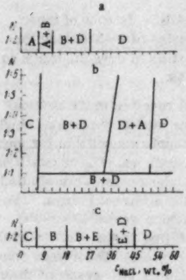

Fig. 1. Regions of stability for phases in the system $CdO-(NH_4)_2HPO_4-NaCl-H_2O$. a) t = 400; b) 450; c) 500°C.

monium hydrogen phosphate. The molar ratio CdO : $(NH_4)_2HPO_4$ employed was 1 : 2 at 400 and 500°C and 1.5:1, 1:2, and 1:6 at 450°C. The crystallization medium was aqueous sodium chloride solution at concentrations of 0 – 60 wt.%, taken at 3 wt.% intervals.

On studying crystallization in the system $CdO-(NH_4)_2HPO_4-NaCl-H_2O$ as a function of temperature, molar ratio of the components in the initial charge, and solvent concentration, five phases were obtained whose individual nature was established by optical, x-ray diffraction, and chemical methods. Tables 1 and 2 present the results from the x-ray diffraction and chemical studies of the single crystals. A large series of experiments enabled us to construct a diagram of the regions of stability of the various phases in composition–solvent concentration coordinates for 400–500°C (see Fig. 1). It is seen from these results that the regular interchange of the crystal phases for 400 and 500°C is controlled only by the concentration of the NaCl solution, but for 450°C this relationship is also associated with the molar CdO:$(NH_4)_2 \cdot HPO_4$ ratio. Thus, analysis of the crystallization processes in the system $CdO-(NH_4)_2HPO_4-NaCl-H_2O$ showed that the phase composition of the system and the interchange of the crystalline phases are determined by temperature, the concentration of the NaCl solution and, finally, by the ratio of the components CdO and $(NH_4)_2HPO_4$ in the initial charge. A brief description of the Cd phosphates prepared and their unit-cell parameters is presented below.[1)]

Phase A. The crystals of phase A ($2CdO \cdot P_2O_5 \cdot 5H_2O$) are orthorhombic (Laue class mmm). The unit-cell parameters are: a = 4.999 ± 0.004; b = 5.824 ± 0.006; c = 8.88 ± 0.01 Å. The crystals are colorless, lamellar, but rather elongated along the c axis. The hydrostatic density is 3.18 g/cm³. It was established experimentally that the yield of this phase is optimal over a NaCl solution concentration range of 33–50 wt.% at 450°C and a CdO : $(NH_4)_2HPO_4$ ratio of 1:2 and 1:6.

Phase B. The crystals of phase B ($Na_2O \cdot 10CdO \cdot 4P_2O_5 \cdot H_2O$) are monoclinic (Laue class 2/m). The unit-cell parameters are: a = 9.686 ± 0.008; b = 9.49 ± 0.01; c = 7.555 ± 0.004 Å; γ = 109.5° ± 0.1. The yield of phase B crystals is a maximum over a NaCl solution concentration range of 6–25 wt.% at 450°C and a CdO:$(NH_4)_2HPO_4$ ratio of 1:2. An increase in the NaCl solution concentration to 33 wt.% for the same experimental conditions leads to a sharp reduction in the yield of phase B. The crystals of this phase are transparent, well-defined, having a glassy luster with a prismatic habit. The hydrostatic density is 4.83 g/cm³.

Phase C. The crystals of phase C ($5CdO \cdot 2P_2O_5 \cdot 3H_2O$) are orthorhombic (Laue class mmm). The unit-cell parameters are: a = 5.111 ± 0.003; b = 5.887 ± 0.002; c = 17.21 ± 0.01 Å. The crystals are deposited at CdO : $(NH_4)_2HPO_4$ ratios of 1:2 and 1:6 over the temperature range 450–500°C. Phase C is formed over only a narrow range of initial NaCl solution concentrations. An increase in the CdO : $(NH_4)_3HPO_4$ ratio to 1.5:1 leads to the appearance of this phase at all NaCl solution concentrations in the form of transparent, colorless, thin needles. The density of this phase is 4.61 g/cm³.

Phase D. The crystals ($2Na_2O \cdot 4CdO \cdot 2P_2O_5$) are also orthorhombic (Laue class mmm). The unit-cell parameters are: a = 5.055 ± 0.002; b = 6.494 ± 0.002_5; c = 10.832 ± 0.004 Å. This, the most stable phase, is formed at all the temperatures studied and over widely varying ratios of the initial components. The yield increases with an increase in the NaCl solution concentration; the single-phase region of its stability is over the range 50–60 wt.% NaCl. The crystals are colorless, transparent, and of lamellar habit. Their density is 4.14 g/cm³.

Phase E. $Cd_5(PO_4)_3Cl$ crystallizes in a hexagonal system (Laue class 6/m). The unit-cell parameters are: a = 9.615 ± 0.006; c = 6.508 ± 0.005 Å. The crystals of this phase are deposited only at 500°C over a NaCl solution concentration range of 18–45 wt.% and for a CdO : $(NH_4)_2HPO_4$ ratio of 1:2. The crystals are transparent, colorless, well-defined, and of acicular habit. The density is 5.47 g/cm³. The closeness of the interplanar distances and the unit-cell parameters, as well as the results from chemical analysis indicate that the E phase has an apatite-type structure.

CONCLUSIONS

1. A study has been made of hydrothermal crystallization in the $CdO-(NH_4)_2HPO_4-NaCl-H_2O$ system at 400–500°C and for NaCl solution concentrations of 0–60 wt.%, with molar CdO : $(NH_4)_2HPO_4$ ratios of 1:2 at 400 and 500°C and 1:2, 1:6, and 1.5:1 at 450°C.

2. The stability regions of the various single-crystal phases have been constructed in N–C coordinates (where N is the molar CdO:$(NH_4)_2HPO_4$ ratio and C is the NaCl solution concentration).

3. Analysis of the crystallization process in the $CdO-(NH_4)_2HPO_4-NaCl-H_2O$ system shows that the phase composition of the system and the subsequent interchanges between the crystalline phases are determined by

temperature, NaCl solution concentration, and the molar ratio of the components in the initial charge.

4. Five single-crystal phases were obtained in the stability regions established, whose chemical compositions, Laue symmetries, and unit-cell parameters have been determined.

---

[1] Determined by the oscillation method in an RKOP-A camera (Mo Kα radiation) and refined on a "Syntex" P1 automatic diffractometer.

[1] M.-T. Averbuch-Pouchot and A. Durif, Mat. Res. Bull., 7, 4 (1969).

[2] M.-T. Averbuch-Pouchot and A. Durif, Bull. Soc. Fr. Minéral. et Cristallogr., 1, 93 (1970).

[3] R. C. Ropp and R. W. Money, J. Amer. Chem. Soc., 82, 4848 (1960).

[4] A. Klement and F. Zureda, Z. Anorgan. und Allgem. Chem., 245, 229 (1940).

[5] R. C. Ropp, R. W. Money, and C. W. W. Hoffman, Anal. Chem., 33, No. 12 (1961).

[6] G. Engel, Z. Anorgan. und Allgem. Chem., 1, 378 (1970).

Indexing of the crystallographic planes in rhombohedral crystals

V. A. Gerken, B. K. Kazurov, and G. M. Tsigel'nitskii

(Submitted July 27, 1972; resubmitted January 31, 1973)
Kristallografiya, 18, 1074 (September-October 1973)

In work with rhombohedral crystals, many research workers, particularly in industrial organizations, make errors in the preparation of single-crystal elements by indexing the crystallographic planes incorrectly. This is due to the fact that for some rhombohedral crystals, before the crystallographic unit cells of these crystals had been determined, mineralogists had indexed their "morphological" cells (cells of the cleavage rhombohedron), and these have appeared in the basic reference literature.

For the "morphological" cell of calcite ($CaCO_3$): a_R = 6.37 Å and $\alpha_R = 101°55'$. The cleavage plane of the rhombohedron for this choice of cell has indices $\{10\bar{1}1\}$ (see Fig. 1). The cleavage rhombohedra in crystals of ruby (α-Al_2O_3) in hexagonal packing with ratio $c/a = 1.365$ have the index $\{10\bar{1}1\}$. For indexing of the planes of ruby crystals in hexagonal packing with ratio $c/a = 2.730$ (for the crystallographic unit cell of the crystal a_R = 5.14 Å and $\alpha_R = 55°17'$) the cleavage rhombohedra have the index $\{10\bar{1}2\}$, as can readily be verified from the calculated Bragg angles θ_{hkil} on an x-ray diffractometer.

The main reference literature notes the absence of cleavage in perfect crystals of corundum (ruby, sapphire, leucosapphire). For most perfect ruby and leucosapphire crystals, however, we observed good cleavage, with a glassy luster, along the $\{10\bar{1}2\}$ rhombohedra.

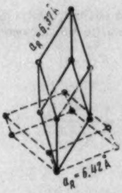

Fig. 1. Cell of the cleavage rhombohedron of the crystal of $CaCO_3$ (calcite) and its crystallographic unit cell.

In the preparation of single-crystal elements from α-Al_2O_3, it is necessary to recognize clearly that at an angle $\rho = 57°36'$ lies the plane of the rhombohedron $\{10\bar{1}2\}$, and not $\{10\bar{1}1\}$, as given in various reference sources. Reference books also give the $\{10\bar{1}1\}$ rhombohedron in crystals of lithium metaniobate (a_R = 5.49 Å; $\alpha_R = 55°42'$), although in a real crystal the reticular rhombohedral planes are the $\{10\bar{1}2\}$ and $\{10\bar{1}4\}$ planes, the normals to which make angles of 57°15' and 37°51' with the optical axis of the lithium metaniobate crystal.

Crystal structure of $La_2Sr_3(BO_3)_4$

G. K. Abdullaev, Kh. S. Mamedov, and S. T. Amirov

Institute of Inorganic and Physical Chemistry, Academy of Sciences of the Azerbaidzhan SSR

(Submitted November 2, 1972)
Kristallografiya, 18, 1075-1077 (September-October 1973)

Single crystals of lanthanum strontium borate, grown from solution in melts of the $La_2O_3-SrO-B_2O_3$ system at 1100°C, were studied by x-ray diffraction in ref. 1. The orthorhombic lattice constants of the crystal are: $a = 8.78$, $b = 16.54$, $c = 7.42$ Å; $z = 4[La_2Sr_3(BO_3)_4]$, $\rho_{cal} = 4.80$ g/cm^3.

The experimental information used for the structural investigation were the hk0−hk3 and 0k*l*−1k*l* scans obtained for unfiltered Cu radiation with an integrating Weissenberg x-ray goniometer. A total of 530 independent nonzero reflections were established, the intensities of which were estimated visually from the blackened lines with a $\sqrt[4]{2}$ measure. When scaling the intensities the Lorentz factor and the polarization factor were taken into account in the structural factor; no correction for absorption was introduced.

When interpreting the structure of lanthanum strontium borate we had to reject the space group Pccn adopted previously[1] and adopt the noncentrosymmetric group $Pc2_1n(Pna2_1)$ as the most probable.

The coordinates of the heavy lanthanum and strontium atoms were found from the three-dimensional Patterson function. The three-dimensional synthesis of the electron density calculated from these coordinates (R = 30%) enabled us to establish the position of eight of the oxygen atoms. The coordinates of the remaining oxygen atoms and the boron atoms were localized with different three-dimensional Fourier syntheses (the lanthanum and strontium atoms being "eliminated"). On including in the calculation the coordinates of all the light atoms found the divergence factor R_{hkl} is reduced to 23%.

The structure was refined by the method of least squares on an M-220A computer from the complete block consisting of 530 F^2_{hkl}, using the programs of B. A. Tarnopol'skii and V. I. Andrianov.[2] After refinement the divergence factor (with an overall isotropic temperature correction[2] $B = 1.2$ Å^2, $\sin\theta/\lambda \le 0.62$ Å^{-1}) was reduced to $R_{hkl} = 14\%$. On taking the individual isotropic temperature factors into account $R_{hkl} = 12\%$.

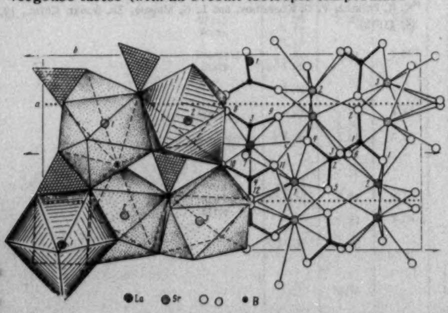

Fig. 1. Projection of the structure of $La_2Sr_3(BO_3)_4$ on the (001) plane.

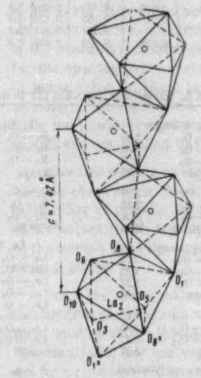

Fig. 2. Chain of La_2 eight-pointed units.

The coordinates of the basis atoms (63 parameters) are presented in Table 1, and the interatomic distances calculated from them are given in Table 2.

The crystal structure consists of isolated BO_3 triangles and oxygen polyhedra of lanthanum and strontium. The principal details of the structure can be seen in Figs. 1 and 2. The lanthanum and strontium atoms are situated within irregular oxygen eight-, nine-, and ten-pointed units. Each of the Sr_1, Sr_2, Sr_3, and La_2 polyhedra, being connected through a common edge and a face with the closest symmetrical equivalent polyhedra, form columns parallel to the c axis (Fig. 1). This would also seem to cause the elongation of the crystals in the direction of the short axis. These columns, being joined together by common edges, faces, and B_1 and B_2 boron−oxygen triangles, form walls perpendicular to the c axis. The latter are joined together by La_1, eight-pointed units, and the B_3 and B_4 boron−oxygen triangles. The pseudosymmetry of the structure is noteworthy. To a rough approximation the walls are connected with each other by the mirror plane of symmetry, i.e., the Pcmn (Pnma) group is the pseudosymmetry group of the crystal.

The interatomic distances in the structure of $La_2Sr_3 \cdot (BO_3)_4$ (Table 2) are in good agreement with the data for other lanthanum strontium borates.[3-9]

Finally, it should be noted that while this paper was being prepared a communication by K. K. Palkina et al. appeared[10] on the crystal structure of $Pr_2Sr_3(BO_3)_4$. A

TABLE 1. Coordinates of the Basis Atoms in the Structure of $La_2Sr_3(BO_3)_4$

Atoms	x/a	y/b	z/c	B	Atoms	x/a	y/b	z/c	B
La_1	0.037	0.544	0.184	0.8	O_7	0.007	0.044	0.151	1.5
La_2	0.169	0.384	0.464	1.5	O_8	0.211	0.484	0.717	0.6
Sr_1	0.148	0.170	0.182	2.2	O_9	0.186	0.625	0.730	1.4
Sr_2	0.181	0.714	0.472	0.8	O_{10}	0.065	0.975	0.530	0.9
Sr_3	0.155	0.924	0.186	0.7	O_{11}	0.074	0.119	0.570	2.0
O_1	0.0433	0.405	0.081	1.4	O_{12}	0.242	0.050	0.894	0.8
O_2	0.201	0.842	0.922	1.6	B_1	0.052	0.840	0.874	0.5
O_3	0.005	0.289	0.252	1.1	B_2	0.042	0.262	0.831	0.6
O_4	0.0604	0.702	0.122	0.9	B_3	0.141	0.550	0.797	0.9
O_5	0.193	0.257	0.871	2.4	B_4	0.138	0.049	0.512	1.3
O_6	0.008	0.309	0.682	0.6					

TABLE 2. Interatomic Distances (Å) in the Structure of $La_2Sr_3(BO_3)_4$

B_1 triangle		B_2 triangle		B_3 triangle	
$B_1 - O_1$	1.40	$B_2 - O_4$	1.38	$B_3 - O_7$	1.36
$B_1 - O_2$	1.36	$B_2 - O_5$	1.36	$B_3 - O_8$	1.38
$B_1 - O_3$	1.35	$B_2 - O_6$	1.38	$B_3 - O_9$	1.39
Average	1.37	Average	1.37	Average	1.38
$O_1 - O_2$	2.38	$O_4 - O_5$	2.40	$O_7 - O_8$	2.37
$O_1 - O_3$	2.32	$O_4 - O_6$	2.36	$O_7 - O_9$	2.33
$O_2 - O_3$	2.39	$O_5 - O_6$	2.31	$O_8 - O_9$	2.34
Average	2.36	Average	2.36	Average	2.35
B_4 triangle		La_1 polyhedron		La_2 polyhedron	
$B_4 - O_{10}$	1.38	$La_1 - O_1$	2.42	$La_2 - O_1$	3.07
$B_4 - O_{11}$	1.35	$La_1 - O_4$	2.65	$La_2 - O_3$	2.65
$B_4 - O_{12}$	1.37	$La_1 - O_7$	2.52	$La_2 - O_6$	2.48
Average	1.37	$La_1 - O_8$	2.44	$La_2 - O_8$	2.53
		$La_1 - O_9$	2.80	$La_2 - O_1$*	2.69
$O_{10} - O_{11}$	2.40	$La_1 - O_{10}$	2.57	$La_2 - O_5$	2.52
$O_{10} - O_{12}$	2.33	$La_1 - O_{11}$	2.41	$La_2 - O_8$*	2.68
$O_{11} - O_{12}$	2.37	$La_1 - O_{12}$	2.52	$La_2 - O_{10}$	2.54
Average	2.37	Average	2.54	Average	2.64
Sr_1 polyhedron		Sr_2 polyhedron		Sr_3 polyhedron	
$Sr_1 - O_3$	2.39	$Sr_2 - O_4$	2.81	$Sr_3 - O_2$	2.41
$Sr_1 - O_5$	2.75	$Sr_2 - O_9$	2.41	$Sr_3 - O_7$	2.38
$Sr_1 - O_7$	2.43	$Sr_2 - O_3$	2.38	$Sr_3 - O_{10}$	2.80
$Sr_1 - O_{11}$	3.07	$Sr - O_3$	2.90	$Sr_3 - O_{12}$	3.10
$Sr_1 - O_{12}$	3.03	$Sr_2 - O_4$*	2.54	$Sr_3 - O_1$	2.66
$Sr_1 - O_4$	2.95	$Sr_2 - O_6$	2.55	$Sr_3 - O_2$*	2.55
$Sr_1 - O_5$*	2.44	$Sr_2 - O_9$*	2.60	$Sr_3 - O_6$	2.57
$Sr_1 - O_9$	3.09	$Sr_2 - O_{11}$*	2.75	$Sr_3 - O_{10}$*	2.84
$Sr_1 - O_{11}$*	2.71	Average	2.62	$Sr_3 - O_{12}$*	2.74
$Sr_1 - O_{12}$*	2.71			Average	2.67
Average	2.76				

*The asterisks indicate atoms connected with basic symmetry operations.

comparison of the preliminary coordinates for the atoms in this structure with the atomic coordinates we found for the structure of $La_2Sr_3(BO_3)_4$ confirms our suggestion[1] that these compounds are isostructural.

---

[1] C. K. Abdullaev and O. A. Aliev, Kristallografiya, 15, 812 (1970) [Sov. Phys.–Crystallogr., 15, 693 (1971)].

[2] B. L. Tarnopol'skii and V. I. Andrianov, Zh. Strukt. Khim., 4, 433 (1963).

[3] J. Ysker and W. Hoffmann, Naturwissenschaften, 57, 129 (1970).

[4] R. Bohlhoff, H. Bambauer, and W. Hoffmann, Z. Kristallogr., 133, 386 (1971).

[5] J. R. Clark, Amer. Mineralogist, 49, 1549 (1964).

[6] L. Kutschabsky, Z. Chem., 5, 110 (1965).

[7] A. Perloff and S. Block, Acta Crystallogr., 20, 274 (1966).

[8] I. M. Rumanova and O. Gandymov, Kristallografiya, 16, 99 (1971) [Sov. Phys.–Crystallogr., 16, 75 (1971)].

[9] J. R. Clark and C. L. Christ, Amer. Mineralogist, 56, 1934 (1971).

[10] K. K. Palkina, V. G. Kuznetsov, and L. G. Mogura, Zh. Strukt. Khim., 13, 341 (1972).

X-ray investigation of some examples of a homologous series of cholesterol ethers in dicarboxylic acid

Ya. I. Dutchak and V. K. Burima

L'vov State University

(Submitted July 3, 1972; September 21, 1972)
Kristallografiya, 18, 1078-81 (September 21, 1972)

A majority of the cholesterol ethers are able to form the so-called cholesteric liquid crystals.[1-3]

We have carried out an x-ray investigation of the short-range order in eight examples of a homologous series of cholesterol ethers of dibasic carboxylic acid. These compounds have the form $C_{27}H_{45}-OOC-(CH_2)_n-COO-C_{27}H_{45}$ (n = 1, 2, 3, 4, 5, 6, 7, 8). It should be noted that they have only recently been synthesized, and as yet there are no data on their structure.

The goal of our work was to find the structural changes in a transition to a higher homolog and also in the transitions from the solid crystal to the liquid crystal and to the isotropic liquid for each compound separately. For the x-ray studies, the samples were placed in thin-walled capillaries. The x-ray measurements were made with Cu Kα radiation in a camera with temperature control. The diameter of the cylindrical casette was 114 mm.

The results of the analysis of the diffraction pattern are given in Table 1. It is evident from a study of the table that with the growth of the alkyl chain, the magnitude of the interplanar spacings, which characterize the intramolecular arrangement of atoms, does not change within the limits of experimental error. Considering that the molecules of the materials being investigated are planar, it is possible to assume that all of the intense reflections in the x-ray diffraction pattern give distances between planes on which the molecules lie. If we follow the change of the character of this spacing, we note a marked tendency for the spacing to decrease as the members of the chain increase—that is, there is a tendency toward a denser packing of the molecules. Only compounds which do not form the liquid-crystal phase $C_{57}H_{92}O_4$ (n = 1); $C_{59}H_{96}O_4$ (n = 3) are not subject to this tendency.

It is interesting to note that the largest number of lines is observed in the diffraction pattern of the cholesteric ether of pimelic acid, which is the first odd member of the series (n-5), beginning with which the odd members of the series have the capability of forming the liquid-crystal phase.

Since the compounds which we studied are stable in the liquid-crystal state, we were able to make x-ray structural studies in the liquid-crystal and isotropic phases. The treatment and analysis of the results were carried out by a procedure described in refs. 5-8.

The experimental intensity curves were corrected for absorption and polarization and then were expressed in electron units. In this calculation, in order to be able to compare the intensity curves of the different samples which we studied, we did not compute the scattering factor F for a single molecule but instead used scattering factors

TABLE 1

Intensity of the lines on the diffraction pattern	n							
	1	2	3	4	5	6	7	8
					1.87			
					2.03			
					2.08			2.06
		2.12			2.16			
Very weak	2.22				2.21			2.25
Very weak	2.42				2.41			2.40
				2.63	2.64			
	2.78				2.70			
Weak	2.98	2.99	2.84	2.98		2.88	2.89	2.85
Weak	3.19		3.13		3.25	3.13	3.08	3.13
	3.35			3.55				
Intermediate	3.87	3.92	3.86	3.85	3.83	3.90	3.85	3.83
	4.08				4.02			
					4.16			
	4.36			4.38	4.37	4.31		
				4.68	4.78			
Strong	4.65	4.72	4.83		4.99	4.93	4.91	4.84
		5.02		5.23				
Very strong	5.38	5.51	5.38	5.55	5.44	5.41	5.31	5.27
		6.07			6.12			
				6.48				
		6.71		6.99	6.75		6.38	6.33
Weak	7.39							
Intermediate	7.50	7.64	7.53			7.71	7.64	7.44
					8.28			
		9.24	9.65					
				10.45				
	11.98	11.36					11.82	11.63
			12.01		12.85	12.14		
				13.68				
				14.12				
		16.15		17.82				
					25.39	26.94	26.14	
				28.87				
								38.41

per average atom. That is, $F^2 = (\sum_{i=1}^{m} f_i^2)/m$, where m is the number of atoms in a molecule, and f_i is the atomic scattering factor of the i-th atom. The normalizing factor k was determined by measuring the areas Q_1 and Q_2 under the curves $s^2 I_e(s)$ and $s^2[F^2(s) + I_j(s)]$ in relation to $k = Q_2/Q_1$, where $s = 4\pi\lambda^{-1}\sin\theta$.

The position of the first maximum on the intensity curves for all compounds in the liquid-crystal phase corresponds to $s = 1.15$ Å^{-1} in the isotropic phase, which indicates a somewhat denser packing of the molecules in the liquid-crystal phase.

Some tendency toward a displacement of the second maximum toward smaller s can be noted, while in the liquid-crystal phase the third maximum is shifted to larger s for even members of the series. No well-defined regular behavior can be observed in the other curves.

The atomic-electron density radial distribution curves (see the figure) corresponding to the above intensity curves were computed from the equation

$$\sum_{j=1}^{m}\sum_{k=1}^{m} K_j 4\pi R^2 \rho_k(R) = \sum_{j=1}^{m} K_j 4\pi R^2 \rho_0 + \frac{2R}{\pi}\int_0^{\infty} s\left(I - \sum_{i=1}^{m} f_i^2 \Big/ f_e^2\right) \sin sR\, ds,$$

where the summation is carried out over all atoms of a molecule, K_j is the effective number of electrons in an atom, ρk and ρ respectively are the true and mean electron densities, and f_e is the scattering function for an electron of a molecule. The position of the maxima in the figure are given in Table 2.

In the analysis of these curves, we note that the first maxima occur at nearly the same position, and the areas under them are nearly the same. The same can be said of the second maxima, despite an increase in their intensity with increasing n. These maxima can be ascribed to intramolecular structure: The first characterizes the covalent bonds C−C, C−O, C = O in the molecule, while the second is connected with the C−C and C−O bonds, which are not covalent.

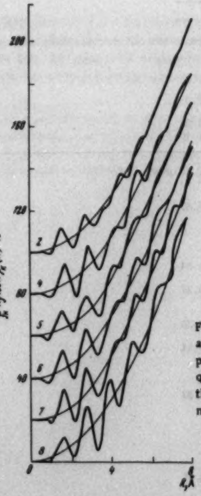

Fig. 1. Atomic-electron density radial distribution curves for the compounds which were studied in the liquid-crystal state. The number on the curve corresponds to the number n of members of the alkyl chain.

TABLE 2. Positions of the Maxima (in Å) on the Radial Distribution Curves for Different Homologs

n					
2	4	5	6	7	8
1.58	1.57	1.50	1.57	1.64	1.56
2.67	2.70	2.70	2.70	2.72	2.71
3.60					3.9
4.45	4.15	4.12	4.30	4.30	
5.50	5.19	5.20	5.25	5.22	5.0
	6.25		6.25	6.20	6.44
				7.14	7.4

The maximum in the neighborhood of 5.0−5.50 Å is in all probability due to intermolecular effects and has a tendency to be displaced toward smaller R as the number of members in the series increases. We also observed a similar tendency in the characteristic interplanar spacing in the solid phase.

Accounting for the fact that the molecules of the compounds being investigated have large dimensions, especially in length (~50 Å, onto any intermolecular peak there must definitely be superimposed the intramolecular peaks which may alter not only the form, but also the position of the former. Consequently, such a distinction into inter- and intramolecular peaks cannot be correct for an analysis of the distribution curves of similar molecules. However, in spite of this difficulty in distiguishing inter- and intramolecular effects, it is possible to note a tendency toward a denser packing in the liquid-crystal phase as n increases. A similar behavior is not found in the isotropic phase.

In order to be convinced of the correctness of relating the first two maxima to the number of intramolecular bonds, we compare the value of the area under these maxima with the values computed from theory for sebacic acid (n = 8) in the liquid-crystal phase. The theoretically computed areas under the first and second maxima are $6.3 \cdot 10^3$ e^2 and $12.7 \cdot 10^3$ e^2, respectively, while the experimentally determined values of the areas under these maxima are $6.79 \cdot 10^3$ e^2 and $16.66 \cdot 10^3$ e^2, respectively.

CONCLUSIONS

1. In the analysis of the packing of the compounds which were studied in the crystalline phase, an increase in the density of molecular packing was observed as the number of members in the alkyl chain increased. The members of the series which do not have a liquid crystal phase do not exhibit this behavior.

2. A similar tendency is also found in the liquid-crystal phase.

3. Intramolecular changes in the transition of the compound from the liquid crystal to the isotropic phases, if they exist, are not appreciable, and they cannot be the basis for the fundamental differences in these phases. Analogous differences were not observed as the number of members of the chain increased.

Evidently, one must seek the fundamental differences of the two liquid phases not in the interactomic or even in the intermolecular distances, but rather in the mutual orientation of the molecules.

---

[1] I. G. Chistyakov and V. N. Aleksandrov, Uch. Zap. Ivanovsk. Gos. Ped. Justo, 77, 34 (1970).

[2] C. W. Gray, J. Chem. Soc. 3733, 1956.

[3] C. Weygand, Z. Naturforsch. 4, 249 (1949).

[4] R. G. Makitra, E. M. Dovbenchyuk, and Ya. M. Tsikanchyuk, Depon. VINITI, No. 3186-71.

[5] A. F. Skryshevskii, Structural Analysis of Liquids (in Russian), Vyashaya Shkola, Moscow, 1971.

[6] V. I. Davidov, A. F. Skryshevskii, Izv. Akad. Nauk SSSR, Ser. Fiz., 2, 187 (1971).

[7] A. F. Skryshevskii, Sb. Nauch. Rabot. Labor. Matellofiz. Akad. Nauk Ukr-SSR, 4, 77 (1953).

[8] V. P. Klochkov, Avtoreferat Dissertatsii, Dnepropetrovsk (1963).

Crystallochemical determination of the structure of $NaTl_3(SO_3)_2$ by means of the method of crystallograms

N. L. Smirnova

M. V. Lomonosov Moscow State University

(Submitted March 28, 1973)
Kristallografiya, 18, 1082 (September-October 1973)

The lattice parameters and the Fedorov group of $NaTl_3 \cdot (SO_3)_2$ were published in ref. 1 : a = 5.74, c = 7.18 Å (c/a = 1.251; $P\bar{3}m1$, Z = 1. Application of the method of crystallograms[2,3] to $NaTl_3(SO_3)_2$ suggests two slightly differing structure versions. One of these is related to the $NaKSO_4$ structure type (c/a = 1.308) and derived from the latter by removing O atoms with a triple axis and replacing one Na atom and two K atoms by Tl atoms (Fig. 1a). The second version (holding when examination reveals reduction of the symmetry group to P3) is related to the structure of Na_2SO_3 (c/a = 1.127) and arises when three Na atoms in the latter structure are replaced by Tl (see Fig. 1b). A refined evaluation of the x-ray diffraction pattern did not suggest changes in the structure of $NaTl_3(SO_3)_2$. The value of c/a for $NaTl_3(SO_3)_2$ is intermediate between the c/a values for the two other structures mentioned, since the sharp reduction of c/a produced by removal of two O atoms is compensated for by the introduction of Tl atoms.

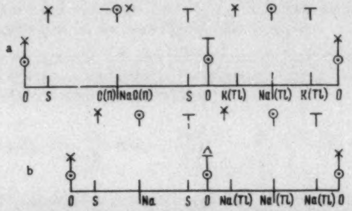

Fig. 1. Dash diagrams of the $NaKSO_4$ (a) and Na_2SO_3 (b) structure types and models derived from them for $NaTl_3(SO_3)_2$; Π) vacancy. The distances between the atom lattices expressed in fractions of c/a are plotted along the horizontal line, the atom coordinates x, y, u (indicated by a cross, dash or circle with dot) in the independent region are represented by vertical lines.[2,3]

Oxidation of a sulfite to a sulfate generally results in replacement of an unpaired electron pair of the S atom by an O^{2-} ion. Ordered or unordered homologous (heteropolytypical) series may form from substances belonging to the considered structure types, in accordance with the construction laws of crystal structures.

---

[1] Y. Oddon, Cl. Caranoni, and T. Aymond, Compt. Rend., C276, 61 (1973).
[2] N. L. Smirnova, Vestn. Mosk. Univ., Ser. Geol., 2, 100 (1967).
[3] N. L. Smirnova, Kristallografiya, 16, 63 (1971) [Sov. Phys.–Crystallogr., 16, 46 (1971)].

Stimulated emission from (Er, Lu)AlO$_3$ crystals containing Ho^{3+} and Tm^{3+} ions

Kh. S. Bagdasarov, A. A. Kaminskii, A. M. Kevorkov, S. É. Sarkisov, and T. A. Tevosyan
Institute of Crystallography, Academy of Sciences of the USSR
(Submitted April 27, 1972)
Kristallografiya, 18, 1083-1084 (September-October 1973)

Aluminates of some elements from group III of the periodic system containing trivalent rare-earth ions as impurities have been used as active media in lasers. Of these the most interesting are YAlO$_3$ − Nd^{3+} (refs. 1-3), YAlO$_3$ − Er^{3+} (ref. 4), YAlO$_3$ − Cr^{3+} and YalO$_3$ − Tm^{3+} (ref. 5), and ErAlO$_3$ containing Ho^{3+} and Tm^{3+} ions.[7] These compounds show less of a twinning effect when prepared from a melt. A brief report[6] has previously been given of the observation of stimulated pulsed emission of Ho^{3+} ions in ErAlO$_3$ at 77°K at a wavelength around 2.1 μ involving the $^5I_7 \rightarrow {}^5I_8$ transition. The erbium in this crystal host is an efficient sensitizer for luminescence of the Ho^{3+} and Tm^{3+} ions. Unfortunately its content is very high in ErAlO$_3$, which makes it hard to achieve a uniform distribution of excitation over the whole volume of the active element. We have thus set out to study the growth conditions in order to investigate the possibility of "diluting" the Er^{3+} ion concentration in this crystal with another kind of ion which does not affect its structural and spectroscopic properties. We chose the spectroscopically neutral Lu^{3+} ions in the ratio 1 : 1 with Er^{3+} ions (in the starting mixture)[1]. The (Er, Lu)AlO$_3$ single crystals thus produced containing Ho^{3+} and Tm^{3+} ions (which contained hardly any twins) were used to prepare active elements (25 mm long and 5 mm in diameter) for studying stimulated emission. As an illustration of the spectroscopic properties of these crystals Fig. 1 shows their luminescence spectra corresponding to the main emission channel. At the frequencies of some of their intense lines (shown by arrows) optical generation was also detected at 77°K. The results of the measurement of some of the spectrocopic and laser properties are given in Table 1.

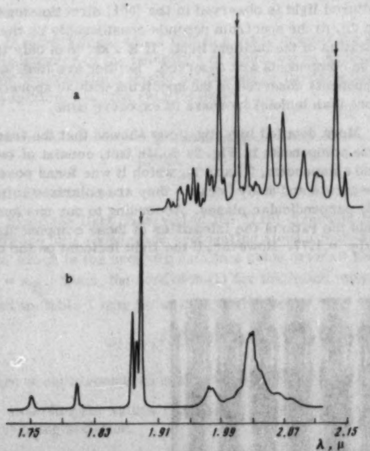

Fig. 1. Luminescence spectrum of (Er,Lu)AlO$_3$ crystals at 77°K: a) containing Ho^{3+} ions ($^5I_7 \rightarrow {}^5I_8$ transition): b) containing Tm^{3+} ions ($^3H_4 \rightarrow {}^3H_6$ transition).

TABLE 1

Activator ion, concentration (at.%)	Transition	λ_Γ^{*}, μ	$\Delta\nu_{lum}^{**}$ cm^{-1}	E_c^{***}, J	E_c^{****}, cm^{-1}
Ho^{3+}, 2—5	$^5I_7 \rightarrow {}^5I_8$	2.0010	6	75	~200
		2.1205	10	30	~570
Tm^{3+}, 2—5	$^3H_4 \rightarrow {}^3H_6$	1.8845	5.5	45	~400

*The precision of the laser wavelength measurement is ± 10 Å.

**The width of the luminescence lines was determined to within ± 0.5 cm^{-1}.

***The excitation threshold is calculated per unit length of crystal, and the values cited for E_t correspond to a transmission of the spherical interference mirror of ~1%; the experiments used a confocal (R = 600 mm) optical resonator and pulsed Xe lamps of the IFP-400 type for excitation.

****The positions of the levels at which the observed induced transitions terminate require further refinement.

In conclusion we indicate that the Ho^{3+} and Tm^{3+} ions have nearly the same spectroscopic properties in ErAlO$_3$ and (Er, Lu)AlO$_3$ crystals. The optical spectra of these compounds are quite strongly polarized, which gives a definite possibility for changing the generation wavelength λ_Γ by choosing the orientation of the generating crystals. The crystals obtained can also evidently be used in lasers operating continuously.

---

[1] We know of no data on the formation of the compound LuAlO$_3$, which is isostructural with ErAlO$_3$.

[1] Kh. S. Bagdasarov and A. A. Kaminskii, ZhETF Pis. Red., 9, 501 (1969) [JETP Lett., 9, 303 (1969)].
[2] M. J. Weber, M. Bass, K. Andringa, R. Monchamp, and E. Comperchio, Appl. Phys. Lett., 15, 342 (1969).
[3] G. A. Massey and J. M. Yarborough, Appl. Phys. Lett., 18, 576 (1971).
[4] M. J. Weber, M. Bass, G. A. de Mars, K. Andringa, and R. R. Monchamp, IEEE J. Quantum Electron., QE-6, 654 (1970).
[5] G. A. Keig and L. G. De Shaser, Laser und Elektro-optik, 3, 45 (1972).
[6] Kh. S. Bagdasarov, G. A. Bogomolova, M. M. Gritsenko, A. A. Kaminskii, and A. M. Kevorkov, Kristallografiya, 17, 415 (1972) [Sov. Phys.—Crystallogr., 17, 357 (1972)].
[7] V. A. Gorbachev, V. L. Zhekov, T. M. Murina, V. V. Osiko, B. P. Starikov, and M. L. Timoshechkin, Kratkie. Soobshch. Fiz., 4, 16 (1973).

Molecular scattering of light in a single crystal of hafnium dioxide

V. I. Aleksandrov, V. F. Kitaeva, I. V. Kozlov, V. V. Osiko,
N. N. Sobolev, V. M. Tatarintsev, and I. L. Chistyi
Physics Institute, Academy of Sciences of the USSR
(Submitted October 18, 1972)
Kristallografiya, 18, 1085-1087 (September-October 1972)

In this paper we present the results of the first studies into the molecular scattering of light in single-crystal cubic HfO_2 and 10% Y_2O_3, the yttrium oxide being added to stabilize the cubic phase. The $HfO_2-Y_2O_3$ crystals were prepared from the melt in air. Their point group was m3m. They have a high refractive index (n = 2.22), a very high density (ρ = 9.65 g/cm^3), and are transparent over the region 3000-70,000 Å. The purpose of the investigations described below was to study special features in the molecular scattering of light and to determine the elastic and photoelastic constants in a single crystal of the cubic solid solution $HfO_2-Y_2O_3$.

The excitation source of the scattered light was the λ = 4880 Å live from an Ar^+ laser. The power of the laser radiation in this line was 0.5 W. A diagram of the experimental arrangement is shown in Fig. 1.

The crystal studied was of good optical quality, having the shape of a parallelepiped (5 × 7 × 16 mm). The shortest edge of the parallelepiped was parallel to the four-fold axis while the longest edge was parallel to the [$\bar{1}$10] direction (case 1) or along [001] (case 2).

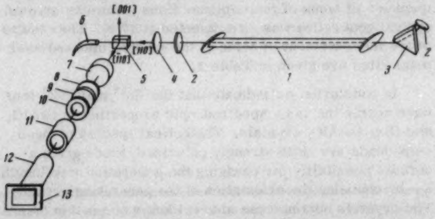

Fig. 1. Experimental arrangement. 1) Gas-discharge tube; 1) resonator mirror; 3) Brewster prism ensuring laser generation at 4880 Å; 4) lens (f = 208 mm); 5) HfO_2 crystal; 6) Wood's horn; 7) collimator (f = 90 mm); 8) 525-21 light filter; 9) interference light filter; 10) diaphragm; 11) Fabry–Perot etalon; 12) camera (f = 350 mm); 13) film holder.

The excitation light was polarized either in the scattering plane[1] (**E** ∥ **kk**') or perpendicular to the scattering plane (**E** ⊥ **kk**'). The plane of polarization was rotated by 90° by means of crystalline quartz wafers.

The spectrum of the scattered light was studied by means of the Fabry–Perot etalon and recorded photographically. The Raman scattering light and the orange–red luminescence from the crystal were cut off by the SZS-21 light filter and the interference light filter to a wavelength of 4880 Å with a transmission bandwidth of 20 Å. Some of the spectrograms obtained are presented in Fig. 2.

Examination of the spectrograms shows that in case 1 (Fig. 2a, b) the intensity of the longitudinal Mandel'shtam–Brillouin scattering components (L) is virtually independent of whether the light is polarized in the scattering plane or perpendicular to it. The transverse Mandel'shtam–Brillouin scattering components (T) are observed clearly only when the excitation light is polarized in the scattering plane (**E** ∥ **kk**'), the intensity of the transverse components being markedly weaker than that of the longitudinal components. For **E** ⊥ **kk**' the transverse components are almost completely masked by parasitic scattering and by a continuous luminescence background which is not completely removed by the light filters. Where the scattered light is observed in the [001] direction (case 2, Fig. 2c, d) the spectrum depends considerably on the polarization of the incident light. If **E** ⊥ **kk**' then only transverse components are observed. Neither are longitudinal components observed in the spectrum with an appreciable (more than tenfold) increase in exposure time.

More detailed investigations showed that the transverse components in Fig. 2c do, in fact, consist of two close components, T_1 and T_2, which it was found possible to separate and study because they are polarized in mutually perpendicular planes. According to our measurements the ratio of the intensities of these components is I_{T_2}/I_{T_1} = 1.77. However, if the light incident on the crys-

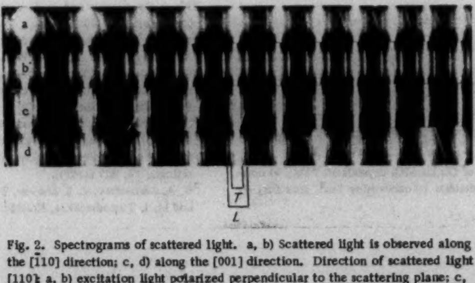

Fig. 2. Spectrograms of scattered light. a, b) Scattered light is observed along the [$\bar{1}$10] direction; c, d) along the [001] direction. Direction of scattered light [110]; a, b) excitation light polarized perpendicular to the scattering plane; c, d) parallel to the scattering plane.

TABLE 1. Direction of Excitation Radiation [110]

Direction of scattered light wave	Wave	Sound velocity, km/sec	Relative intensity		
			E ⊥ kk'	exposure, min	E ∥ kk'
$[\bar{1}10]$	L	6.29±0.04	1.00	←20→	2.1
	T_2	2.50±0.02	Masked by parasitic scattering		0.3
[001]	qL	5.46±0.02	Not observed	←20 | 90→	1.00
	T_2	3.20±0.01	1.8		1.5
	qT_1	3.48±0.04	1.00		

tal is polarized in the scattering plane (E∥kk'), then a spectrum is observed in which longitudinal components of similar intensity to that of the transverse components appear, in addition to the transverse components (T_2).

Processing of the spectrograms involved measuring the relative intensities I of the Mandel'shtam–Brillouin components by the usual method of photographic photometry and their displacement $\Delta\nu$ from the excitation line. The velocity of the hypersonic waves was calculated from the displacement. The results obtained from processing the spectrograms are presented in Table 1.

It is seen from Table 1 that the velocities of the longitudinal and transverse sound waves depend appreciably on the direction of their propagation in the crystal, i.e., a crystal of cubic HfO_2 is highly anisotropic to the velocity of sound. The relative intensities of the longitudinal and transverse Mandel'shtam–Brillouin components in a HfO_2 crystal also depend appreciably on the direction of propagation of the sound wave at which the scattering of light is observed.

It follows from ref. 1 that in a cubic crystal the sum of the squares of the velocities of sound waves having different polarizations should not depend on the direction of propagation, i.e., the relationship

$$\sum_{\gamma=L,T_1,T_2} v_\gamma^2 = \text{const.} \tag{1}$$

should be satisfied.

Since the light observed in the $[\bar{1}10]$ direction is scattered at a sound wave propagating along a four-fold axis, which is the acoustic axis in a cubic crystal, then $\nu_{T_1} = \nu_{T_2}$. Thus, the condition (1) for the sound waves noted in Table 1 may be written in the form

$$v_L^2 + 2v_{T_2}^2 = v_L'^2 + v_{T_1}'^2 + v_{T_2}'^2, \tag{2}$$

where ν corresponds to case 1 and ν' to case 2.

Inserting the values from Table 1 leads to the equality (2) being satisfied.

The measurements of the sound wave velocities were used to calculate the elastic constants c_{11}, c_{44}, and c_{12}. The constants c_{inmj} (in four-index notation) were determined from the equation[1]

$$|c_{inmj}\varkappa_n\varkappa_m - \rho v_\gamma^2\delta_{ij}| = 0. \tag{3}$$

Here $\varkappa_n$ and $\varkappa_m$ are the projections of the directions of the sound waves on the principal axes of the crystal, ρ is the density, ν_γ is the velocity of a sound wave with polarization γ (γ = L, T_1, T_2), and δ_{ij} is a Kronecker symbol.

The values of the elastic constants were calculated and averaged for both the experimentally studied cases of the propagation of sound waves relative to the principal axes of the crystal. The following values were obtained for the elastic constants:

$$c_{11} = 382 \cdot 10^{10}\ \text{dyn/cm}^2,\ c_{44} = 60 \cdot 10^{10}\ \text{dyn/cm}^2$$
$$c_{12} = 108 \cdot 10^{10}\ \text{dyn/cm}^2.$$

From the experimentally measured relative intensities of the Mandel'shtam–Brillouin components, using the dependence of the intensities of the components on the photoelastic constants,[2] the relative values of certain photoelastic constants can be determined. From our experimental data we found that $p_{11} = -1.9\ p_{12}$, $p_{44} = 0.3\ p_{12}$.

However, these values should be considered as preliminary, since the intensities of the transverse components were determined with a large error (particularly in case 1), owing to the strong parasitic scattering at an empirical frequency.

Thus, analysis of the molecular scattering of light in a single crystal of $HfO_2-Y_2O_3$ solid solution shows that one of the interesting peculiarities of this crystal is the comparatively pronounced dependence of the nature of the spectrum on the direction of the sound wave at which light scattering occurs. The orientation of the crystal at which longitudinal waves make virtually no contribution to the scattered light has been found.

The absence of longitudinal Mandel'stam–Brillouin components in the spectrum of scattered light was observed previously for trigonal crystals of sapphire and lithium niobate.[4,5] In the present investigation it has been observed for a single crystal of the cubic solid solution $HfO_2-Y_2O_3$. It must be supposed that this peculiarity in the scattering of light in both trigonal and cubic crystals is due to the shear and compressive deformation created by the sound wave mutually compensating the resulting change in dielectric constant for VV spectra for longitudinal waves.[6]

---

1) We shall indicate the scattering plane by kk', where k and k' are the wave vectors of the incident and scattered light.

---

[1] F. I. Fedorov, The Theory of Elastic Waves in Crystals [in Russian], Fizmatgiz, Moscow (1965).

[2] I. L. Fabelinskii, The Molecular Scattering of Light [in Russian], Fizmatgiz, Moscow (1965).

[3] V. F. Kitaeva and I. L. Chistyi, ZhETP Pis. Red., 13, 611 (1971).

[4] D. F. Kiselev, T. M. Glushkova, and M. M. Firsova, Fiz. Tverd. Tela, 11, 3592 (1969). [Sov. Phys.–Solid State, 12, 101 (1970)]

[5] Z. M. Khashkhozhev, V. V. Lemanov, and R. V. Pisarev, Fiz. Tverd. Tela, 12, 128 (1970) [Sov. Phys.–Solid State 12, 101 (1970)]; Izv. Akad. Nauk SSSR, Ser. Fiz., 35, 987 (1971).

[6] I. L. Chistyi, V. F. Kitseva, N. N. Sobolev, and V. P. Bakhar, Zh. Eksp. Teor. Fiz., 63, 1477 (1972) [Sov. Phys.–JETP, 36, 783 (1973)].

Crystal optics of alkaline-earth metavanadates

M. P. Glazyrin, A. A. Ivakin, and V. A. Gurevich

Chemistry Institute, Urals Scientific Center,
Academy of Sciences of the USSR

(Submitted May 10, 1972; resubmitted September 18, 1972)
Kristallografiya, 18, 1088-1089 (September-October 1973)

The metavanadates $Mg(VO_3)_2 \cdot 6H_2O$, $Ca(VO_3)_2 \cdot 4H_2O$, $Sr(VO_3)_2 \cdot 4H_2O$ and $Ba(VO_3)_2 \cdot H_2O$ have been examined with a MIN-8 microscope and with a differential thermal analysis (dta) apparatus; the refractive indices were measured in standard immersion liquids, the sets being IZh-1 and VIZh. The thermal analyses were made with a heating rate of 10 deg/min. The compounds were made by adding 0.1 M solutions of the alkaline-earth chlorides to 0.1 M solutions of sodium metavanadate. The mixtures were kept at room temperature for 1-2 months. The crystalline products were dried and checked for purity under the microscope.

$Mg(VO_3)_2 \cdot 6H_2O$. The water-clear crystals were short prisms and generally of prismatic habit; a supersaturated solution often gives rise to needles instead. The material is colorless under the microscope, and the water of crystallizaton is lost on heating in two stages. The first three molecules are lost in the range 50-160°C, and the others in the range 300-380°C.

$Ca(VO_3)_2 \cdot 4H_2O$. The crystallographic and optical characteristics have been described in detail[1,2] for this compound; our optical constants were almost exactly the same as those given in the literature. The water of crystallization is lost in three stages on heating: one molecule of H_2O in the range 20-100°C, 0.5 molecule in the range 100-130°C, and 2.5 molecules at 130-170°C. These results agree with published evidence.[3]

$Sr(VO_3)_2 \cdot 4H_2O$. The crystals are prismatic or acicular, and often form stellate intergrowths (Fig. 1). Under the micrsocope they are colorless, but macroscopically they are pale yellow. The crystallographic constants have been given previously.[4] The water of crystallization is lost in two stages on heating; three molecules in the range 80-200°C and one at 280-320°C, which agrees well with published values.[5]

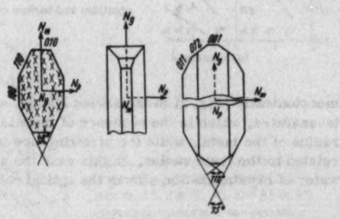

Fig. 1. Optical orientation and general appearance of $Sr(VO_3)_2 \cdot 4H_2O$ crystals.

$Ba(VO_3)_2 \cdot H_2O$. A white crystalline powder, which under the microscope shows colorless fragments of prismatic crystals. See refs. 5 and 6 for the crystallographic characteristics, thermal analysis, and method of synthesis.

Table 1 gives the basic optical characteristics of these vanadates.

The evidence shows that all these compounds apart from $Ca(VO_3)_2 \cdot 4H_2O$ are orthorhombic; one assumes that $Mg(VO_3)_2 \cdot 6H_2O$, $Sr(VO_3)_2 \cdot 4H_2O$ and $Ba(VO_3)_2 \cdot H_2O$ are isostructural. Increased water of crystallization in the compound, e.g., sodium orthovanadate,[7] results in a reduction in the refractive index. On the other hand, increase in the ion radius reduces the refractive index and birefringence in a series of compounds of the same type, e.g., the alkali metavanadates.[8] The amount of water of crystallization falls, while the refractive indices increase

TABLE 1. Principal Optical Constants of Alkaline-Earth Metavanadates

Formula	Simple forms	Cleavage	Optical orientation, elongation (+), (-)	Refractive indices	2V	System
$Mg(VO_3)_2 \cdot 6H_2O$	Rhombic prisms: {011}, 58—60°, {100} Pinacoids: {100} , {010}	(110), moderate (001), appreciable	$N_g \parallel c$ $N_m \parallel b$ $N_p \parallel a$	$N_g = 1.718$ $N_m = 1.670$ $N_p = 1.640$	+79°	Orthorhombic
$Ca(VO_3)_2 \cdot 4H_2O$	—	—	$CN_g = 2-3°$ (+)	$N_g = 1.840$ $N_m = 1.780$ $N_p = 1.710$	—82°	Triclinic
$Sr(VO_3)_2 \cdot 4H_2O$	Rhombic prisms : {110}, 48° {011}, 75° {012}, 68° Pinacoids: {100}, {010} {001}	(110), perfect	$N_g \parallel c$ $N_m \parallel b$ $N_p \parallel a$ (+)	$N_g = 1.843$ $N_m = 1.766$ $N_p = 1.720$	+79°	Orthorhombic
$Ba(VO_3)_2 \cdot H_2O$	Pinacoids: {100}, {010} {001}	(001), moderate	$N_g \parallel c$ $N_m \parallel b$ $N_p \parallel a$ (+)	$N_g = 1.874$ $N_m = 1.786$ $N_p = 1.734$	+79°	Orthorhombic

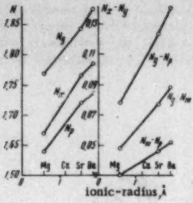

Fig. 2. Effects of cation radius on the optical constants for magnesium, strontium and barium metavanadates.

monotonically (Fig. 2) in the series Mg, Sr, and Ba metavanadates, which is the sequence of increasing ionic radius of the metal, while the birefringence is linearly related to the ionic radius. In this case the amount of water of crystallization affects the optical constants more than does the ionic radius. The optical constants of $Ca(VO_3)_2 \cdot 4H_2O$ do not fit into this relationship, because this compound is triclinic.

---

[1] H. Foshag, Proc. US. Nat. Museum, LXXII, Art, 2, 9 (1927).

[2] E. S. Dana, System of Mineralogy, Vol. 2, part 2, Wiley, New York (1951).

[3] T. Dupuis and V. Lorenselli, J. Thermal Analysis, 1, 15 (1969).

[4] P. Sedlacek and K. Dornberger Schiff, Acta Crystallogr., 18, 407 (1965).

[5] L. Zurkova, J. Corba, and V. Sucha, Chem. Zvesti, 22, 73 (1968).

[6] L. Zurkova, L. Ulicka, and M. Dillinger, Collect. Czech. Chem. Commun., 34, 3835 (1969).

[7] V. Z. Tarasenko, V. D. Ponomareva, A. L. Zazubina, and B. A. Bochkareva, Trudy Inst. Met. Obogashch. AN KazSSR, Khim. Tekhnol. Vanadiya, 27, 58, (1968).

[8] A. A. Fotiev and A. A. Ivakin, Trudy Inst. Khim., Ural. Fil. AN SSSR, "Formation conditions for vanadium compounds of alkali metals", 19, 78 (1970).

Temperature dependence of the elastooptical constants p_{11} and p_{12} of NaCl, KCl, KBr, and KI crystals

A. V. Pakhnev, S. S. Gorbach, and M. P. Shaskol'skaya
Moscow Institute for Steel and Alloys
(Submitted March 16, 1972; resubmitted October 6, 1972)
Kristallografiya, 18, 1090-1091 (September-October 1973)

The theory developed in refs. 1 and 2 allows the calculation of the elastooptical constants p_{11} and p_{12} if the values of the piezooptical constants $(\pi_{11} - \pi_{12})$, which can be measured by the double refraction arising in the crystal under the action of mechanical stresses, are known. For a linear stressed state, the relationship between the stress and double refraction is written in the following manner for stresses which do not exceed the elastic limit:

$$\Delta = C_\sigma^\Delta \sigma, \tag{1}$$

where C_σ^Δ is the optical coefficient of stresses or the photoelastic constant. If double refraction is measured in the (100) plane and the direction of loading coincides with the [001] direction, then the value of C_σ^Δ is related to $(\pi_{11} - \pi_{12})$ by

$$C_{\sigma[001]}^{\Delta[100]} = -{}^1/_2 n_0^3 (\pi_{11} - \pi_{12}), \tag{2}$$

where n_0 is the index of the unstressed crystal. By use of Eq. (2), from the measured function $C_\sigma^\Delta \begin{bmatrix}100\\001\end{bmatrix} = f(T)$ and taking the change of n_0 with temperature into account, the values of $(\pi_{11} - \pi_{12})$ are determined.

Experimentally, it is considerably more complex to measure the quantities p_{11} and p_{12} than $(\pi_{11} - \pi_{12})$; therefore, the existence of a theory which allows the calculation of p_{11} and p_{12} and which allows one to obtain sufficiently good agreement with empirically determined values simplifies the estimation of the degree of change of polarizabilities of the ions with temperature and deformation.[1,2] The derivative of polarizability with respect to deformation allows a judgment as to the portion of ionic character in the bond.[3]

We have measured the piezooptical constants $(\pi_{11} - \pi_{12})$ for KBr and KI crystals in the temperature interval 77-573°K as functions of temperature. Specimens were loaded by the compression method with compensation for birefringence by the Senarmon method for $\lambda = 546$ nm. The method of determination of the constants is described in ref. 4. The precision of measurement amounted to $\pm 0.2 \cdot 10^{-7}$ cm³/kg. The results of measurement of the temperature function are shown in Fig. 1. The values from ref. 5 are plotted here.

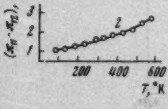

Fig. 1. Piezooptical constants $(\pi_{11} - \pi_{12})$ of KBr (1) and KI (2) crystals as functions of temperature. ○) Our values; △) values obtained in ref. 5.

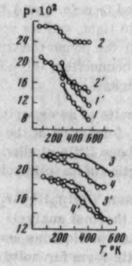

Fig. 2. Elastrooptical constants p_{11} (1-4) and p_{12} (1'-4') for NaCl (1, 1'), KCl (2, 2'), KBr (3, 3'), and KI (4, 4') crystals as functions of temperature.

The elastooptical constants p_{11} and p_{12} were calculated at each temperature by the method suggested in ref. 5. Results of the present study were used during the calculation, and the temperature dependence of the constants $(\pi_{11} - \pi_{12})$ of NaCl and KCl crystals obtained in ref. 4, as well as thermooptical and thermoelastic values taken from refs. 6-14. The temperature functions obtained are shown in Fig. 2.

---

[1] K. G. Bansigir and K. S. Iyengar, Acta Crystallogr., 14, 670 (1961).
[2] K. G. Bansigir and K. S. Iyengar, Acta Crystallogr., 14, 727 (1961).
[3] K. G. Bansigir, Nature, 216, 256 (1967).
[4] S. S. Gorbach, L. A. Deptsova, G. F. Dobrzhanskii, V. Yu. Markovskii, and M. P. Shaskol'skaya, Kristallografiya, 14, 729 (1969) [Sov. Phys.–Crystallogr., 14, 627 (1970)].
[5] L. V. Smushkov, M. S. Kaplan, and V. I. Sumin, Fiz. Tverd. Tela, 12, 1937 (1970) [Sov. Phys.–Solid State, 12, 1540 (1971)].
[6] S. Bhagavantam and Y. Krishna Murty, Proc. Indian Acad. Sci., 25, 481 (1947).
[7] G. N. Ramachandran and I. Radhakrishnan, Phil. Mag., 43, 317 (1952).
[8] A. V. Stepanov and I. M. Éidus, Zh. Eksp. Teor. Fiz., 29, 669 (1955) [Sov. Phys.–JETP, 2, 377 (1956)].
[9] M. H. Norwood and C. V. Briscol, Phys. Rev., 112, 45 (1958).
[10] S. P. Nikanorov and A. V. Stepanov, Fiz. Tverd. Tela, 4, 2576 (1962) [Sov. Phys.–Solid State, 4, 1889 (1963)].
[11] J. K. Galt, Phys. Rev., 73, 1460 (1948).
[12] S. P. Nikanorov and A. V. Stepanov, Zh. Eksp. Teor. Fiz., 37, 1814 (1959).
[13] A. V. Sharko and A. A. Botaki, Fiz. Tverd. Tela, 12, 2702 (1970) [Sov. Phys.–Solid State, 12, 2171 (1971)].
[14] P. J. Reddy and J. Bhimasenachar, Acta Crystallogr., 17, 28 (1964).

Phase diagram of the system $(HgI_2)_x(HgBr_2)_{1-x}$ and some optical properties of its single crystals

I. D. Turyanitsa and V. V. Khiminets
Uzhgorod University

(Submitted March 29, 1972; resubmitted June 12, 1973)
Kristallografiya, 18, 1092-1094 (September-October 1973)

Mercuric iodide, previously studied in refs. 1 and 2, is very sensitive to x rays and visible light, and its optical properties are very nonlinear near the phase transition temperature $D_{4h}^{15}-C_{2v}^{12}$. In this connection, the solid solutions based on HgI_2 are of interest.

In this article we give the results of an experimental investigation of the conditions for formation of the system $(HgI_2)_x(HgBr_2)_{1-x}$, which has been little studied hitherto,[3] together with some properties of its solid solutions.

The phase diagram of the system $(HgI_2)_x(HgBr_2)_{1-x}$ was constructed from differential thermal analysis data and is shown in Fig. 1. We see that the liquidus and solidus curves have the characteristic form for solid solutions with a point of equal concentration at the minimum. The effect of the polymorphic transition observed for HgI_2 at 127°C is also clearly manifested at other compositions ($1 > x \geq 0.9$) in the system, but its character is modified. As the mercuric bromide concentration in the solution increases, the phase transition temperature falls, and owing to the formation of α and β solid solutions the transition itself becomes less sharp, so that there is a marked region of two-phase equilibrium.

The formation of a continuous series of solid solutions $(\beta\text{-}HgI_2)_x(HgBr_2)_{1-x}$ is also confirmed by the results of x-ray structural analysis. Figure 2 shows graphs of the crystal lattice parameters of the solid solutions vs composition, and these obey Vegard's law. Curves a' and c' on the same figure plot the lattice parameters of the system in the tetragonal modification.

Using differential thermal analysis data, we found the conditions for obtaining single crystals of the solid solutions from the gas phase. We used a Pyrex capsule evacuated to 10^{-3} mm Hg, along which we established a gradient of 2 deg/cm; the charge temperature was 10-15°C below the melting point.

To investigate optical absorption we selected homogeneous single-crystal plates 0.3-0.5 cm² in area and with thicknesses from 10 μ to tenths of a millimeter.

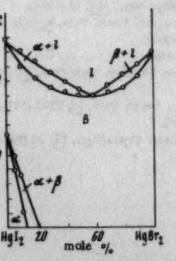

Fig. 1. Phase diagram of system $(HgI_2)_x(HgBr_2)_{1-x}$.

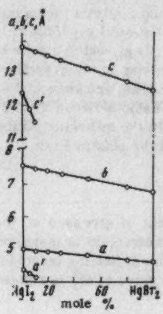

Fig. 2. Lattice parameters vs solution concentration in the system $(HgI_2)_x \cdot (HgBr_2)_{1-x}$. a, b, c) orthorhombic phase. a', c') tetragonal phase.

The absorption coefficients were determined by measuring the transmissions of two crystals of different thicknesses. With the thickness ratios used by us, the relative error of determination of the absorption coefficient[4] did not exceed 10%.

Using the absorption spectrum data, we plotted the forbidden-band width vs composition in the system $(HgI_2)_x \cdot (HgBr_2)_{1-x}$: The curve is shown in Fig. 3. The forbidden-band width increases with the concentration of mercuric bromide in the solid solution. The change in the slope of the concentration dependence of the forbidden-band width in this system is due to the fact that at the measurement temperatures (20°C) the compositions with $x < 0.8$ and $x > 0.8$ belong to different polymorphic modifications with symmetries D_{4h}^{15} and C_{2v}^{12} respectively. In compositions with $x > 0.8$, as in pure mercuric iodide, the phase transition leads to an increase in the forbidden-band width; this is confirmed by its temperature dependence (Fig. 4). Whereas dEg/dT for single crystals of mercuric bromide is linear in the temperature range under investigation, for compositions with $1 > x > 0.8$ there is a sudden change in Eg on the temperature dependence of the forbidden-band width at the phase transition point (type A transition,

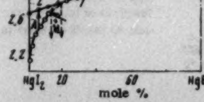

Fig. 3. Forbidden-band width vs composition in the system $(HgI_2)_x(HgBr_2)_{1-x}$. 1) At room temperature in the tetragonal ($x < 0.8$) and orthorhombic ($x > 0.8$) modifications; 2) in the orthorhombic modification with allowance for dEg/dT; 3) extrapolated graph for tetragonal modification.

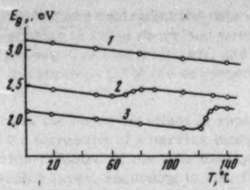

Fig. 4. Temperature dependence of forbidden-band width of single crystals at temperatures between 20 and 140°C. 1) $HgBr_2$; 2) $(HgI_2)_{0.95}(HgBr_2)_{0.05}$; 3) HgI_2.

Fig. 3). This becomes less marked as the phase transition becomes less sharp. These changes in the forbidden-band width and the fall in the phase transition temperature with varying composition are responsible for the nonlinearity of the graph of forbidden-band width vs concentration. Thus the actual concentration dependence of the forbidden-band width of the continuous series of solid solutions $(\beta\text{-}HgI_2)_x(HgBr_2)_{1-x}$ in the region $1 > x > 0.8$ with allowance for the variation of dEg/dT is given by curve 2 in Fig. 3.

The observed temperature dependence of the forbidden-band width in the phase transition region agrees with the theoretical conclusions of Fridkin.[5] It was of interest to investigate the variation of dE_g/dT for compositions with $x < 0.8$, for which the phase transition temperature and the phase transition $D_{4h}^{15}-C_{2v}^{12}$, according to Fig. 3, should lead to inversion of E_g (type B transition), i.e., to a decrease in the forbidden-band width. Owing to the very marked loss of sharpness of the phase transition at these concentrations of the solid solutions, our experiments did not reveal this effect.

On the linear sections of the graphs, the temperature coefficients of the forbidden-band widths of single crystals of HgI_2 and $HgBr_2$ and their solid solutions are of the order of 10^{-3} eV/deg ($HgBr_2$, $2.2 \cdot 10^{-3}$; HgI_2, $3 \cdot 10^{-3}$; $(HgI_2)_{0.95}(HgBr)_{0.05}$, $3.2 \cdot 10^{-3}$ eV/deg). Since $(\partial Eg/dP)_T$ for HgI_2 is[6] $1.6 \cdot 10^{-6}$ eV/atm, we can conclude that the temperature dependence of the forbidden-band width for solid solutions $(HgI_2)x(HgBr_2)_{1-x}$ is mainly due to electron–phonon interactions.

---

[1] D. V. Chepur, Zh. Tekh. Fiz., 25, 2421 (1955).

[2] R. H. Bube, Phys. Rev., 106, 703 (1957).

[3] V. Luchitskii, Zap. Kievsk. O-va Est., 20, 121 (1906).

[4] I. D. Turyanitsa and D. V. Chepur, Ukr. Fiz. Zh., 12, 500 (1967).

[5] V. M. Fridkin, ZhETF Pis. Red., 3, 252 (1966) [JETP Lett., 3, 161 (1966)].

[6] K. Gulyamov, N. A. Tikhomirova, I. D. Turyanitsa, and V. M. Fridkin, Fiz. Tverd. Tela, 7, 2723 (1965) [Sov. Phys.–Solid State, 7, 2201 (1966)].

Surface layer of barium titanate crystals

V. P. Dudkevich, I. N. Zakharchenko, V. S. Bondarenko, R. V. Kolesova, A. G. Stoinov, and E. G. Fesenko
Rostov State University

(Submitted May 22, 1972; resubmitted September 18, 1972)
Kristallografiya, 18, 1095-1097 (September-October 1973)

Hypotheses regarding the peculiar surface condition of barium titanate crystals have been published on various occasions for interpretation of several anomalies.[1-7] In contrast, differences have not been observed between the surface structure and the internal regions of the crystals.[8-10] It is thus possible that, during the electrical measurements which define the surface layer, an electric field acted on the crystal which did not exist during the structural studies. In this connection, it was of interest to study the structural changes in the barium titanate layers at the electrodes during application of a direct field.

The crystals were grown by Remeika's method.[11] The samples were cut in the form of disks (D = 6 mm, d = 0.1-0.5 mm). Metal electrodes (Al, Pt, Ag), were applied by vaporization in vacuum. The liquid electrodes consisted of cigarette paper moistened with a saturated LiCl solution. The crystals in some case were etched in hot (140°C) phosphoric acid prior to application of the electrodes. The studies were performed on a URS-50IM diffractometer (Fe Kα, Cu Kα) with a planar quartz monochromator.

With the cathode as the reflecting face, the shape of the $(00l)$ reflections did not depend on field strength and duration. With the field in the opposite direction, the $(00l)$ reflections were distorted: In addition to the original "fundamental" diffraction maximum, a "lateral" maximum formed on the side of lower θ angles. Changes in shape of the $(00l)$ reflections continued for 30-40 min after the field was turned on (see Fig. 1). When the field was shut off, the process occurred in reverse order. When a field of the opposite direction was applied to a crystal in the "saturated" state (Fig. 1d), all changes faded away, practically instantly. It should be noted that irradiation time did not affect the experimental result. The overall character of the above phenomenon was practically independent of electrode material. There were no observed differences in the behavior of the etched and unetched samples. The effect was also apparent at temperatures above the Curie temperature.

With an increase of the average field E, the intensity I of the "fundamental" reflection decreased, and that of the "lateral" reflection I' increased with a shift to the region of lower θ angles.

Investigations conducted using various reflection orders and radiations (both factors affect the layer thickness contributing to the diffraction maximum) permit the observed effect to be interpreted as the inhomogeneous deformation (increase of the c and decrease of the a parameter) of a thin surface layer, caused by a nonlinear distribution potential. The effective layer thickness may be found from the equation

$$I'/(I'+I) = 1 - \exp(-2\mu h/\sin\theta), \tag{1}$$

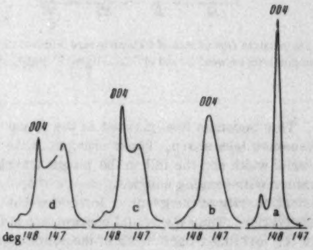

Fig. 1. Time-dependent changes in shape of the 004 diffraction profile (Fe Kα) of a barium titanate crystal. Thickness: d = 0.047, silvered electrodes; E = 19 KV/cm. a) T = 0; b) 4; c) 17; d) 60 min.

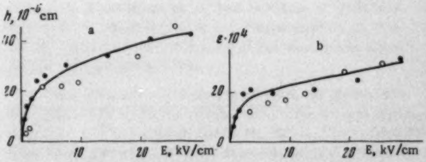

Fig. 2. Dependence of surface layer thickness (a) and its average deformation (b) on electric field strength. ●) crystal of thickness d = 0.042 cm, platinum electrodes. ○) crystal of thickness d = 0.047 cm, silvered electrodes.

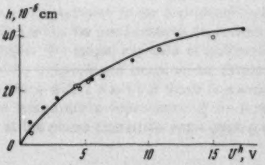

Fig. 3. Dependence of surface layer thickness h on electric field strength incident on the layer U^h.

where h is the layer thickness. With increase of E, there is an increase in the surface layer thickness (Fig. 2a) and in the average deformation of the layer ε_{33} (Fig. 2b) (determined by the angular distance between the "fundamental" and "lateral" maxima). The field at the surface layer E may be calculated from the relationship: $E^h = \varepsilon_{33}/d_{33}$, where d_{33} is the longitudinal piezomodulus. These values depend on the average applied field.

Vol
July
June

The results obtained contradict the data of ref. 12, where effects similar to those described were observed at the side of the negative electrode (Al), and where the surface layer thickness (~ 1.5 μ) did not depend on the applied field.

The nature of the observed effect is apparently associated with the formation of a barrier contact which adjoins a carrier-depleted semiconductor layer. The thickness of such a layer, according to ref. 13, is determined by the equation

$$2\pi enh^2 / K = U_c \pm U_b, \tag{2}$$

where U_b is the potential difference at the contact; U_c is the fraction of the applied strength incident on the barrier; K is the dielectric permeability in the field direction; e is the charge of an electron; and n is the total density of charges in the semiconductor. The asymmetry of the observed effect agrees well with equation (2). Besides this, the experimentally found layer thickness dependence on applied field strength h (U^h) (Fig. 3) approximates a parabola, as follows from Eq. (2).

The existence of a strong field at the surface layer (~ 10^5-10^6 V/cm), permits reconsideration of the lack of correspondence between the theoretical predictions for the coercive field in barium titanate and the experimental data.[14,15] According to theory,[14] for switching by lateral 180° domain-wall motion, fields of the order of 10^5 V/cm are needed. The theory for switching by nuclei formation due to thermal fluctuations[15] gives, at an external field of ~ 500 V/cm, a substantial value for the activation energy of a critical nucleus: ~ 10^8 kT. Besides this, our data show that the field at the surface layer for an average field of 700 V/cm is ~ $1.2 \cdot 10^5$ V/cm. At the same time, the formation energy of a critical nucleus, computed according to ref. 15, decreases to 100 kT.

Study of the surface layer problem is being continued.

---

[1] P. Glogar, V. Janovec, Czech. J. Phys., 13, 261 (1963).

[2] W. J. Merz, J. Appl. Phys., 27, 938 (1956).

[3] S. Triebwasser, J. Phys. Rev., 118, 100 (1960).

[4] V. G. Bhide, R. T. Condhalekar, and S. N. Shringi, J. Appl. Phys., 36, 3825 (1965).

[5] A. G. Chynoweth, J. Phys. Rev., 102, 705 (1956).

[6] V. Janovec, B. Březina, and A. Glanc, Czech. J. Phys., 10, 690 (1962).

[7] H. Toyoda and M. Itakura, J. Phys. Soc. Japan, 17, 924 (1962).

[8] M. E. Drougard and R. C. Landauer, J. Appl. Phys., 30, 1663 (1953).

[9] V. P. Dudkevich, E. G. Fesenko, and V. G. Gavrilyachenko, Elektron. Tekh., Ser. 14, 130 (1970).

[10] M. Tanaka and G. Honjo, J. Phys. Soc. Japan, 19, 954 (1964).

[11] O. I. Prokopalo, V. G. Gavrilyachenko, R. I. Spinko, and V. S. Bondarenko, in: Barium Titanate [in Russian], Izd. Rostovskii Gos Univ., Rostov (1971).

[12] H. Motegi and S. Hoshino, J. Phys. Soc. Japan, 29, 524 (1970).

[13] A. Royce, Fundamentals of Photoconductivity Theory [Russian translation], Izd. Mir Moscow (1966).

[14] W. Kinase and H. Takahasi, J. Phys. Soc. Japan, 12, 464 (1957).

[15] R. Landauer, J. Appl. Phys., 28, 227 (1957).

Dislocation structure of $KMgF_3$ crystals

S. N. Bodrug
M. V. Lomonosov Moscow State University
Tiraspol State Pedagogic Institute
(Submitted September 25, 1972)
Kristallografiya, 18, 1098-1100 (September-October 1973)

$KMgF_3$ crystals provide a convenient matrix for the introduction of impurities, and exhibit characteristic optical properties.[1-3] Crystals of $KMgF_3$ of different quality and with different dimensions are grown by spontaneous crystallization from solution in a melt,[4,5] or by Stockbarger's method.[6] We grew crystals by the Czochralski method. The crystals were pulled from the melt in an inert atmosphere on seed crystals oriented along ⟨100⟩. The rate of rotation of the seed was 20-60 rpm, and the rate of pulling 6-8 mm/h. The diameter of the crystals obtained was 5-15 mm, and their length 10-40 mm. The pure crystals are colorless, transparent, and insoluble in water, and exhibit good cleavage along the {001} planes.

Etching agents for revealing dislocations in $KMgF_3$ crystals. We etched crystals freshly broken along the (001) plane, perpendicular to the direction of pulling. Since etching agents for revealing the dislocations in $KMgF_3$ crystals were not known, we tested the action of hydrofluoric, hydrochloric, nitric, and sulfuric acids. After etching, the specimens were washed with distilled water, dried with filter paper, and studied by means of an MIM-7 metallurgical microscope and an MII-4 interferometer.

The action of these acids on the crystal surface produces etch pits of definite shape. The nature of the effect depends on the duration of etching and the temperature and composition of the etching agent. The best etching agents are concentrated hydrochloric acid (HCl) and dilute sulfuric acid (1 part H_2SO_4 : 3 parts H_2O). The etch figures in these cases have the form of four-sided square pyramids with sides parallel to the ⟨100⟩ directions (Fig. 1, a and b). This shape of etch pit is determined by the fact that the rate of movement of the elementary dissolution steps is smallest in these directions. The shape of the etch pits is the same for pure crystals and for crystals containing impurity.

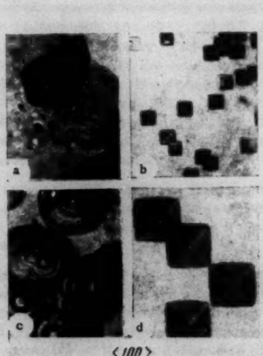

Fig. 1. Etch figures at dislocations on the <100> face of $KMgF_3$ crystals. a) Hydrochloric acid: 100°C, duration of etching 3 min, × 70; b) dilute sulfuric acid, 100°C, 25 sec, × 70; c) nitric acid, 100°C, 30 sec, × 120; d) double etching, first in dilute sulfuric acid (100°C, 30 sec) and then in hydrofluoric acid (100°C, 4 min), × 120.

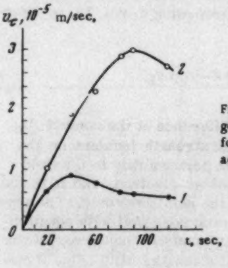

Fig. 2. Time dependence of the tangential rate of selective etching v_T for $KMgF_3$ crystals. 1) Hydrochloric acid; 2) dilute sulfuric acid.

Study of the kinetics of etching showed that the tangential rate of etching v_T is not constant. The change in the rate v_T with time is the same for different etching agents; the magnitude of v_T, however, is much greater for dilute sulfuric acid than for hydrochloric acid (Fig. 2). The decrease in the rate of etching after a long time interval is apparently due to the production of impurity layers on the surface of the crystal.

Repeated successive etching of the same surface with the same etching agents showed that new pits are not formed. It was also noted that not all the pits have the same dimensions, and that the pits with largest dimensions gradually become flat-bottomed. Corresponding analysis showed that pits with pointed ends are formed at the points of emergence of dislocations, and that flat-bottomed pits are formed at microdefects on the fracture surface. On prolonged or repeated etching, the pits on the dislocations remain sharp-ended, and their dimensions increase (Fig. 1, a and d).

Analysis of the distribution of dislocations on the (001) fracture surface showed that the density of dislocations is greater at the edge, at the points of contact between the crystal and the knife blade during cleavage. In the central region of the crystal, the density of dislocations does not exceed 10^4 cm^{-2}.

Influence of annealing and irradiation. Some of the prepared specimens were annealed in a platinum crucible. The annealing conditions were as follows: heating to 950°C over a period of 3 h, heating at this temperature for 3 h, rate of decrease in temperature 10 deg/h. The specimens were annealed in air. It was found that at 950°C the surface of the crystals is covered with an oxide

Fig. 3. Etched $KMgF_3$ crystal after irradiation with x rays. ×70.

film. Only those surfaces which are in contact with the crucible remain clean. Experiments on the etching of these specimens showed that in order to reveal the dislocations, the duration of etching had to be increased by a factor of 3–4. This is possibly due to the formation of a thin film of the compound MgO on the surface of the crystals during annealing. Observation showed that the number of dislocations does not decrease after annealing in this way, that they are not displaced from their previous positions, and that new dislocations are not produced. This may be due to the low mobility of the dislocations. Thus the degree of perfection of $KMgF_3$ crystals cannot be increased by high-temperature annealing.

A number of etched specimens were irradiated with x rays. The irradiation was continued until the crystal acquired a pale-orange color. It was found that irradiation leads to breakdown of the surface of the crystal, so that the distinct shape of the etch pits is lost (Fig. 3). A similar phenomenon was observed after irradiation with protons. Irradiation apparently produces radiation damage in the crystals, analogous to that observed for halide crystals.

Mechanical properties of $KMgF_3$ crystals. The microhardness of the $KMgF_3$ crystals was measured by the indentation method on a PMT-3 instrument. The indentations were produced for two orientations of the diagonal of the indentor: parallel to ⟨100⟩ and parallel to ⟨110⟩; the indentations obtained had convex and concave sides respectively, indicating that the mechanical properties of the $KMgF_3$ crystals are strongly anisotropic. Measurement of the microhardness with different loads showed that for all loads, the microhardness is greater for orientation of the diagonal of the indentor in the ⟨100⟩ direction than for orientation in the ⟨110⟩ direction. Thus, for example, for a load of 100 g the microhardness in the ⟨100⟩ direction is 306 ± 14 kg/mm², and that in the ⟨110⟩ direction is 255 ± 14 kg/mm². Study of the relief of the surface around the indentations by means of an MII-4 interferometer showed that the curvature of the sides of the indentations is due to lowering or raising of the surface, taking place when the indentor is applied. According to Boyarskaya and co-workers,[7] it is for this reason that the microhardness depends on the orientation of the indentations.

Fig. 4. Rosette of etch pits around the imprint (P = 100 g) of the indentor on the {001} plane of $KMgF_3$ crystals. ×120.

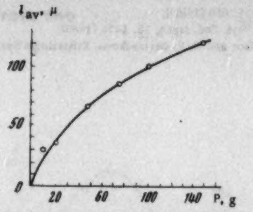

Fig. 5. Dependence of the average length l_{av} of the rays of the rosette on the magnitude of the load on the indentor P.

The surfaces of crystals with indentations with different orientations were etched. It was found that around the indentations there are formed dislocation rosettes consisting of four rays; the form of these rosettes is independent of the orientation of the indentations. The rays of the rosette are oriented along the ⟨110⟩ directions (Fig. 4). Their length is greater, the greater the magnitude of the load on the indentor (Fig. 5). It may therefore be concluded that $KMgF_3$ crystals at room temperature have a low plasticity.

When a given rosette was etched several times, significant changes in the positions of the pits in the long rays of the rosette were not observed; only an increase in size was observed. This suggests that the dislocations corresponding to the long rays of the rosette lie in the {110} planes. To determine more accurately the crystallographic orientation of the glide planes, scratches were applied to the (001) surface by means of a diamond indentor. Etching of the scratches applied along [110] and [100] showed that the ends of the dislocations on the (001) surface move in the [110] or [$\bar{1}$10] directions. On the other hand, etching of the same scratch (or indentation) on the (001) plane and on the adjacent lateral (100) surface showed that the glide lines on the (001) face are directed along [110] and [$\bar{1}$10], and those on the (100) face are directed along [0$\bar{1}\bar{1}$] and [01$\bar{1}$]. From this it may be concluded that the {110} planes in $KMgF_3$ crystals are glide planes.

The author thanks A. A. Predvoditelev for discussion of the results and valuable comments.

---

[1] S. N. Bodrug and V. A. Timoshenkov, Zh. Prikl. Spektrosk., 12, 117 (1970).

[2] S. N. Bodrug, E. G. Valyashko, V. N. Mednikova, R. K. Sviridova, and D. T. Sviridov, Opt. Spektrosk., 34, 312 (1973).

[3] L. E. Johnson, H. J. Guggenheim, and R. A. Thomas, Phys. Rev., 149, 179 (1966).

[4] A. G. Tutov and P. P. Syrnikov, Kristallografiya, 12, 713 (1967) [Sov. Phys.–

Crystallogr., 12, 619 (1968)].

[5] S. Ogawa, J. Phys. Soc. Japan, 15, 1475 (1960).

[6] B. V. Beznosikov and N. V. Beznosikova, Kristallografiya, 13, 1881 (1968) [Sov. Phys.–Crystallogr., 13, 158 (1968)].

[7] Yu. S. Boyarskaya, I. I. Melent'ev, and D. Z. Grabko, Izv. Vyssh. Ucheb. Zaved. Fizika, No. 2, 84 (1971).

Determination of the degree of ordering in liquid crystals from the dichroism of dissolved dyes

V. G. Rumyantsev, L. M. Blinov, and V. A. Kizel'

(Submitted June 27, 1972; resubmitted October 12, 1972)
Kristallografiya, 18, 1101-1103 (September-October 1973)

The study of the optical spectra of dye molecules with anisotropic light absorption in oriented liquid-crystal matrices can give information on the degree of ordering of a liquid crystal, reported by Tsvetkov[1] as

$$S_{lc} = (3\overline{\cos^2\theta_{lc}} - 1)/2; \tag{1}$$

where θ_{lc} is the angle between a given axis of the liquid crystal molecule and the direction of its optic axis.

In addition to the x-ray method used in ref. 2, there are at present two optical methods of determining S_{lc}. One of these[3] requires, in addition to the measurements of the density and refractive index of the material, information on the crystallographic structure and the density and refractive indices of solid single crystals of the same material. The other method is based on the measurements of the dichroism of the absorption vibrational hands of the liquid crystals as in ref. 4 and requires laborious measurements in the spectral region beyond the ir. It is possible to suggest a simpler method for determining S_{lc} using the tendency of liquid-crystal matrices to orient dye molecules which are introduced into the matrix.[5]

The purpose of the present paper is to show that under certain conditions the degree of ordering of the linear dye molecules S_d in a liquid-crystal matrix is equal, to a high degree of accuracy, to the degree of ordering of the liquid crystal itself. By using the results of the measurements of the dye dichroism it is possible to determine S_{lc}.

By analogy with Eq. (1) we introduce the degree of ordering in dye molecules

$$S_d = (3\overline{\cos^2\theta_d} - 1)/2, \tag{2}$$

where θ_d is the angle between the optic axis of the liquid crystal and the direction of the long axis of the dye molecules. In the case of linear molecules of many dyes (particularly azo-, azomethine, and stilbene dyes) the direction of the dipole moment of the optical transition μ is the same as that of the long axis of the molecule.[6] In this case we have

$$\overline{\cos^2\theta_d} = \frac{\int \cos^2\theta_d \, d\Omega}{\int d\Omega} = \frac{\int \mu_\parallel^2 \, d\Omega}{\int \mu^2 \, d\Omega} = \frac{D_\parallel}{3D_0} = \frac{D_\parallel}{D_\parallel + 2D_\perp} \tag{3}$$

where $D_\parallel$ and $D_\perp$ are the optical densities of the dye solution in the liqud crystal for light polarized parallel or perpendicular to the orientation (i.e., with respect to the optical axis of the liquid crystal); D_0 is the optical density of the isotropic solution; and $\mu_\parallel^2 = \mu^2\cos^2\theta_d$ is the square of the projection of the transition moment of a dye molecule onto the orientation direction. Substituting Eq. (3) in (2) we obtain an equation for the experimental determination of the degree of ordering of the dye:

$$S_{lc} = (D_\parallel - D_\perp)/(D_\parallel + 2D_\perp). \tag{4}$$

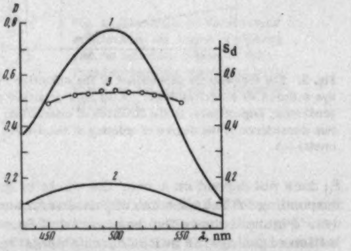

Fig. 1. The optical density of an oriented solution of KI dye in EBCA. Concentration c = 0.2 wt.%; 1) light polarized parallel to the direction of rubbing; 2) polarization perpendicular to this direction; 3) the degree of ordering of the dye (S_d) calculated from the dichroism. Thickness of the cell d = 20 μ; t = 82°C; supercooled phase of EBCA.

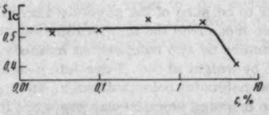

Fig. 2. The dependence of the degree of ordering S_d of the KI dye molecules on their concentration in the EBCA solution. t = 82°C, supercooled phase EBCA.

Using solutions of the dyes KI, KII, and KIII in the liquid crystal p-ethoxybenzylidene-p'-cyananiline (EBCA) it was possible to show that S_d does not depend on the molecular structure or on the dye concentration but is determined by the orientation of the liquid crystal,

KI :
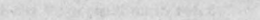

KII :
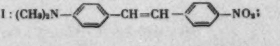

KIII :
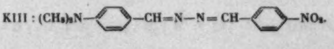

The orientation of the solution was done experimentally by rubbing the walls of a microcell according to the method described in ref. 7. In the nematic phase of $\left(\begin{array}{l} 103^\circ\mathrm{C} \rightarrow \\ \qquad 113^\circ\mathrm{C} \\ 70^\circ\mathrm{C} \leftarrow \end{array}\right)$ the solution had an intense dichroism in the absorption band region of the dye. Figure 1 shows the absorption spectra of the KI dye in EBCA for the two polarizations of the light (parallel or perpendicular to the direction of rubbing) and the graph of the value of S_d as a function of the wavelength (λ) calculated from Eq. (4). It is clear that within the measurement accuracy (~10%),

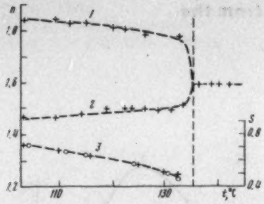

Fig. 3. The temperature dependence of the refractive indices of a 1% KI dye solution in p-azoxyanisole: 1, 2) light polarized parallel and perpendicular, respectively, to the direction of orientation; 3) the temperature dependence of the degree of ordering of the dye (○) and the liquid crystal (+).

S_d does not depend on λ over the whole of the range corresponding to the half-width of the absorption band of the dye. Figure 2 shows the dependence of S_d on the concentration of the dye KI in EBCA, which confirms the consistency S_d up to a concentration of the order of several percent. It was also found that S_d does not depend on the thickness of the microcell, between 5 and 100 μ. The degree of ordering of the KI and KIII dyes in EBCA are the same as S_d of KI (at the same temperature t = 82°C) to an accuracy of 5-6%.

In order to be sure of the absolute agreement between S_d and S_{lc} we measured the temperature dependence of these parameters by two independent methods. We introduced 1% by weight of the KI dye into p-azoxycyanisole (PAA), whose molecular polarizations $\gamma_\parallel$ and $\gamma_\perp$ are well known.[3] The oriented solution was prepared in a microcell with a wedge-shaped gap of 5 μ average thickness. We then measured the temperature dependence of the dichroism of the dye and determined the temperature dependence of the refractive index of the solution ($n_\parallel$ and $n_\perp$) at the wavelength of a helium–neon laser ($\lambda = 0.63\,\mu$) using an interference method.[8] As a result it was possible to measure S_d, $n_\parallel$, and $n_\perp$ in the same specimen.

The calculation of S_d was made using Eq. (4) and of S_{lc} from the ratio

$$S_d = (\alpha_\parallel - \alpha_\perp) / (\gamma_\parallel - \gamma_\perp), \qquad (5)$$

where $\alpha_\parallel$ and $\alpha_\perp$ are the polarizations of the PAA and KI mixture for a direction parallel and perpendicular to the direction of rubbing. The values of $\alpha_\parallel$ and $\alpha_\perp$ were calculated from the refractive indices ($n_\parallel$ and $n_\perp$) and from the density[3] of the PAA. Figure 3 shows the temperature dependence of the refractive indices of the PAA and KI mixture. These are almost identical with the analogous dependence for pure PAA. Figure 3 also shows the calculated values of S_d and S_{lc}, which are virtually the same throughout the entire interval of the nematic phase.

Thus, we can conclude that the measurement of the dichroism of linear, sufficiently long dye molecules dissolved in a liquid crystal is a convenient method of determining its degree of ordering. In this case we do not have to know any other parameters of the liquid crystal and the range of possible structures and concentrations of dye molecules is sufficiently wide. It must also be pointed out that the use of liquid crystals with a known value of S_{lc} makes it possible to solve the problem opposite to that described above, namely, to determine the direction of the dipole moment of the transition for such dye molecules where a certain angle is formed between it and the long molecular axis.

The authors would like to thank V. V. Titov, E. I. Balabanov, V. T. Lazarev, and B. M. Bolotin for the synthesis and purification of the chemical compounds, and I. N. Kompanets for assistance with the refractive index measurements.

---

[1] V. N. Zwetkoff, Acts Phys. Chim., URSS, 16, 132 (1942).

[2] I. G. Chistyakov, "The Structure of Liquid Crystals" [in Russian], Author's Abstract, Dissertation, Institute of Crystallography, Academy of Sciences of the USSR, Moscow (1972).

[3] S. Chandrasekhar and N. V. Madhusudana, J. Phys. Suppl., 30, 4-24 (1969).

[4] V. D. Neff, L. W. Gulrich, and G. H. Brown, Liquid Crystals, Gordon and Breach, New York (1967), p. 21.

[5] G. H. Heilmeier and L. A. Zanoni, Appl. Phys. Lett., 13, 91 (1968).

[6] K. R. Popov and L. B. Smirnov, Opt. Spektrosk., 30, 628 (1971).

[7] P. Chatelain, Bull. Soc. Franc. Mineral., 66, 105 (1943).

[8] I. N. Kompanets, Second All-Union Conf. on Liquid Crystals, Lecture Themes [in Russian], Ivanov (1972).

Orientational order and molecular parameters of liquid crystals with a positive dielectric anisotropy

V. G. Rumyantsev, P. D. Berezin, L. M. Blinov, and I. N. Kompanets

(Submitted July 24, 1972)
Kristallografiya, 18, 1104-1106 (September-October 1973)

Liquid crystals in the p-alkoxy-p'-benzylidene-cyananiline class (ABCA) have a large positive dielectric anisotropy at low frequencies,[1] $\Delta\varepsilon = \varepsilon_{\parallel} - \varepsilon_{\perp} \approx +15$ to 20, where $\varepsilon_{\parallel}$ and $\varepsilon_{\perp}$ are the dielectric constants of the liquid crystal measured parallel and perpendicular to its optical axis. As a result, the electric field applied to the ABCA film can effectively control the value of the double refraction of the liquid crystal[2] and, what is very important in practice, can produce phase modulation of the light beam[3] without causing any significant dynamic light-scatter effect.

The purpose of this paper is to study the temperature dependence of the degree of ordering S and the refractive index ($n_{\parallel}$ and $n_{\perp}$) of p-ethoxy... (EBCA), p-butoxy... (BBCA), and p-heptoxy... (HBCA) -benzylidene-p -cyananilines and to calculate from this data the longitudinal and transverse components of the molecular polarization $\gamma_{\parallel}$ and $\gamma_{\perp}$ and the dipole moments μ of these liquid crystals. The materials used in the study were first purified by two- or threefold recrystallization from solution followed by double sublimation in vacuum. The materials had a specific resistance of 10^{8}-10^{9} $\Omega \cdot$cm in the nematic phase.

In contrast to refs. 4 and 5, where the degree of ordering of liquid crystals (p-azoxyanisole, p-azoxyphenetol, and anisaldazine) was found from the values of $\gamma_{\parallel}$ and $\gamma_{\perp}$ which were known from the optical and crystallographic data for the solid single crystals, we used the reverse procedure and determined S independently from the dichroism of dyes dissolved in the liquid crystals.[6] In accordance with this method, the measurement of the temperature dependence of S, $n_{\parallel}$ and $n_{\perp}$ was made for each crystal on the same thermostatted specimen, as illustrated in Fig. 1.

A wedge-shaped gap was made between two optically polished glass substrates (1) of 40 mm diameter, using a Teflon washer (2) 10 μ thick. Approximately 2/3 of the area was filled with the liquid crystal and added dye (3) (this is the hatched region in Fig. 1). In order to orient the liquid-crystal molecules, the walls of the wedge-shaped gap were rubbed using the method described by Chatelain.[7] The specimen was illuminated by polarized light from a helium-neon laser with a wavelength of λ = 633 nm. The interference pattern which arose in the wedge was examined through a microscope in reflected light. In this case the boundary between the liquid crystal and the air lay within the field of vision of the microscope [region (4) in Fig. 1]. The refractive index of the liquid crystal was given by the ratio between the frequency of the interference bands on the left of the boundary (liquid crystal) and the frequency on its right (air). In order to determine $n_{\parallel}$ and $n_{\perp}$, the specimen was duly rotated around the polarization vector of the laser beam. The addition of 1% by weight of an azo-dye did not have any effect on the measured refractive index of the liquid crystal.

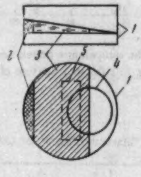

Fig. 1. The design of the unit used to determine the degree of ordering and the refractive indices of the liquid crystals (the thermostat is not shown and the symbols are explained in the text).

The degree of ordering was measured from the value of the dichroism of the azo-dye (p-dimethylamino-p'-nitroazobenzene) which has molecules with a long rod-like shape.[6] For this purpose the spectrum of the optical density of the liquid-crystal solution was recorded (same specimen) in the polarized light of a spectrophotometer. The light beam in this case passed through region (5) (Fig. 1). In the reference channel of the spectrophotometer we placed an analogous specimen with a liquid crystal without any dye in order to compensate for the absorption and scatter of light in the liquid crystal. The calculation of the degree of ordering was carried out using the equation

$$S = (D_{\parallel}^{\max} - D_{\perp}^{\max}) / (D_{\parallel}^{\max} + 2D_{\perp}^{\max}), \tag{1}$$

where $D_{\parallel}^{\max}$ and $D_{\perp}^{\max}$ are the optical densities at the maximum of the absorption band ($\lambda_{\max}$ = 480 nm) of the liquid-crystal solution in the directions parallel and perpendicular to the rubbing.

The temperature dependence of the refractive indices and the degree of ordering for three of the experimental liquid crystals are shown in Figs. 2a, 2b and 3a.

The calculation of the main polarizations of the nematic phase of the liquid crystal ($\alpha_{\parallel}$ and $\alpha_{\perp}$) was made in accordance with the Vuks equation in ref. 8:

$$(n_i^2 - 1) / (\overline{n^2} + 2) = 4\pi N \rho \alpha_i / 3M, \tag{2}$$

where $\alpha_i = \alpha_{\parallel}, \alpha_{\perp}$; $n_i = n_{\parallel}, n_{\perp}$; $\overline{n^2} = (n_{\parallel}^2 + 2n_{\perp}^2)/3$; N is

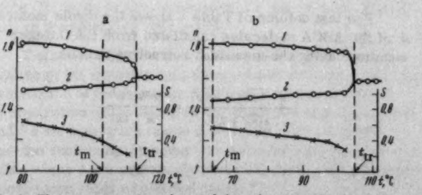

Fig. 2. The temperature dependence of the refractive indices $n_{\parallel}$ (1), $n_{\perp}$ (2), and the degree of ordering S (3) of the liquid crystals EBCA (a) and BBCA (b) (t_m and t_{tr} are the melting and transmissivity points, respectively).

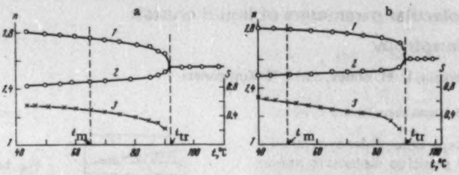

Fig. 3. The temperature dependence of $n_{\parallel}$ (1), $n_{\perp}$ (2) and S (3) for HBCA (a) and a 1 : 1 (by wt.) mixture of EBCA and BBCA (symbols as in Fig. 2).

TABLE 1. Some Characteristics of the Compounds 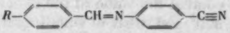

Type of radical, R	M	$t_m - t_{tr}$, °C	ρ (100° C) g/cm³	$\bar{n}$	$\bar{\gamma} \times 10^{24}$ cm⁻³	$\bar{\gamma}_{\parallel} \times 10^{24}$ cm⁻³	$\gamma_{\perp} \times 10^{24}$ cm⁻³	$\gamma_{\parallel}/\gamma_{\perp}$	ε (t, °C)	μ, Debye
C_2H_5O — (EBCA)	254	103—113	1.07	1.60	34.0	55.2	23.2	2.38	15.5 (130° C)	4.32
C_4H_9O — (BBCA)	282	63—104	1.00	1.58	37.3	73.5	19.5	3.76	14.5 (120° C)	4.53
$C_7H_{15}O$ — (HBCA)	324	65—92	1.02	1.54	38.5	76.3	19.7	3.85	11.5 (100° C)	4.20
EBCA + BBCA. 1 : 1	—	50—90	1.04	1.60	—	—	—	—	—	—
Measurement accuracy			±2%	±2%	±3%	±6%	±12%			±10%

Avogadro's number; M the molecular weight; and ρ the density of the material. The values of ρ at 100°C were determined experimentally for all the liquid crystals in our study using a 0.2 cm³ pyrometer. It was found possible in this case also to evaluate the temperature coefficient of the density ($d\rho/dT \approx 10^{-3}$ g/cm³ · deg); this was then used to evaluate the density in the required temperature interval.

Using the relationship $\bar{\alpha} = (\alpha_{\parallel} + 2\alpha_{\perp})/3$ and[5] $S = (\alpha_{\parallel} - \alpha_{\perp})/(\gamma_{\parallel} - \gamma_{\perp})$, it is easy to find the following expressions for the calculations of $\gamma_{\parallel}$ and $\gamma_{\perp}$:

$$\gamma_{\parallel} = \bar{\alpha} + 2(\alpha_{\parallel} - \alpha_{\perp})/3S,$$
$$\gamma_{\perp} = \bar{\alpha} - (\alpha_{\parallel} - \alpha_{\perp})/3S. \quad (3)$$

These results for the three experimental compounds are shown in Table 1. The fourth line of the table refers to a mixture of EBCA and BBCA which is very suitable for practical use. The molecular constants in this case were not determined, but the curves of the temperature dependence of S, $n_{\parallel}$, and $n_{\perp}$ are given for this mixture in Fig. 3b.

The last column of Table 1 shows the dipole moments μ of the ABCA molecules calculated from the Onsager equation[9] using the measured refractive indices

$$\frac{(\varepsilon - \overline{n_0^2})(2\varepsilon + \overline{n_0^2})}{\varepsilon(\overline{n_0^2} + 2)^2} = \frac{4\pi N\rho}{M}\,\frac{\mu^2}{3kT} \quad (4)$$

where ε is the dielectric constant of the isotropic phase of the liquid crystal and $\overline{n_0^2} = 1.1\,\overline{n^2}$ allowing for the atomic polarization. The values of ε for EBCA and BBCA were taken from ref. 1 and we measured the values for HBCA using an R-568. The calculated values of μ for all the ABCA are close to the handbook value for the dipole moment of the C ≡ N bond.[10]

The authors would like to thank V. V. Titov, V. T. Lazarev, and E. I. Balabanov for the synthesis and purification of the experimental compounds; and M. F. Grebenkin for his assistance with the measurements of the dielectric constants of HBCA.

---

[1] M. Shadt, J. Chem. Phys., 56, 1494 (1972)

[2] J. E. Goldmacher and G. H. Heilmeier, US Patent No. 3499702, cl. 350-150 (March 10, 1970).

[3] N. G. Basov, P. D. Berezin, L. M. Blinov, I. N. Kompanets, V. N. Morozov, and V. V. Nikitin, ZhETF Pis. Red., 15, 20 (1972).

[4] S. Chandrasekhar and N. V. Madhusudana, J. Phys. Suppl., 30, 4-25 (1969).

[5] N. V. Madhusudana, R. Shashidhar, and S. Chandrasekhar, Molecular Crystals and Liquid Crystals, 13, 61 (1971).

[6] V. G. Rumyantsev, L. M. Blinov, and V. A. Kizel', Kristallografiya, 18, 1101 (1973) [Sov. Phys.—Crystallogr., 18, 695 (1974)].

[7] P. Chatelain, Bull. Soc., Franc. Mineral., 66, 105 (1943).

[8] M. F. Buks, Opt. Spektrosk., 20, 644 (1966).

[9] H. Fröhlich, Theory of Dielectrics, Oxford Univ. Press, London (1958).

[10] V. I. Minkin, O. A. Osipov, and Yu. A. Zhdanov, Dipole Moments in Organic Chemistry [in Russian], Khimiya, Leningrad (1968).

Nature of the impurity water in synthetic quartz crystals

L. I. Tsinober and V. E. Khadzhi
All-Union Scientific-Research Institute for the Synthesis of Mineral Raw Materials
(Submitted September 28, 1972)
Kristallografiya, 18, 1107-1108 (September-October 1973)

It has previously been shown in refs. 1 and 2 that quartz crystals grown in alkali solutions with high supersaturation retain some nonstructural impurity. These crystals are normally opalescent and become cloudy when heated at temperatures above 500°C. In their original state these crystals, according to the electron microscope data, contain regions of nonuniformity of the order of 200-300 Å. After annealing, spherical inclusions up to 1000 Å in diameter as well as microcracks are formed.[1,3] Clearly, these cause the clouding effect on annealing. The spectrochemical (and also the neutron-activation analysis) showed that the crystals containing the nonstructural impurity are enriched with sodium (or potassium if the crystals were grown in a potassium system) and aluminum. The presence in the IR spectra of a diffusion maximum of ~ 3440 cm^{-1}, which is proportional to the degree of clouding in the crystals on annealing, shows the high concentration of impurity water in them. These results suggest, as in ref. 2, that the nonstructural impurity is in the form of either dispersed colloidal inclusions of aqueous sodium aluminosilicate (water-glass type) or regions of disordering in the quartz structure enriched by water, aluminum, and sodium. It is necessary to point out that in the thermodynamic interval in which such crystals are formed there is liquation of the liquid phase with the separation of the sodium- and silicon-enriched "heavy phase," which can be adsorbed and held by the growing crystal.[4]

It is of interest to examine in greater detail the nature of the impurity water in these crystals on the basis of the IR-spectroscopy data. Crystals were selected for the study which had been grown in 10% aqueous Na_2CO_3 at P = 400 kg/cm^2, T = 335°C, and ΔT = 20°C. There was practically no loss in weight of the quartz observed in the thermogravimetric analysis up to 1100°C. A series of polished disks 3 mm thick were prepared from the ⟨c⟩ pyramid of the crystal. Individual disks were annealed at 500, 600, 700, and 800°C for various periods. As would be expected, the specimens became cloudy on annealing and the degree of cloudiness increased in proportion to the increase in temperature and duration of the anneal. The IR spectra in the 3000-3700 cm^{-1} region were measured at room temperature and at liquid-nitrogen temperature for the untreated and annealed disks (UR-10W spectrometer; cryostat with LiF windows).

The results of the measurements are shown in Figs. 1 and 2. These figures also show for comparison the IR spectra of films of liquid water and ice I according to the data in ref. 5. A comparison of these spectra suggests the following conclusions.

1. In the untreated specimens of quartz enriched with a nonstructural impurity, in addition to the series of discrete bands (3400, 3440, and 3590 cm^{-1}) which are particularly well developed at liquid-nitrogen temperature and are associated with various types of OH defects in the quartz structure,[6] there is a wide diffusion band with a maximum in the ~ 3440 cm^{-1} region. This band may be compared with impurity water in the molecular state. Since at low temperatures, however, the character of the spectrum is not essentially different, it can be assumed that the impurity water does not form an individual phase but enters the composition of the colloidal sodium aluminosilicate inclusions above or of disordered regions of the quartz.

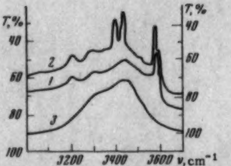

Fig. 1. The IR transmission spectra of the untreated synthetic quartz specimen: polished z-cut disk 3 mm thick from the < c > pyramid; 1) at room temperature; 2) at 80°K; 3) spectrum of film of liquid water from the data in ref. 5: left-hand scale refers to curves 1 and 3; right-hand scale, to curve 2.

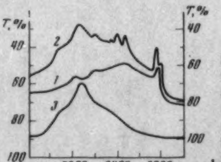

Fig. 2. The IR transmission spectra of the same specimen as in Fig. 1 but annealed at 800°C for 600 h: 1) at room temperature; 2) at 80°K; 3) spectrum of ice film I as in ref. 5: left-hand scale refers to curves 1 and 3; right-hand scale, to curve 2.

2. In the annealed specimens there is a sharp difference between the spectra recorded at room temperature and at low temperatures. While the first are basically identical to the spectra of the untreated specimens (with the maximum characteristic of molecular H_2O in the 3440 cm^{-1} region), there is a shift of the diffusion maximum in the spectra recorded at liquid-nitrogen temperature into the 3230 cm^{-1} region, indicating the presence of impurity ice I. In the case of the annealed specimens a substantial increase in the intensity of the discrete OH bands is also characteristic and is more intense than in the untreated specimens.

Thus, the experimental data suggest that during annealing of the crystals containing a nonstructural impurity destruction of the impurity aggregates occurs followed by separation of the water in the form of a separate phase and its encapsulation inside the crystal. It is possible that the encapsulation occurs in the same spherical globules which were previously observed during the electron-microscope study of clouded quartz.[3]

---

[1] V. E. Khadzhi, Trudy Vses. Nauchn. Institut. P'ezooptich. Mineral. Syr'ya, 6, 31 (1962).

[2] L. I. Tsinober, V. E. Khadzhi, L. A. Gordienko and M. I. Samoilovich, in: Growth of Crystals, Vol. 6, Consultants Bureau, New York (1968).

[3] L. P. Khadzhi and V. E. Khadzhi, Dokl. Akad. Nauk SSSR, 172, 1072 (1967) [Sov. Phys.—Dokl., 12, 116 (1967)].

[4] V. P. Butuzov and L. V. Bryatov, Kristallografiya, 2, 670 (1957) [Sov. Phys.—Crystallogr., 2, 659 (1957)].

[5] D. Eischberg and W. Kauzmann, The Structure and Properties of Water, Clarendon Press, Oxford (1969).

[6] A. Kats, Philips Res. Repts., 17, 133 (1962).

Structure of amorphous indium monochalcogenide films

Yu. G. Poltavtsev, V. P. Zakharov, and T. V. Remizovich

(Submitted September 5, 1972; resubmitted October 23, 1972)
Kristallografiya, 18, 1109-1110 (September-October 1973)

In this work, electron diffraction is used to study the structure of the short-range order of amorphous InSe and InTe films. The films were obtained by thermal sputtering of single-crystal samples on unheated substrates in a vacuum of about 10^{-5} torr.

The results of the investigation of amorphous InSe are given in Fig. 1, which shows the curves of the intensity of electron scattering and the atomic radial distribution curves. The latter curves were computed, as in ref. 1, with different upper integration limits S_{max}. In Fig. 1b it is seen that the atomic radial distribution curve computed with the larger S_{max} value contains more information—the structural maxima in it are better defined than in the curve calculated with a smaller S_{max}.

For amorphous InSe, there are maxima for $r_1 = 2.75$, $r_2 = 3.8$, $r_3 = 4.4$, $r_4 = 5.4$, and $r_5 = 6.15$ Å. The successive symmetric resolution of the second and third structural maxima is shown in Fig. 1b. The right-hand sides of the bell-shaped curves in Fig. 1b were obtained by forming the mirror image of the left branches; the left side of the third maximum was found by subtracting the right side of the second maximum from the radial distribution curve. Then, subtracting the right side of the third maximum from the radial distribution curve, we find a bend in the difference curve, indicating the existence of one more structural maximum at $r_3' = 4.8$ Å.

To find a model of the structure of amorphous indium monoselenide we compute the ratios $r_i/r_1 = 1, 1.38, 1.6, 1.74, 1.96$, and 2.24. The values nearly coincide with the corresponding r_i/r_1 values for the hexagonal close-packed structure: 1, 1.4, 1.63, 1.73, 1.91, 2.0, and 2.24. (The value 1.96 corresponds to the average of 1.91 and 2.0.) The analogy of the statistics of the interatomic distances in the hexagonal close-packed structure and the structure of amorphous InSe thus is established.

Crystalline InSe has a layer structure, composed of distorted hexagonal packets, bounded by Se atoms.[2] Inside a packet, each In atom has three Se atoms at a distance $r_{1k} = 2.50$ Å and one In atom at a distance $r'_{1k} = 3.15$ Å. From Fig. 1b it is seen that only r_{2k} falls in the region of the first maximum of the distribution curve. The area A_1^c under the first maximum, computed for $Z_{Se}(In) = 3$, is equal to 1.4.

An arrangement of atoms is also possible in which $Z_{se}(In) = 2$, $Z_{In}(In) = 1$, and $Z_{In}(Se) = 2$, that is, an arrangement of atoms in hexagonal layers, bounded by Se atoms. For this model, the computed value of A_1^c, the area under the first maximum of the distribution curve, is 2.5.

By allowing a statistical distribution of different kinds of atoms at the points of a normal hexagonal lattice, we

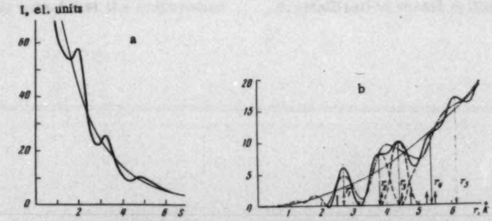

Fig. 1. The intensity of electron scattering (a) and the atomic radial distribution curve $4\pi r^2 \sum_i \sum_j n_i k_i k_j P_{ij}(r)$ in amorphous InSe (b). The dashed line is the curve for $S_{max} = 6.5$ Å^{-1}; the dot–dash curve is for $S_{max} = 4.7$ Å^{-1}. Vertical segments show the two coordination spheres in crystalline InSe.

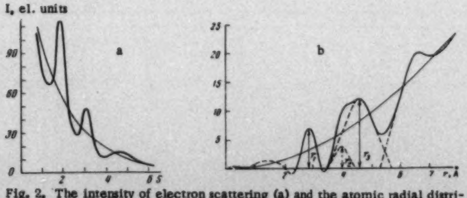

Fig. 2. The intensity of electron scattering (a) and the atomic radial distribution curve (b) in amorphous InTe.

obtain $A_1^c = 2.9$. The value is practically identical to the experimental value $A_1 = 2.8$.

Figure 2 shows the electron scattering data for amorphous InTe films. Crystalline indium monotelluride has a TlS type structure.[2] Monovalent In atoms are placed at the centers of slightly deformed cubes, and trivalent atoms are at the centers of tetrahedra. The coordination numbers are $Z_{Te}(In) = 4$, $Z_{Te}(Te) = 1$, and $Z_{In}(Te) = 1$.

On the distribution curve for amorphous InTe there are maxima for $r_1 = 2.85$, $r_2 = 4$, $r_3 = 4.6$, and $r_4 = 6.6$ Å; the area A_1 under the first maximum is 3.4. The ratios $r_2/r_1 = \sqrt{2}$ and $r_3/r_1 = 1.62$ correspond to the presence of octahedral and tetrahedral packing of nearest neighbors in amorphous InTe, that is, there is a definite analogy between the structures of the crystal and the amorphous film. This is supported by the good agreement of the experimental value A_1 with the computed value $A_1^c = 3.2$, which is obtained by use of the above values of the coordination numbers for the crystal.

---

[1] Yu. G. Poltavtsev, V. P. Zakharov, V. M. Pozdynakova, and L. M. Protas, Kristallografiya, 17, 203 (1972) [Sov. Phys.–Crystallogr., 17, 165 (1972)].

[2] K. Shubert, Crystal Structure of Two-Component Phases [in Russian], Metallurgiya, Moscow (1971).

Simple method for preventing the formation of parasite crystals during the growth of crystals from solution

I. V. Isakov

Branch of the L. Ya. Karpov Physicochemical Scientific Research Institute

(Submitted November 1, 1972)
Kristallografiya, 18, 1111 (September-October 1973)

In the growth of crystals from a solution in an open vessel, in the case of a substance with a very high solubility and a highly volatile solvent which effectively wets the material of the vessel, it is possible to observe rapid propagation of a film of solution over the wall of the crystallization vessel, followed by the appearance of a band of fine precipitated crystallites and subsequent upward movement of this band with an increase in the quantity of polycrystalline mass. Under these conditions the production of single crystals in the solution is excluded. It is nevertheless possible to try to obtain single crystals in an ordinary glass vessel into which, through a stopper, is hermetically fixed a tube which has a diameter equal to half the diameter of the vessel and which descends to a height of several millimeters above the surface of the solution. It is of course necessary to ensure that the solvent does not react with the material of the stopper.

Using a very simple crystallization vessel of this kind, with a capacity of 100 ml, we grew single crystals of acrylamide from solution in chloroform and in alcohol in several days under static conditions at room temperature.

The evaporation process is very slow — less than 0.1 ml of solvent in 24 h — and when single crystals appear the rate of evaporation can be reduced even further by covering the tube. To the extent that the evaporation takes place chiefly from the central area of the surface of the solution, and equilibrium volatilization conditions are preserved in the region of the boundary between the solution and the wall, precipitation of a polycrystalline product at the boundary does not take place. Moreover, if the film of liquid is able to rise up the wall to an appreciable height with the production of a polycrystalline product in the time interval between the introduction of the solution and the fixing of the tube in position, all the precipitated crystals will dissolve in a period of several hours after the tube is fixed in position, the material will be returned to the main bulk of the solution, and the walls of the crystallization vessel will become quite clean.

If crystallization does not begin for a long time after the introduction of the solution, the saturation can be increased by evacuating the solvent vapor by means of a water pump. The solution is cooled, and a polycrystalline product appears on the walls. When the evacuation is stopped, the solution returns to room temperature, and the walls of the crystallization vessel undergo the self-cleaning process. The evacuation should be carried out for several minutes with interruptions to ensure stability of the solution.

This method of crystallization may prove useful where it is not possible to acquire or construct a special crystallization vessel sufficiently quickly.

Conference on anomalous scattering

Kristallografiya, 18, 1112 (September-October 1973)

The commission on crystallographic apparatus of the International Union of Crystallography is organizing a special conference on anomalous scattering in the period between congresses. This conference will be held 23-26 April 1974 in Madrid, Spain in the Research College.

The object of the conference is to evaluate the experimental and theoretical errors arising in measuring and processing data on the anomalous scattering of x rays, neutrons, and electrons.

The conference will consider the following:

1. Accuracy in anomalous-scattering measurement with characteristic x rays and white spectra, as well as x rays near absorption edges, neutrons, and electrons.

2. The effects of the dispersion correction on atomic parameters and the accuracy of the dispersion correction.

3. Anomalous scattering applied to structure determination.

4. The error probability in determining absolute configurations.

5. The relation between atomic positions and tensors for macroscopic quantities.

6. New uses of anomalous scattering in Mössbauer work and electron diffraction.

7. Other applications of anomalous scattering.

The number of participants will be restricted to 125 appropriate specialists. The conference proceedings will be published.

More detailed information can be obtained from S. C. Abrahams, Bell Laboratories, Murray Hill, New Jersey 07974, USA.

Reduction of the Kronecker product of representations of the crystallographic groups. III

B. A. Men', A. N. Men', and V. I. Cherepanov
Institute of Metallurgy, Ural Scientific Center,
Academy of Sciences of the USSR

(Submitted July 25, 1972; resubmitted November 9, 1972)
Kristallografiya, 18, 1117-1125 (November-December 1973)

A procedure is given for constructing functions of appropriate symmetry (for any number of the space of cofactors) for the octahedral group and all crystallographic groups obtained from the direct product of this group and a cyclic group of order 2.

The reduction of the Kronecker product of the representations of all the crystallographic groups apart from the octahedron ($O \approx S_4$) was considered in refs. 1 and 2. In this paper the corresponding problem will be solved for the octahedron.[1)]

Let us write down the table of characters for S_4 and A_4 (Table 1) and select a basis such that the matrices of the degenerate representations Γ_3, Γ_4 and Γ_5 may take the following form:

$$\begin{array}{ccccccc}
 & e & (12)(34) & (13)(24) & (14)(23) & (134) & (123) \\
\Gamma_3 & \begin{pmatrix} 1 & \\ & 1 \end{pmatrix} & \begin{pmatrix} 1 & \\ & 1 \end{pmatrix} & \begin{pmatrix} 1 & \\ & 1 \end{pmatrix} & \begin{pmatrix} 1 & \\ & 1 \end{pmatrix} & \begin{pmatrix} \omega & \\ & \omega^2 \end{pmatrix} & \begin{pmatrix} \omega & \\ & \omega^2 \end{pmatrix} \\
\left.\begin{matrix}\Gamma_4\\ \Gamma_5\end{matrix}\right\} & \begin{pmatrix} 1 & & \\ & 1 & \\ & & 1 \end{pmatrix} & \begin{pmatrix} 1 & & \\ & -1 & \\ & & -1 \end{pmatrix} & \begin{pmatrix} -1 & & \\ & 1 & \\ & & -1 \end{pmatrix} & \begin{pmatrix} -1 & & \\ & -1 & \\ & & 1 \end{pmatrix} & \begin{pmatrix} 0 & 0 & 1 \\ 1 & 0 & 0 \\ 0 & 1 & 0 \end{pmatrix} & \begin{pmatrix} 0 & 0 & 1 \\ -1 & 0 & 0 \\ 0 & -1 & 0 \end{pmatrix} \\
 & (243) & (142) & (143) & (132) & (234) & (124) \\
\Gamma_3 & \begin{pmatrix} \omega & \\ & \omega^2 \end{pmatrix} & \begin{pmatrix} \omega & \\ & \omega^2 \end{pmatrix} & \begin{pmatrix} \omega^2 & \\ & \omega \end{pmatrix} & \begin{pmatrix} \omega^2 & \\ & \omega \end{pmatrix} & \begin{pmatrix} \omega^2 & \\ & \omega \end{pmatrix} & \begin{pmatrix} \omega^2 & \\ & \omega \end{pmatrix} \\
\left.\begin{matrix}\Gamma_4\\ \Gamma_5\end{matrix}\right\} & \begin{pmatrix} 0 & 0 & -1 \\ -1 & 0 & 0 \\ 0 & 1 & 0 \end{pmatrix} & \begin{pmatrix} 0 & 0 & -1 \\ 1 & 0 & 0 \\ 0 & -1 & 0 \end{pmatrix} & \begin{pmatrix} 0 & 1 & 0 \\ 0 & 0 & 1 \\ 1 & 0 & 0 \end{pmatrix} & \begin{pmatrix} 0 & -1 & 0 \\ 0 & 0 & -1 \\ 1 & 0 & 0 \end{pmatrix} & \begin{pmatrix} 0 & -1 & 0 \\ 0 & 0 & 1 \\ -1 & 0 & 0 \end{pmatrix} & \begin{pmatrix} 0 & 1 & 0 \\ 0 & 0 & -1 \\ -1 & 0 & 0 \end{pmatrix}
\end{array}$$

$$\begin{array}{cccccccc}
 & (12) & (34) & (1423) & (1324) & (1234) & (13) & (1432) \\
\Gamma_3 & \begin{pmatrix} & 1 \\ 1 & \end{pmatrix} & \begin{pmatrix} & 1 \\ 1 & \end{pmatrix} & \begin{pmatrix} & 1 \\ 1 & \end{pmatrix} & \begin{pmatrix} & 1 \\ 1 & \end{pmatrix} & \begin{pmatrix} & \omega^2 \\ \omega & \end{pmatrix} & \begin{pmatrix} & \omega^2 \\ \omega & \end{pmatrix} & \begin{pmatrix} & \omega^2 \\ \omega & \end{pmatrix} \\
\Gamma_4 & \begin{pmatrix} 1 & 0 & 0 \\ 0 & 0 & -1 \\ 0 & -1 & 0 \end{pmatrix} & \begin{pmatrix} 1 & 0 & 0 \\ 0 & 0 & 1 \\ 0 & 1 & 0 \end{pmatrix} & \begin{pmatrix} -1 & 0 & 0 \\ 0 & 0 & 1 \\ 0 & -1 & 0 \end{pmatrix} & \begin{pmatrix} -1 & 0 & 0 \\ 0 & 0 & -1 \\ 0 & 1 & 0 \end{pmatrix} & \begin{pmatrix} 0 & 0 & 1 \\ 0 & -1 & 0 \\ -1 & 0 & 0 \end{pmatrix} & \begin{pmatrix} 0 & 0 & 1 \\ 0 & 1 & 0 \\ 1 & 0 & 0 \end{pmatrix} & \begin{pmatrix} 0 & 0 & -1 \\ 0 & -1 & 0 \\ 1 & 0 & 0 \end{pmatrix} \\
\Gamma_5 & \begin{pmatrix} -1 & 0 & 0 \\ 0 & 0 & 1 \\ 0 & 1 & 0 \end{pmatrix} & \begin{pmatrix} -1 & 0 & 0 \\ 0 & 0 & -1 \\ 0 & -1 & 0 \end{pmatrix} & \begin{pmatrix} 1 & 0 & 0 \\ 0 & 0 & -1 \\ 0 & 1 & 0 \end{pmatrix} & \begin{pmatrix} 1 & 0 & 0 \\ 0 & 0 & 1 \\ 0 & -1 & 0 \end{pmatrix} & \begin{pmatrix} 0 & 0 & -1 \\ 0 & 1 & 0 \\ 1 & 0 & 0 \end{pmatrix} & \begin{pmatrix} 0 & 0 & -1 \\ 0 & -1 & 0 \\ -1 & 0 & 0 \end{pmatrix} & \begin{pmatrix} 0 & 0 & 1 \\ 0 & 1 & 0 \\ -1 & 0 & 0 \end{pmatrix}
\end{array}$$

$$\begin{array}{cccccc}
 & (24) & (1243) & (23) & (1342) & (14) \\
\Gamma_3 & \begin{pmatrix} & \omega^2 \\ \omega & \end{pmatrix} & \begin{pmatrix} & \omega \\ \omega^2 & \end{pmatrix} & \begin{pmatrix} & \omega \\ \omega^2 & \end{pmatrix} & \begin{pmatrix} & \omega \\ \omega^2 & \end{pmatrix} & \begin{pmatrix} & \omega \\ \omega^2 & \end{pmatrix} \\
\Gamma_4 & \begin{pmatrix} 0 & 0 & -1 \\ 0 & 1 & 0 \\ -1 & 0 & 0 \end{pmatrix} & \begin{pmatrix} 0 & 1 & 0 \\ -1 & 0 & 0 \\ 0 & 0 & -1 \end{pmatrix} & \begin{pmatrix} 0 & -1 & 0 \\ -1 & 0 & 0 \\ 0 & 0 & 1 \end{pmatrix} & \begin{pmatrix} 0 & -1 & 0 \\ 1 & 0 & 0 \\ 0 & 0 & -1 \end{pmatrix} & \begin{pmatrix} 0 & 1 & 0 \\ 1 & 0 & 0 \\ 0 & 0 & 1 \end{pmatrix} \\
\Gamma_5 & \begin{pmatrix} 0 & 0 & 1 \\ 0 & -1 & 0 \\ 1 & 0 & 0 \end{pmatrix} & \begin{pmatrix} 0 & -1 & 0 \\ 1 & 0 & 0 \\ 0 & 0 & 1 \end{pmatrix} & \begin{pmatrix} 0 & 1 & 0 \\ 1 & 0 & 0 \\ 0 & 0 & -1 \end{pmatrix} & \begin{pmatrix} 0 & 1 & 0 \\ -1 & 0 & 0 \\ 0 & 0 & 1 \end{pmatrix} & \begin{pmatrix} 0 & -1 & 0 \\ -1 & 0 & 0 \\ 0 & 0 & -1 \end{pmatrix}
\end{array} \quad (1)$$

We must construct functions obtained from the tensor product of the representations:

$$\overbrace{\Gamma_1\times\ldots\times\Gamma_1}^{k}\times\overbrace{\Gamma_2\times\ldots\times\Gamma_2}^{l}\times\overbrace{\Gamma_3\times\ldots\times\Gamma_3}^{r}\times\overbrace{\Gamma_4\times\ldots\times\Gamma_4}^{n}\times\overbrace{\Gamma_5\times\ldots\times\Gamma_5}^{p}$$

$$\begin{array}{cccccccccccccccccc}
\downarrow & & \downarrow & \downarrow & & \downarrow & \downarrow & & \downarrow & \downarrow & & \downarrow & \downarrow & & \downarrow \\
\psi_1^{(1)} & \ldots & \psi_k^{(1)} & \psi_1^{(2)} & \ldots & \psi_l^{(2)} & \psi_{11}^{(3)} & \ldots & \psi_{r1}^{(3)} & \psi_{11}^{(4)} & \ldots & \psi_{n1}^{(4)} & \psi_{11}^{(5)} & \ldots & \psi_{p1}^{(5)} \\
\multicolumn{6}{c}{\underbrace{\hphantom{\psi_1^{(1)}\ldots\psi_k^{(1)}\psi_1^{(2)}\ldots\psi_l^{(2)}}}_{\Phi=\prod\limits_{i_1=1}^{k}\psi_{i_1}^{(1)}\prod\limits_{i_2=1}^{l}\psi_{i_2}^{(2)}}} & \psi_{12}^{(3)} & \ldots & \psi_{r2}^{(3)} & \psi_{12}^{(4)} & \ldots & \psi_{n2}^{(4)} & \psi_{12}^{(5)} & \ldots & \psi_{p2}^{(5)} \\
 & & & & & & & & & \psi_{13}^{(4)} & \ldots & \psi_{n3}^{(4)} & \psi_{13}^{(5)} & \ldots & \psi_{p3}^{(5)}
\end{array} \quad (2)$$

TABLE 1

S_4	e	$\{(12)\}$	$\{(123)\}$	$\{(1234)\}$	$\{(12)\ (34)\}$
Γ_1	1	1	1	1.	1
Γ_2	1	−1	1	−1	1
Γ_3	2	0	−1	0	2
Γ_4	3	1	0	−1	−1
Γ_5	3	−1	0	1	−1

A_4	e	$\{(12)(34)\}$	$\{(123)\}$	$\{(132)\}$
Γ_1^1	1	1	1	1
Γ_2^1	1	1	ω	ω^2
Γ_3^1	1	1	ω^2	ω
Γ_4^1	3	−1	0	0

TABLE 2

Splitting of r	Set + and 0	Value of δ (mod 3) a_1	a_2	$\delta = a_1 - a_2$	Form of functions ψ_1 and ψ_2
2 = 2	$\begin{pmatrix} + & + \\ 0 & 0 \end{pmatrix}$	2	0	2	$\psi_{++}^{(\Gamma_3)} = \psi_{11}^{(3)}\psi_{21}^{(3)},\ \psi_{00}^{(\Gamma_3)} = \psi_{12}^{(3)}\psi_{22}^{(3)}$
2 = 1 + 1	$\begin{pmatrix} + & 0 \\ 0 & + \end{pmatrix}$	1	1	0	$\psi_{+0}^{(\Gamma_3)} = \psi_{11}^{(3)}\psi_{22}^{(3)},\ \psi_{0+}^{(\Gamma_3)} = \psi_{12}^{(3)}\psi_{21}^{(3)}$

A. Let us first consider the general case, in which $r \neq 0$, $n+p \neq 0$.

1. Let us take the functions of representations $\Gamma_3 \times \dots \times \Gamma_3$ and from these find possible sets of functions ψ_1 and ψ_2 as in ref. 1. For example, r = 2 (Table 2).

2. Let us now take the function of the representations $\overbrace{\Gamma_4 \times \dots \times \Gamma_4}^{n} \times \overbrace{\Gamma_5 \times \dots \times \Gamma_5}^{p}$ and from this find possible sets of functions ψ_1, ψ_2, ψ_3 as in ref. 2. For example, n+p = 2 (Table 3).

3. Let us set up all possible sets of products of the functions by cross-multiplying the functions $\psi_i^{(\Gamma_3)}\psi_j^{(\Gamma_{4,5})}$ from subsections (1) and (2) and subsequently multiplying by $\psi(2)$. For example, we consider $\Gamma_3 \times \Gamma_3 \times \Gamma_{4,5} \times \Gamma_{4,5}$ (Table 4)

$$\begin{pmatrix} \Gamma_{4,5} = \Gamma_4 \text{ or } \Gamma_5 \to \Gamma_4 \times \Gamma_4, \Gamma_5 \times \Gamma_5, \Gamma_4 \times \Gamma_5, \Gamma_5 \times \Gamma_4 \\ r = 2,\ n+p = 2 \end{pmatrix}$$

4. Let us regroup the sets of functions not containing sets of the form $n+p = a_1 + 0 + 0 + \dots$ in the splitting of n+p. Let us consider two pairs of sets differing from one another simply by the signs of the a_i in n+p (for example, $n+p = a_1 + a_2 - a_3$ and $a_1 - a_2 + a_3$). Let us set out the basis functions of the six-dimensional blocks in the following order:[2]

$$\begin{array}{l}
\psi_1(+\dots|\ \overbrace{0\dots0}^{a_1}\quad \overbrace{+\dots+}^{a_2}\quad \overbrace{-\dots-}^{a_3}) \\
\psi_2(+\dots|+\dots+\quad -\dots-\quad 0\dots0) \\
\psi_3(+\dots|-\dots-\quad 0\dots0\quad +\dots+) \\
\psi_4(0\dots|\ 0\dots0\quad -\dots-\quad +\dots+) \\
\psi_5(0\dots|+\dots+\quad 0\dots0\quad -\dots-) \\
\psi_6(\underbrace{0\dots}_{\Gamma_3}|\underbrace{-\dots-\quad +\dots+\quad 0\dots0}_{\Gamma_{4,5}})
\end{array} \qquad (3)$$

For the example under consideration we obtain $\Gamma_3 \times \Gamma_3 \times \Gamma_{4,5} \times \Gamma_{4,5}$ by using Table 4 (the sets of functions corresponding to the splittings r = 1 + 1, n+p = 2 + 0 and r = 2 + 0, n+p = 2 + 0 remain intact) (Table 5).

5. Let us write down the explicit form of the functions for each of the representations of expansion (2) according to the theorem [l is the number of Γ_2, p the number of Γ_5 in (2)] using the functions derived in Table 5 (here the values of δ_l are chosen from the first lines of Table 5).

I. If all the $\delta_l + \delta_j \equiv 0 \pmod 2$ we have

1) $l+p \equiv 0 \pmod 2$

$$(+)\ \Gamma_1 \to \frac{1}{\sqrt{3}}(\varphi_1 + \omega^{\delta}\varphi_2 + \omega^{\delta}\varphi_3)$$

$$(+)\ \Gamma_3 \to \begin{cases} \frac{1}{\sqrt{3}}[\omega^{-(1+\delta)}\varphi_1 + \omega\varphi_2 + \varphi_3] \\ \frac{1}{\sqrt{3}}[\omega^{-(1+\delta)}\varphi_1 + \varphi_2 + \omega\varphi_3] \end{cases}$$

$$(-)\ \Gamma_2 \to \frac{1}{\sqrt{3}}(\varphi_1 + \omega^{\delta}\varphi_2 - \omega^{\delta}\varphi_3)$$

$$(-)\ \Gamma_3 \to \begin{cases} \frac{1}{\sqrt{3}}[\omega^{-(1+\delta)}\varphi_1 + \omega\varphi_2 - \varphi_3] \\ \frac{1}{\sqrt{3}}[-\omega^{-(1+\delta)}\varphi_1 - \varphi_2 + \omega\varphi_3] \end{cases}$$

2) $l+p \equiv 1 \pmod 2$

$$(+)\ \Gamma_2 \to \frac{1}{\sqrt{3}}(\varphi_1 + \omega^{\delta}\varphi_2 + \omega^{\delta}\varphi_3)$$

$$(+)\ \Gamma_3 \to \begin{cases} \frac{1}{\sqrt{3}}[\omega^{-(1+\delta)}\varphi_1 + \omega\varphi_2 + \varphi_3] \\ -\frac{1}{\sqrt{3}}[\omega^{-(1+\delta)}\varphi_1 + \varphi_2 + \omega\varphi_3] \end{cases}$$

$$(-)\ \Gamma_1 \to \frac{1}{\sqrt{3}}(\varphi_1 + \omega^{\delta}\varphi_3 - \omega^{\delta}\varphi_3)$$

$$(-)\ \Gamma_3 \to \begin{cases} \frac{1}{\sqrt{3}}[\omega^{-(1+\delta)}\varphi_1 + \omega\varphi_2 - \varphi_3] \\ -\frac{1}{\sqrt{3}}[-\omega^{-(1+\delta)}\varphi_1 - \varphi_2 + \omega\varphi_3] \end{cases} \qquad (4)$$

II. If not all the $\delta_l + \delta_j \equiv 0 \pmod 2$ we have

1) $l + p \equiv 0 \pmod 2$ 2) $l + p \equiv 1 \pmod 2$

(+) $\Gamma_4 \to \varphi_1, \omega^{\delta}\varphi_3, \omega^{\delta}\varphi_2$ (+) $\Gamma_5 \to \varphi_1, \omega^{\delta}\varphi_3, \omega^{\delta}\varphi_2$

(-) $\Gamma_5 \to \varphi_1, -\omega^{\delta}\varphi_3, \omega^{\delta}\varphi_2$ (-) $\Gamma_4 \to \varphi_1, -\omega^{\delta}\varphi_3, \omega^{\delta}\varphi_2$

TABLE 3

Splitting of n + p	Form of matrix	δ_1	δ_2 (mod 2)	δ_3	Form of functions ψ_1, ψ_2, ψ_3
2+0	$\begin{pmatrix} 0 & 0 \\ + & + \\ - & - \end{pmatrix}$	0	0	0	$\psi_{00}^{(\Gamma_{4,5})} = \psi_{11}\psi_{21},\ \psi_{++}^{(\Gamma_{4,5})} = \psi_{12}\psi_{22}$ $\psi^{(\Gamma_{4,5})} = \psi_{13}\psi_{23}$
1+1	$\begin{pmatrix} 0 & + \\ + & - \\ - & 0 \end{pmatrix}$	1	1	0	$\psi_{0+}^{(\Gamma_{4,5})} = \psi_{11}\psi_{22},\ \psi_{+-}^{(\Gamma_{4,5})} = \psi_{12}\psi_{23}$ $\psi_{-0}^{(\Gamma_{4,5})} = \psi_{13}\psi_{21}$
1−1	$\begin{pmatrix} 0 & - \\ + & 0 \\ - & + \end{pmatrix}$	1	0	1	$\psi_{0-}^{(\Gamma_{4,5})} = \psi_{11}\psi_{23},\ \psi_{+0}^{(\Gamma_{4,5})} = \psi_{12}\psi_{21},$ $\psi_{-+}^{(\Gamma_{4,5})} = \psi_{13}\psi_{22}$

TABLE 4

Splitting of n + p	Form of matrix	Values of s	δ_1	δ_2	δ_3	Form of functions ψ
$r=2+0$ $n+p=2+0$	$\begin{pmatrix}+&+\\0&0\end{pmatrix}\begin{pmatrix}0&0\\+&+\\-&-\end{pmatrix}$	2	0	0	0	$\psi(++\mid 00)=\psi^{(2)}_{11}\psi^{(2)}_{21}\psi_{11}\psi_{21}$ $\psi(++\mid ++)=\psi^{(2)}_{11}\psi^{(2)}_{21}\psi_{12}\psi_{22}$ $\psi(++\mid --)=\psi^{(2)}_{11}\psi^{(2)}_{21}\psi_{13}\psi_{23}$ $\psi(00\mid 00)=\psi^{(2)}_{12}\psi^{(2)}_{22}\psi_{11}\psi_{21}$ $\psi(00\mid ++)=\psi^{(2)}_{12}\psi^{(2)}_{22}\psi_{12}\psi_{22}$ $\psi(00\mid --)=\psi^{(2)}_{12}\psi^{(2)}_{22}\psi_{13}\psi_{23}$
$r=2+0$ $n+p=1+1$	$\begin{pmatrix}+&+\\0&0\end{pmatrix}\begin{pmatrix}0&+\\+&-\\-&0\end{pmatrix}$	2	1	1	0	$\psi(++\mid 0+)=\psi^{(2)}_{11}\psi^{(2)}_{21}\psi_{11}\psi_{22}$ $\psi(++\mid +-)=\psi^{(2)}_{11}\psi^{(2)}_{21}\psi_{12}\psi_{23}$ $\psi(++\mid -0)=\psi^{(2)}_{11}\psi^{(2)}_{21}\psi_{13}\psi_{21}$ $\psi(00\mid 0+)=\psi^{(2)}_{12}\psi^{(2)}_{22}\psi_{11}\psi_{22}$ $\psi(00\mid +-)=\psi^{(2)}_{12}\psi^{(2)}_{22}\psi_{12}\psi_{23}$ $\psi(00\mid -0)=\psi^{(2)}_{12}\psi^{(2)}_{22}\psi_{13}\psi_{21}$
$r=2+0$ $n+p=1-1$	$\begin{pmatrix}+&+\\0&0\end{pmatrix}\begin{pmatrix}0&-\\+&0\\-&+\end{pmatrix}$	2	1	0	1	$\psi(++\mid 0-)=\psi^{(2)}_{11}\psi^{(2)}_{21}\psi_{11}\psi_{23}$ $\psi(++\mid +0)=\psi^{(2)}_{11}\psi^{(2)}_{21}\psi_{12}\psi_{21}$ $\psi(++\mid -+)=\psi^{(2)}_{11}\psi^{(2)}_{21}\psi_{13}\psi_{22}$ $\psi(00\mid 0-)=\psi^{(2)}_{12}\psi^{(2)}_{22}\psi_{11}\psi_{23}$ $\psi(00\mid +0)=\psi^{(2)}_{12}\psi^{(2)}_{22}\psi_{12}\psi_{21}$ $\psi(00\mid -+)=\psi^{(2)}_{12}\psi^{(2)}_{22}\psi_{13}\psi_{22}$
$r=1+1$ $n+p=2+0$	$\begin{pmatrix}+&0\\0&+\end{pmatrix}\begin{pmatrix}0&0\\+&+\\-&-\end{pmatrix}$	0	0	0	0	$\psi(+0\mid 00)=\psi^{(2)}_{11}\psi^{(2)}_{22}\psi_{11}\psi_{21}$ $\psi(+0\mid ++)=\psi^{(2)}_{11}\psi^{(2)}_{22}\psi_{12}\psi_{22}$ $\psi(+0\mid --)=\psi^{(2)}_{11}\psi^{(2)}_{22}\psi_{13}\psi_{23}$ $\psi(+0\mid 00)=\psi^{(2)}_{12}\psi^{(2)}_{21}\psi_{11}\psi_{21}$ $\psi(0+\mid ++)=\psi^{(2)}_{12}\psi^{(2)}_{21}\psi_{12}\psi_{22}$ $\psi(0+\mid --)=\psi^{(2)}_{12}\psi^{(2)}_{21}\psi_{13}\psi_{23}$
$r=1+1$ $n+p=1+1$	$\begin{pmatrix}+&0\\0&+\end{pmatrix}\begin{pmatrix}0&+\\+&-\\-&0\end{pmatrix}$	0	1	1	0	$\psi(+0\mid 0+)=\psi^{(2)}_{11}\psi^{(2)}_{22}\psi_{11}\psi_{22}$ $\psi(+0\mid +-)=\psi^{(2)}_{11}\psi^{(2)}_{22}\psi_{12}\psi_{23}$ $\psi(+0\mid -0)=\psi^{(2)}_{11}\psi^{(2)}_{22}\psi_{13}\psi_{21}$ $\psi(0+\mid 0+)=\psi^{(2)}_{12}\psi^{(2)}_{21}\psi_{11}\psi_{22}$ $\psi(0+\mid +-)=\psi^{(2)}_{12}\psi^{(2)}_{21}\psi_{12}\psi_{23}$ $\psi(0+\mid -0)=\psi^{(2)}_{12}\psi^{(2)}_{21}\psi_{13}\psi_{21}$
$r=1+1$ $n+p=1-1$	$\begin{pmatrix}+&0\\0&+\end{pmatrix}\begin{pmatrix}0&-\\+&0\\-&+\end{pmatrix}$	0	1	0	1	$\psi(+0\mid 0-)=\psi^{(2)}_{11}\psi^{(2)}_{22}\psi_{11}\psi_{23}$ $\psi(+0\mid +0)=\psi^{(2)}_{11}\psi^{(2)}_{22}\psi_{12}\psi_{21}$ $\psi(+0\mid -+)=\psi^{(2)}_{11}\psi^{(2)}_{22}\psi_{13}\psi_{22}$ $\psi(0+\mid 0-)=\psi^{(2)}_{12}\psi^{(2)}_{21}\psi_{11}\psi_{23}$ $\psi(0+\mid +0)=\psi^{(2)}_{12}\psi^{(2)}_{21}\psi_{12}\psi_{21}$ $\psi(0+\mid -+)=\psi^{(2)}_{12}\psi^{(2)}_{21}\psi_{13}\psi_{22}$

TABLE 5

Splitting of $r, n+p$	Values of δ and δ_1				Form of functions ψ_1
	δ	δ_1	δ_2	δ_3	
$r=2+0$	2	1	1	0	$\psi_1 \equiv \psi(++\|0+) = \psi^{(3)}_{11}\psi^{(3)}_{21}\psi_{11}\psi_{22}$
$n+p=\left\{\begin{smallmatrix}1+1\\1-1\end{smallmatrix}\right.$	2	1	1	0	$\psi_2 \equiv \psi(++\|+-) = \psi^{(3)}_{11}\psi^{(3)}_{21}\psi_{12}\psi_{22}$
	2	1	1	0	$\psi_3 \equiv \psi(++\|-0) = \psi^{(3)}_{11}\psi^{(3)}_{21}\psi_{12}\psi_{21}$
	2	1	0	1	$\psi_4 \equiv \psi(00\|0-) = \psi^{(3)}_{12}\psi^{(3)}_{22}\psi_{11}\psi_{22}$
	2	1	0	1	$\psi_5 \equiv \psi(00\|+0) = \psi^{(3)}_{12}\psi^{(3)}_{22}\psi_{12}\psi_{21}$
	2	1	0	1	$\psi_6 \equiv \psi(00\|-+) = \psi^{(3)}_{12}\psi^{(3)}_{22}\psi_{12}\psi_{22}$
$r=2+0$	2	1	0	1	$\psi_1 \equiv \psi(++\|0-) = \psi^{(3)}_{11}\psi^{(3)}_{21}\psi_{11}\psi_{22}$
$n+p=\left\{\begin{smallmatrix}1-1\\1+1\end{smallmatrix}\right.$	2	1	0	1	$\psi_2 \equiv \psi(++\|+0) = \psi^{(3)}_{11}\psi^{(3)}_{21}\psi_{12}\psi_{21}$
	2	1	0	1	$\psi_3 \equiv \psi(++\|-+) = \psi^{(3)}_{11}\psi^{(3)}_{21}\psi_{12}\psi_{22}$
	2	1	1	0	$\psi_4 \equiv \psi(00\|0+) = \psi^{(3)}_{12}\psi^{(3)}_{22}\psi_{11}\psi_{22}$
	2	1	1	0	$\psi_5 \equiv \psi(00\|+-) = \psi^{(3)}_{12}\psi^{(3)}_{22}\psi_{12}\psi_{22}$
	2	1	1	0	$\psi_6 \equiv \psi(00\|-0) = \psi^{(3)}_{12}\psi^{(3)}_{22}\psi_{12}\psi_{21}$
$r=1+1$	0	1	1	0	$\psi_1 \equiv \psi(+0\|0+) = \psi^{(3)}_{11}\psi^{(3)}_{22}\psi_{11}\psi_{22}$
$n+p=\left\{\begin{smallmatrix}1+1\\1-1\end{smallmatrix}\right.$	0	1	1	0	$\psi_2 \equiv \psi(+0\|+-) = \psi^{(3)}_{11}\psi^{(3)}_{22}\psi_{12}\psi_{22}$
	0	1	1	0	$\psi_3 \equiv \psi(+0\|-0) = \psi^{(3)}_{11}\psi^{(3)}_{22}\psi_{12}\psi_{21}]$
	0	1	0	1	$\psi_4 \equiv \psi(0+\|0-) = \psi^{(3)}_{12}\psi^{(3)}_{21}\psi_{11}\psi_{22}$
	0	1	0	1	$\psi_5 \equiv \psi(0+\|+0) = \psi^{(3)}_{12}\psi^{(3)}_{21}\psi_{12}\psi_{21}$
	0	1	0	1	$\psi_6 \equiv \psi(0+\|-+) = \psi^{(3)}_{12}\psi^{(3)}_{21}\psi_{12}\psi_{22}$
$r=1+1$	0	1	0	1	$\psi_1 \equiv \psi(+0\|0-) = \psi^{(3)}_{11}\psi^{(3)}_{22}\psi_{11}\psi_{22}$
$n+p=\left\{\begin{smallmatrix}1-1\\1+1\end{smallmatrix}\right.$	0	1	0	1	$\psi_2 \equiv \psi(+0\|+0) = \psi^{(3)}_{11}\psi^{(3)}_{22}\psi_{12}\psi_{21}$
	0	1	0	1	$\psi_3 \equiv \psi(+0\|-+) = \psi^{(3)}_{11}\psi^{(3)}_{22}\psi_{12}\psi_{22}$
	0	1	1	0	$\psi_4 \equiv \psi(0+\|0+) = \psi^{(3)}_{12}\psi^{(3)}_{21}\psi_{11}\psi_{22}$
	0	1	1	0	$\psi_5 \equiv \psi(0+\|+-) = \psi^{(3)}_{12}\psi^{(3)}_{21}\psi_{12}\psi_{22}$
	0	1	1	0	$\psi_6 \equiv \psi(0+\|-0) = \psi^{(3)}_{12}\psi^{(3)}_{21}\psi_{12}\psi_{21}$

where $\delta_1+\delta_2$ is even:

$$\begin{array}{ll} (+) & (-) \\ \varphi_1=\frac{1}{\sqrt{2}}(\psi_2+\psi_6) & \varphi_1=\frac{1}{\sqrt{2}}(\psi_2-\psi_6) \\ \varphi_2=\frac{1}{\sqrt{2}}(\psi_1+\omega^{\delta}\psi_5) & \varphi_2=\frac{1}{\sqrt{2}}(\psi_1-\omega^{\delta}\psi_5) \\ \varphi_3=\frac{1}{\sqrt{2}}(\psi_4+\omega^{\delta}\psi_3) & \varphi_3=\frac{1}{\sqrt{2}}(\psi_4-\omega^{\delta}\psi_3) \end{array}$$

$\delta_1+\delta_3$ is even:

$$\begin{array}{ll} (+) & (-) \\ \varphi_1=\frac{1}{\sqrt{2}}(\psi_3+\psi_5) & \varphi_1=\frac{1}{\sqrt{2}}(\psi_3-\psi_5) \\ \varphi_2=\frac{1}{\sqrt{2}}(\psi_2+\omega^{\delta}\psi_4) & \varphi_2=\frac{1}{\sqrt{2}}(\psi_2-\omega^{\delta}\psi_4) \\ \varphi_3=\frac{1}{\sqrt{2}}(\psi_6+\omega^{\delta}\psi_1) & \varphi_3=\frac{1}{\sqrt{2}}(\psi_6-\omega^{\delta}\psi_1) \end{array}$$

$\delta_2+\delta_3$ is even:

$$\begin{array}{ll} (+) & (-) \\ \varphi_1=\frac{1}{\sqrt{2}}(\psi_1+\psi_4) & \varphi_1=\frac{1}{\sqrt{2}}(\psi_1-\psi_4) \\ \varphi_2=\frac{1}{\sqrt{2}}(\psi_3+\omega^{\delta}\psi_6) & \varphi_2=\frac{1}{\sqrt{2}}(\psi_3-\omega^{\delta}\psi_6) \\ \varphi_3=\frac{1}{\sqrt{2}}(\psi_5+\omega^{\delta}\psi_2) & \varphi_3=\frac{1}{\sqrt{2}}(\psi_5-\omega^{\delta}\psi_2) \end{array} \qquad (5)$$

We note that, if all the $\delta_i + \delta_j \equiv 0 \pmod 2$, the choice of functions φ_i is arbitrary. The resultant functions are distinguished by a constant factor, whose modulus was equal to unity.

As an example (see Table 6) we have

$$\Gamma_3\times\Gamma_3\times\Gamma_4\times\Gamma_5=2\Gamma_1+2\Gamma_2+4\Gamma_3+4\Gamma_4+4\Gamma_5. \qquad (6)$$

Let us now consider some particular cases.

B. $r = 0$, $n+p \neq 0$ ($\delta_2 = \delta_3 = 0$). In this case it is easy to obtain the functions of the basis for the splitting $n+p \equiv (n+p)+0+0$ [see ref. 2 taking Eq. (2) into account ($r = 0$)]:

$$\begin{aligned} \varphi_1&=\psi\psi^{(4)}_{11}\ldots\psi^{(4)}_{n1}\psi^{(5)}_{11}\ldots\psi^{(5)}_{p1}, \\ \varphi_2&=\psi\psi^{(4)}_{12}\ldots\psi^{(4)}_{n2}\psi^{(5)}_{12}\ldots\psi^{(5)}_{p2}, \\ \varphi_3&=\psi\psi^{(4)}_{13}\ldots\psi^{(4)}_{n3}\psi^{(5)}_{13}\ldots\psi^{(5)}_{p3}. \end{aligned} \qquad (7)$$

Let us write down the explicit form of the functions for each of the expansions of the representation (2) ($r = 0$) according to the theorem (l is the number of Γ_2, n the number of Γ_4, p the number of Γ_5).

I. $n+p \equiv 1 \pmod 2$:

1) $l+p\equiv 0 \pmod 2$ 2) $l+p\equiv 1 \pmod 2$

$\Gamma_4\rightarrow\varphi_1, \varphi_2, \varphi_3$ $\Gamma_5\rightarrow\varphi_1, \varphi_2, \varphi_3$

II. $n+p\equiv 0 \pmod 2$

$$1)\ l+p\equiv 0 \pmod 2 \qquad\qquad 2)\ l+p\equiv 1 \pmod 2$$

$$\Gamma_1 \to \frac{1}{\sqrt{3}}(\varphi_1+\varphi_2+\varphi_3) \qquad \Gamma_2 \to \frac{1}{\sqrt{3}}(\varphi_1+\varphi_2+\varphi_3)$$

$$\Gamma_3 \to \begin{cases} \frac{1}{\sqrt{3}}(\varphi_1+\omega\varphi_2+\omega^2\varphi_3) \\ \frac{1}{\sqrt{3}}(\varphi_1+\omega^2\varphi_2+\omega\varphi_3) \end{cases} \qquad \Gamma_3 \to \begin{cases} \frac{1}{\sqrt{3}}(\varphi_1+\omega\varphi_2+\omega^2\varphi_3) \\ -\frac{1}{\sqrt{3}}(\varphi_1+\omega^2\varphi_2+\omega\varphi_3) \end{cases}$$

$$r\neq 0, \quad n+p=0. \tag{8}$$

C. r ≠ 0, n = p = 0. In this case it is easy to obtain the functions of the basis for the splitting of r (see ref. 1 allowing for (2) (n = p = 0). Let us write down the explicit form of the functions for each of the expansions of the representation (2) (n = p = 0) according to the theorem (l is the number of Γ_2):

$$\delta\equiv 0 \pmod 3 \qquad\qquad \delta\equiv 1 \pmod 3 \qquad\qquad \delta\equiv 2 \pmod 3$$

$$\Gamma_1 \to \frac{1}{\sqrt{2}}[(-1)^l\psi_1+\psi_2] \qquad \Gamma_3 \to \begin{cases} (-1)^l\psi_1 \\ \psi_2 \end{cases} \qquad \Gamma_3 \to \begin{cases} \psi_2 \\ (-1)^l\psi_1 \end{cases}$$

$$\Gamma_2 \to \frac{1}{\sqrt{2}}[(-1)^{l+1}\psi_1+\psi_2] \tag{9}$$

D. r = 0, n ± p ≠ 0 (apart from B). In this case the scheme of A is entirely retained.

The method of reducing the Kronecker products of the representations set out in the authors' various papers has so far dealt with groups of the trigonal and tetragonal type[1] (I), the tetrahedron[2] (II), and the octahedron (III). The remaining crystallographic groups are obtained from

TABLE 6a

	Representation Γ_i	Splitting of r, $n+p$	$l+p$ mod (2)	Choice of + or −	δ	δ_1	δ_2	δ_3	Form of functions $\Phi_{\Gamma_i}(r,\ n+p,\ \pm)$
	Γ_1	$r\equiv 2+0$ $n+p\equiv 2+0$	1	−	2	0	0	0	$\Phi_{\Gamma_1}(2+0);\ 2+0;\ -)=\frac{1}{\sqrt{3}}(\varphi_1+\omega^2\varphi_2-\omega^2\varphi_3)$
	Γ_2	$r\equiv 2+0$ $n+p\equiv 2+0$	1	+	2	0	0	0	$\Phi_{\Gamma_2}(2+0;\ 2+0;\ +)=\frac{1}{\sqrt{3}}(\varphi_1+\omega^2\varphi_2+\omega^2\varphi_3)$
I	Γ_3	$r\equiv 2+0$ $n+p\equiv 2+0$	1	+	2	0	0	0	$\Phi_{\Gamma_3}(2+0;\ 2+0;\ +)=\frac{1}{\sqrt{3}}(\varphi_1+\omega\varphi_2+\varphi_3)$ $-\frac{1}{\sqrt{3}}(\varphi_1+\varphi_2+\omega\varphi_3)$
	Γ_3	$r\equiv 2+0$ $n+p\equiv 2+0$	1	−	2	0	0	0	$\Phi_{\Gamma_3}(2+0;\ 2+0;\ -)=\frac{1}{\sqrt{3}}(\varphi_1+\omega\varphi_2-\varphi_3)$ $-\frac{1}{\sqrt{3}}(-\varphi_1-\varphi_2+\omega\varphi_3)$
	Γ_1	$r\equiv 1+1$ $n+p\equiv 2+0$	1	−	0	0	0	0	$\Phi_{\Gamma_1}(1+1;\ 2+0;\ -)=\frac{1}{\sqrt{3}}(\varphi_1+\varphi_2-\varphi_3)$
	Γ_2	$r\equiv 1+1$ $n+p\equiv 2+0$	1	+	0	0	0	0	$\Phi_{\Gamma_2}(1+1;\ 2+0;\ +)=\frac{1}{\sqrt{3}}(\varphi_1+\varphi_2+\varphi_3)$
II	Γ_3	$r\equiv 1+1$ $n+p\equiv 2+0$	1	+	0	0	0	0	$\Phi_{\Gamma_3}(1+1;\ 2+0;\ +)=\frac{1}{\sqrt{3}}(\omega^2\varphi_1+\omega\varphi_2+\varphi_3)$ $-\frac{1}{\sqrt{3}}(\omega^2\varphi_1+\varphi_2+\omega\varphi_3)$
	Γ_3	$r\equiv 1+1$ $n+p\equiv 2+0$	1	−	0	0	0	0	$\Phi_{\Gamma_3}(1+1;\ 2+0;\ -)=\frac{1}{\sqrt{3}}(\omega^2\varphi_1+\omega\varphi_2-\varphi_3)$ $-\frac{1}{\sqrt{3}}(-\omega^2\varphi_1-\varphi_2+\omega\varphi_3)$
	Γ_3	$r\equiv 2+0$ $n+p\equiv\begin{cases}1+1\\1-1\end{cases}$	1	+	2	1	1	0	$\Phi_{\Gamma_3}\left(2+0;\ \binom{1+1}{1-1},\ +\right)\to\varphi_1,\ \omega^2\varphi_3,\ \omega^2\varphi_2$
III	Γ_4	$r\equiv 2+0$ $n+p\equiv\begin{cases}1+1\\1-1\end{cases}$	1	−	2	1	1	0	$\Phi_{\Gamma_4}\left(2+0;\ \binom{1+1}{1-1},\ -\right)\to\varphi_1,\ -\omega^2\varphi_3,\ \omega^2\varphi_2$
	Γ_3	$r\equiv 2+0$ $n+p\equiv\begin{cases}1-1\\1+1\end{cases}$	1	+	2	1	0	1	$\Phi_{\Gamma_3}\left(2+0;\ \binom{1-1}{1+1},\ +\right)\to\varphi_1,\ \omega^2\varphi_3,\ \omega^2\varphi_2$
IV	Γ_4	$r\equiv 2+0$ $n+p\equiv\begin{cases}1-1\\1+1\end{cases}$	1	−	2	1	0	1	$\Phi_{\Gamma_4}\left(2+0;\ \binom{1-1}{1+1},\ +\right)\to\varphi_1,\ -\omega^2\varphi_3,\ \omega^2\varphi_2$
	Γ_3	$r\equiv 1+1$ $n+p\equiv\begin{cases}1+1\\1-1\end{cases}$	1	+	0	1	1	0	$\Phi_{\Gamma_3}\left(1+1;\ \binom{1+1}{1-1},\ +\right)\to\varphi_1,\ \varphi_3,\ \varphi_2$
V	Γ_4	$r\equiv 1+1$ $n+p\equiv\begin{cases}1+1\\1-1\end{cases}$	1	−	0	1	1	0	$\Phi_{\Gamma_4}\left(1+1;\ \binom{1+1}{1-1},\ +\right)\to\varphi_1,\ -\varphi_3,\ \varphi_2$
	Γ_3	$r\equiv 1+1$ $n+p\equiv\begin{cases}1-1\\1+1\end{cases}$	1	+	0	1	0	1	$\Phi_{\Gamma_3}\left(1+1;\binom{1-1}{1+1},\ +\right)\to\varphi_1,\ \varphi_3,\ \varphi_2$
VI	Γ_4	$r\equiv 1+1$ $n+p\equiv\begin{cases}1-1\\1+1\end{cases}$	1	−	0	1	0	1	$\Phi_{\Gamma_4}\left(1+1;\binom{1-1}{1+1},\ +\right)\to\varphi_1,\ -\varphi_3,\ \varphi_2$

TABLE 6b

Form of functions φ_i (sign determined by the sign of Φ_{Γ_i})	Form of functions ψ_i
I $\varphi_1=\frac{1}{\sqrt{2}}(\psi_2\pm\psi_6)$ $\varphi_2=\frac{1}{\sqrt{2}}(\psi_1\pm\omega^2\varphi_5)$ $\varphi_3=\frac{1}{\sqrt{2}}(\psi_4\pm\omega^2\psi_3)$	$\psi_1=\psi^{(3)}_{11}\psi^{(3)}_{21}\psi^{(4)}_{11}\psi^{(5)}_{11}$ $\psi_2=\psi^{(3)}_{11}\psi^{(3)}_{21}\psi^{(4)}_{12}\psi^{(5)}_{12}$ $\psi_3=\psi^{(3)}_{11}\psi^{(3)}_{21}\psi^{(4)}_{13}\psi^{(5)}_{13}$ $\psi_4=\psi^{(3)}_{12}\psi^{(3)}_{22}\psi^{(4)}_{11}\psi^{(5)}_{11}$ $\psi_5=\psi^{(3)}_{12}\psi^{(3)}_{22}\psi^{(4)}_{12}\psi^{(5)}_{12}$ $\psi_6=\psi^{(3)}_{12}\psi^{(3)}_{22}\psi^{(4)}_{13}\psi^{(5)}_{13}$
II $\varphi_1=\frac{1}{\sqrt{2}}(\psi_2\pm\psi_6)$ $\varphi_2=\frac{1}{\sqrt{2}}(\psi_1\pm\omega^2\psi_5)$ $\varphi_3=\frac{1}{\sqrt{2}}(\psi_4\pm\omega^2\varphi_3)$	$\psi_1=\psi^{(3)}_{11}\psi^{(3)}_{22}\psi^{(4)}_{11}\psi^{(5)}_{11}$ $\psi_2=\psi^{(3)}_{11}\psi^{(3)}_{22}\psi^{(4)}_{12}\psi^{(5)}_{12}$ $\psi_3=\psi^{(3)}_{11}\psi^{(3)}_{22}\psi^{(4)}_{13}\psi^{(5)}_{13}$ $\psi_4=\psi^{(3)}_{12}\psi^{(3)}_{21}\psi^{(4)}_{11}\psi^{(5)}_{11}$ $\psi_5=\psi^{(3)}_{12}\psi^{(3)}_{21}\psi^{(4)}_{12}\psi^{(5)}_{12}$ $\psi_6=\psi^{(3)}_{12}\psi^{(3)}_{21}\psi^{(4)}_{13}\psi^{(5)}_{13}$
III $\varphi_1=\frac{1}{\sqrt{2}}(\psi_3\pm\psi_6)$ $\varphi_2=\frac{1}{\sqrt{2}}(\psi_1\pm\omega^2\psi_5)$ $\varphi_3=\frac{1}{\sqrt{2}}(\psi_4\pm\omega^2\psi_3)$	$\psi_1=\psi^{(3)}_{11}\psi^{(3)}_{21}\psi^{(4)}_{11}\psi^{(5)}_{12}$ $\psi_4=\psi^{(3)}_{12}\psi^{(3)}_{22}\psi^{(4)}_{11}\psi^{(5)}_{13}$ $\psi_2=\psi^{(3)}_{11}\psi^{(3)}_{21}\psi^{(4)}_{12}\psi^{(5)}_{13}$ $\psi_5=\psi^{(3)}_{12}\psi^{(3)}_{22}\psi^{(4)}_{12}\psi^{(5)}_{11}$ $\psi_3=\psi^{(3)}_{11}\psi^{(3)}_{21}\psi^{(1)}_{13}\psi^{(5)}_{11}$ $\psi_6=\psi^{(3)}_{12}\psi^{(3)}_{22}\psi^{(4)}_{13}\psi^{(5)}_{12}$
IV $\varphi_1=\frac{1}{\sqrt{2}}(\psi_3\pm\psi_5)$ $\varphi_2=\frac{1}{\sqrt{2}}(\psi_2\pm\omega^2\psi_4)$ $\varphi_3=\frac{1}{\sqrt{2}}(\psi_6\pm\omega^2\psi_1)$	$\psi_1=\psi^{(3)}_{11}\psi^{(3)}_{21}\psi^{(4)}_{11}\psi^{(5)}_{13}$ $\psi_4=\psi^{(3)}_{12}\psi^{(3)}_{22}\psi^{(4)}_{11}\psi^{(5)}_{12}$ $\psi_2=\psi^{(3)}_{11}\psi^{(3)}_{21}\psi^{(4)}_{12}\psi^{(5)}_{11}$ $\psi_5=\psi^{(3)}_{12}\psi^{(3)}_{22}\psi^{(4)}_{12}\psi^{(5)}_{13}$ $\psi_3=\psi^{(3)}_{11}\psi^{(3)}_{21}\psi^{(4)}_{13}\psi^{(5)}_{12}$ $\psi_6=\psi^{(3)}_{12}\psi^{(3)}_{22}\psi^{(4)}_{13}\psi^{(5)}_{11}$
V $\varphi_1=\frac{1}{\sqrt{2}}(\psi_3\pm\psi_6)$ $\varphi_2=\frac{1}{\sqrt{2}}(\psi_2\pm\psi_5)$ $\varphi_3=\frac{1}{\sqrt{2}}(\psi_4\pm\psi_3)$	$\psi_1=\psi^{(3)}_{11}\psi^{(3)}_{22}\psi^{(4)}_{11}\psi^{(5)}_{12}$ $\psi_4=\psi^{(3)}_{12}\psi^{(3)}_{21}\psi^{(4)}_{11}\psi^{(5)}_{13}$ $\psi_2=\psi^{(3)}_{11}\psi^{(3)}_{22}\psi^{(4)}_{12}\psi^{(5)}_{13}$ $\psi_5=\psi^{(3)}_{12}\psi^{(3)}_{21}\psi^{(4)}_{12}\psi^{(5)}_{11}$ $\psi_3=\psi^{(3)}_{11}\psi^{(3)}_{22}\psi^{(4)}_{13}\psi^{(5)}_{11}$ $\psi_6=\psi^{(3)}_{12}\psi^{(3)}_{21}\psi^{(4)}_{13}\psi^{(5)}_{12}$
VI $\varphi_1=\frac{1}{\sqrt{2}}(\psi_3\pm\psi_5)$ $\varphi_2=\frac{1}{\sqrt{2}}(\psi_2\pm\psi_4)$ $\varphi_3=\frac{1}{\sqrt{2}}(\psi_6\pm\psi_1)$	$\psi_1=\psi^{(3)}_{11}\psi^{(3)}_{22}\psi^{(4)}_{11}\psi^{(5)}_{13}$ $\psi_4=\psi^{(3)}_{12}\psi^{(3)}_{21}\psi^{(4)}_{11}\psi^{(5)}_{12}$ $\psi_2=\psi^{(3)}_{11}\psi^{(3)}_{22}\psi^{(4)}_{12}\psi^{(5)}_{11}$ $\psi_5=\psi^{(3)}_{12}\psi^{(3)}_{21}\psi^{(4)}_{12}\psi^{(5)}_{13}$ $\psi_3=\psi^{(3)}_{11}\psi^{(3)}_{22}\psi^{(4)}_{13}\psi^{(5)}_{12}$ $\psi_6=\psi^{(3)}_{12}\psi^{(3)}_{21}\psi^{(4)}_{13}\psi^{(5)}_{11}$

those presented here by the direct multiplication of these by a cyclic group of order 2 (apart from the case $D_{6h} = D_6 \times C_i$, $D_6 = D_3 \times \{e, C_6^3\}$). For these the methods of finding the corresponding functions amount to the following: First we have to find the functions transforming according to the representations of the ordinary groups (I, II, III), then we have to act on these functions with the nonunitary element a_{12} of a cyclic group of the second order. If

$$a_{12}\psi=\psi, \qquad (10)$$

we are then concerned with even representations Γ_{ig}; if not we have

$$a_{12}\psi=-\psi \qquad (11)$$

and the representations will be odd, Γ_{iu}.

Let us illustrate this for the group $D_{3h} = D_3 \times C_i$:

$$\Gamma_{3g}\times\Gamma_{3g}\times\Gamma_{3u}=3\Gamma_{3u}+\Gamma_{1u}+\Gamma_{2u}. \qquad (12)$$

If we take the functions given in Table 2 of ref. (I) and act on these with the inversion operation (a_{12}), we obtain case (11). Of course in this case all the representations will have the index "u."

---

[1] The mathematical basis for the procedure was outlined in ref. 3.

[2] It should be remembered that, if any $a_i = 0$, then these signs are simply omitted, and the remaining order of signs is retained. As an example, if $a_2 = 0$ we have $\psi_1(+\ldots|0\ldots0-\ldots-)$, $\psi_2(+\ldots|+\ldots+0\ldots0)$, and so on.

[1] B. A. Men', A. N. Men', and V. I. Cherepanov, Kristallografiya, 18, 669 (1973) [Sov. Phys.–Crystallogr., 18, 421 (1974)].

[2] B. A. Men', A. N. Men', and V. I. Cherepanov, Kristallografiya, 18, 901 (1973) [Sov. Phys.–Crystallogr., 18, 567 (1974)].

[3] B. A. Men', A. N. Men', and V. I. Cherepanov, Dokl. Akad. Nauk SSSR, 203, 776 (1972) [Sov. Phys.–Dokl., 17, 330 (1972)].

"Spectral instability" of multiwave diffraction with coplanar x rays

A. D. Fofanov, A. V. Kuznetsov, and G. A. Karacheva

Petrozavodsk State University

(Submitted June 6, 1972; resubmitted December 7, 1972)
Kristallografiya, 18, 1126-1133 (November-December 1973)

The three-wave approximation of the dynamical theory of scattering is used to treat the "spectral instability" of multiwave x-ray diffraction for coplanar rays. It is shown, using as an example the scattering of x rays by a certain idealized crystal with parameters close to real ones, that for a "thick" crystal the decay of the three-wave diffraction into double two-wave diffraction occurs with a change in the wavelength of the incident radiation within the natural linewidth of the characteristic x radiation.

Although the basic ideas of the dynamical theory of x-ray diffraction were formulated more than 50 years ago, the theory of multiwave diffraction has developed slowly due to its mathematical difficulties. It is true that sometimes investigators turned to it in seeking explanations for observed effects (see refs. 1, 2 for example); however there has been no persistent interest in this theory.

Recently a number of theoretical and experimental studies have appeared in the area of multiwave diffraction. This revival is evidently due to the work of Borrmann and Hartwig,[3] who observed a very interesting phenomenon called the "double Borrmann effect". This phenomenon has found a satisfactory explanation[4-9] on the basis of the three-wave approximation of the dynamical theory. In addition it has been predicted theoretically[9] that there will be a very strong decrease in the effective absorption coefficient when four and six reciprocal lattice sites are located on the Ewald sphere. All of this means that interest in multiwave diffraction is increasing.

In the present work we treat one of the features of x-ray scattering characteristic of multiwave diffraction for coplanar rays. The essence of this feature is the following. While in the two-wave case we obtain the very same diffraction pattern with two different recording conditions: (1) monochromatic radiation and rotating crystal; (2) polychromatic radiation and a stationary crystal; for three or more strong coplanar waves this should not be so. It can be seen from the Ewald construction that three-wave diffraction occurs only for a rigorously fixed wavelength λ_0. If it is measured with a rotation of the crystal there is a gradual decay of the three-wave diffraction into two two-wave diffraction situations.

In the present work we have studied the transition of three-wave diffraction with coplanar rays into two-wave diffraction.

This way of posing the problem requires a solution of the fundamental system of equations of the dynamical theory under conditions where the crystal is rotated relative to the primary beam composed of a set of plane waves having different wavelengths. It is not possible to trace this analytically in a general form. Therefore we have solved the system numerically using a computer. To reduce the volume of calculation we have limited the analysis to the simplest case of multiwave diffraction, three coplanar rays (it has been treated in detail previously[1]).

In the present case the fundamental system of equations of the dynamical theory is composed in general of six linear homogeneous equations, which decompose into two independent systems of three equations corresponding to each polarization direction. Here we concern ourselves only with scattering of plane-polarized radiation with the direction of the electric field vector perpendicular to the plane of incidence. The geometry of the case considered is as follows: A parallel beam of x rays falls perpendicularly on a crystalline plane-parallel plate. Both of the scattered beams make an angle with respect to it of $2\theta_{1B} = 2\theta_{2B} = 60°$. For a plane-polarized beam the fundamental system of equations for the dynamical theory can be put in the form

$$\begin{aligned}(\psi_0-2\delta_0)D_0+\psi_{-1}D_1+\psi_{-2}D_2&=0,\\ \psi_1D_0+(\psi_0-2\delta_1)D_1+\psi_{1-2}D_2&=0,\\ \psi_2D_0+\psi_{2-1}D_1+(\psi_0-2\delta_2)D_2&=0,\end{aligned} \qquad (1)$$

where ψ_H are the expansion coefficients in the Fourier series for the polarizability of the crystal and $(1+\delta_0)$ and $(1+\delta_H)$ are the refractive indices of the incident and reflected waves respectively. The quantities δ_H and δ_0 are related by

$$\delta_H=\delta_0/b_H+\alpha_H/2, \quad H=\pm1, \pm2, \qquad (2)$$

where

$$\frac{1}{b_H}=1+\frac{(\mathbf{n}, \mathbf{B}_H)}{(\mathbf{n}, \mathbf{K}_0)}\simeq\frac{(\mathbf{n}, \mathbf{K}_H)}{(\mathbf{n}, \mathbf{K}_0)}, \qquad \alpha_H=\frac{1}{K_0^2}\{B_H^2+2(\mathbf{K}_0, \mathbf{B}_H)\}.$$

Assuming that nonmonochromatic radiation is incident on a rotating crystal, it is easy to find the following expressions for α_1 and α_2:

$$\alpha_1=2\sin2\theta_{1B}\Delta\theta+4\sin^2\theta_{1B}(\Delta\lambda/\lambda_0),$$
$$\alpha_2=-2\sin2\theta_{2B}\Delta\theta+4\sin^2\theta_{2B}(\Delta\lambda/\lambda_0),$$

where λ_0 is the vacuum wavelength for both of the planes which satisfy the Bragg–Wolf conditions, and θ_{1B} and θ_{2B} are the Bragg angles which correspond to this wavelength.

Thus in our particular case, assuming that $b_1 = b_2 = 2$, Eq. (2) will take the form

$$\delta_1=(\delta_0+\sqrt{3}\Delta\theta+\Delta\lambda/\lambda_0)/2, \quad \delta_2=(\delta_0-\sqrt{3}\Delta\theta+\Delta\lambda/\lambda_0)/2 \qquad (3)$$

for both scattered waves. After substituting Eq. (3) into Eq. (1) we find the working system of equations which is to be solved with the boundary conditions

$$D_0=E_0,\ D_1=D_2=0 \text{ with } t=0. \tag{4}$$

The intensity of each of the three strong waves having a wavelength λ at the exit from the crystal is

$$|D_H(\Delta\theta,\lambda,t_0|^2=\Bigl|\sum_{j=1}^{3} D_0^{(j)}x_H^{(j)}\exp\Bigl[-i2\pi\frac{K_0}{\gamma_0}\delta_0^{(j)}t_0\Bigr]\Bigr|^2, \tag{5}$$

$$\text{with}\quad H=0,1,2,$$

where $K_0 = 1/\lambda_0$, γ_0 is the direction cosine of the incident beam, $\delta_0^{(j)}$ is the solution to the dispersion equation,

$$x_0^{(j)}=1,\qquad x_1^{(j)}=\frac{\psi_{1-2}(\psi_0-2\delta_0^{(j)})-\psi_1\psi_{-2}}{\psi_{-2}(\psi_0-2\delta_1^{(j)})-\psi_{-1}\psi_{1-2}},$$
$$x_2^{(j)}=\frac{\psi_1\psi_{-1}-(\psi_0-2\delta_0^{(j)})(\psi_0-2\delta_1^{(j)})}{\psi_{-2}(\psi_0-2\delta_1^{(j)})-\psi_{-1}\psi_{1-2}}, \tag{6}$$

and $D_0^{(j)}$ is determined from the boundary conditions of Eq. (4).

From the practical point of view the greatest interest lies in the distribution of the intensities of the x rays scattered by a "thick" crystal. We have carried out a calculation for a crystal of thickness t_0 = 1 mm ($\mu_0 t_0$ = 20). With this thickness the distribution of the intensity in both the two- and three-wave cases is a very strongly oscillatory curve. Experimentally one always obtains an averaged curve; therefore in the present work we have calculated only the averaged energy distribution. The averaging was done by the commonly used method.[10] We took account of the fact that the crystal thickness t_0 is only known with some uncertainty.

In the general case the ratio of the power in the scattered beam to that in the primary nonmonochromatic beam is related to $|D_H|^2$ by

$$\frac{P_H(\Delta\theta)}{P}=\frac{1}{|b_H|}\frac{\int I_0(\lambda)\,|D_H(\lambda,\Delta\theta)|^2\,d\lambda}{\int I_0(\lambda)\,d\lambda}, \tag{7}$$

where $I_0(\lambda)$ is the distribution of intensity with respect to wavelength in the primary beam. For monochromatic radiation this is a Dirac delta function.

To study the transition of three-wave diffraction into two-wave diffraction we calculate the distribution P_H/P of the scattered monochromatic x-ray beams having wavelengths different from λ_0, i.e., we assume that $I_0(\lambda) = \delta(\lambda-\lambda_i)$, where λ_i is a certain wavelength close to λ_0. Here the coefficient ψ_H is chosen as follows:

$$\psi_0=-2\cdot10^{-4}-i\,0.5\cdot10^{-6},$$
$$\psi_1=\psi_2=\psi_{-1}=\psi_{-2}=-10^{-4}-i\,0.48\cdot10^{-6},$$
$$\psi_{1-2}=\psi_{2-1}=-0.5\cdot10^{-4}-i\,0.45\cdot10^{-6}. \tag{8}$$

The real part is associated with scattering processes and the imaginary part involves absorption. The different values of the imaginary parts ψ_H are due to the inclusion of thermal motion.

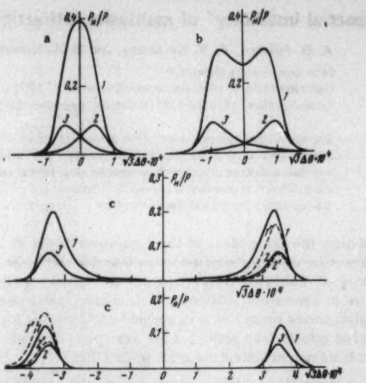

Fig. 1. Change in the energy distribution with a change in the wavelength of the incident radiation for three-wave diffraction. a) Simultaneous reflection from both families of Bragg planes; b, c, d) nonsimultaneous reflection: a) $\Delta\lambda/\lambda_0 = 0$; b) $\Delta\lambda/\lambda_0 = 0.5\cdot10^{-4}$; c) $\Delta\lambda/\lambda_0 = 3\cdot10^{-4}$; d) $\Delta\lambda/\lambda_0 = -4\cdot10^{-4}$; 1) energy distribution in the incident beam; 2, 3) energy distributions in both scattered beams having wave vectors K_2 and K_1 respectively. The dashed lines show the energy distribution for two-wave diffraction: 1' is the transmitted and 2' is the scattered beam.

We have calculated the distribution P_H/P for 16 values of λ_i, one of which coincides with λ_0. Figure 1a shows the distribution of P_H/P for the transmitted and both scattered beams for simultaneous reflection from both families of Bragg planes. Of the remaining diffraction patterns ($\lambda_i \neq \lambda_0$) we only give three here (Figs. 1b, 1c, 1d). Figure 1b shows P_H/P, where $\Delta\lambda/\lambda_0 = (\lambda_i-\lambda_0)/\lambda_0 = 5\cdot10^{-4}$. It can be seen that the curve P_0/P (the transmitted beam) has two maxima already. With increasing $\Delta\lambda/\lambda_0$, the dip and the distance between them increase and the three-wave diffraction decomposes into two two-wave diffraction patterns (Fig. 1c, $\Delta\lambda/\lambda_0 = 3\cdot10^{-4}$). A nearly analogous pattern is also observed with wavelengths $\lambda_i < \lambda_0$. For sufficiently large $|\Delta\lambda/\lambda_0|$ there is also a decomposition of the three-wave diffraction into two two-wave patterns (Fig. 1d). For comparison in the latter two figures we show the distribution of P_H/P for the two-wave case (the dashed curves).

We might expect at first glance that Fig. 1 contradicts common sense. For example, in Figs. 1c-d the reflections from the first and second Bragg planes occur at different angles θ, i.e., the mutual effects of the two reflections on each other are as if they didn't exist, while the energy distribution differs substantially from the pure two-wave case. It should, however, be noted that the width of the distribution depends on the quantity $\mu_0 t_0$ and decreases as the latter increases. For simplicity we can regard the crystal of interest as a set of several thinner crystals, say, 10 crystal plates with $\mu_0 t_0$ = 2. If we consider the first plate then the energy distributions of both reflections will overlap. As one approaches the next plate the distribution will narrow but the presence of an overlap (interaction) in the upper parts of the crystal will manifest itself in a finite distribution of the energy. We have used

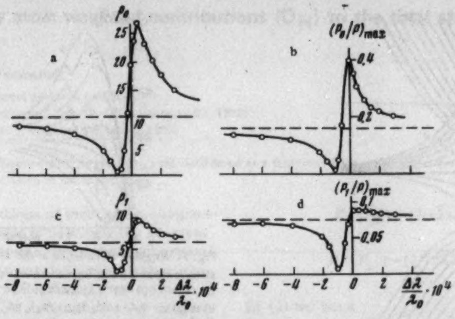

Fig. 2. Variation of the integrated and maximum power as a function of λ. a, b) Transmitted beam; c, d) one of the scattered beams (the curves for the second scattered beam are the same). The dashed lines show the values corresponding to the two-wave diffraction case; in graph a the dashed curve corresponds to $2\int(P_H/P)d(\Delta\theta)$ since in this case there is a "decay" of the three-wave diffraction into two two-wave diffraction patterns; the ordinates of graphs a and c are taken in arbitrary units.

the calculated distributions $P_H/P = f(\Delta\theta)$ to construct the relations $(P_H/P)_{max}$ and $\rho_H = \int (P_H/P)d(\Delta\theta)$ as a function of $\Delta\lambda/\lambda_0$. These relations are shown in Fig. 2. We can see from them that with increasing $|\Delta\lambda/\lambda_0|$ both the energy at the maximum and the integrated energy go asymptotically to values corresponding to the two-wave case (dashed curves).

We also arrive at a similar conclusion if we consider the changes in the dispersion surfaces with varying λ_i. Figure 3b shows cross sections of the dispersion surface for three-wave diffraction ($\Delta\lambda/\lambda_0 = 0$) in the plane of incidence. These cross sections completely determine the dispersion surface, since for coplanar rays it consists of several cylinders. Figure 3a and 3c show the case where $\Delta\lambda/\lambda_0 \neq 0$ [a) $\Delta\lambda/\lambda_0 > 0$; c) $\Delta\lambda/\lambda_0 < 0$]. In both cases we see that the dispersion surface contains dispersion surfaces for two-wave diffraction as a component part. With increasing $|\Delta\lambda/\lambda_0|$ they become ever larger and more separated. However, despite the sameness of the general nature of this change in the cases with $\Delta\lambda/\lambda_0 > 0$ and $\Delta\lambda/\lambda_0 < 0$ they differ essentially from each other. Comparing Figs. 3a and 3c we see that one of the sheets of the dispersion surface at the point $\Delta\theta = 0$ has a minimum in one case and a maximum in the other. To determine the values of λ_i for which there is a change in the nature of the extrema we calculated the dispersion surfaces for several values of λ_i close to each other. These surfaces are shown in Fig. 4. For convenience they are shifted in such a way that the spheres of radius $K_{0i} = 1/\lambda_i$ coincide in the region of the Laue points (line AA' in the figure). It can be seen that when $\Delta\lambda/\lambda_0 = -0.5\cdot 10^{-4}$ one of the sheets of the dispersion surface coincides with its asymptote, i.e., for this wavelength there is a change in the curvature of one of the sheets of the dispersion surface.

However such a change in the shape of the dispersion surface does not fully explain the unusual behavior of the dependence of the integrated and maximum energy on $\Delta\lambda/\lambda_0$. These curves were calculated for an absorbing crystal ($\mu_0 t_0 = 20$); therefore the intensity distributions of both the scattered and transmitted beams are substantially influenced by the nature of the absorption of the wave fields which arise in the crystal. In order to estimate the role of absorption we calculated the relation $P_H/P = f(\Delta\theta, \Delta\lambda/\lambda_0)$ for a nonabsorbing crystal, i.e., in Eq. (8) the imaginary part ψ_H was set equal to zero. Just as in the case of an absorbing crystal, a decay of the diffraction pattern of the three-wave case into two diffraction patterns corresponding to the two-wave case was observed.

We calculated the relation between the integrated and maximum energy of the scattered beam and the wavelength. The curves obtained differ somewhat from the analogous curves calculated for an absorbing crystal. Just as for an absorbing crystal, all of the curves have a minimum when $\Delta\lambda/\lambda_0 = -10^{-5}$ but it is not too strong. With a deviation of $\Delta\lambda/\lambda_0$ from this value all of the curves asymptotically approach a line corresponding to the two-wave case. Such

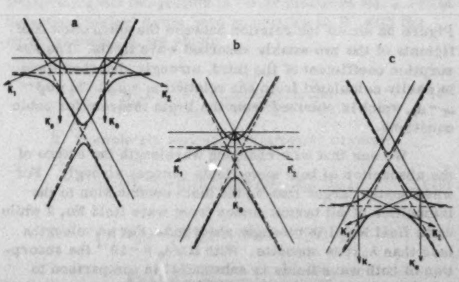

Fig. 3. Variation of the dispersion surface with changing wavelength. a) $\Delta\lambda/\lambda_0 = 3\cdot 10^{-4}$; b), $\Delta\lambda/\lambda_0 = 0$; c), $\Delta\lambda/\lambda_0 = -4\cdot 10^{-4}$; the solid curves show parts of spheres of radius $K_d = 1/\lambda_i$, whose centers are at reciprocal lattice sites, and the dashed curves show the asymptotes of spheres of radius $\sigma_d = K_d(1+\psi_0/2)$.

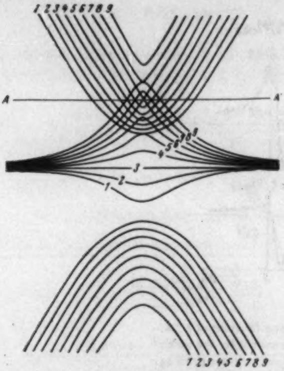

Fig. 4. Change in the shape of the dispersion surfaces with a change in the wavelength of the incident radiation. 1) $\Delta\lambda/\lambda_0 = 0$; 2) $\Delta\lambda/\lambda_0 = -0.25\cdot 10^{-4}$; 3) $\Delta\lambda/\lambda_0 = -0.5\cdot 10^{-4}$; 4) $\Delta\lambda/\lambda_0 = -0.75\cdot 10^{-4}$; 5) $\Delta\lambda/\lambda_0 = -10^{-4}$; 6) $\Delta\lambda/\lambda_0 = -1.25\cdot 10^{-4}$; 7) $\Delta\lambda/\lambda_0 = -1.5\cdot 10^{-4}$; 8) $\Delta\lambda/\lambda_0 = -1.75\cdot 10^{-4}$; 9) $\Delta\lambda/\lambda_0 = -2\cdot 10^{-4}$.

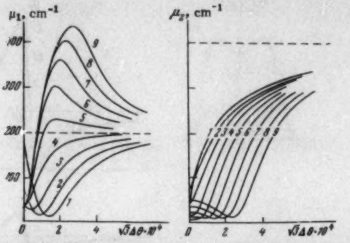

Fig. 5. Angular dependence of the absorption coefficients of the two weakly absorbed wave fields for various wavelengths. 1) $\Delta\lambda/\lambda_0 = -2\cdot 10^{-4}$; 2) $\Delta\lambda/\lambda_0 = -1.5\cdot 10^{-4}$; 3) $\Delta\lambda/\lambda_0 = -10^{-4}$; 4) $\Delta\lambda/\lambda_0 = -0.5\cdot 10^{-4}$; 5) $\Delta\lambda/\lambda_0 = 0$; 6) $\Delta\lambda/\lambda_0 = 0.5\cdot 10^{-4}$; 7) $\Delta\lambda/\lambda_0 = 10^{-4}$; 8) $\Delta\lambda/\lambda_0 = 1.5\cdot 10^{-4}$; 9) $\Delta\lambda/\lambda_0 = 2\cdot 10^{-4}$; both of the relations are symmetric, $\mu_j(\Delta\theta) = \mu_j(-\Delta\theta)$; the dashed line denotes the limiting value of the absorption coefficients. In our case they are just as in the two-wave case.

a change in the integrated and maximum powers of the scattered beams with decay of the three-wave diffraction in a nonabsorbing crystal favors the idea of a "clearing" effect, i.e., a decrease in the intensity of the beam scattered by a single plane when another Bragg plane falls into a reflecting position simultaneously. (The "clearing" phenomenon has been explained by Maeyer.[1])

However, the "clearing" phenomenon does not suffice to explain the behavior of the curves for the dependence of the maximum and integrated power on the wavelength. Therefore we have treated the question of absorption in more detail. In our particular case three wave fields propagate in the direction of each strong wave, each of which has its own refractive index and consequently its own absorption coefficient. This absorption coefficient is related to the imaginary part of the solution to the dispersion equation as follows:

$$\mu_j = -4\pi\delta_{0M}^{(j)}/\lambda. \tag{9}$$

Figure 5a shows the relation between the absorption coefficients of the two weakly absorbed wave fields. The absorption coefficient of the third, strongly absorbed wave is easily calculated from the relation $\mu_3 = \mu_0(1 + b_1 + b_2) - \mu_1 - \mu_2$, which is obtained from the Vieta theorem for cubic equations.

We see that with changing wavelength the nature of the absorption of both wave fields changes strongly. For wavelengths larger than λ_0 the main contribution to the intensities of all beams comes from wave field No. 2 while wave field No. 1 is strongly absorbed. For wavelengths less than λ_0 it is opposite. With $\Delta\lambda/\lambda_0 = -10^{-4}$ the absorption of both wave fields is substantial in comparison to the absorption with $\lambda > \lambda_0$ and $\lambda < \lambda_0$. Thus we can explain the minimum values of $(P_H/P)_{max}$ and ρ_H corresponding to the wavelength $\lambda = \lambda_0(1 - 10^{-4})$ (Fig. 2). The different angular dependences of the absorption coefficients can also be explained, as well as the maxima in the curves of Fig. 2. The maxima of the curves for $\rho_H(\Delta\lambda/\lambda_0)$ (Figs. 2a, c) are explained by the fact that when $\Delta\lambda/\lambda_0 = 0.5\cdot 10^{-4}$ the absorption coefficient for wave field No. 2 remains close to the minimum over a larger angular region than for other values of $\Delta\lambda/\lambda_0$.

Such an unusual change in the diffraction pattern for three-wave diffraction with a change in the wavelength (in the case of two-wave diffraction there is only a shift in the diffraction pattern due to the corresponding change in the Bragg angle) naturally should be reflected in the angular distribution of the intensities of the scattered beams in the case of nonmonochromaticized radiation. In this case even the characteristic radiation cannot be regarded as monochromatic since all of the most important changes in the diffraction pattern occur with a change of the wavelength within the limits of the natural linewidth.

It should be noted that the "decay" of multiwave diffraction into several two-wave diffraction patterns for small changes in the wavelength of the incident radiation will always occur for coplanar rays. For noncoplanar rays it will occur under conditions where the Ewald sphere intersects not less than four reciprocal lattice sites not lying in the same plane.

---

[1] G. Maeyer, Z. Kristallogr., 66, 585 (1928).
[2] M. Renninger, Z. Phys., 106, 141 (1937).
[3] G. Borrmann and W. Hartwig, Z. Kristallogr., 121, 401 (1965).
[4] G. Hildebrandt, Phys. Status Solidi, 24, 245 (1967).
[5] P. P. Ewald and Y. Héno, Acta Crystallogr., A24, 5 (1968).
[6] Y. Héno and P. P. Ewald, Acta Crystallogr., A24, 16 (1968).
[7] P. Penning, Philips Res. Repts., 23, 12 (1968).
[8] W. Uebach and G. Hildebrandt, Z. Kristallogr., 129, 1 (1969).
[9] T. Joko and A. Fukuhara, J. Phys. Soc. Japan, 22, 597 (1967).
[10] W. H. Zachariasen, Theory of X-Ray Diffraction in Crystals, J. Wiley, New York (1945).

Statistical values of heavy atom weighted contributions (D_H) to the total structure amplitude

L. L. Shadyro and I. D. Feranchuk

Concrete and Reinforced Concrete Research Institute

(Submitted July 16, 1971; resubmitted June 12, 1972; February 20, 1973)
Kristallografiya, 18, 1134-1140 (November-December 1973)

All important cases of the difference distributions $P(D_H)$ are considered as a function of the number of atoms and the symmetry of atomic clusters in the crystal.

To facilitate structure calculations of increasing complexity it is sometimes advantageous to separate the absolute values $|F_{HKL}|$, due to heavy atoms, from the total crystal scattering amplitudes. This is carried out by taking into account the change in intense reflections by anomalous scattering or (and) isomorphic substitutions. For single-wave anomalous scatterers or single isomorphic substitutions solving the problem of separating the heavy-atom diffraction contribution requires a statistical approach.[1,2] One of the main aspects of such an approach is the determination of the values of $D_H = |F_H|/(|F_H| + |F_L|)$, where $|F_H|$ and $|F_L|$ are the absolute values of structure amplitudes due to unknown heavy atoms of one kind and to all remaining atoms (mainly light ones), respectively.

The quantity D_H is determined as a function of contributions by atoms of H (heavy) and L (light) types to the total crystal scattering. These contributions are proportional, respectively, to $\Sigma_T = \sum^{H} f_T^2 = \Sigma_L = \sum^{L} f_L^2$, which are assumed known.

In this paper we consider all cases of the important difference distributions $\mathscr{P}(D_H) = P(D_H)dD_H$ as a function of the number of atoms and symmetry of H and L atoms in the crystal. For each of seven cases (three in part I and four in part II) we provide, besides the shape of the distribution function $P(D_H)$, expressions for the most important characteristic of the distribution $\mathscr{P}(D_H)$: $(D_H)_M$, the most probable value of D_H (mode), and $\overline{D}_H$, the center of the $\mathscr{P}(D_H)$ distribution (the mathematical expectation of D_H).

Using the transformation equation of a two-dimensional distribution law,[3] one can obtain the general form for the distribution of the quantity $D_H = |F_H|/(|F_H| + |F_L|)$, under the assumption that $|F_H|$ and $|F_L|$ are independent random quantities with given distributions $\mathscr{P}_1(|F_H|) = P_1(|F_H|)d|F_H|$ and $\mathscr{P}_2(|F_L|) = P_2(|F_L|)d|F_L|$,

$$\mathscr{P}(D_H) = \left\{ (1-D_H)^{-2} \int P_1[D_H|F_L|/(1-D_H)] P_2(|F_L|)|F_L|d|F_L| \right\} dD_H, \tag{1}$$

where $0 \leq D_H \leq 1$ and $P_1[D_H|F_L|/(1-D_H)]$ is the result of replacing the variable $P_1(|F_H|)$ by $|F_H|$ in the original distribution function $D_H|F_L|/(1-D_H)$.

I. GENERAL CASE OF MANY ATOMS OF ARBITRARY TYPE. THE GAUSSIAN APPROXIMATION

The absolute value distribution of structure amplitudes is well known[4] in this approximation. Consider the first three possibilities, related to the symmetries of H and L atomic clusters.

1. A centrosymmetric crystal:

$$P_1(|F_H|) = (2/\sqrt{2\pi\Sigma_H})\exp(-|F_H|^2/2|F_H|), \tag{2}$$

$$P_2(|F_L|) = (2/\sqrt{2\pi\Sigma_L})\exp(-|F_L|^2/2|F_L|). \tag{3}$$

By (1) we have

$$P(D_H) = 2/[(1-D_H)^2\pi\sqrt{\Sigma_H\Sigma_L}] \int_0^\infty \exp\{[(-|F_L|^2/2\Sigma_H)(D_H/(1-D_H))]^2\}$$
$$\times\exp(-|F_L|^2/2\Sigma_L)|F_L|d|F_L| = (2/\pi)\sqrt{\Sigma_H\Sigma_L}[\Sigma_L D_H^2 + \Sigma_H(1-D_H)^2]^{-1}. \tag{4}$$

The value of $(D_H)_M$ is determined from the condition

$$\left.\frac{dP(D_H)}{dD_H}\right|_{D_H = (D_H)_M} = 0. \tag{5}$$

In the case given this leads to the condition

$$\frac{4\sqrt{\Sigma_H\Sigma_L}\{\Sigma_L[1-(D_H)_M] - \Sigma_H(D_H)_M\}}{\pi\{\Sigma_L(D_L)_M^2 + \Sigma_H[1-(D_H)_M]^2\}} = 0, \tag{6}$$

whence

$$(D_H)_M = \Sigma_H/\Sigma_H + \Sigma_L. \tag{7}$$

Since Eq. (1) gives the distribution $\mathscr{P}(D_H)$ in normalized form then we obtain

$$\overline{D}_H = \int_0^1 D_H P(D_H)dD_H = \frac{2\sqrt{\Sigma_H\Sigma_L}}{\pi}\int_0^1 \frac{D_H dD_H}{[\Sigma_H - 2\Sigma_L D_H + (\Sigma_H + \Sigma_L)D^2]}. \tag{8}$$

Performing the integration in (8) by means of Eq. 2.175 of reference tables[5] (from here on denoted G. R. with the equation number), we obtain

$$\overline{D}_H = \frac{\Sigma_H}{\Sigma_H + \Sigma_L} + \frac{\sqrt{\Sigma_H\Sigma_L}}{\pi(\Sigma_H + \Sigma_L)}\ln\frac{\Sigma_L}{\Sigma_H}. \tag{9}$$

2. Completely noncentrosymmetric crystal:

$$P_1(|F_H|) = (2|F_H|/\Sigma_H)\exp(-|F_H|^2/\Sigma_H), \tag{10}$$

$$P_2(|F_L|) = (2|F_L|/\Sigma_L)\exp(-|F_L|^2/\Sigma_L), \tag{11}$$

$$P(D_,) = \frac{4}{(1-D_H)^2\Sigma_H\Sigma_L}\int_0^\infty \frac{D_H}{1-D_H}$$
$$\times\exp\left\{-|F_L|^2\left[\frac{1}{\Sigma_H}\left(\frac{D_H}{1-D_H}\right)^2 + \frac{1}{\Sigma_L}\right]\right\}$$
$$\times|F_L|^3 d|F_L| = 2D_H(1-D_H)\Sigma\,\Sigma_L[\Sigma_L D_H^2 + \Sigma_H(1-D_H)^2]^{-2}. \tag{12}$$

By condition (5) we obtain the equation

$$2(\Sigma_H+\Sigma_L)(D_H)_M^3-3(\Sigma_H+\Sigma_L)(D_H)_M^2+\Sigma_H=0, \tag{13}$$

whence we find

$$(D_H)_M=\frac{1}{2}\left(1-\cos\frac{2}{3}\varphi+\sqrt{3}\sin\frac{2}{3}\varphi\right), \tag{14}$$

where $\varphi=\arctan(\Sigma_H/\Sigma_L); 0<\varphi<\pi/2$. We notice that (7) and (9) are easily expressed in terms of the well-known[6] parameter $r=(\Sigma_H/\Sigma_L)^{1/2}$:

$$(D_H)_M=r^2/1+r^2, \tag{7'}$$

$$\bar{D}_H=\frac{r^2}{1+r^2}\left(1+\frac{1}{\pi r}\ln\sqrt{\frac{1}{r}}\right). \tag{9'}$$

Similarly to the preceding case 1 we find an expression for $\bar{D}_H$:

$$\bar{D}_H=2\Sigma_H\Sigma_L\int_0^1 D_H^2(1-D_H)[\Sigma_L D_H^2+\Sigma_H(1-D_H)^2]^{-2}dD_H$$

$$=\frac{\Sigma_H}{\Sigma_H+\Sigma_L}-\frac{\Sigma_H\Sigma_L}{(\Sigma_H+\Sigma_L)^2}\ln\frac{\Sigma_L}{\Sigma_H}+\frac{\pi}{2}\frac{\sqrt{\Sigma_L\Sigma_H}(\Sigma_L-2\Sigma_H)}{(\Sigma_L+\Sigma_H)^2}. \tag{15}$$

3. Noncentrosymmetric crystal with a centrosymmetric heavy atom cluster. The search for the distribution $\mathcal{P}(D_H)$ is carried out on the basis of Eqs. (1), (2), and (11):

$$P(D_H)=\frac{4}{(1-D_H)^2}\frac{1}{\Sigma_L\sqrt{2\pi\Sigma_H}}$$

$$\times\int_0^\infty \exp\left\{-|F_L|^2\left[\frac{1}{2\Sigma_H}\left(\frac{D_H}{1-D_H}\right)^2+\frac{1}{\Sigma_L}\right]\right\}$$

$$\times|F_L|^2 d|F_L|=2\Sigma_H\sqrt{\Sigma_L}(1-D_H)[\Sigma_L D_H^2+2\Sigma_H(1-D_H)^2]^{-3/2} \tag{16}$$

(see G. R. 3.461).

$(D_H)_M$ is determined from the equations

$$4\Sigma_H-(8\Sigma_H+3\Sigma_H)(D_H)_M+2(2\Sigma_H+\Sigma_L)(D_H)_M^2=0, \tag{17}$$

$$(D_H)_M=[8\Sigma_H+3\Sigma_L-(9\Sigma_L^2+16\Sigma_L\Sigma_L)^{1/2}]/[4(2\Sigma_H+\Sigma_L)], \tag{18}$$

$$\bar{D}_H=2\Sigma_H\sqrt{\Sigma_L}\int_0^1 D_H(1-D_H)[\Sigma_L D_H+2\Sigma_H(1-D_H)^2]^{-3/2}=\frac{2\Sigma_H}{2\Sigma_H+\Sigma_L}$$

$$+\sqrt{\frac{2\Sigma_H}{\Sigma_L}}\frac{\Sigma_L}{2\Sigma_H+\Sigma_L}-\frac{2\Sigma\sqrt{\Sigma_L}}{(2\Sigma_H+\Sigma_L)^{3/2}}\ln\frac{\sqrt{(2\Sigma_H+\Sigma_L)\Sigma_L}+\Sigma_L}{\sqrt{(2\Sigma_H+\Sigma_L)2\Sigma_H}-2\Sigma_H} \tag{19}$$

(see G. R. 2.264)

II. SMALL NUMBER (1,2) OF HEAVY ATOMS (N_H) OF ONE TYPE

The starting equations for the distribution function $P_1(|F_H|)$ are borrowed from Parthasarathy's work,[7] taking into account the identity of notation ($T\equiv p$, $L\equiv Q$, $\Sigma_H\equiv\sigma_p^2$, $\Sigma_L\equiv\sigma_Q^2$; $P_1(|F_H|)$ is the density function $P(|F_p|)$. The number of light atoms per unit cell is assumed sufficient to satisfy all requirements of the Gaussian approximation.

$N_H=1$. One heavy atom. In this case it can always be placed at the origin of coordinates. Two possibilities arise, depending on the symmetry of the surrounding atoms.

1. One heavy atom in a centrosymmetric crystal:

$$P_1(|F_H|)=\delta(|F_H|-\sqrt{\Sigma_H}), \tag{20}$$

where δ is Dirac's delta function. The corresponding expression for $P_2(|F_L|)$ was derived above, see Eq. (3). Performing the transformation (1) we obtain

$$P(D_H)=\frac{1}{(1-D_H)^2}\frac{2}{\sqrt{2\pi\Sigma_L}}\int_0^\infty \delta\left(|F_L|\frac{D_H}{1-D_H}-\sqrt{\Sigma_H}\right)$$

$$\times\exp(-|F_L|^2/2\Sigma_L)|F_L|d|F_L|=[2\sqrt{\Sigma_H}/(D_H^2\sqrt{2\pi\Sigma_L})]$$

$$\times\exp[-\Sigma_H(1-D_H)^2/(2\Sigma_L D_H^2)]. \tag{21}$$

The most probable value $(D_H)_M$ is determined from condition (5), equivalent in this case to the condition

$$\frac{\Sigma_H}{2\Sigma_L(D_H)_M^4}\left[\frac{1-(D_H)_M}{(D_H)_M}\right]-\frac{2}{(D_H)_M^3}=0, \tag{22}$$

which leads to the equation

$$2(\Sigma_L/\Sigma_H)(D_H)_M^2+(D_H)_M-1=0. \tag{23}$$

Taking account during the solution of (23) of the unconditionally positive values of D_H $(0\le D_H\le 1)$, we obtain

$$(D_H)_M=(-1+\sqrt{1+8\Sigma_L/\Sigma_H})/(4\Sigma_L/\Sigma_H). \tag{24}$$

$$\bar{D}_H=\frac{2}{\sqrt{2\pi}}\left(\frac{\Sigma_H}{\Sigma_L}\right)^{1/2}\int_0^1 \exp\left[-\frac{\Sigma_H}{2\Sigma_L}\left(\frac{1-D_H}{D_H}\right)^2\right]D_H^{-1}dD_H$$

$$=\frac{2}{\sqrt{2\pi}}\left(\frac{\Sigma_H}{\Sigma_L}\right)^{1/2}\int_0^\infty \exp\left(-\frac{\Sigma_H}{2\Sigma_L}z^2\right)\Big/(1+Z)^{-1}dD_H$$

$$=\frac{2}{\sqrt{2\pi}}\left(\frac{\Sigma_H}{\Sigma_L}\right)^{1/2}f(x), \tag{25}$$

where

$$z=(1-D_H)/D_H, \tag{26}$$

$$f(x)=\int_0^\infty \frac{\exp(-z^2)}{z+x}dz \tag{27}$$

and

$$X=\sqrt{\Sigma_H}/\sqrt{2\Sigma_L}. \tag{28}$$

$f(x)$ in Eq. (27) is expressed[8] in terms of the tabulated integral I, whose values for $0.1\le x\le 2$ are given in Table 1 with a step of $\Delta x=0.1$.

TABLE 1

x	0.1	0,2	0,3	0.4	0.5	0.6	0.7	0.8	0.9	1.0
I	2.17	1.59	1.30	1.10	0.96	0.86	0.78	0.71	0.65	0.61
x	1.1	1.2	1.3	1.4	1.5	1.6	1.7	1.8	1.9	2.0
I	0.57	0.50	0.53	0.47	0.45	0.42	0.40	0.39	0.37	0.35

2. One heavy atom in a noncentrosymmetric crystal. The starting equations are expressions (11) and (20):

$$P(D_H)=\frac{1}{(1-D_H)^2}\frac{2}{\Sigma_L}\int_0^\infty \delta\left(|F_L|\frac{D_H}{1-D_H}-\sqrt{\Sigma_H}\right)\exp(-|F_L|^2/\Sigma_L)$$

$$\times|F_L|^2\,d|F_L|=(2\Sigma_H/\Sigma_L)[(1-D_H)/D_H^3]\exp[-\Sigma_H(1-D_H)^2/(\Sigma_L D_H^2)]. \tag{29}$$

Similarly to the preceding case 1 we obtain an equation for the required $(D_H)_M$:

$$[2(D_H)_M-3](D_H)_M^2+[2\Sigma_H(1-(D_H)_M)^2]/\Sigma_L=0, \tag{30}$$

whose solution in analytic form is awkward. It is found that

$$(D_H)_M\simeq\frac{\sqrt{\Sigma_H}}{\sqrt{\Sigma_H}+\sqrt{\Sigma_L}}+0.02\frac{\Sigma_H-\Sigma_L}{\Sigma_H+\Sigma_L} \tag{31}$$

[$\delta\le 3\%$ for the practically interesting region $0.1<(\Sigma_H/\Sigma_L)<3$] and

$$\bar{D}_H=\frac{2\Sigma_H}{\Sigma_L}\int_0^1\frac{1-D_H}{D_H^2}\exp\left[-\frac{\Sigma_H}{\Sigma_L}\left(\frac{1-D_H}{D_H}\right)^2\right]dD_H$$

$$=\sqrt{\frac{\pi\Sigma_H}{\Sigma_L}}-\frac{2\Sigma_H}{\Sigma_L}\int_0^\infty\exp\left(-\frac{\Sigma_H}{\Sigma_L}z^2\right)\Big/(1+z)^{-1}\,dD_H=\sqrt{\frac{\pi\Sigma_H}{\Sigma_L}}-\frac{2\Sigma_H}{\Sigma_L}f(x), \tag{32}$$

where z is defined by (26), $f(x)$ by (27), and

$$x=\sqrt{\Sigma_H}/\sqrt{\Sigma_L}\quad. \tag{33}$$

$N_H = 2$. In a noncentrosymmetric crystal a pair of heavy atoms can always be connected by a center of inversion, choosing as origin of coordinates the center of the segment joining the atoms. Two possibilities arise again.

3. Two heavy atoms in a centrosymmetric crystal:

$$P_1(|F_H|)=(2/\pi\sqrt{2\Sigma_H})\sqrt{1-(|F_H|^2/2\Sigma_H)};\quad 0\leqslant|F_H|\leqslant\sqrt{2\Sigma_H}\ . \tag{34}$$

The corresponding expression for $P_2(|F_L|)$ is given above, (see Eq. 3), and

$$P(D_H)=\frac{1}{(1-D_H)^2}\frac{2}{\pi\sqrt{\pi\Sigma_H\Sigma_L}}\int_0^{a_H}\frac{\exp(-|F_L|^2/2\Sigma_L)|F_L|}{[1-(|F_L|D_H)^2/2\Sigma_H(1-D_H)^2]^{1/2}}$$

$$\times d|F_L|=\frac{1}{D_H(1-D_H)}\frac{\sqrt{2}}{\pi\sqrt{\pi\Sigma_H\Sigma_L}}\int_0^{u_H}\frac{\exp(-t/2\Sigma_L)}{[2\Sigma_H(1-D_H)^2/D_H-t]^{1/2}}\,dt, \tag{35}$$

$$a_H=\sqrt{2\Sigma_H}(1-D_H)/D_H, \tag{36}$$

$$u_H=2\Sigma_H(1-D_H)^2/D_H^2, \tag{37}$$

$$t=|F_L|^2. \tag{38}$$

Using Eq. G. R. 3.383, we obtain

$$P(D_H)=2\sqrt{\Sigma_H}/(\pi\sqrt{\pi\Sigma_L}D_H^2)B(1,1/2)\,\Phi\left[1,3/2;-\frac{\Sigma_H}{\Sigma_L}\left(\frac{1-D_H}{D_H}\right)^2\right], \tag{39}$$

where $B(\mu,\nu)$ is the Euler function, and Φ is the confluent hypergeometric function. Denoting

$$\sqrt{\frac{\Sigma_H}{\Sigma_L}}\frac{1-D_H}{D_H}=z \tag{40}$$

and calculating $B(1, 1/2)$ by Eqs. G. R. 8.384-G.R. 8.338 , we obtain

$$P(D_H)=4\sqrt{\Sigma_H}/(\pi\sqrt{\pi\Sigma_L}D_H^2)\,\Phi(1,3/2;-z^2). \tag{41}$$

The interval $0\le D_H\le 1$ corresponds here to the interval $\infty\ge z\ge 0$. By means of Kummer's equation (42) can be transformed from $(-z^2)$ in (41) to positive values of the argument z^2, for which the function Φ is tabulated and represented graphically[9] in the region $0\le z^2\le 4$ (taking into account that $z^2\equiv z$ in ref. 9):

$$\Phi(a,c;z^2)=\exp(z^2)\,\Phi(c-a;c;-z^2), \tag{42}$$

which leads in our case to

$$\Phi(1,3/2;-z^2)=\Phi(1/2,3/2;z^2)/\exp(z^2). \tag{43}$$

For $|z^2|>4$ the large $|z^2|$ asymptotic approximation for Φ can be used, and it is found that for $|z^2|>4$ the equation can be simplified considerably without serious loss in accuracy:

$$\Phi(1,3/2;-z^2)\simeq\frac{1}{2z^2}+\frac{0.25}{z^4}+\frac{0.375}{z^6}. \tag{44}$$

Retaining in the right-hand side of (44) only the first term $z^2/2$ for $|z|\to\infty\,(D_H\to 0)$, we obtain that $P(D_H)$ tends to the finite limit $2\sqrt{\Sigma_L}/\pi\sqrt{\pi\Sigma_H}$ (the reflection probability of a small number of structure amplitudes with $|F_H|=|F_{H1}|-|F_{H2}|=0$). Direct calculations of the distribution (41) for different ratios (Σ_H/Σ_L) also established that to a good approximation ($\delta\le 2\%$) we have

$$(D_H)_M\simeq\frac{\Sigma_H}{2(\Sigma_H+\Sigma_L)}+\frac{\sqrt{2\Sigma_H}}{2(\sqrt{2\Sigma_H}+\sqrt{\Sigma_L})}. \tag{45}$$

By (1) we have

$$\bar{D}_H=\frac{2}{\pi\sqrt{\pi}}\sqrt{\frac{\Sigma_H}{\Sigma_L}}\int_0^1(D_H)^{-1}\Phi\left[1,3/2;-\frac{\Sigma_H}{\Sigma_L}\left(\frac{1-D_H}{D_H}\right)^2\right]dD_H$$

$$=\frac{2}{\pi\sqrt{\pi}}\int_0^\infty\left(1+\sqrt{\frac{\Sigma_H}{\Sigma_L}}\right)^{-1}\Phi(1,3/2;-z^2)\,dz. \tag{46}$$

$\bar{D}_H$ is best calculated by numerical integration of (46).

4. Two heavy atoms in a noncentrosymmetric crystal. The starting equations are (11) and (34):

$$P(D_H)=\frac{1}{(1-D_H)^2}\frac{4}{\pi\Sigma_H\Sigma_L\sqrt{2}}\int_0^\infty\left[1-\frac{|F_L|^2}{2\Sigma_H}\left(\frac{D_L}{1-D_H}\right)^2\right]^{-1/2}$$

$$\times\exp(-|F_L|^2/\Sigma_L)\,|F_L|^2\,d|F_L|=\frac{1}{D_H(1-D_H)}\frac{2}{\pi\Sigma_H}$$

$$\times\int_0^{u_H}(u_H-z)^{-1/2}\sqrt{z}\exp(-z/\Sigma_L)\,dz. \qquad (47)$$

Similarly to the preceding case 3 one can obtain the expression

$$P(D_H)=2\frac{\Sigma_H}{\Sigma_L}\frac{1-D_H}{D_H}\Phi(3/2,2,-z^2), \qquad (48)$$

to be used graphically for $0 \le |z^2| \le 5$ and

$$\Phi(3/2,\,2;\,-z^2)=\Phi(1/2,\,2,\,z^2), \qquad (49)$$

while for $|z^2| > 5$ we have

$$\Phi(3/2,2,-z^2)\simeq\frac{1}{\sqrt{\pi}}\left[\frac{1}{z^3}+\frac{0.75}{z^5}+\frac{2}{z\exp(z^2)}\right], \qquad (50)$$

$$(D_H)_m\simeq 0.92\sqrt{2\Sigma_H}/(\sqrt{2\Sigma_H}+\sqrt{\Sigma_L}), \qquad (\delta\leqslant 3\%), \qquad (51)$$

$$\bar{D}_H=\int_0^\infty\left(1+\sqrt{\frac{\Sigma_H}{\Sigma_L}}\right)^{-1}\Phi(3/2,2;-z^2)\,dz. \qquad (52)$$

Analysis of the distributions $\mathscr{P}(D_H)$ obtained shows that by increasing the number of heavy atoms from 1 to 2 the distributions approach very quickly those of the many-atom case. Thus, for $N_H > 2$ already the difference is insignificant.

---

[1] L. L. Shadyro, Kristallografiya, 18, 69 (1973) [Sov. Phys.—Crystallogr., 18, 43 (1973)].

[2] L. L. Shadyro, 10th Conf. X-Ray Application to Material Science, Inst. of Crystallogr., Academy of Sciences of the USSR, Moscow (1971), p. 43.

[3] A. M. Zaezdnyi, Basic Calculations in Statistical Radio Engineering [in Russian], Svyaz', Moscow, p. 58.

[4] M. A. Porai-Koshits, Practical Course in X-Ray Structural Analysis [in Russian], Izd. MGU (1960), pp. 150-151.

[5] I. S. Gradshtein and I. M. Ryzhik, Tables of Integrals, Sums, Series, and Derivatives [in Russian], Gos. Izd. Fiz.—Matem. Lit., Moscow (1963).

[6] G. A. Sim, Acta Crystallogr., 10, 177 (1957).

[7] S. Parthasarathy, Acta Crystallogr., 18, 1022 (1965).

[8] Quart. J. Mech. Appl. Math., 1, 319 (1948).

[9] E. Janke, F. Emde, and F. Losch, Special Functions [in Russian], Gos. Izd. Fiz. Matem. Lit., Moscow (1969), p. 308.

Key role of analysis of intercation distances in oxygen compounds containing heavy cations (high atomic numbers)

T. M. Polyanskaya, S. V. Borisov, and N. V. Belov
Institute of Inorganic Chemistry, Siberian Branch, Academy of Sciences of the USSR
(Submitted July 4, 1973)
Kristallografiya, 18, 1141-1156 (November-December 1973)

The relationship of the shortest interatomic distances E-E, E-R, and R-R (E is W^{6+} of Mo^{6+} and R is a rare earth or Y) to the type of coordination and the manner in which the coordination polyhedra are joined to one another is analyzed. Examples are given of the use of intercation distances to find the anionic component in four crystal structures.

Descriptive crystal chemistry has amassed sufficient data and established a sufficient number of patterns that it is now necessary to modernize the principle of densest packing, which has traditionally been represented in the form of compact packing of identical spheres. In a broader interpretation,[1] the primary factor is symmetric surrounding of the atoms by others of the same type (in the case of simple structures) and hence overall symmetry of the arrangement of the atomic centers. If one type of cation or anion seems to be the most important, or "leading," in the structure, we can speak of the "rule of 12 neighbors,"[1] i.e., the tendency of the leading atoms to "be arranged in such fashion that each of them is surrounded by the maximum number of equally long vectors to the nearest neighbors, whereupon it turns out that the number of such vectors cannot exceed 12." The best-known structure in which the dominant Ca cations are packed in accordance with the rule of 12 and the larger anions occupying the "small" tetrahedral voids of this packing is the CaF_2 structure.

In real multicomponent crystalline systems, one more frequently observes deviations from the rule of 12 than conformance to it. However, if we limit ourselves to the relative positions and coordination of one or two types of atoms (e.g., heavy and high-valence cations), it is sensible to seek local empirical rules relating the intercation distances to the type of coordination and the manner in which the coordination polyhedra are joined. Such patterns have already been discussed[2] for structures containing the dominant cations W^{6+} and Mo^{6+}. It was shown that analysis of the E−E intercation distances (E is W or Mo) makes it possible to predict the type of heavy-atom coordination and the approximate positions of the anions.

The present article is intended as a description and critical analysis of experimental data on the E−E intercation distances in the structures of oxygen compounds of tungsten and molybdenum with cations in groups I-V of the periodic table; an analysis is also given of the E−R and R−R distances in a number of rare-earth compounds (E is W^{6+} or Mo^{6+} and R^{3+} is a rare earth or Y). Since structural studies usually contain no data on intercation distances, these figures and the unavailable cation−anion and anion−anion distances were calculated from the atomic coordinates. Examples are given of the practical use of the analytic data for interpretation of four structures.

I. GEOMETRIC CHARACTERISTICS OF THE COORDINATION OF W(Mo) ATOMS

1. Experimental data. It was noted in a survey[3] of the crystal chemistry of oxygen compounds of W and Mo that coordination numbers of 4 and 6 are most frequently encountered for W(Mo), c.n. of 5, 7, and 8 being considerably rarer. In addition to the usual tetrahedra and octahedra, the coordination polyhedra can be pentagons in the form of square pyramids (polyoctahedra)

TABLE 1. Experimental Data Pertaining to Tetrahedral Coordination of E (E is W or Mo)

Compound	Distances				Reference
	ΔE (Å)	E − O (Å)	$\overline{E-O}$ (Å)	O − O (Å) in tetrahedron	
K_2MoO_4 *	4.20	1.74—1.78	1.76	2.84—2.97	[4]
K_2WO_4	4.96	1.76—1.80	1.79	2.88—3.04	[5]
$CaWO_4$ *	3.87	1.78	1.78	2.88 • 2.98	[4]
$CdMoO_4$	3.81	1.82	1.82	2.94 • 2.98	[6]
$SrMoO_4$	4.04	1.77	1.77	2.85 • 2.95	[7]
$SrWO_4$	4.03	1.78	1.78	2.87 • 2.97	[7]
$CaMoO_4$	3.87	1.76	1.76	2.82 • 2.96	[7]
$BaWO_4$	4.24	1.78	1.78	2.88 • 2.96	[7]
α-$ZnMoO_4$ *	3.85	1.71—1.84	1.76	2.79—3.01	[4]
$CuMoO_4$ *	>3.85	1.70—1.86	1.77	2.72—3.05	[4]
α-$MnMoO_4$	>4.0	1.72—1.85	1.76	2.75—2.98	[8]
β-$SnWO_4$	4.16	1.75—1.76	1.75	2.84—2.92	[9]
$Cu_3Mo_2O_9$	>3.80	1.69 • 1.86	1.76	2.74—2.99	[10]
α-$Nd_2(MoO_4)_3$	3.95	1.80	1.80	2.90 • 3.03	[11]
β′-$Gd_2(MoO_4)_3$	4.30	1.73—1.80	1.76	2.78—2.91	[12]
$Sc_2(WO_4)_3$ *	>4.00	1.70—1.83	1.76	2.73—3.05	[4]
$Al_2(WO_4)_3$	>4.00	1.76—1.83	1.78	2.83—3.08	[13]
$NaCo_{2.31}(MoO_4)_3$ *	4.24	1.73—1 82	1.77	2.81—3.00	[4]
$Li_2Fe_2(MoO_4)_3$	4.18	1.73—1.80	1.77	2.78—3.04	[14]
$Li_3Fe(MoO_4)_3$	4.17	1.75—1.81	1.78	2.82—2.99	[14]

*The data on these compounds were taken from the original publications, but in order to reduce the size of the bibliography we refer to the survey by M. A. Poral-Koshits et al.,[4] where these works are listed.

TABLE 2. Experimental Data for E with Five-Fold and Six-Fold Coordination

Compound	c.n. E	ΔE(Å)	E − O(Å)	$\overline{E-O}$ (for 4)	$\overline{E-O}$ (for 6)	O − E(Å) for O c.n. of			O − O (Å)	Common edges of E polyhedra	References
						1	2	3			
$Na_2Mo_2O_7$*	I 4 II 6	II—II 3.58 (v) I—II 3.60 (v)	I 1.71; 1.75; 1.78 1.78 II 1.68 : 2.27; 1.68 : 2.27; 1.90 : 1.90	1.75 1.79	1.95	1.68—1.75 av 1.71	1.78—2,27 av 1.96		av 2.87 tetahedra av 2.72 octahedron		[4]
$K_2Mo_2O_7$	I 4 II 6	II—II 3.09 (e) I—II 3.42(в); 3.78 (v)	I 1.75; 1.77; 1.78; 1.80 II 1.75: 2.27; 1.76 : 2.17; 1.83 : 2.10	1.77 1.86	1.96	1.75—1.78 av. 1.76	1.77—2.27 av. 1.99		I 2.82—2.96 II 2.56—2.90	2.56	[15]
$K_2Mo_3O_{10}$*	I 5 II 6	I—I 3.22 (e) I—II 3.25 (e) I—II 4.00 (e)	I 1.66; 1.74; 1.93; 1.96; 2.00 II 1.70 : 2.19; 1.70 : 2.19 1.95 : 1.95	1.82 1.83	I av. for 5 1.86 II 1.95	1.66; 1.70; 1.74 av. 1.70	1.93; 1.95 av. 1.94	1.96; 2.00; 2.19; av. 2.05	I 2.31—3.33 II 2.38—2.92	I—I 2.31 I—II 2.38	[4]
$K_2M_4O_{13}$	6	3.20 (e); 3.28 (e) 3.29 (e); 3.33 (e) 3.38 (e); 3.40 (e) 3.48 (e); 3.52 (e) 3.79 (e); 4.01 (e) 4.08 (e)	I 1.67 : 2,30; 1.74: : 2.35; 1.85 : 1.96 II 1.67 : 2.23; 1.75 : 2.34; 1.90 : 2.02 III 1.71 : 2.11; 1.72 : 2.39; 1.87 : 1.95 IV 1.68 : 2.30; 1.74 : 2.23; 1.92 : 2.07	1.80 1.84 1.81 1.85	1.98 1.98 1.96 1.99	1.67—1.75 av. 1.71	1.71—2.35 av. 1.98	c.n. 3 1.85—2.34 av. 2.08 c.n. 4 1.95—2.30 av. 2.22		2.47; 2.48; 2.49 (×2); 2.53; 2.65 (×2); 2.74	[16]
$MgWO_4$*	6	3.25 (e)	1.80: 2.14; 1.80 : : 2.14; 1.80 : 1.80	1.80	1.94	1W + 2Mg av. 1.80	1.80 и 2.14 av. 1.97		2.50—2.84	2.50	[4]
$CuWO_4$	6	3.17 (e) 3.21 (e)	1.76 : 2.21 1.82 : 1.99 1.85 : 2.03	1.85	1.94		1) 1.82—2.21 2) 1.99, 2.03 av. 2.01		2.41—2.84	2.41; 2.51	[17]
$FeWO_4$*	6	3.21 (e)	1.78 : 2.12 1.78 : 2.12 1.91 : 1.91	1.85	1.94	1W + 2Fe 1.78	2W + 1Fe 1.91, 2.12 av. 2.02		2.55—2.84	2.55	[4]
α-$CoMoO_4$	I 6 II 6	I—II 3.34 (e) II—II 3.80 (e)	I 1.73 : 2.31 (×2) 1.89 : 1.98 II 1.72 : 2,33 (×2) 1.93 : 1.93	1.83 1.82	1.99 1.99	1,72—1,89 av. 1.76	1.93—2.31 av. 2.12	1.98—2.33 av. 2.21	I 2.58—2.84 II 2.58—2.96	2.58 (×4) (~ΔE=3.34) 2.69~ ~ΔE=3.80	[18]
Cu_3WO_6	6	3.97 (isolated)	1.79 : 2.09 (×3)	1.86	1.94	1W + 2Cu 1.79 1W + 3Cu 2.09			2.57—2.80	2.57 (W, Cu)	[19]
$Eu_2(WO_4)_3$*	I 4 II 5	I—I ~4.0 II—II 3.30 (e)	I 1.70 и 1.78 II 1.72; 1.77 1.81(×2); 2.19	1.74 1.78	av. for 5 1.86				I 2.73—3.11 II 2.37—3.33	2.37 (2W) 2.51 (W, Eu)	[8]
α-Bi_2WO_6	6	3.85 (e)	1.69 : 2.30 (×2) 1.82 : 1.82	1.75	1.94	1W + 1Bi 1.83	2W 1,68, 2.28 av. 1.98		2.57—2.81		[20]
$Li_2Fe(WO_4)_2$	6	3.23 (e)	1.78 : 2.28 1.84 : 2.10 1.87 : 2.01	1.87	1.98	1W + 2Fe 1.78, 1.84 av. 1.81	2W + 2Li 1.87, 2.28 av. 2.08 2W + 2Fe 2.01, 2.10 av. 2.05		2.47; 2.63—3.02	2.47; 2.63	[21]
$LiGa(WO_4)_2$	6	3.20 (e)	1.71 : 1.90; 1.88 : 2.26; 1.89 : 2.04	1.85	1.95	1W + 2Ga 1.90 1W + 2Li 1.71	2W + Ga 1.89, 2.26 av. 2.07 2W + Li 1.88, 2.04 av. 1.96		2.47; 2.67—2.88	2.47	[22]
α-$KNd(WO_4)_2$	6	3.23 (e) 3.53 (e)	I 1.74 : 2.18 (×2); 1.91 : 1.91 II 1.73 : 2.15 (×2) 1.84 : 1.95	1.83 1.81	1.94 1.92	1.73—1.74 av. 1.73	1.84—1.95 av. 1.90	2.15—2.18 av. 2.17	I 2.46; 2.55; 2.73—2.84 II 2.46; 2.63—2.81	2.46 2.55	[23]
α-$KY(WO)_2$*	6	3.29 (e) 3.77 (e)	1.72 : 2.36 1.78 : 2.14 1.84 : 1.93	1.82	1.96	1W + 1Y 1.78, 1.84 av. 1.81	2W 1.72; 1.93; 2.14, 2.36; av. 2.04		2.41; 2,59—3.01	2.41	[4]
$ZrMo_2O_7\cdot(OH)_2(H_2O)_2$	6	3.79 (e)	1.72 : 2.31 (H_2O) 1.75 : 2.11 (OH) 1.80 : 2.03 (O)	1.83	1.95	1:72	1Mo + 1Zr 1.76, 1.80	2Mo + 1Zr 2.03	2.45—2.81	2.45 (Mo, Zr)	[24]
$W_2O_3(PO_4)_2$	6	3.66 (e) 3.87 (e)	I 1.72 : 2.14 1.74 : 2.11 1.97 : 2.08 II 1.66 : 2.21 1,94 : 1.98 1.90 : 2.08 III 1.61 : 2.15 1.96 : 2.01 1.76 : 1.98 IV 1.73 : 2.23 1.84 : 1.99 1.93 : 2.24	1.88 1.87 1.83 1.87	1.96 1.96 1.91 1.99	1W 1W+1P 1.74 1.97—2.14 1.66 1.90—2.08 1.61 1.76—2.15 1.73 1.93—2.24	W_1, W_2 1,72, 2.21 av. 1.96 W_3, W_4 1.84, 2.01 av. 1.92		I 2.56—3.15 II 2.40—3.08 III 2.32—3.00 IV 2.40—3.22		[25]
$MoOPO_4$	6	4.29 (e)	1.65 : 2.64 1.98 : 1.98(×2)	1.90	2.03	I Mo + 1P 1.98	2Mo 1.65, 2.64 av. 2.15		2.73—3.03		[26]

TABLE 2 (continued)

Compound	c.n. E	ΔE(Å)	E−O (Å)	$\overline{E-O}$ (for 4)	$\overline{E-O}$ (for 6)	O−E (Å) for O c.n. of 1	2	3	O−O (Å)	Common edges of E polyhedra	References
$W_2O_3(AsO_4)_2$	6	≃3.6 (e)	I 1.68 : 2.15 1.85 : 2.03 1.92 : 1.92 II 1.68 : 2.13 1.92 : 1.92 1.93 : 1.94	1.84 1.86	1.92 1.92	1.68	2Mo 1.85, 1.93 av. 1.89 1Mo + 1As 1.92−2.15 av. 2.01		I 2.57−2.78 II 2.61−2.77		[27]
$LiMoO_2AsO_4$	6	4.89 (isolated)	1.68 : 2.17 1.71 : 2.18 2.01 : 2.06	1.87	1.97	1 Mo 1.68, 1.71 av. 1.69	1Mo + 1As 2.01; 2.06; 2.17, 2.18; av. 2.11		2.63; 2.71−2.83		[28]

---

*See note to Table 1.

or trigonal bipyramids; specific differentiation of these two types of pentagons is rather arbitrary in all the structures that have been investigated, since both polyhedra deviate considerably from ideal form. With c.n. of 7 and 8, the polyhedra are described as pentagonal or hexagonal bipyramids; the latter can also be characterized as cubes compressed along the third axis. The present article will not consider exotic cases involving c.n. of 7 and 8, particularly since they correspond either to "pure" oxides of W and Mo or to compounds where the W(Mo) cations occur in pairs with Nb, Ta, or U; it is probably the pairing that determines the structural geometry.

It should also be noted that both the characteristics of E−O coordination and the intercation distances will be considered solely from the methodological standpoint of their utilization to find the unknown anionic component of the structure. The E−E or E−R distances need only be known to within a few hundred angstroms, while the E−O distances need only be known to tens of angstroms.

Experimental data on the tetrahedral coordination of the E atoms are given in Table 1, while data for c.n. of 5 and 6 are given in Table 2. In each of these tables, we have included 20 reliably determined structures containing, in addition to W and Mo, cations of mono-, di-, and trivalent elements (Table 1); Table 2 also gives data for tetra- and pentavalent elements.

In analyzing the E coordination, we considered the following geometric characteristics.

a) The common vertices (v) or edges (e) of the W and Mo coordination polyhedra and the corresponding distances between adjacent cations (henceforth, the W−W and Mo−Mo distances will be designated as ΔE in the text and tables).

b) The difference in the average cation−anion distances for the major W(Mo) coordinations (tetrahedral, octahedral, and pentagonal) and, in the latter two cases, the difference in the average of the four shortest distances in comparison with the average tetrahedral distance E−O. This is shown in the corresponding columns in Tables 1 and 2.

c) The differential cation−anion distance in the octahedra, over a length dependent on the number of cation partners among which the oxygen atoms is "shared." Table 2 shows the cases of c.n. of 1, 2, and 3 for the O atom.

d) The isometricity of the polyhedra for all coordination numbers of E. This characteristic is related to the lengths of the edges and is qualitatively the reciprocal of the scattering interval for these lengths.

e) The maintenance of the O−O distances for edges common to two polyhedra (the next-to-last columm in Table 2).

2. Intercation distances. Isolated similar E polyhedra not joined to one another are observed with minimum distances ΔE > 3.80 Å in the tetrahedral coordination and ΔE > 3.95 Å in the octahedral coordination.

In all cases where ΔE > 3.80 A, contact of the E polyhedra is obligatory. The development of any contact precludes simultaneous tetrahedral coordination for two adjacent E atoms, and tungstates and molybdates have structures displaying neither chains nor bands of W or Mo tetrahedra such as those in silicates or phosphates. Polymerization of W and Mo polyhedra occurs only with coordinations exceeding 4, although this c.n. need occur for only one of the bound E atoms. The principle of local observation of balance of valence must apparently be considered one factor introducing this type of restriction.

Contacts between polyhedra are also possible with large values of ΔE, up to ΔE = 4.0−4.1 Å. Over the intermediate range 3.8−4.1 Å, octahedra with a common vertex or an octahedron and pentahedron with a common vertex are possible in addition to isolated polyhedra. Rarer cases of bonding of an octahedron and a tetrahedron through a common vertex are encountered at lower values of ΔE (up to ΔE ≈3.4 Å), especially in the presence of large and weakly polarizing "foreign" atoms [$K_2Mo_2O_7$ (ref. 15)]. The most common value of ΔE for bonding of E octahedra at their vertices is 3.70−3.95 Å, but 3.6 Å is also possible.

With ΔE < 3.60 Å, down to about 3.0−3.1 Å (the limit at which we can still assume that use of the concept of ionic rather than metallic bonding is valid), octahedra with a common edge, pentahedra with a common edge, or a pentahedron and an octahedron with a common edge are most probable. The probability becomes a certainty with ΔE < 3.4 Å.

The examples of W and Mo compounds with "foreign" elements as well as oxygen do not include heteroganic compounds, among which a case of a common oxygen face for two Mo octahedra has been reported[29] with ΔE = 3.31 Å [$(NH_4)_2Mo_2O_5(C_6H_4O_2) \cdot 2H_2O$].

3. Cation − anion distances. It can be seen from Table 1 that, regardless of the type and valence of the "foreign" atom participating in the compound, the

tetrahedral W—O and Mo—O distances are comparable and fall into the interval 1.69–1.86 Å. The average tetrahedral distances lie in an even narrower interval, 1.75–1.80 Å, fluctuating around 1.77 Å.

It can be seen from Table 2 that the transition to a c.n. of 6 produces considerable distortion of the octahedra in all structures. According to the survey by Porai-Koshits,[4] we can distinguish three types of distortions characteristic of the octahedral coordination of W and Mo: with one, two, or three shortened W—O or Mo—O bonds, always in the cis position with respect to one another. When the octahedron contains two such pairs of short-long bonds in the trans position (this position in designated by the symbol : in Table 2), there is usually a pair of bonds of intermediate length, also in the trans position with respect to one another. This type of differentiation is often associated with displacement of the W or Mo atom from the center of the octahedron along the corresponding octahedral symmetry axis: For example, differentiation into three short and three long bonds in the Cu_3WO_6 structure[19] develops as a result of displacement of the W atom along the three-fold axis; formation of two short, two long, and two intermediate bonds in the α-Bi_2WO_6 structure[20] is associated with displacement of the W atom along the polar two-fold axis. The latter case is characteristic of structures of the wolframite type, etc. Displacement of the W or Mo along axis 4 of the octahedron segregates the E—O bonds in the proportion of 1 +4 +1, i.e., one short, one long, and four intermediate.

These effects substantially expand the range of values for E—O in the octahedral coordination, to 1.6–2.4 Å; in the structure[26] of $MoOPO_4$ the five-fold coordination of the Mo (1.65–1.98 Å) is augmented by octahedral incorporation into the coordination sphere of a sixth neighbor at a distance of 2.64 Å, which leads to appearance of a common vertex with adjacent Mo octahedra with the distance $\Delta E = 4.29$ Å characteristic of isolated polyhedra. Nevertheless, the average octahedral distances remain within the rather narrow range 1.91–1.99 Å, varying around 1.96 Å.

The intervals for the average tetrahedral and average octahedral distances quite characteristically do not overlap and are even separated by a gap of ~ 0.1Å; calculation shows that the average for the four shortest distances (W—O or Mo—O) in the octahedral coordination is usually above the average upper limit for the tetrahedral coordination ($\geq$ 1.80 Å) or approximates to it. These two facts serve as additional indications of the validity of the presumed coordination and the entire interpretation as a whole when it is, for some reason, not sufficiently accurate.

With an E c.n. of 5, the range of values of E—O is narrower for octahedral coordination and wider for tetrahedral coordination (1.66–2.19 Å in the structures considered); the average E—O distances in the pentagonal arrangement also lie between the averages for the tetrahedral and octahedral conformations, averaging 1.85–1.90 Å.

4. Anion — cation distances. Knowledge of the O—E distances for O c.n. of 1 (E), 2, 3, and 4 is of great importance for x-ray diffraction analysis. The shortest O—E distances usually correspond to terminal O atoms and longer distances to cross-linking O atoms. For a c.n. of 1, the normal O—E distance is 1.7 Å, but participation in the compound of "foreign" cations, whose coordination sphere can include a given "terminal" atom of the E polyhedron, increases this value. Thus, the E—O distance in the divalent magnesium compound[4] $MgWO_4$, which has a wolframite structure, is increased to 1.80 Å; in this case, the terminal atom of the W octahedron serves as a common vertex in the Mg octahedron.

In the compound[22] $LiGa(WO_4)_2$, which contains trivalent gallium and has a structure derived from that of wolframite, the terminal atom of the W octahedron is shared with the Ga octahedron and the corresponding W—O distance is increased to 1.90 Å. In compounds of E with pentavalent phosphorus and arsenic, where the "terminal" atoms of the W or Mo octahedra simultaneously participate in the P and As tetrahedra, the E — O distance is elongated to 2.2 Å (see Table 2).

There is still less regularity in the presence of foreign cations for oxygen c.n. of 2, 3, and 4. Nevertheless, it can be assumed that, on the average, the E—O distances for coordination numbers of 2, 3, and 4 are 1.95 Å, 2.0–2.1 Å, and 2.2 Å respectively.

For a c.n. of 2, the arms of the bridge are usually unequal; the shorter arm can be reduced to 1.71 Å and the longer to 2.35 Å [$K_2Mo_4O_{13}$ (ref. 16)]. The aforementioned tendency toward elongation of the O—E distance with increasing coordination number for the O atom is, on the whole, retained in the presence of any "foreign" cation: The variation range of the O—E distance is quite large, but the lower limit is usually increased.

5. Polyhedron isometricity. The O—O distances for the compounds listed in Table 1 are 2.72–3.08 Å in the tetrahedra and 2.31–3.22 Å in the octahedra (Table 2). The shorter edges in the octahedra generally correspond to the common edges either of two E polyhedra or of an E polyhedron and the polyhedron formed by a "heavy" cation of another type.

Table 2 lists two of the very few compounds containing W and Mo atoms with a coordination of 5: $K_2Mo_3O_{10}$ and $Eu_2(WO_4)_3$ (ref. 4). In both cases, the expansion of the coordination sphere to include five anions is justified by the improved isometricity of the polyhedra or the fact that it permits explanation of the shortened O—O distances in the structure. If one of the two crystallographically independent Mo atoms in $K_2Mo_3O_{10}$ is restricted to tetrahedral coordination (Mo—O distances of 1.66–1.96 Å) and we neglect the fifth neighbor at a distance of 2.04 Å, the isolated tetrahedron has five O—O edges in the range 2.74–2.87 Å and a sixth with a length of 3.72 Å. When the fifth O atom is incorporated into the coordination sphere, the distance of 3.72 Å becomes the inside diagonal of a pentahedron (square pyramid) and the edges supplementing the tetrahedron in the pyramid have lengths of 2.31, 2.38, 3.29, and 3.33 Å. In this case, the 2.31 Å edge joins two W pentahedra and the 2.38 Å edge joins the pentahedron to a W octahedron.

In the $Eu_2(WO_4)_3$ structure, it makes sense to supplement the tetrahedral coordination of one of the two types of W atoms to produce a distorted trigonal bipyramid, incorporating an additional atom at a distance of 2.19 Å in the coordination polyhedron, together with four O atoms at distances of 1.72–1.81 Å. The edge lengths in the tetrahedron are 2.64, 2.77, 2.78, 2.91, 2.91, and 3.33 Å. The bipyramid has additional edges with lengths of 2.37, 2.51, and 2.92 Å; the first edge is common to a pair of newly formed trigonal bipyramids and the second is common to a W bipyramid and an Eu octahedron.

II. E−R AND R−R INTERCATION DISTANCES AND THEIR RELATIONSHIP TO CATION COORDINATION AND THE MODE OF CATION−POLYHEDRON JOINING

The E−R and R−R distances were analyzed for R^{3+}, including Y. Trivalent rare-earth cations were selected because they occupy an intermediate position with respect to size and polarizing capacity among the "foreign" cations that can be present in tungstates and molybdates. The R−R distances were analyzed for a number of other compounds containing rare earths: aluminates, silicates, germanates, niobates, tantalates, rhennates, etc. The corresponding experimental data are given in Tables 3 and 4.

Analysis of Table 3 shows that fixed E−R distances can also serve as an important crystal-chemical characteristic, defining the bonding of the E and R cation polyhedra and sometimes quite unambiguously indicating the arrangment of the linking atoms common to them. The gradual reduction of these distances leads to bending of the linkage and then to appearance of a common edge and even a common face for the E and R polyhedra. Specifically, with E−R distances of 3.63–4.10 Å, the E and R polyhedra at least have common vertices. Distances E−R = 3.38–3.80 Å are usually correlated with common edges for the E and R polyhedra. These values are lower in polyhedra with larger coordination numbers. With E−R distances less than or near the lower limit of the interval (3.38 Å), common faces are possible in the corresponding polyhedra. The only example of this, a common face for the Pr and W octahedra, occurs in the α-$Pr_2W_2O_9$ structure with a W−Pr distance of 3.38 Å (Table 3).

The following principal conclusions can be drawn from our analysis of the structure of oxygen compounds of molybdenum and tungsten containing rare-earth atoms (Tables 3 and 4):

1. Common elements appear in the R polyhedra regardless of the type and coordination number of the other cations in the rare-earth compound being analyzed, with R−R distances lying in the range 3.43–4.30 Å (and possibly less).

2. Generally speaking, the number of common ligands in the coordination spheres of adjacent R polyhedra depends on many factors, particularly the coordination number of the R cation and its ionic radius; rare-earth elements of the cerium group (La−Sm) accordingly have a tendency to form higher c.n. (7, 8, 9, 10) than elements of the yttrium group (Eu−Lu), which are characterized by c. n. of 6, 7, and 8.

As a result, increased R−R distances for elements of the Y group (3.70–3.95 Å) correspond to a common vertex, while the same or an even broader range of R−R distances (3.70–4.10 Å) for elements of the Ce group corresponds to a common edge. In most cases, a common vertex in R polyhedra of the Ce group occurs with R−R distances greater than 4.05 Å; shorter R−R distances corresponds to a common face (3.43–3.70 Å). For elements of the yttrium group with coordination numbers of 6 and 7, almost the same distances are characteristic of a common edge; an increase in the c.n. to 8 with the same ΔR permits a common face (in $Gd_2Ge_2O_7$ with Gd = 3.77 and 3.78 Å, there are common faces for the Gd septahedra and octahedra).[42]

TABLE 3. Experimental Data for Intercation Distances E−R and R−R (E is W or Mo, R is a rare earth or Y)

Compound	c.n. E	c.n. R	Number of common anions in R polyhedra and R−R distances (Å)			R − O (Å)	Number of common anions in R polyhedra and R-R distances (Å)		References
			1	2	3		2	3	
$KY(MoO_4)_2$*	4 (or 5)	8	3.63: 3.65: 3.81	3.81 for c.n. E=5		2.30—2.50	3.98		[4]
α-$KY(WO_4)_2$*	6	8	3.84: 3.94: 3.98	3.55		2.28—2.71	4.08		[6]
α-$Eu_2(WO_4)_3$*	4 (or 5)	8	3.75: 3.85	3.55 for c.n. E = 5		2.36—2.47 av. 2.43	3.90: 4.00		[4]
α-$Nd_2(MoO_4)_3$	4	8	3.75: 3.95			av. 2.50	3.95		[11]
β'-$Gd_2(MoO_4)_3$	4	7	3.65: 3.71: 3.82: 3.87: 3.88: 3.89: 3.90: 3.97: 4.02: 4.07: 4.08			2.27—2.44 av. 2.35	3.90: 3.91		[12]
α-$Pr_2W_2O_9$	6	8 , 9	For octagons 3.82 4.10 For nonagons 3.94	3.53 3.38: 3.40: 3.47	3.38	c.n. 8 2.34—2.63 c.n. 9 2.35—2.77	c.n. R = 9 , 9 4.00 c.n. R = 8 , 9 4.01: 4,07 c.n. R=8 , 8 4.12	c.n. R = 8 and 9 3.82	[30]
$NdWO_4OH$	4 (or 5)	8	3.92: 4.01: 4.05: 4.11	3.65 , 3.72 (for c.n. E = 5)		2.38—2.54	3.97: 3.99: 4.03		[31]
$LiYb(WO_4)_2$	6	6		3.58: 3.63: 3.78: 3.79		2.16—2.38			[32]
α-$KNd(WO_4)_2$	6	8	4.03: 4.06: 4.19	3.53		2.44—2.55	4.21		[29]
α-$RbPr(MoO_4)_2$	4	8	3.95: 3.98			2.47—2.51			[33]
$Na_5Lu(WO_4)_4$	4	8	3.74: 3.76			2.40—2.41 av. 2.41			[34]
α-$CsPr(MoO_4)_2$	4	8	3.75: 3.88			2.38—2.54 av. 2.46	4.13		[35]

---

*See note to Table 1.

TABLE 4. Experimental Data on Coordination and Distances between Rare-Earth Cations

Compound	c.n. E	c.n. R	$R-O$ (Å)	Number of common anions in E and R polyhedra and E-R distances (Å)			References
				1	2	3	
$Eu_4Al_2O_9$	4 (tetrahedron)	I , IV 6 (octahedron II и III 7	I 2.23–2.53 II 2.26–2.38 III 2.31–2.70 IV 2.28–2.38	3.73: 4.17 3.79: 3.89 3.81	c.n. 6 , 6 3.73: 3.68 c.n. 6 , 7 3.60: 3.74: 3.75: 3.82: 3.88: 3.88 c.n. 7 , 7 3.64: 3.76: 3.79		[36]
$Y_3[Si_3O_{10}](OH)_3$	4 (tetrahedron)	I , II 7 III 8	I 2.23–2.44 II 2.24–2.59 III 2.22–2.94	4.06 4.10	c.n. , 7 3.60: 3.71: 3.83: 3.88 c.n. 7 , 8 3,57; 3,78 c.n. 8 , 8 3.62		[37]
$Yb_2Si_2O_7$	4	6	2.21–2.28		3.43: 3.55		[38]
$Er_2Si_2O_7$	4	6	2.23–2.31		3.51: 3.60		[38]
$Gd_2Si_2O_7$	4	7	I 2.27–2.63 II 2.25–2.49	4.29: 4.29: 4.30	3.86: 4.03		[38]
α-Sm_2SiO_7	4	I , III 7 II , IV 9	I 2.35–2.66 II 2.33–2.96 III 2.27–2.66 IV 2.37–2.85	4.05: 4.52 4.80: 4.83 к. ч. 9 и 9 4.76: 4.91	c.n. 7 , 7 3.83 c.n. 7 , 9 3.80: 3.89: 3.89: 4.05: 4.10	c.n. 7 , 9 3.83 c.n. 9 , 9 3.78	[39]
$Nd_2Si_2O_7$	4	8	I 2.37–2.95 II 2.24–2.63		3.93: 4.00: 4.15: 4.18: 4.24: 4.39		[38]
$Sm_{4,67}[SiO_4]_3O$	4	I 7 II 9	I 2.21–2.67 II 2.32–2.74	3.98	c.n. 7 7 3.82: 4.07 c.n. 7 , 9 4.08	c.n. 9 , 9 3.43	[40]
$La_{4,67}[SiO_4]_3O$	4	I 7 II 9	I 2.29–2.75 II 2.49–2.79		c.n. 7 7 3.97: 4.24 c.n. 7 9 4.19	c.n. 9 , 9 3.57	[40]
$La_2Ge_2O_7$	4	8	I 2.40–2.93 II 2.35–2.80 III 2.31–3.33 IV 2.44–2.85	4.31	3.88: 4.01: 4.03: 4.03: 4.03: 4.08: 4.17	3.70: 3.95: 4.11	[41]
$Gd_2Ge_2O_7$	4	7 , 9	к. ч. 7 2.17–2.77 к. ч. 8 2.31–2.66	4.01 (×2) 4.12 4.12: 4.25 4.35	c.n. 7 7 3.63 (×3): 3.75: 3.79 (×2): 3.83 (×2): 3.84: 3.91 (×2): 4.03 c.n. 7 8 3.73: 3.74: 3.75: 3.83(×5): 3,87: 3.88	c.n. 7 , 8 3.77 3.78	[42]
$Er_2Ge_2O_7$	4	7	2.19–2.52		3.57: 3.60 (×2): 3.80		[43]
$NaNd_3Ge$] $]_2(OH)_2$	Na : 6 Ge : 4	7 , 8	c.n. 7 2.33–2.53 c.n. 8 2.37–2.62		c.n. 7 7 4.05 c.n. 7 8 3.83 (×2): 3.84 (×2)		[44]
$Ce(NbTi)_2O_6$	6octahedron	8	2.12–2.46		3.92 (×2)		[45]
$LaTaO_4$	6 octahedron	8	2.40–2.84; cp. 2.54		3.91 (×2): 4.00: 4.14: 4.34		[46]
$YTaO_4$	4 tetrahedron	8	2.25–2.42		3.65: 3.95		[47]
$La_4Re_6O_{19}$ *	6	10	2.50–2.88		4.09		[1]

*See notes to Table 1.

III. PRACTICAL EXAMPLES OF USE OF INTERCATION-DISTANCE ANALYSIS FOR INTERPRETATION OF CRYSTAL STRUCTURES

1. **$Pr_3WO_6Cl_3$ structure.** The positions of the metal and Cl atoms have been sufficiently well determined from analysis of the Patterson function.[48] Judging from the W−Cl distances, the Cl atoms are not incorporated into the coordination sphere of the W, so that the W polyhedron should be of the oxygen type. The minimum W−W distances of 5.37 Å in this case indicates the W polyhedra to be isolated. On the other hand, the nine short distances, W−Pr vectors of 3.57 Å (× 6 and 3.66 Å (× 3), require common oxygen edges for the W and Pr polyhedra. With $P6_3/m$ symmetry, this condition is satisfied in two cases: 1) The ligands surrounding the W atom are located at the vertices of a trigonal prism oriented in such fashion that the W−Pr vectors are, in first approximation, perpendicular to all the edges of this prism, as

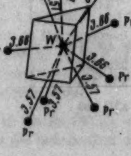

Fig. 1. Structure of $Pr_3WO_6Cl_3$. Diagram showing arrangement of oxygen atoms at vertices of trigonal prism, in conformity with short W−Pr intercation distances.

shown in Fig. 1; 2) the prism orientation differs from that depicted in Fig. 1 by rotation through 60° around the vertical axis 6, which passes through the center of the prism.

There are no examples of oxygen compounds with trigonal-prismatic coordination for W, so that the W − O distances anticipated in this case are unknown. We have given the possible coordinates of the O atoms, proceeding from the average octahedral W− distance of 1.95 Å to calculate the differential (without cations) Fourier synthesis. The electron-density patterns confirmed the first prism orientation, while refinement of the structure led to a slight change in the coordinates of the oxygen atoms and a reduction in the W−O distance to 1.93 ± 0.06 Å.

2. $Nd_2WO_5O = Nd_2WO_6$ structure. In the Nd_2WO_6 structure[49] the minimum W−W distance for atoms joined by the inversion center is 3.88 Å, which might indicate an isolated tetrahedral coordination, as well as an octahedral or pentahedral (with a common vertex) W atom coordination. The octahedral variant did not arise, since at least one anion in a common position from the WO_6 radical should also be coordinated by Nd atoms (see below). From the standpoint of stoichiometry, the octahedral coordination would be possible in this case in the presence of an isolated W_2O_{10} group consisting of two octahedra with a common edge. A ligand common to two pentahedra (O_2) can only be located at an inversion center joining two nearest-neighbor W atoms. However, no confirmation of this variant was obtained in refining the structure. For the localization of the remaining atoms in the W polyhedron, we returned to the interpretation obtained in the first stage for the short W − Nd distances in the tetrahedron consisting of three Nd atoms and one W atom (Fig. 2a). Each of these distances, W − Nd_1 (3.48 Å), W−Nd_2 (3.61 Å), and W−Nd_3 (3.69 Å) corresponded to bonding of the W and N polyhedra through a common edge and this requirement of common edges was only satisfied with one anion (O_2) in the center of a tetrahedron of cations (a W−O_2 distance of approximately 2.1 Å) and the other three anions (O_3, O_5, O_6) located at distances of approximately 1.9 Å from the W atom on lines drawn from the center of the tetrahedron perpendicular to the three short W−Nd vectors.

The next largest distance, W−Nd_2' = 3.85 Å, was an argument in favor of the presence of a common vertex in the corresponding polyhedra. We thus determined the missing fourth vertex (O_4) of the W tetrahedron on the W−Nd_2' line. In this case, the initial O_2 anion, which was attracted to the three Nd cations and lay at the center of one face (O_3, O_5, O_6) of the fixed WO_4 tetrahedron, became a fifth, more distant partner of the W atom.

After assigning positions to the five basis O atoms, we were left with the vacant cation tetrahedron $Nd_2Nd_2'Nd_3'Nd_3$ (Fig. 2b). Its sides of 3.74, 3.78 (× 2), 3.81, 3.83, and 3.97 Å also corresponded to bonding of the Nd polyhedra through common edges. The only possible way to obtain common edges for six pairs of Nd polyhedra with the aid of a single anion was to place it in the center of the cation tetrahedron and this was done for the O_1 anion.

Refinement of the structural model showed that the O_3 atom must also occupy a common position and the W polyhedra are consequently isolated.

3. $Nd_4W_3O_{15}$ structure. The W_1−W_2 (3.77 Å) distances in the $Nd_4W_3O_{15}$ structure[50] indicated that octahedral coordination of the W was most probable; the octahedra are joined by their vertices to form the chain radical $[WO_5]^{4-}$, each subunit containing two W_2 atoms located at the same level on the z axis and one W_1 atom at another level. The restrictions imposed by the symmetry of the $P4_2/nmc$ space group led to unambiguous positioning of the cross-linking O_4 and O_6 anions in the same specular plane as the W cations bound to them (Fig. 3). The deviation of the O atoms from the lines joining adjacent W atoms were calculated on the basis of the average octahedral W−O distance.

In the cationic framework of this structure, we also isolated the four short distances W_2 − Nd_3 (3.31 Å) (I), W_2−Nd_1 (3.44 Å) (I), W_2−Nd_1 (3.44 A) (II), W_1−Nd_2 (3.57 Å) (III), and W_1−Nd_3 (3.61 Å) (IV). The first distance indicated the possibility of a common face for the W_2 and Nd_3 polyhedra, while the other three required at least common edges. A common face was obtained when two oxygen atoms, O_1 and O_2, were added in the plane perpendicular to vector I and passing through the previously fixed O_6 atom. The W_2 octahedron was then fully formed: Two vertices, O_4 and O_6, lay in the specular plane and four vertices, $2O_1$ and $2O_2$, occurred in common positions.

The W_1 octahedron was formed in similar fashion. The missing four vertices were obtained from the O_3 and O_5 anions, which were located in the specular planes on a line perpendicular to vector III, i.e., in conformity with

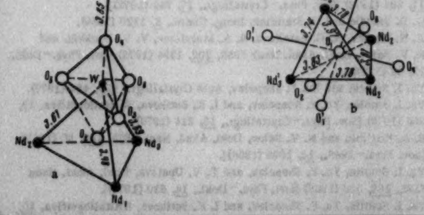

Fig. 2. Structure of Nd_2WO_5O. a) Diagram for determination of positions of oxygen atoms in W pentahedron in accordance with short W −Nd interaction distances; b) diagram showing location of O_1 oxygen atom in "cation" tetrahedron of four Nd atoms.

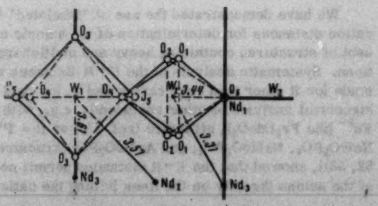

Fig. 3. Diagram showing arrangement of oxygen atoms in $Nd_4W_3O_{15}$ structure. The double lines indicate the horizontal and vertical specular planes. The numbers are the W−Nd distances.

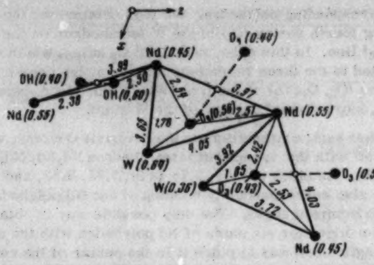

Fig. 4. Diagram for determination of ligand positions in the $NdWO_4OH$ structure. The common oxygen edges of the Nd polyhedra (dash lines) pass through the inversion centers (circles).

the rule of formation of a common edge with the nearest W_1 and Nd_2 polyhedra. This resulted in development of a common edge for the W_2 and Nd_1 polyhedra and a common face for the W_1 and Nd_3 polyhedra $(O_4O_3O_4)$, accounting for the short distances II and IV.

4. $NdWO_4OH$ structure. In interpreting this structure,[31] the intercation distances ΔW of 4.05 and 4.47 Å did not indicate the unambiguous positions of the O atoms and systematic analysis of the rather weak W−O peaks in the Patterson function required confirmation, which was obtained by examination of the distances ΔNd. The cationic framework contained three distances between Nd atoms joined by symmetry centers of 3.97, 3.99, and 4.03 Å, which could be assumed to indicate bonding of the Nd polyhedra through common edges. The two basis O atoms were located in the planes passing through the two corresponding Nd atoms and one W atom, at a distance of 1.8 Å from the W atom and equal distances from the two Nd atoms (Fig. 4). Further refinement of the coordinates showed that the deviations from the calculated coordinates did not exceed 0.2 Å.

The position of the OH group, which participates in the formation of still another common edge of the Nd polyhedra (ΔNd equals 3.97 Å), was determined with an accuracy equivalent to the rotation around the Nd−Nd line and to the "alternating" effect, which was found to be significant on the basis of the final coordinates: The OH−Nd distances were 2.38 and 2.50 Å.

CONCLUSIONS

We have demonstrated the use of "tabulated" intercation distances for determination of the anionic component of structures containing heavy and multicharge cations. Systematic analysis of the E−R distances was not made for R other than rare earths and Y, but data from structural analysis of other compounds, e.g., with R = Fe^{3+} [the $Fe_2(MoO_4)_3$ structure (ref. 51)] or R = P^{5+} [the $NaWO_2PO_4$, $NaMoO_2PO_4$, and $AgMoO_2PO_4$ structures (refs. 52, 53)], showed that the E−R distances permit positioning of the anions directly on the lines joining the cations.

The MLS method and differential Fourier syntheses can be used to verify the validity of the structural models constructed.

---

[1] N. V. Belov, Vestn. Mosk. Univ., Ser. Geol., No. 6, 10 (1971).

[2] S. V. Borisov, Kristallografiya, 17, 5 (1972) [Sov. Phys.−Crystallogr., 17, 1 (1972)].

[3] T. M. Polyanskaya, Dissertation [in Russian], Inst. Neorgan. Khim. Sib. Otd. Akad. Nauk SSSR, Novosibirsk (1971).

[4] M. A. Porai-Koshits, V. N. Vorotnikova, V. S. Sergienko, and V. I. Sokol, Progress in Sciences, Chemistry Series, Crystal Chemistry [in Russian], Vol. 6, Vses. Inst. Nauch. Tekh. Inform., Moscow (1971).

[5] A. S. Koster, F. X. N. M. Kools, and G. D. Rieck, Acta Crystallogr., B25, 1704 (1969).

[6] A. V. Chichagov, L. V. Demyanets, V. V. Ilyukhin, and N. V. Belov, Kristallografiya, 11, 686 (1966) [Sov. Phys.−Crystallogr., 11, 588 (1967)].

[7] E. Gurmen, E. Daniels, and J. S. King, J. Chem. Phys., 55, 1093 (1971).

[8] S. C. Abrahams and J. M. Reddy, J. Chem. Phys., 43, 2533 (1965).

[9] W. Jeitschko and A. W. Sleight, Acta Crystallogr., B28, 3173 (1972).

[10] L. Kihlborg, R. Norrestam, and B. Olivecrona, Acta Crystallogr., B27, 2066 (1971).

[11] K. Nassau, P. B. Jamieson, and J. W. Shiever, J. Phys. Chem. Solids, 30, 1225 (1969).

[12] W. Jeitschko, Acta Crystallogr., B28, 60 (1972).

[13] D. C. Craig and N. C. Stephenson, Acta Crystallogr., B24, 1250 (1968).

[14] R. F. Klevtsova and S. A. Magarill, Kristallografiya, 15, 710 (1970) [Sov. Phys.−Crystallogr., 15, 611 (1971)].

[15] S. A. Magarill and R. F. Klevtsova, Kristallografiya, 16, 710 (1790) [Sov. Phys.−Crystallogr., 16, 645 (1972)].

[16] B. M. Gatehouse and P. Leverett, J. Chem. Soc., A13, 2107 (1971).

[17] L. Kihlborg and E. Gebert, Acta Crystallogr., B26, 1020 (1970).

[18] G. W. Smith and J. A. Ibers, Acta Crystallogr., 19, 169 (1965).

[19] L. Kihlborg and E. Gebert, Acta Chem. Scand., 23, 221 (1969).

[20] R. W. Wolfe, R. E. Newnahm, and M. J. Kay, Solid State Comm., 7, 1797 (1969).

[21] R. F. Klevtsova and S. V. Borisov, Kristallografiya, 14, 610 (1969) [Sov. Phys.−Crystallogr., 14, 515 (1970)].

[22] P. V. Klevtsov, A. V. Demenev, and R. F. Klevtsova, Kristallografiya, 16, 520 (1971) [Sov. Phys.−Crystallogr., 16, 440 (1971)].

[23] R. F. Klevtsova and L. M. Volkova, Kristallografiya, 17, 859 (1972) [Sov. Phys.−Crystallogr., 17, 751 (1973)].

[24] A. Clearfield and R. H. Blessing, J. Inorg. Nucl. Chem., 34, 2643 (1972).

[25] P. Kierkegaard and S. Asbrink, Acta Chem. Scand., 18, 2329 (1964).

[26] P. Kierkegaard and J. M. Longo, Acta Chem. Scand., 24, 427 (1970).

[27] M. Westerlund-Sun, Acta Chem. Scand., 24, 427 (1970).

[28] B. Linnros, Acta Chem. Scand., 24, 3711 (1970).

[29] L. O. Atovmyan, V. V. Tkachev, and T. G. Shishova, Dokl. Akad. Nauk SSSR, 205, 609 (1972).

[30] S. V. Borisov and R. F. Klevtsova, Kritsallografiya, 15, 38 (1970) [Sov. Phys.−Crystallogr., 15, 28 (1970)].

[31] R. F. Klevtsova and S. V. Borisov, Kristallografiya, 14, 904 (1969) [Sov. Phys.−Crystallogr., 14, 776 (1970)].

[32] R. F. Klevtsova and N. V. Belov, Kristallografiya, 15, 43 (1970) [Sov. Phys.−Crystallogr., 15, 32 (1970)].

[33] R. F. Klevtsova and P. V. Klevtsov, Kristallografiya, 15, 466 (1970) [Sov. Phys.−Crystallogr., 15, 395 (1970)].

[34] R. F. Klevtsova, L. A. Glinskaya, L. P. Kozeeva, and P. V. Klevtsov, Kristallografiya, 17, 768 (1972) [Sov. Phys.−Crystallogr., 17, 672 (1973)].

[35] R. F. Klevtsova, V. A. Vinokurov, and P. V. Klevtsov, Kristallografiya, 17, 284 (1972) [Sov. Phys.−Crystallogr., 17, 240 (1972)].

[36] C. D. Brandle and H. Steinfink, Inorg. Chem., 8, 1320 (1969).

[37] A. N. Kornev, N. G. Batalieva, B. A. Maksimov, V. V. Ilyukhin, and N. V. Belov, Dokl. Akad. Nauk SSSR, 202, 1324 (1972) [Sov. Phys.−Dokl., 17, 88 (1972)].

[38] Yu. I. Smolin and Yu. F. Shepelev, Acta Crystallogr., B26, 484 (1970).

[39] Yu. I. Smolin, Yu. F. Shepelev, and I. K. Butikova, Kristallografiya, 15, 256 (1970) [Sov. Phys.−Crystallogr., 15, 214 (1970)].

[40] E. A. Kuz'min and N. V. Belov, Dokl. Akad. Nauk SSSR, 165, 88 (1965) [Sov. Phys.−Dokl., 10, 1009 (1966)].

[41] Yu. I. Smolin, Yu. F. Shepelev, and T. V. Upatova, Dokl. Akad. Nauk SSSR, 187, 322 (1969) [Sov. Phys.−Dokl., 14, 630 (1970)].

[42] Yu. I. Smolin, Yu. F. Shepelev, and I. K. Butikova, Kristallografiya, 16, 911 (1971) [Sov. Phys.−Crystallogr., 16, 790 (1972)].

[43] Yu. I. Smolin, Kristallografiya, 15, 47 (1970) [Sov. Phys.−Crystallogr., 15, 36 (1970)].

[44] A. V. Chichagov, V. S. Kovalenko, V. I. Ponomarev, and N. V. Belov,

Dokl. Akad. Nauk SSSR, 189, 88 (1969) [Sov. Phys.—Dokl., 14, 1037 (1970)].

[45] V. B. Aleksandrov, Dokl. Akad. Nauk SSSR, 142 181 (1962).

[46] T. A. Kurova and V. B. Aleksandrov, Dokl. Akad. Nauk SSSR, 201, 1095 (1971) [Sov. Phys.—Dokl., 16, 1023 (1972)].

[47] G. M. Wolten, Acta Crystallogr., 23, 939 (1967).

[48] T. M. Polyanskaya, S. V. Borisov, and N. V. Belov, Dokl. Akad. Nauk SSSR, 187, 1043 (1969) [Sov. Phys.—Dokl., 14, 733 (1970)].

[49] T. M. Polyanskaya, S. V. Borisov, and N. V. Belov, Dokl. Akad. Nauk SSSR, 193, 83 (1970) [Sov. Phys.—Dokl., 15, 636 (1971)].

[50] T. M. Polyanskaya, S. V. Borisov, and N. N. Belov, Kristallografiya, 15, 1135 (1970) [Sov. Phys.—Crystallogr., 15, 991 (1971)].

[51] L. M. Polyanskaya, S. V. Borisov, and N. V. Belov, Kristallografiya, 15, 1135 (1970) [Sov. Phys.— Crystallogr., 25, 991 (1971)].

[52] P. Kierkegaard, Arkiv Kemi, 18, 553 (1962).

[53] P. Kierkegaard and S. Holmen, Arkiv Kemi, 23, 213 (1965).

X-ray diffraction study of naphthaloimide

A. N. Sobolev, L. A. Chetkina, G. A. Gol'der,
Yu. G. Fedorov, and V. E. Zavodnik
L. Ya. Karpov Scientific-Research Physicochemical Institute
Institute of Applied Mathematics, Academy of Sciences of the USSR
(Submitted November 9, 1972)
Kristallografiya, 18, 1157-1161 (November-December 1973)

Naphthaloimide crystallizes in a monoclinic habit in the $P2_{1/a}$ space group with unit-cell parameters a = 15.968, b = 5.41, c = 10.999 Å, β = 111°49', N = 4; 1616 independent reflections with sin θ/λ ≤ 0.7 were measured in an automatic diffractometer. The structure was determined by the "dip" method and refined by the method of least squares and three dimensional electron-density syntheses (to R = 0.127). The molecule is slightly deformed, although the naphthalene ring and the heterocyclic ring are individually planar. The average bond lengths and valence angles are: $C_{arom}-C_{arom}$ = 1.40 Å, $C_{arom}-C_{carb}$ = 1.46 Å, C−N = 1.39 Å, C = O = 1.22 Å, CCC = 120°, CCO = 124.2°, CCN = 115.9°, and CNC = 126.7°. The structure is composed of centrosymmetric dimers formed by hydrogen bonds (N−H...O) 2.85 Å long.

X-ray diffraction analysis of anhydrides and imides of naphthalic acid began comparatively recently. Among imide derivatives, structural determinations have been made only for crystalline 5-bromo-N-oxynaphthaloimide.[1] Naphthaloimide and its derivatives have been studied by various physicochemical methods (dipole moments and infrared and ultraviolet spectra).[2,3] The present article gives the results obtained in determining the structure of naphthaloimide. This compound has the following structural formula:

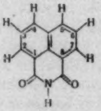

EXPERIMENTAL METHOD AND STRUCTURAL DETERMINATION

Single crystals of naphthaloimide $C_{12}H_7O_2N$ were obtained from solution in n-xylol in the form of clear colorless needles. The unit-cell constants obtained previously[4] were refined in a DRON-1 diffractometer and are given below together with other crystal-chemical data:

$a = 15.968 \pm 0.002$ Å
$b = 5.41 \pm 0.01$ Å
$c = 10.999 \pm 0.002$ Å
$\beta = 111°49' \pm 01'$
$V = 882.1$ Å^3
$N = 4$

Space group $P2_1/a$
$d_{meas} = 1.43$ g·cm^{-3}
$d_{cal} = 1.48$ g·cm^{-3}
$F(000) = 408$
$T_m = 305°$ C

The integrated intensity of the reflections from the naphthaloimide crystal was measured in a DARM-2 automatic x-ray diffractometer.[5] The diffractometer program was compiled and the integrated-intensity results subjected to primary processing in a Minsk-22 computer at L. Ya. Karpov Scientific-Research Physicochemical Institute.

The diffractometer measurements were made with a crystal 0.13 × 0.24 × 0.5 mm in size. The mosaic angle of the crystal, determined from the formula in the literature,[6] was 25'. Using molybdenum radiation and limiting ourselves to the sphere sin θ/λ = 0.7, because of the rapid decrease in reflection intensity, we measured the integrated intensities of 1616 independent reflections (528 zero-order reflections) from six layer planes (h0l − h5l). Pri-

TABLE 1. Basis-Atom Coordinates,* Individual Isotropic Temperature Factors, and Maximum Amplitudes (probable errors in parentheses)

Atom	Initial model			Final results				
	x	y	z	x	y	z	B, Å^2	ρ, el/Å^3
C_1	0.057	0.576	0.289	0.0583(5)	0.5721(16)	0.2925(8)	2.65(12)	9.5
C_2	0.042	0.714	0.386	0.0432(5)	0.7099(16)	0.3869(7)	3.11(13)	7.9
C_3	0.099	0.909	0.448	0.1018(5)	0.9093(16)	0.4505(8)	3.68(14)	7.6
C_4	0.173	0.966	0.412	0.1721(5)	0.9682(16)	0.4128(8)	3.51(14)	8.1
C_5	0.232	0.884	0.280	0.2648(5)	0.8755(15)	0.2786(8)	3.16(13)	8.6
C_6	0.278	0.745	0.183	0.2821(5)	0.7311(17)	0.1908(7)	3.43(14)	8.0
C_7	0.220	0.550	0.122	0.2232(5)	0.5371(16)	0.1268(8)	3.12(13)	8.4
C_8	0.146	0.494	0.157	0.1483(5)	0.4871(16)	0.1596(8)	2.46(11)	9.7
C_9	0.189	0.827	0.316	0.1895(5)	0.8303(16)	0.3167(8)	3.10(13)	9.1
C_{10}	0.131	0.632	0.254	0.1312(5)	0.6325(16)	0.2533(8)	2.37(11)	10.0
C_{11}	−0.003	0.374	0.225	−0.0042(5)	0.3719(16)	0.2268(8)	3.18(13)	8.5
C_{12}	0.087	0.232	0.093	0.0865(5)	0.2920(16)	0.0902(8)	2.81(12)	8.9
O_1	−0.066	0.325	0.256	−0.0672(3)	0.3080(10)	0.2564(5)	3.89(10)	10.3
O_2	0.100	0.172	0.009	0.0944(3)	0.1668(10)	0.0030(5)	3.62(10)	11.3
N	0.013	0.235	0.128	0.0157(4)	0.2447(11)	0.1312(6)	2.99(11)	10.5
H_2				−0.015	0.667	0.414	4	
H_3				0.083	0.015	0.527	4	
H_4				0.216	0.129	0.459	4	
H_5				0.313	0.029	0.329	4	
H_6				0.342	0.777	0.166	4	
H_7				0.238	0.423	0.054	4	
H_N				0.028	0.107	0.085	4	

*The number of the hydrogen atoms correspond to the numbers of the carbon atoms to which they are bound.

mary processing of the experimental data resulted in conversion of the reflection intensities to structural factors, taking into account the Lorentz and polarization factors.

In order to convert $F^2(hkl)$ to an absolute scale, normalization was conducted by Wilson's method[7] (using the program of Andrianov et al.[8]) and by Vainshtein's method. The normalization constants obtained by the two methods were similar.

The structure of the naphthaloimide was determined by the method of nonlocal search for a minimum in a function of many variables,[10] using the modifications described previously.[11] In seeking a structural model, it was assumed that the molecule is planar and that its geometric characteristics are similar to those obtained for the 5-bromo-N-oxynaphthaloimide structure.[1] The search was first carried out with a small number of the strongest reflections in the region of small values of $\sin\theta/\lambda$. The 64 strongest reflections at the minimum point yielded the value $R_{64} = 0.10$. Then, without removing the presumed bonds from the model, the value $R_{250} = 0.127$ was obtained for 250 reflections. This was the original model and its atomic coordinates are given in Table 1. The preliminary-model search required about one hour in a large computer.

The structure was refined by the method of least squares in the full-matrix isotropic approximation over several cycles, to an R factor of 0.135. When the positions of the hydrogen atoms were taken into account, basing them on the usual geometric considerations (C−H = 1.09 Å, N−H = 1.00 Å, bonds directed along the diagonals of hexagonal rings), the divergence factor was reduced to 0.127. Subsequent localization of the electron-density maxima made virtually no change in the R factor, although the atomic coordinates were somewhat modified; these coordinates were taken as the final values. Table 1 gives the atomic coordinates, temperature factors B ($B_{tot} = 3.1$ Å^2, B = 4 Å^2 was assumed for the H atoms), and the maximum amplitudes from the three-dimensional electron-density synthesis. The probable errors are given in parentheses, as calculated from the reciprocal matrix during refinement of the structure by the method of least squares. The structural numbering of the atoms is used in Table 1 and henceforth. All the calculations involved in refinement of the structure and determination of the geometric parameters were made with the Roentgen program.[12]

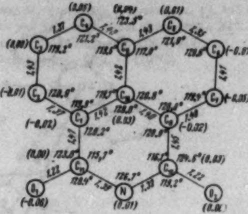

Fig. 1. Bond lengths and valence angles. The deviations of the atoms (in Å) from the median plane of the molecule are given in parentheses.

DISCUSSION OF RESULTS

The naphthaloimide structure is composed of centrosymmetric dimers formed by hydrogen bonds of the N−H...O type. The molecular geometry is shown in Fig. 1. The bond lengths and valence angles in the molecule are shown in Table 2 (the indicated probable errors were calculated from the errors in the atomic coordinates). Although the molecule occupies a common position in the unit cell, it can be seen from Fig. 1 that, within the limits of experimental error, the molecule is symmetric with respect to the central C_9-C_{10} bond. The corresponding figures for the naphthalene rings of the naphthaloimide and naphthalene molecules[13] are similar. As is to be expected, the geometry of the heterocyclic ring and carbonyl groups is similar for the compound under investigation and 5-bromo-N-oxynaphthaloimide. Thus, the bond lengths for the imide linkage to the naphthalene ring (1.45 and 1.47 Å) are somewhat shorter than for a normal sp^2-sp^2 single bond,[14] the C−N bonds (1.39 Å) are intermediate, and the carbonyl-group bonds C = O (1.22 Å) are those usual for organic compounds. The valence angles at the C_{11} and C_{12} atoms are nonequivalent, as found previously.[1] The CNC angle is 126.7°. Values similar to those obtained for the C−N bond length and CNC valence angle of

TABLE 2. Bond Lengths d and Valence Angles ω in Molecule (probable errors in parentheses)

Bond	d, Å	Angle	ω
C_1-C_2	1.370(13)	$C_1C_2C_3$	120°55′(49′)
C_2-C_3	1.429(11)	$C_2C_3C_4$	119°13′(48′)
C_3-C_4	1.371(13)	$C_4C_9C_{10}$	119°34′(47′)
C_4-C_9	1.403(13)	$C_9C_{10}C_1$	119°03′(47′)
C_5-C_9	1.434(13)	$C_{10}C_1C_2$	119°56′(44′)
C_5-C_6	1.348(13)	$C_3C_4C_9$	121°11′(43′)
C_6-C_7	1.410(11)	$C_9C_5C_6$	121°51′(42′)
C_7-C_8	1.398(13)	$C_5C_6C_7$	120°49′(47′)
C_8-C_{10}	1.402(13)	$C_6C_7C_8$	119°23′(47′)
C_9-C_{10}	1.420(11)	$C_7C_8C_{10}$	120°01′(43′)
C_1-C_{11}	1.468(11)	$C_8C_{10}C_9$	120°51′(49′)
C_8-C_{12}	1.453(10)	$C_{10}C_9C_5$	116°56′(46′)
$C_{11}-N$	1.389(11)	$C_{10}C_1C_{11}$	120°15′(45′)
$C_{12}-N$	1.388(9).	$C_{10}C_8C_{12}$	120°56′(44′)
$C_{11}-O_1$	1.217(11)	$C_1C_{10}C_8$	119°57′(43′)
$C_{12}-O_1$	1.218(9)	$C_1C_{11}N$	115°40′(44′)
C_1-C_{10}	1.421(13)	$C_8C_{12}N$	116°04′(35′)
		$C_{11}NC_{12}$	126°43′(33′)
		$C_1C_{11}O_1$	123°47′(47′)
		$C_8C_{12}O_2$	124°39′(38′)
		$O_1C_{11}N$	120°25′(40′)
		$O_2C_{12}N$	119°14′(32′)
		$C_4C_9C_5$	123°29′(42′)

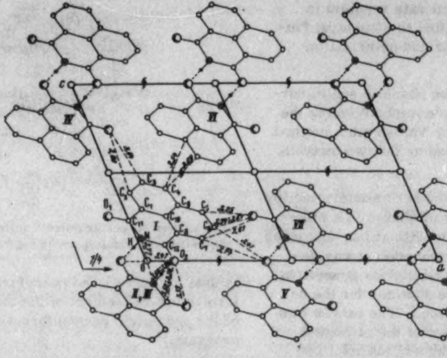

Fig. 2. Arrangement of molecules in crystal and intermolecular distances (without taking into account hydrogen atoms).

TABLE 3. Shortest Intermolecular Distances d in Å*

Atoms	d	Atom	d
C_2(I)...O_1(VIII)	3.67	C_6(I)...C_1(X)	3.34
C_2(I)...O_1(IV)	3.80	C_6(I)...O_2(V)	3.41
C_3(I)...C_{11}(VIII)	3.44	C_7(I)...O_1(VII)	3.61
C_3(I)...O_1(VIII)	3.47	C_7(I)...O_2(V)	3.74
C_3(I)...N(VIII)	3.75	O_1(I)...O_2(II)	3.73
C_3(I)...O_1(IV)	3.64	O_2(I)...C_9(IX)	3.67
C_4(I)...C_4(VIII)	3.72	O_2(I)...C_1(III)	3.58
C_4(I)...C_{11}(VIII)	3.50	O_2(I)...C_{11}(III)	3.52
C_4(I)...C_{12}(VIII)	3.71	O_2(I)...C_{11}(II)	3.78
C_4(I)...N(VIII)	3.52	O_2(I)...N(III)	3.68
C_4(I)...C_5(VI)	3.69	O_2(I)...N(II)	2.85
C_4(I)...C_3(VI)	3.54	O_2(I)...O_2(II)	3.47
C_5(I)...C_{12}(VIII)	3.62	N(I)...C_9(IX)	3.58
C_5(I)...O_2(VIII)	3.60	N(I)...C_8(III)	3.54
C_5(I)...O_1(X)	3.25	N(I)...C_{12}(III)	3.45
C_6(I)...O_2(VIII)	3.74	N(I)...N(II)	3.77
C_6(I)...O_1(VII)	3.67		

*The molecular positions are as follows: I) x, y, z; II) $\bar{x}$, $\bar{y}$, $\bar{z}$; III) $\bar{x}$, 1 − y, $\bar{z}$; IV) $\bar{x}$, 1 − y, 1 − z; V) $^1/_2 - x$, $^1/_2 + y$, $\bar{z}$; VI) $^1/_2 - x$, $^1/_2 + y$, $1 - z$; VII) $^1/_2 + x$, $^1/_2 - y$, z; VIII) x, 1 + y, z; IX) x, − 1 + y, z; X) $^1/_2 + x$, $(1/2 - y) + 1$, z.

the heterocyclic ring were found in the molecules of 5-bromo-N-oxynaphthaloimide[1] (1.40 Å and 124°), cyanuric acid[15] (1.372 Å and 124.7°), and uracil[16] (1.373 Å and 126.7°). The equations for the planes passing through the entire molecule and individual segments of it showed that, although the naphthalene and heterocyclic rings are individually planar, the molecule as a whole is slightly deformed. The deviations of individual atoms from the median plane of the molecule, $5.281x - 3.441y + 5.767z = 0.006$, are 0.06–0.07 Å and are shown in Fig. 1.

Figure 2 shows the molecular packing in the crystal, as projected on the (010) plane. The shortest intermolecular distances are given here and in Table 3. It can be seen from Fig. 2 that the molecules in the crystal are joined into centrosymmetric dimers by intermolecular hydrogen bonds (N−H... O) 2.85 Å long. In the 5-bromo-N-oxynaphthaloimide structure,[1] similar dimers are formed through O−H... O bonds located around the 2_1 axis. The observed hydrogen bond is a medium bond, since the generally accepted range of N−H... O distances[17] is 2.6–3.2 Å. The remaining intermolecular distances are normal. The molecular coordination number is 12.

The authors wish to thank É. M. Smelyanskii for assisting in the calculations for the preliminary structural model and V. L. Plakidina for furnishing the subject crystals.

[1] Le Nguyen Shok, G. A. Gol'der, L. A. Chetkina, and M. A. Davydova, Kristallografiya, 16, 923 (1971) [Sov. Phys.–Crystallogr., 16, 801 (1972)].

[2] C. M. Lee and W. D. Kumler, J. Organ. Chem., 27, 2055 (1962).

[3] V. L. Plakidin and P. P. Gnatyuk, Zh. Org. Khim., 6, 2312 (1970).

[4] Le. Nguyen Shok and G. A. Gol'der, Zh. Strukt. Khim., 11, 939 (1970).

[5] D. M. Kheiker, É. L. Lube, A. V. Mirenskii, N. I. Komyak, O. V. Maklakov, L. Z. Tatkin, É. N. Gurevich, and V. S. Rogachev, Apparat. Metody Rentgen. Anal., 3, 130 (1968).

[6] É. L. Lube and D. M. Kheiker, Apparat. Methody Rentgen. Anal., 3, 145 (1968).

[7] A. J. Wilson, Nature, 150, 152 (1942).

[8] V. I. Andrianov, Z. Sh. Safina, and B. L. Tarnopol'skii, Zh. Strukt. Khim., 12, 1052 (1971).

[9] B. K. Vainshtein, Zh. Eksp. Teor. Fiz., 27, 44 (1954).

[10] I. M. Gel'fand, E. B. Vul, S. L. Ginzburg, and Yu. G. Fedorov, The Dip Method in X-Ray Diffraction Analysis [in Russian], Nauka, Moscow (1966).

[11] Le Nguyen Shok, L. A. Chetkina, M. G. Neigauz, G. A. Gol'der, É. M.

Smelyanskaya, and Yu. G. Fedorov, Kristallografiya, 16, 500 (1971) [Sov. Phys.–Crystallogr., 16, 423 (1971)].

[12] B. L. Tarnopol'skii and V. I. Andrianov, Zh. Strukt. Khim., 4, 433 (1963).

[13] D. W. Cruickshank and R. A. Sparks, Proc. Roy. Soc., A258, 270 (1960).

[14] O. Bastiansen and M. Tratteberg, Tetrahedron, 17, 147 (1962).

[15] G. C. Verschoor and E. Keulen, Acta Crystallogr., B27, 134 (1971).

[16] B. M. Craven, Acta Crystallogr., 23, 376 (1967).

[17] L. H. Jensen, Polymer Sci., C29, 47 (1970).

Crystal and molecular structures of octafluoroanthraquinone

L. A. Chetkina and E. G. Popova

L. Ya. Karpov Physicochemical Scientific Research Institute

(Submitted December 14, 1972)
Kristallografiya, 18, 1162-1168 (November-December 1973)

Crystals of octafluoroanthraquinone belong to the monoclinic system, with a = 9.350 Å, b= 20.870 Å, c = 5.906 Å, γ = 91°46', N = 4, and space group $P2_1/b$. The structure was deciphered by the direct Sayer–Zachariasen–Cochran method and refined by the least squares method in isotropic approximation from 1960 independent nonzero reflections. Lengths of the C–F bonds average 1.34 Å. The quinoid ring has the "basin" [boat] configuration, and the carbonyl groups stick out of the plane of the central ring at 13 and 19°. The molecule as a whole takes on the "butterfly" conformation, the dihedral angle between the end rings of the nucleus being 160°.

Fluoroanthraquinone compounds, mainly intermediates and dyes, have been studied very little as yet. The exceptionally high reaction capability of fluorine results in special properties of fluoroanthraquinone dyes.[1] Polyfluoro aromatic compounds have also been found to be more suitable for the study of mechanisms of chemical reactions.[2] Of the fluoro derivatives of anthraquinone, up to this time x-ray structure investigation has been done only for 1,5-difluoroanthraquinone.[3] For octafluoroanthraquinone, the synthesis of which is described in ref. 4, it was of interest to study the influence of fluorine on the coplanarity of the molecule upon the replacement of all hydrogen atoms by fluorine.

EXPERIMENTAL PROCEDURE

Single crystals of octafluoroanthraquinone, $C_{14}F_8O_2$, were grown from acetic acid solution in the form of transparent pale yellow needles, elongated along the c axis. The unit-cell parameters determined earlier[5] were refined on a DRON-1 diffractometer, and the density of the crystals was found again by the method of flotation (in Thoulet's liquid). Unlike the case in ref. 5, in this work another setting of the crystal (c is the monoclinic axis) was chosen. Crystallographic data for the compound studied were

$a = 9.350 \pm 0.003$ A
$b = 20.870 \pm 0.006$ A
$c = 5.906 \pm 0.005$ A
$\gamma = 91°46' \pm 2'$
$V = 1151.9$ Å^3
$N = 4$

space group $P2_1/b$
$d_{meas} = 2.02\ g \cdot cm^{-3}$
$d_{calc} = 2.03\ g \cdot cm^{-3}$
F(000) = 688
$\mu(Cu\,K\alpha) = 22.6\ cm^{-1}$
$T_f = 342°C$

A crystal of dimensions 0.2 × 0.1 × 1.1 mm was used for taking the patterns on a Weissnberg x-ray goniometer. The hk0-hk5 layer lines, in all 1960 independent nonzero reflections, were obtained by use of unfiltered Cu radiation. Intensities of the reflections were estimated visually from a blackening scale with correction for Lorentz and polarization factors. Some of the reflections were also measured on the DRON-1 diffractometer, and of them, 54 reflections were used for reduction of the group to a common scale, and more precise values of the intensities were found for the 34 strongest reflections.

DETERMINATION AND REFINEMENT OF THE STRUCTURE

The structure was solved by the Sayre–Zachariasen–Cochran direct statistical method of correspondence of signs and by use of a program worked out in the Institute of Chemical Physics Branch, Academy of Sciences of the USSR.[6–8] The structure factors were reduced to an absolute scale on an electronic computer by the Wilson method[9] and the normalized structure amplitudes $|E(hkl)|$ were calculated. Comparison of experimentally obtained statistical mean values and the distribution of normalized structure amplitudes with theoretical values for centrosymmetric and noncentrosymmetric crystals[10,11] is made in Table 1. Of a total number of 2264 reflections (with subtraction of 304 reflections which were not observed, to which were assigned values of $F^2 = \frac{1}{3}F_{min}^2$), 340 reflections were chosen with $|E_h| \geq 1.4$ and 1417 third derivatives with $|E_h E_{h'} E_{h''}| \geq 8.3$ and probability of $P_{min} = 0.95$ were compiled. In this case the expected estimated values[6] $R_0 = 0.928$ and $\nu_0 = 120$ were obtained. The quantity σ is 0.108 for octafluoroanthraquinone. Of the reflections with a large number of bonds q_i (this is the number of third derivatives into which the value E enters), three were chosen according to the determining rule[12] which were independent of parity of coordinate reflection and were given plus signs; we also chose six reference reflections (Table 2). In all, there were $2^6 = 64$ variants of signs for the given $P_{min} = 0.99$ and $\delta = 0.75$ (ref. 6), from which one variant was clearly distinguished with the best appraisable factors: n = 271, R = 0.945, and ν = 84. The closest variant had the estimates n = 259, R = 0.923, and ν = 115. Thus, 280 signs of structure amplitudes (271 + 9 reference) were determined. Not one of them was changed after refinement of the structure.

The positions of all 24 atoms were found from the three-dimensional E synthesis, constructed from 280

TABLE 1. Statistical Mean Values and Distribution of Normalized Structure Amplitudes

Value of amplitude	Experimental	Theoretical		Value of amplitude	Experimental	Theoretical	
		$\bar{1}$	1			$\bar{1}$	1
$\langle \lvert E \rvert^2 \rangle$	0.993	1.000	1.000	$\lvert E \rvert > 1.4$	0.150	0.162	0.141
$\langle \lvert E^2 - 1 \rvert \rangle$	0.978	0.968	0.736	$\lvert E \rvert > 1.6$	0.101	0.110	0.078
$\langle \lvert E \rvert \rangle$	0.788	0.798	0.886	$\lvert E \rvert > 1.8$	0.072	0.072	0.039
$\lvert E \rvert > 1$	0.298	0.320	0.368	$\lvert E \rvert > 2$	0.046	0.050	0.018
$\lvert E \rvert > 1.2$	0.216	0.230	0.237	$\lvert E \rvert > 3$	0.004	0.003	0.0001

TABLE 2. Reference Group of Reflections

$\|E\|$	hkl	φ_1
3.06	224	68
2.59	271	59
2.30	532	43
3.53	180	31
2.89	643	44
2.84	311	56
2.80	4.12.3	45
2.42	341	42
2.09	123	37

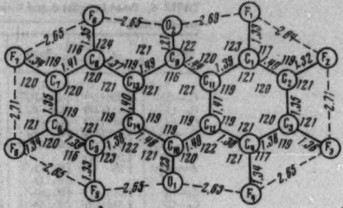

Fig. 1. Bond lengths (in Å) and valence angles (in degrees) in the molecule.

reflections. The divergence factor was 0.41 for these atomic coordinates and the entire set of $|F(hkl)|$ values. The structure was refined by the least squares method and full-matrix isotropic approximation to an R factor of 0.18 with account being taken of the weighted function according to Cruickshank:[13]

$$W = 1/a + |F_e| + c|F_e|^2,$$

where

$$a = 2|F_{\min}| = 3.26,\ c = 2/|F_{\max}| = 0.015.$$

Atomic coordinates and thermal factors B with their probable errors, calculated from the reciprocal matrix during structure refinement by the least squares method, are given in Table 3. The heights of maxima given there are those from the three-dimensional electron density synthesis. All calculations were done by the "Roentgen" program.[14]

GEOMETRY OF THE MOLECULE AND PACKING IN THE CRYSTAL

Dimensions of the molecule are given in Fig. 1 and Table 4. Standard deviations, calculated from the errors given in Table 3 in atomic coordinates, amount to 0.010-0.013 Å for the bond lengths and 0.7-0.8° for the valence angles. The C−F bond lengths (average of 1.34 Å) are close to those obtained for 1,5-difluoroanthraquinone[3] (average of 1.35 Å), fluoranil[15] (1.333 Å), and the fluorine derivatives of benzene[16] (average 1.328 Å), but less than those found in o-fluorobenzoic acid[17] (1.368 Å) and decafluorodiphenyl[18] (1.38 Å). The rest of the bond lengths are similar to those obtained in the anthraquinone molecule,[19] with the exception of the slightly shortened distance for the C_2-C_3 and C_6-C_7 bonds.

Steric hindrances exist in the octafluoroanthraquinone molecule between F and O atoms which are not linked by valences: The F...O distance in the ideal model of the molecule (2.45 Å) is less by 0.38 Å than the sum of the van der Waals radii of these atoms ($r_F = 1.47$ Å, $r_0 = 1.36$ Å). However, unlike the case with 1,5-difluoroanthraquinone,[3] these steric hindrances exist along both directions from the oxygens of the carbonyl groups under the stiffening action of the F atoms in the β positions. Deformation of the external valence angles occurs as the result of repulsion of neighboring F and O atoms, especially for F atoms in the α positions (see Fig. 1 and Table 4), and disturbance of the planarity of the molecule also occurs. The degree of disturbance of coplanarity of the molecule cannot be explained by geometrical factors alone, but evidently can also be the result of interaction of the more electronegative F atoms (E = 3.9 eV) and O atoms (E = 3.5 eV).

TABLE 3. Atomic Coordinates, Individual Thermal Factors, and Heights of Maxima (probable errors in parentheses)

Atom	x	y	z	B, Å²	ρ, el/Å³
C(1)	0.2564(29)	0.3471(13)	0.6378(49)	3.93(14)	7.4
C(2)	0.3435(29)	0.3941(13)	0.5343(50)	3.93(14)	7.3
C(3)	0.4070(30)	0.3817(14)	0.3342(51)	4.14(15)	7.2
C(4)	0.3904(27)	0.3223(12)	0.2352(47)	3.41(13)	7.3
C(5)	0.2484(26)	0.0928(12)	0.3153(44)	3.17(12)	7.8
C(6)	0.1959(29)	0.0431(13)	0.4526(50)	3.86(14)	7.5
C(7)	0.1294(29)	0.0571(13)	0.6479(49)	3.94(14)	7.2
C(8)	0.1074(25)	0.1214(11)	0.7087(49)	2.94(11)	8.3
C(9)	0.1400(26)	0.2380(12)	0.6473(46)	3.28(12)	8.2
C(10)	0.2896(27)	0.2093(12)	0.2322(43)	3.20(12)	8.2
C(11)	0.2358(25)	0.2871(12)	0.5389(45)	3.33(13)	8.4
C(12)	0.3041(27)	0.2747(12)	0.3312(45)	3.27(12)	8.3
C(13)	0.1597(26)	0.1702(12)	0.5755(45)	3.22(12)	8.2
C(14)	0.2323(27)	0.1562(12)	0.3749(47)	3.33(13)	8.2
F(1)	0.1945(18)	0.3632 (8)	0.8308(28)	4.71(10)	11.7
F(2)	0.3636(19)	0.4503 (8)	0.6342(30)	5.14(10)	10.8
F(3)	0.4948(18)	0.4263 (8)	0.2346(30)	4.99(10)	11.3
F(4)	0.4596(17)	0.3128 (8)	0.0394(28)	4.55 (9)	12.2
F(5)	0.3148(18)	0.0755 (8)	0.1266(29)	4.75(10)	11.7
F(6)	0.2148(17)	−0.0179 (8)	0.3911(29)	4.72(10)	11.2
F(7)	0.0799(18)	0.0100 (8)	0.7841(30)	4.93(10)	11.6
F(8)	0.0376(17)	0.1300 (8)	0.9067(29)	4.47(10)	12.1
O(1)	0.3256(20)	0.1999 (9)	0.0354(33)	4.18(11)	10.6
O(2)	0.0462(20)	0.2519 (9)	0.7782(32)	4.08(10)	10.8

TABLE 4. Bond Lengths d and Valence Angles ω in the Molecule (probable errors in parentheses).

Bond	d, Å	Bond	d, Å	Angle	ω, degree	Angle	ω, degree
C_1—C_2	1.396(12)	C_5—F_5	1.332(10)	$C_1C_2C_3$	119.9(8)	$C_5C_6F_6$	119.7(8)
C_2—C_3	1.351(13)	C_6—F_6	1.342(10)	$C_2C_3C_4$	120.4(8)	$C_7C_6F_6$	120.8(8)
C_3—C_4	1.375(12)	C_7—F_7	1.341(11)	$C_3C_4C_{12}$	121.4(8)	$C_6C_7F_7$	120.5(8)
C_4—C_{12}	1.382(11)	C_8—F_8	1.354(11)	$C_4C_{12}C_{11}$	118.8(8)	$C_8C_7F_7$	119.1(8)
C_{11}—C_{12}	1.411(12)	Average	1.34	$C_1C_{11}C_{12}$	118.7(8)	Average	120
C_1—C_{11}	1.390(11)			$C_2C_1C_{11}$	120.7(7)		
Average	1.38	$F_4...O_1$	2.634(8)	Average	120	$C_2C_1F_1$	116.5(8)
		$F_5...O_1$	2.650(8)			$C_3C_4F_4$	117.2(7)
C_5—C_6	1.393(12)	$F_1...O_2$	2.687(8)	$C_5C_6C_7$	119.5(8)	$C_6C_5F_5$	116.2(7)
C_6—C_7	1.346(13)	$F_8...O_2$	2.654(8)	$C_6C_7C_8$	120.3(8)	$C_7C_8F_8$	115.5(7)
C_7—C_8	1.411(12)	Average	2.66	$C_7C_8C_{13}$	120.2(8)	Average	116
C_8—C_{13}	1.365(11)			$C_8C_{13}C_{14}$	119.8(7)		
C_{13}—C_{14}	1.401(12)	$F_1...F_2$	2.639(8)	$C_5C_{14}C_{13}$	118.9(8)	$C_{11}C_1F_1$	122.8(8)
C_5—C_{14}	1.382(11)	$F_3...F_4$	2.646(8)	$C_6C_5C_{14}$	121.2(8)	$C_{12}C_4F_4$	121.4(7)
Average	1.38	$F_5...F_6$	2.647(8)	Average	120	$C_{14}C_5F_5$	122.6(8)
		$F_7...F_8$	2.649(8)			$C_{13}C_8F_8$	124.2(8)
C_9—C_{11}	1.485(11)	Average	2.65	$C_9C_{13}C_{14}$	120.8(7)	Average	123
C_9—C_{13}	1.494(11)			$C_{10}C_{14}C_{13}$	119.5(7)		
C_{10}—C_{12}	1.487(11)	$F_2...F_3$	2.714(9)	$C_9C_{11}C_{12}$	121.0(7)	$C_{11}C_9O_2$	122.3(7)
C_{10}—C_{14}	1.479(11)	$F_6...F_7$	2.713(9)	$C_{10}C_{12}C_{11}$	118.8(7)	$C_{13}C_9O_2$	121.3(7)
Average	1.49	Average	2.71	Average	120	$C_{12}C_{10}O_1$	120.1(7)
						$C_{14}C_{10}O_1$	121.0(7)
C_9—O_2	1.211(10)			$C_{11}C_9C_{13}$	116.2(7)	Average	121
C_{10}—O_1	1.228(10)			$C_{12}C_{10}C_{14}$	118.9(7)		
Average	1.22			Average	118	$C_1C_{11}C_9$	120.3(8)
						$C_8C_{13}C_9$	119.4(8)
C_1—F_1	1.327(11)			$C_1C_2F_2$	119.5(8)	$C_4C_{12}C_{10}$	122.2(8)
C_2—F_2	1.321(10)			$C_3C_2F_2$	120.6(8)	$C_5C_{14}C_{10}$	121.6(8)
C_3—F_3	1.356(11)			$C_2C_3F_3$	120.5(8)	Average	121
C_4—F_4	1.343(10)			$C_4C_3F_3$	118.9(8)		

TABLE 5. Deviations of Atoms of the Molecule (in hundredths of Å) from Mean Planes

Plane No.	Atom																					
	C_1	C_2	C_3	C_4	C_5	C_6	C_7	C_8	C_9	C_{10}	C_{11}	C_{12}	C_{13}	C_{14}	O_1	O_2	F_1	F_2	F_3	F_4	F_5	F_6	F_7	F_8
1	+06	+25	+19	−00	+03	+23	+24	−01	−40	−36	−16	−20	−19	−17	−63	−79	+09	+48	+41	−01	+05	+44	+45	+01
2	+24	+43	+39	+19	+22	+41	+41	+16	−23	−17	+02	−02	−02	+02	−43	−63	+26	+67	+61	+19	+25	+61	+61	+17
3	+00	−00	−03	+00							+01	−00					−01	+02	−00	+01				
4					−00	−01	+01	−02					+00	+02							−00	−01	+02	−01

1) $7.883x - 3.970y + 3.024z = 2.512$ (through all atoms of the molecule); 2) $7.919x - 3.955y + 2.988z = 2.327$ (through atoms $C_{11} - C_{14}$); 3) $7.467x - 7.500y + 2.954z = 1.191$ (through atoms $C_1 - C_4$, C_{11}, C_{12}, $F_1 - F_4$); 4) $8.139x - 0.385y + 2.906z = 2.903$ (through atoms $C_5 - C_8$, C_{13}, C_{14}, $F_5 - F_8$).

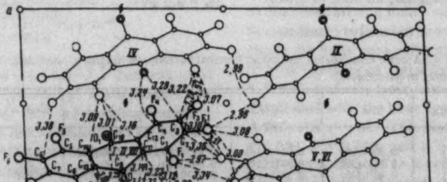

Fig. 2. Arrangement of molecules and intermolecular distances in the crystal.

Equations of the planes through the molecule and specific fragments of it are given in Table 5. For a description of the real conformation of the molecule, the deviations of all atoms from the plane passing through four carbon atoms of the central ring (plane No. 2 of Table 5) were obtained. It can be seen that the outer

TABLE 6. Shortest Intermolecular Distances d, in Å*

Atoms	d	Atoms	d	Atoms	d
$C_1(I)...C_4(II)$	3.78	$C_{13}(I)...O_2(III)$	3.10	$O_2(I)...F_8(III)$	3.41
$C_1(I)...F_4(II)$	3.13	$C_{14}(I)...F_8(VII)$	3.35	$F_1(I)...F_4(II)$	2.99
$C_1(I)...F_8(III)$	3.12	$C_{14}(I)...O_2(III)$	3.33	$F_1(I)...F_6(VI)$	2.97
$C_2(I)...F_5(IV)$	3.28	$C_{14}(I)...F_4(IV)$	3.09	$F_1(I)...F_7(VI)$	3.34
$C_2(I)...F_8(V)$	3.36	$C_{10}(I)...O_2(III)$	3.28	$F_1(I)...F_8(III)$	3.32
$C_3(I)...O_1(IV)$	3.29	$C_{10}(I)...F_4(IV)$	3.01	$F_2(I)...F_3(IX)$	2.96
$C_3(I)...F_5(IV)$	3.22	$C_5(I)...F_8(VII)$	3.22	$F_2(I)...F_5(V)$	3.08
$C_3(I)...F_6(V)$	3.10	$C_6(I)...C_7(VIII)$	3.68	$F_2(I)...F_5(IV)$	3.07
$C_4(I)...F_1(VII)$	3.14	$C_6(I)...F_3(IV)$	3.38	$F_2(I)...F_6(VI)$	3.21
$C_4(I)...O_1(IV)$	3.24	$C_6(I)...F_7(VIII)$	3.11	$F_2(I)...F_7(VI)$	3.00
$C_{12}(I)...O_2(III)$	3.32	$C_7(I)...F_5(II)$	3.33	$F_3(I)...F_5(IV)$	2.92
$C_{12}(I)...F_4(IV)$	3.16	$C_7(I)...C_7(VIII)$	3.77	$F_3(I)...F_6(V)$	2.99
$C_{11}(I)...O_2(III)$	3.14	$C_7(I)...F_8(VIII)$	3.30	$F_5(I)...F_7(VII)$	3.26
$C_{11}(I)...F_8(III)$	3.23	$C_8(I)...O_1(II)$	3.22	$F_5(I)...F_8(VII)$	3.14
$C_9(I)...C_{10}(II)$	3.78	$C_8(I)...F_5(II)$	3.30	$F_6(I)...F_7(VIII)$	2.95
$C_9(I)...O_1(II)$	3.00	$O_1(I)...O_2(VII)$	3.24	$F_7(I)...F_7(X)$	2.98
$C_9(I)...O_2(III)$	2.80	$O_1(I)...F_8(VII)$	3.12		
$C_{13}(I)...O_1(II)$	3.18	$O_2(I)...O_2(III)$	3.08		

*Positions of molecules: I) x, y, z; II) x, y, 1 + z; III) $\bar{x}$, $^1/_2 - y$, $-^1/_2 + z$; IV) 1 − x, $^1/_2 - y$, $^1/_2 + z$; V) x, $^1/_2 + y$, $^1/_2 - z$; VI) x, $^1/_2 + y$, $(^1/_2 - z) + 1$; VII) x, y, −1 + z; VIII) $\bar{x}$, $\bar{y}$, 1 − z; IX) 1 − x, 1 − y, 1 − z; X) $\bar{x}$, $\bar{y}$, 1 + (1 − z).

rings of the nucleus, along with their F atoms, leave the plane of the central ring at 10° in one direction, forming a dihedral angle of 160°. The quinoid ring of the molecule has the "basin" [boat] conformation, since the carbonyl groups deviate from this plane in the other direction (the C_{11}, C_9, C_{13}, O_2 group at an angle of 19°, and the C_{12}, C_{10}, C_{14}, O_1 group at an angle of 13°). The molecule as a whole takes on the "butterfly" conformation.

The molecules of 10-dicyanomethyleneanthrone[20] (dihedral angle between outer rings of 152°, and angle of inclination of the carbonyl system to the plane of the central ring of 11°) and dianthrone[21] (corresponding angles of 148 and 14°) have the analogous "butterfly" conformation and deviation of groups without a visible cause of steric nature.

In the equilibrium conformation of octafluoroanthraquinone, the distances between F...O atoms not bonded by valence (average 2.66 Å) and F...F (average 2.65 and 2.71 Å) (see Table 4) remain shortened in comparison with the sum of the van der Waals radii (2.83 Å for F...O, and 2.94 Å for F...F).

Packing of the molecules in the crystal in (010) projection is shown in Fig. 2. The shortest intermolecular distances are given there also and in Table 6. Of the closer intermolecular contacts, the distances $C_9(I)...O_2(III)$ of 2.80 Å (shortening $\Delta = 0.38$ Å) and $C_{10}(I)...F_4(IV)$ of 3.01 Å ($\Delta = 0.18$ Å) should be noted. The van der Waals radius of the F atom, obtained from the F...F distances given in Table 6, is ~1.5 Å, which corresponds to the value of 1.47 Å accepted earlier.[22] The molecular coordination number is equal to 10. The packing coefficient of the molecules in the crystal is 0.717.

The authors express their deep thanks to G. A. Gol'der for continual attention to the work, to G. G. Yakobson for submitting the interesting compound for study, to V. E. Zavodnik and E. G. Mirevich for carrying out part of the experiment on the diffractometer, to V. P. Glushkova for growing the single crystals, and to A. N. Nikolaeva and G. A. Ilyukhina for help in the work.

---

[1] N. S. Dokunikhin and Z. Z. Moiseeva, Zh. Vses. Khim. Obshchestva, 11, 35 (1966); N. S. Dokunikhin and B. V. Salov, Symposium on Organic Intermediates and Dyes. 4. Chemistry of Anthraquinone /in Russian/, Khimiya, Moscow (1969), p. 80.

[2] N. N. Vorozhtsov, Zh. Vses. Khim. Obshchestva, 15, 52 (1970).

[3] L. A. Chetkina, Kristallografiya, 12, 42 (1967) [Sov. Phys. – Crystallogr. 12, 33 (1967)].

[4] G. G. Yakobson, V. N. Odinokov, and N. N. Vorozhtsov, Tetrahedron Lett., 49, 4473 (1965).

[5] L. A. Chetkina, O. A. Mikhno, G. A. Gol'der, E. G. Popova, M. A. Davydova, and V. P. Glushkova, Kristallografiya, 15, 1244 (1970) [Sov. Phys.–Crystallogr., 15, 1085 (1971)].

[6] V. I. Andrianov, B. L. Tarnopol'skii, and R. P. Shibaeva, Zh. Strukt. Khim., 10, 116 (1969).

[7] V. I. Andrianov, Dissertation, Institute for Crystallography, Academy of Sciences of the USSR (1969).

[8] V. I. Andrianov, Z. Sh. Safina, and B. L. Tarnopol'skii, Zh. Strukt. Khim., 12, 1052 (1971).

[9] A. J. C. Wilson, Nature, 150, 152 (1942).

[10] J. L. Karle, K. S. Dragonette, and S. A. Brenner, Acta Crystallogr., 19, 713 (1965).

[11] F. Hanic, Acta Crystallogr., 21, 332 (1966).

[12] K. Lonsdale and H. J. Grenville-Wells, Acta Crystallogr., 7, 490 (1954).

[13] D. W. J. Cruickshank, D. F. Pilling, A. Bujosa, F. M. Lovell, and M. R. Truter, Computing Methods and the Phase Problem in X-Ray Crystal Analysis, Pergamon, Oxford (1961), p. 45.

[14] B. L. Tarnopol'skii and V. I. Andrianov, Zh. Strukt. Khim., 4, 433 (1963).

[15] A. W. Hanson, Acta Crystallogr., 16, 1147 (1963).

[16] Tables of Interatomic Distances and Configuration in Molecules and Ions, Chem. Soc., Burlington House, Suppl. L (1965).

[17] J. Krausse and H. Dunken, Acta Crystallogr., 20, 67 (1966); G. Ferguson and K. M. S. Islam, Acta Crystallogr., 21, 1000 (1966).

[18] N. N. Neronova, Zh. Strukt. Khim., 9, 147 (1968).

[19] A Prakash, Acta Crystallogr., 22, 439 (1967).

[20] J. Silverman and N. F. Yannoni, J. Chem. Soc., 194 (1967).

[21] E. Harnic and Y. M. J. Schmidt, J. Chem. Soc., 3295 (1954).

[22] A. Bondi, J. Phys. Chem., 68, 441 (1964).

Determination of the crystal structure of the hexagonal phase β^{III} in the copper–tellurium system by electron diffraction

R. V. Baranova, A. S. Avilov, and Z. G. Pinsker

Institute of Crystallography,
Academy of Sciences of the USSR

(Submitted August 11, 1972; resubmitted November 15, 1972)
Kristallografiya, 18, 1169-1176 (November-December 1973)

The crystal structure of the hexagonal phase β^{III}-Cu$_{\sim 1.81}$Te is determined. The lattice constants are a = 8.37 ± 0.01, c = 21.6 ± 0.2 Å, Fedorov group P3m1 (C_{3v}^1), ρ (calc) 7.45 g/cm^3. The structure is disordered and is characterized by its own structural type; it contains 36 independent atoms, of which there are 24 Cu atoms (three of these occupy their positions with a probability of ~50%) and 12 Te atoms, altogether having 54 independent position parameters. The atoms are distributed among four types of particular positions: 1(a)(00z), 1(b)($^1/_3\,^2/_3$z), 1(c)($^2/_3\,^1/_3$z), and 3(d)(x$\bar{x}$z, . . .). The interatomic distances exhibit a severe scatter accompanied by considerably shortened bond lengths. There are 41 (each different) Cu–Cu and 41 Cu–Te distances in the ranges 2.20-3.49 and 2.27-2.98 Å, respectively, and eight Te–Te distances in the range 2.48-2.77 Å. In the crystal-chemical aspect this phase is similar to the earlier studied hexagonal phases β^I-Cu$_{1.75}$Te and β^{II}-Cu$_{1.75\pm0.04}$Te.

The crystal structure of the hexagonal phases[1)] β^I-Cu$_{1.75}$Te and β^{II}-Cu$_{1.75\pm0.04}$ were determined by electron diffraction in refs. 1-3. The lattice constants of these phases occur in multiple relations: β^I: $a \approx 2a_0$, c ≈ c$_0$; β^{II}: $a \approx a_0$, c ≈ 3c$_0$, where $a_0 \approx 4.15$, c$_0$ ≈ 7.2 Å. Despite the multiplicity of the periods and the overlapping of the ranges of concentration within which these phases exist, they nevertheless belong to different and fairly complex structural types with a large number of positional parameters, and are described by the noncentrosymmetric Fedorov groups P3m1–C_{3v}^1(β^I) and P$\bar{6}$m2–D_{3h}^1(β^{II}). However, both phases are similar in the crystal-chemical respect, being characterized by a somewhat blurred coordination, a severe spread of the interatomic distances, and the existence of several considerably shortened bond lengths (relative to the sum of the atomic or covalent radii).

We found that, if these phases were represented as consisting of specific atomic groupings or clusters, each containing within itself the shortest Cu–Te bonds, their structural similarity could easily be established. We found by an appropriate choice of hexagonal cells of roughly equal volumes that the structures of the two phases were composed of an equal number either of predominantly octahedral (β^I) or trigonal–prismatic (β^{II}) clusters. The transition from one phase to the other lay in the rearrangement of some of these clusters with respect to one another by a 60° rotation of one of their triangular faces.

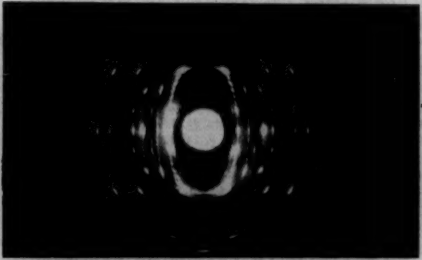

Fig. 1. Electron-diffraction pattern of the β^{III} phase (oblique texture with the [0001] axis, angle fo recording ~60°).

In view of this, we thought it would be interesting, in order to develop the cluster representation further, to determine the structure of yet another hexagonal copper telluride, which we denoted β^{III}, the lattice constants of which were also related in a multiplicative way to the constants of the β^I and β^{II} phases, namely, $a \approx 2a_0$, c ≈ 3c$_0$.

Film samples of this compound were prepared in vacuo (10^{-4} mm Hg) by sputtering the elements Cu and Te from different sources and then condensing them on cleaved NaCl. The resultant films were annealed at about 100°C for 2-3 h. Electron-diffraction patterns of the oblique texture kind with a [0001] texture axis (Fig. 1) were recorded in a horizontal ÉG-1 electron-diffraction camera with an accelerating voltage of up to 75 kV.

For the β^{III} phase we obtained the following parameters of the hexagonal lattice: a = 8.37 ± 0.01, c = 21.6 ± 0.2 Å, Ω = 1310 Å^3. We indexed 120 independent reflections up to $(\sin\theta/\lambda)_{\max}$ = 0.65 Å^{-1}. In addition to this, for the ellipses with odd h and k we found some 30 "excess" re-

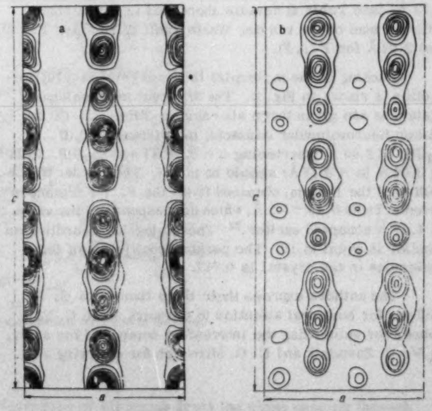

Fig. 2. Cross sections of the interatomic function at v = 0 (a) and ~1/6 (b) for β^{III} phase in the Cu–Te system.

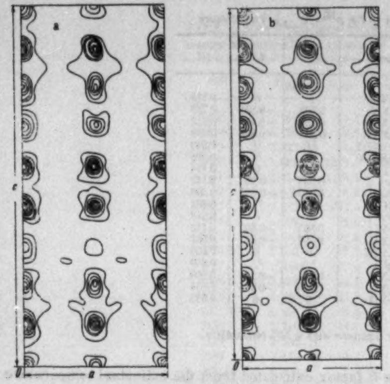

Fig. 3. Fourier potential cross sections for the β^{III} phase of composition $Cu_{\sim 1.8}Te$: a) $\varphi_{exp}(x0z)$; b) $\varphi_T(x0z)$. General temperature correction B = 2.0 Å^2.

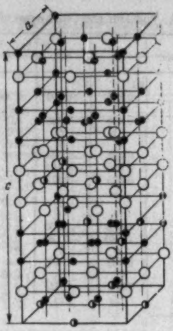

Fig. 4. Schematic view of the structure of the hexagonal β^{III} phase in the Cu–Te system.

flections, corresponding, as it were, to a double c axis. These reflections had a greater elongation along the ellipses and a very low intensity (the intensity ratio of the strongest reflections respectively belonging to the excess and main sets was 0.14). Also for large $\sin\theta/\lambda$ there was a weak splitting of the reflections, into principal and auxiliary components. In view of this, the whole set of additional (auxiliary) reflections was ascribed to some unknown phase differing from the main β^{III} phase, and was not taken into account in the structural analysis. The intensities of the reflections from the β^{III} phase were estimated visually. The transition to structure amplitudes was based on the kinematic equations.

In calculating the Patterson syntheses, the structure factors for those reflections merging in the electron-diffraction pattern were assumed to be equal, in view of the fact that the space group was not actually known. In the cross sections of the interatomic function at v = 0 (Fig. 2a) and 0.5, strong peaks lie at intervals of $\Delta w = 0.11$, while in the cross sections at v = 0.17 (Fig. 2b) and 0.33 strong peaks lie at $w \approx 0.17$ and 0.5 and weak peaks at $w \approx 0$, 0.05, 0.3, and 0.4. The blurring of the peaks of the interatomic function indicates a large scatter of the interatomic distances, which is evidently characteristic of all the hexagonal copper tellurides.

The character of the Patterson function indicates a similarity between the structure in question and the structure of β^I-$Cu_{1.75}Te$, on the one hand, and the structure of β^{II}-$Cu_{1.75 \pm 0.04}Te$ on the other. This is also indicated by the absence of extinctions on the electron-diffraction patterns of the β^{III} phase (an absence also characteristic of the β^I and β^{II} phases), and also by the fact that the unit cells of these phases have lattice constants in multiple ratio.

Since the *a* spacing of the phase under consideration is twice as long as the *a* spacing of the disordered phase β^{II}, it was considered that the structure of the β^{III} phase differed from that of the β^{II} phase in that the positions in the planes parallel to the (xy0) at z = 0.32 and 0.18 were completely occupied by Cu atoms, and also in that there was no layer[2] at z = 0.5, since peaks at w = 0.5 were absent from the Patterson syntheses[2)] in the sections $v \approx$ 1/6 and 1/3.

The variance factors R_{hkl} of this model calculated within the framework of the noncentrosymmetric Fedorov groups $P\bar{6}m2 - D^1_{3h}$ (the Fedorov group for β^{II}) and $P3m1 - C^1_{3v}$ (the Fedorov group for β^I) indicated a preference for the latter. Nevertheless, the first version of the structure with the higher symmetry was refined by Fourier syntheses and by the method of least squares. This yielded a composition corresponding to the range of existence of tetragonal ricardite,[3] several extremely short interatomic distances (much shorter than in the structures of the β^I and β^{II} phases), and also a negligible degree of occupation of the positions by one of the Cu atoms (as compared with the error in determining the potential). This version was accordingly rejected.

The second version of the structure of the model was refined within the P3m1 group by the method of successive approximations with respect to the Fourier syntheses (Fig. 3a, b). In the case of reflections of the type $h0\bar{h}l$, $h0\bar{h}l$ and $hkil$, $hki\bar{l}$ (these pairs not being equivalent as regards $|\Phi|$, but merging into a single reflection), at every state the experimental intensities were divided up in the same ratio as the theoretical intensities, using an electronic computer.[4] The number of structure amplitudes thus rose to 197. In order to estimate the effect of truncation, and in particular its nonuniformity, Fourier syntheses were calculated every time from the computed structure amplitudes (Fig. 3b). Thus the peaks were identified by comparing the "experimental" and "theoretical" syntheses.

The structure was not refined by the method of least squares because of the separation of the structure factors associated with the merging reflections which would be required at each stage. Only the general temperature correction, equal to 2.0 Å^2, was refined by this method.

Figure 4 illustrates the final model of the structure, which contains 24 independent Cu atoms and 12 Te atoms.

TABLE 1. Positions and Coordinates of the Atoms in the β^{III}-$Cu_{\sim 1.81}Te$ Structure

Atoms	x/a	y/b	z/c	Atoms	x/a	y/b	z/c
Cu *I	0.500	—0.500	0.000	CuXIX	0	0	0.778
CuII	$^2/_3$	$^1/_3$	0.045	CuXX	0.505	—0.505	0.779
CuIII	0.835	—0.835	0.061	CuXXI	0.163	—0.163	0.932
CuIV	$^1/_3$	$^2/_3$	0.062	CuXXII	0.828	—0.828	0.939
CuV	0	0	0.225	CuXXIII	$^1/_3$	$^2/_3$	0.940
CuVI	0.496	—0.496	0.225	CuXXIV	0	0	0.998
Cu *VII	0.162	—0.162	0.254	TeI	0	0	0.114
CuVIII	0.825	—0.825	0.270	TeII	0.505	—0.505	0.115
CuIX	$^1/_3$	$^2/_3$	0.271	TeIII	0.835	—0.835	0.390
CuX	0	0	0.327	TeIV	$^1/_3$	$^2/_3$	0.392
CuXI	$^2/_3$	$^1/_3$	0.368	TeV	0	0	0.442
Cu *XII	0.830	—0.830	0.499	TeVI	0.505	—0.505	0.442
CuXIII	0.160	—0.160	0.620	TeVII	0.497	—0.497	0.557
CuXIV	0	0	0.672	TeVIII	0	0	0.558
CuXV	0.495	—0.495	0.675	TeIX	$^1/_3$	$^2/_3$	0.609
CuXVI	$^2/_3$	$^1/_3$	0.697	TeX	0.825	—0.825	0.609
CuXVII	0.835	—0.835	0.731	TeXI	0.495	—0.495	0.884
CuXVIII	$^1/_3$	$^2/_3$	0.732	TeXII	0	0	0.885

*The atoms marked with an asterisk occupy their positions with a 50% probability.

These are distributed over the single positions (00z), ($^1/_3{}^2/_3$z), and ($^2/_3{}^1/_3$z) and the three-fold positions (x$\bar{x}$z, x2xz, and 2$\bar{x}\bar{x}$z) – Fedorov group P3m1 (Table 1).

The structure of the β^{III} phase as a whole is characterized by 54 independent positional parameters. Characteristics of the structural motif include the alternation (in a nonuniform manner along the z axis) of groups of approximately equal numbers of Cu and Te atoms, and also a certain polarity in the distribution of the atoms with respect to different z levels (nonequivalence of the upper and lower parts of the cell). It is an interesting fact that the motif of the rejected version of the structure (within the P$\bar{6}$m2 group) is extremely similar to this final version. The chief difference lies in the absence of atoms from the positions 1(c)($^2/_3{}^1/_3$z) and 3(d) (x$\bar{x}$z) at x ≈ 1/6 for the first version.

A comparative analysis of the heights of the peaks on the "experimental" and "theoretical" potential syntheses and calculations of the R factor showed that some of the Cu atoms occupied their positions incompletely.[3] In Table 1 these atoms are indicated by asterisks. For a 50% occupation of their positions by the atoms Cu I, Cu VIII, and Cu XII, the composition of the phase corresponds to the formula $Cu_{\sim 1.81}Te$, ρ (calc.) = 7.45 g/cm³. Here the $R_{hkl}^{(1)}$ factor, obtained from the independent moduli of the structure amplitudes for coinciding reflections, equals 17.8%, while the $R_{hkl}^{(2)}$ obtained from the reflection intensities equals 24%. Table 2 gives the experimental and calculated intensities. Assuming the complete occupation of all the positions by the Cu atoms (state of complete order in the structure), the composition is determined by the formula Cu_2Te, ρ(calc.)[4] = 7.89 g/cm³, and the $R_{hkl}^{(1)}$ factor equals 23%.

However, because of the already mentioned very nonuniform truncation, the comparatively low accuracy in the visual estimation of the intensities, and the possible influence of the additional reflections, any conclusions as to the partial occupation of their positions by some of the Cu atoms may be shown to be ambiguous; one possible explanation for the reduction in the heights of these atoms on the syntheses, and for the associated improvement in the R factor, may then be an intensification in the thermal motion of these atoms, leading to an increase in the individual temperature corrections relative to B_{gen} = 2.0 Å². The R factor calculated from the individual temperature correction B_{j*} = 3.0 Å² for all the starred Cu atoms in Table 1 equalled 21.7%. However, in the experimental Fourier syntheses calculated from the structure amplitudes, obtained after the introduction of the individual temperature corrections (assuming a complete state of order in the structure), the general tendency for certain potential peak heights of the starred copper atoms to fall remains intact, which once again confirms a deviation of the composition from stoichiometric. At the time, the difference between the potentials of the Cu* atoms in the Fourier syntheses calculated for a 50% occupation of their positions by these atoms, using $B_{j*} = B_{gen}$ = 2.0 Å² in the one case and B_{j*} = 3.0 Å² in the other, remained within the range of the error committed in determining the heights of the peaks. In order to secure the final model we therefore took the nonstoichiometric composition (~50% occupation of their positions by the Cu* atoms) and a general temperature correction of B_{gen} = 2.0 Å².

An analysis of the interatomic distances (Table 3) shows a severe scatter in their values, while there are also a number of distances lying substantially below the sums of the atomic or covalent radii. Thus there are 41 different Cu–Cu and 41 different Cu–Te distances in the ranges 2.20-3.49 and 2.27-2.98 Å, respectively, and eight Te–Te distances in the range 2.48-2.77 Å.

We mentioned earlier that analogous effects had been found in the structures of the β^{I} and β^{II} phases studied in a previous investigation. In the first of these Cu–Te bonds predominate (57 different distances in the range 2.39–3.18 Å); there are also six Cu–Cu distances from 2.38 to 3.28 and four Te–Te between 2.86 and 2.92 Å. In the second phase the number of different Cu–Te, Cu–Cu, and Te–Te distances is approximately the same (7, 8, and 8), but the scatter is more severe for Cu–Cu and Te–Te. The interatomic distances in β^{II} lie in the ranges 1.82–2.74 (Cu–Cu), 2.49–2.80 (Cu–Te), and 2.68–2.73 Å (Te–Te).

The majority of authors[5-8] who have studied the Cu–Te system indicate that the hexagonal phases exist chiefly in the range of compositions $Cu_{1.75}Te$–$Cu_{1.83}Te$. The existence of a stoichiometric hexagonal form of Cu_2Te with the minimum lattice constants (a_0 = 4.245 and c_0 =

TABLE 2. Comparison between the Experimental and Calculated Intensities (oblique-texture electron-diffraction pattern) for β^{III}-Cu$_{\sim 1.81}$Te

hkil	d_{calc}	I_{exp}	I_{calc}
$10\bar{1}0$	7.249	24.5	41.5
$11\bar{2}0$	4.185	10.8	8.3
$11\bar{2}3$	3.617	24.5	59.3
$20\bar{2}0$	3.624	1273.1	1216.5
$20\bar{2}1$	3.574	29.4	42.9
$20\bar{2}2$	3.436	8.8	16.6
$20\bar{2}3$	3.236	685.5	460.8
$20\bar{2}4$	3.008	24.5	8.9
$20\bar{2}5$	2.775	39.2	26.0
$20\bar{2}6$	2.552	107.7	99.9
$20\bar{2}7$	2.348	97.9	105.8
$20\bar{2}8$	2.163	24.5	21.0
$20\bar{2}9$	1.999	781.3	1265.5
$20\bar{2}.10$	1.854	9.8	16.9
$21\bar{3}0$	2.740	44.1	5.3
$21\bar{3}3$	2.560	4.9	24.2
$21\bar{3}6$	2.179	48.9	46.2
$21\bar{3}.12$	1.503	2.9	3.6
$30\bar{3}0$	2.416	5.9	4.0
$30\bar{3}3$	2.250	24.5	21.7
$22\bar{4}0$	2.093	1762.6	1522.2
$22\bar{4}1$	2.083	2.9	9.2
$22\bar{4}2$	2.054	2.9	7.7
$22\bar{4}3$	2.009	9.8	12.7
$22\bar{4}4$	1.951	12.7	14.8
$22\bar{4}5$	1.883	0.3	1.7
$22\bar{4}6$	1.808	132.2	117.0
$22\bar{4}7$	1.731	0.2	1.4
$22\bar{4}8$	1.653	0.9	4.8
$22\bar{4}9$	1.576	4.9	4.2
$22\bar{4}.12$	1.363	4.9	13.8
$22\bar{4}.15$	1.185	3.9	4.2
$22\bar{4}.16$	1.133	14.7	16.2
$31\bar{4}0$	2.010	2.9	1.3
$31\bar{4}3$	1.936	3.9	6.8
$31\bar{4}5$	1.822	0.2	0.4
$31\bar{4}6$	1.755	3.8	4.3
$40\bar{4}0$	1.812	127.3	82.5
$40\bar{4}1$	1.806	3.9	3.1
$40\bar{4}2$	1.787	1.0	0.9
$40\bar{4}3$	1.757	53.9	35.8
$40\bar{4}4$	1.718	1.9	0.7
$40\bar{4}5$	1.671	3.9	2.7
$40\bar{4}6$	1.618	13.7	10.2
$40\bar{4}7$	1.562	15.7	12.8
$40\bar{4}8$	1.504	2.9	2.8
$40\bar{4}9$	1.445	146.9	181.8
$43\bar{7}6$	1.131	2.4	3.0
$52\bar{7}0$	1.161	1.0	0.7
$52\bar{7}3$	1.146	6.8	3.2
$52\bar{7}6$	1.105	0.4	0.5
$61\bar{7}0$	1.105	0.3	0.1
$61\bar{7}3$	1.093	0.2	0.4
$61\bar{7}6$	1.057	0.1	0.1
$61\bar{7}9$	1.004	0.2	0.2
$44\bar{8}0$	1.046	11.7	37.7
$44\bar{8}3$	1.035	0.2	0.4
$44\bar{8}6$	1.005	4.9	4.0
$44\bar{8}.15$	0.846	0.3	0.4
$44\bar{8}.16$	0.827	0.5	1.2
$44\bar{8}.18$	0.788	1.9	3.6
$40\bar{4}.11$	1.331	0.4	0.5
$40\bar{4}.12$	1.276	3.9	2.3
$40\bar{4}.13$	1.224	1.1	1.7
$40\bar{4}.14$	1.174	1.9	0.7
$40\bar{4}.15$	1.126	7.8	10.4
$40\bar{4}.16$	1.082	1.2	1.0
$40\bar{4}.17$	1.039	1.0	0.7
$32\bar{5}0$	1.663	2.9	1.1
$32\bar{5}3$	1.620	2.5	3.3
$32\bar{5}6$	1.509	1.0	0.5
$32\bar{5}9$	1.366	1.9	1.2
$32\bar{5}.12$	1.221	1.0	1.8
$32\bar{5}.15$	1.088	2.5	0.7
$41\bar{5}0$	1.582	1.9	1.4
$41\bar{5}3$	1.545	6.8	6.6
$41\bar{5}6$	1.448	1.0	1.8
$41\bar{5}9$	1.320	1.2	0.7
$41\bar{5}.12$	1.187	0.1	0.1
$41\bar{5}.15$	1.064	0.5	0.5
$50\bar{5}0$	1.450	4.9	0.3
$50\bar{5}3$	1.421	0.6	1.2
$50\bar{5}6$	1.345	3.4	4.2
$33\bar{6}0$	1.395	1.5	0.3
$33\bar{6}3$	1.369	0.7	0.7
$42\bar{6}0$	1.370	39.2	40.8
$42\bar{6}1$	1.367	0.5	1.5
$42\bar{6}2$	1.359	0.5	0.5
$42\bar{6}3$	1.346	22.5	24.8
$42\bar{6}5$	1.306	1.9	1.6
$42\bar{6}6$	1.280	5.9	5.7
$42\bar{6}7$	1.252	5.9	7.4
$42\bar{6}8$	1.221	1.5	1.7
$42\bar{6}9$	1.189	107.7	110.7
$42\bar{6}.10$	1.156	1.0	1.7
$42\bar{6}.12$	1.050	2.4	1.7
$42\bar{6}.15$	0.992	5.9	7.7
$42\bar{6}.18$	0.902	7.8	7.2
$51\bar{6}0$	1.302	0.5	0.2
$51\bar{6}3$	1.281	0.5	0.8
$51\bar{6}6$	1.224	1.5	2.3
$51\bar{6}9$	1.144	0.1	0.2
$60\bar{6}0$	1.208	88.1	93.7
$60\bar{6}3$	1.191	0.5	0.7
$60\bar{6}6$	1.145	7.8	9.2
$60\bar{6}.16$	0.900	1.9	2.4
$60\bar{6}.18$	0.851	1.9	7.3
$43\bar{7}0$	1.192	1.5	0.2
$62\bar{8}0$	1.005	6.8	6.5
$62\bar{8}3$	0.996	3.9	2.9
$62\bar{8}6$	0.968	0.7	0.9
$62\bar{8}7$	0.956	0.5	1.4
$62\bar{8}8$	0.942	0.2	0.3
$62\bar{8}9$	0.927	17.6	19.7
$62\bar{8}.15$	0.824	1.5	1.7
$62\bar{8}.16$	0.806	0.3	0.2
$62\bar{8}.18$	0.770	1.5	1.8
$70\bar{7}0$ $53\bar{8}0$	1.036	0.7	0.1
$70\bar{7}3$ $50\bar{5}3$	1.025	0.5	0.2

---

*The experimental and calculated intensities are reduced by a factor of 10^3 relative to the absolute scale and rounded off to an accuracy of 0.1.

TABLE 3. Interatomic Distances in the Structure of β^{III}-$Cu_{\sim 1.81}Te$ in Å

Cu—Cu	Cu—Te	Te—Te	Cu—Cu	Cu—Te	Te—Te
2.200	2.269	2.483	2.687	2.637	
2.248	2.308	2.502	2.707	2.651	
2.286	2.352*	2 624	2.710	2.653	
2.430*	2.374*	2.633	2.716	2.657*	
2.436	2.376	2.642	2.718*	2.662	
2.464	2.3[illegible]4	2.643	2.741*	2.677	
2.472*	2.437	2.712	2.745	2.693	
2.475	2.447	2.765	2.751	2.720*	
2.503*	2.459		2.759	2.739	
2.511*	2.481		2.761*	2.742	
2.533	2.482*		2.762*	2.751	
2.548	2.486		2.800	2.752	
2.558	2.502		2.819	2.754*	
2.577	2.503*		2.828*	2.774*	
2.579	2.524		2.850*	2.788	
2.598	2.545		2.936	2.789	
2.604*	2.571		3.120	2.798	
2.608	2 592		3.271	2.835	
2.632	2.610		3.360	2.878	
2.633	2.622		3.486	2.978	
2.646	2.636				

*Distances between atoms, one of which is disordered.

7.289 Å) at room temperature was established in ref. 9 and its structure was determined. A phase with similar lattice constants was also observed in ref. 9 at high temperatures (340-475°C) over a wide range of concentrations ($Cu_{1.94}Te$-$Cu_{1.77}Te$).

All the foregoing leads us to assert with some confidence that the β^{III} phase deviates from the stoichiometric composition of Cu_2Te (33.3 at.% Te) as far as $Cu_{\sim 1.81}Te$ (~35.6 at.% Te).

All the calculations were carried out in the M-220 computer of the Institute of Crystallography, Academy of Sciences of the USSR, using the "Kristall" set of programs.

The authors wish to thank R. M. Imamov for discussing the work.

---

[1] The thermodynamic properties of the compounds in question were not studied either in our earlier papers[1-3] or here; however, we shall use the word "phase" meaning a specific crystal structure.

[2] The latter assertion is ambiguous, since of course the general background may screen individual peaks. This explains why in the final model of the structure a disordered layer of Cu atoms occurs at z = 0.5.

[3] Owing to the very nonuniform truncation, no comparison was made between the heights of the potential peaks obtained from the syntheses and the potential values in the centers of the atoms calculated by the Vainshtein equation.

[4] Comparison with the densities of other known copper tellurides (fluctuating over the range 7.4-7.5 g/cm³) indicated a preference for the composition $Cu_{\sim 1.81}Te$, which corresponds to a density in the middle of this range.

[1] R. V. Baranova, Kristallografiya, 12, 266 (1967) [Sov. Phys.–Crystallogr., 12, 221 (1967)].

[2] R. V. Baranova, Kristallografiya, 13, 803 (1968) [Sov. Phys.–Crystallogr., 13, 695 (1969)].

[3] R. V. Baranova and Z. G. Pinsker, Zh. Strukt. Khim., 11, 690 (1970).

[4] L. I. Man and R. M. Imamov, Kristallografiya, 17, 757 (1972) [Sov. Phys.–Crystallogr., 17, 663 (1973)].

[5] K. Anderko and K. Schubert, Z. Metallkunde, 45, 371 (1954).

[6] M. Kieu van con and H. Rodot, Compt. Rend., 260, 1908 (1965).

[7] M. Hansen and K. Anderko, Constitution of Binary Alloys, Vol. 2, McGraw-Hill (1958).

[8] A. L. N. Stevels, Philips Res. Repts. Suppl., 1-120 (1969).

[9] H. Nowotny, Z. Metallkunde, 37, 40 (1946).

Neutron-diffraction refinement of the structure of alpha lithium iodate

A. Émiraliev, A. G. Kocharov, I. I. Yamzin, and V. A. Lyubimtsev
Institute of Crystallography,
Academy of Sciences of the USSR

(Submitted October 4, 1972; resubmitted December 27, 1972)
Kristallografiya, 18, 1177-1181 (November-December, 1973)

Using single-crystal and polycrystalline samples, the positions of the Li and O atoms in the structure of α-$LiIO_3$ are refined by neutron diffraction. The interatomic distances and angles are found. The parameters of the anisotropic thermal vibrations are determined. It is shown that the oxygen polyhedra around the Li and I atoms are distorted.

Recent x-ray structural studies of α-$LiIO_3$ showed[1,2] that the crystals of this compound belonged to the $P6_3$ space group, and not the $P6_322$ space as indicated in ref. 3. The coordinates of the atoms in general form are: Li(0, 0, z; 0, 0, $z + 1/2$), I($1/3$, $2/3$, 0; $2/3$, $1/3$, $1/2$), O(x, y, z, etc.). Figure 1 gives a schematic impression of the structure of α-$LiIO_3$.

It was found in refs. 1 and 2 that the oxygen octahedra surrounding the I atoms were considerably distorted. At the same time the oxygen polyhedra around the Li ion were distorted according to ref. 1, but regular (within the limits of experimental error) according to ref. 2. The difficulties encountered in finding by x-ray diffraction the positions of light atoms in the presence of heavy ones are generally understood.

The aim of the present investigation was to refine the positions of the Li and O atoms in the structure of α-$LiIO_3$ by neutron diffraction. The use of this method should in principle give more reliable results, owing to the fact that the amplitude of the coherent neutron scattering is greater for oxygen than for iodine (5.77 and 5.2f respectively), while the scattering amplitude for lithium has a negative sign (−1.94f).

We used a DN-500 neutron-diffraction system in the heavy-water reactor of the Institute of Theoretical and Experimental Physics, and measured the neutron scattering intensity of powdered and single-crystal samples of α-$LiIO_3$ (λ = 1.24 Å, T = 293°K). The powder was obtained by crushing α-$LiIO_3$ single crystals and was fed into a thin-walled cylindrical vanadium container 12 mm in diameter and 60 mm high. The single-crystal sample had natural $\{10\bar{1}1\}$ and ~ $\{20\,0\,\bar{20}\,\bar{1}\}$ faceting with dimensions of about 8 mm along and normal to the hexagonal axis. The neutron-diffraction pattern of the powdered sample (Fig. 2) was obtained by scanning every 10' with a set of neutron pulses operating for 400 sec at each point with a continuous rotation of the sample around its axis. Sixteen reflections were recorded.

For the single-crystal sample the ω method was employed (point by point, every 2.5'); we measured the scattering intensity at the Bragg maxima with the beginning and end of the scan at the background level. The pulse collection time was 28-280 sec, depending on the intensity of the reflection. Altogether the intensity of 104 reflections was measured, but since the difference in the

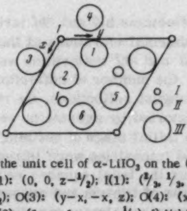

Fig. 1. Projection of the unit cell of α-$LiIO_3$ on the (001) plane. Coordinates of the ions: Li(1): (0, 0, $z-1/2$); I(1): ($2/3$, $1/3$, $1/2$); O(1): x, y, z); O(2): (y, $y-x$, $z + 1/2$); O(3): ($y-x$, $-x$, z); O(4): ($x-y$, x, $z + 1/2$); O(5): ($1-y$, $1 + x-y$, z); O(6): ($1-x$, $1-y$, $z + 1/2$); I) lithium ions; II) iodine; III) oxygen.

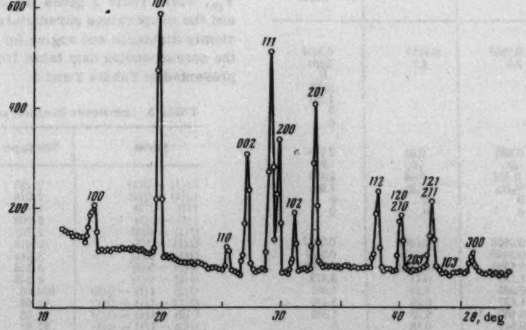

Fig. 2. Powder neutron-diffraction recording of α-$LiIO_3$.

TABLE 1. Comparison between the Calculated and Measured Structure Amplitudes for an α-LiIO$_3$ Single Crystal

hkl	$10\|F_m\|$	$10\|F_c\|$	$10\,A_c$	$10\,B_c$	hkl	$10\|F_m\|$	$10\|F_c\|$	$10A_c$	$10B_c$
100	6.41	5.71	−5.71	0	402	3.78	3.64	−3.44	−1.21
200	16.40	18.23	−18.23	0	502	4.37	3.68	−1.81	−3.21
300	11.11	11.92	11.92	0	112	12.23	11.22	−7.80	−1.44
400	8.81	8.72	−8.72	0	212	6.55	5.37	−3.32	−4.22
500	8.48	9.38	−9.38	0	122	17.92	17.95	−11.98	13.36
110	8.05	6.17	−6.17	0	222	7.78	6.65	2.80	6.04
210	15.04	14.81	−14.81	0	322	4.37	3.81	−2.25	−3.08
310	14.01	16.45	−16.45	0	422	7.14	9.50	−6.32	7.09
410	3.49	3.96	3.96	0	332	6.38	6.89	6.18	−3.05
510	4.75	3.97	3.97	0	242	3.12	2.76	−2.27	−1.57
120	9.01	7.51	7.51	0	103	1.80	1.26	−0.49	1.16
220	10.52	11.58	11.58	0	203	18.56	20.72	−1.08	−20.69
320	9.72	10.42	−10.42	0	303	1.95	1.42	0.10	1.41
420	5.26	4.00	4.00	0	403	6.31	5.76	−0.29	5.75
130	10.97	11.80	11.80	0	503	9.51	11.49	−0.86	−11.46
230	7.81	8.07	−8.07	0	113	12.65	13.36	−1.47	−13.28
330	2.66	0.65	−0.65	0	213	1.80	1.29	−0.36	1.24
140	1.59	0.17	−0.17	0	123	9.21	7.56	−0.06	−7.56
240	7.48	6.89	−6.89	0	223	5.11	4.02	0.58	3.98
150	4.72	4.77	−4.77	0	004	14.24	14.80	−5.76	−13.63
101	12.79	14.37	−6.69	12.71	104	5.11	5.36	−5.22	1.20
201	15.32	15.57	−15.50	1.46	204	8.23	7.33	−0.14	7.32
301	2.49	1.84	1.57	−0.95	304	4.60	3.02	2.93	−0.73
401	6.21	5.82	0.79	5.77	404	4.17	3.54	−1.84	3.03
501	8.04	8.08	−8.08	0.16	114	12.70	13.61	10.74	8.36
111	16.78	17.32	−14.67	9.21	214	7.03	5.64	−0.77	5.58
211	12.84	12.23	−5.57	10.88	124	10.39	10.15	−8.86	−4.95
121	7.83	6.71	−1.42	−6.56	224	4.49	3.59	3.29	−1.43
221	6.49	5.21	4.38	−2.82	105	7.34	7.22	3.34	6.40
321	5.17	4.91	1.32	4.73	205	8.23	7.84	7.70	−1.48
421	4.18	4.12	−1.13	−3.96	305	0	0.84	−0.77	−0.34
231	8.12	7.18	−7.08	−1.20	115	8.53	7.96	7.50	2.65
331	8.25	9.15	−7.82	4.76	215	7.17	6.20	2.76	5.55
241	7.62	7.87	−3.63	6.99	125	4.65	4.26	0.77	−4.19
002	24.46	30.26	−6.85	29.47	225	0	2.40	−2.30	−0.67
102	11.10	9.73	−8.58	4.58	006	14.47	16.11	16.11	−0.21
202	7.65	6.59	−2.63	−6.04	106	0	1.63	−0.47	1.56
302	9.18	7.49	3.63	6.55	116	1.95	2.67	1.32	2.32

intensities of reflections h0*l* and 0h*l* (arising solely from the anisotropic thermal vibrations of the O atoms) was under 5%, the h0*l* and 0h*l* reflections were treated as one. In this way the number of reflections was reduced to 76; the 20 strongest reflections, the intensity of which was certainly distorted by extinction, were left out of consideration in the initial stage of refining the structure. The remaining 56 intensities were introduced into a program designed for the least-squares refinement of the atomic coordinates of lithium and oxygen in the M-220 computer. The original atomic coordinates were taken from ref. 1. The extinction corrections were introduced by the Zachariasen method after the first refining cycle. The extinction-corrected intensities of all 76 reflections took part in the second cycle of least-squares structure refinement. At the second stage we refined (or for lithium, determined) the parameters of the anisotropic thermal vibrations of the atoms, considering the temperature factor as taking the form

$$\exp\{-\tfrac{1}{4}[(h^2B_{11}+k^2B_{22}+2hkB_{12})a^{*2}$$
$$+2l(hB_{13}+kB_{23})a^*c^*+l^2B_{33}c^{*2}]\}.$$

The final convergence factor $R = \Sigma\|\,|F_m| - |F_c|\,\|\cdot(\Sigma|F_m|)^{-1}$ was 0.12. Table 1 gives a comparison between the calculated and measured structure amplitudes F_c and F_m, while Table 2 gives the coordinates of the atoms and the temperature parameters; Table 3 gives the interatomic distances and angles for α-LiIO$_3$. For comparison the corresponding data taken from refs. 1 and 2 are also presented in Tables 2 and 3.

TABLE 2. Coordinates of the Atoms (Å) and Temperature Parameters (Å^2)

Atoms	Coordinates and temperature parameters	[1]	[2]	This paper
Li	z	0.8907	0.9110	0.9461
	B_{11}	2.0	1.0	3.381
	B_{22}			B_{11}
	B_{33}			2.005
	B_{12}			1.267
	B_{13}			0
	B_{23}			0
I	B_{11}	0.833	0.53	2.169
	B_{22}	B_{11}	B_{11}	B_{11}
	B_{33}	0.853	0.46	2.393
	B_{12}	$\frac{1}{2}B_{11}$	$\frac{1}{2}B_{11}$	1.204
	B_{13}	0	0	0
	B_{23}	0	0	0
O	x	0.0936	0.0940	0.0957
	y	0.3440	0.3425	0.3437
	z	0.1698	0.1652	0.1618
	B_{11}	1.190	0.71	3.479
	B_{22}	0.985	1.11	3.055
	B_{33}	1.157	0.99	3.470
	B_{12}	0.180	0.28	1.542
	B_{13}	0.541	0.18	0
	B_{23}	0.419	0.22	0.174

TABLE 3. Interatomic Distances and Angles (Deg) in α-LiIO$_3$

Atoms	This paper	[1]	[2]
Li(1) − O(1)	2.235	2.038	2.11
Li(1) − O(2)	2.019	2.220	2.13
I(1) − O(2)	1.795	1.817	1.809
I(1) − O(3)	2.908	2.873	2.892
O(1) − O(5)	2.751	2.756	2.763
O(1) − O(3)	2.915	2.925	2.908
O(1) − O(2)	3.085	3.085	3.082
O(2) − O(5)	3.538		3.535
O(3) − O(4)	4.245		4.012
O(2) − I(1) − O(6)	100.00	98.65	99.50
O(1) − I(1) − O(6)	94.62		94.73
O(2) − I(1) − O(3)	78.03		78.24
O(3) − I(1) − O(5)	87.57		87.85
O(3) − I(1) − O(6)	165.30		165.73

On comparing our own results with those of refs. 1 and 2 we see that the greatest differences occur, as we should expect, in the z coordinates of lithium and to a lesser extent in the z coordinate of oxygen. Our Li–O distances indicate a displacement of the Li atom relative to the center of the oxygen octahedron by 0.0343 Å along the Z axis, whereas according to ref. 2 the lithium lies in the center of the oxygen octahedron (within the limits of experimental error), and according to ref. 1 the displacement of the Li atom is 0.0291 Å, but in the opposite direction along the Z axis.

Unfortunately we did not have a program for determining the standard errors in the coordinate values, and correspondingly the interatomic distances and angles. However, an estimate based on the equations given in ref. 4 showed that for the Li atoms the error was no greater than 0.008 and for the O atoms ~0.007. This suggested that the difference between our own results and those of refs. 1 and 2 lay outside the limits of experimental error, while our lithium and oxygen coordinates and Li–O distances were quite reliable. This cannot be said of our parameters for the anisotropic thermal vibrations of the atoms, since the 76 reflections were evidently insufficient for their exact determination. On the other hand, we were able to find the parameters of the anisotropic thermal vibrations of the Li atoms, which is practically impossible to do by the x-ray diffraction method in a structure such as α-LiIO$_3$.

TABLE 4. Comparison between the Calculated and Measured Intensities for α-LiIO$_3$ Powder

hhl	$10F^2_m$	$10F^2_c$	hhl	$10F^2_m$	$10F^2_c$
100	5.07	3.26	201	30.15	24.24
101	17.49	20.65	112	20.67	18.69
110	4.39	3.81	210, 120	32.41	35.34
002	91.79	91.57	202	0	4.34
111	30.43	30.00	211, 121	18.20	19.46
200	37.94	33.23	103	0	0.16
102	8.74	9.47	300	11.15	14.21

The use of the resultant coordinates for calculating the powder neutron-diffraction pattern gave an R factor of 0.01 (with respect to F^2). Table 4 gives the comparison between the calculated and measured intensities for the α-LiIO$_3$ powder.

The authors are grateful to G. F. Dobrzhanskii for presenting the crystals and L. A. Muradyan for the program used in refining the parameters of the anisotropic thermal vibrations of the atoms.

---

[1] A. Rosenzweig and B. Morosin, Acta Crystallogr., 20, 758 (1966).

[2] J. L. de Boer, F. van Bolhuis, Roeli Olthof-Hazekamp, and Aafje Vos, Acta Crystallogr., 21, 841 (1966).

[3] W. H. Zachariasen and F. A. Barta, Phys. Rev., 37, 1626 (1931).

[4] I. D. Datt, N. V. Rannev, and R. P. Ozerov, Kristallografiya, 15, 25 (1970) [Sov. Phys.–Crystallogr., 15, 18 (1970)].

Relationships of structure types.
New representatives of the homologous classes corundum, spinel, and amesite

N. L. Smirnova, S. D. Polzikov, and N. A. Rebrova
M. V. Lomonosov Moscow State University
(Submitted September 20, 1971; resubmitted January 3, 1973)
Kristallografiya, 18, 1182-1191 (November-December 1973)

New structure types of the homologous classes corundum, spinel, and amesite have been examined by the method of crystallograms. As had been suggested, they are constructed from the six basic free structural minals characteristic of these classes: AB and AA for spinel, AB and AA for corundum, and amesite I and II.

The relationships among various objects are determined by features which unite them in groups and assume the existence of an ancestor and genealogical hierarchy, i.e., the existence of a system. Within the limits of the system, all objects which are possible in principle and the laws of their formation are revealed, and the evolutional growth from the simplest to the complex is traced.

There is a series of approaches to the study of the family relationships in the various groups of structure types.[1-6] All approaches supplement one another, illuminating the connection between structure types from various positions. At the base of a study of family relationships,[7-9] we have assumed a unified approach, which allows us to combine the multiplicity of structure types in a system on the assumption that the reorganization of some structure types into others proceeds as the result of ordering (in the homologous sense, i.e., polytypy and heteropolytypy), adoption, and deformation. These transitions, for which a smooth (martensitic, topotaxial) change of atomic coordination is possible, are called constructional.[10] They are revealed by the basic laws of evolutional reorganization of crystal structures by the laws of succession.

Another position, which is put on the basis of analysis of the family relationships of structure types, is the representation of structure types as complex formations, each constructed of a small number (1-3) of different details or partial structures, otherwise known as structural minals (s-minal).[8,11-16] By s-minal (a quantum of crystal space) is understood a portion cut out of a unit cell of a layer parallel to some plane (hk*l*) which is present as a whole in different structure types. For example, the s-minal of Mg (≡ Cu), which represents half the unit cell of the hexagonal close packing, is contained in the structure types of Mg, Cu, and other n-layer packings, and in CdI_2, $CdCl_2$, Fe_3S_4, etc. The s-minal is bounded by (hk*l*) planes and is characterized by linear and angular parameters. An s-minal is named on the basis of the name of the structure types which it forms, or on the basis of composition; for example, the BaO_3 s-minal in $BaAl_2Si_2O_8$. An s-minal can be simple or combined (a cs-minal). The latter is combined from simple s-minals (for example, $CdI_2 = Mg \cdot NiAs$, i.e., the cs-minal of CdI_2 consists of the NiAs and Mg s-minals). If the s-minals are the same, then the cs-minal will be monotypic (a cms-minal). Thus, upon selection of a cell in close packing with $a = a'\sqrt{3}$ or $2a'$, etc. (where a' is the shortest distance between atoms of a layer), cms-minals of the Mg_3, Mg_4 types, etc., containing three, four, etc., s-minals of Mg, are formed. chs-Minals, consisting of different s-minals, will be heterotypic (for example, $CdI_2 = Mg \cdot NiAs = Cu \cdot NaCl$). A structure type can be heterotype on the basis of relationship to a simple s-minal ($CdI_2 = Mg \cdot NiAs$), but a monotype on the basis of relationship to a combined one (CdI_2).

In different directions, the same structure type can consist of different s-minals with different coupling areas: a minal base, or m base. For the Cu, α-Fe structure type, the s-minal has a hexagonal m base with parameter a in the [111] direction, a tetragonal one ($a/\sqrt{2}$) in the [100] direction, and a rhombic one (a, $a\sqrt{2}$) in the [110] direction. The value of the m base can be estimated, in particular, by the number of atoms in the cell of the layer (for example, Mg, Mg_2, Mg_3, Mg_4, etc.). A structure type with an m-base of minals the same in value belongs to one homologous class (the G_n^m class), in which polytypic and heteropolytypic series of structure types can be isolated (n and m are indices which depend on choice of direction and value of the m base, respectively). In the first case, all terms of the polytypic (homeotectic) series are constructed from one type, and the second from a different type of s-minals (Mg, Cu, La, Sm; $CdI_2 = Mg \cdot NiAs$, $Fe_3S_4 = Mg \cdot 3NiAs$, NiAs). All structure types are terms of these or other existing or potentially possible homologous series, and therefore at their limits will be homologs (or Cs structures), i.e., polytypes and heteropolytypes.

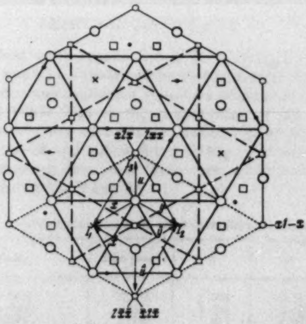

Fig. 1. Nets possible in the G classes α-Fe−Cu (○, −, ×), corundum, spinel, and amesite. Atoms of structure types of these classes can be projected only in the nearest vicinity of points of these nets. Types of nets: I_1 small cross, I_2 fine line, I_3 light small circle (A, B, Ċ); light coarse circle X(000), heavy coarse circles $X(\hat{0}\hat{0}\hat{0})$ (A_{3C}, B_{3C}, C_{3C}); light small squares X(1/6, 1/6, 0), heavy coarse squares X(1/6, 0, 1/6) (A_{3sp}, B_{3sp}, C_{3sp}); small blackened circles X(x0u).

Each s-minal has permanent (skeletal) and changeable (topotaxial) parts.[16] In the Mg s-minal, the skeletal part is the close-packed atoms, and the topotaxial part is the atoms which occupy the vacancies. The combination of s-minals with the same skeletal but different topotaxial part belongs to the same free structural minal (fs-minal). The fs-minal must be considered to be hypothetical, since the simultaneous filling of all vacancies in it cannot be accomplished. But all s-minals which belong to it represent derivatives d_q of s-minals of different generations (q). Thus, the Mg fs-minal has its d_0, d_1, and d_2 s-minal derivatives: Mg = Cu (zero generation), NiAs = NaCl (first generation), ZnS, CaF_2 (second generation) in the direction of the type 3 axis. The order of the generation is determined by the ratio of coordination numbers.

The combination of s-minals forming the structure type carries in itself complete information about the structure type and its formation from the s-minals (CdI_2 = Mg · NiAs, Fe_3S_4 = Mg · 3NiAs). The value of the parameters of the s-minals in the structure types serves as the criterion of complexity of the structure type. If the parameters of the structure type are small, then the structure type and s-minals cannot be complex. However, the reverse statement is not valid. If the parameters of the structure type are small, then either structure types are formed with complex s-minals or the structure type represents the n-th term (n can be a rather large number) of a homologous series.

During the study of the evolution of structure types from simple to complex ones we start from a structure type with small lattice parameters and the same isotropic coordination of atoms, and later we shall study their development into a structure type with large parameters, complex groupings, and various anisotropic coordinations of atoms. The simplest s-minals are cut out from the lattice with four basic polymorphic forms which transform from one to another: the cubic face-centered, body-centered, primitive, and the hexagonal (c/a = 1) with minimal m-base in the (001), (111), and (110) planes. The combination of structure types of different G_n^m classes formed from s-minals of one designation we shall call the F_p^q class, where q is the order of the generation, and p is determined by the s-minals, which are the ancestors. The F_1^0 class is the zero generation (q = 0) and contains the structure types with an s-minal of zero generation (Cu; Mg; Sm; γ-Mn; Cu_3; Ti_1; Pa; etc.), and class F_1^1 (the first generation) contains structure types of more complex s-minals (s-minals of zero generation are secondary and rudimentary, and can be combined with s-minals of first generation): NaCl, CdI_2, PbO_2, Fe_2N, Al_2O_3, BiI_3, TiO_2, and NiAs.

Layers and rods correspond to s-minals. Therefore, for the appearance of composition s-minals all structure types, independently of this, would be molecular, insular, layers, or carcasses, and they are scanned by the method of crystallograms (projective, lettered, graphic line diagrams), at the basis of which lies the representation of the structure type in the form of layers corresponding to the s-minals.[8–16]

Since a series of simplifications of the line-diagram method was accomplished in later works,[13–16] it is expedient to summarize the general principle of this method. During use of the line-diagram method, the structure types of the hexagonal and cubic systems (in the hexagonal aspect) are represented in the form of linear spectra. The structure types are characterized by the basic and superstructure spectra. Into the basic spectrum enter the lines retained from one structure type to another, and the superstructure spectrum is represented by lines which change in this case. The basic spectrum corresponds to the skeletal part of the fs-minals, and the variable spectrum corresponds to the topotaxial part. The line-diagram method is only possible when all structure types are constructed from a small number of plane nets genetically related among themselves.[11,12] The cell parameter determines the possibility of appearance of the various nets and their combinations, and seems to be the most important criterion in the system of structure types.[11] For $a \sim 3$ Å, in the hexagonal and cubic systems the points of nets parallel to the (0001) plane lie only on type 3 axes (Fig. 1), i.e., they form nets denoted by the symbol[12] I, and the close-packed layers, combinations of which form all structure types[13] of the G_1^1 class α-Fe–Cu, including the ancestral structure types: α-Fe; Cu; Hg_1; Sn_6 (Sn*), which is the simple hexagonal lattice, and[8] α-Po. For $a \sim 5$–6 Å, aside from the I nets, both the so-called X nets[12] with three points on the m base and not lying on type 3 axes participate in the formation of the structure type. During construction of the line diagram, use is made of one of the points of the X net in an independent region bounded by the lines **x2x**, **2xx**, **$\bar{x}2\bar{x}$**, and **$2\bar{x}\bar{x}$** and shared with the lines x and 1 − x in two subregions with origin of coordinates at ⅓, ⅓ and ⅔, ⅔ and atomic coordinates xyuz and $\hat{x}\hat{y}\hat{u}z$, respectively (Fig. 1).

Let us represent the coordinates of each atom on the line diagrams in the form of a graph: At the right we put down the value zc/a, and above the values x, y, u or $\hat{x}$, $\hat{y}$, $\hat{u}$, represented, respectively, by a cross, a line, and a circle with or without a caret.

Coordinates equal to zero are not represented, with the exception of the case where all three coordinates are zero. Under the mark is placed the symbol of the element whose atoms form a net, and an independent layer is isolated by the lines more precisely than its unit cell. In the direction of the z axis the marks of the line diagram of the independent layer are shifted by reflection or translation operations:[14] m and t are reflection and translation; m't' ($xyu \rightarrow \hat{x}\hat{y}\hat{u}$ and the reverse); m_u, t_u ($xyu \rightarrow yxu$), m'_u, t'_u ($xyu \rightarrow \hat{y}\hat{x}\hat{u}$), $t3_1$ ($xyu \curvearrowright$), $t3_2$ ($xyu \curvearrowleft$), $t' \cdot 3_1$ ($xyu \rightarrow \hat{y}\hat{u}\hat{x} \rightarrow uxy$). The distance between nets (corresponding to marks of the line diagram) is called the interlayer distance [$h = c(z_2 - z_1)/a$]. Letter crystallograms, on which the nets are denoted by letters, are convenient during examination of specific G_n^m classes. In the G_1^1 or α-Fe–Cu class,[13] the six letters A, B, C, *a*, b, and c, to which the I_1, I_2 and I_3 nets with coordinates, ⅓, 0, 0 $\curvearrowright$ correspond, are sufficient.

In the G_1^1 class, these fs-minals are designated: The Mg(Cu) fs-minal is Abc*a*B (h between A and B is ~0.8, b and *a* are tetrahedral vacancies, and c are octahedral vacancies); the (Sn*) fs-minal is Ab + *a* + cA is a section from a layer of trigonal prisms (h ~ 1, b and c are centers of prisms, and *a* are centers of edges of prisms).

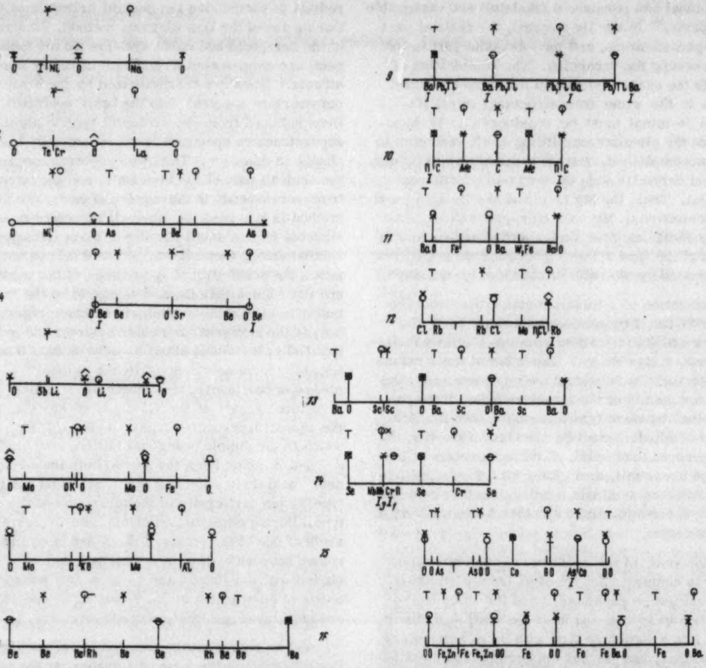
1
0 I Ni Na 0
2
0 Te Cr 0 La 0
3
0 Ni 0 As 0 Ba 0 As 0
4
0 Be Be 0 Sr Be 0 Be
I I
5
0 Sb Li 0 Li Li 0
6
0 Mo 0 K 0 Mo 0 Fe 0
7
0 Mo 0 K 0 Mo Al 0
8
Be Be Be Rh Be Be Rh Be Be Be
9
Ba Pb,Tl Ba Pb,Tl Pb,Tl Ba Pb,Tl Ba
I I I
10
h C Me C Me h C
I I
11
Ba 0 Fe 0 Ba W,Fe Ba 0
12
Cl Rb Rb Cl Mo h Cl Rb
I
13
Ba Sc Sc 0 Ba Sc 0 Ba Sc Ba 0
I
14
Se Nb h Cr R Se Cr Se
I₃ I₁
15
0 0 As As 0 0 Co 0 0 As Co 0 0
I
16
0 0 Fe,Zn Fe Fe,Zn 0 0 Fe 0 0 Fe Fe Ba 0 Fe 0 Ba

Fig. 2. Line diagrams of structure types of corundum, spinel, and amesite G classes. 1) NaNiIO$_6$, P312, m'; 2) LaCrTeO$_6$, P$\bar{3}$m1, m$_u$'; 3) BaNi(AsO$_4$)$_2$, R$\bar{3}$, m$_x$'·3$_1$; 4) SrBe$_3$O$_4$, P$\bar{6}$c2, mm$_u$; 5) Li$_7$SbO$_6$, R3, t·3$_1$; 6) KFe(MoO$_4$)$_2$, P$\bar{3}$c1, m$_u$'m$_u$; 7) KAl·(MoO$_4$)$_2$, P$\bar{3}$m1, m$_u$'; 8) Rh$_3$Be$_{16-x}$, P$\bar{6}$m2, m; 9) Ba(Pb$_{0.8}$, Tl$_{0.2}$)$_3$, P6$_3$/mmc, mm$_u$; 10) Me$_8$C$_3$, R3m, t·3$_1$; 11) BaFe(Fe, W)$_2$O$_9$, P6$_3$/mmc, mm$_u$; 12) Rb$_3$Mo$_2$Cl$_6$(Cl$_2$, h$_1$), P$\bar{6}$2c, mm$_u$; 13) Ba$_3$Sc$_4$O$_9$, R$\bar{3}$m, m$_x$·3$_1$; 14) Nb$_4$CrSe$_4$, P6$_3$/mmc, m$_u$m; 15) (Co$_3$h$_1$)·As$_3$O$_{16}$, R$\bar{3}$m, m$_x$·3$_2$; 16) Ba$_2$(Zn$_1$, Fe$_1$)Fe$_{16}$O$_{22}$, R$\bar{3}$m, m$_y$·3$_1$ (h denotes a hole or vacancy, Me denotes a metal).

Upon the superposition of nets of type AB and for h 0.4, the α-Po fs-minal is formed (here c are the centers of cubes), and for h ~ 0.2 the α-Fe fs-minal is formed; and upon the superposition of type AA nets and for h = 0.5, the Sn$_1$* s-minal is formed. In the G$_1^2$ class of corundum ($a = a'\sqrt{3}$, three atoms of a close-packed layer per cell) and the G$_1^3$ spinel class ($a = 2a'$, four atoms of a close-packed layer per cell, where a' is the distance between closest points of the net),[12,16] triple and quadruple monotypic s-minals of the G$_1^1$ α-Fe–Cu class (for example, Mg$_3$, Mg$_4$) appear, which we shall later call the corundum and spinel AB and AA, with interlayer distances h = 0.806, 0.408, and 0.204. In the G$_1^2$ corundum class[12,16] the close-packed layer is denoted by A$_{3c}$, B$_{3c}$, and C$_{3c}$ (the index c denotes corundum, and the index 3 denotes three atoms of the X net) if the layer is formed by X(000) and X(000) nets, and by A + B + C or a + b + c if the layer is formed by the nets I$_1$ + I$_2$ + I$_3$. In the G$_1^3$ spinel class[12,16] the X nets have coordinates $\sim 1/6, 1/6, 0$ ⤵ and are combined with I$_3$, I$_2$, and I$_1$ nets with the formation of close-packed layers of composition A + A$_{3sp}$, B + B$_{3sp}$, etc. (sp denotes spinel). Aside from the four basic fs-minals of the corundum and spinel AA, AB types with the superposition of layers of the types A$_{3c}$B$_{3c}$ (A$_{3c}$$a$ + b + cb$_3$$a_3$A + B + C), A$_{3c}A_{3c}$, A + A$_{3sp}$B + B$_{3sp}$, and A + A$_{3sp}$A + A$_{3sp}$, in the C$_1^4$ amesite (micaceous) class[12,16] are possible two more fs-minals: the amesitic I, A + A$_{3sp}$$a$ + b + cA + B + C (b and a are tetrahedral vacancies, and a is a position above the center of the hexagonal ring) and amesitic II, A + A$_{3sp}$$a$ + b + cB$_{3c}$ (a is a tetrahedral vacancy, and b and c are octahedral vacancies). The amesitic fs-minals can be combined both with each other and with the basic spinel and corundum fs-minals, but in addition the formation of double amesitic fs-minals is possible: A + A$_{3sp}$$a$ + b + cA + B + Ca' + b + c' and A + A$_{3sp}$$a$ + b + cB$_{3c}$$a'$ + b' + c' (shortened to A + A$_{3sp}$$aa'$·bb'cc'A + B + C and A + A$_{3sp}$$aa'$bb'cc'B$_{3c}$). Doubling of amesitic fs-minals I and II is also possible along the nets A + A$_{3sp}$ (the doubled amesitic fs-minals I' and II'). All these combinations are accomplished not only in the hexagonal and cubic structure types, but also in structure types with other symmetries. Examination of the fs-minals and their combinations was introduced earlier,[12] and it was assumed that structure types of new fs-minals with $a \approx$ 5–6 Å do not exist.

TABLE 1. Letter Crystallograms of Structure Types of G_1^2 Corundum Class*

Structure Type	s-Minal composition of structure type	A_{3c}	oh *a* +	oh *b* +	oh *c*	B_{3c}	oh *a* +	oh *b* +	oh *c*			
$NaNiIO_6$	$Al'Al''O_3 \cdot Fe_3N$	O_3	Ni	I		O_3			Na			
$LaCrTeO_6$	$Al'Al''O_3 \cdot Fe_3N$	O_3	Cr	Te		O_3			La			
$CrCl_3$	$Al_2O_3 \cdot Cu_3$	Cl_3	Cr	Cr		Cl_3						
Me_2C_3	$Fe_3N \cdot Fe_3S_3$	Me_3			C	Me_3	C	C	C			
Li_6ReO_6	$Fe_3'Fe''S_3 \cdot Fe_3'S_3$	O_3	Li	Li	Re	O_3	Li	Li	Li			
CrO_3	Fe_3N	O_3			Cr							
$AlCl_3$	$Al_2O_3 \cdot Cu_3$	Cl_3	Al	Al		Cl_3						
			oh	oh	oh		**th**	oh	**th**			
		A_{3c}	*a* +	*b* +	*c*	B_{3c}	$\mathbf{a_{3c}}$	c_{3c}	$\mathbf{b_{3c}}$			
Li_7SbO_6	$Al'Al''O_3 \cdot Ca_3F_6$	O_3	Sb	Li		O_3	**Li_3**		**Li_3**			
			oh	oh	oh		**th**	th	th			
		A_{3c}	*a* +	*b* +	*c*	B_{3c}	*bb'*	*aa'*	*cc'*	*A* +	*B* +	*C*
Ga_2S_3	Ga_2S_3					S_3		Ga	Ga			
$SrBe_3O_4$	$BeBe_3O_3OSr$					O_3	**Be**	BeBe'		O		Sr
$Be_2BO_3(OH)_1, (H_2O)_1$	$BBe_2O_3(OH)_1, (H_2O)_1$					O_3	**B**	Be	Be'			
$BaNi_2(AsO_4)_2$	$Al_2O_3 \cdot As_2O_3BaO_3$	O_3		Ni	Ni	O_3		As	As'	O	Ba	O
$2Ca(OH)_2Ca(OCl)_2$	$Fe_3S_1'S_2'' \cdot Ga_2S_1'S_2''$		Ca	Ca	Ca	$(OH)_3$		Cl	Cl	O	OH	O

*Notation: oh denotes octahedral holes, and th denotes tetrahedral or triangular (bold type) holes. Primes in the eighth and succeeding columns denote holes of the second half of their s-minal and the atoms which occupy them; Me denotes a metal.

TABLE 2. Letter Crystallograms of Structure Types of G_1^3 Spinel Class*

Structure type	s-Minal composition of structure type	*A* +	A_{3sp}	oh *c* +	oh c_{3sp}	*B* +	B_{3sp}	oh *c* +	oh c_{3sp}				
$Ba(Pb_{0.8}Tl_{0.2})_3$	Cu_3Au	Ba	Pb_3										
Me_6C_5	$Na_3Cl_4 \cdot Fe_4N$	*Me*	Me_3	C	C_3	*Me*	Me_3	C					
$Ba_3Fe(Fe, W)_2O_9$	$CaTi'O_3 \cdot 2CaTi''O_3$	Ba	O_3	Fe		(Ba	O_3	$W)_2$					
$Rb_3Mo_2Cl_9(Cl_2, h_1)$	$CaTiO_{1.5}''O_{1.5}' \cdot Cu_3Au$	Rb	Cl_2, h_1			(Rb	Cl_3	$Mo)_2$					
$CsCuCl_3$	$CaTiO_3$	Cs	Cl_3	Cu									
				th	**th**	oh	oh	**th**	**th**			oh	oh
		A +	A_{3sp}	*b* +	$\mathbf{b_{3sp}}$	*c* +	c_{3sp}	*a* +	$\mathbf{a_{3sp}}$	*B* +	B_{3sp}	*c* +	c_{3sp}
$(Co_8, h_1)As_3O_{16}$	$Cu_4O_2 \cdot 2W_3N_4 \cdot Na'Na_3''Cl_4$	O	O_3	As						O	O_3		Co_3
		O	O_3			As	Co_3	As		O	O_3		Co_3
$Ba_2(Zn_1, Fe_1)Fe_{10}O_{22}$	$Co_1'Co_2''S_4 \cdot 2W_3N_4$	O	O_3	Zn		Fe		Zn		O	O_3		Fe_3
	$\cdot 2Zn'Zn''O_{0.5}'O_{3.5}'' \cdot CaTiO_3$	O	O_3			Fe		Zn		Ba	O_3	Fe	**
								ph *a* +	*b* +	ph *c* +	ph a_{3sp}+	b_{3sp}+	ph c_{3sp}
TaN	TaN_3Ta_2					Ta	N_3	Ta		Ta			
$Ba_3Sc_4O_9$	$2CaTiO_3 \cdot BaO_3Sc_2$	(Ba	O_3	$Sc)_2$		Ba	O_3	Sc		Sc			
$(\Pi_1, Cr_1)Nb_2Se_4$	$Fe_4N \cdot SeSe_3NbCrNb_3$	Se	Se_3	Cr		Se	Se_3	Nb		Cr	Nb_3		
MoN	$MoMo_3N_22N_3 \cdot MoMo_3$					Mo	Mo_3	N		N	N_3		N_3
						Mo	Mo_3						
MoN	$MoMo_32N_3 \cdot MoMo_3N_2$					Mo	Mo_3				N_3		N_3
						Mo	Mo_3	N		N			

---

*Notation is the same as in Table 1; ph denotes prismatic hole, h denotes hole or vacancy.

The OO_3FeZn and OO_3Fe_3 s-minals again follow after the BaO_3Fe s-minal.

Definite structure types are given again in Fig. 2 and Tables 1-3, along with part of the structure types not examined earlier in the form of line diagrams and letter crystallograms. New fs-minals are not observed, but a few derived s-minals, combining with those examined earlier, form structure types recently published in the literature and not examined earlier. The difference lies only in the combinations of possible derived s-minals. The formula of the compound is given in the first column of the tables, and the s-minals which enter into the composition of the structure type are given in the second. For example, $NaNiIO_6$ consists of two s-minals: the superstructure to the $Al_2O_3-Al'Al''O_3$ s-minal and the Fe_3N s-minal. In the succeeding columns, combinations of s-minals are examined with the isolation of the nets which form them, and the distribution of atoms along these nets is designated. The purpose of the tables is to demonstrate the similarity of the composition s-minal of various structure types, types of condensation of the s-minals not being taken into account. Therefore, a few of the first nets (three, as a rule) reflect the absolute arrangement of the atoms. Notation of the following nets is arbitrary in character, i.e., it names the type of nets and vacancies, but not always the orientation relative to the first net. The combined s-minals (muscovitic, talc) are alternated with $O_{1.5}OH_{1.5}$ derived from the amesite II fs-minal and with O_3 and KO_3 derived from the $A + A_{3sp}A + A_{3sp}$ spinel fs-minal. In the KO_3 s-minal, the center of the ring of the second layer is located above points of the A_{3sp} net, which is possible in the absence of the type 3 axis. A system of notations of possible polytypes has been worked out for mica[17] which may also be used for the structure types of the G_1^m spinel, corundum, and amesite classes.

During the transition of amesitic I and II fs-minals into the fs-minal, the corundum A_{3sp} net becomes A_{3c}

TABLE 3. Letter Crystallograms of Structure Types of the G_1^4 Amesite Class*

Structure type	s-Minal composition of structure type	A	$A_{\bar{3}sp}$	oh $c+$	oh c_{3sp}	B+ or bb'	B_{3sp}	th aa'	th cc'	$A+$	$C+$	B	oh $a+$	oh $a+$	oh a	B_{3c}
$KFe(MoO_4)_2$	$ReO_3 \cdot Mo_2O_3KO_3$		O_3	Fe			O_3	Mo	Mo'	O	O	K				
$KAl(MoO_4)_2$	$ReO_3 \cdot Mo_2O_3KO_3$		O_3	Al			O_3	Mo	Mo'	O	O	K				
$NaBa_3Si_2O_7OH$	$CaTiO_3 \cdot BaSi_2O_3OBaOH$	Ba	O_3	Na		Ba	O_3	SiSi'		O	OH	Ba				
$RhBe_x$: $Rh_{1-x}Rh_3Be_{18}Be_{1x}$	$Zr'(Zr'', Al_3) \cdot 2PdBe_3$					BeBe'	Be_3 $(Be_3$			Be Be	Rh Be	 $Rh)_3$				
$KAl_2(Al_1, Si_3O_{10})(OH)_2$, Muscovite	$2[Si_2O_{2.5}(OH)_{0.5}] \cdot Al_2O_1'O_2'' \cdot KO_3$				K**		$(O_3$	Si	Si	O	O	$OH)_3$	Al	Al		2
$KMg_3(Al_1, Si_3O_{10})(OH)_2$, Phlogopite	$2[Si_2O_{2.5}(OH)_{0.5}] \cdot Fe_3S_1'S''_2 \cdot KO_3$				K**		$(O_3$	Si	Si	O	O	$OH)_3$	Mg	Mg	Mg	2
$KLi_2Al(Si_4O_{10})(F, OH)_2$, Lepidolite	$2[Si_2O_{2.5}(OH)_{0.5}] \cdot Fe_1'Fe_2''S_1'S_2'' \cdot KO_3$				K**		$(O_3$	Si	Si	O	O	$OH)_3$	Li	Li	Al	2
$KLiAlFe(Al_1, Si_3O_{10})(F, OH)_2$, Zinnwaldite	$2[Si_2O_{2.5}(OH)_{0.5}] \cdot Fe'Fe''F'''S_1'S_2''$				K**		$(O_3$	Si	Si	O	O	$OH)_3$	Li	Fe	Al	2
$Al_2(Si_4O_{10})(OH)_2$, Pyrophyllite	$2[Si_2O_{2.5}(OH)_{0.5}] \cdot Al_2O'_1O''_2 \cdot O_3$						$(O_3$	Si	Si	O	O	$OH)_3$	Al	Al		2
$Mg_3(Si_4O_{10})(OH)_2$, Talc	$2[Si_2O_{2.5}(OH)_{0.5}] \cdot Fe_3S'_1S''_2 \cdot O_3$						$(O_3$	Si	Si	O	O	$OH)_3$	Mg	Mg	Mg	2
$(Mg_2, Al_1)(Si_1, Al_1)O_5(OH)_4$, Amesite	$Si_2O_{2.5}(OH)_{0.5} \cdot Fe_3S'_1S''_2 \cdot O_{1.5}(OH)_{1.5}$						O_3	Si	Si	O	O	OH	Mg_1	Mg_1	Al_1	$(OH)_3$
$Al_2(Si_2O_5)(OH)_4$, Kaolinite	$Si_2O_{2.5}(OH)_{0.5} \cdot Al_2O_1'O_2'' \cdot O_{1.5}(OH)_{1.5}$						O_3	Si	Si	O	O	OH	Al	Al		$(OH)_3$
$Mg_3, Al_2(Si_2O_5)(OH)_8$, Chlorite	$2[Si_2O_{2.5}(OH)_{0.5}] \cdot Fe_3S_1'S_2'' \cdot O_{1.5}(OH)_{1.5} \cdot Al_2O_3$						$(O_3$	Si	Si	O OH	O OH	$OH)_3$ OH	Mg Mg	Mg Mg	Mg	2 $(OH)_3$

*See Table 1 for notation; 2 is the local axis of homology, which connects the two halves in the muscovitic s-minal.

**K is in prismatic defect holes.

(it is trigonalized) and the hexagonal A vacancy becomes triangular. The change of type of vacancies and the appearance of new ones can be seen from the formulas of the s-minals in Tables 1 and 3. During this transformation the double amesitic I and II s-minals become double trigonalized (t-amesitic I or II) s-minals with formulas $A_{3C}aa'bb'cc'A + B + C$ and $A_{3C}aa'bb'cc'B_{3C}$, which are composed of s-minals of the G_1^2 corundum class. Aside from n-gonalization is the general principle of transformation of fs-minals from one to another,[11,12] which in this case is accomplished as the result of transformation of the hexagon into four triangles, and a transition with change of c/a ("montmorization") is possible, which results[13] in the transition $AB(h = 0.8) \rightarrow AB(h = 0.4) \rightarrow AB(h = 0.2)$. In the fs-minals of the G_1^m α-Fe–Cu, spinel, corundum, and amesite classes, this transition is observed for many intermediate structure types. For example, increase of c/a in the spinel fs-minal $A + A_{3sp}a + b + cB + B_{3sp}$ transforms it into the double amesite I s-minal, $A + A_{3sp}A + B + CB + B_{3sp}$ (transition from TaN to CoSn).

Crystallograms and line diagrams allow prediction of the structures of new substances. In particular, for $a \sim 5$–6 Å the cations can only be located on type 3 axes ($\bar{3}$, 6_3, $\bar{6}$), and anions will be partly located on these same axes or will have coordinates $\sim 1/6, 1/6, 0 \ulcorner$, 000, or 000. The corundum and spinel AB and AA and the amesite I and II fs-minals will lie at the base of all structure types. Study of the G_n^m and F_p^q classes is being continued.

The authors thank N. V. Belov and A. A. Voronkov for discussion of the results of the work.

---

[1] W. L. Bragg, The Structure of Silicates, Akademische Verlags gesellschaft, Leipzig (1930).
[2] N. V. Belov, Crystal Chemistry of Silicates with Large Cations [in Russian], Izd. Akad. Nauk SSSR, Moscow (1961).
[3] G. B. Bokii, Crystal Chemistry, Nauka, Moscow (1971).
[4] P. I. Kripyakevich and E. E. Cherkashin, Izv. Sekt. Fiz. Khim. Analiza, Inst. Obshch. Neorgan. Khim. SSSR, 24, 59 (1954).
[5] P. I. Kripyakevich, Author's Abstract, Dissertation, Izd. L'vovsk. Univ. (1972).
[6] P. M. Zorkii, V. K. Bel'skii, S. G. Lazareva, and M. A. Porai-Koshits, Zh. Strukt. Khim., 8, 312 (1967).
[7] N. L. Smirnova, Zap. Vses. Mineralog. Obshchestva, 87, 627 (1958).
[8] N. L. Smirnova, Kristallografiya, 4, 13, 20 (1959) [Sov. Phys.–Crystallogr., 4, 10, 17 (1960)].
[9] N. L. Smirnova, Tr. Mineralog. Muzeya. Akad. Nauk SSSR, 15, 162 (1964).
[10] N. L. Smirnova and N. V. Belov, Geokhimiya, 11, 1291 (1962).
[11] N. L. Smirnova and L. S. Mezhueva, Zh. Strukt. Khim., 7, 566 (1966).
[12] N. L. Smirnova, Vestn. Mosk. Univ., Ser. Geol., 2, 100 (1967).
[13] N. L. Smirnova, T. V. Mel'chakova, and R. E. Chigar'kova, Zh. Strukt. Khim., 10, 1076 (1969).
[14] N. L. Smirnova, V. I. Artyushina, and M. P. Anisimova, Vestn. Mosk. Univ., Ser. Geol., 1, 73 (1969).
[15] N. L. Smirnova, R. E. Chigar'kova, and T. A. Demidova, Problems in Crystallography [in Russian], Izd. MGU (1971), p. 74.
[16] N. L. Smirnova, Kristallografiya, 15, 63 (1971).
[17] B. B. Zvyagin, Electron Diffraction and Structural Crystallography of Clay Minerals [in Russian], Nauka, Moscow (1964).

Binary molybdates and tungstates of alkali metals with bismuth, $M^+Bi(TO_4)_2$

P. V. Klevtsov, V. A. Vinokurov, and R. F. Klevtsova

Institute of Inorganic Chemistry, Siberian Branch,
Academy of Sciences of the USSR

(Submitted October 25, 1972)
Kristallografiya, 18, 1192-1197 (November-December 1973)

Spontaneous crystallization from solution in molten alkali-metal dimolybdates and ditungstates was employed to synthesize binary bismuth molybdates and tungstates $M^+Bi(TO_4)_2$, where M^+ is Li, Na, K, Rb, or Cs and T is Mo or W; the structural types and thermostabilities of these compounds were investigated. In addition to the well-known scheelite structural type, five other structural types were detected. Of these, $RbBi(MoO_4)_2$ crystallizes in a new structural type. We determined the crystal symmetry and unit-cell parameters.

The first data on binary bismuth-containing molybdates appeared in 1943, when Sillen and Sundvall synthesized $M^+Bi(MoO_4)_2$ (where M^+ was Li, Na, and K) by fusion of oxides with an excess of the alkali metal chloride or molybdate.[1] X-ray diffraction analysis led to the conclusion that all three compounds crystallize in a tetragonal structure of the scheelite ($CaWO_4$) type, in the space group $C_{4h}^6 = I4_1/a$. Mokhosoev and Aleikina[2] produced sodium-bismuth molybdate by solid-phase synthesis, while Karapetyan and Morozov[3] obtained single crystals of this compound, both pure and neodymium-activated, and investigated their optical characteristics; the crystals were pulled from a melt.

Binary bismuth molybdates with heavy alkali elements were unknown until recently. The present authors reported growth of $CsBi(MoO_4)_2$ crystals by the solution-melt method[4] and found them to be isostructural to rhombic cesium-rare earth molybdates of the $CsPr(MoO_4)_2$ type.[5,6] The only known binary bismuth tungstate is $NaBi \cdot (WO_4)_2$, which was produced by solid-phase synthesis and assigned to the scheelite structural type on the basis of x-ray diffraction data.[2]

The present article reports the results of an investigation of the crystallization from molten solutions of binary molybdates and tungstates of alkali elements (Li, Na, K, Rb, and Cs) with bismuth and of studies of these compounds by the x-ray diffraction, thermal, and other methods. The observed structural types were first discovered and characterized from x-ray powder patterns.

SYNTHESIS OF CRYSTALS

The crystallization experiments and solid-phase syntheses were conducted with the following chemical reagents: spectral-analysis grade MoO_3 and WO_3, chemically pure Bi_2O_3, and chemically pure alkali-metal carbonates $M_2^+CO_3$. The solvents were alkali-metal dimolybdates and ditungstates $M_2^+[Mo(W)_2O_7$, which are the lowest-melting compounds of this type and permit crystallization of binary molybdates and tungstates over a relatively broad temperature range. The charge consisted either of previously prepared sintered cakes of the binary compounds or of mechanical mixtures of the oxides MoO_3 or WO_3, Bi_2O_3, and $M_2{}^+O(M_2{}^+CO_3)$ in a stoichiometric ratio; the molar ratios of the charge to the solvent were 1:1 and 1:2. When the amount of solvent was increased, there was a large decrease in the yield of binary molybdate crystals, especially for crystallization of $RbBi(MoO_4)_2$. When the charge:solvent ratio was 1:3 or less, we were unable to detect formation of $M^+Bi \cdot (MoO_4)_2$ binary molybdates.

Crystallization was conducted by slow reduction of the molten-solution temperature, with spontaneous nucleation. The system was heated to 800-900°C and held at the maximum temperature for 12-18 h; programmed cooling was conducted at a rate of 3-6 deg/h. The crystals were separated from the solidified solution by boiling in water.

We synthesized binary molybdates and tungstates of the $M^+Bi[Mo(W)O_4]_2$ type (where M^+ was Li, Na, K, Rb, and Cs) under these conditions. The crystals of these compounds were identified by comparison of their x-ray powder patterns, infrared spectra, and thermograms (DTA) with those of sintered cakes prepared from the corresponding oxides in a stoichiometric ratio. In a number of cases, we measured the density of the compounds and compared it with that calculated from the x-ray diffraction data.1)

STRUCTURE AND THERMOSTABILITY

Binary molybdates $M^+Bi(MoO_4)_2$. Four structural types were detected among the binary bismuth molybdates. The LiBi and NaBi molybdates crystallized with a structure of the scheelite type. The faceted single crystals of these compounds had the form of tetragonal dipyramids. The lattice parameters, calculated from the x-ray powder patterns, are given in Table 1. They were in satisfactory agreement with the data in the literature.[1] Neither compound underwent a polymorphic transformation on heating. In view of the fact that low-temperature modifications exist among binary tungstates and molybdates of the rare earths, however, including a transition in scheelite[7,8] that is irreversible on heating (to 600-800°C), we conducted control experiments involving synthesis of $LiBi(MoO_4)_2$ and $NaBi(MoO_4)_2$ (as well as K, Rb, and Cs molybdates) by solid-state reactions at the minimum temperatures where the reactions would take place. It was found that the LiBi and NaBi molybdates also formed a scheelite structure at 500°C.

The KBi molybdate was not obtained in a scheelite modification, which was not in agreement with the results of Sillen and Sundvall.[1] Regardless of the method used to obtain the crystals (crystallization from a molten solution or melt and solid-state synthesis), the KBi molybdate had a $KSm(MoO_4)_2$ structure. This was shown by the x-ray powder patterns and infrared spectra. The crystal structure of this modification was not studied. The crystals we obtained were unsuitable for x-ray diffraction analysis, because of their tendency toward twinning. A similar situation occurred in crystallization of the potassium-samarium molybdate.[9] Nevertheless, it can be assumed on the basis of the x-ray powder patterns that the structure

TABLE 1

Compound	Lattice parameters				z	Density, g/cm³		Space group	Structural type	T_M, °C (±20°)
	a, Å	b, Å	c, Å	β, deg		d_x	d_{mea}			
$LiBi(MoO_4)_2$	5.23		11.49		2	5.68		$C_{4h}^6 = I4_1/a$	$CaWO_4$	645
$NaBi(MoO_4)_2$	5.28		11.60		2	5.69		$C_{4h}^6 = I4_1/a$	$CaWO_4$	840
$KBi(MoO_4)_2$									$KSm(MoO_4)_2$	710
$RbBi(MoO_4)_2$	11.63	12.09	5.28	92.5	4	5.52	5.44	$C_{2h}^5 = P2_1/c$	$RbBi(MoO_4)_2$	640
$CsBi(MoO_4)_2$	9.45	5.14	8.21		2	5.53	5.46	$D_{2h}^3 = Pccm$	$CsPr(MoO_4)_2$	675
$LiBi(WO_4)_2$	10.06	6.07	4.99	92.5	2	7.79	7.69	$C_{2h}^4 = P2/n$	β-$LiYb(WO_4)_2$	780
$NaBi(WO_4)_2$	5.28		11.50		2	7.57	7.52	$C_{4h}^6 = I4_1/a$	$CaWO_4$	920
$KBi(WO_4)_2$	8.25	10.60	7.62	93.8	4	7.46	7.41	$C_{2h}^6 = I2/c$	α-$KY(WO_4)_2$	750

TABLE 2. X-Ray Data on $RbBi(MoO_4)_2$

hkl	d, Å	I	hkl	d, Å	I
100	11.64	45	232, 52$\bar{1}$	2.040	2
110	8.40	35	322, 530	2.015	2
120	5.36	5	40$\bar{2}$, 042	1.987	20
300	3.877	2	14$\bar{2}$, 44$\bar{1}$, 41$\bar{2}$	1.966	3
12$\bar{1}$	3.733	2	142	1.947	2
310	3.681	2	402	1.917	18
22$\bar{1}$	3.327	100	16$\bar{1}$, 450	1.858	2
221	3.236	80	540	1.841	4
31$\bar{1}$, 131	3.064	3	26$\bar{1}$	1.798	10
040	3.023	30	261	1.782	13
400	2.903	40	62$\bar{1}$, 51$\bar{2}$	1.762	13
23$\bar{1}$, 410, 32$\bar{1}$	2.824	3	342, 630	1.747	2
321	2.738	5	541, 621, 25$\bar{2}$	1.721	10
002	2.637	10	550, 63$\bar{1}$	1.677	2
33$\bar{1}$, 112	2.493	2	44$\bar{2}$, 700, 270	1.659	8
411, 331	2.452	5	22$\bar{3}$	1.636	8
21$\bar{2}$	2.389	2	442	1.618	8
241, 150	2.368	2	13$\bar{3}$, 223	1.605	8
500, 212	2.321	5	72$\bar{1}$	1.548	3
510, 22$\bar{2}$	2.280	3	54$\bar{2}$	1.532	2
250	2.232	2	41$\bar{3}$, 721, 080	1.512	5
222, 051	2.201	2	371, 452	1.506	3
31$\bar{2}$, 13$\bar{2}$, 43$\bar{1}$	2.179	3	36$\bar{2}$, 542, 73$\bar{1}$	1.491	2
440	2.095	25	800	1.453	10

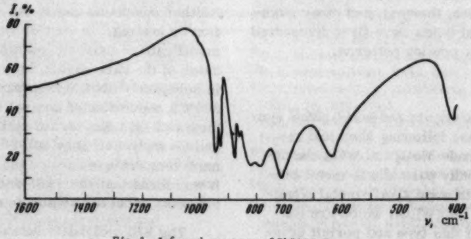

Fig. 1. Infrared spectrum of $RbBi(MoO_4)_2$.

of the KBi molybdate was apparently a distorted scheelite type with reduced symmetry. We did not detect transformation of this modification to a "pure" scheelite structure.

The compound $RbBi(MoO_4)_2$ crystallized in a new type of structure not previously encountered. This structure exhibited the powder pattern for which data are given in Table 2. The single crystals had a prismatic appearance and a monoclinic habit. The lattice parameters, which were determined from the vibratory x-ray patterns and the Weissenberg patterns and refined from the powder diffraction pattern, were $a = 11.63$, $b = 12.09$, $c = 5.28$ Å, $\beta = 92.5°$. The cell contained four formula units (the density was $d_{mea} = 5.44$ g/cm³ and $d_{cal} = 5.52$ g/cm³). Analysis of the extinction in the Weissenberg patterns yielded the space group $C_{2h}^5 = P2_1/c$. The infrared spectrum of the RbBi molybdate (Fig. 1) indicated that the structure probably had octahedral coordination of the molybdenum atom with respect to oxygen.

The aforementioned CsBi molybdate crystallized in the fourth structural type [$CsPr(MoO_4)_2$]. It formed laminated tabular crystals with perfect cleavage along the (100) plane. Less perfect cleavage occurred along the (001) plane.

Differential thermal analysis and x-ray diffraction analysis showed that the M^+Bi molybdates did not have high-temperature polymorphism. The binary molybdates of lithium, sodium, and potassium with bismuth melted without noticeable decomposition. Their thermostability made it possible to grow single crystals from melts. The compounds $RbBi(MoO_4)_2$ and $CsBi(MoO_4)_2$ obviously dissociated on melting and partially decomposed. When these compounds were chilled and reheated, their differential thermal curves displayed additional thermal effects pertaining to the decomposition products.

Binary tungstates $M^+Bi(WO_4)_2$. These compounds, with M^+ = Li, Na, K, Rb, and Cs, like the analogous molybdates, crystallized in several structural types, but not all of them were identical to those of the molybdates. The scheelite structure was common to both groups of compounds and $NaBi(WO_4)_2$ crystallized in it. The faceted crystals of the sodium compound had a tetragonal-dipyramidal form. The powder pattern was typical of a scheelite structure. The unit-cell constants (Table 1), which were determined from the diffraction patterns obtained for ground crystals, were in good agreement with the data in the literature[2] and indicated that the crystal composition was close to stoichiometric. The compound melted at 920°C without decomposing.

The $LiBi(WO_4)_2$ was characterized by light yellow prismatic crystals. Single-crystal and powder diffraction patterns showed the symmetry to be monoclinic and provided a basis for calculating the unit-cell constants. The LiBi tungstate crystallized in one of the tungstate-structure modifications observed for binary tungstates,[10,11] i.e., that of β-$LiYb(WO_4)_2$ (see Table 1). Heating of the LiBi tungstate to its melting point (780°C) did not lead to any change in its crystal structure. The compound decomposed in the molten state.

It was established from the infrared spectra and x-ray diffraction patterns[12,13] that the potassium–bismuth tungstate was isostructural to monoclinic α-$KY(WO_4)_2$. The unit-cell dimensions are given in Table 1. In contrast to its countertype, $KBi(WO_4)_2$ did not undergo a polymorphic transition when heated and decomposed on melting (at 750°C). Analysis of the differential thermal analysis curves and diffraction patterns recorded from fused specimens showed that $KBi(WO_4)_2$ decomposed into the potassium tetratungstate $K_2W_4O_{13}$ ($K_2O \cdot 4WO_3$) and the oxide Bi_2O_3. The decomposition process was the reverse of the synthesis process: During sintering from the oxides, the binary tungstates (and molybdates) were formed through alkali-metal tetracompounds ($M_2^+[W(Mo)]_4O_{13}$). The RbBi and CsBi tungstates were obtained in single-crystal form.

All the bismuth compounds synthesized were thus characterized by relatively low melting points. The binary molybdates melted over the temperature range 640–840°C, while the tungstates melted at slightly higher temperatures.

In conclusion, it should be noted that bismuth-containing molybdates and tungstates are similar in their crystal-chemical nature to the corresponding compounds of rare earths. Bismuth and rare earths form isostructural compounds with alkali metals. Formal replacement of the Bi in $M^+Bi[Mo(WO_4)]_2$ by the corresponding rare earth does not alter the crystal structure of the compound. Thus, LiBi and NaBi molybdates and NaBi tungstate crystallize with a scheelite structure. A whole series of rare earth molybdates with Li and Na and tungstates with Na are known to crystallize in this structure. The structural analogy between other binary compounds of bismuth and the rare earths can be seen from Table 1. It is only for $RbBi(MoO_4)_2$ that there is no known isostructural compound among the corresponding rare earths. On the other hand, the structural types characteristic of molybdates and tungstates $M^+R^{3+}[Mo(W)O_4]_2$ of nonrare-earth trivalent metals (R^{3+} = Al, Fe, In, Sc, etc.)[14–16] have not been observed for compounds with bismuth.

[1)] The x-ray powder patterns were recorded in a URS-50I diffractometer in filtered Cu radiation, with crystalline silicon or germanium added to the specimens as a standard. The infrared spectra were recorded in a two-channel UR-10 spectrometer, while the DTA curves were recorded with an HTP-62 apparatus. The densities were measured by the pycnometric method.

---

[1] L. G. Sillen and H. Sundvall, Arkiv Kemi, Mineral. Och Geol., A17, 1(1943).

[2] M. V. Mokhosoev and S. M. Aleikina, Izv. Akad. Nauk SSSR, Neorgan. Mat., 2, 2084 (1966).

[3] V. E. Karapetyan and A. M. Morozov, Izv. Akad. Nauk SSSR, Neorgan. Mat., 4, 2039 (1968).

[4] P. V. Klevtsov and V. A. Vinokurov, Izv. Akad. Nauk SSSR, Neorgan. Mat., 9, 156 (1973).

[5] V. A. Vinokurov and P. V. Klevtsov, Kristallografiya, 17, 127 (1972) [Sov. Phys.–Crystallogr., 17, 102 (1972)].

[6] R. F. Klevtsova, V. A. Vinokurov, and P. V. Klevtsov, Kristallografiya, 17, 284 (1972) [Sov. Phys.–Crystallogr., 17, 240 (1972)].

[7] P. V. Klevtsov and L. Yu. Kharchenko, in: Growth of Crystals, Vol. 7, Consultants Bureau (1969).

[8] P. V. Klevtsov and L. Yu. Kharchenko, Izv. Akad. Nauk SSSR, Neorgan. Mat., 6, 1454 (1970).

[9] P. V. Klevtsov and L. P. Kozeeva, Izv. Akad. Nauk SSSR, Norgan. Mat., 8, 1379 (1968).

[10] R. F. Klevtsova and N. V. Belov, Kristallografiya, 15, 43 (1970) [Sov. Phys.–Crystallogr., 15, 32 (1970)].

[11] L. P. Kozeeva, Dissertation [in Russian], Inst. Neorgan. Khim., Sib. Otd. Akad. Nauk SSSR, Novosibirsk (1972).

[12] P. V. Klevtsov, L. P. Kozeeva, and R. F. Klevtsova, Izv. Akad. Nauk SSSR, Neorgan. Mat., 4, 1147 (1968).

[13] S. V. Borisov and R. F. Klevtsova, Kristallografiya, 13, 517 (1968) [Sov. Phys.–Crystallogr., 13, 420 (1968)].

[14] R. F. Klevtsova and P. V. Klevtsov, Kristallografiya, 15, 294, 953 (1970) [Sov. Phys.–Crystallogr., 15, 245 (1970); 15, 829 (1971)].

[15] P. V. Klevtsov and R. F. Klevtsova, J. Solid State Chem., 2, 278 (1970).

[16] R. F. Klevtsova and P. V. Klevtsov, Kristallografiya, 16, 292 (1971) [Sov. Phys.–Crystallogr., 16, 241 (1971)].

Irradiation-induced phase transition in quartz

E. V. Kolontsova, É. E. Kulago and N. A. Tomilin

M. V. Lomonosov Moscow State University

(Submitted August 2, 1972)
Kristallografiya, 18, 1198-1201 (November-December 1973)

The changes in the magnitude and distribution of the x-ray diffuse scattering intensity observed in quartz single crystals which had been irradiated with neutrons (10^{19}, $4\cdot 10^{19}$, and $6\cdot 10^{19}$ fast neutrons/cm^2) were studied using the shapes of the scattering regions. Studies were also done during heating of unirradiated samples between 20 and 670°C. It was shown that the dose dependence of the change is similar to the temperature dependence, which indicates the existence of an irradiation-induced transition at $4\text{-}5\cdot 10^{19}$ n/cm^2 of the same kind as the $\alpha\to\beta$ transition.

At a certain stage of neutron irradiation, the structure of quartz changes substantially.[1,2] The available data suggest that the irradiation-induced structural changes are similar to the structural changes during the $\alpha\to\beta$ transition.[3–5] The present paper gives the results of a study of the shapes of the x-ray diffuse scattering regions for irradiated and heated quartz single crystals and shows the existence of an irradiation-induced phase transition like the $\alpha\to\beta$ transition in quartz. The data obtained permitted us to determine the nature of the atomic shifts in the irradiated crystals and to trace the atomic displacements during heating in unirradiated crystals over a broad temperature range, which included the transition temperature. It is necessary to carry out such an investigation due to the lack of a common viewpoint on the effect of irradiation on quartz[5–7] and the nearly complete absence of data on the mechanism of the irradiation-induced structural changes.

It is not possible to carry out investigations of the effect of irradiation and heating on a single sample due to the twinning of quartz crystals during cooling, beginning at a temperature close to the transition temperature (T_t= 575°C). Therefore it was first shown that the treatment of the crystals during sample preparation, changes in the dimensions and shapes of the single crystals which we studied, and the inevitable misorientation of 3 to 5' did not effect the intensity distribution of the diffuse scattering.

To study the effect of irradiation we used samples given doses of about 10^{19}, $4\cdot 10^{19}$, and $6\cdot 10^{19}$ n/cm^2 (fast neutrons). The effect of heating was studied on the very same sample; the studies for $T \leq 500$°C were carried out during cooling to room temperature, while between 500 and 679°C they were done without intermediate cooling. The high-temperature x-ray photography was done in a RKSO camera using an attachment described previously[8] with the intensities being derived photometrically. Monochromatic Mo Kα radiation obtained by reflection from a single-crystal topaz plate was used. The x-ray patterns to be compared were taken at the same time. We used the linear region of the blackening curve of the film to estimate the intensities. We corrected the photometric data for the polarization of the radiation and the geometry of the x-ray photography. Calculations of the scattering regions in reciprocal lattice space were carried out on a "Mir-1" computer using equations derived (in contrast to ref. 9) without transforming to orthogonal coordinates and simplified for the chosen crystal orientation with [210] along the rotation axis of the goniometer. The rotation angle γ was reckoned from the position in which [001] is parallel to the x-ray beam.

For a sample irradiated with a dose of 10^{19} n/cm^2 the intensity distribution of the diffuse scattering for different orientations did not differ from the intensity distribution for unirradiated single crystals at room temperature. A comparison of the general pattern of diffuse scattering for samples which received a dose $\geq 10^{19}$ n/cm^2 and for heated crystals and a comparison of the scattering regions constructed for the 30$\bar{3}$1 and 03$\bar{3}$1 sites show that the scattering by crystals irradiated with $4\cdot 10^{19}$ n/cm^2 is similar within experimental error to the scattering by unirradiated crystals at ~ 560°C. This conclusion refers not only to the maxima, but also to the subsidiary pattern of streak-like intensity distribution most pronounced at certain orientations during heating at $T \geq 500$°C in crystals irradiated with doses > 10^{19} n/cm^2 (see Fig. 1).

In considering the orientations of the streaks, their shapes and widths in the interval which we studied from $\gamma = 0$ to 26° and $\gamma = 67$, 69, and 90°, we can distinguish seven families of streaks. All of them are elongated along the [100] and [101] directions bu the intensity distribution in reciprocal lattice space differs for the same streak orientation. Correspondingly (from the regions constructed) the streaks can be divided into two types:1) I) rod streaks parallel to [100] of differing intensities, elongations, and widths ($\varnothing \gtrsim 0.4c^* - 0.4b^*$); II) streaks whose scattering regions can be represented as partially overlapping, elongated along [100] nonequal-axis regions (Fig. 2). Some of the streaks can be seen in Fig. 1.

The behavior of all seven families with a change of temperature is also very complex and varies. Some of the type I and II streaks were noted at room temperature. Upon heating, their intensities changed somewhat differently (Fig. 3). The intensities of the type II streaks, in agreement with the changes in the magnitude and distribution of the intensity in the diffuse maxima,[10] increased relatively sharply between 500 and 585°C. The changes observed here in the intensity distribution in the longitudinal and transverse cross sections of the scattering regions also follow the temperature dependences mentioned above (Fig. 2). A similar redistribution of the intensity, as seen from the figure, is also observed under irradiation (the dose is $4\cdot 10^{19}$ n/cm^2).

Some of the type I streaks behave like type II streaks. The others have uniform temperature dependences over the whole investigated temperature range (Fig. 3), in which the diameters of all of the rods change insignificantly upon heating.

The intensities of the type I and II streaks which show up during heating beginning at temperatures of ~ 450 to

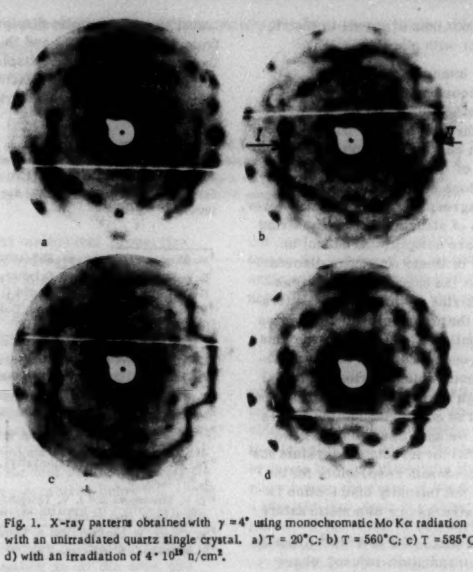

Fig. 1. X-ray patterns obtained with $\gamma = 4°$ using monochromatic Mo Kα radiation with an unirradiated quartz single crystal. a) T = 20°C; b) T = 560°C; c) T = 585°C; d) with an irradiation of $4 \cdot 10^{19}$ n/cm^2.

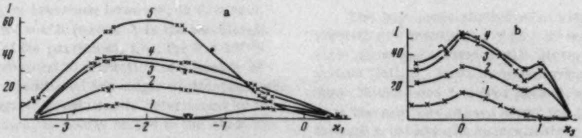

Fig. 2. Variation in the intensity distribution upon heating and during irradiation for type II streaks in the longitudinal (a) and transverse (b) cross sections. $\varkappa_1$, $\varkappa_2$, and $\varkappa_3$ are the coordinates in the reciprocal lattice. a) $\varkappa_2 = 3.9$ and $\varkappa_3 = 1$; b) $\varkappa_1 = 1.5$, $\varkappa_2 = 3.9$. 1) T = 20°C; 2) T = 500°C; 3) $4 \cdot 10^{19}$ n/cm^2; 4) T = 560°C; 5) 585°C.

500°C increase more sharply than those of equivalent streaks which are observed at room temperature, which brings them to equal intensities upon approaching T_t, in agreement with the transition from c_3 to c_6 symmetry (Fig. 1).

Note that our results on the streaklike distributions of intensity do not fully agree with data in the literature.[11,12] Comes et al.[11] noted a strengthening of type II streaks (in our terminology) in irradiated ($3 \cdot 10^{19}$ n/cm^2) quartz crystals and suggested that this strengthening is related to line disorder since they assumed that the regions of the streak intensity distribution in reciprocal lattice space are planes. Arnold,[12] in studying the temperature dependence of this kind of streak in unirradiated crystals, proposed that planar disorder is responsible for the increased intensity (the scattering regions are rods). There is no indication in those papers of the applicability of the cross section method for obtaining the intensity distribution in reciprocal lattice space.

Our data show that the scattering regions constructed from the cross sections in such a way that the Ewald sphere touches the streaks at their centers, where the contribution from the "bell-shaped" intensity distribution of the diffuse maxima is nearly absent, are qualitatively the same for the irradiated and heated crystals and do

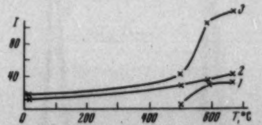

Fig. 3. Characteristic temperature dependences of the streaklike intensity distributions. 1 and 2 correspond to type I streaks, which pass through $0\bar{3}31-\bar{1}\bar{3}41-\bar{2}\bar{3}51$ and $\bar{1}3\bar{2}2-03\bar{3}2$ maxima; 3 corresponds to type II streaks, which pass through $04\bar{4}0-\bar{1}4\bar{3}0-\bar{2}4\bar{2}0-\bar{3}4\bar{1}0-\bar{4}400$ maxima. The measurements were carried out with $\gamma = 0°$ between $0\bar{3}31$ and $\bar{1}\bar{3}41$ maxima (1), with $\gamma = 16° 30'$ between $0\bar{3}32$ and $\bar{1}3\bar{2}2$ maxima (2), and between $\bar{2}4\bar{2}0$ and $\bar{3}4\bar{1}0$ maxima (3).

not coincide for type II streaks, nor with rods in the rigorous sense of this word, nor with planes.

Most of the streak-like intensity distributions, in agreement with the calculations of Arnold,[12] can be explained by an arrangement of the effective scattering centers along chains in ⟨100⟩ directions under conditions where there is a correlation between the atomic displacements and the magnitudes of the shifts and the dimensions of the correlation regions depend on temperature and the irradiation dose in agreement with Fig. 2. However, it is evident that the pattern of structural changes during $\alpha \rightarrow \beta$ transition is much more complex and cannot be described by simple models of linear or planar disorder. It is clear from our data that the changes in the streak-like intensity distributions during heating and under irradiation are closely related to the previously noted[10] changes of the intensity and distribution of the diffuse maxima and correspond to a single general complex model of cooperative atomic displacements, which carries the initial structure of α-quartz through several intermediate states to the β-quartz structure. The comparison of the diffuse scattering intensities which we have carried out at two temperatures (293 and 100°K) in irradiated crystals has shown that the atomic displacements responsible for the strengthening and change in the intensity distribution in the diffuse maxima and the streaks are of a static nature.

Thus our data show that doses of 4 to $6 \cdot 10^{19}$ n/cm^2 in quartz crystals produce an irradiation-induced phase transition due to static displacements of atoms arising from radiation defects and there is a complete analogy in the nature of the atomic displacements with irradiation and heating. The general scheme of the displacements is complex and needs more work.

---

1) We were unable to construct the scattering regions for one family of very sharp narrow streaks parallel to [100] due to the low intensity, and for a family of streaks parallel to [101] due to the insufficient number of cross sections.

---

[1] M. Wittels, Phys. Rev., 89, 657 (1953).

[2] E. V. Kolontsova and I. V. Telegina, Dokl. Akad. Nauk SSSR, 147, 592 (1962) [Sov. Phys.—Dokl., 7, 1034 (1963)].

[3] V. G. Zubov and Lp. P. Osipova, Dokl. Akad. Nauk SSSR, 156, 300 (1964) [Sov. Phys.—Dokl., 9, 383 (1964)].

[4] J. Mayer and M. Lecomte, J. Phys. et Radium, 21, 846 (1960).

[5] E. V. Kolontsova and I. V. Telegina, Fiz. Tverd. Tela, 7, 2730 (1965); 8, 3412 (1966) [Sov. Phys.—Solid State, 7, 2207 (1966); 8, 2733 (1967)].

[6] M. Wittels and F. Sherril, Phys. Rev., 93, 1117 (1954).

[7] R. Roy and C. P. Buhsmer, J. Appl. Phys., 36, 331 (1965).

[8] E. V. Kolontsov and É. E. Kulago, Apparat. i Metody Rentg. Anal., 7, 64 (1970).

[9] Yu. A. Bagaryatskii, Kristallografiya, 4, 919 (1959) [Sov. Phys.—Crystallogr., 4, 875 (1960)].

[10] E. V. Kolontsova and I. V. Telegina, Dokl. Akad. Nauk SSSR, 173, 1045 (1967) [Sov. Phys.—Dokl., 12, 350 (1967)].

[11] R. Comes, M. Lambert, and A. Guinier, Acta Crystallogr., A26, 244 (1970).

[12] H. Arnold, Z. Kristallogr., 121, 145 (1965).

Use of the double-crystal neutron spectrometer to study the low-temperature decomposition in niobium single crystals saturated with hydrogen

M. Kalanov, S. Sh. Shil'shtein, and V. A. Somenkov

(Submitted May 15, 1972; resubmitted December 25, 1972)
Kristallografiya, 18, 1202-1206 (November-December 1973)

The low-angle scattering of neutrons (scattering angle of the order of 10-20") caused by hydride precipitates, which have the form of plates and dimensions from a fraction of a micron to 1.5-2 μ, has been observed in single crystals of niobium containing 3% deuterium at liquid-nitrogen temperature. The decomposition process is characterized by strong hysteresis effects, since heating to 50°C does not result in complete dissolution of the precipitate.

Anomalies in the physical and mechanical properties caused by the precipitation of hydrogen dissolved in the metal, which can be very small in amount, of the order of a fraction of an atomic percent, have been observed at low temperatures in a series of transition metals (see, for example, ref. 1). The neutron diffraction method allows determination of the composition and atomic structures of the precipitates. Thus, the decomposition of the Nb + 3%D solid solution, accompanied by the formation of particles of hydride of composition $NbD_{0.65}$ having macroscopic dimensions (> 10^{-5} cm), was observed in ref. 2. Determination of these dimensions metallographically is not always simple in view of the fact that the decomposition process takes place at temperatures below 0°C, which is generally characteristic for solutions of hydrogen in low concentration and, in addition, there is the risk of uncontrolled absorption of hydrogen during the etching process. In principle, information as to the size and shape of the precipitates can be obtained by study of the low-angle scattering of neutrons; however, in this case the scattering angles $\theta \approx \lambda/R$ (where λ is the wavelength and R is the radius of the particles), i.e., for $R = 10^{-4}$ cm and λ = 1 Å, correspond to a fraction of a minute of arc. Therefore, the traditional low-angle scattering methods, in which the angular resolution is determined by the width of the collimators, is poorly suited to the study of such macroscopic precipitates (the upper limit of sizes in this case[3] amounts to 10^{-5} cm). In this work the low-angle scattering of neutrons by crystals of hydrogenated niobium, which was studied earlier by the neutron diffraction method, was studied by the use of a double-crystal spectrometer. The specimen was placed between two perfect crystals of germanium and low-angle scattering was carried out to the appearance of "tails" on the reflection curve, for which, in this experiment, angular resolution amounts to a few seconds of arc.[4]

The complete cross section for low-angle scattering of neutrons by one particle of precipitate is[5]

$$\sigma = \pi R^4 (Na - N_0 a_0)^2 \lambda^2 / 2, \tag{1}$$

where N and N_0 are the numbers of unit cells in 1 cm³ of precipitate and matrix, and a and a_0 are the total coherent scattering amplitudes calculated per unit cell of precipitate and matrix, respectively. The integrated low-angle scattering intensity for a specimen of thickness l is

$$\int I(\theta)\, d\theta = I_0 [1 - \exp(-N'\sigma l)], \tag{2}$$

where I_0 is the intensity of the primary beam, $N' = 3\xi \cdot (4\pi R^3)^{-1}$ is the number of particles of precipitate in one cm³, and ξ is the ratio of the total volume of the precipitate to the volume of the specimen. The intensity of low-angle scattering as a function of angle is approximated according to the Guinier method[3] by the exponent

$$I(2\theta) \sim \exp\left[-\frac{4\pi^2 R_g^2}{\lambda^2} (2\theta)^2\right], \tag{3}$$

where R_g is a radius of gyration, equal to $R/\sqrt{5}$, but for a parallelepiped $R_g = t/2\sqrt{3}$, where t is the dimension of the side parallel to the scattering vector. If this approximation is valid, then for scattering angles 2θ which are rather large in comparison with the angular width of the primary beam, the graph of the function log $I(4\theta^2)$ represents a straight line, from the slope of which R_g can be determined. If the shape of regularly oriented precipitates is anisotropic or if there are several characteristic sizes of the particles, the experimental curve represents the sum of several exponents.

The specimens studied were single-crystal plates of niobium of dimensions 2 × 16 × 30 mm, oriented along the (110) plane and saturated with deuterium[2] to the concentration $NbD_{0.03}$. Measurements were carried out for the three thicknesses 2, 4 (two plates), and 16 mm (in this case the neutrons passed along the plane of the plate through a narrow slit approximately equal to its thickness). The wavelength of the neutrons was 1.45 Å, and the width of the rocking curve in the absence of low-angle scattering was 3.2". The specimens were placed in the cryostat described in ref. 6. Cooling to liquid-nitrogen temperature, even for small thicknesses, resulted in a noticeable low-angle scattering effect (Fig. 1), the inten-

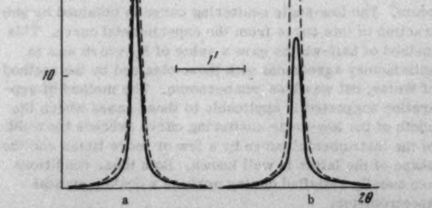

Fig. 1. Curves of low-angle scattering of neutrons at liquid-nitrogen temperature. Solid lines are experimental curves, and dashed lines are intrinsic low-angle scattering curves: a) l = 4 mm ($I_{max} = 92 \cdot 10^3$ neutrons/min); b) l = 2 mm ($I_{max} = 108 \cdot 10^3$ neutrons/min).

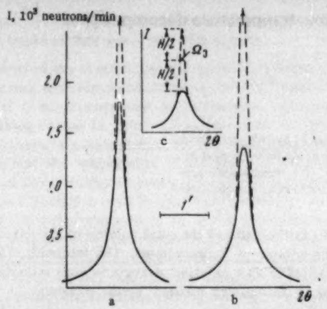

Fig. 2. Low-angle scattering curves for l = 16 mm. a) Liquid-nitrogen temperature ($I_{max} = 4.3 \cdot 10^3$ neutrons/min); b) room temperature ($I_{max} = 8.6 \cdot 10^3$ neutrons/min); c) scheme for separation of diffracted and transmitted beams by the half-width method ("tails" of experimental curves corresponding to low-angle scattering were not completely symmetrical, and the curves presented were made symmetrical by averaging the right- and left-hand portions of the experimental curves).

sity at the maximum of the reflection curve decreasing by 15-20% as compared with that at room temperature. Approximately half of the neutrons were scattered by the 16-mm thickness, and low-angle scattering did not disappear upon heating to room temperature (Fig. 2).

For a quantitative treatment of the results, it was necessary to separate the experimental curve into parts corresponding to the diffracted and the transmitted beams. Weiss[5] suggested a method for this separation, the basic idea of which is that the ratio of integrated intensities of the diffracted and transmitted beams is estimated by Eq. (2), and the separation is done graphically from this ratio, the width of the scattering curve then being determined from Eq. (3) for the radius of gyration of the particles. For estimation of the integrated intensity, it is necessary to assign a "seed" value of R_g, so this procedure is essentially repetitious. It was necessary to carry out three or four cycles of calculations for the determination of R_g during treatment of our results. It was found that the separation could be done by use of the following procedure: An ordinate corresponding to a width equal to the width of the original reflection curve (3.2") is found on the experimental curve; then the distance H/2 from this point to the maximum of the experimental curve is accepted as half the width of the curve corresponding to the passed beam. The low-angle scattering curve is obtained by subtraction of this curve from the experimental curve. This method of half-widths gave a value of R_g which was in satisfactory agreement with those obtained by the method of Weiss, but was less cumbersome. The method of separation suggested is applicable to those cases where the width of the low-angle scattering curve exceeds the width of the instrumental curve by a few or more times and the shape of the latter is well known. Both these conditions are usually satisfied during work on a double-crystal spectrometer.

Low-angle scattering by hydride precipitates in niobium is concentrated mainly in the region of angles from 10-20" (Figs. 1 and 2). Low angle scattering curves are not exponential, and the function log I($4\theta^2$) approximates linearity only for the smallest and largest θ (Fig. 3). The hydride precipitates usually have the shape of plates with lengths in tens or more microns,[7,8] so that low-angle scattering by plates oriented with long edges along the scattering vector is not resolved even by the double-crystal spectrometer. Therefore, from the curves of Fig. 3 it follows that there is a distribution of thicknesses of the plates. The values of minimum (t_{min}) and maximum (t_{max}) thickness are determined, respectively, from the slopes of the final and initial portions of the curve log I($4\theta^2$). The quantity t_{max} can also be determined from the half-width of the central portion of the low-angle scattering curve (values are given in Table 1 in the column t_{max}'). The values of t_{max}' and t_{max} are in satisfactory agreement. [Values mainly for specimen thickness of 16 mm and partly for thickness of 4 mm (for $4\theta^2 < 200 \cdot 10^{-10}$, where the low-angle scattering intensity is great enough for reliable separation from the primary beam) are used in Table 1; an estimation of multiple scattering effects[9] shows that their influence is not substantial.]

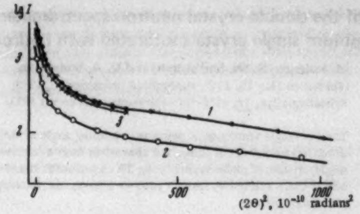

Fig. 3. Low-angle scattering curves on the scale log I($4\theta^2$). 1) Thickness of specimen 16 mm, liquid-nitrogen temperature; 2) thickness of specimen 16 mm, room temperature, after cooling; 3) thickness of specimen 4 mm, liquid-nitrogen temperature.

A distribution of thicknesses from one fourth to 1.5-2 μ was observed at both temperatures. There was a tendency toward decrease in thickness of the plates at room temperature, though it hardly extended beyond the limits of error.

The dimensions given above agree in order of magnitude with the dimensions of precipitates formed during the decomposition of the V + 3.5% H solution[8] (1-2 μ). Coarser hydride plates[10] (thickness of tens of microns) have been found in niobium hydrogenated at high temperatures (300-600°C), but information as to concentration was not presented in that work.

The processes of decomposition of the hydrogen solid solutions of metals of Group V are characterized by clearly pronounced hysteresis: Precipitation of the hydride occurs within a few minutes, but the reverse process of solution of the hydride is not fully complete after several hours even upon superheating of tens of degrees. Although

TABLE 1. Thicknesses of Hydride Plates (μ)

Temperature	t_{min}	t_{max}	t_{max}'
Liquid-nitrogen	0.30	1.6	1.8
Room	0.26	1.6	1.4

the presence of hysteresis contradicts the data of Velekis cited in Goldschmidt's book,[7] it was clearly confirmed by the results of low-angle scattering obtained in this work. Heating to room temperature (Fig. 2) and to 40-50°C does not result in complete disappearance of low-angle scattering. At the present time, it is customary to consider that the hydrogen embrittlement of transition metals is caused by decomposition processes. From the results presented it follows that brittleness can appear not only at low temperatures, but also at room temperature if the metal was previously subjected to cooling.

In conclusion, we note that one of the virtues of the double-crystal spectrometer method is the possibility of simultaneous measurement of the intensities of the diffracted and direct beams. Therefore, a representation of the integrated scattering effect can be obtained by determining the decrease in intensity of the previous beam. Consequently, for observation of the low-angle scattering it is sufficient to compare the transmissions of two single crystals, in one of which heterogeneity is lacking. The sensitivity of the method depends on the ratio of the scattering powers of the matrix and precipitate, and amounts to the order of magnitude of the volume percent fraction (the results presented above correspond to concentration of precipitate $\xi = 5\%$, so the integrated effect for thickness $l = 2$ mm should be the same as in the case $\xi = 0.5\%$ and $l = 20$ mm).

Thus, upon cooling to liquid-nitrogen temperature, hydride precipitates in the shape of plates of thicknesses of a fraction of a micron to 1.5-2 μ are formed in single crystals of niobium containing 3% hydrogen. The decomposition process is characterized by strong hysteresis effects: Heating to 50°C does not result in complete dissolution of the precipitates.

---

[1] D. G. Westlake, Trans. AIME, 239, 1341 (1967).
[2] V. A. Somenkov, V. F. Petrunin, S. Sh. Shil'shtein, and A. A. Chertkov, Kristallografiya, 14, 617 (1969) [Sov. Phys.—Crystallogr., 14, 522 (1970)].
[3] A. Guinier, X-Ray Diffraction in Crystals, Imperfect Crystals, and Amorphous Bodies, Freeman (1963).
[4] S. Sh. Shil'shtein, V. I. Marukhin, M. Kalanov, and V. A. Somenkov, Prib. Tekh. Eksp., 3, 70 (1971).
[5] R. J. Weiss, Phys. Rev., 83, 379 (1951).
[6] I. V. Naumov, M. Kalanov, and V. S. Bondarevskii, Prib. Tekh. Eksp., 6, 223 (1969).
[7] H. J. Goldschmidt, Interstitial Alloys, Plenum (1968).
[8] D. G. Westlake, J. Less-Common Metals, 23, 89 (1971).
[9] D. L. Dexter and W. W. Beeman, Phys. Rev., 76, 1782 (1949).
[10] H. W. Paxton, J. M. Sheehan, and W. J. Babyak, Trans. AIME, 215, 725 (1959).

KIO_3: the first ferroelectric permitting just a 120° shift in the ferroelectric polarization

L. A. Shuvalov, N. R. Ivanov, O. A. Chikhladze, and A. N. Izrailenko

Institute of Crystallography, Academy of Sciences of the USSR
Institute of Cybernetics, Academy of Sciences of the Georgian SSR

(Submitted June 3, 1973)
Kristallografiya, 18, 1207-1213 (November-December 1973)

It was established that KIO_3 is the first crystal which has one spontaneous polarization component P_s which cannot be reoriented (the pyroelectric P_s) and another, perpendicular to the first one, which can be oriented by just 120° (the ferroelectric P_s). Some characteristics of the 120° shift were investigated. Temperature dependences of certain optical properties and of the ferroelectric P_s, which confirm the presence of a number of phase transitions for KIO_3, were investigated. It is proposed that the low-temperature phase ε, just like the β, γ, and δ phases, is ferroelectric, and the nature of its ferroelectric behavior is predicted.

1. INTRODUCTION

The existence of ferroelectric properties for KIO_3 was reported for the first time more than 10 years ago.[1] However, recently, in spite of a number of serious investigations by Helg and Granicher[2–4] and Salje,[5,6] a clearly defined interpretation of the contradictory data concerning the quite peculiar ferroelectric behavior and other physical properties of KIO_3 has remained extremely difficult. This is explained by the fact that due to the difficulties in growing sufficiently large and homogeneous KIO_3 crystals, either the crystal symmetry was incorrectly determined below the Curie point[1–6] (T_C = 212°C) or was not taken into consideration, or the fundamental effect of the existence of both the unusual shift in the domain structure and the choice of the polarity of the measuring or shifting electric field on the behavior of the crystal was incorrectly taken into consideration.

Only recently did Crane[7] establish sufficiently unambiguously that KIO_3 changes at 212°C from the low-temperature R3m rhombohedral phase to the Cm monoclinic phase while retaining this symmetry at room temperature.1) Unfortunately, Crane did not analyze the ferroelectric properties of KIO_3.

Meanwhile, it can be shown on the basis of Crane's data as compared with Helg and Granicher's results that KIO_3 is representative crystallographically of an entirely new type of ferroelectric crystal and the general character of its ferroelectric properties can be predicted. Let us dwell on this important problem in more detail.

Until recently, the reversibility of the spontaneous polarization P_s in the ferroelectric phase under the effect of an external field E was felt to be a necessary property of any ferroelectric crystal, which distinguished it among the pyroelectrics. It was distinctly demonstrated for the first time in ref. 9 (see also ref. 10) that when the P_s arises at the Curie point in the usual polar direction of the high temperature (original) phase of the crystal, there are no 180° domains in the ferroelectric phase in it and reversion of the P_s is impossible. This case was discussed independently in detail later by Aizu,[11] and shortly after, Schmid[12] established that the trigonal R3c phase of boracites (original phase $F\bar{4}3c$) is an example of such a ferroelectric phase in accordance with the prediction in ref. 13. Thereby, it was experimentally shown that the reversibility of P_s in the ferroelectric phase is not a necessary property of ferroelectrics; only the reorientability of P_s by a fixed angle, not necessarily equal to 180°, is obligatory.

Two types of ferroelectric phases with a reorientable irreversible P_s are thus possible.[11,14] No component of the P_s can be distinguished for the first type (the original phase is nonpolar), which always keeps its orientation fixed during the reorientation of the P_s (for example, the trigonal boracites). On the other hand, it is certain that such an unreorientable component of the P_s, which behaves as a purely pyroelectric one and coincides in its direction with the polar axis of the original phase, exists for the second type (the original phase is polar). It is practically impossible to distinguish this component in the background of the pyroelectric P_s, which exists in the original polar phase, although the orientation of the vector of the overall P_s in such a ferroelectric phase should certainly vary with temperature in accordance with its symmetry (cm or C1). The overall P_s will of course be reoriented from the effect of an external field, but if one excludes its unreorientable component P_{sp}, only the component which is always perpendicular to the polar axis of the original phase will remain. It is precisely this reorientable component of the overall P_s that can be called the ferroelectric component of the spontaneous polarization P_{sf}, and a crystal in such a ferroelectric phase, if you will, can be called ferropyroelectric.

The monoclinic Cm phase of KIO_3 should be an example of such a ferroelectric phase and, furthermore, the first example. According to the classification proposed in ref. 14, it will belong to the 3m(3/2)AmFm species (3mFm by the abbreviated designations) and have the following general properties. The pyroelectric (component) P_{sp} is parallel to axis 3 of the original R3m polar phase; the ferroelectric (component) P_{sf} lies in the m plane and is perpendicular to axis 3 of the original phase; the number of P_s axes is three; the number of P_{sf} axes evidently also is three; they are polar, and lie at an angle of 120° to each other; the number of different orientations of the domains also equals three; only a 120° reorientation of the P_{sf} is allowable.

The results of a detailed investigation of the physical properties of KIO_3 are described in this paper, and these preliminary conclusions are confirmed.

2. SAMPLES

Potassium iodate crystals approximately 10×10×10 mm in size were grown by the isothermal method from

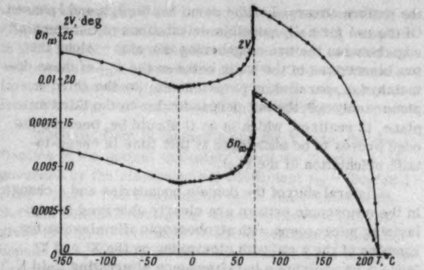

Fig. 1. Temperature dependences of the angle of the optical axes and the birefringence in the z cut of a KIO_3 crystal. ●) Calculation from 2V (T); x) direct measurements.

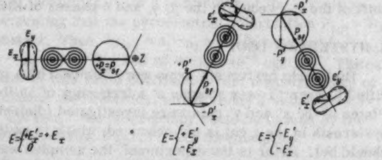
E_y
E_x
$+P_x' = P_{sf}$
Z
E_y'
E_x'
$+P_y'$
P_{sf}
$-P_x'$
$-P_x'$
P_{sf}
$-P_y'$
E_y'
E_x'
$E = \begin{cases} +E_x' = +E_x \\ 0 \end{cases}$
$E = \begin{cases} +E_y' \\ -E_x' \end{cases}$
$E = \begin{cases} -E_y' \\ -E_x' \end{cases}$

Fig. 2. Orientation of the indicating surface of the dielectric constant, conoscopic pattern, and ferroelectric spontaneous polarization vector P_{sf} in an electric field.

an aqueous solution.

The orthogonal system of coordinates we used was chosen in the following way: The Z axis is parallel to axis 3 of the high-temperature phase (the [111] pseudocubic axis), the X axis lies in the m plane, the Y axis is perpendicular to the m plane. It proved to be convenient to consider the directions of the P_{sp} and P_{sf} vectors respectively to be the positive directions of the Z and X axes.

It is not difficult to understand that when all the physical properties of KIO_3 are to be investigated (even those depicted by tensors of even rank), the samples must be made single-domain in directions different from axis 3 (sometimes the contribution of the reorientation of the domains can be taken into consideration through the calculating system if there is assurance of their complete shift). The samples were made single-domain by a uniaxial mechanical compression along the normal to one of the three m planes while cooling them below 212°C (as was done in ref. 7). Subsequently, we discovered that this same result could be obtained with a field acting on the sample and directed along the positive X semiaxis of one of the domains.

The crystallophysical system of X, Y, Z coordinates, which is closely related to the crystallographic system, is turned by 120° about the Z axis when the initially single-domain sample is shifted, because of the specific character of the crystal shift (the case where there is only complete shifting is intended). Therefore, in order to depict and understand the experiments, still another fixed system of coordinates X', Y', Z, which coincides with the initial X, Y, Z system of the single-domain sample and which ceases to coincide with it after its shifting, must be introduced.

The samples used for the optical measurements were cut from suitable portions of the crystal and oriented with their edges along only the X', Y', Z axes (approximate dimensions 2×2×4 mm). Thin plates with their principal faces normal to the X', Y', or Z axes were used for the dielectric measurements. Silver paste was used as the electrode material.

3. THERMOOPTICS AND PHASE TRANSITIONS

The crystals in the high-temperature phase (above T_C = 212°C) are optically uniaxial and negative. They become optically biaxial below 212°C. At this time, the acute bisectrix of the angle of the optical axes proves to be parallel to the Z axis (axis 3), and the obtuse one parallel to the X axis. Upon appearing at 212°C, the angle of the optical axes increases continuously (Fig. 1), which permits one to consider the transition at the Curie point to be a transition of the second type. In contrast to the data in ref. 7, no anomaly is detected on the curve at 150°C. A jump in 2V(T) with a temperature hysteresis of 0.5°C is observed at 72°C, which confirms the data in refs. 1-7 on the presence of a phase transition and shows it to be one of the first type. An inflection without a jump is observed on the 2V(T) curve at −15°C, confirming the data in refs. 1-6 on the presence of a phase transition. Evidently, this transition is one of the second type.

The temperature dependence of the birefringence in the z cut (Fig. 1) demonstrates a similar behavior, whereby the curve calculated from 2V(T) agrees well with that measured by the interference method.

The dependence of $P_{sf}(T)$ obtained from the measurements of the dielectric hysteresis loops (see below)

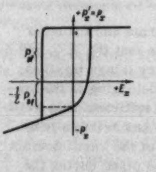

Fig. 3. Dielectric hysteresis loop for a sample of the x cut of a KIO_3 crystal.

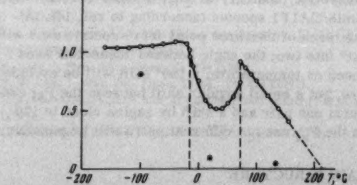

Fig. 4. Temperature dependence of the ferroelectric spontaneous polarization P_{sf} of a KIO_3 crystal. The asterisks represent the data in ref. 4.

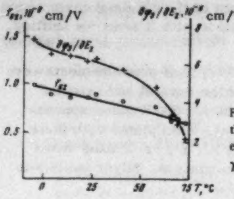

Fig. 5. Temperature dependence of the magnitude of $\partial\varphi_3/\partial E_2$ and the electrooptical coefficient f_{62} for the γ phase of a KIO_3 crystal.

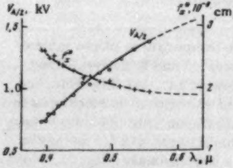

Fig. 6. Dispersion of the effective electrooptical coefficient f_x^* and of the corresponding halfwave voltage $V_{\lambda/2}$ of a KIO_3 crystal at T = 20°C.

agrees completely with the data from the thermooptical measurements both in relation to the position on the temperature scale and with regard to the type of transitions.

It should be mentioned that at low temperatures approaching that of liquid nitrogen, crystallooptical measurements become impossible because the conoscopic pattern is washed out due to the division of the single-domain sample into small domains. This fact could serve as confirmation of the data in refs. 1 and 5 that there is still another phase transition (at −163°C according to ref. 5).

Thus, according to our measurements and the literature data, the KIO_3 crystal has the following sequence of phase transitions (the designations of the phases according to Salje[5] are used):

$$\varepsilon \xleftrightarrow{-163^\circ} \delta \xleftrightarrow{-15^\circ} \gamma \xleftrightarrow{72^\circ} \beta \xleftrightarrow{212^\circ} \alpha \text{ phase} .$$

The nature of the conoscopic forms and the other data we obtained (see below) indicate that the β, γ, and δ phases have the same point symmetry (class m); thus, all three phases are ferroelectric, belonging to the 3m · (3/2)A,Fm species. We do not have sufficient data available relative to the ε phase to make any reliable judgments. However, if the emergence of the small domain structure we observed actually takes place during the δ → ε transition, this quite reliably points to a decrease to triclinic symmetry, and then the ε phase should also be ferroelectric (contrary to Salje's assertion[5]) and belong to the 3m(6/2)A1F1 species (according to ref. 14). At this time, each of the three polar ferroelectric axes will be "split" into two; the angle between these two axes will depend on temperature; a 180° shift will be excluded as before, but a small angular shift between the P_{sf} axes which form one pair and a shift by angles close to 120° between the P_{sf} axes of different pairs will be possible.

4. DOMAIN STRUCTURE

In samples which have not been made single-domain, domain-triplets are clearly observed in the z cut, whereby the pattern observed is the same for the β, γ, and δ phases. Of the two formally possible orientations of the domain edge between the two neighboring domains — along the two bisectrices of the angle between the P_{sf} of these domains, i.e., parallel or perpendicular to the third m plane — only one, the one perpendicular to the third m plane, is realized, which is as it should be, because the edge proves to be uncharged at this time (a "head-to-tail" orientation of the P_{sf}).

A lateral shift of the domain boundaries and a change in the conoscopic pattern are clearly observed in a polarizing microscope with stroboscopic illumination for samples of the z cut with electrodes on the X' and Y' faces upon applying a low-frequency alternating field E_{x}' or E_{y}'. If the sample is originally single domain, the transition to another single-domain state (Fig. 2) takes place abruptly. These observations completely confirmed the conclusion concerning the existence of only a 120° shift of the P_{sf} vector in the β, γ, and δ phases of KIO_3.

5. HYSTERESIS LOOPS

Dielectric hysteresis loops were detected by a modified Sawyer—Tower scheme at a frequency of 50 Hz. Plates of the x' and y' cuts were investigated (dielectric hysteresis in the z cut is not observed, which is as it should be). Prior to the experiment, the samples were made single domain. The loops for the x' cut (Fig. 3) are unsymmetrical, whereby the measurable portion of the P_{sf} in the $+E_x'$ field equals $+P_{sf}$ and in the $-E_x'$ field, it equals[2)] $-(1/2)\,P_{sf}$. The loops are symmetrical for samples of the y' cut, and the measurable portion of the P_{sf} in the $\pm E_y'$ field equals $\pm\sqrt{3/2}\,P_{sf}$. The results obtained agree completely with the model of the 120° shift. Calculations show very good agreement in the 0–150°C range of the $P_{sf}(T)$ curves obtained from measurements of the hysteresis loops on samples of the x' and y' cuts (Fig. 4) (measurements at T > 150°C are complicated by an increase in the conductivity of the crystal; discrepancies of up to 20% are also observed in the region of the γ— δ transition).

The model of the 120° shift permits one to explain the specific hysteresis loops of the dielectric constant that Helg and Granicher[3] obtained. Further, upon analyzing these data, the principal components of the tensor of the dielectric constant for KIO_3 at room temperature can be calculated:[3] $\varepsilon_x = 37$, $\varepsilon_y = 81$ ($\varepsilon_z = 11.5$).

Because the shift in the domains is accompanied by a marked change in the shape of the sample, the sample vibrates during cyclic repolarization, and individual sharp clicks are audible during repolarization in a quasistatic field.

6. ELECTROOPTICAL PROPERTIES

Salje[6] reported that KIO_3 possesses a strong electrooptical effect, and found that the half-wave voltage $V_{\lambda/2} \approx 3.5$ kV for a sample in the shape of a cube for the transverse effect. However, the field in these experiments was not applied along the principal directions and the absence of any shifting of the domains was not guaranteed. Therefore, Salje's data should be considered only to be estimated.

We investigated the linear induced electrooptical effect of mechanically free single-domain KIO_3 samples in the γ phase. The deflection of the optical indicatrix was measured on a precision photoelectric spectropolarimeter. The change in the birefringence was calculated from the magnitude of the shift in the interference spectra.

When the field is applied along the Y axis, the deflection of the optical indicatrix about the Z axis, φ_3, is governed by the electrooptical coefficient $f_{62} = (\partial\varphi_3/\partial E_2) \cdot (1/n_1^2 - 1/n_2^2)$. The relationship $f_{62}(T)$ constructed from the data obtained during the measurements of $\varphi_3(T)$ is given in Fig. 5. The experiment shows that φ_3 does not depend on λ, therefore, the dispersion of f_{62} is completely governed by the dispersion of n_1 and n_2.

The magnitude of the effective electrooptical coefficient r_X^* when the wave vector is directed along the Z axis can be calculated right from the thermooptical data (Fig. 1), assuming P_X is a parameter of the transition and assuming that the pyroelectric polarization $P_{sp} = P_Z$ is constant. Then, $\delta n_{(Z)} = n_2 - n_1 = (n_2^3/2)[r_{21} - (n_1^3/n_2^3) r_{11}] \cdot P_X = -(n_2^3/2) r_X^* P_{sf}$ and $r_X^* = -1.1 \cdot 10^{-6}$ cgs esu. The calculation of this same coefficient from measurements of the induced electrooptical effect yields a value of $-2.0 \cdot 10^{-6}$ cgs esu. The discrepancy could be caused by the contribution from $P_{sp}(T)$ to the thermooptics.

The dispersion of the effective electrooptical coefficient $f_X^* = (\varepsilon_1 - 1) r_X^*/4\pi$ calculated from the measurements of the induced effect $[\delta n_{(Z)} = (n_2^3/2) f_X^* E_X)$ and also the dispersion of the corresponding $V_{\lambda/2}$ calculated for a cubic shaped sample are given in Fig. 6.

7. CONCLUSION

Thus, KIO_3 is the first ferroelectric crystal with an original polar phase (R3m symmetry) to be found. According to the classification in ref. 14, the ferroelectric phases for this type of original phase can belong to the 3m(3/2)AmFm species or to the 3m(6/2)A1F1 species. The entire collection of experimental data unambiguously shows that the β, γ, and δ phases of KIO_3 have the same monoclinic point symmetry and, consequently, belong to the 3m(3/2) AmFm species. Accordingly, the ferroelectric behavior of KIO_3 in its β, γ, and δ phases is qualitatively the same, and from this point of view, they can be considered to be one ferroelectric phase. Let us stress once more the number of unusual features of the ferroelectric properties of KIO_3, especially the fact that we are the first ones to have encountered in this example a type of ferroelectric phase that had not yet been encountered.

The ferroelectric spontaneous polarization vector, which appears at T_C = 212°C in one of the m planes of the crystal, should, generally speaking, change its orientation in this plane with temperature. At this time, it is impossible to distinguish the unreorientable component of the ferroelectric polarization directed along polar axis 3 of the original phase from the purely pyroelectric polarization, which still exists in the original phase and is directed along this same axis, and, of course, is retained in the ferroelectric phase; one can only speak of the temperature dependence in the ferroelectric phase of the combined unreorientable spontaneous polarization directed along the Z axis (axis 3 of the original phase). Therefore, it is expedient to consider the overall spontaneous polarization P_s and its two components: the unorientable one directed along the polar axis of the original phase, i.e., the pyroelectric one (P_{sp}), and the reorientable one, which is perpendicular to the first, i.e., the ferroelectric one (P_{sf}), for KIO_3 and, in general, for ferroelectric phases of such a type. The abnormality of KIO_3 is in the fact that $P_{sp} \gg P_{sf}$ ($P_{sp} \approx 30\ \mu C/cm^2$, see ref. 7).

The 3m(3/2)AmFm species of KIO_3 in the ferroelectric phase has three P_s axes and three P_{sf} axes. Because these axes are polar in the original phase, a 180° shift of P_s and P_{sf} is impossible; the P_{sf} axes lie at an angle of 120° to each other, and, therefore, only a 120° shift of P_{sf} is possible; the angle between the P_s axes varies with temperature, depending on $P_{sf}(T)$ and $P_{sp}(T)$.

The low-temperature ε phase of KIO_3 is also probably ferroelectric and belongs to the 3m(6/2)A1F1 species, which is of that type having six P_s axes and six P_{sf} axes and a correspondingly more complex behavior (see Sec. 3 above).

The authors thank L. N. Rashkovich and G. F. Dobrzhanskii and especially L. M. Belyaev for their support of this effort in all of its stages.

---

1) Various assertions concerning the symmetry of KIO_3 at room temperature (from rhombohedral[8] to triclinic[1-4]) had appeared in the literature prior to this. See ref. 7 for a review of these data.

2) When measuring the P_{sf} from the dielectric hysteresis loops (including using a modified Sawyer–Tower scheme), it is necessary to take into consideration the fact that portions of the dielectric hysteresis loop in the $+E_X'$ and $-E_X'$ fields have different slopes because of the difference in the dielectric constants in the positive and negative directions of the X' axis (Fig. 2).

---

[1] F. Herlach, Helv. Phys. Acta, 34, 305 (1961).
[2] U. Helg, Proc. Intern. Meeting on Ferroelectricity, Vol. 1, Prague (1966), p. 300.
[3] U. Helg and H. Granicher, J. Phys. Soc. Japan, Suppl., 28, 169 (1970).
[4] U. Helg, Z. Kristallogr., 132, 241 (1970).
[5] E. Salje, Z. Kristallogr., 134, 107 (1971).
[6] E. Salje, Z. Kristallogr., 136, 135 (1972).
[7] G. R. Crane, J. Appl. Crystallogr., 5, 360 (1972).
[8] R. P. Ozerov, N. V. Rannev, V. I. Pakhomov, and G. S. Zhdanov, Kristallografiya, 7, 620 (1962) [Sov. Phys.–Crystallogr., 7, 499 (1963)].
[9] L. A. Shuvalov, Kristallografiya, 8, 617 (1963 [Sov. Phys.–Crystallogr., 8, 495 (1964)].
[10] I. S. Zheludev and L. A. Shuvalov, Kristallografiya, 1, 681 (1956) [Sov. Phys.–Crystallogr., 1, 537 (1956)].
[11] K. Aizu, J. Phys. Soc., Japan, 23, 794 (1967).
[12] H. Schmid, J. Phys. Soc. Japan, Suppl., 28, 354 (1970).
[13] L. A. Shuvalov, Lectures read at Czechoslovak Academy of Sciences (1967).
[14] L. A. Shuvalov, J. Phys. Soc. Japan, Suppl., 28, 38 (1970).

Phase transition, dielectric anomaly, and domain structure in hydrosodalite

N. R. Ivanov and V. Yu. Galitskii

Institute of Crystallography, Academy of Sciences of the USSR

(Submitted March 27, 1973; resubmitted May 22, 1973)
Kristallografiya, 18, 1214-1217 (November-December 1973)

A phase transition in hydrosodalite $Na_8[Al_6Si_6O_{24}](OH)_2 \cdot 6H_2O$ at -120°V has been detected for the first time and investigated. We studied the anomalous behavior of the temperature functions ε(T) and tan δ(T) in [100], [110], and [111] sections. For purposes of comparison, we studied the corresponding functions in crystals of partially (≈ 50%) deuterated hydrosodalite and chlorosodalite. Polarized-light microscopy showed that there is a decrease in symmetry in the low-temperature phase; the domain boundaries and the boundaries for coexistence of the two phases coincided with the {110} planes. The temperature discontinuity and hysteresis of δn(T) indicate that the observed transition is of type I.

Intensive research has recently been conducted on the structure and physical properties of crystals of hydrosodalite $Na_8[Al_6Si_6O_{24}](OH)_2 \cdot 6H_2O$. The successes achieved in growing large single crystals[1] have permitted practical use of electrooptical,[2] piezoelectric,[3] and photochromic[4] aspects of the properties of hydrosodalite.

The crystal structure of hydrosodalite at room temperature belongs to the $P\bar{4}3n$ space group; the cell parameter[5] is $a_0 = 8.88$ Å. Investigation of hydrosodalite by the proton magnetic resonance (PMR) method[6] showed that the reorientation and diffusion mobility of the water molecules and hydroxyl groups located within the voids of the alumosilicate framework virtually disappeared at temperatures below −135°C. The second moment of the PMR line underwent a severe change near this temperature. The dielectric and optical studies made in the present investigation showed that the hydrosodalite crystal undergoes a phase transition in this temperature region.

Specimens were cut from large faceted single crystals grown by O.K. Mel'nikov at the Institute of Crystallography, Academy of Sciences of the USSR, using the hydrothermal method; the specimens consisted of tabular (100), (110), and (111) sections 0.2–0.3 mm thick and 1–4 cm² in area. Silver-paste electrodes were applied to the polished large facets. The dielectric permeability and the tangent of the dielectric-loss angle were measured with an R589 ac bridge under an automatic tracking regime. The anomalies in ε and δ remained almost unchanged when the ac measurement voltage was reduced. The temperature was measured with copper–constantan thermocouples, the experiments being conducted with a slow temperature variation (0.5 deg/min) for both heating and cooling. The optical observations were made in an MIN-8 polarized-light microscope with an attachment for low-temperature operation. The deuterium content of the deuterosodalite crystals was not determined, but the initial solution contained 50% D_2O.

The results obtained in investigating the dielectric properties of hydrosodalite and deuterosodalite are shown in Fig. 1, from which it can be seen that ε and tan δ exhibited an anomalous trend, which obviously indicated the occurrence of a phase transition. The transition temperature was −125 ± 5°C. Dielectric measurements could not provide a more accurate figure for the transition temperature, because of mechanical stresses, which altered the transition temperature from specimen to specimen (and at different points in the same specimen) and especially because of the lack of a sharp maximum in the ε(T) curves.

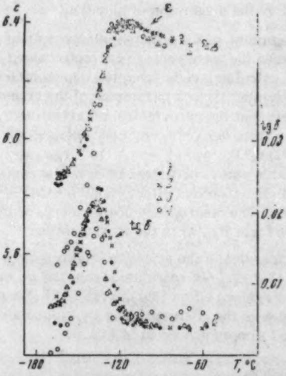

Fig. 1. Dielectric permeability ε and tangent of dielectric-loss angle tan δ as functions of temperature for hydrosodalite (1-3) and deuterosodalite (4). Frequency of 1000 Hz. 1) [100] direction; 2) [110]; 3) [111]; 4) [100].

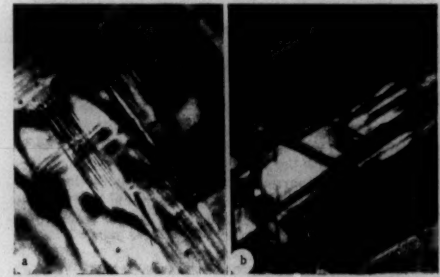

Fig. 2. Domain structure of hydrosodalite at −140°C in different sections: a) (100) section; b) (111) section. In addition to domains, the (100) section exhibits a system of interference bands, which indicates additional mechanical stresses arising as a result of the change in the unit-cell parameter during the transition to the low-temperature phase.

We did not detect any noticeable temperature hysteresis for the transition in measuring ε(T) and tan δ (T), i.e., there was no discrepancy in the transition temperatures during cooling and heating (within a range of ± 5°). The tan δ (T) curves had a maximum 10° below the transition

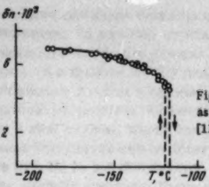

Fig. 3. Birefringence of hydrosodalite as a function of temperature in the [110] section.

temperature. The maximum of tan δ corresponded to the region of greatest curvature for the ε(T) curve and could evidently be correlated with the region of most rapid structural rearrangement. As can be seen from Fig. 1, ε and tan δ varied little between −110 and −40°C, but they increased noticeably when the temperature was further raised to the room level or above.

The deuterated crystal exhibited no noticeable shift in the transition temperature in comparison with the hydrogen-containing crystal, thus providing still another example of the absence of an isotopic transition shift. However, the curve representing the drop in ε(T) below the transition temperature ran considerably lower (Fig. 1), which can apparently be attributed to the fact that the degree of crystal deuteration was rather high. At the same time, the function tan δ(T) for the same crystal differed little from the corresponding function for hydrosodalite. We did not detect a dielectric hysteresis loop in any of the sections in fields of up to 40 kV/cm.

Polarized-light microscopy showed the phase transition to be accompanied by development of a twinned (domain) structure (Fig. 2). The point symmetry was obviously reduced as a result of the transition, but we do not as yet have sufficient information to determine the symmetry of the low-temperature phase. The domain structure was most distinct in the (111) section. Good visible-domain contrast was provided by the fact that the extinction position formed an angle of 30° with the domain boundary. The domain patterns differed for different sections. The domain boundaries intersected at an angle of 90° in the sections of type (100) and at an angle of 60° in the sections of type (111). The domain boundaries were naturally the same in both cases, coinciding with the {110} symmetry planes of the high-temperature phase.

A detailed polarization-optical investigation conducted with a (110) section made it possible to determine the dependence of the birefringence produced during the transition on temperature. The measurements were made with "single-domain" specimens. The birefringence was measured with a Berek compensator in specimens 314 μ thick in white light (with an effective wavelength of 550 mμ). As can be seen from Fig. 3, the δn(T) curve exhibited a discontinuity during the phase transition, which amounted to 66% of the total change in δn; according to the optical data, the phase transition had a temperature hysteresis of 2.0°. These measurements enabled us to find the transition temperature more accurately than the dielectric measurements, yielding −121 ± 0.3°C during cooling and −119 ± 0.3°C during heating.

The results obtained in studying the function δn(T) clearly show that the phase transition in hydrosodalite is of type I. Additional confirmation was provided by the phase front observed in (110) specimens and the coexistence of the two phases at a fixed temperature within the transition hysteresis region. It was often possible to observe two phase fronts in this section, intersecting at an angle of 71° and coinciding with the $(0\bar{1}1)$ and (011) planes. The phase front thus was always a plane of the (110) type, which was also the cleavage plane of the crystal. It is interesting to note that these planes were also the twinning boundaries.

We attempted preliminary measurements of the functions tan δ (T) and ε(T) in a natural chlorosodalite specimen of arbitrary orientation. The ε(T) curve apparently had no anomaly, but there was a broad tan δ peak in the vicinity of −60°C, which hampered determination of the behavior of ε(T) in this region. Using only these data, it would be difficult to say whether the anomaly in tan δ could be correlated with the phase transition. However, polarization-microscopy examination showed that the crystal remained cubic down to the temperature of liquid nitrogen. It can thus be concluded that, in contrast to hydrosodalite, there is no phase transition in a natural chlorosodalite crystal.

Proceeding from the results of the present investigation and NMR data,[6,7] it can be concluded that the observed phase transition in hydrosodalite is of the "composite type," in which there is displacement and skewing of the heavy structural subunits as a result of changes in the dynamics of the light subsystem; in our case, this took the form of disappearance of the orientational lability of the the water molecules and OH groups as a result of ordering of the protons in the hydrogen bonds.

The authors wish to thank O. K. Mel'nikov, who provided the crystals, and L. A. Shuvalov, who supported this work.

---

[1] V. I. Ivanov, Outlines of Physicochemical Petrology [in Russian], Nauka, Moscow (1970), p. 158.

[2] Yu. V. Shaldin, O. K. Mel'nikov, V. V. Nabatov, and Yu. V. Pisarevskii, Kristallografiya, 10, 574 (1965) [Sov. Phys.−Crystallogr., 10, 484 (1966)].

[3] V. I. Bukin and E. S. Makarov, Geokhimiya, 1, 31 (1967).

[4] K. L. Bye and E. A. D. White, J. Crystal Growth, 6, 355 (1970).

[5] N. V. Belov, Crystallography of Silicates Containing Large Cations [in Russian], Izd. Akad. Nauk SSSR, Moscow (1961), p. 38.

[6] V. Yu. Galitskii, V. N. Shcherbakov, and S. P. Gabuda, Kristallografiya, 17, 788 (1972) [Sov. Phys.−Crystallogr., 17, 691 (1973)].

[7] V. Yu. Galitskii, V. N. Shcherbakov, and S. P. Gabuda, Kristallografiya, 18, 5 (1973) [Sov. Phys.−Crystallogr., 18, 1 (1973)].

Domain boundaries, antiphase boundaries, and dislocations in gadolinium molybdate single crystals

V. A. Meleshina, V. L. Indenbom, Kh. S. Bagdasarov, and T. M. Polkhovskaya

Institute of Crystallography, Academy of Sciences of the USSR

(Submitted September 30, 1971; resubmitted September 19, 1972, May 17, 1973)
Kristallografiya, 18, 1218-1226 (November-December 1973)

Gadolinium molybdate is used as an example to examine the specific characteristics of the domain structure which develops in nonintrinsic ferroelectrics during phase transitions involving a change in the number of atoms in the unit cell. Group-theory considerations dictate the necessity for the existence of four types of domains and two types of boundaries (domain walls and antiphase boundaries) in the polar phase of gadolinium molybdate. Possible reactions among the domain boundaries, antiphase boundaries, and dislocations are considered. The selective-etching method was used to make an experimental study of the characteristics of the interaction of the domain boundaries with the antiphase boundaries and dislocations. It was shown that the antiphase boundaries adhere to the domain boundaries and move together with them. Annihilation at the domain boundaries causes disappearance of the antiphase boundaries, which are replaced by the master dislocations that produced them; these reactions determine the character of the change in the pattern formed by all the boundaries (domain and antiphase) and the macroscopic repolarization characteristics.

INTRODUCTION

The molybdates of rare earths (Gd, Tb, Sm, and Eu) belong to a new class of so-called nonintrinsic ferroelectrics, whose existence was predicted previously.[1] In contrast to ordinary ferroelectrics, spontaneous polarization in nonintrinsic ferroelectrics is manifested only as a secondary effect during a phase transition, which accounts for the specific physical properties of these crystals. The increased interest in research on molybdates is also due to the prospects for their practical application in optical electronics and holography. Investigation of the domain-structure characteristics of nonintrinsic ferroelectrics is of interest both for practical applications and for analysis of the repolarization mechanism. As a typical example, the present article will consider gadolinium molybdate $Gd_2(MoO_4)_2$, for which all the nceessary x-ray diffraction data are available[2,3] and a selective-etching method has been developed that permits sufficiently reliable visualization of the real structure of the crystal.[4]

Observations of domain-boundary movement during repolarization of gadolium molybdate[5,6] indicate the presence of an additional (in comparison with ordinary ferroelectrics) mechanism for domain-boundary deceleration: The trigger stress, i.e., threshold field, increases with the total boundary movement time before a given start, while the domain-boundary velocity after the start increases linearly with the applied field. In addition to etch jogs corresponding to the ferroelectric domain boundaries and etch pits corresponding to dislocations, selective etching of polar (001) sections of $Gd_2MOO_4)_3$ crystals reveals unusual etch grooves, which form closed loops running from one domain to another or joining dislocation etch pits. Since these etch grooves stop dislocations existing to the specimen surface, it has been hypothesized[4] that they correspond to dislocations lying directly beneath the etched surface. More detailed study of the selective etching pattern, however, cast doubt on whether these grooves correspond to any linear defects. Successive etching of a fracture showed that grooves were present and persisted in domains of both signs in both halves of the fracture. It was thus found that etch grooves develop not at dislocations (and not at linear defects in general) but at certain surface defects that intersect the fracture surface and run into the interior of the specimen.

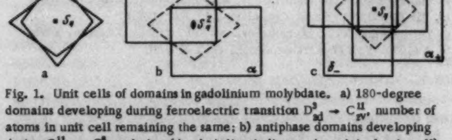

Fig. 1. Unit cells of domains in gadolinium molybdate. a) 180-degree domains developing during ferroelectric transition $D_{2d}^{3} \rightarrow C_{2v}^{11}$, number of atoms in unit cell remaining the same; b) antiphase domains developing during $C_{2v}^{11} \rightarrow C_{2v}^{8}$ ordering (the dash line indicates the original unit cell); c) four types of domains developing during $D_{2d}^{3} \rightarrow C_{2v}^{8}$ phase transition in nonintrinsic ferroelectric (the dash line indicates the original D_{2d}^{3} unit cell).

Study of the changes in the etching pattern resulting from movement of domain boundaries (under the action of an electric field or mechanical shear stresses) showed that the defects corresponding to the etch grooves were highly mobile and exhibited a definite correlation with the domain boundaries. Purely morphological investigations thus demonstrated that, in addition to stationary growth dislocations, the domains of both components in gadolinium molybdate single crystals contain certain labile defects that are, on one hand, fixed near dislocations, and, on the other, undergo changes in conformation when the domain boundaries move. These observations become comprehensible if we take into account the specific characteristics of the structure of nonintrinsic ferroelectrics.

DOMAIN STRUCTURE OF NONINTRINSIC FERROELECTRICS

Since spontaneous polarization is not a transition parameter and does not define the change in crystal symmetry in nonintrinsic ferroelectrics, neither does it define the difference in the domains produced by the phase transition. Specifically, translational domains with generally identical physical properties must arise during phase transitions involving a change in the number of atoms in the unit cell.[7] The twinning elements for such domains are translations that disappear during the transition. An example of such translational domains is the so-called antiphase domains that develop during ordering processes. In an ideal crystal, the antiphase-domain boundaries divide the crystal into differently ordered regions, in a manner wholly analogous to ordinary domain boundaries dividing a crystal into regions with different physical properties. However, this analogy breaks down for a real crystal, which contains dislocations: The antiphase boundaries can be interrupted at dislocations and the crystal is not divided into different (isolated) regions, i.e., strictly speaking, there are no antiphase domains.[1]

According to x-ray diffraction data,[2,3] gadolinium molybdate undergoes a change in space group ($D_{2d}^3 - C_{2v}^8$) during the transition, this corresponding to: a) halving of the order of the point symmetry group (the inversion center, S_4 axis, and two V_2 axes perpendicular to the S_4 axis disappear); b) doubling of the unit-cell volume (the translations **a** and **b** = $S_4 \times$ **a** disappear and the vectors corresponding to **a** + **b** and **a** − **b** become the new elementary translation vectors).

The change in symmetry (a) itself corresponds to the ordinary ferroelectric transition $D_{2d}^3 \rightarrow C_{2v}^{11}$ to a higher polar subgroup, which involves halving of the group order and appearance of two (positive and negative) domain systems (see Fig. 1a). The twinning elements for these domains are the expansion of the initial D_{2d}^3 group into contiguous classes for the C_{2v}^{11} group:

$$D_{2d}^3 = C_{2v}^{11} + S_4 C_{2v}^{11}, \tag{1}$$

i.e., in addition to S_4, the twinning elements are the products of S_4 by all symmetry elements of the C_{2v}^{11} group. The change in symmetry (b) itself corresponds to the ordering transition $C_{2v}^{11} \rightarrow C_{2v}^8$, which results in formation of antiphase domains in each antiparallel domain component (Fig. 1b). The expansion into contiguous classes1)

$$C_{2v}^{11} = C_{2v}^8 + S_4^2 C_{2v}^8 \tag{2}$$

yields all the twinning elements: in addition to S_4^2, the $S_4^2 C_{2v}^8$ class includes the translations to S_4^2, the $S_4^2 C_{2v}^8$ class includes the translations ±**a** and ±**b** equivalent to S_4^2. The ordering represented by Eq. (2) occurs in each of the domains in Eq. (1). This results in development of four types of domains: α_+, β_+, γ_-, and δ_- (Fig. 1c), which are related by the twinning operations; the latter can be obtained by expanding the D_{2d}^3 group for the C_{2v}^8 group. Substituting Eq. (2) into Eq. (1), we find

$$D_{2d}^3 = C_{2v}^8 + S_4 C_{2v}^8 + S_4^2 C_{2v}^8 + S_4^3 C_{2v}^8. \tag{3}$$

The first contiguous class converts the positive domain α_+ to the negative domain γ_-, the second type to the antiphase positive domain β_+, and the third type to the negative domain δ_- antiphase with respect to the domain γ_-. (The first class differs from the third only in the direction of rotation by 90°). Generally speaking, the domains of the above four types could yield six different types of domain boundaries, but it follows from Eq. (3) that only two types of domain boundaries differ in symmetry: a) ordinary 180-degree domain boundaries, $(\alpha_+|\gamma_-)$, $(\beta_+|\gamma_-)$ $(\alpha_+|\delta_-)$, and $(\beta_+|\delta_-)$.

The 180-degree boundaries (domain boundaries) divide the crystal into positively and negatively polarized regions and therefore cannot be interrupted within the crystal. The antiphase boundaries can be continuous, can be interrupted at dislocations, or, as follows from symmetry considerations, can form a triple point (node) in the network of antiphase and domain boundaries. For example, the antiphase boundary $(\alpha_+|\beta_+)$, exiting to the 180-degree boundary $(\beta_+|\gamma_-)$, should change the type of the latter at the junction point from $(\beta_+|\gamma_-)$ to $(\alpha_+|\gamma_-)$. This triple boundary junction corresponds to annihilation of the antiphase boundary at the domain boundary:

$$(\alpha_+|\beta_+) + (\beta_+|\gamma_-) = (\alpha_+|\gamma_-), \tag{4}$$

which should proceed from left to right, liberating the energy of the antiphase boundary undergoing annihilation, since coherent 180-degree boundaries oriented along the unit translation vectors of the paraelectric phase are crystallographically equivalent. As will be shown below, reaction (4) is more complex under real conditions, involving formation of a combined (domain and antiphase) boundary. It is apparently necessary to take into account the structure of both the intersecting domains and the domain boundaries themselves, which may prove (e.g., in the case of boundaries of the Bloch type) nonequivalent for the initial boundary $(\beta_+|\gamma_-)$ and the composite boundary of type (4). The equivalence of boundaries of types $(\beta_+|\gamma_-)$ and $(\alpha_+|\gamma_-)$ also breaks down when the boundary plane deviates from the direction of the unit translations vectors of the paraelectric phase. Differences in the structure and energy of these boundaries can affect the electrical balance of reaction (4).

An antiphase boundary, whether of the $(\alpha_-|\delta_-)$ or $(\alpha_+|\beta_+)$ type, is interrupted at dislocations when and only when the Burgers dislocation vector (with an accuracy of the order of the translation vector of the ferroelectric phase) coincides with the vector **a** and equals, e.g., + **a** or + **b**. Dislocations with such Burgers vectors necessarily serve as sources of antiphase boundaries, i.e., the boundaries cannot be separated from the dislocations regardless of the transformations undergone by the domain structures. Observation of the antiphase boundaries and the dislocations with which they are associated can therefore materially facilitate interpretation of the dislocation structure of crystals, particularly in distinguishing screw dislocations exiting to the surface of (001) planes, since antiphase boundaries should not interact with them.

If a dislocation lies on the domain boundary itself, it can form either a triple junction between an antiphase boundary and a domain boundary or a double junction of the $(\alpha_+|\gamma_-)$ or $(\beta_+|\gamma_-)$ type without a physically discrete boundary between the domains α_+ and β_+. In the latter case, after separating from the dislocation, the 180-degree boundary remains joined to it by an antiphase boundary, e.g., of the $(\alpha_+|\beta_+)$, $(\alpha_+|\gamma_-)$, $(\beta_+|\gamma_-)$.

In addition to annihilation of an antiphase boundary at a domain boundary, we might point out the reaction by which an antiphase boundary is formed during the annihilation of 180-degree boundaries:

$$(\alpha_+|\gamma_-) + (\gamma_-|\beta_+) = (\alpha_+|\beta_+). \tag{5}$$

The energy contribution made by this reaction is undoubt-

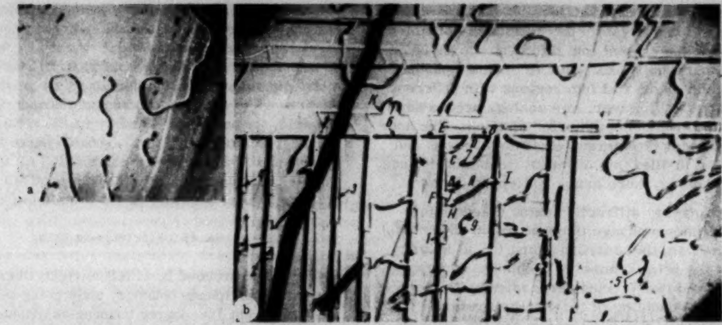

Fig. 2. Antiphase-boundary configurations characteristic of monodomain (a) and polydomain (b) regions of gadolinium molybdate, × 50. Selective etching, surface of (001) fracture.

edly positive and exceeds the yield of reaction (4) by twice the difference in the energies of the 180-degree boundary and the antiphase boundary.

DOMAIN STRUCTURE AND ANTIPHASE BOUNDARIES IN GADOLINIUM MOLYBDATE

The foregoing gives rise to a simple explanation for the selective-etching pattern of gadolinium molybdate. The etch grooves connecting the dislocation etch pits or forming closed loops (Fig. 2) are undoubtedly the tracks of antiphase boundaries of the $(\alpha_+|\beta_+)$ or $(\gamma_-|\gamma_-)$ type, depending whether they are located in a domain with positive or negative polarization respectively.

As can be seen from Fig. 2b, the dislocation pits and antiphase boundaries in domains of different signs have different sizes and depths. This difference in the etching rates and pit faceting for dislocations in domains of different signs is known to occur for ferroelectrics.[8-9] They are usually assumed to be due to the influence of bound spontaneous-polarization charges on selective etching. Experimentation[3,6,10] showed the chemical polishing rate in domains of one sign to be so high that there was not sufficient time for the etching patterns of the defects in these domains (dislocations and antiphase boundaries) to persist. As a result, the real structure is shown by selective etching only for domains of one sign, for which the chemical polishing rate is sufficiently low. As can be seen from Fig. 2b, the etchant we used[4] showed the antiphase boundaries and dislocations at the (001) surface of the domains of both components, in contrast to other studies.[3,6,10]

Observations have shown that single-domain and polydomain regions of gadolinium molybdate are characterized by significantly different antiphase-boundary configurations. In single-domain regions (i.e., in large domains), the antiphase boundaries have a free form: closed loops and semiloops connecting two nearby or distant dislocations (see, for example, Fig. 2a, the semiloop in the upper right-hand corner). The free form of the antiphase boundaries is modified in the immediate vicinity of the domain boundaries: closed loops within a single domain are "attracted" to the domain boundary (boundaries 1–4, Fig. 2b); closed loops in two domains of different signs develop segments that adhere to the domain boundary separating the antiparallel domains (loop 6, Fig. 2b); semiloops joining two nearby dislocations can acquire a very complex form (loop ABCDEFJHI, Fig. 2b). Adhesion of antiphase boundaries of the $\alpha_+|\beta_+$ type to 180-degree domain boundaries results in formation of triple junctions (junction K, loop 6, Fig. 2b); judging from the etching relief, the triple junction in this case is formed by boundaries of the $(\alpha_+|\beta_+|$ and $(\beta_+|\gamma_-)$ types and a composite $(\alpha_+|\beta_+; \beta_+|\gamma_-)$ boundary, which is not equivalent to the $(\alpha_+|\gamma_-)$ boundary that should be formed when reaction (4) goes to completion. Since such composite boundaries are observed not only in cuneate domains with noncoherent boundaries, but in other regions as well, it can be assumed that incomplete structural relaxation cocurs during reactions of the type in Eq. (4).

Unusual changes in the pattern of antiphase and composite boundaries take place during formation of domains and movement of domain boundaries. Under the action of thermal factors, an electric field, or thermoelastic stresses, new domains develop in the form of a thin wedge-shaped interlayer, which subsequently increases in width. The rearrangement of the antiphase boundaries that occurs in this case is illustrated by Fig. 3, which shows regions I and II separated by a domain boundary (DB). This region was produced by thermoelastic shock. Region I re-

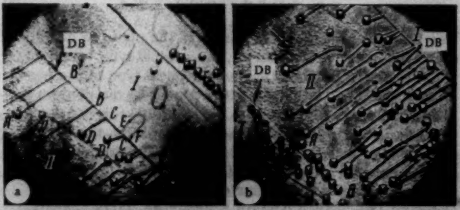

Fig. 3. Antiphase boundaries and dislocations in regions one of which I has retained its polarity and the other (II) has been repolarized; DB) domain boundary; × 50.

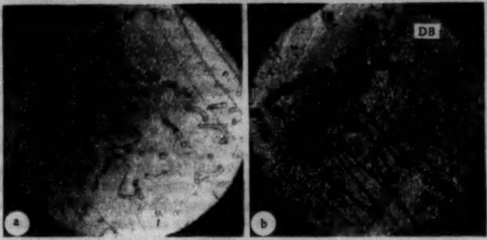

Fig. 4. Antiphase boundaries and dislocations before (a) and after (b) movement of domain boundary (DB). Identical numbers indicate mirror-symmetric etch pits at dislocations.

tained its polarity and the antiphase-boundary pattern was the same as after the phase transition during cooling after crystal growth. In region II, the boundaries moved during enlargement of the domain wedge and all the antiphase boundaries were elongated in the direction of boundary movement, i.e., perpendicular to the boundary, while part of the boundary adhered to the domain wall (boundaries ABB'A and DCEFC'D', Fig. 3a, and boundary ABC, Fig. 3b).

The behavior of the individual antiphase boundaries during repolarization can also be studied by comparing mirror-symmetric fracture surfaces: Half the crystal is retained as a specimen and the other half is subjected to repolarization. Figure 4 is an example of such a pair of fracture surface. The movement of one boundary of a newly developing domain was checked at an aggregate of growth dislocations. The second domain boundary (outside the picture) moved in the direction indicated by the arrow. As a result of its movement, the curved boundaries became straight. The dislocations free of antiphase boundaries remained the same as after the domain boundary passed through them (Fig. 4b, dislocation 1). The antiphase boundaries, a considerable proportion of which had a similar orientation in the (001) plane to the boundaries of the newly developing wedge, were rearranged in such fashion that individual antiphase boundaries changed direction (Fig. 4b, antiphase boundaries at dislocations 2-3 and 4-5).

The domains of the displaced component undergo retrogression with respect to the growing component and are converted from bands to thin wedges in the (001) plane. In this case, the antiphase boundaries adhering to the walls of the narrowing wedge usually retain their orientation along the wedge walls (Fig. 5a) After complete displacement of one component the newly developing monodomain region (of one polarity) acquires an unusual antiphase-boundary pattern as a result of a reaction of type (5): The fracture surfaces match along the annihilation sites of the displaced-component domain boundaries (Fig. 5b).

It follows from the above examples of the changes in domain structure during repolarization of gadolinium molybdate that adhesion of the antiphase boundaries to the domain boundaries is characteristic of their interaction. Regions in which there has been no movement of domain boundaries of the types $(\alpha_+|\gamma_-)$, etc. have free antiphase boundaries of the $(\alpha_+|\beta_+)$ and $(\gamma_-|\delta_-)$ types, both closed (Fig. 2a) and terminating at dislocations (Fig. 2b, semiloops 5). If the antiphase boundaries have a complex pattern, it can be concluded that they have acquired it as a result of interaction with the moving antiparallel-domain boundaries, regardless of whether these boundaries are retained at the time of the observations (compare loop ABCDEFJHI, Fig. 2a, which joins two nearby dislocations, and Fig. 5b).

The behavior of the antiphase boundaries depends on their orientation with respect to the moving domain boundary. Boundaries located along the domain walls undergo the greatest rearrangement. A typical pattern is shown in Fig. 6a-d. The antiphase-boundary semiloop fixed at dislocations 1-2 adheres to the domain boundary passing through the loop and is drawn along by it. If the next loop,

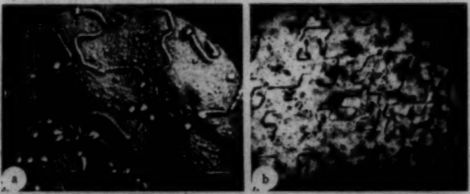

Fig. 5. Antiphase boundaries of regions becoming single-domain under the action of mechanical compressive stress along the [010] direction, × 50. a) Boundaries near narrowing domain wedge; b) boundaries after annihilation of several domain boundaries.

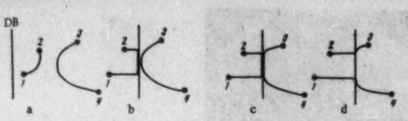

Fig. 6. Successive stages of movement of domain wall (DW) through half-loops formed by antiphase boundaries fixed at dislocations (1, 2, 3, and 4).

fixed at dislocations 3-4, enters the vicinity of the combined boundary, which is of the type $(\alpha_+|\beta_+;\ \beta_+|\delta_-)$, the reaction

$$(\alpha_+|\beta_+;\ \beta_+|\delta_-)+(\delta_-|\gamma_-)=(\alpha_+|\gamma_-) \tag{6}$$

apparently results in: a) annihilation of the combined and antiphase boundary and restoration of the initial domain boundary; b) paired combination of the remnants of the antiphase boundaries and consequent exchange of the host dislocations; c) formation of new protuberances (adhering to the walls) as a result of the presence of unreacted portions of the initial antiphase boundaries. It is clear that the overall pattern of the rearranged antiphase configurations depends on the relative positions of the dislocation pairs giving rise to the boundaries and that the antiphase boundaries of several pairs of dislocations can be exchanged simultaneously at a moving domain boundary.

It has been shown[6] that gadolinium molybdate specimens do not crack and can withstand up to 10^9 repolarization cycles if domain-wall movement occurs in a limited volume, so that the boundary does not leave this region and hence no new domains are formed. The advantages of this empirically selected regime become understandable if we take into account the reaction among the domain boundaries, antiphase boundaries, and dislocations shown in Eq. (6) (Fig. 6). Most of the antiphase boundaries adhering to the domain boundary obviously follow the latter only during the first half-cycle of its movement, when reactions of type (6) occur at it. When rearrangement of the antiphase boundaries and dislocation exchange is complete and the antiphase boundaires are elongated in the direction of domain-boundary movement, the same rearranged antiphase boundaries, fixed at dislocations (and other defects) follow the domain boundary and react during all subsequent domain-wall movement cycles.

Our investigation thus showed that the effects of the interaction of antiphase boundaries with domain walls and dislocations apparently govern the specific properties of nonintrinsic ferroelectrics of the class in question (including increased sensitivity of electrical properties to the real crystal structure). It is understandable that the dislocation configurations produced at the phase-transition point as a result of crystal growth and cooling to a considerable extent determine both the configuration of the antiphase boundaries and the possible reactions between the antiphase boundaries and domain boundaries, i.e., the macroscopic repolarization characteristics.

The authors wish to express their deep gratitude to A. P. Levanyuk and D. G. Sannikov for their helpful discussion of our results and their valuable comments.

After this article was submitted, we learned of the study made by Barkley and Jeitschko,[11] who also investigated domain boundaries, antiphase boundaries, and dislocations in crystals of rare earth molybdates. These authors had an etchant that showed the antiphase boundaries only in domains of one sign, so that a number of their conclusions are speculative and do not agree with our data.

---

1) We are using the notation S_4^2 so as not to confuse the twinning axis with the C_2 axis, which is retained in the C_{2v}^8 group.

[1] V.L. Idenbom, Izv. Akad. Nauk SSSR, Ser. Fiz., 24, 1180 (1960).
[2] E. T. Keve, S. C. Abrahams, and J. L. Bernstein, J. Chem. Phys., 54, 3185 (1971).
[3] W. Jeitschko, Acta. Crystallogr., B28, 60 (1972).
[4] Kh. S. Bagdasarov, G. A. Bogomolova, A. A. Kaminskii, V. A. Meleshina, T. M. Prokhortseva, and L. A. Shuvalov, Izv. Akad. Nauk SSSR, Ser. Fiz., 35, 1849 (1971).
[5] A. Kumada, H. Jumoto, and S. Ashida, Proceedings of the Second International Meeting on Ferroelectricity, Kyoto (1969), p. 351.
[6] J. R. Barkley, L. H. Brixner, E. M. Hogan, and R. K. Waring, Ferroelectrics, 3, 191 (1972).
[7] V. L. Indenbom, in: Physics of Crystals Containing Defects: Proceedings of a Symposium on the Theory of Defects in Crystals and Radiation Damage [in Russian], Vol. 1, Akad. Nauk GSSR, Tbilisi (1966).
[8] V. A. Meleshina, Kristallografiya, 16, 557 (1972) [Sov. Phys.-Crystallogr., 16, 475 (1971)].
[9] A. Savada and R. Abe, Japan. J. Appl. Phys., 8, 202 (1969).
[10] I. Bohm and H. D. Kursten, Kristall und Technik, 6, 213 (1971).
[11] J. R. Barkley and W. Jeitschko, J. Appl. Phys., 44, 938 (1973).

High-temperature phase transitions in crystals of Rb $(D_xH_{1-x})_2PO_4$

V.A. D 'yakov, V.A. Koptsik, I.V. Lebedeva, A. V. Mishchenko, and L. N. Rashkovich

M. V. Lomonosov Moscow State University

(Submitted August 1, 1972; resubmitted October 12 and November 20, 1972)
Kristallografiya, 18, 1227-1233 (November-December 1973)

It is shown that RbH_2PO_4 crystals experience phase transitions of the first kind at 93 and 115°C. The heat of the transition is 1500 and 50 cal/mole respectively. The molar volume increases by 1.8% in the first transition. With increasing degree of deuterization the temperature of this transition falls to ~ 40°C. The low-symmetry phase formed in the first transition may exist for a long time in a dry medium at room temperature; with increasing humidity of the medium the time required for its transition into the tetragonal phase falls to a few minutes. The second transition is easily reversible, the structure of the crystal changing very little. No changes occur in the weight of the samples during the transitions.

Recently observed high-temperature phase transitions of the first kind in KH_2PO_4, KD_2PO_4, and RbH_2PO_4 crystals have provided new information as to the role of hydrogen bonds in ferroelectric crystals of the KH_2PO_4 group.[1-4] It was shown in ref. 1, in particular, that above the transition temperature the lines characteristic of the hydrogen bonds vanished from the infrared spectra. In addition to this, at this temperature the activation energy of the electrical conductivity changed sharply.[2] It was suggested in ref. 1 that during the high-temperature phase transition the hydrogen bond ruptured and the protons were drawn to the upper and lower oxygens of each PO_4 structural tetrahedron, or even jumped over into the planes of the faces of the tetrahedron. No systematic study of these high-temperature transitions has yet been carried out.

In this paper we shall present the results of fresh study of the behavior of tetragonal $Rb(D_xH_{1-x})_2PO_4$ $(0 \le x \le 0.9)$ crystals between room temperature and 150°C. Single crystals were grown by the method described in ref. 5. The degree of deuterization was determined to an accuracy of ± 0.02.

High-temperature transitions had earlier been observed in RbH_2PO_4 at 86 and 175°C. We ourselves studied the first of these.

Visual observation was carried out by means of a binocular MBS-3 microscope, its object table accommodating a small furnace, enabling the sample temperature to be maintained to an accuracy of ±2°. The rate of heating could be varied from 1 to 10 deg/min. Samples of cross section 5×5 mm and under were studied by transmission in the direction of the crystallographic axes in ordinary and polarized light. On gradual heating, the crystals first revealed microscopic cracks in the form of dark spots; these quickly became more evident, and then intensive cracking of the crystal set in, making it completely opaque. The temperature at the onset of cracking (the appearance of spots) did not depend on the rate of heating the samples. The temperature corresponding to the onset of cracking was considerably affected by the size of the samples and the part of the single crystal from which they had been cut. Furthermore, it was considerably easier to detect the onset of cracking in the thicker samples than in the thin ones, and it was in fact detected at a lower temperature. In plates ~ 0.2 mm thick it was impossible to detect the appearance of the "spots", and the transformation temperature was correspondingly high. Figure 1 illustrates the results of experiments as to the effect of the degree of deuterization on the temperature corresponding to the onset of cracking. The thickness of the samples was of the order of 1 mm.

Independently of the orientation of the samples in the furnace, the system of cracks in the crystal always formed a group of planes parallel to the optic axis of the crystal.

Examination of the conoscopic pattern (the sample in the furnace being illuminated with a laser beam) showed that, within the limits of experimental error, the sample remained uniaxial up to the point that it was completely clouded over.

The x-ray investigations were carried out by the powder method in a URS-50IM instrument with a heater attachment. We used Cu Kα radiation. Samples with degrees of deuterization x = 0 and 0.85 were prepared in the form of pressed blocks 15×15×5 mm in size. The temperature was changed in steps and held constant to an accuracy of ± 0.2°C. The reflections were recorded in the angular range $2\theta = 20\text{-}60°$. Typical curves are shown in Fig. 2. We see from the figure that the x-ray diffraction patterns sharply reveal a change in sample structure. This process takes place in two stages. For the RbH_2PO_4 crystals a new group of lines appears in the range $2\theta = 38\text{-}41°$ between 100 and 110°C; on the x-ray diffraction pattern taken at 120°C a new line occurs at d = 3.68 Å, while the (200) reflection has vanished. In the tetragonal $Rb(D_{0.85}H_{0.15})_2PO_4$ crystals the corresponding temperatures are 90 and 100°C. Further heating the samples (to 150°C) makes no difference in the form of the x-ray diffraction patterns. The new structure formed at ~100°C is metastable at room temperature and apparently has a reduced symmetry (Fig. 1 compares the corresponding x-ray diffraction patterns with those of the monoclinic phase). In

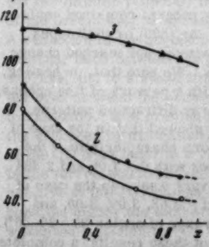

Fig. 1. Effect of the degree of deuterization on the temperature corresponding to the onset of sample cracking (1), the temperature of the large endothermic effect A (2), and the temperature of the small endothermic effect B (3).

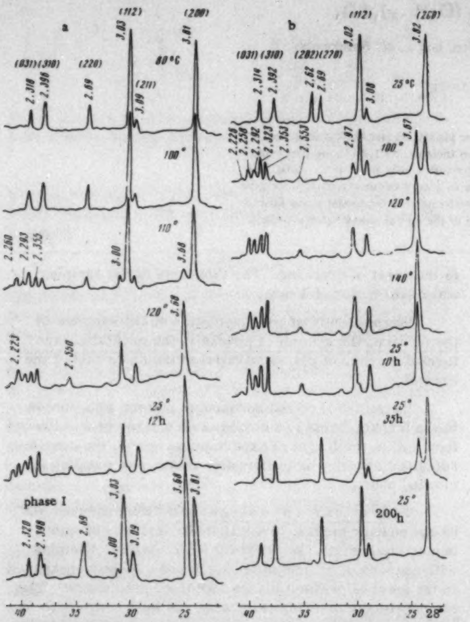

Fig. 2. Debye patterns of the samples recorded at different temperatures. a) RbH_2PO_4; b) $Rb(D_{0.85}H_{0.15})_2PO_4$. The recording temperature is indicated above each curve, together with the time of holding the sample after cooling it to room temperature.

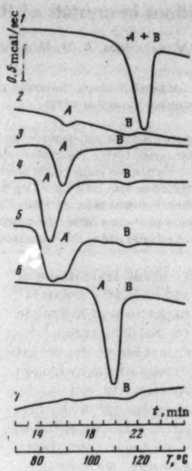

Fig. 3. Thermograms of RbH_2PO_4 taken at different times after previous heating. The samples were stored at room temperature. 1) First heating; 2) 4; 3) 5; 4) 16; 5) 24; 6) 350; 7) 100 h over P_2O_5.

air at room temperature there is a gradual transition of the low-symmetry into the original tetragonal phase; in contrast to the changes observed on heating, all the new reflections vanish simultaneously.

We found that, if the RbH_2PO_4 powder heated to 120°C is held after cooling for 30 min in saturated water vapor, its x-ray diffraction pattern indicated a complete transition into the tetragonal phase.

On recording diffraction patterns from single-crystal RbH_2PO_4 plates (z and x cuts) we found that, after heating the samples to 120°C, with a subsequent period of holding over H_2O, the form of the x-ray paterns remained unaltered; as before, reflections of the (h00) or (00*l*) types (h = 2n, *l* = 4n) were recorded without any marked change in their half-width and intensity. We note that, on heating, the sample becomes covered with a network of fine cracks, but remains one piece. The x-ray diffraction patterns recorded directly after heating showed that in the case of the x cut nearly all the reflections characteristic of the powder appeared except the lines with d = 3.09 and 2.854 Å, the latter being in any case very weak. In the case of the z cut only reflections with d = 3.68, 3.09, 3.00, and 2.355 Å were recorded (in the range of angles $2\theta = 20\text{–}40°$). We are as yet unable to interpret these results; a complete x-ray structural investigation with special recording conditions would be required for this.

It is interesting to note that the x-ray diffraction pattern of monoclinic crystals of $Rb(D_{0.9}H_{0.1})_2PO_4$ (phase I in terms of ref. 5) recorded at room temperature is almost identical with the x-ray diffraction patterns of the tetragonal phases heated above the transition temperature (Fig. 1). As noted in ref. 5, phase I is also metastable at room temperature and gradually passes into the tetragonal form.

The sample density measurements were effected by hydrostatic weighing in toluene. The density of RbH_2PO_4 was 2.879 ± 0.005 and that of $Rb(D_{0.85}H_{0.15})_2PO_4$ – 2.892 ± 0.005 g/cm^3. After heating the samples to 120°C and cooling in a dry medium the density was 2.827 ± 0.005 and 2.849 ± 0.005 g/cm^3 for samples with x = 0 and 0.85, respectively. Thus in the course of the phase transition the density falls by $1.80 \pm 0.35\%$ (x = 0) and $1.48 \pm 0.35\%$ (x = 0.85). Storing the samples in air leads to an increase in density to the original value. We also note that the density of the phase I samples (according to ref. 5) is practically equal to the density of the deuterized tetragonal crystal heated to 120°C.

The thermal analysis was carried out in a differential scanning calorimeter, the "Termoflex". The sensitivity of the calorimeter was varied over the range 10-40 mcal/sec. The accuracy of temperature recording was ± 0.2°C. The samples included both fragments of crystals and crushed powder 10-20 mg in weight; the loss of weight was monitored to an accuracy of 0.05 mg (≈ 0.5 wt.%). The rate of heating and cooling was 5 deg C/min. As a standard we used Al_2O_3. Heating was carried out both in air and in water vapor. In all the experiments over the temperature range of interest no changes in the weight of the samples were observed (within the limits of experimental error indicated).

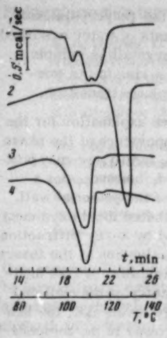

Fig. 4. Thermograms of RbH_2PO_4 taken in air (1,2) and in a water-vapor atmosphere (3,4). The dislocation density in the samples corresponding to curves 1, 3 is two orders of magnitude higher than in the case of curves 2 and 4.

The thermograms show two endothermic effects: a large one (A) of about 1.5 kcal/mole and a small one (B) at a slightly higher temperature (~50 cal/mole). The B effect is reversible but is often masked by the A effect on the heating curves.

The magnitude and temperature of appearance of the A effect on second heating depends on the conditions of storing the samples. Figure 3 illustrates this fact for single-crystal samples with x = 0. If the samples are stored in air at room temperature after the first heating, at least ~ 4 h holding are required for this effect to appear. If the samples are stored in a dry medium the effect fails to appear even after several days storage (lower curve in Fig. 3). An analogous result is obtained if the samples are stored at high temperature (~ 60°C). On the other hand, if after heating to 130°C the crystal is placed in a moist medium (over a water surface at 20°C), a few minutes are sufficient for the original magnitude of the effect to be restored.

The form of the thermograms recorded in air is greatly affected by the nature of the samples, whether these are single-crystal fragments or powder obtained by preliminary crushing of the crystal. In the first case the results are irreproducible if there is any difference in the defect content of the samples. The reproducibility becomes good if the thermograms are recorded in an atmosphere of water vapor, as in Fig. 4. In the second case reproducible results can only be obtained if the crushing is carried out in a dry medium (in a P_2O_5 dessicator). We note that none of the foregoing pertains to the B effect; its magnitude and temperature are independent of the factors discussed.

The manner in which the temperature corresponding to the onset of the two endothermic effects depends on the degree of deuterization is shown in Fig. 1 [the thermograms were recorded in saturated (below 100°C) water vapor]. The magnitude of the B effect hardly changes at all on deuterization. The A effect in samples with x = 0.8-0.9 is roughly half as large as in the nondeuterized samples.

The results of the thermal analysis show that two phase transitions are occurring within these samples. The first transition is described in the literature as a transition at 86°C (in our own experiments, using samples with x = 0, it occurred at 93°C). The second is a reversible transition (taking place at 115°C for nondeuterized samples) not earlier studied.

The phase formed after the first transition is metastable at room temperature and gradually transforms into the original tetragonal phase. The x-ray data indicate that the formation of this high-temperature phase takes place in two stages.

The phase formed after the second transition does not exist at room temperature. The fact that the x-ray diffraction patterns of samples heated above 130°C remain intact after cooling the samples indicates that this phase differs in only small structural details from the first.

The dielectric measurements of the crystals were carried out with the help of an ac R-5004 bridge at a frequency of 1 kHz. We studied RbH_2PO_4 plates of the x and z cut type (5×4×0.5 mm). The sample holder was placed in a thick-walled hermetically sealed copper cylinder, kept in an oil thermostat. The temperature was stabilized to an accuracy of ±0.1°. The sample and holder were flooded with transformer oil.

At room temperature $\varepsilon_1 = 45 \pm 1$, $\varepsilon_3 = 32 \pm 1$ (data for five samples). Heating first led to a slight fall in ε (about 3%); at 92±1°C the electric constant fell sharply by 35-40% of the original value; on further heating the constant ε rose slightly. Cooling the samples led to a slight reduction and then a slight increase in ε. After 10-15 days of storing the sample in oil the dielectric constant rose to almost its original value. During the phase transition, at the same time as the fall in ε there was an increase in the tangent of the dielectric loss angle (about two orders of magnitude). The activation energy of the electrical conductivity was 0.45 eV before the phase transition and about 1 eV above it.

Discussion of results. We showed earlier that the first of our high-temperature phase transitions was accompanied by a considerable change in the structure of the tetragonal phase and by the cracking of the crystal. The relationship between this, the degree of deuterization, and the water-vapor content of the atmosphere indicates that the transition is largely due to the behavior of the hydrogen (deuterium) in the structure of the crystal.

It is well known that in the structure of crystals of the KH_2PO_4 family the protons lie on lines connecting the closest oxygen atoms of neighboring PO_4 tetrahedra. As a result of the tunneling mechanism in a potential well with the two minima proposed in refs. 1, 4, and 6, the position of the proton may be spread out along the line of the bond. A reduction in the degree of tunneling should lead to a stronger bond between the proton and one of the neighboring oxygens, and to a weakening of the hydrogen bond, i.e., the bond between the proton and the oxygen of the other tetrahedron. It is precisely this which occurs on replacing hydrogen by deuterium. The increase in the strength of the OD bond leads to a rise in the Curie temperature. In the ferroelectric phase, in fact, the protons are ordered relative to the PO_4 groups, and the stronger the OH (OD) bond the higher the temperature at which this may be weakened sufficiently. On the other hand, further increase of the temperature should lead to the breakdown of the

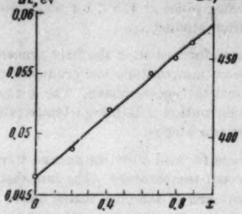

Fig. 5. Effect of the degree of deuterization on the splitting energy of the ground state in the asymmetrical potential well with a double minimum.

hydrogen bonds. In the deuterized crystals the hydrogen bond is weakened; hence the temperature at which the OD...O bond breaks should be lower than in the case of the OH...O bond.

The results of the present investigation may be largely explained on the foregoing basis.

The nonsimultaneous two-stage rearrangement of the proton subsystem may be associated with the fact that the structure of the crystal at the level of this subsystem is more complicated than generally accepted. The prolonged metastable existence of the high-temperature phase is due to the slowness of the diffusion processes taking place in the solid phase.

It is logical to assume that water vapor initiates the restoration of the hydrogen bonds in this phase. Being adsorbed on the surfaces and the microcracks of the crystal and diffusing into the latter, the water weakens the bond of the protons with the neighboring oxygens of the PO_4 tetrahedra. This weakening of the (OH) bond explains the fall in the temperature of the transition from the tetragonal to the high-temperature phase, which is observed on recording the thermograms in a water-vapor atmosphere.

The difference between the thermograms of the single-crystal and polycrystalline samples is associated both with the greater defect content of the polycrystalline material and with the different amounts of water adsorbed throughout the thickness of the polycrystalline sample. These circumstances should lead to a rise in the temperature and to a diffuseness of the phase transition.

In order to provide a qualitative explanation for the influence of deuterization on the temperature of the phase transitions in crystals of the KH_2PO_4 family, we may proffer the theory of Imry,[6] who assumed, however, not a steady-state structural asymmetry of the potential well, as in ref. 6, but a statistically distributed local asymmetry of the proton subsystem, not detected by x-ray diffraction (Chapter 12 in ref. 7). The main conclusions of the theory of ref. 6 remain intact within the framework of this modified model: The greater the asymmetry of the well and the greater the splitting of the energy levels ΔE, the less marked is the tunneling and the narrower is the temperature range in which it takes place.

Using the solution of the corresponding equation (Fig. 2 in ref. 2), the dependence of T_C on the degree of deuterization of the RbH_2PO_4 crystals,[8] and the data presented in Fig. 1, we calculated the value of ΔE as a function of the degree of deuterization (Fig. 5). This relationship is practically linear.

The authors wish to thank V. G. Vaks for interest in the work and for discussion of the results.

---

[1] J. Grünberg, S. Levin, I. Pelah, and D. Gerlich, Phys. Status Solidi, B49, 857 (1972).

[2] M. O'Keeffe and C. T. Perring, J. Phys. Chem. Solids, 28, 1086 (1967).

[3] E. Rapport, J. Chem. Phys., 53, 311 (1970).

[4] R. Blinc, D. E. O'Reilly, E. M. Peterson, and J. M. Williams, J. Chem. Phys., 50, 5408 (1969).

[5] A. V. Mishchenko and L. N. Rashkovich, Kristallografiya, 16, 1064 (1971) [Sov. Phys.–Crystallogr., 16, 940 (1972)].

[6] J. Imry, I. Pelah, and E. Wiener, J. Chem. Phys., 43, 2332 (1965).

[7] V. A. Koptsik and A. V. Shubnikov, Symmetry in Science and Art [in Russian], Nauka, Moscow (1972).

[8] E. N. Volkova, B. M. Berezhnoi, A. N. Izrailenko, A. V. Mishchenko, and L. N. Rashkovich, Izv. Akad. Nauk SSSR, Ser. Fiz., 35, 1858 (1971).

Relaxational internal friction in crystals of KH_2PO_4 with chromium added

S. A. Gridnev. L. N. Kamysheva, and N. F. Romanova
Voronezh Polytechnic Institute
Voronezh State University

(Submitted July 7, 1972; resubmitted October 11, 1972 and December 18, 1972)
Kristallografiya, 18, 1234-1239 (November-December 1973)

The internal friction of single crystals of potassium dihydrophosphate with chromium ions added was studied at vibration frequencies of the order for several hertz. A new relaxational internal-friction maximum was detected over the temperature range from −180 to −150°C, its amplitude and temperature depending on the additive concentration and the strength of the applied dc electric field. The results obtained are interpreted within the framework of the mechanism of the interaction of stationary domain boundaries with charged point defects.

One source of the loss of mechanical-vibration energy in ferroelectric crystals is interaction of domain boundaries with point defects. By varying the defect concentration through introduction of additives during crystal growth, it is therefore possible to study the mechanisms of the interaction between the defects and domain boundaries.

In continuing our previous investigation[1–3] of the characteristics of internal friction in various ferroelectric crystals, we studied the internal friction and shear modulus of potassium dihydrophosphate crystals over the temperature range from −190 to −140°C with different Cr^{3+} concentrations under the action of various external factors.

The internal friction and shear modulus were measured by the inverted torsional-pendulum method[4] at frequencies of from 1 to 20 Hz. This frequency range was selected on the basis of the following considerations. The relaxation time of the processes responsible for reorganization of the domain structure, which is controlled by diffusion of impurities and lattice vacancies, can be of the order of several seconds.[1] In this case, we can expect the appearance of a mechanical-loss maximum in the curve representing the internal friction as a function of temperature at a frequency of the order of several hertz. As the internal friction criterion Q^{-1}, we selected the logarithmic attenuation decrement divided by π. Our apparatus enabled us to measure the logarithmic attenuation decrement of the free oscillations of the pendulum system automatically, with a differential amplitude selector; the error was no more than 5%. The signal form was monitored with an S1-19 low-frequency oscillograph. The vibration period of the pendulum was measured with an electronic ChZ-4 frequency meter to within 0.1%. The apparatus working chamber was chilled to −190°C with liquid nitrogen; the temperature was raised and held constant with a nichrome heating element. Special measures enabled us to obtain a temperature gradient along the specimen length not exceeding $0.50\ \mathrm{deg \cdot cm^{-1}}$. All the measurements were made while raising the temperature at a rate of less than $0.5\ \mathrm{deg \cdot min^{-1}}$. The resultant thermoelastic deformations were at least an order of magnitude less than the amplitude of the specimen deformations used in the experiment ($\sim 5 \cdot 10^{-5}$). The pendulum drive was kept in a vacuum of $\sim 10^{-2}$ torr.

The KH_2PO_4 crystals, which were grown from aqueous solutions containing chromium ions as an impurity (in the form of the compound $CrCl_3 \cdot 6H_2O$, 0.001 mole%), had a nonuniform green coloration. The (100) and (010) faces were most intensely colored. Spectral analysis of specimens cut from portions of the crystal with different colorations showed that the weakly colored specimens contained 0.0054 mole% Cr^{3+} ($\sim 10^{23}\ M^{-3}$), while the dark green specimens contained 0.27 mole% ($\sim 10^{25}\ M^{-3}$). The crystals were sawed into bars 20 × 3 × 2 mm in size by the wetted-filament method; the bars were then rubbed with a damp cloth and polished with glycerol. In view of the fact that KH_2PO_4 crystals have materially different dielectric, piezoelectric, and elastic properties in the directions of the X and Z axes,[5] our investigations were conducted with two groups of specimens. The first group consisted of specimens whose longest axis was parallel to the ferroelectric Z axis of the crystal; the electrodes were applied to faces perpendicular to the X axis (Z sections). In the second group, the long axis of the specimen was parallel to the X axis and the electrodes were applied to faces perpendicular to the Z axis (X sections). Silver electrodes were vacuum-deposited on the largest faces of the specimens. The finished specimens were glued into brass holders with epoxy resin and the holders were inserted into the clamps of the apparatus.

The electrical boundary conditions are known to have a material influence on the internal friction in KH_2PO_4 crystals.[6] Experiments conducted at frequencies of the order of several Hz showed that the Q^{-1} level of short-circuited X-section crystals was 15–20% higher than that of disconnected specimens. In the ferroelectric phase, this effect was apparently due to the fact that, in the case of an isolated crystal (electrodes disconnected), domain repolarization under the action of mechanical stresses was hampered by the presence of depolarizing field, so that the contribution of the domain mechanism to the internal friction was reduced. The result of this effect was similar to that of a constant electric field on Q^{-1}. In those cases where no external field was applied to the specimens, all the curves were determined under electrode short-circuit conditions. Short-circuiting of the electrodes in Z-section specimens had no effect on Q^{-1}.

Exposure of the specimens to a varying field with a strength of $400\ \mathrm{V \cdot cm^{-1}}$ and a frequency of 50 Hz at a temperature near the Curie point for 10 min caused no change (within the limits of experimental error) in the Q^{-1} background. As a result, our subsequent measurements were made with specimens not subjected to preliminary "rejuvenation."

The temperature functions of internal friction Q^{-1} and the shear modulus G for Z- and X-section specimens are shown in Figs. 1 and 2. It can be seen that, in addition to the known peaks at the phase-transition temper-

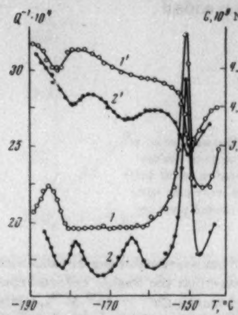

Fig. 1. Temperature functions of Q^{-1} and shear modulus G of Z-section specimens of KH_2PO_4 crystals at frequency of 6.2 Hz. 1, 2) Q^{-1}; 1', 2') G; 1, 1') pure crystal; 2, 2') chromium ion concentration of ~ 10^{24} m^{-3}.

ature (− 150°C) and the temperature corresponding to "freezing" of the domain structure[6,7] (− 180°C), the $Q^{-1}(T)$ curves determined for specimens with Cr^{3+} added displayed a new Q^{-1} peak in the temperature interval between them; the amplitude and temperature of which depended on the additive concentration. The temperature function of the shear modulus in the vicinity of the new Q^{-1} peak underwent a characteristic change only when the specimens contained Cr^{3+} ions. It should be noted that the anomalous behavior of Q^{-1} and G occurred for specimens of both sections; the amplitude of the Q^{-1} peaks and the changes in G were also identical for different sections.

The different Q^{-1} background levels for curves 1 and 2 in Fig. 1 and curves 1-3 in Fig. 2 cannot be attributed solely to the different chromium ion concentrations, since the measurements were made with different specimens. In this case, different degrees of specimen compression in the clamps, differences in specimen centering, the influence of the cement, etc., could have led to a change in the instrumental background. In discussing the experimental results, we will consider not the absolute value of Q^{-1} and the behavior of the Q^{-1} background but only the excess above the background. Since the Q^{-1} background varies monotonically with temperature,[3] the peaks Q^{-1}_m could be isolated by subtracting the instrumental and specimen background in processing the measurement results.

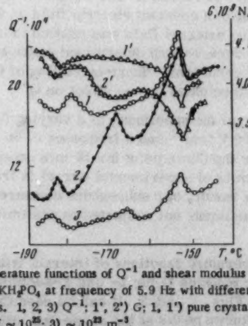

Fig. 2. Temperature functions of Q^{-1} and shear modulus G of X-section specimens of KH_2PO_4 at frequency of 5.9 Hz with different chromium ion concentrations. 1, 2, 3) Q^{-1}; 1', 2') G; 1, 1') pure crystal; 2, 2') chromium ion content of ~ 10^{25}; 3) ~ 10^{23} m^{-3}.

Because of the lack of experimental data, the present article will not consider the characteristics of the internal-friction peaks at the Curie point and the "domain-freezing" temperature but will be limited to examination of the new Q^{-1} maximum associated with addition of Cr^{3+} ions to KH_2PO_4.

The displacement of this Q^{-1} peak by 15° toward higher temperatures when the specimen vibration frequency was increased from 2.4 to 15.8 Hz indicated its relaxational character. Assuming a single relaxation time, the temperature displacement of the Q^{-1} peak with varying frequency was used to calculate the activation energy of the process, yielding 0.11 ± 0.01 eV. Assuming that the temperature function of the relaxation time is described by the well-known Arrhenius equation $\tau = \tau_0 \exp(H/kT)$, experimental data yield $\tau_0 \sim 10^{-7}$ sec. The linear function ln $\tau(1/T)$, plotted from experimental results, indicates that the process responsible for the peak is thermally activated and has a single relaxation time.

A constant electric field applied parallel to the polarization axis of an X-section specimen markedly reduced the amplitude of the peak in question and shifted it toward lower temperatures (Fig. 3). The field also attenuated the peaks Q^{-1}_m at the Curie point and in the vicinity of the "domain-freezing" temperature. The inhibition of the Q^{-1} maximum at −180°C by an external electric field confirms the hypothesis that it is of domain origin.[6,8]

As noted above, the new relaxation peak in Q^{-1} was observed only in KH_2PO_4 specimens containing Cr^{3+} ions and was absent in pure specimens. Measurements made at frequencies of the order of 1 kHz should show the peak to be shifted into the temperature region corresponding to the paraelectric state. The absence of a relaxation maximum in tan δ in the para-phase in control dielectric measurements and the noticeable dependence of the amplitude and temperature of the peak Q^{-1}_m on $E_=$ indicate that it is related to the presence and state of the domain structure. The internal-friction maximum under consideration is evidently produced by the interaction of point defects (chromium ions) and 180-degree domain boundaries.

The model of the interaction of stationary domain boundaries with charged point defects proposed previously[9] can be employed to account for the nature of this peak. Although this model was developed for 90-degree domain boundaries, it was subsequently shown[10] that it is also applicable to 180-degree domain boundaries. In conformity with this mechanism, a bound electric charge develops as a result of the piezoeffect when shear stresses act on the domain boundaries; charges of opposite sign develop on adjacent walls. The development of bound charges is accompanied by appearance of an electric field. The compensation of this field resulting from the electrical conductivity produced by movement of the chromium ions and their diffusional redistribution in the bound-charge field leads to a change in the electric field within the domain. The field decreases in strength with time,

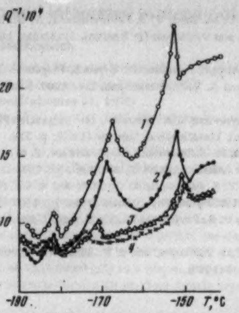

Fig. 3. Dependence of Q^{-1} on temperature for X-section specimen of KH_2PO_4 crystal at frequency of 5.9 Hz. Chromium ion concentration of $\sim 10^{25}\ m^{-3}$. 1) $E_= = 0$; 2) 0.8; 3) 1.5; 4) 2 $kV \cdot cm^{-1}$.

which is accompanied by additional deformation of the crystal as a result of the reverse piezoeffect, i.e., mechanical relaxation occurs. The internal friction in this case can be found from the equation[10]

$$Q^{-1}=\frac{4q^2 d_{15}^2 CD}{\pi^2\varepsilon^2\varepsilon_0^2 kTS}\frac{\omega\tau^2}{1+\omega^2\tau^2}, \tag{1}$$

where the relaxation time τ is defined by the expression

$$\tau=\frac{1}{D}\left(\frac{\pi^2}{L^2}+\frac{q^2C}{\varepsilon\varepsilon_0 kT}\right)^{-1} \tag{2}$$

Here q is the charge on the chromium ion, C is the ion concentration, D is the diffusion constant, L is the domain width, S is the yield factor for shear deformation, d_{15} is the piezomodulus, ε is the dielectric permeability, ε_0 is the electric constant, k is Boltzmann's constant, and T is the absolute temperature.

Equations (1) and (2) are valid on condition that the interaction energy for a point defect and a domain boundary is substantially less than kT, i.e.,

$$q\rho L/kT\varepsilon\varepsilon_0 \ll 1, \tag{3}$$

where $e = \sqrt{2}\sigma d_{15}$ is the bound-charge density at the domain boundary and σ is the shear stress. Assuming[5] $L \sim 10^{-7}$ m, $d_{15} = 4 \cdot 10^{-11}\ C \cdot N^{-1}$, $q = 4.8 \cdot 10^{-19}$ C, T = 108°K, and $\varepsilon \sim 10^3$, we obtain $3 \cdot 10^{-2} \ll 1$, i.e., Eq. (3) is well satisfied.

According to Eqs. (1) and (2), the amplitude of the internal-friction peak at small point-defect concentrations is proportional to the concentration; it is independent of concentration when the latter is large. The concentration can be considered small if $(q^2L^2C/\pi^2\varepsilon\varepsilon_0 kT) < 1$, and large if this inequality is reversed. Our experiments were conducted with specimens having a chromium ion concentration of $\sim 10^{23}$ or $\sim 10^{25}\ m^{-3}$. We obtain $0.4 < 1$ for specimens of the first type and $40 \gg 1$ for those of the second type; a concentration of $\sim 10^{23}\ m^{-3}$ can therefore be considered moderate and that of $\sim 10^{25}\ m^{-3}$ large. We experimentally observed (Fig. 2) an increase in Q_m^{-1} with rising defect concentration of less than two orders of magnitude (a factor of 3.2), the latter being the figure that should have been observed at small concentrations. This confirms previous estimates that $C \sim 10^{23}\ m^{-3}$ corresponds to the transition region from small to large concentrations. At a concentration of $\sim 10^{25}\ m^{-3}$, the internal fraction should be at the saturation level. This conclusion is borne out by estimates of the peak amplitudes at both concentrations, which yield values of the same order of magnitude, $Q_m^{-1} \sim 10^{-4}$, which is in good agreement with experimental results.

According to Eq. (2), the relaxation time is inversely proportional to the concentration when the defect concentration is sufficiently large. The dependence of τ on T can be defined in terms of the quantities T, ε, and D in Eq. (2). Under our conditions, the temperature function of τ is governed principally by the term $D = D_0 \exp \cdot (-H/kT)$, since $H/kT \gg 1$; the dielectric permeability ε of KH_2PO_4 crystals over the temperature range in question is virtually independent of temperature ("plateau" region), i.e., it can be assumed that $\tau = \tau_0 \exp(H/kT)$. It should be noted that the internal-friction measurements at different frequencies also confirm this $\tau(T)$ relationship. When the chromium-ion concentration is increased, the internal-friction peak should be shifted toward lower temperatures, which is in agreement with the experimental data (Fig. 2).

This model can also be used to account for the change in the amplitude of the maximum Q_m^{-1} and its position on the temperature scale when a traveling electric field was applied to the specimen. According to Eq. (1), the amplitude of the Q^{-1} peak is proportional to the square of the distance between the domain boundaries L^2, which varies under the action of an electric field. It has been shown[11] that the domains in a KH_2PO_4 crystal break up as $E_=$ is increased from zero to 5 $kV \cdot cm^{-1}$. Since the field strength did not exceed 2 $kV \cdot cm^{-1}$ in our experiments, it was sensible to expect a decrease in the Q^{-1} peak with increasing $E_=$, a phenomenon that was actually observed experimentally (Fig. 3). It can also be seen from Fig. 3 that the internal-friction peak was displaced toward lower temperatures by 7° when a field with $E_= = 2\ kV \cdot cm^{-1}$ was applied to the crystal. This can be explained by the fact that, when the distance between the domain walls decreases, the relaxation time τ is reduced and this, for the reasons considered above, should lead to displacement of the Q^{-1} peak toward lower temperatures. An estimate made with Eq. (2), on the assumption[11] that the domain width changes to $0.5 \cdot 10^{-8}$ m in a field with $E_= = 2\ kV \cdot cm^{-1}$, yields a displacement of ~ 9°, which is of the same order of magnitude as the measured shift.

According to the model under consideration, the Q^{-1} relaxation peak should be observed for both types of KH_2PO_4 sections, since, when external shear stresses act on X- and Z-section specimens, the bound charges at the domain boundaries are due to the action of the same piezomodulus d_{15}. The experimental results presented in Figs. 1 and 2 confirm the absence of any dependence of the Q^{-1} peak on orientation.

CONCLUSIONS

1. A new relaxation peak appears in the curve representing internal friction as a function of temperature for KH_2PO_4 single crystals when Cr^{3+} ions are added.

2. The behavior of this peak with varying chromium-ion concentration, vibration frequency, and constant electric-field strength can be explained by the interaction of point defects (chromium ions) and stationary domain boundaries.[9]

The authors wish to thank L. A. Shuvalov for his interest in this work and his discussion of the results.

---

[1] V. S. Postnikov, V. S. Pavlov, S. A. Gridnev, S. K. Turkov, and L. A. Shuvalov, Izv. Akad. Nauk SSSR, Ser. Fiz., 33, 1200 (1969).

[2] S. A. Gridnev, B. M. Darinskii, and V. S. Postnikov, Fiz. Khim. Obrabot. Mat., 5, 99 (1969).

[3] S. A. Gridnev, B. M. Darinskii, and V. S. Postnikov, in: Mechanisms of Relaxation Phenomena in Solids [in Russian], Nauka, Moscow (1972), p. 206.

[4] V. S. Postnikov, V. M. Lubé, V. S. Pavlov, and S. A. Gridnev, in: Prevention of Noise and Vibrations [in Russian], Stroiizdat, Moscow (1966), p. 407.

[5] F. Jona and D. Shirane, Ferroelectric Crystals, Pergamon (1962).

[6] L. A. Shuvalov and A. V. Mnatsakanyan, Izv. Akad. Nauk SSSR, Ser. Fiz., 29, 1974 (1965).

[7] A. V. Mnatsakanyan and L. A. Shuvalov, in: Relaxation Phenomena in Solids [in Russian], Metallurgiya, Moscow (1968), p. 518.

[8] L. N. Kamysheva, N. A. Burdanina, O. K. Zhukov, B. M. Darinskii, and L. N. Sizova, Izv. Akad. Nauk SSSR, Ser. Fiz., 34, 2612 (1970).

[9] V. S. Postnikov, V. S. Pavlov, S. A. Gridnev, and S. K. Turkov, Fiz. Tverd. Tela, 10, 1599 (1968) [Sov. Phys.—Solid State, 10, 1267 (1968)].

[10] V. S. Postnikov, V. S. Pavlov, and S. K. Turkov, J. Phys. Chem. Solids, 31, 1785 (1970).

[11] V. V. Gladkii, I. S. Zheludev, and E. V. Sidnenko, Izv. Akad. Nauk SSSR, Ser. Fiz., 33, 300 (1969).

Polarization and integrated intensity of x rays scattered by silicon crystals

N. M. Olekhnovich

Institute of Solid State and Semiconductor Physics,
Academy of Sciences of the Belorussian SSR

(Submitted December 25, 1972)
Kristallografiya, 18, 1240-1245 (November-December 1973)

Results given for measurements of the polarization ratio $(\rho_\parallel/\rho_\perp)$ (111 reflection) and the integrated intensity $(\rho_\perp)$ (111 and 333 reflections) of x rays scattered by silicon crystals of various degrees of perfection, which, according to the values of $\rho_\perp$, range over the whole region from a perfect crystal to an ideal mosaic crystal. The studies were done using Cu Kα_1 plane-polarized radiation (using the 333 Bragg reflection from a perfect Ge crystal). For the majority of the crystals studied, which covered the whole range of $\rho_\perp$, $\rho_\parallel/\rho_\perp > |\cos 2\vartheta|$ $(\rho_\parallel/\rho_\perp = |\cos 2\vartheta|$ corresponds to a perfect nonabsorbing crystal). A relation between $\rho_\parallel/\rho_\perp$ and $\rho_\perp$ was experimentally established. The analysis which we carried out showed that the theory of extinction describes the relation established only in a narrow range of $\rho_\perp$ values $(0.75\ \rho_{\perp c} < \rho_\perp \leq \rho_{\perp c})$ where $\rho_{\perp c}$ is the integrated intensity of the reflection for an ideal mosaic crystal.

It is well known that x radiation scattered by a crystal is always polarized to some degree. The degree of polarization is defined as $(1 - \rho_\parallel/\rho_\perp)$, where $\rho_\parallel$ and $\rho_\perp$ are respectively the integrated reflections for the parallel and perpendicular components of the electric vector of the unpolarized radiation incident upon the crystal. The ratio $\rho_\parallel/\rho_\perp$, called the polarization ratio, depends on the degree of perfection of the crystal of interest. It is known, for example, that for an ideal mosaic crystal $\rho_\parallel/\rho_\perp = \cos^2 2\vartheta$, while for a perfect nonabsorbing crystal $\rho_\parallel/\rho_\perp = |\cos 2\vartheta|$. For real crystals this ratio depends on the nature of the mosaic structure. In the approximation of the extinction theory it has been shown[1] that for real crystals with distinct mosaic structure the polarization ratio can be greater than for ideal nonabsorbing crystals, i.e., $\rho_\parallel/\rho_\perp > |\cos 2\vartheta|$. This is in qualitative agreement with the results of direct experimental measurements. Thus investigations of LiF crystals[2] (the 200 reflection) and Ge crystals[3] (the 111 reflection) used as monochromator crystals for Cu Kα_1 radiation have shown that the measured values of the polarization ratio for LiF is 0.722 with $\cos 2\vartheta = 0.707$ while for Ge $\rho_\parallel/\rho_\perp = 0.94$ with $\cos 2\vartheta = 0.888$.

Up to the present time there have been no systematic experimental studies of the x-ray polarization in real crystals, although this kind of study is of great interest both from the viewpoint of the structure of real crystals themselves and from the viewpoint of the development of a theory of x-ray scattering in imperfect crystals.

In the present work we have undertaken an investigation of the polarization of x radiation scattered by silicon crystals with varying degrees of perfection, which, according to the magnitudes of their integrated reflections, occupy the whole range from perfect up to ideal mosaic crystals. The measurements were done on silicon crystal plates cut along a (111) plane. Samples with a varying degree of perfection were prepared as follows. The initial plane-parallel silicon plates with a dislocation density of approximately 10^2 cm^{-2}, cut along a (111) plane, were subjected to plastic single or double bending across cylindrical or spherical surfaces with various radii of curvature and subsequently restored to their original shape. The plastic deformation of the plates was carried out at 1100°C in a purified argon atmosphere. Then from the plates subjected to this treatment we prepared samples for x-ray investigations using the usual methods (mechanical lapping and polishing, vacuum annealing, and chemical polishing). The precision of the (111) plane alignment was within ± 10'.

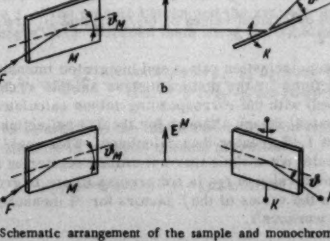

Fig. 1. Schematic arrangement of the sample and monochromator for azimuthal (a) and equatorial (b) placements of the sample.

To measure the polarization ratio and the intensity of the integrated reflection of the samples studied we used a plane-polarized source of Cu Kα_1 radiation. This source was the 333 reflection of a perfect germanium crystal, whose angle 2ϑ was 90° 2' so that the electric vector $\mathbf{E}^M$ of the reflected radiation is rigorously perpendicular to the scattering plane FMK (Fig. 1). The collimation system used ensured that we extracted only the Cu Kα_1 line and formed a quite narrow parallel beam, whose size at the sample was approximately 0.3× 0.3 mm.

The intensity measurements were done using a scintillation counter [NaI(Tl)] according to the number of counted pulses.

The aperture for the URS-50IM diffractometer which we constructed allowed us to carry out measurements of the integrated intensity with azimuthal and equatorial positioning of the sample. The schemes for the arrangement of the monochromator and the sample for azimuthal and equatorial arrangements are shown in Figs. 1a and 1b respectively. The measurements of the integrated intensity of the reflections from the samples were done by rotating the sample with the counter held still. To measure the integrated intensity $\rho_\parallel$ with the azimuthal arrangement, the sample was rotated at a constant angular velocity about an axis perpendicular to the electric vector $\mathbf{E}^M$ while for measurements of the integrated intensity $(\rho_\perp)$ with the equatorial arrangement of the sample it was rotated with the same velocity but about an axis parallel to $\mathbf{E}^M$.

TABLE 1. Experimental Values of the Polarization Ratio and Integrated Intensity of the Silicon Reflections

Sample No.	111			333	w_{111}, ′	w_{333}, ′	$N_d \cdot$cm^{-2}
	$\rho_\parallel/\rho_\perp$	$\rho_\perp \cdot 10^5$	$\rho_\perp/\rho_{\perp c}$	$\rho_\perp \cdot 10^5$			
1	0.866	4,30	0,127	1,06	—	—	0
2	0.886	5.08	0,151	1,43	2.62	1,66	$2 \cdot 10^5$
3	0,892	7.49	0,222	2.46	2.64	1.84	$2 \cdot 10^6$
4	0.924	9.52	0,282	3,39	4.33	2,18	$3 \cdot 10^6$
5	0.914	10,94	0.324	3,42	8,61	3.31	$5 \cdot 10^6$
6	0.927	10,35	0.307	3.52	7.61	3.50	$5 \cdot 10^6$
7	0.920	16,25	0.481	4.17	9.09	6,29	$1 \cdot 10^7$
8	0.925	16,40	0.486	4.27	8.97	7.47	—
9	0.916	17,06	0.506	4.27	9,79	8,95	—
10	0.888	19.4	0,574	4.37	6.80	4.71	—
11	0.863	21,5	0,636	4.77	34.1	23,60	—
12	0.841	22.2	0.657	4.73	10.7	9.49	—
13	0.796	29.7	0.878	4.74	30.9	29,0	—
14	0.785	30,2	0,894	4.78	47.2	34.2	—

The polarization ratio ($\rho_\parallel/\rho_\perp$) was determined from $\rho_\parallel$ and $\rho_\perp$ measured in relative units. The measurements of $\rho_\parallel$ and $\rho_\perp$ were carried out for 111 reflections with the following measurements sequence. Initially the integrated intensity of the reflection $\rho_\perp$ was measured with the equatorial arrangement of the sample, and then the sample was placed in the azimuthal arrangement and $\rho_\parallel$ was measured. After this a second measurement of $\rho_\perp$ was carried out. For both arrangements of the sample the counter was placed such that the maximum of the reflected intensity fell upon the same region of the crystal scintillator. In each sample position the measurements were repeated up to 10 times. The mean arithmetic error in the determination of $\rho_\parallel/\rho_\perp$ did not exceed 0.8%.

Absolute measurements of the integrated intensity $\rho_\perp$ of the 111 and 333 reflections and also their integrated widths (w) were carried out with the equatorial sample arrangement. The reflection curves for all of the samples were smooth and close to Gaussian; w was defined in the usual way ($w = \rho_\perp/I_{max}$). The integrated intensity was defined as the mean of the values obtained with the two arrangements of the sample relative to the monochromator, (m, −n) and (m, n). The intensities for these two sample positions differed very little.

To determine the absolute value of $\rho_\perp$ we measured the integrated intensity of the primary beam (I_0) incident upon the crystal studied. In measuring I_0 we used attenuating filters with an attenuation coefficient no more than 10.

The mean errors in the absolute measurements of $\rho_\perp$ for the 111 reflection were less than 1% and for the 333 reflection they amounted to 1 to 1.2%. In all we studied 14 samples. The measured results are presented in Table 1, in which the sample numbers are arranged in sequence of increasing integrated intensity of the 111 reflection. Sample 1 is a dislocation-free crystal. For samples 2-7 the last column of Table 1 indicates the dislocation densities estimated from etch pits. The dislocation densities in samples 8 to 14 could not be directly estimated due to their high values. However, we can assume that they increase with increasing sample number since the radii of the formers used in the plastic bending of the initial plates during sample preparation decreased in the same sequence.

In analyzing the results obtained we calculated the polarization ratio and intensity of the integrated reflection in the approximations of a perfectly absorbing and an ideal mosaic crystal.

According to the dynamical theory of x-ray scattering[4,5] the intensity of the integrated reflection of a perfect absorbing crystal (the case of symmetric Bragg reflection) for perpendicular polarization of the incident radiation can be determined from

$$\rho_{\perp D} = \frac{e^2}{mc^2} \frac{\lambda^2}{\pi V \sin 2\theta} |F_H| e^{-M} R_{H\perp}^y. \qquad (1)$$

The polarization ratio of this case can be written as

$$\rho_\parallel/\rho_\perp = |\cos 2\theta| R_{H\parallel}^y / R_{H\perp}^y, \qquad (2)$$

where $R_{H\parallel}^y$ and $R_{H\perp}^y$ are the Prins corrections, which take account of the effect of absorption during scattering from a perfect crystal respectively with parallel and perpendicular polarization of the incident radiation. $R_{H\parallel}^y$ and $R_{H\perp}^y$ can be calculated using tables.[6]

For an ideal mosaic crystal, according to the kinematic theory of scattering, the integrated intensity of the reflection is given by

$$\rho_{\perp c} = \left(\frac{e^2}{mc^2}\right)^2 \frac{\lambda^3 |F_H|^2 e^{-2M}}{2\mu V^2 \sin 2\theta}. \qquad (3)$$

Calculations of $\rho_{\perp D}$, $\rho_{\perp c}$, and $(\rho_\parallel/\rho_\perp)_D$ were carried out for room temperature, where the investigations were done. In making these calculations the atomic scattering factors were taken as $f_{111} = 11.12$ (ref. 7) and $f_{333} = 6.50$ (ref. 8); the dispersion correction was $\Delta f' = 0.2$, and the temperature factor was $B = 0.446$ Å^{-2}.

The calculated values of $(\rho_\parallel/\rho_\perp)_D$ and $\rho_\perp$ are given in Table 2.

The polarization ratios and integrated intensities of the reflections for the dislocationless sample (Table 2) agreed well with the corresponding values calculated using the dynamical theory although for the 333 reflection $\rho_{\perp exp}$ was about 1.4% greater than calculated. This could be because we did not include thermal diffuse scattering and the assumed value of f_{333} is not precise (there is great scatter in the values of the f factors for Si measured by different workers[9]).

The integrated intensity of the 333 reflection in the

TABLE 2

hkl	Experiment (sample 1)		Dynamical theory taking absorption into account				Kinematic theory	
	$\rho_\parallel/\rho_\perp$	$\rho_\perp\cdot 10^6$	$\rho_\parallel/\rho_\perp$	$\rho_\perp\cdot 10^6$	$R^y_{H\parallel}$	$R^y_{H\perp}$	$\rho_\parallel/\rho_\perp=\cos^2 2\vartheta$	$\rho_\perp\cdot 10$
111	0.866	4.30	0.8682	4.29	2.4095	2.4393	0.7728	33.76
333	—	1.06	—	1.045	—	2.2870		4.75

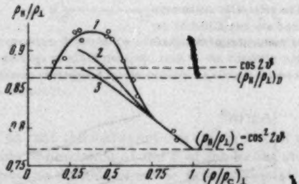

Fig. 2. Polarization ratio for scattered radiation as a function of the integrated intensity of the 111 silicon reflection. 1) Experiment; 2-3) calculation.

sequence of samples considered (Table 1) increases rapidly and, beginning for the 11th sample, reaches saturation with a value equal to $\rho_{\perp c}$ for an ideal mosaic crystal.

Attention is drawn to the fact that for the majority of the samples studied, occupying a broad range of $\rho_\perp$ values, the polarization ratio exceeds the values of $\rho_\parallel/\rho_\perp$ corresponding to a perfect crystal. As follows from analysis of Table 1 there is a definite functional relation (Fig. 2, curve 1) between the polarization ratio $\rho_\parallel/\rho_\perp$ and the integrated intensity of the 111 reflection. With an increase of the integrated intensity from the value $\rho_{\perp D}$ corresponding to a perfect crystal to values close to $\rho_{\perp c}$ the polarization ratio initially increases, reaches a smooth maximum, and then fairly rapidly drops. As $\rho_\perp$ approaches $\rho_{\perp c}$, $\rho_\parallel/\rho_\perp$ goes to a value $\cos^2 2\vartheta$ corresponding to an ideal mosaic crystal.

No unique correlation was observed between the polarization ratio and the integrated broad reflections (as follows from Table 1).

We will compare the experimental relation between the polarization ratio and the integrated intensity with the dependences of these quantities which follow from the extinction theory. In calculating the primary extinction we limit ourselves to the Darwin equation[10] and for the secondary extinction we use the Kuznetsov approximation.[11] Then the polarization ratio can be expressed in terms of the size L of the mosaic blocks and the average misorientation angle $\sqrt{2\pi\varphi^2}$ between them using the equation

$$\rho_\parallel/\rho_\perp=\cos 2\theta\,\frac{\mathrm{th}\,(x_0\cos 2\theta)}{\mathrm{th}\,x_0}\left[\frac{1+y_\perp-y_\perp^2L\mu/2\sin\theta}{1+y_\parallel-y_\parallel^2L\mu/2\sin\theta}\right], \tag{4}$$

while the intensity of the integrated reflection referred to the intensity of an ideal mosaic crystal is

$$\rho_\perp/\rho_{\perp\text{м}}=\mathrm{th}\,x_0/x_0(1+y_\perp-y_\perp^2L\mu/2\sin\theta), \tag{5}$$

where

$$y_\perp=gBQ_\perp\,\mathrm{th}\,x_0/\mu x_0,\quad y_\parallel=gBQ_\parallel\,\mathrm{th}\,(x_0\cos 2\theta)/\mu x_0\cos 2\theta,$$

$$x_0=\frac{L}{\sin\theta}\sqrt{Q_\perp\sin 2\theta/\lambda},\qquad B=2L\cos\theta/\lambda\sqrt{1+8\pi\varphi^2L^2(\cos^2\theta/\lambda^2)}.$$

The calculations of $\rho_\parallel/\rho_\perp$ and $\rho_\parallel/\rho_{\perp c}$ were carried out for a broad range of block sizes for two limiting values of the misorientation angle between them, 15" and ∞. The first case corresponds to the presence of primary extinction with the greatest possible value of the secondary extinction and the second case corresponds to only primary extinction (there is no secondary). These two cases allow one to judge the range of possible $\rho_\parallel/\rho_\perp$ values which follow from the extinction theory.

The results of the calculation for the cases considered are presented in Fig. 2 as curves 2 and 3 respectively. As we see, these curves (with $\rho_\perp/\rho_{\perp c} > 0.75$) nearly coincide with each other and with the experimental curve 1 for comparatively low values of the extinction. Here the tangent to the slope merges with the curve of interest at the point $\rho_\perp/\rho_{\perp c}=1$ and has the same value, equal to $\cos^2 2\vartheta\ \sin^2 2\vartheta$. For values of the integrated intensity $(\rho/\rho_c)_\perp$ less than 0.75, both of the calculated curves are substantially lower than the experimental one.

The results obtained show that the extinction theory only describes a small part of the observed curve for the polarization ratio of x rays scattered by a real crystal. This part of the curve corresponds to crystals with integrated intensities of the reflections which are little different from those for an ideal mosaic crystal.

We thank Academician N. N. Sirota, Academy of Sciences of the Belorussian SSR, for valuable advice.

---

[1] N. M. Olekhnovich, Kristallografiya, 14, 840 (1969) [Sov. Phys.–Crystallogr., 14, 724 (1970)].
[2] L. D. Jennings, Acta Crystallogr., A24, 472 (1968).
[3] N. M. Olekhnovich, Kristallografiya, 14, 261 (1969) [Sov. Phys.–Crystallogr., 14, 203 (1969)].
[4] W. H. Zachariasen, Theory of X-ray Diffraction in Crystals, Wiley, New York, (1945).
[5] P. B. Hirsch and G. N. Ramachandran, Acta Crystallogr., 3, 187 (1950).
[6] J. J. DeMarco and R. J. Weiss, Acta Crystallogr., 19, 68 (1965).
[7] L. D. Jennings, J. Appl. Phys., 40, 5038 (1969).
[8] J. J. DeMarco and R. J. Weiss, Phys. Rev., 137, A1868 (1965).
[9] N. N. Sirota, Acta Crystallogr., A25, 223 (1969).
[10] R. James, Optical Principles of the Diffraction of X Rays, Cornell (1948).
[11] A. V. Kuznetsov, Kristallografiya, 7, 121 (1962) [Sov. Phys.–Crystallogr., 7, 97 (1962)].

Anisotropy of the molar refraction of liquid-crystal alkoxybenzoic acids

E. I. Ryumtsev, A. P. Kovshik, I. P. Kolomiets, and V. N. Tsvetkov

Physical Institute, Leningrad State University

(Submitted January 12, 1973)
Kristallografiya, 18, 1246-1249 (November-December 1973)

The refractive indices of nematic and amorphous liquids of the homologous series of alkoxybenzoic acids are measured with a prism refractometer. The molar refraction and the anisotropy of the molar refraction are calculated for each homolog over the whole range of existence of the nematic phase. The refraction anisotropy is presented as a function of the structure of the molecules; the relationships so obtained are explained by assuming a certain flexibility in the molecules, this being a phenomenon well known in molecules of the chain type.

The temperature dependence of the refractive indices of the nematic and isotropic liquid phases of the esters of a homologous series of pp'-dialkoxyazoxybenzenes was determined in ref. 1 by means of a prismatic refractometer. This paper is a continuation of the crystal-optical study of homologous series of nematic liquid crystals. Our subject for study is a series of p-alkoxybenzoic acids having the following structural formula:

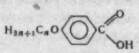

where n varies from 3 to 10 or equals 12. The temperatures at which the substances pass into the isotropic phase, T_0, are presented in Table 1. The values obtained for T_0 were close to those given in ref. 2.

We used the earlier-described[1] method of preparing the specimens and measuring the absolute values of the ordinary and extraordinary refractive indices of the anisotropic-liquid phase n_o and n_e, as well as n_{il}, the refractive index of the isotropic liquid.

The refractive indices of the liquid layer were determined by the method of total internal reflection at the glass–liquid interface, using right-angled prisms with a refracting angle of 60°. The refractive index of the glass of the prisms, measured independently by reference to the angle of minimum deviation, equalled $N = 1.746 \pm 0.001$ (at $\lambda = 546$ mμ).

The experimental values of n_o, n_e, and n_{il} for various acids are given in Table 1. It should be noted that the absolute values of the refractive indices of butyl oxybenzoic acid measured in ref. 3 practically coincided with our own data. Using the tabulated results we calculated the molar refractions R associated with the corresponding refractive indices, using the relations

$$R_{o,e,il} = \frac{n^2_{o,e,il} - 1}{n^2_{o,e,il} + 2}\frac{M}{\rho}, \qquad (1)$$

$$R_{il} = (R_e + 2R_o)/3, \qquad (2)$$

where M is the molecular weight. We measured the acid densities ρ required for the determination of R by means of a two-capillary pycnometer with a volume of 0.3 cm³ (error ± 0.001 g/cm³); the results are shown in relation to the temperature in Fig. 1. It should be noted that the values of R_{il} calculated from the experimental n_{il}, using Eq. (1), and the values of R_o and R_e calculated from Eq. (2) agreed to within 1%. Figure 2 shows the dependence of R_{il} on the number of methylene groups n in the acid molecules. The values of the refraction in the isotropic-liquid phase do not depend on the temperature, but increase linearly with increasing length of the molecules. This gives a good illustration of the additivity rule for the molar refraction of liquids. The value of R_{CH_2} calculated from the slope of the experimental curve of Fig. 2 was 4.66 cm³, almost coinciding with the corresponding tabulated values.

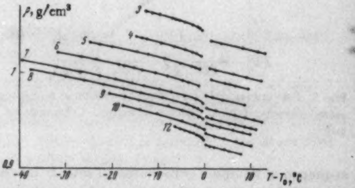

Fig. 1. Density ρ of alkoxybenzoic acid as a function of temperature, reckoned from the point of transition into the isotropic state T_0. The numbers on the curves correspond to the number of carbon atoms in the alkyl chain of the molecules of the homologs.

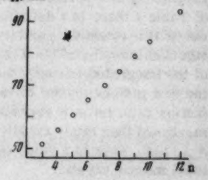

Fig. 2. Molar refraction R_{il} of alkoxybenzoic acid in the isotropic liquid state as a function of the number of methylene groups in the molecules.

The anisotropy of the molar refraction $\Delta R = R_e - R_o$ of a nematic substance is directly related to the anisotropy of the polarizability of its molecules Δb and the degree of order S characterizing the molecular axes[4] of the nematic mesophase:

$$\Delta R = \frac{4\pi}{3} N_A \Delta b S. \qquad (3)$$

Figure 3 shows the temperature dependence of ΔR for members of our homologous series of alkoxybenzoic acids. For each homolog Δb is constant and independent of tem-

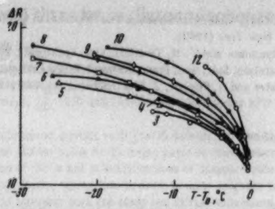

Fig. 3. Temperature dependence of the anisotropy of the molar refraction ΔR of the homologs of alkoxybenzoic acid in the nematic state. The numbers of the curves correspond to the number of carbon atoms in the alkyl chain of the molecules.

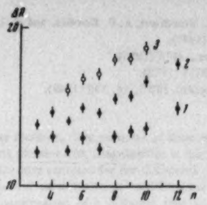

Fig. 4. Dependence of ΔR on the number of carbons in the alkyl chain of the alkoxybenzoic acid molecules. ΔT, deg: 1)−2; 2)−7; 3)−20.

perature, so that the different curves in Fig. 3 reflect the temperature dependence of the S of the acids studied. For each sample the degree of order falls with rising temperature, suddenly collapsing to zero at the point T_0 at which the substances pass into the isotropic phase.[4]

We see from the results presented in Fig. 4, which gives the values of ΔR as a function of the number of carbon atoms n in the aliphatic chains of the molecules at three fixed temperatures $\Delta T = T - T_0$ (−2, −7, −20°C), that the refraction anisotropy ΔR increases with increasing n. As already noted (Fig. 2), the values of the refraction in the isotropic phase R_{il} also increase with increasing molecular weight of the acids. However, the ratio

$$\frac{\Delta R}{R_{il}} = \frac{\Delta b}{\bar{b}} S, \qquad (4)$$

where $\bar{b}$ is the average polarizability of the molecule at a fixed temperature ΔT, on the average falls with increasing length of the molecular chain of the homologs (Fig. 5).

We obtained an analogous experimental $\Delta R / R_{il} = f(n)$ relationship for a homologous series of dialkoxyazoxybenzenes earlier,[1] and explained this as being due to a certain flexibility of the molecules under consideration. As a result of this flexibility, the optical anisotropy of the molecule Δb in the homologous series increases rather more slowly than its mean polarizability $\bar{b}$; this is

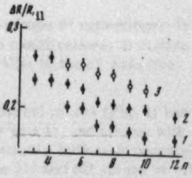

Fig. 5. Dependence of the ratio $\Delta R/R_{il}$ on the length of the molecules in the homologs of alkoxybenzoic acid. ΔT, deg: 1)−2; 2)−7; 3)−20.

the reason for the fall in $\Delta b/\bar{b}$ and hence in $\Delta R / R_{il} = f(n)$ in both cases under consideration. Evidently the deviations of the alkoxybenzoic acid molecules from stick-like form may be associated with a certain flexibility in the aliphatic parts of the molecules. Another very likely cause may be the presence of dimers in the anisotropic liquid phase of alkoxybenzoic acid,[5,6] formed by virtue of intermolecular hydrogen bonds, the energy of which is much lower than the energy of true chemical bonds.

It follows in principle from Eq. (3) that the reduction in the ratio $\Delta R / R_{il}$ with increasing n may also be associated with a change in the degree of order S within the homologous series. However, it is well known that the higher homologs of the dialkoxybenzenes and alkoxybenzoic acids are capable of forming a smectic mesophase,[5] characterized by a higher degree of order than the nematic state. It is therefore unlikely that S falls with increasing length of the molecules at constant temperature; under these conditions it is more reasonable to expect an increase in the degree of order.[7,8]

TABLE 1. Refractive Indices of the Liquid-Crystal and Amorphous Phases of Alkoxybenzoic Acids

$T - T_0$, °C	n = 3	4	5	6	7	8	9	10	12
	T_0 = 150,5	161	150,5	152,5	147,5	148,5	140,5	143,5	139
					n_e				
−1	1.600	1.590	1.575	1.565	1.550	1.547	1.540	1.540	1.535
−5	1.617	1.605	1.590	1.582	1.569	1.566	1.562	1.560	1.555
−10	1.632	1.620	1.602	1.595	1.580	1.578	1.574	1.571	
−20			1,620	1.610	1.600	1.595	1.588	1.585	
−30					1.611	1.608	1.599		
					n_o				
−1	1.463	1.455	1.461	1.457	1.457	1.455	1.456	1.454	1.453
−5	1.458	1.452	1.457	1.453	1.453	1.451	1.452	1.450	1.449
−10	1.457	1.451	1.456	1.453	1.452	1.450	1.451	1.448	
−20			1.456	1,453	1.452	1.450	1.451	1.450	
−30					1.453	1.453	1.454		
					n_{il}				
+1	1.501	1.494	1.494	1.488	1.484	1.482	1.480	1.477	1.475
+10	1,496	1.488	1.488	1.482	1.479	1.476	1.475	1.472	1.470

Note: The numbers of the columns correspond to the number of carbon atoms in the alkyl chain of the molecules.

[1] V. N. Tsvetkov, E. I. Ryumtesev, I. P. Kolomiets, A. P. Kovshik, and N. L. Gantseva, Opt. Spektrosk., 35, No. 5 (1973).
[2] G. W. Gray and B. Jones, J. Chem. Soc., 4179 (1953).
[3] J. Falgueirettes, Compt. Rend., 234, 2619 (1952).
[4] V. Tsvetkov (Zwetkoff), Acta Physicochim. URSS, 16, 132 (1942).
[5] G. W. Gray, Molecular Structure and Properties of Liquid Crystals, Academic Press, New York (1962).
[6] E. I. Ryumtsev and V. N. Tsvetkov, Opt. Spektrosk., 26, 607 (1969).
[7] P. Chatelain, Bull. Soc. Franc. Mineral. et Cristallogr., 60, 280 (1937).
[8] W. Maier and G. Englert, Z. Electrochem., 64, 689 (1960).

One-dimensional disorder in diazoaminobenzene

V. F. Gladkova

State Institute of Applied Chemistry

(Submitted November 9, 1972)
Kristallografiya, 18, 1250-1257 (November-December 1973)

Diazoaminobenzene crystals with growth defects are investigated by x-ray methods. The presence of sharp reflections and diffuse bands in the x-ray patterns indicates one-dimensional disorder with irregularities in the superposition of the α and β modifications of diazoaminobenzene. An intensity equation for the disordered layers of both forms, taking into account nearest neighbor interactions and two partial-error probabilities, made it possible to interpret both the sharp and diffuse reflections. A layer concentration of a different type was determined approximately for four imperfect crystals.

INTRODUCTION

Diazoaminobenzene (D) $C_6H_5-NH-N=N-C_6H_5$, which forms two crystal modifications (α with space group[1,2] $P2_1$ and β with space group[3] $P2_1/c$), very seldom crystallizes in one of these forms, and it is especially difficult to obtain α-D. Usually a D crystal, grown from solutions in various organic solvents (benzene, alcohol, ether, etc.), contains a sufficiently large coherent scattering region of both modifications, and their x-ray patterns are superpositions of the diffraction patterns of both the α-D and the β-D. In several x-ray reflection patterns one observes not only sharp but also diffuse bands on node lines parallel to one of the axes.[4] In this paper we attempt to explain these anomalies in x-ray patterns of D, starting from features of the α- and β-modification crystal structures.

EXPERIMENTAL INTENSITY DISTRIBUTION

Needle-shaped D crystals, 2-3 mm long and with transverse measurements of 0.1-0.2 mm, yielding anomalous x-ray diffraction patterns, were obtained by cooling for two days a D solution saturated in benzene and heated to +50°C.

To explain this type of disorder we photographed x-ray rotation patterns, scanning the h0*l*, h1*l*, h2*l* reciprocal lattice planes of various crystals by x-ray reflection (RG-28 and KFOR-4 cameras, Cu Kα,β radiation, a Ni filter, a slit diaphragm of 0.25 mm). A kforogram* of h0*l* planes of crystal 1 with two-dimensional effects is given in Fig. 1. The diffraction patterns of the h0*l*, h1*l*, h2*l* planes, obtained by photographing the reciprocal lattice and by Sauter's method, contained two groups of reflections: 1) sharp reflections of the α and β modifications; 2) diffuse interferences on node lines parallel to the c* axis (the β-D arrangement).

Fig. 1. Kforogram of h0*l* planes of reciprocal lattice 1.

The diffraction pattern of the h0*l* planes (Fig. 1) has diffuse bands at odd arrays (h = 2n + 1), and arrays with even h contain only sharp reflections. Diffuse broadening was observed in the scans of the h1*l* and h2*l* planes on all arrays parallel to the c* axis, except the zero terms. The intensity distribution I(ζ) along the 10*l* and 30*l* arrays was measured on the Sauter pattern of crystal 1 by means of an MF-2 microphotometer. A photometric curve of the 10*l* array is represented in Fig. 2 in relative units, after accounting for diffuse background. Anomalous diffuse (superlattice) maxima are present between even reflections of α- and β-D on node lines sensitive to lattice defects usually occurring close to reflections of α-D. They divide the interval between sharp peaks in the ratio 2:3 approximately. The intensity and half-width of diffuse maxima of various crystalline objects vary within quite broad limits. Photometric curves for the 10*l* array of several crystals are given in Fig. 3. The intensity is in relative units, its scale varying for the different crystals. The vividly expressed superlattice maxima of the x-ray patterns are matched with a drastic lowering of the even reflections of one of the modifications. The α-D reflections (crystal 1 in Figs. 1, 2; crystal 2 in Fig. 3a) are reduced most of the time, while those of β-D (crystal 3 in Fig. 3b) are reduced very seldom. For close reflection intensities of both modifications the diffuse broadening is usually much weaker and more uniform (crystal 4 in Fig. 3c).

THEORETICAL INTENSITY DISTRIBUTION

The characteristic location of diffuse bands on the x-

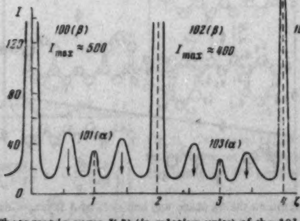

Fig. 2. Photometric curve I(ζ) (in relative units) of the 10*l* array on the Sauter pattern of crystal 1.

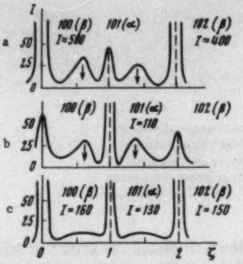

Fig. 3. Photometric curves I(ζ) of the 10*l* array on Sauter patterns of 2(a) 3(b), and 4(c) crystals.

ray goniometric photographs implies one-dimensional disorder in the c-axis direction of D crystals. Molecular layers, parallel to the *a*b plane of the β-D structure (Figs. 4, 5), were distinguished in these photographs at associated structures[2,3] of α- and β-D. One of the layers (of the basic A' layer) is identical in both modifications, and the structures differ in the packing of the second layer. In the α-D structure the second B' layer, identical to the main one, is displaced by *a*/2 with respect to its neighboring layer, while in the β-D structure the second C' layer is formed by inversion of the main one. Both can be considered structure layers with successive A'B'A'B'... (A-D) and A'C'A'C' (β-D) layers. The absence of appreciable structural distortions in transitions of one modification to the other, related to structural features of α- and β-D molecular layers,[3] creates favorable conditions for their simultaneous growth and makes it possible to assume an incorrect layer alternation of these modifications in imperfect D crystals.

As a model of disorder we use in first approximation only those layer arrangements (and their combinations) which are experimentally observed in the ordered D modifications: A' is the main layer, B' is the main layer displacement by *a*/2, and C' is inversion of the main layer. The relatively large width of a single molecular layer (9.2 Å) allows one to restrict the discussion to interactions between successive layers only (the case s = 1). The possibility of any two of the layers mentioned above being nearest neighbors was analyzed from the point of view of packing. The combinations A'B' and A'C' are allowed, while B'C' and the superposition of identical layers are forbidden.[1)]

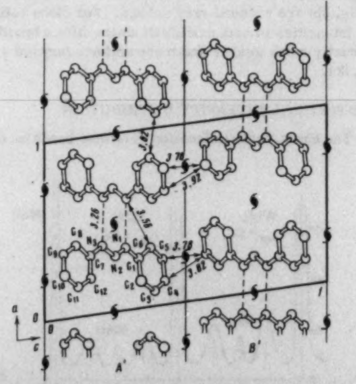

Fig. 4. Projection on the xz plane and unit cell of A layer. Continuous thin lines separate the identical molecular layers A' and B', arrows indicate intermolecular contacts, and dashed lines are hydrogen bonds.

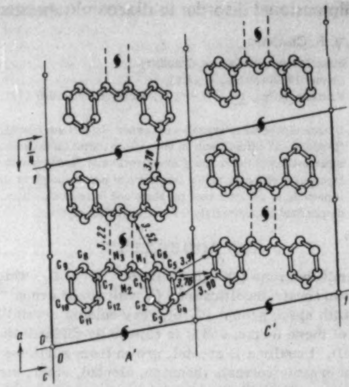

Fig. 5. Projection on the xz plane and unit cell of a B layer. Continuous thin lines separate the identical molecular layers A' and C', arrows indicate intermolecular contacts, and dashed lines are hydrogen bonds.

The incompatibility of B' and C' layers excludes the application to imperfect D of such models as the disordered arrangements A', B', C', allowing in the case where s = 1 a neighborhood of any nonidentical layers. In the suggested disordered model the transition from α- to β-D and vice versa is realized by interposing the A' layer between them: A'B'A'C'A'B'..., with packing errors consisting of inclusion of layers of one modification close to those of the other. We consider two-layer packets A'B' and A'C' of two kinds of layers A and B with structure amplitudes F_1 and F_2, respectively, and we introduce two partial probabilities: α, the error probability in the sequence AAA..., and β, the error probability in the sequence BBB....

The x-ray diffraction intensity for the case under consideration[5,6] (disorder of layers of two shapes, correlation between neighboring layers) can be represented as follows:

$$I=L\left\{\frac{1}{(\alpha+\beta)^2}(\beta F_1+\alpha F_2)^2\frac{\sin^2 N_3\pi\zeta}{\sin^2\pi\zeta}+\frac{\alpha\beta}{(\alpha+\beta)^2}\frac{N_3(1-\varkappa^2)(F_1-F_2)^2}{1+2\varkappa\cos 2\pi\zeta+\varkappa^2}\right\}, \tag{1}$$

where

$$L=\frac{\sin^2 N_1\pi\xi}{\sin^2\pi\xi}\frac{\sin^2 N_2\pi\eta}{\sin^2\pi\eta};$$

N_1, N_2, N_3 are the translation numbers along the x, y, z axes, ξ, η, ζ are the coordinates of the diffraction space points, and

$$\varkappa=(\alpha+\beta)-1 \tag{1a}$$

is the short-range order parameter ($0 \leq \varkappa \leq 1$). The structure amplitudes of A and B layers (whose unit cells are shown in Figs. 4 and 5) are expressed by the following general equations:[2)]

$$F_1=\sum_{j=1}^{N} f_j \exp[2\pi i k y_j]\{\exp[2\pi i(hx_j+\zeta z_j)] \times [1+\exp[\pi i(h+\zeta)]] + \exp[-2\pi i(hx_j+\zeta z_j)][\exp[\pi i(h+k)]+\exp[\pi i(k+\zeta)]]\}; \tag{2}$$

$$F_2=2\sum_{j=1}^{N} f_j\{\cos 2\pi(hx_j+ky_j+\zeta z_j) + \exp[\pi i(k+\zeta)]\cos 2\pi(hx_j-ky_j+\zeta z_j)\}; \tag{3}$$

F_1 and F_2 are the structure amplitudes of the α and β modifications in the β-D arrangement.[3)]

According to (1), both three-dimensional (sharp reflection) and two-dimensional (diffuse rods) diffraction occur in one-dimensional scattering by a disordered crystal of a given type. The three-dimensional diffraction [the first term in (1)], represented by the sum of α- and β-D diffraction patterns with intensity

$$I(hkl)=\frac{1}{(\alpha+\beta)^2}(\beta F_1+\alpha F_2)^2 N_1^2 N_2^2 N_3^2 \tag{4}$$

in the reciprocal lattice nodes, corresponds, both in location and in relative intensities, to the experimentally observed sharp reflections hk*l*, these being reflections of α- and β-D or their superposition. Peaks of α-D and β-D do not overlap [Eqs. (2), (3)] on h0*l* node lines with even h, and refer to α-D for $l = 2n + 1$ ($F_2 = 0$) and to β-D for $l = 2n$ ($F_1 = 0$). The intensity ratio of such reflections equals, by (4),

$$\frac{I_1}{I_2}=\frac{\beta^2}{\alpha^2}\frac{F_1^2}{F_2^2}. \tag{5}$$

In h0*l* nodes with even h and in h1*l*, h2*l* with even h + 1 [Eqs. (2), (3)] we have superpositions of α-D and β-D spots, while h1*l* and h2*l* with odd h + *l* correspond to β-D reflections ($F_1 = 0$).

The second term in (1) describes two-dimensional diffraction. Diffuse rods are located on node lines parallel to the c* axis. The theoretical intensity distribution along the rod axis is nonequilibrium and is characterized by the presence of broadened superlattice maxima of intensity

$$I_{\max}=\frac{\alpha\beta}{(\alpha+\beta)^2}(F_1-F_2)^2\frac{1+\varkappa}{1-\varkappa}N_1^2 N_2^2 N_3 \tag{6}$$

and half-width[7]

$$\eta_\zeta=2\frac{1-\varkappa}{\sqrt{2\varkappa}} \tag{7}$$

between nodes of the reciprocal lattice [$\zeta = (2n + 1)/2$].

The extinction law of diffuse reflections, determined by the difference of structure amplitudes ($F_1 - F_2$) [Eqs. (2), (3)], forbids their appearance on arrays with even h ($F_1 - F_2 = 0$). Two-dimensional diffraction on h0*l* lines with odd h and h1*l*, h2*l* arrays with any h are not restricted ($F_1 - F_2 \neq 0$). The location of diffuse bands on x-ray patterns of the h0*l* (Fig. 1), h1*l*, h2*l* planes corresponds to the general extinction law obtained. The latter does not explain the absence of visible diffuse broadening on the 01*l* and 02*l* axes.[4)]

The presence of nonoverlapping α-D and β-D reflections on the h0*l* planes of the reciprocal lattice allows us to estimate, by their intensity ratio (5) and by the diffuse maxima half-width (7), preliminary values of the parameters α, β, $\varkappa$ for real crystals, assuming they are completely disordered in the first approximation. Below are the given results, obtained from the Sauter patterns of h0*l* planes of crystal 1.

The intensities of sharp reflections, measured by an MF-2 microphotometer, were corrected for angular and temperature factors (B = 4.0 A²). The structure amplitudes F_1 and F_2 were calculated by (2), (3) from the coordinates of the β-D atoms.[3] An average value $\alpha/\beta = 4.5$ was obtained from four ratios (5) of eight 10*l* and 30*l* reflections (only nearest neighbor reflections were compared). The short-range order parameter $\varkappa$ was calculated by (7) from the experimental half-widths of diffuse maxima, related to the theoretical values by

$$\eta_\zeta^2=\eta_e^2-\eta_0^2; \tag{8}$$

η_0 is the half-width of instrumental reflection, being in the given case sharp reflections of Sauter patterns ($\eta_0 = 0.3$ rad). The average experimental half-width of the eight diffuse reflections (some of them shown in Fig. 2), $\eta_e = 1.51$ rad, corresponds to the value $\varkappa = 0.4$. We hence obtain, taking into account (1a) and $\alpha/\beta = 4.5$, $\alpha = 1.1$, $\beta = 0.3$.

The intensity distribution along the 10*l* array in the interval $0 < \zeta < 2$ (Fig. 6a) was calculated by Eq. (1) (the

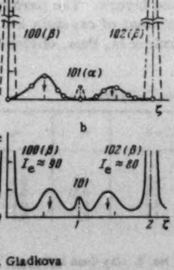

Fig. 6. Calculated (a) and experimental (b) curves of the intensity distribution along the 10*l* array of crystal 1.

TABLE 1. Dependence of $|F_1 - F_2|$ on ζ on the 10l Node Line

ζ	0	0.25	0.40	0.50	0.60	0.75	1.00	1.25	1.40	1,50	1.60	1.75	2.00
$\|F_1 - F_2\|$	36	250	290	280	254	187	36	80	206	180	150	90	36

expression in braces), by the layer structure factors (2), (3), and from the coefficients α, β, $\varkappa$ found above. The calculated number of layers $N_3 = 300$ was obtained by equating the theoretical [Eqs. (4) and (6)] and experimental (Fig. 2) ratios of the maximum heights of sharp and diffuse reflections. The intensity curve of two-dimensional diffraction is given in Fig. 6a by continuous lines. The quantity $|F_1 - F_2|$, calculated from Eqs. (2), (3) and by the coordinates of β-D atoms,[3] is given in Table 1. In the interval $0 < \zeta < 2$ it reached maximum values at ζ = 0.4 and 1.4. Sharp reflections are shown schematically on Fig. 6a (dashed lines): Their intensity was calculated by (4), the structure amplitudes of 100, 101, 102 reflections were assumed identical in view of their close absolute values and were equal to $|F_B|_{av} = 36.0$, and the half-width of reflections was conveniently augmented by the instrumental correction $\eta_0 = 0.3$ rad. Introducing such a correction, the half-width of diffuse maxima (8) increased insignificantly (by ~2%). Comparison of the calculated and experimental intensity curves, reduced on Figs. 6a and 6b to the same scale, indicates an agreement of their general behavior: The position of one of the diffuse maxima ($\zeta = 1.4$) coincides with the experimental values, and that of the second ($\zeta = 0.4$) differs somewhat from the observed value.

The parameter values α and β allow one to draw conclusions about the concentration of A and B layers in a disordered crystal of a given type, since[5] $\alpha/\beta = w_2/w_1$, where w_1 is the probability that any chosen layer is of A type (A layer concentration probability) and w_2 is the analog concentration probability of B layers.

For crystal 1 (Table 2) $w_1 = 0.2$, $w_2 = 0.8$, i.e., a concentration error (of A layers) in the main BBB... sequence consists of 20% approximately. Approximate parameters of crystals 2-4 (Fig. 3), given in Table 2, were calculated similarly to crystal 1.

Crystals 1-3, yielding quite sharp superlattice maxima (Figs. 2, 3a, b) on the x-ray patterns, have α or β parameters (Table 2) close to unity, which indicates proximity of these structures to order with regular layer alternation. For crystal 1, for example, the sequence ABBBBABBBBAB... is possible. Diffuse broadening with weak modulation (crystal 4, Fig. 3c) corresponds, on the contrary, to disordered superposed layers. The parameter $\varkappa$ is 1.5-2 times smaller than that of crystals 1-3. The sharpness of superlattice maxima is, thus, obviously related to regularities in alternating A and B layers in imperfect D crystals.

TABLE 2. Parameters of Several Disordered D Crystals

Crystal No.	$\varkappa$	α	β	α/β	w_1	w_2
1	0.4	1.1	0.3	4.5	0.2	0.8
2	0.3	1.0	0.3	3.5	0.25	0.75
3	0.3	0.5	0.8	0.6	0.6	0.4
4	0.2	0.6	0.6	1.1	0.5	0.5

CONCLUSION

The correspondence between experimental and theoretical results implies the existence of the suggested growth errors with alternating α- and β-modification layers in one-dimensional disordered D crystals. The intensity equation (1) for disordered layers of two types, including the interaction between neighboring layers and two partial-error probabilities, allows us to explain in general outline the geometry of the observed diffraction patterns (the location and extinction law of three-dimensional set of sharp reflections and diffuse bands) as well as several deviations from the theoretical laws mentioned above.

From experimental data on h0l planes of the reciprocal lattice we managed to estimate in first approximation the parameters and layer concentrations of various types in four imperfect D crystals. For one crystal we calculated, for the sake of illustration, the intensity distribution curve along the 10l array, which compares well with the photometric curve. The theoretical curve was obtained by (1). For more accurate, quantitative correspondence one must evaluate total intensities, taking into account a number of corrections.

Several deviations between observed and theoretical two-dimensional diffraction, noted above, can be due to approximations both in the simplified disorder model considered and in its solution. The starting assumption about uniform disorder of the whole crystal is, probably, valid only for very preliminary estimates. A real crystal may contain an impurity of the ordered α or β modification, possibly more complex than the mixed nature of disorder itself.[5)] In this case, however, the suggested more general disorder model would include the more probable error type described, as it is constructed only on layer combinations, experimentally found in regular D modifications, and the anomalous diffraction created by such errors corresponds to that observed on x-ray patterns.

The author is deeply grateful to Prof. A. I. Kitaigorodskii, Yu. D. Kondrashev, and R. A. Zvinchuk for discussing the results of this work.

---

*Publisher's note: A kforogram is similar to a pattern taken with a precision camera.

[1)] For the excluded combinations the interatomic distances at the contact points between layers were smaller than the sums of carbon intermolecular radii $2R_C = 3.60$ Å.

[2)] Using Eqs. (2) and (3) for sharp reflections, the continuous parameter ζ is replaced by the integral index l.

[3)] The unit cell of layer A is twice as large as the unit cell[2] of α-D. The unit cell of layer B is displaced by $a/2$ with respect to the cell[3] of β-D.

[4)] Pseudoextinctions of sharp β-D reflections were also observed on the 01l and 02l node lines.

[5)] A possible complication of a disorder model is to include in it one quarter of a theoretically admissible position of a main layer, D', inversion + displacement by $a/2$. An intensity equation for such a disorder model, not considered in the literature to the best of our knowledge, can be obtained, for example, by a matrix method[8] with the use of symmetry operators.[9]

---

[1] V. F. Gladkova and Yu. D. Kondrashev, Kristallografiya, 13, 1076 (1968) [Sov. Phys.—Crystallogr., 13, 936 (1969)].

[2] V. F. Gladkova and Yu. D. Kondrashev, Kristallografiya, 16, 929 (1971) [Sov. Phys.—Crystallogr., 16, 806 (1972)].

[3] V. F. Gladkova and Yu. D. Kondrashev, Kristallografiya, 17, 33 (1972) [Sov. Phys.—Crystallogr., 17, 23 (1972)].

[4] Yu. D. Kondrashev, Kristallografiya, 3, 617 (1958) [Sov. Phys.—Crystallogr., 3, 622 (1959)].

[5] H. Jagodzinski, Acta Crystallogr., 2, 201 (1949).

[6] A. I. Kitaigorodskii, X-Ray Analysis of Microcrystalline and Amorphous Bodies [in Russian], Gos. Izd. Tekh.-Teor. Lit., Moscow—Leningrad (1972), Chap. 3.

[7] A. Guinier and R. Griffoud, Acta Crystallogr., 1, 188 (1948).

[8] S. B. Hendricks and E. Teller, J. Chem. Phys., 19, 147 (1942).

[9] H. Jagodzinski, Acta Crystallogr., 7, 17 (1954).

Determination of the activation energy of forward and reverse reactions during crystal growth

E. B. Treivus
Leningrad State University

(Submitted April 7, 1972; resubmitted October 11, 1972)
Kristallografiya, 18, 1258-1262 (November-December 1973)

Experimental data on the kinetics of crystallization in aqueous solutions were used to compute the rate of reverse reaction and the rate coefficient of forward reaction at different temperatures. This allowed the calculation of the activation energy of the forward and reverse processes. The difference between both activation energies agrees with the heats of crystallization of the corresponding materials. On the basis of the data obtained, it is concluded that the active group during crystallization of the materials considered consists of one molecule.

According to ref. (1), if one considers experimental data as a polynomial with respect to degree of chemical affinity

$$V=a\frac{A}{RT}+b\left(\frac{A}{RT}\right)^2, \tag{1}$$

then $a = \overleftarrow{V}_0$, $b = (\overleftarrow{V}_0+2\overleftarrow{V}_0')/2$, where $\overleftarrow{V}_0$ is the reverse reaction rate and $\overleftarrow{V}_0'$ is the derivative of the reverse reaction rate at coordinate zero.

At equilibrium we have

$$\overrightarrow{V}_0=\overleftarrow{V}_0=\overrightarrow{k}_0 a_0 a_\omega^r=\overrightarrow{k}_0/K, \tag{2}$$

where $\overrightarrow{V}_0$ is the forward reaction rate, $\overrightarrow{k}_0$ is the rate coefficient of forward reaction, a_0 and a_ω are the activities, respectively, of the electrolyte and water in the saturated solution, r is the number of water molecules in the crystal hydrate, and K is the equilibrium constant. Equations (1) and (2) afford the possibility of calculating the activation energies of forward and reverse reactions $\overrightarrow{E}$ and $\overleftarrow{E}$, strictly speaking, at equilibrium.

We note that at present the activation energy is usually computed either from the growth rate taken at the same relative supersaturation Δc/c, or from the rate taken at the same absolute supersaturation Δc. In the first instance an approximate value of $\overleftarrow{E}$ is obtained, since Δc/c ~ A/RT; in the second case, an approximate value of $\overrightarrow{E}$, since Δc ~ Δ*a*. We emphasize that neglect of the exact values of the contributing forces in some cases can produce a substantial discrepancy in E. Sometimes the activation energy is also determined from the growth rate taken at a constant supercooling. It is cumbersome to interpret the specific activation energy in such a way.

To appraise the feasibility calculation for $\overrightarrow{E}$ and $\overleftarrow{E}$, we may take the expression:[2] $\overrightarrow{E} - E = MQ$, where Q is the heat of crystallization, M is the molecularity of the process, equal to one or two (number of particles in an active group). In the absence of experimental data on the heat of crystallization, it is not difficult to calculate the exact enthalpy of the equilibrium phase transformation.[3]

Here we determine both activation energies from our data on crystallization of potash alum and $FeSO_4 \cdot 7H_2O$ from aqueous solutions, and from the data of ref. 4 for the case of sucrose. The chemical affinity of potash alum solutions up to the saturation concentration was computed on the basis of the information on $\gamma_\pm$ and a_ω in ref. 5, and then by linear extrapolation to a supersaturated solution. The activity coefficients of $FeSO_4$, known only for 25°C, practically agree[6,7] with the $\gamma_\pm$ for $CuSO_4$ and $NiSO_4$. For this reason, the $\gamma_\pm$ of $CuSO_4$ solution[8-11] at 0-35°C, and of $NiSO_4$ at[12-13] 25°C were used. The increase of $\Delta\mu_\omega$ for $FeSO_4$ solutions was approximated on the basis of the Gibbs–Duhem equation. Although the solutions contained about 5 wt.% of free H_2SO_4 during crystallization, the computations were done for a system not containing H_2SO_4, since the error in evaluation is insignificant. The values of A/RT calculated for a 1-deg supersaturation at temperatures of 30, 40, and 50°C for $KAl \cdot (SO_4)_2 \cdot 12H_2O$ are, respectively, 0.086, 0.070, and 0.058; for $FeSO_4 \cdot 7H_2O$, at temperatures of 13, 19, and 25.5°C they are, respectively, 0.044, 0.039, and 0.033.

Table 1 gives the $\gamma_\pm$ and a_ω values of saturated $FeSO_4$ solutions necessary for calculation of the equilibrium constant. The activity of water is indicated with a correction of 0.02 for the H_2SO_4 content. The correction was calculated on the assumption that the Zdanov law of linear isoactivity of water holds in the given system at a small H_2SO_4 concentration (data on equilibria in this system are in ref. 14). In the calculations for sucrose, the same data as in ref. 4 were used for the solubility; the equations for the γ dependence of sucrose on concentration and temperature were from ref. 15. The magnitude of A/RT for sucrose increases practically linearly with supersaturation. The maximum attainable A/RT value varies from 0.80 at 21°C (supersaturation 820 g/kg H_2O) to 0.25 at 70.5°C (supersaturation 390 g/kg H_2O).

The growth-rate measurements were performed on the (111) face of potash alum and on the (110) face of $FeSO_4 \cdot 7H_2O$ using a forced convection regime in an apparatus similar to that described in ref. 16 and 17. The measurements were performed under a microscope with an ocular micrometer. The crystal size was 1-3 mm, and the solution velocity was 20-25 cm/sec. The face was positioned vertically, i.e., parallel to the solution flow, and the solution current was from top to bottom. The

TABLE 1. Thermodynamic Parameters of Saturated Aqueous Ferrous Sulfate Solutions

t, °C	m_s	$\gamma_\pm$	a_ω
13	1.47	0.038	0.954
19	1.72	0.036	0.947
25	1.97	0.034	0.940

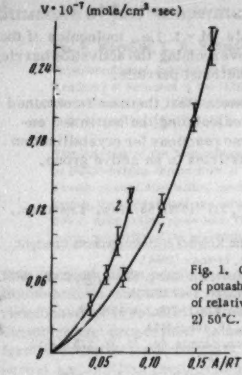

Fig. 1. Growth rate of the (111) face of potash alum crystals as a function of relative chemical affinity: 1) 40°C; 2) 50°C.

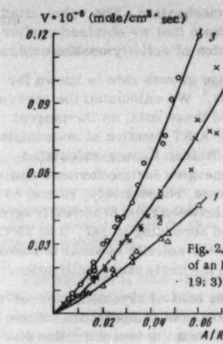

Fig. 2. Growth rate of the (110) face of an $FeSO_4 \cdot 7H_2O$ crystal. 1) 13; 2) 19; 3) 25.5°C.

TABLE 2. Crystallization Parameters of Investigated Crystal Hydrates

Parameters	12	19	25.5	30	35	39	40	50
	$FeSO_4 \cdot 7H_2O$			$KAl(SO_4)_2 \cdot 12H_2O$				
$\overleftarrow{V}_0 \cdot 10^7$	6.3	7.8	11.2	0.12	0.20**	0.20***	0.26	0.45
$\overleftarrow{V}_0 \cdot 10^7$	—	—	—	0.08*	—	—	0.30*	0.53*
$\overleftarrow{V}_0' \cdot 10^6$	1.7	6.8	15.6	0.41	—	—	0.70	1.30
$\overrightarrow{k}_0 \cdot 10^4$	2.8	3.0	3.8	0.060	—	—	0.074	0.087
p	3.2	9.2	14.5	35	—	—	28	30
K	390	330	300	600	—	—	270	165
$\overrightarrow{E}$	4300			2500				
$\overleftarrow{E}$	8200			15000				
ΔH	5100			14500				

* Computation according to data of ref. 18.

** According to data of ref. 17.

*** According to data of ref. 19.

The coefficient $\overrightarrow{k}_0$ for the alums is calculated on the basis of the average $\overleftarrow{V}_0$ values we obtained, determined according to the method of ref. 18. The error in determining $\overleftarrow{V}_0$ and $\overrightarrow{k}_0$, calculated for the assumed confidence interval, does not exceed 5-7% for $FeSO_4 \cdot 7H_2O$ and 20-25% for alum.

TABLE 3. Crystallization Parameters of Sucrose

Parameters	21	31	41	51	60.5	70.5
$\overleftarrow{V}_0 \cdot 10^7$	0.04	0.14	0.31	0.57	0.92	1.94
$\overrightarrow{k}_0 \cdot 10^9$	0.22	0.72	1.50	2.45	3.50	6.40
K	0.056	0.053	0.049	0.043	0.038	0.033

total error in determining and maintaining the supercooling was 0.1°C. The temperatures of the individual experiments lie over an interval of ± 0.5°C about the average temperature indicated below.

The results of the measurements are given in Figs. 1 and 2. For the potash alum, 10 to 15 runs were performed for each supersaturation at 40°C, and six to nine runs at 50°C. Figure 1 gives the average rates and the interval for a probability of 95%. The data were treated using the method of least squares according to Eq. (1), and values of $\overleftarrow{V}_0$ and $\overrightarrow{K}_0$ were then computed (Table 2). Here, however, the index of nonlinearity according to ref. 1 is $p = b/a$. As seen from the resulting data, the nonlinearity noticeably increases with temperature for $FeSO_4 \cdot 7H_2O$, but shows practically no change for the alum. The data on alum in Table 2 are taken from ref. 1. The results of the $\overrightarrow{E}$, $\overleftarrow{E}$, and ΔH calculations are given in cal/mole in Table 2. The difference between ΔE and ΔH is in the range 10-20%, which is not large. The value of $\overrightarrow{E}$ we obtained is close to the activation energy in refs. 17 and 19, which was calculated on the basis of equations corresponding to some actual growth mechanism. The value cited here substantially differs from that we obtained earlier (ref. 20) without consideration of activity coefficients.

For sucrose, the average growth rate is known for intensively stirred solutions.[4] We calculated the reverse reaction rate on the basis of these data, as the tangent of the slope angle of the V ~ A/RT function at coordinate zero. Afterwards, the coefficient $\overrightarrow{k}_0$ was calculated (Table 3). The activation energies for the forward and reverse reactions approximate, respectively, 13 and 15 kcal/mole. The difference between them practically agrees with the ΔH value calculated according to ref. 3 at 25°C (using the data of ref. 21 on the activity of water in sucrose solutions), and according to the heats of crystallization.[22,23]

According to ref. 22, the heat of crystallization of sucrose increases with increase of temperature. Consequently, the difference between the two activation energies should increase; this, however, is impossible to observe with the available precision of data. There is an observed tendency for a decline of the sucrose activation energy with temperature, which is possibly caused by an increase in the limiting action of diffusion.[4,15,24] However, it should be noted that the reverse reaction rate and the rate coefficient for forward reaction are proportional to the number of active growth sites on the crystal surface. It is therefore still possible that the decrease in activation energy is only apparent, and is associated with a change in the number of active sites with temperature. In principle the activation energy during crystallization may be computed as a function of the logarithm of the reciprocal of temperature only approximately, which has apparently gone unnoticed.

The following should also be mentioned. The number of growth sites generally changes with departure from equilibrium at a different rate for various temperatures. It is therefore necessary to approach the activation energy determination strictly according to the rate taken at a given supersaturation. As was earlier noted, this is especially so if there is a different nonlinearity of the growth rate dependence on supersaturation for different temperatures.

For all three materials M = 1, i.e., molecules of the considered materials, in overcoming the activation barrier, do not need to annex an additional particle.

In summary, we emphasize that the results obtained confirm the possibility of calculating the activation energy of forward and reverse reactions for crystallization with a known number of particles in an active group.

---

[1] E. B. Treivus, Kristallografiya, 17, 211 (1972) [Sov. Phys.–Crystallogr., 17, 171 (1972)].

[2] S. L. Kiperman, Introduction to the Kinetics of Heterogeneous Catalytic Reactions [in Russian], Izd. Nauka, Moscow (1964).

[3] A. N. Kirgintsev and A. V. Luk'yanov, Zh. Neorg. Khim., 12, 2302 (1967).

[4] B. M. Smythe, Australian J. Chem., 20, 1087 (1967).

[5] S. S. Odokienko and V. V. Serdyuk, VINITI File No. 4086-72.

[6] B. Fedorov, Ann. Chimie, Ser. 11, 16, 155 (1941).

[7] N. Demassieux and B. Fedorov, Ann. Chimie, Ser. 11, 16, 215 (1941).

[8] Gmelins Handbook, 60, B, 1, 549 (1958).

[9] F. E. W. Wetmore and A. R. Gordon, J. Chem. Phys., 5, 60 (1937).

[10] A. R. Tourky and S. E. S. Elwakkad, J. Chem. Soc., 740 (1948).

[11] D. S. Dhillon and R. L. Blokhra, Indian J. Chem., 5, 340 (1967).

[12] L. E. Voznesenskaya, in: Problems in the Physical Chemistry of Electrolyte Solutions [in Russian], Izd. Khimiya, Leningrad (1968), p. 172.

[13] I. E. Voznesenskaya and G. L. Mikulin, in: Problems in the Physical Chemistry of Electrolyte Solutions [in Russian], Izd. Khimiya, Leningrad (1968), p. 361.

[14] A. P. Belopol'skii, V. N. Kolycheva, and S. Ya. Shpunt, Zh. Prikl. Khim., 21, 794 (1968).

[15] A. Van Hook, Indust. and Engr. Chem., 36, 1042 (1944).

[16] W. L. McCabe and R. P. Stevens, Chem. Engr. Progr., 46, 168 (1951).

[17] G. D. Botsaris and E. G. Denk, Indust. and Engr. Chem. Fundam., 9, 276 (1970).

[18] K'uang Han-Hang, Study of the Growth Kinetics of Potash Alum Crystal Faces, Dissertation Register, Leningrad (1968), Table 2.

[19] P. Bennema, R. Kern, and B. Simon, Phys. Status Solidi, 19, 211 (1967).

[20] E. B. Treivus, Kristallografiya, 14, 355 (1969) [Sov. Phys.–Crystallogr., 14, 290 (1969)].

[21] R. Robinson and R. Stokes, Solutions of Electrolytes [Russian translation], IL, Moscow (1963).

[22] E. J. Kilmartin and A. Van Hook, Sugar J., 45, 34 (1950).

[23] N. Tikhomiroff, F. Pultrini, F. Heitz, and M. Gilbert, Compt. Rend., 261, 334 (1965).

[24] A. Van Hook, Indust. and Engr. Chem., 37, 782 (1945).

Structure of low-temperature "amorphous" bismuth films

Yu. F. Komnik, L. A. Yatsuk, A. A. Motornaya, M. L. Bolotina, and B. I. Belevtsev

Physicotechnical Institute of Low Temperatures,
Academy of Sciences of the Ukrainian SSR

(Submitted July 17, 1972; resubmitted November 2, 1972)
Kristallografiya, 18, 1263-1271 (November-December 1973)

The structure of the "amorphous" bismuth films formed by the condensation of molecular beams on a substrate at liquid-helium temperature is studied by low-temperature electron diffraction. Construction of the radial atomic density distribution function reveals considerable changes in the coordination structure of the films on raising the temperature and increasing the film thickness, as well as structural transformations in films ~400-500 Å thick taking place after final condensation. An explanation is offered for the manner in which the electrical properties of the low-temperature bismuth films vary with their thickness and temperature.

Thin bismuth films condensed on a substrate cooled to liquid-helium temperature differ very considerably from rhombohedral crystalline bismuth films as regards both structure and properties. In contrast to the rhombohedral form existing in large crystals (not subject to high pressures) and in films condensed at room temperature, the low-temperature phase in the bismuth films is superconducting with a critical temperature of $T_c \sim 5$-6°K, as indicated in refs. 1-3. This low-temperature phase transforms into rhombohedral form on heating, the transition temperature being higher, the smaller the film thickness.[3,4] The low-temperature phase is not restored on cooling.

According to the extremely limited structural investigations which have so far been carried out, low-temperature bismuth films have a very nearly amorphous structure. The electron-diffraction patterns obtained by Buckel[5] contained diffuse haloes at $\sin\vartheta/\lambda = 0.158$; 0.231; 0.318; 0.478 $Å^{-1}$. Richter and Steeb[6] analyzed Buckel's data for the intensity distribution in the diffraction pattern and obtained the radial atomic density distribution by the Fourier-transformation technique. According to Richter[7] the structure of the low-temperature films was similar to that of liquid bismuth.

Fujime[8] presented an analysis of the electron-diffraction pattern which he obtained from a bismuth film 200 Å thick; he concluded that the low-temperature condensate was an amorphous substance, the number of atoms in the first coordination sphere being much smaller than in the liquid metal at the melting point of bismuth. In structure the amorphous bismuth was similar to the supercooled liquid metal. In an earlier paper Takagi[9] showed that on supercooling bismuth films the number of atoms in the first coordination sphere diminished. The results of different authors pertaining to the amorphous and liquid bismuth are presented in Table 1.

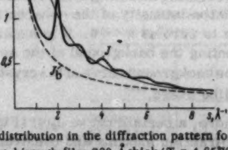

Fig. 1. Intensity distribution in the diffraction pattern for a low-temperature bismuth film 290 Å thick (T = 4.65°K).

The structural data should explain a number of peculiar characteristics of the physical properties found in "amorphous" bismuth films. Thus, according to Buckel and Hilsch,[2] the low-temperature phase in bismuth films has a greater conductivity and a greater Hall carrier concentration than the rhombohedral form, i.e., it is more "metallic" than the ordinary form of bismuth. The property of superconductivity arises, not immediately after the condensation of the film, but after a short interval,[10] this being the longer, the greater the film thickness.[11] This indicates structural changes taking place in time after the condensation of the film.

The specific electrical resistance of "amorphous" bismuth films increases with diminishing thickness, this effect occurring in a range of thicknesses within which the defectiveness of the structure of the condensate does not determine the resistance.[4] On raising the temperature, thin films (less than 100 Å) exhibit a drop in resistance; the thinner the film, the more pronounced is the "negative" movement of the resistance.[4] The temperature dependence of the resistance in amorphous and liquid metals, in contrast to crystals, is not associated with the temperature dependence of the various electron-scattering mechanisms (by phonons, other electrons, impurity atoms, crystal boundaries, etc.), but is mainly determined by structural changes taking place in the short-range coordination spheres of the disordered samples.[12] It may well be considered that the changes taking place in the specific resistance of "amorphous" bismuth films with thickness and temperature are also associated with structural transformations.

The aim of the present investigation was a detailed study of the structural characteristics of the low-temperature phase in bismuth films of various thicknesses at various temperatures. To this end we developed a special method of low-temperature electron diffraction.

EXPERIMENTAL METHOD

We used an ÉG electron-diffraction camera of the type constructed by Z. G. Pinsker and B. K. Vainshtein, furnished with a low-temperature adapter. The latter constituted a helium cryostat with a specimen holder. The temperature of the copper block was determined by means of an Allen–Bradley carbon resistance. In order to improve the degree of vacuum the electron-diffraction camera was furnished with a cryogenic sublimation pump, on using which the pressure fell to $(7\text{-}10) \cdot 10^{-7}$ mm Hg.

The materials for study were condensed inside the actual electron-diffraction camera on a substrate held at liquid-helium temperature. As substrates we used acetate lacquer or aluminum films. Because of the oxide layer on its surface the aluminum film formed a neutral substrate with a fairly high thermal conductivity. One considerable advantage of the aluminum substrate lay in the fact that the diffraction pattern of the aluminum itself constituted a small number of sharp maxima, which could easily be eliminated from the diffraction pattern. Electron-diffraction pictures were also obtained at temperatures above the helium point as the low-temperature attachment underwent a slow temperature drift.

The film thickness was determined by reference to a standard, using multiple-beam interferometry, or else from a calibration curve relating the optical density of the bismuth films to their thickness.

COMPUTING METHOD

The structure of liquid and amorphous substances is described by the radial atomic density distribution function. The construction of this function from electron-diffraction data may be achieved by making a Fourier transformation of the intensity-distribution curve J(s) describing the scattering of electrons by the sample in question [$s = 4\pi(\sin\vartheta)/\lambda$, 2ϑ is the scattering angle, λ is the electron wavelength]. Whereas the experimental measurements determine the intensity J_c simply associated with the coherent scattering, expressed in units of f^2 (f is the atomic scattering factor of the electrons), subsequent calculation of a nonatomic substance lies in finding the function $i(s) = (J_c - f^2)/f^2$, after which the radial atomic density distribution function may be constructed:

$$4\pi r^2\rho(r)=4\pi r^2\rho_0+\frac{2r}{\pi}\int\limits_0^\infty si(s)\sin sr\,ds. \tag{1}$$

These calculations may be performed in a computer to a very great accuracy. The degree of reliability of the results obtained is determined mainly by the accuracy achieved in executing the operations preceding the integration: the separation of the substrate's contribution to the diffraction, the method of allowing for the background, and the normalization of the coherent scattering intensities. We shall now give some detailed attention to our own methods.

Determination of the substrates's contribution to the diffraction. Let us assume that in the diffraction pattern actually observed there is an additive superposition of the intensity distributions arising from the substrate (J_{sub}) and from the metal under test(J). Let the coefficient α determine the ratio of the intensities attributable to the substrate in the complete diffraction pattern to the corresponding intensities in the electron-diffraction pattern of the clean substrate (i.e., in the absence of the sample). For the intensity I in the observed diffraction pattern we have the equation

$$I=\alpha J_{\mathrm{sub}}+J, \tag{2}$$

or

$$\alpha J_{\mathrm{sub}}=I-J. \tag{2a}$$

Let us write down this equation for three values of s:

$$\alpha J_{\mathrm{sub}\,1}/J_{\mathrm{sub}\,1}=I_1-J_1, \tag{3a}$$

$$\alpha J_{\mathrm{sub}\,1}/J_{\mathrm{sub}\,2}=I_2-J_2, \tag{3b}$$

$$\alpha J_{\mathrm{sub}\,1}/J_{\mathrm{sub}\,3}=I_3-J_3. \tag{3c}$$

Here in addition to α the unknown quantities include J_1, J_2, and J_3. Let us take the ratios of (3a), (3b), and (3c):

$$a=J_{\mathrm{sub}\,2}=(I_1-J_1)/(I_2-J_2), \tag{4a}$$

$$b=J_{\mathrm{sub}\,3}=(I_1-J_1)/(I_3-J_3), \tag{4b}$$

$$c=J_{\mathrm{sub}\,3}=(I_2-J_2)/(I_3-J_3). \tag{4c}$$

Using electron-diffraction patterns from the pure substrate we may determine the coefficients a, b, and c. Then by solving the system of equations (4) we may find the intensity J for three values of s.

The calculations simplify if we may assume that for two similar values of s the intensities due to the substrate differ considerably from each other, while intensities due to the metal under consideration are practically equal. This requirement is easily realized in our particular materials (especially for large s), for which the diffraction from the aluminum substrate gives sharp peaks, whereas the "amorphous" low-temperature films give diffuse haloes. In the region of the aluminum peaks the conditions $J_1 \approx J_2$ and $a = J_{\mathrm{sub}1}/J_{\mathrm{sub}2} \neq 1$ may be realized; in this case we obtain the following from (4a):

$$J=(aI_2-I_1)/(a-1). \tag{5}$$

Having set up several values of J, we may then find the average coefficient for the particular electron-diffraction pattern in question, and using this we may subtract the substrate component from the overall diffraction pattern. This procedure may best be carried out separately for the envelope and the profile of the aluminum lines. As we shall shortly show, the background from the substrate lying below the envelope to the intensity curve for pure aluminum need not be specially separated; it will be automatically separated together with the background for the samples under examination.

Elimination of the background from the intensity curves, and normalization of the latter. In electron diffraction the background is formed from incoherently scattered electrons and also electrons repeatedly scattered in the test object and substrate, by the edges of the diaphragm, and so forth. The intensity of the incoherent scattering is large for small s and falls off as $\gamma/s^4 (\gamma \sim s)$. From the general properties of the curve representing the background on the diffraction pattern of an amorphous substance, it is known that this does not coincide with the envelope but passes slightly below the latter. For small s the curve of total intensities and the curve representing the background should come closer together, since the intensity of the coherently scattered electrons falls to zero as $s \to 0$. It is assumed that the curve representing the background of the amorphous phase is similar to the background curve of the crystalline phase.[8,13]

of the crystalline phase.[8,13]

Furthermore, a certain curve $J_0(s)$ (Fig. 1) passing through the diffraction maxima and constructed above the background should constitute a function of $f^2(s)$, taken with a scale factor c. Using this factor, we may carry out the normalization of the curve for the intensities of the coherent electrons, in which the following condition should be satisfied:[14]

$$\int_0^\infty (J_\text{c}-f^2)s^2\,ds=0. \tag{6}$$

In calculating the integrals in (1) and (6) the upper limit of integration is assumed finite ($s_\text{max} \sim 8$–10). Close to s_max the oscillations in intensity are, as a rule, very small; we may therefore consider that the curve $J_0(s)$ approaches the intensity curve $J(s)$. All the foregoing requirements are allowed for in our method of eliminating the background and normalizing the $J(s)$ curve.

After eliminating the diffraction maxima due to the aluminum substrate, all further calculations were carried out in an electronic computer, using a special program. The following mathematical problem was solved. We determined the curve $J_\text{b}(s)$ for the background, the form of which was specified and contained two independent parameters. The curve has to pass through two points: One of them – at small s ($s \sim 0.4$–0.8) – coincides with the total intensity, while the second – at large s ($s \sim 9$) – lies below the total intensity by an amount ε. Furthermore the curve

$$J_0(s)=J_\text{b}(s)+cf^2(s) \tag{7}$$

should coincide with the intensity curve for large s, while the function $J_\text{c}(s) = [J(s) - J_\text{b}(s)]/c$ should satisfy Eq. (6). Thus the problem has to be solved in respect of two unknown parameters describing the background curve, subject to the variation of another two mutually related quantities ε and c. Calculations showed that the solution (if it exists) is unique.

It was suggested in refs. 8, 9, and 15 that the background on the electron-diffraction pattern of an amorphous substance might be obtained if an electron-diffraction picture of the crystalline phase were taken in the same sample:

$$J_\text{b}^\text{am}(s)=bJ_\text{b}^\text{cr}(s)+b_1. \tag{8}$$

Here the two unknown quantities are b and b_1, in which b_1 is small or zero. Our calculations based on the scheme just set out showed that this assumption could not be strictly justified. Thus the similarity between the backgrounds of the crystalline and amorphous phases is not exact. Hence in order to describe the background we analytically specified a function with two unknown parameters, providing a satisfactory approximation to the background for the crystalline phase. Of the various possible forms of this function [for example, $a\exp(-\alpha s)$, $a_1s^{c_1}$ + $a_2s^{c_2}$, etc.] the most suitable was $J_\text{b} = as^{-\alpha}$. The suitability of this approximation was discussed in ref. 16. The power index is usually close to unity; it depends on the substance under study and changes slightly on passing from the crystalline to the amorphous material.

All other sources of errors in the calculation (the restriction of the limit of integration to s_max, the propinquity of the background to the total intensity curve at $s_\text{min} \sim 0.4$–0.8 and not $s = 0$, etc.,[1)] also have a less serious influence on using a reasonably consistent method of background separation and normalization.

EXPERIMENTAL RESULTS AND DISCUSSION

Figure 1 shows a typical picture for the intensity distribution on the diffraction pattern of an "amorphous" bismuth film (the sharp diffraction maxima from the aluminum are eliminated, the incoherent background from the aluminum amounts to 30% and enters into the pattern illustrated). In the majority of cases in our electron-diffraction patterns the maxima at $s \simeq 2.05$, 2.95, 4.00, 4.95, 6.0, ~ 7, ~ 8 are sharply distinguished in our electron-diffraction patterns. On the pattern obtained by Fujime[8] (Table 1) maxima were observed at s = 2.1, 3.8, 4.24, 6.3, 8.3. By comparing these we see that, instead of the maximum at s = 4.24, there are actually two maxima, at s = 4.0 and 4.9. In thin films (L < 100 Å), and sometimes in thicker films, these two maxima often form a single plateau on the electron-diffraction patterns.

The position of the diffraction maxima is not strictly fixed, but varies slightly with the film thickness and temperature. For thick films (L ~ 400-500 Å) a considerable change takes place in the diffraction pattern on holding after condensation; thus, in particular, the intensity ratio of the maxima changes; at first the intensity of the background increases sharply (for medium values of s), then the background intensity falls again and the position of the maxima changes slightly at large s (Fig. 2).

The heating of "amorphous" bismuth films leads to crystallization and the appearance of the diffraction pattern corresponding to the ordinary rhombohedral form of bismuth. The change taking place in the temperature of the transition with changing film thickness, as derived from the electron-diffraction data, agrees with that based on electrical measurements (Table 2). The phase transition is extended in temperature, lasting over a range of 3-5°K. In certain cases we were able to record a diffraction pattern on which broad maxima corresponding to the rhombohedral bismuth appeared on a background of diffuse haloes from "amorphous" bismuth. After the completion of crystallization the bismuth maxima are narrow and no signs of texture appear (in contrast to films con-

TABLE 1. Electron-Diffraction Data of Various Authors for "Amorphous" and Liquid Bismuth in Films

Author	T, °K	sin θ/λ, Å⁻¹				Radial distribution (r, Å)			
						r_1	n_1	r_2	r_3
Buckel (ref. 5)	4.2	0.158	0.231	0.318	0.478	—	—	—	—
Richter (ref. 7)	4.2	0.161	0.236	0.323	0.472	3.32	6.7	4.7	6.7
Fujime	4.2	0.166	0.244	0.336	0.500	3.28	5	4.5	6.7
Takagi	544	0,159	—	0.328	0.510	3.3	8	—	6.5
Takagi	383	0,159	0,230	0.318	0.485	3.3	6	4.5 5.6	6.5

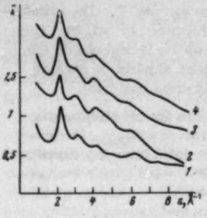

Fig. 2. Change in the diffraction pattern of a bismuth film 450 Å thick with time: 1) immediately after condensation; 2) 12 min later; 3) 18 min; 4) 31 min. Curves 2, 3, and 4 are shifted upward along the scale of intensities by 0.1, 0.65, and 0.825 relative units respectively (T = 4.7°K).

densed with the substrate at room temperature).

In order to construct the radial atomic density distribution function we carried out a computer integration, in accordance with Eq. (1), for the function i(s), plotted in steps of $\Delta s = 0.04168$ Å over the range $s_0 = 0.4$ to ~ 10 Å^{-1}. The integration was carried out between 0 and 7 Å^{-1} (for $s < s_0$ we took $i = -1$). The upper limit of integration was limited (truncated) so as to exclude the "tail" of the intensity curve from the calculations, this tail usually being determined with a poor relative accuracy. The influence of truncation effects on the coordination numbers and the half-widths of the coordination maxima was taken into account by the method of ref. 17. The radial distribution function was constructed in steps of 0.1 Å over the range 2-10 Å. The density of "amorphous" bismuth was taken very close to the density of the crystalline rhombohedral phase, as in ref. 8, equal to 0.0283 atoms/Å^3.

Figures 3-5 illustrate the characteristic curves of the radial atomic density distribution in "amorphous" bismuth films of various thicknesses and at various temperatures. In films thicker than 100 Å, after holding at the condensation temperature (~4.6°K), we find an approximately monotypic coordination structure, which we call "typical" (Table 3). The characteristic feature of this structure consists of the following: After a well-expressed maximum, defining the first coordination sphere, with n ~ 5-6, there follow two less sharp maxima containing altogether 16 atoms, and then a coordination sphere containing over 20 atoms is clearly discerned.

We see from Fig. 3 that for films with a thickness L > 100 Å raising the temperature makes little difference to the radial distribution curve. There is a slight blurring of the coordination structure, the width of the first coordination maxima increasing slightly as the temperature rises (Table 3). We note that the "typical" structure of low-temperature bismuth films differs from the structure of liquid supercooled bismuth (Table 1): It is characterized by a greater number of sharply expressed short-range coordination spheres, the first sphere contains fewer atoms than in the liquid metal, and so forth. In addition to this, we note a similarity between the "typical" structure of "amorphous" bismuth and the coordination structure of liquid bismuth supercooled in the form of thin films (Takagi[9]).

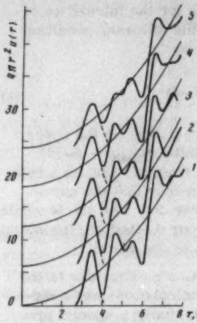

Fig. 3. Radial atomic density distribution curves in a low-temperature bismuth film 120 Å thick: 1) T = 4.65; 2) 17.5; 3) 24.5; 4) 35; 5) 39.5°K.

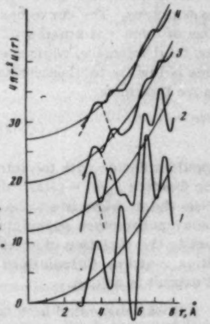

Fig. 4. Radial atomic density distribution curves in a bismuth film 15 Å thick: 1) T = 4.6; 2) 22; 3) 92; 4) 151°K.

In very thin films (L < 100 Å) the initial structure differs from the "typical." The radial atomic density distribution curve for such films contains a small number of sharply featured maxima, which indicates a high degree of structural order (Fig. 4). With rising temperature the radial atomic density distribution curve changes, and the structure approaches the "typical" case (Fig. 4, curve 2). With decreasing thickness of the films the temperature of the transition into the crystalline phase rises sharply (Table 2), as a result of which for very thin films a change in the coordination structure may be followed over a wide temperature range. Raising the temperature leads to the blurring of the coordination structure; this is clearly illustrated by the curves of Fig. 4. Data in relation to the change in the half-width of the coordination sphere with

TABLE 2. "Amorphous" Phase—Crystal Transition Temperature as a Function of the Thickness of Bismuth Films

Thickness, Å	16	32	34	40	60	68	113	122	140	158	250	375
Temperature, °K	190	120	129	115	102	83	50	45	34	24	21	12
Method	ED	ED	R	ED	R	R	ED	ED	ED	R	R	ED

ED) electron diffraction, R) jump in resistance.

TABLE 3. Coordination Structure of Low-Temperature Bismuth Films

Thicknesses	T, °K	r_1, Å	n_1	r_2	n_2	r_3	n_3	r_4	n_4	$A_{1/2,\infty}$	Type of structure
15	4.6	3.8	9			5.1	11	6.6	~21		Initial
	22	3.53	8	4.6	9	5.5	~ 5	6.6	~18	0.68	Typical
	92	3.65	5.5	4.8	10	6.6		7.3		1.29	»
	151	3.8	6	4.8						1.63	»
	203	~4								1.96	»
32	4.6			4.7	16			6.7	~30		Initial
	5.4	3.55	7	4.78	9	5.9	9	7	~24	0.63	Typical
	33.5	3.53	5.8	4.6	7	5.5	10	6.7	~20	0.87	»
	41	3.5	6.1	4.7	8.8	5.8	~12	7	~25	1.09	»
	96	3.5	5.5	4.7	9	5.9	~12	7	~22	1.05	»
70	4.5	3.45	6	4.67	8.4	5.7	8	6.7	~20	0.9	»
113	4.6	3.45	5.5	4.67	9	5.5	7	6.8	~22	1.2	»
120	4.6	3.42	6.2	4.6	8	5.5	7.8	6.7	~20	0.76	»
	17.5	3.47	5	4.63	8	5.5	8	6.7	~19	0.63	»
	24.5	3.43	5.8	4.67	8.5	5.5	8	6.6	~19	0.9	»
	35	3.43	6	4.6	7.4	5.5	8	6.7	~20	0.96	»
	39.5	3.45	5.9	4.62	7.5	5.45	8	6.7	~20	1.09	»
290	4.65	3.5	5.3	4.7	8	5.7	10	6.9	~22	0.78	»
450*	4.7; 0′	3.55	7	4.5	8	5.5	9	6.6	~18		Initial
	12′	3.43	4	4.5	6	5.3	7				Transitional
	18′	3.53	4.7	4.57	7.2	5.3	7.5	6.6			
	30′	3.5	4.4	4.5	6.8	5.5	10	6.5	~22		Typical

*Time delay. $A_{1/2\infty}$ is the half-width of the first coordination maximum, corrected as in ref. 17.

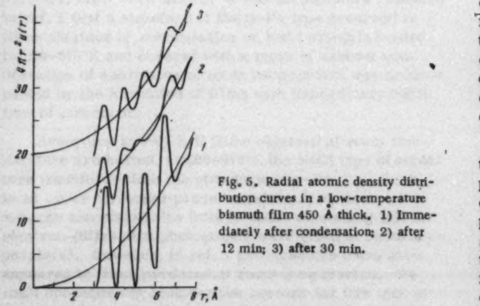

Fig. 5. Radial atomic density distribution curves in a low-temperature bismuth film 450 Å thick. 1) Immediately after condensation; 2) after 12 min; 3) after 30 min.

increasing temperature are contained in Table 3.

In thick films, as indeed in very thin films, the structure recorded immediately after the end of condensation (Fig. 5) is distinguished from the "typical" structure by the fact that the coordination spheres are sharply defined. After a holding period this initial structure transforms into the "typical" structure; it follows from the observations already made that this process passes through a stage of disordering (Fig. 2). The "typical" structure in films of different thicknesses is characterized by similar radial atomic density distribution curves and the same position of the maxima; there is a tendency for the number of atoms in the first coordination sphere to diminish with increasing film thickness.

Thus the results here obtained show that in very thin films the spatial coordination of the atoms is more sharply defined than in thick low-temperature bismuth films. Evidently in the first case there is a tendency toward a certain two-dimensional (surface) ordering in the short-range coordination. On raising the temperature or increasing the film thickness, when the influence of surface coordination weakens, the initial coordination structure vanishes. On producing a thick layer, the structure characteristic of very thin layers is reproduced, first of all, while the process of rearrangement into the "typical" structure lags behind and is only completed after condensation has ended.

This variability in the coordination structure of low-temperature bismuth films may serve as a basis for explaining the peculiar characteristics of the physical properties of these materials noted in the introduction, in particular the dependence of the resistivity and critical superconconducting temperature T_C on the film thickness, the appearance of superconductivity after holding the film for a certain period after the end of condensation, the reduction in the resistance of thin films with rising temperature, and so on.

CONCLUSION

In the condensation of molecular beams of bismuth at liquid-helium temperature a low-temperature phase is created; its structure may be considered amorphous if measured by the smallness of the regions of coherent electron scattering. Nevertheless, at any rate for very thin films, there is a tendency toward the formation of a sharply expressed coordination in the immediate surroundings of any particular atom.

---

1)It should be remembered that for our particular materials oscillations in J practically vanish at $s \sim 8$; as $s \to 0$ the coherent intensity tends to zero asymtotically; however, it also enters into all the calculations with a factor s, which renders the situation unimportant for small s.

[1] R. Hilsch, Rec. Intern. Conf. Low Temp. Phys., Oxford (1951).
[2] W. Buckel and R. Hilsch, Z. Phys., 138, 109 (1954).
[3] N. V. Zavaritskii, Dokl. Akad. Nauk SSSR, 86, 687 (1952); 91, 787 (1953).
[4] B. I. Belevtsev, Yu. F. Komnik, and L. A. Yatsuk, Fiz. Tverd. Tela, 14, 2177 (1972) [Sov. Phys.—Solid State, 14, 1887 (1973)].

[5] W. Buckel, Z. Phys., 138, 136 (1954).
[6] H. Richter and S. Steeb, Naturwissenschaften, 51, 512 (1968).
[7] H. Richter, Z. Phys., 172, 530 (1963).
[8] S. Fujime, Japan. J. Appl. Phys., 5, 764 (1966).
[9] M. Takagi, J. Phys. Soc. Japan, 11, 396 (1956).
[10] B. G. Lazarev, E. E. Semenenko, and A. I. Sudovtsev, Fiz. Met. Metalloved., 28, 954 (1969).
[11] V. V. Postnikov, Dissertation [in Russian], Voronezh. Politekh. Inst. (1971).
[12] J. M. Ziman, Phil. Mag., 6, 1013 (1961).
[13] L. I. Tatarinova, Electron Diffraction of Amorphous Substances [in Russian], Nauka, Moscow (1972).
[14] B. K. Vainshtein, Kristallografiya, 2, 29 (1957) [Sov. Phys.—Crystallogr., 2, 24 (1958)].
[15] R. Leonhardt, H. Richter, and W. Rossteutscher, Z. Phys., 165, 121 (1961).
[16] Yu. F. Komnik, Kristallografiya, 11, 213 (1966) [Sov. Phys.—Crystallogr., 11, 205 (1966)].
[17] A. I. Andrievskii, I. D. Nabitovich, Ya. I. Stetsiv, and Ya. V. Voloshchuk, Ukr. Fiz. Zh., 13, 1596 (1968).

Structure of thin lead telluride films

E. V. Rakova and S. A. Semiletov
Institute of Crystallography,
Academy of Sciences of the USSR
(Submitted January 3, 1973)
Kristallografiya, 18, 1272-1274 (November-December 1973)

A detailed electron-diffraction study of the structure of thin PbTe films obtained by vacuum condensation of NaCl substrates covered with a layer of carbon and on celluloid films at temperatures of 20-570°K was carried out. By analyzing the intensities of the reflections on the electron-diffraction patterns taken at different angles to the surface of the film and comparing them with the theoretical intensities calculated for the cases of the ordered (NaCl-type) and disordered (α-Po type) structure of PbTe, it is shown that the absence of reflections with odd indices on the normal photographs is associated with the predominant orientation of the crystals on the substrate and the formation of a [001] texture, and not with the existence of a disordered structure of the α-Po type.

Like its closest analogs, lead sulfide and selenide, lead telluride has a structure of the NaCl type (a = 6.46 Å). However, according to certain authors[1,2] a structure of the α-Po type with a primitive cubic cell (a = 3.21-3.23 Å) arises in thin films, the Pb and Te atoms being arranged in a disordered manner in the same crystallographic position. The authors of the papers cited came to this conclusion as a result of an analysis of electron-diffraction patterns, in which only reflections with even indices were observed, while all the reflections with odd indices (111, 311, 331, etc.) were absent. It was furthermore indicated in ref. 2 that a structure of the α-Po type occurred in films obtained by condensation on NaCl crystals heated to 500-570°K and covered with a layer of carbon; condensation of substrates at room temperature was accompanied by the formation of films with the ordinary NaCl type of structure.

According to ref. 2, if films obtained at room temperature are heated, at 500-570°K the NaCl type of structure transforms into the structure of α-Po, i.e., there is an order–disorder phase transition.[2] However, the reverse transformation fails to occur on cooling (all the electron-diffraction photographs were taken at room temperature). However, in ref. 1 the structure α-Po also appeared in films produced at room temperature. We shall subsequently consider the reasons for this lack of agreement.

The structure of α-Po with its primitive cubic lattice is of fundamental interest; this interest is associated with the fact that for lead telluride there may be a phase transition into the ferroelectric state due to the order–disorder transition. On the other hand, structures with the cubic primitive cell are extremely rare, so that the possible existence of such a structure in thin PbTe films calls for meticulous verification.

In view of this we made a detailed electron-diffraction study of the structure of thin (100-600 Å) PbTe films. The samples for study were obtained (as in refs. 1 and 2) by vacuum condensation on a substrate heated to 500-570°K or else held at room temperature. The substrates were NaCl crystals covered with a carbon film (as in ref. 2), or else celluloid films (as in ref. 1). In order to discover the possibility of a texture being created we recorded the patterns at an angle and analyzed the intensities of the reflections. We shall now present the results obtained by studying two series of films (T_S = 500-570 and 300-350°K).

HIGH-TEMPERATURE FILMS

On the electron-diffraction patterns of such samples taken at an angle of 90° to the surface (Fig. 1a, normal photographs), as in the films presented in ref. 2, reflections with odd indices are completely absent. However, on the photographs taken at an angle of 45° (oblique recordings, Fig. 1b) weak (111), (311), and (511) reflections may easily be seen.

Thus the vanishing of the reflections with odd indices in the photographs taken at an angle of 90° is in this case associated, not with a statistical disposition of the Pb and Te atoms, but with a preferred orientation of the PbTe crystallites (face of the cube parallel to the substrate), i.e., with the creation of texture.

We note that the possibility of texture formation was considered in ref. 2; however, it was eliminated because the 222 and 422 rings appeared on the photographs taken at normal incidence, while x-ray diffraction patterns taken at different angles revealed no texture. The 222 and 422 rings are also present on our own electron-diffraction patterns, yet nevertheless the patterns recorded at 45° to the beam quite clearly indicate the presence of texture. As regards the x-ray patterns which supposedly exhibited no texture, this remains uncertain.

Nevertheless, in order to leave no doubts as to the possible influence of the conditions of film deposition in our own experiments and in ref. 2 on the structure, we

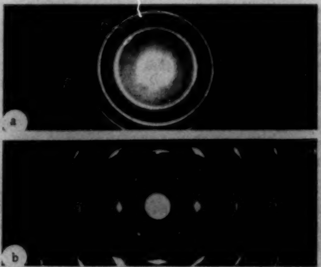

Fig. 1. Electron-diffraction patterns of high-temperature PbTe samples. a) Normal recording; b) recording at an angle of 45°; the 111, 311, and 511 reflections may be seen.

TABLE 1. Intensities of the Reflections for a Structure of the α-Po Type

hkl	d, Å	I_{exp} (ref. 2)	I_{theo}
100	3.23	v.v.s.	272
110	2.28	v.s.	176
111	1.86	v.w.	54
200	1.61	m.,s	23
210	1.44	s.	58
211	1.31	w.	40
220	1.14	m.	10

TABLE 2. Reflection Intensities for the NaCl Type of Structure

hkl	d, Å	I_{theo}	I_{exp} (ref. 2)	I_{exp} (ref. 1)	I_{exp} (our data)
111	3.72	11	v.w.	—	—
200	3.23	272	v.v.s.	v.v.s.	v.v.s.
220	2.28	176	v.s.	v.s.	v.s.
311	1.95	5	m.	—	—
222	1.86	54	w.	m.s.	s.
400	1.61	23	s.	w.	m.
331	1.48	2	—	—	—
420	1.44	58	m.s.	s.	
422	1.31	40	w.	m.s.	m.s.
333 511	1.24	1	—	—	—

analyzed the intensities of the electron-diffraction rings given in ref. 2 (Fig. 1c). For this purpose we calculated the theoretical intensities of the reflections for a structure of the α-Po type (Table 1) and compared them with the experimental intensities.

We found that in the electron-diffraction pattern in question all the reflections of the hk0 type were intensified (or the reflections with $l \neq 0$, i.e., the 111 and 311, weakened). In particular, the 111 ring was much weaker than the 200 (v.w. and m.s. according to ref. 2), although in the structure of α-Po, as in the NaCl structure (in which these rings have indices 222 and 400), the calculated intensities have values of 54 and 23, i.e., their ratio is reversed. This can only be explained by assuming that in the films studied by Chopra[2] there was a preferential orientation of the crystallites with the (100) face parallel to the substrate, i.e., a [001] texture. A comparison between the intensities of the other reflections in ref. 2 and those calculated for the α-Po structure showed that no agreement existed between them at all (Table 1).

Thus the conclusion arrived at in ref. 2 to the effect that a disordered structure of the α-Po type existed in PbTe films and that order–disorder transitions were taking place must clearly be refuted.

FILMS PRODUCED AT ROOM TEMPERATURE

In this case it was especially vital to establish the reason for the disagreement between the results of refs. 1 and 2. An analysis of the electron-diffraction patterns presented in these papers showed that the discrepancy was associated with an error in indexing the pattern of Fig. 1a in ref. 2: The ring with indices 311 should really have been given the indices 222. The diameter of this ring is about 20 mm, while the diameter of the 311 ring should be 19 mm; apart from this the intensity of the 311 ring cannot be higher than that of the 222 (NaCl structure); their calculated intensities are 5 and 54 (Table 2), while in ref. 2 they were estimated as m. and w., i.e., the first was stronger than the second. Actually these rings should be given the indices 222 and 400, then come 420, 422, and so forth.

As regards the ring with indices (111) (d = 3.72 Å), it is more reasonable to regard this as having been derived from the paraffin which is very often present in diffraction patterns and has a very similar value of d (3.73 Å). Hence in the photograph presented in ref. 2 reflections with odd indices are absent, in agreement with ref. 1.

In our own electron-diffraction patterns obtained with normal and oblique incidence the reflections in question are also missing (Fig. 2a, b), and we may therefore conclude that at room temperature the α-Po structure with a statistical distribution of atoms is indeed formed. A conclusion of this kind was arrived at in ref. 1, although, as we ourselves think, this was premature.

Our own analysis of the intensities showed that, despite the absence of a clearly expressed texture, a partial orientation of the crystallites with the (100) face parallel to the substrate nevertheless occurred, and the absence of weak reflections with odd indices from the photographs (the intensity of such reflections is proportional to the square of the difference of the atomic amplitudes of lead and tellurium, in contrast to the even reflections, in which it is proportional to the square of the sum of the atomic amplitudes) could thus be associated with that very fact. It should be remembered that in the patterns obtained from the films prepared at room temperature a strong background appears and this considerably impedes the detection of the reflections with odd indices. Results which we obtained with PbS films also bear witness to the truth of this conclusion.

It is asserted in ref. 2 that in these (PbS) films a structure of the α-Po type with a disordered disposition of the atoms is also formed; however, every one of our own PbS patterns contained reflections with odd indices. This is due to the fact that the intensities of these reflections are considerably greater than those of the PbTe films, in agreement with the greater difference between the atomic numbers of Pb and S. However, the intensities

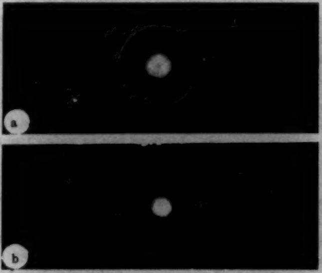

Fig. 2. Electron-diffraction patterns of low-temperature PbTe samples. a) Normal recording; b) recording at an angle of 45°; rings with even indices are stretched out into arcs.

of these reflections are lower than the theoretical values in this case also, in view of the partial orientation of the crystallites with the (100) face parallel to the substrate. The condensation of PbS on heated substrates is always, however, accompanied by the formation of texture; hence reflections with odd indices are missing in this case as well.

---

[1] A. Feltynowski, I. Glass, and L. Grelewicz, Exptl. Tech. Phys., 6, 17 (1958).

[2] K. L. Chopra, R. H. Duff, and W. J. Mallio, Seventh Intern. Congress of Electron Microscopy, Vol. 2, Grenoble (1970), p. 425.

Structures of leucophoenicite, $Mn_7[SiO_4]_2[(SiO_4)(OH)_2]$, and synthetic Cd orthogermanate, $Cd_3[GeO_4](OH)_2$

E. L. Belokoneva, M. A. Simonov, and N. V. Belov
M. V. Lomonosov Moscow State University

(Submitted July 9, 1973)
Kristallografiya, 18, 1275-1277 (November-December 1973)

Two peculiarities stand out in the crystal structure of monoclinic leucophoenicite, $Mn_7[SiO_4]_2[(SiO_4)(OH)_2]$, which was worked out rather recently by Moore,[1] and has parameters $a = 10.842 \pm 0.019$ Å, $b = 4.826 \pm 0.006$ Å, $c = 11.324 \pm 0.009$ Å, $\beta = 103.93 \pm 0.09°$, Z = 4, and space group $P2_1/a$ (determined with λ Mo Kα radiation from 1207 independent nonzero reflections, final value $R_{hkl} = 0.07$). The first and more interesting peculiarity is a crystal-chemical one: the coupling of two Si_1 tetrahedra along an edge with statistical distribution of only one Si_1 atom in them and also with statistical replacement of two O atoms in the tetrahedron by (OH) groups.[1)] The second feature – a more geometrical one – pertains to the motif of joining the Mn octahedra into a new form of cation chains, which are different from the chains of octahedra in representatives of the humite group, from which leucophoenicite was first taken in accordance with the formula $Mn(OH)_2 \cdot 3Mn_2SiO_4$. In minerals of the humite group (olivine, chondrodite, clinohumite) (Figs. 1a-1c), a band of "generalized" olivine type appears to be a variable foundation. Comparing the chains of octahedra in leucophoenicite (Fig. 1d) with the olivine–chondrodite bands (Figs. 1a-1c), Moore assumed a hypothetical silicate structure (Fig. 1e) with a band which had been established earlier in kotoite, $Mg_3(BO_3)_2$, and its $Mn_2(BO_3)_2$ analog[2] and which, like olivine, should in its variation characterize the whole family of minerals including the observed representative, leucophoenicite (Fig. 2). The chemical formula of the hypothetical photomineral is $Mn_3[(SiO_4)(OH)_2]$, and the orthorhombic cell parameters are $a = 9.0$ Å, $b = 4.8$ Å, $c = 5.3$ Å, Z = 2. It is most important that the Si atoms, as in leucophoenicite, be located in tetrahedra joined along an edge and statistically half-populated.

The cation bands of octahedra predicted by Moore are observed in the structure of orthorhombic Cd orthogermanate, $Cd_3[GeO_4](OH)_2$, obtained by Duderov and Dem'yanets during a study of crystallization in the $Na_2O-CdO-GeO_2-H_2O$ system. We have solved this structure, which has parameters[3] $a = 9.89 \pm 0.01$ Å, $b = 5.784 \pm 0.004$ Å, $c = 5.036 \pm 0.004$ Å, Z = 2. The space group first established, P2nn (crystals with weak piezoelectric effect), actually required statistical distribution of one Ge atom in two tetrahedra joined along an edge, which in silicates, until the structure of leucophoenicite was worked out, was supposed to exist only in fibrous β-quartz.[4] A detailed P(uvw) analysis substantiated the assumption of an n_y glide plane as a pseudoplane, and finally another form of oriented group of the same class (horseshoe) $C_{2v}^7 - Pm2_1n$ was chosen. The refined structure model is quite compatible with the structure of Moore's hypothetical mineral $Mn_3[(SiO_4)(OH)_2]$. The Cd octahedra in the orthogermanate $Cd_3[GeO_4](OH)_2$ are built into the same chain which was assigned to the hypothetical silicate. The Ge atoms are found in isolated tetrahedra formed by O atoms and fill

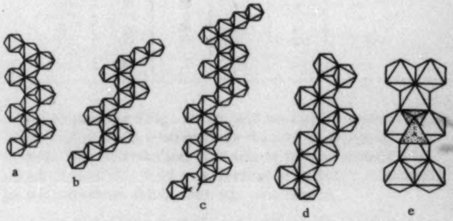

Fig. 1. Cation chains of octahedra in the simplest orthosilicates.

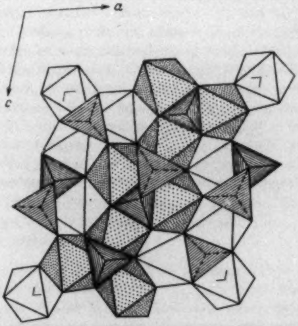

Fig. 2. Leucophoenicite, $Mn_7[SiO_4(OH)_2]$. xz projection of the structure.

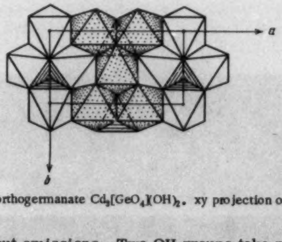

Fig. 3. The orthogermanate $Cd_3[GeO_4](OH)_2$. xy projection of the structure.

them without omissions. Two OH groups take part in the formation of a neighboring tetrahedron joined along an O–O edge, but it remains empty (Fig. 3).

Thus, the synthetic Cd orthogermanate $Cd_3[GeO_4](OH)_2$ has been found to be compatible with the hypothetical Mn protosilicate $Mn_3[(SiO_4)(OH)_2]$, with an analogous triad of orthorhombic cell parameters (allowance being made for the difference in ionic radii for the pairs Cd–Mn and Ge–

Si) and with a compatible general structural motif. However, within space group $Pm2_1n$ it is rather probable that only one neighboring tetrahedral vacancy along the edge is filled, the more so that the corresponding tetrahedra in the group C_{2v}^7 are not associated with the symmetry.

[1)] Two pairs of such double tetrahedra with two Si atoms statistically distributed in them are contained in the cell.

[1] P. D. Moore, Am. Mineralogist, 55, 1146 (1970).

[2] T. Watanabe, A. Kato, T. Matsumoto, and I. Ito, Japan Acad. Proc., 39, 170 (1963).

[3] E. L. Belokoneva, M. A. Simonov, and N. V. Belov, Dokl. Akad. Nauk SSSR, 207, 850 (1972)[Sov. Phys.—Dokl., 17, 1124 (1973)].

[4] G. V. Kukolev, Physical Chemistry of Silicon and Physical Chemistry of Silicates [in Russian], Vysshaya Shkola, Moscow (1966).

Crystal structures of $RbNbO(SO_4)_2$ and $NH_4NbO(SO_4)_2$

A. A. Kashaev, G. E. Postoenko, and É. A. Zel'bst
Irkutsk State Pedagogical Institute

(Submitted September 8, 1972; resubmitted December 27, 1972)
Kristallografiya, 18, 1278-1280 (November-December 1973)

As noted earlier,[1] the double niobium sulfates with rubidium and ammonium are isostructural with $CsNbO(SO_4)_2$. The results of the refinement of atomic coordinates in the $RbNbO(SO_4)_2$ and $NH_4NbO(SO_4)_2$ structures are reported in this work.

Experimental values of F_{hkl} were obtained from the h0l and hk0–hk4 layer lines on a Weissenberg goniometer with Mo radiation (the crystals had the shape of fibers not exceeding 0.1-0.2 mm in diameter). During calculation of the F_{hkl} values, corrections for the Lorentz and polarization factors were introduced.

The atomic coordinates were first established from three-dimensional electron density syntheses. The final refinement was done for the centrosymmetric space group $Pnam$, which was preferred over the group $Pna2_1$ on the basis of analysis of the arrangement of peaks on the xz Patterson projection.[1]

Atomic coordinates for $RbNbO(SO_4)_2$ are given in Table 1 (R_{hkl} = 0.167 for 540 independent reflections), and the major interatomic distances are given in Table 2. Analogous data for $NH_4NbO(SO_4)_2$ are located in Tables 3 and 4 (R_{hkl} = 0.131 for 460 reflections).

The principal details of the structure of the sulfates which were studied are close to those established in $CsNbO(SO_4)_2$. The projection of the ammonium sulfate on the xy plane is shown in Fig. 1, for which the numbers inside the polyhedra indicate the values of the z coordinates of the cation, and NH_4^{1+} ions are denoted by circles. A fragment of the structure of a layer, which gives a representation of the nature of the linking of the octahedra and tetrahedra, is illustrated in Fig. 2.

As in the double sulfate of cesium, in the $RbNbO(SO_4)_2$ and $NH_4NbO(SO_4)_2$ structures the niobium cation is dis-

TABLE 1. Atomic Coordinates in the $RbNbO(SO_4)_2$ Structure (a = 16.96 Å, b = 8.76 Å, c = 5.16 Å)

Atoms*	x/a	y/b	z/c	B
Rb	0.0602	0.1600	0.25	0.97
Nb	0.3100	0.0783	0.25	0.59
S_1	0.3056	0.4793	0.25	0
S_2	0.4298	0.1260	0.75	0.221
O_1	0.2239	0.0655	—0.0253	1.50
O_2	0.3779	0.1684	—0.0246	1.43
O_3	0.2708	0.3282	0.25	1.03
O_4	0.0440	0.4788	0.25	1.03
O_5	0.5088	0.7539	0.25	1.03
O_6	0.3931	0.4829	0.25	1.03
O_7	0.8356	0.6109	0.25	1.03

*The multiplicity of the O_1 and O_2 atoms is 8, and for the rest of the atoms it is 4.

TABLE 2. Interatomic Distances (in Å) in the $RbNbO(SO_4)_2$ Structure.

S_1-tetrahedron	S_2-tetrahedron	Nb-octahedron
$S_1 - O_1 = 1.48$ (2)	$S_2 - O_2 = 1.50$ (2)	$Nb - O_1 = 2.04$ (2)
$S_1 - O_3 = 1.45$	$S_2 - O_4 = 1.37$	$Nb - O_2 = 1.99$ (2)
$S_1 - O_6 = 1.48$	$S_2 - O_5 = 1.48$	$Nb - O_3 = 2.28$
Average 1.48	Average 1.47	$Nb - O_7 = 1.71$
$O_1 - O_1 = 2.32$	$O_2 - O_2 = 2.32$	$O_1 - O_1 = 2.84$
$O_1 - O_3 = 2.38$	$O_2 - O_4 = 2.42$	$O_2 - O_2 = 2.84$
$O_1 - O_6 = 2.44$	$O_2 - O_5 = 2.35$	$O_1 - O_3 = 2.78$
$O_3 - O_6 = 2.48$	$O_4 - O_5 = 2.42$	$O_1 - O_7 = 2.84$
		$O_2 - O_3 = 2.70$
	$Rb - O = 2.81-3.86$	$O_2 - O_7 = 2.91$
		$O_1 - O_2 = 2.76$

TABLE 3. Atomic Coordinates in the $NH_4NbO(SO_4)_2$ Structure (a = 27.01 Å, b = 8.69 Å, c = 5.13 Å)

Atoms*	x/a	y/b	z/c	B
N	0.0470	0.1408	0.25	0.88
Nb	0.3094	0.0814	0.25	0.84
S_1	0.3080	0.4800	0.25	0.88
S_2	0.4324	0.1308	0.75	0.88
O_1	0.2199	0.0749	—0.0221	0.88
O_2	0.3786	0.1653	—0.0265	0.88
O_3	0.2717	0.3310	0.25	0.88
O_4	0.0413	0.4664	0.25	0.88
O_5	0.4997	0.2488	0.75	0.88
O_6	0.3886	0.4845	0.25	0.88
O_7	0.1663	0.3986	0.75	0.88

*The multiplicity of the O_1 and O_2 atoms is 8, and for the rest of the atoms it is 4.

TABLE 4. Interatomic Distances (in Å) in the $NH_4NbO(SO_4)_2$ Structure

S_1-tetrahedron	S_2-tetrahedron	Nb-octahedron
$S_1 - O_1 = 1.51$ (2)	$S_2 - O_2 = 1.47$ (2)	$Nb - O_1 = 2.07$ (2)
$S_1 - O_3 = 1.44$	$S_2 - O_4 = 1.50$	$Nb - O_2 = 1.98$ (2)
$S_1 - O_6 = 1.45$	$S_2 - O_5 = 1.54$	$Nb - O_3 = 2.26$
Average 1.48	Average 1.49	$Nb - O_7 = 1.64$
$O_1 - O_1 = 2.36$	$O_2 - O_2 = 2.31$	$O_1 - O_1 = 2.81$
$O_1 - O_3 = 2.42$	$O_2 - O_4 = 2.48$	$O_2 - O_2 = 2.86$
$O_1 - O_6 = 2.32$	$O_2 - O_5 = 2.46$	$O_1 - O_3 = 2.66$
$O_3 - O_6 = 2.39$	$O_4 - O_5 = 2.56$	$O_1 - O_7 = 2.84$
		$O_2 - O_3 = 2.71$
	$NH_4 - O = 2.83-4.16$	$O_2 - O_7 = 2.70$
		$O_1 - O_7 = 2.81$

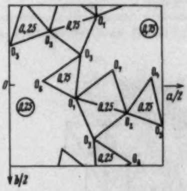

Fig. 1. Projection of the $NH_4NbO(SO_4)_2$ structure.

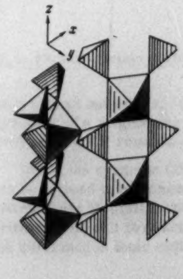

Fig. 2. Fragment of the $NH_4NbO(SO_4)_2$ structure.

TABLE 5. Some (Cs, Rb, NH_4)−O Interatomic Distances (in Å)

Oxygen atom	Cation		
	Cs	Rb	NH_4
O_1	3.33	3.22	3.30
O_4	3.04	2.81	2.83
O_5	3.08	2.95	2.87
O_6	3.15	3.09	2.89
O_6'	3.39	3.12	3.09

placed substantially from the center of the octahedron in the direction toward the free vertex O_7. However, the octahedron has nearly regular shape and, in particular, the sum of the Nb−O_3 and Nb−O_7 interatomic distances in all three compounds is close to twice the Nb−O distance in other directions (~4 Å). Displacement of the niobium from the center of the octahedron evidently is associated with the fact that the O_7 atom expends the greater part of its valence force on the bond with this cation, since it is located at a great distance from the alkali cations (3.70, 3.72, and 3.96 Å for Cs, Rb, and NH_4 sulfates, respectively) and does not have contact with sulfur atoms. The strong Nb−O_7 bond results in increase of the distance of the octahedral cation from the opposite O_3 vertex, i.e., a weakening of the Nb−O_3 bond. Under these conditions, atom O_3 should expend a large part of its valence force on the bond with the S_1 atom, which also finds expression in the decrease of the length of the S_1−O_3 bond. For all three sulfates studied, this bond is the shortest in the S_1 tetrahedron (see Table 3 in ref. 1 and Tables 2 and 4 of this paper).

The alkali cations in the structure are located in surroundings of differently removed oxygen atoms. Values of some of the cation−oxygen distances for the three sulfates studied are given in Table 5. The values of the table confirm the generally known fact that the Rb^{1+} and NH_4^{1+} cations are approximately equal in size and are noticeably smaller than the Cs^{1+} cation. This circumstance also seems to explain the difference in parameters of the unit cell and atomic coordinates of the Cs sulfate, on the one hand, and the Rb and NH_4 sulfates on the other, as well as the closeness of structures of the two latter sulfates. The small difference in atomic coordinates in the Rb and NH_4 sulfate structures evidently is caused by the anisotropy of shape of the NH_4^{1+} cation.

---

[1] A. A. Kashaev and G. V. Sokolova, Kristallografiya, 18, 620 (1973) [Sov. Phys.—Crystallogr., 18, 388 (1973)].

Unit-cell parameters and space groups of several pyridino-anthraquinones

O. A. Mikhno, Z. I. Ezhkova, and M. I. Evstratova
Scientific-Research Institute of Raw Materials and Pigments

(Submitted December 7, 1972)
Kristallografiya, 18, 1281-1282 (November-December 1973)

During an x-ray diffraction study of the heterocyclic derivatives of anthraquinone,[1,2] we determined the unit-cell parameters and space groups of three anthraquinone derivatives containing a pyridine cycle (Table 1). These data were obtained from rotation and Weissenberg x-ray film patterns using Cu radiation.

I. 6-Chlornaphtho[2,3-h]-quinoline-7-12-dion(6-chlor-α-pyridinoanthraquinone). The synthesis of this compound (as in the case of compound II) is described in ref. (3). Crystals grown from a solution in chlorobenzene are in the form of elongated prisms of reddish-brown color and 0.2×0.2 mm cross section.

II. 5-Chlornaphtho[2,3-h]quinoline-7,12-dion(5-chlor-α-pyridinoanthraquinone). Crystals of this compound were grown as pale yellow needles 0.1×0.1 mm in cross section from a solution in dimethylformamide.

III. 7,14-dioxybenzo[1,2-h:4,5-h']diquinoline. This compound was synthesized by reduction of the respective quinone (benzo[1,2-h : 4,5-h') diquinoline-7,14-dion). Needle-like crystals of a reddish-brown color were grown from a solution in dimethylformamide. Crystals of all the compounds were grown at room temperature from weakly supersaturated solutions.

For the 6-chlor-α-pyridinoquinone, we visually measured the intensities of 620 hk0-hk4 reflections, and determined the molecular structure. The x and y coordinates of the Cl atom were found from a P(u, v) Patterson projection. On the basis of these coordinates we obtained several possible variations for arrangement of a molecular projection in the (001) plane. The smallest discrepancy factor R for one of the variations was 0.580. Refinement by the least-squares method was carried out to R = 0.140. The refined atomic coordinates are given in Table 2.

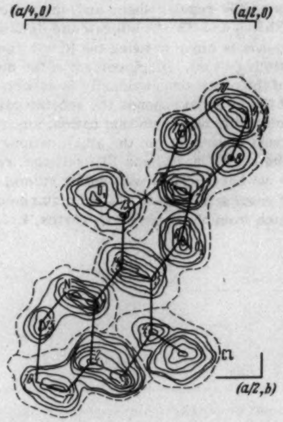

Fig. 1. Projection of the 6-chlor-α-pyridinoquinone molecule on the (001) plane.

TABLE 1. X-Ray Diffraction Data for Three Anthraquinone Derivatives Having a Pyridine Cycle

Sample number	Structural formula	Unit-cell parameters	Number of molecules per unit cell	X-ray density (g·cm^{-3})	Space group
I	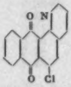	$a = 23.87 \pm 0.06$ A $b = 8.85 \pm 0.02$ A $c = 5.96 \pm 0.02$ A $\beta = 94°20' \pm 10'$ $V = 1255$ A^3	4	1.56	$P2_1/a$
II	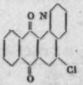	$a = 36.69 \pm 0.10$ A $b = 3.82 \pm 0.02$ A $c = 38.76 \pm 0.10$ A $\beta = 109°10' \pm 10'$ $V = 5134$ A^3	16	1.61	$C2/c$
III	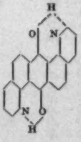	$a = 13.50 \pm 0.03$ A $b = 14.08 \pm 0.03$ A $c = 3.79 \pm 0.02$ A $\beta = 101° \pm 10'$ $V = 707$ A^3	2	1.47	$P2_1/a$

TABLE 2. Atomic Coordinates of 6-Chlor-α-pyridinoquinone

Atom	x	y	Atom	x	y
Cl	0.418	0.937	C_8	0.468	0.372
O_1	0.316	0.465	C_9	0.485	0.251
O_2	0.422	0.617	C_{10}	0.457	0.213
N	0.288	0.757	C_{11}	0.416	0.308
C_1	0.318	0.795	C_{12}	0.400	0.433
C_2	0.316	0.945	C_{13}	0.352	0.525
C_3	0.350	0.984	C_{14}	0.351	0.680
C_4	0.380	0.876	C_{15}	0.262	0.860
C_5	0.381	0.728	C_{16}	0.260	0.014
C_6	0.411	0.604	C_{17}	0.285	0.054
C_7	0.427	0.467			

The numerical legend of the atoms in Table 2 corresponds to Fig. 1, which shows the electron density projection on the (001) plane, calculated according to the coordinates of Table 2. It is apparent from the projection that the molecule is not planar. The rings of nuclei are twisted with respect to each other.

---

[1] L. A. Chetkina, O. A. Mikhno, and Z. I. Ezhkova, Zh. Strukt. Khim., 12, 187 (1971).

[2] O. A. Mikhno, L. A. Chetkina, and Z. I. Ezhkova, Kristallografiya, 17, 297 (1972) [Sov. Phys.—Crystallogr., 17, 251 (1972)].

[3] M. V. Gorelik, M. I. Evstratova, and I. Ya. Koshcheeva, Zh. Organ. Khim., 4, 1465 (1968); M. V. Gorelik and M. I. Evstratova, Zh. Organ. Khim., 5, 758 (1969)

Hydrothermal synthesis, x-ray diffraction, and thermogravimetric study of rare-earth hydroxychlorides $Ln(OH)_2Cl$

L. N. Dem'yanets, V. I. Bukin, E. N. Emel'yanova, and V. I. Ivanov

Institute of Crystallography,
Academy of Sciences of the USSR

(Submitted February 24, 1972; resubmitted July 11, 1972).
Kristallografiya, 18, 1283-1286 (November- December 1973)

Within the confines of the general problem of rare-earth behavior under hydrothermal conditions, we studied the systems $Ln_2O_3-R-H_2O$ (Ln is La, Pr, Nd, Sm, Eu, Gd, Tb, Dy, and Ho, and R is NH_4Cl). The literature[1-6] records the synthesis and x-ray diffraction study of the hydroxychlorides of yttrium and the specific rare earths Nd, Sm, Gd, and La. The structures of the orthorhombic and monoclinic forms of $Y(OH)_2Cl$ were determined by x-ray methods, and the relation was established between them.[2-4,7,8] The structures were also determined[9,10] for the monoclinic forms of $Sm(OH)_2Cl$, $Er(OH)_2Cl$, and $Gd(OH)_2Cl$, and the lattice parameters of the hydroxychlorides of Y, La, Nd, Sm, and Gd were ascertained.[6] The thermal decomposition process was only examined for several rare-earth hydroxychlorides.[6,8]

The goal of the present work was to obtain a complete picture of the synthesis of the entire series of rare-earth hydroxychlorides, and of the change in lattice parameter as a function of lanthanide atomic number.

Hydrothermal crystallization of the rare-earth hydroxychlorides was performed in systems which practically excluded the effect of other ions on crystallization of the respective compounds. (In a number of the works, rare-earth hydroxychlorides occurred as a secondary phase during the crystallization of other compounds.)

The experimental conditions were as follows: temperature, 450-500°C; fill coefficient, 0.7-0.8; and temperature differential ΔT, 10-20°C. The charge consisted of rare-earth oxides or chlorides; calculated amounts of $La_2O_3(LaCl_3)$, NH_4Cl (dry weight), and H_2O were introduced into the autoclave. The solvent concentration was 10-15 wt.%; the volume ratio of the charge to the aqueous solution varied from 1:2 to 1.7.

The $Ln(OH)_2Cl$ crystals obtained as a result of hydrothermal treatment under an isothermal regime with subsequent slow cooling (Ln = rare earth from La to Ho) usually have a prismatic habit. They are thickly prismatic for the compounds of Nd, Sm, and Ho; platelike prismatic for La, Tb, and Dy; and acicular for Pr and Gd. It should be noted that the crystal habit at C_{NH_4Cl} = constant depends on the temperature conditions. In absence of a temperature gradient, spontaneous formation of needlelike crystals is observed on slow cooling; however, crystals of a thickly prismatic habit are obtained under conditions of a small thermal gradient ΔT(5-10°C).

The possibility was previously shown, as exemplified for the case of $Nd(OH)_2Cl$, of growing single crystals of $Ln(OH)_2Cl$ on a seed by method.[11]

For all the rare-earth hydroxychlorides synthesized (from La to Ho), x-ray powder patterns were obtained (RKD-57 camera, sample diameter 0.3 mm, Fe radiation, Mn filter; or on a URS-50IM diffractometer, Cu radiation Ni filter).

The isostructural nature of the resulting hydroxychlorides was established on the basis of the correspondence of powder patterns and subsequent single-crystal determinations.

The analysis of x-ray data obtained on a $Nd(OH)_2Cl$ crystal established a monoclinic symmetry with the unit-cell dimensions $a = 6.21$, $b = 3.88$, $c = 6.82$ Å, $\beta = 113°$, and space group $P2_1-C_2^2$, or $P2_1/m-C_{2h}^2$. The rare-earth hydroxychlorides of the composition $La(OH)_2Cl$ from La to Ho are thus isostructural to the known[4] monoclinic modification of $Y(OH)_2Cl$.

The unit-cell parameters of all the compounds synthesized (Table 1) clearly express the effect of the lanthanide contraction in the rare-earth hydroxychloride series. The b parameters were measured according to x-ray diffraction rotation photographs, obtained with a calibrated RKV-86 camera. In addition, for crystals rotated around the b axis on a URS-50I diffractometer (cali-

TABLE 1. Results of X-Ray Investigation of $Ln(OH)_2Cl$ Hydroxychlorides

Ln	Unit-cell parameters				Density ρ (calculated)	Unit-cell volume V (Å³)
	a, Å	*b*, Å	*c*, Å	β		
La	6.320	3.98	6.932	113°55′	4.366	159.4
Pr	6.243	3.91	6.846	113°23′	4.581	153.4
Nd	6.213	3.876	6.821	113°11′	4.727	151.0
Sm	6.186	3.81	6.753	112°15′	4.984	147.3
Eu	6.166	3.79	6.734	112°52′	5.066	146.0
Gd	6.150	3.75	6.704	110°41′	5.237	144.6
Tb	6.180	3.71	6.661	109°39′	5.305	143.8
Dy	6.197	3.65	6.626	107°53′	5.433	142.6
Ho	6.198	3.61	6.603	107°04′	5.545	141.2
Y*	6.14	3.62	6.60	107°	3.77	

---

*According to data of ref. (4).

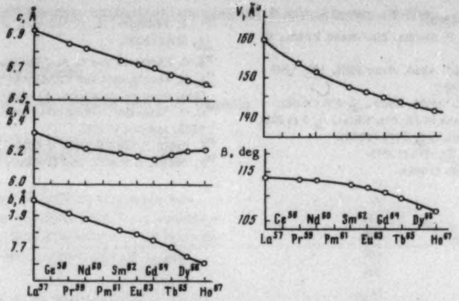

Fig. 1. Change of $Ln(OH)_2Cl$ unit-cell parameters as a function of rare-earth atomic number.

brated to a crystal of quartz), we determined values of the *a* and c parameters, and the monoclinic angles β. The following radiation was used: $\lambda Cu\ K\alpha = 1.54051$, $\lambda Cu\ K\beta = 1.39217$, $\lambda Mo\ K\alpha = 0.70926$, and $\lambda Mo\ K\beta = 0.63225$ Å.

Figure 1 shows graphically the change of the hydroxychloride unit-cell parameters as a function of rare-earth atomic number. The effect of the lanthanide contraction is reflected insignificantly for the *a* parameter, but more sharply for the b and c parameters and angle β, which is apparently associated with the structural peculiarities of the hydroxychlorides. The tendency for a break at gadolinium[12] in the plot of the change of unit-cell parameters of the rare earths not having a first region of crystallochemical instability is only observed for the *a* parameter in the hydroxychlorides.

The hydroxychlorides synthesized were studied thermogravimetrically on a derivatograph similar to the system of F. Paulik, J. Paulik, and L. Erdey.[13,14] The charges were 60–200 mg. Due to the small quantity of large crystals of the Gd, Dy, and Ho compounds, we used in the thermal analysis their mixture with the overall charge mass. Several subsidiary effects thus occured on the DTA and DTG curves of these three hydroxychlorides, indicating the inhomogeneity of the sample. An oxychloride of the composition LnOCl forms as a result of thermal decomposition of the hydroxychlorides, with loss of a molecule of H_2O. Comparison of the experimental and calculated weight loss on heating the hydroxychlorides resulted in preliminary data on the composition of the second phase for a nonsingle-phase sample. For the Gd, Dy, and Ho hydroxychlorides, such phases are apparently the $Ln(OH)_3$ hydroxides and $Ln(OH)_2Cl$ hydroxychlorides of the orthorhombic modification. The presence of the latter phase does not alter the weight loss and appears only as supplementary peaks on the DTA and DTG curves. The results of the thermogravimetric study are presented in Table 2. As an example, Fig. 2 shows the derivatogram of $Nd(OH)_2Cl$.

TABLE 2. Results of Thermal Analyses of Hydroxychlorides

Ln	Temperature of water evolution (°C)	Theoretical weight loss (%)	Weight loss from DTA* (%)	Notes
La	430	8.65	8.7	
Pr	400	8.56	8.5	
Nd	400	8.43	8.4	
Sm	410	8.20	8.2	
Eu	410–440	8.14	8.2	
Gd	430–440	7.95	8.0	$Gd(OH)_3$ impurity (400°C peak)
Tb	440–460	7.89	7.8	
Dy	450	7.77	8.4	$Dy(OH)_3$ impurity (380°C peak)
Ho	390	7.69	7.6	Mixture of two orthorhombic phases (440°C peak) and monoclinic $Ho(OH)_2Cl$

*Accuracy of determination: ± 0.3%.

PRINCIPAL RESULTS

1. Single crystals of rare-earth hydroxychlorides of the composition $Ln(OH)_2Cl$ (Ln = La, Pr, Nd, Sm, Eu, Gd, Rb, Dy, and Ho) were synthesized under hydrothermal conditions.

2. X-ray and thermogravimetric methods were used to study the course of their thermal decomposition. The unit-cell parameters of $Ln(OH)_2Cl$ were measured, and an isostructurality was established to the monoclinic modification of $Y(OH)_2Cl$.

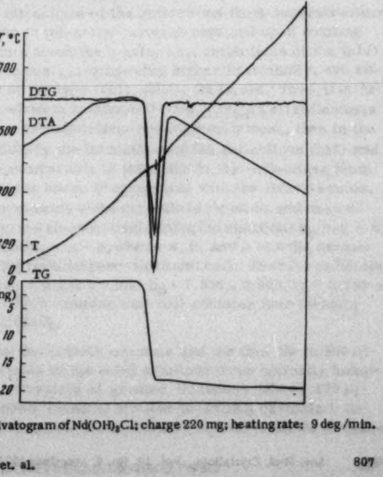

Fig. 2. Derivatogram of $Nd(OH)_2Cl$; charge 220 mg; heating rate: 9 deg/min.

---

[1] N. V. Aksel'rud, Usp. Khim., 32, 800 (1963).

[2] P. V. Klevtsov, R. F. Klevtsova, and L. P. Sheina, Zh. Strukt. Khim., 6, 469 (1965).

[3] R. F. Klevtsova and P. V. Klevtsov, Dokl. Akad. Nauk SSSR, 162, 1049 (1965) [Sov. Phys.—Dokl., 10, 487 (1965)].

[4] R. F. Klevtsova and P. V. Klevtsov, Zh. Strukt. Khim., 7, 556 (1966).

[5] P. V. Klevtsov, Izv. Sib. Otdel. Akad. Nauk SSSR, Ser. Khim., 7, 3 (1963).

[6] F. L. Carter and S. Levinson, Inorg. Chem., 8, 2788 (1969).

[7] K. Dornberg-Schiff, Acta Crystallogr., 22, 435 (1967).

[8] P. V. Klevtsov, Compt. Rend., C266, 385 (1968).

[9] T. M. Tarkhova, N. N. Mironov, and I. A. Grishin, Zh. Strukt. Khim., 11, 556 (1970).

[10] R. F. Klevtsova and L. A. Glinskaya, Zh. Strukt. Khim., 10, 494 (1969).

[11] L. N. Dem'yanets and E. N. Emel'yanova, Kristallografiya, 14, 753 (1969) [Sov. Phys.—Crystallogr., 14, 654 (1970)].

[12] G. A. Bandurkin, Dissertation, Inst. Obshch. Neorg. Khim. Akad. Nauk SSSR, Moscow (1967).

[13] F. Paulik, J. Paulik, and L. Erdey, Acta Chim. Hungar., 10, 61 (1950).

[14] F. Paulik, J. Paulik, and L. Erdey, Z. Analyt. Chem., 160, 241 (1958).

Growth and investigation of binary cadmium oxides with structures of the perovskite type.

II. Cadmium stannate and zirconate

R. I. Spinko, V. N. Lebedev, R. V. Kolesova, and E. G. Fesenko

Rostov State University

(Submitted June 19, 1972; resubmitted November 22, 1972)
Kristallografiya, 18, 1287-1288 (November-December 1973)

The synthesis and investigation of $CdHfO_3$ crystals has been reported previously. The present work is a continuation of the study of cadmium oxides with perovskite-type structures, in particular of $CdSnO_3$ and $CdSn_xZr_{1-x}O_3$ crystals.

SYNTHESIS AND GROWTH OF THE CRYSTALS

Attempts to synthesize cadmium stannate and zirconate by reaction between the corresponding oxides in the solid phase did not give positive results. We established that it is only possible to produce a limited range of solid solutions in the system $CdSn_xZr_{1-x}O_3$. As can be seen from Fig. 1, x assumes values from 0.9 to 0.4. We then turned to synthesis in a solution in molten low-melting-point salts and oxides. The fluxes used were KF, $KF-CdF_2$, $CdO-PbF_2$, and $CdO-PbF_2-B_2O_3$. Using the first two fluxes we synthesized $CdSnO_3$ in the form of a light yellow powder.

The reaction goes nearly to completion after 1 to 1.5 h at 1000°C. Cadmium zirconate was not synthesized in these systems up to temperatures close to the boiling point of KF.

$CdSnO_3$ crystals, as previously,[1] were grown from the $CdO-SnO_2-PbF_2-B_2O_3$ system, whose components were taken in the following molecular ratios: $CdO : SnO_2 : PbF_2 : B_2O_3 = (10 \text{ to } 15) : 1 : 10 : 7$. The process was carried out in platinum crucibles of volume 100 cm^3. The maximum experimental temperature did not exceed 1150°C. The crystallization was done by a method described previously.[2]

Under these conditions we produced platelike and needle-shaped light brown cadmium stannate crystals with linear dimensions up to 8 mm and thicknesses from 20 to 100 μ. In view of the fact that $CdZrO_3$ does not crystallize in this system we attempted to produce crystals of solid solutions in the $CdSn_xZr_{1-x}O_3$ system with as large a cadmium zirconate content as possible. As a result we produced crystals of the solid solution with a minimum value of $x = 0.2$. The compositions of the crystals produced were determined by x-ray structural analysis.

X-RAY STRUCTURAL INVESTIGATIONS AND OPTICAL OBSERVATIONS OF THE PHASE TRANSITIONS

The reduced (containing a single formula unit) perovskite unit cell of $CdSnO_3$ and all of the solid solutions $CdSn_xZr_{1-x}O_3$ which we produced have monoclinic distortion. The reduced unit cell parameters are given in Table 1.

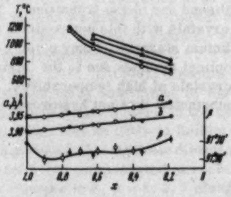

Fig. 1. Unit-cell parameters (○ – ceramic; ● – crystal) and phase transition temperatures (○ and ● show the first phase transition and Δ and ▲ show the second phase transition respectively during heating and cooling) in the system $CdSn_xZr_{1-x}O_3$.

TABLE 1

Crystal composition	Parameters		
	a, c, Å	b, Å	β
$CdSnO_3$	3.905	3.945	91°29′
$CdSn_{0.9}Zr_{0.1}O_3$	3.910	3.944	91°
$CdSn_{0.8}Zr_{0.2}O_3$	3.906	3.945	91°4′
$CdSn_{0.76}Zr_{0.24}O_3$	3.915	3.954	91°12′
$CdSn_{0.7}Zr_{0.3}O_3$	3.915	3.946	91°16′
$CdSn_{0.63}Zr_{0.37}O_3$	3.923	3.958	91°10′
$CdSn_{0.6}Zr_{0.4}O_3$	3.921	3.958	91°16′
$CdSn_{0.5}Zr_{0.5}O_3$	3.930	3.965	91°20′
$CdSn_{0.4}Zr_{0.6}O_3$	3.940	3.970	91°16′
$CdSn_{0.36}Zr_{0.64}O_3$	3.934	3.974	91°9′
$CdSn_{0.2}Zr_{0.8}O_3$	3.944	3.989	91°34′

From x-ray rotation patterns taken using Cu Kα radiation and rotating $CdSnO_3$ and $CdSn_xZr_{1-x}O_3$ ($x = 0.2$) crystals around their *a*, b, and c axes we determined the reduced unit cell (as in the case of $CdHfO_3$) to have all three identity periods doubled.

The intensities of the reflections from superstructure layer lines in the x-ray patterns obtained upon rotating the crystals about the b axis, i.e., reflections of the (h1*l*) and (h3*l*) types..., noticeably higher in intensity, are reflections of the type (1k*l*), (3k*l*), (hk1), etc. Thus, if in the case of cadmium hafnate and $CdSn_{0.2}Zr_{0.8}O_3$ all reflections of the superstructure lines are extremely weak, then in the case of $CdSnO_3$ the intensities of the reflections (h1*l*) and (h3*l*) are comparable in intensity to the reflections from the even layer lines. In agreement with the Bravais rules, the true symmetry of the crystals is rhombic, and one can transform to a rhombic basis using the equations $a_p = a + c$, $b_p = 2b$, and $c_p = a - c$, where *a*, b, and c are the parameters of the reduced perovskite unit cell. Thus for cadmium stannate $a_p = 5.451 \pm 0.003$, $b_p = 7.886 \pm 0.003$, $c_p = 5.596 \pm 0.003$ Å. This rhombic unit cell contains four formula units of $CdSnO_3$.

All of the $CdSnO_3$ crystals and the thin (20 to 100 μ) crystal plates of the solid solutions were optically homogeneous. Crystals of greater thickness (above 150 μ) have complex twinning similar to $CdHfO_3$ crystals.[1] In studying the phase transitions by optical methods in transmitted polarized light in $CdSn_xZr_{1-x}O_3$ crystals we observed two high-temperature transitions as in $CdHfO_3$ (ref. 1). The phase transitions were accompanied by a change in the interference color and a discontinuous change in the twinning pattern during heating and cooling of the crystals.

Figure 1 shows the phase transition temperature as a function of the composition. We see that with increasing x the phase transition temperatures increase. In $Zr_{0.24}O_3$ we only established one phase transition. The second transition in crystals with this composition and the transitions in cadmium stannate (if they exist) could not be observed by optical methods due to the intrinsic fluorescence of the crystals at high temperatures. It should be noted that a substantial thermal hysteresis is seen for both transitions, amounting to 50 to 60 deg.

Thus we have made the first synthesis of $CdSnO_3$ and $CdSn_xZr_{1-x}O_3$; crystals. We have noted the details of the superstructure and determined the true symmetry and the unit cell parameters. $CdSn_xZr_{1-x}O_3$ crystals show phase transitions whose temperatures drop with increasing zirconium content in them.

---

[1] R. I. Spinko, V. N. Lebedev, R. V. Kolesova, and E. G. Fesenko, Kristallografiya, 18, 849 (1973) [Sov. Phys.–Crystallogr., 18, 536 (1974)].

[2] E. G. Fesenko, V. G. Gavriyachenko, R. I. Spinko, M. A. Martynenko, E. A. Grigor'eva, and A. D. Feronov, Kristallografiya, 17, 153 (1971) [Sov. Phys.–Crystallogr., 17, 122 (1972)].

Thermooptical and dielectric properties of $(NH_4)_2BeF_4$ in the neighborhood of the ferroelectric transition

A. T. Anistratov and S. V. Mel'nikova

Institute of Physics, Siberian Branch,
Academy of Sciences of the USSR

(Submitted January 4, 1973)
Kristallografiya, 18, 1289-1291 (November-December 1973)

Ammonium fluoroberyllate single crystals suffer a ferroelectric transition of the first kind,[7] lying close to one of the second kind, at about −97°C. Many published data relating to the crystal structure and certain physical properties of ammonium fluoroberyllate are extremely unusual and somewhat contradictory when compared with such intensively studied ferroelectrics as KDP, TGS, $BaTiO_3$, etc. Thus, according to refs. 2 and 3, ammonium fluoroberyllate is isomorphic with respect to ammonium sulfate at room temperature (space group D_{2h}^{16}), whereas according to ref. 4 it has a superstructure and belongs to the group D_{2h}^{18}. For the dielectric constant ε_b the Curie−Weiss Law is only satisfied in the immediate neighborhood (~ 1°) of T_C, while the Curie constant is very low.[5] The anomaly in ε_b is small, and so is the spontaneous polarization[5]; however, the changes taking place in the birefringence at the transition point are considerable.[6,7] Finally, the spontaneous changes in Δn are three orders of magnitude greater than the changes in birefringence which might be expected by virtue of the electrooptical effect.[7] These and a number of other interesting facts have as yet not received any exhaustive explanation.

It was suggested in ref. 8 that one possible reason for these unusual physical properties lay in the fact that the ferroelectric transition in $(NH_4)_2BeF_4$ was accompanied by a change in the number of atoms in the unit cell, and was described, not by the polarization vector, but by certain parameters having different transformation characteristics. Analysis of the thermodynamic potential[8] shows that in this case there are stable solutions corresponding to two asymmetrical phases, and spontaneous polarziation may arise during a transition between these phases. Recently, fresh measurements were made in relation to the specific heat and volumetric thermal expansion of ammonium fluoroberyllate; two anomalies in c_p and (apparently) three anomalies in β_V were discovered.[9] On the basis of the thermal measurements, and bearing the analysis of ref. 8 in mind, it was accordingly suggested in ref. 9 that there was at least one other phase transition, separated from the ferroelectric transition by an interval of 6°. In view of these data, it is interesting to pursue further precision investigations into the properties of ammonium fluoroberyllate.

In this paper we shall present some measured values of the temperature-induced changes in birefringence; these were recorded with a view to revealing the proposed phase transition. In these measurements we used the method of the Senarmon compensator[10], the sensitivity of which was two orders of magnitude greater than the Berek compensator used in refs. 6 and 7. For control purposes we measured the dielectric constant ε_b at the same time as the thermooptical measurements.

The ammonium fluoroberyllate crystals, were grown from aqueous solutions by evaporation at 25°C. Over a period of three months we grew transparent colorless crystals up to 50 × 30 × 10 mm in volume. For the measurements we cut rectangular plates 5 × 3 × 3 mm in extent along the [100], [010], and [001] directions, respectively, the directions being determined by the x-ray method, using a URS-50I diffractometer. In the thermooptical measurements, light from an OKG-11 helium−neon laser ($\lambda = 6328$ Å) was propagated along these directions. The natural birefringence was compensated at room temperature, while the changes in Δ_i ($i = 1, 2, 3$ along the three principal directions of the orthorhombic crystals respectively) were established by means of a photoelectric reading system[10]. The dielectric measurements were made on a 1007 RFT capacity bridge. As electrodes we used gold leaf applied to the (010) face. The sample temperature was determined with a copper−constantan thermocouple, the readings of which were measured to an accuracy of ±0.1° with a P-306 potentiometer. The temperature−time gradient in the most interesting region of −80 to −100°C was 0.05 deg/min. The measurements were carried out between room temperature and −110°C.

The measurements showed that, up to a temperature of approximately −90°C, the birefringence of ammonium fluoroberyllate varied almost linearly with temperature (curves 1-3 in Fig. 1). In the region of −90°C there is a break in the $\Delta i(T)$ relationships, this being most marked in $\Delta_1(T)$ (curve 2). There are no singularities of $\varepsilon_b(T)$ at this point (curve 4). There is an anomaly in the dielectric constant at −97°C. On the $\Delta_i(T)$ curves, slight bends appear at this temperature. In contrast to the thermal-expansion data of ref. 9, we found no singularities in the region of −83°C.

The absence of any marked anomalies of $\Delta_i(T)$ at the Curie point may at first glance seem surprising. However, a calculation of the changes taking place in the birefringence in terms of the electrooptical constants and spontaneous polarization gives a value[7] of $\sim 10^{-7}$, which is much lower than the sensitivity of the method employed. Nevertheless, for verification purposes we made additional measurements of $\Delta_i(T)$ on a sample cut from a crystal in which two anomalies of c_p appeared in ref. 9. The results of these measurements practically coincided with the data relating to our own crystals, and are presented for purposes of comparison in Fig. 1.

Thus the simultaneous measurements of the thermooptical and dielectric characteristics of ammonium fluoroberyllate confirm the assumption made in ref. 9 as to the existence of a phase transition separated from the already known ferroelectric transformation by an interval of 6-7°. The existence of a such a transition (of a nonferroelectric nature) at any rate qualitatively explains the deviations characterizing the behavior of the optical

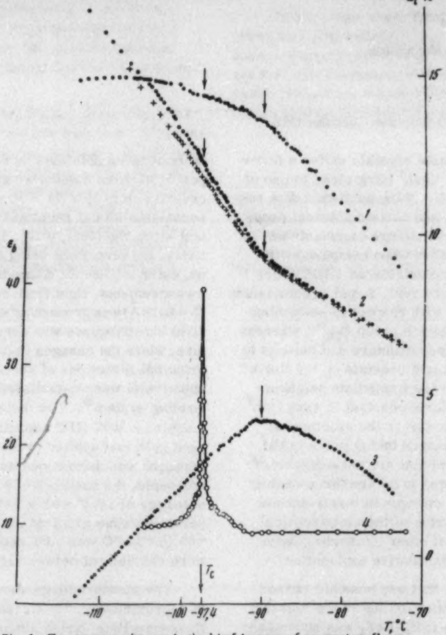

Fig. 1. Temperature changes in the birefringence of ammonium fluoroberyllate, measured with the light propagating along the [001] (1), [100] (2), [010] (3) directions, and also in the dielectric constant (4) ●) Our own crystals, +) those of B. A. Strukov.

properties mentioned at the outset. These deviations are in fact associated, not with the development of spontaneous polarization, but apparently with certain rearrangements taking place in the crystal lattice, and should in fact be described by different characteristic parameters. However, a final solution of the problem as to the nature of the two asymmetrical phases will demand a low-temperature structural analysis of ammonium fluoroberyllate.

The authors wish to thank K. S. Aleksandrov for interest in the work, A. I. Rostuntsova and T. A. Leibovich for growing the crystals, and B. A. Strukov for the crystal used in the control measurements.

---

[1] F. Jona and D. Shirane, Ferroelectric Crystals, Pergamon (1962).

[2] P. L. Mukherjee, Indian J. Phys., 18, 148 (1944).

[3] V. V. Udalvoa, Kristallografiya, 6, 629 (1961) [Sov. Phys.–Crystallogr., 6, 504 (1962)].

[4] Y. Okaya, K. Vedam, and R. Pepinsky, Acta Crystallogr., 11, 307 (1958).

[5] B. A. Strukov, N. D. Gavrilova, and V. A. Koptsik, Kristallografiya, 6, 780 (1961) [Sov. Phys.–Crystallogr., 6, 625 (1962)].

[6] B. A. Strukov, N. D. Gavrilova, and V. A. Koptsik, Kristallografiya, 6, 780 (1961) [Sov. Phys.–Crystallogr., 6, 625 (1962)].

[7] A. T. Anistratov, Rev. Phys. Appl., 7, 77 (1972).

[8] A. P. Levanyuk and D. G. Sannikov, Zh. Eksp. Teor. Fiz., 55, 256 (1958) [Sov. Phys.–JETP, 28, 134 (1969)].

[9] B. A. Strukov, T. P. Skomorokhova, V. A. Koptsik, A. A. Boiko, and A. N. Izrailenko, Kristallograifya, 18, 143 (1973) [Sov. Phys.–Crystallogr., 18, 86 (1973)].

[10] N. M. Melankholin, Methods of Studying the Optical Properties of Crystals [in Russian], Nauka, Moscow (1970).

Optical activity in monoclinic sodium zincogermanate Na_2ZnGeO_4

S. P. Kozyrev, A. B. Gil'varg, B. N. Grechushnikov, and N. V. Belov
Institute of Crystallography, Academy of Sciences of the USSR
(Submitted November 27, 1972; resubmitted January 11, 1973)
Kristallografiya, 18, 1292 (November-December 1973)

In the crystallographic m class, optical activity has only heretofore been observed in the ferroelectric $LiH_3(SeO_3)_2$, converted into single-domain form by an electric field.[1] The present note concerns the detection of a rotation of the plane of polarization in a class m Na_2ZnGeO_4 crystal. The sodium zincogermanate was synthesized when studying hydrothermal crystallization in the $Na_2O - ZnO - GeO_2 - H_2O$ system.[2] Single-crystal samples were presented for our investigation by I. P. Kuz'mina (Hydrothermal Synthesis Laboratory, Institute of Crystallography, Academy of Sciences of the USSR). The monoclinic cell parameters[3] were $a = 7.27$, $b = 5.60$, $c = 5.33$ Å, $\beta = 90°$ (space group Pn). The position of the optic axes relative to the unit cell was determined in a polarization microscope, an x-ray diffraction photograph of the same sample being recorded subsequently. The directions of the optic axes approximately coincide with the [110] and [1$\bar{1}$0] directions, the m plane is perpendicular to the plane of the optic axes, and the angle $2V \approx 80°$ (Fig. 1). In the external facing of the sodium zincogermanate crystals, the $\{110\}$ and $\{1\bar{1}0\}$ faces are the most fully developed. We cut plates, 3 × 5 mm in size and 0.6–1.5 mm thick, parallel to these faces. The normal to the plane of the plates was inclined to the optic axis by ~ 12°. For purposes of control measurement, one plate was cut along the normal to the optic axis.

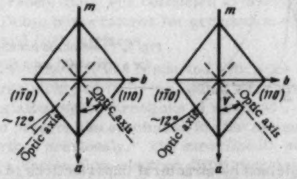

Fig. 1. Positions of the optic axes in the biaxial Na_2ZnGeO_4. The m plane is perpendicular to the [010] direction; the angle 2V ≈ 80°.

The orientation of the optic axis of the sample was determined by reference to the conoscopic pattern, and the angle of rotation of the plane of polarization was measured along the optic axis in the light beam of a helium–neon laser. Using a quarter-wave plate, it was shown that the light passing through the crystal plate in the direction of the optic axis was linearly polarized. The experimentally measured angle of rotation of the plane of polarization was proportional to the thickness of the plates in different crystals (both left- and right-handed rotations of the plane of polarization were observed, with the same absolute magnitude), and amounted to 16.2 ± 0.5 deg/mm (for λ = 6328 Å). The same value of specific rotation was also obtained for the plate cut normally to the optic axis.

The authors wish to thank V. V. Ilyukhina for help in this work.

---

[1] H. Futama and R. Pepinsky, J. Phys. Soc. Japan, 17, 725 (1962).

[2] I. P. Kuz'mina, O. K. Mel'nikov, and B. N. Litvin, in Hydrothermal Synthesis of Crystals, Vol. 1 [in Russian], Nauka, Moscow (1968).

[3] É. A. Kuz'min, V. V. Ilyukhin, and N. V. Belov, Kristallografiya, 13, 976 (1968) [Sov. Phys.–Crystallogr., 13, 848 (1969)].

SbSI thin films with a ferroelectric phase transition

A. A. Agasiev, A. Kh. Zeinally, and V. G. Sil'vestrov

Azerbaidzhan State University

(Submitted May 29, 1972; resubmitted January 4, 1973)
Kristallografiya, 18, 1293-1294 (November-December 1973)

The simultaneous existence of ferroelectric and semiconducting properties in $A^VB^{VI}C^{VII}$ compounds has made them the subject of wide investigation. The properties of single crystals of these compounds, especially SbSI, have been intensively studied.[1,2] However, at present the literature contains no data on studies of SbSI films having ferroelectric properties.

The difficulty in making such films, first, involves the need to preserve the composition of a complex compound which decomposes upon evaporation. We studied the following methods for making the films: 1) flash or discrete evaporation[3] with a continuous feed of powder into an oven whose temperature is high enough to evaporate the least volatile component; 2) annealing SbSi films made by thermal evaporation in iodine vapor; 3) crystallization from the gas phase in vacuum in a sealed vessel.[4]

All attempts to produce ferroelectric films by these methods were unsuccessful. To avoid decomposition of the SbSI we used vacuum sublimation with a small gap between the vapor source and the substrate.[5] The SbSI crystals were placed on a heater; the substrate was placed at a small distance (1 to 2 mm) above the crystal. The process was carried out with a pressure of $\sim 10^{-5}$ torr. The oven was heated such that there was intense evaporation and a temperature gradient was created for deposition onto the substrate. The best results were obtained with direct contact between the substrate and the crystal; therefore we call it the contact method. The whole film deposition process lasted two to three minutes. The substrates were both nonoriented (glass, fused quartz, and glass ceramic) and oriented (NaCl, LiF, mica) materials. The temperatures of the oven and substrate were measured using calibrated Copperler* thermocouples with a precision of 0.5 to 1°. Under the corresponding conditions we obtained a single crystal (which is shown by the electron-diffraction pattern in Fig. 1) SbSI film 4 to 6 μ thick.

Study of the properties of our films showed the presence of a ferroelectric phase transition. This was established by the observation of pyroelectric current along the film. At a temperature above the Curie point we applied a field of $1.5 \cdot 10^4$ V/cm and then cooled the sample down to −80°C. The ends were short-circuited and the sample was held in this state for 5 to 10 minutes. Then it was connected to the input of an electrometer and heated. We observed a pyrocurrent during this time. The pyroelectric current curves for crystals and films are shown in Fig. 2. It follows from these curves that, in contrast to crystals, the films have a smeared phase transition taking place over a range 15 to 30°C wide. This can be explained by structural imperfections in the films, which are created by the nonequilibrium deposition process. The polarization, which is determined by the area under the pyrocurrent curve, amounts to 1.2 μC/cm^2.

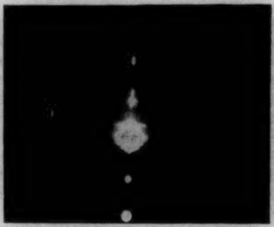

Fig. 1. Reflection electron-diffraction pattern from a SbSI film produced by the contact method on mica.

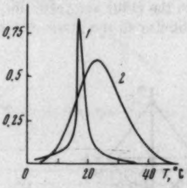

Fig. 2. Pyroelectric current curves for a crystal (1) and a film (2).

Thus the use of the contact method allowed us to produce single-crystal films having a phase transition. We also used this method to produce single-crystal films of other complex materials, for example, CdS and Sb_2S_3.

---

*Publisher's note: This may be an alloy of American origin, or it may be the Russian alloy Copel (55% Cu, 45% Ni).

[1] V. M. Fridkin, L. M. Belyaev, A. A. Grekov, I. I. Groshik, V. A. Lyakovitskaya and A. I. Rodin, Proceedings of the Ninth International Conference on Semiconductor Physics, Vol. 2, Nauka, Moscow (1969), pp. 1328-1332.
[2] K. Kreher, Ferroelectrische Halbleiter, Wiss. Z. Karl-Marx Univ. Leipzig, Math-naturwiss, R20, 287 (1971).
[3] J. L. Richards, P. B. Gareth, and E. K. Muller, in: Single-Crystal Films, M. H. Francombe and H. Sato (eds.), Pergamon (1963).
[4] R. N. Sheftal', A. G. Zhdan, K. V. Nikitin, and E. S. Artobolevskaya, Fiz. Tverd. Tela, 11, 2669 (1969) [Sov. Phys.–Solid State, 11, 2158 (1970)].
[5] Z. A. Magomedov, Abstract to Dissertation, Institute of Crystallography, Academy of Sciences of the USSR, Moscow (1968).

Reflection intensity as a function of temperature during diffraction of slow electrons from (111) and (100) faces of germanium

B. Z. Ol'shanetskii, A. I. Volokitin, and S. M. Repinskii
Institute of Semiconductor Physics, Siberian Branch,
Acadmy of Sciences of the USSR

(Submitted July 31, 1972; resubmitted January 15, 1973)
Kristallografiya, 18, 1295-1297 (November-December 1973)

Use of slow electrons makes it possible to determine the effective Debye temperature at a crystal surface as a function of the electron energy and hence of the depth of the surface layer contributing to diffraction.[1-4]

The temperature function of the reflection intensity during diffraction of electrons is described by the expression[3,4]

$$I = I_0 \exp\left[-\frac{12h^2T}{mk\Theta^2}\left(\frac{\sin\varphi}{\lambda}\right)^2\right], \tag{1}$$

where I_0 is the intensity of diffraction from an ideal lattice of 0°K, h and k are the Planck and Boltzmann constants, m is the atomic mass, T is the absolute temperature of the crystal, Θ is the effective Debye temperature, λ is the electron wavelength, and φ is half the sum of the angles formed by the incident and reflected beams with the surface plane.

The present study was conducted to determine the effective Debye temperatures for germanium atoms at the (111) and (100) surfaces.

Our investigation was conducted with p-Ge specimens having a resistivity of 20 Ω · cm, which were oriented in given crystallographic directions to within 30′. The method used to prepare the specimens for the measurements was described previously.[5] The experiments were conducted in a Varian slow-electron diffractometer. After ion bombardment and simultaneous heating of the specimens to 550°C, we observed the Ge(111)-8 and Ge(100)-4 structures characteristic of atomically pure germanium surfaces. The temperature of the test specimen was determined by passage of a dc current and measurement of the resistivity. As in other studies,[6] passage of dc current through the specimen did not distort the measurement results.

The reflection intensity was measured with an $IV^{1/2}$ point photometer on a luminescent screen. The background intensity was subtracted from the reflection intensities. The Debye–Waller factor was determined for a (00) specular beam with electron energies that corresponded to the intensity maxima of this reflection. The angle of incidence of the primary beam was no less than 82° with respect to the surface. The lowest electron energy at which the temperature functions were determined was 10 eV for the (111) face and 11 eV for the (100) face. No corrections were made for the contact potential difference and the internal potential of the crystal. The intensity of the diffraction peaks from both faces investigated was high in comparison with the background.

The brightness and sharpness of these reflections apparently also indicate that they are primary Bragg peaks, whose intensity cannot be greater than the contribution made by the secondary scattering, so that the temperature function should be well described by the kinematic approximation in Eq. (1).

Unfortunately, the intensity maxima of the (00) reflection over the measured temperature range at high energies were comparable to the background intensities, which reduced the accuracy of the measurements at these energies. This was especially true of the (100) face, where the maximum electron energy at which the temperature function could be determined was 280 eV.

The data presented in Fig. 1 show that Eq. (1) was satisfied over a broad temperature range. The curves for temperatures above 800°K exhibited an inflection, which was apparently due to a large increase in the contribution made by the anharmonic components of the atomic vibrations.

The effective Debye temperatures, which characterize the atomic-vibration components normal to the surface, were determined from the slope of curves analogous to those in Fig. 1.

The effective Debye temperatures are shown as a function of the incident-electron energy for the (111) and (100) faces in Fig. 2. The value of $\Theta_\perp$ for the first maximum of the (00) reflection at an energy of 10 eV was 95 ± 5°K, while the value of the (100) face (an energy of 11 eV) was 75 ± 5°K. The values of $\Theta_\perp$ determined for the (111) face with beams with energies above 300 eV were close to the Debye temperature determined for a germanium crystal from data on heat capacity or neutron scattering. The characteristic Debye temperatures given in the literatures[7,8] range from 290 to 370°K. The values determined for low-energy reflections characterize the dynamics of surface-atom vibrations. The mean square amplitudes of the atomic displacements normal to the surface are related to $\theta_\perp$ by the expression

$$\bar{u}_\perp{}^2 = 3h^2T/4\pi^2 mk\Theta_\perp{}^2. \tag{2}$$

If we assume the interior of the crystal to have a Debye temperature[8] of 360°K, it follows from our experimental data that the ratio of the mean square displace-

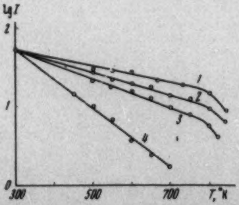

Fig. 1. Logarithm of intensity of (00) reflection from (111) face as a function of temperature. 1) Energy of 10 eV; 2) 21 eV; 3) 68 eV; 4) 158 eV.

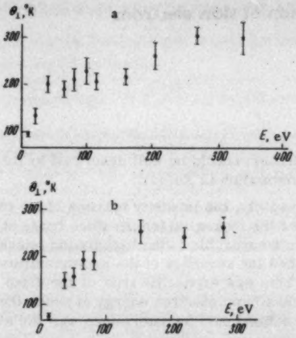

Fig. 2. Effective Debye temperature $\theta_\perp$ as a function of primary-electron energy. a) (111) face; b) (100) face.

ment amplitudes at the surface and in the interior $\bar{u}_{s\perp}^2/\bar{u}_\infty^2$ amounts to 13 for the (111) face and 23 for the (100) face. The lower Debye temperatures for the (100) face than for the (111) face may mean that the constant quasielastic forces acting on the atoms at the (100) face are less than the forces acting on the more densely packed (111) face. This phenomenon has also been described for platinum.[6]

It is noteworthy that the mean square displacements of the atoms at the germanium surface exceed the values obtained for metals in similar calculations. It can be assumed that this results from the specific characteristics of the bonding in semiconductor crystals and the material difference between the bonding of surface atoms and that of internal atoms. This is in agreement with the results obtained by Nesterenko and Borodkin[2] for silicon.

---

[1] D. Tabor, J. M. Wilson, and T. G. Bastow, Surf. Sci., 26, 471 (1971).

[2] B. A. Nesterenko and A. D. Borodkin, Fiz. Tverd. Tela, 12, 2042 (1970) [Sov. Phys.—Solid State, 12, 1621 (1970); B. A. Nesterenko, A. D. Borodkin, and O. V. Snitko, Fiz. Tverd. Tela, 13, 1238 (1971)[Sov. Phys.—Solid State, 13, 1036 (1971)].

[3] R. James, Optical Principles of the Diffraction of X-Rays, Cornell Univ. Press (1968).

[4] E. R. Jones, J. T. McKinney, and M. B. Webb, Phys. Rev., 151, 476 (1966).

[5] B. Z. Ol'shanetskii, N. I. Makrushin, and A. I. Volokitin, Fiz. Tverd. Tela, 14, 3175 (1972)[Sov. Phys.—Solid State, 14, 2713 (1973)].

[6] H. B. Lyon and G. A. Somorjai, J. Chem. Phys., 44, 3707 (1966).

[7] B. F. Ormont, Introduction to the Physical Chemistry and Crystallization of Semiconductors [in Russian], Vysshaya Shkola, Moscow (1968), p. 188.

[8] F. Blatt, Physics of Electronic Conduction in Solids, McGraw-Hill, New York (1968).

Influence of impurities on the photoelastic constants of potassium chloride crystals

M. P. Shaskol'skaya, A. V. Pakhnev, S. S. Gorbach, and N. M. Malikova
Moscow Institute of Steel and Alloys

(Submitted October 9, 1972; resubmitted February 26, 1973)
Kristallografiya, 18, 1298 (November-December 1973)

In a continuation of our investigations of the photoelasticity of alkali halide crystals[1,2] we studied the influence of divalent cationic impurities on the photoelastic constants of KCl crystals. A linear stress pattern was set up by compression. The birefringence was compensated for by the Senarmon method at $\lambda = 546$ nm. The photoelastic constants were determined by the method described earlier.[1]

Impurities of Pb, Sn, Sr, Mg, and Zn in amounts of 0.1 wt.% increased the constant[1)] $C^{\Delta[100]}_{\sigma[001]}$ of "pure" KCl (containing $< 10^{-3}$ wt.% impurities). The increase amounted to from 29% for Pb to 62% for Zn.

We also measured the constant $C^{\Delta[001]}_{\sigma[110]}$ for KCl : Pb crystals (0.01 wt.%). The photoelastic constants $C^{\Delta[100]}_{\sigma[001]}$ and $C^{\Delta[001]}_{\sigma[110]}$ for these crystals were $3.6 \cdot 10^{-7}$ cm²/kgf and $-6.4 \cdot 10^{-7}$ cm²/kgf, while the corresponding values for pure KCl are $2.4 \cdot 10^{-7}$ cm²/kgf and $-8.6 \cdot 10^{-7}$ cm²/kgf respectively. The quantity $\beta = 1 - |C^{\Delta[100]}_{\sigma[001]}/C^{\Delta[001]}_{\sigma[110]}|$, which characterizes the anisotropy of photoelastic properties in the (100) plane, was 0.7 for "pure" KCl and 0.4 for KCl: Pb. The presence of a lead impurity in KCl thus materially reduces its photoelastic anisotropy.

The trend of the photoelastic constants with temperature over the range 293–583°K differed (see Fig. 1) for KCl and KCl: Pb. The greatest difference was observed over the range 293–473°K, where there is a change[3,4] in the state of impurity Pb in KCl. It can be assumed that the polarization-optics method is sensitive to changes in the state of impurities.

Cationic impurities can thus be used to control the photoelastic effect in a KCl crystal. By measuring the temperature function of the photoelastic constants, it is evidently possible to determine the temperature range over which the state of the impurity changes.

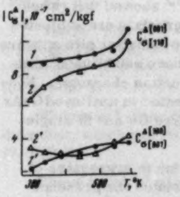

Fig. 1. Photoelastic constants as a function of temperature for KCl (1, 1') and KCl : Pb (2, 2') single crystals. 1, 2) $C^{\Delta[001]}_{\sigma[110]}$; 1', 2') $C^{\Delta[100]}_{\sigma[001]}$.

[1)] The superscript represents the observation direction and the subscript represents the loading direction. The photoelastic constants are related to the piezooptical constants by the expressions $C^{\Delta[100]}_{\sigma[001]} = -\frac{1}{2}(n^0)^3(\pi_{11} - \pi_{12})$ and $C^{\Delta[001]}_{\sigma[110]} = -\frac{1}{2}(n^0)^3\pi_{44}$, where n^0 is the refractive index of the undeformed crystal. We did not convert C^{Δ}_{σ} to π_{ij}, since the n^0 values for the impure crystals were not known.

---

[1] S. S. Gorbach, G. F. Dobrzhanskii, L. A. Deptsova, V. Yu. Markovskii, and M. P. Shaskol'skaya, Kristallografiya, 14, 729 (1969) [Sov. Phys.–Crystallogr., 14, 627 (1970)].
[2] S. S. Gorbach, V. Yu. Markovskii, A. V. Pakhnev, and M. P. Shaskol'skaya, Transactions of the Fourth All-Union Conference on the Polarization-Optical Method for Investigation of Stresses [in Russian], Vol. 4, Izd. EstSSR, Tallin (1971), p. 128.
[3] L. Ya. Melik-Gaikazyan and M. I. Ignat'eva, Kristallografiya, 11, 410 (1966) [Sov. Phys.–Crystallogr., 11, 362 (1966)].
[4] O. V. Obukhova, M. M. Tagieva, and M. P. Shaskol'skaya, Kristallografiya, 14, 948 (1969) [Sov. Phys.–Crystallogr., 14, 825 (1970)].

Nature of small etch pits in tellurium-alloyed GaAs single crystals

S. S. Shifrin, V. B. Osvenskii, M. G. Mil'vidskii, L. M. Morgulis, and S. P. Grishina

State Scientific-Research and Planning Institute of the Rare Metals Industry

(Submitted August 28, 1972; resubmitted December 12, 1972)
Kristallografiya, 18, 1299-1302 (November-December 1973)

Previous structural investigations[1,2] showed that, when highly alloyed n-type GaAs single crystals are subjected to chemical etching, a background of smaller pits appears together with dislocations. It has been established[1] that the small etch pits have a nondislocation character. Nondislocation etch pits have been detected in unalloyed GaAs single crystals[3,4] and dislocation-free Ge and Si single crystals.[5-7]

These pits are believed to be due to aggregates of vacancies; specifically, de Kock[7] relates the presence of small pits to vacancy clusters formed from vacancy–oxygen complexes during crystal cooling. In all these instances, however, conclusions regarding the nature of the defects responsible for the appearance of small etch pits were drawn on the basis of indirect data.

In the present investigation, the formation mechanism and nature of the small etch pits in GaAs single crystals alloyed with tellurium were studied with the aid of scanning and transmission electron microscopy, as well as ordinary optical microscopy. This combination of research methods permitted direct identification of the defects responsible for appearance of small etch pits.

We investigated GaAs crystals grown by the Czochralski method and alloyed with tellurium to carrier concentrations of from $3 \cdot 10^{17}$ cm^{-3} (~ $3 \cdot 10^{17}$ atoms · cm^{-3}) to $1 \cdot 10^{19}$ cm^{-3} ($5 \cdot 10^{19}$ atoms/cm^3). The microstructure was visualized by chemical etching in a boiling HNO_3-H_2O solution (1:3) for 4 sec. Figure 1 shows a typical example of the structure observed in the optical microscope.

Special statistical processing of the results of metallographic analysis of GaAs single crystals highly alloyed with tellurium showed that the threshold carrier concen-

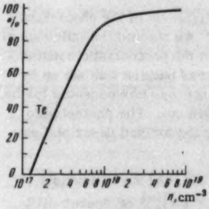

Fig. 2. Probability of appearance of fine-pitted background in GaAs single crystals as a function of Te concentration.

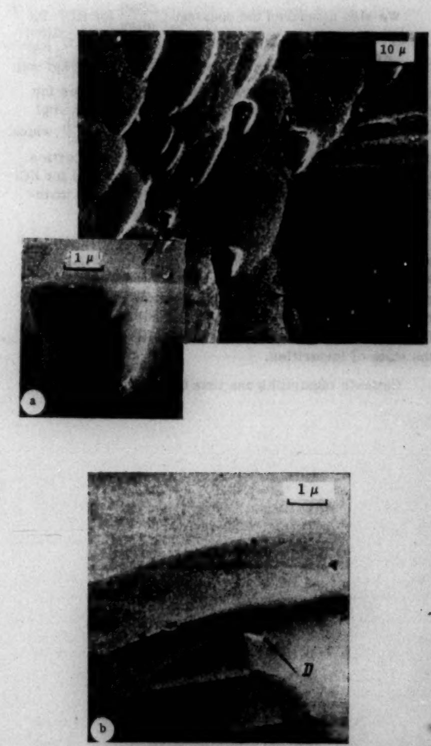

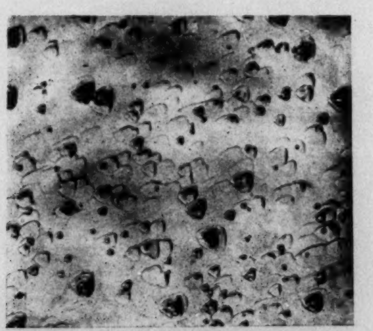

Fig. 1. Microstructure of GaAs alloyed with Te (~ $5 \cdot 10^{18}$ cm^{-3}) under optical microscope; Ga (111) surface, × 200.

Fig. 3. Etching patterns of GaAs alloyed with Te under scanning electron microscope; Ga (111) surface.

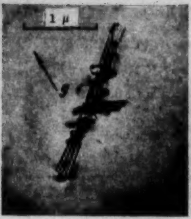

Fig. 4. Transmission electron photomicrograph of structural defect responsible for appearance of a small nondislocation etch pit; (111) plane of foil; **g**) <220> diffraction vector.

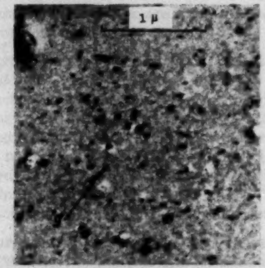

Fig. 5. Aggregates in GaAs alloyed with Te to concentration of $\sim 9 \cdot 10^{18}$ cm^{-3}, responsible for appearance of "subsmall" etch pits (transmission electron microscopy); **g**) <200> diffraction vector.

tration above which a background of small etch pits appeared was $\sim 3 \cdot 10^{17}$ cm^{-3}. Figure 2 shows a curve characterizing the probability of development of small pits in GaAs crystals grown in the [111] direction and containing different tellurium concentrations. Analysis of this relationship indicated that, with all other conditions equal, the probability of the presence of small pits increased with the alloying-impurity concentration and that a "fine-pitted" background was almost always present in Te-containing GaAs crystals at a carrier concentration of $4 \cdot 10^{18}$ cm^{-3}.

The chemical etching pattern could vary in character at small tellurium concentrations: Some crystals had a "fine-pitted" background and others had none at the same impurity concentration. This indicated that the probability of appearance of small (nondislocation) pits in alloyed single crystals is determined not only by the impurity concentration, but apparently also by slight variations in the crystal-growth thermal conditions, primarily the rate at which the crystals are cooled from the melting point.

In order to establish the nature of the small etch pits in GaAs crystals alloyed with Te, we conducted experiments on annealing with different cooling rates. Analysis of the etching pattern for heat-treated GaAs specimens showed that the nondislocation pits were not produced by coagulation of nonequilibrium vacancies, as in unalloyed crystals,[4] but by segregation of impurity atoms (e.g., precipitation of a second phase).

Useful information about defect character can be obtained by electron-microscope study of the ultrastructure of highly alloyed GaAs single crystals. Using a scanning electron microscope, it was found that there are several types of nondislocation pits, which can be classified in the following manner:

Small pits with a tapering bottom, from 0.8 to 4 μ in diameter, formed at the exit sites of defects to the surface examined (Fig. 3a, B); the dislocation-pit size at a given magnification can be evaluated from a fragment (Fig. 3a, A).

"Large" pits with a flat bottom, from 2 to 50 μ in diameter (Fig. 3a, C), formed as a result of etching out of a defect. It is these pits that are usually seen under the optical microscope (see Fig. 1).

"Subsmall" pits (Fig. 3b, D), from 0.03 to 0.1 μ in diameter, which can only be seen at high magnifications ($\geqslant 10,000$).

These types of pits were present in all the crystals investigated, but it was rather difficult to detect the "subsmall" pits in crystals with a carrier concentration of $\leq 10^{18}$ cm^{-3}, because of their low density. It was established that the density of the small and "subsmall" pits increased with the alloying-impurity concentration and amounted to $\sim 5 \cdot 10^{7}$ and $\sim 10^{9}$ cm^{-2} respectively at a carrier concentration of $\sim 1 \cdot 10^{19}$ cm^{-3}. The density of the "large" pits varied with the impurity concentration to a considerably less marked degree and amounted to $\sim 10^{5}$–10^{6} cm^{-2} at $n \sim 10^{19}$ cm^{-3}. We observed certain specific characteristics of the surface relief of the specimens examined after etching. The surface relief in GaAs specimens alloyed with tellurium to a carrier concentration of $> 5 \cdot 10^{18}$ cm^{-3} was relatively "smooth." At a carrier concentration of $> 5 \cdot 10^{18}$ cm^{-3}, the surface was characterized by an "irregular" relief. The observed relief characteristics were most probably due to the state of the impurity in the interior of the crystal.

In order to identify the defects responsible for the appearance of nondislocation etch pits, we investigated the same specimens under scanning and transmission electron microscopes. Thin films oriented along the {111} plane were prepared for examination in the transmission electron microscope by chemical thinning in a selective etchant with the composition H_2SO_4:H_2O_2:H_2O. This preparation procedure enabled us to observe both structural defects in the interior of the crystal (by transmission microscopy) and the corresponding etch pits at the Ga {111} surface (by scanning microscopy) in the same specimens.

It was found that the small pits corresponded to aggregates having the contrast of packing defects and lying in the oblique {111} planes. Figure 4 is a transmission electron photomicrograph of the specimen region corresponding to a small etch pit.

When examined in the transmission electron microscope, the crystals with "subsmall" pits exhibited dispersed inclusions, whose volumetric density corresponded to the density of the "subsmall" pits, reaching $\sim 10^{13}$–10^{14} cm^{-3} in GasAs crystals with a Te concentration of about 8–$9 \cdot 10^{18}$ cm^{-3} (Fig. 5). This makes it possible to conclude that the "subsmall" pits were produced by the small inclusions observed in the transmission electron microscope. The inclusions were visible as a result of their strong deformation contrast, similar to that of small prismatic loops; they were apparently fine tabular inclusions containing Te atoms. However, the electron-diffraction patterns did not display additional reflections associated with the presence of these aggregates, which make it difficult to draw any final conclusions regarding their nature.

---

[1] M. G. Mil'vidskii, V. B. Osvenskii, V. I. Fistul', É. M. Omel'yanovskii, and S. P. Grishina, Fiz. Tekh. Poluprov., 1, 969 (1967) [Sov. Phys.–Semicond., 1, 813 (1968)].

[2] N. S. Belyatskaya, S. P. Grishina, E. V. Lopatin, M. G. Mil'vidskii, V. B. Osvenskii, and V. G. Fomin, Kristallografiya, 17, 158 (1972) [Sov. Phys.–Crystallogr., 17, 126 (1972)].

[3] V. O. Petrusevich, E. S. Solyartinskaya, and S. Sh. Shil'shtein, in: Metal-Working and Processing of Nonferrous Metals and Alloys [in Russian], Vol. 24, Metallurgiya, Moscow (1965), p. 38.

[4] S. Sh. Shil'shtein and I. V. Matveev, in: Gallium Arsenide [in Russian], Izd. Tomsk. Univ., Tomsk (1968), p. 440.

[5] S. Sh. Shil'shtein and G. I. Simonova, Kristallografiya, 10, 580 (1966) [Sov. Phys.–Crystallogr., 10, 490 (1966)].

[6] F. Secco d' Aragona, Phys. Status Solidi, a7, 577 (1971).

[7] A. J. deKock, Appl. Phys. Lett., 16, 100 (1970).

Formation of trigons at the {111} faces of natural diamond during etching

O. N. Grigor'ev

Institute of Metal Physics, Academy of Sciences of the Ukrainian SSR

(Submitted April 5, 1972; resubmitted December 12, 1972)
Kristallografiya, 18, 1303-1305 (November-December 1973)

Etching of the {111} faces of diamond usually results in formation of triangular pits, whose orientation coincides with that of the octahedral face. Etch pits with this positive orientation (Franks' terminology[1]) are formed, for example, during etching in KNO$_3$. There are also etchants[2,3] in which etch pits oriented opposite to the configuration of the octahedral face are formed, hence having negative[1] orientation.

The trigons, i.e., triangular depressions, detected in the natural {111} faces of natural diamonds have a negative orientation and differ in a number of features from the pits formed in etching experiments.[1,4,5] The problem of the origin of the trigons has not as yet been solved and there are two directly opposed viewpoints: 1) the trigons are formed during growth;[4–9] 2) the trigons are formed during natural etching of the crystals.[10–14] Trigon formation has not been observed in the etchants studied to date.

The present article describes experiments on etching in an NiS alloy, in which trigon formation during crystal solution was observed.

Our investigation was conducted with natural colorless diamonds of jewelry grade 1. We etched cleavage planes and mechanically polished (111) planes. The etchant was a eutectic NiS melt. Etching was carried out at 700°C in an alundum crucible.

Areas with etch pits of positive and negative orientation were formed on the (111) cleavage surface of a crystal cleaved immediately before etching in NiS (Fig. 1). Etching was more rapid in the areas with negatively oriented etch pits. The difference in the etching rates of the segments with pits having positive and negative orientations was of the order of $0.5\ \mu$/h. During further etching, the boundaries of the regions containing etch pits with the two orientations in question were displaced over the crystal surface and the area occupied by etch pits with a negative orientation generally increased. When the etching time was increased, the positively oriented pits did not acquire the round shape characteristic of the pits formed during etching[4] in KnO$_3$ but remained sharply tapered (Fig. 2). In this case, we observed overlapping of the pits and nonuniform etching of the portions of the crystal surrounding the pit.

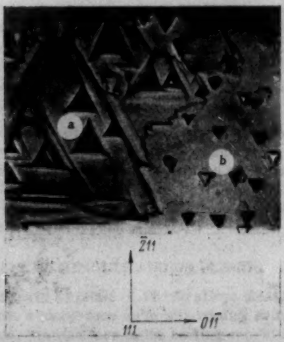

Fig. 1. Fracture plane after etching in NiS (700°C, 1 h), ×1600. Etch pits with negative (a) and positive (b) orientations can be seen.

The pits with both positive and negative orientations were pyramidal or flat-bottomed. However, the negatively oriented pits had a number of special features typical of trigons. Overlapping of negatively oriented etch pits was not detected in any case (Figs. 1 and 3). In a number of cases, these pits were elongated in one direction; the sides of the triangles were always straight. We often observed close contact between the vertex of one pit and the side of another; in some instances, a "salient" or ridge[1,5] rose from the contact point and led in the $\langle 112\rangle$ direction. Hence, trigons were formed on the (111) cleavage planes of the crystal during etching.

An increase in etching time did not lead to overlapping of the trigons. In some cases, further etching resulted in a decrease in the number of "old" trigons and

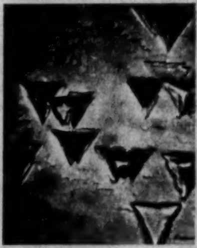

Fig. 2. Positively oriented pits on cleavage surface, etching for 2 h, ×1600.

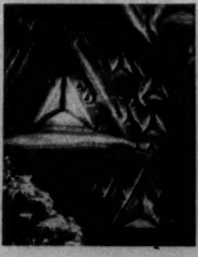

Fig. 3. Trigons visualized on cleavage surface by etching for 2 h, ×800.

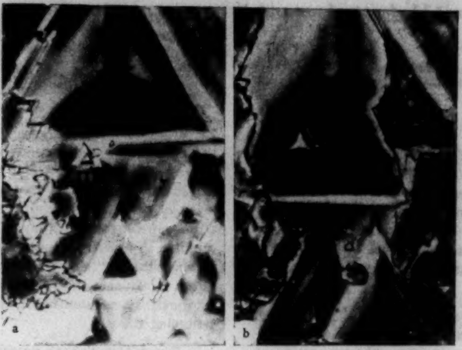

Fig. 4. Cleavage surface after etching, × 800. a) 700°C, 2 h; b) 700°C, 3 h.

no change in shape, this process extending as far as disappearance of the "old" trigons and appearance of new ones.

X-ray diffraction analysis, x-ray topographic analysis, and optical microscopy revealed no twinning in the crystals. The development of regions of the crystal surface with etch pits having both orientations therefore was not due to the presence of twins. This was also indicated by the different morphologies of the etch pits with positive and negative orientations and different etching rates. The two observed etching mechanisms were also not related to a nonuniform impurity distribution in the crystals, since the distribution of the regions of positively oriented pits and trigons did not coincide with the distribution of regions of different impurity concentrations. It can be assumed that the difference in the etching mechanisms was due to inhomogeneity of the etchant.

Etching in an NiS-alloy melt thus leads to formation of trigons (together with the usual positively oriented etch pits), which confirms the possibility of formation of trigons on the octahedral faces of diamond during solution under natural conditions.

---

[1] F. C. Frank, K. E. Puttick, and E. M. Wilks, Phil. Mag., 3, 1262 (1958).

[2] T. Evans and D. H. Sauter, Phil. Mag., 6, 429 (1961).

[3] A. R. Patel and S. Ramanathan, Phil. Mag., 7, 1306 (1962).

[4] S. Tolansky, Physical Properties of Diamonds, Clarendon Press, Oxford (1965).

[5] C. K. R. Varma, Phil. Mag., 16, 611 (1967).

[6] A. E. Fersman, Crystallography of Diamond [in Russian], Izd. Akad. Nauk SSSR, Moscow (1955).

[7] A. Halperin, Proc. Phys. Soc., 67, 538 (1954).

[8] M. A. Gnevushev, Mineral. Sb. L'Vov. Geol. Obshch., No. 9, 25 (1955).

[9] C. K. R. Varma, Phil. Mag., 16, 959 (1967).

[10] F. C. Frank and K. E. Puttick, Phil. Mag., 3, 1273 (1958).

[11] Yu. A. Orlov, Morphology of Diamond [in Russian], Izd. Akad. Nauk SSSR, Moscow (1963).

[12] A. R. Patel, K. W. Goswami, and C. C. Desai, Phil. Mag., 10, 931 (1964).

[13] A. R. Lang, Proc. Roy. Soc., A278, 234 (1964).

[14] A. R. Patel and N. Ramachandran, Ind. Diamond Rev., 26, 549 (1966).

Forms of antimony crystal growth in alloys of the eutectic type

I. V. Salli, L. V. Samoilenko, and V. Z. Dolinskaya
Dnepropetrovsk Branch, Institute of Mechanics,
Academy of Sciences of the Ukrainian SSR

(Submitted June 9, 1972; resubmitted September 20, 1972)
Kristallografiya, 18, 1306-1308 (November-December 1973)

During structuring of alloys and growth of single crystals, the crystal–liquid interface can be flat or rounded. A rounded interface has been correlated with an atomically rough surface. A flat interface is formed in the case of an atomically smooth surface, at which growth occurs through formation of two-dimensional nuclei or rapid overgrowth of jogs formed by dislocations.

Jackson[1,4,5] gives a very approximate calculation of the conditions for formation of a rough surface and proposes the following criterion for the form of crystal growth: A flat interface develops if the entropy of fusion of the material is more than 4 and the interface is rounded if the entropy of fusion is less than 4.

The Jackson criterion has been tested experimentally.[6-8] Miller and Chadwick[6] assert that this criterion cannot characterize the growth form and demonstrate that, in some cases, the calculated equilibrium structure does not agree with experimental observations of equilibrium forms. According to other data, however, such substances as Ge, In, Sb, and Bi, for which $\Delta S > 4$, retain a flat-faceted form over all concentration and supercooling regions investigated.[7,8]

In the present investigation, we studied the growth forms of antimony ($\Delta S > 2R$) as a function of the cooling conditions and the composition of binary alloys of the eutectic type.

The morphology of primary antimony crystals was studied during crystallization of noneutectic Pb–Sb, In–Sb, Ga–Sb, Ge–Sb, Zn–Sb, and Cd–Sb alloys. The alloys were prepared from high-purity initial materials with a principal-component concentration of 99.999%. The alloys investigated were melted in quartz crucibles in an inert-gas (argon) atmosphere and cooled under different regimes: 1) with the furnace, at cooling rates of 0.1, 1, and 5 deg/min to a temperature 5-10 deg above the eutectic point; 2) with the furnace to a temperature 30-50 deg below the eutectic point; 3) in a copper mold with a cooling rate of $6 \cdot 10^3$ deg/min; 4) in quartz capillary tubes with a cooling rate of $6 \cdot 10^4$ deg/min. Cooling was arrested by quenching in water.

The structure of the resultant specimens was studied metallographically. The following etchants were used for identification of the primary crystals: a mixture of 2 g of $FeCl_3$, 60 ml of HCl, and 38 ml of H_2O for the Pb–Sb and In–Sb alloys and 80% H_2NO_3 solution for the Ge–Sb, Ga–Sb, Zn–Sb, and Cd–Sb alloys.

EXPERIMENTAL RESULTS AND DISCUSSION

The primary crystals of Pb–Sb alloys containing 15% antimony had a plane-face form with cooling rates of $3 \cdot 10^3$ deg/min. An increase in the cooling rate to $6 \cdot 10^4$ deg/min did not cause any change in the form of the primary Sb crystals but increased the structural dispersion.

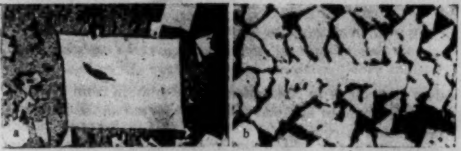

Fig. 1. Growth forms of Sb crystals during crystallization from solution in Pb–Sb melt. a) 70% Sb, $V_{cool} = 1$ deg/min, ×40; b) 70% Sb, $V_{cool} = 3 \cdot 10^3$ deg · min^{-1}, ×800.

In the alloys with the highest antimony content (70% Sb), the antimony crystals also had a plane-face form (Fig. 1a) at low cooling rates (1 deg/min). When the cooling rate was increased to $3 \cdot 10^3$ deg/min, the Sb crystals ramified and acquired a skeletal form, retaining the same faceting and vertex angles (Fig. 1b).

Thus, primary antimony crystals grow from solution in a lead melt with distinct faceting over the entire concentration and cooling-rate range studied.

Figure 2, a and b, shows the change in the morphology of antimony crystals in an In–Sb melt as a function of concentration during cooling at a rate of $3 \cdot 10^3$ deg/min. Alloys containing 90% Sb exhibited curvature of the flat crystal faces, formation of protuberances, and some smoothing out of the angles at the vertices (Fig. 2a). When the Sb content was reduced to 80%, the antimony crystals ramified and acquired a skeletal form. A further decrease in the Sb content to 72% caused the antimony to form dendrites (Fig. 2b). During crystallization of antimony from solution in an indium melt with a cooling rate of $3 \cdot 10^3$

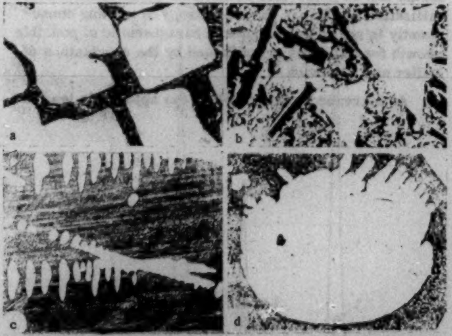

Fig. 2. Growth forms of Sb crystals during crystallization from solution in In–Sb melt. a) 90% Sb, $V_{cool} = 3 \cdot 10^3$ deg/min, ×800; b) 72% Sb, $V_{cool} = 3 \cdot 10^3$ deg/min, ×300; c) 72% Sb, $V_{cool} = 0.1$ deg/min, × 100; d) 72% Sb, $V_{cool} = 1$ deg/min, ×200.

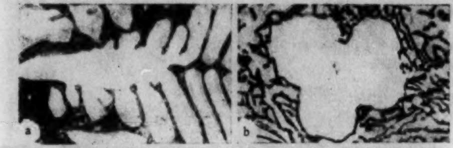

Fig. 3. Growth forms of Sb crystals during crystallization from solution in melts, × 800. a) Ge−Sb (87%), $V_{cool} = 3 \cdot 10^3$ deg/min; b) Ga−Sb (94%), $V_{cool} = 3 \cdot 10^3$ deg/min.

deg/min, there is consequently a transition from faceted growth forms to skeletal and round forms as the Sb concentration is reduced.

The change in the antimony growth form as a function of cooling rate was studied in In−Sb alloys (72-80% Sb). Figure 2, c and d, shows the transition from plane-face growth forms to rounded forms in an alloy containing 72% Sb. Faceted Sb crystals were observed at low cooling rates, ~0.1 deg/min (Fig. 2c). An increase in the cooling rate to 1 deg/min led to a transition from anisotropic to isotropic growth, the antimony crystals acquiring a rounded shape (Fig. 2d). In alloys containing 80% Sb, an increase in the cooling rate from $3 \cdot 10^3$ to $6 \cdot 10^4$ deg/min caused the primary Sb crystals to grow in the form of dendrites and no faceted surfaces were observed. Thus, during crystallization of alloys in the In−Sb system, an increase in the cooling rate was accompanied by a transition from faceted antimony growth forms to rounded forms; the more dilute the solution, the lower was the cooling rate at which this transition occurred.

The change in the morphology of the primary antimony crystals during crystallization from solution in Ge, Ca, Zn, and Cd melts was similar to that observed in the In−Sb system. Figure 3, a and b, shows that the Sb crystals grown from liquified Ge and Ga solutions with a cooling rate of $3 \cdot 10^3$ deg/min took the form of dendrites.

Our investigation thus showed that, although the entropy of fusion of antimony is more than 4, its growth forms can be plane-face or rounded under different crystallization conditions and the entropy of melting consequently is not an unambiguous characteristic of possible growth forms. This is confirmed by the conclusions of Miller and Chadwick.[6]

An increase in supercooling can apparently lead to rapid formation of two-dimensional nuclei on the crystal surface, which in turn is responsible for development of roughness and a macroscopically rounded interface. The same conclusion follows from Chernov's work.[9]

Our investigation enables us to draw the following conclusions: 1) The growth forms of antimony crystals ($\Delta S > 4$) during crystallization of the binary In−Sb, Ga−Sb, Ge−Sb, Zn−Sb, and Cd−Sb systems depend on the cooling rate and composition: The crystals can be faceted or rounded; 2) during crystallization of the Pb−Sb system, the antimony grows in faceted form over the entire range of cooling rates and composition investigated (an increase in the Sb content of the alloy to 70% with a cooling rate of $3 \cdot 10^3$ deg/min leads to a transition from plane-face to skeletal growth); 3) the Jackson criterion, which by nature predicts the equilibrium crystallization front structure, cannot be unambiguously employed to characterize the growth form of primary-phase crystals during crystallization of binary systems.

---

[1] C. A. Jackson, Liquid Metals and Their Solidification [Russian translation], Metallurgizdat, Moscow (1962), p. 200.

[2] H. W. Kerr and W. C. Winegard, Crystal Growth, Pergamon (1967), p. 179.

[3] V. V. Voronkov and A. A. Chernov, Crystal Growth, Pergamon (1967), p. 593.

[4] C. A. Jackson, Problems of Crystal Growth [Russian translation], Mir, Moscow (1968), p. 13.

[5] C. A. Jackson, D. Uhlman, and J. Hant, Problems of Crystal Growth [Russian translation], Mir, Moscow (1968), p. 27.

[6] W. A. Miller and G. A. Chadwick, Growth Forms and Equilibrium Shapes of Crystals in the Melt: Solidification of Metals, London (1968).

[7] I. V. Salli and E. V. Finagina, in: Metal Physics [in Russian], Naukova Dumka, Kiev (1968), No. 22, p. 104.

[8] A. M. Ovrutskii and I. V. Salli, Kristallografiya, 15, 533 (1970) [Sov. Phys.−Crystallogr., 15, 449 (1970)].

[9] A. A. Chernov, Usp. Fiz. Nauk, 100, 277 (1970) [Sov. Phys.−Usp., 13, 101 (1970)].

Effect of the crystallization mechanism on boron diffusion in silicon–germanium solid-solution epitaxial films

K. L. Lyutovich, F. A. Gimel'farb, P. B. Orlov, and T. A. Ukhorskaya
Institute of Electronics, Academy of Sciences of the Uzbek SSR
State Scientific-Research and Design Institute for the Rare Metal Industry

(Submitted October 9, 1972; resubmitted January 17, 1973)
Kristallografiya, 18, 1309-1311 (November-December 1973)

When single-crystal films of silicon–germanium solid solutions are grown epitaxially from the gas phase on silicon substrates strongly doped with boron (boron concentrations above 10^{17} atoms/cm^3) inversion of the conductivity type in n-type epitaxial films into p-type is often observed. On lightly doped substrates (boron concentrations below 10^{16} atoms/cm^3) no inversion is observed.

The purpose of this report is to explain the nature of these phenomena, which we believe to originate in the crystallization mechanism of silicon–germanium solid solutions. If the process temperature is kept below the solidus line during crystallization of epitaxial Si–Ge films from the gas phase, the growth occurs by the vapor–solid mechanism. If the process temperature is above the solidus line, then the growth occurs by the vapor–liquid–solid mechanism. Depending on the ratio of the components of the solid solution it is possible to have crystallization by different mechanisms at the same temperature. During crystallization by the vapor–liquid–solid mechanism onto a strongly boron doped substrate one can have accelerated boron diffusion through the liquid phase and inversion of the conductivity type of the Si–Ge films (boron overcompensation of n-type material).

To check this hypothesis we have carried out epitaxial growth of Si–Ge solid solutions of various compositions on strongly and weakly doped substrates by methods described previously.[1] The conductivity type of the films produced was determined using a thermal probe and the distribution of the resistivity over the film thickness was determined by the single-probe method from the spreading resistance at a point contact. The measurements were done on an angle-polished section at an angle of 6° with respect to the growth surface, with a probe interval corresponding to 2 microns of film thickness. The silicon and germanium contents in the films and the uniformity of their distribution over thickness and over the surface of the film were determined by the local x-ray structural analysis method which we have described previously.[1] The nature of the boron distribution and its dependence on the crystallization conditions were studied by ion microanalysis using AI-86 apparatus.[2] The boron in the surface layer was detected from the B_{11}^{+} peak in the mass spectrum and its relative content was determined from the magnitude of this peak. The distribution of boron over the thickness of the layer was studied by a continuous tracing of the secondary ion current during ion etching of the epitaxial film by a beam of primary argon or oxygen ions. The x-ray structural methods were used to determine the structural perfection of the epitaxial films and metallographic methods were used to study the surface morphologies of the films.

The epitaxial growth temperatures of the films, depending on the composition of the solid solution, varied from 1000 to 1300 deg C. For the same initial process temperature, compositions were grown lying below, on, and above the solidus line in the phase diagram. In the latter case, due to liquation processes during crystallization, the composition was not uniform in silicon and germanium.

During growth on silicon substrates containing less than 10^{16} atoms/cm^3 of boron no inversion of the conductivity type was observed and n-type Si–Ge solid solution epitaxial films were produced over the whole range of growth temperatures and compositions.

In many cases we produced p-type films during growth on substrates doped with boron to concentrations greater than 10^{17} atoms/cm^3. A comparison of the film compo-

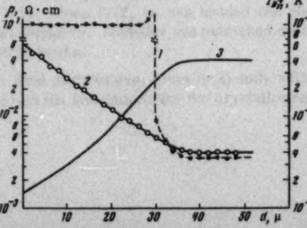

Fig. 1. Variation in the resistivity (1 and 2) and the magnitude of the secondary B_{11}^{+} current (3) within the epitaxial film. 1) $Si_{0.90}Ge_{0.10}$ 2, 3) $Si_{0.81}Ge_{0.19}$.

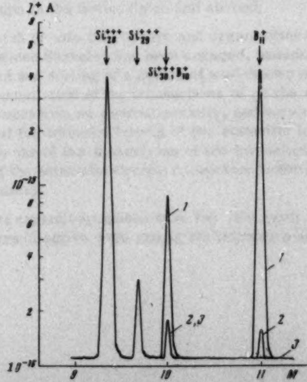

Fig. 2. Mass spectrum of the substrate (1) a $Si_{0.81}Ge_{0.19}$ film (2) and a $Si_{0.90}Ge_{0.10}$ film (3).

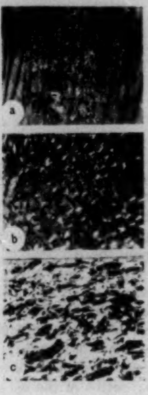

Fig. 3. Surface morphologies of silicon-germanium solid solution epitaxial films, × 600. a) $Si_{0.90}Ge_{0.10}$; b) $Si_{0.85}Ge_{0.15}$; c) $Si_{0.81}Ge_{0.19}$.

sition and the process temperature with the Si−Ge phase diagram showed that inversion only occurred in those cases where the initial process temperature was above the solidus line.

As an example we studied samples grown at 1300 deg C on silicon substrates doped with boron to $5 \cdot 10^{19}$ atoms · cm^{-3} and containing 10 at.% (12 wt. %) germanium ($Si_{0.90} \cdot Ge_{0.10}$) and 19 at.% (38 wt.%) germanium ($Si_{0.81}Ge_{0.19}$). The $Si_{0.90}Ge_{0.10}$ sample was n-type while the $Si_{0.81}Ge_{0.19}$ sample was p-type. The variation of the resistivity within these films is shown in Fig. 1 (curves 1 and 2). An estimate of the carrier concentration from the resistivity, taking account of the concentration dependence of the carrier mobility,[3] showed that it varies from $\sim 5 \cdot 10^{19}$ cm^{-3} in the substrate to $\sim 5 \cdot 10^{14}$ cm^{-3} in $Si_{0.90}Ge_{0.10}$ and to $\sim 1 \cdot 10^{18}$ cm^{-3} in $Si_{0.81}Ge_{0.19}$. At the surface of the $Si_{0.81}Ge_{0.19}$ sample the mass spectrum showed a B_{11}^{+} signal (Fig. 2, curve 2) although substantially weaker than in the substrate (Fig. 2, curve 1). At the surface of the $Si_{0.90}Ge_{0.10}$ sample no analogous signal was seen (Fig. 2, curve 3). During ion etching of the $Si_{0.81}Ge_{0.19}$ sample we traced the magnitude of the secondary ion current in the epitaxial film by tuning for detection of B_{11}^{+} (Fig. 1, curve 3). The change in the magnitude of the secondary ion current corresponds to the boron concentration profile over the film thickness and is close to the nature and value of the change in resistivity due to the variation in the carrier concentration (Fig. 1, curve 2).

The anomalous diffusion of boron in the $Si_{0.81}Ge_{0.19}$ sample can only be explained by diffusion through a liquid phase during crystallization by the vapor−liquid−solid mechanism. Additional support for the vapor−liquid−solid mechanism of crystallization comes from study of morphology of the epitaxial films. Figure 3a shows the usual growth steps in the surface of a $Si_{0.90}Ge_{0.10}$ epitaxial film and Fig. 3b shows a certain melting-down on the surface of a $Si_{0.85}Ge_{0.15}$ epitaxial film while Fig. 3c shows a strongly molten surface in a $Si_{0.81}Ge_{0.19}$ film which also indicates the liquid-phase crystallization mechanism.

---

[1] K. L. Lyutovich, T. A. Ukhorskaya, and F. A. Gimel'farb, Kristallografiya, 15, 1263 (1970) [Sov. Phys.−Crystallogr., 15, 1109 (1971)].

[2] Ya. M. Fogel', Usp. Fiz. Nauk, 91, 75 (1967) [Sov. Phys.−Usp., 10, 17 (1967)].

[3] Ya. A. Fedotov, Fundamentals of Semiconductor Device Physics [in Russian], Sov. Radio, Moscow (1969)

Lev Aleksandrovich Shuvalov (on his 50th birthday)

Kristallografiya, 18, 1312-1313 (November-December 1973)

November 15, 1973 marked the 50th birthday of Lev Aleksandrovich Shuvalov, Doctor of Physicomathematical Sciences, a noted Soviet crystallographer and one of the leading specialists in ferroelectricity.

Having completed secondary school in Moscow a few days before the outbreak of World War II, Shuvalov joined the Soviet Army with his Young Communist League unit, fought at Moscow and Stalingrad and on other fronts, and was in Prague at the end of the war.

Shuvalov entered the Physics Faculty of Moscow University in 1945 and completed his course in 1950. For the next five years, he worked at the S. Ya Zhuk All-Union Planning and Scientific–Research Institute, where he was occupied in the development of equipment for investigating the physical characteristics of hydraulic equipment on a full scale and with models. He simultaneously studied under A. V. Shubnikov in the correspondence graduate school of the Institute of Crystallography, Academy of Sciences of the USSR; the scientific views and interests of the young Shuvalov were formed under the direct influence of this mentor.

In 1956, Lev Aleksandrovich transferred to the Institute of Crystallography, where all his subsequent scientific work has been conducted. In 1961, he wrote his candidate's dissertation; his doctoral dissertation was completed in 1971. Since 1972, he has headed the phase-transition laboratory. Shuvalov has published more then 120 scientific works.

In his first publications, Shuvalov (jointly with I. S. Zheludev) laid the foundations for the crystallography of ferroelectrics. Development of the symmetry aspects of the theory of ferroelectricity was subsequently the main thrust of his work. The formulation and solution of the problem of changes in symmetry during ferroelectric phase transitions, establishment of the general patterns of domain structure and its role in the variation of different physical properties, and development of a crystal-physical classification of ferroelectrics, as well as demonstration of the heuristic possibilities of the latter, are among the results that have been included in Shuvalov's monographs and textbooks.

A second area of Shuvalov's scientific activity, closely related to the first, has been experimental research on the physical properties of ferroelectrics. Together with his colleagues, he has conducted an outstanding series of studies of the unique family of alkali trihydroselenite crystals and discovered a number of new phenomena: a series of effects occurring during repolarization of various ferroelectrics, autostabilization of the temperature of ferroelectric elements in the vicinity of the Curie point, asymmetry of pulse switching, development of metastable domain boundaries, etc. Shuvalov has also established and studied the contribution made by domains to internal friction and conducted the first systematic investigations of the spontaneous and induced rotary electrooptical effects in ferroelectrics, as well as making a number of other widely known studies.

Shuvalov has devoted much effort to the training of specialists: He has been adviser to eight candidates. He has been directly responsible for the organization of groups to study ferroelectricity at Kalinin University, the Voronezh Polytechnic Institute, the Volgograd Institute of Civil Engineers, and other institutions.

The great authority and respect that Shuvalov enjoys among specialists has led to extensive cooperation in research projects between Shuvalov and his colleagues and many groups in the Soviet Union and abroad.

We wish to note the literary and organizational activities in which Shuvalov has been engaged, including the translation and editing of a series of well-known monographs, compilation of the transactions of all the All-Union Conferences on Ferroelectricity, and service as a member of the editorial boards of two scientific journals. He is also one of the supervisors of the ferroelectricity section of the Scientific Council on Semiconductor Physics and Chemistry.

Soviet crystallographers wish Lev Aleksandrovich many years of active work among his students and friends.